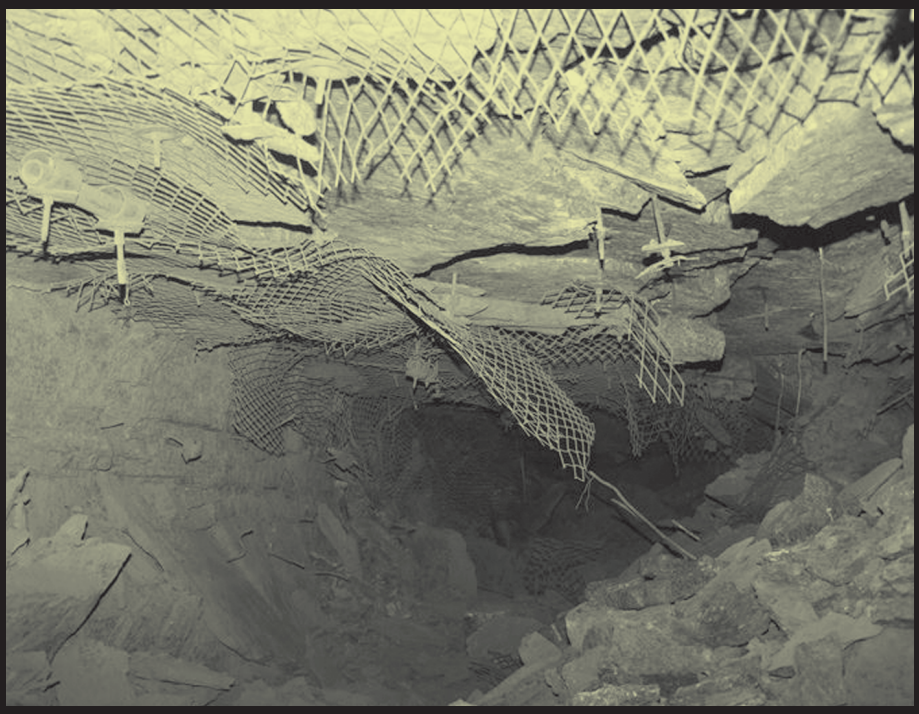
EUROCK 2013



Rock Mechanics for Resources, Energy and Environment

MAREK KWAŚNIEWSKI
DARIUSZ ŁYDŻBA
EDITORS

CRC Press
Taylor & Francis Group
A BALKEMA BOOK

ROCK MECHANICS FOR RESOURCES, ENERGY AND ENVIRONMENT

The photograph on the cover of this book shows a mine excavation at a depth of 950 m in the Rudna copper mine in the Legnica-Głogów Copper Region, Poland, where a mine tremor with a duration of 10 s and an energy of 1.6×10^8 J occurred on 19 March 2013. An area of 400 m × 150 m was affected. Fragmented rock was ejected from side walls of the mine workings and a massive floor heave occurred, while the roof was damaged to a lesser extent.

Photo credit: Courtesy of the State Mining Authority (WUG).

PROCEEDINGS OF EUROCK 2013 – THE 2013 ISRM INTERNATIONAL SYMPOSIUM
WROCŁAW, POLAND, 23–26 SEPTEMBER 2013

Rock Mechanics for Resources, Energy and Environment

Editors

Marek Kwaśniewski
Silesian University of Technology, Gliwice, Poland

Dariusz Łydżba
Wrocław University of Technology, Wrocław, Poland

CRC Press
Taylor & Francis Group
Boca Raton London New York Leiden

CRC Press is an imprint of the
Taylor & Francis Group, an **informa** business

A BALKEMA BOOK

CRC Press/Balkema is an imprint of the Taylor & Francis Group, an informa business

© 2013 Taylor & Francis Group, London, UK

Typeset by MPS Limited, Chennai, India
Printed and bound in Great Britain by CPI Group (UK) Ltd, Croydon, CR0 4YY.

All rights reserved. No part of this publication or the information contained herein may be reproduced, stored in a retrieval system, or transmitted in any form or by any means, electronic, mechanical, by photocopying, recording or otherwise, without written prior permission from the publishers.

Although all care is taken to ensure integrity and the quality of this publication and the information herein, no responsibility is assumed by the publishers nor the author for any damage to the property or persons as a result of operation or use of this publication and/or the information contained herein.

Published by: CRC Press/Balkema
P.O. Box 11320, 2301 EH, Leiden, The Netherlands
e-mail: Pub.NL@taylorandfrancis.com
www.crcpress.com – www.taylorandfrancis.com

ISBN: 978-1-138-00080-3 (Hardback + CD-ROM)
ISBN: 978-1-4822-2907-3 (eBook PDF)

Rock Mechanics for Resources, Energy and Environment – Kwaśniewski & Łydżba (eds)
© 2013 Taylor & Francis Group, London, ISBN 978-1-138-00080-3

Table of contents

Preface XIII
Committees XV

The 2013 ISRM Franklin lecture

Engineering aspects of geotechnical tunnel design 3
A. Goricki

Keynote lectures

The mechanical behavior of salt and salt caverns 17
P. Bérest

The mechanisms and consequences of strong mining tremors that occur in Polish hard coal and copper mines 31
J. Dubiński

Geomechanical aspects of shale gas development 39
M.B. Dusseault

An overview of underground rock engineering risk 57
J.A. Hudson

Optimization, sensitivity and robustness analysis – Applications and trends in geomechanics 69
H. Konietzky & R. Schlegel

Geomechanical modeling of CO_2 storage in deep saline aquifers – A review 79
X. Li, W. Yuan, B. Bai, M. Liu & H. He

1. Rock mass characterization

A preliminary geoengineering assessment of Bazda antique underground quarries in Şanlıurfa, Turkey 93
C. Ağan, M.İ. Yeşilnacar, M. Geniş, S. Kulaksız, R. Ulusay, Ö. Aydan & M.D. Yücel

The geological and geotechnical susceptibility of Jurassic and Cretaceous units; A case study from Central-Western Portugal 99
P.S. Andrade, H. Ventura & P.M. Callapez

Characterisation and propagation of epistemic uncertainty in rock engineering: A slope stability example 105
A. Bedi & J.P. Harrison

Characterization of the "Chaotic Complex" (Northern Apennines, Italy) 111
M. Coli & M. Tanzini

Impact of expertise on rock fall assessment – An original study 117
A. Delonca, T. Verdel & Y. Gunzburger

Seismic reflections around a tunnel "viewed" through waveguides – A case study 123
J.M. Descour & H. Hume

Comparison between different estimators of the degree of rock mass fracturing 129
A.M. Ferrero, M.R. Migliazza & G. Umili

Passive three-dimensional microseismic imaging for mining-induced rock-mass degradation 135
J.-W. Huang, J.M. Reyes-Montes & R.P. Young

ERMR system and correlations with known rock mass rating systems 141
M. Jovanovski & I. Peshevski

Assessing the mechanical properties of a rock using indentation tests 145
H.-T. Le, F. Descamps, J.-P. Tshibangu, J.-F. Nauroy, O. Vincké & L. Cangémi

Rock mechanical aspects for cavern stability 151
T. Pilgerstorfer, H. Wannenmacher, K. Grossauer, A. Stucki & B. Schwegler

Study of the relation between cracks and the elastic properties of rock mass 157
I. Stan-Kłeczek & A.F. Idziak

Rock physical interpretation of the seismic properties of the excavation disturbed zone 161
T. Takahashi & S. Tanaka

Depth distribution of lithospheric strength determined by the self-unbalancing shear rupture mechanism 165
B.G. Tarasov

Geomechanical attributes of reconstituted Indian coals under carbon dioxide saturation 171
V. Vishal, P.G. Ranjith & T.N. Singh

Adjustment of rock mass strength parameters using direct shear tests carried out on large blocks 175
G.J. Zapata & A.P. Assis

Determination of the extent of fractured zones around mine openings using the resistivity and GPR methods 181
B. Żogała, M.J. Mendecki, W.M. Zuberek, T. Gołębiowski & W. Antonik

2. *Laboratory and in-situ testing*

On the accuracy of the in-situ Schmidt hammer test on carbonate rocks 189
H. Arman, W. Hashem, O. Abdelghany & A. Aldahan

Rockfall: Scaling factors for the Coefficient of Restitution 195
P. Asteriou, H. Saroglou & G. Tsiambaos

Nano-indentation tests on partially satured argillite: Experimental device and measurements 201
C. Auvray, R. Giot & D. Grgic

Measuring stress induced electric field in sandstone and granite using the Electric Potential Sensor 207
A. Aydın, M.R. Dobbs, H.J. Reeves, C.C. Graham & M.P. Kirkham

Characterization of the distribution of physical and mechanical properties of rocks at the Tutupan coal mine, South Kalimantan, Indonesia 213
M.A. Azizi, S. Kramadibrata, R.K. Wattimena & I.D. Sidi

Experimental study of the permeability evolution of a rock fracture under THMC conditions 217
A. Blaisonneau, M. Peter-Borie & S. Gentier

Simulation of single cutter experiments in evaporite using the discrete element method 223
C. Carrapatoso, S.A.B. da Fontoura, I.M.R. Martinez, N. Inoue, A. Lourenço & D. Curry

Damage and plasticity rate dependence of Luna limestone in uniaxial compression 233
J. Cieślik

Effective stresses in cohesive discontinuous rocks around a vertical drill hole 239
P. Ciobanu

A database to manage rock mechanical properties and assess formation abrasiveness for drilling 245
F. Descamps, J.-P. Tshibangu, N. da Silva & S. Regnard

Effect of an increase in rotation in a wear test to predict the durability of rock materials 251
J.L.E. Dias Filho, G.C. Xavier & P.C.A. Maia

The elastic wave velocity in rocks under triaxial stress at high pressure and temperature 255
A. Dziedzic & J. Pinińska

Environmental characterization of the stress-corrosion cracking of rockbolts in underground coal mines using laboratory and in-situ testing 261
E. Elias, D. Vandermaat, A. Crosky, S. Saydam, P. Hagan, B.K. Hebblewhite & P. Craig

Effect of constant and varying mean stress levels of cyclic loading on the indirect tensile strength of rocks 267
N. Erarslan

Tensile fracturing of anisotropic Brisbane phyllite 271
N. Erarslan, D.J. Williams & A. Shokouhi

A new test for the characterization of highly jointed rock masses 275
C. González-Nicieza, M.B. Prendes-Gero, R. Fernandez-Rodriguez & F. Lopez-Gayarre

Influence of chemo-mineralogical transformations on micro/macro-mechanical properties of ironstone 281
D. Grgic

Influence of water vapor pressure in surrounding environment on strength and fracture toughness of rocks 287
M. Kataoka, Y. Obara & H.S. Jeong

Susceptibility of rock materials used in the construction of monuments to long-term salt crystallization 293
A.K. Kłopotowska & P.J. Łukaszewski

Beachrock mapping by geophysical exploration: Application to Yagaji Island in Okinawa, Japan 299
R. Kubo, S. Kawasaki, K. Suzuki, S. Yamaguchi & T. Hata

Physical and mechanical characterization of weak schistose rocks 305
T. Le Cor, D. Rangeard, V. Merrien-Soukatchoff & J. Simon

Thermal conductivity of rocks under high pressure conditions 311
W. Lin, O. Tadai, T. Hirose, W. Tanikawa, M. Kinoshita, H. Mukoyoshi & M. Takahashi

Developing a high capacity direct shear apparatus for the large scale laboratory testing of rock joints 315
Z. Moradian, C. Gravel, A. Fathi, G. Ballivy, P. Rivard & M. Quirion

Some remarks on the experimental determination of the Biot coefficients 321
A. Nowakowski & J. Walaszczyk

Dynamic and static rock mechanical properties of heavy oil sandstones 325
C. Rabe, P. Perdomo & J. Cherrez

Selection and interpretation of shear strength parameters for weak phyllites 331
G.V. Ramana, Shashank Pathak & Nripendra Kumar

Evaluation of specific cutting energy in the circular sawing with the elastic parameters of rocks 337
N. Sengun, I. Ugur, S. Demirdag & R. Altindag

Strength behaviour of reinforced natural jointed rock 343
L.P. Srivastava & M. Singh

Estimation of the effects of the centrifugal hydraulic conductivity of impermeable rocks under constant head conditions 347
M. Takahashi, W. Lin & M. Kato

An in-situ monitoring system for natural temperature and relative humidity 351
A.J. Taylor, J.C. Cripps & S.D. Clarke

Micro-textural controlled variations of the geomechanical properties of andesites 357
Ö. Ündül, F. Amann, N. Aysal & M. Plötze

Loss slake index evaluation and its applicability to marl 363
G. Vlastelica, P. Miščević & D. Salvezani

Effect of scratch length on the Cerchar abrasivity index 369
O. Yaralı, H. Aydın, H. Duru & A. Özarslan

3. *Constitutive models and numerical modeling*

Strain-softening characterization of granitic rocks and numerical simulation of servo-controlled strength tests 379
J. Arzúa, J. Barbiero & L.R. Alejano

A constitutive model for jointed rock mass 385
A. Azami, T. Yacoub, J. Curran & D. Wai

Numerical investigation of asperity degradation in the direct shear test of rock joints 391
M. Bahaaddini, P. Hagan, R. Mitra & B.K. Hebblewhite

Micromechanics of geocomposites: CT images and FEM simulations 399
R. Blaheta, R. Kohut, A. Kolcun, K. Souček & L. Staš

The coupled hydro-mechanical approach for fluid compressibility problems in porous media 405
S.R.C. Brant, M.P. Cordão Neto & I. Fernandes Gomes

Rheological behavior of jointed rock masses inferred from an analogue laboratory testing approach 411
M.E. Discenza, S. Martino, G. Scarascia Mugnozza, L. Stedile, A. Bretschneider & M. Teodori

Numerical simulation of the impact of a rock fall impact on a flexible barrier using Abaqus/Explicit 6.12 417
J.P. Escallón, C. Wendeler & M. Mrozik

Global methodology for the evaluation of the stress field in a rock mass from in-situ tests. Application to the Salamonde II powerhouse cavern 425
M. Espada, L. Lamas, N. Leitão & B. Figueiredo

Influence of rock mass creep on tunnel loading 431
P. Fortsakis, A. Kalos, V. Despotaki & M.J. Kavvadas

A new time-dependent constitutive model and its application in underground construction 437
M. Karami & A. Fahimifar

Efficient and numerically stable anisotropic failure criterion for micro layered rock 441
M. Kawa & D. Łydżba

An extended Lemaitre's viscoplastic model 447
X. Lei & F.L. Pellet

Modeling fault activation due to the evolution of remote stresses 453
M.T. Myers, V.A. Dunayevsky & M.B. Bennett

A case study of large scale rock mass preconditioning by confined blasting 461
I. Onederra, A. Catalan & G. Chitombo

Back analysis of rock mass behavior of the Quintner Limestone at the Gonzen mine near Sargans, Switzerland 473
M.A. Perras, E. Ghazvinian, M.S. Diederichs, F. Amann & H. Wannenmacher

Numerical simulation of the water jet excavation of soft rock saturated with water 479
K. Sakaguchi, Y. Yumoto & A. Kizaki

Elastic response of laterally loaded rock sockets using 3D finite element analyses 485
K.P. Tzivakos, M.J. Kavvadas & D.G. Kaltsas

The influence of the type of pore fluid in two-phase media on the form of consolidation equations 491
A. Uciechowska & T. Strzelecki

A Weibull distribution-based constitutive model of creep of salt rock 497
H.W. Zhou, J.Y. Ding, J.D. Liu & J.F. Liu

4. *Mathematical modeling of coupled T-H-M processes in rocks*

Definition and implementation of a fully coupled THM model for unsaturated rocks 507
A. Haxaire, V. Galavi & R.B.J. Brinkgreve

A study on shear characteristics of a smooth rock surface under different thermal, hydro and mechanical conditions 513
T. Kim, N. Zhang & S. Jeon

Periodic character of failure near openings in high-stress rock mass conditions 519
V.V. Makarov, L.S. Ksendzenko, N.A. Opanasyuk & A.M. Golosov

Three-dimensional modeling of a coupled shear-flow test on soft sedimentary rock 525
H. Park, K. Ito, M. Takahashi, M. Osada & G. Smolnik

Study of thermo-hydro-mechanical processes at the potential site of an Indian nuclear waste repository 531
A.K. Verma, T.N. Singh & R.K. Bajpai

Numerical modeling of induced seismicity associated with fluid injection and withdrawal using 2D discrete element fracture network model 537
J.S. Yoon, A. Zang, G. Zimmermann & O. Stephansson

5. *Mine design and ground control*

Strength of faults – A concern for mining engineers? 545
M. Alber

Critical energy and mine rockburst potential 551
M. Al Heib, G. Lafont, C. Didier, Y. Gunzburger, J.P. Piguet, W. Pytel & H. Mitri

The design and results of an innovative instrumentation method for monitoring and improving the excavation of a road tunnel in a highly fractured and strained rock mass 557
M.I. Álvarez-Fernández, M.B. Prendes-Gero, I.N. Álvarez-Garcia & A.O. Oliva-González

The shape effect and rock mass structural control for mine pillar design 563
L.A. Ayres da Silva, A.L.M. Ayres da Silva & E.C. Sansone

The residual risk of an abandoned mine 569
D. Brambilla, L. Longoni, M. Papini, D. Arosio & L. Zanzi

Analysis of the consequences of mining exploitation in substantially disturbed strata based on spatial measurements of a building's tilt 575
L. Florkowska & A. Kanciruk

Geomechanical and geotechnical evaluation of maingate No. 080 5253 monitoring in the conditions of the Paskov mine 581
R. Kukutsch, K. Souček, P. Koníček, J. Ptáček, P. Waclawik & R. Šňupárek

Stability analysis of deep coal mine main roadways for pumped hydropower lower reservoir storage 587
A. Özarslan, H.Y. Aydıner, E. Köken & M. Alber

Overburden deformation and damage caused by the construction of a hard rock tunnel – An analysis and countermeasures 593
G. Yu, S. Lu, D. Meng & G. Ouyang

6. *Underground storage and waste disposal*

Modeling the Excavation Damaged Zones in the Bátaapáti radioactive waste repository 603
F. Deák, L. Kovács & B. Vásárhelyi

Quantitative roughness profiling of fracture surfaces of a granitic host rock at a radioactive waste disposal site 609
Á. Krupa, F. Deák, P. Görög, I. Buocz & Á. Török

Rock mechanics for gas storage caverns with respect to optimization of operation 615
B. Leuger, K. Staudtmeister & D. Zapf

Feasibility and behavior of a full scale disposal cell in a deep clay layer 621
J. Morel, F. Bumbieler, N. Conil & G. Armand

Temporal analysis of fracturing using acoustic emissions at the Aspö Pillar Stability Experiment 627
H.C. Moretti, J.M. Reyes-Montes, J.R. Haycox & R.P. Young

7. *Slope and open pit stability*

Conditions of stability in a marl and limestone opencast mine 635
Z. Bednarczyk

An on-line landslide monitoring system in flysch Carpathians 641
Z. Bednarczyk

Swelling rocks in an open pit mine 647
M.E. Bilir & E. Aydıngun

The role of shear surface geometry in the definition of deep-seated gravitational slope deformation thresholds 653
D. Brambilla, L. Longoni, M. Papini, D. Arosio & L. Zanzi

Large scale field tests for slope stabilizations made with flexible facings 659
M. Cala, M. Stolz, P. Baraniak, A. Rist & A. Roduner

Application of stochastic methods for the strain and stability analysis of a slope 663
E. Hrubešová, B. Luňáčková & T. Petřik

Physical modeling and simulation of slope failure by means of centrifuge acceleration 669
S. Kramadibrata, R.K. Wattimena, M.A. Azizi, Y. Wicaksana & I.D. Sidi

A safety inspection system for large-scale slopes in Korea 673
J.G. Lee, B.S. Jang, S.W. Bae, J.S. Moon, H.J. Sin & J.H. Park

Basic kinematic analysis of a rock slope using terrestrial 3D laser scanning on the M-22 highroad pilot site 679
M. Marjanović, B. Abolmasov, U. Djurić, S. Zečević & V. Šušić

Microseismicity due to gravity-induced rock-mass deformations and a related alarm system 685
S. Martino, A. Prestininzi, S. Rivellino, L. Lenti & A. Paciello

Comparison between the mechanical behavior of barriers against rock fall vs debris flows 691
A. Segalini, R. Brighenti, A.M. Ferrero & G. Umili

Rock fall modeling for protection barrier design and validation in the Sungun copper mine 697
R. Tajaddodian Far, N. Behi & F. Alilou

Slope optimization and design based on geotechnical and hydrogeological assessments for a new deep open pit coal mine 703
R. Ulusay, M. Ekmekci, E. Tuncay & N. Hasancebi

Influence of accuracy in specifying design input data on stability safety factors for excavated slopes in an open pit mine 709
V.K. Vavilova

Monitoring unstable slopes using Persistent Scatterers Interferometry: opportunities and challenges 713
J. Wasowski, F. Bovenga, D. Nitti & R. Nutricato

8. *Dynamic phenomena in rock masses*

Large scale field tests of rock bolts and high-tensile steel wire mesh subjected to dynamic loading 721
M. Cala, A. Roth & A. Roduner

Unifying energetic approach for the control of ground vibrations 727
C. Dinis da Gama

A numerical study on the ground amplifications in areas above abandoned room and pillar mines and old longwall mines 733
M. Geniş & Ö. Aydan

Spatio-temporal analysis of the influence of mining on the surface – A case study from the Ostrava-Karviná Coal Field 739
E. Jiránková & P. Waclawik

Control of rockburst risk in hard coal longwall mining – A case study 745
P. Koníček, R. Kukutsch, J. Ptáček, K. Souček, L. Staš & P. Waclawik

Integration of geomechanical and geophysical analysis methods for the prediction of seismic events in underground mining 751
B. Orlecka-Sikora & W. Pytel

Determination of dynamic rock strength to assess blasting efficiency 757
F.L. Pellet, V.K. Dang, C. Baumont, M. Dusseux & G.J. Huang

Dynamic modelling of a mining-induced fault slip 763
A. Sainoki & H. Mitri

The estimation of the effectiveness of torpedo blasting based on an analysis of focal mechanisms of induced mining tremors in the Bielszowice coal mine 769
Ł. Wojtecki, M.J. Mendecki, A. Talaga & W.M. Zuberek

9. Design methodology in rock engineering

Rock engineering design and the evolution of Eurocode 7 777
L.R. Alejano, A. Bedi, A. Bond, A.M. Ferrero, J.P. Harrison, L. Lamas, M.R. Migliazza, R. Olsson, Á. Perucho, A. Sofianos, H. Stille & D. Virely

Risk management approach for the design of underground constructions 783
B. Amusin & J. Eisenberg

A new design approach for rockfall barriers 789
A. Grimod & G. Giacchetti

Influence of in-situ stress variation on results of back analyses – an open pit case study 795
M. Grošić, D. Vidović & Ž. Arbanas

The contribution of rock mechanics to small-scale mining in Indonesia 801
P.N. Hartami, B. Nugroho, S. Mayangsari & Nurhardono

Index of time-dependency for rock and its application for the assessment of the long-term stability of underground structures 807
K. Hashiba & K. Fukui

Rock ledge support design. A deterministic and stochastic approach 813
J. Jakubowski & J.B. Stypulkowski

Protection of a tunnel entrance from rockfall risk 819
C. Mignelli, K. Daneshmand & D. Peila

Infrared thermography methodology applied to detect localized rockfalls in self-supporting underground mines 825
M.B. Prendes-Gero, F.J. Suárez-Domínguez, C. González-Nicieza & M.I. Álvarez-Fernández

Are classification systems outdated? 831
W. Schubert

Sensitivity analysis of the generalized Hoek-Brown failure criterion 835
P. Ván & B. Vásárhelyi

Analysis and treatment of a diversion tunnel in adverse geological conditions: A case study from south-western China 841
J.K. Yang, Y.F. Wang & D.F. Chen

Excavation and monitoring of the main tailrace tunnels of the Xiangjiaba underground power station 847
Z. Yi

Periphery mapping in NATM tunnels 853
B. Yilmaz & H. Keskin Citiroglu

10. Mechanical breakage of rocks

Investigations on the fracture behaviour of rocks in a triaxial compression test 861
L. Baumgarten & H. Konietzky

The relationships between Drilling Rate Index (DRI), physico-mechanical properties and specific cutting energy for some carbonate rocks 867
G. Ekincioglu, R. Altindag, N. Sengun, S. Demirdag & A. Guney

A new small scale rock cutting test 875
M. Entacher, S. Lorenz, R. Galler & G. Winter

Emission analysis of the cutting tools used for hard rock cutting with regard to status monitoring 881
K. Nienhaus, C. Kuchinke & D. Röllinger

3D elastic solutions for point load and Brazilian indirect tensile strength tests 887
M. Serati, H. Alehossein, N. Erarslan & D.J. Williams

11. Rock tunnel excavation and support

Underground construction at high altitudes: A case history on Mont Blanc in Italy 895
G. Bragonzi, P. Cancelli, R. Castellanza & G. Frigerio

Evaluation of geological conditions ahead of a tunnel face using the Tunnel Seismic Prediction method (TSP) – Lesson learned from the Pahang-Selangor raw water transfer tunnel, Malaysia 901
M.A.M. Ismail, R. Azit, S.M. Ng, H. Zabidi, N. Bakhudin & Z. Nordin

Tunnel behaviour and support in molassic rocks. Experience from 12 tunnels in Greece 909
V. Marinos, G. Prountzopoulos & P. Fortsakis

New yielding elements for tunnel linings: Design requirements, layout and influence on system behavior 915
W. Schubert & N. Radončić

A Rock Mass Rating system for predicting TBM utilization 921
S. Yagiz, T. Kim, O. Frough & S.R. Torabi

12. Petroleum rock mechanics

Observations of the intrinsic acoustic anisotropy of sands in various geologic settings 929
L.A. Hathon & M.T. Myers

Well stimulation on the basis of preliminary triaxial tests of reservoir rock 935
V.I. Karev & Yu.F. Kovalenko

Evaluation of stress changes due to multi-stage hydraulic fracturing – Consideration of field results 941
N.B. Nagel, F. Zhang, M.A. Sanchez-Nagel & B. Lee

Analysis of the hydromechanical behavior of fault zones in petroleum reservoirs 947
G.L. Righetto, C.E.R. Lautenschläger, N. Inoue & S.A.B. da Fontoura

13. Geological CO_2 sequestration

AE monitoring of hydraulic fracturing experiments conducted using CO_2 and water 957
T. Ishida, Y. Nagaya, S. Inui, K. Aoyagi, Y. Nara, Y. Chen, Q. Chen & Y. Nakayama

Effects of vertical stress on fracture propagation using super critical carbon dioxide 963
A. Kizaki, K. Ohashi, H. Tanaka & K. Sakaguchi

Assessing the geomechanical effects of CO_2 injection in a depleted gas field in Poland by field scale modelling 969
B. Orlic, M. Mazurowski, B. Papiernik & S. Nagy

Subject index 977
Author index 981

Rock Mechanics for Resources, Energy and Environment – Kwaśniewski & Łydżba (eds)
© 2013 Taylor & Francis Group, London, ISBN 978-1-138-00080-3

Preface

This book is a peer-reviewed and edited volume that contains papers that were received for EUROCK 2013 – The 2013 ISRM International Symposium, which will be held in the city of Wrocław POLAND on 23–26 September, 2013. The Symposium was organized by the Polish Society for Rock Mechanics and the Institute of Geotechnics and Hydrotechnics of the Wrocław University of Technology with the main objective of providing a forum for engineers, researchers and students to meet, to integrate industry professionals and scientific research communities, to create opportunities to update and improve knowledge and to present the most recent contributions in the area of rock mechanics and rock engineering.

EUROCK 2013 is the latest symposium in the series of annual European rock mechanics symposia that started in 1992 with the memorable symposium "Rock Characterization" that was held in Chester UK. It was preceded last year by EUROCK 2012, which was held in Stockholm SWEDEN, and will be followed next year by EUROCK 2014, which will be held in Vigo SPAIN.

EUROCK 2013 is the second major ISRM event that will be held in Poland. The previous one, which was devoted to the subject of "Protection Against Rock Fall", was held in the city of Katowice, the capital of the Upper Silesia, which is the center of the Polish hard coal mining industry, in October 1973. It was organized by the Polish Committee for Rock Mechanics, the Association of Mining Engineers and Technicians and the Central Mining Institute. Three hundred and seventy participants from 24 countries, including M. Borecki (Chairman of the Organizing Committee), H. Denkhaus, G. Everling, C. Fairhurst, H. Filcek, A. Kidybiński, P. Knoll, G.N. Kuznetsov, L. Obert (President of the ISRM), J.F. Raffoux, A. Silverio (Secretary-General of the ISRM), L. Šiška and B.N. Whittaker, to name but a few, took part in the Symposium. Thirty-six papers, which covered a variety of topics ranging from methods for the detection of loosened rocks that are liable to fall to the criteria for the selection of suitable supports for mine workings were presented.

We are proud and pleased that the Polish community of rock scientists and engineers has been given the opportunity to host colleagues from Europe and other parts of the world again after 40 years.

EUROCK 2013 was planned to focus on recent developments in the field of rock mechanics with an emphasis on the application of rock mechanics to the extraction of natural resources, securing energy supplies and protecting of the environment surrounding rock that is subjected to engineering activities. To this end, six keynote lectures will be presented by leading international experts on mining-induced dynamic phenomena that occur in rock masses (J. Dubiński), the geomechanical aspects of *in situ* energy development (M.B. Dusseault), the storage of hydrocarbons in salt caverns (P. Bérest), the geological sequestration of carbon dioxide (X. Li), reliable modeling of rocks and rock masses (H. Konietzky) and the risks associated with underground rock engineering (J.A. Hudson).

In total, 285 abstracts were received for EUROCK 2013 from universities, research institutes, consulting firms and industrial enterprises in 40 countries. Of these, 260 were tentatively accepted for the Symposium. The full papers that arrived in fewer numbers were reviewed by members of the International Scientific Committee in order to determine their eligibility for publication in the Symposium Proceedings and subsequent presentation during the Symposium. Finally, 144 papers from 33 countries were accepted. These include contributions from Asia (27), Australia (8), Europe (92), North America (10) and South America (7), with the greatest number of papers coming from Poland, Italy, Japan, Turkey and France (in this order).

These Symposium proceedings have been published in a single volume and contain the 2013 ISRM Franklin lecture, six keynote lectures and 144 technical papers classified under the following 13 themes: Rock mass characterization; Laboratory and *in situ* testing; Constitutive models and numerical modeling; Mathematical modeling of coupled T-H-M processes in rocks; Mine design and ground control; Underground storage and waste disposal; Slope and open pit stability; Dynamic phenomena in rock masses; Design methodology in rock engineering; Mechanical breakage of rocks; Rock tunnel excavation and support; Petroleum rock mechanics and Geological sequestration of CO_2.

Much effort was devoted to improving the English language of papers written by non-native speaking Authors who had no possibility to attend to the quality of the language themselves. The contribution of Ms. Michele Simmons to this endeavor was essential. Unfortunately, due to the time limitations, not all of the papers could be proofread and corrected, which we sincerely regret.

We would like to thank everyone who contributed to the organization of EUROCK 2013 and the publishing of this volume. Our thanks and words of gratitude go to the Board of the International Society for Rock Mechanics,

members of the Council of the ISRM and members of the International Advisory Committee with special words of appreciation and gratitude to Prof. Xia-Ting Feng and Prof. John A. Hudson, the present and former presidents of the ISRM, Prof. Frederic Pellet and Dr. Nuno F. Grossmann, the present and former vice-presidents of the ISRM for Europe, to Dr. Luís N. Lamas, Secretary-General of the ISRM and to Ms. Sofia Meess, Executive Secretary of the ISRM. We equally warmly thank the members of the International Scientific Committee who so generously contributed their expertise and time to review the abstracts and the full papers that were received for the Symposium. We also gratefully acknowledge Mr. Janjaap Blom, the Senior Publisher, Mr. Léon Bijnsdorp, the Editor 'Conference Proceedings', and Messrs. Lukas Goosen and Richard Gundel, the Production Managers at CRC Press/Balkema – Taylor & Francis Group for their excellent cooperation and commitment during the entire editorial and publishing process. Last, but not least, we wish to express our appreciation to our secretaries: Dr. Adrian Różański and Dr. Grzegorz Smolnik and all of the members of the Organizing Committee with special emphasis on the staff of the Institute of Geotechnics and Hydrotechnics at the Faculty of Civil Engineering of Wrocław University of Technology.

Finally, we would like to extend our best wishes to all of the participants of EUROCK 2013. Thank you for attending and we hope that you will enjoy the Symposium. We wish you a pleasant stay in Wrocław!

Marek Kwaśniewski
Dariusz Łydżba
Editors of this volume

Rock Mechanics for Resources, Energy and Environment – Kwaśniewski & Łydżba (eds)
© 2013 Taylor & Francis Group, London, ISBN 978-1-138-00080-3

Committees

EUROCK STEERING COMMITTEE

Giovanni Barla
Claus Erichsen
Dominique Fourmaintraux
Nuno F. Grossmann
John A. Hudson
Marc Panet
Frédéric Pellet, Chairman
Manuel Romana
Pekka Särkkä
Wulf Schubert
Luís Sousa
Ove Stephansson
Ivan Vrkljan
Walter Wittke

ADVISORY COMMITTEE

Xia-Ting Feng, President of the ISRM
John A. Hudson, Immediate Past President of the ISRM
Frédéric Pellet, Vice-President of the ISRM for Europe
Nuno F. Grossmann, Immediate Past Vice-President of the ISRM for Europe
Ivan Vrkljan, Vice-President of the ISRM at Large
Luís Lamas, Secretary General of the ISRM

Wulf Schubert	Austria
Jean-Pierre Tshibangu	Belgium
Sabid Zekan	Bosnia and Herzegovina
Predrag Miščević	Croatia
Petr Koniček	Czech Republic
Erik Johansson	Finland
Jian-Fu Shao	France
Claus Erichsen	Germany
Alexandros Sofianos	Greece
Giovanni Barla	Italy
Dominique J.M. Ngan-Tillard	The Netherlands
Charlie Chunlin Li	Norway
Carlos Dinis da Gama	Portugal
Erast Gaziev	Russia
Milan Tričković	Serbia
Claudio Olalla	Spain
Håkan Stille	Sweden
Jian Zhao	Switzerland
Reşat Ulusay	Turkey
Robert Zimmerman	United Kingdom

ORGANIZING COMMITTEE

Irena Bagińska	Wrocław University of Technology, Wrocław
Marek Cała	AGH University of Science and Technology, Cracow

Andrzej Dulski	Wrocław University of Technology, Wrocław
Lucyna Florkowska	Strata Mechanics Research Institute, PAS, Cracow
Józef Kabiesz	Central Mining Institute, Katowice
Marek Kawa	Wrocław University of Technology, Wrocław
Ewa Koszela-Marek	Wrocław University of Technology, Wrocław
Paweł Łukaszewski	University of Warsaw, Warsaw
Dariusz Łydżba (Chairman)	Wrocław University of Technology, Wrocław
Andrzej Nowakowski	Strata Mechanics Research Institute, PAS, Cracow
Joanna Pieczyńska	Wrocław University of Technology, Wrocław
Adrian Różański (Secretary)	Wrocław University of Technology, Wrocław
Maciej Sobótka	Wrocław University of Technology, Wrocław
Joanna Stróżyk	Wrocław University of Technology, Wrocław
Stanisław Szweda	Silesian University of Technology, Gliwice
Matylda Tankiewicz	Wrocław University of Technology, Wrocław

INTERNATIONAL SCIENTIFIC COMMITTEE

Leandro Alejano	Vigo, Spain
Ömer Aydan	Shizuoka, Japan
Marco Barla	Turin, Italy
Pedro Bernardo	Lisbon, Portugal
Radim Blaheta	Ostrava, Czech Republic
Dieter Brückner	Leipzig, Germany
Mirosława Bukowska	Katowice, Poland
Piotr Czaja	Cracow, Poland
Jan Drzewiecki	Katowice, Poland
Józef Dubiński	Katowice, Poland
Sylvie Gentier	Orléans, France
Giovanni Grasselli	Toronto, Canada
Jerzy Hoła	Wrocław, Poland
Eva Hrubešová	Ostrava, Czech Republic
Adam F. Idziak	Sosnowiec, Poland
Ryszard J. Izbicki	Wrocław, Poland
Jacek Jakubowski	Cracow, Poland
Waldemar Korzeniowski	Cracow, Poland
Danuta Krzysztoń	Cracow, Poland
Marek Kwaśniewski (Chairman)	Gliwice, Poland
Cezary Madryas	Wrocław, Poland
Tadeusz Majcherczyk	Cracow, Poland
Wolfgang Minkley	Leipzig, Germany
Mariusz Młynarczuk	Cracow, Poland
José Muralha	Lisbon, Portugal
Paweł Nawrocki	Abu Dhabi, UAE
Stanisław Pietruszczak	Hamilton, Canada
Joanna Pinińska	Warsaw, Poland
Till Popp	Leipzig, Germany
Witold Pytel	Wrocław, Poland
Jakub Siemek	Cracow, Poland
Grzegorz Smolnik (Secretary)	Gliwice, Poland
Ove Stephansson	Potsdam, Germany
Jan Walaszczyk	Cracow, Poland
Saffet Yagiz	Pamukkale, Turkey
Wacław M. Zuberek	Sosnowiec, Poland

The 2013 ISRM Franklin lecture

This page intentionally left blank

Rock Mechanics for Resources, Energy and Environment – Kwaśniewski & Łydżba (eds)
© 2013 Taylor & Francis Group, London, ISBN 978-1-138-00080-3

Engineering aspects of geotechnical tunnel design

A. Goricki
3G Gruppe Geotechnik Graz ZT GmbH, Graz, Austria

ABSTRACT: The geotechnical design of underground structures deals with the interaction between the ground and the structure. The key element of this behavior is the potential failure mode of the ground, which mainly depends on the ground conditions including ground parameter, water and primary stress condition as well as the excavation geometry. Typical ground behaviors for underground structures are discussed and engineering design methods are presented. To deal with the uncertainties of the ground and the complexity of the subsurface buildings a behavior based design methodology is discussed in combination with the risk management process as described in ISO 31000. The integration of the processes leads to a sound design process, which allows the application of individual and problem-oriented engineering design tools as well as the adaptation of the design during the construction phase to minimize the geological and geotechnical risks if required.

1 INTRODUCTION

The "geotechnical design of underground structures" can be described as the design dealing with the interaction between the ground and the structure. With focus on an economic construction according to its pre-defined specifications the geotechnical design mainly covers the design of the excavation and the primary support but also additional measures such as lowering of the ground water level or injections to change the ground properties. Generally the geotechnical design includes all aspects, which deal with the ground interactions.

Underground structures are often complex structures with geometrically different elements such as shafts, tunnels or caverns. These structures are excavated in various ground conditions concerning geological units, overburden, primary stresses or ground water with different levels of uncertainties of the predictions. Due to this the geotechnical design of underground structures is often very complex and requires comprehensive understanding of the geological, geotechnical and structural designs and its interactions.

At the moment a comprehensive method for the geotechnical design of underground structures, especially in rock mass, is neither defined in standards nor internationally accepted as state of the art. Various different approaches are applied based on regional experience or specifications of local clients and authorities. The typical methods applied for geotechnical design are discussed by various authors (e.g. Hudson 2001, Palmstrom & Stille 2007 or Feng & Hudson 2011) and can be summarized as

- Empirical methods based on experience from comparable projects;
- Closed form solutions;
- Numerical analyses; and
- Combinations of the methods mentioned above.

Independent of the applied method, the most important aspect of the geotechnical design of underground structures is the interaction between the ground and the structure. This "behavior" can be described as the reaction of the ground to any change of the natural in situ conditions due to construction works such as excavation, support installation or ground improvement. It is obvious that this behavior is dominated by the ground conditions such as rock mass parameters, ground water or primary stress condition as well as by the excavation process, the type of support measures and the applied installation process. It is the result of the complex interaction within the system ground, excavation and support and consequently a key element of any geotechnical design.

In the following a systematic structure for the geotechnical design of underground structures is presented, including general design principles, rock mechanical aspects concerning failure mechanisms and ground behavior as well as aspects of risk management. Additionally focus is set on the applicability of the geotechnical design during all design stages including the construction phase of the underground structure.

2 GROUND BEHAVIOR – BASIS FOR GEOTECHNICAL DESIGN

The failure mechanism, or more general, the behavior is often the key element in engineering design procedures. In structural engineering, for example, it is typical that different design approaches are applied for different loading conditions, which lead to different modes of failure. In the design of reinforced

concrete structures (CEN 2011) it is a matter of course that different design processes and analyses are used depending on the loading, which causes different failure mechanisms of the structural element. Consequently the design analyses are different for tension, pressure or torsion due to the different modes of failure.

Also in soil and rock mechanics the potential failure mechanisms as well as the behavior of the ground are used as the key factors for the development of geotechnical designs. In rock slope design, for example, it is state of the art to use different design approaches depending on the expected slope failure mode such as plane failure, wedge failure, circular failure or toppling. The applied models and analyses are adapted to the expected slope behavior and different and independent design approaches are used.

Also for the design of underground structures the logical engineering design approach is to predict the potential behavior without support and then develop measures to change or modify it to the required behavior of the compound system ground-excavation-support.

The behavior of the ground varies significantly depending on the ground properties such as rock, discontinuity or rock mass parameters but also primary stress condition and ground water condition. It is important to recognize that different combinations of the parameters can lead to absolutely different behavior of the rock mass. For example, with the increase of primary stresses the behavior of hard massive rock could change from stable to spalling or rock burst. Fractured rock mass might show progressive gravitational failure in case of very low stresses and change its behavior with increasing stresses to limited gravitational failure (due to increasing confinement pressure), local shear failure and a kind of "plastic" behavior in case of very high stresses compared to the rock mass strength. Additionally ground water may change the behavior depending on pressure and quantity of inflow.

Besides ground properties also the geometry of the underground structure has a significant impact onto the behavior. The span of a tunnel or cavern or the geometry of the excavation has a major influence on the development of failure modes. A rectangular excavation, for example, shows more stress induced failure than an excavation with a round profile and gravitational block failure is more probable and has larger volume if the excavation becomes bigger.

Such simple examples show that the behavior of an underground excavation can change due to variations of the ground and boundary conditions. This underlines the importance of the geological and geotechnical investigation and prediction as another important aspect of the geotechnical design by defining the precision of the relevant design parameters. For the construction of a second tunnel tube of an infrastructure tunnel for example, very detailed information is available from the investigation and especially from the construction of the first tunnel. Besides the detailed geological data from tunnel documentation also observations of the actual behavior and the effectiveness of support concepts are existing (for example Metsovo Tunnel see Goricki & Rachaniotis 2011). On the other hand only very limited data with high uncertainties might be available in case of a deep tunnel in remote mountainous area, where field mapping or drilling is not possible due to topographical reasons (for example Rohtang tunnel see Reichenspurner 2013). This might lead to basic differences in the structure and methodology of a geotechnical design only due to the quality and precision of the available input data.

For the sound development of a geotechnical design it is necessary to separate the underground structure into sections with homogeneous or comparable geometrical and geotechnical conditions. Due to this split into smaller tasks it becomes possible to develop the ground behavior of any underground structure, independent of its geometrical complexity or extension and independent of the heterogeneity of the ground. Based on the ground behavior, developed for each section with comparable conditions, the geotechnical design can be developed and excavation and support measures can be designed. Considering the big variety of possible parameter combinations and conditions for underground structures in general, it is obvious that different design approaches in terms of models and analyses must be used to capture all the different possible behaviors and modes of failure. Therefore a geotechnical design procedure based on ground behavior is required to prepare a framework for all different tasks, which have to be performed during a geotechnical design of an underground structure in general.

3 GEOTECHNICAL DESIGN PROCEDURE – BASED ON GROUND BEHAVIOR

In the past various design procedures for underground structures were developed (e.g. Hoek & Brown 1980, ITA 1988 or Bieniawski 1992), more detailed discussion and further developments of these methods are given for example in Goricki (2003) or Palmstrom & Stille (2007). In the following the "Guideline for the geotechnical design of underground structures with conventional excavation" published by Austrian Society for Geomechanics (2010) is introduced briefly. It consists of two consistent design procedures, one for the design phase and another for the adaptation of the design during the construction phase.

3.1 *Geotechnical design during design phase*

The design procedure consists of mainly 5 steps starting with the description of the basic geologic architecture and proceeds by defining geotechnical relevant key parameters for each ground type. The

key parameter values and distributions are determined from available information and/or estimated with engineering and geological judgment. The values are constantly updated as pertinent information is obtained. Ground Types are then defined according to their key parameters.

The second step involves the evaluation of the potential ground behaviors considering each Ground Type and local influencing factors, including the relative orientation of relevant discontinuities to the excavation, ground water conditions, stress situation, etc. This process results in the definition of project specific Ground Behavior Types. The ground behavior has to be evaluated for the full cross sectional area without considering any modifications including the excavation method or sequence and support or other auxiliary measures. Eleven general categories are listed in the guideline.

- Stable;
- Potential of discontinuity controlled block fall;
- Shallow failure;
- Voluminous stress induced failure;
- Rock burst;
- Buckling;
- Crown failure;
- Raveling ground;
- Flowing ground;
- Swelling ground; and
- Ground with frequently changing deformation characteristics.

In case more than one Ground Behavior Type is identified in one of the general categories, sub types can be assigned. The Ground Behavior Types form the basis for determining the excavation and support methods as well as assist in evaluating monitoring data during the excavation.

In the third to fifth step, different excavation and support measures are evaluated and acceptable methods are determined based on the Ground Behavior Types. The System Behavior is a result of the interaction between the ground behavior and the selected excavation and support schemes. The evaluated System Behavior has to be compared to the defined requirements. If the System Behavior does not comply with the requirements, the excavation and/or support scheme has to be modified until compliance is obtained. It is emphasized, that different boundary conditions or different requirements may lead to different support and excavation methods for the same Ground Behavior Type even within one project.

In the sixth step, based on steps 1 through 5 the alignment is divided into "homogeneous" regions with similar excavation and support requirements. A framework plan indicates the excavation and support methods available for each region, and contains limits and criteria for possible variations or modifications on site.

In the final step of the design process the geotechnical design must be transformed into a cost and time estimate for the tender process.

3.2 *Geotechnical design adaptation during construction phase*

Due to the fact that in many cases the ground conditions cannot be defined with the required accuracy prior to construction, a continuous updating of the geotechnical model and an adjustment of excavation and support to the actual ground conditions during construction is required. The final determination of excavation methods, as well as support type and quantity is often only possible on site. In order to guarantee the required safety, a safety management plan needs to be followed.

Step 1: To be able to determine the encountered Ground Type, the geological documentation during construction has to be targeted to collect and record the relevant parameters that have the greatest influence on the ground behavior. The geological and geotechnical data collected and evaluated on site are the basis for the extrapolation and prediction of the ground conditions into a representative ground volume, which determines the behavior.

Step 2: Based on the predicted ground conditions the system behavior in the section ahead has to be assessed and compared with the framework plan. Particular attention has to be paid on potential failure modes.

Step 3: To determine the appropriate excavation and support the criteria laid out in the framework plan have to be followed. Consequently, the actual ground conditions continuously have to be compared to the prediction for compliance. Based on the additional data obtained during construction the excavation and support methods are determined to achieve economic and safe tunnel construction. The System Behavior is predicted for the next excavation sections, considering ground conditions and the chosen construction measures. Both, excavation and support, to a major extent, have to be determined prior to the excavation. After the initial excavation only minor modifications, like additional bolts, are possible. This fact stresses the importance of a continuous short-term prediction.

Step 4: By monitoring the system behavior the compliance with the requirements and criteria defined in the geotechnical safety management plan is checked. In case of differences between the observed and predicted behavior occur, the parameters and criteria have to be reviewed. When the displacements or support utilization are higher than predicted, a detailed investigation into the reasons for the different System Behavior has to be conducted, and if required improvement measures (like increase of support) ordered. In case the System Behavior is more favorable than expected, the reasons have to be analyzed as well, and the findings shall be used to modify the design accordingly.

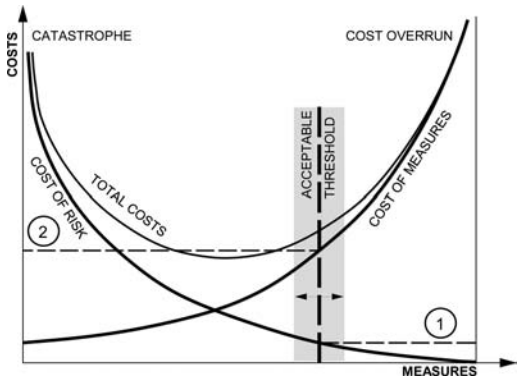


Figure 1. Interaction between risk, measures and costs.

4 GEOTECHNCIAL DESIGN AND RISK MANAGEMENT

4.1 *General*

The main goal of a geotechnical design is the definition of measures to construct a safe and economic underground structure. Due to the uncertainties of the ground, the risks related to construction methods and the usual demand for cost reduction also the results of the geotechnical design are affected by uncertainties and risks. To deal with these risks it is proposed to apply the principles of risk management and combine it with the typical procedures of geotechnical design as presented above (Goricki et al. 2002, Schubert 2011). For such approach it is important to clearly differentiate between basic condition, measures and effect of measures.

In the design of underground structures the behavior of the ground is evaluated and, if the predicted ground behavior is not acceptable, e.g. in case of predicted ground instabilities, measures such as bolting or shotcreting are designed to achieve an acceptable and stable behavior. In terms of risk management, a not acceptable risk was reduced due to measures to fulfill the risk criteria and became acceptable. Additionally a pre-defined factor of safety is usually considered in engineering designs, which also influences the risk level.

The interaction between risk, measures and costs is shown quantitatively in Figure 1. Without any measures the probability for occurrence of damages is highest and might lead to catastrophic conditions. If intensive measures are implemented, the risk decreases to a minimum but the costs for the measures will increase significantly and might lead to unreasonable high costs. With a decrease of the risk due to measures the costs for possible damages decrease, while the costs for measures develop opposite to the costs of risk. At a certain point the total costs, calculated as the sum of costs from possible damages and costs for mitigation measures, show a minimum. Independent to these minimum total costs an "acceptable mitigation threshold" is introduced, which defines the balance between acceptable residual risk (1) and the necessary costs (2) to align this residual risk. In a technical design this threshold can also be described as the minimum design criteria. Additionally any kind of uncertainties or a factor of safety can be considered by moving the threshold, which influences the risk as well as the measures and their costs. Besides this defined minimum safety or maximum risk level also definitions concerning the costs can set the boundary conditions.

By applying the principles of risk management to geotechnical designs it can easily be seen that the design of excavation and support to control the ground behavior follows these correlations in general. If a ground, for example, has a potential for gravitational discontinuity controlled over break of rock blocks, the design of an underground structure can be developed with various options. Without any rock support progressive failure with systematic voluminous over break will occur, which requires intensive and costly repair works (unacceptable risk without costs for measures). In case of forepoling with spiles the applied support measures are generally cheap and only minor over break occurs, which leads to a well balance between risk reduction and costs for measures (acceptable risk with some costs for measures).

In a third scenario the excavation is supported with heavy pipe umbrella forepoling with high costs and slow progress, which results in cero potential for overbreak (acceptable risk with high costs). This simple example shows that the application of risk management to geotechnical design does fully comply with the design approach based on ground behavior and additionally supports the engineering design decisions.

4.2 *Risk management according to ISO 31000*

The ISO 31000 (International Organization for Standardization 2009) provides a generic approach in terms of principles and guidelines for managing any form of risk in a systematic and logical process. Risk is defined as the uncertainty on objects, which is often expressed in term of a combination of consequences of an event and the associated likelihood of occurrence. Risk management is defined as coordinated activities to direct and control something with regard to risk. The process of risk management as an integrative part of the management consists mainly of systematic application of management policies, procedures and practices to activities of communicating, consulting, establishing the context, and identifying, analyzing, evaluating, treating, monitoring and reviewing risk.

Figure 2 shows the process risk management with its main elements and their interaction. In the beginning the overall context including objective, internal and external influencing parameters, boundary conditions, strategies and risk criteria shall be defined. Then the risks are assessed by using tools of risk identification, risk analysis and risk evaluation. Based on this understanding the risk treatment is developed, which involves the selecting and implementing of one or

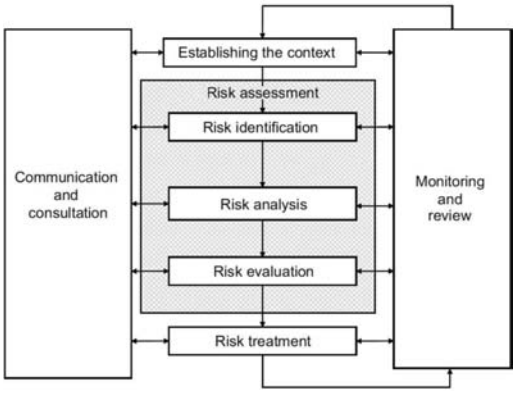


Figure 2. General risk management process; from ISO 31000.

more option for modifying the risks. The risk treatment is a cyclic process of developing a treatment, assessing a treatment, deciding about acceptable residual risk levels and checking the effectiveness of that treatment by comparing with risk level. The risk treatment options can include avoiding a risk, taking or increasing a risk, removing a risk source, changing the likelihood, changing the consequences, sharing a risk or retaining a risk. A risk treatment plan describes the implementation of the chosen treatment options.

Finally, both monitoring and review should be planned as part of the risk management process and shall ensure

- control in design and operation;
- obtain further information to improve risk assessment;
- analyzing and learning lessons from events, changes, trends, successes and failures;
- detection of changes in the context including risk criteria or risk itself; and
- identifying emerging risks.

4.3 *Geotechnical design as risk management procedure*

By comparing the geotechnical design procedure as described in chapter 3 with the risk management procedure from ISO 31000 it can be seen, that the geotechnical design procedure does generally contain all relevant elements of a risk management process.

Figure 3 shows the procedure of geotechnical design in the center and the main elements of risk management at the sides in dark beams. In the design stage the description of the ground conditions and the evaluation of the ground behavior covers the elements of risk identification, risk analysis and risk evaluation which can be summarized as risk assessment. Based on the results of this risk assessment the construction concept, the excavation and the support is designed in a way that the behavior fulfills the previously defined requirement.

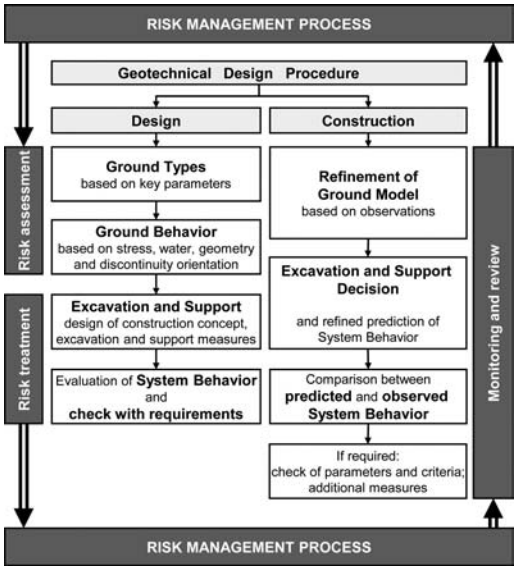


Figure 3. Integration of the geotechnical design procedure (as defined in chapter 3) in the risk management process as defined in ISO 31000.

These requirements are risk criteria and the process of design and check of the modified behavior equals the process of risk treatment. During construction many input data but also the behavior of the ground with measures can be observed and interactive process of monitoring and reviewing must be executed.

4.4 *Monitoring and review*

A key element in the geotechnical design as well as in the risk management is the monitoring and review process. It allows to verify the success of the applied measures and if necessary to modify the measures to gain the expected result. In geotechnical design there are two main sources for uncertainties, the characterization of the ground and the geotechnical design models for behavior without and with measures. The monitoring of the ground conditions during construction (geological and geotechnical documentation) allows the observation of the actual condition and usually leads to an increase of the ground data in quantity and quality. Due to this a verification of the predicted ground conditions can be done. Additionally the behavior of the ground influenced by the applied measures can be observed and compared with the predicted behavior of the system ground with measures.

The difficulties to characterize ground materials and the complexity of modeling underground excavations and support measures might lead to an actual behavior deviating from the predicted. In such a case it is essential to modify the measures once defined according to the actual ground conditions, behavior and construction specific conditions. This must be done on site and requires a clear structure and full

implementation of a design representative on site as described in general in the risk management process.

The step of monitoring and review is not limited to the construction phase. Also during the different design phases the design decisions have to be reviewed in case of additional data or more detailed information is available for example from additional investigation.

During monitoring and reviewing it is again essential to focus on the basic failure modes, the behavior of the ground. If the variations in ground conditions change the behavior of the underground excavation, for example due to higher primary stresses or due to water inflows, the measures have to be adapted to the new potential failure modes. By, for example changing the bolting according to the stress orientation or by locally lowering the water pressure, stable conditions can be developed more successful than by simply adding unspecific support.

The elementary demand for a geotechnical design is to adapt the relevant measures to the actual ground condition and behavior and hence control the ground related risks continuously during all project phases. Consequently the geotechnical design is the continuous evaluation of ground behavior (check of risks), the design of a proper excavation and support system (definition of measures and check of risk reduction) and the comparison with design criteria and boundary conditions to reach a balance between required safety level and costs.

5 TYPICAL GROUND BEHAVIOR AND ENGINEERING METHODS

5.1 *General*

In the chapters above the importance of the ground behavior as basis for the geotechnical design of underground structures is pointed out. In the following the most important types of ground behavior are described and engineering methods for evaluation, analysis and design of measures are discussed briefly. As the ground behavior is highly depending on the project specific ground and boundary conditions, the descriptions below shall be used as a general guidance for a design engineer.

The classification into different behavior types must be done project specific depending on the detailing of the design due to the heterogeneity of and the knowledge about the underground conditions as well as due to the project phase, the importance of the project and the costs of the underground structure. Most important for the grouping into ground behavior types is the consideration of the potential soil or rock mechanical failure mechanisms. Consequently, basic behavior types can be defined, which create the basis for the project specific work. In the past various authors have developed grouping or classification of behavior types for underground structures (e.g. Hoek et al. 1995, Goricki 2003, Palmstrom & Stille 2007).

In the following a classification of the main behavior types by considering the potential failure modes due to gravity, stress, water and swelling is given. Each type of ground behavior is discussed briefly including the basic mode of failure, the important parameters and the typical methods for design and analysis with and without measures. The excavation and support measures itself are not discussed in this context. Due to this it is important to understand that the modes of failures are theoretical and will be avoided by the design and installation of the proper excavation and support system. Consequently the theoretical modes of failure – the plain ground behavior – cannot be observed during construction.

The models used for analyses, evaluation of the behavior and design of measures are not limited to any method but must be applicable for the problem, the behavior and the mode of failure respectively. Therefore also empirical methods can be used if the experience is comparable with the geometrical, ground and boundary conditions. Additionally it is required that the data are collected from technically successful and economically traceable projects during the design and construction phases.

5.2 *Gravity induced behavior – discontinuity controlled blocks*

Mechanism: gravity induced falling, sliding or rotating of blocks into the excavation, along discontinuities with potential for local shear failure. The kinematic freedom and the exceeding of the tension and shear strength along the discontinuities are the basic prerequisite for this behavior (Goodman & Shi 1985, Pötsch 2011). The blocks can fail locally or systematically with various depths and volumes.

Important parameters: number, orientation and distance of discontinuities or degree of fracturing; waviness, roughness persistence, aperture and fillings of discontinuities or tension and shear strength in general; strength and deformability of the rock material, water pressure, primary stress conditions. Additionally the excavation geometry and the secondary stress condition around the excavation do also have significant importance especially for the estimation of the over break volume.

Methods for design and analysis: for the evaluation of this behavior kinematic and mechanical models are used. Depending on the project specific problem only kinematic models, kinematic models in combination with mechanical methods, or 2D and 3D numerical distinct element methods are used. Depending on the available ground data and the geometry of the underground structure a systematic (e.g. for a tunnel) or a discrete (e.g. for a cavern) excavation and support system can be developed.

Comment: the behavior of gravity induced block failure is generally very sensitive to the discontinuity properties and the stress condition. Due to this the knowledge about the ground conditions has a significant impact onto the predictability of the behavior. In case of shallow underground structures it might be possible to use a distinct model while for deep tunnels only

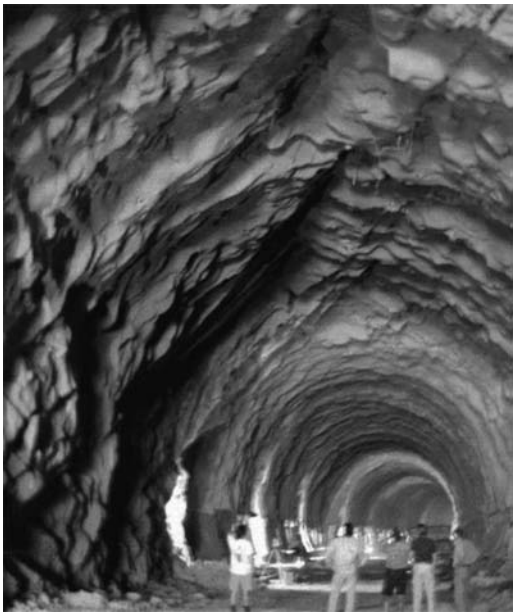


Figure 4. Gravity induced, discontinuity controlled block failure in a tunnel; photo by W. Schubert.



Figure 5. Raveling of highly fractured rock mass (Peridotite/Serpentinite) in the beginning stage of a progressive failure after local instabilities during works at the bench/side wall; photo by Goricki.

a random prediction of this behavior might be used and final support decisions depend on the observations of the ground conditions during construction.

5.3 *Gravity induced behavior – raveling ground*

Mechanism: gravity induced raveling and falling of generally dry soil material or highly fractured and poorly interlocked rock mass (e.g. fault material) into the excavation; the ground has no or low cohesion and the failure occurs usually progressively.

Important parameters: degree of fracturing, interlocking, grain size distribution, discontinuity fillings, cohesion or tension and shear strength in general; primary stress condition.

Methods for design and analysis: the mechanism mainly depends on the tension between the particles and consequently on the parameter cohesion, in case of applying Mohr-Coulomb failure criterion. Especially in soil mechanics many analytical models have been developed, from simple comparison of cohesion with free span or height of excavation surfaces to sophisticated numerical DEM models.

Comment: The exact prediction of the limit state of raveling (detaching of a particle) is generally difficult but tendencies and scenarios can be developed from the models as well as from observations during site investigation such as collapse of drill holes or collapse of exploratory pit side walls. In case of fractured rock mass the limit between the behaviors of gravity induced falling of discontinuity controlled blocks and gravity induced raveling of particles is difficult to define. The main difference could be described by the influence of bolting, if distinct bolting concepts can avoid failure or not.

5.4 *Stress induced behavior*

Mechanism: the loading of the rock mass due to secondary stresses around the underground excavation exceeds the rock mass strength. This leads to the development of fractures along discontinuities and through intact rock. Depending on the stress condition and the rock mass properties the stress induced failures can occur differently from plastic to brittle.

Important parameters: deformation and strength parameters of intact rock, discontinuities and rock mass; the significance of the parameters highly depends on the detailed mode of stress induced failure.

Methods for design and analysis: closed form solutions and numerical models, which describe the strain/stress condition, the utilization of the ground surrounding the excavation or more detailed fracture propagation are the typical methods for modeling. Therefore it is important that the relevant ground parameters are considered and that the applied model can reproduce or represent the potential failure mechanism. Anisotropic ground properties for example or distinct zones of weakness must be considered in the applied model if the behavior of the ground is triggered by these influences (Goricki et al. 2005).

As mentioned above, different modes of stress induced failure may propagate due to different combinations of ground parameters, stress conditions and excavation geometry. In the following typical types of stress induced failure are discussed briefly.

5.4.1 *Stress induced behavior – shear failure in low stress environment*

Even with generally low stress magnitudes the loading of the rock mass exceeds the rock mass strength. Especially due to low confinement stresses (e.g. in case of shallow overburden) progressive shear failures lead to voluminous over break in the crown area and



Figure 6. Day-lighting shear failure of a tunnel in rock mass (weathered gneiss) with shallow overburden, upper photo from surface, lower photo from tunnel; photos by Goricki.

chimney like roof failures. Figure 6 shows the result of a progressive shear failure, which developed up to the ground surface. The failure occurred during the bench excavation in weathered gneiss material with an overburden of approx. 5 m plus a 1.5 m thick upper soil layer.

This mode of failure can usually be observed in soil material with shallow overburden but can also propagate in highly fracture or weathered rock mass or in rock mass with steeply dipping discontinuities and low shear strength.

5.4.2 *Stress induced behavior – shear failure in high stress environment*

The loading of the rock mass exceeds the rock mass strength and the rock mass is significantly utilized. Due to the high stress level and the triaxial loading condition around the excavation shear failures develop. Figure 7 shows the development of a discrete shear failure at the side wall of a tunnel top heading. With increasing confinement pressure the shear fractures become more distributed in the rock mass, which leads to "plastic behavior" (Jaeger et al. 2007) in combination with large and uniform displacements of the excavation surfaces. The anisotropic properties of the rock mass have a significant influence on the development of the behavior and must be considered properly in the model.

Modeling of this type of behavior was published by various authors in the past (e.g. Schubert 1996, Goricki et al. 2006, Anagnostou & Cantanieni 2007, Radoncic et al. 2009, Hoek & Marinos 2009, Barla et al. 2010).



Figure 7. Shear failure at the right top heading side wall, temporary stabilization with tree trunks; photo by G. Feder.



Figure 8. Rock burst in deep tunnel in massive rock mass; from (Ortlepp 2000).

5.4.3 *Stress induced behavior – brittle failure in high stress environment*

The loading of hard, massive and brittle rock mass exceeds the high rock or rock mass strength. The brittle failure develops close to the excavation surface due to the generally uniaxial loading condition in this area. The failure, which mainly depends on the rock mass properties, the stress level and the orientation of the primary stresses can propagate within a wide variety from local spalling to violent rock burst. The fractures develop parallel to the principle stress and create thin rock plates. Figure 8 shows the result of a rock burst of a small tunnel in massive rock mass. The modeling of this behavior can either be done by evaluation of relevant rock mass parameter (such as uniaxial compression strength, post failure behavior or elastic parameters) in combination with the primary and secondary stress condition or by applying numerical models with appropriate failure criteria. Different models and approaches are published concerning a proper and realistic analysis of this type of behavior (e.g. Hoek et al. 1995, Kaiser et al. 1996, Martin & Christiansson 2009, Kaiser 2010).



Figure 9. shows a typical failure of a tunnel floor due to swelling.

5.5 *Swelling ground*

Mechanism: Swelling is the volumetric increase of rock or rock mass due to chemical processes in combination with water. Swelling pressure can develop if the volumetric strains are kinematically limited. The behavior is time dependent and dominated by the interaction between water, rock mass mineralogy and the stress environment. Considering equilibrium the swelling process can start by adding water and/or reducing the stress level.

Important parameters: mineralogy of the rock and rock mass, water, permeability, primary and secondary stress condition.

Methods for design and analysis: One method is to determine the swelling pressure based on ground condition, mineralogical condition and specific laboratory tests (ISRM 1999) in combination with the potential infiltration of water. These loads can then be used for typical design methods such as closed form solutions or numerical analysis. Another method is the direct implementation of the swelling behavior in the analysis by using specifically developed constitutive laws for example in combination with numerical models. The mechanism and models are discussed in literature such as Einstein (1996), Wittke-Gattermann & Wittke (2004), Rauh (2009), Anagnostou et al. (2010) or Steiner et al. (2010).

Comment: Swelling, especially anhydrite swelling can lead to large deformations of the ground in combination with high stresses on underground structures. The timely development can continue through years and even small variations of the environment can again change the behavior. To handle such behavior two basically different design approaches, stiff and ductile, were developed. The decisions about the support system as well as the applied design models must be done project specific based on engineering understanding of the potential swelling behavior, especially considering the significant impact of measures onto the development of the behavior itself.



Figure 10. Flowing ground in a tunnel due to intensive water inflow; reference unknown.

5.6 *Flowing ground*

Mechanism: flowing of intensively fractured rock mass or soil material into the excavation due to high water content. The initial water pressure is higher than the interlocking, cohesion or bonding strength of the soil and rock mass particles. The failure occurs usually progressively.

Important parameters: water pressure and quantity, permeability, degree of fracturing, interlocking, grain size distribution, cohesion or tension and shear strength.

Methods for design and analysis: A simple method is to compare the tensile strength or cohesion of the rock mass with the predicted ground water conditions. Such simple evaluation is often sufficient in rock tunneling to decide about measures to reduce the ground water inflow or pressure or to increase the rock mass strength. More detailed models are developed in soil mechanics especially in combination with shallow urban tunneling.

Comment: In hard and fractured rock mass water inflows, independent to quantities and quantities do often only affect the construction progress but not create significant ground failure. Such water inflows without influence on the excavation stability are not discussed in this context as the ground can be classified as stable with mainly contractual impact.

6 IMPLEMENTATION OF BEHAVIOR BASED DESIGN IN CONSTRUCTION PROCESS

In the following it is assumed that an underground structure in natural ground is under excavation at any random position within the project.

In the design phase construction measures including construction method, process and materials were defined. Additionally a prediction of the behavior of the structure and the surrounding environment was prepared. This includes the stability as well as the serviceability and covers for example loading, utilization and strain of structural elements as well as underground and surface displacement, maximum water inflows and more. Additionally the monitoring system

was defined in the design and expected as well as alert and maximum allowable values were quantified.

Before the excavation of the next cycle, a decision about the final layout of excavation and support system need to be done. Therefore some fundamental works concerning the update of the design to the site conditions are necessary.

In a first step a geological and geotechnical prognosis for the next few excavation meters needs to be done. This prognosis is an update of the existing design due to the information gained from the already preformed excavation and/or from additional investigations e.g. ahead of the tunnel face. It has to include geological conditions, ground parameters, stress and water conditions as well as a prediction of the theoretical ground behavior due to excavation without any support (potential failure mechanism). This short term prognosis can be similar, slightly or significantly different to the descriptions in the original design.

In a second step the applicability of the design for the ground as described in the short term prediction must be verified. Therefore the basic design assumptions including ground conditions, tunnel geometry and boundary conditions such as maximum surface displacements or lowering of ground water table must be checked.

In a third step observations of the ground behavior from already constructed tunnel section in comparable conditions are evaluated, if available. The data from the observations can be used to re-evaluate the potential failure modes of the ground and the predicted behavior as the effects of the interaction between ground, excavation and support.

In the fourth step, the data as described in the previous steps, the updated short term prediction, the design assumptions for this particular section and the experience gained from previous observations, are used to evaluate the original design. In case of deviations the geotechnical design for the next excavation must be adapted, modified or maybe entirely re-designed.

Any change of the geotechnical design must fulfill the same criteria as applied during the design phase including analysis in case of significant changes. Additionally a detailed description of the expected behavior due to the changes must be given. The design changes must be done by qualified engineers who are aware of the design as well as in the construction. Small adaptations and modifications must be part of the routine work on site while sever design changes might be done by an additional design team ideally supervised by an onsite design engineer.

The above described decision making process must be fully integrated part of the project risk management process. This guarantees that the design and its adaptation to the actual ground conditions is always integrative part of the on-site decisions and that the basic focus of the design always remains the mitigation of unacceptable risks to acceptable conditions by application of measures.

During excavation the actual ground conditions are compared with the prediction and, in case of deviations, modifications can immediately be developed by following the procedure as described above starting with step 1 for the actual excavation round.

After construction the observation and evaluation of the behavior of the ground and the structural elements continues. The experience shall be used for the optimization of future construction works as described in step three. In case of deviations from the predicted behavior an evaluation must be done and, if required measures must be developed based on the principles of project risk management.

7 CONCLUSIONS

The geotechnical design of underground structures mainly deals with the interaction between the ground and the structure in the different construction stages. It often has to deal with difficult and complex conditions due to differences and uncertainties within the ground, the structures and the boundary conditions. In order to develop an economic and safe underground structure it is essential to develop a sound geotechnical design during all project phases.

The behavior of the ground is the key element for the development of the geotechnical design. With the understanding of the interaction between ground and construction works including mechanisms and potential failure modes, a proper design and modeling techniques can be applied. Depending on the specific conditions any engineering method representing the state of the art in soil and rock mechanics as well as in structural mechanics can be used to investigate the mechanisms and develop the required geotechnical measures concerning excavation and support.

For a systematic development of the geotechnical design during all project phases, including construction, it is necessary to follow a general procedure, which allows systematic adaptation of the design to the different levels of information. It is proposed to use the process of risk management as described in ISO 31000, which provides a comprehensive framework for the development of the geotechnical design. By considering the potential modes of ground failure as risks and the designed ground support as mitigation measures, the actual risks of underground structure can be evaluated and controlled in any project phase. Especially the adaptation of the geotechnical design during the construction phase due to possible changes of the ground conditions, collection of additional ground data and the observation of the actual behavior can be developed very well within the risk management process.

The proposed methodology provides a consistent design approach for the development, adaptation and application of the geotechnical design in any project phase. Based on the predicted ground behavior the proper engineering design method and tool can be selected and within the framework of the risk management process the geotechnical design can be developed

independent of the difficulty of the ground conditions or the complexity of the underground structure. The design modifications, due to additionally gained information, become an integrative part of the decision making process on-site independent to the design and construction method.

REFERENCES

Anagnostou, G., Cantieni, L. 2007. Design and analysis of yielding support in squeezing ground. In: The second half century of rock mechanics, 11th ISRM Congress Lisbon, Vol. 2: 829–832.

Anagnostou, G., Pimentel, E., Serafeimidis, K. 2010. Swelling of sulphatic claystone – some fundamental questions and their practical relevance. Geomechanics and Tunnelling 3 (2010), No. 5: 567–572.

Austrian Society for Geomechanics. 2010. Guideline for the geotechnical design of underground structures with conventional excavation. Salzburg.

Barla, G., Bonini, M., Debernardi, D. 2010. Time Dependent Deformations in Squeezing Tunnels. International Journal of Geoengineering Case Histories. Vol. 2, Issue 1: 40–65.

Bieniawski, Z.T. 1992. Design methodology in rock engineering: theory, education and practice. Balkema, Rotterdam

CEN European Committee for Standardisation. 2011. EN 1992-1-1 Eurocode 2: Design of concrete structures — Part 1-1: General rules and rules for buildings.

Einstein, H.H. 1996. Tunnelling in Difficult Ground – Swelling Behavior and Identification of Swelling Rocks. Rock Mechanics and Rock Engineering 29 (3): 113–124.

Feng, X.T. & Hudon, J.A. 2011. Rock Engineering Design, CRC Press.

Fröhlich, B. & Dauwe, L. 2006. Part renovation of the Weinsberg Tunnel in swelling gypsum Keuper rock. Mitteilung für Ingenieurgeologie und Geomechanik, Vienna University of Technology, Vol. 7 (2006): 3rd Colloquium "Rock Mechanics – theory and practice": 177–190.

Goodman, R.E., Shi, G-H. 1985. Block Theory and its Application to Rock Engineering. Prentice-Hall, New Jersey.

Goricki, A., Schick, K.J., Steidl, A. 2002. Quantification of the Geotechnical and Economic Risk in Tunneling. Probabilistics in Geotechnics: Technical and Economic Risk Estimation, Graz, Austria, Sept. 2002: 483–489.

Goricki., A. 2003. Classification of Rock Mass Behaviour based on a Hierarchical Rock Mass Characterization for the Design of Underground Structures. Doctoral thesis, Graz University of Technology, Austria.

Goricki, A., Button, E., Schubert, W., Poetsch, M., Leitner, R. 2005. The Influence of Discontinuity Orientation on the Behaviour of Tunnels. Felsbau 23 (5), 12–18.

Goricki, A., Rachaniotis, N., Hoek, E., Marios, P., Tsotsos, S., Schubert, W. 2006. Support Decision Criteria for Tunnels in Fault Zones. Felsbau, 24 (2006) Nr 5: 51–57.

Goricki, A. & Rachaniotis, N. 2011. NATM Designs for Challenging Tunnel Projects in Northern Greece. In: Kolic, D. (ed.). Using underground space, 1st International Congress on Tunnels and Underground Structures in South-East Europe, Dubrovnik, Croatia: 56–57.

Hoek, E. & Brown, E.T. 1980. Underground Excavation in Rock. Institution of Mining and Metallurgy, London.

Hoek, E., Kaiser, P.K., Bawden, W.F. 1995. Support of Underground Excavations in Hard Rock. Balkema, Rotterdam.

Hoek, E., Marinos, P.G. 2009. Tunnelling in overstressed rock. In: Vrkljan, I. (ed). Rock Engineering in Difficult Ground Conditions – Soft Rocks and Karst. Taylor and Francis Group, London: 49–60.

Hudson, J.A. 2001. Rock engineering case histories: key factors, mechanisms and problems. Keynote lecture. In: P. Särkkä, P. Eloranta (eds.), Rock Mechanics a Challenge for Society, ISRM Reg. Symp. Eurock 2001, Espoo, Finland: 13–20.

ISRM. 1999. Suggested methods for laboratory testing of swelling rock. Int. J. Rock Mech. Min. Sci. & Geomech. Vol 36 (1999): 291–306.

International Organization for Standardization. 2009. ISO 31000:2009(E) Risk management – Principles and guidelines. Switzerland.

ITA Working Group on General Approaches to the Design of Tunnels. 1988. Guideline for the Design of Tunnels. Tunnelling and Underground Space Technology 3: 237–248

Jaeger, J.C., Cook, N.G.W., Zimmerman, R.W. 2007. Fundamentals of Rock Mechanics, Fourth Edition. Blackwell Publishing.

Kaiser, P.K., McCreath, D.R., Tannant, D.D. 1996. Canadian Rockburst Support Handbook. Mininig Research Directorate, Sudbury.

Kaiser, P.K., Diederichs, M.S., Martin, C.D., Sharp, J., Steiner, W. 2000. Underground Works in Hard Rock Tunnelling and Mining. In: Ervin, M.C. (ed.), GeoEng 2000; Proc. intern. symp., Melbourne: CD.

Kaiser, P.K., with contributions by Amann, F. & Steiner, W. 2010. How highly stressed brittle rock failure impacts tunnel design. EUROCK 2010, Lausanne: 27–38.

Martin, C.D. & Christiansson, R. 2009. Estimating the potential for spalling around a deep nuclear waste repository in crystalline rock. Int. J. Rock Mech. Min. Sci., 36 (2009): 219–228.

Ortlepp, D. 2000. Rock Fracture and Rockbursts, An Introspective Review. ISRM News Journal Vol.6 (2): 23–27.

Palmstrom, A. & Stille, H. 2007. Ground behaviour and rock engineering tools for underground excavations, Tunnelling and Underground Space Technology 22 (2007): 363–376.

Poetsch, M. 2011. The analysis of rotational and sliding modes of failure for slopes, foundations and underground structures in blocky, hard rock mass, Doctoral thesis, Graz University of Technology, Austria.

Radoncic, N., Schubert, W., Moritz, B. 2009. Ductile support design. Geomechanics and Tunnelling 2 (2009), No. 5: 561–577.

Rauh, F. 2009. Untersuchungen zum Quellverhalten von Anhydrit und Tongesteinen im Tunnelbau. Münchner Geowissenschaftliche Abhandlungen. Verlag Dr. Friedrich Pfeil, München.

Reichenspurner, P. 2013. Rohtang Praying for Rock. Tunnels, January 2013: 22–26.

Schubert, W. 1996. Dealing with Squeezing Conditions in Alpine Tunnels. Rock Mechanics and Rock Engineering Vol. 29, No. 3: 145–153.

Schubert, W. 2011. Risk oriented design and construction of tunnels. In: Qian, Q. & Zhou, Y. (eds.), Harmonising Rock Engineering and the Environment, 12th ISRM International Congress on Rock Mechanics, 2011, Beijing, China: 127–139.

Steiner, W., Kaiser, P.K., Spaun, G. 2010. Role of brittle fracture on swelling behavior of weak rock tunnels: hypothesis and qualitative evidence. Geomechanics and Tunnelling 3 (2010), No.5: 583–596.

Wittke-Gattermann, P., Wittke, M. 2004. Computation of strain and pressure for tunnels in swelling rocks. ITA-AITES congress: E14 1–8.

This page intentionally left blank

Keynote lectures

This page intentionally left blank

Rock Mechanics for Resources, Energy and Environment – Kwaśniewski & Łydżba (eds)
© 2013 Taylor & Francis Group, London, ISBN 978-1-138-00080-3

The mechanical behavior of salt and salt caverns

Pierre Bérest
LMS, Ecole Polytechnique ParisTech, Palaiseau, France

ABSTRACT: Several remarkable features of the mechanical behavior of salt caverns are presented. How these features can be explained by laboratory experiments and micro-mechanical investigations is discussed. Other aspects of the mechanical behavior of salt (slow strain rates, humidity, temperature, stress triaxiality, transient creep and salt failure) are analyzed.

1 INTRODUCTION

The mechanical behavior of salt can be studied at various scales: the scale of crystals, at which dislocations climb, glide and pile up; the scale of grains and the interface between grains, where micro-cracks can form; and the scale of the salt formation, in which the salt, clay or anhydrite layers generate specific interactions. These scales are provided by Nature. Two other scales are man-made. The first of these is the laboratory scale, which is quite helpful but not fully relevant — laboratory tests alone cannot provide a full picture of salt mechanical behavior. The most significant scale is the scale of the body under study: mine, cavern, or repository. To start the discussion, the next Sections are devoted to a brief overview of salt-cavern behavior.

2 ELASTIC BEHAVIOR OF A SALT CAVERN

The elastic behavior of a brine-filled cavern can be observed easily when an additional amount of brine (v_{inj}) is injected in the cavern: the resulting cavern-pressure increase, or p_c, is proportional to the injected volume of brine, $\beta V p_c = v_{inj}$, where V is the cavern volume. The slope of the curve, or βV, is called the cavern compressibility (in m^3/MPa or bbls/psi). An example of such a test is described in Thiel (1993) and illustrated in Figure 1. The cavern compressibility coefficient, β, is the sum of the brine-compressibility coefficient (which is $\beta_b = 2.7\ 10^{-4}$/MPa) and of the "hole" compressibility coefficient, β_c, which can be written $\beta_c = 3(1+\nu)f(\Omega)/2E$, depending on the elastic properties (E, ν) of the salt formation and on cavern shape (Ω) (Bérest et al. 1999). When the cavern is a perfect sphere, $f(\Omega) = 1$; for a perfect cylinder, $f(\Omega) = 4/3$; when the cavern is "flat", $f(\Omega)$ is much larger than 1. A typical value is $\beta_c = 1.3 \times 10^{-4}$/MPa, which proves that the *in situ* elastic modulus of salt is $E = 15$ GPa or so, a figure that is consistent with the results of laboratory experiments. For instance, Hansen et al. (1984) measured the elastic moduli of natural rock-salt samples from ten different locations in the U.S.; mean values were in the range $E = 24$–32 GPa.

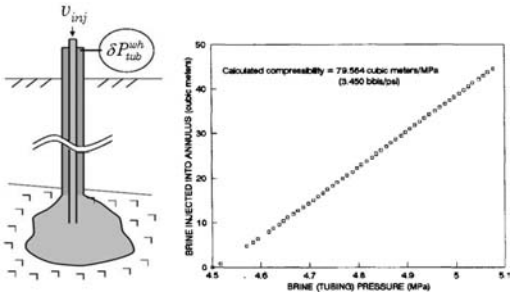


Figure 1. Measurement of cavern compressibility. After Thiel (1993).

Cavern compressibility plays a significant role in various phenomena: the mechanical-integrity test, pressure build-up in a closed cavern, or blow-out scenarios (Bérest et al. 1999).

3 CREEP CLOSURE, SPALLING AND SLUFFING IN SALT CAVERNS

3.1 *Introduction*

Several caverns experience spalling, sluffing, breakouts and fast creep closure. In most cases, these caverns are deep gas-storage caverns in which gas pressure was low when the gas inventory was small. The driving force for cavern creep closure is the gap between geostatic pressure (P_∞) and cavern pressure (P_c). In a liquid-filled cavern, this gap is a linear function of cavern depth, and is $P_\infty - P_c = 10$ MPa at a depth 1000 m. In a gas-filled cavern, when gas inventory (and pressure) is small, the gap can be much larger than in a liquid-filled cavern.

Only creep closure leads to cavern volume loss. Measuring cavern shape evolution is not an easy task. Sonar surveys can be run occasionally, but their accuracy is a couple of % points. In a brine cavern, the rate of flow expelled from an open cavern, or, more conveniently, the pressure increase in a closed cavern ("shut-in test") can be measured accurately; however, the brine-flow rate, or pressure increase, often is governed by cavern brine warming rather than by cavern closure. In a gas cavern, some brine is left at the cavern bottom, and the rise of the gas-brine interface provides some information on the evolution of cavern shape. Such a rise, however, can be generated both by block fall and by cavern bottom creep closure. Various "mass balance" techniques based on the measurement of gas pressure, temperature and inventory also can be used to assess cavern "free" volume (accessible to gas), but uncertainties are unavoidable.

A couple of examples are discussed below. The analysis focuses on cavern depth, cavern shape, cavern internal pressure; rate, frequency and amplitude of pressure cycles, and temperature changes as possible factors explaining cavern behavior.

3.2 *Creep closure: Tersanne, France and Eminence, Mississippi*

Cavern TE02 belongs to the Tersanne (France) gas-storage facility operated by Storengy. Cavern depth is 1400 to 1550 m, a depth at which the geostatic pressure is approximately $P_\infty = 32$MPa. This cavern was leached out in February 1970, at which time the "sonar" volume was $V = 91600 \pm 4300\,\mathrm{m}^3$ (Boucly & Legreneur 1980). The cavern was filled with gas and experienced 9 pressure cycles between $P_c = 22$ MPa and $P_c = 8$ MPa during the period 1970–1979. The measured cavern gas temperature during that period fluctuated between 32°C and 69°C. In July 1979, it became clear that cavern had lost significant volume: the cavern bottom had risen by 5.8 m. It was decided to fill the cavern with brine and perform a sonar survey. Cavern volume had decreased to $V = 58\,200 \pm 2300\,\mathrm{m}^3$, a loss of 1/3 loss over a 9-year period. In addition, the gas-brine interface had risen: *"In order to explain the gas-brine interface rising it is not possible to exclude the fall of the blocks following the failure of the overhanging banks visible on the February 1970 reading; the January 1980 reading has a much smoother appearance*" (Boucly & Legreneur 1980, p. 256). Brine then was removed, and the cavern was used again for gas storage. In April 2005, the cavern was filled again with brine (Hévin et al. 2007) and a sonar survey run. The overall cavern loss was 60% after 35 years of operation. Volume loss had been much faster in the lower part of the cavern (Fig. 2a).

A somewhat similar example is provided by Cavern #1 of the Eminence Salt Dome, Mississippi (Baar 1977, Serata & Cundey 1979). Its depth was between 1725 m and 2000 m, and the geostatic pressure was $P_\infty \approx 40$ MPa. The first gas injection was completed by mid-1970. Starting in October 1970, the gas pressure was lowered to $P_c = 6$ MPa and kept constant for two months, after which it was increased to $P_c = 28$ MPa. A similar pressure cycle was performed in 1971. By April 1972, the cavern bottom had been raised by 36 m. A sonar survey was performed at that time that showed a cavern volume loss of 40%. It was noticed, however, that the cavern roof had remained intact (Fig. 2b). It is difficult to assert whether, in addition to cavern loss, sluffing and spalling took place. It is obvious, again, that a large part of the volume loss must be attributed to bottom heave. Bérest et al. (1986) suggest that, in addition to possible block falls, this non-symmetrical behavior can be explained at least partly by the larger overburden pressure and warmer temperature in the lower part of the rock mass. Note, also, that the gas depressurization rate was not overly fast in this cavern.

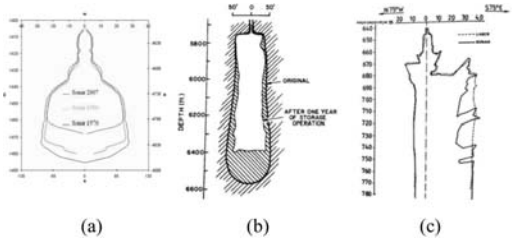
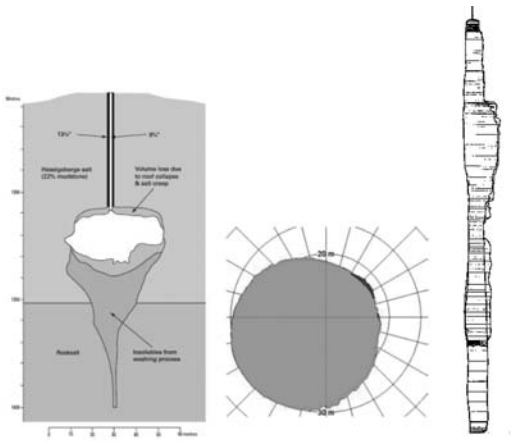


Figure 2. From left to right: 2a. TE02 cavern shape evolution (Acknowledgement: Grégoire Hévin, Storengy); 2b. Cavern #1, Eminence Salt Dome, Mississippi (Serata & Cundey 1979); 2c. Huntorf Cavern (Quast 1983).

3.3 *Blocks fall: Huntorf, Kiel, Germany, Lille-Torup, Denmark and Big Hill, Texas*

Crotogino et al. (2001) described "*more than 20 years of successful operation*" of the CAES storage facility at Huntorf (Germany). Two caverns with depths between 650 m ($P_\infty = 14.5$ MPa) and 800 m were operated. Air pressure varied between $P_c = 4.3$ MPa and $P_c = 7$ MPa. The fastest depressurization rate was 5 MPa/hr. Between 1978 and 1986, there were 200 starts/yr (cycles/yr), and less than 100 starts/yr in the 1990s. Quast (1983) compared two vertical cross-sections of the NK1 cavern, which had been run in 1976 and in 1980, i.e. before and after the first gas injection (Fig. 2c). Salt "curtains", still present in 1976 when the cavern was filled with brine, broke and fell to cavern bottom during the first gas injection (during which the cavern bottom rose by 16 m). Later, the depth of the brine-air interface remained almost constant, and Crotogino et al. (2001) state that "*evaluation over the whole operational period shows practically no changes that can be attributed to roof falls"* (p. 356).

The Kiel 101 cavern (Fig. 3a) had been leached out at a depth between 1305 m and 1400 m ($P_\infty \approx$ 30 MPa). The amount of insolubles in the salt formation was high, resulting in a large sump at the cavern bottom. After leaching was completed, a submersible



(a) (b) (c)

Figure 3. From left to right: 3a. Kiel Cavern, Germany (British Geological Survey 2008); 3b. Lille-Torup, Denmark (Rokahr et al. 2007); 3c. Markham Cavern #5 (Cole 2002).

pump was lowered to the bottom of the well. *"Starting about 1 November 1967, the pressure at the roof of the cavity was lowered from 15.6 MPa to practically zero by pumping the brine out of the access well"* (Baar 1977, p. 147). In fact, when cavern pressure was lowered from $P_c = 13.1$ MPa to $P_c = 6.5$ MPa over 5 days, the cavern roof collapsed (Fig. 3a). A sonar survey was performed at the end of the testing period. The volume accessible to sonar had decreased from 36,600 m^3 to 32,100 m^3. An additional loss of 1900 m^3 was observed five months later. Many factors could have played a role in this evolution — e.g., a heterogeneous salt formation, a flat roof, and rapid depressurization (more than 1 MPa/day). However, fluid cooling cannot be a factor. (During depressurization, the brine temperature drops adiabatically by 0.03°C/MPa, a very small figure.)

Rokahr et al. (2007) described a remarkable rock-mechanics test performed in a cavern of the Lille-Torup (Denmark) gas-storage facility. The average cavern depth was 1460 m ($P_\infty \approx 32$ MPa). During the test, the cavern pressure dropped from $P_c = 21$ MPa to $P_c = 6$ MPa in three months. Two high-resolution (laser) sonar surveys were performed on January 16, 2005 and March 31, 2005, a period of time over which the cavern gas pressure dropped from $P_c = 14$ MPa to $P_c = 6$ MPa. The increase in cavern cross-section is clearly visible on Figure 3b: *"The enlargement of the cavern in this sector is interpreted as a consequence of local failure of the rock salt at the cavern wall, that means that spalling had occured locally."* (Rokahr et al. 2007, p. 137).

Munson et al. (2004) described a salt fall event involving two – million cubic feet in a Big Hill cavern of the Strategic Petroleum Reserve in Texas. They suggest that linear and / or planar features in the salt dome represent either sites of preferential leaching or localized spalling.

3.4 *Creep closure and block falls: Markham, Texas*

Cole (2002) describes two gas caverns in the Markham storage field in Texas. These caverns were cycled 8 to 10 times per year, and withdrawal rates were 3–4 times faster than injection rates. The cavern tops are at 1050 m and 1075 m ($P_\infty = 23$ MPa), and the original cavern heights were 530 m and 696 m, respectively. The first gas injections were in June 1992 (Cavern #2) and October 1995 (Cavern #5). Cavern operation resulted in cavern-volume loss, and salt sluffing from the walls and roof of the cavern. Brine-gas interface surveys were run every year. As of January 2002, the caverns had lost 89 m and 128 m of their depths. A "material balance" test also had been performed in 2001 to assess the cavern "free" volume, and natural gas sonars were run in January 2002. Comparison of these various methods suggests that cavern closure was approximately 5% of the initial volume; however, a similar volume of salt had fallen from the walls to the bottom of the caverns. Comparison of sonar profiles shows vertical profile overlay of sonars performed in May 1995 and January 2002 (Fig. 3c). Note the bottom heave and possible break-outs at the cavern wall. However, "*no large sections of salt from one area of the caverns fell to the bottom creating the fill ... the salt was removed in thin layers over large areas of the caverns ... horizontal cavern closure occurred ... thus closing in part of the area created by the salt falling*." (Cole 2002, p. 82).

3.5 *Slow creep closure at shallow depth: Gellenoncourt and Etrez, France*

Brouard et al. (2013) measured closure rate in a 250-m deep cavern ($P_\infty = 5.5$ MPa) operated by CSME at Gellenoncourt, France. This brine-filled cavern ($P_c = 3$ MPa) had been kept idle for 30 years: thermal equilibrium between the rock mass and the cavern brine was reached, and brine thermal expansion could be disregarded. To assess cavern closure rate, brine outflow, which results from cavern creep closure, was measured over a period of 10 months; this test was followed by a 6-month shut-in test during which the pressure build-up rate was measured. Both tests proved that the cavern closure rate was less than $\dot{V}/V = 10^{-5}$/yr. A similar test is described by Brouard (1998), who proved that closure rate was $\dot{V}/V = 3 \times 10^{-4}$/yr in a 950-m deep, brine-filled cavern creep at Etrez (France).

3.6 *Depth and creep closure rate: Vacherie salt dome, Louisiana*

The significance of depth was illustrated clearly by Thoms & Gehle (1983): "*In early 1978, exploratory boreholes were drilled to depths of 5,000 feet* [1600 m] *in the North Louisiana salt domes of Vacherie and Rayburn's. The exploratory boreholes were logged several times with 4-arm caliper 'tools' over a time period of approximately four years*" (p. 28). Closure data

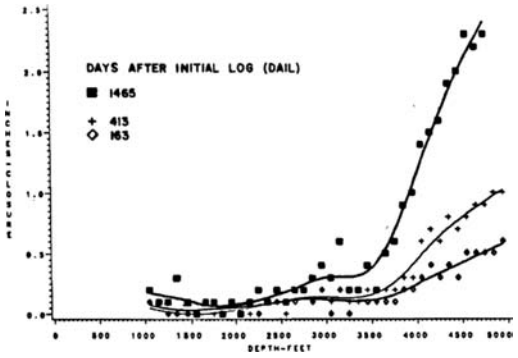


Figure 4. Borehole diameter as a function of depth and time: The borehole closure rate is faster when the depth is greater than 3500 ft or 1000 m. (Thoms & Gehle, 1983).

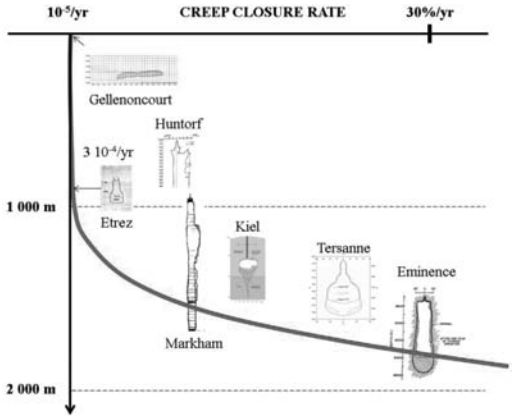


Figure 5. Cavern creep closure rate versus cavern depth: Gellenoncourt, Huntorf, Etrez, Markham, Kiel, Tersanne, Eminence. The curve represents cavern convergence rate as a function of depth for a typical brine-filled cavern.

for the Vacherie salt dome are provided in Figure 4. A considerable variation of borehole closure with depth and time can be observed.

3.7 *Conclusions*

Large creep closures (respectively, 3%/yr and 30%/yr) were observed at Tersanne and Eminence, two gas storage sites with depths of 1450 m and 1900 m, respectively. In these gas storages, depressurization rates were relatively slow. Spalling also took place, but it is believed to have been small. At Kiel, a 1450-m deep cavern, the somewhat flat roof fell when the cavern pressure dropped abruptly to zero. At the CAES Huntorf site, overhanging blocks fell during the first gas injection, which may be attributed to the reduction in Archimedes thrust, when fluid density drastically drops after brine withdrawal. No, or small, further spalling was observed despite fast depressurization rates. Block falls certainly occurred at Lille – Torup, even if the pressure – drop rate was slow (5 MPa/month or so). Markham is a remarkable case, as many pressure cycles were performed (8–10/year), and both cavern creep closure and wall sluffing were observed. The Big Hill case proves that, in addition to loading conditions, geological features and heterogeneities can play significant roles. From this a couple of conclusions can be drawn. Salt cavern behavior exhibits both brittle (roof fall, spalling, sluffing) and ductile (cavern closure) features. Creep closure rate is a (highly) non-linear function of depth: it is 10^{-5}/yr at a 250-m depth, 3×10^{-4}/yr at a 1000-m depth, and several 10^{-2}/yr at a 2000-m depth (see Figure 6). Generally speaking, gas caverns (in which gas pressure is small when gas inventory is low) are more creep-prone than liquid-filled caverns (in which liquid pressure is almost constant and halmostatic — i.e., proportional to depth). Volume loss is larger in the deepest part of the cavern (Tersanne, Eminence, Markham); this is partly due to rock fall, but larger temperature and deviatoric stresses values in the deeper part of the cavern also are important factors. The role of depressurization rate in a gas cavern (which is accompanied by the onset of temperature drop and tensile thermal stresses) is still unclear: rates were relatively slow during the Lille-Torup test, but rates were fast during the Kiel test. However, in this case, temperature drop was not a factor, as the cavern was filled with brine. In the next Sections, it will be proved that these features are consistent with the conclusions drawn from laboratory tests.

4 LABORATORY EXPERIMENTS

Salt testing in the laboratory raises some specific problems, which are addressed, for instance, in Guessous et al. (1988) and Wawersik & Preece (1984). The issue of room-temperature fluctuations is discussed in Section 7.3.

Few other rocks have given rise to such a comprehensive set of laboratory experiments (see, for instance, the seven proceedings of the Conferences on the Mechanical Behavior of Salt). While a full description of these efforts is beyond the scope of this paper, the results that are widely accepted by rock mechanics experts are listed below.

When constant triaxial load and temperature are applied to a rock sample, the observed strain is the sum of three parts: the elastic (instantaneous) strain, the transient strain and the steady state strain:

$$\dot{\varepsilon}_{ij} = \dot{\varepsilon}^{el}_{ij} + \dot{\varepsilon}^{ss}_{ij} + \dot{\varepsilon}^{tr}_{ij} \tag{1}$$

The immediate response to a load change is elastic; it can be described by a linear relation between $\dot{\varepsilon}^{el}$ and $\dot{\sigma}$.

The steady-state part is characterized by a constant strain rate, or $\dot{\varepsilon}^{ss}$, reached after some days or weeks: in the long term, rock salt flows. Steady-state rate is a highly non-linear function of applied deviatoric stress and temperature. In principle, the mean stress has no influence on strain rate, and no volumetric change is

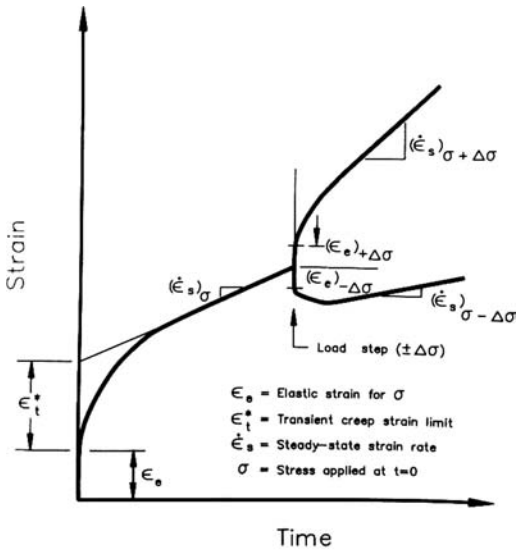


Figure 6. Strain and strain rate as functions of time during a creep test: during the first step the applied stress is σ; at the beginning of the second step it is increased (or decreased) by $\Delta\sigma$ ($-\Delta\sigma$). (From Van Sambeek et al. 1993).

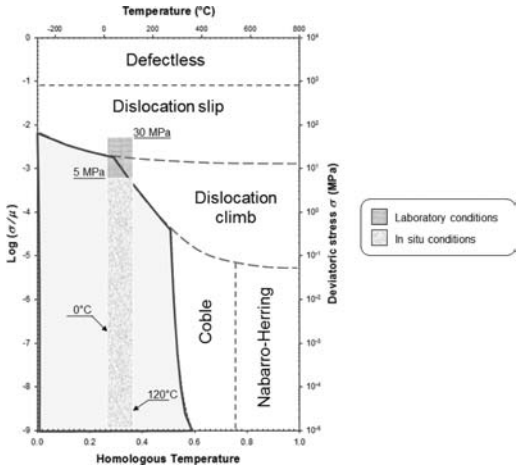


Figure 7. Micromechanism map, after Munson & Dawson (1984).

observed, except when a dilation criterion is exceeded, as explained below.

The transient part describes rock behavior before steady state is reached. Any change in applied loading (or temperature) triggers transient creep, or $\dot{\varepsilon}^{tr}$. It is characterized by fast initial rates following a load increase and by slow initial rates — or even "reverse" initial rates — following a load decrease, or "stress drop"; see Figure 7. These transient rates slowly decrease or increase to reach steady-state creep. Micro-mechanisms can explain some of these characteristic features.

5 MICROMECHANISMS GOVERNING SALT CREEP

Usually, creep tests last several months. The question is whether such a period of time is sufficient to provide a strong basis for extrapolation at the much longer periods of interest when considering such problems as cavern abandonment (centuries) or waste repository design (dozens of centuries). Langer (1984) stated that "*Reliable extrapolation of the creep equations over long period of time and at low deformation rates can only be carried out on the basis of deformation mechanisms. The construction of a deformation-mechanism map is an essential preliminary",* an issue discussed by Hunsche (1984), Munson & Dawson (1984) and Blum & Fleischman (1988).

A deformation-mechanism map, adapted from Munson & Dawson (1984), is presented in Figure 8. It was derived (when possible) from theoretical models of deformation, as well as from empirically determined constitutive equations and from "interpolation, extrapolation or conjecture" (Munson & Dawson, 1984, p. 719). On Figure 8, the governing creep-mechanism (defectless flow, dislocation climb or glide, diffusional creep) is indicated for each domain of the Temperature-Deviatoric Stress plane.

Two rectangles also are drawn; the rectangle [0–120°C] × [5–20 MPa] is the domain in which laboratory tests generally are performed. As explained below, the rectangle [0–120°C] × [0–5 MPa] is the domain of temperature and deviatoric stress *actually* experienced in the vicinity of a salt cavern during most of its lifetime. Except for the upper part of the first rectangle, in which dislocation climb is the dominant mechanism, the micro-mechanism that governs creep in these two rectangles is poorly known. As a first approximation, in this domain, creep rate is described by a power law whose exponent is $n > 1$ (see Section 6). In fact, Spiers et al. (1990) suggested that, in the lower stress range, pressure solution and recrystallization are the most significant mechanisms and that the exponent of the power law should be close to $n = 1$. As seen in Section 8.2, researchers recently have investigated the micro-mechanisms that govern the dilatant behavior of salt (micro-cracks creation, coalescence and interaction).

6 CONSTITUTIVE MODELING

Several constitutive models for the mechanical behavior of salt have been published in the literature, among which are Munson & Dawson (1984), Langer (1984), Aubertin (1996), Cristescu & Hunsche (1998) and Hampel (2012). A synthetic overview of the models developed in Germany can be found in Schultze et al. (2007) and Salzer et al. (2012).

Munson & Dawson (1984) suggest that, in the stress and temperature domains of interest for conventional mines and solution-mined caverns, the

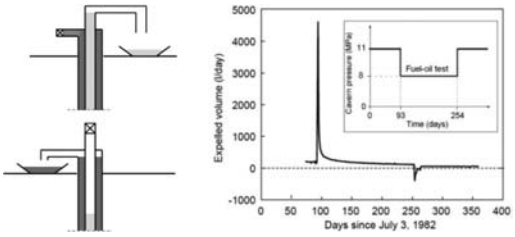


Figure 8. Hydrocarbon Outflow Test: brine (or hydrocarbon) outflow is measured at ground level (Hugout 1988).

so-called "undefined mechanism" is especially active, and steady-state strain rate can be written:

$$\begin{cases} \dot{\varepsilon}^{ss} = A\exp(-\dfrac{Q}{RT})\sigma^n \quad \text{or} \\ \dot{\varepsilon}_{ij}^{ss} = \dfrac{3A}{2}\exp(-\dfrac{Q}{RT})(\sqrt{3J_2})^{n-1}s_{ij} \end{cases} \tag{2}$$

where A, Q/R, n are three constants to be determined in the laboratory: n is in the 3–6 range; Q/R is in the 3000–10 000/K range (Brouard & Bérest, 1998); and A is such that when the applied deviatoric stress is $\sigma =$ 10 MPa, the steady-state strain rate typically belongs to the range $\dot{\varepsilon} = 3 \times 10^{-11} - 3 \times 10^{-10}\ \mathrm{s}^{-1}$. Consider the case of an idealized spherical cavern of radius a, leached out at depth H, where the overburden pressure is P_∞ and the internal cavern pressure is P_c. Steady-state closure rate and deviatoric stresses at cavern wall are:

$$\frac{\dot{V}}{V} = -\frac{3}{2}\left(\frac{3}{2n}\right)^n A\exp\left(-\frac{Q}{RT}\right)\left(P_\infty - P_c\right)^n \tag{3}$$

$$\sqrt{3J_2}\Big|_{ss}^{NH} = \frac{3}{2n}\left(P_\infty - P_c\right)\left(\frac{a}{r}\right)^{3/n} \tag{4}$$

This "Norton-Hoff" law explains, at least qualitatively, most of the features observed in the behavior of salt caverns: when the cavern is deeper, both temperature and deviatoric stresses are larger, and a much faster cavern closure rate can be expected. However, a couple of less intuitive consequences of Equations (3) and (4) also must be noted. Cavern closure rate is a decreasing function of the exponent (n) of the power law; deviatoric stresses are significantly smaller (They are divided by n.) than in the case of the elastic behavior of a rock mass (see Section 7.1), and, in most cases, are smaller than 5 MPa (see, also, Œlizowski & Urbañczyk, 2007, p. 365). Last but not least, computations prove that cavern steady-state is reached after a long period of time (longer when n is higher). This transient effect is said to be *geometrical* (see Section 7.5). Such a simple constitutive law does not account for all the aspects of salt mechanical behavior; some other aspects are discussed in the Sections below.

7 OTHER ASPECTS OF SALT CREEP BEHAVIOR

7.1 *Slow strain rates*

It was noted, in Section 6, that steady-state deviatoric stresses at a cavern wall are low. When extrapolated to low stresses, Equation (2) predicts exceedingly slow strain rates. For instance, assuming $n = 3$ and $\dot{\varepsilon}^{ss} = 10^{-10}\ \mathrm{s}^{-1}$ when $\sigma = 10$ MPa leads to $\dot{\varepsilon}^{ss} = -10^{-16}\ \mathrm{s}^{-1}$ when $\sigma = 0.1$ MPa. Little laboratory evidence is available. For example, to measure accurately such rates, room temperature fluctuations must be kept smaller than 1/100°C (to prevent too large thermo-elastic strains rates from blurring test results). However, Hunsche (1988) and Bérest et al. (2005) applied axial stresses as low as $\sigma = 0.57$ MPa (over 10 days) and $\sigma = 0.1$ MPa (for one year) to salt samples; the observed strain rates were $\dot{\varepsilon} = -7 \times 10^{-12}\ \mathrm{s}^{-1}$ and $\dot{\varepsilon}^{ss} = -1.4 \times 10^{-12}\ \mathrm{s}^{-1}$, respectively — much faster than anticipated. Spiers et al. (1990) suggested that, in the stress-temperature domain of interest, in addition to dislocation creep, pressure-solution creep is the dominant mechanism, especially when stress is significantly smaller than 10 MPa. Theoretical findings strongly suggest that, for this mechanism, the relation between deviatoric stress and strain rate is linear. In fact *"... the relative importance of each process depends strongly on variables such as temperature, confining pressure, grain size, solid solution impurities and second phase content and, importantly, on the presence of sufficient water in grain boundaries to enable solution-precipitation phenomena"* (Uraï & Spiers, 2007, p.151), and the Norton-Hoff law typically should be modified in such a way that

$$\dot{\varepsilon}^{ss} = A\exp\left(-\frac{Q}{RT}\right)\sigma^n + \frac{b}{TD^3}\exp\left(-\frac{\bar{Q}}{RT}\right)\sigma \tag{5}$$

where b and $\bar{Q}/R$ are constants, and D is the grain diameter.

Computations easily prove that using (5) instead of (2) leads to significantly different predictions when cavern closure rate is concerned. However, monitoring cavern behavior does not provide strong evidence for (or against) any type of governing mechanism in the low-stress range, because, as mentioned above, accurate measurements are difficult. A comprehensive discussion of available evidence, both from laboratory experiments and field observations, can be found in Uraï & Spiers (2007).

7.2 *Humidity*

The influence of water vapor on salt creep during laboratory tests has been investigated by several authors, among which are Horseman (1988), Spiers et al. (1990), Le Cléac'h et al. (1996) and Hunsche & Schulze (1996, 2002). Hunsche & Schulze proved that steady-state creep rate increases by a factor of 90 when relative air humidity varies from 0% RH to

75% RH (the limit above which salt dissolves in air water vapor); they also proved that this effect was much more pronounced during uniaxial tests and, more generally, when the sample experienced dilation. Dilation increases salt porosity and permeability; vapor can diffuse through micro-cracks and open grain boundaries; at contact areas, where stresses are high, solubility rises and creep is faster. Bérest et al. (2012) performed two series of uniaxial creep tests in a mine gallery under very small stresses (0.1 MPa), where hygrometry of the ventilation air was 55% RH to 75% RH, respectively. No hygrometry influence was observed. One possible explanation for this is that the applied stresses were so small that no dilation took place, impeding any effect of the water vapor contained in the ventilation air.

A practical consequence is that moisture influence should be limited to a relatively thin "disturbed zone" at the wall of galleries or caverns where dilation takes place, with minor overall influence on creep closure. However, Van Sambeek (2012) observed a clear correlation between room-closure rate (which was slow) and relative humidity in a 600-m deep salt mine.

One can expect that brine influence be even more significant. Spiers et al. (1990) and Cosenza et al. (2002) proved that, when saturated brine is added at the periphery of a salt sample submitted to a moderate mechanical loading (say, 10 MPa), creep rate immediately accelerates. However, when mines are flooded with brine, it seems, in most cases, that the brine-filled mine is more stable than the dry mine had been. [See Van Sambeek & Thoms (2000), who observed that subsidence rate above the Jefferson Island Mine decreased by a factor of 10 after the mine was flooded, or Feuga (2003), who performed a sonar survey in an old flooded mine at Dieuze to find that actual mine geometry was exactly the same as what was expected from a map drawn by the miners 130 years before.] These results suggest that creep acceleration only exists in a relatively thin damaged zone at pillar walls and that the favorable effect of the increase in mine internal pressure (from atmospheric to halmostatic) is much more significant from the perspective of mine stability.

7.3 *Temperature*

The role of temperature is two-fold. On one hand, creep rate is a function of the sample temperature; on the other hand, salt warming or cooling generates thermal expansion or contraction.

$$\dot{\varepsilon}_{ij} = \frac{1+\nu}{E}\dot{\sigma}_{ij} - \frac{\nu}{E}\dot{\sigma}_{kk}\delta_{ij} + \alpha\dot{T}\delta_{ij} + \frac{3A}{2}\exp\left(-\frac{Q}{RT}\right)\left(\sqrt{3J_2}\right)^{n-1}s_{ij} + \dot{\varepsilon}^{tr}_{ij} \tag{6}$$

The influence of temperature on the steady-state strain rate is captured through the term: $\exp(-Q/RT)$, and $\dot{\varepsilon}^{ss}_{,T}/\varepsilon^{ss} = Q/RT^2 \approx 3 - 10 \times 10^{-2}/^{\circ}\mathrm{C}$ when $T = 300$ K. (Transient strain rate is also temperature-dependent.) However, several authors (for instance, Tijani, CEC Cosa Report, 1987, unpublished.) underlined that such a formulation is likely to be too simple. Hunsche (1984) mentioned that for a given testing temperature, the creep rate is slower after a step during which temperature was higher than it was before that step. A possible explanation for this is that some brine is removed from the sample when the temperature is high. In a cavern, temperature of the stored fluid may change by several dozens of °C, with possible effects on rock temperature and the creep closure rate of the cavern, but this effect does not seem to be large enough to be detected; the same cannot be said of a repository of heat-generating wastes.

The thermo-elastic effect of temperature is captured through the coefficient of thermal expansion, which is larger than for most rocks, $\alpha \approx 4 \times 10^{-4}/^{\circ}\mathrm{C}$. Daily fluctuations in room temperature by $\pm 1^{\circ}\mathrm{C}$, or $\dot{T} \approx 10^{-5}\ \mathrm{s}^{-1}$ can blur the results of a creep test when the steady-state strain rate is slower than $\dot{\varepsilon} \approx 10^{-9}\ \mathrm{s}^{-1}$.

It is known that, in an idealized spherical or cylindrical cavern, a change in cavern temperature has no effect on cavern volume — a counter-intuitive result that remains approximately true even when a more realistic cavern shape is considered (Karimi-Jafari et al. 2007). Conversely, tangential stresses, or σ_{tt}, are generated at the cavern wall. Their order of magnitude is $\sigma_{tt}/\Delta T = -E\alpha/(1-\nu) \approx 0.8\ \mathrm{MPa}/^{\circ}\mathrm{C}$, a high value. These tangential stresses are compressive when the cavern fluid is warmed and tensile when the cavern fluid is cooled. Because the tensile strength of salt is low (1–2 MPa), the effect of fluid cooling can be especially important. In fact, prompted by the needs of gas traders, withdrawal rates from gas caverns tend to be faster; cavern gas cools down by several dozens of °C during withdrawal. This effect has been discussed by several authors (Wallner & Eickemeier 2001, Pellizzaro et al. 2011, Bérest et al. 2012, Zapf et al. 2012, Lux & Dresen 2012). It was feared that such a temperature drop would generate fractures at the cavern wall. However, computations prove that, in most cases, only a thin salt layer at cavern wall experiences severe temperature drops and tensile stresses (Bérest et al. 2012).

7.4 *Stress triaxiality*

It is assumed in Equation (2) that strain rate is a function of stress through the second invariant of the stress tensor, or J_2. In fact, most laboratory tests are the so-called "triaxial" tests during which the two main stresses are equal, which means that the influence of the third invariant of the stress tensor, or J_3, cannot be investigated. Liu & Hunsche (1988) performed "true" triaxial tests on cubic samples and proved that "*within the limits of precision of the measurements, the behavior is isotropic*" (p. 235). Mellegard et al. (2007) performed creep tests under alternating compressive ($0 > \sigma_2 = \sigma_3 > \sigma_1$) and extensive ($0 > \sigma_1 > \sigma_2 = \sigma_3$) states of stresses and observed that while creep rate

depends on $|\sigma_1 - \sigma_2|$ only, "*each time the Lode angle was changed, a significant transient response (not predicted by constitutive models) was observed"* (p. 9). Munson et al. (1992), however, proved that closure displacements in a 655-m deep room of the WIPP repository was explained better when, instead of $\sqrt{3J_2}$, the viscoplastic potential was expressed in terms of $|\sigma_1 - \sigma_3| = 2\cos\psi\sqrt{J_2}$ (the Tresca criterion, ψ is the Lode angle). Tests performed on hollow cylinders seem to confirm this choice.

7.5 *Transient creep*

As Figure 7 schematically suggests, the creep rate is much faster (by one order of magnitude or more) immediately after a load is applied to a salt sample than it will be several weeks or months later, when steady-state creep is reached. A significant decrease in applied load leads to "reverse" creep: sample height increases even if the applied load is compressive (Lux & Heusermann 1983, Hunsche 1988, Bérest et al. 2005).

Munson & Dawson (1984) proposed a constitutive model that accounts for most aspects of transient creep:

$$\dot{\varepsilon}^{tr} = F\dot{\varepsilon}^{ss} \qquad \dot{\zeta} = (F-1)\dot{\varepsilon}^{ss} \qquad \varepsilon_t^f = K_0 e^{cT}\sigma_{eq}$$
$$F = \; <\varepsilon_t^f - \zeta> \exp\left[\Delta\left(1-\zeta/\varepsilon_t^f\right)^2\right] \qquad (7)$$
$$+ <\zeta - \varepsilon_t^f> \exp\left[-\delta\left(1-\zeta/\varepsilon_t^f\right)^2\right]$$

Note that transient creep in this model is faster (and longer) when the load change is larger. "Reverse" creep modeling was addressed in Munson et al. (1996) (see, also, Karimi-Jafari et al. 2006).

Transient or reverse creep also is observed in salt caverns. Hugout (1988) performed a test in a 8000-m^3, 950-m deep cavern of the Etrez site operated by Storengy: three months after leaching was completed (while brine thermal expansion was still quite active), he measured the flow of brine expelled from the cavern. On day 93 (Fig. 8), he vented the light hydrocarbon contained in the annular space. The brine-air interface dropped to a depth of 293-m below ground level, resulting in a cavern-pressure drop of 3.5 MPa or so. Hydrocarbon flow jumped to a rate of 5000 liters/day (instead of 200 liters/day before venting) and rapidly decreased. The annular space was closed 161 days later, and brine was poured in the central tubing to restore halmostatic pressure, triggering a "reverse" transient brine flow: brine was added for 5–6 days to keep the air-brine interface at ground level; after two additional weeks, the brine flow was steady again.

Interpretation of such a test is not straightforward. The thermodynamic behavior of a cavern is much more complex than the behavior of a sample. According to the Le Chatelier-Braun principle, any pressure change triggers phenomena that tend to restore the pre-existing equilibrium: they involve transient permeation, cooling following the initial adiabatic temperature increase and, above all, additional dissolution — all effects that can be quantified. However, among all these factors, transient creep plays a major role (Bérest et al. 2007a).

Note that transient creep in a cavern is the sum of two components: the "rheological" transient creep, which can be described, for example, by (7), and the "geometrical" transient creep, associated with the slow redistribution of stresses in the rock mass from its initial to final steady-state distribution, an effect that does not exist when an idealized triaxial creep test is performed on a rock sample. Computations predict that the "geometrical" transient creep can be several decades long (Karimi et al. 2006) [See, also, Munson et al. (1992, p.445) and Munson (1999).]

"Reverse" creep and, more generally, transient creep must be taken into account when interpreting tightness tests (Bérest et al. 2007a).

8 ROCK SALT FAILURE

8.1 *Introduction*

Numerous shallow, brine-filled caverns collapsed, leading to the formation of a crater at ground surface. In most cases, the cavern diameter was too large, and cavern brine pressure was not able to support the full weight of the overburden. Salt mechanical properties do not play a major role in such a context. Generally speaking, no collapse of a deep salt cavern was described in the literature. (Block fall, spalling and sluffing were observed, as explained in Section 2; they are local phenomena.) A remarkable exception is the 1100-m deep Oxy-3 cavern at Bayou Corne, Louisiana; it is suspected that this cavern was too close to the edge of the dome and that unstable materials slid along the salt dome to fill the cavern. In fact, in the laboratory or in boreholes, salt failure is observed in several circumstances.

8.2 *Dilation*

When an increasing deviatoric stress is applied to a salt sample, onset of "dilation" can be observed: (inelastic) volumetric strain rate becomes positive, a clear sign of the development of multiple micro-fractures. These micro-fractures are oriented in the direction of the most compressive stress. Onset of dilation is easier when the confining pressure is smaller. Dilation generally is accompanied by a loss of material strength, an increase in permeability and acoustic emission, a decrease in ultrasonic wave velocities (Popp et al. 2007, 2012), and a strong influence of external humidity on strain rate (see above). It is widely accepted that rock dilation is a relevant indicator of damage (Cristescu & Hunsche, 1996). Several authors suggest that the onset of dilation characterizes the long-term strength of the rock.

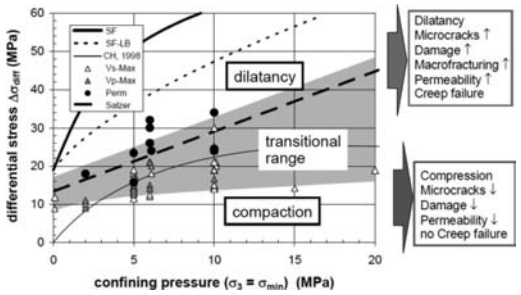


Figure 9. Dilation criterion in the $\sigma_2 = \sigma_3, \sigma_1 - \sigma_3$ plane (from Popp et al., 2007).

Onset of dilation can be predicted by a stress criterion (Spiers et al. 1990) obtained during short-term tests, often described by $\eta = \sqrt{J_2}/(aI_1 + b) < 1$ where η is called the *dilation index*. For Gulf Coast salt, Van Sambeek et al. (1993) suggest $b = 0, a = -0.27$. (Compressive stresses are negative.) Advanced criteria, taking into account stress triaxiality (through Lode's angle) were proposed by DeVries et al. (2006). Generally speaking, as was underlined by Schultze (2007), the dilation criterion must be seen as a band (in the σ-plane) rather than a line, as the onset of volume increase does not coincide with the onset of changes in ultrasonic wave velocities (Popp et al. 2002 and Figure 9).

There is strong evidence that the dilation criterion must be modified when, instead of a single monotonous loading, dozens of cycles are applied to the sample (see Arnold et al. 2011 and Düsterloh et al. 2012). DeVries & Mellegard (2010) proved that variability of dilation onset was strongly related to preconditioning procedures.

It must be noted that the dilation criteria mentioned above do not depend on the stress *rate*, a possible flaw when rapid stress changes are discussed. Schultze (2007) noted that at this time no author mentioned such a dependency when the dilation index is concerned. However Wallner (1984), speaking of rock strength rather than dilation criterion, stated that "*the strength besides the well-known dependence on the stress also depends on the strain rate*" (p. 745), a concept that should be revised in the new context of rapid pressure changes in salt caverns.

8.3 *Tensile stresses*

It is known that most rocks exhibit poor tensile strength. The tensile strength of salt typically is 1–2 MPa (Hansen et al. 1984), smaller than uniaxial compressive stress by one order of magnitude. In most cases, contrary to the case of a mine gallery, no tensile stresses are generated at a cavern wall. Even in a gas cavern, when the gas inventory is small, stresses at cavern wall are compressive, except perhaps at some specific locations such as overhanging parts or a flat roof. Blocks may fall, and cavern shape is rearranged; overall cavern stability is not at stake. However, when high-amplitude rapid cycles are conducted, gas temperature experiences large changes, and tensile "thermal stresses" are generated at the cavern wall. This topic was addressed in Section 7.3.

8.4 *Tensile effective stress – Hydraulic Micro-fracturing*

When, at the wall of a borehole, gas — or brine — pressure (P) is larger than the least compressive stress($\sigma_{\max} < 0$) by, say, $T = 2$ MPa or, $\sigma_{\max} + P > T$, a fracture is created. The onset of such a fracture allows the assessment of *in situ* stresses in rock formations (Durup 1994, Rummel et al. 1996, Doe & Osnes 2006). The pioneering works of Kenter et al. (1990) and Fokker (1995), however, proved that, before the onset of such a discrete fracture, in the pressure domain: $-t < \sigma_{\max} + P < T$ (tensile failure criterion; t is small or null), micro-fractures develop, and salt permeability increases significantly. This mechanism has important practical consequences. It is known that when a tight, brine-filled cavern is abandoned, cavern pressure increases to geostatic pressure and above (Wallner & Paar 1997), raising fears of tightness loss and brine migration. Micro-fracturing allows pressure release and brine seepage in the immediate vicinity of the cavern — a much less severe scenario. The SMRI has put this problem at the centre of its research program (Ratigan 2003, Rokahr & Staudtmeister 2003, Bérest 2007b). In the long term, a similar problem is raised in a radioactive waste repository, when anaerobic corrosion generates gases whose pressure increases (the "gas-frac scenario", Popp et al. 2007 and 2012).

An abundant literature has been dedicated to laboratory experiments (see for instance Peach 1991, Alkan & Pusch 2002), and studies raise experimental difficulties. Bérest et al. (2001) performed tests on hollow spheres and proved that permeability starts increasing slightly before the condition $\sigma_{\max} + P = 0$ is met. Popp et al. (2012) observed that such micro-fracturing is accompanied by small, or no, acoustic emission and a small increase in salt porosity. The micro-fractured zone develops in a direction perpendicular to the minimum compressive stress (Wolters et al. 2012), and "*micro-cracks and associated permeability develop anisotropically with strain*" (Popp et al. 2002, p. 109).

When these notions are applied to an actual salt cavern, two additional problems appear. The first problem lays in the computation of the least compressive stress. This stress is low (making the onset of micro-fractures easier) in two circumstances:

(i) In a gas or liquid-filled cavern after a rapid pressure increase following a long period of time during which the cavern was kept idle [A flat roof raises specific problems, as the vertical stress is such that: $(\sigma_{zz} + P)_{,z} = (\rho_{salt} - \rho_{fluid})g > 0$, and the effective stress is larger in the rock mass than it is at cavern wall]. This idea was mentioned by Wallner (1988) and Wawersik & Stone (1989); a comprehensive discussion can be found

in Brouard et al. (2007) and Djizanne et al. (2012) and,

(ii) In a gas-filled cavern after a rapid pressure decrease, as noted by computations recently published in the literature (see Section 7.3). The second problem is the modeling of the post-micro-fracturing behavior.

8.5 *Post failure behavior*

In the previous sections, the onset of dilation or hydro-mechanical fracturing were discussed. How these notions can be applied to the dimensioning of a cavern or a mine raises difficult problems. The simplest approach consists of simply drawing the zone in which the dilation criterion or the tensile failure criterion is met, without attempting to model the rock behavior after the onset of damage. This approach was applied successfully to back-calculate the behavior of salt mines in which collapse or loss of tightness had been observed (Bauer et al. 2000, Bérest et al. 2008) or to design salt caverns (DeVries, 2006). It should be noted that, in a cavern with constant pressure, delayed onset of dilation is not expected. Equation (2) can be rewritten:

$$\dot{\varepsilon} = \dot{\varepsilon}^{el} + \dot{\varepsilon}^{vp} = M \cdot \dot{\sigma} + \dot{\Phi} \tag{8}$$

where $\Phi = A \exp(-Q/RT)(\sqrt{3J_2})^{n+1}/(n+1)$ is an increasing function of J_2. In the rock mass, $div\dot{\sigma} = 0$ in Ω and $\dot{\sigma} \cdot n = 0$ on $\partial\Omega$, $\int_\Omega \dot{\Phi}\, d\Omega = -\int_\Omega \dot{\sigma} \cdot M \cdot \dot{\sigma}\, d\Omega < 0$: when averaged throughout the entire rock mass, the deviatoric stress, J_2, is a decreasing function of time, and the dilation criterion will never be met when it is not met from the start.

It must be said that at this time, however, that there is no consistent theoretical basis that allows for predicting failure through a dilation criterion. (Such a basis exists, for instance, when a perfect plastic criterion is used). The adopted approach is more empirical: a dilated zone may appear at the wall of a cavern or a dry mine pillar, but to prevent generalized failure, the dilated zone must remain confined inside a non-dilated zone. In a dry mine, for example, a significant part of the core of the pillars must remain non-dilated. Such a prudent approach seems to provide a conservative assessment.

Various attempts were made to describe the "post-dilation" behavior of salt mathematically. Several modeling strategies can be used to account for volume increase. Thorel & Ghoreychi (1993), Serata & Fuekenjorn (1993) and Brückner et al. (2012) treat the dilation criterion as a plastic-like criterion: the flow rule can be associated, or not. Pudewills (2012) introduces a second viscoplastic potential that, in addition to the second invariant J_2, depends on the first invariant I_1.

Volume increase is related to porosity increase (Stormont & Daemen 1992, Pusch & Alkan 2002), which, in turn, is related to permeability change through a modified Coseny-Carman relation (Popp et al. 2012). However, this approach might be too simple, as the "secondary" permeability clearly is not isotropic. In addition, the material loses some strength (weakening), and viscoplastic strain rates are faster. Chan et al. (1996) and Thorel & Ghoreychi (1993) use Kachanov's damage theory, in which the constitutive law is a function of Kachanov's "effective stress", $\tilde{\sigma} = \sigma/(1-D)$, where D is a damage parameter increasing from 0 (virgin state) to 1. In such a context localization is likely and may raise difficult numerical problems. Strain softening is an alternative modeling strategy, successfully used by Kamlot et al. (2007) to compute dilatancy in the Asse II salt mine in Germany. A remarkable dynamic analysis was provided by Minkley & Menzel (1996) in the case of mine excavated in a salt formation with brittle behavior.

When gas or brine can enter the micro-fractures, the poro-mechanical problem is fully coupled. Whether the notions of Darcy flow and Biot's coefficient (classical notions in Reservoir Engineering) apply is an open question (see Pfeifle & Hurtado, 2000 and Cosenza et al. 2002). When gas is concerned, the notion of a capillary pressure (two-phase flow) does not apply, as micro-fracturing creates new voids (Brine must not be removed by gas.), which provides a possible explanation for the results of a micro-fracturing test performed in a wellbore by Durup (1994). Most of these comments apply to post-tensile micro-fracturing and dilation as well. Interpretation of laboratory tests becomes more difficult, because, the development of dilation and fluid permeation cause the state of stress in the sample to be non-uniform. In addition, it is believed that, to some extent, a dilated material can "heal" and restore its initial strength (Chan et al. 1996; Popp et al. 2012; Wolters et al. 2012). In this sense, one must distinguish between *compaction*, which refers to permeability decrease observed when an isotropic stress is applied, and true *healing*, which means that any memory of past damage has been lost. These research fields are being pursued actively, and new developments are expected.

ACKNOWLEDGEMENTS

The author benefited from discussions with many colleagues during SMRI Meetings and Conferences on the Mechanical Behavior of Salt. Special Thanks to Benoît Brouard, Hippolyte Djizanne and Kathy Sikora.

REFERENCES

Alkan, H. & Pusch, G. 2002. Definition of the Dilatancy Boundary Based on Hydro-Mechanical Experiments and Acoustic Detection, *Proc. SMRI Fall Meeting*, Bad Ischl, Austria: 9–24.

Arnold, R.D., DeVries, K.L., Nieland, J.D. & Tiruneh, H. 2011. Cyclic Fatigue Effects on the Mechanical Properties of Salt. In *Proc. SMRI Spring Meeting, Galveston, Texas*: 51–64.

Aubertin, M. 1996. On the physical origin and modeling of kinematic and isotropic hardening of salt. In Mehdi

Ghoreychi, Pierre Bérest, H. Reginald Hardy Jr, Michael Langer (eds), *Proc. 3rd Conf. Mech. Beh. of Salt*: 3–17. Clausthal-Zellerfeld; Trans TechPub.

Baar, C.A. 1977. *Applied salt-rock mechanics. Vol. I. Developments in Geotechnical Enginnering.* 16-A . Amsterdam: Elsevier Science.

Bauer, S.J., Ehgartner, B.L. & Neal, J.T. 2000. Geotechnical Studies Associated with Decommissioning the Strategic Petroleum Reserve Facility at Weeks Island, Louisiana: A Case History. In *Proc. SMRI fall meeting, San Antonio*: 145–156.

Bérest, P., Ghoreychi, M., Fauveau, M. & Lebitoux, P. 1986. Mechanism of Creep in Gas storage Caverns. Effect of gravity forces. In H.L Hartman (ed), *Proc. 27th Rock Mech. US Symp.*: 789–794. Littleton, Colorado: Soc. Min. Eng. Inc.

Bérest, P., Bergues, J. & Brouard, B. 1999. Review of Static and dynamic compressibility of deep underground caverns. *Int. J. Rock Mech. Min. Sci.* (36):1031–1049.

Bérest, P., Brouard, B. & de Greef, V. 2001. Salt Permeability Testing. The Influence of Permeability and stress on Hollow Salt Samples. *SMRI Research Project Report n° 2001-8.*

Bérest, P., Blum, P.A., Charpentier, J.P., Gharbi, H. & Valès, F. 2005. Very slow creep tests on rock samples. *Int. J. Rock Mech. Min. Sci.* (42): 569–576.

Bérest, P., Brouard, B., Karimi-Jafari, M. & Van Sambeek, L., 2007a. Transient behavior of salt caverns – Interpretation of mechanical integrity tests. *Int. J. Rock Mech. Min. Sci.* (44):767–786.

Bérest, P. 2007b. Questions on the Prediction of the long-term behaviour of underground openings. In *Proc. ISRM Congress, Lisbon, Vol.3:* 1413–1425.

Bérest, P., Brouard, B., Feuga, B. & Karimi-Jafari, M. 2008. The 1873 Collapse of the Saint-Maximilien Panel at the Varangéville Salt Mine. *Int. J. Rock Mech. Min. Sci.* 45 (7): 1025–1043.

Bérest, P., Béraud, J.F., Bourcier, M., Dimanov, A., Gharbi, H., Brouard, B., DeVries, K. & Tribout, D., 2012. Very slow creep tests on rock samples. In Pierre Bérest, Mehdi Ghoreychi, Faouzzi Hadj-Hassen, Michel Tijani (eds), *Proc. Mechanical Behavior of Salt VII:* 81–88. London: Taylor & Francis.

Bérest, P., Djizanne, H., Brouard, B. & Hévin, G. 2012. Rapid depressurizations: can they lead to irreversible damage? In *Proc. SMRI Fall Meeting, Regina*: 64–83.

Blum, W. & Fleischman, C. 1988. On the deformation-mechanism map of rock salt. In H. Reginald Hardy, Jr & Michael Langer (eds.), *Proc. 2nd Conf. Mech. Beh. of Salt*: 7–23. Clausthal-Zellerfeld: Trans TechPub.

Boucly, Ph. & Legreneur, J. 1980. Hydrocarbon storage in cavities leached out of salt formations. In Magnus Bergman (ed), *Subsurface SpaceProc. Int. Symp. (Rockstore '80), Stockholm, Sweden*: 251–257. Pergamon Press.

British Geological Survey 2008. An appraisal of underground storage technologies and incidents, *Research Report RR605*.

Brouard, B. 1998. Sur le comportement des cavités salines. *Ph.D. Thesis*, Ecole Polytechnique, Palaiseau, France. [in French]

Brouard, B. & Bérest, P. 1998. A tentative classification of salts according to their creep properties. In *Proc. SMRI Spring Meeting, New Orleans, Louisiana:* 18–38.

Brouard, B., Karimi-Jafari, M. & Bérest, P. 2007. Onset of Tensile effective Stresses in Gas Storage Caverns. In *Proc. SMRI Fall Meeting, Halifax, Canada:* 119–135.

Brouard, B., Bérest, P., de Greef, V., Beraud, J.F, Lheur, C. & Hertz, E. 2013. Creep closure rate of a shallow salt cavern at Gellenoncourt, France. *Int. J. Rock Mech. Min. Sci.* (62):42–50.

Brückner, D., Minkley, W. & Lindert, A. 2012. The improved IfG gas storage cavern design concept. In Pierre Bérest, Mehdi Ghoreychi, Faouzzi Hadj-Hassen, Michel Tijani (eds), *Proc. Mech. Beh. of Salt VII:* 391–398. London: Taylor & Francis.

Chan, K.S., Munson, D.E., Fossum, A.F. & Bodner, S.R. 1996. A constitutive model for representing coupled creep, fracture and healing in rock salt. In Michel Aubertin & H. Reginald Hardy, Jr (eds), *Proc. 4th Conf. Mech. Beh. of salt*: 221–247. Clausthal-Zellerfel: Trans Tech Pub.

Cole, R. 2002. The long Term Effects of High Pressure Natural Gas Storage on Salt Caverns. In *Proc. SMRI Spring Meeting, Banff, Canada:* 75–97.

Cosenza, Ph., Ghoreychi, M. & Chanchole, S. 2002. Effects of fluid-rock interaction on mechanical behavior of rock salt. In Nicolaie D. Cristescu, H. Reginald Hardy Jr, R. Olivian Simionescu (eds), *Proc. 5th Conf. Mech. Beh. of Salt:* 57–72. Lisse, Swets & Zeitlinger.

Cristescu, N.D. & Hunsche, U. 1998. *Time Effects in Rock Mechanics*. Series: Materials, Modelling and computation. Chichester, UK: John Wiley & Sons Ltd.

Crotogino, F., Mohmeyer, K.U. & Scharf, R. 2001. Huntorf CAES: More than 20 Years of Successful Operation. In *Proc. SMRI Spring Meeting, Orlando, Florida*: 351–362.

DeVries, K.L. 2006. Geomechanical Analyses to Determine the Onset of Dilation Around Natural Gas storage Caverns in Bedded Salt. In *Proc. SMRI Spring Meeting, Brussels*: 132–148.

DeVries, K.L. & Mellegard, K.D. 2010. Effects of specimen preconditioning on salt dilation onset. In *Proc. SMRI Fall Meeting, Leipzig, Germany:* 60–65.

Djizanne, H., Bérest, P. & Brouard, B. 2012. Tensile effective stresses in hydrocarbon storage caverns. In *Proc. SMRI Fall Meeting, Bremen, Germany*: 223–240.

Doe, Th. & Osnes, J. 2006. In Situ Stress and Permeability Tests in the Hutchinson Salt and the Overlaying Shale, Kansas. In *Proc. SMRI Fall Meeting, Rapid City:* 182–213.

Durup, JG. 1994. Long term tests for tightness evaluations with brine and gas in salt. In *Proc. SMRI Fall Meeting, Hannover.*

Düsterloh, U., Lerche, S. & Lux, K.H. 2012. Cyclic loading effects on the dilation and healing properties of rock salt from Avery Island Louisiana – 250 days cyclic loading tests and numerical back analysis. In *Proc. SMRI Fall Meeting, Bremen, Germany*: 3–32.

Feuga, B. 2003. Old salt mine at Dieuze (France) revisited 150 years after being abandoned. In *Proc. SMRI Fall Meeting, Chester*: 114–128.

Fokker, P.A. 1995. The behavior of salt and salt caverns. *PhD thesis*, Delft University of Technology, The Netherlands.

Guessous, Z., Ladanyi, B. & Gill, D.E. 1988. Effects of Sampling Disturbance on Laboratory Determined Properties of Rock Salt. In H. Reginald Hardy, Jr & Michael Langer (eds.), *Proc. 1st Conf. Mech. Beh. of Salt:* 137–158. Clausthal-Zellerfeld: Trans TechPub.

Hampel, A. 2012. The CDM constitutive model for the mechanical behaviour of rock salt: Recent developments and extensions. In Pierre Bérest, Mehdi Ghoreychi, Faouzzi Hadj-Hassen, Michel Tijani (eds), *Proc. Mechanical Behavior of Salt VII:* 45–56. Taylor & Francis Group, London.

Hansen, F.D., Mellegard, K.D. & Senseny, P.E. 1984. Elasticity and strength of ten natural rock salts. In H. Reginald Hardy, Jr & Michael Langer (eds.), *Proc. 1st Conf. Mech. Beh. of Salt*: 71–83. Clausthal-Zellerfeld: Trans Tech Pub.

Hévin, G., Caligaris, C. & Durup, J.G. 2007. Deep salt cavern abandonment: a pilot experiment. In *Proc. SMRI Fall Meeting, Halifax, Canada:* 16–25.

Horseman, S.T. 1988. Moisture content – A major uncertainty in storage cavity closure prediction. In H. Reginald Hardy, Jr & Michael Langer (eds.), *Proc. 2nd Conf. Mech. Beh. of Salt*: 53–68. Clausthal-Zellerfeld: Trans Tech Pub.

Hugout, B. 1988. Mechanical behavior of salt cavities -in situ tests- model for calculating the cavity volume evolution. In H. Reginald Hardy, Jr & Michael Langer (eds.), *Proc. 2nd Conf. Mech. Beh. of Salt*: 291–310. Clausthal-Zellerfeld: Trans Tech Pub.

Hunsche, U. 1984. Results and interpretation of creep experiments on rock salt. In H. Reginald Hardy, Jr & Michael Langer (eds.), *Proc. 1st Conf. Mech. Beh. of Salt:* 159–167. Clausthal-Zellerfeld: Trans Tech Pub.

Hunsche, U. 1988. Measurement of creep in rock salt at small strain rates. In H. Reginald Hardy, Jr & Michael Langer (eds.), *Proc. 2nd Conf. Mech. Beh. of Salt*: 187–196. Clausthal-Zellerfeld: Trans Tech Pub.

Hunsche, U & Schultze, O. 1996. Effect of Humidity and Confining pressure on creep of rock salt. In Mehdi Ghoreychi, Pierre Bérest, H. Reginald Hardy Jr, Michael Langer (eds), *Proc. 3rd Conf. Mech. Beh. of Salt:* 237–248. Clausthal-Zellerfeld: Trans Tech Pub.

Hunsche, U. & Schultze, O. 2002. Humidity induced creep and its relation to the dilatancy boundary. In Nicolaie D. Cristescu, H. Reginald Hardy, Jr, & R. Olivian Simionescu (eds), *Proc. 5th Conf. Mech. Beh. of Salt*: 73–87. Lisse, Swets & Zeitlinger.

Kamlot, P., Günther, R.M., Stockmann, N. & Gärtner, G. 2007. Modeling of strain softening and dilatancy in the mining system of the southern flank of the Asse II salt mine. In Manfred Wallner, Karl-Heinz Lux, Wolgang Minkley & H. Reginald Hardy, Jr (eds), *Proc. 6th Conf. Mech. Beh. of Salt:* 327–336. London: Taylor & Francis.

Karimi-Jafari, M., Bérest, P. & Brouard, B. 2006. Some aspects of the transient behaviour of salt caverns. In *Proc. SMRI Fall Meeting, Rapid City, South Dakota:* 254–270.

Karimi-Jafari, M., Bérest, P. & Brouard, B. 2007. Thermal effects in salt caverns. In *Proc SMRI Spring Meeting, Basel, Switzerland:* 165–177.

Kenter, C.J., Doig, S.J., Rogaar, H.P., Fokker, P.A. & Davies D.R. 1990. Diffusion of brine through rock salt roof of caverns. In *Proc. SMRI Fall Meeting*, *Paris, France*.

Langer, M. 1984. The rheological behaviour of rock salt. In H. Reginald Hardy, Jr & Michael Langer (eds.), *Proc. 1st Conf. Mech. Beh. of Salt*: 201–240. Clausthal-Zellerfeld: Trans TechPub.

Le Cléac'h, J.M., Ghazali, A., Deveughele, M. & Brulhet, J. 1996. Experimental study of the role of humidity on the thermomechanical behaviour of various halitic rocks. In Mehdi Ghoreychi, Pierre Bérest, H. Reginald Hardy Jr, Michael Langer (eds), *Proc. 3rd Conf. Mech. Beh. of Salt: 231–236.* Clausthal-Zellerfeld: Trans Tech Pub.

Liu, X. & Hunsche, U. 1988. Creep behavior of salt under true triaxial stress. In H. Reginald Hardy, Jr & Michael Langer (eds.), *Proc. 2nd Conf. Mech. Beh. of Salt*: 235–243. Clausthal-Zellerfeld: Trans Tech Pub.

Lux, K.H. & Dresen, R. 2012. Design of salt caverns for high frequency cycling of storage gas. In Pierre Bérest, Mehdi Ghoreychi, Faouzzi Hadj-Hassen, Michel Tijani (eds), *Proc. Mech. Beh. of Salt VII:* 371–380. London: Taylor & Francis.

Lux, K.H. & Heusermann, S. 1983. Creep tests on rock salt with changing load as a basis for the verification of theoretical material laws. In B. Charlotte Schreiber, H. Lincoln Harner (eds), *Proc. 6th Int. Symp. on Salt,* Vol. I: The Salt Institute: 417–35.

Mellegard, K.D., De Vries, K.L. & Callahan, G.D. 2007. Lode angle effects of salt. In Manfred Wallner, Karl-Heinz Lux, Wolgang Minkley & H. Reginald Hardy, Jr (eds), *Proc. 6th Conf. Mech. Beh. of Salt:* 9–15. London: Taylor & Francis.

Minkley, W. & Menzel, W. 1996. Local Instability and System Instability of Room and Pillar Fields in Potash Mining. In Mehdi Ghoreychi, Pierre Bérest, H. Reginald Hardy Jr, Michael Langer (eds), *Proc. 3rd Conf. Mech. Beh. of salt:* 497–510. Clausthal-Zellerfeld: Trans Tech Pub.

Munson, D.E. 1999. Transient analysis for the multi-mechanism-deformation parameters of several domal salts. In *Proc. SMRI Fall Meeting, Washington DC, 1999:* 275–298.

Munson, D.E. & Dawson, P.R. 1984. Salt constitutive modeling using mechanism maps. In H. Reginald Hardy, Jr & Michael Langer (eds.), *Proc. 1st Conf. Mech. Beh. of Salt:* 717–737. Clausthal-Zellerfeld: Trans Tech Pub.

Munson, D.E., De Vries, K.L., Schiermeister, D.M., De Yonge, W.F. & Jones R.L. 1992. Measured and calculated closures of open and brine filled shafts and deep vertical boreholes in salt. In J.R. Tillerson and W. Wawersik (eds), *Proc. 33rd US Rock Mech. Symp.* 439–448. Rotterdam: Balkema.

Munson, D.E., De Vries, K.L., Fossum, A.F. & Callahan, G.D. 1996. Extension of the Munson-Dawson model for treating stress drops in salt. In Mehdi Ghoreychi, Pierre Bérest, H. Reginald Hardy Jr, Michael Langer (eds), *Proc. 3rd Conf. Mech. Beh. of Salt:* 31–44. Clausthal-Zellerfeld: Trans Tech Pub.

Munson, D.E., Ehgartner, B., Bauer, S., Rautman, C. & Myers, R. 2004. Analysis of a salt fall in Big Hill Cavern 103, and a preliminary concept of salt dome structure. In *Proc. SMRI Spring Meeting, Wichita, Kansas*: 57–72.

Peach, C.J. 1991. Influence of deformation on the fluid transport properties of salt rocks. *Ph.D. Thesis*, University of Utrecht, the Netherlands.

Pellizzaro, C., Bergeret, G., Leadbetter, A. & Charnavel, Y. 2011. Thermomechanical behavior of Stublach Gas Storage Caverns. In *Proc. SMRI Fall Meeting, York, UK*: 161–178.

Pfeifle, T.W. & Hurtado L.D. 2000. Effect of Pore Pressure on Damage Accumulation in Salt. In Rob M. Geertman (ed.), *Proc 8th World Salt Symposium. Vol. I*: 307–312. Elsevier.

Popp, T., Kern, H. & Schultze, O. 2002. Permeation and development of dilatancy in rock salt. In Nicolaie D. Cristescu, H. Reginald Hardy Jr, R. Olivian Simionescu (eds), *Proc. 5th Conf. Mech. Beh. of Salt:* 95–124. Lisse: Swets & Zeitlinger.

Popp, T., Wiedemann, M., Kansy, &. Pusch, G. 2007. Gas transport in dry rock salt – implications from laboratory investigations and field studies. In Manfred Wallner, Karl-Heinz Lux, Wolgang Minkley & H. Reginald Hardy, Jr (eds), *Proc. 6th Conf. Mech. Beh. of Salt*: 17–26. London: Taylor & Francis.

Popp, T., Minkley, W., Salzer, K. & Schulze, O. 2012. Gas transport properties of rock salt – synoptic view. In Pierre Bérest, Mehdi Ghoreychi, Faouzzi Hadj-Hassen, Michel Tijani (eds), *Proc. Mechanical Behavior of Salt VII:* 143–153. London: Taylor & Francis.

Pudewills, A. 2012. Numerical simulation of coupled Thermo-Hydro-Mechanical processes in rock salt. In Pierre Bérest, Mehdi Ghoreychi, Faouzzi Hadj-Hassen, Michel Tijani (eds), *Proc. Mechanical Behavior of Salt VII:* 115–122. London: Taylor & Francis.

Pusch, G. & Alkan, H. 2002. Gas Permeation Models Related to Dilatancy Development Under Deviatoric Stress conditions. *Proc. SMRI Fall Meeting,* Bad Ischl, Austria, 213–232.

Quast, P. 1983. L'installation de Huntorf : plus de trois années de fonctionnement de cavernes à air comprimé. *Annales des Mines* (190ème année, n° 5–6, mai-juin 1983): 93–102. [in French]

Ratigan, J. 2003. The SMRI Cavern Sealing & Abandonment Research Program Summary. In *Proc. SMRI Spring Meeting, Houston, Texas:* 141–164.

Rokahr, R., Staudtmeister, K. & Zander-Schiebenhöfer, D. 2003. High Pressure Cavern Analysis. In *Proc. SMRI Spring Meeting, Houston:* 88–113.

Rokahr, R., Staudtmeister, K., Zander-Schiebenhöfer, D. & Johansen, J.I. 2007. In-situ Test with a Gas Storage Cavern as a Basis for Optimization. In *Proc*. *SMRI Spring Meeting, Basel, Switzerland*: 84–97.

Rummel, F., Benke, K. & Denzau, H. 1996. Hydraulic Fracturing Stress Measurements in the Krummhörn Gas Storage Field, Northwestern Germany. In *Proc. SMRI Spring Meeting*, *Houston.*

Salzer, K., Günther, R.M., Minkley, W., Popp, T., Wiedemann, M., Hampel, A., Pudewills, A., Leuger, B., Zapf, D., Staudtmeister, K., Rokahr, R., Herchen, K., Wolters, R. & Lux, K.H. 2012. Joint projects on the comparison of constitutive models for the mechanical behavior of rock salt. In Pierre Bérest, Mehdi Ghoreychi, Faouzzi Hadj-Hassen, Michel Tijani (eds), *Proc. Mechanical Behavior of Salt VII:* 221–240. London: Taylor & Francis.

Schultze, O. 2007. Investigations on damage and healing in rocks. In Manfred Wallner, Karl-Heinz Lux, Wolgang Minkley & H. Reginald Hardy, Jr (eds), *Proc. 6th Conf. Mech. Beh. of Salt:* 33–44. London: Taylor & Francis.

Schultze, O., Heemann, U., Zetsche, F., Hampel, A., Pudewills, A., Günther, R.M., Minkley, W., Salzer, K., Hou, Z. Wolters, R., Rokahr, R. & Zapf, D. 2007. Comparison of advanced models for the mechanical behavior of rock salt – results from a joint research project. In Manfred Wallner, Karl-Heinz Lux, Wolgang Minkley & H. Reginald Hardy, Jr (eds), *Proc. 6th Conf. Mech. Beh. of Salt*: 77–98. London: Taylor & Francis.

Serata S. & Cundey T.E. 1979. Design Variables in Solution Cavities for Storage of Solids, Liquids and Gases. In Alan H. Coogan & Lkas Hauber (eds), *Proc. 5th Symposium on Salt: Vol. II,* 161–170, The Northern Ohio Geological Society, Inc.

Serata, S. & Fuenkajorn, K. 1993. Formulation of a Constitutive Equation for Salt. In Hidekate Kakihana, H. Reginald Hardy. Jr, Takeshi Hoshi, Ken Toyokura (eds.), *Proc. 7th Symp. on Salt*, *Vol. I*: 483–488. Amsterdam, Elsevier.

Ślizowski, J. & Urbañczyk, K.M. 2007. Influence of effective stress on strain rate around the gas storing cavern. In Manfred Wallner, Karl-Heinz Lux, Wolgang Minkley & H. Reginald Hardy, Jr (eds), *Proc. 6th Conf. Mech. Beh. of Salt:* 363–368. London: Taylor & Francis.

Spiers, C.J., Schutjens, P.M. T.M., Brzesowsky, R.H., Peach, C.J., Liezenberg, J.L. & Zwart, H.J. 1990. Experimental determination of the constitutive parameters governing creep of rocksalt by pressure solution. In Knipe R.J. & Rutter E.H. (eds), *Deformation Mechanisms, Rheology and Tectonics. Geological Society special Publication* 54: 215–227.

Stormont, J.C & Daemen, J.J.K. 1992. Laboratory study of gas permeability changes in rock salt during deformation. *Int. J. Rock. Mech. Min. Sci.* 29 (4): 325–342.

Thiel W.R. 1993. Precision Methods for Testing the Integrity of Solution Mined Underground Storage Caverns. In Hidekate Kakihana, H. Reginald Hardy Jr, Takeshi Hoshi, Ken Toyokura (eds.), *Proc. 7th Symp. on Salt*, *Vol. I*: 377–383. Amsterdam, Elsevier.

Thoms, R.L. & Gehle, R.M. 1983. Borehole Tests to Predict Cavern Performance. In B. Charlotte Schreiber & H. Lincoln Harner (eds), *Proc. 6th Symp. on Salt Vol. 2:* 27–33. The Salt Institute.

Thorel, L. & Ghoreychi, M. 1993. Rock salt damage. Experimental results and interpretation.In Mehdi Ghoreychi, Pierre Bérest, H. Reginald Hardy Jr, Michael Langer (eds), *Proc 3rd Conf. Mech. Beh. of Salt*: 175–189. Clausthal-Zellerfeld: Trans Tech Pub.

Uraï, J.L. & Spiers, C.J. 2007. The effect of grain boundary water on deformation mechanisms and rheology of rocksalt during long-term deformation. In Manfred Wallner, Karl-Heinz Lux, Wolgang Minkley & H. Reginald Hardy, Jr (eds), *Proc. 6th Conf. Mech. Beh. of Salt*: 149–158. London: Taylor & Francis.

Van Sambeek, L. 2012. Measurements of humidity-enhanced salt creep in salt mines: Proving the Joffé effect. In Pierre Bérest, Mehdi Ghoreychi, Faouzzi Hadj-Hassen, Michel Tijani (eds), *Proc. Mechanical Behavior of Salt VII:* 179–184. London: Taylor & Francis.

Van Sambeek, L. & Thoms, R. 2000. Pre- and Post-Flooding Surface Subsidence Rates at the Retsof, Belle Isle, Jefferson Island Salt Mines. In *Proc. SMRI Fall Meeting, San Antonio:* 75–85.

Van Sambeek, L., Fossum, A., Callahan, G. & Ratigan, J. 1993. Salt Mechanics: Empirical and Theoretical Developments. In Hidekate Kakihana, H. Reginald Hardy Jr, Takeshi Hoshi, Ken Toyokura (eds.), *Proc. 7th Symp. on Salt*, *Vol. I*: 127–134. Amsterdam, Elsevier.

Wallner, M. 1984. Analysis of thermomechanical problems related to the storage of heat producing radioactive wastes. In H. Reginald Hardy, Jr & Michael Langer (eds.), *Proc. 1st Conf. Mech. Beh. of Salt*: 739–763. Clausthal-Zellerfeld: Trans Tech Pub.

Wallner, M. 1988. Frac-Pressure risk for cavities in rock salt. In H. Reginald Hardy, Jr & Michael Langer (eds.), *Proc. 2nd Conf. Mech. Beh. of Salt:* 645–658. Clausthal-Zellerfeld: Trans Tech Pub.

Wallner, M. & Eickemeier, R. 2001. Subsidence and Fractures Caused by Thermo-Mechanical Effects. In *Proc. SMRI Spring Meeting, Orlando, Florida*: 363–371.

Wallner, M. & Paar, W.A. 1997. Risk of progressive pressure build up in a sealed cavity. In *Proc. SMRI Fall Meeting, El Paso, Texas:* 177–188.

Wawersik, W.R. & Preece, D.S. 1984. Creep Testing of Salt – Procedures, Problems and Suggestions. In H. Reginald Hardy, Jr & Michael Langer (eds.), *Proc. 1st Conf. Mech. Beh. of Salt*: 421–449. Clausthal-Zellerfeld: Trans Tech Pub.

Wawersik W. & Stone C.M. 1989. A characterization of pressure records in inelastic rock demonstrated by hydraulic fracturing measurements in salt. *Int. J. Rock Mech. Min. Sci.:* 613–627.

Wolters, R., Lux, K.H. & Düsterloh, U. 2012. Evaluation of rock salt barriers with respect to tightness: influence of thermomechanical damage, fluid infiltration and sealing/healing. In Pierre Bérest, Mehdi Ghoreychi, Faouzzi Hadj-Hassen, Michel Tijani (eds), *Proc. Mechanical Behavior of Salt VII:* 425–434. London:Taylor & Francis.

Zapf D. Staudtmeister K. & Rokahr R.B. 2012. Analysis of thermal induced fractures in salt. In *Proc. SMRI Spring Meeting, Regina, Saskatchewan:* 47–62.

This page intentionally left blank

Rock Mechanics for Resources, Energy and Environment – Kwaśniewski & Łydżba (eds)
© 2013 Taylor & Francis Group, London, ISBN 978-1-138-00080-3

The mechanisms and consequences of strong mining tremors that occur in Polish hard coal and copper mines

J. Dubiński
Central Mining Institute, Katowice, Poland

ABSTRACT: In this paper, a rockburst is considered as a complex physical and rock mechanical process. The dynamic stress generated by the seismic load that is caused by a seismic event has to be added to the static stress in the rock mass in order to create this phenomenon. The seismic load near to underground workings is directly related to the source mechanism and radiation directivity of seismic tremors. The relation between the seismic load and the directivity of the seismic source radiation is presented and analysed using several cases of rockbursts in Polish coal and copper mines. The method, which utilizes directivity of seismic waves resulting from different source mechanisms, contributes significantly to increase our knowledge of the rockburst phenomenon and provides an explanation of its origin.

1 INTRODUCTION

Rockbursts belong to a group of natural hazards, the occurrence of which has the characteristics of a mining disaster. Rock masses that are suddenly thrown into the mine workings cause a chain reaction of mechanical damage to the support and equipment and pose a threat to the crew; roof fall is also a frequent occurrence. As a result of rockbursts there is a loss of the functionality of workings, interruptions in production and various types of property damage and injuries to the mining crew (Dubiński & Konopko 2000). The proximate cause of the occurrence of a rockburst is always a seismic disturbance. It is connected with a dynamic release of seismic energy, typically of a high magnitude, which reaches the mine workings in the form of seismic waves, thus affecting their stability and causing rockbursts in the form of the above-mentioned effects.

The phenomenon of a rockburst occurs in many mining basins around the world, both in hard coal and metal ore mines. In Poland, the seismicity induced by mining activities and the accompanying rockbursts occur in the hard coal mines in the Upper Silesian Coal Basin (the USCB) and the copper ore mines in the Legnica-Głogów Copper Region (LGOM).

Research that was aimed at understanding the causes and mechanisms of rockbursts and the development of technological solutions for the reduction and mitigation of their impact has been carried out in various countries for many decades. These include multi-directional activities using geomechanical and geophysical methods and specialized mining technologies. It should be emphasized that the problem of mining seismicity and rockbursts is within the sphere of the widest application of rock mechanics solutions as well as selected methods of mining geophysics. These refer both to projections and current assessments of seismic risk, as well as the prevention of rockburst hazards. There has been significant progress in the study of the physical nature of seismic events that are induced by mining activities and in the development of rockburst prevention technologies (Konopko 2010). In the area of geophysical methods, progress has been made in particular through the development of specialized measuring equipment and the widespread introduction of computer technology to process and interpret measurement data. Today, there are mine geophysical stations that continuously observe the behavior of the rock mass in all Polish mines where there is a risk of seismic hazards. They fall within the scope of rockburst departments that deal with the complex issues of seismic and rockburst hazards as they are related to occupational safety.

In this paper, the results investigations of the relationship between the focal mechanism of mining tremors and the effects of the rockbursts that took place after their occurrence are presented on the example of Polish mines. They confirm the existence of such a relationship, which is important not only from a cognitive point of view, but also from a practical one when assessing the risk and prevention of rockbursts.

2 CHARACTERISTICS OF SEISMICITY INDUCED BY MINING ACTIVITIES IN POLAND AND THE ACCOMPANYING RISK OF ROCKBURSTS

Research in the area of seismicity induced by the mining activities of the Polish hard coal and copper mines have their own long history, which dates back to the late 1940s in the case of the mines of the Upper Silesian Coal Basin. Later, in the 1970s, research began in copper ore mines. Today, it is an indisputable fact

Table 1. Data characterizing the seismic and rockburst hazards in Polish hard coal and copper mines for the years 1977–2012.

	Hard coal mines				Copper ore mines			
Year	Number of tremors $E \geq 10^5$ J	Number of rockbursts	Number of fatalities	Total number of accidents	Number of tremors $E \geq 10^5$ J	Number of rockbursts	Number of fatalities	Total number of accidents
1977	3798	20	12	74	40	1	0	0
1980	3432	22	7	54	213	5	3	8
1985	2480	15	8	31	327	4	1	9
1990	1038	16	6	30	447	2	2	6
1995	465	7	6	34	474	7	2	13
2000	1088	2	0	0	512	4	2	10
2005	1451	3	1	13	786	3	1	22
2006	1170	4	4	20	872	2	0	5
2007	885	3	0	10	1011	3	4	14
2008	883	5	0	26	785	2	1	19
2009	741	1	0	6	474	4	1	11
2010	1203	2	2	2	581	8	6	46
2011	1034	4	1	7	601	1	0	5
2012	1022	1	1	2	526	1	0	8

that this seismicity always appears in these basins with the increasing depth of mining carried out in an environment of rocks that are capable of storing elastic energy that originates from deformation processes and with the development of the extraction over time (Marcak 2012). Nowadays, virtually all Polish hard coal and copper ore mines are characterized by the presence of mining seismicity, although not all of these result in rockbursts. In these mines, seismic monitoring is carried out by the mine seismic network, which is supported in the case of hard coal mines by a seismo-acoustic observation system. Moreover, in works in the USCB, a superior mine network surveillance system in the form of the Silesian Regional Seismological Network is in place (Stec 2001).

Table 1 lists the energy-quantitative characteristics of seismicity that occurs in the above-mentioned mining basins and data on the existing rockbursts and their effects in the form of mining accidents that have involved mining crews. In order to show their variation prior to 2000, data are provided only for selected years, as well as for every year since 2000.

The seismicity that is induced by mining activities, which is recorded by the mine seismic networks falls within an energy range of 10^2–10^9 J. The strongest mining tremors of seismic energy $E \geq 10^9$ J have a local magnitude of about 4.0 and on the surface; they create the sense similar to that of a weak earthquake among the area's inhabitants. Moreover, the energy level of seismic the activity that occurs in the copper mines is significantly higher and differs in its frequency characteristics from the tremors in hard coal mines in the Upper Silesian Coal Basin. Undoubtedly, these differences are due to the different geological structures of these mining regions (Dubiński & Mutke 2011).

A characteristic feature of the seismic activity that are observed in these two different basins is its bimodality, and therefore, the presence of two different distributions of tremors. In the case of seismic events of lower energies, their origin is usually associated with a highly extracted seam or its close surroundings, while in the case of strong tremors; the foci are located in the strong and thick roof rock complexes. The bimodality also indicates different mechanisms of these shock foci (Dubiński & Stec 2001).

The most common effects of tremors take the following forms (Dubiński & Konopko 2000):

- damage, which in some cases includes the destruction of the support of mine workings, particularly as a result of the mechanical shock caused by the ejected rock mass, as well as the excessive static load of the support due to the loss of the self-support of the fractured rock mass and the dynamic load that results from the vibrations connected with a seismic wave,
- damage to machinery and equipment in the area within the rockburst,
- a sudden convergence of the working, which loses its functionality,
- the caving-in of workings,
- incidents involving the workers present in the workings in which the above-mentioned effects of the rockburst took place, including serious and fatal accidents.

In addition, rockbursts can cause a significant increase in the methane content in workings where mining is carried out in areas with a high risk of methane as well as an increase in dustiness and air blasts due to the rapid convergence of workings.

3 THE METHODOLOGY FOR DETERMINING THE FOCAL MECHANISM OF MINING TREMORS

The development of modern, digital seismic networks in Polish mines can significantly extend the processing

of the input seismic signals and the physical interpretation of the processes associated with actual mining tremors. Therefore, one of the interpretative tasks was to determine the mechanisms of the tremor foci (Stec 2009).

It should be noted that in its assumptions this methodology is based on the overall achievements of the seismology for earthquakes. Mining tremors, like earthquakes, are the result of certain systems of forces that act on a particular piece of rock medium. As a result of this action a tremor focus is initiated. In addition, when properly oriented in space, systems of forces determine the specific development and course of the dynamic processes in the tremor focus, which are the source of seismic radiation that has well-defined characteristics in the form of the emission of seismic waves. Thus, the recorded seismograms contain "coded" information about this system of forces that is acting on the tremor focus as well as the course of the dynamic processes that are involved. They determine the mechanism of the tremor focus.

Tremor foci as seismic sources are commonly described by models of equilibrant forces. These are defined as certain systems of forces that generated displacement at points of seismological registration, which are identical to the displacements caused by actual forces that are acting in the tremor focus (Gibowicz & Kijko 1994). The use of computer technology and digital processing of data that is measured has given rise to a new approach in dealing with the mechanisms of tremor foci. Thanks to this, it has become possible to check all of the possible solutions for their conformity with the data that is observed. In the case of the shocks that are induced by mining activities, in addition to the dominant shear processes on fault planes or other planes with a weakened structure of the rock mass, there are also other mechanisms of foci, such as explosion or implosion.

Modern solutions for determining the focal mechanism of mining tremors use the method of the seismic moment tensor inversion. This tensor fully describes the system of forces that are acting in the seismic source, and which are a linear combination of force couples with the moment. It is understood that the displacement in the far field u_k, which is caused by the system of forces that are acting in the tremor focus, is the sum of the displacements caused by the particular force couples (Aki & Richards 1980), which can be written as follows:

$$u_k = M_{ij} \frac{\partial G_{ki}}{\partial \xi_j} = M_{ij} * G_{ki,j} \tag{1}$$

where M_{ij} – the moment of the force couples acting in the direction of the x_i axis of the arm in line with the x_j axis; G_{ij} – Green's function, which describes the impulse response of the medium for the distance travelled by the seismic wave; * – convolution operation.

The method of the seismic moment tensor inversion assumes a point nature of the tremor source, since the size of the source is usually significantly reduced compared to the length of the seismic waves that are observed. It is also assumed that all of the seismic moment tensor components depend on time in the same way as that described by the source function. Therefore, it is a synchronous source that generates the same changes in time in all directions. In that case, the displacement field described in Equation (1) can be written as:

$$u_k(x,t) = M_{ij}\left[G_{ki,j} * s(t)\right] \tag{2}$$

where: $s(t)$ – the function of the source that, characterizes the emission of a seismic source in time.

Thus, the displacement field u_k is a linear function of the components of the seismic moment tensor and the terms written in square brackets. With the assumption that the source function is described by the Dirac function, the displacement field u_k can be expressed as follows:

$$u_k(x,t) = M_{ij}\, G_{ki,j} \tag{3}$$

The set of all nine components M_{ij} can be written in the form of a matrix M with dimensions of 3×3, representing a seismic moment tensor:

$$M = \begin{bmatrix} M_{11} & M_{12} & M_{13} \\ M_{21} & M_{22} & M_{23} \\ M_{31} & M_{32} & M_{33} \end{bmatrix} \tag{4}$$

The diagonal components, for which $i = j$, describe the force couples without moments, directed along the respective axes of the coordinate system.

An important benefit of using the seismic moment tensor in the determination of the focal mechanism of mining tremors is that it enables decomposition into the isotropic part, which describes the change in volume in the focal point of the tremor and the deviatoric part, including a double force couples (DBCP) and compensated linear vector dipole (CLVD). Thus, the seismic moment tensor decomposition into the abovementioned components is the most commonly used description of the mechanism of a tremor focus (Stec 2001). In practice, this operation is done using special computer programs, such as Wiejacz's SMP (Wiejacz 1991) or Kwiatek's FPCI (Kwiatek 2009).

In this paper, in order to determine the focal mechanism of selected mining tremors, a specialized program was used (FPCI), which permits three models of tremor foci to be obtained, which differ in their mechanisms, and which are described by the three types of seismic moment tensors, namely:

- general tensor,
- deviatoric tensor,
- pure shear tensor.

The general tensor has the isotropic component I., which describes the changes in volume in the focus (explosion /+/ or implosion /−/), the CLVD component corresponding to uniaxial compression /−/ or

tension /+/ and the DBCP component described by the double couple of forces. The deviatoric tensor, on the other hand, (associated with a change in shape or volume) has two components: CLVD and DBCP. However, the pure shear tensor only has a component of DBCP.

The explosive or implosive model of tremor focus corresponds to the process of the volume destruction of the structure of the medium, for example, due to shooting at the selected layer of the deposit or in its immediate vicinity, and also as a result of pressure in overlying layers. The linear, compensated dipole vector corresponds – in approximation – to uniaxial compression or tension and may involve the destruction of the pillars. However, the model and the mechanism described by a double force couple corresponds to tremors associated with that cracking of the thick and dense strata with a high degree of stiffness and strength, or the displacement of their fragments. It most often refers to undermined complexes of roof rocks. The characteristic distribution of the displacement field in the case of a seismic focus described using the shear model can be expressed by the values that determine the spatial orientation of the so-called nodal planes. The nodal planes are two perpendicular planes separating the two areas of compression and dilatation, of which one is the actual focal plane. The spatial location of these planes is described by angles ϕ, δ, λ, which mean:

1. ϕ – strike or cracking plane strike,
2. δ – cracking plane dip,
3. λ – shear angle or displacement angle.

The solution for this model of focus can also aid in determining the dimensional position of the principal stress axis, and therefore, compressive stress P and tensile stress T. It is described by similar angles of the azimuth ϕ and dip δ.

4 AN ANALYSIS OF THE MECHANISMS OF SELECTED TREMORS AND THE EFFECTS OF THE TREMORS THAT OCCURRED

In order to show that there is a reciprocal relationship between the focal mechanism of mining tremors and the effects in the form of rockbursts that occur as a result of these tremors, two examples were selected that will be analysed in this section. As was shown above, the focal mechanism identifies the type of forces that are acting in the tremor focus and shows the directivity of the seismic radiation. These two elements are essential for the localization of the effects of a rockburst and their nature.

4.1 *An example from the "Rydułtowy-Anna" hard coal mine*

A rockburst occurred in the area of the driven inclined drift III-1200-E2 in seam $713/_{1\text{-}2}$ $+712/_{1\text{-}2}$ on 10/21/2010 at $10^{28'48''}$ p.m. that had been caused

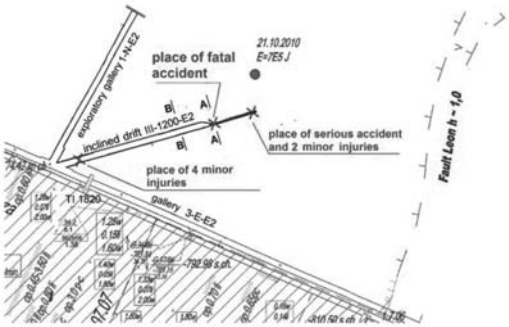


Figure 1. Situation in the region of the rockburst that occurred in driven inclined drift III-1200-E2 in seam $13/_{1\text{-}2}$ $+712/_{1\text{-}2}$ in the Rydułtowy-Anna hard coal mine.

by the occurrence of a tremor with a seismic energy of $E = 7 \cdot 10^5$ J. The seam was deemed to exhibit a rockburst hazard of the third degree, due to:

- the great depth of the exploitation (800–1100 m),
- the existence of strong rocks in the roof in the form of thick layers of sandstone,
- the existence of residue and edges that had formed in the neighboring overlying the seams,
- the well developed fault tectonics,
- as also due to methane hazard category IV.

Seismicity at an average level is observed in this part of the mining area, which means that the strongest seismic tremors have an energy of 10^6J and occur sporadically. During the driving of the inclined drift III-1200-E2, 26 seismic tremors took place with energies of 10^2–10^3 J, some of which were induced by blasting. The construction of inclined drift III-1200-E2 comprised a double, yieldable steel arch support ŁP/V32/A that was built every 0.8 m. In addition, the support was stabilized with steel sprags and tremors of such energies do not affect the condition of such a support. On the day of the rockburst, the inclined drift was driven using an AM-50 shearer to reach a length of 169 m.

Figure 1 presents a section of the seam map that shows the area of the rockburst that occurred, the position of tremor focus and the locations of accidents.

The rockburst that occurred in this region as a result of a clearly stronger tremor in terms of energy ($E = 7 \cdot 10^5$ J) on 10/21/2010, had the following effects:

- of the eight miners who were in this area, six had a minor accident, one a severe accident and one a fatal accident,
- there was a strong outflow of methane,
- there were slides at the junctions of the support components that caused deformations,
- the support was destroyed, especially from the northern side wall, which was subject to a lateral convergence; some of its side wall components were upturned and covered with excavated material,



Figure 2. View of the inclined drift support III-1200E2 after the rockburst on 10/21/2010.

– there was a decrease in the cross-section to a height of about 0.85 m as a result of the damage and floor upheaval.

The working lost its functionality at a distance of 125 m from the inclined drift exit and effects of the damage to the support were found at a distance of about 30 m and the effects of this damage over a distance of 26 m.

The photograph below was taken during the site visit and shows the effects of the rockburst that clearly display the nature and extent of the changes that occurred in the inclined drift III-1200-E2.

In line with the methodology for determining the focal mechanism of the tremors presented, seismogram analyses of the tremor with energy $7 \cdot 10^5$ J were performed, based on the data registered by the seismological network of the "Rydułtowy-Anna" mine, which had caused the rockburst in the inclined drift III-1200-E2. The focal mechanism of the tremor was determined based on the amplitudes of the occurrences of the first P-wave and taking into account the directions of the first deflections in the time domain. The results are shown in Figure 3. where: ϕA and ϕB – azimuth of nodal planes A and B; δA and δB – dip of nodal planes A and B; ϕP and ϕT – azimuth of axis P and T; δP and δT – dip of axis P, T; P – compressive principal stress axis; T – tensile principal stress axis; Q – solution quality factor; M_{ij} – components of the seismic moment; M_0 – scalar seismic moment; M_T – total seismic moment; I – the percentage part of the isotropic component; CLVD – the percentage part of the component corresponding to the uniaxial compression /–/ or tension /+/; DBCP – the percentage part of the shear component; ERR – error of the moment tensor components.

There is a clear dominance of the isotropic component (I = 54%), which indicates an explosive type of focal mechanism. With increased accuracy (on the basis of the value of coefficient Q), the depth of the location of the tremor focus indicates that the location of the tremor focus is in the seam or in its immediate vicinity. The focus must have been located in close proximity to the face of the driven inclined drift III-1200-E2, in the part of the seam between the inclined drift and the exploratory gallery 1-N-E2. An explosion in the seam itself could have been the primary cause of the rock cracking of the direct roof, as is evidenced by the value of the component corresponding

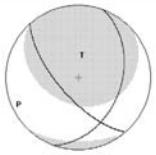
Date	Time	Energy, J	Coordinates, m
10/21/2010	10:28 p.m.	$7.0 \cdot 10^5$	x=36153 y = 31170 z= -790
Full solution			
			*Explosive mechanism*
	M_{ij}, Nm		
0.603E+11 -0.575E+11 0.146E+11	-0.575E+11 -0.625E+12 0.252E+12		0.146E+11 0.252E+12 -0.158E+11
I, % 54.7	**CLVD, %** 30.1		**DBCP, %** 16.2
M_0, Nm 0.196E+11		M_T, Nm 0.224E+11	
ϕA, ° 139	δA,° 68	ϕB,° 20	δB,° 39
ϕP,° 253	δP,° 16	ϕT,° 7	δT,° 54
Q, % 52		**ERR, Nm** 0.216E+11	

Figure 3. The solution for the mechanism of the tremor focus on 10/21/2010 at 10:28 p.m.

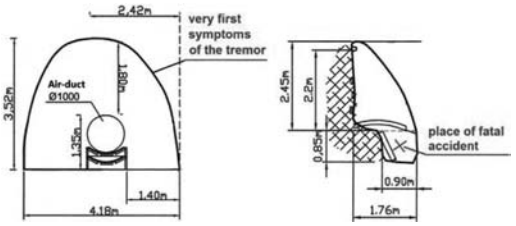


Figure 4. Changes in the shape of the inclined drift III-1200-E2 in seam $713/_{1\text{-}2}$ +$712/_{1\text{-}2}$ that occurred as a result of the tremor and a rockburst on 10/21/2010 at 10:28 p.m.

to the uniaxial tensile strength (CLVD = 30%). The emission of seismic energy had a clear direction from north to south, which correlates well with the characteristic damage to the arches of the roadway support and the very inclined drift III-1200-E2 as is shown in Figure 3. This is confirmed by sketches along cross-sections AA (at 130 m along the inclined drift) and BB (at 113 m along the inclined drift), which were made during the site visit after the rockburst as is shown in Figure 4.

4.2 *An example from the "Rudna" copper mine*

A rockburst took place in exploitation panel XVII/1 in department G-22 in the "Rudna" copper mine . The immediate cause of the rockburst was a high-energy tremor with a seismic energy of $E = 1.5 \cdot 10^8$ J that occurred on 12/30/2010 at 9:56 a.m. The exploitation

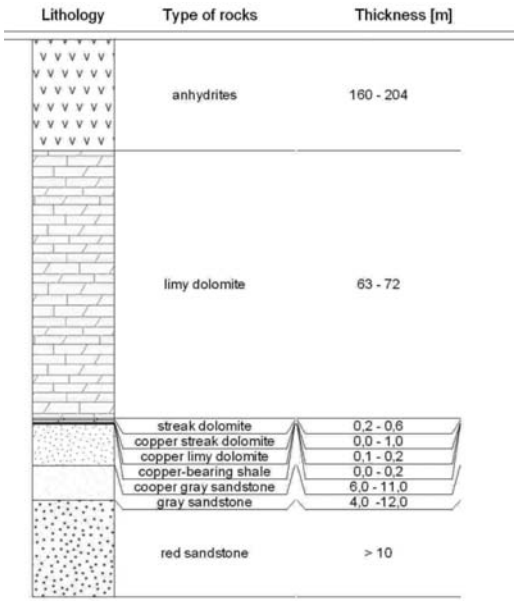


Figure 5. A typical geological profile of the strata in a copper ore deposit.

area was classified as a third degree rockburst hazard due to:

– the great depth of the exploitation, about 1050 m,
– the presence of thick, strong complexes of dolomite-limestone rocks and anhydrite rocks with a uniaxial compressive strength of over 130 MPa (Fig. 5).
– the presence of fault dislocations and a strong tectonic engagement of the rock mass,
– the relatively large thickness of the extracted deposit, from 4 to 13 m.

The high rockburst hazard was confirmed by recorded seismicity in the area of extraction. During the years 2005–2010, during which the extraction was carried out, there were more than 30 high-energy seismic events with energies above 10^7 J, as is shown below in Table 2. Such high seismic activity resulted in the frequent stressing of the rock mass and there were a number of rockbursts that had an impact on the underground workings and caused accidents that involved the crews (including fatal accidents).

Exploitation of a deposit of up to 7 m thick took place using the room and pillar mining system, along with making the deposit more compliant and the additional protection of the roof, while for thicknesses exceeding 7 m, the room and pillar system with hydraulic backfilling was used. The length of the exploitation front in the main part of the panel was 750 m.

The rockburst that occurred resulted in the following effects:

– a serious accident that included three fatalities and 13 minor injuries,

Table 2. Energy and quantitative characteristics of seismicity induced by mining activities in the panel XVII/1 in G-22.

Year	Seismic energy E, J 10^5	10^6	10^7	10^8	Number of seismic events	Seismic energy – sum, [10^8 J]
2005	6	2	1	1	10	2.63
2006	19	10	4	0	33	1.25
2007	36	13	7	1	57	3.46
2008	30	18	3	0	51	1.59
2009	33	15	9	0	57	2.70
2010	20	5	5	1	31	2.91
Sum	144	63	29	3	239	14.5

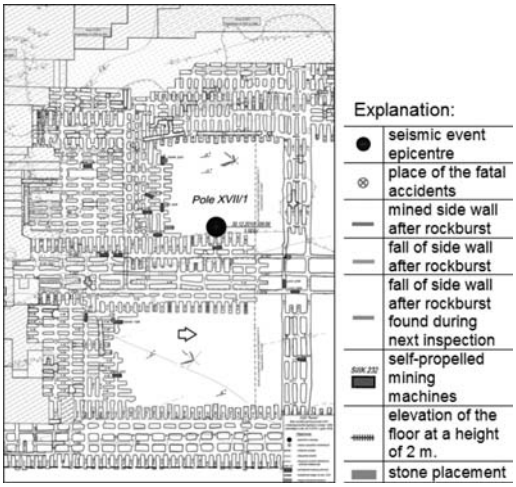


Figure 6. The situation in the area of rockburst occurring in panel XVII/1, department G-22 in the copper mine "Rudna" on 12/30/2010.

– crumbling of the side walls in numerous workings in panel XVII/1,
– fragmentation of the side walls in a few headings and chambers,
– a roof collapse,
– the uplift of the floor in cross-cut 7/T-243a at a height of approximately 2.0 m and along the whole front in two belts close to the unmined copper to a height of 0.5 to 1.5 m.

As a result of the dynamic displacement of large masses of rock into the mine workings, several machines that were located in this area of operation were buried, damaged or destroyed. Figure 6 presents the situation after the rockburst in panel XVII/1, along with the location of the effects listed above. A photograph (Fig. 7) that was taken during the site visit shows one of the areas in which the effects of the rockburst were visible.

As in the case of the tremor in the "Rydułtowy-Anna" mine, the methodology for determining the mechanism of tremor foci was applied to the seismic



Figure 7. A view of the area where the effects of the rockburst occurred.

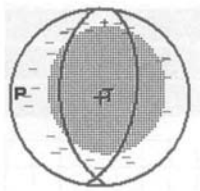
Date 12/30/2010	Time 09:56 a.m.	Energy, J $1.5 \cdot 10^8$	Coordinates
Full solution			
			*Complex mechanism - a large part of the implosive component that was connected with the shear component on the reversed fault*
	M_{ij}, Nm		
-0.786E+14	0.781E+13		0.457E+14
0.781E+13	-0.133E+15		0.603E+14
0.457E+14	0.603E+14		0.295E+15
I, %	**CLVD, %**		**DBCP, %**
14.1	56.8		29.1
M_0, Nm		M_T, Nm	
0.225E+15		0.248E+15	
ϕA,°	δA,°	ϕB,°	δB,°
175.27	53.08	9.58	37.79
ϕP,°	δP,°	ϕT,°	δT,°
271.48	7.70	48.92	79.59
Q, %		**ERR, Nm**	
74		0.54E+13	

Figure 8. The solution to the mechanism of tremor focus on 12/30/2010 at 9:56 a.m.

phenomena that caused the rockburst in panel XVII/1 in the "Rudna" mine. Based on the seismogram analysis of the tremor, which had seismic energy equal to $1.5 \cdot 10^8$ J as registered by the seismological network of the "Rudna" mine, a complete solution for the focal mechanism of the tremor in question was determined as is shown in Figure 8. where: ϕA and ϕB – azimuth of nodal planes A and B, δA and δB – dip of nodal planes A and B; ϕP and ϕT – azimuth of axis P and T, δP and δT – dip of axis P, T; P – compressive principal stress axis; T – tensile principal stress axis; Q – solution quality factor; M_{ij} – components of the seismic moment; M_0 – scalar seismic moment; M_T – total seismic moment; I – the percentage part of the isotropic component; CLVD – the percentage part of the component corresponding to the uniaxial compression /−/ or tension /+/; DBCP – the percentage part of the shear component; ERR – error of the moment tensor components.

There is clear dominance of the tension component CLVD = 56.8% with a slightly lower shear component DBCP = 29.1%, which indicates that the development processes in the focal zone had the form of a thrust slip fault combined with uniaxial tension. This indicates a complex focal mechanism. The shearing process occurred here along one of the two nodal planes that run NE-SW, thus they are close to the direction of the fault dislocation, which is situated in the area of extracted panel XVII/1. When analysing the geological and mining situation, a solution that better correlates with the effects of the rockburst that occurred is nodal plane A, whose break plane is inclined above the workings from the directions W and SW. This indicates a significantly higher seismic emission on the upper part of panel XVII/1, which is reflected in the greater effects as is shown in Figure 6. Nevertheless, the high energy of the rockburst caused effects that also occurred elsewhere in the exploitation front.

The examples of the results of the correlation of the focal points of mining tremors with the effects of rockbursts that are caused by these tremors, which have been presented, clearly indicate that the nature of the physical processes that occur in the focus shapes the direction of the emission of seismic energy, and thus affects the location as well as the size and nature of the effects that occur in the mine workings. It should be recognized that these are interesting research results, which permit a more accurate determination of the origin of the mining-induced tremors that occur in mine strata.

5 CONCLUSIONS

1. Modern equipment and computer technology permit the development of new research methods that can bring about a better understanding of the development and the course of the physical processes that occur in the focal points of tremors that are induced by mining activities and thereby aid in the determination of their origin in the event of a rockburst.
2. There exists a certain correlation between the type of focal mechanism and the type of damage that occurs in mine workings as a result of a rockburst.
3. The examples of the analyses of the two tremors from a hard coal mine and a copper mine suggest that this correlation may have its own geomechanical interpretation.
4. The promising results of the research initiated in this area indicate the possibility of further development as well as a the practical use of this type of work in indentifying seismic hazards and mitigating the effects of tremors.

REFERENCES

Aki K., Richards P.G. 1980. *Quantitative Seismology – Theory and Methods*. Ed. W.H. Freeman & Co. Vol. 1, 2. San Francisco.

Dubiński J., Konopko W. 2000. *T'pania. Ocena – Prognoza – Zwalczanie*. [Rockrockbursts. Assessment – Forecast – Prevention] Wyd. GIG, Katowice.

Dubiński J., Stec K. 2001. Modalnoœæ sejsmicznoœci górniczej w œwietle badań mechanizmu ognisk wstrząsów. Mat. Konferencji „*Nauki o Ziemi w badaniach podstawowych, złożowych i ochronie środowiska na progu XXI wieku".* [Seismic Modality in the Light of Studying Focal Points of Tremors. Materials of Conference *'Earth Sciences in Basic Research, Deposit Research and the Environmental Protection at the Beginning of 21st Century'*] Wyd. AGH, Kraków, pp. 331–334.

Dubiński J., Mutke G. 2011. Selected relations between earthquakes and mining seismic events recorded in Polish coal mines. Proceedings of the 22nds World Mining Congress. Vol. I. Istanbul, Ed. TNC/WMC, pp. 359–365.

Gibowicz S., Kijko A. 1994. *An introduction to mining seismology*. Intern. Geophysics Series. Vol. 55.

Konopko W. 2010. Warunki bezpiecznej eksploatacji pokładów węgla zagrożonych metanem, tąpaniami i pożarami endogenicznymi. [Conditions for Safe Exploitation of Coal Deposits Endangered with Methane, Rockbursts and Spontaneous Fires] Wyd. GIG., Katowice.

Kwiatek G. 2009. Foci – Tensor momentu sejsmicznego – Parametry Spektralne. www.sejsmologiagórnicza.pl/foci. [Foci – Seismic Moment tensor – Spectral Parameters. www.sejsmologiagórnicza.pl/foci]

Marcak H. 2012. Seismicity in mines due to roof bending. Archives of Mining Sciences. Vol. 57, issue 1, pp. 229–250.

Stec K. (2001): Rozwój i wykorzystanie Górnośląskiej Regionalnej Sieci Sejsmologicznej, [w]: *„Badania geofizyczne w kopalniach".* [Development and the Use of the Silesian Regional Seismological Network [in]: *"Geophysical Studies in Mines"*] Wyd. IGSMiE PAN, Kraków, pp. 179–184.

Stec K. 2009. Metody wyznaczania mechanizmu ognisk wstrząsów. [Methods for Determining the Mechanism of Tremors Foci] Prace Naukowe GIG „Górnictwo i Środowisko", no. 4/1/2009. pp. 223–236, Katowice.

Wiejacz P. 1991. *Badania mechanizmów wstrząsów górniczych przy wykorzystaniu tensora momentu sejsmicznego*. *[Studies on Mechanisms of Mining Tremors with the Use of Seismic Moment Tensor]* Wyd. Instytutu Geofizyki PAN, Warszawa.

Rock Mechanics for Resources, Energy and Environment – Kwaśniewski & Łydżba (eds)
© 2013 Taylor & Francis Group, London, ISBN 978-1-138-00080-3

Geomechanical aspects of shale gas development

Maurice B. Dusseault
Department of Earth and Environmental Sciences, University of Waterloo, Waterloo, Canada

ABSTRACT: Shale gas development involves aggressive hydraulic fracturing of a naturally fractured rock mass to generate an interconnected open fracture network with a large internal surface area for gas drainage. Conventional hydraulic fracture design software cannot cope adequately with fracture propagation in naturally fractured rock, and it is not clear what form a better design software environment will take, but activity in a number of directions is taking place. Several preliminary options are discussed herein, along with a review of shale gas occurrence and the geomechanical aspects of its development.

1 INTRODUCTION

Decades ago, natural gas occurrence was noted during drilling through the naturally fractured black shales of Appalachia (Ohio Shale, Marcellus Shale, Utica Shale – Charpentier et al. 1995) and Texas. However, these fine-grained Naturally Fractured Rocks – NFRs – were considered poor prospects for economic production, despite considerable attention paid to them in the 1980's and 1990's by the United States Department of Energy and Gas Research Institute (e.g. Kruuskaa et al. 1998, Curtis 2002). Persistence in their development and the implementation of large volume propped Hydraulic Fracturing (HF) methods in vertical wells led to limited production of the gas in the Antrim Shale (Michigan Basin), Barnett Shale (Fort Worth Basin) and Ohio Shale (Appalachian Basin) during the 1990's and into the first part of the decade of the 2000's. Massive improvements in drill bit technology, top-drive drilling rigs, and down-hole steerable drilling motors made the emplacement of horizontal wells >1 km long economical by the late 1990's. This was followed by development of new well completion techniques – Multi-Stage Hydraulic Fracturing – MSHF – in the period 2000–2008. With these technologies, the "shale gas revolution" had arrived in the United States and Canada, but it was not until about 2010–2012 that the full economic impact was realized.

The key factor was that although shale gas had been produced for decades (anecdotally, the first commercial use of natural gas in the USA was sourced from NFRs in Appalachia in the early 1800's), long horizontal wells developed with MSHF proved to be so highly productive that large-scale shale gas commercialization because possible. To achieve this commercialization and improve the effectiveness of HF in NFRs, special techniques such as slickwater fracturing (water with a friction reducer), high rate ($>8\ m^3/m$) viscous fluid HF with proppant, and microseismic monitoring to gauge effectiveness and HF extent were developed alongside more rapid drilling methods. Seemingly suddenly, vast regions underlain by shale gas suddenly became exploitable, and activity moved from the original fields (mainly the Barnett Shale in the Dallas-Ft. Worth Basin) to deposits in northeastern USA, in northeastern British Columbia, and elsewhere. The price of natural gas was soon driven down from over $10.00/MMbtu to less than $4.00/MMbtu by 2009, many coal-fired power plants were put on hold or cancelled in favor of gas turbine generations, US gas imports from Canada declined, American CO_2 emissions dropped, and, because of the sister resource (shale oil) and natural gas liquids accompanying shale gas, US oil imports plummeted. The economic impact on the USA has been profound, and the sharp economic recovery in the USA from the 2008 World Financial Crisis is attributed in no small part to the surge in shale gas and shale oil development (Jacoby et al. 2011).

In the period 2005–2008 it was recognized that MSHF technology being perfected for shale gas was applicable to shale oil deposits – conventional oil trapped in fine-grained rocks, usually the source rocks from whence the oil was generated (in contrast to more conventional reservoirs to where some of the oil migrated after being generated). First in the Bakken Formation of the Williston Basin (Lolon et al. 2009), then in the Eagle Ford of the Western Gulf Basin (Bazan et al. 2012), the application of MSHF in long horizontal wells has led to the sharpest leap in the history of US oil production: an unprecedented 10^6 barrels of production were added in the USA in the calendar year 2012 (BP 2013).

Shale gas and shale oil development depends on successful MSHF, and this area of rock mechanics has become of great interest to research and practitioners as it is apparent that a great deal remains to be learned about the behavior of naturally fractured low-permeability rock masses when subjected to aggressive HF activity. Specifically, our discipline needs to develop better HF design tools, based on the physics

of the problem, not an excessively simplified set of assumptions. Currently, the widely-used commercial HF modeling tools are based solely on mathematical modeling of single planar vertical fractures induced in layered weak rocks that are assumed to be unfractured and linear elastic.[1] No provision for interaction with a NFR medium is made. Even in conditions that correspond reasonably well to the assumptions, i.e. strong unfractured rock masses such as homogeneous sandstones), they serve only as rough approximations that must be carefully calibrated in individual regions, and even in different regions within a given field. At worst, HF modeling tools used too liberally can lead to poor design, production misestimates, and so on.

This review article is an introduction to the broad issue of mechanics and HF in stiff, naturally fractured rocks.

2 SHALE GAS PROVENANCE AND OCCURRENCE

Shale gas is defined as natural gas of biogenic or thermogenic origin trapped in the fine-grained host rock where it was generated. In contrast, tight gas sands are low-permeability porous reservoirs to which biogenic or thermogenic gas migrated from a source rock generally found down-dip or below the tight gas reservoir. Biogenic shale gas was generated by anaerobic bacterial decomposition of carbohydrates (plant matter), generally at depths less than 2000 m; thermogenic gas was generated by the anaerobic and thermally activated decomposition of lipids and other algal matter at depths generally greater than 2500 m. In some cases, such as the Colorado Group shallow gas in Alberta (Rice and Claypool 1981), biogenic gas is found in zones comprising fine-grained organic-rich source strata alternating with thin tight gas sands, and even thin coal streaks, with all three lithologies being potential contributors to production, although the tight sands dominate the well behavior. These relatively shallow gas occurrences are dominantly of biogenic origin but because thermogenic gas may have seeped upward during geological history from deeper strata, the natural gas in the reservoirs may be of mixed provenance. However, the shale gas occurrences that are the focus of greatest attention in the United States and Canada are thermogenic in origin, geologically old, and may well be locally rich in C2+ molecules which are economically much more valuable and lead to the search for these "sweet spots".

Major shale gas deposits that are currently being exploited commercially include the Barnett (Texas), Haynesville (Louisiana), Marcellus (eastern USA NW of the Appalachian Mountains), Horn River Shale (NE BC) and the Montney Shale (NE BC and NW Alberta).

3 GEOLOGICAL CHARACTERISTICS OF SG RESERVOIRS

Each reservoir is different, but all reservoirs have similarities. This means that outlines and summaries of the characteristics of thermogenic SG reservoirs are useful for the general assessment of geomechanical properties and for the empirical development of best practices for HF in NFRs through correlative methods. SG reservoirs that are thermogenic in nature are almost invariably black shales, the color resulting from high residual carbon content because of an originally high organic content (Tourtelot 1979). They are marine shales (much more rarely lacustrine) laid down in foreland basins in thicknesses up to 200–500 meters (e.g. maximum H over 150 m for the Horn River SG in BC, over 400 m for thicker parts of the Montney Shale in western Alberta), although most SG reservoirs being exploited in the USA range from perhaps 20 m to 60 m in thickness). The thickness is an important aspect of development, as the implementation of HF treatments to try and cover a SG reservoir over a 200 m height is challenging.

SG reservoirs are generally quartz-illite shales containing little to no swelling clay, and they are of low porosity (<10%) with a microDarcy matrix permeability. Deep burial and great geological age mean that smectitic clay minerals likely laid down with the original sediments have been diagenetically altered to illite and precipitated quartz. This means that the silica content of the SG strata is high (over 40%) and the clay mineral content, dominantly illite, is low (10–40%). This transition is considered to be the major reason that SG strata are naturally fractured (see mechanical properties below) because the smectite-to-illite transition is associated with a substantial volume diminution. Note that if smectite is present, even in small amounts, swelling can have significantly negative effects on HF results using aqueous fluids.

The SG plays being exploited at the present time may be considered as non-tectonic from a structural point of view. Although there are local faults, in general the strata are relatively flat-lying and unfolded. For example, the Marcellus Shale lies under much of the Appalachian Basin (Roen and Kepferle 1993) to the northwest of the Appalachian Mountains, and the SG prospective region stretches from the middle of New York state to the southernmost part of West Virginia, and extends from the disturbed belt (northwestern Appalachian thrust belt) to eastern Ohio and Michigan, underlying about a quarter million square kilometers. It is thicker in the southeast against the thrust belt, but as the formation is more and more deformed and intersected by faults, the gas content is less. To the northwest, the Marcellus Shale tends to have more liquids and C2+ molecules, and therefore be a more desirable target. Probably ¾ of the

[1] This critique applies to the great majority of available software, but only to the geomechanics part, not the cost-benefit analysis and other parts. I have avoided being specific because different software environments have somewhat different limitations, and any user is advised to evaluate products carefully to make sure the product meets the need at hand.

Table 1. Petrophysical properties of three selected shale gas deposits.

Shale gas play name	Porosity %	Permeability milli-darcies	Clay content %	Organic matter %	Silica content %
Barnett	3–6[5]	0.2–0.10[6]	Below 35[1]	3–10[1]	35–50[1]
Marcellus	6–10[4]	0.13–0.77[7]	10–35[4]	2–10[4]	10–60[4]
Horn River	3.2–6.2[8]	0.0003[9]	20–40[8]	0.5–6.0[8]	45–65[8]

Table 2. Mechanical properties of three selected shale gas deposits.

Shale gas play name	Static Young's modulus GPa	Static Poisson's ratio	Natural fracture descriptions	Velocity information
Barnett	20–80*	0.18–0.32*	Strike and dip are N50°W80–85°[2,3]	v_P 3.9–4.2 km/s; v_S 2.5–2.6 km/s, $v_P/v_S = 1.6$**
Marcellus	15.5***	0.16–0.18[12]	One set NE, another striking NW[4]	
Horn River	18–31[10]			$v_P/v_S = 1.7$[10]

*at confining stress 50 MPa[2,3]
**at stress of 45 MPa[2,3]
***at a confining stress of 16 MPa[11]

[1] Montgomery, S.L., Jarvie, D.M., Bowker, K.A., and Pollastro, R.M. 2005. Mississippian Barnett Shale, Fort Worth basin, north-central Texas: Gas-shale play with multitrillion cubic foot potential: AAPG Bulletin, v. 89, pp. 155–175.
[2] Vermylen, J.P. 2012. Geomechanical Studies of the Barnett Shale, Texas, USA, PhD Thesis, Stanford University.
[3] Sone, H. 2012. Mechanical Properties of Shale Gas Reservoir Rocks and its Relation to the In-situ Stress Variation Observed in Shale Gas Reservoirs, PhD Thesis, Stanford University.
[4] Bruner, K.R. and Smosna, R. 2011. A Comparative Study of the Mississippian Barnett Shale, Fort Worth Basin, and Devonian Marcellus Shale, Appalachian Basin: U.S. Department of Energy, DOE/NETL-2011/1478.
[5] Johnston, D. 2004. Technological Advances Expand Potential Play: Oil and Gas Journal, accessed at following webpage http://www.ogj.com/display_article/196507/7/7/ARCHI/none/none/1/Technological-advances-expand-potential-pay/.
[6] Jarvie, D. 2004. Evaluation of Hydrocarbon Generation and Storage in the Barnett Shale, Fort Worth basin, Texas.
[7] Zielinski, R.E., and Nance, S.W. 1979. Physical and Chemical Characterization of Devonian Gas Shale, Quarterly Status Report (January 1–March 31, 1970): MLM-ML-79-43-0004, MLM-EGSP-TPR-Q-009, 166 p.
[8] National Energy Board of Canada, 2009. Energy Briefing Note: A Primer for Understanding Canadian Shale Gas.
[9] Reynolds, M.M. and Munn, D.L. 2010. Development Update for an Emerging Shale Gas Giant Field-Horn River Basin, British Columbia, Canada, SPE 130103.
[10] Chou, Q., Gao, J., and Somerwill, M. 2011. Analysis of Geomechanical Data for Horn River Basin Gas Shales, NE British Columbia, Canada, SPE 142498.
[11] Li, Y., and Ghassemi, A. 2012. Creep Behavior of Barnett, Haynesville, and Marcellus Shale, ARMA 12–330.
[12] Eshkalak, M.O., Mohaghegh, S.D., and Esmaili, S. 2013. Synthetic Geomechanical Logs for Marcellus Shale, SPE 163690.

Marcellus is undeformed and unfaulted, but naturally fractured. Similar conclusions may be drawn for the Utica Shale that underlies the Marcellus Shale, and also stretches up into the St Lawrence River lowlands in Quebec (Dykstra and Longman 1995). By extension, similar issues such as deformation, faulting, richness in liquids, and so on, extend to other SG deposits.

4 MECHANICAL CHARACTERISTICS OF SHALE GAS RESERVOIRS

There are three major issues related to the mechanical properties of shale gas reservoirs: the rock mass deformation properties, the transport properties, and the fabric properties related to the disposition of discontinuities in the rock mass. In particular, the latter is not only difficult to quantify, it is not clear how this system responds to stimulation, and the uncertainty of the fabric condition of the rock mass *in situ* is a contentious issue. The SG targets being pursued in the USA and Canada are considered to be fractured shales (e.g. Gale et al. 2007).

brief sum-

maries of some of the properties of three major SG plays in North America.

These table values are ranges and do not contain the most extreme values reported. Many issues including anisotropy in properties such as stiffness, permeability, resistivity and acoustic response are not addressed. The effects of anisotropy, strain, stress level and microfabric on rock deformation properties are critical factors, and are the subjects of intensive studies (e.g. Fjaer et al. 2013). Young's modulus, for example, can be as much as 50% lower in unconfined conditions, compared to *in situ* stress conditions, largely because of the effects of stress-relief-induced microcracking during coring and specimen preparation.

An economically important aspect of SG (and shale oil) production is that the matrix permeability is highly sensitive to effective stress (drawdown), especially in less stiff shales, and that this effect is largely irreversible because it is associated with the anelastic closure of microfissures (Aldin 2013). The effect is far less pronounced in stiff SG strata, which are usually quartz-illite shales with low clay contents and no swelling clay, whereas the softer SG strata tend to have higher clay contents with perhaps some swelling clay. The important observation is that rapid drawdown of a wellbore may cause microfissure closure and sharp reduction of the matrix permeability in rocks adjacent to the induced HF and natural fractures. This means the well would experience better early-time production, but worse long-term production, resulting in a loss of recovery factor (but perhaps a better cash-flow situation). This is an important geomechanics-related optimization issue, demonstrating that there are important lithological, mineralogical and microfabric aspects of the mechanical properties of gas shales.

The table data refer to small scales (cm), and the important properties of SG reservoirs tend to be at the scale of metres or 10's of metres, and include the effects of fractures and large-scale anisotropy. For example, slight differences in flat-lying lithologies give rise to a large-scale anisotropy as well as heterogeneity. A priori, one would expect mechanical factors such as cohesion, UCS and stiffness to be well-correlated to rock physics factors such as porosity, water content (related to porosity for saturated shales), clay content, cation exchange capacity (related to clay content and type), cementation ratio (from logs), and so on (Dewhurst et al. 2008, David 2007).

5 NATURAL FRACTURES

Up-scaling of geomechanics data is a significant challenge, particularly in the case of NFRs. This section discusses some aspects of the presence and behavior of natural fractures.

Are the natural fractures open or closed at depth? This is not an easy question, and there are many natural fracture states that can be noted in semi-quantitative descriptions: open, closed, incipient, cemented, persistent, oriented . . . If a fracture can easily be observed in a borehole geophysical log (e.g. formation microimager resistivity log, borehole acoustic televiewer, acoustic fracture detection log using backscattered radiation analysis), there is no doubt that it exists; likely these fractures, upon examination in core, show surface alterations and mineral deposits that verify that the fracture acted as a flow path deep in the ground. However, core examination often shows fractures that have opened during the rough handling of core, and although the fracture is clearly a planar surface of geological origin that cuts across bedding surfaces, no visible alterations of the fracture surface can be noted. This fracture is what is called an "incipient fracture" (Dusseault et al. 2011) that would, at the surface, be opened by weathering processes, but which at depth is closed and at best is only partially debonded across its surface area. An incipient fracture cannot be detected at depth because the intimate contact and high stress do not lead to a slight opening that would lead to backscatter of seismic energy or otherwise be amenable to detection. Apparently, there is no method to quantify the relative importance of incipient fractures in the case of NFRs, but their importance seems to be significant.

The origin of natural fractures that are open or that are incipient (a weakness plane not fully opened) must arise from a tendency for lateral shrinkage in the rock at some time during its geological history, or because of the generation of large internal pressures that led to natural hydraulic fracturing. The major mechanisms are discussed here.

When organic (algal or vegetal matter) shales are laid down as organic muds, burial takes place, and much water is expelled from the shales. As burial of thick shale sequences continues, pore pressures build up from the vertical loading (the source of the overpressure in the Gulf of Mexico), and if $p_o > \sigma_{hmin}$, vertical hydraulic fracturing will occur as the only way to relieve the excess pressures. In fact, the flow of this expelled water at high pressures leads to pressurization of sand bodies that are isolated from regional flow regimes, leading to highly pressurized conditions (occasionally $p_o > 0.95 \cdot \sigma_v$). Vertical strains in a non-tectonic compacting environment lead directly to vertical subsidence, but the no-lateral-strain condition associated with flat-lying strata being dewatered leads to a diminution of σ_{hmin}, leading to internal HF, which leads in great part to the NFR fabric that we note in so many locations.

When burial of carbohydrates (vegetable matter) or lipids (algal matter) takes place, bacterial action breaks down the carbohydrates into CH_4, CO_2 and H_2O, leaving carbon behind, and thermogenesis breaks down the lipids (called Type II kerogen) into hydrocarbons and carbon (hence black shales). The conversion of a semi-solid substance such as kerogen to a fluid (liquid and perhaps gaseous HCs) involves pressurization of the liquid as the matrix stress is thrown on to the fluids as pressure. As above, when $p_o > \sigma_{hmin}$, vertical hydraulic fracturing will occur, and part of the oil and gas can escape to migrate into porous, permeable reservoirs. Once the pressure is largely relieved, the remaining oil and gas can stay in the source rock, and these may, if the organic content is sufficient, form shale gas and shale oil reservoirs in rocks that are now naturally fractured.

A third important mechanism is the conversion of smectite to silica, illite, and water over geological time at depth. Not only is water generated which can increase the pore pressure early in this transition process, but the mineralogical change involves a volumetric shrinkage that can be as high as several percent (>10% if the shale was originally pure smectite). Lateral shrinkage, even a very small amount, has a large consequence on the horizontal stress because

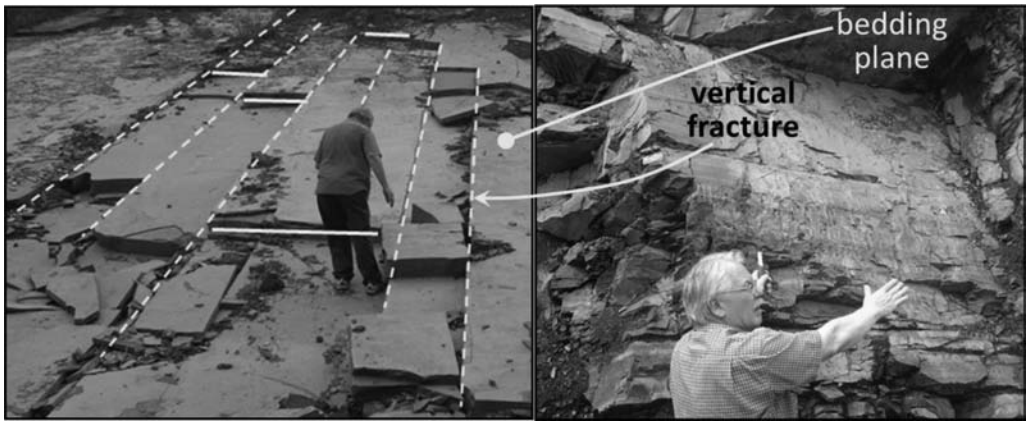


Figure 1. Joint Sets in Outcrops of the Oil Source Rock, Central Sumatra Basin.

of the no-lateral-strain condition in flat-lying strata undergoing uniform changes. In an analogy to thermoelastic shrinkage, if there is a uniform lateral strain taking place in a laterally extensive stratum, then $\Delta\sigma'_{\mathrm{h}} \approx \varepsilon_h \cdot \mathrm{E}/(1-\nu)$. Here, the change in lateral effective stress is proportion to the product of the linear strain – $\varepsilon_h = \Delta\mathrm{L}/\mathrm{L}$ – and Young's modulus, divided by $(1-\nu)$, where ν is Poisson's ratio. Even for relatively soft rocks before full induration, say with a value of $\mathrm{E} = 5$ GPa, a 1% shrinkage ($\varepsilon = 0.01$) leads to a loss of effective lateral stress of $\Delta\sigma'_h \approx \varepsilon_h \cdot \mathrm{E}/(1-\nu) \approx 0.01 \cdot 5000\,\mathrm{MPa}/(1-0.33) \approx 70$ MPa. The rock mass has no choice but to develop vertical fractures when the horizontal effective stresses become tensile, and this often happens in nature in a regular pattern, a joint set (Figure 1).

Figure 1 shows an outcrop of the source rock that is found 2600–3000 m beneath the center of the Central Sumatra Basin, where it generated oil and gas that migrated to a number of reservoirs in the northeastern part of the basin. The rock shows a very strong and regularly spaced joint set pointing to the nearby mountains, and it is likely that the direction 90° to the major joint set was the direction of $\sigma_{\mathrm{hmin}} (= \sigma_3)$ at the time the joints formed, parallel to the mountains, which is the commonly observed minimum stress direction at depth in foreland basins. Deeper in the basin, this rock is a black shale, it is undoubtedly fractured, and is considered prospective for shale oil and shale gas (depending on the depth of burial); here at the outcrops near the mountains, it has never been deeply buried, and this lacustrine formation contains zones of 3–12% algal TOC, and there are nearby coal seams and coaly residues in the shale (leaf and stem fragments).

6 WELL ORIENTATION AND STRESS STATE

To maximize reservoir contact area, the horizontal section of the well is drilled parallel to σ_{hmin}, which is usually assumed to also be σ_3 (an assumption that in most cases is correct). This means that in the virgin stress condition, the dominant plane of the fracture network will propagate at 90° to the wellbore axis. Hence, it is important to determine the orientation of the principal stresses at depth.

Although large-scale tectonic fabric gives a first-order estimate of the stress orientations, local effects such as gentle doming or basin subsidence may alter the regional stress fields, and it is best early in development planning to more precisely determine stress orientations. The preferred method for orientation reliability is tiltmeter-based deformation measurement during HF (Fisher et al. 2002), as this approach eliminates near-wellbore effects. Microseismic monitoring, particularly of the first fracture in a horizontal wellbore, can also give good constraints as to the fracture orientation and the tendency for vertical fracture rise, as the microseismic "cloud" tends to form an ellipsoid with the short axis in the direction of σ_{hmin}. In an interesting development in Apache Energy Corporation's Horn River Basin horizontal well drilling, the first handful of wells was drilled parallel to the mountain front, a reasonable expectation for the orientation of σ_{hmin}; measurements later led them to rotate their well layout by 30° CCW, to correspond to the σ_{hmin} direction that had been determined (public-domain slides, Apache).

Because the distribution of σ_{hmin} with depth is a vital factor in HF behavior and is a first-order input to any quantitative design process, refinement of methods to determine σ_{hmin} and to also get an estimate of the $\sigma_{\mathrm{hmin}}/\sigma_{\mathrm{HMAX}}$ ratio is necessary in practice to develop a regional stress orientation map. Because precise and properly conducted leak-off tests to determine σ_{hmin} are expensive, it is necessary to include models that use borehole acoustic data to correlate to stresses, and these correlative models are undoubtedly SG basin-dependent. Use of uncalibrated acoustic measurements to build a σ_{hmin} profile is less desirable. Similar comments (e.g. Fjaer 2006) can be applied to acoustic-based predictions of static moduli and UCS, as the static moduli are also first-order inputs to HF simulation, and the Young's modulus is highly

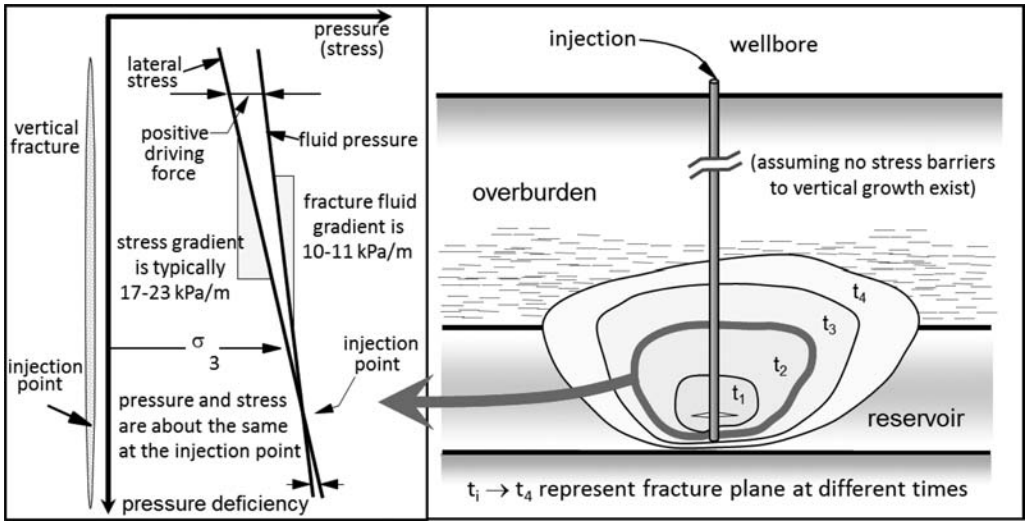


Figure 2. Fractures rise to minimize work because of different stress and pressure gradients.

stress-sensitive in NFR (note that there may also be substantial rate-dependent stiffness effects in the HF process).

Finally, it is important to recall that during active HF, the induced fractures will rise because the density of the fluid is less than the lateral stress gradient ($d\sigma_{hmin}/dz$) (Figure 2); thus, to minimize work for the volume injected, it is easier to grow upward than downward. The amount of rise is of great interest to operators because there is no economic value to the vertical propagation of induced fractures into non-productive horizons. Current HF models are not good predictors of height in the case of high-rate viscous fluid fracturing or gas fracturing of NFRs.

7 FRACTURING AND SHEAR DILATION

In the case of a single HF induced in a non-fractured continuum that has a high cohesion, the work is the combination of the fracture resistance that is overcome, the work of opening of the HF against a stress field, and the viscous fluid flow losses. Work of opening a fracture against the stress field is conceptually expressed for an impermeable rock as $W = F \cdot d \approx (p_f - \sigma_{hmin}) \cdot A \cdot \widetilde{\omega}$, where p_f is the pressure in the fracture and σ_{hmin} is the minimum principal stress, A is area of the fracture, and $\widetilde{\omega}$ is a measure of the mean fracture width (aperture). The product $A \cdot \widetilde{\omega}$ is actually the volume, and because the HF is very thin and planar, only the net stress $(p_f - \sigma_{hmin})$ need be considered. It is instructive to compare this first-order approximation for the work in opening a fracture with the seismic moment equation in earthquake geophysics; they express the same work concept, albeit for shear versus normal displacement. To be complete, a work equation for fracturing should include the viscous energy losses and the work of fracture. However, the work of fracture increases with the square of the length but the work of opening increases with the cube of the length (i.e. the volume), it is apparent that after a relatively small amount of injection, the work of fracture is negligibly small, and essentially all of the work in HF is associated with volume growth and friction losses.

In real fracturing operations, σ_{hmin} is not constant (Dusseault and Simmons 1982), especially for the high-rate viscous fluid injection phase of the HF operation; the fracture is shorter and wider because of the high viscous energy losses down the crack, and the aperture growth in the horizontal direction for a vertical fracture reacts against the rock mass, leading to a stress concentration, evidenced as an increase in σ_{hmin}. Thus, also accounting for the viscous fluid energy losses, the injection pressure will show an increase with time, and this is widely observed in all waste solids injection operations and most large HF treatments. Furthermore, HF operations in sandstones that were initially monitored in the 1980's (e.g. Talebi et al. 1991) showed that the microseismic energy release was associated with shearing (Figure 3), with almost no energy detectable from tip parting (confirmed by others in the 1990's, e.g. Warpinski et al. 1998).

Stress changes in cases of previous production or thermal stimulation (e.g. Dusseault et al. 1988, 2007) may have a major effect on fracture propagation behavior, as well as the effects of previous fracture stages, a subject of current great interest. This occurs at a large scale, but small-scale changes also take place. Consider the propagation of a vertical hydraulic fracture in a NFR such as a SG reservoir, where the matrix blocks have a high resistance to fracturing, but there are natural fractures that are open or incipient, with the dominant fabric sets rotated at some angle to the directions of the principal stresses, which are somewhat different one from the other. The fracture plane

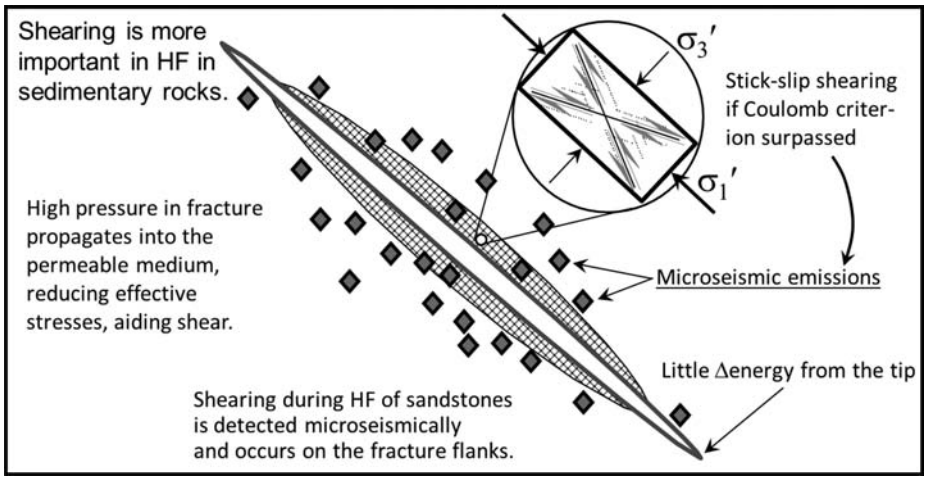


Figure 3. The energy release from shearing dominates microseismic emissions.

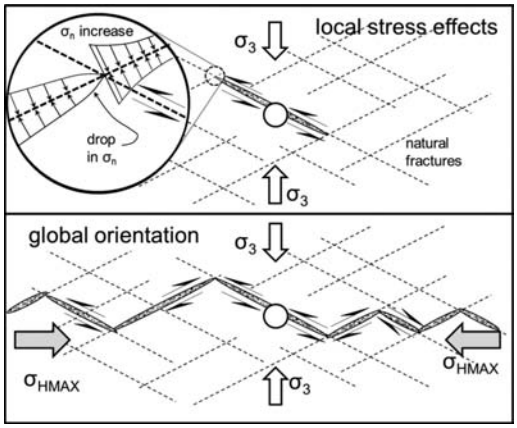


Figure 4. Local and large-scale effects on fracture propagation in NFR.

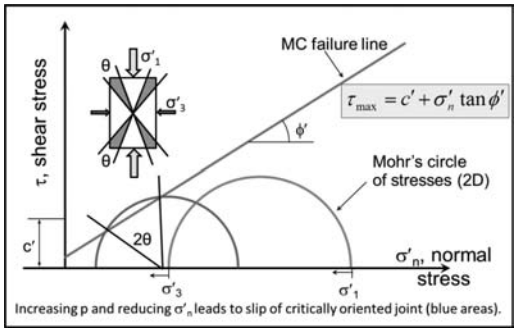


Figure 5. Properly oriented joint surfaces will slip before opening during injection.

follows the local fabric from a work point of view, but as a fracture that is inclined to the orthogonal stress field is opened, it undergoes slip, and the deformation shown in Figure 4 creates a loading condition on the intersected fracture that causes it to be easier to change direction than to continue propagating in the same direction. The longer the fracture length in the deviated direction, the greater the stress that tries to turn the fracture around, something shown previously for continuum fracturing (Mogilevskaya et al 2000a and b) and for HF (Warpinski and Teufel 1987). The inset in the figure shows the normal stress that develops across the offset fracture because of the shear motion of the first opened natural fracture. So, at the local scale, a fracture will tend to follow appropriately oriented natural fractures rather than break through fresh rock because of the need to minimize local work, but overall, at the large-scale, the fracture will tend to remain on average at 90° to the direction of σ_{hmin} because of global work minimization requirements.

It was previously mentioned that microseismic shear events were observed to accompany HF, and these shear events in a material such as an unfractured sandstone appear to arise because of a reduction of the confining stress as the pore pressure percolates into the medium. Do such shear events occur in SG MSHF? Yes they do, and mapping them has proven to be highly useful to understand what is actually happening during HF. However, the understanding and interpretation of the microseismic emissions remains semi-quantitative because no models coupling the stress evolution explicitly to the stick-slip events generating MS have been developed in practice.

Appropriately oriented natural fractures in a SG HF operation in a differential stress field will exhibit shear displacement if the pore pressures within them are increased, if the normal effective stress across them is reduced, and most likely it takes place as a combination of the two processes. This is shown for a simple Mohr-Coulomb case in Figure 5. In this case, a combination of pressure increase and normal effective stress decrease led to an intersection of the stress state with the slip criterion of the joints (of course, only one

MC failure line is shown, whereas in principal it is a probabilistic issue). Joints oriented in the blue orientations plotted on the small triaxial model inset will have slipped. Since shear in a stiff system with some component of brittle (strain-weakening) behavior is a stick-slip process, microseismic emissions will be generated, and these are used to map the region of shear slip.

The mechanisms that arise to increase the permeability of a naturally fractured rock during HF are two-fold:

(i) Opening or wedging of natural fractures tales place, and generally, it is desirable to have these fractures propped with a high permeability granular agent.
(ii) When shear displacement takes place, remnant increased conductivity is left behind after the stick-slip event through a process of self-propping (although this conductivity increase does partially disappear with time (creep) and effective stress (partial closure and crushing of asperities).

The wedging of a crack in a stiff NFR leads to an opening of a crack far in advance of the wedge, if the wedge is a solid; if the wedge is the injected fluid under HF conditions, of course the injected fluid can be much closer to the tip of the wedged portion.

This knowledge, in the context of the discussion above, helps explains the strategy of initially using a viscous fluid at extremely high injection rates ($>8\,m^3$/min) containing high concentrations of proppant.

This process wedges open many natural fractures, and most importantly, because of wedging and opening, additional fractures are opened so that a high-connectivity propped fracture zone is created. The proppant lags behind the fluid, even if it is high viscosity, because of the narrowness of the opened paths (frictional retardation, arching, etc.). So, in the absence of any shear dilation, the zone that is generated has a central region where the fracture apertures are wide and propped (at least partially) with granular proppant. Surrounding this is a region where the rigid blocks have rotated slightly, so that there are aperture openings that increase the fracture conductivity, generating an ellipsoid (approximately) defining an enhanced fracture conductivity region of high internal surface area which helps increase the CH_4 diffusion to the fractures, to flow to the wellbore.

However, the MS emissions that were observed around HFs in the 1980's and 1990's were, in cases involving NFR, clearly taking place far from where the sand was reaching, and arguably even in conditions where the pore pressure had not yet penetrated. This led eventually to the concept of shearing along natural fractures, with a remnant conductivity arising because of shear dilation of the rough fracture surface (Figure 6). Indeed, a shear displacement as small as 1 mm is sufficient in a hard rock to increase the conductivity by an order of magnitude or more if the original fracture was largely closed.

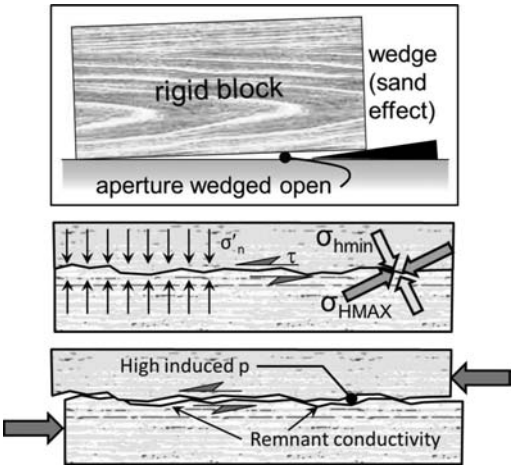


Figure 6. Wedging and shear dilation and conductivity increase.

Once this effect was realized, a new approach, high-rate slickwater fracturing, became widely used, usually after the viscous fluid fracturing phase with proppant, to try and stimulate the SG reservoir far from the propped region. Slickwater is water with a small amount of a friction reducing substance such as a polyacrylamide. This permits a dramatic lowering of the resistance to flow, so that, in principle, water and elevated pore pressures can propagate far from the propped zone. MS monitoring has demonstrated conclusively that this is taking place, as the ellipsoid of MS events during slickwater fracturing is much fatter and extensive than for the high-viscosity HF phase. The flow paths can be thin, and if the leak-off potential of the SG rock mass is low, the shear dilation effect can propagate out 200–300 m in some cases, developing a region around the sand-propped zone that is much larger in volume than the sand propped zone. The increase in conductivity of the natural fractures that have been sheared gives again a much greater surface area from which the gas to slowly diffuse. So, there is a differentiation between the "propped volume" (or "sand zone") and the "stimulated volume", which can be many times the volume of the sand zone (Figures 7 and 8 show the shearing and the rigid block displacement concepts at the field scale).

It is important to determine how large of a stimulated zone can be generated in real cases because this will help dictate the optimum well spacing, whether an additional upper row of wells is needed in a thick reservoir, the best spacing of fracture sites along the wellbore, what is the optimum size and rate of the HF treatment, at what depth in the reservoir should the wells be drilled, and so on.

In this decision-making process, many other factors must also be considered, such as whether the shale is water sensitive (a gas or gelled propane may alternatively be used as the fluid at much greater expense), whether the first fractures affect the behavior of the subsequent fractures along the wellbore, whether there

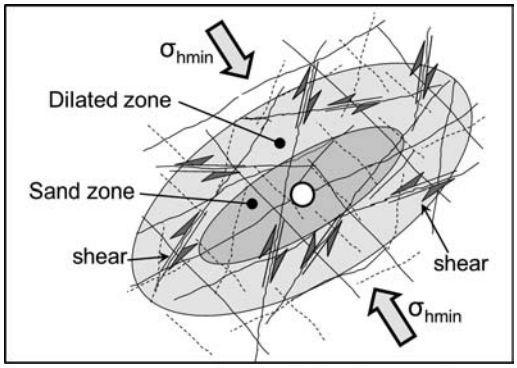


Figure 7. The sand-propped zone and the stimulated (dilated) zone.

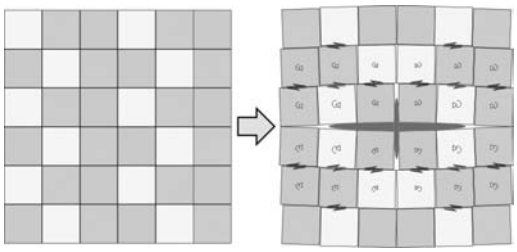


Figure 8. The concept of rigid block movements in high pressure HF with sand wedging.

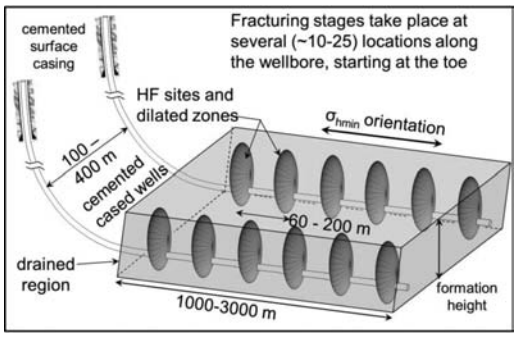


Figure 9. Well placement and optimization issues.

may be advantages to simultaneously or alternately fracturing adjacent wells, and so on. Figure 9 shows, in a simple manner, the disposition of two wells in a SG development, with ellipsoids representing the stimulated volumes.

8 MODELING INDUCED FRACTURING

Classical approaches to HF design in the industry involve closed-form solutions, semi-analytical or integral solutions, and numerical methods based on some form of boundary discretization. Closed-form approaches include the Sneddon penny-shaped crack or elliptical variants, 2-D approximations such as the Geertsma-de Klerk-Kristianovic approach (e.g. Geertsma and de Klerk, 1969) and the Perkins-Kern-Nordgren approach (e.g. Nordgren 1972), modified crack solutions such as the Barenblatt-Dugdale method to eliminate the stress singularity associated with a sharp crack, the Eshelby solution, integral hypersingular methods (Mogilevskaya et al. 2000a and b), and various integrated and modified versions of these methods. Fracture initiation criteria at the borehole wall dealt with solutions for stresses around boreholes in cases of elastoplastic rocks or elastic rocks, some solutions coupled, some not (Wang and Dusseault 1991 a&b), and with some solutions it was found that fracture initiation a short distance within the borehole wall was possible. However, these and related solutions failed to address fracture propagation in a naturally fractured rock mass, although attempts to explain the physical processes involved with natural stresses and fabric, including stress changes, were quite common (Dusseault 1977, 1989, Dusseault and Simmonds 1982). Here I only cite mainly my own articles, but there are dozens of excellent articles following 1980 by Pollard, Rice and others, and over 8800 articles involving hydraulic fracturing in the Society of Petroleum Engineering library base alone, including both Journal and Conference articles.

The advent of Discrete Element Methods allowed the study of fractures in granular media with differential stresses and cohesive bonding between grains (e.g. Thallak et al. 1991), and these are undergoing rapid development for HF in NFR's.

More recently, mathematical models that are more rigorously coupled and that can incorporate strong fabric elements (faults, natural fractures that are strongly or weakly persistent …) have been developed and used. Some of these are based on Discrete Element Methods, on Extended Finite Element analysis, and on various hybrid formulations. Here, the current work of two students is briefly presented: one is a DEM investigation of strong fabric using UDEC™ (an Itasca Product), the second is a new hybrid model for thermal-hydraulic-mechanical (THM) coupling using a hybrid Displacement Discontinuity – Finite Difference coupled formulation.

9 SOME RESULTS USING 2-D DEM MODELS

The software UDEC™ is being used to look at the impact of strong fabric on the propagation of hydraulic fractures (Pirayehgar 2013). UDEC™ is a discrete element formulation widely used in rock mechanics to simulate the response of a jointed rock mass. The effect of strong rock fabric on the propagation of hydraulic fractures in a NFR can be explored as a set of numerical experiments, using models with different types of fabric and varying differential principal compressive stresses. The medium is constructed with strong fabric comprising joint surfaces that are frictional, or they can be frictional-cohesive with strain-weakening, whereas the matrix blocks cannot be fractured.

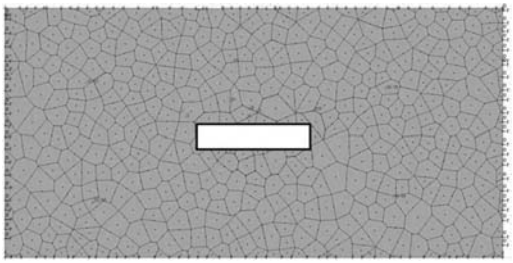


Figure 10. A Voronoi tessellation with a central opening subjected to injection Well placement and optimization issues.

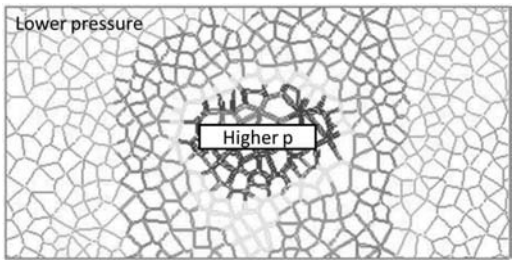


Figure 11. Pressure diffusion into a Voronoi-style fracture system.

The model is hydraulically coupled, as flow in the joints (1-D cracks) is linked to the mean joint aperture that changes during the simulations.

Figure 10 shows a Voronoi tessellation, which represents a 2-D rock mass with intersecting joints connected at nodal points. Such an array might be taken to represent a random array of joints but with no dominant orientation (no strong fabric). Alternatively, one may design a fracture array with strong oriented fabric of various types to explore the interaction of joint fabric and the directions of the principal stresses. In these simulations, numbers have been deliberately left off so that only the general results are shown for a few of the cases being studied. The outside of the array is subjected to a stress, isotropic or differential, and the rectangular opening is subjected to a boundary pressure greater than the far-field pressure, so that pressure diffusion takes place, as shown in Figure 11, which is a realization of pressure diffusion into the fracture system, and it is to be noted that if a stronger differential stress is applied, there is greater anisotropy in the distributions of the pore pressure, as fractures approximately normal to the minimum principal stress open more easily than those at 90° , and the differential behavior magnitude is related to the stress difference in a non-linear manner.

Figure 12 shows some of the effects that can be studied, whether injection takes place along a line, at a point, or, in this case, along the boundaries of an opening.

On the left-hand side is a plot of joints that have undergone sufficient displacement that they are not in

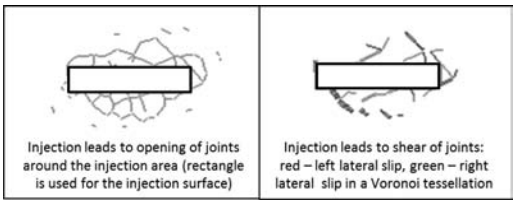


Figure 12. Opening of fractures and slip along favorably oriented fractures.

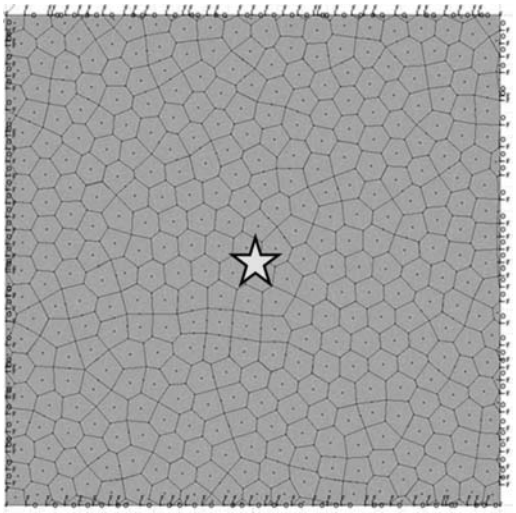


Figure 13. Injection at a point (star is centered on the center of a joint surface and represents the injection point in a Voronoi tessellation).

direct contact; i.e., they have "opened" in response to the hydraulic injection. Of greater interest in the context of SG stimulation is the propensity for shearing. In these simulations, slip has occurred along a number of favorably oriented surfaces, with right- and left-lateral shear (conjugate shear), and one might suppose that in each case a microseismic event has occurred and a discrete amount of energy consumed (as work). The amount of energy associated with the stick-slip even is small compared with the work done to generate the distortions in the mass (UDEC permits the displacements to all be tracked, so that work calculations – $F \cdot d$ – can be undertaken). An energy formulation for the energy release of the slip event is being explored.

Here, another tessellation in a differential stress field is subjected to injection at a point, Figure 13. The yellow star is centered at the midpoint of a joint surface in the array, and HF is initiated by injecting at an increasing pressure that becomes greater than the minimum principal stress – at which point joint surfaces near the borehole that are close to 90° to σ_{hmin} should open. In fact, that is exactly what is observed in the simulations. The black line in Figure 14 is sketched to emphasize the region where the fracture is opened.

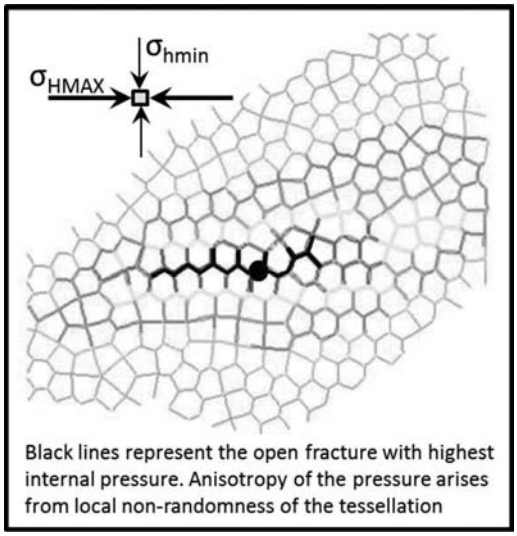


Figure 14. Injection at a point leading to HF, the pressure distribution is plotted. The black lines have been added to emphasize the HF location and the propagation path.

We now see a number of effects that could have been anticipated from a careful consideration of the physical effects:

- The fracture opening follows the local joints (of course, in this case the matrix blocks cannot fracture) to form an "average orientation" that is normal to σ_{hmin}.
- Branching can occur, although shortly thereafter, one of the branches dominates and the other is suppressed.
- The beginning of a fracture network is seen, and short vertical paths are close to opening and could likely be opened and "propped" if the injection pressure can be made large enough.

In the next set of pictures (Figure 15), some results are shown for a case of the presence of a strong fabric element. There has been concern expressed that HF near an existing fault can trigger slip along the fault and generate a seismic event of significance (e.g. Richter Magnitude 2.5 or larger). The second row of figures shows the pore pressure progression on the left, with the fractures that have been opened hydraulically in black. The right hand figure shows the elements that

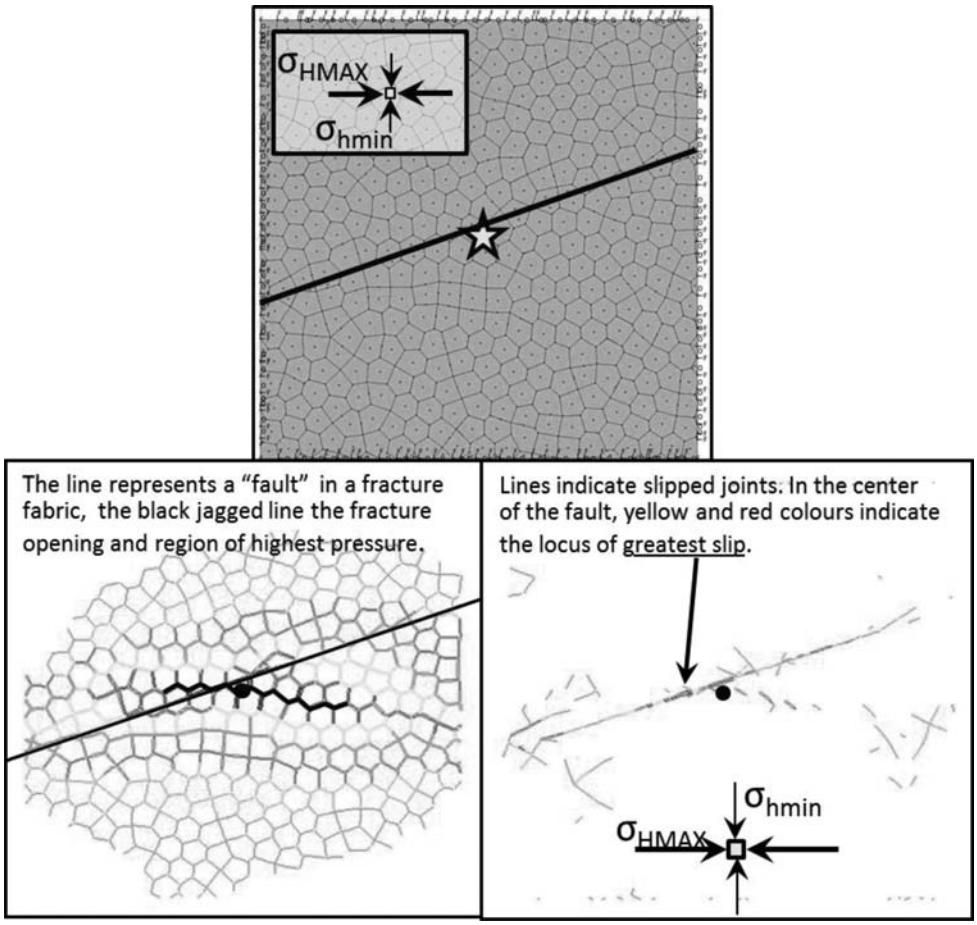


Figure 15. A DEM realization of HF in a rock mass with a nearby fault plane.

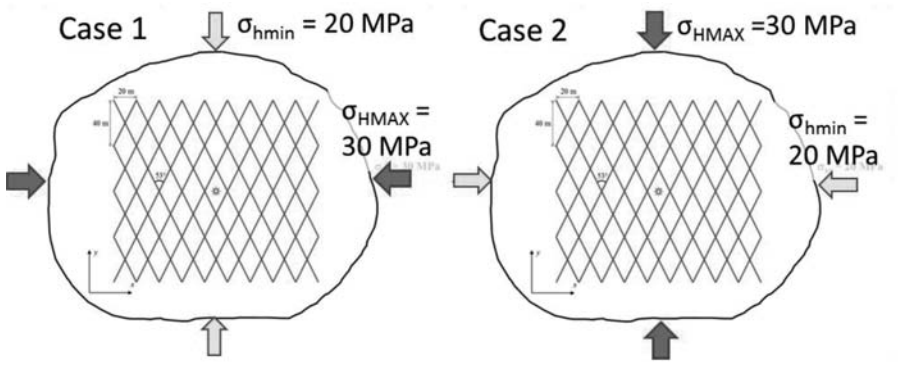


Figure 16. Fractured medium with strong mis-aligned fabric and differential stress field. The fracture array is effectively a fractured region embedded into a 2-D poroelastic infinite continuum, therefore issues of scale will arise (block size versus array size).

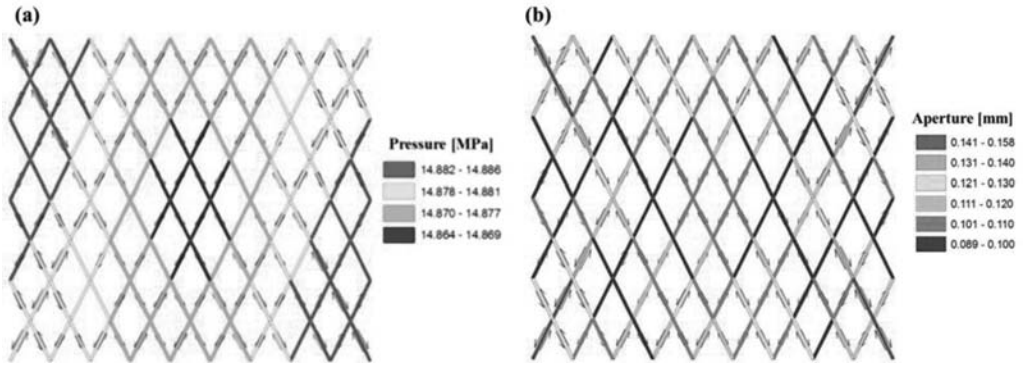


Figure 17. Pressure response (a) and aperture (b) after 5 days of constant rate production from Case 1 model (fracture network embedded in a 2-D continuum).

have slipped, and clearly the presence of the fault has led to a large amount of slip focused on the fault plane, with the strongest slip displacement occurring near the injection borehole. In this simulation, slip occurred before the opening of the hydraulic fracture, and the slight rotation of the fracture away from the plane is because of stress field modifications associated with the fault slip.

In principle, the DEM approach can be used to determine the seismic moment, and the impact on shear slip propagation of the constitutive law for the fault (cohesion – friction law with strain weakening) can be explored. Work calculations can be undertaken to look at the various sources of energy storage (elastic strain energy) or dissipation (slip), and likely the energy losses from viscous dissipation could be clarified as well, helping to clarify HF processes in NFRs.

The DEM method holds considerable promise for clarification of the effects of strong fabric and differential stress fields, opening of cracks, and shear dilation; there is also the possibility of including inertial effects in crack slip, at least at a macroscopic scale. Some deficiencies include impermeable elastic matrix blocks, the lack of thermal flux capability, and issues associated with the nature of the constitutive laws for the joint stiffness and conductivity relationships. For large arrays, the DEM is computationally demanding, and for 3-D problems it remains beyond the capability of design engineering efforts, although, as with all computational engineering problems, this limitation gradually becomes less over time.

10 SOME RESULTS USING A NOVEL THM COUPLED FD-DD FORMULATION

Figures 16, 17 and 18, along with the simulation parameters in Table 3, show some results from a new hybrid 2-D approach based on Displacement Discontinuity – DD – treatment of the fractures and a Finite Difference – FD – approach for the flow network and seepage into rock blocks (Jalali 2013).

In addition to flux, the average pressure in each fracture segment is calculated using the FD method, based on a cubic fracture flow law, then the pressures are incorporated into the DD calculations to determine aperture, and iterations performed to fully couple

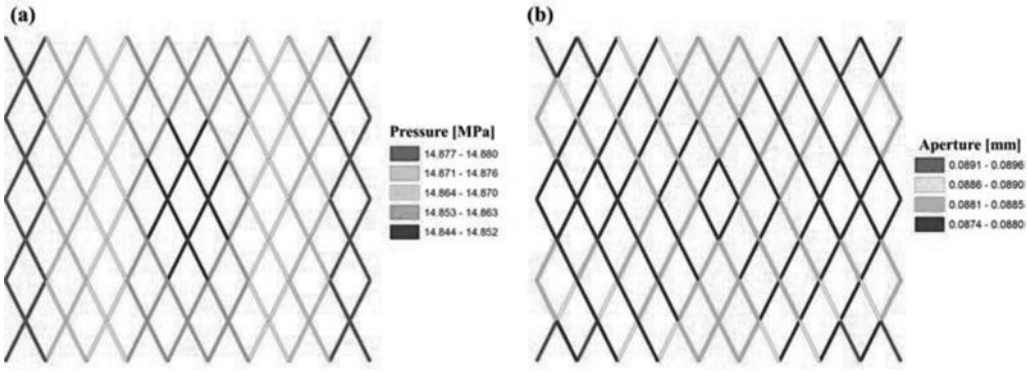


Figure 18. Pressure response (a) and aperture (b) after 5 days of constant rate production showing the direction of slip along fracture surfaces, arrow size scaled to displacement.

Table 3. Properties for the simulations in the next two figures.

Drained Poisson's ratio (ν)	0.25
Young's modulus (E)	20 GPa
Initial fracture aperture (w_0)	0.1 mm
Fracture normal stiffness (K_n)	10 GPa/m
Fluid compressibility (c_f)	7×10^{-10} 1/Pa
Production fluid rate (Q_{prod})	10^{-5} m^3/s
Matrix permeability (k_m)	0.05 mD
Biot's coefficient	0.8
Cohesion (c)	0
Undrained Poisson's ratio (ν)	0.35
Initial pressure (p_0)	16 MPa
Fracture maximum closure (w_{res})	50 μm
Fracture shear stiffness (K_s)	10 GPa/m
Fluid dynamic viscosity (μ)	1 cP
Fluid density (ρ_f)	1000 kg/m^3
Matrix porosity (ϕ_m)	0.25
Dilation angle (ψ)	5
Friction angle (ϕ)	30

the stress and the hydraulic conditions. In the example chosen, after five days, the aperture has decreased about 3%, with an effect on the conductivity.

The amount of aperture compliance is set by a constitutive stiffness law based on Bandis et al. (1983), and the stiffness can be varied to simulate non-elastic compliance as long as the pressure changes are monotonic.

Although geometrically regular arrays are shown, a Voronoi tessellation or a non-homogeneous distribution of fractures can be implemented, as well as different strongly oriented rock joint fabric systems. Figure 19 is an example of the aperture evolution with fluid injection or production into a brick array (differential orientation of strong fabric with continuous joints in the x direction but discontinuous ones in the y direction, but the same external stresses). On the right hand side, note how the apertures are large because the fractures are embedded into a continuum, so issues of scaling have arisen (the numbers of fractures would have to be much larger as well as the overall model size to avoid this effect). Because the DD-FD method is computationally efficient, it is possible to explore issues of scale with reasonable computational effort, although we have not yet done so.

The DD method exploits influence functions for an elastic rock, and the displacements at the fracture intersection points between adjacent elements are made compatible mathematically so that the elastic stresses may be solved quickly at any point in the rock mass, without further discretization of the rock blocks or the surrounding rock mass (see for example Dusseault et al. 2007). Similarly, for the matrix blocks, boundary flow elements are used to predict the pressure propagation with the rock blocks.

In addition, the new formulation was designed to include the effects of temperature through the use of convective-conductive heat transfer calculations using boundary elements for heat flow, conduction of heat into the matrix blocks, cooling of the liquid flow through the fractures, and the thermoelastic strains induced in the matrix and how this affects the stresses and the fracture aperture. Because the changes of fracture aperture are linked through the FD calculations to the fluid flux and pressure, a full thermo-hydromechanical (THM) coupling is achieved. In general, when realistic fracture constitutive laws and thermoelastic matrix block properties are used, the thermal effects of fracture aperture (increasing for cooling, decreasing for heating) are dominant for realistic cases such as cold water injection into a deep reservoir ($\Delta T \approx -40$–$100°$ C), thermal injection for heavy oil viscosity reduction in a fractured carbonate (e.g. Shafiei et al. 2013), liquid nitrogen injection (no gas capability yet) or geothermal exploitation (although the model cannot accommodate steam injection or production at this stage).

The use of influence functions for the solution to heat flow, fluid flow, stresses and displacements leads to computational speed far greater than any method that involves block discretization. Of course,

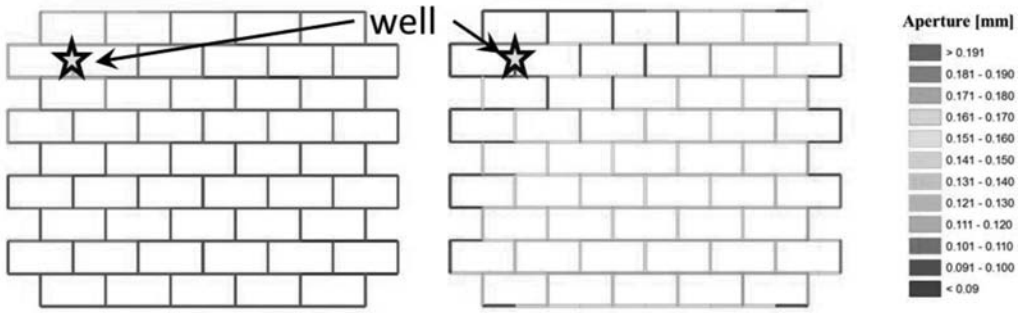


Figure 19. Injection or production in a brick model of a fractured medium embedded in a continuum with an off-centre well. Left: aperture distribution after one day of cold fluid injection. Right: aperture distribution after four days of fluid production.

Table 4. Model parameters, single 40 m fracture, differentially stressed poroelastic medium.

Drained Poisson's ratio (ν)	0.25
Young's modulus (E)	10 GPa
In-situ vertical stress (σ_{yy})	20 MPa
Initial pressure (p_0)	10 MPa
Initial fracture aperture (w_0)	0.1 mm
Fracture normal stiffness (K_n)	100 GPa/m
Fluid compressibility (c_f)	7×10^{-10} 1/Pa
Fluid thermal conductivity (k_{Tf})	0.6 J/m°Ks
Fluid specific heat (c_f)	4200 J/kg°K
Matrix permeability (k_m)	1 mD
Fluid thermal expansion (B_f)	2.4×10^{-5} 1/°K
Biot's coefficient	0.8
Cohesion (c)	0
Injection fluid rate (Q_{inj})	2×10^{-6} m^3/s
Undrained Poisson's ratio (ν)	0.35
In-situ horizontal stress (σ_{xx})	30 MPa
In-situ shear stress (σ_{xy})	0
Initial temperature (T_0)	80°C
Fracture maximum closure (w_{res})	50 μm
Fracture shear stiffness (K_s)	100 GPa/m
Fluid dynamic viscosity (μ)	1 cP
Fluid density (ρ_f)	1000 kg/m^3
Rock heat diffusivity (c^T)	5×10^{-5} m^2/s
Matrix porosity (ϕ_m)	0.25
Rock thermal expansion (B_s)	2.1×10^{-5} 1/°K
Dilation angle (ψ)	0
Friction angle (ϕ)	30
Injection temperature (T_{inj})	50°C

computational efficiency is, to some degree, at the expense of an ability to incorporate internal block heterogeneity, anisotropy, plasticity or other non-linear processes. In addition to solutions such as these for various cases of stipulated rock fabric and properties, this method can be used as an efficient "quick-assessment" method to study parametric variability and stochastic property cases to assess risk. Parametric variation analysis can be used to determine the sensitivity of the case to various inputs such as joint compliance, the nature of the joint flow law, rock matrix properties and so on. Different types of fabric can be studied, and this may give insight, for example, to the shearing behavior discussed previously (in these THM coupled simulations, a constant dilation angle is used). Furthermore, stochastic simulation (e.g. Monte Carlo simulation) using different distribution functions of properties can be carried out in a reasonable time, giving guidance as to what problem domains are worthy of more detailed analyses incorporating some forms of non-linearity.

The following figures show some results for the injection of cool water into a single fracture in a poroelastic medium to demonstrate some of the model capabilities.

In Figure 20, the fracture aperture as the result of cooling is plotted on the bottom, and the fracture pressure and temperature in the fracture along the top. The contours represent pressures and temperatures within the rock matrix. Because of the thermoelastic effect on the aperture, the impact of thermal rock matrix strains is strong in fractured rock masses.

Figure 21 shows various displacements and stresses generated during the simulation for a single fracture. It is not possible to show all the details here, but we have found that there are subtle but important effects that are difficult to "conceptually predict" in advance because of the interplay of the various coupled processes that affect fracture aperture, flow rate, pressure, volume change, stresses, shear displacement and dilation, changes in fracture conductivity, and so on.

A potential application of the method is to serve as a "first-order coupling" with a petroleum reservoir simulator. The term "first-order coupling" is intended to convey the idea that integrating the new method with a petroleum simulator does achieve a great level of coupling for a fractured medium, but with the limitations stipulated previously. The approach would be the following: reservoir 3-phase simulators are based on 3-D grid blocks with the corners defined by finite difference nodes; the reservoir model would be constructed as well so that the surfaces of the 3-D grid blocks correspond to natural fracture surfaces; the DD-FD simulation would be geometrically identical; and, iteration between the two models at appropriate time steps can give a far more realistic result that a conventional grid block simulator.

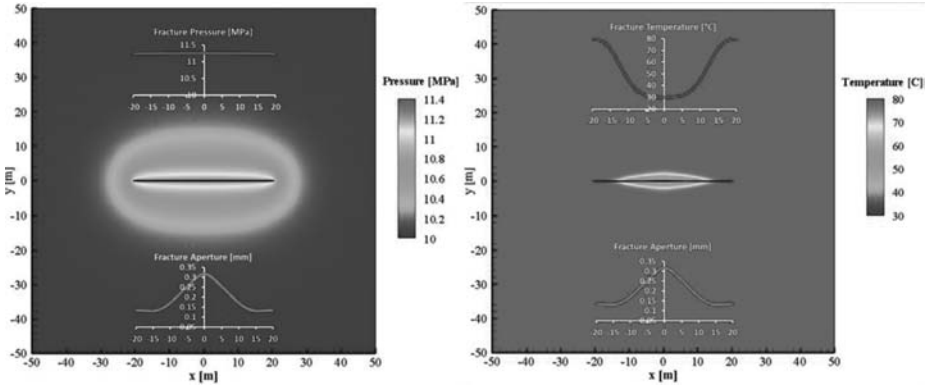


Figure 20. Pressure and temperature after 10 hours of cold fluid injection.

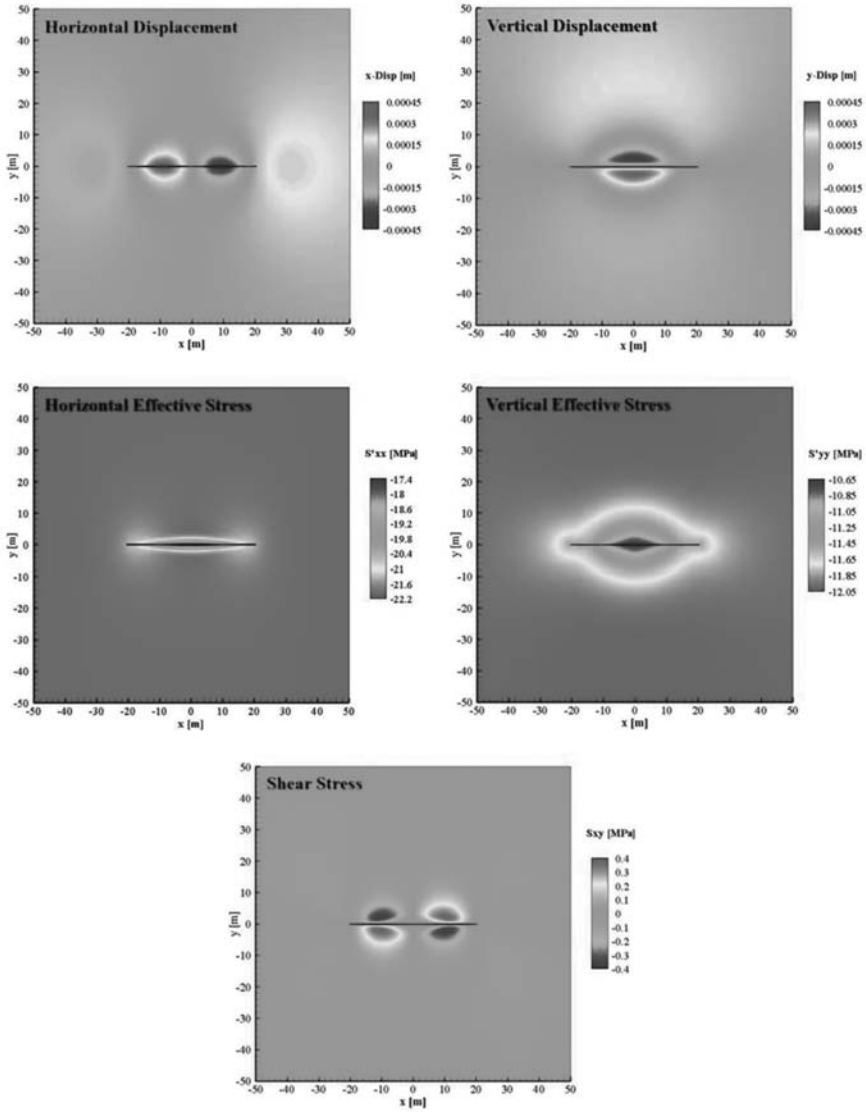


Figure 21. Displacements (horiz, vert), stresses (σ'_h, σ'_v, τ_{xy}) for the case stipulated above.

11 CONCLUSIONS

Optimization of HF design in NFRs requires development of hydromechanically coupled mathematical models that can reasonably simulate induced fracture network development in rock masses with strong fabric (weak joints in a strong rock). In many cases, these should be thermally coupled models as well. Some of the outstanding questions that are relevant to the engineering planning of MSHF might include:

- What is the effect of penetrative oriented defects (persistent joint sets) on the interconnected fracture network creation?
- How does stress anisotropy impact interconnected fracture network characteristics (aspect ratio, branching. . .)?
- Can the interaction between stress anisotropy and a joint system that deviates from the principal stress directions be rationally quantified for practical application?
- How might a single massive-scale planar feature (through-going fault) modify interconnected fracture network development?
- Can we realistically simulate the impact of stress changes that are induced by early fracture stages on the later stages, and how these changes might modify the major interconnected fracture network characteristics?
- Will HF and MSHF simulations in NFRs become genuinely predictive tools or will they always have to be calibrated extensively with *in situ* measurements (deformations, MS emissions)?

The DEM method has current limitations that may be at least partially resolved in future realizations. It is highly useful for understanding in a conceptual and semi-quantitative manner how HF can interact with natural fracture systems, how remote slip occurs under injection without fracture opening, and likely for work estimates. A DD-FD approach developed by Jalali (2013) holds promise as a computationally efficient means of exploring THM coupling in complex naturally fractured systems. The combined effects of thermal and poromechanical strains under different thermohydraulic loading, different fabric types and stress fields, and differing material parameters lead to some subtle effects that are now amenable to more rapid study. The DD-FD model can be coupled with other approaches iteratively (using geometric similarity), or as a rapid "first-look" to study parametric sensitivity and stochastic realizations. Both these methods have promise in evolving toward a design aid for HF in NFR.

Future developments will include extended finite element methods to track details of fracture propagation, including the possibility of tensile rupture through intact rock blocks. Eventually, an explicit link based on energy calculations will be made between the slip that can be simulated in these various mathematical approaches and the MS emissions in the field, with the potential for more rigorous elastic inversion of the MS emissions to delineate approximate stress field evolution during fracturing. For the first time, through the use of appropriate constitutive laws, we may be able to monitor an evolving stress field through the MS emissions.

For all of these methods, going to a full 3-D model realization carries challenges, not only computationally, but in terms of data input and data display. Good visualization tools have greatly improved mining and reservoir engineering, and development of good tools to examine stresses, displacements, joint slip locations and direction, temperatures, pressures and flow rates. Incorporation of geological heterogeneity, with all of its attendant uncertainties, is another challenge, common to all parts of geomechanics, and especially in NFRs.

Design is a multi-faceted exercise integrating many tools, not the least of which are experience and a deep understanding of mechanics. Mathematical models are a valuable aid to design in determining quantitative recommendations, but also in informing the design engineer of the mechanisms and consequences. They will never replace judgment, but better models make the design process more rational, reducing uncertainty in several important ways.

Shale gas has changed the energy picture in the world. Now, shale oil (also in naturally fractured rocks that require HF stimulation) is contributing new petroleum resources in North America, and soon in the rest of the world (primary estimates suggest an increase of 20% in recoverable reserves already – http://energy.usgs.gov/OilGas/ReserveGrowth/ReserveGrowthPublications.aspx – with much data to be collected and analyzed in decades to come. In the Middle East, the vast naturally fractured reservoirs that are gradually approaching the end of their first productive cycle because of water encroachment will soon begin redevelopment using horizontal wells, hydraulic fracturing, and gravity-stabilized drainage. All these resources depend on good hydraulic fracture design for optimization of recovery: that is the purview, in large part, of the specialist in Petroleum Geomechanics.

ACKNOWLEDGEMENTS

Several active PhD graduate students contributed results and reviews to this article: Li Ruiqiang in geosciences and mechanical properties, Atena Pirayehgar provided UDEC™ simulations, and Reza Jalali (PhD 2013) developed a 2-D FD-DD code for thermohydromechanical coupling of hot or cold fluid injection into fractured rock masses. ITASCA Inc. generously contributed licenses for the use of UDEC and 3-DEC software. Schlumberger Canada helped support Reza, the Centre of Excellence in Mining Innovation supports Atena, and Ruiqiang is partially supported by the Chinese government on a scholarship. The rest of the support for Reza and Ruiqiang comes from the Canadian government through the Natural Sciences and Engineering Research Council.

REFERENCES

Aldin, M. 2013. Personal communication on shale gas testing results. Metarock Laboratories Ltd. http://www.metarocklab.com/

Bandis, S., Lumsden, A., and Barton, N. (1983). Fundamentals of Rock Joint Deformation. *International Journal of Rock Mechanics and Mining Sciences & Geomechanics Abstracts*. 20 (6), 249–268.

Bazan, L.W., Lattibeaudiere, M.G. and Palisch, T.T. 2012. Hydraulic Fracture Design and Well Production Results in the Eagle Ford Shale: One Operator's Perspective. SPE America's Unconventional Resources Conference, Pittsburgh, Pennsylvania. SPE #155779.

BP 2013. *BP Statistical Review of World Energy 2013*. http://www.bp.com/en/global/corporate/about-bp/statistical-review-of-world-energy-2013.html

Charpentier, R.R., deWitt, W., Claypool, G.E., Harris, L.D., Mast, R.F., Megeath, J.D., Roen, J.B. and Schmoker, J.W., 1993. Estimates of unconventional natural gas resources of the Devonian shales of the Appalachian basin, *in* Roen, J.B., and Kepferle, R.C., 1993, *Petroleum geology of the Devonian and Mississippian black shale of eastern North America: U.S. Geol. Surv. Bull. 1909B*, p N1–N20.

Curtis, J.B. 2002. Fractured shale-gas systems. *Bulletin of the American Association of Petroleum Geologists* 86(11), 1921–1938.

David, C. 2007. *Rock Physics & Geomechanics in the Study of Reservoir & Repositories - Special Publication no 284*. The Geological Society of London, 232 p.

Dewhurst, D.N., Siggins, A.F., Kuila, U., Clennell, M.B., Raven, M.D. and Nordgård-Bolås, H.M. 2008. Elastic, Geomechanical and Petrophysical Properties of Shales. Proc. 42nd ARMA Conference, San Francisco, Paper 08-208.

Dusseault, M.B. 1977. Stress state and hydraulic fracturing in the Athabasca Oil Sands. *J. of Canadian Petroleum Technology* 16(3), 19–27.

Dusseault, M.B. 1989. Behaviour of induced fractures in sand and friable sandstones, J. of Hydrology, Spec. Vol., *Proceedings 4th Can/Am. Conference on Hydrogeology*, 3–10.

Dusseault, M.B. and Simmons, J.V. 1982. Injection-induced stress and fracture orientation changes, *Canadian Geotechnical J.* 19(4), 483–493.

Dusseault, M.B., McLennan, J. and Shu, J. 2011. Massive multi-stage hydraulic fracturing for oil and gas recovery from low mobility reservoirs in China. *Petroleum Drilling Techniques* 39(3), 6–16.

Dusseault, M.B., Wang, Y. and Simmons, J.V. 1988. Induced stresses near a fireflood front, *AOSTRA J. of Research* 4(2), 153–170.

Dusseault, M.B., Yin, S., Rothenburg, L., and Han, H.X. 2007. Seismic monitoring and geomechanics simulation. *Leading Edge* 26(5) (May), 610–620.

Dykstra, J.C.F. and Longman, M.W. 1995. Gas Reservoir Potential of the Lower Ordovician Beekmantown Group, Quebec Lowlands, Canada. *AAPG Bulletin* 79(4), 513–530.

EIA 2013. *Technically Recoverable Shale Oil and Shale Gas Resources: An Assessment of 137 Shale Formations in 41 Countries outside the United States*. Energy Report by Advanced Resources International, primary authors: Kruuskaa, V.A.; Stevens, S.H. and Moodhe, K.D. 730 pp including appendices and cover pages.

Fisher, M.K. and six other authors. 2002. Integrating Fracture Mapping Technologies to Optimize Stimulation in the Barnett Shale. *Proc. SPE Annual Technical Conf.*, San Antonio, SPE #77441, 7 p.

Fjær, E. 2007. Geomechanics and geophysics for reservoir management. Revue Européenne de Génie Civil 10(6–7), 703–730.

Fjær, E., Stroisz, A.M. and Holt, R.M. 2013. Elastic Dispersion Derived from a Combination of Static and Dynamic Measurements. *Rock Mech. & Rock Eng.* 46(3). 611–618.

Gale, J.F.W., Reed, R.M. and Holder, J. 2007. Natural fractures in the Barnett Shale and their importance for hydraulic fracture treatments: *AAPG Bulletin* 91, 603–622.

Geertsma, J. and de Klerk, F. 1969. A Rapid Method of Predicting Width and Extent of Hydraulically Induced Fractures, *J. of Petroleum Tech.* 21(12), 1571–1581.

Jacoby, H. D. and seven others. 2011. The future of U.S. natural gas production, use, and trade. *Energy Policy* 39(9), 5309–5321

Jalali, M. R. 2013. Thermo-Hydro-Mechanical Behavior of Conductive Fractures using a Hybrid Finite Difference – Displacement Discontinuity Method. PhD Dissertation University of Waterloo, Department of Earth and Environmental Sciences, 151 p plus appendices.

Kuuskraa, V.A., Koperna, G., Schmoker, J.W. and Quinn, J.C. 1998. Barnett Shale rising star in Fort Worth Basin. *Oil and Gas Journal* (May), Part 5 of a 1998 6-Part Series on Emerging U.S. Gas Resources; pp. 67–76.

Lolon, E.P., Cipolla, C.L., Weijers, L., Hesketh, R.E. and Grigg, M.W. 2009. Evaluating Horizontal Well Placement and Hydraulic Fracture Spacing/ Conductivity in the Bakken Formation, North Dakota. *Proc. SPE 2009 Annual Technical Conference and Exhibition*, 4–7 October, New Orleans, Louisiana, SPE #124905, 12 p.

Mogilevskaya, S.G., Rothenburg, L. and Dusseault, M.B. 2000b. Growth of pressure-induced fractures in the vicinity of a wellbore. *Int. J. of Fracture* 104, L25-L30.

Mogilevskaya, S.G., Rothenburg, L. and Dusseault, M.B., 2000a. Interaction between a circular opening and fractures originating from its boundary in a piecewise homogeneous plane. *Int. J. of Numerical and Analytical Methods in Geomechanics* 24, 947–970.

Nordgren, R.P. 1972. Propagation of a Vertical Hydraulic Fracture, *Soc. of Petroleum Engineers J.* 12, 306–314.

Pirayehgar, A. 2013. DEM approaches to simulate hydraulic fractures in rock masses with strong fabric. PhD Proposal, University of Waterloo,Waterloo, Ontario.

Rice, D.D. and Claypool, G.E. 1981. Generation, accumulation, and resource potential of biogenic gas: *AAPG Bulletin* 65(1), 5–25.

Rivard, C., Molson, J.W., Soeder, D.J., Johnson, E.G., Grasby, S.E., Wang, B. and Rivera, A. 2012. A review of the Noovember 24–25, 2011 shale gas workshop. Calgary Alberta – 2. Groundwater resources. *Geological Survey of Canada Open File 7906*, 205 p.

Roen, J.B. and Kepferle, R.C. 1993. Petroleum geology of the Devonian and Mississippian black shale of eastern North America: *U.S. Geological Survey Bulletin 1909*, 434 p.

Shafiei, A. and Dusseault, M.B. 2013. Geomechanics of thermal viscous oil production in sandstones. *Journal of Petroleum Science and Engineering* 103, 121–139.

Shafiei, A., Zendehboudi, S., Dusseault, M.B. and Chatzis, I. 2013. A 3-D mathematical model for steamflooding in naturally fractured carbonate heavy oil reservoirs. *Ind. Eng. Chem. Res.*, 52(23), 7993–8008.

Talebi, S., Young, R.P., Vandamme, L. and McGaughey, W.J. 1991. Microseismic Mapping of a Hydraulic Fracture. *Proc. 32nd U.S. Symposium on Rock Mechanics*, July 10–12, Norman, Oklahoma, Publisher A.A. Balkema, Rotterdam, Paper 91-461.

Thallak, S., Rothenburg, L. and Dusseault, M.B. 1991. Hydraulic fracture simulation in granular assemblies using the discrete element method. *AOSTRA J. of Research*, 141–153.

Tourtelot, H.A. 1979. Black Shale–Its Deposition and Diagenesis 1. *Clays and Clay Minerals* 27(5), 313–321.

Wang, G., Dusseault, M.B., Rothenburg, L. and Pindera, J. 1994. Influence of Subsurface Fractures on Surface Deformation of an Elastic Half-space. *Int. J. of Analytical and Numerical Methods in Geomechanics*, 18, 287–303.

Wang, Y. and Dusseault, M.B. 1991a. Borehole yield and hydraulic fracture initiation in poorly consolidated rock strata – Part I. Impermeable Media, *Int. J. Rock Mechanics Mining Science and Geomechanical Abstracts 28*, 235–246.

Wang, Y. and Dusseault, M.B. 1991b. Borehole yield and hydraulic fracture initiation in poorly consolidated rock strata – Part II. Permeable Media, *Int. J. Rock Mechanics Mining Science and Geomechanical Abstracts 28*, 247–260.

Warpinski, N.R. and Teufel, L.W. 1987. Influence of Geologic Discontinuities on Hydraulic Fracture Propagation (includes associated papers SPE #17011 and #17074). *J. of Petroleum Technology* 39(2), 209–220.

Warpinski, N.R., Branagan, P.T., Peterson, R.E., Wolhart, S.L. and Uhl, J.E. 1998. Mapping Hydraulic Fracture Growth and Geometry Using Microseismic Events Detected by a Wireline Retrievable Accelerometer Array. *Proc. SPE Gas Technology Symposium*, Calgary, Alberta. SPE #40014.

Rock Mechanics for Resources, Energy and Environment – Kwaśniewski & Łydżba (eds)
© 2013 Taylor & Francis Group, London, ISBN 978-1-138-00080-3

An overview of underground rock engineering risk

J.A. Hudson
Department of Earth Science and Engineering, Imperial College, London, UK

ABSTRACT: The paper begins by noting that many of the contributions to the EUROCK2013 Symposium deal directly with risk. An explanation of epistemic and aleatory uncertainty then follows with further notes on risk analysis techniques and 'black swan' events. Three illustrative rock engineering application examples are discussed in some detail: shale gas extraction, CO_2 storage, and radioactive waste disposal—with the emphasis being on successfully achieving the project objectives. The paper concludes with ten recommendations, concentrating on the further development of the subjects of uncertainty and risk as they apply to rock mechanics and rock engineering. Especially important is the need to validate coupled numerical modelling and to make the programs more accessible to practitioners. This, together with the wider application of the techniques used for the design of radioactive waste repositories, will significantly reduce the impact of uncertainties and risks inherent in all rock engineering modelling, design and construction.

1 INTRODUCTION

1.1 *Uncertainty in rock engineering modelling, design and construction*

In order to be able to coherently design an underground rock engineering project, one has to be able to predict the future. For example, what will happen when a tunnel of this diameter, at this depth, excavated in this direction, in this rock mass, is constructed? Will rock blocks fall into the tunnel, will the concentrated rock stress damage the tunnel, will the tunnel encounter any major faults? If one is unable to answer questions such as these, indicating that the future cannot be predicted, the design of the project is subject to some level of uncertainty and risk. Since, we cannot yet obtain full information about any rock mass, all rock engineering projects are subject to uncertainty and hence risk. Reduction of the risks is directly related to reduction of the uncertainties and so, for improved rock engineering design, we must concentrate on the uncertainties involved. In the worst case, lack of attention to this subject could endanger lives and prejudice the functionality of the completed project.

1.2 *Risk in the topics discussed in the EUROCK2013 papers*

There are risks in all aspects of rock engineering projects, as is illustrated by the list of topics covered by this EUROCK2103 Symposium: i.e., rock mass characterisation, laboratory and *in situ* testing, constitutive models and numerical modelling, mathematical modelling of T-H-M processes in rocks, mine design and ground control, petroleum rock mechanics, geological CO_2 sequestration, underground storage and waste disposal, slope and open pit stability, dynamic phenomena in rock masses, new materials and technologies in geo-engineering, design methodology in rock engineering, mechanical breakage of rocks, and rock tunnel excavation and support.

This paper focusses on the physical uncertainties and hence risks that are related to underground rock engineering (as opposed to the associated financial risks) and hence has strong links with the subjects of the other five Keynote lectures at this Symposium: by P. Berest on rock salt rheology, J. Dubiński on mining tremors in hard coal and copper mines, M. Dusseault on shale gas exploitation, H. Konietzky on design optimisation, X. Li on underground carbon dioxide storage and the topic of the 2013 ISRM Franklin Lecture given by A. Goricki.

Uncertainty has a ubiquitous presence in all the aspects of rock engineering from initial conceptright through to the use of the finished facility. Aspects of the uncertainty and risk subjects are explicitly covered in several papers at this Symposium, as evidenced by the following titles: "Characterisation and propagation of epistemic uncertainty in rock engineering: a slope stability example" by A. Bedi and J. P. Harrison; "Risk management approach for the design of underground constructions" by B. Amusin and J. Eisenberg; "Control of rockburst risk in hardcoal longwall mining—a case study" by P. Koníček, R. Kukutsch, J. Ptáček, K. Souček, L. Staš and P. Waclawik; "The residual risk of an abandoned mine" by D. Brambilla, L. Longoni, M. Papini, D. Arosio and L. Zanzi; "Protection of a tunnel entrance from rockfall risk" by C. Mignelli, K. Daneshmand and D. Peila.

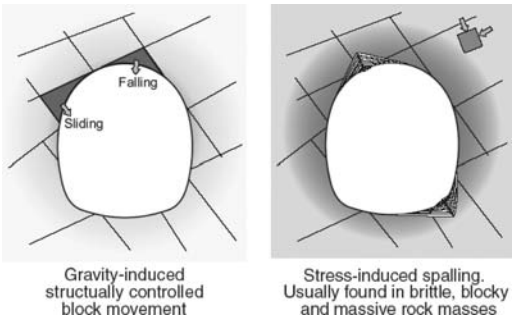


Figure 1. Rock block falls and stress-induced damage (from D. Martin).

1.3 *The current work of the International Society for Rock Mechanics (ISRM) Design Methodology Commission*

Over the last 50 years of the ISRM and elsewhere, a great deal has been achieved in understanding the hazards encountered during underground construction (Brown, 2012a). In particular, we now know much more about the potential for rock block falls and damage induced by the concentrated *in situ* stress (Figure 1) and predictions of these events have been considerably improved. However, other aspects, such as the likelihood of encountering major water inrushes or whether the completed construction work will in fact fulfil the functional project objective can be much more problematic.

During the period 2007–2011, the ISRM Design Methodology Commission researched many subjects relating to the design of rock engineering structures, including the ways ahead for rock engineering design methodologies, flowcharts for the associated modelling and design, the related information required, technical auditing of the modelling and design, and applied the results to a large surface project and a large underground project. The work resulted in the book "Rock Engineering Design" (Feng & Hudson, 2011).

During the current 2011–2015 ISRM Presidential period, the themes of the Design Methodology Commission are uncertainty and risk in rock engineering. We are concentrating on the concepts of epistemic and aleatory uncertainty, and the implications for the various phases of rock engineering, particularly site investigation, modelling, design and construction.

* * * * *

The purpose of this paper is to discuss underground rock engineering risk by highlighting the uncertainty and risk concepts and describing three rock engineering applications relating to achieving the overall project objective: the process of shale gas extraction; the storage of CO_2 gas; and the design of an underground radioactive waste repository.

2 UNCERTAINTY AND RISK

2.1 *Books relating to rock engineering risk*

There are many books on the subject of risk, dealing with both the subject of risk in general and risk directly connected with rock engineering. The following useful general books on the subject of risk are highlighted: "Risk" by Adams (2001); "A Practical Guide to Risk Management" by Coleman (2011); and "Fundamentals of Risk Management" by Hopkin (2012). There are also books directly or indirectly relating to rock engineering/geotechnical risk: "Risk and Reliability in Ground Engineering" edited by Skipp (1994); "Managing Geotechnical Risk" by Clayton (2001); "Geotechnical Risk in Rock Tunnels" edited by Campos e Matos, Ribeiro e Sousa, Kleberger& Lopes Pinto (2006); "Geotechnical Baseline Reports for Construction" by Essex (2007); and "Risk Management for Design and Construction" by Cretu, Stewart and Berends (2011).

In his book "Risk", Adams (2001) notes in the wider risk context that, "Rarely are risk decisions made with information that can be reduced to quantifiable probabilities." This is also true in rock engineering because of the difficulties of both the epistemic and aleatory uncertainties inherent in understanding and quantifying the variability of rock masses and their response to engineering perturbations. Adams refers to the Royal Society (1983, 1992) reports on risk assessment highlighting the differences of opinion between physical and social scientists concerning the nature and meaning of risk. These reports define risk as the probability that a particular adverse event occurs during a stated period of time, and distinguish between objective and perceived risk.

2.2 *Two types of uncertainty: epistemic and aleatory*

The understanding of uncertainty is clarified through consideration of the two types of uncertainty, epistemic and aleatory, which are characterised by their distinct features, as listed in Tables 1a and 1b.

Thus, epistemic uncertainty, e.g., relating to lack of fundamental knowledge about the rock conditions, can be reduced through systematic structural geology studies, site investigation and during the construction itself. On the other hand, aleatory uncertainty, e.g. when the next water inrush will occur, relates more to specific difficult-to-predict factors.

Kahyaoglu (2012) provides an intriguing tunnelling example—which has been slightly modified by the current author—of reduction in epistemic uncertainty through structural geology understanding. Consider that a tunnel is being driven from right to left in Figure 2. At chainage point A, all is going well with steeply inclined strata being intersected. The same conditions are still encountered at point B, but at point C conditions worsen and there are roof falls. This continues until point D when steeply inclined strata are again encountered—but these are at a different orientation.

Table 1a. The characteristics of epistemic uncertainty.

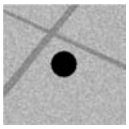
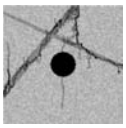
Epistemic Uncertainty
Relating to knowledge, from the Greek, *episteme,* for knowledge
Subjective uncertainty, reducible uncertainty
Due to lack of knowledge of processes or quantities in the rock engineering system
Reducible through further investigation
Reducible through expert information
Generally has one value, but this is not known
Conceptually resolvable
Can be expressed as a 'degree of belief' probability distribution (Bayesian approach)
Sensitivity analysis can reduce epistemic uncertainty
Relates to assumptions made about rock mechanics processes in the computer model. For example, the inclusion of fractures when studying the stresses around a circular hole in an inhomogeneous rock.
 Numerical model, vertically applied stress  Failure induced by hole and fractures
Example: Lack of understanding of coupled phenomena, lack of data
Example: What type of geological structure will be encountered by the tunnel?
Example: Will an earthquake damage the tunnel?
Problem: Knowing all the factors involved

Table 1b. The characteristics of aleatoryuncertainty.

Aleatory Uncertainty
Dependent on chance, an uncertain outcome, from the Latin, *alea,* game of chance, dice
Random uncertainty, irreducible uncertainty
Due to chance, intrinsic randomness in the rock engineering system
Modelled via probability, statistics
Not reducible through expert information
Generally has more than one value
Conceptually not resolvable
Usually expressed as a probability density or cumulative distribution function
Sensitivity analysis can reduce aleatory uncertainty using probability density functions
Relates to varying the material parameters in the computer model, e.g. the background variation in the rock micro-/meso-structure following, e.g., the Weibull probability density distribution, as in the numerical model below.

Example: Variability in fracture density, variation in life of tunnel boring machine cutters
Example: At exactly what chainages will water-bearing fractures be encountered by the tunnel?
Example: When will the next earthquake occur?
Problem: Appropriately representing variability
Both epistemic and aleatory uncertainties are unavoidable and ubiquitous in rock engineering projects
Both epistemic and aleatory uncertainty reduce as construction proceeds

The geological advice is now updated with the information *that a box fold is being traversed*, indicating that future tunnelling conditions will now revert to be similar to those encountered in the A–B region. At point D, knowledge of the rock structural conditions has been significantly enhanced, epistemic uncertainty has been reduced, and the rest of the tunnel length becomes a risk that can be identified and quantified from the knowledge gained. This was not the case at the earlier points A and B. This example illustrates the point in the last row of Table 1b—that both epistemic and aleatory uncertainty reduce as construction proceeds.

2.3 *Risk analysis techniques*

The subjects of risk and the risk analysis techniques available have recently been highlighted in the paper by E. T. Brown (2012b) on "Risk assessment and management in underground rock engineering—an overview". Brown provides "brief overviews for some of the risk analysis and evaluation tools that are commonly used in geotechnical engineering and tunnelling, and may be suitable for use in large underground construction projects", specifically fault tree analysis (FTA), event tree analysis (ETA), consequence or cause-consequence analysis, bowtie diagrams, probabilistic risk analysis (PRA), decision analysis, multi-risk analysis, analytical hierarchy process (AHP), Bayesian networks, and fuzzy logic and other artificial intelligence (AI) methods. Brown (2012) notes that, "It is important to recognise that in geotechnical engineering, including in underground rock engineering, many of the risk sources or hazards arise from geotechnical uncertainty or error". The risk subject is continuing to be studied in the context of different applications, e.g., the paper by Barton (2012) on "Reducing risk in long deep tunnels by using TBM and drill-and-blast methods in the same project—the hybrid solution".

In the overview paper, "Rock engineering, uncertainty and Eurocode 7: implications for rock mass characterisation", by Harrison (2012), the subjects of epistemic and aleatory uncertainties, interval analysis, fuzzy numbers, probability boxes, Bayesian statistics, selecting the uncertainty model, EUROCODE 7 and



Figure 2. Example of reduction in epistemic uncertainty as a tunnel is being driven, with the full structural geology context becoming apparent at chainage point D.

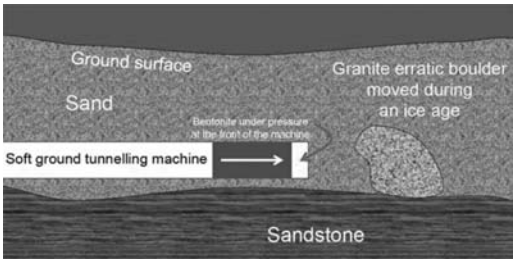


Figure 3. 'Black Swan' event: a large granite boulder unexpectedly encountered by a shallow soft ground tunnelling machine in the UK.

limit state design, and rock mass characterisation are described. Harrison and Hadjigeorgiou (2012) further discuss the challenges in selecting appropriate input parameters for numerical models and conclude that, ". . . not only does the challenge of obtaining appropriate input parameters remain, it may even be growing due to the increased sophistication of numerical techniques."

2.4 *'Black Swan' events*

Another aspect is the occurrence of either highly unlikely and/or completely unexpected conditions and/or events.In his book, "The Black Swan: The Impact of the Highly Improbable", Taleb (2007, 2010) points out that there can be outliers which are not included in probability distributions—the Black Swan events that lie "outside the realm of regular expectations". They have low predictability together with large impact and represent our epistemic knowledge limitation.

One such event is illustrated in Figure 3. A soft-ground tunneling machine with pressurisedbentonite at the face excavating through sand in the UK unexpectedly encountered a large granite boulder, resulting in considerable machine damage and difficulty. The tunnel was just above an old land surface on which the erratic boulder had come to rest after being transported there in earlier geological times by a glacier.

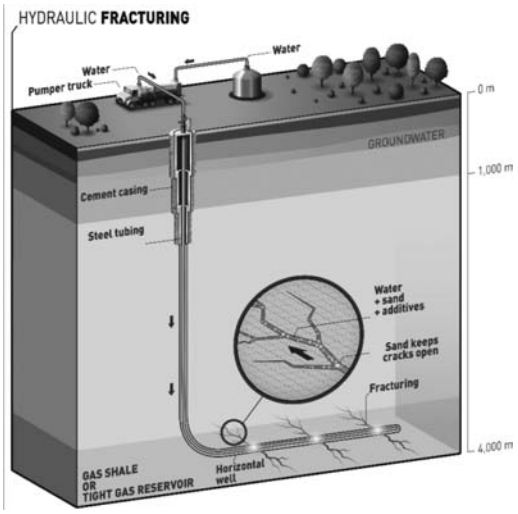


Figure 4. The process of extracting shale gas at depth via hydraulic fracturing of the strata (from http://www.skifergas.dk/en/technical-guide/what-is-hydraulic-fracturing.aspx).

Another such Black Swan event, perhaps more related to regulations but still completely unexpected, occurred in January 2013 when 27 tonnes of brown cheese caught fire when being transported by truck through the Brattli Tunnel in Tysfjord, Norway (Tunnels and Tunnelling, 2013). Brown cheese is made from whey containing up to 30% fat which caused the fire to last for five days and toxic gases to fill the tunnel. The Black Swan aspect of this event is that "Since such foodstuffs are not 'dangerous goods' they do not fall within the Sixth Issue of the ADR Directive Road Tunnels controls but, in reality, they can present a far more likely tunnel fire hazard than do petrochemical fuels." KjellBjoernVinje, of the Norwegian Public Roads Administration, said it was the first time he could remember cheese catching fire on Norwegian roads. The accident occurred near one of the tunnel exits and no one was injured.

* * * * *

3 ROCK ENGINEERING APPLICATION EXAMPLE 1: SHALE GAS EXTRACTION

3.1 *Extraction of shale gas by hydraulic fracturing*

Shale gas, i.e., methane, is sometimes present within shale deposits—in the natural fractures, within the rock pores, and adsorbed onto organic material. Some of this gas will have already escaped but much of it remains in the shale strata which have a relatively low permeability. In order to extract the methane, this permeability has to be increased by the creation of additional fractures formed by hydraulic fracturing, a process known as 'fracking', Figure 4.

The use of hydraulic fracturing is well known in rock mechanics studies through its use in rock stress

measurement, both for fracturing intact rock and for opening pre-existing fractures, to provide estimates of the stress tensor components. However, in the present context, the purpose is to provide a set of fractures within the rock mass to enable the methane to escape and be collected, hopefully under controlled engineering circumstances. Water, sand and chemicals are pumped under high pressure into the production well creating fractures which can extend hundreds of metres into the shale formation, with the injected sand holding the fractures open. Depressurising the well then allows the shale gas to travel to the surface.

There are large resources of shale gas in the world, with, in order of the magnitude of their resources, China, USA, Argentina, Mexico, S. Africa, Australia and Canada having the most. The UK does not have a large resource in comparison to these countries (although its value is currently estimated to be £1.5 trillion), but this is more than enough for economic production to be considered and to have stimulated a joint Royal Society/Royal Academy of Engineering RS/RAE report (2012). In the UK, the gas belongs to the Crown Estate.

3.2 *Risks associated with shale gas extraction*

Environmental concerns relating to shale gas production have been expressed by many organisations, especially with regard to global warming (because methane has a greater global warming potential than carbon dioxide), contamination of ground water and hence drinking supplies, and seismic events. Malin (2012) in a Talking Point feature in Ground Engineering considers the uncertainties and risks involved in 'fracking' and notes that controlling the impacts is a function of the predictability of an individual 'fracking' activity. He notes that, "... fracking' is controlled primarily by natural fractures and these do not lend themselves to any type of average description. As a consequence, local physical property measurements at a given site do not predict anything about a nearby one, even though the two sites might be geologically and mechanically connected." In other words, this is both aleatory and epistemic uncertainty. He goes on to say that, "Even taking into account obvious factors such as sub-surface depth and rock type, the erratic nature of fracture flow paths renders frack-drive flow improvement and leak avoidance unpredictable."

This means that the actual extraction operation needs to be adequately controlled. For example, the surface operation should ensure that there are no significant spills of the water-based fracturing fluid (which contains additives). This is accomplished by the use of an impermeable site lining. Similarly, the series of casings in the well itself must be sufficient for the purpose (the conductor casing near the ground surface, the 'surface' casing that isolates the well from any fresh groundwater, the intermediate casing that isolates the well from non-fresh water, and the production casing itself which is installed into the production strata). The risk of blowouts is rare for shale gas wells because the shale strata have a low permeability.

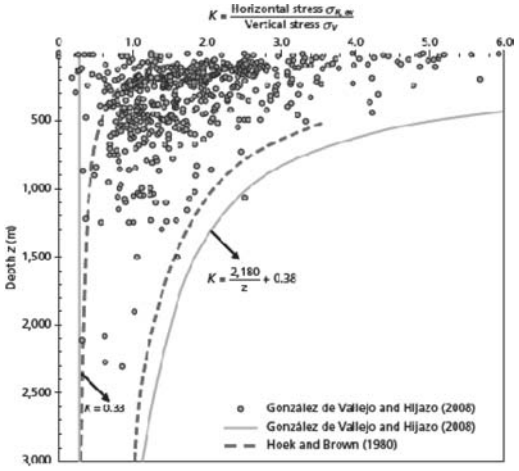


Figure 5. Variation in the relation between the mean of the horizontal stress components and the vertical stress component (from Gonzalez de Vallejo and Ferrer, 2011).

The development and orientation of rock fractures initiated by the hydraulic fracturing process (and which can be seismically monitored) depends to a large extent on the rock stress at the shale strata location. Near the surface, rocks tend to have the greatest stress component acting horizontally but, as the depth increases, so does overburden and hence the vertical stress component, so that eventually the vertical stress component exceeds the horizontal stress component (Figure 5).

From Figure 5, and assuming that fractures propagate perpendicular to the least principal stress (following the least work principle), we would expect horizontal fractures to develop near the surface, where the horizontal stresses tend to be high compared to the vertical stress, $k > 1$, and vertical fractures to develop below that. However, it should be remembered that the magnitude and orientation of the *in situ* stresses are a function of the local geology, especially the presence of any major discontinuities such as faults, see Figure 6. Although the mod-elling illustration in Figure 6 refers to a depth of only 150 m, such stress perturbations can occur at any depth depending on the nature of the geological discontinuities. Fracturing at one site in the UK (Bowland trough) occurred at 1700–3100 m where we could expect the vertical and horizontal principal stresses to be similar.

The fractures produced by the fracking process may be irregular because of the rock mass inhomogeneity, but the idea is to maximise the fracture surface area. Various techniques are used to maximise this fracture area, given the nature of the shale formation. At present, the environmental regulator does not permit fracturing below freshwater aquifers. The other concern relating to hydraulic fracturing is that it could cause seismicity. Naturally, the fracturing process itself will induce low intensity seismicity; the danger is that it will reactivate an existing fault causing an earthquake, as is thought to have occurred during

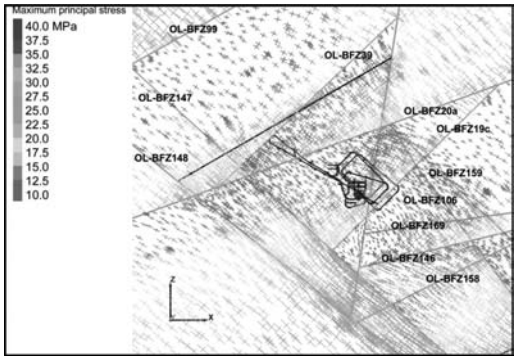


Figure 6. Computer simulation of the variation in the maximum principal stresses at a depth of 150 m in the gneissic rocks at Olkiluoto, western Finland, as affected by brittle fault zones, the OL-BFZ features in the display (from Valli *et al*., 2012).

exploitation of the Bowland shale in the UK. However, and in the context of hydraulic fracturing in shale formations, there are several factors mitigating against the stimulation of a large earthquake—mainly that the shale is a relatively weak rock, the volume of rock involved is relatively small, and the pressure of the hydraulic fracturing fluid is limited, controllable, and only sustained for a relatively short time.

3.3 *The approach to risk management of shale gas extraction*

In 2012, a study of the safety of shale gas extraction using hydraulic fracturing was completed jointly by the Royal Society and the Royal Academy of Engineering (RS/RAE 2012). The report, stimulated by the risks associated with this engineering process, discusses the many aspects of the subject and specifically addresses "the major risks associated with hydraulic fracturing as a means to extract shale gas in the UK, including geological risks, such as seismicity, and environmental risks, such as groundwater contamination." The report also considers whether and how these risks can be effectively managed. Although this report was written in the UK context, its explanations and conclusions apply generally to the fracking process.

The RS/RAEng (2012) report highlights the Offshore Installations and Wells Regulations 1996 as follows: they state that wells should be designed and constructed so that 'as far as is reasonably practicable, there can be no unplanned escape of fluids from the well; and risks to the health and safety of persons from it or anything in it, or in strata to which it is connected, are as low as is reasonably practicable'. The report also mentions the need to develop a more 'goal-based approach to environmental protection': "Operatorsare forced to identify and assess risks in a way that fosters innovation and continuous improvements in risk management". This has advantages over a prescriptive approach based upon standards which "tends to support routine practices and limit innovation in risk management". The report also states that, "Operators should also ensure mechanisms are put in place to audit their risk management processes"—which is directly in line with the auditing procedure recommended by Feng & Hudson (2011) for all rock engineering design and construction work, as developed during the 2007–2011 period of the ISRM Design Methodology Commission.

The RS/RAE report (2012) makes two important recommendations: "To manage environmental risks:

- an Environmental Risk Assessment (ERA) should be mandatory for all shale gas operations, involving the participation of local communities at the earliest possible opportunity; and
- the ERA should assess risks across the entire lifecycle of shale gas extraction, including the disposal of wastes and well abandonment. Seismic risks should also feature as part of the ERA."

The first recommendation, to involve the participation of local communities at the earliest possible opportunity, which might not be the first aspect being considered during a technical evaluation, is particularly important—as radioactive waste implementers have found to their cost in different countries over the years. The second recommendation, to consider the entire lifecycle, is also important as this then includes all environmental factors.

The RS/RAE report (2012) goes on to recommend that, "Co-ordination of the numerous bodies with regulatory responsibilities for shale gas extraction should be maintained. A single body should take the lead. Consideration should be given to: clarity on roles and responsibilities; mechanisms to support integrated ways of working; more formal mechanisms to share information; joined-up engagement of local communities; and mechanisms to learn from operational and regulatory best practice internationally." The report concludes that more research is required to address the uncertainties involved in both exploratory and production activities, and discusses research funding options.

* * * * *

This case study of shale gas extraction has also highlighted the need in a risk assessment for a 'corporate memory' of existing data and experiences as baseline information for the design of extraction. In the context of understanding the evolution of the shale gas extraction process, the example further reinforces the need for an integration of the relevant technical subjects, e.g., structural geology, rock mechanics, fluid flow, coupled numerical modelling, etc., when developing the design. In terms of the practicalities of risk evaluation, a more 'goal-based approach to environmental protection' has been recommended. Additionally, a technical and operational auditing procedure should be implemented concurrently with the various stages of the process, from concept to abandonment. All these aspects assist in reducing the uncertainty and hence risk.

4 ROCK ENGINEERING APPLICATION EXAMPLE 2: UNDERGROUND CARBON DIOXIDE STORAGE

'*sequester*':
1. To cause to withdraw into seclusion.
2. To remove or set apart; segregate
(from www.thefreedictionary.com)

4.1 *The purpose of underground carbon dioxide storage*

The purpose of storing carbon dioxide in the ground is to 'create a closed carbon loop', i.e., to return the carbon generated by the use of fossil fuels back into rock masses. Whilst the exact reasons for climate change are subject to debate, there is no question that the release of significant quantities of carbon dioxide into the atmosphere and subsequently the oceans must have some effects. For this reason, the underground sequestration of carbon dioxide is being promoted and researched. The proposal is that the CO_2 should be captured at coal- and gas-fired power stations and other industrial facilities such as cement plants, transported to a storage location, and then injected into a rock mass for long-term storage.

Considerable research has already been undertaken in assessing the viability of the concept in different geological formations, in identifying suitable geological formations in different countries, in computer modelling of such storage, and in pilot storage schemes. In addition, and because CO_2 emission is of global concern, networks have been established to co-ordinate related information and research results, e.g. the European Commission's CO_2GeoNet European Network of Excellence.

Because the proposal is to store the CO_2 underground and hence perturb the rock mass, there are risks associated with such a storage concept—in a similar manner to shale gas extraction, except that, for CO_2 storage, a material is being injected into the rock mass rather than being extracted from it. In both cases, the rock stresses are being anthropogenically altered and the overall entropy level is being increased with the associated risks. In this Section on CO_2 storage, the principle will be explained first and then the potential risks discussed.

4.2 *The principle of underground carbon dioxide storage*

To store the CO_2 underground, it is cheaper to utilise naturally occurring containment such as a depleted gas/oilfield, a saline aquifer, or another type of natural trap such as a dome formed by folded rock strata having a relatively impermeable cap rock and an absence of faulting, see Figure 7.

As illustrated in Figure 7, the relatively impermeable caprock traps the CO_2 within the rock mass. There are also subsidiary effects such as trapping of the CO_2 in small pores, dissolution in which some CO_2 becomes dissolved in water which sinks, and mineralisation in which, for example, the presence of the CO_2 can lead to precipitation of calcite.

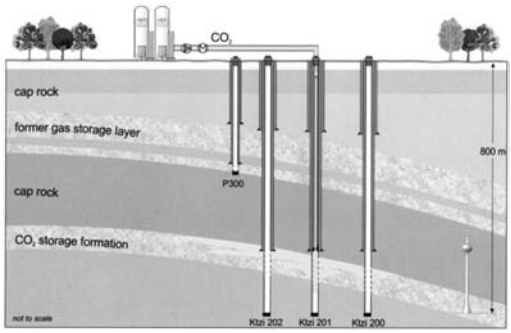


Figure 7. Underground storage of CO_2 beneath an impermeable caprock stratum (from GFZ German Research Centre for Geosciences). The two deep boreholes to the left and right of the injection borehole are observation boreholes. For scale, the 368 m high Berlin television tower is included at the lower right.

4.3 *The Ketzin Pilot Site for CO_2 disposal*

At Ketzin, near Potsdam west of Berlin in Germany, an *in situ* pilot scale experiment operated by the GFZ German Research Centre for Geosciences has been underway since 2008. The purposes of the experiment have been to "improve the scientific understanding of the geological storage of CO_2, and to study the sub-surface processes of the CO_2 injection and distribution". The CO_2 has been injected at 650 m into porous sandstone of the Stuttgart formation which is locally in the shape of a dome and below a 210 m thick shalycaprock, see Figure 7. More than 50,000 tonnes have been injected. The CO_2 storage tanks can be seen in Figure 8. Seismic measurements and numerical computer simulation models support the pilot scale experiment and enable assessments of the distribution of the injected CO_2.

4.4 *The risks in storing carbon dioxide*

There are two main categories of risk associated with the general underground storage of CO_2: the CO_2 could leak from the site; and the alteration of the pressure within the reservoir and hence the stress state within the surrounding rock mass could lead to earthquakes (Figures 9 & 10). Leakage from the reservoir requires a pathway—which could be natural, through one or more major fractures in the overlying strata, or man-made through the injection and other wells. Such leakage could be locally dangerous to humans if the resultant CO_2 concentrations are sufficiently high. Naturally, the prime CO_2 storage function of the reservoir could be prejudiced if such leakage occurs. However, leakage should not occur if the site is sufficiently well geologically understood and if care has been taken with the engineering procedures.



Figure 8. Large cylindrical CO_2 storage tanks (visit to the Ketzin CO_2 pilot site by members of the DECOVALEX project, 2012).

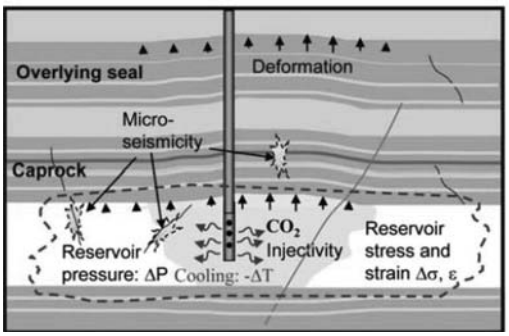


Figure 9. Injection-induced stress, strain and deformation resulting from CO_2 injection into rock strata (from Rutqvist, 2012).

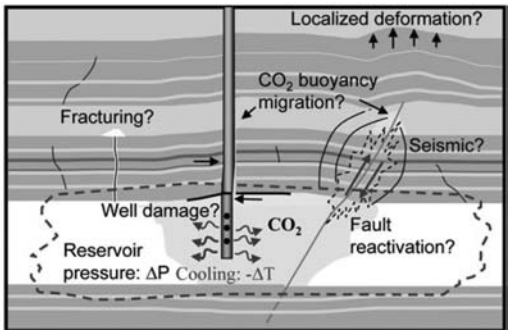


Figure 10. Unwanted mechanical changes resulting from CO_2 injection into rock strata (from Rutqvist, 2012).

The injection of fluids and CO_2 into rock formations during fracking and sequestration processes and the consequential alteration of the natural rock stresses can lead to 'earth tremors', which has been experienced in Lancashire in the UK. In a paper on "Earthquake triggering and large-scale geologic storage of carbon dioxide", Zoback and Gorelick (2012) argue that, ". . . there is a high probability that earthquakes will be triggered by injection of large volumes of CO_2 into the brittle rocks commonly found in continental interiors. Because even small- to moderate-sized earthquakes threaten the seal integrity of CO_2 repositories, in this context, large-scale CCS is a risky, and likely unsuccessful strategy for significantly reducing greenhouse gas emissions." However, this view has been challenged on the basis that experience from injection activities worldwide related to oil and gas, geothermal, waste disposal and storage operations does not show the triggering of large scale earthquakes or the breach of cap rock integrity, and that the possibility of breaching the seal by injection of CO_2 is a risk factor that is routinely assessed in both the preliminary characterisation of storage sites and in the risk management plan that drives the lifecycle of a storage project. Thus, a potential injection site that was found to have a significant risk will not therefore proceed to development in any case. However, in Europe, where country sizes are smaller than the USA and the areal population densities much higher, any earth tremors are more likely to be felt and have a strong psychological effect on the population—and hence on the granting of any future permissions for fracking or CO_2 storage.

In terms of the design life of a CO_2 storage reservoir, we note that the design life of rock engineering projects varies within the spectrum of a few days to a million years, depending on the project. In a longwall coal mine in which an advancing face where the coal is being extracted moves forward, the superincumbent strata behind the advancing face are designed to collapse so that the region in the immediate vicinity of the face can remain open and move forward with the advancing face. Thus, at any particular time, the opening at the coal face should only remain clear for a few days. At the other end of the spectrum, the design life of a repository for underground disposal of radioactive waste is based on the criterion that unacceptable quantities of radionuclides should not return to the biosphere and the regulators of such a facility can recommend a design life of a million years (see Section 5). Within this extremely wide time spectrum, what should be the design life of a CO_2 storage reservoir?

The main steps in such a storage project (see the CO_2GeoNet) are site selection, site characterisation, storage design and construction, injection operations and site closure—a period of about 45 years—but how long should the monitored post-closure design phase be? In the case of radioactive waste disposal, the objective is to ensure safe *disposal*, i.e., no monitoring should be required. Can we apply this philosophy to the underground disposal of CO_2 or do we need to continuously monitor the disposal facility for escaping CO_2 via one of the potential escape mechanisms illustrated in Figure 11?

Wilson *et al*. (2003) reviewed the risks and regulatory history of deep underground injection on the U.S. mainland and the surrounding continental shelf. They focus on geological sequestration implemented by injecting CO_2 into porous sedimentary formations

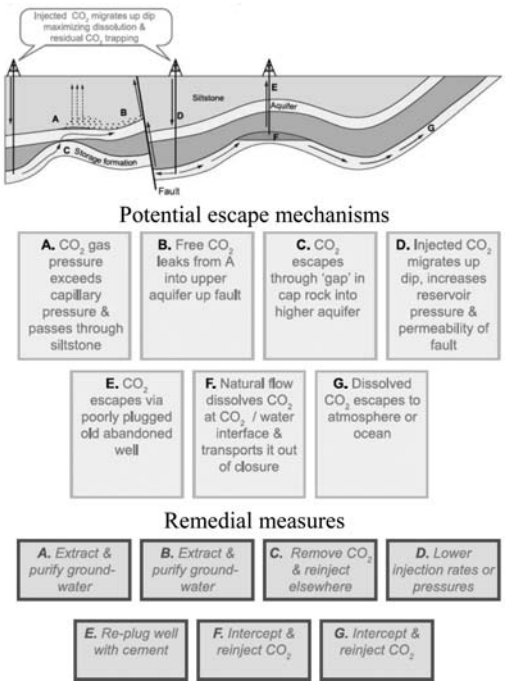


Figure 11. Some potential escape routes for CO_2 injected into saline formations and the associated remedial measures (from Metz *et al*., 2005).

deeper than one kilometer using drilling and injection technologies derived from the oil and gas industry. They state that, "At almost all plausible injection sites, CO_2 will be less dense than the displaced brines, so buoyancy-driven flow will carry the CO_2 upward until it rests against the underside of Low permeability cap-rock."

* * * * *

This case example of CO_2 storage, like the previous case example of shale gas extraction, has highlighted the risks involved and, in this CO_2 case, particularly in terms of whether the project objective can be successfully achieved. There are powerful arguments both for and against the ability to successfully store CO_2 underground, but the way forward must be to enhance the understanding of the risks and their mitigation, and the implementation of the aspects mentioned at the end of Section 3.

5 ROCK ENGINEERING APPLICATION EXAMPLE 3: DESIGN OF AN UNDERGROUND REPOSITORY FOR RADIOACTIVE WASTE DISPOSAL

5.1 *The unique combination of characteristics of an underground radioactive waste repository*

The ultimate example of a long design life in underground rock engineering projects is a repository for the disposal of radioactive waste. Moreover, the design of

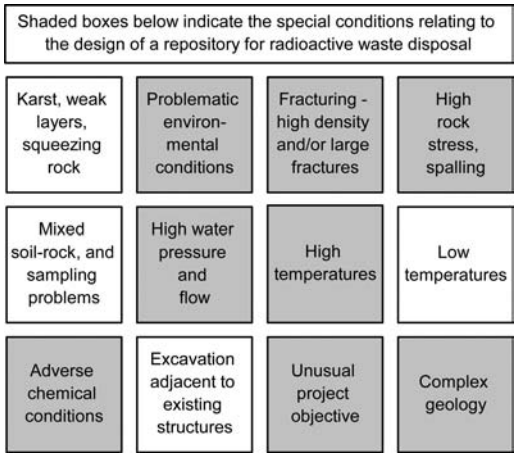


Figure 12. Some of the rock engineering special conditions (shaded) which are associated with designing a repository for radioactive waste disposal.

such a repository involves an unusual combination of factors because

- from a *technical* point of view, the repository can be located anywhere suitable, as opposed to other structures such as transport tunnels and mines which have to be located in specific places,
- the function of the repository is that of isolation of the waste, i.e., there is no active function such as, for example, transport of people or ore extraction,
- the design involves understanding the coupled geological-thermal-hydrological-mechanical-chemical-biological processes to a much greater degree than for other rock engineering projects, and
- the design life of the repository is measured in hundreds of thousands of years.

Within a presentation of some of the special conditions that can be involved in rock engineering design, some of the special conditions for the case of radioactive waste disposal are highlighted by the dark squares in Figure 12.

The key to the design of such a repository is that unacceptable quantities of radionuclides should not migrate from the repository to the biosphere. This means that, in the case of a repository for high-level waste, the regulators insist on designing for a very long period, i.e., of the order of one million years. There are many ramifications of this, not least are that all the possible features, events and processes (FEPs) must be evaluated, much more site investigation is required (e.g., 50 km of cored boreholes at a potential site), and that the supporting design programme from concept to approval can take 20–30 years.

In order to be able to predict the potential migration of radionuclides over such a long time period, it is necessary to understand and be able to characterise the hydrogeologically connected fracture network. The repositories are anticipated at depths of ~400–500 m (e.g., Figure 13) which means that there will be a

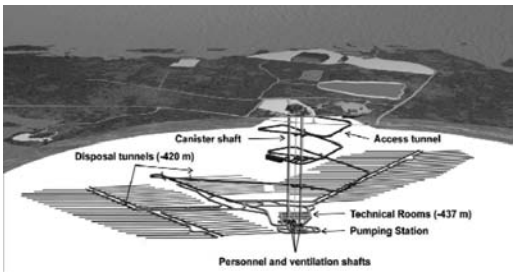


Figure 13. The layout of a radioactive waste repository, as illustrated by one of PosivaOy's schemes at the Olkiluotosite in Western Finland (from PosivaOy, Finland).

high rock stress compared to other civil engineering projects and rock spalling then becomes a possibility. The same applies to the water pressure at these depths. High-level waste is significantly heat emitting so that, after a period of ~50–100 years, the maximum thermal load can induce additional rock stresses of the order of 25 MPa and hence further spalling of the excavations. Also, given the long design life, it is necessary to be able to model long-term effects, which then include chemical effects.

5.2 *The design process*

Needless to say, all these aspects cannot be simulated in one computer model; nor can the results of individual sub-models be validated (i.e. confirmed by the actual rock behaviour) because of the long design life required. Accordingly, the repository design has to be based on a systems overview methodology.

There are two main rock engineering design aspects: developing a design that will ensure safe disposal; and developing the construction operations for excavation and disposal. In terms of the rock mechanics contributions, these aspects include the following:

- obtaining the rock properties at the chosen site (*in situ* stress, intact rock, fractures, thermal properties, etc.);
- using/developing coupled numerical models to assess the effects of different design options;
- designing the underground excavations, given the characteristics of the site and the required openings;
- understanding the short- and long-term results of excavation; and
- understanding the short- and long-term effects of the disposal of radioactive waste at elevated temperatures, i.e., up to 100°C.

There will have to be extensive *in situ* and laboratory tests. Additionally, an underground research laboratory (URL) is generally required so that tests can be conducted on a representative scale, see Figure 14.

5.3 *Validation of numerical models*

Also, and because much of the support for the design of an underground radioactive waste repository is

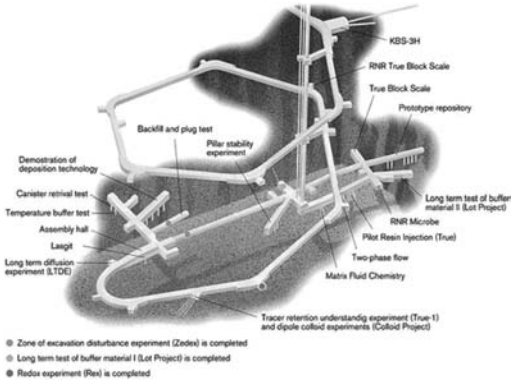


Figure 14. The Äspö Hard Rock Laboratory in Sweden and the many experiments conducted therein (from SKB, Sweden).

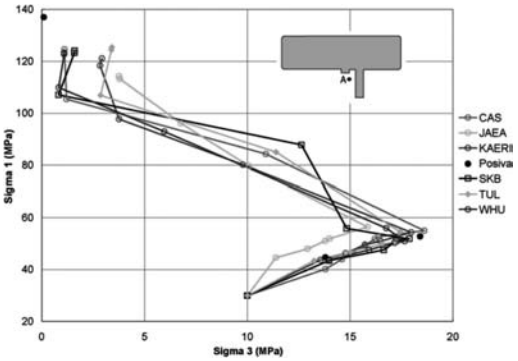


Figure 15. Modelling the stress path during excavation—by seven different international teams from China, Japan, Korea, Finland, Sweden, Czech Republic, and another from China (from the DECOVALEX programme).

provided through thermo-hydro-mechanical-chemical coupled numerical modelling, it is crucial to ensure that the modelling is reproducible and has been technically audited. This is to check that all the necessary factors are included and that the technical work is correct within the limits of the site information and current scientific knowledge.

An interesting approach to establish the reproducibility of numerical modelling was conducted within the 2007–2011 phase of the DECOVALEX research programme (DEmonstration of COupled models and their VALidation against EXperiment). In this Test Case example, the principal stress alterations caused by excavation of two small diameter shafts at the Äspö Hard Rock Laboratory in Sweden (Figure 15) were numerically modelled by separate teams from China, Japan, Korea, Finland, Sweden, Czech Republic, and another from China and compared with the actual results. As is evident from Figure 15, the stress path results obtained using different numerical models are approaching sufficiently close reproducibility for the results to be considered adequate for engineering purposes. Continuing studies

through the DECOVALEX project (Hudson & Jing, 2013) will improve the agreement.

* * * * *

The case examples of underground CO_2 storage and radioactive waste disposal have highlighted whether the project objective can be successfully achieved. As explained, in the case of high-level radioactive waste disposal, the objective is to ensure that unacceptable quantities of radionuclides do not migrate to the biosphere for the next million years—this design life being required by the regulators. In order to achieve this aim, many risks are involved, through understanding the host geology, the hydrogeological regime, the effects of excavation, the security of the waste containers, the effects of canister heating of the rock mass, potential migration of the radionuclides, etc. The design of such a radioactive waste disposal facility thus represents an extreme example of rock engineering design, not only in terms of the required design life but also in terms of the time required for the design: around 20–30 years.

Considerable effort has already been spent by many countries in evaluating the associated risks and developing the necessary design procedures. These techniques, suitably streamlined, could be used to great advantage for all rock engineering projects.

6 CONCLUSIONS

From the general discussion on uncertainty and risk, plus the three rock engineering application case examples presented, a variety of conclusions are evident, as follows.

1. The subject of uncertainty and risk requires much more development so that the concepts can be built into all the aspects of rock mechanics and rock engineering, i.e., through rock characterisation, modelling and design. There is considerable literature available on the philosophies and techniques to support such development, both in general and as related to rock engineering, as summarised by Brown (2012b).
2. In particular, it is helpful to study uncertainty through the two concepts of epistemic and aleatory uncertainties. These two concepts (the former dealing with lack of knowledge but reducible uncertainty, and the latter dealing with intrinsic randomness) should be implemented in design procedures.
3. Both epistemic and aleatory uncertainty reduce as excavation proceeds—indicating that, where possible, the rock engineering design should have built-in flexibility so that it can be adapted to the continually improving knowledge and understanding. This supports the inclusion of design flexibility and the 'observational method' in design and construction.
4. The three rock engineering application examples, of shale gas extraction, CO_2 storage and radioactive waste disposal, are all cases where the overall project objective could be prejudiced by a lack of understanding of, for example, the geology, the fluid flow, or the long-term behaviour of the facilities. Thus, for all three of the case examples presented in this paper, the risks should be assessed through the entire lifecycle of the project.
5. Such comprehensive risk assessment has been extensively undertaken by many countries for the case of radioactive waste disposal—and the associated techniques could be most usefully applied when suitably streamlined to all major rock engineering projects.
6. Rock engineering design should specifically include consideration of potential 'black swan' events. Application of Conclusion 5 above should assist in this process, even if such events are mainly aleatory in nature.
7. Further work is required to establish the validity of thermo-hydro-mechanical-chemical coupled numerical models in order to reduce the risks of incomplete conceptual understanding and/or inaccuracy in the predicted values of physical variables as excavation proceeds.
8. Additionally, more information about the coupled numerical models should be made available and procedures established to make their wider use more practical.
9. An international, corporate knowledge database should be established for rock engineering projects to enhance the information available for all projects and hence reduce the uncertainty and thus the risks.
10. There is a conflict between the enhanced study of uncertainty and risk as recommended in this paper and the necessity to follow a code of practice, such as EUROCODE7, which may not be appropriate, either for rock engineering or for the particular project in hand. Therefore, pressure should be applied through the ISRM or by other means to modify such codes of practice so that they are indeed suitable and do include the concepts of uncertainty and risk in an appropriate manner for rock engineering.

REFERENCES

Adams, J. 2001. *Risk*. London:Routledge, Taylor & Francis, 228p.

Brown, E.T. 2012a. Fifty years of the ISRM and associated progress in rock mechanics. In Qian Q. & Zhou Y. (Eds.), *Proc. Harmonising Rock Engineering and the Environment: 12th ISRM International Congress on Rock Mechanics*, 18–21 October 2011, 29–45. London: Taylor & Francis Group.

Brown, E.T. 2012b. Risk assessment and management in underground rock engineering—an overview. *J. Rock Mech. Geotech. Eng*. 4 (3): 193–204.

Campos e Matos, A., Ribeiro e Sousa, L., Kleberger, J. & Lopes Pinto, P. (Eds). 2006. *Geotechnical risk in rock tunnels*. London: Taylor & Francis, 191p.

Clayton, C.R.I. 2001. *Managing geotechnical risk*. London: Thomas Telford, 80p.

Coleman, T.S. 2011. *A practical guide to risk management.* The Research Foundation of CFA Institute, 212p.

Cretu, O., Stewart, R. & Berends, T. 2011. *Risk management for design and construction*. Hoboken, N.J., USA: John Wiley, 261p.

Essex, R. J. 2007. *Geotechnical baseline reports for construction: suggested guidelines*. Reston, Virginia, USA:ASCE, American Society of Civil Engineers.

Feng, X.T. & Hudson, J.A. 2011. *Rock engineering design*. London: CRC Press, Taylor & Francis. 468p.

Gonzalez de Vallejo, L.I., Ferrer, M. Geological Engineering. London: CRC Press, Taylor & Francis Group, 678p.

Harrison, J.P. 2012. Rock engineering, uncertainty and Eurocode 7: implications for rock mass characterisation. In *Proc. XIV Ciclo di Conferenze di Meccanica e IngegneriaDelleRocce: NuoviMetodi di IndagineMonitoraggio e ModellazioneDegliAmmassiRocciosi*. Torino, Italy, 21–22 Nov. 2012.

Harrison, J.P. & Hadjigeorgiou, J. 2012. Challenges in selecting appropriate input parameters for numerical models. *Proc. 46th US Rock Mech. & Geomech. Symp.*, Chicago, 24–27 June.ARMA.

Hopkin, P. 2012. *Fundamentals of risk management*. Kogan Page (2nd Edn.) 419p.

Hudson, J.A. & Jing, L. 2013. Demonstration of coupled models and their validation against experiment: the current phase—DECOVALEX 2015. In Feng, X.T., Hudson, J.A. & Tan, F (Eds.) *Proc. ISRM SINOROCK2013 Symp*., London: Taylor & Francis.

Kahyaoglu, H. 2012. The profit in risk. *Tunnels & Tunnelling*, 16 Oct., 45–51.

Malin, P. 2012. Talking Point. *Ground Engineering*, UK, September, p. 7.

Metz, B., Davidson, O., de Coninck, H., Loos, M. & Meyer, L. (Eds.), 2005.*Carbon dioxide capture and storage. Report of the intergovernmental panel on climate change*. UK: Cambridge University Press. 431p.

Royal Society. 1983. *Risk assessment: a study group report.* London.

Royal Society. 1992. *Risk: analysis, perception and management*. London.

RS/RAE. 2012.*Shale gas extraction in the UK: A review of hydraulic fracturing.* Report by the Royal Society and the Royal Academy of Engineering, 75. Download available from www.raeng.org.uk/news/publications/list/reports/Shale_Gas.pdf

Ruqvist, J. 2012. The geomechanics of CO_2 storage in deep sedimentary formations. *Geotech. Geol. Eng.* 30: 525–551.

Skipp B.O. (Ed.). 1994. *Risk and reliability in ground engineering*. London: Thomas Telford, 304p.

Taleb, N.N. 2007 & 2010. *The black swan: the impact of the highly improbable.* London: Penguin Books, 444p.

Tunnels and Tunnelling. 2013. International Edition. Truckload of burning cheese closes Norway tunnel. March. pp. 7.

Valli, J., Hakala, M, & Kuula, H. 2011. *Modelling of the* in situ *stress state at the Olkiluoto site, western Finland.* Posiva Working Report.

Wilson, E.J., Johnson, T.L. & Keith, D.W. 2003. Regulating the ultimate sink: managing the risks of geologic CO_2 storage. *Environ. Sci. Technol.* 37: 3476–3483.

Zoback, M.D. & Gorelick, S.M. 2012. Earthquake triggering and large-scale geologic storage of carbon dioxide. *Proc. Nat. Acad. Sci*. www.pnas.org/cgi/doi/10.1073/pnas.1202473109.

Rock Mechanics for Resources, Energy and Environment – Kwaśniewski & Łydżba (eds)
© 2013 Taylor & Francis Group, London, ISBN 978-1-138-00080-3

Optimization, sensitivity and robustness analysis – Applications and trends in geomechanics

H. Konietzky
Geotechnical Institute, TU Bergakademie, Freiberg, Germany

R. Schlegel
Dynardo GmbH, Weimar, Germany

ABSTRACT: The paper summarizes the state-of-the-art in Robust Design Optimization in geomechanics with special emphasis on sensitivity and robustness analysis as well as optimization. An academic example related to roof anchorage of an underground opening is used to illustrate the general procedure. A thermo-mechanical analysis of a dam is used to illustrate the application of sensitivity analysis in the engineering practice followed by exemplary robustness analysis for a dynamic loaded foundation plate.

1 INTRODUCTION

Today the rock mechanical engineer is forced to develop safe and economic designs for systems, which are characterized by many influencing factors (technical parameters, rock mass parameter, economical parameters, environmental parameters etc.). In such systems it is more and more difficult to find optimal solutions and to define those parameters, which are really decisive. Therefore, classical procedures like parameter studies, 'trial-and-error'-procedures and simple parameter fitting is replaced more and more by so-called mathematical optimization techniques. These techniques involve the following analysis methods:

- Sensitivity analysis
  Within a sensitivity analysis the influence of individual input parameters on the model output is investigated. Based on the sensitivity analysis insignificant parameters can be excluded from further design and interaction of different parameters can be revealed.
- Uncertainty analysis
  Uncertainty analysis investigates the uncertainty of input variables and their impact on the model response. Uncertainty estimates are used to assess the confidence of model results.
- Robustness analysis
  Within the robustness analysis it is estimated how robust the model response is in relation to uncertainty in the input parameters or in other words: how stable is our model response if the input variables scatter in a certain manner.
- Reliability analysis
  Reliability analysis investigates the boundary violation of output due to the variability of input parameters. Reliability analysis can either predict the failure probability or proof, that all constraints scatter within defined boundaries.
- Optimization
  Optimization means the mathematical based selection of best fitting object in respect to defined criteria. This leads to the maximizing or minimizing of functions by choosing input values/functions from a certain parameter set or range. Different deterministic and stochastic optimization schemes are available. Popular deterministic approaches are: response surface methods, hill climbing methods or gradient based strategies. Typical stochastic approaches are: evolutionary algorithms, neural network approaches, particle swarm algorithms or the Fuzzy logic theory based methods. Of great importance is multi-objective optimization, where an optimum is searched not only for one parameter or function, but for several and sometimes also contradictionary objective functions (Pareto-Optimization).
- Parameter identification
  Parameter identification is a reverse optimization procedure (inverse parameter identification), where parameters and/or constitutive relations are determined in such a way, that the model with this parameters/constitutive relations predicts results, which are close to measurements/observations (automatic model calibration).
- Data mining
  Data mining is a process to extract hidden information from existing data.

The application of the above mentioned mathematical based procedures demands the existence or development of a model (analytical, empirical or numerical), which describes the rockmechanical

problem (e.g. a tunnel construction, a slope instability, the stress-strain behavior of a rock sample etc.). Such a model is characterized by input and output parameters or functions. Although the huge potential of optimization techniques is recognized and already extensively used in engineering in general, the break through in geomechanics has not yet taken place. Only on the academic level several publications illustrate the potential, e.g. Beiki et al. 2010, DeGagne 2011, Garvey & Ozbay 2011, Keshavarzi & Jahanbakhski 2011, Kim et al. 2012, Moel et al. 2012, Shao & Su 2010, Tran & Abousleiman 2010, Wainwright et al. 2012, Xu et al. 2013, Yoon 2007.

2 BASIC STRATEGY

The basic strategy of solving rockmechanical problems by using optimization schemes consists of 2 steps: Sensitivity analysis first, followed by optimization.

Within the sensitivity analysis it is analyzed which input parameters are relevant for the considered output. On the basis of the evaluation of the sensitivity analysis unimportant parameters can be eliminated during the subsequent optimization, which makes the optimization easier to perform, faster and robuster. The rockmechanical problems under consideration often contain much more than 10 input-parameters. Also their influence can be non-linear and the input parameters can influence each other. This all makes it impossible to estimate the influence of the input parameters on the output by just the engineering judgment/experience or simple parameter studies. The most logical alternative is the use of a mathematical based sensitivity study. This has to be based on stochastic sample algorithms, which means that sets of input parameters have to be created, which should cover the whole possible range of parameter constellations. The most strait forward procedure is the Monte Carlo Sampling, but it leads to an extremely high number of model sets. Therefore, alternatives like the Latin Hypercube Sampling, were developed, which require fewer sampling points to cover the whole design space. Our experience has shown, that for even high order design spaces (several dozen of input parameters) only about 50 up to a few hundred model runs are necessary, if Latin Hypercube Sampling is used.

In the following a simplified rockmechanical problem is used to illustrate the several steps for a **R**obust **D**esign **O**ptimization (RDO). This example was performed using Optislang [optiSLang 2012] and FLAC [Itasca 2012]. optiSLang is a software for sensitivity analysis, multidisciplinary and multiobjective optimization, robustness evaluation and reliability analysis. optiSLang include the **M**etamodel **o**f Optimal **P**rognosis (MoP) and the **C**oefficient **o**f **P**rognosis (CoP) as key algorithms for quantifiable solutions of RDO. The CoP/MOP approach provides a specific benefit by automatic variable reduction and verification of the forecast quality with a minimum of solver calls.

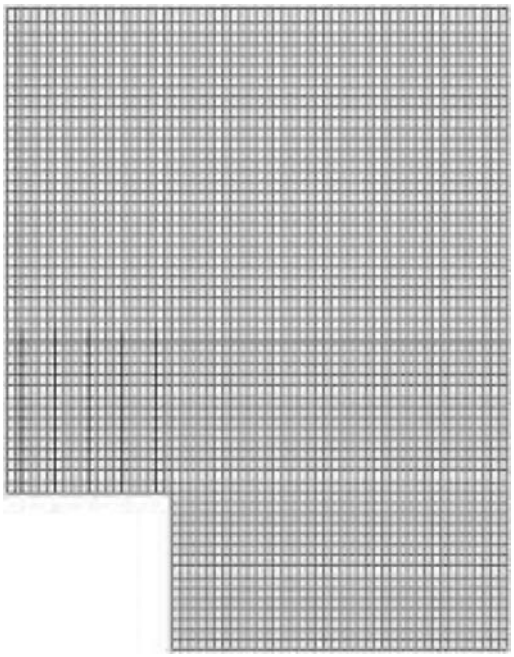


Figure 1. Numerical model deduced from the rockmechanical problem of roof anchorage (mesh with 5 roof anchors).

2.1 *Step 1: Conversation of the rockmechanical problem into a numerical model*

The rockmechanical problem may be the design of an anchor scheme for the roof of an underground chamber with rectangular cross section. Corresponding initial and boundary conditions, constitutive laws for the rock mass, the anchors and the interaction between anchors and rock mass have to be specified.

To demonstrate the whole procedure a simple 2-dimensional numerical model as shown in Figure 1 is used. The model represents half of a chamber 10 m wide and 5 m high. Due to the symmetry conditions, a half-space model was used. The model has a vertical symmetry line at the left boundary and contains 5 roof anchors. The rock mass was modeled using the classical elasto-plastic Mohr-Coulomb model with tension cut-off and non-associated flow rule. The virgin principal stress state is characterized by 10 MPa vertical stress and 5 MPa horizontal stress. The outer model boundaries are fixed in the normal directions.

2.2 *Step 2: Specification of input and output parameters and definition of objective function*

According to the specified constitutive laws a basic parameters set and a corresponding parameter range for the sensitivity analysis have to be defined (Tab. 1 and 2).

Table 1. Basic parameter set for rock mass, anchor and grout.

Parameter	Description	Unit	Value
Rock mass			
E	Young's-modulus	Pa	10^9
ν	Poisson's ratio		0.3
φ	Friction angle	°	30
ψ	Dilation angle	°	10
C	Cohesion	Pa	10^5
Ft	Uni. tens. strength	Pa	0
ρ	Density	kg/m^3	2500
Anchor			
length_anker	Anchor length 1–5	m	5
Dxdirec	Distance between anchors	m	1
e_anker	Young's modulus of anchor steel	Pa	10^{10}
yield_anker	Yield point of anchor steel	Pa	10^7
radius_anker	Anchor radius	m	0.01
Interaction between anchors and rock mass (FLAC, 2006)			
cs_ncoh/cs_scoh	Cohesion normal/shear	Pa	$10^5/10^5$
cs_sfric	Friction angle	°	10
cs_nstiff/cs_sstiff	Grout stiffness normal/shear	Pa	$10^7/10^7$
grout_thick	Grout thickness	M	0.01

Table 2. Input parameters with lower and upper bounds for sensitivity analysis.

Name	Description	Unit	Lower bound	Upper bound
length_anker	length of anchor	m	1.0	5.0
radius_anker	radius of anchor	m	0.01	0.1
e_anker	E-Modulus of anchor	Pa	10^{10}	$2.0*10^{11}$
cs_ncoh	grout normal cohesion	Pa	10^5	$5.0*10^6$
cs_scoh	grout shear cohesion	Pa	10^5	$5.0*10^6$
cs_sfric	friction angle	°	10	60
cs_sstiff	Grout shear stiffness	Pa	10^7	10^8
cs_nstiff	Grout normal stiffness	Pa	10^7	10^8
yield_anker	yield stress of anchor material	Pa	10^8	10^9
grout_thick	grout thickness	m	0.01	0.1

2.3 *Coupling between optimization tool and numerical code (master-salve-modus)*

The numerical model and the optimization tool have to communicate with each other in a master-slave mode. The optimization tool has to specify and change, respectively, the input-parameters for the individual model runs and has to get specific model response data from the numerical model for further evaluation (Fig. 2). This communication can be performed by special interfaces or simply by using ASCII-files, which will be written and read by the two codes in communication.

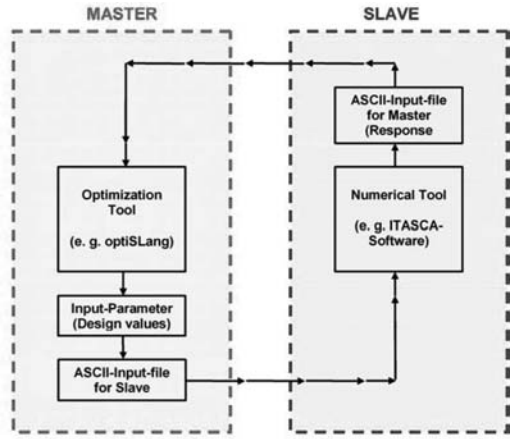


Figure 2. Work flow of optimization tool and numerical solver in form of a master-slave-modus.

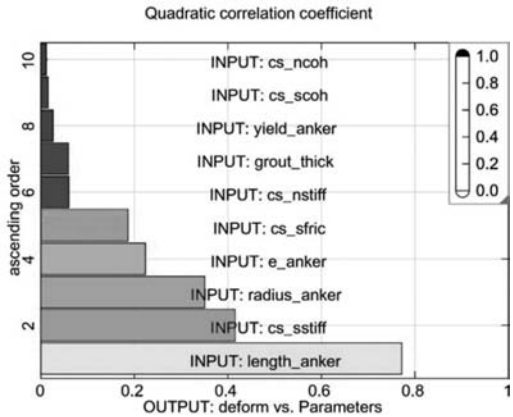


Figure 3. Quadratic correlation coefficient.

2.4 *Step 4: Execution of sensitivity analysis*

First of all, a sensitivity analysis was performed to investigate the impact of the individual parameters on the roof subsidence. The most important parameters according to Table 2 were used. A stochastic sampling method, the Latin Hypercube sampling, was used to define the input parameter sets. Only 50 model runs were necessary to derive the linear and quadratic correlation coefficients and coefficients of determinations, respectively.

Exemplary, the Anthill-Plot for the anchor length versus the obtained maximum roof settlement is shown in Figure 6.

The example is based on the simplified assumption, that all anchors have the same length and that

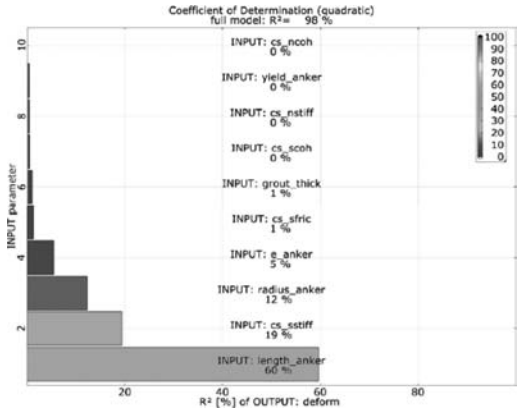


Figure 4. Coefficient of determination.

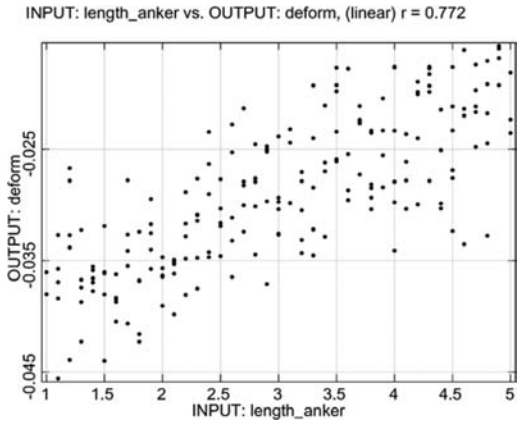


Figure 5. Anthill-plot: anchor length (m) versus output (maximum roof settlement in m).

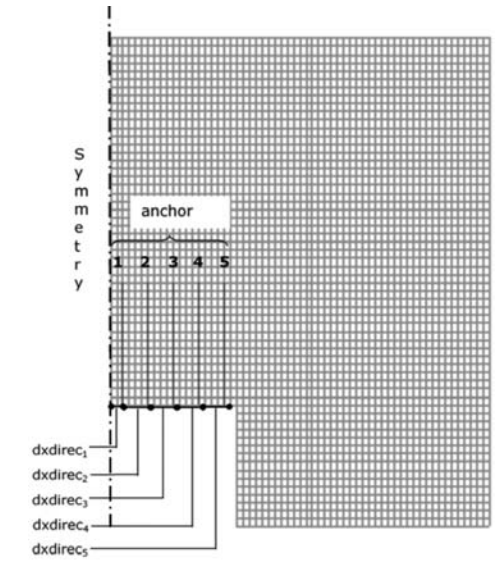


Figure 6. Numerical model set-up with variable anchor locations.

Table 3. Input parameters with lower and upper bounds for sensitivity analysis.

Name	Description	Unit	Lower bound	Upper bound
length1	length of anchor 1	m	1.0	5.0
length2	length of anchor 2	m	1.0	5.0
length3	length of anchor 3	m	1.0	5.0
length4	length of anchor 4	m	1.0	5.0
length5	length of anchor 5	m	1.0	5.0
dxdirec1	distance between symmetry axis and anchor 1	m	0.25	2.5
dxdirec2	distance between anchor 1 and 2	m	0.5	2.5
dxdirec3	distance between anchor 2 and 3	m	0.5	2.5
dxdirec4	distance between anchor 3 and 4	m	0.5	2.5
dxdirec5	distance between anchor 4 and 5	m	0.5	2.5

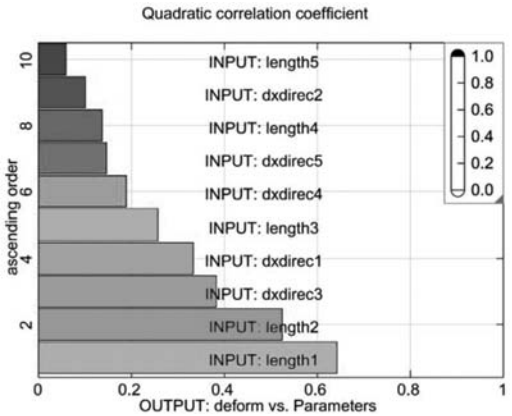


Figure 7. Quadratic correlation coefficient.

the distance between the anchors is fixed. The plot of the coefficient of determination of the maximum roof settlement (Fig. 5) shows, that 60% of the roof settlements can be explained by the anchor length alone. All other input parameters have less than 40% influence. As expected the maximum roof subsidence decrease with increasing anchor length.

Based on the knowledge, that the anchor length plays a dominant role, a second sensitivity analysis was performed, there both, the parameters for the rock mass as well as the parameters for the interaction between the rock mass and the anchors were fixed. Instead of fixed anchor locations, now the anchors are allowed to move along the roof and the anchor length can be different for each anchor within the values of 1 to 5 m (Table 3). This sensitivity analysis shows that the anchors 1 and 2 have by far the strongest influence on the roof subsidence. The length of the anchor 5 (nearest to the side wall) shows no correlation to the maximum roof subsidence (Fig. 7 and 8).

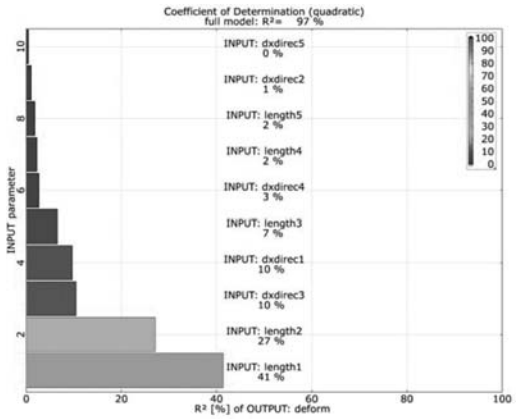


Figure 8. Coefficients of determination.

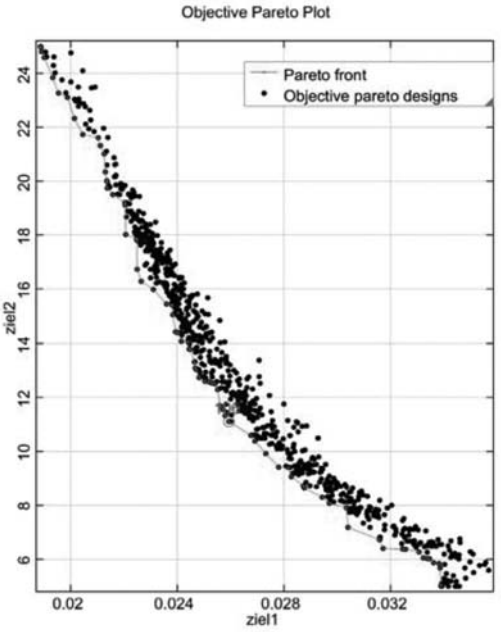


Figure 9. Roof settlement [ziel1, m] versus accumulated anchor length [ziel2, m].

2.5 *Step 5: Pareto-Optimization*

After getting detailed knowledge about the sensitivity of the input parameters optimization can start. First of all an objective function has to be specified. Here, for simplicity two contradictionary objectives were considered: besides the technical (safety) objective f1 (= maximum allowable roof settlement) a second (economic) objective f2 (= minimum of total anchor length) was defined:

1. objective: f1 = maximum roof subsidence → min
2. objective: f2 = Σli → min

with the constraint: Σdxdirec ≤ 4.5 m

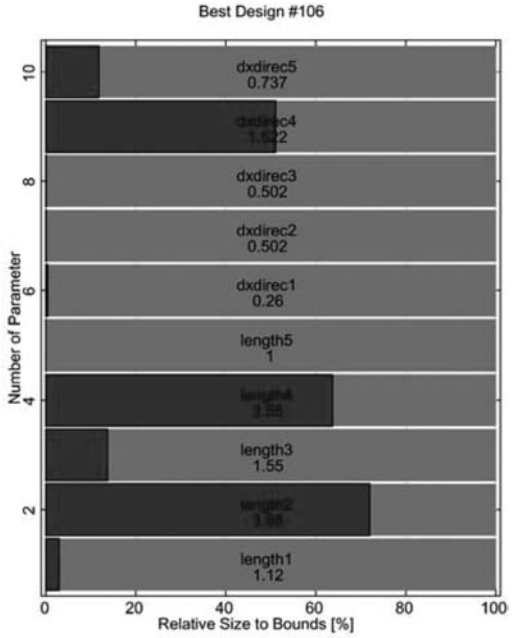


Figure 10. Parameters for best design.

1000 runs were performed. The Pareto-Optimization automatically results in the maximum anchor length (5 × 5 m) at the left upper corner and minimum anchor length (5 × 1 m) at the right lower corner of the Pareto-front (see Fig. 9). The best design gives an accumulated anchor length of 11 m for 2.5 cm roof subsidence (see Fig. 10). Along the Pareto-front all other optimum designs can be obtained. The minimum roof subsidence is reached with the anchor lengths l (1–5) = 5 m and the respective minima for the anchor distances. The interesting point is, that both, anchor length and location are strongly inhomogeneous for the optimum designs. This is caused by the inhomogeneous secondary stress field, the nonlinearities of rock behavior (plastifications) and the interaction between rock mass and anchors. A more detailed analysis of the Pareto-optimized solutions is necessary in conjunction with practical restrictions (available anchor lengths, limitations in technology to install anchors of different lengths, incorporation of financial aspects in terms of anchors with different lengths etc.) to recommend an optimum anchor scheme. Finally, it would make sense to add a robustness analysis to investigate to what extent smaller unavoidable changes in the input parameters influence the output.

3 PRACTICAL EXAMPLES

The following examples were performed using the optimization software optiSLang [2012] and the finite element simulation tool ANSYS [2012].

Table 4. Input parameters and their variations for sensitivity analysis.

Input parameter	Name	Type	Variation MIN	Variation MAX
start date of RCC	BauAnfang	Discr.	1.4./1.5/1.6/1.7./1.8.	
initial temp. fresh concrete	IniBeton Temp	Cont.	10°C	20°C
thermal quantity of concrete	BetonWarme Menge	Cont.	17000 J/kg	28000 J/kg
thermal conduct. of concrete	IniBeton Leitfahig	Cont.	1.4 $W \cdot m^{-1} \cdot K^{-1}$	2.4 $W \cdot m^{-1} \cdot K^{-1}$
special heat conductivity of concrete	IniBeton Kapazitat	Cont.	750 $J \cdot kg^{-1} \cdot K^{-1}$	250 $J \cdot kg^{-1} \cdot K^{-1}$
density of concrete	Beton Dichte	Cont.	2100 $kg \cdot m^{-3}$	2500 $kg \cdot m^{-3}$
heat coeff. of concrete expansion	niBeton Ausdehnung	Cont.	0.000014 K^{-1}	0.000020 K^{-1}
concrete quality	Druckfest365	Cont.	15 MPa	25 MPa
distance joints	BlockLange	Conti.	15 m	30 m
heat transfer coefficient	AlfaKonv	Conti.	20 $W \cdot m^{-2} \cdot K^{-1}$	45 $W \cdot m^{-2} \cdot K^{-1}$

3.1 *Sensitivity analysis: Thermo-mechanical analysis of a RCC dam*

Some challenging aspects that need to be faced during the design and construction of the 40 m high RCC dam are the short construction period (3 months) and the relatively extreme environmental conditions at the site during winter time. The use of a high fly-ash RCC mix concept has been proposed to reduce the heat generated in the concrete mass and to extend the setting time of the mix. A preliminary thermal and structural analysis was conducted in order to analyze the sensitivity of various parameters in the dam design.

The numerical simulations were conducted as transient thermo-mechanical coupled analyses on the 3D model of the dam structure and a connected rock section. The non-linear finite element analysis considers the evolution of temperature and mechanical resistance depending on time and location within the dam structure. The calculations were carried out as load history calculations simulating the progress of dam construction in each of the 30 cm thick layers as well as the subsequent five years of operation.

Due to the complexity of the interaction between material parameters and the nonlinear analysis, the FE model was built parametrically. Within the sensitivity analysis, 100 designs were calculated using Latin Hypercube sampling.

Here, all input parameters (see Table 4) were changed in each design to have on optimal resolution of the design space as well as minimum correlation errors in the correlation analysis, which identifies the most import input variable. The goal of this sensitivity analysis was:

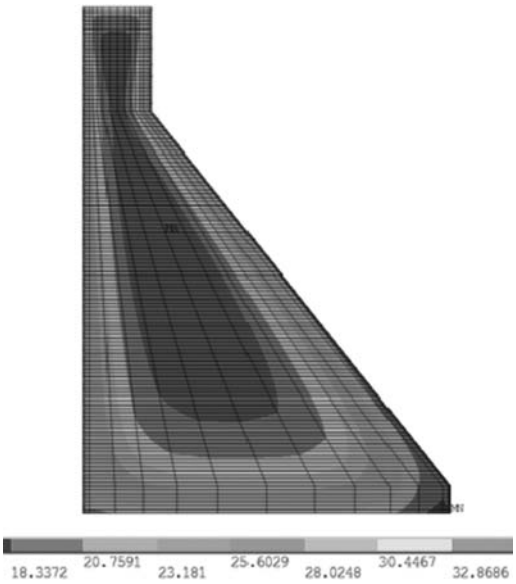


Figure 11. Estimated temperature distribution after RCC placement.

- to identify those input parameters which influence mainly the concrete tensile stress forced by hydration,
- to analyze trends, such as changes in input parameters modifying the concrete tensile stress,
- to provide meaningful variation ranges for the input parameters.

The predictive quality of the calculation results of the sensitivity analysis exceeds clearly those of a single calculation. The evaluation of the results considers particularly the tensile stresses in the concrete due to hydration. For this, at each time step, the current main tensile stresses in the dam were compared with the current concrete tensile strength.

As a result of the sensitivity analysis, it became obvious that the amount of maximum tensile stress on the outside (water- and air-side) of the concrete as a result of hydration especially dependents on (see Figure 13-left):

- the horizontal distance between the vertical joints,
- the start of placing the concrete, and
- the coefficient of thermal expansion.

Thus, the major influences are structural and techno-logical parameters. Furthermore, the results show that the maximum tensile stress on the concrete in the inner structure as a result of hydration is particularly influenced by (see Figure 13-right):

- the specific heat capacity of the concrete,
- the heat quantity of the concrete, and
- the coefficient of thermal expansion,

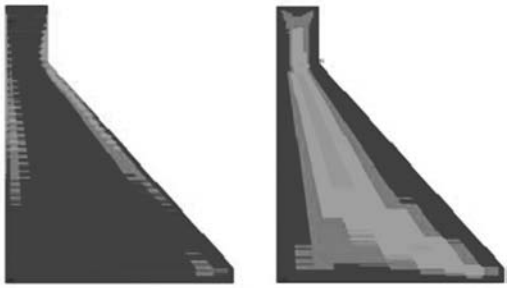


Figure 12. Distribution of tensile stresses: left after RCC placement, right: after 5 years.

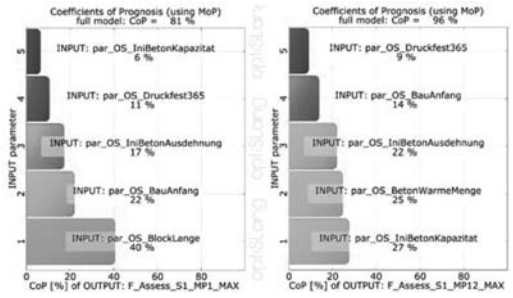


Figure 13. Coefficients of prognosis for the most important parameters responsible for the maximum hydration caused tensile stresses, left: on the outside (water- and air-side), right: in the inner structure.

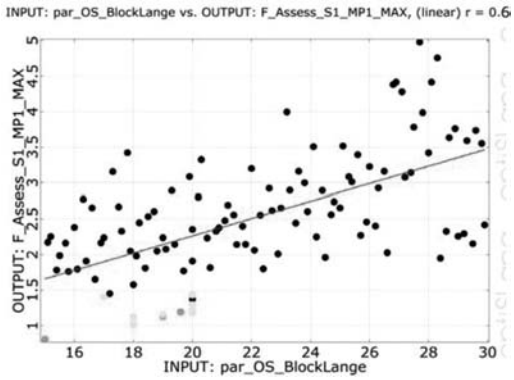


Figure 14. Anthill plots: assessment of hydration caused tensile stresses [MPa] versus distance of joints [m].

and mostly depends on the mixture and quality of the concrete. Only with this degree of diagnostic characterization of the thermo-mechanical analysis it is possible to truly understand the evolution of the tensile stresses and concrete tensile strength over time. With this approach, a predictive model for the evaluation and design of RCC dams is developed. By use of the predictive model, the RCC design as well as technological aspects can be optimized to provide the required safety levels.

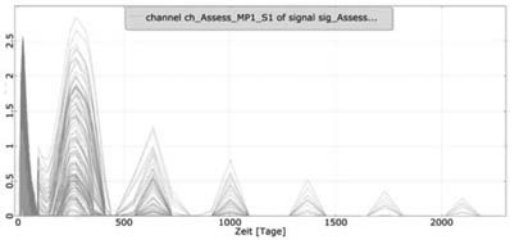


Figure 15. Tensile stresses [MPa] versus time [days].

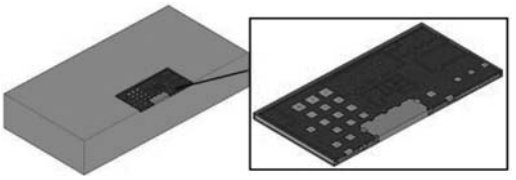


Figure 16. Foundation plate of research laboratory.

3.2 *Robustness evaluation of the serviceability of a dynamic loaded foundation plate*

The following robustness analysis was conducted to ensure the serviceability of a foundation plate constructed for a research laboratory (Fig. 16). In this building, high-resolution measuring instruments with accuracy in the micrometer range will be installed. The smallest vibrations caused by dynamic effects, such as pedestrian traffic in the building, road traffic outside, building equipment or machinery operating in a repair shop area nearby, can affect these instruments and make research results worthless. The foundation plate is structured of different areas, which were dynamically decoupled from each other by different insolation materials.

Individual deterministic analyses for a safe dimensioning of vibration absorbing building structures are not sufficient, which is typical for such dynamic issues. In fact, different load constellations have to be analyzed within different frequency ranges. Robustness evaluation using stochastic analysis is necessary to assess adequately the reliability of the construction.

For the robustness of the foundation, the following 43 input parameter variations were analyzed:

- Material parameters (stiffness, density, Poisson's ratio, absorption coefficient) of the soil as well as sand and gravel layers above
- Material parameters (E-modulus, density, Poisson's ratio) of the reinforced concrete of the foundation plate
- Material parameters (E-modulus, density, Poisson's ratio, loss factor) of the isolation material (foam glass, Sylomer, Ethafoam)
- Material parameters (stiffness, density, Poisson's ratio, loss factor) as well as the thickness of bitumen layer nearby the laboratory building.

For the definition of the distribution function, the upper and lower limits of the input parameters reported

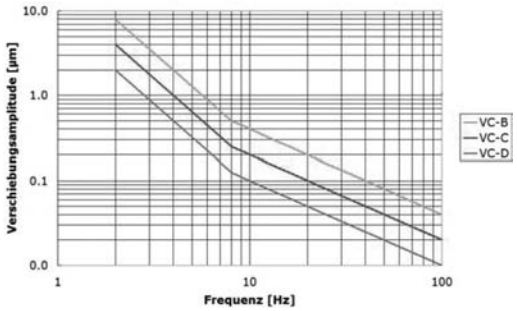


Figure 17. Maximum permissible amplitude as function of frequency.

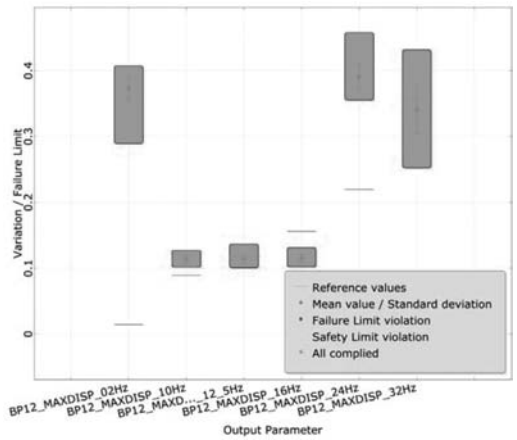


Figure 18. Variation interval of oscillation amplitude subject to excitation frequency.

by the operator and construction manager have been specified according to 2-sigma values and the probability density functions (normal distribution) were defined and scaled at these constraints. The external effects (pedestrian loads, equipment loads, traffic) were considered as deterministic variables with constant amplitude and given frequency in the calculation. As response variables, the amplitudes of vibration were analyzed at selected measuring points (planned positions of measuring instruments) on the foundation plate. In Figure 17, the maximum permissible amplitude of vibration as a function of frequency and the requirement classes VC-B, VC-C, and VC-D are shown for various planned locations of measuring instruments.

For the robustness evaluation, 100 designs were generated by the stochastic Latin Hypercube Sampling method.

In Figures 18 and 19, the results of the robustness evaluation are shown exemplarily for measurement point BP12. Figure 18 depicts the interval variation of the maximum oscillation amplitude for different excitation frequencies. For all frequencies, the permissible limits are met as shown in Figure 17. Figure 19

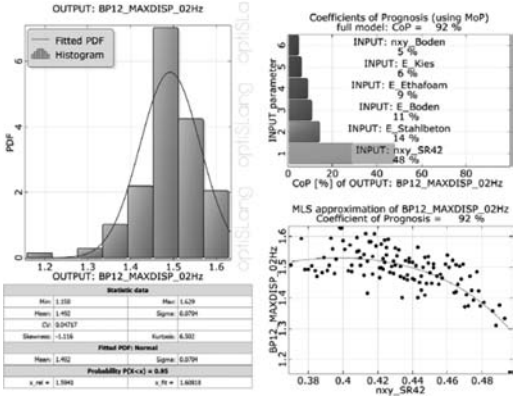


Figure 19. Results of measurement point BP12, excitation frequency 2 Hz; Left: Frequency distribution of the maximum oscillation amplitude; top right: CoP values; bottom right: Anthill plot of the most important input parameter nxy_SR42 vs. response value of the maximum oscillation amplitude BP12.

shows exemplarily the results of maximum oscillation amplitude for an excitation frequency of 2 Hz (pedestrian) BP12-02Hz. The frequency distribution of the maximum oscillation amplitude can be seen in Figure 19 (left). This is very important for the immediate assessment of the serviceability. Figure 19 (top right) shows the input parameters responsible for the scattering of the oscillation amplitude. Here, the **C**oefficient **o**f **P**rognosis (CoP) indicates the percentage of how strongly the scattering response values (oscillation amplitude) are affected by the scattering respective input parameter. In the case shown, the parameter nxy_SR42 (Poisson's ratio of the isolating material for dynamic decoupling) shows the greatest influence on the maximum oscillation amplitude. Figure 19 (bottom right) depicts the corresponding Anthill plot of this input parameter. Both results shown in the plots of Figure 19 are of great importance for explaining the causes of the scatter of the maximum oscillation amplitude at BP12-02Hz. With the help of this information, it is possible to assess the effectiveness of the planned measures for vibration isolation.

4 CONCLUSIONS AND OUTLOOK

Optimization, sensitivity analysis and robustness evaluation are modules of a virtual design process that can be also used very successfully in rock mechanics. In contrast to the deterministic analysis, stochastic or variation-based analysis provides not only the option of assessing result values but also the consideration of their scatters, effectiveness and complex interactions towards other input and output parameters.

Due to its highly advanced assessment potential in comparison to deterministic calculations, stochastic analyzing methods will be increasingly applied to many projects in rock mechanics (e.g. planning,

cost optimization, system and parameter identification). Here, the option of combining the introduced modules sensitivity analysis, optimization and robustness evaluation are very important. In recent years, there has been rapidly advancing process automation by applying numerical simulation programs (e.g. simplification of processing a CAD geometry and its automatic mesh generation in the fields of FEM, FDM and DEM). Also, parameter optimization and stochastic analysis have been improved concerning process automation. Using wizard technologies, it is conceivable that a standard optimization starting with the input of design space and objective function and using a sensitivity analysis and subsequent optimization methods can be conducted in a fully automated mode. A manual setting or interaction by the user is no longer necessary.

REFERENCES

Beiki, M. et al. 2010. Genetic programming approach for estimating the deformation modulus of rock mass using sensitivity analysis by neural network, *Int. Journal Rock Mechanics and Mining Sciences*, 47: 1091–1103

DeGagne, D.O. et al. 2011. Estimation of tunnel squeezing inanisotropic stress fields using a FLAC-based neural network, In: D. Sainsbury et al. (eds), *Continuum and Distinct Element Numerical Modeling in Geomechanics*, Itasca Int. Inc., Minneapolis, Minnesota, USA, 143–151

FLAC 2012. *Manuals*, Itasca Consulting Group, Inc., Minneapolis, Minnesaota, USA

Garvey, R. & Ozbay, U. 2011. Computer-aided calibration of PFC3D coal sample using genetic algorithm, In D. Sainsbury et al. (eds), *Continuum and Distinct Element Numerical Modeling in Geomechanics*, Itasca Int. Inc., Minneapolis, Minnesota, USA, 493–499

Keshavarzi, R. & Jahanbakhski, R. 2011. A neural network-based sensitivity analysis of reservoir-related parameters during laser perforation in downhole conditions in limestone, *Proc. 45. US Rock Mechanics Symposium*, ARMA, 11–116

Kim, H.-M. et al. 2012. Parametric sensitivity analysis ofground uplift above pressurized underground rock cavern, *Engineering Geology*, 135–136: 60–65

Moel, H. et al. 2012. Uncertainty and sensitivity analysis ofcostal flodd damage estimates in the west of the Netherlands, *Natural Hazard and Earth Sciences*, 12: 1045–1058

optiSLang 2012. *Manuals,* DYNARDO GmbH, Weimar, Germany

Shao, G. & Su, J. 2010. Sensitivity and inverse analysis methods for parameter intervals. *Journal Rock Mechanics and Geotechnical Engineering*, 3: 274–280

Tran, M.H. & Abousleiman, Y.N. 2010. The impacts of failure criteria and geological stress states on the sensitivity of parameters in wellbore stability analysis, *Proc. 44. US Rock Mechanics Symposium*, ARMA, 10–328

Wainwright, H. M. et al. 2012. Itough2 global sensitivity analysis module: applications to CO2 storage system, *Proc. TOUGH Symposium*, Lawrence Berkeley National Laboratory, 1–8

Xu, L.M. et al. 2013. Fuzzy C-means cluster analysis based on mutative scale chaos optimization algorithm for grouping of discontinuity sets, *Rock Mechanics Rock Engineering*, 46: 189–198

Yoon, J. 2007. Application of experimental design and optimization to PFC model calibration in uniaxial compression simulation, *Int. Journal Rock Mechanics and Mining Sciences*, 44: 871–889

This page intentionally left blank

Rock Mechanics for Resources, Energy and Environment – Kwaśniewski & Łydżba (eds)
© 2013 Taylor & Francis Group, London, ISBN 978-1-138-00080-3

Geomechanical modeling of CO_2 storage in deep saline aquifers – A review

X. Li, W. Yuan, B. Bai, M. Liu & H. He
State Key Laboratory of Geomechanics and Geotechnical Engineering, Institute of Rock and Soil Mechanics, Chinese Academy of Sciences, Wuhan, China

ABSTRACT: CO_2 storage in deep saline aquifers is one of the most promising options for reducing the atmospheric emissions of CO_2 and the geomechanical issues associated with this approach, such as injection-induced stress-and-strain changes, ground surface deformation, cap-rock and well-bore integrity, existing fault reactivation and potential notable seismic events, have received increasing attention from researchers, policy-makers and the general public. In order to address these challenges, many analytical methods, including analytical analyses, numerical modeling and response surface strategies, have been proposed and implemented. In particular, numerical modeling is a widely used approach because of its feasibility for the modeling of large-scale and complex geometry. Thus, this paper provides a review of the numerical modeling of the geomechanics associated with CO_2 storage in deep saline aquifers. The paper first provides a brief introduction of coupled Thermo-Hydro-Mechanical-Chemical (THMC) processes in porous media and the common constitutive models that are used in that simulation followed by the existing categories of coupling methods for a numerical simulation. Secondly, the geomechanical aspects of CO_2 storage in deep saline aquifers that result from numerical modeling are summarized in detail. Finally, some of the weaknesses that exist in the current simulators and simulation approaches are discussed and improvement measures are recommended.

1 INTRODUCTION

Geological CO_2 storage (GCS), particularly in deep saline aquifers, is considered to be a promising technology to reduce the CO_2 emissions into the atmosphere due to the burning of fossil fuels. Large-scale and long-term CO_2 sequestration is a significantly coupled thermal-hydraulic-mechanical-chemical (THMC) process, which may cause a series of mechanical issues, including ground surface deformation, reduced integrity of the cap-rock and well-bore and the reactivation of fault or seismic events (Rutqvist 2012, Li et al. 2006). For example, in a GCS project in Salah, Algeria, an uplift of 2.5 cm at a rate of 5 mm per year has been observed. In addition, at Weyburn, approximately 100 micro-seismic events with magnitudes ranging from -1 to -3 have been detected since 2004. Fortunately, no grave security issues associated with CO_2 storage systems have yet been reported. However, serious accidents caused by the injection of fluid into a deep geologic formation have been reported. For instance, a geothermal project in Basel was shut down after a 3.4 magnitude seismic event was induced by a water injection. Water injection is similar to CO_2 injection; hence, the potential for a large-scale CO_2 injection to cause serious accidents in the future cannot be ruled out. Thus, it is vital to comprehensively assess the geomechanical issues associated with CO_2 sequestration (Rutqvist 2012).

The approaches for analyzing the THMC processes in CO_2 sequestration can be summarized into three categories: analytical analysis, numerical modeling and response surface strategy (Song & Zhang 2013). Numerical modeling is the most widely used method because of its feasibility at large-scales and with complex geometry. Thus, this review focuses on the numerical modeling of the geomechanical issues associated with CO_2 sequestration systems and provides a brief introduction to the coupled THMC process and numerical modeling methods. In particular, a more detailed review of the geomechanics of CO_2 storage that results from numerical modeling is performed. Finally, the defects of the present numerical modeling methods are described and measures for improvement are recommended.

2 NUMERICAL SOLUTIONS OF THE THMC PROCESSES IN POROUS MEDIA

2.1 *Brief introduction to the THMC processes in porous media*

Injecting supercritical CO_2 into deep porous media causes an increase in the pore pressure and a decrease in the effective stress of the rock-mass that results in stress-strain changes in and around the injection zones. These alterations may lead to changes in the porosity and permeability of the strata, thus affecting the migration and injectivity of the CO_2, which may in turn affect the deformation of the rock mass. Moreover, any changes in temperature resulting from the

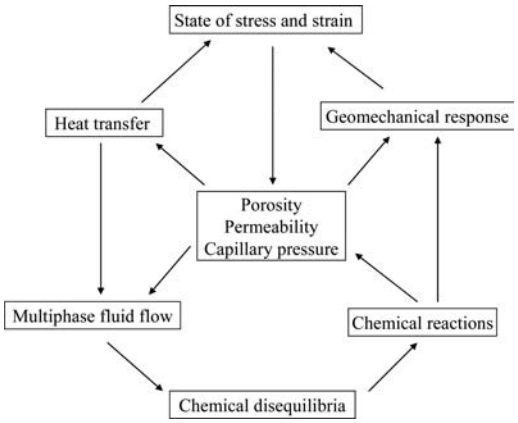


Figure 1. Schematic of the coupled THMC processes (modified from Johnson et al. 2004).

injection of CO_2 will also induce changes in stress-strain, fluid density and viscosity, which will have an indirect impact on the migration and injectivity of CO_2. For long-term CO_2 sequestration in deep saline aquifers, the effect of the CO_2-water-rock reaction on the geomechanics of the CO_2 sequestration system cannot be ignored. CO_2-water-rock reactions dominate the dissolution and precipitation of minerals, and affect the leakage pathways and physical properties of the fluid and geological formations, which in turn affect the progress of the CO_2-water-rock reactions.

In conclusion, mass CO_2 injection into saltwater layers induces a range of coupled thermal, hydraulic, mechanical and chemical processes (THMC), including heat transfer, multiphase fluid flow, geomechanical response, solute transport and geochemical reactions between the fluids and the minerals contained in the strata (Yin et al. 2012). A schematic of the coupled THMC processes is shown in Figure 1.

2.2 *Constitutive models for the THMC processes in porous media*

Existing constitutive models for depicting rock masses can be classified into four primary categories: (1) elastic constitutive models, (2) elastoplastic constitutive models, (3) rheological constitutive models and (4) damage constitutive models. Each category contains various constitutive models, some of which are specially developed for describing anisotropic (i.e., anisotropic elastoplastic constitutive models) or jointed rock (i.e., elastoplastic constitutive models, damage constitutive models, modified soil constitutive models, empirical constitutive models, dual porosity models) (Oka et al. 2002, Gens et al. 1990, Zhu et al. 2003, Souley et al. 1995, Ladanyi & Archambault 1970, Bower & Zyvoloski 1997).

However, only a small number of models, including poroelastic constitutive models, elastoplastic models, viscoplastic constitutive models and dual porosity models, have been applied to the geomechanical modeling of CO_2 storage. Poroelastic constitutive models are commonly used due to their simplicity and easy coupling (Rutqvist et al. 2008). Because the mechanical behavior of some soft porous rocks, such as many types of sandstone or chalks, differs greatly from linear elastic behavior, an elastoplastic constitutive model is adopted. Among the elastoplastic constitutive models in existence, the critical state model (CSM) is perceived to be the most advantageous for (1) considering a non-linear bulk modulus, (2) presenting a yield surface to define any change between the elastic regime and the plastic regime and (3) introducing a plastic variable associated with the degradation of the cement and the generation of water meniscuses between the solid particles to describe the mechanisms of plastic deformation (Alonso et al. 2012b). Because of the creep phenomena of reservoirs induced by CO_2-water-rock interactions, Vilarrasa et al. (2011) used a viscoplastic constitutive model to describe the combined effect of creep and plasticity. To reproduce the undrained loading behavior of a fractured rock mass during water-rock-CO_2 reactions, Taron et al. (2009) applied a dual porosity model to simulate the jointed rock-mass.

2.3 *Coupling modeling methods and softwareet al for THMC processes in porous media*

To accurately simulate THMC processes in CO_2 sequestration systems, many numerical methods, including the finite element method, the finite differential method, the finite volume method and the discrete element method, have been developed and applied and several commercial software products have been widely used to simulate the process of CO_2 injection into deep sedimentary formations, although the process is too complex to obtain an appropriate analytical solution. In brief, such numerical modeling methods can be classified into three categories: full coupling, partial coupling and one-way coupling. A more detailed summary of these numerical simulation methods is given below.

2.3.1 *Full coupling*

Full coupling refers to the simultaneous solution of all of the partial differential equations. This is the highest level coupling method, in which all of the parameters are updated in each iteration and at each time step and their changes are directly accounted for in the stiffness matrix for the computation of the next iteration step (Preisig & Prevost 2011, Rutqvist 2011). Full coupling is clearly a relatively accurate approach compared with the other two coupling methods. However, there may be serious numerical stability problems in certain situations and full coupling always requires a long period of time in order to acquire stable results due to its heavy computational requirements. Thus, relatively simple physical and mathematical models with some simplifications and assumptions are considered when full coupling is used to solve the partial

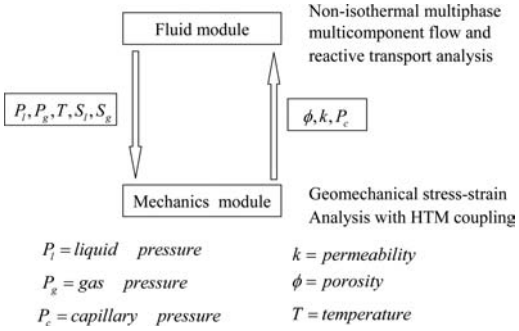


Figure 2. Schematic for linking separate codes for coupling computation (modified from Rutqvist & Tsang 2003).

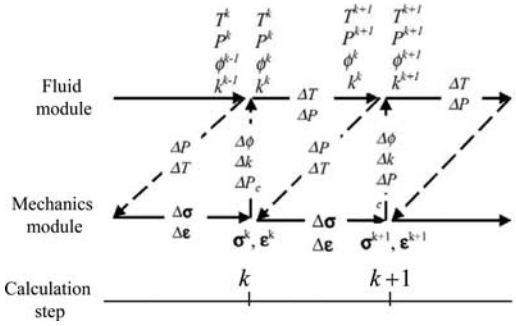


Figure 3. Numerical procedure and data communication of the linked codes (from Rutqvist & Tsang 2003).

differential equations that depict the THMC processes of CO_2 storage in deep saline aquifers. Commercial software products, including CodeBright (Olivella et al. 1996), OpenGeoSys (Kolditz et al. 2012), FEMH (Bower & Zyvoloski 1997), DYNAFLOW (Prevost 1981), GeoSim (TAURUS) and COMSOL (Alonso et al. 2012b, Li et al. 2009), perform full coupling simulations of the THMC processes in CO_2 storage systems.

2.3.2 *Partial coupling*

In partial coupling, the fluid module and geomechanics module are implemented separately and the parameters of these two computation modules are corrected at the end of each iteration step or each time step for the next calculation step. Partial coupling can be divided into iterative coupling and time-step coupling. To a certain extent, time-step coupling can be considered to be a special case of iterative coupling in which only one iteration per time-step is performed (Settari & Walters 1999, Rutqvist 2011). One of the main advantages of this coupling method is that separate codes for the fluid module and the geomechanics module, running separately in a specific order, can be linked through data communication (Preisig & Prevost 2011). Coupling simulators that link two established codes have been developed, such as Tough2-Flac3D (Rutqvist et al. 2002, Yuan et al. 2013), Tough2-Code_Aster (Seyedi et al. 2009), SIMED II-Flac3D (Connell & Detournay 2009), NUFT-GEODYN_L (Morris et al. 2011a), ATHOS-VISAGE (Longuemare et al. 2002), ToughReact-Flac3D (Taron et al. 2009) and Retraso-CodeBright (Liu & Kvamme 2008). Moreover, some single codes can also perform partial coupling, such as Eclipse (Smith et al. 2011) and Abaqus (Li et al. 2006). Figure 2 depicts a schematic for linking separate codes for coupling computation and Figure 3 shows the numerical procedure and data communication of the linked codes.

2.3.3 *One-way coupling*

In practice, one-way coupling, which is commonly considered to be the simplest case of partial coupling, refers to a minimal coupling method in which the fluid flow problem is solved first followed by the use of

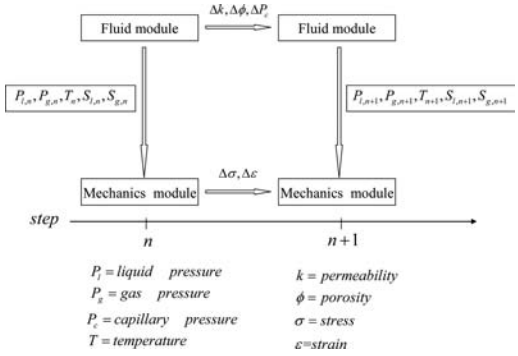


Figure 4. Schematic of one-way coupling.

updated pore pressure as the external load in order to solve the geomechanical problem and there is no feedback of the mechanical results to the fluid module; in other words, the mechanical effects on the hydraulic properties are not considered (Vidal-Gilbert et al. 2009; Rohmer & Seyedi 2010). Although it is the most elementary coupling approach, one-way coupling can be useful under special circumstances, e.g., in the case of an embedded pumped aquifer in a mechanically homogeneous half-space or when calibrating an uncoupled model to fit existing data (Levis 1991).

Two different grids and physical models can be coupled for simulation by linking two separate codes, such as ECLIPSE/300-VISAGE (Olden et al. 2012), NUFT-LDEC (Johnson et al. 2004), FEMH-ABAQUS (Li et al. 2005) and ATHOS- Abaqus (Vidal-Gilbert et al. 2009). Figure 4 illustrates a schematic of one-way coupling.

3 SIMULATION OF THE GEOMECHANICAL ISSUES INDUCED BY THE INJECTION OF CO_2

3.1 *Injection-induced stress-strain and pore pressure changes*

CO_2 injection impacts the initial pore pressure field and any pressure changes can induce stress changes in

and around the injection zones; increasing pore pressure decreases the effective stress of the rock-mass during CO_2 injection and migration. In contrast, the expansion of the pore volume due to the decrease in the effective stress facilitates the evolution of pore pressure.

The *in situ* stress field may not remain constant but, rather, may evolve along with the evolution of the pore pressure. In general, due to the variation in the pore pressure, horizontal and vertical effective stress decrease and the decrease in the vertical effective stress is much greater than the decrease in the horizontal effective stress. Moreover, the total vertical stress remains nearly constant, equal to the gravity of the over-burden, whereas the total horizontal stress changes significantly. This effect occurs because, from a mechanical point of view, the rock mass is free to expand in the vertical direction, but lateral expansion is confined (Vidal-Gilbert et al. 2009; Rutqvist et al. 2008). For a hypothetical reservoir model (i.e., a thin, homogeneous and laterally extensive reservoir), the magnitude of the change in the total horizontal stress is a function of the geological conditions and the pressure variation, which is depicted in Eq. (1) (Hettema et al. 2000; Hawkes et al. 2005):

$$\Delta\sigma_h = \left(b\frac{1-2\upsilon}{1-\upsilon} \right) \cdot \Delta p \qquad (1)$$

where b is Biot's coefficient, usually assumed to be 1.0 and υ is Poisson's ratio. If the reservoir is homogeneous, $\Delta\sigma_h$ is a linear function of Δp. However, the changes in *in situ* stresses are not correlated with the changes in pore pressure in the simulation of a real engineering project because of the heterogeneity of the mechanical properties and the structural shape of the reservoir (Vidal-Gilbert et al. 2009).

Pore pressures increase significantly ahead of the fully developed capillary fringe. Once the pore pressure exceeds the capillary pressure, CO_2 continues to displace the brine and the pressure begins to drop slightly. Thus, a pressure "shoulder" can be observed from the pressure curve, which is a function of the distance from the injection well (Vilarrasa et al. 2010). Pore pressure in and around the injection zones will rise as a result of long-term CO_2 injection. A comparison of a coupling simulation with a hydraulic simulation concluded that a coupling simulation leads to a lower increase in pore pressure than does a hydraulic simulation (Alonso et al. 2012a, Vilarrasa et al. 2010). Moreover, the evolution processes of the pore pressure in the aquifer cause a minor difference between a coupling simulation and a hydraulic simulation when the storage coefficient is evaluated well, although this difference may be notable in the cap-rock, indicating that monitoring the pore pressure in the cap-rock is optional for identifying hydromechanical processes (Vilarrasa et al. 2010). In addition, other effects on the evolution of pore pressure, including mechanical constitutive models (elastic and elastic-plastic), boundary conditions (open, closed, semi-closed), burial history and aquifer geometry, have been studied (Alonso et al. 2012a; Alonso et al. 2012b).

Temperature and chemical reactions can also affect the stress and pore pressure fields. In general, the CO_2 that is injected into the stratum is cooler than the rock mass surrounding the injection zones; thus, cooling effects (shrinkage) may occur and reduce the compressive stress, particularly the tensile stress. Once the tensile stress exceeds the tensile strength of the rock, a fracture is formed. When the temperature difference between the CO_2 and rock mass is much greater, the scope of the tensile stress or fractures is much more extensive (Preisig & Prevost 2011, Yin et al. 2012, Goodarzi et al. 2012). Chemical effects on stress fields take three forms: (1) the dissolution or precipitation of minerals leading to increased porosity and permeability, directly impacting the pore pressure field and indirectly affecting the stress fields (Yin et al. 2012, Rutqvist 2012, Liu & Kvamme 2008); (2) the reactions of the CO_2-water-rock weakens the mechanical properties of the rock skeleton, thus also affecting the state of stress (Orlic et al. 2011, Nguyen et al. 2011, Espinoza et al. 2011); and (3) the aperture change of the fractures induced by the chemical reaction, which is regarded as an equivalent strain in calculating the stress (Taron et al. 2009).

3.2 *Ground surface deformation*

Injection-induced pore pressure increases give rise to decreases in the effective stress of the rock mass, resulting in volumetric expansion in the injection zones. This volumetric expansion, combined with the extrusion force that comes directly from the bended cap-rock, squeezes the overlying rock mass, and finally determines the ground-surface deformation. (Rutqvist et al. 2010, Yuan et al. 2013, Vidal-Gilbert et al. 2009; Cappa et al. 2009, Vilarrasa et al. 2011).

Due to the restriction of the overburden, the upward displacement near the ground surface is always relatively small compared with the uplift at the top of the injection zones. Furthermore, the stiffness of the overburden has a remarkable influence on the ground-surface uplift, whereas the Poisson ratio of the overburden and the height of the overburden and the basement are not critical for the uplift (Goodarzi et al. 2012, Yuan et al. 2013). The influence of other factors on the ground-surface deformation has also been studied; for example, the increase in the uplift is directly associated with the increased permeability of the cap-rock (Rutqvist et al. 2010, Vilarrasa et al. 2011) and the surface displacement in the thermal model is less than that in the isothermal model because of the reduction of the compressive stress due to the effect of temperature (Goodarzi et al. 2012).

3.3 *Mechanical integrity of the cap-rock and well-bore*

Leakage through networks of fractures or faults is one of the main modes for the escape of CO_2 and

the fractures are generally induced in intact rock or pre-existing fractures by geo-mechanical, geochemical and cooling shrinkage actions (Song & Zhang 2013); leakage through the faults will be discussed in the next section. In general, for new fractures, once the elastic-plastic cap-rock yields (Olden et al. 2012), the stress of the elastic intact cap-rock meets the shear or tensile failure criterion (Smith et al. 2011), the accumulated total plastic strain of the visco-plastic cap-rock element increases to a critical value (Vilarrasa et al. 2010), the nodal of the cap-rock ruptures (Johnson et al. 2004) or the permeability of the cap-rock varies sharply (Longuemare et al. 2002) and the integrity of cap-rock is thought to suffer the damage. For pre-existing fractures, the Mohr-Coulomb model without bonding is used. If the shear-slip of the pre-existing fracture occurs, the integrity of the cap-rock may also be weak (Smith et al. 2011).

The state of initial stress in geologic formations is the main factor that affects the failure mode of the cap-rock. In the elastic constitutive model, a high potential for shear failure exists under both the extensional stress regime (horizontal stress is less than vertical stress) and the compressional stress regime (horizontal stress is greater than vertical stress) and the shear failure surface occurs throughout the cap-rock much more steeply under the extensional stress regime than under the compressional stress regime. Moreover, the potential for tensile failure near the bottom of the cap-rock under the extensional stress regime is much higher than under the compressional stress regime and shear failure most likely occurs earlier than tensile failure under both stress regimes. (Rutqvist et al. 2007, Seyedi et al. 2009). In the elastic-plastic model, the yield surface is reached earlier under the extensional stress regime than under the compressional stress regime (Alonso et al. 2012b). For the visco-plastic model, the plastic strain concentrates only between the bottom of the cap-rock and the top of the aquifer under the compressional stress regime, whereas the plastic strain runs through the entire cap-rock under the extensional stress regime (Vilarrasa et al. 2010). Therefore, the elastic-plastic and visco-plastic models indicate that the compressional stress regime is a better initial stress state for the integrity of the cap-rock; however, this conclusion is not consistent with the results of analyses based on the elastic model (Rutqvist et al. 2007, Seyedi et al. 2009). The factors that affect the stress-strain and pore pressure noted above can have a similar influence on the failure patterns of the cap-rock, including the strength of the rock-mass, the boundary conditions, the burial history, the temperature and the chemical reactions (Song & Zhang 2013).

In general, it is difficult to determine a leakage pathway from the failure location of the cap-rock. For instance, Smith et al. (2013) reported that CO_2 could escape from the reservoir when a percolating network of fractures exists from one side of the region to the other in the cap-rock. Yuan et al. (2013) suggested that the leakage pathway comprises the failure elements. Vilarrasa et al. (2011) stated that plastic strain propagating throughout the entire cap-rock creates a passageway for CO_2 in the reservoir. Each of these assertions represents a qualitative assessment of the risk of CO_2 leakage without considering the hydraulic behavior of the different fractures. For example, Alonso et al. (2012b) concluded that dilatant shear bonds act as flow pathways, whereas compressive shear bonds act as flow barriers. Gutierrez et al. (2000) showed that the permeability of a fracture in shale may decrease depending on the increase in the normal stress of the fractures.

3.4 *Existing fault reactivation and seismic events*

Faults, acting as discontinuity structures of a geologic formation, are generally depicted as interfaces or joint elements (Vidal-Gilber et al. 2009), isotropic solid elements with weak strength and stiffness parameters (Rutqvist et al. 2007, Cappa & Rutqvist 2011a) or ubiquitously fractured media (Ouellet et al. 2011). CO_2 migrating into a fault may cause an increase in pore pressure that is associated with a reduction in the effective stress and strength in fault segments, thereby causing the instability of the fault, especially in seismic events that are associated with the escape of CO_2. Thus, research on the influence of faults on CO_2 storage systems involves three important subjects: the reactivation of the fault, the risk of the CO_2 leakage and the sustaining injection pressure.

The failure criteria of a fault simulation for CO_2 storage in deep saline aquifers are essentially all based on Mohr-Coulomb criteria without any consideration of the cohesive strength; in particular, the coefficients of the static friction fall in the range $0.6 \leq \mu \leq 0.85$. Moreover, most of the constitutive models of the faults are based on the elastic-perfectly plastic theory. Other constitutive models have also been developed and applied to other aspects. For example, a model representing shear dilation and a decrease in constant stress once slippage occurs was created for fluid injection-induced seismicity at Soultz-sous-Forets (Baisch et al. 2010); a stick-slip and creep-slip model with constant stress drops was applied to simulate and reproduce the repeating earthquakes at Parkfield (Beeler et al. 2001). Such factors as pore pressure, the orientation of the stress and the magnitude of the geologic formation and the orientation and frictional strength of the fault can have an important influence on the reactivation of the fault (Streit & Hillis 2004). The local safety factor and the slip tendency have been defined to identify the potential reactivation of every segment of the fault. The methods used to define the safety factor are also variable (Li et al. 2006, Vilarrasa et al. 2010). The slip tendency is defined as the ratio of the shear stress to the normal effective stress that acts on the fault (Streit & Hillis 2004), as shown in Eq. (2):

$$T_s = \frac{\tau}{\sigma_n - p_f} \tag{2}$$

where σ_n, τ and p_f are the normal total stress, shear stress and pore pressure that act on the fault,

respectively. Once the safety factor or the tendency of one segment of the fault is outside the secure range, this region of the fault is considered to have failed and the stress will be redistributed throughout the storage system. The residual shear loads will be supported by the other regions, resulting in the progressive failure of the fault and even in the reactivation of the entire fault. Cappa & Rutqvist (2011b) evaluated the seismic magnitude based on the following formulas:

$$M_o = \mu A d \tag{3}$$

$$M = \left(\log_{10} M_o / 1.5\right) - 6.1 \tag{4}$$

where M is the seismic magnitude, μ is the shear module, A is the reactive area and d is the slip distance. However, substantial uncertainties (i.e., the *in situ* stress and the strength of the fault), combined with the defective method of analysis, led to difficulty in drawing an exact analytical conclusion regarding fault reactivation (Rutqvist 2012). However, the action of a fault can be reflected through ground-surface motion (Morris et al. 2011b); thus, the monitoring of ground-surface displacement is a valid measure to assess the motion of a fault.

Faults can influence fluid flow both positively and negatively. To reflect the changes in the permeability of the fault along with any variation in stress, several flow models for faults have been proposed. If a fault is considered as two parallel plates corresponding to an interface or joint element, the flow capacity based on the cubic law is depicted as follows (Bower & Zyvoloski 1997; Cappa & Rutqvist 2011a):

$$Q = \frac{b^3}{12\mu} \cdot \frac{\Delta P}{\Delta L} \tag{5}$$

where b is the fault aperture based on the stiffness and stress state, μ is the dynamic viscosity for the fluid and $\Delta P / \Delta L$ is the pore pressure gradient. In addition, if the fault is treated as a solid element with weak stiffness and strength, the permeability of the fault can be regarded as a function of the strain or stress, as in the following formulas (Cappa & Rutqvist 2011a, Taron et al. 2009):

$$\begin{cases} \phi = 1 - (1 - \phi_i)\exp(-\varepsilon_v) \\ \phi = (\phi_i - \phi_r)\exp(a \cdot \sigma'_M) + \phi_r \end{cases} \tag{6}$$

$$\begin{cases} k = k_i \left(\dfrac{\phi}{\phi_i}\right)^n \\ k = k_i \left(\dfrac{1-\phi_i}{1-\phi}\right)^2 \left(\dfrac{\phi}{\phi_i}\right)^3 \\ k = k_i \exp\left[b \cdot \left(\dfrac{\phi}{\phi_i} - 1\right)\right] \end{cases} \tag{7}$$

where ϕ_i and k_i are the initial porosity and permeability, respectively; ε_v is the volumetric strain; σ'_M is the mean effective stress; and a, b and n are the empirical parameters. Finally, if the fault is treated as ubiquitously fractured media, the following equation can be used to display the permeability of the fault (Cappa & Rutqvist 2011a):

$$\frac{k}{k_i} = \left[\frac{a}{c\left(c\sigma'_n + 1\right)} \frac{1}{b_{hi}} + \frac{e_{ftp} + e_{fsp} \tan\psi}{f_d b_{hi}} \right]^3 \tag{8}$$

where ψ is the dilation angle; e_{fsp} and e_{fstp} are the plastic strain caused by shear and tensile failure, respectively; f_d is the fracture frequency; and b_{hi} is the initial fracture aperture. For some faults, the permeability normal to the fault is much lower than that parallel to the fault and can even be significantly lower than the surrounding formations. In these cases, the fault may act as a flow barrier and when the CO_2 encounters the fault, it may gather on one side and migrate parallel to the fault. Thus, the fault is not always considered be a leakage pathway for CO_2 escape (Morris et al. 2011a). However, the activation of the fault enhances the permeability of the fault, thus increasing the risk of CO_2 escape (Song & Zhang 2013).

The maximum injection pressure that will not create new fractures, not cause pre-fractures to slip or open and not reactivate the fault, is defined as the maximum sustainable injection pressure (Rutqvist et al. 2007). The maximum sustainable injection pressure can be determined simply by the site-specific fracture-close pressure obtained from direct or indirect testing (Rutqvist 2012). In addition, this pressure can be determined using Eq. (2) before the injection of CO_2. The upper bound of the pore pressure, which is provided by progressively increasing the pore pressure in Eq. (2) up to the critical state for fault slip, is regarded as the maximum sustainable injection pressure. This analytical approach is based on the pre-injection and remote stress field. However, the injection of CO_2 can disturb the stress state around the fault, thereby changing the normal and shear stress on the fault and leading to a substantially different maximum sustainable injection pressure. Thus, numerical modeling, simulating the change in stress with the injection of CO_2, may be advisable in these instances (Rohmer & Seyedi 2010, Rutqvist et al. 2007). Certainly, the factors that affect the stability of the fault have a similar influence on the maximum sustainable injection of CO_2.

4 CONCLUSIONS AND DISCUSSION

The paper reviews the numerical modeling of geomechanical issues associated with CO_2 storage in deep saline aquifers. All of the details discussed above are summarized in Table 1. The following conclusions can be derived from this table:

(1) At present, the numerical coupling methods for THMC processes in porous media can be divided into three categories: full coupling, partial coupling and one-way coupling. Full coupling, the

Table 1. Summary of the present methods for simulation of CO_2 sequestration systems.

Software			CodeBright	OpenGeoSys	FEMH	Geosim	DYNAFLOW	COMSOL	Eclipse(Abaqus)	Tough2-Flac3D	ToughReact-Flac3D	SIMEDII-Flac3D	Retraso-CodeBright	Tough2-Codes_Aster	NUFT-GEODYN_L	ATHOS-VISAGE	Eclipse/300-VISAGE	NUFT-LDEC	ATHOS(FEMH)-ABQUS
character istic	Coupling method	Full coupling	▲	▲	▲	▲	▲	▲											
		Partial coupling							▲	▲	▲	▲	▲	▲	▲	▲			
		One-way coupling															▲	▲	▲
	Numerical method	FEM	★	★	★	★	★	★	(★)				★	★	★	★	★		★
		FDM							★	★	★	★			★	★	★	★	★
		FVM								★	★			★					
		DEM																★	
	Constitutive model	elasticity		◆	◆	◆	◆		◆	◆	◆	◆		◆		◆			◆
		elastoplasticity						◆	(◆)	◆	◆	◆			◆		◆	◆	◆
		viscoplasticity	◆										◆						
		dual porosity poroelasticity								◆	◆								
	Additional factors	temperature	※	※	※	※	※	※	※	※	※	※	※	※	※	※	※	※	※
		chemistry		※	※				※		※		※		※		※	※	
application	stress and pore pressure change		⋆	⋆	⋆	⋆	⋆	⋆	⋆	⋆	⋆	⋆	⋆	⋆	⋆	⋆	⋆	⋆	⋆
	ground-surface deformation					△	△	△	△	△	△	△	△	△	△	△	△	△	△
	cap-rock integrity	①		●	●	●	●		●	●	●	●		●		●			●
		②						●	(●)	●	●				●		●		●
		③	●										●						
		④																●	
	fault stability	interface element							(□)	□				□					□
		weak solid element							(□)	□					□	□			□
		ubiquitously fracture media								□							□		□
remarks	numerical methods: FEM: finite element method; FDM: finite difference method; FVM: finite volume method; DEM: discrete element method cap-rock integrity: ①The cap-rock is presented as an intact elastic model, and new fractures are hypothesized to occur when the stress meets the shear or tensile criterion. The fractures are not explicitly addressed in the real model. ②The cap-rock is presented as an elastic-plastic model, and new fractures are expressed as the failure element. ③The cap-rock is presented as a visco-plastic model, and new fractures are expressed as the plastic strain. ④The cap-rock is presented as nodal cohesive elements, and new fractures occur with the nodal rapture. The fractures are explicitly addressed in the model.																		

highest-level coupling method, is suitable for relatively simple physical and geometrical modeling because of its large calculation cost and serious numerical stability problems. One-way coupling is primarily used for studying the problem by only focusing on the mechanical response. Partial coupling, which has an accuracy and calculation speed that falls between those of full coupling and one-way coupling, is the most widely used method of the three coupling methods.

(2) Isotropic elastic and elastic-plastic models are widely used for numerical modeling in CO_2 storage systems. Temperature can be considered in all of the methods, whereas only some of the methods consider chemical reactions.

(3) Any changes in stress-strain and pore pressure can be simulated by all of the models. However, the large-scale model (i.e., simulating a ground-surface deformation) and the complex model (i.e., involving a fault) are rarely simulated using the full coupling method.

(4) The intact elastic model is the most widely used method for simulating the integrity of the cap-rock. In this model, new fractures are hypothesized to occur where the stress meets the shear or tensile failure criterion. These fractures are not explicitly addressed in the model and the stress field is not affected by the new fractures. The cohesive element model, which is applied only in the discrete element method, can simulate crack propagation exactly, but changes in permeability are not coupled in the mechanical analysis.

(5) Fault stability can be simulated by linking two separate codes and the accuracy and complexity of the simulation are primarily based on the mechanical method. A single method, coupling the THMC processes to simulate a fault in a CO_2 storage system, has not yet been established.

Great progress has been made in the numerical modeling of the geomechanical issues that are associated with the storage of CO_2 in deep saline aquifers. However, the following issues may need to be explored further:

(1) At present, almost all geologic formations are considered to be isotropic materials. These constitutive models can describe the behavior of the rock during CO_2 injection to some extent, but they rarely consider the mechanical properties of the sedimentary rocks in saline aquifers. The saline aquifers that are suitable for CO_2 storage occur almost exclusively in sedimentary basins because they have a tremendous pore volume and connectivity and are widely distributed. Sedimentary rocks have a key mechanical property, namely, transverse isotropy, in which the mechanical properties remain the same horizontally and change vertically. However, the currently available simulations and their corresponding constitutive models usually assume that the deformation of the rock is isotropic, which differs from transverse isotropy. Thus, transverse isotropic models should be used for simulating the THMC processes in CO_2 storage systems in future studies.

(2) Some unexpected results may be obtained based on different mechanical constitutive models (i.e., elastic and elastic-plastic models). For example, according to the elastic model, the mechanical failure of the cap-rock is much more likely under a compressive stress regime than under an extensional stress regime. However, a completely opposite result can be derived from the elastic-plastic model. Thus, new constitutive models are needed in light of the influence of CO_2 on rock behavior. CO_2 can dissolve in the aqueous phase and produce weak acids, which could constitute a threat to the carbonate frame in the rock and the compaction or failure of the reservoir. If this process occurs, there is a possibility of a change in the characteristics of the reservoir with respect to porosity, specific surface, pore stiffness, wettability, mineralogy and mechanical failure. However, at present no constitutive model considers these effects. Constitutive models that specifically describe the rock under the conditions of CO_2-H_2O as two-phase fluids are needed. However, at present, the critical state model is the best available.

(3) It is not certain that existing fracture networks in the cap-rock lead to CO_2 leakage because it is difficult to predict how much change in fracture permeability will be induced by CO_2 injection. Recent research has either focused on the stress changes that are induced by CO_2 injection causing shear or tensile failure in the cap-rock without considering any change in the permeability of the cap-rock or on any change in fracture permeability without examining the effect of the fractures on the stress field. Thus, current research involves only a qualitative analysis of the integrity of the cap-rock. Thus, simulations should be developed to investigate the propagation of multiple cracks coupled with HTMC in order to assess the integrity of the cap-rock.

(4) At present, the simulations of a fault are primarily based on the Mohr-Coulomb criterion and the elastic perfectly plastic model. Because of the complex action of faults that are associated with the migration of CO_2, fault models that have been successfully applied in the other conditions should also be used for reference in CO_2 storage systems. In addition, because of the great amount of uncertainty regarding the properties and *in situ* stress of faults, probability analysis and sensitivity analysis, combined with the existing deterministic analysis, should be used in any compressive analysis of faults.

(5) Almost all of the current geomechanical analyses are focused on CO_2 sequestration systems with a single cap-rock. Thus, the geomechanical issues associated with the presence of a composite

cap-rock in a CO_2 sequestration system should be studied in the future.

(6) Although a geomechanical analysis of CO_2 storage systems has been performed to acquire a basic understanding, a perfect evaluation system and procedure for the stability analysis of an entire site is lacking. Such an evaluation system should be developed and used for site selection in the future.

ACKNOWLEDGEMENTS

The authors gratefully acknowledge the support of the National Science Foundation of China (NSFC). Project No. 41172285.

REFERENCES

Alonso, J., Navarro, V., Calvo, B. & Asensio, L. 2012a. Hydro-mechanical analysis of CO_2 storage in porous rocks using a critical state model. International Journal of Rock Mechanics & Mining Sciences 54:19–26.

Alonso, J., Navarro, V., Calvo, B. 2012b. Flow path development in different CO_2 storage reservoir scenarios a critical state approach. Engineering Geology 127:54–64.

Baisch, S., Voros, R., Rother, E. et al. 2010. A numerical model for fluid injection induced seismicity at Soultz-sous-
Forets. International Journal of Rock Mechanics & Mining Sciences 47:405–413.

Beeler, N.M., Lockner, D.L. & Hickman, S.H. 2001. A Simple Stick-Slip and Creep-Slip Model for Repeating Earthquakes and its Implication for Microearthquakes at Parkfield. Bulletin of the Seismological Society of America 91(6):1797–1804.

Bower, K.M. & Zyvoloski, G.1997. A numerical model for thermo-hydro-mechanical coupling in fractured rock. Int. J. Rock Mech. Min. Sci. 34(8):1201-1211.

Cappa, F. & Rutqvist, J. 2011a. Modeling of coupled deformation and permeability evolution during fault reactivation induced by deep underground injection of CO_2. International Journal Green Gas Control 5:336–346

Cappa, F. & Rutqvist, J. 2011b. Impact of CO_2 geological sequestration on the nucleation of earthquakes. Geophys Research Letters, Article first published online: 15 Sept. 2011.

Cappa F., Rutqvist, J. 2012. Seismic rupture and ground accelerations induced by CO_2 injection in the shallow crust. Geophysical Journal International. Doi: 10.1111/j.1365- 246X.2012.05606.x

Cappa, F., Rutqvist, J. & Yamamoto, K. 2009. Modeling crustal deformation and rupture processes related to upwelling of deep CO_2-rich fluids during the 1965–1967 Matsushiro earthquake swarm in Japan, J. Geophys. Res. 114, B10304.

Chang, K.W. & Bryant, S.L. 2007. Dynamics of CO_2 plumes encountering a fault in a reservoir. In Proceedings of the National Energy Technology Laboratory 6th Annual Conference on Carbon Capture and Sequestration, Pittsburgh, PA, 2007.

Connell, L.D. & Detournay, C. 2009. Couple flow and geomechanical processes during enhanced coal seam methane recovery through CO_2 sequestration. International Journal of Coal Geology 77:222–233.

Espinoza, D.N., Kim, S.H. & Santamarina, J.C. 2011. CO_2 geological storage-Geotechnical implications. KSCE J Civ Eng 15:707–719

Ferronato, M., Gambolati, G., Janna, C. et al. 2010. Geomechanical issues of anthropogenic CO_2 sequestration in exploited gas fields. Energy Conversion and Management 51:1918–1928.

Gens, A., Carol, I. & Alonso, E.E. 1990. A constitutive model for rock joints formulation and numerical implementation. Computers and Geotechnics 9(1):3–20.

Goerke, U.J., Park, C.H., Wang, W., Singh, A.K. & Kolditz, O. 2011. Numerical simulation of multiphase hydromechanical processes induced by CO_2 injection into deep saline aquifers. Oil & Gas Science and Technology – Rev. IFP Energies nouvelles 66(1):105–118.

Goodarzi, S., Settari, A. & Keith, D. 2012. Geomechanical modeling for CO_2 storage in Nisku aquifer in Wabamun Lake area in Canada. International Journal of Greenhouse Gas Control 10:113–122.

Gutierrez M., Øyno, L.E. & Nygård, R. 2000. Stress-dependent permeability of a demineralised fracture in shale. Mar Pet Geol 17:895–907.

Hawkes, C.D., McLellan, P.J. & Bachu, S. 2005. Geomechanical factors affecting geological storage of CO_2 in depleted oil and gas reservoirs. J Can Pet Technol 44:52–61.

Hettema, M.H.H., Schutjens, P.M.T.M. et al. 2000. Production compaction of a sandstone reservoir: the strong influence of stress path, SPE 65410. SPE Reservoir Eval. Eng. 3 (August (4)).

Johnson, J.W., Nitao, J.J. & Morris, J.P. 2004. Reactive transport modeling of cap rock integrity during natural and engineered CO_2 storage. Carbon dioxide capture for storage in deep geologic formations (two-volume set published by Elsevier: ISBN 0080445705).

Kanamori, H. & Anderson, D.L. 1975. Theoretical basis of some empirical relations in eismology. Bull Seism Soc Am 65:1073–1095 .

Kanamori, H. & Brodsky, E.E. 2001. The physics of earthquakes. Physics Today (June 2001):34–40.

Kolditz, O., Bauer, S., Bilke, L. et al. 2012. OpenGeoSys: an an open-source initiative for numerical simulation of thermo-hydro-mechanical/chemical (THM/C) processes in porous media. Environ Earth Sci 67:589–599.

Kvamme, B. & Liu, S. 2009. Reactive transport of CO_2 in saline aquifers with implicit geomechanical analysis. Energy Procedia 1:3267–3274.

Ladanyi, B. & Archambault, G. 1970. Simulation of the shear behaviour of a jointed rock mass. In Proc 11th US Symposium on Rock Mechanics, Berkeley, 1970. pp. 105–25.

Lewis, R.W. 1991. Coupling versus uncoupling in soil consolidation. International Journal for numerical and analytical methods in Geomechanics 15:533–548.

Li, Q., Ito, K. Wu, Z.S., Lowry C.S. & and Loheide II S.P. 2009. COMSOL Multiphysics: A Novel Approach to Groundwater Modeling, Ground Water, 47(4):480–487.

Li, Q., Wu, Z.S., Li, X.C. et al. 2006. Site geomechanics analysis of CO_2 geological sequetsration. IAEG 2006 Paper number 129.

Li, Q., Wu, Z.S., Y. Murakami, Y., Satoh, T. & Lei X.-L. 2005. Hydraulic and Geomechanical Simulation of Fractured Porous Media under Geo-Sequestration of Carbon Dioxide, in Poromechanics III – Biot Centennial (1905–2005), edited by Y. Abousleiman, A. H. D. Cheng and F.-J. Ulm, pp. 669–674, Taylor & Francis, Norman, Oklahoma, USA.

Li, X.C & Liu Y.F. 2006. Ranking and screening of CO_2 saline aquifer storage zones in China. Chinese Journal of Rock Mechanics and Engineering 25(5):963–968 (in Chinese).

Liu, S. & Kvamme, B. 2008. Improved Newton Raphson Method- An effective tool in solving flow-mechanical-chemistry equations of CO_2 storage in Saline aquifers. American conference on applied mathematics (MATH 08), Harvard, Massachusetts, USA, March 24–26, 2008.

Longuemare, P., Mainguy, M. & Lemonnier, P. et al. 2002. Geomechanics in reservoir simulation: overview of coupling methods and field case study. Oil & Gas Science Technology-Rev. IFP, 57(5):471–483.

Morris, J.P., Detwiler, R.L., Friedmann, S.J. et al. 2011a. The large-scale geomechanical and hydrogeological effects of multiple CO_2 injection sites on formation stability. International Journal of Greenhouse Gas Control 5:69–74.

Morris, A., Ferril, D.A. & Henderson, D.B. 1996. Slip tendency analysis and fault reactivation. Geology 24(3): 275–8.

Morris, J.P., Hao, Y., Foxall, W. & McNab, W. 2011b. A study of injection-induced mechanical deformation at the In Salah CO_2 storage project. International Journal of Greenhouse Gas Control 5:270–280.

Morris, J., Johnson, S., & Friedmann, S.J. 2008. Geomechanical Simulations of Caprock Integrity Using the Livermore Distinict Element Method. Seventh Annual Conference on Carbon Capture and Sequestration Pittsburgh, PA, United States May 5–8, 2008.

Nguyen, M.T., Bemer, E. & Dormieux, L. 2011. Micromechanical modeling of carbonate geomechanical properties evolution during acid gas injection. Proc 45th US Rock Mech/Geomech Symp, San Francisco, California, USA, June 27–June 30, 2011.

Oka, F., Kimoto, S., Kobayashi, H. et al. Anisotropic behavior of soft sedimentary rock and a constitutive model. Soils and foundations 42(5):59–70.

Olden, P., Pickup, G., Jin, M. et al. 2012. Use of rock mechanics laboratory data in geomechanical modelling to increase confidence in CO_2 geological storage. International Journal of Greenhouse Gas Control 11:304–315.

Olivella, S., Gens, A., J. Carrera, J. & Alonso, E.E. 1996. Numerical Formulation for a Simulator (CODE_ BRIGHT) for the Coupled Analysis of Saline Media, Engineering Computations 13(7):87–112.

Orlic, B. ter Heege, J. & Wassing, B. 2011 Assessing the integrity of fault- and top seals at CO_2 storage sites. Energy Procedia 4:4798–4805.

Ouellet, A., Bérard, T., Desroches, J. et al. 2011. Reservoir geomechanics for assessing containment in CO_2 storage: a case study at Ketzin, Germany. Energy Procedia 4:3298–3305.

Park, C.-H., Taron, J., Gorke, U.-J. et al. 2011. The fluidal interface is where the action is in CO_2 sequestration and storage: Hydromechanical analysis of mechanical failure. Energy Procedia 4:3691–3698.

Preisig, M. & Prevost, J.H. 2011. Coupled multi-phase thermo-poromechanical effects. Case study: CO_2 injection at In Salah, Algeria. International Journal of Greenhouse Gas Control, 5:1055–1064.

Prevost, J.H. 1981. DYNAFLOW: A Nonlinear Transient Finite Element Analysis Program.Department of Civil and Environmental Engineering, Princeton University, Princeton, NJ. http://www.princeton.edu/dynaflow/

Rohmer, J. & Seyedi, D.M. 2010. Coupled large scale hydromechanical modeling for cap-rock failure risk assessment of CO_2 storage in deep saline aquifers. Oil & Gas Science and Technology- Rev. IFP. 65:503–517.

Rutqvist, J. 2011. Status of the TOUGH-FLAC simulator and recent applications related to coupled fluid flow and crustal deformations. Computers & Geosciences 37: 739–750.

Rutqvist, J. 2012. The geomechanics of CO_2 storage in deep sedimentary formations. Geotech Geol Eng 30:525–551.

Rutqvist, J., Birkholzer, J.T. & Tsang, C.-F. 2008. Coupled reservoir–geomechanical analysis of the potential for tensile and shear failure associated with CO_2 injection in multilayered reservoir-caprock systems. International Journal of Rock Mechanics & Mining Sciences 45:132–143.

Rutqvist, J., Birkholzer, J., Cappa, F. & Tsang, C.F. 2007. Estimating maximum sustainable injection pressure during geological sequrestration of CO_2 using coupled fluid flow and geomechanical fault-slip analysis. Energy Conversion and Management 48:1798–1807.

Rutqvist, J. & Tsang, C.-F. 2003. Tough-Flac: A numerical simulator for analysis of coupled thermal-hydrologic-mechanical processes in fractured and porous geological media under multi-phase flow condition. Proceeding, TOUGH Symposium 2003, Lawrence Berkeley National Laboratory, Berkeley, California, May 12–14, 2003.

Rutqvist, J., Vasco, D.W. & Myer, L. 2010. Coupled reservoir-geomechanical analysis of CO_2 injection and ground deformations at In Salah, Algeria. International Journal of Greenhouse Gas Control 4:25–230.

Rutqvist, J., Wu, Y.S., Tsang, C.F. & Bodvarsson, G. 2002. A modeling approach for analysis of coupled multiphase fluid flow, heat transfer and deformation in fractured porous rock. International Journal of Rock Mechanics & Mining Sciences 39:429–442.

Settari, A. & Walters, D.A. 1999. Advances in coupled geomechanical and reservoir modeling with applications to reservoir compaction. In: SPE Reservoir Simulation Symposium, Vol. SPE 74142, pp. 334–342.

Seyedi, D., Ducellier, A., Foerster, E. et al. 2009. Coupled hydromechanical modeling to study the integrity and safety of geological storage of CO_2. Energy Procedia 1:2541–2548.

Shi, J.-Q. & Durucan, S. 2009. A coupled reservoir-geomechanical simulation study of CO_2 storage in a nearly depleted natural gas reservoir. Energy Procedia 1:3039–3046.

Smith, J., Durucan, S., Korre, A. & Shi, J.-Q. 2011. Carbon dioxide storage risk assessment: Analysis of cap-rock fracture network connectivity. International Journal of Greenhouse Gas Control 5:226–240.

Song, J. & Zhang, D. 2013. Comprehensive review of caprock sealing mechanisms for geologic carbon sequestration. Environ. Sci. Technol. 47:9–22.

Souley, M., Homand, F. & Amadei, B. 1995. An extension to the Saeb and Am,adei constitutive model for rock joints to include cyclic loading paths. International Journal of Rock Mechanics and Mining Sciences & Geomechanics Abstracts 32(2):101–109.

Streit, J.E. & Hillis, R.R. 2004. Estimating fault stability and sustainable fluid pressures for underground storage of CO_2 in porous rock. Energy 29:1445–1456.

Taron, J., Elsworth, D. & Min, K.-B. 2009. Numerical simulation of thermal-hydrologic-mechanical-chemical processes in deformable, fractured porous media. International Journal of Rock Mechanics & Mining Sciences 46:842–854.

TAURUS Reservoir Solutions Ltd. Reservoir and Geomechanical Simulation and Engineering. http://www.taurusrs.com/geosim.html

Vidal-Gilbert, S., Nauroy, J.-F. & Brosse, E. 2009. 3D geomechanical modeling for CO_2 geologic storage in the Dogger carbonates of the Paris Basin. International Journal of Green Gas Control 3:288–299.

Vilarrasa, V., Bolster, D., Olivella, S. et al. 2010. Coupled hydromechanical modeling of CO_2 sequestration in deep

saline aquifers. International Journal of Greenhouse Gas Control 4:910–919.

Vilarrasa, V., Olivella,S. & Carrera, J. 2011. Geomechanical stability of the caprock during CO_2 sequestration in deep saline aquifers. Energy Procedia 4:5306–5313.

Yin, S., Dusseault, M.B. & Rothenburg, L. 2012. Coupled THMC modeling of CO_2 injection by finite element methods. Journal of Petroleum Science and Engineering, 80:53–60.

Yuan, W., Li, X. & Bai, B. 2013. The application of the strength reduction method in site stability analysis of CCS. Clean Energy Systems in the Subsurface: Production, Storage and Conversion Springer Series in Geomechanics and Geoengineering 2013, pp. 265–280.

Zhu, W., Zhang, Q., Li, S. et al. 2013. Brittle Elastoplastic Damage Constitutive Model for Jointed Rockmasses and Computation Concerning Bolt-Reinforcement. International Journal of Damage Mechanics 12(1):65.

This page intentionally left blank

1. Rock mass characterization

This page intentionally left blank

Rock Mechanics for Resources, Energy and Environment – Kwaśniewski & Łydżba (eds)
© 2013 Taylor & Francis Group, London, ISBN 978-1-138-00080-3

A preliminary geoengineering assessment of Bazda antique underground quarries in Şanlıurfa, Turkey

C. Ağan & M.İ. Yeşilnacar
Departments of Civil and Environmental Engineering, Harran University, Şanlıurfa, Turkey

M. Geniş
Department of Mining Engineering, Bülent Ecevit University, Zonguldak, Turkey

S. Kulaksız & R. Ulusay
Departments of Mining and Geological Engineering, Hacettepe University, Ankara, Turkey

Ö. Aydan
Institute of Oceanic Research and Development, Tokai University, Shizuoka, Japan

M.D. Yücel
Bahcelievler Mah., Aydogan Sitesi, Adapazarı, Turkey

ABSTRACT: Geoengineering evaluation of man-made antique underground structures improves and provides important information on such structures. Harran City in Şanlıurfa Province of Turkey was constructed probably during Sumerian period BC 3000 (5000 years BP). The building stones consisting of limestones of Harran City were extracted from open-pit and underground quarries known as Bazda quarries. Bazda antique underground quarry pillars suffer some structural stability problems in terms of splitting of high pillars, roof falls, plane or wedge sliding and large sinkholes. The authors have initiated a collaborative integrated research program to map the antique underground quarries having working levels up to four floor, in-situ rock characterization, identification of stability problems, some geomechanical properties of surrounding rock. This paper describes the first preliminary studies on Bazda antique underground quarries and discusses its implications in modern geomechanics and geoengineering.

1 INTRODUCTION

The long-term performance of underground openings is of great importance for civil engineering utilization and also the nuclear waste disposal. Therefore, the geoengineering evaluation of man-made antique underground structures improves and provides important information on such structures. There are several geoengineering studies on such antique underground structures in literature. Turkey also has a number of antique underground openings, such as those in the Cappadocia Region and in Şanlıurfa Province. Harran City in the Şanlıurfa Province was constructed probably during Sumerian period BC 3000 (5000 years BP). The building stones of Harran City, where there is no rock outcrop, were extracted from open-pit and underground quarries in Tek-Tek Mountain and they are called as Bazda quarries, which are the oldest underground quarry known in Turkey as well as in the world. These quarries are about 7–8 km away from the city and the extracted stones are Eocene aged limestone. Stone blocks from Bazda quarries were used in the construction of Harran ancient city, the temple of Moon and Sun God and the nearby historical Hanel Ba'rür caravanserai and Şuayb City. Underground rooms in Bazda extend more than 50 m and pillars are mostly in rectangular or nearly square shape. These quarries have greatest importance for both underground excavation techniques in the past as well as the long-term performance of underground mining.

Bazda antique underground quarry pillars suffer some structural stability problems in terms of splitting of high pillars, roof falls, plane or wedge sliding and large sinkholes. Therefore, it provides a great variety of stability problems, which may develop in short and long-term. The authors have initiated a collaborative integrated research program to map the antique underground quarries having working levels up to four floors, in-situ rock characterization, identification of stability problems, some geomechanical properties of surrounding rock. This paper describes the first preliminary studies on Bazda antique underground quarries and discusses its implications in modern geomechanics and geoengineering. For the purpose, plans of some underground quarries were

prepared based on laser meter measurements, rock mass characteristics were determined, rock blocks from some quarries for geomechanical testing were collected, rock mechanics tests were conducted and preliminary assessments on the observed instabilities were performed.

2 ENGINEERING GEOLOGICAL CHARACTERISTICS OF THE QUARRIED ROCK

Limestones are abundant in the Şanlıurfa Province and the majority of which are reef limestones of Middle-Upper Eocene age (Turgut & Yeşeilnacar 2008). Their thickness ranges between 50 and 300 m and they include fossils. Some small karstic features in the limestones are also observable. The limestones can easily be cut with a hand-held saw. Prior to the use of reinforced concrete structures, limestone was the main building material for major construction in the province. However, it is still used to a limited extent as structural material or external cladding.

As a part of the study, thin-sections of four specimens collected from different quarries were examined. Thin-section studies indicated that all samples were micritic or micro-sparitic or sparitic limestones and include abundant amount of calcite mineral with some fossils. In some samples, calcites are not matured and have formed under pressure. In addition, X-ray diffraction analyses of these samples were also conducted. The XRD diffractograms showed that calcite was the dominant mineral in the limestone samples. However, in two samples (B1 and B2), small amount of dolomite ranging between 12 and 23% were also observed.

Limestone at Bazda quarries is very thickly and horizontally bedded (with spacing between 4- and 8 m) and intersected by mutually orthogonal widely spaced main two joint sets, which are vertical or subvertical. The joint surfaces are free from infill material, generally unweathered and very rough. In addition, some normal faults with left/right lateral offsets and generally dips of 70° are also observed.

3 HISTORY OF THE BAZDA QUARRIES

In view of recent findings in Göbekli Tepe in Şanlıurfa, the quarrying of limestone in the region extends at least 11000 BP. It is estimated that Harran City was established, at least 5000 years ago, during the period of Sumerians, who came from Central Asia to Mesopotamia about 7000 years ago and governed the area until BC 2270. Sumerians were the pioneers in all aspects of the modern science, engineering, technology, culture and religion of mankind including the cunical scripts (Kramer 1956). It is known that building stones used in this city were extracted from open-pit and underground quarries in Tek-Tek Mountain and they are known as Bazda quarries. Although it is well-known that the underground quarries existed in Qurna (Luxor, Egypt), the scale and antiquity of

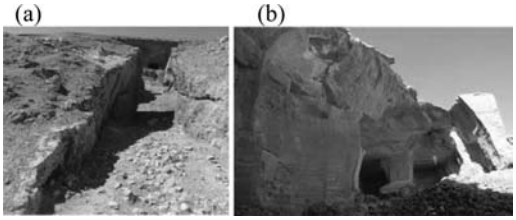


Figure 1. Remnants of open-pit and underground quarries during the early stages of excavations: (a) Pathway leading to the quarries, (b) initial underground quarries.

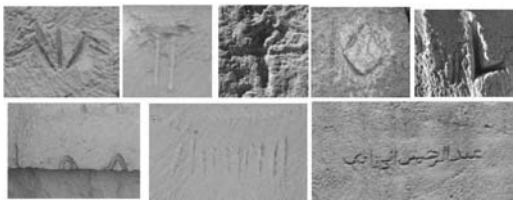


Figure 2. Examples of scripts observed in Bazda underground quarries.

Bazda underground quarries are probably larger and older than those in Qurna underground quarry in Luxor region of Egypt (Kulaksız & Aydan 2010).

The limestone blocks were initially extracted at Bazda quarries through open-pit quarries. It seems that the engineers in ancient times also used structural discontinuities in rock mass to their favour for extraction of stones as noted in Figure 1a. However, as the overburden increased and limestone was more massive at depth, the quarrying method changed to underground extraction using room and pillar technique (Figure 1b). One can also infer numerous underground quarries next to each other from the wall left between adjacent quarries. It is unknown when the excavation was changed from open-pit quarrying to underground quarrying. One can recognize symbols of similar to numerals used by Sumerians' and following civilizations in Mesopotamia. Figure 2 shows several symbols and scripts found at underground quarries.

4 LAYOUT, EXCAVATION TECHNIQUES AND ENVIRONMENTAL CONDITIONS

The underground Bazda quarries have been excavated using the room and pillar method and have different dimensions. Their lengths from the entrances range between 35 and 105 m, widths and heights are between 15–50 m and 4 and 25 m, respectively. The thickness of the overburden varies from place to place and is between 4 and m. Pillar and room arrangement types are regular, random or isolated panels containing board pillars. Pillar shapes are square or rectangular. The distances between the pillar range between 4 and 10 m and pillar sizes (2.7×3.3 m, 2.2×2.1 m, 2.8×1.75 m) are different. There are three floors in a few quarries. Schematic plan view of one of the underground quarries, and some views from underground

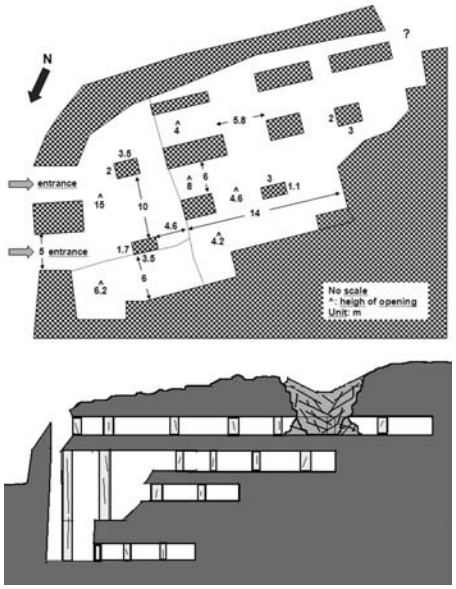


Figure 3. Layout plan and its cross-section of one of the underground quarries in Bazda.

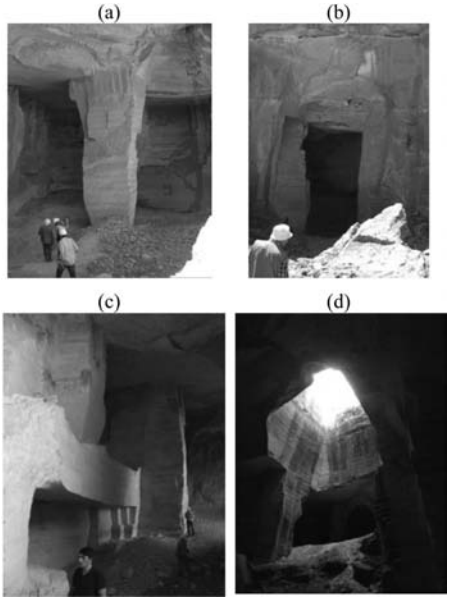


Figure 4. Some views from the Bazda underground quarries: (a) pillars, (b) gate, (c) openings and floors, (d) ventilation shaft.

open stops, pillar quarry entrance and pillar shape arrangements are shown in Figures 3 and Figure 4, respectively. Except a very large underground quarry involving three floors (Figure 4d), the quarries have no ventilation shaft. However, a shaft is recognized in the largest quarry.

Based on the observations by the authors, the cutting tools of blocks in the quarries were mostly chisels hammer. In their some parts, the authors observed

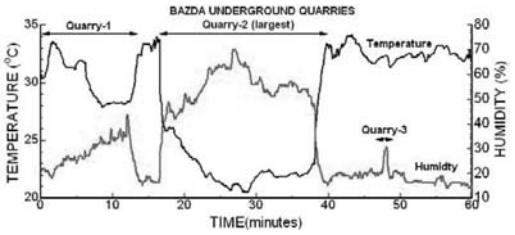


Figure 5. Temperature and humidity variations during site investigations of quarries (Date: September 14, 2012).

traces of saw blade at the top of the openings. Nearly rectangular shaped trenches in the openings (15–20 cm × 2 cm × 15 cm) have probably been used for wedge type block cutting method.

During site investigations, some environmental conditions such as temperature, humidity and air pressure were also measured using an ONDOTORI TR-73U device produced by TANDD. The sampling rate was 15 seconds. Figure 5 shows the temperature and humidity variations in underground quarries during the site-exploration. The largest underground quarry is about 150 m long and 50 m wide. The temperature was about 20.5°C and RH was 70% at the deepest point from the entry of the quarry while temperature and humidity was 34.4°C and 14% outside the largest quarry. In other words, there is huge temperature and humidity variations, to which rock mass is subjected. Temperature and humidity in quarries vary depending upon their size.

5 MECHANICAL PROPERTIES OF THE SUROUNDING ROCK AND EFFECTS

5.1 *Short-term properties*

Short-term tests involved the determination of unit weight, porosity, void ratio, P-wave velocity, uniaxial compressive strength (UCS), tensile strength, cohesion and internal friction angle, modulus of elasticity and Poisson's ratio and Schmidt hammer rebound value of the surrounding limestone as rock material under both dry and fully saturated conditions at the rock mechanics laboratories of Hacettepe and B. Ecevit Universities (Turkey) and Tokai University (Japan). These tests were carried out in accordance with the test procedures suggested ISRM (2007). The test results including range of parameters, their mean values and the number of specimens tested are given in Table 1.

The limestone is susceptible to large water content variations. Experiments at Tokai University indicated that limestone can absorb 14–18% water and its strength characteristics are greatly affected by the water content. The UCS and tensile strength can be reduced up to 40% of those under dry states. Figure 6 shows the water content variation of limestone with time. It generally takes about 3 days to dry under conductive type drying environment.

Table 1. Physical, strength and deformation properties of tuff in dry and saturated conditions.

Material properties	Average value ± SD (n: test number)
Dry unit weight (kN/m^3)	17.5 ± 0.8 (n = 126)
Saturated unit weight (kN/m^3)	20.2 ± 0.7 (n = 33)
Porosity (%)	25.4 ± 3.9 (n = 37)
Void ratio	0.37 ± 0.14 (n = 38)
Water absorption by weight (%)	15.0 ± 1.1 (n = 8)
Specific gravity	2.64 ± 0.04 (n = 8)
UCS (dry) (MPa)	14.1 ± 2.4 (n = 39)
UCS (saturated) (MPa)	5.62 ± 1.21 (n = 34)
Brazilian tensile strength (dry) (MPa)	1.83 ± 0.21 (n = 22)
Brazilian tensile strength (saturated) (MPa)	0.81 ± 0.09 (n = 19)
Bending strength (dry) (MPa)	3.77 ± 0.56 (n =4)
Bending strength (saturated) (MPa)	1.47 ± 0.19 (n =3)
Young's modulus (GPa)	13.1 ± 3.5 (n = 11)
Poisson's ratio	0.22 ± 0.03 (n = 8)
P-wave velocity (dry) (m/s)	2729 ± 106 (n = 105)
P-wave velocity (saturated) (m/s)	2533 ± 517 (n = 19)
S-wave velocity (dry) (m/s)	1424 ± 176 (n = 14)
(S-wave velocity (saturated) (m/s)	1170 ± 50 (n = 8)
Cohesion (MPa)	3.64 ± 0.89 (n = 4)
Internal friction angle (°)	38.5 ± 7.1 (n = 4)
Slake durability index Id_2 (%)	87.5 ± 2.8 (n = 9)
Schmidt rebound value	12.6 ± 0.6 (n = 58)

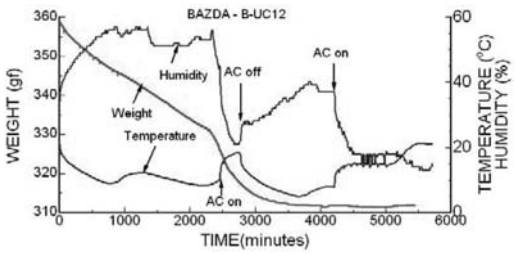


Figure 6. The variation of water content during drying process of the Bazda limestone.

5.2 *Long-term properties*

A series of bending, Brazilian and uniaxial compression creep tests has been carried out at Tokai University and Toyota National College of Technology. In some experiments, specimens were initially dry and saturated during creep experiments. During experiments, acoustic emission responses are also monitored in addition to the displacement measurements. Some preliminary results of Brazilian and bending creep tests at Tokai University have been obtained and the results are shown in Figure 7. Figure 8 shows the relation between the normalized failure time an applied stress ratio. Although the results shown in Figure 8 are still few, the general trend of the experimental data follow the empirical relation proposed by Aydan & Nawrocki (1998).

The slake durability and wetting and drying tests, known as accelerated weathering tests, are carried out

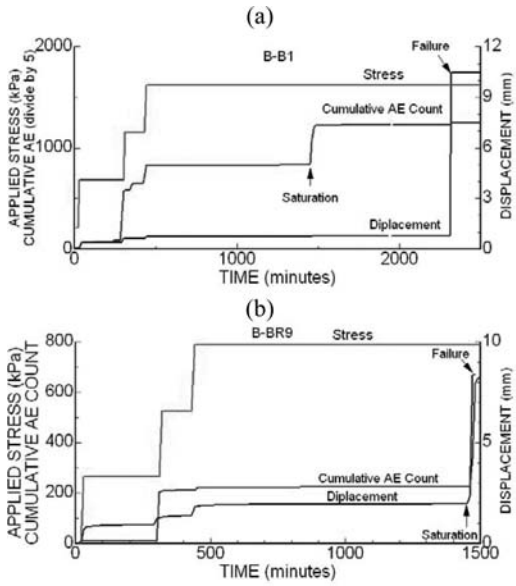


Figure 7. Responses of samples in (a) bending creep test, and (b) Brazilian indirect tensile creep test.

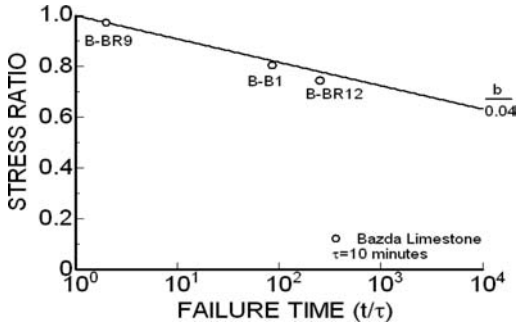


Figure 8. Relation between creep failure time and applied stress ratio in bending and Brazilian creep experiments and their comparison with the empirical law of Aydan & Nawrocki (1998).

to assess the durability of the surrounding rock under different environmental conditions. The experimental results on cyclic wetting and drying experiments indicated that the rock is not very sensitive to such cycles. The slaking durability tests are indicated the rock has almost none slaking characteristics.

6 IN-SITU STRESS STATE IN BAZDA AND ITS VICINITY

There is no in-situ stress measurement at this site yet. However, preliminary experiments on the samples from the site indicated that the Kaiser effect, which is used in in-situ stress estimations, is clearly observed. Therefore, the oriented sampling at this site should provide some information on the possible stress-state.

Table 2. Inferred crustal stresses for striation and large earthquakes for Bazda quarries.

		Fault 1	Fault 2	2102 Bozova E.	2010 Hilvan E.
σ_1	σ_1/σ_v	1.05	1.06	1.45	1.43
	d_1	178	187	206	17
	p_1	69	67	8	12
σ_2	σ_2/σ_v	0.72	0.73	1.00	0.98
	d_2	32	33	72	218
	p_2	19	21	77	77
σ_3	σ_3/σ_v	0.35	0.35	0.48	0.48
	d_3	65	299	297	108
	p_3	8	9	8	5
	σ_h/σ_v	0.36	0.37	0.50	0.48
	σ_H/σ_v	0.76	0.77	1.45	1.41
	θ	337	27	27	17

Preliminary stress state inferences for the site and its close vicinity have been done using the method of Aydan (Aydan 2000; Aydan & Kim 2002; Aydan et al. 2002) from the striations of the faults at Bazda quarries and focal mechanism solutions of some recent earthquakes in the close vicinity of the site. The inferred stress states for faults and some recent earthquakes are given in Table 2. As noted from the table, the maximum horizontal stress is almost north-south and the vertical stress is close to the maximum principal stress inferred from fault striations. The horizontal stress ratio ranges between 0.36 and 0.5. Therefore, it is expected that the overburden stress would be the dominant factor governing the stability of the quarries. The overburden at underground quarries ranges between 3 to 35 m.

7 INSTABILITY PROBLEMS AND THEIR CAUSES

Rock mass observed in the Bazda Quarries was classified using RMR (Bieniawski, 1989) and Q-System (Barton et al. 1974) rock classifications. Kulaksız & Aydan (2010) classified Bazda limestone as massive and thickly bedded limestone. In addition, thinly bedded limestone layers are also observed at the roofs of the underground quarries visited by the authors and roof falls are generally associated with these layers. Furthermore, some normal faults are observed and the rock mass in the close vicinity of the faults are heavily fractured and include some clayey materials. The results of evaluations done in this study are given in Table 3 together with those by Kulaksız & Aydan (2010).

There are various forms of instability observed in Bazda underground quarries (Figures 9 and 10). When the excavation ratio is large or pillars are high, shearing and/or splitting failure of pillars are observed (Figure 9). As the limestone is bedded and has vertical or subvertical joints, roof falls occur either due to the tensile separation or free fall of blocks of layers from upper layers (Figure 10). As there are many recent large fallen

Table 3. Rock classifications of Bazda underground quarries.

	Kulaksız & Aydan (2010)		This study
Condition	RMR	Q-Value	RMR
Massive limestone	80–90	5–50	77–82
Thickly bedded limestone	60–80	5–25	64–74
Thinly bedded limestone	–	–	59–69
Fault zone	–	–	29–33

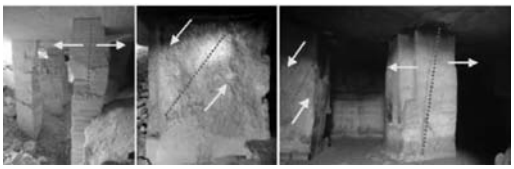


Figure 9. Shearing and/or splitting failure of pillars.



Figure 10. Some examples of roof failures.

rock blocks, they may be due to the creep failure under tensile stress regime and/or seismic events taking place from time to time. In addition, some huge blocks are fallen in the close vicinity of quarry entries when they are crossed by faults. Furthermore, a huge sinkhole was observed and its diameter was more than 39 m (Figure 10).

Aydan & Tokashiki (2011) described several methods to analyse the stability of natural and man-made underground openings. Figure 11 shows the stability assessment of pillars and roof of the underground quarries using the method of Aydan & Tokashiki (2011) together with some observations. It seems that some stability problems occur when the unsupported span is wider than 8 m and RMR value ranges between 60 and 70. The data for collapsed locations shown in Figure 11(b) imply that unsupported span cannot be more than 30 m for RMR value ranging between 60 and 70. These results are surprisingly similar to the estimations from empirical relations proposed Aydan & Tokashiki (2011). Although the computational results are consistent with observations, further studies and exact geometry of underground quarries and topography are necessary for better assessments including more sophisticated techniques.

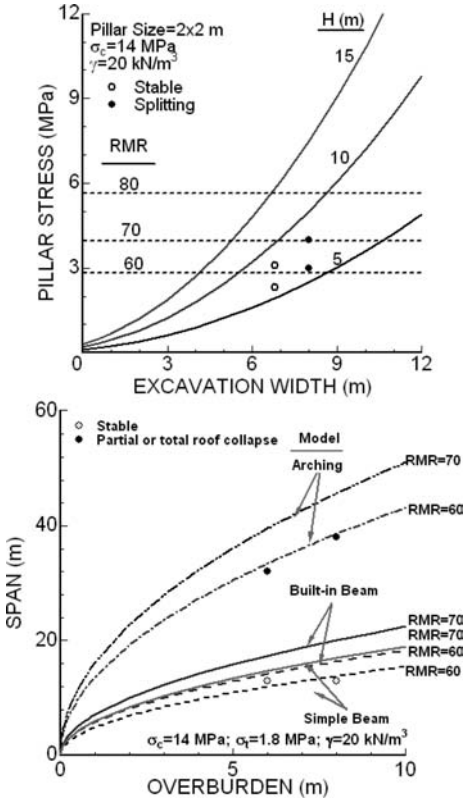


Figure 11. The stability assessment of pillars and openings of Bazda underground quarries and comparisons with observations.

8 CONCLUSIONS AND FURTHER STUDIES

The Bazda underground quarries are important cultural assets of mankind and it should also provide important information on the long-term behaviour of rock masses, which may be very valuable for underground space utilization as well as nuclear disposal sites in rock. This paper is just a preliminary study and further detailed studies are needed. Nevertheless, some of preliminary conclusions may be summarized as follow:

1) Limestone is quite susceptible to water absorption and its geomechanical properties are greatly reduced by increase in its water content.
2) Bazda underground quarries suffer some structural stability problems in terms of splitting of high pillars, roof-falls, plane or wedge sliding and formation of large sinkholes.

As mentioned previously, since this is a preliminary study, and there are some rooms for further studies, which are as follow:

1) The geometry of the underground quarries and topography of the area are necessary for better evaluations of the state of underground quarries in long-term.
2) Experiments on the long-term mechanical characteristics of limestone are necessary. Such experiments should clarify several aspects on the long-term stability of Bazda underground quarries.
3) Although the overburden of the Bazda underground quarries is less than 30 m, the evaluation of in-situ stress state and its variation in time in the close vicinity of these quarries are necessary. Nevertheless, it is expected that the overburden stress is the major principal stress and lateral stress coefficient should be around 0.45.
4) Although the Bazda underground quarries are in an aseismic region of Turkey, further studies are necessary to clarify the situation in relation to their stability during earthquakes.

REFERENCES

Aydan, Ö. 2000. A stress inference method based on structural geological features for the full-stress components in the earth' crust. *Yerbilimleri* 22: 223–236.

Aydan, Ö. & Nawrocki, P. 1998. Rate-dependent deformability and strength characteristics of rocks. *Geotechnics of Hard Soils-Soft Rocks, Proc. intern. symp.*, Napoli, Vol. 1, pp. 403–411.

Aydan, Ö. & Kim, Y. 2002. The inference of crustal stresses and possible earthquake faulting mechanism in Shizuoka Prefecture from the striations of faults. *J. School of Marine Science and Technology*, *Tokai University* 54: 21–35.

Aydan Ö., Kumsar H. & Ulusay R. 2002. How to infer the possible mechanism and characteristics of earthquakes from the striations and ground surface traces of existing faults. *Earthquake and Structural Engineering/Earthquake Engineering, JSCE* 19 (2): 199–208.

Aydan, Ö. & Tokashiki, N. 2011. A comparative study on the applicability of analytical stability assessment methods with numerical methods for shallow natural underground openings. *The 13th International Conference of the International Association for Computer Methods and Advances in Geomechanics*, Melbourne, Australia, pp. 964–969.

Barton, N., Lien, R. & Lunde, I. 1974. Engineering classification of rock masses for the design of tunnel supports. *Rock Mechanics* 6 (4): 189–239.

Bieniawski, Z.T. 1989. *Engineering Rock Mass Classifications*. New York, John Wiley & Sons.

ISRM, 2007. *The Complete ISRM Suggested Methods for Rock Characterization, Testing and Monitoring: 1974–2006*. Suggested Methods Prepared by the Commission on Testing Methods, International Society for Rock Mechanics, R. Ulusay & J.A. Hudson (eds.), Compilation Arranged by the ISRM Turkish National Group, Ankara, Turkey.

Kramer, S.N. 1956. *History Begins at Sumer: Thirty-Nine Firsts in Man's Recorded History*. University of Pennsylvania Press.

Kulaksız, S. & Aydan, Ö. 2010. Characteristics of ancient underground quarries of Turkey and Egypt and their comparison. *22nd World Mining Congress*, Istanbul, pp. 607–614.

Turgut, P. & Yesilnacar, M.I. 2008. Physico-thermal and mechanical properties of Sanliurfa limestone, Turkey. *Bulletin of Engineering Geology and the Environment* 67: 485–490.

Rock Mechanics for Resources, Energy and Environment – Kwaśniewski & Łydżba (eds)
© 2013 Taylor & Francis Group, London, ISBN 978-1-138-00080-3

The geological and geotechnical susceptibility of Jurassic and Cretaceous units; A case study from Central-Western Portugal

P.S. Andrade
Department of Earth Sciences/Geotechnology-FCT, University of Coimbra, Coimbra, Portugal

H. Ventura
Department of Earth Sciences, University of Coimbra, Coimbra, Portugal

P.M. Callapez
Department of Earth Sciences /Geographical Institute of the University of Coimbra-FCT, University of Coimbra, Coimbra, Portugal

ABSTRACT: The purpose of this work is to present a study of the geologic and geotechnical susceptibility of units located in the Figueira da Foz municipality (Central-Western Portugal). A geological and geotechnical susceptibility classification was established to evaluate rock masses which are constituted by Jurassic and Cretaceous rocks (limestones, marls and sandstones). The classification, divided into qualitative and quantitative parameters and sub-parameters, was applied in 43 outcrops located in the study area. The main parameters are the historical record, lithology, geological structures, geomorphology, floods and *in situ* stress relief. The sum of the several parameters varies from 0 to 100. The results can be grouped in classes, from very low to very high degree of susceptibility. Two outcrops showed low susceptibility. The majority of the sites scored between 40 and 60 and belong to the medium susceptibility class. The high susceptibility degree is located on costal and quarry areas.

1 INTRODUCTION

1.1 *Concepts*

The concepts of 'hazard', 'susceptibility', 'vulnerability' and 'risk' have all been used in studies on natural phenomena, corresponding to catastrophic events. Several recent publications have been based on natural hazards and their impact on human activity.

UNDRO (United Nations Disaster Relief Organization), in collaboration with UNESCO (United Nations Educational, Scientific and Cultural Organization), carried out a study aimed at clarifying the concepts of 'hazard', 'susceptibility' and 'risk' (Varnes 1984). 'Hazard' refers to situations or events which pose a threat to man, society or the environment (Bell 2002). According to Cantos & Ayala-Carcedo (2002), 'susceptibility' is the propensity of an area to be affected by a hazard, compared to other areas which have been previously affected. 'Susceptibility' can also be defined as the probability of a given area to be affected by a process, which can be classified using qualitative methods (Vallejo & Ferrer 2011).

'Hazards' can be defined as natural, technological or a mixture of both (Schmidt-Thomé & Kallio 2006). 'Risk' refers to exposure to a hazard and can be defined as the product of probability and loss (Smith 2001).

2 GEOGRAPHY AND GEOLOGY

2.1 *Geographical setting*

The area of study is located on the Atlantic coast of central-western Portugal in the region of Figueira da Foz, a municipality situated 200 km northward of Lisbon. The Figueira da Foz municipality belongs to the Coimbra district and has a recent census of 62,105 inhabitants. The study area is bordered by the National Road 596 to the north, the Mondego river to the south, the Atlantic Ocean to the west, and the Highway A17 to the east (Figure 1).

The study area is approximately 29.6 km^2 and includes urban zones of Figueira da Foz, the neighborhood settlements of Buarcos and Tavarede, the Cape Mondego promontory and the Serra da Boa Viagem calcareous massif.

2.2 *Geologic setting*

From a geological point of view, this area displays great lithological diversity of carbonated and siliciclastic rocks and surface deposits belonging to the Meso-Cenozoic infill of the western Portuguese continental margin (Figure 2). The local tectonic setting lies on the dependence of the Serra da Boa Viagem

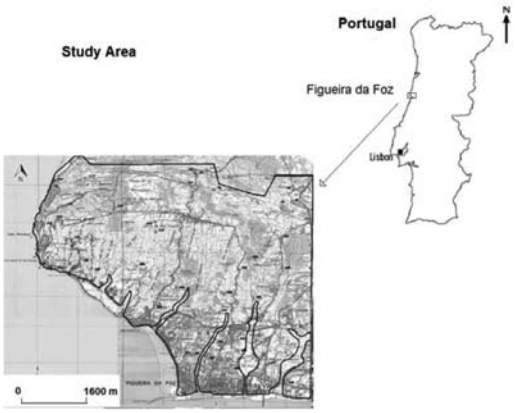


Figure 1. Study area location.

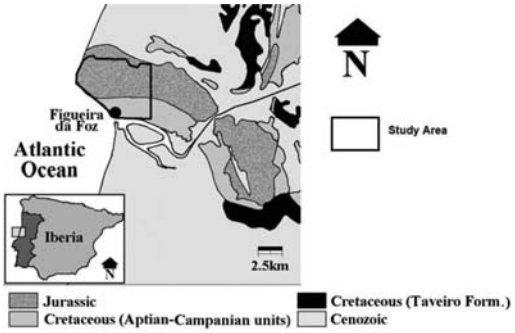


Figure 2. Geology of the study area.

fault, a thrust structure that has generated the uplift of the calcareous massif and its Jurassic units, during the Plio-Pleistocene. As a consequence, the Jurassic and Cretaceous sedimentary succession has been deformed as a large monocline gently deepening southwards, towards the Mondego River estuary.

The younger geological units are alluvial and estuarine deposits from this river and its tributaries, and sandy beaches along the shoreline. There is also evidence of several terrace and raised beach deposits with clastic and argillaceous sediments.

The Cretaceous formations are present on the southern section of the study area. They include a succession of Cenomanian and Lower Turonian platform carbonates (Costa d'Arnes Formation (Fm.)), well exposed in the main urban area. These marine carbonate sediments overlie a thicker unit of Lower Cretaceous coarse sandstones and conglomerates (Figueira da Foz Fm.) generated by the progradation of braided alluvial systems.

The Jurassic rocks occur in the Northern section of the research area, where they include several units with ages ranging from the uppermost Lias to the Malm. The older beds of this succession outcrop on the northern flank of the calcareous massif as a thick sequence of marly rich strata recording carbonated ramp sedimentation during the Toarcian stage

Table 1. Geological and geotechnical rock mass classification.

Parameters		Classification
Historical record and evidence of instability		0–12
Lithology		0–13
	Orientation	0–8
	Joint set number	0–4
Geological structures	Joint spacing	0–4
	Cavities	0–5
	Seismic activity	0–10
	Dip	0–6
Geomorphology	Presence of water	0–8
	Erosion	0–9
	Vegetation	0–5
Floods		0–9
In situ stress relief		0–7

(São Gião Fm.). They are overlaid by several hundred meters of rhythmic sequences with marine limestones, marly limestones and marls of Middle Jurassic age (Cape Mondego Fm.). The following Upper Jurassic succession begins with Upper Oxfordian marginal marine and freshwater, carbon rich, carbonates locally designated as "Carbon Complex", "Hydraulic Limestone" and "Bivalve rich marine beds". They are covered by an almost 600 m thick succession of deltaic coarse sandstones and red lutites with paleosoils, recording the Kimmeridgian-Tithonian (Boa Viagem Fm.).

3 METHODOLOGY

The geological and geotechnical susceptibility classification used in this work was only applied to rock masses, and a qualitative and quantitative analysis was carried out using different parameters. This classification was defined, using classifications by Bieniawski (1984), Flenje et al. (2000), Ko Ko et al. (2004) and Narciso & Andrade (2011). A field survey was conducted to study the different sites and geotechnical tests were carried out.

The classification applied on the municipality of Figueira da Foz considered six main parameters: historical record and evidence of instability, lithology, geological structures, geomorphology, floods and "*in situ*" stress relief. The parameters, geological structures and geomorphology, were subdivided into several sub-parameters. The characteristics defined in this classification related to records of potentially hazardous events. A weighting approach to the classification parameters was adopted to study the field survey. Each parameter has its own evaluation criteria and weighted classification (Table 1). The sum of the six parameters and their respective sub-parameters allowed the researchers to obtain a weighted total value

and to define a susceptibility degree for each of the sites studied. The results of the geological and geotechnical susceptibility classification were between 0 and 100 points. The uppermost values pertained to outcrops that showed a greater susceptibility to geological and geotechnical problems.

The parameter, historical record and evidence of instability, is associated with the deformations, failures and instability such as slope movements, tilting trees, cracks in structures, differences in vegetation and fractures. The values in this parameter were lower when there were no signs of slope movement, tension fractures or deformations on the outcrops.

Lithology corresponds to the identification of the rock material, its weathering degree and strength. According to Ko Ko et al. (2004), sedimentary rocks show strength ranging from very high to low; igneous rocks show very high or low strength; and metamorphic rocks have very high, high or low strength. The classification of weathering degree followed ISRM (1981) recommendations, with five different weathering degrees. Geotechnical tests, such as the Schmidt Hammer tests and the Point Load tests, were used to characterize rock strength and to compare their values with those identified in the field survey. For the Schmidt hardness test, an L-type hammer was used with 0.735 Nm of impact energy and the procedures followed ISRM (1981) recommendations. The Point Load tests were also based on ISRM (1985) and were performed using irregular lumps. The purpose of these tests was to determine the point load strength index, corrected to a specimen diameter of 50 mm (I_{s50}).

The geological structures parameter is subdivided into five sub-parameters: discontinuity orientation, joint set number, joint spacing, presence of caves and seismic activity.

For the discontinuity orientation parameter, an adapted version of the Ko Ko et al. (2004) model was used. For outcrops with favorable orientation, the parameter value was between 0 and 2 points, while for the most unfavorable, it was 8. The joint set number was obtained through stereographic projection analysis. The discontinuity study also included joint spacing, corresponding to the perpendicular distance between discontinuity surfaces belonging to the same set. In this work, joint spacing was defined using modal values. Its interval values are presented in Table 2.

The existence of cavities indicated the probability of vertical movements such as subsidence or collapses.

Seismic activity identified the seismic susceptibility of the outcrops and consequently of the study area. The definition of this parameter was obtained through the use of seismic hazard maps (RSA 1983), (CT-115 2009) and (Cabral & Ribeiro 1988) and an analysis of the correlations between seismicity, lithology and the degree of weathering; fault presence and earthquake location; and time, magnitude, focal depth and failure extension.

The geomorphology parameter was made up of four sub-parameters: dip, the presence of water, erosion and vegetation.

Table 2. Joint spacing sub-parameter.

Joint spacing m	Classification
>3	0
1–2	1–2
0.3–1	2–3
<0.3	3–4

Table 3. Vegetation sub-parameter.

Vegetation	Classification
Absence of vegetation	5
Graminoids	4
Medium and small-sized trees and moderate vegetation	1–3
Large and medium-sized trees and moderate to dense vegetation	0–1

In the present work two distinct kinds of dip were adopted: the cut slope dip angle or the natural slope dip. There was a direct correlation between the dip angle and the rating values of this sub-parameter.

The presence of water was linked to the position of the water table and water flow. In a rock mass, water flow was essentially found along discontinuities. The rock mass permeability was greatly influenced by the joint set number, joint spacing, aperture and infilling material.

The erosion sub-parameter was further subdivided into two types: soil and weathered rock erosion, and coastal erosion. The latter occurred on the coast, and referred to weathering caused by wind, water and gravity. The vegetation sub-parameter was based on the lithological and geometrical characteristics of the sites studied; this classification of this parameter included various vegetation types shown in Table 3.

The floods parameter corresponded to the probability of flooding in the area being studied. For this parameter, it was necessary to study the local area, and its proximity to water streams and flood records.

The parameter, "*in situ*" stress relief, was defined as absent, low, medium or high. This parameter pertained to the presence of relief joint or stress actions.

Slope movements occurring on the sites studied were classified in order to define the kind of landslide, velocity, states of activity, dimension, consequences, and external and internal causes.

4 RESULTS

4.1 *Results of the susceptibility classification*

The rock mass classification was applied to 43 sites located in the study area to determine the geological and geotechnical susceptibility. The interval values results of the classification are shown in Table 4.

Table 4. Geological and geotechnical rock mass classification results.

Parameters		Classification
Historical record and Evidence of instability		3–12
Lithology		5–11
	Orientation	0–6
	Joint set	1–3
Geological structures	Joint spacing	0–4
	Cavities	0–2
	Seismic activity	3–4
	Dip	0–6
Geomorphology	Presence of water	0–5
	Erosion	2–8
	Vegetation	0–5
Floods		0–2
In situ stress relief		1–7

Table 5. Hardness and strength results.

Parameters	R	I_{s50} (MPa)
Cape Mondego Fm.	33.6–63.0	2.8–3.9
Carbon Complex and Hydraulic limestones	45.7–47.2	
Boa Viagem sandstones	13.0–47.2	0.7–1.1
Figueira da Foz Fm. (sandstones)	16.2–22.5	
Costa d'Arnes Fm. (limestones)	35.0–45.9	2.8

For the parameter, historical record and evidence of instability, the values were between 3 and 12, with lower values reported in sites located on coarse sandstone levels of the Boa Viagem Fm. where there was little or no evidence of instability. The highest values were recorded from an outcrop with limestone and marly levels of the Cape Mondego Fm., which showed evidence of rock falls and constant slope movements.

The lithological classification was associated to rock strength, in particular with regard to the results of laboratory and '*in situ*' tests. The minimum value in this parameter was 5, pertaining to rock material with a low degree of weathering. Higher values, such as 11, corresponded to low to medium strength sandstone (Boa Viagem Fm.) and colluvial deposits (Figueira da Foz Fm.).

The lowest values in the discontinuity orientation sub-parameter were found in sub-horizontal formations or where there was a dip direction towards the rock mass. The highest results pertained to outcrops with discontinuities dipping towards the face slope.

For 40 out of the 63 sites, the joint set number was 3. The results for joint spacing were very varied; however the most common values (0.3–1.0 m) corresponded to 3 points.

Cavities only occurred in 9 sites and its impact was defined as null or of medium importance.

The seismic activity was influenced by seismic zonation and intensities. The Figueira da Foz area showed a maximum seismic intensity of VII, and its seismicity was classified as moderate to low. Three out of the 63 sites studied are located near a major regional fault (The Quiaios Fault).

The geomorphology parameter was divided into 4 sub-parameters: dip, presence of water, erosion and type of vegetation. A declivity map of the area studied was drawn up, and the dip slope '*in situ*' measurements revealed angles of between 26° to 90° (sub-vertical).

The presence of water pertained to the water table and percolation; a slope exposition map was produced in order to evaluate this sub-parameter. In most parts of the sites studied, where there was no presence of water, the value was zero (0); in some outcrops of the Figueira da Foz Fm., where the water table was detected, the result was 4 or 5.

Results on the erosion sub-parameter ranged from 2 to 8 points, corresponding to the absence of erosion and to high susceptibility to erosion, respectively. Coastal erosion was linked to the energetic SW and W swell direction, particularly in winter.

There was greater variability with regard to vegetation. The absence of vegetation, graminoid cover and dense vegetation, was observed in 6 (14%), 18 (42%) and 3 (7%) sites, respectively.

For the majority of the studied outcrops there were no records of floods: in this case the respective score was zero. Only four out of the sites studied were classified as more prone to flooding.

The '*in situ*' relief showed generally low to medium evidence.

The results of rebound hardness (R) were greater for the limestone levels of the Cape Mondego Fm. with the highest values ranging from 56 to 63. In general, limestone showed higher R values than sandstone (Table 5).

The limestone levels of the Cape Mondego Fm. showed the highest I_{s50} values (2.8–3.9 MPa) and the Boa Viagem sandstone the lowest (0.7–1.1 MPa), with positive correlation to R results (Table 5).

4.2 *Slope movements*

In addition to the application of the susceptibility classification, a slope stability characterization analysis was carried out. This study was useful for the historical record and evidence of instability parameter.

Various kinds of instability were identified; the most frequent were rock falls. Other kinds of movement occurring were planar and wedge failure, toppling, debris fall and complex movements. Some of the slopes showed more than one kind of slope movement. 42% of the slopes studied did not show any evidence of instability, 53% showed rock falls, 9.3% and 4.7%, respectively, revealed planar and rotational failures, and an equal proportion of 2.3% showed toppling failures and complex movements, respectively.

Table 6. Geologic and geotechnical susceptibility classes.

Classes	Geologic and geotechnical degree
80–100	Very High
60–80	High
40–60	Medium
20–40	Low
0–20	Very Low

In 93% of the sites studied, there was no evidence of stabilization or remediation works. The planar failures were generally associated with stratification. Rotational failures were present in the sandstone units, soil and weathered material.

The velocity of slope movement was defined as very fast (>3 m/min) for 15 slopes and fast (1.8 m/h to 3 m/min) for 10 slopes.

42% of the sites were considered stable, 2% showed signs of instability but were considered stable, while 12% showed signs of suspended instability and 44% corresponded to active instability. The most common size of the falling rock blocks was 1000 cm^3; they can sometimes reach 1 300 000 cm^3.

The greatest impact of slope movement was on roadways, which occurred in 32% of the sites studied; in 2%, they damaged homes and/or buildings; in 24%, they disturbed forests and uninhabited areas; but in 42%, there was no evidence of instability.

Slope movement can be caused by various external factors. In this study, these factors were considered to be the increase in dip slope (9% of the sites), rainfall infiltration (23% of the sites), and vibrations and superficial erosion (35% of the sites). Similar to external factors causing slope instability, more than one internal cause may be present in the outcrops studied. The lithology, the geological structures, the pore pressure water, the reduction of strength and the '*in situ*' relief were considered to be internal causes for slope movement in 35%, 44%, 16%, 14% and 28% of the sites studied, respectively.

4.3 *Results classification evaluation*

A final classification of the geological and geotechnical susceptibility was established through the use of parameters defined by the field survey and in '*in situ'* and laboratory tests. The results can be grouped in classes, from a very low to a very high degree of susceptibility (Table 6).

In this study, there were no sites classified as having very high or very low susceptibility. Among the outcrops that showed low susceptibility (20-40) one belong to limestone and marly levels of the Cape Mondego Fm.; two (2) to the "Carbon Complex" and "Hydraulic Limestone" units; seven (7) to coarse sandstone and lutitic levels of the Boa Viagem Fm., two (2) to coarse sandstones of the Figueira da Foz Fm and two (2) to carbonate beds of the Costa d'Arnes Fm. The low susceptibility classification corresponded to areas of low declivity and the occurrence of limestone and sandstone of medium to high strength.

The majority of the sites scored between 40 and 60, and belong to the medium susceptibility category: one of them is found on the São Gião Fm., nine are situated on the Cape Mondego Fm., one belongs to the "*Bivalve rich marine beds*" (Upper Oxfordian), eleven are located on the Boa Viagem Fm. and six are found on the coarse sandstones of the Figueira da Foz Fm. Medium susceptibility sites are characterized by suspended to active slope movement, intermediate rock strength and higher declivity than lower susceptibility sites.

The high susceptibility degree is concentrated in the northwest section of the study area (Cape Mondego and Teimoso zone) and is represented by an outcrop located on the Boa Viagem Fm. High susceptibility is linked to active slope instability such as rock falls and planar failures, high declivity, geological heterogeneity and coastal erosion. The latter is associated with winter storms, energetic swell and littoral drift direction.

5 CONCLUSIONS

The area studied was chosen for its geological diversity and to verify the proposed susceptibility classification.

'*In situ*' tests and laboratory tests, such as the Schmidt hammer test and the Point Load test, were carried out to validate the lithological characterization and its strength. The results showed a direct correlation between the Schmidt hammer and Point Load tests values. The rock material of the Cape Mondego Fm. had the highest results on the R and I_{s50}, respectively, equal to 63.0 and 3.9 MPa. Sandstone revealed lower values in strength and hardness than limestone with the same weathering degree.

The analysis of slope movement highlighted the absence of signs of instability in 42% of the sites studied; 53% revealed rock falls; 9.3% showed planar failures and 4.7% revealed rotational failures. Toppling failures and complex movements appeared in an equal proportion of 2.3% of the outcrops studied.

The analysis of the study area and the use of the classification permitted the definition of geological and geotechnical susceptibility. 30% of the sites studied showed low susceptibility. These are located in the Northern part of the study area (the upper zone of the Boa Viagem calcareous massif) and in Figueira da Foz city. 63% of the studied outcrops were identified as having medium susceptibility, which corresponds to an intermediate hazard probability for the population and existing infrastructures. Only 2% of the sites showed evidence of high susceptibility; the potential hazards are mainly associated with coastal erosion, steep slopes and landslides; however, the areas demonstrating high susceptibility are largely uninhabited.

The classification here presented was intended to identify the degree of geological and geotechnical susceptibility in order to establish alerts and protective measures for the population. The susceptibility classification can be used for town planning, contributing to an appropriate use of land and a proper design of the municipal area. The study can provide information for risk maps, improve civil protection and emergency planning, and reduce geological and geotechnical hazards.

REFERENCES

Bell, F.G. 2002. *Geological hazards: their assessment, avoidance and mitigation*. Spon Press: London.

Bieniawski, Z.T. 1984. *Rock mechanics design in mining and tunneling*. Balkema: Rotterdam.

Cabral, J. & Ribeiro, A. 1988. *Carta Neotectónica de Portugal escala 1/1 000 000*. Serviços Geológicos de Portugal: Lisbom.

Cantos, J.O. & Ayala-Carcedo, F.J. 2002. *Riesgos naturales. Conceptos fundamentales y classificación*. Ariel Ciência: Barcelona.

CT-115 2009. *Eurocódigos Estruturais NP EN 1998-1*. Comissão Técnica Portuguesa de Normalização. LNEC: Lisbon.

Flentje, P.; Chowdhury, R. & Ko Ko, C. 2000. A matrix approach for assessing landslide risk in the context of a comprehensive strategy. *Proc. Geo-Eng 2000, an international conference on geotechnical and geological engineering*, *Melbourne, 19–24 November 2000*. Technomic Publishing: Melbourne.

Ko Ko, C.; Flentje, P. & Chowdhury, R. 2004. Landslide qualitative hazard and risk assessment method and its reliability. *Bulletin of Engineering Geology and the Environment*, 63(2): 149–165.

ISRM 1981. *Rock characterization testing & monitoring. ISRM suggested methods*. E. T. Brown (ed.). Published for the Commision on Testing Methods. Pergamon Press: Oxford.

ISRM 1985. Suggested method for determining point load strenght. *Int. J. Rock Mechanics and Mining Science and Geomech*, 22 (2): 51–60.

Narciso, J. & Andrade, P.S. 2011. Geotechnical Suceptibility Analysis.. In J. Lourenço, A. Alencoão, A. Sousa Oliveira, L. Sousa, R. Teixeira (eds). *Proc. VI RGAOT, Vila Real, 6–8 October 2011*. University of Trás-os-Montes e Alto Douro (UTAD): Vila Real.

RSA 1983. *Regulamento de segurança e acções para estruturas de edifícios e pontes*. Decreto-lei n° 235/83 de 31 de Maio. Impressa Nacional – Casa da Moeda: Lisbon.

Schmidt-Thomé, P. & Kallio, H. 2006. Natural and Technological Hazard maps of Europe. In P. Schmidt-Thomé (ed). *Natural and Technological Hazards and Risks in European Regions*: Special Paper 42. Geological Survey of Finland: Espoo.

Smith, K. 2001. *Environmental Hazards: Assessing risks and reducing disaster*. Routledge: London.

Vallejo, L.I.G. & Ferrer, M. 2011. *Geological Engineering*. CRC Pess/Balkema: Leiden.

Varnes, D.J. 1984. *Landslide hazard zonation: a review of principles and pratice*. UNESCO.

Rock Mechanics for Resources, Energy and Environment – Kwaśniewski & Łydżba (eds)
© 2013 Taylor & Francis Group, London, ISBN 978-1-138-00080-3

Characterisation and propagation of epistemic uncertainty in rock engineering: A slope stability example

A. Bedi
Imperial College, London, UK

J.P. Harrison
University of Toronto, Canada

ABSTRACT: In this paper we show how the appropriate uncertainty model to apply in an analysis depends on the nature of the available information. We explore this through the analysis of a rock slope using probabilistic models that incorporate alternative subjectively assigned probability distributions. These alternatives mimic the opinion of multiple experts. The results are shown to depend strongly on the shape of the input distributions, and hence the expert opinion utilised. We conclude by showing that an analysis using fuzzy mathematics is more appropriate than a probabilistic approach when objective data are limited or absent, and present a novel technique for decision making using the results of a fuzzy analysis.

1 INTRODUCTION

In rock engineering, practitioners are often required to make critical decisions based on little or no objective data. This lack of information requires subjective estimation of parameters used in any analysis, and thus introduces uncertainty.

Some have suggested that even with little or no information, stochastic methods can be used to make pragmatic decisions by adopting a subjective view of probability (Aven 2010, Lindley 2000). This forms the basis of the Bayesian approach, which suggests that expert opinion can be applied to assign precise probability distributions (so-called 'priors') based solely on the knowledge or judgement of an expert. Within this framework, a probability distribution function (PDF) represents an expert's subjective degree of belief in a value's probability of occurrence. However, others argue that the subjective assignment of priors can lead to misinformed decisions and dissonance amongst experts (Ferson & Ginzburg 1996). In this paper, we investigate the latter argument via a case study on slope stability – that of the previously published Sau Mau Ping Road slope in Hong Kong (Hoek 2007).

In this paper we compare the results from Monte-Carlo simulation based on a subjectivist approach to probability and a non-probabilistic approach using fuzzy sets. We show the significant differences in design decisions that may result depending on the model adopted to characterise and propagate uncertainty.

2 MODELLING UNCERTAINTY AND VARIABILITY

The distinction between epistemic uncertainty and aleatory variability can be made through an understanding of the current level of knowledge, given the available information (Bedi & Harrison 2013, Zimmermann 2000), as shown in Figure 1. This figure shows how complete ignorance is one extreme of epistemic uncertainty, and that as knowledge increases so it may be possible to recognise that aleatory variability exists.

Ascertaining the current level of knowledge, and thus whether one is dealing with epistemic uncertainty or aleatory variability, requires consideration of both the quantity and quality of information available by which the parameter or system in question is being characterised (Bedi & Harrison 2013, Zimmermann 2000).

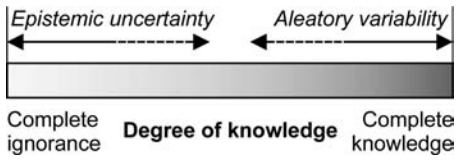


Figure 1. Uncertainty, variability and degree of knowledge (after Guo & Du 2007).

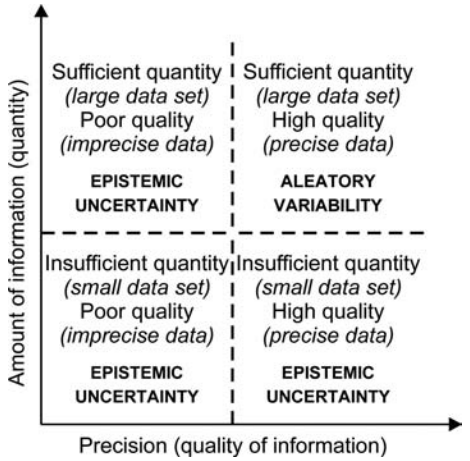


Figure 2. Qualitative and quantitative assessment of available information required to determine current level of information (from Bedi & Harrison 2013).

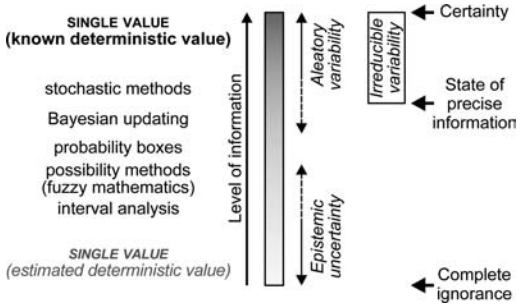


Figure 3. Level of information concept (after Wenner & Harrison 1995).

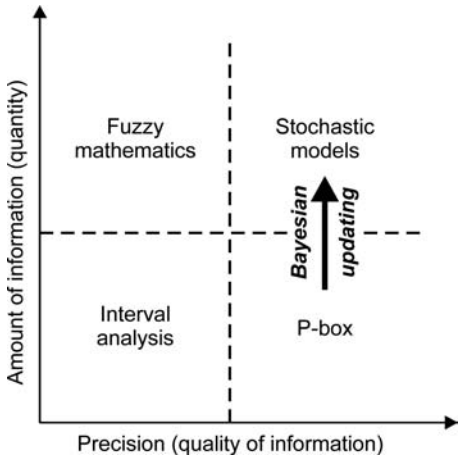


Figure 4. Appropriate uncertainty models with respect to quantity and quality of information (from Bedi & Harrison 2013).

2.1 *Quality and quantity of available information*

Figure 2 summarises the link between quantity and quality of information with respect to uncertainty characterisation. This figure shows that aleatory variability can only be invoked once a sufficient quantity of precise information is available. These constraints are necessary in order to objectively fit a probability distribution to the data (Dubois & Guyonnet 1996). The figure also confirms that a transition from epistemic uncertainty to aleatory variability can be achieved by gathering either more or better information. However, attaining this additional information is not always possible, in which case – and regardless of the quality of data – the uncertainty must be characterised as epistemic.

Once the unpredictability has been characterised as either aleatory or epistemic, an uncertainty model should be selected that faithfully propagates the available information through the analytical process. This suggests that for any given amount of knowledge – and hence degree of uncertainty – there is an optimal model that should be applied. This concept was conjectured some time ago (Wenner & Harrison 1995) as a 'level of information', and – together with some of the concepts that were introduced in Figure 1 – is illustrated in Figure 3.

In this framework, an interval requires nothing more than a (possibly) subjective assessment of upper and lower bounds, whereas a stochastic model requires sufficient understanding and data to be able to select and characterise a specific probability distribution. Intermediate levels of information may be modelled by fuzzy sets or probability boxes (p-boxes).

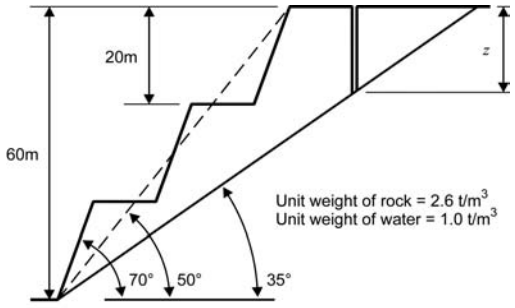
In Figure 4 the appropriate uncertainty models are arranged with respect to the quantity and quality of available information. Two important conclusions with immediate ramifications for our work in rock mechanics and rock engineering are demonstrated by this figure. Firstly, stochastic methods can only be applied when there is a sufficient quantity of precise data. Secondly, Bayesian methods are appropriate where the measurements are precise and additional information can be obtained which will allow convergence to an aleatory model through the updating process, using Bayes' Theorem (Ang & Tang 2006).

In order to validate these concepts, we now present an example that illustrates the consequences of subjectively assigning an aleatory model to characterise a state of information that is actually epistemic.

3 CASE STUDY: PLANAR SLOPE STABILITY

Following a series of landslides in Hong Kong that were triggered by exceptionally heavy rains, the stability of a rock slope on Sau Mau Ping Road in Kowloon – located immediately across the road from two blocks of apartments, each housing approximately 5,000 people – was brought into question (Hoek 2007).

Given the critical nature of this slope, a study was required to investigate the factor of safety (FoS) of the slope under normal conditions and under conditions



Random variables	PDF	Mean	St. Dev.
Sliding surface friction, ϕ (deg)	Normal	35°	5°
Sliding surface cohesion, c (t/m^2)	Normal	10	2
Tension crack depth, z (m)	Normal	14	3
Tension crack water depth, z_w (m)	Exponential	z/2	max = z
Horizontal seismic accln. factor, α	Exponential	0.08	max = 2α

Figure 5. Planar slope stability analysis: Sau Mau Ping Road (after Hoek 2007).

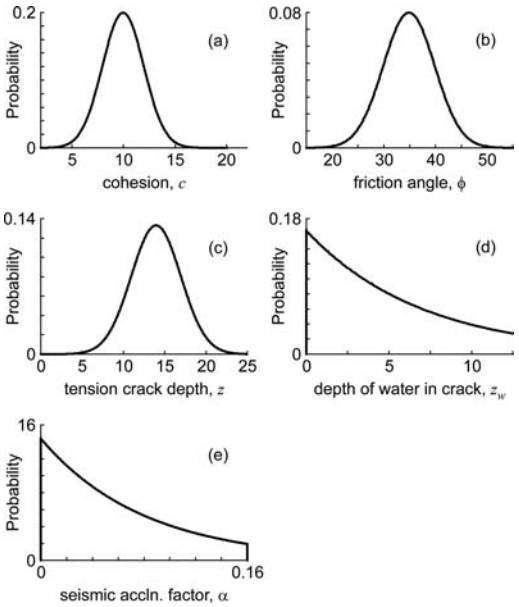


Figure 6. PDFs of non-deterministic parameters used in Monte-Carlo simulation (after Hoek 2007).

that could occur during an earthquake or during exceptionally heavy rains. Unfortunately – and as is often the case in geotechnical engineering – no objective data (i.e. laboratory or field observations and measurements) were available at the time of undertaking the study. Consequently, critical input parameters for the analysis had to be determined from expert judgement and previous experience (Hoek 2007). The geometry of the slope, as well as those parameters for which no objective data were available – referred to herein as the non-deterministic parameters – are shown in Figure 5.

3.1 *Sau Mau Ping Road: Aleatory or epistemic?*

With respect to Figure 2, the absence of objective data with which to fit a PDF for each non-deterministic parameter constitutes a quantitative lack of information. Figure 2 to Figure 4 suggest that the non-deterministic parameters must therefore be classified as epistemic and propagated using an appropriate, non-stochastic uncertainty model. However, and contrary to these concepts, Hoek (2007) suggests that even in the absence of objective information the non-deterministic parameters can be modelled as random variables (i.e. aleatory) defined solely from expert judgement or experience. On this basis, Hoek (2007) undertook a probabilistic assessment of the factor of safety of the Sau Mau Ping slope. Given the absence of any objective information, and with respect to the concepts presented in Section 2, this approach is questionable.

3.2 *Critical review of data characterisation as random variables*

Recalling the 'level of information concept' presented in Figure 3, the simple act of defining a probability of occurrence when faced with epistemically uncertain parameters introduces a significantly greater level of knowledge than is actually available. Of most importance is not the magnitude of the selected minimum, maximum or mean values, but rather the shape of the PDF chosen to define them (Ferson & Gizburg 1996).

Although a full justification for the choice of distributions used to define the non-deterministic parameters of Figure 5 is provided in Hoek (2007), the general suggestion was that a normal distribution be the usual choice in the absence of information on the actual distribution. Thus, the shear strength parameters (c and ϕ) were modelled using truncated normal distributions (see Figure 6) with the mean and standard deviation estimated subjectively based on literature reports (Hoek & Bray 1974) of back analysed slope failures in similar rock types. Hoek (2007) states the minimum and maximum truncation limits were arbitrarily chosen to allow for a wide range of values in the analysis. Similarly, the lack of access to inspect the crests of the slopes for the presence of tension cracks meant the PDF defining their depth was also speculative, as were the PDFs for tension crack water depth and seismic acceleration.

In this example, there is no evidence to suggest that the shear strength parameters and tension crack depth are better defined with normal distributions rather than, say, triangular or beta distributions. Consequently, dissonance between experts may well result in others opting for alternative distributions; the triangular distribution is a common choice. For these reasons, the Bayesian view contends that 'non-informative' PDFs (i.e. uniform distributions between the estimated lower and upper bounds) may be assigned in the absence of information on the shape of the distribution.

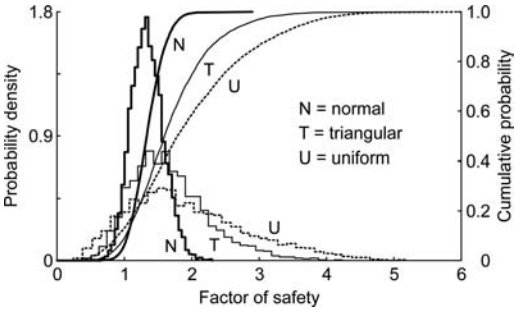


Figure 7. Comparison of three Monte-Carlo simulations.

Irrespective of the whether non-informative or other distributions are chosen to model the non-deterministic parameters, Figures 2 to 4 suggest an aleatory model represents the highest level of information requiring a sufficient quantity of precise data to justify the choice of PDF. Furthermore, Figure 4 suggests that the Bayesian approach is only suitable when further data collection is planned with which to update the initial (i.e. prior) distributions to 'posterior' distributions, using Bayes Theorem (Ang & Tang 2006). In the case of this analysis the sufficiency criterion was not fulfilled, nor was it possible to obtain further objective data. Therefore, the non-deterministic parameters should have been characterised as epistemic. The following exemplar calculations investigate the effect on calculated factor of safety obtained by Monte-Carlo simulation when using various subjectively assigned PDFs.

3.3 *Effect of the choice of the prior distribution*

Figure 7 compares the results of three Monte-Carlo (MC) simulations, each with a different PDF defining the non-deterministic shear strength parameters (c and ϕ) and the depth of the tension crack (z). The first MC simulation uses the PDFs shown in Figure 6, the second adopts triangular distributions that approximate the parameters of Figure 6(a–c), and the final simulation adopts the Bayesian philosophy and assigns non-informative priors to these parameters. In each simulation the minimum, maximum and mean values shown in Figure 5 and Figure 6 are used.

Figure 7 demonstrates how the choice of the input PDFs has a significant influence on the output of the Monte-Carlo simulations. Most importantly, despite the input distributions having the same minimum, maximum and mean values, the different shapes of the PDFs have resulted in significant differences in the bounds and fractile values of the output.

These differences result from the varying degree of information contained purely in the shape of the selected PDF. However, in this example, there is simply no evidence to warrant the selection of one PDF over another. In fact, this dispute on the selection of an appropriate PDF in the absence of any knowledge on the parameters which define it, dates back to Laplace's principle of indifference, which itself dictates the use of uniform distributions (Ferson & Ginzburg 1996).

Table 1. Statistics computed from Monte-Carlo simulations.

Simulation	Type of PDF	Min FOS	Lower 5%	Mean	Max FOS	P (FoS ≤ 1)
1	Normal	0.59	0.97	1.34	2.31	6.4%
2	Triangular	0.46	0.88	1.68	4.59	9.5%
3	Uniform	0.25	0.70	1.94	5.21	14%

In this example, the results of the three MC simulations presented in Figure 7 can be considered a reflection of the subjective opinions of three different experts. The question then becomes, how do the views of each of these experts differ with respect to the FoS of the slope and what influence has this in determining remedial measures, if any?

3.3.1 *Effect on decision making*

In terms of stability of the Sau Mau Ping slope, a FoS of safety less than 1 indicates the slope is unstable; a FoS of 1 can be thought of as the 'limit state'. In civil engineering, a 5% probability of occurrence of the limit state is often considered as the threshold of acceptable risk.

Table 1 presents a summary of various statistics for the FoS, calculated from the results of the three analyses presented in Figure 7. The final column in this table presents the calculated probability of the FoS being less than 1, i.e. the probability of occurrence of the limit state.

The results of Simulation 1 indicate that the probability of a FoS less than 1 is 6.4%. Hoek (2007) suggests that, in the short term, this represents a low risk of slope failure. Simulations 2 and 3 (triangular and uniform PDFs, respectively) indicate that the probability of a FoS less than 1 is 9.5% and 14%. These are both substantially more than that obtained in Simulation 1, and suggest that the slope may not be stable. Note also that there are significant differences in the other calculated values.

These simulations demonstrate how differing views on the stability of the slope may be obtained when a subjective approach to assigning probability distributions is applied. As subjective distributions are determined by expert opinion, the question could be raised: '*which expert should I believe?*' The definitive answer to this would require objective measurements to confirm the correct distribution of the input parameters, by which juncture an expert opinion would not be required.

3.4 *Possibility analysis*

The analysis presented in the preceding section used non-deterministic parameters that were defined as random variables (i.e. aleatory) around a common minimum, maximum and mean value. Regardless of these commonalities, the calculated performance of

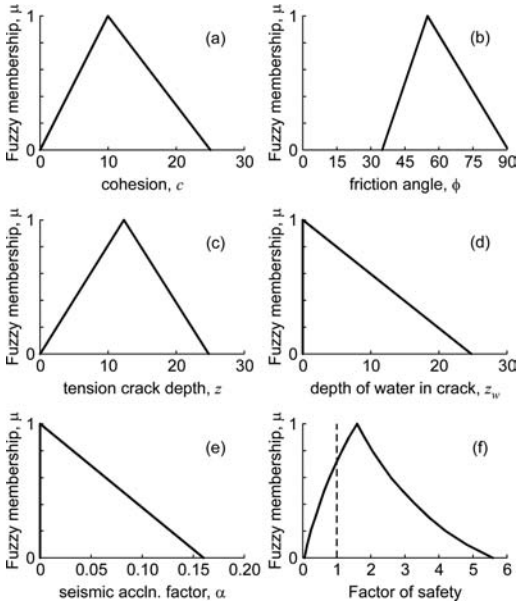


Figure 8. Fuzzy inputs and computed fuzzy factor of safety.

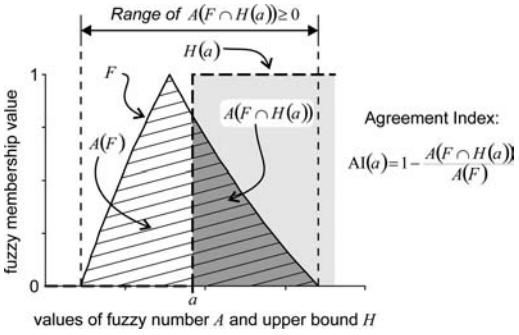


Figure 9. Defuzzification of a fuzzy number using the agreement index (after Harrison & Hudson 2010).

the slope varied with the chosen shape of the input PDFs. In cases such as this, a more appropriate uncertainty model is one that uses only the minimum, maximum and 'most typical' value of any of the non-deterministic parameter. Such a model may be constructed using fuzzy mathematics.

A fuzzy number may be viewed as a possibility distribution, analogous to the way a probability distribution is associated with a random variable (Kaufmann & Gupta 1991). Fuzzy numbers may take any shape, although these should be justified by the available information; triangular fuzzy numbers (TFNs) are most commonly used (Dubois & Prade 1989). For the Sau Mau Ping slope, where only minimum, maximum and mean values are available, most experts would, arguably, agree that triangular fuzzy numbers are most appropriate. Figure 8 shows the TFNs constructed to characterise the non-deterministic parameters of Figure 5. It is important to realise that the TFNs are different to triangular PDFs, in that they contain a lower level of information. The fuzzy numbers do not define precise probabilities of occurrence for values of the parameter they characterise, but rather encode preferences of imprecise measures. The resulting fuzzy factor of safety (*Fôs*) is shown at the lower right of Figure 8.

In comparison with the results of the earlier analyses (see Table 1), fuzzy arithmetic ensures that the resulting fuzzy factor of safety correctly bounds the minimum and maximum possible values, however improbable they may be (Kaufmann & Gupta 1991). Thus, the fuzzy number faithfully represents the full range of uncertainty. *Fôs* also depicts the *most possible* factor of safety, so the result shown in Figure 8(f) may be expressed linguistically as *"A FoS less than 0.05 or greater than 5.58 is considered impossible. Values close to these bounds are considered least possible; the most possible FoS is 1.58. The median FoS is likely to lie in the interval [0.63, 2.93]"*.

Although fuzzy analysis faithfully propagates epistemic uncertainty, the imprecise output means pragmatic decision making is awkward. One way to overcome this issue is to use a defuzzification measure, as we show below.

3.5 *Defuzzification and decision making*

Kaufmann & Gupta (1991) present a defuzzification procedure using the concept of an 'agreement index', which is a measure of the proportion of the fuzzy number, by area, less than a certain upper bound, as shown in Figure 9. An agreement index of 0 represents a condition where every value of the fuzzy number is greater than the upper bound, and an agreement index of 1 represents the case in which every part of the fuzzy number is less than the upper bound. By using the factor of safety as the value of the upper bound, we compute an '*agreement curve*' by calculating the agreement index for a range of factor of safety values. Figure 10 shows a comparison between the agreement curve and the cumulative probability distribution functions from the Monte-Carlo simulations.

The agreement curve is interpreted as follows. Figure 8(f) shows that the most possible FoS is 1.58. Now, using the agreement curve in Figure 10, we can see that there is 35% agreement that the FoS will be less than or equal to this value. Similarly, there is a 15% agreement that the FoS will be less than or equal to 1. Comparing the 5% agreement index with the lower 5% fractile value obtained from the three Monte-Carlo simulations (Table 1), the fuzzy analysis indicates a FoS of 0.55 at this level.

When comparing the agreement of the limit state with the probability of occurrence based on the Monte-Carlo simulations, the fuzzy analysis indicates more conservative conclusions. This is perhaps warranted given the little objective information on which to base critical decisions. However, it is not clear what agreement index could be deemed acceptable in terms of rock engineering designs.

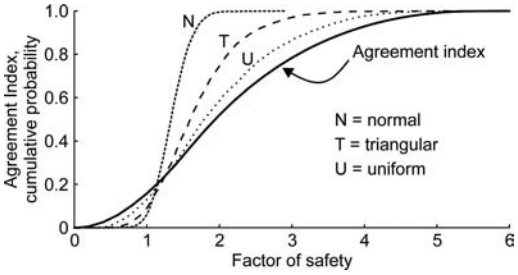


Figure 10. Defuzzification of a fuzzy number using agreement index.

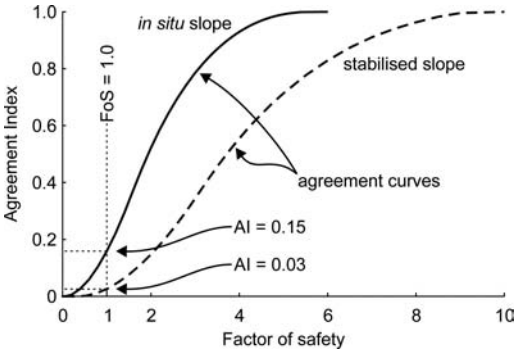


Figure 11. Agreement curves for *in-situ* and stabilised slope.

As all the analyses predict potential instability of the slope, stability may be improved using various remedial measures, such as installation of rock bolts. Using the fuzzy approach, Figure 11 compares the agreement curve obtained from a further analysis with a support force of 1000 t per metre of slope (applied via rock bolts inclined 30° counterclockwise from the normal to the sliding plane) with the *in-situ* condition. This figure shows that the installation of rock bolts reduces the minimum *Fôs* to 0.33, with a most possible value of 3.10 and a maximum of 10.34. Figure 11 also shows that the agreement index at a FoS = 1 falls from 15% to 3% with the applied support. It is on these bases that we suggest the proposed agreement curve may be useful for comparing design scenarios during the decision making stage.

4 CONCLUSIONS

We have shown the importance of differentiating between aleatory variability and epistemic uncertainty by considering the quality and quantity of the information available. Aleatory variability can be invoked only when there is enough measurements that are sufficiently precise to objectively fit a probability distribution to the data using statistical methods.

The re-analysis of the Sau Mau Ping Road slope presented in this paper demonstrates the substantial variability in results that can occur when subjective assignment of probability distributions is used to handle epistemic uncertainty. We have shown that by subjectively assuming a prior probability density function we are implying a greater level of information than is actually available: the greater level of information is in the definition of the shape of the PDF. The significantly different results can be taken to represent the subjective views of different experts.

We have shown how non-probabilistic analyses using fuzzy mathematics are more suitable for the characterisation and propagation of epistemic uncertainty. Associated with this, we have presented a new measure to defuzzify the output of such an analysis and thus assist in decision making. As a result, we have shown how a possibility analysis may give more meaningful results than subjective probability in the face of epistemic uncertainty.

REFERENCES

Ang, A.H-S. and Tang, W.H. (2006). *Probability concepts in engineering: emphasis on applications in civil and environmental engineering. 2nd ed*. London: John Wiley & Sons Ltd.

Aven, T. 2010. On how to define, understand and define risk. *Reliab. Eng. Syst. Safe.* 95: 623–631.

Bedi, A. & Harrison, J.P. 2013. A taxonomy for characterisation of epistemic uncertainty and aleatory variability in rock mechanics and rock engineering. *Rock Mech. Rock. Eng*. IN PREPARATION.

Dubois, D. & Guyonnet, D. 2011. Risk-informed decision-making in the presence of epistemic uncertainty. *Int. J. Gen. Syst.* 40 (2): 145–167.

Dubois, D. & Prade, H. 1989. Fuzzy sets, probability and measurement. *Eur. J. Oper. Res*. 40: 135–154.

Ferson, S. & Ginzburg, L. R. 1996. Different methods are needed to propagate ignorance and variability. *Reliab. Eng. Syst. Safe.* 54 (2–3): 133–144.

Guo, J. & Du, X. P. 2007. Sensitivity analysis with mixture of epistemic and aleatory uncertainties. *AIAA Journal*. 45: 2337–2349.Lindley, D.V. 2000. The philosophy of statistics. *J. Roy. Stat. Soc. D-Sta.* 49(3): 293–337.

Hoek, E. (2007). *Practical rock engineering. Chapter 7: A slope stability problem in Hong Kong; and Chapter 8: Factor or safety and probability of failure*. In: http:/www.rocscience.com/hoek/PracticalRockEngineering.asp.

Hoek E. & Bray, J.W. 1974. *Rock Slope Engineering*. London: Instn Min. Metall.

Kaufmann, A. & Gupta, M.M. 1991. *Introduction to fuzzy arithmetic: theory and applications*. New York: Van Nostrand Reinhold.

Lindley, D.V. 2000. The philosophy of statistics. J. Roy. Stat. Soc. D-Sta. 49(3): 293–337.

Wenner, D. & Harrison, J.P. 1996. Techniques to cope with uncertain parameters in geomechanics on different levels of information. In Proc. Eurock '96, Torino, Italy, Vol. 1, 327–334.

Zimmermann, H.-J. 2000. An application-oriented view of modelling uncertainty. *Eur. J. Oper. Res*. 122: 190–198.

Rock Mechanics for Resources, Energy and Environment – Kwaśniewski & Łydżba (eds)
© 2013 Taylor & Francis Group, London, ISBN 978-1-138-00080-3

Characterization of the "Chaotic Complex" (Northern Apennines, Italy)

M. Coli
Dipartimento di Scienze della Terra, Firenze University, Italy

M. Tanzini
Spea Ingegneria Europea S.p.A., Milano, Italy

ABSTRACT: The "Chaotic Complex" is a mélange largely present in the Northern Apennines (Italy). It resembles both sedimentary, olistostromes, and tectonic mélanges, which geostructural assemblage ranges from "broken formation" to "scaly fabric". The Chaotic Complex (CC) is characterized by a clayey matrix including calcareous rock blocks which size can range from coarse sand to boulders and huge fragments of a formation. In this paper its geomechanical characterization has been faced with these criteria: a) Classical geotechnical approach; b) GSI approach; c) Bimrock approach. In general it results that Mohr-Coulomb data from GSI cover a wider range than those from lab tests, while the Bimrock approach resulted into higher values of friction angle and lower values of cohesion.

1 INTRODUCTION

The Chaotic Complex (hereafter called as CC) is widely present in the Northern Apennines orogenic chain, Italy. It is a redefinition (Abbate & Sagri 1970) of the classical term "Argille Scagliose" introduced by Salmojraghi (1881) in a paper facing the geological concerns encountered by the "new" Napoli-Foggia rail-line, Southern Apennines, where it is also largely present and known as "Varicoloured Shales". Since that experiences, which led to the introduction of the classical "Italian Method" to drive a tunnel through complex squeezing and swelling rock-mass, many tunnels, large mine and civil excavations were executed into the CC, every time with severe concerns (short-term response in terms of strong swelling and squeezing) regarding both the stability of the excavations and how to face that problems by a correct rock-mass characterization and parameters definition.

In almost all those experiences, the classical geotechnical approach, which implies the definition of the mechanical parameter of the shaly component of the CC on reconstructed samples, was applied.

Recently, the Bimrock (Medley 1994) and GSI (Hoek et al. 1998, Marinos & Hoek 2001) approaches were introduced in order to define the rock-mass parameters to be used in the design for tunnels and large civil and mine excavations.

In this paper, on the basis of published data and personal experience, we compare results from these three different approaches in order to outline the advantages and difficulties in defining the best approach suitable to be used for CC in tunnelling and excavations.

2 GEOLOGICAL BACKGROUND

Some authors consider the CC as a stack of olistostromes (*sensu* Flores 1955) and attribute its origin to sedimentary submarine mass movements, like debris-flows and mud-flows (Trevisan 1965, Gorler & Reutter 1968, Sestini 1968, Elter & Trevisan 1973, Castellucci & Cornaggia 1980, Abbate et al. 1981), others as tectonic melanges (tectonosomes), which originated from the dismemberment of pre-existing formations due to the over-thrusting of tectonic nappes during the Apennine orogenic phases (Castellarin et al. 1986, Bonini 1999, Boccaletti et al. 1999. Bonini & Sani, 2002). Bettelli & Panini (1987), Bettelli et al. (1996) and Pini (1999) outline the presence in the CC of rock-mass of both these origins, in complex relationships between them.

2.1 *Texture*

Despite its origin the texture of the CC consists of huge chaotic assemblage of heterogeneous and heterometric randomly distributed slices, blocks and broken formation bodies, mostly marly-calcareous, deriving from pre-existing formations incorporated into a highly shared, until scaly fabric, clayey matrix. Post-genesis tectonic movements, superimposed on the original fabric, caused in turn the formation of a late pervasive fissility and the presence of many shear planes.

In the field the CC appears as a dark grey body, highly tetanised, with heterometric marly-calcareous blocks randomly distributed in the clayey matrix with a matrix-supported fabric, in which the following lithological components can be identified:

– Matrix: dark-light grey shale and clay subdivided into centimetric and millimetric thin lenticular

laminae by pervasive and polished fissility planes.
- Marly-calcareous blocks: light grey marly-calcareous heterometric blocks, from a few millimeters to tens of a meter in size, well graded. Block shapes range from tabular to sub-spherical, with angular to sub-rounded edges. Blocks are randomly distributed in the clayey matrix in a chaotic manner, with a preferred orientation parallel with the main tectonic surfaces.
- Broken-formations: strata or pack of strata characterized by the alternation of limestone and dark pelitic beds, ranging from some meters to a few tens of a meters in size, without lateral continuity and randomly distributed in the CC rock-mass.

The clayey matrix presents a pervasive fissility (from "S-C" tectonites to scaly-fabric) which subdivides the matrix in thin sigmoidal and prismatic scales. Two order of scales (scale-in-scale structure) can be identified: the first order is characterized by centimetric to millimetric scales originating from the intersection of two or more discontinuity sets (disjunctive cleavage); the second order is represented by millimetric scales originating from an anatomizing continuous cleavage.

Marly-calcareous blocks and broken-formations are characterized by an intense jointing; tabular blocks are often boudinaged and dislocated by block-scale fractures.

Clayey matrix and broken-formations can present mesoscopic disharmonic folds, with inclined or recumbled axis planes, often rootless, related with a flexural slip deformational mechanism.

2.2 *Mineralogical composition*

Compositional analysis on the clay matrix (Barla et al. 1980, Coli & Bruni 1989) give around: quartz 15%, feldspar 5% and clay minerals 75%. Smectites, which can adsorb large amount of water and increase their volume up to 200%, represent about the 50% of the clay minerals. The activity index values are in the order of:

$$I1 = (I + IS)/(S + IS + ClV + V) \approx 0.60$$
$$I2 = (S + IS + ClV + V) \approx 70\%$$

where: I = Illite, IS = Illite-Smectite, S = Smectite, ClV = Clorite-Vermiculite, V = Vermiculite

These values classify the CC as strongly swelling, with a potential swelling pressure up to 2 MPa.

3 GEOMECHANICS CHARACTERIZATION

The CC represents a classic Structurally Complex Rock Mass of which it is difficult to define the physical-mechanical parameters due to its small- and large-scale heterogeneity (Morgensten & Eigenbrod 1974, A.G.I. 1979, Houska 1982, Meyerhof 1982, Picarelli 1986).

In the last decades too, many authors faced with this problem during the design of tunnels or large mine and civil excavation in CC, the main projects related with this problem were: the San Donato rail-tunnel, the Santa Barbara open-pit coal-mine, some urban settlements in the outskirts of Firenze, some tunnels of the new High-Speed rail-line Bologna-Firenze and of the renewed A1 Highway (Esu 1976, Berry et al. 1977, Barla et al. 1980, 1986, D'Elia et al. 1984, 1986, 1988, Lunardi et al. 1990, Cotecchia et al. 1993, Santaiola & Cancelli 1997, Lunardi & Pantaleone 2000, Garzonio & Sfalanga 2003, Pigorini et al. 2004, D'Elia 2006, Lunardi 2006).

In most of these projects the designers applied the classical geotechnical approach which consists in the determination of the physical properties by means of lab tests run onto samples reconstructed from the clayey matrix. The GSI approach was also used for the most recent tunnels and for the reclaiming design of the Santa Barbara open-pit coal-mine. In this last case the Bimrock approach, with also the execution of "non conventional *in situ* shear tests" (Coli et al. 2011), was also applied.

On the basis of our personal experience, hereafter we outline the main features and parameters which concern to these three different approaches.

3.1 *Geotechnical approach versus GSI approach and back analyses*

As aforementioned, the CC is constituted by argillites and marls with intercalations of calcareous blocks and, due to tectonic stresses, this heterogeneous formation shows a highly fractured and erratic structure and the clay particles has a preferred orientation in the plane of the tectonic movement, on this plane the shear resistance has residual value.

As use, on both disturbed and undisturbed samples, taken from boreholes, the following lab tests have been carried out on classical sized core samples: mineralogical analysis, classification tests, consolidated drained triaxial tests, unconsolidated undrained triaxial tests, direct shear tests, ring-shear tests, unconfined compression tests. In some of the analysed projects, in order to investigate the behaviour below high overburdens, triaxial tests have been performed at the Ponts et Chaussées Laboratory, in Paris, in a special cell able to reach high confining pressure.

Some lab test results have shown a marked strain-softening behaviour mobilising the peak strength for low strain levels and a considerable difference between peak and residual shear strength while some other test results have shown non appreciable strain-softening beyond peak.

The curved Mohr shear strength envelopes obtained from the lab tests indicated the dependence of the strength parameters on the confining stress. Peak shear strength values indicated, mainly, two different strength envelopes according to the depth of samples, with a higher cohesion for the samples deeper than 250 m (Fig. 1).

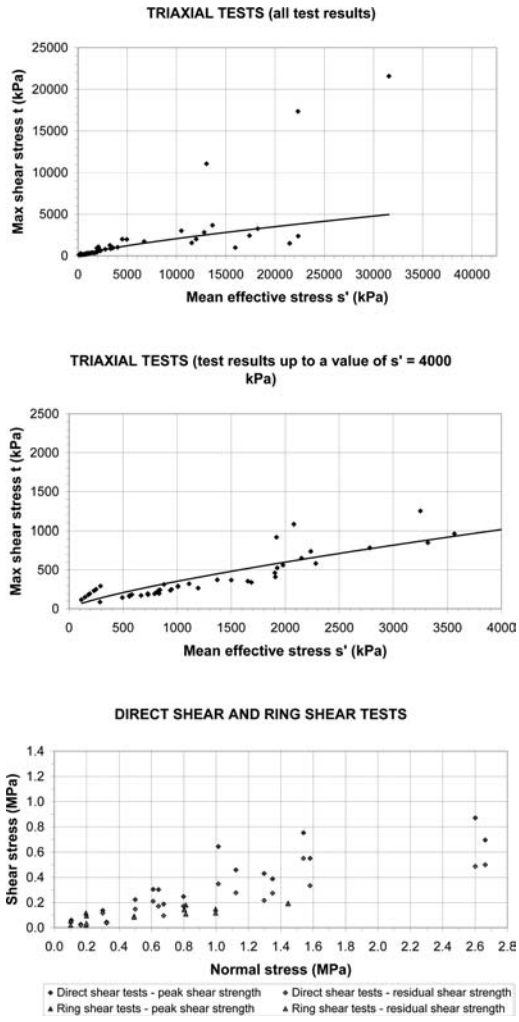


Figure 1. Lab strength measurements of clay shale samples.

The constant *in situ* monitoring of face extrusion and tunnel wall convergences have been analysed and correlated with construction phases and geomechanical ground conditions. Calculations have been performed by using closed–form analytical solutions, FEM as well as empirical relationships proposed by Marinos & Hoek (2001) and Hoek et al. (2002) that were used to determine the sensitivity of the radial strain during the excavation due to the variation of the GSI, σ_{ci} and m_i values.

The maximum radial strains obtained from the measured convergences and the radial strains calculated for appropriate values of the Hoek & Brown failure criterion parameters (GSI, σ_{ci} and m_i), fit as well as possible the measured values (Fig. 2).

On the basis of the radial strain values, a comparison between lab and ground strength parameters, obtained from back analyses, was done (Fig. 3).

Lab data are lower of the mobilized geotechnical parameters i.e. calculations based on lab data lead to

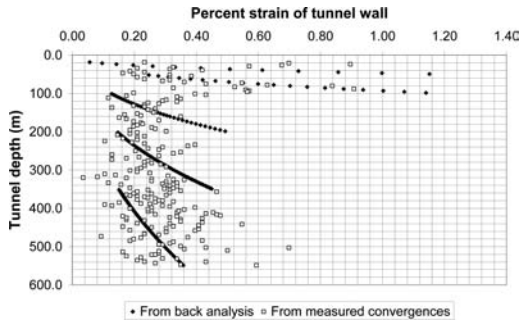


Figure 2. Raticosa tunnel: comparison between radial strains obtained from the measured convergences and calculated by back analyses adopting the Hoek & Brown failure criterion with values for the parameters GSI, σ_{ci} and m_i obtained from the examination of the rock mass at the tunnel face and geomechanical tests on blocks from the tunnel face.

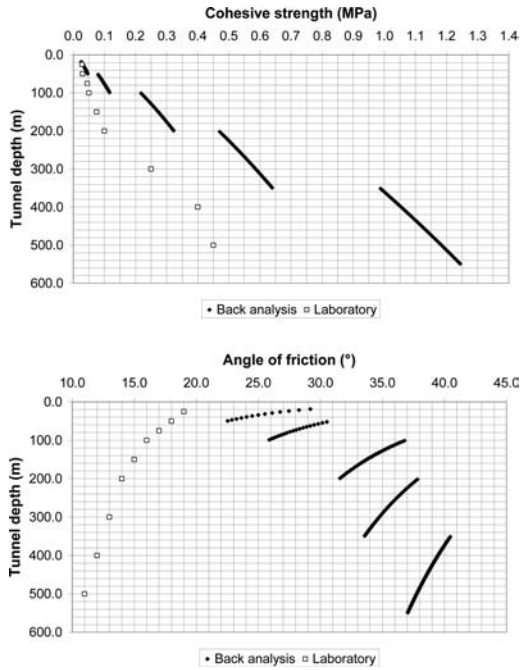
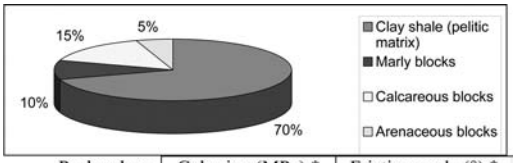


Figure 3. Raticosa tunnel: comparison between shear strength from lab tests and back analyses.

assess unrealistically high displacements around the tunnel. On the basis of these results it can be inferred that the prediction of tunnel performance based on lab test results is not reliable. In conclusion, in general, the lab data cannot be used directly to assess the tunnel behaviour because of the high sensitivity of the pervasively fissured material to sampling disturbance. In fact, the shear strength of the tectonized shales is strongly affected by the network of fissures.

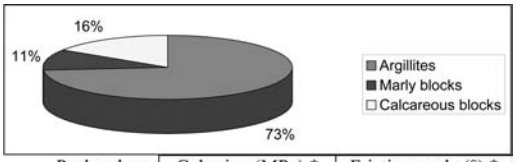
For this type of rock mass the GSI approach, adopting the Hoek & Brown failure criterion, has given reliable shear strength parameters, to correctly assess the tunnel behaviour. The GSI has been estimated from



Peak values	Cohesion (MPa) *	Friction angle (°) *
Lab tests	0.028 ÷ 0.45	12 ÷ 19
Back analyses	0.03 ÷ 1.25	23 ÷ 40
Bimrock model	0.03 ÷ 0.38	15 ÷ 24

* the lower and upper limits refer to the assumed stress ranges as a function of the tunnel overburden (maximum overburden of 500m)

Figure 4. Raticosa tunnel: mechanical properties, comparison for shear strength parameters obtained by: (1) lab tests, (2) back analyses based on the Hoek & Brown failure criterion and GSI values and (3) bimrock model.



Peak values	Cohesion (MPa) *	Friction angle (°) *
Lab tests	0.025 ÷ 0.04	16 ÷ 18
Back analyses	0.030 ÷ 0.065	19 ÷ 25
Bimrock model	0.025 ÷ 0.035	20 ÷ 23

* the lower and upper limits refer to the assumed stress ranges as a function of the tunnel overburden (maximum overburden of 70 m)

Figure 5. Other railway and highway tunnels: mechanical properties, comparison for shear strength parameters obtained by: (1) lab tests, (2) back analyses based on the Hoek & Brown failure criterion and GSI values and (3) bimrock model.

visual examination of the rock mass exposed in outcrops, in surface excavations such as road cuts and in tunnel faces and borehole cores. According with the blocks/matrix ratio the GSI ranges from 17 up to 30.

3.2 *The Bimrock approach*

Bimrock (block-in-matrix-rock; Medley, 1994) is a mixture of strong competent blocks of rock surrounded by a matrix of weak rocks. In a Bimrock the geomechanical behaviour is related with the volumetric block proportion (VBP): for VBP < 25% it is mainly controlled by the matrix properties, for VBP > 75% it is mainly controlled by the properties of the block assemblage. More in detail, blocks orientation, shape and size distribution also play a role in the bimrock mechanical behaviour.

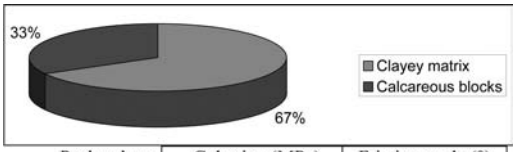
The threshold value between matrix and blocks is related with the scale of the problem.

The CC, mainly composed by pelitic matrix with dispersed block of limestone, marl and sandstone, with a VBP varying between 0 and some tens %, resembles a typical bimrock.

The geotechnical characterization of the clay shale is carried out by means of lab tests while the geometrical properties can be inferred by in-situ sieving tests or directly on the outcrops by a detailed indirect non–destructive characterization of geometrical properties by means of advanced images and geostatistical analyses. The rock mass Mohr–Coulomb parameters have been obtained from: (1) cohesion and internal friction angle of the clay shales matrix, c_{matrix} and ϕ_{matrix} from lab test results, (2) UCS of the blocks from lab tests, (3) volumetric block proportion (VBP) and (4) angle of repose for blocks (see in: Coli et al. 2008, 2009).

The bimrock cohesion, $c_{bimrock}$, and friction angle, $\phi_{bimrock}$, have been calculated, according to the solutions proposed by Sonmez et al. (2006, 2009) (Figures 4 to 6). These data come respectively from: (1) the Raticosa railway tunnel, (2) other railway and highway tunnels and (3) a high mine slope in the disused Santa Barbara open pit mine.

For the last example, it has been possible to compare the shear strength obtained from lab tests, in situ non



Peak values	Cohesion (MPa)	Friction angle (°)
Lab tests	50 ÷ 100 *	20 ÷ 25 *
In situ shear tests	10 ÷ 29	38 ÷ 44
Back analyses	20 ÷ 175	22 ÷ 34
Bimrock model	0.04 ÷ 0.08	26 ÷ 33

* in the stress range of $0.05 < \sigma'_n < 1.2$ MPa

Figure 6. Santa Barbara open pit mine: mechanical properties, comparison for shear strength parameters obtained by: (1) lab tests, (2) in situ non conventional shear tests (Coli et al. 2011), (3) back analysis (D'Elia et al. 1988), (4) bimrock model.

conventional shear tests (Coli et al. 2009, 2011) and results of back analyses of a rotational slide characterized by a maximum depth of 70–80 m that occurred when the mine was active and the cut slope was 205 m in height (D'Elia et al. 1988).

4 DISCUSSION AND FINAL REMARKS

The geological strength index (GSI) has been revealed appropriate in describing/characterizing difficult rock mass such as the CC. Its joint use with the Hoek & Brown failure criterion has been revealed useful to evaluate the strength and deformation characteristics of CC interested by tunnel excavations, with particular reference to high overburden situations with high confining and major principal stresses. This approach has been validated on the basis of detailed back analyses of numerous railway and highways tunnels excavated in the CC.

The intact rock strength of the clay shale has been initially obtained from lab tests to be used in the Hoek & Brown failure criterion. However, experience collected during tunnel excavations has shown that the lab tests underestimate the shear strength of the rock mass because of the difficulty to recover samples for lab testing in a tectonically disturbed and pervasively

fissured rock mass, where discontinuities are included in the lab sample; also the samples cannot be prepared, typical for the poor quality, due to infirmity to form adequate cores. Moreover, lab tests do not take into account the contribution of the blocks to the the rock mass strength.

In conclusion, we think that the GSI approach, integrated with lab tests on matrix and blocks, represents the best suitable method in order to characterize the CC, both at a preliminary stage of a project and for the executive design.

The Bimrock approach is promising in order to identify shear strength parameters representative of the in-situ mobilized shear strength values for slopes as well as shallow tunnels while for deep tunnels there is a considerable underestimation of the cohesion values.

Recent developments (Coli et al. 2012) have opened new insights for a possible future more consistent application of the Bimrock approach to deep tunnel by using FEM lab test large scale simulations to define the parameters of a Bimrock.

REFERENCES

Abbate, E. & Sagri, M. 1970. The eugeosyncline sequences. In G. Sestini ed., "Development of the Northern Apennine geosyncline. *Sedimentary Geology*, 4, 521–557.

Abbate, E., Sagri, M., Bortolotti, V. 1981. Excursion No.5: Olistostromes in the Oligocene Macigno Formation (Florence area). Introduction: An approach to Olistostrome interpretation. In. F. Ricci Lucchi (ed.) *In International Assiciation of Sedimentologists, 2nd European Regional Meeting, Excursion guidebook, Bologna, 1981*, 165–185. Bologna: Tecnoprint.

A.G.I. 1979. Some Italian experiences on the mechanical characterization of structurally complex Formations. *Proc. IV I.C.R.M.*, Montreaux 1979, 1, 827–846.

Barla, G., Pazzagli, G. & Travaglini, S. 1980. Fenomeni di swelling verificatisi in Argille Scagliose. *Nota tecnica, XIV Conv. Naz. Geotecnica, Firenze 28 ottobre*, 22 pp.

Barla, G., Pazzagli, G., Rabagliati, U., Travaglini, S. (1986). The San Donato Tunnel (Florence). In *"Large Underground Openings"*, *Proc. Int. Congress* Firenze 1986, 1, 61–69.

Berry, P., Brizzolari, E., Pantaleoni, G., Ribacchi, R. & Sciotti, M. 1977. Static behaviour of a tunnel excavated in a complex mudrock formation. *A.G.I., The Geotechnics of Structurally Complex Formations*, Capri.

Bettelli, G. & Panini, F. 1987. I Melanges dell'Appennino Settentrionale dal T. Tresinaro al T. Sillaro. *Mem. Soc. Geol. It.*, 39, 187–214.

Bettelli, G., Capitani, M., Panini, F. & Pizzaiolo, M. 1996. Le rocce caotiche dell'Appennino Emiliano: metodi sperimentali di rilevamento stratigrafico, esempi e nomenclatura. *Accad. Naz. Sc. Lett. Arti di Modena, Collana di Studi 15, Miscellanea Geologica*, 189–220.

Boccaletti, M., Bonini, M., Moratti, G. & Sani, F. 1999. Compressive Neogene-Quaternary tectonics in the hinterland area of the Northern Apennines. *Journal of Petroleum Geology*, 22, 37–60.

Bonini, M. 1999. Basement-controlled Neogene polyphase cover thrusting and basin development along the Chianti Mountains ridge (Northern Apennines, Italy). *Geological Magazine*, 136: 133–152.

Bonini, M. & Sani, F. 2002. Extension and compression in the Northern Appennines (Italy) hinterland: evidence from the late Miocene-Pliocene Siena-Radicofani Basin and relations with basement structures. *Tectonics*, 21(3) 2–35.

Castellarin, A., Pini, G.A., Crestana, G., Rabbi, E. 1986. Caratteri strutturali mesoscopici delle Argille Scagliose dell'Appennino Bolognese. *Memorie di Scienze Geologiche*, 38: 459–477.

Castellucci, P. & Cornaggia, F. 1980. Gli olistostromi nel Macigno dei Monti del Chianti: analisi stratigrafico-strutturale. *Mem. Soc. Geol. It.* 21: 171–180.

Coli, M. & Bruni, P. 1989. *Studio geologico-strutturale, sedimentologico e geomeccanico della galleria "Bellosguardo" tra Signa e Montelupo (Firenze), cunicolo pilota – Nota preliminare.* Copisteria San Gallo, Firenze, 86 pp.

Coli, N., Berry, P., Boldini, D. & Castellucci, P. 2008. Analysis of the block-size distribution in the shale–limestone chaotic complex (Tuscany, Italy). In *Proceedings of the 42nd US rock mechanics symposium,* San Francisco, paper ARMA 08-233.

Coli, N., Berry, P., Boldini, D. & Bruno, R. 2009. Investigation of block geometrical properties of the shale–limestone chaotic complex bimrock of the Santa Barbara open pit mine (Italy). *In: Proceedings of the 3rd Canada–US rock mechanics symposium*, Toronto 2009, paperARMA09-3999.

Coli, N., Berry, P. & Boldini, D. 2011. In situ non conventional shear tests for the mechanical characterisation of a bimrock. *Int. J. Rock Mech. & Min. Sc.*, 48, 95–102.

Coli, N., Boldini, D., Bandini, A. & Lopes, D.S. 2012. Modeling of complex geological rock misture under triaxial testing conditions. In *Proceeding EUROCK-2012*, Stockholm 28-30/5/2012

Cotecchia, V., Monterisi, L. & Salvemini, A. 1993. Analysis of a mass movement in structurally and geotechnically complex arenaceous marly formation. In Chowdhury & Sivakumar (eds), *Environmental Management, Geo-Water & Engineering Aspects,* Balkema, Rotterdam.

D'Elia, B., Di Stefano, D., Federico, G. & Oliva, S. 1984. Full-scale study of a high cut in a structurally complex formation. *Proceedings of the 4th International Symposium on Landslides*, Toronto, Canada, 16–21 September 1984, University of Toronto Press. 2, 57–62.

D'Elia, B., Di Stefano, D., Esu, F. & Federico, G. 1986. Slope movements in Structurally Complex Formations. In *Engineering in Complex Formations, Proceedings of the International Symposium*, 3–7 November 1986, Beijing, China, Science Press. XIV, 430-436.

D'Elia, B., Di Stefano, D., Esu, F. & Federico, G. 1988. Deformations and stability of high cuts in a structurally complex formation: Analysis and prediction. In *Proceedings of the 5th international symposium on landslides*, Lausanne, 10–15 July 1988. 1, 699–604.

D'Elia, B. 2006. Esperienze sul comportamento di alti fronti di scavo (Memories on the behaviour of high mine slopes). *Rivista Italiana di Geotecnica* 2, 12–47.

Elter, P. & Trevisan, L. 1973. Olistostromes in the tectonic evolution of the Northern Appennines. In K.A. De Jong & R Scholten (eds.) *Gravity and tectonics*, New York, John Wiley & Sons, 175–188.

Esu, F. 1976. Problemi di stabilità dei pendii naturali in argille sovra consolidate e fessurate italiane. *Atti dell'Istituto di Scienza delle Costruzioni,* Politecnico di Torino, 315, 35 pp.

Flores, G. 1955. Discussion. In Beneo E. "Les resultats des études pour la recherche pétrolifere en Sicilie. In *Proc. IV world Petroleum Congr.*, Rome, Sec.I/A/2, 109–124.

Garzonio, C.A. & Sfalanga, A. 2003. Geomechanical characterization of a tectonized shaly complex in the hill area around Florence. *Bull. Eng. Geol. Env*. 62, 289–297.

Gorler, K. & Reutter, K.J. 1968. Entstehung und Merkmale Olistostrome, *Geologishe Rundschau*, 53, 73–85.

Hoek, E., Marinos, P. & Benissi, M. 1998. Applicabilità of the geological strength index (GSI) classification for very weak and sheared rock masses. The case of the Athens Schist Formation. *Bull. Eng. Env*., 57, 151–160.

Hoek, E., Carranza-Torres, C. & Corkum, B. 2002. Hoeck-Brown failure criterion – 2002 Edition. Proc. NARMS-TAC Conference, Toronto (CA), 267–273.

Houska, J. 1982. Proceedings of the international symposium on the geotechnics of structurally complex formations. *Eng. Geol.*, 19 (1), 78–79.

Lunardi, P. 2006. *Progetto e costruzione di gallerie*. Hoepli, Milano, 577 pp.

Lunardi, P., Aiello, E., Rizzo, S. & Mongliardi, E. 1990. Una frana in terreni geologicamente e strutturalmente complessi interessante l'abitato della Presura di Impruneta (Firenze). *Quarry & Construction*, Aprile 1990, 1–13.

Lunardi, P. & Pantaleone, V. 2000. Problematiche affrontate nello scavo delle gallerie Bellosguardo e San Vito, Quadruplicamento ferroviario Firenze-Empoli, tratta Signa-Montelupo. *Quarry & Construction*, Ottobre 2000, 63–82.

Marinos, P. & Hoek, E. 2001. Estimating the geotechnical properties of heterogeneous rock mass such as flysch. *Bull. Eng. Geol. Env.* 60, 85–92.

Medley, E. 1994. *The engineering characterization of melanges and similar block_in_matrix rocks (bimrocks).* Dept of Civil Engineering, University of California, Berkley, California, PhD diss., UMI Diss. Svc., Ann Arbor, NI.

Meyerhof, G.G. 1982. The geotechnics of structurally complex formations. *Eng. Geol*., 19 (1), 63.

Morgensten, A. & Eigenbrod, P. 1974. Classification of argillaceous soils and rocks. *ASCE, J. Geotech. Eng. Div*., 100, 1137–1156.

Picarelli, L. 1986. Caratterizzazione geotecnica dei terreni strutturalmente complessi nei problemi di stabilità dei pendii. *Atti XVI Convegno Nazionale Geotecnica*, Napoli, 15–16 Maggio.

Pigorini, A., Puccinelli, M., Caldini, S. & Giovannini, R. 2004. Linea ferroviaria Pontremolese tra progettazione e costruzione: superamento di passaggi difficili sulla via di Parma, parte prima. *Gallerie e grandi opere sotterranee*, 72, 62–72.

Pini, G.A. 1999. Tectonosomes and olistostromes in the argille scagliose of the Northern Apennines, Italy. Geological Society of America, Special Paper, 335: 1–69.

Salmojraghi, F. 1881. Alcuni appunti geologici sull' Appennino fra Napoli e Foggia. *Bollettino del R. Comitato Geologico d'Italia*, 12, 102–106.

Santaiola, F. & Cancelli, A. 1997. Landslide evolution around Mt Campastrino (Northern Apennines, Italy): a complex and composite gravitational movement. *Eng. Geo*., 47, 217–232.

Sestini, G. 1968. Notes on the internal structure of the major Macigno olistostrome (Oligocene, Modena and Tuscany Apennines). *Boll. Soc. Geol. It*., 87, 57–63.

Sonmez, H,, Altinsoy, H., Gokceoglu, C. & Medley, E.W. 2006. Considerations in developing an empirical strength criterion for bimrocks. In *Proceedings 4th Asian Rock Mechanics Symposium*, Nov. 6–10 2006, Singapore.

Sonmez, H,, Kasapoglu, K.E. & Coskun, A. 2009. A conceptual empirical approach for the overall strength of unwelded bimrocks. In *Proceedings ISRM Regional Symp. "Rock Eng. in Difficult Ground Conditions, Soft Rock and Karst"*, Dubrovnik, Croatia, 29–31 Oct. 2009.

Trevisan, L. 1965. aspetti e problemi del complesso delle "Argille Scagliose" ofiolitifere nei suoi affioramenti occidentali (Toscana marittima e Liguria). *Boll. Soc. Geol. It*., 75, 21–40.

Rock Mechanics for Resources, Energy and Environment – Kwaśniewski & Łydżba (eds)
© 2013 Taylor & Francis Group, London, ISBN 978-1-138-00080-3

Impact of expertise on rock fall assessment – An original study

A. Delonca, T. Verdel & Y. Gunzburger
Université de Lorraine, GeoRessources, Nancy, France

ABSTRACT: The mapping assessment of rock fall probability is mostly based on qualitative observations. For this reason, expertise is of great importance in determining to which hazard class a sub-area belongs. Consequently, the resulting hazard map may depend on the person in charge of the field study. We present an experiment that was realized in order to evaluate the importance of subjective assessment: three populations, with different level of expertise (students in geosciences, researchers in geosciences and confirmed experts) have been asked to assess rock fall hazard on a test site divided in three different sectors. Their first assessment of the probability of a rock fall was given without using any method. Then, they used the "Laboratoire des Ponts et Chaussées" (LPC) method, which is a qualitative method frequently used in France and the "Slope Mass Rating" (SMR) method which is a more quantitative approach, resulting from the classifications of rock masses. An analysis of results variance shows that there is a significant influence of the method used on the assessment of rock fall probability, but a non-significant influence of the expertise level of the population. The SMR method seems highly sensitive to the presumed instable volume and exhibits an important dispersion on the results. To the contrary, with the LPC qualitative method, the results are similar.

1 INTRODUCTION

Rock fall instabilities are a major risk for population, human activities and infrastructure (Bell & Glade 2004, Moreiras 2006). It is thus necessary to evaluate the level of rock fall hazard and propose hazard maps in order to manage risk in urban areas. Construction in some high hazard areas is excluded, or requires geotechnical engineering assessment of slope stability (Fell et al. 2008). In some parts of the world, landslide hazard and risk maps are introduced across the country. They provide different hazard classes as for example the PPR ("Plans de Prevention des Risques Naturels Previsibles") in France (Laboratoire des Ponts et Chaussées 1999) and the "Cartes de Dangers" in Switzerland (Leroi et al. 2005). This evaluation will also allow to establish a monitoring system of rock mass movement or a suitable protection. It must be as accurate as possible (not underestimated neither overestimated) and reproducible.

Rock fall hazard can be defined as the probability that a specific location at the toe of a studied slope is reached by a rock fall of a given intensity (Jaboyedoff et al. 2001). What ever is the intensity of the expected rock fall, the previous probability can be divided in two terms as (Hantz 2011): the probability of detachment (or probability of failure) and the propagation probability.

Various methods exist to simulate the trajectory of rock mass after rupture and assess the propagation probability (Dorren 2003). However, in the present state of knowledge, there is no fully reliable method to estimate the probability of failure (Hantz 2007). Some of the existing methods are quantitative and based on historical inventory (Dussauge-Peisser et al. 2002, Hungr et al. 1999, Luckman 1976). However, most of the time, such an inventory is not available, and qualitative assessment methods are thus used, mainly based on expert judgment (Hantz et al. 2003, Jaboyedoff et al. 2001, Laboratoire des Ponts et Chaussées 2004). These methods are based on the qualitative study of two different kinds of parameters: internal parameters (IP), which are intrinsic features of the slopes (e.g. the geology of the site, the mechanical properties of rock and soil or the fracturing), and external factors (EF) (e.g. water circulation or human activities,Volkwein et al. 2011). They allow the instable volume and the occurrence probability of rock fall to be defined. Consequently, experts have a key role in hazard assessment.

The present paper presents an experiment developed to evaluate the influence of subjective judgments in the process of expertise in rock fall assessment. This experiment is based on the comparison of the results obtained after evaluation of the hazard level on a test-site by three populations having different levels of expertise. Two different methods for rock fall assessment are tested. Results are presented and discussed in a second part.

2 EXPERIMENTAL PROTOCOL

2.1 *Selection of the test site*

The experiment was realized on a cliff situated in Liverdun (close to Nancy, France), that has been

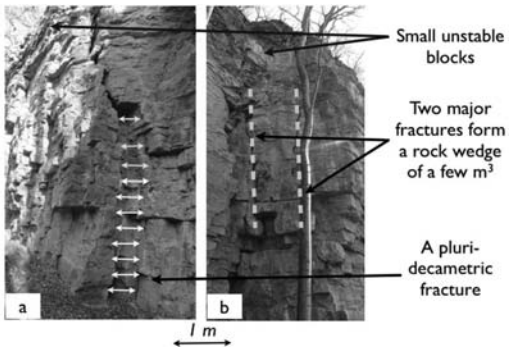


Figure 1. Sector 1 (a) and sector 2 (b) and their mean characteristics.

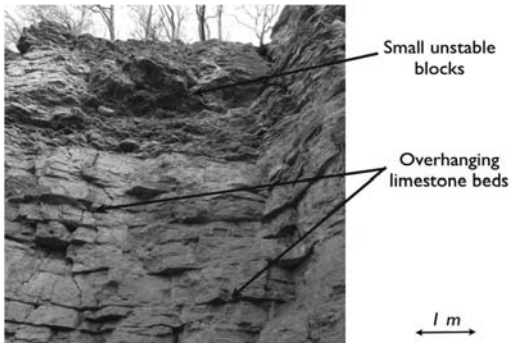


Figure 2. Sector 3 and its mean characteristics.

previously classified as presenting a high level rock fall hazard (Moiriat et al. 2008). The site is a 50-meters cliff of Jurassic limestone. It is made up by massive blocks in the base, and small blocks in the upper part.

Three sectors were identified:

- Sector 1 presents a massive wall with well-defined stratification beds. A pluri-decametric fracture isolates a rock panel of several hundred of m^3. On the top, small unstable blocks can be noticed (Figure 1).
- On sector 2, two major fractures form a rock wedge of a few m^3. Small unstable blocks are present in the upper part (Fig. 1).
- On sector 3, limestone beds are overhanging and some blocks at the top are unstable (Figure 2).

2.2 *Population*

Three populations were defined:

- 25 first year master students in geosciences who were confronted to a risk assessment study for the first time. These students may be later asked for making hazard or risk maps, in internships for e.g.
- 10 researchers in geosciences who work in risk assessment field. This population is not accustomed to regular rock fall assessment studies
- 6 confirmed experts who benefit from a long experience in field rock fall hazard and risk study.

Table 1. Assessment of the probability of failure with the LPC method.

Predisposition intensity	Very low	Low	Medium	High	Very high
$<0.001\,m^3$	L	L	L	M	M
0.001 to $0.01\,m^3$	L	L	M	M	H
0.01 to $1\,m^3$	L	M	M	H	H
1 to $100\,m^3$	M	M	H	H	H
$>100\,m^3$	M	H	H	H	H

L : Low – M : Moderate – H : High

The comparison of the rock fall hazard evaluation obtained by each population will highlight the influence of the level of expertise on rock fall hazard assessment.

2.3 *Methods used in the rock fall assessment*

At first, an "a-priori" hazard level was ask to each population, without making use of any method. Then two rock fall assessment methods were used: the "Laboratoire des Ponts et Chaussées" (LPC) method which is a qualitative method frequently used in France and the "Slope Mass Rating" (SMR) method which relies on a more quantitative approach.

2.3.1 *LPC method*

The LPC method is detailed in Laboratoire des Ponts et Chaussées (2004). It proposes three main steps:

(i) Localize and identify potential instabilities using the following parameters:
  - Nature of the studied blocks:
    - Description of the instable rock mass;
    - Lithology;
    - Hydraulic and hydrologic data;
  - Geometrical parameters: geometry and dimensions of the potentially instable compartment;
  - Geomechanical parameters of discontinuities: frequency, roughness, discontinuities aperture, filling, orientation of critical discontinuities. . .
  - Triggering factors: interstitial water, rainfall, high temperature variation, freeze-thaw cycles, vegetation. . .

  This step helps to determine the unstable volume and the mechanism of failure.

(ii) Define of the failure probability. The study of the previously parameters helps determining potentially instable volumes. For each of these, a temporal probability (annual frequency or return period) and an occurrence probability is associated. The combination of these two data gives a level of the predisposition at the instability, which, coupled with the corresponding volume, determines the probability of failure (Table 1).

(iii) The next step would be to determine the probability of propagation, but this step was not considered in this study, its objective being only to study the probability of failure.

2.3.2 *SMR method*

The Slope Mass Rating (SMR) index, proposed by Romana (1985), is a geomechanical classification commonly used for the characterization of rock slope. It is obtained by:

$$SMR = RMR_b(F_1 \times F_2 \times F_3) + F_4 \quad (1)$$

where:

- RMR_b is the basic RMR index resulting from Bieniawski's rock mass classification without any correction (Bieniawski 1989). The later is obtained by adding rating values for five parameters: (i) strength of intact rock; (ii) RQD; (iii) spacing of discontinuities; (iv) condition of discontinuities; and (v) water inflow through discontinuities and/or pore pressure ratio;
- F_1 depends on the parallelism between joint azimuth and slope face strike. It ranges from 0.15 to 1.00 according to the relationship: $F_1 = (1 = \sin(A))^2$ where A denotes the angle between the strike of slope face and that of the joints;
- F_2 refers to joint dip angle. For a plane sliding mechanism, its value varies from 1.00 to 0.15, according to the relationship: $F_2 = \tan(B_j)^2$ where B_j denotes the joint dip angle. For a toppling mode of failure, F_2 is equal to 1.00;
- F_3 reflects the relationship between slope and joints dips. This parameter retains the Bieniawski adjustment factors that vary from 0 to -60 points and expresses the probability of discontinuity outcropping on the slope face for planar and wedge failure;
- F_4 is an adjustment factor for taking into account the method of excavation (natural slope, presplitting, smooth blasting, blasting or mechanical and deficient blasting). Is value varies from −8 to 15, and it is fixed empirically.

The SMR calculation leads to five stability classes (Romana 1985). Then, based on the work of El-Shayeb (1999), a level of the site activity is evaluated. There are four different levels of activity corresponding to:

(i) Dormant: morphological traces are faded, and there is no alteration of rock mass;
(ii) Inactive: morphological traces are evolved, and there is superficial alteration;
(iii) Low active: recent morphological traces, and the rock mass are altered;
(iv) Active: numerous morphological traces, and the rock mass are profoundly altered.

The combination of the SMR classes and the site activity provides a level of occurrence probability (Table 2), which in turn is coupled to the volume of unstable masses to obtain the hazard level (Table 3).

2.4 *Tools for the statistical treatment*

Each individual evaluated three levels of rock fall hazard: "a-priori" assessment, assessment with the LPC method and with the SMR method. After a first statistical treatment in order to compare the results, they were analyzed using the analysis of variance (ANOVA) method (Scheffé 1959) in order to assess the influence of the level of expertise, and the method on the final hazard level.

Table 2. Assessment of the occurrence probability with the SMR method.

SMR Activity	VF	F	M	U	VU
Dormant	VL	L	L	M	M
Inactive	L	L	M	M	H
Low active	L	M	M	H	H
Active	M	M	H	H	H

SMR : VF : Very Favorable – F : Favorable – M : Moderate
U : Unfavorable – VU : Very Unfavorable
VL : Very Low – L : Low – M : Moderate – H : High

Table 3. Assessment of the probability of failure with the SMR method.

Occurrence probability Intensity	Very low	Low	Medium	High
$<0.01\ m^3$	VL	L	L	M
0.01 to $1\ m^3$	L	L	M	M
1 to $10\ m^3$	L	M	M	H
$>10\ m^3$	M	M	H	H

VL : Very Low – L : Low – M : Moderate – H : High

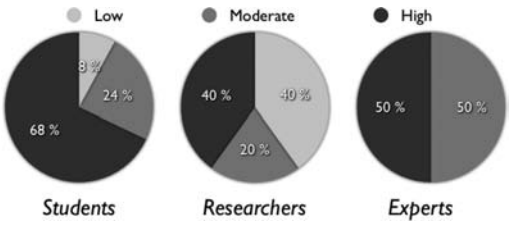


Figure 3. Rock fall hazard level with the "a-priori" assessment – Sector 2.

3 RESULTS

3.1 *First statistical treatment*

For this part, the results are only presented for the sector 2, which is a good representation of the global results.

The first statistical treatment shows that:

- With an "a-priori" assessment, there is a wide dispersion in the results, in particularfor the students and the researchers (Fig. 3);
- With the LPC method, the results are similar regardless the population groups; Experts give a lower

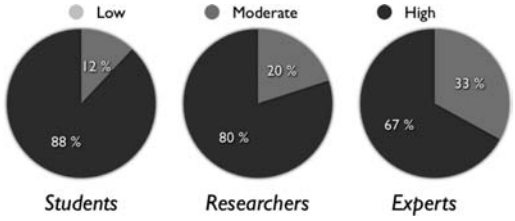


Figure 4. Rock fall hazard level with the LCP method – Sector 2.

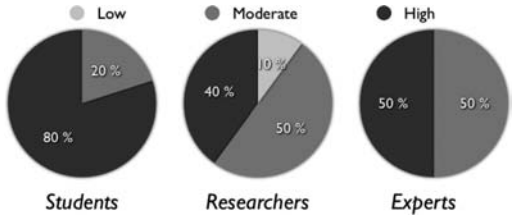


Figure 5. Rock fall hazard level with the LCP method – Sector 2.

level of rock fall hazard. A decrease of the proportionof high rock fall hazard level is observed, parallel to the increase of the level of expertise (Fig. 4).

For comparison, random samplingwas conducted using the LPC matrix (predisposition – intensity). The five levels of predisposition and intensity have been quantified from 1 to 5. Then, 100 000 random values were generated for these two parameters. It gave the following results: 24% of low rock fall hazard level, 36% of moderate rock fall hazard level and 40% of high rock fall hazard level;

- With the SMR method, the results exhibit a wide dispersion too. The mean hazard level is lower than with the LPC method (Fig. 5).

For comparison, random sampling conducted using the SMR matrix (Occurrence probability – Intensity) gave the following results: 24% of low rock fall hazard level, 51% of moderate rock fall hazard level and 25% of high rock fall hazard level.

3.2 *Analysis of the variance (ANOVA)*

In order to use the analysis of variance (ANOVA) method, the three hazard levels of rock fall have been transformed into a quantitative variable: low hazard level has been coded to '1', moderate level to '2' and high level to '3', seeing that it reflects the increase of the hazard in a familiar and convenient way. Therefore, several quantification methods have been tested which did not changed the following conclusions.

Reminding that the influence of a factor is considered as significant when the probability to exceed the F-value is lower than 5%, the ANOVA method shows the significant influence of the factor "method", and the non-significant influence of the factor "expertise" nor the interaction between these 2 factors, on the level of rock fall hazard assesses (Table 4, Table 5 & Table 6).

Table 4. Results of ANOVA: influence of the level of expertise and the choice of the method on the level of rock fall hazard – Sector 1.

	DF	Sum of Squares	Mean square	F value	Prob(X > F)
Method	2	7.317	3.66	8.52	0.00036
Expertise	2	2.645	1.32	3.08	0.0499
Method-Expertise	4	0.946	0.24	0.55	0.699
Residuals	114	47.684	0.43		
TOTAL	122	58.592	5.65		

Table 5. Results of ANOVA: influence of the level of expertise and the choice of the method on the level of rock fall hazard – Sector 2.

	DF	Sum of Squares	Mean square	F value	Prob(X > F)
Method	2	5.463	2.73	8.62	0.00033
Expertise	2	1.174	0.59	1.85	0.161
Method-Expertise	4	1.834	0.46	1.45	0.223
Residuals	114	36.113	0.32		
TOTAL	122	44.584	5.1		

Table 6. Results of ANOVA: influence of the level of expertise and the choice of the method on the level of rock fall hazard – Sector 3.

	DF	Sum of Squares	Mean square	F value	Prob(X > F)
Method	2	6.455	3.23	12.11	1.70e-5
Expertise	2	1.694	0.85	3.18	0.0455
Method-Expertise	4	2.204	0.55	2.07	0.0875
Residuals	114	30.395	0.27		
TOTAL	122	40.748	4.9		

4 DISCUSSION AND CONCLUSIONS

During the experiment, three methods were tested: (i) the "a-priori" assessment, (ii) the use of the LPC method and (iii) the use of SMR method. This order allowed each participant to assess the rock fall hazard with their own experience at first, then with a qualitative method (LPC method)then with a quantitative method (SMR method).

The results show dispersion in the hazard level for the "a-priori" assessment, especiallyfor the students and researchers, explained by their non-experience in this type of exercise. The guidance in LPC method helps the user to identify the blocks mass potentially mobilisable, its intensity and helps to reflect on its probability occurrence. Consequently, this method seems applicable for all the populations. Note that the experts give a lower overall level than the two other populations, which suggests that the experts do not overestimate the final hazard level. This remark deserves to be validated by further work.

SMR method showssimilar results to those obtained by the LPC method for students. However, for the researcher and expert populations, the dispersion in the results is important. The choice of the joint family and the volume of the potentially unstable rock mass can explain it.

REFERENCES

Bell, R. & Glade, T., 2004. Multi-hazard Analysis in Natural Risk Assessment, *in: International Conference on Computer Simulation in Risk Analysis and Hazard Mitigation, edited by: Brebbia, C. A.: WIT Press*, 26–29 September, Rhodes (GR), 197–206.

Bieniawski, Z.T., 1989. *Engineering Rock Mass Classification*, John Wiley and Sons Inc.

Dorren, L.K., 2003. A review of rockfall mechanics and modelling approaches. *Progress in Physical Geography*, 27(1), pp. 69–87.

Dussauge-Peisser et al. 2002. Probabilistic approach to rock fall hazard assessment: potential of historical data analysis. *Natural Hazards And Earth System Science*, 2(1/2), pp. 15–26.

El-Shayeb, Y. 1999. *Apport à la logique floue à l'évaluation de l'aléa "Mouvement de Terrain des sites géotechniques": propositions pour une méthodologie générale*. Ecole des mines de Nancy: Institut National Polytechnique de Lorraine.

Fell, R. et al. 2008. Guidelines for landslide susceptibility, hazard and risk zoning for land use planning. *Engineering Geology*, 102(3-4), pp. 85–98.

Hantz, D. 2007. *Contribution à l'évolution de l'aléa éboulement rocheux – Approche multidisciplinaire et multiéchelles.* Mém. De Diplôme d'Habilitation à Diriger des Recherches, Université Joseph Fourier, Grenoble 1, 79 p.

Hantz, D. 2011. Quantitative assessment of diffuse rock fall hazard along a cliff foot. *Natural Hazards and Earth System Sciences*, 11(5), pp. 1303–1309.

Hantz, D., Vengeon, J.M. & Dussauge-Peisser, C. 2003. An historical, geomechanical and probabilistic approach to rock-fall hazard assessment. *Natural Hazards and Earth System Sciences*, 3(6), pp. 693–701.

Hungr, O., Evans, S.G. & Hazzard, J. 1999. Magnitude and frequency of rock falls and rock slides along the main transportation corridors of southwestern British Columbia. *Canadian Geotechnical Journal*, 36(2), pp. 224–238.

Jaboyedoff, M. et al. 2001. *Prévention des mouvements de versants et des instabilités de falaises?: confrontation des méthodes d'étude des éboulements rocheux dans l'arc alpin*, Suisse: Programme INTERREG II.

Laboratoire des Ponts et Chaussées, 2004. *Les études spécifiques d'aléa lié aux éboulements rocheux*, Paris: Laboratoire Central des Ponts et Chaussées.

Laboratoire des Ponts et Chaussées, 1999. *Plans de prévention des risques naturels (PPR) – Risques de mouvements de terrain*, Paris: Laboratoire Central des Ponts et Chaussées.

Leroi, E. et al. 2005. Risk assessment and management. *Landslide risk management*, pp. 159–198.

Luckman, B.H. 1976. Rockfalls and rockfall inventory data: Some observations from surprise valley, Jasper National Park, Canada. *Earth Surface Processes*, 1(3), pp. 287–298.

Moiriat, D., Colin, S. & Dufrenoy, R. 2008. *Aléa chute de blocs sur le territoire de Meurthe et Moselle (54) – Etat des connaissances et cartographie au 1/50000*, BRGM.

Moreiras, S.M. 2006. Frequency of debris flows and rockfall along the Mendoza river valley (Central Andes), Argentina: Associated risk and future scenario. *Quaternary International*, 158(1), pp. 110–121.

Romana, M. 1985. New adjustment ratings for application of Bieniawski classification to slopes. *In Proceedings of the International Symposium on the Role of Rock Mechanics in Excavations for Mining and Civil Works.* Zacatecas: International Society of Rock Mechanics, pp. 49–53.

Scheffé, H. 1959. *The Analysis of Variance*, John Wiley & Sons.

Volkwein, A. et al. 2011. Rockfall characterisation and structural protection-a review. *Natural Hazards and Earth System Sciences*, 11.

This page intentionally left blank

Rock Mechanics for Resources, Energy and Environment – Kwaśniewski & Łydżba (eds)
© 2013 Taylor & Francis Group, London, ISBN 978-1-138-00080-3

Seismic reflections around a tunnel "viewed" through waveguides – A case study

J.M. Descour
C-Thru Ground, Inc., Littleton, CO, USA

H. Hume
Yeh and Associates, Inc., Denver, CO, USA

ABSTRACT: A two-lane tunnel on a busy highway will be expanded. Reflected seismic waves were used to map structural features in the surrounding rock from the inside of the tunnel. The results of seismic imaging, largely in accord with the geological investigation, provided 3D characterization of the rock mass useful for the expansion project. Parts of the concrete liner of the tunnel had separated from damaged rock. This posed a challenge to conducting the seismic ground characterization from inside the tunnel. The uniqueness of the seismic survey approach was not the use of a small, hand-held source driving a swept frequency signals into the rock which allowed conducting the survey without stopping the traffic; nor was it the use of high sensitivity, broad-band accelerometers for detecting seismic waves in the rock. It was the fiberglass waveguides (1 meter long), anchored to the rock via holes drilled through the liner that introduced the uniqueness. These waveguides provided reliable coupling to the rock mass for sources and receivers mounted inside the tunnel near the inner surface of the liner. The sources and receivers, in interchanging arrays, formed 14 sets of "directional seismic antennae" along the tunnel, each deployed around the liner circumference within the limits of having to leave one lane open to traffic. Each "antenna" was used for imaging its own section of the rock mass around the tunnel. Overlapping ground images were then joined to successfully map the whole length of the tunnel.

1 INTRODUCTION

A decision was made to widen the east-bound (EB) tunnel for one of the short double tunnels in Colorado. To assure an optimal design and a safe and economical construction, a comprehensive geotechnical investigation of the rock mass around and south of this tunnel was launched. The investigation included using reflected seismic waves for imaging anomalous rock mass conditions associated with possible fractures, faults, weathered rock etc.

The major obstacles for this investigation were:

- Elevated attenuation levels particularly for shorter/higher frequency seismic waves due to often disturbed and fractured rock mass;
- Disruption caused by the traffic in the tunnel; and,
- Concrete liner blocking access for coupling seismic sources and receivers to the competent parts of the native rock over 1 meter behind the inner surface of the liner.

Using very sensitive accelerometers significantly improved detection of the weakest seismic waves by the digital data acquisition system.

The noise problem associated with the traffic was overcome by using a swept frequency seismic source. At the same time the controlled wide spectrum of the source signal enhanced detection of shorter reflected waves, improving the resolution of seismic imaging.

And the access to the native ground for sources and receivers was provided through fiberglass rods (waveguides) anchored to the rock through holes in the liner.

The seismic investigation generated a complex 3D image of structural anomalies in the rock mass which appeared matching the expression of tectonic features on the surface above the tunnels. The alignment of these anomalies complemented the pattern of tectonic features identified by the other geotechnical investigation.

2 BACKGROUND

The Tangential Reflector Tracing (TRT) uses seismic waves generated and detected at the perimeter of the natural tunnel walls for imaging structural anomalies (fractures, voids, water saturated zones etc.), in the rock mass ahead and around advancing or existing tunnels or shafts. Small amounts of the incident energy coming from a seismic source become reflected from structural anomalies (Neil et al. 1999, Descour et al. 2012), and can be detected by an array of sufficiently sensitive receivers.

The strength of reflected seismic waves is defined by the change of seismic impedance across the boundary of an anomaly (Aki & Richards 1980, Descour et al. 2012), the orientation and shape of that boundary, and the ratio between the size of the anomaly and the length of incident seismic waves.

The waves reflected particularly from a zone of fractured, deteriorated ground are often very weak and "fragmented" compared to direct waves from the source. Consequently the reflected waves are usually impossible to identify visually in raw seismic records.

The TRT utilizes the reflected waves to construct digital images of respective structural anomalies in the ground by transposing spatial expression of those waves back to the location of their origin.

The images are generated within a predetermined volume formed of orthogonal matrix of nodal points and of known seismic velocity distribution.

For each seismic source-receiver pair of known location within such a volume, the travel times for recorded reflected waves are converted through the velocity to form 3D ellipsoidal virtual waves (Fig. 1) (Ashida 1993 & 2001, Neil et al. 1999).

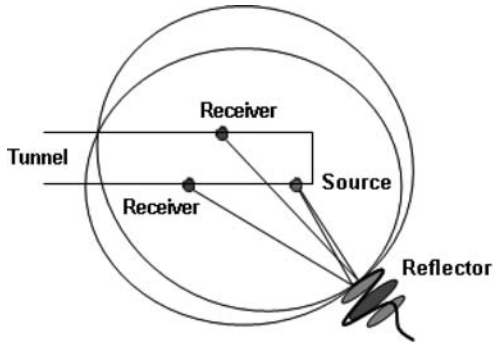


Figure 1. Principal idea of using reflected waves for imaging seismic reflectors.

With a sufficient number and spatial spread of sources and receivers all the ellipsoidal waves for the same anomaly tend to match in phase and add together at each anomaly's true location to form characteristic 3D wave-like patterns (Fig. 1).

Typically a color code is used to indicate the wave swings.

3 SURVEY STEP

The main objective for the survey was to image weakened ground conditions around and over the planned expansion zone to the south of the EB tunnel. Plan view of the perimeter of the image block and the horizontal outline of sources and receivers used for this survey (RA# and SA# sets of dots respectively), are shown in Figure 2.

In the EB tunnel the source and the receiver points were deployed in reciprocating arrays, each formed of 3 rings of 4 points per ring. Two magnified tunnel profiles (Fig. 2 – insert) show the arrangement of sources and receivers and their numbering sequence in each of the three rings of a respective array. Also two rows of 10 source points each were deployed on the south wall of the westbound (WB) tunnel, one row near each portal and facing the nearest receiver array in the EB tunnel. Similarly two arrays of source points were deployed at the base of the rock outcrop south of the EB tunnel.

The walls of both tunnels were formed of the concrete liner approximately half-meter thick with an old steel and wood support. The rock, immediately behind the liner was often in a poor condition. In some locations the rock was separated from the liner.

The fiberglass rods (waveguides), approximately 1.2 m long and 20 mm in diameter were anchored to the native rock through holes in the liner (Fig. 3). Polyurethane foam was injected around each rod to dampen the lateral vibrations.

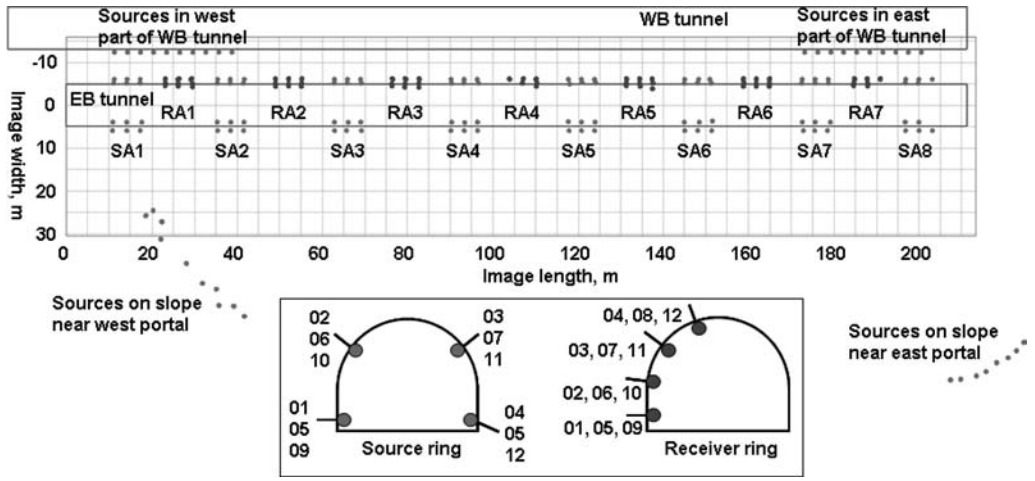


Figure 2. Plan view of image base with arrays of seismic sources (SA#) and receivers (RA#) along EB tunnel, arranged in three rings per array (insert, due east), and additional sources outside EB tunnel.

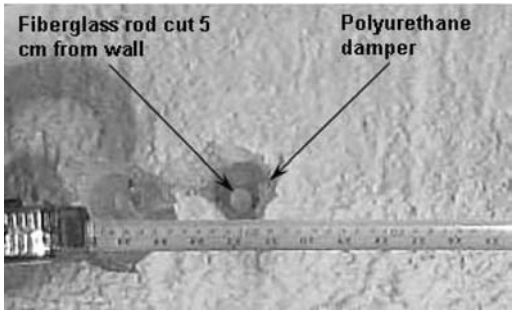


Figure 3. View of outer end of the fiberglass rod/seismic waveguide.

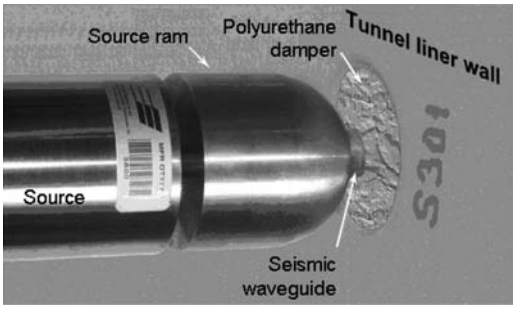


Figure 4. Hand-held seismic swept frequency source applied at outer end of a waveguide.

The source points at the base of the rock outcrop south of the EB tunnel were selected directly at the surface of exposed and competent rock layers.

In general, the holes for the fiberglass rods were drilled nearly perpendicular to the concrete liner inner surface. However the holes for the bottom sources on the south side of the EB tunnel, and for the sources in the WB tunnel were inclined approximately 30 degrees down from horizontal.

The purpose of the incline was to improve the directional characteristics for S-waves toward the south.

4 EQUIPMENT

At each source point a hand-held magnetostrictive source (Fig. 4) powered by a swept frequency signal was pressed axially at the outer end of the fiberglass rod or directly at the rock surface (outcrop) (Yamamoto et al. 2006). In each case the resulting seismic waves were polarized nearly parallel to the source alignment (Descour et al. 2012).

The 2-seconds long swept frequency signal ranging from 100 to 3000 Hz was delivered via a light cable from the source driving assembly.

The accelerometers (receivers) of sensitivity approximately 0.1 V/m/s^2 were coupled to the fiberglass rods using screw-on PVC couplers (Fig. 5). They were connected to a multi-channel digital seismograph via a separate coax cable each.

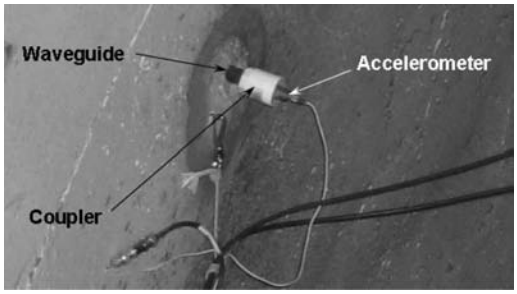


Figure 5. Accelerometer coupled to a waveguide.

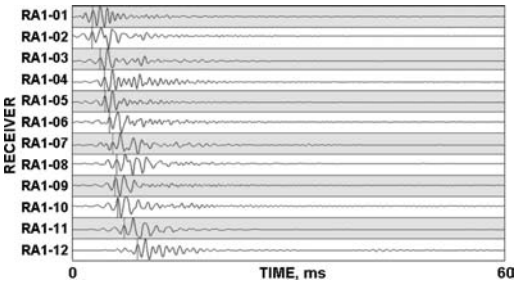


Figure 6. Accelerometer records for array RA1 cross-correlated with the source signal.

Triggering the source signal simultaneously activated recording by the seismograph of both the source (pilot) signal and the signals from the accelerometers.

The software on board the seismograph performed correlation of the signals from the accelerometers with the pilot signal, converting each record to an equivalent of an impact source (Fig. 6). Using the swept frequency signal effectively suppressed the noise from the traffic.

5 DATA ACQUISITION

The TRT survey was conducted by recording seismic waves for all neighboring pairs of sources and receivers arrays along the EB tunnel. This routine produced the total of fourteen overlapping sets of seismic records covering together the entire survey area, with up to 144 seismic traces for individual source-receiver pairs per set.

The records between sources in the WB tunnel and the closest receiver arrays in the EB tunnel produced good quality seismic data for measuring seismic velocity between the tunnels. However the records between the source points on the outcrop and the closest arrays of receivers to assess velocity toward south were weak and difficult to identify.

6 DATA PROCESSING

6.1 *Seismic velocity evaluation*

The preliminary assessment of seismic velocity along EB tunnel was done through linear regression of

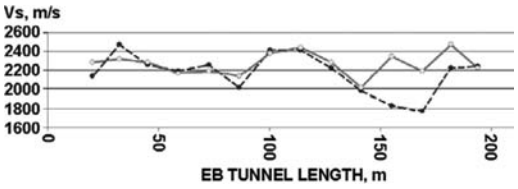


Figure 7. Preliminary (dashed), and refined through iteration (solid) S-wave velocity along EB tunnel.

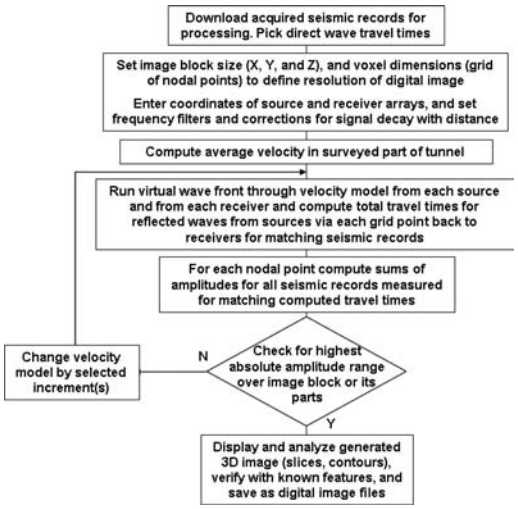


Figure 8. Simplified flow chart for TRT data processing.

travel times vs. distance for seismic records acquired between neighboring arrays of sources and receivers. The S-wave velocity refined later through iteration ranged from 1980 to 2470 m/s (Fig. 7).

The velocity tomography using seismic records across the pillar between the tunnels and also between the EB tunnel and the sources on the outcrop to the south produced the velocity ranging from 2130 to 4270 m/s. The upper velocity values were consistent with the expected P-waves, and the lower values likely represented the S-waves.

Overall, the velocity values along and lateral to the EB tunnel were interpreted as indicative of rather insignificant directional velocity anisotropy.

6.2 *Tangential Reflector Tracing (TRT)*

Figure 8 presents a simplified block schematic of the TRT data processing flow.

TRT survey data were processed to image the ground features within a rectangular block 46 m wide (X), 210 m long (Y) (Fig. 2), and 21 m high (Z was measured up from the road pavement).

Due to the limit for the number of nodal points which the software could process (less than 55,000), and to assure the desired resolution (+/−0.5 m), the

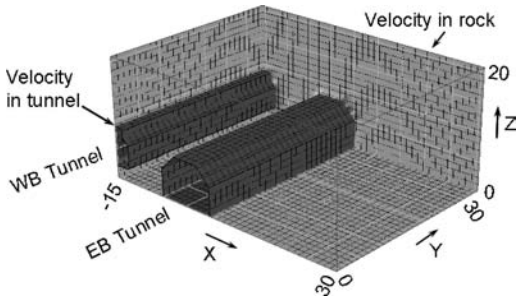


Figure 9. S-wave velocity model for a single TRT segment with zero velocity in tunnel cavities.

image was generated in 14 separate, overlapping segments. Each segment was matching the X and Z dimensions of the block, while extending only 34 m along the EB tunnel alignment (Y). Also each segment included, and was centered with respect to the pair of two neighboring source and receiver arrays which produced the survey data used to generate the TRT image for that segment.

Using the preliminary velocity evaluation, individual average velocity models were built for each segment (Fig. 9). Each model incorporated voids representing both tunnels. Subsequently, the ground image for each segment was generated using TRT procedure while refining the average velocity model through iteration (Fig. 8).

Finally, the TRT images generated for each segment were "fused" together along the overlapping zones to produce the overall image of structural features around and south of the EB tunnel.

According to other geotechnical data, the dominant structural features in the ground were associated with fractures and joints. Hence, to improve the clarity, the TRT images were rectified, and their polarity was inversed to represent detected features as blue (negative) anomalies typically characteristic for reflections from weaker rocks and voids.

7 REVIEW OF RESULTS

Figure 10 shows plan view of TRT defined anomalies in the ground, along with a pattern of recently mapped joints superimposed on the topographic map of the ground surface above the tunnels.

This superposition demonstrates a correlation between the plan view of the TRT anomalies, the known joints, and the ground features on the surface. Some additional possible alignments of ground features identified by the TRT images are marked with dotted lines.

These additional directions were identified by rotating the TRT images and searching for apparent planes of alignment for sets of individual contour anomalies (Fig. 11).

The planes of alignment appear related to tectonic and structural fractures criss-crossing the rock mass.

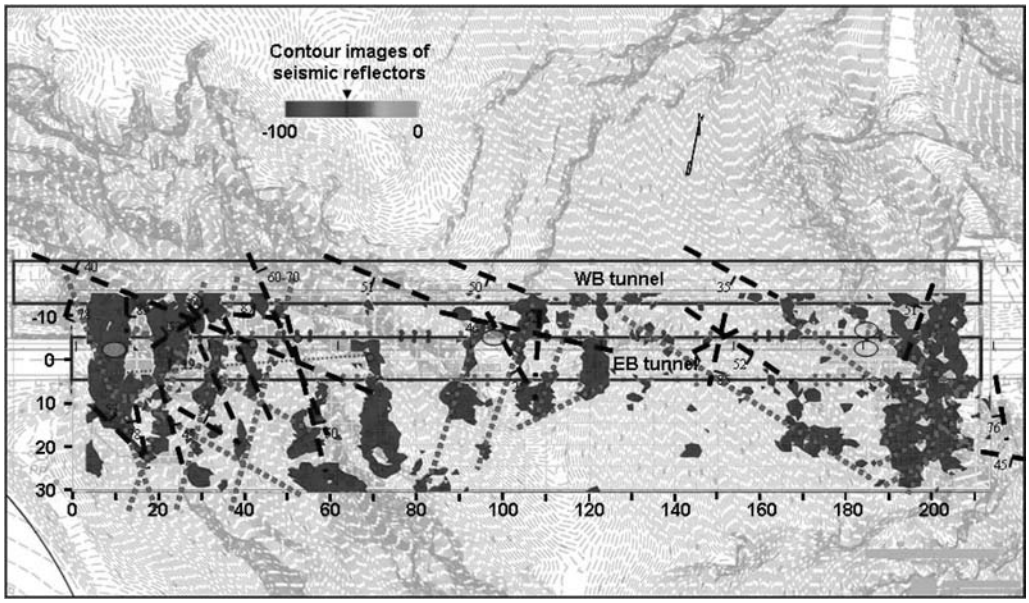


Figure 10. Plan view of TRT anomalies (contour images) and joints from geological survey (dashed lines), compared to surface map above the tunnels. Dotted lines are interpreted as additional TRT features.

Many alignment planes appear to correlate with the orientation of fracture zones mapped recently at the site. The TRT survey did not identify any explicit fault line near the west portals of the tunnels.

Patterns of anomalies along the alignment planes near both the west and the east portals of the EB tunnel appear matching the features on the rock face (Fig. 12).

The bulkier blue contour anomalies in Figure 10 represent general locations of possible more intensely fractured and weathered parts of the rock structures.

Slimmer anomalies could indicate joints or fractures. Their dimensions/extent may be exaggerated due to the coarseness of images proportional to the length of detected reflected waves. Also the confinement of sources and receivers to the tunnel profile in rock and a relatively flat pattern of receiver arrays in the EB tunnel could have contributed to a possible tangential elongation of detected anomalies with respect to the tunnel alignment.

In general, the overall distribution of the anomalies in the planned expansion zone south of the EB tunnel could potentially affect stability of the rock mass at the following ranges measured from the west portal: 5 to 30 m, 90 to 130 m, and 190 to 205 m.

8 CONCLUSIONS

– The distribution of imaged contour anomalies forms a zigzagging zone which appears to correlate with the topographic expression of tectonic features on the surface (Figs 10 & 12).

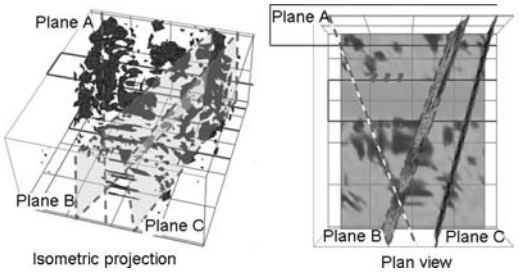


Figure 11. Identifying possible alignment planes by rotating three-dimensional TRT images.

– This correlation lends credibility to the TRT survey results obtained using waveguides, and merging partially overlapping images.
– The lateral distribution of the anomalies along the EB tunnel appears to correlate with voids and joints mapped by the other geotechnical investigation.
– The images appear to represent local weakness zones in the rock structure possibly associated with fractured and weathered rock mass. They provide 3D complementary support for an assessment of the ground integrity needed for the construction work.
– Using swept frequency source significantly reduced interference from the noise primarily associated with ongoing traffic in the tunnel.
– Orienting the source and the receivers to generate and record seismic waves of amplitude normal to the tunnel perimeter was designed for, and successfully generated well defined S-waves which are typically the most effective for imaging structural features in the ground.

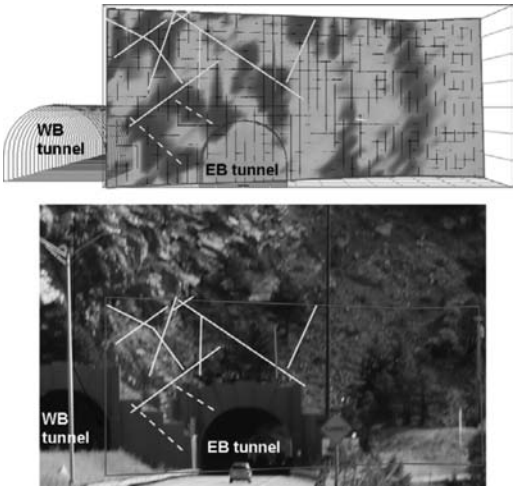


Figure 12. Comparing alignment of anomalies (white lines) in TRT vertical profile and the surface relief features near west portals of both tunnels.

REFERENCES

Aki, K. & Richards, P. G. 1980. Quantitative seismology. Theory and methods. Vol. 1. N. York: W. H. Freeman and Co.

Ashida, Y. & Sassa, K. 1993. Depth transform of seismic data by use of equi-travel time planes. Exploration Geophysics 1993; 23:341–6.

Ashida, Y. 2001. Seismic imaging ahead of a tunnel face with three-component geophones. International Journal of Rock Mechanics & Mining Sciences 38 (2001) 823–831.

Descour, J.M., Morino, A., Maffucci, M., Pinheiro, F. & Elsner, P. 2012. Ten Months of Ground Imaging Ahead of TBM Using Seismic Reflector Tracing. In Proceedings of 46th US Rock Mechanic/Geomechanics Symposium, Chicago, IL, USA

Neil, D.M., Haramy, K.Y., Descour, J.M. & Hanson, D. 1999. Imaging ground conditions ahead of the face. World Tunneling, V. 12, No. 9, November, pp. 425–429.

Yamamoto, T., Shirasagi, S., Murakami, K., Nishioka, K. & Descour, J. 2006. Imaging Changing Ground in Front and Above a TBM Using Seismic Reflector Tracing; A Case Study. In Proceedings of 41st U.S. Symposium on Rock Mechanics, Golden, Colorado.

Rock Mechanics for Resources, Energy and Environment – Kwaśniewski & Łydżba (eds)
© 2013 Taylor & Francis Group, London, ISBN 978-1-138-00080-3

Comparison between different estimators of the degree of rock mass fracturing

A.M. Ferrero
Department of Earth Sciences, University of Turin, Italy

M.R. Migliazza
Department of Earth Sciences "A. Desio", University of Milan, Italy

G. Umili
Department of Civil, Environmental and Territory Engineering, University of Parma, Italy

ABSTRACT: The evaluation of the degree of fracturing of a rock mass is a major starting point for any rock engineering design. There are different methods available in literature for the evaluation of the rock mass degree of fracture. Among the most popular we have considered: the J_v estimation by Palmström (1996) and the P_{32} estimation by Dershowitz (1985). The first one considers the total number of discontinuities in a certain volume weighed by the joint persistence whilst the second method consider the joint area computed by a statistical analysis of the traces under the hypothesis of different joint shape.

A comparison between the two different approaches firstly developed on simplified synthetic schemes and then on real rock mass data has been the topic of this work.

In particular a rock slope of the Mount Blanc massif and the excavation faces of the Marta-Giulia tunnel have been analysedto highlight the influence of scale effects on the rock mass degree of fracturing evaluation.

1 INTRODUCTION

A rock mass is a discontinuous medium made of rock blocks delimited by discontinuities, which generally are the subjects of in situ surveys. Different characteristics, defined by the International Society of Rock Mechanics (ISRM, 1978), have to be included in the description of discontinuities: orientation, spacing, continuity or persistence, roughness, wall strength, opening, filling and infiltrations. The first three types of characteristics are geometrical magnitudes that can be measured using the compass or non-contact techniques. From these it is possible to obtain evaluations on the degree of fracturing of a rock mass and on the dimensions of the blocks that can be formed. Such evaluations can be made in either a deterministic or statistical manner, whenever the collected data sample is sufficiently representative.

The key point of the correct evaluation of the degree of fracturing and the characterisation of the rock mass is the correct identification of the effects of the observation window that could significantly influence results and lead to a totally different quality rate. The size of the observation window is sometime influenced by external boundaries such as the dimension of the excavation front in a tunnel that cannot be enlarged. In these cases is particularly important to quantify the scale effect in the evaluation of the degree of fracturing.

Moreover, although discontinuities are 3D planes, we often observe their traces on the rock wall and we can only measure their apparent orientation between the discontinuity and the observation window. These two kinds of limitations (dimensions and orientation) can both influence the rock mass fracturing estimation and these errors also depends upon the chosen methodology as shown in the following chapters.

2 TWO ESTIMATORS OF THE DEGREE OF FRACTURING: J_V AND P_{32}

Two different approaches are here described: the J_v estimation by Palmström (1996) and the P_{32} estimation by Dershowitz (1985), both of them applicable to the case of a 2D survey window.

Volumetric joint count J_v is defined as the number of joints in a unit volume:

$$J_V = \frac{N_V}{V} \tag{1}$$

For a survey conducted on a window of area A, the areal frequency of the joints N_a is defined as the number of joints that emerge in the surveyed window and

J_v can be estimated by applying the following formula (Palmström 1996):

$$J_V = K_P \cdot Na = K_P \cdot \frac{\sum_i \left(na_i \frac{L_i}{\sqrt{A}} \right) + Na_j}{\sqrt{A}} \quad (2)$$

in which K_P is a correlation factor ($K_P = 1–2.5\ m^{-2}$), $\sqrt{A}$ is the equivalent dimension of the window, na_i is the number of joints with shorter dimensions than that of the window and Na_j is the number of discontinuities with a longer length of the traces than the dimension of the window. The counting of the number of not completely persistent joints is carried out considering a "weight" lower than unity, which is a function of the relationship between the length of the discontinuity L_i and that of the survey. It should be pointed out that the scale effect that conditions the value of J_v is mitigated by normalising the value with respect to the dimensions of the survey, and that the persistence of the joints is taken into account through the length of the traces and not considering the areal extension; they are therefore considered to be extended infinitively in the third dimension.

The other considered estimator is fracture intensity P_{32}, which is defined as the sum of the surface fracture areas present in the volume unit (Dershowitz 1985):

$$P_{32} = \frac{\sum_i A_i}{V} \quad (3)$$

For a survey conducted on an observation window, P_{32} can be calculated as (Zhang & Einstein 2000):

$$P_{32} = \frac{N_T E(S)}{V} \quad (4)$$

where N_T is the total number of sampled discontinuities, E(S) is the mean joint area and V is the reference volume.

2.1 *Comparison between the methods for the estimation of the degree of fracturing*

If a simulated rock mass portion containing known joints is considered and an observation window is used to infer data from a reference volume in that rock mass, it is possible to calculate deterministically the values of J_v and P_{32} by considering their definitions, and to estimate them by applying equations 2 and 4. In order to examine in depth such evaluations, a simplified geometrical scheme was assumed and formulations were all expressed in term of discontinuity spacing, trace length, persistence and dimension of the observation window. This scheme is shown in Figure 1: a rock mass portion in which 3 orthogonal joint systems are present, each characterised by spacing S_i, trace length L_i, rock bridges length R_i and persistence p_i, which are assumed to be known. Persistence is defined as:

$$p_i = \frac{L_i}{L_i + R_i} \quad (5)$$

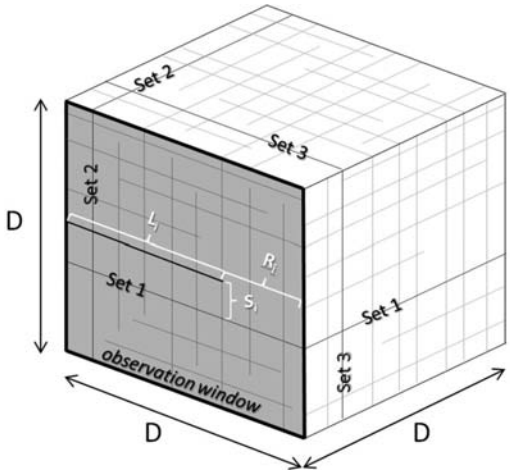


Figure 1. Reference volume and survey window for the estimation of the J_v and P_{32} values. Three orthogonal discontinuity sets intersect the volume.

and can vary between 0, absence of joints, and 1, continuous joints.

In order to verify whether the determination of J_v and P_{32} is affected by a scale effect and if so, whether it is determined by the observation dimension, a cubic volume of characteristic dimensions D has been considered, with a square observation window of side D. The discontinuity surface area A_j, with a trace length L_i, can be estimated as:

$$A_j = k_j L^2 \quad (6)$$

where k_j represents the shape factor of the discontinuity surface, which is equal to 1 for square shaped discontinuities and equal to $\pi/8$ for semi-circular shapes.

According to the method proposed by Dershowitz (1985), the volume for the estimation of P_{32} is equal to:

$$V = k_{VOL} D^3 \quad (7)$$

in which k_{VOL} represents the shape factor of the volume, which is equal to 1 for a cube and equal to $\pi/8$ for a semi-cylinder, both of which develop behind the observation window.

Considering the scheme in Figure 1, the following relations can be used to calculate J_v with equations 1 and 2:

$$N_{a_i} = \frac{D}{(L_i + R_i)} \cdot \frac{D}{S_i} = \frac{pD^2}{L_i S_i} \quad (8)$$

$$N_{v_i} = \left(\frac{D}{L_i + R_i} \right)^2 \cdot \frac{D}{S_i} = \frac{p^2 D^3}{L_i^2 S_i} \quad (9)$$

The formulations that can be obtained for the estimation of J_v and P_{32}, considering both the direct

Table 1a. Equations to determine J_v and P_{32} from a direct measurement on the reference volume.

	DIRECT MEASUREMENT from VOLUME			
	CONTINUOUS		DISCONTINUOUS	
J_v	$\frac{1}{D^2}\sum_i \frac{1}{S_i}$	(10)	$\sum_i \frac{p_i^2}{L_i^2 S_i}$	(11)
P_{32}	$k_j \sum_i \frac{1}{S_i}$	(12)	$k_j \sum_i \frac{p_i^2}{S_i}$	(13)

Table 1b. Equations to determine J_v and P_{32} from an indirect measurement on an observation window.

	INDIRECT MEASUREMENT from OBSERVATION WINDOW			
	CONTINUOUS		DISCONTINUOUS	
J_v	$K_P \sum_i \frac{1}{S_i}$	(12)	$K_P \sum_i \frac{p_i}{S_i}$	(13)
	Palmström			
P_{32}	$\frac{k_j}{k_{VOL}} \sum_i \frac{1}{S_i}$	(16)	$\frac{k_j}{k_{VOL}} \frac{1}{D} \sum_i \frac{p_i L_i}{S_i}$	(17)
	Zhang & Einstein			

measurement of the discontinuities in the considered volume and the indirect measurement made on the observation window (equations 2 and 4), are reported in Table 1a and Table 1b. The joints are assumed to have their trace length longer than the observation dimension D; they are considered continuous if persistence is equal to 1, discontinuous otherwise. Summations refers to the fact that each discontinuity set contributes to the global value of the considered estimator.

From the formulations reported in Table 1a and 1b, it is possible to observe that dimension of the estimators are verified (parameter K_P in equations 12 and 13 is the one used in equation 2 and its dimension in m^{-2}). An important consideration to be done is how the two formulations are affected by a scale effect (that is, the dimension D of the observation window appears in the formula) in relation to the methodology that is used and to the persistence characteristics of the discontinuities. In particular, for joints which are continuous with respect to the observation window (that is, with persistence p_i equal to 1), the value of J_v determined from the direct measurement of the number of joints in the considered volume is inversely proportional to D^2 (equation 10); this scale effect affects directly the definition of J_v. On the other hand, the procedure proposed by Palmström (equation 12) does not suffer from such an effect, even though J_v values calculated with equation 13 and 11 for the case of discontinuous joints are different. Anyway, equations 12 and 10 coincide for $K_P = 1/D^2$, while relation between equation 13 and 11 is far more complex.

Table 2. Characteristics of the discontinuity sets.

Discontinuity Set	F_1	F_2	F_3
Spacing S_i [m]	1	1	1
Trace length L_i [m]	2	1	3
Rock bridge length R_i [m]	1	1	1
Persistence p_i [–]	0.67	0.50	0.75

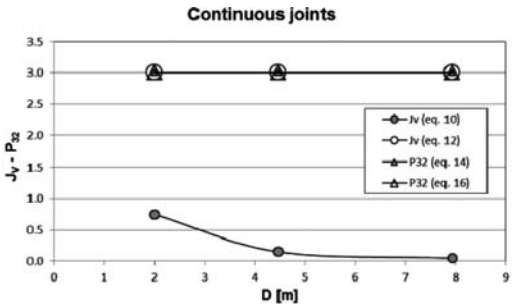


Figure 2. Comparison between J_V and P_{32} values obtained considering continuous joints.

As far as the P_{32} value is concerned, it should be observed that this value never suffers from a scale effect, except for the case of discontinuous joints and estimation through an indirect analysis conducted on the observation window (equation 17). In this case, however, it is sufficient to choose a reference volume equal to $D^2\bar{L}$, in which the depth $\bar{L}$ is equal to the mean traces length, in order to minimize or even annul the scale effect. In particular, in the case of discontinuity systems characterized by the same trace length L_i, L is equal to L_i and the ratio $L_i/(k_{VOL} \cdot D)$ would result to be equal to 1. Equation 17 becomes equal to equation 13 except for the different coefficients k_j and K_P.

One can observe that equation 14 and 16 coincide for $k_{VOL} = 1$, while relation between equations 15 and 17 is far more complex.

A simulated rock mass with three orthogonal discontinuity sets geometrically known was assumed (Table 2) in order to make all the comparisons between the two estimators of the degree of fracturing. Observation window dimension D has been varied to consider the scale effect. Figure 2 shows the comparison between J_v and P_{32} values obtained considering continuous joints. Figure 3 shows the comparison between J_v and P_{32} values obtained considering discontinuous joints.

3 CASE HISTORIES

3.1 *Application to the Marbrée massif*

The crest of the Aiguilles Marbrées (3477 m a.s.l.) is part of the Monte Bianco massif and is made up of a series of peaks and walls of heights that reach and sometimes exceed 100 metres. From a

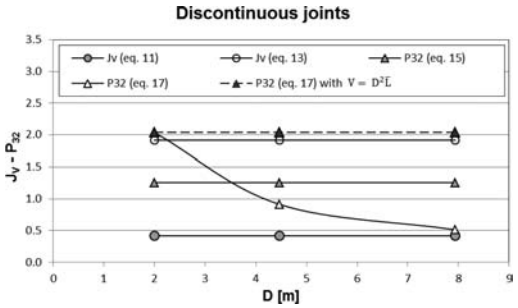


Figure 3. Comparison between J_V and P_{32} values obtained considering discontinuous joints.

geological-structural point of view, the Aiguilles du Marbrées is considered to be part of the Swiss-Ultraswiss system and, in particular, the part that is the subject of this study belongs to the bedrock of the Swiss Unit of Monte Bianco. It is characterised by the presence of medium-coarse grain granites and some porphyry rock.

A series of rock falls, some of which were serious, occurred in the summer of 2007 on the North face of the Aiguilles Marbrées. This induced the local administration to finance a series of measurements and monitoring, which are described hereafter.

A series of geostructural surveys, adopting both conventional techniques and photogrammetry, has been carried out since 2007. A photogrammetric survey has been carried out using digital cameras together with GPS in order to obtain a georeferenced-Digital Surface Model (DSM) of the rock mass.

This activity has been conducted for many reasons: The first DSM that was obtained was used as a "zero-situation" model for comparison purposes with the subsequent monitoring surveys, in order to identify rock falls. Moreover the DSMallowed to make a more detailed study of the geometry and kinematics that led to the rock fall occurred in 2007. It was in fact possible to identify discontinuity sets, estimate their persistence and establish the volume that could be mobilised as well as study its instability.

During the traditional survey, measurements were made of the attitude, dip and spacing as well as of the strength of the wall on some fractures (using Schmidt hammer) and roughness profiles were established (using Barton comb). Two scanlinesof about 25 m were materialised at the foot of the wall.

The measurements that were conducted were then used to verify those obtained through the application of Rockscan software (Ferrero et al., 2009) to the DSM of the rock face (Fig. 4a). The identification and the measurement of the traces were conducted using the automatic method CurvaTool (Umili et al., 2013) (Fig. 4b).

The mean attitude values of the families identified using the traditional and photogrammetric methods, which confirm the good agreement between their results, are reported in Table 3. The frequency

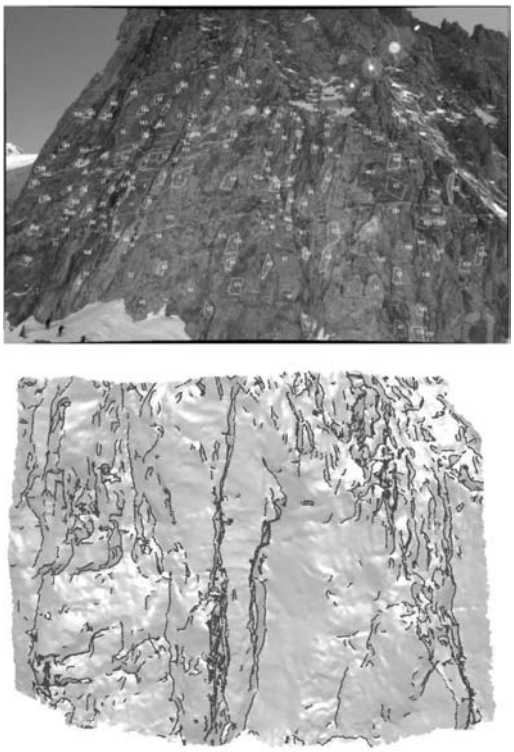


Figure 4. The North face of Aiguille du Marbrèes a) image used as interface in Rockscan code, b) DSM analysed with CurvaTool code.

Table 3. Comparison between set orientation obtained with traditional survey and Rockscan code

Set	Traditional survey	Rockscan survey	Differences
1	82/284	75/296	(+)7/(−)12
4	75/000	80/029	(−)5/(−)29
2	05/166	15/084	(−)10/(+)82
3	71/323	70/325	(+)1/(−)2

distribution of the trace lengths identified by means of CurvaTool is shown in Figure 5.

The consistency of the data acquired with the previously described software also made it possible to determine the trend of the P_{32} and J_v values for an increase in the sampling window (Fig. 6) and the frequency distribution of the volume of blocks which the intersection of the discontinuities that are present determines on the rock wall (Fig.7).

From an analysis of Figures 6 and 7, it is possible to observe how, from the great deal of information that can be gained on the geometric properties of the discontinuities, it is possible to verify, in a statistical manner, the influence of any scale effects on both the fracture degree of the rock mass and, as a consequence, on the dimensions of the potentially unstable blocks.

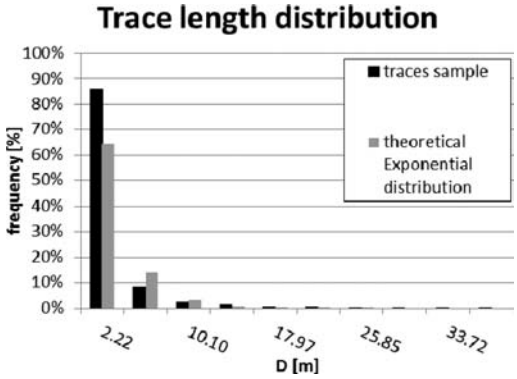


Figure 5. Frequency distribution of the trace lengths identified by means of CurvaTool code.

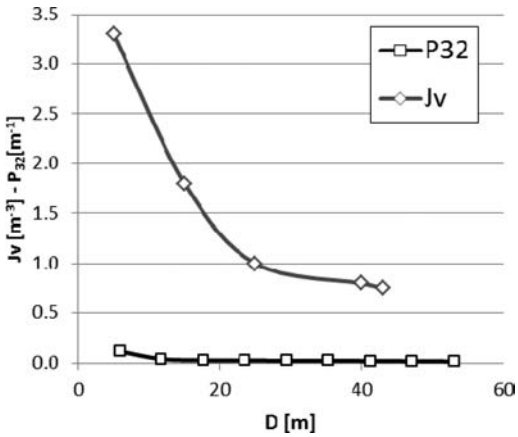


Figure 6. J_v and P_{32} values vs observation window dimension.

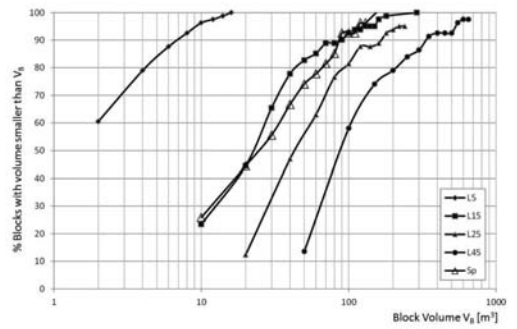


Figure 7. Frequency distribution of the volume of blocks.

3.2 *Application to the Marta Giulia tunnel*

The previously described method has been applied to the MartaGiulia tunnel, whose construction is part of the Pontremolese Infrastructure Development works for the doubling of the Solignano-Osteriazza (PR) section.

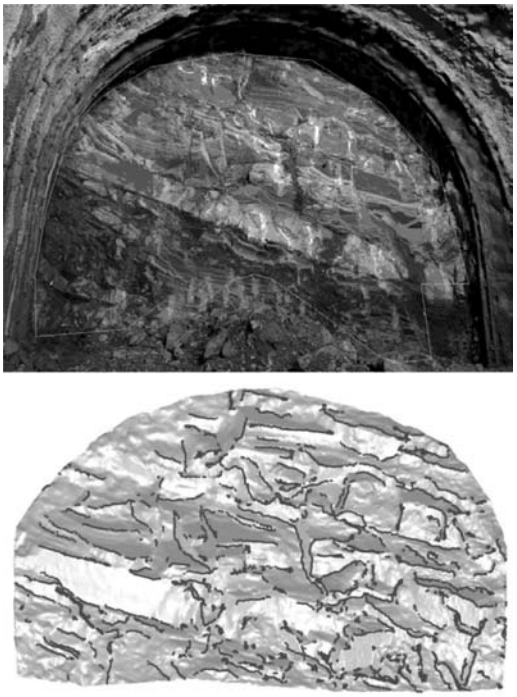


Figure 8. Marta Giulia tunnel face a) image used as interface in Rockscan code, b) DTM analysed with CurvaTool code.

The tunnel alignment crosses through low mountain areas and passes under reliefs with somewhat steep slopes, characterised by the presence of Solignano and Monte Cassio Flysch and Varicoloured Clays. The excavation zone passes entirely through Solignano Flysch reliefs made up of orderly parallel alterations of plain geometry turbid layers of a thickness that varies from just a few millimetres up to some tens of metres and it is characterised by the presence of another two conjugated joint systems.

The tunnel design was drawn up according to the ADECO-RS method, on the basis of the analysis and monitoring of the deformations in the rock mass subject to excavation. The tunnel face was surveyed using the photogrammetric method and the obtained data were compared to data obtained by means of traditional method. The planes were identified using Rockscan code on 3 images of the excavation face, one central (Fig. 8a) and two side images,and the relative georeferenced DSM (Fig. 8b), in order to have as complete a view as possible of the excavation face.The planes were therefore established through a manual choice of the various excavation face portions; the image with the most suitable view was chosen for each portion, while paying attention not to choose the same zone more than once in order to prevent conditioning the statistical analysis of the poles distribution and therefore the identification of the discontinuity families. The orientation angles of 135 planes were determined.

Table 4. Comparison between set orientation obtained with traditional survey and Rockscan code.

Set	Traditional survey	Rockscan survey	Differences
LAYER	39/031	57/045	(+)18/(+)14
J1	48/180	70/195	(+)22/(+)15
J2	86/240	58/247	(−)28/(+)7
FRONT	89/034	90/033	(+)1/(−)1

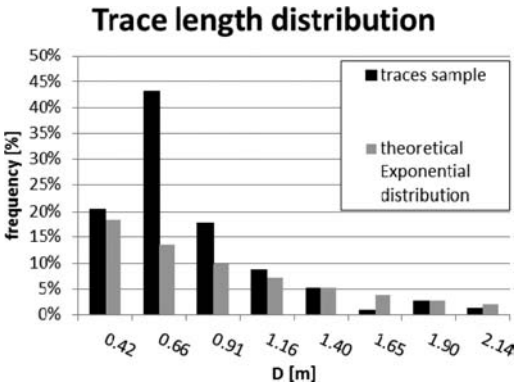


Figure 9. Frequency distribution of the trace lengths identified by means of CurvaTool code.

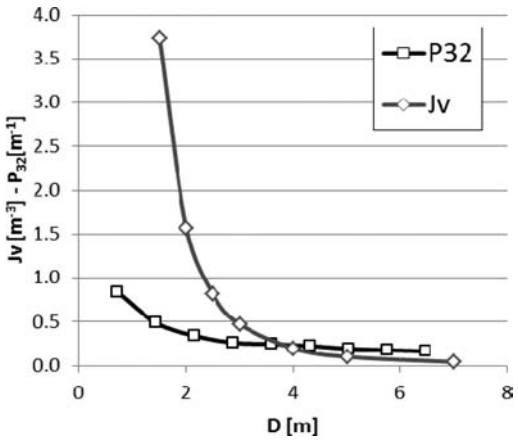


Figure 10. J_v and P_{32} values vs observation window dimension.

As expected, three discontinuity systems were revealed: the layer plane and the two conjugated joint systems, in good agreement with the data obtained using the traditional survey with a compass (22 different data) (Table 4).

The frequency distribution of the trace lengths identified by means of CurvaTool is shown in Figure 9; Figure 10 shows the trend of the P_{32} and J_v values for an increase in the sampling window.

4 CONCLUSIONS

The present note has shown, using the most common estimators of the degree of fracturing used in the rock mechanics sector (P_{32} and J_v), how it is important to be able to analyse the scale effects of the survey and to verify whether a representative volume (REV) has been obtained for the characterisation of the rock mass. The assumed simplified geometrical scheme allowed us to set up synthetic formulations in function of discontinuity spacing, trace length, persistence and dimension of the observation window. These formulations simplified the comparison between the two different approaches, highlighting two cases affected by a scale effect represented by the dimension D of the observation window.

REFERENCES

Dershowitz, W. 1985. Rock Joint Systems. Ph.D. Thesis, Massachusetts Institute of Technology, Cambridge, MA., 987 pp.

Ferrero, A.M., Forlani, G., Roncella, R. & Voyat, H.I. 2009. Advanced Geostructural Survey Methods Applied to Rock Mass Characterization. *Rock Mech Rock Eng* 42: 631–665.

Ferrero, A.M. & Umili, G. 2011. Comparison of Methods for Estimating Fracture Size and Intensity: Aiguille du Marbrée (Mont Blanc). *International Journal of Rock Mechanics and Mining Sciences* 48: 1262–1270.

ISRM 1978. Commission on standardization of laboratory and field tests. Suggested methods for the quantitative description of discontinuities in rock masses. *Int. J. Rock Mech. Min. Sci. & Geomech. Abstr.* 15: 319–368.

Palmström, A. 1996. The rock mass index (RMi) applied in rock mechanics and rock engineering. *Journal of Rock Mechanics and Tunnelling Technology* 11(2): 1–40.

Umili, G., Ferrero, A.M. & Einstein, H.H. 2013. A new method for automatic discontinuity traces sampling on rock mass 3D model. *Computers & Geosciences* 51: 182–192.

Zhang, L. & Einstein, H.H. 2000. Estimating the intensity of rock discontinuities. *International Journal of Rock Mechanics and Mining Sciences* 37: 819–837.

Rock Mechanics for Resources, Energy and Environment – Kwaśniewski & Łydżba (eds)
© 2013 Taylor & Francis Group, London, ISBN 978-1-138-00080-3

Passive three-dimensional microseismic imaging for mining-induced rock-mass degradation

J.-W. Huang & J.M. Reyes-Montes
Applied Seismology Consultants Ltd, Shrewsbury, UK

R.P. Young
University of Toronto, Toronto, Ontario, Canada

ABSTRACT: Mine development imposes stress changes in the surrounding rock that typically induce or trigger seismicity with a wide range of magnitudes. Seismic monitoring can provide insight into the rock deformation and give critical feedback to the on-going operations. We have developed a passive seismic imaging algorithm based on earthquake seismology to jointly locate induced microseismic events and update the velocity of the rock model illuminated by the seismicity. We calculate travel-time based on the fast sweeping method to account for complex 3D distribution of velocity and use the adjoint method to transform the inverse problem to a forward problem which can also be solved by the fast sweeping method. In this paper, we demonstrate the efficiency and robustness of the fast sweeping and adjoint method based travel-time tomography in monitoring fracture evolution and dynamic velocity variations.

1 INTRODUCTION

During the development of a mine site, monitoring of induced seismicity is generally used to provide insight into the rock fracturing and deformation processes and to give critical feedback to the on-going operations. Passive microseismic (MS) monitoring applications are often restricted to imaging induced fractures using source locations assuming a velocity model and ignoring the time-lapse variation of velocity with complex structures. We have adapted the seismic tomography technique from earthquake seismology (e.g. Thurber, 1983) and developed a passive seismic inverse algorithm to jointly locate induced MS events and update rock velocity model traveled by the ray paths. Honoring the coupling between the event location and the velocity model, passive imaging can provide a more realistic image of the rock velocity structure, its time-lapse variation and more accurately locate events. Recent advancement includes the double-difference tomography using S-P times in addition to both absolute and relative P- and S-wave arrival times (Zhang *et al*., 2009), and velocity tomography only using the absolute arrival time of P- and S-wave to derive 3D v_p, v_p/v_s as well as quality factor Q_P (Tselentis *et al*., 2011). However, both methods calculate the travel times using conventional ray tracing which cannot treat complex velocity shapes and arbitrary discontinuities commonly observed in mines. We propose to use the fast sweeping method (Zhao, 2004) to account for complex 3D distribution of velocity. Furthermore, poorly covered region included in the model introduces additional unstable issues to the conventional linearized travel-time inversion. Damped least square method can stabilize the inversion but scarifies the model resolution. The adjoint method-based tomography (Huang & Bellefleur, 2012) formulates an inverse problem as a forward problem and only updates the region with adequate coverage. In the following section, we first briefly introduce the background of the fast sweeping and the adjoint method. We then demonstrate the performance of the fast sweeping and adjoint method-based travel-time tomography in locating MS events and recovering velocity variations using synthetic data based on field well logs and a sample of the seismicity induced during the caving development of Lift 2 of Northparkes mine. We demonstrate that the fracture evolution and dynamic velocity variations at Northparkes mine is well detected by the tomographic velocity model.

2 METHODOLOGY

2.1 *Fast sweeping and adjoint method*

Fast sweeping method (FSM) is a finite difference method directly solving the following Partial Differential Equation (PDE), also known as Eikonal equation:

$$|\nabla T(\boldsymbol{x})|^2 = 1/c^2(\boldsymbol{x}),\ \boldsymbol{x} \in \mathbf{R}^3 \backslash \boldsymbol{x}_s \tag{1a}$$

with boundary condition

$$T(\boldsymbol{x}_s) = \tau_0, \tag{1b}$$

where $T(\boldsymbol{x})$ is the travel-time and $c(\boldsymbol{x})$ the propagation velocity at location $\boldsymbol{x}$, respectively. The operator |.| is

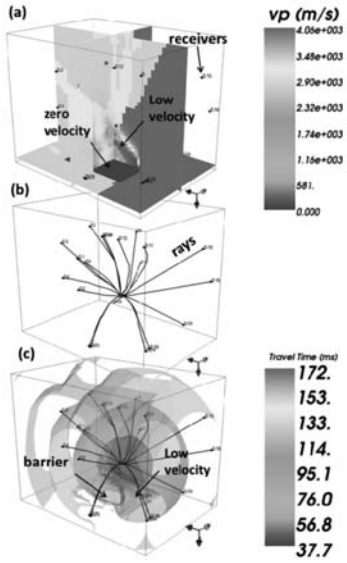


Figure 1. (a) The velocity model constructed from yield zone modelling of a developing underground caving mine (Reyes-Montes et al., 2012), (b) the seismic rays traced based on the gradient of travel time and (c) the contour of the travel time rendered as isosurfaces. The full computation time is less than 5 seconds using a single CPU.

the vector norm and ∇ the gradient. The point source is located at $\boldsymbol{x}_s$ with initial time τ_0 with respect to a reference time.

This grid-based method presents numerous advantages over conventional ray tracing. For example, it assigns a travel time to each grid point and thus avoids shadow zone problems. In addition, unlike shooting or bending methods in ray tracing, it is formulated as a forward problem, which is highly stable for first arrival travel time calculations. We demonstrate the modelling power of FSM by simulating a point source in a complex velocity model as shown in Figure 1.

The velocity of the model ranges from 0 to 4 km/s with the low velocity region representing air gap and mobility zone. The zero velocity is treated as barriers in which the travel time is undefined. The model contains $\sim 10^4$ grid points and the total computation time is less than 5 seconds on a single CPU core. Seismic rays can be traced following the gradient of the travel time field and provide the modelled polarization as well as travelling distance for both P- and S-wave to any geophone locations (Figure 1b and 1c).

The adjoint method was initially developed to efficiently compute the gradient of the misfit function in the field of control theory (Lions, 1971). It formulates the inverse problem as the minimization of the misfit function under the constraint of the PDE, and an adjoint PDE is obtained to avoid intensive computation of the Fréchet derivative. In our case, we obtain the following adjoint PDE:

$$\nabla \cdot (-\lambda \nabla T) = 0, \boldsymbol{x} \in \mathbf{R}^3 \backslash \boldsymbol{\Gamma} \tag{2a}$$

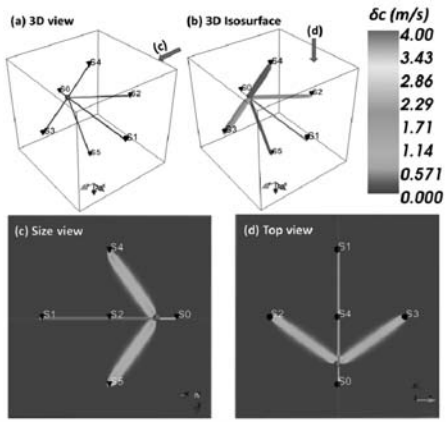


Figure 2. (a) A 3D view of the source (red dot) and geophone stations (black cones). The source and stations are connected by straight lines. (b) The isosurface plot of the velocity perturbation. The colour bar represents the value of velocity perturbation shown in (c) and (d). The spatial pattern of δc is consistent with the ray path between the source and stations. The velocity along the ray path shall be increased due the low initial velocity (2 km/s) comparing to the true velocity (3 km/s).

with the boundary condition

$$(\mathbf{n} \cdot \nabla T)\lambda = T^* - T, \boldsymbol{x} \in \boldsymbol{\Gamma} \tag{2b}$$

where **n** is the normal vector to the surface Γ where the sensors are deployed, λ is the adjoint solution and the equation itself is called the adjoint equation, which can be solved using the fast sweeping method as well.

The velocity perturbation δc and the updated velocity c_{n+1} are then calculated using:

$$\delta c = -\lambda / c^3 \text{ , and} \tag{3a}$$

$$c_{n+1} = c_n + \alpha \delta c, \tag{3b}$$

where α is the step size. The velocity perturbation (∂c) is usually not smooth and may cause unstable inversion results or render models trapped in local minima. To eliminate spikes and avoid local minima, we regularize the model perturbation by a low pass filter. The uncertainty and resolution of the tomographic image can be obtained using a checkerboard model. The details can be found in Huang & Bellefleur (2012).

As an example, Figure 2 shows the velocity perturbation calculated using equation 3a for a point source surrounded by 6 geophones in a homogeneous velocity model (3 km/s). Using 2 km/s as the initial velocity, the spatial pattern of δc shows the ray coverage and indicates that the value along the ray paths shall be increased whereas the area outside remains unchanged. This example demonstrates that the adjoint method is able to update the model adaptive to the ray coverage.

2.2 *Passive seismic tomography*

Passive seismic imaging is a well-established technique in earthquake seismology (Thurber, 1983; Kissling, 1988) to simultaneously locate hypocenter of earthquakes and update a portion of the velocity model illuminated by earthquakes. According to Thurber (1981), the fundamental recipe of simultaneous location of earthquake and velocity inversion using first arrival time of P- or S-wave involves the following steps:

a) Select *a priori* model for the P- or S-wave velocity structure appropriate for the area being investigated;
b) Make an initial estimate of the earthquake location and initial time (hypocentral parameters);
c) Calculate theoretical P- or S-wave travel times from the estimated location to observing stations, and compute the corresponding arrival-time residuals;
d) Evaluate derivatives of the arrival time residuals with respect to variations of the hypocentral parameters and with respect to variations in the velocity;
e) For a set of events, find adjustments to both the hypocentral and velocity parameters which will minimize the arrival time residuals, and obtain a new estimate of the earthquake locations and the velocity structure.

Steps of c) to e) are performed iteratively until the travel-time residuals are minimized to a target level.

We first define the travel-time residual as the L^2 norm of the arrival time differences:

$$E(c,t_0,\mathbf{s}) = \frac{1}{2}\sum_g \left(T\left(c,g;t_0,s_x,s_y,s_z\right) - T^*\left(g\right)\right)^2 \qquad (4)$$

where $T(c, g; \tau_0, s_x, s_y, s_z) = T(c, g; s_x, s_y, s_z) = \tau_0$, c is the propagation velocity, τ_0 is the initial time of the source, (s_x, s_y, s_z) is the coordinate of the source location, T is the calculated theoretical arrival from the source, and T^* is the observed arrival time at the geophone g with respect to the chosen zero time. The total error is the summation of all the travel-time residuals for all geophones.

If the variation of the velocity ∂c and the hypocentral parameters $(\partial x, \partial y, \partial z, \partial\tau_0)$ cause a corresponding change in arrival time ∂T, then the change of the travel-time residual can be expressed as

$$\partial E = \sum_g \left(T - T^*\right)\partial T\,. \qquad (5)$$

The partial derivative of the residual E with respect to the variation of location, initial time, and velocity can be expressed as

$$\frac{\partial E}{\partial s_i} = \sum_g \left(T - T^*\right)\frac{\partial T}{\partial s_i}, \qquad (6a)$$

$$\frac{\partial E}{\partial \tau_0} = \sum_g \left(T - T^*\right)\frac{\partial T}{\partial \tau_0} = \sum_g \left(T - T^*\right), \qquad (6b)$$

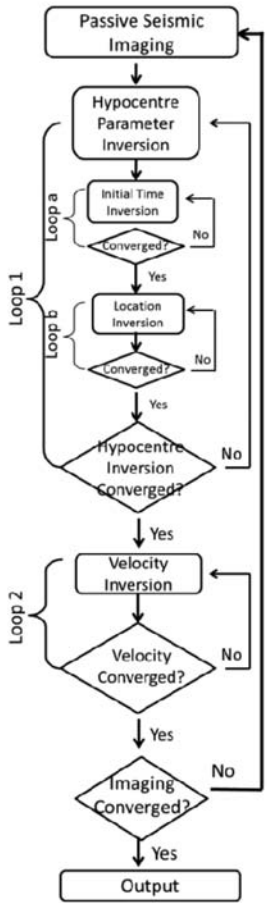


Figure 3. The workflow of passive seismic imaging consists of two loops of inversion, one for hypocenter parameter and the other for velocity. The hypocenter parameter inversion is performed in two sub-loops, i.e., inverting for the initial time before the location. At the end of iteration, if the decrease of residual is larger than the target threshold, the two loops are repeated till the convergence criterion is satisfied.

$$\frac{\partial E}{\partial c} = \int_{\mathbf{R}^3} d\mathbf{x}\cdot\frac{\lambda}{c^3}, \qquad (6c)$$

where $s_i = s_x$, s_y, or s_z, and the adjoint variable λ is obtained from section 2.1. Given a velocity model, the vector field of $-(\partial E/\partial \mathbf{s},\ \partial E/\partial\tau_0)^T = -(\partial E/\partial s_x,\ \partial E/\partial s_y,\ \partial E/\partial s_z,\ \partial E/\partial\tau_0)^T$ points towards the true location of the earthquake in the 4D hypocentral space. Thus we choose the perturbation $\delta s_i = -\partial E/\partial s_i$, and $\delta\tau_0 = -\partial E/\partial\tau_0$.

Considering that the residual E has different degree of sensitivity to the variation of τ_0, $\mathbf{s}$, and c, we update them individually within each iteration step. The workflow is shown in Figure 3. At the end of the iteration, if the RMS residual $\bar{E} = \sqrt[2]{2E/N}$ (where N is the number of observed travel-times) reaches a plateau, i.e., the percentage of reduction is less than a target threshold, the inversion is considered converged and the

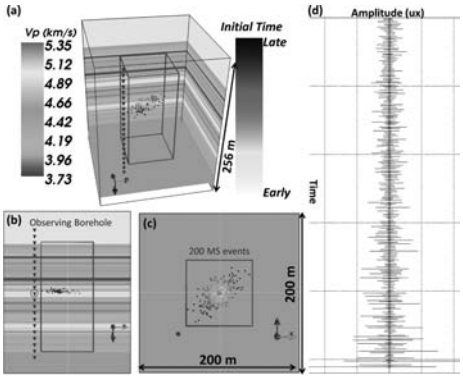


Figure 4. The 3D perspective (a) plan (b) and side (c) views of the velocity model and the monitoring array geometry using a string of borehole geophones (blue cones). The red box marks the monitoring volume and the dots inside show the true location of the modeled 200 MS events. The left colour bar in (a) represents the P-wave velocity and the right colour bar shows the MS event initial time with respect to a chosen reference time. (d) An example of the waveform recorded by the geophone circled in (b).

final hypocenter parameters and velocity are output. In the following section, we demonstrate the performance of our algorithm on a synthetic data set from a single borehole monitoring project and a subset of the seismicity induced during the caving of Lift 2 of Northparkes Mine.

3 RESULTS

3.1 *Synthetic data from a single monitoring borehole*

The numerical MS monitoring survey using 21 triaxial borehole geophones is conducted on a layered 3D model (200 m × 200 m × 256 m with 2 m grid interval) based on field well logs (Figure 4) from a hydrocarbon reservoir. The red box marks the monitoring volume, with the dots representing 200 MS events induced by the stress changes imposed by hydraulic injection at the center point. The source mechanism for all events is a mixture of tensile and shear crack with primary frequency of ∼150 Hz. Figure 4d shows the synthetic waveform along the horizontal north (x) component.

Using a homogeneous velocity (4.65 km/s), we process the waveform data following the conventional microseismic processing workflow (e.g., Pettitt & Young, 2007) and locate all 200 MS events together with their arrival time as shown in Figure 5a, 5b, and 5c. It is easy to verify that the processing locates the majority of events to the right region and recovers the true fracture development along the north-east ($x - y$) direction. The homogeneous velocity and the initial hypocenter positions are then input into the passive seismic imaging workflow (Figure 3) as the initial model. The discrepancy between the calculated travel-time and the picked travel-time from waveform is used to update both velocity and hypocentral parameters.

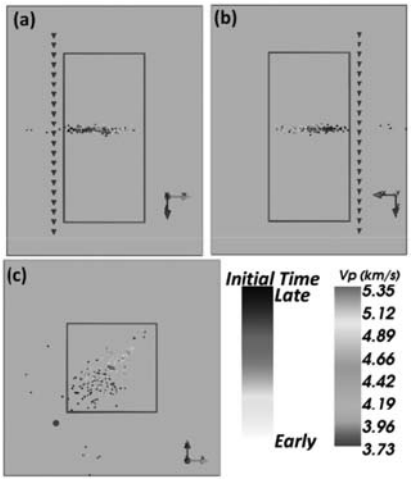


Figure 5. All 200 MS events are triggered and located using a homogeneous velocity as shown in the side view looking North (a), side view looking East view (b), and the plan view (c). The majority of the events are located to the right position within the monitoring volume. The homogeneous velocity and the located events are then supplied to the passive seismic imaging workflow and the tomographic velocity and the relocated MS events are shown in Figure 6.

After four iterations, the RMS residual decreases from 49.7 ms to the plateau of 0.40 ms with reduction less than 2% and the inversion is thus considered converged.

The final velocity and the location of all MS events are shown in Figure 6. Comparing to the true velocity well logs along the borehole (Figure 6b), the tomographic velocity recovers multiple velocity layers penetrated by the borehole. In addition, comparing to the true velocity in Figure 4, the high-velocity region where the MS events occur is also recovered.

The error between the relocated events and the true events is quantified in the histogram which shows the major events differ from the true hypocenter <5 ms in the initial time (Figure 7a) and <40 m in the location (Figure 7b). A few outliers introduced from the initial model stay in local minima due to the initial large distance away from the true location. The travel-time in the final tomographic velocity is calculated and the difference between the observation and the calculation in Figure 7c shows a normal distribution with 0.027 ms mean value and 0.43 ms standard deviation.

3.2 *Field data from Northparkes cave mine*

The microseismic (MS) events used in this study were recorded during the monitoring of the early stages development and caving of Lift 2 the E26 orebody at Northparkes Mine. The undercut level at Lift 2 of Northparkes Mine locates at a depth of 830 m and covers a footprint of approximately 200 m in diameter. With 27 monitoring stations deployed around the projected cave volume, we have located 1525 events in

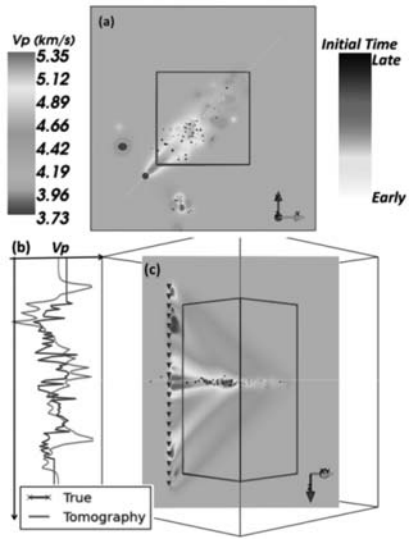


Figure 6. The plan view (a) and the side view looking northwest (c) of the tomographic velocity after passive seismic imaging. Two colour bars represent the velocity and the initial time of the events, respectively. The inverted velocity (green line) along the borehole is compared to the true velocity well logs (blue line) in (b). Our passive imaging algorithm recovers multiple velocity layers penetrated by the borehole. In addition, comparing to true velocity in Figure 4, the high velocity in the area of the MS events is also recovered.

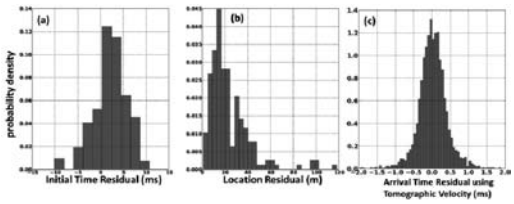


Figure 7. Histograms of the residual in the initial time (a) and the location (b) for the 200 synthetic MS events. (c) The travel-time error between the calculation and the observation.

a period of 10 days at early stages of cave development using a homogeneous velocity model (3.9 km/s). Due to the wide azimuth coverage, events within the volume surrounded by the monitoring stations are usually located with the lowest uncertainty. Therefore we exclude events outside and only use the 869 events for passive seismic imaging (Figure 8). A diorite body (grey shape) within the target volume is shown together with the initially located MS events (dots) and the undercut floor map (blue outlines). Each event is colour-coded indicating its occurring time and the uniform color of the volume is associated with the homogeneous velocity value.

The size of the model is 320 m wide, 715 m long and 685 m height with 5 m grid interval. After two iterations, the RMS travel-time residual decreases from 531.6 ms to the plateau of 7.7 ms with a reduction less than 5% and is thus considered as converged. Unlike

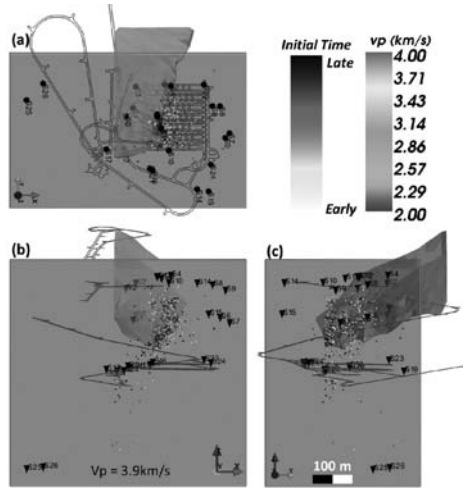


Figure 8. Three different views of Lift 2 of Northparkes Mine showing the geophone locations (black cones), and the mine infrastructure (blue lines). (a) is viewing from the top, (b) towards North and (c) towards West. The axis x, y, and z are pointing in East, North and Upward direction, respectively. Only 869 MS events surrounded by the 27 stations are used for passive seismic imaging. The subset corresponds to early stages of caving, with most of the events occurred close to the east side of the dioritic body (grey surface).

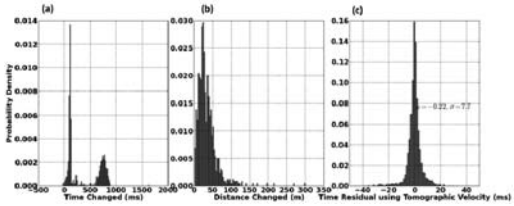


Figure 9. (a) The initial time changed from the starting model. (b) the location changed from the starting model. (c) The error in the arrival time between the observation and the calculation using the tomographic velocity primarily follows a normal distribution with 0.22 ms mean value and 7.7 ms standard deviation.

the synthetic case in section 3.1 where the true model is known, we here compare the final model with the starting model and show the changes in the initial time and the location in Figure 9a and 9b. The travel-time in the final tomographic velocity is calculated and the difference between the observation and the calculation shows that the residual primarily follows a normal distribution with -0.22 ms mean value and 7.7 ms standard deviation (Fig. 9c).

The isosurface visualization of the tomographic velocity in Figure 10 reveals a low velocity region ($\sim$3 km/s) developed close to the dioritic body around which most early activity concentrates induced by the caving operation within the selected period. The high velocity region ($\sim$4.2 km/s) inside the dioritic body suggests a different geomechanical behavior of this body. The same structure can be observed in Figure 11

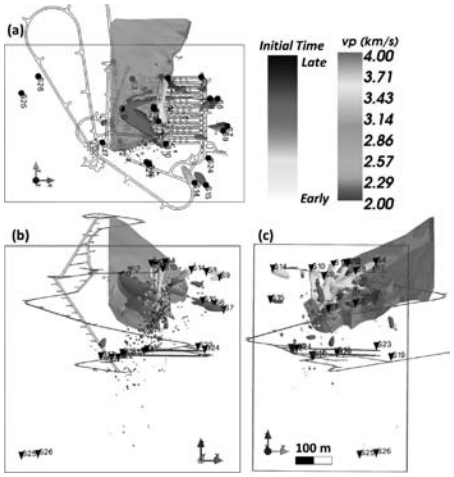


Figure 10. The isosurface visualization of the final velocity from passive seismic tomography. (a) plan view from the top, (b) side towards North and (c) side towards West. The axis *x*, *y*, and *z* are pointing in East, North and Upward direction, respectively. The low velocity region (in yellow) around the dioritic body is induced by the caving operation whereas the high velocity region (in red) partially overlapped within the dioritic body indicates it may have higher velocity than the surrounding rock and a different geomechanical behavior.

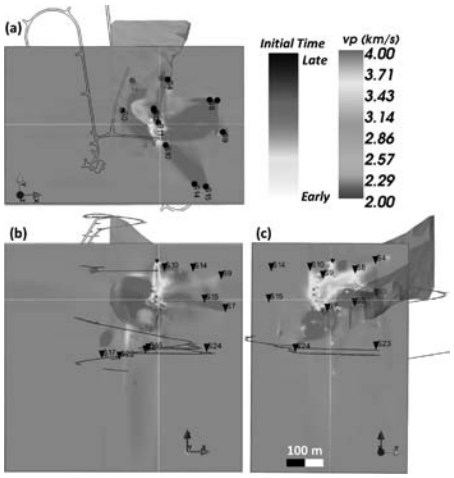


Figure 11. The tomographic velocity after inversion. (a) is plan view from the top, (b) side towards North and (c) side towards West. The axes *x*, *y*, and *z* are pointing in the East, North and Upward direction, respectively.

except that the velocity variation is represented by color. Increases in transmission velocity can be associated with local stress concentrations during the caving process, an observation that will require a time-lapse processing of seismic data.

4 CONCLUSIONS

In this study, we present a new algorithm to monitor the velocity changes caused by damages during the development of a mine site. Although similar to the seismic tomography in earthquake seismology, our method is based on the recent advancement of travel-time calculation using fast sweeping method and adjoint inversion. Superior to conventional ray tracing methods, the fast sweeping method is able to handle complex velocity model commonly observed in the mining environment. Unlike classical tomography formulating the inverse problem as a sequence of linear problems, the adjoint method transforms the inversion problem to a forward problem which can be solved efficiently by the fast sweeping method. In addition, it updates the velocity model according to the ray coverage and eliminates the issue of null-space.

We demonstrate the performance of our algorithm using synthetic data based on a borehole monitoring project and the field data from Northparkes cave mine. We show that applying this algorithm at multiple occasions during the block caving process is an efficient method to monitor the fracture evolution and the time-lapse velocity variations caused by cave development.

ACKNOWLEDGEMENTS

This research is funded by the SMI Mass Mining Technology II project. The authors would like to thank Northparkes Mines and Rio Tinto Group for providing the data for this study.

REFERENCES

Huang, J.-W. & Bellefleur, G. 2012. Joint transmission and reflection travel-time tomography using the fast sweeping method and the adjoint-state technique, *Geophys. J. Int.* 188: 570–582 doi: 10.1111/j.1365-246X.2011.05273.x.

Kissling, E. 1988. Geotomography with local earthquake data. *Rev. Geophys.* 26: 659–698, doi: 10.1029/RG026i004p00659.

Lions, J. L. 1971. *Optimal Control of Systems Governed by Partial Differential Equations*, translated by S. K. Mitter, Springer, 396 pages.

Pettitt, W.S. & Young, R.P. 2007. *InSite seismic processor: User operations manual version 2.14.* Applied Seismology Consultants Ltd.

Tselentis, G-A., Martakis, N., Paraskevopoulos, P. & Lois, A. 2011. High-resolution passive seismic tomography for 3D velocity, Poisson's ratio *v*, and P-wave quality QP in the Delvina hydrocarbon field, southern Albania. *Geophysics* 76, B89; http://dx.doi.org/10.1190/1.3560016.

Thurber, C.H. 1981. *Earthquake locations and three-dimensional crustal structure in the Coyote Lake area, central California, PhD thesis,* MIT.

Thurber, C.H. 1983. Earthquake locations and three-dimensional crustal structure in the Coyote Lake area, central California, *J. Geophys. Res.* 88: 8226–8236, doi: 10.1029/JB088iB10p08226.

Zhang, H., Sarkar, S., Toksöz, M.N., Kuleli, H.S. & Al-Kindy, F. 2009. Passive seismic tomography using induced seismicity at a petroleum field in Oman. *Geophysics* 74(6), WCB57–WCB69, doi: 10.1190/1.3253059.

Zhao, H.-K.. 2004. A fast sweeping method for Eikonal equations. *Math. Comput.* 74: 603–627.

Rock Mechanics for Resources, Energy and Environment – Kwaśniewski & Łydżba (eds)
© 2013 Taylor & Francis Group, London, ISBN 978-1-138-00080-3

ERMR system and correlations with known rock mass rating systems

M. Jovanovski & I. Peshevski
Faculty of Civil Engineering, University "Sts Cyril and Methodius" Skopje, R. Macedonia

ABSTRACT: Excavation Rock Mass Rating (ERMR) system is developed on the basis of numerous investigations for different civil engineering and mining projects in R. Macedonia. In this system, all Rock Masses are divided in seven classes. For each class, an adequate technology of excavation is suggested. Beside other analyses, the correlation of ERMR with known rock mass systems is given in order to have data for parallel use in solving of different practical problems. Notes about possible practical application of the system are analyzed and results presented in short. It can be underlined, that the ERMR system is more adequate for assessment of type of excavation technology for soft and hard rock, while for coarse grained sedimentary rocks, somewhat modified classification can be used.

1 INTRODUCTION

One of the main problems in rock engineering is to predict ease of excavation of rock masses in an appropriate manner. This is very significant in earthworks for civil engineering works and in surface mines because of the quantity of excavation masses. In fact, this is one of the key problems in organization and technology of excavation, prediction of costs and safety aspects.

Several authors give effort to establish acceptable methodologies for practical use in this important scientific and practical field, as: Franklin et al. (1971), Weaver (1975), Kirsten (1982), Abdullatif & Cruden (1983), Pettifer & Fookes (1994), Singh et al. (1987), Jovanovski (2001), Tsiambaos & Saroglou (2010).

In general, in all classifications, main parameters for assessment of excavatability are uniaxial compressive strength, weathering degree, spacing of discontinuities, hardness, seismic velocity, continuity, aperture, orientation and roughness of joints etc. Anyhow, no particular method is universally accepted because of the complex nature of the rock masses and difficulties in determination of the input parameters.

Having this in mind, a classification system called ERMR (Excavation Rock Mass Rating) is presented.

The classification is developed on the bases of numerous investigations for different structures, with a main idea to have possibility to determine easy of excavation for non-coherent and coherent soils, weak and hard rock masses in one method (Jovanovski 2001).

Beside the analyses, several correlations of ERMR with known rock mass systems are given in order to have basis for parallel usage of the system for different practical problems.

2 BASICS OF ERMR SYSTEM

The system is based on scoring, where the selection of classification parameters is done respecting principles that input parameters shall be obtained with quick and relatively simple tests, they should be relevant for the properties of the rock masses and that same property should not be taken into the evaluation twice or more times (Bieniawski 1974).

Input parameters are related and representative for the characteristics of the rock massif from one and intact rock parts from the other side.

As characteristics of the intact rock the uniaxial compressive strength (σc) or point load strength (Js) alternatively, bulk density (γ) and hardness are considered. Hardness, can be qualitatively expressed trough the Moss scale relative hardness (M) and quantitatively with value of Schmidt Hammer Rebound Value (SHRV). The correlation is defined with following equation after Jovanovski (2001):

$$SHRV = 8.72M - 0.04 \quad (1)$$

where SHRV = Schmidt Hammer Rebound Value; and M = hardness after Moss scale of relative hardness.

Characteristics of rock massif are presented with average joint spacing (Ls) or as alternative with rock quality designation parameter (RQD), condition of fracture walls (continuity, aperture, roughness, infill material etc).

Combining the ranges of values for individual parameters, the total rating is defined (Jovanovski 2001). The range of values for each rock mass class and ERMR class is presented in Table 1.

For all evaluation factors correlative curves are defined, with a main goal to have possibility to assign an adequate rating for all parameters. One example for bulk density is given with following equation, while the details are explained by Jovanovski (2001).

$$Rating\ (BD) = 0.7832 * BD - 18.32 \quad (2)$$

where Rating (BD) = an adequate value for rating for some value of bulk density; BD = bulk density of the rock mass in kN/m^3.

Table 1. ERMR class, rating and suggested excavation method.

ERMR class	ERMR rating	Excavation
I	<10	Easy digging
II	10–25	Digging
III	26–40	Hard digging
IV	41–50	Ripping
V	51–60	Hard ripping
VI	61–80	Blasting
VII	81–100	Hard blasting

In general, up to class III, the excavation method will be digging, for class IV and V ripping is dominant excavation method, while classes VI and VII are for blasting.

In a practice, several special cases can occur. For example, for coarse grained non-coherent rock masses, large boulders can be secondary blasted. In certain cases, selection of excavation method depends on the available mechanization. For an example, if we have a bulldozer type D9 or D9G, the media will be excavated with hard ripping, and in opposite we will apply blasting procedure.

Sometimes, excavation method depends on the morphology of the terrain and the type of structure. For an example, ripping is rarely used in tunnelling, in difficult morphological conditions and tight excavations for bridge foundations and concrete dams, even if the properties of the media allow it.

In cases when conditions for blasting are extremely hard, where the specific consumption of explosives is increased and where closely spaced blast holes are needed, special cases for payment should be agreed.

It is obvious that for each specific problem, evaluation of other external factors is needed, which can affect choice of method of excavation, and which are not included in the criteria of the classification itself.

3 CORRELATIONS OF ERMR AND OTHER CLASSIFICATION SYSTEMS

In the rock engineering practice, it is useful when several classification methods are used in parallel. The idea is to perceive the degree of correlation between different approaches, because the rock mass classification systems have some common parameters, therefore a link might be expected between the ERMR and other well known rating systems.

The established correlations are presented with the following equations:

$$ERMR = 0.76RMR + 17.98 \quad (3)$$

$$ERMR = 11.68 \log Kr + 27.77 \quad (4)$$

$$ERMR = 0.87RMR(w) + 1.48 \quad (5)$$

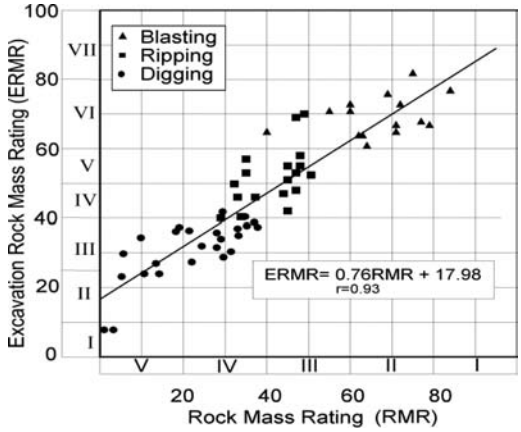


Figure 1. Correlation between ERMR value and Rock Mass Rating after Bieniawski.

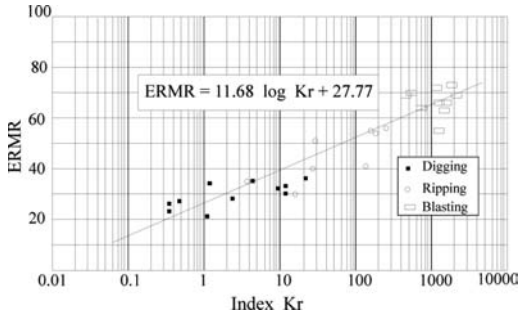


Figure 2. Correlation between ERMR value and Kr-value from Kirsten classification.

$$ERMR = 25.67 + 9.66 * Vp$$
$$ERMR = 26.43 * Vp \quad (6)$$

where ERMR = Excavation Rock Mass Rating; Kr = Rippability index after Kirsten: RMR = Rock Mass Rating after Bieniawski; RMR (w) = Ripability Mass rating after Weawer; and Vp = value of P-wave velocity in km/s.

Graphical presentation of the defined correlations is given in Figures 1–4.

It can be noted that determination coefficient for all cases has very high values from $R^2 = 0.8$ to $R^2 > 0.95$ which indicates a very strong connection between the analysed parameters.

The data for correlation are obtained from more than 45 case histories for large civil and mining projects, so it is considered that for initial phases of planning, the method can be very useful for practical application.

4 PRACTICAL APPLICATION OF ERMR SYSTEM

The proposed classification method can be used at a first place to choose adequate technology of

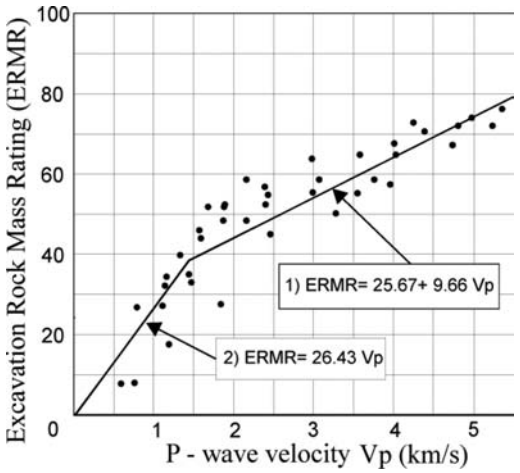


Figure 3. Correlation between ERMR and velocity of P-waves.

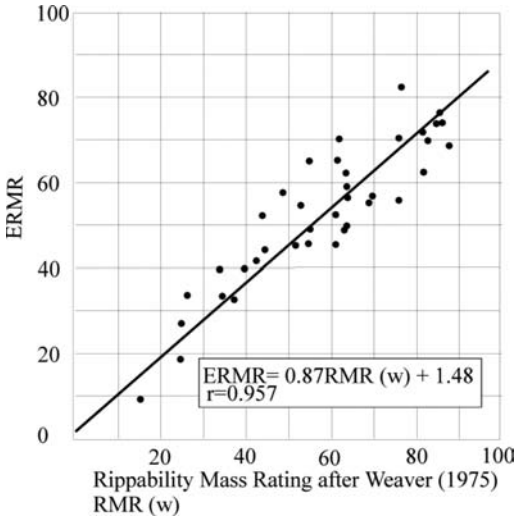


Figure 4. Correlation between ERMR and Rippability Mass Rating after Weaver (1975).

excavation. It can be noted that blasting is required when ERMR values are higher than ERMR = 60. Successful ripping is generally achieved for rock masses with ERMR values between ERMR = 40–60. However, there are cases when alternative methods for excavations are possible.

Another important aspect for defining of excavation cost is possibility to connect ERMR value with the unit price for excavation per cubic meter (Fig. 5).

The diagrams are obtained using prices from several large civil engineering projects, as a lower and upper envelope. It is clear that this can be only method for fast prediction of the cost of excavation,

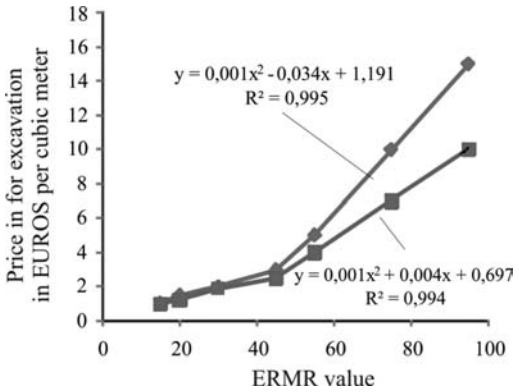


Figure 5. Prediction of unit price per meter cubic using ERMR value.

while the tendering price or real price of excavation shall be prepared according to the market and field conditions.

5 CONCLUSIONS

Based on numerous investigations for specific structures, Excavation Rock Mass Rating classification system is developed. All rock masses are divided in seven basic classes, and for them a recommendations for possible method of excavation, mechanisation etc. is given.

The system well correlates with other classification systems (RMR after Bieniawski, value of longitudinal seismic Vp-waves propagation, Kirsten method and others).

Having in mind that the empirical methods are based on certain level of experience, the philosophy of the methodology it should be subjected to critical reviewing in time, and should be used in combination with other methods.

Anyhow, it can help a lot in defining of technology of excavation, selection of excavation equipotent and cost of excavation.

REFERENCES

Abdullatif, O.M. & Cruden, D.M. 1983. The relationship between rock mass quality and ease of excavation. *Bull IAEG* 28(1):183–187.

Bieniawski, Z.T. 1974. Geomechanics classification of rock masses and its application to tunneling. In *Proc. 3rd Int. Congr. Rock Mech.*, Denver, Colorado: I(A), 27–32. Washington, DC: National Academy of Sciences.

Franklin, A.J. 1970. Observations and tests for engineering description and mapping of rock. In *Proc. 2nd Int. Congr. Rock Mech.,* Belgrade: Paper 1–3, 1–6.

Kirsten, H. 1982. A classification system for excavation in natural materials. *Civ Eng S Afr* 24: 293–308.

Jovanovski, M. 2001. Methodology for investigation of Rock Masses a working media, Doctoral thesis, University "Sts Cyril and Methodius", Faculty of Civil Engineering, Skopje.

Jovanovski, M., Zileska-Pancovska, V. & Peshevski, I. 2011. ERMR System – an useful tool in defining technology of excavation. *Organization, Technology and Management in Construction, An International Journal* 3(2): 302–307.

Pettifer, G.S. & Fookes, P.G. 1994. A revision of the graphical method for assessing the excavability of rock. *Q J Eng Geol* 27: 145–164.

Tsiambaos, G. & Saroglou, H. 2010. Excavatability assessment of rock masses using the Geological Strength Index (GSI). *Bull Eng Geol Environ* 69(1): 13–27.

Weaver, J.M. 1975. Geological factors significant in the assessment of rippability. *Civ Eng S Afr* 17(12): 313–316.

Rock Mechanics for Resources, Energy and Environment – Kwaśniewski & Łydżba (eds)
© 2013 Taylor & Francis Group, London, ISBN 978-1-138-00080-3

Assessing the mechanical properties of a rock using indentation tests

H.-T. Le, F. Descamps & J.-P. Tshibangu
UMONS-University of Mons, Mons, Belgium

J.-F. Nauroy, O. Vincké & L. Cangémi
IFP Energies Nouvelles (IFPEN), Rueil-Malmaison, France

ABSTRACT: Instrumented indentation devices allow testing of materials at small scales (micro and nano-indentation). In this framework, IFPEN has developed a new indentation system under confining conditions: this is a lightweight tool called Mechanicalab, which can perform simultaneously uniaxial strain test and indentation tests with a 7 mm diameter flat indenter. This paper describes the tests carried out on clayey silt (Transinne Kaolin, Belgium) under different moisture contents both with this new equipment and with standard geomechanical devices (triaxial tests and uniaxial strain tests). Furthermore, indentation tests are carried out with the Mechanicalab and a classical indentation device working under atmospheric conditions.

1 INTRODUCTION

In the field of oil production, standard indentation tests have been widely used in order to characterize the formations, especially the overburden because of a lack of cores for standard tests. Indentation tests can be carried out with a small amount of material, do not require a specific sample shape or size and are easy to operate. The results depend on the test method, especially the indenter geometry and indentation parameters.

Whereas standard indentation systems operate under atmospheric conditions, IFPEN has developed a new indentation device called Mechanicalab in order to investigate the behavior of materials under confining conditions. The system first performs a uniaxial strain test on the material and then flat cylindrical indenters are forced into the sample.

In this paper, we investigate the behavior of clayey silt by means of conventional and indentation techniques. The results will be discussed by comparing on one hand indentation tests with triaxial compressive tests, and, on the other hand, Mechanicalab experiments with standard indentation tests.

2 SELECTED MATERIAL AND ITS MECHANICAL PROPERTIES

2.1 *Transinne Kaolin*

The material that we consider in this study is clayey silt called Transinne Kaolin. It is mined out in an open pit quarry in the South-East of Belgium and is used in the production of white cement.

This soft rock was chosen because of its availability and its clay content. Indeed, clay minerals are typical of cap formations and exhibit particular behavior which needs to be assessed in the frame of CO_2 storage for example. Figure 1 shows a typical SEM micrograph of the rock which consists of 10% kaolinite, 50% quartz, 40% of illite/muscovite and other minor elements. In order to characterize more deeply this material, some physical properties were determined. Its dry density is 2.7 g/cm^3 and its relative porosity ranges between 10 and 20%.

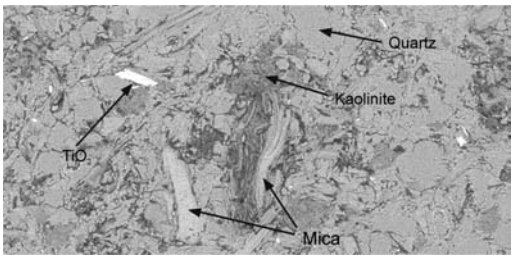


Figure 1. SEM micrograph of Transinne Kaolin showing quartz, mica and kaolinite with some traces of TiO_2.

2.2 *Triaxial compression tests*

In order to investigate the mechanical properties of this rock, triaxial compressive tests have been carried out on instrumented cylindrical rock samples. As the first tests revealed scattering in the material behavior, the samples were observed by X-ray CT scan (Fig. 2) and only most homogeneous samples were selected for the experiments reported in this paper.

As the moisture content can have a big influence on the mechanical behavior of clay materials, the triaxial tests were performed for two cases in terms of

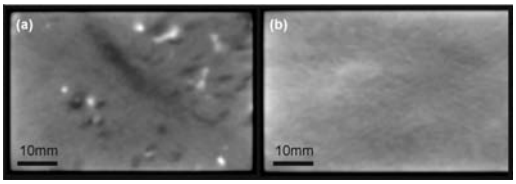


Figure 2. X-ray CT scan images on 2 different samples cored within the same block. (a) Heterogeneous sample. (b) Homogenous sample.

Table 1. Mechanical properties determined from triaxial compression tests. The Young's modulus was determined during unloading.

σ_3 (MPa)	E (MPa)	ν	σ_e (MPa)	σ_r (MPa)
0	–	0.26	6	20
1	16690	0.18	18	24
5 (dry)	20770	0.20	33	55
5 (saturated)	6880	0.25	9	27
20	30180	0.25	65	102

with σ_e elastic limit and σ_r failure limit.

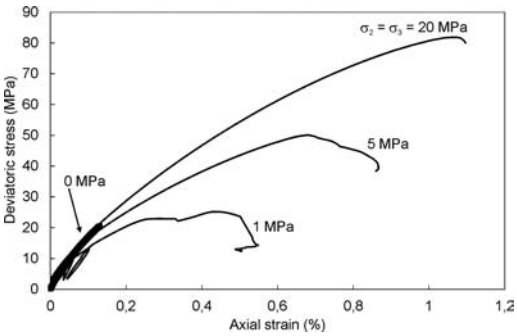


Figure 3. Triaxial compression tests on dry Transinne Kaolin.

moisture: either dry or saturated samples. In the first case, the samples have been placed in an oven at 60° C during 24 hours, whereas in the second case, they were placed under vacuum in a controlled humidity environment.

Triaxial experiments were performed with a loading rate of 0.01 MPa/s. The results are given in Table 1 and Figure 3 for tests in dry conditions. Transinne Kaolin exhibits large plastic strain before a maximum strength is reached. The Young' modulus increases with the confining pressure whereas the Poisson's ratio does not seem to be very sensitive to the effect of confining pressure. The intrinsic curve is not linear; therefore the internal friction angle and cohesion of the Mohr-Coulomb criterion can be approached by different values depending on the confining stress at which they are assessed, as shown in Table 2.

We also compared the behavior of dry and saturated samples. An example is given on Figure 4 for

Table 2. Evolution of the cohesion and internal friction angle with the confining pressure for dry Transinne Kaolin.

σ_3 (MPa)	Cohesion (MPa)	Internal friction angle (°)
≤ 5	3.8	48.6
>5	11.1	31.1

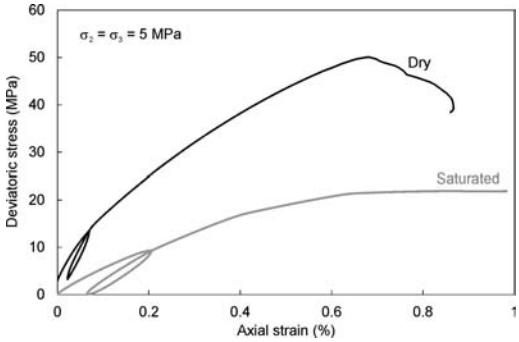


Figure 4. Triaxial compression tests on Transinne Kaolin in dry and saturated conditions.

a confining pressure $\sigma_2 = \sigma_3 = 5$ MPa. Those experiments indicate that the behavior of Transinne Kaolin is strongly dependent on its moisture content, dry samples exhibiting much stiffer behavior and higher strength.

3 INDENTATION TESTS IN ATMOSPHERIC CONDITIONS

Indentation tests have been performed in atmospheric conditions in the Rock Mechanics laboratory of the University of Mons. The device uses tungsten carbide indenters (Tshibangu 1987, Tshibangu et al. 1999, Descamps & Tshibangu 2004, Descamps et al. this conference). The tests deliver curves of the load on the indenter versus its displacement. Among the computed parameters, the punching strength (or indentation strength) R_p is the ratio of the load at failure F_{max} on the section of the indenter; it is well correlated with UCS (Tshibangu et al. 1999). Another interesting parameter for assessing mechanical properties of rocks is the elastic parameter defined as:

$$\frac{E}{1-\nu^2} = \frac{F_{\max}}{2a\,d_e} \tag{1}$$

where a is the indenter diameter and d_e is the elastic part of the displacement at F_{max}.

In our case, we used flat cylindrical indenters (4 mm diameter). The results are plotted in Figure 5. The curves indicate a brittle failure but also emphasize the influence of the loading rate on the slope of indentation curves.

Indentation parameters are computed in Table 3. UCS computed from its correlation with R_p

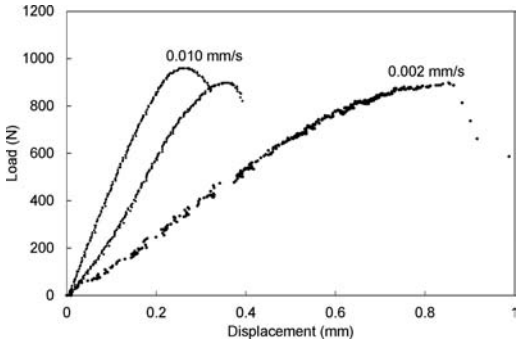


Figure 5. Standard indentation tests on Transinne Kaolin at two different loading rates.

Table 3. Results of indentation tests in atmospheric conditions on Transinne Kaolin.

Sample	R_p (MPa)	Elastic parameter $= E_{max}$ (MPa)	E_{min} (MPa)
1	76	1129	847
2	71	821	616
3	70	343	257

(Tshibangu et al. 1999) ranges between 3.2 and 3.5 MPa, which is much lower than UCS determined by conventional testing on dry sample.

This can be explained by the range of strengths on which the R_p-UCS correlation was established ($300 < R_p < 8000$ MPa): Transinne Kaolin is a much softer material than the ones we use to characterize. In addition, this correlation usually does not give good results for claystones and shales and Transinne Kaolin contains 10% kaolinite.

By considering that the Poisson's ratio ranges between 0 and 0.5, the elastic parameter can be used to compute the minimum and maximum values of the Young's modulus, E_{min} and E_{max}. Those values are particularly low in comparison with triaxial experiments. They cannot be explained by the difference in loading rate as it is higher during indentation test and this would lead to a stiffer behavior. A possible cause of the low values of Young's modulus could be a poor quality in measuring the indenter displacement; this deserves an in-depth discussion about interpretation despite the good calibration of the machine.

4 PRESENTATION OF THE MECHANICALAB

Indentation tests are generally performed in atmospheric conditions. However, if we aim to study the behavior of rocks at depth with such a test, it is necessary to incorporate the effect of confining pressure. That is why a new indentation device has been developed by IFPEN (Fig. 6).

The system is designed to test cylindrical samples (40 mm diameter and 60 mm height) and includes two

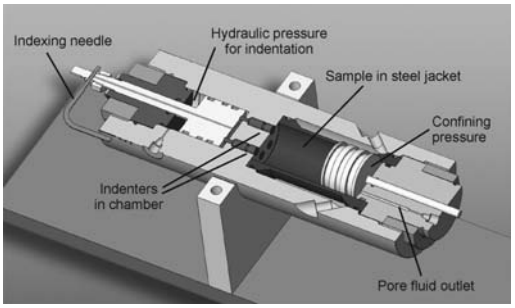


Figure 6. The Mechanicalab device, developed by IFPEN.

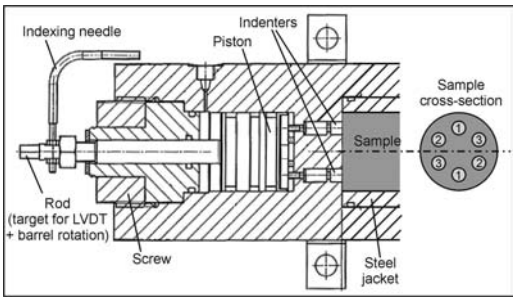


Figure 7. Detailed view of the indentation system on the Mechanicalab. The sample cross-section shows the position of pairs of indenters.

different functions: the application of a confining pressure on the sample through uniaxial strain loading (oedometric loading path) and its indentation by flat cylindrical indenters. The sample is first placed in a steel jacket which in turn is inserted in the testing cell.

In order to apply a confining pressure, a volumetric pump is used to activate a hydraulic cylinder which compresses the sample under uniaxial strain conditions. Strain gages placed on the steel jacket allow checking the radial strains and computing the radial stress (σ_3). During indentation, two boundary conditions can be set on the piston thanks to the pressure regulation: (1) fixing the piston position or (2) keeping a constant pressure on the piston. An external LVDT records the displacement of the piston while a pressure sensor gives the axial stress on the sample (σ_1). The maximum allowable axial stress is 100 MPa; it will be called "confining pressure" in the following. Provisions for pore fluid are also included to allow drainage of the sample.

The indentation system acts on the opposite side of the sample with respect to the confining piston. Six flat cylindrical indenters (7 mm diameter) are placed in a cylindrical chamber such that they are equally distributed on the section of the sample (Fig. 7). An indexing needle is used to activate a barrel system in order to choose a pair of diametrically opposed indenters for a test. The indentation pressure is given by a piston driven by a volumetric pump and then measured via a pressure sensor. The displacement of the

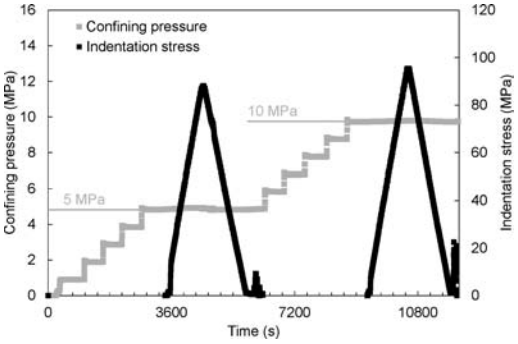


Figure 8. Example of a testing sequence on a sample with two indentation tests at two different confining stresses (5 and 10 MPa).

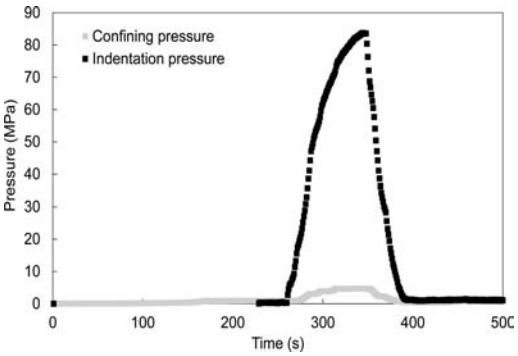


Figure 9. Indentation test on the Mechanicalab with confining piston in fixed position.

indenters is given by a LVDT sensor placed at the back end of the piston (outside the cell).

Up to three successive indentation tests can thus be performed on a same sample. Figure 8 gives an example in which two indentations are performed at two different confining pressures. At the beginning of the test, a pressure ramp is imposed in the confining circuit until the desired pressure is reached (here, 5 MPa). Then, the confining pressure is kept constant while a pair of indenters is forced in the sample. After this indentation phase, the indenters are left in the sample but the pressure on them is released. A new pair of indenters is selected, the confining pressure is further increased (10 MPa in Figure 8) and a new indentation phase is performed.

The example of Figure 8 deals with indentation at controlled confining pressure. In order to maintain this confining pressure at a constant value, the confining piston is allowed to move backwards during the indentation phase. It is also possible to perform indentation tests with the confining piston in fixed position as stated earlier. In this case, the confining pressure increases. Figure 9 illustrates such a case where the confining pressure equals 1 MPa when the indentation begins and reaches 5 MPa at the end of the indentation test.

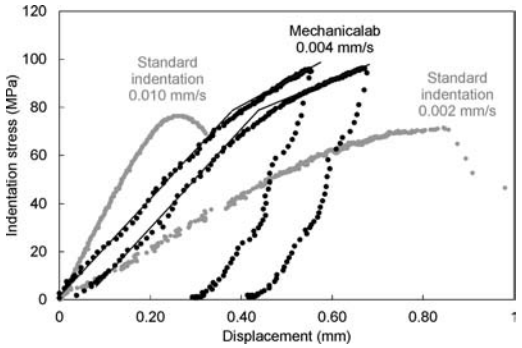


Figure 10. Comparison of standard indentation test in atmospheric conditions and indentation tests on the Mechanicalab with a constant confining pressure of 1 MPa.

In comparison with indentation in atmospheric conditions, the boundary conditions on the Mechanicalab are very particular. After the confining phase, the sample is in uniaxial strain conditions ($\sigma_1 > \sigma_3$ and $\varepsilon_1 > \varepsilon_3 = 0$). During the indentation process, the two end faces of the cylindrical sample are in contact with two rigid bodies: the confining piston on one side, and the frame bearing indenters on the opposite side.

5 RESULTS OBTAINED WITH THE MECHANICALAB AND DISCUSSION

5.1 *Indentation tests*

In order to compare the indentation results of the Mechanicalab with standard indentation tests, experiments were performed at low confining pressure on the Mechanicalab (1 MPa). The results are given on Figure 10. In standard tests, brittle failure is observed with limited plastic strain before failure whereas, with the Mechanicalab, the rock exhibits strain hardening (the maximum stress of the curves is the maximum value allowed by the device before unloading occurs).

The difference in behavior can be explained by the confining effect of the cell. As shown by the conceptual sketch of Figure 11, when working in atmospheric conditions, the behavior of the rock under the indenter can be assumed as analogous to a cylinder in triaxial compression.

When failure occurs, the confining effect of the surrounding material vanishes suddenly as cracks propagate towards the free surface. If the indented material is ductile, material upsetting can occur around the indenter. In the Mechanicalab, as the sample is confined between two rigid bodies, the confining pressure does not drop even when failure occurs, leading to strain hardening.

In addition, if we compare the initial slopes of the curves, the results of the Mechanicalab are consistent with tests in atmospheric conditions in terms of the influence of the loading rate; this emphasizes the viscous behavior of Transinne Kaolin.

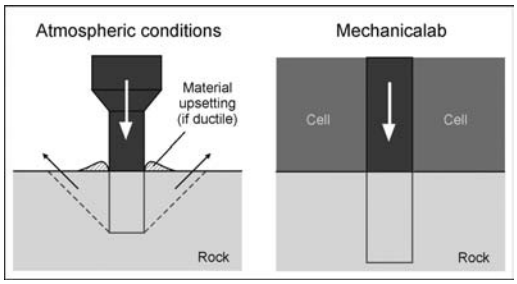


Figure 11. Conceptual sketch of the indentation mechanism in atmospheric conditions and with the Mechanicalab.

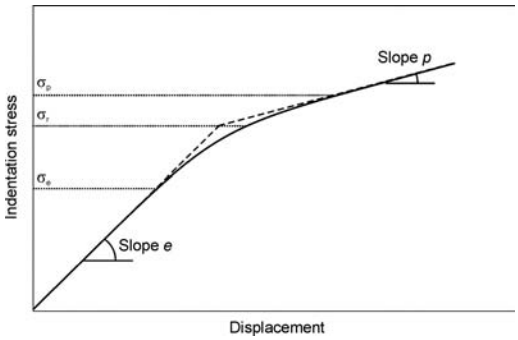


Figure 12. Parameters to be identified on the indentation curve in order to asses E, ν, cohesion and internal friction angle, according to the method developed by Onaisi & Bargui (1998). The indentation strength is also indicated on the curve.

Onaisi & Bargui (1998) developed an analytical model in order to assess mechanical properties from indentation curves showing strain hardening (Figure 12). Their method is based on the analogy between the indentation problem and the case of superficial and deep foundations. From the identification of four parameters on the indentation curve (slopes e and p, stresses σ_e and σ_p), it is possible to estimate E, ν, the cohesion and internal friction angle. Using this method, we computed the properties of Table 4 for Transinne Kaolin at different confining pressures. In addition, we also computed the indentation strength as indicated on Figure 12.

The Young's modulus determined by indentation tests is of the same order of magnitude both in atmospheric conditions (Table 3) and with the Mechanicalab (Table 4). The effect of the confining pressure on the Young's modulus is also well expressed with the Mechanicalab.

Even if those values are not consistent with conventional triaxial experiments, indentation experiments can be used to compare material stiffness under different conditions. The values of the Poisson's ratio seem to be reliable. The indentation strength does not really vary for the tested confining pressures and are similar to the ones given by tests in atmospheric conditions. Even if the values of cohesion and internal friction angle are not equal to the ones reported in Table 2, they already constitute encouraging results.

Table 4. Interpretation of indentation tests on the Mechanicalab.

σ_3	E (MPa)	ν	R_p (MPa)	C (MPa)	φ (°)
1 (dry)	1869	0.18	71	0.8	38.9
1 (saturated)	1059	0.2	64	1.4	33.3
5	9711	0.17	72	0.7	39.2

with C, cohesion and φ, internal friction angle.

Table 5. Results of the uniaxial strain tests performed with the Mechanicalab.

Test	E_{oedo} (MPa)	N	E (MPa)
1	10737	0.03	10700
2	8200	0.03	8150

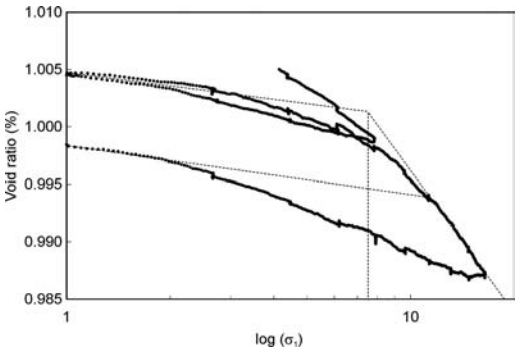


Figure 13. Uniaxial strain test performed with the Mechanicalab on dry Transinne Kaolin.

In Table 5, we also report results on a saturated sample at 1 MPa confining pressure. The effect of moisture content on the behavior of Transinne Kaolin is well expressed by the Mechanicalab: lower Young's modulus, strength and internal friction angle.

5.2 *Uniaxial strain tests*

Uniaxial strain tests have also been performed on Transinne Kaolin with the Mechanicalab. Figure 13 shows a typical result obtained on a dry sample. The general trend of the void ratio versus log (σ_1) curve is typical of such test, with a consolidation pressure of 7.5 MPa.

We tried to estimate the Young's modulus and Poisson's ratio from these uniaxial strain tests. An oedometer modulus is computed from the axial strain-axial stress curves whereas the Poisson's ratio is obtained from the slope of σ_3–σ_1 curves. Both values are then used to compute the Young's modulus (Table 5). Even if the Poisson's ratio is too low, it does

not have much influence on the computation of the Young's modulus from oedometric modulus. However, Young's modulus values are lower than the ones given by triaxial experiments (Table 1). A possible reason for this is found in the evolution of radial strains with time: the contact of the sample with the lateral surface of the steel jacket is only confirmed when axial stress reaches about 10 MPa.

6 CONCLUSIONS

In this paper, we presented a new original device developed by IFPEN in order to perform indentation tests under confining pressure. The general principle of the system is to place a rock sample under uniaxial strain conditions before indenting it with a pair of flat cylindrical indenters. Up to three tests can be performed on a same sample, with a different confining pressure and at different periods for each test; this potentially allows taking a lot of information from a single sample.

For the purpose of this research, Transinne Kaolin, a clayey silt, was selected and characterized by conventional triaxial tests. For confining pressures ranging between 0 and 20 MPa, this soft rock exhibits large plastic strains before a maximum strength is reached. Its behavior is time-dependent and also influenced by its moisture content.

Indentation tests with flat cylindrical indenters were first performed in atmospheric conditions in order to compare the results of conventional indentation with triaxial experiments. The loading rate dependence has been emphasized but the mechanical properties are not in agreement with the ones obtained in triaxial testing.

Indentation tests with the Mechanicalab were first performed at 1 MPa confining pressure in order to compare them with conventional indentation. The indentation curves are consistent with conventional indentation in terms of the effect of the loading rate and the indentation strength is similar. The main difference is the behavior mode: strain hardening is observed with the Mechanicalab. This is explained by the confining effect of this system which is maintained even when failure propagates through the sample. When working in atmospheric conditions, the surrounding rock brings some confining effect on the material under the indenter but this effect disappears when failure shear bands propagate.

In addition, tests with the Mechanicalab emphasized the effect of saturation on the mechanical properties of Transinne Kaolin (decrease of Young's modulus and strength) and allowed assessing the cohesion and internal friction angle by using an analytical model developed by Onaisi & Bargui (1998).

Those first results seem particularly encouraging in the potential of this device for assessing the behavior of rocks. Some aspects need to be further examined. Therefore, we plan to use numerical modeling in order to better understand the effect of the boundary conditions on the indentation mechanism.

REFERENCES

Descamps, F. & Tshibangu, J-P. 2004. Determination of rock properties using the punching test. In Y. Ohnishi & K. Aoki (eds), *Proceedings of the ISRM International Symposium 3rd ARMS*, Kyoto, 30 November–2 December 2004, pp. 953–958. Rotterdam: Millpress.

Onaisi, A. & Bargui, 1998. Rapport sur l'essai de poinçonnement développé par Total.

Tshibangu, J-P. 1987. *L'essai de poinçonnage des roches – Quelques aspects théoriques du procédé*, internal report, Faculté Polytechnique de Mons, Mons, Belgium.

Tshibangu, J-P., Lamine, E. & Charlier, R. 1999. Mécanismes de destruction des roches et conception des outils de forage. In G. Vouille & P. Berest (eds), *Proceedings of the 9th International Congress on Rock Mechanics, Paris, August 25–28, 1999,* Vol. 2, pp. 1245–1249. Rotterdam: Balkema.

Rock Mechanics for Resources, Energy and Environment – Kwaśniewski & Łydżba (eds)
© 2013 Taylor & Francis Group, London, ISBN 978-1-138-00080-3

Rock mechanical aspects for cavern stability

T. Pilgerstorfer
Amberg Engineering AG, Regensdorf, Switzerland

H. Wannenmacher
Amberg Engineering AG, Sargans, Switzerland

K. Grossauer
Amberg Engineering AG, Regensdorf, Switzerland

A. Stucki
AF-ConsultSwitzerland AG, Baden, Switzerland

B. Schwegler
KWO Kraftwerke Oberhasli, Innertkirchen, Switzerland

ABSTRACT: The extension of Grimsel 3 hydropower project (600 MW) entailsthe construction of a 2.5 km long tailrace tunnel, a machine and a transformer cavern as well as a new 600 m deep vertical shaft connecting the existing conduit with the Räterichsboden reservoir. Generally high in-situ stress conditions are expected for the construction of the extension of Grimsel 3 hydropower project within the massive Grimsel granodiorite and granite. Due to higher ground coverage for the cavern structure, brittle rock mass behaviour is expected influencing the constructionin the course of the relocation for the vertical shaft. The specific intact rock and rock mass conditions as well as the stress conditions were investigated by means of 600 m deep core drillings in order to obtain the geomechanical conditions and parameters at cavern structure level. The investigation included detailed analyses of brittle rock parameters as well as in-situ hydro-fracturing tests. Brittle parameters of rock were utilised for the two and three dimensional finite element analyses to determine the depth of spalling and fracturing expected for the construction. The variances of the two and three dimensional finite element analyses as well as the influence of brittle parameters influencing the analyses are discussed.

1 INTRODUCTION

The Grimsel 3 pump storage plant (PSP) will connect the existing pressure tunnels of the Grimsel 2 PSP, built in the late 1970s, with the reservoir of Räterichsboden. The installed capacity of the Grimsel 3 PSP is approximately 660 MW with an expected flow rate of 130 m^3/s. The major construction elements of the pump storage scheme to develop are the approximately 550 m deep vertical pressure shaft, the tailrace tunnel with a length of about 2.5 km and the power house complex.

2 PLANT LAYOUT

Due to the utilisation of a vertical shaft instead of an inclined shaft as initially foreseen (Wannenmacher 2013), the galleries of Grimsel 3 are situated deep within the ridge of the "Schwarze Nollen". The overburden at the cavern structure is approximately 650 m. The cavern layout foresees a separation of the machine and the transformer cavern, which is situated above the tailrace galleries in-between. The caverns are connected via three small galleries. Three variable speed pumping turbines will be used for electricity production and pumping. The ratio of width to height and length for the machine cavern is 27.6*46.6*92.5 m and 18.1*30.9*112.6 m for the transformer cavern. The machine cavern also hosts three upstream spherical valves, where else the three butterfly valves are situated in the transformer cavern. All access tunnels to the underground structure are connected to the existing structures of the KWO, guaranteeing access all overthe year within this alpineconstruction area. The access tunnels are further utilised for ventilation, drainage, escape paths and energy transmission.

The main elements of the structure are (Fig. 1):

① Cavern structure Grimsel 2
② Pressure tunnel upstream
③ Surge shaft Grimsel 2 and Grimsel 3
④ Vertical shaft upstream
⑤ Cavern structure Grimsel 3

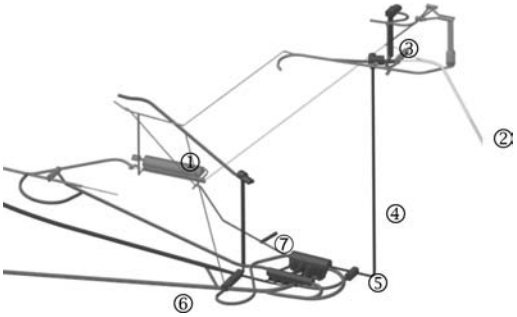


Figure 1. Grimsel 3 overall layout.

⑥ Tailrace tunnel
⑦ Surge shaft downstream.

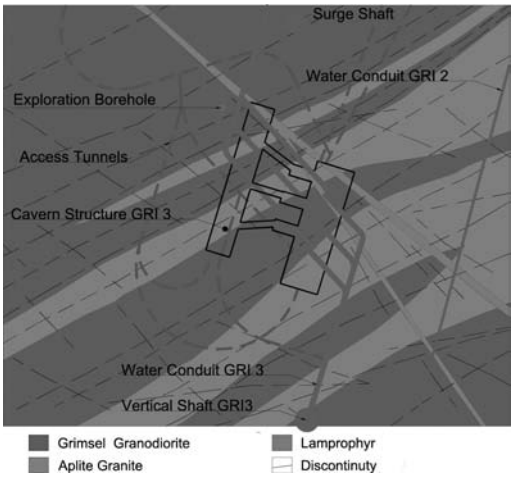


Figure 2. Geological conditions.

3 GEOLOGICAL CONDITIONS

The project area is completely situated within the Swiss Aarmassif. The rock units comprise magmatides, which intruded into the crystalline rock mass. The intake structure in the lake of Räterichsboden to the north is located at the boundary of the central "Aaregranite" and the intruded "Grimselgranodiorite" in the south. In order to establish a reliable geological and geotechnical model, a vertical borehole extending to the depth of the planned cavern structure of Grimsel 3 was drilled to investigate the conditions below the existing structure of Grimsel 2. The rock structure, as encountered, is characterised by a subdominant parallel foliation texture due to alpine deformation. The foliation is dipping steeply to SSE. The fracture intensity is very low and the overall rock-mass conditions are massive with large interlocking blocks with a generally low permeability in the range of $10E^{-9}$ m/s up to $10E^{-14}$ m/s. Due to the dense characteristic of the rock mass, no crack water table is expected in the area, with overall dry and damp conditions for the tunnelling works.

The orientation of the geological structures towards the cavern orientation is of subordinate influence on gravitational driven stability problems.

3.1 *Rock types*

The main rock types within the area are granodiorites, coarse-grained gneiss and minor aplitic medium grained, slightly foliated gneiss. The brittle behaviour of these rock types wasinvestigated by intense rock mechanical testing performed at the ETH Zurich and EPFL Lausanne. The rock types show a generally small variationof intact rockstrength. The typical values for the mechanical properties of intact rockare summarised for granodiorite and aplitic gneisses in Table 1.

Crack initiation for the rock types is found at approximately 50% of the intact rock strength.

Table 1. Typical values for rock types.

	Unit	Granodiorite	Aplitic Gneisses
UCS, dry	[MPa]	130–150	180–190
UCS, wet	[MPa]	∼110	∼180
BT	[MPa]	7.0–12.5	9.0–12.0
Unit weight	[g/cm^3]	2.73	2.61
Porosity, 48 h	[%]	0.26	0.31
Porosity, 4 mo.	[%]	0.34	0.51
E50, tangent, dry	[GPa]	56	56
E50, tangent, wet	[GPa]	49	53

4 GEOMECHANICAL MODEL

The construction of Grimsel 2 as well as the output of NAGRA test facility give a detailed insight into the geomechanical boundary conditions for the design of the Grimsel 3 hydropower extension. The Grimsel area is well-known for its high tectonic stresses, which is indicated by various surface parallel detachments and sudden bursts during open excavation works. Egger (1980) reports on stress-induced failure (surface-parallel spalling) which occurred during the construction of Grimsel 2 cavern at the transition of the sidewalls to the invert. Numerical back calculations could reproduce the spalling mainly located at the stress raisers of the shallow-placed cavern structure. All underground structures of the KWO are situated more or less close to the surface, allowing no precise prediction of stress development for Grimsel 3 cavern structure. Minor water ingress occurred during the heading of the access tunnel of Grimsel 2.

4.1 *Initial stress conditions*

Especially in steep alpine morphologies, the primary stress state is influenced by the shape of the valley

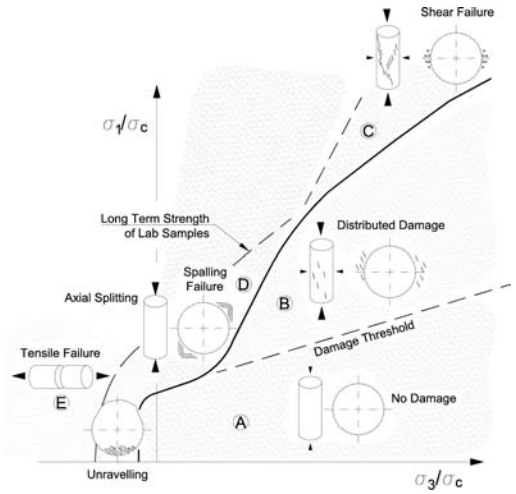


Figure 3. Compilation of strength envelopes for brittle rocks (modified from Diederichs 2002).

Table 2. Magnitude and orientation of the stress state.

Grimsel 3	Primary Stress Regime
Magnitude	$s_h = z^*(0.035618 \pm 0.00544)$ $s_H = z^*(0.05653 \pm 0.0116)$ (pore-pressure considered) $s_H = z^*(0.066624 \pm 0.0116)$ (no pore-pressure considered)
Orientation	Azimuth s_h [°] = 171 (average values) Azimuth s_H [°] = 81 (average values)

(absence of lateral confines of the slope), the tectonic history and the elastic properties of the gneisses.The initial stress conditions (magnitude and orientation) may significantly affect the cavern stability in case of unfavourable orientation. In total, seven hydraulic fracturing tests were conducted at the 600 m deep exploration borehole providing essential information onthe local stress. The orientation of the stress field varies within the area, where else the magnitude of the stress data is in line with the overall stress regime. The general orientation of the major horizontal stress is about E–W with a magnitude of two (in fractured zones) to three times (in massive zones) exceeding the vertical stressatthe depth of the cavern. Minorlocal borehole breakouts at the depth of the cavern prove the orientation of the hydraulic fracturing analyses.

The minimum primary stress is oriented more or less parallel to the vertical axis of the shaft with a magnitude of ~17.5 MPa at the low point, corresponding to an overburden of 650 m (Fig. 3).

The hydraulic fracturing analysis indicates the following for the stress state (Evans 2012, Tab. 2).

The stress measurements fit in well with the general trends of the Grimsel area, with documented measurements from NAGRA test site (Bräueret al. 1989) and various investigation campaigns and construction phases of hydropower plants in the area in the past few decades.

Table 3. Brittle failure analysis criteria after Diederichs & Carvalho (2007).

	GSI			
σ_{ci}/σ_t	<55	55–65	65–80	>80
<8	GSI	GSI	GSI	GSI
9–15	GSI	GSI	GSI	GSI/SP
15–20	GSI	GSI/SP	SP/GSI	SP
>20	GSI	GSI/SP	SP	SP

GSI … rock mass strength according to GSI-value
SP … brittle failure analysis

5 GEOTECHNICAL DESIGN

The geotechnical design was carried out according to Swiss Code SIA 199 (1998) in combination with the Austrian guideline for geotechnical design of underground structures (Austrian Society for Geomechanics 2008).

The geotechnical design considers the unsupported underground facility, the stress state and the orientation of the structures as well as groundwater conditions for stability analyses for the identification of hazard scenarios.

System behaviour is considered as the underground structure with all temporary or permanent rock support elements.

5.1 *Rock mass behaviour*

The expected rock mass behaviour for the construction of the caverns and adjacent structures is mainly associated to brittle failure (spalling and rock burst) and minor structural controlled overbreaks due to gravitational sliding and falling of blocks.

5.1.1 *Brittle failure (spalling, rock burst)*

Brittle failure such as spalling and rock burst is generally associated with massive rock mass conditions and high stress regimes. Brittle failure is triggered by the exceedance of the tensile strength (Martin 1997, Diederichs 2002), with a failure pattern oriented parallel to the tunnel surface. Brittle failure is governed by the ratio of intact tensile (σ_t) and compressive (σ_{ci}) rock strength, crack initiation of intact rock strength as well as blockiness of the rock mass GSI > 75 (Diederichs & Carvalho 2007), characterised by theblock volume in relation to the underground opening.

As a criteria for brittle failure analyses, Diederichs & Carvalho (2007) suggest a relationship of the ratio of σ_{ci} and σ_t and the GSI value (Tab. 3).

The ratio of the tensile to the compressive strength in regard to the very massive ground conditions highlights the potential for stress induced failure.

Table 4. Rock mass parameters Grimsel Granodiorite.

Rock mass parameters		Unit	Value
Rock mass strength	σ_{cm}	[MPa]	44
Tensile strength rock mass	σ_{tm}	[MPa]	−0.9
Young's Modulus rock mass	E_m	[GPa]	30
Friction angle	φ	[°]	48
Cohesion	c	[MPa]	14
Unit weight	γ	[kN/m^3]	27
Poisson's ratio	ν	[–]	0.19
Rock mass permeability	k	[m/s]	1 × E-9
Dilatancy angle	ψ	[°]	0

Table 5. Formulation of the brittle failure criteria.

Damage threshold	$\sigma_1 = (d_i)\sigma_c + (1.0)\sigma_3$ *damage initiation* $d_i = 0.5$
Spalling limit	$\sigma_1 = (10)\sigma_3$
Shear failure (HB)	$\sigma_1 = \sigma_3 + \sigma_{cm}\ (m_b * \sigma 3/\sigma_{cm} + s)^a$ *for GSI* = 80, σ_{ci} = 130 MPa, σ_{cm} = 44 MPa, m_i = 29, a = 0.501, m_b = 14.197 and s = 0.1084[1]
Tensile failure	σ_t = 10 MPa

[1](calculation according to Hoek and Brown failure criterion (Hoek et al. 2002).

Table 6. Principle failure modes after Diederichs (2002).

Ⓐ No failure	Stress points do not exceed the damage initiation threshold.
Ⓑ Damage initiation	Stress points exceed the spalling limit and aresituated above the damage threshold and below the shear failure line.
Ⓒ Shear failure	Stress points aresituated above the shear failure line.
Ⓓ Spalling failure	Stress point is above damage threshold, left of spalling limit and below the shear failure line
Ⓔ Tensile failure	Stress points exceed the tensile strength of intact rock.

5.1.2 *Constitutive law for estimation of spalling in highly stressed rock mass*

For the assessment of brittle failure, the strength parameters at lower boundary of the distribution as well as values with the highest confidence are considered.

The brittle failure analysis reconciles the history of the stress points, determined by a numerical 3D analysis, with the tri-linear constitutive law, as proposed by Diederichs (2002).

The formulation of the individual failure criteria for damage initiation, spalling limit, tensile and shear failure is given in Table 5.

Following principle failure modes can be distinguished within the s_1 and s_3 quadrant (Tab. 6).

Figure 3 depicts three regions – upper strength limit at high compression (shear failure), lower strength limit at low compression (in-situ strength), and limit at the passage to spalling failure.

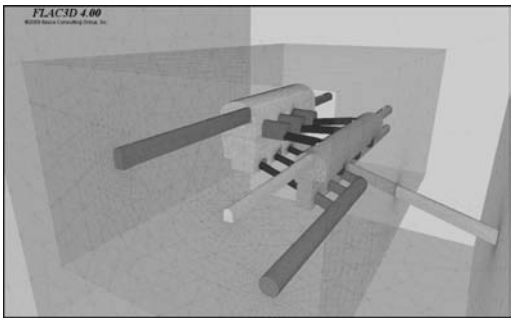


Figure 4. Overview 3D numerical model.

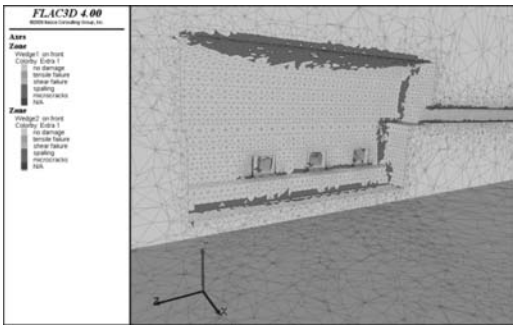


Figure 5. Contour plot brittle failure analysis for the machine cavern (viewing direction headwater).

5.1.3 *Numerical analyses*

A three-dimensional numerical calculation was performed utilising the finite difference program FLAC^{3D} (Itasca 2009) to investigate rock mass behaviour and define support requirements. The rock mass features a linearly elastic material behaviour. This simplification was deemed to be valid, since the rock mass strength is relatively highand plastification of the rock mass is not expected. Beside cavern structure and the water conduit, the model considers some of the major access tunnels (Fig. 5).

5.1.3.1 Results of brittle failure analysis

The results of the brittle failure analysis are depicted as contour plots, where the different colours represent certain failure types (Fig. 6). The results show a plausible and for such rock mass conditions a typical and coherent behaviour.

Brittle failure (shallow overstressing of the rock mass) and spalling are present in the crown towards the haunches and, somewhat less pronounced in the invert due to the high rock mass quality in combination with the dominating stress situation.

The highest tangential stresses are expected to occur in the crown/invert region (due to the orientation of the major normal stress σ_h situated orthogonal to the cavern axis). In the corner zones of the cavern, an exceedance of the tensile strength can be observed.

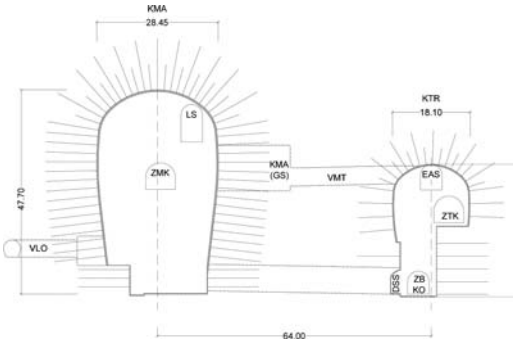


Figure 6. Simplified section of machine cavern (KMA) and transformer cavern (KTR).

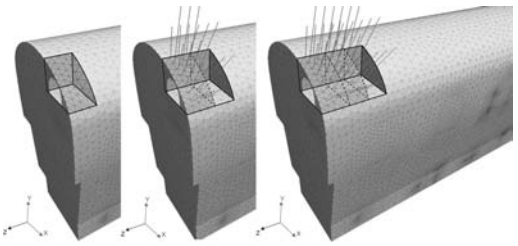


Figure 7. Sequential installation of initial widening of cavern.

The rock mass in such zones features lower cohesion, whereasthe frictional properties generally remain the same (Martin 1997).

Since all failure modes mentioned above appear just in the vicinity of the excavations, the system behaviour can be deemed as stable without far reaching problems in a rock mechanical aspect or for the excavation.

The results of the calculation with the parameters of the granodiorite with pre-existing joints show slightly less zones with occurrence of brittle failure. This is as expected since stress redistribution diminishes on the pre-existing discontinuities.

5.1.3.2 Support measures

The support concept of the cavern considers mainly potential wedge failure and effects of stress-induced failure withresulting dead loads.

A shotcrete lining consisting of four layers of shotcrete, each ten centimetres, with wire-mesh and staggered rock bolts with a length of 6 m and 12 m in the crown and 12 m at the side-walls. The grid of the bolts in the crown is 1.7*1.7 m and widened to 2.0*2.0 m at the sidewalls (Fig. 7).

The shotcrete was modelled as shell element, which allows bearing of normal forces and bending moments, featuring linearly elastic material behaviour. The parameters for the shotcrete considered are given in Table 7.

The rock bolts are modelled as cable elements. The material behaviour is described by the behaviour of the steel and the grout independently.

Table 7. Shotcrete properties.

Shotcrete properties		Unit	Value
Young's Modulus	E_{SC}	[MPa]	7000
Compressive strength	$\sigma_{c,SC}$	[MPa]	30
Tensile strength	$\sigma_{t,SC}$	[MPa]	0.2
Poisson's ratio	ν		0.2
Unit weight	γ	[kN/m^3]	25

Table 8. Anchor mortarparameters.

Anchor mortar parameters		Unit	Value
Diameter borehole	d_B	[mm]	51
Young's modulus	E_M	[MPa]	30,000
Comprstrength (24 h)	σ_M	[MN]	25
Shear strength	τ_M	[MN]	0.32
Cohesion	c_M	[MPa/m]	2.00
Shear stiffness	G_M	[MPa]	11,000

Table 9. Bolt properties.

Bolt properties		Unit	Value
Diameter	d_A	[mm]	25
Young's modulus	E_A	[MPa]	210,000
Tensile load at yield stress	$F_{A,eh}$	MN	0.32
Unit weight	γ	[kN/m^3]	78.50

The bond stiffness and the bond strength between bolt, mortar and rock mass are considered in this formulation. The parameters for the mortar and the bolts are shown in Table 8 and Table 9, respectively.

The excavation steps of the caverns and adjacent access tunnels were modelled by a sequential removal of predefined clusters.

The support is installed step by step in order to derive a realistic system behaviour of the excavation works (Fig. 8).

Three main phases of the cavern excavation considering expected displacements as well as shotcrete and rock bolt utilisation are analysed regarding system behaviour. The investigated phases for the machine cavern are as follows:

- Phase A: Top heading excavation and support installation finished
- Phase B: Top heading and bench (level KMA) excavation and support installation finished (Fig. 9)
- Phase C: Excavation and support installation finished

The shotcrete is only used to a minor extent utilisation during the top heading excavation (Phase A). Maximum normal forces to occur at the haunches are expected within the range of 2.0 MN. Maximum anchor loads in the haunches are expected with a maximum of 65 kN, which is up to a utilisation of 20 %

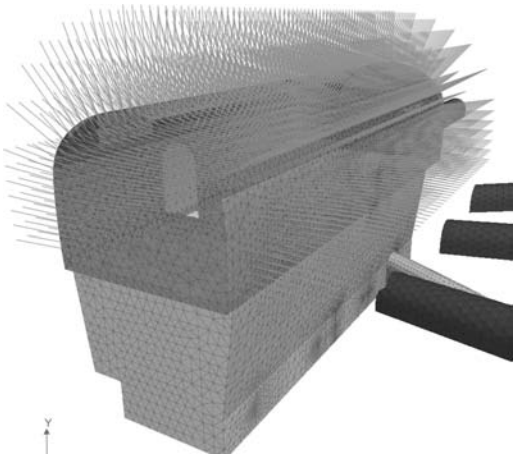


Figure 8. Excavation and support installation KMA Phase B.

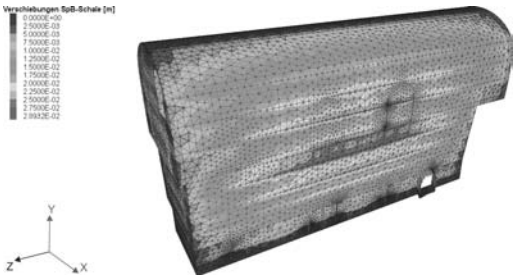


Figure 9. Displacements, Phase C.

of the tensile load at yield strength. Normal forces will increase to about 3.0 MN in the haunches, where else no significant increase of normal force is found in the crown. The results are reasonable and in line with the orientation and magnitude of the initial stress state normal to the side wall. Due to displacements at the sidewalls in the range of 16 mm, some tensile stress is arising in the range of 2.5 MN. The crown area experiences no further stress rises at this stage. Maximum anchor loads at the haunches will increase to approximately 90 kN.

Displacements will further rise to a maximum value of about 30 mm at the sidewalls, expected at half height of the cavern. Displacements at the crown will stabilise at a range of 2.5 to 3.0 mm (Fig. 10).

Maximum normal loads of 3 MN are expected upon full excavation in the crown region. Tensile stress at the side wall will rise to a magnitude of about 2–4 MN, without no major moments occurring in the lining. Maximum anchor loads will be expected within a range of 90 kN at the haunches towards half height of the cavern. Anchors will be utilised at local areas up to a level of about 30% of tensile load at yield strength.

6 CONCLUSION

The detailed analyses of ground behaviour utilising 3D finite element modelling is a valuable method for the design of large underground structures. The output of the 3D finite element calculation compared with the standard 2D finite element calculation provides a more realistic view on expected rock mass behaviour. The implementation of brittle failure analyses within FLAC^{3D} proved as a valuable analysis for rock mass behaviour and further on sufficient separation and alignment of underground structures.

ACKNOWLEDGEMENTS

The assistance of Dr F. Amann in discussing brittle failure is highly appreciated. All works for the design of the hydropower plant Grimsel 3were performed by the engineering joint venture GRI3 (AF-Consult AG, Gruner Ltd and Amberg Eng. Ltd.

REFERENCES

Austrian Society for Geomechanics. 2008. Guideline for the geotechnical design of underground structures with cyclic excavation. 2nd revised edition. Salzburg.

Bräuer, V., Kilger, B. & Pahl, A. 1989.Nagra Technical Report NTB 88-37E. Nagra, Baden.

Diederichs, M.S. & Carvalho, J.L. 2007. A modified approach for prediction of strength and post yield behavior for high GSI rock masses in strong, brittle ground. *Proc. 1st Canada/U.S. Rock Mech. Symp. 2007*.

Diederichs, M.S. 2002. Keynote – stress induced accumulation and implications for hard rock engineering. In: Hammah R, Bawden WF, Curran J, Telsnicki M (eds.). Proc. NARMS 2002. Toronto: University of Toronto Press; 2002. pp. 3–14.

Egger, P. 1980. Schlussbericht über die durchgeführten felsmechanischen Untersuchungen (in German), KWO AG.

Evans, K. 2012. Evaluation of stress estimates, Kraftwerke Oberhasli AG.

Hoek, E., Carranza-Torres, C. & Corcum, B. 2002. Hoek-Brown criterion – 2002 edition. Proc. NARMS-TAC Conference, Toronto, 2002, 1, 267–273.

Itasca Consulting Group, Inc. 2009. FLAC^{3D} Fast Lagrangian Analysis of Continua in 3 Dimensions, manual, 4th edition. Minnesota, USA.

Martin, C.D. 1997. The effect of cohesion loss and stress path on brittle rock strength, Canadian Geotechnical Journal Vol. 34, No. 5.

Swiss Code SIA 199. 1998. Erfassen des Gebirges im Untertagbau

Wannenmacher, H., Stucki, A., Bauert, M., Rüegg, Ch. & Schwegler, B. 2013. Geomechanical Influences on Shaft Construction for Hydropower Projects. In G. Anagnostou & H. Ehrbar (eds), *Underground – the way to the future! Proc. World Tunnel Congress 2013, Geneva, Switzerland.*

Rock Mechanics for Resources, Energy and Environment – Kwaśniewski & Łydżba (eds)
© 2013 Taylor & Francis Group, London, ISBN 978-1-138-00080-3

Study of the relation between cracks and the elastic properties of rock mass

I. Stan-Kłeczek & A.F. Idziak
Faculty of Earth Sciences, University of Silesia, Sosnowiec, Poland

ABSTRACT: The crack systems which exist in rocks decide about their physical properties. Especially, they have an essential influence on velocity of seismic waves propagating through the fractured rock mass. The aim of the present study was to verify if fracturing is an important factor affecting the elastic properties of rock masses, particularly, generating the anisotropy of dynamic elastic moduli in sedimentary rocks from the southern part of Poland. The seismic anisotropy of the rock mass were measured using P.A.S.I. Seismograph (Mod. 16S24-N). The research was made along precise oriented radial seismic profiles. P-waves and S-waves velocities were established from recorded seismograms and then the values of dynamic elastic moduli were calculated for all profiles. The diagrams of azimuth distribution of elastic moduli showed an anisotropy of elastic properties of the investigated rocks. The maximal values of moduli agree with orientation of main crack sets or potential directions of weakening of the rock mass. Seismic methods, enabling the determination of dynamic elastic modulus are a useful tool to study the degree of fracturing and rock massifs quality assessment for engineering purposes. An important element is the fact that they are relatively inexpensive and fast.

1 INTRODUCTION

Fracturing is very common feature of the rock mass which influences physical properties of rocks. The main consequence of the existence of cracks for the elastic wave propagation is the development of seismic anisotropy due to the anisotropic distribution of crack orientation. There are a lot of theoretical and experimental papers which concern the relationship between fracture parameters and seismic wave velocity (e.g., Bamford & Nunn 1979, Idziak 1992, Gueguen & Schubnel 2003, Stan-Kłeczek 2010). Preferred orientation of crack systems involves a velocity anisotropy. The velocity of the P-wave is maximum for a wave propagating parallel to the crack strike and is minimum for a wave propagating perpendicular to it. If two or more systems of parallel cracks exist in rocks, the minimum value of velocity is observed for the wave propagating diagonally to crack systems. This dependence allowed to develop a method of seismic anisotropy measurements to study the crack pattern in a rock mass. Velocity of P- and S-waves can be also used to assign dynamic elastic moduli of rock mass. On the other hand, it is possible to calculate the effective moduli of cracked rocks from crack tensor describing geometry of crack sets (Oda 1986, 1993, Stan-Kłeczek & Idziak 2008).

The aim of presented research was to establish directional changes of dynamic elastic moduli in Triassic sedimentary rocks and compare them with effective moduli obtained from the crack tensor. Investigation was carried out in three quarries (Fig. 1).

Site A and site B are located on the Wilkoszyn syncline in the south-eastern part of the Upper Silesia Coal Basin. The "Sadowa Góra" (site A) is a limestone quarry located on the south-western limb of syncline and the "Gródek" (site B) is a dolomite quarry placed on the north-eastern syncline limb.

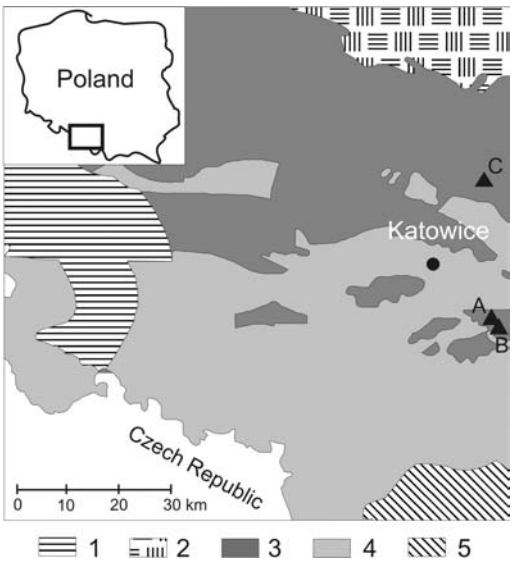


Figure 1. Geological map of the investigated area: A – deposit 1, B – deposit 2, C – deposit 3. 1 – Cretaceous, 2 – Jurassic, 3 – Triassic, 4 – Carboniferous, 5 – Devonian, A, B and C – measuring sites.

The "Ząbkowice Będzińskie" (site C) is an open pit in which Triassic dolomite covered by quaternary

sediments exist. The pit is located in north-eastern border of the Upper Silesian Coal Basin.

2 DYNAMIC ELASTIC MODULI

The knowledge of longitudinal and shear waves velocities allows to calculate the values of dynamic elastic moduli according to the relations (Plewa & Plewa 1992, Burger 1992):

Young's modulus:

$$E = \frac{\rho V_S^2\left(3V_P^2 - 4V_S^2\right)}{2\left(V_P^2 - V_S^2\right)} \tag{1}$$

Shear modulus:

$$\mu = \rho V_S^2 \tag{2}$$

Bulk modulus:

$$k = \rho\left(V_P^2 - \frac{4}{3}V_S^2\right) \tag{3}$$

Poisson's constant:

$$\nu = \frac{V_P^2 - 2V_S^2}{2\left(V_P^2 - V_S^2\right)} \tag{4}$$

where ρ is bulk density of rock, V_P and V_S are velocities of longitudinal and shear wave, respectively.

3 EFFECTIVE MODULI

Oda (1986) introduced the model which allowed to use a second rank crack tensor to calculate values of effective Young's modulus for different directions of seismic waves propagation. Directional changes of the effective modulus E^* can be present as a quotient effective modulus and its isotropic modulus E:

$$\frac{E^*}{E} = \frac{1}{1 + \ell\left(F_1 \cos^2\alpha + F_2 \sin^2\alpha\right)} \tag{5}$$

where ℓ is the geometrical parameter of cracks (for elliptical cracks $\ell = \pi/2$), F_1 and F_2 are the eigenvalues of second rank crack tensor, α is the angle between direction of wave propagation and longer axis of crack tensor. In anisotropic medium, the highest value of effective Young's modulus exists in the direction perpendicular to the longer axis of crack tensor, the modulus smallest value – along this axis.

4 FIELD STUDY

The direct mezostructure observations and seismic measurements were made in three quarries (site A – limestone, site B – dolomite and site C – dolomite).

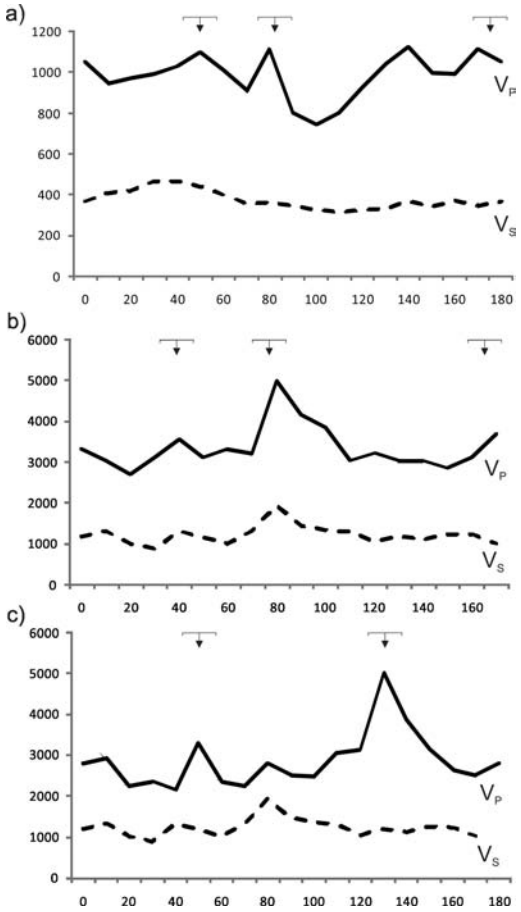


Figure 2. Comparison of the azimuth of maximum P and S waves velocities to orientation of the main crack systems: a) site A, b) site B, c) site C.

The P.A.S.I. seismograph was used for recording of seismic waves propagating trough the surface layers of rock mass. The measurements were made along precisely oriented, 33-meter long, radial seismic profiles. The azimuth interval between profiles was 10°. The seismic waves, generated by an eight kilogram hammer, were digitally recorded by twelve geophones uniformly placed along the profile. Accuracy of seismic velocity measurement depended on the precision of apparatus and local wave velocity changes along the profile. The first breaks of P-waves and S-waves were read from the recorded seismograms.

Wave velocities were calculated from a slope of head wave hodographs obtained by least-squares fitting to the experimental data.

In each quarry, strike azimuth and dip angle of visible cracks were measured with a geological compass.

In all investigated sites, the azimuth distributions of seismic wave velocity are characterized by the occurrence of velocity maxima at specific directions agreed with the measured directions of main crack systems (Fig. 2a, 2b and 2c).

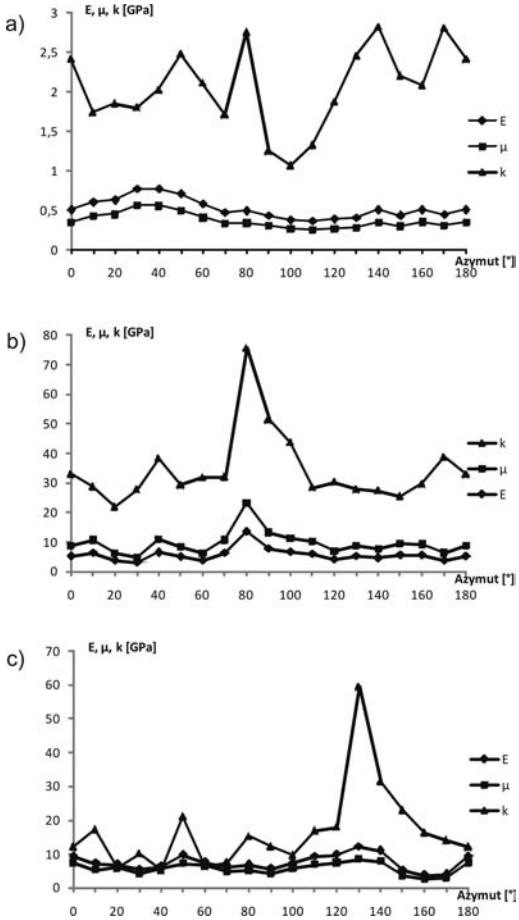


Figure 3. Azimuth distribution of dynamic elastic moduli: a) site A, b) site B, c) site C.

Results of field measurements allowed to estimate components of 2-nd rank crack tensor and velocity tensor (Idziak et al. 2010, Stan-Kleczek et al. 2012). Crack tensor allowed to calculate effective Young's modulus.

5 RESULTS AND DISSCUSION

Characteristic azimuth distributions of the dynamic elastic moduli obtained for investigated sites are presented on Figure 3. This figure shows the variations of elastic moduli for different directions of seismic wave propagation involved by the anisotropy of elastic properties of rocks under study.

The results obtained for a limestone from the site A show that azimuth distribution of bulk modulus k have three maxima agreed with main crack systems (Fig. 3a). The fourth maximum is not connected with any crack set existing in the rock mass. Probably, it reflects potential direction of the rock mass weakening. The azimuth distribution of Young's modulus E and shear modulus μ are rather constant.

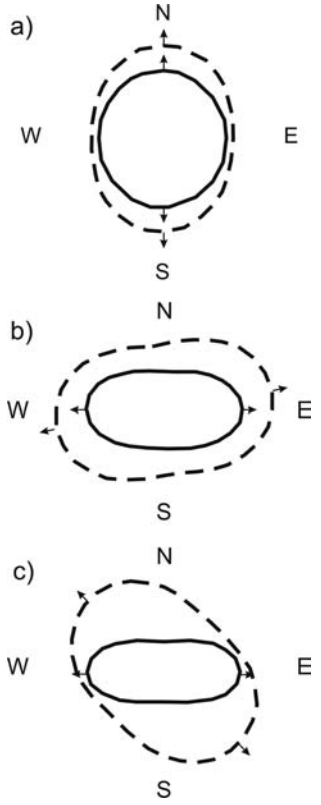


Figure 4. Relation between the distribution of squared P-wave velocity (dashed line) and the effective Young's modulus (solid line) in the investigated rock mass: a) site A, b) site B, c) site C.

Different situation we can observe for a dolomite from the site B (Fig. 3b). Azimuth distributions of all the dynamic moduli are characterized by presence of one maximum and two smaller peaks corresponding to strike of three existing crack systems.

For a dolomite from the site C, Young's modulus E and shear modulus μ are rather constant (Fig. 3c). On the distribution of bulk modulus k we can observed two maxima corresponding to fracture orientations.

Calculated from the crack tensors directional distributions of effective Young's modulus showed distinct similarity to the distributions of squared P-wave velocity, described by the second rank velocity tensor, for the two of three investigated deposits (Fig. 4). The both distributions obtained for the rock mass at site C differ because of incompatibility between a number of measurable crack systems and a number of peaks visible on the azimuth distribution of P-wave velocity.

6 CONCLUSIONS

The obtained results proved that fracturing is the important factor influences elastic properties of rocks. Seismic measurements carried out along oriented seismic profiles allow to establish azimuth distribution

of longitudinal and shear waves velocities and thus to calculate spatial distribution of effective dynamic moduli.

The effective bulk modulus k is the significant indicator of elastic anisotropy of investigated carbonate rocks. The anisotropy of effective Young's modulus and shear modulus is rather small.

If the existing crack systems are nearly perpendicular to themselves, maximum effective elastic moduli agree with the resultant directions of cracks strike but if the crack systems cut across under a small angle, maximum values of the effective elastic moduli are observed for the directions diagonal to the crack strikes.

In some rock mass it is possible to assign anisotropy of elastic parameters directly from the crack tensor.

The azimuthal distribution of effective dynamic elastic moduli calculated from seismic velocity distributions shows not only crack systems existing in the rock mass but also potential directions of rock mass weakening in which new crack systems can appear, for example during the surface mining.

REFERENCES

Bamford, D. & Nunn, K.R. 1979. In situ seismic measurement of crack anisotropy in the carboniferous limestone of North-West England. *Geophys. Prosp*. 27(2): 322–338.

Burger, H.R. 1992, Exploration geophysics of the shallow subsurface, Prentice Hall PTR: 7–20.

Gueguen, Y. & Schubnel, A. 2003. Elastic wave velocities and permeability of cracked rocks. *Tectonophysics* 370: 163–176.

Idziak, A.F. 1992. Seismic Wave Velocity Anisotropy and its Relation to Crack Orientation of Rock Masses, Silesian Univ. Publishing. Katowice (in Polish with English abstract).

Idziak, A., Stan-Kłeczek. I. & Pilarek, A. 2010. Study of rock anisotropy involved by cracks using combined geophysical methods. In J. Zhao, V. Labiouse, J.P. Dudt & J.F. Mathier (eds). *Rock Mechanics in Civil and Environmental Engineering*. Leiden: CRC Press/Balkema.

Oda, M., Yamabe, T. & Kamemura, K. 1986. A crack tensor and its relation to wave velocity anisotropy in jointed rock masses. *In. J. Rock Mech. Min Sci. & Geomech. Abstr.* 23 (6): 387-397.

Oda, M., Yamabe, T., Ishizuka, Y., Kumasaka, H., Tada, H. & Kimura, K. 1993. Elastic stress and strain in jointed rock masses by means of crack tensor analysis. *Rock Mech. Rock Engng.* 26(2): 89–112.

Plewa, M. & Plewa, S. 1992. Petrofizyka. Wydawnictwa Geologiczne: 273–309.

Stan-Kłeczek, I., Sutkowska, K., Stan, D. & Zolich, M. 2012. The study of the relationship between cracks and seismic parameters of rocks. *Acta Geodyn. Geomater.* Vol. 9, No. 2 (166): 137–142.

Stan-Kłeczek, I. 2010. Wpływ spękań na anizotropię prędkości fal sejsmicznych w wybranych masywach skalnych. Silesian Univ. Publishing. Katowice (in Polish with English abstract).

Stan-Kłeczek, I. & Idziak, A.F. 2008. Anisotropy of elastic properties of rock mass induced by cracks. *Acta Geodyn. Geomater.* Vol. 5, No. 2(150): 153–159.

Rock Mechanics for Resources, Energy and Environment – Kwaśniewski & Łydżba (eds)
© 2013 Taylor & Francis Group, London, ISBN 978-1-138-00080-3

Rock physical interpretation of the seismic properties of the excavation disturbed zone

T. Takahashi & S. Tanaka
Fukada Geological Institute, Tokyo, Japan

ABSTRACT: For modeling and interpreting seismic velocity reduction due to loosening in the Excavation Disturbed Zone (EDZ), we have studied the Kuster-Toksoz model (K-T model) which has been widely used as an inclusion model for a cracked rock. The K-T model can represent seismic velocity of a cracked rock based on seismic scattering theory due to cracks within the rock. The K-T model is first described mathematically and then used for calculating P-wave velocity vs. porosity relation in a cracked granitic rock. Assuming the porosity and aspect ratio of the crack, model calculations are compared to actual observations in many tunnels in different types of rocks. These comparisons reveal that seismic velocity reduction strongly depends on porosity and the aspect ratio of the crack in the rock and the rock physics model such as the K-T model can be used for predicting seismic velocity reduction due to loosening in the EDZ.

1 INTRODUCTION

In site characterization of a planned tunnel route, a seismic refraction survey is commonly performed for designing a tunnel support system through seismic velocities. However a tunnel support pattern determined based on a rock mass classification using seismic velocities obtained a seismic refraction survey before tunnel excavation often significantly differs from that after excavation (Kimura & Ohashi 2002). It has been recognized that the seismic velocity before excavation represents a rock state with confinement and often differs from that after excavation without confinement, especially for a rock with large loosening. Kimura & Ohashi (2002) conducted seismic velocity measurements at many tunnels before and after excavations for studying a rational way of design of the tunnel support pattern considering reduction of seismic velocity due to loosening of a tunnel wall. Figure 1 shows the seismic velocities for various types of rocks before and after excavations they measured. It should be noted that seismic velocity reduction is larger as rock mass quality is higher.

For interpreting the seismic properties of the excavation disturbed zone (EDZ) as above, we have studied rock physics models which have been aggressively used in modeling seismic properties of oil and gas reservoir rocks (Mavko et al. 2009). In this study Kuster-Toksoz model (K-T Model) (Kuster & Toksoz 1976) is applied to represent seismic P-wave velocity of a rock. This model is one of inclusion models, which has been widely employed for modeling a cracked rock. In this paper we first describe how to calculate model parameters following Saito et al. (1983) and then discuss how to model and interpret the EDZ seismic properties.

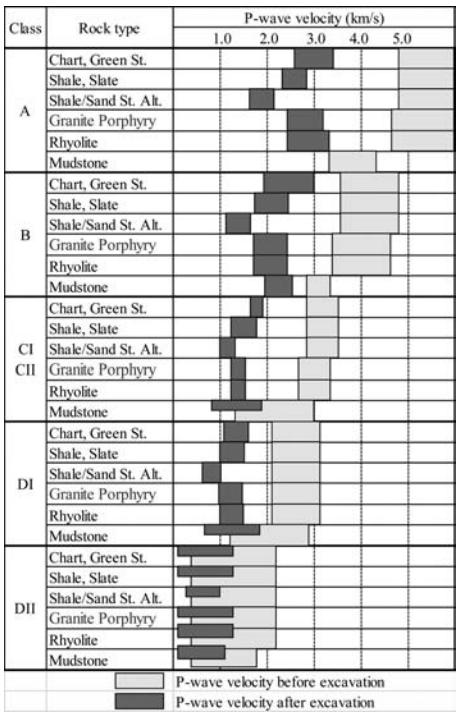


Figure 1. P-wave velocities before and after tunnel excavation for different rock types and rock quality classes.

2 ROCK PHYSICS MODEL FOR A CRACKED ROCK

The K-T model is commonly employed for modeling a rock with inclusions like cracks as shown in Figure 2.

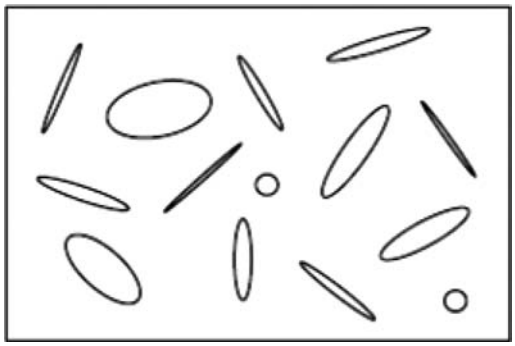


Figure 2. Schematic diagram of the inclusion model Cracks as inclusions have different shape (aspect ratio).

In the K-T model, bulk (K) and shear (G) moduli of a rock with inclusions are expressed as (Kuster & Toksoz 1976):

$$K = \frac{4PGs + Ks(3Ks + 4Gs)}{3Ks + 4Gs - 3P} \tag{1}$$

$$G = \frac{5Gs^2(3Ks + 4Gs) + QGs(9Ks + 8Gs)}{5Gs(3Ks + 4Gs) - 6Q(Ks + 2Gs)} \tag{2}$$

where *Ks* and *Gs* are bulk and shear moduli of rock matrix. *P*and *Q* are parameters determined by elastic properties of the rock matrix and inclusions as well as their shapes. Details of their calculations are described in the APPENDIX.

3 MODELING AND INTERPRETATION OF EDZ

For modeling the EDZ, loosening of the tunnel wall due to excavation is defined as 1) the confining stress surrounding the tunnel is released and 2) ground water is lowered and the tunnel wall becomes unsaturated. These phenomena are modeled as 1) porosity of the rock becomes larger because confining stress decreases and 2) inclusion of the crack changes from water to air, resulting in large reduction of bulk modulus of the inclusion.

The change of porosity due to change of confining stress can be expressed as (Toksoz et al.,1976)

$$\frac{d\phi}{\phi} = -\frac{P}{K^*}/[E_1 - E_2E_3/(E_3 + E_4)] \tag{3}$$

$$E_1 = \frac{6GI}{2\pi(3K + 4G)} \tag{4}$$

$$E_2 = \frac{6G}{4\pi(3K + 4G)}(3I - 4\pi) \tag{5}$$

$$E_3 = \frac{\alpha^2(3 - 9I/4\pi)(6K + 2G)}{2(1 - \alpha^2)(3K + 4G)} + \frac{6GI}{8\pi(3K + 4G)} \tag{6}$$

$$E_4 = \frac{1}{2}\left\{\frac{(3 - 9I/4\pi)(6K + 2G)}{2(1 - \alpha^2)(3K + 44G)} - \frac{3G(1 - I/\pi}{3K + 4G)}\right\} \tag{7}$$

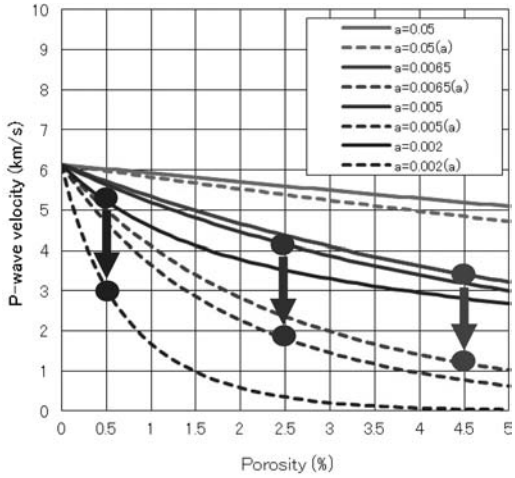


Figure 3. P-wave velocity – porosity relations calculated by the K-T model for the rocks with four different aspect ratios (0.002, 0.005, 0.0065 and 0.05), and before and after loosening due to excavation. Each arrow indicates velocity reduction due to loosening for the rocks of quality A, B and CI/CII.

Table 1. Parameters used in this calculation.

Ks	46.2 GPa	Bulk modulus of the rock matrix
Gs	28.1 GPa	Shear modulus of the rock matrix
Ki	2.25 GPa	Bulk modulus of the crack (water)
Gi	0.0 GPa	Shear modulus of the crack (water)

$$I = \frac{2\pi\alpha}{(1 - \alpha^2)^{3/2}}\left\{\cos^{-1}\alpha - \alpha(1 - \alpha^2)^{1/2}\right\} \tag{8}$$

where P is the confining stress, K* is the bulk modulus of the rock including cracks, K and G are bulk and shear moduli of the rock with cracks excluding cracks with the aspect ratio of α. Assuming that the size of crack is unchanged due to the stress change, the change of aspect ratio is defined as (Toksoz et al. 1976):

$$\frac{d\alpha}{\alpha} = \frac{d\phi}{\phi} \tag{9}$$

Assuming the rock is a cracked rock and the overburden above the tunnel is 100 m which determines the confining stress, we can calculate P-wave velocity against porosity using the K-T model together with the equations (3) to (9) for the rock with and without the EDZ. Figure 3 shows P-wave velocity vs. porosity relation calculated for the rock with aspect ratios 0.002, 0.05, 0.065 and 0.01 with and without the EDZ. The EDZ is modeled as 1) the confinement corresponding to 100 m deep overburden is released to zero and 2) the inclusion of crack changes from water to air. The parameters used in this calculation are shown in Table 1. This calculation indicates that the reduction of seismic velocity due to loosening at the EDZ is larger

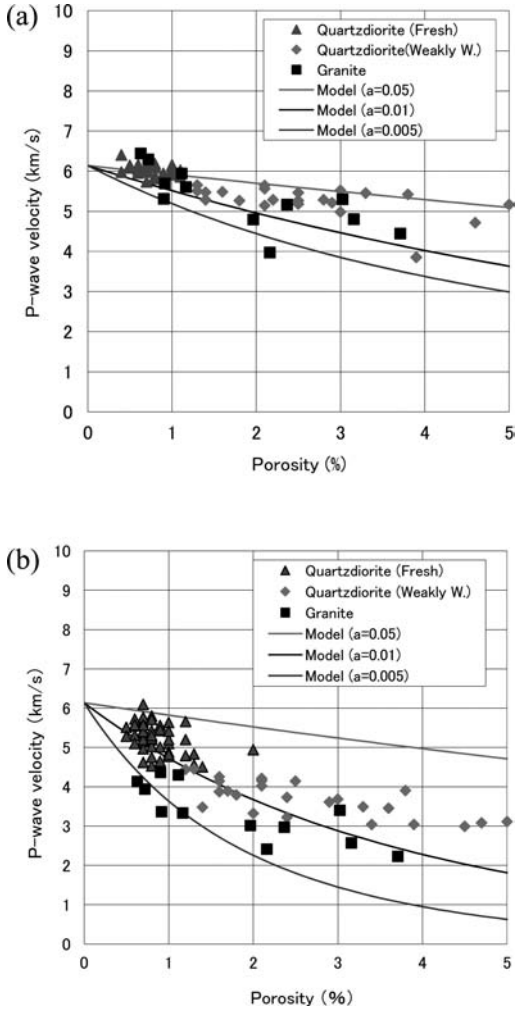


Figure 4. Ultrasonic P-wave velocity vs. porosity relations for (a) dry (unsaturated) and (b) water saturated granitic rocks. Three curves are calculations by the K-T model for the rocks with three different aspect ratios (0.005, 0.01 and 0.05).

as the aspect ratio of the crack is smaller. In this calculation we assume that the rock with the porosity of 0.5 and the aspect ratio of 0.002 be the rock quality A shown in Figure 1, porosity 2.5 and aspect ratio 0.005 for quality B and porosity 4.5 and aspect ratio 0.0065 for quality CI/CII. This comparison reveals that the observed reduction of P-wave velocity for the tunnel in granite porphyry is well predicted by the model proposed here. This indicates that the rock physics model can be used for predicting seismic velocity reduction due to loosening at the EDZ.

Very careful observation of this calculation indicates that most of reduction of P-wave velocity is caused that the rock becomes unsaturated. To prove it, we have compared ultrasonic velocity measurements on the saturated and unsaturated rocks. Figure 4 shows such comparisons of P-wave velocities for three kinds of granitic rocks (fresh and weakly weathered quartzdiorites and granite). The theoretical predictions calculated by the K-T model with the similar parameters as Table 1 are overlain on the measurement data. In this case, the three aspect ratios of 0.005, 0.01 and 0.05 are used. This figure clearly shows that the model rock with the aspect ratio of 0.01 well represents the ultrasonic P-wave velocity changes due to water saturation changes.

4 CONCLUSIONS

The K-T model as a rock physics models is studied for modeling and interpreting seismic velocity reduction due to loosening in the EDZ. Model calculated P-wave velocity vs. porosity relation for a granitic rock reveals that velocity reduction strongly depends on porosity and aspect ratio of the crack in the rock. If both properties of the rock can be obtained, seismic velocity reduction due to loosening on the EDZ can be predicted by using a rock physics model such as the K-T model.

The K-T model assumes small crack density and its homogeneous distribution in the rock. Although it, therefore, should be carefully applied to real rocks, this study proves its high applicability. However more applications to more rock types should be conducted for making its applicability much clearer.

REFERENCES

Kimura, M. & Ohashi, H. 2002. Selection of rational support in consideration of reduction of elastic wave velocity. OYO Technical Report 2002: 117–125. *(in Japanese)*

Kuster, G.T. & Toksoz, M.N. 1976. Velocity and attenuation of seismic waves in two phase media. *Geophysics* 39: 587–618.

Mavko, G., Mukeruji, T. & Dvorkin, J. 2009. *Rock Physics Handbook*, New York: Cambridge University Press.

Saito, T., Abe, M. & Sato, S., 1983. On the estimation of elastic constants for the application of theory of composite materials to crystalline rocks. *Buturi-Tanko* 36: 1–15. *(in Japanese)*

Toksoz, M.N., Cheng, C.H. & Timur, A., 1976. Velocities of seismic waves in porous rocks. *Geophysics* 41: 621–645.

APPENDIX

Parameters P and Q in the equations (1) and (2) are calculated as (Saito et al. 1983):

$$P = \frac{\phi}{3}(Ki - Ks)Tiijj \quad \text{(A1)}$$

$$Q = \frac{\phi}{5}(Gi - Gs)(Tijij - \frac{1}{3}Tiijj) \quad \text{(A2)}$$

$$Tiijj = \frac{3F_1}{F_2} \quad \text{(A3)}$$

$$Tijij - \frac{1}{3}Tiijj = \frac{2}{F_3} + \frac{1}{F_4} + \frac{F_4F_5 + F_6F_7 - F_8F_9}{F_2F_4} \quad \text{(A4)}$$

$$F_1 = 1 + A\left\{\frac{3}{2}(E+D) - C\left(\frac{3}{2}E + \frac{5}{2}D - \frac{4}{3}\right)\right\} \quad \text{(A5)}$$

$$F_2 = 1 + A\left\{1 + \frac{3}{2}(E+D) - \frac{C}{2}(3E+5D)\right\} + B(3-4C) + \frac{A}{2}(A+3B)(3-4C)\left\{E - D - C(E-D+2D^2)\right\} \quad \text{(A6)}$$

$$F_3 = 1 + \frac{A}{2}\left\{C(2-D) + \frac{1+\alpha^2}{\alpha^2}E(C-1)\right\} \quad \text{(A7)}$$

$$F_4 = 1 + \frac{A}{4}\left\{3D + E - C(E-D)\right\} \quad \text{(A8)}$$

$$F_5 = A\left\{C(E+D-\frac{4}{3}) - E\right\} + BD(3-4C) \quad \text{(A9)}$$

$$F_6 = 1 + A\left\{1 + E - C(E+D)\right\} + B(1-D)(3-4C) \quad \text{(A10)}$$

$$F_7 = 2 + \frac{A}{4}\left\{9D + 3E - C(5D+3E)\right\} + BD(3-4C) \quad \text{(A11)}$$

$$F_8 = A\left\{1 - 2C + \frac{E}{2}(C-1)\right\} + \frac{D}{2}(5C-3) + B(1-D)(3-4C) \quad \text{(A12)}$$

$$F_9 = A\left\{E(C-1) - CD\right\} + BD(3-4C) \quad \text{(A13)}$$

$$A = \frac{Gi}{Gs} - 1 \quad \text{(A14)}$$

$$B = \frac{1}{3}\left(\frac{Ki}{Ks} - \frac{Gi}{Gs}\right) \quad \text{(A15)}$$

$$C = \frac{3Gs}{3Ks - 4Gs} \quad \text{(A16)}$$

$$D = \frac{\alpha}{(1-\alpha^2)^{3/2}}\left\{\cos^{-1}\alpha - \alpha(1-\alpha^2)^{1/2}\right\} \quad \text{(A17)}$$

$$E = \frac{\alpha^2}{1-\alpha^2}(3D-2) \quad \text{(A18)}$$

where K_i and G_i are the bulk and shear moduli of the inclusion (crack), ϕ is the porosity and α is the aspect ratio of the crack.

Once the bulk and shear moduli of the rock including cracks are estimated, their seismic velocities can be calculated as:

$$Vp = \sqrt{\frac{K + 4G/3}{\rho}} \quad \text{(A19)}$$

$$Vs = \sqrt{\frac{G}{\rho}} \quad \text{(A20)}$$

$$\rho = \phi\rho_f + (1-\phi)\rho_s \quad \text{(A21)}$$

where ρ, ρ_f and ρ_s are the densities of the cracked rock, water and rock matrix, respectively.

Rock Mechanics for Resources, Energy and Environment – Kwaśniewski & Łydżba (eds)
© 2013 Taylor & Francis Group, London, ISBN 978-1-138-00080-3

Depth distribution of lithospheric strength determined by the self-unbalancing shear rupture mechanism

B.G. Tarasov
University of Western Australia, Perth, Australia

ABSTRACT: It is generally accepted that the frictional strength of pre-existing faults represents a lower limit on rock shear strength in the seismogenic layer. The paper proposes an alternative concept based on a recently identified shear rupture mechanism (fan-mechanism). The fan-mechanism creates paradoxical effect providing the formation of new faults in intact rock mass at shear stress levels significantly below the frictional strength. This indicates that the lower limit of lithospheric strength is not restricted by the frictional strength. The varying efficiency of this mechanism with depth provides a specific depth distribution of lithospheric strength.

1 INTRODUCTION

Earthquakes are normally related to pre-existing faults, which implies an essential role of them in earthquake activity. It is assumed that the Earth's crust is riddled with faults. Modern understanding of the nature of earthquakes is that the primary mechanism comprises stick-slip instability on pre-existing faults, along which the frictional strength represents a lower limit on rock shear strength in the lithosphere (Scholz 2002). Depth distribution of the lithospheric shear strength within the seismogenic layer is determined by the Byerlee's law (Byerlee 1978) in consideration of enhanced temperature at great depths (Brace & Kohlstedt 1980).

The paper proposes an alternative concept based on a recently identified self-unbalancing 'fan-head' shear rupture mechanism (Tarasov 2008, 2010, Tarasov & Randolph 2011, Tarasov & Guzev 2013). The fan-mechanism is activated at stress conditions corresponding to the seismogenic layer and can provide the formation of new faults in intact rock mass at shear stress levels significantly below the frictional strength. This indicates that the lower limit of lithospheric strength is not restricted by the frictional strength. An important feature is that in nature the fan-mechanism nucleates in the vicinity of pre-existing discontinuities (boundaries between tectonic plates, faults, deep mines, etc.) which serve as local stress concentrators necessary for the initial formation of the fan-structure. The proximity of the pre-existing faults to the area of instability caused by the fan-mechanism creates the illusion of stick-slip instability on the pre-existing faults, thus concealing the real situation. The new concept proposes a new mode of instability in the Earth's crust in addition to the generally accepted frictional stick-slip instability. The varying efficiency of this mechanism with depth provides a specific depth distribution of lithospheric strength.

2 FAN-HEAD SHEAR RUPTURE MECHANISM

Shear is a universal form of intact rock failure under confined compression of any scale, from laboratory specimens to earthquake faults. A fundamental feature of any fault is a specific structure known as 'book shelf' or 'domino' structure (Peng & Johnson 1972, King & Sammis 1992, Reches & Lockner 1994, Ortlepp 1997). This structure is represented by an echelon of inclined blocks (slabs) separated by tensile cracks. Such a domino-structure is subjected to rotation at shear displacement along the fault.

It was proposed that the domino-structure plays an essential role in determination of rock strength and brittleness at failure (Tarasov 2008, 2010, Tarasov & Randolph 2011, Tarasov & Guzev 2013). Depending on the strength and geometry of the domino-blocks they can collapse at rotation, creating normal friction within the fault, or can operate as hinges decreasing dramatically friction between the fault faces.

An analysis of post-peak behavior of hard rocks (uniaxial strength above 300 MPa) under highly confined conditions led to the hypothesis that domino-blocks at these conditions create a fan-structure, representing the head of a propagating shear rupture (Tarasov 2008, 2010). Figure 1 illustrates the fan-head of shear rupture propagating through the intact material from left to right. A mathematical model (Tarasov & Guzev 2013) shows that the fan-head represents a self-unbalancing structure which causes inevitably spontaneous rupture development. The fan-head propagates though the intact material as a wave creating new shear rupture. Due to rotation of domino-blocks involved in the head the fault faces are subjected to relative displacement.

The character of spontaneous shear rupture propagation due to the fan-mechanism corresponds to pulse-like mode rupture propagation observed for earthquakes and in laboratory experiments (Heaton

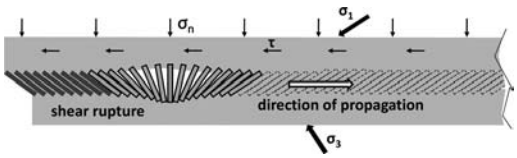


Figure 1. Fan-head domino structure.

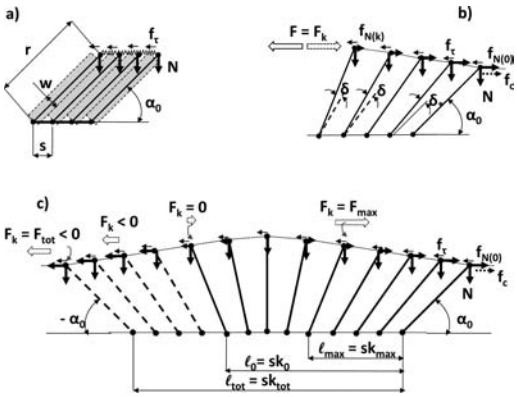


Figure 2. Elements of the fan-head mechanism.

1990, Ohnaka et al. 1986). At any given time during rupture propagation, slip occurs over only a narrow band (fan-head) along the fault. This slip pulse propagates forward as the fault proceeds. This process is analogous to pulling a large, heavy carpet across a floor by introducing a small wave, or ruck, that propagates the entire length of the carpet. Eventually the entire carpet will be translated from its original position, but at any one time only a small ripple is in motion.

Unfortunately direct observations of the fan-structure are not possible due to the spontaneous and violent character of the failure process caused by this mechanism. This is the reason why the fan-structure has not been experimentally detected and studied before.

A brief introduction of the mathematical model (Tarasov & Guzev 2013) is presented below. Figure 2 illustrates principles of the model. The domino-blocks are located between two layers. At the initial position (Figure 2a) surfaces of neighboring blocks are in contact providing a very compact (monolithic) structure. To simulate the resistance of neighboring blocks to splitting(separation) at rotation we assume that the blocks are glued to each other.

For simplicity all domino-blocks in the model are represented by rods of length r inclined at the initial angle α_0 and distanced from each other by s. The distance $s = w/\sin\alpha_0$, where w is the block width. Both ends of each rod are connected to the upper and lower layers by joints. For simplicity we assume that the upper layer is represented by an elastic material (elastic connector) while the lower layer and the rods are stiff. Each rod is loaded by the same normal, N, and horizontal (shear), f_τ, elementary forces representing the evenly distributed normal σ_n and shear τ stresses applied to the whole structure. The meaning of the elementary forces is as follows: $N = \sigma_n s1$; $f_\tau = \tau s1$, where depth (or thickness) of the model is equal to unity (1). The value of τ is less than the shear stress necessary for displacement of the upper layer against the lower.

The fan-structure in this model can be formed if in addition to the existing evenly distributed stresses a local supplementary force (or stress) is applied. Figures 2b and 2c illustrate the main principles of interaction between the blocks at different stages of the fan-head formation when a supplementary horizontal force F is applied to the upper end of the leftmost rod. The force F causes consecutive rotation of rods against lower joints. Forces from each prior rod are transmitted to the next rod via the stretched upper elastic connector. Shear resistance of relative displacement of the rupture faces due to the fan-mechanism is determined by the sum of all horizontal elementary forces applied to all rods involved in the fan-structure.

Horizontal components $f_N = N/tg\alpha$ of normal forces N (shown by bold arrows) and forces f_τ (shown by thin arrows) are applied to all rods of the fan-structure. Force f_c representing the reduced resistance of tearingoff the front rod-0from the basis is applied to the rod-0 only (shown by dotted arrow). Elementary forces resisting displacement of the top rupture face against the bottom one are directed to the right, while forces assisting displacement are directed to the left. Equation (1) describes shear resistance of the completed fan-structure involving k_{tot} domino-blocks taking into account friction in joints of the rotated domino-blocks (see details in Tarasov & Guzev 2013).

$$F_{k(tot)} = \frac{N}{\delta}\ln\left|\frac{\sin(\alpha_0 + k_{tot}\delta)}{\sin(\alpha_0)}\right| - f_\tau k_{tot} + f_c + 0.85\frac{w}{r}\mu N k_{tot} \quad (1)$$

The first member of Equation (1) reflects the effect of elementary forces f_N and stretching of the elastic connectors (face material) on shear resistance of the fan-structure. The stretching is characterized by angle δ between any two neighboring rods. Angle δ is a function of elastic properties and cross-section of the elastic connector. It is established that angle δ is the same between any two neighboring rods of the fan-structure.

An essentially important feature of the fan-structure is the fact that the resistance f_N of each rod decreases with increasing angle α. It reaches zero at $\alpha = 90°$ and becomes negative at $\alpha > 90°$. For the completed fan-structure the united shear resistance caused by elementary forces f_N is equal to zero due to self-balancing. Hence, the first member of the Equation (1) is equal to zero.

The third member f_c of Equation (1) representing the reduced resistance of tearing off the front domino-block from the intact material is extremely small because it is applied to the front rod only. Estimations show that it corresponds approximately to 0.001 of the common frictional strength.

The last member of Equation (1) represents the united resistance provided by friction within the 'joints' of all k_{tot} rotating hinges. Here: μ is the coefficient of sliding friction; and w/r is the ratio width/length of domino-blocks. The last member of Equation (1) shows that the existence of hinges decreases the friction between the rupture faces proportionally to the ratio w/r. For example, for domino-blocks with the ratio $w/r = 0.1$ the frictional resistance of the fan-head τ_{fan} is less than the frictional resistance of sliding faces in a common fault τ_f by a factor of ten: $\tau_{fan} \approx 0.1\tau_f$.

The second member of Equation (1) represents an active united force assisting displacement and caused by the evenly distributed shear stress τ applied to the material.

The conducted analysis shows that the united shear resistance of the fan-head τ_{fan} is actually determined solely by friction within the joints (Equation (2)). It is a function of the ratio w/r (width/length of domino-blocks) and can be significantly less than the frictional strength τ_f.

$$\tau_{fan} = 0.85\tau_f \frac{w}{r} \qquad (2)$$

At stress levels applied to the material $\tau > \tau_{fan}$ the fan-structure is self-unbalancing. It propagates through intact rock mass as a wave providing inevitably spontaneous and violent failure process.

It means that the instability due to creation of a new fault in intact rock mass by the fan-mechanism can occur at stress levels significantly below the frictional strength of pre-existing faults. This feature of the fan-head mechanism provides a paradoxical effect contradictory to the classical rock mechanics: shear strength of intact rock involving the fan-structure is less than frictional strength of pre-existing fault at the same confined conditions.

It must be emphasized that this feature is true for situation when the fan-structure has completed. However, for the initial formation of the fan-structure a high local shear stress is required corresponding to the fracture material strength τ_u. This is due to a specific variation of shear resistance described by the first member of Equation (1). At the initial stage of the fan formation it increases up to a maximum value (pre-peak stage of loading) and then decreases to zero (post-peak stage of loading).

Figure 3 illustrates this feature. Figure 3a shows a fragment of the rock mass loaded by stresses presented in Figure 3b. The whole rock mass is loaded by low distributed shear stress representing the field scale stress τ_A. We suppose that this stress is below the frictional stress $\tau_A < \tau_f$. Levels of the both stresses are shown in Figure 3b by horizontal lines.

The fan-head can be generated by a locally applied high shear stress. The graph OPABC shows shear resistance of the fan-head at different stages of its formation. At the formation of the first half of the fan-structure the local stress increases from τ_A to the

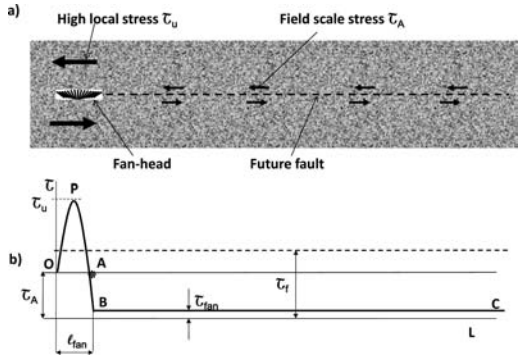


Figure 3. Features of nucleation and propagation of the fan-head in nature.

fracture strength τ_u (OP stage). The stage PB corresponds to the formation of the second half of the fan-head. The horizontal line τ_{fan} reflects shear resistance of the completed fan-head propagating through the rock mass. During the stage OPA the fan-structure can develop in stable regime. However, after point A due to the self-unbalancing condition further formation of the fan-head (AB) and its propagation through the rock mass will be inevitably spontaneous. As shown in (Tarasov and Guzev, 2013) the length of the fan-head ℓ_{fan} is a function of the fault thickness. It is estimated that for primary ruptures ℓ_{fan} may be of the order of a few centimeters while for faults with thickness of a few centimeters the corresponding fan-head length is some two orders of magnitude greater (so some meters).

High stresses necessary for the initial formation of the fan-structure in intact rock mass of the Earth's crust can be generated in the vicinity of pre-existing faults (boundaries between tectonic plates, fault, deep mines, etc.) representing stress concentrators.

According to the new approach:

- Pre-existing faults play the role of stress concentrators, but instability occurs mainly due to development of new faults in the intact rock mass.
- By creating new faults this mechanism increases the intensity of rock fracturing in earthquake active zones, making these zones finally riddled with faults.
- It also explains the spatial distribution of earthquakes: new faults are generated in intact rock at new locations.
- The proximity of the pre-existing faults to the area of instability caused by the fan-mechanism creates the illusion of stick-slip instability on the pre-existing faults, thus concealing the real situation.

It was shown experimentally (Tarasov 2010, Tarasov & Randolph 2011) that efficiency of the fan-mechanism is a function of confining stress σ_3. In accordance with Equations (1) and (2) the efficiency of the fan-mechanism increases with the decrease of the ratio w/r. In real rocks, however, the situation is more complicated. The efficiency of the fan-mechanism is

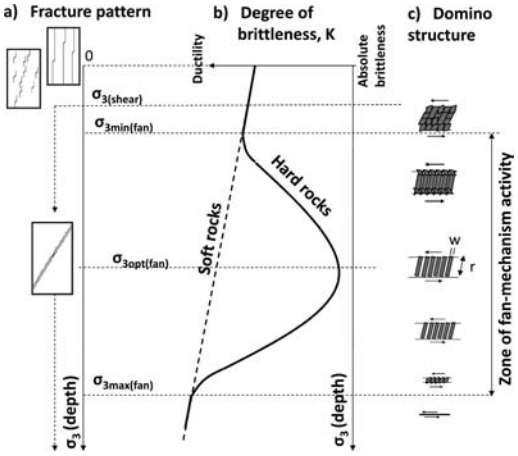


Figure 4. Influence of confining pressure σ_3 (depth) on a) fracture pattern, b) rock brittleness, and c) domino-structure.

determined also how perfect and uniform the fault structure is. The point is that long and thin domino-blocks cannot withstand rotation without collapse preventing formation of the fan-head. Experiments conducted on hard rocks at different levels of confining pressure σ_3 showed a specific variation of the fan-mechanism efficiency with rising σ_3. Figure 4 helps to discuss this question.

It is known that confining pressure influences the fracture patterns (Kirby & McCormick 1984, Shimada 2000). At uniaxial compression and low confinement shear ruptures cannot propagate in their own plane. The fracture patterns at these conditions are associated with creation of long tensile cracks. Increase in σ_3 decreases the length of tensile cracks leading to variation in fracture pattern as illustrated in Figure 4a (with σ_3 increasing top-down). Starting from a certain level of confining pressure $\sigma_{3(shear)}$ (different for different rocks) rocks fail due to formation of a plane macroscopic shear rupture capable of propagating in its own plane due to consecutive creation of short tensile cracks and domino-blocks between them in the tip of the propagating rupture.

For relatively soft rocks friction is mobilized in all types of developing ruptures. Due to this rock brittleness decreases with rising confining pressure σ_3 as symbolically shown by inclined dotted line in Figure 4b. Hard rocks can also exhibit similar behavior at relatively low levels of $\sigma_3 < \sigma_{3min(fan)}$ where long domino-blocks collapse at rotation. Within the pressure range $\sigma_{3min(fan)} - \sigma_{3max(fan)}$ the domino-blocks operate as hinges with different efficiency affecting rock brittleness as shown symbolically in Figure 4b by solid line (Tarasov 2010, Tarasov & Randolph 2011). The brittleness index K was estimated as the ratio between post-peak rupture energy dW_r and post-peak elastic energy dW_e released from the failing rock: $K = dW_r/dW_e$ (see Tarasov & Potvin 2013).

Variation in brittleness within the pressure range $\sigma_{3min(fan)} - \sigma_{3max(fan)}$ is caused by the fan-mechanism and reflects the efficiency of the mechanism operation. At the lower end of this pressure range, when the relative length of rotating blocks is still large, the blocks are subjected to partial destruction as they rotate. Figure 4c illustrates features of domino-blocks with rising σ_3. At higher σ_3, with shorter blocks, this imperfection decreases rendering the fan-mechanism more efficient. The optimal efficiency takes place at $\sigma_{3opt(fan)}$ when the blocks rotate with minimum destruction. At greater σ_3 the efficiency reduces because shorter blocks gradually lose any potential operating as hinges in accordance with Equations (1) and (2). Finally very short blocks lose this capability completely and the rock behavior returns to the conventional frictional mode. For hard rocks the maximum efficiency can take place at σ_3 of about 300 MPa (or higher) which correspond to depth of about 10 km (or greater).

3 STRENGTH OF THE LITHOSPHERE

Figure 5 illustrates a new concept of the lithospheric strength associated with the fan-mechanism. Figures 5a,b,c show relative depth distributions of earthquake frequency (number of earthquakes), lithospheric strengths (including frictional, creep, fracture and fan), and rock brittleness. In Figure 5b the fracture strength curve represents strength of intact rock. The fan-strength curve is plotted by analogy with the curve reflecting the variation of rock brittleness with depth (Figure 5c) as estimated on the basis of experimental results. Both curves (fan-strength and brittleness) reflect the efficiency of the fan-mechanism operation with depth. The maximum efficiency of the fan-mechanism defines the depth-position of minimum fan-strength and maximum rock brittleness and earthquake frequency. The curves in Figures 5a,b,c illustrate the principal relation between various strength parameters without consideration of the temperature effect with depth.

Figure 5b shows that at shallow depths frictional strength along pre-existing faults represents the lower limit of rock strength and determines the lithospheric strength. Within the depth region where fan-strength is less than frictional strength the situation is very specific, as explained in Figures 5d,e which show schematic curves illustrating rock properties at field scale. Figure 5d shows variations of fracture strength τ_u, frictional strength τ_f and fan-strength τ_{fan} versus confining stress σ_3. The fan-strength line indicates potential lithospheric strength determined by shear resistance of the fan-mechanism. To understand the situation within the range of confining stress $\sigma_{3(B)} < \sigma_3 < \sigma_{3(C)}$ we should keep in mind that the fan-strength line corresponds to the resistance of the completed fan-head. However, for formation of the fan-head, high local stresses equal to the fracture strength must be generated in the intact rock mass. Before these localized high stresses have been created the limit of lithospheric strength within the

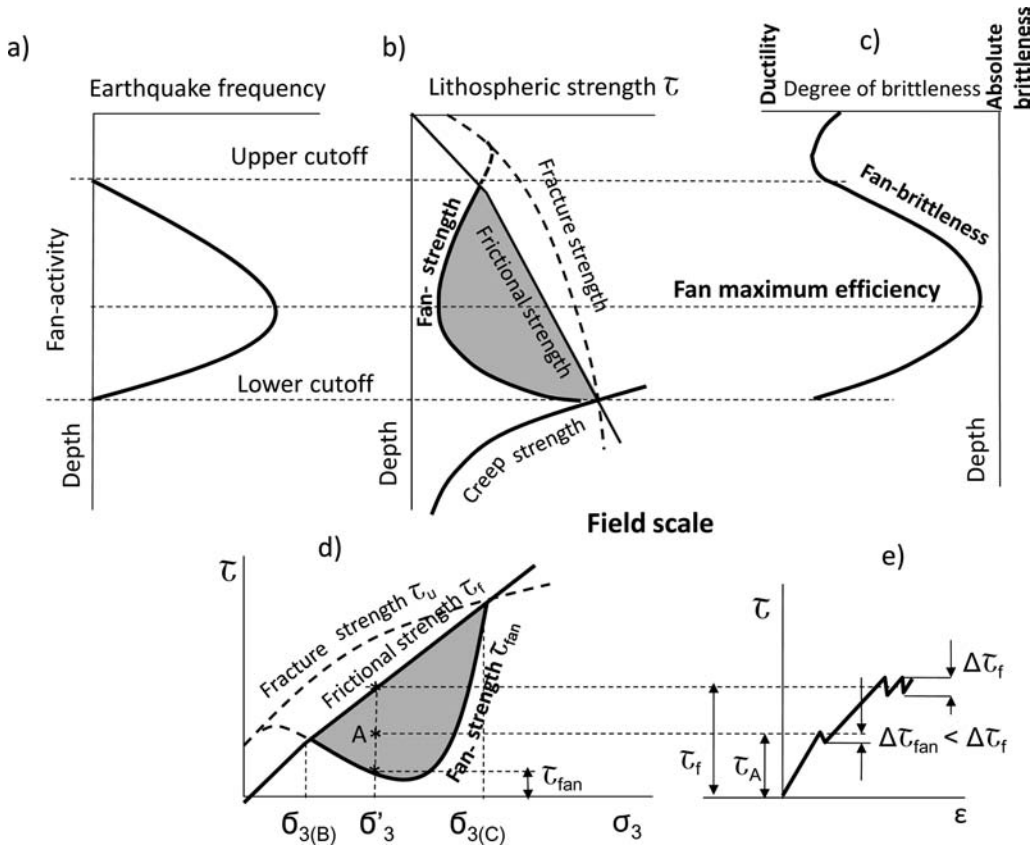


Figure 5. Relative depth distribution of: a) earthquake frequency (number of earthquakes); b) lithospheric strength; and c) rock brittleness. d) Variation of fracture strength τ_u, frictional strength τ_f, and fan-strength τ_{fan} versus confining stress σ_3 for field scale rock mass. e) Schematic stress τ – strain ε curve for field scale rock mass.

range $\sigma_{3(B)} < \sigma_3 < \sigma_{3(C)}$ is determined by the frictional strength.

Nucleation of the fan-head in a zone of local stress concentration can occur at any level of lithospheric (field scale) stress within the grey area located between the frictional and fan-strength curves. Let us consider the situation when the field stress corresponds to point A in Figure 5d ($\sigma_3 = \sigma'_3$ and $\tau = \tau_A$). The graph in Figure 5e represents a speculative stress τ – strain ε curve corresponding to loading of the field scale rock mass at confining stress $\sigma_3 = \sigma'_3$. Stress τ_A on the graph corresponds to lithospheric stress at which the fan-head was generated and propagated through the rock mass. The failure process is accompanied by corresponding stress drop $\delta\tau_{fan}$. The stress drop associated with the failure at stress level τ_A will be less than the stress drop caused by frictional instability at τ_f because of the difference in levels of lithospheric stresses: $\delta\tau_{fan} < \delta\tau_f$. The closer the stress τ_A to τ_f the larger the stress drop accompanying the instability. It is important that after failure at the stress level τ_A the failed rock mass can be loaded further up to frictional strength τ_f.

It should be emphasized that instability in the Earth's crust caused by the fan-mechanism in intact rock is more likely (or preferable) compared to frictional stick-slip instability on pre-existing faults because the fan-instability can be generated at lithospheric stresses below the frictional strength. Because of this we can suppose that in the majority of cases the fan-mechanism actually defines the seismogenic layer in the Earth's crust. Frictional stick-slip instability within the confining pressure range $\sigma_{3(B)} < \sigma_3 < \sigma_{3(C)}$ can occur if the stress level in the lithosphere reaches the frictional strength and the fan-mechanism is not activated.

In accordance with the new concept the relation between the depth distributions of earthquake frequency, lithospheric strength and brittleness is absolutely logical: the lower the strength and higher the brittleness, the higher is the propensity of rocks in the seismogenic layer for dynamic unstable shearing.

The new concept comprising two forms of instability caused by the fan-mechanism and by the conventional stick-slip mechanism provides more comprehensive understanding of lithosphere strength and earthquake instability and can explain a number of earthquake features which previously had not been fully resolved.

4 CONCLUSIONS

The paper proposes a new concept of lithospheric strength and earthquake mechanism based upon the hitherto unknown self-unbalancing shear rupture mechanism. The mechanism causes paradoxical effects, contradicting conventional knowledge: 1) it makes rocks more brittle with depth; 2) it makes strength of intact rocks less than the frictional strength of pre-existing faults; 3) it makes preferred earthquake instability due to creation of new faults in intact rock mass rather than stick-slip instability on pre-existing faults. The varying efficiency of this mechanism with depth explains the relationship between the depth distribution of earthquake hypocenters (frequency) and lithospheric strength and brittleness.

The new concept can provide alternative explanations for many features observed in earthquakes, for example:

- Typical hypocenter depth distribution (increase—maximum—decrease).
- Creation of new faults in seismically active zones, making this zone riddled with faults.
- Spatial distribution of earthquakes.
- Depth positions of upper and lower cutoffs and maximum earthquake frequency.
- Instability at low lithospheric stress.
- Small stress drop caused by instability.
- The absence of strong depth dependence of stress drop.
- Pulse-like mode of fault propagation.
- New instability mechanism – the fan-head mechanism in hard rock in addition to the accepted velocity weakening mechanism.

ACKNOWLEDGEMENTS

This work has been supported by the Centre for Offshore Foundation Systems (COFS) at the University of Western Australia. This support is gratefully acknowledged.

REFERENCES

Brace, W.F. & Kohlstedt, D. 1980. Limits on lithospheric stress imposed by laboratory experiments. *Journal of Geophysical Research* 85:6248–6252.

Byerlee, J.D. 1978. Friction of rocks. *Pure Appl. Geophys*. 116: 615–626.

Heaton, T.H. 1990. Evidence for and implications of self-healing pulses of slip in earthquake rupture. *Physics of Earth Planet International* 64(1): 1–20.

King, G.C.P. & Sammis, C.G. 1992. The mechanisms of finite brittle strain. *PAGEOPH* 138(4): 611–640.

Kirby, S.H.& McCormick, J.W. 1984. Inelastic properties of rocks and minerals: strength and rheology. In R.S. Carmichael (ed.),*CRC Handbook of Physical Properties of Rocks*, Boca Raton, Florida: CRC Press, Vol. 3, pp. 139–280.

Ohnaka, M., Kuwahare, Y., Yamamoto, K. & Hirasawa, T. 1986. Dynamic breakdown processes and the generating mechanism for hi-frequency elastic radiation during stick-slip instabilities. In S. Das, J. Boatwright & C.H. Scholz (eds), *Earthquake Source Mechanics, Geophys. Monogr. Ser*., Vol. 37, pp. 13–24, AGU, Washington, D.C.

Ortlepp, W.D. 1997. *Rock fracture and rockbursts*. Johannesburg: The South African Institute of Mining and Metallurgy.

Peng, S. & Johnson, A.M. 1972. Crack growth and faulting in cylindrical specimens of Chelmsford granite. *International Journal of Rock Mechanics and Mining Sciences* 9: 37–86.

Reches, Z. & Lockner, D.A., 1994. Nucleation and growth of faults in brittle rocks. *Journal of Geophysical Research* 99(B9): 18159–18173.

Scholz, C.H. 2002. *The Mechanics of Earthquakes and Faulting*. Cambridge: Cambridge University Press.

Shimada, M. 2000. *Mechanical Behaviour of Rocks under High Pressure Conditions*. Rotterdam: Balkema.

Tarasov, B.G. 2008. Intersonic shear rupture mechanism. *International Journal of Rock Mechanics and Mining Sciences* 45(6): 914–928.

Tarasov, B.G. 2010. Superbrittleness of rocks at high confining pressure. In *Fifth International Seminar on Deep and High Stress Mining*, Santiago, Chile, pp. 119–133.

Tarasov, B.G.& Randolph, M.F. 2011. Superbrittleness of rocks and earthquake activity. *International Journal of Rock Mechanics and Mining Sciences* 48: 888–898.

Tarasov, B.G. & Potvin, Y., 2013. Universal criteria for rock brittleness estimation under triaxial compression. *International Journal of Rock Mechanics and Mining Sciences* 59: 57–69.

Tarasov, B.G. & Guzev, M.A. 2013. Self-unbalancing shear rupture mechanism—the most energy efficient rock failure mechanism at confined compression. In *8th International Symposium on Rockbursts and Seismicity in Mines*. S-Petersburg-Moscow, Russia, 1–7 September 2013 (in press).

Rock Mechanics for Resources, Energy and Environment – Kwaśniewski & Łydżba (eds)
© 2013 Taylor & Francis Group, London, ISBN 978-1-138-00080-3

Geomechanical attributes of reconstituted Indian coals under carbon dioxide saturation

V. Vishal
IITB Monash Research Academy, IIT Bombay, Powai, Mumbai, India

P.G. Ranjith
Department of Civil Engineering, Monash University, Clayton, Australia

T.N. Singh
Department of Earth Sciences, IIT Bombay, Powai, Mumbai, India

ABSTRACT: Geologic sequestration of anthropogenic greenhouse gases into deep geological reservoirs like coal seams has caught attention worldwide. The potential of coal to adsorb CO_2 and preferentially release methane partly offsets the cost of capture, transport and storage of the gases. For such projects, it is important to understand the influence of geomechanical properties of coal on cap rock integrity and long term safety. However, coal being highly heterogeneous from basin to basin, seam to seam, and those within the seam, it is difficult to determine the properties of the complete seam. This makes it difficult to characterize and understand the coal properties for developing ideal models for optimization of sequestration process and generating useful correlations. Therefore, in this study, reconstituted bituminous coals were used in the laboratory experiments to overcome the problem of heterogeneity. It was found that the mechanical properties of reconstituted coal like density, strength, etc. were quite homogenous as compared to the natural samples. The samples were tested for their geomechanical attributes after sustained exposure in a carbon dioxide environment. The saturated strength of coal were nearly 3–4% lesser than the strength of intact reconstituted coal specimens. This study may be very useful and extended for further investigation on coals overcoming the difficulty of the heterogeneity.

1 INTRODUCTION

Geologic sequestration of anthropogenic greenhouse gases is being viewed as one of the most feasible options for preventing their release in the atmosphere (Bachu 2002, Perera et al. 2011, Shukla et al. 2010, Vishal et al. 2013a,b). Deep seated coal seams offer opportunities for storage of carbon dioxide for geologically significant periods of time. The unmineable coal seams may have potential for production of coalbed methane (CBM). The economics analysis states that the recovery of the partly offsets the cost of CO_2 capture, compression, transport and storage. During enhanced CBM recovery, CO_2 is injected into the coal seams and is used to extract methane. Injected CO_2 reduces the partial pressure of methane and enhances its desorption from the matrix (White et al. 2005). Furthermore, CO_2 is preferentially adsorbed onto the porous surface of the coal thereby displacing methane from adsorption sites. In coals where the quantities of methane are not significant, injection of CO_2 may be carried out solely for storage purposes. Understanding the geotechnical characteristics of coal is key to successful sequestration operations. The major challenge to understand coal behaviour is due to its high anisotropy and heterogeneity. Therefore, in this study, reconstituted Indian coals were developed and the same were treated with CO_2 exposure and the changes in coal characteristics were monitored.

2 DEVELOPMENT OF RECONSTITUTED INDIAN COAL SPECIMENS

Coal samples collected from Jharia coalfield, India were stored in environment chamber to prevent any influence of atmosphere on their characteristics. The coal blocks were crushed using milling machine into fine powder. The crushed coal was passed through mechanical sieving machine. The sample powder less than mess size 60 of ASTM standard (0.250 mm) was collected and stored in sealed plastic containers. Moulds made of steel were used to develop reconstituted coal samples. A cylindrical compaction ram of appropriate dimension was fit atop the filled in mould and connected to Universal Testing Machine (UTM) from Wykeham Farrance. Compaction was achieved in one attempt by using predetermined volume of coal powder. The crushed coal along with the moulds and



Figure 1. The four cylinder moulds for the raw materials, chiefly the powdered coal and distilled water, mixed in specific proportion of weights and the freshly developed reconstituted coal specimen at a compaction load of 20 MPa.



Figure 2. Experimental set-up to develop the reconstituted coal specimens; four set of samples developed simultaneously under the UTM where the load was predefined in each case.

a freshly developed reconstituted coal specimen at 20 MPa confining pressure are shown in Figure 1. Equal amounts of coal were put in the moulds and loaded at a constant rate under constant load to develop most homogenous/uniform assembly of specimens for comparative analysis and testing (Fig. 2). Finally, the samples were extruded from the moulds and covered in plastic bags and stored in environment chambers till testing. This methodology was successfully developed and implemented by Jasinge et al. (2008, 2009) for Australian coal varieties.

3 GEOMECHANICAL CHARACTERISTICS OF RECONSTITUTED COAL SPECIMENS

The basic geomechanical characteristics of reconstituted coal (RC) specimens, developed at different loading conditions were determined. It was observed that the density and uniaxial compressive strength of coal specimens increased with increasing loading stresses. The coal specimens developed at 22 MPa and 24 MPa load were closest in terms of strength of natural coal. The RC specimens had an average density of 1.35 g/cc and 1.42 g/cc and an average UCS of 5.41 MPa and 5.88 MPa for those developed at



Figure 3. High strength steel chamber used for CO_2 saturation.

Table 1. The UCS values and changes in the UCS of saturated reconstituted coal specimens developed at 22 MPa and 24 MPa loading stresses.

RC type	22 MPa RC Type I		24 MPa RC Type II	
Condition	UCS (MPa)	ΔUCS (%)	UCS (MPa)	ΔUCS (%)
Natural	5.40		5.88	
CO_2	5.16	4.4	5.70	3.1

loading stresses of 22 MPa (referred as Type I) and 24 MPa (referred as Type II) respectively. These two varieties were chosen for further experiments on saturation behaviour of reconstituted coals in a pure CO_2 environment at a pressure of 3.0 MPa.

4 BEHAVIOUR OF RECONSTITUTED COAL SPECIMENS UNDER CO_2 SATURATION

The coal specimens developed at 22 MPa and 24 MPa loading stresses were chosen for further studies, primarily since their mechanical attributes were the closest to natural coal. Four samples of each were subjected to saturation with gaseous CO_2 for a period of three weeks using the saturation chamber as shown in Figure 3. All the samples were tested under UTM at a load displacement rate of 3.0 mm/min and failure load value was simultaneously recorded using the data acquisition system.

The average UCS values obtained for both varieties of RC specimens at natural and saturated conditions are listed in Table 1. A failed reconstituted coal specimen is also shown in Fig. 4. It was observed that CO_2



Figure 4. Failure of reconstituted coal sample under the UTM platens.

saturated samples experienced a reduction of nearly 4.4% and 3.1% in the two varieties of specimens respectively. This reduction is lower as compared to the natural coal specimens.

The less change in strength of the developed specimens due to saturation may be due to the high compaction of coal particles which leads to minimal conduits for the fluids. Hence, most of the specimens remained largely intact within while only the outer boundary seemed to be affected by the flow of CO_2. Presence of fractures allows easy passage of fluids to deep interiors of coal where the sorptive phases such as CO_2 are easily picked up by matrix carbon. This path is hindered in reconstituted specimens and hence, lesser adsorption of CO_2 takes place, leading to minimal changes in strength. The interaction of CO_2 and coal is limited in the core of the specimens; hence, the overall strength of the specimens remains intact.

5 CONCLUSIONS

This study was carried out to understand the geomechanical response of reconstituted coal specimens after saturation with gaseous CO_2. The methodology on developing RC specimens was followed to overcome the heterogeneity in coal samples. It was observed that the specimens developed at 22 MPa and 24 MPa loads respectively were closest in terms of strength and density of natural coal samples. These two varieties of RC specimens when subjected to CO_2 saturation indicated decline in strength by nearly 3–4%. This reduction in coal strength in coal is attributed to the gas sorption induced coal weakening phenomenon. For detail studies and correlation of results from one basin to another, this methodology is expected to prove useful.

REFERENCES

Bachu, S. 2002. Sequestration of carbon dioxide in geological media in response to climate change: road map for site selection using the transform of the geological space into the CO_2 phase space, Energy Conver Manag, 43(1): 87–102.

Jasinge, D., Ranjith, P.G., Choi, S.K., Kodikara J., Arthur M. & Li H. 2009, Mechanical properties of reconstituted Australian black coal, *J Geotech Geoenv Eng* 135(7): 980–985.

Jasinge, D., Ranjith, P.G., Choi, S.K. & Kodikara, J. 2008. Effect of carbon dioxide injection on the mechanical properties of synthetic brown coal, 1st Southern Hemisphere Int Rock Mech Symp, pp. 301–308.

Perera, M.S.A., Ranjith, P.G. & Peter M. 2011. Effects of saturation medium and pressure on strength parameters of Latrobe valley brown coal: carbon dioxide, water and nitrogen saturations. *Energy* 36: 6941–6947.

Shukla, R., Ranjith, P., Haque, A. & Choi, X. 2010. A review of studies on CO_2 sequestration and caprock integrity. *Fuel* 89(10): 2651–2664.

Vishal, V., Singh, L., Pradhan, S.P., Singh, T.N., Ranjith, P.G. 2013a. Analog modeling of Gondwana coal seams in India as coalbed methane reservoirs substituted for carbon dioxide sequestration. *Energy* 49: 384–394.

Vishal, V., Ranjith, P.G., Singh, T. N., 2013b, CO_2 permeability of Indian bituminous coals: Implications for carbon sequestration. *Int J Coal Geol* 105: 36–47.

White, C.M., Smith, D.H., Jones, K.L., Goodman, A.L., Jikich, S.A., LaCount, R.B. et al., 2005, Sequestration of carbon dioxide in coal with enhanced coalbed methane recovery – A review. *Energy & Fuels* 19(3): 659–724.

This page intentionally left blank

Rock Mechanics for Resources, Energy and Environment – Kwaśniewski & Łydżba (eds)
© 2013 Taylor & Francis Group, London, ISBN 978-1-138-00080-3

Adjustment of rock mass strength parameters using direct shear tests carried out on large blocks

G.J. Zapata & A.P. Assis
University of Brasilia, Brasilia, Federal District, Brazil

ABSTRACT: Due to the complex nature of rock masses, geomechanical classifications are often used to estimate indirectly strength parameters, such as the Geological Strength Index(GSI), developed by Hoek. This work intends to compare the rock mass strength parameters assessed by the GSI index with those obtained in direct shear tests carried out on large blocks. The rock mass in study is characterized by the dominant presence of carbonaceous phyllite, by the intense folding and weathering, by its ductile behavior and by presenting a dominant failure mode controlled by the rock mass properties. The tests were conducted in a servo controlled direct shear equipment on four undisturbed samples of $30 \times 30 \times 30$ cm^3. It was found that the rock mass strength parameters assessed by the GSI index were significantly conservative compared to the results of the shear tests. Based on these results, the input parameters of the generalized Hoek & Brown failure criterion were calibrated using the RocLab software.

1 INTRODUCTION

Due to the complex nature of rock masses, geomechanical classifications are often used to estimate indirectly their strength parameters, such as the Geological Strength Index (GSI).

Nowadays, this tool is globally recognized and it is widely used in the definition of projects which involve the mechanical behavior of rock masses.

However, as it is suggested on these methodologies, itis necessary to check if during the construction, the geotechnical structure behaves according to the initial predictions. Otherwise, modifications on the models must be performed in order to obtain a more realistic representation.

This work intends to verify the rock mass strength parameters assessed using the GSI index by comparing these results with those obtained in direct shear tests carried out on large blocks (large enough to be considered representative of the rock mass in study).

The rock mass in study is mainly composed by carbonaceous phyllite and its particular characteristics, described in the further sections, made possible to obtain reasonable samples, representative of the rock mass.

2 THE GENERALIZED HOEK & BROWN FAILURE CRITERION

The original Hoek & Brown failure criterion (Hoek & Brown 1980a,b) was an attempt to provide input data for analyses required in the design of underground excavations in hard rock. The criterion was derived from results of brittle failure of intact rocks performed by Hoek and on model studies of jointed rock mass behavior by Brown. The criterion starts from the properties of the intact rock and then some factors are added in order to reduce these properties according to the characteristics of the joints in the rock mass (Hoek et al. 2002).

The main contribution that Hoek and Brown made was to link the criterion to geological observations by means of rock mass classifications, choosing initially, the Rock Mass Rating published by Bieniawski in 1976. Therewith, it was possible to consider in a practical way the effect of the discontinuities on the intact rock.

However, the criterion evolved through time (Hoek 1983, Hoek 1994, Hoek & Brown 1997, Hoek 1999, Hoek et al. 2002) and it extended its application for poor and good quality rock masses. Among other enhancements, it was also introduced the Geological Strength Index as substitute of Bieniawski's rock mass classification.

The GSI index measure the quality of the structure and the discontinuities conditions of the rock mass. Currently, this index is assessed by visual inspection of the geological characteristics of the rock mass and through abacus proposed by the authors.

The GSI was initially proposed by Hoek (1994). However, it evolved through time (Hoek & Brown, 1997, Hoek et al. 1998, Marinos & Hoek 2000, Marinos & Hoek 2001, Marinos et al. 2005) in order to expand its applicability for several rock mass conditions not considered in the initial proposal.

Nowadays, the criterion is known as the generalized Hoek & Brown failure criterion and it can be applied

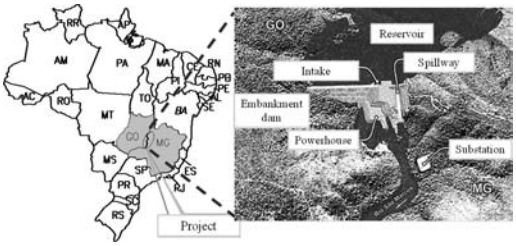


Figure 1. Location of the study area.

for the intact rock or the rock mass. The criterion is expressed as:

$$\sigma_1' = \sigma_3' + \sigma_{ci}\left(m_b\frac{\sigma_3'}{\sigma_{ci}} + s\right)^a \quad (1)$$

with

$$m_b = m_i \exp\left(\left(\mathrm{GSI}-100\right)/\left(28-14D\right)\right) \quad (2)$$

$$s = \exp\left(\left(\mathrm{GSI}-100\right)/\left(9-3D\right)\right) \quad (3)$$

$$a = \frac{1}{2} + \frac{1}{6}\left(\exp^{-\mathrm{GSI}/15} - \exp^{-20/3}\right) \quad (4)$$

where σ_1' and σ_3' are the major and minor effective principal stresses at failure; σ_{ci}' is the uniaxial compressive strength of the intact rock; m_b, a and s are the rock mass strength parameters; m_i is an intact rock strength parameter; GSI is the Geological Strength Index; D is a factor which measures the disturbance of the rock mass due blast damage and stress relaxation.

Furthermore, from the generalized Hoek & Brown failure criterion it is possible to obtain equivalent Mohr-Coulomb cohesion (c′) and friction angle (ϕ') for the rock mass (Hoek 1990, Hoek 1994, Hoek & Brown 1997). Currently, this is done by fitting an average linear relationship to the curve generated by solving Equation 1 for a range of minor principal stress values. The maximum value of this range is calculated according to the type of application defined by the authors: general, slopes and tunnels.

In this work the equivalent Mohr-Coulomb strength parameters are set for applications in slopes. This demands, additionally, the definition of the unit weight (γ) of the rock and the height of the slope (H).

3 DESCRIPTION OF THE STUDY AREA

The rock mass in study is part of a hydropower station located in San Marcos River, between the states of Minas Gerais and Goias, Brazil (Fig. 1).

The hydroelectric is projected to have 52 MW of installed capacity. It forms a reservoir covering a surface area of 138 km^2, with a storage capacity of 1782 million m^3 of water.



Figure 2. General view of the rock mass in study.

The hydroelectric is composed by a concrete dam located on the left side of the river (with the direction going from upstream to downstream). On the right side, there is a geotechnical embankment dam with a maximum height of 50 m.

The rock mass in study is the one located on the left side of the river, which sustain the concrete dam and their respective structures, like spillway, powerhouse, hydraulic circuits etc.

These structures involve superficial excavations (i.e. slopes) and underground excavations (i.e. tunnels and caverns) in the rock mass. Consequently, a good characterization of the rock mass is important, as it is the basis for defining several aspects of the project, such as the kind and the quantity of support, the sequence of the excavation etc.

3.1 *Geology*

The rock mass in study presents three main litotypes. All of them are classified as metamorphic rocks and they are referred to as phyllite, carbonaceous phyllite and quartzite. However, it is noticed a dominant presence of carbonaceous phyllite.

All litotypes present foliation, characterized by the preferential arrangement of minerals which confers certain anisotropy in the rock.

Historical tectonic events of extension and compression which took place in the region developed intense folding and high level of fracture in the rock mass. The Figure 2 shows a general view of the rock mass in study.

Also, this rock mass is highly weathered. Even in some cases, the rock can be broken manually (Fig. 3). This is product of the intensetropical weathering of the region and the proximity of the rock mass to the San Marcos river course.

Several kinds of discontinuities can be identified in the rock mass (joints, foliations, foldings etc.). Still, it was defined that only the foliation can represent a threat to the stability of the slopes.

Therefore, considering the particular characteristics of the rock mass, two possible failure mechanisms were established in the slopes of the rock mass.



Figure 3. Highly weathered carbonaceous phyllite.

The first one occurs when the direction given by the foliation is unfavorable with respect to the excavation face. In that case, the strength properties of the discontinuities given by the foliation will govern the failure mechanism, possibly generating planar or wedge type of failure.

The second one takes place when the direction of the foliation it is such that does not represent any threat to the slope stability. In other words, the failure mechanism is not controlled by the discontinuity. In this case, the rock mass properties govern the failure mechanism, possibly generating a circular type of failure. In this case it is possible to estimate the rock mass strength parameters using the GSI index.

However, considering the high variability of the direction of the foliation due to the intense folding, the highly weathered condition of the rock mass and its ductile behavior, it is conclude that the second type of failure is dominant in the rock mass.

4 INTACT ROCK CHARACTERIZATION

Visually, the carbonaceous phyllite is characterized by presenting a grey to dark-grey color and foliation. In the ABGE (1998) system, the rock has a weathering level of C3/A3. This means that the rock has a poor coherence and that is intensely altered. In other words, this rock is highly weathered and tends to have low mechanical properties.

X-ray diffraction tests performed in a diffractometer SIEMENS, model D5000, revealed the mineralogical composition of the rock. Thus, the main mineral of the rock is quartz and the secondary minerals are kaolinite and muscovite.

Different types of tests were performed in order to characterize several properties of the rock. Those tests were executed in Furnas laboratory, located in Aparecida de Goiânia, Goiás, Brazil, by trained technicians and following the ISRM (2007) recommendations and the ASTM norms.

The properties obtained for the intact rock characterization are: porosity, absorption of water, dry density, saturated density, void ratio, velocity of the longitudinal wave, dynamic Young modulus, perpendicular point load index, parallel point load index, point load anisotropy index, Unconfined Compressive Strength (UCS) and secant Young modulus. In Table 1, all information related to the intact rock properties is gathered.

Table 1. Intact rock properties.

Properties	# of tests	Mean	Standard deviation
Porosity, n (%)	3	15.7	1.5
Absorption of water (%)	3	7.0	0.8
Dry density, ρ_d (kg/m^3)	3	2250.1	58.3
Saturated density, ρ_s (kg/m^3)	3	2407.1	54.6
Void ratio, e	3	0.19	0.02
Velocity of P-wave, v_p (m/s)	6	809.0	214.7
Dynamic Young modulus (GPa)	6	1.58	0.88
Parallel point load index, $I_{s(50)\ //}$ (MPa)	3	0.32	0.05
Perpendicular point load index, $I_{s(50)\ \perp}$ (MPa)	3	0.39	0.35
Point load anisotropy index, $I_{a(50)}$	–	1.10	–
UCS, σ_{ci}(MPa)	4	3.85	1.09
Secant Young modulus, E_s (GPa)	4	0.32	0.08

With exception of the point load test, no tests were conducted defining a particular angle between the direction of the foliation and the load application. However, as observed, the point load anisotropy index is very close to the unity, indicating that the rock material tends to behave as isotropic for this level of weathering. According to the ISRM (1981) classification, this rock has a poor anisotropy. Also, according to the UCS value and the ISRM (2007), this rock is classified as a weak rock.

5 ROCK MASS STRENGTH ASSESSED BY THE GSI INDEX

In this section, the rock mass strength parameters are estimated using the GSI index. So, both Hoek & Brown and Mohr-Coulomb rock mass strength parameters are assessed. As stated before, the equivalent Mohr-Coulomb strength parameters are set for slopes applications. The assessment of the rock mass strength parameters was performed with help of the software RocLab, created by the Rocscience.

Initially, the input parameters of the generalize Hoek & Brown criterion must be defined. Thus, the basic parameters required are: σ'_{ci}, m_i, D, GSI, γ and H.

The unconfined compressive strength is defined according to the value reported in Table 1, so $\sigma'_{ci} = 3.85$ MPa. Due to the lack of triaxial tests in the intact material it was not possible to obtain directly the m_i parameter. However, Marinos & Hoek (2000) show a list of suggested values of this parameter for different types of rock. Thus, for phyllites $m_i = 7 \pm 3$. Also, taking into consideration the good quality of blasting

Table 2. Rock mass strength parameters.

Input	Value	Output	Value
σ_{ci} (MPa)	3.85	σ'_{3max} (MPa)	0.46
GSI	30	m_b	0.21
m_i	10	s	3.93E-05
D	0.7	a	0.52
γ (kN/m^3)	24.0	c′ (kPa)	50.32
H (m)	30	ϕ' (°)	19.49

performed on the rock mass in study and following the guidelines proposed by Hoek (2007), the disturbance factor is defined as $D = 0.7$.

According to the abacus proposed by Marinos & Hoek (2000), the rock mass can be fit in the intersection region defined by the category blocky/disturbed/seamy structure and poor discontinuities conditions. Consequently, the Geological Strength Index can be defined as GSI $= 30 \pm 5$. These categories describe the rock mass as folded, highly weathered, highly fractured and with persistence of schistosity. Those descriptions have a good fit with the observed geological conditions of the rock mass.

The unit weight of the rock is defined according with the value reported in the Table 1, so $\gamma = 24$ kN/m^3. The height of the slope is defined as $H = 30$ m. This height value can be considered representative for several slopes in this rock mass.

Thus, with the input parameters defined, initially the sensibility of the equivalent Mohr-Coulomb strength parameters in relation to the GSI and the m_i is determined. Subsequently, a representative rock mass strength envelope is defined for comparative purposes with the laboratory tests.

Figure 4 shows the rock mass equivalent cohesion and friction angle, and their behavior depending on the GSI and the m_i parameter. It is observed that the variation of the equivalent cohesion is about 28–59 kPa and the variation of the internal friction angle is 12–22°.

A representative rock mass strength envelope is selected taking GSI $= 30$ and $m_i = 10$. These are typical values adopted in this project.

The Table 2 gathers the input and output parameters generated by the RocLab software. The output data shows the rock mass strength parameters estimated for the Hoek & Brown and the equivalent Mohr-Coulomb criterion. The Figure 5 shows the plot of the envelope for both failure criteria.

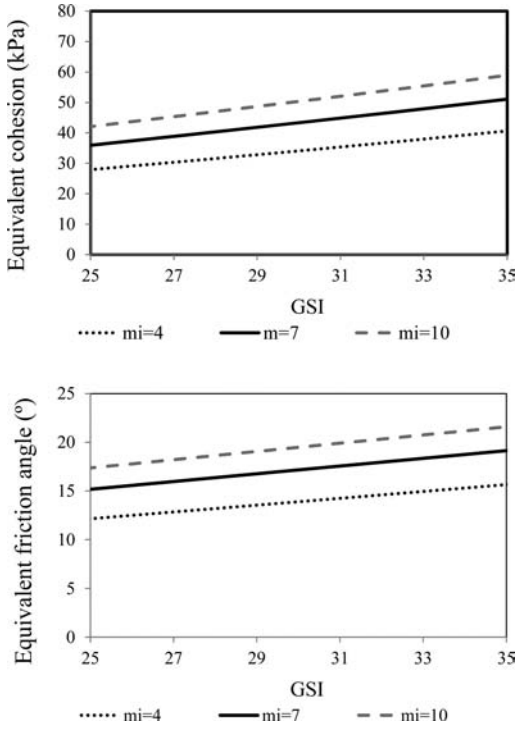


Figure 4. Equivalent cohesionand internal friction angle for different GSI and m_i values.

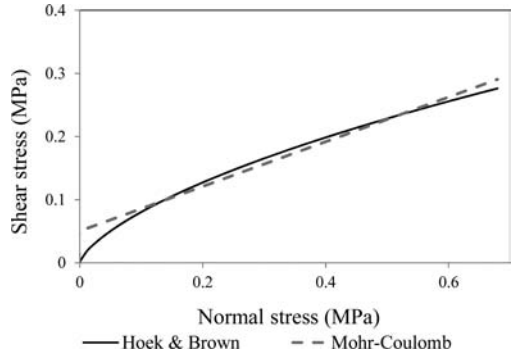


Figure 5. Rock mass strength envelopes: Hoek & Brown and Mohr-Coulomb.

6 ROCK MASS STRENGTH ASSESSED BY DIRECT SHEAR TEST ON LARGE BLOCKS

The shear test was performed in undeformed blocks of carbonaceous phyllite with dimensions of approximately $30 \times 30 \times 30$ cm^3 (Fig. 6).

Taking into account the particular characteristics of the rock mass, it could be considered that this size of sample is representative of the rock mass.

The test was performed at Laboratory for rock mechanics in Furnas and following the ASTM D5607.

The test was executed in a servo-controlled equipment with a maximum capacity of 490 kN of normal load and 980 kN of shear load (Fig. 7). The shear load was applied perpendicular to the foliation and with a speed of 0.2 mm/min. The normal stresses applied were approximately 200, 400, 800 and 1600 kPa. The specimens were submitted to immersion in water for at least 24 h.

The Figure 8 shows the relation between shear stress and horizontal displacement in the four samples.

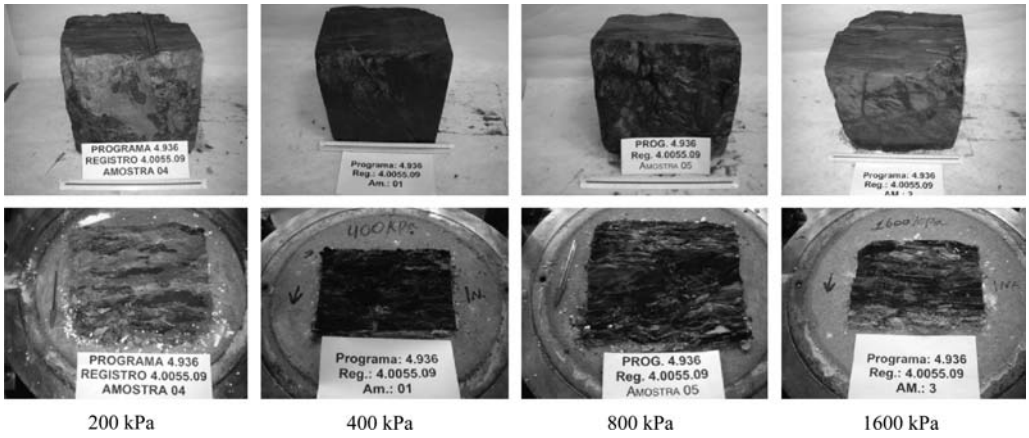


Figure 6. Cubic samples for the shear test, before and after the test; and their respective normal load.



Figure 7. Shear test equipment.

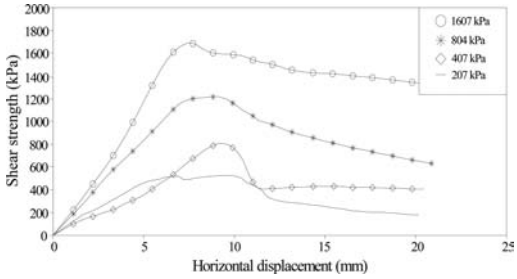


Figure 8. Shear stress vs. horizontal displacement.

The Figure 9 shows the peak and residual envelopes. From the results, it can be observed a friction angle of 39° and cohesion of 485.7 kPa. These values are taken as the experimental rock mass strength parameters.

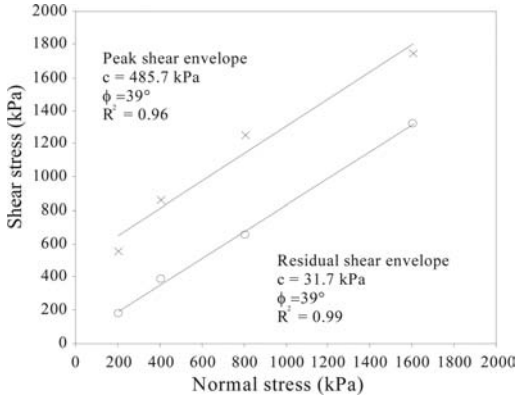


Figure 9. Experimental rock mass strength envelope.

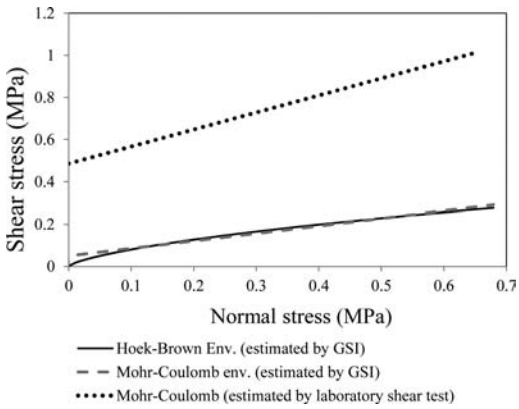


Figure 10. Comparison between the rock mass strength parameters assessed via GSI index and via laboratory shear test.

7 COMPARISON BETWEEN RESULTS AND CALIBRATION OF PARAMETERS

The Figure 10 shows the comparison between the rock mass strength envelopes obtained via GSI and via laboratory shear tests. It can be observed that the rock mass strength parameters assessed by the GSI index were significantly conservative compared with those obtained in the shear tests.

Also, based on the results, the input data of the generalized Hoek & Brown criterion were calibrated using

Table 3. Input parameters calibrated and resultant rock mass strength parameters.

Input	Value	Output	Value
σ_{ci} (MPa)	3.85	σ'_{3max} (MPa)	0.57
GSI	91	m_b	4.11
m_i	6	s	0.33
D	0.3	a	0.5
γ (kN/m^3)	0.024	c′ (kPa)	487.0
H (m)	30	φ' (°)	39.00

the RocLab software. Thus, it was possible to obtain a strength envelope similar to that obtained in the direct shear tests.

The calibration was performed only in the GSI, m_i, and D parameters. These values were modified until a good approximation to the Mohr-Coulomb parameters obtained in the laboratory test was reached. Table 3 shows the calibrated input data and the resultant rock mass strength parameters obtained from the generalized Hoek & Brown criterion.

8 CONCLUSIONS

Due to the complex nature of rock masses, empirical geomechanical classifications are often used to estimate indirectly their strength parameters. However, further verification and investigation must be performed in order to obtain more accurate parameters.

This paper shows the estimation of the rock mass strength parameters following the methodology proposed by Hoek and coworkers. These parameters were compared to those obtained in laboratory shear tests performed in representative samples of the rock mass. It was observed that the strength parameters assessed by the GSI index were significantly conservative compared to those obtained in the shear tests.

Since the rock mass strength parameters are the basis for defining aspects like kind and quantity of support, slope models can be redefined taking into account these experimental values and the project can be benefited in terms of economy, time and safety.

ACKNOWLEDGEMENTS

The authors would like to acknowledge the support given by Brazilian research organizations CAPES, CNPQ, FINATEC and University of Brasília. Also, to the Furnas Rock Mechanics laboratory that allowed access into the project database and made possible this academic analysis.

REFERENCES

ABGE. 1998. Geologia de engenharia. Associação brasileira de geologia de engenharia, M.S. Santos, & N.A. Alves (Eds.), São Paulo, Brasil, pp. 211–226.

Hoek, E. & Brown, E.T. 1980a. *Underground Excavations in Rock.* London: Institution of Mining and Metallurgy.

Hoek E. & Brown, E.T. 1980b. Empirical strength criterion for rock masses. *J. Geotech. Engng Div., ASCE* 106(GT9): 1013–1035.

Hoek, E. 1983. Strength of jointed rock masses. 23rd. Rankine Lecture. *Géotechnique* 33(3): 187–223.

Hoek, E. 1990. Estimating Mohr-Coulomb friction and cohesion values from the Hoek-Brown failure criterion. *Int. J. Rock Mech. Min. Sci. & Geomech. Abstr.* 12(3): 227–229.

Hoek E. 1994. Strength of rock and rock masses. *ISRM News Journal* 2(2): 4–16.

Hoek E. & Brown, E.T. 1997. Practical estimates of rock mass strength. *Int. J. Rock Mech Min Sci.* 34(8): 1165–1186.

Hoek, E., Marinos, P. & Benissi, M. 1998. Applicability of the Geological Strength Index (GSI) classification for very weak and sheared rock masses. The case of the Athens Schist Formation. *Bull. Eng. Geol. Env.* 57(2): 151–160.

Hoek, E. 1999. Putting numbers to Geology – an Engineer's Viewpoint. The Second Glossop Lecture. *Quarterly Journal of Engineering Geology* 32(1): 1–19.

Hoek E., Carranza-Torres C. & Corkum B. 2002. Hoek-Brown criterion – 2002 edition. Proc. NARMS-TAC Conference, Toronto, 2002, 1: 267–273.

ISRM, 1981. *Rock Characterization, Testing and Monitoring. ISRM Suggested Methods.* Oxford: Pergamon Press.

ISRM, 2007. *The Complete ISRM Suggested Methods for Rock Characterization, Testing and Monitoring: 1974–2006.* R. Ulusay & J.A. Hudson (eds), 628 p.

Marinos, P. & Hoek, E. 2000. GSI – A geologically friendly tool for rock mass strength estimation. Proc. GeoEng2000 Conference, Melbourne, pp. 1422–1442.

Marinos, P. & Hoek, E. 2001. Estimating the geotechnical properties of heterogeneous rock masses such as flysch. *Bull. Eng. Geol. Env* 60: 85–92.

Marinos, V., Marinos, P. & Hoek, E. 2005. The geological Strength index: applications and limitations. *Bull. Eng. Geol. Environ* 64: 55–65.

Rock Mechanics for Resources, Energy and Environment – Kwaśniewski & Łydżba (eds)
© 2013 Taylor & Francis Group, London, ISBN 978-1-138-00080-3

Determination of the extent of fractured zones around mine openings using the resistivity and GPR methods

B. Żogała, M.J. Mendecki & W.M. Zuberek
Faculty of Earth Sciences, University of Silesia in Katowice, Sosnowiec, Poland

T. Gołębiowski & W. Antonik
Faculty of Geology, Geophysics and Environmental Protection, AGH University of Science and Technology, Kraków, Poland

ABSTRACT: The goal of research was to determine the spatial distribution of the fractures and to recognize the electric properties of the rock mass around the mining openings in the O/ZG "Polkowice – Sieroszowice" underground copper mine (the Lower Silesian region, Poland). The measurements were carried out with the multielectrode resistivity ABEM Lund Imaging system and georadar equipment produced by MALA Geoscience.

The measurements were conducted on the side walls of the two selected mining openings, i.e. inclined drift A5F and dip road D2. On each side wall 3 measurement profiles of the 40 m length were designed. The profiles were located in the lower, middle and upper parts of the side walls.

Applying inverse combined algorithm the resistivity changes were recognized to the depth of approx. 8 m from the side walls. The results of resistivity imaging have indicated the occurrence of the increasing resistivity zones in the vicinity of the side walls. They can be related to the fractured and loose zones of the rock mass. The obtained resistivity values change in the range from approx. 15 Ωm to over 100 Ωm. It has also been observed that the depth of the fractured zones changes and depends on the side walls height. In the both openings the fractured zones extensions increased up to 6–7 m of depth near the roofs and were the lowest near the floors, reaching 2–3 m. The deeper, not disturbed zones of the rock mass showed the resistivity below 10 Ωm.

The GPR reflection measurements with the use of 500 MHz and 250 MHz antennas delivered information about fractured zones distribution to the depth of 5.0 m and 10.0 m, respectively. The results of measurements obtained for the both antennas were similar, therefore in the paper only recordings for 250 MHz antenna are presented. The results of GPR surveys were correlated to the depth of about 8 m with the results obtained for the resistivity method. The majority of fractures has been located by the GPR method near the openings' roofs in this way confirmed the results from the resistivity method.

1 INTRODUCTION

The aim of the geophysical research was analysis of ability of resistivity imaging (RI) and georadar reflection technique (GPR) application for detection of natural fractured zones surrounding openings and fractures induced by mining activity. Due to the fact that the GPR and RI methods base on different physical fields, therefore in the interpretation only some regions with anomalies may be correlated for both methods and so-called quantitative interpretation may be carried out.

The georadar and the resistivity imaging surveys were carried out in two galleries chosen by the O/ZG "Polkowice-Sieroszowice" copper mine (belonging to the KGHM Polska Miedź S.A. mining company), i.e. in the inclined drift A5F, region SR-14 (Fig. 1a) and in the dip road D2, region Jm-21 (Fig. 1b).

2 SURVEY METHODS

2.1 Resistivity imaging

The resistivity measurement (for more details see: Binley and Kenmna, 2005; Cegrell and Martensson 2008; Loke, 2004; Telford et al. 1990), were carried out by the 41-electrodes imaging system created by Swedish firm of ABEM Lund (www.abem.se). The equipment consists of SAS4000 terrameter, electrode selector, multicore cables and stainless steel electrodes. Relative length of profiles was 40.0 m with minimum electrode spacing 1.0 m. Data were collected by SAS4000 terrameter which allowed to set measurement parameters such as: maximal direct current: 200 mA, minimal direct current 10 mA, numbers of stacks: 2–4, average value: median, acquisition time 0.5 s, delay time 0.2 s. During survey the Wenner-Schlumberger array was applied.

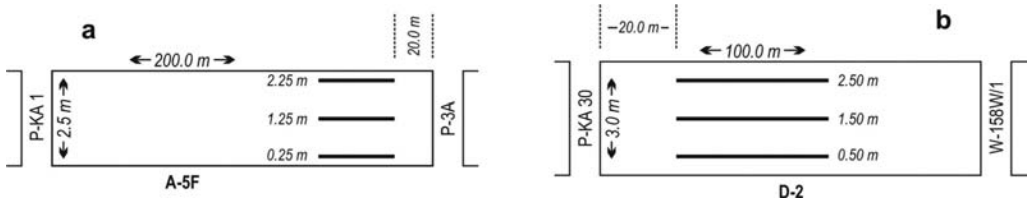


Figure 1. Location of survey profiles on the side walls: (a) the inclined drift A5F, region SR-14 and (b) the dip road D2, region Jm-21. Thick black horizontal lines indicate the location of profiles, the number near the profile is its distance from the floor.

2.2 *Ground Penetrating Radar*

The georadar method (GPR) is a geophysical method which uses of electromagnetic waves in the frequency range from 10 MHz to a few GHz. This method is used for non-invasive detection of underground objects (among them, fractures) and geological structures. The standard technique of terrain surveys is constant-offset reflection profiling (Annan, 2001) and this measurement technique was applied for collection of presented data. The GPR surveys were carried out with the use of multi-channel, digital georadar PROEX produced by Swedish firm of MALA Geoscience (www.malags.se). For measurements the antenna with frequency of 250 MHz (max. depth penetration equals 10 m and mean resolution equals 0.1 m) was used (MALA 2003).

Measurements along the profiles were conducted with constant distance interval $\Delta x = 0.05$ m. The results of GPR surveys were correlated to the depth of about 8 m with the results obtained for resistivity imaging method, which was conducted on the same profiles. For GPR measurements 100-metres-length profiles were designed and surveys using of RI technique were carried out only from $x = 204$ m to $x = 60$ m of the selected profiles; therefore, correlation of the results obtained for both methods was carried out for 40-metres-length profiles (Figs 1a, 1b).

3 DATA PROCESSING

3.1 *Resistivity inversion*

The resistivity data were processed in Res2Dinv software (Loke, 2004; www.geotomosoft.com). Apparent values of resistivity were converted into true values by an application of the combined inversion technique which uses solutions from the Marquardt – Levenberg algorithm and smooth-constrained least square method. The inversion algorithm is solved iterative. In this case the algorithm was stopped on 5th iteration, if RMS error decreased below 5%.

3.2 *GPR data processing*

All radargrams presented in the paper were shown in a normalized form, i.e. normalization to max. amplitude of so-called Direct Air Wave was applied. For better visualization of anomalies in the radargrams exaggeration of vertical axis was used. All radargrams were processed digitally with the use of computer program ReflexW, delivered by SandmeierGeo firm (ReflexW 2012). Time-depth conversion of radargrams was carried out for mean velocity adequate for rocks in the surveys sites, i.e. $v_{mean} = 0.12$ m/ns.

4 RESULTS

4.1 *The inclined drift A5F, region SR-14*

In general, three different zones can be distinguished on all resistivity cross-section presented in this paper. The highest resistivity zone with values greater than 40 Ωm is observed near the surface of side wall of the gallery. The second zone can by marked as an area with resistivity values range of 10–40 Ωm and is located deeper, behind the high-value zone. Considering resistivity values of these two areas and sxtent of its occurrences, it can be assumed that they are related to the fractured zone with different intensity of cracking (Schön, 1996). The last zone which is characterized by the lowest values of resistivity (less than 10 Ωm) is located deeper and probably is connected to non-cracked rock mass.

Resistivity imaging results (Figs 2A, 2C and 2E) show a change in horizontal zones of fracturing and color scale indicates a change in their intensity (because higher resistance values are associated with more cracked area). Some similarities can be noticed in Figures 2B, 2D and 2F where horizontally correlated reflections may be distinguished. They deliver information about course of main fractures in the rock mass generated by mining activity. Analyzing resistivity results from region SR14 (Figs 2A, 2C and 2F) it can be found that mentioned zones are observed on all profiles but the range of the first two zones is decreasing with height. The same feature may be noticed in radargrams recorded in the same region SR-14 where the decrease of high amplitude anomalies (Figs 2B, 2D and 2F – red and black colours) in the successive radargrams from the roof profile to bottom one is also observed.

Near the excavation roof, the fracture zone is the most developed (Fig. 2A). The range of high resistivity (>15 Ωm) zone on distance from the side wall to interior of the rock mass (z-axis) is up to 5–6 m. This boundary is not linear. Also the highest resistivity anomaly (>40 Ωm) is distinct in the cross-section

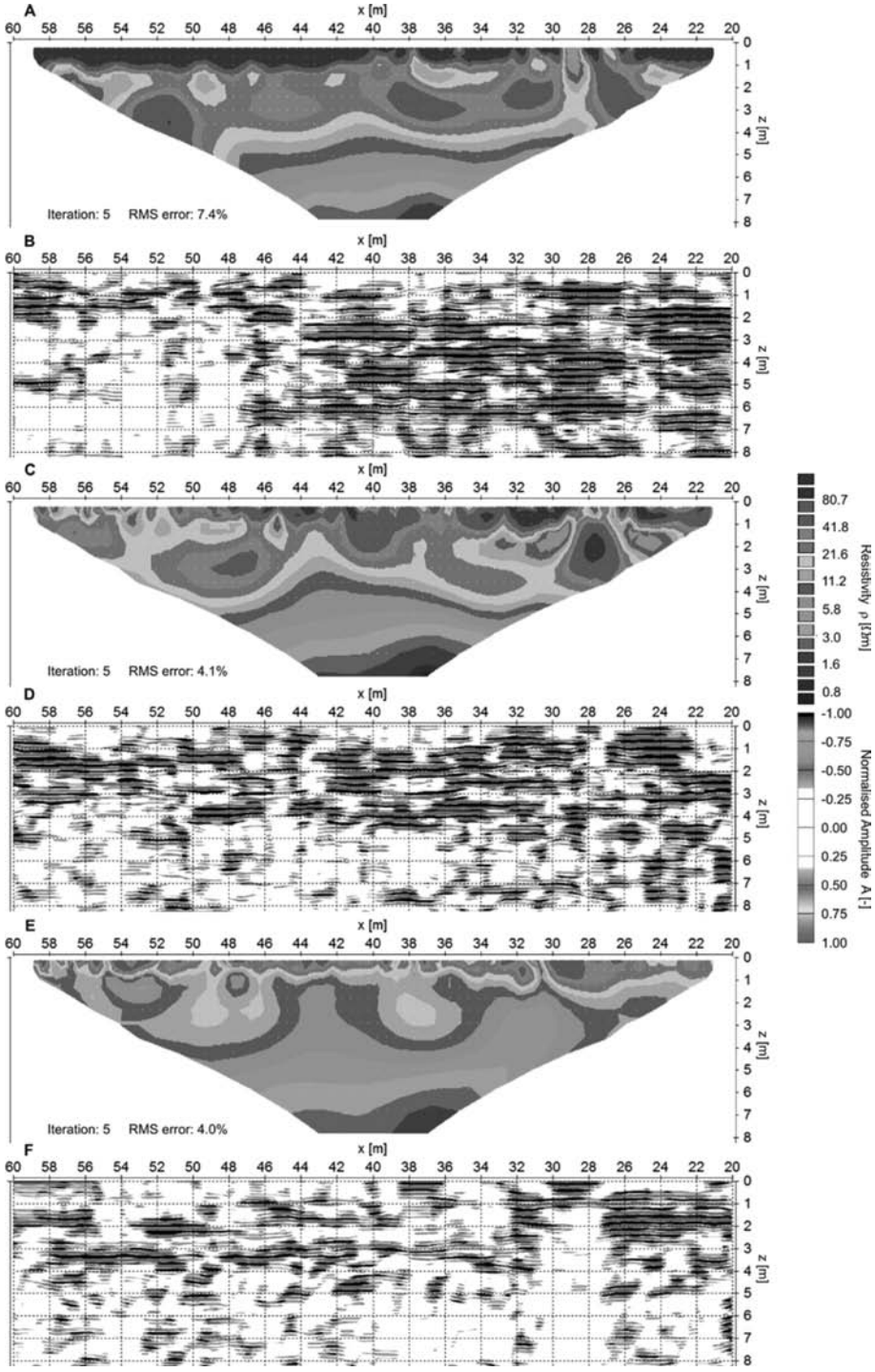


Figure 2. The results of geophysical surveys carried out in the side wall of the inclined drift A5F, in region SR-14, along: profile by the roof for RI technique (A) and GPR method (B), profile in the middle of excavation for RI technique (C) and GPR method (D), profile by the floor for RI technique (E) and GPR method (F).

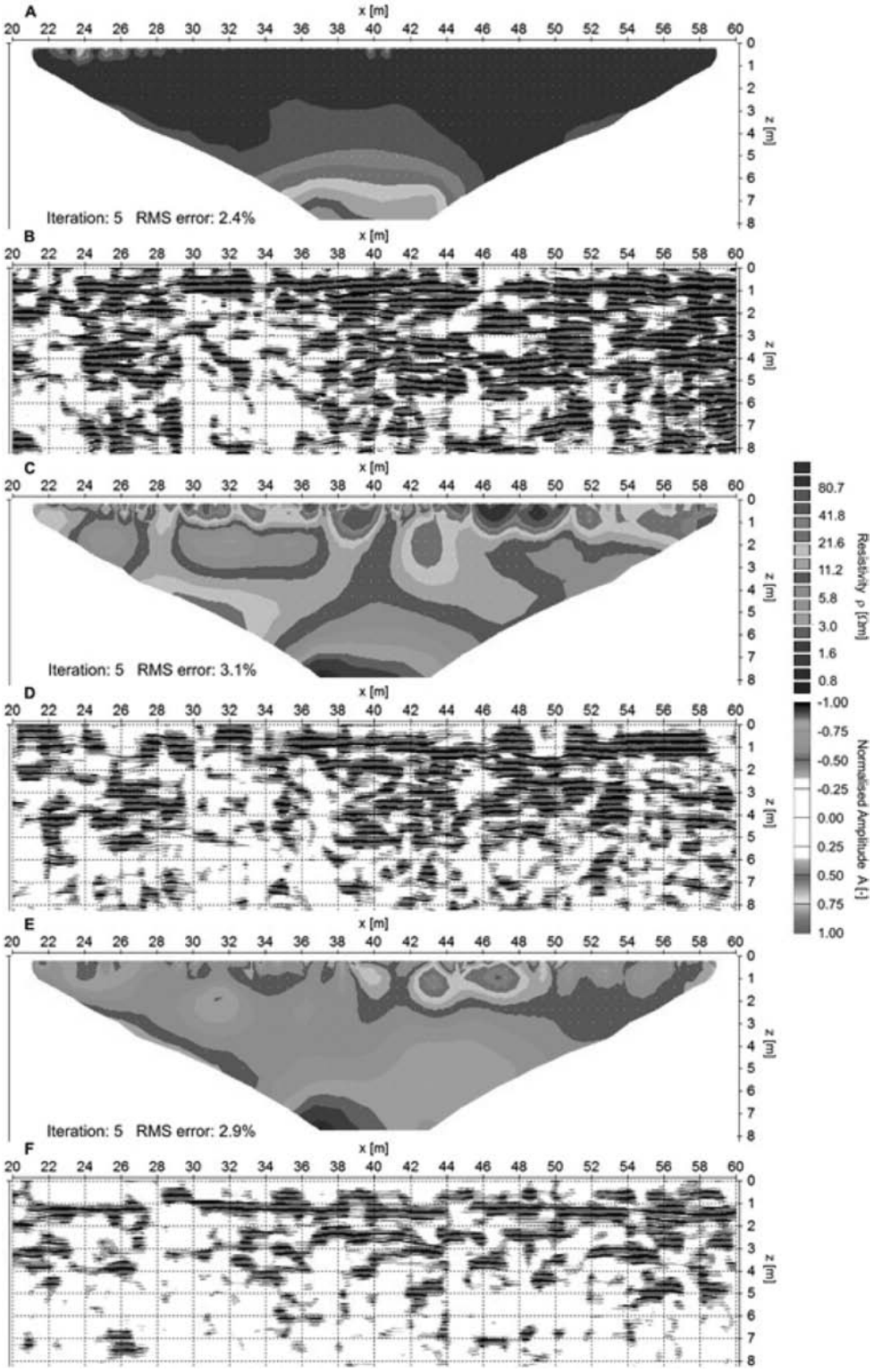


Figure 3. The results of geophysical surveys carried out in the side wall of the dip road D2, in region Jm-21, along: profile by the roof for RI technique (A) and GPR method (B), profile in the middle of excavation for RI technique (C) and GPR method (D), profile by the floor for RI technique (E) and GPR method (F).

near the excavation roof. This is thin, cracked and loose zone which had been observed during the survey near to excavation roof. In the mine this loose rock zone can generate rockslides which can be danger for miners. However, this shallow zone is not noticed in Figure 2B, but high amplitude reflections to the depth "z" equals about 7 m are recorded; deeper a slight decrease of amplitudes of reflections may be also noticed as it is observed on the RI cross-section, so it might be assumed that the range of the fractured zone in the excavation roof was equal c.a. 7 m.

Comparing the middle resistivity profile (Fig. 2C) to the roof resistivity profile (Fig. 2A) some similar anomalies can be found. The boundary between fractured and non-cracked zones is irregular and it stretches at the depth 4–5 m. The GPR result confirms it, because high amplitude zones, interpreted as fractured zones, in the middle of excavation have similar distribution along the whole profile (Fig. 2D) and depth range of fractures is equal as RI interpreted depth. At the beginning of the profile, between $x = 20.0$ m and $x = 36.0$ m additional anomalies in deeper part of the rock mass were recorded; they origin from the highly fractured geological medium and concentration of fractures in this part of rock mass is caused by the presence of crossing of excavations at $x = 0.0$ m. An influence of crossing of excavations on the fractures distribution is also clearly visible in Figure 2B where high amplitude reflections are recorded at the beginning of radargram, up to $x = 47.0$ m.

Analysis of anomalies distribution in Figures 2E and 2F allows to interpret thickness of fractured zone generated by mining activity; fractures spread from the side wall to depth of about 3–4 m on both cross-sections. Resistivity imaging RI (Fig. 2E) shows the same pattern of higher resistivity anomalies as these which are observed on the other sections (Figs 2A, 2C) from this side wall. Additionally high amplitude reflections, originated from fractures located by the crossing of excavations, are visible up to distance $x =$ 37.0 m and to the depth $z = 3.0$ m.

4.2 *The dip road D2, region Jm-21*

General characteristic of anomalies distribution in the geophysical recordings in region Jm-21 (Figs 3A-F) is the same that described for region SR-14; high resistivity anomalies and high amplitude reflections in the excavation roof are caused by highly fractured rock mass and moving towards the floor of the dip road fractures disappear.

Resistivity cross-section at the excavation roof consists of high-fractured area which covers almost all sections (Fig. 3A). Only at the depth about 7 m the low resistivity zone can be noticed and it is probably connected to non-cracked rock. Besides, the high resistivity zone has a characteristic pattern from $x = 26.0$ m to $x = 34.0$ m which can be compared with GPR result for the roof profile, presented in Figure 3B, where in a vertical strip from $x = 29.0$ m to $x = 37.0$ m a decrease of amplitudes of reflections is easily observed. This can be related to an effect of less fractured rock mass. A similar strip may be noticed between $x = 20.0$ m and $x = 24.0$ m; small areas of solid rock mass (Fig. 3B – white areas) are located also in the second part of the profile. But these GPR anomalies cannot be compared with the resistivity section, because survey geometry did not cover the utmost parts of measured profile.

Sections from the middle part of side wall (Figs 3C and 3D) present lower values of increased resistivity anomalies and also lower high amplitude reflections. It might be assumed that fractures reached to the depth of about 4–5 m when we compare result from the middle profile to the roof profile (Figs 3A and 3B). Between depths $z = 1$–5 m and in the vertical strip from $x = 29.0$ m to $x = 38.0$ m the low fractured zone may be interpreted more clear (Fig. 3C – light green area and Fig. 3D – white area). This low fractured anomaly correlated with the same area in the roof sections. The resistivity anomalies indicate that intensity of fracturing is lower than in drift A5F, region SR-14.

In Figures 3E and 3F the concentration and depth range of fractures is much lower than in previous profiles. Resistivity imaging RI shows that fractured zones almost disappear, only in the vertical strip section from $x = 40.0$ m to $x = 60.0$ m relative high resistivity anomalies can be observed up to $z = 3.0$ m depth. Moreover, georadar linear anomalies located at $z = 1.5$ m depicted at continuous crack close by the side wall and GPR amplitudes indicate fractured zone extension up to about 2–3 m depth.

5 CONCLUSIONS

Comparison of the results of resistivity imaging and ground penetrating radar has enabled to investigate the changes in the cracked rock area surrounding the excavation side wall. However, due to the fact that GPR and RI methods base on different physical fields, the study shows that in the interpretation only some regions with detected anomalies may be correlated for both methods. It cannot be excluded that some of the resistivity anomalies, unconfirmed by the GPR, are caused by changes in lithology, which in turn is not clearly visible on radargrams and vice versa.

The unknown is also the distribution of humidity appearing in rock mass which can influence resistivity values and GPR amplitudes.

Nevertheless, the research points it out that the horizontal range of the fractured zone in the rock changes with the height of opening. Near the excavations' roofs the rock mass is more cracked than near the floor. This result can be related to the stress distribution of the rock mass surrounding the opening. Future research also can focus on quantitative calculation of intensity of fracturing using information obtained from resistivity values and from georadar signals amplitudes. Knowledge of fractured zone extent and intensity of fracturing might be useful information for future design of exploitation and for rockburst prevention.

ACKNOWLEDGEMENTS

The work performed under the agreement No.: KGHM-KP-U-0340-2011 (AGH-UST agreement No.: 5.5.140.096).

REFERENCES

Annan, A.P. 2001. *Ground Penetrating Radar – Workshop Notes*. *Sensor & Software company*, Mississauga, Canada.

Binley, A. & Kenmna, A. 2005. DC Resisitivity and Indcuced Polarization Methods. In Y. Rubin & S.S. Hubbard (eds), *Hydrogeophysic*, 129–156, 50, Springer.

Cegrell, M. & Martensson, J. 2008. *Resistivity and IP measurements at the Bolmen Tunel and Adalsbanan, Sweden*. No 231 (*master thesis*) Departament of Geology Lund University, Sweden.

Loke, M.H. 2004. *Tutorial: 2-D and 3-D electrical imaging surveys*. www.geoelectrical.com.

MALA 2003. *Basic and Advance Radar Theory*. Mala GeoScience AB, Sweden.

ReflexW 2012. *User Manual*. SandmeierGeo firm, Karlsruhe, Germany.

Schön, J.H. 1996. *Physical Properties of Rocks: fundamentals and principles of petrophysics*. Pergamon Press Oxford.

Telford, W.M., Geldart, L.P. & Sheriff, R.E. 1990. *Applied Geophysics*. Cambridge University Press, Second Edition.

Website: www.malags.se

Website: www.abem.se

Website: http://www.geotomosoft.com

2. Laboratory and in-situ testing

This page intentionally left blank

Rock Mechanics for Resources, Energy and Environment – Kwaśniewski & Łydżba (eds)
© 2013 Taylor & Francis Group, London, ISBN 978-1-138-00080-3

On the accuracy of the in-situ Schmidt hammer test on carbonate rocks

H. Arman, W. Hashem, O. Abdelghany & A. Aldahan
United Arab Emirates University, Al-Ain, UAE

ABSTRACT: The handy and practical Schmidt Hammer (SH) has been used for both in-situ and laboratory measurements of hardness and estimate of the Unconfined Compressive Strength (UCS) of rocks. Geological features such as structure, texture and mineralogy influence the mechanical properties of rock masses and these factors should be carefully evaluated for each testing location. In the work presented here, a case study was chosen to demonstrate and discuss the effectiveness of particular geological circumstances on in-situ SH test results concerning different carbonate rocks. Three different types of limestones, chalky, marly and dolomitic are available in the Tertiary carbonate sequences at the studied area which is Jabal Hafit, south of Al Ain city, United Arab Emirates (UAE). The results clearly show that rapid changes in carbonate rocks structure, texture and even mineralogy always create problems in generalizing the mechanical properties which are essential parameters in geological and engineering practices.

1 INTRODUCTION

The measurement of rock strength and characteristics of discontinuities (mainly fractures) are essential tasks in engineering constructions. In general, rock strength is defined as the ability to withstand stress or deformation; the quality of bodies by which they endure the application of force without breaking. In engineering terms, rock strength may be defined as the inherent strength of an isotropic rock under specific conditions – notably wet or dry. However rock masses are anisotropic and as a consequence, the strength of rocks is influenced both by the presence of impurities, weak zones and/or discontinuities (Hawkins 1998). Carbonate rocks represent large exposure of rock masses in the United Arab Emirates (UAE) and are targeted in the study presented here.

Rapid (on meter scale) changes in carbonate rocks structures (layering, fractures, faults, folds), texture (grain size, fossil content, cementation, dissolution) and even mineralogy (dolomitization, percent of clay minerals, silicification) have always created problems in generalizing an overall bulk physical properties such as rock strength, porosity and permeability. Thus, mass homogeneity may only exists at small scale (a few decimeter cubes) and rock failure problems are faced by the oil companies, construction engineering companies and environmental agencies when the size of the rock mass gets larger. The results of such rapid change in the physical properties cause unexpected rock failure or formation of karst (surface and subsurface caves and sinkholes) that are sometimes difficult to predict. Rock mass changes in homogeneity become even worse when it is combined with water. All these factors suggest that it is essential to measure the rock strength. In-situ measurements of rock strength when possible can provide a relatively accurate and simple estimate of changes in rock physical properties.

In laboratory, determination of either compressive strength or deformability of a rock material, is time consuming and relatively expensive. Generally, a great number of specimens have to be tested and involve destructive tests in order to produce a representative value for a large rock exposure. For these reasons, substitution of these tests with a quick, non-destructive, and of acceptable reliability test, as Schmidt hammer (SH) test would be valuable for at least, the preliminary stage of designing a structure or for rock exposure zoning (Sachpazis 1990).

SH test is not only non-destructive and quick but also can be easily performed under both field and laboratory conditions. Since the early 1960s, it has been used in rock engineering and numerous studies have been reported on the relationships between the Schmidt hardness values and both strength and the deformability characteristics of various rock types (Arman et al. 2007, Aydin & Basu 2005, Buyukbagis and Goktan 2007, Kahraman 2001, Katz et al. 2000, Palchik & Hatzor 2004, Tsiambaos & Sabatakakis 2004, Tugrul & Zarif 1999, Yagiz 2009, Xu et al. 1990).

The study area, city of Al-Ain, is one of the fastest urbanized cities in the UAE and is located in the eastern part of Abu Dhabi Emirate, UAE, near the international border with Oman (Figure 1). Jabal Hafit and the surrounding hills are selected as target sites for this study since the area suffers from slope instability and common occurrence of landslides, karsts and caving. The geology of the area is relatively well documented in terms of lithology, structural features and major stress-strain fields. In addition, most of the

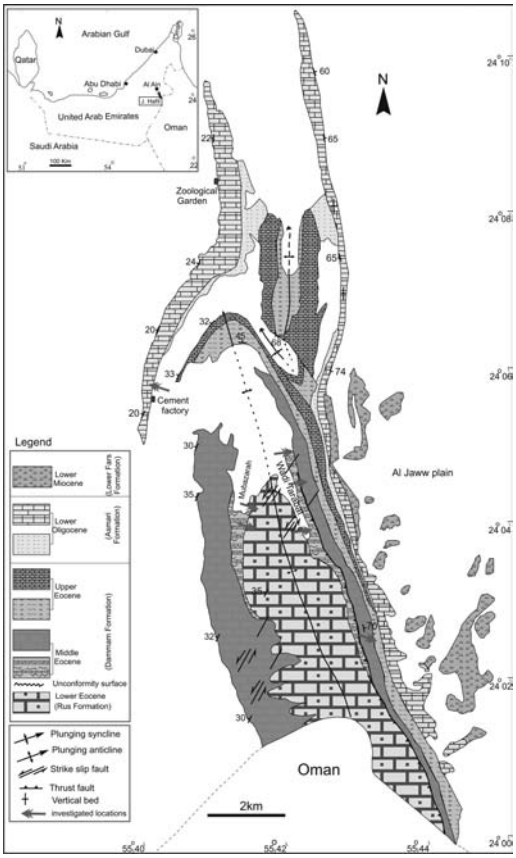


Figure 1. Location map of the study area (rectangle) within the UAE. Enlargement of part of the study area showing geology of the northern part of Jabal Hafit (modified from Abdelghany 2002) and investigated locations (red arrows).

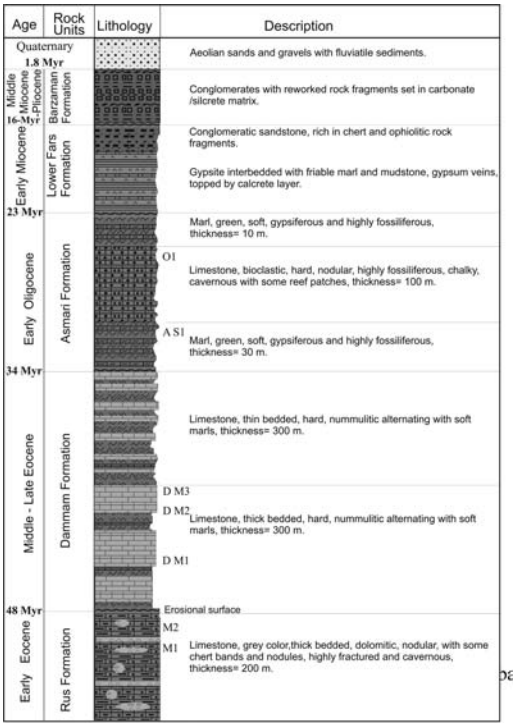


Figure 2. The generalized stratigraphic sequences of Jabal Hafit in Al Ain area.

area was accessible for the planned extensive measurements program. Therefore, the main objective of this study is to compare the in-situ SH measurements with laboratory Uniaxial Compressive Strength (UCS) test.

2 GEOLOGICAL SETTINGS

The geological setting of the study area considered here is dominated by Jabal Hafit anticline which is about 29 km long and 5 km wide with a maximum elevation of about 1240 m above sea level. Structurally, Jabal Hafit is a huge doubly plunging highly asymmetric anticline that is developed over two large thrust faults underlying its eastern and western limbs. The beds on the eastern limb dip steeply (70°–90°) toward the northeast, whereas those on the western limb dip gently (20°–30°) toward the southwest (see Figure 1). The faults and fractures are generally trending between northwest-southeast (parallel to the fold) and east-west (orthogonal to the fold), in addition to subordinate northeast-southwest (Warrak 1996, Noweir 2000, Styles et al. 2006). Some of these structures are thought to be rejuvenated during the different passed geologic times.

The mountain (Jabal Hafit) is classified into three main rock units (Figures 1 and 2) that are composed mainly of different types of carbonate rocks. The oldest rock unit is the Rus Formation (Early Eocene 55-49 Myr). It consists of about 200 m thick of grayish white, thick-bedded to massive limestone beds. The lower part of the formation has subordinate brownish grey thin layers of dolomite and abundant chert nodules and bands that have colored as grey, white and brown. Faults and fractures are common with different scales as well as caves and cavities. Fractures and cavities may be empty or filled with calcite crystals. Measurement of rock strength along with documentation of rock properties was performed in the lower part of the Rus Formation at Mubazarah area (Figures 1 and 2, two locations indicated with red arrows in Figure 1).

The next rock unit in Jabal Hafit is the Dammam Formation (Middle to Late Eocene 49-34 Myr) which is about 600 m thick. The lower part is composed of grayish thick-bedded fractured and rarely cavernous limestone that changes locally to be chalky or dolomitic. This part is regularly interbedded with thick soft marl beds. The top of this part consists of thinly-bedded yellowish colored regularly interbedded nummulitic limestone and marl. Calcite veins are encountered within the limestone beds while gypsum

veins are found within the marl beds. SH measurements were acquired on the eastern limb of Jabal Hafit, where the Dammam beds are steeply dipping. The younger (upper) part of the Dammam Formation is composed of yellowish brown to orange colored thinly-bedded clastic limestone (calcarenite) that has interlayers of soft marl. The limestone beds are extensively fractured in some locations. The data of bed strengths were collected from the limestone observed at one of the excavation, close to industrial area, south of Al-Ain city (Figures 1 and 2, three locations indicated with red arrows in Figure 1).

The third rock unit in Jabal Hafit is the Asmari Formation (Early Oligocene 34-29 Myr) which is about 140 m thick and shows variations in lithologies between two parts. The lower part is 30 to 40 m thick and consists of greenish, gypsiferous mudstone and brownish nummulitic marly limestone. The upper part is composed of thick-bedded chalky limestone with some layers of dolomitic limestone and marl. The limestone is highly fossiliferous with nummulites, pelecypods, algae and corals that form separated large coral heads and algal mats. The abundance of variable sizes of cavities and paleokarsts (few centimeters to tens of meters wide) is the prominent characteristic feature of the chalky beds of this unit. This unit has been observed near the surface at some excavations within Al-Ain city (Figures 1 and 2, two locations indicated with red arrows in Figure 1). The SH measurements were acquired from the chalky limestone beds within inside and outside the caves but far enough from the large skeletal fossils remains.

3 ROCK TYPES DESCRIPTION

Microscopic examinations and point-counting of thin sections of the rock samples used for the SH and UCS measurements indicate made up of either skeletal grains embedded in partially recrystallized micritic groundmass and/or variable grain sizes. In many of the samples micro fracture and veins may occur as single or in groups and mostly filled with calcite and dolomite crystals. These different fractures may influence the mechanical properties of rock masses.

4 EXPERIMENTAL STUDY

4.1 *Sampling and data collection*

A total of seven locations were used for the in-situ SH measurements and encompass all the three rock units described in section on geological setting. The locations within the Rus Formation are M1 and M2. Three locations were selected within the Dammam Formation; DM1, DM2 and DM3 and two locations within Asmari Formation, O1 and AS on the eastern and western fold limbs (see Figures 1 and 2). It is worth mentioning that each of these sites was represented by a number of SH measurements. A number of representative rock block samples (approximately $0.25 \times 0.25 \times 0.25$ m in size) were collected from each site. Then, a number of NX core specimens were drilled in each rock block sample with a length to diameter ratio of approximately 2:1. UCS tests were performed on those core samples.

The examined rocks block of the Rus Formation (M1 and M2) are composed of dolomitic limestone that is relatively hard, thick-bedded to massive and range between gray to white in color, with subordinate reddish color ferruginous-rich bands. These rocks have very common lenses and concretions of white to brownish chert. Dolomitization of these carbonate rocks is a characteristic property around this area and in this stratigraphic interval. The rock type is dominated by paleokarstic and fracture cavities that were filled later forming variable sizes and shapes of calcite geodes and veins in many locations (Figures 1 and 2).

The rocks sequence of the Dammam Formation has more lithological variability, so three sites were selected for the study of this rock unit. The sampled rock blocks (DM1, DM2 and DM3) are composed of limestones that are interbedded with layers of marl. The limestone beds are slightly chalky or dolomitic, white to orange in color, relatively hard and partly cavernous (Figures 1 and 2).

Two sites (O1 and AS) were selected in the Asmari Formation where the rock blocks are chalky limestone that is bedded to massive, white in color, highly fossiliferous. The most characteristic feature of this interval of the Asmari Formation in both areas is the abundance of the cavities that have different sizes. The obtained samples and measurements of these sites were collected from beds inside one of the relatively large caves (Figures 1 and 2).

4.2 *In-situ SH measurements*

Extensive SH measurements (thousands) were performed in seven selected test sites (Figure 1). Generally, the position of the rock hammer was horizontal except in some rare cases where vertical position was used. The average corrected Schmidt hardness rebound (SHR_{cor}) value of each test location was determined and reported according to ASTM D5873-95.

5 RESULTS AND DISCUSSION

The results of in-situ SH measurements, SHR_{cor}, on carbonate rocks indicate wide range ($N_{cor} = 16–55$) of distribution even at the same location. However, the maximum SHR_{cor} value is recorded in test site Mubazarah area (M2) which belongs to Rus Formation dolomitic limestone. The high values of SHR_{cor} in this site may relate to nodular nature and occurrence of chert bands in the dolomitic limestone. The minimum SHR_{cor} value is observed in test site (O1) which is Asmari Formation of chalky limestone. However, corresponding data ($N_{cor} = 16–52$) is still in very

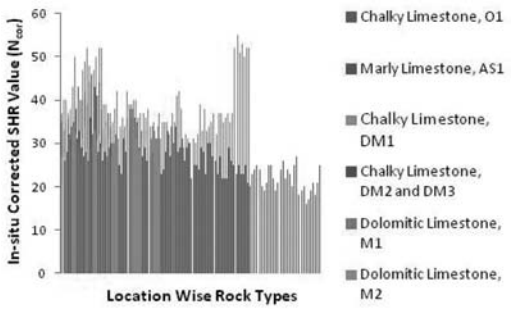


Figure 3. Distribution of in-situ corrected SHR (N_{cor}) with rock types for different locations.

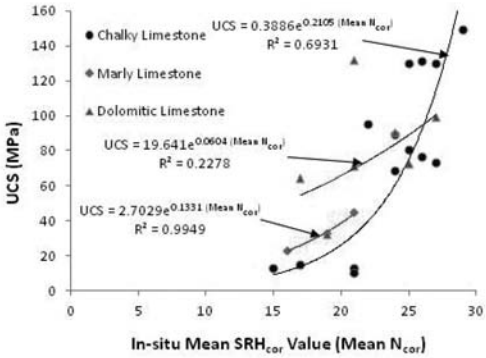


Figure 4. Relationship between in-situ mean SHR_{cor} value (Mean N_{cor}) and the UCS for three types of rocks.

wide range due to hard nodular and fossiliferous characteristic of chalky limestone. It is also interesting to recognize that mode of chalky limestone is almost same as dolomitic limestone in some location. Distribution of all SHR_{cor} values based on rock types for all test locations is presented in Figure 3. As clearly seen in the figure, data are highly scattered with respect to rock types as expected.

Furthermore, in order to be able to describe, the relationships between the mean SHR_{cor} value (Mean N_{cor}) and the UCS values for core samples, regression analyses were performed for three different types of rocks available in the study area. The equation of the best-fit line and the correlation coefficient were determined for each regression analysis and shown in Figure 4. The R^2 values are clear indicative of moderate and weak relationships for chalky and dolomitic limestone with scattered data points. On the other hand, there is a strong relationships for dolomitic limestone with limited data.

6 CONCLUSION

The results of extensive SH measurements, the mean SHR_{cor} value and UCS in seven selected locations within the carbonate dominated rocks indicate variable relationship (moderate, weak to strong) between the two parameters. This variability is attributed to compositional and textural inhomogeneity of the rocks on macro- and micro-scales. The implications of these results are that generalizing of rock mechanical properties should be restricted to well specified rock type and in a relatively of small extension. Such practice will enhance both better recognition of foundation substrata as well as safety aspects of engineering constructions.

ACKNOWLEDGEMENT

The authors wish to express their sincere appreciation to the Research Affairs office at the United Arab Emirates University for providing financial support for this project (Grant # FOS/IRG-16/11).

REFERENCES

Abdelghany, O. 2002. Biostratigraphy (Turborotalia cunialensis/Cribrohantkenina inflata Concurrent-Range Zone, P16) of the Late Eocene Dammam Formation, west of the Northern Oman Mountains. *Micropaleontology* 48: 209–221.

Arman, H., Ramazanoglu, S. & Akinci, A. 2007. Mechanical and physical properties of the Kandira Stone, Kandira, Turkey. *Bulletin of Engineering Geology and the Environment* 66: 331–333.

ASTM, 2001. Standard test method for determination of rock hardness by rebound hammer method D 5873-95, 693–695.

Aydin, A. & Basu, A. 2005. The Schmidt hammer in rock material characterization. *Engineering Geology* 81: 1–14.

Buyuksagis, I.S. & Goktan, R.M. 2007. The effect of Schmidt hammer type on uniaxial compressive strength prediction of rock. *International Journal of Rock Mechanics and Mining Sciences* 44: 299–307.

Hawkins, A.B. 1998. Aspects of rock strength. *Bulletin of Engineering Geology and the Environment* 57: 17–30.

Kahraman, S. 2001. Evaluation of simple methods for assessing the uniaxial compressive strength of rock. *International Journal of Rock Mechanics and Mining Sciences* and Geomechanics *Abstract* 38: 981–994.

Katz, O., Reches, Z. & Roegiers, J.C. 2000. Evaluation of mechanical rock properties using a Schmidt Hammer. *International Journal of Rock Mechanics and Mining Sciences* and Geomechanics *Abstract* 37: 723–728.

Noweir, M.A., 2000. Back-thrust origin of the Hafit structure, Northern Oman Mountain Front, United Arab Emirates. *GeoArabia* 15–228.

Palchik, V. and Hatzor, Y.H., 2004. The influence of porosity on tensile and compressive strength of porous chalk. *International Journal of Rock Mechanics and Mining Sciences* and Geomechanics *Abstract* 37(4): 331–341.

Sachpazis, C.I. 1990. Correlating Schmidt hardness with compressive strength and Young's modulus of carbonate rocks. *Bulletin of Engineering Geology and the Environment* 42: 75–83.

Styles, M.T., Ellison, R.A., Arkley, S.L.B., Crowley, Q., Farrant, A., Goodenough, K.M., Ckervey, J.A., Pharaoh, T.C., Philips, E.R., Schofield, D. & Thomas, R.J. 2006.

The geology and geophysics of the United Arab Emirates. Geology, *Ministry of Energy, United Arab Emirates* 2: 1–351.

Tsiambaos, G. & Sabatakakis, N. 2004. Considerations on strength of intact sedimentary rocks. *Engineering Geology* 72: 261–273.

Tugrul, A & Zarif, I.H. 1999. Correlation of mineralogical and textural characteristics with engineering properties of selected granitic rocks from Turkey. *Engineering Geology* 51: 303–317.

Yagiz, S. 2009. Predicting uniaxial compressive strength, modulus of elasticity and index properties of rocks using the Schmidt hammer. *Bulletin of Engineering Geology and the Environment* 68: 55–63.

Xu, S., Grasso, P. & Mahtab, A. 1990. Use of Schmidt hammer for estimating mechanical properties of weak rock. *Proc. of 6th Int. IAEG Cong., Rotterdam*, Balkema, 511–519.

Warrak, M. 1996. Origin of the Hafit structure: implication for timing the Tertiary deformation in the northern Oman Mountains. *Journal of Structural Geology* 803–818.

This page intentionally left blank

Rock Mechanics for Resources, Energy and Environment – Kwaśniewski & Łydżba (eds)
© 2013 Taylor & Francis Group, London, ISBN 978-1-138-00080-3

Rockfall: Scaling factors for the Coefficient of Restitution

P. Asteriou, H. Saroglou & G. Tsiambaos
Geotechnical Department, School of Civil Engineering, National Technical University of Athens, Greece

ABSTRACT: Rockfalls poses a significant hazard on human activities and infrastructure. In order to design remedial measures, simulation programs are used to define the rockfall trajectory. The most significant input parameter is the Coefficient of Restitution which describes the response of the falling block at impact. This parameter is commonly adjusted to the incident velocity with the use of a scaling factor, but the effect of the block mass is usually neglected. A laboratory investigation using artificial materials to account for the influence of the mass and the incident velocity of the falling blocks is presented. Experimental results show that the coefficient values decrease with both the increase of the block mass and the impacting velocity. The various scaling methods in literature are evaluated. Additionally, a momentum based scaling approach was found to be consistent with the present experimental results.

1 INTRODUCTION

1.1 *Coefficients of Restitution*

In general, the coefficient of restitution (COR) is defined as the decimal fractional value representing the ratio of velocities before and after an impact of two colliding entities. Theoretically, a COR that equals one corresponds to a perfect elastic collision, a COR less than unity defines an inelastic collision and a COR that equals zero is obtained when the object instantaneously stops at the surface area without bouncing which corresponds to a perfectly plastic behavior (Goldsmith, 1960).

When in contact with the slope, the block's magnitude of velocity changes according to the COR value. Hence, for rockfall engineering practice, COR is assumed to be an overall value that takes into account all the characteristics of the impact; including deformation, sliding at contact, transformation of rotational moments into translational and vice versa (Giani, 1992).

Various definitions on the coefficients of restitution have been proposed, such as the kinematic, kinetic or energy coefficients of restitution, but it seems that there is no consensus on which of them is more appropriate for rockfall trajectory prediction (Chau et al., 2002).

The kinematic approach, which is derived from the inelastic collision of particles in the Newtonian mechanics, is the most commonly used due to its overall simplicity. The definition of the COR for an object which impacts on a steadfast surface is simplified as:

$$v_{COR} = \frac{v_r}{v_i} \tag{1}$$

where v_i = incident velocity; v_r = rebound velocity; and v_{COR} = kinematic coefficient of restitution.

The most common COR definition is derived from the normal and tangential projections of the velocity vector on the impact surface, according to:

$$n_{COR} = \frac{v_{r,n}}{v_{i,n}} \tag{2}$$

$$t_{COR} = \frac{v_{r,t}}{v_{i,t}} \tag{3}$$

where the subscripts after the comma n = normal component; t = tangential component; n_{COR} = normal coefficient of restitution; and t_{COR} = tangential coefficient of restitution.

Another COR definition found in literature is given in energy terms:

$$E_{COR} = \frac{0.5\left(mv_r^2 + I\omega_r^2\right)}{0.5\left(mv_i^2 + I\omega_i^2\right)} \tag{4}$$

where I = moment of inertia; ω = angular velocity; and E_{COR} = energetic coefficient of restitution.

It can be seen from the aforementioned equations that E_{COR} yields the square root of the v_{COR} when angular velocity is zero, which is valid for the case of a free fall impact, while the n_{COR} is equivalent to v_{COR}. However, t_{COR} cannot be defined according to Equation 4 since the denominator is zero, which results to an undefined expression. Thus, in the present paper v_{COR} is used and is denoted as COR.

The parameters which influence the bouncing phenomenon, and subsequently the COR values, are summarized in Table 1.

Table 1. Parameters assumed to influence the bouncing phenomenon (Labiouse & Heidenreich, 2009).

Slope characteristics	Block characteristics	Kinematics
Strength	Strength	Translational velocity
Stiffness	Stiffness	Rotational velocity
Roughness	Weight	Collision angle
Inclination	Size	Configuration of block

1.2 *Review of scaling factors*

COR depends amongst others on incident velocity and mass, as seen in Table 1. Various scaling factors have been proposed in order to take these parameters into account in the analysis of rockfalls with computer codes.

Pfeiffer & Bowen (1989) introduced the CRSP rockfall simulation program, in which both normal and tangential COR values are scaled according to the incident velocity. The scaled normal COR value is calculated by multiplying the literature suggested value by the scaling factor (Eq. 5), while a relevant expression for scaling the tangential COR is also available.

$$B_v = \frac{1}{1+\left(v_{i,n} / v_{ref}\right)^2} \tag{5}$$

where v_{ref} = reference velocity; and B_v = scaling factor.

According to Equation 5, the scaling factor is equal to 0.5 when incident velocity is equal to the reference velocity, which was defined in CRSP as 9.14 ms^{-1}. Richards et al. (2001) suggested a reference velocity equal to 5 ms^{-1} based on laboratory investigation. This scaling factor is adopted by many simulation codes. However, very little information is available concerning the calibration of this equation with experiments using blocks of different sizes (Bourrier & Hungr, 2011).

An alternate velocity scaling factor (Eq. 6) was used by Rammer et al. (2010) in which scaling is applied for incident velocities higher than 10 ms^{-1}. Since literature suggested values, which are commonly used, originate from testing with lower incident velocities, scaling is included.

$$k = \begin{cases} 1, & v_i \le 10 ms^{-1} \\ 10^{0.25} v_i^{-0.25}, & v_i > 10 ms^{-1} \end{cases} \tag{6}$$

where k = scaling factor.

This scaling factor originates from an equation proposed by Johnson (1985), according to which COR is proportional to $v_i^{-0.25}$. The aforementioned scaling factors, which are all dependent on incident velocity, show a significant variation as presented in Figure 1.

A momentum based COR definition has recently been proposed by Bourrier & Hungr (2011) based on intuition. COR is represented by a hyperbolic function which yields unity in 'soft' impacts and zero in 'heavy' impacts, where all energy dissipates due plastic deformation.

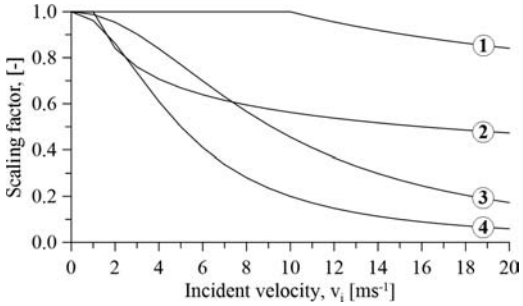


Figure 1. Scaling factors versus incident velocity originating from: 1- Rammer et al. (2010); 2- Johnson (1985); 3- Pfeiffer & Bowen (1989); and 4- Richards et al. (2001).

$$k' = \frac{M_{0.5}}{M_n + M_{0.5}} \tag{7}$$

where M_n = normal incident momentum; $M_{0.5}$ = reference momentum; and k' = scaled coefficient of restitution.

A scaling factor dependent on mass, which presents a similar trend with scaling factor B_v, is also available in RocFall software (RocScience, 2003). However, no information concerning the definition of this factor is available. According to the software developers, it is not advised to use simultaneously mass and velocity scaling factors, since it results in unrealistic rock paths.

$$B_m = \frac{1}{1+\left(m / m_{ref}\right)^2} \tag{8}$$

where m_{ref} = reference mass; and B_m = mass scaling factor.

2 EXPERIMENTAL SETUP

The rebound angle for a normal and frictionless impact between a sphere and steadfast surface should be theoretically equal to 90 degrees. However, when performing free fall tests with randomly shaped blocks, the rebound trajectory presents a wide deviation from the fall direction. Block shape has been found to pose a significant effect on the rebound angle and subsequently to the obtained COR value (Asteriou et al., 2012). In order eliminate the effect of the block shape effect and the other parameters shown in Table 1; spherical blocks and free fall drops were used in the experiments.

2.1 *Apparatus*

The surface area, upon which the impact of the spherical blocks occurred, was a smooth and planar plate

Table 2. Properties of used materials.

Material properties	Cement grout	Epoxy resin
Density, ρ (kN/m^3)	21.9	20.4
Compressive strength, σ_{ci} (MPa)	37.4	86.5
Young's modulus, E_t (GPa)	15.7	11.0
Poisson's ratio, v	0.11	0.38
Tensile strength, σ_t (MPa)	7.5	15.6
P-wave velocity, v_p (m/s)	4335	4125
S-wave velocity, v_s (m/s)	2575	2430
Schmidt Hardness, R	33	42

formed by the same material. The plate had a thickness of 5 cm with 15 cm side length, fixed in a massive dead weight base which ensured the preservation of the momentum caused by the impact.

Prior to the experiment, the block was held by suction produced by a vacuum pump and was released to a free fall drop by switching the vacuum pump off. Consequently, the block developed only vertical translational velocity prior to impact. The trajectory of the block was recorded with a digital high-speed video camera, at a capture speed of 500 fps and a resolution of 440 × 330 pixels, installed 1 m away from the impact surface. A high contrast background was installed in order to make the block distinguishable.

2.2 *Materials*

Preparing spheres from natural rock is expensive and time consuming, which are hardly ever perfectly spherical. Thus, artificial materials were chosen, as they present advantages: they can be casted in any shape and size and their mechanical properties can match those of natural materials. For casting the spherical blocks, custom silicon molds were created, able to reproduce boulders with diameters of 3, 4, 5 and 6 cm. The materials chosen were a cement based grout and a high strength epoxy resin. Both materials were stable and cohesive, exhibiting zero segregation and were shrinkage compensating, resulting in uniform samples. The physical and mechanical properties of these materials, presented in Table 2, were determined according to ISRM suggested methods (ISRM, 2007).

Asteriou et al. (2013) have used these materials for investigating the effect of material properties of free falling blocks with cubical shape along with eight natural rock materials commonly found in Greece.

2.3 *Data acquisition*

A video file is a sequence of still images displayed at a constant rate (fps). A grayscale digital image forms an array of pixels the size of which is described by the image resolution. Each element obtains a numerical value from 0 (black) to 255 (white) representing the intensity of the pixel, which is described by a matrix, easily manipulated within MATLAB environment.

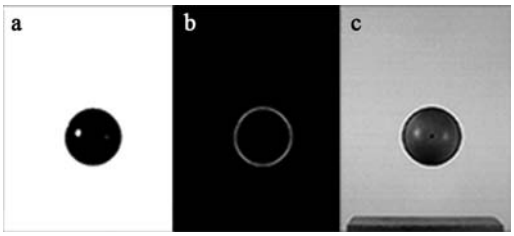


Figure 2. Tracking algorithm stages: a. conversation into a binary image resulting discretization of the block; b. boundary recognition and acquisition of x_i, y_i coordinates; and c. calculation of block's geometrical properties.

Initially, each frame was converted to a binary image (black-and-white) discretizing the block from the background (Fig. 2a). The near end projection of the block in the capture plan resembles a circular shape. Hereafter, an edge recognition algorithm (Canny, 1986) was used providing the boundary between the circular projection and the background (Fig. 2b). The coordinates of each pixel defining the boundary line were used in order to calculate the center point and the radius of the boulder using Pratt (1987) least squares method (Fig. 2c). According to this method, the geometric properties of a circle are calculated according to Equation 9.

The determination of the trajectory of the block was done by repeating the aforementioned process for all captured frames.

$$SS(X,Y,R)=\sum_{i=1}^{n}\left(R-\sqrt{(x_i-X)^2+(y_i-Y)^2}\right)^2 \quad (9)$$

where x_i, y_i = coordinates of boundary points; X, Y = coordinates of the center point; and R = circle radius.

Further on, the trajectory was separated in the pre and post impact stages. For each stage a 2nd degree regression analysis of the Y coordinates over time was performed, which resulted to a constant acceleration. The impact point and time were calculated as the intersection of the pre and post trajectory curves and the line representing the impact surface.

The points defining block's boundary include a positioning error, due to the finite pixel size. The error in the determination of the center point coordinates was less than the pixel size, due to the large number of boundary points used in Pratt's method.

The error in the measurements of position between frames due to change of velocity caused by the acceleration was diminished by using a high frame rate and a 2nd degree regression. However, the high frame rate increases drastically the velocity error caused by the positioning uncertainty (Feng et al., 2011). When velocity is calculated by the position measurements an uncertainty of δy is included, while the time interval between the two positions is Δt, then the error in velocity is $2(\delta y/\Delta t)^2$. It is apparent that as Δt reduces, when the frame rate increases, the error in velocity determination also increases. In order to increase the time

interval and reduce the error, incident velocity was calculated by Equation 10 as the average of the velocities calculated from the impact point and each measured point. A more analytical presentation of the error analysis is beyond the scope of the present paper. However, after implementing this methodology, the relative error in the calculated COR value is less than 5%.

$$v = \frac{1}{n}\sum_{i=1}^{n}\left[0.5g\Delta T + \frac{\Delta Y}{\Delta T}\right] \quad (10)$$

where n = number of measurements; ΔY = vertical movement of center point between point i and impact point; ΔT = flight time between measurement point i and impact point; and g = gravitational constant.

The trajectory of the block in the impacts following the first one deviated from verticality which resulted in horizontal and angular velocities additional to the vertical. In order to deduct the effect of both horizontal and rotational velocity, only the initial impacts were taken into account. This deviation can be attributed to grain boundaries and micro fissures, since the surfaces of the colliding entities were not perfectly smooth (Imre et al., 2008). The maximum deviation from the vertical was less than 5 degrees, which results in a difference of less than 0.4% between the normal component and the total velocity.

2.4 *Experimental program*

In order to address the effect of impact velocity and mass of the block on COR values and evaluate the proposed scaling factors, free fall drop tests were conducted with spherical blocks of two artificial materials. Spheres were prepared from the cement grout material with diameters of 3, 4 and 5 cm and from the epoxy resin with diameters of 3, 4, 5, and 6 cm. All spheres were dropped from heights of 0.1, 0.25, 0.5, 1.0, 2.0, 3.0 and 4.5 m. In order to account for the randomness of the impact, each test was repeated five times. Thus, the experimental procedure consisted of 49 series of tests.

3 PRESENTATION OF RESULTS

The calculated COR values for epoxy resin and cement grout are presented in figures 3 and 4 respectively. The average value of each test series is presented on the graphs. It becomes evident that COR is dependent on both incident velocity and mass and reduces with increasing incident velocity and mass.

The trend lines presented in figures 3 and 4 are described by multivariate linear regressions. The overall regression coefficients have high values, denoting that the data are well correlated. However, extending those correlations for larger blocks and higher velocities is problematic. Using higher values for mass and velocity, but still low compared to real scale rockfalls, those correlations produce negative COR values, which are unacceptable.

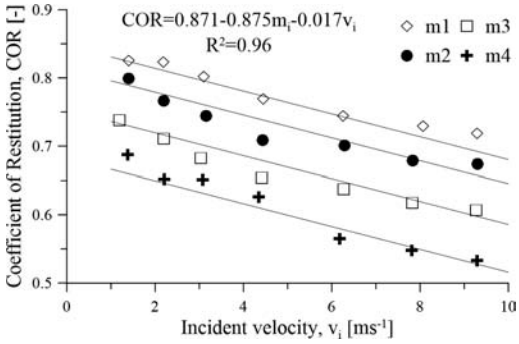


Figure 3. COR values versus incident velocity for the epoxy resin blocks.

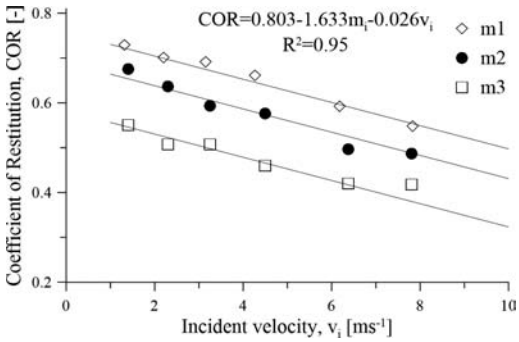


Figure 4. COR values versus incident velocity for the cement grout blocks.

Additionally, the presented linear correlations do not to predict the COR values for impacts in the elastic regime, where COR should be approximately equal to unity independently of the mass. According to Hertzian theory of collinear impact, a COR value equal to unity is derived when incident velocity is less than the yield velocity, which is defined as the velocity where plastic deformation within the colliding blocks initiates. Johnson (1985) has shown that yield velocity is a function of density, Young's modulus and material's strength. However, even in high strength rock materials, yield velocity is significantly lower than the velocities encountered in real scale rockfalls, which implies that it is practically impossible to observe an impact with COR equal to unity. However, the upper COR boundary should theoretically approach unity when incident velocity approaches to zero. This demonstrates that COR is connected to the mass and velocity with a nonlinear function.

The experimentally derived COR values for both materials are plotted against incident momentum (Fig. 5), which is the product of the mass and incident velocity of the block. A strong correlation between momentum and COR is applicable, which is defined by a non-linear function in the form of:

$$COR = a\left(mv_i\right)^{-b} \quad (11)$$

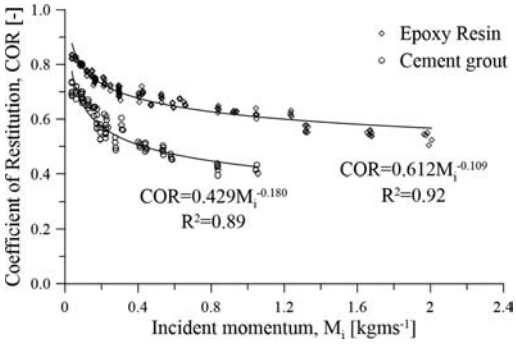


Figure 5. Coefficient of restitution values from all tests versus incident momentum.

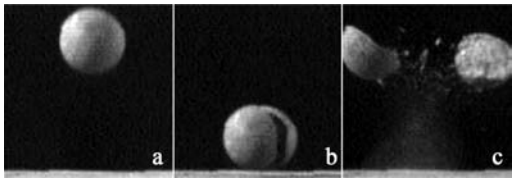


Figure 6. Image sequence of a fracture; 3 cm diameter concrete block released from a height of 4.5 m; a. $t_a = 0.000$ s; b. $t_b = 0.008$ s; and c. $t_c = 0.024$ s.

where a and b are parameters which are assumed to be controlled by the material properties, such as strength, elastic properties etc. since they were the only parameters that differed between the two tested materials. However, in order to determine these parameters, additional tests with more materials and larger blocks are required. This forms part of on-going research of the authors.

An interesting observation arises from the tests with cement grout blocks. All blocks were fractured for a release height of 4.5 m, by splitting along the loading direction (fig. 6), which is similar to the failure mode of Brazil test, implying that fracture is controlled by the tensile strength. Moreover, the calculated COR values for these impacts were lower than their prediction obtained by extending the results of tests performed with lower release heights. Fracture of the blocks occurred after 3 to 4 drops and a lower COR value was calculated after each test, denoting that internal cracking developed and propagated. However, until fracture there were no macroscopically visible signs of cracking on the surface of the blocks. These tests were not included in the present analysis as they concern the fracture phenomenon.

4 EVALUATION OF RESULTS

The present data are significant for the evaluation of the proposed scaling models and their calibration. The model used in the majority of computer programs is presented by Equation 4 and incorporates incident velocity, reference COR value and reference velocity. However, from figures 3 and 4 it is evident that COR value depends significantly also on the block's mass. Thus, this model lacks the ability to predict the scaling factor for blocks whose size varies.

This is also true with the model proposed by Rammer et al. (2010). Additionally, in this model COR is not scaled for incident velocities less than 10 ms^{-1}, due to the fact that COR value is selected by the literature suggested values, which are determined from experimental studies performed within that velocity range, thus already including the scaling factor. However, based on the present study, the velocity effect on the COR value is significant for the range between zero and 10 ms^{-1}. Additionally, the model omits the mass dependency for the whole velocity range. Hence, this model cannot be used to describe the trends produced by the presented experimental data.

The momentum based COR definition suggested by Bourrier & Hungr (2011) matches well with trend of the present experimental results. However, the proposed hyperbolic function (Eq. 7) could not be calibrated; the term $M_{0.5}$ presents a wide scatter, although it is defined as a constant parameter. Furthermore, a model defined in terms of incident momentum seems to be appropriate for the simultaneous scaling of COR values according to incident velocity and mass.

5 CONCLUSIONS

In the present paper the COR value dependency on mass and velocity was examined for spherical blocks of various sizes impacting on a horizontal surface. The blocks consisted of two artificial materials and the free fall experiments were conducted from different release heights, up to 4.5 m resulting incident velocities up to 9.5 ms^{-1}.

According to the experimental results, it is shown that the COR value reduces by increasing both incident velocity and mass. Additionally, the rate of decrease seems to be a function of the mechanical properties of the blocks. For instance, in the tests conducted with epoxy resin blocks, increasing the incident velocity approximately 10 times COR is reduced by 17%. On the other hand, by increasing mass 8 times, COR is reduced by 20%.

The COR scaling factors found in literature are mainly focused on the effect of incident velocity, and therefore lack the ability to fit to the present data. However, using a momentum based scaling factor, expressed by a power function, seems capable to address both mass and velocity effects. This function could also incorporate parameters connected to material properties, such as strength and Young's modulus.

Besides the uncertainty introduced by the scaling factor, a more important issue is the uncertainty of the reference values. In literature, suggested values are given mostly by the material type, based on laboratory, in situ investigations and back analysis of known rockfall trajectory paths, which present a large

scatter. According to present results this scatter can be attributed -beyond other parameters- to the different testing conditions applied, such as incident velocity and mass of the blocks.

Further research on the size and velocity dependency on COR is under progress in the Rock Mechanics laboratory of the School of Civil Engineering at the National Technical University of Athens. Larger blocks and different materials are tested, whereas also shape and incident angle are altered. Additionally research has been recently extended in the field, by conducting tests in real scale, in order to establish sound methods and correlations for predicting rockfall trajectories more accurately.

ACKNOWLEDGEMENTS

Authors would like to express their gratitude to Mr. Dario Stefanou, Craftsman-Artist, for the construction of the silicon molds and to Sika Hellas SA for providing the materials used in this research.

REFERENCES

Asteriou, P., Saroglou, H. & Tsiambaos, G. 2012. Geotechnical and kinematic parameters affecting the coefficients of restitution for rock fall analysis. *International Journal of Rock Mechanics and Mining Sciences*, 54, 103–113.

Asteriou, P., Saroglou, H. & Tsiambaos, G. 2013. Rockfalls: Influence of Rock Hardness on the Trajectory of Falling Rock Blocks. *Bulletin of the Geological Society of Greece*, XLVII.

Bourrier, F. & Hungr, O. 2011. Rockfall Dynamics: a Critical Review of Collision and Rebound Models. In S. Lambert & F. Nicot (eds), *Rockfall Engineering*: Hoboken, NJ – London: Wiley – ISTE.

Canny, J. 1986. Computational Approach to Edge Detection. *IEEE Transactions on Pattern Analysis and Machine Intelligence*, PAMI-8, 679–698.

Chau, K. T., Wong, R. H. C. & Wu, J. J. 2002. Coefficient of restitution and rotational motions of rockfall impacts. *International Journal of Rock Mechanics and Mining Sciences*, 39, 69–77.

Feng, Y., Goree, J. & Liu, B. 2011. Errors in particle tracking velocimetry with high-speed cameras. *Review of Scientific Instruments*, 82.

Giani, G. P. 1992. *Rock Slope Stability Analysis*. Rotterdam: Balkema.

Goldsmith, W. 1960. Impact: The theory and physical behavior of colliding solids. *Edward Alrnold, London*.

Imre, B., Räbsamen, S. & Springman, S. M. 2008. A coefficient of restitution of rock materials. *Computers & Geosciences*, 34, 339–350.

ISRM 2007. *The Complete ISRM Suggested Methods for Rock Characterization, Testing and Monitoring: 1974–2006*. R. Ulusay & J.A. Hudson (eds)

Johnson, k. L. 1985. *Contact Mechanics*, UK, Cambridge University Press.

Labiouse, V. & Heidenreich, B. 2009. Half-scale experimental study of rockfall impacts on sandy slopes. *Natural Hazards and Earth System Science*, 9, 1981–1993.

Pfeiffer, T. J. & Bowen, T. D. 1989. Computer simulation of rockfalls. *Bulletin – Association of Engineering Geologists*, 26, 135–146.

Pratt, V. 1987. Direct Least-Squares Fitting Of Algebraic Surface. *Computer Graphics (ACM)*, 21, 145–152.

Rammer, W., Brauner, M., Dorren, L. K. A., Berger, F. & Lexer, M. J. 2010. Evaluation of a 3-D rockfall module within a forest patch model. *Natural Hazards and Earth System Science*, 10, 699–711.

Richards, L. R., Peng, B. & Bell, D. H. 2001. Laboratory and field evaluation of the normal Coefficient of Restitution for rocks. *Proceedings of Proc. ISRM Regional Symposium EUROCK2001*, 149–155.

RocScience. 2003. Advanced Tutorial: Determining Input Parameters for A RocFall Analysis. *www.rocscience.com*.

Rock Mechanics for Resources, Energy and Environment – Kwaśniewski & Łydżba (eds)
© 2013 Taylor & Francis Group, London, ISBN 978-1-138-00080-3

Nano-indentation tests on partially satured argillite: Experimental device and measurements

C. Auvray, R. Giot & D. Grgic
GéoRessources, UMR 7359, Université de Lorraine, CREGU, Vandoeuvre les Nancy, France

ABSTRACT: Callovo-Oxfordian argillite from the underground laboratory of ANDRA (Meuse/Haute-Marne, France) corresponds to a multiphase material. This material is highly influenced by fluids as already shown by many mechanical tests under different variable hygrometry. Indeed, argillite is made of a clayey matrix with quartz and carbonates inclusions. The present study was devoted to the development of an experimental device of nanoindentation under variable hygrometry. An experimental methodology for nanoindentation, allowing the determination of micromechanical properties of the different phases under variable hygrometry was proposed. A process for samples preparation was established. A parametric study taking into account the axial loading rate, the penetration depth of the indenter tip and the distance between two indentation points was performed for different hydrous conditions. This allows an objective comparison of results. Many measurements were performed under a hygrometry of 50% and 95% and a constant temperature of 20°C.

1 INTRODUCTION

The argillite rocks of Callovian-Oxfordian, from the ANDRA underground research laboratory in Meuse/ Haute-Marne (France), are called multiphase material. Water sensitivity, paramount feature of this material, was also demonstrated with numerous mechanical tests under variable humidity (Escoffier 2002, Hoxha et al. 2007). Indeed, this material is composed of a clay matrix (presence of swelling clays such as smectite) with inclusions of quartz and carbonates few tens of microns. The matrix itself is multiphase: there are between the layers of clay micrometric inclusions of quartz and carbonates (Robinet 2008, Robinet et al. 2012). To understand the behavior of each of these phases, a nanoindentation test campaign was performed. The set of elastic parameters of the various components already estimated in Magnenet (Magnenet et al., 2011) will be used to power various models already developed or under development. For example, the elastoplastic or viscoelastic behavior will be apprehended using the approach due to Dao (Dao et al., 2001), or to Seltzer in the case of Drucker-Prager model (Seltzer et al. 2011) or even using models of Vandamme (Vandamme & Ulm 2006) and Feng (Ngang et al. 2005).

This study consisted in developing a standard apparatus for nanoindentation (CSM Instruments SA) with a climatic chamber (Vötsch Industrietechnik GmbH) to allow carrying out tests under variable hygrometry. An experimental methodology of nanoindentation was developed to define the micromechanical properties of the different phases (matrices and inclusions) in variable water conditions, that is to say under partially saturated conditions. A sample preparation process was developed allowing to preserve the physico-mechanical properties of the material but also ensuring reproducibility of processing. A parametric study, taking into account the speed of axial loading, the depth of penetration of the indenter and the distance between two points indentation was performed in order to establish an experimental protocol for different water conditions ensuring an objective comparison of results. Several measurement campaigns were carried out under humidities of 50% and 95% at a constant temperature of 20°C.

In order to validate the experimental methodology, the spatial 2D micromechanical properties, which is the outcome of measurement campaigns, was compared to an image obtained by optical microscopy. Water sensitivity of the clay phase was also observed. A good correlation was noted between the moduli isovalues map and location of inclusions observed in the photograph of the surface of the sample.

2 EXPERIMENTAL APPARATUS

In order to perform nanoindentation tests under imposed constant humidity, we decided to place the test bench in a climatic chamber. This was achieved by deporting the bench support outside the enclosure to eliminate any vibrations due to mechanical mixing of the air in the room. Another modification of the enclosure was necessary: the motor-compressor was also deported from the enclosure, once again to be free of vibrations. Indeed, the nanoindentation tests must always be carried out in an undisturbed environment.



Figure 1. Nanoindentation tester installed in a climatic chamber.

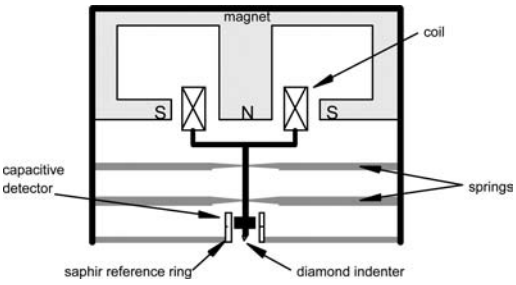


Figure 2. Schematics of the measurement head of the CSM Instruments SA nanoindentation tester.

Otherwise, the forces that are a few mN would be very noisy. To complement this, the nanoindentation bench is placed on a table with air cushion to remove the last unwanted vibrations but also to ensure a perfect horizontality of the device. The details of this device are given in Figure 1.

The nanoindentation test bench is composed of a first module with the nanoindenter and a second module with an optical microscope to visualize the surface of the sample. Moving the sample between the two modules is provided by a motorized table that also enables indentation matrices.

The indentation technique used consists of digging in an indent on the surface of a sample by applying an increasing normal load. When the value of the normal force reaches a set value, a partial discharge followed by a loading to a maximum value is achieved. This procedure is performed repeatedly at various points on the sample surface, with a constant interval along the abscissa and ordinate. The load is directly applied by an electromagnet assembly to a vertical rod, the end of which houses a standard Berkovich diamond indenter (Fig. 2). Displacement of the rod is measured by a capacitive detector and the rod is supported by two guide springs. The system has load and displacement resolutions of 10 μN and <1 nm respectively (Randall et al. 1997).

To determine the elastic modulus of the material, we use the model developed by Oliver & Pharr (1992).

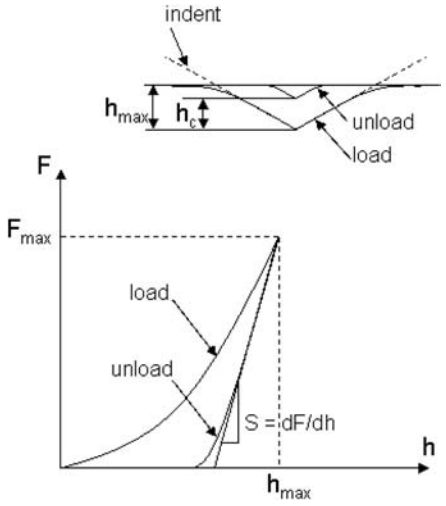


Figure 3. Typical load-displacement curve.

Table 1. Indentation tester specifications.

Load range	0.1–500 mN
Load resolution	0.04 μN
Maximum depth	200 μm
Depth resolution	0.04 nm
Maximum load rate	0.5 N/min
XY stage	120 × 20 mm
XY resolution	0.25 μm

This model is suitable for materials with elastoplastic behavior. It notably allows to estimate the penetration hardness H_{it} as well as Young's modulus E_{it} of the indented area from the force-penetration curve (Fig. 3).

Hardness H_{it} and Young's modulus E_{it} are assessed using equations (1) and (2):

$$H_{it} = \left(\frac{F_{max}}{Ap(hc)} \right) \quad (1)$$

where F_{max}: maximal load; A_p (h_c): projected contact area of the indent, function of hc: depth of contact.

$$\frac{1}{E_r} = \frac{1-\nu_s^2}{E_{it}} + \frac{1-\nu_i^2}{E_i} \quad (2)$$

$$E_r = \frac{S\sqrt{\pi}}{2\beta\sqrt{Ap(hc)}} \quad (3)$$

where S tangent to the unloading curve; β indent shape factor; E_i and ν_i Young's modulus and Poisson's ratio of the indent; ν_s Poisson's ratio of the indented area (0.30 for the whole sample).

The technical features of the apparatus are given in Table 1.

3 SAMPLE PREPARATION

Our equipment allows a test matrix by setting the difference between two measurements and the number of rows and columns. Millimeter surface is thus taken into account to perform all the tests.

The state of the sample surface must be perfectly smooth and the lack of parallelism between the substrate and the surface of the sample must not exceed 5 μm (Fig. 5). These processing requirements are systematic in the preparation of samples, but even more difficult to carry out nanoindentation tests (Vandamme 2008, Miller et al. 2008).

These two basic conditions require specific and rigorous preparation of samples: i) the first step is to cut a sample of 5 cm long, 3 cm wide with a thickness of 7 mm ii) the second step is to rectify a perfectly parallel sample (the surface resting on the substrate must be perfectly parallel to the surface where tests will be carried out). The crude sample is placed in a lathe to machine the sides against each other with an accuracy of 1 μm iii) the final step is to polish the surface to be indented. To achieve this aim, the sample is placed in a polishing lathe with an abrasive to obtain a surface with defects below 5 μ m.

After this processing step, the flatness of the sample is checked by carrying out measurements using a comparator with an accuracy of 1 μm. The difference in flatness along the length and width must not exceed 5 μm, so that the sample can be used for the test.

4 RESULTS

4.1 *Parametric study*

Constantinides & Ulm (2007) argued that the statistical processing of nanoindentation tests is only relevant if the typical size of inclusions d is much larger than the typical penetration depth value h. If $d << h$, the material can be viewed as homogeneous (see Figure 2 in Constantinides & Ulm, 2007), whereas the condition $d << h$ implies that the mechanical behaviour of each constituent could be important. Regarding argillite, the choice of the indentation depth was particularly problematic because of the high dispersion of inclusion sizes and the limited number of specimens. It was indeed possible to distinguish between two characteristic sizes of inclusions, the first being close to 1. Contrary to Abou-Chakra Guéry et al. (2008), we distinguished between this first kind of inclusions and the "bigger" and classically considered inclusions of quartz and calcite, with sizes between 1 μm and 10 μm. In this study, we needed to account for these inclusions of 1 μ m to choose a relevant value for h. Thus, to focus on characterizing the homogeneous argillaceous behavior of the matrix, we needed to fulfil the following condition (Magnenet et al. 2011):

$$1\mu m \leq h \leq 5\mu m \quad (4)$$

meaning that the considered scale was such that (i) the matrix can be viewed as homogeneous but with the possibility of (ii) distinguishing between the constituents of the biggest inclusions. Finally, an approximate maximal value of 2 μm was chosen for the maximal indentation depth (Fig. 4).

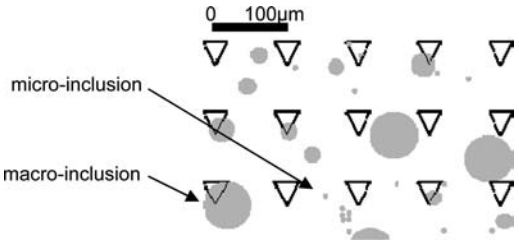


Figure 4. Comparison of typical lengths. The triangles represent the imprint of the (Magnenet et al. 2011).

Table 2. Indentation tester specifications.

Pitch (x & y)	100 μm
Load/unload rate	30 mN/min
Max. depth (constant)	2.5 μm

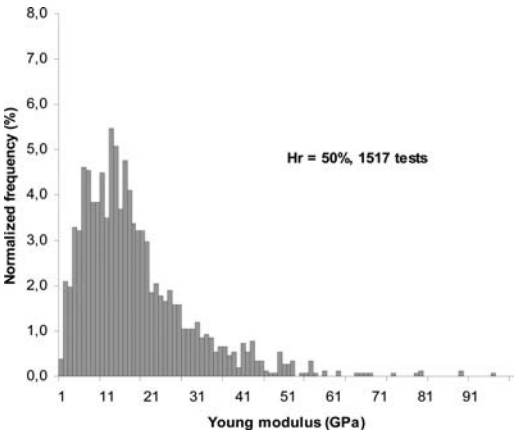


Figure 5. Experimental frequencies of Young's modulus (Hr = 50%).

4.2 *Measurements campaigns*

Two measurement campaigns were carried out on material previously saturated, with 50% humidity and then with a relative humidity of 95%.

The first series of measurements was performed with a relative humidity of 50%. The test parameters are given in Table 2.

With such humidity, the matrix has an elastic modulus of 10 and 30 GPa. In contrast, macro-carbonate inclusions have a modulus of 70 GPa. We also exhibited measures of intermediate moduli corresponding to the presence of more or less important micro-inclusions in the clay matrix (Fig. 5).

The second set of measurements was performed with a relative humidity of 95%. The test parameters

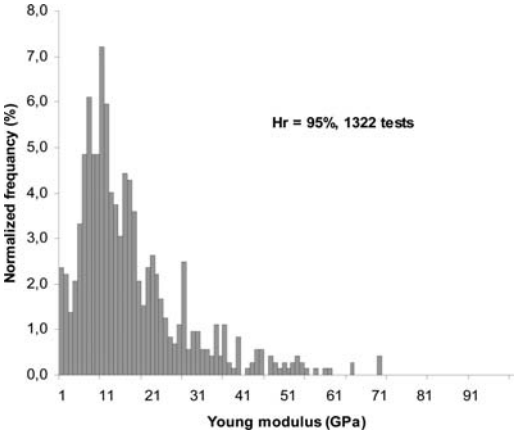


Figure 6. Experimental frequencies of Young's modulus (Hr = 95%).

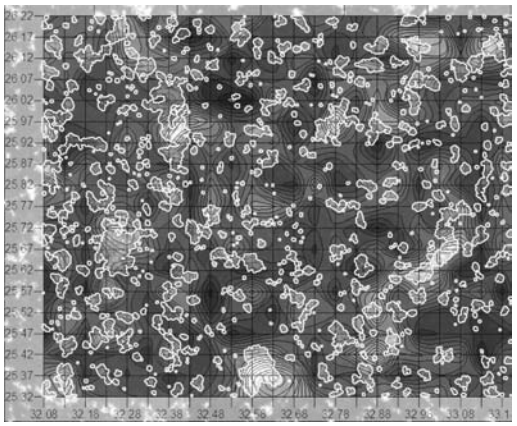


Figure 7. Map of Young's modulus (Hr = 50%) with a photograph of the indented surface.

are given in Table 2. Matrix in such a hydric environment exhibits a viscoelastic behavior with a modulus of deformability less than 10 GPa. Measures of macro-inclusions moduli are difficult to obtain: we only have a few points with moduli around 40 GPa. As with the first series, we obtain a spread distribution of moduli which must correspond to the more or less dense presence of micro-inclusions (Fig. 6).

4.3 *Interpretation & conclusions*

From the tests carried out under a constant humidity of 50%, a map of isolines was plotted in order to highlight the areas of inclusions and therefore stronger moduli. This map was superimposed on the photograph of the indented surface which has micro-and macro-inclusions highlighted (Fig. 7).

We can see that the strong moduli correspond in most cases to a highlighted area. However, we have areas that do not coincide with the strong moduli. The hypotheses for these differences are as follows: i) The measured modulus is high but one cannot see any inclusion. A thin layer of clay matrix covers inclusion; ii) The measured modulus is small but one can see a macro-inclusion or a cluster of micro-inclusions. The inclusion is only a few nanometers thick, and the measured modulus does not match that of the inclusion, but that of the clay matrix.

From these two assumptions, we can extrapolate and thus obtain a range of intermediate moduli corresponding to different thicknesses of matrix or different thicknesses of inclusion. All these moduli measured therefore exhibit a more or less normal distribution where different classes of moduli are more or less discriminated (Fig. 5).

Considering the results of the tests performed under a relative humidity of 95%, so with an almost saturated material, the inclusions are not indented but indent themselves the matrix which has very low strength but mostly a very low stiffness. In this case we obtain a tightened distribution of moduli compared to that obtained with a material highly desaturated (Fig. 6).

So, the role of humidity on the material behavior was highlighted. Discrimination of the different phases (matrix and inclusions) remains delicate with a material close to saturation. However, the elastic moduli of the inclusions can be measured on a strongly desaturated matrix. These first results allow to consider complementary experimental measurement campaigns: i) conducting creep levels ii) by testing relaxation, to address the deferred behavior of this material under different hydro-mechanical solicitations.

REFERENCES

Abou-Chakra Guery, A., Cormery, F., Shao, J. & Kondo, D. 2008. A micromechanical model of elastoplastic and damage behaviour of a cohesive geomaterial. International Journal of Solids and Structures 45(5): 1406–1429.

Constantinides, G. & Ulm, F-J. 2007. The granular nature of C-S-H. *Journal of the Mechanics and Physics of Solids* 55: 64–90.

Dao, M., Chollacoop, N., Van Vliet, K.J., Venkatesh, T. A. & Suresh, S. 2001. Computational modelling of the forward and reverse problems in instrumented sharp indentation. *Acta Mater.* 49: 3899–3918.

Escoffier, S. 2002. Caractérisation expérimentale du comportement hydromécanique des argilites de Meuse/Haute-Marnes. *Ph. D. Thesis, INPL Nancy France*.

Hoxha, D., Giraud, A., Homand, F. & Auvray, C. 2007. Satured and unsatured behaviour modelling of Meuse/Haute-Marnes argillite. *Int. J. of Plasticity* 23(5): 733–766.

Magnenet, V., Auvray, C., Francius, G. & Giraud, A. 2011. Determination of the matrix indentation modulus of Meuse/Haute-Marne argillite. *Applied Clay Science* 52: 266–269.

Miller, M., Bokko, C., Vandamme, M. & Ulm, F-J. 2008. Surface roughness criteria for cement paste nanoindentation. *Cement and Concrete Research* 38(4): 467–476.

Ngan, A.H.W., Wang, H.T., Tang, B. & Sze, K.Y. 2005. Correting power-law viscoelastic effects in elastic modulus measurement using deplth-sensing indentation. *Int. J. of Solids and Structures* 42: 1831–1846.

Oliver, W.C. & Pharr, G.M. 1992. An improved technique for determining hardness and elastic modulus using load and displacement sensing indentation experiments, *Journal of Materials Research* 7: 1564–1583.

Robinet, J-C., Davy, C., Ghayaza, M., Skoczylas, F., Troadec, D., Sardini, P. & Talandier, J. 2012. Direct observations of the 3D pore network of a callovo-oxfordien claystone. *5th Int. Meeting on clays in Natural and Engineered barriers for radioactive waste management*.

Randall, N.X., Julia-Schmutz, C., Soro, J.M., Von Stebut, J. & Zacharie, G. 1997. Novel nanoindentation method for characterising multiphase materials. *Thin Solid Films* 308–309: 297–303.

Robinet, J-C. 2008. Minéralogie, porosité et diffusion de solutés dans l'argilite du callovo-oxfordien de Bure (Meuse/Haute-Marnes, France) de l'échelle centimétrique à l'échelle métrique. *Ph. D. Thesis, Université de Poitiers* France.

Seltzer, R., Cisilino, A.P., Frontini, P.M. & Mai, Y.W. 2011. Determination of the Drucker-Prager parameters of polymers exhibiting pressure-sensitive plastic behaviour by depth-sensing indentation. *Int. J. of Mechanical Sciences* 53: 471–478.

Vandamme, M. & Ulm, F-J. 2006. Viscoelastic solutions for conical indentation. *Int. J. of Solids and Structures* 43: 3142–3165.

Vandamme, M. 2008. The nanogranular origin of concrete creep: a nanoindentation investigation of microstructure and fundamental properties of calcium-silicate-hydrate. *Ph. D. Thesis, Massachussetts Institute of Technology* USA.

This page intentionally left blank

Rock Mechanics for Resources, Energy and Environment – Kwaśniewski & Łydżba (eds)
© 2013 Taylor & Francis Group, London, ISBN 978-1-138-00080-3

Measuring stress induced electric field in sandstone and granite using the Electric Potential Sensor

A. Aydın
University of Sussex, Brighton, UK

M.R. Dobbs, H.J. Reeves, C.C. Graham & M.P. Kirkham
British Geological Survey, Keyworth, UK

ABSTRACT: Electromagnetic phenomena associated with rock deformation have been detected using various electrical measurement methods. Studies demonstrate that this includes electric field. A recent approach to this is enabled through a new, low cost sensor technology, the Electric Potential (EP) Sensor. The EP Sensor has previously measured complementary electric field signals extant with stress-induced currents in marble and granite. This paper presents preliminary research, measuring stress-induced electric field changes in uniaxial compressive stress tests on sandstone and granite until failure. The result is a unique data-set that reveals stress-induced electric field, which increases in amplitude and frequency simultaneously, up to the point of failure. It is seen that the electric field is sensitive to two factors controlled in these tests, specifically lithology and drying condition (moisture content). The findings are important since they provide information regarding stress state and fracture processes occurring. This technology has potential for application to rock at the field-scale.

1 INTRODUCTION

Since the 1970's, evidence for pre-earthquake electromagnetic phenomena has been growing and many of these attribute this to rock deformation (Mizutani et al. 1976) (Hayakawa et al. 1994) (Tzanis et al. 2001). This viewpoint is supported by laboratory-based studies, which have found the flow of electric currents and the detection of electric potential in rock are associated with their deformation and the application of stress (Brady et al. 1986) (Aydan et al. 2001) (Freund 2002) (Hadjicontis et al. 2004) (Eccles et al. 2005) (Triantis et al. 2006) (Takeuchi et al. 2011). All have made measurments with laboratory based electrometers that are expensive and draw current from the rock specimen.

While these studies have demonstrated the existence of pressure stimulated currents (Anastasiadis et al. 2004), the precise mechanism/mechanisms responsible are still debated. There are also factors that may inhibit application of these techniques to *in situ* field studies. Inherit problems include low level currents (pico Amps level) and the closed loop system configuration requiring ends to be some arbitrary width apart for the measurement.

One technology that could resolve many of these issues is the Electric Potential Sensor (EPS or EP Sensor) developed and patented by the University of Sussex (Prance et al. 2000). EP Sensor technology has already been successfully applied in a number of diverse fields including microscopic imaging (Prance et al. 1998) electrophysiology (Harland et al. 2002) and nuclear magnetic resonance (Prance et al. 2007). Recent work has shown that it may also be transferable to the detection of changes in the electric potential field of rocks subjected to a compressive stress (Aydin et al. 2009). The EPS is based on an ultra-high input impedance amplifier system, which gives it its unique properties that comprise; no real current drawn and therefore a capability of detecting very small changes in electric field; a broad frequency response, ranging from quasi dc to >100 MHz; capability of single ended (ground referenced) acquisition, making it potentially ideal for deployment in the field; and low cost due to its makeup of standard components.

In this paper, we present results from recent experiments to measure stress induced changes in the electric potential field of rock specimens using a high capacity servo-controlled load frame. Four ISRM-type standard uniaxial compressive stress tests were undertaken on specimens of sandstone and granite until failure occurred. The specimens were instrumented with EP Sensors and strain gauges. Specimens were tested under strain control with different drying conditions, being air-dry and oven-dry.

A control test was also undertaken on a cylindrical specimen of aluminium in order to verify that the change in electric potential measured was derived from the rock specimens and not the surrounding environment.

2 TESTING METHODOLOGY

2.1 *Specimen preparation and instrumentation*

Cylindrical rock specimens approximately 108 mm in length and 54 mm in diameter were extracted from block samples or borehole core using a water-fed diamond core drill bit. The ends of each specimen were trimmed and ground to ensure they were flat, parallel and perpendicular to their long axis, in general accordance with ISRM suggested methods (2007).

The porosity and density of each specimen was calculated using standard ISRM saturation and buoyancy techniques (Ulusay & Hudson 2007). The specimens were then either: i) placed in an oven at 105°C until dry and then left to cool in a desiccator prior to testing; or ii) left to air dry for a period of 2 weeks at 20°C. Prior to instrumentation, the exact physical characteristics of each specimen were measured, and are summarised in Table 1. This table also includes the characteristics for the aluminium control sample.

All specimens were prepared with 25 mm × 25 mm copper strips to act as electrodes for the EPS. Kapton® polyimide film was placed between the specimen and electrodes to ensure they were electrically isolated from the specimen. EP Sensors were then aligned and fixed to each electrode using rubber bands, encircling the specimen to ensure contact between the EPS and the electrodes. Two such EP Sensor arrangements were used on each specimen in order to make a differential measurment.

The instrument setup, including EPS and strain gauges, can be seen in Figure 1. The EPS, together with its associated signal conditioning and acquisition system are simplified in Figure 2 and are referred to as the EPS system.

The EP Sensors were configured with a gain of five, applied to the signal induced on the electrode. Each of the EPS channels were low pass filtered at 140 kHz to reduce aliasing, before digitization using a PC based National Instruments data acquisition system.

The EPS signals were recorded and then processed using this unit. This EPS system was triggered by the load frame controller in order to determine time domain signal features for later comparison.

Two direct contact axial strain gauges were attached to the sides of the specimen using rubber bands. A direct contact circumferential strain gauge was also fitted around the centre of the specimen.

A 4,600 kN capacity servo-controlled hydraulic load frame (MTS 815) was used to perform the loading of the specimens. Load was measured using a high resolution load cell and recorded together with the strain data.

The instrumented specimens were placed in the load frame with FR-4 copper-clad printed circuit board plates, above and below the specimen, in order to electrically isolate it from the load frame. Shielding techniques were used to reduce sources of noise.

The MTS servo-controller was connected to a PC separate from the EPS system. This PC operated the

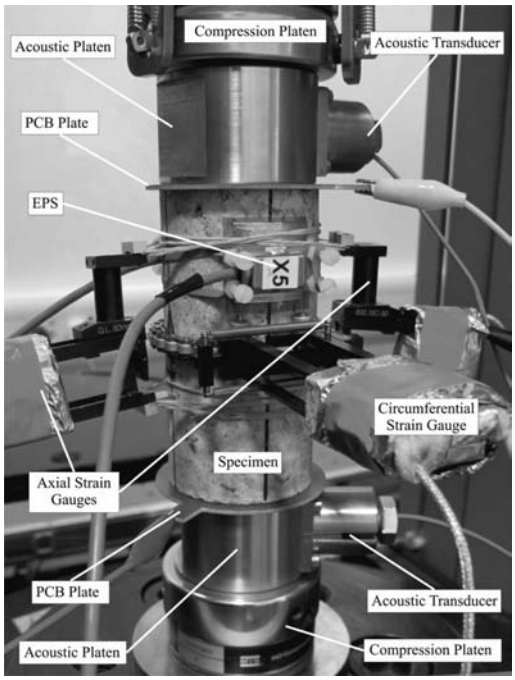


Figure 1. Instrumented granite specimen.

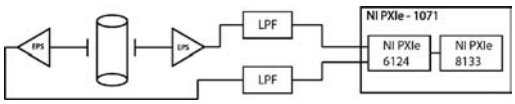


Figure 2. EPS signal conditioning and data acquisition configuration.

Table 1. Properties for granite and sandstone specimens tested.

Sample no.	Lithology	Diameter (mm)	Length (mm)	Porosity (%)	Dry density (Mgm^{-3})	Drying condition	Load/Strain rate	Time to failure (s)	Peak stress (MPa)
C81_8	Granite	54.9	107.8	1.20	2.59	Air dry	$6.5 \times 10^{-6}\ s^{-1}$	411.1	109.4
C81_3	Granite	54.9	107.3	1.20	2.62	Oven dry	$6.5 \times 10^{-6}\ s^{-1}$	495.2	137.5
S4_1	Permian Sandstone	54.7	107.9	15.5	2.24	Oven dry	$8.0 \times 10^{-6}\ s^{-1}$	419.1	46.9
S4_3	Permian Sandstone	54.3	107.8	17.20	2.19	Air dry	$8.0 \times 10^{-6}\ s^{-1}$	371.8	39.2
Alu	Aluminium	50.0	100.0	N/A	N/A	N/A	$1.00\ kNs^{-1}$	938.1*	234.4

servo-controlled hydraulic actuator and was also used to record and visualise the stress and strain data for each experiment.

2.2 *Experimental configuration and testing procedure*

Prior to commencing each test, an initial 1 kN load was applied to ensure the specimen and compression platens were appropriately seated. Four rock specimens were subjected to an increasing uniaxial compressive stress until failure occurred. For the granite specimens, a constant axial strain rate of $6.5 \times 10^{-6}\ s^{-1}$ was used. For the sandstone specimens, a strain rate of $8.0 \times 10^{-6}\ s^{-1}$ was used. For each lithology, an air dry and oven dry specimen was tested, as given in Table 1. The aluminium control sample was subjected to a single cycle stress ramp test at a constant loading rate of $1.0\ kN\ s^{-1}$, up to a peak stress of 234 MPa (460 kN load) before being returned to 0.5 MPa (1 kN load) at a constant rate of $1\ kNs^{-1}$.

3 RESULTS

The electric field measured using the EP Sensors for the experiments conducted are presented in this section, along with the stress and strain data for all specimens, including the aluminium control sample. Acoustic emission data is also available but its presentation does not form the focus of this paper and will be presented elsewhere. Specimen properties, including lithology, dimensions, porosity, density, drying condition, experimental load/strain-rate, peak stress and time to failure, are summarised in Table 1.

The stress is calculated from the applied load and specific specimen cross-sectional area. The volumetric strain data is calculated as the sum of the average axial strain (from two gauges) plus two times the circumferential strain as set out by Ulusay and Hudson (2007). The EPS signals greater than 1 kHz are presented and are arithmetic differential results of the two digitised EP Sensor channels. A colour, joint time and frequency plot is used to display the Fast Fourier Transform of the differential signal over time. The color intensity indicates the magnitude of the specific frequency signal at a given time. It is important to note that all joint time and frequency plots have a fixed intensity scale in order to make a direct comparison between test outputs. The frequency intensities below 1 kHz, shown as a high magnitude strip at the bottom of each plot and may be discounted as the FFT resolution is insufficient causing the false intensities.

Figure 3 and Figure 4 show the stress, strain and differential EP Sensor data for granite lithology specimens. The single variation between these is the drying condition, where Figure 3 is for air dried granite, and in Figure 4, is for oven dried.

Figure 5 and Figure 6 show the stress, strain and differential EP Sensor data for sandstone lithology specimens. The variation between these is the drying condition, where Figure 5 is for oven dried sandstone, and Figure 6 is for air dried.

Figure 7 depicts the stress, strain and differential EPS data for the aluminium control specimen.

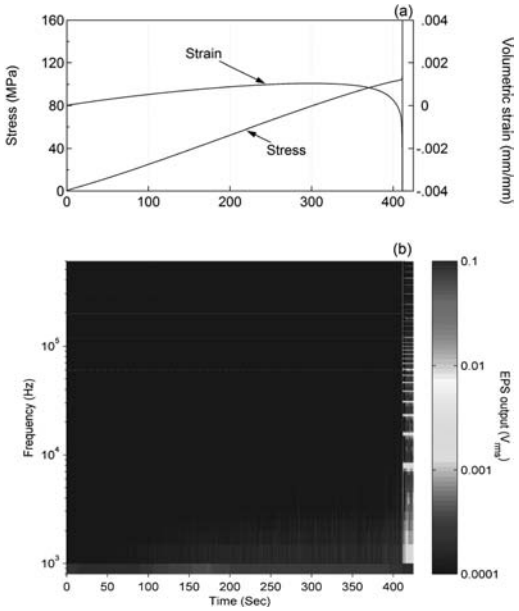


Figure 3. Result for air-dry granite, specimen C81_8. (a) stress and strain plot; (b) differential EPS singal.

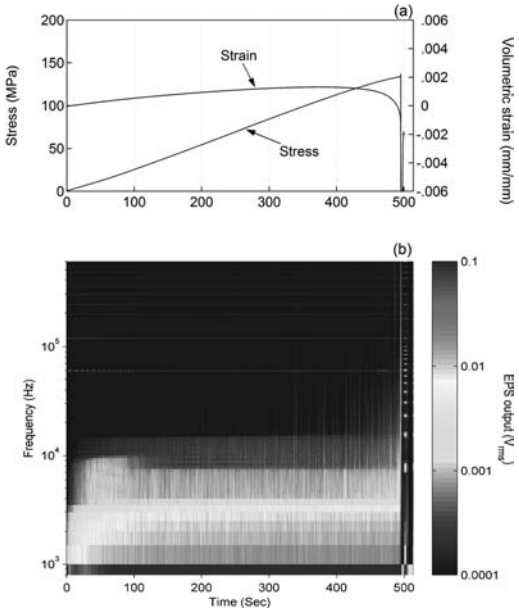


Figure 4. Result for oven-dry granite, specimen C81_3. (a) stress and strain plot; (b) differential EPS singal.

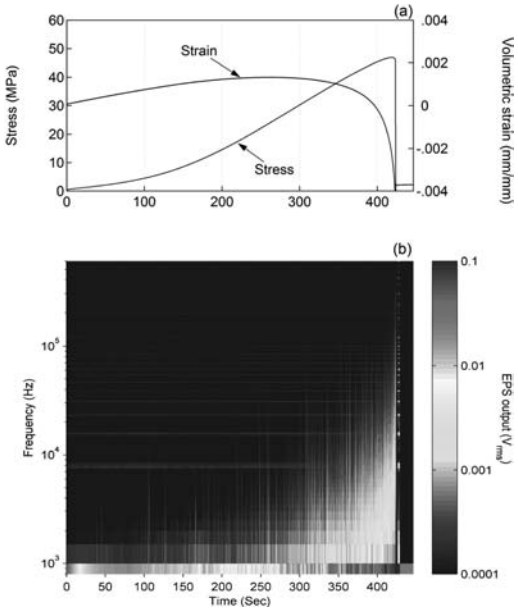


Figure 5. Result for oven-dry sandstone, specimen S4_1. (a) stress and strain plot; (b) differential EPS singal.

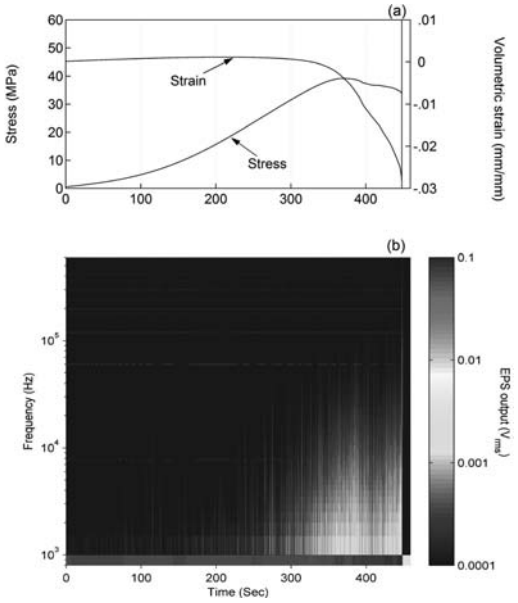


Figure 6. Result for air-dry sandstone, specimen S4_3. (a) stress and strain plot; (b) differential EPS singal.

4 DISCUSSION

Electric field signals were detected for all specimens that varied in signal intensity, the level of which was dependent on their drying condition. The fixed intensity scale for the electric field detected using the EP Sensor allowed a direct comparison of the relative signal intensities.

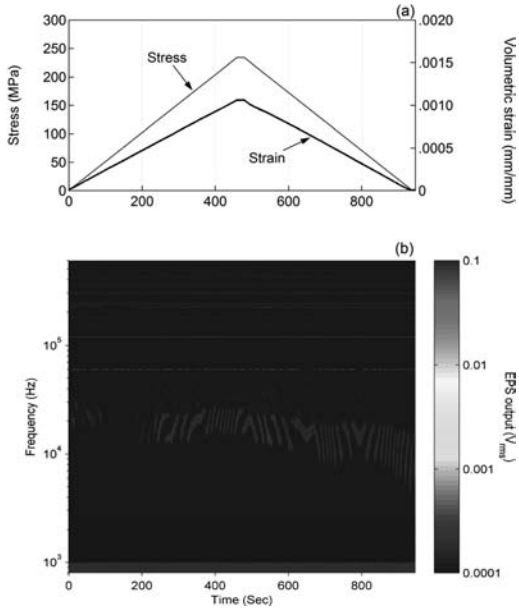


Figure 7. Result for aluminium control specimen. (a) stress and strain plot; (b) differential EPS singal.

Both granite samples followed an expected strain profile, however, the resulting electric field was markedly different between the two drying conditions. The air dried specimen contained a relatively low electric field which gained some frequency bandwidth over the test. The intensity remained constant but low. This result can be improved for intensity by using a more sensitive scale. Feint high bandwidth spikes are seen in the run up to failure. The oven dried granite specimen contained a comparatively greater intensity and frequency band of signal throughout the test when juxtaposed with the air dried specimen. It also contains a much greater number of high bandwidth spikes throughout the test. The oven dried sandstone specimen followed a normal strain profile before failure. The electric field detected for this test revealed a buildup of signal in both frequency and intensity as the loading tended to failure. Numerous spikes of broadband signals are also seen throughout the run. For the air dried specimen, the strain profile exhibits a peak stress observed before the formation of catastrophic sample failure. The electric field signals detected contain increasing frequency content with less intensity than in the oven dried specimen. The non-ideal approach to catastrophic failure highlights the sensitivity of the EPS technique to peak stress. This is seen where the changing strain is coincident with a change in electric field frequency content in Figure 6.

The control test on the aluminium specimen discloses no electric field bar an anomalous semi-oscillatory signal in a 10–30 kHz frequency band. This is possibly attributed to the use of a conductor control specimen, approximating a pickup antenna. This

is not observed in other tests therefore, it may be concluded that the electric field signals in the rock tests do originate from the specimens.

5 CONCLUSIONS

Uniaxial compressive tests were conducted on two lithology types, granite and sandstone. Measurements of the stress and strain were made, together with a new quality, the electric field produced in a wide band, made possible using the Electric Potential Sensor (EPS or EP Sensor). Tests were administered under a strain control stress regime for the two lithology types. For each type, two tests were carried out which varied the drying condition of the specimen; oven-dried and air-dried. This condition is thought to be the cause of the difference seen in electric field content detected in addition to the lithology. The main trend was less intensity and frequency band for air dried specimens. Moisture content of similar air dried specimens tested (sandstone and granite of the same lithology) showed variations between 0.25% and 0.5%. All tests exhibited a number of high bandwidth spikes during the test. The authors would like to attribute these to fracture development however, these are also seen in the elastic phase of deformation in all tests. Observations from one of the sandstone samples indicates a clear sensitivity to peak stress. More studies are needed to quantify the exact effect on electric field of a fuller range of moisture content, as well as comparison of acoustic emission data.

ACKNOWLEDGEMENTS

The authors would like to thank all colleagues involved at the British Geological Survey and the University of Sussex for their input to the work, in particular R.J. Prance, D.A. Gunn, L.P. Field and S.J. Holyoake. We would also like to acknowledge: the Engineering and Physical Sciences Research Council (grant ref.: EP/J015938/1) and the Natural Environment Research Council for providing the funding for the project. This paper is published with the permission of the Executive Director of the British Geological Survey (NERC).

REFERENCES

Anastasiadis, C., Triantis, D., Stavrakas, I. & Vallianatos, F. (2004) Pressure Stimulated Currents (PSC) in marble samples. *Annals of Geophysics*, 47, 21–28.

Aydan, Ö., Minato, T. & Fukue, M. (2001) An experimental study on the electrical potential of geomaterials during deformation and its implications in Geomechanics. *38th US Rock Mechanics Symposium.* Washington.

Aydin, A., Prance, R. J., Prance, H. & Harland, C. J. (2009) Observation of pressure stimulated voltages in rocks using an electric potential sensor. *Applied Physics Letters*, 95, 124102.

Brady, B. T. & Rowell, G. A. (1986) Laboratory Investigation of the Electrodynamics of Rock Fracture. *Nature*, 321, 488–492.

Eccles, D., Sammonds, P. R. & Clint, O. C. (2005) Laboratory studies of electrical potential during rock failure. *International Journal of Rock Mechanics and Mining Sciences*, 42, 933–949.

Freund, F. (2002) Charge generation and propagation in igneous rocks. *Journal of Geodynamics*, 33, 543–570.

Hadjicontis, V., Mavromatou, C. & Ninos, D. (2004) Stress induced polarization currents and electromagnetic emission from rocks and ionic crystals, accompanying their deformation. *Natural Hazards and Earth System Sciences*, 633–639.

Harland, C. J., Clark, T. D. & Prance, R. J. (2002) Electric potential probes-new directions in the remote sensing of the human body. *Measurement Science and Technology*, 13, 163–163.

Hayakawa, M. & Fujinawa, Y. (1994) *Electromagnetic Phenomena Related to Earthquake Prediction*, Terra Scientific Publishing Company.

Mizutani, H., Ishido, T., Yokokura, T. & Ohnishi, S. (1976) Electrokinetic phenomena associated with earthquakes. *Geophysical Research Letters*, 3, 365–368.

Prance, R. J. & Aydin, A. (2007) Acquisition of a nuclear magnetic resonance signal using an electric field detection technique. *Applied Physics Letters*, 91, 044103.

Prance, R. J., Clark, T. D., Prance, H. & Clippingdale, A. (1998) Non-contact VLSI imaging using a scanning electric potential microscope. *Measurement Science & Technology*, 9, 1229–1235.

Prance, R. J., Debray, A., Clark, T. D., Prance, H., Nock, M., Harland, C. J. & Clippingdale, A. J. (2000) An ultra-low-noise electrical-potential probe for human-body scanning. *Measurement Science & Technology*, 11, 291–297.

Takeuchi, A., Aydan, Ö., Sayanagi, K. & Nagao, T. (2011) Generation of electromotive force in igneous rocks subjected to non-uniform loading. *Earthquake Science*, 24, 593–600.

Triantis, D., Stavrakas, I., Anastasiadis, C., Kyriazopoulos, A. & Vallianatos, F. (2006) An analysis of pressure stimulated currents (PSC), in marble samples under mechanical stress. *Physics and Chemistry of the Earth*, 31, 234–239.

Tzanis, A. & Vallianatos, F. (2001) A critical review of Electric Earthquake Precursors. *Annali Di Geofisica*, 44, 429–460.

Ulusay, R. & Hudson, J. A. (2007) *The complete ISRM suggested methods for rock characterization, testing and monitoring: 1974–2006*, Ankara, Turkey, Commission on Testing Methods, International Society of Rock Mechanics.

This page intentionally left blank

Rock Mechanics for Resources, Energy and Environment – Kwaśniewski & Łydżba (eds)
© 2013 Taylor & Francis Group, London, ISBN 978-1-138-00080-3

Characterization of the distribution of physical and mechanical properties of rocks at the Tutupan coal mine, South Kalimantan, Indonesia

M.A. Azizi
Mining Engineering Department, Institut Teknologi Bandung, Indonesia
Mining Engineering Department, Trisakti University, Indonesia

S. Kramadibrata & R.K. Wattimena
Mining Engineering Department, Institut Teknologi Bandung, Indonesia

I.D. Sidi
Civil Engineering Department, Institut Teknologi Bandung, Indonesia

ABSTRACT: Uncertainties of factors that influence slope stability have been acknowledged by many geotechnical engineers, and these are drawn from the characterization of the geotechnical parameters of the slope. The characterization is associated with a process of identifying the distribution of random variable values used in the design of a single slope of an open mine, and also part of the probabilistic method which is an alternative approach in estimating the stability of a slope with a Failure Probability value (FP). This paper explains the characterization process using the Kolmogorov-Smirnov (K-S) method, which will determine the most appropriate function for the distribution of the random variable. The characterization results can be used in determining the Safety Factor including the level of confidence and Probability of Failure based on the best fitting function.

1 INTRODUCTION

Slope design has over the years become the domain of geotechnical engineers. While this has benefited the technology of theslope design processes, it has also separated the the mine design engineers from the responsibility of the risk versus reward relationship.

Given the uncertainties that prevail within the geotechnical discipline, there always exists a probability that a slope may not perform aspredicted, and in the worst case can result in a catastrophic failure.

The rock slope stability analysis affected by the random input parameters such as internal friction angle, cohesion, water pressure, seismic acceleration and density, which cannot be properly represented by a single value as input parameters in slope stability analysis. The uncertainty in the values of rock mass properties is a major factor in slope stability analysis.

Each input parameter has a certain distribution function. There are several methods used in characterizing a data distribution, namely: Chi-Square Method, Kolmogorov-Smirnov method, and the method of Anderson Darling. This paper uses the Kolmogorov-Smirnov method. The principle of this method is based on a comparison between the experimental cumulative distribution function and cumulative distribution theoretical assumptions.

The 4 assumptions of the cumulative distribution function will be compared with the empirical distribution functions, namely: normal, lognormal, beta, gamma.

The results of the characterization process will be used for the calculation of the safety factor and failure probability of slopes, and the distribution data are obtained from Tutupan Coal Mine, South Kalimantan, Indonesia.

2 BASIC THEORY

2.1 *Probability distribution function*

Probability distribution function describes the spread of a random variable that is used to estimate the probability of the occurrence of a parameter value. It has typical and unique properties of distribution that make one function different from others. But this does not rule out the possibility that a distribution function is a derivative from another function. For example, the exponential distribution function is a special form of the gamma distribution function withshape parameter (a) is 1. Likewise, a uniform distribution function is a special form of the beta distribution function with shape parameter values $\alpha = 1$ and $\beta = 1$. A triangular distribution function is also a special form of the beta distribution function with shape parameter values $\alpha_1 = 1$ and $\alpha_2 = 2$.

This paper employs 4 assumed continuous distribution functions, i.e. normal, lognormal, beta, and

Table 1. Assumed probability density function (Tse, 2009).

Distribution	Probability density function	Mean & Varians
Normal	$f_x(x) = \frac{1}{\sigma\sqrt{2\pi}} e^{-\frac{1}{2}\left(\frac{x-\mu}{\sigma}\right)^2}$ $-\infty < x < \infty$	μ σ^2
Lognormal	$f_x(x) = \frac{1}{x\sigma\sqrt{2\pi}} e^{-\frac{1}{2}\left(\frac{\ln x-\mu}{\sigma}\right)^2}$ $x > 0$	$e^{\mu+\frac{1}{2}\sigma^2}$ $e^{2\mu+\sigma^2}(e^{\sigma^2-1})$
Beta	$f(x) = \frac{x^{\alpha_1-1}(1-x)^{\alpha_2-1}}{B(\alpha_1,\alpha_2)}$; $0 \le x \le 1$ $f(x) = 0$, x others	$\frac{\alpha_1}{\alpha_1+\alpha_2}$ $\frac{\alpha_1\alpha_2}{(\alpha_1+\alpha_2)^2(\alpha_1+\alpha_2+1)^2}$
Gamma	$f(x) = \frac{x^{\alpha-1}e^{-x/\beta}}{\beta^\alpha\Gamma(\alpha)}$; $x > 0$ $f(x) = 0$, x others	$\alpha\beta$ $\alpha\beta^2$

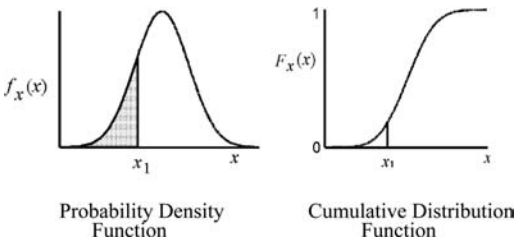


Figure 1. Probability Distribution Function.

gamma. These are considered to represent the properties of the distribution of the random variables (see Table 1).

Figure 1 describes a Probability Density Function (PDF) and Cumulative Distribution Function (CDF). Probability density functionsexplains the area in which the relative probability of a random number can be assumed to be a unique value compared to the other value. Failure probability (FP) is determined from the distribution of the safety factor. The area under the curve (FK < 1) is defined as a failure probability value.

2.2 *Fitting distribution function*

If a theoretical distribution has been assumed, then the validity of the assumed distribution could be confirmed or refuted by a statistical test with goodness of fit. There are several methods to test the goodness of fit of some assumed distribution functions, i.e. Chi Square method, Kolmogrov-Smirnov (K-S) method, and Anderson-Darling method. This paper only discusses the K-S method. The basic procedure of this method includes a comparison between experimental and theoretical cumulative frequency distribution of the types of assumed distributions. If the difference of both frequencies is higher than those of a certain sample size, the assumed theoretical distribution will be rejected. The equation of this cumulative distribution function is as follows:

Table 2. Critical value (Tse, 2009).

Significance level α	0.10	0.05	0.01
Critical value	$\frac{1.22}{\sqrt{n}}$	$\frac{1.36}{\sqrt{n}}$	$\frac{1.63}{\sqrt{n}}$

$$S_n(x) = \begin{cases} 0 & x < x_1 \\ \frac{k}{n} & x_k \le x < x_{k+1} \\ 1 & x \ge x_n \end{cases} \quad (1)$$

$x_1, x_2, \ldots, x_n$ are the values of the sample data that is already set, and n is the sample size.

In the K-S test, the maximum difference between $S_n(x)$ the and F(x) for all ranges of x is a measure of the difference between assumed theoretical distributions and experimental data distribution. The maximum difference of both distributions can be written as follows:

$$D_n = max_x|F(x) - S_n(x)| \quad (2)$$

Theoretically D_n is a random variable whose distribution depends on n. To a certain significance level α, K-S test compares the maximum difference of the observations in above equation with the critical value D_n^α. Table 2 describes the critical value with a particular significance level α. Thus with a significance level α, the null hypothesis is rejected if D_n is higher than the critical value. To facilitate this method assisted with Matlab software Ver.7.12.0.

When all functions have a D_n value lower than the critical value, it can be retested using 2 indicators, i.e. Akaike Information Criteria (AIC) and Bayesian Information Criteria (BIC). The Akaike information criterion, denoted by AIC, proposes to penalize large models by subtracting the number of parameters in the model from its log-likelihood. Thus, AIC is defined as:

$$AIC = \log L(\hat{\theta};\mathbf{x}) - p \quad (3)$$

where $\log L(\hat{\theta}; \mathbf{x})$ is the log-likelihood and p is thenumber of estimated parameters in the model. Based on this approach the modelwith the largest AIC is selected.

The above problem of the AIC can be corrected by imposing a differentpenalty on the log-likelihood. The Schwarz information criterion, also calledthe Bayesian information criterion, denoted by BIC, is defined as:

$$BIC = \log L(\hat{\theta};\mathbf{x}) - \frac{p}{2}\log n \quad (4)$$

The details of these methods can be seen in Tse (2009).

2.3 *Monte Carlo simulation*

This method effectively simulates the response of the SF performance function to randomly select discrete values of the component variables. The process is repeated many times to obtain an approximate discrete PDF of the resulting SF values. The component random variables for each calculation are selected from a sample of random values that are based on the selected PDF of the random variables. Although the PDFs can take on any shape, the normal, lognormal, beta and gamma distributions are among the most favored for the analysis.

It should be noted that each Monte Carlo simulation will use a different sequence of random values, and the resulting probabilities, means, variances, and histograms will be slightly different. As the number of trials increases, the differences will become smaller.

Because the Monte Carlo simulation requires a large number of calculations, it often has been viewed as a less desirable option than the Taylor series or point estimation method. However, with the general availability of faster desktop computers, the Monte Carlo approach has gained wider acceptance due to its inherent simplicity and the ability to use existing computer programs with only minor modifications. Details of this method can be read in Abramsom et al. (2002), Baecher et al. (2003), and Tse (2009).

3 DATA COLLECTION & METHODOLOGY

Data gathering of the physical and mechanical properties of the lithology (coal, mudstone and sandstone) of Tutupan coal mines, South Kalimantan, Indonesia was carefully conducted. These properties include unit weight, cohesion, and internal friction angle. The number of data from each lithology consists of 10, 33 and 16 for coal properties data, mudstone properties data, and sandstone properties data respectively.

Furthermore, the fitting test of K-S method was done using Matlab software Ver.7.12.0. By using equation [1], the empirical data representation can be done by sorting the data from smallest to highest value, which produces a histogram in the form of CDF (See Figure 2).

In the K-S method, the empirical distribution function was compared with the 4 assumptions in the theoretical distribution function, i.e. normal, lognormal, beta, and gamma. If the distribution function of the data is not actually, then D_n has a considerable value. Thus, with a significance level $\alpha = 5\%$, the null hypothesis is rejected if D_n is greater than the critical value. The critical value for $\alpha = 5\%$ is $1.36/\sqrt{n}$. For example, a fitting test was conducted on the cohesion distribution of mudstone (see Figure 3). The amount of data is 33 and $\alpha = 5\%$, the critical value is 0.237. To declare the assumptions of the functions fit and the hypothesis is accepted, the D_n value must be smaller than the critical value. The results of the fitting test on cohesion distribution of mudstone indicates that the 4 assumed theoretical distribution functions have a D_n value smaller than the critical value, the hypothesis is then accepted.

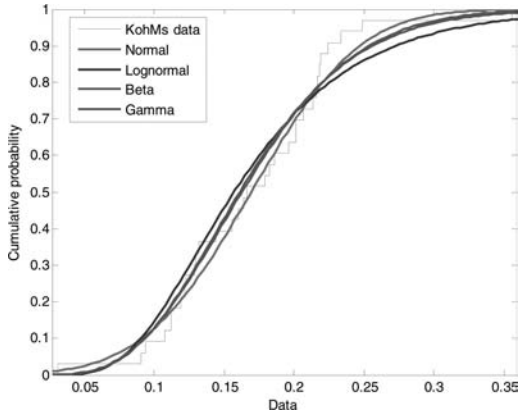


Figure 2. Empirical CDF.

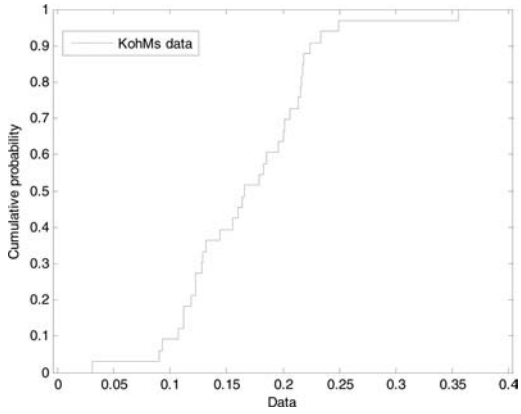


Figure 3. Overlay empirical and assumed theoretical CDF.

Table 3. The results of fitting test on cohesion of mudstone.

Statistical parameter	Normal	Lognormal	Beta	Gamma
Mean	0.191	0.193	0.191	0.191
D_n	0.096	0.118	0.095	0.096
Critical value	0.237	0.237	0.237	0.237
Log-likelihood	46.111	42.632	45.543	45.147
AIC	44.111	40.632	43.543	43.147
BIC	44.593	41.113	44.024	43.629

Besides that, we also have to see the AIC and BIC values of the 4 assumed theoretical distribution functions. By using equation [3] and [4], AIC and BIC values can be determined. The largest value of that distribution is normal distribution, i.e. respectively 44.111 and 44.593. Thus, it can be said that the most appropriate distribution function is the normal distribution (see Table 3).

Table 4. The result of fitting test in rock properties of tutupan coal mine.

Statistical parameter	c (MPa)	ϕ (Deg.)	γ (kN/m^2)
Mudstone			
Mean	0.169	23.6	22.68
Variance	0.004	23.5	0.38
Std. Deviation	0.061	4.8	0.62
D_n	0.096	0.090	0.324
Critical Value	0.237	0.237	0.237
Log-likelihood	46.11	−98.38	−30.42
AIC	44.11	−100.38	−32.42
BIC	44.59	−99.82	−31.93
Distribution	Normal	Normal	Normal
Sandstone			
Mean	0.191	27.8	21.48
Variance	0.003	33.1	–
Std. Deviation	0.057	5.8	–
D_n	0.144	0.121	–
Critical Value	0.340	0.340	–
Log-likelihood	23.54	−50.20	–
AIC	21.54	−52.20	–
BIC	22.34	−51.40	–
Distribution	Normal	Normal	–
Coal			
Mean	0.241	34.1	12.36
Variance	0.003	5.4	–
Std. Deviation	0.051	2.3	–
D_n	0.190	0.120	–
Critical Value	0.430	0.430	–
Log-likelihood	15.77	−22.13	–
AIC	13.77	−24.13	–
BIC	14.77	−23.13	–
Distribution	Gamma	Normal	–

Table 4 presents the summary of the characterization test of rock properties distribution on 3 lithology of rock. Only the cohesion of coalthat has gamma distribution, while others have normal distribution.

4 DISCUSSION

Based on the characterization results using K-S method, each fitted distribution was included in the calculation of the safety factor. Given any variation in the random variable that is used in the determination of SF, then FP was also be generated.

Characterization data can also be used to predict failure probability when the slope failed. This is possible when there is a strength decrease (see Table 5).

Table 5. The results of failure probability.

Lithology	Coal	Mudstone	Sandstone
Slope Height (m)	15	15	15
Slope Angle (deg.)	70	70	70
SF Deterministic	5.5	2.7	2.8
SF Mean	5.5	2.8	2.8
Cohesion (kPa)	241	169	191
Cohesion (kPa) Back Analysis	57	68	66
Deterioration (%)	76.3	59.8	65.4
FP (%)	0	1.3	0
FP (%) Back Analysis	56.5	46.2	49.8

5 CONCLUSIONS

Several points can be concluded from the results of this study, and is as follows:

- KS method is the most practical method to obtain the most suitable distribution.
- The results of the characterization of the properties of 3 rock lithology produce all types of variables tested had a normal distribution, except for the cohesion of coal that has a gamma distribution.
- Characterization results are used to estimate the value of the safety factor following the data distribution, which would further strengthen the confidence level of the FK value.

ACKNOWLEDGEMENT

The authors would like to thank the committee ISRM which gives the opportunity to present this paper, and PT Adaro Indonesia for the support in providing data.

REFERENCES

Abramson, L.W., Lee, T.S., Sharma, S. & Boyce, G.M. 2002. Slope Stability and Stabilization Methods, second edition, John Wiley & Sons.

Ang, A.H-S., & Tang, W.H. 1984. Probability Concepts in Engineering Planning and Design – Vol. II Decision, Risk and Reliability John Wiley & Sons.

Azizi, M.A., Kramadibrata, S., Wattimena, R.K. & Arif, I. 2010. Application of Probabilistic Approach on Slope Stability Analysis, Annual Meeting of Indonesian Mining Professionals Association (PERHAPI) XIX 2010, Balikpapan.

Azizi, M.A., Kramadibrata, S., Wattimena, R.K. & Arif, I. 2011. Application of probabilistic approach on single slope stability analysis using limit equilibrium method, National conference of Statistical 2011, organized by Statistical Department, Faculty of Science, University of Diponegoro, Semarang, Indonesia.

Azizi, M.A., Kramadibrata, S., Wattimena, R.K., Suhedi & Basuki, S. 2011. Probabilistic approach on single slope stability analysis using Bishop Method, National Conference of Mining 2011, organized by mining department, faculty of engineering, University of Lambung Mangkurat, South Kalimantan.

Baecher, G.B., & Christian, J.T. 2003. Reliability and statistics in geotechnical engineering. Wiley, Chichester, U.K.

Hoek, E., Factor of Safety and Probability of Failure, Chapter 8 – Rock Engineering.

Tse, Y.K. 2009. Nonlife Actuarial Models, Theory, Methods and Evaluation, Cambridge University Press.

Rock Mechanics for Resources, Energy and Environment – Kwaśniewski & Łydżba (eds)
© 2013 Taylor & Francis Group, London, ISBN 978-1-138-00080-3

Experimental study of the permeability evolution of a rock fracture under THMC conditions

A. Blaisonneau, M. Peter-Borie & S. Gentier
BRGM, Georessources Division, Geothermal Energy Department, Orleans Cedex 2, France

ABSTRACT: The goal of the development of reactive percolation tests in fracture under Thermo-Hydro-Mechanical conditions is to improve the understanding of fluid/rock interactions and their role on the fracture permeability evolutions. Indeed, these permeability evolutions of the fractures are a key point in the life duration of a geothermal exchanger in EGS (Enhanced Geothermal System) sites.

1 INTRODUCTION

In the framework of the development of EGS (Enhanced Geothermal System) technology, a better understanding of fluid/rock interactions in the deep fractured reservoir will allow to improve the management of the heat exchanger and to optimize its life duration. Indeed, beyond the stimulation step of the reservoir, the evolution of fracture permeability is strongly related to chemical processes due to fluid/rock interactions in a system with varying mechanical, hydraulic and thermic conditions, depending on the distance from injective and productive wells. These chemical processes can lead either to an increase of the permeability, due to dissolution phenomenon, or to a decrease of the permeability because of precipitation phenomenon. This is to improve the understanding of these fluid/rock chemical interactions and their impact on the fluid flow in the fracture that reactive percolation tests in fracture in Thermo-Hydro-Mechanical (THM) conditions are developed.

2 DESCRIPTION OF PERCOLATION TESTS IN FRACTURE

2.1 *Experimental device*

The principle of the reactive percolation test is to perform a fluid flow in a fracture of a rock sample in THM conditions determined and controlled (Fig. 1):

- A cylindrical rock sample is drilled to get the mean plane of the fracture perpendicular to the axis of revolution;
- A normal stress is applied to the rock sample, perpendicular to the fracture plane;
- The fluid, whose chemical composition is calculated, is injected with a determined flow rate at the center of the fracture. In the fracture, the flow is radial divergent. The fluid, flowing through the fracture, is collected in an annulus tank surrounding the rock sample.

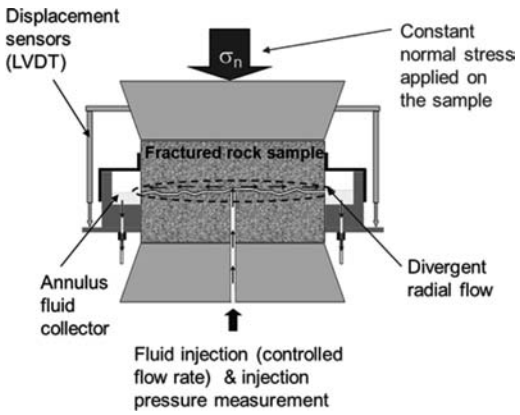


Figure 1. Principle of the THM reactive percolation test (cross-sectional view).

The test is performed inside a thermodynamic cell, settled under a mechanical press. The thermodynamic cell is pressurized and includes a heating device to impose the temperature. The pressurization is made by water saturated azote with a controlled humidity to avoid fluid evaporation during the test.

The fluid is expulsed *via* capillary tubes out of the fluid collector tank of the cell thanks to the difference of pressure between inside and outside the cell. It is then driven through a system of electro-valves either to a weighing system to check up the outflow or to a collector of fluid sample for chemical analysis.

During the test, the parameters fixed by the operator are: the normal stress, the injection flow rate, temperatures both in the cell and of the injected fluid.

The parameters measured during the test are: the closure/aperture of the fracture by means of four LDVT displacements sensors (Fig. 1), the fluid pressure at the injection point at the center of the fracture, the temperature at several points (center of the fracture, in the upper part of the rock sample, in the annulus fluid collector tank, in the cell). The outflow is checked to ensure that there is an admissible conservation of the fluid mass in order to make fluid balance.

During the test, the pH and the redox potential Eh are measured online outside of the thermodynamic cell and allow verification of the chemical processes reactivity. The evolutions of the chemical composition of the fluid during the test are determined by the analysis of the collected fluid samples.

2.2 *Methodology*

In order to achieve a better understanding of fluid/rock interactions and their influence on the evolution of the fracture permeability, a complete methodology has been developed in parallel to the implementation of the experimental device. The methodology is based on a set of characterizations and tests made before and after the reactive percolation test *stricto sensu,* in order to determine the evolutions of physical and morphological characteristics of the fracture, and its rock walls, and also the evolutions of the hydraulic behavior of the fracture.

The following physical and morphological characterizations are made:

- Analysis and visual description of the minerals on the fracture walls and in the rock matrix;
- Mapping of the fracture voids (Gentier & Billaux 1989) by image analysis of voids molding;
- Mapping of the topography of the fracture walls by means of profiles made with a laser profilometer;
- Mapping of chemical elements by X-ray microflurescence of the fracture walls.

To characterize the hydraulic behavior of the fracture, injection tests under different levels of normal stress are made, before and after reactive percolation test. For these tests, unlike during the reactive percolation test, the chemical composition of the injected fluid is determined to be non-reactive with the minerals on the fracture and in the rock matrix.

3 TEST ON A GRANITIC FRACTURED ROCK SAMPLE

3.1 *Description of the initial fractured rock sample*

The test presented here has been performed on a granitic fractured rock sample (70 mm in diameter) and formed in a core from the EPS1 drilling of Soultz-sous-Forêt (France). The core comes from 1890 m in depth. The rock is porphyritic granite containing pinkish multi centimeter mega crystals of potassium-feldspar (K-spar) in a matrix made of gray to greenish

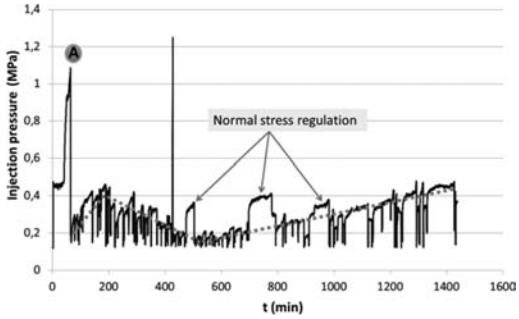


Figure 2. Evolution of the injection pressure during the first day of the reactive percolation test.

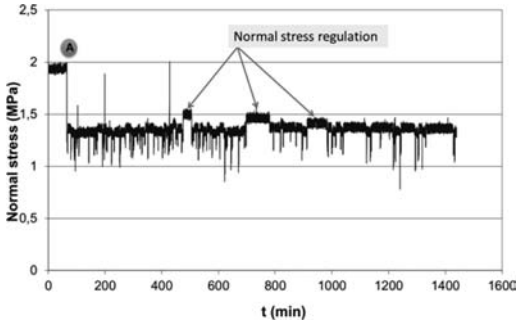


Figure 3. Evolution of the normal stress during the first day of the reactive percolation test.

medium-sized grains of quartz, plagioclase, K-spar, biotite and metal oxides. The fracture walls show a very thin coating of calcite extended, infra millimeter thick.

The full set of mapping (voids, topography maps and chemical elements) has been made on the walls and the fracture before the installation of the rock sample in the experimental device.

3.2 *Reactive percolation test*

For the reactive percolation test, a synthetic brine has been injected with an injection flow rate of 30 ml/h. The chemical composition of the brine is calculated to be close to that of *in situ* Soultz-sous-Forêt site fluid but with lower concentrations of some elements to avoid precipitation of secondary mineral phases and clogging of pipes.

The test lasted 17 days with a temperature near of 85°C at the injection point. At the beginning of the test, a 1.9 MPa normal stress has been applied. Nevertheless, during the first hour, the injection pressure increased rapidly and exceeded 1 MPa after one hour (point A in Figure 2). To limit every risk of hydraulic fracturing of the rock sample, the level of normal stress was a little bit decreased, from 1.9 to 1.35 MPa (point A in Figure 3), in order to decrease the level of injection pressure.

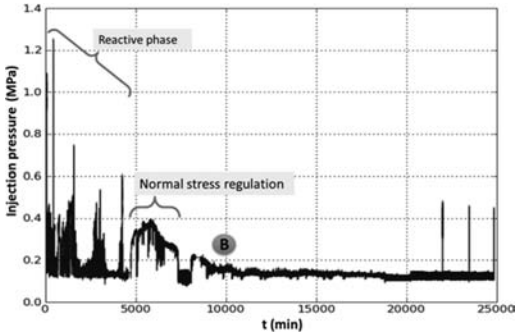


Figure 4. Evolution of the injection pressure during the 17 days percolation test.

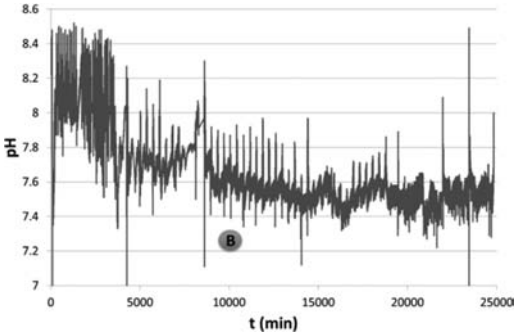


Figure 5. Evolution of the pH during the 17 days percolation test.

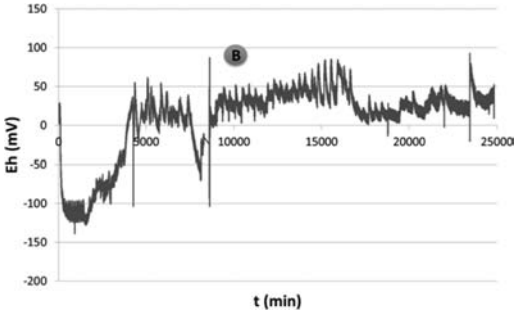


Figure 6. Evolution of the Eh potential during the 17 days percolation test.

After the decrease (point A) during the first day of the test, the mean evolution of the injection pressure shows (Fig. 2) an increase between 60 and 200 minutes, then a decrease between 200 and 600 minutes, then an increase again between 600 and 1400 minutes. This mean evolution, underlined by the dotted line in Figure 2, can be explained by an alternation of dissolution/precipitation processes in the fracture. For the evolutions at a lower scale (briefs peaks or shutting down of the injection pressure), it's more difficult to separate physical causes from experimental artifacts: for example artifacts induced by the normal stress regulation are highlighted in Figures 2 and 3.

After the first day, the alternation of decrease/increase of the mean evolution of the injection pressure continues (reactive phase on Figure 4). After the 7th day of the test, the pressure is stabilized around 0.15 MPa (point B in Figure 4).

Most of the recorded parameters during the test show a similar tendency to those of the injection pressure: the main changes occur during the first seven days of the test, then there is a stabilization of the phenomenon. This can indicate that the main chemical interactions occur at the beginning of the test. This looks to be corroborated by the recorded evolutions of the pH (Fig. 5) and Eh potential (Fig. 6): the main changes occur during the first seven days (point B in figures) then a relative stabilization around a pH value of 7.5 and a potential Eh of 25 mV.

3.3 *Evolution of the rock sample*

The visual description of the fracture walls shows mainly dissolution of the calcite coating and dissolution of plagioclase, locally strongly rounded, and an alteration of biotite. K-spar and quartz look intact and unaffected by alteration processes.

The full set of mapping has been made on the rock sample after its disassembly from the experimental device. The comparison with those made before allows to characterize the physical evolution of the fracture.

Figure 7 shows the map of the void thickness variation of the fracture achieved by subtracting the initial map of voids from those done after the reactive percolation test.

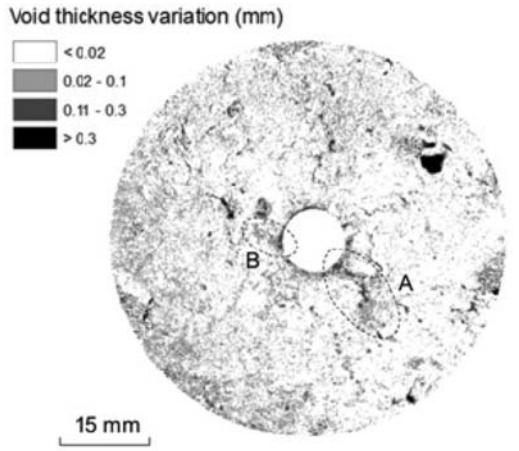


Figure 7. Map of the difference between voids thickness before and after the percolation test.

In the two areas noted A and B on Figure 7, increases of void thickness are observed so as to form channels which meander from the injection area to a maximal distance of 8 mm for A. These channels are characterized by a thickness greater than a millimeter and so most likely do not result of errors in adjustments of the final and initial void maps. They are interpreted as the consequences of rock wall local erosion linked

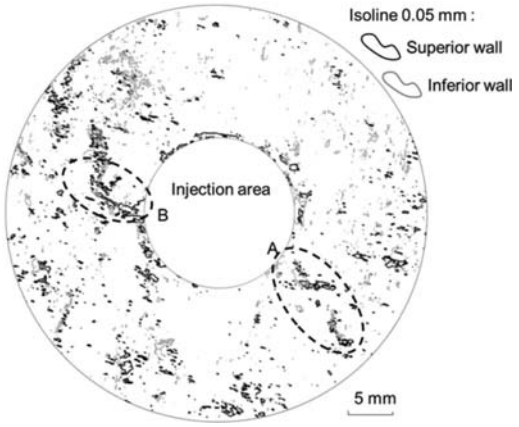


Figure 8. Variation of the elevation of the walls of the fracture: Isoline of an erosion of 0,05 mm (zoom on the center part of the fracture).

to percolation test. This interpretation is corroborated by the evolution of the topography of the walls of the fracture as shown by Figure 8.

Quantitative analysis is performed by computing directional variograms (equiangularly distributed axes) of the void thickness before and after the percolation test. Several variograms are computed on rings of increasing radius and neighboring the injection area (radius of the smaller circle constant). Regardless of the studied direction, and until a radius of the ring of 9 mm, the sill of variograms computed on the void thickness after the percolation test is more important than the sill of variograms computed on the void thickness before the percolation test. It indicates that variations of the void thickness in the sub-centimetric area neighboring the injection area are more important after percolation than initially.

Whether it is by qualitative observation of the maps or quantitative analysis (variogram analysis), it appears that the measurable evolution of the morphology of the fracture concerns a centimetric-thick ring neighboring the injection area.

3.4 *Evolution of the mechanical behavior of the fracture*

The mechanical behavior of the fracture has been characterized under normal stress before and after the reactive percolation test. Figures 9 and 10 show the evolution of displacements (recorded by the four LVDT sensors) as a function of the normal stress applied on the rock sample, respectively before and after the reactive percolation test.

The overall trend of the evolution of the recorded incremental displacements versus the increment of normal stress looks similar before and after the reactive percolation: under an increment of normal stress of 7 MPa the recorded closure of the fracture is roughly of 0.03 mm. Usually, the fracture behavior under normal stress exhibits a phase for low stress range (below

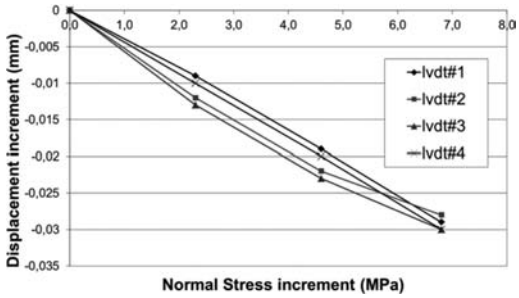


Figure 9. Evolution of the displacements with normal stress before the reactive percolation test.

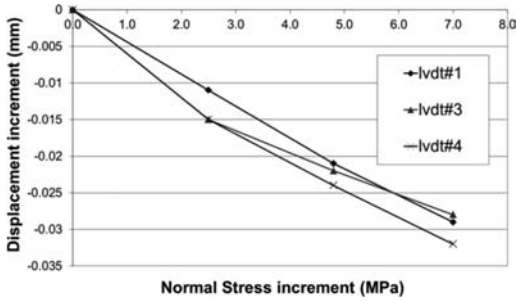


Figure 10. Evolution of the displacements with normal stress after the reactive percolation test.

8–10 MPa) where the evolution of closure as a function of with normal stress is linear. This phase is followed by a non-linear phase corresponding to a locking of the fracture. The major part of recorded fracture closure looks to be in the linear phase except the closure recorded by LVDT#3 (Fig. 10) which exhibit a non-linear evolution. Based on these data, it seems that the mechanical behavior of the fracture is weakly affected by the chemical interactions occurring during the reactive percolation test.

Note that from the reactive percolation test the LVDT#2 was out.

3.5 *Evolution of the hydraulic and hydromechanical behavior of the fracture*

In order to characterize the hydraulic behavior of the fracture, injection tests with non-reactive fluid are made: the injection pressure is measured under increasing flow rate steps. These injection tests are performed under increasing levels of normal stress in order to characterize the hydraulic behavior evolution under normal stress. Figures 11 and 12 illustrate the collected data, respectively before and after the reactive percolation test.

Figure 11 shows that for the lowest normal stress (2.6 MPa) the evolution of the injection pressure versus injection flow rate looks linear, indicating a laminar flow regime. For higher normal stresses (4.9, 7.2 and 9.4 MPa), despite the small number of experimental points, the curves look nonlinear. Moreover, Figure 11

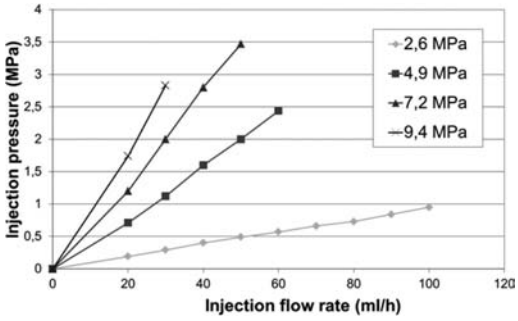


Figure 11. Evolution of the injection pressure with respect to the injection flow rate under increasing levels of normal stress before the reactive percolation test.

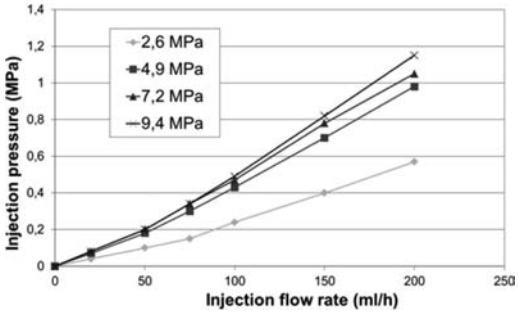


Figure 12. Evolution of the injection pressure with respect to the injection flow rate under increasing levels of normal stress after the reactive percolation test.

exhibits that an increase of the normal stress induces an increase of the injection pressure for the same injection flow rate: for the highest level of normal stress (9.4 MPa) the injection pressure is just below 3 MPa for an injection flow rate of 30 ml/h whereas for the lowest level of normal stress (2.6 MPa), it is about 0.3 MPa. Thus, the mechanical loading induces a significant reduction of the fracture permeability.

After the reactive percolation, the hydraulic behavior of the fracture (Fig. 12) looks different. First, even for the lowest normal stress, the curves of injection pressure versus flow rate look nonlinear. Moreover, the levels of injection pressure are lower after reactive percolation (Fig. 12) than before (Fig. 11) whereas the injection flow rates are higher.

Concerning the influence of normal stress on the hydraulic behavior, for the three highest levels of normal stress (4.9, 7.2 and 9.4 MPa) the evolutions of injection pressure versus injection flow rate (Fig. 12) are very close. It looks that the mechanical loading has little influence on the hydraulic behavior.

Another way to illustrate the evolution of the hydraulic behavior of the fracture under the mechanical loading is to represent the evolution of the intrinsic transmissivity of the fracture with respect to the increment of normal stress (Fig. 13). This physical parameter can be estimated from the equation 1 by making the

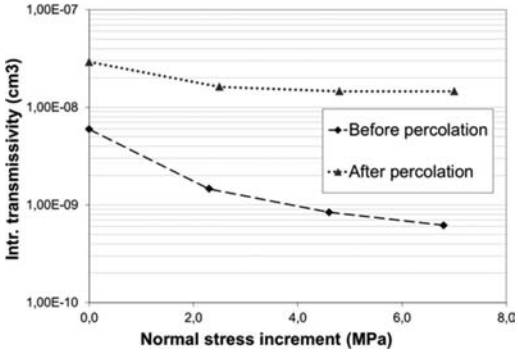


Figure 13. Evolution of the intrinsic transmissivity (logarithmic representation) with respect to the normal stress increment before and after the reactive percolation test.

assumption of radial laminar divergent flow between two circular planes (Gentier 2002):

$$k_f e = - (\eta/2\pi) (Q/\Delta P) \text{ Ln } (R_i/R_e) \quad (1)$$

where η is the dynamic viscosity of the fluid (Pa.s), Q is the mass flow (cm^3/s), ΔP is the delta pressure (Pa) between the center of the fracture (injection point) and its periphery (at the pressure of the confining cell), R_i and R_e (in mm) are respectively the inner radius (radius of the injection drilling) and outer radius (radius of the rock sample). The intrinsic transmissivity $k_f e$ has the dimension of a volume, expressed here in cubic centimeter.

Before the reactive percolation test, the intrinsic transmissivity of the fracture decreases with the normal stress increment (Fig. 13) and reaches a minimal value of 6×10^{-10} cm^3 at the increment of normal stress of 7 MPa. After the percolation, there is a decrease on the intrinsic transmissivity for the first normal stress increment then a stabilization for upper increments at 1.4×10^{-8} cm^3. It looks that the reactive percolation test has induced a decrease of the mechanical impact on intrinsic transmissivity of the fracture. Moreover, the intrinsic transmissivity of the fracture has been drastically increased, roughly of one order of magnitude (Fig. 13), by the reactive percolation test, indicating an increase of the fracture permeability.

3.6 *Conclusions of the test*

For this reactive percolation test, the evolutions of parameters, such as injection pressure or pH, show reactivity focused on the first seven days of the test, followed by a stabilization of the phenomena.

The set of physical characterizations and tests made on the fracture before and after the reactive percolation highlights changes induced by chemical fluid/rock interactions during the reactive test:

– The visual observation of the fracture walls shows mainly dissolution of the calcite coating and dissolution of plagioclase, locally strongly rounded, and an alteration of biotite;

– The morphological characterizations (map of the fracture voids, map of the topography of the rock walls) show the creation of "channels", which meander from the injection area to a distance of 8 mm with a thickness greater than a millimeter;
– The closure of the fracture under normal stress looks unaffected by the chemical interactions occurring during the reactive percolation test;
– The reactive percolation test has induced a decrease of the impact of the mechanical loading on the hydraulic behavior of the fracture;
– The intrinsic transmissivity of the fracture has been drastically increased, roughly of one order of magnitude, by the reactive percolation test.

Based on these results, a probable hypothesis to explain the increase of the fracture permeability (highlight by intrinsic transmissivity evolution) is that fluid/rock interactions have induced a deepening of pre-existing channels, at least in an area around the injection point, without affecting the contact points of the fracture, which determine the mechanical behavior of the fracture.

4 CONCLUSION AND PERSPECTIVES

Reactive percolation tests in fracture under Thermo-Hydro-Mechanical conditions allow a better understanding of fluid/rock interactions and of their influence on the flow in fracture. A percolation test performed on a fractured granitic sample has shown that fluid/rock interaction under fixed THM conditions have induced an increase of the fracture permeability without affecting significantly the mechanical behavior under normal stress of the fracture. Such results are of great interest in order to estimate the fracture permeability evolutions during the life duration of EGS exploitation.

Of course, the experimental device and the associated methodology are still in progress of development. Several points have to be improved in order to refine the understanding of the fracture behavior, for example:

– Improve the hydraulic test to characterize the flow regime in the fracture;
– Improve the characterization of the mechanical behavior of the fracture by enlarging the applied normal stress range .

Moreover, the data collected during the test are not sufficient to say if the observed behavior corresponds more to behavior on the whole fracture than a behavior on local areas in the fracture. To help for answering that question, in parallel to experimental works, modeling works are in progress to better understand:

– the mechanical behavior of the fracture with models based on the map of contact points in the fracture deduced from topography of the rock walls;
– the hydraulic behavior of the fracture with a hydraulic model constructed on the basis of the voids map.

The results of these models would permit to compare the location and the evolution of the contact points to the location and the evolution of the flow channels in the fracture.

ACKNOWLEDGEMENTS

This work has been funded by the French Agency for Environment and Energy Management (ADEME).

REFERENCES

Gentier S., Billaux D. (1989) – Caractérisation en laboratoire de l'espace fissural d'une fracture, Rock at great depth, Pau, France, V. Maury and D. Fourmaintreaux (Eds), Balkema, pp. 425–431.

Gentier S. (2002) – Fractures dans les roches cristallines – Effet des déformations sur les circulations de fluides, Collection Sciences et Techniques, édité par l'ANDRA.

Rock Mechanics for Resources, Energy and Environment – Kwaśniewski & Łydżba (eds)
© 2013 Taylor & Francis Group, London, ISBN 978-1-138-00080-3

Simulation of single cutter experiments in evaporite using the discrete element method

C. Carrapatoso, S.A.B. da Fontoura, I.M.R. Martinez & N. Inoue
ATHENA – Computational Geomechanics Group, GTEP – Group of Technology in Petroleum Engineering PUC-Rio – Pontifical Catholic University of Rio de Janeiro, Brazil

A. Lourenço & D. Curry
Baker Hughes Inc., Houston, USA

ABSTRACT: The discovery of large oil reservoirs under salt layers is motivating the study of drilling optimization of wells in many basins, notably in Brazil and West Africa. The aim of this paper is to present the laboratory experiments carried out to cut evaporite samples in the so-called single cutter configuration. These tests are meant to generate results to improve the understanding of the mechanics of drill bit – rock interaction. The paper also describes the use of a numerical tool based upon the discrete element method to model the experiments.

The laboratory experiments consist in obtaining the forces acting upon a cutter during its penetration and cutting of a groove in a sample of evaporite. These forces are transformed into Mechanical Specific Energy, MSE. The tests were carried out under different depths of cut and back-rake angles. The results indicate that MSE decreases with the increase of depth of cut until a certain limit when it stabilizes. The experiments also indicate that changing cutter inclination changes the cutting forces and mechanisms, and the paper explores these findings. Triaxial confining tests were carried out in cylindrical samples of the same evaporite used in the cutting experiments. The results of these tests were used to create a virtual rock to be treated by the discrete element method. This is an important step in the workflow and is also described in the paper. Finally, the laboratory experimental results are compared with the results produced by numerical simulation. Both 2D and 3D modeling of the single cutter experiments were carried out under atmospheric conditions and satisfactory results were obtained, revealing the importance of the developed methodology in understanding rock cutting mechanisms.

1 INTRODUCTION

Distinct element method is a numerical technique developed to model problems of interaction between circular particles and has been explored in this work to model rock behavior. This study aims to modeling numerically the cutting action (drilling) of evaporites by a single polycrystalline diamond cutter using the aforementioned technique through the software PFC^{2D} and PFC^{3D}. The modeling work is considered an important step to understand the interaction between the drill bit and the rock and consequently optimize rate of penetration while drilling for oil and gas.

Single cutter laboratory experiments are used to simulate drilling action and assist drill bits cutter design and testing by measuring forces acting on the cutter and drilling efficiency. A single polycrystalline diamond cutter (PDC) cuts a groove as a sample of rock rotates at certain angular velocity against it. Several passes over the same groove (single track) occur as drilling progresses. These experiments can be simulated through numerical methods to analyze the effects of changing relevant conditions affecting drilling efficiency. Mechanical Specific Energy (MSE) is commonly used to evaluate cutting efficiency and is defined as the amount of work required for removing a unit volume of rock. This parameter is used as reference to identify what needs to be changed to improve the drilling.

The numerical models developed in this study assume that the cutting is carried out using a perfectly sharped PDC cutter and the cutter surface does not wear off during the test. Therefore, the mechanical specific energy obtained from the simulations considers only the energy used to cut the rock without taking into account the energy dissipation associated with friction between the cutter surface and the rock.

This paper presents the calibration procedure that was implemented to properly simulate the evaporite rock mechanical behavior numerically, including changes to the contact model to create the softening behavior of the observed biaxial/triaxial stress-strain curve. In addition, a set of simulations was carried out

with different cutter geometrical conditions in order to study the cutting process. Two-dimensional and three-dimensional simulations were performed under atmospheric conditions. Both depth of cut (DOC) and cutter back-rake angle were changed during the simulations and their influence on the mechanical specific energy was analyzed.

The experimental work, i.e., single cutter experiments as well as triaxial load experiments were carried out at Baker Hughes laboratories. High strain rate triaxial compression tests were performed on samples of the same material used for the single cutter tests to assess the material mechanical behavior (constitutive equation). This information was used to independently calibrate rock behavior (compressive tests) and later compare MSE results obtained experimentally with those predicted numerically.

The use of discrete element method to simulate single cutter tests was reported by some researchers. Lei et al. (2004) simulated rock cutting using DEM to investigate the effects of various parameters on the cutting force. The effect of brittle and ductile failure on drilling efficiency was also investigated through numerical modeling (Block & Jin 2009, Huang et al. 2012). Mendoza et al. (2011) modeled scratching tests using a three-dimensional distinct element program. They studied the influence of depth of cut on the cutting forces and found that shallow cuts do not always lead to ductile failure as earlier established by Huang & Detournay (2008). Akbari et al. (2011) studied the influence of dynamic loads on the drilling efficiency. They created a cutting environment using a two dimensional distinct element program and applied a vertical velocity that could be constant (representing weight on bit) or oscillatory (representing vibration assisted rotary drilling).

2 MICRO PARAMETERS FOR EVAPORITES

The discrete element method implemented in PFC describes the real rock as a package of particles connected together at their contacts. The properties at the contacts are described by micro parameters. Whenever PFC is used, macro parameters are output data obtained by a calibration process where the inputs are set by micro parameters. The procedure to obtain the proper set of micro parameters for a given virtual rock is an iterative process that ends when the predicted real rock properties (its macro parameters such as Young's modulus, Poisson's Ratio, unconfined compressive strength) are equivalent to those obtained at laboratory tests. In this paper the calibration process was carried out using, as reference, the results of unconfined compression test performed in the target evaporite, i.e., halite.

In the discrete element method, the Newton's second law is applied to each particle, providing its position and velocity. The contact forces are calculated from the relative particle displacements and from the constitutive model used in the contacts.

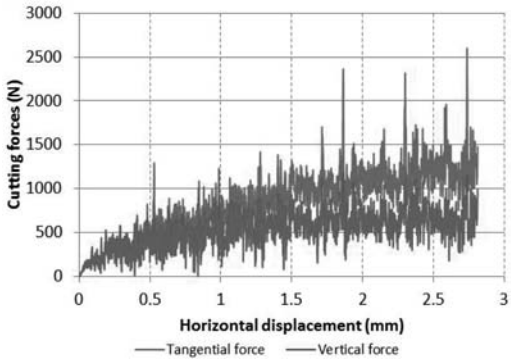


Figure 1. Experimental cutting forces under no confinement.

The magnitude of the normal contact force is calculated as presented in Equation 1 where k_n is the normal stiffness at the contact. k_n is determined from the current contact stiffness model.

$$F_n = k_n \cdot U_n \tag{1}$$

The shear force at the contact is computed in an incremental fashion. When the contact is formed, the total shear contact force is equal to zero. Each subsequent shear displacement increases the shear stress. In this way, to determine the shear strength it is necessary to compute the force generated by the translational displacement of the contact and the force generated by the rotation of the particles.

Figures 1 and 2 present the cutting forces from single cutter experiments and the stress-strain curve corresponding to an unconfined compressive test carried out under a strain rate of 10%/min. At the beginning of stress application, the curve displays an inelastic, concave-upward interval and this happens because fissures and pores begin to close (Goodman 1989). On halite, this interval is large compared to other rocks because rock salt experience greater deformation under loading. Otherwise, this phase is almost inexistent for confined tests, probably because of counteracting confinement forces preventing the development of fissures and pores. The decrease of the tangent modulus with increasing axial strain is evident, suggesting a softening response.

A calibration process is needed to model the rock in PFC. Laboratory experiments such as triaxial compression test, Brazilian test, direct shear and tension tests (Itasca, 1999) can assist in obtaining the micro parameters. In this paper the triaxial test was selected.

To generate the PFC model for the evaporite rock, using the stress strain curve shown in Figure 2, the linear contact model combined with parallel bond was chosen as a first approximation. After some iteration, a synthetic specimen was modeled in PFC^{2D} and its stress-strain curve was compared with the experimental curve shown in Figure 2.

The synthetic sample stress-strain curve shows an elastic behavior until failure. After the peak, the

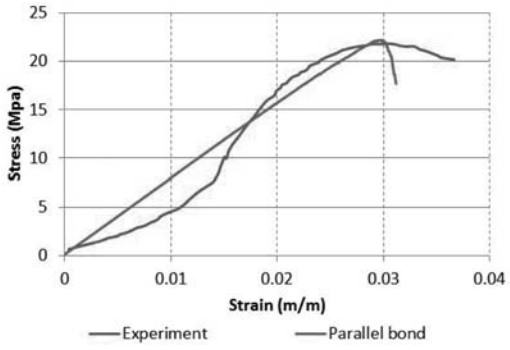


Figure 2. Laboratory test stress-strain curve and model calibration using linear contact model– PFC^{2D}.

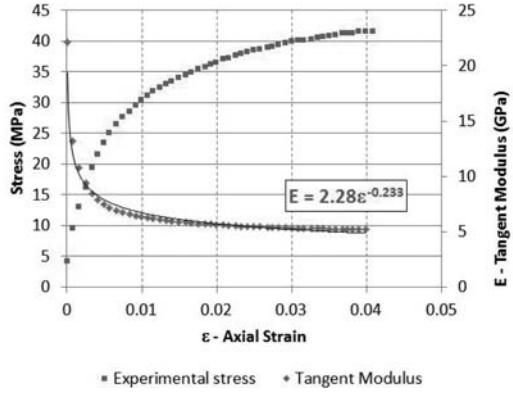


Figure 3. Experiment stress-strain curve and its derivate curve – 2 MPa of confinement.

material has a brittle behavior. The linear model combined with parallel bond has been used in many studies (Kaitkay & Shen 2004, Akbari et al. 2011, Block et al. 2009, Martinez et al. 2011, Mendoza et al. 2011, Rajabov et al. 2012) to represent the cutting of brittle rocks like marble, sandstone and shale with good results.

Analyzing Figure 2, it is clear that this contact model does not represent the real experimental curve since the evaporite sample shows a ductile behavior. Other contact models available in PFC^{2D} and PFC^{3D} were applied (like simple ductile model and simple viscoelastic model) without success in obtaining the hardening behavior.

To solve this problem, a modification was made on the linear model combined with parallel bond. The parallel bond contact stiffness was modified in each cycle, assigning decreasing contact stiffness as a function of disc overlap. This technique converts the linear model available on PFC in a different model with nonlinear behavior, standing as a new methodology to obtain a representative contact model of rocks with nonlinear stress-strain behavior.

2.1 *Methodology of micro parameters calibration*

The proposed methodology is composed of 3 steps that summarize the validation of the new model.

First, it is necessary to understand how the evaporite sample stiffness changes during the triaxial/uniaxial test. In PFC, the relation between the stiffness and the elastic modulus at a single contact bond is found as in Equation 2, where k_s is the tangent stiffness at the contact, t is sample thickness and R is the particle radius.

$$k_n = k_s = 2E_c \begin{cases} t, & (PFC^{2D}) \\ 2\tilde{R}, & (PFC^{3D}) \end{cases} \quad (2)$$

It is possible to find a relationship between tangent modulus and sample strain from the experimental stress-strain curve. Figure 3 illustrates this relationship for a 2 MPa confined test. Assuming that the value of the laboratory sample tangent modulus is roughly the same of the contact modulus, this last parameter can replace the sample tangent modulus in the relation shown in Figure 3. This relation represents the tangent modulus variation of each point in the curve according to the sample axial strain. It is important to note that this procedure is done for each specific stress-strain curve. In the case of halite, Equation 3 shows this relationship for a confined test of 2 MPa, where Ec (in GPa) is the contact elastic modulus and ε is the axial strain of the laboratory sample (triaxial/uniaxial test).

$$E_c = 2.28 \cdot \varepsilon^{(-0.233)} \quad (3)$$

Knowing that contact elastic modulus is equivalent to twice the contact stiffness multiplied by stiffness on PFC^{2D}, and is equivalent to four times the contact stiffness multiplied by particle radius on PFC^{3D} (Equation 1), it is possible to rewrite Equation 3 as Equation 4 and 5. The particle ratio is kept constant and with equivalent values on all numerical simulations.

$$k_n = 4.56 \cdot \varepsilon^{(-0.233)} \cdot t \quad \left(\text{PFC}^{2\text{D}}\right) \quad (4)$$

$$k_n = 9.12 \cdot \varepsilon^{(-0.233)} \cdot R \quad \left(\text{PFC}^{3\text{D}}\right) \quad (5)$$

The second step consists in using the relationship shown in Equations 4 and 5 to modify the linear contact model. In order to do this, it was necessary to create a code that calls this function at each simulation cycle. Thus, the contact stiffness will always be a function of the synthetic sample axial strain obtained in the previous step of the test. The stiffness at the contact decreases with the axial strain and hence the triaxial/biaxial test is continuously simulated in order to check if the numerical curve is close to the experimental one.

The use of macro parameters (sample strain, for example) as an input for calibration is not the conventional way to work with PFC because the particle size

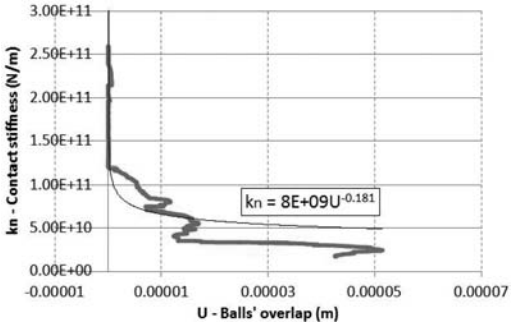


Figure 4. Contact stiffness versus ball's overlap, U, of a single contact – triaxial simulation.

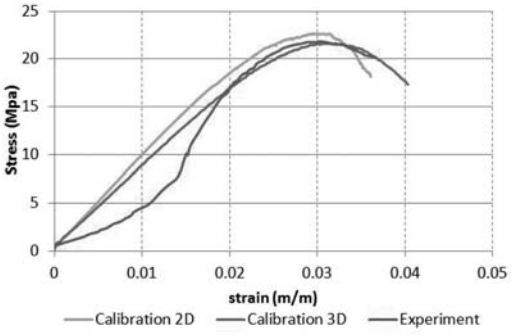


Figure 5. Laboratory triaxial test and model calibration using nonlinear contact model – PFC^{2D} and PFC^{3D}.

and the packing arrangement affect the model behavior. Also, it is not possible to use Equations 4 and 5 in single cutter simulation because an axial sample strain is not observed. Having said that, a retro-analysis of the calibration was performed. Some contacts were monitored during simulation to observe how micro parameters were changing (balls' overlap and contact's normal stiffness). It is worth mentioning that an additional code was written in order to monitor the contacts since PFC is unable to automatically identify them. Figure 4 presents the relationship found between contact stiffness and balls' overlap for a single contact during a triaxial simulation. Equation 6 presents the final relationship between contact stiffness and balls' overlap used to represent numerically the nonlinear behavior of the evaporite rock:

$$k_n = -8E09 \cdot U^{(-0.181)} \quad (6)$$

At this point, the simulation of the triaxial/biaxial test is repeated using Equation 6 at each simulation cycle. A new stress-strain curve is found that correlates well with the laboratory test curve. Figures 5 and 6 present the final calibration (PFC^{2D} and PFC^{3D}) and volumetric strain obtained in the three-dimensional modeling. Table 1 shows the micro parameters found

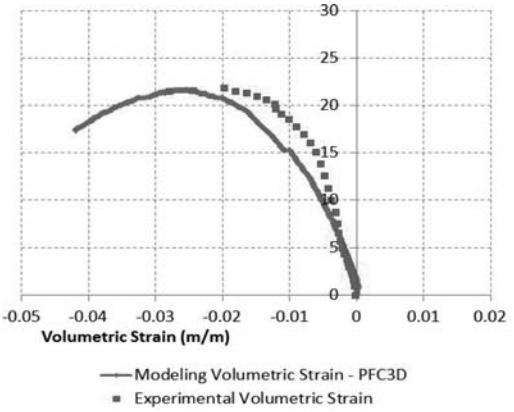


Figure 6. Volumetric strain versus axial stress – PFC^{3D}.

Table 1. Micro-properties established on final calibration using the new contact model.

Parameters	Symbol	Value	
		PFC^{2D}	PFC^{3D}
Sample Height (mm)	H	66.6	66.6
Sample width (mm)	W	37.97	37.97
Minimum ball radius (mm)	R_{min}	0.1	0.1
Ball size ratio	R_{max}/R_{min}	1	1
Ball density (kg/m^3)	ρ	2125	2125
Ball – ball contact modulus (GPa)	E_c	3	3
Ball stiffness ratio (GPa)	K_n/K_s	3	3
Parallel bond modulus (GPa)	$\overline{E}_c$	3	3
Parallel bond stiffness ratio	$\overline{k}_n/\overline{k}_s$	3	3
Ball friction coefficient	μ	1	1
Parallel bond normal strength, mean (MPa)	$\overline{\sigma}_{c,\,mean}$	22	14.5
Parallel bond normal strength, std. dev. (MPa)	$\overline{\sigma}_{c,\,std.\,dev.}$	12	9
Parallel bond shear strength, mean (MPa)	$\overline{\tau}_{c,\,mean}$	22	14.5
Parallel bond shear strength, std. dev. (MPa)	$\overline{\tau}_{c,\,std.\,dev.}$	12	9

after calibration procedure. These data and Equation 6 were used to simulate the evaporate behavior during the single cutter modeling.

3 SINGLE CUTTER MODEL

This part of the paper describes the modeling of the single cutter experiment and uses the parameters found in the calibration procedure to represent the salt rock. The model geometry is defined by a cutter that moves along the length of a synthetic rock with a fixed velocity. Depth of cut (DOC) can be changed or kept constant during simulations. In the two-dimensional simulation, the cutter is represented as a sharp edged pair

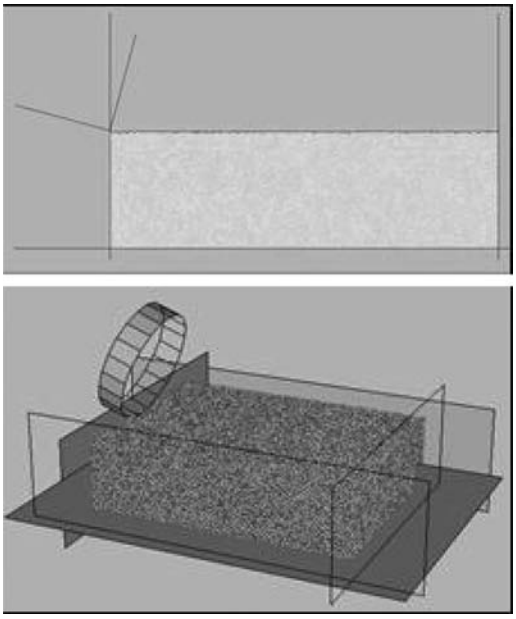


Figure 7. Cutting configuration – PFC^{2D} and PFC^{3D}.

of walls, and the particles are represented as discs. In the three-dimensional scenario the cutter is composed of a set of faces that form a cylinder and particles are represented as spheres.

Figure 7 shows the simulation set implemented in PFC^{2D} and PFC^{3D}.

4 VALIDATION OF THE CUTTING MODEL

Initially, a two-dimensional rock cut model was developed using the same features of the single cutter experiments. The objective was to reproduce the experimental results as close as possible. The numerical cutter had constant horizontal velocity of 1 m/s and vertical velocity of 0.060 m/s. To reduce the simulation time, these velocities are higher than those applied in the actual experiments (horizontal velocity = 0.44 m/s and vertical velocity = 0.0008 m/s). It is believed that the lower cutter velocities in the experiments may have been responsible for the observed MSE values stabilizing at higher depths of cut than those predicted by the simulations. Figures 8 and 9 show the calculated forces and mechanical specific energy, respectively.

Figure 8 shows that the profile of both vertical and horizontal forces is in good agreement with experiments. However, the order of magnitude is substantially higher than the observed in the experimental curve (847 N) and it is also higher when compared to results obtained for Carthage marble (Kaitkay e Shen, 2004). One possible explanation is that halite experiences greater deformation before it fails and this probably leads to higher cutting forces. In addition, the modeling is carried out on a two-dimensional

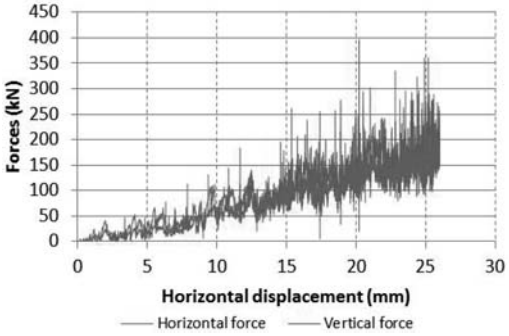


Figure 8. Horizontal and vertical forces of the PFC^{2D} rock cut modeling.

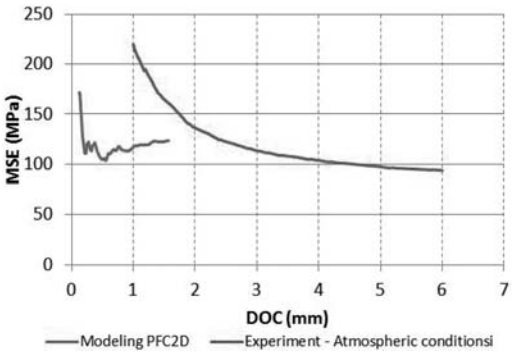


Figure 9. Comparisons between single cutter test and PFC^{2D} rock cut modeling – atmospheric conditions.

environment and forces generated are not of the same magnitude of those generated by a three dimensional cutter.

Figure 9 exhibits the comparison between calculated and measured MSE as a function of the depth of cut (DOC). Note that for computation reasons, simulations were performed at smaller depth of cuts, but the calculated curve exhibits similar shape as the experimental curve. However, its final value is higher than the experimental one. The final calculated specific energy was 125 MPa against 92 MPa in the experiments.

The cutting model considered a specimen with 5 cm of length and the test is run until 2.5 cm of length is reached. This is smaller than in the experiments, where the cutter reaches 2 m of total displacement through grooves produced on the sample. Because of that, the rate of penetration is higher in the simulations aiming at reaching the same order of magnitude as of the experiments. Despite of differences between simulated and real cutter geometry, the specific energy profile was similar to observed during experiments. The specific energy tends to initially decrease with DOC until it stabilizes at a certain value. Another observation is that a larger displacement is needed for the specific

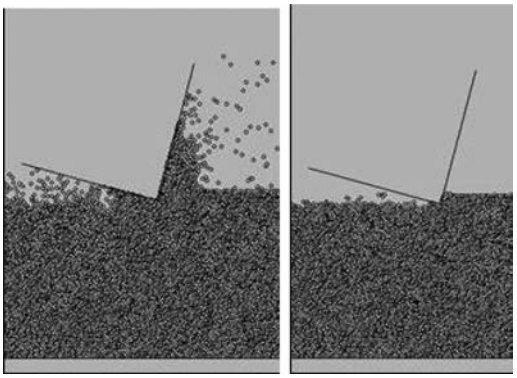


Figure 10. (a) Cutting view; (b) Cutting view with particle removal from cutter's face.

energy to stabilize. In order to make reliable comparisons between modeling and experimental results, a single value of specific energy was used as reference: the end value in the curve after it stabilizes.

A discrepancy between the reference calculated and experimental values of specific energy were observed (Figure 9). Two possible explanations are given here: the contact model does not properly represent halite or the particles that remain ahead of the cutter during simulation are leading to higher specific energy estimations. The last assumption is more likely to be the reason because in a numerical simulation carried out under atmospheric conditions, see Figure 10(a), a lot of particles (that simulates the crushed material) accumulate in front of the cutter, creating extra forces against the cutter movement. Its influence on the generated mechanical work must be investigated in order to adjust it for reproducing real experimental conditions. In confined experiments, cuttings remain in front of the cutter during test as ribbon like structures before detaching. However, cuttings are ejected away under atmospheric conditions due to the release of elastic energy (Ledgerwood III, 2009). In order to solve this problem and obtain better numerical results, a change was made into the PFC^{2D} rock cutting code. Particles ahead of the cutter are deleted using a particle position criterion. It works as all particles with broken bonds disappear from the cutter's face at a certain position. Figure 10(b) shows a cutting view using this modification and Figures 11 and 12 show the simulation results.

Figure 11 exhibits the cutting forces for the simulation considering crushed material (particles ahead of the cutter) removal. It can be seen that the forces are significantly smaller than those presented in Figure 8. The removal of particles ahead of the cutter led to an average 22% reduction in calculated forces.

Figure 12 compares the calculated specific energy without particles removal (red curve) and for the case with partial removal of particles ahead of the cutter (blue curve). Specific energy stabilized during simulation in the value of 96.35 MPa that represents a much better agreement with the 92 MPa from experiments.

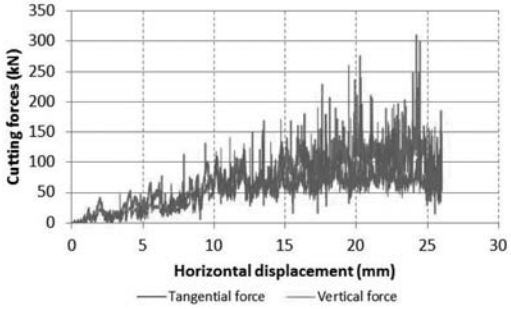


Figure 11. Forces of the PFC^{2D} rock cut modeling with particle removal from cutter's face.

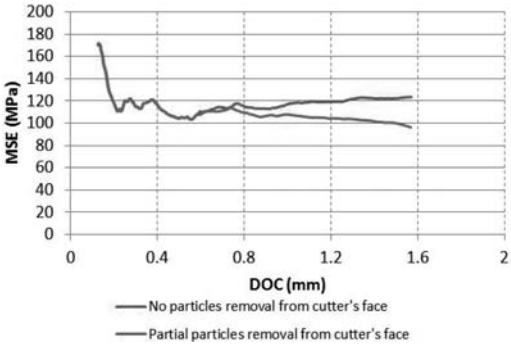


Figure 12. Comparison between numerical simulations with and without partial removal of particles ahead of cutter – PFC^{2D}.

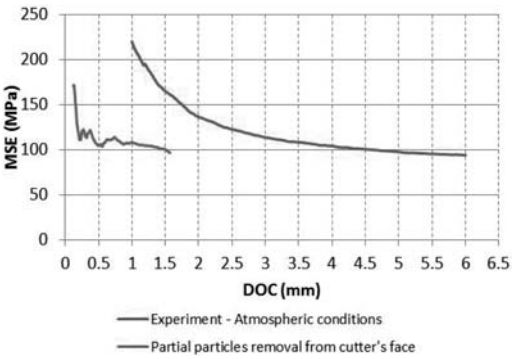


Figure 13. Comparisons between single cutter test and PFC^{2D} rock cut modeling considering removal of particles ahead of the cutter – atmospheric conditions.

Based on Figure 12, it is clear that specific energy decreases with the removal of crushed material in front of the cutter once any additional matter is reworked and wastes mechanical energy that otherwise would go into cutting rock.

Similarly, Figure 13 compares theoretical and experimental results for the same case. The result

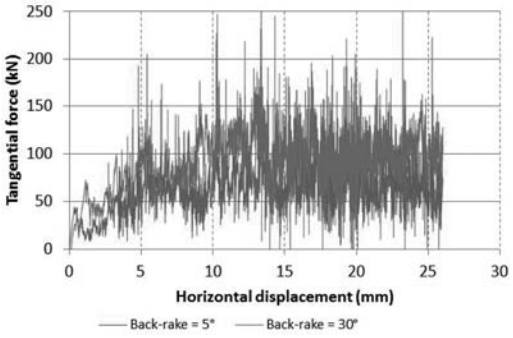


Figure 14. Increased contact area and cutting forces when the back rake angle increases – PFC^{2D}.

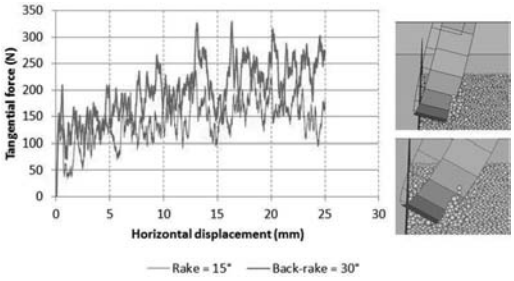


Figure 15. Increased contact area and cutting forces when the back rake angle increases – PFC^{3D}.

(together with calibration) seems to validate the approach of using the new contact model combined with particles removal criterion for the two-dimensional modeling carried out under atmospheric conditions.

5 INFLUENCE OF BACK RAKE ANGLE ON ROCK CUTTING

PFC^{2D} and PFC^{3D} rock cutting algorithms were used to analyze the influence of cutter's back-rake angle on rock cutting efficiency. The modeling were carried out under atmospheric conditions, using a depth of cut of 0.8 mm and varying back-rake angle from 5° to 30°. The cutter had constant horizontal velocity of 3 m/s for 3D-simulations and of 1 m/s for 2D simulations. As commented previously, higher velocities are used for modeling than those applied in the actual experiments (horizontal velocity = 0.44 m/s) in order to reduce the simulation time. It is important to emphasize that a new contact model was created to better represent salt behavior numerically.

Figure 14 and 15 display the cutting forces for two simulations using back-rake angles of 5° and of 30° at PFC^{2D} and PFC^{3D}, respectively. The average tangential forces are of 59 kN and 89 kN for the two-dimensional simulations and 134.08 kN and 190.87 kN for PFC^{3D}, respectively.

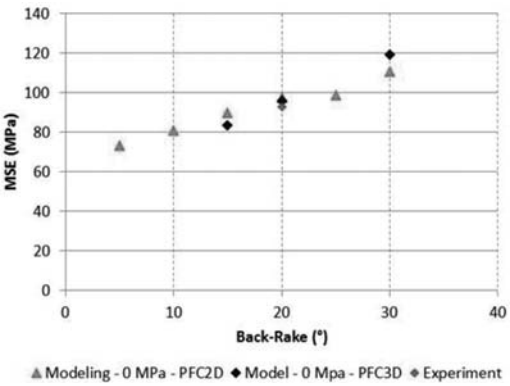


Figure 16. Effect of back-rake angle: results for halite at atmospheric conditions in 2D and 3D models.

The area of the cutter in contact with the material (groove area) increases with the increase of back-rake angle. Because of this fact, the cutter has to push more material resulting in higher forces observed on simulations with higher back-rake angles. Figure 14 illustrates the phenomenon. The reason for the increase of forces at higher back-rake angles is the increased degree of difficulty to remove cuttings from cutter front at large back-rake angles. Similar behavior was reported by Kaitkay and Shen (2004).

Figure 16 present the effect of back-rake angle on MSE for two-dimensional (green points) and three-dimensional (black points) simulations. The specific energy increases with the cutter inclination. Modeling on PFC^{2D} shows that mechanical specific energy has almost equivalent values when using back-rake angles of 20° and 25°. MSE continues to increase at higher angles as it happened at lower angle ranges (5°, 10° and 15°). Experiments were carried out using a back-rake angle of 20° under atmospheric condition and result is shown in Figure 16 and the reference MSE value of 92 MPa was measured. Three-dimensional modeling yielded better results than the two-dimensional approach. Table 2 shows the comparison.

It is important to remember that cutter wear is disregarded during simulations. Hence, we can state that cutting efficiency improves when low back-rake angles are used in a frictionless cutter-rock system since the values are closer to the unconfined compressive strength of salt (22 MPa).

Unfortunately no similar works involving DEM applied to simulating cutting in evaporite could be found in the literature. In spite of that a few works on other types of rocks are highlighted here. Rajabob et al. (2012) performed single cutter tests on Carthage marble, changing back-rake angle from 5° to 40°. They observed that the mechanical specific energy may double its value when the back-rake increases. Ghoshouni and Richard (2008) while performing scratch tests

Table 2. Comparison between experimental single cutter test and numerical modeling.

	Experiment	Modeling 2D	Modeling 3D	Error 3D (%)	Error 2D (%)
MSE (MPa)	92	98	96.04	4.4	6.5

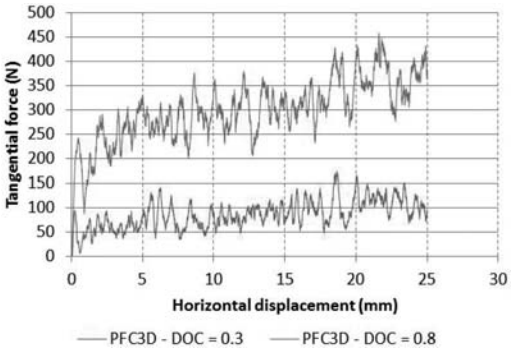


Figure 17. Cutting forces – depths of cut of 0.3 mm and of 0.8 mm.

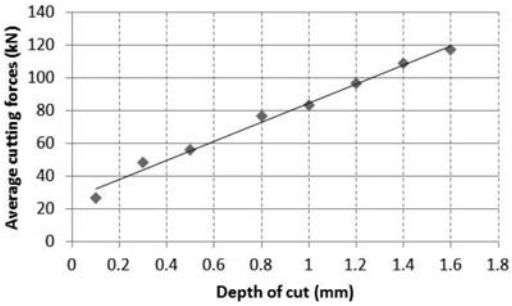


Figure 18. Average cutting forces versus depth of cut – PFC^{2D}.

on some brittle rocks also observed an increase on specific energy with increasing back-rake angle.

6 EFFECT OF DEPTH OF CUT

The effect of DOC on rock cutting efficiency is discussed in this section. Analogously to the previous section, simulations were carried out under atmospheric conditions, but now using a constant back-rake angle of 20°, the same as in the single cutter experiments.

Figure 17 shows the horizontal force for the three-dimensional modeling. Simulations were performed at DOC of 0.3 and 0.8 mm. Results show an increase of cutting forces with the increase in DOC. Figures 18 and 19 show the average forces for all simulations

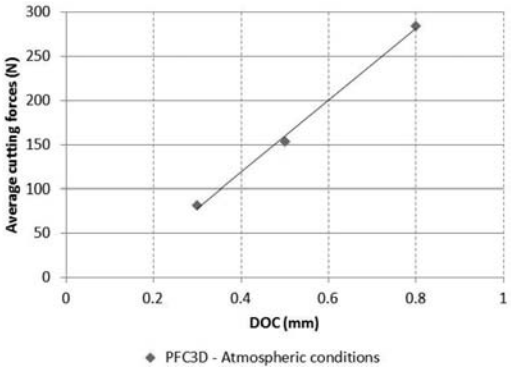


Figure 19. Average cutting forces versus depth of cut – PFC^{3D}.

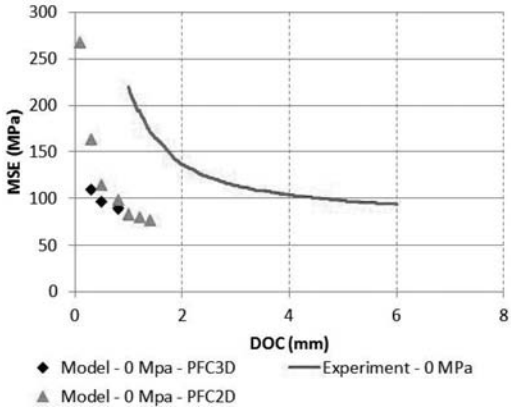


Figure 20. Specific energy final values for modeling with different depth of cut (PFC^{2D} and PFC^{3D}).

with different DOC for the two and three-dimensional modeling. The average horizontal forces increased linearly with DOC that is in agreement with results of similar studies on Carthage marble presented by Mendoza et al. (2011). Richard et al. (1998) demonstrated that cutting forces are proportional to the cross sectional area of the cut geometry for shallow depths of cut which is coherent with the observed linear trend between cutting forces and DOC. The authors stress that this relationship is expected when cutting happens in ductile regime.

Figure 20 shows the calculated mechanical specific energy for two and three-dimensional modeling using different DOC. In spite of that, DOC was constant during a particular simulation. Results reveal a decrease of specific energy with the increase of DOC. Similar results were found by Rajabov et al. (2012) on experiments carried out on Torrey Buff sandstone with DOC up to 0.8 mm. Jianyong (2012) also found analogous results while working with Carthage marble. Figure 20 shows that specific energy decreases until the depth of

cut of 1.4 mm to further stabilize around a value of 77 MPa.

For every rock type, there is a DOC range where drilling is optimum. This range varies depending on bit type and bit wear off characteristics.

It is important to emphasize that some results produced in this study are indicative of the specific behavior of the studied target rock: halite. Finally, acknowledging all model assumptions, Figure 20 suggests that the efficient drilling for modeling occurs for DOC greater than 0.8 mm.

7 CONCLUSIONS

A Discrete Element Modeling methodology on evaporite drilling was proposed that involved setting micro properties of spherical discrete elements and the establishment of relationship between contact stiffness and ball's overlap for the same discrete element set. A new method to calibrate the parameters affecting the mechanical behavior of a virtual material in order to reproduce realistic compressive mechanical behavior of halite samples based on the triaxial test data was also presented. The model was tested against single cutter experimental data and drilling efficiency analysis was performed based on the effects of different cutter back-rake angles and depths of cut.

The calibration process was challenging given the fact PFC does not have contact models readily available for the target scenario. A complementary code was developed based on a linear model combined with parallel bond technique. A new artifice was employed and the parallel bond contact stiffness was changed in each simulation cycle, assigning decreasing contact stiffness as a function of balls overlap. This artifice converted the linear model available on PFC in a different model with nonlinear behavior. As a result, a new stress-strain curve was found that correlated well with the lab test curve.

A relevant aspect concerning the physics of rock cutting was implemented in the model leading to better agreement between calculated and experimental drilling mechanical specific energy. Particles ahead of the cutter were deleted using a particle position criterion for 2D-simulations.

A second set of modeling was performed to understand the impact of changing back-rake angle on the mechanical specific energy. The increase in back-rake angle increases the specific energy and cutting efficiency improves when low back-rake angles are used since the values approximate with the unconfined compressive strength of salt (22 MPa).

Furthermore, the study on the effect of depth of cut on specific energy revealed that specific energy decreases with the increase of depth of cut until a particular point from where specific energy stabilizes.

Initial results from the frictionless model suggest that for halite drilling using a sharp PDC bit, DOC higher than 0.8 mm and up to 1.6 mm were considered optimum.

ACKNOWLEDGEMENTS

The authors would like to thank Baker Hughes Incorporated for authorizing the publication of this work. The authors also wish to express their gratitude to Russell Maharidge and to the staff of the Baker Hughes Pressure Pumping division in Tomball, Texas, for performing the triaxial tests; Barrett Scrivener, Paul Lutes and Wesley Moore from the Baker Hughes Drilling Laboratory in The Woodlands, Texas, for performing the single cutter experiments.

REFERENCES

Akbari, B.; Butt, S. D.; Munaswamy, K.; Arvani, F. 2011. Dynamic Single PDC Cutter Rock Drilling Modeling and Simulations Focusing on Rate of Penetration Using Distinct Element Method. ARMA 11-379, *45th US Rock Mechanics/Geomechanics Symposium,* San Francisco, CA.

Block, G.; Jin, H. 2009. Role of Failure Mode on Rock Cutting Dynamics. SPE 124870, *2009 SPE Annual Technical Conference and Exhibition*, USA.

Ghoshouni, M.; Richard, T. 2008. Effect of Back Rake Angle and Groove Geometry in Rock Cutting. *ISRM International Symposium*, Iran.

Goodman R. E. 1989. Introduction to Rock Mechanics. *John Wiley & Sons, 2 Ed., Cap 2–5*.

Höfer, K. H.; Thoma, K. 1968. Triaxial Tests on Salt Rocks. *International Journal of Rock Mechanics & Mining Sciences* 5:195–203.

Huang, H.; Detournay, E. 2008. Intrinsic length scales in tool-rock interaction. *International Journal of Geomechanics* 8(1):39–44.

Huang, H.; Lecampion, B.; Detournay, E. 2012. Discrete element modeling of tool-rock interaction I: Rock cutting. *International Journal for Numerical and Analytical Methods in Geomechanics.*

Itasca, 1999. Fish in PFC3D. *Itasca Consulting Group, Minneapolis, Minnesota 55401 USA, first edition*.

Jianyong, P. 2012. Interpretation of Single Cutter Tests for Rock Mechanical Properties. ARMA 12-142. *46TH US Rock Mechanics/Geomechanics Symposium held in Chicago, IL, USA, 24–27 June 2012*.

Ledgerwood III, L. W. 2009. Discrete Modeling of Rock Destruction Under High Pressure Conditions. *Patent Application Publication US 2009/0132218 A1. Texas*.

Lei, S.; Kaitkay, P.; Shen, X. 2004. Simulation of Rock Cutting Using Distinct Element Method – PFC2D. *Numerical Modeling in Micromechanics via Particle Methods, London.*

Liang, W.; Yang, C.; Zhao, J. L.; Dusseault, M. B. 2006. Experimental Investigation of Mechanical Properties of Bedded Salt Rock. *International Journal of Rock Mechanics & Mining Sciences* 44:400–411

Martinez, I.M.R.; Fontoura, S.; Inoue, N.; Pinto, C. 2011. Numerical Simulation of Drill Bit Rock Interaction. *Iberian Latin American Congress on Computational Methods in Engineering* – CILAMCE XXXII. Ouro Preto.

Martinez, I.M.R.; Fontoura, S.; Inoue, N.; Carrapatoso, C. M.; Lourenço, A.; Curry, D. 2013. Simulation of Single Cutter Experiments in Evaporites through Finite Element Method. *SPE/IADC Drilling Conference and Exhibition held in Amsterdam, The Netherlands, 5–7 March 2013.*

Mendoza, J. A.; Gamwo, I. K.; Zhang, W.; Lin, J. S. 2011. Considerations for Discrete Modeling of Rock Cutting. *ARMA 11-210, 45th US Rock Mechanics/Geomechanics Symposium, San Francisco, CA*

Potyondy, D.; Cundall, P. 2004. A Bonded-Particle Model for Rock. *International Journal of Rock Mechanics & Mining Sciences* 41:1329–1364.

Rajabov, V.; Miska, S.; Mortimer, L.; Yu, M.; Ozbayoglu, E. 2012. The Effects of Back Rake and Side Rake Angles on Mechanical Specific Energy of Single PDC Cutters with Selected Rocks at Varying Depth of Cuts and Confining Pressures. *IADC/SPE 151406, 2012 IADC/SPE Drilling Conference and Exhibition, USA*.

Zhang, W.; Whipple, G. R.; Lindner, E. N.; Thornton, J. D. 2011. The initial Single Cutter Test of the NETL Ultra Deep Drilling Simulator. *ARMA 11-500, 45th U.S. Rock Mechanics/Geomechanics Symposium, San Francisco, CA*.

Rock Mechanics for Resources, Energy and Environment – Kwaśniewski & Łydżba (eds)
© 2013 Taylor & Francis Group, London, ISBN 978-1-138-00080-3

Damage and plasticity rate dependence of Luna limestone in uniaxial compression

J. Cieślik
Faculty of Mining and Geoengineering, AGH University of Science and Technology, Kraków, Poland

ABSTRACT: Paper presents the results of mechanical tests of carbonate rock samples under quasistatic uniaxial compression. The main objective of the work was to identify two different dissipative processes following failure of rock samples in pre and post critical loading range. Two micro mechanical processes fracture of rock and grain slips were identified as damage and plastic dissipation. These micro mechanical failure processes and related energy changes were presented for various strain rate loading conditions.

1 DAMAGE AND PLASTIC DISSIPATION AS A MICRO AND MACRO MECHANICAL PROCESSES EFFECTS

Rock damage is a process of nucleation and propagation of initial flaws and microfractures of rock leading to macroscopic failure of samples. This process is strongly related to initial heterogeneous and discontinuous structure of rock. Microfractures initiate from local stress concentrations at flaws tips, grain boundaries (Tapponnier & Brace 1976, Olsson & Peng, 1976) or pores (Sprunt & Brace, 1974, Kranz, 1979), and propagate in a direction of the major principal compressive stress (Wawersik & Brace 1971, Kranz 1979, Wong 1982).

In the case of uniaxial compression, in the cracks and fractures oriented in accordance with the loading direction shear slips[1] occur, with result of tensile stress concentrations located at the crack tips. Propagation of cracks in a form of the so-called wing cracks on the direction of the loading is the consequence of this state (Ashby & Sammis 1990, Horii & Nemat-Nasser 1985). Cracks whose direction is perpendicular to the direction of the loading remain "deactivated" and do not take part in the process of the damage growth.

In the uniaxial compression conditions rock samples behave brittle, often with axial splitting failure mode in the post critical loading range. Despite this phenomenon in the pre and post critical loading range after unloading of rock sample, the permanent strains, and the hysteresis on stress strain characteristics are clear visible (Fig. 1). Permanent strain in the uniaxial compression and hysteresis are a plasticity effects which can be explained on the basis of micromechanical analysis (Jaeger et al. 2007).

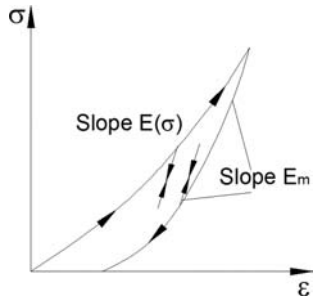


Figure 1. Hysteresis of stress-strain characteristic for rock containing random oriented cracks (after Jaeger et al. 2007).

Jaeger, Cook and Zimmerman explained the hysteresis and permanent strain as a effect of frictional resistance along the microcracks faces and the energy dissipation trough frictional sliding. These micromechanical phenomena observed in the pre critical loading range on grain boundaries and microfractures (Tapponnier and Brace 1971) are also observed in the post critical loading regime. Following the macrofracture formation the permanent strain and hysteresis in this range may be explained as a result of frictional sliding on the boundary of broken pieces of rock sample.

2 ENERGY DISSIPATION DUE TO DAMAGE AND PLASTICITY

Accepting that the elastic strain energy accumulated in rock sample is dissipated on frictional sliding on grain

[1] According to the so-called sliding crack model, used in micro mechanical analysis of rock, confirmed by microscopic observations (Paterson and Wong 2005, Rawling et al. 2002)

boundaries and micro and macrofractures (plastic dissipation) and fracturing process (damage dissipation) the loading process energy changes may be determined on the ground of non-linear fracture mechanics (Broek 1988, Saxena 1998). Following the principle of energy conservation the work performed per unit time by the applied loads $\dot{W}$ must be equal to the rates of change of the internal elastic energy $\dot{U}_{el}$, plastic energy $\dot{U}_{pl}$, kinetic energy $\dot{K}$ of the body, and the energy per unit time $\dot{\Gamma}$ spent on increasing the crack area (Wang 1996).

$$\dot{W} = \dot{U}_{el} + \dot{U}_{pl} + \dot{K} + \dot{\Gamma} \tag{1}$$

In the quasistatic case when the crack grows slowly the kinematics energy K is negligible and can be omitted and all changes with respect to time are caused by fracture surface A changes. When the potential energy of the system Π is expressed as difference between elastic energy U_{el} and work of external forces W, then the principle of energy conservation can be written as:

$$-\frac{d\Pi}{dA} = \frac{d\Gamma}{dA} + \frac{dU_{pl}}{dA} \tag{2}$$

The change of potential energy of system is equal to the energy dissipated in plastic work and for new surface creation.

For an ideally brittle material (when the energy dissipated in plastic work is negligible) Griffith in 1921 gave the equation:

$$-\frac{d\Pi}{dA} = \frac{d\Gamma}{dA} \tag{3}$$

witch in the final form can be written as:

$$G = -\frac{d\Pi}{dA} = 2\gamma \tag{4}$$

where γ is a energy required to form new unite surface area (usually called surface energy) and G is energy release rate per crack tip (Broek 1988).

The potential energy changes caused by crack propagation (the energy release rate G) is dependent on sample loading conditions. Considering a uniaxial compression test the most interesting case is the general case, when the crack extends under changing load and displacement (Fig. 2). Based on potential energy changes $\Delta\Pi$

$$\Delta\Pi = -\frac{1}{2}\left(F_1 u_2 - F_2 u_1\right) \tag{5}$$

and measurements of the crack extension Δa it is possible to determine the energy release rate G.

$$G = \frac{area\Delta OAB}{\Delta a} = 2\gamma \tag{6}$$

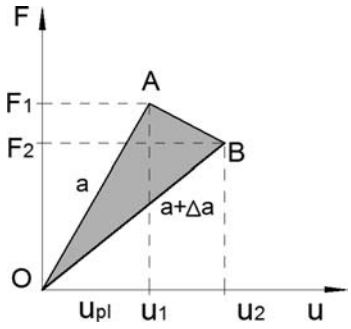


Figure 2. Load–displacement relation for cracked body (crack extension under changing load and displacement).

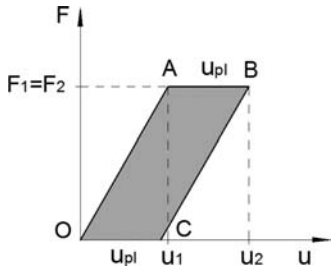


Figure 3. Load–displacement relation for elastic ideally plastic body.

Under conditions of uniaxial compression tests of rocks samples, measurements of microcrack extensions on a certain load level are not possible directly. Because of this fact, the surface energy or energy release rate, as a material parameter, cannot be determined directly in this type of tests. Some attempts using computer tomography were made by Landis et al. (1999) but the results are acceptable only for advanced loading and sample cracking stage. Despite this limitations using a standard stress-strain characteristics (with unloading on certain load levels) one can determine energy consumed on fracture propagation (triangle *OAB* surface – Fig. 2).

In the opposite case for elastic ideally plastic body (without any crack) the whole energy is consumed on plastic dissipation (Fig. 3).

$$\Delta\Pi = -F\left(u_2 - u_1\right) \tag{7}$$

For a general case of the elastic-plastic body with crack there is a overlap of two cases described earlier. The change of potential energy in that case equals the sum of plastic and damage (fracture) dissipation energies (Fig. 4).

$$\Delta\Pi = U_{pl} + U_{dam} \tag{8}$$

$$U_{dam} = \frac{1}{2}\varepsilon'\left(\sigma_1 - \sigma_y\right) \tag{9}$$

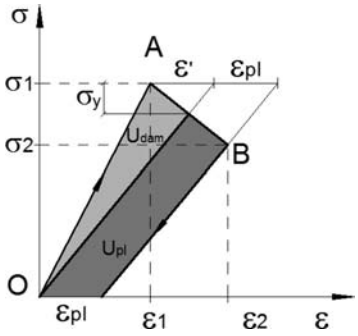


Figure 4. Schematic stress–strain relationship for cracked elastic–plastic body and the energy relations.

$$U_{pl} = \sigma_2 \varepsilon_{pl} + \frac{1}{2}\varepsilon_{pl}\left[(\sigma_1 - \sigma_2) - \sigma_y\right] \tag{10}$$

$$\sigma_y = \frac{\varepsilon'(\sigma_1 - \sigma_2)}{\varepsilon' + \varepsilon_{pl}} \tag{11}$$

3 MECHANICAL TESTS OF LUNA LIMESTONE SAMPLES

The Luna limestone is a micritic rock with a porosity of 12%, from the area of south Spain. The laboratory investigation was performed on twelve cylindrical samples with dimension of 34 mm diameter and 70 mm high, all cut out from a tick rock plate.

Uniaxial compression tests were performed with Multi-purpose Rock and Concrete Testing System MTS 815. Radial displacements were determined through the measurement of changes of the sample circumference with a chain put around it, axial with extensometers installed between compression plates. All tests were performed with axial strain rate control of rock samples, and four axial strain rates of $1 \times 10^{-5}\,s^{-1}$, $1 \times 10^{-4}\,s^{-1}$, $5 \times 10^{-4}\,s^{-1}$, $1 \times 10^{-3}\,s^{-1}$.

4 DAMAGE AND PLASTICITY STRAIN RATE DEPENDENCE

The uniaxial strength and Young modulus (determined as secant modulus from unloading $\sigma - \varepsilon$ path) of Luna limestone (Figs. 5 and 6), are clearly strain rate dependent in quasistatic loading conditions. But the main subject of this work was to show how the damage and plastic energy dissipation change with the different strain rates.

Following the procedure proposed earlier the increments of plastic, damage and potential energy are shown on Figures 7 and 8.

As it was presented before the change of the potential energy is the sum of the energy dissipated on damage and plastic deformation (Fig. 8).

Plastic and damage dissipation processes begin each at different loading level. Plastic dissipation

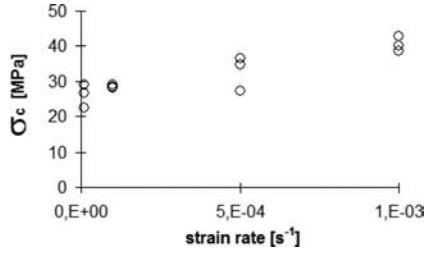


Figure 5. Uniaxial strength σ_c strain rate dependence for Luna limestone.

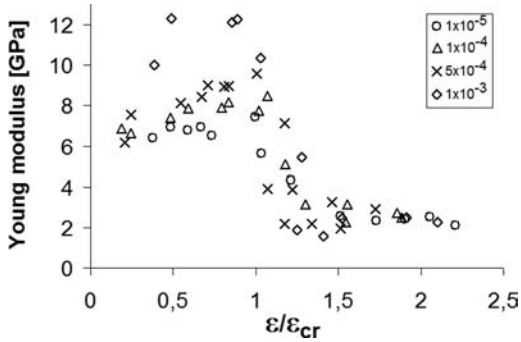


Figure 6. Changes of the Young modulus through loading and it's strain rate dependence for example Luna limestone samples.

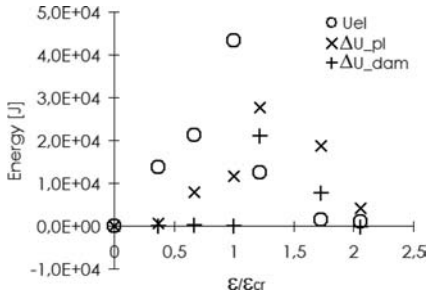


Figure 7. The increments of plastic, damage and elastic energy determined for example sample with strain rate of $1 \times 10^{-4}\,s^{-1}$.

begins at about 1/3rd critical strain of rock samples, but damage dissipation begins at about critical strain. It is caused by the method of damage energy dissipation measurement, determined by local Young modulus changes (it's maximum values are reached close to the critical strain, see Figure 6). It should be noted that in pre critical loading range plastic dissipation is much more intensive than damage, witch is very small or zero. In the post critical loading range damage increments are initially rising, then falling down and fading about sample residual strength level. Plastic dissipation increments in the post critical range are falling down and stabilizing at the residual strength level (Fig. 7).

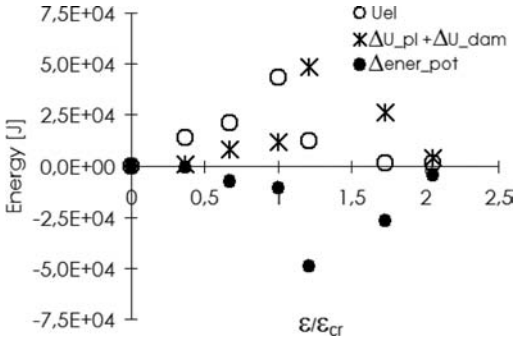


Figure 8. The increments of plastic, damage and potential energy determined for example sample with strain rate of 1×10^{-4} s^{-1}.

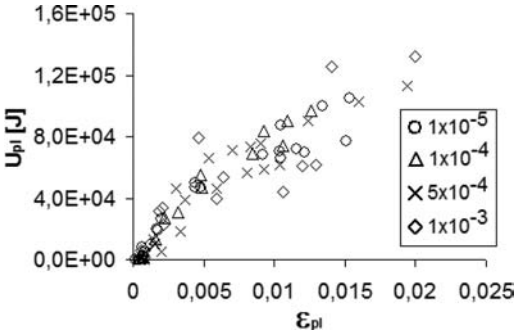


Figure 9. The plastic energy dissipation at different strain rates of limestone samples.

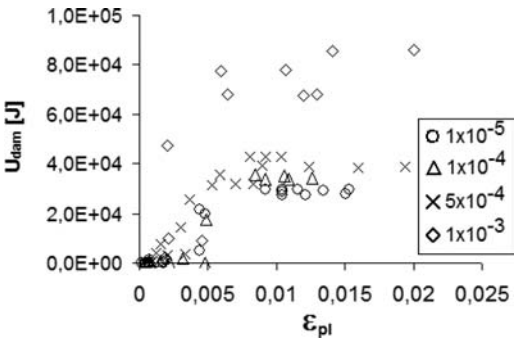


Figure 10. The damage energy dissipation at different strain rates of limestone samples.

Figures 9 and 10 show summarized plastic and fracture dissipated energies during loading process as the function of plastic strain.

Only in the case of damage dissipation rate dependence is clearly visible (Fig. 10). Because the change of potential energy is a sum of fracture and plastic dissipation, the potential energy changes are also rate dependent. Test results showed, that the plastic dissipation, was strain rate independent, in analyzed range of strain rates.

5 CONCLUSIONS

Accepting that the elastic strain energy accumulated in a rock sample is dissipated on frictional sliding on grain boundaries and micro and macrofractures (plastic dissipation) and fracturing process (damage dissipation) the loading energy changes may be determined on the ground of non-linear fracture mechanics (Broek 1988, Saxena 1998, Wang 1996). For typical uniaxial compression tests results with unloading and some geometrical dependencies of $\sigma - \varepsilon$ characteristic (Cieślik 2011) it is possible to determine the energy changes caused by plastic and damage dissipation.

Only in the case of damage dissipation, a rate dependence is clear visible. In the analyzed range of axial strain rates of rock samples, the plastic dissipation was strain rate independent. Observed effects are the result of the axial stiffness reduction strain rate dependence (Fig. 6) which plays dominate role in damage process.

ACKNOWLEDGEMENTS

This work have been supported by statutory research funds of the AGH University of Science and Technology, Faculty of Mining and Geoengineering within the framework of the research program Nº 11.11.100.197.

REFERENCES

Ashby, M.F. & Sammis, C.G. 1990. The Damage Mechanics of Brittle Solids in Compression. *Pure Appl. Geophys*. 133 (3): 489–521.

Broek, D. 1988. *The practical use of fracture mechanics*. Kluwer Academic Publishers.

Cieślik, J. 2011. Energy changes with damage and plastic dissipation process under uniaxial and triaxial compression test of sandstone samples. *Mining and Geoengineering* 35 (4): 25–32.

Horii, H. & Nemat –Nasser, S. 1985. Compression-Induced Microcrack Growth in Brittle Solids:Axial Splitting and Shear Failure. *J. Geophys. Res*. 90 (B4): 3105–3125.

Jaeger J.C., Cook N.G.W. & Zimmerman R. W. 2007. *Fundamentals of Rock Mechanics*. Fourth edition, Blackwell Publishing.

Kranz, R.L. 1979. Crack-crack and crack-pore interactions in stressed granite. *Int. J. Rock Mech. Mining Sci*. 16: 37–47.

Landis, E.N. & Nagy, E.N. 2000. Three-dimensional work of fracture for mortar in compression. *Engineering Fracture Mechanics* 65:223–234.

Moore, D.E. & Lockner, D.A. 1995. The role of microcracking in shear-fracture propagation in granite. *J. Struct. Geol*. 17: 5–114.

Olsson, W. & Peng S. 1976. Microcrack nucleation in marble. *Int. J. Rock Mech. Min Sci. & Geomech. Abstr.* 13: 53–59.

Paterson, M S. & Wong T-F. 2005. *Experimental rock deformation – the brittle field*. Second Edition: Springer.

Rawling, G.C., Baud, P. & Wong, T-F. 2002. Dilatancy, brittle strength and anisotropy of foliated rocks: experimental deformation and micromechanical modeling. *J. Geophys. Res.* 107: 2234.

Saxena, A. 1998. *Nonlinear fracture mechanics for engineers*. CRC Press.

Sprunt E. & Brace, W.F. 1974. Direct observation of microcavities in crystalline rocks. *Int. J. Rock Mech. Mining Sci.* 11: 139–150.

Tapponnier, P. & Brace, W.F. 1976. Development of stress induced microcracks in Westerly granite. *Int. J. Rock Mech. Mining Sci.* 13: 103–112.

Wang, C.H. 1996. *Introduction to Fracture Mechanics*. Published by DSTO Aeronautical and Maritime Research Laboratory. Australia.

Wawersik, W.R. & Brace, W.F. 1971. Post-failure behavior of granite and diabase. *Rock Mech.* 3: 61–85.

Wong, T.F. 1982. Micromechanics of faulting in Westerly granite. *Int. J. Rock Mech. Min. Sci. & Geomech. Abstr*. 19: 49–64.

This page intentionally left blank

Rock Mechanics for Resources, Energy and Environment – Kwaśniewski & Łydżba (eds)
© 2013 Taylor & Francis Group, London, ISBN 978-1-138-00080-3

Effective stresses in cohesive discontinuous rocks around a vertical drill hole

P. Ciobanu
Petroleum-Gas University, Ploiesti, Romania

ABSTRACT: The author of this paper has published in recent years a concept for defining and developing mathematical models for calculating the effective stress in cohesive rocks. The present paper describes two applications of this concept on cohesive, porous and non-fractured rocks. The first application shows the evaluation methodology for constants of the material and geometrical parameters, quantifying pores' size, shape, distribution and arrangement. The second application shows the effective stress distribution around a vertical drill hole. In both applications, the author's results are compared with those obtained by Terzaghi model – one of the models commonly used in similar situations.

1 INTRODUCTION

The first appeared (published in 1936) and one of the most known and used calculation models of effective stresses in discontinuous rocks is Terzaghi model (Terzaghi & Peck 2010):

$$\sigma' = \sigma - p \ , \quad \tau' = \tau \qquad (1), (2)$$

where σ and τ are apparent values of normal, respectively tangential stress, σ' and τ' are the real (effective) stress values, and p is the fluid pressure in pores. Usually, the apparent values are called apparent stresses, and real values – effective stresses.

Terzaghi developed the model based on experimental research studies conducted on soils, grounds and – mostly, on non-cohesive rocks. Later and so far, some experts used this model for any type of rock, including cohesive rocks. Besides Terzaghi model, in published literature there are other effective stress models, but – it seems that there is no general valid concept to define used notions and to regulate development of calculation mathematical models for any situation, as type of rock and mechanical loading.

Starting from known principles of *Deformable Solid Mechanics* – which are used to define and evaluate stress in continuous materials, the author of this paper proposes a concept of definition and evaluation of effective stresses in discontinuous cohesive rocks materialized by the following rules (Ciobanu 2011a): 1) – Within calculation of effective stresses to be included all mechanical loadings, both external forces – acting on the boundary that separates the gross volume of rock, and internal forces acting on the surface of existing discontinuities within rock. 2) – Internal forces must be calculated in compliance with the rules used in case of external and known forces in *Mechanics*. 3) – The parameters and measurement techniques of rock discontinuities shall be improved for a more accurate assessment of the effective area whereby transmitting internal tensions of material.

Based on these rules, for a discontinuous cohesive rock and its division plane with a total area A, the apparent stresses are given by relations:

$$\sigma = N_{ext} / A \ , \quad \tau = T_{ext} / A \ , \qquad (3), (4)$$

and effective stresses – by relations:

$$\sigma' = \left(N_{ext} + N_{int}\right) / A' \ , \quad \tau' = \left(T_{ext} + T_{int}\right) / A' \ . \qquad (5), (6)$$

N_{ext}, T_{ext} and N_{int}, T_{int} represent the normal and tangential components of resultant of external forces – marked by *ext*, respectively the resultant of internal forces – marked by *int*. With A' it was marked the real area defined as difference between total area A and pores' area A_p, meaning: $A' = A - A_p$ or $A' = A(1-a)$, where a is the relation $a = A_p / A$.

From (3), (4) results: $N_{ext} = \sigma \ A$, respectively $T_{ext} = \tau \ A$ and based on them, the relations (5) (6) can also be written as:

$$\sigma' = \frac{\sigma + \left(N_{int} / A\right)}{1-a} \ , \quad \tau' = \frac{\tau + \left(T_{int} / A\right)}{1-a} \ . \qquad (7), (8)$$

Out of the external mechanical loadings – most commonly found at rocks in geosphere, are mentioned: weight of top layers, in case of rocks making up the walls of underground excavations may be pressure strengths and frictional forces fluid-rock when within excavations is a pressure fluid, respectively when the fluid moves. The most common internal forces are: forces generated by fluid pressure saturating the rock, frictional forces solid-solid (rock-rock) on closed fractures' plane or frictional forces solid – liquid even if the

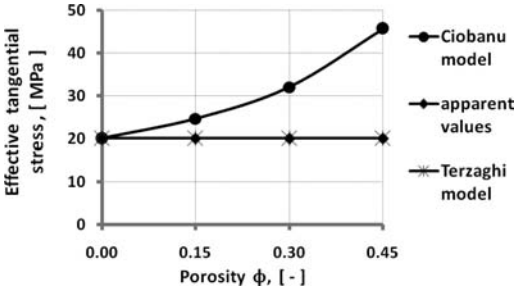


Figure 1. Influence of porosity on effective tangential stress.

fluid runs through discontinuities in internal structure of the rock.

In this paper, the external mechanical loadings and their parameters N_{ext}, T_{ext}, respectively σ and τ are considered known, and out of the internal mechanical loadings it is considered the situation when only F_p is present, being generated by pressure p of the fluid in pores, calculated by relation: $F_p = pA_p$. In this case we have: $N_{int} = F_p$ and $T_{int} = 0$; and this is because the pore fluid was considered non-viscous, not producing the shear stress, but the normal stress. Using the sign convention by assigning positive values to compressive stress and negative values to tension stress, and customizing relations (7), (8) for above statement, it results:

$$\sigma' = \frac{\sigma - ap}{1-a}\ , \qquad \tau' = \frac{\tau}{1-a}\ . \qquad (9), (10)$$

Given that the parameter marked by a – in general, it is very difficult to measure it, it is introduced and used another parameter marked by c defined by relation $c = a/\varphi$ in order to quantify the shape and distribution of pores. With φ was noted overall porosity defined as relation between volume V_p of all pores in rock and its total volume (gross) V ($\varphi = V_p/V$). Using the relation $a = c\varphi$, the relations (9), (10) can also be written as:

$$\sigma' = \frac{\sigma - c\phi p}{1-c\phi}\ , \qquad \tau' = \frac{\tau}{1-c\phi}\ . \qquad (11), (12)$$

From these relations it is found that the effective stress values are influenced (determined) by the following units: 1) – external forces measured by the apparent stress σ and τ; 2) – pore geometric parameters, respectively a or c and φ; 3) – pore fluid pressure p only for values of σ'.

In Figures 1, 2 and 3 are shown the influences of parameters φ and p over effective stresses for the values: $c = 1.25$ (the case $c > 1$ or $a > \varphi$), $\sigma = 10$ MPa and $\tau = 20$ MPa. The case $c = 1$ or $a = \varphi$ it is presented in Ciobanu 2011b.

2 THE PROPOSED METHOD FOR EVALUATION OF ROCK PARAMETERS

It is considered a rock wherefore deformations achieved before breaking are small enough so the

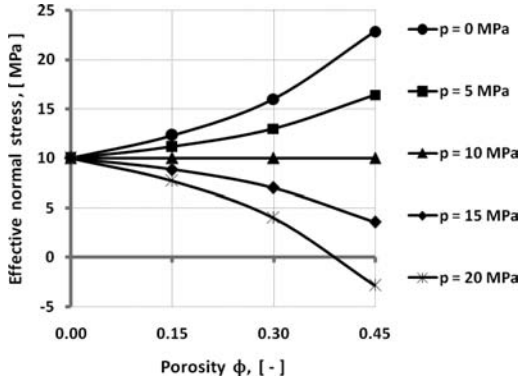


Figure 2. Influence of porosity on effective normal stress for various values of pore pressure p.

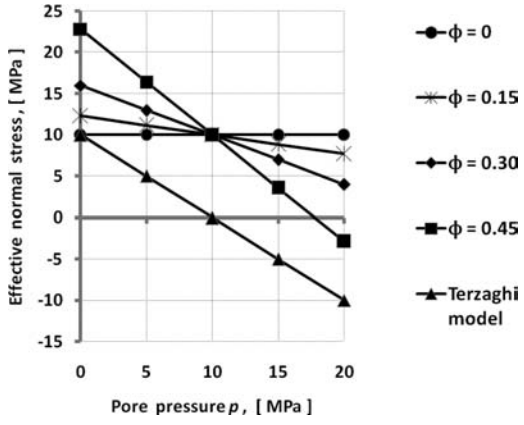


Figure 3. Influence of pore pressure on effective normal stress for various values of porosity φ.

relations (11), (12) to be complied with (true) when breaking. This means that when breaking, the effective stresses σ' and τ' reached the ultimate strength by tension U_0, respectively – by shearing S_0 of solid phase within rock, and apparent stresses σ and τ reached the ultimate strength U, respectively S of porous rock.

In other words, U_0 and S_0 represent values of U and S strengths when rock's porosity decreases to zero ($\varphi \to 0$). Under these conditions, the relations (9), (10) applied to rock breaking moment after tension and, respectively shearing stresses, we will have:

$$U_0 = \frac{U + ap}{1-a}\ , \qquad S_0 = \frac{S}{1-a}\ , \qquad (13), (14)$$

or

$$U = (1-a)U_0 - ap\ , \quad S = (1-a)S_0\ . \qquad (13'), (14')$$

If within volume occupied by analyzed rock there are two areas with different values for porosity φ, marked by φ_1, φ_2, than these areas shall have for breaking strengths the values U_1, S_1 and, respectively U_2,

Table 1. Measured values S_m and U_m for strength *S*and, respectively U.

Parameter name	U. M.	Lot (group) number of specimens				
		1	2	3	4	5
Apparent density, ρ	kg/m^3	1596.7	1519.5	1475.3	1442.2	1377.5
Shear strength, S_m	MPa	6.73	5.91	5.49	5.12	4.43
Tensile strength, U_m	MPa	3.68	3.28	2.98	2.81	2.45

Table 2. Calculated values S_c and U_c for strength S,respectively U, and for relative deviations ΔS, respectively $\Delta U$of their from measured values S_m, respectively U_m.

Parameter name	U. M.	Lot (group) number of specimens				
		1	2	3	4	5
Total porosity, φ	%	9.38	13.76	16.27	18.15	21.82
Area coefficient, a	%	20.48	30.04	35.52	39.62	47.63
Shear strength, S_c	MPa	6.66	5.86	5.4	5.05	4.38
Tensile strength, U_c	MPa	3.59	3.16	2.91	2.73	2.37
Relative deviation, ΔS	%	1.1	0.92	1.69	1.3	1.06
Relative deviation, ΔU	%	2.32	3.59	2.19	2.88	3.39

S_2, and between them shall be created a relationship similar to (13′)(14′). Meaning:

$$U_1 = (1-a_1)U_0 - a_1 p\ , \quad S_1 = (1-a_1)S_0\ , \qquad (15), (16)$$

$$U_2 = (1-a_2)U_0 - a_2 p\ , \quad S_2 = (1-a_2)S_0\ . \qquad (17), (18)$$

After solving the system comprised by equations (15)–(18) results that- as solution, the relations (19)–(23):

$$a_1 = \frac{1-s}{\varphi - s}\ , \quad a_2 = \varphi\frac{1-s}{\varphi - s}\ , \qquad (19), (20)$$

$$U_0 = \frac{u-\varphi}{1-\varphi}U_1\ , \quad S_0 = \frac{s-\varphi}{1-\varphi}S_1\ , \qquad (21), (22)$$

$$c = \frac{1-s}{\varphi - s}\left(\frac{1}{\phi_1}\right)\ , \qquad (23)$$

$$a = \frac{1-s}{\varphi - s}\left(\frac{\phi}{\phi_1}\right)\ . \qquad (24)$$

In these relations were used the notations: $\phi = \varphi_2/\varphi_1$, $s = S_2/S_1$, $u = U_2/U_1$.

For a specific rock it is accepted that parameter c is a constant for the material ($c = a/\varphi = $ constant) which leads to the equality: $a_1/\varphi_1 = a_2/\varphi_2$ and it represents the fifth equation of the system (15)–(18). For any other value of porosity φ, the value of parameter a can be calculated by relation (24).

This method was checked by the author by a laboratory experiment described – briefly as follows: from cement, water and a foaming agent it was prepared a slurry – after homogenization it was divided into five parts (portions) of equal mass and volume. In each portion it was injected a certain amount of air different from the one injected in the other portions. After homogenization, setting (solidification) and removing pore water – by drying, there were obtained five groups of specimens with different porosity values φ marked by φ_i, where $i = 1, 2, 3, 4, 5$. Each group of specimens – out of the available ones, was subject to breaking tests by indirect tensile test (Brazilian Tension Test), and breaking tests by shearing. The values of breaking strengths per group, marked by U_{mi} and, respectively S_{mi}, are given in Table 1. Using data in table, corresponding to two of the five groups, by relations (19)–(23) have been calculated the values: $a_1 = 0.204$, $a_2 = 0.301$, $S_0 = 8.37$ MPa, $U_0 = 4.51$ MPa and $c = 2.18$. The values have been used to check if equality of relations (13)–(14) is also kept for values measured on the other three groups of specimens. Among measured values – in Table 1, and values calculated in the presentation in Table 2 can be observed deviations less of 3.59 %. The values φ_i for porosity of the five groups of specimens were calculated by $\varphi_i = 1 - \rho_i/\rho_0$, where ρ_i is the apparent density of the cement stone, and ρ_0 is the density of its solid phase, meaning the cement stone for $\varphi = 0$. The values of ρ_i have been measured by gravimetric method, and the ρ_0 value – by pycnometer method.

3 DISTRIBUTION OF EFFECTIVE STRESSES AROUND A VERTICAL DRILL HOLE

It is considered a drill hole drilled by hydraulic-rotary drilling method. The drill hole has a linear trajectory, it is vertically oriented and crosses a horizontal layer

made up by a cohesive, porous, non-fractured and pressure fluid – saturated rock.

It is considered a depth H near layer mentioning: p –fluid pressure in pores, p_w – fluid pressure in well and b – radius of the drill hole. The horizontal normal stress in a state of nature – at this depth and long distance from well's axis, has the same value σ_h in any direction.

For depth H it's graphically illustrated – for comparison reason, the variation with distance r against well's axis of effective stresses, meaning radial σ_r' and circumferential σ_θ' stresses provided by Terzaghi and Ciobanu models. For both models are used the distribution laws of apparent stresses σ_r, σ_θ given by known relations (Aadnøy&Looyeh 2011, Fjaer et al. 2008, Watson et al. 2003):

$$\sigma_r = \sigma_h - (\sigma_h - p_w)\left(\frac{b}{r}\right)^2, \tag{25}$$

$$\sigma_\theta = \sigma_h + (\sigma_h - p_w)\left(\frac{b}{r}\right)^2. \tag{26}$$

Using the relations, from equation (1) results effective stresses σ'_r, σ_θ', corresponding to Terzaghi model (Aadnøy&Looyeh 2011, Fjaer et al. 2008, Watson et al. 2003):

$$\sigma_r' = (\sigma_h - p) - (\sigma_h - p_w)\left(\frac{b}{r}\right)^2, \tag{27}$$

$$\sigma_\theta' = (\sigma_h - p) + (\sigma_h - p_w)\left(\frac{b}{r}\right)^2. \tag{28}$$

Similarly, by equation (9) results effective stresses σ_r', σ_θ', obtained by Ciobanu model:

$$\sigma_r' = \frac{1}{1-a}\left[(\sigma_h - ap) - (\sigma_h - p_w)\left(\frac{b}{r}\right)^2\right], \tag{29}$$

$$\sigma_\theta' = \frac{1}{1-a}\left[(\sigma_h - ap) + (\sigma_h - p_w)\left(\frac{b}{r}\right)^2\right]. \tag{30}$$

Radial variation charts for effective stresses, calculated by relations (25)–(30) for $H = 3000$ m, are given in Figures 4 and 5.

Variation charts with depth for effective stresses σ_r', σ_θ' calculated for $r = b$ and for σ_z' are given in Figures 6-8. For above situation has: $\sigma_z = \sigma_v$. From relation (1) result $\sigma_z' = \sigma_z - p$,and from relation (11) $\sigma_z' = (\sigma_z - c\,\varphi p)/(1 - c\,\varphi)$.

In calculations needed for elaborating such charts have been used – for example, values: $\sigma_v = 0.025H$, $\sigma_h = 4.90 + 0.020H$, $p = 0.0103H$, $p_w = 0.0123H$, for H €[2900 – 3100]m and $a = 0.1$.

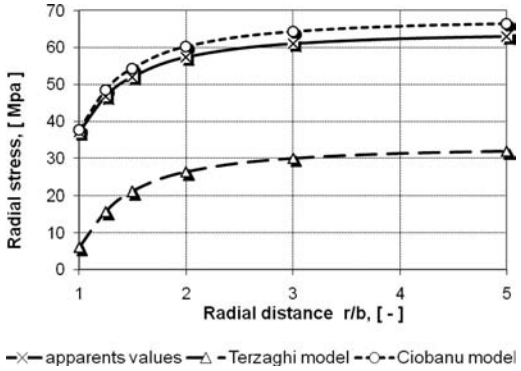


Figure 4. Radial variation charts of radial stress.

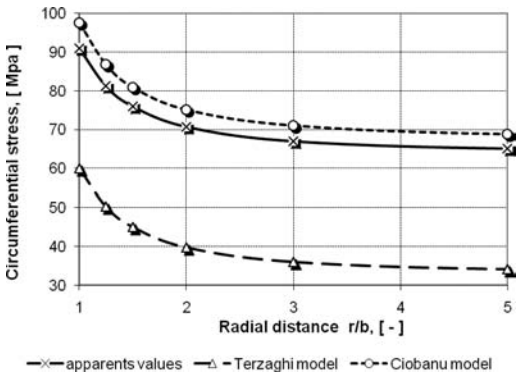


Figure 5. Radial variation charts of circumferential stress.

4 CONCLUSIONS

1. The experiments performed by Terzaghi and his model show that for non-cohesive rocks the effective stresses are influenced by the exterior forces (quantified by apparent stresses) and by the pressure from pores p for stress σ'. For this type of rocks the geometrical parameters of the porosity property do not influence the effective pressures.
2. For cohesive rocks, the effective stresses are influenced by the same factors (same as for non-cohesive rocks), the only difference is that in this case the influences of porosity and of its geometrical parameters are present. For the cohesive rocks, the influence of porosity of parameter A_p is present two times: once when quantifying the internal force F_p of the pore pressure ($F_p = pA_p$), and second time when quantifying the effective area A' ($A' = A – A_p$).
3. In Figures 1, 2, 3, by the illustrated graphs, the effect of the parameters a or c and φ are presented over the effective stresses in a cohesive rock, and these results are compared with the ones obtained from Terzaghi model. The differences between the values of the effective stresses obtained by Terzaghi and Ciobanu models increases along with the increase of porosity, more for the lower values of c and less for its higher values.
4. For the porous cohesive rocks that have high values for the deformation moduli (for instance Young modulus), that gets a little bit deformed before breaking, the mathematic model (11), (12) can be used to evaluate the breaking strength for the solid

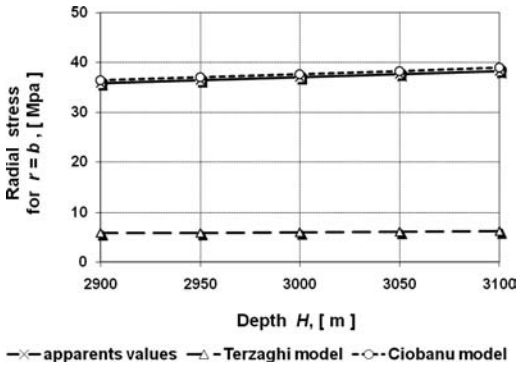


Figure 6. Variation charts with depth for radial stress.

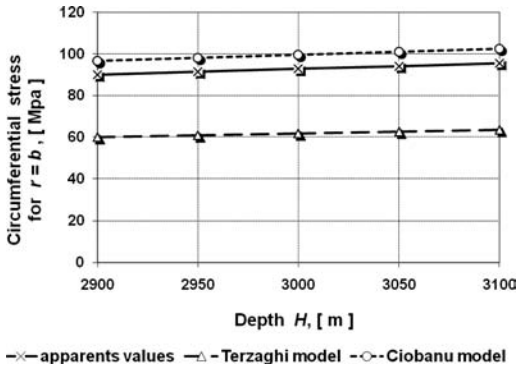


Figure 7. Variation charts with depth for circumferential stress.

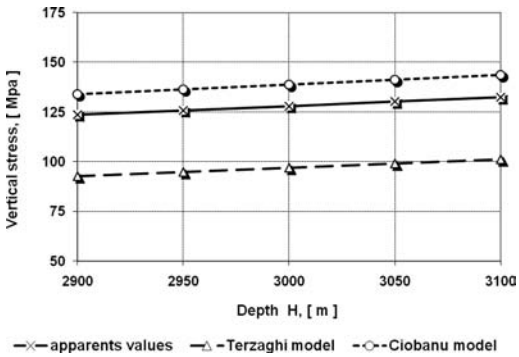


Figure 8. Variation charts with depth for vertical stress.

stage of the rocks (S_0, U_0), but also the shape coefficient of the pores noted by c (see connection (23)).

5. By the experiment performed by the author, using specimens made of foamed cement paste, it has been noted that the calculated values using the relations (13′). (14′) shows that there are relative deviations less than 3.59% than the measured values (see Table 1 and 2).
6. The effect of the porosity over the effective stresses is illustrated in Figures 4–8, as well, for the rocks situated around a drill hole. Here, huge differences can be noted between the value obtained by Terzaghi and Ciobanu models, for both radial stress σ_r' – Figures 4 and 6, for the circumferential stress σ_θ' – Figures 5, 7 and for the vertical stress σ_z' – Figure 8.
7. The results presented in Chapter 2 are valid and can be used for the porous cohesive rocks that have higher values for the deformation moduli and for which the coefficient c has a constant value (c is not affected by porosity φ). But the results presented in Chapter 1 and 3 can be used, as well, for rocks that do not meet the conditions presented in Chapter 2.
8. The concept for the effective stresses presented at the beginning of this abstract offers new possibilities for enhancing and increasing accuracy of the models when calculating effective stresses in cohesive rocks. Such a model for a particular fissured rock has been presented by the author at the *Geological Congress*- 2012 edition (Ciobanu 2012), and it is in progress to be published. Other different projects of the author, related to ways to apply the concept in solving issues for *Rocks Mechanics*, are at different stages of development.
9. Parameter a, in general, is difficult to be measured and, thus, makes difficult the evaluation of effective stresses using models (9), (10). For this reason the author proposes to introduce the coefficient c that characterizes the shape, distribution in space and distributions of pores by sizes. For a certain rock, having a certain structure and texture, it is obvious that coefficient c is approximately constant. If c is constant, by applying the proposed method in Chapter 2, its value can be calculated as wells as parameter a (relation (24)).
10. Generally, effective stresses are higher than apparent stresses and – from Figures 4-8 one can note that the obtained values using Ciobanu model follow this rule. But – for the obtained values using Terzaghi model, the effective values are less than apparent values. Therefore, the case presented in Chapter 3 is an additional argument that supports the idea that the validity domain of Terzaghi model must be limited to non-cohesive rocks.

5 SYMBOLS AND UNITS

A – total area of the rock, in the plane of sectioning considered in m^2;

A' – effective area of the rock, in the plane of sectioning considered in m^2;

A_p – pore area in the plane of sectioning considered in m^2;

b – drill hole radius in m;

a – pore area coefficient, dimensionless;

c – pore shape coefficient, dimensionless;

F_p – the force generated by the pore fluid pressure in N;

H – depth in m;

N – normal component of the resultant forces acting on the rock, in N;

p – pore pressure in N/m^2 or Pa;

p_w – drill hole fluid pressure in N/m^2 or Pa;

r – radial distance measured from the probe axis (distance r against well's axis) in m;

S – rock shear strength (without compression), in N/m^2 or Pa;

S_0 – shear strength rock solid phase, and the raw rock it only in areas free of pores – where porosity is zero, in N/m^2 or Pa;

s – value ratio S_2/S_1, dimensionless;

T – tangential component of the resultant forces acting on the rock, in N;

U – rock tensile strength by simple traction in N/m^2 or Pa;

U_0 – tensile strength rock solid phase, and the raw rock it only in areas free of pores – where porosity is zero, in N/m^2 or Pa;

u – value ratio U_2/U_1, dimensionless;

V – total (gross) occupied by rock considered (analyzed), in m^3;

V_p – volume of all pores existing in the rock volume V, in m^3;

σ – apparent value for normal stress, in N/m^2 or Pa;

σ' – effective value for normal stress, in N/m^2 or Pa;

σ_h – *in-situ* horizontal stress in the earth's crust, in N/m^2 or Pa;

σ_v – vertical overburden stress in the earth's crust, in N/m^2 or Pa;

σ_z, σ_r, σ_θ – apparent values for normal stress after vertical directions, respectively radial, respectively circumferential or rocks in the around of the drill hole in N/m^2 or Pa;

σ'_z, σ'_r, σ'_θ – effective values for normal stress after vertical directions, respectively radial, respectively circumferential or rocks in the around of the drill hole in N/m^2 or Pa;

τ – apparent value for tangential stress in N/m^2 or Pa;

τ' – effective value for tangential stress in N/m^2 or Pa;

φ – total porosity of the rock, dimensionless;

ϕ – value ratio φ_2/φ_1, dimensionless;

ρ – bulk density of the rock, in kg/m^3;

ρ_0 – density of solids from rock, in kg/m^3;

Indices:

ext, *int* – subscripts notation N and T for external forces, respectively internal;

i – subscript used for calculated or measured values of parameters (ρ_i, ϕ_i, a_i, S_i, U_i, ΔS_i, ΔU_i) corresponding to one of five groups of samples used for the experiment presented in Chapter 2, $i = 1, 2, 3, 4,5$;

c, m – use subscripts for calculated values (S_c, U_c), respectively measured (S_m, U_m), of parameters S and U corresponding to each of the five groups of samples used for the experiment presented in Chapter 2.

ΔS_i, ΔU_i – relative deviations of calculated values, from measured values of parameters S_i, respectively U_i, dimensionless. $\Delta S_i = (S_{ci} - S_{mi})/S_{mi}$, and $\Delta U_i = (U_{ci} - U_{mi})/U_{mi}$ (see Tables 1 and 2).

REFERENCES

Aadnøy, B.S. & Looyeh, R. 2011. *Petroleum Rock Mechanics: Drilling Operations and Well Design*. Oxford, UK: Elsevier, pp. 95–100, 162–163, 173–199.

Ciobanu, P. 2011a. A new concept and model of evaluating the effective stresses designed for the cohesive, porous and cracked rocks. Hi-Tech (XI International Scientific – Practical Conference "Basic and Applied Research, Development and Application of High Technologies in Industry") Conf. Proc. 2011, St. Petersburg, Russia, pp. 317.

Ciobanu, P. 2011b. About mechanical strength of porous materials. *American Institute of Physics Conf. Proc*. 1400, 453 (2011).

Ciobanu, P. 2012. About ultimate strength of layered and cracked rocks. 34*th International Geological Congress* – 34*IGC*, Brisbane, Australia: (in press).

Fjaer, E., Holt, R.M., Horsrud, P., Raaen, A.M. & Risnes, R. 2008. *Petroleum Related Rock Mechanics*. Oxford, UK: Elsevier, pp.135–174, 369–390.

Terzaghi, K., & Peck, R.B. 2010. *Soil Mechanics in Engineering Practice*. Milton Keynes, UK: Lightning Source UK Ltd.

Watson, D., Brittenham, T. & Moore, P.L. 2003. Advanced Well Control. *SPE Textbook Series vol* 10. Richardson, Texas: Hans Juvkam-Wold, Texas A&MU, pp. 27–37, 93–112.

Rock Mechanics for Resources, Energy and Environment – Kwaśniewski & Łydżba (eds)
© 2013 Taylor & Francis Group, London, ISBN 978-1-138-00080-3

A database to manage rock mechanical properties and assess formation abrasiveness for drilling

F. Descamps & J.-P. Tshibangu
UMONS-University of Mons, Mons, Belgium

N. da Silva & S. Regnard
Halliburton, Drogenbos, Belgium

ABSTRACT: The design of drilling tools for deep wells requires a minimum knowledge of petrophysical and mechanical properties of the reservoir, but also of the overburden formations in case of difficult drilling. A specific working method was developed in the rock mechanics lab of the University of Mons (Belgium) to obtain maximum geomechanical characteristics from a small piece of rock. A large number of samples have been processed for a global oil and gas service company which develops drilling bits. The typical analysis includes a petrographical description, petrophysical characterization, mechanical tests (punching, uniaxial compression…) to draw mechanical properties, and abrasiveness test (FPMs method). A database is created to emphasize the potential driving parameters in understanding the wear behavior and cutting efficiency of drill bits. We present the working method and some results obtained from the data analysis and their relationship with the measured abrasiveness.

1 INTRODUCTION

When drilling in difficult conditions, an appropriate bit design requires particular care in assessing mechanical and petrographic properties of drilled formations (reservoir and overburden). In addition, those characterizations have generally to be done from a small amount of rock material, which implies a specific testing program based on few or even non-destructive techniques. This particular methodology, coupled with the long-term collaboration with Halliburton's drill bits and core heads design and development team, involved the processing of a large number of samples and led to the development of a database in order to manage all the collected data and, especially, assess abrasiveness and its relation with other properties.

2 PRESENTATION OF THE DATABASE

2.1 *Overview*

The information collected from laboratory tests in the framework of the collaboration between UMONS and Halliburton has been gathered on a long time period, more than fifteen years, and deals with tests on core samples coming from all over the World (Algeria, Argentina, Australia, France, Germany, Japan, Norway, Oman, Poland, Russia, Saudi Arabia, USA, Venezuela,…). In this context, the collected data are generally associated with difficult drilling conditions for which specific analyses were required in order to explain the wear and improve the performance of the drilling tools. Therefore the tested rock samples are not statistically representative of geological conditions encountered in oil and gas drilling. In addition, the long time period over which data have been accumulated implies that different people have worked, sometimes with different methodologies (technical progress, new laboratory equipments). This required a consolidation of the data.

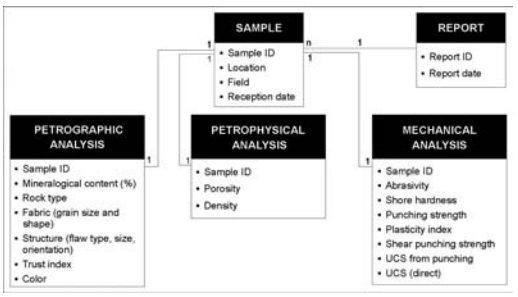


Figure 1. Overview of the structure of the database.

The results are now organized in a database (Fig. 1) which allows the analysis of the data. It includes information about the origin of the rock samples (country and field), their petrographic description, their petrophysical and mechanical properties. Each parameter has been quantified, either on an absolute (e.g. the rock strength) or a relative scale (e.g. granulometric classes).

2.2 *Petrographic description*

Our petrographic description is based on a macroscopic observation coupled with a thin section analysis (35mm x 40 mm x 300 μm) with a polarizing microscope. A picture of the sample and some micrographs under normal and polarized light are generally included in the reports, keeping the possibility for future analyses.

2.2.1 *Mineralogical analysis*

The mineralogical content is given as volume percentages. We identified more than 30 different components (generally mineral species but also rock fragments like silts and phyllite, rock clasts, organic matter, fossils…) which are distributed into two groups: (i) the grains, crystals and rock clasts, (ii) the cement or matrix.

In Table 1, minerals are organized in 6 categories according to Franklin's classification (1970). They represent common rock-forming mineral assemblages that control the mechanical properties of rocks in engineering projects, by decreasing order of quality from quartzo-feldspars to pellitic. Quartz is by far the dominant mineral species in the data base. The other frequent components are feldspars, micas, calcite and phyllite. Quartzo-feldspars represent about 50% of the encountered minerals (in terms of occurrence) whereas micaceous, carbonates and pellitic minerals account each for about 15%. Lithic/basic and saline minerals are not frequent in the database due to their oil and gas field of application and the type of samples typically selected, usually corresponding to "difficult drilling" conditions.

In terms of mineralogical content, it is important to identify the potentially abrasive minerals. Quartz is not only the most frequent mineral but it is also one of the most abrasive. Quartz, and more generally silica, occurs under various forms in our samples (Table 1): among grains, crystals and rock clasts, we find quartz, chert and siliceous tuff, but also silica in the matrix phase. All those four components are referred as "total silica content" in the following.

However, some other mineral species, even if they are not as abrasive as quartz, may have a significant contribution to the rock abrasiveness. The concept of an equivalent content in quartz in relation with abrasiveness problems has been investigated by several authors (Suana & Peters 1981, Atkinson 1993, Thuro 1996, Bruland 1998). Our database also incorporates "equivalent quartz contents" by using either the Cerchar Abrasiveness Index (CAI) of minerals (Suana & Peters 1981) or their Vickers hardness (Bruland 1998) as a weighing factor. We note those indices EqQtzC and EqQtzV respectively.

More than 40 rock types have been identified. The most frequent ones are sandstones and quartzites which represent about two thirds of the samples. Some qualifiers like silty, sandy, carbonated are thus useful to further identify the rock.

Inspired from Table 1, five other rock families are defined in order to group the samples: plutonic rocks, volcanic rocks, carbonates, siltstones, and finally shales and claystones. The samples which do not enter one of those families are grouped in a seventh category, labeled "other rocks". Figure 2 gives an overview of the distribution of the samples among rock families. Additional information about the trust index is also given on this figure; it will be explained in Section 3.

Table 1. Abundance of mineralogical components (mineral assemblages or minerals) among the tested samples (number of occurrences) after Franklin's classification (1970). Graphite, iron oxide, pyrite, epidote, dense minerals, ferruginous, amorphous, vitreous, organic matter and fossils are not listed.

Category	Components
Quartzo-feldspars (553)	Quartz (257); feldspars (160); chert (39); siliceous tuff (27); siltstone (16); silica matrix/cement (70)
Lithic-basic (36)	Pyroxenes (14); amphiboles (12); olivine (5); mafics (5)
Micaceous (165)	Micas (138); chlorite (27)
Carbonate (149)	Calcite (137); dolomite (12)
Saline (21)	Sulphates *s.l.* (5); anhydrite (9); barite (1); apatite (6)
Pellitic (184)	Phyllite (68); clay minerals (64); glauconite (35); serpentine (1)

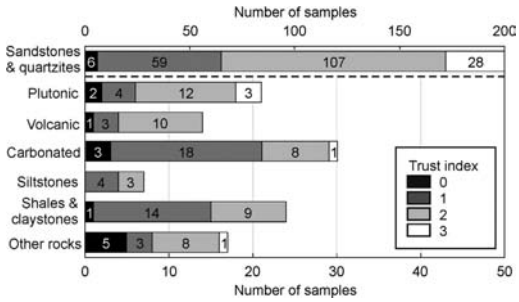


Figure 2. Distribution of the samples among the various rock families, by trust index.

2.2.2 *Fabric*

In terms of texture, we collected information about grain size and shape from micrographs observation as it is suggested that those features influence the potential abrasiveness of rocks (Verhoef et al. 1990).

For the grain size, we defined ten classes covering the range from clay to pebbles. Their definition is inspired from Wentworth's classification (1922). This classification is originally developed for detrital rocks but the definitions have also been extended to other rock types in order to simplify and standardize our database to allow further numerical statistical processing. In this case, grain and crystal sizes are entered in the same database field. Currently, all the considered samples are inbetween the sizes of silts and sands (from 4 μm to 2 mm). Some statistical estimators have also been associated for each rock: the minimum, maximum, and mean values as well as the grain size range.

Table 2. Definition of the roundness scale describing grain shape.

Class	Descriptive term
1	Rounded
2	Sub-rounded
3	Sub-angular
4	Angular

Table 3. Definition of sorting classes.

Class	Descriptive term
1	Very well sorted
2	Well sorted
3	Moderately sorted
4	Poorly sorted
5	Very poorly sorted

Even if estimators exist to quantify grain shape and sorting (Sneed & Folk 1958, Ersoy & Waller 1995, Selley 2000, Stachowiak 2000), it was not possible to assess them in our case. However grain shape and sorting are estimated in the database by means of qualitative scales, as shown in Tables 2 and 3. Additional scales have also been integrated to account for the presence of particular flaws or structures (laminations, microcracks …), their size and orientation, in the thin sections.

2.3 *Petrophysical analysis*

The petrophysical analysis mainly deals with porosity which was generally determined from thin section observation, and occasionally by weighing dry and saturated samples and determining the total volume. Porosity data are organized in five classes.

2.4 *Mechanical properties*

The uniaxial compression test to yield the unconfined compressive strength (UCS) is probably the most important test to mechanically characterize a rock material. However, for samples usually available from oil fields, it is not always possible to have samples big enough in order to perform this test. Following a long collaboration between Halliburton and the Mining Engineering Department of the University of Mons, Belgium, three mechanical tests have been identified and two of them specifically developed in order to process small samples: FPMs abrasiveness, Shore hardness and punching tests.

The FPMs abrasiveness test was developed by Brych (Brison & Brych, 1971). It is based on the understanding of the rock destruction process in a rotary drilling. A flat cylindrical steel tool rotates on the rock sample under a load of 72 N with a speed of 120 rpm. The FPMs abrasiveness is defined as the ratio of the powers consumed by the tool and by the rock. As the load keeps the same value in both cases, the calculation becomes a ratio of the tool volume (V_t) to the rock volume (V_r).

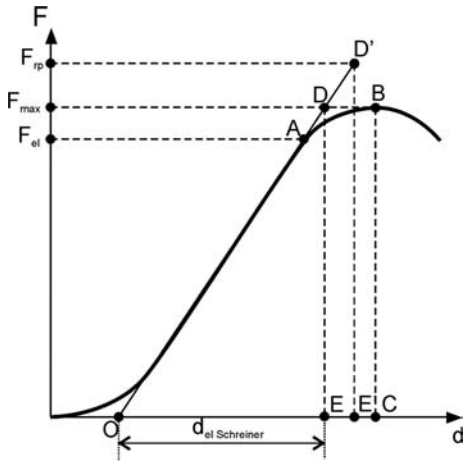


Figure 3. Typical indentation curve showing the force on the indenter (F) versus its displacement (d).

The Shore hardness is determined by dropping a small diamond-tipped indenter on the specimen and measuring its rebound height (Bamford et al. 1978). Due to the small size of the indenter and the heterogeneous nature of rock materials, a large number of tests are conducted to obtain a significant average. The Shore hardness can be used to estimate the unconfined compressive strength (UCS) of weak rocks.

Altindag and Güney (2006) reported results of studies that tried to correlate the Shore hardness and the UCS (Judd & Huber 1961, Deere & Miller 1966).

Punching tests are another easy mean to determine a mechanical property of a rock with small samples. The machine that we developed is based on Schreiner's theory and uses a flat cylindrical indenter (generally 1.4 mm in diameter) which is forced into the rock under an increasing load and at constant rate (Tshibangu 1987, Tshibangu et al. 1999, Descamps & Tshibangu 2004). The indentation curve gives the load on the indenter versus its vertical displacement (Fig. 3). Punching parameters are then computed, the main one being the punching strength R_p:

$$R_p = \frac{F_{max}}{S} \quad (1)$$

with F_{max}, the load at failure, and S, the cross-section of the indenter. Many other parameters can be calculated to understand the mechanical behavior of the tested rock and assess the energy spent during the destruction process (drilling, drifting…). The plasticity index for instance is a property intended to evaluate drillability in terms of energy. It is defined as the ratio between the total destruction work (OABC) to the elastic part of this work (ODE).

Ten to twelve tests are generally performed on a sample to give a good estimate of its punching strength.

Table 4. Indicative scale for the "trust index".

Class	Classification	Description
0	Low trust	Major data missing
1	Moderate trust	Part of data missing
2	Good trust	Some data not clear or not detailed; some interpretation needed
3	Very good trust	No interpretation at all

After testing more than 50 different rocks, Tshibangu et al. (1999) got a good linear correlation between R_p and the uniaxial compressive strength.

3 ANALYSIS OF DATA

3.1 *Quality of the information*

In an ideal case, a material sample registered in the database is completely identified in terms of origin, mineralogical content, petrographic and mechanical properties. However, the complete information is not always available, particularly for the thin section analysis. Indeed, for the last ten years analysis, the results were directly stored in the database while older ones required paper reports review and sometimes, an interpretation to fit to the format of the database (for instance if the mineral species are identified but not clearly quantified).

Therefore, an additional parameter was defined in order to account for the reliability of the information. This allows, depending on the data selected, to assess the reliability of the various interpretations and conclusions. We named it the "trust index", which ranges from "low trust" to "very good trust", from 0 to 3 according to Table 4 (da Silva, unpubl.). As shown on Figure 2, most of the data have a trust index of 2.

3.2 *Overview of the data*

Two filtering criteria were applied before analyzing the data. The first one is the reliability of the information: only records with trust index 2 or 3 will be considered. The second criterion is the availability of the information: the analysis is not performed according to UCS (only 18 direct measurements), porosity (only 38 evaluations) nor flaw type, size and orientation (23 referenced cases).

Among the remaining data, a first question arises: which kind of rocks do we have in this database? From a mineralogical point of view, we already showed that quartzo-feldspars are the dominant minerals. In fact, 80% of the analyzed rocks belong to the shale-sand series. In terms of grain size, about 40% of the analyzed samples are in the range 250-500 microns, corresponding to medium coarse sands in Wentworth's classification (1922).

From a mechanical point of view, based on the punching strength measurements, 85% of the tested rocks have moderate to high strength. The plasticity index (Fig. 4) also indicates that a wide majority of rocks exhibit brittle failure during the punching test

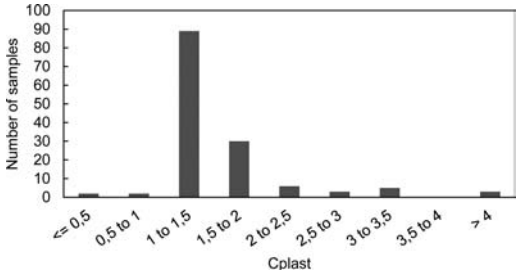


Figure 4. Plasticity index distribution among the samples of the database.

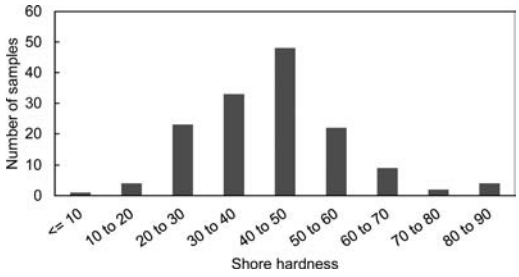


Figure 5. Shore hardness distribution among the samples of the database.

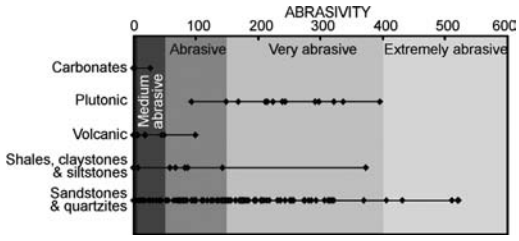


Figure 6. Distribution of abrasiveness in our dataset among rock families.

with 64% of samples having a plasticity index between 1 and 1.5. The Shore hardness (Fig. 5) follows a Gaussian distribution with a mean value of 43 and a standard deviation of 14.

Our abrasiveness scale (from 0 to 600, Fig. 6) is completely covered by the data, with values ranging between 0 and 522; most of the samples being abrasive (34%) to very abrasive (41%), as their potential abrasiveness was generally the reason why the rocks were characterized.

Hence, we can state that the data are representative of difficult drilling formations that is, typically in oil and gas, shaly to sandy rocks with moderate to high strength, and abrasive to very abrasive.

3.3 *Analysis method*

In the field, when a given section is to be drilled, the most suitable bit will be chosen according to available data. The rock type determination is the first step of our methodology as it is the first information coming from the field. This already gives an idea of the potential

Table 5. Correlation coefficients between abrasiveness and mechanical properties of the database.

Rock family	Abrasiveness versus Shore	R_p	C_{plast}
Carbonated	0.688	0.973	0.088
Plutonic	0.765	0.145	−0.511
Volcanic	0.775	0.853	−0.151
Shales-argilites-siltstones	0.558	0.882	−0.339
Quartzites and sandstones	0.336	0.123	−0.331
All rocks	0.470	0.276	−0.311

abrasiveness of the material: sandstones are a priori more abrasive than limestones (Figure 6).

In order to point out the driving parameters in the wear of drilling tools, we then identify few mechanical and petrographic properties to correlate with abrasiveness, in analogy with Schimazek's wear factor (Schimazek & Knatz 1970).

Among mechanical properties, we evaluate the relationships between abrasiveness and the Shore hardness, the punching strength and the plasticity index. Among petrographic properties, mineralogical content and grain size will be correlated with abrasiveness.

3.4 *Abrasiveness versus mechanical properties*

Table 5 gives the correlation coefficients between abrasiveness and other mechanical properties. The overall correlation with abrasiveness is quite poor for the three studied properties. However, when the rocks are classified according to their nature, some interesting results appear: the punching strength is well correlated with abrasiveness for carbonates, for volcanic rocks and for shales, claystones and siltstones (Fig. 7).

For plutonic rocks, a fairly good correlation exists between abrasiveness and Shore hardness. In the case of sandstones and quartzites, we also identify the Shore hardness as the mechanical property which best correlates with abrasiveness for this type of rock but the correlation is quite poor.

Those results can be compared with other works. On one hand, the relation between abrasiveness and punching strength is analogous to the results published by Kahraman et al (2010) who correlated the CAI with UCS. The idea that rock strength influences abrasiveness is also used by Plinninger (2001) for defining the Rock Abrasiveness Index. On the other hand, Oparin & Tanaino (2009) related abrasiveness to hardness, which is in agreement with our results on sandstones and quartzites. Our results indicate that the mechanical properties correlated to abrasiveness of rocks may differ from one rock type to another.

3.5 *Abrasiveness versus petrophysical properties*

Table 6 examines the correlation coefficients between abrasiveness and some estimators of the grain size. By considering the good correlation between abrasivity and the punching strength for carbonates and shales-claystones-siltstones, we will only focus on this property for those rocks.

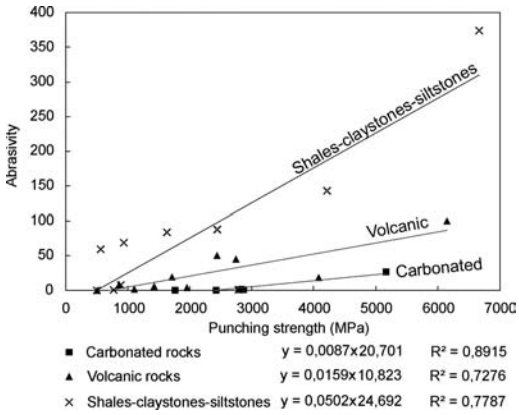


Figure 7. Correlation between abrasiveness and punching strength for three rock families.

Table 6. Correlation coefficients between abrasiveness and grain size estimators.

Rock family	Abrasiveness versus Min*	Mean*	Max*	Range*
Carbonated	−0.277	0.067	0.065	0.076
Plutonic	0.568	0.265	0.220	0.765
Volcanic	−0.393	0.025	0.036	0.775
Shales-claystones-siltstones	−0.257	0.005	0.012	0.558
Quartzites & sandstones	0.403	0.039	−0.006	0.336
All rocks	0.487	0.182	0.138	0.470

*Min: minimum grain size. Mean: mean grain size. Max: maximum grain size. Range: grain size range.

In the case of plutonic and volcanic rocks, the difference between the maximum and minimum crystal size (range) is well correlated with abrasiveness. It means that the presence of (probably hard) big mineral crystals among smaller ones or a matrix will influence the rock abrasiveness.

For quartzites and sandstones, the minimum grain size best correlates with abrasiveness, despite the low correlation coefficient.

The mineralogical composition was also considered by studying the correlation between abrasiveness and silica content, as shown in Table 7.

Carbonated rocks were not assessed here due to their nature.

Plutonic rocks are the typical case where other minerals than quartz/silica influence the abrasiveness. The correlation coefficient for EqQtzV is much higher than the one considering only silica.

For the volcanic rocks samples considered, there is limited silica content and therefore only EqQtzV and EqQtzC make sense but their correlation coefficients with abrasiveness remain low in comparison with the interesting correlation obtained for the punching strength.

The case of quartzites and sandstones is particular. Most of the samples have a high silica content. Except

Table 7. Correlation coefficients between abrasiveness and silica content.

Rock family	Abrasiveness versus		
	Total SiO_2	EqQtzV*	EqQtzC*
Plutonic	0,397	0,607	0,529
Volcanic	−0,020	0,449	0,502
Shales-claystones-siltstones	−0,287	−0,320	−0,325
Quartzites & sandstones	0,287	0,300	0,309
All rocks	0,326	0,396	0,402

*EqQtzV: equivalent quartz content using the Vickers hardness of minerals. EqQtzC: equivalent quartz content using the Cerchar abrasiveness index of minerals.

for the cement/matrix phase, the correlations between abrasiveness and silica content are of the same order of magnitude for the various estimators. The best results are found with EqQtzC. In fact, for these rocks, the Shore hardness, the minimum grain size and equivalent content in quartz estimated from the CAI have to be considered to estimate the abrasiveness.

4 CONCLUSIONS

In this paper we have shown how samples coming from difficult drilling formations have been processed in order to assess their mechanical and petrographic properties, and particularly their abrasiveness. The large amount of collected data has been organised in a database which incorporates quantitative as well as qualitative scaling of properties.

Depending on the rock type, we found that different mechanical and/or petrographic properties can be correlated to abrasiveness:

- in carbonates and shales-claystones-siltstones, only the punching strength is considered as an important property for the abrasiveness;
- in volcanic rocks, the punching strength is identified as the mechanical property which best correlates with abrasiveness but the grain size range and EqQtzV may also be considered;
- in plutonic rocks, abrasiveness seems to be related to several properties : Shore hardness combined with grain size range and EqQtzV;
- in sandstones and quartzites, several properties also need to be considered for explaining abrasiveness: Shore hardness associated with minimum grain size and EqQtzC.

In the future, we plan to refine those results by integrating tests on selected materials having specific properties in order to complete the dataset and draw more general trends.

REFERENCES

Altindag, R. & Güney, A. 2006. ISRM Suggested Method for determining the Shore Hardness value for rock, *Int. J. Rock Mech. Min. Sci.* 43:19–22.

Atkinson, H. 1993. Hardness tests for rock characterization. In Hudson, J. (ed.-in-chief), *Comprehensive rock engineering. Principles, practise &* projects. Vol. 3: Rock testing and site characterization, Oxford, New York: Pergamon.

Bamford, W.E., Van Duyse, H., Nieble, C., Rummel, F., Broch, E., Franklin, J.A., Atkinson, R.H., Tarkoy, P.J. & Deere D.U. 1978. Suggested methods for determining hardness and abrasiveness of rocks, ISRM, Commission on Standardization of Laboratory and Field Tests. *Int. J. Rock Mech. Min. Geomech. Abstr.*, 15: 89–98.

Brison, L. & Brych, J. 1971. Influence des propriétés physico-mécaniques sur le processus de découpage des roches. *Extrait des annales des mines de Belgique*, Année 1971, 2ème livraison.

Bruland. A. 1998. Project report 13A-98 – Hard rock tunnel boring: Drillability Test methods. NTNU Trondheim.

Deere, D.U. & Miller, R.P. 1966. Engineering classification and index properties of intact rock. *Urbana*, IL : Department of Civil Engineering, University of Illinois, pp. 90–101.

Descamps, F. & Tshibangu, J-P. 2004. Determination of rock properties using the punching test. In Ohnishi & Aoki (eds), *Proceedings of the ISRM International Symposium 3rd ARMS*, Kyoto, 30 November–2 December 2004, Rotterdam: Millpress.

Ersoy, A. & Waller, M.D. 1995. Textural characterisation of rocks. *Engineering Geology* 39: 123–136.

Judd, W.R. & Huber, C. 1961. Correlation of rock properties by statistical methods. In Clarke, G. (ed), *International Symposium on Mining Research*, Rolla, Missouri, February 1961, Oxford: Pergamonn.

Plinninger, R.J. 2001. *Klassifizierung und Prognose von Werkzeugverschleiß bei konventionellen Gebirgslösungsmethoden im Festgestein*. Ph.D.thesis TU Munich.

Schimazek, J. & Knatz, H., 1970. The influence of rock structure on the cutting speed and pick wear of heading machines. *Gluckauf*, 106: 274–278 (in German).

Selley, R. 2000. *Applied Sedimentology*, Academic Press.

Sneed, E.D. & Folk, R.L. 1958. Pebbles in the lower Colorado River, Texas, a study of particle morphogenesis. *Journal of Geology* 66(2):114–150.

Stachowiak, G.W. 2000. Particle angularity and its relationship to abrasive and erosive wear. *Wear* 241: 214–219.

Suana, M. & Peters, Tj. 1981. The Cerchar Abrasivity Index and Its Relation to Rock Mineralogy and Petrography. *Rock Mechanics* 15, 1–7.

Verhoef, P.N.W., van den Bold, H.J. & Vermeer, T.W.M. 1990. Influence of microscopic structure on the abrasivity of rock as determined by the pin-on-disc test. In Price, D.G. (ed), 6th International IAEG Congress, Amsterdam, 6–10 Augustus 1990. Rotterdam: Balkema.

Thuro, K. 1997. Drillability prediction: geological influences in hard rock drill and blast tunneling. *Geol Rundsch* 86: 426–438.

Tshibangu, J-P. 1987. *L'essai de poinçonnage des roches – Quelques aspects théoriques du procédé*, internal report, Faculté Polytechnique de Mons, Mons, Belgium.

Tshibangu, J-P., Charlier, R. & Lamine, E. 1999. Mécanismes de destruction des roches et conception des outils de forage. In Vouille, G. & Berest, P. (eds), 9th ISRM Congress, Paris, Augustus 1999, Rotterdam : Balkema.

Wentworth, C.K. 1922. A scale of grade and class terms for clastic sediments. *Journal of Geology* 30: 377–392.

Rock Mechanics for Resources, Energy and Environment – Kwaśniewski & Łydżba (eds)
© 2013 Taylor & Francis Group, London, ISBN 978-1-138-00080-3

Effect of an increase in rotation in a wear test to predict the durability of rock materials

J.L.E. Dias Filho, G.C. Xavier & P.C.A. Maia
Laboratory of Civil Engineering from Universidade Estadual do Norte Fluminense 'Darcy Ribeiro' – UENF, Campos dos Goytacazes, Rio de Janeiro, Brazil

ABSTRACT: This paper presents a study in wear tests with a gneiss from Santo Antônio de Pádua/RJ/BR and includes analysis of the rotation increase by testing Slake Durability (SD) and Micro-Deval (MD) tests. To evaluate the influence of the rotation in these tests was set up laboratory equipment that allows varying the speed of 7 rpm to 238 rpm. This study could be implemented in wide variety of rock materials and thus target it according to their lifetime in the project. With varying the wear levels it was observed increasing weight loss until the inertia moment holding the specimens in the wall of the machine. The results indicate an increase in linear mass loss. These procedures allow a more precise analysis of durability at a range approximately from various regions of the world.

1 INTRODUCTION

The civil engineering studies to evaluate of the durability characteristics in rock materials are common to use wear tests. In these test there is a relationship between the rotation speed of the degradation drum and the material durability characteristics. The determination of this relationship is fundamental for characterization a material in the long term, considering that the rotation speed is related to the energy of environmental degradation.

Among the existing building materials, highlight particular deserve the rocks by the frequent use in the projects. According to Salles & Maia (2004), these materials before they are extracted from mines or quarries, it presents in a balanced alteration state with the environment, which was achieved in a geological time-interval, that is, from hundreds to thousands of years. After extraction and application in a work, change occurs in the middle. Then, the rock begins to undergo transformations seeking a new equilibrium condition. The speed of change in the new environment depends on the rock susceptibility to alteration, in the others words, the alterability. Thus, the rock alterability will depend on the material characteristics, the external environment and the exposure time. Depending on the alterability characteristics, the rock can change it in an interval of time that can vary from thousands of years to a few months.

This paper presents the wear results of gray gneiss, from an ornamental stone extraction region in Santo Antônio de Padua, which is a Brazilian city that is located in the Northwest of the Rio de Janeiro state (Fig. 1).

A universal wear equipment, specially built at the Universidade Estadual do Norte Fluminense (UENF),

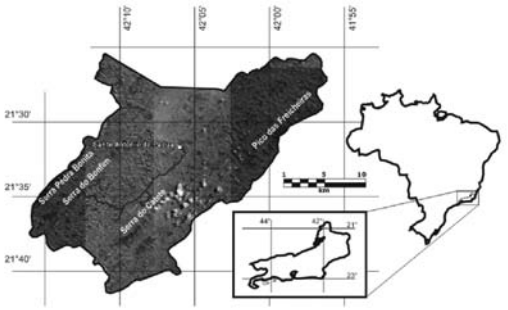


Figure 1. Location of gneiss in the "Serra do Bonfim".

was used in this study. In the apparatus, it is possible to control the rotation speed of the wear drum. It was evaluated the effect of the rotation increase in two wear tests used to predict the durability in rock materials: the slake durability and micro-Deval. These tests allow for differentiated analyzes of the wear evaluation on materials. While the SD test one promotes wear in the materials surface, the MD wear is more intense and occurs particle breaking. The literature mentions examples of similar studies and procedures to analyze the behavior of rocks resulting from rocks used in construction using this tests (Table 1).

2 MATERIAL AND METHODS

2.1 *Material of study*

The rock material analyzed came from a quarry in "Serra do Bonfim", located in Santo Antonio de Pádua city, in the northern region of the State of Rio de

Table 1. Some works developed in degradation with slake durability and micro-Deval test with rocks.

Reference	Material	Analysis	Note
Agustawijaya (2003)	Weak rocks	Slake durability test	Significant changes in the results according to the specimen's geometry.
Fuenkajorn & Scri-in (2007)	Various rocks	Slake durability test	Physical alterations in the materials and change in strength. Durability satisfactory.
Lane et al. (2011)	Various rocks	micro-Deval	Modifying the duration time of the test
Yagiz (2010)	Carbonate rocks	Slake durability test	Correlation between of the slake cycles quantity in the results analysis.
Keaton & Mishra (2010)	Sedimentary rock	Slake durability test	Modifying the duration time of the test and removal of the drying process.
Dias Filho et al. (2012)	Gneiss	Slake durability test and micro-Deval	Durability study using special laboratory equipment.
Erichsen et al. (2011)	Various rocks	micro-Deval, Los Angeles and Nordic test	Comparison of the test methods for different test fraction
Allam & Ebrahimpour (2013)	Sedimentary rock	micro-Deval and Idaho degradation test	Repeatability of the tests

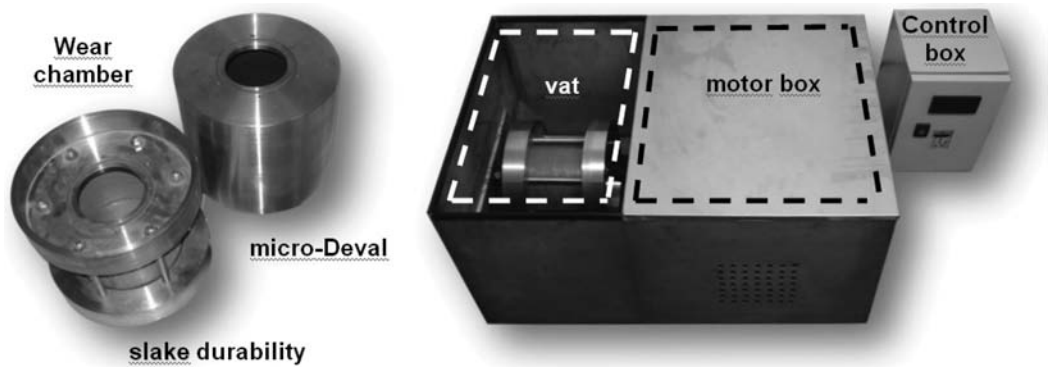


Figure 2. Universal Wear Equipment built at the Universidade Estadual do Norte Fluminense.

Janeiro. Note that the rock studied is used for ornamental purposes and it is commercially called "Pedra Olho do Pombo" (Augen gneiss). It is medium-grained mylonitic gneiss with white orthoclase porphyroblasts and rich in quartz present throughout the "Serra do Bonfim" alignment. The commercial name originated from these characteristics because the minerals on the gneiss surface remind us of a pigeon's eye. Dias Filho et al. (2012), Salles et al. (2008) and Salles & Maia (2004) conducted some studies to classify the physical and mechanical characteristics of the rock material from this region.

2.2 *Method formulation*

The methodology for study the effect of the rotation increase in wear test to predict the rock materials durability consist in a comparison between the slake durability test and micro-Deval, on the intact material, changing the rotation speed by the wear equipment.

For evaluation of material durability in some cases are sufficient shows an index with the intact material parameters. The mainly parameters is de loss mass in the choice test. For deeper analysis of the material behavior, considering that in other regions where it will be applied the conditions to weathering are different, then it is necessary to produce samples for testing at different levels wear.

2.3 *Experimental program*

The material parameter studied was the weight loss by wear. The wear equipment used for this study is shown in Figure 2. This equipment has physical characteristics according to the Standard Rock Characterization of Testing and Monitoring, ISRM (1981). In the apparatus the sample is placed inside a hollow cylindrical metal chamber, which rotates about a horizontal axis. Each test has singular characteristics. While the SD test promoting the shock of rock particles with each other, the MD abrasion promotes the similar situation, but the wear is more intense, because there are steel balls in the drums.

The tests allow contact of the particles with the water, favoring the disintegration. In the study, the variation in the wear energy was done by controlling the rotation speed of the chamber. Six levels of rotation

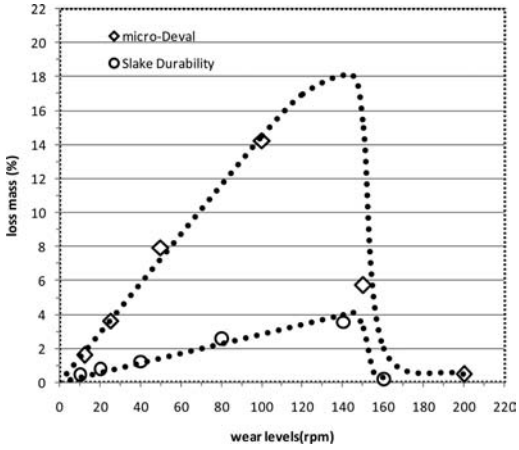


Figure 3. Results of SD and MD test in six different rotations.

were used in the SD tests: 10, 20, 40, 80, 140 and 160 revolutions per minute (rpm), where the standard rotation is 20 rpm. Similarly, six different rotation speeds: 12.5, 25, 50, 100, 150 and 200 rpm, where the standard rotation is 100 rpm, were used in the MD tests.

These tests were conducted in the Laboratory of Engineering Civil at the UENF.

3 RESULTS AND DISCUSSION

The experimental results indicate that the weight loss increases with wear levels. For the results from SD test shows results of the 5° cycles for each increase rotation.

Based on the experimental results it is possible to determine the mass loss variation with the rotations number (Fig. 3). Note in these figures that the weight loss increases with the rotation number. However, from a given revolutions number is noted tendency to stabilization and then a subsequent abrupt reduction of mass loss with increasing revolutions number. This behavior is explained by the increase centrifugal force which causes the reduction in relative mobility between the particles up to the limit where the particles are completely immobilized and trapped in the chamber wall. At this point the test loses efficiency and no longer represents a condition field.

The determination of the theoretical rotations number can be done through the forces balance at the critical moment of the particle movement in the chamber (Fig. 4). Thus, the moment that the friction is equal the weight force has the critical rpm (see Equation 1).

$$W = F_c \cdot \mu \tag{1}$$

where:

$$W = \text{weight force} = m \cdot g \tag{2}$$

$$F_c = \text{centrifugal force} = \frac{m \cdot v^2}{r} \tag{3}$$

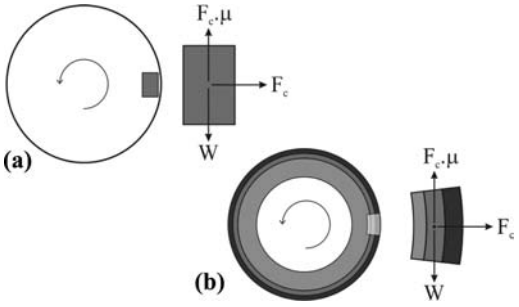


Figure 4. Critical position of the particle in the chamber and its equilibrium equation in SD (a) and MD (b).

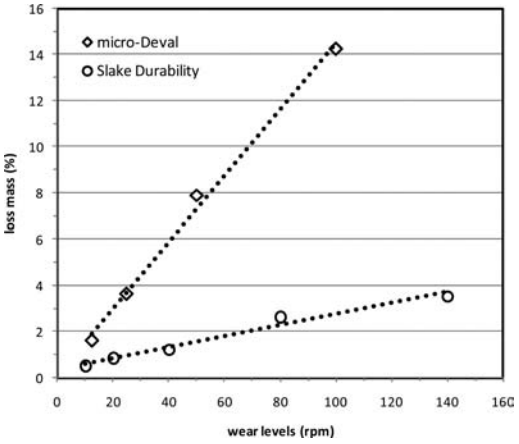


Figure 5. Results of SD and MD test in six different rotations.

$$\mu = \text{friction coefficient} = \tan\varphi \tag{4}$$

By substituting Equations 2, 3 and 4 in Equation 1 v can be isolated:

$$v = \frac{\sqrt{g \cdot r}}{\tan\phi} \tag{5}$$

The division of v by the speed at the chamber wall gives the test critical speed. The value found is close to 165 rpm in SD and 145 in MD.

The analytical theory determination to critical rotation is next to experimental values. However, for SD test in 140 rpm the curve presents results in a sharp fall contradicting the idea of the increasing mass loss until the total inertia of the particle in the chamber wall and that the theoretical rotation critical was bigger. But in the MD test the value was between 100 and 150 rpm, where will be necessary to do others testing to confirm. The main reason can be the reduction of the friction between the particles in the chamber observed during the test, thus, in the Figure 5 shows only the data that can be correlated in future research ensuring more accurate data.

4 CONCLUSIONS

This work contributes to a critical analysis about topic, hoping therefore to understand the relationship between the wear energy and the rock materials durability studied. In this sense, the methodology allowed the assessment of the durability considering the effect of varying the wear energy characteristic from Campos Goytacazes, a city of Rio de Janeiro. It also allows estimating the behavior in other regions, with different wear energies.

It was observed with the wear levels variation, a mass loss increasing until the moment that because of centrifugal force, the particles cling to the wall of the equipment.

The results indicate a wear increase with the rotation speed in the degradation drum. Note that the relationship between the drum rotations number and the wear follows an approximately linear relationship. Thus, considering that the increased of the drum rotation represents increased wear energy from environment, it can be concluded that the wearing speed of the rock is greater in environments with higher degradation energy and the wear level can follow a linear function with the degradation energy of the environment.

ACKNOWLEDGEMENTS

The authors thank CAPES, UENF and Serraria Olho do Pombo for support of this research.

REFERENCES

Agustawijaya, D. S. 2003. Modeled Mechanisms in The Slake-Durability Test For Soft Rocks. *Lecturer, Department of Civil Engineering, Faculty of Engineering – Mataram University. Dimensi Teknik Sipil* 5(2): 87–92.

Allam, L. & Ebrahimpour, A. 2013. Comparative Analysis of Idaho and Micro-Deval Aggregate Degradation Test Methods. *J. Mater. Civ. Eng.* DOI: 10.1061/(ASCE)MT.1943-5533.000077.1

Dias Filho, J.L.E; Maia, P.C.A; Xavier, G. de C. & Fernandes, P.A.M. 2012. "Study of the Wear Energy Effect in the Durability Predicting of Ornamental Gneiss from Pádua-RJ." *XVI Brazilian Congress of Soil Mechanics and Geotechnical Engineering, Porto de Galinhas/PE 14–18 September 2012. 7p.*

Erichsen, E.; Ulvik, A. & Sævik, K. 2010. Mechanical Degradation of Aggregate by the Los Angeles-, the Micro-Deval- and the Nordic Test Methods. *Rock Mech Rock Eng* 44: 333–337. DOI 10.1007/s00603-011-0140-y.

Fuenkajorn, K. & Sri-in, T. 2007. Slake durability index and strength testing of some rocks in Thailand. *Geomechanics Research Unit, Suranaree University of Technology, Thailand. 15p.*

ISRM – International Society for Rock Mechanics. 1981. Rock Characterization Testing and Monitoring. *ISRM Suggested Methods,* Ed. E.T. Brown, Pergamon Press, Oxford, pp.1–212.

Keaton, J.R. & Mishra, S.K. 2010. Modified Slake Durability Test for Erodible. *International Conference on Scour and Erosion (ICSE-5).*

Lane, D.S., Druta, C., Wang, L. & Xue, W. 2011. Modified Micro-Deval Procedure for Evaluating the Polishing Tendency of Coarse Aggregates. *TRB 2011 90th Annual Meeting.*

Miscevic, P. 2011. Durability Characterization of Marls from the Region of Dalmatia, Croatia. *Geotech Geol Eng* 29:771–781. DOI 10.1007/s10706-011-9416-y.

Salles, R.O. & Maia, P.C.A. 2004. Experimental Evaluation of Alterability of Ornamental Rocks from North of the State of Rio de Janeiro. 1^{rt} *Brazilian Symposium on Geotechnical Young. São Carlos/SP, 2004. 6p.*

Salles, R.O; Maia, P.C.A & Sayão, A.S.F.J. Effect of Degradation in Stiffness of Geotextile Fabric after Exposure in the Field and Laboratory. *XIV Brazilian Congress of Soil Mechanics and Geotechnical Engineering, Armação de Búzios/RJ 23–26 September 2008. 7p.*

Yagiz, S. 2010. Correlation between slake durability and rock properties for some carbonate rocks. *Bull Eng Geol Environ* (2011) 70:377–383. DOI 10.1007/s10064-010-0317-8.

Rock Mechanics for Resources, Energy and Environment – Kwaśniewski & Łydżba (eds)
© 2013 Taylor & Francis Group, London, ISBN 978-1-138-00080-3

The elastic wave velocity in rocks under triaxial stress at high pressure and temperature

A. Dziedzic & J. Pinińska
Department of Geomechanics, Faculty of Geology, University of Warsaw, Warsaw, Poland

ABSTRACT: The aim of this paper are the relations between static and dynamic indexes of rock deformation at great depths on the basis of laboratory geomechanical studies under conditions of high pressure and temperature. In the studies the high-capacity MTS-815 Rock Test System with a thermo-pressure cell and recording the ultrasonic waves was used. The tested were six types of rocks, subjected to triaxial compression with confining pressure 0 to 90 MPa and temperature 22 to 120°C. The tests shown variable dynamics of increase of the wave velocity (V_p) with an increase of pressure. Therefore the wave velocity in sedimentary rocks can reach the value close to velocity characteristic for granite under low pressure. The comparison of the longitudinal wave velocity (V_p) and the phases of deformation indicates main increase of velocity in the phase of compaction and in the phase of elasticity. The wave velocity reaches its maximum value near the threshold of absolute dilatancy but with discrepancies, depending on the lithology and depth modeled by pressure and temperature.

1 INTRODUCTION

Rock features at great depths are identified mainly by geophysical methods where lithological layers, tectonic structures and engineering parameters are established on the basis of measuring the velocity of seismic waves. However, wave velocity registered at the given depth is not an unequivocal feature of lithology, and thus of geomechanical properties of the rocks at the unknown conditions (Birch 1961, Wolarowich et al. 1964). Seismic wave velocity depends on the stress and temperature and in the given rock is variable at the various depths (Wepfer & Christensen 1991). Therefore the appropriate correlation of seismic data with geomechanical parameters, requires detail research, the importance of which was clearly stated by Barton (2000, 2007), as a key topic for rock engineering courses of research.

The range of fluctuations in geomechanical and geophysical properties determination under varying conditions of temperature and pressure was tested in a laboratory on a lithologicaly well-identified rocks from various regions of Poland. Samples were subjected to compression strength tests under triaxial conditions, during which the changes in longitudinal wave velocity were simultaneously recorded. The aim of the study was to link dynamic parameters describing the characteristics of the rocks obtained in geophysical studies, with parameters characterizing their mechanical properties, obtained in static laboratory compression tests. Thus, the properties of rocks at the stress and temperature modeling the conditions of increasing depth, were being determined in two separate research ways. Further, the comparative data and correction factors, necessary in identification of rock massive behaviour at a great depths, have been acquired.

The both methods: of mechanical deformability and of elastic wave velocity changes, were directly connected with the analysis of deformation mechanisms in each, studied type of the rock. It was analysed, inter alia, if the state of stress at which the elastic wave reaches its maximum velocity ($\sigma_{1\ Vpmax}$), is equivalent to the stress state on the threshold of absolute dilatancy ($\sigma_{1\ TD}$). Using two independent tests: the ultrasonic, which is laboratory equivalent to seismic survey, and the laboratory triaxial mechanical testing, it was being observed if the phenomenon of stability loss in the rock structure, is recorded simultaneously on the both way of studies and whether in the same type of the rock the processes of stability loosing are similar at the various levels of pressure and temperature. In both cases, the impact of lithological diversity in the studied rocks was evaluated.

2 RESEARCH METHODOLOGY

2.1 *Rock material*

The study was performed on 6 varieties of sedimentary and igneous rocks. The first group was represented by clastic flysch sandstones from Cieżkowice and Mucharz quarries, and anhydrites and dolomites surrounding the copper-shale deposit in the Legnica-Głogów Copper District. The second group was represented by Sudetes granites from Strzelin quarry and basalts from Wilków quarry.

Clastic sedimentary rocks differed in their degree of diagenesis and grain size. Poorly consolidated Ciężkowice sandstones, are built of mixed coarse, medium and fine grains of 0.06 to more than 1 mm fraction, with the quartz grains domination, cemented by iron-clay matter, locally passing in carbonate. Sandstones from Mucharz (Krosno sandstones) are the rocks much more diagenetically formed, composed of medium and fine, mainly quartz grains ranging from 0.2 to 0.4 mm. Numerous lithoclasts of size up to 1 mm are come together. Detrital material is tightly bonded with abundant carbonate conglomerate. The rock is laminated and is characterized by linear, parallel arrangement of non-transparent ironic minerals.

The tested anhydrites are fully-crystallized rock structures, with grain sizes ranging from 0.05 to 0.8 mm, built almost entirely of anhydrite developed in the form of mosaics and tightly interlocking crystals. Dolomites are made of well-sorted, dolomitized carbonate matter, with the grain size of 0.03 – 0.06 mm, which interlock tightly and mosaic-like, forming a dense, non-porous, micro-crystalline mass.

Igneous rocks selected to the study are extrusive basalts of alkaline mineral composition, and deep granite rocks classified as acidic. Basalt rock is black in colour, of a phenocryst structure, with large single plagioclases and pyroxenes and fine-crystallized rock matrix filling the entire space between the phenocrysts**.** Granite is a medium-grained rock of a fully-crystallized structure, with mineral components tightly, mosaic-like interconnected. The dominant minerals are quartz, potassium feldspar, plagioclases and micas.

In terms of internal structure, the studied types of rocks formed a group of distinct crystalline rocks, (sandstone and granite), and a group of cryptocrystalline rocks (anhydrite, dolomite, basalt). This division is reflected in their bulk density (ρ_s). Laboratory tests shown $\rho_{s,}$ ranging at an atmospheric pressure and room temperature, from 2300 to over 2600 kg/m^3 for the first rock group, and much higher 2800 to 3000 kg/m^3 for the second group.

In the prior laboratory conditions, the velocity of an ultrasonic longitudinal wave (V_{p0}) varied also, depending on the lithology. Rocks with a clear, granular structure were characterized by average V_{p0} value of 1728 m/s (Ciężkowice sandstone) to 3691 m/s (Krosno sandstone), and 4739 m/s (granite). The cryptocrystalline rocks recorded a higher average V_{p0} velocity value, from 5820 m/s (anhydrite) to 5933 m/s (dolomite), and 6456 m/s (basalt).

2.2 *Testing and management equipment*

In order to determine the course of the deformation under the loading, cylindrical rock samples with a diameter of about 50 mm and slenderness of about 2 were subjected to triaxial conventional compression tests under the high temperature and pressure. The study used the MTS Co. equipment based on the high-capacity MTS-815 Rock Test System with the TestStar II electronic control, thermo-pressure cell and the module for registration of the longitudinal ultrasonic wave velocity, authorized by Department of Geomechanics and synchronized with the whole system (Dziedzic & £ukaszewski 2010). This set allowed, for each performed test at each level of the selected confining pressure and temperature, a simultaneous recording of both: the changes of deformation and the changes of elastic wave velocity, as a function of stress, from the baseline until the final destruction of rock structure. In the course of tests the paths of axial (ε_z), circumferential (ε_c) and volumetric (ε_v) strain were recorded. Therefore the range of deformation phases after Hallbauer et al. (1973) for each rock types was established. As a result for each test, the relationships between the characteristics of the deformation and changes in the velocity of a longitudinal ultrasonic wave (V_p) were determined (Piniñska & Dziedzic 2011). Particular attention was paid to registered values of stress on the absolute dilatancy threshold, heralding the emergence of inelastic damage of the rock structure.

Table 1. Depth levels modeled by pressure and temperature in thermo-pressure cell.

Level	Depth m (b.g.l.)	Pressure MPa	Temperature °C
1	0	0	22
2	500	12	25
3	1000	25	30
4	1500	37	45
5	2000	50	60
6	2500	62	75
7	3000	75	90
8	3500	90	120

Classical, single triaxial tests were performed for each variety of rocks, with the aim to model conditions from the earth surface to the depth of 3.5 km at 500 m intervals. Conditions of confining pressure and temperature (P & T) corresponding to the programmed this way, eight different depth levels were created in a thermo-pressure cell. Confining pressure (P) values in the range of 0 to 90 MPa and the temperature (T) in the range of 22 to 120°C corresponding to the depth levels are summarized in Table 1.

The tests were performed in two stages. In stage I in the cell in which the rock samples were placed, the temperature was gradually increasing, together with increase of a confining pressure at the constant velocity of 10 MPa/min to the desired level of P & T. In stage II, after the modeled test conditions were stabilized, the sample was loaded with a constant axial strain increase at 10^{-5} s^{-1}. In both stages changes in the longitudinal ultrasonic wave velocity (V_p) were registered in the direction of the major principal stress σ_1 by using ultrasonic heads with the frequency of 1 MHz, arranged at the basis of cylindrical rock samples.

The stress-strains curves ($\sigma_1 - \varepsilon_z$, ε_c, ε_v) obtained from the mechanical studies formed the basis for determining the pre-critical deformation phases described and associated with them critical threshold values of stress and strain. The data were correlated with the recorded values of longitudinal wave velocity (V_p).

A detailed analysis of the value of the stress at the maximum velocity of the wave ($\sigma_{1\ Vpmax}$) and at the absolute dilatancy threshold ($\sigma_{1\ TD}$) allowed to determine the integrity stress ratio ($I_{Vp} = \sigma_{1\ Vpmax} - \sigma_{1\ TD}$). According to research, the value of this index can be above or below zero, depending on the litho-logy of the rock and for the same rock types, on the applied pressure.

3 RESEARCH RESULTS

3.1 V_p *changes*

The study shows that with an increase of principal stress, a wave velocity gradually rises, both, in a stage I (unstable conditions of P & T) and in a stage II (P & T stable and major principal stress σ_1 arising). For all the samples, the curves of velocity growth can be, in general, considered to be co-shaped with stress – volumetric strain curves (Fig. 1).

At each level of the depth modeled by pressure (P) and temperature (T), in most of the varieties of the examined rocks the velocity increase was continuous. The wave velocity reaches its maximum ($V_{p\ max}$) at a certain limit value of stress ($\sigma_{1\ Vpmax}$). After exceeding it, a wave attenuation takes place, manifesting a severe damage at the structure of the material. The state of stress for the maximum wave velocity ($\sigma_{1\ Vpmax}$) is not always identical with a state of stress/strain, acquired through mechanical tests, which is demarcating the threshold of absolute dilatancy ($\sigma_{1\ TD}$). These discrepancies, depend on the type of the rock and the depth modeled by pressure (P) and temperature (T).

Although the differences, noted in laboratory conditions, between the values of V_p registered on the threshold of absolute dilatancy and the value $V_{p\ max}$ at the threshold of attenuation are not high and reach up to 150 m/s, but associated with them discrepancy of the stress and strain value are conside-rable. It means that the critical stress/strain state causing the loss of continuity of the rock medium, established through geophysical and mechanical methods are different. In case, at the same type of the rock, such as e.g. granites, velocity $V_{p\ max}$ recorded at the threshold of attenuation can in some conditions "overtake" absolute dilatancy threshold or appear as "delayed" (Fig. 1a, b).

The main increase of wave velocity in all studied varieties of rocks occurs in stage I (Fig. 2), during the increase in confining pressure (P) and temperature (T). These changes can be seen as an indicator of continuous compaction of the rock structure. At this stage occurs about 30 to 80% of the total increase in velocity, from its initial value (V_{p0}) to the maximum value ($V_{p\ max}$). This is consistent with the thesis

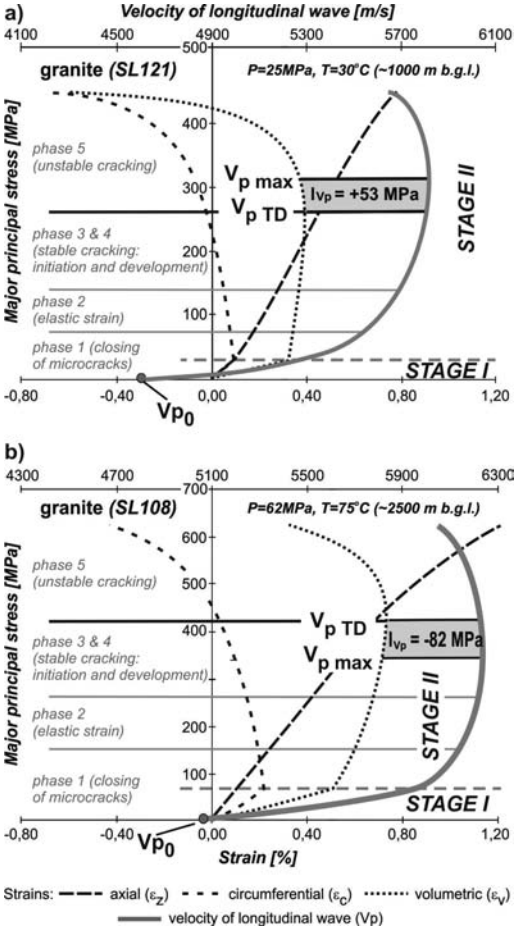


Figure 1. Simultaneously recorded curves of deformation and of longitudinal wave velocity in granites: a) maximum of velocity wave (V_{pmax}) "overtake" absolute dilatancy limit (Vp TD), b) maximum of velocity wave (V_{pmax}) "delayed" absolute dilatan-cy limit (Vp TD).

Karato (2008) that the increase of a wave velocity depends mainly on the pressure. In Ciężkowice sandstones the increase is even higher from the initial velocity (V_{p0}) of about 1700 m/s at the confi-ning pressure 12 MPa (500 m b.g.l.) the velocity increases up to about 3500 m/s and at a pressure of 37–62 MPa (1500–2500 m b.g.l.) to nearly 5000 m/s. Therefore, without any damage to the structure (stage I) the Ciężkowice sandstone may reach velo-city characteristic to velocity of the Krosno sandstones (average $V_{p0} = 3690$ m/s, $V_{p\ max}$ about 5700 m/s). The example of the Ciężkowice and Krosno sandstones also indicates that clastic rocks subjected to confining pressure may have a considerable potential for the structure compaction, without loss of continuity. It results in significant increase of a wave velocity at great depths, making difficult the correct identification of some rocks with the assistance of indirect geophysical methods only.

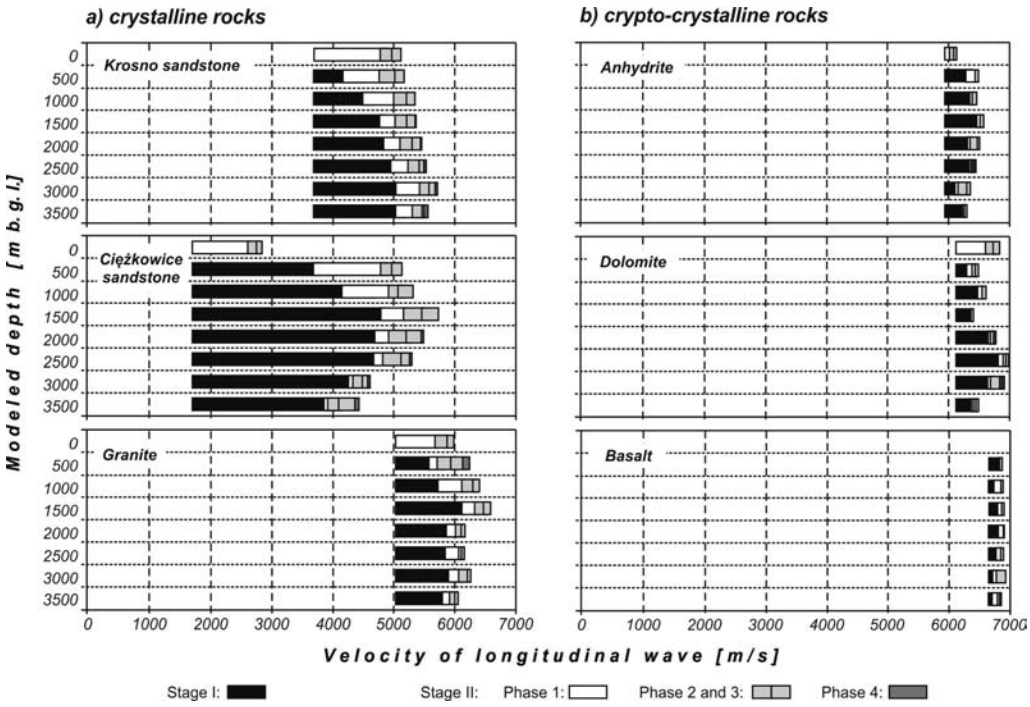


Figure 2. Longitudinal wave velocity changes at the Stage I and Stage II related to the average value of V_{p0}: a) crystalline rocks, b) crypto-crystalline rocks.

The increase of wave velocity in the Ciężkowice and Krosno sandstones in a stage I to an average value of about 5000 m/s makes them similar to granites, in which recorded at atmospheric pressure an average value of V_{p0} is 5000 m/s and increases in stage I to the maximum 6200 m/s. In the other examined varieties of rocks a wave velocity changes in stage I are considerably lower and do not exceed 1000 m/s, which indicates the limited capacity of these rock media for the compaction. For basalts, a maximum velocity increase in stage I reaches only about 200 m/s, and for anhydrites and dolomites less than 1000 m/s.

The results of the research also indicate that the general correlation the raise of a wave velocity with the increase of depth, modeled by confining pressure (P) and temperature (T), is not linear. In majority of the examined rocks, maximum values of V_p is achieved in the modeled conditions, at the corres-ponded depths range of 1500 to 2500 m below the ground rather than to extreme depths at 3500 m. As the studies indicate, only in the Krosno sandstones a velocity increased gradually up to 3000 m below the ground level. Thus, changes in registered velocity V_p depends on rocks structure and under certain conditions of P & T, rocks material undergo deformations and in the discontinuous media wave velocity decreases. This is consistent with the observations of Silaeva & Bayuk (1967), who on the basis of a well logging stated that the increase of wave velocity in rocks can reach several thousand m/s, but takes place mainly to the depth of 1000 m.

In a stage II, in stabilized conditions of P & T, with the axial compression applied, the wave velo-city change with a fluctuating dynamics and depends on a phase of deformation (Fig. 2). The main ve-locity raise is recorded in the compaction phase (Phase 1) as a continuation of a stage I, i.e. further thickening of the material. With the increase of the modeled depth, in the compaction phase the velocity increases relatively less.

In subsequent phases of deformation, changes of the longitudinal wave velocity are determined to a large extent by lithology. Changes in poorly consolidated clastic rocks, starting from the Phase 1, are apparently larger, than in the rocks of considerable density. In the phase of elastic deformation (Phase 2) a velocity increases continuously but slightly, and there are no clear trends following the depth. During the initiation and growing of stable cracking (Phases 3 and 4), a wave velocity can further increase despite of the initial unidirected micro-cracking heralded by volumetric strain (ε_v) growth at the stress/strain curve. Until the opening of microcracks transverse to the wave propagation, the attenuation does not occur. Often, in the multidirection cataclased rocks, the wave velocity remains also high due to compensation of internal and external microcracking by high confining pressure (P).

3.2 *Stress integrity index (I_{Vp})*

Comparative analysis of the mechanical destruction of a rock structure shown on the deformation curves and

the changes of the elastic wave velocity indicates that the value of critical stress at the initiation moment of the rocks structure damaging may vary, depending on a research methodology.

As well the stress characterizing the occurrence of unstable growth of cracks at the absolute dilatancy threshold, does not always result in elastic wave attenuation. The further increase of wave velocity, even after the rock medium is damaged, may be due to the anisotropy rupture – directional orientation of microcracks, directional compaction of cracked rock fragments or, the rotation of grains and their array in the deformation process. This results in a higher density of rock material at high confining pressure, mainly in the crypto-crystalline rocks.

The discrepancy in determining the level of critical stress at the transition of the rock medium from the continuous to the not continuous state, observed on the both tests, has been expressed by the stress integrity index ($I_{Vp} = \sigma_{1\ Vpmax} - \sigma_{1\ TD}$). This index characterizes the difference between the stress registered at a maximum velocity of elastic wave ($\sigma_{1\ Vpmax}$) which signals the critical stress that causes the destruction of structure and those observed by means of mechanical deformation at the absolute dilatancy treshold ($\sigma_{1\ TD}$). The index may take positive or negative values. A positive value indicates the increase in wave velocity in spite of a mechanical damage to the rock structure, and the negative value represents earlier attenuation, despite the absence of mechanical symptoms signaling rock damage. Gene-rally, the index is dependent on the lithology of rock and its susceptibility to damage in the given conditions of pressure and temperature (Fig. 3).

In polimineral, distinct crystalline rocks (sandstones and granites) the I_{Vp} index value is positive in a part or along a complete considered depth profile. Therefore, a delay in the attenuation of wave occurs in spite of a mechanical damage to the rock structure. In the Krosno sandstones the positive IVp index occurs to the modeled by P & T depth, of about 3500 m b.g.l.; in granites and the Ciężkowice sandstones it occurs only to a depth 1500 to 2500 m b.g.l. In the latter the transgranular cracking is, probably initiated at earlier stage, what causes a wave attenuation. But, earlier intragranular, distributive microcrackings of resistant quartz grains without displacements do not reduce the wave propagation (Piniñska 2008). In the crypto-crystalline rocks – basalts, dolomites and anhydrites the opposite effect is observed. The I_{Vp} index is negative or close to zero at a low pressure corresponding to the depths of 1500 m b.g.l., or even, as in the case of basalts, along the in the whole analyzed depth profile. It is probable that a random distribution of cracks result in a suppression of the wave earlier than the recorded clear volume changes which characterize absolute dilatancy. Increasing confining pressure, in turn, reduces the opening of developing microcracks, what contributes to the elastic wave propagation over a threshold of the absolute dilatancy.

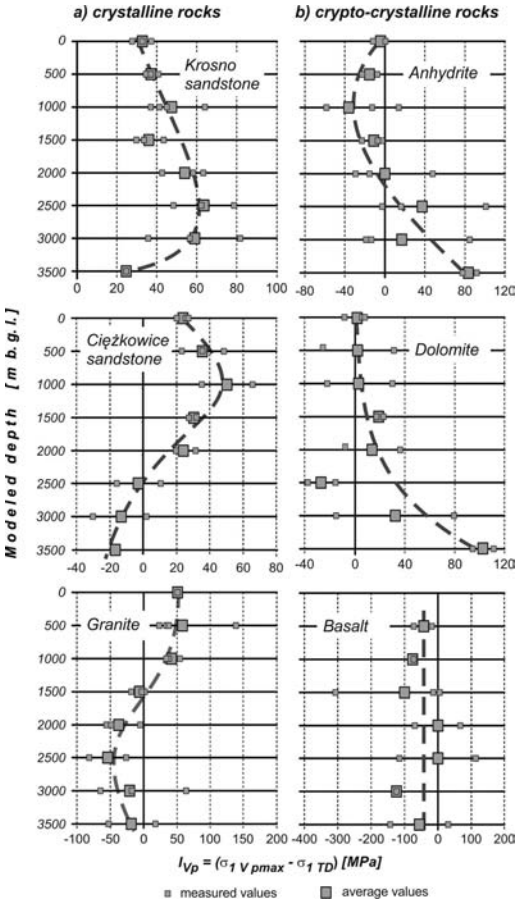


Figure 3. Stress integrity index (I_{Vp}) changes with a depth mo-deled by pressure (P) and temperature (T): a) crystalline rocks, b) crypto-crystalline rocks.

4 SUMMARY

The conducted studies show that under the influence of increasing pressure and temperature longitudinal wave velocity (V_p) in rocks can increase by several thousands of m/s. In the case of studied Ciężkowice sandstones the increase is over 250% of the initial value (V_{p0}) registered in surface conditions. At a great depth sedimentary rock can therefore be characterized by the wave velocity close to the velocity characteristic of igneous rocks such as granite. This feature may sometimes hinder, in the complex conditions of pressure and temperature, the accurate identification of lithological layers on the basis of seismic surveys at depths of several kilometers.

Changes in the longitudinal wave velocity, observed in the conducted laboratory tests, in the same rock types under the same pressure and thermal conditions depend on the phase of rock deformation. The largest increase in V_p occurs during the increa-sing density of rock material, in particular as a result of the confining pressure and temperature raise du-ring the compaction

phase at the stage of axial compression in stabilized P & T conditions. Hence, the greatest changes of V_p occur in less dense rock media.

The variability of a propagation properties of ultrasonic waves in deformed rocks is apparent, both, in the vertical and lateral profiles. Depending on the susceptibility of the rock structure to continuous and discontinuous deformation, the natural pores and microcracks may be subject to closures or openings in different directions (Rasolofosaon et al. 2000). That results in significant deviations of the actual, experimentally measured wave velocity from the velocity considered as typical for given rocks in surface conditions, where the structure is intact.

Depending on the type of a rock lithology, and the stress and temperature conditions, the maximum increase in a wave velocity precedes occurrence of the absolute dilatancy threshold or, is delayed to it. Thus, measurements of the longitudinal wave velo-city (V_p) are a sensitive tool which enables detect the beginning of a destruction, as long as mechanisms of rock structure destruction are well recognized.

The impact of the micro-structural factors on the mechanical properties of rocks, observed in the experiments cause a non-linear V_p changes in the depth profile. It is therefore necessary, as previously stated by Barton (2000, 2007), to constantly carry out a comprehensive correlation of seismic surveys with the indicators obtained in the mechanical and ultrasonic laboratory tests, conducted under modeled va-rying conditions of temperature and pressure due to different depth levels of the Earth crust.

REFERENCES

Barton, N. 2000. Some new Q-value correlations to assist in site characterization and tunnel design. *Int. J. Rock Mech. Min Sci. & Geomech. Abstr.*, 39/2. 185–216.

Barton, N. 2007. *Rock Quality, Seismic velocity, Attenuation and Anisotropy*. Rotterdam: Balkema.

Birch, F. 1961. The velocity of compressional waves in rocks to 10 kilobars. *Jurnal of Geophysical Research* 66 (2): 2199–2224.

Dziedzic, A. & Łukaszewski, P. 2010. Ultrasound wave velocity measurements in triaxial compressional tests. *Górnictwo i Inżynieria: Kwart. AGH* 34(2): 223–230 (in polish).

Hallbauer, D.K., Wagner, H., Cook N.G.W. 1973. Some observations concerning the microscopic and mechanical behaviour of quartzite specimens in stiff, triaxial compression tests. *Int. J. Rock Mech. Min. Sci.* 10: 713–726.

Karato, S. 2008. *Deformation of Earth Materiale. An Introduction to the Rheology of Solid Earth*. New York: Cambridge University.

Piniñska, J. 2008. Models of rock deformation under uniaxial compression conditions. *Geologija* 50: 108–115.

Piniñska, J. & Dziedzic, A. 2011. Volume density and longitudinal wave velocity changes of the Ciężkowice and Krosno flysch sandstones under high pressure and temperature in the triaxial test condition. *Arch. of Civ. Eng.* 57(1): 73–85.

Rasolofosaon, P.N.J., Rabbel, W., Siegesmund, S. & Vollbrecht, A. 2000.Characterization of crack distribution: fabric analysis versus ultrasonic inversion. *Geophys. J. Int.*141 (2): 425–453.

Silaeva, O.I. & Bayuk, E.I. 1967. On the nature of anisotropy of elastic properties of rocks, *Izv. Akad. Nauk SSSR, Fiz. Zemli* 12:22–29 (in russian)

Wepfer, W.W. & Christensen, N.I. 1991. A seismic velocity-confining pressure relation, with applications. Technical note. *Int. J. Rock Mech. Min. Sci. & Geomech. Abstr.* 28 (5): 451–456.

Wolarowich, M.N. & Lebykin, A.N. & Galdin, N. 1964. Study of longitudinal wave velocities in rock samples at pressure up to 20 000 kg/cm^2. *Dokl. Akad. Nauk SSSR* 157 (6): 1349–1351.

Rock Mechanics for Resources, Energy and Environment – Kwaśniewski & Łydżba (eds)
© 2013 Taylor & Francis Group, London, ISBN 978-1-138-00080-3

Environmental characterization of the stress-corrosion cracking of rockbolts in underground coal mines using laboratory and in-situ testing

E. Elias, D. Vandermaat, A. Crosky, S. Saydam, P. Hagan & B.K. Hebblewhite
The University of New South Wales, New South Wales, Australia

P. Craig
Jennmar Australia Pty Ltd and The University of New South Wales, New South Wales, Australia

ABSTRACT: This paper describes a program that has been developed for stress corrosion cracking testing of rockbolt steels both in-situ in underground mines and in a controlled laboratory environment. Two types of double bent beam specimen have been used, a pin loaded specimen stressed to just above the yield stress, and a bar loaded specimen stressed almost to the ultimate tensile strength. Testing of the specimens in an acidified 3.5% sodium chloride solution containing hydrogen sulfide has verified the efficacy of both designs.

1 INTRODUCTION

1.1 *Stress corrosion cracking principles*

Underground coal mines rely extensively on effective ground control through the use of resin-grouted rock bolts. Consequently, any failure of rock bolts drastically decreases the stability of the roof, which has serious implications for both mine operations and personnel safety. In recent years it has been recognized that a substantial proportion of rock bolt failures, at least in the Australian context (Crosky et al. 2002, 2004, 2012), have resulted from stress corrosion cracking (SCC). It is considered that strata movement disrupts the protection provided by the grouting resin, exposing the rock bolts to groundwater. The combined action of the corrosive environment provided by the ground water, and installation and/or service-induced stresses, causes cracks to initiate and grow, eventually leading to catastrophic failure of the rock bolts.

SCC cracks can initiate at surface flaws that either preexist, or are formed during service by corrosion, wear and other related processes. These cracks then propagate by either a transgranular or intergranular model. In some cases both transgranular and intergranular crack propagation can occur.

As SCC is a delayed failure process, the cracks in the material initiate and propagate at slow rates (for example 10^{-9} to 10^{-6} m/s) (Jones & Ricker 1992) until the stress in the remaining ligament of metal exceeds the fracture strength. The main stages leading to SCC failure are as follows (Jones & Ricker 1992):

- crack initiation (Stage 1)
- steady state crack propagation (Stage 2)
- final failure (Stage 3)

It is noted that SCC is not simply the result of mechanical failure from the stress concentration at corrosion-generated surface flaws when a critical value of stress concentration, K_{crit}, is reached. Even though stress corrosion does initiate at surface flaws, the stress concentration at these flaws is generally well below the critical value required to cause mechanical fracture of the material in an inert environment, consequently, $K_{SCC} < K_{crit}$ (Jones & Ricker 1992).

1.2 *In-situ mine site characterization*

Environments that cause SCC are usually aqueous and can be either condensed layers of moisture or bulk solutions. SCC is alloy/environment specific, that is, it is frequently the result of a specific chemical species in the environment. However, an environment that causes SCC in one alloy may not cause it in another. Changing the temperature, the degree of aeration and/or the concentration of ionic species in solution may change a harmless environment into one that has the potential to cause SCC failure. In addition, a given alloy can be either immune or susceptible to SCC depending on its heat treated condition. In view of these factors, care must be exercised when assessing the potential of SCC at different mine sites.

In the present study, mine water analysis has been carried out on samples collected from five different mine sites. The mine waters can be classified into two distinctly different types, given in Table 1. These are referred to here as near neutral pH (pH values of 5–8) and high pH (pH values of 8–10).

In addition to the difference in pH there is a huge difference in the level of sulfate with only 0–130 mg/l being detected in the near neutral mine water but 82000 mg/l being detected in the high pH mine water.

Table 1. Different types of mine water.

	Units	Near-Neutral SCC[1]	High pH SCC[2]
pH	pH units	5–8	8–10
Total Dissolved Solids	mg/L	100–9500	≈500
Dissolved Oxygen	mg/L	4–10	≈7
Sulfate	mg/L	0–130	≈82000
Chloride	mg/L	5–290	≈15
Alkalinity (Total)	mg/L	10–8500	≈2890
Carbonate	mg/L	0	≈203
Bicarbonate	mg/L	10–8500	≈2687

[1] found in four of the five mines
[2] found in one of the five mines

Several of the other species present have a significant effect on corrosion. Dissolved solids increase the electrical conductivity of the water (Rawat 1976). Chloride ions increase corrosivity due to their ability to remove any protective layer forming on the steel's surface (Rawat 1976). Carbonates lead to a tendency for the solution to passivate the steel surface and cause SCC (Rawat 1976).

Another important factor to consider is the amount of dissolved oxygen, as the corrosion rate of iron in water is proportional to the concentration of dissolved oxygen and is found to drop to a low value below a certain critical concentration of oxygen (Rawat 1976). Moreover, previous studies have noted that the corrosion effects due to dissolved oxygen are greatly increased in waters with a low pH (Rawat 1976).

It is noted that the values given in Table 1 are the global composition of the mine water and are not necessarily representative of the environment present at a crack tip.

2 COUPON SPECIMENS

2.1 *Design*

Coupon testing is being undertaken both in-situ in the mines and in the laboratory using double bent beam test specimens based on a design developed by Parrott (Crosky et al. 2002). These specimens were manufactured from a 200 mm length of rockbolt with a 10 mm wide slot machined into the centre of the specimen, as shown in Figures 1 and 2.

Two different levels of loading were used. In the first case, an oversize pin was inserted into the slot while in the second case a stressing bar was used.

In the first method, the pin was tapered at one end (Fig. 1) and then inserted, tapered end first, into the centre of the slot using a hydraulic press, forcing the two sides of the slot apart. A pin diameter of 18 mm was chosen, which caused slight permanent deformation of the adjoining region, so as to stress the material just beyond yield.

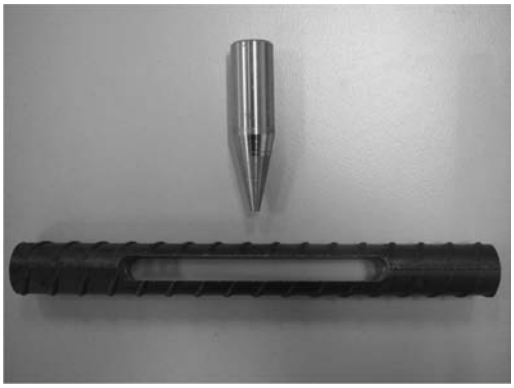


Figure 1. Tapered pin with specimen.



Figure 2. Tapered stressing bar with specimen.

The stressing bar, Figure 2, was used to produce substantially higher stress in the steel than could be obtained using a pin. Rockbolt steels show substantial work hardening and this effect could be exploited to substantially increase the level of elastic strain in the sample. As for the loading pins, a tapered design was used for the loading bar. The bar was initially parallel sided with width of 67 mm, but then tapered outward to a second parallel sided region, 75 mm in width (Fig. 2). The width of the second parallel sided region was selected such that the steel would be loaded to just below its ultimate strength when the stressing bar was inserted to its full width.

To insert the stressing bar, the slotted specimen was loaded in compression. This caused the two ligaments on either side of the slot to buckle outwards, inducing a large tensile strain in the outer radius of the bends. Once the desired width was reached, the load was paused and the small end of tapered bar inserted into the specimen. The specimen was then unloaded, during which elastic springback occurred causing the specimen to clamp onto the loading bar. A hydraulic press was then used to push the tapered loading bar into the specimen to its full width. This ensured that the elastic strain lost during springback was fully reintroduced back into the test specimen.

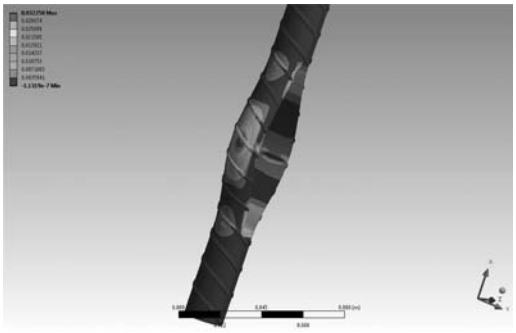


Figure 3. Finite Element Analysis on coupon sample showing areas of high stress.

Table 2. Stress calculation for specimen with tapered pin.

Specimen thickness	Ixx	Deflection	Stress
5.75 mm	1.3 mm^4	4 mm	898 MPa

2.2 *Stress calculations*

A finite element analysis was undertaken to determine the tensile stress in the outer fiber of the pin loaded coupon specimen using the method described previously by Vandermaat et al. (2012) for determination of stress in 3-point and 4-point bending jig specimens.

Each side of the slotted coupon can be thought of as two separate specimens. As such, each side of the slot is assumed to have no stress interaction with the other.

Figure 3 shows the results of the finite element analysis. The loaded bar can be seen to be most highly stressed at the widest point (adjacent to the pin) and at the inside ends of the slot. Table 2 gives the deflection and peak stress from the analysis.

The same method could not be used to determine the stress in the bar-loaded specimen, since it had been stressed well beyond the elastic limit. However, based on the lateral deflection required to cause failure of the slotted specimen under compression loading, it was estimated that the stress was approximately 90–95% of the ultimate strength.

3 TESTING PROTOCOL

3.1 *Coupon specimen material*

The two different types of rockbolt steel are being used for the coupon testing. These are 840 grade and AISI 1355 steel, which have the compositions shown in Table 3. These were chosen as spanning the range of microstructures observed in rockbolt steels, with the 840 grade (0.4% carbon) having a mixed ferrite/pearlite structure, and AISI 1355 (0.55% carbon) having an almost fully pearlitic structure.

Table 3. Chemical composition of 840 grade and AISI 1355 grade steel.

	Weight percent	
Element	840 Grade	AISI 1355
Carbon	0.39	0.56
Manganese	1.53	1.63
Silicon	1.08	0.26
Nickel	0.02	0.05
Chromium	0.03	0.15
Molybdenum	0.004	0.011
Sulfur	0.019	0.035
Phosphorus	0.017	0.014
Copper	0.01	0.21
Vanadium	0.038	0.002
Tungsten	0.014	0.023
Titanium	0.001	0.001
Aluminum	0.004	0.004

3.2 *Specimen preparation*

In order to simulate service conditions, the coupons were tested with the surface of the coupon in the as-manufactured condition of the rockbolt. In particular it was desired to preserve the mill scale in the as-manufactured condition since prior studies of pipeline failures have indicated that its presence is significant to SCC (Public Inquiry Concerning Stress Corrosion Cracking on Canadian Oil and Gas Pipelines).

3.3 *Testing environment*

The test coupons are being exposed to mine water of both the near neutral and high pH types, both in underground mines and in a laboratory test rig. The laboratory testing involves alternate immersion and drying, with each cycle of one hour duration, and is being undertaken in the purpose-built UNSW Controlled Mine Environment Laboratory, which simulates the temperature and relative humidity of underground mines.

3.4 *Reproducibility*

Several test coupons are being installed in mines of both groundwater types while all laboratory testing is being carried out using duplicate specimens.

4 PRELIMINARY RESULTS AND DISCUSSION

4.1 *Design verification*

In order to verify the efficacy of the test coupon design, specimens of both configurations, made from both steels, were tested by static immersion in an acidified 3.5% sodium chloride solution containing hydrogen sulfide. This hydrogen sulfide was introduced by the reaction between acetic acid in the electrolyte solution and sodium sulfide when added to the electrolyte



Figure 4. Failed pin loaded specimen.

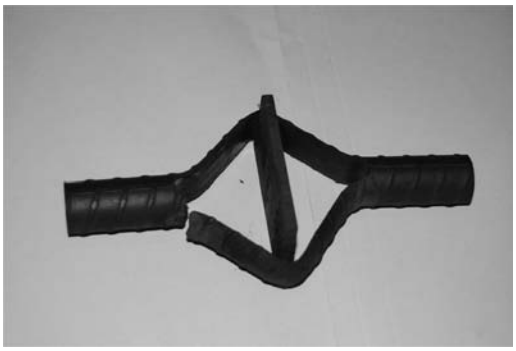


Figure 5. Failed wedge loaded specimen.

solution. This solution is commonly used for inducing stress corrosion cracking in carbon steels. In particular, it has been used previously by Parrott to induce SCC in rockbolts (Crosky et al. 2002).

Rockbolts of both steels failed for the bar loaded specimens while the AISI 1355 pin loaded specimen also failed, with the failure times being from 2-24 hours. However, the 840 pin loaded specimen showed no sign of SCC even after one month. A duplicate specimen is yet to be run. Examples of the failed coupons are shown in Figures 4 and 5.

4.2 *Analysis of fracture surface*

An optical fractograph showing the fracture surface of one of the test coupons is given in Figure 6. The fracture surface exhibits a discolored region produced during the propagation of the stress corrosion crack, followed by a bright region produced by the final catastrophic overload failure. Additionally, the fracture surface exhibits orange-coloured "tide marks" which suggest that propagation of the stress corrosion crack had paused at these points allowing for buildup of the corrosion product. Similar orange "tide marks" have been seen on some failed rockbolts.

Scanning electron microscopy (SEM) fractographs of the SCC region and the overload region are shown in Figures 7 and 8, respectively. The two regions are distinctly different, with Figure 7 showing features characteristic of SCC while Figure 8 shows features characteristic of mixed ductile/brittle overload failure, similar to that seen in previous studies of service failed rockbolts.

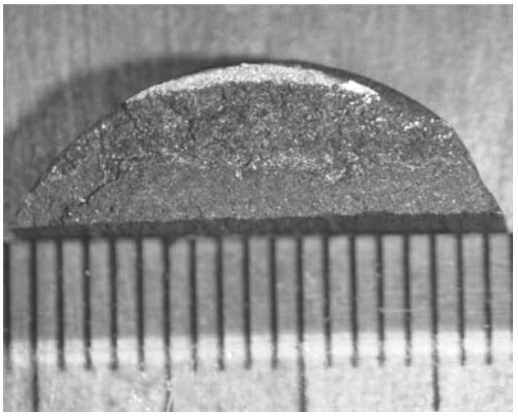


Figure 6. Optical fractograph of failed coupon specimen fracture surface.

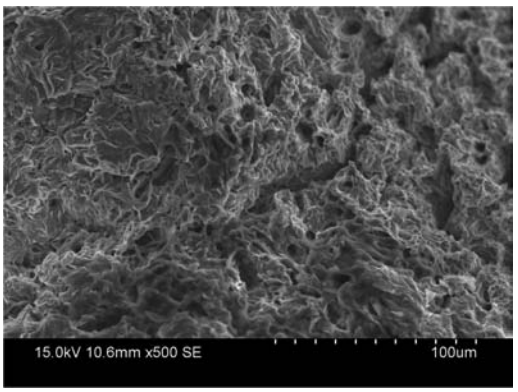


Figure 7. SEM fractograph showing SCC region in failed coupon specimen.

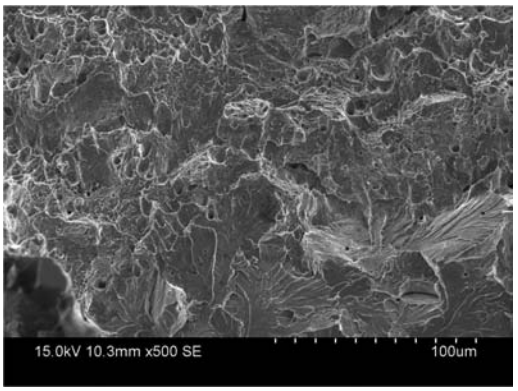


Figure 8. SEM fractograph showing overload region in failed coupon specimen.

5 CONCLUSIONS

SCC test coupons which can be installed in underground mines have been developed. Laboratory testing of the coupons in acidified 3.5% sodium chloride containing hydrogen sulfide has validated the specimen design.

ACKNOWLEDGEMENTS

Financial assistance from the following organisations and companies is gratefully acknowledged:

- Australian Research Council (ARC)
- Jennmar Australia Pty Ltd
- Centennial Coal Pty Ltd
- Xstrata Coal Pty Ltd
- Whitehaven Coal Pty Ltd
- Anglo American Metallurgical Coal

REFERENCES

Crosky, A., Smith, B., Elias, E., Chen, H., Craig, P., Hagan, P., Vandermaat, D., Saydam, S. and Hebblewhite 2012. Stress corrosion cracking failure of rockbolts in underground mines in Australia, in Proceedings AIMS 2012 – 7th International Symposium of Rockbolting and Rock Mechanics in Mining, 30–31 May 2012, Aachen, Germany.

Crosky, A., Fabjanczyk, M., Gray, P. and Hebblewhite, B. 2004. "Premature rock bolt failure Stage 2". ACARP Project No. C12014, final report, Australian Coal Association Research Program, August 2004.

Crosky, A., Fabjanczyk, M., Gray, P., Hebblewhite, B. and Smith, B. 2002. "Premature Rock bolt Failure". ACARP Project No. C8008, Final report Australian Coal Association Research Program, April 2002.

Jones, R.H. & Ricker, R.E. 1992. Mechanisms of Stress-Corrosion Cracking. Stress-Corrosion Cracking. ASM International.

National Energy Board 1996. Public Inquiry Concerning Stress Corrosion Cracking on Canadian Oil and Gas Pipelines. National Energy Board, Report No. MH-2-95.

Rawart, N.S. 1976. Corrosivity of Underground Mine Atmospheres and Mine Waters: A Review and Preliminary Study, *British Corrosion Journal*, 11, 86–91

Vandermaat, D., Elias, E., Craig, P., Crosky, A., Hagan, P., Hebblewhite, B. 2012. Coupon Testing for Field Assessment of Stress Corrosion Cracking of Rock Bolts, in Proceedings The Thirty First International Conference on Ground Control in Mining, T.M. Barczak (eds), West Virginia, United States.

This page intentionally left blank

Rock Mechanics for Resources, Energy and Environment – Kwaśniewski & Łydżba (eds)
© 2013 Taylor & Francis Group, London, ISBN 978-1-138-00080-3

Effect of constant and varying mean stress levels of cyclic loading on the indirect tensile strength of rocks

N. Erarslan
Geotechnical Engineering Centre, The University of Queensland, Brisbane, Queensland, Australia

ABSTRACT: The design and construction of underground openings, supports and rock pillars, as well as drilling and blasting, are based on an understanding of the mechanical behaviour of rocks under various loading conditions. The Brazilian indirect tensile tests described in the paper were carried out on Brisbane tuff, a host rock of Brisbane's first motorway tunnel, from which core samples were obtained. Three different types of cyclic loading were used in this research. The main purpose of performing the three types of cyclic loading was to find the most damaging cyclic loading type. The indirect tensile strength of Brisbane tuff was reduced from the static value of 10.8 to 7 MPa as a result of Type I cyclic loading. Comparing the results of the sinusoidal, Type I and II cyclic loading tests, the maximum BITS reduction was obtained with the highest amplitude in Type I and smallest amplitude Type II cyclic loadings.

1 INTRODUCTION

1.1 *Type area*

The study of brittle fracture and its relationship to material damage, fatigue and strength is central to many rock engineering problems, including rock fracture and damage mechanics, rock cutting, drilling and blasting techniques for the design and construction of underground openings, supports and rock pillars. Mechanical behavior of rock under static loading has been thoroughly investigated. However, rock reaction to cyclic, repetitive stresses resulting from dynamic loads has been generally neglected, with the exception of a few rather limited studies (Attewell & Farmer 1973, Bagde & Pedros 2005, Costin & Holcomb 1981, Evans & Fuller 1974, Haimson & Kim 1971, Haimson 1978, Tao & Mo 1990). The tensile strength of rock is one of the most important parameters influencing its deformability and fracture toughness. An impressive outcome of this study is the observation of the effect of tensile cyclic loading on the indirect tensile strength (ITS). The difficulties associated with performing a direct uniaxial tensile test on a rock specimen have led to a number of indirect methods for assessing tensile strength. In 1978, the Brazilian test was officially proposed by the International Society for Rock Mechanics (ISRM) as a suggested method for determining the tensile strength of rock materials (ISRM 1978).

2 EXPERIMENTAL PROCEDURE AND TESTS

2.1 *Sample Preparation*

Tests described herein were carried out on Brisbane tuff, which is a host rock of Brisbane's first motorway tunnel, CLEM7, from which core samples were obtained. Brisbane tuff is a fine-grained, massive rock of rhyolitic composition with coarser grains imparting a porphyritic texture. The ITS sample preparation and testing procedure conformed to the requirements of the ISRM (1978); that is, cylindrical specimens 52 mm in diameter and 26 mm in thickness, to give a thickness to diameter ratio of 0.5. The Brazilian disc specimen in Figure 1 has two strain gauges attached to its perpendicular faces, aligned (vertical) with and transverse (horizontal) to the load applied to the specimen.

2.2 *Static and Cyclic Tests*

For the static ITS loading tests, the ISRM (1978) suggests that the load be applied via two steel loading jaws in contact with a disc-shaped rock specimen. The tensile strength of the five rock specimens tested using the standard Brazilian jaws were calculated using the formula given by the ISRM (1978).

Three different types of cyclic loading were used in this study: 1) cyclic loading with constant mean level and constant amplitude, termed sinusoidal cyclic loading (Fig. 2a); 2) cyclic loading with four amplitude values start at same increasing valley value with different increasing mean stress level, termed Type I increasing cyclic loading (Fig. 2b); and 3) cyclic loading with four amplitude values have same mean level value with different valley values, termed Type II increasing cyclic loading (Fig. 2c).

The main purpose of applying three types of cyclic loading was to find the most damaging cyclic loading type for the same amplitudes. It is known that applying a load provides energy for crack initiation and



Figure 1. Brazilian ITS test specimen with strain gauges placed between loading jaws.

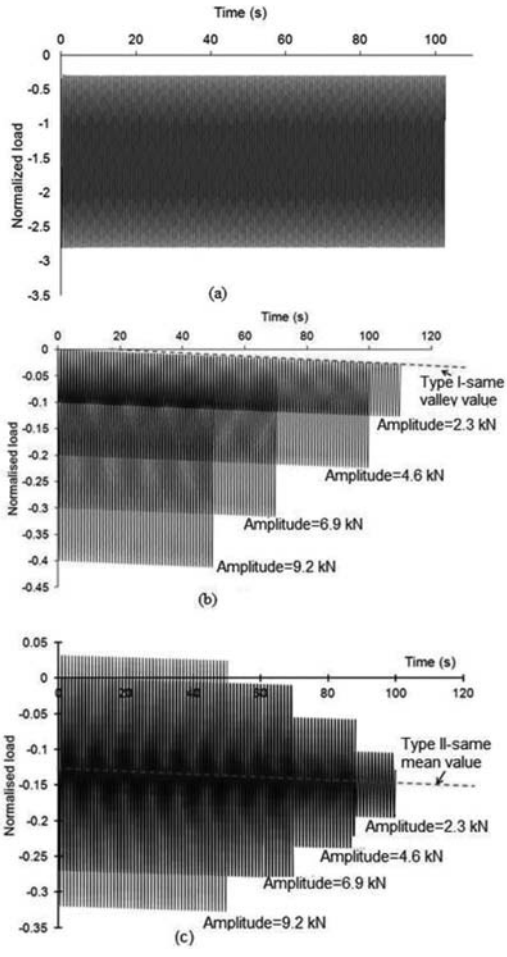


Figure 2. (a) Sinusoidal (b) Type I and (c) Type II increasing cyclic loading.

propagation. By removing the load, the energy driving crack propagation is discontinued and the remaining excess energy in the system dissipates through crack propagation processes. Hence, it was believed that the fracturing energy balance in a specimen being tested depends on the stress level when the unloading stops.

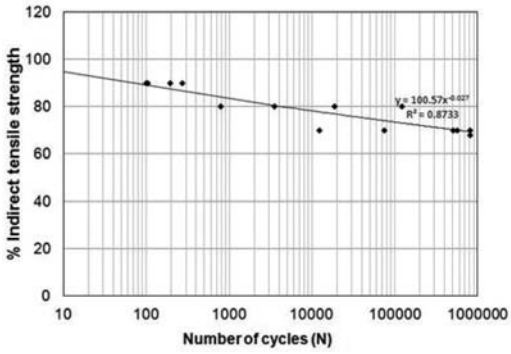


Figure 3. S–N curve for indirect tensile strength of Brisbane tuff.

3 RESULTS OF TESTS

The first important conclusion of the sinusoidal cyclic loading tests was that the failure load used in the calculation of the ITS is weakened 30% by repetitive loading. Figure 3 shows a relationship, between the number of cycles (N) and the reduction of applied stress amplitude (S), for the ITS of Brisbane tuff.

The cyclic loading used in the Type I and Type II tests was, diametral compressive cyclic loading as ramp wave form with increasing mean level. Four different amplitudes were chosen to investigate the effect of fatigue on the ITS of Brisbane tuff; 2.3 kN, at 10% of the Static Ultimate Load (SUL); 4.6 kN (20% SUL); 6.9 kN (30% SUL) and 9.2 kN (40% SUL) (Fig. 2).

The series of Type I diametral compressive dynamic cyclic loading tests were performed on 12 Brisbane tuff disc specimens. The ITS of Brisbane tuff was reduced from 10.8 to 7 MPa as a result of the cyclic loading. The reduction in ITS due to cyclic loading is shown in Table 1, in comparison with static ITS values.

For a clear understanding of the effect of fatigue on rock damage mechanisms, a comparison between static and dynamic tensile cyclic loading tests is shown in Figure 4 by plotting both results on the same axes. Comparing these figures, diametral axial strain under both static and cyclic loading is larger when compared with diametral lateral strain. However, the contribution of plastic strain to the diametral lateral strain plot under cyclic loading is much more than that under monotonic loading. Moreover, diametral lateral plastic strain accumulation obtained by using strain gauges is highest as a result of loosening of the during the final cycles up to failure. During cyclic loading, diametral lateral deformation develops faster than diametral axial deformation. This behaviour indicates the development of cracking in the specimen, due to dilatancy.

Figure 5 shows the Brazilian disc specimens after testing under static and cyclic loading. It is obvious that much more crushed rock material and debris was produced with cyclic loading compared with static loading. It is explained in literature that rock fatigue under cyclic loading induces many more micro-cracks

Table 1. Results of Type I cyclic loading tests performed on Brazilian disc specimens.

Sample	Amp. % SUL	Ultimate load (kN)	No. of cycles up to failure	ITS (MPa)	Reduction of ITS (%)
Rp1	10	17.4	2583	8.2	24.1
Rp2	10	15.6	2384	7.3	32.5
Rp3	10	18.1	2723	8.5	21.3
Avr.		17.03	2563	8.0	25.9
Rp1	20	17.5	2195	8.2	24.1
Rp2	20	15.4	1887	7.2	33.4
Rp3	20	14.6	1679	6.8	37.1
Avr.		15.9	1920	7.4	31.5
Rp1	30	17.3	1906	8.1	25.0
Rp2	30	15.2	1334	7.1	34.3
Rp3	30	16.1	1556	7.5	31.0
Avr.		16.2	1598	7.6	30.1
Rp1	40	14.0	738	6.5	39.9
Rp2	40	14.4	992	6.7	38.0
Rp3	40	16.8	1227	7.9	27.0
Avr.		15.0	985	7.0	36.0

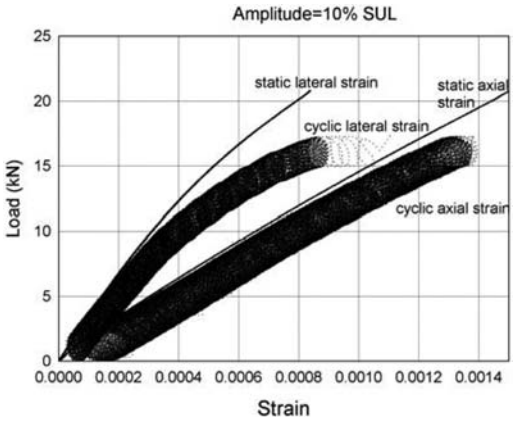


Figure 4. Comparison of load–strain curves for Brazilian disc specimens tested under static and Type I cyclic loading.

compared with failure under static loading (Costin & Holcomb 1981, Hadley 1976, Erarslan & Williams 2012).

Type II diametral compressive cyclic loading tests were also performed on 12 Brisbane tuff Brazilian disc specimens, and the results are given in Table 2.

Comparing the results of the Type I and II cyclic loading tests, the maximum reduction in ITS was obtained with the smallest amplitude for Type II, whereas the maximum reduction in ITS was obtained with the highest amplitude for Type I.

Load–strain and strain–number of cycles plots are given in Figure 6.

An example of Type I and II cyclic loading tests repeated under highest amplitude is given in Figure 6. In general, there was not a big difference in the amount

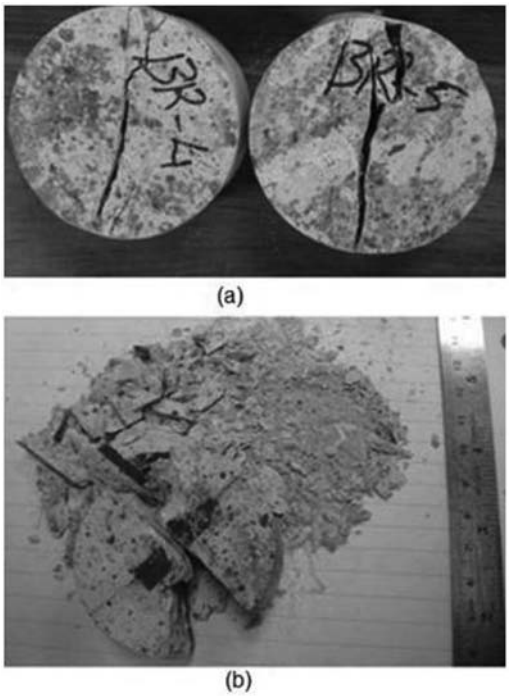


Figure 5. Brazilian disc specimens tested under: (a) static loading, and (b) cyclic loading.

Table 2. Results of Type II cyclic loading tests performed on Brazilian disc specimens.

Sample	Amp. % SUL	Ultimate load (kN)	No of cycles up to failure	ITS (MPa)	Reduction of ITS (%)
Rp1	10	14.6	735	6.87	36.4
Rp2	10	16.7	1106	7.86	27.3
Rp3	10	14.0	551	6.59	39
Avr.		15.1	797	7.10	34.2
Rp1	20	18.3	1049	8.61	20.3
Rp2	20	13.9	355	6.54	39.5
Rp3	20	17.2	955	8.09	25.1
Avr.		16.4	786	7.74	28.3
Rp1	30	13.8	241	6.49	40
Rp2	30	18.3	895	8.61	20.3
Rp3	30	15.3	435	7.07	35
Avr.		15.8	523	7.39	31.8
Rp1	40	16.1	384	7.58	30
Rp2	40	18.2	738	8.56	20.8
Rp3	40	17.2	513	8.07	25.3
Avr.		17.2	545	8.07	25.04

of total strain produced under either Type I or Type II cyclic loading. However, measurements of permanent strain damage show that both the axial and lateral strain damage curves increased with increasing damage increments, but at different rates, in both types

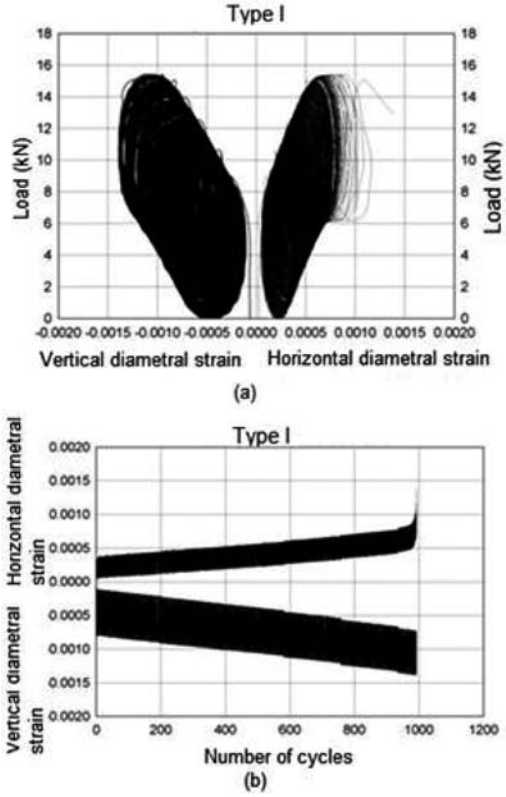


Figure 6. Type I diametral cyclic loading with highest loading amplitude = 9.2 kN (40% SUL).

of cyclic tests. In general, the converse trends near failure result from the fact that lateral strain increases more rapidly than axial strain. It can be concluded that Type II cyclic loading produces the same amount of irreversible damage as Type I cyclic loading in a specimen under both the smallest and the highest loading amplitude. Thus, equivalent damage in rock is possible with fewer cycles and less energy with Type II cyclic loading compared with Type I cyclic loading.

4 CONCLUSIONS

The response of the Brazilian rock disc to cyclic loading was found to be different to that under monotonic loading, resulting in a lower ultimate load and different fracturing mechanisms. In the current study, various experimental observations from sinusoidal, Type and Type II increasing cyclic loading tests, with varying amplitudes, have shown that increasing cyclic loading is more effective in degrading the ITS of rocks than sinusoidal cyclic loading. The reduction in ITS was found to be 30% with sinusoidal loading, whereas Type I and II increasing cyclic loading caused a maximum reduction in ITS of 36%. However, comparing the results of Type I cyclic loading with Type II cyclic loading, one of the maximum ITS reduction was obtained with the Type II cyclic loading with the smallest amplitude, whereas the maximum reduction of ITS was obtained with the Type I cyclic loading with highest amplitude.

Damage was be quantified as the accumulation of permanent strain in Brisbane tuff disc specimens with each cycle of loading, since micro-fracturing introduces nonlinearity into the supposedly elastic behavior of the rock. A continuous irreversible accumulation of damage was observed in the dynamic cyclic loading tests carried out at different amplitudes and mean stress levels.

REFERENCES

Attewell, P.B. & Farmer, I.W. 1973. Fatigue behavior of rock. *Int. J. Rock Mech. Min.* 10(1): 1–9.

Bagde, M.N. & Pedros, V. 2005. Fatigue properties of intact sandstone samples subjected to dynamic uniaxial cyclical loading. *Int. J. Rock Mech. Min.* 42(2): 237–50.

Costin, L.S. & Holcomb, D.J. 1981. Time-dependent failure of rock under cyclic loading. *Tectonophysics* 79(3–4): 279–96.

Erarslan, N. & Williams, D.J. 2012. Mechanism of Rock Fatigue Damage in Terms of Fracturing Modes. *Int. J. of Fatigue* 43: 76–89.

Evans, A.G. & Fuller, E.R. 1974. Crack propagation in ceramic materials under cyclic loading conditions. *Metall. Trans.* 5(1): 27–9.

Hadley, K. 1976. The effect of cyclic stress on dilatancy: another look. *J. Geophys. Res.* 81(14): 2471–4.

Haimson, B.C. & Kim, C.M., 1971. Mechanical behaviour of rock under cyclic fatigue. *Rock Mechanics* 3: 845–63.

Haimson, B.C. 1978. Effect of cyclic loading on rock. In *Dynamic Geotechnical Testing ASTM STP* 654, pp. 228–45.

ISRM, 1978. International Society for Rock Mechanics. Suggested methods for determining tensile strength of rock materials. *Int. J. Rock Mech. Min. Sci. Geomech. Abs.* 15: 99–103.

Tao, Z. & Mo, H. 1990. An experimental study and analysis of the behaviour of rock under cyclic loading. *Int. J. Rock Mech. Min. Sci. Geomech. Abs.* 27: 51–56.

Rock Mechanics for Resources, Energy and Environment – Kwaśniewski & Łydżba (eds)
© 2013 Taylor & Francis Group, London, ISBN 978-1-138-00080-3

Tensile fracturing of anisotropic Brisbane phyllite

N. Erarslan, D.J. Williams & A. Shokouhi
Geotechnical Engineering Centre, The University of Queensland, Brisbane, Queensland, Australia

ABSTRACT: Rocks are generally more or less anisotropic, depending on their structure at the scale of interest. The anisotropic rocks in civil and mining engineering projects cause non-symmetric deformation and their behaviour is unpredictable. The authors present the results of Brazilian Indirect Tensile (BIT) strength and Cracked Chevron Notched Brazilian Disc (CCNBD) tests for the determination of the fundamental tensile fracturing parameters of Brisbane phyllite specimens. In general, the influence of orientation angle (ψ) and foliation-loading angle (β) were found to influence both fracturing and the failure load.

1 INTRODUCTION

Anisotropy is a characteristic of foliated metamorphic rock masses (gneisses, phyllites and schists), and intact stratified or bedded sedimentary rocks (coal, shales, sandstones, siltstones, limestones, etc.). At a larger scale, rock mass anisotropy is found in volcanic formations and in sedimentary formations consisting of alternating layers or beds of different rock types and in rock formations cut by one or several regularly-spaced joint sets. Since the deformation and fracture of these rocks is of importance to engineers concerned with the design of mining excavations or of foundations for civil engineering structures, it is obvious that research into the effects of anisotropy on rock behavior is necessary (Hoek, 1964; Chen & Hsu, 2001; Cho et al., 2012).

As in the case of the original Griffith criterion (Griffith, 1924), it is generally assumed that the specimen contains a sufficient number of randomly-oriented cracks for fracture to initiate from those cracks, which are inclined at an angle. If, however, the cracks are oriented preferentially, as in the case of a highly antistrophic material, it is necessary to consider the inclination of the cracks with respect to the applied stress system (Hoek, 1964). Brace (1961) presented evidence indicating that the cracks, from which fracture of the rock propagates, probably lie within the grain boundaries of the rock. Even in rocks of sedimentary origin, which exhibit marked foliation and planar anisotropy, the constituent bedding planes are made up of grains that are cemented together and hence randomly-oriented grain boundary cracks are likely to be present (Brace, 1960).

In the case of an anisotropic rock, two distinct systems of inherent cracks can be visualised: (a) a set of relatively large preferentially-oriented cracks that lie along bedding planes; and (b) a randomly-oriented matrix of grain boundary cracks that are probably several times smaller than the bedding plane cracks (Hoek, 1964).

Whenever the fracture pattern deviates from classical central splitting, the interpretation of the peak strength in terms of tensile strength should be performed with great caution, because the stress state as well as the fracture type might deviate significantly from the assumptions underlying the classical evaluation procedure (Barla and Innaunato, 1972; Chen & Hsu, 2001; Ke et al., 2008; Dinh et al., 2013). Dinh et al (2013) found that the anisotropy ratio of the peak (tensile) strength can reach values of up to 2.65 and 5.24 for Gneiss and Slate respectively.

Crack propagation is generally tensile by nature and tensile fractures within rock can be generated under both tensile and compressive stress fields, and hence are very common. However, due to their random orientations, pre-existing cracks in intact rock and discontinuities in rock masses are seldom subjected to pure tensile (Mode I) loading; rather, they are subjected to compressive, shear sliding (Mode II) or mixed mode (Mode I–II) loading.

2 EXPERIMENTAL STUDY

2.1 *Sample preparation and tests*

Brisbane tuff and phyllite are targeted rock types in the Brisbane area for their strength and stability in tunnelling and excavation applications. Tests described herein were carried out on Brisbane phyllite with clear white–black foliations, which is one of the host rocks of Brisbane's first motorway tunnel, CLEM7, from which core samples were obtained. Brazilian Indirect Tensile (BIT) strength and mode I (tensile) and mixed mode I-II (tensile-shear) tests were conducted on specimens prepared from these core samples.



Figure 1. Prepared BIT disc specimens (left) and CCNBD specimens (right).

The BIT sample preparation and testing procedure conformed to the requirements of the ISRM (1978). The core samples were trimmed to form disc specimens 52 mm in diameter and 26 mm in thickness, to give a thickness to diameter ratio of 0.5. The Cracked Chevron Notched Brazilian Disc (CCNBD) sample preparation and specimen geometries used in this study were in the valid ranges indicated by the ISRM (1995). A circular 40 mm diamond saw was used to cut the required notch. The notch in the CCNBD specimens was made by cuts from both sides of the disc along the designed foliation orientation direction, on the same diametral cutting plane. All geometrical dimensions are converted to dimensionless parameters with respect to the specimen radius and diameter. The two most important dimensions: the dimensionless final notched crack length (α_1) and the dimensionless quantity (α_B) must fall within the range outlined in the suggested ISRM methods (ISRM, 1995) in order to have a valid test. The thickness of the notches (t) was 1.5 mm, the thickness of the specimens (B) was 26 mm, and the radius of the specimens (R) was 26 mm. The internal chevron notch crack length, $2a_0$, was 16 to 18 mm and the external chevron notch crack length, $2a_1$, was 36 to 37 mm (Figure 1).

For the static BIT loading tests, the ISRM (1978) suggests that the load be applied via two steel loading jaws in contact with a disc-shaped rock specimen, with the two steel loading jaws designed to make contact with the specimen at diametrically opposed surfaces over an arc of contact of approximately 10° at failure. The static load was applied by a stiff hydraulic Instron loading frame, with a loading rate of 200 N/s applied to the standard loading jaws, as suggested by the ISRM (1978). The experimental arrangement for the BIT tests is conducted with respect to the orientation of the foliation planes. The orientation angle (ψ) is the angle between the sample axis and the structural plane, and the foliation-loading angle (β) is the angle between the loading direction and structural plane. The foliation planes were found to be the true planes of weakness, characterized by reduced cohesive and reduced tensile strength.

3 TEST RESULTS

The BIT tests were carried out in order to determine the tensile strength in directions relative to the planes of schistosity, ranging from 0° to 90° . For each orientation 2 to 3 specimens were tested. In general, the expected central tensile cracks were not obtained with the anisotropic phyllite disc specimens (Figure 2a, b). However, loading isotropic disc specimens with the Brazilian jaws caused central tensile cracking at the centre of the disc specimens (Figure 2c). Mixed tensile splitting and shear were observed in certain cases. Two major modes of failure were observed: (i) tensile splitting along the loaded diameter was the dominant mode of failure occurring when β was between 0° and 30° , (ii) mixed tensile splitting and shear failure along the layers with or without branching was dominant when $45° < \beta < 90°$ and $30° < \psi < 45°$. Due to the

Table 1. Average failure load of BIT tests (kN).

β (°)	$\psi = 0°$	$\psi = 45°$	$\psi = 60°$
0	9.5	10.1	10.1
30	11.4	11.3	12.8
45	11.7	15.3	13.4
60°	16.3	16.9	15.1
90	22.5	17.2	14.7



Figure 2. (a, b) failed anisotropic Brisbane phyllite IBT specimens (c) failed isotropic Brisbane tuff specimens.

Table 2. Average failure load from CCNBD tests (kN).

β (°)	$\psi = 0°$	$45° < \psi < 60°$
0	6.5	7.88
30	7.6	8.53
45	10.18	11.41
60	10.26	12.43

shear failure mode for the inclined foliations, those relative failure load values cannot be used to determine the indirect tensile strength of rocks by using the proposed ISRM (1978) standards. However, even in this case a theoretical relationship must still be established in order to define the dependence of the tensile strength on β. The result obtained for the phyllite required a different method of testing to be used in order to induce a true tensile failure in this rock.

The failure loads are given in Table 1. The minimum failure load is obtained with disc specimens having orientation and foliation-loading angles $\psi = 0°$ and $\beta = 0°$, respectively. Needless to say, the maximum failure load and the tensile strength are affected significantly by the existence of a foliation or schistose plane that is perpendicular or parallel to the maximum tensile stress direction.

The CCNBD tests were carried out in order to determine the mode and mixed mode I-II fracturing behaviour in directions relative to the planes of schistosity, ranging from 0 to 90° . From the failure loads recorded for discs oriented with an initial crack inclined at 0° , 30° , 45° and 60° to the planes of schistosity, the critical stress intensity factor (SIF) or fracture toughness (K_C) in mode I, mode II and mixed-mode I–II (K_{IC} and K_{IIC}) can be determined (Ke et al., 2008).

Table 2 gives the maximum failure load at different notch crack inclination angles β and foliation orientation angles ψ.

In this research, mode I and mixed mode I-II rock fracturing is investigated rather than the fracture toughness value of the anisotropic Brisbane phyllite specimens tested. The determination of fracture toughness requires the calculation of a stress concentration factor, SIF, which represents the stress state at the tip of the notch crack. When a rock is isotropic, the value of SIF is a function only of the disc and notch crack dimensions. For anisotropic rocks, however, SIF is more complex and depends on the rock elastic constants, the inclination angle with the planes of rock anisotropy, and the size of the notch crack.

Failed CCNBD specimens are shown in Figure 3. Although tensile splitting was the dominant failure mode in most of cases, the shear failure planes along the foliation planes and smaller branching cracks normal to foliation planes occurred simultaneously at $30° < \beta < 60°$. However, the $\beta = 45°$ inclined notch crack showed very different failure behaviour (Figure 3c). Wing crack initiation at the tip of the notch crack,

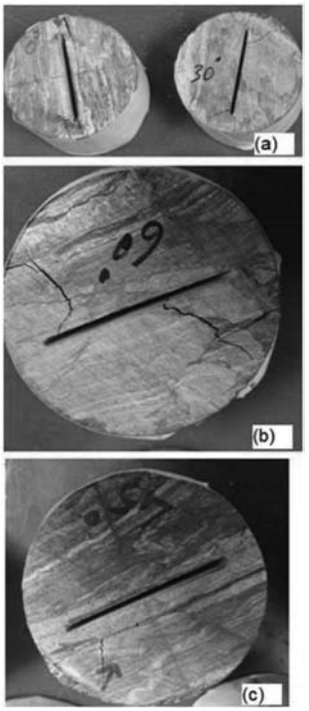


Figure 3. Tested CCNBD specimens with various notch crack inclination angles.

as found on testing isotropic rocks at same inclination angle, did not occur with the anisotropic phyllite. Instead, one major failure plane occurred parallel with notch crack plane.

In general, it was observed experimentally that progressive slip on the interface reduces the failure load. When using the CCNBD test to examine the interaction between foliation planes (called interfaces) and the notch crack), two important observations were made. Firstly, the expected wing crack initiation points at the tip of the notch crack differ along the notch crack mouth because the stress distribution induced adjacent to the interface causes different fracture pattern to that observed in specimens with no slip (Figure 3a, b). Secondly, when slip occurs on an interface, local asperities can form nucleation centers for the initiation of extra fractures, rather than the expected wing cracks. It was observed that the extension fractures initiating in this manner usually propagate on only one side of the interface (Figure 3c).

4 CONCLUSIONS

The laboratory tests reported herein have shown that the anisotropy has a strong influence on the measured peak failure load and tensile fracturing obtained in the BIT and CCNBD specimens. The fracture patterns in BIT specimens were found deviated from the classical

central splitting. Anisotropic BIT phyllite disc specimens show distinct tensile cracks along the centreline when β is between 0° and 30° . In contrast to the later, the fracture pattern is more complicated and composed of mixed-mode cracks along the weak planes and the matrix when $45° < \beta < 90°$ and $30° < \psi < 45°$. The interpretation of the peak strength in terms of tensile strength should be performed with great caution as the stress state deviate significantly from the assumptions underlying the classical evaluation procedure.

The mode I type fracture occurs when β is 0° . On the other hand, mixed mode I-II fracturing patterns were found to be dependent on the plane of anisotropy. The usual wing cracks (mixed mode I-II cracks) observed with isotropic rocks were not observed with anisotropic Brisbane phyllite CCNBD specimens inclined at $30° < \beta < 60°$. Rather, extra branch fractures were observed around the notch cracks.

In general, the influence of orientation angle (ψ) on fracturing was found to be much larger than that of foliation-loading angle (β), for both BIT and CCNBD specimens. On the other hand, the influence of orientation angle (ψ) on failure load was found less than that of foliation-loading angle (β).

ACKNOWLEDGEMENTS

Acknowledgement is made to Leighton Contractors who provided core samples of Brisbane phyllite from the CLEM7 Project and to Golder Associates Pty Ltd for their assistance in obtaining the core samples. The first author was supported by an Australian Postgraduate Award/UQRS and the Golder Geomechanics Centre during the duration of the doctoral research on which this paper is based.

REFERENCES

Barla, G & Innaurato, N. 1972. Indirect Tensile Testing of Anisotropic Rocks. *Rock Mechanics* 5: 215–230.

Brace, W.F. 1961. Dependence of fracture strength of rocks on grain size. Bulletin of Mineral Industries Experimental Station. *Penn. State University*, No. 76, 99–103.

Chen, C.S. & Hsu, S.C. 2001. Measurement of Indirect Tensile Strength of Anisotropic Rocks by the Ring Test. *Rock Mech. & Rock Eng.* 34(4): 293–321.

Cho, J.W, Hanna, K. & Seokwon, J. 2012. Deformation and strength anisotropy of Asan gneiss, Boryeong shale, and Yeoncheon schist. *Int. J. Rock Mech. Min. Sci.* 50: 158–169.

Dinh Q.D, Heinz, K. & Martin, H. 2013. Brazilian tensile strength tests on some anisotropic rocks. *Int. J. Rock Mech. Min. Sci.* 58: 1–7.

Griffith, A.A. 1924. The theory of rupture. *In Proceedings of the First International Congress for Applied Mechanics (pp.55–63), Biezeno, Delft. C.B., Burgers, J.M. & Waltman, J. (Eds.).*

Hoek, E. 1964. Fracture of anisotropic rock. *J. S. Afr. Inst. Min. & Metall.* 64(10): 501–518.

ISRM, (Coordinator: Fowell, R. J.), 1995. Suggested method for determining mode I fracture toughness using cracked chevron notched Brazilian disk (CCNBD) specimens. *Int. J. Rock Mech. & Min. Sci. Geomech. Abs.* 32(1): 57–64.

ISRM, 1978. International Society for Rock Mechanics. Suggested methods for determining tensile strength of rock materials. *Int. J. Rock Mech. & Min. Sci. Geomech. Abs.* 15: 99–103.

Ke, C.C., Chen, C.S. & Tu, C.H. 2008. Determination of Fracture Toughness of Anisotropic Rocks by Boundary Element Method. *Rock Mech. & Rock Eng.* 41(4): 509–538.

Rock Mechanics for Resources, Energy and Environment – Kwaśniewski & Łydżba (eds)
© 2013 Taylor & Francis Group, London, ISBN 978-1-138-00080-3

A new test for the characterization of highly jointed rock masses

C. González-Nicieza, M.B. Prendes-Gero, R. Fernandez-Rodriguez & F. Lopez-Gayarre
University of Oviedo, Asturias, Spain

ABSTRACT: The task of characterizing highly jointed rock masses correctly is often complex due to errors resulting from the scale effect in the majority of laboratory tests. Furthermore, current methods of on-site characterizations pose logistical, technical and even problems, while geomechanical classifications are not precise enough for this kind of rock mass. With the aim of contributing with a new method of analysis for this type of terrain, we describe a novel, easily applied on-site test that calculates the strength values of a weak rock mass while minimizing the scale effect. This new methodology was applied to the characterization of large slopes in an opencast coal mine. The existing mine slopes were back-analysed using classical methods to test the reliability of the results obtained using this new test.

1 INTRODUCTION

The determination of the global mechanical properties of a jointed rock mass remains one of the most difficult tasks in rock mechanics. Many researchers have developed constitutive models to describe the strength and deformation behaviors of jointed rock masses (e.g., Amadei 1988 and Cai & Horii 1992). Because there are so many parameters that affect deformability and strength, it is generally impossible to develop a universal model that can be used to predict a priori the strength of a rock mass.

Among the existing on-site tests to determine the cohesion and friction of a rock mass there are two main ones which, while highly effective, are only implemented in large-scale works owing to methodological difficulties, logistics and cost. The two tests are the direct shear test on rock joints (Uriel 1964) and the triaxial test (Taheri & Tani 2008). A third on-site direct shear test (Ramírez-Oyanguren et al. 2008) is used to determine the friction for specific types of materials. Other tests are used to analyse the deformability of the rock mass, including the presiodilatometer test (Nihat et al. 2008), the plate load method (Ünal 1997) and the seismic method (Denver & Steffenssen 1989). All these tests present problems when applied to jointed rock masses, owing to the fact that the results are greatly influenced by the scale effect and also because they are not cost effective.

Another method widely used for determining the characteristics of rock masses is geomechanical classification, which continues to be applied successfully in underground mining (Bieniawski 1989, Grimstad & Barton 1993, Laubscher 1990). However, classification systems, when applied to slopes, do not produce good results. Some years ago, the Hoek-Brown failure criterion (Hoek & Brown 1980) was adapted to the Rock Mass Rating (RMR) classification system (Bieniawski 1989) to analyse the shear resistance of surface rock masses. This methodology has also been used by other authors (Pender & Free 1993, Singh & Gahrooee 1990) in various slope stability analyses. The Slope Mass Rating (SMR) method proposed by Romana (1993) uses approximately the same parameters as the RMR, but also provides data on slope failure. These classification systems may be suitable for good quality rock masses and those with well-defined fractures, but are less useful for highly jointed rock masses.

In order to improve the characterization of such terrains, we describe a method to implement an on-site test called the hydraulic cylinder test (HCT). It offers significant advantages over conventional tests from a technical point of view, first of all, given the amount of information that can be obtained regarding the materials tested, but also from a logistical point of view, as the only excavation work necessary is to dig a trench.

2 USING HCT TESTS TO CALCULATE STRENGTH PROPERTIES

In order to characterize masses in a reliable and simple way, a test device was developed, based on the application of stress to the ground using a hydraulic cylinder. This device obtains the stress-strain curve for the tested terrain, and the resulting data can be used to determine different parameters of the material.

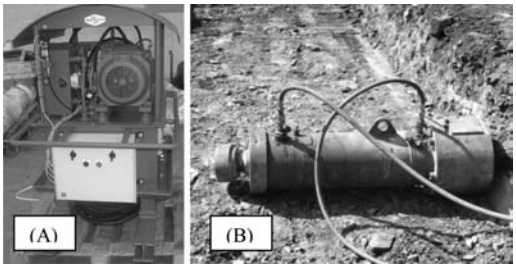


Figure 1. Hydraulic unit (A) and cylinder (B).



Figure 2. Data capture system.

2.1 *Test equipment*

The device is composed of the following four components:

1. A hydraulic unit (Figure 1-A) with a variable hydraulic pump with A10VSO axial piston that is capable of exerting stress of up to 25 MPa.
2. A hydraulic cylinder (CRB M F4 250/140/500 1x/1CON UW), 1.5-m long and with a 500-mm piston stroke (Figure 1-B). This is the element that exerts pressure. It has flat bases at each end (diameters 420 mm and 205 mm) and contains a 0-to-500-mm displacement sensor with a signal outlet.
3. High-pressure hoses that transmit the pressure created by the hydraulic unit pump to the cylinder.
4. An automatic data capture system. The stress and displacement sensors transmit an electrical signal which is continuously recorded by a data acquisition module. Data capture frequency (minimum, 2 s) is regulated by means of a computer application. The data recorded on-site are transferred to a laptop computer for subsequent processing and interpretation in the laboratory. Figure 2 shows the control box connected to the hydraulic unit.

2.2 *Test implementation*

HCT tests are stress-strain tests that consist of applying stress to the ground (using equipment like that described in the previous section) and measuring the deformation produced by said stress. To perform the test, a trench approximately 1.5 m wide is first excavated in the material. The equipment is then positioned in this trench and the cylinder is positioned perpendicular to the walls, as shown in Figure 3.



Figure 3. Hydraulic cylinder positioned in the trench.



Figure 4. Ground failure during testing.

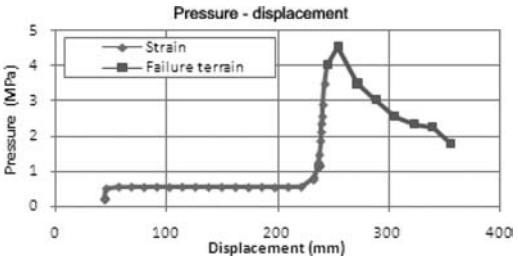


Figure 5. Pressure-displacement diagram obtained from a HCT test.

Once the cylinder has been positioned, pressure is applied and gradually increased. The stress is transmitted perpendicularly to the ground by the cylinder's piston, by means of a hinge joint. Pressure is increased until ground failure takes place; the stress applied is reduced rapidly and the piston penetrate in the ground. Numerous cracks also tend to appear which propagate rapidly, causing the walls of the trench to collapse. Figure 4 depicts the moment at which ground failure takes place during testing.

The stress-strain curve can be used to calculate the failure stress for each analysed material and to estimate peak and residual resistance. An estimate can also be made of the penetration experienced by the hydraulic cylinder when it begins to exert stress, until ground failure takes place (Figure 5). These data are of crucial importance for analysing the properties of the mine materials and for designing slopes, since they quantify the materials' resistance to failure as well as any post-failure residual resistance.

Figure 5 shows four phases: the first stage (horizontal) corresponding to the piston's stroke up to the

Table 1. Strength properties determined based on the results of HCT tests.

	Strength properties					
	Minimum			Average		
Material	σ_f MPa	c kPa	Φ °	σ_f MPa	c kPa	Φ °
Sandstone	1.1	50	17	2.1	120	27
Lutite	3.0	20	20	5.8	48	24
Coal	0.7	15	19	1.2	33	22

point when the hydraulic cylinder makes contact with the trench walls; the second stage, when the cylinder connects with the trench walls; the third phase (slope ascent) when the hydraulic cylinder exerts pressure on the trench walls (material elasticity); and the final phase, when ground failure occurs.

Below we examine the applicability of this test to a real case, specifically an evaluation of the slopes in an opencast coal mine.

3 HCT TEST APPLICATION STUDY

3.1 *Description of the study area*

The studied opencast coal mine is situated in the province of Leon in northern Spain. Its slopes are made up of alternating layers of lutite, sandstone and coal. The slopes are large, measuring between 100 m and 350 m. Mine banks are 10 m high and berms are between 5 m and 6 m wide.

In order for coal mining activity to continue at this site, the mine needs to be enlarged. This enlargement will involve redesigning and increasing the size of the existing slopes. It is therefore crucial to ascertain the resistance properties of the rock mass. The HCT tests were carried out, given the problems associated with the typology of the materials and the fact that they are highly jointed, as result not only of the effects of blasting, but also of subsidence caused by ongoing underground mining beneath the opencast mine in question.

3.2 *Testing*

A total of 20 HCT tests were carried out to ensure that all the different lithologies were included. Once stress-strain graphs were calculated for the implemented tests, based on failure stress (σ_f) — and considering the dimensions of the trench and the depth at which each test was implemented — we could calculate terrain cohesion (c) and friction (Φ) in accordance with the classical formula for calculating bearing capacity (Terzaghi 1956, Meyerhof 1961, Meyerhof 1963, Brinch 1961). Table 1 shows the values obtained in this way.

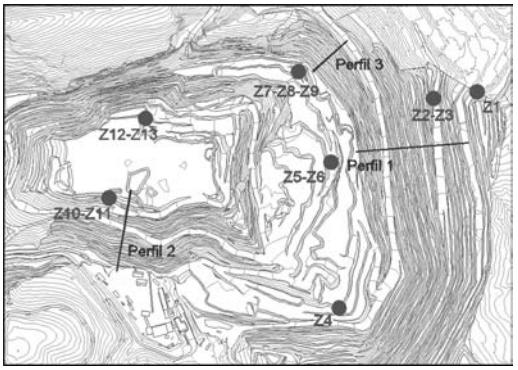


Figure 6. Location of profiles and trenches.

4 VERIFYING TEST RELIABILITY: BACK-ANALYSIS

Once the resistance parameters were obtained, the reliability and accuracy of results had to be tested before the method could be applied to any study of the design and stability of the mine. A two-dimensional stability analysis of the mine's current slopes was carried out using the SLOPE computer programme (Geo-Slope International 2004). In this study, Bishop's Simplified has been used as calculus method.

When a profile of an area where sliding has taken place is modelled, the stability analysis should produce a safety factor lower than 1, for sliding of the type observed in reality. If this safety factor value is obtained, it means that the values assigned to each material by the model match the real values. We applied this kind of analysis, called back-analysis, to confirm the HCT test values calculated for the sandstone, lutite and coal.

Areas with local sliding or incipient cracks were located throughout the mine and were analysed using SLOPE and the results obtained were compared with the values obtained for the HCT tests. Three transversal profiles (called 1, 2 and 3) were created, following the line of maximum gradient in the slopes. Figure 6 shows the location of these profiles and also the trench position where the HCT tests were carried out.

Below we summarize the results for the simulations for each of the profiles.

4.1 *Profile 1*

This profile is located in the east slope of the mine, running across an area, mainly of lutite, where sliding has affected the intermediary berms. The groundwater level in this area was measured in a borehole — after sliding took place — that established that the slope was not saturated. Figure 7 shows the area affected by sliding and the point where the groundwater level was measured.

Cohesion of 51 kPa and friction of 25° — very similar values to those obtained for the HCT tests of the lutite, namely, cohesion 48 kPa and friction 24° — were introduced into the model generated for this



Figure 7. Sliding affecting the mine's east slope.

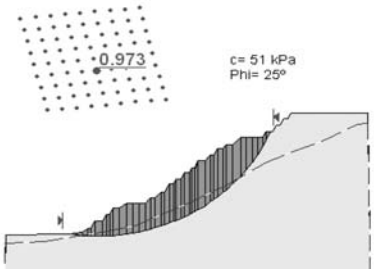


Figure 8. Profile 1: sliding in lutite.



Figure 9. South slope of the mine.

profile and, bearing in mind the groundwater level in accordance with the measurements made, a slip surface with a safety factor of 0.97 was modelled (Figure 8).

Analysis of this slip surface corroborates the cohesion and friction data obtained by the HCT tests, it being possible to reproduce what happened in reality in the theoretical stability calculation model.

4.2 *Profile 2*

This profile is located in the south slope of the mine, in a predominantly sandstone area showing signs of incipient instability (Figure 9); as a result, we attempted to estimate a slip surface with a safety factor slightly higher than 1.

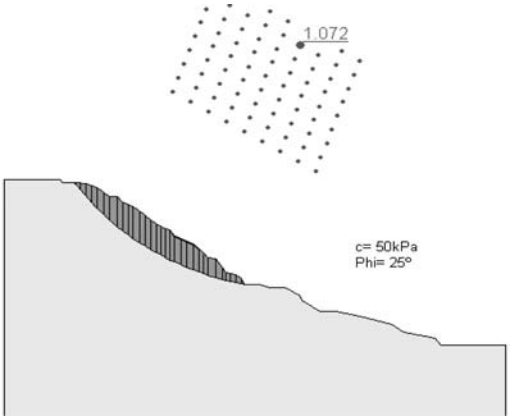


Figure 10. Profile 2: sliding in sandstone.



Figure 11. Sliding in the northeast slope.

Figure 10 shows the desired slip surface, modelled in a dry sandstone area with cohesion of 60 kPa and friction of 25°.

These values are rather similar to the minimums obtained in the HCT tests, namely 50 kPa cohesion and 17° friction, although friction was, in fact, closer to the average value of 27°. The fact that the back-analysis values are closer to the test minimums can be explained by the fact that, in the area analysed, alternating with the sandstone are strata of lutite, whose average values are lower than for sandstone.

4.3 *Profile 3*

Profile 3, runs along the northeast slope of the mine, where small-scale sliding has been detected in carboniferous materials topped with backfill (Figure 11).

To determine the triggering conditions for incipient sliding in this area of the mine, SLOPE was used to simulate Profile 3 under different conditions. The first simulation was for a terrain without water. Note, however, that piezometric data recorded for the area indicate that this area can occasionally experience sudden increases in the phreatic level. In the simulation for terrain without water, the coal values necessary

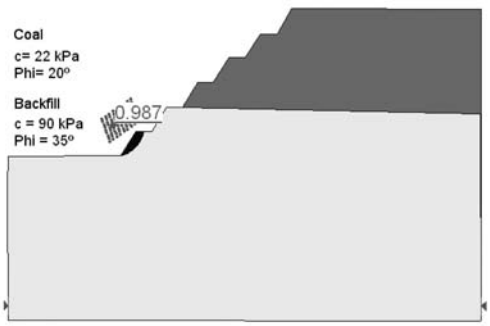


Figure 12. Profile 3: sliding in coal.

Table 2. Comparison of HCT tests and back-analysis results.

	Average properties HCT		Back-analysis	
Materials	c kPa	Φ °	c kPa	Φ °
Sandstone	120	27	60	25
Lutite	48	24	51	25
Coal	33	22	35	22

to reproduce the sliding that took place in reality were slightly lower than the minimums obtained in the HCT tests. On the other hand, considering a phreatic level close to the surface, the coal values were fairly close to the average values obtained in the HCT tests. Thus, the model values calibrated for coal cohesion and friction were 35 kPa and 22° respectively (Figure 12), compared with the average HCT test values of 37 kPa and 22°, respectively.

Note that even though the backfill is included in the profile, it did not affect the calibration, as the desired slip surface is located exclusively in the coal seam and the backfill is merely an overload. Therefore, the values assigned to the backfill are standard values obtained from tests on similar materials.

5 CONCLUSIONS

The calibration results obtained for the three profiles as resistance values obtained coincide with average or minimum values obtained in the HCT tests performed on each material in the mine (Table 2). In the case of the back-analysis carried out for the sandstone, the fact that the calibrated values were closer to the minimums than to the averages was due to the sandstone being intercalated with lutite.

The fact that the values obtained using such different methods were so similar demonstrates that the results were quite accurate and close to the real values for the materials. This would indicate that the test methodology is useful for defining the values of a rock mass on a real scale. In other words, representative values can be obtained for the whole rock mass and not just the intact rock. Such data could be used to design the safe slopes that are required to enlarge this particular mine.

The HCT test is easily and rapidly implemented, and only requires, in addition to the testing equipment, a back-shovel to dig the trench in which to perform testing. The test can therefore be easily used several times as the mining front advances. Slope stability can thus be monitored continuously, without disrupting the mining works and at a minimal cost for the company.

REFERENCES

Amadei, B. 1988. Strength of a regularly jointed rock mass under biaxial and axisymmetric loading. *International Journal of Rock Mechanics & Mining Sciences*. *Geomech. Abstr*. 25(1): 3–13.

Bieniawski, Z. T. 1989. *Engineering Rock Mass Classification*. New York: John Wiley and Sons.

Brinch Hansen, J. 1961. A general formula for bearing capacity. *Geoteknisk Institut. Institute Akademict for de Tekniske Videuskaber*, *Bulletin No 11.* Copenhagen.

Cai, M & Horii H. 1992. A constitutive model of highly jointed rock masses. *Mechanics of Materials* 13: 217–46.

Denver, H & Steffensen, H. 1989. Ground moduli determined by seismic methods. *Proceedings 12th International Conference on Soil Mechanics and Foundation Engineering*, *Rio de Janeiro, 13–18 August 1989* V1: 215–218. Rotterdam: Balkema.

Geo-Slope International, 2004. *SLOPE User Manual*.

Grimstad, E. & Barton, N. R. 1993. Updating the Q-System for NMT. *Proceedings International Symposium on Sprayed Concrete – Modern use of wet mix sprayed concrete for underground support, Fagernes*. Oslo: Kompen, Opsahl and Berg. Norwegian Concrete Association.

Hoek, E. & Brown, E. T. 1980. Empirical strength criterion of rock masses. *Journal Geotechnical Engineering Division American Society of Civil Engineers.* 106: 1013–1035.

Laubscher, D. H. 1990. A geomechanics classification system for the rating of rock mass in mine design. *Journal of the South African Institute of Mining and Metallurgy*, 90(10): 257–273.

Meyerhof, G.G. 1961. The ultimate bearing capacity of wedge-shaped foundations. *V Congreso Internacional de Mecánicas de Suelos e Ingeniería de Cimentaciones*. Vol. II, París.

Meyerhof, G.G. 1963. Some recent research on the bearing capacity of foundations. *Canadian Geotechnical Journal*. Vol. I, n° 1.

Nihat, S. I., Resat, U., Vedat, D. 2008. Deformation modulus of heavily jointed–sheared and blocky greywackes by pressuremeter tests: Numerical, experimental and empirical assessments. *Engineering Geology* 101(3–4): 269–282.

Pender, M.J. & Free, M.W. 1993. Stability assessment of slopes in closely jointed rock masses. *Proceedings Eurock'93*. A. Sousa and P. Grossmann. A. A. Balkema, pp. 863–870.

Ramírez Oyanguren, P., González-Nicieza, C., Álvarez Fernández, M.I. & González Palacio, C. 2008. Stability

analysis of Llerin Rockfill Dam: An in situ direct shear test. *Engineering Geology* 100(3–4): 120–130.

Romana, M. 1993. A geomechanical classification for slopes: Slope Mass Rating. In J.A. Hudson (ed.), *Comprehensive Rock Engineering*, Vol. 3, Ch. 22, 575–599. Oxford: Pergamon Press.

Singh, R. N. & Gahrooee, D. R. 1990. Deterministic stability and sensitivity analyses of slopes in jointed rock masses. *Mining Sciences and Technology* 10(10): 265–286.

Taheri, A. & Tani, K. 2008. Development of an apparatus for down-hole triaxial tests in a rock mass. *International Journal of Rock Mechanics & Mining Sciences* 45: 800–806.

Terzaghi, K. 1956. *Theoretical Soil Mechanics*. Cap VIII. John Wiley and Sons.

Ünal, E. 1997. Determination of in situ Deformation Modulus: New Approaches for Plate-Loading Tests. *International Journal of Rock Mechanics & Mining Sciences* 34(6): 897–915.

Uriel, S. 1964. La geotecnia aplicada a las grandes presas. *Revista de Obras Públicas*, tomo I (2988): 493–510.

Rock Mechanics for Resources, Energy and Environment – Kwaśniewski & Łydżba (eds)
© 2013 Taylor & Francis Group, London, ISBN 978-1-138-00080-3

Influence of chemo-mineralogical transformations on micro/macro-mechanical properties of ironstone

D. Grgic
GeoResources Laboratory, University of Lorraine/CNRS/CREGU, Vandoeuvre-lès-Nancy, France

ABSTRACT: A study on the mineralogical ageing of iron ore rock was performed. During mining, oxidizing conditions were imposed in the mines for a century and chemo-mineralogical transformations occurred in iron ore pillars: chemical alteration of reduced minerals (siderite and berthierine) in the inter-oolithic cement, recrystallization of berthierine and neo-crystallization of a hematite crust. This corrosion occurred at a large scale in old pillars exposed to the mine atmosphere for 70–100 years. Because of the alteration of the inter-oolithic cement, which is not compensated by the neo-mineralizations, the cohesion decreased, thus resulting in a decrease in micro- and macro-mechanical properties (from the millimetric scale of micro-indentation tests to the decimetric scale of triaxial tests). This chemical weathering of anthropic-origin plays a major role in the long-term behaviour of ironstone. It is probably one of the main causes explaining collapses of underground iron mines in Lorraine (France).

1 INTRODUCTION

This paper focuses on the problem of underground iron mines collapses in Lorraine (North-Eastern France). A partial extraction method (i.e., room and pillar system) was used under sensitive zones with houses and surface infrastructures until 1980. Some of these safety pillars were left in a state of abandon for a hundred years. In these areas of partial extraction, many collapse occurred often because of the failure of iron ore pillars. Underground iron mines are in shallow (∼200 m) environments with hydrous conditions which evolve in time: saturation under a water-table before the mining, partial saturation during mining because of the ventilation of rooms ($hr = 85$–100%), resaturation at the end of mining due to the water-table rising and thus the mine flooding. Some of the mine collapses occurred during this flooding stage.

Knowledge of the long-term strength of rocks is of prime importance for estimating the stability of such man-made structures. In chemically reactive environments (e.g., iron ore exposed to O_2 and water in the mine) and in the brittle regime relevant to *in situ* mine conditions (low temperature and confining pressure), time-dependent behaviour of rocks depends on the physiochemical mechanism of sub-critical stress corrosion cracking (e.g., Atkinson 1984, Heap et al. 2009, Nara et al. 2007) and on chemical reactions responsible for mineralogical transformations. Ageing of rocks results from the chemical and/or physical weathering of mineralogical, geochemical, geomechanical and petrophysical properties. Previous studies on ageing/weathering were carried out to characterize building materials such as concrete, granite, calcareous shale and basalt (e.g., Nandi & Whitelaw 2009, Moon & Jayawardane 2004), to analyse landslides (e.g., Zhao et al. 2011) and (reservoir and cap) rocks of underground constructions such as storage sites (e.g., Tu et al. 2005, Oztoprak & Pisirici 2011) and to study the mechanisms of rock-soil transition (e.g., Begonha & Braga 2002, Arel and Onalp 2004). In the case of ironstone, ageing is an important parameter to take into account when performing mine stability analysis.

The present work is devoted to the study of the ageing of iron ore exposed to a mine atmosphere as compared to healthy iron ore located in a zone without mining workings. To determine how the iron ore evolved during the period of exposure to the mine atmosphere, chemo-mineralogical and micro/macro-mechanical analyses are performed. A mineralogical ageing model will be proposed and the impact on mechanical behaviour of ironstone will be analysed.

2 EXPERIMENTAL METHODS

2.1 *Description of intact iron ore*

The intact (i.e., "healthy") oolithic-type ironstone has an average grain (ooliths) size of 0.2 mm (Fig. 1). The oolithic cortices are made of concentric layers of goethite (ferric oxide-hydroxide) whose formation would be related to biochemical processes (Burkhalter 1995, Konhauser 1998). The inter-oolithic cement is made up of diagenetic calcite, siderite (iron carbonate), magnesite, iron oxides and berthierine (hydrous magnesium iron phyllosilicate) in varied proportions.

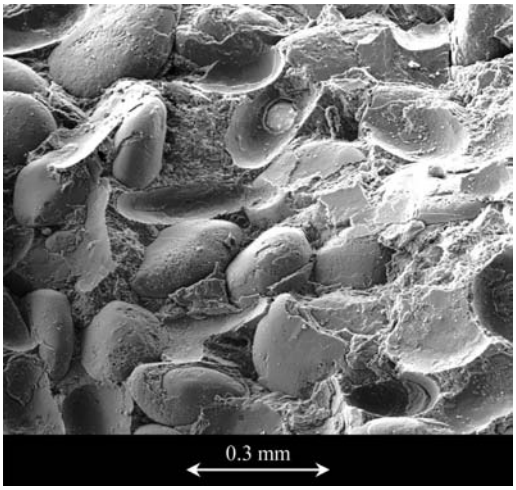


Figure 1. SEM observation on a crack surface showing oolithic structure of intact iron ore: oolithes are cemented by siderite.

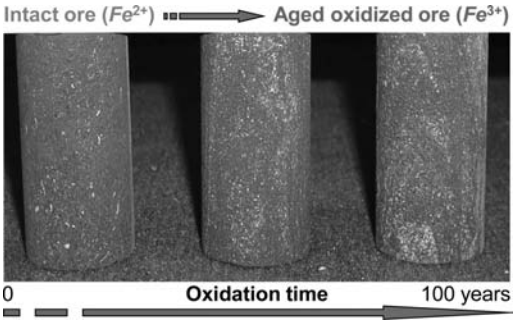


Figure 2. Macroscopic samples of intact and aged iron ore.

Calcite bioclasts are abundant in the cement where a small amount of pyrite can also be found. Ironstone is a very porous rock: the total (i.e., inter-granular and intra-granular) porosity is about 30%. The porous network of iron ore is mainly composed of mesopores of radii between 0.002 μm and 0.05 μm in size.

The most common facies is a ferriarenite (i.e., iron-rich rock). Some layers of calcarenite (i.e., calcite-rich rock) are locally intercalated. From a macroscopic point of view (Fig. 2), intact iron ore has a green/grey colour due to the large amount of Fe^{2+} in the inter-oolithic cement (siderite and berthierine). Aged iron ore (exposed to the mine atmosphere for 70–100 years) has a red colour due to the oxidation of Fe^{2+} to Fe^{3+}.

2.2 *Experimental techniques*

Some vertical core drillings were carried out from the land surface in a non-mined area and in a zone where they cross the centre of large rectangular (20 × 30 m) pillars to study intact iron ore. For the study of aged iron ore, horizontal cores were carried out in 4 pillars

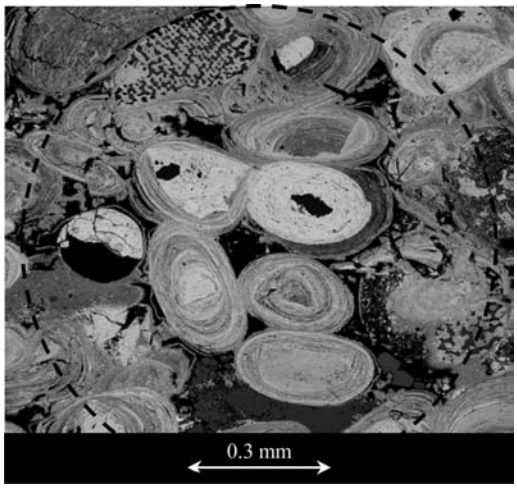


Figure 3. SEM observation on a polished thin section of intact iron ore showing the size ($\varphi = 1$ mm) of the micro-indenter tip.

(up to one meter depth) for which the time of exposition to the mine atmosphere was known to be 10, 30, 70 and 100 years.

Mineral phases and chemical compositions were identified using: SEM (Scanning Electron Microscopy) with the EDS (Energy Dispersive X-ray Spectroscopy) method, X-ray diffraction, Mössbauer spectroscopy for the determination of the Fe^{2+}/Fe^{3+} ratio, Inductively Coupled Plasma (ICP) spectroscopy for the analysis of the chemical composition of the mine mud (made from the weathering of iron ore), determination of the amount of calcite and siderite in the inter-oolithic cement by chemical reaction with hydrochloric acid (HCl).

Multi-scale mechanical tests were carried out on both intact and aged (70-100 years) iron ore:

- Macro-compression triaxial tests on decimetric cylindrical samples ($h = 7.6$ cm, $\varphi = 3.8$ cm).
- Micro-compression triaxial tests on centimetric cylindrical samples ($h = 10$ mm, $\varphi = 5$ mm).
- Micro-indentation tests at millimetric scale. The size of the cylindrical indenter tip ($\varphi = 1$ mm) was chosen to be representative of the micro-structure of the oolithic rock (Fig. 3).

3 RESULTS

3.1 *Mineralogical and geochemical analyses*

Figure 4 illustrates the first step of the weathering of inter-oolithic siderite. When siderite is entirely weathered, contacts between oolithes become direct and many oolithes are crushed (Fig. 5). When pillars are 70–100 years old, oolithes are covered by neo-crystallized crust of rust (Figs. 5 and 6) which results from the oxidation of the inter-oolithic siderite. This

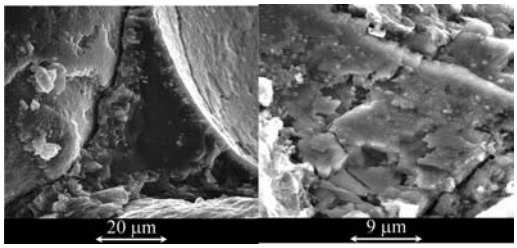


Figure 4. SEM observations showing intact interoolithic siderite on the left and slightly weathered siderite on the right.

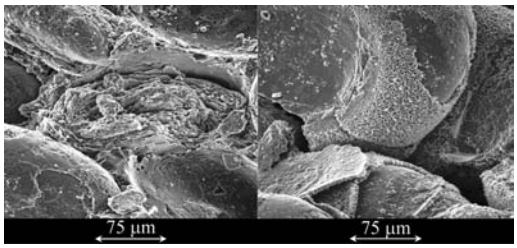


Figure 5. SEM observations on aged iron ore. On the left: oolithes are directly in contact and crushed. On the right: oolithes are covered by neo-crystallized ferric oxide crust.

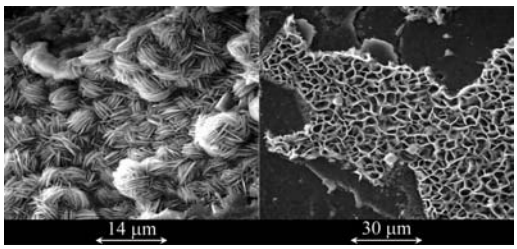


Figure 6. Detailed views (SEM) of the neo-crystallized minerals. On the left: "petals" of berthierine in the inter-oolithic cement. On the right: honeycombed ferric oxide crust on oolithe.

Iron(III) oxide (i.e., ferric oxide) crust gives the red colour to the aged iron ore (Fig. 2). Recrystallized "petals" of iron phyllosilicates (berthierine) are also observed in the inter-oolithic cement (Fig. 6).

Table 1 represents the mean chemical composition of some (diagenetic and neo-crystallized) minerals in intact and aged iron ore obtained from EDS semi-quantitative absorption spectra. The diagenetic phyllosilicate, which was identified as berthierine with X-ray diffraction, is a very ferriferous species and generally contains a proportion of SiO_2 approximately twice higher than the proportion of Al_2O_3.

The Fe^{2+}/Fe^{3+} ratio was determined using Mössbauer spectroscopy (Tab. 2). During ageing, the proportion of Fe^{2+} was found to decrease which is mainly due to the weathering of diagenetic siderite. Conversely, the proportion of Fe^{3+} was found to increase during ageing which is mainly due to the oxidation of Fe^{2+} and the neo-crystallization of hematite (ferric oxide), i.e. the honeycombed crust covering oolithes of aged iron ore (Figs. 5 and 6).

Table 1. Mean chemical composition of some minerals in intact and aged iron ore. EDS analysis for minerals and ICP spectroscopy for the mine mud.

Oxide	SiO_2	Al_2O_3	MgO	P_2O_5	FeO
Intact iron ore					
Oolithic cortices (goethite)	9%	11%	3%	5%	70%
Berthierine	32%	18%	6%	n.s.	43%
Transformations in aged iron ore					
Berthierine	28%	20%	5%	n.s.	46%
Honeycombed iron oxide crust	5%	9%	5%	n.s.	78%
Mine mud in mg/g of oxide	63	47	184	20	10

n.s.: not significant.
n.b.: all iron is expressed in FeO.

Table 2. Fe^{2+}/Fe^{3+} repartition in healthy (10 years old pillar) and aged (70 years old pillar) iron ore. Mössbauer spectroscopy analysis.

Age of pillars	10 years	70 years
Total Fe^{2+}	14%	4%
Berthierine[a]	7%	4%
Siderite	7%	n.d.
Total Fe^{3+}	86%	96%
Goethite	81%	88%
Berthierine[a]	n.d.	3%
Not identified[b]	5%	n.d.
Hematite	n.d.	5%

[a]: berthierine may contain Fe^{3+}.
[b]: probably a phyllosilicate.
n.d.: not detected.

The amount of carbonates (calcite and siderite) in the inter-oolithic cement was determined by considering its chemical reaction with hydrochloric acid (HCl). Figure 7 shows the evolution of the percentage of siderite in the inter-oolithic cement as a function of exposition time to the oxidizing mine atmosphere and distance to the pillar's border. The relative content of siderite was found to decrease as the time of exposition to the oxidizing mine atmosphere increased. In addition, the relative content of siderite is more significant one meter inside pillars than close to the border (15 cm depth).

3.2 *Micro-macro mechanical properties*

Figures 8 and 10 show the macro- and micro-triaxial failure points of intact and aged iron ore (ferriarenite) in the principal stresses plane. The ageing is responsible for a significant decrease in the strength of the

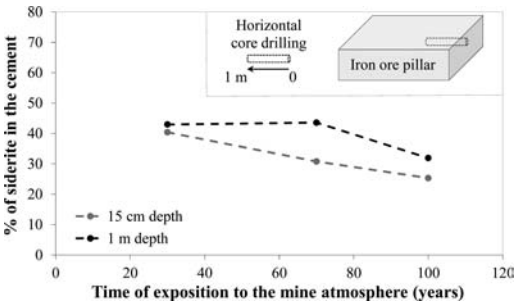


Figure 7. Evolution of the relative content of siderite in the inter-oolithic cement as a function of the time of exposition to the mine atmosphere. Iron-rich (ferriarenite) facies of iron ore.

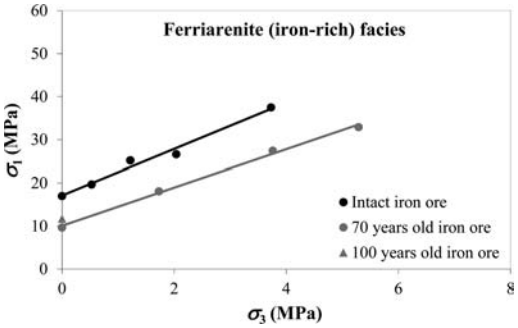


Figure 8. Failure points of intact and aged iron ore (ferriarenite) in the principal stresses plane. Macro-compression triaxial tests on decimetric cylindrical samples.

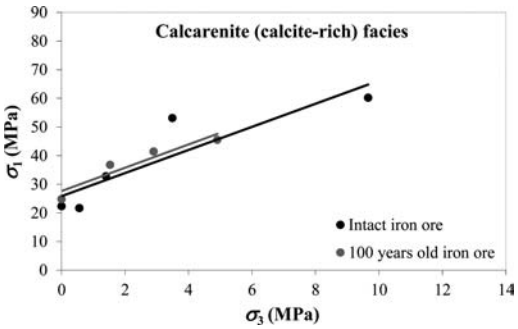


Figure 9. Failure points of intact and aged iron ore (calcarenite) in the principal stresses plane. Macro-compression triaxial tests on decimetric cylindrical samples.

ferriarenite. Conversely, the triaxial strength of the calcarenite facies did not evolve during ageing (Fig. 9). Figure 10 shows the Young's modulus E of intact and aged iron ore (ferriarenite) measured with micro-indentation tests at millimetric scale. The Young's modulus of aged iron ore is about twice smaller than the Young's modulus of intact iron ore.

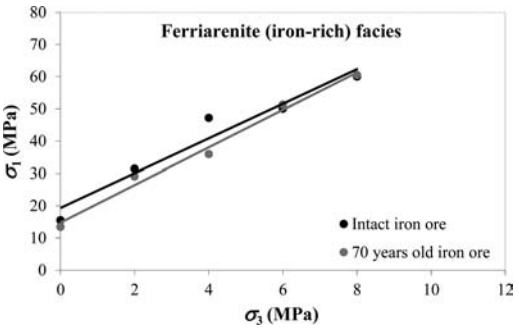


Figure 10. Failure points of intact and aged iron ore (ferriarenite) in the principal stresses plane. Micro-compression triaxial tests on centimetric cylindrical samples.

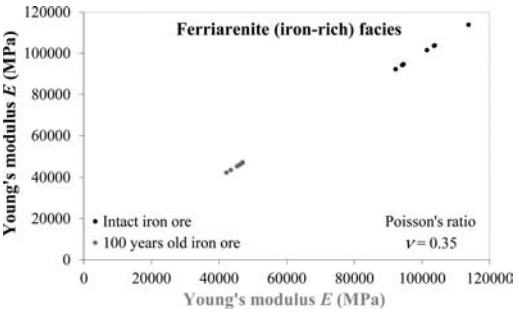


Figure 11. Young's modulus E of intact and aged iron ore (ferriarenite). Micro-indentation tests at millimetric scale.

4 DISCUSSION

4.1 *Mineralogical ageing model for iron ore*

After geological formation and burying, the chemical conditions corresponded to a reducing medium and the cement grew rich in siderite and berthierine during its diagenesis. Before mining, over a period of 180 million years, rocks were saturated under a water-table and interstitial water was chemically equilibrated with rocks. The pH was neutral due to the high carbonates content and no oxidation reaction occurred because of the anaerobic conditions. During mining, galleries were ventilated thus inducing a modification of the chemical balances in the medium which became oxidizing. The anthropogenic evolution of iron ore can be presented in two steps, namely alteration of ferrous minerals and reorganization-neoformation of ferric minerals

In the first step, berthierine (Fe^{2+}, Fe^{3+}, Al, $Mg)_{2-3}(Si,Al)_2O_5(OH)_4$ and siderite $FeCO_3$, i.e. minerals that cement oolithes and ensure the cohesion of ironstone, are weathered through hydrolysis reactions. Siderite was probably the first to react:

$$FeCO_3 + CO_2 + H_2O \rightarrow Fe^{2+} + 2HCO_3^- \quad (1)$$

Ferrous ions Fe^{2+}, which were released from the dissolution of inter-oolithic siderite and berthierine,

were immediately oxidized because of the aerobic environmental conditions (Eq. 2). This oxidation is probably aided by chemolithotrophic bacteria such as *Gallionella ferruginea*, *Leptotrix* and *Thiobacillus ferrooxidans* (Konhauser 1998, Ferris et al. 1989).

$$Fe^{2+} + \frac{1}{2}O_2 + 2H^+ \rightarrow Fe^{3+} + H_2O \quad (2)$$

The weathering of iron ore is well illustrated in Table 3 which gives the chemical composition of the mine mud. This mud is rich in *Si*, *Al* and *Fe* which result from the weathering of the inter-oolithic cement. Since Fe^{2+}-rich minerals (i.e., siderite and berthierine) contained in the inter-oolithic cement more or less disappeared (Fig. 4), the diagenetic links (between carbonates and oolithes) ensuring the mechanical cohesion of ironstone were broken and many oolithes are now directly in contact and so stressed and crushed (Fig. 5, on the left).

In the second step, the released Fe^{2+} ions hydrolyse when they come in contact with H_2O and form ferric hydroxide (Eq. 3) then hematite (Eq. 4), the most dehydrated ferric oxide, which precipitate:

$$2Fe^{2+} + \tfrac{1}{2}O_2 + H_2O + 4OH^- \rightarrow 2Fe(OH)_3(s) \quad (3)$$

$$2Fe^{2+} + 4HCO_3^- + \tfrac{1}{2}O_2 + 4H_2O \rightarrow Fe_2O_3(s) + 4CO_2 + 6H_2O \quad (4)$$

The neo-crystallized hematite (cf. Tabs. 1 and 2) corresponds to the residue of the siderite alteration. This rust coats all mineral supports (oolithes, carbonates, phyllosilicates) as a honeycombed crust (Figs. 5 and 6, on the right) and gives a red colour to old and "corroded" iron ore (Fig. 2). This ferric oxide contains aluminium (Tab. 1) thus suggesting that it partly results from the hydrolysis of berthierine:

$$-SiO - Fe^{2+} + 2H^+ \rightarrow Fe^{2+} + 2HO - Si \quad (5)$$

The evolution of diagenetic berthierine to recrystallized berthierine (Fig. 6, on the left), which has already been observed in iron ore rocks (Velde 1989), shows a moderate SiO_2 loss and a small iron gain (Tab. 1). In addition, Mössbauer spectroscopy analysis (Tab. 2) shows a decrease in the Fe^{2+}/Fe^{3+} ratio, again providing evidence that a large fraction of the iron is in an oxidized form in aged ironstone. Such a transformation of siliceous berthierine to ferric berthierine can be written as follows:

$$Fe^{2+}{}_{1.5}\, U_{0.5}\, Al_{1,0}\, Si_{2,0} \rightarrow Fe^{2+}{}_{2,0}\, (Al,\, Fe^{3+})_{1,0}\, (Si, Al)_{2,0} \quad (6)$$

These mineralogical processes are of anthropogenic origin given that they began with the start of mining. Since aerobic conditions were imposed in the mines for almost one century, chemical weathering developed on a large scale, not only at the border of abandoned pillars but up to one meter depth at least. In addition, its amplitude was found to be progressively less significant when we move from the border to the core of the abandoned pillars (Fig. 7) and increasingly significant as the time of exposition to the oxidizing mine atmosphere increases. Indeed, mineralogical transformations are more significant at the border of 70–100 years old pillars.

The remaining mineralogical structures were reorganized in place and new material was added. Such an evolution is commonplace and is similar to those undergone in several well-known diagenetic or pedologic alterations. At the end of mining activity, the mine drainage pumping was stopped which caused the water-table to rise and rocks to be resaturated. From that moment, oxidation reactions no longer occurred because of the anaerobic conditions.

4.2 *Impact of the chemo-mineralogical transformations on mechanical properties of iron ore*

The chemo-mineralogical reactions described in §4.1 correspond to a weathering and corrosion of iron ore in a mining environment (presence of H_2O and O_2), thus inducing the decrease in the inter-oolithic cohesion. Indeed, the alteration of the inter-oolithic cement (mainly siderite) was not compensated by the neo-crystallization of the honeycombed ferric oxide crust. In other words, the cementation induced by this crust is not as strong as the initial cementation supplied by the diagenetic bonds between oolithes and interoolithic cement. As illustrated in Figure 5 (on the right), the ferric oxide crust does not adhere strongly on oolithes which are easily removed from the inter-oolithic cement.

These mineralogical transformations result in the decrease in the micro- and macro-mechanical properties of iron ore. Figure 8 shows that the macroscopic (i.e., decimetric scale) triaxial strength and therefore the failure surface of the ferriarenite decrease significantly because of ageing. The calcite-rich facies is not affected by ageing (Fig. 9) since corrosion reactions are limited compared to that observed in iron rich facies. At the centimetric scale corresponding to the micro-compression triaxial tests, the triaxial strength and the failure surface decrease as well (Fig. 10), again providing evidence of the mechanical impact of mineralogical ageing. At the millimetric scale corresponding to the size of a few oolithes (Fig. 3), the micro-indentation tests showed that the Young's modulus of aged (100 years) iron ore is two times lower that the Young's modulus of the intact iron ore (Fig. 11).

These phenomena are amplified by the stress redistribution. Indeed, during the long geological period before underground mining began, the natural and almost isotropic stress state ensured the ironstone cohesion and the stability of the ore mineral paragenesis. After excavation, the stress state became brusquely and strongly anisotropic in pillars, thus inducing the damage of pillars. Multiple cracks developed, from the

microscopic scale of minerals to the macroscopic scale of pillars, promoting the leaching/alteration of the diagenetic inter-oolithic cement and thus inducing a loss of cohesion.

5 CONCLUSIONS

During the long geological period before the underground mining (180 million years), the paragenesis of ironstone was preserved under reducing conditions. Aerobic (i.e., oxidizing) conditions were then imposed in the mines of Lorraine (France) for more than a century and chemo-mineralogical transformations, triggered or activated by chemical and biochemical processes (including bacteria), occurred in iron ore pillars. These processes were: chemical alteration of reduced minerals (siderite and berthierine) in the inter-oolithic cement, recrystallization of berthierine in the inter-oolithic cement and neo-crystallization of a honeycombed hematite crust (i.e., rust) on all mineral surfaces. These evolutions of anthropogenic origin, which differ from diagenetic evolution, correspond to a chemical weathering and corrosion of ironstone and occurred at a large scale in pillars (up to one meter depth from the border at least), especially in very old pillars exposed to the oxidizing mining atmosphere for 70–100 years.

Because of the alteration of the inter-oolithic cement, which was not compensated by the crystallisation of new minerals, the ironstone cohesion decreased strongly as well as micro- and macro-mechanical properties (from the millimetric scale of micro-indentation tests to the decimetric scale of triaxial tests). All these chemo-mineralogical processes, along with mechanical pore pressure effects (during the transient stage of mine flooding) and physiochemical mechanism of subcritical stress corrosion cracking, result in the ageing of iron ore and therefore play a major large-scale role in the long-term behaviour of pillars. They are probably the main mechanisms responsible for many mine collapses in Lorraine. Therefore, the characterization of this chemical weathering resulting in iron ore ageing is important for estimating the long-term stability of such rock structures.

ACKNOWLEDGEMENTS

This research was carried out thanks to subsidies from the Ministries for Industry and Research and the Lorraine Region within the GISOS (www.gisos.org) framework. The authors express their gratitude to these organizations.

REFERENCES

Arel, E. & Onalp, A. 2004. Diagnosis of the transition from rock soil in a granodiorite. *J. Geotech. Geoenviron*. 130(9): 968–974.

Atkinson, B.K. 1984. Subcritical crack growth in geological materials. *J. Geophys. Res.* 89(B6): 4077–4114.

Begonha, A. & Braga, S.M.A. 2002. Weathering of the Oporto granite: geotechnical and physical properties. *Catena* 49(1–2): 57–76.

Burkhalter, R.M. 1995. Ooidal ironstones and ferruginous microbialites: origin and relation to sequence stratigraphy (Aalenian and Bajocian, Swiss Jura mountains). Sedimentology 42: 57–74.

Ferris, F.G., Tazaki, K. & Fyfe, W.S. 1989. Iron oxides in acid mine drainage environments and their association with bacteria. *Chem.Geology* 16: 149–152.

Heap, M.J., Baud, P., Meredith, P.G., Bell, A.F. & Main, I.G. 2009. Time dependent brittle creep in Darley Dale sandstone. *J. Geophys. Res*. 114(B07203).

Jeong, H.-s., Kang, S.-s. & Obara, Y. 2007. Influence of surrounding environments and strain rates on the strength of rocks subjected to uniaxial compression. *Int. J. Rock Mech. Min. Sci.* 44: 321–331.

Konhauser, K.O. 1998. Diversity of bacterial iron mineralization. *Earth-Science Reviews* 43: 91–121.

Moon, V., & Jayawardane, J. 2004. Geomechanical and geochemical changes during early stages of weathering of Karamu Basalt, New Zealand. *Engineering Geology* 74(1–2): 57–72.

Nandi, A. & Whitelaw, M. 2009. Effect of Physico-Chemical Factors on the Disintegration Behavior of Calcareous Shale. *Environmental & Engineering Geoscience* 15(4): 273–285.

Nara, Y., M. Takada, T. Igarashi, N. Hiroyoshi & Kaneko, K. 2007. Subcritical crack growth in rocks in an aqueous environment. *Exploration Geophysics* 40(1): 163–171.

Oztoprak, S. & Pisirici, B. 2011. Effects of micro structure changes on the macro behaviour of Istanbul (Turkey) clays exposed to landfill leachate. *Engineering Geology* 121(3–4): 110–122.

Tu, X.B., Jian, B., Wang, S.J., Bian, H.Y., Wang, J. & Li, S.G. 2005. Swelling behavior induced by alteration in granite and its implications on underground excavation. *Tunnelling And Underground Space Technology* 20(4): 378–389.

Velde, B. 1989. Phyllosilicate formation in berthierine peloids and iron oolites. *Spec. Publ. geol. Soc. London* 46: 3–8.

Zhao, Y., Cui, P., Hu, L.B. & Hueckel, T. 2011. Multi-scale chemo-mechanical analysis of the slip surface of landslides in the Three Gorges, China. *Science China-Technological Sciences* 54(7): 1757–1765.

Rock Mechanics for Resources, Energy and Environment – Kwaśniewski & Łydżba (eds)
© 2013 Taylor & Francis Group, London, ISBN 978-1-138-00080-3

Influence of water vapor pressure in surrounding environment on strength and fracture toughness of rocks

M. Kataoka & Y. Obara
Kumamoto University, Kumamoto, Japan

H.S. Jeong
NEXGEO Inc., Seoul, South Korea

ABSTRACT: In this paper, firstly, uniaxial compression test and Brazilian test of rock were conducted to investigate the influence of surrounding non-atmospheric environments on uniaxial compressive strength and tensile strength. The environments used in this paper were organic vapor, inorganic gas and water vapor. As the results, it was founded that water vapor is the most effective agent which promotes stress corrosion for rocks. Then, a series of uniaxial compression tests, Brazilian tests and Semi-Circular Bend tests of rocks under various water vapor pressures was conducted to investigate the influence of the surrounding water vapor environment on uniaxial compressive strength, tensile strength and fracture toughness. The rocks used in this paper were Kumamoto andesite, African granodiorite and Korean granite. It was made clear that rock strengths and fracture toughness of these rocks are dependent on the water vapor pressure in the surrounding environment and decrease with increasing the pressure.

1 INTRODUCTIONS

Strengths of a rock are dependent on not only the properties of rock itself but also the surrounding environment, such as temperature, humidity, confining pressure and so on. Furthermore, it has been known that fracture of a rock takes place owing to the subcritical crack growth caused by stress corrosion under the stress state below the strengths of the rock. The stress corrosion is the chemical reaction activated by stress concentration at a crack tip. The water vapor is considered to be a chemical reaction agent in the stress corrosion for silicate materials like a rock (Freiman 1984, Atkinson & Meredith 1979). Therefore it is desired that the influence of the water vapor on rock strengths is taken into account based on the results obtained from various experiments.

In this paper, firstly, uniaxial compression (UC) test and Brazilian test were conducted on Kumamoto andesite to investigate the influence of surrounding non-atmospheric environments on uniaxial compressive (UC) strength and tensile strength (Jeong et al. 2007). The environments used in this paper were methanol, ethanol and acetone vapor as organic vapor, argon, nitrogen and oxygen as inorganic gas and water vapor, using special vacuum chamber. Then it was found that the water vapor is the most effective environment which promotes decreasing of the strengths, namely stress corrosion for rocks. Secondly, fracture toughness of various types of rock was estimated under various water vapor pressures in surrounding environment, as well as UC and tensile strengths. Semi-Circular Bend (SCB) test (Chong & Kuruppu 1984) was adopted to estimate the fracture toughness of rock for its simplicity of specimen preparation, equipment and testing procedure. The Kumamoto andesite, African granodiorite and Korean granite were used in the SCB test (Kataoka et al. 2011).

2 EXPERIMENTAL METHODS

2.1 *SCB testing method*

The geometry of SCB specimen and loading is shown in Figure 1. The specimen is loaded at three points including lower two points with span of 2*s* and upper single point.

Fracture toughness of mode I K_{IC} is represented by the following equation (Lim et al. 1994).

$$K_{IC} = \frac{P_{max}\sqrt{\pi a}}{2rt} Y_I \tag{1}$$

where P_{max} is the maximum load, a is an artificial notch length, r is a radius and t is a thickness of the specimen. The normalized stress intensity factor Y_I is the dimensionless stress intensity factor given as a function of the dimensionless notch length a/r and the support span ratio s/r (Kuruppu et al. in press). In this paper, $a/r = 0.5$ and $s/r = 0.8$ is used. The value of Y_I is 6.65 in this case.

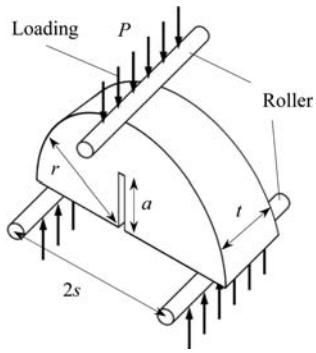


Figure 1. SCB specimen and loading.

2.2 *Apparatus and procedure*

Figure 2(a) shows a vacuum chamber used in the tests to control surrounding environment of a specimen. The chamber, which is made of SUS304 steel, has six ports and a valve to inject gases. In these ports, two ports are to lead the output from strain gauges or a load cell. Another two ports are used to measure the vapor or gas pressure in the chamber by two types of pressure gauges, namely a penning pressure gauge with a measurement range of 10^{-6} to 10^{0} Pa and a pirani pressure gauge with the range of 10^{-1} to 10^{5} Pa. One port is a window for observing inside of the chamber and the last port with a valve is connected to an evacuation system through a flexible tube as shown in Figure 3. The evacuation system consists of two vacuum pumps, namely a turbo molecular pump and a rotary pump.

The chamber has upper and lower flanges with loading rods and the specimen is set up between these rods as shown in Figure 2(b),(c). For the Brazilian test, the specimen is adjusted in a jaw made according to ISRM suggested method (Bieniawski & Bernede 1978). The SCB specimen is placed on two rollers and a loading plate can move up and down vertically by guide rods. Then the chamber is placed at a MTS servo-controlled testing machine with a capacity of 500 kN for UC test and 100 kN for Brazilian test and SCB test. The specimen is loaded with the rods by pressing up the lower flange using the testing machine. The load application is controlled by constant strain rate of 1.2×10^{-6} to 1.4×10^{-5}/s for UC test and displacement rate of 4.6×10^{-5} to 1.0×10^{-3} mm/s for Brazilian test, 1.7×10^{-4} mm/s for SCB test. The load is recorded using the load cell equipped at the testing machine for UC test and Brazilian test and placed on the loading plate for SCB test.

In these tests, it is necessary that the air in the chamber is exhausted and that various vapor or gas pressures are provided. Figure 4 shows the change of the pressure in the chamber before the test. At first, the air in the chamber is exhausted by using two pumps until the pressure decreases to less than 10^{-2} Pa. The distilled organic liquid, inorganic gas or distilled water is then injected through the injection valve to the pressure of about 10^{3} Pa. As the result, the pressure in the chamber

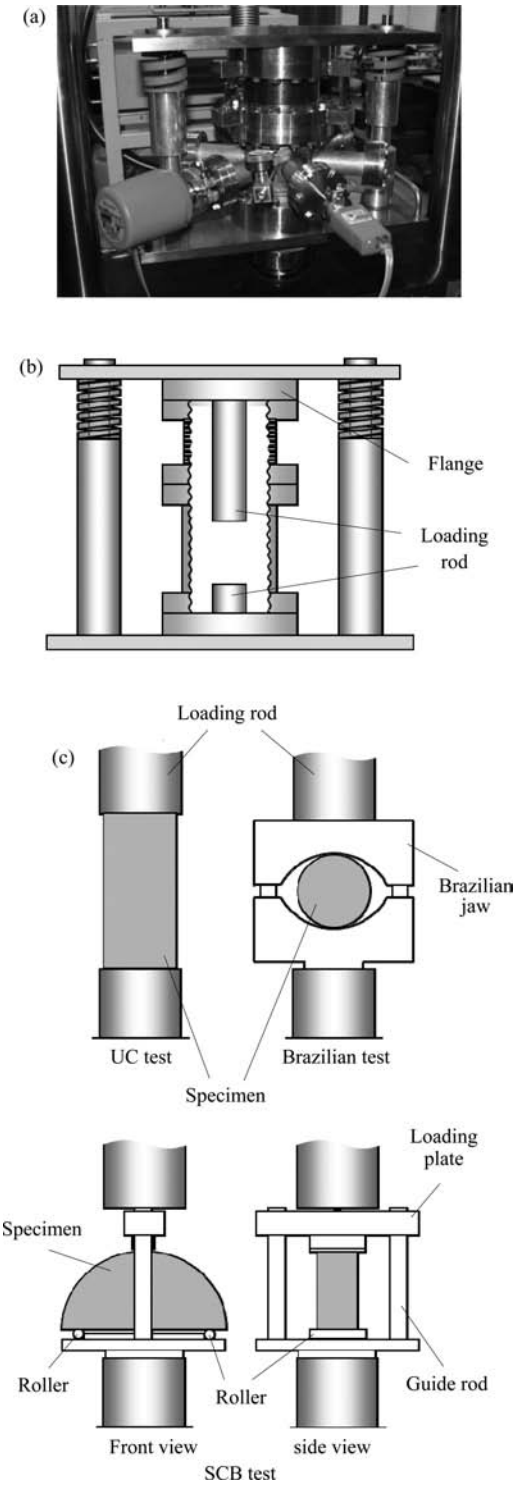


Figure 2. Vacuum chamber: (a) View, (b) Schematic view of inside, (c) Setup of specimen for UC, Brazilian and SCB tests.

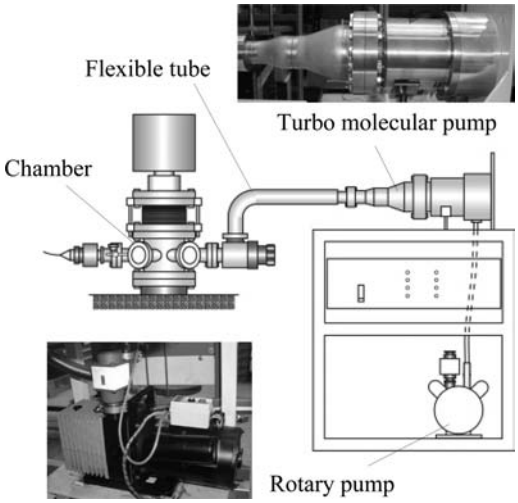


Figure 3. Evacuation system.

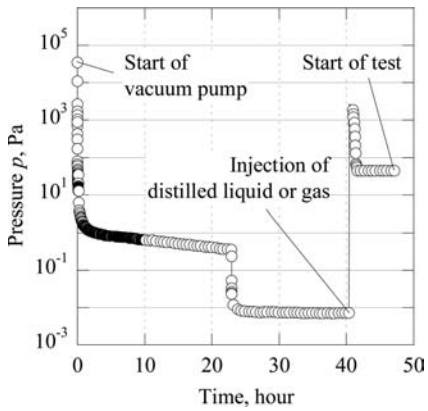


Figure 4. Change of pressure in the chamber.

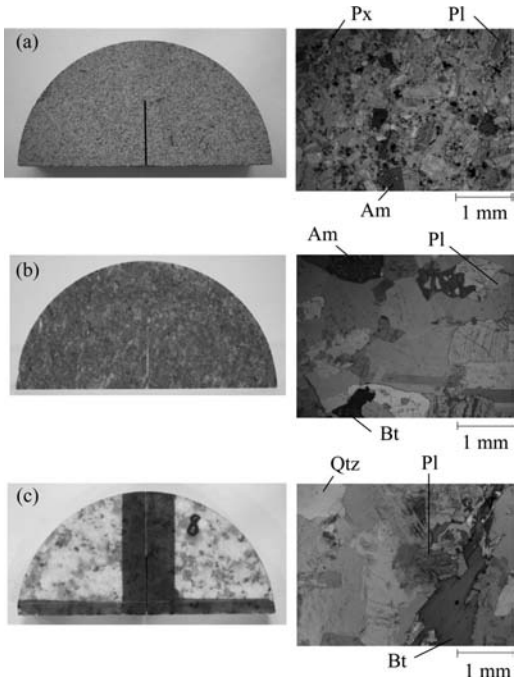


Figure 5. Photographs of SCB specimen and its thin section (open nicol): (a) Kumamoto andesite (KA), (b) African granodiorite (AG), (c) Korean granite (KG): in thin section, Px: Pyroxene, Pl: Plagioclase, Am: Amphibole, Bt: Biotite, Qtz: Quartz.

Table 1. Elastic wave velocity and defined axes.

	Elastic wave velocity, m/s		
African granodiorite (AG)	6760	6580	6540
Korean granite (KG)	2640	2590	2580
	Axis-1	Axis-2	Axis-3

becomes the saturated vapor or gas pressure at room temperature and the chamber is filled with only the vapor or gas. Then the vapor or gas pressure in the chamber is modulated to a test condition by the evacuation system. Having the required pressure maintained for about 6 hours, the test is conducted.

3 SPECIMEN

3.1 *Preparation of specimen*

The rocks used in this paper were Kumamoto andesite (KA), African granodiorite (AG) and Korean granite (KG) shown in Figure 5. These rock blocks were tested for elastic wave velocity in three normal directions. For KA, the three directions are almost the the same velocity of approximately 4500 m/s (Obara et al. 1992). On the other hand, AG and KG have anisotropic properties of the velocity as shown in Table 1. Then the directions were defined as Axis-1, Axis-2 and Axis-3 in order of the velocity. The velocity in the direction of Axis-1 is higher than that in the other two directions for both rocks. These results show that the direction of Axis-1 has lower resistance to the wave propagation.

The size of the specimen is 35 mm in diameter and 70 mm in length for the UC test and 35 mm in diameter and 20 mm in thickness for the Brazilian test. For preparation of the SCB specimen, a disk of 75 mm in diameter and 20 mm in thickness was cut into halves. Then an artificial notch was made by a diamond blade with a thickness of 0.4 mm. The size of SCB specimen is: $r = 37.5$ mm, $t = 20$ mm and $a/r = 0.5$ where r, t and a are defined in Figure 1. The specimens were prepared from arbitrary direction for KA. On the other hand, two types of SCB specimen were prepared for AG and KG, namely Type-1 and Type-3 as shown in Figure 6. The figure of the type represents the direction of the artificial notch.

It is necessary that water in the specimen is removed to investigate influence of the surrounding environment of the specimen. In order to achieve complete

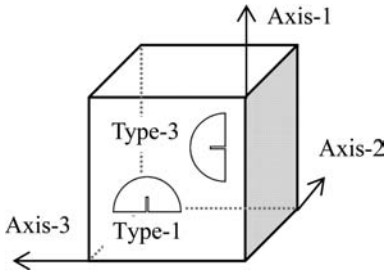


Figure 6. Definition of axes and orientation of SCB specimens: Axis-1 is the direction of the fastest elastic wave velocity, Axis-2 is intermediate and Axis-3 is the lowest.

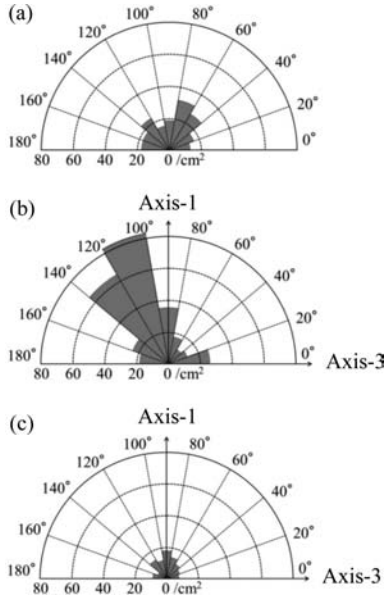


Figure 7. Micro crack density in rose diagram: (a) Kumamoto andesite (KA), (b) African granodiorite (AG), (c) Korean granite (KG).

dry condition of the specimens, they were kept in an electric drier oven at more than 100°C for about 80 days for UC specimen, 30 days for Brazilian specimen SCB specimen before the tests.

3.2 *Observation of thin section*

Observation of thin sections was performed using a polarization microscope. Figure 5 shows photographs of the thin section for the rocks. The thin section was prepared in arbitrary plane for KA. On the other hand, it was in the plane normal to Axis-2 for AG and KG.

In order to make clear distribution of inherent micro cracks, the direction of each micro crack was measured. Then its density in the direction, that is number per unit area, was drawn in rose diagrams with an interval of 20 degrees as shown in Figure 7. The densities are similar to each direction for KA and KG. On the other hand, many micro cracks are almost oriented to the direction of Axis-1 for AG. It shows that the inherent micro cracks are rather oriented normal to Axis-3 for AG and the tendency of the results is the same as the measurement of elastic wave velocity described above.

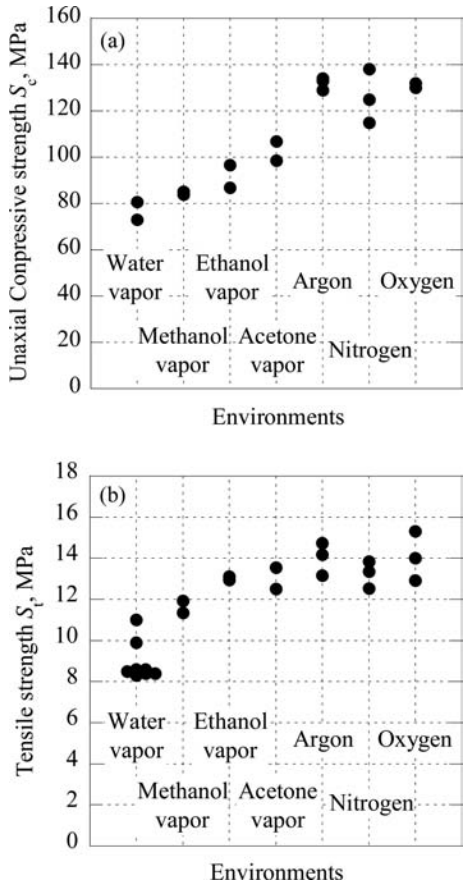


Figure 8. Influence of surrounding environments on (a) UC strength and (b) tensile strength.

4 RESULTS AND DISCUSSION

4.1 *Effect of surrounding environment on uniaxial compressive strength and tensile strength of rock*

The UC strength and the tensile strength of each environment are shown in Figure 8. UC test and Brazilian test were performed in 7 kinds of surrounding environments, namely water vapor, organic vapors and inorganic gases. The vapor or gas pressure in the chamber is approximately 10^3 Pa. Two to eight specimens of KA were used in the test under each environment.

As the results shown in Figure 8(a), the UC strength in inorganic environments of argon, nitrogen and oxygen is greater than the others and decrease in order of acetone, ethanol, methanol and water vapor environments. The average of the strength in inorganic

environments is 1.7 times of that in water vapor environment. The results in Figure 8(b) shows that the tensile strength in water vapor environment is the lowest and others are similar although that in methanol vapor is slightly low. The average strength in inorganic environments is 1.5 times of that in water vapor of the lowest strength.

The decrease of the strengths is considered to be due to stress corrosion. The stress corrosion is the reaction between strained silicate minerals and environmental agent at a crack tip in rocks. The surface energy of a crack tip is dropped due to the stress corrosion so that cracks propagate easier. The reaction of the stress corrosion is represented by the following equation:

$$\mathrm{H\text{-}O\text{-}H} + [\equiv \mathrm{Si\text{-}O\text{-}Si}] \;\Leftrightarrow\; 2[\equiv \mathrm{Si\text{-}OH}] \qquad (2)$$

This is the chemical reaction of hydroxyl groups and Si-O bonds at a crack tip (Scholz 1972, Freiman 1984). According to this reaction, it is clear that the stress corrosion in water vapor environment is the most effective agent on the strengths of rocks. Moreover, the stress corrosion cannot occur in inorganic environment since there are no hydroxyl groups in inorganic gases.

The molecule of methanol and ethanol has hydroxyl groups. The silica is essentially insoluble in methanol and ethanol under standard conditions (Iler 1979). However, since the energy state at the crack tip is considered to be very high under loading, the following reaction may take place in these environments:

$$\mathrm{SiO_2} + 4\mathrm{CH_3OH} \rightarrow \mathrm{Si(OCH_3)_4} + 2\mathrm{H_2O} \qquad (3)$$

$$\mathrm{SiO_2} + 4\mathrm{C_2H_5OH} \rightarrow \mathrm{Si(OC_2H_5)_4} + 2\mathrm{H_2O} \qquad (4)$$

Water is generated from this reaction and is used for the reaction of stress corrosion represented by the reaction (2).

Therefore it is considered that the strengths are the lowest in water vapor environment and the highest in inorganic environment and that strengths in alcohol environments exist between those. It is concluded that water is the most effective agent which promotes stress corrosion of rock and that the strengths are influenced by the stress corrosion.

4.2 *Effect of water vapor pressure on uniaxial compressive strength, tensile strength and fracture toughness of rock*

A series of UC tests, Brazilian tests and SCB tests were conducted under water vapor environment. 10 specimens of KA were used in UC test and Brazilian test. In SCB test, 9 specimens for KA, 25 specimens for AG and 32 specimens for KG were used. The range of water vapor pressure in the test was from 4.2×10^{-3} to 1.2×10^{3} Pa.

The relations between (a) UC strength S_c, (b) tensile strength S_t and (c) fracture toughness K_{IC} and water vapor pressure p is shown in Figure 9. These strengths vary almost linearly against the water vapor pressure

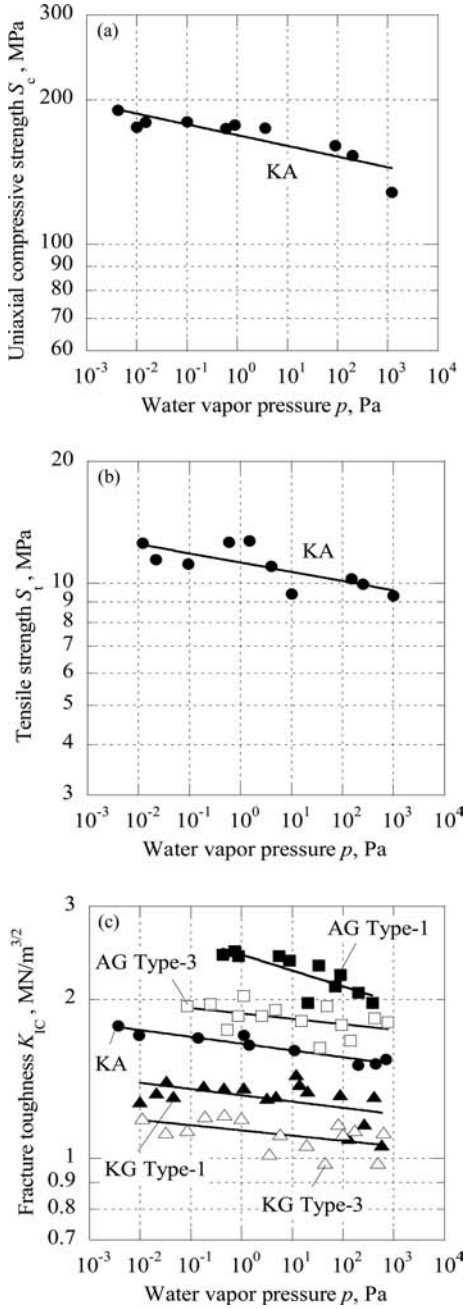


Figure 9. Relations between (a) uniaxial compressive strength, (b) tensile strength, (c) fracture toughness and water vapor pressure.

on the logarithmic graphs. The strengths decrease with increasing the water vapor pressure. Lines drawn using the least square approximation are also shown in each strength and each kind of rocks. The equation of the lines is represented as:

$$S_c, S_t, K_{IC} = \beta p^{-m} \qquad (5)$$

where β is a constant and m is an inclination of the line. The parameter m is considered to represent the degree of stress corrosion and its values are: 0.0223 for the UC strength, 0.0227 for the tensile strength and 0.0129 for the fracture toughness in KA and 0.0301 for Type-1, 0.0102 for Type-3 in AG, 0.0119 for Type-1 and 0.0098 for Type-3 in KG for the fracture toughness. As the results, the values for the UC strength and tensile strength are almost the same in KA. For the fracture toughness, that of AG Type-1 is larger than the others. Therefore the influence of the water vapor pressure on the fracture toughness for Type-1 of AG is stronger. Moreover, the values of the fracture toughness of Type-1 are larger than that of Type-3 through the whole range of the water vapor pressure for AG and KG. Both rocks have anisotropic properties of the fracture toughness.

The decrease of the strengths is due to the stress corrosion promoted by water vapor as described above. It is found that not only the UC strength and tensile strength but also the fracture toughness is influenced by the stress corrosion.

For the fracture toughness, the m values are almost the same although that for AG Type-1 is greater. As the results described in Sections 3, the density of inherent micro cracks oriented to Axis-1 for AG is greater. The stress corrosion is the reaction occurred at a crack tip in rocks. The effect of the stress corrosion on inherent micro cracks can be more severe. Therefore the resistance to crack propagation decreases rapidly in the case that the water vapor pressure is increasing. It is concluded that the stress corrosion has a sensibility for the orientation and the distribution of inherent micro cracks and that the m value is dependent on the inherent micro crack density.

5 CONCLUSIONS

In this paper, firstly, uniaxial compression test and Brazilian test were conducted on Kumamoto andesite to investigate the influence of surrounding non-atmospheric environments on the uniaxial compressive strength and the tensile strength. Then the fracture toughness of the andesite, African granodiorite and Korean granite was estimated under water vapor environment to investigate the influence of the water vapor in the surrounding environment on these strengths. The obtained results are summarized as follows:

1) The uniaxial compressive strength and the tensile strength were independent on inorganic environments and the lowest in water vapor environment;
2) Water vapor is the most effective environment which promotes stress corrosion of rocks and the strengths of rocks decreases due to the stress corrosion;
3) The uniaxial compressive strength, the tensile strength and the fracture toughness of rocks are dependent on the water vapor pressure in the surrounding environment and decrease with increasing the water vapor pressure. The sensitivity of the influence is dependent on the orientation and the density of inherent micro cracks of the rocks.

REFERENCES

Atkinson, B.K. & Meredith, P.G 1979. The theory of subcritical crack growth with applications to minerals and rocks. In B.K. Atkinson (ed.), *Fracture Mechanics of Rock*: 111–166. London: Academic Press.

Bieniawski, Z.T. & Bernede, M.J. 1978. Suggested methods for determining tensile strength of rock materials. *Int. J. Rock Mech. Min. Sci.* 15: 99–103.

Chong, K.P. & Kuruppu, M.D. 1984. New specimen for fracture toughness determination for rock and other materials. *Int. J. Fract.* 26: 59–62.

Freiman SW. 1984. Effects of chemical environments on slow crack growth in glasses and ceramics *J Geophys Res* 89: 4072–4076.

Iler, R.K. 1979. *The Chemistry of Silica: Solubility, Polymerization, Colloid and Surface Properties, and Biochemistry.* New York: Wiley-Interscience Publication.

Jeong, H.S., Kang, S.S., & Obara, Y. 2007. Influence of surrounding environments and strain rates on strength of rocks under uniaxial compression. *Int. J. Rock Mech. Min. Sci.* 44: 321–331.

Kataoka, M., Obara, Y. & Kuruppu, M. 2011. Estimation of fracture toughness of anisotropic rocks by SCB test and visualization of fracture by means of X-ray CT. In Q. Qian & Y. Zhou (eds), *Harmonising Rock Engineering and the Environment, Proceedings of the 12th International Congress on Rock Mechanics*: 667–670. Leiden: CRC Press/Balkema.

Kuruppu, M.D., Obara, Y., Ayatollahi, M.R., Chong, K.P. & Funatsu, T. ISRM suggested method for determining the mode I static fracture toughness using semi-circular bend specimen. (in press)

Lim, I.L., Johnston, I.W., Choi, S.K. & Boland, J.N. 1994. Fracture testing of a soft rock with semi-circular specimens under three-point bending, Part 1-mode I. *Int. J. Rock Mech. Min. Sci. & Geomech. Abstr.* 31(3): 185–197.

Obara, Y., Sakaguchi, K., Nakayama, T. & Sugawara, K. 1992. Anisotropy effect on fracture toughness of rock. In J.A. Hudson (ed.), *Rock Characterization, Proc. ISRM Symp. Eurock '92, Chester, UK*: 7–12. London: British Geotechnical Society.

Scholz, C.H. 1972. Static fatigue of quartz. *J Geophys. Res* 86: 9299–9311.

Rock Mechanics for Resources, Energy and Environment – Kwaśniewski & Łydżba (eds)
© 2013 Taylor & Francis Group, London, ISBN 978-1-138-00080-3

Susceptibility of rock materials used in the construction of monuments to long-term salt crystallization

A.K. Kłopotowska & P.J. Łukaszewski
Department of Geomechanics, Faculty of Geology, University of Warsaw, Warsaw, Poland

ABSTRACT: The paper takes the issue of susceptibility of rock materials used in historic and contemporary buildings to long-term salt crystallization. The influence of long-term action of salt crystallizing from water solutions on the rock material was studied by means of artificial accelerated aging tests. Out of the rock materials used in stone engineering objects two lithological types were chosen, which represent the sedimentary clastic rocks. The result of the performed tests were the structural changes, stress and strain changes as well as mass changes which occurred under influence of a temporary action of selected destructive factor. The quality assessment of deterioration was conducted through macro- and microscopic observations and the quantitative changes were determined on the basis of indicative assessment of geomechanical parameters that distinguishes the primary rock from the damaged one.

1 INRODUCTION

One of the most common and extensive sources of deterioration of stone is the consequence of crystallization phenomena that take place in pores and cracks at near exposed surfaces. The greatest damage of stone monuments is caused by salts crystallizing at variable amounts of crystallization water when the temperature that determines the transformations is within the ambient temperatures. Some easily soluble sulfates, which often occur in the monuments also, have this ability. As a result of water evaporation, these salts deposit in the pores as hydrates: mirabilite – $Na_2SO_4 \times 10H_2O$, epsomite – $MgSO_4 \times 7H_2O$, gypsum – $CaSO_4 \times 2H_2O$. For the salts in anhydrous or hydrated state the transition from one state to another is dependent on the temperature and the relative humidity of the air.

The commonly found in buildings sodium sulfate, which comes from rain and ground water as well as from cement binding the individual architectural details, is one of the most damaging salts. At temperatures above 32.4°C the sodium sulfate crystallizes in an anhydrous form (Na_2S0_4 – thenardite). At lower temperatures it crystallizes first in the form with 7 molecules of water ($Na_2S0_4 \times 7H_2O$) and below 24.3°C the amount of crystallization water increases to 10 molecules ($Na_2S0_4 \times lOH_2O$ – mirabilite). These transformations are accompanied by one of the biggest changes in volume, which in the case of the transition of sulfate from the anhydrous to the decahydrate form is about 400% (Domasłowski 1993, Jarmontowicz et al. 1994).

2 CHARACTERIZATION OF THE ROCK MATERIALS

The research materials were sandstones from Śmiłów and Żerkowice often used in monumental buildings.

The analyzed sandstones from Śmiłów exploited in the Świętokrzyski region are characterized by a very fine/fine- and equigranular structure (Fig. 1a). The placement of the rock components is random and undirected. There are numerous and well communicating with each other pores visible in the microscopic image. The dominant component of the rock is quartz with well sorted grains of mostly isometric type ranging in size from 0.08–0.16 mm. The quartz grains are partially regenerated and covered with more and less complete regenerative overgrowths. Other components of the rock are fragments of quartz rocks, small and elongated plates of mica (muscovite) and a few grains of feldspars. Small and rounded grains of zircon and tourmaline also occur occasionally. All detrital components are conglomerated by poor silica-clay cement that fills only a part of the intergranular space. Clay cement occurs locally in form of irregular clusters of small plates/packets of kaolinite as well as clusters of a dark brown iron-clay substance. According to the classification by Pettijohn the discussed rocks were identified as the quartz arenite.

The analyzed sandstones from Żerkowice, exploited in the north Sudeten depression, are characterized by a fine- and equigranural structure and disordered texture (Fig. 1b). The composition of the rock is dominated by well separated, poorly or average rounded, detrital

quartz grains of irregular and isometric type, ranging in size from 0.12 to 0.20 mm. Small amounts of polycrystalline quartz, fragments of quartz rocks, elongated plates of muscovite and grains of partially transformed feldspars. Among the accessory components, small grains of zircon and tourmaline as well as oxides of Fe and Ti can be distinguished. Detrital components are conglomerated rarely occurring silica-clay cement that fills only a small part of the intergranular space. Occasionally – small, irregular clusters consisting of small plate packets of kaolinite as well as clusters of a yellow-brown iron-clay substance occur. According to the classification by Pettijohn the discussed rocks were identified as the quartz arenite.

The mineralogical differentiation of the studied rocks is reflected in the physical and mechanical properties, which have been identified in Table 1.

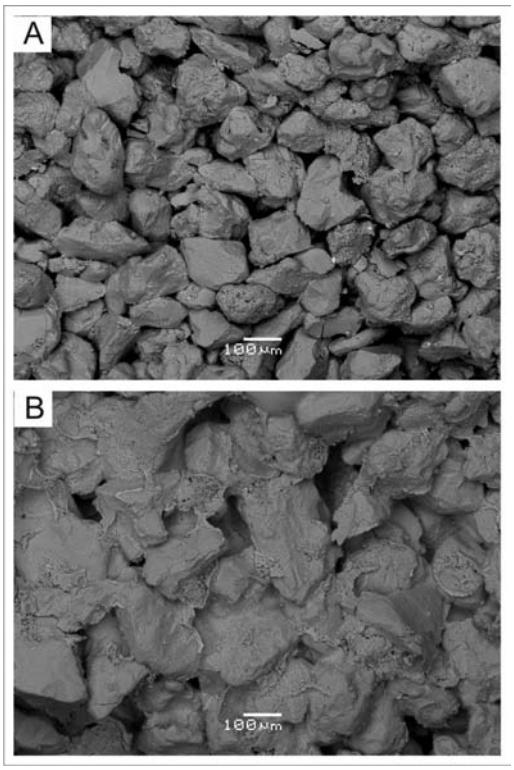


Figure 1. SEM images of the structure of analyzed sandstone before the treatment: a) sandstone from Śmiłów; b) sandstone from Żerkowice.

3 METHODS

The determination of resistance to salt crystallization was performed on the basis of the PL-EN 12370-2001 standard. After the samples had been dried and weighed, they were immersed in a 14% decahydrate solution of sodium sulfate for 2 hours. Then they were dried for 18 hours gradually increasing the temperature at initially high relative humidity. The drying temperature was modified to 70°C, whereas the temperature recommended by the PL-EN 12370-2001 standard is 105°C. It is due to the fact that the maximum temperature for stones used in monumental buildings under natural conditions is about 70°C even when they are dark and exposed to a strong and direct sunlight. Afterwards, the samples were saturated again with sodium sulfate. The saturating and drying cycle was repeated 15 times. Diagram of the study is presented in Figure 2.

After all the cycles had been performed, the samples were immersed in water for 24 hours and then they were washed under running water, dried and weighed. The results are shown in percents as a relative weight difference (weight loss or gain) in relation to the initial dry weight of the sample according to the formula:

$$\Delta m = \left(\frac{m_a - m_b}{m_b} \right) \quad (1)$$

where m_b – weight of the dry sample before the test (g); m_a – weight of the dry sample after the test (g).

While performing the tests, the longitudinal wave propagation velocity was recorded (Vp). Changes of

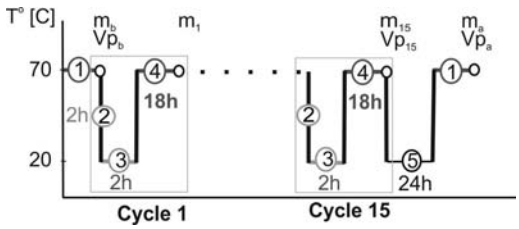


Figure 2. Diagram of the study: 1- drying to a constant weight, 2- cooling to a room temperature, 3- immersion in a 14% solution of sodium sulfate, 4- drying, 5- immersion in distilled water.

Table 1. Physical and mechanical properties of the studied rocks.

Type of stone	Bulk density* kg/m^3	Apparent (skeletal) density* kg/m^3	Effective porosity* %	Hysteresis* %	Longitudinal wave velocity m/s	Uniaxial compressive strength MPa
Sandstone from Śmiłów	2070	2620	20.8	18	2598–2894	47–69
Sandstone from Żerkowice	1960	2640	25.7	5	3694–3808	49–52

*result of the mercury intrusion porosimetry.

the longitudinal wave velocity in relation to the initial longitudinal wave velocity of a dry sample were determined according to the

$$\Delta Vp = \left(\frac{Vp_x - Vp_b}{Vp_b} \right) * 100\% \quad (2)$$

where Vp_b – longitudinal wave velocity of a dry sample before test [m/s] and Vp_x – longitudinal wave velocity of a dry sample during test [m/s].

Changes in the properties of the rock under influence of salt crystallizing from water solutions in the modeled test were described with an acoustic integrity index (I_s). This index describes the change of the longitudinal wave velocity recorded for the material after the action of sodium sulfate in reference to the longitudinal wave velocity measured in air-dry state (before the test) and it is designated by a general formula:

$$I_s = \left(\frac{Vp_a}{Vp_b} \right)^2 \quad (3)$$

where I_s – index of the longitudinal wave velocity change after the action of sodium sulfate [–]; Vp_a – longitudinal wave propagation velocity after test [m/s] and Vp_b – longitudinal wave propagation velocity before the test (in the air-dry state) [m/s].

After the modeling of the action of sodium sulfate from water solutions, the samples were subjected to the uniaxial compressive strength test. The test was performed in the stiff loading machine MTS-815 in reference to the Polish standard PN-EN 1926: 2007 and suggestions of ISRM. Based on the acquired values of Rc, the coefficient of resistance (w_S) to salt crystallizing was determined according to a general formula:

$$w_s = \frac{Rc_a}{Rc_b} \quad (4)$$

where w_s – coefficient of resistance to salt crystallizing [–]; Rc_a – uniaxial compressive strength of a sample after completing the test of resistance to salt crystallizing [MPa] and Rc_b – uniaxial compressive strength of a sample before test in the natural state [MPa].

In order to illustrate the microstructural changes, the additional observations under the scanning electron microscope (SEM) were performed after the tests have been finished, that is after the final rinsing with water. The monitoring of changes was performed on the samples sprayed with gold. The recognition of the chemical composition of the crystallized minerals was performed using Energy Dispersive X-Ray Spectroscopy (EDS).

4 RESULTS

As the result of the performed tests for the crystallization of sodium sulfate, the clear differences in behavior of the both analyzed sandstone types have been found (Fig. 3). The progressive deterioration was more visible in the case of the sandstone from Śmiłów. The loss of mineral grains resulting in formation of cavities on the surface of the sandstone was observed. In many places, the surface layer was sugaring. Initially sharp and clear edges became rounded. In the case of the sandstone from Żerkowice only the rounded edges were observed.

The nucleation of the salt crystals from the solution during repeated hydration and dehydration of the sodium sulfate (mirabilite-thenardite-mirabilite) caused the relaxation of the structure and the formation of internal defects in the rock material. The greatest destruction occurred during the successive cycles of immersing the samples in a salt solution, during which the hydration of the crystallized in the course of drying anhydrous sodium sulfate took place. It resulted in the increase of the salt volume and consequently in generating a destructive pressure. Many scientists (Winkler & Wilhelm 1970, Tsui et al. 2003, Steiger & Asmussen 2008) claim, that the pressure associated with the phase transformation of the salt from anhydrous into hydrated is much larger and more abrupt than the crystallization pressure of an anhydrous salt (e.g. thenardite).

Observations under the scanning electron microscope (SEM) after the tests had been finished showed the presence of numerous thenardite crystals that formed aggregates both on the surface as well as in the porous space of the examined sandstones. The porous space, after the final rinsing with water, showed signs of strong disintegration and the loss of cement (Fig. 4).

This phenomenon was more visible in the case of the sandstone from Śmiłów. In both sandstones, the observed thenardite crystals usually took isometric and spheroidal forms (Fig. 5a); however feathery and granulose forms were also observed. Among other forms of thenardite found in the analyzed sandstones also the dendroid forms created by elongated crystals were observed (Fig. 5b). In the SEM image mainly of the surfaces of the samples from Żerkowice, the tabular or needle gypsum crystals often embedded in the thenardite aggregates were observed.

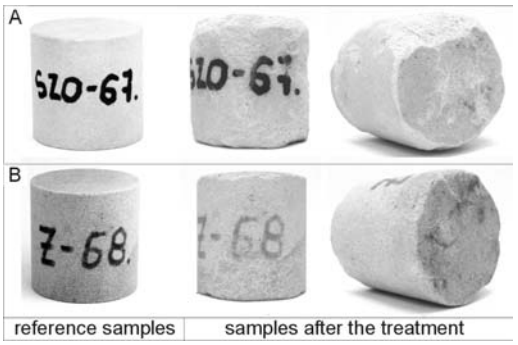


Figure 3. The appearance of the samples after completing the test of resistance to salt crystallization: a) sandstone from Śmiłów; b) sandstone from Żerkowice.

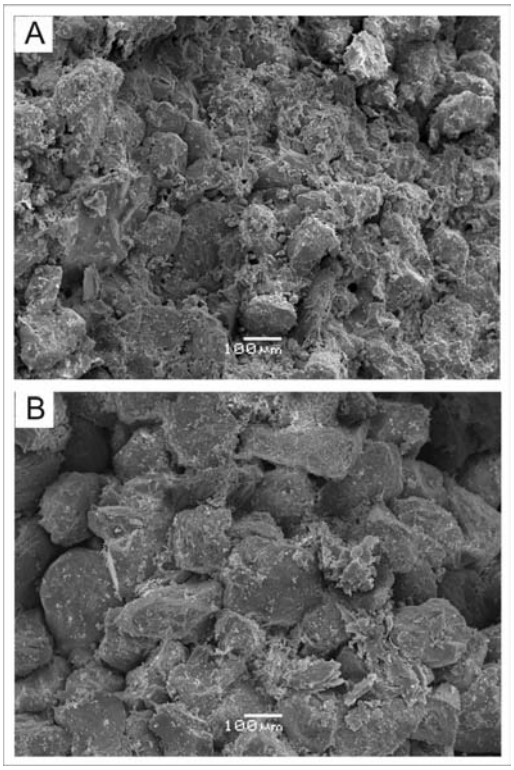


Figure 4. SEM images of the structure of analyzed sandstones after the treatment: a) sandstone from Śmiłów; b) sandstone from Żerkowice.

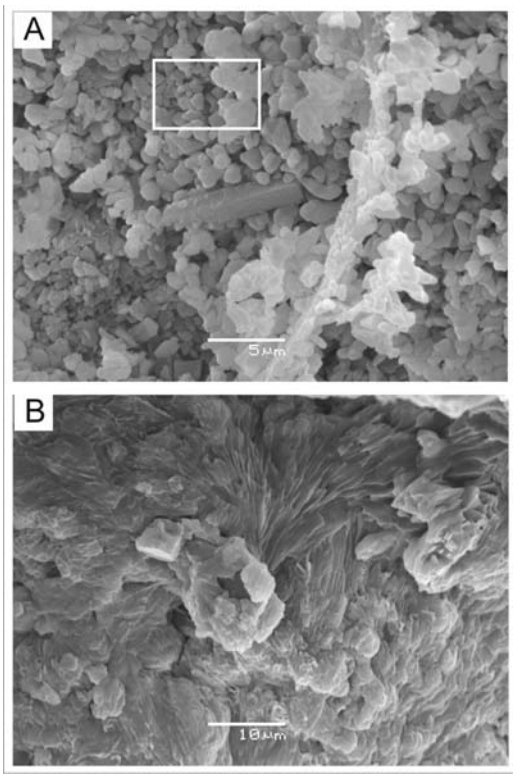


Figure 5. SEM images of the structure of analyzed sandstones after the treatment: a) isometric, spheroidal crystals of thenardite in form of aggregates hermetically filling the porous space; b) dendroid forms created by elongated crystals of thenardite.

After the samples had been rinsed with water and dried to a constant weight, for all samples treated with the sodium sulfate the weight loss was recorded. It was relatively small for the sandstones from Żerkowice and ranged from 0.2 to 0.6%, whereas it was quite significant for the sandstones from Śmiłów, in which the weight loss ranged from 2.6 to 7.3%. The comparison of the average weight loss values during the described accelerated aging tests for the sandstones from Żerkowice and Śmiłów is presented in Figure 7.

The cyclic ultrasonic measurements carried out during the accelerated aging tests indicate that the crystallizing from a solution sodium sulfate results in the decrease of the longitudinal wave in the sandstones from Śmiłów ranges from 2% to 7% (Fig. 8a). In the case of the sandstones from Żerkowice both a small increase as well as a decrease of the longitudinal wave velocity was recorded and the values were similar to those obtained under air-dry conditions (Fig. 8b).

The values of the integrity index (I_S) calculated on the basis of the longitudinal wave velocity changes in the samples treated with the sodium sulfate also clearly differentiate the analyzed sandstones (Fig. 9). The values of the index that are close to 1 indicate, that the sandstones from Żerkowice are resistant to the crystallization of sodium sulfate, whereas the values between 0.88–0.92 obtained for the sandstones from Śmiłów

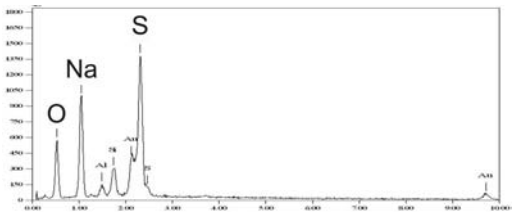


Figure 6. Energy dispersive spectrum (EDS) of thenardite form (white rectangle in the Figure 5).

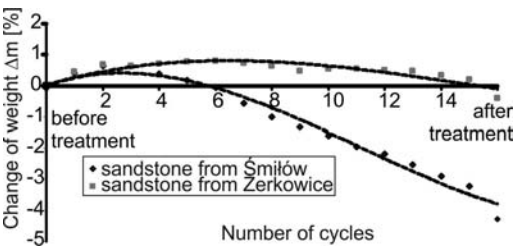


Figure 7. Change of mass during the test of salt crystallization.

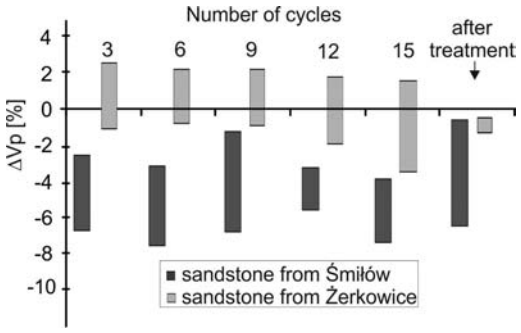


Figure 8. Change of longitudinal wave velocity during the test of salt crystallization.

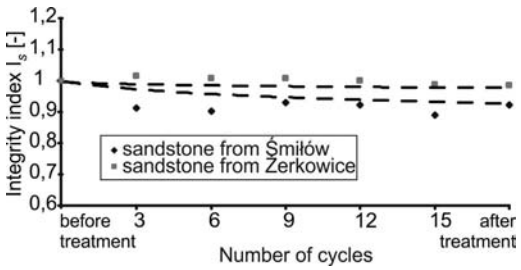


Figure 9. Average values of the integrity index during the test of salt crystallization.

confirm their lower resistance to the crystallization of the sodium sulfate.

The process of the salt crystallization in the porous space leads to the reduction of the uniaxial compressive strength both in the case of the sandstone from Śmiłów as well as from Żerkowice with regard to the resistance of these rocks in the air-dry state. However it must be noted that in the case of the sandstones from Śmiłów the coefficient of resistance to the crystallization of salt was on average 0.59, whereas in the case of the sandstones from Żerkowice it was 0.91.

5 CONCLUSIONS

The performed accelerated aging tests indicated, that the sodium sulfate crystallizing from a solution does not cause significant changes in the appearance of the sandstone from Żerkowice, whereas in the case of the sandstone from Śmiłów the nucleation of salt leads to the relaxation of the structure and the formation of internal defects that are visible in the SEM image, which consequently causes the surface layers of the stone to come off and the granular disintegration of the material. The reason for such a different responses to sodium sulfate may be the pore size distribution. As the porosimetry studies have shown, the both sandstones are rocks with a high effective porosity of about 21–26%. However, the sizes of hysteresis of the curves of the increasing and the decreasing pressures are significantly different in the two types of rocks. The research shows that the sandstone from Żerkowice has a very low hysteresis (5%), reflecting the cylindrical shape of the pores in the rock. This model allows the free flow of water in the rock, reducing the probability of the salt crystallization in the pores (Labus 2009). However, the pressure generated by the crystallization of salt in the porous space resulted in lower mechanical resistance to compression both in the case of the sandstones from Żerkowice, as well as from Śmiłów. All the performed tests indicate that the sandstones from Żerkowice are characterized by the resistance to the salt crystallization and the sandstones from Śmiłów do not have this feature. Although none of the samples of the sandstone from Śmiłów was completely damaged during the testing, however the weight loss of up to 7% is very significant.

REFERENCES

Domasłowski, W. 1993. (eds) Profilaktyczna konserwacja kamiennych obiektów zabytkowych. Wydawnictwo UMK. Toruń: 1–253.

Fairhurst, C.E. & Hudson, J.A. 1999. Draft ISRM suggested method for the complete stress-strain curve for intact rock in uniaxial compression, *International Journal of Rock Mechanics and Mining Sciences* 36: 279–289.

Jarmontowicz, A., Krzywobłocka-Laurów, R. & Lehmann, J. 1994. Piaskowiec w zabytkowej architekturze i rzeźbie. Wydanie 1. Biblioteka Towarzystwa Opieki nad Zabytkami. Warszawa: 1–88.

Labus, M. 2009. Parametry porozymetryczne górnokredowych piaskowców ciosowych jako czynnik warunkujący ich odporność na wietrzenie. Geologia: Kwartalnik Akademii Górniczo-Hutniczej 35(2): 263–275.

Polska Norma PN-EN 1926, 2007. Metody badań kamienia naturalnego. *Oznaczenie wytrzymałości na ściskanie*. PKNiM. Warszawa.

Polska Norma PN-EN 12370, 2001. Metody badań kamienia naturalnego. *Oznaczenie odporności na krystalizację soli*. PKNiM. Warszawa.

Steiger, M. & Asmussen, S. 2008. Crystallization of sodium sulfate phases in porous materials: The phase diagram Na_2SO_4–H_2O and the generation of stress, *Geochimica et Cosmochimica Acta* 72: 4291–4306.

Tsui, N., Flatt, R.J. & Scherer, G.W. 2003. Crystallization damage by sodium sulfate. *Journal of Cultural Heritage* 4: 109–115.

Winkler, E.M. & Wilhelm, E.J. 1970. Salt burst by hydration pressures in architectural stones in urban atmosphere, *Geological Society of America Bulletin* 81: 567–572.

This page intentionally left blank

Rock Mechanics for Resources, Energy and Environment – Kwaśniewski & Łydżba (eds)
© 2013 Taylor & Francis Group, London, ISBN 978-1-138-00080-3

Beachrock mapping by geophysical exploration: Application to Yagaji Island in Okinawa, Japan

R. Kubo & S. Kawasaki
Hokkaido University, Sapporo, Japan

K. Suzuki
Central Research Institute of Electric Power Industry, Abiko, Japan

S. Yamaguchi
Nihon Chikatansa, Osaka, Japan

T. Hata
Toyama Prefectural University, Imizu, Japan

ABSTRACT: Beachrock, a type of sedimentary bedrock composed of beach deposits, is expected to restrain coastal erosion by preventing the outflow of sand. To artificially create beachrocks, we need data on the chemical and physical properties of this rock. In this study, we conducted a Direct Current (DC) electrical survey and a seismic surface wave survey to investigate the underground structures of the beachrock in Yagaji Island, Okinawa, Japan. In order to estimate the effectiveness of the geophysical surveys, we conducted laboratory tests to measure the resistivity, the shear wave velocity, and the porosity of beachrock samples collected from the study site. On the basis of these results, we estimated the beachrock structure as follows: The beachrock is detected as a high resistivity and high velocity zone, which is 1–2 m thick. A sand layer under the beachrock is represented as a low resistivity and low velocity zone.

1 INTRODUCTION

Sea-level rises, triggered by global heating, cause coastal erosion owing to the outflow of sand across the world. Concrete armor units have been used as a revetment for preventing coastal erosion, but this method has the drawback that it affects the environment and landscape adversely. In addition, the continuing decline in the expenditure on Japanese public works projects means that new methods of bank protection are required to minimize the maintenance and operation cost of such projects. For the above reasons, we studied the formation process of beachrocks to develop a new method of bank protection that has the ability to repair itself.

Beachrock is a type of sedimentary formation that generally occurs in tropical and subtropical beaches as result of intertidal lithification of loose beach sands and gravels by carbonate cementation (Ginsburg 1953) (Fig. 1). The cement materials of beachrocks are mainly high-magnesium calcite and aragonite. The most widely held theory of is that the deposition of $CaCO_3$ between coral sand and gravel by evaporation of seawater leads to the formation of bedrocks (Ginsburg 1953). Bedrocks are formed over a long period of time, but it has been reported that the formation periods of some beachrocks were only a few

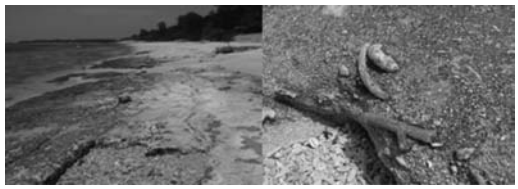


Figure 1. Beachrocks.

decades (Danjo & Kawasaki 2012). Many studies, both in Japan and in other countries, have reported on beachrocks, but the majority of these studiesfocused on their geochemistry. In particular, the underground structures of beachrocks are not yet well understood. One of the few studies of this aspect focused on the application of electrical resistivity tomography to map the beachrocks in Thassos Island, Greece, by Psomiadis et al. (2009). In spite of the general claim that it is absolutely imperative to comprehend beachrocks' underground structures to elucidate its formation process, existing research has been restricted to areas around the surface of seashores out of consideration for avoiding damage to the landscape from boring exploration. In this study, we conducted a seismic surface wave survey and a DC electrical survey in Yagaji Island, Okinawa, Japan. To the best of our

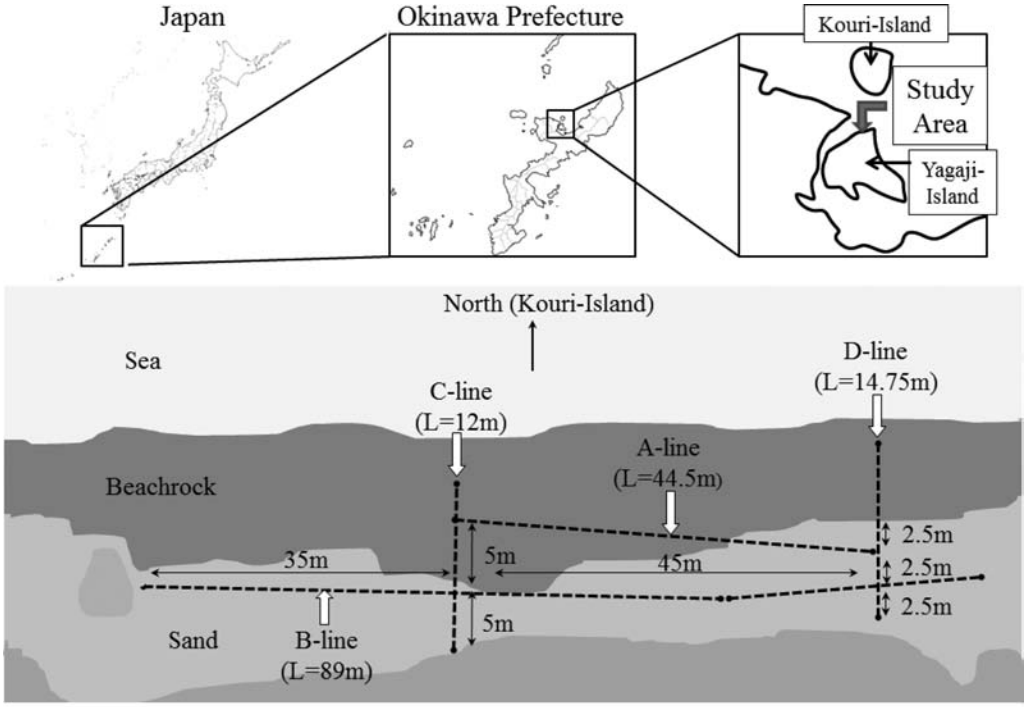


Figure 2. A location map of the survey lines and beachrock.

knowledge, this is the world's first report on the mapping of the underground structures of beachrocks by more than one geophysical exploration method. A view of the underground structure around the seashore up to a depth of more than 10 m was obtained through these surveys. Laboratory tests were conducted to measure the resistivity, S wave velocity, and porosity of the beachrock samples gathered from the study site to estimate the effectiveness of surveys. Its underground structures were estimated by comparing the resistivity sections, the S wave velocity sections, and the values measured in the laboratory tests. Furthermore, this study addresses the effectiveness of geophysical exploration methods to comprehend the underground structures of beachrocks.

2 STUDY AREA

The study site is located on the north coast of Yagaji Island and to the west of Kouri bridge (see Figure 1). Yagaji Island is one of a number of islands located in the northern part of Okinawa Prefecture, Japan. Okinawa Prefecture is an island that lies in the subtropical zone between the Pacific and the East China Sea. The bedrock comprises old limestone and volcanic rocks. The upper bedrock is composed of sand, shingle, and coral reef deposits. Beachrocks extend up to about 100 m in the east-west direction and about 10 m in the north-south direction in this site. According to Omoto (2007), the sea level of this area has not changed for about 1000 years. The inclination of the beachrocks is about 3° towards the sea.

In the seismic surface wave survey as well as the DC electrical survey, two survey lines (A- and B-lines) were set horizontal to the seashore, and two lines (C- and D-lines) were set perpendicular to the seashore (Fig. 2). The lengths of A-, B-, C-, and D-lines were 44.5 m, 89 m, 12 m, and 15 m, respectively. The outcrop beachrocks on A- and B-lines run from the western edge of A-line to 27.3 m east of it and from 27 m east of the western edge of B-line to 43 m east of it (Fig. 2). On the D-line, they run from the land edge to 7.25 m seaward. In addition, they are interspersed above the B-line. GPS systems determined the GPS position coordinates of the survey lines.

3 METHODS

A DC electrical survey and a seismic surface wave survey in the field show the resistivity and the S wave velocity sections. In addition, the influence of saturation on the resistivity and, the P and S wave velocities of the beachrock samples collected from the study site were determined from laboratory tests.

3.1 *DC electrical survey*

Archie (1942) showed a correlation between resistivity, pore water resistivity, porosity, and the degree of saturation of rocks. Thereafter, many researcher shave

conducted research into the relationship between electrical resistivity and the physical characteristics of rocks.

Archie's law states:

$$\rho_R = a \cdot \varphi^{-m} \cdot S^{-n} \cdot \rho_W \quad (1)$$

Here, ρ_R = rock resistivity, φ = porosity, S = water saturation, ρ_W = the pore water resistivity, and a, m and n are constants that depend on rock type.

According to this law, there is a relationship between rock resistivity and pore water resistivity, and a negative correlation exists between rock resistivity and rock's water content. The rock resistivity increases as pore water resistivity increases and as the water content decreases. In general, unconsolidated sands have low resistivity. Furthermore, the resistivity section obtained by a DC electrical survey can be converted into sections of other physical properties, if each physical property is substituted using Archie's law (Suzuki et al. 2001). For the above property, a DC electrical survey is used to determine vertical and lateral variations in the ground's conductivity by measuring electrical potential differences. The exploration depth is determined by the intervals of electrodes driven into the ground.

In this survey, the nails used as the electrodes are about 5 mm in diameter and 0.15 m long. The electrodes were driven in with a hammer to a depth of about 4 cm in the sand and about 1 cm in the beachrocks. The number of electrodes on A-, B-, C-, and D-lines were 90, 90, 48 and 60, respectively, and the intervals on each line were 0.5, 1.0, 0.25, and 0.25 m, respectively. The resistivity sections were analyzed from the measured data using the 2D inversion technique. This method consists of numerical calculation of an electric field and a constrained smoothing non-linear least-squares method.

3.2 *Seismic surface wave survey*

In spite of the fact that the S wave velocity has a recognized relationship with mechanical physical properties of rocks, elastic (especially S) wave velocity has been widely used for ground exploration in the fields of civil engineering and construction (Kavazanjian et al. 1996). In general, harder rocks show higher the wave velocities. S wave velocities are affected by the strength and pore structure of sand rock, meaning that the rock's geological structure is correlated with the S waves that propagate through it. The frequency of the surface wave determines the exploration depth. Compared with the seismic refraction method, this survey has the advantage of easy measurement and being fairly resistant to noise. However, its exploration precision is not so good for small-scale vertical structures because the analysis condition requires a horizontal multi-layer structure.

At most, 24 geophones (4.5 Hz) were deployed on each line at 1.0 m intervals. Multiple geophones were used in this survey (Land streamer, Geostuff, USA). These geophones were attached to a cloth belt, thus increasing work efficiency through that high mobility. The source point was located at distance of 2.0 m from the rear geophone against the direction of movement. The measured data obtained in this survey was analyzed by the 1D inversion technique (SeismicImager/SW, OYO Corporation, Japan). Furthermore, the measured surface wave velocity was converted into the S wave velocity section by analytic work.

3.3 *Laboratory tests*

Beachrock samples were collected from a point on the western edge of the A-line to about 27 m east of the A-line for laboratory tests. After being brout back to the laboratory, the samples were cut into rectangular parallelepiped pieces (dimensions: $2.7 \times 2.4 \times 5.8$ cm) using a rock-cutting machine; this shape was used as beachrock falls to pieces after coring. The specimens were soaked in artificial seawater (AQUAMARIN for metal corrosion test, Yashima pure chemicals CO., LTD., Japan) for 24 h in a vacuum. The specimens were tested for changes in resistivity, P and S wave velocity, and mass during natural evaporation at 25°C room temperature. Once the evaporation process slowed down, these tests were continued while the specimen was heated to then held at 40°C in a constant-temperature drying oven. Finally, tests were carried out with the specimen heated to 110°C for 24 h. The methods are as follows.

The saturated density of the specimen was measured by "test method for bulk density of rock" (JGS 2132-2009) and its resistivity by a resistivity meter (miniOHM, OYO Corporation, Japan) three times at each water content. The P and S wave velocities were determined from several measurements (Sonic Viewer SX, OYO Corporation, Japan), two times at each water content. In measuring resistivity, the specimen was placed between two sets (one set is made up of two electrodes that are less than 0.5 mm thick and the other set is made up of two filter papers alternately facing upward and downward soaked in the artificial seawater in which the specimen had been immersed) on the paper side.

4 RESULTS

4.1 *Field tests*

Figure 3 shows the resistivity sections on both A- and B-lines. In Figure 4, (c) and (d2) show the resistivity sections on C- and D-lines, and (d1) shows the velocity section. The pink grid-line in Figure 4 (d1) represents the areas of resistivity sections on the same lines.

As will be shown below, the underground structure of beachrocks was detected by the DC electrical survey and the seismic surface wave survey. The higher resistivity areas (more than 4.0 Ωm) are observed at about 0–32 and 39–43 m (A-line), 38–42 and 62–88 m (B-line), 0–12 m (C-line), and 0–15 m (D-line) (Figs 3, 4(c), (d1)). In the velocity sections of the D-line, the near-surface areas showing the highest velocity (more than 325 m/s) are between about 12–14 m (Fig.

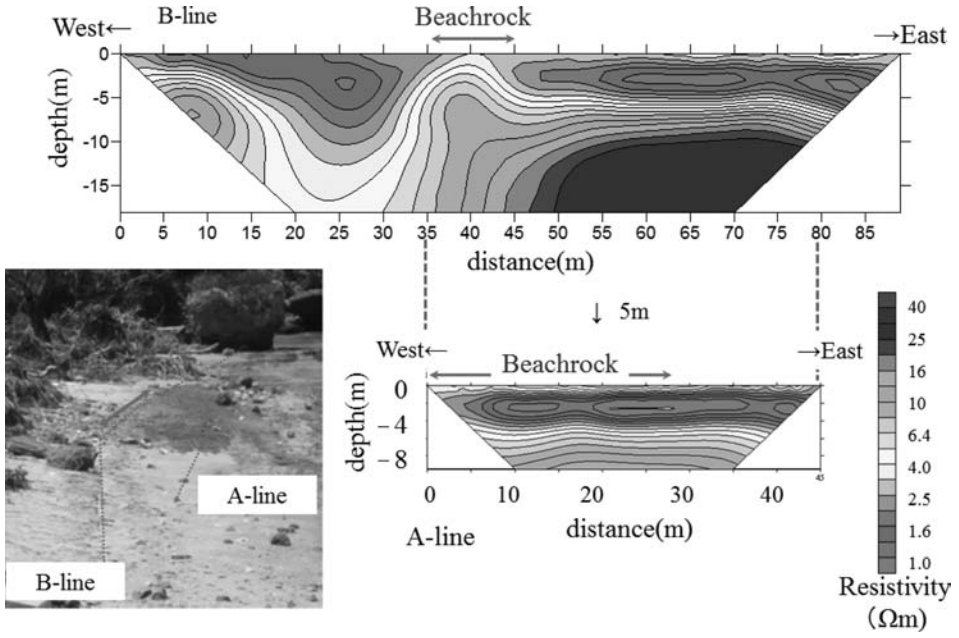


Figure 3. Results of the resistivity survey (A-, B-line).

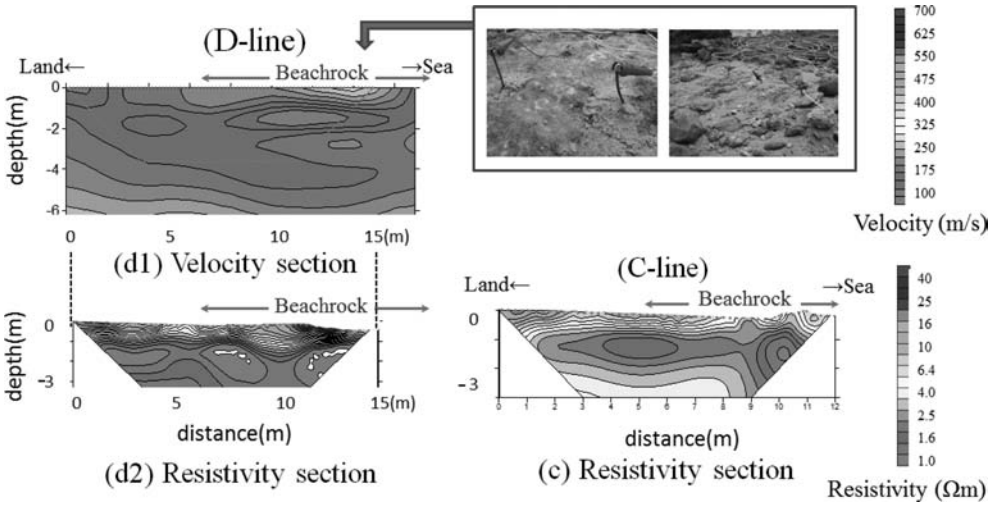


Figure 4. Results of velocity and resistivity survey (C-, D-line).

4(d1)). As mentioned in Chapter 3, the harder the rock, the higher both its resistivity and S wave velocity. The high velocity areas coincide relatively well with the high resistivity areas and the observed outcrops of beachrock (Fig. 4(d1) and Chapter 2). Furthermore, it was very likely able to detect the buried beachrocks. The examples are the surface areas at about 27–44.5 and 43–89 m on A- and B-lines, respectively. The area on the D-line is assumed to be between about 7.25–12 m because the resistivity of the higher surface area (more than 16 Ωm) between 0–4 m is too high in spite of not observing a beachrock outcrop, and this is due to the drying of sand by evaporation. The surface area between 0–2 m on C-line is similar.

From the above, it is believed that the two surveys detected beachrocks. Likewise, it was assumed that the thickness of beachrock in this study area is about 1 m, its surface wave velocity is about 300–350 m/s, and its resistivity is about 4–40 Ωm.

In the next location, it was assumed that the geological structure of this study area is as follows:

1) The follow results roughly agree with the result of the geological surveyor that explored for the construction of Kouri bridge. It is very possible that lower resistivity (less than 2.5 Ωm) and lower velocity (less than 250 m/s) zones indicate unconsolidated sand saturated with seawater.

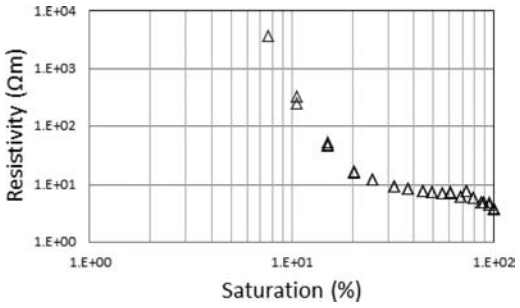


Figure 5. Relationship between saturation and resistivity.

2) There are higher velocity (more than 400 m/s) and higher resistivity (more than 6.4 Ωm) areas at depths greater than about 10–15 m. This is believed to be detection of the bedrock.

4.2 *Laboratory tests*

The results of the laboratory tests are as follows. The volume of the specimen is 38.6 cm^3; dry mass, 77.0 g; wet mass, 87.8 g; dry density, 1.99 g/cm^3; wet density, 2.27 g/cm^3; and porosity, 27.4%. The results of this experiment are shown in Figure 3. This Figure indicates the relationship between the saturation, P and S wave velocity, and electrical resistivity of the specimen. It was found that the electrical conductivity and the specific gravity of the solution saturating the specimen were 5.85 S/m and 1.021 g/cm^3 respectively. Its S wave velocity was about 1.3 km/s and not affected by the saturation, unlike the P wave velocity. Its electrical resistivity was about 5.0 Ωm at 100% saturation and increased when the saturation fell under about 20% (Fig. 5). The saturation and electrical resistivity of rock can be approximated by a log-log linear regression in the case that its electrical resistivity accords with Archie's law (1942). However, its linear relationship was confined to under about 20% in this test.

5 DISCUSSION

5.1 *Applying geophysical exploration to a geological survey of beachrocks*

This is the first domestic or international study involving two types of surveys on beachrocks. In this study, the velocity sections coincide relatively well with those of resistivity, in spite of each survey measuring a completely different physical property. In the seismic surface wave survey of beachrocks, there is a big difference between the S wave velocity that had been assumed to detect beachrocks in the field (about 0.3 km/s) and the S wave velocity in the laboratory tests (about 1.3 km/s). The cause of this discrepancy is believed to be that the highest frequency area on the survey line, or the highest velocity area, could not be detected because of the attenuation of this frequency by only putting the geophones on the beachrocks. As a countermeasure against the above, it is proposed to place the sensitive geophones into holes made on the ground. In the DC electrical survey, the nails used as electrodes could not be hammered into the harder surface of outcrop beachrocks to a depth of more than about 1.0 cm. However, the same current value (300 mA) was carried steadily from all nails because of their low grounding resistance (less than 100 Ω).

The time taken for the work on the A- and B-line is about 3 h and that on C- and D-lines is shorter than the other surveys. Furthermore, there is every possibility of detecting buried beachrocks. The reliability of the results is improved by comparison with multiple surveys. A proposed future task for both surveys is to address the interval between electrodes or geophones. It is necessary to shorten the interval to under 25 cm for the DC survey on D-line since the thickness of beachrocks in this area is about 1 m. On the D-line (Fig. 4 (d2)), it was possible to observe the distribution of resistivity in the high resistivity area (more than 16 Ωm). Finally, the possibility of probing by boring exploration is limited because the area around these beachrocks is a tourist spot. It is considered that geophysical prospecting, in which underground structures can be surveyed without damaging the landscape, is an extremely effective way to study the distribution of beachrocks. In addition, the relationship between the results of geophysical prospecting and laboratory tests are described in detail in Suzuki et al. (in press).

5.2 *Characteristics of beachrocks in this study area*

First, the resistivity of beachrocks in Yagaji island, Japan is about 4–40 Ωm (Figs 3, 4 (d2)), whereas that in Thassos island, Greece is about 2–15 Ωm, reported in Psomiadis et al. (2009). It is assumed that the former beachrocks are harder than the latter. Their thicknesses in both study areas are similar, about 1 m.

Second, it is considered that the beachrocks at this site were not solidified horizontally against the coast line. From the location map of this study site (Fig. 2) and the resistivity sections (Figs 3, 4), it is assumed that there are buried beachrocks from 43 m east of the western edge of B-line to over 89 m east and between 7.25–12 m of D-line seaward from the land edge. This section describes the porosity of beachrocks at this site. From the following, it was assumed that the porosity of beachrocks in the field is about 30%. The resistivity of the site where the sample of beachrocks was collected (from the western edge of A-line to about 27 m east) is about 6.4 Ωm (Fig. 3). The resistivity roughly matched with the result of laboratory tests when the porosity was more than 20% (Fig. 5).

It is believed that the reason why the linear relationship between the saturation and specific resistivity of rock was confined to under about 20% saturation in this test (Fig. 5), is that the interior of the specimen was not unsaturated and homogenous during its natural evaporation at 25°C room temperature. That is to say, it is assumed that a saturated columnar area remained inside the specimen as a circuit until less than about 20% saturation was reached. In future research,

the resistivity could be converted into porosity using Archie's law (1942).

Finally, this section describes a comparison of the result of our surveys with existing opinion on the origin of beachrocks. It is widely believed that beachrocks were solidified by repeated immersion in seawater and the subsequent evaporation of seawater (Ginsburg 1953). The results of this study support this opinion. First, the beachrocks situated nearer to the seaward side (the north side) show a thicker area of higher resistivity compared to the resistivity sections of each survey line (Figs 3, 4(d2)). Comparing the resistivity sections of the A- and B-lines, the resistivity of the surface area that revealed the outcrop of beachrocks between 0–27 m on the A-line (nearer to the sea than the B-line) is higher than that of the B-line. This tender is the same as that of D-line except for the unsaturated area between about 0–5 m. In particular, the higher resistivity area (more than 16 Ωm) is shown between about 10–15 m on the D-line, and the thickness is over 0.5 m. On the C-line, the thickness is almost same. From the findings above, it is deduced that the harder beachrocks are, the longer the time during which they have been immersed in sea water. Second, there are no observed beachrocks in the area that is always saturated by sea water. The sandy area on the bedrock is assumed to be saturated from the results of each survey and is not considered likely to solidify (Figs 3, 4) because there is sea water inside this areas regardless the rise and fall of the tides (Riedl 1971). From the above reasons, it is highly likely that repeated immersion in sea water and the evaporation of the liquid is important to solidify the sand into beachrocks.

6 CONCLUSIONS

1) The features of beachrocks at this site are as follows. Their S wave velocity was found to be about 350 m/s, and their resistivity was about 4–40 Ωm. Their thickness was about 1.0 m and had a tendency to become thicker closer to the sea. In order to solidify the sand, it is highly likely that it is important for the sand to be repeatedly immersed in seawater, resulting in repeated evaporation of the liquid.
2) The results of the first attempt to use multiple geophysical surveys for detecting the underground structure of beachrocks are as follows: there was a good correlation between the results from the seismic surface wave survey and the DC electrical survey. These two surveys detected buried beachrocks over a wide area without damaging the landscape of the study area, which highlights the utility of this approach in studying rock formations in areas where disruption of the terrain is not possible for social, economic, or environmental reasons. Further, the resistivity of beachrocks could be converted into the porosity using Archie's law (1942) in future research.

REFERENCES

Archie, G.E. 1942. The electrical resistivity log as an aid in determining some reservoir characteristics. *Trans. A.I.M.E.* 146: 54–62.

Danjo, T. & Kawasaki, S. 2012. Characteristics of beachrock based on bibliographical research – Toward the development of man-made beachrock. *J. Japan Soc. Eng. Geol.* 53(3): 129–141 (in Japanese).

Ginsburg, R.N. 1953. Beach rock in South Florida. *J. Sediment. Petrol.* 23: 85–92.

Kavazanjian, E., Jr., Matasovic, N., Stokoe, K.H. II, & Bray, J.D. 1996. In-situ shear wave velocity of solid waste from surface wave measurements. *Proceedings of the 2nd International Congress on Environmental Geotechnics* 1: 98–102. Rotterdam: Balkema.

Omoto, K. 2007. Significance of the Oldest Beach Rock Collected from the Nansei Islands, Southwest of Japan. *The Bulletin of the Institute of Natural Sciences, Nihon University College of Humanities & Sciences* 42: 1–14 (in Japanese, with English abstract).

Psomiadis, D., Tsourlos, P. & Albanakis, K. 2009. Electrical resistivity tomography mapping of beachrocks: application to the island of Thassos (N. Greece). *Environmental Earth Science* 59: 233–240.

Riedl, R.J. 1971. How much seawater passes through sandy beaches? *Int. Rev. ges. Hydrobiol.* 56: 923–946.

Suzuki, K., Ohie, Y., Yamaguchi, H. & Noguchi, K. 2001. Estimation of physical properties of reclaimed ground with coal ash using resistivity, IP, and micro-gravity surveys. *Buturi-Tansa* 54(5): 277–289 (in Japanese with English abstract).

Suzuki, K., Kawasaki, S., Kubo, R., Yamaguchi, S. & Hata, T. 2013. Geological structure of beachrock using electrical resistivity and surface wave surveys – Application to the coastal area at Yagaji island in Nago-shi, Okinawa. *Proceedings of the 128th SEGJ Conference* (in Japanese with English abstract) (in press).

Rock Mechanics for Resources, Energy and Environment – Kwaśniewski & Łydżba (eds)
© 2013 Taylor & Francis Group, London, ISBN 978-1-138-00080-3

Physical and mechanical characterization of weak schistose rocks

T. Le Cor
INSA Rennes, Groupe Dacquin, France

D. Rangeard
INSA Rennes, France

V. Merrien-Soukatchoff
Université de Lorraine, CNRS, CREGU, GeoResources UMR 7359, France

J. Simon
Groupe Dacquin, France

ABSTRACT: The anisotropic behaviour of schistose rocks is rarely considered in the conception of retaining structures (diaphragm wall, soldier piles wall …) in this type of rocks. Brioverian shales are often encountered underground the city of Rennes (Brittany France) and its surrounding area. They are fractured, altered and folded along a vertical plane which lead to lateral variations of facies and alteration changes on short distances. Consequently of the numerous construction projects, including the excavation of the second subway line, the physical and mechanical knowledge of this material has to be improved to help structure design.

This paper presents the results of physical and mechanical characterization on schistose rocks extracted from several locations in the Rennes area. Some of the methods employed were classical geotechnical tests (X-ray diffraction, thin sections observations, uniaxial compression tests and shear tests along open joints) whereas others were modified tests usually used in the road construction fields (grindability test based on LCPC abrasiveness test and Micro Deval test used on prismatic samples). This characterization showed an important heterogeneity of the mechanical properties of the Brioverian shales despite homogeneity in their mineralogical contain. The important sensitivity to water of the material was revealed.

1 INTRODUCTION

Brioverian shales can be encountered undeground a large part of Brittany (West of France, Jegouzo 1973, Dabard 1990). The unpredictable anisotropic behaviour of these rocks during construction projects can be a real problem. Indeed, those shistose rocks present a high level of fracturation and alteration that leadsto important lateral variations on short distances. The most common problems encountered are: deviation during drilling (piles used as foundations or retaining structures, diaphragm wall), collapsing between vertical elements of a retaining structure during excavation, higher ground pressures than expected in calculations leading to unacceptable displacements or moments of the structure …

Numerous underground construction projects are under view in the Rennes Metropole area and the construction of a second subway line will begin in 2014 through these schistose formations.

Considering those expected projects in this type of ground, the physical and mechanical knowledge of this material have to be improved to help structure design. Rock samples, from different sites in the city of Rennes, were extracted during excavation steps of different construction sites. The physical characterization consisted in X-ray diffraction analyses on shale powders, thin section observations, grindability tests on aggregates and a modified Micro Deval test on prismatic samples. The mechanical characterization used uniaxial compression tests and direct shear tests along open joints. An overview of the results obtained so far is presented in the next pages.

2 PHYSICAL CHARACTERIZATION

2.1 *Localization*

The extraction sites of the samples were spread over Rennes (Fig. 1) on different construction sites.

For each site, samples were taken at different depths varying from 2 to 8 metres. Sample sites are named from A to L. Subcategories, for the same site, representing variations of visual facies are numbered (examples: L1 and L2) in the results presented in this paper.

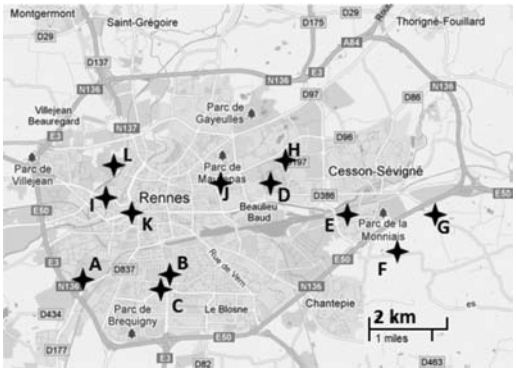


Figure 1. Localization map of the sampling sites spread over Rennes (Source: Google maps).

2.2 *X-ray diffraction analysis and thin sections observations*

Thin section observationis a usual technique used to study anisotropic rocks (Behrestaghi 1996, Wenk et al. 2010). Thin sections parallel and perpendicular to the schistosity were made for each sample. Observations through microscopes revealed that the granulometry of all the samples tested was small (lower than 60 μm) but some were smaller than others: B, D and G with a granulometry lower than 30 μm. Schistosity direction can be, generally, easily identified,yet stratigraphy cannot always be recognized or differentiate from schistosity. Oxides (goethite and leucoxene) were identified in important quantities in some samples (A, B and C3) which reveal their important alteration degrees. The main minerals presented in all the samples are quartz and phyllosilicates. Samples D to G also contained feldspars (plagioclase and orthose). Examples of thin sections perpendicular to schistosity are shown in Figures 2a and 2b.

X-ray diffraction analyses (Fig. 3a), regularly used in the rock mechanics field (Gy et al. 1995, Nasseri 2003), were lead on powder of schistose rocks in order to evaluate the quantities of quartz and clayey minerals.

According to Figure 3b, samples can be divided in two categories. The first one includes samples D, E, F, H, I, J3 to K3 which contain the lowest quantity of clays relative to the quartz. The second category includes samples A, B, C, G, J2 and L with clay quantities in the same range or larger than quartz. Complementary treatment (glycerol saturation) was conducted on samples B, D and L that confirmed the suspected presence of expansive clay (smectite) revealed by the observed fractures of the samples after water immersion.

2.3 *Modified tests: Grindability and Micro Deval tests*

Simple tests were elaborated in an attempt to evaluate the alteration degree of the Brioverian shales. These tests, relevance to estimate mechanical strength of rocks, are discussed hereinafter.

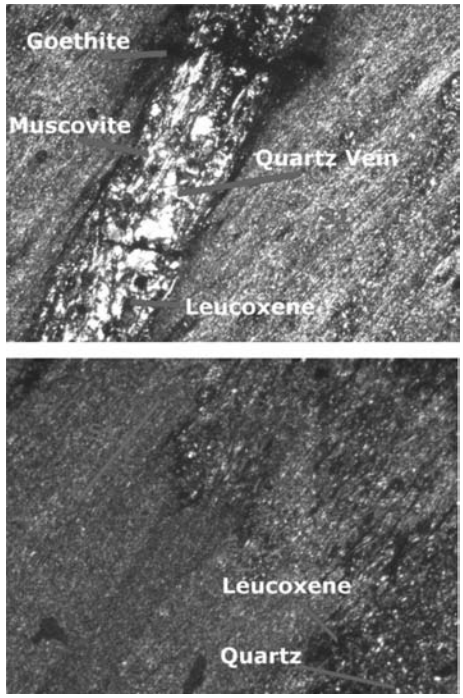


Figure 2. Thin sections of two different samples. Top (a): B sample zoom × 25. Bottom (b): F sample zoom × 25.

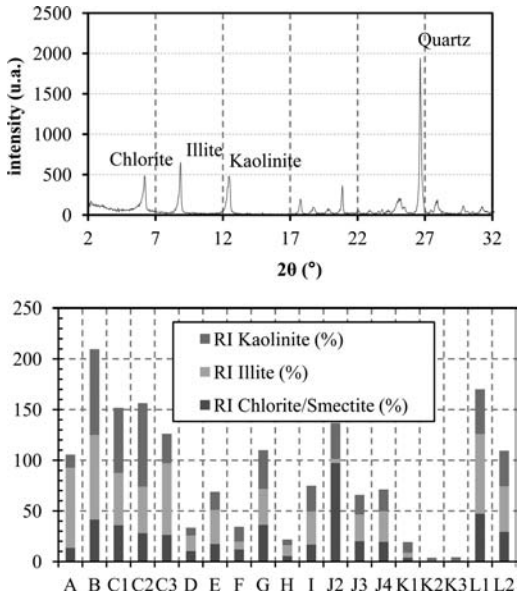


Figure 3. Intensity peaks of clays and quartz for each sample. Top (a): X ray diffraction results for one sample (I). Bottom (b): Relative intensity of the clays compared to quartz.

2.3.1 *Description of the tests*

The first test performed was the grindability test on aggregates based on an existing test (AFNOR 1990).

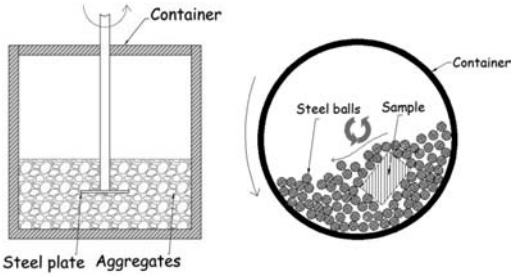


Figure 4. Drawing of the modified tests. Left (a): Grindability test. Right (b): Micro Deval test.

It consisted in subjecting the aggregates to the action of a rotating steel plate (Fig. 4a). Initially, the only measure of the test was the quantity of fine elements (<1.6 mm) produced by the crushing action of the plate after 15 minutes. As our material was completely crushed after a shorter duration, the test was shortened to 5 minutes and fractionated to realize a measure every 15 seconds during the first 90 seconds.

The second test developed is based on the Micro-Deval test usually used to characterize wear resistance of aggregates. The modified version of the test is based on the adaptation proposed by Takarli (2007) to test granite aggregates. It consists in exposing plane-parallel samples (instead of aggregates) to the abrasive action of steel balls (Ø10 mm). Sample and steel balls are placed in a rotating container at a constant speed (100 rev/min) during 120 minutes (Fig. 4b). The weight loss of the sample is measured (and divided by the surface of the sample exposed to the abrasive load) during the test and the evolution of the loss is used to calculate two parameters: final wear corresponding to the weight loss after 120 minutes of testing and the wear factor which is the slope of the linear part of the plot.

2.3.2 *Results of the tests*

The grindability index (GI) for each sample is calculated according Equation 1.

$$GI(t) = \frac{m_{fines<1.6mm}(t)}{m_{initial}} \times 100 \quad (1)$$

where $m_{fines<1.6mm}(t)$ = weight of fine elements passing through a riddle of 1.6 mm at t time; $m_{initial}$ = initial weight of aggregates tested (200 g).

After each measure, the weight of aggregates reintroduced in the container was measured in order to consider the loss during manipulations (average of 5 g at the end of the test) in the calculation of the GI. The resulting weight loss is called homogenized weight loss (Eq. 2).

First, a repeatability study was carried out on samples A, C and D (these were available in larger quantities than the others). Test was repeated 4 times for each sample and it showed a maximum deviation, for the same sampling site, lower than 7%. Consequently, each sample was tested at least ones andaverage values

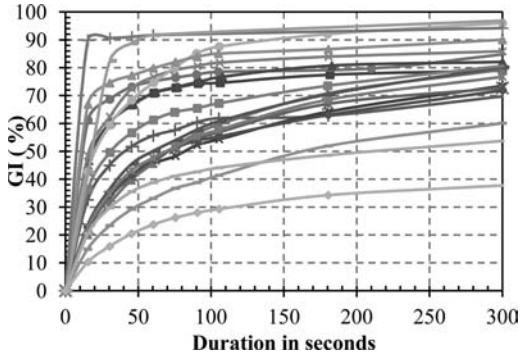


Figure 5. Evolution of the grindability index (GI) for all the samples.

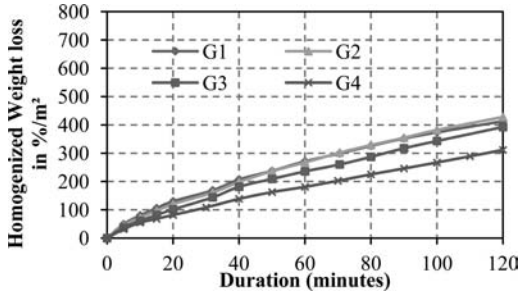


Figure 6. Evolution of the homogenized weight loss for four samples from the same site.

of the grindability index were established for the ones that were tested several times. The results of the grindability tests of all the sampling sites are presented on Figure 5.

The grindability index increases during the test for all the samples, however, the speed of the rise and the value reached at the end of the test varies a lot from one sample to another. It appears that the differences between samples are more significant in the first 90 seconds of the test and are reduced at the end of the test. Most of the samples reached a grindability index between 75 and 90% after 300 seconds. The most pertinent indicative parameters for this test is the grindability index after 30 seconds (differences between samples more important than after 300 seconds).

During the wear test based on the Micro Deval test, the sample can break into pieces (especially the weakest samples presenting visible joints). In this case, the additional area exposed to abrasion was included in the calculation of the homogenized weight loss (ΔM_S) as expressed in the subsequent formulation (Eq. 2).

$$\Delta M_S = \frac{M_i - M_t}{M_i} \times 100 \times \frac{1}{S_{exposed}} \quad (2)$$

where M_i is the initial weight of the sample; M_t is the weight of the samples at t time; $S_{exposed}$ is the surface of the samples exposed to the abrasion.

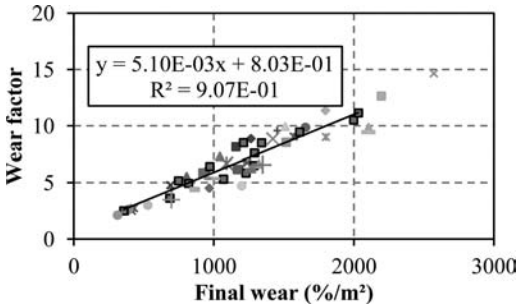


Figure 7. Relation between the final wear and the wear factor. Dark squares represent the average wear factor and final wear for each sampling site.

At least three samples persite were tested. The evolutions of the homogenized weight loss of each sample during the tests are displayed in Figure 6 for site G.

The parameters inferred from the Figure 6 are the homogenized weight loss after 120 minutes (Final wear) and the slope of the linear (wear factor) part of the curves (from 50 minutes to 120 minutes). The link between the two parameters is quite linear as shown on Figure 7 (this result is observable only if the additional area exposed to abrasion is considered in the calculation).These parameters will be correlated to the results of the compression tests presented in part 4.

3 MECHANICAL CHARACTERIZATION TESTS

Two types of mechanical tests were carried out on the Brioverian shales: uniaxial compression tests and direct shear tests.

3.1 *Uniaxial compression tests*

Uniaxial compression tests were performed on plane-parallel samples (approximate size: 60 mm × 30 mm × 30 mm) from each sites. Due to the difficulties of preparation (fracturing of the material during the cut) and the limited quantities of material available, we were unable to respect the ISRM recommendations (ISRM 2007) regarding the shape, the size, the planarity and parallelism of the loading faces of samples. Surface treatment with plaster was experimented in order to obtain a good planarity of the surfaces but it appeared that the same results were obtained by using a ball joint between the loading plate and the loading axe (which required much less preparation since the loading plate does not need to be perpendicular to the loading axe). This last technique was then used for all the tests. For each site, at least six samples were tested: three "dry" samples (dried for a week at ambient temperature, water content lower than 1%) and three "wet" samples (obtained by immersing the samples in water for a week, water content varying from one sample to another) and the density of each sample was calculated. The load was appliedalongside the schistosity because it was not possible to cut samples perpendicular to it. Two parameters

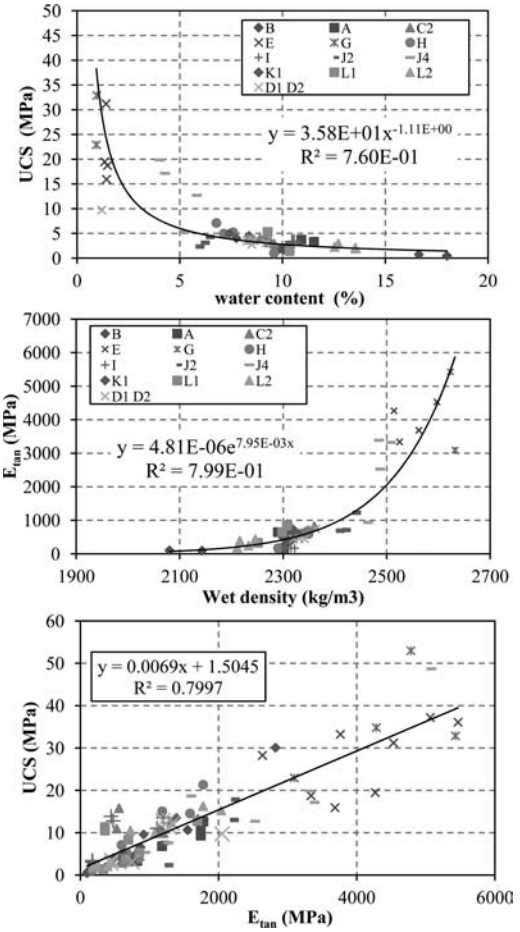


Figure 8. Top (a): Evolution of the UCS with the water content of the samples Center (b): Evolution of the tangent Young's modulus with the density Bottom (c): Evolution of UCS with tangent Young's modulus.

were extracted from the tests: the uniaxial compressive strength (UCS) and the tangent Young's modulus (E_{tan}). Previous studies on anisotropic rocks (Hoek 1968, Kwasniewski & Nguyen 1986, Nasseri 2003) revealed that loading parallel to schistosity usually lead to the highest E_{tan} but not to the highest UCS (can be higher if the loading is perpendicular to schistosity). In the case of our study it means that we obtained the highest E_{tan} but not necessarily the highest UCS. The water content of the sample was measured after each test.

As displayed in Figures 8a and 8b, the mechanical characteristics of the samples decreased with the water content and increased with the wet density. Correlations between mechanical characteristics and water content and density are good but non linear. Exponential and hyperbolic relationships were observed on metamorphic rocks presenting various degrees of alteration (Sousa et al. 2005, Marques et al. 2010, Vásárhelyi & Ván 2006). The correlation between UCS and E_{tan} is linear (Fig. 8c).

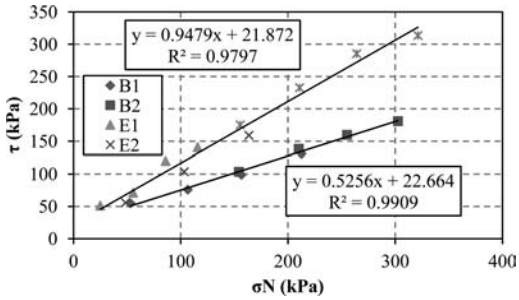


Figure 9. Direct shear tests results. Each sample was tested for different normal stresses (τpeak represented however it was really closed to τ residual).

The samples containing expansive clay (B, D1, D2, L1, L2) are the ones with the lowest mechanical characteristics combined with the highest water content and the lowest density (Figs 8 a, b).

3.2 *Direct shear tests*

Failure in Brioverian shales happened mainly along joints or fractures. In order to characterize the joints behaviour, direct shear tests were carried outon opened joints from two different sites (B and E, respectively, the sites where the weakest and the strongest samples were extracted). The two parts of each sample (dimensions about 60 mm × 30 mm) were embedded in mortar in order to be perfectly maintained and to compensate any planarity faults (ISRM 2007). During each test, the sample was sheared in one direction at a constant speed (0.5 mm per minute) and sheared back to its original position before increasing the normal stress and start again. This procedure was repeated at least three times for each sample (test results are presented in Figure 9).

Cohesions obtained are almost the same for the two sites (approximately 22 kPa) but the samples were very different: joints of the E samples presented a lot of iron oxides whereas the samples from the B site were clayey. However the angle of friction is more important in the case of the E site samples: around 43° against 28° for the B site samples.

4 RELATIONS BETWEEN PHYSICAL AND MECHANICAL CHARACTERISTICS

In section 3, it has been shown that mechanical characteristics were well correlated to the wet density and the water content.

Attempts to correlate directly UCS to quartz or clay content (deduced from X-ray analyses) were unsuccessful. Yet, when the proportion of clay (combining all types of clay) is greater than the proportion of quartz (Σ $I_{clays} > I_{quartz}$), the UCS seems to have an upper-bound around 15 MPa (Fig. 10). Underneath a ratio of 100% (Σ $I_{clays} > I_{quartz}$), the UCS increases with the percentage of clay.

Correlations between UCS and the results of the grindability tests were inconclusive (Fig. 11), but

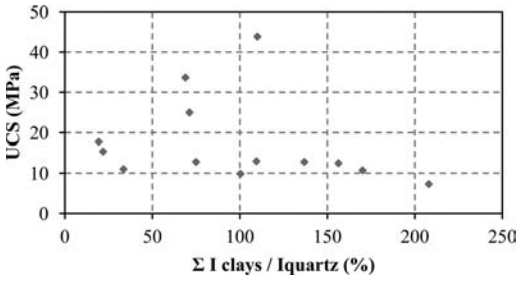


Figure 10. Evolution of the UCS with the relative quantities of clay homogenized by the quantity of quartz.

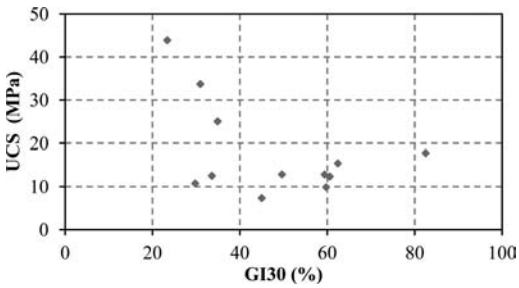


Figure 11. Evolution of the UCS with the grindability index after 30 seconds of testing.

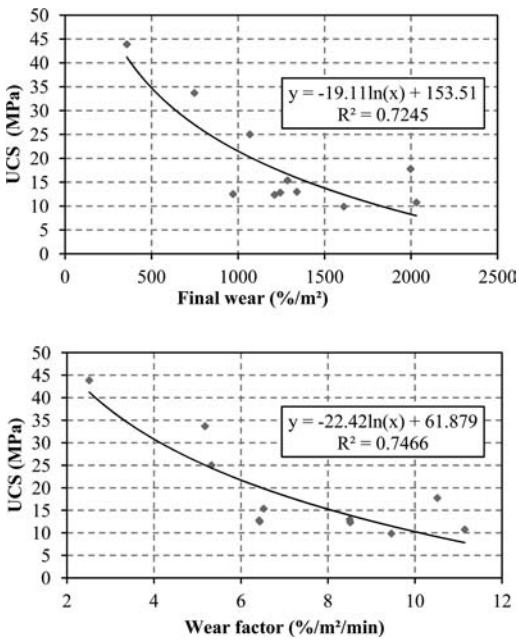


Figure 12. Relations between UCS and the results of Micro Deval tests. Top (a): Wear factor. Bottom (b): Final wear.

correlations ($r^2 > 0.7$) were observed between UCS and the wear factor (or the final wear) as displayed in Figures 12a and 12b.

A decrease of the UCS with the increase of the wear factor and the final wear is observed. However,

shales seem to reach a lower bound for the UCS: above 1000%/m^2 (all samples except E, G and C2) and an increase of wear parameters do not lead to a decrease in the UCS. The correlation between the UCS and the final wear is as good as the correlation with the wear factor but the wear factor requires measuring the weight loss regularly, while the final wear only requires one measure at the end of the test. However, the accuracy of this last measure depends on the precision of the monitoring of the samples surface exposed to abrasion. Thus, it is necessary to perform the measures of weight loss and surface evolution in order to have conclusive results.

Not enough shear tests were made to draw any conclusions about the correlations possible with the other tests. However, the two sampling sites tested (which revealed to be the ones with the most extreme UCS) presented differences concerning the angle of friction showing that joint characterization is justified and need to be studied more precisely.

5 CONCLUSIONS

Brioverian shale is a complex material. It cannot be classified as a soil because it has a cohesive structure but, depending on its alteration degree, it can barely be classified as a rock.

Mineralogical characterizationby X-ray diffraction and thin section observations revealed the presence of common minerals in all the samples (quartz, clay, oxide) but in variable quantities from one sample to another. The mineralogical composition seems to have a slight influence on the mechanical strength of the samples excepted, in some samples (B, D and L), when swelling clay is identified. For these last sampling sites, a high sensitivity to water was observed and implied a high decrease in the mechanical strength of the samples with the water content.

Complementary tests were developed in order to characterize the alteration degree of the shales by measuring their grindability and abrasion resistance. These two tests are characteristic of the sampling site. However, only the Wear test (adapted from micro-Deval)is well correlated to the uniaxial compressive strength. This may be due to a solicitation more adapted to the material in the case of the Wear test (the grindability test being may be too "violent" for this type of material).

The uniaxial compression tests, performed on "wet" and "dry" samples confirmed the important sensitivity to water on the material. The water content and the density, which is easy data to obtain, can be used to quickly estimate the UCS of Brioverian shales in a first approach.

The direct shear tests showed that the friction angle varied from a site to another but the cohesions obtained were almost the same. However more tests on other sites need to be done to confirm these first results.

Besides collecting more data to improve the knowledge of the Brioverian shales through the tests presented in this paper, several other tests are to be investigated: ultrasound wavepropagation immersed direct shear tests on joints.

ACKNOWLEDGEMENTS

The authors would like to thank the geotechnical company Dacquin for financing this research work. Acknowledgements also go to Marie-Pierre Dabard and Magali Sevenier from the Geosciences Department of the University of Rennes for their scientific support regarding this work.

REFERENCES

AFNOR 1990. *P18-579. Granulats – Essai d'abrasivité et de broyabilité.* Paris: AFNOR.

Behrestaghi, M. 1996. Engineering geological and geotechnical responses of schistose rocks from dam project areas in India. *Engineering Geology* 44(1–4): 183–201.

Dabard, M.P. 1990. Lower Brioverian formations (Upper Proterozoic) of the Armorican Massif (France): geodynamic evolution of source areas revealed by sandstone petrography and geochemistry. *Sedimentary Geology* 69: 45–58.

International Society for Rock Mechanics 2007. *The Complete ISRM Suggested Methods for Rock Characterization, Testing and Monitoring: 1974–2006*. ISRM, 628 pp.

Gy, O.L., Bhasin, R., Barton, N., Grimstad, E. & Chryssanthakis, P. 1995. Engineering geological characterization of low strength anisotropic rocks in the Himalayan region for assessment of tunnel support Jutogh Group Pre-Cambrian Jeori-Wangtu Gneissic Complex. *Engineering Geology* 40: 169–193.

Hoek, E. 1968. Brittle failure of rock. In K.G. Stagg & O.C. Zienkiewicz (eds) *Rock Mechanics in Engineering Practice*: 99–124. London: Wiley.

Jégouzo, P. 1973. *Petrographical and structural study on lower Vilaine shales and granites*, Ph.D. thesis, Rennes University (in French).

Kwasniewski, M. & Nguyen, V.H. 1986. Experimental studies on anisotropy of the time-dependent behaviour of bedded rocks. *Proc. of the Int. Symp. on Eng. in Complex Rock Formations*: 325–337. Beijing: Pergamon Books Ltd. and Science Press.

Marques, E. A. G., Barroso E., MenezesFilho, A.P. and Vargas, E.D.A. 2010. Weathering zones on metamorphic rocks from Rio de Janeiro – Physical, mineralogical and geomechanical characterization. *Engineering Geology* 111(1–4), 1–18.

Nasseri, M. 2003. Anisotropic strength and deformational behavior of Himalayan schists. *International Journal of Rock Mechanics and Mining Sciences* 40(1): 3–23.

Sousa, L.M.O., Del Rio, L.M.S., Calleja, L., Argandoña, V.G.R. & Rey, A.R. 2005. Influence of microfractures and porosity on the physic-mechanical properties and weathering of ornamental granites. *Engineering Geology* 77: 154–168.

Takarli, M. 2007. *Behavior of constitutive materials of rock dams: Mineralogical, physical, mechanical characterization and alteration*. Ph.D. thesis, INSA, Rennes (in French).

Vásárhelyi, B. & Ván, P. 2006. Influence of water content on the strength of a rock. *Engineering Geology* 84: 70–74.

Wenk, H.-R., Kanitpanyacharoen, W., & Voltolini, M. 2010. Preferred orientation of phyllosilicates: Comparison of fault gouge, shale and schist. *Journal of Structural Geology* 32(4): 478–489.

Rock Mechanics for Resources, Energy and Environment – Kwaśniewski & Łydżba (eds)
© 2013 Taylor & Francis Group, London, ISBN 978-1-138-00080-3

Thermal conductivity of rocks under high pressure conditions

W. Lin
Japan Agency for Marine-Earth Science and Technology (JAMSTEC), Nankoku, Japan

O. Tadai
Marin Works Japan LTD, Nankoku, Japan

T. Hirose, W. Tanikawa & M. Kinoshita
Japan Agency for Marine-Earth Science and Technology (JAMSTEC), Nankoku, Japan

H. Mukoyoshi
Marin Works Japan LTD, Nankoku, Japan

M. Takahashi
National Institute of Industrial Science and Technology (AIST), Tsukuba, Japan

ABSTRACT: To exactly evaluate thermal conductivity of a rock specimen taken from a great depth, pressure effects have to be taken into consideration. We developed a new measurement system of thermal conductivity of rock specimens under high confining pressure and high pore-fluid pressure. This system consists of a commercial thermal conductivity meter, a high pressure vessel in which the rock specimen, sensors of thermal conductivity measurements were installed and two high resolution syringe pumps. One of the syringe pumps is for controlling confining pressure; and the other is for pore-fluid pressure. Both the pumps are able to monitor fluid flow rate and cumulative volume change of pore fluid in rock specimen assembly during testing. We examined the effects of high pressure on thermal conductivity in rock specimens of five terrestrial rock types. Thermal conductivity clearly increased with increasing effective pressure for both dry and wet (water saturated) samples.

1 INTRODUCTION

In case of the geological disposal of high-level radioactive waste at a large depth in underground, thermal conductivity of rocks under in-situ pressure and temperature conditions is the most important key parameter for estimations of temperature increasing of the rocks around the canisters associated to generation of heat by radioactive materials. The physical properties of rocks, including thermal conductivity, are dependent on pressure and temperature (Schön 1998), so in situ pressure and temperature conditions should be simulated in laboratory measurements of the thermal conductivity of drill core samples from great depths.

General, thermal conductivity of rock samples are measured at atmospheric pressure condition in civil and geotechnical engineering fields. Several previous studies on thermal conductivity at high confining pressure were found in mining and geoscience fields (e.g. Horai and Susaki 1989; Abdulagatova et al. 2009), but almost of them did not take pore-fluid pressure into consideration. We developed a new apparatus capable of measuring the thermal conductivity of a rock sample at both high confining pressure and high pore-fluid pressure conditions based on our previous system which was able to measure the thermal conductivity under high confining pressure condition only (Lin et al. 2011).

2 METHODS

2.1 *Measurement method of thermal conductivity under high pressure conditions*

Our measurement system under high pressure conditions consists of a thermal conductivity meter QTM-500, a high hydrostatic pressure vessel in which the rock specimen, sensors for thermal conductivity measurements were installed and two high resolution syringe pumps (Fig. 1). One of the syringe pumps is for controlling confining pressure up to 138 MPa; and the other is for pore-fluid pressure with a pressure limitation of 52 MPa. Both the pumps are able to monitor fluid flow rate and cumulative volume change of pore fluid in rock sample assembly during testing. This apparatus will be further modified in the future to allow measurement of thermal conductivity at high temperatures.

The commercial thermal conductivity meter QTM-500 we used is based on transient heating of a half-space sample by a line source (Sass et al. 1984). This approach is usually used for tests at atmospheric pressure with a cased box-type line-source sensor probe. For high-pressure thermal conductivity measurements, it is necessary to place the sample and sensor in a high-pressure vessel. Because commercial box-probe cannot be used under high pressures, we instead used a wire-type line-source sensor consisting of a line heater and a thermocouple to measure temperature changes at the center of the line heater during heating (Fig. 2A).

2.2 *Sample assembly*

In the sample assembly (Fig. 2), the wire sensor was placed between a halved cylindrical rock sample (50 mm diameter, 100 mm length) and a matching piece of Teflon (0.29 W/mK) of the same dimensions. We installed the wire sensor through a dielectric end piece at the top of the sample, from where it ran between the sample and the Teflon. We used the end piece at the bottom of the sample to allow pore water to drain from the sample and to control pore pressure. Filter papers were placed between the rubber jacket and the rock sample and between the bottom end piece and the sample to promote drainage of pore water.

This sensor type of line source measures the thermal conductivity in a direction perpendicular to the line source, i.e. core sample axis in our sample assembly. If the core sample was taken from vertical drilling, the measured thermal conductivity is in horizontal direction. If it is possible to make up two or more samples from the same rock in the same dimension (a halved cylindrical sample with 50 mm diameter and 100 mm length) but in different directions, we can examine anisotropy of thermal conductivity under high pressure of the rock.

2.3 *An example of thermal conductivity measurement*

For thermal conductivities measured with transient line-source devices such as the QTM-500, the lower the thermal conductivity of the test sample, the steeper the increase of temperature during heating. Thus, the apparent thermal conductivity (λ_{app}) for the rock and Teflon combination we used can be calculated as:

$$\lambda_{app} = KQ[\ln(t_2) - \ln(t_1)]/4\pi(T_2 - T_1) \quad (1)$$

where K is a constant dependent on the measurement apparatus, Q is the quantity of heat, and T_1 and T_2 are temperatures at times t_1 and t_2, respectively, during transient heating. Our high-pressure measurements showed an almost linear relationship at semi-log scale between temperature and heating time (Fig. 3). The gradient decreased as confining pressure increased, indicating that apparent thermal conductivity increased with increasing confining pressure. We used the temperature increasing data ranged between 20–90 second which is more stable than in the early part of 0–20 second for calculating apparent thermal conductivity. By using a calibration curve derived from several standard samples, the thermal conductivity of the rock sample can be determined from the apparent thermal conductivity.

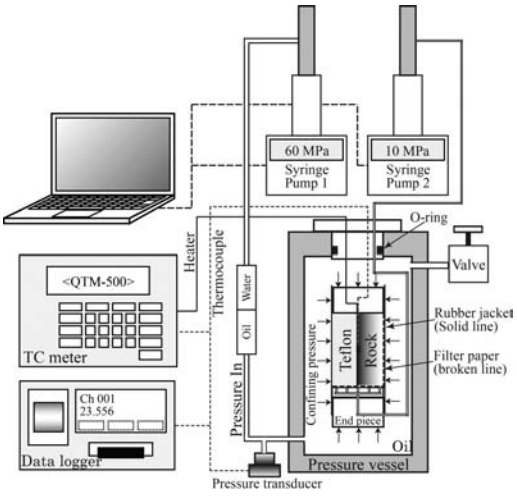


Figure 1. Schematic diagram of the apparatus developed in this study for measurements of thermal conductivity under high confining pressure and pore fluid pressure conditions.

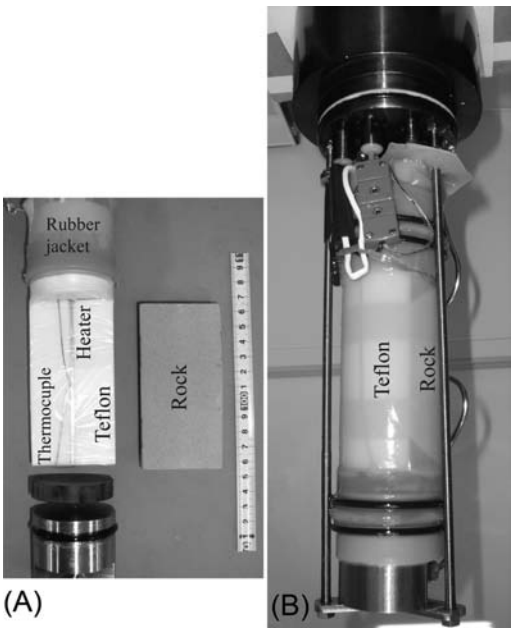


Figure 2. Photos of sample assembly for thermal conductivity measurements under high pressure. (A) before setup and (B) after setup.

2.4 *Examination of measurement system under high-pressure conditions*

First, to examine measured thermal conductivity values by our high-pressure measurement apparatus, we conducted the measurements for a fused silica specimen at several steps in increasing and decreasing confining pressure. The reason that we used the fused silica sample is that its thermal conductivity may not change distinctly with pressure. The average values of thermal conductivity showed a small increasing with increasing confining pressure because better closeness between the combination of sensor, fused silica and the Teflon under higher pressures, but the change with pressure was very limited (Fig. 4A). In addition, no hysteresis was recognized during the cycle of increasing and decreasing confining pressure. Because the fused silica is very hard to deform, changes of confining pressure have almost no effect on thermal conductivity (Fig. 4A). This result indicates that our thermal conductivity measurements were not influenced by the high pressures except the pressure effects on thermal conductivity of samples.

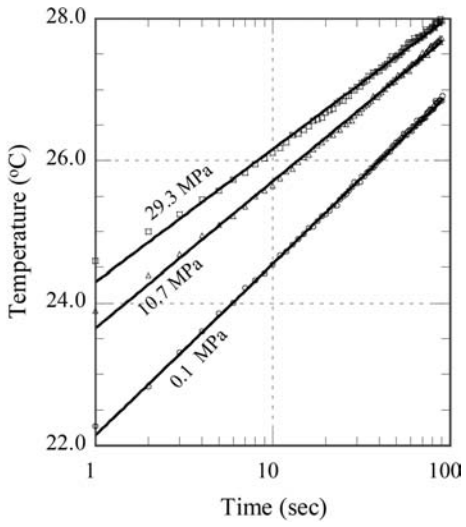


Figure 3. Examples of thermal conductivity measurements for a rock sample at three different confining pressures and a constant pore pressure of 0.1 MPa. The gradient of each data series at semi-log scale is inversely proportional to the thermal conductivity.

3 PRESSURE EFFECTS ON THERMAL CONDUCTIVITY OF ROCKS

3.1 *Rock samples*

To examine the general relationships of thermal conductivity to effective confining pressure for various rocks, we performed high-pressure tests on five rock types. The rock samples were fine-grained Aji Granite (porosity 0.85%, wet bulk density 2.64 g/cm^3 determined by the buoyancy method) from Kagawa, Japan; Rajasthan sandstone (10.6%, 2.45 g/cm^3) from India; Shirahama sandstone (13.5%, 2.43 g/cm^3), a Miocene rock from Kii Peninsula in Wakayama, Japan; Berea sandstone (19.7%, 2.31 g/cm^3) from Ohio, USA; and Tage welded tuff (31.9%, 2.03 g/cm^3) from the Miocene Oya formation in Tochigi, Japan (Lin et al. 2010).

Basically we prepared dry samples for the five rocks dried in an oven at 110°C for more than 24 hours and then moved into a dried desiccator for cooling to room temperature and keeping dry state until thermal conductivity tests. To compare the pressure effects on thermal conductivity for dry and wet samples, we also prepared fully water-saturated samples for Shirahama sandstone. The samples were soaked in ion-exchanged water in a vacuumed desiccator for more than three days for water saturation just before the thermal conductivity test.

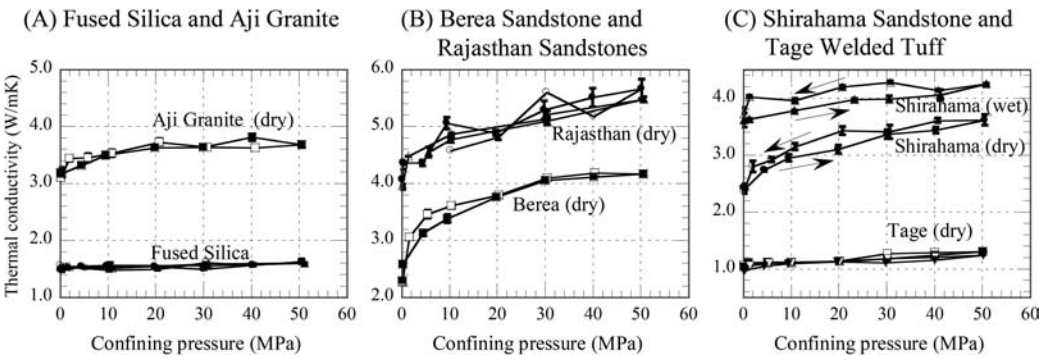


Figure 4. Relationship between thermal conductivity and confining pressure at 0.1 MPa pore pressure for all samples tested of fused silica and five rocks. The thermal conductivity was measured two or three times at each pressure. Symbols show aver-age thermal conductivity at each pressure; error bars show the range of values. Solid symbols are for stepwise increasing pres-sure; open symbols are for stepwise decreasing pressure. Arrows indicate the loading path for stepwise changes of confining pressure.

3.2 *Relationship between thermal conductivity and effective pressure*

We measured thermal conductivities of the rock samples for both increasing and decreasing stepwise changes of confining pressure. At each step of increasing pressure, the samples contracted (elastic deformation and anelastic consolidation); for each step of decreasing pressure, the samples expanded. At each step, we kept the confining pressure constant over several hours after stepwise pressure loading or unloading; and then measured thermal conductivity of the samples two or three times before proceeding to the next pressure step.

The thermal conductivity of the dry Aji granite sample increased with increasing confining pressure, but the rate of increase decreased with increasing pressure (Fig. 4A). Granites generally contain numerous microcracks, even for fresh and intact samples. It is possible that the microcracks close mainly at the lower pressure range, which would explain the decrease of the rate of thermal conductivity change with increasing pressure.

The pressure dependencies of thermal conductivity for dry samples of Rajasthan, Shirahama and Berea sandstones were similar (Figures 4B and 4C), and also similar to those of several previous studies for dry sandstones (e.g., Abdulagatova et al., 2009). However, the thermal conductivities for each rock type were different, reflecting their different mineral compositions, porosities, environments of deposition, and geological ages.

One water-saturated sample of Shirahama sandstone showed a similar relationship of thermal conductivity to pressure (Fig. 4C). This monotonous increasing relationship was similar to those of the dry samples, but the rate of thermal conductivity change was lower. In addition, the steep changes of thermal conductivity we observed for the dry samples of the sandstone at pressures lower than 10 MPa were not observed for the wet sandstone samples. In addition, the thermal conductivities of the wet sample were clearly higher than those of the dry samples for the same pressure conditions. This data also show that the rate of thermal conductivity change with pressure for a dry sample is higher than that for a wet sample.

The effect of pressure on thermal conductivity for the dry Tage welded tuff sample was much weaker than for the other rock samples (Fig. 4). Moreover, the thermal conductivities of the tuff were much lower than those of the other rocks. Repeat measurements confirmed the original results for the tuff, suggesting that the characteristics that control thermal conductivity of the tuff were different from those of the other samples. The tuff had a higher porosity than the sandstones, but the median pore size of the tuff determined by mercury intrusion porosimetry was smaller than those of the sandstones (e.g. Lin et al. 2011). The pore structure (lower pore size distribution) and mineral composition (presence of numerous clay minerals including smectite) of the tuff may also have contributed to its markedly lower thermal conductivity and muted thermal conductivity changes in response to increasing pressure.

4 SUMMARY

We developed a new apparatus to measure thermal conductivity of rock samples at high pressure conditions. The thermal conductivity of samples tested in this study clearly increased with increasing effective confining pressure. Our results suggest that it is important to measure thermal conductivities of drill core samples from great depths under in situ pressure conditions. In this study, we have not taken into account the effects of temperature on thermal conductivity. We are currently planning further experiments to address both high pressure and high temperature conditions at depth.

ACKNOWLEDGEMENTS

A part of this work was supported by Grants-in-Aid for Scientific Research (21107006) of the Japan Society for the Promotion of Science (JSPS), Japan.

REFERENCES

Abdulagatova, Z., Abdulagatov, I.M. & Emirov, V.N. 2009. Effect of temperature and pressure on the thermal conductivity of sandstone. *Int. J. Rock Mech. Min. Sci.* 46: 1055–1071, doi:10.1016/j.ijrmms.2009.04.011.

Horai, K. & Susaki, J. 1989. The effect of pressure on the thermal conductivity of silicate rocks up to 12 kbar. *Phy. Earth Planetary Interiors* 55: 292–305.

Lin, W., Tadai, O., Takahashi, M., Sato, D., Hirose, T. & Tanikawa, W. 2010. Comparison of bulk densities and porosities of various rock samples measured by different techniques. In A.L. Williams et al. (eds), *Geologically Active*, *Proceedings of the 11th IAEG Congress, Auckland, New Zealand, 5–10 September, 2010*: 2081–2086. London: Taylor & Francis Group.

Lin, W., Tadai, O. Hirose, T. Tanikawa, W. Takahashi, M. Mukoyoshi, H. & Kinoshita M. 2011 Thermal conductivities under high pressure in core samples from IODP NanTroSEIZE drilling site C0001. *Geochem. Geophys. Geosyst.* 12, Q0AD14, doi:10.1029/2010GC003449.

Sass, J.H., Stone, C. & Munroe, R.J. 1984. Thermal conductivity determinations on solid rock—a comparison between a steady-state divided bar apparatus and a commercial transient line-source device. *Jour. Volcanol. Geotherm. Res.* 20: 145–153.

Schön, J.H. 1998. Thermal properties of rocks. In *Physical Properties of Rocks*, *Handbook of Geophysical Exploration: Seismic Exploration*, Vol. 18 (2nd edn): 323–378. Pergamon.

Rock Mechanics for Resources, Energy and Environment – Kwaśniewski & Łydżba (eds)
© 2013 Taylor & Francis Group, London, ISBN 978-1-138-00080-3

Developing a high capacity direct shear apparatus for the large scale laboratory testing of rock joints

Z. Moradian, C. Gravel, A. Fathi, G. Ballivy & P. Rivard
Département de Génie Civil, Université de Sherbrooke, Sherbrooke, Québec, Canada

M. Quirion
Hydro-Québec Production, Unité Expertise en barrages, Montréal, Québec, Canada

ABSTRACT: The reliable determination of the shear strength parameters of rock joints is one of the most critical problems in geomechanics. Because of scale effects, there is no simple method for the determination of in situ shear strength parameters from the results of the laboratory tests conducted on small rock joint specimens; for this reason in situ tests on large rock joints have been developed and are sometimes conducted. However these tests are expensive and time consuming; consequently there is a great interest for simulating in situ shear tests in laboratory by developing high capacity apparatus and testing large rock joint samples. For this purpose, a new direct shear test apparatus has been developed in the Laboratoire de mécanique des roches et de caractérisation non destructive at the Université de Sherbrooke, Québec, Canada. This new system offers high shear load (up to 1000 kN) and normal load (up to 250 kN) for testing different samples with surface sizes ranging from 30 × 30 cm to 100 × 100 cm. The servo-controlled loading system allows testing of the joints by controlling the force or the displacement under cyclic loading (up to 300 cycles) and dynamic loading (with frequency 3–4 Hz) both in horizontal and vertical directions. This paper presents the characteristic of the apparatus, experimental methodology and some results of the tested joints. A procedure for the preparation of replicas from in situ rock surfaces with a Room Temperature Vulcanizing silicone (RTV) is described. These replicas are used as samples to be tested with the new shear apparatus.

1 INTRODUCTION

The province of Quebec (Canada) is one of the world largest producers of hydroelectricity. During last decades, more than 6000 dams have been constructed and are distributed all over the province territory. However, some dams are old as they were built in the 1920–1930 and they are still in service. As a consequence, older concrete gravity dams (those over fifty years) are systematically studied by Hydro-Quebec, as a part of the dam safety program in place. However, in some cases, special attention may be paid to the foundation and the rock-concrete interface.

For safety evaluation, all the causes are considered and among them are those related to the foundations mainly the shear strength along discontinuities or dam-rock interfaces. This requires taking into account the most accurate quantification available of the shear strength parameters of these discontinuities.

If possible, the shear strength of discontinuities should be measured using the results of in situ tests, as they essentially take into account the scale effect. However, in situ tests are always time consuming in terms of preparation of the specimens and transportation of the equipment and hence, quite expensive. As a result, only a small number of in situ tests can be performed for a given project. To investigate larger samples under stress environments, higher forces are necessary and high capacity loading systems have to be developed (Bidaut et al. 2006, Konietzky et al. 2012).

The aim of this project is to bring the concept of in situ direct shear tests performed on dam sites into the laboratories by replicating the real surface roughness of a discontinuity. The paper describes the components, set-up and technical data of an in-house developed system which is capable of testing large samples up to 100 cm × 100 cm under different monotonic and dynamic loading conditions.

2 LARGE SCALE DIRECT SHEAR TEST APPARATUS

The large scale direct shear test apparatus was fabricated in Laboratoire de mécanique des roches et de caractérisation non destructive at the Université de Sherbrooke, Québec, Canada in 2012 (Fig. 1).

The system consists of a steel base plate having dimensions of 170 cm × 120 cm × 5 cm in thickness to sit the lower sample parts with its supports (Fig 2). This base plate contains several holes to accommodate samples of sizes ranging from 30 cm × 30 cm up to 100 cm × 100 cm.

A total of eight threaded steel rods (ø = 40 mm, L = 110 cm) are used to rigidly fix the plate on the concrete slab of the laboratory floor. The system also consists of two supports made of a plate (106 cm × 50 cm × 5 cm) on which are perpendicularly welded to 4 steel triangles serving for the reinforcement.

The plate and the triangle reinforcements are bolted to the base plate with 6 screws (ø 1.5″ × 3″). The support plate is connected to an adjustment plate (100 cm × 49 cm × 5 cm) with 3 adjustable screws (ø 1.5″ × 6″). The adjustable plate is used to fix and position the sample in the frame. This set up has been designed to be used with rectangular samples. If the sample is not rectangular or one wants to increase the stiffness of the set up (in the case of higher stresses) two steel moulds with two different sizes have been constructed for such an application. In this case, the irregular or the regular shape sample is placed in the mould and is fixed with grouting.

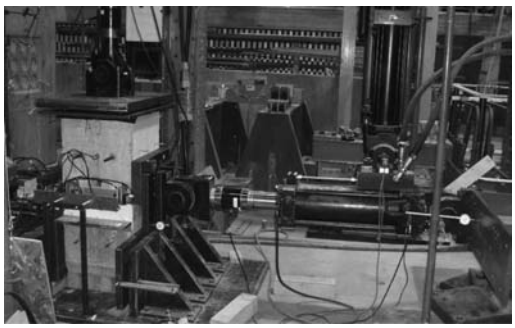


Figure 1. The large scale direct shear test apparatus is capable of testing rock and concrete joint surfaces up to 100 cm × 100 cm. The horizontal MTS actuator has a capacity of 500 kN (it can be replaced with a 1000 kN actuator) and the vertical actuator has a capacity of 250 kN.

Two steel plates are located between vertical jack and the upper block and a system of rollers is placed in between allowing the upper block to move freely in the shearing direction. Normal and tangential loads are generated by two hydraulic actuators with capacities of 250 and 500 kN respectively and are controlled by the software. Actuators can reach a frequency up to 4 Hz. The loads are read by the two load cells integrated in the actuators. The direction of the horizontal (shear) load was considered to pass through the interface in order to minimize the rotation of the specimen.

Displacements of the samples in the three orthogonal directions are read by eight laser extensometers having a range of 120 mm and an accuracy of 8 μm. Four laser extensometers are used to measure the dilation of the upper sample, two for measuring shear displacement and two for measuring the lateral displacement. The displacements of the frame base plate and supports are recorded by 4 portable Fissuro Loggers (SITES) having an accuracy of 3 μm. The lateral movement of the joint sample is fixed by two rolling holders in two sides of the upper block.

Since the capacity of the vertical jack is 250 kN, it was decided to apply normal loads of 50 kN, 100 kN, 150 kN and 200 kN during testing of the samples. The displacement rate of 0.10 mm/min was considered

The servo-controlled system used is designed for the standard procedures described in the following:

– *Shearing at constant normal force*: in this case the normal load is constant; however, due to the change in contact area during the test the normal stress doesn't remain constant.

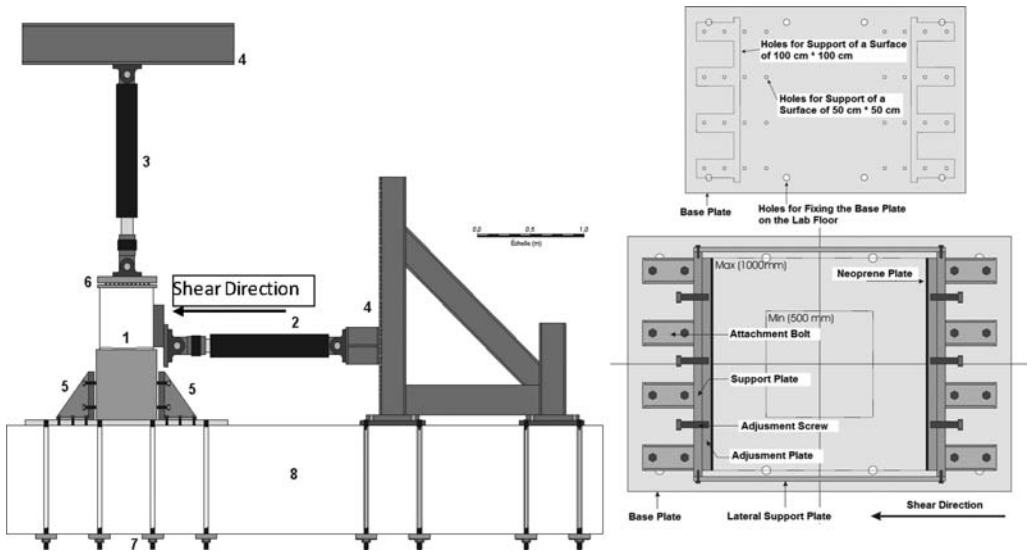


Figure 2. Several parts of the laboratory large scale direct shear test apparatus 1) Joint surface, 2) Horizontal (shear) actuator 500 kN, 3) Vertical (normal) actuator 250 kN, 4) Supports, 5) Supports of the lower sample casted in a steel mold, 6) Sliding rollers, 7) Bolts, 8) Concrete Slab of the lab floor.

– *Shearing at constant normal stress*: in order to have constant normal stress during the test, the normal load and the area have to be constant For this case the lower surface must be larger than the upper surface so that the contact area always remains constant (Muralha 2012).
– *Shearing at constant normal stiffness*: constant change of normal stress versus normal relative displacement ratio. In this case, a series of springs with constant stiffness have to be put between the upper half and the plate of the vertical jack.

Acoustic emissions (AE) generated by the asperity degradations during the test were recorded by fourteen AE sensors (Fig. 3). An AE system was used for the recording of AE events. The frequency range of sensors was 40–100 kHz with a resonance frequency of 55 kHz. The sampling rate was set to 1 MSPS, amplification of pre-amplifier was 40 dB, and AE exceeding 45 dB was measured.

The sample surface was scanned before and after testing with a laser profilometer having a resolution of 15 μm (Fig. 3). These scans allow performing a 3D analysis of surface roughness parameters. This analysis will be combined with the location of damaged areas obtained from acoustic emission (Moradian et al. 2012).

3 SPECIMENT PREPARATION AND METHODOLOGY

Joint samples for large scale direct shear tests should be preferably collected in situ. Concerning the shape of the sheared area, rectangular shapes are the most suitable because any error in the evaluation of the area results in an error in the shear strength (Muralha 2012).

Obtaining a rectangular rock-rock joint sample with a desired dimension (100 cm × 100 cm) may become rapidly time consuming and somehow difficult: precise drilling and cutting is required and might not be always successful.

An alternative was considered for this project and consists to construct a concrete-concrete joint sample in the laboratory that represents the in situ rock-rock joint. To reach this goal, the following step were taken into account:

1) Selecting the in situ joint surface (preferably more than 1 m^2) and preparing the surface.
2) Pouring the silicon on the joint surface to copy the roughness.
3) Obtaining rock cores of the rock mass or getting some rock blocks for coring in the laboratory in order to carry out basic rock mechanics laboratory tests.
4) Selecting an appropriate mortar mix in order to fabricate concrete samples with similar physical and mechanical parameters to the rock samples tested at section 3.
5) Pouring mortar prepared from the selected mix on the silicon surface for fabricating the concrete-concrete joints. In this way the morphological and mechanical characteristics of the replica are very close to the in situ joint surface and the rock mass.

The use of joint surfaces replicas allows performing many mechanical tests with various experimental conditions, while still keeping the same surface morphology. Thus, for a given surface, multiple orientations of the shear directions can be considered to create a database of the mechanical behavior (anisotropy) of discontinuities.

Making of the appropriate concrete replica is not a straightforward process. Indeed, there must be a number of criteria to be checked (Flamand 2000):

– Grain size of the mortar should be comparable to that of minerals in the rock;

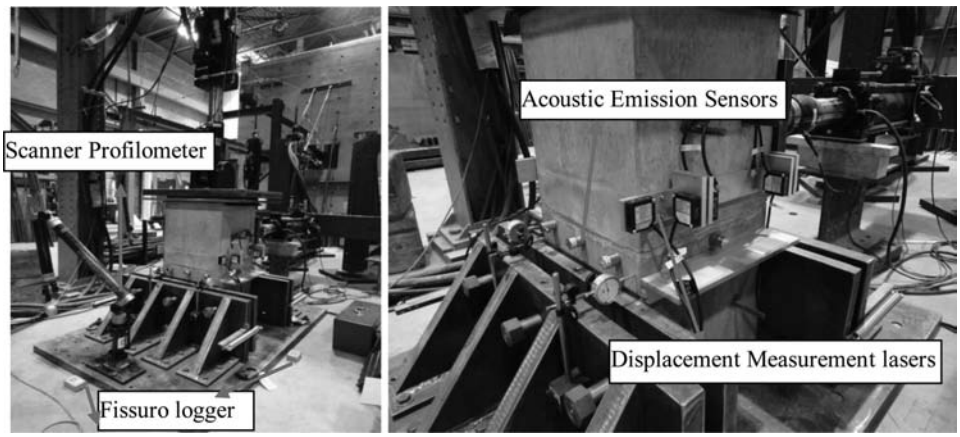


Figure 3. The experimental set up, scanner profilometer is placed near to the test set up for scanning the upper and the lower joint surfaces before and after the test, fissuro loggers for measuring the probable movement of the base plate and other part of the set up, acoustic emission sensors for detecting the signals as a precursor of the joint failure and localizing the asperity damaged zones and displacement lasers for measuring the horizontal, vertical and lateral displacements of the joint specimen precisely.



Figure 4. Natural granite joint surface used to make concrete replica. Samples are fabricated for every window size and the large scale test is carried on to investigate the scale effect on joint roughness and its shear parameters.

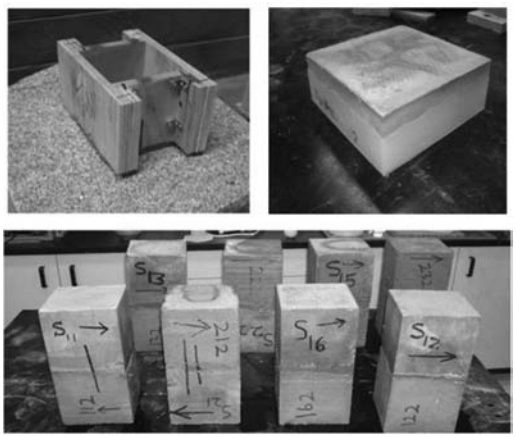


Figure 5. Several steps in fabricating concrete replica from granite joint surface.

- Permeability of the mortar should be as close as possible to that of the rock;
- Compressive strength of the mortar must be at least 50% of the rock. When the shear tests are performed under low normal stress (less than 2 MPa), a mortar with a lower resistance may be used;
- Mortar should be sufficiently vibrated, so that there is no air voids at the interface between the surface and the mortar;
- Once the replicas are completed, they must reach their full strength explaining why the tests are generally carried out after 28 days.

A rock joint surface from Stanstead granite, Quebec, Canada was selected to prepare the replica (Fig. 4). Figure 5 shows the successive milestones of preparation of a sample, starting from the original rock joint to the final mortar replica.

The mortar experienced a very small shrinkage during the preparation of the sample. The size of the grains of mortar is small enough to reproduce the details of the granite surface roughness. The mortar used is Sika 212 which reaches a compressive strength of 55 MPa at 14 days. The molds used are made of silicone RTV 1556 which faithfully reproduces the micron size of rock surfaces.

4 RESULTS

4.1 *Surface roughness measurement*

Roughness is one of the key parameters affecting the shear strength of the discontinuities. This parameter increases the friction angle and consequently the shear strength of the discontinuities significantly. Many parameters have been proposed to characterize the roughness of the discontinuities in 2D and 3D dimensions (Tatone & Grasselli 2012). The most challenging issue related to roughness is its scale dependency.

Some researchers have addressed the increasing of the roughness by increasing of the scale. Others have demonstrated that roughness decrease by increasing of the scale (Tatone & Grasselli 2012).

Fardin et al. (2001) showed that the scale effect related to the roughness is neutralized after passing a specific dimension of the surface area. This particular point was named "stationarity threshold" which was around 50 cm for their tested sample.

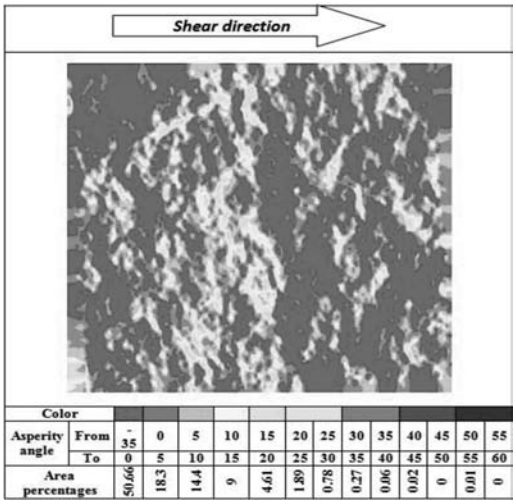
Another important factor regarding shear strength of discontinuities is the joint matching percentage of the upper and lower surfaces. This index is based on the percentage of joint surface in contact. The joint matching is an important factor governing the aperture, normal closure, stiffness, shear strength, and hydraulic conductivity of the joints.

Recently, researchers expressed that the effective contact on shear resistance could only occur between asperities facing to the shear direction. Furthermore, only the steepest surfaces can be involved in the shearing and they will ultimately be deformed, sheared or crushed, depending on the applied normal load. Accordingly, the identification of the potential sliding areas only requires the determination of the areas facing to the shear direction and steep enough to be involved in the shearing process (Grasselli 2006).

In this study, the joint surfaces (upper and lower) of samples have been scanned using profilometer scanner in order to identify the steepest asperities in the shear directions. For achieving this, a computer program was developed by using C++ programming language.

This program allows the user to draw 2D profile and 3D view of the surface in different directions. Furthermore, it enables calculating of shear parameters for different directions. This program can calculate the asperity angle and show their distribution on the joint surface using ArcGIS software.

In this research, steepest asperities in 4 directions (0, 90, 180 and 270 degree) were determined using the above program and then the distribution of the steepest asperities was calculated. Using two types of representation, topography and asperities distribution, one can have a better evaluation of the asperities that have a significant role during shear process. For example, one of the results exported from ArcGIS is shown in Figure 6.



Color														
Asperity angle	From	-35	0	5	10	15	20	25	30	35	40	45	50	55
	To	0	5	10	15	20	25	30	35	40	45	50	55	60
Area percentages		50.66	18.3	14.4	9	4.61	1.89	0.78	0.27	0.06	0.02	0	0.01	0

Figure 6. Asperity angle distribution of a joint surface. Area percentages of each angle have been shown in the above table.

Table 1. Some of roughness parameters of the surface. They vary with sampling interval.

Dimension	Parameter	Interval (mm)	Amount
2D	Z_2	1	0.194
		0.8	0.221
		0.6	0.294
		0.4	0.401
		0.2	0.659
	R_p	1	1.018
		0.8	0.972
		0.6	1.025
		0.4	1.030
		0.2	1.040
3D	R_s	1	1.018
		0.8	1.021
		0.6	1.025
		0.4	1.030
		0.2	1.040

Almost 50% of asperities are facing to shear direction (positive angles) and 50% are against shearing direction. It means that 50% participate in shearing process and 50% do not. Therefore, the efficient contact area is 50%.

Table 1 shows some of the roughness parameters measured for the surface displayed in Figure 6. R_P is defined as the ratio of the true profile length, to the nominal profile length (El-Soudani 1978) and R_S is the 3D analog of R_P, defined as the ratio of the true surface area to the nominal surface area. The parameter Z2 represents the root mean square of the first derivative of the height of a 2D profile (Tse & Cruden 1979).

These results are used for fully understanding of the asperity degradation and shear mechanism of the rock joints and evaluating the developed shear failure criteria for the tested samples. Afterward, the best criterion

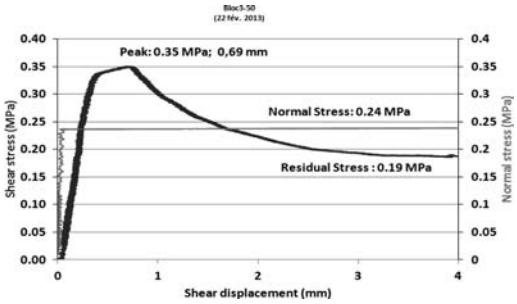


Figure 7. Shear stress and normal stress versus shear displacement of the first large sample. The applied constant normal load was 50 kN (medium normal stress of 0.24 MPa). The sample showed the max shear strength of 0.35 MPa and residual shear strength of 0.19 MPa.

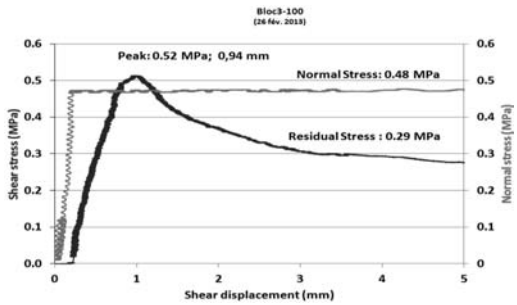


Figure 8. Shear stress and normal stress versus shear displacement of the second large sample. The applied constant normal load was 100 kN (medium normal stress of 0.48 MPa). The sample showed the max shear strength of 0.52 MPa and residual shear strength of 0.29 MPa. By increasing normal load, the second sample reached the peak later (0.94 mm comparing to 0.69 mm for the first sample) with a brittle failure.

that matches better with the results is chosen or modified. If such criterion is not available a new one will be proposed in the next steps of this research project.

4.2 *Shear behavior and shear parameters of large scale joints*

Shear behavior and shear strength parameters are significantly subjected to scale effect. Many researchers have pointed out a negative effect of scale on shear strength of discontinuities (Tatone & Grasselli 2012).

The results of two different sample sizes from one joint surface are presented in the following. Large replica samples with dimensions of 50 cm × 50 cm were tested under constant normal load tests.

Figures 7 and 8 show the shear stress vs. shear displacement of the two samples tested under normal stress of 0.25 MPa and 0.50 MPa respectively. Figure 9 and 10 present dilation vs. shear displacement for the tested samples. It can be seen from these figures that the shear stress is increasing with the constant slope (shear stiffness Kn) until the maximum shear strength; and then decreases down to a constant residual value.

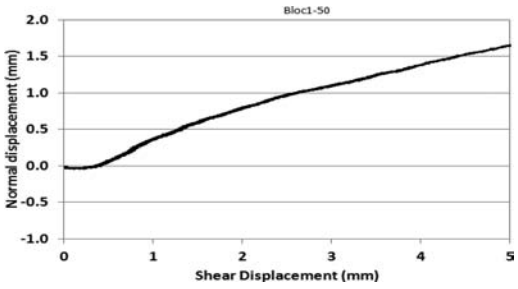


Figure 9. Normal displacement (dilation) of the first large sample versus shear displacement. For a shear displacement of 5 mm, the maximum dilation of the sample was 1.7 mm.

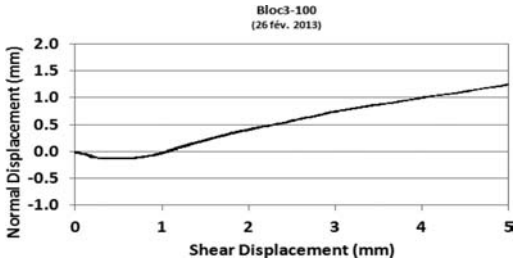


Figure 10. Normal displacement (dilation) of the second large sample versus shear displacement. For a shear displacement of 5 mm, the maximum dilation of the sample was 1.3 mm. Increasing of the normal load decreased the dilation.

Regarding the effect of the normal load on the dilation; the joint is first slightly contracted and then dilated.

5 CONCLUSIONS

It has been demonstrated that for precise determination of the morphological and mechanical properties of rock joints in the laboratory and in the field, samples of size equal to or larger than "stationarity threshold" are needed. Samples of smaller size are not representative for the in situ rock joints.

For this purpose, a new high capacity direct shear system was developed and successfully tested, which provides new testing possibilities, especially in relation to large forces, larger sample sizes, as well as cyclic and dynamic testing. The system has been fabricated for force, displacement, dilatancy and stiffness-controlled testing conditions.

A variety of joint sizes and types can be tested with the system. Interfaces can have irregular or regular surfaces and can be either natural or artificial.

The proposed research program will certainly contributes in the determination of more realistic values of shear strength of discontinuities to be used for stability analysis and numerical modeling. Future work are planned to study the influence of the shear roughness and shear direction on the hydraulic conductivity of the fluid on large joint surface and possibly testing repaired discontinuities by grout injection.

ACKNOWLEDGEMENT

This study was made possible by the financial participation of Hydro-Quebec and the Natural Sciences and Engineering Research Council of Canada (NSERC) grant. The authors would like to thank Danick Charbonneau for his valuable assistance and Groupe de structure for the testing material.

REFERENCES

Bideaut, P., Durville, J.L., Guillemin, P., Richard, J.C. & Vitorovitch, M. 2006. Essais de cisaillement sur discontinuités rocheuses armées par ancrages passifis: utilisation d'une boîte de cisaillement de grandes dimensions. *Bulletin des Laboratoires des ponts et chaussées* 263–264: 7–18

El Soudani, S.M. 1978. Profilometric analysis of fractures. *Metallography* 11: 247–336

Fardin, N. & Stephansson, O. & Jing, L. 2001. The scale dependence of rock joint surface roughness. *Int. J. Rock Mech. Min. Sci.* 38: 659–669.

Flamand, R. 2000. Validation d'une loi de comportement mécanique pour les fractures rocheuses en cisaillement. *Thèse de doctorat. Université du Québec à Chicoutimi. Ca.* 470 p.

Grasselli, G. 2006. Shear strength of rock joints based on quantified surface description. *Rock Mech. Rock Eng.* 39(4): 295–314.

Konietzky, H. & Frühwirt, T. & Luge, H. 2012. A new large dynamic rockmechanical direct shear box device. *Rock Mech. Rock Eng.* 45: 427–432.

Moradian, Z.A., Ballivy, G. & Rivard, P. 2012. Correlation between acoustic emission source locations and damage zones of rock joints under direct shear test. *Canadian Geotechnical Journal* 49(6): 710–718.

Muralha, J. 2012. Rock joint shear tests, Methods, results and relevance for design. EUROCK 2012, Stockholm, Sweden, May 28–30, 2012.

Tatone, B.S.A. & Grasselli, G. 2012. An investigation of discontinuity roughness scale dependency using high-resolution surface measurements. *Rock Mech. Rock Eng.* 46(4): 657–681.

Tse, R. & Cruden, D.M. 1979. Estimating joint roughness coefficients. *Int. J. Rock Mech. Min. Sci.* 16: 303–307.

Rock Mechanics for Resources, Energy and Environment – Kwaśniewski & Łydżba (eds)
© 2013 Taylor & Francis Group, London, ISBN 978-1-138-00080-3

Some remarks on the experimental determination of the Biot coefficients

A. Nowakowski & J. Walaszczyk
Strata Mechanics Research Institute Polish Academy of Sciences, Kraków, Poland

ABSTRACT: The Biot consolidation theory allows the formulation the effective stress law in the form of equation binding the components of the stress tensor with the value of pore pressure. This equation contains certain factors (the so-called Biot coefficients) which are mathematical functions of the rock porosity (n), rock bulk modulus (K) and bulk modulus (K_S) of rock solid phase (matrix). The article is devoted to the study of the impact of the pore fluid type on the values of Biot coefficients.

Some specimens cut from two rocks: sandstone and gaize were tested in the laboratory. At first the specimens were tested in pycnometer to determine their bulk and helium densities. Then, on the basis of the measured densities porosity of the studied rocks were calculated.

Compressibility tests were performed at four different pore fluids: two liquids (distilled water and kerosene), and the two gases (nitrogen and carbon dioxide). The K modulus was determined on the basis of experiments in which the pore fluid pressure was equal to atmospheric pressure, and K_S modulus was based on experiments in which the pore fluid pressure was equal to the confining pressure. All compressibility tests were drained ones.

Experiments results have shown that the values of K and K_S moduli (and thus the values of the Biot coefficients) depend on a relatively small extent on the type of fluid filling the pore space of the rock specimen. It seems that these values are determined by two main factors: the degree of filling the rock pore space with fluid and filtering capabilities of fluid in the rock pore space. The tests have indicated, that the Biot coefficients can be determined correctly only when the entire pore space is filled with fluid and porous fluid filtration is free within the sample.

1 INTRODUCTION

The term "effective stress" was introduced into soil mechanics by the turn of the XIX century by Paul Fillunger (1913–1915) and Karl von Terzaghi (1923). It gave grounds to build a mathematical model of some phenomena taking place in soil with pore fluid under pore pressure p_p. Maurice Biot (1941) developed Terzaghi's concept by using Hooke's law equations and introducing proprietary sets of equations for elastic, homogeneous and isotropic porous medium given by (see Paterson & Wong (2005) – pp. 149–152, Fabre & Gustkiewicz (1998), Gustkiewicz (1989)):

$$\varepsilon_{ij} = \frac{(1+\nu)}{E}\sigma_{ij} + \frac{\nu}{E}\sigma_{ii}\delta_{ij} - \frac{1}{3H}p_p\delta_{ij} \quad i,j=1,2,3 \tag{1a}$$

$$\zeta = \frac{\sigma_m}{H} - \frac{p_p}{R} \tag{1b}$$

$$\frac{1}{H} = \frac{1}{K} - \frac{1}{K_S} \tag{1c}$$

$$\frac{1}{R} = \frac{1}{K} - \frac{1+n}{K_S} \tag{1d}$$

where E and ν = Young's modulus and Poisson's ratio, respectively, n = medium's porosity, K = its bulk modulus, K_S = bulk modulus of its solid phase, ζ = change in the volume of pore space of considered medium, and H and R = some material constants.

Nur and Byerlee (1971) noticed, by expanding on Biot's concept, that should $i = j$ in set of equations (1a), we get three Biot's medium equations for three main directions. By adding sides of all equations we get:

$$\varepsilon_{ii} = \frac{3(1+\nu)}{E}\sigma_{ii} + \frac{3\nu}{E}\sigma_{ii} - \frac{1}{H}p_p \qquad i,=1,2,3 \tag{2}$$

Then, by using the equation (2), Nur and Byerlee obtained the so-called effective stress law for porous medium satisfying the equation (1a). That law is expressed by:

$$'\sigma_{ij} = \sigma_{ij} - \alpha_1 p_p\delta_{ij} \qquad i, j = 1, 2, 3 \tag{3a}$$

$$\alpha_1 = 1 - \frac{K}{K_S} \tag{3b}$$

where $'\sigma_{ij}$ = so-called effective stress tensor.

What Nur and Byerlee did next, was to rearrange the equation (1b) similarly to equation (1a). In effect, they obtained the law of effective stress for pore space of considered medium, which satisfies the equation (1b). In this case, said law is given by

$$'\sigma_{ij} = \sigma_{ij} - \alpha_2 p_p\delta_{ij} \qquad i, j = 1, 2, 3 \tag{4a}$$

$$\alpha_2 = 1 - \frac{nK}{K_S - K} \tag{4b}$$

In conclusion, Nur and Byerlee proved, starting with Biot's consolidation theory, that effective stress in porous medium may be defined by the following relationship:

$$'\sigma_{ij} = \sigma_{ij} - \alpha\, p_p \delta_{ij} \qquad i, j = 1, 2, 3 \tag{5}$$

where the value of so-called effective pressure coefficient α is given by the formula (3b) for the entire porous medium or formula (4b) for deformation of that medium's pore space. Based on relationships (3b) and (4b) as well as interdependencies between n, K and K_S, Gustkiewicz (1989) proved that the following is true:

$$0 \le \alpha_1 \le 1 \wedge \qquad 0 \le \alpha_2 \le 1 \tag{6}$$

2 SUBJECT MATTER AND METHODOLOGY

Since the effective stress law (5) is derived from Biot's relationships, it implies that effective stress is the stress which controls volumetric change of the medium relative to pore stress and pressure. This is all the more apparent, after studying relationships (3b) and (4b). The material constants K and K_S they include are quantities linking together medium stresses with volume changes. Hence to determine the form of relationship (3b) and (4b) it is necessary to determine given rock's porosity and bulk moduli.

Porosity is a property which may be determined in course of pycnometry testing. In case of rock formed as a solid matrix and so-called pore space, the following types of density are to be considered: helium density ρ_S and bulk density ρ_0. The former determines density of solid phase i.e. the so-called mineral matrix of the rock. When determining bulk density the total specimen volume is considered, which includes both the volume of mineral matrix and volume of the pores. The type of pore fluid (either gas or liquid) is key for determining density, because density depends to a large extent on mineral composition of the material, porosity and quantity of pore fluid.

Measurements of density where carried out using Micromeritics pycnometers. AccuPyc II 1340 gas pycnometer facilitates measuring volume of rock specimen's matrix by deploying helium. It penetrates well the inner rock structure and fills all pores connected with external surface of the specimen. Thanks to helium pycnometer the helium density of the rock may be determined without excluding isolated pores which could not be reached by the gas.

GeoPyc 1360 apparatus determines bulk density of rock specimen by measuring its volume using quasi-liquid DryFlo substance. Based on helium and bulk density, porosity n of tested rocks may be determined from the following equation:

$$n = 1 - \frac{\rho_o}{\rho_S}, \tag{7}$$

Detailed description of the pycnometer can be found in the paper by Dutka et al. (2007).

As aforementioned, for purposes of the Biot's theory, it is necessary to determine bulk moduli of the rock (K) and its matrix (K_s). The K modulus is determined through the compressibility experiment, where the pore space is open and pore pressure equals barometric pressure and strain in tested specimen equals total strain of its matrix and pores. The immediate conclusion is that the greater rock porosity the greater its strain, thus lower K modulus. To determine the K_s modulus the compressibility test is employed, where pore pressure constantly equals hydrostatic pressure. Notice, the entire pore space needs to be filled with pore fluid. The computational error when determining the K_S increases with percentage of the so-called isolated pores i.e. pores without connections with other cavities surrounded completely by rock mass. Detailed information concerning procedures of carrying out the tests at the Laboratory of Rock Deformation of the Strata Mechanics Research Institute of the Polish Academy of Sciences is given in Gustkiewicz's paper (1989).

At this stage is must be emphasized that neither Biot nor Nur, Byerlee or indeed any other – to the authors' best knowledge – paper concerning this subject matter (e.g.: Rice & Cleary (1976), Zienkiewicz & Shiomi (1984), Detournay & Cheng (1993), Roegiers et al. (1998), Lade & de Boer (1997)) did not unequivocally state, what fluid shall fill pore space during the compressibility experiment. The referred to on numerous occasions Gustkiewicz (1989) suggests to determine the K modulus when it is filled with air (dry air state). The K_S on the other hand when it is filled with kerosene. Even this author, however, takes no interest in considering the impact of the fluid type on test results. Hence, a decision was made to determine K and K_S moduli of rock specimens whose pore space was filled with different pore fluids – both liquids and gases. Therefore, a number of compressibility tests were carried out, using the following liquids as pore fluids:

a) kerosene – inert liquid,
b) distilled water (H_2O) – non-inert liquid,
c) nitrogen (N_2) – inert gas,
d) carbon dioxide (CO_2) – non-inert gas,

Experiments were carried out under the following conditions: pore pressure equal to barometric pressure ($p_p = 0$); pore pressure equal to hydrostatic pressure ($p_p = p$). Determined through those experiments bulk moduli (K and K_S respectively) were then used to determine Biot's coefficients according to formulae (3b) and (4b). Presented below (Fig. 1) is an example compressibility test result obtained for kerosene impregnated sandstone specimen. The figure displays the curves: "$p_p = 0$" and "$p_p = p$" and how their K and K_S moduli are determined.

3 SOME PROPERTIES OF TESTED ROCKS

Subjected to testing were two rocks: sandstone – henceforth referred to as "sandstone 8348" and gaize –

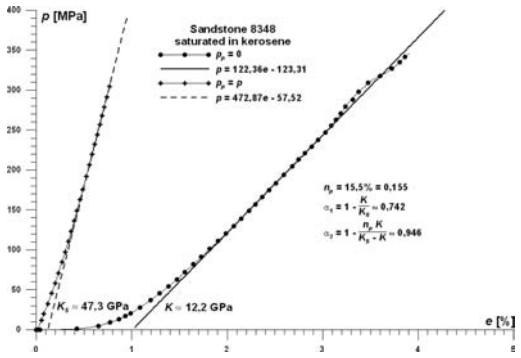


Figure 1. Example compressibility test results: kerosene impregnated sandstone 8348.

marked as "gaize 9166". Sandstone is created through a mechanical process of sedimentation whereas gaize through chemical process of precipitation. The sandstone 8348 was a grey and yellow medium-grained rock, poorly sorted, bonded with cement. The gaize was a grey rock combining carbonate phase and silica (opal, chalcedon) and a compact matrix (carbonate components did not leach).

Said rocks were used to produce 16 specimens of each. They were cylinders 22.5 cm in diameter and 45.0 mm in height. Both helium and bulk densities were obtained for all specimens. Porosity was calculated. The value of porosity n necessary in formula (4b) was taken as mean of all void fractions obtained for each specimen. The n value was taken as:

for sandstone 8348 – $n = 15.9\%$
for gaize 9166 – $n = 7.4\%$.

4 RESULTS OF LABORATORY EXPERIMENTS

The experimentally determined values of bulk modulus and Biot's coefficient are displayed in Tables 1 and 2. By studying these values, the following conclusions were drawn:

i) The type of pore fluid has no significant influence on the Biot's coefficient α_2 derived using the formula (4b). Since this coefficient is supposed to determine the influence pore pressure has on volumetric deformation of medium's pore space. it is fair to say that volumetric deformation of that space. by and large. does not depend on the fluid.
ii) In case of α_1 coefficient calculated from the formula (3b). it is more complicated. Values of α_1 obtained for the sandstone would suggest. that volumetric deformation of the rock is more "susceptible" to pore pressure where pore fluid is a liquid (non-compressible medium) as opposed to compressible gas. Notice. however. the differences are insignificant. On the other hand. results for the gaize indicate relatively high α_1 value and considerably smaller α_1 for the liquid. It would seem that the factor. which determines the value of the α_1 coefficient is the efficiency of space filling of specimen pore space with pore fluid and filtering of that fluid within that space. The condition required to determine the K_S modulus is: pores completely filled with fluid and its "speedy" filtration – necessary to maintain equal confining and pore pressures. In an extreme case. when pore space consisted solely of isolated pores. we could have $K_S/K = 1$ (i.e. $\alpha_1 = 0$) plainly because pores remain empty and there would be no way of correctly determining the K_s modulus.

Table 1. Bulk moduli and Biot coefficients; sandstone 8348.

		Sandstone 8348						
		n [%]	K [MPa]	K_S [MPa]	$K : K_S$	α_1	α_2	$\alpha_1 : \alpha_2$
Pore fluid	kerosene	15.5	12.2	47.3	1 : 3.9	0.742	0.946	1 : 1.3
	H_2O		12.0	41.9	1 : 3.5	0.714	0.938	1 : 1.3
	N_2		9.5	25.6	1 : 2.7	0.629	0.909	1 : 1.5
	CO_2		13.2	38.1	1 : 2.9	0.653	0.917	1 : 1.4

Table 2. Bulk moduli and Biot coefficients; gaize 9166.

		gaize 9166						
		n [%]	K [MPa]	K_S [MPa]	$K : K_S$	α_1	α_2	$\alpha_1 : \alpha_2$
Pore fluid	kerosene	7.6	14.4	28.8	1 : 2.0	0.493	0.923	1 : 1.9
	H_2O		21.5	33.6	1 : 1.6	0.360	0.865	1 : 2.4
	N_2		12.8	54.0	1 : 2.4	0.763	0.976	1 : 1.3
	CO_2							

In order to correctly interpret above numbers. results produced by Dutka et al. (2008) through studying properties of rocks in presence of gas i.e. the time it takes pore space to fully fill up and probability of sorptive effects. the sandstone's pore space was fully filled with inert gas (helium) in approx. 200 s. CO_2 took longer i.e. 50 min before the pressure p_p had stabilised. Gaize was not tested using helium. whereas CO_2 took approx. 120 min. to fill 50% of pore space with gas. No sorptive effects were observed which could influence the process. What does it mean from the viewpoint of compressibility testing? Firstly – in case of gaize there is no guarantee the entire specimen's pore space was filled with pore fluid. secondly – even if the entire pore space was filled with gas. The filtration processes are sluggish enough to make keeping confining pressure and pore pressure the same throughout the experiment impossible. Thereby the K_S modulus could not be determined correctly. Also. notice that if filling the specimen with gas was that difficult. filling it with liquid must have been more troublesome. ergo empirical K_S values must have been more erroneous than in case of gas used as pore fluid.

To summarise the above discussion it is fair to say that dependence of Biot's coefficient α_1 on pore

medium is to a significant extent contingent on the structure and texture of analysed rock. In case of high porosity clastic rock where pore fluid filters easily. type of that fluid plays a lesser role. whereas in case of low porosity hard rock that coefficient values might diverge significantly depending whether gas or liquid was used as the pore medium.

REFERENCES

Biot, M.A. 1941. *General theory of three dimensional consolidation*. J. Appl. Phys. 12: 155–168.

Detournay, E. & Cheng, A.H.-D. 1993. *Fundamentals of Poroelasticity.* In: C. Fairhurst (ed.), "Comprehensive Rock Engineering: Principles. Practice & Projects". Vol. II, pp. 113–171. Oxford: Pergamon Press.

Dutka, B., Kudasik, M. & Wierzbicki, M. 2007: *Nowe metody i narzędzia dla badania zjawiska nagłego wyrzutu węgla i gazu*. Transactions of the Strata Mechanics Research Institute 9(1–4): 137–147.

Dutka, B., Lizak, Z., Nowakowski, A., Nurkowski, J. & Wierzbicki, M. 2008. *Zależność wartości współczynnika Biota od rodzaju medium porowego.* Transactions of the Strata Mechanics Research Institute 10(1–4): 3–15.

Fabre, D. & Gustkiewicz, J. 1998. *Influence of rock porosity on the Biot's coefficient*. In: Thimus et al. (eds.), "Poromechanics – A Tribute to Maurice A. Biot". Proc. of the Biot Conf. on Poromech. Louvain-la-Neuve (Belgium). 14–16 Sept. 1998. Rotterdam: Balkema.

Fillunger, P. 1913. *Der Auftrieb in Talsperren.* Österr. Wochenschrift für den öffentlichen Baudienst. 19: 532–556, 567–570.

Fillunger, P. 1914. *Neuere Grundlagen für die statische Berechnung von Talsperren*. Zeitschrift des Österr. Ing.- und Arch.- Vereines. 23: 441–447.

Fillunger, P. 1915. *Versuche über die Zugfestigkeit bei allseitigem Wasserdruck*. Österr. Wochenschrift für den öffentlichen Baudienst. 29: 443–448.

Gustkiewicz, J. 1989. *Objętościowe deformacje skały i jej porów*. Arch. Min. Sci. 34(3): 593–609.

Lade, P.V. & Boer de, R. 1997. *The concept of effective stress for soil, concrete and rock*. Géotechnique 47(1): 71–67.

Nur, A. & Byerlee, J.D. 1971: *An Exact Effective Stress Law for Elastic Deformation of Rock with Fluids*. J. Geophys. Res. Vol. 76. No. 26. pp. 6414–6419.

Paterson, M.S. & Wong, T.-f. 2005. *Experimental Rock Deformation – The Brittle Field*. Berlin Heidelberg: Springer-Verlag, 347 p.

Rice, J.R. & Cleary, M.P. 1976. *Some basic stress diffusion solutions for fluid-saturated elastic porous media with compressible constituents*. Reviews of Geophysics and Space Physics. 14(4): 227–241.

Roegiers, J.-C., Cui, L. & Bai, M. 1978. *Poroelasticity applications*. In: H.-P. Rossmanith (ed), Mechanics of Jointed and Faulted Rock. Proc. of the MJFR-3 Int. Conf., Vienna, 6–9 April 1998, pp. 39–46. Rotterdam: Balkema.

Terzaghi, von. K. 1923. *Die Berechnung der Durchlässigkeitsziffer des Tones aus dem Verlauf der Spannungserscheinungen*. Sitzungsber. Akad. Wiss. Wien Math.-Naturwiss. Kl.. Abt. 2A. 132. 105.

Zienkiewicz, O.C. & Shiomi, T. 1984. *Dynamic behaviour of saturated porous media; the generalized Biot formulation and its numerical solution.* Int. J. Num. Anal. Meth. Geomech. 8: 71–96.

Rock Mechanics for Resources, Energy and Environment – Kwaśniewski & Łydżba (eds)
© 2013 Taylor & Francis Group, London, ISBN 978-1-138-00080-3

Dynamic and static rock mechanical properties of heavy oil sandstones

C. Rabe & P. Perdomo
Baker Hughes, Rio de Janeiro, Brazil

J. Cherrez
Petroleos de Venezuela S.S., Puerto la Cruz, Anzoategui, Venezuela

ABSTRACT: This article describes consolidated drained triaxial tests to determine the acoustic and mechanical properties of heavy oil sandstone from shallow, high-temperature boreholes in the Eastern Venezuela basin. The purpose of this laboratory campaign is to create physical correlations between rock under in-situ conditions and the severe temperatures generated during steam injection. These tests will be used for modeling the impact of Steam-Assisted Gravity Drainage (SAGD), in unconsolidated sandstones.

1 INTRODUCTION

For most oil and gas reservoirs, temperature effects on rocks during the life of the well are incorrectly thought to have aminimal effect, compared to the effects of hydrostatic or injected fluid pressures such as from completion fluids or drilling muds. However, this is clearly not the case where steam is injected for heavy oil reservoir stimulation. In these situations there is a tremendous elevation in the bottom hole temperature, resulting in changes in the rock structure and its elastic properties and rock strength.

Thermal properties of rocks are very complex. Their thermal parameters depend on mineralogy, density, and grain size distribution in addition toporosity and permeability and static and dynamic in-situ temperature effects that include the reservoir geothermal base temperature plus induced by the enhanced oil recovery (EOR) process. Steam-assisted gravity drainage (SAGD) processes generally disturb the stress field, stress direction and rock properties. High thermal conductivity results in a wide range of temperature distribution, improving the porosity, permeability and stiffness of the rock (Rabe et al. 2008).

Among the 9–13 trillion barrels of oil that presently constitute the world oil reserves, 30% correspond to conventional oil (greater than 22.3° API), 15% to heavy oil (between 22.3 and 10° API), and 55% correspond to extra-heavy oil, bituminous sands and bitumen (Alboudwarej et al. 2006). Many thermal processes have been developed to increase the recovery factor of heavy oil and extra-heavy oil reservoirs around the world. Chalaturnyk & Li (2004) concluded that steam stimulation is one of the most successful thermal processes that can affect the rock formations. Indeed, steam stimulation can reduce the effective stresses by varying the pore pressure, inducing oil sands to shear, generating compaction or surface dilation, reducing the strength of the formation around the steam chamber and occasionally causing in rock failure. To properly evaluate the impact of geomechanics on the SAGD process in the Faja del Orinoco study area, it was necessary to understand the rock properties and porepressure behavior, the stress state as well as the fracture gradient during steam injection to predict wellbore instability, design the casing shoe, correctly locate the well pairs and predict accurately the recovery factor as well as the volume of heavy oil that could be extracted in the studied field (Rabe et al. 2008, Perdomo et al. 2010). The purpose of this paper is to provide a fundamental geomechanical data set of the studied area to optimize and mitigate risks in SAGD projects elsewhere.

2 ORINOCO BELT

The Orinoco Belt is one of the largest heavy oil reservoirs in the world. It is found near the southern border of the Eastern Venezuelan basin. The subsurface rocks date from the Precambrian to the recent and were affected by several tectonic periods that caused regional events; the combinations of which favored large stratigraphic accumulations of oil. Regionally, the most interesting intervals are those of the Tertiary. In some locations the area of interest extends to the Cretaceous where important accumulations of heavy oil and bitumen are found.

3 MINERALOGICAL COMPOSITION AND PARTICLE SIZE DISTRIBUTION

The qualitative and quantitative identification of the minerals present in the sands were evaluated. The results indicated that quartz is the dominant mineral (95%, with high content of medium and fine fractions

Table 1. Mineralogical composition.

Mineral	Percentage
Quartz	
Course	23.0%
Medium	46.0%
Fine (<1.15)	26.0%
Kaolinite	2.0%
Albite	1.0%

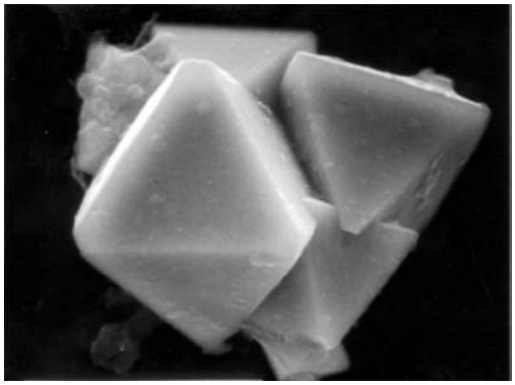


Figure 1. Over-grown poly-crystalline quartz with fine grained materials.

of sands). Kaolinite is the secondary mineral, and there is a minor amount of albite, muscovite and siderite (Table 1).

4 DESCRIPTION OF SAND MICROSTRUCTURES

The description of the sand microstructures was made through the study of images from scanning electron microscopy (SEM) thin-sections and energy dispersive spectroscopy (EDS). Results presented in Figure 1 indicate a high content of quartz sands, monocrystalline saturated on the border by oil with clay minerals identified in the pore space. Pyrite has also been identified. Fractured and poly-crystalline quartz grains were also identified. Grains of quartz are overgrowing and are distributed throughout the sample, representing the foremost mineral (estimated around 87 to 97%).

Figures 1 and 2 show the results of electronic microscopy, indicating a well-developed primary porous space. EDS was useful for identifying and analyzing fine particles t, the results of which indicated quartz was also the predominant mineral in the fines, along with smaller amounts of kaolinite, albite and muscovite.

5 IMMERSION TEST

Immersion tests were performed with some organic and inorganic fluids to evaluate the potential of

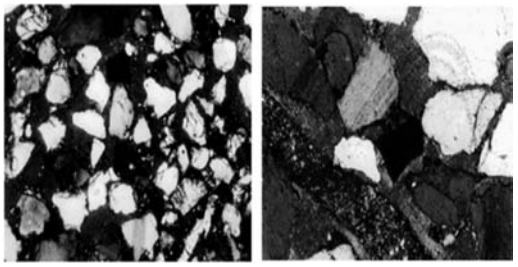


Figure 2. Quartz identified as the main mineral in the pore space.

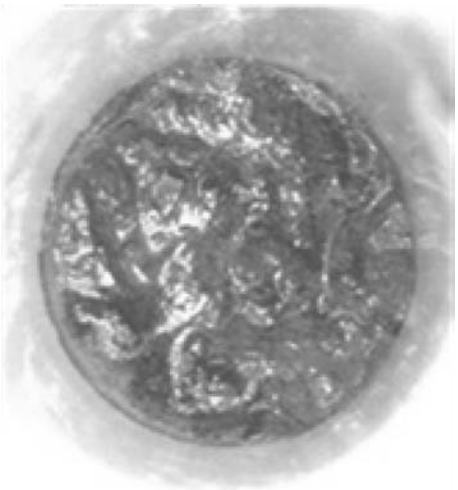


Figure 3. Immersion test (sandstone).

reactivity between the drilling fluid, pore fluid and deionized water used during the steam stimulation process. These tests are crucial to evaluate the stability of wells in shale formations as well as the impact of steam injection in shale interlayers. The samples were previously collected and stored in the laboratory without contact with any fluids. The immersion test was performed for 48 hours. Figure 3 shows that unconsolidated sandstone samples present a low degree of superficial disintegration and chemical reactivity between the rock sample saturated with heavy oil and the super-heated injection fluid (deionized water). The upper shale samples were affected by immersion in water, indicating a high potential of reactivity due to high concentrations of expansible clay minerals (mainly smectite and illite). The sodium formate (organic fluids) showed good potential for inhibition for the shale.

6 PORE VOLUME COMPRESSIBILITY TESTS (PVC)

Uniaxial-strain PVC tests were performed using samples of 3.81 cm nominal diameter by approximately 7.62 cm long. Samples were saturated with laboratory

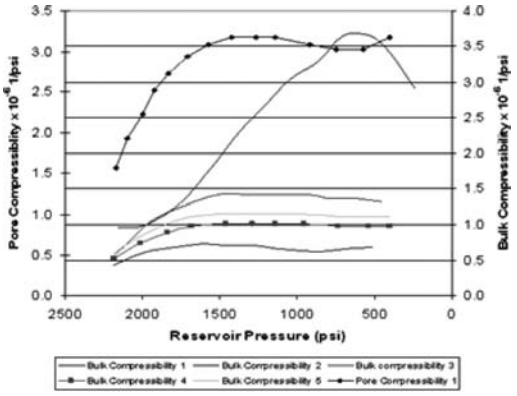


Figure 4. Pore and total compressibility.

oil mineral under ambient conditions. The tests were performed considering the confining pressure estimated from logs and depth under high in-situ conditions. Compaction was analyzed considering the drawdown effect in the pore pressure at a constant rate of 0.67 kPa/s (0.1 psi/s). The confining stress develops naturally due to the imposed uniaxial-strain boundary conditions. Results show that the sample has low pore compressibility, around 0.464 GPa^{-1} (3.2×10^{-06} psi^{-1}) at 9.8 MPa (1424 psi), and a total compressibility around 0.145 GPa^{-1} (1.0×10^{-06} psi^{-1}) at reservoir conditions (Fig. 4).

7 TRIAXIAL TEST CAMPAIGN AT LABORATORY TEMPERATURE CONDITIONS

Mechanical tests were carried out using triaxial test equipment. The cylindrical samples (2.54 cm diameter and 7.62 cm long) were saturated with mineral oil and tests were performed at 22°C. Due to the nonconsolidated nature of the sands in the reservoir, nitrogen was used to cylindrically model the samples. Triaxial compression tests were conducted on cores from one offset well using a servo-controlled testing apparatus that subjected the samples to the desired stress state at controlled strain rates. Prior to the testing, each test sample was placed between two end-caps and jacketed with polyolefin sleeve. To avoid damage to the equipment caused by heavy oil, a top cap adapted with a small pressure transducer was developed to measure pore pressure due to low fluid mobility. Samples were placed inside the triaxial cell and transducers were used to measure axial and radial displacements. The previous saturation of the side drain protected the sample from air-drying and allowed the fluid flow to remove air bubbles trapped along the fluid pressure system. Confining pressure and pore pressure at the base of the sample were adjusted to start the consolidation process, followed by the opening of the drainage valves. The rock testing facility consists of a servo-controlled and fully automated load application system. The load application system consists of a rigid 45,000 kN reaction frame, triaxial cell designed for high temperature and high pressure (HTHP), and a fluid pressure controlling system capable of applying up to 150 MPa of confinement.

Table 2. Rock properties from triaxial tests campaign.

Lithology	Depth m	φ °	Static μ	Static E GPa
Shale	706.5	30.1	0.32	1.4
Sandstone	629.3	26.2	0.42	7.1

where φ is internal friction angle, μ is Poisson's ratio and E is Young's modulus.

The saturation and consolidation phases are carried out under elevated backpressure. After applying the backpressure the specimen is consolidated isotropically before undrained shearing. The heavy oil reduces the intrinsic permeability of the sands. Static and cyclic loading can be performed as stress-controlled or strain-controlled. The specimen was subjected to varying cyclic stress or strain levels. For failure characterization, suites of single-stage triaxial compression tests were conducted on vertical samples to construct Mohr stress circles and calculate Coulomb parameters for peak compressive strength corresponding to initial failure of the intact rock, and the residual effective compressive corresponding to quasi-stable frictional sliding on the newly formed fracture at the end of each test.

The drained shear phase is conducted at slow axial strain rate that is selected to enable adequate redistribution of pore pressure throughout the samples. Three consolidated triaxial tests were conducted under a range of confining pressure ranging from 0 to 20.68 MPa (3000 psi) with 3.44 MPa (500 psi) of backpressure. The triaxial tests show that the sandstone has a low internal friction angle and Young's modulus. Shale (overburden) also presents low internal frictional angle and high static Young's modulus. The Poisson's ratio of these formations is around 0.32 for sandstones and around 0.43 to shales (Table 2).

8 METHODOLGY DEVELOPED FOR THE ULTRASONIC TRIAXIAL TEST CAMPAIGN AT HIGH TEMPERATURES

Coring and sampling friable and unconsolidated heavy oil sandstones cause much damage to the rock samples. One reason is the expansion caused by gas evolution. All samples suffer a severe reduction of apparent cohesion under atmospheric pressure when impregnated by oil and gas due to gas expansion (Fig. 5). This effect was also identified when the samples were heated inside the triaxial cell. To avoid these problems several procedures were implemented.

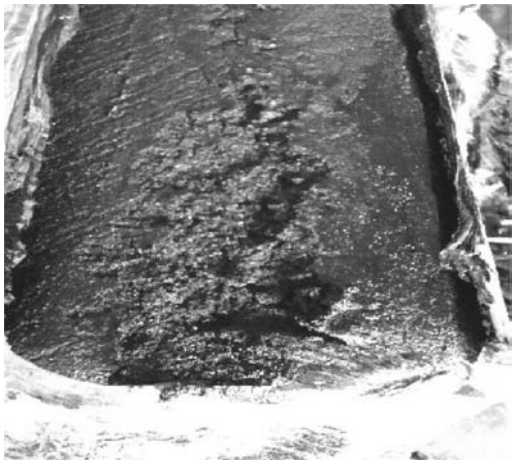


Figure 5. Sample of heavy oil under atmospheric pressure.

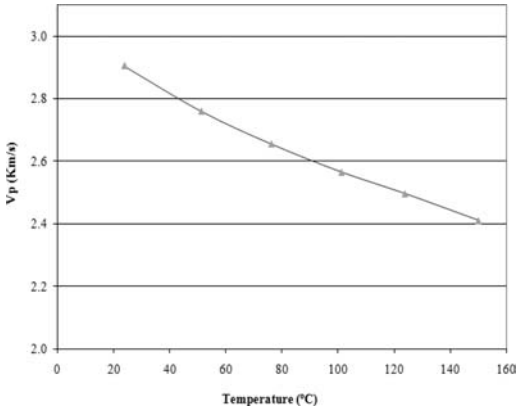


Figure 6. Effect of temperature in the compressional velocity in the studied heavy oil sandstone.

Mechanical restraint and freezing of the samples using nitrogen seemed to be very useful in reducing the effects of sample microcracks and dilation. After the sample preparation each core was carefully reviewed using a scanner installed in the laboratory. The x-ray CT system had high-penetration capacity, penetrating up to 15.24 cm diameter cylinders at high resolution (up to 6 μm)

The x-ray CT scanner identified a severe loss of sample integrity during its modeling at laboratory temperature. At ambient laboratory temperatures, visco-plastic behavior, especially close to the shale interlayers, was high. Nitrogen was useful in minimizing this disturbance by reduction of the visco-plastic behavior of the unconsolidated sandstone.

An ultrasonic test campaign was performed to evaluate the impact of high temperature on the rock sample properties using low frequencies. Mechanical tests using heavy oil samples at high temperature presented severe limitations in terms of integrity of the triaxial equipment (especially transducers and strain gages). To avoid damage to the equipment caused by heavy oil, a new top cap adapted with a small pressure transducer was developed. This solution is still under development and the preliminary results show a maximum high temperature limitation of 150°C.

The pore fluid pressure line was filled with an inert fluid to avoid reactions between the pore fluid and the saturation fluid at high temperatures. In the laboratory test campaign it was decided to use a fluid with a chemical activity close to the chemical activity of the pore fluid. The mechanical laboratory test campaign was performed at high temperatures, soit was also performed at undrained conditions. The tests were also performed at in-situ levels of pore pressure and radial/axial confining pressures. The apparatus enables propagating compressional waves to simulate high temperatures through the core samples. The test rig analytical tool could also generate and measure the pore pressure and confining pressure and calculate acoustic velocity.

Results show (Fig. 6) a reduction in the compressional velocities. In general, high temperatures induced by a probe weaken the rock. This is due to fracture development and mineral dehydration and vaporization that result in an increase in the void space. Results indicated increasing temperature led to a reduction of compressional velocity of about 20.5% at 150°C (Fig. 6). At this high temperature, quartz grains expand by approximately 1.00% of their original size.

9 DISCUSSION

Sample preparation and heating these samples of friable and unconsolidated heavy oil sandstones caused much damage in the rock matrix. The main reason for this was from the expansion of gas trapped within the heavy oil samples. The original gas adsorbed in the samples was liberated during the pressure reduction (coring process) and the temperature increase (during the consolidation stage). The consequences were clearly seen in the samples by using the SEM equipment. The apparent porosity of the samples increased as well the permeability. The minerals, like micas and feldspars, were rearranged in the porous media. The dilation process in unconsolidated rocks is very complex.

In the case of full grain contact (low void space), grains have no place to expand. The expansion results in microfractures, which also increase the void space. Unconsolidated samples supposed not be so susceptible to this effects, but in presence of heavy oil, its permeability is severely affected.

Micro-cracks are also formed during the grain cooling phase, so bringing the samples to surface lowers the temperatures. The second topic is the mineralogy affecting fracture gradient. Clays contain water, which will escape in the form of vapor when subjected to high temperatures. This increases the volume and pressure in the pore and can cause fractures. The reduction of

the fracture gradient exposes the samples for tensile loads under low pressures.

Acoustic velocities reduce as temperature increases. The main factors to explain this behavior depends on temperature, porosity, composition and cementing. The magnitude of this decrease ranges usually from 2 to 10% in dry rocks as temperature increases by 100°C (Han et al. 1996). In rocks saturated with fluids, the temperature is dependent on acoustic velocity.

Acoustic velocities in rocks are also affected by the properties of pore fluids. The main factors to explain this fluid behavior are compressibility, viscosity, phase, and density. The heavier oil, as is found in the Orinoco Belt, presents higher acoustic velocity and lower compressibility. Therefore, the acoustic velocity in a rock saturated with heavier oil is usually higher than the same rock saturated with lighter oil.

A small amount of gas (2% by volume) in the pores can dramatically decrease the compressional velocity, whereas in partially gas or liquid-saturated rocks the amount of gas only slightly affects compressional and shear velocities. This variation of compressibility can be explained by increases of gas in the rock. Gassmann (1951) and Biot (1956) established the theory of acoustic wave propagation in porous media. The Gassmann equation and the Biot theory predict that completely replacing the gas by decrease liquid in the pores increases the compressional velocity but has little effect on the shear velocity. The laboratory campaign identified that at low frequency the temperature dependence of ultrasonic velocities can be described by Gassmann theory for temperatures >100°C, whereas velocity-dispersion effects must be taken into account at lower temperatures.

10 CONCLUSIONS

This article describes the results of ultrasonic triaxial tests performed at high temperature to simulate the impact of steam-assisted gravity drainage (SAGD) projects on the rock properties of a heavy oil reservoir from Venezuela. The mineralogical analysis indicated that quartz is the dominant mineral, with kaolinite as the secondary mineral. Grains of quartz are overgrowing, micro-fractured and distributed throughout the sample. The sands present low-reactivity potential, mainly due to the very low content of expandable clay minerals.

The saturation and consolidation phases are carried out under elevated backpressure and increasing temperature. To avoid damage to the equipment caused by heavy oil, a new top cap adapted with a small pressure transducer was developed. The strength behavior for this heavy oil sandstone can be described using the linear Mohr-Coulomb strength criterion. The triaxial tests showat laboratory temperature that the heavy oil sandstone has a low internal friction angle (27°), low static Young's modulus (7.1 GPa) with a Poisson's ratio (0.23). Temperature reduced the compressional velocity in around 20.5% under high temperature (150°C), showing a considerable variation for rock strength prediction using velocities. The analysis indicated that the Skempton coefficient and the compressibility measurements are much more severe affected under a high temperature test.

ACKNOWLEDGEMENT

The authors thank PDVSA for permission to publish this paper.

REFERENCES

Alboudwarej H., Felix J. & Taylor S. 2006. Highlighting heavy oil. *Oilfield Review*, Summer 2006: 34–53.

Biot, M.A. 1956. Theory of propagation of elastic waves in fluid saturated porous solid, 1-Low frequency range-higher frequency range. *J. Acoustic. Soc. Am.* 28: 168–191.

Chalaturnyk, R.J. & Li, P. 2004. When is it important to consider geomechanics in SAGD operations? *Journal of Canadian Petroleum Technology* 43(4): 53–61.

Gassmann, F. 1951, Elastic waves through a packing of spheres. *Geophysics* 16: 673–685.

Han, D., Nur, A., & Morgan, F.D. 1986. Effects of porosity and clay content on wave velocities in sandstone. *Geophysics* 51: 2093–2107.

Perdomo, P., Rabe, C. & Fontoura, S. 2010. Laboratory test and logging campaign for geomechanical application in SAGD process for heavy oil reservoirs in Venezuela. In J. Zhao et al. (eds), *Rock Mechanics in Civil and Environmental Engineering, Proceedings of EUROCK 2010 – The ISRM Regional Symposium* (Lausanne, 15–18 June 2010). Leiden: CRC Press/Balkema.

Rabe, C., Piña, J.A. & Valbuena, E. 2008. Impact of Geomechanics on SAGD process for Heavy Oil Reservoir in Venezuela. *SEG/EAGE Summer Research Workshop*, Vancover, Canada, 7–11 September, 2008.

This page intentionally left blank

Rock Mechanics for Resources, Energy and Environment – Kwaśniewski & Łydżba (eds)
© 2013 Taylor & Francis Group, London, ISBN 978-1-138-00080-3

Selection and interpretation of shear strength parameters for weak phyllites

G.V. Ramana, Shashank Pathak & Nripendra Kumar
Central Spil and Materials Research Station, Olof Palme Marg, Hauz Khas, New Delhi, India

ABSTRACT: Hydroelectric power projects are pollution free and renewable sources of energy. These projects involve the construction of dams across the flowing stream of water. Construction of dams in rock regions requires stability analysis of the foundation and the supporting rocks at the banks of the reservoir area. Stability of the concrete foundation over the rocky strata and stability of the banks depend upon the shear strength of the concrete-rock and rock-rock interfaces, respectively. Therefore, evaluation of shear strength parameters (cohesion and friction angle) at rock-rock and concrete-rock interface is the most important primary step for stability analysis and design of dams. Determination of shear strength parameters involves the in-situ tests in drifts on the dam axis site and interpretation of test results. In view of the above, site-specific shear strength parameter interpretation is carried out for Amochu hydroelectric power project site, Bhutan. This project envisages construction of 175 m high concrete gravity dam across river Amochu. The existing rock type on both left and right banks of the site is observed to be weathered Phyllites. From the analysis of 20 field tests in 2 drifts, it has been found that for rock-rock interface shear strength values are approximately 50% higher at the right bank as compared to the left bank. On the other hand, for concrete-rock interface, this variation is around 10% only. Therefore, seeing the large variation of estimated shear strength in rock-rock interface, it is proposed to use individual bank stability analysis whereas, marginal variation in concrete-rock interface suggests the use of the combined analysis of the data from both the banks for foundation stability analysis.

1 INTRODUCTION

The design of foundations of dams in rocky strata includes determination of bearing capacity, settlement analysis and sliding/slope stability analysis. Bearing capacity and settlement analysis involve the ability of the rock foundation to support the imposed loads without shear failure and without excessive settlements. Sliding stability analysis involves the ability of the rock foundation or slope to resist the imposed loads without shearing or sliding. Both analyses must be coordinated and satisfied in the design. For performing theses analyses shear strength parameters viz. cohesion and friction-angle are used as input parameters. There are two major categories of analysis, a) Analysis at the concrete foundation and rock joint interface and b) Analysis at the rock-rock interface. Henceforth, determination of shear strength parameters is required for the concrete over rock (C/R) interface as well as rock over rock (R/R) interface on the project site. Former is for stability analysis of concrete dam resting over rocky strata while later is concerned with the ability of the surrounding rocks to hold the reservoir.

2 GEOLOGY OF THE REGION

The Exploratory drift on the right bank of the river is located on the dam axis at an elevation 263.00 m, i.e. about 28.0 m above the river level. The drift has encountered fine grained dark gray quartzite- phyllite. The rocks in the drift are also traversed by 7 sets of joints as given in Table 1.

Table 1. Details of joint sets in right bank drift.

Sl.	Joint	Orientation	Description
1	J1 (foliation joint)	N0° to N350°/40°–70°	Smooth planar
2	J2	N335° to N340°/50°–80°	Rough planar
3	J3	N90° to N100°/65° to 85°	Rough planar
4	J4	N290° to N310°/60° to 80°	Rough planar
5	J5	N290° to N310°/35° to 50°	Rough planar
6	J6	N10° to N30°/20° to 40°	Rough planar
7	J7	N30° to N60°/40° to 75°	Rough planar

The Exploratory drift on the left bank of the river is located on the dam axis at an elevation 245.00 m. The drift has encountered fine grained dark gray quartzite-phyllite. The rocks in the drift are also traversed by 9 sets of joints as given in Table 2.

3 TEST PROCEDURE

In-situ shear tests at rock-rock and concrete- rock interfaces are conducted at the dam axis site of proposed

Table 2. Details of joint sets in left bank drift.

Sl.	Joint	Orientation	Description
1	J1 (foliation joint)	N0° to N350°/20° to 80°	Smooth planar
2	J2	N40° to N60°/40° to 80°	Rough planar
3	J3	N185° to N200°/17° to 45°	Rough planar
4	J4	N240° to N270°/65° to 80°	Rough planar
5	J5	N240° to N260°/10° to 20°	Rough planar
6	J6	N160° to N180°/80° to 85°	Rough planar
7	J7	N330° to N335°/40° to 75°	Rough planar
8	J8	N130°/70°	Rough planar
9	J9	N155° to N165°/35° to 40°	Rough planar

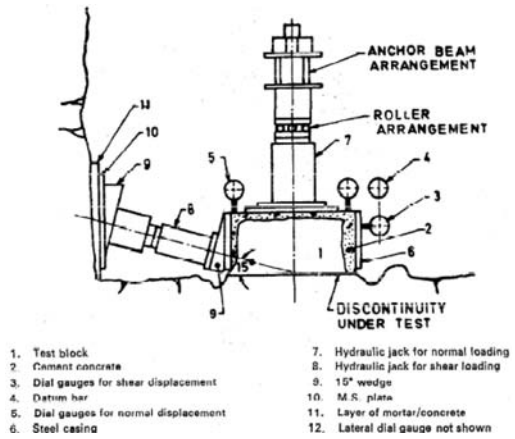


Figure 1. Schematic diagram of in-situ shear test set-up (IS 7746:1991).

hydroelectric project at Amochu (Bhutan). The tests are conducted in two drifts named as DR-5 on right bank and DL-6 on left bank. Blocks of rock mass for R/R interface test and concrete blocks for C/R interface test are prepared for testing purpose as per provisions of IS 7746:1996 and ISRM: 1981. Fig. 1 shows the schematic diagram of the test-setup as given in IS 7746:1996.

Following step by step testing procedure is carried out on the site:

a) Diamond wheel chisel and hammer along with rock breakers are used to separate the rock mass of block size (0.70 m × 0.70 m × 0.35 m) from the parent rock to create R/R interface. Steel frame of 0.020 m thickness MS plate is placed over the block and then it is filled with cement grout.

Following step by step testing procedure is carried out on the site:

b) Diamond wheel chisel and hammer along with rock breakers are used to separate the rock mass of block size (0.70 m × 0.70 m × 0.35 m) from the parent rock to create R/R interface. Steel frame of 0.020 m thickness MS plate is placed over the block and then it is filled with cement grout.

c) For C/R interface, the rock surface is leveled as much as possible by removing all undulations with the help of a chisel and a hammer. The rock breaker is also used in case of hard rock. After leveling the rock surface, the concrete blocks (0.70 m × 0.70 m × 0.35 m) are prepared by using steel mould. All the blocks are cured for 28 days before the test.

d) 0.020 m thick MS plates are used to prepare side and top reaction pads and strengthened by RCC. The care is taken to keep the top and side reaction pads concentric with the block. It should be noted that the horizontal reaction pad has to be prepared such that it does not break during the application of horizontal thrust.

e) Vertical load is applied using a 2000 kN capacity hydraulic jack. Hallow cylinders of aluminum alloy are used to fill up the gap between the top reaction pad and the hydraulic jack. Shear force is applied by another 2000 kN capacity hydraulic jack from the side reaction pad

f) Table 3 shows the applied normal loads in the five tests, respectively. The shear load is applied at an angle of 15° with the horizontal so that the sheared plane coincides with a plane of weakness in the rock. This is achieved by two wooden wedges of appropriate geometry placed across the jack.

g) Five such blocks for R/R interface and C/R interface are prepared. Each block is tested for a particular normal stress which is kept constant during the test. The shear force and displacement of block are measured and recorded during the test. The vertical, horizontal, and lateral displacements of the block, produced during the test are measured by 9 dial-gauges, 4 for normal displacement, 3 for shear displacement, and 2 for lateral displacement.

h) The observations are recorded till failure and continued even after the failure at which no further rise or fall in shear strength is observed with increasing shear displacement to get the information regarding residual frictional resistance.

4 ASSUMPTIONS

Interpretation of the test results are based on the following assumptions:

a) Effect of pore water pressure is implicitly taken as the tests are conducted in the saturated condition.
b) Complete interface area is involved in the process of shearing.
c) Shear strength is governed by Mohr-Coulomb criteria only.
d) All the reaction pads are infinitely stiff and not prone to any deformation.
e) The rock mass has been considered to be ideally intact *i.e.* without cracks and voids.

Table 3. Applied normal load and corresponding test sequence.

Test No.	Normal load (kN)
Test No. 1	200
Test No. 2	250
Test No. 3	300
Test No. 4	350
Test No. 5	400

5 FORMULATION

Normal stress (σ_n) and shear stress (τ) are obtained, respectively, from applied normal load (P_{na}) and applied shear load (P_{sa}) during the test, using the Eq. 1 and 2.

$$\tau = \frac{P_s}{A} = \frac{P_{sa}\cos\alpha}{A} \quad (1)$$

$$\sigma_n = \frac{P_n}{A} = \frac{P_{na} + P_{sa}\sin\alpha}{A} \quad (2)$$

where, P_s, P_n, A, and α, are net shear force, net normal force, gross cross-sectional area of the interface, and inclination of the applied shear force, respectively. It is worth mentioning here that to keep the normal stress constant (as required in the specified test procedure), the applied normal force is reduced by an amount P_{sa} sin α after each increment in the applied shear force.

6 TEST RESULTS AND DISCUSSION

The test data is collected in terms of applied shear load and observed shear displacement at the applied constant vertical load. This exercise is then repeated for five vertical loads as shown in Table 3.

The collected data is used to derive the shear stress (using Eq. 1) and corresponding shear displacement. Further, the plots of shear stress versus shear displacement are prepared for R/R interface at right bank drift (after here DR-5), R/R interface at left bank drift (after here DL-6), C/R interface at DR-5, and C/R interface at DL-6 as shown in Figs. 2 to 5, respectively.

Figures 2 to 5 are clear depiction of the shear behavior of the interfaces. Initially, required shear stress for shear displacement increase and it reaches at a peak value that is known as peak shear strength. After this point, curves start showing an asymptotic behavior and shear stress reduces to a value known as residual shear stress. Table 4 shows the shear displacement achieved at the peak shear stress, values of peak shear stress and residual shear stress for specified normal load, corresponding to R/R interfaces.

Similarly, Table 5 above shows the shear displacement achieved at the peak shear stress, values of peak shear stress and residual shear stress for specified normal load, corresponding to C/R interfaces. The

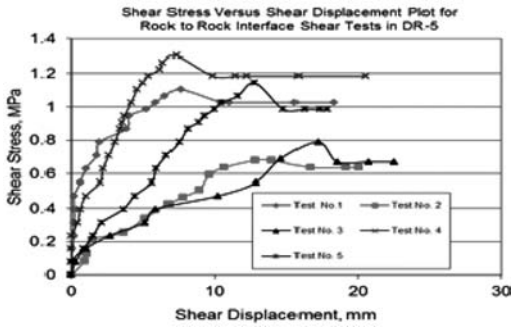


Figure 2. Shear stress V/S shear displacement plot or R/R interface shear tests in drift DR-5 (CSMRS 2011).

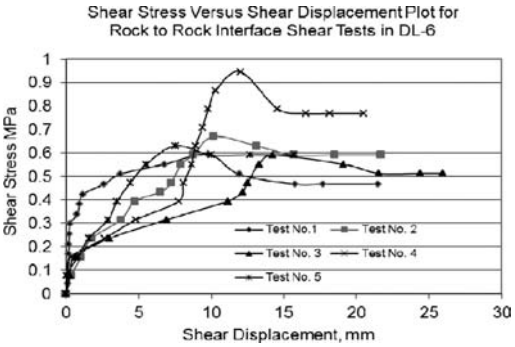


Figure 3. Shear stress V/S shear displacement plot for R/R interface shear tests in drift DL-6 (CSMRS 2011).

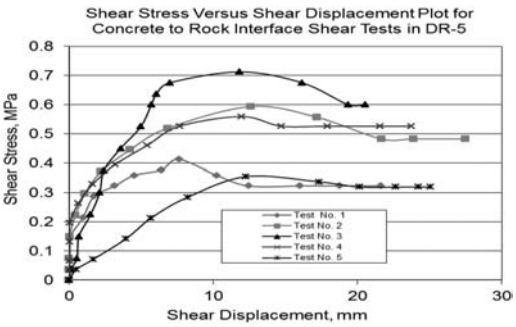


Figure 4. Shear stress V/S shear displacement plot for C/R interface shear tests in drift DR-5 (CSMRS 2011).

comparative study based on the Figs. 2 to 5 and Tables 4 & 5 leads to following important observations:

a) There is no definite trend of observed shear displacement (at peak shear stress) with applied vertical load. The reason might be the presence of discontinuity on the rock surface in the form of joints or cracks.
b) There is an increasing trend (not necessarily monotonous for example See DR-5) in peak shear stress with the applied vertical stress.
c) Similarly there is an increasing trend in residual shear stress with the applied vertical stress.

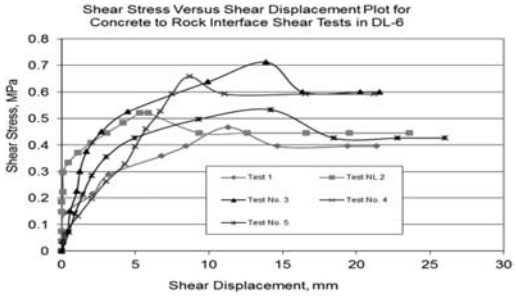


Figure 5. Shear stress V/S shear displacement plot for C/R interface shear tests in drift DL-6 (CSMRS 2011).

Table 4. Comparison of shear displacement curves for various normal loads at R/R interface.

Applied normal load kN	Shear displacement at peak shear stress (mm)		Peak shear stress (MPa)		Residual shear stress (MPa)	
	DL 6	DR 5	DL6	DR5	DL6	DR5
200	9.80	12.86	0.59	0.68	0.47	0.64
250	14.21	17.20	0.59	0.79	0.51	0.67
300	1.17	7.60	0.67	1.10	0.59	1.03
350	7.53	12.84	0.63	1.14	0.59	0.99
400	12.01	9.89	0.95	1.30	0.77	1.18

Table 5. Comparison of shear displacement curves for various normal loads at C/R interface.

Applied normal load kN	Shear displacement at peak shear stress (mm)		Peak shear stress (MPa)		Residual shear stress (MPa)	
	DL 6	DR 5	DL6	DR5	DL6	DR5
200	11.30	7.59	0.47	0.41	0.40	0.32
250	5.19	12.61	0.52	0.59	0.45	0.48
300	14.20	12.26	0.53	0.36	0.43	0.32
350	8.69	11.96	0.66	0.56	0.59	0.53
400	13.88	11.81	0.71	0.71	0.60	0.60

Observation (b) and (c), suggest that the peak and residual shear strength of the rock mass increases with the applied normal stress. This conclusion supports the use of Mohr-Coulumb criteria in the determination of shear strength parameters at the interface.

7 SHEAR STRENGTH PARAMETERS

In selecting shear-strength parameters for rock, the analysis should not be limited to a single approach, rather should incorporate several approaches into the selection process. Comparison of values obtained from several alternative approaches, together with a thorough understanding of rock-mechanics principles and prerequisites will provide the necessary basis for selection of meaningful shear-strength parameters. However, as discussed above in the present paper, the Mohr-Coulumb criterion of shear strength (τ_f) is used as given in Eq. 3.

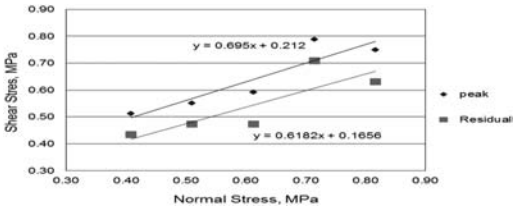


Figure 6. Shear stress V/S normal stress plot for C/R interface in drift DL-6.

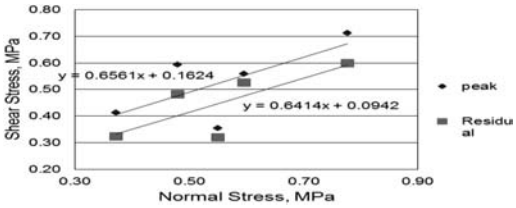


Figure 7. Shear stress V/S normal stress versus plot for C/R interface in drift DR-5.

$$\tau_f = c + \sigma_n \tan\phi \tag{3}$$

where, c is cohesion, σ_n is applied normal stress, and φ is angle of friction at the interface, is used as the governing behavior for the interpretation of the shear test results in the present study. The shear stresses at the failure and the residual shear stresses are plotted against the corresponding normal stresses. Then, this data set is used to fit the Equation 3 and to determine the cohesion (c) and friction angle (φ). Figs. 6 to 11, show the scatter plots of shear stress (τ_f) (peak and residual) versus normal stress (σ_n) and the best fit lines for C/R interface in DL-6, DR-5 and combined DL-6 & DR-5, R/R interface in DL-6, DR-5, and combined DL-6 & DR-5, respectively. The constant term of the best fit line represents the cohesion (c) and the slope is tangent of friction-angle (tan φ).

Values of the peak and residual shear strength parameters are tabulated below in Tables 6 & 7 for R/R and C/R interfaces, respectively. The data shows large variations among the shear strength parameters *i.e.* cohesion and friction-angle for both R/R and C/R interfaces. There are also variations in peak and residual shear strength parameters. These variations show that there are abrupt changes in various geological and mechanical rock mass properties from one bank to other. However, there are cases where the shear strength parameters are almost similar in magnitude on the left bank and the right bank for both R/R and C/R interfaces (Singh 2009). Further, it is recommended

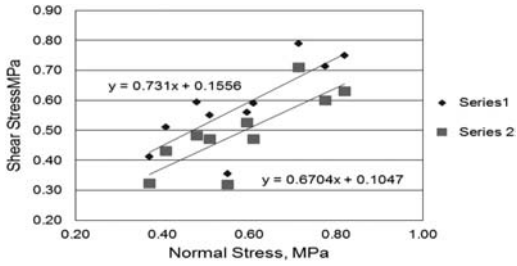


Figure 8. Shear stress V/S normal stress plot for C/R interface in combined DR-5 & DL-6.

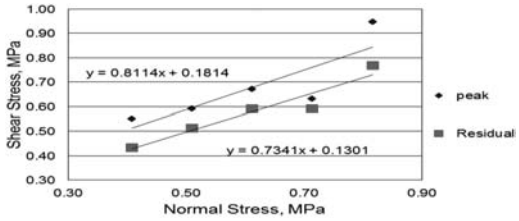


Figure 9. Normal stress V/S shear stress plot for R/R interface in drift DL-6.

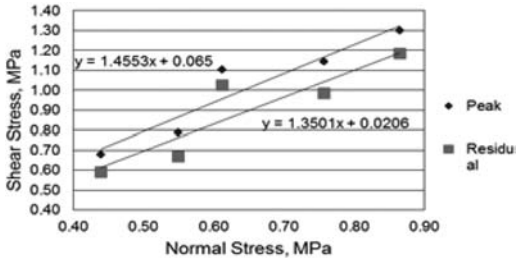


Figure 10. Shear stress V/S normal stress plot for shear tests on R/R interface in drift DR-5.

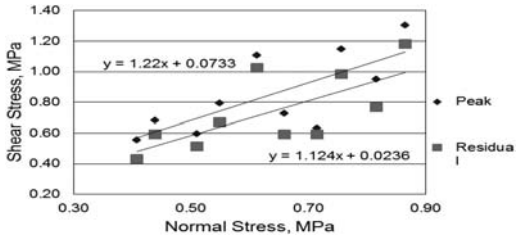


Figure 11. Shear stress V/S normal stress plot for R/R interface in combined DR-5 & DL-6.

that the average values for a particular dam site may be obtained by plotting data from both the banks together rather than taking an arithmetic average of cohesion and friction values from both the banks as it may give better representative values (See Figs. 8 &11).

Further, it is recommended that the average values for a particular dam site may be obtained by plotting data from both the banks together rather than taking an arithmetic average of cohesion and friction values from both the banks as it may give better representative values (See Figs. 8 & 11).

Table 6. Shear Strength Parameters on rock-rock interface.

Location of Drift		Peak Shear Strength Parameters		Residual Shear Strength Parameters	
Drift. No.	RL (m)	Cohesion, c (MPa)	Friction Angle, φ (degree)	Cohesion, c_r (MPa)	Friction Angle, φ_r (degree)
DR-5	263.00	0.07	55.50	0.02	53.50
DL-6	245.00	0.18	39.10	0.13	36.00
Combined DR-5 & DL-6		0.07	50.70	0.02	48.30

Table 7. Shear Strength Parameters on concrete-rock interface.

Location of Drift		Peak Shear Strength Parameters		Residual Shear Strength Parameters	
Drift. No.	RL (m)	Cohesion, c (MPa)	Friction Angle, φ (degree)	Cohesion, c_r (MPa)	Friction Angle, φ_r (degree)
DR-5	263.00	0.16	33.30	0.09	32.70
DL-6	245.00	0.21	34.80	0.17	31.70
Combined DR-5 & DL-6		0.16	36.10	0.11	33.82

Table 8. Shear strength on rock to rock interface (for 400 kN of vertical load).

Location of Drift	Peak Shear Strength (MPa)	Residual Shear Strength (MPa)
DR-5	1.25	1.12
DL-6	0.85	0.72
Combined DR-5 & DL-6	1.07	0.94

8 INTERPRETATION OF SHEAR STRENGTH PARAMETERS

Two *major design* issues viz. stability of the rock and stability of the dam over rock are of central importance during the dam construction. Thus, R/R interface values are required for stability analysis of the rocks while C/R interface values are required for the stability of the dam foundation.

Being on the conservative side, designer may like to use the lowest observed values of shear strength parameters for the above two cases. However, this may not be the case as the rock mass is not homogeneous throughout the dam axis. In view of this, a combined analysis of the values obtained from left and right bank is proposed in the present study. For illustration purpose, Tables 8 & 9 show the shear strength of R/R

Table 9. Shear Strength on concrete to rock interface (for 400 kN of vertical load).

Location of Drift	Peak Shear Strength (MPa)	Residual Shear Strength (MPa)
DR-5	0.70	0.62
DL-6	0.78	0.67
Combined DR-5 & DL-6	0.75	0.65

and C/R interfaces, respectively, for 400 kN of vertical load (which is applied on 0.70 m × 0.70 m block). These values are determined using Eq. 3 and using the shear strength parameters as given in Tables 6 & 7.

In case of R/R interface, the right bank values are 47.97% higher as compared to the left bank values. Similarly, values determined by residual shear strength parameters are 55.93% higher as compared to the left bank values. Therefore, it seems better to use individual bank stability analysis due to this large relative variation in the shear strength for R/R interface. For C/R case, the relative variation is quite small as compared with R/R case. Variation is of the order of 10%. Hence, the combined values of shear strength parameters may be used instead of using separate values on separate banks for foundation design. Lesser variation in concrete over rock may be due to uniformity in the concrete surface as compared to the rock over rock case. Residual shear strength parameters may be utilized for long term stability analysis.

9 CONCLUSIONS

Based on the present study, following important conclusions may be drawn for the test drift at Amochu hydroelectric project site, Bhutan.

1. The drifts have been encountered for fine grained, dark gray quartzites and phyllites. Most of the joints observed to be rough planar.
2. Values of cohesion coefficient vary between 0.02 MPa to 0.18 MPa for R/R interface with a combined value (right and left bank together) of 0.07 MPa and 0.02 MPa for peak and residual shear strengths, respectively. For C/R interface, it varies between 0.09 MPa to 0.02 MPa with a combined value of 0.16 MPa and 0.11 MPa for peak and residual shear strengths, respectively.
3. Values of friction-angle vary between 36.00° to 55.50° for R/R interface with a combined value of 50.70° and 48.30° for peak and residual shear strengths, respectively. For C/R interface, it varies between 31.70° to 34.80° with combined values of 36.10° and 33.82° for peak and residual shear strengths, respectively.
4. The use of individual bank stability analysis is recommended as in case of R/R interface, the right bank values of example shear strength are around 50% higher as compared to the left bank values. On the other hand, for C/R case, the relative variation is only around 10%. Hence, the combined values of shear strength parameters may be used for foundation design on both the banks.

REFERENCES

CSMRS Report, 2011. In-Situ Shear Strength Parameters of Rock Mass in Right Bank Drifts at Dam Site of Amochu Project, Bhutan.

IS 7746, 1996. Indian Standard code of practice for in-situ shear test on rock, Bureau of Indian Standards.

ISRM Part 1, 1981. Suggested methods for determining shear strength.

ISRM, 1987. International Society for Rock Mechanics Suggested Methods for Rock bolt Testing.

Singh, Rajbal, 2007. Field Shear Test, Chapter 11 in *Engineering in Rocks for Slopes, Foundations and Tunnels*, Ed. Prof. T. Ramamurthy, pp. 256–264.

Rock Mechanics for Resources, Energy and Environment – Kwaśniewski & Łydżba (eds)
© 2013 Taylor & Francis Group, London, ISBN 978-1-138-00080-3

Evaluation of specific cutting energy in the circular sawing with the elastic parameters of rocks

N. Sengun, I. Ugur, S. Demirdag & R. Altindag
Department of Mining Engineering, Süleyman Demirel University, Isparta, Turkey

ABSTRACT: In this study, laboratory tests were carried out on 15 different volcanic and carbonate rocks collected from the marble processing plants to determine the specific cutting energy value in cutting operation with circular saw of each rock. Circular sawing measurements were performed on a specially designed high precision rock block cutter. All rock specimens used in the cutting tests were having a length of 50 × 100 × 200 mm section. The sawing analyses were performed in the down cutting mode. The main sawing parameters which are peripheral speed of the saw blade (60 m/s), cutting depth (20 mm) and workpiece traverse speed (0.5 m/min) was kept constant in the cutting tests. To calculate elastic parameters of rocks, the velocities of *P* and *S*-waves were measured using the high frequency ultrasonic pulse technique instrument. The ultrasonic elastic parameters such as modulus of elasticity, shear modulus, bulk modulus and Poisson's ratio of rocks were calculated from the measured wave velocities and the bulk density according to ASTM D 2845. Specific cutting energy and rock elastic properties were evaluated using simple regression analysis by statistical methods. Regression analysis showed that high correlations exist between specific cutting energy and elastic parameters of rocks.

1 INTRODUCTION

With the increasing demand of natural stone as constructional and ornamental material, circular sawing with segmented diamond blades is the most commonly used process for natural stone such as granite and marble. The prediction of rock sawability is very important in cost estimation and process planning. Specific cutting energy (SCE) in cutting processes is derived from the amount of energy required to remove a given volume of rock and has been successfully used in the diamond tool industry. The SCE is one of the most widely used parameters to measure the efficiency of a rock cutting system within a given rock. The lower value of SCE indicates the more efficient sawability of the rocks.

In the stone processing industry, the SCE can be used to monitor the efficiency of a sawing process and for estimating the power requirements. However, SCE is not a fundamental intrinsic property of rock. It is mainly influenced by the operational parameters (cutting depth, saw blade peripheral speed, feed rate, cutting mode, blade specifications, etc.), and the rock properties (strength, hardness, mineralogy, etc.).

Ultrasonic techniques are non-destructive and easy to apply, in both for site and laboratory conditions. In rock engineering, ultrasonic velocity techniques have increasingly been used to determine the dynamic properties of rocks. The ultrasonic velocity of a rock mass is closely related to the intact rock properties and measuring the velocity in rock masses interrogates the rock structure and texture. The important influencing factors are rock type, mineralogical composition, rock texture and structure, grain size and shape, density, porosity, anisotropy, porewater, confining pressure, temperature, weathering and alteration zones, bedding planes and joint properties (Yasar & Erdogan 2004).

The SCE is derived from the amount of energy required to a given volume of rock and has been successfully used in the diamond tool industry. There have been many studies on the sawing performance and the mechanism of the circular diamond saw (Walker & Wood 1971, Wright & Cassapi 1985, Wright 1986, Wright & Jennings 1989, Luo & Liao 1995, Tönshoff & Ashe 1997, Ceylanoglu & Gorgulu 1997, Xu 1999, Tönshoff & Hillmann-Apmann 2002, Brook 2002, Konstanty 2002, Wang & Clausen 2002, Buyuksagis 2007, Ersoy & Atici 2007, Kahraman & Gunaydin 2008, Sengun 2009, Guney 2011, Sengun & Altindag 2013). The most of these studies are related to basic rock properties. There is a few study on related to the influence of rock elastic parameters on the performance of circular diamond sawing for rocks. The relationships between *P* and *S*-wave velocities and rock characteristics have been studied by many researchers. Inoue & Ohomi (1981), Babuska et al. (1984), Gaviglio (1989), Kern (1993), Barruol & Kern (1996), Karpuz & Pasamehmetoglu (1997), Kahraman (2001, 2002) and Yagiz (2011) have studied the relations between rock properties and ultrasonic velocity and they have found that the sound velocity is closely related to rock properties such as uniaxial compressive strength, Brazilian tensile strength, porosity, unit volume weight, hardness, etc.

In this paper, relationships between ultrasonic elastic parameters such as modulus of elasticity, shear modulus, bulk modulus and Poisson's ratio of rocks and SCE of some selected rocks, determined during circular sawing experiments are presented.

2 ELASTIC PARAMETERS OF ROCKS

The elastic constants of rocks can be obtained from a stress-strain experiment (static test) or from a wave propagation experiment (dynamic test). From dynamic experiments, instead of measuring stress-strain relationships, the velocity of compressional (Vp) and shear (Vs) waves are measured.

The elastic parameters of rocks such as modulus of elasticity, shear modulus, bulk modulus and Poisson's ratio are described as follows;

- Young's modulus (E) describes tensile elasticity, or the tendency of an object to deform along an axis when opposing forces are applied along that axis. It is often referred to simply as the elastic modulus.
- The shear modulus or modulus of rigidity (G) describes an object's tendency to shear (the deformation of shape at constant volume) when acted upon by opposing forces; it is defined as shear stress over shear strain.
- The bulk modulus (K) describes volumetric elasticity, or the tendency of an object to deform in all directions when uniformly loaded in all directions; it is defined as volumetric stress over volumetric strain, and is the inverse of compressibility. The bulk modulus is an extension of Young's modulus to three dimensions.
- Poisson's ratio measures the ratio of lateral strain to axial strain, at linearly-elastic region.

The propagation velocities of the compression and shear waves, *Vp* and *Vs* respectively, are calculated from the measured travel time and the distance between transmitter and receiver by using the following equations:

$$V_p = \frac{L}{t_p} \tag{1}$$

$$V_s = \frac{L}{t_s} \tag{2}$$

where, *Vp* is the velocity of the compressional wave, *Vs* is the velocity of the shear wave, *tp* and *ts* are times which *P* and *S*-wave, respectively, took to travel the distance *L*.

The relations between *P* and *S*-waves velocities and the Poisson's ratio (ν) and the Young's modulus (E) are given by Equation 3 and 4 (ASTM D 2845, 2005).

$$\nu = \frac{\left(V_p^2 - 2V_s^2\right)}{2\left(V_p^2 - V_s^2\right)} \tag{3}$$

$$E = \frac{\rho V_s^2\left(3V_p^2 - 4V_s^2\right)}{\left(V_p^2 - V_s^2\right)} \tag{4}$$

Other useful elastic parameters that can be obtained from the dynamic or static tests are the bulk and shear module or modulus of rigidity, K and G, respectively. According to ASTM D 2845 (2005), K and G can be determined as follows:

$$K = \frac{\rho\left(3V_p^2 - 4V_s^2\right)}{3} = \frac{E}{3(1-2\nu)} \tag{5}$$

$$G = \rho V_p^2 = \frac{E}{2(1+\nu)} \tag{6}$$

where, ν is Poisson's ratio, ρ is density in kg/m^3, E is Young's modulus of elasticity in Pa, K is bulk modulus in Pa and G is modulus of rigidity or shear modulus in Pa.

3 EXPERIMENTAL STUDIES

Blocks of 15 different volcanic and carbonate rocks were collected from the marble processing plants and brought to the laboratory in order to process and test for the determination of specific cutting energy in circular sawing and elastic parameters of rocks. Marble blocks were inspected to confirm that they do not contain any alteration and major fracture zones. Then the samples were prepared from these blocks. During sampling, rock types having no bedding planes were selected to eliminate any anisotropic effects on the measurements. The name, the location and the class of the collected rocks are given and shown in Table 1.

3.1 *Density test*

The density of rock samples were determined using saturation and buoyancy techniques, as recommended by ISRM (2007). The weight of the specimen was determined by a balance, capable of weighing to an accuracy of 0.01 g. The density of samples was calculated by dividing the dry weight of samples to the bulk volumes. The arithmetical average values of density with standard deviations of the rocks are given in Table 2.

3.2 *P and S-wave measurements*

To calculate elastic parameters of rocks, the velocities of *P* and *S*-waves were measured using the high frequency ultrasonic pulse technique instrument. *P* and *S*-wave measurements were carried out on the five prismatic test samples for each rock type having an approximate dimension of 5 × 10 × 20 cm. The ultrasonic velocity testing method determines the velocity of propagation of elastic waves in laboratory conditions. Transmitter and receiver transducers and a nominal frequency of 1 MHz are used. The receiver

Table 1. Details on rocks tested.

Rock code	Rock name	Rock type	Rock class	Location
R1	Lymra	Lymra	Sedimentary	Antalya-Demre
R2	Bucak Travertine	Travertine	Sedimentary	Burdur-Bucak
R3	Denizli Travertine	Travertine	Sedimentary	Denizli-Kaklik
R4	Tundra Grey	Limestone	Sedimentary	Afyon-Cay
R5	Burdur Emprador	Limestone	Sedimentary	Burdur-Karamanli
R6	Burdur Beige	Limestone	Sedimentary	Burdur-Karamanli
R7	Aglasun Beige	Limestone	Sedimentary	Isparta-Aglasun
R8	Karaman Beige	Limestone	Sedimentary	Karaman
R9	Devrekani Beige	Limestone	Sedimentary	Kastamonu-Devrekani
R10	Marmara Grey	Marble	Metamorphic	Balikesir-Marmara Island
R11	Tiger skin	Marble	Metamorphic	Afyon-İscehisar
R12	Mugla White	Marble	Metamorphic	Mugla-Yatagan
R13	Isparta Andesite	Trachy-andesite	Magmatic	Isparta-Sav
R14	Gönen Andesite	Trachyte	Magmatic	Isparta-Gonen
R15	Isparta Basalt	Basalt	Magmatic	Isparta-Kayi

Table 2. *P* and *S*-waves velocities, specific cutting energy and density values of rocks tested.

Rock code	*Vp* (m/s)	*Vs* (m/s)	SCE (j/mm^3)*	ρ (kg/m^3)*
R1	4270 ± 147	2140 ± 155	0.38 ± 0.03	2377 ± 22
R2	4257 ± 196	2187 ± 33	0.52 ± 0.08	2485 ± 18
R3	4425 ± 199	1974 ± 65	0.48 ± 0.03	2384 ± 39
R4	5868 ± 51	2323 ± 76	0.98 ± 0.08	2652 ± 25
R5	5090 ± 299	2288 ± 109	0.62 ± 0.14	2616 ± 44
R6	5705 ± 235	2413 ± 56	1.11 ± 0.07	2677 ± 70
R7	5521 ± 162	2481 ± 45	0.88 ± 0.15	2682 ± 20
R8	5814 ± 152	2373 ± 51	0.89 ± 0.19	2701 ± 3
R9	6121 ± 134	2149 ± 77	0.93 ± 0.15	2692 ± 3
R10	3577 ± 240	2010 ± 59	0.70 ± 0.04	2706 ± 2
R11	4720 ± 216	2122 ± 90	0.69 ± 0.10	2710 ± 2
R12	4408 ± 254	2445 ± 103	0.74 ± 0.10	2715 ± 7
R13	4214 ± 263	1938 ± 93	0.38 ± 0.06	2298 ± 26
R14	2885 ± 45	1617 ± 64	0.28 ± 0.07	2296 ± 7
R15	4595 ± 294	1943 ± 58	0.75 ± 0.06	2655 ± 19

Vp and *Vs*: *P* and *S*-waves velocities, SCE: specific cutting energy, ρ: density (*from Sengun 2009)

is positioned on a plane opposite to the plane which the transmitter pressed. The transducers are placed in face to face contact with soft lead foil placed between them to ensure good acoustic contact.

The velocities of the *P* and *S*-wave velocities are calculated from the measured travel time and the distance between transmitter and receiver. In order to measure a ultrasonic velocity value, the Pundit testing machine was used. The average value of P and S wave velocities with standard deviations of the collected rocks are given in Table 2.

The ultrasonic elastic parameters such as modulus of elasticity, shear modulus, bulk modulus and Poisson's ratio of rocks were calculated from the measured wave velocities and the bulk density according to ASTM D 2845 (2005) and the results are given in Table 3.

3.3 *Specific cutting energy*

In this study, laboratory tests were carried out on 15 different rocks collected from the marble processing plants to determine the SCE value in cutting operation with circular saw of each rock. Circular sawing experiments were conducted on a specially designed high precision rock block cutter (Fig. 1). All rock specimens used in the cutting tests were having a length of $5 \times 10 \times 20$ cm section. The sawing experiments were performed in the down cutting mode. The main sawing parameters which are peripheral speed of the saw blade (60 m/s), cutting depth (20 mm) and workpiece traverse speed (0.5 m/min) were kept constant in the cutting tests. Thus the specific removal rate (Q), which is equal to cutting depth times workpiece traverse speed, was fixed at 100 cm^2/min. City water was used as the cutting fluid in the sawing tests.

SCE which is defined as the energy consumed per unit volume of material removal, was computed for the rocks from the following equations.

$$F_T = \frac{P_n}{V_p} \tag{7}$$

Table 3. Calculated elastic parameters of rocks tested.

Rock code	ν	E (GPa)	K (GPa)	G (GPa)
R1	0.33	29.0	28.8	10.9
R2	0.32	31.4	29.2	11.9
R3	0.38	25.6	34.3	9.3
R4	0.41	40.3	72.2	14.3
R5	0.37	37.6	49.5	13.7
R6	0.39	43.4	66.3	15.6
R7	0.37	45.4	59.7	16.5
R8	0.40	42.6	71.0	15.2
R9	0.43	35.6	84.3	12.4
R10	0.27	27.8	20.0	10.9
R11	0.37	33.5	44.1	12.2
R12	0.28	41.5	31.1	16.2
R13	0.37	23.6	29.3	8.6
R14	0.27	15.3	11.1	6.0
R15	0.39	27.9	42.7	10.0

ν: Poisson's ratio, E: modulus of elasticity, K: bulk modulus, G: shear modulus



Figure 1. The view of the sawing test machine.

$$SCE = \frac{F_T V_p}{h W_s V_w} \quad (8)$$

where SCE is specific cutting energy (J/mm^3), P_n is net power (W), F_T is tangential force (N), V_p is peripheral speed of the sawblade (m/min), h is cutting depth (mm), W_s is the width of the sawblade segments (mm) and V_w workpiece travel speed (mm/min). Each test was repeated six times under same cutting conditions and the average specific energy values of each cutting with standard deviations are calculated and summarized in Table 2.

4 RESULTS AND DISCUSSION

Specific cutting energy values derived from cutting operation and elastic parameters of rocks calculated from *P* and *S*-waves velocities were correlated using least squares regression technique. Because of linear relationships were found between these rock properties, linear curve fitting was undertaken.

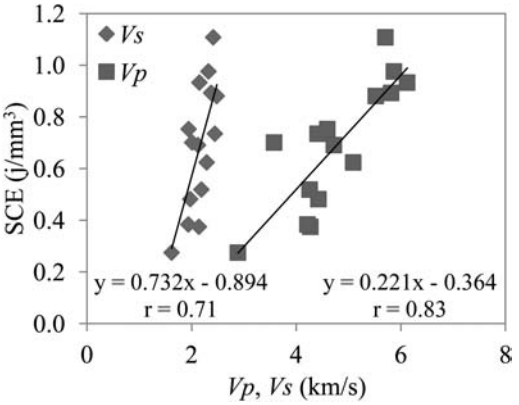


Figure 2. Relationships between *P* and *S*-waves velocities and SCE.

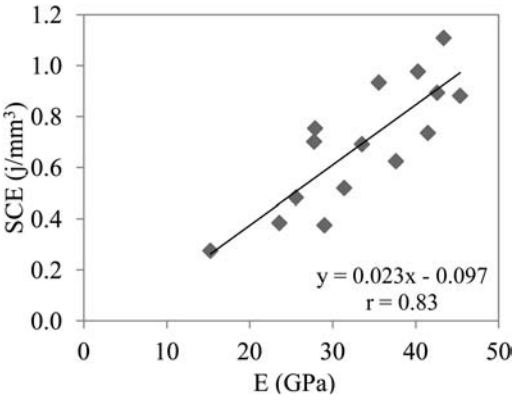


Figure 3. Relationships between Young's modulus and SCE.

Relationships between *P* and *S*-waves and SCE were evaluated and the plot of ultrasonic wave velocities as a function of SCE values is shown in Figure 2. A meaningful linear relationship exists between *Vp* and SCE. There is also a good linear correlation between the *Vs* and SCE. The correlation coefficients between *Vp*, *Vs* and SCE of rocks are obtained as 0.83 and 0.71, respectively. The clear trend is that an increase in the SCE increases the velocities of *P* and *S*-waves.

Figures 3 and 4 also revealed increasing linear relationships between SCE and Young's modulus of elasticity and bulk modulus of rocks with strong correlation coefficients, 0.83 and 0.84, respectively.

As seen in Figure 5, there is a good correlation between shear modulus of rocks and SCE. The SCE increases with increasing shear modulus of rocks. The correlation coefficient between G and SCE is 0.78.

5 CONCLUSIONS

From the analyses, performed on a special high precision circular diamond sawing machine, SCE value was tried to be related with the elastic rock parameters such

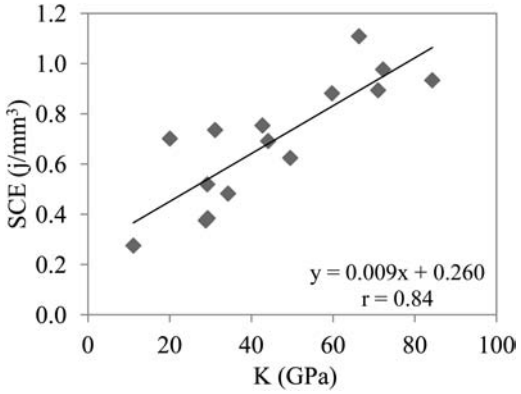


Figure 4. Relationships between bulk modulus and SCE.

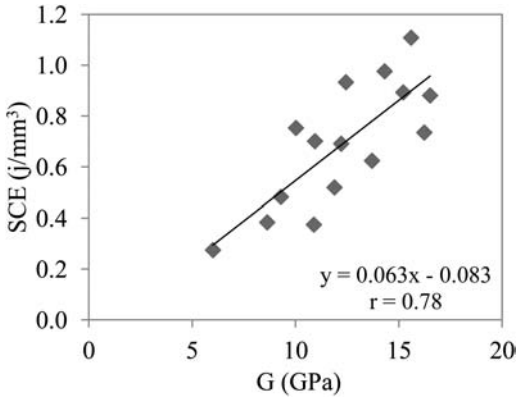


Figure 5. Relationships between shear modulus and SCE.

as modulus of elasticity, shear modulus, bulk modulus and Poisson's ratio in the down cutting mode by kept constant the main sawing parameters. In the study reported here, the velocities of *P* and *S*-waves were measured using the high frequency ultrasonic pulse technique with Pundit Plus instrument for 15 types of volcanic and carbonate rocks and the following conclusions were drawn:

- Higher *Vp* and *Vs* values will demand more specific cutting energy consumption;
- Regression analysis showed that good correlations exist between SCE and elastic parameters of rocks including E, K and G.
- Lower elastic rock parameters will demand less specific cutting energy consumption

For the further researches related with this subject, it may be advised that, elastic parameters of the rocks defined above must be taken into consideration besides the main rock parameters.

REFERENCES

ASTM D 2845, 2005. Standard Test Method for Laboratory Determination of Pulse Velocities and Ultrasonic Elastic Constants of Rock.

Babuska, V. & Pros, Z. 1984. Velocity anisotropy in granodiorite and quartzite due to the distribution of microcracks. *Geophys J R Astron Soc* 76: 121–127.

Barruol, G. & Kern, H. 1996. Seismic anisotropy and shear-wave splitting in lower-crustal and upper mantle rocks from the Ivrea zone experimental and calculated data. *Phys Earth Planet Inter* 95: 175–194.

Brook, B. 2002. Principles of diamond tool technology for sawing rock. *Int J Rock Mech Min Sci* 39: 41–58.

Buyuksagis, I.S. 2007. Effect of cutting mode on the sawability of granites using segmented circular diamond sawblade. *J Mater Process Tech* 183: 399–406.

Ceylanoglu, A. & Gorgulu, K. 1997. The performance measurement results of stone cutting machines and their relations with some material properties. In V. Strakos et al. (eds), *Proceedings of the 6th International Symposium on Mine Planning and Equipment Selection*: 393–398. Rotterdam: Balkema.

Ersoy, A. & Atici, U. 2007. Correlation of P and S-waves with cutting specific energy and dominant properties of volcanic and carbonate rocks. *Rock Mech Rock Eng* 40: 491–504.

Gaviglio, P. 1989. Longitudinal waves propagation in a limestone: the relationship between velocity and density. *Rock Mech Rock Eng* 22: 299–306.

Guney, A. 2011. Performance prediction of large-diameter circular saws based on surface hardness tests for Mugla (Turkey) marbles. *Rock Mech Rock Eng* 44: 357–366.

Inoue, M. & Ohomi,. M. 1981. Relation between uniaxial compressive strength and elastic wave velocity of soft rock. In K. Akai et al. (eds), *Weak Rock – Soft, Fractured and Weathered Rock, Proceedings of the International Symposium on Weak Rock, Tokyo*: 9–13. Rotterdam: Balkema.

ISRM, 2007. *The Complete ISRM Suggested Methods for Rock Characterization, Testing and Monitoring: 1974–2006*, (Ulusay, R. & Hudson, J.A., Editors), Kozan Ofset, Ankara, Turkey, 628 p.

Kahraman, S. 2001. Evaluation of simple methods for assessing the uniaxial compressive strength of rock. *Int J Rock Mech Min Sci* 38: 981–994.

Kahraman, S. 2002. Estimating the direct P-wave velocity value of intact rock from indirect laboratory measurements. *Int J Rock Mech Min Sci* 39: 101–104.

Kahraman, S. & Gunaydin, O. 2008. Indentation hardness test to estimate the sawability of carbonate rocks. *Bull Eng Geol Environ* 67: 507–511.

Karpuz, C. & Pasamehmetoglu, A.G. 1997. Field characterization of weathered Ankara andesites. *Eng Geol* 46: 1–17.

Kern, H. 1993. P- and S-wave anisotropy and shear-wave splitting at pressure and temperature in possible mantle rocks and their relation to the rock fabric. *Phys Earth Planet Inter* 78(3–4): 245–256.

Konstanty, J. 2002. Theoretical analysis of stone sawing with diamonds. *J Mater Process Tech* 123: 146–154.

Luo, S.Y. & Liao, Y.S. 1995. Study of behaviour of diamond sawblade in stone processing. *J Mater Process Tech* 51: 296–308.

Sengun, N. & Altindag, R. 2013. Prediction of specific energy of carbonate rock in industrial stones cutting process. *Arab. J Geosci* 6: 1183–1190.

Sengun, N. 2009. The Effects of Fracture Toughness and Brittleness of Rocks on Sawing Efficiency with Circular Discs. Ph.D. Thesis, Süleyman Demirel Univ., Isparta, 182 p. (in Turkish)

Tonshoff, H.K. & Hillmann-Apmann, H. 2002. Diamond tools for wire sawing metal components. *Diam Relat Mater* 11(3–6): 742–748.

Tonshoff, H.K. & Ashe, J. 1997. Wear of metal-bond diamond tools in the machining of stone. *Ind Diamond Rev* 1: 7–13.
Walker, R.D. & Wood, M.G. 1971. Granite sawing techniques *Ind Diamond Rev* 31: 4–7.
Wang, C.Y. & Clausen, R. 2002. Marble cutting with single point cutting tool and diamond segments. *Int J Mach Tools Manuf* 42: 1045–1054.
Wright, D.N. 1986. The prediction of diamond wear in sawing of stone. *Ind Diamond Rev* 5: 213–216.
Wright, D.N. & Cassapi, V.B. 1985. Factors influencing stone sawability. *Ind Diamond Rev* 2: 84–87.
Wright, D.N. & Jennings, M. 1989. Guidelines for sawing stone. *Ind Diamond Rev* 2: 70–75.
Xu, X. 1999. Friction studies on the process in circular sawing of granites. *Tribol Lett* 7: 221–227.
Yagiz, S. 2011. P-wave velocity test for the assessment of some geotechnical properties of rock materials. *B Mater Sci* 34: 943–957.
Yasar, E. & Erdogan, Y. 2004. Correlating sound velocity with the density, compressive strength and Young's modulus of carbonate rocks. *Int J Rock Mech Min Sci* 41: 871–875.

Rock Mechanics for Resources, Energy and Environment – Kwaśniewski & Łydżba (eds)
© 2013 Taylor & Francis Group, London, ISBN 978-1-138-00080-3

Strength behaviour of reinforced natural jointed rock

L.P. Srivastava & M. Singh
Department of Civil Engineering, Indian Institute of Technology Roorkee, Roorkee, India

ABSTRACT: The rocks encountered in civil and mining engineering applications are invariably jointed. The presence of joints in rock makes them anisotropic and weak in strength behaviour. One of the techniques for enhancing the rock mass strength is to provide rock bolts. Assessment of strength of reinforced jointed rock is a challenging task before the geotechnical engineers. The strength of reinforced jointed rock depends on characteristics of intact rock, joint and rock bolt. An experimental study has been conducted to assess the mechanism of strength enhancement in jointed rocks due to provision of rock bolts. NX size cylindrical specimens of natural rocks having natural joints at variable orientation have been tested under uniaxial loading condition. Tests were also conducted on the bolted specimens. The results have been used to come out with an expression, which correlates the strength and deformation of intact rock to that of jointed rock without, and with reinforcement.

1 INTRODUCTION

Rock bolts are used as a primary support in many rock structures. Bolts increase the stiffness of the rock mass against external tensile or shear forces. In past, several studies have been conducted by researchers to evaluate the strength of jointed rock reinforced with rock bolts. The strength of reinforced rock has been reported to be dependent on various factors like strength of the parent rock (Egger & Zabuski 1991, Pellet & Egger 1996, and Sakurai 2010), joint orientation, angle of inclination between joint and bolt, and diameter of bolt (Bjurström 1974, Ludvig 1983, Pellet & Egger 1996, Grasselli et al. 1999, and Grasselli 2005). Effect of failure mode on engineering response of jointed rock has been emphasized by Singh (1997) and Singh et al. (2002) which is also an important factor in the case of jointed rocks. In present work, the effect of joint orientation on the strength and deformation behaviour of unreinforced and reinforced natural joint rock has been investigated.

2 EXPERIMENTAL STUDY

The experimental study has been performed by conducting uniaxial compression strength tests on natural cylindrical rock specimens of NX size. The rock specimens were retrieved from cores drilled from a project site in Garhwal region of the Indian Himalayas. Tests have been conducted on intact, jointed unreinforced and reinforced specimens. Height to diameter ratio of the specimens has been kept roughly equal to two. The joint orientation ($\theta°$) of the specimens has been varied between 0° to 90°, where θ is the angle between normal to the joint plane and the specimen axis (Fig. 1). The reinforced jointed rock specimens were prepared by installing rock bolt (Fig. 2). A hole of 6 mm diameter was drilled normal to the axis of cylindrical specimens and a 4 mm diameter bolt was installed into the drilled hole. The bolt was grouted with cement–sand slurry. The tensile strength of the bolt is about 550 MPa. Table 1 shows the joint orientations for which specimens have been tested. The rocks in Himalayan region exhibit heterogeneous character, hence intact rock specimens were extracted from same depth from where the jointed specimens were obtained.



Figure 1. Unreinforced specimens of jointed rock.

The specimens were tested in a strain-controlled machine. The rate of application was so adjusted that failure occurred within about 10 to 15 minutes. Axial load and axial displacement were recorded during the experiment. Triaxial tests were also performed on intact rock specimens at minor principal stress of 5, 20, and 40 MPa to obtain shear strength parameters



Figure 2. Reinforced specimens of jointed rock.

Table 1. Number of specimens tested.

	Unreinforced		Reinforced	
(θ°)	Jointed	intact	Jointed	intact
0–10	1	1	–	–
10–20	1	1	–	–
20–30	1	1	1	1
30–40	1	1	1	1
40–50	1	1	1	1
50–60	1	1	1	1
60–70	1	1	1	1
70–80	1	1	1	1
80–90	1	1	1	1

Table 2. Properties of intact material.

Unit weight (kN/m^3)	26
Uniaxial compressive strength (σ_{ci}), MPa	67
Tangent modulus (E), MPa	8500
Cohesion (c_i), MPa	14
Angle of internal friction, φ_i°	38
Brazilian tensile strength, MPa	10
Deere-Miller classification (1966)	CL

of intact rock. In addition Brazilian tests were also conducted on intact rock specimens.

3 RESULTS AND DISCUSSION

3.1 *Intact rock properties*

The physical and engineering properties of the intact rock are presented in Table 2. The uniaxial compressive strength and tangent modulus values reported in this table are average values obtained from UCS tests conducted on intact rock specimens.

3.2 *Failure modes*

Failure modes play important role in giving the engineering response of jointed rocks. They have direct influence on the strength and deformability. The modes

Table 3. Failure modes observed.

Joint orientation (θ°)	Failure mode observed	
	Unreinforced	Reinforced
Intact	Splitting/Shearing	–
0–10	Splitting/Shearing	–
10–20	Splitting/Shearing	–
20–30	Splitting/Shearing	Splitting/shearing
30–40	Sliding	Splitting/shearing
40–50	Sliding	Splitting/shearing
50–60	Sliding	Splitting/shearing
60–70	Sliding	Splitting/shearing
70–80	Sliding	Splitting/shearing
80–90	Splitting/Shearing	Splitting/Shearing



Figure 3. Failure of reinforced jointed rock under uniaxial compression.

have been observed after the specimen failed in all cases of UCS tests. The modes observed in intact, unreinforced and reinforced jointed rock are listed in Table 3. The intact rock shows splitting and shearing modes of failure. The unreinforced jointed rock exhibit sliding, shearing and, splitting modes of failure. Splitting/shearing has been observed in case of specimens having joint orientation less than 30° and more than 80°. For the range $\theta = 30°–80°$, sliding mode of failure has been observed. In case of reinforced rock, only two modes i.e. shearing and splitting were observed for all specimen tested i.e. $\theta > 20°$. It is observed from Table 3 that the failure mode changes from sliding to splitting/shearing for orientations $\theta = 30°–80°$ when rock bolt is installed. Figure 3 shows typical failure of reinforced jointed rock under uniaxial compression.

3.3 *Yielding of bolt*

The yielding of the bolt has been observed in case of joint orientations between $\theta = 30°–80°$. These orientations exhibited sliding mode of failure in unreinforced case. In case of critical joint orientation i.e. $\theta = 40°–50°$ complete shearing of the bolt has been observed. Visual inspection of failed specimens has

Table 4. Yielding of bolt observed.

Joint orientation (θ°)	Yielding observed
20–30	No yielding
30–40	Slight yielding
40–50	Complete shearing
50–60	Significant yielding
60–70	Significant yielding
70–80	Significant yielding
80–90	No yielding

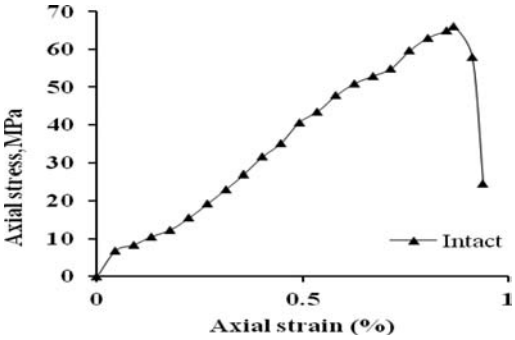


Figure 4. Axial stress vs axial strain curve for intact rock.

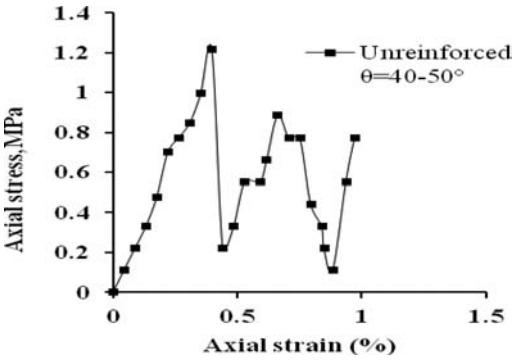


Figure 5. Axial stress vs axial strain curve for unreinforced rock at $\theta = 40$–50°.

revealed that significant yielding of bolt occurred for $\theta = 50°$–480° while slight yielding of bolt occurs for $\theta = 30°$–40° (Table 4).

3.4 *Uniaxial compressive strength and tangent modulus*

Axial stress vs axial strain curves were plotted for all the tests conducted on jointed specimens. Few typical stress vs strain curves are plotted in Figures 4 to 6. Values of uniaxial compressive strength (UCS) and tangent modulus (E_{t50}) of unreinforced and reinforced specimens are listed in Table 5. The results indicate that the strength as well as the tangent modulus of reinforced rock is greater than the strength of unreinforced rock, but it is less than the strength of intact

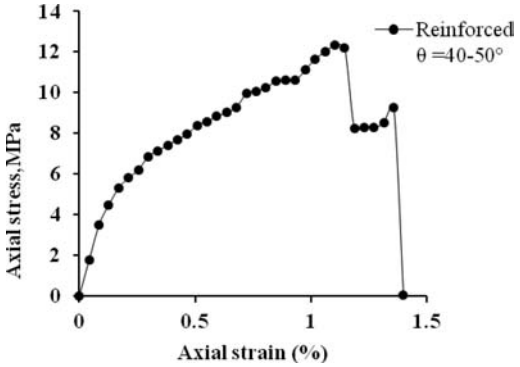


Figure 6. Axial stress vs axial strain curve for reinforced rock at $\theta = 40$–50°.

Table 5. Values of UCS and E_{t50} for unreinforced (U) and reinforced (R) specimens of jointed rock.

	UCS, MPa		E, MPa	
θ°	U	R	U	R
0–10	44.69	–	4920	–
10–20	47.01	–	5593	–
20–30	32.02	34.47	3798	4827
30–40	6.55	18.05	905	4487
40–50	1.22	12.32	322	744
50–60	1.08	5.97	156	1633
60–70	1.03	7.78	56	503
70–80	0.56	46.05	38	5770
80–90	21.52	23.69	4367	4382

material. For all joint orientations, the reinforced rock has greater strength as compared to unreinforced rock.

4 CLASSIFICATION OF UNREINFORCED AND REINFORCED JOINTED ROCK

The laboratory strength and tangent modulus of the unreinforced and reinforced specimens are presented in the form of Deere-Miller (1966) classification charts (Fig. 7 and 8) as suggested by Ramamurthy & Arora (1993). Deere-Miller (1966) classify the rock by two lettered symbols: the first letter represents the range of the uniaxial compressive strength (UCS) and the second letter represents the modulus ratio. The classification is very helpful in designing as it gives idea of both the strength and deformability of the rock. It is interesting to see that for both unreinforced and reinforced specimens the data points are scattered around an empirical line starting from intact rock position (shown by letter I).

The gradient of empirical lines shown in Figures 7 and 8 may be used to assess the strength of unreinforced and reinforced rock as given below:
From Figure 7

$$Gradient\ of\ line = \frac{\log E_i - \log E_{ju}}{\log \sigma_{ci} - \log \sigma_{cju}} \quad (1)$$

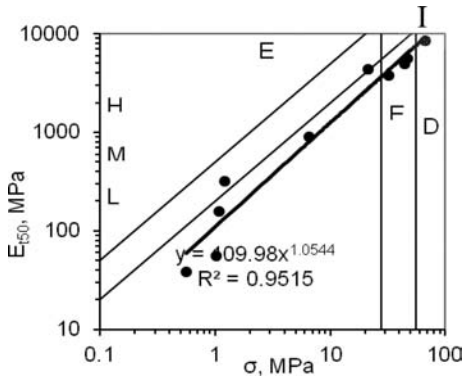


Figure 7. Strength and tangent modulus values for unreinforced joined rock.

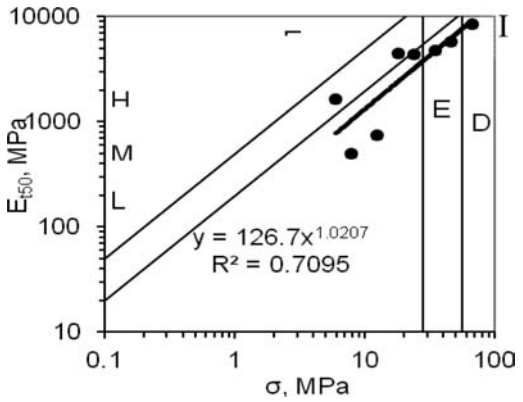


Figure 8. Strength and tangent modulus values for reinforced joined rock.

$$\Rightarrow \frac{\sigma_{cju}}{\sigma_{ci}} = \left(\frac{E_{ju}}{E_i}\right)^{\frac{1}{Gradient\ of\ line}} = \left(\frac{E_{ju}}{E_i}\right)^{0.95} \quad (2)$$

Similarly from Figure 8

$$\frac{\sigma_{cjr}}{\sigma_{ci}} = \left(\frac{E_{jr}}{E_i}\right)^{\frac{1}{Gradient\ of\ line}} = \left(\frac{E_{jr}}{E_i}\right)^{0.98} \quad (3)$$

where σ_{ci} and E_i = uniaxial compressive strength and tangent modulus of intact rock; σ_{cju} and E_{ju} = uniaxial compressive strength and tangent modulus of unreinforced rock; σ_{jr} and E_{jr} = uniaxial compressive strength and tangent modulus of intact rock.

In the field, the deformability tests are relatively easier to conduct. The value of E_{ju} will therefore be known. The above expression may be used for rough estimation of the strength of jointed rock for unreinforced and reinforced conditions.

5 CONCLUDING REMARKS

Experiments have been conducted on cylindrical specimens of jointed rocks. The tests have been conducted for unreinforced as well as reinforced condition. The joint orientation has been varied in this study. It is observed that, on Deere-Miller classification chart the position of jointed rock specimens are scattered around an empirical line starting from intact rock position. The position of reinforced specimens has also been found to be scattered around the same line starting from intact rock position, though scattered for reinforced specimen was found to be little larger. The empirical lines thus obtained can be used to correlate strength and deformability of unreinforced and reinforced jointed rocks with those of intact rock. These correlations can be used for rough estimation of strength properties of the reinforced jointed rocks, which otherwise are difficult to obtain though field-testing.

REFERENCES

Bjurström, S. 1974. Shear strength of hard rock joints reinforced by grouted untensioned bolts. In *Proc. 3rd Int. Congr. Rock Mech.*, Denver, Colorado: II(B), 1194–1199. Washington, DC: National Academy of Sciences.

Deere, D.U. & Miller, R.P. 1966. Engineering Classification and Index Properties for Intact Rock, Technical Report No. AFNL-TR-65-116. Air Force Weapons Laboratory, New Mexico.

Egger, P. & Zabuski, L. 1991. Behaviour of rough bolted joints in direct shear tests. In W. Wittke (ed.), *Proc. 7th Int. Congr. Rock Mech.,* Aachen, Germany: 1285–1288. Rotterdam: Balkema.

Ferreroq, A.M. 1995. The shear strength of reinforced rock joints. *Int. J. Rock Mech. Min. Sci. & Geomech. Abstr.* 32(6): 595–605.

Grasselli, G. 2005. 3D behaviour of bolted rock joints: experimental and numerical study. *Int. J. Rock Mech. Min. Sci.* 42: 13–24.

Grasselli, G., Kharchafi, M. & Egger, P. 1999. Experimental and numerical comparison between fully grouted and frictional bolts. In G. Vouille & P. Bérest (eds), *Proc. 9th Int. Congr. Rock Mech.,* Paris, France: 903–907.

Ludvig, B. 1983. Shear tests on rockbolts. *Proceedings of the International Symposium on Rock Bolting*, Abisko: 113–123. Rotterdam: Balkema.

Pellet, F. & Egger, P. 1996. Analytical model for the mechanical behaviour of bolted rock joints subjected to shearing. *Rock Mech. Rock Eng.* 29(2): 73–97.

Ramamurthy, T. & Arora, V.K. 1993. A classification for intact and jointed rocks. In A. Anagnostopoulos et al. (eds), *Geotechnical Engineering of Hard Soils – Soft Rocks*: 235–242. Rotterdam: Balkema.

Sakurai, S. 2010. Modeling strategy for jointed rock masses reinforced by rock bolts in tunneling practice. *Acta Geotechnica* 5: 121–126.

Singh, M. & Rao, K.S. 2005. Empirical methods to estimate the strength of jointed rock masses. *Engineering Geology* 77: 127–137.

Singh, M. 1997. *Engineering behaviour of jointed model materials.* PhD thesis, IIT Delhi, India.

Rock Mechanics for Resources, Energy and Environment – Kwaśniewski & Łydżba (eds)
© 2013 Taylor & Francis Group, London, ISBN 978-1-138-00080-3

Estimation of the effects of the centrifugal hydraulic conductivity of impermeable rocks under constant head conditions

M. Takahashi
Geological Survey of Japan, Higashi, Tsukuba, Ibaragi, Japan

W. Lin
JAMSTEC, Nangoku, Kouchi, Japan

M. Kato
Hokkaido University, Kitaku, Sapporo, Japan

ABSTRACT: The advantage of using centrifugal acceleration as a fluid driving force is that it acts as a body force in a way that is similar to that of gravity. To compare the saturated hydraulic conductivity of impermeable rocks, constant head tests under centrifugal acceleration and gravity, and Transient Pulse tests were conducted. Shirahama sandstone and Kabasan granite were used as specimens for determining the hydraulic conductivity. The centrifugal constant head method proved to be low hydraulic conductivity value by an order of 1 or 2 than that by the gravity Transient Pulse method. The reason was assumed to be that an unsaturated region occurred in the bottom of the specimen because the centrifugal force is greater near the bottom (downstream side) than the top of the specimen. To avoid unsaturation inaccuracies as much as possible, appropriate specimen length and sufficient water pond will be necessary for the loading bucket assembly.

1 INTRODUCTION

Transport ability of rocks are evaluated either by hydraulic conductivity, which is an index of liquid flow smoothness, or by storage coefficient, which indicates rock's capacity to store or to extract of liquid. Because the reservable amount of liquid under hydrostatic condition is usually negligibly small compared to the total volume of a specimen, water permeation tests may focus only on hydraulic conductivity. In permeation tests on low-permeability rocks, measuring techniques and apparatus that take account of very small porosity of samples are used. Several methods have been proposed for this kind of water permeation tests. These are Transient Pulse method (Brace et al. (1968)), Flow Pump method (Olsen et al. (1985)) and Sinusoidai method (Bennion and Goss (1971), Kranz et al. (1990)). Esaki et al. (1996) and Zhang et al. (2000a, 200b) have proposed a technique that determines both hydraulic conductivity and specific storage coefficient at the same time by using exact solution which takes compressibility of apparatus into account.

While experiments which use these techniques are conducted under acceleration of free fall (normal gravity, 1g), Nimmo and Mello (1991) have proposed a technique that utilizes centrifugal force which can determine hydraulic conductivity from amount of fluid which passes through specimen under given rotational velocity. They used as specimen ceramics and argillacious samples obtained from 5 to 8 m depth at a site in Menlo Park. Hydraulic conductivity of them under saturated condition were reported to be between from 10^{-8} to 10^{-10} m/s. They discuss that these measurements show differences of less than 20% from those obtained through conventional falling-head and constant-head permeability tests.

To measure hydraulic conductivities of Shirahama sandstone and Kabasan granite, we chose constant-head permeability test method among those techniques which utilize centrifugal force. While conventional water permeation tests, which use techniques such as Transient Pulse method, can measure hydraulic conductivity up to about 10^{-12} cm/s, the measurement limit of water permeation tests by centrifugal method is considered to be 10^{-8} cm/s. We examined whether centrifugal method can be applied to specimens whose hydraulic conductivity is two orders smaller than this value.

2 EXPERIMENTAL EQUIPMENT

The apparatus of our test was basically categorized as UFA (Unsaturated Flow Apparatus). Though the term "UFA" contains the word "unsaturated", it is now used also for saturated conditions. The term is also applied to flow measurements of specimens under any given acceleration or under condition of centrifugal loading.

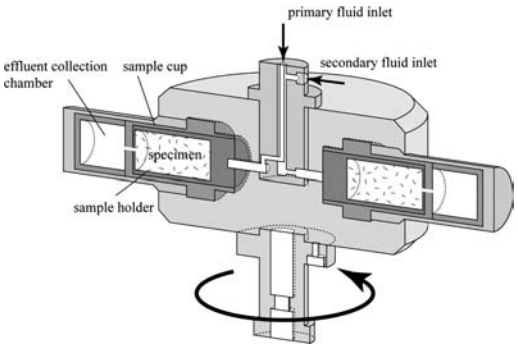


Figure 1. Schematic view of the UFA rotor.

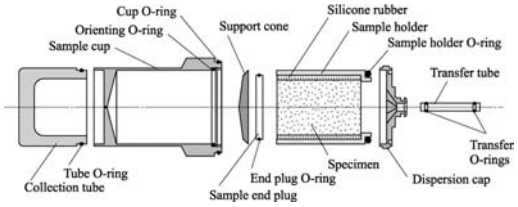


Figure 2. Loading bucket assembly.

Figure 1 shows a schematic diagram of apparatus we used. It mainly consisted of centrifugal-loading part and a flow-control part which provided or retrieved fluid from specimens. The rotational speeds of the centrifugal loading part could be set from 100 to 3000 rpm in increments of 20 rpm. This part could be continually operated up to 99 hours. Rotor chamber had a diameter of 58 cm. Two specimens could be placed in it at intervals of 180°. In the flow-control part, pipes from low-flow micro pump reached to the rotor through rotating seal. This part consisted of, from the rotational axis to outside, dispersion cup, specimen, sample holder, sample cup, effluent collection chamber, and sample bucket (metal bucket). When the rotational speed was set to a particular value and fluid was released from the center of rotor at any desired flow speed, water flux rate at every time segment could be directly read through stroboscope which was synchronized with the rotational speeds.

Figure 2. is a cross section of fluid cell we adopted in the test. When the type of specimen is rock sample, there is a possibility of facial flow, in which water flows outside of the specimen. To prevent facial flow from happening, the space between sample and sample holder was sealed with silicon rubber, as illustrated in Figure 3. Since the purpose of our test was to clarify changes in liquid phase composition of flux and to measure hydraulic conductivity at the same time. Therefore, we placed a reservoir on the flow-control part which could reserve fluid three orders larger than the water flux rate of a specimen. Since this large reservoir allowed water level above a specimen to stay constant throughout the test by providing flux through rotor, we measured hydraulic conductivity using constant head test.

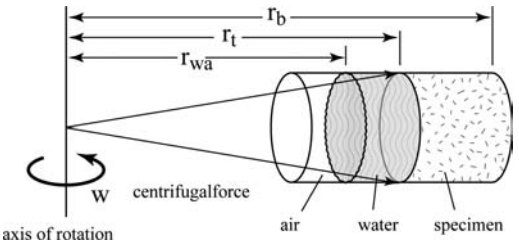


Figure 3. Schematic view of physical model in UFA.

3 CALCULATION OF HYDRAULIC CONDUCTIVITY

We chose in the test constant-head centrifugal loading method, in which water head pressure on a specimen stays constant. When hydraulic conductivity is measured by this method, the experimental condition can be illustrated as shown in Figure 3. The upper boundary condition is atmospheric pressure at air-water interface, positioned at r_{wa} from the axis of rotation. The lower boundary condition is atmospheric pressure at the bottom of specimen, positioned at r_b from the axis of rotation.

Darcy's law holds at any point of a specimen when fluid flux q is equivalent to the product of hydraulic conductivity K and driving force. Fluid driving force under centrifugal loading includes matric potential gradient dp/dr and centrifugal force per unit volume ($\rho\omega^2 r$). Therefore, Darcy's law is expressed by

$$q = K_{sat}\left(-\frac{dp}{dr} + \rho\omega^2 r\right) \tag{1}$$

The equation for the whole sample is given as

$$q = K_{sat}\left(-\frac{dp}{dr} + \rho\omega^2 r\right) \tag{2}$$

Therefore,

$$p_t - p_b = \frac{1}{2}\rho\omega^2\left(r_t^2 - r_b^2\right) - \frac{q}{K_{sat}}\left(r_t - r_b\right) \tag{3}$$

$$\begin{cases} p_t = \int_{r_{wa}}^{r_t} \rho\omega^2 r dr = \frac{1}{2}\rho\omega^2\left(r_t^2 - r_{wa}^2\right) \\ p_b \to 0. \end{cases}$$

Substitution of these conditions into equation (3) yields

$$\therefore K_{sat} = \frac{2qL}{\rho\omega^2\left(r_b^2 - r_{wa}^2\right)} \quad \left(L = r_b - r_t\right) \tag{4}$$

where q is fluid flux (equivalent to water flux rate per unit time, ml/hour), p is pressure (matric potential, Pa), dp/dr is matric potential gradient (Pa/cm), $p\omega^2 r$ is centrifugal force per unit area, K is hydraulic conductivity (cm/s), ρ is density of water (gm/cm^3), ω is angular velocity (rad/s), and L is height of specimen (cm).

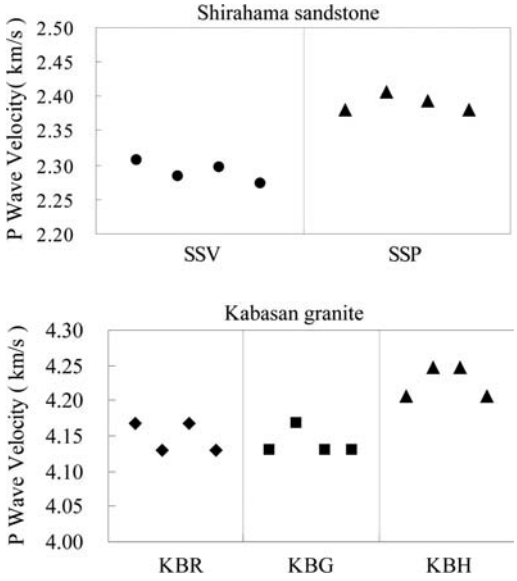


Figure 4. P wave velocity in Shirahama sandstone and Kabasan granite.

Though matric potential gradient is counted as driving force in equation (1), here fluid migration is supposed to be caused only by centrifugal force, as seen from equation (4). Improving Equation (4) requires development of techniques for measuring and clarifying matric potential inside rocks.

4 THE TEST RESULTS

All test specimens were shaped into cylindrical form, 32 mm in diameter and 45 mm in height. These dimensions were adopted to attain handling easiness and appropriate flux time length in water flow test with a given size of the sample holder.

Figure 4 shows elastic wave velocity distribution of each specimen in normal conditions before the test. Among Shirahama sandstone samples, approximately 0.1 km/sec differences in elastic wave velocity were detected between specimens with bedding plane was perpendicular to major axis (SSV) and ones whose bedding plane was parallel to major axis (SSP). As for Kabasan granite samples, specimens with major axis perpendicular to rift plane (the plane of easiest splitting) or grain plane (next easiest splitting) showed slower velocity values than one to hardway plane (the hardest plane). No clear differences can be seen between specimens with major axis being perpendicular to rift plain and ones to grain plane. Granite has this kind of anisotropy which results from preexisting microcrack orientation. The anisotropy was used to classify Kabasan granite samples in the test.

Figure 5 shows the relationship between accumulated effluent of water flow test on Shirahama sandstone (proportional to total flux time) and hydraulic

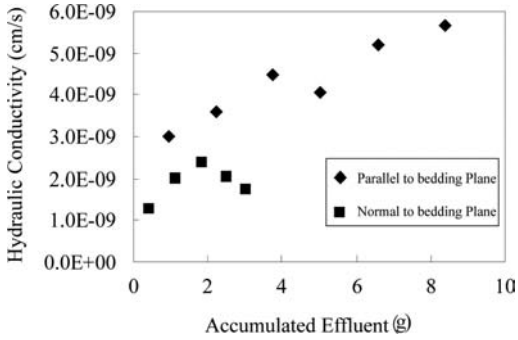


Figure 5. Permeability vs accumulated effluent on Shirahama sandstone.

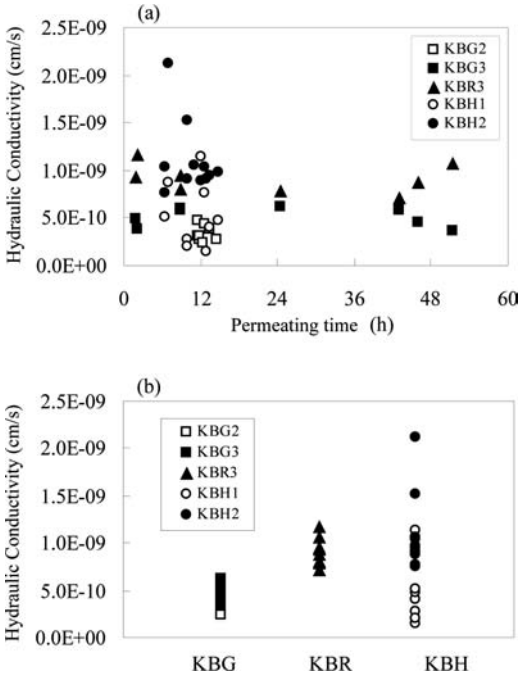


Figure 6. (a) Permeability vs permeating time, (b) Permeability distribution of Kabasan granite at three different orientations.

conductivity obtained from Equation (4). On specimens whose major axis was parallel to bedding plane, hydraulic conductivity increased as total flux time increased. This relationship was not clear in perpendicular specimens.

Figure 6 shows (a) hydraulic conductivities of Kabasan granite and (b) their distribution in each specimen group with different preexisting orientation. In contrast to Shirahama sandstone, their hydraulic conductivity showed no clear dependence on flux time. KBH1 and KBH2 were specimens whose major axis was perpendicular to hardway plane. KBH1 showed smaller hydraulic conductivity. KBH specimens showed wider distributional range of hydraulic

conductivity than KBR or KBG specimens on the whole.

5 PROBLEMS IN MEASURING HYDRAULIC CONDUCTIVITY UNDER CENTRIFUGAL CONDITION

Nimmo and Mello (1991) have examined the relationship between hydraulic conductivities obtained in usual constant-head test and those obtained in centrifugal loading tests. Three different kinds of tests were conducted on the same samples. These are constant-head test under atmospheric pressure, constant-head and falling-head tests under centrifugal loading. Hydraulic conductivities were evaluated as functions of centrifugal force. They were reported to have declined slightly as centrifugal force increased. Also, the values obtained in constant-head test under normal gravity were reported to be lower than those values extrapolated from the results of constant-head and falling-head tests under centrifugal loading. Nimmo and Mello also reported that ceramic plates showed almost same values of hydraulic conductivity in these three kinds of water permeation test.

In contrast with their results, in our case, those values of Shirahama sandstone measured in centrifugal loading test were lower than those determined in Transient Pulse water permeation test. Most probable cause of this discrepancy was the generation of unsaturated region in the lower part of specimens under centrifugal rotation. Since all specimens had heights of 45 mm, their upper part and lower part had different distances from the axis of rotation when set to the apparatus, which resulted in yielding different centrifugal force on two parts. This difference in centrifugal force seems to have led to phenomena such as dehydration from the bottom of specimens. Other possible causes of unsaturation were much less likely to have occurred. Sample assembly were vacuumed before the tests to make them completely saturated, Shirahama sandstone for 4 days and Kabasan granite for 1 week. Then they were quickly moved from water into the apparatus, which kept the amount of evaporation negligibly small.

The specimens were sized a little larger this time to increase reaction area of liquid phase and rock's framework structure in the water flow test. However, it is necessary to minimize the difference of centrifugal forces acting on different parts of a specimen in order to avoid the generation of unsaturated region mentioned above. While this may be attained by enlarging head at the top of specimen, the most practical option is to prepare them in disk-shaped form by lowering the height of specimens while keeping the diameter in the same length. In order to determine the shape and dimensions of specimens that are appropriate for both water permeation test and water flow test for detecting liquid phase change, further examination on experimental conditions is necessary which takes porosity of specimens and rotational velocity into account.

6 CONCLUSIONS

We conducted hydraulic conductivity measuring test with centrifugal loading apparatus, using Shirahama sandstone and Kabasan granite as specimens. The resultant values of hydraulic conductivity were lower than those obtained through the tests which are conducted under normal gravity, employing other techniques such as Transient Pulse method. Most probable reason for this is the generation of unsaturated region in the lower part of specimens, which is caused by excessive length (height) of the specimens used. Accurate measurements of hydraulic conductivity under centrifugal loading require appropriate height of specimens. We also confirmed that analysis by flow examination of changes in liquid phase, for which centrifugal loading is originally used, is effective technique to examine time effect.

REFERENCES

Bennion, D.W. & Goss, M.J. 1971. A sinusoidal pressure response method for determining the properties of a porous medium and its in-situ fluid, Soc. Petrol. Engng, paper SPE 3541.

Brace, W.F., Walsh, J.B. & Frangos, W. T., 1968. Permeability of granite under high pressure. *J. Geophys. Res.* 73: 2225–2236.

Esaki, T. & Zhang, M. 1996. Rigorous Theoretical Analysis of a Flow Pump Permeability Test. *Geotechnical Testing Journal* 19(3): 241–246.

Kranz, R.L., Saltzman, J.S. & Blacic, J. D. 1990. Hydraulic diffusivity measurements on laboratory rock samples using an oscillating pore pressure method. *Int. J. Rock. Mech. Min. Sci. & Geomech. Abstr.* 27(5): 345–352.

Nimmo, J.R. & Mello, K.A. 1991. Centrifugal Techniques for Measuring Saturated Hydraulic Conductivity. *Water Resources Research* 27(6): 1263–1269.

Olsen, H.W., Morin, R.H. & Nichols, R.W. 1985. Flow pump applications in triaxial testing, Advanced Triaxial Testing of Soil and Rock. In: Donaghe, R.T., Chaney, R.C. & Silver, M.L. (Eds.), ASTM STP 977, Philadelphia, pp. 68–81.

Zhang, M., Takahashi, M., Morin, R.H. & Esaki, T. 2000a. Evaluation and Application of the Transient-Pulse Technique for Determining the Hydraulic Properties of Low-Permeability Rocks – Part 1: Theoretical Evaluation. *Geotechnical Testing Journal* 23(1): 83–90.

Zhang, M., Takahashi, M., Morin, R.H. & Esaki, T. 2000b. Evaluation and Application of the Transient-Pulse Technique for Determining the Hydraulic Properties of Low-Permeability Rocks – Part 2: Experimental Application. *Geotechnical Testing Journal* 23(1): 91–99.

Rock Mechanics for Resources, Energy and Environment – Kwaśniewski & Łydżba (eds)
© 2013 Taylor & Francis Group, London, ISBN 978-1-138-00080-3

An in-situ monitoring system for natural temperature and relative humidity

A.J. Taylor, J.C. Cripps & S.D. Clarke
Department of Civil and Structural Engineering, University of Sheffield, Sheffield, UK

ABSTRACT: Oxidation of pyrite-rich, carbonaceous mudrocks used as fill beneath ground bearing floor slabs is currently causing significant problems to domestic and other properties in Ireland. Due to the precipitation of gypsum and other minerals the fill expands and this causes heave of slabs, together with distortion and cracking of the structure. Temperature is known to have an effect on both the rate and amount of this expansion; however, the full impact of human habitation on this process is not fully understood. The paper gives details of the development and testing of a system for monitoring temperature, humidity and pressure conditions within the material. This system is designed to minimise cost and disruption to the homeowner, whilst facilitating reliable measurements over period of 3 to 12 months.

1 INTRODUCTION

Oxidation of framboidal pyrite is known to be the cause of several problems in ground engineering. A particular problem occurs when sulfuric acid produced as part of the oxidation process reacts with calcium-bearing minerals also present in the parent rock. This can eventually lead to the expansive precipitation of sulfate minerals such as gypsum.

In Ireland, particularly in the Dublin area, pyrite-rich, Carboniferous age mudstone was extensively used in the late 20th Century as fill material beneath the ground supported concrete floor slabs of residential properties. Many of these properties are now showing evidence of damage such as uplift and cracking of the floor slab, which is attributed to heave of the fill material.

Although laboratory tests studying the nature and behaviour of the material are ongoing, little data currently exists detailing the behaviour of the material under field conditions. Information about the temperature and humidity conditions, both of which are recognised as key controlling factors of the reaction process, will assist with the interpretation of the lab tests and the relationships In addition the monitoring of temperature and humidity at various depths in the fill, it is also possible to record vertical stress conditions in the fill for periods between 3 and 12 months duration.

2 PROBLEM IN IRELAND

It is currently estimated that as many as 60,000 residential properties in Ireland are, or may potentially be, subject to damage caused by expansion of pyritic fill. Although the damage seen is varied, including sticking of doors, bulging of internal walls, cracking of wall and floor finishes; in the majority of cases these effects can be attributed to heave of the floor slab caused by the expansion of the underlying fill.

3 CAUSE OF THE PROBLEM

3.1 *The pyrite reaction process*

The form of pyrite most prevalent in these problematic mudrocks is small disseminated grains commonly between 0.1 and 0.5 μm in diameter or larger clusters of grains known as framboids, which are often between 2 and 40 μm in diameter and are shown in Figure 1. Both have a large specific surface and are therefore more reactive than other forms of pyrite (Hawkins & Pinches 1992). When exposed to oxygen and water, oxidation readily occurs leading effectively to production of sulfuric acid and eventual precipitation of gypsum.

The initial reaction between pyrite, water and air leads to the production of $SO4^{2-}$, Fe^{2+} and H^{+} ions, which in turn react to form sulfuric acid and ferrous sulfate, as represented by reaction 1.

$$2FeS_2 + 2H_2O + 7O_2 \rightarrow 2FeSO_4 + 2H_2SO_4 \quad (1)$$

Although the reaction can continue naturally from this point, it is typically slow but can be catalysed by the presence of bacteria of the species *Thiobacillus ferrooxidans*, which aids the conversion of Fe(II) to Fe(III) as well as the conversion of sulfides to sulfates, as is shown in reaction 2. These bacteria thrive in warm, acidic environments, such as that found beneath the floor slab of a domestic property once sulfuric acid

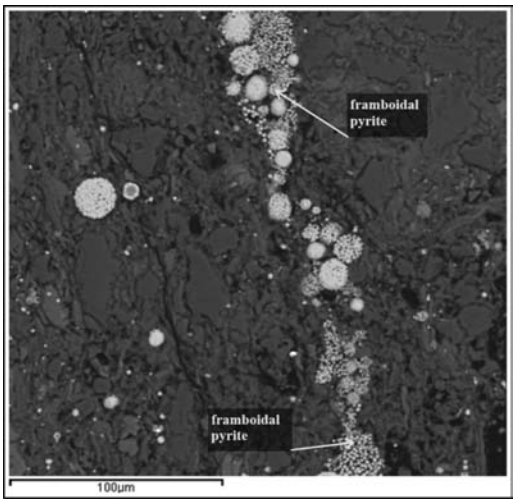


Figure 1. Horizon of pyritic framboids found in an Irish mudrock (image used with permission of Sandberg Consulting Engineers, London).

has begun to be produced by phase one of the reaction process (Hawkins & Pinches 1987b; Hawkins & Pinches 1992).

$$4FeSO_4 + O_2 + 2H_2SO_4 \rightarrow 2Fe_2(SO_4)_3 + 2H_2O \quad (2)$$

The ultimate result of these reactions is that the water present within the system is now low in pH and rich in sulfates. Movement of this water, even over small distances, allows it to react with other minerals, such as calcite ($CaCO_3$), or with engineering materials such as concrete, leading to sulfate attack. It should be noted that at the time of writing, very little evidence of chemical attack on concrete has been found at the sites in Ireland.

The reaction with calcite results in the precipitation mainly of gypsum, as is summarised in Equation 3.

$$H_2SO_4 + CaCO_3 + 2H_2O \rightarrow CaSO_4.2H_2O + H_2O + CO_2 \quad (3)$$

Although workers in Canada studying similar problems with expansion of pyrite-rich mudrocks have discovered cases of jarosite precipitation leading to expansion, this is only rarely found in Irish cases and never in large amounts. This is believed to be due to the presence of calcite in the Irish mudrocks.

The gypsum formed by the reaction process precipitates between and within the laminae and fractures in the fill particles. Studies in Canada (Penner et al 1973) and the UK (Nixon 1978, Hawkins & Pinches 1987a) confirm that this process can result in a net increase in volume of the fill and thus be the cause of expansion and heave. Example of gypsum crystals apparently formed by this process in Irish fills is illustrated in Figure 2.

The precipitation and growth of these crystals within the rock causes an increase in pressure within

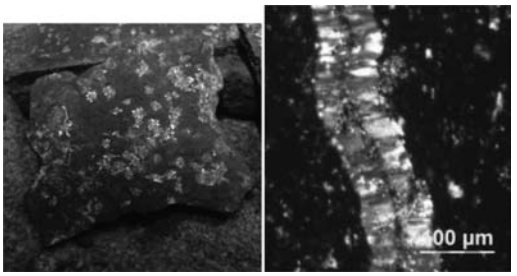


Figure 2. Occurrences of gypsum crystals in Irish mudrocks. Left: gypsum rosettes on the surface of a mudrock particle. Right: gypsum growth along a fracture in a mudrock particle (image used with permission of Sandberg Consulting Engineers, London).

Table 1. Implied pressures induced within systems showing expansion of pyritic mudrock.

	Pressure
Lutenegger et al. (in Bérubé et al., 1986)	28 kPa
Quigley et al. (in Bérubé et al., 1986)	72 kPa
Quigley & Vogan, 1970	74 kPa
Fasiska et al. (in Bérubé et al, 1986)	500 kPa
Maher et al., 2011	600 kPa

the system. The amount of heave is influenced by several factors, most notably precipitation location and crystal habit. For example a needle-like, acicular crystal forming within a laminated mudrock particle will exert more pressure than a flat, tabular crystal developing upon the surface of the particle. Although this pressure has not yet been measured directly under laboratory conditions, as summarized in Table 1, various workers have back-calculated values from site measurements and other tests.

The results presented by Bérubé et al (1986) and Quigley & Vogan (1970) are back-calculated from damage seen on sites in Canada, where the material was pyritic bedrock. The value presented by Maher et al (2011) is from a test carried out with Irish mudrocks re-compacted into a concrete tube, and is the value estimated to be required to cause cracking of the tube as seen during testing. It is unclear from the evidence presented whether or not changes in the stress on the outside of the tube was accounted for when calculating this value, and the figure should, therefore, be considered an upper value for pressure induced by pyritic expansion.

3.2 *Factors affecting expansion*

As can be expected from processes described above, there are many factors that affect the reaction process and pressures produced. These include, but are not limited to:

- Rock lithology/composition
- Depth/amount of fill

– Temperature
– Density of fill – amount and availability of void space
– Ground pressures
– Water content
– Grading of fill

Although it is understood, from both site observations and ongoing laboratory testing, that many of these factors play an important part, especially in the rate of the reaction, research into how much of an impact each factor has on both rate and amount of expansion is still ongoing

Recent research by Sutton et al (2013) points to the importance of environmental conditions on the rate of heave. With reference to temperature, Sutton et al (2013) point out that in certain parts of Canada, where heave is a common problem and temperatures range from an average maximum of 27˚ C to an average minimum of −15°C, damage to structures is typically noted within 10–15 years or more of construction (CTQ-M200 2001). However, for many of the properties in Ireland, where the average maximum temperature is around 20°C but the average minimum is around 4°C, significant signs of damage develop over a timescale of less than 10 years, with most buildings showing signs within 5–8 years of fill placement. As noted above the availability of water is liable to be another significant controlling factor, and there is much uncertainty over the magnitude of the uplift pressure generated by the processes.

4 FIELD LOGGING

Although laboratory tests looking at the effects of factors such as temperature and density upon the rate of reaction are ongoing, the focus herein is the behavior of the material in field conditions. The investigations carried out in order to determine the cause of damage to structures in connection with insurance claims provides an opportunity to determine the conditions typically experienced within the fill placed below floor slabs. Of particular relevance are the seasonal changes in temperature and moisture content and the influence of internal and external temperatures on the variation of these conditions with depth.

To do this, monitoring systems will be installed within occupied and unoccupied properties at the time of sampling for the geological testing of the fill. As this sampling is normally carried out after a structural survey of the property, buildings that are suspected to be suffering pyritic expansion, based upon details recorded in the structural survey, will be selected.

Although the finer details vary, geological sampling usually entails forming a hole (approximately 0.4 by 0.4 meters) through the concrete floor slab, insulation and damp proof membrane/ radon barrier. Any blinding sand and then the fill material is removed. Under normal procedures, the hole is then backfilled, the damp proof membrane made secure and the insulation and concrete replaced.

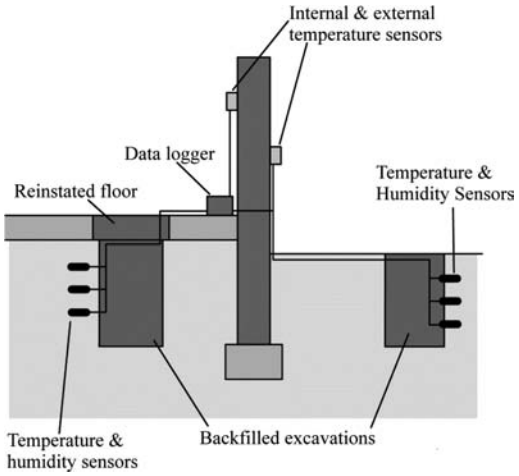


Figure 3. Basic schematic layout of sensors within a domestic property.

As Figure 3 shows, it is proposed to install temperature, pressure and humidity sensors, housed in protective cases, into the fill material in the side of the excavated hole. The hole would then be backfilled with matching fill and the insulation and slab reinstated around a tube protecting the connecting wires. Additional sensors will be used to monitor the internal and external air temperatures and at two or three properties per development, sensors will also be placed outside the property to enable the effects of the presence of the building on the ground environment conditions to be investigated.

Typically, in proven cases of pyritic heave, remediation is carried out 6 months to one year after sampling. At present it is planned to install the system in around 12 properties, for periods of around 6 months. Installation will be staggered in time so that there is enough overlap between sites to determine how the ground conditions change over a full annual cycle.

The equipment is designed to be easily adaptable dependent upon where within the property the excavation will be sited. The data will be recorded using a data logger that is based upon an Arduino microcontroller, shown in Figure 4. This will be programmed to log the information from each sensor at hourly intervals and record it to an SD card. If necessary this card can be retrieved by site engineers during the logging process.

The main criteria when selecting equipment both for the data logger and for the sensors was to minimise disruption to the homeowners when logging within an occupied property. The recording devise is small, robust, and relatively cheap and does not require frequent visits to retrieve data. The data logger in its present configuration requires mains power for use, although this power drain is low and the system could conceivably be adapted to run from batteries when used in unoccupied properties.

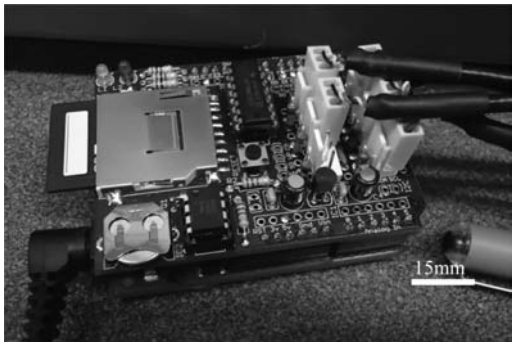


Figure 4. The Arduino microcontroller currently in use for laboratory testing.

Removal of the sensors will take place when the properties are remediated, as this entails removal of the floor slab and all the fill material. At this time, additional characterization and testing of the fill will take place for comparison with field logging and laboratory data.

5 LABORATORY TESTING

5.1 *Test set up*

Prior to beginning field logging, the system was tested in the laboratory as part of an ongoing suite of tests on pyritic material from a housing estate just North of Dublin.

The material used in this test was removed from the foundations of a property beginning remediation in May 2012. As such it had already begun to react and was therefore anticipated to react further once set up under laboratory conditions. After removal from the property, the material was sealed in bags for transport and then stored in an outdoor, insulated storage unit whilst at the university.

The material was described during initial geological testing as being a dark grey to black, calcareous siltstone to mudstone, with the latter being clearly laminated and making up around 40% of the material. The initial tests gave a pyrite content, as of June 2009, of 1.8% by weight and a gypsum content between 1.7 and 2.5% by weight. Although chemical testing has not yet been carried out on the samples held at the university, initial assessment confirms the physical description, and testing is planned to fully characterise the material.

The swelling tests are being carried out in 850 mm high by 225 mm diameter tubes containing fill compacted in several layers, as shown in Figure 6. Hence it is easy to install the sensor system proposed for the field tests in the material being used in the laboratory experiments. The design was adapted from that used by Sutton et al (2013) and it is intended to investigate the effects of differing initial conditions on the swell process.

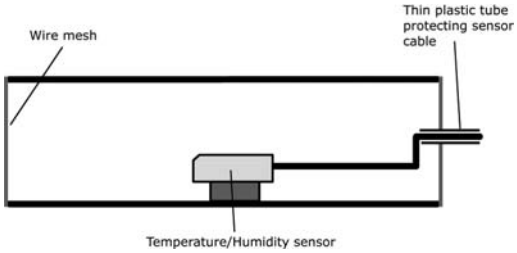


Figure 5. Schematic layout of sensor placement in protective tubes (not to scale).

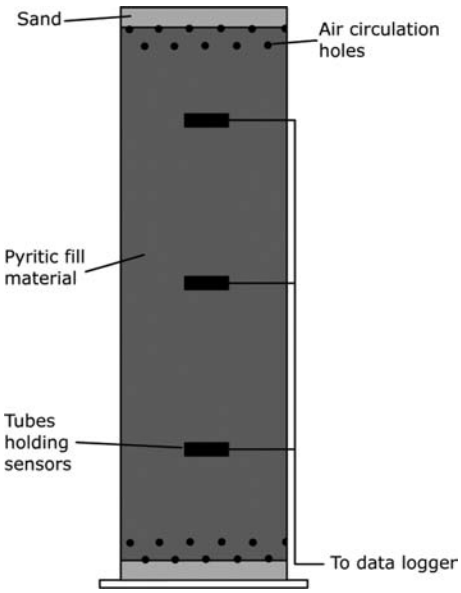


Figure 6. Schematic layout of test tube containing field logging system (not to scale).

The combined temperature and relative humidity sensors were housed within 25 mm diameter rigid plastic tubing with fine wire mesh on either end to prevent material entering the tube and still allow air circulation. These smaller tubes containing the sensors, indicated in Figure 5, were placed at three, evenly-spaced levels during the compaction process. A compacted density of 2010 kg/m^3 was achieved for the sample with an average moisture content of 8.0%.

In both field and laboratory investigations, the sensors are connected to the Arduino, which was coded to record data from the sensors every 15 minutes. Considering the volume of data recorded, and the way that temperature and humidity were seen to change, this sampling time can be reduced to once every hour for the field measurements.

5.2 *Initial results*

Data was recorded from the sensors such that it could be accessed as a spreadsheet, from which the data

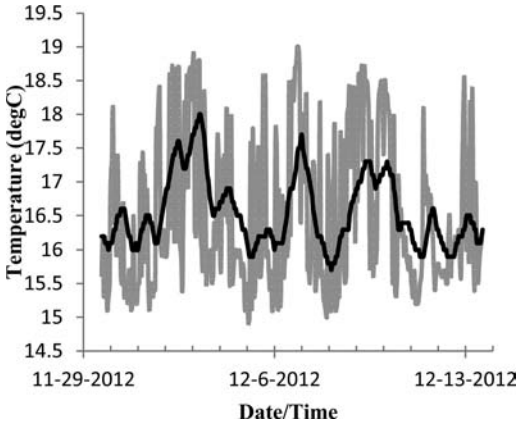


Figure 7. Temperature data obtained from laboratory tests. Pale grey represents the laboratory air temperature; black represents the data recorded from the sensor within the fill.

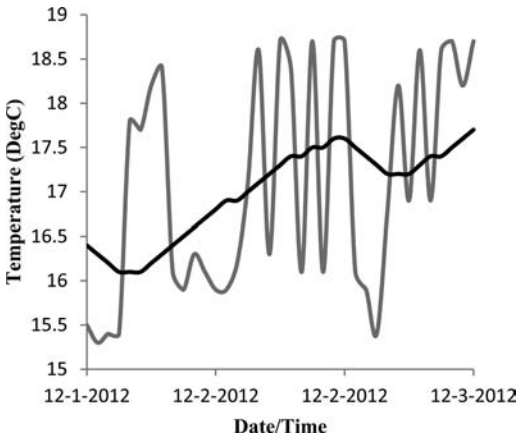


Figure 8. Data obtained over two days showing the way in which the fill temperature (black line) mirrors changes in the laboratory air temperature (grey line).

could be plotted and analysed graphically. Figure 7 shows the first set of temperature data obtained.

The sensors located at the base and top of the tube recorded similar temperature values, such that only the value from the lower-most sensor is presented here for ease of viewing. The sensor placed in the middle of the fill was malfunctioning and consistently recorded temperatures higher than those recorded in the laboratory. For this reason, the results from this sensor were excluded from the initial analysis.

From Figure 7 it is possible to see that the sensors compacted within the sample mirror the temperature changes recorded in the laboratory air temperature, although at a lesser rate.

In order to look more closely at this effect, Figure 8 shows a much smaller dataset, with the laboratory air temperature and the lower-most fill sensor data obtained over two days.

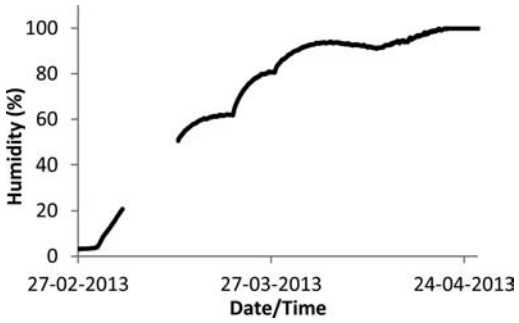


Figure 9. Humidity increases with addition of water to dry material. The gap in data collection was caused by a power cable being knocked loose. This issue has been addressed in the laboratory and the cable will be fixed more securely for field logging.

During the test period it was discovered that the sensors were returning humidity values of 100%, although the functioning temperature sensors seemed to be behaving normally. In order to determine the source of this problem the sensors were excavated from the sample.

Once two of the sensors had been removed from the sample, the other left in place as a control for temperature logging, data collection recommenced and the sensors were allowed to normalise to laboratory levels.

As the sensors recorded values consistent with laboratory humidity levels within 24 hours of removal from the fill material, it was determined that the problem was related to either the sensor set up or an excess of moisture within the sample. As the material in the laboratory test had a moisture content of 8% and many of the samples returned from affected sites show moisture content values of between 2 and 12%, this is a significant problem.

In order to improve understanding of the data, one of the sensors was placed within a modified tube in which only one end was open to air movement via a mesh, and the other end was sealed. This was then placed vertically within a dry sample, with the mesh at the base and several days logging data recorded.

Over the next several weeks water was added to the sample at intervals, with the intention of monitoring the results until a humidity reading of 100% was reached, or the moisture content exceeded 15%. The water was introduced to the surface layers of material and around the edges of the box so as to allow the moisture to move through the material while preventing it moving too close to the sensor.

Once the humidity readings reached 100%, as shown in Figure 9, and were determined to be constant, the test was dismantled and the final moisture content of the material determined. This value was returned as 2.5%.

As this moisture content overlaps the minimum that may reasonably be expected under site conditions, it may be possible to insulate the sensors to further limit the amount of humidity that can access

the sensors. Although such as system could be tested and calibrated by recording data from samples of a known moisture content, it is likely that this method would simply reduce the responsiveness of the instrumentation, thus decreasing its effectiveness. It seems unlikely that humidity sensors will prove viable for this application and small dielectric sensors are being investigated.

6 CONCLUSIONS

Although testing is still ongoing at the time of writing, and field testing has not yet commenced, initial results suggest that the temperature sensors will be a viable option for field logging purposes. The temperature values obtained from the sample clearly reflect the temperature as recorded in the laboratory and show the insulating effect of the material.

The humidity sensors, however, do not work over a sufficiently large range of moisture contents with the current set up and an alternate layout is currently being tested. Initial results confirm that humidity sensors will operate satisfactorily at very low moisture contents. However, alternative monitoring methods based on dielectric sensors are being investigated to ensure that accurate values are measured given the expected moisture content range.

REFERENCES

Bérubé, M-A., Locat, J., Gélinas, P. & Chagnon J-Y. 1986. Black shale heaving at Sainte-Foy, Quebec, Canada. *Canadian Journal of Earth Sciences* 23: 1774–1781.

CTQ-M200. 2001. Appraisal Procedure for Existing Residential Buildings. Version 2.0. *Comite Technique Quebecois D'Etude des Problemes de Gonflement Associes a la Pyrite*.

Hawkins, A.B. & Pinches, G.M. 1987a. Cause and significance of heave at Llandough Hospital, Cardiff – a case history of ground floor heave due to gypsum growth. *Q. J. Eng. Geol.* 20: 41–57.

Hawkins, A.B. & Pinches, G.M. 1987b. Sulphate analysis on black mudstones. *Geotechnique* 37: 191–196.

Hawkins, A.B. & Pinches, G.M. 1992. Understanding sulphate generated heave from pyrite degradation. *International Conference on the Implications of Ground Chemistry and Microbiology for Construction*.

Maher, M.L.J., Azzie, B., Grey, C. & Hunt, J. 2011. A large scale laboratory swell test to establish the susceptibility to expansion of crushed rock containing pyrite. *Proceedings 2011 Pan-Am CGS Geotechnical Conference*.

Nixon, P.J. 1978. Floor heave due to the use of pyritic shales as fill material. *Chemistry & Industry*, March, pp. 160–164.

Penner, E., Eden, W.J. & Gillott, J.E. 1973. Floor heave due to biochemical weathering of shale. *Proceedings 8th International Conference on Soil Mechanics and Foundation Engineering*, Vol 2, Part 2, Session 4, pp. 151–158.

Quigley, R.M. & Vogan, R.W. 1970. Black shale heaving at Ottawa, Canada. *Canadian Geotechnical Journal* **7**: 106–115.

Sutton, D., McCabe, B., O'Connell, A. & Cripps, J. 2013. A laboratory study of the expansion of pyritic mudstone/siltstone fill material. *Engineering Geology* 152: pp. 194–201.

Rock Mechanics for Resources, Energy and Environment – Kwaśniewski & Łydżba (eds)
© 2013 Taylor & Francis Group, London, ISBN 978-1-138-00080-3

Micro-textural controlled variations of the geomechanical properties of andesites

Ö. Ündül
Geological Engineering Department, Istanbul University, Istanbul, Turkey,
Engineering Geology, Swiss Federal Institute of Technology, Zurich, Switzerland

F. Amann
Engineering Geology, Swiss Federal Institute of Technology, Zurich, Switzerland

N. Aysal
Geological Engineering Department, Istanbul University, Istanbul, Turkey

M. Plötze
Institute for Geotechnical Engineering, Swiss Federal Institute of Technology, Zurich, Switzerland

ABSTRACT: Micro-textural variations are essential for understanding variation in strength and failure behavior of rock material. Therefore the effects of petrography and mineralogy on geomechanical properties have been widely investigated. In this study andesitic rock samples with different micro-textural characteristics from three different locations in Turkey were selected. Unconfined compressive strength tests revealed substantial variations in Unconfined Compressive Strength (UCS) and the micro-crack initiation (σ_{CI}) threshold. Detailed petrophysical, petrographic and mineralogical analysis (XRD) were used to understand these strength variations. The synthesis of strength, petrographic, micro-structural and mineralogical data suggest, that both, the peak strength and crack initiation threshold are strongly influenced by the distribution of plagioclase, amphibole and biotite phenocrystals, and the mineral composition of the fine-grained matrix.

1 INTRODUCTION

Petrographic, mineralogical and microstructural features constitute the heterogeneous and anisotropic rock fabric. Basically strength and deformation characteristics of rocks (e.g. unconfined compressive strength (UCS) and micro-crack initiation (σ_{CI})) rely on these constituents. The effect of micro-texture (including mineralogical composition, grain sizes, microstructure etc.) on the UCS and micro-cracking was investigated by Rigopoulos et al. (2011), Nicksiar & Martin (2013) and others utilizing modal analysis. Additional to previous studies, detailed quantitative mineralogical and petrographic analyses were performed before and after unconfined compression tests to improve our understanding of micro-crack initiation and strength variations in andesitic rocks.

2 METHODS

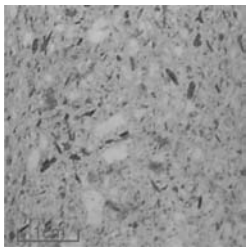
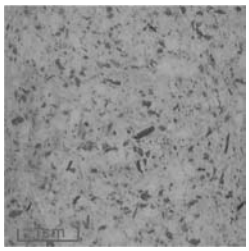
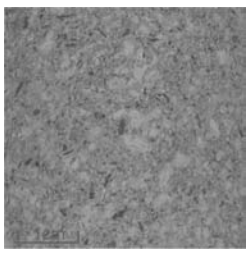
2.1 *Sample description*

The andesitic rock samples for this study were obtained from 3 different locations in NW of Turkey. These rocks belong to Miocene aged volcanic sequence. The samples were in fresh or slightly weathered state according to ANON (1995). Unconfined compression tests were performed on 43 mm diameter samples. These rocks were generally composed of plagioclase, amphibole, biotite phenocrystals and fine grained groundmass (Table 1).

2.2 *Unconfined compression tests*

For the unconfined compressive strength tests a 2000 kN Walter and Bai servo-hydraulic rock testing device with digital feedback control was utilized. Axial and circumferential strain gages were mounted onto the specimen at half of the specimen height to eliminate the influence of end effects on the strain measurements (Fig. 1). Two axial strain gages (Type BD 25/50, DD1) were firmly attached on opposite sides of the specimens. The measurement base-length was 50 mm. The radial strain was calculated from the displacement measured by a single gage (Type 3544-150M-120m-ST) attached to a chain wrapped tightly around the specimen (Fig. 1). The radial displacement rate was utilized as the controlling feedback signal. The selected rate was 0.03 mm/min. Before testing of the rock specimens strain gages and the load cell were calibrated.

Table 1. Overview of basic mechanical, mineralogical and petrographical properties of samples taken from three different locations in Turkey.

	Overview of the specimen	XRD (%)	UCS (MPa) (Min-Max)	σ_{CI}(MPa) (Min-Max)	P + A/Gm (Min-Max)	Biotite area (%)
1)		Q: 10.2-12.1 P: 25-28.9 Orth: 24-25.1 A:17.6-19.4 Other: 19.3-21.3	102-199	43-79	0.53-0.77	4.5-134
2)		Q: 14-14.6 P: 35.9-39.4 Orth:21.2-21.9 A:15.2-17.1 Other: 10.9-13.2	148-288	61-123	0.39-1.12	0.3-12.7
3)		Q: 10.8-11.5 P: 40.9-42.7 Orth: 21-22.7 A: 5.7-6.9 Other: 16.6-19.6	144-162	63-68	0.56-0.88	1.2-9.1

Q: Quartz, P: Plagioclase, Orth: Orthoclase, A: Amphibole,
P + A, represents the sum of the areas of plagioclase and amphibole. Gm represents the groundmass area

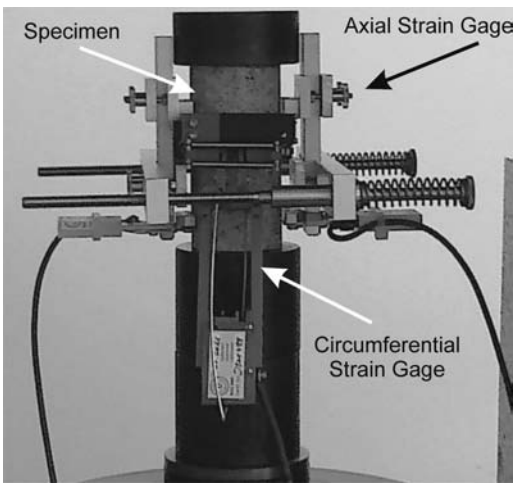


Figure 1. Set-up for unconfined compressive strength tests.

2.3 *Determining crack initiation under compressive stress*

In this study three methods were used to determine the crack initiation stress. The first method was suggested by Brace et al. (1966) and is based on identifying the point where the volumetric strain curve deviates from the early linear portion at low axial strain (Fig. 2). The second method was proposed by Lajtai (1974) and relies on defining σ_{CI} by the stress level where the stress-radial strain curve deviates from linearity (Fig. 3). The third method utilized was proposed by Nicksiar & Martin (2012) (Fig. 4).

2.4 *Mineralogical analyses*

Mineralogy of the samples was determined on randomly oriented powder specimens with X-ray powder diffraction analysis. First, the samples were crushed with a jaw breaker <0.4 mm and homogenized. A representatively split aliquot of 2 g was milled in ethanol

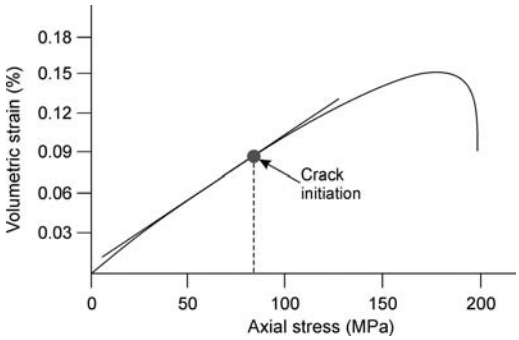


Figure 2. Volumetric strain method proposed by Brace et al. (1966).

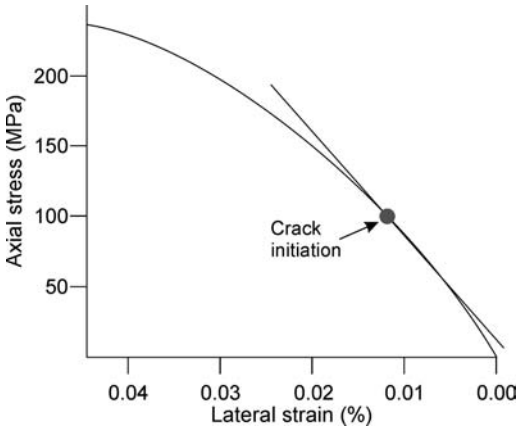


Figure 3. Lateral strain method proposed by Lajtai (1974).

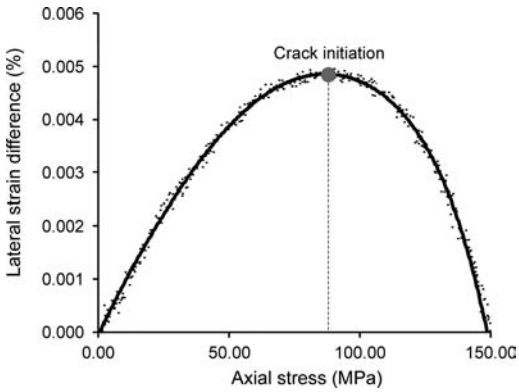


Figure 4. Lateral strain response method proposed by Nicksiar & Martin 2012.

to a grain size below 20 μm with a McCrone micronizing mill. X-ray diffraction measurements were made with a Bragg-Brentano diffractometer (Bruker AXS D8) using Co Kalpha radiation. The powder samples were step-scanned at room temperature from 2.5 to 80° 2alpha (step width 0.02° 2alpha, counting time 4 s per step). The qualitative phase composition was determined with the software DIFFRACplus (BRUKER AXS). The mineral phases were identified in comparison to the ICSD data base. The quantitative mineral composition of the samples was determined with the Rietveld program AutoQuan (GE SEIFERT).

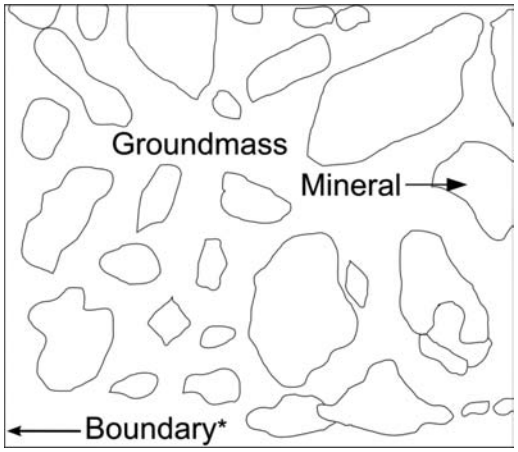


Figure 5. Schematic view of elements used for quantitative petrographic measurements. (*) : reference boundary.

2.5 *Thin section preparation*

Thin sections for quantitative petrographic analyses were prepared either before or after mechanical perturbation. After mechanical perturbation thin sections were prepared from the sections where macro scale fractures were observed on the core. Prior to thin section preparation, a low viscous, blue stained epoxy resin was drawn into the samples under a moderate vacuum to allow a better identification of newly formed cracks under the microscope.

2.6 *Quantitative petrographic studies*

Boundaries of individual grains of minerals were traced on high resolution digital images to quantify the area and distribution of different minerals (e.g. plagioclase, amphibole, biotite). The image processing software ImageJ v1.46 developed by National Institute of Health, USA (Rasband 2012) (Fig. 5) was used.

3 RESULTS AND DISCUSSION

3.1 *Rock fabric and mineralogy*

Macroscopically, the tested samples include varying amounts of plagioclase, amphibole and very rare biotite as phenocrysts and groundmass. Similar phenocrystals were determined by quantitative petrographic studies. The average content of plagioclase, amphibole and biotite phenocrystals within the reference boundaries were 23.9%, 14.6% and 5.3% respectively.

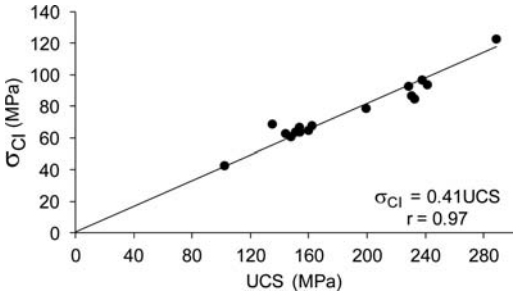


Figure 6. The relationship between crack initiation and peak stress.

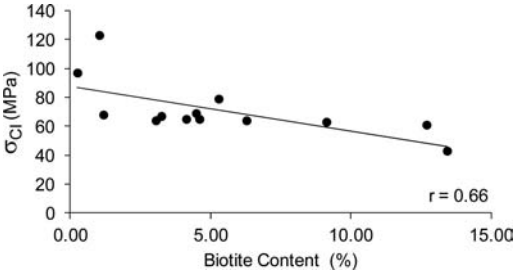


Figure 7. The influence of biotite content on the crack initiation stress.

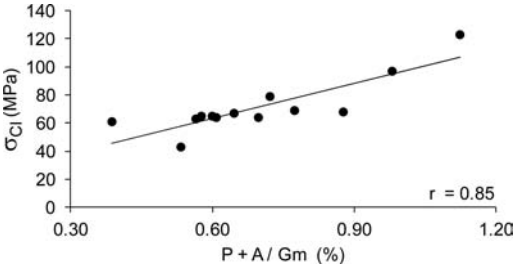


Figure 8. The influence of the ratio of selected phenocrystals to groundmass on σ_{CI}. P + A, represents the sum of the areas of plagioclase and amphibole. Gm represents the groundmass area.

The mineralogical composition of the fine-grained matrix (called groundmass) could not be identified or quantified using thin section analyses. However, the XRD analyses revealed mineralogical constitutes which do not form phenocrysts. These results suggest that the dominant mineralogical constitutes in the groundmass are orthoclase, quartz, zeolite and clay minerals. The mass fractions of these minerals are on average 22.5% (ortho), 12.2% (quartz), 6.3% (zeolite) and 3.4% (clay minerals) respectively.

3.2 *Strength characteristics*

The unconfined compressive strength of the specimens (UCS) ranges from 102.5 to 288.9MPa depending on the mineralogical composition. The crack initiation stress levels for the same specimen ranges between 43 to 123 MPa.

The ratio of crack initiation to peak stress for the studied andesitic rocks is presented in Figure 6. The relationship between UCS and σ_{CI} obtained from least square linear regression gives a value of 0.41 (e.g. 0.41UCS). Similar findings were reported by Nicksiar & Martin (2013). They analyzed various crystalline rocks with a broad range of mineralogical composition, σ_{CI} and UCS. Even though the variations in strength and mineralogical composition were substantial, they found that crack initiation occurred consistently at a stress level of 0.46UCS.

The results in Table 1 and Figures 7 indicate that lower strength values were obtained from specimens having higher biotite content. Nicksiar & Martin (2013) and Mahabadi et al. (2012) found a similar dependency for igneous rocks. Mahabadi et al. (2012) suggested that the softer biotite may have an substantial effect on the fracture formation and propagation.

It was also observed in this study that with an increasing ratio of the total area of plagioclase and amphibole phenocrysts to the area of the groundmass, CI and UCS increase (Fig. 8).

A clear relationship between quartz content and σ_{CI} or UCS was not found in this study. The coefficient of correlation between Quartz content and UCS was 0.58, between quartz and σ_{CI} 0.56 only.

3.3 *The effect of micro-texture on cracking and the stiffness variation*

Biotite can be found as phenocrystals and as very fine grains distributed within the groundmass. Biotite has lower stiffness compared to the other two major phenocrystals. As a consequence the existence of biotite causes stiffness heterogeneities within the tested specimens. It is assumed that upon loading these stiffness heterogeneities may cause stress or strain heterogenities which may promote micro-cracking, crack propagation and peak strength (Fig. 7).

Biotite is however not limited to phenocrystal. Low stiffness minerals such as biotite, zeolite and clay minerals can also be found in the groundmass. The mass fraction of these compliant minerals in the ground mass was 17% on average. Stiffness variations are therefore to be expected in the groundmass depending on the spatial distribution of these minerals. As a consequence stress and strain heterogeneities may develop upon loading between the groundmass and phenocrystals. The boundary between these two different stiffness compounds may affect crack growth and crack propagation. This is shown for example in Figure 9 which shows a crack following the boundaries of a stiff amphibole and a compliant groundmass.

Biotite is however not limited to Phenocrsystal. Low stiffness minerals such as biotite, zeolite and clay minerals can also be found in the groundmass. The mass fraction of these compliant minerals in the ground mass was 17% on average. Stiffness variations are

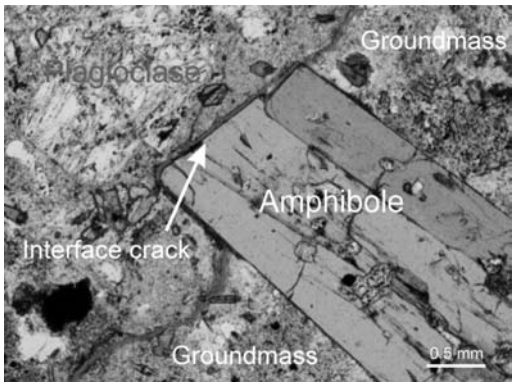


Figure 9. Photomicrograph after mechanical test showing the crack propagated along the boundary of amphibole and groundmass (direction of loading is vertical).

therefore to be expected in the groundmass depending on the spatial distribution of these minerals. As a consequence stress and strain heterogeneities may develop upon loading between the groundmass and phenocrystals. The boundary between these two different stiffness compounds may affect crack growth and crack propagation. This is shown for example in Figure 9 which shows a crack following the boundaries of a stiff amphibole and a compliant groundmass.

4 CONCLUSIONS

In this study variation in micro textural properties on crack initiation and peak strength of andesitic rocks was investigated. Compressive strength tests, high-resolution strain measurements in combination with petrographic and mineralogical analyses were utilized. The following conclusions were obtained:

The average ratio between crack initiation and peak stress was 0.41.

The content of biotite phenocrysts has a negative correlation to both the crack initiation and peak stress.

The ratio of the total content of plagioclase and amphibole to groundmass effects the strength parameters of andesitic rocks in a substantially positive manner.

REFERENCES

ANON 1995. The description and classification of weathered rocks for engineering purposes. *Quaterly Journal of Engineering Geology* 28: 207–242.

Brace, W.F., B.R. Paulding, & Scholz, C. 1966. Dilatancy in fracture of crystalline rocks. *Journal of Geophysical Research* 71(16): 3939–3953.

Eberhardt, E., Stimpson, B. & Stead, D. 1999. Effect of grain size on the initiation and propagation threshold of stress-induced brittle fracture. *Rock Mechanics and Rock Engineering* 32(2): 81–99.

Lajtai, E.Z. 1974. Brittle fracture in compression. *International Journal of Fracture* 10(4): 525–536.

Mahabadi, O.K., Randall, N.X., Zong, Z. & Grasselli, G. 2012. A novel approach for microscale characterization and modeling of geomaterials incorporating actual material heterogeneity. *Geophysical Research Letters* 39(1), doi:10.1029/2011GL050411.

Nicksiar, M. & Martin, C.D. 2012. Evaluation of methods for determining crack initiation in compression tests on low-porosity rocks. *Rock Mechanics and Rock Engineering* 45(4): 607–617.

Nicksiar, M & Martin, C.D. 2013. Crack initiation stress in low porosity crystalline and sedimentary rocks. *Engineering Geology* 154: 64–76.

Rasband, W.S. 2012. ImageJ, *U. S. National Institutes of Health, Bethesda, Maryland, USA, http://imagej.nih.gov/ij/, 1997–2012*.

Rigopoulos, I., Tsikouras, B., Pomonis, P. & Hatzipanagiotou, K., 2011. Microcracks in ultrabasic rocks under uniaxial compressive stress. *Engineering Geology* 117: 104–113.

This page intentionally left blank

Rock Mechanics for Resources, Energy and Environment – Kwaśniewski & Łydżba (eds)
© 2013 Taylor & Francis Group, London, ISBN 978-1-138-00080-3

Loss slake index evaluation and its applicability to marl

G. Vlastelica, P. Miščević & D. Salvezani
Faculty of Civil Engineering, Architecture and Geodesy, University of Split, Split, Croatia

ABSTRACT: Some of the main soft rock characteristics are relatively rapid deterioration and degradation of strength when soft rock is exposed to atmospheric agents. For this study marl samples from Eocene flysch formation found in Dalmatia region in Croatia are selected. When weathered, marl tends to degrade into a fine-graded soil-like material with high compressibility and low shear strength. Current methods of predicting behavior of marl (i.e. slake durability index) when exposed to weathering process are sometimes unreliable, therefore there is a necessity to establish new durability index. This study is an effort to try to implement loss slake index developed by Bryson et all. on shale samples as a new index for marl. In this case samples are taken from a coastal area, therefore information about natural moisture level could not be used to make a valid correlation analysis. Results show that loss slake index, as a method of evaluating durability, could be also applied on marl.

1 INTRODUCTION

Flysch is a rock mass that is most frequently encountered during engineering constructions in the region of Dalmatia, Croatia. One of the major components of the Eocene flysch in the Split region is marl. Problems such as slope stability and settlement of embankments made of crushed marl are very common in these materials (Miščević & Vlastelica 2012). The susceptibility to weathering upon exposure is the main cause of problems with clay bearing rocks. Weathering can induce a rapid change in rock material from initial properties to soil-like properties.

The sensitivity of a rock type against weatherability is usually described by a durability parameter, such as the slake durability index – SDI (Franklin & Chandra 1972). However, marl resistance is not always detected satisfactorily by SDI thus modifications of this test are often suggested. Some authors suggested additional criterions such as plasticity index (Gamble 1971), modifying the durability test by using only one wetting and drying cycle with different cycle time (Hopkins & Deen 1984), sieved slake durability test (Richardson & Long 1987), etc. Bryson et al. (2012) developed a new durability index (loss slake index – LSI) that better characterizes the durability behavior of shales which is based on Hopkins & Deen (1984) observations.

Results by Gokceoglu et al. (2000) and Miščević & Vlastelica (2011) also indicate that durability of clay-bearing rocks would most likely be better captured by increasing either the number or the duration of the slaking cycles for the durability test. This study is an effort to better understand and implement LSI developed on shale as a new index for marl.

2 GEOLOGY AND SITE LOCATIONS

In the context of this study, the term "marl" is used in a generic sense to refer to a broad class of fine-grained sedimentary rocks that are megascopically distinguished from breccia and sandstone by their smoother texture and absence of abundant visible grains. By means of x-ray diffraction, the following mineralogical compounds are detected: calcite, dolomite, quartz, plagioclase, smectite, illite and muscovite. Calcite usually dominates in ranges 40–80%, and smectite and illite ranges from 15 up to 40% (Miščević & Vlastelica 2011). Marl is usually classified according to $CaCO_3$ content, which is very important for its engineering behavior. Marl with lower $CaCO_3$ have lower shear strength and lower durability, i.e., degradation processes in those marl occur more rapidly (Šestanović et al. 2012).

The existence of marl in many different forms, ranging from clay rich marl to calcareous marl, makes collection and preparation of samples rather difficult. Therefore, stone cutting saw without use of water had to be used to ensure that there is no initial deterioration before tests were carried out.

For this study total of eight samples of marl with varying percentage of clay and carbonate mineral content are used.

Samples are taken from the benches of the slopes at construction sites and from drill cores from coastal

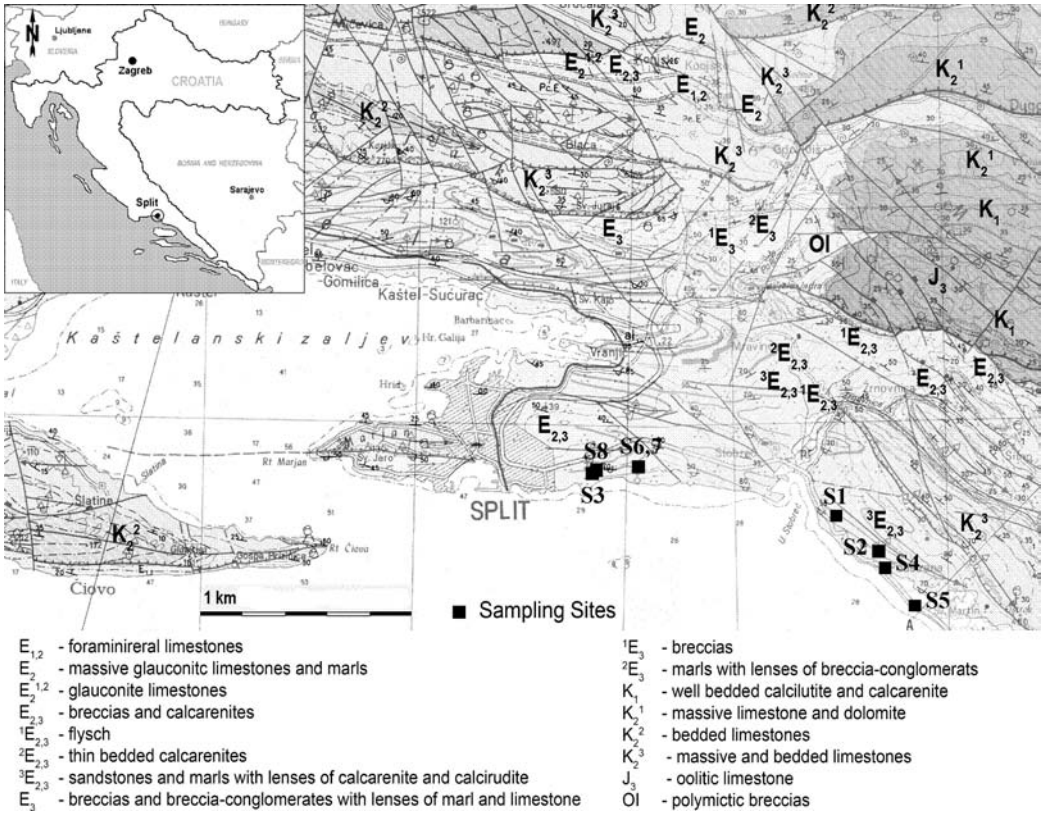


Figure 1. Location map of the sampling sites with the geological map of an area around town Split.

area around the town of from Split, Dalmatia (Fig. 1). The color of samples varies yellow-brown to blue-grey.

3 LABORATORY TESTING PROCEDURES

All index testing used for this study were performed according to ASTM procedures. Water contents were determined in accordance with ASTM D2216, specific gravity ASTM D854 and the slake durability test ASTM D4644-04. Furthermore, water absorption was estimated as the weight of water absorbed by the rock after 24 hours of immersion in water, divided by its oven-dried weight, expressed as a percentage of its oven-dried weight in accordance with ASTM C97-02.

Instead from XRD analyses, the relative quantity of carbonate minerals of all analyzed samples was also determined by the standard procedure ASTM D4373-02 which determines the amount of $CaCO_3$.

3.1 *Slake durability*

The resistance to deterioration or the durability of the studied marl was characterized by using the standard slake durability test. The slake durability index, I_{dn} was calculated as:

$$I_{dn} = \frac{m_n}{m_0} \times 100\,(\%) \qquad (1)$$

where m_0 is the mass of the oven-dried sample before the first cycle; m_n is the mass of the oven-dried sample retained after the n cycles.

As a standard two cycles index – I_{d2} is usually used because it gives a consistent indication of durability. Harder – more durable rock have higher I_{d2} values. However, sometimes for some types of weak rock it is necessary to go up to four cycles or more or vary with the duration of the slaking cycles for the durability test (Gokceoglu et al. 2000).

Hopkins & Deen (1984) modified the durability test by using only one wetting and drying cycle. The same wire drum is used as is for the standard test, however the duration of each test is changed to 10, 25, 60 and 120 min, respectively. These modified slake durability index values for a given time cycle were calculated as

$$SDI_{(time)} = \frac{m_{(time)}}{m_0} \times 100\,(\%) \qquad (2)$$

where $m_{(time)}$ is the mass of the oven-dried sample retained after the first "time" cycle for a given cycle time; $SDI_{(time)}$ is the slake durability index for a given cycle time (i.e., SDI_{60} is the slake durability index for 60 min).

As it can be seen from Equation 1 & 2 both SDI and modified SDI values are basically ratios of the

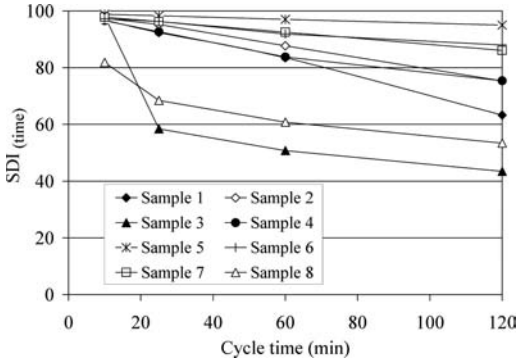


Figure 2. Influence of the duration of slaking cycles on the slake durability index of the marl samples used in this study.

amount of material retained in the rotating wire mesh drum after specific number of cycles and cycle time, relative to the initial amount placed in the drum. Initial amount is around 500 g (±50 g), formed in 10 oven-dried lumps which weigh about 50 g each.

3.2 *Loss slake index*

When the ratio of $SDI_{10}/SDI_{(time)}$ is plotted versus cycle time (t) it can be noticed that the degree of curvature of the regression curve is different for each material and more importantly, the degree of curvature increases as a function of decreasing durability (Bryson et al. 2012). Therefore, using regression analyses of the data the relationship between aforementioned can be described by a common logarithmic function:

$$\log\left(\frac{SDI_{10}}{SDI_{(time)}}\right) = LSI\,(t-10) \qquad (3)$$

where LSI is a new durability index called the Loss Slake Index. When plotted on a semilog scale it represents the slope of the line going through the origin. When compared to I_{d2} values it can be seen that LSI values are bigger for less durable materials. Therefore, it can be stated that the lesser the durability the greater is the LSI value.

4 RESULTS

The results obtained from the SDI test, modified SDI test, $CaCO_3$ and LSI values are presented in Table 1. The variation of the $SDI_{(time)}$ versus the cycle duration of each marl sample is plotted in Figure 2. From Figure 2 it can be observed that the amount of material retained in the drum in the later cycle times is a function of material retained after the first cycle. Also, it can be noticed that samples with steeper SDI versus time curves are less durable than marls with relatively flatter curves.

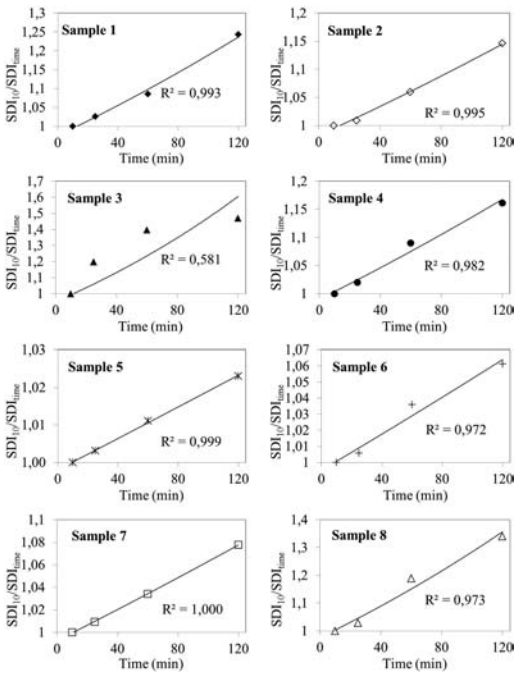


Figure 3. Relationship between $SDI_{10}/SDI_{(time)}$ and the duration of cycle time of the marl samples used in this study.

In Figure 3 plots of the $SDI_{10}/SDI_{(time)}$ ratio versus cycle time are shown for each sample. It shows that the degree of curvature is different for each sample. More important, when calculated LSI values are compared with I_{d2} and I_{d4} in Table 1, it is clear that the degree of curvature increases as a function of decreasing durability.

LSI values are consistent with I_{d2} and I_{d4}, however the logarithmic scale of LSI emphasizes the differences more. For example, difference between I_{d2} for Sample 2 and Sample 6 is only 0.2, while LSI is almost double for Sample 2.

LSI results are also more consistent with amount of $CaCO_3$ in each sample as it can be seen in Figure 4. In this case coefficient of determination R^2 suggest a very strong correlation (0.98), while in case of I_{d2} and I_{d4} it is less than 0.6. Other authors (Beyhan & Emir 2010, Miščević & Vlastelica 2011) have also tried to correlate SDI results and $CaCO_3$, however in those cases R^2 was also poor.

Additionally, one more variation of SDI tests was made. Except modifying SDI test by increasing the number of cycles or cycle time, the third option is to do both. Therefore, the SDI test was repeated for each cycle time duration up to four times. Results for Sample 1 are presented as plots of the $SDI_{10}/SDI_{(time)}$ ratio in Figure 5 and as LSI values for all samples used in this study in Table 2.

The data presented in Figure 5 shows that the degree of curvature is more evident by increasing the number of cycles, however the interrelation of LSI values for these eight samples is the same (Table 2). Therefore,

Table 1. Summary of index testing and Slake durability index values for the eight unweathered marl samples used in this study.

Sample no.	$CaCO_3$ (%)	Slake Durability Index		Modified Slake Durability Index (time cycle)				Loss Slake Index
		I_{d2}(%)	I_{d4}(%)	SDI_{10} (%)	SDI_{25} (%)	SDI_{60} (%)	SDI_{120} (%)	LSI (%)
1	47.9	96.8	94.8	98.7	96.2	90.9	79.4	0.083
2	51.6	97.4	95.8	98.9	98.1	93.4	86.3	0.052
3	40.2	95.3	87.8	98.8	82.5	70.7	67.2	0.181
4	51.8	96.7	94.0	98.0	96.0	89.9	84.4	0.061
5	80.9	98.9	98.0	99.3	99.0	98.2	97.0	0.009
6	65.6	97.2	96.4	98.2	97.6	94.8	92.5	0.025
7	65.0	97.9	97.2	98.6	97.7	95.4	91.5	0.029
8	45.8	81.9	62.2	90.0	87.5	75.7	67.2	0.120

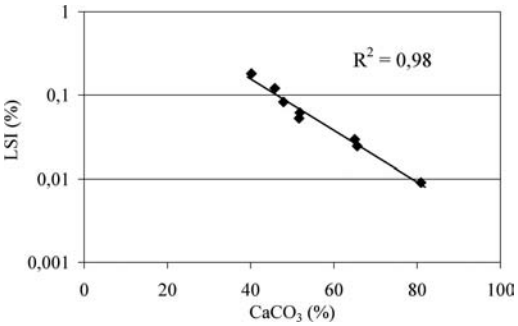


Figure 4. Correlation between Loss Slake Index and $CaCO_3$ content of the marl samples used in this study.

Table 2. LSI values for multiple time cycles.

Sample no.	Loss Slake Index		
	$LSI_{1.cycle}$ (%)	$LSI_{2.cycles}$ (%)	$LSI_{4.cycles}$ (%)
1	0.083	0.160	0.288
2	0.052	0.099	0.181
3	0.181	0.368	0.378
4	0.061	0.103	0.183
5	0.009	0.015	0.027
6	0.025	0.041	0.073
7	0.029	0.050	0.086
8	0.120	0.189	0.231

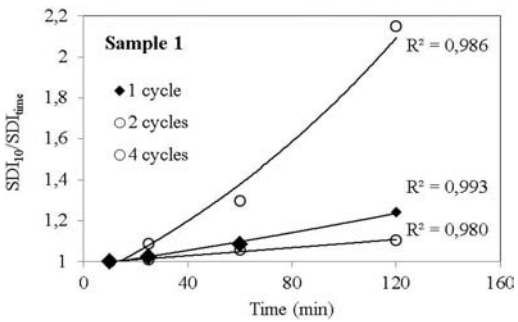


Figure 5. Relationship between $SDI_{10}/SDI_{(time)}$ and the duration of cycle time for Sample 1. For each cycle time duration 1, 2 and 4 repetitions are presented.

additional cycles for calculating LSI values are not necessary.

5 CONCLUSIONS

This study presents analysis of LSI developed by Bryson et all. in effort to apply it to other soft rock. Two basic inexpensive tests are made ($CaC0_3$ content and different SDI tests) in effort to analyze and evaluate LSI. The tests that are presented in this study indicate that this method of durability evaluation can be applied also on marl. LSI values are consistent with results of SDI, however the logarithmic scale which LSI uses emphasizes the differences more.

This study was also performed on limited number of samples (as the original study), therefore additional testing should be performed.

In combination with other index testing, i.e. clay fraction content, natural water content, swelling and even critical friction state angle, empirical expressions could be made to estimate those values via LSI.

ACKNOWLEDGEMENTS

The presented results derive from the research project, Development of the Weathering Model for the Design Purpose of Geotechnical Constructions in Flysch, implemented due to support of the Ministry of Science, Education and Sports, Republic of Croatia.

REFERENCES

ASTM (D4644-04) 2004. Standard test method for slake durability of shales and similar weak rocks.

ASTM (D4373-02) 2004. Standard Test Method for Rapid Determination of Carbonate Content of Soils.

ASTM (C97-02) 2004. Standard Test Methods for Absorption and Bulk Specific Gravity of Dimension Stone.

ASTM (D2216) 2004. Test Methods for Laboratory Determination of Water (Moisture) Content of Soil and Rock by Mass.

Beyhan, S. & Emir, E. 2010. Effect of calcium carbonate content on engineering properties of marl. In J. Zhao et al. (eds), *Rock Mechanics in Civil and Environmental*

Engineering, Proceedings of the European Rock Mechanics Symposium (EUROCK) 2010, Lausanne, 15–18 June 2010: 71–74. Leiden: CRC Press/Balkema.

Bryson, L.S. Gomez-Gutierrez, I.C. & Hopkins, T.C. 2012. Development of a new durability index for compacted shale. *Engineering Geology* 139–140: 66–75.

Franklin, J.A. & Chandra, R. 1972. The slake durability test. *International Journal of Rock Mechanics and Mining Sciences* 9: 325–341.

Gamble, J.C. 1971. Durability-Plasticity classification of shales and other argillaceous rocks. *Ph.D. Thesis,* University of Illinois at Urbana-Champaign, Urbana, IL USA.

Gokceoglu, C. Ulusay, R. & Sonmez, H. 2000. Factors affecting the durability of selected weak and clay-bearing rocks from turkey, with particular emphasis on the influence of the number of drying and wetting cycles. *Engineering Geology* 57(3–4): 215–237.

Hopkins, T.C. & Deen, R.C. 1984. Identification of shales. *ASTM Geotechnical Testing Journal* 7(1): 10–18.

Miščević, P. & Vlastelica, G. 2011. Durability Characterization of Marls from the Region of Dalmatia, Croatia. *Geotechnical and Geological Engineering* 29(5):771–781

Miščević, P. & Vlastelica, G. 2012. Time-dependant stability of slopes excavated in marl. *Građevinar* 64(6): 451–461

Richardson, D.N. & Long, J.D. 1987. Sieved slake durability test. *Bulletin of the Association of Engineering Geologists* 24(2): 247–258.

Šestanović, S. Toševski, A. Mihalié, S. Dečman, A. & Ferić, P. 2012. Preliminary Data for Development of the Engineering Geological Map of the City of Split (Croatia). *Environmental Earth Sciences* 66: 1547–1556.

This page intentionally left blank

Rock Mechanics for Resources, Energy and Environment – Kwaśniewski & Łydżba (eds)
© 2013 Taylor & Francis Group, London, ISBN 978-1-138-00080-3

Effect of scratch length on the Cerchar abrasivity index

O. Yaralı, H. Aydın, H. Duru & A. Özarslan
Mining Engineering Department, Bülent Ecevit University, Zonguldak, Turkey

ABSTRACT: Cerchar Abrasivity Index test (CAI) is widely used for determining the abrasiveness of rocks. This test provides an index value that can be used as a gauge for the abrasiveness of rocks in order to estimation of bit life and wear in various mining and tunneling applications. In this study, changes in CAI with the changes in scratch length were investigated by the use of West apparatus to determine the effects of length on CAI. The tests were carried out on 6 different rock types (3 types of sandstone, limestone, granite and quartzite) where on rough and saw cut surfaces with a scratch length between 2 mm to 20 mm with an increment of 2 mm. It has been found that about 60% of the final Cerchar index (at a 20 mm sliding) was observed at the first 2 mm scratch and continued at a constant rate up to 16–18 mm, then rests around 20 mm sliding distance. This initial high tip wears may partly depend on the deformation and shear failure at the tip of pins. It has been also observed that 87% of the final Cerchar index was reached at 10 mm sliding distance while 97% of the final Cerchar index at the 15 mm sliding distance. Since initial wear at the 2 mm sliding distance is not dependent on the amount of abrasive material in the host rock. Approximately 35% of the Cerchar index can be attributed to the abrasion effect which corresponds to the final 8 mm of sliding distance. However if the sliding distance is increased to 15 mm then 45% of the Cerchar index can be attributed to the rock abrasion effects. This is very important for the tool life estimation in tunneling applications.

1 INTRODUCTION

1.1 *Previous studies*

Abrasion can be defined as the wearing or tearing away of particles from the surface. Abrasion is a process causing removal or displacement of material at a solid surface; which will lead to wear, especially in tools which use in mining, drilling, and tunneling applications (Atkinson 1993).

Tool wear is an important parameter in mechanized tunneling and is highly affected by rock abrasiveness. Rock abrasiveness has a direct relationship with the wear occurring in the bits of drills, road headers, tunnel boring machines and other equipment, and has been researched (Bilgin et al. 2012). Knowledge of abrasiveness of rocks in mechanical excavation (TBM, roadheader) and drilling is very important to determine pick consumption. Cerchar abrasivity index test is widely used for estimation of pick consumption in engineering projects.

There are numerous tests to identify the rock abrasivity. One of the widely used rock abrasion tests is the Cerchar abrasivity index (CAI). CAI has become widely accepted and has been used for cutter life and cost estimation for excavation machines (Plinninger et al. 2003, Yaralı et al. 2008). Nevertheless, an in-depth examination of specific test procedures and equipment used has highlighted the significant impact of these parameters upon results. Although the test results varying from lab to lab and the variation in values rendered by different laboratories and equipment could create major errors in related estimates (Plinninger et al. 2003, Rostami et al. 2005, Michalakopoulos et al. 2006, Stanford & Hagan 2009, Oparin & Tananio 2009, Cardu et al. 2013).

Cerchar abrasivity index test was developed for the first time by Cerchar Institute in France in 1970s and the results were published by Valantin (1973). This test instrument is passed into literature as a first generation machines. Cerchar Institute suggested a standard numbered of NF P94-430-1 in 1986 for this test due to expansion of the application of this test method and the differences have been seen in the efforts of various researchers. However, as these standards are prepared only for formal, this test has not been accepted by a lot of researchers and the trouble in this area is continuing. This state is reported in ISRM Testing Methods Commission' report in dated 2009 and the Commission has decided that the establishment of a new Working Group (WG) on the "Abrasivity Test" would be useful (ISRM 2009). The test is simple and can be considered for field applications. However, there are some differences in the test results related to experimental procedure used in test, the type of used test device, test samples of the surface conditions, operator skills, direction of scratch, hardness of pins, metallurgical properties and evaluation of the pin wear flat.

There are mainly two types of apparatus which are in use today (Fig. 1). One of them is the original Cerchar test device (Fig. 1a) which was suggested

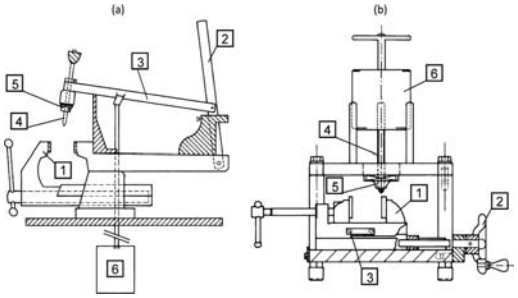


Figure 1. The Cerchar machines. (a) Original Cerchar device: 1, sample vice; 2, hand lever; 3, arm; 4, steel pin; 5, pin chuck; 6, weight. (b) West's apparatus : 1, sample vice; 2, handwheel; 3, scale; 4, steel pin; 5, holder; 6, weight (after Plinninger et al. 2003).

Table 1. The classification of abrasiveness (after Cerchar 1986).

Cerchar Abrasivity Index	Classification
0.3–0.5	Not very abrasive
0.5–1.0	Slightly abrasive
1.0–2.0	Medium abrasiveness to abrasive
2.0–4.0	Very abrasive
4.0–6.0	Extremely abrasive

by Laboratoire du Centre d'Etudes et Recherches des Charbonnages (Cerchar) de France (Valantin 1973). The other test device was West apparatus (Fig. 1b) which was designed by West (1989) and it is a widely used system in commercial and laboratory application. This apparatus is named after him but being marketed by a company in the UK (Ergo Tech).

In both cases, the rock specimen is securely held in a vice (1) and a steel pin is applied on the surface of a rock specimen under a load of 70 N and scratched on a distance of 10 mm. In the original design (Fig. 1a), the steel pin is scratched over the rock surface (freshly broken or saw cut) by moving the testing lever whereas, in West's apparatus (Fig. 1b), a hand crank moves the sample below the pin. The results are different testing velocities; 10 mm/s in the original machine and 1 mm/s for West's apparatus. The abrasiveness of the rock is obtained by measuring the wear on the tip of steel stylus with a cone shape under a microscope. The unit of abrasiveness is defined as a wear flat of 0.1 mm diameter. Pins should be re-sharpened before each test.

Five scratches, each time with a new or re-sharpened stylus, should be made on a single specimen of rock to give a reasonable mean value for the rock abrasiveness. Both devices are estimated to give equivalent values of the CAI (Plinninger et al. 2003). However, if the testing surface is extremely rough or coarse grained, the steel pin may bounce and the testing velocity has to be reduced (Plinninger et al. 2004). A classification of rock abrasiveness proposed by Cerchar (1986) is given in Table 1.

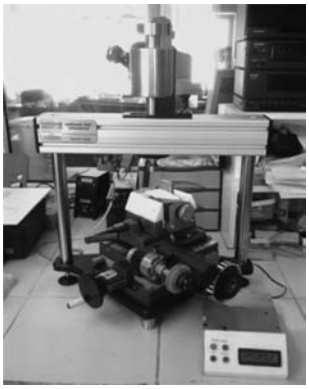


Figure 2. West apparatus used in this study.

Cerchar abrasivity index (CAI) has been examined by several researchers. They investigated the effects of petrographic properties from thin section analyses (such as grain size, mineralogical composition, degree of cementation, quartz content, the equivalent quartz content, matrix properties) and geomechanical properties (such as strength, young modulus, etc.) on Cerchar abrasivity index (CAI) (Suana & Peters 1982, Al-Ameen & Waller 1994, West 1986, Deketh 1995, Plinniger et al. 2003, Mathier & Gisiger 2003, Plinninger et al. 2004, Yaralı 2005, Yaral*ı* et al. 2008, Thuro & Kasling 2009, Kahraman et al 2010, Lassnig et al. 2011, Deliormanlı 2012). Alber (2007) demonstrated that the CAI was definitely stress-dependent. A novel test procedure in which the CAI tests was conducted on samples in a triaxial cell shows the stress dependency for various rock types by higher CAI values upon confining pressure.

Other researchers have made experiments with different hardness and different metallurgical properties of pins using Cerchar abrasivity index. These researchers have also emphasized that hardness of pin effects results of Cerchar abrasivity index (Suana & Peters 1982, West 1989, Al-Ameen & Waller 1994, Pilinninger et al. 2003, Rostami et al. 2005, Michalakopoulos et al. 2006, Yaralı et al 2008, Stanford & Hagan 2009, Cardu et al. 2013). ASTM D (7625) it is recommended to use a stylus of hardness 55HRC. In some cases (e.g. when testing low abrasive rocks), other steel qualities might be preferred (ASTM 2012).

1.2 *Length of scratch*

According to the testing procedures outlined in the original Cerchar document, the scratching distance on the rock sample is defined to be 10 mm (Plinninger et al. 2003).

Al-Ameen & Waller (1994) performed some test using various lengths (1, 2, 3, 5, 7 and 10 mm). They concluded that within initial horizontal movement of the stylus (≈1 mm), the cone tip tends to deform and shear off due to the dead load and the resistance to

horizontal movement, and a flat-ended tip is formed. This flat area formed at the beginning of the test is not dependant on the amount of abrasive material in the host rock. It is due entirely to deformation and shear failure at the tip of the pins (EN3 with 225 Vickers hardness), and its magnitude should be related to the rock strength and the stylus material. They also observed that the Cerchar index related to a 1 mm sliding distance is about two thirds of the final Cerchar index at a 10 mm sliding distance for most of rock types. Approximately 30% of the Cerchar index can be attributed to the abrasion effect which corresponds to the final 9 mm of sliding distance. These findings are of great importance. They clearly show that the CAI value is highly influenced by rock strength and also the test is not representative of the 10 mm but 1–2 mm of the rock, although 10 mm is also very small and questionable (Ghasemi 2010).

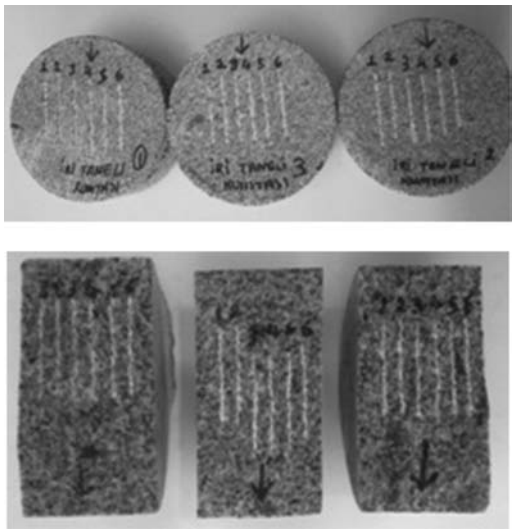


Figure 3. Samples, saw cut and rough surfaces.

2 EXPERIMENTAL STUDIES

In this study, in order to determine effects of scratch distance, Cerchar abrasivity index tests were carried out on six different rock types (sandstone (fine gr.), sandstone (medium gr.), sandstone (coarse gr.), limestone, granite, quartzite). The tests were made both on rough and saw cut surfaces with a scratch length between 2 mm to 20 mm, with a stepwise increment of 2 mm. West apparatus (from Ergo Tech, England, Fig. 2) were used in tests.

Before each test, the tip of the stylus (Rockwell hardness of HRC 54–56, tensile strength of 2000 MPa) was sharpened to achieve a conical tip angle of 90°. Experiments were three times repeated with five scratch for each rock sample (sample size is 54 mm in diameter, 30 mm in height, Fig. 3). Pin wear surface were examined with a digital microscope (magnification 35×) and tip wear surface captured with a digital imaging software for the measurement. Stylus tip wear examination were carried both vertically and horizontally and averaged for the final Cerchar index.

3 EVALUATION OF RESULTS

Summary findings of these experiments are illustrated in Table 2, Figure 4 and Figure 5. Table 2 and the figures indicated that 60% of the final Cerchar index (at a 20 mm sliding) was observed at the first 2 mm scratch and continued at a constant rate up to 16–18 mm, then rests around 20 mm sliding distance. It has been also found that 87% of the final Cerchar index was observed at 10 mm sliding distance while

Table 2. Changes in CAI with the change in scratch length (54/56 HRC stylus).

		Scratch Length (mm)						
Sample Surface	Rock Type	2 (CAI)	(%)	10 (CAI)	(%)	15* (CAI)	(%)	20 (CAI)
Smoot	Fine Grain Sandstone	1.07	56.32	1.57	82.63	1.78	93.42	1.90
	Medium Grain Sandstone	1.05	54.12	1.50	77.32	1.86	95.62	1.94
	Coarse Grain Sandstone	1.41	58.51	2.13	88.38	2.36	97.93	2.41
	Limestone	1.32	76.30	1.52	87.86	1.71	98.84	1.73
	Granite	2.36	66.11	3.35	93.84	3.52	98.60	3.57
	Quartzite	2.82	73.82	3.51	91.88	3.77	98.69	3.82
Rough	Fine Grain Sandstone	1.42	66.05	1.98	92.09	2.11	98.14	2.15
	Medium Grain Sandstone	0.96	37.94	2.10	83.00	2.40	94.66	2.53
	Coarse Grain Sandstone	1.60	63.24	2.28	90.12	2.48	98.02	2.53
	Limestone	1.33	75.14	1.58	89.27	1.73	97.74	1.77
	Granite	2.73	68.42	3.54	88.72	3.90	97.74	3.99
	Quartzite	3.33	63.43	4.98	94.86	5.19	98.86	5.25
Standard Deviation		0.81	10.70	1.10	5.10	1.11	1.79	1.11
Average		1.78	63.28	2.50	88.33	2.73	97.36	2.80

* average of 14 and 16 mm scratch length

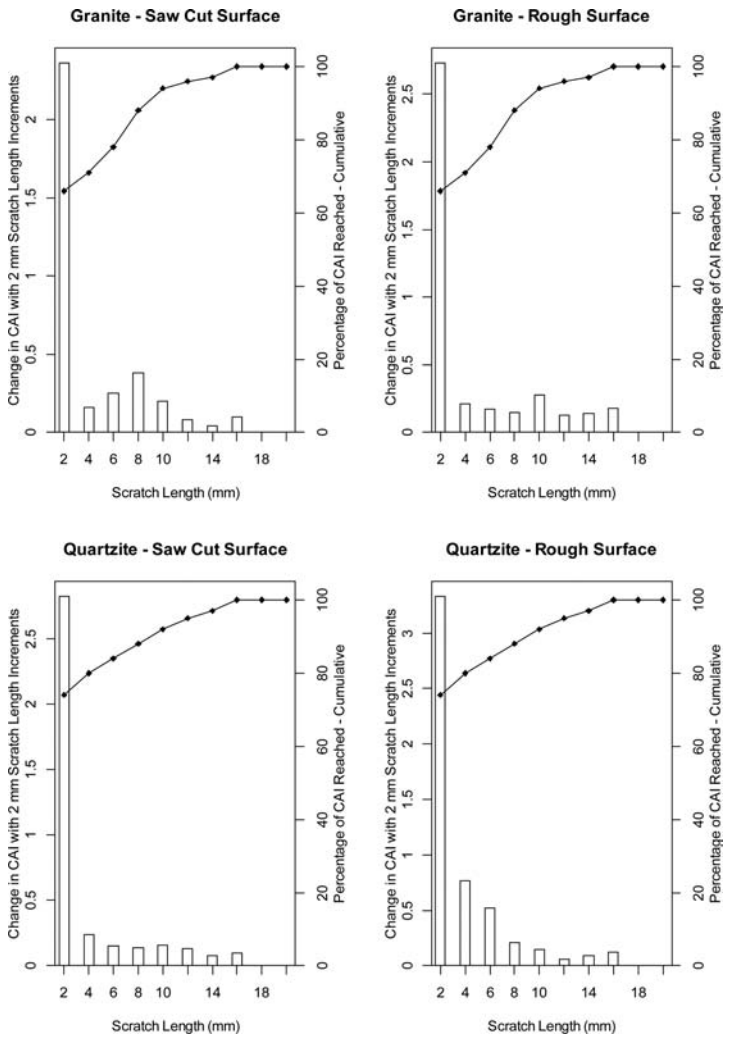


Figure 4. Changes in CAI with the changing scratch length in rocks (granite, quartzite).

97% of the final Cerchar index at the 15 mm sliding distance.

Regression analysis is also carried out to investigate the relationship between CAI values of 10 mm and 15 mm scratch length. It has been found that there is linear relation (Eq. 1) with a good fit ($R^2 = 0.995$) between sliding distance. From this relation, equivalent CAI values for the 15mm scratch length can be calculated from the 10 mm scratch length (Fig. 6).

$$CAI_{(15mm)} = 0.209 + 1.008.CAI_{(10mm)} \quad (1)$$

where $CAI_{(15\,mm)}$ = equivalent CAI values for the 15 mm scratch length; $CAI_{(10\,mm)}$ = measured CAI values for the 10 mm scratch length.

4 CONCLUSIONS

In this study, six different rock types (3 types of sandstone, limestone, granite and quartzite) were tested in laboratory for the investigation effect of scratch length on CAI test values. The tests were carried out by the use of West apparatus and rock samples on rough and saw cut surfaces with a scratch length between 2 mm to 20 mm with an increment of 2 mm.

It has been found that about 60% of the final Cerchar index (at a 20 mm sliding) was observed at the first 2 mm scratch and continued at a constant rate up to 16–18 mm, then rests around 20 mm sliding distance. It has been also observed that 87% of the final Cerchar index was reached at 10 mm sliding distance while 97% of the final Cerchar index at the 15 mm sliding distance. This initial high tip wears probably partly

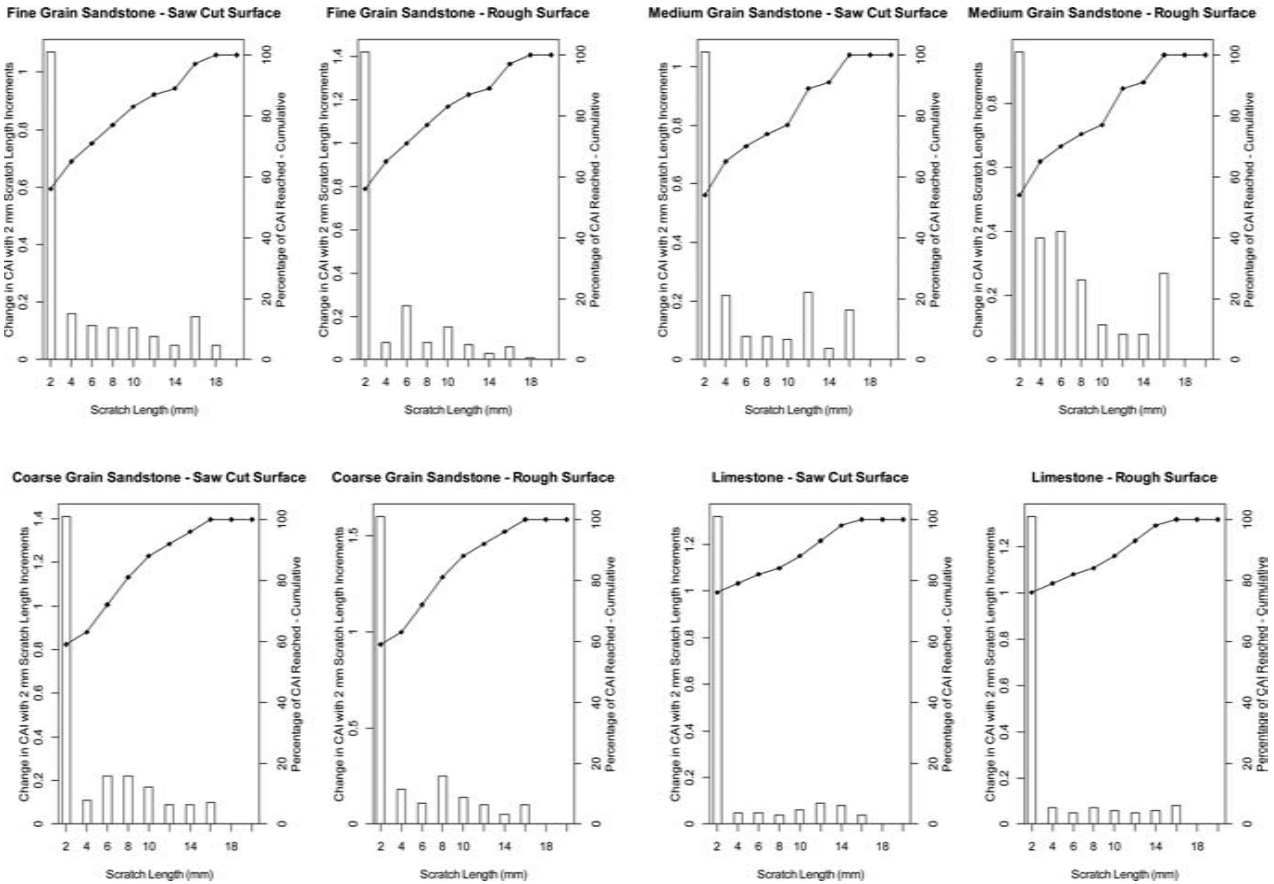


Figure 5. Changes in CAI with the changing scratch length in rocks (sandstone, fine, medium, coarse grain, limestone).

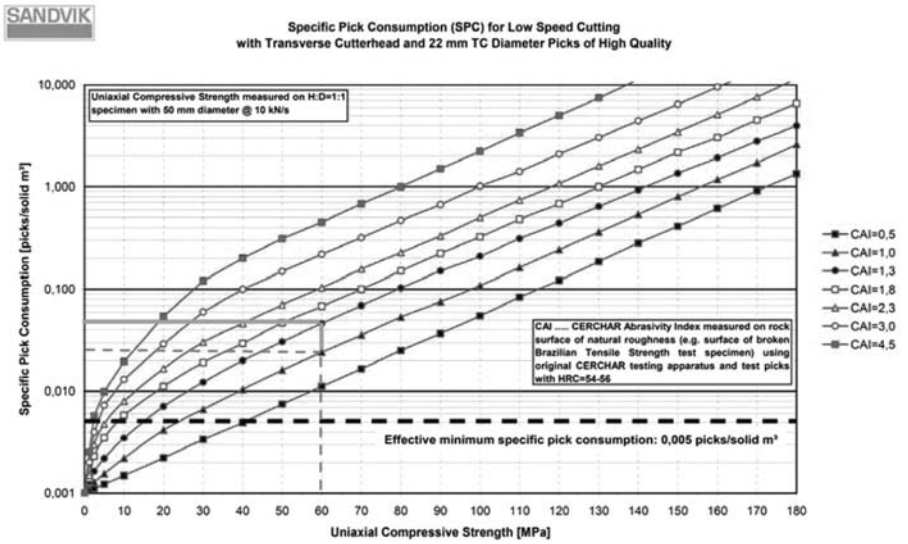


Figure 6. Spesific pick consumption for MT720 as function of UCS and CAI (after Restner and Pichler 2007).

depend on the deformation and shear failure at the tip of pins and therefore is not dependent on the amount of abrasive material in the host rock. So, the remaining Cerchar index that can be attributed to the abrasion effect corresponding to the final 8 mm of sliding distance was observed to be 35% of the total Cerchar index. However if the sliding distance is increased to 15 mm then 45% of the Cerchar index can be attributed to the rock abrasion effects. This situation is very important for researchers and applicators to predict real tool consumption. Since, small increase (0.1) in CAI of the rock will lead to bigger tool consumption in the tunnel excavation (see Figure 6). According to this experiment 15 mm scratch length should be enough to capture almost all the stylus wear. With this adjustment, the abrasivity class of the rock will increase and therefore will improve predictability of real tool wear.

ACKNOWLEDGEMENTS

This study was supported by TUBITAK under the project number of 110M579. The authors also gratefully acknowledge Bülent Ecevit University.

REFERENCES

Al-Ameen, S.I. & Waller, M.D. 1994. The influence of rock strength and abrasive mineral content on the Cerchar abrassive index. *Engineering Geology* 36 (3–4): 293–301.

Alber, M. 2007. Stress dependency of the Cerchar abrasivity index (CAI) and its effects on wear of selected rock cutting tools. *Tunnelling and Underground Space Technology* 23(4): 351–359.

Atkinson, T., Cassapi, V.B. & Singh, R.N. 1986. Assessment of abrasive wear resistance potential in rock excavation machinery *International Journal of Mining and Geological Eng*ineering 3:151–163.

ASTM, 2012. *Standard test method for laboratory determination of abrasiveness of rock using the CERCHAR method. Designation 7625-10*. United States: ASTM International.

Bilgin, N., Copur, H. & Balci, C. 2012. Effect of replacing disc cutters with chisel tools on performance of a TBM in difficult ground conditions. *Tunnelling and Underground Space Technology* 27(1): 41–51.

Cardu, M., Giraudi, A., Rocca, V. & Verga, F. 2012. Experimental laboratory tests focused on rock characterisation for mechanical excavation. *International Journal of Mining, Reclamation and Environment* 26(3): 199–216.

CERCHAR, 1986. *The Cerchar Abrasiveness Index*. Centre d' Etudes et Recherches de Charbonnages de France, 12 p.

Deketh, H.J.R. 1995. *Wear of Rock Cutting Tools, Laboratory Experiments on the Abrasivity of Rock*. Rotterdam: A.A. Balkema.

Deliormanlı, A.H. 2012. Cerchar abrasivity index (CAI) and its relation to strength and abrasion test methods for marble stones. *Construction and Building Materials* 30: 16–21.

Ghasemi, A. 2010. *Study of Cerchar abrasivity index and potential modifications for more consistent measurement of rock abrasion*. M.Sc. Thesis, Department of Energy and Mineral Engineering, The Pennsylvania State University.

ISRM 2009. ISRM Testing Methods Commission: Report for 2009. *News Journal,* Vol. 12, December 2009: 54–59.

Kahraman, S., Alber, M., Fener, M. & Günaydin, O. 2010. The usability of Cerchar abrasivity index for the prediction of UCS and E of Misis Fault Breccia: Regression and Artificial Neural Networks Analysis. *Expert Systems with Applications* 37(12): 8750–8756.

Lassnig, K., Latal, C. & Klima, K. 2008. Impact of grain size on the Cerchar abrasiveness test. *Geomechanics and Tunnelling* 1(1): 71–76.

Mathier, J.F. & Gisiger, J.P. 2003. Abrasivity of Icelandic basalts. In *Technology Roadmap for Rock Mechanics, Proceedings of the 10th International Congress on Rock Mechanics* 1: 809–812. Johannesburg: The South African Institute of Mining and Metallurgy.

Michalakopoulos, T.N., Anonostou, V.G., Bassanou, M.E. & Panagiotou, G.N. 2006. The influence of steel stylus hardness on Cerchar abrasiveness index value. *International Journal of Rock Mechanics and Mining Sciences* 43: 321–328.

Oparin, V.N. & Tanaino, A.S. 2009. Assessment of abrasivity by physico-mechanical properties of rocks. *Journal of Mining Science* 45(3): 240–249.

Plinninger, R., Kasling, H., Thuro, K. & Spaun, G. 2003. Testing conditions and geomechanical properties influencing the Cerchar abrasiveness index (CAI) value. *International Journal of Rock Mechanics and Mining Sciences* 40: 259–163.

Plinninger, R., Kasling, H. & Thuro, K. 2004. Wear prediction in hardrock excavation using the Cerchar abrasiveness index (CAI) value. In W. Schubert (ed.), *Proceedings of the ISRM Regional Symposium EUROCK 2004 & 53rd Geomechanics Colloquy*: 599–604. Essen: Verlag Glueckauf GmbH.

Restner, U. & Pichler, J. 2007. Mont Cenis Tunnel modification project-lowering of tunnel invert with SANDVIK tunnel miner MT620. In N. Bilgin (ed.). *Proc the 2nd Symp. on Underground Excavations for Transportation, Ýstanbul, 15–17 November 2007*. Ýstanbul: ÝTÜ.

Rostami, J., Özdemir, L., Bruland, A. & Dahl, F. 2005. Review of issues related to Cerchar abrasivity testing and their implications on geotechnical investigations and cutter cost estimates. In J.D. Hutton & W.D. Rogstad (eds), *Proceedings of the 2005 Rapid Excavation and Tunnelling Conference (RETC), Seattle WA, USA*: 15–29. Littleton: Society for Mining, Metallurgy and Exploration.

Stanford, J. & Hagan, P. 2009. An assessment of the impact of stylus metallurgy on the Cerchar abrasiveness index value. *Proceedings of the Coal Operators' Conference*: 347–355. University of Wollongong.

Suana, M. & Peters, T. 1982. The Cerchar abrasivity index and its relation to rock mineralogy and petrography. *Rock Mechanics* 15(1): 1–6.

Thuro, K. & Kasling, H. 2009. Classification of the abrasiveness of soil and rock. *Geomechanics and Tunnelling* 2(2): 179–188.

Valantin, A. 1973. An examination of the various conventional procedures to determine the resistance of rock to mechanized winning. Development and exploratory techniques in coal mines. Commission of the European Communities, Luxembourg: 177–193.

West, G. 1986. A relation between abrasiveness and quartz content for some coal measures sediments. *International Journal of Mining and Geological Engineering* 4:73–78.

West, G. 1989. Rock abrasiveness testing for tunneling. *International Journal of Rock Mechanics and Mining Sciences & Geomechanics Abstracts* 26(2): 151–160.

Yaralı, O. 2005. Zonguldak Taşkömür Havzası kömür çevre kayaçlarinin aşindiricilik özelliklerinin araºtirilmasi. *Türkiye Uluslararası 19. Madencilik Kongresi Kitab*ı. TMMOB Maden Müh. Odası Yayını: Ýzmir. Turkey: 243–251. (in Turkish)

Yaralı, O., Yasar, E., Bacak, G. & Ranjith, P.G. 2008. A study of rock abrasivity and tool wear in coal measures rocks. *International Journal of Coal Geology* 74(1): 53–66.

This page intentionally left blank

3. Constitutive models and numerical modeling

This page intentionally left blank

Rock Mechanics for Resources, Energy and Environment – Kwaśniewski & Łydżba (eds)
© 2013 Taylor & Francis Group, London, ISBN 978-1-138-00080-3

Strain-softening characterization of granitic rocks and numerical simulation of servo-controlled strength tests

J. Arzúa, J. Barbiero & L.R. Alejano
Department of Natural Resources & Environmental Engineering, University of Vigo, Spain

ABSTRACT: The main objective of this study regards the analysis of results of a series of compressive strength tests on granite rocks carried out on a press with servo-controlled loading in order to characterize their strain-softening behavior. We pay particular attention to the evolution of failure criteria from peak to residual strength that obviously presents plastic strain dependence. A graphical methodology was used to link strength with plastic strain all along the process of plastic yield and for different levels of confining pressure. It was possible to fit a mathematical expression, which is able to reflect this relation and which also allows obtaining evolving strength criteria (cohesion and friction values). We have also accounted for the post-failure dilation behavior of these rocks, studied elsewhere. The derived model has been implemented in a numerical code, and some simple simulations are carried out. These models have been able to reproduce the initial experimental results reasonably well.

1 INTRODUCTION

The relevance of a thorough knowledge of the complete stress-strain curve in rock has frequently been highlighted in the rock mechanics field, and most particularly, in its earlier breakthroughs (Hudson et al., 1971). The aim of the present research is to study the actual behavior of rocks and propose strain-softening and dilation models able to better represent the observed stress-strain response of rock samples.

It is widely acknowledged that rocks, and also rock masses, suffer a strain softening or strength weakening process after achieving a peak stress. This is a complex behavior, so even simple strain softening models need a good number of parameters to reproduce its most relevant features.

Simple strain-softening models for rocks require at least elastic parameters (E and ν), peak and residual strength envelopes (typically two parameters each, as for instance c^{peak}, ϕ^{peak}, c^{res} and ϕ^{res}) and two post-failure parameters (for instance drop modulus M and dilatancy ψ). These 8 parameters serve to recover the main features of this type of behavior (see upper graphs of Fig. 1). However, one must admit that this representation is still not very similar to the actual stress-strain response of rock tests, as it can be derived from the comparison of this representation to actual test results, as shown in the lower graphs of Figure 1. In this paper we investigate a possible approach to provide a more accurate model to simulate strain-softening behavior of granitic rocks as observed in the lab.

To study this behavior we have performed in our lab 3 series of around thirty unconfined and confined triaxial tests (σ_3 in the range 0–12 MPa) in three different granitic rocks named Amarelo País, Blanco Mera and Vilachán, respectively (Fig. 2). To do this, a servo-controlled press was modified to control the axial stress in triaxial tests and also to measure the volume of hydraulic fluid displaced from Hoek's cell, so that the volumetric strain in the sample can be computed.

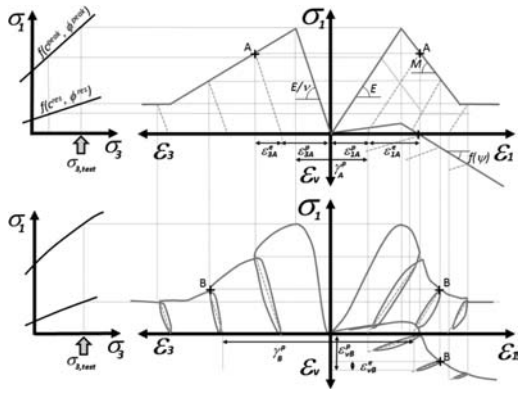


Figure 1. Theoretical (simple strain-softening) and actual stress–strain response of rock sample submitted to a triaxial test in the laboratory.

As a result we have obtained complete stress strain curves for different confinements in three different granitic rocks, as it is shown in Figure 3.

In what follows we propose a methodology to characterize this type of behavior in order to obtain numerical parameters able to reproduce the behavior observed in the lab.

In strain-softening behavior models, a softening parameter η controls strength capacity. Although η can



Figure 2. Tested samples in our lab.

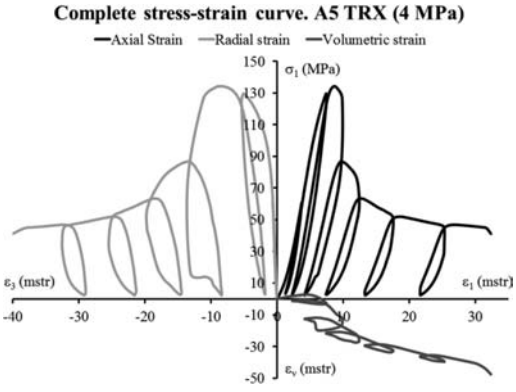


Figure 3. Complete stress-strain curve from a triaxial test.

be defined in a number of ways, the most widely used variable is shear plastic strain, obtained as the difference between the major and minor principal plastic strains, as follows:

$$\gamma^p = \varepsilon_1^p - \varepsilon_3^p \tag{1}$$

This variable can be computed as shown in Fig. 1.

2 METHODOLOGY

2.1 *Correlation between strength and plastic strain*

Based on results in confined tests (three or four tests for every granite and every confining stresses of 2, 4, 6, 10 and 12 MPa) as shown in Figure 4, we have marked the values of σ_1 corresponding to pre-peak (the point where the line σ_1-ε_1 loses its linearity, related to the so-call transition between stable and unstable crack propagation also called long term UCS). We have also computed the values of peak and residual σ_1, and intermediate points between these values (25, 50 and 75%).

We have finally estimated the plastic shear strain values associated to all of these points, as illustrated on Figure 4. In this way for each test we have of some pairs of values σ_1-γ^p representing yield envelopes for different levels of plasticity.

See for instance in Figure 5 the graph of these results for $\sigma_3 = 4$ MPa for one of the tested granites.

Starting from these series of data points, we have looked for a curve to adjust to these results and we have found in the literature that a curve as this one presented

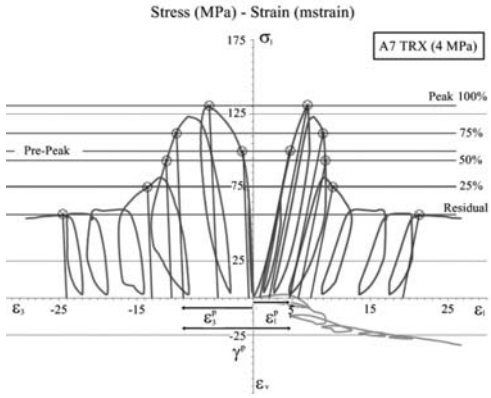


Figure 4. Estimate of relevant σ_1-γ^p points from stress-strain complete curves as explained in the main text.

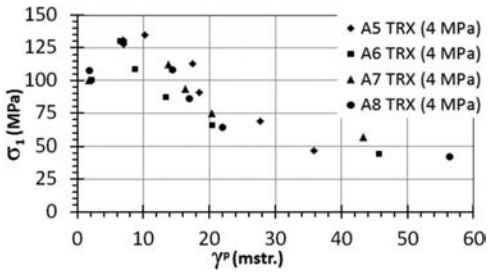


Figure 5. Representation of σ_1-γ^p points for triaxial tests with $\sigma_3 = 4$ MPa for Amarelo País granite.

in eq. (2) can accommodate our results reasonably well.

$$\sigma_1 = a\left[1 - e^{-b\cdot\gamma^p} - \frac{c}{c+d}\left(1 + \frac{b e^{-(c+d)\gamma^p} - (c+d)\cdot e^{-b\cdot\gamma^p}}{c+d-b}\right)\right] \tag{2}$$

where a, b, c and d are constants that can be fitted for every rock and confinement level. These values have been fitted and we have represented the values of these constants against the confinement stress for every granite type. In this way we have obtained the values of these parameters as a function of σ_3 for every granite type as shown in Table 1. In fact those are yield functions depending on σ_3 and the level of plasticity suffered by the sample in terms of γ^p.

Results of these curves for the three different granites analyzed and for various confinement levels are presented in Figure 6 to 8, together with the original σ_1-γ^p points derived from actual tests.

2.2 *Correlation between dilatancy and plastic strain*

For rocks the dilation angle is smaller than friction angle (Vermeer & De Borst, 1980). These authors proposed as a suitable way to assess dilatancy:

$$\psi = \arcsin\frac{\dot{\varepsilon}_v^p}{-2\dot{\varepsilon}_1^p + \dot{\varepsilon}_v^p} \tag{3}$$

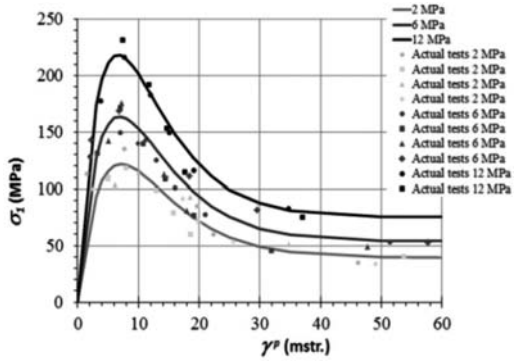


Figure 6. Fitted curves relating σ_1 and γ^p for different confining stress together with points derived from tests on Amarelo País granite samples.

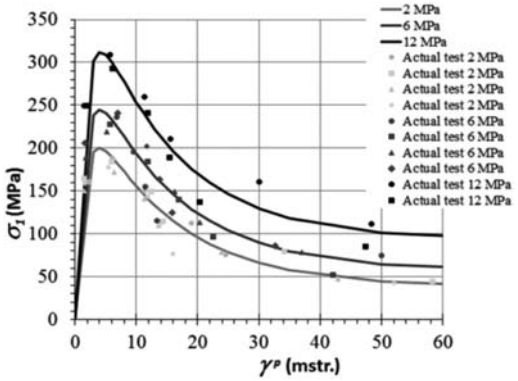


Figure 7. Fitted curves relating σ_1 and γ^p for different confining stress together with points derived from tests on Blanco Mera granite samples.

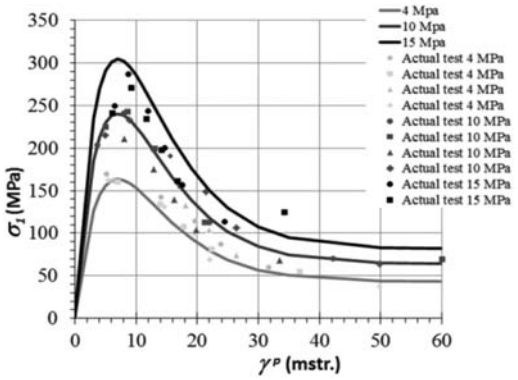


Figure 8. Fitted curves relating σ_1 and γ^p for different confining stress together with points derived from tests on Vilachán granite samples.

This formulation is valid for the interpretation of triaxial tests. The plastic axial strain can be obtained as shown in Figures 1 and 4. Some loading-unloading cycles (as we have done) are necessary to obtain more or less accurate value of the plastic volumetric strain (Fig. 1). Linking the points of minimum strain in every cycle, the so-called irrecoverable volumetric strain locus is obtained, and from it, values of ε_v^p can be recovered. Based on this line, we can obtain a number of ψ-γ^p pairs, for every test.

Table 1. Fit of parameters a, b, c and d dependent on σ_3 for the three different tested granites.

Amarelo País	R^2	
a =	$28.078 \cdot \sigma_3 + 212.74$	0.967
b =	$-0.0011 \cdot \sigma_3 + 0.1835$	0.437
c =	$0.0034 \cdot \sigma_3 + 0.1154$	0.385
d =	$0.0004 \cdot \sigma_3 + 0.0200$	0.139
Blanco Mera		
a =	$13.918 \cdot \sigma_3 + 224.62$	0.933
b =	$-0.0031 \cdot \sigma_3 + 0.0828$	0.156
c =	$-0.0004 \cdot \sigma_3 + 0.0610$	0.034
d =	$0.0004 \cdot \sigma_3 + 0.0091$	0.441
Vilachán		
a =	$31.968 \cdot \sigma_3 + 292.93$	0.968
b =	$0.00003 \cdot \sigma_3 + 0.1011$	0.00003
c =	$0.0001 \cdot \sigma_3 + 0.1441$	0.0007
d =	$0.00002 \cdot \sigma_3 + 0.0167$	0.007

This has been done elsewhere (Arzúa & Alejano, 2013) and dilatancy has been estimated according to the approach developed by Zhao & Cai (2010), which relates dilation angle with plastic shear strain (expressed in percentage of deformation):

$$\psi = \frac{a'b'\left[\left(\exp\left(-b'\gamma^p\right) - \exp\left(-c'\gamma^p\right)\right)\right]}{c' - b'} \tag{4}$$

where moreover a', b' and c' fit the following expressions:

$$\begin{aligned} a' &= a'_1 + a'_2 \exp\left(\frac{-\sigma_3}{a'_3}\right) \\ b &= b'_1 + b'_2 \exp\left(\frac{-\sigma_3}{b'_3}\right) \\ c' &= c'_1 + c'_2 \left(\sigma_3\right)^{c'_3} \end{aligned} \tag{5}$$

Using equations (5) another 3 coefficients are necessary to fit each confining dependent parameter in equation (4). These coefficients have been fitted following the ideas by Zhao & Cai (2010) and they are presented in Table 2.

There exist more simple models of dilatancy depending on confinement stress and plasticity such as that proposed by Alejano & Alonso (2005). However, our results on granite samples do not seem to fit very well this model that was initially developed back-analyzing test results on samples of sedimentary rocks, such as coal, mudstone, siltstone and sandstone.

3 MODEL RESULTS

With this information of evolving yield criteria, as in eq. (2) and Table 1, and dilation, as in eq. (4) and

Table 2. Parameters of the plastic shear strain and confining pressure dependent dilation angle model as proposed by zhao & Cai (2010) for the three studied granitic rocks.

	Amarelo País	Blanco Mera	Vilachán
a'_1	29.01	21.13	3.79
a'_2	28.05	36.71	53.65
a'_3	4.76	4.92	4.46
b'_1	8.26	20.63	10.38
b'_2	17.49	29.44	49.69
b'_3	1.5	2.97	2.19
c'_1	0.014	0.047	0.058
c'_2	0.0749	0.049	0.050
c'_3	0.711	0.589	0.295

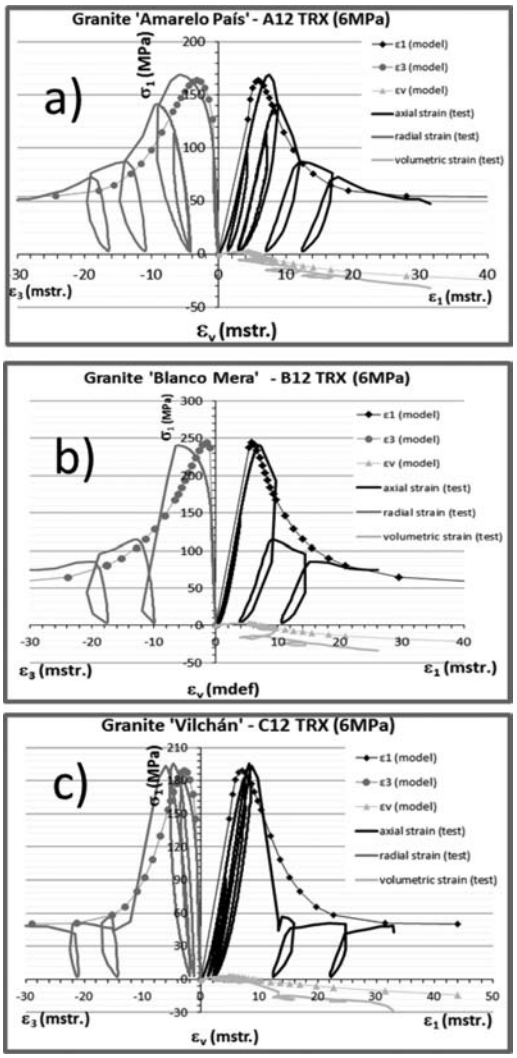


Figure 9. Model and actual complete stress-strain curves of tests for samples of the threes studied granites a) Amarelo País, b) Blanco Mera and c) Vilachán, submitted to a confinement stress of 6 MPa.

Table 2, and once also derived the elastic parameters (E and ν), it is possible to model or reproduce results of tests by means of calculation sheets, and compare them against actual results.

We will start with the elastic phase, and then when arriving at pre-peak, we recover the values of σ_1 according to eq. (2) and the values of ψ according to eq. (4) for every value of γ^p. Then and accounting for:

$$\gamma^p = \varepsilon_1^p - \varepsilon_3^p = \varepsilon_1^p - \frac{K_\psi}{2}\varepsilon_1^p = \left(1 - \frac{K_\psi}{2}\right)\cdot\varepsilon_1^p \tag{6}$$

$$K_\psi = \frac{1+\sin\psi}{1-\sin\psi}$$

it is possible to obtain the values of ε_1^p and ε_3^p associated to every σ_1:

$$\varepsilon_1^p = \gamma^p \Big/ \left(1 - \frac{K_\psi}{2}\right) \quad \& \quad \varepsilon_3^p = \frac{K_\psi}{2}\cdot\varepsilon_1^p \tag{7}$$

The corresponding elastic counterpart, ε_1^e and ε_3^e, are derived from the elastic constants:

$$\varepsilon_1^e = \sigma_1 \Big/ E \quad \& \quad \varepsilon_3^e = \sigma_1 \Big/ \frac{E}{\nu} \tag{8}$$

So we can obtain the corresponding ε_1 and ε_3, associated to every σ_1, as well as the corresponding value of value of ε_v:

$$\varepsilon_1 = \varepsilon_1^e + \varepsilon_1^p \;,\; \varepsilon_3 = \varepsilon_3^e + \varepsilon_3^p \quad \& \quad \varepsilon_v = \varepsilon_1 + 2\varepsilon_3 \tag{9}$$

In this way, the model of the complete stress-strain curve of any test can be obtained. Examples of model and actual tests for samples of the threes studied granites are shown in Figure 9.

This representation of results is much more accurate and realistic than the typical simple strain-softening models usually used for standard modeling, as that presented in the upper graphs of Fig. 1.

4 NUMERICAL APPROACH

The code FLAC (Itasca, 2009) has been used to try to reproduce test results. In order to model numerically the laboratory triaxial strength tests, it is first necessary to implement the presented behavior model in the selected code.

4.1 *Implementation of behavior model*

Code FLAC, implements an incremental plastic parameter e_{ps}, whose incremental form is:

$$\Delta e^{ps} = \left\{\frac{1}{2}(\Delta\varepsilon_1^{ps} - \Delta\varepsilon_m^{ps})^2 + \frac{1}{2}(\Delta\varepsilon_m^{ps})^2 + \frac{1}{2}(\Delta\varepsilon_3^{ps} - \Delta\varepsilon_m^{ps})^2\right\}^{\frac{1}{2}} \tag{10}$$

where, $\Delta\varepsilon_m^{ps} = \frac{1}{3}\left(\Delta\varepsilon_1^{ps} + \Delta\varepsilon_3^{ps}\right)$ and $\Delta\varepsilon_j^{ps}$ j = 1, 2, 3 are the principal increments of the shear plastic strain. This incremental plastic parameter can be related to the more standard γ^p or plastic shear strain. If an elasto-plastic strain-softening material with constant dilation angle is considered, in addition characterized by a plastic potential $g = \sigma_1 - K_\psi \sigma_3$, then the following relationship between γ^p and η_{FLAC} can be deduced (Alonso et al., 2003):

$$\eta_{FLAC} = \frac{\sqrt{3}}{3}\sqrt{1 + K_\psi + K_\psi^2}\,\frac{\gamma^p}{1 + K_\psi} \tag{11}$$

The reader can check how for null dilation $\eta_{\mathrm{FLAC}} = \gamma^p/2$.

On the other hand and in order to obtain the evolving failure criteria starting from eq. (2) and parameters in Table 1 it is possible to obtain strength values for any confinement and for different values of γ^p. This has been done and linear strength envelopes have been fitted for a number of values of γ^p (from 3 to 13 mstr. 1 by 1, from 13 to 25 mstr. 3 by 3 and 25, 30, 35, 50 and 70 mstr). For these linear envelopes, estimates of cohesion (c) and friction (ϕ) were obtained.

Also for every value of γ^p (σ_3 and type of granite) we can compute dilatancy as per eqs. (4) and (5) with parameters in Table 2. And with dilatancy and γ^p it is possible to obtain η_{FLAC} as in eq. (10). An internal language subroutine has been created to update dilatancy values following Zhao & Cai's (2010) dilatancy angle model every certain number of steps.

To introduce the behavior model and parameters in FLAC, we use pairs of points (c, η_{FLAC}) and (ϕ, η_{FLAC}) for the failure criteria as those shown in Table 3, for the case of Vilachán granite.

Table 3. Values of friction and cohesion for different values of the plastic parameters (first, γ^p, and then, e^{ps}, obtained from γ^p, and dilatancy) for the case of Vilachán granite submitted to a confinement stress of 6 MPa (similar tables are obtained for different confinements and for the two other granites).

Granite 'Vilachán'				
	6 MPa			
γ^p (mstr.)	K_ψ	$e^{ps} = \eta_{\mathrm{FLAC}}$	ϕ (°)	c (*MPa*)
3	1.81	0.0015	57.87	11.17
4	1.81	0.0020	59.94	11.96
5	1.80	0.0025	61.03	12.40
6	1.79	0.0030	61.54	12.61
7	1.77	0.0035	61.69	12.65
8	1.76	0.0040	61.58	12.57
9	1.74	0.0046	61.28	12.40
10	1.73	0.0051	60.83	12.17
11	1.71	0.0056	60.26	11.51
12	1.70	0.0061	59.60	11.61
13	1.69	0.0066	58.86	11.29
16	1.65	0.0081	56.31	10.32
19	1.61	0.0096	53.48	9.41
22	1.58	0.0111	50.62	8.63
25	1.55	0.0126	47.94	7.99
30	1.50	0.0151	44.24	7.24
35	1.46	0.0176	41.68	6.79
50	1.35	0.0251	38.74	6.34
70	1.25	0.0351	38.27	6.28

4.2 *FLAC models*

Simple models of triaxial tests have been created resorting to the axi-symmetric geometrical possibilities of FLAC. Models present the half section of the cylindrical specimens with a rotation axis in its left part (Fig. 10). The servo-control has been modeled by means of a subroutine which induces a constant velocity (5e-8 m/step) in the upper and lower faces of the sample. Additionally, a confinement stress is induced on the right hand side (Fig. 10). Models corresponding to confinement stresses of 2, 6 and 10 MPa are run for every type of granite and for 5 different mesh sizes including 10 × 40, 15 × 60, 20 × 80, 25 × 100 and 40 × 160 (Fig. 10), in order to control and study the role of mesh in test result, which is known to control strain-softening numerical models.

4.3 *FLAC results*

As a sample of the numerical results obtained we represent the numerical results with mesh size 15 × 60 of two triaxial tests (2 and 6 MPa) on Blanco Mera granite together with actual test results in Fig. 11.

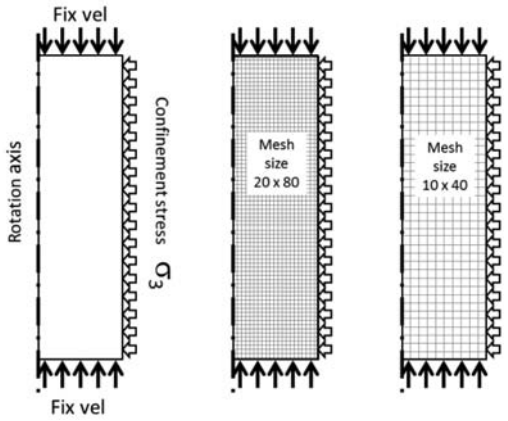


Figure 10. Boundary conditions and example of two grids used to model numerically the triaxial tests.

Fig. 12 illustrates the numerical results of a triaxial test (6 MPa, Blanco Mera) together with FLAC results in this case for three different mesh sizes.

The obtained numerical results can be considered a reasonably similar representation of tests even if, as usually happen in rock mechanics, there are slight discrepancies, so a number of points are to be remarked and some comments are in order.

Strength is well represented by models. Peak strength values observed in models tend to be slightly

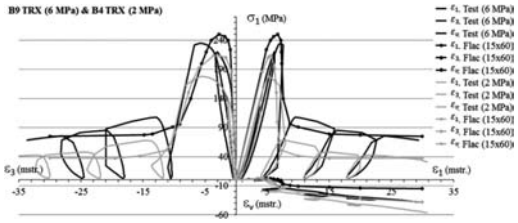


Figure 11. Complete stress-strain curve (σ_1-ε_1, σ_1-ε_3 and ε_v-ε_1) for two triaxial tests (2 and 6 MPa) in Amarelo País granite. Actual tests and FLAC results with mesh size 15×60.

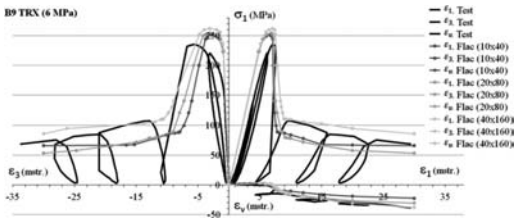


Figure 12. Complete stress-strain curve (σ_1-ε_1, σ_1-ε_3 and ε_v-ε_1) for a triaxial test (6 MPa) in Blanco Mera granite. Actual test and FLAC results with meshes 10×40, 20×80 and 40×160.

larger than those observed in tests. This trend is more marked for smaller meshes. Residual strength values are generally well captured by tests, particularly for average mesh sizes (15×60 and 20×40). Smaller meshes tend to overestimate the observed residual values. In the radial strain (ε_3) branch, the model does not capture well the large deformation in the phase between the elastic part and the peak. This is difficult to capture for every model and it is due to the 'negative dilatancy' of this phase.

The drop phase, between the peak and residual stage, is usually steeper in the models than in the tests in the axial branch (ε_1), especially for larger meshes. However, in the radial branch actual tests and results are more alike. The behavior of this drop phase is partially controlled by the occurrence of shear bands, particularly for finer meshes. Some results concerning the orientation of shear bands are being derived, but for the sake of briefness they are not presented in this study.

Volumetric strain (ε_v) is in general well reflected in many tests, although in some cases, it is slightly underestimated. This fact can be associated to the steeper response of the axial strain in the drop phase.

Certainly, mesh size affect results, as it is well known for the case of strain-softening (Varas et al., 2005) and, there are a number of differences highlighted in the previous paragraphs. Most of these differences are however, within the limits of the natural variability of tests. All in all, the obtained results are more realistic than those derived by means of standard simple strain-softening approaches, as that shown in the upper part of Figure 1.

5 CONCLUSIONS

In this study and starting from servo-controlled triaxial compressive strength tests with loading and unloading cycles on granite samples, a strain-softening behavior model is proposed where evolving strength (from peak to residual values) is related to a plastic parameter and where dilation is a confinement stress and plastic shear strain dependent parameter.

Three different granite types are characterized according to the above indicated behavior models and simple computations are performed, able to represent the complete stress-strain curve as observed in the laboratory for granite samples with a good level of accuracy.

Moreover, this non-simple behavior model has been implemented in FLAC in our best possible way and accounting for the particularities of this code (different plastic parameter, evolving failure criteria in Mohr-Coulomb terms …). Axi-symmetric models of the tests in the different granites with different mesh sizes have been run to find out that numerical results of the complete stress-strain curve are a reasonably accurate representation of the actual observed behavior.

ACKNOWLEDGMENTS

The authors thank the Spanish Ministry of Science and Technology for financial support awarded, under Contract Reference Number BIA2009-09673, which funded developments in this paper. This contract has been partially financed by means of ERDF funds of the EU.

REFERENCES

Alejano LR, Alonso E 2005. Considerations of the dilatancy angle in rocks and rock masses. International Journal of Rock Mechanics & Mining Sciences. 42(4): 481–507.

Alonso, E., Alejano, L.R., Varas, F., Fdez-Manin, G., Carranza-Torres, C. 2003. Ground Reaction Curves for tunnels in strain-softening rock masses. Int. J. Numer. & Anal. Meth. Geomech. 27: 1153–1185.

Arzúa J, Alejano LR. 2013. Dilation in granite during servo-controlled strength tests. International Journal of Rock Mechanics & Mining Sciences. In press. DOI: 10.1016/j.ijrmms.2013.02.007.

Hudson, J.A., Brown, E.T., Fairhurst, C. 1971. Shape of the complete stress-strain curve for rock. Proc. 13th Symp. on Rock Mechanics, University of Illinois, 1971.

ITASCA. 2009. User manual for FLAC, Version 5.0. Itasca Consulting Group Inc, Minnesota.

Varas F, Alonso E, Alejano LR, Fdez.-Manin G. 2005. Study of bifurcation in the problem of unloading a circular excavation in a strain softening material. Tunnelling and underground Space Technology, 20: 311–322.

Vermeer PA, De Borst R. 1984. Non-associated plasticity for soils, concrete and rock. Heron. 29 (3): 64.

Zhao XG, Cai M 2010. A mobilized dilation angle model for rocks. International Journal of Rock Mechanics & Mining Sciences. 47(3): 368–384.

Rock Mechanics for Resources, Energy and Environment – Kwaśniewski & Łydżba (eds)
© 2013 Taylor & Francis Group, London, ISBN 978-1-138-00080-3

A constitutive model for jointed rock mass

A. Azami & T. Yacoub
Rocscience Inc., Toronto, Ontario, Canada

J. Curran
Rocscience Inc., Toronto, Ontario, Canada
Civil Engineering, University of Toronto, Canada

D. Wai
Rocscience Inc., Toronto, Ontario, Canada

ABSTRACT: The effects of strength anisotropy of rock masses in slope stability problems are the focus of this paper. The source of the strength anisotropy can be attributed to many factors and the motivation of this study is to concentrate on the effects of planes of weakness, such as joints and bedding planes on the slope stability analysis. The limit equilibrium approach and finite element with shear strength reduction method are used for numerical simulations of slope stability problems. The finite element simulations take advantage of a constitutive model with embedded weak planes. The results obtained from the two methods are compared with each other.

1 INTRODUCTION

Natural soils and sedimentary rocks, such as shale, limestone and mudstone, are typically formed by deposition and progressive consolidation during formation. Such formations usually have a distinct internal structure, which is characterized by the appearance of multiple sedimentary layers. Besides the bedding planes, the geometric layout of networks of joints and other types of discontinuities in a rock mass are significant contributors to the complex behavior of such geomaterials (e.g. Hoek & Brown 1980, Hoek 1983, Zienkiewicz & Pande 1977). The presence of these fissures and planes of weakness significantly influence the response of geotechnical structures such as slopes, tunnels and excavations (Goodman et al, 1968, Bandis et al, 1983).

2 JOINTED ROCK MASS

The jointed rock mass here is considered to be composed of an intact material that is intercepted by up to three sets of weak planes. The spacing of the weak planes is such that the overall effects of the sets can be smeared and averaged over the control volume of the material. Such a configuration with two sets of weak planes is illustrated in Figure 1 where the weak planes are oriented at an arbitrary angle θ_1 and θ_2 in the rock mass.

In this paper, it is assumed that the failure of the matrix can be described by the Generalized Hoek-Brown criterion presented in Equation 1. The strength criterion of the weak planes is formulated by a simple Coulomb criterion as in Equation 2.

$$\sigma_1 - \sigma_3 - \sigma_{ci}\left(m_b \frac{\sigma_3}{\sigma_{ci}} + s\right)^a = 0 \tag{1}$$

$$\tau = \sigma_n \tan\varphi + c \tag{2}$$

In the above, σ_1 and σ_3 are the major and minor principal stresses, σ_{ci} is the uniaxial compressive strength of the intact rock material, and

$$m_b = m_i \exp\left(\frac{GSI - 100}{28 - 14D}\right) \tag{3a}$$

$$s = \exp\left(\frac{GSI - 100}{9 - 3D}\right) \tag{3b}$$

$$a = \frac{1}{2} + \frac{1}{6}\left[\exp\left(\frac{GSI}{15}\right) - \exp\left(\frac{-20}{3}\right)\right] \tag{3c}$$

m_i is an intact rock material property, GSI is the geological strength index, and D is the disturbance factor (Hoek et al 2002). τ and σ_n are the tangential and normal components of the traction vector on a weak plane, ϕ is the friction angle and c is the cohesion of the weak plane.

According to Equation 3, the strength of the rock mass is related to the strength of the intact rock that

is factored by GSI and D parameters. In general, the presence of weak planes contributes to these two factors. In this work however, since the weak planes are considered in the modeling separately, the GSI and D parameters are selected to be very close to that of the intact rock. This will help capture the anisotropic effects caused by dominant weak planes in a rock mass.

3 CONSTITUTIVE MODEL

The constitutive model developed for the commercial finite element package, *Phase*[2] (Rocscience Inc. 2011), considers the Generalized Hoek-Brown model for the matrix and can include up to three sets of Coulomb weak planes. Tension cut offs are also considered for the matrix and the weak planes. In the formulation of this constitutive model, the total number of yield functions adds up to eight, not all of which needs to be active simultaneously. In the following sections the integration procedure of the constitutive equations and some application examples are presented.

3.1 *Integration of the constitutive equations*

Considering a multi-yield surface constitutive model where $F_\alpha(\sigma_{ij}) = 0$ is a set of yield surfaces and $Q_\alpha(\sigma_{ij}) = const.$, the corresponding set of plastic potentials, the basic elasto-plastic equations are:

$$\dot{\varepsilon}_{ij} = \dot{\varepsilon}^e_{ij} + \dot{\varepsilon}^p_{ij} \tag{4a}$$

$$\dot{\sigma}_{ij} = D^e_{ijkl}\dot{\varepsilon}^e_{kl} \tag{4b}$$

$$\dot{\varepsilon}^p_{ij} = \sum_\alpha \left(\dot{\varepsilon}^p_{ij}\right)_\alpha = \sum_\alpha \dot{\lambda}_\alpha \frac{\partial Q_\alpha}{\partial \sigma_{ij}} \tag{4c}$$

where $\dot{\varepsilon}_{ij}$ is the increment of strain tensor, $\dot{\sigma}_{ij}$ is the increment of stress tensor, D^e_{ijkl} is the fourth order elastic tensor, subscript α stands for each yield surface, $\dot{\lambda}$ is the plastic multiplier and superscripts e and p indicate elastic and plastic, respectively. Equations 4 represents the additivity postulate, Hooke's law and flow rules for each yield mechanism (Vermeer 1978, Simo et al. 1988, Hofstetter et al. 1993, Simo & Hughes 1998). The total rate of plastic strain in Equation (8) is the summation of the rate of plastic strain calculated for all the mechanisms. Note that the constitutive model presented here is an elasto-perfect-plastic model with no hardening parameter. That is why the hardening parameter and hardening/softening rules are not included in the set of Equations 4.

For any process of loading/unloading, the Kuhn-Tucker conditions (Luenberger 1984) must be satisfied for all the mechanisms:

$$F_\alpha(\sigma_{ij}) \le 0 \quad ; \quad \dot{\lambda}_\alpha \ge 0 \quad ; \quad \dot{\lambda}_\alpha F_\alpha = 0 \tag{5}$$

The plastic potential for the Generalized Hoek-Brown yield surface has a similar function as in Equation 1 with a dilation factor m_q replacing the m_b. For the weak planes, a constant dilation angle is considered and the plastic potential function has the same form as the Coulomb criterion in Equation 2. The tension cutoffs have associated flow rules.

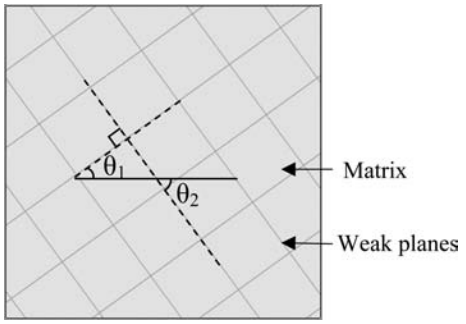


Figure 1. Typical control volume of a material with two sets of perpendicular weak planes with inclination angle θ_1 and θ_2.

3.2 *Example I: Uniaxial compression tests*

As an example, Figure 2 shows the anisotropic effects induced by one and two sets of weak planes on the maximum axial strength of a rock mass sample tested in a biaxial tests configuration. The material properties for the matrix and the weak planes are listed in Table 1. Weak planes set I is oriented at angle θ_1 and set II is perpendicular to set I at angle $\theta_2 = 90° - \theta_1$. The results include the cases where only one set of the weak planes (either set I or set II) exists in the medium and the case that both sets are present. The variation of maximum axial stress with the inclination angle of the weak planes from both the analytical solution and the finite element simulations are presented in Figure 2. The analytical solutions are from a simple evaluation of failure functions for the weak planes and the matrix for different configurations of the model under uniaxial loading (Pietruszczak 2010). Similar patterns for the variation of maximum axial stress with inclination angle have been reported by many researchers both in numerical and experimental investigations (e.g. Hoek & Brown 1980, Zienkiewicz & Pande 1977).

3.3 *Example II: Circular excavation*

This example presents the numerical results obtained for a circular excavation in a jointed rock mass. Two types of simulations have been performed. In the first one, the weak planes are simulated by joint networks in the finite element mesh, i.e. the joints are modeled explicitly. The second simulation takes advantage of the proposed constitutive model with embedded weak planes. The domain of the problem is a circular disk with a radius of 5 m, and the circular excavation is located at the center of the disk with the radius of 1m. The simulations are plane strain and the boundary condition at the external boundary is pinned. The initial stress field is hydrostatic with a pressure equal to

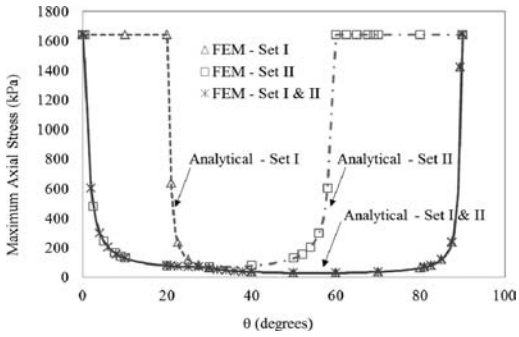


Figure 2. Variation of maximum axial stress of the rock mass sample intercepted by two sets of perpendicular weak planes.

Table 1. Properties for the matrix and weak planes.

Characteristics of the matrix	Value
Unit Weight	$20\,kN/m^3$
Elastic Modulus	$50\,MPa$
σ_{ci}	$5\,MPa$
m_b, m_q	3.42679
s	0.108368
a	0.500593
GSI	80
D	0
m_i	7
Weak Planes Set I	**Value**
Friction & Dilation Angle	20°
Cohesion	$10\,kPa$
Weak Planes Set II	**Value**
Friction & Dilation Angle	30°
Cohesion	$20\,kPa$

100 kPa, and the body force is not included in the analysis. The material properties of the intact rock are taken from Table 1, and the weak planes have the properties of weak plane set I in that table.

In one set of simulations only one set of weak planes oriented at $\theta = 45°$ is considered, and in the second set two sets of perpendicular weak planes with $\theta_1 = 45°$ and $\theta_2 = 135°$ (see Figure 3).

Figure 4 and 5 show the results of simulations for the case where the rock mass has only one set of weak planes with inclination angle $\theta = 5°$. Figure 4(a) shows the contours of total displacement in the domain from the simulation with the new constitutive model. Figure 4(b) shows the results obtained from the simulation that uses a joint networks. Figure 5 shows the failure pattern observed in these two simulations. The "+" symbols in Figure 5(a) are indications of failure along the weak planes at Gaussian integration points. The bold red lines in Figure 5(b) represent the slip along the

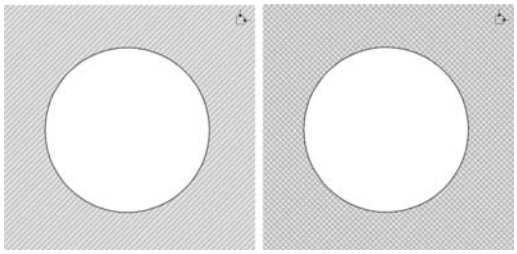


Figure 3. Circular excavation in a rock mass with one and two sets of weak planes (illustration of the explicit joint networks).

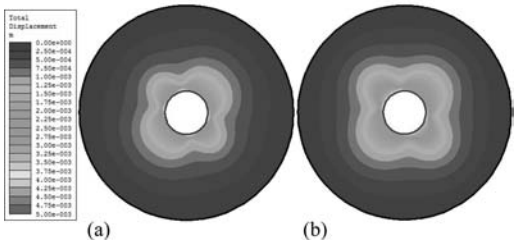


Figure 4. Contours of total displacement for the case of one set of weak planes oriented at $\theta = 45°$; (a) Constitutive model with embedded weak planes and (b) joint network.

explicit joints. In these simulations the plastic deformation is in the form of slips along the weak planes and no failure was observed in the intact rock.

Figures 6 and 7 present the numerical results for the case where two sets of weak planes exist at $\theta_1 = 45°$ and $\theta_2 = 135°$. Note that the properties of both sets of weak planes are the same as weak planes set I in Table 1. Figure 6 shows the contours of mean principal stress and Figure 7 illustrates the failure pattern.

Note that in these simulations since the geometry is symmetric and the field stress is constant, if the material was isotropic the results would have been symmetric as well. The asymmetry observed in the numerical results is the result of anisotropic effects induced by the weak planes.

Clearly there is a good agreement between the two approaches in modeling the weak planes in a finite element analysis.

4 SLOPE STABILTY IN JOINTED ROCK MASS

The finite element method with the shear strength reduction (SSR) method (Azami et. al. 2012, Hammah et. al. 2006, Dawson et al. 1999, Griffiths & Lane 1999) is used to evaluate the safety factor of slopes against failure. In this method, finite element analyses are used systematically to search for a strength reduction factor (SRF), i.e. the factor of safety, which brings a slope to the point of failure. Here, the SRF is applied to both the Generalized Hoek-Brown criterion for the matrix and the Coulomb criterion for the weak planes.

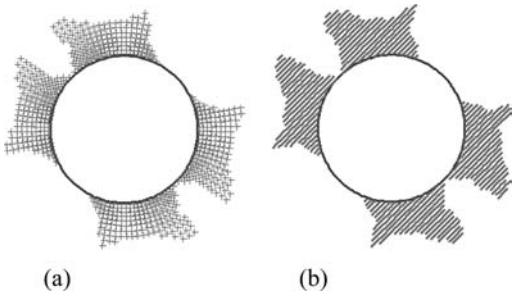


Figure 5. Failure pattern around the excavation for the case of one set of weak planes oriented at $\theta = 45°$; (a) Constitutive model with embedded weak planes and (b) joint network.

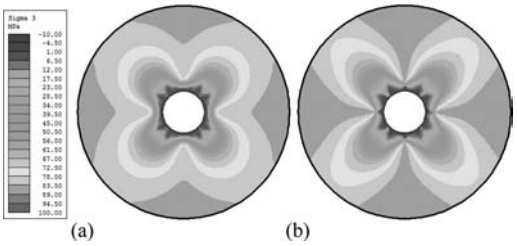


Figure 6. Contours of mean principal stress for the case of two sets of weak planes oriented at $\theta_1 = 45°$ and $\theta_2 = 135°$; (a) Constitutive model with embedded weak planes and (b) joint network

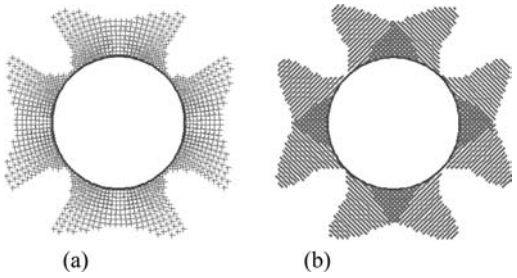


Figure 7. Failure pattern around the excavation for the case of two sets of weak planes oriented at $\theta_1 = 45°$ and $\theta_2 = 135°$; (a) Constitutive model with embedded weak planes and (b) joint network.

4.1 *SSR for the new constitutive model*

Application of SRF to the Coulomb criterion is rather straight forward. It would suffice to divide the right hand side of Equation 2 by the scalar value that is the SRF. However, for the Generalized Hoek-Brown model this task is more challenging.

There are number of approaches for applying the SRF to the Generalized Hoek-Brown model in the literature, most of which rely on some sort of a fitting procedure. In some, the Hoek-Brown criterion is locally fitted using a Mohr-Coulomb criterion based on the stress level at the material calculation point (e.g. Dawson et al 2000). In the approach proposed

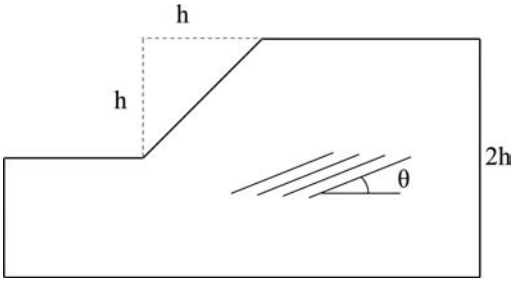


Figure 8. Geometry of the slope analyzed in this study.

by Hammah et al. (2005), a new and reduced Generalized Hoek-Brown criterion is formulated based on the locally fitted Mohr-Coulomb criterion. The approach selected in this paper is based on the work of Benz et al (2008). In this approach, the yield function is modified to incorporate a SRF in its definition (see Equation 6). The simplicity and computational efficiency of this method are the reasons for this selection.

$$\sigma_1 - \sigma_3 - \frac{1}{\eta}\sigma_{ci}\left(m_b\frac{\sigma_3}{\sigma_{ci}} + s\right)^a = 0 \tag{6}$$

In above η is a factor that is related to the SRF as follows:

$$\eta = \frac{1}{2}\left[SRF\left(2+\tilde{f}'\right)\sqrt{1+\frac{\left(SRF^{-2}-1\right)\tilde{f}'^2}{\left(2+\tilde{f}'\right)^2}} - \tilde{f}'\right] \tag{7}$$

$$\tilde{f}' = \frac{\partial\left[\sigma_{ci}\left(m_b\frac{\sigma_3}{\sigma_{ci}} + s\right)^a\right]}{\partial\sigma_3} \tag{8}$$

4.2 *Numerical results and discussion*

The rock mass material considered for the slope stability analysis consists of the intact material intercepted by only one set of weak planes. The material properties of the rock mass are presented in Table 1 and the properties of the weak planes corresponds to the weak planes set I in that table.

Figure 8 shows the geometry of the problem where θ is the orientation of the planes with respect to the horizontal plane and h=150m. The finite element simulations are carried out in two-dimensional plane strain configuration using 6-noded triangular elements. The external boundary of the model is constrained in both horizontal and vertical directions.

In finite element SSR simulations, θ varies from $\theta = 0°$ to $\theta = 180°$ with steps of $\Delta\theta = 5°$. On top of these, another simulation is carried out considering only the intact material with no weak planes.

Limit equilibrium analyses (Spencer 1967, Balmer 1952) were carried out using *Slide* (Rocscience Inc.

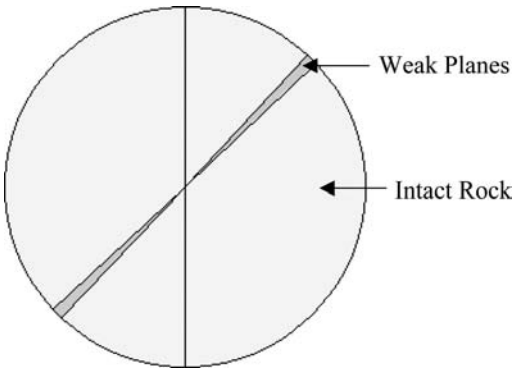


Figure 9. The composite material with generalized anisotropic strength properties used in limit equilibrium analysis ($\theta = 45°$).

2010). The generalized anisotropic behavior was considered for the simulations where the composite material had the properties of the weak planes with orientations ranging of $\theta \pm 2°$, and the properties of the intact rock for orientations other than that range. The configuration for $\theta = 45°$ is illustrated in Figure 9. Note that in limit equilibrium analysis, for the weak planes to have any effect on the stability, they should be aligned in the direction of slip surface (Zienkiewicz & Pande 1977). Thus for $\theta > 90°$ and even close to this value, the weak planes will show no effect on the stability of slope in a typical limit equilibrium analysis. In this set of simulations, θ varies from $\theta = 0°$ to $\theta = 65°$ with steps of $\Delta\theta = 5°$. Similar to the finite element simulations, an additional analysis is carried out considering only the intact material with no weak planes.

Figure 10 presents the results of a set of finite element SSR simulations. The figures show distributions of maximum shear strain (distortion) for the SRF at failure. The results presented here are for the cases of no weak planes and one set of weak planes oriented at θ equal to 0°, 15°, 35°, 50° and 55°, respectively. The slip surface predicted by the limit equilibrium analysis is also included in each figure.

The high intensity of distortion indicates the location of the slip surface. The first observation is that the shape of the failure surface is highly dependent on the orientation of weak planes. In the absence of weak planes, the slip surface has its classical circular shape (see Figure 10a). In the absence of weak planes, the finite element SSR predicts a safety factor of 2.12 for the slope, while the limit equilibrium analysis evaluates the safety factor to be 2.20. The presence of weak planes forces the failure surface to deviate from its original circular form. For $\theta = 0°$ and $\theta = 35°$, the noncircular failure surface and the influence of weak planes is very clear.

The evaluated safety factors are also highly affected by the inclination angle as they vary from 2 to about 0.4. Evidently, the safety factor is higher in the absence of weak planes. Clearly by not considering the weak planes and their configuration in the slope stability

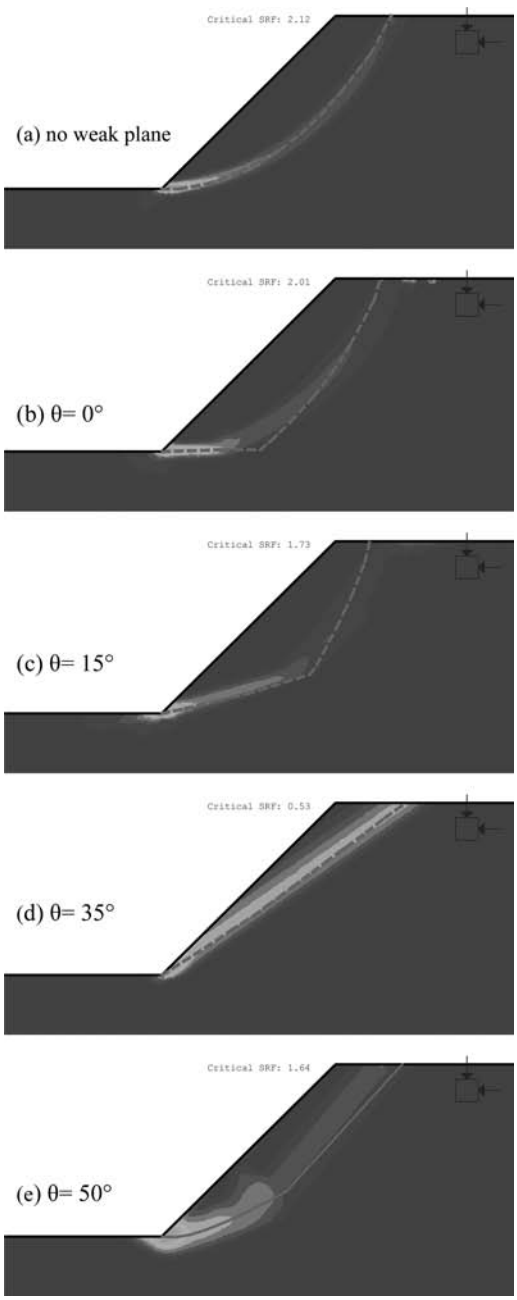


Figure 10. Numerical simulation results; the distribution of distortion in the domain obtained from finite element analyses using the constitutive model with embedded weak planes, and the slip surface predicted by limit equilibrium analysis, for the cases of no weakness planes and θ equal to 0°, 15°, 35°, 50° and 55°.

simulations, the evaluation of safety factor would be far from being safe.

The variation of safety factor with the orientation of the weak planes is presented in Figure 11. There is a good agreement between the finite element SSR

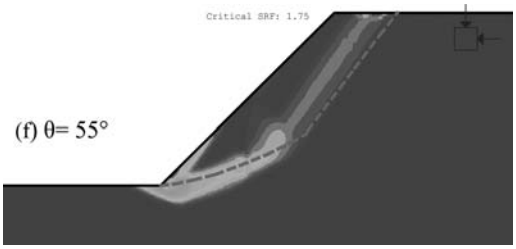


Figure 11. Variation of factor of safety with the inclination angle of weak planes.

results with the limit equilibrium results in cases where the weak planes are aligned in the direction of the slip surface, i.e. $0° \leq \theta \leq 60°$. Based on that, it can be concluded that for other orientations, where the limit equilibrium approach cannot estimate an accurate safety factor, the finite element SSR results are valid.

5 CONCLUSION

The effects of strength anisotropy of geomaterials due to the presence of weak planes in the material on the stability of slopes were studied in this paper. To utilize this investigation, a constitutive model was developed based on the notion of the multi-yield-surface elasto-plastic constitutive framework. The constitutive model is composed of 4 major shear failure mechanisms, i.e. Generalized Hoek-Brown for intact material and three sets of Coulomb weak planes, and their corresponding tension cut off criteria. The multi-yield surface plasticity model was programmed as an extension to a finite element program and was used in finite element SSR simulations to calculate the safety factor of slopes in such materials. The results of finite element SSR simulations were verified by limit equilibrium analysis where possible. It was shown that the stability of slopes is highly dependent on the presence and configuration of the weak planes in the material. The shape of the possible slip surface is also influenced by the orientation of the weak planes.

REFERENCES

Azami A., Yacoub T. & Curran J., 2012. Effects of strength anisotropy on the stability of slopes. *65th Canadian Geotechnical Conference, CGS Geo-Manitoba*, Winnipeg, Manitoba, Canada.

Balmer, G. 1952. A general analytical solution for Mohr's envelope. *American Society for Testing and Materials*, (52): 1260–1271.

Bandis, S.C., Lumsden, A.C. & Barton, N.R., 1983. Fundamentals of rock joint deformation. *International Journal of Rock Mechanics, Mining Sciences & Geomechanics Abstracts*, 20(10): 249–268.

Benz, T., Schwab, R., Kauther, R.A. & Vermeer, P.A. 2008. A Hoek–Brown criterion with intrinsic material strength factorization. *International Journal of Rock Mechanics & Mining Sciences*, 45: 210–222.

Dawson, E.M., Roth, W.H. & Drescher, A. 1999. Slope stability analysis by strength reduction, *Geotechnique*, 49(10): 835–840.

Goodman, R.E., Taylor, R.L. & Brekke, T.L., 1968. A model for the mechanics of jointed rock. *Journal of the Soil Mechanics and Foundations Division*, ASCE, 637–659.

Griffiths, D.V., & Lane, P.A. 1999. Slope stability analysis by finite elements, *Geotechnique*, 49(3): 387–403.

Hammah, R.E., Yacoub, T.E., & Curran, J.H. 2006. Investigating the performance of the shear strength reduction (SSR) method on the analysis of reinforced slopes. *In Proceedings of the 59th Canadian Geotechnical and 7th Joint IAH-CNC and CGS Groundwater Specialty Conferences – Sea to Sky Geotechnique*, Vancouver, Canada.

Hoek, E. (1983), Strength of jointed rock masses. *Geotechnique*, 33(3): 187–205.

Hoek, E. and Brown, E.T. 1980. *Underground Excavations in Rock*. London, Insiyute of Min. Metal, England.

Hoek, E., Carranza-Torres, C., Corkum, B. 2002. Hoek-Brown failure criterion—2002 edition. In: *Proceedings of the 5th North American symposium*, NARMS-TAC, Toronto.

Hofstetter, G., Simo, J.C. & Taylor, R.L. 1993. A modified cap model: closest point solution algorithm. *Computers and Structures*, 46(2): 203–214.

Luenberger, D.G. 1984. *Linear and Nonlinear Programming. Reading*, Massachusetts, Addison-Wesley.

Pietruszczak S. 2010. *Fundamentals of Plasticity in Geomechanics*. CRC Press/Balkema, The Netherlands.

Rocscience Inc. 2011, *Phase*^{2} Version 8.0 – Finite Element Analysis for Excavations and Slopes. www.rocscience.com, Toronto, Ontario, Canada.

Rocscience Inc. 2010, *Slide* Version 6.0 – 2D Limit Equilibrium Slope Stability Analysis. www.rocscience.com, Toronto, Ontario, Canada.

Simo, J.C. & Hughes T.J.R. 1998. *Computational Inelasticity*: Springer Verlag.

Simo, J.C., Kennedy, J.G. & Govindgee, S. 1988. Non-smooth multisurface plasticity and viscoplasticity, Loading/unloading conditions and numerical algorithms. *International Journal of Numerical Methods in Engineering*, 26(10): 2161–2185.

Spencer E. 1967. Method of analysis of the Stability of Embankments Assuming Parallel Inter-Slice Forces, *Geotechnique*, 17(1): 11 –26.

Vermeer P.A. 1978. A double hardening model for sand. *Geotechnique*, 28(4): 413–433.

Zienkiewicz, O.C. & Pande G.N. 1977. Time-dependent multilaminate model of rocks-A numerical study of deformation and failure of rock masses, *International Journal for Numerical and Analytical Methods in Geomechanics*, 1(3): 219–247.

Rock Mechanics for Resources, Energy and Environment – Kwaśniewski & Łydżba (eds)
© 2013 Taylor & Francis Group, London, ISBN 978-1-138-00080-3

Numerical investigation of asperity degradation in the direct shear test of rock joints

M. Bahaaddini
School of Mining Engineering, University of New South Wales, Sydney, Australia,
Shahid Bahonar University of Kerman, Kerman, Iran

P. Hagan, R. Mitra & B.K. Hebblewhite
School of Mining Engineering, University of New South Wales, Sydney, Australia

ABSTRACT: This paper investigates the progressive shear behavior and asperity degradation of rock joints in the direct shear test using PFC2D. PFC is a discrete element code in which the intact material is represented by assemblies of circular particles bonded together. Traditionally, joints have been modeled in PFC by removing bond between particles or the smooth joint model. However, these approaches are not able to reproduce the shear behavior of rock joints in the direct shear test. A new developed method called "shear box genesis" is used in this study to study the shear behavior of rock joints. Three saw-tooth triangular joint profiles with the base angles of 15°, 25° and 35° are generated and the mechanism of asperity degradation of these profiles under different normal stresses are studied. Three mechanisms of sliding, asperity wearing and shearing are observed in the numerical models and it observed that as the asperity base angle increases, the transition from sliding to shearing mechanism takes place at a lower normal stress. A good agreement is found between the peak shear strength of numerical models and Patton and Ladanyi and Archambault models. In order to study the process of asperity degradation during the shear test on a real rock joint profile, direct shear test on standard profile of *JRC* 18–20 is carried out. The peak shear strength of numerical models under different normal stresses are compared against the Barton model and a good agreement is found.

1 INTRODUCTION

The stability of near-surface rock structures such as rock slopes and crown pillars in blocky condition is strongly dependent on the shear behavior and mobilization of the friction of joints (Swan and Zongqi, 1985). Understanding the shear mechanism of rock joints in a given situation is not easy to ascertain and depends on several parameters such as joint surface roughness, the properties of intact material, loading conditions, weathering of the joint surface and infilling materials. A number of studies have been carried out to experimentally and analytically investigate the effect of joint roughness on the shear behavior of rock joints. Patton (Patton, 1966), Ladanyi and Archambault (Ladanyi and Archambault, 1980) and Barton (Barton and Choubey, 1977) models are the most widely used models for estimation of the shear strength of rock joints. However, a robust method to consider the effect of joint roughness on the shear behavior of rock joints is still not available. Quantitative description of the joint roughness and unknown mechanism of asperity degradation during the shearing process are the main challenges in understanding the shear behavior of rock joints.

Some studies have been carried out to numerically investigate the shear behavior of rock joints using constitutive models. However, these approaches suffer from special difficulties in generation and modeling of real rough rock joints and also they are not able to track the asperity degradation during the shearing process.

This paper tries to study the effect of joint roughness on the shear behavior of rock joints and investigate the process of asperity degradation in the direct shear test using a discrete element code, PFC2D. Particle flow code (PFC) is a promising approach to explicitly study the shear behavior of rock joints. The mechanical behavior of materials in PFC is simulated by displacement and force interaction of collection of circular disks in PFC2D and spherical particles in PFC3D. These particles can be glued together with bonds and the composite of these glued particles is called bonded particle model (BPM) (Itasca Consulting Group Inc. 2008). The macroscopic behavior of the BPM is controlled by the microscopic properties of bonds and particles as input parameters. By breakage of bonds under loading, micro-cracks are produced in the sample and by propagation and coalescence of micro-cracks, macroscopic fractures are generated. Therefore, it produces a scientific tool to consider the

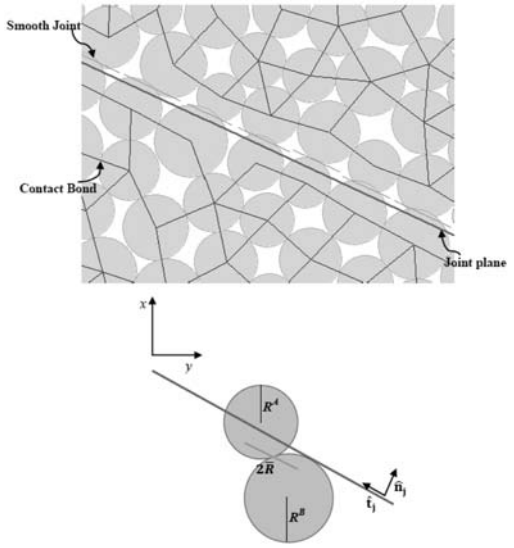


Figure 1. The smooth joint model (Bahaaddini et al. 2013).

macroscopic behavior of rock under complex loading situations based on microscopic properties of components (particles and bonds).

Traditionally, joints have been simulated in PFC by removing bonds between particles along the joint plane, called the bond removal method. Removing bond between particles results in a micro-scale roughness of the joint surface due to circular shape, non-uniform distribution and unequal size of particles. This leads to unrealistic increase of the shear strength and dilation (Bahaaddini et al. 2012).

In order to overcome the shortcoming of micro-scale roughness in the bond removal method, the smooth joint (SJ) model was introduced (Pierce et al., 2007). In the SJ model, slip surfaces (smooth joints) are assigned at contacts between particles lying on the opposite sides of the joint plane. Particle pairs intersected by a smooth joint may overlap and pass through each other. The application of smooth joint at contact between particles is shown in Figure 1.

Bahaaddini et al. (2012) investigated the ability of the SJ model in reproducing the shear behavior of rock joints. It was found that the SJ model suffers from particle interlocking at shear displacements larger than the minimum particle size (D_{min}). This problem is related to the inability of detection of upper and lower particles of the shear box blocks and proper application of smooth joints. A new method called "shear box genesis" is proposed to solve this problem that will be explained in Section 2.

This paper studies the shear behavior of rock joints using the shear box genesis approach. Three saw-tooth triangular joint profiles with base angles of 15°, 25° and 35° are prepared and direct shear tests under different normal stresses are carried out. In order to investigate the ability of this method in reproducing the peak shear strength, results of numerical models are compared against Patton and Ladanyi and Archambault models. The asperity degradation of these profiles under different normal stresses are studied. In order to study the process of asperity degradation in a real rock joint profile during shearing process, direct shear test on the standard joint roughness coefficient (*JRC*) profile of 18-20 is carried out.

2 SHEAR BOX GENESIS APPRAOCH

As mentioned above, the main deficiencies of the SJ model in reproducing the shear behavior of rock joints are identifications of particles of upper and lower shear box blocks and the proper applications of smooth joint between particles. The shear box genesis method is proposed to solve these problems. The process of undertaking direct shear test in this approach is as follows:

A) The upper and lower blocks vessels are generated separately. Each vessel consists of four frictionless walls (Figure 2a). B) The upper and lower vessels are filled separately by assemblies of randomly placed particles and the system is allowed to reach the static equilibrium (Figure 2b). C) A specified isotropic stress is applied between particles to reduce the magnitude of locked-in stresses. Five measurement circles are placed in each block and the isotropic stress inside of these blocks are calculated in cycling process to reach the specified value (Figure 2c). D) The particles with less than three contacts (floaters) are eliminated (blue balls in Figure 2d). E) Parallel bond is installed between the particles that are in physical contact (Figure 2e). F) In the above mentioned steps, the upper and lower blocks are generated separately and the particles of these blocks can be recognized easily in all stages of the test. In the final stage, the interface walls are removed and a specified normal load is applied to upper block and allowing the system to reach the static equilibrium. By stepping, new contacts are generated between the particles of upper and lower blocks. Smooth joints are applied between the particles of these blocks in an orientation parallel to the predefined joint profile (Figure 2f). This approach can be applied for generation of real rough joint profiles and solves the problem of particle interlocking.

3 NUMERICAL SIMULATION OF DIRECT SHEAR TEST

In the numerical direct shear tests, specimens having length of 100 mm and height of 40 mm are generated, as shown in Figure 3. Each sample consists of around 38,000 particles and direct shear tests under constant normal load (CNL) is carried out on these samples. The normal load is applied vertically on the upper block and by using a servo-control mechanism the normal load is kept constant during the test. The lower block is kept stationary during the test and upper block is

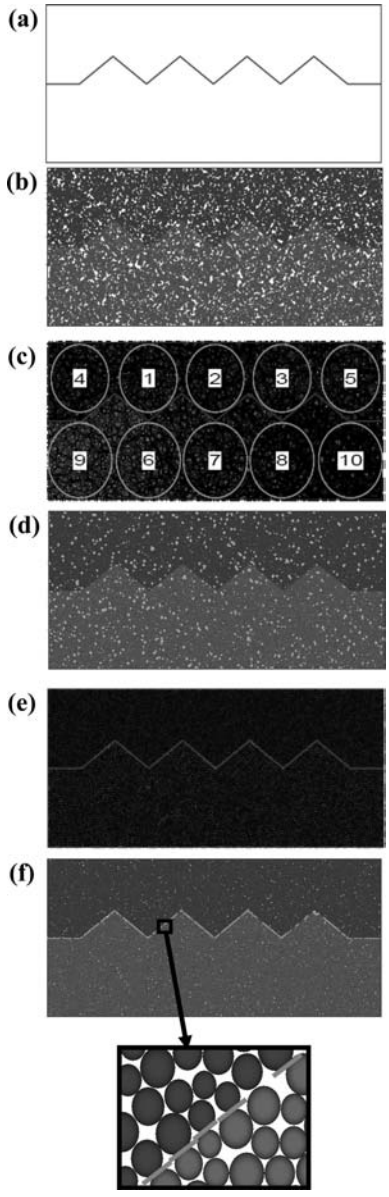


Figure 2. Process of undertaking direct shear test in shear box genesis method.

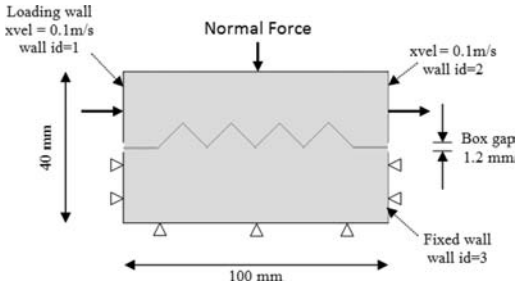


Figure 3. Simulation of direct shear test under CNL condition.

Table 1. Micro-properties of the calibrated model.

Particles properties		Parallel bonds properties	
R_{min} (mm)	0.14	$\overline{E}_c$ (GPa)	2.8
R_{max}/R_{min}	1.5	Normal strength (MPa)	20
Ball density (kg/m^3)	2205	S.D.* Normal strength (MPa)	4.5
E_c (GPa)	2.8	Shear strength (MPa)	20
Coefficient of friction	0.6	S.D.* Shear strength (MPa)	4.5
k_n/k_a	1.45	$\overline{k}_n/\overline{k}_a$	1.45

* S.D.: Standard deviation

Table 2. Results of experimental and numerical uniaxial compression tests.

	UCS (MPa)	*E* (GPa)	ν
Experimental	27.4	4.2	0.2
Numerical	27.45	4.25	0.198

moved horizontally by a velocity of 0.1 m/sec. Preliminary study shows that this velocity is slow enough to ensure that the system remains in the quasi-static condition. Horizontal displacement is recorded by the horizontal displacement of upper block and the normal displacement is measured by vertical displacement of the upper wall. The shear stress is measured by reaction force on wall id 3 divided by the joint length.

4 CALIBRATION OF THE MICRO-PROPETIES

4.1 *Calibration of bonded particle model*

In order to generate a numerical model similar to real rock, the micro-properties of the BPM is calibrated against the Hawkesbury sandstone. Hawkesbury sandstone dominates the Sydney region and a number of civil and mining structures have been constructed in it.

BPM samples with width of 42 mm and height of 84 mm are generated and the micro-properties of material are calibrated to reproduce the uniaxial compressive strength (*UCS*), Elastic modulus (*E*) and Poisson's ratio (ν) measured in laboratory experiments (for more details about the procedure of calibration refer to (Potyondy & Cundall 2004, Itasca Consulting Group Inc. 2008)). The calibrated micro-properties are presented in Table 1. The results of numerical uniaxial compression test are compared against experimental tests in Table 2 and shows that the results are in good agreement.

4.2 *Calibration of smooth joint parameters*

The smooth joint parameters are SJ normal stiffness, SJ shear stiffness and SJ coefficient of friction and these parameters need to be calibrated before undertaking the shear test (Bahaaddini et al., 2013). The

calibration process is carried out in two stages. Firstly, the SJ normal stiffness is calibrated against the normal deformability test on planar joints of Hawkesbury sandstone. Numerical normal deformability tests are carried out on single planar joint and the SJ normal stiffness is varied by trial and error to recover the experimental normal stiffness. Secondly, the SJ shear stiffness and SJ coefficient of friction are calibrated against experimental direct shear test on planar joints of Hawkesbury sandstone. The calibrated SJ parameters are presented in Table 3. Results of numerical and experimental normal deformability and direct shear tests are depicted in Table 4.

Table 3. Calibrated smooth joint parameters.

Smooth joint parameters	Calibrated value
SJ normal stiffness (MPa/mm)	200
SJ shear stiffness (MPa/mm)	50
SJ coefficient of friction	0.78

Table 4. Results of numerical and experimental normal deformability and direct shear tests.

	Experimental	Numerical
System normal stiffness (MPa/mm)	28.77	28.766
System shear stiffness (MPa/mm)	6.42	6.417
Friction angle (deg)	37.62°	37.81°

5 NUMERICAL DIRECT SHEAR TEST ON SAW-TOOTH TRIANGULAR JOINTS

In order to study the shear behavior of saw-tooth triangular joints under different normal stresses, three saw-tooth triangular joint profiles with base angles of 15°, 25° and 35° are generated. Direct shear tests under the constant normal stresses in the range of 0.5 MPa to 5 MPa are carried out. The peak shear strength of these samples are measured and compared against the Patton (Patton, 1966) and Ladanyi and Archambault (Ladanyi and Archambault, 1969, Ladanyi and Archambault, 1980) models. Results of this comparison are shown in Figure 4. Due to unknown value of joint cohesion, the Patton model is shown for only sliding mode.

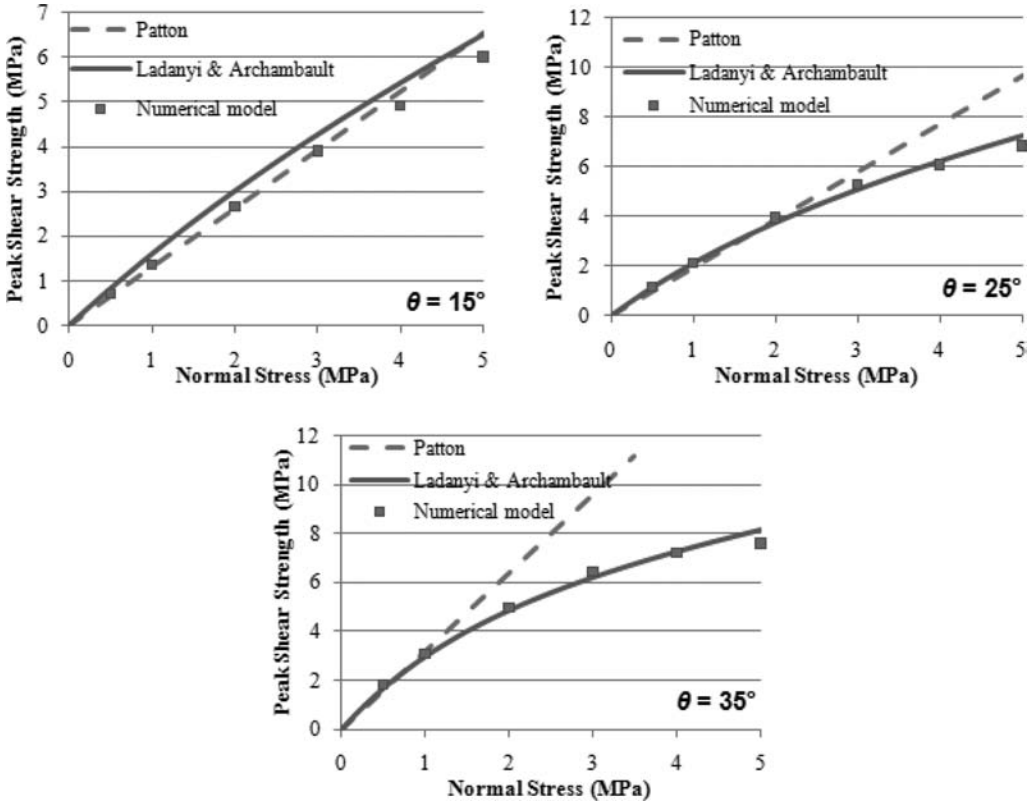


Figure 4. Results of numerical direct shear tests under different normal stresses on saw-tooth triangular joints with the base angles of 15°, 25° and 35°.

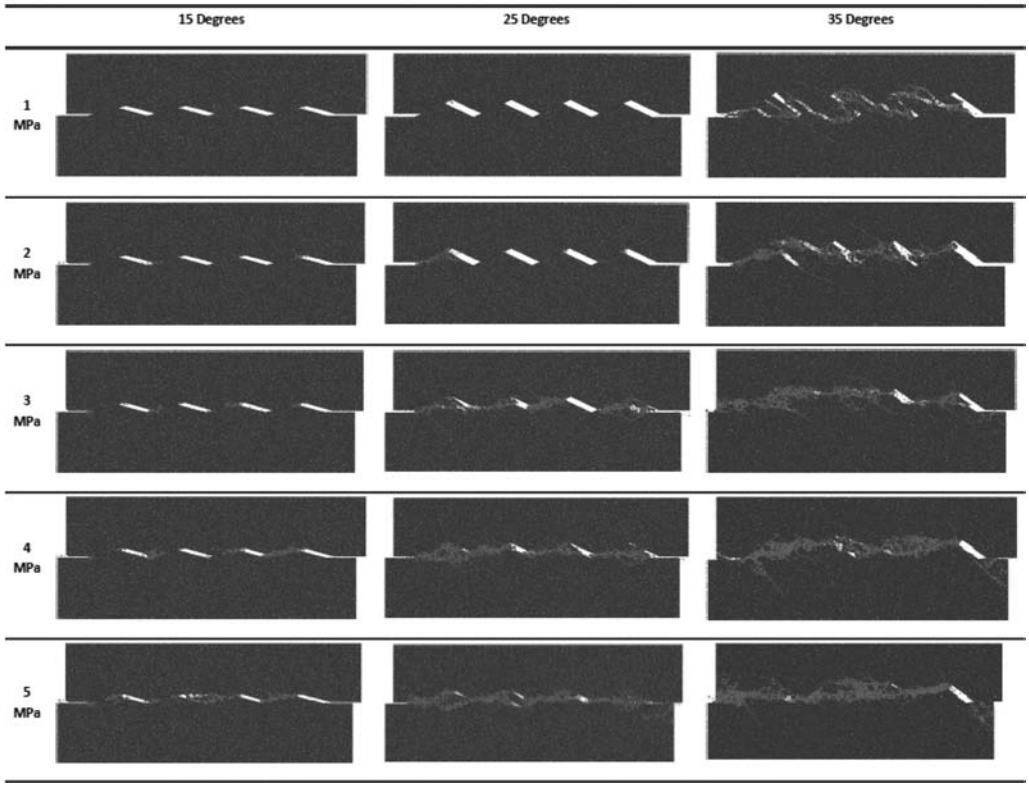


Figure 5. Asperity degradation of saw-tooth triangular joints in direct shear test under different normal stresses.

The asperity degradation of these triangular joints under different normal stresses is presented in Figure 5. Tensile and shear cracks are shown by red and blue colors, respectively. The results of numerical experiments on saw-tooth triangular joint with the base angle of 15° shows that when the normal stress is less than 4 MPa, the shear behavior is controlled by sliding along the joint surface and there is a good agreement between the peak shear strength of numerical model and Patton model. The asperity wearing is observed at the normal stresses of 2 and 3 MPa but the transition from sliding to shearing is observed at the normal stresses close to 4 MPa. When the normal stress exceeds 4 MPa, tensile cracks propagate inside the intact material and results in shearing of the asperity. For the saw-tooth triangular joints with the base angle of 25°, a good agreement is found between the peak shear strengths of the numerical models and Ladanyi and Archambault model and the transition from sliding to shearing takes place at normal stress of around 2 MPa. For the saw-tooth triangular joint with the base angles of 35°, the sliding mode is observed only at the normal stress of 0.5 MPa and shearing takes place at higher normal stresses. A good agreement is found between the peak shear strength of numerical models and Ladanyi and Archambault model.

These results show that as the asperity base angle of triangular joints increases, the peak shear strength increases and transition from sliding to shear mode takes place at a lower normal stress.

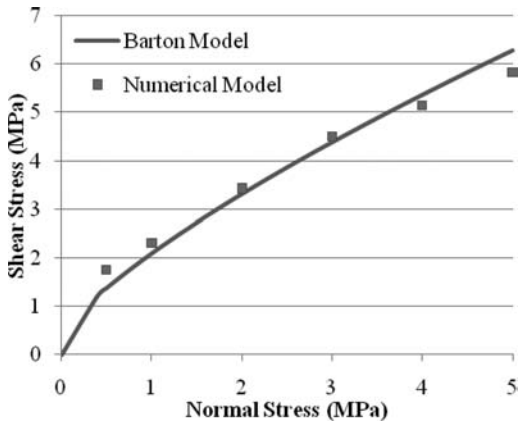


Figure 6. Results of numerical direct shear tests on standard JRC 18-20.

6 ASPERITY DEGRADATION OF A ROUGH JOINT DURING THE SHEARING PROCESS

In order to study the process of asperity degradation of a rough joint profile, the standard *JRC* 18-20 profile

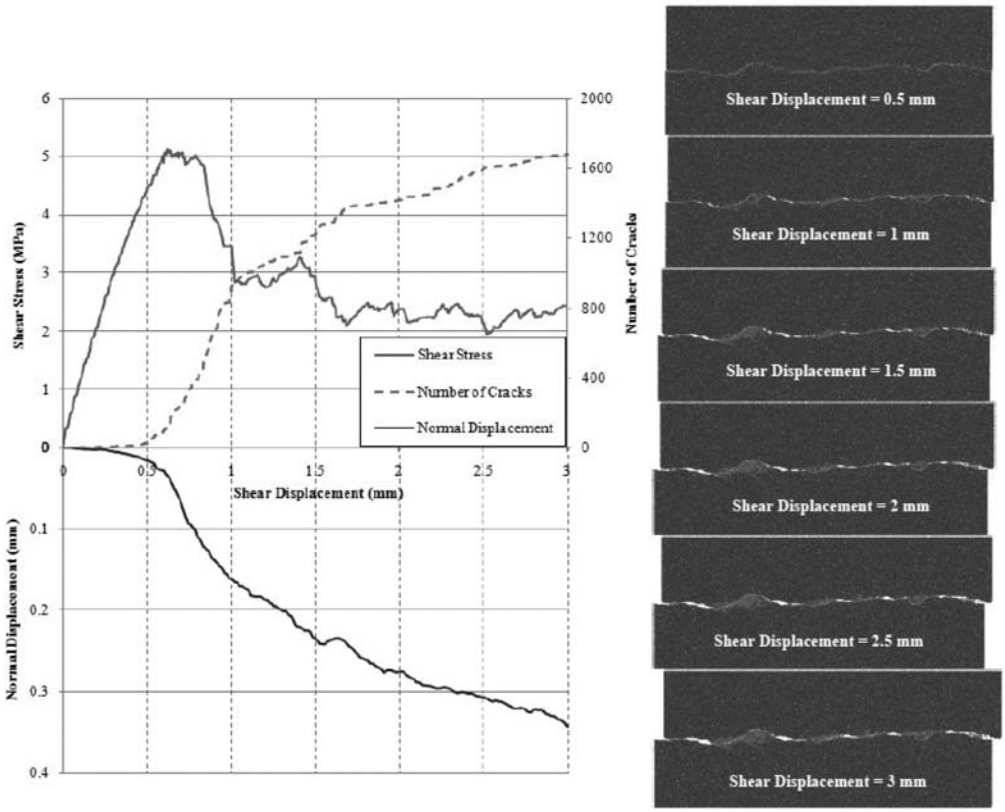


Figure 7. Process of asperity degradation during the shear test on standard JRC 18–20 under the constant normal stress of 4 MPa.

is digitized and based on the procedure explained in Section 2, the shear box is generated. Direct shear tests under different normal stresses are carried out and the peak shear strength of numerical models are compared against the Barton model (Barton et al., 1974, Barton and Choubey, 1977). The results are depicted in Figure 6 and shows that the peak shear strengths of numerical experiments are in good agreement with the Barton model.

The process of asperity degradation for this profile under the constant normal stress of 4 MPa is shown in Figure 7. Tensile and shear cracks are shown in red and blue colors, respectively and smooth joints are shown in green color. In the pre-yield region, the shear behavior is controlled by elastic deformation of the intact material and joint and only minor cracks takes place in the sample.

At the shear displacement close to 0.5 mm, sign of yielding is observed by departing from linear elastic behavior. As the shear stress reaches the peak shear strength, the surface damage becomes more extensive and the number of cracks increases rapidly. At the shear displacement of 0.62 mm, the shear stress reaches the peak strength of 5.13 MPa and the normal displacement increases rapidly from the peak shear displacement. Reduction of contact area results in stress concentration at effective asperities and breakage of bonds at these asperities. This leads to the decrease of shear strength. Tensile cracks propagate inside the intact material and followed by progressive shearing of first-order asperities. By breakage of first-order asperities, the shear stress reaches the residual strength and the rate of bond breakage decreases.

7 CONCLUSIONS

In this study, the shear behavior of rock joints are studied numerically using PFC2D. The shear box genesis approach is used to model the joints. Triangular joints with base angles of 15°, 25° and 35° are generated and direct shear test under different normal stresses is carried out. The peak shear strengths of numerical models are compared against Patton and Ladanyi and Archambault models and a good agreement is observed. The mechanisms of shearing in these profiles are studied and it is observed that at low normal stresses, the shear behavior is controlled by sliding along the asperities. At the medium normal stresses, breakage of bonds at the surface of asperities takes place and results in asperity wearing. At high normal stresses, shearing of asperities occurs. As the asperity base angle increases,

the transition from sliding to shearing takes place at a lower normal stress.

The asperity degradation of standard *JRC* 18–20 profile under the constant normal stress of 4 MPa during the shearing process is studied and it is found that at the pre-yield stage the shear behavior of rock joint is controlled by elastic deformation of the system. As the yield stress exceeds, the contact area decreases and stress concentration at major asperities results in progressive asperity degradation.

REFERENCES

Bahaaddini, M., Sharrock, G., Hebbelwhite, B. & Mitra, R. 2012. Direct shear tests to model the shear behaviour of rock joints by PFC2D. *46th U.S. Rock Mechanics/Geomechanics Symposium.* Chicago, USA, American Rock Mechanics Association.

Bahaaddini, M., Sharrock, G. & Hebblewhite, B. K. 2013. Numerical investigation of the effect of joint geometrical parameters on the mechanical properties of a non-persistent jointed rock mass under uniaxial compression. *Computers and Geotechnics*, 49, 206–225.

Barton, N. & Choubey, V. 1977. The shear strength of rock joints in theory and practice. *Rock Mechanics,* 10, 1–54.

Barton, N., Lien, R. & Lunde, J. 1974. Engineering classification of rock masses for the design of tunnel support. *Rock Mechanics and Rock Engineering,* 6, 189–236.

Itasca Consulting Group Inc 2008. *PFC2D manual, version 4.0.,* Minneapolis, Minnesota.

Ladanyi, B. & Archambault, G. 1969. Simulation of shear behavior of a jointed rock mass. *The 11th US Rock Mechanics Symposium (USRMS).* Berkeley, CA.

Ladanyi, B. & Archambault, G. 1980. Direct and indirect determination of shear strength of rock mass. *Preprint number 80–25 AIME Annual Meeting.* Las Vegas, Nevada.

Patton, F. D. 1966. Multiple modes of shear failure in rock. *1st ISRM Congress.* Lisbon, Portugal.

Pierce, M., Cundall, P., Potyondy, D. & Mas Ivars D 2007. A synthetic rock mass model for jointed rock. *Rock Mechanics: Meeting Society's Challenges and Demands, 1st Canada-U.S. Rock Mechanics Symposium.* Vancouver, London, Taylor & Francis Group.

Potyondy, D. O. & Cundall, P. A. 2004. A bonded-particle model for rock. *International Journal of Rock Mechanics and Mining Science,* 41, 1329–1364.

Swan, G. & Zongqi, S. 1985. Prediction of shear behaviour of joints using profiles. *Rock Mechanics and Rock Engineering,* 18, 183–212.

This page intentionally left blank

Rock Mechanics for Resources, Energy and Environment – Kwaśniewski & Łydżba (eds)
© 2013 Taylor & Francis Group, London, ISBN 978-1-138-00080-3

Micromechanics of geocomposites: CT images and FEM simulations

R. Blaheta, R. Kohut, A. Kolcun, K. Souček & L. Staš
Institute of Geonics AS CR, Ostrava, Czech Republic

ABSTRACT: By micromechanics of geocomposites, we understand an analysis of mechanical properties of modified geomaterials by numerical testing of digitalized samples with complicated microstructure but known local material properties. We touch several important and interacting topics –numerical upscaling and understanding of its results; application of X-ray computed tomography (CT) for visualization of structure of geomaterials; processing the digital image data for constructing FEM models of test samples; numerical testing of digitalized samples for obtaining homogenized properties and study of sensitivity to changes in local material properties, micro-level structure and FE mesh; validation of numerical results by comparison with laboratory testing of samples; use of identification technique for refining the local material properties and calibration of the upscaling procedure.

1 INTRODUCTION

We follow a two-scale view on the behaviour of geomaterials. The macro-scale corresponds to the use of material in engineering applications, whereas the micro-scale considers the microstructure with much smaller dimensions of inclusions, grains, cracks etc. The micromechanics then represents an analysis of elastic and inelastic plastic or damage material behaviour based on micro-scale information about the microstructure. We assume that the continuum mechanics models can be used on both scales.

Our aim is to derive the macro-scale properties using the information on microstructure geometry and local material properties. We can call this process as upscaling or homogenization, as the heterogeneous microstructure will not be further visible at the macro-level. Our computational procedure, shortly described in the sequel, is a numerical analogue to the classical laboratory testing on samples with heterogeneous microstructure and with dimensions proper for getting representative macro-scale behaviour. We shall first describe such computational upscaling for the case of elasticity and later discuss possible extension of such procedure for investigation of inelastic material behaviour including damage.

X-ray computed tomography (CT) is used as asuitable tool for getting information about the geo-metry of the microstructure and, with some level of uncertainty, about the inner material composition. We shall show that CT scanning can be used for construction of finite element meshes for computational upscaling.

After introduction the basic ideas of analysis of elastic behaviour, we consider questions of uncertainty arising from proper interpretation of CT scans and using the local material properties. Finally, we discuss the questions of simulation of inelastic behaviour and efficient computing.

The suggested procedures are applied and tested on analysis of the behaviour of coal-polyurethane geocomposite arising from coal seam grouting for improving resistance to dynamic events.

2 NUMERICAL MATERIAL TESTING PROCEDURE

The procedure for investigation of influence of micro-level structure to macro-level material properties starts with definition of the test volume (TEV) Ω as a macro-level size sample of the material involving micro-level structure. In our conception, the testing volume corresponds to a size of sample, which is otherwise used for laboratory testing of the material properties. It means that it can besomewhat smaller than the real representative volume (REV), but still providing useful information, allowing assessing the importance of individual microstructure characteristics etc. Let us assume that the test volume Ω is given with information about the microstructure (geometry and local material properties). Then the macro-scale characterization is obtained from boundary loading of the test volume. If we assume linear elastic material behaviour, which is given by elastic behaviour of the constituents and no occurrence of debonding between the constituents (material phases), then the micro-level stresses and strains in Ω are described by the boundary value problem

$$\text{div}\,(\sigma) = 0, \sigma = C : \varepsilon, \varepsilon = (\nabla u + (\nabla u)^T/2 \text{in} \Omega$$
$$+ \text{boundary conditions on the boundary } \delta\Omega.$$

Above, σ, ε, C are stress, strain and elasticity tensors, respectively. The boundary conditions can be of different types

- uniform strain $(x) = \varepsilon_0 x$ on $\delta\Omega$
- uniform stress $(x) \cdot n(x) = \sigma_0 \cdot n(x)$ on $\delta\Omega$

with given (constant) ε_0 or σ_0, or periodic or mixed boundary conditions, e.g. a uniaxial boundary conditions for cubical or cylindrical samples Ω with

- prescribed pressure $\sigma \cdot n = 0$ on the side, $u \cdot n = d$, $\sigma_t = 0$ with $d \neq 0$ on the top and $d = 0$ on the bottom.

The macro-scale elasticity tensor $\overline{C}$ can be then obtained from averaged strains and stresses

$$\bar{\sigma} = \langle\sigma\rangle = |\Omega|^{-1} \int_\Omega \sigma(x)dx, \tag{1}$$

$$\bar{\varepsilon} = \langle\varepsilon\rangle = |\Omega|^{-1} \int_\Omega \varepsilon(x)dx \tag{2}$$

with $|\Omega| = \int_\Omega 1\, dx$ by using the condition

$$\|\bar{\sigma} - \bar{C}\bar{\varepsilon}\|_F \to \min_{\bar{C}}, \tag{3}$$

$$\|\eta\|_F = \sqrt{\eta : \eta},\ \eta : \zeta = \textstyle\sum_{ij} \eta_{ij}\zeta_{ij}\,. \tag{4}$$

We shall apriori determine if we assume some material symmetries or if we are looking for generally anisotropic material. For an isotropic material, we get

$$\bar{C}\varepsilon = \bar{C}_{iso}\varepsilon = 3K\varepsilon_{vol} + 2G\varepsilon_{dev}, \tag{5}$$

where K is the bulk modulus, G is the shear modulus, ε_{vol} and ε_{dev} are the volumetric and deviatoric part of ε. Then

$$\|\bar{\sigma} - \bar{C}_{iso}\bar{\varepsilon}\|_F^2 =$$
$$= \|\bar{\sigma}_{vol} - 3K\bar{\varepsilon}_{vol}\|_F^2 + \|\bar{\sigma}_{dev} - 2G\bar{\varepsilon}_{dev}\|_F^2. \tag{6}$$

It allows to determine K, G as

$$K = \frac{tr(\bar{\sigma})}{3tr(\bar{\varepsilon})}, \qquad G = \frac{\bar{\sigma}_{dev} : \bar{\varepsilon}_{dev}}{2\|\bar{\varepsilon}_{dev}\|^2},$$

by minimizing the first and second term in (6), respectively.

For description and analysis of the procedure of determination of the elasticity tensor in the case of material anisotropy, we shall use the Voight notation and represent the stress and strain by vectors (taking into account the symmetry of tensors),

$$\bar{\sigma}_V = (\sigma_{11}, \sigma_{22}, \sigma_{33}, \sigma_{12}, \sigma_{13}, \sigma_{23})^T,$$
$$\bar{\varepsilon}_V = (\varepsilon_{11}, \varepsilon_{22}, \varepsilon_{33}, 2\varepsilon_{12}, 2\varepsilon_{13}, 2\varepsilon_{23})^T.$$

The general elasticity tensor is now represented by 6×6 symmetric matrix C_V, which can be further rearranged as a vector $\boldsymbol{C_{VF}} \in R^{36}$ contained all elements of C_V arranged row by row. Moreover, due to symmetry of C_V, $\boldsymbol{C_{VF}} = TC_{VS}$, where $\boldsymbol{C_{VF}} \in R^{21}$ is the vector of 21 independent elasticity constants and $\boldsymbol{T}$ is a full rank transformation matrix. The longer vector representation is more suitable for expression of the minimization condition

$$\|\bar{\sigma} - \bar{C}\bar{\varepsilon}\|_F \sim \|\bar{\sigma}_V - \bar{C}_V\bar{\varepsilon}_V\| = \|\bar{\sigma}_V - \boldsymbol{E}\overline{\boldsymbol{C}}_{\boldsymbol{VF}}\|, \tag{7}$$

where $\sim$ is the equivalence between the Frobenius norm of tensor and Euclidean norm of its Voight representation, $\boldsymbol{E}$ is a 6×36 matrix with 6×6 blocks of dimension 1×6. The diagonal blocks are equal to $\bar{\varepsilon}_V^T$, all other are equal to zero,

$$\boldsymbol{E} = \begin{bmatrix} \bar{\varepsilon}_V^T & 0 \cdots & 0 \\ \vdots & \ddots & \vdots \\ 0 & \cdots 0 & \bar{\varepsilon}_V^T \end{bmatrix}.$$

The minimization problem (7),

$$\|\bar{\sigma}_V - \bar{C}_V\bar{\varepsilon}_V\| \to \min_{\bar{C}_V} \tag{8}$$

leadsnow to the linear least square problem

$$\|\bar{\sigma}_V - \boldsymbol{E}\boldsymbol{T}\overline{\boldsymbol{C}}_{\boldsymbol{VS}}\| \to \min_{\boldsymbol{C_{VS}}}, \tag{9}$$

which is equivalent to the solution of normal system

$$\boldsymbol{T^T E^T E T}\overline{\boldsymbol{C}}_{\boldsymbol{VS}} = \boldsymbol{T^T E^T}\bar{\sigma}_V. \tag{10}$$

This system has an unique solution if $\boldsymbol{E}$ has linearly independent column, which is not the case here.

To obtain uniqueness of the anisotropic elasticity tensor described by the minimization problem, it is necessary to perform $n > 1$ tests providing averaged stresses $\bar{\sigma}^k$ and strains $\bar{\varepsilon}^k$ for $k = 1, \ldots, n$ and seek $\overline{C}$ from the overall minimization

$$\sum_k \|\bar{\sigma}^k - \bar{C}\bar{\varepsilon}^k\|_F^2 \sim \sum_k \left\|\bar{\sigma}_V^k - \bar{C}_V\bar{\varepsilon}_V^k\right\|^2 \to \min_{\bar{C}_V}.$$

This condition can be also written in the linear least squares form and consequently in the form

$$\boldsymbol{T^T E^T E T}\overline{\boldsymbol{C}}_{\boldsymbol{VS}} = \boldsymbol{T^T E^T S}, \tag{11}$$

where $\boldsymbol{E}$ is now $6n \times 36$matrix, n is the number of tests, $\boldsymbol{S} = ((\bar{\sigma}_V^1)^T, \ldots, \bar{\sigma}_V^n)^T)^T$. The uniqueness of the resulting elasticity tensor is guaranteed e.g. by existence of six linearly independent strain vectors $\bar{\varepsilon}_V^k$ providing by the tests.

Note that different material symmetries with respect to the chosen coordinate systems can be easily treated by using a proper transformation matrix $\boldsymbol{T}$. In the case of material symmetries with respect to a rotated coordinate system, we have to seek for the proper rotation, which provide a nonlinear least squares problem.

If Ω is smaller than the representative volume, then the choice of boundary conditions can substantially influence the obtained elasticity tensor $\overline{C}$. Especially,

if C_ε, C_σ and C_m come from strain and stress driven testing and testing with mixed boundary conditions, then C_ε, C_σ provide some limits in an energetic sense see(Blaheta et al., submitted). The difference $C_\sigma - C_\varepsilon$ indicates how much is the REV property violated for the volume Ω.

The micro-level stress and strain are computed numerically, mostly by the finite element (FE) method, which easily allows to take into account material heterogeneity in the microstructure. In our case, the computations were done by an in-house FE software GEM (Blaheta et al. 2010), which is suitable for this application from two reasons. First, it is oriented to regular meshes, like voxel meshes or their deformation. Second, it is equipped by fast iterative solvers, which enable the use of voxel meshes without a special care about mesh coarsening for decreasing the number of degrees of freedom. Note that the GEM software divides the voxel elements, each into six tetrahedral and uses piecewise linear finite element functions.

Note that the FEM is a common tool when the material is assumed as continuous, but a discontinuous model of the sample behaviour can also be used.

3 COAL-PUR GEOCOMPOSITES

The described material testing procedure was used for analysis of coal-PUR geocomposites, which results from polyurethane (PUR) grouting of the coal seam for improving the stability behaviour during mining. More detail can be found e.g. in (Souček et al. 2008).

4 CT IMAGE BASED FINITE ELEMENT ANALYSIS

In geosciences, CT images are increasingly used for determination of the microstructure of geomaterials and preparation of meshes for subsequent FE analysis of processes as the mechanical deformation, flow in porous structure etc., see e.g. (Ketcham & Carlson 2001), (Baker et al. 2012). The application of CT to investigation of coal-PE geocomposites is especially suitable due to a good contrast between the main components. This application begun owing to a collaboration with X-Earth Centre of Kumamoto University, see (Souček et al. 2006). At present a new GeoCT lab was also open at the Institute of Geonics AS CR, which allows scanning samples up to about 100 kg mass on one side and small cubic centimeter volume samples with resolution of order of microns on the other side (Fig. 1).

There is a number of techniques for preparation of FE meshes based on CT images, among which we can distinguish direct voxel oriented methods and methods exploiting segmentation with surfaces aligned to segment boundaries and subsequent tetrahedralization of the segmented parts.

We use a relatively straightforward procedure for preparing voxel mesh. Despite of this, the way from the



Figure 1. CT laboratory at the Institute of Geonics equipped with XTH 225 ST and XTH 450 2D/3D Nikon Metrology tomographswith X-ray focal size 80μm and 3μm reflex mode/1μm transmission mode, respectively. Flat detectors with 4 mil. pixels are available.

Table 1. An example of etalon data (slice n.038).

Etalon		CT values of etalons: Min value	Max value	Avrg value	Prescribed value
1	Empty	7	21	13	0
2	Oil	89	104	97	100
3	H_2O	104	122	113	120
4	Carbon	145	162	154	180

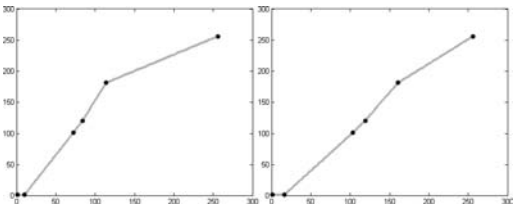


Figure 2. Rescaling of two slices (n.018, n.056) – horizontal axes – original CT values, vertical axes - rescaled CT values.

CT scan to FEM mesh is not trivial and fully automatic. The adopted procedure includes three steps:

1. etalon based scaling of the CT-values,
2. (global) coarsening of the voxel mesh,
3. segmentation with assigning information about local material properties to the finite elements.

In the case of coal-PE geocomposite, we started with CT images arranged as a voxel rectangular mesh with voxel dimensions $0.1 \times 0.1 \times 1.125$ mm.

The first scaling step, which is especially required when the scanning of sample is interrupted, then uses four etalons (Table 1) and results in substantial rescaling of the CT-values (Fig. 2).

Further modification is mesh coarsening. In our case, a mesh of $623 \times 633 \times 56$ voxels, representing the geocomposite sample after rotation and clipping, was coarsened to the mesh of $103 \times 105 \times 56$ voxels by averaging the squares of 6×6 voxels in each slice. This coarsening was done for economy of computations as well as for a better aspect ratio of the

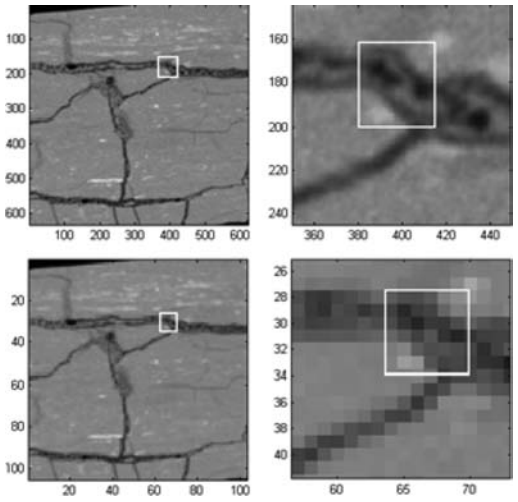


Figure 3. The slice n.007 and detail: for the original fine mesh (first row) and for thecoarsened mesh (second row).

Table 2. A comparison of material constants from uniaxial laboratory and numerical tests (average over three samples) in the case of uniaxial loading boundary conditions.

Load direction	Uniaxial lab test		Uniaxial numerical test	
	E[MPa]	ν	E[MPa]	ν
x	1472	0.27	1415	0.29
y	1121	0.21	1415	0.29
z	1353	0.23	1423	0.29

resulting finite elements. The coarsening is illustrated in Figure 3.

Finally, a segmentation is performed by thresholding for obtaining a realistic material distribution (Fig. 4). We found that constructing a right thresholding is very important and our procedure was not fully automated, exploiting visualization of segmentation obtaining from use of different thresholds (Fig. 4).

Figure 5 shows a 3D visualization of the coal-PE sample and the FE mesh. Note that generally a lot of work in converting 3D image data into computational models and use of such models was done, e.g. (Mishnaevsky 2005), (Young et al. 2008), (Wirjadi 2007) and several open source (OOF, iso2mesh) as well as commercial software products appeared (Simpleware, Avizo Fire, etc.)

5 VERIFICATION OF NUMERICAL TESTS

First, we compare numerical and laboratory testing results for three coal-PUR specimens prepared in laboratory with a satisfactory agreement, see Table 2 and (Blaheta et al. submitted).

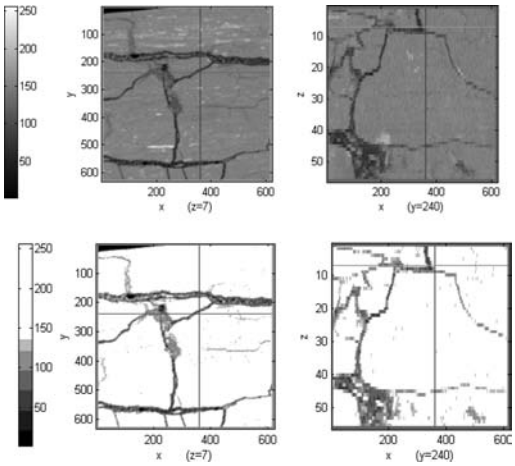


Figure 4. Digital model of a cubic sample of coal-polyurethane geocomposite. Top: slice visualization, bottom: segmentation – material separation by proper thresholding.

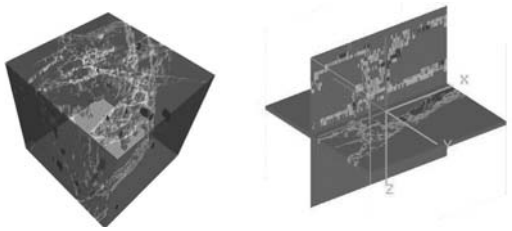


Figure 5. Visualization of 3D microstructure of a coal geocomposite sample and its FEM representation.

We also tested and evaluated an influence of different factors on the computed response of coal-PUR geocomposite samples. Our experience shows a higher sensitivity to thresholding for interpretation of material interfaces and to the definition of local material properties. The computed results also depend on the boundary conditions used for testing. More details can be found in (Blaheta et al., submitted), which confirm the energetic ordering of elasticity tensors computed under different types of boundary conditions. As mentioned in Section 2, the use of uniform stress and uniform strain boundary conditions provides the lower and upper limits, respectively.

6 LOCAL MATERIAL PROPERTIES, IDENTIFICATION AND CALIBRATION

There are several ways for determination of local material properties:

– the constituents allow to prepare homogeneous samples and it is possible to get the material properties from laboratory testing of the samples of these constituents,

Table 3. An example of a model calibration via identification of local elastic parameters (E, ν) of coal.

	Properties			
	Local forcoal		Global for gecomposite	
	E[MPa]	ν	E[MPa]	ν
1lab test	–	–	1371	0.27
2coal apriori	2200	0.23	1507	0.278
3coal identified	1933	0.22	1370	0.274

*Row 1 – global properties of a sample from lab test. Row 2 - computed global properties using the local properties of coal from a priori lab tests. Row 3 – local properties of coal are modified by parameter identification based on the global lab testing data from Row 1 and the corresponding computed global properties.

– indentation techniques can be used for getting local material information without decomposition into constituents,
– only the experimental testing of the composite samples is possible and local material properties should be determined by numerical parameter identification methods.

Note that any combination of the described techniques (i) – (iii) is highly recommended to use if it is possible.

The numerical parameter identification methods are based on minimization of the objective function

$$F(p) = \sum_k \left(\left\| \hat{\varepsilon}^{(k)} - \left\langle \varepsilon^{(k)}(p) \right\rangle \right\|^2 + \left\| \hat{\sigma}^{(k)} - \left\langle \sigma^{(k)}(p) \right\rangle \right\|^2 \right) \quad (12)$$

where p is the vector of material parameters to be determined, $\hat{\varepsilon}^{(k)}$, $\hat{\sigma}^{(k)}$ are constant strain and stress fields corresponding to the response of homogeneous sample with elastic modules provided by laboratory testing to a given load, $\varepsilon^{(k)}(p)$, $\sigma^{(k)}(p)$ are micro-level strains and stresses obtained from micromechanics computations, angle brackets stands for volume averaging. The index k denotes possibi-lity of including more than one loading case into the minimization. The evaluation of $F(p)$ then requires one or more finite element calculations of micro-level strains and stresses. The minimization itself can be done by different optimization methods and the papers (Blaheta et al. 2012, 2013) describe our experience in this respect, including the use of parallel computations.

The identification of local material parameters can be also used as a way of calibration of the numerical testing procedure, see Table 3.

7 INELASTIC ANALYSIS

So far we discussed the case, when the material response on both micro and macro level is elastic.

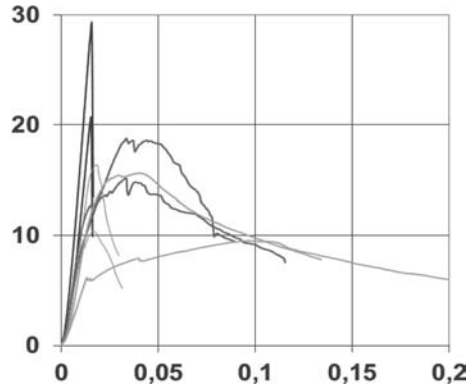


Figure 6. Stress (vertical axis, MPa) – strain (horizontal axis) curve showing a quasi-brittle behaviour of coal-PUR geoposites (orange and red curves) in contrast to the brittle behaviour of coal (blue). The different strength levels result from using different samples; the qualitative behaviour is more important.

It is not always true, as the micro-level components and their bonds can possess different plastic or damage behaviour. Correspondingly, the macro-level response is nonlinear and the nonlinear behaviour can be described by different models. These models describe the qualitative behaviour and should be selected apriori, e.g. for the coal-PUR geocomposite we could expect a quasi-brittle behaviour, see Figure 6 and (Souček et al. 2008).Consequently, a continuous damage model can be selected for this case, which requiresto determinevarious parameters.

The macroscale model parameters can be derived from the complete stress-strain curve obtained either from laboratory test with controlled loading or by analogous numerical experiments. Such simulations can use damage model for coal and plasticity model for the polyurethane at micro level, see e.g. (Wang & Liu 2011), (Qin et al. 2006). A similar type of modelling can be found in (Wriggers & Moftah 2006), (Hain & Wriggers 2008), (Charlebois et al. 2010).

8 CONCLUSIONS

This contribution discusses our experience with the two-level analysis of heterogeneous elastic geocomposites using CT for description of the microstructure and the finite element method for computations of the macro-level elastic response. More details can be found in (Blaheta et al. submitted). Note that such computation can be demanding (we use voxel grids with millions of elements) and therefore a high performance computing and methods were used.

The computed results were compared with laboratory testing of geocomposite samples with a good agreement. These tests were also used for a calibration of a model by identification of local material properties, see again (Blaheta et al. submitted).

Future work will concern the analysis of inelastic material behaviour, which is much more difficult for simulation. The idea of this work is outlined in Section 7.

The numerical testing is performed on 3D computational grids with millions of degrees of freedom. It itself means that the computations are suitable for parallel processing – in our case parallel assembling of stiffness matrix, conjugate gradient iterative methods with parallel matrix by vector computations and parallelizable additive Schwarz method as preconditioner are used for solving the eleasticity problems. The efficiency of the Schwarz type preconditioners is enhanced by use of aggregation based coarse problem. Moreover, a special situation with solving of singular systems arises in the case of uniform stress boundary conditions. For details of the used numerical methods, see (Blaheta et al. 2010), (Blaheta et al. 2013). The computational requirements are further enhanced when identification techniques are used, see (Blaheta et al. 2012). The computational requirements for inelastic analysis will be treated in a future.

ACKNOWLEDGEMENTS

This work was supported by the European Regional Development Fund in the IT4Innovations Centre of Excellence project (CZ.1.05/1.1.00/02.0070) and the GACR project n.13-18652S.

REFERENCES

Baker, D.R. et al. 2012.An introduction to the application of X-ray microtomography to the three-dimensional study of igneous rocks. Lithos 148, pp. 262–276.

Blaheta, R. et al. 2010.GEM – A Platform for Advanced Mathematica lGeosimulations. R. Wyrzykowski et al. (Eds.): PPAM 2009, Part I, Springer-Verlag LNCS 6067, pp. 266–275.

Blaheta, R. et al. 2012. Material parameter identification with parallel processing and geo-applications. In: R. Wyrzykowski et al. (Eds.): PPAM 2011, Part I, Springer-Verlag LNCS 7203, pp. 366–375.

Blaheta, R., Jakl, O., Starý, J. & Turan, E. 2013. Parallel Solvers for Numerical Upscaling.P. Manninen and P. Öster (Eds.): PARA 2012, Springer-Verlag LNCS 7782, pp. 375–386.

Blaheta R. et al. submitted. Digital Image Based Numerical Micromechanics of Geocomposites with Application to Chemical Grouting. Int. J. Rock Mech. Min. Sci.

Charlebois, M., Jirasek ,M. & Zysset, P.K. 2010. A nonlocal constitutive model for trabecular bone softening in compression. Bio-mechanics and Modeling in Mechanobiology 9, pp. 597–611.

Hain, M. & Wriggers, P. 2008.Numerical homogenization of hardened cement paste. Comput Mech. 42, pp. 197–212.

Ketcham, R.A. & Carlson, W.D. 2001. Acquisition, optimization and interpretation of X-raycomputed tomographic imagery: applicationsto the geosciences. Computers & Geosciences 27, pp. 381–400.

Mishnaevsky, L.L. Jr. 2005.Automatic voxel-based generation of 3D microstructural FE modelsand its application to the damage analysis of composites. Materials Science and Engineering A 407, pp. 11–23.

Otani, J., Watanabe, Y. & Chevalier, B. 2010.Introduction of X-ray CT application in geotechnical engineering – theory and practice. OP Conf. Ser.: Mater. Sci. Eng. 10, 10 pp.

Qin, S., Jiao, J.J., Tang, C.A. & Li, Z. 2006.Instability leading to coal bumps and nonlinearevolutionary mechanisms for a coal-pillar-and-roof system.International Journal of Solids and Structures 43,pp. 7407–7423.

Souček, K., Staš, L., Obara, Y. & Fukahori, D. 2006. X-ray CT observation of failure in coal geo-composites.Darve, F. ed. Advances in Geomaterials and Structures AGS'06. Commission universitaire pour le development, Tunis, ISBN 978-9973-61-317-2, pp. 269–274.

Souček, K., Staš, L., Ščučka, J. & Martinec, P. 2008. Chemical Grouting – Laboratory Study of Chemical Grouts and Geocomposites Properties, In: Singh D. ed., International Conference IACMAG/12./. Bombay: Indian Institute of Technology Bombay, pp. 3567–3574.

Wang, Y. & Liu, X. 2011. Investigations on theLawof AE EnergyAccumulation and DamageEvolutionofthe-Coal and Rock.Journal of Liaoning Technical University, n.1, 6 pp.

Wirjadi, O. 2007. Survey of 3d image segmentationmethods. Rep. Fraunhofer ITWM, Nr. 123, 29 pp.

Wriggers, P. & Moftah, S.O. 2006.Mesoscale models for con-crete: Homogenisation and damage behaviour. Finite Elements in Analysis and Design 42, pp. 623–636.

Young, P.G. et al. 2008. An efficient approach to converting three-dimensional image data into highly accurate computational models. Phil. Trans. R. Soc. A 366, 3155–3173.

Avizo Fire – 3D Analysis Software for Materials Science http://www.vsg3d.com/avizo/fire.iso2mesh – a free matlab/octave-based mesh generation and processing toolbox. http://iso2mesh.sourceforge.net

MAVI -Modular Algorithms for Volume Images http://www.itwm.fraunhofer.de/en/departments/image-processing/microstructure-analysis/mavi.html OOF: Object-Oriented Finite Element Analysis of Real Material Microstructures http://www.ctcms.nist.gov/oof

Simpleware – conversion of 3D image data into high-quality CAD, Rapid Prototype, CFD and Finite Element models http://www.simpleware.com/

Rock Mechanics for Resources, Energy and Environment – Kwaśniewski & Łydżba (eds)
© 2013 Taylor & Francis Group, London, ISBN 978-1-138-00080-3

The coupled hydro-mechanical approach for fluid compressibility problems in porous media

S.R.C. Brant & M.P. Cordão Neto
Universidade de Brasília, Brasilia, Brazil

I. Fernandes Gomes
Universidade Federal de Pernambuco, Recife, Brazil

ABSTRACT: Numerical modeling for geotechnics use formulations which take into consideration simplifying hypotheses for porous media physical behavior. However, these simplifications neglect effects which could contribute in model's accuracy. In this paper, a fully coupled hydro-mechanical formulation considering fluid and solids compressibility is presented. This formulation was tested for a two-dimensional consolidation case. A sensitivity analysis for the fluid compressibility parameter was performed, with comparison of the simulation results to Biot's analytical solution. Results show that the values of vertical displacements are lower to cases with compressible fluids than to those with incompressible fluids. Instantaneously after load application, fluid pressure increases to a maximum value and it dissipates as load is gradually transferred to solid matrix. For compressible fluids, however, there is a delay in fluid pressure dissipation, which makes effective stress lower than expected. Therewith, stress-strain relations are affected, with low soil strain rate values, justifying vertical displacement decrease.

1 INTRODUCTION

1.1 *Context*

When evaluating physical behavior of porous media, such as soils and rocks, one can observe that stress-strain state is affected by fluid pressures and vice-versa. Therewith, it is intuitive the understanding that both mechanical and hydraulic effects are interconnected. This proves the importance of coupled analyses, which describe more precisely how mechanical and hydraulic behavior are related.

Using numerical modeling for behavior prediction is largely employed in geotechnics, more specifically in geomechanics. Formulations are previewed to reproduce porous media behavior. However, the complexity of the phenomena evaluated may induce some simplification of the numerical models. This may interfere in model responses, with simulation results not correspondent to the observed behavior of the studied case.

The compressibility of the solids which form the solid matrix of a porous medium and the compressibility of the fluids within this medium are not taken into account in traditional models in geotechnics or related areas, such as reservoir geomechanics, in petroleum engineering. This type of consideration could enhance modeling, contributing to more accurate results in behavior prediction.

1.2 *Objectives*

When solids and fluid compressibility are considered for porous media physical behavior evaluation, a different approach for mechanical and hydraulic behavior must be presented.

A fully coupled hydro-mechanical formulation with this consideration was presented by Jesus (2012). This formulation was fully described by the author, followed by its implementation, validation and calibration in ALLFINE (Farias 1993, Cordão Neto 2005, Jesus 2012).

Results of a sensitivity analysis for fluid compressibility are presented in this paper. The tests are performed for a two-dimensional consolidation problem, based on the analytical solution proposed by Biot (1940).

With this model assumption, a theoretical case of consolidation is analyzed, with verification of vertical displacements of the soil surface.

2 FORMULATION

The presented formulation was fully described by Jesus (2012). Here, a brief summary of the equations and their solution is shown.

2.1 *Equilibrium equation*

The equilibrium equation for a porous medium can be described as:

$$\frac{\partial \sigma_{ij}}{\partial x_j} + b_i = 0 \tag{1}$$

where: σ_{ij} is the stress tensor, b_i is the body forces vector and x_j corresponds to the coordinate system.

The stress-strain relation used for this numerical model is based on the definition of the generalized effective stress, with consideration of the influence of solids compressibility on solid matrix stress state. The effective stress principle is defined as (Li et al. 1999):

$$\{\sigma'\} = \{\sigma\} - \alpha_b \{m\} p \tag{2}$$

where: $\{\sigma'\}$ is the effective stress vector, $\{\sigma\}$ is the total stress vector, α_b is the Biot parameter, $\{m\}^{\mathrm{T}} = \{1\,1\,1\,0\,0\,0\}$ for a 3D analysis and p is the fluid pressure (for a saturated analysis).

The Biot parameter (α_b) is defined by the following expression:

$$\alpha_b = 1 - \frac{\{m\}^T \left[D^{ep}\right] \{m\}}{9k_s} \tag{3}$$

where: $[D^{ep}]$ is the constitutive matrix and k_s is the bulk modulus of solids.

The Principle of Virtual Work is employed to solve the equilibrium equation in space using FEM (Zienkiewicz, 1977).

The matrixes that represent the solved equilibrium equation are assembled and may be written as:

$$[K]\{\dot{u}\} + [C]\{\dot{p}\} = \{\dot{F}\} \tag{4}$$

where:

$$[K] = \int_{\Omega} [B]^T [D][B]\, d\Omega$$

$$[C] = \int_{\Omega} [B]^T \alpha_b \{m\} \left[N^p\right] d\Omega$$

$$\{\dot{F}\} = \int_{\Omega} [N]^T \{\dot{b}\}\, d\Omega + \int_{\Gamma} [N]^T \{\dot{t}\}\, d\Gamma$$

$[K]$ is the stiffness matrix, $\{\dot{u}\}$ is the nodal displacements rate vector, $[C]$ is the solids-fluid coupling, $\{\dot{p}\}$ is the nodal fluid pressure rate vector and $\{\dot{F}\}$ is the external forces rate vector.

2.2 *Mass conservation equation*

The mass conservation equation previewed for this formulation involves both liquid and solid phases. The mass conservation equation for the liquid phase is defined by the following expression:

$$\frac{\partial}{\partial t}\left(\theta \rho^f\right) + \frac{\partial}{\partial x_i}\left(\theta \rho^f \dot{U}_i\right) = 0 \tag{5}$$

where: θ is the volumetric water content, ρ^f is the fluid density and $\dot{U}_i$ is the real fluid velocity.

The real fluid velocity assumption implies on taking into account the effects of porosity changes in the porous medium. It can be expressed as:

$$\dot{U}_i = \dot{u}_i + \frac{w_i^f}{\theta} \tag{6}$$

where: $\dot{U}_i$ is the real fluid velocity vector, $\dot{u}_i$ is the velocity of the solids vector, w_i^f is the fluid velocity due to percolation vector and θ is the volumetric fluid content of the medium.

The evolution law for liquid fluids density (Peaceman 1977, Rosa et al. 2006) is expressed as:

$$\frac{d\rho^f}{\rho^f} = \frac{1}{k_f} dp \tag{7}$$

where: ρ^f is the fluid density, k_s is the bulk modulus of the fluid and p is the fluid pressure.

The mass conservation equation for the solid phase may be presented as:

$$\frac{\partial}{\partial t}\left[\left(1-\phi\right)\rho^s\right] + \frac{\partial}{\partial x_i}\left[\left(1-\phi\right)\rho^s \dot{u}_i\right] = 0 \tag{8}$$

where: ϕ is the material porosity, ρ^s is the solids density and $\dot{u}_i$ is the solids velocity vector.

The evolution law of solids density (Li et al., 1999) is:

$$\frac{\left(1-\phi\right)}{\rho^s}\frac{D\rho^s}{Dt} = \left[\frac{\left(\alpha_b - \phi\right)}{k_s}\frac{Dp^R}{Dt} - \left(1-\alpha_b\right)\dot{u}_{i,i}\right] \tag{9}$$

where: ρ^s is the solids density, k_s is the bulk modulus of rock crystals, α_b is the Biot parameter, ϕ is the porosity of the rock and p^R is the pressure of the fluids (for saturated medium $p^R = p$).

In order to represent the mass conservation of porous media, the volume of solids and the volume of fluid within a finite element should be balanced in a total element volume approach (Li et al. 1999).

The spatial solution for the mass conservation equation via FEM can be made with Galerkin method, a weighted residual method (Zienkiewicz, 1977).

The matrixes that represent the solved mass conservation equation are assembled and written as:

$$[M]\{\dot{p}\} + [L]\{\dot{u}\} + [R]\{p\} = \{Q\} \tag{10}$$

where:

$$[M] = \int_{\Omega} \left[N^p\right]^T \left[\frac{\left(\alpha_b - \phi\right)}{k_s} + \frac{\phi}{k_f}\right] \left[N^p\right] d\Omega$$

$$[L] = \int_{\Omega} \left[N^{p}\right]^{T} \alpha_{s} \{m\}^{T} [B] d\Omega$$

$$[R] = \int_{\Omega} \left[N^{p}\right]^{T} \left[\frac{(\alpha_{s} - \phi)}{k_{s}} \{\dot{u}\} + \frac{\phi}{k_{f}} \left(\{\dot{u}\} + \frac{\{w^{f}\}}{\phi} \right) \right] \left[B^{p}\right] d\Omega +$$

$$\int_{\Omega} \left[B^{p}\right]^{T} \frac{[K]}{\mu} \left[B^{p}\right] d\Omega$$

$$\{Q\} = \left[\int_{\Omega} \left[B^{F}\right]^{T} \frac{[K]}{\mu} \rho_{f} \{g\} (\nabla . y) d\Omega \right] - \int_{\Gamma_{2}} \left[N^{F}\right]^{T} \overline{q} d\Gamma$$

$[M]$ is the mass matrix, $\{\dot{p}\}$ is the nodal fluid pressure rate vector, $[L]$ is the fluid-solids coupling matrix, $\{\dot{u}\}$ is the nodal displacements rate vector, $[R]$ is the flow matrix, $\{p\}$ is the nodal fluid pressure vector and $\{Q\}$ is the external discharges vector.

2.3 *Coupling of equations and time solution*

The spatial solution of equilibrium and mass conservation equations may be gathered in a system of equations. This system allows the time solution of the problem at a later stage. Considering Equations 4 and 10, we have:

$$\begin{bmatrix} 0 & 0 \\ 0 & [R] \end{bmatrix} \begin{Bmatrix} \{u\} \\ \{p\} \end{Bmatrix} + \begin{bmatrix} [K] & [C] \\ [L] & [M] \end{bmatrix} \begin{Bmatrix} \{\dot{u}\} \\ \{\dot{p}\} \end{Bmatrix} = \begin{Bmatrix} \{\dot{F}\} \\ \{Q\} \end{Bmatrix} \quad (11)$$

Thus, the system of equations is expressed as:

$$[W]\{x\} + [Y]\{\dot{x}\} = \{Z\} \quad (12)$$

Considering the studied phenomenon is transient, this system of equations should be solved in time. Finite Difference (FDM) was the chosen method for the time discretization of the system of equations, already solved in space. This choice was based on the ease of application of FDM for that matter. Evaluating Equation 12 in time stage $t + \alpha \Delta t$, the solution of the equation system is:

$$\left[\Delta t \alpha [W]_{t+\alpha\Delta t} + [Y]_{t+\alpha\Delta t}\right] \{\Delta x\} = \Delta t \{Z\}_{t+\alpha\Delta t} - \Delta t [W]_{t+\alpha\Delta t} \{x\}_{t} \quad (13)$$

3 METHODOLOGY

The presented formulation has been implemented on ALLFINE (Farias, 1993; Cordão Neto, 2005; Jesus, 2012). The validation of the proposed formulation is done by the comparison of the results achieved with the simulations and the analytical solution for a consolidation problem. Then, the formulation is tested with fluid compressibility sensitivity tests.

A two-dimensional consolidation problem is studied: an infinitely deep layer of soil is analyzed in a plane-strain situation, with x, z as the in-plane axes.

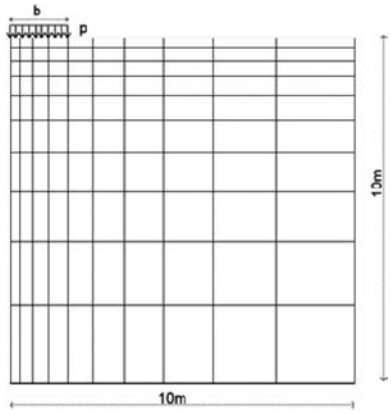


Figure 1. Two-dimensional consolidation problem (modified Cordão Neto, 2005).

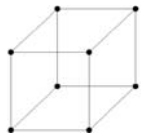


Figure 2. 8-noded 3D element.

The porous medium hydro-mechanical behavior is analyzed with the application of an uniform load, infinite in one direction (y) and limited on the other (from $x = -b$ to $x = b$), as shown in Figure 1. The soil is considered totally saturated and it is subjected to a geostatic initial stress state. Also, the fluid is assumed to escape freely at the surface. This case is also based on simulations performed by Farias (1993) and Cordão Neto (2005).

The studied domain is discretized in 200 three-dimensional 8-noded elements (Figure 2), making up a mesh with a total of 462 nodes. The division of the domain follows an exponential distribution in both directions (x and y). The configuration of the finite element mesh is shown in Figure 1.

When fluid bulk modulus is large enough (compared to solids bulk modulus), fluid is considered incompressible. So, using values for these parameters correspondent to the condition of incompressibility, results should match the analytical solution of the problem, proposed by Biot (1940).

The comparison of the simulation results to the analytical solution has its results presented in terms of normalized displacements. This normalization is made by dividing the surface displacements results by w_{inf} (Eq. 14), correspondent to the initial uniform displacement the surface would suffer if the load extended from $x = -\infty$ to $x = \infty$.

$$w_{\text{inf}} = \frac{apl}{4\sqrt{\pi}} \quad (14)$$

Table 1. Parameters for calculating the initial uniform displacement w_{inf}.

a	0.0001 kPa^{-1}
Load (p)	100 kPa
Extension of application of the load (b)	1.68 m
l ($l = 2b$)	3.36 m

Table 2. Parameters for two-dimensional consolidation problem.

Young modulus (E)	10000 kPa
Poisson coefficient (ν)	0
Initial void ratio (e_0)	0.90
Density of the solids (ρ_f)	2.65 kg/m^3
Solids bulk modulus (k_s)	1.0×10^{15} kPa
Density of the fluid (ρ_s)	1.00 kg/m^3
Fluid bulk modulus (k_f)	1.0×10^{12} kPa
	3.7×10^{6} kPa
	1.0×10^{3} kPa
	5.0×10^{2} kPa
Permeability (k)	1.0×10^{-6} m/s

where: w_{inf} is the initial uniform displacement, p is the load and l is the double of the extension in which the load is applied ($l = 2b$).

In Equation 14, a is defined as:

$$a = \frac{(1-2\nu)(1+\nu)}{E(1-\nu)} \tag{15}$$

where: E is the Young modulus and ν is the Poisson coefficient.

For the fluid compressibility sensitivity analysis, the values of displacements are not normalized. The initial uniform displacement (w_{inf}) is calculated for a linear elastic model response, with incompressible fluid. Therefore, using the normalization procedure for compressible fluids does not have any physical meaning for the analysis.

The time factors for which the results are presented correspond to those based on classic consolidation theory. The value of the time factor is maintained constant for all simulations, permitting a comparison of results at the same stage of analysis.

The presented results permit an evaluation of the hydro-mechanical behavior of the porous medium in a consolidation analysis, verifying the applicability of the enhanced version of ALLFINE, with the compressibility hypothesis considered.

4 RESULTS AND DISCUSSION

The parameters required for the calculation of the initial uniform displacement are related in Table 1 and the parameters used for the simulations are disposed in Table 2.

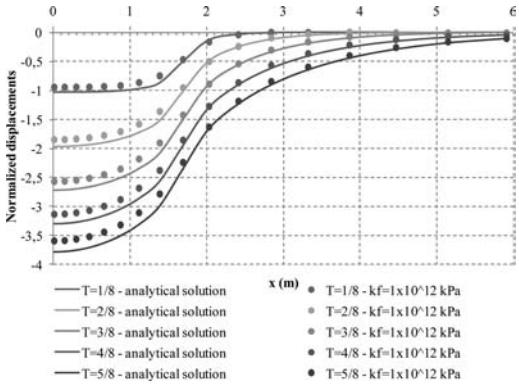


Figure 3. Comparison between analytical solution and results of simulation with ALLFINE for a two-dimensional consolidation problem.

4.1 *Validation of the formulation for the two-dimensional consolidation case*

The validation of this formulation is made with the comparison of simulation and analytical results for the two-dimensional consolidation problem.

In order to properly compare the results, the simulation is performed with incompressible fluid bulk modulus ($k_f = 1.0 \times 10^{12}$ kPa) and linear elastic model.

The vertical displacements results presented in Figure 3 correspond to five different time factor values, T = 1/8, 2/8, 3/8, 4/8 and 5/8. These time factors refer to the analytical solution of Terzaghi's consolidation problem analysis and are only employed to facilitate the visualization of the results for each simulation over time.

The values of displacement to the initial time stage correspond to an undrained behavior of the soil, not being representative of the consolidation phenomenon. The results have been normalized by the initial uniform displacement w_{inf} (Eq. 14).

It may be noticed that the responses achieved with ALLFINE are satisfyingly close to the analytical solution for the problem, with minimum error associated to the numerical solution.

The difference between the responses of analytical solution and simulation may be explained by considerations made in the numerical modeling. In this case, the domain of the problem is finite, limited in all directions, x, y and z, differently than the conditions of the analytical solution, which preview an infinite semi-space. This induces the results of the simulations to values not so close to the analytical solution as they could be.

Also, the discretization made on the domain of the numerical solution requires boundary conditions which contribute to the noticed difference between the model results and the analytic response of the problem.

4.2 *Sensitivity analysis for fluid compressibility*

The simulations were now performed for different values of fluid bulk modulus, in order to evaluate the

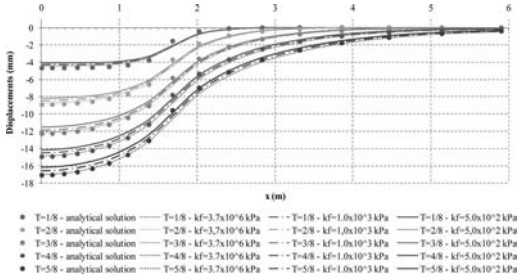


Figure 4. Results of displacements for different values of fluid bulk modulus.

effects of fluid compressibility in results of vertical displacement in the porous medium. These values of displacement are not normalized, but the displacement referent to the undrained loading condition (initial stage, $T = 0$) is deducted.

The results of the simulations are shown in Figure 4. The values of fluid bulk modulus employed in the simulations are presented in Table 2.

It can be noticed that when fluid bulk modulus is decreased under $k_f = 3.7 \times 10^6$ kPa the results of vertical displacements start to be influenced. The surface displacements decrease for fluids with higher compressibility (lower k_f), when considering the same time factor.

Instantaneously after load application, the entire load goes to the fluid, increasing fluid pressure to a maximum value. Over time, fluid pressure tends to dissipate, as load is gradually transferred to solid matrix. This stress transference is more expressive with incompressible fluids.

However, in cases in which fluid compressibility is significant, stress transference from the fluid to the solid matrix is delayed. The initial increase of fluid pressure reduces fluid volume. Thus, fluid pressure increases more than with incompressible fluids. This delay in fluid pressure dissipation makes the effective stress lower (fluid pressure is higher). Therewith, one can deduce that the stress-strain relations of the porous medium are affected. For lower stress, the strain rate of the soil is lower as well, justifying the decrease in the values of vertical displacement as fluid compressibility is increased.

5 CONCLUSIONS

In this paper, the effects of fluid compressibility during a consolidation process were investigated.

The presented formulation has been tested for the two-dimensional consolidation problem, with evaluation of vertical displacements of the soil surface. Firstly, a validation of the formulation was performed, with comparison of the numerical and the analytical solutions of the problem. Then, a sensitivity analysis of fluid compressibility was carried out.

It has been shown that the proposed numerical model is adequate to reproduce the effects of consolidation for this type of simulation, with linear elastic model and other assumptions made.

The results of fluid compressibility sensitivity analysis show that there was less displacement of the soil surface when fluid is more compressible. This is explained by the reduction of effective stress (due to fluid pressure increase). Consequently, the observed soil straining is much less significant, resulting in less vertical displacement.

ACKNOWLEDGEMENTS

The authors would like to acknowledge the support given by Brazilian research organizations CAPES and CNPq and University of Brasília.

REFERENCES

Biot, M. A. (1940). *General theory of three-dimensional consolidation*. J. Appl. Phys., 12:155–164.

Cordão Neto, M. P. (2005). *Análise hidro-mecânica de barragens de terra construídas com materiais colapsíveis.* Doctorate thesis, G.TD – 028/05, Civil and Environmental Engineering Department, University of Brasília, Brasília, DF, 152 p.

Farias, M. M. (1993). *Numerical analysis of clay core dams*. Ph.D. Thesis, University of Wales – University College of Swansea. 161 p.

Jesus, S. R. C. B. P. de (2012). *Coupled Hydro-mechanical Analysis Considering Fluid and Solids Compressibility*. Master dissertation, G.DM-207/12, Civil and Environmental Engineering Department, University of Brasília, Brasília, DF, 124 p.

Li, X., Thomas, H. R., Fan, Y. (1999). Finite element method and constitutive modeling and computation for unsaturated soils. *Computer methods in applied mechanics and engineering*. 169: 135–159.

Peaceman, D. W. (1977). *Fundamentals of numerical reservoir simulation*. Elsevier, Amsterdan, Netherlands. 192p.

Rosa, A. J., Carvalho, R. de S., Xavier, J.A.D. (2006). *Engenharia de reservatórios de petróleo*. Interciência, 1 ed. 808 p.

Zienkiewicz, O. C. (1977). *The Finite Element Method*. McGraw-Hill, London, United Kingdom, 3 ed., 787 p.

This page intentionally left blank

Rock Mechanics for Resources, Energy and Environment – Kwaśniewski & Łydżba (eds)
© 2013 Taylor & Francis Group, London, ISBN 978-1-138-00080-3

Rheological behavior of jointed rock masses inferred from an analogue laboratory testing approach

M.E. Discenza, S. Martino, G. Scarascia Mugnozza & L. Stedile
Dipartimento di Scienze della Terra e Centro di Ricerca Previsione, Prevenzione e Controllo dei Rischi Geologici (CERI), "Sapienza" Università di Roma, Roma, Italy

A. Bretschneider
Institut Français des Sciences et Technologies des Transports, de l'Aménagement et des Réseaux (IFSTTAR), Nantes, France

M. Teodori
Autostrade per l'Italia S.p.A., Roma, Italy

ABSTRACT: The aim of this study is to investigate the rheological behavior of jointed rock masses involved in large space-time scale deformational processes. The analysis is based on both, an experimental approach consisting of an analogue laboratory testing approach which allowed to investigate the mechanical behavior of hypothetical rock masses with different joint characteristics with overlapping effects of creep along these interfaces. Several uniaxial strength and creep lab-tests were performed on artificial specimens of concrete mixtures whose rheological properties were selected according to physic-analogical scaling criteria. The specimens were realized to represent both intact rock and jointed rock masses. Different geometrical configurations were adopted to reproduce pervasive joint sets. The laboratory results were analyzed considering the jointed rock mass as an equivalent continuum medium with a visco-plastic rheological behavior. The study allowed to correlate the major mechanical properties of the jointed rock masses to both the properties of the intact rock and the geometrical configurations of joints.

1 INTRODUCTION

Jointed rock masses present a very complex rheology, strictly related to their discontinuous, heterogeneous and anisotropic nature. As a consequence, the overall rock mass stress-strain behavior is strictly controlled by properties of both intact rock and discontinuities (Sridevi & Sitharam 2000; Sitharam et al. 2001; Peng & Zhang 2007).

In the study of gravity induced deformations affecting the natural rock mass slopes at a large space-time scale the joint sets play a fundamental role on the creep processes which drive the deformational phenomenon. More in particular, the rheological properties of rock, the structural setting, the jointing conditions and the joint alteration strongly influence of creep phenomenon and the consequent time-stress-deformations (Chigira 1992).

In the case of the above mentioned phenomena a discrete solution for representing the involved rock mass is not reliable due to the difficulty of taking into account all the joint sets and their properties. This encourages to consider the rock mass as a continuum medium (Ramamurthy 1994; Sridevi & Sitharam 2000; Sitharam et al. 2001; Martino et al. 2004; Esposito et al. 2007; Discenza et al. 2011), i.e. in which the properties of the joints and of the rocky matrix are merged to obtain equivalent parameter values referable to the jointed rock mass. According to such an approach, rock mass strength and stiffness can be obtained by rheological models that take into account the geometrical and mechanical properties of both intact rock and joints.

The main goal of this study is the analysis of rheological behavior of jointed rock masses involved in large space-time scale deformational processes. At this aim, an extended experimental laboratory testing was performed by using artificial materials which are physically scaled with respect to natural prototypes, consisting on limestone which widely outcrop in the Italian Apennines and are often involved in gravitational slope-scale deformations. The laboratory tests allowed to define the influence of the joint geometrical characteristics on the mechanical and time-dependent behavior of rock masses. The specimens were composed of a concrete mixture, which mechanical-rheological properties were properly scaled according to physic-analogical criteria to represent the rheological properties of Apennines limestone.

Such an approach allowed to examine the influence of the joint dip and spacing on the strength and stiffness of the rock masses as well as the influence of the joint properties on the rock mass creep behavior.

2 EQUIVALENT CONTINUUM APPROACHES

Jointed rock mass behavior can numerically be represented with two different approaches: the "discrete approach" and the "equivalent continuum approach". The "discrete approach" considers the rock masses as discontinuous media. Under this assumption, the mechanical behavior is influenced by characteristics of both intact rock and discontinuities. The joints are considered as independent elements with a their own constitutive law. On the other hand, the "continuum equivalent approach" considers the rock masses as continuum media whose mechanical characteristics can be obtained by integrating intact rock e discontinuities properties. The advantage of the "discrete approach" consists on representing the physical discontinuities of the rock masses but, due to the requested geomechanical constraints, such an approach is reliable only for meter scale rock mass slopes (e.g. cut slopes, cliff slopes, and so on). On the other hand, the "continuum equivalent approach", which does not represent individual discontinuities, can represent rock masses at a larger slope scale (i.e. dimensioned several ten or hundred of meters).

In the last decade many equivalent continuum approaches were developed to attribute mechanical characteristics to jointed rock masses. The Hoek-Brown's failure criterion (Brown 2002) is the most applied equivalent continuum approach for defining the rock mass strength by assuming an elastic-plastic behavior. It's based on the mechanical properties of intact rock and joints, these last ones attributed according to the Geological Strength Index (Hoek 1994).

Furthermore, many other literature approaches define the mechanical behavior of jointed rock masses according to an equivalent continuum assumption (Singh 1973a,b, Zienkiewicz et al. 1977, Gerrard 1982, Fossum 1985, Wei & Hudson 1986, Amadei et al. 1988, Kawamoto et al. 1988, Chen 1989, Cai & Horii 1992, Oda et al. 1993, Priest 1993, Verman et al. 1997, Zhang & Einstein 2004). Among these approaches, the stiffness-equivalent approach proposed by Sitharam et al. (2001) is particularly adapt for numerical modelling applications. This approach is based on results from standard laboratory tests and traditional geomechanical surveys, to define the Joint Factor of the rock mass (Ramamurthy 1994, Sridevi & Sitharam 2000).

While several applications were carried out to consider at a lab-scale the direct influence of joints on specimen strength (Parsons et al. 1993; Wong et al. 2001; Kumar & Das 2002; Singh et al. 2002; Rao et al. 2003; Tiwari & Rao 2003; Singh & Rao 2005; Ghazvinian & Hadei 2012), no specific studies were carried on so far for analyzing the rheological behavior of natural rock masses by using artificial materials after a physical properties scaling. In this regard, the here presented study proposes an application of laboratory testing on analogue material with different jointing characteristics. This allows to evaluate in uniaxial and creep tests the representative material parameters of rock masses at slope scale.

3 LABORATORY TESTING

The laboratory tests were performed on physical-scaled analogical specimens composed of concrete mixture, in intact and jointed conditions. This allowed to determine the rheological behavior of jointed rock masses in relation to jointing conditions.

3.1 *Physical scaling of specimens*

A space-time scaling was applied to attribute physical and mechanical properties to the artificial mixture representative for natural limestone. At this aim, preliminary tests on intact specimens were performed in order to determine the mechanical parameters of the artificial mixture used for reproducing the natural prototype. More in particular, the physical scaling was based on the characteristics of limestone widely outcropping in the Italian Apennines and often involved in gravity-induced deformational processes (Martino et al. 2004, Maffei et al. 2005, Discenza et al. 2011, Lenti et al. 2012). Fixed the scale ratios for dimensions and density, a scaling ratio of 10^{-2} was then calculated. Being the viscosity scaling ratio between the concrete mixture and the limestone of 10^{-4}, the expected result about the strain-rate ratio was of 10^{-2}.

3.2 *Specimen preparation*

In order to evaluate the influence of joints on the rheological behavior of the rock mass, different geometrical characteristics were reproduced in the specimens. To make possible to realize these elements, prismatic specimens were used. In particular, for the UCS tests $14 \times 6 \times 6$ cm specimen dimensions were used, while for the creep tests they were used $10 \times 6 \times 6$ cm specimen dimensions.

The joints were introduced using hard elements (e.g. metal plates) in the concrete mixture. The concrete mixture has a density of 2030 kg/m^3, a UCS of 1.15 MPa a cohesion of 170 kPa and a friction angle of 27° (Fig. 1). The removal of metal plates, during the phase of maturation, generated weak planes within the mixture which reproduced the discontinuities of the specimen.

Due to the difficulties in the specimen realization it has been possible to reproduce only one pervasive jointing system.

More in particular, two geometrical parameters of the joints were selected for analyzing their effect on the rock mass behavior: the joint dip (0°, 30°, 45°, 60°) and the joint spacing (2.0 cm, 2.5 cm, 3.0 cm).

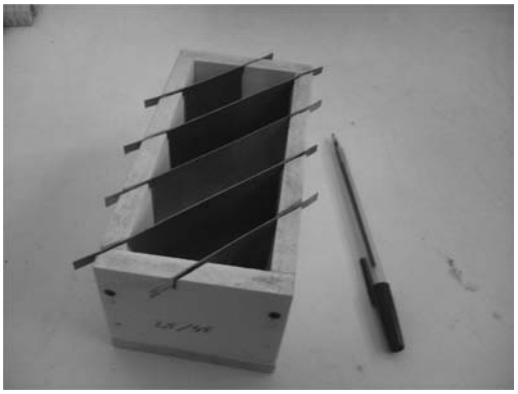


Figure 1. Example of the plexiglass box with the metallic sets used for reproducing the joints within the specimens.

Table 1. Summary of the specimen joint configuration considered for the UCS and creep laboratory tests.

Specimens Spacing (cm)/Dip (°)	UCS n. test	Creep n. test
Intact	5	9
2.0/0	3	1
2.0/30	3	1
2.0/45	3	1
2.0/60	3	1
2.5/0	3	1
2.5/30	3	1
2.5/45	3	1
2.5/60	3	1
3.0/0	3	1
3.0/30	3	1
3.0/45	3	1
3.0/60	3	1

All the possible combinations of joint dip and spacing restituted the different test conditions summarized in Table 1.

3.3 *Scheduled laboratory tests*

Five UCS tests and nine creep tests on cylindrical specimens realized by pouring the liquid mortar within cylindrical tubes (with the standard dimensions of a triaxial test) were preliminary performed on specimens of intact concrete mixture to obtain the all parameters necessary for setting the physical scaling.

Afterward, several UCS and creep tests were performed on jointed specimens by reproducing all the combinations of dip and spacing reported in Table 1. In particular, 36 UCS tests at all were carried out on jointed specimens (Fig. 2). The UCS tests were performed on groups of 3 specimens with the same geometrical configuration. The tests were carried out using a strain-controlled uniaxial testing device, and setting a strain rate of about 0.002 mm/s.

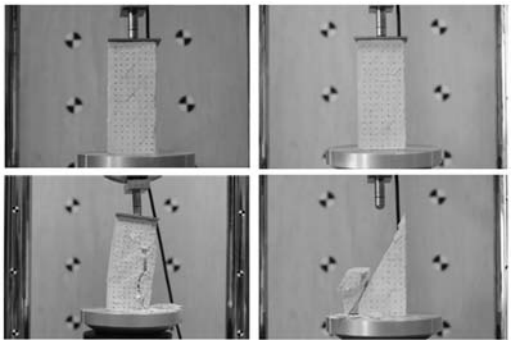


Figure 2. Example of UCS tests on jointed specimen with 45° (left) and 60° (right) joint dip and with 2.0 cm joint spacing: the images are taken before (up) and after (down) failure.

The UCS tests were performed by a Belladonna device equipped with a load ring Wykeham & Farrance LVDT transducer (max load 1000 kg and resolution of 0.3% f.s.). The data logger consists in a Campbell Scientific measurement and control system CR1000 (test displacement velocity 0.010 mm/min equal to an axial strain rate equal to 0.4%/hour).

This not standard value was selected in order to allow an efficient stress redistribution into the specimens in a sufficient time scale.

Moreover, 12 creep tests were carried out on jointed specimens by considering the different conditions of Table 1. In these tests one only sample for each configuration was analyzed. The jointed samples have been loaded up to about 50% of the uniaxial compression strength measured in the intact specimens.

4 TESTS RESULTS

The performed laboratory tests allow to define the rheological behavior of the jointed specimens (specially about the strength and deformability properties) as well as to identify the relations between the joint geometries and the mechanical properties of the jointed medium.

4.1 *UCS tests*

The results obtained from the UCS tests show a significant influence of joints on the mechanical behavior of the specimens (Fig. 3).

At small strain level some irregularities of the stress-strain curve are particularly evident during the specimen compression, which can be related to the major displacements along the joints (Fig. 3b).

The resulting UCS values are of about 1.14 MPa for the intact specimens and vary in the range 1.04–1.40 MPa for the jointed specimens; the resulting Young modulus values (measured at low strain level) are of about 8.7 GPa for the intact specimens and vary in the range about 5.5–7.5 GPa for the jointed specimens.

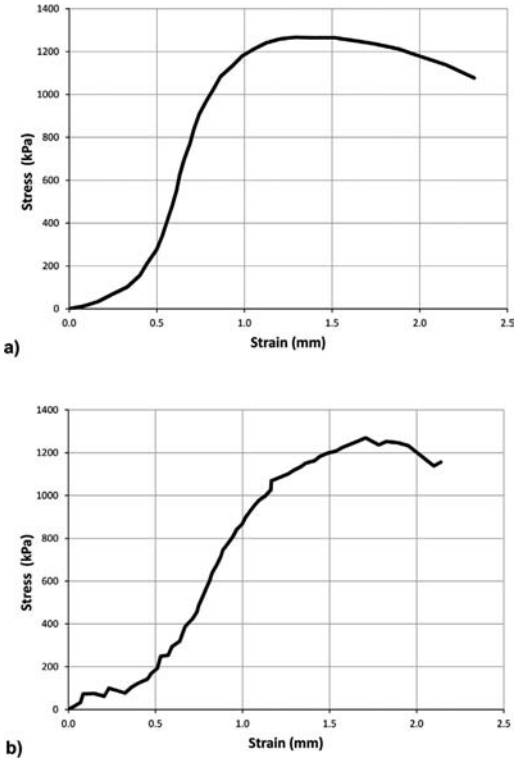


Figure 3. Example of results from UCS tests on a jointed specimen with 30° joint dip and 2.5 cm joint spacing (a) and with 30° joint dip and 2.0 cm joint spacing (b).

Even if the resulting UCS values for intact and jointed samples are almost similar, the UCS tests on the jointed specimens demonstrated the role played by the joints (Fig. 4) since at decreasing joint spacing and at increasing joint dip the UCS and the stiffness values decrease.

This trend is particularly evident for the specimens with the highest dip joints, which also show a sliding failure along individual joints (Fig. 2).

With regard to the stiffness (measured by the Young modulus at a low strain level) of the jointed specimens, the results output decreasing values with decreasing spacing and increasing dip of the joints.

4.2 *Creep tests*

The creep tests started 8 months ago' and are still in progress. For all these tests some lag of measurement, due to instrumental problems, make it difficult to derive the rheological values up to now. Nevertheless, it is always evident low-frequency trend of the measured strains (Fig. 5) inferred from both the seasonal thermal variations and the accuracy of the used sensors. By comparing the results of the creep tests on the intact rock and on the jointed specimens it is evident the influence of joints on the time-dependent behavior. The strain values are higher for the jointed specimens with respect to the intact ones; such result

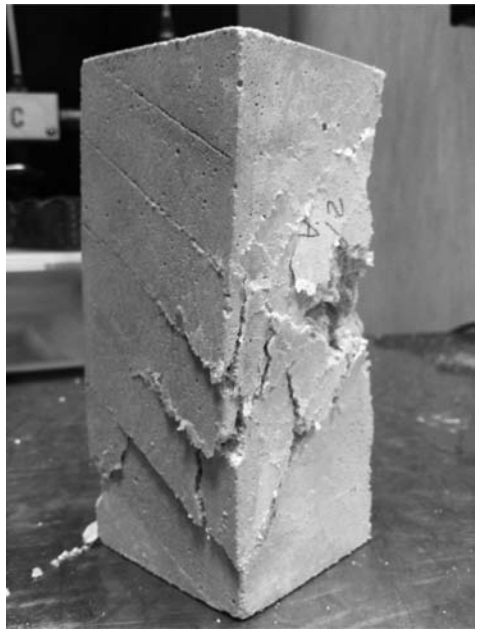


Figure 4. Example of a specimen with 30° dip and 2.5 cm spacing after the UCS failure.

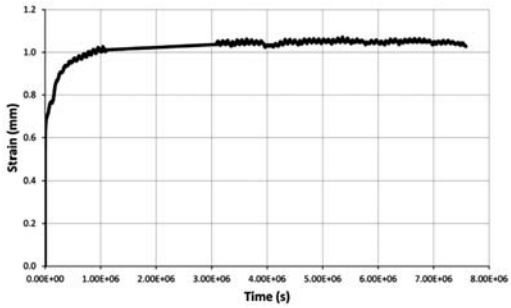


Figure 5. Results of a creep test performed on a jointed specimen with 45° dip and 3.0 cm spacing.

is mainly referred to the strain rate of the "secondary creep" stage (in the order of 10^{-9}–10^{-10} s^{-1}), while for the "primary creep" stage the measured values of strain rate (in the order of 10^{-3} s^{-1}) do not show significant differences. For the "primary creep" the test results are quite similar, i.e. they don't show a significant relation with dip and spacing of the joints. Based on this finding it seems that at low strain levels the role of the joints on the analogue rock mass behavior can be neglected. This can be related to the joint asperities reproduced within the samples which avoid sliding along discontinuities to occur at small loads and low strain rates.

In the case of the "secondary creep" the performed tests output an evident increase of the strain rate with increasing joint dip and a moderate increase for decreasing joint spacing.

5 SUMMARY AND CONCLUSIONS

This study based on experimental investigations on analogue material allowed to characterize the influence of geometrical parameters of joint sets (i.e. dip and spacing) on the rheological behavior of jointed specimens. With respect to reversibility of different tests, these artificial specimens were realized by a concrete mixture whose rheological properties have being scaled to be representative for limestone which widely outcrops in the Italian Apennine. A particular attention was paid on the mechanical influence of the principal features of the joints. Several UCS and creep tests were performed on both the intact and the jointed specimens, by considering different joint configurations. The obtained results demonstrate that the jointed specimens present, in any case, a lower strength if compared to the intact ones, as an effect of the mechanical influence of the pervasive jointing. For the same reason, the measured stiffness of the jointed specimens result significantly lower with respect to the intact ones. Also the creep behavior of the jointed specimens result to be significantly controlled by the presence of the joints since the strain rate results higher in case of pervasive jointing than in the case of intact material. More in particular, an increase of the joint dip and a decrease of the joint spacing determine an increase of strain rate values (whose scaling ratio is in the order of 10^{-2}). These results are more evident in the case of "secondary creep" stage rather than in the "primary creep" one. Considering the outputs of creep tests and UCS tests, it is possible to deduce that for quickly applied loads (i.e. UCS tests) and low strain values (i.e. "primary" creep) the rheological role of the joints is negligible with respect to the rock matrix one. On the other hand, with constant loads and higher strain levels (i.e. creep tests in the "secondary" stage) the joints start to play a mechanical role, contributing to the strain field and controlling the rheological behavior of the samples. Future perspectives for this study consist on deriving the rheological constitutive law which best fits the experimental data in order to upscale this behavior to natural case histories.

In this regard, it is worth stressing that the here obtained preliminary results encourage to model different rheological behaviors of rock masses in case of short time or long time loading effects, i.e. due to quick morphological evolutions or to stationary ones.

REFERENCES

Amadei, B., Swolfs, H.S. & Savage, W.Z. 1988. Gravity-induced stresses in stratified rock masses. *Rock Mechanics and Rock Engineering* 21(1): 1–20.

Brown, E.T. 2002. *A brief history of the development of the Hoek-Brown failure-criterion*. Rocscience Inc.

Cai, M. & Horii, H. 1992. A constitutive model of highly jointed rock masses. *Mechanics of Material* 13(3): 217–246.

Chen, E.P. 1989. A constitutive model for jointed rock mass with orthogonal sets of joints. *Journal of Applied Mechanics* 56(1): 25–32.

Chigira, M. 1992. Long-term gravitational deformation of rocks by mass rock creep. *Engineering Geology* 32(3): 157–184.

Discenza, M.E., Esposito, C., Martino, S., Petitta, M., Prestininzi, A. & Scarascia Mugnozza, G. 2011. The gravitational slope deformation of Mt. Rocchetta ridge (central Apennines, Italy): geological-evolutionary model and numerical analysis. *Bulletin of Engineering Geology and the Environment* 70(4): 559–575.

Esposito, C., Martino, S. & Scarascia Mugnozza, G. 2007. Mountain slope deformation along thrust fronts in jointed limestone: an equivalent continuum modelling approach. *Geomorphology* 90(1): 55–72.

Fossum, A.F. 1985. Effective elastic properties for a randomly jointed rock mass. *International Journal of Rock Mechanics and Mining Sciences & Geomechanics Abstract* 22(6): 467–470.

Gerrard, C.M. 1982. Elastic models of rock masses having one, two and three sets of joints. *International Journal of Rock Mechanics and Mining Sciences & Geomechanics Abstract* 19(1): 15–23.

Ghazvinian, A. & Hadei, M.R. 2012. Effect of discontinuity orientation and confinement on the strength of jointed anisotropic rocks. *International Journal of Rock Mechanics and Mining Sciences* 55: 117–124.

Kawamoto, T., Ichikawa, Y. & Kyoya, T. 1988. Deformation and fracturing behaviour of discontinuous rock mass and damage mechanics theory. *Int. Journal for Numerical and Analytical Methods in Geomechanics* 12(1): 1–30.

Kumar, D. & Das, S.K. 2002. Experimental investigations into floor bearing strength of jointed and layered rock mass. In Y.H. Hatzor (ed), *Stability of Rock Structures; Proceedings of the 5th International Conference on Analysis of Discontinuous Deformation, Beer Sheva, 6–10 October 2002*. Taylor & Francis.

Hoek, E. 1994. Strength of rock and rock masses. *ISRM News Journal* 2(2): 4–16.

Lenti, L., Martino, S., Paciello, A., Prestininzi, A. & Rivellino, S. (2012). *Microseismicity within a karstified rock mass due to cracks and collapses triggered by earthquakes and gravitational deformations*. Natural Hazards, 64: 359–379.

Maffei, A., Martino, S. & Prestininzi, A. (2005). *From the geological to the numerical model in the analysis of the gravity-induced slope deformations: an example from the Central Apennines (Italy)*. Engineering Geology, 78: 215–236.

Martino, S., Prestininzi, A. & Scarascia Mugnozza, G. (2004). *Geological-evolutionary model of a gravity-induced slope deformation in the carbonate central Apennines (Italy)*. Quarterly Journal of Engineering Geology and Hydrogeology, 37(1): 31–47.

Oda, M., Yamabe, T., Ishizuka, Y., Kumasaka, H., Tada, H. & Kimura, K. 1993. Elastic stress and strain in jointed rock masses by means of crack tensor analysis. *Rock Mechanics and Rock Engineering* 26(2): 89–112.

Parsons, G.C., Reddish, D.J. & Whittaker, B.N. 1993. Rock failure and deformation development around mining tunnels with reference to seam inclination. In A.G. Pasamehmetoglu, B.N. Whittaker, O. Aydan & Kawamoto T. (eds), *Assessment and Prevention of Failure Phenomena in Rock Engineering; Proceedings of the International Symposium on Assessment and Prevention of Failure Phenomena in Rock Engineering, Istanbul, 5–7 April 1993*. Balkema.

Peng, S. & Zhang, J. 2007. *Engineering geology for underground rocks*. Springer.

Priest, S.D. 1993. *Discontinuity analysis for rock engineering*. Chapman & Hall.

Ramamurthy, T. 1994. Strength and modulus response of anisotropic rocks. In J.A. Hudson (ed), *Comprehensive rock engineering*: 313–329. Pergamon.

Rao, K.S., Shrivastava, V.K. & Tiwari, R.P. 2003. Numerical simulation of jointed block mass under uniaxial stress condition. In J.N. Merwe (ed), *Technology roadmap for rock mechanics, Proceedings of the 10th International Congress of the International Society for Rock Mechanics, Johannesburg, 8–12 September 2003*. The South African Institute of Mining and Metallurgy.

Singh, B. 1973a. Continuum characterization of jointed rock masses: Part I – The constitutive equations. *International Journal of Rock Mechanics and Mining Sciences & Geomechanics Abstract* 10(4): 311–335.

Singh, B. 1973b. Continuum characterization of jointed rock masses: Part II – Significance of low shear modulus. *International Journal of Rock Mechanics and Mining Sciences & Geomechanics Abstract* 10(4): 337–349.

Singh, M. & Rao, K.S. 2005. Empirical methods to estimate the strength of jointed rock masses. *Engineering Geology* 77(1): 127–137.

Singh, M., Rao K.S., & Ramamurthy T. 2002. Strength and deformational behaviour of a jointed rock mass. *Rock Mechanics & Rock Engineering* 35(1): 45–64.

Sitharam, T.G., Sridevi, J. & Shimizu, N. 2001. Practical equivalent continuum characterization of jointed rock masses. *International Journal of Rock Mechanics and Mining Sciences* 38: 437–448.

Sridevi, J. & Sitharam, T.G. 2000. Analysis of strength and moduli of jointed rocks. *Geotechnical and Geological Engineering* 18: 3–21.

Tiwari R.P. & Rao K.S. 2003. Physical and engineering response of artificially manufactured model material and its use for rock mass testing. In S.K. Singh & A. Sinha (eds), *Geomechanics and Ground Control; Proceedings of National Seminar on Geomechanics and Ground Control, New Delhi, 24–25 September 2003*. Allied Publishers

Verman, M., Singh, B., Viladkar, M.N. & Jethwa, J.L. 1997. Effect of tunnel depth modulus of deformation of rock masses. *Rock Mechanics and Rock Eng.* 30(3): 121–341.

Wei, Z.Q. & Hudson, J.A. 1986. Moduli of jointed rock masses. In K.H.O. Saari (ed), *Large rock caverns; Proceedings of the International Symposium on Large Rock Caverns, Helsinki, 25–28 August 1986*. Pergamon.

Wong, R.H.C., Li, E.Y.M., Wong, P.C.W. & Chau, K.T. 2001. The evolution of damage around an opening in non-persistent jointed rock mass. In K.K.S. Ho & K.S. Li (eds), *Geotechnical Engineering; Proceedings of the 14th Southeast Asian Geotechnical Conference, Hong Kong, 10–14 December 2001*. Taylor & Francis.

Zhang, L. & Einstein, H.H. 2004. Using RQD to estimate the deformation modulus of rock masses. *International Journal of Rock Mechanics and Mining Sciences* 41(2): 337–441.

Zienkiewicz, O.C., Kelly, D.W. & Bettess, P. 1977. The coupling of the finite element method and boundary solution procedures. *International Journal for Numerical Methods in Engineering* 11(2): 355–375.

Rock Mechanics for Resources, Energy and Environment – Kwaśniewski & Łydżba (eds)
© 2013 Taylor & Francis Group, London, ISBN 978-1-138-00080-3

Numerical simulation of the impact of a rock fall impact on a flexible barrier using Abaqus/Explicit 6.12

J.P. Escallón
WSL Institut, Davos, Switzerland

C. Wendeler
Geobrugg Technical Department, Romanshorn, Switzerland

M. Mrozik
Geobrugg Poland, Kraków, Poland

ABSTRACT: This paper presents a rock-fall impact calculation of a flexible barrier used in an open pit mine. The design of this barrier is based on the barrier prototypes tested according to the European Standards (ETAG 027 guidelines). These prototypes have successfully met the guidelines and now have official ETA approval and CE marking. A series of quasi-static tests on flexible chain-link net specimens and small-scale impact tests were carried out to check the material model assumptions and to calibrate the input data. Furthermore, a prototype of one of the ETA barriers was numerically simulated. The calculations are performed with Abaqus/Explicit 6.12. The rock-fall barrier model accounts for many complex physical processes that occur during the rock-fall stopping process: high-speed impact, contact with sliding friction and strain-rate dependent material behavior. The match between the simulation results and the test results allowed us to assess numerically a rock-fall barrier prototype specially developed for mining applications.

1 INTRODUCTION

Flexible steel wire-net rock-fall protection systems main components are: ultra-high strength (UHS) steel wire nets supported by spiral rope steel cables with inelastic brake elements and steel posts. They are used to stop falling rocks in mountain regions in order to protect people and infrastructure.

The rock-fall system investigated in this paper has been tested according to the European Standards (ETAG027, 2008). The fulfillment of the standards has allowed the manufacturer to obtain the CE marking of the product. This paper presents results of a FE simulation of the kinetic maximum energy level (MEL) test carried out in Walenstadt (SG, Switzerland). The MEL to which the barrier prototype was tested is equal to 502 kJ, which corresponds to a 1590 kg impactor with 25.12 m/s velocity at contact.

The numerical results are compared to the test data. The agreement of the simulation results allowed us to adapt the system for a mining application in Sishen, South Africa. Rock-fall events in open-pit mines occur mainly on steep pit walls without berms. However, in order to increase the profitability of the mines, the berm width can be decreased when installing rock-fall protection barriers on the berms (Balg et al. 2012).

The investigated prototype intercepting structure consists of a chain-link net, composed of wire bundles which are in contact to each other. The mechanical behavior of these nets has been studied by performing quasi-static tensile tests and impact tests (Von Boetticher 2012). The numerical approach used on this paper relies on the general contact algorithm of the FE Abaqus/explicit code (Abaqus Analysis User's Manual).

FE rock-fall simulations based on a general contact algorithm taking into account shear contact forces on the intercepting structures have been carried out in LS-dyna (Yiu et al. 2012) and Abaqus/Explicit (Escallón & Wendeler, in press).

In this paper the UHS steel components are studied introducing additional physical details, such as strain-rate hardening, sliding friction, damage initiation and evolution, which have broadened the current knowledge of the dynamical behavior of rock-fall systems. These aspects have been studies using the FE code Abaqus/Explicit 6.12.

2 ROCK-FALL TEST ACCORDING TO ETAG027

2.1 *Test setup*

The tested rock-fall prototype consists of three modules (Fig. 1). The installation of the prototype and the dropping of the boulder are carried out using a 16-ton

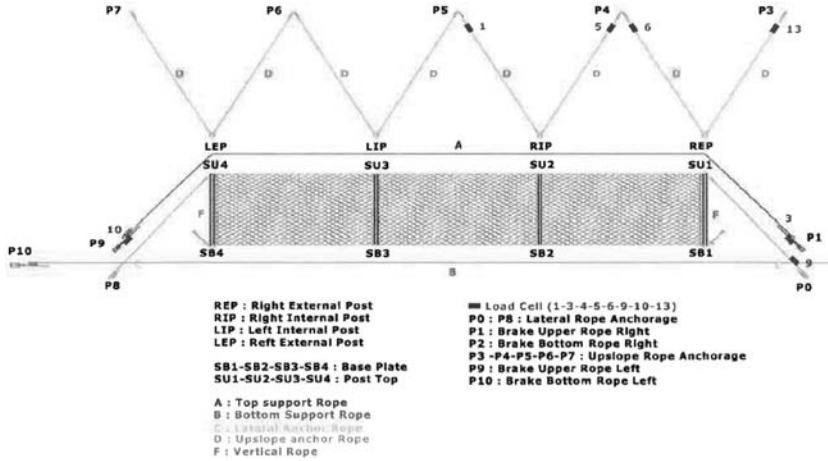


Figure 1. Arrangement of the tested prototype with positions of the load cells and energy dissipating devices (ETA-09/0085).

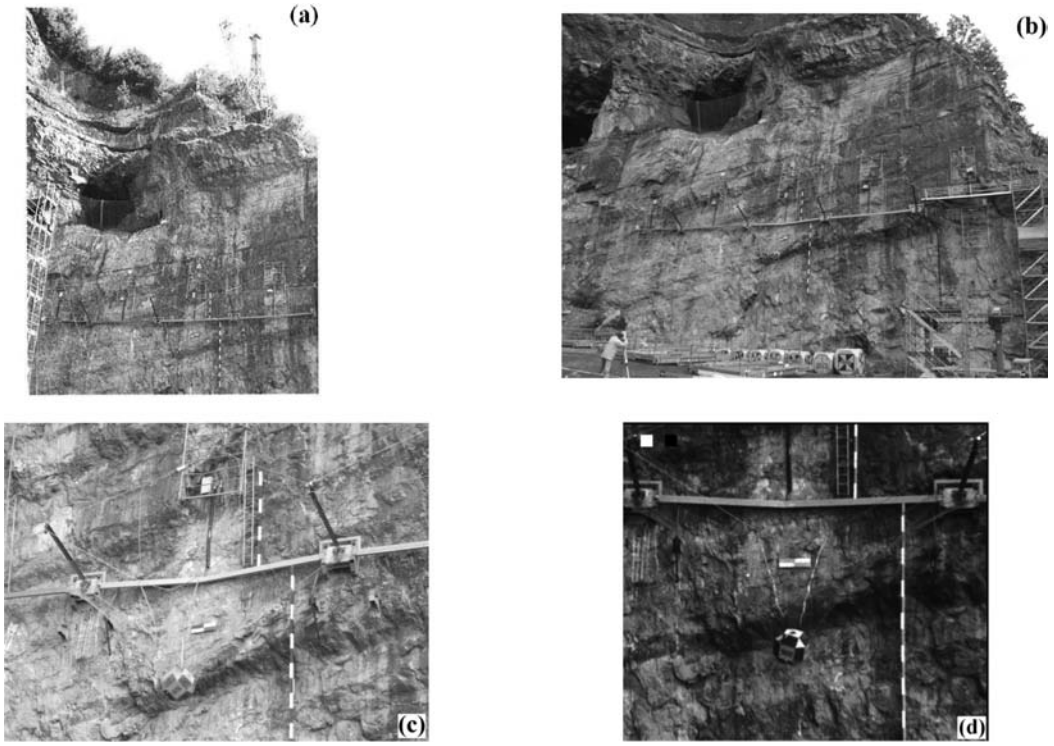


Figure 2. The test site in Walenstadt (SG, Switzerland): (a) general view, (b) lateral view, (c) oblique front view, and (d) picture taken after the MEL impact test.

crane (Fig. 2a). The test site consists of a vertical rock wall (Figs 2b, c). Load cells were installed to measure the cable forces. Two digital high-speed cameras, one placed on the front of the prototype and the other one on its side at suitable height and distance, record the rock-fall event. The barrier maximum elongation Sm and braking time tb are determined by the analysis of the frames collected during the

2.2 *Test procedure*

The rock-fall prototype is replaced after the two serviceability energy level tests (SEL). The weight of the impactor for the MEL test was 1590 kg. The drop height was 32.68 m, and the impactor velocity before contact was 25.12 m/s. In Figure 2d, a general view of the barrier after the MEL test is shown.

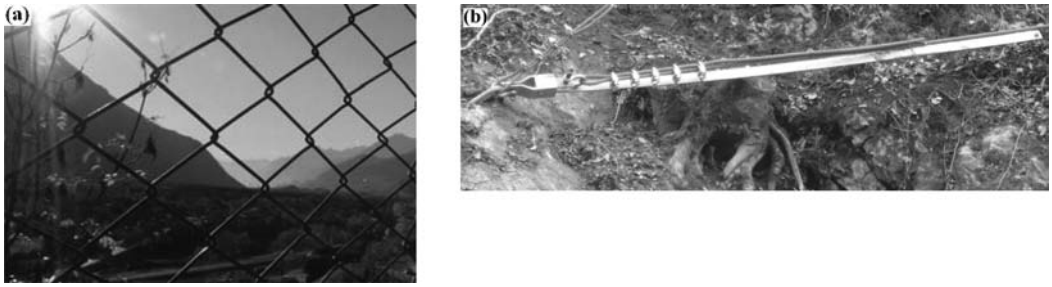


Figure 3. (a) chain-link UHS steel wire net, and (b) energy dissipating devices.

2.3 *Barrier prototype*

The tested steel wire-net rock-fall protection system consists on: a chain-link UHS steel wire net (Fig. 3a) supported by spiral rope UHS steel cables with energy dissipating devices (Fig. 3b), steel posts, and connecting components.

3 THE FEM NUMERICAL APPROACH

3.1 *General aspects*

The numerical scheme used in the present paper relies on the general contact algorithm of the Abaqus finite element code. The hard contact behavior was approximated by the penalty contact algorithm in Abaqus. This algorithm approximates contact enforcement using penalty stiffness. It adjusts automatically the stiffness of the normal force – overclosure relationship allowing a small amount of penetration.

For the numerical analyses Abaqus/Explicit v. 6.12 has been used. The explicit codes have proved to efficiently solve rock-fall impact problems provided the simulated total dynamic response time is only a few orders of magnitude longer than the stability limit (Volkwein 2004, Gentilini 2012). Furthermore, explicit codes are also suitable for the simulation of quasi-static tests by properly using the mass-scaling approach (Chung 1998, Han 2007).

The explicit codes do not require the assembly of the global stiffness matrix, and the global equilibrium is not checked. This allows the solution to proceed without iterations, and without the requirement of tangent stiffness matrices to be formed (Abaqus Analysis User's Manual). It also simplifies the treatment of contact. The time increments are dictated by the stability limit, which is given in terms of the highest eigenvalue in the FE model. From a conservative point of view, the stable time increment is given by the minimum value from all the elements. Therefore, the stable time increment is proportional to the smallest element size in the numerical domain and inversely proportional to the dilatational wave speed across the element.

The chain-link rhomboidal net geometry is modeled as a composition of wire bundles which can come into contact with one another as in the real ring net system. This detailed approach allows a deep understanding of the mechanics of the knots where contact takes place. The wire bundles are discretized by linear beam elements. Bundle-to-bundle normal and shear contact forces are taken into account.

Sliding-friction was included in the general contact model. In order to calculate shear stresses at the contact interfaces the isotropic Coulomb friction model with the penalty method was used. The penalty method approximates the ideal no slip (relative sliding) during stick with a stiff elastic behavior. A reduction of the friction coefficient with increasing slip velocity and increased pressure may be assumed for the ring-to-ring contact (Philippon, 2004 and Chowdhury, 2008). The cables-to-net and bundle-to-bundle friction coefficient used for the numerical simulations was 0.1. The impactor – chain-link net friction used for the numerical simulations was 0.3.

3.2 *Modeling of the supporting structures*

The posts were treated as rigid bodies, because the prototype design avoids normal forces on the posts to exceed their buckling capacity. Furthermore, the impact occurs at the middle of the intercepting structure, and therefore deformation takes place exclusively in the chain-link net, cables and brake elements. The base plates are also declared as rigid bodies, and hinge connectors allow modeling the post-to-base plate kinematic connections. The posts and the base plates are modeled using continuum elements, for the purpose of having contact facets interacting with the shackles.

3.3 *Modeling of wire-spiral cables*

The mechanical properties of the cable elements have been determined by means of quasi-static tension tests. The steel allow composing the strands forming the cables is the same steel type used for the manufacture of the chain-link wire nets, which has a Young modulus of 210 GPa, and yield strength of at least 1770 MPa. The cables are modeled as a macro-equivalent structure with a single cross section. However, based on tension tests, the Young modulus of the macroscopic structure is equal to 112 GPa.

The cables are discretized by means of linear beam elements. The strain-rate version of the von Mises elastic-plastic hardening model is the constitutive law assigned to the cable section. Figure 4a shows the elastic and plastic part of the stress vs strain behavior in tension in the cable for a strain rate less or equal to

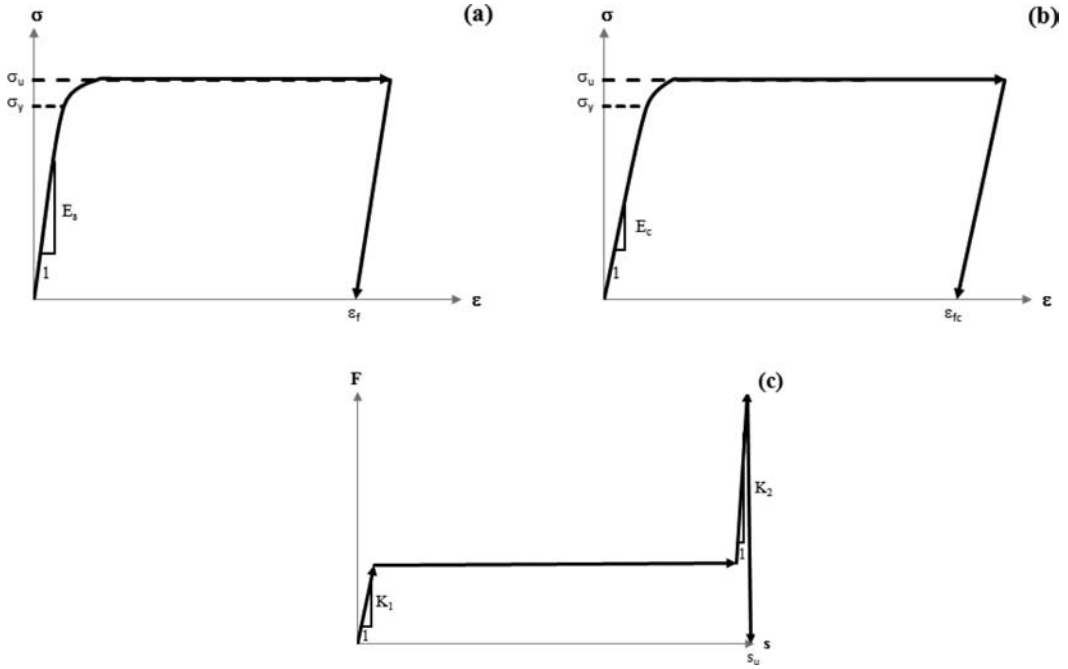


Figure 4. (a) stress-strain behavior in tension for the wire-rope cables, (b) stress-strain behavior in tension for the wire-nets, and (c) load-displacement behavior during impact for the U-brakes.

$1e^{-4}\ s^{-1}$. It was assumed that the yield and ultimate stress increase with strain rate as in the case of the ES-1c steel alloy (Boyce & Dilmore 2009). Based on this experimental data, a set of tension yield curves were obtained and used as material input to model the cables and the wire nets. It has been proved that this assumption allows a close match of test data and FE numerical simulation results (Escallón & Wendeler, in press).

3.4 *Modeling of the chain-link wire net*

The mechanical description of the knot where bundle-to-bundle contact takes place shows that in the region around it, contact shear forces and bending moments take place (Von Boetticher 2012). To verify this mechanical description a fully 3D model of the chain-link wire net bundles was carried out. Furthermore, bundle-to-bundle contact is taken into account to calculate contact pressures and contact shear forces.

The chain-link bundles are discretized by linear beam elements, and the same constitutive model used to model the cable elements is used to model these elements. The strain at failure ε_f (Fig. 4b) has been calibrated based on quasi-static and impact tests. When the plastic strain ε_p reaches ε_f, a ductile damage model describes the decay of tensile strength with plastic displacement (Escallon & Wendeler, in press).

3.5 *Modeling of the energy dissipating devices*

The mechanical description of ring brake systems are described by Volkwein (2001). Several FE algorithms have been developed to compute these ring brake systems (Volkwein, 2001). Dissipating devices in general, however, can be idealized using connector systems (Gentilini et al., 2012) following an axial load-displacement law (Fig. 4c).

3.6 *Structure connections*

The cables are generally connected to the net by means of steel clips which were treated as rigid bodies. Both the top and bottom cables are threaded through the net in the same places of the real structure. Furthermore, the cables are connected to the posts by means of shackles which were treated as rigid bodies as well. Contact shear forces are taken into account by this realistic FE model.

3.7 *Modeling of the impactor*

For rock-fall simulations, the impactor is much stiffer than the net and it behaves as an undeformable body; therefore, the impactor was treated as a rigid body. However, the rigid body was discretized into finite elements with the purpose of having facets to interact with the net.

4 MODEL ASSESSMENT

The model of the barrier prototype described in the previous section was subjected to a series of simulations to calibrate contact friction, and damage energy of the deformable steel components (cables and net). Furthermore, these series of impact tests allowed the

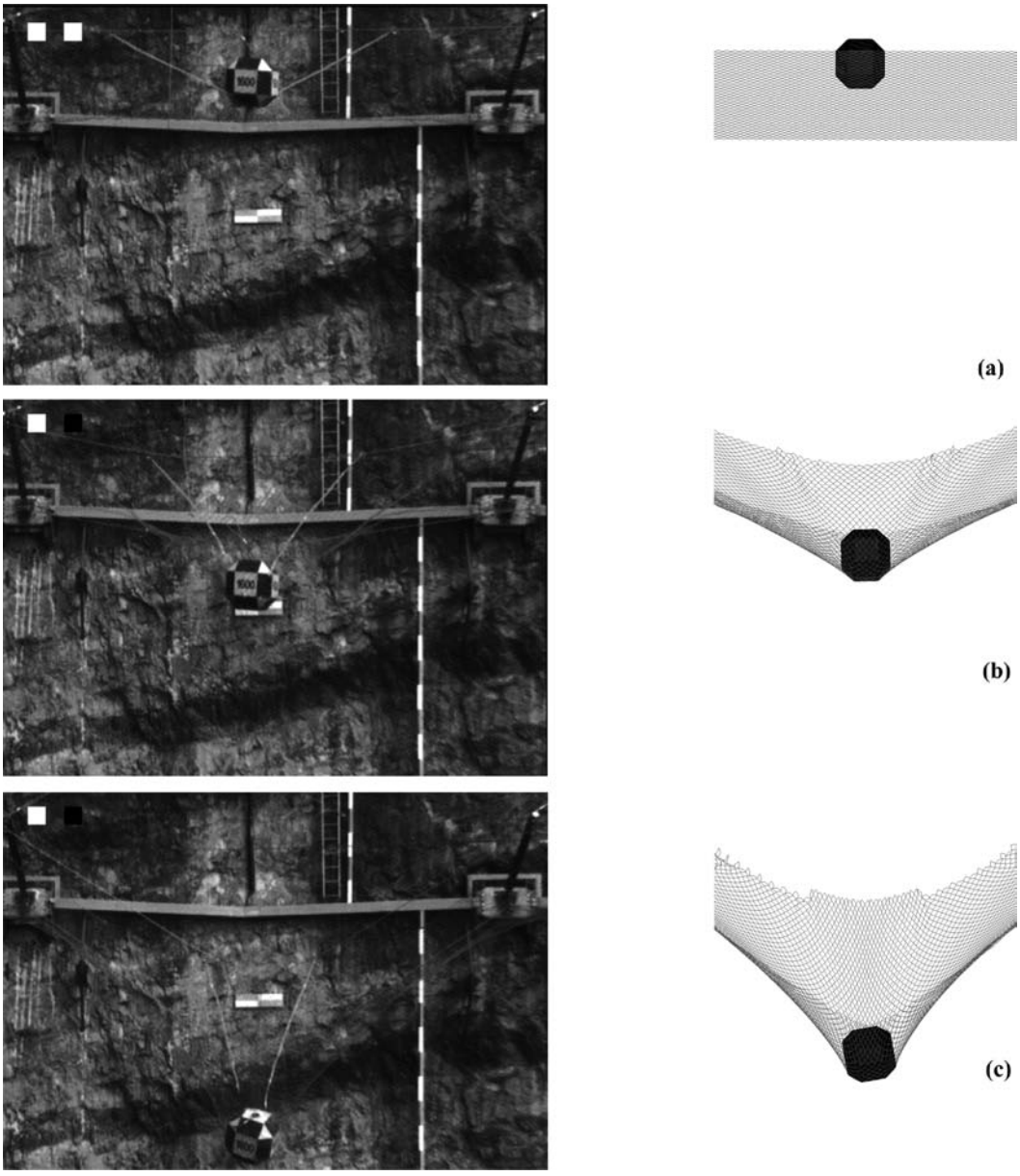


Figure 5. Barrier response during impact (left), and numerical response of the net (right): (a) t = 0 (contact), (b) t = ts/2, and (c) t = ts.

adjustment of the strain at failure ε_f of these components taking into account their dynamic behavior and the loading paths during impact.

Mesh convergence studies were also carried out during this process. After calibration and mesh convergence definition the MEL test was simulated.

4.1 *Net elongation*

Figure 5 compares the test and numerical response of the net during the MEL test. Camera frame pictures taken from the front are compared to the corresponding model deformed frames.

The maximum net elongation during the MEL test was equal to 5 m approximately. However, due to geometrical simplifications of the net-support cables connections, the numerical model computes a maximum deflection of 5.7 m. Furthermore, the computed value is also bigger because the effect of the initial net sag caused by gravity was neglected, and this effect causes a slightly stiffer behavior of the net (Escallón & Wendeler, in press).

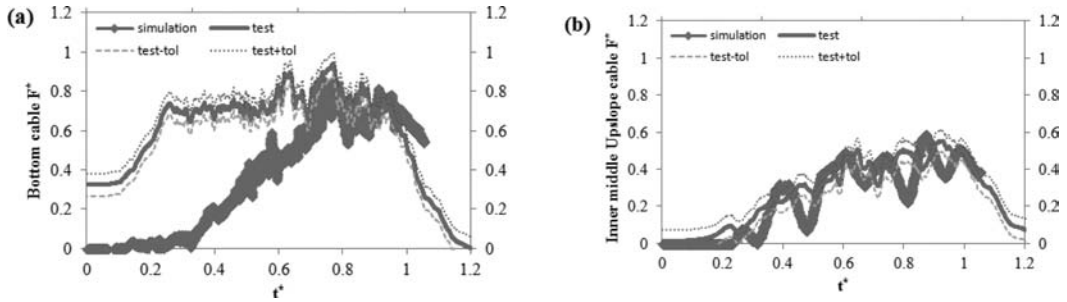


Figure 6. Normalized cable forces: (a) bottom cable, and (b) inner middle upslope cable.

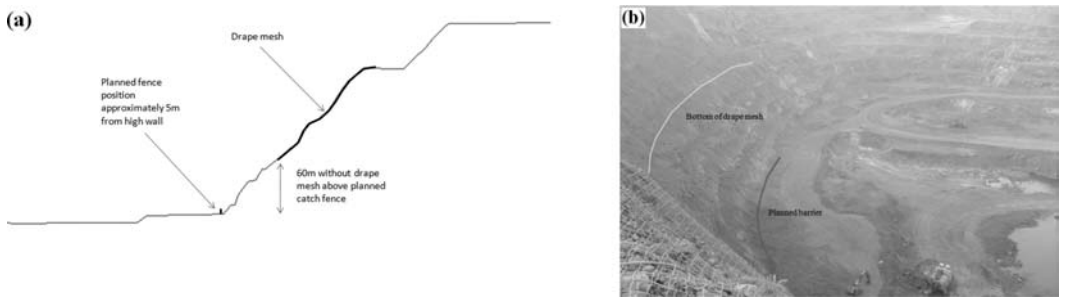


Figure 7. Mine in Sishen, South Africa: (a) lateral view, and (b) general view.

4.2 *Cable forces (F)*

Wire-rope UHS steel cables have little bending and shear resistance, due to their geometry. Additionally the rock-fall process causes big tension forces and shear forces and bending moments are negligible. It is convenient to perform the comparison with test data, in terms of dimensionless quantities (Gentilini et al. 2012):

$$t^* = \frac{t}{t_s}; \qquad F^* = \frac{F}{E_{km}} S_m$$

where t_s = experimental braking time; E_{km} = energy level; and S_m = experimental maximum elongation.

Figure 6a, b shows the test vs numerical results of bottom support (load cell 9) and the inner middle upslope cables (load cell 1). The load cells tolerance was evaluated as ±6% (ETA-09/0085). Therefore Figure 6a, b includes this uncertainty.

The fact of disregarding the static sag caused by gravity in the numerical simulations influences more the support cables in comparison to the upslope cables (Fig. 6a, b). The computed tension forces on the upslope cables are basically inside the test tolerance range during the whole time span. In the case of the bottom support cable, the computed tension forces are inside the test tolerance for a smaller time span. However, in both cases the maximum computed tension forces are inside the test tolerance range, which shows the tremendous prediction capacity of the developed FE model.

5 MINING APPLICATION

The agreement of the FE simulation results allowed us to adapt the system for a mining application in Sishen, South Africa. The anchor points of the new prototype are then adjusted to the topography described in Figure 7a, b. The rock impact is not vertical in this case and based on the topography a 60 degrees angle respect to the berm plane is considered.

The position of the barrier is roughly indicated (Fig. 7b). The length of the barrier is 100 m approximately, and is about 5 m away from the wall. The height of the wall above the barrier without drape mesh is about 60 m. The maximum size of the possible falling boulders has been estimated in 0.125 m^3. However, for the FE numerical simulation the same impactor size and kinetic energy of the test previously discussed will be taken into account.

Figure 8 shows the computed normalized tension forces on the bottom cable. The tension forces are compared with the test case (Fig. 8), showing similar results. However, the peak force of the mining application barrier is 20% approximately higher than in the case of the tested barrier, because the impact angle causes the bottom cable to be subjected to a slightly higher peak force.

6 CONCLUSIONS AND DISCUSSION

This paper has presented explicit FEM simulation results of a maximum energy level rock-fall test on a flexible rock-fall barrier according to the European

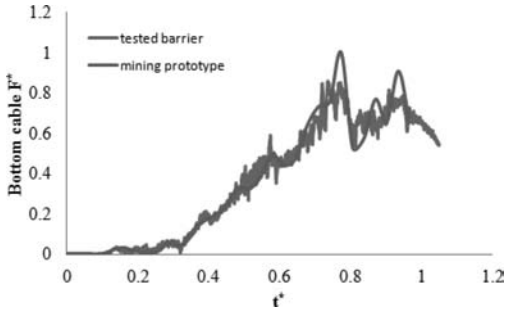


Figure 8. Normalized bottom cable force histories: mining application prototype vs. ETA barrier values.

Guidelines ETAG027. The model has taken into account important physical effects such as ductile damage, and strain rate sensitivity.

The numerical scheme relies on the general contact algorithm in Abaqus/Explicit. Sliding-friction was included in the general contact model. The applied friction coefficients allow the best match with test data and they are consistent with the physical parameters which influence friction.

Future work will be to make model simplifications to optimize computational time, without sacrificing current prediction capabilities. For instance, post-cable abstract connections will be considered. Furthermore, the shear forces and bending moments in the bundle-to-bundle knot area will be analyzed, which probably could lead to a simplified chain-link wire mesh FE model.

The agreement of the FE simulation results with test data has demonstrated the model's predictive capabilities as a powerful tool for prototyping and modifications to rock-fall barrier design.

Rock-fall protection barriers can be used to increase the profitability of mines, because they allow a reduction in berm width, which can potentially increase yield in addition to reducing the risks of rock-falls.

REFERENCES

Abaqus Analysis User's Manual, Version 6.12-1, Dassault Systémes Simulia Corp., Providence, RI.

Balg, C., Sims, G & Schoevaerts, B. 2012. Rockfall mitigation and slope stabilization measures in opencast mines, and a mechanized installation of high-tensile chain-link mesh for underground support to reduce rockfall risk and increase productivity. The Southern African Institute of Mining and Metallurgy Southern Hemisphere International Rock Mechanics Symposium SHIRMS 2012. South Africa.

Boyce, B.L. & Dilmore, M.F. 2009. The dynamic tensile behavior of tough ultrahigh-strength steels at strain rates from 0.0002 s-1 to 200 s-1, *International Journal of Impact Engineering* 36: 263–271.

Chowdhury, M.A. & Helali, Md. M. 2008. The effect of amplitude of vibration on the coefficient of friction for different materials. Science direct, pages 307–314.

Chung, W.J., Cho, J.W. & Belytschko, T. 1998. On the dynamic effects of explicit FEM in sheet metal forming analysis, *Engineering Computations* 15(6): 750–776.

Escallón, J.P. & Wendeler, C. 2013. Numerical simulations of quasi-static and rockfall impact tests of ultra-high strength steel wire-ring nets using Abaqus/Explicit, Simulia Community Conference, Vienna (in press).

European Organisation for Technical Approvals. ETAG 27. Guideline for European Technical Approval of Falling Rock Protection Kits. Edition 2008 – 02 -01.

Gentilini, C., Govoni. L., de Miranda, S., Gottardi, G & Ubertini, F. 2012. Three- dimensional numerical modelling of falling rock protection barriers, *Computers and Geotechnics* 44: 58–72.

Gentilini, C., Gottardi, G., Govoni, L., Mentani, A. & Ubertini, F. 2012. Design of falling rock protection barriers using numerical models. *Engineering Structures* (in press).

Han, H., Taheri, F. & Pegg, N. 2007. Quasi-static and dynamic crushing behaviors of aluminum and steel tubes with a cutout. *Thin-Walled Structures* 45: 283–300.

Volkwein, A. 2004. Numerische Simulation von flexiblen Stein schlagschutzsystemen, PhD. Diss. Swiss Federal Inst. of Technology Zurich, Switzerland.

Von Boetticher, A. 2012. Flexible Hangmurenbarrieren: Eine numerische Modellierung des Tragwerks, der Hangmure und der Fluid-Struktur-Interaktion PhD. Diss. Technische Universität München, Germany.

Yiu, J., Huang, Y., Pappin, J., Sturt, R., Kwan, J.S.H & Ho, K.K.S. 2012. Landslide Mobility and Flexible Barrier Numerical Modeling Using LS-DYNA, 12th International LS-DYNA® Users Conference.

This page intentionally left blank

Rock Mechanics for Resources, Energy and Environment – Kwaśniewski & Łydżba (eds)
© 2013 Taylor & Francis Group, London, ISBN 978-1-138-00080-3

Global methodology for the evaluation of the stress field in a rock mass from in-situ tests. Application to the Salamonde II powerhouse cavern

M. Espada, L. Lamas, N. Leitão & B. Figueiredo
National Laboratory for Civil Engineering (LNEC), Lisbon, Portugal

ABSTRACT: This paper presents the results of *in situ* stress measurements and the application of a global interpretation model for evaluation of the most likely *in situ* stress field in the rock mass of the underground powerhouse cavern of the Salamonde II re-powering scheme, located in a mountainous zone of the North of Portugal. The objective of the study was to obtain the stress field prior to the powerhouse cavern excavation, for design purposes. Overcoring tests were performed in boreholes, before construction started. During early construction stages, when direct access to the vicinity of the cavern was created, flat jack tests were performed. For estimating the most likely state of stress in the rock mass, a global inverse analysis was carried out, which combined the overcoring and the flat jack tests results, using an appropriate methodology and a three dimensional numerical model. In order to assess the influence of time dependent effects on the *in situ* stresses, a viscoelastic gravitational analysis was also performed using the same numerical model. The results obtained are compared and discussed.

1 INTRODUCTION

In situ stress tests in rock masses for the design of underground caverns or tunnels are necessarily performed in a limited number of locations and their results are scarce for evaluating the stress field in a representative rock mass volume. Several factors influence the *in situ* stresses, such as topography, nearby excavations, rock mass heterogeneity, tectonic forces or time dependent effects at the geological scale. Thus, for evaluation of the most likely natural stress field at a specific site, it is important to use global interpretation models, that consider the influence of those factors and integrate the results of all tests conducted at different locations, preferably using more than one testing method.

Several *in situ* stress measurements were carried out for design of the Salamonde II hydroelectric scheme, which corresponds to the re-powering of a 50-years old scheme, located in a mountainous zone in the North of Portugal. In 2009, before construction started, six overcoring (STT) tests were carried out in two boreholes and a preliminary analysis of the stress field was done, but it was decided to complement them with additional tests, using flat jacks, as soon as access to the zone of the powerhouse cavern would exist. For this purpose, ten flat jack (SFJ) tests were performed in 2012, at three locations.

A large three dimensional numerical model was developed-which simulates the topography and the underground openings-and an appropriate inversion methodology was implemented in order to integrate all the test results and to estimate the most likely state of stress in the Salamonde II rock mass.

2 SALAMONDE II RE-POWERING SCHEME

The Salamonde II re-powering hydroelectric scheme, promoted by the owner Energies of Portugal – EDP, includes a new, 2 km long underground hydraulic conduit and a powerhouse cavern. A comprehensive geotechnical characterization programme took place for design purposes. The rock mass is a good quality, homogeneous, coarse grained granite, intersected by several fault zones. The state of stress in the vicinity of the powerhouse is influenced by the complex topography of the ground, with elevations that range between 193 m and 350 m.

The powerhouse cavern, is 66 m long, 26.5 m wide and 56 m high at the turbine hall, and is located 150 m to the South, on the left river bank, and 150 m below the ground surface (COBA 2009). Figure 1 shows a longitudinal profile along the hydraulic conduit. Figure 2 shows the location of the new powerhouse with respect to the old one and to the Cávado river, where the Salamonde dam is located, as well as to a tributary, the Mau river. Also shown a 3D perspective of the excavations around the powerhouse cavern.

3 OVERCORING TESTS

Overcoring tests (STT) were performed in two boreholes (LNEC 2009). Borehole S8 is vertical and starts

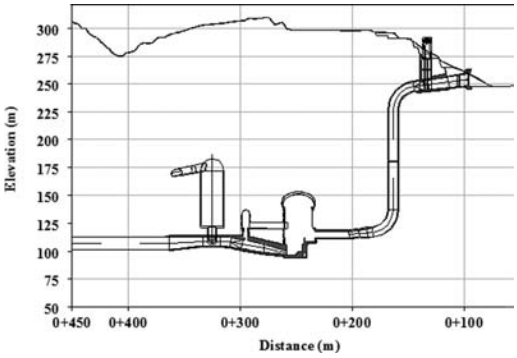


Figure 1. Longitudinal profile along the hydraulic circuit.

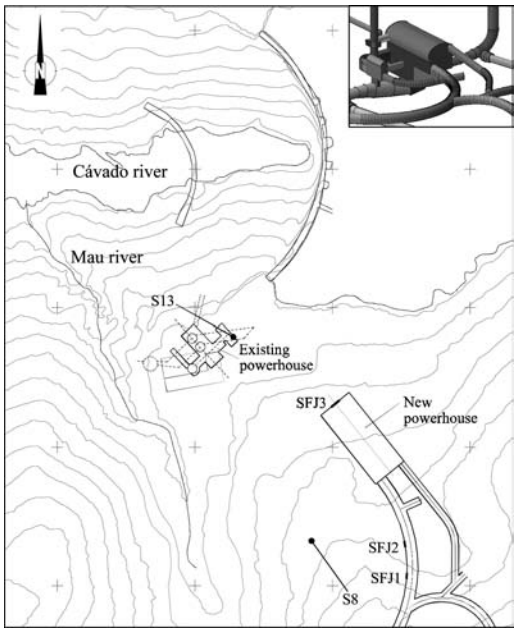


Figure 2. Salamonde II re-powering scheme and the existing powerhouse.

at the ground surface, while S13 starts at the existing valve chamber, close to the original powerhouse, at a depth of 121 m, and dips at 70° (Fig. 2). Three tests were carried out in each borehole, at depths between 79 m and 96 m in S8, and between 28 m and 48 m in S13. However, the results obtained in two tests in borehole S8 were doubtful, due to an intersected rock joint, and they had to be discarded.

From tests conducted on the overcored rock, the values of the elastic constants needed for interpreting the test results were obtained: E = 50 GPa, $\nu = 0.21$.

In both boreholes the maximum principal stress obtained is subvertical, with values around 7 MPa in S13 and around 4 MPa in S8. The sub-horizontal minimum principal stress is around 3 MPa for the three tests of S13 and around 2 MPa for the test in S8.

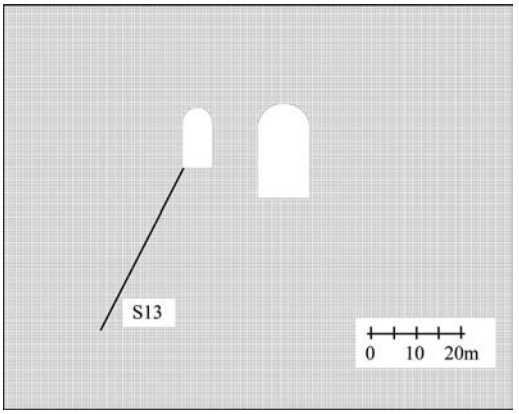


Figure 3. 2D mesh detail and location of borehole S13.

For a global interpretation of the three tests of borehole S13 a 2D numerical model was used, that represents a cross section of the existing powerhouse caverns. Figure 3 shows the FLAC mesh, where these caverns and borehole S13 are represented.

For calculation of the most probable values of the *in situ* stresses with this 2D model and the overcoring results from borehole S13, a specific inversion analysis was carried out (see Lamas et al. 2010) and the following assumptions were considered:

- the rock mass is continuous, linearly elastic, homogeneous and isotropic, with $\gamma = 27\,\text{kN/m}^3$;
- plane strain conditions;
- the vertical and horizontal stresses prior to excavation of the caverns vary linearly with depth;
- one principal stress is vertical.

The most probable values of the *in situ* stresses prior to excavation of the caverns, obtained with this analysis are: vertical stress 1.4 times the overburden weight and horizontal stresses 0.7 times the vertical stress, both in the plane and normal to the plane.

The fact that the value obtained for the vertical stress is higher than the gravitational stress, can be due to topography effects, that were not considered in this simple model, but may also result from the overestimation of the stresses along the borehole axis, that was reported by several authors for overcoring tests. Therefore, additional tests were recommended for the construction phase.

4 SMALL FLAT JACK TESTS

The small flat jack tests (SFJ) were conducted in three locations identified in Figures 2–4 as SFJ1, SFJ2 and SFJ3 (LNEC 2012a). SFJ1 and SFJ2 were in the left wall of the powerhouse access tunnel and SFJ3 in the powerhouse North top wall, close to the roof. When the tests in SFJ3 were performed, the excavation of the powerhouse was in its initial stages, with the configuration shown in Figure 5, with two side drifts, three transverse galleries and three rock pillars.

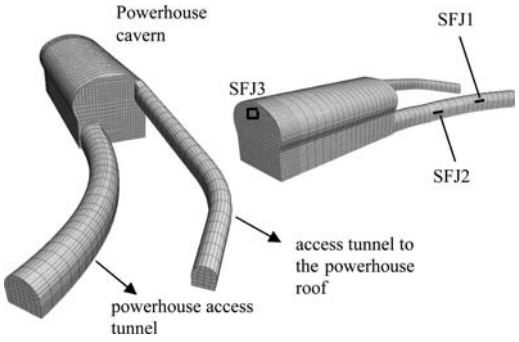


Figure 4. Perspective of the underground works.

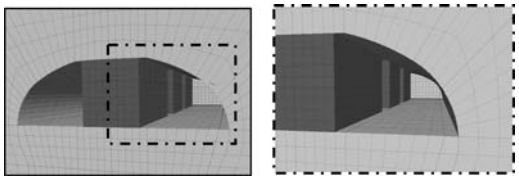


Figure 5. Detail of the excavation of the powerhouse roof.

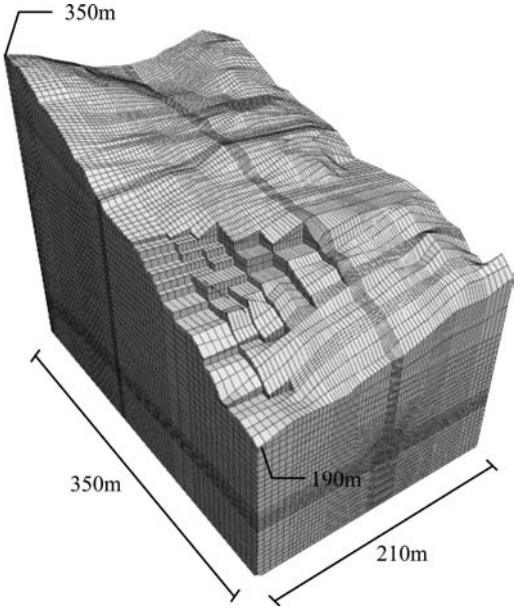


Figure 6. Global perspective of the 3D model.

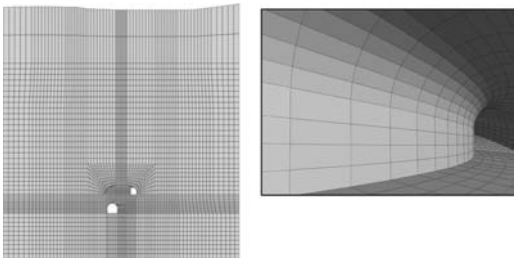


Figure 7. Cross section close to the powerhouse cavern with the tunnel's excavations. Detail of the powerhouse access tunnel.

The results obtained in locations SFJ1 and SFJ2, were analysed together due to their proximity and similar lithology. The maximum and minimum principal stresses obtained are approximately 16 MPa and 6 MPa, with dip direction and dip 173°/72° and 353°/18°, respectively. In location SFJ3 the maximum and minimum principal stresses were approximately 8 MPa and 6 MPa, with dip direction and dip 225°/56° and 45°/34°, respectively.

5 STRESS STATE ANALYSIS

5.1 *Three-dimensional model description*

A 3D numerical model of the rock mass volume of interest for the stress state analysis was developed with the finite difference FLAC3D program, in order to apply a global interpretation methodology of the overcoring and SFJ test results (LNEC 2012b).

The 3D mesh represents the powerhouse cavern, part of the powerhouse access tunnel and the access tunnel to the powerhouse roof (Fig. 4). The topography was also represented, because is an important factor for evaluation of the stress field.

Figure 6 presents a global perspective of the 3D numerical model developed. Figure 7 shows a vertical section through both access tunnels and a detail of the powerhouse access tunnel.

It was assumed that the rock mass is continuous, linearly elastic, homogeneous and isotropic, with an elastic modulus of 35 GPa, close to the average value obtained in the SFJ tests. However, for the stress analysis only the value of the Poisson's ratio is relevant. The value of 0.20 that was considered is close to the average obtained in overcoring tests. The unit weight was set to $\gamma = 27\,\text{kN/m}^3$.

5.2 *Methodology for the stress field evaluation*

For a global interpretation of the stress measurement results several assumptions are usually made regarding the principal stress directions and the variation of the stress values. It is common to consider that the vertical and horizontal stresses increase linearly with depth, since the stresses are, in a large proportion, due to the weight of the overlaying ground (Lamas et al. 2010). In this study, given the 3D analysis and the influence of the topography, it was considered that the state of stress in the rock mass, before the excavations, is given by a linear combination of the states of stress, resulting from the application of the following loadings in the numerical model:

– initial vertical normal stress (Z-axis), equal to the weight of the overlaying ground ($\sigma_3^0 = \gamma h$);

– initial horizontal normal stresses (X-axis and Y-axis), equal to the weight of the overlaying ground ($\sigma_1^0 = \gamma h$ and $\sigma_2^0 = \gamma h$);
– initial shear stress in the horizontal plane, equal to the weight of the overlaying ground ($\sigma_4^0 = \gamma h$).

By applying these loadings separately in the numerical model, it is possible to obtain, at each point of the rock mass, the stresses σ_{im}, where i denotes the six stress components and m the four loadings. Two types of boundary conditions had to be considered. For initial normal stress loadings, the displacements normal to lateral boundaries were restricted and in the lower boundary all displacements restricted. For the initial shear stress loading in the horizontal plane, the horizontal displacements were fixed in the lateral boundaries and in the lower boundary all displacements were restricted.

The values of σ_{im} obtained for the locations where the tests were carried out can be grouped in the matrix A_{lm}, where ℓ denotes the N stress measurements made and m the four loadings.

Assembling in vector M_l the stress values in the N measurements, the linear combination of the states of stress resulting from the four loads considered can be expressed by the following set of equations:

$$\sum_m A_{lm} k_m = M_l \qquad (\ell = 1,\ldots N)\ (m = 1,\ldots 4) \qquad (1)$$

The resolution of this set of equations was performed using the least squares method, thus allowing calculating the parameters k_m, which characterise the most likely *in situ* state of stress in the rock mass. Thus, the *in situ* state of stress in a specific location corresponds to the following sum for the m loads:

$$\sigma_i = \sum_m k_m \sigma_{im} \qquad (i = 1,\ldots 6)\ (m = 1,\ldots 4) \qquad (2)$$

For application of this methodology, it was further assumed that the parameter k_3 is unitary, which corresponds to the usual hypothesis of considering that the vertical stress is equal to the weight of the overlaying ground. This constraint has been introduced, because in the overcoring tests the vertical stress component (approximately normal to the boreholes axis) was considered overestimated, which is a problem common to overcoring tests.

Considering the SFJ tests performed in the access tunnel to the powerhouse and in the powerhouse top wall (six equations), the test performed in borehole S8 at depth of 93.48 m (six equations) and the three STT tests performed in S13 borehole (18 equations), the following values of the k_m parameters were obtained: $k_1 = 0.88$, $k_2 = 0.98$, $k_3 = 1.00$ and $k_4 = 0.31$.

5.3 *Stress state analysis results*

By combining the stress fields calculated for each loading and using the values of the k_m parameters, the most probable stress field prior to the excavation was calculated. Figure 8 presents a cross section through the middle of the powerhouse cavern with the 3D principal stress tensor (in perspective). The rotation of the obtained sub-vertical principal stress is consistent with the expected influence of the Mau river (Fig. 2).

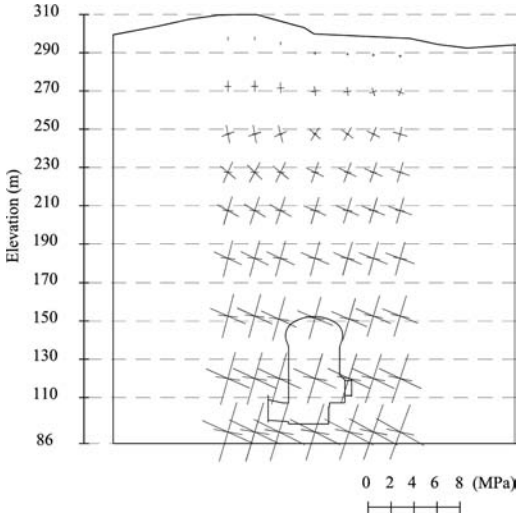


Figure 8. Cross section through the middle of the powerhouse cavern with principal stresses.

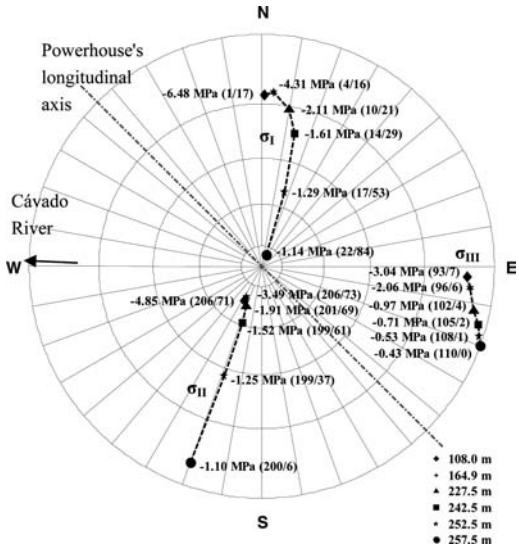


Figure 9. Principal directions and stresses for various depths.

Figure 9 shows a stereographic projection (lower hemisphere) of the principal directions and stresses for various depths. There is a clear rotation of the maximum (σ_I) and intermediate (σ_{II}) principal stresses with depth. After the superficial zone, affected by local topographic effects, σ_I becomes sub-horizontal and normal to the direction of the Cávado river, while σ_{II} becomes sub-vertical. The minimum principal stress

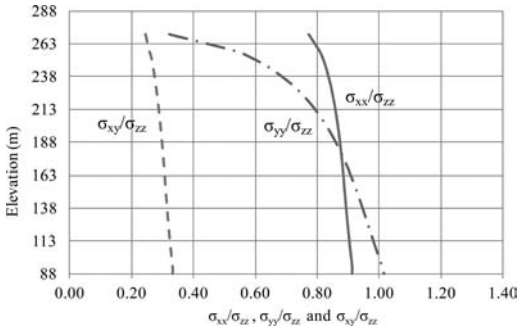


Figure 10. Ratio between horizontal stresses, σ_{xx}, σ_{yy}, σ_{xy}, and the vertical stress σ_{zz}.

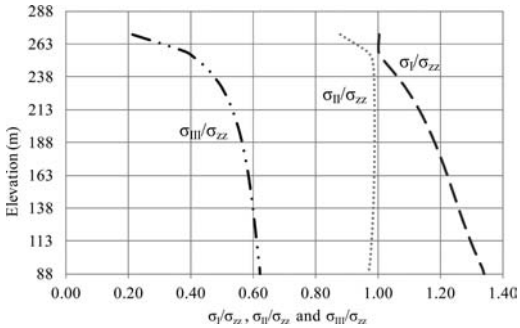


Figure 11. Ratio between the principal stresses and the vertical stress σ_{zz}.

(σ_{III}) is sub-horizontal and parallel to the direction of the Cávado river. The σ_I to σ_{III} ratio is approximately 2.

Figure 10 presents the ratio between the stresses in the horizontal plane (σ_{xx}, σ_{yy}, and σ_{xy}) and the vertical stress (σ_{zz}) for several elevations along a vertical axis in the middle zone of the powerhouse, where the ground surface elevation is 299.9 m. As a general trend, these ratios vary fast near the ground surface, influenced by the effect of topography, and then become more stable in depth.

Figure 11 shows the ratio between the principal stresses and the vertical stress along the same vertical axis in the middle zone of the powerhouse. After the superficial zones, the ratio of the maximum principal stress (σ_I) to the vertical stress varies between 1.0 and 1.3, the intermediate principal stress (σ_{II}) is approximately equal to the vertical stress and the ratio of the minimum principal stress (σ_{III}) to the vertical stress varies between 0.5 and 0.6. Thus, at the depth of the powerhouse, σ_I and σ_{III} are sub-horizontal, with ratios to the vertical stress of 1.3 and 0.6 respectively, and σ_{II} is sub-vertical.

Figure 12 is a contour plot of the maximum principal stress along a longitudinal section through the top part of the powerhouse top, showing the excavation as it was during the SFJ tests. The vertical stress concentration in the three rock pillars is notorious.

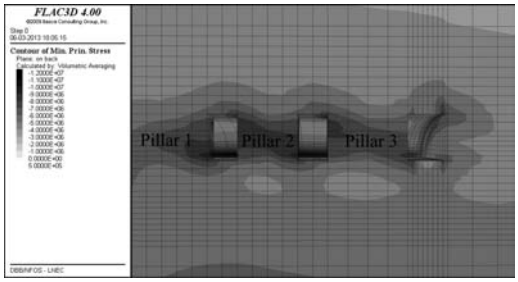


Figure 12. Contour of maximum compressive principal stress along a longitudinal section in the powerhouse.

5.4 *Consideration of time dependent effects*

The analysis done so far considered the rock mass as a linear elastic material. This is usually valid at the time scale of the construction projects, but, at the geological time scale, time dependent effects may play an important role in the distribution of the *in situ* stresses, due to creep or relaxation of the rock mass. If time dependency is considered, the stress field that results from a gravitational analysis is different and has higher horizontal stresses.

Time dependent effects in rock masses can be simulated by a Maxwell viscoelastic model (Amadei & Stephansson 1997), by increasing the Poisson's ratio and decreasing the elastic modulus. In the limit, a Poisson's ratio of 0.5 would result in hydrostatic stresses, which is the limit to which Maxwell's viscoelastic model tends for an infinite time. The elastic modulus would tend to zero, but in stress analysis such as this one, its value is irrelevant.

In order to investigate to which extent time dependent effects could contribute to the horizontal stresses calculated in the previous section, which are higher than those obtained in a gravitational analysis with the "short term" value of $\nu = 0,20$ that was used, new calculations were carried out with the 3D numerical model. These were gravitational analyses, but with increasing values of ν, so that the resulting minimum horizontal stress coincides with the minimum horizontal stress obtained in the previous section, *i.e.*, approximately 0.6 times the vertical stress at the depth of the powerhouse. The "long term" Poisson's ratio obtained by this process was 0.40, which is the double of the "short term" value.

Figure 13 presents the principal stresses obtained in a horizontal section through the middle of the powerhouse cavern for the two types of analysis performed. On the left hand side are the results obtained with the inverse analysis of the test results presented in the previous section. On the right hand side are the results of a simple gravitational analysis with $\nu = 0.40$. In this latter analysis, a nearly hydrostatic horizontal stress field was calculated, and therefore the stress orientations are not very well defined.

Figure 14 shows the ratio between the principal stresses and the vertical stress for the gravitational, time dependent analysis. Comparison of

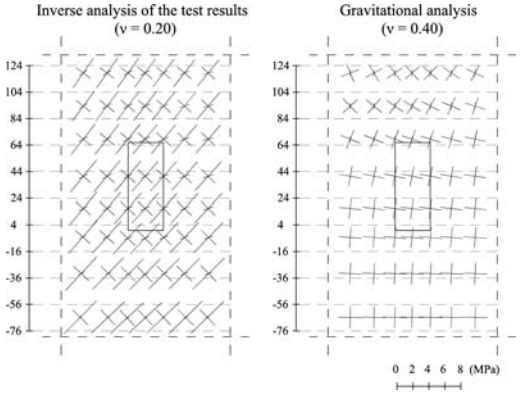


Figure 13. Principal stresses in a horizontal section through the middle of the powerhouse cavern.

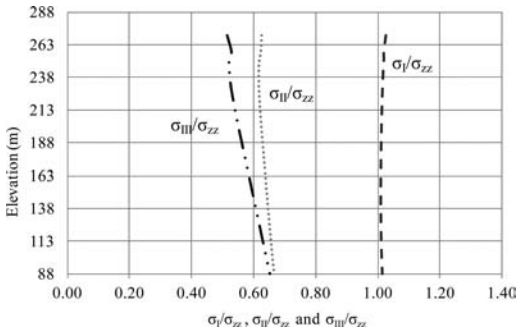


Figure 14. Ratio between the principal stresses and the vertical stress for a gravitational analysis with a Poisson's ratio of 0.40.

Figures 11–14 suggests that the *in situ* stress state, at a specific location, is influenced by the topography and has a component due to gravity and time dependent effects, superimposed with stresses of other origins, such as tectonic forces, or resulting from the effect of important discontinuities, or heterogeneities.

6 CONCLUSIONS

In this work the three-dimensional numerical model of the rock mass, which includes the main excavations and the ground topography, for estimating the initial state of stress in the rock mass of the new powerhouse of Salamonde II, was presented.

An inverse methodology using this global model that integrates the results of all stress measurements, namely the overcoring tests and the small flat jack tests, was also presented. This methodology includes assumptions regarding the stress field, which are reasonable approximations of reality.

It was concluded that, below the superficial zone of the rock mass, the maximum and minimum principal stresses are sub-horizontal. They are, respectively, 1.30 and 0.60 times the weight of the overlaying ground, and oriented normal and parallel to the Cávado river. The intermediate principal stress obtained is subvertical and corresponds to the weight of overlaying ground.

A calculation with consideration of the time dependent effects was also presented, by applying in the 3D model relaxed elastic properties. The results obtained evidence that, at a specific location, the *in situ* stresses are influenced by the topography and have a component due to gravity and time dependent effects, superimposed with stresses of other origins, such as tectonic forces, or resulting from the effect of important discontinuities, or heterogeneities.

ACKNOWLEDGEMENTS

Permission from EDP – Energies of Portugal, S.A. to publish the information regarding the Salamonde II hydroelectric scheme is greatly acknowledged.

REFERENCES

Amadei, B. & Stephansson, O. 1997. *Rock Stress and its measurement*. Chapman & Hall.

COBA 2009. *Design of the Re-powering of the Salamonde Hydroelectric Scheme*. Lisbon.

Lamas, L., Muralha, J. & Figueiredo, B. 2010. Application of global model for assessment of the stress field for engineering purposes. In Xie (ed.), *Rock Stress and Earthquakes*; *Proc. 5th Int. Symp. on In-Situ Rock Stress, Beijing*: 631–636. London: Taylor & Francis.

LNEC 2009. *Repowering of Salamonde. Overcoring tests for determination of stress (in Portuguese). Report 403/09 – NFOS*. Lisbon: LNEC.

LNEC 2012a. *Salamonde repowering scheme. Small flat jack tests for measurement of the state of stress during construction (in Portuguese). Report 340/12 – NFOS*. Lisbon: LNEC.

LNEC 2012b. *Salamonde repowering scheme. Model for interpretation of the initial state of stress (in Portuguese). Report 348/12 – NFOS*. Lisbon: LNEC.

Rock Mechanics for Resources, Energy and Environment – Kwaśniewski & Łydżba (eds)
© 2013 Taylor & Francis Group, London, ISBN 978-1-138-00080-3

Influence of rock mass creep on tunnel loading

P. Fortsakis, A. Kalos, V. Despotaki & M.J. Kavvadas
National Technical University of Athens, Greece

ABSTRACT: Rock mass creep in tunnelling through weak rock masses under high overburden may lead to the potential development of significant convergence. Should this convergence be restrained by a rigid support shell, tunnel loading tends to increase. Although, such increase could be significant, it is often not taken into account in design, due to uncertainties in the calculation procedure. This paper proposes a simplified approach for estimating the additional creep loads on the lining of circular tunnels excavated in one phase. This is achieved by performing a parametric set of 2D numerical analyses with the finite element code ABAQUS. The rock mass is modeled as an elasto-plastic material yielding according to the Drucker-Prager criterion, with time-dependent characteristics described by the Singh-Mitchell creep model. The time-dependent behaviour is initially formulated upon the assumption of a new set of parameters. Typical ranges of these parameters are estimated using creep experiments from the literature.

1 INTRODUCTION

In tunnel design and construction through weak rock masses under high overburden the role of rock mass creep may prove important for the final wall convergence and ground loads exerted on temporary support or final lining. However, this time-dependent behaviour is usually not considered in design, due to the large uncertainties of creep and the need for complex laboratory tests and constitutive models.

In tunneling, the time-dependent behaviour of the rock mass is not typical creep, since deformation does not freely develop under constant state of stress. The construction of the support shell restrains the potential creep deformation, leading to increased tunnel loads and rock mass creep evolves with varying stresses. Moreover, the rock mass creep in tunnelling can be separated in two categories (this separation is only in relation to the specific project which determines the time scale):

- Short-term creep. Creep deformation influences the excavation procedure and the temporary support.
- Long-term creep. Creep deformation develops during the tunnel service life leading to increased ground loads on final lining.

There are several case studies in literature, of tunnels that experienced large deformation and in some cases severe failures due to the short-term creep behaviour of the surrounding rock mass (e.g. the Saint Martin La Porte access adit, along the Torino – Lyon Base Tunnel and the Lötschberg Tunnel). Debernardi (2008) describes the case of the Saint Martin La Porte, where up to 2.0 m convergence developed during the excavation. Using back analysis the dominant role of the creep of the surrounding rock mass was revealed. Moreover, Barla et al. (2010) presented stress measurements in the final lining, clarifying that the increase of the stresses due to the rock mass creep varied from 70% to 100%. Sandrone et al. (2006) employed three different models to simulate the very large time-dependent convergence (up to 80 cm) developed when the tunnel crossed the base sediments of sandstone and siltstone and up to 1.0 m thick beds of carbon and anthracite.

The influence of creep on the surrounding geomaterial has been studied by several researchers in literature using either analytical (e.g. Sulem et al. 1987, Pan & Dong 1991, Nomikos et al. 2011), numerical (e.g. Ghaboussi & Gioda 1977, Boidy et al. 2002, Debernardi 2008, Fortsakis 2012), statistical (e.g. Sandrone 2006; Kontogianni et al. 2005) or experimental (e.g. Yu 1998) methods.

The present paper investigates the influence of rock mass creep on the final lining loads of circular tunnels. Based on results of viscoplastic 2D numerical analyses a simplified approach is proposed for the estimation of the increased tunnel loads due to rock mass creep.

2 ROCK MASS CREEP

Creep is a relatively well defined phenomenon in principle. However, establishing a well-defined constant effective stress to account for the effect of creep deformation is rather illusive. Considering that creep deformation accumulates with evolving time, the pore pressures tend to increase and then dissipate thus leading to a fluctuation of the effective stress.

Throughout the literature creep has been simulated through a series of empirical (e.g. semi-logarithmic

law, Singh-Mitchell creep model) or rheological models (e.g. Maxwell, Bingham) and general theories (e.g. Perzyna 1966, Naghdi & Murch 1963). However, the time-dependent mechanical behaviour experienced in oedometer and triaxial or unconfined compression tests tends to describe different aspects of creep.

Oedometer tests activate the volumetric component of creep thus leading to an increase of strength stemming from the chemical bonding experienced. Regardless whether we tend to neglect or silently disregard any significance of the aforementioned creep characteristic, it tends to dominate the overall mechanical behaviour considering the formation of the rock mass throughout the geological history. The only solace we can receive is that the problem at hand is addressing a relatively small time window while the volumetric creep strain effects on rock mass strength become significant only over extensive periods of time.

Triaxial or unconfined compression tests however, reveal the deleterious effects of deviatoric creep strain component on the rock mass strength. Although the primary and secondary creep stages, inherently associated with crystal and microfabric reconstruction, can be described relatively accurately by most empirical and even rheological models under specific loading conditions, they tend to neglect the final primal role of deviatoric creep strain component characterized as tertiary creep. The tertiary creep stage portrays the deleterious effects of deviatoric creep through strength degradation leading ultimately to creep induced failure.

Next, we will be focusing solely on the deviatoric creep strain component and investigate the effect of primary and secondary stages on the overall mechanical behaviour in tunneling by employing a relatively well established empirical relation.

3 CREEP MODEL AND PARAMETERS

In the frame of the present paper the rock mass creep behaviour is initially formulated upon the assumption of a new set of parameters (φ_{cr}, $t_{50\%}/t_d$). These parameters can easily be correlated with most of the widely used creep models and, as it will be shown from the results of the numerical analyses, they can be further employed on the development of a simplified approach for the estimation of creep loads on the tunnel. More specifically these parameters are:

– Creep factor φ_{cr}: This factor represents the magnitude of the potential creep strain for a given stress state (q/q_f) in a specific time period (t). For instance the time period may correspond to the duration of a laboratory test or the project service life or an arbitrary moment. The creep factor is equal to the ratio of the creep deformation at the specific time and stress state to the elastic deformation at the same stress state assuming linearly elastic – perfectly plastic behaviour ($\sigma_c = 2c \cdot \tan(45 + \varphi/2)$, c: rock mass cohesion, φ: rock mass friction angle, E: deformation modulus, q: deviatoric stress, q_f: maximum deviatoric stress for a specific value of the mean stress p).

$$\varphi_{cr}\left(\frac{q}{q_f}, t\right) = \frac{\varepsilon_{cr}(t = t_d)}{\left(\frac{q}{q_f}\right)\frac{\sigma_c}{E}} \tag{1}$$

– Ratio $t_{50\%}/t_d$: This factor determines the rate of increase of the potential creep strain. The parameter $t_{50\%}$ is the time period required for the 50% of the final creep deformation to be developed according to the creep mode and t_d is the total time of the analysis.

The following equations illustrate the procedure for the calculation of the Singh-Mitchell (Singh & Mitchell 1968) parameters from the values of the creep factor φ_{cr} and the ratio $t_{50\%}/t_d$. The equations for the two time values t_d and $t_{50\%}$ are:

$$\varepsilon_{cr}\left(t = t_d\right) = \frac{A}{1-m} e^{\alpha\frac{q}{q_f}} \left(\left(\frac{t_d}{t_1}\right)^{1-m} - 1\right) \tag{2}$$

$$\varepsilon_{cr}\left(t = t_{50\%}\right) = \frac{A}{1-m} e^{\alpha\frac{q}{q_f}} \left(\left(\frac{t_{50\%}}{t_1}\right)^{1-m} - 1\right) \tag{3}$$

The m parameter of the Singh-Mitchell model is calculated by dividing the two previous equations. It is evident that the m value is not influenced by the values of the creep factor.

$$\frac{\varepsilon_{cr}\left(t = t_{50\%}\right)}{\varepsilon_{cr}\left(t = t_d\right)} = \frac{1}{2} \Rightarrow \left(\frac{t_d}{t_1}\right)^{1-m} - 2\left(\frac{t_{50\%}}{t_1}\right)^{1-m} + 1 = 0 \tag{4}$$

By substituting the creep deformation ε_{cr} in Eq. 1 the creep factor can be expressed through Eq. 5.

$$\varphi_{cr}\left(t = t_d, q/q_f\right) = \frac{\frac{A}{1-m} e^{\alpha\frac{q}{q_f}} \left(\left(\frac{t_d}{t_1}\right)^{1-m} - 1\right)}{\left(\frac{q}{q_f}\right)\frac{\sigma_c}{E}} \tag{5}$$

Since the creep potential depends significantly on the imposed stress state, two different creep factors should be determined for different values of the q/q_f ratio (Eqs. 6, 7).

$$\varphi_{cr1}\left(t = t_d, (q/q_f)_1\right) = \frac{\frac{A}{1-m} e^{\alpha\left(\frac{q}{q_f}\right)_1} \left(\left(\frac{t_d}{t_1}\right)^{1-m} - 1\right)}{\left(\frac{q}{q_f}\right)_1 \frac{\sigma_c}{E}} \tag{6}$$

$$\varphi_{cr2}\left(t = t_d, (q/q_f)_2\right) = \frac{\frac{A}{1-m} e^{\alpha\left(\frac{q}{q_f}\right)_2} \left(\left(\frac{t_d}{t_1}\right)^{1-m} - 1\right)}{\left(\frac{q}{q_f}\right)_2 \frac{\sigma_c}{E}} \tag{7}$$

Finally from the above relationships the values of the parameters a, A of the Singh-Mitchell model can be calculated as follows:

$$\alpha = \frac{\ln\left[\left(\frac{\varphi_{cr2}}{\varphi_{cr1}}\right)\frac{\left(\frac{q}{q_f}\right)_2}{\left(\frac{q}{q_f}\right)_1}\right]}{\left(\frac{q}{q_f}\right)_2 - \left(\frac{q}{q_f}\right)_1} \quad (8)$$

$$A = \frac{\sigma_c}{E}\frac{(\varphi_{cr2} - \varphi_{cr1})(1-m)}{\left(\left(\frac{t_d}{t_1}\right)^{1-m} - 1\right)\left[\frac{e^{\alpha\left(\frac{q}{q_f}\right)_2}}{\left(\frac{q}{q_f}\right)_2} - \frac{e^{\alpha\left(\frac{q}{q_f}\right)_1}}{\left(\frac{q}{q_f}\right)_1}\right]} \quad (9)$$

4 DESCRIPTION OF NUMERICAL ANALYSES

The problem was investigated via 2D numerical analyses using finite element code ABAQUS. The section of the tunnel was assumed to be circular with diameter D = 10 m and the overburden height equal to 10D = 100 m (Fig. 1). The soil was simulated with 4-sided, 4-noded solid elements and the support with linear beam elements.

The surrounding rock mass was modeled as isotropic linearly elastic – perfectly plastic material following the Drucker-Prager failure criterion. The initial selection of the geotechnical parameters was made in terms of the Hoek-Brown failure criterion (Hoek et al. 2002), which better describes rock materials and the rock mass deformation modulus was calculated according to Hoek et al. (2002). The steps of the numerical analyses are:

- Step 1: Geostatic stress state (hydrostatic stress field K = 1.0)
- Step 2: Simulation of the preconvergence development (Chern et al. 1998)
- Step 3: Full face excavation and activation of the temporary support (shotcrete thickness $d_{sh} = 20$ cm, $E_{sh} = 20$ GPa)
- Step 4: Activation of final lining (thickness $d_{FL} = 60$ cm, $E_{FL} = 29$ GPa)
- Step 5: Deactivation of temporary support
- Step 6: Simulation of the rock mass creep behaviour

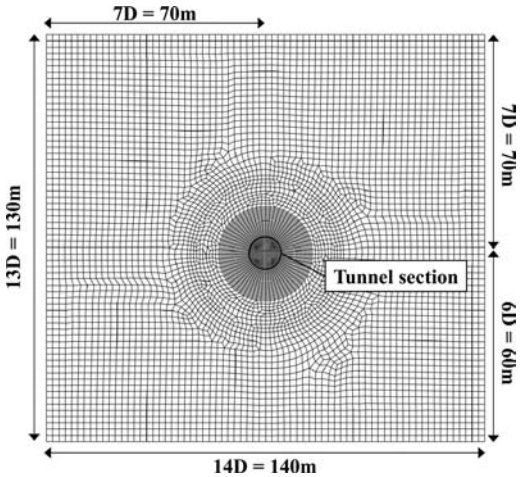


Figure 1. Numerical model.

The selection of the φ_{cr} values was mainly based on a large number of creep experiments from the PhD dissertations of Aristorenas (1987) and Debernardi (2008). However, the φ_{cr} values which are calculated from an experimental procedure should be considered as a lower limit of the values that should be adopted in the design since (a) they correspond to the duration of the experiment which is significantly shorter than the tunnel service life and (b) the creep tests are usually carried out using intact rock samples and therefore the role of the discontinuities in the time-dependent deformation is neglected.

Regarding the time-rate parameters ($t_{50\%}/t_d$ and m parameter of the Singh-Mitchell model) the selection was based on the co-evaluation of the experimental results and the proposed m values from the literature that are summarized by Hunaj-Sarihan (2009): 0.70–0.80 (Tavenas et al. 1978), 0.50–1.30 (Lacasse & Berre 2005) and 0.90–1.3 (Mansour et. al. 2008). Finally, the value of m = 0.80 was chosen for the analyses, which corresponds to $t_{50}\%/t_d \sim 0.10$ via Eq. (4). All rock mass parameters are summarized in Table 1.

The range of the rock mass strength and deformability parameters was chosen so as to correspond to weak materials and potentially unfavourable geotechnical conditions for the specific overburden height (low values of σ_c/σ_o ratio, σ_c: uniaxial compressive strength of the rock mass, σ_o: geostatic stress). The φ_{cr} values have been set for $q/q_f = 30\%$ and 70%, since

Table 1. Numerical analyses parameters.

Parameter	Range	Units
GSI	20–30	
(Marinos & Hoek 2000, Marinos et al. 2005)		
σ_{ci}	4–15	MPa
m_i	6	
D	0	
γ	25	kN/m^3
σ_o	2.5	MPa
σ_c/σ_o	0.11–0.30	
$\varphi_{cr}(q/q_f = 30\%)$	0.20–2.00	
$\varphi_{cr}(q/q_f = 70\%)$	0.30–3.00	
$\varphi_{cr}(q/q_f = 70\%)/\varphi_{cr}(q/q_f = 30\%)$	1.25,	1.50
m (Singh-Mitchell model)	0.80	
t_d	1200	months
$t_{50\%}/t_d$	0.10	

σ_{ci}: intact rock uniaxial compressive strength, m_i: geomaterial constant, D: disturbance factor, γ: rock mass unit weight, $\sigma_c = 2c\tan(45 + \varphi/2)$, σ_o: initial geostatic stress, c: rock mass cohesion, φ: rock mass friction angle, φ_{cr}: creep factor, t_d: tunnel service life.

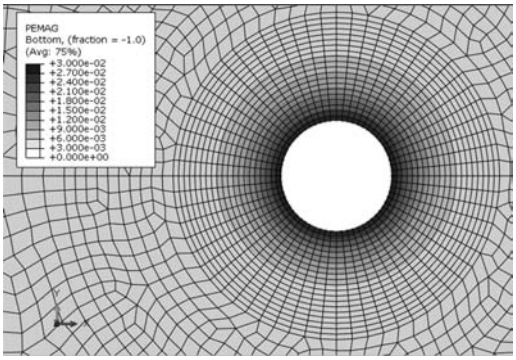


Figure 2. Plastic deformation around the tunnel section. The dark areas correspond to high values of plastic strain (GSI = 20, $\sigma_{ci} = 8$ MPa, $\sigma_c/\sigma_o = 0.14$, $\varphi_{cr1} = 0.60$, $\varphi_{cr2} = 0.75$).

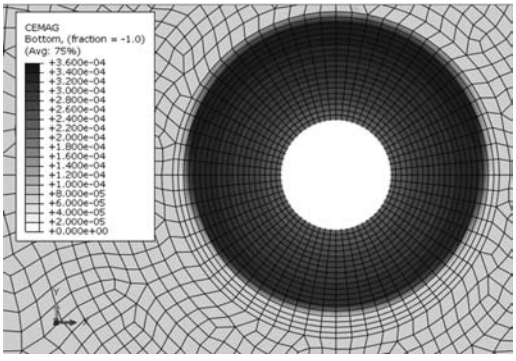


Figure 3. Creep deformation around the tunnel section. The dark areas correspond to high values of creep strain (GSI = 20, $\sigma_{ci} = 8$ MPa, $\sigma_c/\sigma_o = 0.14$, $\varphi_{cr1} = 0.60$, $\varphi_{cr2} = 0.75$).

(a) in this range creep experiments can be carried out to study the primary and secondary creep without creep failure (b) the creep potential is considered to be low for $q/q_f < 30\%$ and (c) this is the range that has been proposed my Singh & Mitchell (1968).

5 RESULTS OF NUMERICAL ANALYSES

The simulation of all the construction stages in the numerical analyses allows for the monitoring of the tunnel loads evolution, from the excavation and temporary support phase to the end of the project service life after the development of the assumed creep deformation. The main symbols which are used for the presentation of the numerical analyses results are summarized here below:

- p_{sh}: average pressure on the shotcrete shell of the temporary support
- p_{FL}: average pressure on the final lining before the rock mass creep simulation
- p_{cr}: average pressure on the final lining after the rock mass creep simulation

Figures 2 and 3 illustrate the distribution of plastic and creep deformation around the tunnel section. The maximum values of the plastic deformation are developed near the tunnel, whereas the maximum values of the creep deformation are developed at the edge of the plastic zone.

This can be explained via the following diagrams which show the development of the stress component in the rock mass at the tunnel edge. In the beginning of the step of the creep simulation the ratio q/q_f is equal to 1.0, since the specific finite element is in the plastic zone (Fig. 4). However, the potential creep deformation cannot be freely developed due to the tunnel final lining leading to the increase of the tunnel load, but also to the increase of the mean stress and the decrease of the deviatoric stress in the rock mass (Fig. 5). This decrease of the ratio q/q_f leads to a decrease of the creep strain rate. As the distance of the tunnel increases

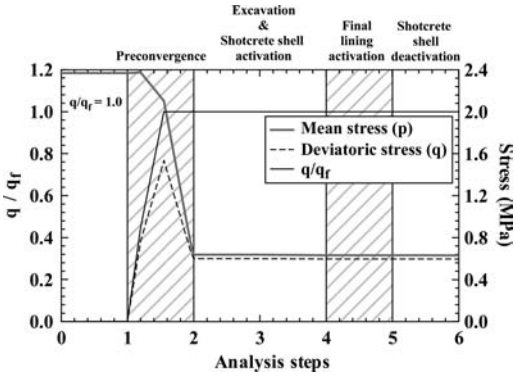


Figure 4. Development of the mean stress (p), the deviatoric stress (q) and the ratio (q/q_f) before the creep simulation in the rock mass at the tunnel edge (GSI = 20, $\sigma_{ci} = 8$ MPa, $\sigma_c/\sigma_o = 0.14$, $\varphi_{cr1} = 0.60$, $\varphi_{cr2} = 0.75$).

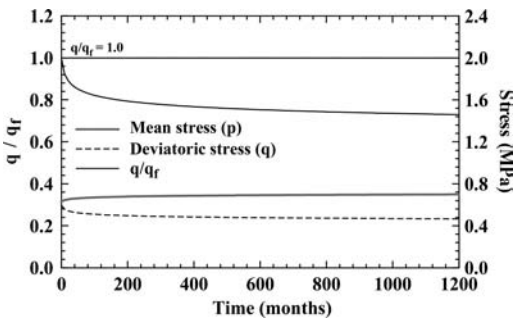


Figure 5. Development of the mean stress (p), the deviatoric stress (q) and the ration (q/q_f) during the creep simulation in the rock mass at the tunnel edge (GSI = 20, $\sigma_{ci} = 8$ MPa, $\sigma_c/\sigma_o = 0.14$, $\varphi_{cr1} = 0.60$, $\varphi_{cr2} = 0.75$).

and this stress redistribution decreases, the maximum creep strains are developed at the edge of the plastic zone. It is also highlighted that, due to the low σ_c/σ_o ratio and the high rigidity of the final lining section in

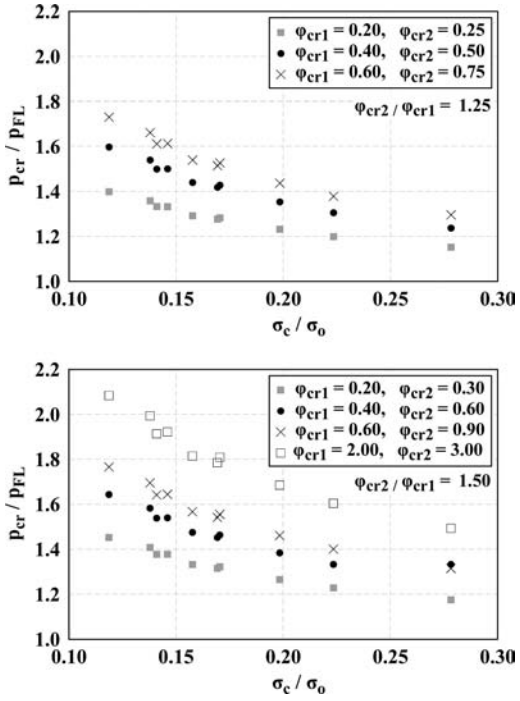


Figure 6. Distribution of the p_{cr}/p_{FL} ratio as a function of the geotechnical conditions ratio σ_c/σ_o for different combinations of the creep factors.

all cases, the percentage of load transfer from the temporary support to the final lining is higher than 93% ($p_{FL}/p_{sh} > 0.93$).

The ratio p_{cr}/p_{FL} can be used to quantify the effect of the rock mass creep on the final lining load. The diagrams in Figure 6 portray the distribution of this ratio as a function of the geotechnical conditions ratio σ_c/σ_o and the φ_{cr} values. As the rock mass quality improves the p_{cr}/p_{FL} ratio decreases, considering that the width of the plastic zone is smaller and the values of the stress factor q/q_f that influences the creep potential are lower. Moreover the increase of the φ_{cr} values tends to reveal an increase of the p_{cr}/p_{FL}. However, this increase has a decreasing rate, due to the increase of the load and the mean stress, which has already been described. For the range of the geotechnical and creep parameters that has been assumed, the increase of the final lining loads varies from 15% to 70% for $\varphi_{cr2}/\varphi_{cr1} = 1.25$ and from 20% to 110% for $\varphi_{cr2}/\varphi_{cr1} = 1.50$.

In order to investigate the sensitivity of the ratio p_{cr}/p_{FL} to the rate of increase of the creep deformation a sensitivity analysis was carried out for $m = 0.60$–0.90 that corresponds to $t_{50\%}/t_d = 0.05$–0.20. The results illustrated in Figure 7 show that higher m values – for the same φ_{cr} values – result to higher rate of increase in the beginning of the analysis, but ultimately lower final values. Nevertheless, the maximum difference for the p_{cr}/p_{FL} ratio at the end of the analysis is 3%.

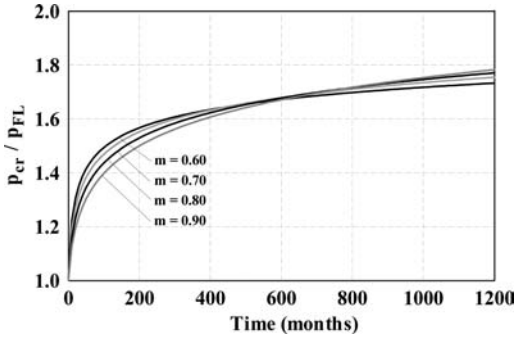


Figure 7. Development of the p_{cr}/p_{FL} ratio for different values of the m parameter of the Singh-Mitchell creep model (GSI = 25, $\sigma_{ci} = 4$ MPa, $\sigma_c/\sigma_o = 0.12$, $\varphi_{cr1} = 0.60$, $\varphi_{cr2} = 0.75$).

6 CONCLUSIONS

The role of rock mass creep can be significant, and sometimes critical, in tunnel analysis, especially in cases of unfavourable geotechnical conditions. However, often it is neglected in the analysis, until it becomes evident from construction monitoring data that there is a significant development of phenomena associated with time-dependent behaviour of the rock mass (e.g. delayed convergence, cracking on the support shell).

Based on the results of numerical analyses, the most critical creep parameter for the estimation of the additional tunnel loads is the potential creep strain that would develop in a tunnel with yielding support during the design life. This parameter also controls the magnitude of the deformation restrained by the tunnel shell, resulting to the increased tunnel loads. The rate of creep deformation increase proved to be insignificant for the long-term tunnel loads.

In the proposed framework, two parameters were introduced in order to quantify the rock mass creep behaviour (φ_{cr} and $t_{50\%}/t_d$). The ratio of the average final lining load after and before the creep simulation (p_{cr}/p_{FL}) can be correlated very well with the values of φ_{cr} and the geotechnical conditions ratio. The resulting normalized diagrams can be used for the estimation of the additional creep loads. For the examined range of geometrical, geotechnical and creep parameters, the long-term increase of loads may reach up to 110% in some cases.

In case of tunnels that exhibit short-term creep phenomena with available pressure cells measurements, these diagrams may also be used to back calculate the rock mass creep parameters, so as to estimate the long-term final lining load and subsequently use it for the dimensioning of the concrete section. It is noted that these diagrams are based on the assumption of elastic behaviour of the temporary support and final lining. In the case of squeezing conditions and temporary support failures the measured loads may be significantly lower due to the increased shotcrete flexibility associated with shell failures.

REFERENCES

Aristorenas, G. 1987. *Time dependent behaviour of tunnels excavated in shale*. PhD thesis, Massachusetts Institute of Technology, USA.

Barla, G., Bonini, M. & Debernardi, D. 2010. Time dependent deformations in squeezing tunnels. *International Journal of Geoengineering Case Histories* 2(1): 40–65.

Boidy, E., Bouvard, A. & Pellet, F. Back analysis of time-dependent behaviour of a test gallery in claystone. *Tunnelling and Underground Space Technology* 17(4): 415–424.

Chern, J.C., Shiao, F.Y. & Yu, C.W. 1998. An empirical safety criterion for tunnel construction. *Proceedings of the Regional Symposium on Sedimendary Rock Engineering, Taipei*: 222–227.

Debernardi, D. 2008. *Viscoplastic behaviour and design of tunnels*. PhD thesis, Politecnico di Torino, Italy.

Fortsakis P. 2012. *Investigation of the static interaction of the surrounding soil/rock with the tunnel final lining*. PhD thesis, National Technical University of Athens (NTUA), School of Civil Engineering, Department of Geotechnical Engineering, Athens (in Greek).

Ghaboussi, J. & Gioda, G. 1977. On the time-dependent effects in advancing tunnels. *International Journal for Numerical and Analytical Methods in Geomechanics* 1: 246–269.

Hoek, E., Carranza-Torres, C. & Corkum, B. 2002. Hoek-Brown failure criterion. *Proceedings of the 5th North American Rock Mechanics Symposium and 17th Tunnelling Association of Canada, Toronto, Canada*, 1: 267–273.

Hunaj-Sarihan, N. 2009. Creep movements of reactivated landslides. In Baligh, F., Adbelmohsen, H., Abouseeda, H. & Abdelghani, K. (eds), *Proceedings of the 4iYGEC: 4th International Young Geotechnical Engineers Conference. Alexandria, Egypt, 3–6 October*, 325–328.

Kontogianni, V., Psimoulis, P. & Stiros, S. 2005. What is the contribution of time-dependent deformation in tunnel convergence? *Engineering Geology* 82: 264–267.

Lacasse, S. & Berre, T. 2005. Undrained creep suspectibility of clays. *Proceedings of the 16th International Conference on Soil Mechanics and Geotechnical Engineering*, Osaka, Japan: 531–536.

Mansour, M.F., Martin, C.D. & Morgestern, N.R. 2008. Characterization of creep movements at the Little Chief Slide, BC. *Proceedings of the Canadian Geotechnical Conference & 9th Joint CGS/IAH-CNC Groundwater Conference*, *Edmonton, Canada, 21–24 September*, 461–468.

Marinos, P. & Hoek, E. 2000. GSI: a geologically friendly tool for rock mass strength estimation. *Proceedings of the GeoEng2000 at the International Conference on Geotechnical and Geological Engineering*, *Melbourne, Australia*: 1422–1446. Lancaster: Technomic publishers.

Marinos, V., Marinos, P. & Hoek, E. 2005. The geological strength index: applications and limitations. *Bulletin of Engineering Geology and the Environment* 64: 55–65.

Naghdi, P. & Murch, S. 1963. On the mechanical behavior of viscoplastic/plastic solids. *Journal of Applied Mechanics* 30(3): 321–328.

Nomikos, P., Rahmannejad, R. & Sofianos, A. 2011. Supported axisymmetric tunnels within linear viscoelastic Burgers rocks. *Rock Mechanics and Rock Engineering* 44: 553–564.

Pan, Y.W. & Dong, J.J. 1991. Time-dependent tunnel convergence – I. Formulation of the model. *International Journal of Rock Mechanics and Mining Sciences & Geomechanical Abstracts* 28(6): 469–475.

Perzyna, P. 1966. *Foundamental Problems in Viscoplasticity*. Advances in Applied Mechanics 9: 244–377.

Sandrone, F., Dudt, J.P., Labiouse, V. & Descoeudres, F. 2006. In Van Cotthem, Charlier, Thimus & Tshibangu (eds) *Analysis of delayed convergences in a carbon zone of the Lötschberg Tunnel. Proceedings of the EUROCK 2006 – Multiphysics Coupling and Long Term Behaviour in Rock Mechanics. Liege, Belgium 9–12 May*.

Singh, A. & Mitchell, J.K. 1968. General stress-strain-time functions for soil. *Journal of the Soil Mechanics and Foundations Division*, 94, Proceedings paper 5728, 21–46.

Sulem, J., Panet, M. & Guenot, A. 1987b. An analytical solution for time-dependent displacements in a circular tunnel. *International Journal of Rock Mechanics and Mining Sciences & Geomechanical Abstracts* 24(3): 155–164.

Tavenas, F., Leroueil, S., La Rochelle, P. & Roy, M. 1978. Creep behaviour of an undisturbed lightly overconsolidated clay. *Canadian Geotechnical Journal* 15(3): 402–423.

Yu, C.W. 1998. *Creep characteristics of soft rock and modelling of creep in tunnel*. PhD thesis. University of Bradford, Great Britain.

Rock Mechanics for Resources, Energy and Environment – Kwaśniewski & Łydżba (eds)
© 2013 Taylor & Francis Group, London, ISBN 978-1-138-00080-3

A new time-dependent constitutive model and its application in underground construction

M. Karami & A. Fahimifar
Department of Civil and Environmental Engineering, Amirkabir University of Technology, Tehran, Iran

ABSTRACT: Based on the classic visco-elastic Burgers model, a new visco-elastoplastic creep model is proposed in this paper, introducing a viscoplastic unit accounting the irreversible creep strain. The viscoplastic unit consists of a dashpot element and the Mohr-Coulomb slider element, which are connected in parallel. By connecting the viscoplastic unit and the viscoelastic Burgers unit in series, the new model can compute the elastic and plastic creep deformation of rock.

The governing equation of the proposed model is implemented in the numerical finite difference code (FLAC^{2D}) using its built-in FISH language for constitutive models, and then applied on a real tunnel accounting for the delayed deformation of rock mass around tunnel. A discussion is presented comparing the numerical results and the monitoring data of the time-dependent convergence developed in the tunnel.

1 INTRODUCTION

Regarding the creep behavior of geomaterials, various kinds of constitutive equations have been developed, following different assumptions and principals. Elastic or reversible deformation is one of the assumptions which are considered in classic models. These visco-elastic models have been used by researchers through analytical formulations to obtain tunnel convergence (Kontogianni et al. 2006, Dai 2004, Sakurai 1978, Pan & Huang 1994, Fahimifar et al. 2010). Subsequently, elastoplastic time-independent components have been added to visco-elastic models by other researchers (Minkley et al. 2001, Swift et al. 2003, Guan et al. 2008, Barla et al. 2010). Furthermore, considering the irreversible creep behavior of rocks, many rheological models have been developed accounting for visco-plastic behavior of rocks typically using slider unit and dashpot unit connected in parallel named as the Bingham unit (Tomanovic 2006, Erichsen & Werfling 2003, Malan 1999, Sterpi & Gioda 2007).

For an acceptable prediction of time-dependent feature of rocks and rock masses, a proper description of elastic and plastic creep feature of rock materials should be taken into account. As a matter of fact, a simultaneous elastic and plastic creep response, which can be exhibited in different stress levels in various types of rocks, should be assumed in a creep model. Thus, some modifications to previous rheological models are necessary. Regarding to this fact, on the basis of the classic visco-elastic Burgers model, a new visco-elastoplastic rheological model is proposed in this paper. The proposed model consists of the Burgers model and of a viscoplastic unit, which are connected in series. Thus, the reversible time-dependent strains of Kelvin unit explain the primary stage of creep curve, and the strains associated with the secondary stage of rocks modeled by both elastic and plastic deformations.

The constitutive laws of the model are worked out for the triaxial stress condition and are implemented in numerical finite difference code FLAC^{2D} using the built-in FISH language for constitutive models. The potential applicability of the model is examined through a numerical simulation of a tunnel which experienced time-dependent convergence. A comparison between the model prediction and the convergence data is illustrated.

2 THE VISCO-ELASTOPLASTIC MODEL

2.1 *The classic visco-elastic Burgers model*

The deviatoric and volumetric behaviors of the Burgers model are characterized by a viscoelastic and an elastic constitutive law, respectively. The deviatoric behavior of Burgers model is schematically illustrated in Figure 1, which is composed of the Kelvin unit and of the Maxwell unit connected in series.

The Kelvin unit is characterized by Kelvin shear modulus G^k and Kelvin viscosity η^k, and the Maxwell unit is characterized by Maxwell shear modulus G^M and Maxwell viscosity η^M. As a result, the relationship between deviatoric strain rates can be formulated as Eq. 1, where e_{ij} is the deviatoric component derived from the strain tensor. The superscripts K and M refer

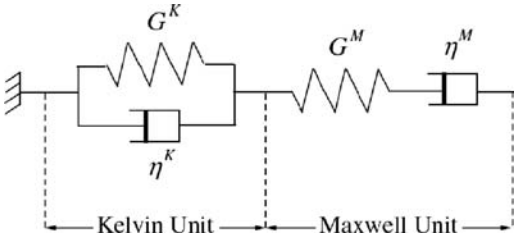


Figure 1. Rheological Burgers model for deviatoric behavior.

to the Kelvin and Maxwell components of the corresponding variables, and the superposed dot denotes time derivative. Eqs 2 and 3 represent the constitutive laws of the deviatoric behavior of Kelvin and Maxwell units, respectively. S_{ij} is the deviatoric component of stresses derived from the stress tensor. The constitutive law of the volumetric behavior, which is defined by a linear elastic spring, is presented as Eq. 4, where K is the bulk modulus of the rock mass.

$$\dot{e}_{ij} = \dot{e}_{ij}^{M} + \dot{e}_{ij}^{K} \tag{1}$$

$$S_{ij} = 2\eta^{K}\,\dot{e}_{ij}^{K} + 2G^{K}e_{ij}^{K} \tag{2}$$

$$\dot{e}_{ij}^{K} = \frac{S_{ij}}{2G^{M}} + \frac{S_{ij}}{2\eta^{M}} \tag{3}$$

$$\dot{\sigma}_{kk} = 3K\,\dot{\varepsilon}_{kk} \tag{4}$$

By constitutive equations presented above the primary and secondary creep stages of rocks can be defined as reversible time–dependent strains, associated with Kelvin and Maxwell units, respectively. However, as mentioned, experimental studies show that plastic or irreversible creep deformation may occur even at low stress level. Therefore, modeling of plastic deformations, which is commonly contributed to the failure process of rock, is of paramount importance.

2.2 *The visco-elastoplastic model*

To introduce failure threshold in rheological models, slider element is commonly used. This element has a specific failure strength which imposes a threshold beyond which irreversible deformations occur.

In this paper, time-dependent irreversible deformations are produced using a viscoplastic unit composed of a Mohr-Coulomb plastic slider and of a dashpot element connected in parallel. By connecting this unit to the Burgers model, the new visco-elastoplastic model is obtained as schematically illustrated in Figure 2.

2.3 *Model formulation*

The constitutive equations of the model can be worked out as follows. By adding the viscoplastic unit to the

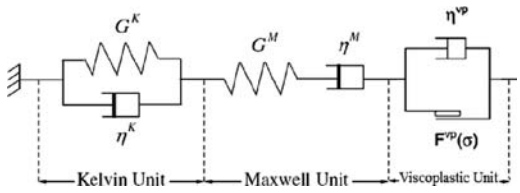


Figure 2. schematical representation of the proposed model.

Burgers model the relationship between stain rates of units incorporated in the model can be written as Eq. 5:

$$\dot{\varepsilon}_{ij}^{t} = \dot{\varepsilon}_{ij}^{M} + \dot{\varepsilon}_{ij}^{K} + \dot{\varepsilon}_{ij}^{vp} \tag{5}$$

where, $\dot{\varepsilon}_{ij}^{t}$ is the total strain rate, $\dot{\varepsilon}_{ij}^{M}$ is Maxwell strain rate, $\dot{\varepsilon}_{ij}^{K}$ is Kelvin strain rate, and $\dot{\varepsilon}_{ij}^{vp}$ is the visco-plastic strain rate.

The Maxwell and Kelvin strain rates incorporated in Eq. 5 are equal to those described in Eq. 1. In the viscoplastic unit, the amount of the strain rate contributed to the slider element is described by the flow rule:

$$\dot{\varepsilon}_{ij}^{vp} = \dot{\lambda}\frac{\partial Q(\sigma)}{\partial \sigma_{ij}} \tag{6}$$

In Eq. 6, $Q(\sigma)$ is the plastic potential function which is a function of the portion of the total stress carried by the slider. $\dot{\lambda}$ is a plastic multiplier.

As mentioned, the Mohr Coulomb plastic slider and a viscous element are used to describe the viscoplastic unit. For this unit the failure criterion f_s, and the plastic potential Q with a non-associated flow rule are expressed as Eq. 7 and Eq. 8, respectively.

$$f_s = \sigma_1 - \sigma_3\frac{1+\sin\phi}{1-\sin\phi} + 2C\sqrt{\frac{1+\sin\phi}{1-\sin\phi}} \tag{7}$$

$$Q = \sigma_1 - \sigma_3\frac{1+\sin\psi}{1-\sin\psi} \tag{8}$$

where σ_1 and σ_3 are the major and minor principal stresses, and $\sigma_1 < \sigma_2 < \sigma_3$ for an assumption of negative compressive stresses, and C, ϕ and ψ are cohesion, internal friction angle and dilation angle, respectively.

The viscous element is described by the constitutive relation as Eq. 9. Where $\dot{e}_{ij}^{vp}$ is the deviatoric strain rate contributed in the visco-plastic unit, S_{ij}^{vp} is the portion of the total deviatoric stress carried by the viscous element, and η^{vp} is the viscosity of this element.

$$\dot{e}_{ij}^{vp} = \frac{S_{ij}^{vp}}{2\eta^{vp}} \tag{9}$$

To calculate the strain of the viscoplastic unit, the stresses contributed to the slider and viscous elements and the value of $\dot{\lambda}$ must be obtained. These unknown values can be calculated by three equations of the viscoplastic unit, namely: deviatoric strain rate equilibrium, stress equilibrium and the failure criterion.

Because of the parallel connection of the slider and the viscous elements, the deviatoric strain rates of these two elements are equal. Considering this equilibrium in the parallel with the stress equilibrium principal, the stress components carried by the slider element are obtained as Eqs. 10.

$$\begin{aligned}\sigma_1' &= \sigma_1 - 2\eta^{vp}\dot{\lambda}\left(\frac{2}{3}+\frac{N(\psi)}{3}\right)\\ \sigma_2' &= \sigma_2 - 2\eta^{vp}\dot{\lambda}\left(\frac{N(\psi)}{3}-\frac{1}{3}\right)\\ \sigma_3' &= \sigma_3 + 2\eta^{vp}\dot{\lambda}\left(\frac{1}{3}+\frac{2N(\psi)}{3}\right)\end{aligned} \tag{10}$$

where

$$N(\psi) = \frac{1+sin(\psi)}{1-sin(\psi)}$$

In Eq. 10, σ_i' is the slider stress and σ_i is total stress component. The slider stresses calculated through Eqs. 10, fulfill the plastic limit conditions to produce the plastic strain. By substituting them in Eq. 7 in the state of $f_s = 0$, unknown parameter $\dot{\lambda}$ is obtained as:

$$\dot{\lambda} = \frac{\sigma_1(1-sin\,\phi)-\sigma_3(1-sin\,\phi)+2C\,cos\,\phi}{2\eta^{vp}\left(1+N\psi+\frac{N\psi}{3}sin\,\phi-\frac{sin\,\phi}{3}\right)} \tag{11}$$

With the calculation of $\dot{\lambda}$, the components of viscoplastic strain rate can be computed using the flow rule described in Eq. 6:

$$\begin{aligned}\dot{\varepsilon}_1^p &= \dot{\lambda}\\ \dot{\varepsilon}_2^p &= \dot{\lambda} * 0 = 0\\ \dot{\varepsilon}_3^p &= \dot{\lambda} * (-N\psi)\end{aligned} \tag{12}$$

Eqs. 12 induce the irreversible strain rates for the Eqs. 12 induce the irreversible strain rates for the steady state of the creep curve. The starting point of this plastic strain is controlled by the Mohr Coulomb criterion and the viscosity coefficient of the dashpot element controls the strain rate magnitude.

As long as, the stress level is below the threshold described by the slider element, the proposed model behaves like the viscoelastic Burgers model. For the higher stress level, where the plastic limit condition is satisfied, the viscoplastic unit is activated, and the corresponding plastic strain is calculated and is added to the elastic Burgers strain, resulting the total visco-elastoplastic strain.

The governing equation presented above is implemented in numerical finite difference code (FLAC^{2D}) using its built-in FISH language for constitutive models, and can be applied on different geotechnical construction accounting for the delayed deformation of rocks and rock masses.

3 MODEL APPLICATION

The existing geotechnical monitoring data of the Lyon-Turin Base Tunnel presented by Barla (2010) is considered here to verify the potential applicability of the proposed model. The model is applied to the rock mass surround the tunnel face to estimate the creep convergence of the excavated section. The analysis is carried out in a plane strain and hydrostatic stress condition. In addition, because of the symmetry by the vertical access, half of the tunnel face is generated and analyzed.

Table 1. Constitutive parameters used for the proposed model (Barla et al. 2010).

Parameters	Value	Unique
Bulk modulus, K	942	MPa
Cohesion, c	0.61	MPa
Friction angle, φ	28	degree
Dilatancy angle, ψ	0	degree
Tensile strength, σ_t	8.5E-3	MPa
Maxwell shear modulus, G^M	566	MPa
Maxwell viscosity, η^M	27.98	MPa.year
Kelvin viscosity, η^K	4.26	MPa.year
Kelvin shear modulus, G^K	498.1	MPa

According to the information mentioned by Barla, the equivalent radius for the cross section is 5.5 meters. With the overburden depth of 310 m, the isotropic stress σ_0 is 8.4 MPa. The influence of the primary lining and of the reinforcement system is neglected. The rock mass elastic modulus is assumed to be 1180 MPa. The constitutive parameters used for the proposed model are shown in Table 1.

The parameters presented above, which were obtained through laboratory creep tests, with an additional parameter value equals to 0.64 MPa.year for the viscoplastic dashpot element η^{vp}, are used to run the proposed model for 160 days after tunnel excavation. The face excavation is simulated in two steps. Following initialization, the top heading excavation is simulated with a stress relaxation equals to 87% of the initial stress state and then analyzed for 40 days using the proposed model to describe the creep behavior of rock mass. Afterwards, the invert excavation is operated and the analysis continues up to 160 days. Figure 3 shows the computed convergence plot versus time obtained from the analytical simulation.

It can be observed that the numerical results and the monitored data have a satisfactory agreement in magnitude and trend.

4 SUMMARY AND CONCLUSION

Based on the classic visco-elastic Burgers model, a new elastic-viscoplastic model is proposed in this paper. The Mohr-Coulomb element in parallel with a dashpot element is used to present the viscoplastic threshold. The governing equations of the proposed model are worked out for the three dimensional stress conditions. The model can simulate the time-dependent deformation of geomaterials as the primary and secondary stage of the creep curve. As a result, the

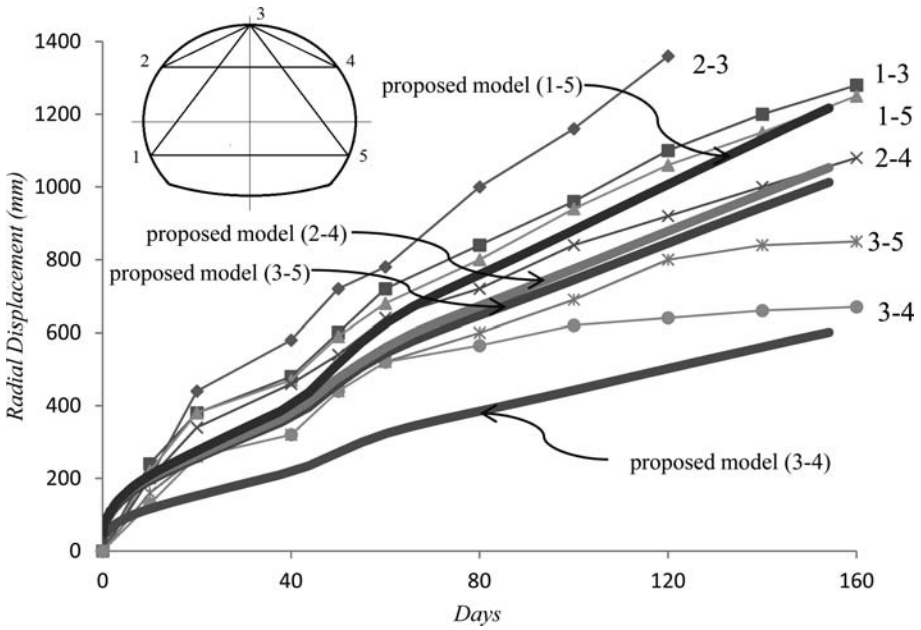


Figure 3. Computed (proposed model) versus monitored radial displacements.

primary stage is described by the Kelvin unit, while the secondary stage includes both elastic and plastic creep strain.

The constitutive equations of the model are implemented in the numerical finite difference code FLAC^{2D} using its built-in FISH language for constitutive models. To verify the applicability of the model, a tunnel section presented in the literature is examine to calculate the convergence after excavation. Satisfactory agreement is obtained between the numerical result and the monitored displacements for different parts of the tunnel face.

REFERENCES

Barla, G., Bonini, M. & Debernardi, D. 2010. Time-dependent deformations in squeezing tunnels. *International Journal of Geoengineering Case Histories* 2(1): 40–65.

Dai, H.L. 2004. Theoretical model and solution for the rheological problem of anchor-grouting a soft rock tunnel. *International Journal of Pressure Vessels and Piping* 81: 739–748.

Erichsen, C. & Werfling, J. 2003. Stability of underground openings in rock salt. In *ISRM 2003 – Technology Roadmap for Rock Mechanics (Proceedings of the 10th Congress of the ISRM*) 1: 301–304. Johannesburg: The South African Institute of Mining and Metallurgy.

Fahimifar, A., Monshizadeh Tehrani, F., Hedayat, A. & Vakilzadeh, A. 2010. Analytical solution for the excavation of circular tunnels in a visco-elastic Burger's material under hydrostatic stress field. *Tunnelling and Underground Space Technology* 25(4): 297–304.

Guan, Z. et al. 2008. A new rheological model and its application in mountain tunnelling. *Tunnelling and Underground Space Technology* 23(3): 292–299.

Kontogianni, V., Psimoulis, P. & Stiros, S. 2006. What is the contribution of time-dependent deformation in tunnel convergence? *Engineering Geology* 82: 264–267.

Malan, D.F. 1999. Time-dependent behaviour of deep level tabular excavations in hard rock. *Rock Mech. Rock Engng.* 32 (2): 123–155.

Minkley, W., Menzel, W., Konietzky, H. & te Kamp, L. 2001. A visco-elasto-plastic model and its application for solving static and dynamic stability problems in potash mining. In *Proceedings of the 2nd International FLAC Symposium* (Lyon, 29–31 October): 21–27.

Pan, Y.W. & Huang, Z.L. 1994. A model of the time-dependent interaction between rock and shotcrete support in a tunnel. *International Journal of Rock Mechanics and Mining Sciences & Geomechanics Abstracts* 31(3): 213–219.

Sakurai, S. 1978. Approximate time-dependent analysis of tunnel support structure considering progress of tunnel face. *International Journal for Numerical and Analytical Methods in Geomechanics* 2(2): 159–175.

Sterpi, D. & G. Gioda, G. 2007. Visco-plastic behaviour around advancing tunnels in squeezing rock. *Rock Mech. Rock Engng.* 42: 319–339.

Swift, G.M. et al. 2003. Numerical modelling of time-dependent deformation around an underground mine in rock salt. *Trans. Instn. Min. Metall.* A 110: 107–113.

Tomanovic, Z. 2006. Rheological model of soft rock creep based on the tests on marl. *Mech. Time-Depend. Mater.* 10(2): 135–154.

Rock Mechanics for Resources, Energy and Environment – Kwaśniewski & Łydżba (eds)
© 2013 Taylor & Francis Group, London, ISBN 978-1-138-00080-3

Efficient and numerically stable anisotropic failure criterion for micro layered rock

M. Kawa & D. Łydżba
Wroclaw University of Technology, Faculty of Civil Engineering, Wrocław, Poland

ABSTRACT: The paper deals with formulation and numerical implementation of anisotropic strength condition for micro layered rock. Periodically layered two–constituent microstructure is considered. The failure criterion of the constituents is assumed to be governed by Drucker-Prager strength condition. The macroscopic criterion is derived based on the micro-mechanics approach. It appears that a microstructure failure function can be satisfactory described by the conjunction of Jaeger critical plane condition and Pariseau anisotropic criterion. The formulation derived is then implemented into the commercial codes FLAC and FLAC3D. Numerical integration scheme, i.e. an elastic predictor and a plastic corrector of the failure function proposed are discussed in details, in the paper. Efficiency and numerical stability of the model proposed are verified against a series of numerical examples. The proposed model is also compared with "Ubiquitous Joints": a classical Jaeger critical plane approach available in FLAC environment. The presented results show that the model in some cases provides more precise description of micro-layered rock then Jaeger criterion.

1 INTRODUCTION

In many rocks one can recognize a characteristic pattern: two or more constituents appear in a form of thin, periodically repeating layers. These rocks are sometimes referred as "micro layered". The microstructure especially often occurs in sedimentary rocks: sandstone, claystone and schist are the most typical examples. The main consequence of the presence of micro layers in the material is its strong anisotropy in both elastic and inelastic range.

The micro layered rocks are usually considered in civil engineering practice as a problematic case for foundations. From the other hand necessity of structures foundation in such condition continues to grow. New structures are usually designed based on numerical calculations performed with some commercial codes. Identification and implementation of adequate, numerically efficient model of micro layered rock to one of these codes is an important and complex task.

A number of researchers focused on formulating a macroscopic anisotropic strength criterion for micro layered rocks based, mainly, on a phenomenological approach. Brief review of some of these criteria is presented in a work of Duveau et al. (1997). Two of these criteria are especially worth noting, i.e. Pariseau criterion (Pariseau 1972) which is an extension for the case of anisotropy of Drucker-Prager isotropic criterion, and Jaeger criterion (Jaeger 1960) which can be interpreted as a basis of a so-called critical plane approach.

The above mentioned Jaeger criterion is implemented as yield function for one of the plastic models available in FLAC and FLAC 3D codes. The model referred as "Ubiquitous Joints" is one of the few most popular models of micro layered rock.

Over the last few decades a rapid development of so-called homogenization techniques took place. These techniques are based, in general, on analysis of stress and strain fields at the level of a microstructure. Suqet (1987) showed that using this technique, an identification of a macroscopic failure surface of a medium with periodic microstructure consists in solving a yield design problem formulated at the level of a single periodic cell. This approach has been also successfully used for sedimentary rocks (e.g., Lydzba et al. 2003).

The main focus of this work is to present formulation and implementation of macroscopic failure criterion for micro layered rock, identified based on results obtained with micro mechanics analysis. The proposed criterion is a conjunction of the Jaeger critical plane approach and the Pariseau anisotropic criterion. As will be shown in the following sections the proposed model is in a very good agreement with micromechanics results and implemented into FLAC code is also the efficient tool for numerical calculations.

2 MACROSCOPIC FAILURE CRITERION

2.1 *Numerical identification of microstructure loading carrying capacity*

Macroscopic strength criterion can be defined as a closure of a set of admissible macro stress states. Macro stress state, in terms of micro mechanics, is admissible if associated micro stress field is self-equilibrated and does not violate the respective failure criterion for

all constituents involved (Suqet 1987). In addition the micro stress field has to be locally periodic for periodic structures. Above formulation can be written as:

$$f(\sigma_{ij}) \le 0 \Leftrightarrow \{\sigma_{ij}\} \in A = \{ < \tau_{ij} > | \exists \tau_{ij}(y) : \frac{\partial \tau_{ij}(y)}{\partial y} = 0, f(\tau_{ij}(y), y) \le 0, \tau_{ij}(y) - periodic \} \quad (1)$$

where σ_{ij}, $\tau_{ij}(y)$ represent macro stress tensor and associated micro stress field respectively, $f(\tau_{ij}(y),y)$ is a local strength criterion and V_{RVE} is a volume of periodic cell. Symbol <.> denotes operation of volume averaging over a periodic cell.

For all constituents of considered micro layered rock local criterion of failure has been assumed to be the Drucker-Prager one:

$$f(\tau_{ij}^{(\alpha)}) = a_\alpha I_1(\tau_{ij}^{(\alpha)}) + \sqrt{J_2(\tau_{ij}^{(\alpha)})} - k_\alpha \le 0 \quad (2)$$

where $I_1(\tau_{ij}^{(\alpha)})$ and $J_2(\tau_{ij}^{(\alpha)})$ denote first invariant of the micro stress tensor and the second invariant of the micro stress deviator for constituent α and a_α, k_α are Drucker-Prager strength parameters corresponding to constituent α.

The closure of the set defined by (1) represents, in space of principal macro stresses, a so-called macroscopic failure surface. This surface can be specified in a discrete manner by solving a set of optimization problems. Numerical procedure used by the authors is not discussed in the paper. The final results of the numerical calculation are only presented.

Two-constituent structure with equal volume fractions of constituents $t1 = t2 = 0.5$ is considered. Strength parameters of criterion are assumed to be: $k1 = 100$ kPa, $k2 = 20$ kPa, $a1 = 0.15$, $a2 = 0.05$. Results, plotted in forms of cross-sections of failure surface by octahedral plane are presented in Figures 1–3. The variables α and β measure the angles between principal load direction and material principal directions. Different shapes of cross-sections corresponding to different values of angles α and β indicate a strongly anisotropic behaviour of material studied.

2.2 *Identification of the macroscopic criterion*

The results presented in the previous section have been used for identification of the phenomenological model. The macroscopic criterion is proposed in the form of conjunction of the Pariseau anisotropic criterion:

$$f^{(1)}(\sigma_{ij}) = A_{ij}\sigma_{ij} + \sqrt{A_{ijkl}\sigma_{ij}\sigma_{kl}} - 1 \le 0 \quad (3)$$

and the Jaeger critical plane equation, which for Drucker-Prager material can be expressed as:

$$f^{(2)}(\sigma_{ij}) = \sqrt{\sigma_{12}^2 + \sigma_{13}^2} + \frac{3 a_c \sigma_{11} - k_c}{\sqrt{1 - 12 a_c^2}} \le 0 \quad (4)$$

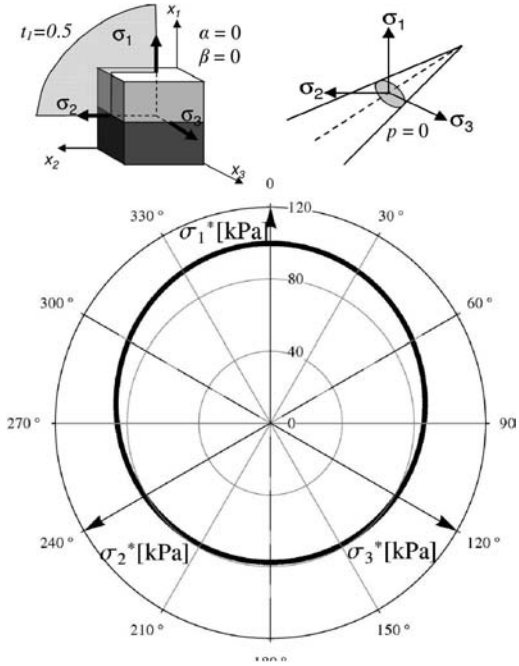


Figure 1. Macroscopic strength surface on octahedral plane for two-constituent micro layered rock with constituents governed by Drucker-Prager criterion.

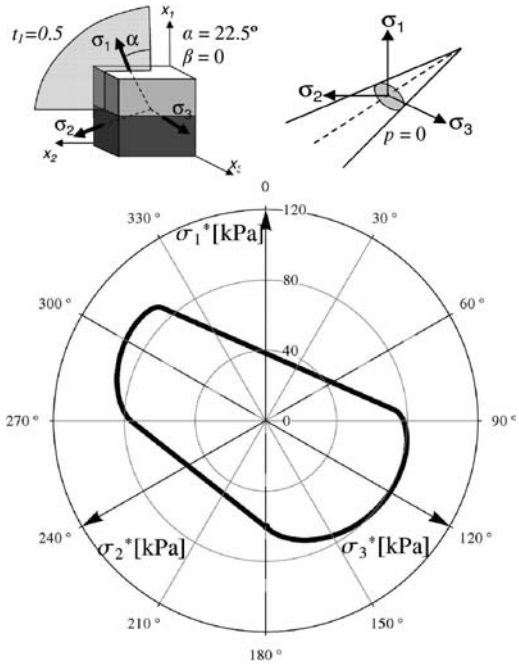


Figure 2. Macroscopic strength surface on octahedral plane for two-constituent micro layered rock with constituents governed by Drucker-Prager criterion.

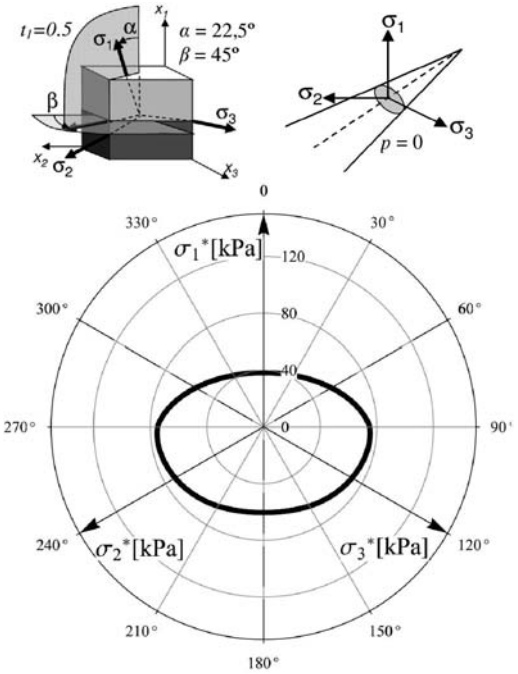


Figure 3. Macroscopic strength surface on octahedral plane for two-constituent micro layered rock with constituents governed by Drucker-Prager criterion.

In the above formulas A_{ij} and A_{ijkl} are anisotropic material tensors of the Pariseau criterion and a_c, k_c are strength parameters of critical plane equation. Note also that in the equation (4) notation of stress components assumes direction 1 to be as perpendicular to lamination direction.

All the parameters of proposed criterion, i.e. all components of A_{ij} and A_{ijkl} tensors and a_c, k_c can be identified as a function of strength parameters of the microstructure constitutes and its volume fraction.

In Figures 4–6 approximation of the criterion proposed against numerical results of the micro-mechanical analysis is shown. Results of the homogenization technique, presented before in Figures 1–3 are drawn with gray bold line and the approximation used is drown by a dashed line. As it can be seen the criterion proposed almost ideally agrees with the micromechanics predictions.

The comparison between proposed criterion and failure surface obtained with homogenization technique has been also tested for different values of confining pressure p and volume fraction t_1. In all these cases the fitting obtained is similar to the ones presented in Figures 4–6.

3 NUMERICAL IMPLEMENTATION OF THE MODEL PROPOSED

3.1 Numerical integration procedure

The proposed anistropic criterion has been implemented into FLAC and FLAC3D codes as plasticity

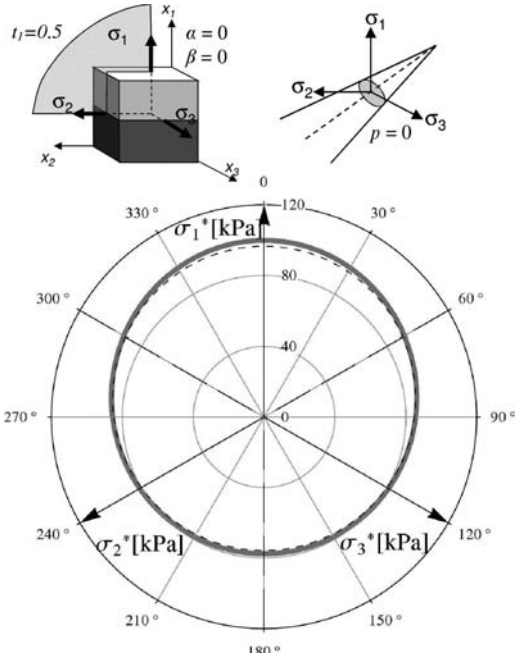


Figure 4. Comparison of proposed criterion (thin dashed line) with results of micro-mechanics (gray bold line).

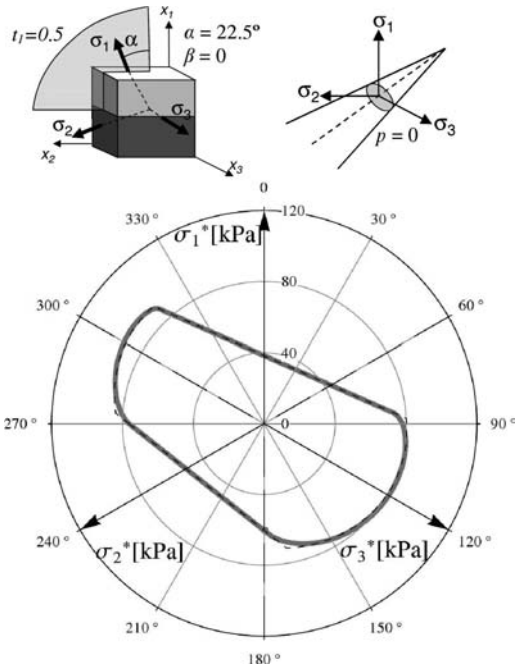


Figure 5. Comparison of identified criterion (thin dashed line) with results of micro-mechanics (gray bold line).

function for elastic-perfectly plastic model of material. Associated flow rule and small deformations have been assumed in the implementation. Following the methodology of FLAC environment user defined

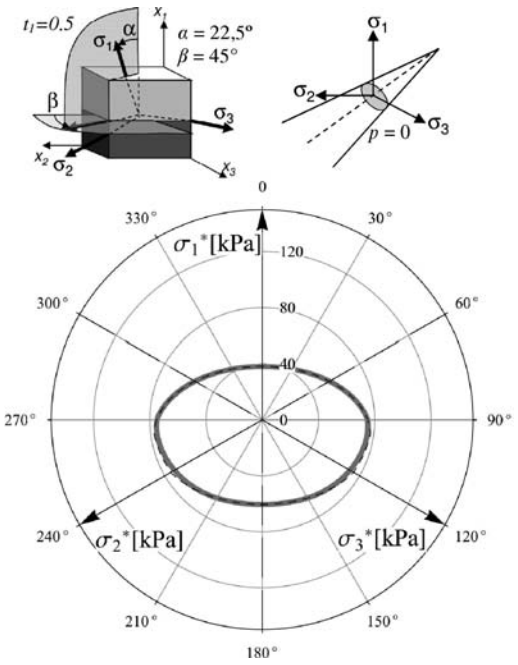


Figure 6. Comparison of identified criterion (thin dashed line) with results of micro-mechanics (gray bold line).

constitutive model written by authors in C++ language utilizes explicit method of time integration and incremental formulation of stress-strain relation. In this formulation plastic deformations of material can be expressed as:

$$\Delta\varepsilon_{ij}^{\ P} = \Delta\lambda \frac{\partial f(\sigma_{ij})}{\partial \sigma_{ij}} \tag{5}$$

where $\Delta\varepsilon^P$ denotes the increment of plastic strain tensor and $\Delta\lambda$ is the Lagrange multiplier.

Since for assumed small deformations total strain increment is a sum of elastic and plastic strain increments:

$$\Delta\varepsilon_{ij} = \Delta\varepsilon_{ij}^{\ E} + \Delta\varepsilon_{ij}^{\ P}, \tag{6}$$

the form of stress strain relation can be written as:

$$\Delta\sigma_{ij} = C_{ijkl}\Delta\varepsilon_{kl} - \Delta\lambda C_{ijkl}\frac{\partial f(\sigma_{kl})}{\partial \sigma_{kl}}, \qquad \sigma_{ij}^{\ n+1} = \sigma_{ij}^{\ n} + \Delta\sigma_{ij} \tag{7}$$

where σ_{ij}^n and σ_{ij}^{n+1} are the stress tensors in actual and following time step, respectively.

Using $\sigma_{ij}^{n+1\,trial} = \sigma_{ij}^n + C_{ijkl}\Delta\varepsilon_{kl}$ formulas (7) can be expressed as a sum of elastic predictor (elastic "guess") and a plastic corrector, i.e.:

$$\sigma_{ij}^{\ n+1} = \sigma_{ij}^{\ n+1\,trial} - \Delta\lambda C_{ijkl}\frac{\partial f(\sigma_{kl}^{\ n+1})}{\partial \sigma_{kl}^{\ n+1}} \tag{8}$$

It can be proved that for sufficiently small time step the following relation holds true (Kawa and Lydzba 2007):

$$\frac{\partial f^k(\sigma_{ij}^{\ n+1})}{\partial \sigma_{ij}^{\ n+1}} = \frac{\partial f^k(\sigma_{ij}^{\ n+1\,trial})}{\partial \sigma_{ij}^{\ n+1\,trial}} \tag{9}$$

The value of parameter $\Delta\lambda$ is determined by substituting (8) into (9) and requiring that the new stress point in plastic state is located on yield surface. The final form of numerical integration formulas can be written as follows:

$$\begin{aligned} &1^o \text{ when } f(\sigma_{ij}^{\ n+1\,trial}) \le 0 \\ &\Delta\lambda^k = 0,\ \sigma_{ij}^{\ n+1} = \sigma_{ij}^{\ n+1trial} \end{aligned} \tag{10}$$

$$\begin{aligned} &2^o \text{ when } f(\sigma_{ij}^{\ n+1\,trial}) > 0 \\ &\Delta\lambda^k = \frac{f^k(\sigma_{ij}^{\ n+1\,trial})}{\dfrac{\partial f^k(\sigma_{ij}^{\ n+1trial})}{\partial \sigma_{ij}^{\ n+1\,trial}} C_{ijkl} \dfrac{\partial f^k(\sigma_{kl}^{\ n+1trial})}{\partial \sigma_{kl}^{\ n+1\,trial}}} \\ &\sigma_{ij}^{\ n+1} = \sigma_{ij}^{\ n+1\,trial} - \Delta\lambda C_{ijkl}\frac{\partial f^k(\sigma_{kl}^{\ n+1})}{\partial \sigma_{kl}^{\ n+1}} \end{aligned} \tag{11}$$

When the stress path passes through the intersection of two functions involved in the criterion proposed, Koiter's rule (Koiter 1953) is applied in the implementation:

$$\Delta\varepsilon_{ij}^{\ P} = \sum_{i=1}^{2} \Delta\lambda \frac{\partial f^k(\sigma_{ij})}{\partial \sigma_{ij}} \tag{12}$$

3.2 *Conditions of numerical stability*

As has been mentioned in previous section the formulas (11) are correct only if time step used in calculations is small enough for equation (9) to be satisfied. A large number of numerical tests performed by the authors have shown that some additional conditions must be met by user in order to obtain correct results. These conditions are mainly due to the characteristics of FLAC codes and must be met also for other models used in this environment:

i) As a result of explicit integration method, time step must be small enough to ensure that the information will not be passed from one node to another in this interval. In the problems involving the determination of the bearing capacity of the structure this can be satisfied by using sufficiently small velocity of displacement (Fig. 7a) When this velocity is too high stress path often crosses the critical load value and then reaches it "from the above" (Fig. 7b).

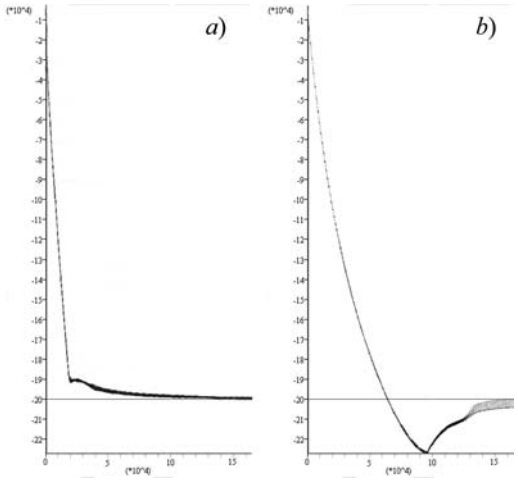


Figure 7. The compressive stress under foundation in problem of determination of bearing capacity. a) proper stress path b) stress path when the velocity of displacement is too high.

ii) The modeled problems are often mesh-dependent. If the localized shearing can occur in the problem, the gridlines should be parallel to lamination direction. If gridlines run differently, the zones close to localization of shearing often block each other, artificially increasing the critical load. For more complicated problems and finer grids it is usually of minor importance, but each time it should be checked.

3.3 *Comparision with ubiqiutous joints model*

As it has been mentioned above FLAC environment already includes model of micro layered rock. This model refered as "Ubiquitous Joints" uses Jaeger criterion (Jaeger 1960) as a plasticity function. The Jaeger criterion can be expressed, in a similar way that has been presented for the proposed model. It is a conjunction of isotropic Mohr Coulomb criterion and Mohr-Coulomb critical plane function. Since the model proposed by the authors bases on Drucker-Prager criterion (and its anisotropic extension) the results obtained with these two models differ, especially in 3D case.

Aside of these differences the proposed model is much more precise and flexible. As it has been shown in the section 2.2 the model perfectly agrees with results obtained with homogenization technique even if the rock has a significant (for example close to 0.5) volume fraction of the weaker component. A characteristic feature of these rocks is that their strength in a direction perpendicular and parallel to the plane of the lamination is usually much different especially if friction coefficient strongly differs in its individual components. In many cases Jaeger model doesn't provide a precise description of such rocks: The best fit of the micro mechanics results by the Jaeger model is presented in Figure 8.

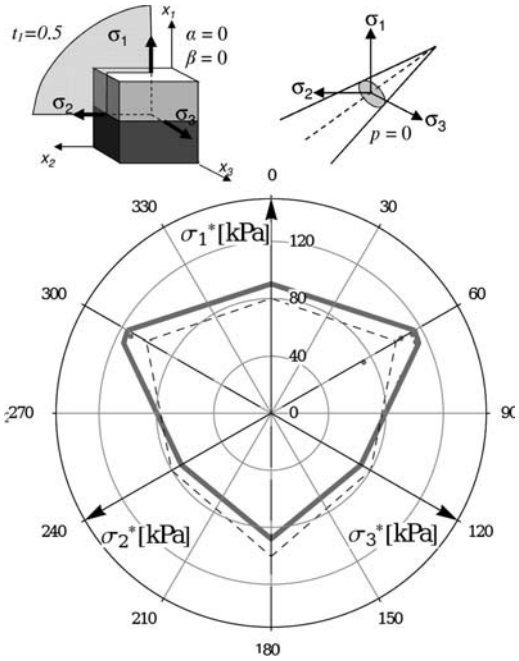


Figure 8. Comparison of Jaeger criterion (thin dashed line) with macroscopic strength surface for micro layered rock with Mohr-Coulomb constituents.

4 EXAMPLE APPLICATION: STRIP AND SQUARE FOOTINGS ON MICROLAYERED ROCK

The implementation of the model proposed has been applied to the boundary value problem of bearing capacity of microlayerd rock under rigid foundation. The parameters of microstructure has been assumed identical as for proeviously presented macroscopic failure surfaces, i.e. $k1 = 100$ kPa, $k2 = 20$ kPa, $a1 = 0.15$, $a2 = 0.05$. The volume fraction of both constitutents has been also assumed as equal: $t1 = t2 = 0.5$.

Two diffrent foundation problems have been considered: 2D problem of rock bearing capacity in plane strain state under strip footing and 3D bearing capacity of the rock under squre footing. The FLAC code as well as FLAC 3D program have been used respectively.

In 2D analysis the width of the footing has been assumed as equal to 1 [m]. A series of boundary value problems for diffrent values of lamination orientation parmeter α (defined on Figure 9a) has been solved. The obtained solution has been presented as function of α angle in Figure 10. As can be seen in this figure, anisotropic strength of rock strongly influences solution of boundary value problem.

In 3D problem the footing dimensions has been assumed also as equal to 1 [m]. This time lamination direction has been oriented by two angles α and β defined on Figure 9b. The result obtained for diffrent values of angles has been presented in Figure 11. As can be seen the value of dip angle α strongly affects

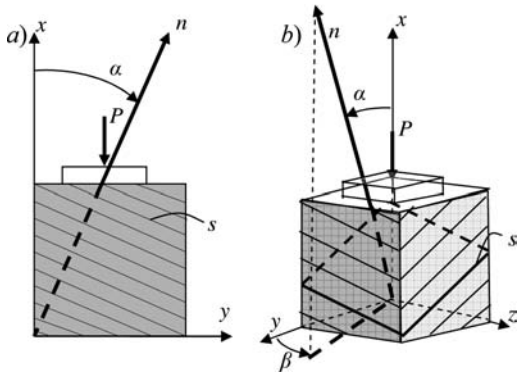


Figure 9. Definition of angles orienting lamination plane in 2D (a) and 3D (b) case.

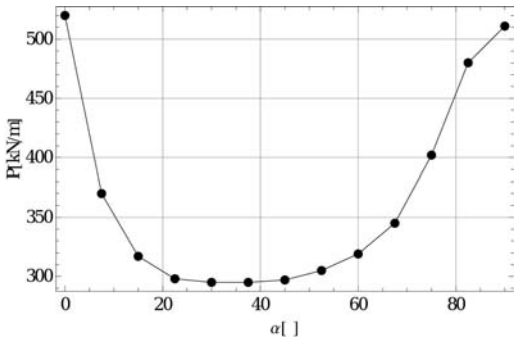


Figure 10. Bearing capacity of micro layered rock under strip foundation as a function of angle α orienting lamination plane.

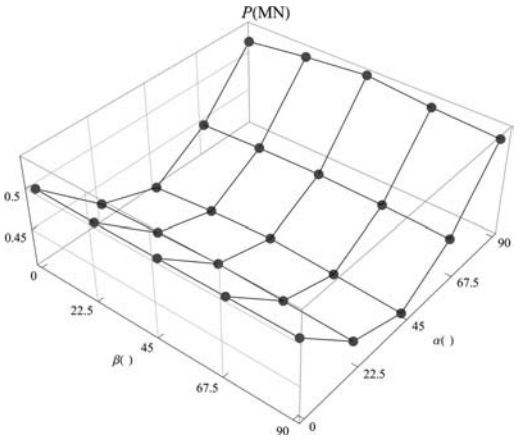


Figure 11. Bearing capacity of micro layered rock under square footing as a function of angles α and β orienting lamination plane.

the obtained solution whereas the azimuth angle β has a minor importance.

5 FINAL REMARKS

In this work strength anisotropic criterion for micro layerd rock derived by micro-mechanics approach has been proposed. Verification of the criterion proposed shows a very good agreement between identified criterion and micromechanics results.

The criterion has been implemented by authors into FLAC and FLAC3D codes. The details of implementation, conditions of numerical stability and comparison with different anisotropic model available in FLAC environment is discussed in the paper. It seems that presented model provides precise and numerically stable tool for geotechnical calculations.

The implementation assumes small strain and associated flow rule.

REFERENCES

Duveau, G., Shao, J.F. & Henry, J.P. 1998. Assessment of some failure criteria for strongly anisotropic rocks. *Int. J. Numer. Anal. Meth. Geomech*. 3(1): 1–26.

Jaeger, J.C. 1998. Shear failure of anisotropic rocks. *Geol. Mag.*. 97(1): 65–72.

Kawa, M. & Lydzba, D. 2007. Usefulness of Hill criterion for description of strength of layered geomaterials (in Polish), *Proceedings of the XXXth Winter School of Rock Mechanics*.

Koiter, W.T. 1953. Stress-strain relations, uniqueness and variational theorems for elastic-plastic materials with a singular yield surface. *Q. Appl. Math*. 11: 350–354.

Lydzba, D., Pietruszczak, S. & Shao, J.F. 2003. On anisotropy of stratified rocks: homogenization and fabric tensor approach. *Comput. Geotech*. 30(4): 289–302.

Pariseau, W.G. 1968. Plasticity theory for anisotropic rocks and soils. *Proceedings of 10th Symposium on Rock Mechanics*, Austin: American Rock Mechanics Association.

Suquet, P. 1987. Elements of homogenisation for inelastic solid mechanics, *Lecture Notes in Physics* 272: 193–278.

Rock Mechanics for Resources, Energy and Environment – Kwaśniewski & Łydżba (eds)
© 2013 Taylor & Francis Group, London, ISBN 978-1-138-00080-3

An extended Lemaitre's viscoplastic model

X. Lei & F.L. Pellet
INSA-University of Lyon, France

ABSTRACT: Lemaitre's viscoplastic model is widely used to model the long-term behavior of rocks, especially argillaceous rocks that are being considered as host rocks for radioactive waste repositories. However, this model has marked disadvantages, such as pressure independency and no volumetric viscoplastic strain, which greatly limit its ability to reproduce the complex phenomena in underground structures. In view of these, based on thermodynamic principles, Lemaitre's phenomenological viscoplastic model is extended in this paper. Two equivalent surfaces are introduced in the *p-q* stress plane in order to consider the contribution of hydrostatic stress on the viscoplastic strain and damage respectively. The inherent concept is that the stress points located on the same equivalent surface share the same intensity for both viscoplastic strain and damage. Moreover, in this model, the non-associated flow rule is assumed and a hyperbolic viscoplastic potential is used to reproduce volumetric viscoplastic deformation. The time dependent damage evolution law is also modified to rely on inelastic strain. In order to verify the constitutive model and to study the newly added parameters, several numerical procedures were performed corresponding to quasi-static tests, creep tests and relaxation tests. Finally, a detailed discussion about the influences of these parameters on both compression and tension cases is presented.

1 INTRODUCTION

Lemaitre's viscoplastic model is widely used to characterize the long-term behavior of argillite (Souley et al. 2011) as well as to model the time dependent evolution of the Excavation Damage Zone (EDZ) around underground openings (Pellet et al. 2009). However this constitutive model assumes that the hydrostatic stress has no influence on the viscoplastic behavior and it imposes no volumetric viscoplastic strain. These are obvious drawbacks in its ability to model geomaterial behavior.

In this paper, an extension of Lemaitre's model that will overcome these drawbacks is presented. Based on thermodynamic principles, two equivalent surfaces are introduced to take into account the influence of hydrostatic stress on both the evolution of viscoplastic strain and damage. In addition, the volumetric viscoplastic strain is introduced by using a hyperbolic viscoplastic potential. The time dependent damage evolution law is also modified to be dependent on inelastic strain. This model is implemented into the finite element software ABAQUS 6.10, and detailed studies of the new parameters are performed by modeling quasi-static tests, creep tests and relaxation tests.

2 EXTENSION OF THE LEMAITRE MODEL

2.1 *Brief description of Lemaitre's model*

Lemaitre's constitutive model is a viscoplastic model that includes damage and it was initially developed for metal (Lemaitre 1996). This model unified both short-term and long–term behavior into a unique elasto-viscoplastic model. The total strain is divided into elastic, ε_e, and viscoplastic ε_{vp} parts and it is assumed that the viscous phenomena are developed simultaneously with plasticization:

$$\dot{\boldsymbol{\varepsilon}} = \dot{\boldsymbol{\varepsilon}}_e + \dot{\boldsymbol{\varepsilon}}_{vp} \tag{1}$$

The elastic behavior is supposed to be linear isotropic and from the generalized Hooke's law, the elastic strain rate is defined as:

$$\dot{\boldsymbol{\varepsilon}}_e = \frac{1+\nu}{E}\dot{\boldsymbol{\sigma}} + \frac{\nu}{E} tr(\dot{\boldsymbol{\sigma}}) \cdot \boldsymbol{I} \tag{2}$$

where E is the elastic modulus and ν the Poisson's ratio.

The viscoplastic strain rate is given by the following expression:

$$\dot{\boldsymbol{\varepsilon}}_{vp} = \dot{p}\frac{\partial q}{\partial \boldsymbol{\sigma}} = \frac{3}{2}\left(\frac{q}{Kp^{1/M}}\right)^N \frac{\boldsymbol{S}}{q} \tag{3}$$

This law takes a hardening effect into account through the parameter p, and the hardening rate is given by

$$\dot{p} = \left(\frac{q}{Kp^{1/M}}\right)^N \tag{4}$$

where K, M and N are the viscoplastic parameters of the model.

This viscoplastic model is usually extended by coupling with the continuum damage theory to model the progressive failure phenomena and rupture in the tertiary creep stage. Based on the concept of effective stress proposed by Kachanov (1959), the equivalence principle is applied by replacing the nominal stress tensor σ with effective stress tensor $\tilde{\sigma}$.

$$\tilde{\boldsymbol{\sigma}} = \frac{E}{\tilde{E}}\boldsymbol{\sigma} = \frac{\sigma}{1-D} \tag{5}$$

The damage parameter D ranges between 0 and 1; $D = 0$ corresponds to the intact state of material and $D \# 1$ to failure. Moreover, the evolution law of damage is expressed by the Rabotnov-Kachanov equation (Kachanov 1959, Rabotnov 1969):

$$\dot{D} = \left\langle \frac{\chi(\sigma)}{A} \right\rangle^r (1-D)^{-k} \tag{6}$$

where $\langle\ \rangle$ are the Macaulay brackets and A, $r$and k the damage law parameters. The equivalent damage stress is given by:

$$\chi(\sigma) = \zeta max\sigma_i + \xi 3\sigma_m + (1-\zeta-\xi)\sigma_{eq} \tag{7}$$

in which $0 < \zeta + \xi < 1$

The coupled viscoplastic damage law is now expressed as:

$$\dot{\varepsilon}_e = \frac{1+\nu}{E}\cdot\frac{\dot{\sigma}}{1-D} + \frac{\nu}{E}\cdot\frac{tr(\dot{\sigma})}{1-D}\cdot\boldsymbol{I} \tag{8}$$

$$\dot{\varepsilon}_{vp} = \frac{3}{2(1-D)}\left(\frac{q}{(1-D)Kp^{1/M}}\right)^N \frac{S}{q} \tag{9}$$

Lemaitre's viscoplastic damage model is a phenomenological model whose parameters can be divided into three groups: the elastic constants E and ν; viscoplastic parameters K, M and N, and damage parameters A, r and k. A complete identification and discussion is given in Pellet et al. (2005). The parameter K represents the viscoplastic stiffness, N is the viscosity exponent and M is the strain-hardening exponent. The damage parameter, A, is called the tenacity coefficient; the role played by A in the damage process is comparable to those played by the coefficient K in viscoplasticity. The parameter r is the damage exponent, and k is the damage progression parameter (Pellet et al. 2009).

2.2 *Extension of Lemaitre's model*

As mentioned above, the Lemaitre model has two obvious drawbacks when modeling geomaterials:

1. There is no dependence on hydrostatic stress. However, under different confining pressures, geomaterials show some significantly different behaviors. In triaxial compression tests, if the confining pressure is increased, the strength increases simultaneously and also brittle-ductile transitions, contraction and dilation transitions happen in this process. Also creep tests conducted under uniaxial conditions give different responses than those tests conducted with a confining pressure.
2. Dilatation has been observed in many types of rock (Cristescu & Hunsche 1998). Depending on the stress state, the volume of a specimen increases or decreases due to overall micro-cracking (opening or closing). When dilation occurs, the permeability of the rock is increased (Selvadurai & Selvadurai 2010). Therefore, the inelastic compressibility/dilation is of utmost importance to assess the sealing efficiency of rocks around an Excavation Damaged Zone.

In view of the above drawbacks, some extensions have been made to the original Lemaitre viscoplastic damage model. The extended model keeps the assumption of strain partition, (i.e. the strain rate tensor is divided into elastic and viscoplastic parts), as expressed by equation (1). However, for the elastic behavior, the total stress-strain relationship is adopted, and can be expressed as:

$$\boldsymbol{\sigma} = \boldsymbol{E}:(\boldsymbol{\varepsilon} - \boldsymbol{\varepsilon}_{vp}) \tag{10}$$

This is partially due to its convenience for implementation and intuitive physical significance when coupled with damage. The other detailed processes are presented as follows.

2.2.1 *Extended viscoplastic model*

In this part, Lemaitre's viscoplastic model without damage is extended first. In order to consider the influence of hydrostatic stress, it is assumed that in the p-q stress plane, a series of equivalent viscoplastic surfaces exist, and thus all the stress points located on the same viscoplastic surface will share the same viscoplastic intensity. Therefore, the so-called equivalent viscoplastic stress $\bar{\sigma}_{vp}$ is defined as:

$$\bar{\sigma}_{vp} = q - \alpha_{vp}\cdot p \tag{11}$$

where α_{vp} is the slope of the equivalent viscoplastic surfaces in p-q stress plane. A new equivalent viscoplastic potential is therefore expressed as:

$$\Omega_{vp} = \frac{K}{N+1}\cdot\left(\frac{\bar{\sigma}_{vp}}{K}\right)^{N+1}\cdot\bar{\varepsilon}_{vp}^{-N/M} \tag{12}$$

where K, N and M are the same parameters as in the original models and $\bar{\varepsilon}_{vp}$ is the equivalent viscoplastic strain. The equivalent viscoplastic strain rate (or the viscoplastic intensity on the equivalent viscoplastic surface) can be defined as:

$$\dot{\bar{\varepsilon}}_{vp} = \frac{\partial\Omega_{vp}}{\partial\bar{\sigma}_{vp}} = \left(\frac{\bar{\sigma}_{vp}}{K\bar{\varepsilon}_{vp}^{1/M}}\right)^N \tag{13}$$

So far, only the viscoplastic intensity is defined and a viscoplastic potential is still needed to control the flow direction. Thus a hyperbolic function is adapted to depict the viscoplastic potential G_{vp}, and is given by:

$$G_{vp} = \sqrt{(\delta\tan\psi)^2 + q^2} - p\tan\psi \tag{14}$$

where ψ is the angle of dilation.

With the adoption of a hyperbolic function, the viscoplastic potential is continuous and smooth. It ensures that the flow direction is always uniquely defined. The function approaches a parallel to its asymptotic line $G = q - p\tan\psi$ at high confining pressure and intersects the hydrostatic pressure axis at a right angle. δ is a small value which is related to the rate of this process.

The viscoplastic flow rule is then defined in such a way that

$$\dot{\varepsilon}_{vp} = \frac{\dot{\bar{\varepsilon}}_{vp}}{f_{vp}}\frac{\partial G_{vp}}{\partial \sigma} = \frac{\dot{\bar{\varepsilon}}_{vp}}{f_{vp}}\left(\frac{3S}{2\sqrt{(\delta\tan\psi)^2+q^2}} + \frac{1}{3}tan\psi\, \boldsymbol{I}\right) \quad (15)$$

where Warning: f_{vp} is an intermediate variable, which is introduced in the process of extending the uniaxial case to a triaxial case. Based on the thermodynamics principle, the mechanical power Φ_{vp} dissipated by the viscoplastic process can be expressed as:

$$\Phi_{vp} = \bar{\sigma}_{vp} \cdot \dot{\bar{\varepsilon}}_{vp} = \boldsymbol{\sigma} : \dot{\boldsymbol{\varepsilon}}_{vp} \quad (16)$$

By substituting equation (15) into (16), f_{vp} is then defined by:

$$f_{vp} = \frac{1}{\bar{\sigma}_{vp}}\boldsymbol{\sigma} : \frac{\partial G_{vp}}{\partial \sigma} = \frac{\bar{\sigma}_{vp}}{\sqrt{(\delta\tan\psi)^2+\bar{\sigma}_{vp}{}^2}} \quad (17)$$

Finally, the viscoplastic flow without damage is expressed as:

$$\dot{\boldsymbol{\varepsilon}}_{vp} = \frac{\dot{\bar{\varepsilon}}_{vp}\sqrt{(\delta tan\,\psi)^2+\bar{\sigma}_{vp}{}^2}}{\bar{\sigma}_{vp}}\left(\frac{3S}{2\sqrt{(\delta\tan\psi)^2+q^2}} + \frac{1}{3}tan\psi\, \boldsymbol{I}\right) \quad (18)$$

2.2.2 *Extended viscoplastic damage model*

Similar to Lemaitre's original damage model, the assumptions of effective stress and isotropic damage are still used. The isotropic elastic Hooke's law is then redefined as:

$$\boldsymbol{\sigma} = (1-D)\boldsymbol{E} : (\boldsymbol{\varepsilon} - \boldsymbol{\varepsilon}_{vp}) \quad (19)$$

In the same way as in the Rabotnov-Kachanov equation, the hardening variable of the evolution of damage is replaced by the equivalent viscoplastic strain rate, and the equivalent damage stress function is replaced by a simplified form:

$$\dot{D} = \left(\frac{\bar{\sigma}_d}{A}\right)^r \left(\dot{\bar{\varepsilon}}_{vp}\right)^\chi \quad (20)$$

$$\bar{\sigma}_d = q - \alpha_d \cdot p \quad (21)$$

where α_d is the slope of the equivalent damage surfaces in p-q stress plane.

In the viscoplastic formulation, the damage effect can be represented by the influence of the equivalent viscoplastic function. Thus the only part affected by damage is the equivalent damage stress function in the dissipation potential. The other variables remain unchanged. Thus the potential coupled with damage is written as:

$$\tilde{\Omega}_{vp} = \frac{K}{N+1}\cdot\left(\frac{\tilde{\bar{\sigma}}_{vp}}{K}\right)^{N+1}\cdot \bar{\varepsilon}_{vp}{}^{-N/M} \quad (22)$$

$$\tilde{\bar{\sigma}}_{vp} = \tilde{q} - \alpha_{vp}\cdot\tilde{p}$$

$$\tilde{q} = \sqrt{\frac{3}{2}\tilde{S}:\tilde{S}} \quad (23)$$

where $\tilde{q} = \sqrt{\frac{3}{2}\tilde{S}:\tilde{S}}$ is the equivalent effective stress, with the effective stress deviator $\tilde{S} = \tilde{\sigma} + \tilde{p}I$, and the effective volumetric stress $\tilde{p} = -\frac{1}{3}tr(\tilde{\delta})$.

When the viscoplastic dissipation potential is coupled to damage, the equivalent viscoplastic strain rate is redefined as:

$$\dot{\tilde{\varepsilon}}_{vp} = \frac{\partial\tilde{\Omega}_{vp}}{\partial\tilde{\bar{\sigma}}_{vp}} = \frac{\partial\tilde{\Omega}_{vp}}{\partial\tilde{\bar{\sigma}}_{vp}}\frac{\partial\tilde{\bar{\sigma}}_{vp}}{\partial\bar{\sigma}_{vp}} = \frac{1}{1-D}\left(\frac{\bar{\sigma}_{vp}}{(1-D)K\bar{\varepsilon}_{vp}{}^{1/M}}\right)^N \quad (24)$$

The viscoplastic flow rule coupled with damage is then expressed as:

$$\dot{\varepsilon}_{vp} = \frac{\dot{\bar{\varepsilon}}_{vp}}{f_{vp}}\frac{\partial\tilde{G}_{vp}}{\partial\tilde{\sigma}} = \frac{\dot{\bar{\varepsilon}}_{vp}}{f_{vp}}\left(\frac{3\tilde{S}}{2\sqrt{(\delta\tan\psi)^2+\tilde{q}^2}} + \frac{1}{3}\tan\psi\, I\right) \quad (25)$$

The viscoplastic potential coupled with damage is given by:

$$\tilde{G}_{vp} = \sqrt{(\delta\tan\psi)^2 + \tilde{q}^2} - \tilde{p}\tan\psi \quad (26)$$

The mechanical power dissipated by the viscoplastic process can still be computed by the following equation:

$$\Phi_{vp} = \tilde{\bar{\sigma}}_{vp}\cdot\dot{\tilde{\varepsilon}}_{vp} = \tilde{\sigma}:\dot{\varepsilon}_{vp} \quad (27)$$

By substituting equation (25) into (27), f_{vp} can be solved as:

$$f_{vp} = \frac{1}{\bar{\sigma}_{vp}}\tilde{\sigma}:\frac{\partial\tilde{G}_{vp}}{\partial\tilde{\sigma}} = \frac{\tilde{\bar{\sigma}}_{vp}}{\sqrt{(\delta\tan\psi)^2+\tilde{\bar{\sigma}}_{vp}{}^2}} \quad (28)$$

Finally, the viscoplastic flow with damage is expressed as

$$\dot{\varepsilon}_{vp} = \frac{\dot{\bar{\varepsilon}}_{vp}}{f_{vp}}\left(\frac{3S}{2\sqrt{\left(\frac{\delta\tan\psi}{1-D}\right)^2+q^2}} + \frac{1}{3}\tan\psi\, I\right) \quad (29)$$

$$f_{vp} = \frac{\sigma_{vp}}{\sqrt{\left(\frac{\delta\tan\psi}{1-D}\right)^2+\bar{\sigma}_{vp}{}^2}} \quad (30)$$

3 DISCUSSION OF THE NEW MODEL

The main features of the extended Lemaitre model compared to the original are the introduction of two equivalent surfaces and the hyperbolic viscoplastic

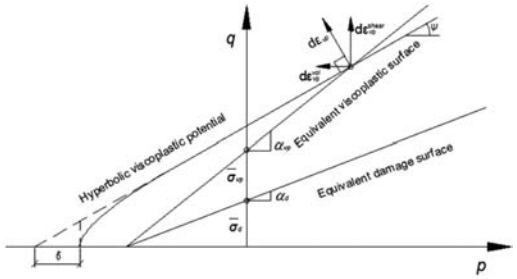


Figure 1. Schematic of key surfaces in the *p-q* stress plane.

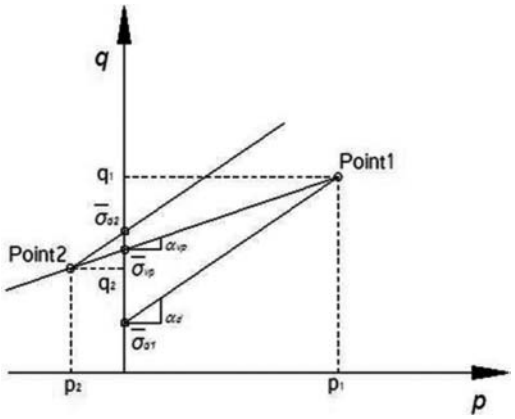


Figure 2. Scheme of equivalent method on equivalent surfaces.

potential, as shown in Figure 1. Using this extension, the original model becomes more suitable for modeling the complex behavior of geomaterials.

In order to consider the influence of hydrostatic pressure, a family of equivalent surfaces is assumed to exist in the *p-q* stress plane both for the viscoplastic and damage strength. In order to explain this basic concept, a demonstration case is presented in Figure 2. Two points located at the positive and negative parts of the hydrostatic stress axis represent the compression and tension stress state separately. In this case, Point 1 and Point 2 will have the same viscoplastic rate, so they have the same equivalent viscoplastic stress $\bar{\sigma}_{vp}$. However, Point 2 is much closer to failure than Point 1, which has a larger equivalent damage stress ($\bar{\sigma}_{d2} > \bar{\sigma}_{d1}$). Numerous models for geomaterials show that in this model, the slope of the equivalent damage curve should be larger than the one for the equivalent viscoplastic curve. Figure 2 also shows that when two points experience the same viscoplastic strain in tension and in compression their apparent strength will be different (i.e. the compressive strength is larger than the tensile strength).

The model extension adds three new parameters to the original (i.e. the slopes of the equivalent surfaces in the *p-q* stress plane α_{vp} and α_d plus the dilation angle ψ). A parametric study for these three new

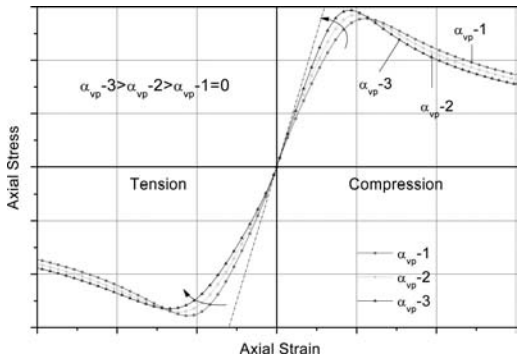


Figure 3. Strain-Stress curves of uniaxial quasi-static tests with different α_{vp}.

parameters is presented below. The discussion on the other parameters can be found in Pellet et al. (2005).

3.1 *On the parameter α_{vp}*

When the slope α_{vp} is changed, different intensities of the hydrostatic pressure will be obtained. This is true for all stress points located on the same equivalent viscoplastic surface (i.e. that share the same intensity of viscoplastic potential).

Figure 3 shows how the hydrostatic pressure influences the viscoplastic deformation in both quasi-static compression and quasi-static tension tests. When $\alpha_{vp} = 0$ (i.e., there is no dependence on hydrostatic pressure), the strain-stress curve show no difference between compression and tension. It is common knowledge that higher hydrostatic stress will reduce the viscoplastic effect. Therefore, from equation (11) and for the case $\alpha_{vp} \neq 0$, greater α_{vp} means smaller viscoplastic potential in compression test ($p > 0$). However, it will increase the viscoplastic intensity in tension tests ($p < 0$). As a result, a strain-stress curve with a larger α_{vp} is closer to the elastic line, which means a smaller viscoplastic strain in compression tests (Fig. 3). The opposite phenomena can be found in tension tests.

It should be also noted that the peak strengths are larger when the strain-stress curves are closer to the elastic line. This is because the lines closest to the elastic line have less viscoplastic strain in the same loading period; this has the same effect as increasing the loading rate.

In Figure 4, a larger α_{vp} shows greater creep strain in tension and smaller creep strain in compression, which means that the hydrostatic pressure can reduce the creep deformation in compressive creep tests and increase the creep deformation in tensile creep tests. As α_{vp} is always positive in this model, geomaterials subjected to the same constant load in tension will have larger creep deformation than in compression. Hence failure will be reached earlier.

When subject to constant displacement, larger viscoplastic strains will lead to larger stress relaxation. In Figure 5, a larger α_{vp} in compressive relaxation test

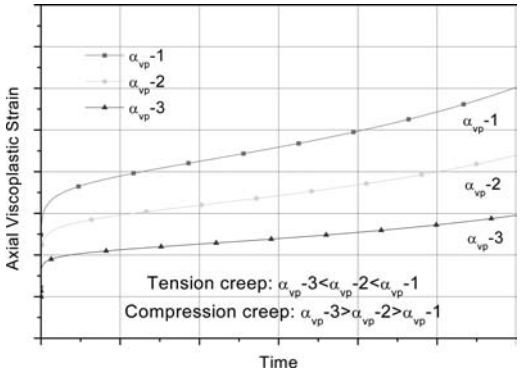


Figure 4. Simulation of creep tests with different α_{vp}.

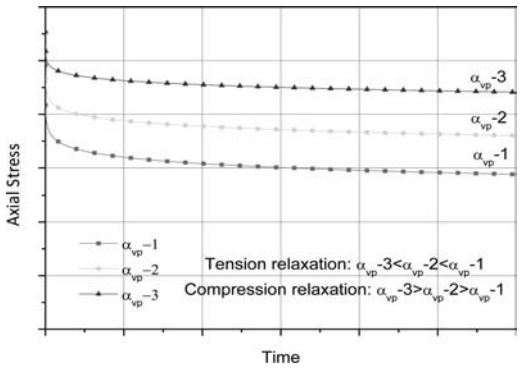


Figure 5. Simulation of relaxation test with different α_{vp}.

represent a smaller viscoplastic strain in the same time period, which leads to lower stress drops. However in the tensile relaxation test, a larger α_{vp} allows faster stress drops.

3.2 *On the parameter α_d*

Using the same notion of an equivalent viscoplastic surface, all the stress points on the same equivalent viscoplastic surface (iso-damage surface) share the same intensity of damage potential. Therefore, this parameter can be used to control the dependence of damage on the hydrostatic pressure.

Positive hydrostatic stress can reduce the evolution of micro-cracks in geomaterials, whereas negative hydrostatic stresses lead to an increase in micro-cracks. In Figure 6, these effects on short-term behavior lead to a higher strength when taking into account more hydrostatic effects (a larger α_d) in the compression test. In the tension test a larger α_d accelerates the damage evolution, which represents a lower material strength. Hence, by choosing a suitable α_d, the difference between the strength in compression and in tension can be considered.

Similarly to the short-term behavior, Figure 7 shows that under the same constant load, three different values of α_d lead to three different stages of creep curves.

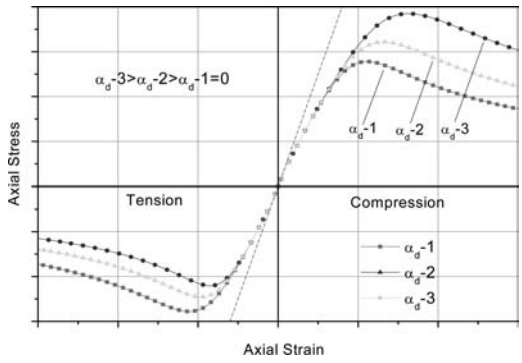


Figure 6. Strain-Stress curves of uniaxial quasi-static tests with different α_d.

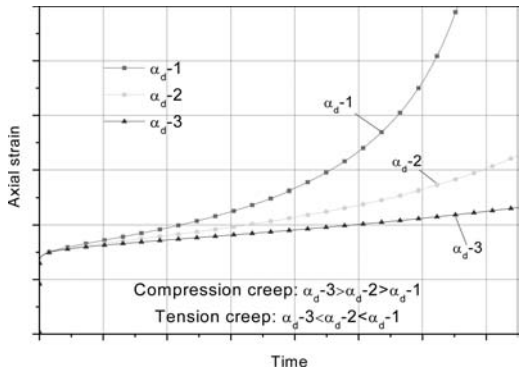


Figure 7. Simulation of creep test with different α_d.

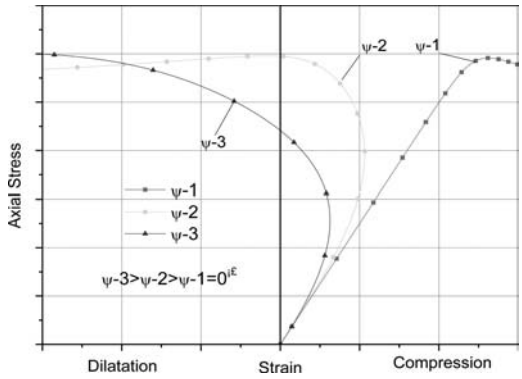


Figure 8. Simulation of uniaxial quasi-static test with different ψ.

These results show how important the hydrostatic stress is in contributing to the evolution of damage.

3.3 *On the dilation angle ψ*

For the sake of simplicity, the angle of dilation ψ is introduced to consider irreversible volumetric strains. The results of a series of uniaxial quasi-static and creep tests are presented in Figures 8 and 9. By increasing

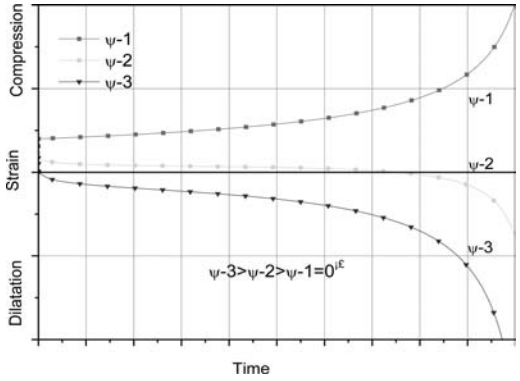


Figure 9. Simulation of uniaxial creep test with different ψ.

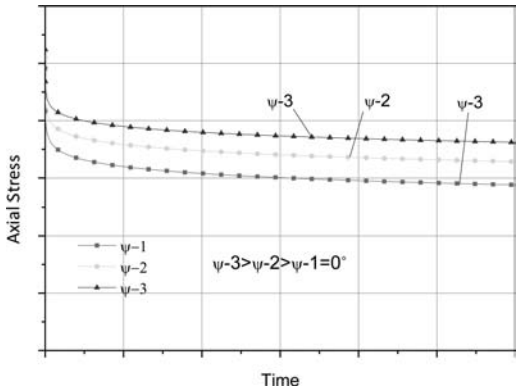


Figure 10. Simulation of uniaxial relaxation test with different ψ.

the value of the dilation angle ψ, the volumetric strain goes from negative to positive, which means more dilatation.

In the uniaxial relaxation tests, the dilatation resulting from the constant strain loading translates into lateral viscoplastic strain. Hence it will lead to a reduction in the axial viscoplastic strain, as shown in Figure 10, where a larger value of the dilation angle leads to less stress relaxation.

4 SUMMARY AND CONCLUSIONS

In order to better model the complex long-term behavior of rocks, the rate-dependent, strain hardening, damage coupled phenomenological viscoplastic-Lemaitre model was extended specifically to overcome its drawbacks of pressure independency and no volumetric viscoplastic strain. First, based on thermodynamic principles, the influence of hydrostatic pressure for the viscoplastic and damage strength is considered by introducing two different equivalent surfaces. Secondly, the original von Mises-type flow rule is replaced by the hyperbolic viscoplastic potential; thus volumetric inelastic strain can be taken into account. Finally, the time-dependent Rabotnov-Kachanov equation for damage evolution is modified to depend on the inelastic strain.

Numerical experiments including quasi-static tests, creep tests and relaxation tests were performed to study the newly added parameters. By choosing a suitable slope for the equivalent viscoplastic and damage surfaces, the influence of hydrostatic pressure can be consider qualitatively both in compression and extension cases. The inequality of deformation and strength between compression and tension in geomaterials can also be properly represented. The dilation angle makes the extended model capable of accounting for the dilatation effects in isotropic cases.

From a preliminary study, the newly extended model is now suitable for modeling the complex time-dependent behavior of soft rocks. The model still needs to be validated by modeling the complex phenomena of underground structures, and the effects of pore pressure should also be considered in the future.

REFERENCES

Cristescu, N. Hunsche, U. 1998. Time Effects in Rock Mechanics. Wiley. New York.

Kachanov, M. 1959. Effective elastic properties of cracked solid: critical review of some basic concepts. Applied Mechanics Reviews 45: 304–335.

Lemaitre, J. 1996. A Course on Damage Mechanics. Second ed. Springer, Berlin, Heidelberg, New York.

Pellet, F., Hajdu, A., Deleruyelle, F., Besnus, F. 2005. A Viscoplastic model including anisotropic damage for the time dependent behavior of rock. International Journal for Numerical and Analytical Methods in Geomechanics, 29(9): 941–970.

Pellet, F., Roosefid, M. Deleruyelle, F. 2009. On the 3D numerical modeling of the time-dependent development of the damage zone around underground galleries during and after excavation. Tunneling and Underground Space Technology, 24(6): 665–674.

Rabotnov, Y.N. 1969. Creep rupture. Proc of the 12th International Congress on Theoretical and Applied Mechanics (ICTAM). Springer: Stanford, CA, U.S.A..; 342–349.

Selvadurai, A.P.S. Selvadurai, P.A. 2010. Surface permeability tests: Experiments and modelling for estimating effective permeability, Proceedings of the Royal Society, Mathematical and Physical Sciences Series A, 466: 2819–2846.

Souley, M. Armand, G. Su, K. Ghoreychi, M. 2011. Modeling the viscoplastic and damage behavior in deep argillaceous rocks. Physics and Chemistry of the Earth, Parts A/B/C, 36(17–18): 1949–1959.

Rock Mechanics for Resources, Energy and Environment – Kwaśniewski & Łydżba (eds)
© 2013 Taylor & Francis Group, London, ISBN 978-1-138-00080-3

Modeling fault activation due to the evolution of remote stresses

M.T. Myers, V.A. Dunayevsky & M.B. Bennett
Shell International E&P, Houston, Texas, USA

ABSTRACT: The Eshelby like approach is used to successfully model the stress and strain fields associated with a fault subject to evolving remote stresses. A modified Cam-Clay material model is implemented as the constitutive equations for the fault material. The exterior of the fault is modeled as an infinite homogeneous linear elastic material and body forces are not considered. These assumptions allow a semi-analytical approach to be applied. The stresses exterior to the fault are induced by evolving either the vertical or horizontal remote stresses. The fault is represented as an elastic-plastic (modified Cam-Clay) high aspect ratio ellipsoidal inclusion loaded by the calculated exterior stress field. Two mechanisms are discussed as criteria for fault activation, runaway instability and negative rate of work of plastic strains. Two initial conditions are considered for the fault material model. First where the parameters for the material model are supplied by the user. Second where the initial effective mean stress and shear stress are assumed to be in the immediate vicinity of the intersection of the critical state line and yield surface. The differing predictions that follow from these two assumptions are discussed.

1 INTRODUCTION

Commonly used methods to investigate fault stability do not account for the stress and strain field inside the fault. They equate the stresses and strains inside and outside and use a simple failure criteria such as Mohr-Coulomb to assess when faults activate. A typical approach is to assume two frictional surfaces with cohesion. This level of approximation becomes questionable, particularly for sharp material contrasts between the host and fault material.

We propose in the following work a more sophisticated model for fault activation. The approach taken here is to represent the fault as a thin ellipsoidal inclusion in an infinite elastic host. The constitutive behavior of the interior of the ellipsoidal is modeled by a Cam-Clay material. Homogeneous material properties are assumed in the interior of the fault, and therefore, due to ellipsoidal geometry, the stress-strain fields in the fault will be uniform. These fields are calculated using the Eshelby approach (Eshelby 1957). This allows a material properties mismatch between the host rock and the fault to be taken into account.

The exterior of the fault is modeled as an infinite homogeneous linear elastic material and body forces are not considered. The stresses exterior to the fault are produced by varying the remote external stresses.

This approach leads to a system of differential equations for the evolution of the internal stress and strain fields interior to the fault due to these varying external stresses. Continuous traction and displacements are assumed at the interface between the fault and the host rock.

Two initial stress states are considered for the fault. The first case considered is where the MCC material model parameters are completely unconstrained. The second case is where the effective mean stress and shear stress are assumed to be near the intersection of the critical state line and yield surface. This assumption implies that the stresses have not evolved significantly after the creation of the fault. This assumption determines two of the parameters in the MCC material model, i.e. preconsolidation stress and the position of the critical state line.

Following a brief introduction to the MCC model, we will consider two mechanisms of fault activation, negative rate of work of plastic strains (NRW) and runaway instability (RAI). Another mechanism for fault instability, the formation of deformation bands, will be explored elsewhere.

2 MODIFIED CAM-CLAY

The general formulation of the Modified Cam-Clay (MCC) material model is shown in Figure 1, where deviatoric stress is plotted against mean stress (P-Q plot). Here P is the effective mean stress, Q is the stress deviator, and P0 is the preconsolidation stress. The preconsolidation stress is defined as the maximum historic mean stress that has been applied to the material. The key features of this model are regions of negative and positive hardening, separated by a critical state line (CSL). It is the presence of a region of negative hardening that allows at least two different modes of failure to occur (Charlez 1991).

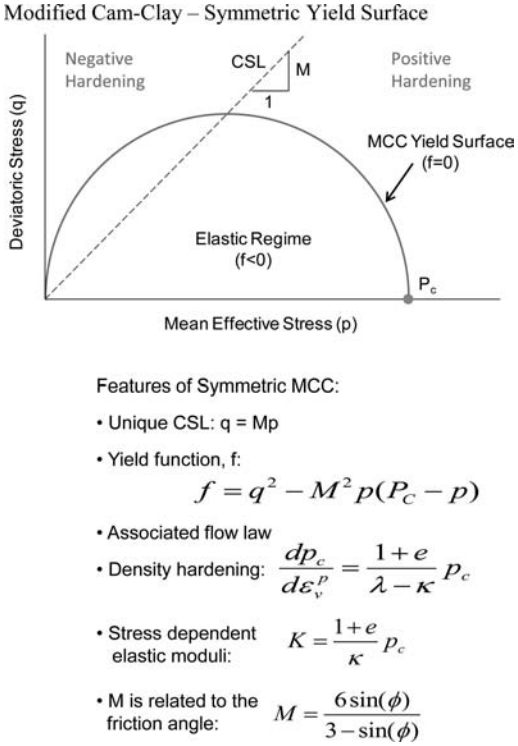


Figure 1. The p-q plot for a Modified Cam-Clay (MCC) model is shown above. The Critical State Line (CSL) separates a region of positive hardening from a region of negative hardening. K is the bulk modulus. λ and κ are cam-clay parameters.

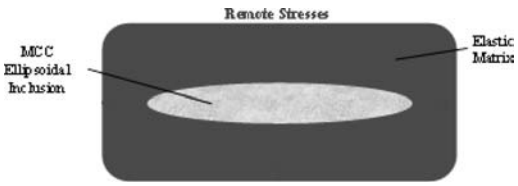


Figure 2. A MCC ellipsoid inside the elastic host matrix.

3 ELASTO-PLASTIC INCLUSION MODELS

The fault is an elastic-plastic (MCC) ellipsoids imbedded in an infinite linear elastic host matrix (Fig. 2). The stresses and strains evolve due to the change of a single parameter called the "loading parameter". This may be either a horizontal or a vertical remote stress.

The assumptions of the model include:

- The continuity of displacements and tractions is imposed on the host/inclusion interface.
- Homogeneous material properties for the host and the inclusion.
- Infinite host medium.
- No body forces applied.

4 FAILURE MECHANISMS

Runaway instability (RAI) and negative rate of work of plastic strains (NRW) are explored as candidates for the mechanism for fault activation.

RAI was first discussed by Rudnicki (1977). Within the framework of the MCC model, it occurs when the stress path approaches the critical state line, where the fault experiences infinitely growing strains.

Another mechanism of instability is related to the rate of work of plastic strains. The rate of work of plastic strains is defined as follows:

$$\dot{w} = \sigma_{ij}\dot{\varepsilon}_{ij} = \left(q^2 + M^2 p^2\right)\Lambda \tag{1}$$

where q is the stress deviator, p the mean effective stress, M defines the position of critical state line, and Λ is the plastic multiplier. Application of the Clausius-Duhem theory gives (Charlez 1991):

$$\dot{S} = \frac{1}{T}\sigma_{ij}\dot{\varepsilon}_{ij} > 0 \tag{2}$$

The second law of thermodynamics requires entropy to increase as depletion proceeds. Therefore, a negative plastic multiplier in Eq. (1) implies a violation of the second law of thermodynamics. The plastic multiplier may become negative, which contradicts to Eq. (2).

The conventional interpretation would be an elastic unloading of the material. For an ellipsoidal inclusion, because of the assumption of monotonically evolving stress, a negative rate of work cannot be interpreted as unloading. Because we are on the yield surface, we cannot continue with purely elastic strains. NRW is therefore interpreted as delamination of the fault from the host material.

5 ELLIPSOIDAL INCLUSION WITH REMOTE STRESSES

We investigate a single ellipsoidal inclusion embedded in an infinite host matrix subject to evolving remote stresses, as in Figure 2. The loading parameter is either vertical or horizontal stress. We examine the stress and strain evolution of the inclusion and the failure mechanisms that results for a variety of different scenarios.

5.1 *Maximum principal stress vertical stress changing (normally consolidated)*

In Figure 3 and Figure 4 we consider a fault with its normal oriented parallel to the vertical remote stress. This fault does not activate, but as expected the stresses interior to the fault follow a stress path represented by the zero lateral strain stress path. To the left of the CSL, NRW may occur.

As we increase the angle between the normal and the critical stress, we find that the induced strains increase,

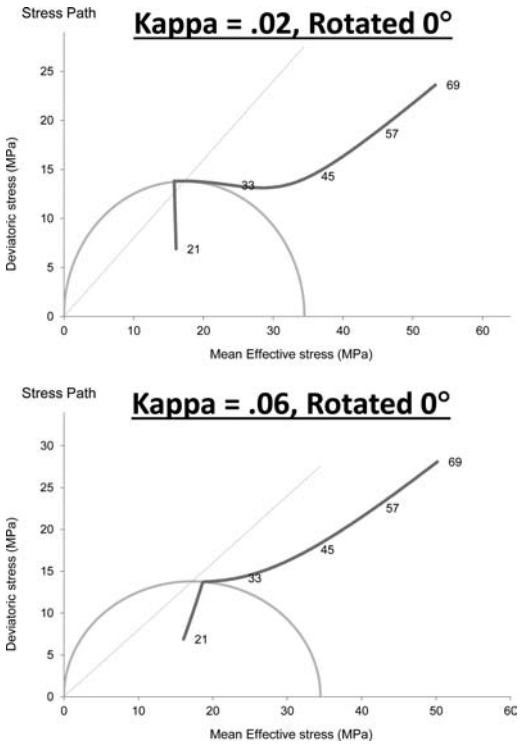


Figure 3. With the fault oriented horizontally, we approach zero lateral strain behavior. The loading parameter is increasing vertical remote stress. The stress path encountered the yield surface and moves to the right. RAI occurs when the stress path encounters the CSL. In this case, the material property kappa = 0.02. The numbers along the stress path are the values of the evolving loading parameter (vertical stress).

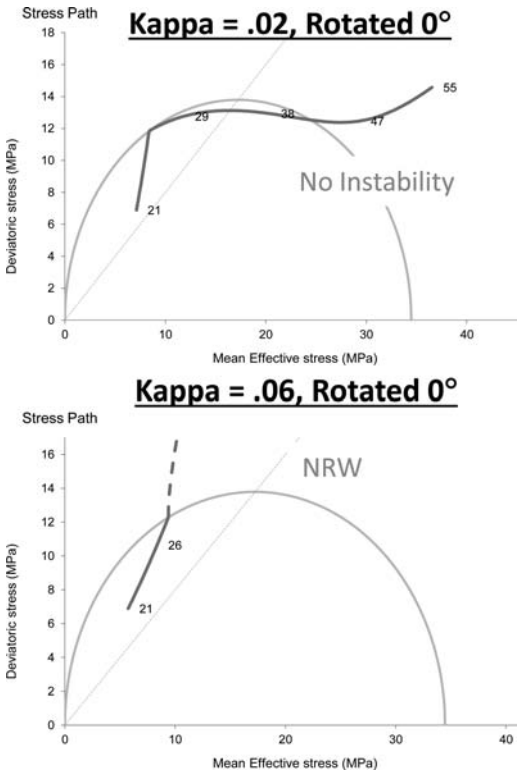


Figure 4. To the left of the CSL, with a horizontal fault (the zero lateral strain case), NRW may be encountered.

but we still don't interpret this as failure since the strains don't approach infinity at a finite stress (Fig. 5).

However, at angles above 60°, the situation changes dramatically and we find failures occur (Fig. 6). The details depend on materials parameters such as kappa. With increasing kappa, the stress at which failure occurs goes down. The existence of a "critical angle" can be explained by the interaction between shear stress and dilation. A maximum in shear stress resolved along the plane of the fault occurs at 45°. In addition, mean stress interior to the fault start to reduce at higher angles, directing stress paths toward the critical state line and a RAI failure mechanism. The exact value of the critical angle depends on the details of the material parameters and the angles between the fault and the remote stresses. This reduction in mean stress is somewhat unexpected and a clear difference between this and traditional approaches to the fault activation problem.

For angles significantly above this "critical angle" RAI no longer occurs. This is attributed to a reduction in shear stresses resolved along the plane of the fault (Fig. 7).

In Figure 8 and Figure 9, we explore the behavior of the model by changing different material parameters. A lower kappa results in RAI occurring more quickly (Fig. 8). A higher compaction coefficient (Cm) of the host matrix also results in RAI occurring more quickly (Fig. 9).

In Figure 10, we look at examples of vertical compaction were the stress path encounters the yield surface to the left of the CSL. Here, we find the NRW often occurs when the stress path encounters the yield surface. Changing the value of kappa may change the results from a stable fault to one which fails due to NRW.

In Figure 11 and Figure 12, we show examples were the loading parameter is decreasing vertical stress (vertical extension). This kind of stress regime could be found in a fault located above or below a depleting reservoir. In these cases, the stress path is moving to the right. When the stress path encounters the yield surface to the right of the CSL, the stress path crosses the CSL with no instability encountered (Fig. 11). To the left of the CSL, changing the material property kappa change the mode of failure from NRW to RAI (Fig. 12).

5.2 *Maximum principal stress horizontal (e.g. extensional basin)*

Here, we consider situations where the evolving remote stress is a horizontal stress. An example is

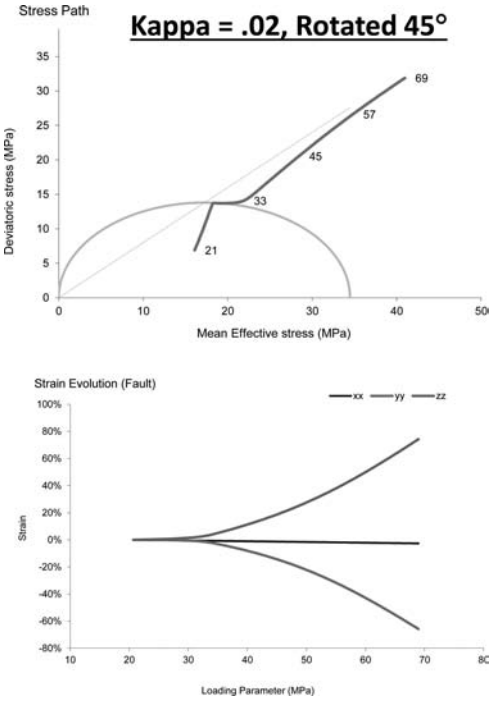


Figure 5. With the fault rotated at 45° as compared to Figure 3 and with kappa = 0.02, the CSL is approached. We still don't interpret this as failure since the strains don't approach infinity at a finite stress.

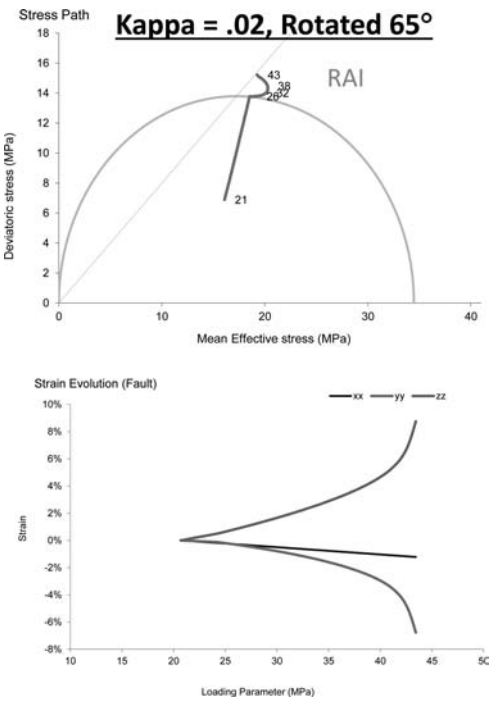


Figure 6. With the fault rotated at 65° as compared to Figure 3 and with kappa = 0.02, RAI occurs.

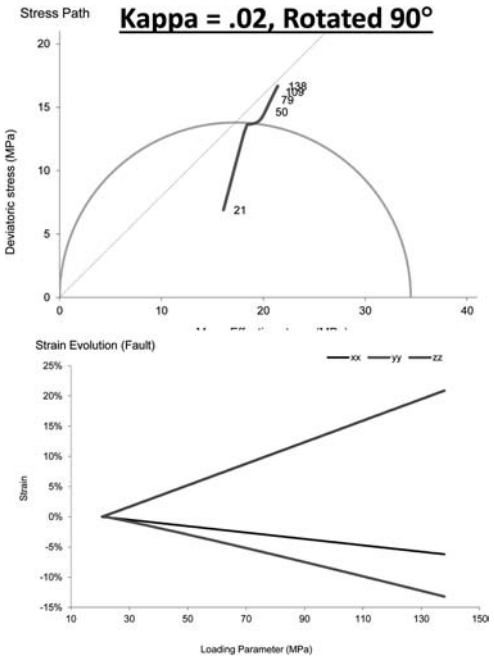


Figure 7. With the fault oriented vertically as compared to Figure 3 and with kappa = 0.02, RAI no longer occurs. This is attributed to a reduction in shear stresses resolved along the plane of the fault.

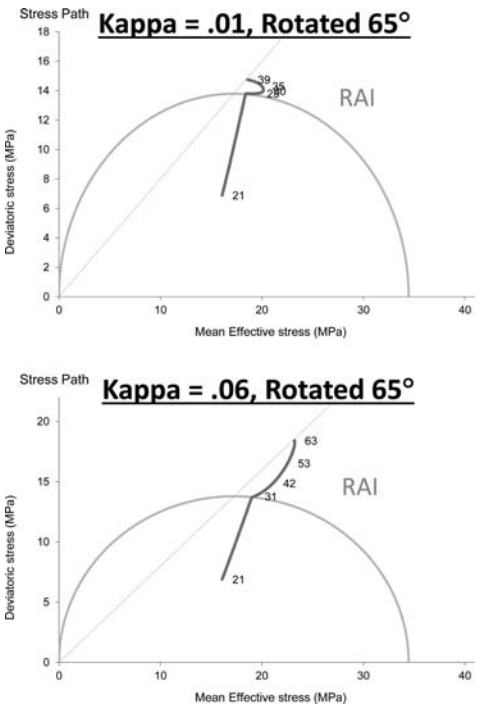


Figure 8. With a lower kappa as compared to Figure 6, RAI is encountered more quickly (left figure). With a higher kappa, RAI occurs more slowly (right figure).

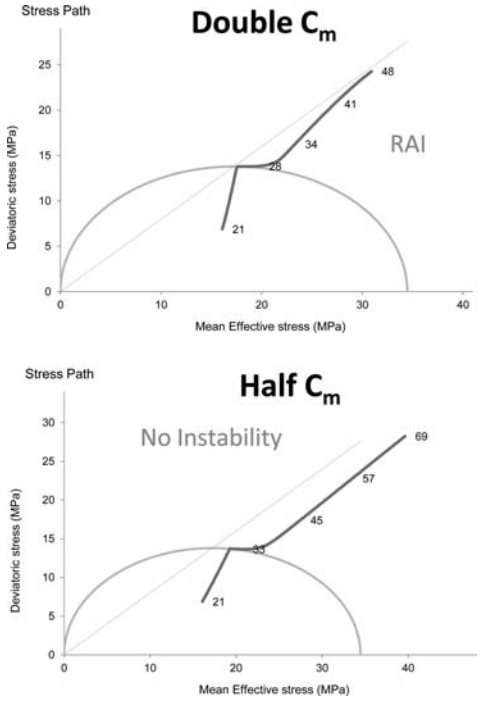


Figure 9. Here we modify the compaction coefficient (C_m) of the host matrix as compared to Figure 5. To the left, we double C_m, resulting in RAI. To the right we reduce Cm by half, resulting in no instability.

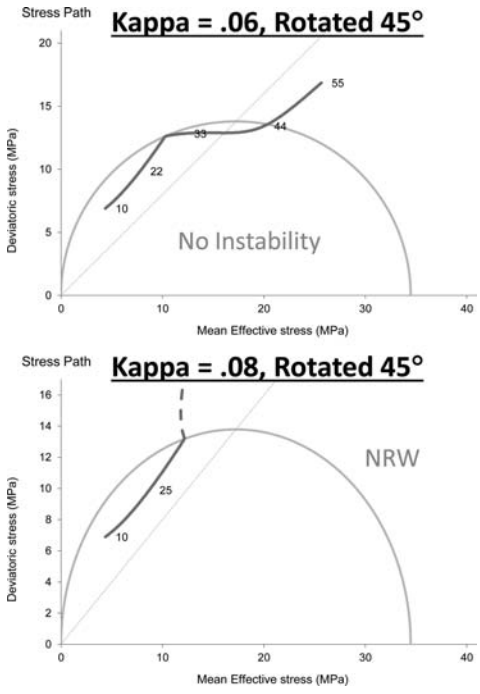


Figure 10. To the left of the CSL, NRW may occur. In the example on the left, with kappa = 0.06, we have no instability. On the right, with kappa increased to 0.08, NRW occurs.

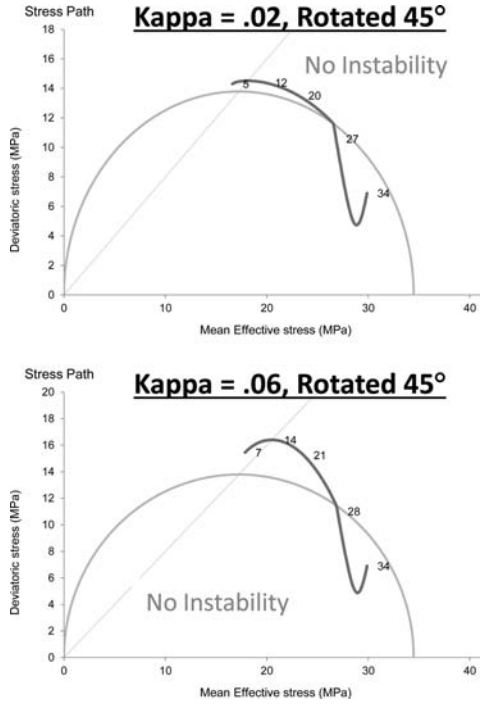


Figure 11. With vertical extension as the loading parameter, when the stress path is encountered to the right of the CSL, the stress path proceeds across the CSL into the region of negative hardening.

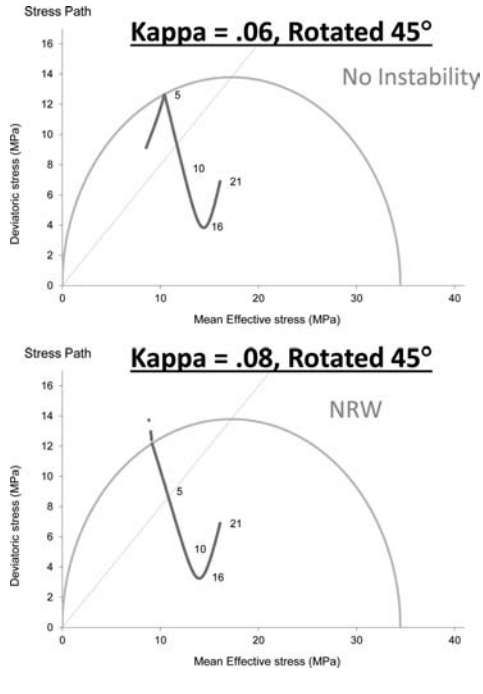
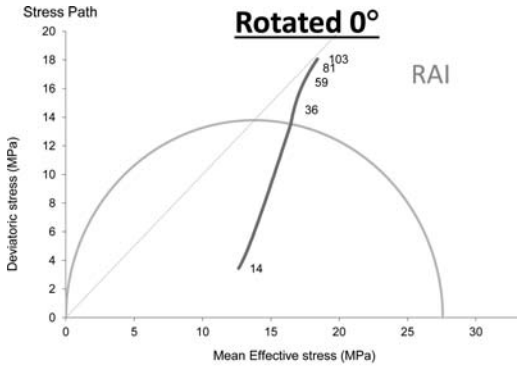


Figure 12. To the left of the CSL, NRW may occur. As in Figure 11, vertical extension is the loading parameter. In the figure on the left, with kappa = 0.06, we have no instability. On the right, with kappa increased to 0.08, NRW occurs.



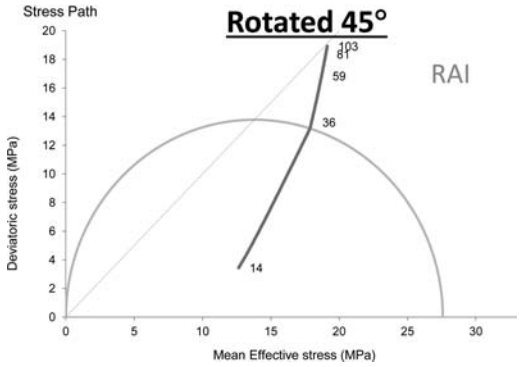
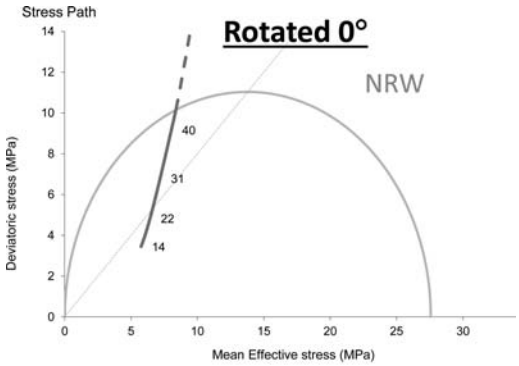


Figure 13. Here the loading parameter is compression along a single horizontal axis. RAI occurs as the stress path approaches the CSL. In the figure to the left, the ellipsoidal is flat horizontal. In the figure to the right, the ellipsoid has been rotated by 45° around the horizontal axis. The stress path approaches the CSL even more quickly.



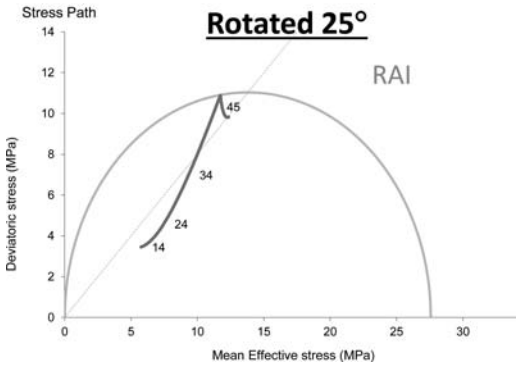


Figure 14. As in Figure 14, the loading parameter is compression along a single horizontal axis. Here, however, the stress path encounters the yield surface to the left of the CSL. In the figure on the left, NRW occurs immediately when the stress path encounters the yield surface. In the figure to the right, with the fault rotated by 25°, the stress path encounters the yield surface and then rebounds down to the CSL, resulting in RAI.

shown in Figure 13. The loading parameter is increasing horizontal stress (horizontal compaction). This could approximate a thrust fault stress regime. RAI is typical in this situation. With the ellipsoid rotated at 45°, RAI is encountered even more quickly.

In Figure 14, we look at cases were the stress path encounters the yield surface to the left of the CSL. In this case, with the fault horizontal, NRW occurs. With the fault rotated 25°, RAI occurs.

In Figure 15, we consider the case of horizontal extension. This kind of stress regime could be found in an extensional basin. In the first case, the stress path encounters the yield surface to the right of the CSL. It then crosses the CSL and no instability is encountered. In the second case, by shifting the initial stresses to lower mean stress, the stress path encounters the yield surface to the left of the CSL, and again, no instability is encountered. In the third case, with the initial mean stress even lower, NRW occurs immediately when the stress path encounters the CSL.

5.3 *Modeling fault activation, initial state determined*

Here we assume that the insitu stresses have not evolved significantly since the creation of the fault. This allows us to calculate the position of the critical state line and preconsolidation stress. This frame-work addresses a major difficulty with modeling fault activation, since usually the material properties for the fault are unknown.

In Figure 16, we show an example of applying this approximation. In compression, no fault activation criteria are met. With further compression, the fault would activate due to RAI. If the same fault is subject to extension rather than compression, NRW is encountered. The stress path starts on the critical state line and results in fault activation due to the NRW criteria when the stress path encounters the yield surface.

These two mechanisms are very different in terms of their physical interpretation. RAI would tend to smear material into the fault, which would lead to decreased transmissibility. NRW, i.e. delamination of the fault, would lead to increased transmissibility. This is to our knowledge the first time that two mechanisms have been identified corresponding to very different physical effects observed in the sub-surface.

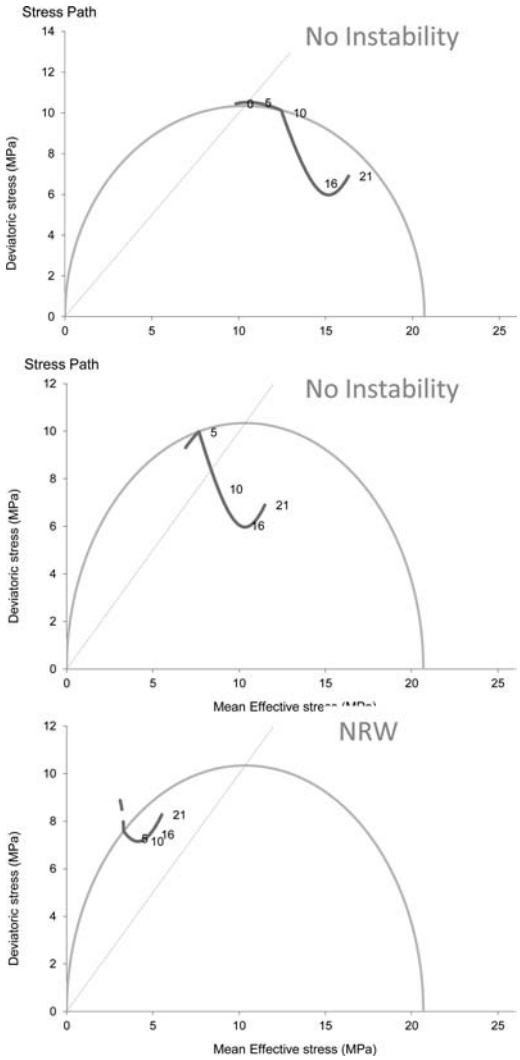


Figure 15. Here the loading parameter is extension along a single horizontal axis. In the first figure, the stress path encounters the yield surface to the right of the CSL. It then crosses the CSL and no instability is encountered. In the second figure, the stress path encounters the yield surface to the left of the CSL, and again, no instability is encountered. In the third figure, with the stress path further to the left of the CSL, NRW occurs immediately when the stress path encounters the CSL.

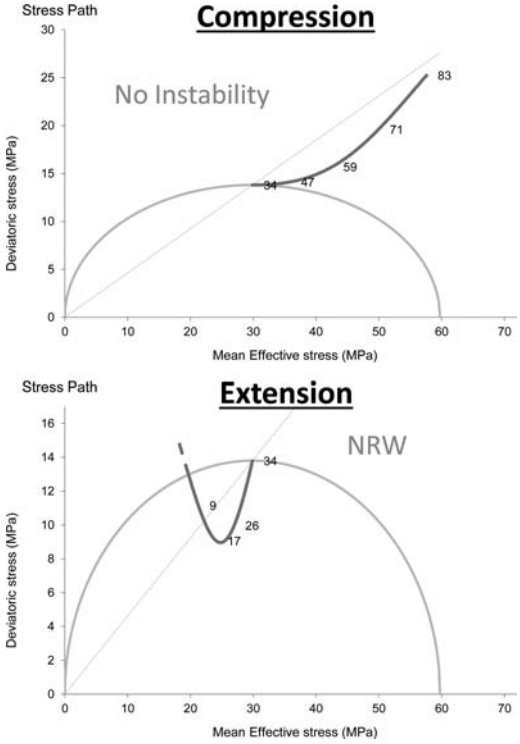


Figure 16. Fault with Initial State Determined. In compression, the fault is stable. Further compression would lead to RAI. In extension, the NRW fault activation criteria is met when the material yields.

6 CONCLUSIONS

It is found that fault activation is sensitive to material properties, fault orientation, and initial external stresses. Preconsolidation is a key factor for activation of a fault due to the negative rate of work criteria. The assumption of the fault being near the critical state is an important technique to narrow the range of possible parameters, and therefore the critical conditions for fault activation.

We have identified two independent mechanisms for fault activation due to two very different physical mechanisms. RAI is associated with smearing the material and decreasing transmissibility. NRW, on the other hand, is associated with delamination of the fault and increased transmissibility.

With the critical state assumption for the fault, we should be able to determine the initial dimensions of the fault. The fault has to be in a stable equilibrium with the initial external stresses. It would then be possible to investigate the post critical evolution of the fault, particularly the final new equilibrium dimensions.

This work represents a simple and computationally efficient way of addressing the effects of plasticity on fault activation. A typical model may be run in seconds allowing multiple scenarios to be run and the full impact of changing parameters, stress fields, etc. to be explored. In many situations an ellipsoid may be a sufficiently accurate approximation to the geometry. Even in simple geometries, we find significant effects due to plasticity.

A MCC material model is applicable to a wide range of materials where sufficient amounts of cements have formed. Therefore, it presents a useful tool for geomechanical analysis of failure.

REFERENCES

Eshelby, J.D. 1957. The determination of the elastic field of and ellipsoidal inclusion, and related problems. *Proc. Roy. Soc. Lond.* A241(1226): 376–396.

Rudnicki, J.W. 1977. The inception of faulting in a rock mass with a weakened zone. *Journal of Geophysical Research* 82(5): 844–854.

Charlez, P.A. 1991. *Rock Mechanics*, Vol. 1. Paris: Editions Technip.

Rock Mechanics for Resources, Energy and Environment – Kwaśniewski & Łydżba (eds)
© 2013 Taylor & Francis Group, London, ISBN 978-1-138-00080-3

A case study of large scale rock mass preconditioning by confined blasting

I. Onederra
CRC Mining, University of Queensland, Australia

A. Catalan
Minera Esperanza, Antofagasta Minerals Group, Chile. Formerly of Newcrest Mining Limited, Australia

G. Chitombo
WH Bryan Mining & Geology Research Centre, Sustainable Minerals Institute, University of Queensland, Australia

ABSTRACT: A number of caving operations are expected to be in deposits or geological systems located at much greater depths than current. These deposits are characterised by strong rock masses and higher stress regimes. These conditions will impose greater technical and mining challenges and therefore risks in terms of the caving processes, cave establishment and subsequent production. In order to mitigate such potential risks, rock mass "preconditioning" techniques are being implemented into mine design and planning. The term "preconditioning" has been adopted within the mining industry to describe the process of "modifying" a rock mass to enable better control or management of the cave mining process. It is currently achieved through techniques such as hydraulic fracturing, confined blasting or a combination of both. This paper summarises the results of a comprehensive geotechnical; monitoring and advanced blast modelling program involving large scale confined blasting tests at the first of a series of panel caves in the Cadia East mining complex in New South Wales, Australia. One of the objectives of this program was to obtain information to calibrate and evaluate the application of a newly developed explosive-rock interaction model. Results from the modelling work were used to understand the complex mechanisms at play under fully confined blasting conditions. In addition they helped identify improvements in explosive charge initiation and blasthole layouts to enhance the extent of rock mass preconditioning within the existing mining geometry and production constraints.

1 INTRODUCTION

The term preconditioning has since been adopted within the caving mining industry to describe the process of "modifying" a rock mass to enable better control or management of the cave mining process. The term "modifying" is used in this context to mean the process of artificially inducing changes to the rock mass through either hydraulic fracturing or large scale confined blasting of the rock mass volume to be caved. These processes involve treating/modifying the characteristics of the rock mass using fluid injection or confined blasting. Current industry experience is mainly with the use of hydraulic fracturing (Chacón et al. 2002), (Chacon et al. 2004), (Araneda & Sougarret 2007), (Van As & Jeffrey 2000), (Van As et al. 2004). Codelco Chile now applies the HF method almost "routinely" at a number of its caving operations including El Teniente and El Salvador. There are now discussions to combine HF and Confined blasting for the preconditioning. The latter methodology is referred to within Codelco as DDE for "Debilitamiento Dinamico con Explosivos" which can be literary translated to mean "Dynamic Weakening with Explosives" ((Chacón et al. 2002), (Molina et al. 2008)). This paper deals with the application of this confined blasting methodology in the Cadia East mining complex.

2 THE CADIA EAST (CE) MINING COMPLEX

The Cadia East ore body is located in Cadia Valley approximately 25 km south east of Orange in New South Wales, Australia. It is 100% owned by Newcrest Mining Ltd. The Cadia East ore body was discovered in 1985 and studies into the viability of the Cadia East resource commenced in the early 1990's ((Malone, 2011)). The Cadia East resource, located adjacent to the Cadia Hill open pit, is a massive low grade gold-copper porphyry deposit covered by up to 200 m of overburden. The system is up to 600 m wide and extends to 1.9 km below the surface.

The Cadia East Underground Project is concerned with the development of the massive Cadia East deposit into Australia's first panel cave. The mine will be the deepest panel cave in the world and Australia's largest underground mine. Newcrest's mining studies identified panel caving as the method likely to deliver

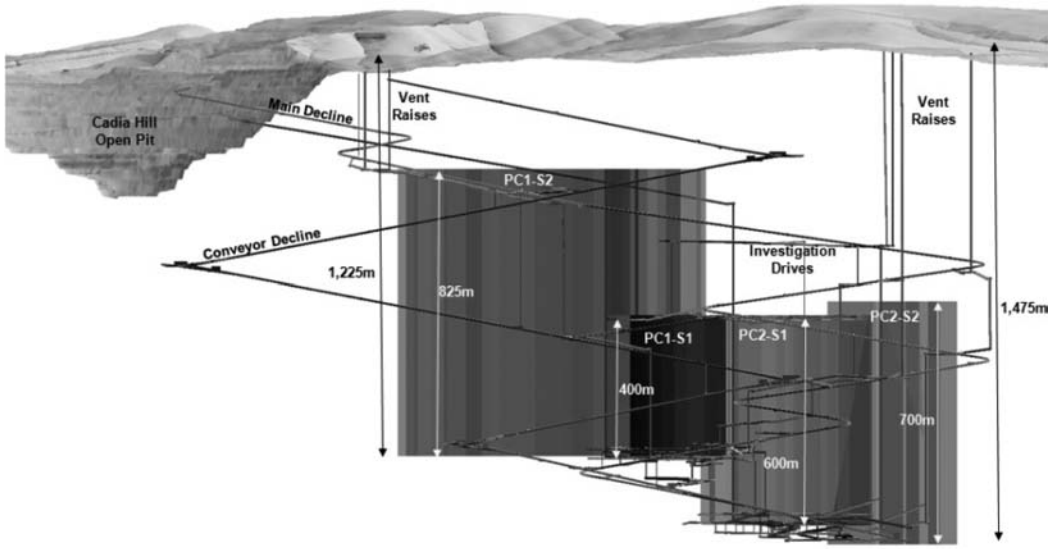


Figure 1. East-West looking North section through the Cadia East project.

the optimum technical and economic outcomes from the deposit.

2.1 *Mining method and production plans*

As shown in Figure 1, the Cadia East mining complex is implementing a series of panel caves designated as PC1 and PC2. The first level (PC1) is located approximately 1200 m below surface and the PC2, 1450 m also below surface. Both panels will be mined simultaneously. The total mining inventory is of the order of 1073 Mt @ 0.60g/t AU and 0.32% Cu. Based on current mine plans, the following are some the key mining parameters:

- Production to start in the latter part of 2012
- Production rate: maximum 26 Mpta
- Mine life: +35 years
- Lift 1 extraction level at ∼1225 m depth
- Lift 2 extraction level at ∼1475 m depth
- El Teniente extraction level layout
- High and Post undercutting strategy
- Jaw – gyratory crushers located within close proximity to footprint
- Materials handling system: conveyor belt 1.5 m
- ∼200 km horizontal development
- Untethered LHD production (Electric or Diesel)

2.2 *Geotechnical environment*

The geotechnical domains within the Cadia East mining complex were delineated based on lithology, alteration and structural interpretations. From this, three major units (Sedimentary, Volcanic-Stratified and Igneous) were defined. As shown in Figure 2, these units have been subdivided further and a 3D geotechnical model has been constructed for the whole Cadia East operation. Pre-existing surfaces, drillholes as well as underground mapping data were used to define the limits and/or contacts for the different geotechnical domains in NS cross sections 25 m apart. In total 121 cross sections were interpreted inside the limits of the 3D model area (Catalan and Suarez, 2010).

2.2.1 *Structural characterisation*

For the geotechnical analysis of the CE complex, structural information was grouped together in two categories: 1) major structures (major structural system) which are the continuous structures (Faults and Shear Zones), and 2) intermediate and minor structures (intermediate structural system) which are Fractures, Joints and Veins. These two major groups were separated using the rank typification defined with the use of the Acoustic Televiewer data. Table 1 summarises the distribution of structural patterns defined for Lift-1 (i.e. intermediate structural system).

2.2.2 *Intact rock classification*

Considering the Engineering Classification of Intact Rock (Deere and Miller, 1966), the main geotechnical units were grouped according to laboratory modulus of deformability (E) and uniaxial compressive strength (UCS). Figure 3 shows the typical ranges of values of igneous rocks.

2.2.3 *In-situ stress field*

In-situ stress measurements as well as their orientation are summarised in Table 2 below (Lee, 2012).

2.2.4 *Geotechnical rock mass classification*

The Cadia East rock mass was classified or rated using RMR-Bieniawski (Bieniawski, 1989), Q′-Barton (Barton, 1990), GSI (values obtained from GSI = RMRB89-5), RMR-Laubscher and MRMR classification schemes (Laubscher, 1990). The data used was

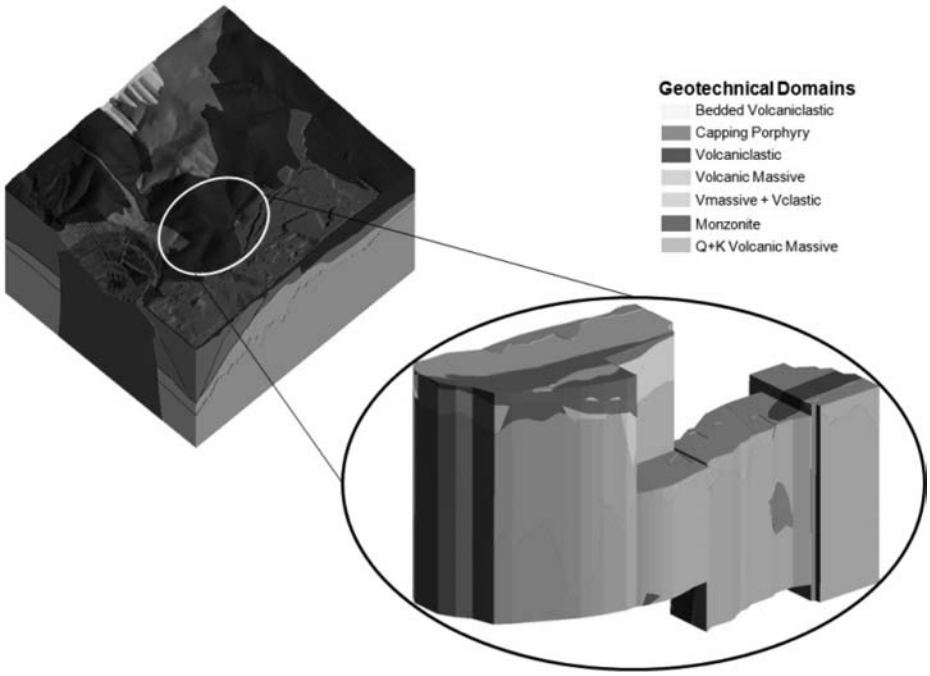


Figure 2. Geotechnical domains 3D model for Cadia East project.

Table 1. Structural patterns PC1-S1 block, Cadia East project.

Set	Dip (°)	Dip Dir (°)	n	PO (%)
S1	76 ± 33	348 ± 66	8735	50%
S2	64 ± 26	130 ± 52	2998	17%
S3	54 ± 51	219 ± 101	5923	33%

Note: n is the number of structures mapping belong to the structural system and PO is the probability of occurrence of the structural system in the specific domain.

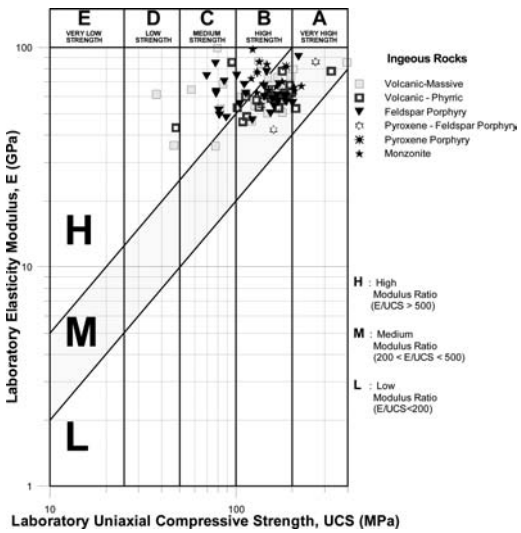


Figure 3. Intact rock classification for the igneous rocks.

Table 2. In situ stress field at Cadia East project.

Orientation (plunge/trend)
$\sigma 1 = 0°/074°$
$\sigma 2 = 0°/164°$
$\sigma 3 = 90°/074°$
Magnitudes (MPa)
$\sigma 1 = 5 + 0.0479 \times$ depth (m)
$\sigma 2 = 0 + 0.0344 \times$ depth (m)
$\sigma 3 = 0 + 0.0297 \times$ depth (m)

mainly from underground and surface drillholes which intersected the main geotechnical domains. The calculated average values and corresponding ranges are summarised in Figure 4.

3 BLAST PRECONDITIONING TRIALS

As illustrated in Figures 5 and 6, full-scale blast preconditioning trials and monitoring programs were conducted at Cadia East with the following objectives:

- To establish optimal operational procedures;
- To collect accelerations, velocity and attenuation data to calibrate an advanced numerical blasting model (i.e. HSBM);
- Through the application of a calibrated model, help establish optimal blast preconditioning design parameters including spacing, booster placement and stemming lengths; as well as quantify the impact

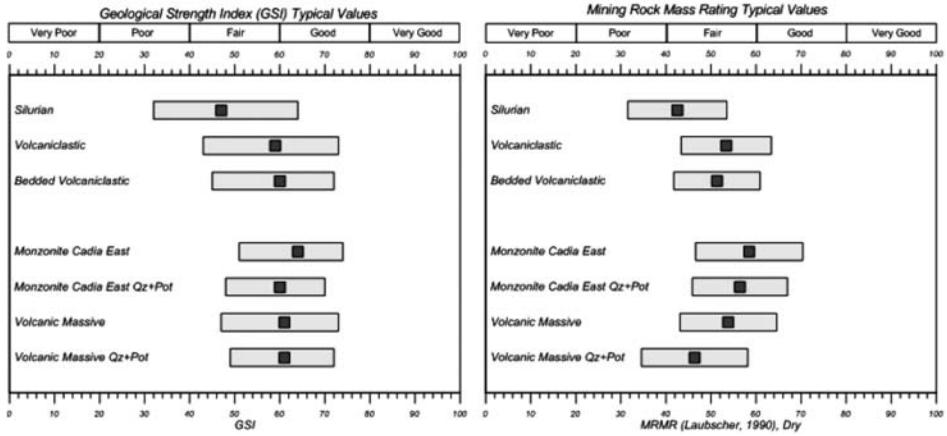


Figure 4. Average values and ranges of GSI and MRMR.

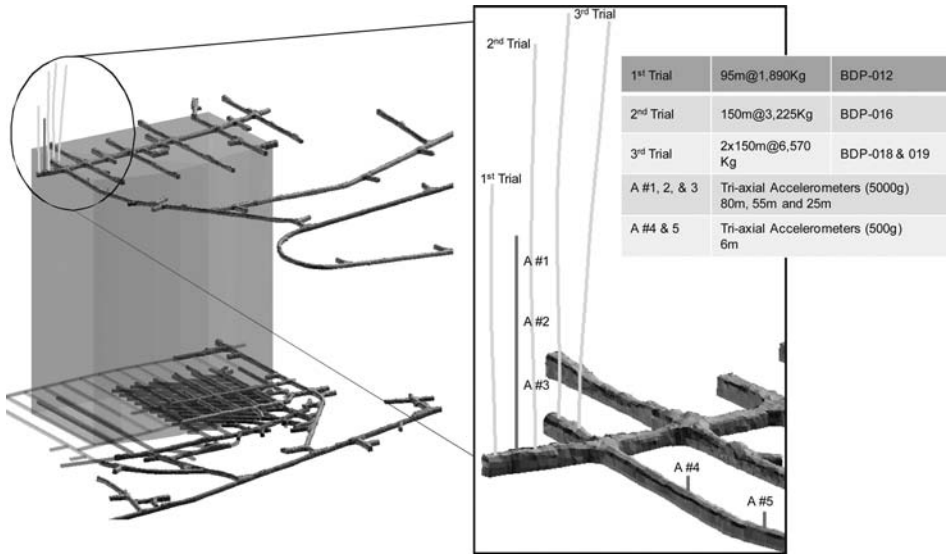


Figure 5. Preconditioning by blasting full-field trials configuration.

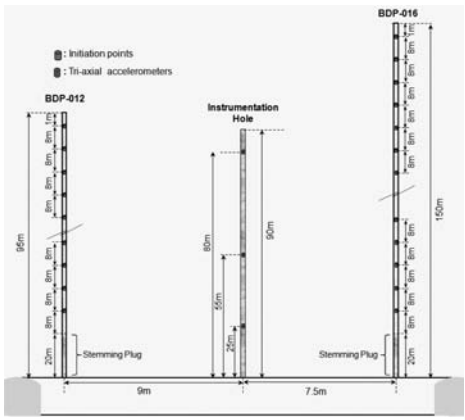


Figure 6. Field trial design blast preconditioning holes.

of the different designs in terms of the degree of rock mass modification observed (e.g. damage zone).

The blast monitoring program consisted of near field acceleration measurements from two up holes (95 m and 150 m long). The explosive used was a solid GMB sensitised emulsion manufactured by Dyno Nobel. A network of 3 tri-axial accelerometers (PCB Piezotronics, Inc, USA) with a measurement range of ±5,000 g and higher broadband resolutions were installed between both holes to monitor the peak particle acceleration and through signal integration calculate the peak particle velocity at a given point. Additionally, two far-field tri-axial accelerometers (i.e. 500 g) were also installed 80 m and 130 m from these preconditioning holes to further evaluate the attenuation characteristics of the rock mass.

4 MODELLING FRACTURING, DISTURBED AND INTERACTION ZONES

As discussed earlier, in order to assist with the assessment and modelling of large scale confined blasting, the Hybrid Stress Blasting Model (HSBM) was calibrated and applied. The HSBM is a numerical model of the complete blasting process jointly developed by the University of Queensland and Itasca (USA). The model represents a rock mass in terms of a "lattice Scheme" (Furtney et al., 2009) (Cundall, 2011, Onederra et al., 2009). It takes into account the mechanical properties of the rock, structures and stresses. In addition the HSBM uses an in-built non-ideal detonation code (Braithwaite et al., 2009) to calculate the forces (stresses and gasses) from the explosive products used.

Table 3. Intact rock properties.

Material properties	Mean values	Stand. Dev.
Density (kg/m^3)	2790	70
Tensile strength (MPa)	14.9	7.5
UCS (MPa)	133	70.5
Young's modulus (GPa)	67.5	19.1
Poisson's ratio	0.32	0.14
P-wave (m/s)	5904	212
S-wave (m/s)	3151	231

Table 4. In situ stress field.

Orientation (plunge/trend)	Magnitudes (MPa)
$\sigma 1 = 6°/083°$	$\sigma 1 = 32.2$
$\sigma 2 = 5°/174°$	$\sigma 2 = 23.8$
$\sigma 3 = 83°/302°$	$\sigma 3 = 13.6$

The primary purpose of applying the HSBM was to get a better insight or understanding into the otherwise complex process of confined blasting. The HSBM was expected to at least provide symptomatic results or likely outcomes of the different design parameters and shed some light into the mechanisms of preconditioning by blasting.

The mechanical properties which have been used as input into the HSBM numerical analyses are summarised in Table 3. These values are based on the work discussed by (Catalan et al., 2012) and also applied by (Onederra et al., 2012).

The in situ stress field which was adopted as input into HSBM models is summarised in Table 2 below. This is also based on direct measurements reported by (Catalan et al., 2012).

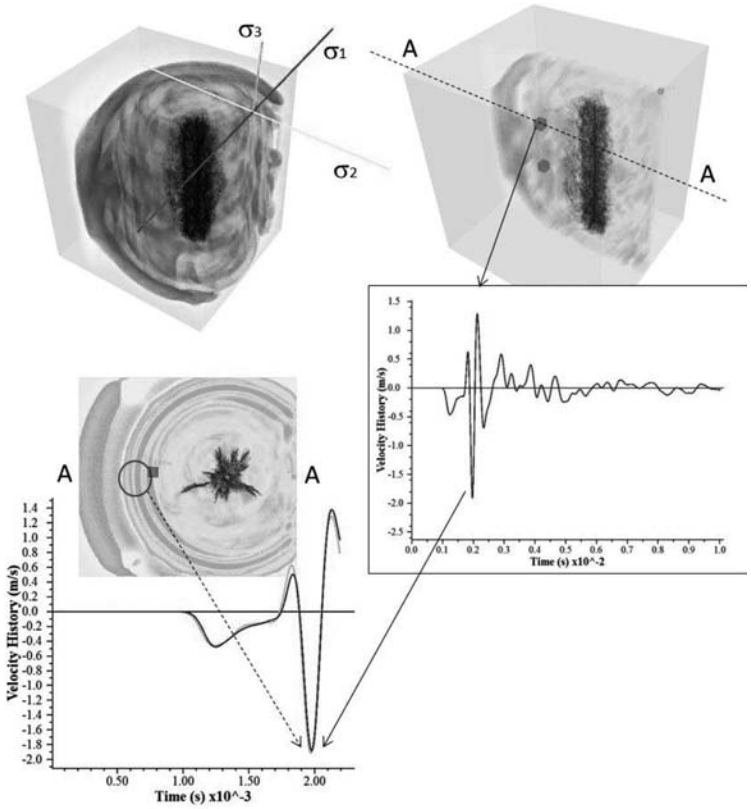


Figure 7. Results of calibration tests where the radial peak particle velocity is approximately 1900 mm/sec.

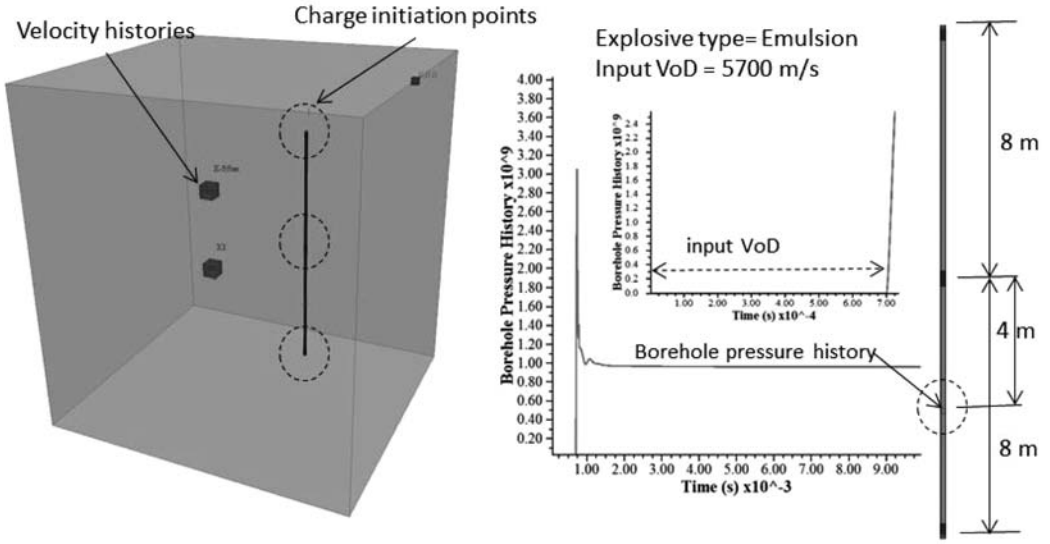


Figure 8. Geometry and explosive charging configuration showing borehole pressure history and velocity of detonation.

4.1 *Model calibration*

The fully instrumented blast preconditioning trials enabled the calibration of the HSBM boundary conditions and the definition of model solution parameters. Near field peak velocity measurements were calculated from measured acceleration records. Once a close match was obtained and the model was numerically stable, the calibrated model was configured and used to investigate the extent of disturbed zones given by different blasthole pattern layouts and the given in situ stress field.

Figure 7 depicts the results of a preliminary calibration test where the radial peak particle velocity is approximately 1900 mm/s 7.5 m away from the closest explosive charge. This peak value closely matched the range of recorded values at that distance (e.g. 1000 mm/s to 2500 mm/s) and was considered appropriate for modelling purposes. Figure 8 also describes the output from a borehole pressure history point located inside the charge to check that explosive input parameters such as velocity of detonation (VOD) and density were adequately considered in the model. This figure also shows that the model is stable within the test simulation timeframe of 10 ms when all wave transients have dissipated. From a practical point of view, the measured and modelled peak radial velocities are consistent with the range of peak particle velocities that can be estimated by more simplistic empirical models (Holmberg and Persson, 1980). This provided a justifiable basis for adopting a "disturbed zone" criterion that combines both the HSBM bond contact tensile failure criteria and a practical peak particle velocity based approach.

4.2 *Disturbed or damage zone criterion*

A "disturbed" or "damage zone" criterion has been proposed and can be described as a region which combines both the final state of the affected intact rock (e.g. lattice node contact failure) and the irreversible deformation or micro fracturing caused by a stress transient. This stress transient is assumed to be directly related to the radial peak particle velocity component. In this case, particle velocity is used as an index to define the potential areas of the rock mass which are likely to be disturbed by the propagation and interaction of stress waves from detonating charges. These are represented in the model by field velocity contours.

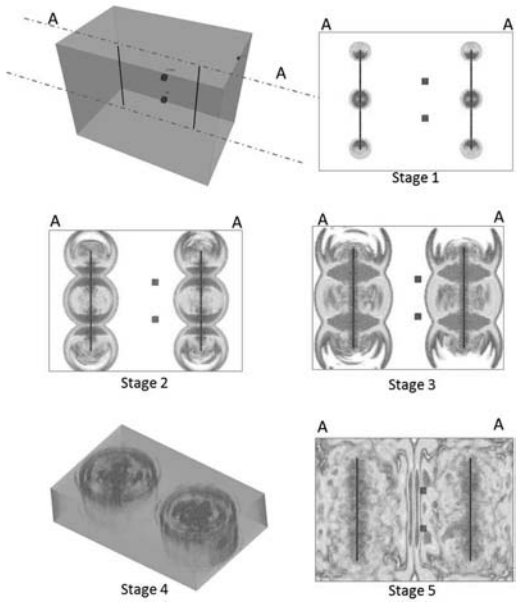


Figure 9. Two blasthole configuration describing the main numerical modelling stages in confined blasting conditions.

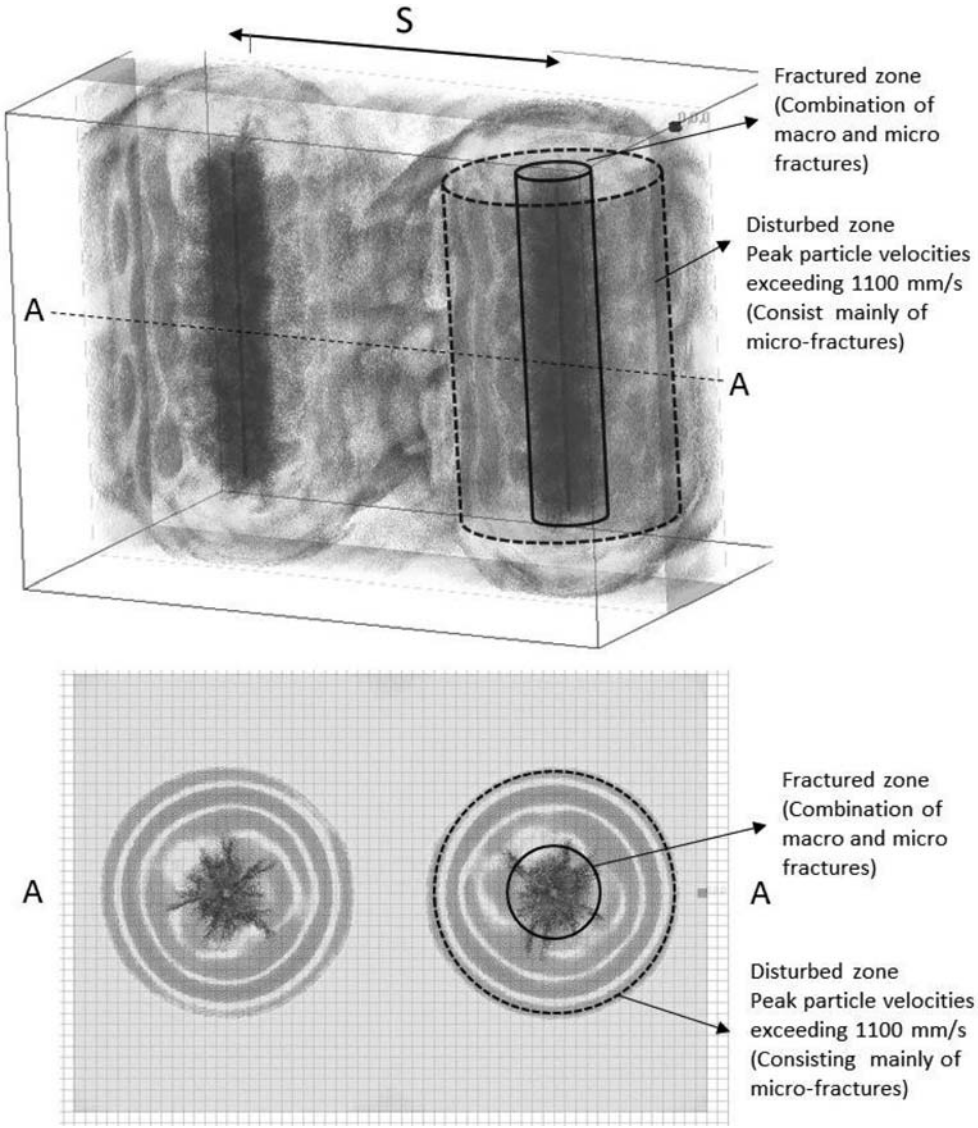


Figure 10. Isometric and plan section views describing the criteria used to define macro fracturing and disturbed zones.

The application of peak particle velocity as an index to estimate damage has been previously demonstrated by researchers and practitioners including (Holmberg and Persson, 1980), (Onederra and Esen, 2003), (Lu and Hustrulid, 2003).

4.3 *Interpretation of confined blasting modelling output*

To help explain the proposed disturbed zone criterion, Figure 9 shows a long section of a two blasthole configuration and describes the different stages and therefore the mechanisms which are assumed in order to model disturbed zones in confined blasting conditions. In this example, primers or initiation points are located every 8 m along the length of each blasthole. During stages 1 and 2 in the figure, the detonation process begins and the stress waves interact along the length of each blasthole after the consumption or detonation of approximately 4 m of the explosive charge. Immediately after the interaction of the detonation fronts described in stage 2 and immediately after the explosive column has been consumed, the gas logic in the HSBM model is activated (stage 3). It should be noted that in the numerical approach implemented in HSBM, the combined effect of the shock and gas, produces the stress wave imparted into the "virtual" rock mass which is depicted in an isometric view in stage 4. This stage shows, in red, the radial velocity field with amplitudes exceeding 1100 mm/s after approximately 1.8 ms. These particle velocities attenuate with distance and may interact with other incoming

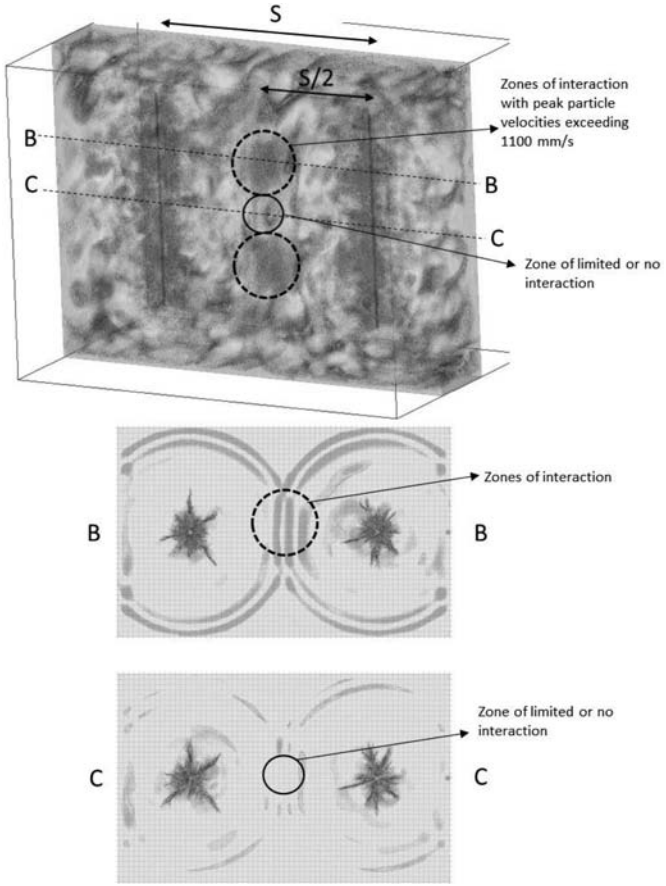


Figure 11. Isometric and plan section views describing the criteria used to define disturbed zones from stress interaction/ superposition.

waves of adjacent charges as described in the long section depicted in stage 5. This shows that for any given spacing between charges, the positive superimposition and therefore positive reinforcement of stress or blast waves can still contribute to disturbances in the rock. The extent and location of this interaction will depend on the level of attenuation; the distance between charges; and the initiation/detonation times assigned to these charges. As shown in stage 5, the probability of positive interaction is high for the chosen distance as the degree of disturbance is continuous along the charge and covers the volume of interest.

4.3.1 *Fracturing, disturbed and interaction zones criterion*

Figures 10 and 11 illustrate the proposed criterion which is also used to interpret the output generated by subsequent HSBM models discussed in this paper. Currently the HSBM is only able to display the final state of a point in the rock mass represented by lattice node contacts (i.e. either failed or intact). This is not necessarily valid when identifying regions that may have experienced transient stress loads that could cause micro fracturing or irreversible damage to intact rock. Because of the ability of HSBM to dynamically display velocity fields in three dimensions, this particular output was used to identify at different stages of the stress propagation and attenuation process, the potential extent of disturbed zones at given distances; and also define whether interaction or stress superposition is achieved between blastholes. An index of incipient damage of 1100 mm/s was estimated from average intact properties and used to display the extent of potential disturbed zones as well as interaction caused by the simultaneous initiation of confined charges. As shown in Figures 10 and 11, this envelope is expected to have different degrees of damage, ranging from a fractured zone near the blasthole (mainly consisting of both macro and micro fracturing) to disturbed zones further away from the blasthole (consisting mainly of micro fracturing of intact rock). Figure 11 depicts the potential interaction zones between blastholes generated after the further propagation and interaction of stresses. In this case, at the point of initiation (primer location C-C plane) the interaction is limited when compared to the plane half way in the explosive charge where two detonation fronts are expected to meet (e.g. B-B plane).

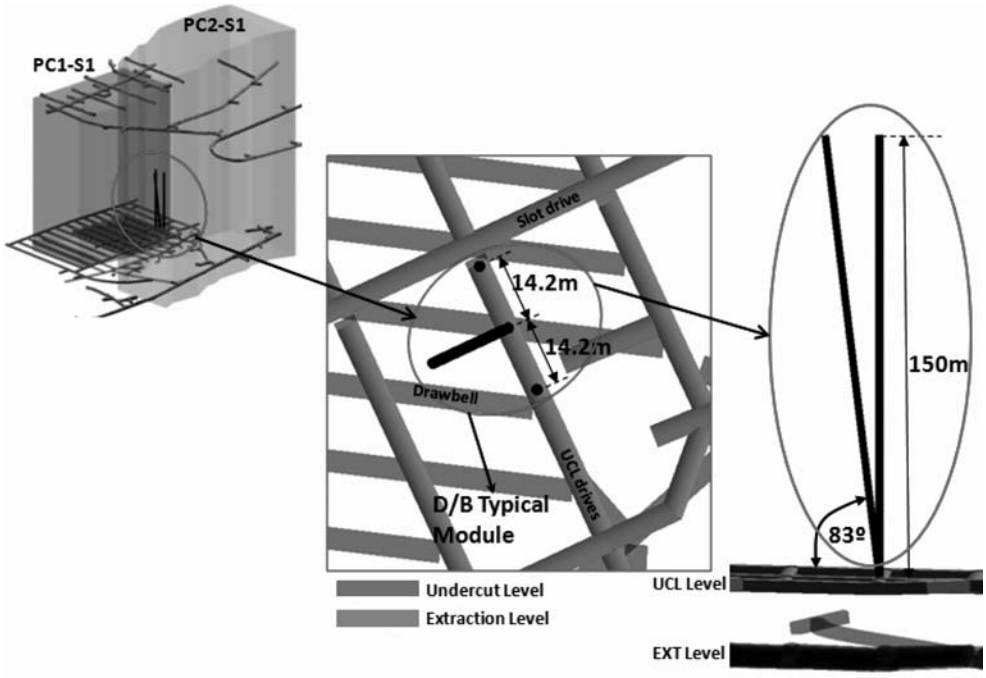


Figure 12. Preconditioning by blasting drilling pattern at CE project.

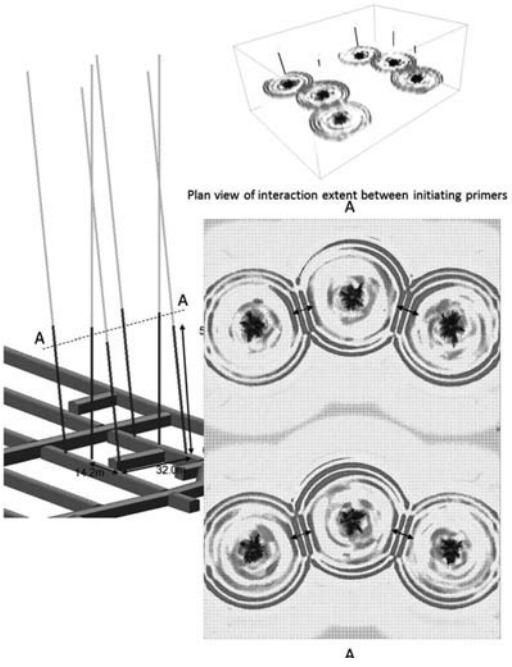


Figure 13. Preconditioning by blasting drilling pattern at CE project.

4.4 *Modelling results of multiple blasthole layouts*

A number of drilling layouts and charging configurations patterns were evaluated as part of the Cadia East blast preconditioning project. Figure 12 shows the basic test configuration comprising two vertical blastholes and one inclined blasthole. Part of the analysis involved the evaluation of a number of different alternatives associated with a repeating pattern of this basic three blasthole module. In this paper we present and discuss the modelling results of a six hole pattern configuration drilled from the undercut level. Figure 13 and 14 depicts the modelling output estimating the expected fracturing, disturbed and interaction zones in the lower region (i.e. 50 m from the collar) and the upper region (i.e. 150 m from the collar) of the volume of interest. As shown in Figure 13, at blasthole spacings of 14.2 m there is notable evidence of interaction and hence disturbance of the intact rock between charges. As stress waves propagate and attenuate further, Figure 14 shows that there is some evidence of disturbance due to interaction between the centre charge and diagonally opposing charges. There are however "blind areas" where no interaction or disturbance is expected within the volume. These areas are highlighted by the dashed circles. It is important to note that in the model, inclined holes are assumed to have no deviation. If blasthole deviation is high, then the potential for interaction is expected to be reduced, particularly in the upper region of the target volume. Further analysis indicated that a layout with only vertical blastholes would be more appropriate to maximise the potential for interaction. However due to mining layout constraints, in order to enable appropriate coverage, a six hole pattern configuration would need to include long hole drilling from both the undercut and the lower extraction level of the mine.

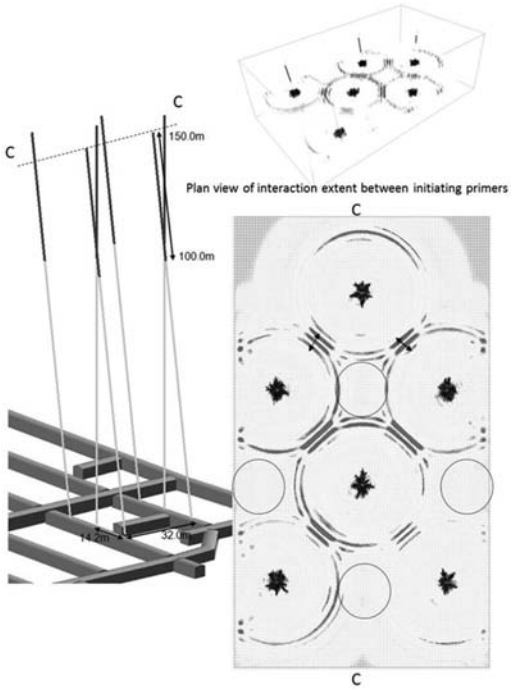


Figure 14. Preconditioning by blasting drilling pattern at CE project.

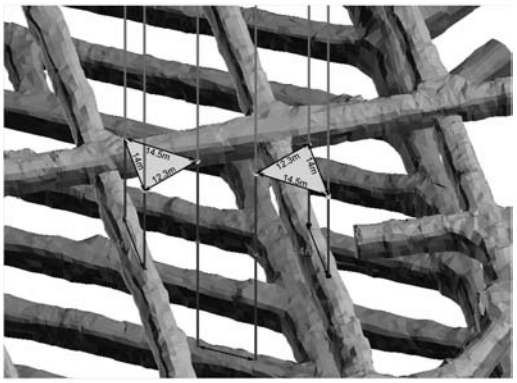


Figure 15. Proposed blasthole layout including blastholes drilled from the drawpoint brow of the extraction level.

The recommended configuration is illustrated in Figure 15. This includes two vertical holes drilled from the drawpoint brow of the extraction level and four holes from the undercut level. At the time of writing this paper, modelling of this configuration was underway and preliminary results indicated that stress interaction would be achieved between primer positions and the volume expected to be disturbed would be greater than that achieved with inclined blastholes drilled only from the undercut level. The risk of blasthole deviation influencing the extent of disturbance could also be minimised with this improved layout. Work continues in order to evaluate and validate modelling results by measuring the degree of disturbance of the intact rock from core samples taken after blasting utilising acoustic emission techniques.

5 CONCLUSIONS

This paper summarises the results of a comprehensive geotechnical; monitoring and advanced blast modelling program involving large scale confined blasting tests at the first of a series of panel caves in the Cadia East mining complex in New South Wales, Australia. Full-scale blast preconditioning trials together with detailed monitoring programs were conducted with the view to establish optimal operational procedures as well was collect all the necessary information to calibrate and evaluate the application of a newly developed explosive-rock interaction model designated as the HSBM.

The blast modelling results discussed in this paper were used to understand the complex mechanisms at play under fully confined blasting conditions and helped identify improvements in explosive charge initiation and blasthole layouts to enhance the extent of rock mass preconditioning within the existing mining geometry and production constraints. A disturbed zones criterion was established and adopted in the numerical modelling analysis. This criterion combined both a lattice bond contact tensile failure criteria and a practical peak particle velocity based approach. Because of the ability of HSBM to dynamically display velocity fields, this particular output was used to identify at different stages of the stress propagation and attenuation process, the potential extent of disturbance at given distances; and also define whether interaction is achieved between blastholes. An index of incipient damage was adopted to display the extent of potential disturbance as well as interaction caused by the simultaneous initiation of confined charges. Three zones were defined which are expected to have different degrees of damage, ranging from a fractured zone near the blasthole to disturbed zones further away from the blasthole consisting mainly of micro fracturing of intact rock.

Modelling results of a six hole pattern configuration showed that at blasthole spacings of 14.2 m there is evidence of interaction and hence expected disturbance of the intact rock between charges. As stress waves propagate and attenuate further, there is still evidence of disturbance between the centre charges and diagonally opposing charges. However there are “blind areas” where no interaction or disturbance is expected within the volume of interest.

Further analysis has indicated that a layout with only vertical blastholes would be more appropriate to maximise the potential of interacting stresses. The improved configuration includes two vertical blastholes drilled from the drawpoint brow of the extraction level. At the time of writing this paper, modelling of this configuration was underway, preliminary results

indicated that interaction would be achieved between primer positions and the volume expected to be disturbed would be greater than that achieved with inclined blastholes drilled only from the undercut level. The risk of blasthole deviation influencing the extent of disturbance could also be minimised with this improved layout.

Work continues in order to evaluate and validate modelling results by measuring the degree of disturbance of the intact rock from several core samples taken before and after blast preconditioning tests.

REFERENCES

Araneda, O. & Sougarret, A. 2007. Lessons Learned in Cave Mining: El Teniente 1997–2007. First International Symposium on Block and Sub-Level Caving Cave Mining, October, Cape Town, South Africa. 59–72.

Barton, N. 1990. Scale effects or sampling bias? Int. Workshop Scale Effects in Rock Masses. Rotterdam. A. A. Balkema, 31–55.

Bieniawski, Z. T. 1989. Engineering Rock Mass Classifications. New York: Wiley: New York.

Braithwaite, M., Sharpe, G. & Chitombo, G. 2009. Simulation of real detonations as an energy source term for the Hybrid Stress Blasting Model. *In:* Sanchidrián, J. A., ed. 9th International Symposium on Rock Fragmentation by Blasting, Granada, Spain. 327–333.

Catalan, A., Onederra, I. & Chitombo, G. A. 2012. proposed methodology for evaluation of the preconditioning by blasting at the Cadia East panel cave mine 6th International conference and exhibition on mass mining, MassMin 2012, June 10–14, Sudbury, ON, Canada. Laurentian University and Canadian Institute of Mining, Metallurgy and Petroleum, 1–13.

Catalan, A. & Suarez, C. 2010. Geotechnical Characterisation – Cadia East panel caving project, NSW, Australia. *In:* Potvin, Y., ed. Proceedings Caving 2010, 20–22 April, Perth, Australia. 371–387.

Chacon, E., Barrera, V. & Jeffrey, R. 2004. Hydraulic fracturing used to precondition ore and reduce fragment size for block caving. *In:* Alfaro, A. K. a. M., ed. MassMin 2004, 22–25 August, Santiago, Chile. 529–534.

Chacón, E., Quiñones, L., González, J. & Barrera, V. 2002. Pre-acondicionamiento de Macizos Rocosos Competentes para la Explotación por Métodos de Hundimiento. *Revista Minerales*, 57, 19–34.

Cundall, P. 2011. Lattice method for modeling brittle, jointed rock. *In:* Sainsbury, H., Detournay & Nelson, ed. Continuum and Distinct Element Numerical Modeling in Geomechanics – 2011, FLACDEM, Melbourne, Australia. Itasca International Inc., Minneapolis, 1–9.

Deere, D. V. & Miller, R. P. 1966. Engineering clas-sification and index properties for intact rock. New Mexico. USA.

Furtney, J. K., Cundall, P. A. & Chitombo, G. P. 2009. Developments in numerical modeling of blast induced rock fragmentation: updates from the HSBM project. 9th International Symposium on Rock Fragmentation by Blasting, Granada, Spain. Taylor & Francis Group, 335–342.

Holmberg, R. & Persson, P. A. 1980. Design of tunnel perimeter blast hole patterns to prevent rock damage. *Transactions of the Institute of Mining and Metallurgy,* 89, A37–A40.

Laubscher, D. H. 1990. A geomechanics classification system for the rating of rock mass in mine design. *Trans. S. Afr. Inst. Min. Metall.,* 90.

Lee, M. 2012. Cadia East – Review Stress Measurements. *In:* 111153, A. C. R. A. (ed.). New South Wales, Australia.

Lu, W. & Hustrulid, W. A. 2003. The Lu-Hustrulid approach for calculating the peak particle velocity caused by blasting. 2nd World Conference on Explosives and Blasting Technique, 10–12 September, Prague, Czech Republic. 291–300.

Malone, E. 2011. The Cadia Valley Mines. A Mining Success Story. *In:* Metallurgy, T. a. I. O. M. (ed.) *The Cadia Valley Mines. A Mining Success Story.* Melbourne, Australia: The Australasian Institute of Mining Metallurgy.

Molina, R., Cerrutti, C., Henriquez, J., Morales, R. & Apablaza, R. 2008. Preconditioning implementation on rock bulks in Codelco Chile and its results. *In:* Nordlund, H. S. a. E., ed. MassMin 2008, 9–11 June, Lulea, Sweden.

Onederra, I., Catalan, A. & Chitombo, G. 2012. Modelling fracturing, disturbed and interaction zones around fully confined detonating charges. *Mining Technology (TIMM A),* Vol 122, 1, 20–32.

Onederra, I., Chitombo, G., Cundall, P. A. & Furtney, J. 2009. Towards a complete validation of the lattice scheme in the Hybrid Stress Blasting Model (HSBM). 9th International Symposium on Rock Fragmentation by Blasting, Granada, Spain. Taylor & Francis Group, 343–351.

Onederra, I. & Esen, S. 2003. An alternative approach to determine the Holmberg-Persson constants for modelling near field peak particle velocity attenuation. *Fragblast: International Journal of Blasting and Fragmentation,* 8, 61–84.

Van As, A. & Jeffrey, R. 2000. Hydraulic Fracturing as a Cave Inducement Technique at Northparkes Mines. *In:* Chitombo, G., ed. MassMin 2000, November, Brisbane, Australia. 165–172.

Van As, A., Jeffrey, R., Chacón, E. & Barrera, V. 2004. Preconditioning by hydraulic fracturing for block caving in a moderately stressed naturally fractured orebody. *In:* Alfaro, A. K. a. M., ed. MassMin 2004, 22–25 August, Santiago, Chile. 535–541.

This page intentionally left blank

Rock Mechanics for Resources, Energy and Environment – Kwaśniewski & Łydżba (eds)
© 2013 Taylor & Francis Group, London, ISBN 978-1-138-00080-3

Back analysis of rock mass behavior of the Quintner Limestone at the Gonzen mine near Sargans, Switzerland

M.A. Perras, E. Ghazvinian & M.S. Diederichs
Queen's University, Kingston, Ontario, Canada

F. Amann
Swiss Federal Institute of Technology, Engineering Geology, Zurich, Switzerland

H. Wannenmacher
Amberg Engineering Ltd., Sargans, Switzerland

ABSTRACT: Iron ore has been mined from Gonzen mine, in Sargans, Switzerland, since Roman times. The mine has been inactive since it closed in 1966. Observations of different failure types have been used to calibrate the likely stress field using continuum models. Observed failures included, pillar instability averaging 0.7 m deep, intersection spalling, roof collapse, and stope collapse. The latter two being localized observations. A K_o (horizontal/vertical stress) ratio between 0.8–0.9 was found to adequately capture the observed depths of failure for the pillar and intersection models. The localized roof and stope collapse models required the inclusion of bedding weakness planes to induce and localize yielding which could correctly capture the region of failure, however, the dimensions could not be correctly captured. The 2-dimensional models calibrated to the pillar instability and intersection spalling can be used as a starting point for more complex 3-dimensional models, which can represent the complex stress field, influenced locally by the mine openings and faulting. This work is part of a large study of the behavior of limestone, with a particular focus on the long term influences on excavation stability.

1 INTRODUCTION

Gonzen mine is located within Gonzen Mountain near the city of Sargans, Switzerland. The mountain is part of the Alvier mountain chain which runs along the east side of Switzerland. Folding and faulting during mountain building exposed the iron ore at high elevations of Gonzen Mountain.

1.1 *Mining History*

It is here that the Roman's likely first encountered the iron ore and began mining, near the peak of Gonzen Nappe, Figure 1 (Hugger 1991). The long history has been documented by Hugger (1991) and the last stage of mining was conducted between 1919 and 1966, which ceased due to poor economic conditions (Pfeifer et al. 1988). Recently a portion of the mine was re-opened as a tourist attraction.

2 GEOLOGICAL HISTORY

The hematitie-manganese ore body is contained within the folded sequence of the Quinterner limestone. The ore is interbedded at the base of the Platten unit, above the top of the lower Quintner unit. The Platten, a marl band, transitions into the more compotent upper Quintner unit, for a total thickness of approximately 350 m (Heim 1917). The foundation of the mountain includes the Schilt and Reischiben formations of the Dogger Epoch, which are not exposed in the mine. The stratigraphy is shown in Figure 1, in relation to the ore horizon mined.

2.1 *Deposition*

The sediment forming the Quintner limestone was deposited in relatively deep waters (100–1000 m) and is therefore predominately a dark gray biomicritic lime-mudstone. The iron ore formed by hydrothermal venting on the sea floor (Pfeifer 1988). The contact is transitional from minor hematite inclusions away from the main ore body, however, in the main ore zone the contact is sharp between the limestone and the massive ore (Pfeifer et al. 1988).

Pfeifer et al. (1988) indicated that the hydrothermal origin would require reactivation of a local fault system; however, the only evidence is breccia beds occurring above and below the ore zone. Otherwise, the faults are due to post-depositional tectonics.

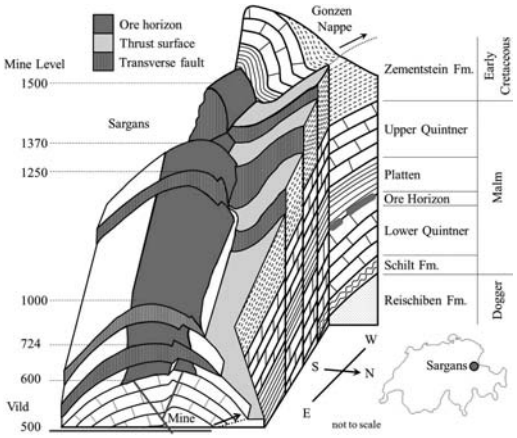


Figure 1. Block diagram showing the Gonzen Mountain with transverse faults, the ore deposit and the stratigraphy.



Figure 2. Calcite veins parallel to bedding and parallel to the axial plane of a fold observed in Gonzen Mine.

Table 1. Properties of the Quintner Limestone. CI (crack initiation), CD (crack damage), UCS (unconfined compressive strength), and E_{50} from Perras et al. 2012. Tensile strength (T) estimated from point load and Brazilian test results and m_i is estimated.

	CI (MPa)	CD (MPa)	UCS (MPa)	T (MPa)	E_{50} (GPa)	m_i (–)
Average	43.6	77.4	112.0	5.9	52.3	12
Minimum	32.0	43.0	53.1	0.6	22.0	10
Maximum	67.0	105.0	143.2	10.4	73.0	15

2.2 *Tectonics*

The Alvier mountain chain is formed from a series of imbricated nappes. Pfiffner (1981) indicates that a transition from imbricated thrusting to folding occurs between the Alvier Mountains in the West and Gonzen Mountian, which are separated by the Santis Thrust. The peak of Gonzen Mountain is itself an anticline with the fold axes generally striking SW-NE (Stadlin 2010). Differential movement along individual thrust surfaces was accommodated by strike-slip movement on transverse faults (see Fig. 1) during tertiary thrusting and folding (Pfiffner 1981). The deformations weakly metamorphosed the formations and calcite veined developed along bedding and within extensile fractures, (Fig. 2). These deformation events also influence the rock mass properties and control the stress field.

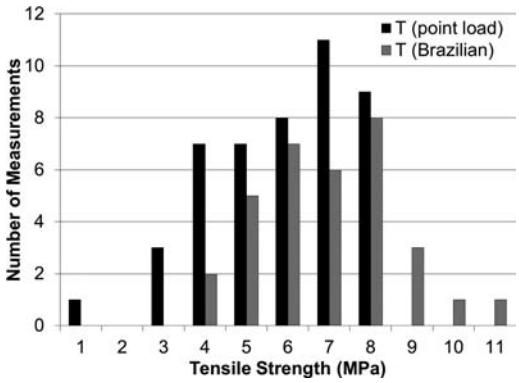


Figure 3. Tensile strength estimated from point load test results compared with Brazilian Tensile results.

2.3 *Quintner limestone properties*

Testing of intact laboratory samples for crack damage thresholds, including crack initiation (CI), critical damage (CD) and Unconfined Compressive Strength (UCS), was conducted previously by the authors (Perras et al 2012). Tensile strength has also been determined from laboratory studies, as part of the practicum program at the Geological Institute at ETH, Zurich, using Brazilian and point load tests. Included in the point load testing results presented in Figure 3 are samples from field investigations for this study. UCS and tensile strength (T) estimates were made using $UCS = 25I_{s50}$ and $T = 1.25I_{s50}$, where I_{s50} is the corrected point load strength (I_s) to an equivalent specimen with a diameter of 50 mm (ISRM 1985). The average values in Table 1, have been used in the modeling.

The values for the Brazilian test results are plotted against the point load estimates in Figures 3. There is a consistent distribution between the two methods, although the point load results appear to truncate at 8 MPa. The average value for the Brazilian tests was 6.4 MPa and the estimation from the point load tests was 5.4 MPa. A value of 5.9 MPa, in between the above results, was used in the modeling.

In some cases the results were influenced by calcite veins in the samples, which caused lower estimates of the tensile strength. When the vein was oriented parallel to the loading direction, for Brazilian tests, the

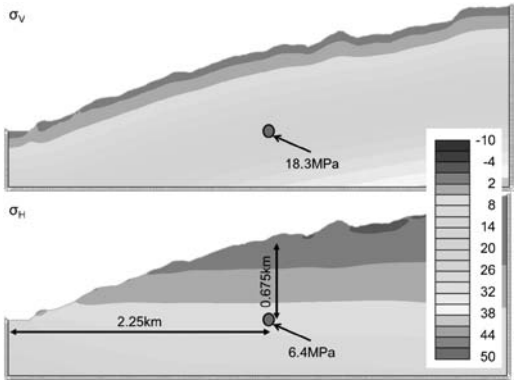


Figure 4. Topographic elastic model along the access tunnel, elevation 500 m a.s.l., showing the vertical (top) and horizontal (bottom) stress contours.

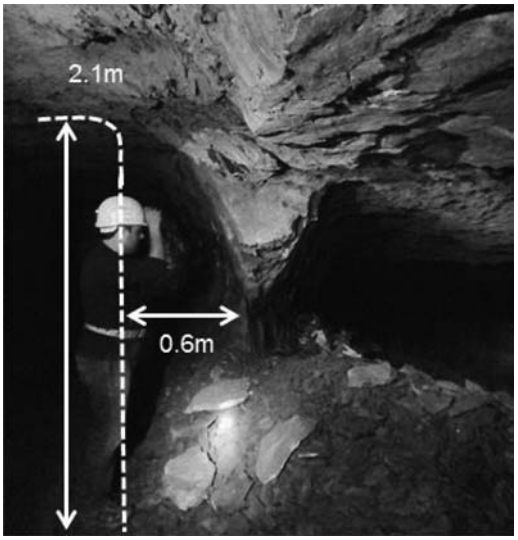


Figure 5. Complete collapse with estimated depth of failure measured from the approximate edge of the original pillar.

tensile strength was 2.5 MPa. This value was used for the tensile strength of the joint elements to represent weakness planes in some of the numerical models.

2.4 *Regional and local stress field*

The new Linth-Limmern hydro-power plant is being constructed in the Quintner limestone at a similar depth to the Gonzen mine. At this project the primary vertical to horizontal stress ratio (K_o) was estimated to range between 0.28 and 0.70 (Marclay et al. 2010). In an effort to narrow the range of stress values an elastic topographic model of Gonzen Mountain was created. This model (Fig. 4) ignores the influence of tectonic locked-in stresses, faulting, and other heterogeneities of the rock mass which can have a large influence on the stress; however, the results can be used as a lower limit of the stress ratio.

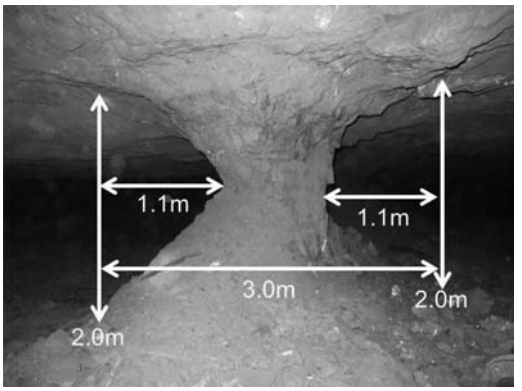


Figure 6. Largest depth of pillar failure on a ~3 m wide pillar.

2.4.1 *Local stress field modelling*

The topography along the access adit was used in an elastic model to determine the stress contours due to the weight of the over lying rock mass (Fig. 4). The vertical and horizontal stresses were determined to be 18.3 MPa and 6.4 MPa, respectively, at the main mine level. This results in a K_o ratio of 0.35. This should reflect the lower bound since other influences on the stress field have been neglected and represents a starting point for calibration based on observed failure at different locations in the mine.

3 OBSERVATIONS FROM GONZEN MINE

Observations by the authors have been conducted at the mine over the last several years, building on the work of Stadlin (2010). The geomechanical behaviour can be related to three main areas; pillar and intersection stress induce failure, roof collapse in room and pillar areas and inclined stope collapse. There also appears to be more recent failure for all modes, which can be easily identified by the fresh gray or red surfaces that distinctly contrast with the reddish brown dust coating presumably from the mining process, when comparing Figures 5 and 6. This observation is supported by accounts of red dust from the mine being similar to coal dust (Hugger 1994).

The pillar instabilities ranged from thin sheets of spalled rock with the pillar largely intact to complete crushing (Fig. 5). Observations indicated that the average room width is approximately 7.7 m with 2.2 m wide pillars in between, in the section of the mine studied. The minimum pillar width is estimated to have been originally 1 m wide, shown in Figure 5, which exhibits failure past the mid-point. The maximum depth of pillar failure observed was 1.1 m (Fig. 6). Measuring surveyed room and pillar widths from a mine plan drawing, compiled by Swisscom in 2009, indicated average widths of 8 m and 2 m, respectively. These measurements likely represent the in-situ conditions at the time of surveying and not the as built dimensions. The pillar stability was used as the first

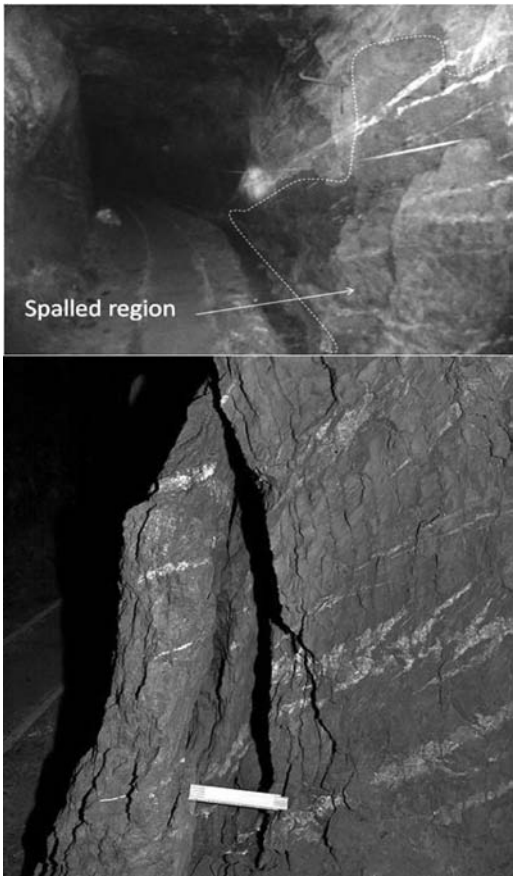


Figure 7. Spalling at a 60 degree intersection of equally sized 2 × 2 m adits, with the top photo showing the spalled region diminishing away from the intersection and the bottom photo showing the depth of damage (scale is 0.2 m) (Stadlin 2010).

calibration geometry for the stress state, as this was the most common failure observed.

Intersections represent a unique opportunity to determine the influence of the distance between excavations on spalling behavior. The distance away from the intersection where spalling terminated shown in Figure 7 was 3 m. The spalled region was approximately 0.5–0.8 m thick and composed of multiple slabs, as shown in the bottom of Figure 7.

Roof collapse in the room and pillar area observed was isolated to one location where the span of the room was greater than 12 m. The roof collapse is a post mining failure, as indicated by the fresh dark gray surfaces which contrast with the reddish brown dust coatings at the top edge of Figure 8.

Similarly a post-mining collpase in a steeply inclined stope was observed (Fig. 9). The main stope area, in between cross pillars at the base, was measured to be 10.3 m wide and 13.0 m high. The contrast between the fresh spall surfaces and the intact stope walls can be clearly seen in Fig. 9.



Figure 8. Roof collapse, over 10–12 m distance, with approximately 0.25–0.5 m slabs. Total span approximately 20 m.



Figure 9. Stope collapse on the 505 level of Gonzen mine.

Following the empirical approach of Potvin (1988), with a hydraulic radius ranging between 3–6 and a modified stability number ranging between 4–65 (extreme values) only the maximum stope dimensions fall into the transition zone between stable and caving, supporting a post-mine collapse interpretation. The post-mining collapses are possibly due to stress corrosion, creep on planes of weakness, or in combination with seismic activity and/or differential strains on existing faults over time.

4 MODELLING

Models were constructed to simulate the various observations. The models use the average properties, outline in Table 1, in combination with the brittle approach of Diederichs (2007). The residual rock mass parameter, m, was set to 10. The stress field was first calibrated using the pillar observations.

4.1 *Pillar stability*

A slightly inclined, 10° from horizontal, room and pillar arrangement, where the majority of the pillar

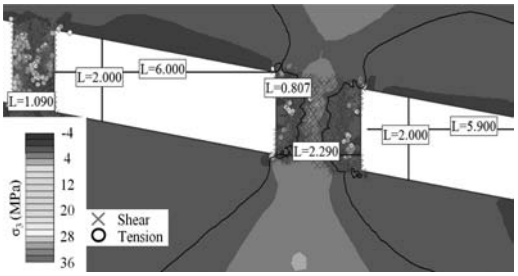


Figure 10. Model results for K_{Hv} of 0.8 (in plane) and K_{hv} of 0.9 (out of plane), which minimizes roof yielding.

observations were conducted, was used to determine the stress state which gave rise to yielding similar to that observed. The K_o ratio was varied from 0.35, the topographic model ratio, up to 1.0. As roof failure was only locally observed, it was used as the limiting factor to calibrate the stresses.

Minimal roof yielding was found to occur for a K_o between 0.8–0.9, demonstrating that the topographic model underestimated the horizontal stress magnitude. There is also an influence of the out of plane stress, which when larger than the horizontal in plane stress gives slightly better results.

The calibrated stress field used was $K_{hv} = 0.8$ (in plane) and $K_{Hv} = 0.9$. The pillar stability model is shown in Figure 10, with depths of failure indicated by the de-stressed contour (black line at $\sigma_3 = 1$ MPa) and tensile yielding, which for example is 0.8 m for the wider pillars. The dimensions of failure in the model are in good agreement with the observations, which showed that pillars of ∼2.2 m wide had an average depth of failure of 0.7 m.

4.2 *Adit intersection*

The same stress field was used for a series of models representing the intersection observations. To adits, 2×2 m square, were modeled at increasing distance from each other. Plastic yielding in the models was found to cease at a distance of 2.0 m between excavations. This corresponds to 2.0 m away from the intersection and the point where the spall slab height decreases significantly, as shown in Figure 11.

The spalled slabs were observed to arrest along or close to calcite veins, which have not been captured in the models. More detailed analysis could more accurately capture the influence of calcite veins on the yielding and therefore more accurately capture the observed geometry, however the distance between adits agrees with the observations.

4.3 *Roof collapse*

The roof collapse was a localized observation in an area which had a large span and according to the mine plane drawing was close to a fault. A homogenous continuum model, with the calibrated stresses, shows little roof yielding, with localized tensile yielding only in the corners between excavation stages up to spans

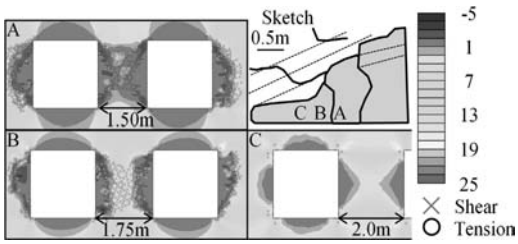


Figure 11. Models showing increasing distance bewteeen the 2×2 m adits, representing the adit intersection, with decreasing yield and increasing stress flow (σ_3) between the adits. The sketch shows the observed spalling, moving away from the intersection at the right, with detached slabs (gray), spall fractures (solid black lines), and calcite veins (dashed lines).

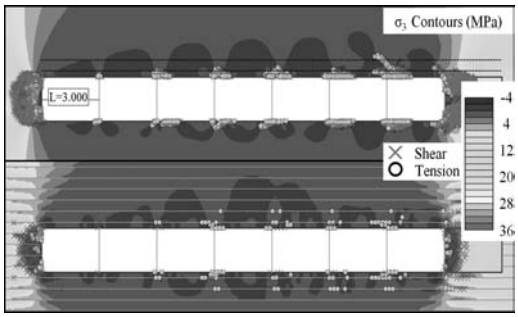


Figure 12. Roof collapse models showing homogenous (top) and bedded models (bottom), with 3 m excavation stages and a 21 m span excavated. The bed positions are shown for reference (dashed lines) to show how the beds minimize yield depth.

of 9 m (Fig. 12 top). For larger spans the yield extends further up, reaching a maximum depth of over 0.75 m with a span of 21 m.

In the roof collapse area bedding was observed to be parallel to the roofand can act as planes of weakness. These can be included numerically using joint elements. The stiffness of the rock simulated in between the joint elements has to compensate for the normal stiffness of the joint element, such that the stiffness of the system is comparable to the homogenous case, using methods such as suggested by Brady & Brown (2006). The joint properties were taken as the Mohr-Coulumb equivalent envelop, generated by the brittle parameters, derived from the minimum values reported in Table 1. A residual friction angle of 15° was used, with the rest set to zero.

The joints minimize the depth of yielding (Fig. 12 bottom) by absorbing strains and focusing the stresses along the first beam. This model demonstrate the influence of bedding to reduce the depth of yielding, however, wide spread yielding is absent. This is consistent with the localized collapse observed, since the observed failure was possibly influenced by a more complex interaction with a fault in the vicinity and other factors controlling the local stress field.

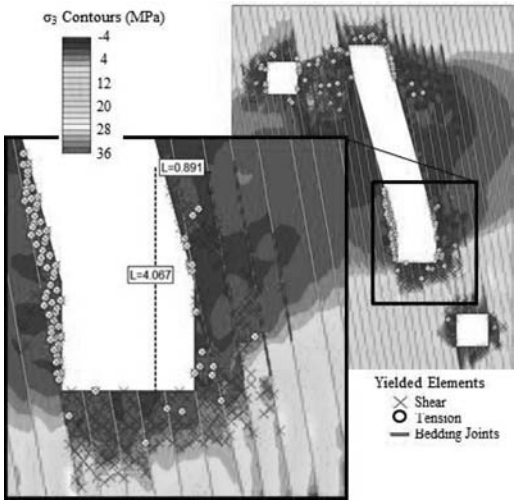


Figure 13. Stope model with inclined bedding dipping at 80°. Inset shows a close up of yield at the toe of the stope.

4.4 *Stope collapse*

The stope model (Fig. 13), with the calibrated stresses, indicates a region of yield in the same area where spalling was observed, at the toe of the stope (Fig. 9). The observed spall was, at its maximum extent, 9 m high and 1.3 m deep and the model indicates roughly 4 m high and 0.9 m deep. Also the numerical yielding occurs around the access adits to a greater extent than observed. In order to induce plastic yielding joint elements were used and the cohesion had to be dropped to 2 MPa, below that used for the roof collapse model.

Despite inadequate height of yielding, the depth is close to that observed. However, in this case the depth is controlled by the bedding (angle and spacing). A complete sensitivity analysis of the rock mass properties, joint element angle and properties is required. A more complex stress field and structural influence, as well as, stress corrosion could be part of the in-situ scenario, which has not been adequately captured numerically in 2-dimension.

5 DISCUSSION AND CONCLUSIONS

The numerical modeling presented here demonstrates the potential range of the stress ratios, $K_o = 0.8–0.9$, that give similar yielding in the models to observations. The pillar stability observations showed the most consistent behavior throughout the mine, which was similarly captured in the numerical models. The intersection models demonstrated that the correct width could be captured; however the exact dimensions are controlled by structural features. Joint elements were used in the roof and pillar models, however, the exact geometry could also not be captured. More complex structures and mine induced stresses are required to correctly capture the geometry of roof and stope collapses.

The calibrated stress regime can be used in more complicated 3D models to further investigate the controlling factors on the failures observed. This work provides an opportunity to understand the long term behavior of excavations in limestone, which in Canada is a potential rock type for the storage of high level nuclear waste. Understand the long term behavior in this context is critical.

ACKNOWLEDGEMENTS

The authors would like to thank the staff at Gonzen mine there help with the research trips. The authors would also like to acknowledge the students from the Engineering Geology Department of ETH Zurich, who tested the samples as part of their Rock Mechanics course. They are Marco Pally, Sophie Gschwind, Dominic Stadlin, Marc Hugentobler, and Katrin Wild.

REFERENCES

Brady & Brown. 2006. *Rock Mechanics for Underground Mining* (3rd edn). Dordrecht: Springer

Diederichs, M.S. 2007. The 2003 Canadian Geotechnical Colloquium: Mechanistic interpretation and practical application of damage and spalling prediction criteria for deep tunneling. *Canadian Geotechnical Journal* 44: 1082–1116.

Heim, A. 1917. Monographie der Churfirsten-Mattstock-Gruppe. Beitrag zur geologischer Karte der Schweiz. 20 p.

Hugger, P. 1994. 2000 Jahre Bergbaukultur am Gonzen. Schweizerisches Archiv für Volkskunde, 90(1): 131–143.

ISRM 1985. International Society for Rock Mechanics Commission on Testing Methods – Point Load Test Method. *International Journal of Rock Mechanics and Mining Sciences & Geomechanics Abstracts* 22(2): 51–60.

Marclay, R., Hohberg, J.-M., John, M., Marcher, T., & Fellner, D. 2010. The new Linth-Limmern hydro-power plant – design of caverns under 500 m overburden. In J. Zhao et al. (eds), *Proceedings of Eurock 2010* (Lausanne, Switzerland). Leiden: CRC Press/Balkema.

Perras, M.A., Diederichs, M.S. & Amann, F. 2012. Fracture initiation and propagation in the Quintner Limestone. In *Proceedings of the 46th US Rock Mechanics/Geomechanics Symposium* (Chicago, 24–27 June 2012), ARMA 12–401.

Pfeifer, H.-R., Oberhansli, H., & Epprecht, W. 1988. Geochemical evidence for synsedimentary hydrothermal origin of Jurassic iron-manganese deposits at Gonzen (Sargans, Helvetic Alps, Switzerland). *Marine Geology* 84: 257–272.

Pfiffner, O.A. 1981. Fold-and-thrust tectonics in the Helvetic Nappes (East-Switzerland). *Geological Society, London, Special Publications* 9: 319–327.

Potvin, Y. 1988. *Empirical Open Stope Design in Canada.* Ph.D. Thesis, Dept. Mining and Mineral Processing, University of British Columbia, 343 p.

Stadlin, D. 2010. Strukturheterogenitäten im Quintnerkalk und deren Relevanz im Untertagebau. Masterarbeit, Ingenieurgeologie Departement Erdwissenschaften ETH, Zurich.

Rock Mechanics for Resources, Energy and Environment – Kwaśniewski & Łydżba (eds)
© 2013 Taylor & Francis Group, London, ISBN 978-1-138-00080-3

Numerical simulation of the water jet excavation of soft rock saturated with water

K. Sakaguchi
Graduate School of Environmental Studies, Tohoku University, Japan

Y. Yumoto
Central Japan Railway Company

A. Kizaki
Graduate School of Environmental Studies, Tohoku University, Japan

ABSTRACT: The excavation performance of Water Jet (WJ) technology is affected by many parameters. Therefore, many experiments are required for the development and application of WJ technology. If a realistic numerical simulation of WJ excavation could be produced, we might be able to identify the optimum conditions for excavation, which could reduce the cost of developing new WJ technology. In this study, we focused on the Smoothed Particle Hydrodynamics (SPH) method, which is a type of particle method, for the numerical simulation of WJ excavation of soft rock saturated with water. The main results can be summarized as follows: (1) We developed a three-dimensional SPH simulation code for WJ excavation of soft rock saturated with water. (2) We clarified the usefulness of this numerical simulation code by comparing the calculated results with those from excavation experiments in soft rock saturated with water.

1 INTRODUCTION

Water jet (WJ) technology is an effective approach to rock excavation. WJ can be used in many fields, such as in the precision machining of solid materials, medical fields and the food industry. In WJ technology, many parameters influence excavation performance. These parameters include the driving pressure, ambient pressure, nozzle geometry, standoff distance, presence or absence of an abrasive, the properties of the excavated material, etc. Therefore, many experiments are necessary for the development and application of WJ technology. However, both the cost and time needed to develop new WJ technology increase with an increase in the number of experiments required. If a realistic numerical simulation of WJ excavation could be produced, we might be able to identify the optimum conditions for excavation rapidly and at low cost, and thus reduce the overall cost of developing WJ technology.

The WJ excavation of rock is a moving boundary problem in which water penetrates the rock, since the interfaces between the solid and liquid are greatly deformed. Therefore, in this study, we used the SPH (Smoothed Particle Hydrodynamics) method (Monaghan 1988), which is a particle method, to numerically simulate the WJ excavation of rock. The SPH method was originally developed to model astrophysical phenomena, and was later widely extended to problems involving continuum solid and fluid mechanics (Liu & Liu 2003). The SPH method is now being applied in various fields, such as in the analysis of the impact of a solid (Komurasaki et al. 1998, Shintate & Sekine 2002) and in the analysis of the large deformation of a solid (Cleary et al. 2006).

Some previous studies have used the SPH method to examine the interaction between a fluid and solid. These studies have examined, for example, the cutting of a soft material by WJ (Shinohara et al. 2004), the cutting of wood by WJ (Sato et al. 2008), the excavation of soil by WJ (Bui et al. 2007), the deformation/failure of a metal by WJ (Potapov et al. 2009), and a coupling simulation of the SPH method (for WJ) and FEM (for solid) (Ma et al. 2008). However, these studies have not considered the application of WJ to rock. Sakaguchi et al. (2012) proposed a method for simulating rock excavation by the SPH method. They also proposed a fracture criterion, which is based on the tensile strain between a particle and a neighboring particle, of rock to simulate rock excavation by WJ. However, that study only considered dry conditions; they did not consider rock excavation under wet conditions.

In this study, we sought to develop a method for the numerical simulation of WJ excavation of rock saturated with water. We developed numerical simulation code based on SPHysics (Gesteira et al. 2008), which is an open-source code for the SPH method.

2 SIMULATION METHOD USING SPH

2.1 *Essential formulation of the SPH*

A physical quantity $\phi(\boldsymbol{r})$ at an arbitrary point $\boldsymbol{r}$ in a continuous body is given by

$$\phi(\boldsymbol{r}) = \int_{\Omega} \phi(\boldsymbol{r}') \cdot \delta(\boldsymbol{r} - \boldsymbol{r}') d\boldsymbol{r}', \tag{1}$$

where $\delta(\boldsymbol{r} - \boldsymbol{r}')$ is the Dirac delta function, and Ω is the volume of the integral that contains $\boldsymbol{r}$. If the Delta function $\delta(\boldsymbol{r} - \boldsymbol{r}')$ is replaced by a smoothing function $W(\boldsymbol{r} - \boldsymbol{r}', h)$, Equation (1) can be given by

$$\langle \phi(\boldsymbol{r}) \rangle = \int_{\Omega} \phi(\boldsymbol{r}') \cdot W(\boldsymbol{r} - \boldsymbol{r}', h) d\boldsymbol{r}', \tag{2}$$

where

$$\phi(\boldsymbol{r}) = \lim_{h \to 0} \langle \phi(\boldsymbol{r}) \rangle. \tag{3}$$

$W(\boldsymbol{r} - \boldsymbol{r}', h)$ is the so-called kernel function, which must satisfy three properties:

$$\lim_{h \to 0} W(\boldsymbol{r} - \boldsymbol{r}', h) = \delta(\boldsymbol{r} - \boldsymbol{r}'), \tag{4}$$

$$\int_{\Omega} W(\boldsymbol{r} - \boldsymbol{r}', h) d\boldsymbol{r}' = 1, \tag{5}$$

$$W(r - r', h) = 0 \qquad \text{for} \qquad |r - r'| \geq h. \tag{6}$$

where h is the smoothing length that defines the area of influence of the kernel function.

There are many possible choices of kernel functions that satisfy Equations (4)–(6). In this study, we chose the cubic spline interpolation function (Gesteira et al. 2008), since this function is independent of the smoothing length h (Hongbin & Xin 2005). The cubic spline function has the following form:

$$W(\boldsymbol{r} - \boldsymbol{r}', h) = \alpha_D \begin{cases} 1 - \frac{3}{2}s^2 + \frac{3}{4}s^3 & 0 \leq s \leq 1 \\ \frac{1}{4}(2 - s^3) & 1 \leq s \leq 2 \\ 0 & s \geq 2 \end{cases}, \tag{7}$$

where $s = |\boldsymbol{r} - \boldsymbol{r}'|/h$. In one-, two-, and three-dimensional space $\alpha_D = 2/3h$, $10/7\pi h^2$ and $1/\pi h^3$, respectively.

The spatial derivative of Equation (2) is represented by the spatial derivative of the kernel function:

$$\frac{\partial}{\partial r} \langle \phi(\boldsymbol{r}) \rangle = \int_{\Omega} \phi(\boldsymbol{r}') \cdot W(\boldsymbol{r} - \boldsymbol{r}', h) d\boldsymbol{r}'. \tag{8}$$

The calculation object is now divided into N volume elements. These volume elements will be called particles. If the region occupied by the j-th particle (particle j) and the position vector of the center of gravity of the particle are represented by Ω_j and $\boldsymbol{r}_j$ Equation (2) can be approximated as

$$\langle \phi(\boldsymbol{r}) \rangle \approx \sum_{j}^{N} \phi_j \cdot W(\boldsymbol{r} - \boldsymbol{r}_j, h) \cdot V_j \ , \tag{9}$$

where $\phi_j = \phi(\boldsymbol{r}_j)$ and $V_j = \int_{\Omega_j} d\boldsymbol{r}'$. Thus, ϕ_j and V_j represent the value of ϕ for particle j and the volume of particle j, respectively. If we use Equation (9), the particle approximation for a function at particle i can be written as

$$\phi_i = \sum_{j}^{N} \phi_j \cdot W_{ij} \cdot V_j = \sum_{j}^{N} m_j \cdot \frac{\phi_j}{\rho_j} \cdot W_{ij} \ , \tag{10}$$

where $\phi_i = \phi(\boldsymbol{r}_i)$, $W_{ij} = W(\boldsymbol{r} - \boldsymbol{r}_j, h)$, and ρ_j and m_j are the density and mass of particle j. If we follow the same argument, when the orthogonal Cartesian co-ordinate axes are represented by x^{α} (in three-dimensional space, $\alpha = 1, 2, 3$), the particle approximation for the spatial derivative of the function at particle i can be written as

$$\left(\frac{\partial \phi}{\partial x^{\alpha}} \right)_i = \sum_{j}^{N} m_j \cdot \frac{\phi_j}{\rho_j} \cdot \frac{\partial W_{ij}}{\partial x^{\alpha}} \ . \tag{11}$$

Equations (10) and (11) are the discretization equations of the SPH method. In this study, Greek superscripts, such as α, β, γ, denote the co-ordinate direction, and subscripts, such as i and j, denote the particle number. In addition, the Einstein convention for summation over repeated indicates is applied to the superscripts.

2.2 *SPH model for a water jet*

Water is modeled as a Newtonian fluid with weak compressibility, since a WJ is a high-velocity fluid. The governing equations for fluid flow are the continuity equation (Equation (12)), the momentum-conservation equation (Equation (13)) and the equation of state (Equation (14)):

$$\frac{D\rho}{Dt} = -\rho \frac{\partial v^{\alpha}}{\partial x^{\alpha}} \ , \tag{12}$$

$$\frac{Dv^{\alpha}}{Dt} = \frac{1}{\rho} \frac{\partial \sigma^{\alpha\beta}}{\partial x^{\beta}} + f^{\alpha} \ , \tag{13}$$

$$P = B \left[\left(\frac{\rho}{\rho_0} \right)^n - 1 \right], \tag{14}$$

where t is the time, v^{α} is the x^{α} component of the velocity, $\sigma^{\alpha\beta}$ is the total stress tensor, f^{α} is the x^{α} component of the external force, P is the isotropic pressure, ρ is the density of the fluid, and ρ is the reference density. n is a constant that is set to 7 in most circumstances (Monaghan 1994), B is a problem-dependent parameter, and D/Dt is the Lagrange differential operator.

If we discretize Equation (12) for particle i using Equation (11), the continuity equation (Equation (12)) is given by

$$\frac{D\rho_i}{Dt} = \sum_j^N m_j \left(v_i^\alpha - v_j^\alpha\right) \frac{\partial W_{ij}}{\partial x^\alpha}. \quad (15)$$

If we follow the same argument, the Equation (13) can be rewritten as

$$\frac{Dv^\alpha}{Dt} = \sum_j^N m_j \left(\frac{\sigma_i^{\alpha\beta}}{{\rho_i}^2} + \frac{\sigma_j^{\alpha\beta}}{{\rho_j}^2} \right) \frac{\partial W_{ij}}{\partial x^\beta} + f_i^\alpha \ . \quad (16)$$

The total stress tensor $\sigma^{\alpha\beta}$ normally consists of two parts: an isotropic pressure term and a viscous term, since water is a Newtonian fluid; i.e.,

$$\sigma^{\alpha\beta} = -P\delta^{\alpha\beta} + \mu T^{\alpha\beta}, \quad (17)$$

where μ is the viscosity. Moreover, $T^{\alpha\beta}$ is the shear strain rate.

If we substitute Equation (17) into Equation (16) and solve for the acceleration of the particle, and then apply a time integration to the acceleration, we can obtain the velocity v_i^α of particle i. In this study, we used the velocity $\hat{v}_i^\alpha$ which was subjected to the XSPH correction (Monaghan 1989) to move the particle at a velocity that is close to the average velocity in its neighborhood:

$$\hat{v}_i^\alpha = v_i^\alpha + \kappa \sum_j^N \frac{m_j}{\overline{\rho}_{ij}} \left(v_j^\alpha - v_i^\alpha\right) w_{ij}, \quad (18)$$

where $\overline{\rho}_{ij} = (\rho_i + \rho_j)/2$. $\kappa = 0.5$.

2.3 *SPH model for a rock*

The procedure used to model the behavior of rock with the SPH method is similar to that used for WJ. The continuity equation (Equation (12)) (the SPH form is Equation (15)) and the momentum-conservation equation (Equation (13)) (the SPH form is Equation (16)) are still used to estimate the density and motion of rock particles. The difference between these two models is the calculation of the total stress tensor in Equation (17). The total stress tensor $\sigma^{\alpha\beta}$ of rock is made up of two parts: isotropic pressure P and deviatoric stress $s^{\alpha\beta}$,

$$\sigma^{\alpha\beta} = -P\delta^{\alpha\beta} + s^{\alpha\beta}. \quad (19)$$

In the SPH method, the pressure is calculated using an equation of state. Since rock is assumed to have elastic behavior, the pressure equation of rock will obey Hooke's law,

$$P = K\eta = K\left(\frac{\rho}{\rho_0} - 1\right), \quad (20)$$

where K is the bulk modulus, η is the volumetric strain and ρ is the initial density. The temporal differentiation (the stress rate tensor $\dot{s}^{\alpha\beta}$) of the deviatoric stress $s^{\alpha\beta}$ can be estimated by Equation (21) using the Jaumann stress rate to consider the rotation of the material:

$$\dot{s}^{\alpha\beta} = 2G\left(\dot{\varepsilon}^{\alpha\beta} - \frac{1}{3}\delta^{\alpha\beta}\dot{\varepsilon}^{\gamma\gamma}\right) + s^{\alpha\gamma}\omega^{\beta\gamma} + s^{\gamma\beta}\omega^{\alpha\gamma} \quad (21)$$

where G is the shear modulus, $\dot{\varepsilon}^{\alpha\beta}$ is the strain rate tensor and $\omega^{\alpha\beta}$ is the rotation rate tensor. The strain rate tensor $\dot{\varepsilon}^{\alpha\beta}$ and the rotation rate tensor $\omega^{\alpha\beta}$ can be written as

$$\dot{\varepsilon}^{\alpha\beta} = \frac{1}{2}\left(\frac{\partial v^\alpha}{\partial x^\beta} + \frac{\partial v^\beta}{\partial x^\alpha}\right), \dot{\omega}^{\alpha\beta} = \frac{1}{2}\left(\frac{\partial v^\alpha}{\partial x^\beta} - \frac{\partial v^\beta}{\partial x^\alpha}\right). \quad (22)$$

By substituting these equations into Equation (21), the deviatoric stress components $s^{\alpha\beta}$ can be calculated. The total stress tensor $\sigma^{\alpha\beta}$ can be obtained by substituting calculated $s^{\alpha\beta}$ into Equation (19). As in the case of WJ, if we then substitute the obtained $\sigma^{\alpha\beta}$ into Equation (16) and solve for the acceleration of a rock particle, and then apply a time integration to this acceleration, we can obtain the velocity of particle i. In addition, we used the velocity that was subjected to the XSPH correction, as in the case of WJ.

2.4 *Artificial viscosity*

In the SPH method, an artificial viscosity Π_{ij} has been used in the momentum-conservation equation to prevent the unphysical penetration of particles (Monaghan 1992, Sakaguchi et al. 2012).

2.5 *Boundary condition*

In this study, a rigid plate is set under a rectangular rock block model to prevent downward movement of the rock model. To prevent rock and water particles from passing through the rigid plate, particles that approach the rigid plate are subjected to repulsive force (Gesteira et al. 2008, Sakaguchi et al. 2012).

2.6 *Modeling of rock saturated with water*

To express the WJ excavation of rock saturated with water, we should consider the pore pressure in the rock. Here, we introduce the pore pressure following Bui et al. (2007). The pore pressure P_{pore} acting on a particle i of rock can be expressed as

$$P_{pore} = -\sum_{a=1}^{N} m_a \frac{p_a}{\rho_i \rho_a} \frac{\partial W_{ia}}{\partial x^\beta}, \quad (23)$$

where a is the number of particles of water. If we add the above formula and the artificial viscosity Π_{ij} into Equation (16), the momentum-conservation equation

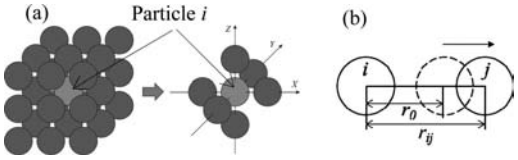


Figure 1. Arrangement of particles and definition of movement. (a) Neighboring particles around particle i in a < simple cubic lattice. (b) Distance between particles i and j.

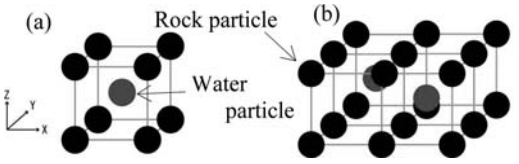


Figure 2. Arrangement of water particles. (a) Body-centered cubic lattice. (b) Checkered pattern.

of rock, the momentum-conservation equation can be given as

$$\frac{Dv_i^\alpha}{Dt} = \sum_j^N m_j \left(\frac{\sigma_i^{\alpha\beta}}{\rho_i^2} + \frac{\sigma_j^{\alpha\beta}}{\rho_j^2} + \Pi_{ij} \right) \frac{\partial W_{ij}}{\partial x^\beta} - \sum_{a=1}^N m_a \frac{p_a}{\rho_i \rho_a} \frac{\partial W_{ia}}{\partial x^\beta} + f_i^\alpha . \quad (24)$$

2.7 *Fracture criterion*

In this study, we defined "fracture" as when a particle of rock was separated from the rock matrix due to impact of the water jet. We assumed the following fracture criterion following Sakaguchi et al. (2012).

(1) Tensile strain criterion
A particle of rock is fractured when the tensile strain between particle i and a neighboring particle j exceeds a critical strain $\varepsilon_{\max}$: $r_{ij} - r_0/r_0 \geq \varepsilon_{\max}$ (=0.3) (Fig. 1), where r_{ij} is the distance between particle $i$and particle j, and r is the initial distance between particles i and j.

3 MODEL FOR NUMERICAL SIMULATION

3.1 *Method for arranging water particles in rock*

It is considered that the method used to arrange water particles in rock will affect the performance of WJ excavation. In this study, we propose two methods for arranging water particles in rock:

(1) Body-centered cubic lattice arrangement
In this method, single water particles are placed at the center of cubes, which are composed of eight rock particles, as shown in Fig. 2(a). This method roughly simulates a state of full saturation.
(2) Checkered pattern arrangement
In this method, water particles are decimated in a checkered pattern from state (1), as shown in Fig. 2(b). This method roughly simulates a state of 50% saturation.

3.2 *Conditions*

In this study, the initial distance between particles was 0.1 mm for water particles and 0.5 mm for rock particles to reduce the calculation time. The smoothing lengths h for both water and rock were 1.5 times the diagonal length of their respective simple cubic lattices (Fig. 1). Therefore, the number of particles was 52,052 for water and 20,480 for rock. The jetting time was $5.4*10^{-4}$ sec because of the limited number of water particles. Other parameters for the simulation are shown in Table 1. Figure 3 shows a model of the simulation and the boundary conditions.

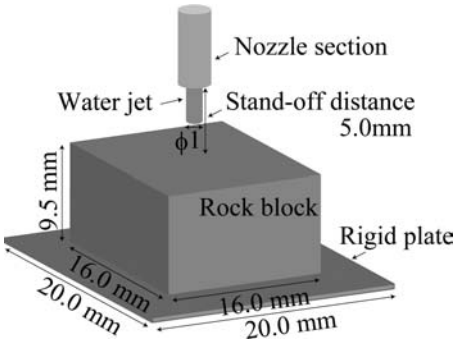


Figure 3. A model of the simulation.

Table 1. Parameters for the numerical simulation.

Density of water [kN/m^3]	10
Viscosity of water [Ns/m^2]	0.001
Unit weight of rock [kN/m^3]	25
Poisson's ratio of rock	0.3
Young's modulus of rock [GPa]	1.0
Water jet nozzle diameter [mm]	1.0
Flow speed of water jet [m/s]	200
Standoff distance [mm]	5.0

4 CASE EXAMPLES OF THE NUMERICAL SIMULATION

(1) Results for the Body-centered cubic lattice arrangement.
Figure 4 shows the excavated borehole. Figure 5 shows the excavation process. In this figure, small gray dots represent water particles and slightly bigger filled circles represent rock particles. Slightly bigger gray circles represent rock particles that have been fractured. Figure 4(a) and Figure 5 show a cross-section along the center axis of the borehole. The borehole is cylindrical. In addition, Figure 5 confirms that pore water particles gather in the direction of the borehole. This is probably because the stress acting on the adjacent particles of the fractured particles is reduced

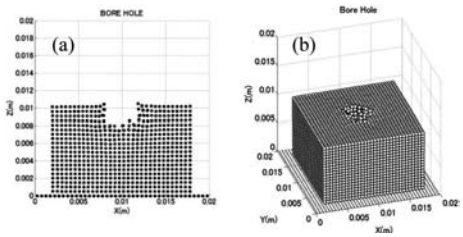


Figure 4. The results of views of the excavated borehole in case of Body-centered cubic lattice arrangement. (a) a cross-section along the center axis of the borehole. (b) 3D image.

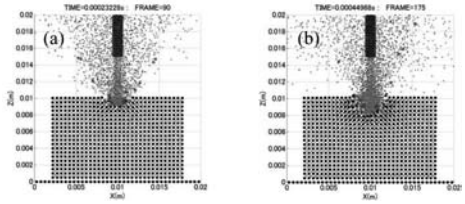


Figure 5. The views of excavation process. (a) $t = 2.32*10^{-5}$, (b) $t = 4.50*10^{-5}$.

by the water jet. As a result, pore water particles gather in the direction of low pressure. It is considered that the rock could be easily excavated because the pore pressure acting on rock particles close to the borehole wall is increased, and thereby the effective stress is reduced and the binding force between rock particles is reduced. In this case, 0.698% of all rock particles were excavated.

(2) Results for the Checkered pattern arrangement

Figure 6 shows the excavated borehole. Figure 7 shows the excavation process. The shape of the borehole is still cylindrical, as with the Body-centered cubic lattice arrangement. Figure 7 confirms that pore water particles gather in the direction of the borehole. However, there are fewer water particles than with a Body-centered cubic lattice. In this case, 0.479% of all rock particles were excavated.

For comparison, dry conditions gave a value of 0.371%. Thus, the amount of pore water affects the amount of excavation. This result shows that pore water affects the mechanism of rock excavation.

5 VERIFICATION OF THE DEVELOPED SIMULATION CODE

We performed a laboratory experiment for the WJ excavation of rock saturated with water to verify the developed numerical simulation code. In addition, we also performed an experiment using dry rock for comparison. We used Kimachi sandstone (Young's modulus 7.7 GPa, Poisson's ratio 0.2 and unit weight 20 kN/m^3) for this experiment. Figure 8 shows the

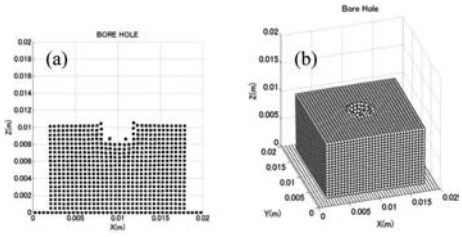


Figure 6. The results of views of the excavated borehole in case of Checkered pattern arrangement. (a) a cross-section along the center axis of the borehole. (b) 3D image.

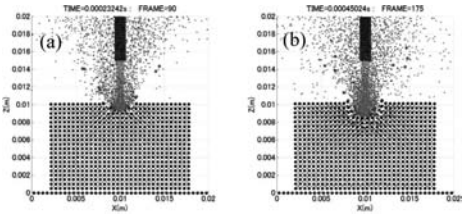


Figure 7. The views of excavation process. (a) $t = 2.32*10^{-5}$, (b) $t = 4.50 * 10^{-5}$.

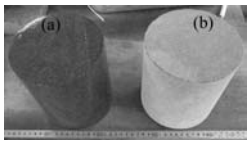


Figure 8. The specimen of Kimachi sandstone. (a) Wet condition. (b) Dry condition.

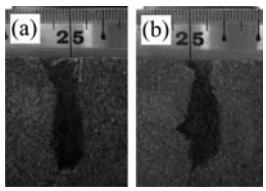


Figure 9. A cross-sectional view of the borehole after WJ excavation. (a) Wet condition. (b) Dry condition.

specimens used in the laboratory experiment. Figures 8(a) and 8(b) show the wet and dry specimens, respectively. The wet specimen had been soaked in water for two days.

The nozzle diameter of the WJ was 1 mm, the driving pressure was 30 MPa and the standoff distance was 5.0 mm. The WJ was applied perpendicularly to the surface of the rock specimen. The excavation time was 60 seconds.

Figure 9 shows a cross-sectional view of the borehole. Figures 9(a) and 9(b) show the results under wet and dry conditions, respectively. In the case of wet rock, the entrance to the borehole is greater than that with dry rock. This is because the rock can be easily excavated because the pore pressure increases, and thereby the effective stress is reduced and the

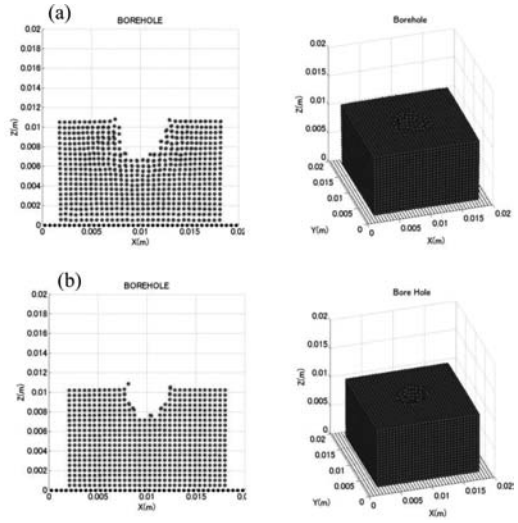


Figure 10. The results of views of the numerical simulation. (a) Wet condition. (b) Dry condition.

binding force between rock particles is reduced. In the dry condition, the entrance to the borehole is enlarged, and the diameter of the borehole narrows before it increases again with depth. Near the bottom of the borehole, its diameter becomes small again. On the other hand, the shape of the borehole is roughly cylindrical, although the diameter near the entrance is smaller than elsewhere.

For comparison with these results from a laboratory experiment, we performed a numerical simulation of the excavation of Kimachi sandstone in wet and dry conditions. Young's modulus, Poisson's ratio and the density were set to be the same of those of Kimachi sandstone. The water particles were given a Checkered pattern arrangement, and the jetting time was $1.5*10^{-3}$ s.

Figure 10 shows the excavated borehole. Figures 10(a) and 10(b) show the results under wet and dry conditions, respectively. The diameter of the borehole in the dry condition gradually decreases along the borehole axis. However, that in the wet condition remains roughly uniform along the borehole axis. These results are consistent with the experimental results. The depth of the borehole under the wet condition is greater than that under the dry condition.

6 CONCLUSIONS

We performed this study to develop numerical simulation code for the WJ excavation of soft rock saturated with water. The main results can be summarized as follows:

(1) We developed code for the three-dimensional numerical simulation of WJ excavation of soft rock saturated with water.
(2) To verify the usefulness of this code, we performed both a laboratory experiment and a numerical simulation using Kimachi sandstone. In the laboratory experiment, the entrance to the borehole in the case of saturated rock was larger than that for dry rock. This is because the rock could be easily excavated, since the pore pressure increases and thereby the effective stress is reduced and the binding force between rock particles is reduced. In the numerical simulation, the diameter of the borehole in the dry condition gradually decreased along the borehole axis. However, in the wet condition, the diameter remained roughly uniform along the borehole axis. This result is consistent with the results of the laboratory experiment.

REFERENCES

Bui, Ha H., Sako, K. & Fukugawa, R. 2007. Numerical simulation of soil-water interaction using smoothed particle hydrodynamics (SPH) method. *J. Terramech.* 44: 339–346.

Cleary, P.W., Prakash, M. & Ha, J. 2006. Novel applications of smoothed particle hydrodynamics (SPH) in metal forming, *J. Mater. Process. Technol.* 177: 41–48.

Gesteira, M.G., Rogers, B.D., Dalrymple, R.A., Crespo, A.J.C. & Narayanaswamy, M. 2008. SPHysics, *Users Guide for the SPHysics Code*

Hongbin, J. & Xin, D. 2005. On criterion for smoothed particle hydrodynamics kernels in stable field. *J. Comp. Phys.* 202: 699–709.

Komurasaki, K. et al. 1988. Numerical simulation of high-speed impacts on brittle materials using the particle methods, *J. Soc. Mat. Sci. Japan* 47: 825–829.

Libersky, L.D., Petschek, A.G., Garney, T.C., Hipp, J.R. & Allahdadi, F.A. 1993. High Lagrangian hydrodynamics *J. Comput. Phys.* 109: 67–75.

Liu, G.R. & Liu, M.B. 2003. *Smoothed Particle Hydrodynamics: A Meshfree Particle Method*, World Scientific Publishing Co. Pte. Ltd.

Ma, L, Bao, R.H. & Guo, Y.M. 2008. Waterjet penetration simulation by hybrid code of SPH and FEA. *Int. J. Impact Eng.* 35: 1035–1042.

Monaghan, J.J 1988. An introduction to SPH. *Comput. Phys. Commun.* 48: 89–96.

Monaghan, J.J. 1989. On the problem of penetration in particle methods. *J. Comp. Phys.* 82: 1–15.

Monaghan, J.J. 1992. Smoothed particle hydrodynamics *Annu. Rev. Astron. Appl.* 30: 543–574.

Monaghan, J.J. 1994. Simulating free surface flows with SPH. *J. Comp. Phys*. 110: 399–406.

Potapov, S., Maurel, B., Combescure, A. & Fabis, J. 2009. Modeling accidental-type fluid-structure problem with the SPH method. *Comput. Struct.* 87: 721–734.

Sakaguchi, K. Yumoto, Y. & Kizaki, A. 2012. Numerical simulation of water jet excavation of rock using Smoothed Particle Hydrodynamics, *Proc. of the 7th ARMS*, USB.

Sato, Y. et al. 2008. Three-dimensional simulation of water-jet cutter by the Smoothed Particle Hydrodynamics method, *J. Inst. Sci. Eng. Chuo Univ.* 14: 7–17.

Shinohara, T., Okabe, K. & Nakayama, T. 2004. Numerical simulation of water-jet cutting of a solid body, *J. Inst. Sci. Eng. Chuo Univ.* 10: 21–32.

Shintate, K. & Sekine, H. 2002. Proposal of new particle generation technique in SPH analysis of hypervelocity impacts, *The Japan Society of Mechanical Engineering*, A, 68: 132–138.

Rock Mechanics for Resources, Energy and Environment – Kwaśniewski & Łydżba (eds)
© 2013 Taylor & Francis Group, London, ISBN 978-1-138-00080-3

Elastic response of laterally loaded rock sockets using 3D finite element analyses

K.P. Tzivakos, M.J. Kavvadas & D.G. Kaltsas
National Technical University of Athens, Greece

ABSTRACT: The paper presents a numerical study of the elastic response of laterally loaded rock sockets. Sockets are loaded at the top with transverse forces and bending moments and the corresponding displacements and rotations are calculated. 3D finite element analyses are carried out to investigate the effects of shaft length, relative stiffness of socket to rockmass and the ratio of the applied moment to shear force. The rockmass is assumed to be linearly elastic, as rock sockets rarely reach the rockmass strength. However, socket-ground interface elements are used along the periphery and at the socket base in order to simulate separation and lift-up effects on the response. The results of the analyses are compiled in semi-empirical dimensionless relationships giving the socket stiffness in terms of the important parameters. The produced results show significant differences compared to the results of numerical analyses reported by Carter & Kulhawy (1992) where separation and lift-up effects were not included.

1 INTRODUCTION

Rigid sockets are nowadays an effective foundation type of structures founded with tall piers. The specific foundation undertakes significant horizontal loads and bending moments, thus it undergoes considerable horizontal displacement and rotation on its head.

Two different approaches are met in common engineering practice for the estimation of the aforementioned socket head deformation. One approach involves the subgrade reaction methods, including numerous methodologies of p-y curves for rock that serve the presence of non-linear, horizontal springs along the socket (Reese 1997, Gabr et al. 2002). On the other hand stands the elastic continuum theory, which treats the rigid socket as an equivalent spring with three independent degrees of freedom for the prescribed loading conditions (Douglas & Davis 1964, Carter & Kulhawy 1992).

The scope of the present paper is the evaluation of the socket head deformation predictions proposed by the most recent methodology of the latter approach. Furthermore it is attempted to derive corresponding closed-form equations through 3D finite element analyses, taking into account the frictional behavior and the possible separation between the laterally loaded rock socket and the surrounding rockmass.

2 THE CARTER & KULHAWY METHOD

2.1 *Assumptions*

In the present chapter, a thoroughly determined methodology is described for the calculation of horizontal displacement and rotation of the socket head, namely the Carter & Kulhawy method (1992). The specific methodology has provided the engineering community with closed-form equations for the calculation of the aforementioned deformation, referring to rigid and flexible shafts. The present study investigates the behavior of rigid rock sockets, therefore only the part of the Carter & Kulhawy method with respect to rigid shafts is presented herein.

The socket is simulated by a hollow, cylindrical shaft of effective Young's modulus (E_e), Poisson's ratio (v_e), length (L) and diameter (D). For a rigid socket with stiffness $(EI)_e$ – (E) for the Young's modulus of the socket construction material – the effective Young's modulus (E_e) is calculated according to Equation 1.

$$E_e = \frac{(EI)_e}{(\pi D^4/64)} \tag{1}$$

The rock socket is considered perfectly elastic, installed in a homogenous, isotropic, elastic rockmass space with Young's elasticity modulus E_r and Poisson's ratio v_r. Thereafter, the socket head is subjected to prescribed lateral loading (H) and bending moment (M).

The study of Carter & Kulhawy (1992) uncovered that the effect of the rockmass Poisson's ratio (v_r) is represented by the secant shear modulus of the rockmass, defined by Equation 2.

$$G^* = G_r\left(1+\frac{3v_r}{4}\right) \tag{2}$$

where G_r = the shear modulus of the isotropic rockmass.

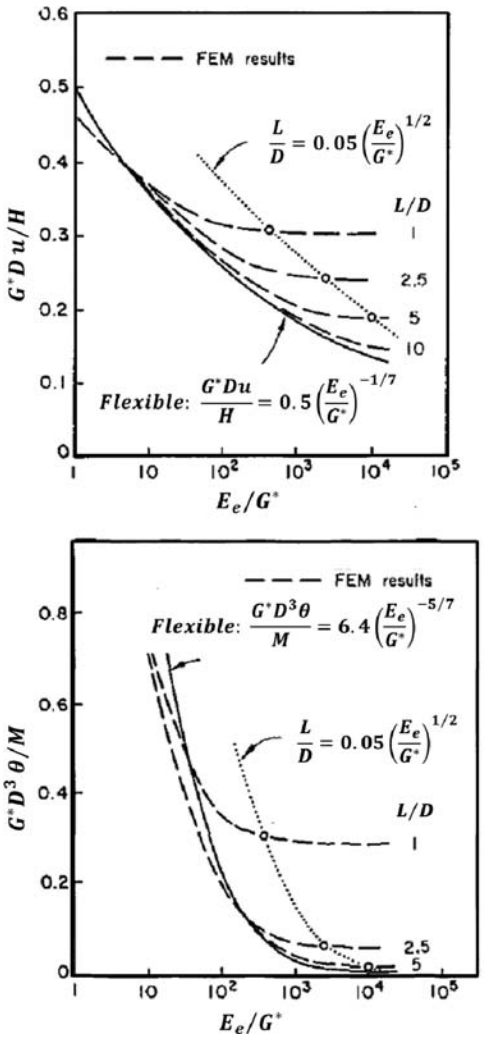


Figure 1. Lateral load-displacement (up) and moment-rotation (down) relations according to Carter & Kulhawy (1992).

For homogenous rockmass, it was determined that the deformation of the shaft head at the level of the rock surface depends on the relative moduli of the shaft and the surrounding rockmass (E_e/G^*) and the geometry of the shaft (L/D). Especially for rigid shafts, the graphs of Figure 1 were formed from the finite element analyses carried out by Carter & Kulhawy (1992), demonstrating the dimensionless shaft head displacement or rotation against the shaft-rockmass relative stiffness (E_e/G^*). The pointed curves indicate that a laterally loaded shaft shall behave as rigid when the condition of the mathematical formulation $(L/D) \leq 0.05(E_e/G^*)^{1/2}$ is met.

2.2 *Prediction of the response of rigid shafts*

Since the rock socket meets the rigidity conditions of Figure 1, it is considered rigid according to the aforementioned methodology. The closed-form solutions for head displacement (u) and rotation (θ) of such sockets are described according to Carter & Kulhawy (1992) by Equations 3 and 4 respectively.

$$u = 0.32\left(\frac{H}{G^*D}\right)\left(\frac{L}{D}\right)^{-\frac{1}{3}} + 0.16\left(\frac{M}{G^*D^2}\right)\left(\frac{L}{D}\right)^{-\frac{7}{8}} \quad (3)$$

$$\theta = 0.16\left(\frac{H}{G^*D^2}\right)\left(\frac{L}{D}\right)^{-\frac{7}{8}} + 0.25\left(\frac{M}{G^*D^3}\right)\left(\frac{L}{D}\right)^{-\frac{5}{3}} \quad (4)$$

3 THE 3D FINITE ELEMENT SIMULATION

Numerous 3D finite element models of the single, free-head, laterally loaded socket are designed in the commercial code ABAQUS. Solid, 8-node, full integration finite elements are used to model the rockmass and the rock socket. The boundaries of the model are set to 6.5D, 2.5D and 5D from the center of the socket head along x, y and z axis respectively, where D is the socket diameter. At this point, it is important to clarify that the socket is simulated by a solid, elastic, reinforced concrete shaft of diameter D = 5 m with Young's modulus E = 25 GPa. Therefore, the effective Young's modulus according to Equation 1 is $E_e = E$. Various socket-rockmass relative stiffness ratios have been analyzed, namely $E/G^* = 10$, 50, 100, 150, 500, 750, 1000 in order to examine the rigidity criteria of the sockets involved in the specific analyses. Furthermore, rock sockets with slenderness ratios L/D = 1, 1.2, 1.5, 1.8, 2, 3 are included in the present study. However, not all the combinations of slenderness ratios and relative stiffness ratios refer to rigid sockets. Therefore, a specific procedure is carried out aiming at the determination of cases that shall contribute to the formation of the desired closed-form equations for the response of rigid sockets (see Section 4).

The rock socket is loaded with a concentrated lateral head load H = 20 MN – the load is applied in specific load increments. Moreover, concentrated head moment M = 0, 300, 600 MNm is applied in equivalent increments, standing for eccentricity values e = M/H = 0, 15, 30 m respectively.

With respect to the socket-rockmass interaction, two different approaches are simulated in the finite element code. Initially, a hard contact is modeled between the rock socket and the surrounding rockmass in order to verify the predictions of the Carter & Kulhawy method for the rigid shaft response. The specific simulation is adopted, due to lack of shaft-rockmass separation effects in the finite element analyses carried out by Carter & Kulhawy (1992). The second approach involves the simulation of socket-rockmass separation and friction through specially calibrated surface interactions. An exponential clearance-pressure law is incorporated for the surface interaction in the normal direction, allowing for the separation of the socket from the surrounding rockmass and the lift-up effects of the socket base (Fig. 2). The Mohr-Coulomb friction criterion is applied to simulate the

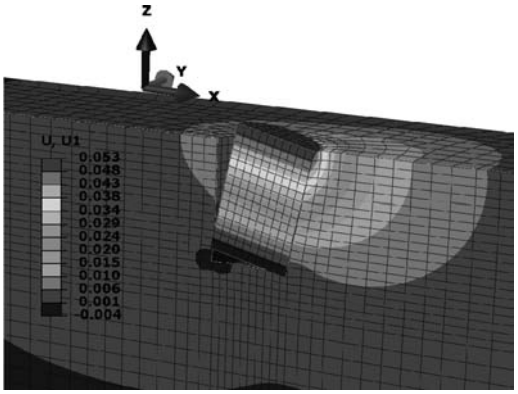


Figure 2. The 3D FEM model with socket-rockmass surface interaction (cut along the loading axis of the socket).

shear stresses developed between the rockmass and the socket. The friction angle of the specific interaction is considered $\delta = (2/3)\phi$, where $\phi =$ the internal friction angle of the rockmass with values ranging between 30°–45°, depending on the rockmass properties.

4 PREDICTION OF RIGID SOCKET ELASTIC RESPONSE

The predictions of the present study for the elastic response of rigid rock sockets are demonstrated in the current section. Output from both hard contact and friction-separation approaches is presented herein, referring to the socket-rockmass interaction. Thus, the predicted elastic response of rigid sockets for the two aforementioned simulations is available for direct comparison. Furthermore, a comparative depiction of the predictions proposed by the present study against the solutions suggested by Carter & Kulhawy (1992) is attempted.

4.1 *The effect of the surface interaction simulation*

Although the problem under consideration is linear in terms of materials, certain non-linearity occurs due to the complicated socket-rockmass surface interaction (see Section 3). A parametric study of the eccentricity is carried out in order to determine whether the surface interaction affects the calculated socket head deformation. More specifically, graphs of horizontal socket head displacement (u) and rotation (θ) against the eccentricity (e) are plotted for certain slenderness ratios (L/D) and various socket-rockmass relative stiffness ratios (E/G^*) (Fig. 3). A linear distribution of socket head deformation against the load eccentricity is observed. Consequently, the socket-rockmass surface interaction does not affect the linearity of the calculated socket head deformation.

4.2 *Determination of rigid sockets*

In the following paragraph, all the possible comparisons of socket-rockmass relative stiffness ratios

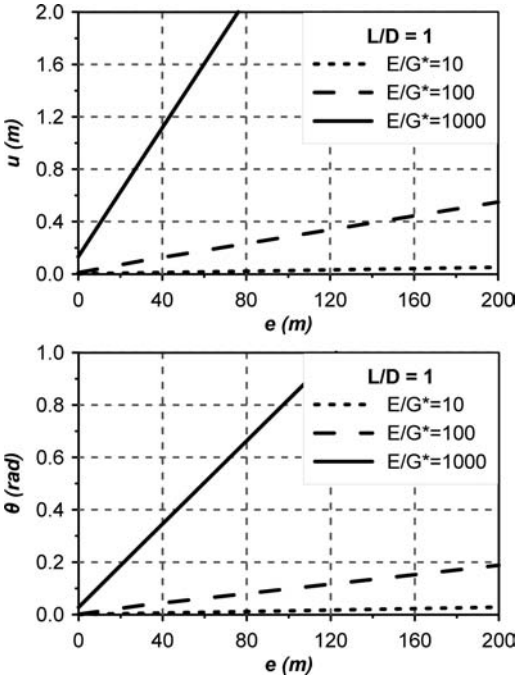


Figure 3. Linear distribution of socket head horizontal displacement (up) and rotation (down) with load eccentricity.

(E/G^*) and socket geometries (L/D) are taken into account in order to define perfectly rigid sockets, according to the finite element analyses results. In line with the procedure demonstrated by Carter & Kulhawy (1992), the rigid sockets of the present study exhibit head deformation that is independent of the socket-rockmass relative stiffness (E/G^*).

Each deformation results from two components: the deformation due to the lateral load (H) and the corresponding one due to socket head moment (M). The general form of the socket head displacement (u) and rotation (θ) is depicted by Equations 5–6 respectively.

$$u = u_H + u_M \tag{5}$$

$$\theta = \theta_H + \theta_M \tag{6}$$

where u_H and θ_H are computed by numerical analyses without the application of any bending moment ($M = 0$) on the socket head. On the other side, u and θ are computed by the analyses carried out for any desired eccentricity value (e).

Specific graphs are designed, illustrating dimensionless mathematical formulations of the socket head horizontal displacement and rotation against the socket-rockmass relative stiffness ratio (E/G^*). Figure 4 depictsthat the dimensionless deformation tends to depend less on the stiffness ratio (E/G^*) with the increase of the latter.

As a consequence, for each socket slenderness ratio (L/D) certain values of stiffness ratio (E/G^*) are set as lower boundaries for the characterization of rigid sockets, as demonstrated in Table 1.

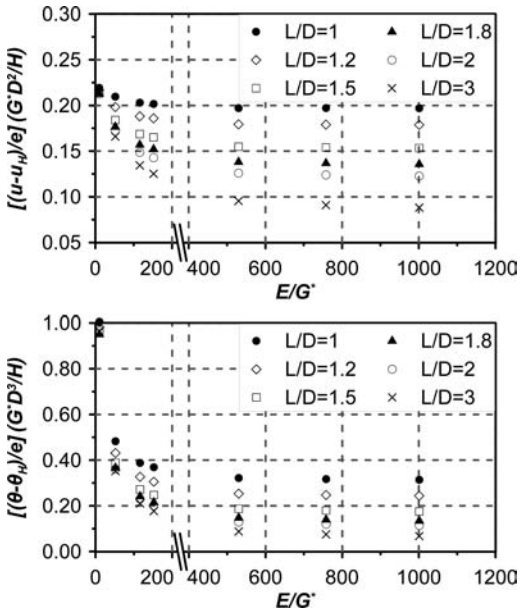


Figure 4. Dimensionless deformation against relative stiffness for the hard contact surface interaction approach.

Table 1. Lower relative stiffness boundaries for rigid sockets.

Slenderness ratio (L/D)	Relative stiffness Hard contact (E/G*)	Relative stiffness Interface (E/G*)
1	100	150
1.2	150	150
1.5	750	150
1.8	750	150
2	750	500
3	750	750

4.3 *Proposed socket head deformation equations*

The aforementioned cases of rigid sockets are processed in order to develop closed-form mathematical formulations for the prediction of socket head deformation, assuming either hard contact or sliding and separation effects between the foundation and the surrounding rockmass. The derived equations shall have the general form of Equations 7–8.

$$u = A\left(\frac{H}{G^{*}D}\right)\left(\frac{L}{D}\right)^{a} + B\left(\frac{M}{G^{*}D^{2}}\right)\left(\frac{L}{D}\right)^{b} \quad (7)$$

$$\theta = B\left(\frac{H}{G^{*}D^{2}}\right)\left(\frac{L}{D}\right)^{b} + C\left(\frac{M}{G^{*}D^{3}}\right)\left(\frac{L}{D}\right)^{c} \quad (8)$$

Consequently, the coefficients **A, a, B, b, C, c** have to be determined. In the previously presented equations it is obvious that coefficients **B, b** are common for displacements and rotations, thus representing the coupled spring stiffness.

Three separate charts are drawn from the finite element analyses output of each socket-rockmass

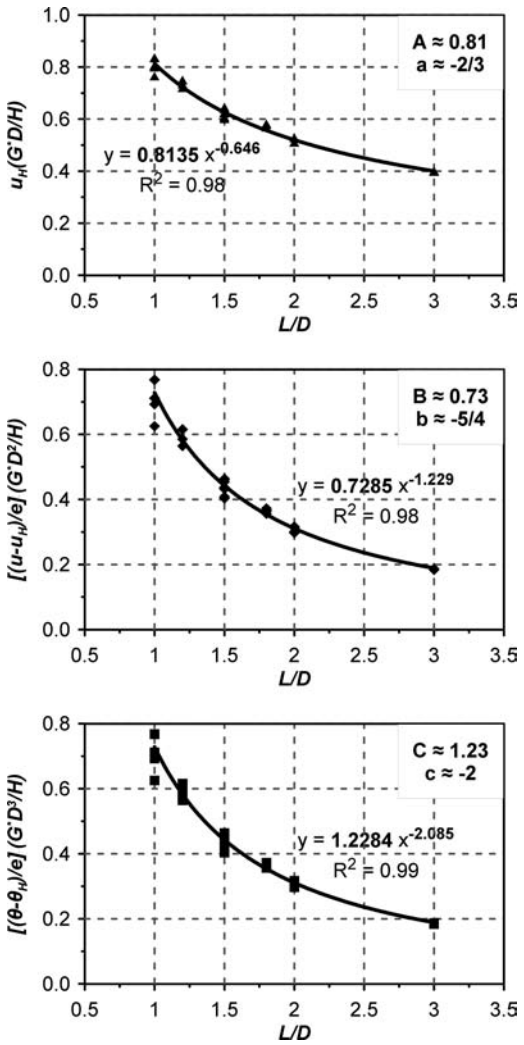


Figure 5. Calculation of the coefficients A, a, B, b, C, c for the friction-separation surface interaction approach.

interaction approach (hard contact or separation and sliding) in order to determine these coefficients. The graphs of Figure 5 depict dimensionless forms of u_H, u, θ_H, θ on the vertical axis against the slenderness ratios (L/D) of the rigid sockets selected in paragraph 4.2 on the horizontal axis. Thereafter, hyperbolic trendlines are drawn aiming at calculating the aforementioned coefficients. Figure 5 demonstrates the calculation procedure of **A, a, B, b, C, c** for the friction-separation surface interaction approach.

As a result, the closed-form Equations 9–12 of the present study are derived, referring to rock socket head deformation for:

(I) socket-rockmasshard contact

$$u_I = 0.29\left(\frac{H}{G^{*}D}\right)\left(\frac{L}{D}\right)^{-\frac{1}{5}} + 0.20\left(\frac{M}{G^{*}D^{2}}\right)\left(\frac{L}{D}\right)^{-\frac{3}{4}} \quad (9)$$

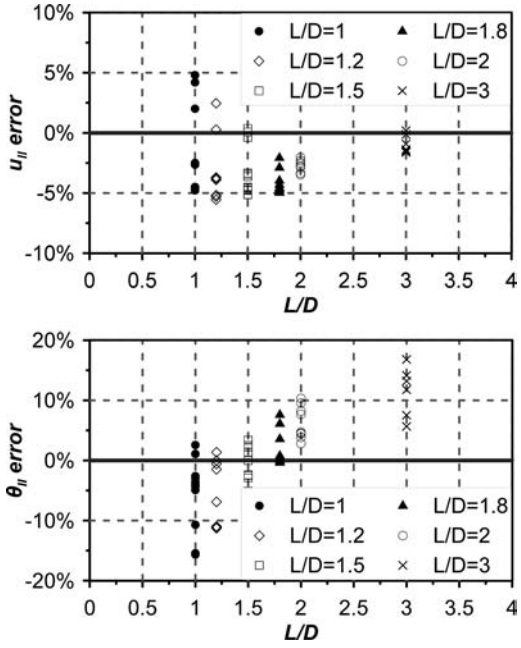


Figure 6. Fractional difference between the proposed displacement (up)/ rotation (down) and the corresponding FEA results.

$$\theta_I = 0.20\left(\frac{H}{G^*D^2}\right)\left(\frac{L}{D}\right)^{-\frac{3}{4}} + 0.35\left(\frac{M}{G^*D^3}\right)\left(\frac{L}{D}\right)^{-\frac{3}{2}} \quad (10)$$

(II) socket-rockmass surface interaction

$$u_{II} = 0.81\left(\frac{H}{G^*D^2}\right)\left(\frac{L}{D}\right)^{-\frac{2}{3}} + 0.73\left(\frac{M}{G^*D^2}\right)\left(\frac{L}{D}\right)^{-\frac{5}{4}} \quad (11)$$

$$\theta_{II} = 0.73\left(\frac{H}{G^*D^2}\right)\left(\frac{L}{D}\right)^{-\frac{5}{4}} + 1.23\left(\frac{M}{G^*D^3}\right)\left(\frac{L}{D}\right)^{-2} \quad (12)$$

4.4 *Verification of the proposed deformation predictions – Rigidity criterion*

The derived closed-form predictions of the previous paragraph are verified in the present section. Initially, the fractional differencebetween the predicted deformation and the one calculated directly through the finite element analysis is investigated. Figure 6 shows that the expected error for the predicted rigid socket head horizontal displacement and rotation is lower than 5% and 15% respectively. For the loading conditions imposed to the sockets of the 3D finite element analyses, the calculated socket head rotations were significantly lower in numerical terms than the horizontal displacements. Therefore, higher numerical errors of the predicted rotation are occasionally expectable and acceptable.

Subsequently, all the sockets analyzed in the finite element code ABAQUS are incorporated in the graphs of Figure 7 in order to locate cases of sockets that can be characterized as rigid, although they do not meet

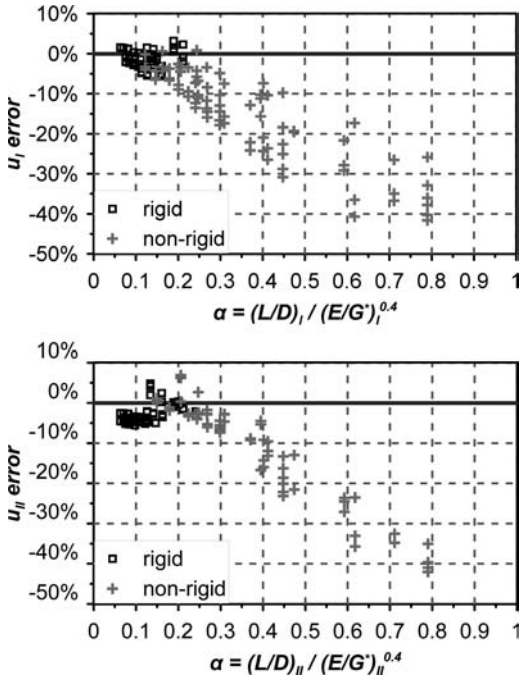


Figure 7. Determination of the criterion for socket rigidity.

the conditions of Table 1. Figure 7 depicts the possibility of expanding the rigidity criteria of paragraph 4.2, with an acceptable error ±10%. An attempt is made to define a numerical formulation of the form $(L/D) \leq \alpha(E/G^*)^{\beta}$ between the slenderness ratio (L/D) and the relative stiffness ratio (E/G*) of the socket. The specific procedure involves the determination of coefficients α, β through charts of the variation of the closed-form predictions from the finite element analyses results against the quantity $\alpha = (L/D)/(E/G^*)^{\beta}$, concerning the horizontal displacement.

For the specific graphs, various values of the parameter β are tested, ranging between 0.2–0.5. Finally, aiming at the incorporation of the largest possible amount of (L/D)-(E/G*) combinations in the rigidity criterion, Equations 13 and 14 occurred for rigid socket determination of both socket-rockmass interaction approaches (see Section 3).

$$\left(L/D\right)_I \leq 0.20\left(E/G^*\right)^{0.4} \quad (13)$$

$$\left(L/D\right)_{II} \leq 0.30\left(E/G^*\right)^{0.4} \quad (14)$$

4.5 *Differences from the Carter & Kulhawy method*

The fractional difference between the proposed closed-form predictions of the present study and the ones proposed by Carter & Kulhawy (1992) are depicted in the graphs of Figure 8. The specific difference is plotted against the slenderness ratio (L/D) for all the cases considered rigid according to Carter &

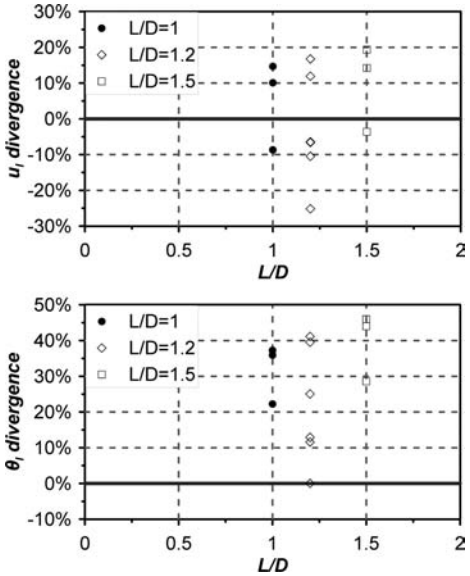


Figure 8. Fractionaldifference between the proposed predictions of the current methodology and the predictions of Carter & Kulhawy (1992).

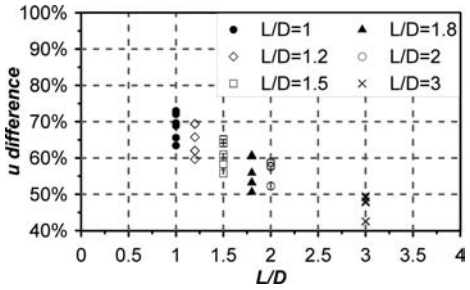


Figure 9. Fractional difference between the socket head horizontal displacement with and without surface interaction.

Kulhawy. A peak divergence of 20% is observed between the compared displacements, while the corresponding difference for the rotations is about 40%.

4.6 *Differences between the predictions of the hard contact and the friction-separation approach*

The fractional difference between the calculated socket head deformation of the hard contact approach and the friction-separation simulation is depicted in Figure 9. Evidently, a divergence is observed, ranging between 40%–80% for the horizontal displacement – similar difference is noticed for the rotation. The aforementioned differences are attributed to the separation and sliding effects simulated by the socket-rockmass surface interaction.

4.7 *Prediction of deformation with interface from hard contact output*

A final contribution of the present study is to propose a specific numerical procedure for the prediction of socket head deformation by utilizing the output from hard contact finite element analyses and the closed-form equations derived from analyses with interface properties on the socket-rockmass surface interaction. Thus, significant computational cost shall be spared. Specific multiplying factors are proposed for each component of Equations 9 and 10 in order to calculate the deformation of the socket head. Equations 15–16 present the aforementioned factors.

$$u_{II} \approx 2.8\left(\frac{L}{D}\right)^{-\frac{7}{15}} \cdot \left(u_H\right)_I + 3.7\left(\frac{L}{D}\right)^{-\frac{1}{2}} \cdot \left(u_M\right)_I \qquad (15)$$

$$\theta_{II} \approx 3.7\left(\frac{L}{D}\right)^{-\frac{1}{2}} \cdot \left(\theta_H\right)_I + 3.5\left(\frac{L}{D}\right)^{-\frac{1}{2}} \cdot \left(\theta_M\right)_I \qquad (16)$$

5 CONCLUSIONS

A thorough study has been carried out on the elastic response of laterally loaded rigid rock sockets. The deformation of the socket head is investigated and specific closed-form predictions for the respective horizontal displacement and rotation are proposed, derived from 3D finite element analyses of the commercial code ABAQUS. Furthermore, a direct comparison of the aforementioned equations to the predictions of Carter & Kulhawy (1992) for rigid sockets is attempted. The conclusion is drawn that the estimations of the present method are more conservative. This observation is attributed to the simulation of sliding, separation and lift-up effects of the socket against the surrounding rockmass in the present study. Finally, a set of multiplying factors are delivered in order to predict the rigid socket head deformation from finite element analyses output without socket-rockmass surface interaction.

REFERENCES

Carter, J.P. & Kulhawy, F.H. 1988. Analysis and design of drilled shaft foundations socketed into rock. *Report EL-5918.* Palo Alto, Calif: Electric Power Research Institute.

Carter, J.P. & Kulhawy, F.H. 1992. Analysis of laterally loaded shafts in rock. *Journal of Geotechnical Engineering* 118 (6): 839–855.

Douglas, D.J. & Davis, E.H. 1964. The movements of buried footings due to moment and horizontal load and the movement of anchor plates.*Geotechnique* 14 (2): 115–132.

Gabr, M.A. et al. 2002. *P-y Curves for Laterally Loaded Drilled Shafts Embedded in Weathered Rock.* North Carolina: Department of Civil Engineering, North Carolina State University.

Reese, L.C. 1997. Analysis of laterally loaded piles in weak rock. *Journal of Geotechnical and Geoenvironmental Engineering*123(11): 1010–1017.

Simulia Abaqus 6.10 Documentation

Zhang, L. 2004. *Drilled Shafts in Rock.* London: Balkema.

Rock Mechanics for Resources, Energy and Environment – Kwaśniewski & Łydżba (eds)
© 2013 Taylor & Francis Group, London, ISBN 978-1-138-00080-3

The influence of the type of pore fluid in two-phase media on the form of consolidation equations

A. Uciechowska & T. Strzelecki
Institute of Geotechnics and Hydrotechnics, Wrocław University of Technology, Wrocław, Poland

ABSTRACT: In this paper various approaches to a modeling medium consisting of an elastic skeleton with gas-filled pores are presented. Classic equations of the poroelasticity model by Biot are cited, with the modifications considering the presence of not only liquid, but also gas in the pores of the medium. Apart from the isothermal models, models including temperature changes and the resulting changes of effective parameters of porous medium are presented. This model can be used in modeling phenomena in soil during underground coal gasification, where as a result of high temperatures water undergoes a phase transition into water vapor.

1 INTRODUCTION

One cannot mention modeling porous media such as soils and rocks without the influence of the type of pore fluid. Generally, calculations taking into account pore fluid concern water. At high temperatures (for instance near generators in the underground coal gasification process) water changes its phase, and consequentlyits parameters change. In this paper various approaches to modeling porous media will be presented, with skeletons filled not only with liquid, but also gas, and the proposed equations, which, in the authors' opinion, may be the foundation of the model of media partially filled with liquid and gas.

2 TWO-PHASE MEDIA WITH AN ELASTIC SKELETON FILLED WITH LIQUID

In 1941, M.A. Biot proposed constitutive equations for porous media filled with liquid. Apart from the strain resulting from Hooke's law, Biot took into account the strain caused by a change of stress in pore fluid. These equations have the form:

$$\theta = \frac{\sigma_m}{H} + \frac{\sigma}{R} \tag{1}$$

$$\varepsilon = \frac{\sigma_m}{K} + \frac{\sigma}{H} \tag{2}$$

where θ = volumetric strain of fluid; ε = volumetric strain of the skeleton; σ_m = stress in the skeleton; σ = stress in fluid; H^{-1}defines soil compressibility caused by a change in fluid pressure; R^{-1}defines the change of fluid content resulting from a change in pressure; Q^{-1} = coefficient defining the amount of fluid that can be forced into the body without changing its volume; K = bulk modulus of the skeleton $K = A + {}^2/_3 N$ (according to Biot); N = shear modulus of the skeleton; A = bulk modulus of a skeleton filled with fluid.

Constitutive equations of poroelastic medium under the isothermal conditions may be shown in the classical form as:

$$\sigma_{ij} = 2N^{sg}\varepsilon_{ij} + \left(A^{sg}\varepsilon + Q^{sg}\theta\right)\delta_{ij} \tag{3}$$

These equations have following form for volumetric strain:

$$\sigma_m^s = K\varepsilon + Q\theta \tag{4}$$

$$\sigma^f = R\theta + Q\varepsilon \tag{5}$$

Biot & Willis (1957) proposed the coefficient $\alpha = K/H$, called later the Biot-Willis coefficient, defined as the change of the volume of fluid to the volumetric strain of the element, under drained conditions ($\sigma = 0$). The Biot-Willis coefficient cannot be less than zero ($\alpha = 0$ for incompressible fluid) or larger than ($\alpha = 1$ for incompressible skeleton). This allows one to write Equation (2) in the form:

$$\varepsilon = \frac{1}{K}\left(\sigma_m - \alpha p_p\right) \tag{6}$$

Introducing the additional coefficient M, called the Biot modulus, it is possible to write the relation for pressure in the form:

$$p = -\alpha M\varepsilon + M\theta \tag{7}$$

The Biot modulus is the inverse of the storage coefficient, defined as the change in the pore fluid volume

as a result of the increase of the pore pressure under constant volumetric strain and temperature.

$$\frac{1}{M}=\left.\frac{\partial\theta}{\partial p}\right|_{\varepsilon} \tag{8}$$

With Skempton's parameter, defined as B = R/H; 0 < B < 1 it is possible to write the relation for fluid in the form:

$$\theta=\frac{1}{R}\left(\sigma+\frac{\sigma_m}{B}\right) \tag{9}$$

3 CONSTITUTIVE RELATIONS FOR A MEDIUM CONSISTING OF A SKELETON AND GAS FILLING ITS PORES

3.1 *Saturated and unsaturated flow*

Coussy (2007, 2010) has dealt with topic of the flow of mixtures in his work. He assumed two kinds of flow – saturated (with pores filled with one kind of fluid), and unsaturated (consisting of two phases: liquid and its vapor, or three phases: liquid, its vapor and additional gas (air)).

Constitutive equations for this case can be obtained from the balance of free energy. For saturated fluid flow, this balance can be written as:

$$\sigma d\varepsilon-\varphi dp+s_{ij}de_{ij}-d\eta_s=0 \tag{10}$$

where $\varphi=\phi-\phi_0$ is the change of Lagrangian porosity (strain results from the change in porosity $\varepsilon=(1-\phi_0)\varepsilon_s+\varphi$, in case of accepting the assumption of an incompressible skeleton $\varepsilon=\varphi$), ϕ refers the current porous volume to the reference volume; η_s = free energy; s_{ij} = stress deviator tensor, e_{ij} – strain deviator tensor.

State equations have the form:

$$\sigma=\frac{\partial\eta_s}{\partial\varepsilon};\quad \varphi=-\frac{\partial\eta_s}{\partial p};\quad s_{ij}=\frac{\partial\eta_s}{\partial e_{ij}} \tag{11}$$

Hence, constitutive equations for isothermal conditions can be written as:

$$\sigma=K\varepsilon-bp \tag{12}$$

$$\varphi=b\varepsilon+\frac{p}{N} \tag{13}$$

$$s_{ij}=2Ge_{ij} \tag{14}$$

In the case of non-isothermal conditions with unsaturated flow (of two fluids) and after taking into account the effects between the two phases:

$$\sigma_{ij}=\left(K-\frac{2}{3}G\right)\varepsilon\delta_{ij}+2G\varepsilon_{ij}-\alpha\left[\chi p_1+(1-\chi)p_2\right]\delta_{ij}-3aKT\delta_{ij} \tag{15}$$

$$\varphi=\varphi_1+\varphi_2=\alpha\varepsilon+\frac{(\alpha\chi-\phi_0S_1)p_1+\left[\alpha(1-\chi)-\phi_0S_2\right]p_2}{M(\alpha-\phi_0)}+3a_\varphi T \tag{16}$$

where χ = constant depending on saturation S; T = temperature; a, a_ϕ = volumetric thermal dilation coefficients; α = Biot-Willis coefficient; M = Biot modulus; K = bulk modulus; G = shear modulus.

3.2 *Consideration of sorption*

While classic poromechanics assumes only mechanical interaction between phases, Łydżba (1991) presents a different approach in his paper. He proposed the adoption of Biot's model to a coal-gas system with sorption and desorption phenomena. The dilatancy of the skeleton in the proposed constitutive relations is dependent, apart from the elastic strain, upon the amount of sorbed gas.

$$\theta_s=\theta_k+\theta_p \tag{17}$$

where θ_k = skeleton dilatancy resulting from elastic stress; θ_p = skeleton dilatancy resulting from sorption,

$$\theta_p=a_1+a_2\ln\left(\frac{\tilde{p}}{p_0}\right)F(\tilde{p}) \tag{18}$$

where F(p) = sorption isotherm; p = equilibrium pressure; a_1, a_2 = parameters of sorption swelling.

The model assumes no mechanical interaction between the gas in the pores and the coal skeleton. The influence of gas on the dilatancy involves only the sorption phenomena.

3.3 *Laboratory tests conducted at the Strata Mechanics Research Institute of Polish Academy of Sciences*

As a result of laboratory tests on rocks with pores filled by air, Fabre & Gustkiewicz (1997) suggested the dependence ofthe Biot-Willis coefficient on porosity:

$$\alpha=1-e^{-a\cdot\tan\left(\frac{\pi}{2}\phi\right)} \tag{19}$$

where *a* is a coefficient depending on the type of rock.

In a selection of samples, the parameters of the bulk modulus of the skeleton and medium (based on which Biot-Willis coefficient can be calculated) were determined in normal conditions and after being heated to 450°C, for the purpose of studying the influence of microcracks on the material parameters. In the tested sandstone samples after the temperature treatment,the porosity increased, the bulk modulus of a skeleton decreased slightly, and the bulk modulus of the rock decreased significantly.

The results of the laboratory tests for various pore fluids were published by Nowakowski (2012). The pore fluid for the tested samples of sandstone and limestone was kerosene, distilled water, nitrogen and

carbon dioxide. Skempton's parameter was similar for gases and liquids, either for limestone or sandstone, hence the conclusion that the influence of the pore pressure on the dilatation of the pore space does not depend on the kind of medium filling the pores. However, the value of the Biot-Willis coefficient, which determines the influence of the pore pressure on the dilatation of the sample, was lower for gases in sandstone, and higher in limestone. The author suspects that this discrepancy is caused by differences in the texture and structure of the rock – as rocks with low porosity resulted in a restricted possibility of filtration, the differences of the value of the coefficient are larger than for rocks with high porosity.

3.4 *Flow through the cracks and micropores*

A model that differs on gas contained in cracks and macropores, and filling micropores, was proposed by Podil'chuk (1976). This is because Darcy's law applies to theflow through cracks and macropores. The constitutive equation for gas is described by Clapeyron's equation:

$$\frac{p_2}{\rho_2} = zRT \tag{20}$$

The equation of motion has the form:

$$\frac{\partial}{\partial t}\frac{fp_2}{zRT} + \frac{\partial}{\partial x_j}\left[\frac{k}{\mu ZRT}\, p_2 \frac{\partial p_2}{\partial x_i}\right] + g = 0 \tag{21}$$

where g is the rate of overflow of gas from the system of blocks into the crack system.

In the flow through micropores, an amount of gas is absorbed by the medium, and the relation between the amount of absorbed and free gas is described by the Langmuir formula:

$$V_a = \frac{a_0 k_u c}{1 + k_u c} \tag{22}$$

where V_a = value of adsorption; a_0, k_u = constants, c = concentration of gas in micropores:

$$c = \frac{p}{zRT} \tag{23}$$

The flow through the micropores, Podil'chuk treated as diffusion, as described by Fick's law:

$$\rho mv = -D\frac{\partial(c + V_a)}{\partial x_j} \tag{24}$$

The equation of motion has the form:

$$\frac{\partial(c + V_a)}{\partial t} - divD\ grad(V_a + c) - g = 0 \tag{25}$$

The exchange of gas between blocks and cracks is described by the equation:

$$q = k(p_2^2 - p_1^2) \tag{26}$$

where k is the gas-transfer coefficient.

The relationship between stress and strain is described by the equations:

$$\begin{aligned} \sigma_{ij} &= 2\mu\varepsilon_{ij} + \delta_{ij}\left(\lambda e - C_1\theta_1 - C_2\theta_2\right) \\ \sigma_1 &= -C_1\varepsilon + M_1\theta_1 + N\theta_2 \\ \sigma_2 &= -C_2\varepsilon + M_2\theta_2 + N\theta_1 \end{aligned} \tag{27}$$

where ε_{ij} = strain tensor, λ = Lamé's first parameter, μ = Lamé's second parameter, θ_1, θ_2 = change of gas volume in cracks and micropores.

In the case of omitting flow through micropores, the equations simplify to those given by Biot (1941).

3.5 *Modification of constitutive equations*

Strzelecki et al. (1993) proposed usage in poroelasticity following the relationship for gas:

$$\frac{p_a}{1 + \theta} = p \tag{28}$$

where p_a = atmospheric pressure.

The equations taking into account the interaction between phases have the form:

$$\begin{aligned} \varepsilon &= \frac{\sigma_m}{K} + \frac{\sigma}{B} \\ \theta &= \frac{\sigma_m}{B} + \frac{\sigma_a}{\sigma} - 1 \end{aligned} \tag{29}$$

where K = bulk modulus of the skeleton; B = modulus of interaction between phases, $\sigma_a = -\phi p$, ϕ = porosity.

By using constitutive equations for dilatational strain, it is possible to determine the dilatancy of the skeleton.

Inverse equations to (29) have the form:

$$\begin{aligned} \sigma_s &= \frac{K}{2}\varepsilon + \frac{B}{2}(\theta + 1) - \frac{B}{2}\sqrt{\left[(\theta + 1) - \frac{K}{B}\varepsilon\right]^2 + 4\frac{K}{B^2}\sigma_a} \\ \sigma_g &= \frac{B}{2}\varepsilon + \frac{B^2}{2K^*}(\theta + 1) + \frac{B^2}{2K^*}\sqrt{\left[(\theta + 1) - \frac{K^*}{B}\varepsilon\right]^2 + 4\frac{K^*}{B^2}\sigma_a} \\ e_{ij} &= \frac{1}{2G}s_{ij} \end{aligned} \tag{30}$$

After the expansion into Maclaurin series, for linear terms of gas:

$$\begin{aligned} \sigma_s(e_1, \theta) &= \frac{K}{2}\left(1 + \frac{\Psi_0}{\Phi_0}\right)e_1 + \frac{B}{2}\left(1 - \frac{\Psi_0}{\Phi_0}\right)\theta \\ \sigma_g(e_1, \theta) &= \frac{B}{2}\left(1 - \frac{\Psi_0}{\Phi_0}\right)e_1 + \frac{B^2}{2K}\left(-1 + \frac{\Psi_0}{\Phi_0}\right)\theta + \sigma_a \end{aligned} \tag{31}$$

where:

$$\Phi_0 = 1 + \frac{K\sigma_a}{B^2}, \quad \Psi_0 = 1 - \frac{K\sigma_a}{B^2}$$

In this way, the parameters of linear constitutive equations have been obtained in the form:

$$\sigma_{ij} = 2N^{sg}\varepsilon_{ij} + \left(A^{sg}\varepsilon + Q^{sg}\theta\right)\delta_{ij} - \frac{K^{sg}}{B^{sg}}\sigma_a \tag{32}$$

$$\sigma = Q^{sg}\varepsilon + R^{sg}\theta + \sigma_a \tag{33}$$

where superscript sg concerns model of skeleton filled with gas:

$$K^{sg} = \frac{K}{2}\left(1 + \frac{\Psi_0}{\Phi_0}\right);$$

$$Q^{sg} = \frac{B}{2}\left(1 - \frac{\Psi_0}{\Phi_0}\right);$$

$$R^{sg} = \frac{B^2}{2K}\left(-1 + \frac{\Psi_0}{\Phi_0}\right); \tag{34}$$

$$M^{sg} = A^{sg} - \frac{\left(Q^{sg}\right)^2}{R^{sg}};$$

$$A^{sg} = K^{sg} - \frac{2}{3}N^{sg}$$

3.6 *Methods of asymptotic homogenization*

Auriault et al. (1990) used theory of homogenization for porous media filled with gas. The following equations have been used for compressible fluid flowing at constant temperature through a rigid porous medium:

– the momentum balance:

$$\mu\Delta\vec{v} + (\lambda + \mu)grad\, div\,\vec{v} - gradp = \rho\left(\frac{\partial\vec{v}}{\partial t} + (\vec{v}grad)\vec{v}\right) \tag{35}$$

where $\vec{v}$ = fluid velocity;

– the mass balance of liquid phase:

$$\frac{\partial\rho}{\partial t} + div\rho\vec{v} = 0 \tag{36}$$

– the adherence condition:

$$\vec{v}\,|_\Gamma = 0 \tag{37}$$

– the equation of state for barotropic flow:

$$f(p,\rho) = 0 \tag{38}$$

For deformable porous medium authors assumed, that the solid is linearly elastic and that the deformations are small. Description was completed with boundary conditions: normal stresses and displacement were continuous on boundary Γ.

Equation of continuity of flow was obtained in the form:

$$div_x\left(\rho^{(0)}\left\langle\vec{v}^{(0)}\right\rangle\right) + \vec{u}^{(0)}v^{(0)}\,grad_x p^{(0)} + \rho^{(0)}\left(\chi e_x\left(\vec{u}_\varepsilon^{(0)}\right) + \beta p^{(0)}\right) = -n\frac{\partial p^{(0)}}{\partial t} \tag{39}$$

where χ, β = a tensor and a vector, same as used for description of consolidation with slightly compressible fluid. The tensor ν is a new coefficient which accounts for the compressibility of the fluid. This interacts with the mass balance which is strongly non-linear.

Under the assumption of incompressible fluid, authors obtained classical consolidation description:

$$\sigma = ce_x\left(\vec{u}^{(0)}\right) - \vec{\beta}p^{(0)} \tag{40}$$

where c is the tensor of elastic modules, e is a strain tensor, dependent on strain vector u.

4 PROPOSED ASSUMPTIONS FOR THE MODEL OF A MEDIUM WITH A POROUS GAS-FILLED SKELETON

For setting the model, the constitutive equations proposed by Strzelecki et al. (1993) were used:

$$\varepsilon = \frac{\sigma_m}{K} + \frac{\sigma}{B}$$
$$1 + \theta = \frac{\sigma_m}{B} + \frac{\sigma_a}{\sigma} \tag{41}$$

The line of thinking of the authors was followed, the inverse equations to (41) were obtained in the form:

$$\sigma = \frac{B^2}{2K}\left[-(\theta+1) + \frac{K}{B}\varepsilon + \sqrt{\left[(\theta+1) - \frac{K}{B}\varepsilon\right]^2 + 4\frac{K}{B^2}\sigma_a}\right]$$
$$\sigma_m = \frac{B}{2}\left[\frac{K}{B}\varepsilon + (\theta+1) - \sqrt{\left[(\theta+1) - \frac{K}{B}\varepsilon\right]^2 + 4\frac{K}{B^2}\sigma_a}\right] \tag{42}$$

Relationships expanded to Maclaurin series have the form:

$$\sigma = \frac{B^2}{K}\left(\sqrt{1+4\frac{K}{B^2}\sigma_a} - 1\right) + \frac{B}{2}\left(1 - \frac{1}{\sqrt{1+4\frac{K}{B^2}\sigma_a}}\right)\cdot\varepsilon - \frac{B^2}{2K}\left(1 - \frac{1}{\sqrt{1+4\frac{K}{B^2}\sigma_a}}\right)\cdot\theta +$$
$$+\frac{K}{2}\cdot\frac{\sqrt{1+4\frac{K}{B^2}\sigma_a} - \frac{1}{\sqrt{1+4\frac{K}{B^2}\sigma_a}}}{2\cdot\left(1+4\frac{K}{B^2}\sigma_a\right)}\cdot\varepsilon^2 + \frac{B^2}{2K}\cdot\frac{\sqrt{1+4\frac{K}{B^2}\sigma_a} - \frac{1}{\sqrt{1+4\frac{K}{B^2}\sigma_a}}}{1+4\frac{K}{B^2}\sigma_a}\cdot\theta^2$$

$$\sigma_m = B\cdot\left(1 - \sqrt{1+4\frac{K}{B^2}\sigma_a}\right) + \frac{K}{2}\left(1 + \frac{1}{\sqrt{1+4\frac{K}{B^2}\sigma_a}}\right)\cdot\varepsilon + \frac{B}{2}\left(1 - \frac{1}{\sqrt{1+4\frac{K}{B^2}\sigma_a}}\right)\cdot\theta + \tag{43}$$
$$+\frac{K^2}{2B}\cdot\frac{\frac{1}{\sqrt{1+4\frac{K}{B^2}\sigma_a}} - \sqrt{1+4\frac{K}{B^2}\sigma_a}}{2\cdot\left(1+4\frac{K}{B^2}\sigma_a\right)}\cdot\varepsilon^2 - \frac{B}{2}\cdot\frac{\sqrt{1+4\frac{K}{B^2}\sigma_a} - \frac{1}{\sqrt{1+4\frac{K}{B^2}\sigma_a}}}{2\cdot\left(1+4\frac{K}{B^2}\sigma_a\right)}\cdot\theta^2$$

For the purpose of simplifying the notation, the substitution:

$$\Phi_0 = \sqrt{1+4\frac{K}{B^2}\sigma_a} \tag{44}$$

has been used. The equations reduced to two first terms ofthe series may be written in a form that differs from that presented by Strzelecki et al. (1993).

$$\begin{aligned}\sigma_m &= B\left(1-\Phi_0\right)+\frac{K}{2}\left(1+\frac{1}{\Phi_0}\right)\varepsilon+\frac{B}{2}\left(1-\frac{1}{\Phi_0}\right)\theta\\ \sigma &= \frac{B^2}{K}\left(1+\Phi_0\right)+\frac{B}{2}\left(1-\frac{1}{\Phi_0}\right)\varepsilon-\frac{B^2}{2K}\left(1-\frac{1}{\Phi_0}\right)\theta\end{aligned} \tag{45}$$

Hence, the material parameters of the constitutive equations have the form:

$$\begin{aligned}&Q^{sg} = \frac{B}{2}\left(1-\frac{1}{\Phi_0}\right);\quad K^{sg} = \frac{B^2}{2K}\left(1-\frac{1}{\Phi_0}\right);\\ &R^{sg} = \frac{K}{2}\left(1+\frac{1}{\Phi_0}\right); A^{sg} = K^{sg} - \frac{2}{3}N^{sg};\\ &M^{sg} = A^{sg} - \frac{Q_{sg}^2}{R^{sg}}\end{aligned} \tag{46}$$

The equations complemented by segments related with temperature have the form:

$$\begin{aligned}\sigma_{ij} &= 2N^{sg}\varepsilon_{ij} + \left(A^{sg}\varepsilon + Q^{sg}\theta\right)\delta_{ij} + a_1\vartheta\\ \sigma^{l} &= R\theta + Q\varepsilon + a_3\vartheta\end{aligned} \tag{47}$$

where a_1, a_3 = material constants, determined under the assumption of dislocations only resulting from the influence of temperature,

$$a_1 = -\left(3K\alpha_T^s + Q\alpha_T^{ls}\right) \tag{48}$$

where α_T^s = thermal expansion the coefficient of the skeleton; α_T^{ls} = coefficient defining the influence of volumetric expansion of the skeleton on fluid expansion,

$$a_3 \cong -\frac{\rho c_v}{T_0}.$$

Considering that $T_0\dot{s} = -q_{i,i}$, and Fourier's law of thermal conduction $q_i = -\lambda_T\vartheta_i$,

$$T_0\dot{s} = -\lambda_T\nabla^2\vartheta \tag{49}$$

where λ_T = coefficient of thermal conductivity for the medium.

Equations (45), as limited to two first terms of a series, are linear. Equations (47), including temperature-related segments, are non-linear, which better describes non-linear behavior, and is highly depending on the temperature of gas.

5 CONCLUSIONS

Most of the cited models are isothermal. The proposed model includes segments considering thermal expansion. For an interpretation of the phenomena taking place in soils at high temperatures (e.g. underground coal gasification) the change in the mechanical parameters of the medium and density with the temperature have to be considered. Gas density is a variable resulting from equation of state of gas: $pV = nRT$.

The proposed model may be used for interpretation of laboratory tests; however, so far the amount of experimental data for two-phase media with gas-filled pores in variable temperature is small.

REFERENCES

Auriault, J.-L., Strzelecki, T., Bauer, J. & He, S. 1990. Porous deformable media saturated by a very compressible fluid: quasi-statics, *Eur. J. Mech., A/Solids* 9(4): 373–392.

Biot, M.A. 1941. General theory of three-dimensional consolidation, *J. Appl. Phys*. 12: 155–164.

Biot, M.A. & Willis, D.G. 1957. The elastic coefficients of the theory of consolidation, *J. Appl. Mech*. 24: 594–601.

Coussy, O. 2007. Revisiting the constitutive equations of unsaturated porous solids using a Lagrangian saturation concept, *Int. J. Numer. Anal. Meth. Geomech*. 31: 1675–1694

Coussy, O. 2010. *Mechanics and Physics of Porous Solids*, John Wiley.

Detournay, E. & Cheng, A.H.-D., 1993. Fundamentals of Poroelasticity*, Comprehensive Rock Engineering: Principles, Practice and Projects, Vol. II, Analysis and Design Methods,* pp. 113–171. Oxford: Pergamon Press.

Fabre, D. & Gustkiewicz, J. 1997. Poroelastic properties of limestones and sandstones under hydrostatic conditions, *Int J. Rock Mech. Min. Sci.* 34(1): 127–134.

Łydżba, D. 1991. Constitutive equations of gas-coal medium, *Studia Geotechnica et Mechanica* 13(3–4): 51–62.

Nowakowski, A. 2012. The law of effective stress for rocks in light of results of laboratory experiments, *Arch. Min. Sci*. 57(4): 1027–1044.

Podil'chuk, Yu.N. 1976. Strain in gas-saturated porous media, *Soviet Applied Mechanics* 12(11): 1237–1241.

Skempton, A.W. 1954. The pore pressure coefficients A and B, *Geotechnique* 4: 143–147.

Strzelecki, T., Bauer, J. & Auriault, J.L. 1993. Constitutive equation of a gas-filled two-phase medium, *Transport in Porous Media* 10: 197–202.

Strzelecki, T., Kostecki, S. & Żak, S. 2008. *Modeling of flows through porous media*, Lower Silesia Educational Publishers. (in Polish)

This page intentionally left blank

Rock Mechanics for Resources, Energy and Environment – Kwaśniewski & Łydżba (eds)
© 2013 Taylor & Francis Group, London, ISBN 978-1-138-00080-3

A Weibull distribution-based constitutive model of creep of salt rock

H.W. Zhou, J.Y. Ding & J.D. Liu
State Key Laboratory of Coal Resources and Safe Mining, China University of Mining and Technology, Beijing, China

J.F. Liu
College of Water Resource and Hydropower, Sichuan University, Chengdu, China

ABSTRACT: A modeling approach to creep behavior of salt rock is of great significance for long-term operation of underground facilities in salt rock. A computer-controlled creep setup is employed to investigate creep behavior of salt rock under the condition of triaxial compression. In addition, suppose the evolution of the internal defects correspond to be the Weibull distribution, a new variable-viscosity Abel dashpot is established by means of definition of damage variable. By replacing a Newtonian dashpot in the classical Nishihara model with the variable-viscosity Abel dashpot, a new creep constitutive model is proposed on the basis of damage evolution and fractional derivative. Furthermore, the parameters in the new constitutive model are determined by fitting analysis of experimental data. The comparison of modeling approach with experimental data indicates that the fractional derivative constitutive model can reflects the three stages of creep of salt rock, especially the tertiary one.

1 INTRODUCTION

Salt rock has been recognized as an ideal medium for the underground strategic energy storage, permanent repositories of CO_2 and disposal of high-level radioactive wastes (Urai et al. 1986), with its extremely low porosity, low permeability and high solubility in water. However, owing to the time-dependent creep behavior of salt rock, large deformation of effective storage volume may influence the stability of the salt caverns in their long-term service. An increasing studies indicate the time dependent behavior of the salt rock induce a loss of cavern volume. As a result, a research for the creep behavior of salt rock is of great importance for deformation controlling of the salt rock caverns.

Generally the achievements in the creep properties of salt rock include several aspects, *i.e.*, creep experimental studies, creep constitutive relations of salt rock and long-term stability of salt caverns. In last decades, most of the effects have been devoted to modeling of salt rock creep, and three approaches to the creep constitutive models of salt rock have been proposed, namely, empirical models, component models and mechanism-based creep constitutive models (Zhou et al. 2011). In order to describe the accelerated creep stage (the tertiary stage) of creep of rock, the function of creep parameters with the time is usually suggested to be nonlinear. Many efforts have been devoted to application of micro-mechanics theory (Miura et al. 2003) or endochronic theory (Auberin et al. 1991) to creep constitutive models. Hou and Lux proposed a damage variable creep constitutive model of salt rock called Hou/Lux model, which shows the development of dilatancy, damage and healing of salt caverns (Hou et al. 1999, 2003). Wang (2004) proposed a new creep constitutive model based on the theory of damage mechanics and described the creep and damage of salt rock. Adolfsson et al. (2005) proposed a fractional order viscoelastic model based on the concept of internal variables which find out that the corresponding rate equations can be formulated by the fractional order integrals rather than the fractional order derivatives.

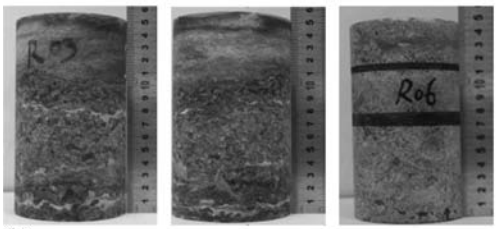
The theory of fractional calculus is which focuses on the study of calculus of any order. An increasing research has been devoted to the application of fractional calculus in many fields. Rogers (1983), Bagley & Torvik (1983, 1985), and Koeller (1984) established a solid foundation in fractional derivative models. Based on the TIBI diagram, Beda and Chevalier (2004) identified the rheological parameter for fractional derivative modeling of viscoelastic materials. Chen et al. (2013) proposed a new variable-order fractional diffusion equation model to describe the coupled chloride diffusion-binding processes in reinforced concrete. Fu et al. (2013) developed a novel boundary meshless approach (LTBPM) for numerical modeling of time fractional diffusion equations. By replacing a Newtonian dashpot in the classical Nishihara model with the fractional derivative Abel dashpot, Zhou et al. (2012) proposed a new creep constitutive model on the basis of time-based fractional derivative,

and the results estimated by the new model are in better agreement with the experimental data.

In this paper, a computer-controlled creep setup is employed to investigate creep behavior of salt rock under the condition of triaxial compression. In addition, based on the Weibull distribution, a new variable-viscosity Abel dashpot is established by means of definition of damage variable. By replacing a Newtonian dashpot in the classical Nishihara model with the new variable-viscosity Abel dashpot, a new creep constitutive model is proposed on the basis of damage evolution and fractional derivative. Furthermore, the parameters in the new constitutive model are determined by fitting analysis of experimental results of creep tests on salt rock. The comparison of modeling approach with experimental results indicates that the fractional derivative constitutive model can better reflects the three stages of creep of salt rock, especially the tertiary one.



(a)



(b)

Figure 1. Experimental equipment and specimens of creep test (a) computer-controlled creep setup; (b) salt rock specimens.

2 TRIAXIAL CREEP TESTS OF SALT ROCK

2.1 *Experimental equipment and salt rock specimens*

The creep tests were carried out in Sichuan University using the computer-controlled creep setup (Fig. 1a), with the laboratory experimental parameters: axial load: 0∼600 kN; confining pressure: 0∼30 MPa; temperature = 22°C. The salt rock specimens identified by R03, R04, R06 were taken from the Chuwang Well No.1, Jianghan Oilfield, Hubei Province. The dimension of the specimens was 75 mm in diameter and 150 mm in height (Fig. 1b). The creep tests were carried out by using the multi-stage axial load, and each stage of the loading time is about 20 days.

2.2 *Analysis of experimental results*

The loading time and the loading scheme of each salt rock specimen are shown in Table 1, in which I ∼ V indicate the first stage to the fifth stage axial

The experimental data of the creep tests are given in Table 1. It is indicated that the steady state creep strain rate increases with the increasing of the axial load and the loading time, which leads to the dislocation, glide and climb of the salt grain. Furthermore, deviatoric stress plays an important role in the initiation and the expansion of microcrack in the plastic

Table 1. Loading time and loading scheme of the creep tests

Specimen number	Confining pressure $\sigma_1 = \sigma_3$ MPa	Axial load σ_1 MPa	Steady state creep strain rate h^{-1}	Loading time h
R03	15	**I**: 27	0.11×10^{-5}	477
	15	**II**: 39	4.19×10^{-5}	475
	15	**III**: 51	8.46×10^{-5}	582
	15	**IV**: 63	13.42×10^{-5}	475
	15	**V**: 75		20
R04	25	**I**: 41	0.26×10^{-5}	475
	25	**II**: 57	8.77×10^{-5}	476
	25	**III**: 73	27.94×10^{-5}	582
	25	**IV**: 86	52.80×10^{-5}	358
R06	20	**I**: 34	0.17×10^{-5}	477
	20	**II**: 48	0.19×10^{-5}	477
	20	**III**: 62	0.22×10^{-5}	582
	20	**IV**: 76	0.26×10^{-5}	475
	20	**V**: 90	0.42×10^{-5}	497

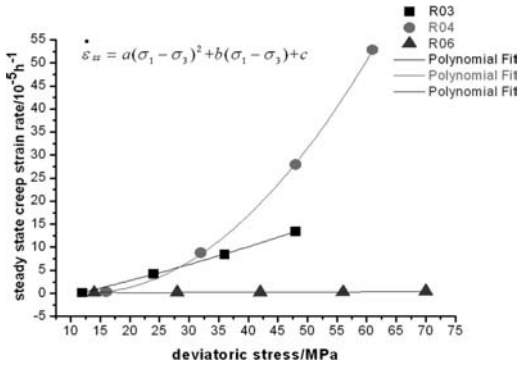


Figure 2. Fitting analysis of the experimental.

Table 2. Parameters determined by fitting analysis.

Sepecimen	a	b	c	R
R03	0.22	3.32	−3.045	0.9999
R04	4.0755	−2.7585	−1.3175	0.9992
R06	0.0207	−0.0673	0.226	0.9653

deformation of the salt rock. With the development of the microcrack, the internal damage of the salt rock is assumed to be increased in time and stress level during accelerated stage of creep tests. Figure 2 shows the relationship between the steady state creep strain rate and the deviatoric stress, which can be fitted by polynomial. The parameters of the fitting analysis are as shown in Table 2.

Figure 3 shows the creep curves of salt rock under triaxial creep tests. Considering the discreteness of the rocks, the strain values of the creep test are different, but the law of the creep curves to the loading time is uniform. In each stage axial load of the creep tests, the specimens of salt rock all pass through the attenuation creep stage and the steady creep stage, and in the last stage axial load, the specimens all pass through the accelerated creep stage. The curve of R04 (the red one) is a typical one including the three stages of creep, so using the experimental data of creep deformation of R04, the parameters of the creep constitutive model of salt rock can be determined by fitting analysis. Figure 4 gives the CT images of the R04, which including the top, the middle and the bottom of the specimen before and after creep test. Comparison of the two images shows that new damage is induced and the number of failed element increases with the loading time.

3 WEIBULL DISTRIBUTION-BASED FRACTIONAL DERIVATIVE CREEP MODEL OF SALT ROCK

The constitutive relation of the Abel dashpot is given by (after Scott Blair 1947)

$$\sigma(t) = \eta^{\gamma} D_t^{\gamma}\left[\varepsilon(t)\right] \ (0 \le \gamma \le 1) \tag{1}$$

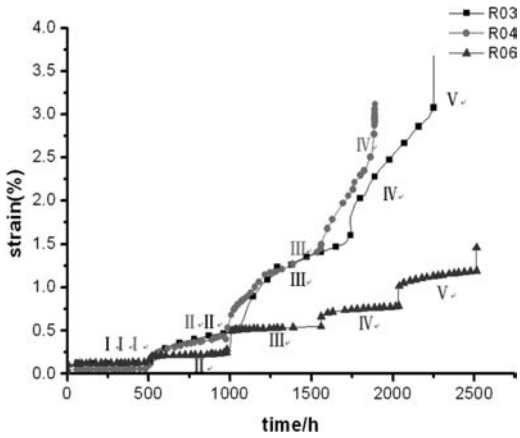


Figure 3. The creep curves of salt rock.

where η^{γ} is the viscosity coefficient. If $\gamma = 0$, the Abel dashpot becomes the Hookean model and Equation 1 gives the stress-strain relation of an ideal solid; if $\gamma = 1$, the Abel dashpot becomes the Newtonian dashpot and Equation 1 represents the stress-strain relation of an ideal fluid. As a result, if $0 \le \gamma \le 1$, Equation 1 characterizes the creep property of the soft material whose rheological property is between the elastic Hookean model and the Newtonian dashpot.

If the Newtonian dashpot in the Nishihara model is replaced by Abel dashpot, the new model can describe the creep characteristic of rock, but cannot explain the characteristics of three stages of creep of salt rock from the micro-mechanism point of view. Chen et al. (2011) indicated that four types of micro-structure changes can be distinguished during the creep test, including the closing of crack, adjustment of weak grain boundary, micro-scale failure and adjustment of tough grain boundary. If the stress in rock is lower than the yield limit of materials, the former two types of changes will be induced; if the stress is larger than the yield limit, all four types of changes will simultaneously be induced. The elastic deformation is generated when a loading is applied to the sample, and the closing of crack corresponds to the attenuation creep stage; the adjustment of weak grain boundary corresponds to the steady creep stage; the micro-scale failure and adjustment of tough grain boundary result in the accelerated creep stage.

From the mentioned-above, if the stress is lower than the yield limit, the viscoelastic strain of rock induces non-accumulation of damage; if the stress is larger than the yield limit, the damage threshold reaches with the unrecoverable damage accumulation, and the rock reaches the accelerated creep stage. In the Nishihara model, when the stress in salt rock reaches the yield limit, the viscoplastic strain continuously increases linearly with time in the Newtonian dashpot connected in parallel with the plastic body as the viscosity coefficient is a constant. However, the linear increase of the viscoplastic strain doesn't coincide with the actual accelerated creep stage of creep of rock.

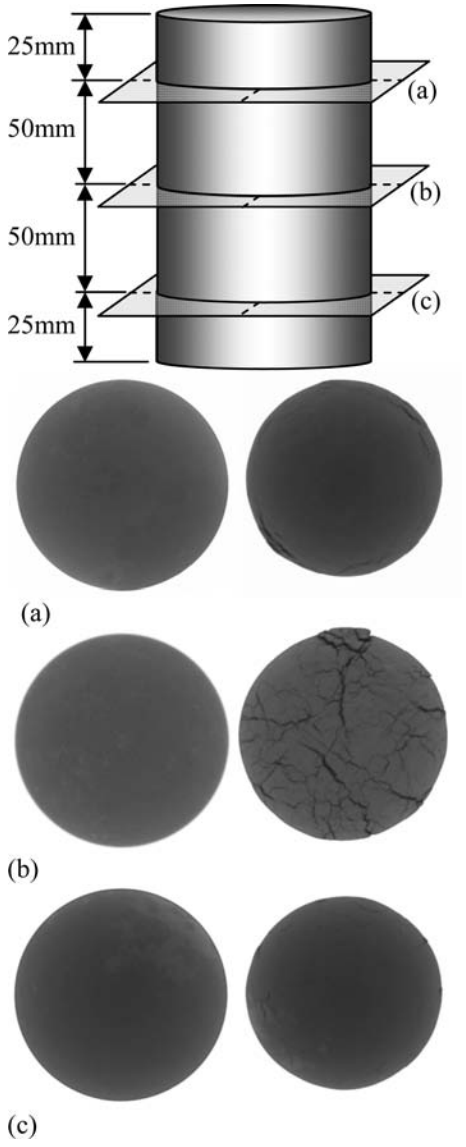


Figure 4. CT sections and images before and after creep test (a) The top of the specimen; (b) the middle of the specimen; (c) the bottom of the specimen.

So based on the Abel dashpot, the viscosity coefficient η_2^{γ} in the viscoplastic body in Figure 6 is defined as a damage accumulation-related variable.

$$\eta_2^{\gamma'} = (1-d)\cdot\eta_2^{\gamma} \tag{2}$$

where d is the damage variable.

Based on the micro-damage mechanics, a representative volume element (RVE) is studied, and the evolution of the internal defects indicates a function with the Weibull distribution, so the damage evolution is a time-dependent continuous process. Suppose

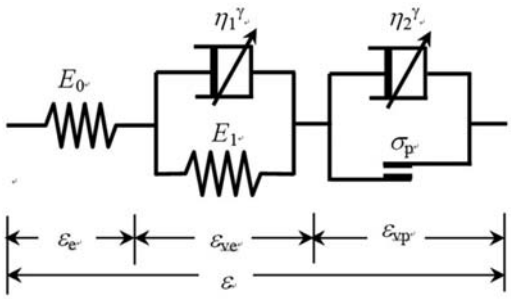


Figure 5. Fractional derivative model of rock salt (Zhou et al. 2012).

the time-dependent behavior of the probability density function of RVE failure can be written as

$$P(t) = \frac{m}{a}\left(\frac{t}{a}\right)^{m-1} e^{-\left(\frac{t}{a}\right)^m} \tag{3}$$

where α and m are parameters associated with the mechanical properties of the material.

In any time interval $[t, t+dt]$, the number of failed RVE is given by $NP(t)dt$, in which N indicates the total number of RVE during the creep test. So until a certain time t, the total number of the failed RVE is given by

$$N_s(t) = \int_0^t NP(t)dt = N\left[1 - e^{-\left(\frac{t}{\alpha}\right)^m}\right] \tag{4}$$

The damage variable d is defined by $d = N_s/N$. Combining Equation 4 with the definition of the damage variable, namely,

$$d = 1 - e^{-\left(\frac{t}{\alpha}\right)^m} = 1 - e^{-\beta t^m} \tag{5}$$

In the Weibull distribution, m is referred to the shape parameter. From the mentioned-above, parameter m indicates the trend of the loading time-dependent change in the number of the failed RVE.

Combining Equation 5 with Equation 2, namely,

$$\eta_2^{\gamma'} = (1-d)\cdot\eta_2^{\gamma} = \eta_2^{\gamma} e^{-\beta t^m} \tag{6}$$

Combining Equation 6 with Equation 1, a constitutive equation of the Weibull distribution-based Abel dashpot is given by

$$\sigma(t) = (\eta_2^{\gamma} e^{-\beta t^m}) D_t^{\gamma}[\varepsilon(t)] \quad (0 \le \gamma \le 1) \tag{7}$$

In Figure 5, if the strains of Hooke body (H), the viscoelastic body (N/H) and viscoplastic body (N/St.V) are assumed to be ε_e, ε_{ve} and ε_{vp}, then the total strain of the constitutive model is

$$\varepsilon = \varepsilon_e + \varepsilon_{ve} + \varepsilon_{vp} \tag{8}$$

The strain-stress relation of the Hooke body (H) is

$$\varepsilon_e = \frac{\sigma}{E_0} \tag{9}$$

where E_0 is the elastic modulus of the spring in the mechanical model of a Hooke body.

The strain-stress relation of the viscoelastic body (N/H) is given by (Zhou et al. 2011)

$$\varepsilon_{ve} = \frac{\sigma}{\eta_1^{\gamma}} \sum_{k=0}^{\infty} \frac{\left(-\frac{E_1}{\eta_1^{\gamma}}\right)^k t^{\gamma(1+k)}}{\gamma(1+k)\Gamma[(1+k)\gamma]} \tag{10}$$

where E_1 and η_1^{γ} are the elastic modulus of the spring and the constant viscosity coefficient of the Abel dashpot in the mechanical model of the viscoelastic body.

In the mechanical model of a viscoplastic body (N/St.V), the stress σ_p carried by the plastic element is given by

$$\sigma_p = \begin{cases} \sigma, & \sigma < \sigma_s \\ \sigma_s, & \sigma \geq \sigma_s \end{cases} \tag{11}$$

where σ_s is the yield limit.

The total stress will be the sum of the stress applied on the dashpot and the plastic element:

$$\sigma = \sigma_d + \sigma_p \tag{12}$$

where σ is the total stress, σ_d is the stress applied on the dashpot with variable viscosity coefficient and σ_p is the stress by the plastic element.

If $\sigma < \sigma_s$, combining Equation 11 with Equation 12, one gets $\sigma_d = 0$, then considering Equation 7

$$\varepsilon_{vp} = 0 \tag{13}$$

If $\sigma > \sigma_s$, combining Equation 11 with Equation 12, one gets $\sigma_d = \sigma - \sigma_s$, then considering Equation 7

$$\sigma = (\eta_2^{\gamma} e^{-\beta t^m}) d^{\gamma}(\varepsilon_{vp}) + \sigma_s \tag{14}$$

Solving Equation 14 with the method of fractional order differential equations (Kilbas et al. 2006), namely,

$$\varepsilon_{vp} = \frac{\sigma - \sigma_s}{\eta_2^{\gamma}\Gamma(\gamma)} \int_0^t (t-x)^{\gamma-1} e^{\beta x^m} dx \tag{15}$$

So the constitutive relationship of the viscoplastic body (N/St.V) is given by

$$\varepsilon_{vp} = \begin{cases} 0, & \sigma < \sigma_s \\ \dfrac{\sigma - \sigma_s}{\eta_2^{\gamma}\Gamma(\gamma)} \displaystyle\int_0^t (t-x)^{\gamma-1} e^{\beta x^m} dx, & \sigma \geq \sigma_s \end{cases} \tag{16}$$

By substituting Equations 9–10 and Equation 16 into Equations 8, the constitutive relationship of the Weibull distribution-based fractional derivative creep model of salt rock.

$$\varepsilon(t) = \frac{\sigma}{E_0} + \frac{\sigma}{\eta_1^{\gamma}} \sum_{k=0}^{\infty} \frac{\left(-\frac{E_1}{\eta_1^{\gamma}}\right)^k t^{\gamma(1+k)}}{\gamma(1+k)\Gamma[(1+k)\gamma]} (\sigma < \sigma_s) \tag{17a}$$

$$\varepsilon(t) = \frac{\sigma}{E_0} + \frac{\sigma}{\eta_1^{\gamma}} \sum_{k=0}^{\infty} \frac{\left(-\frac{E_1}{\eta_1^{\gamma}}\right)^k t^{\gamma(1+k)}}{\gamma(1+k)\Gamma[(1+k)\gamma]} + \frac{\sigma - \sigma_s}{\eta_2^{\gamma}\Gamma(\gamma)} \int_0^t (t-x)^{\gamma-1} e^{\beta x^m} dx \quad (\sigma \geq \sigma_s) \tag{17b}$$

Equation 17a and Equation 17b can be expressed as

$$\varepsilon(t) = \frac{\sigma}{E_0} + \sigma \sum_{k=0}^{\infty} \frac{(-E_1)^k \left(\frac{t}{\eta_1}\right)^{\gamma(1+k)}}{\gamma(1+k)\Gamma[(1+k)\gamma]} (\sigma < \sigma_s) \tag{18a}$$

$$\varepsilon(t) = \frac{\sigma}{E_0} + \sigma \sum_{k=0}^{\infty} \frac{(-E_1)^k \left(\frac{t}{\eta_1}\right)^{\gamma(1+k)}}{\gamma(1+k)\Gamma[(1+k)\gamma]} + \frac{\sigma - \sigma_s}{\Gamma(\gamma)} \int_0^t \left(\frac{t-x}{\eta_2}\right)^{\gamma} \frac{e^{\beta x^m}}{t-x} dx \quad (\sigma \geq \sigma_s) \tag{18b}$$

Equation 18a and Equation 18b are the non-dimensional constitutive equation (Koeller 1984, 2010) of the Weibull distribution-based fractional derivative creep model of salt rock.

4 DETERMINATION OF PARAMETERS FOR WEIBULL DISTRIBUTION-BASED CREEP MODEL

We use least-squares fitting method for the parameters determination of the fractional derivative model, and the parameters in Equation 18 as well as the classical Nishihara model are presented in Table 3. The fitting curves by fractional derivative model given in this paper and the classical Nishihara model are shown in Figure 6. The comparison of modeling approach with experimental data indicates that the fractional derivative constitutive model can better reflects the three stages of creep of salt rock, especially the tertiary one.

If $\gamma = 1$, $\beta = 0$ $m = 1$, then Equation 18a and Equation 18b can be written as

$$\varepsilon(t) = \frac{\sigma}{E_0} + \frac{\sigma}{E_1}\left(1 - e^{-\frac{E_1}{\eta_1}t}\right) \quad (\sigma < \sigma_s) \tag{19a}$$

Table 3. Parameters fitting of fractional derivative model.

	$\frac{E_0}{\text{GPa}}$	$\frac{E_1}{\text{GPa}}$	$\frac{\eta_1^{\gamma}}{GPa \cdot \text{h}^{\gamma}}$	$\frac{\eta_2^{\gamma}}{\text{GPa} \cdot \text{h}^{\gamma}}$	γ	$\frac{\beta}{h^{-1}}$	m	LSF errors
Fractional derivative model	4.32	7.10	85.79	136.28	0.35	0.0061	0.96	6.3281×10^{-6}
Nishihara model	4.21	155.77	227.73	747.90	1	0	1	2.0678×10^{-5}

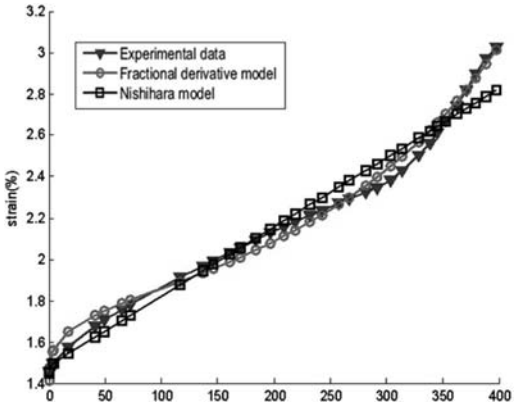


Figure 6. The fitted curves based on the experimental data.

$$\varepsilon(t)=\frac{\sigma}{E_0}+\frac{\sigma}{E_1}\left(1-e^{-\frac{E_1}{\eta_1}t}\right)+\frac{\sigma-\sigma_s}{\eta_2}t \quad (\sigma \geq \sigma_s) \quad (19b)$$

which is the classical Nishihara constitutive model, so the classical Nishihara model has been proved as a special case of the constitutive model given in this paper

5 CONCLUSIONS

In this paper, a new variable-viscosity Abel dashpot is established by means of definition of damage variable based on the micro-mechanics and Weibull distribution. By replacing the Newtonian dashpot in the classical Nishihara model with the variable-viscosity Abel dashpot, a new creep constitutive model is proposed on the basis of fractional derivative, and the parameters are determined by fitting analysis. The main conclusions are as follows:

(1) Three stages are included in the full creep regions of salt rock, and the relationship between the steady state creep strain rate and the deviatoric stress can be fitted by polynomial.
(2) Suppose the evolution of the internal defects correspond a function with the Weibull distribution, and by means of definition of damage variable, a new variable-viscosity Abel dashpot is established.
(3) Based on the method of fractional order differential equations, a new creep constitutive model is proposed, which is the fractional derivative model, and the parameters in the new constitutive model are determined by fitting analysis of experimental data of creep tests on salt rock. The fractional derivative constitutive model can better reflects the three stages of creep of salt rock, especially the tertiary one.

ACKNOWLEDGEMENTS

The present work is supported by the National Natural Science Foundation of China (11172318, 51120145001) and the 973 Program (2009CB724602). The financial supports are gratefully acknowledged.

REFERENCES

Adolfsson, K., Enelund, M. & Olsson, P. 2005. On the fractional order model of viscoelasticity. *Mechanics of Time-Dependent Materials* 9: 15–34.

Aubertin, M., Gill, D.E. & Ladanyi, B. 1991. An internal variable model for the creep of rocksalt. *Rock Mechanics and Rock Engineering* 24(2): 81–97.

Bagley, R.L. & Torvik, P.J. 1983. Fractional calculus – a different approach to the analysis of viscoelastically damped structures. *AIAA Journal* 21(5): 741–748.

Bagley, R.L. & Torvik, P.J. 1985. Fractional calculus in the transient analysis of viscoelastically damped structures. *AIAA Journal* 23(5): 918–925.

Beda, T. & Chevalier, Y. 2004. New methods for identifying rheological parameter for fractional derivative modeling of viscoelastic behavior. *Mechanics of Time-Dependent Materials* 8:105–18.

Chen, W., Zhang, J.J. & Zhang, J.Y. 2013. A variable-order time-fractional derivative model for chloride ions sub-diffusion in concrete structures. *Fractional Calculus and Applied Analysis* 16(1): 76–92.

Chen, W.L., Zhao, F.S. & Gong, H.J. 2011. Study of creep parameters of mica-quartzose schist during triaxial creep test. *Chinese Journal of Rock Mechanics and Engineering* 30(Supp. 1): 2810–2816. (in Chinese)

Fu, Z.J., Chen, W. & Yang, H.T. 2013. Boundary particle method for Laplace transformed time fractional diffusion equations. *Journal of Computational Physics* 235: 52–66.

Hou, Z.M. & Lux, K. 1999. A material model for rock salt including structural damages as well as practice-oriented applications. In N.D. Cristescu, H.R. Hardy, & R.O. Simionescu (eds), *Basic and Applied Salt Mechanics, Proceedings of the Fifth Conference on Mechanical Behavior of Salt (MECASALT V), Bucharest, Romania, 9–11 August* 1999: 55–59. Rotterdam: Balkema.

Hou, Z.M. 2003. Mechanical and hydraulic behaviour of salt in the excavation disturbed zone around underground facilities. *International Journal of Rock Mechanics and Mining Sciences* 40(5): 725–738.

Kilbas, A.A., Srivastava, H.M. & Trujillo, J.J. 2006. *Theory and Applications of Fractional Differential Equations*. Amsterdam: Elsevier.

Kiryakova, V. & Al-Sauabi, B. 1999. Explicit solutions to Hyper–Bessel integral equations of second kind. *Computers & Mathematics with Applications* 37:75–86.

Koeller, R.C. 1984. Application of fractional calculus to the theory of viscoelasticity. *Journal of Applied Mechanics-American Society Of Mechanical Engineers* 51: 299–307.

Koeller, R.C. 2010. A theory relating creep and relaxation for linear materials with memory. *Journal of Applied Mechanics* 77(3):1–9.

Miura, K., Okui, Y. & Horii, H. 2003. Micromechanics-based prediction of creep failure of hard rock for long-term safety of high-level radioactive waste disposal system. *Mechanics of Materials* 35: 587–601.

Rogers, L. 1983. Operators and fractional derivates for viscoelastic constitutive equations. *Journal of Rheology* 27(4): 351–372.

Scott Blair, G.W. 1947. The role of psychophysics in rheology. *Journal of Colloid Science* 2: 21–32.

Urai, J.L., Spiers, C.J., Hendrik, H.J., Zwart, H.J. & Lister, G.S. 1986. Weakening of rock-salt by water during long-term creep. *Nature* 324: 554–557.

Wang, G.J. 2004. A new constitutive creep-damage model for salt rock and its characteristics. *International Journal of Rock Mechanics and Mining Sciences* 41(Supp. 1): 61–67.

Zhou, H.W., Wang, C.P., Han, B.B. & Duan, Z.Q. 2011. A creep constitutive model for salt rock based on fractional derivatives. *International Journal of Rock Mechanics and Mining Sciences* 48(1): 116–121.

Zhou, H.W., Wang, C.P., Duan, Z.Q., Zhang, M. & Liu, J.F. 2012. Time-based fractional derivative approach to creep constitutive model of salt rock. *Scientia Sinica Physica, Mechanica & Astronomica* 42: 310–318. (in Chinese)

This page intentionally left blank

4. Mathematical modeling of coupled T-H-M processes in rocks

This page intentionally left blank

Rock Mechanics for Resources, Energy and Environment – Kwaśniewski & Łydżba (eds)
© 2013 Taylor & Francis Group, London, ISBN 978-1-138-00080-3

Definition and implementation of a fully coupled THM model for unsaturated rocks

A. Haxaire & V. Galavi
Plaxis bv, The Netherlands

R.B.J. Brinkgreve
Faculty of Civil Engineering and Geosciences, Delft University of Technology, The Netherlands

ABSTRACT: A Thermo-Hydro-Mechanical (THM) model for partially saturated rocks is developed and implemented. The hypothesis of constant air pressure simplifies the equations and improves efficiency of calculation while still allowing the description of vapor flow. The implementation uses a fully coupled approach. Comparison against experimental data is performed. Results are promising, yet additional comparisons are required to fully validate the model and its implementation.

1 INTRODUCTION

The necessity of THM modeling appeared in the nineties within the framework of nuclear wastes storage in deep geological formations. Models have then been extended to include the effects of temperature on the mechanical and the hydraulic behavior of rocks (Rutqvist et al. 2001, Collin et al. 2002). Accurate description but also the implementation of such coupled phenomena still remains a challenge. After defining a THM model for partially saturated rocks, its implementation is described then compared to experimental results.

2 GOVERNING EQUATIONS

In this section the governing equations of fully coupled thermo-hydro-mechanical analysis are briefly described. This is an extension to the previous work in which fully coupled hydro-mechanical analysis has been implemented (Galavi et al. 2011, Galavi 2011). Here, non-isothermal unsaturated groundwater flow, heat transport and deformation are considered. Similar to the previous work, we assume a constant gas pressure. Therefore, only one independent unknown in the fluid mass balance equation is needed which is pore water pressure. This study is based on the assumption of local thermodynamic equilibrium which means that all phases have the same temperature, i.e. only one equation of total energy is required. Consequently, the four primary variables are displacements ($\underline{v}$), pore water pressure (p_w) and temperature (T).

2.1 *Non-isothermal unsaturated water flow*

An extended Richard's model is applied to describe non-isothermal unsaturated flow. The mass flux of water is defined as:

$$\underline{J}_w = \rho_w \left(\frac{k_{rel}}{\mu} \underline{\underline{\kappa}}^{\text{int}} \left(\nabla p_w + \rho_w \underline{g} \right) \right) \tag{1}$$

where μ is the dynamic viscosity of the fluid and $\underline{\underline{\kappa}}^{int}$ is the intrinsic permeability of the porous medium. The dynamic viscosity depends on the type of fluid and temperature and the intrinsic permeability is a function of porous structure. In an unsaturated state the coefficient of permeability depends on the soil saturation. The relative permeability $k_{rel}(S)$ is defined as the ratio of the permeability at a given saturation to the permeability in saturated state. The vector of gravitational acceleration is $\underline{g} = (0, -g, 0)^{\mathrm{T}}$. n and S are porosity and degree of saturation, respectively.

Due to the effects of temperature, vapor flow effects need to be considered in non-isothermal processes. The mass flux of vapor is defined as (Rutqvist et al., 2001):

$$\underline{J}_v = -D_v \nabla \rho_v = D_{pv} \nabla p_w - D_{Tv} \nabla T \tag{2}$$

where T is the local equilibrium temperature of the porous medium in Kelvin, f_{Tv} is thermal diffusion enhancement factor, and D_{pv} and D_{Tv} are the hydraulic and thermal diffusion coefficients defined as:

$$D_{pv} = D_v \left(\frac{\partial \rho_v}{\partial p_w} \right) = \frac{D_v \rho_v}{\rho_w RT} \tag{3}$$

$$D_{Tv} = f_{Tv} D_v \left(\frac{\partial \rho_v}{\partial T} \right) = f_{Tv} D_v \left(\theta \frac{\partial \rho_{vS}}{\partial T} + \frac{\rho_v p_w}{\rho_w R T^2} \right) \quad (4)$$

D_v is the vapor diffusion coefficient in a porous material which depends on temperature, gas pressure, and medium tortuosity. ρ_v is the vapor density and ρ_{vS} is the saturated vapor density. The relative humidity θ is defined as:

$$\theta = \exp\left(\frac{-p_w}{\rho_w R T} \right) \quad (5)$$

where R is the specific ideal gas constant. The vapor density ρ_v is related to the temperature dependent saturated vapor density ρ_{vS} by the relative humidity following (Rutqvist et al. 2001):

$$\rho_v = \theta \rho_{vS} \quad (6)$$

The saturated vapor density is a function of temperature only. Here the empirical relationship from Wang et al. (2009) is adopted, where ρ_{vS} is in kg/m^3 and T in K:

$$\rho_{vS} = 10^{-3} \exp(19.891 - 4974/T) \quad (7)$$

2.2 *Mass balance equation*

The water mass balance can be written in the following form (Rutqvist et al. 2001):

$$n \frac{\partial}{\partial t} \left(S \rho_w + (1-S) \rho_v \right) + \left(S \rho_w + (1-S) \rho_v \right) \left[\frac{\partial \varepsilon_v}{\partial t} + \frac{(1-n)}{\rho_s} \frac{\partial \rho_s}{\partial t} \right] = -\nabla \cdot \left(\underline{J}_w + \underline{J}_v \right) \quad (8)$$

The water density is related to water pressure and temperature through the water compressibility β_{wP} and the volumetric thermal expansion of water β_{wT}:

$$\frac{\rho_w}{\rho_{w0}} = 1 - \beta_{wP} (p_w - p_{w0}) - \beta_{wT} (T - T_0) \quad (9)$$

By expanding the two terms on the left-hand side of equation (8) and substituting equation (9), we obtain:

$$\left[n(\rho_w - \rho_v) \frac{\partial S}{\partial p_w} - nS\rho_w \beta_{wP0} - n(1-S) \frac{\rho_v}{\rho_w R_v T} \right] \frac{\partial p_w}{\partial t} + \left[\begin{array}{l} n(\rho_w - \rho_v) \frac{\partial S}{\partial T} - nS\rho_w \beta_{wT0} \\ + n(1-S) \left(\theta \frac{\partial \rho_{vS}}{\partial T} + \frac{\rho_v p_w}{\rho_w R_v T^2} \right) \\ - \left(S\rho_w + (1-S)\rho_v \right)(1-n)\beta_{sT} \end{array} \right] \frac{\partial T}{\partial t} + \left(S\rho_w + (1-S)\rho_v \right) \frac{\partial \varepsilon_v}{\partial t} + \nabla \cdot \left(J_w + J_v \right) = 0 \quad (10)$$

where β_{sT} is the volumetric thermal expansion coefficient of soil grains.

It should be noted that the term $(1-S)\rho_v$ can be neglected for saturated state and low temperature in comparison with $S\rho_w$. However, in the case of very dry and high temperature, this term may be significant.

2.3 *Non-isothermal deformation*

For a representative elemental volume of the soil the linear momentum balance is given by:

$$\nabla \cdot (\boldsymbol{\sigma}) + ((1-n)\rho_s + nS\rho_w + n(1-S)\rho_g)\underline{g} = 0 \quad (11)$$

where ρ is the density of the multiphase medium, ρ_s, ρ_w and ρ_g are the density of the solid, the water and the gas densities respectively.

In Eq. (13) $\boldsymbol{\sigma}$ is the total stress. For partially saturated soils the total stress can be written in the following form:

$$\boldsymbol{\sigma} = \boldsymbol{\sigma}' + P\mathbf{m} \quad (12)$$

where $\mathbf{m}$ is the identity tensor, $\boldsymbol{\sigma}'$ is the effective stress and P is the average pore pressure, which is a function of the pore water pressure, pore gas pressure, degree of saturation of water and degree of saturation of gas:

$$P = S_w p_w + S_g p_g = S p_w + (1-S) p_g \quad (13)$$

By substituting this average pore pressure into Eq. (12) we have:

$$\boldsymbol{\sigma} = \boldsymbol{\sigma}' + \left(S p_w + (1-S) p_g \right)\mathbf{m} \quad (14)$$

If the degree of saturation is replaced by the matric suction coefficient χ, the well-known Bishop's stress is obtained:

$$\boldsymbol{\sigma} = \boldsymbol{\sigma}' + \left(\chi p_w + (1-\chi) p_g \right)\mathbf{m} \quad (15)$$

χ is an experimentally determined factor which depends on degree of saturation, porosity, and the matric suction. As the pore gas pressure is assumed to be constant and equal to the atmospheric pressure, the pore gas pressure can be neglected. Therefore the Bishop's stress can be simplified as:

$$\boldsymbol{\sigma} = \boldsymbol{\sigma}' + \chi p_w \mathbf{m} \quad (16)$$

The constitutive relation using the effective stress $\boldsymbol{\sigma}'$ is written in the following form:

$$d\boldsymbol{\sigma}' = \mathbf{M} : \left(d\boldsymbol{\varepsilon} - d\boldsymbol{\varepsilon}_T \right) \quad (17)$$

$\mathbf{M}$ represents the material stress-strain matrix. $\boldsymbol{\varepsilon}$ is the total strain of the skeleton and $\boldsymbol{\varepsilon}_T$ is thermal strain

caused by temperature increase. The thermal strain can be found from:

$$d\boldsymbol{\varepsilon}_T = \mathbf{B}_{DT}\mathbf{m}\cdot dT = \begin{bmatrix} \beta_{DT,x} & 0 & 0 & 0 & 0 & 0 \\ 0 & \beta_{DT,y} & 0 & 0 & 0 & 0 \\ 0 & 0 & \beta_{DT,z} & 0 & 0 & 0 \\ 0 & 0 & 0 & 0 & 0 & 0 \\ 0 & 0 & 0 & 0 & 0 & 0 \\ 0 & 0 & 0 & 0 & 0 & 0 \end{bmatrix} \mathbf{m}\cdot dT \quad (18)$$

where $\beta_{DT,x}$, $\beta_{DT,y}$ and $\beta_{DT,z}$ are the drained linear thermal expansion coefficient of soil skeleton (1/K) in x, y and z directions, respectively, which vary between 0.5×10^{-6} and 12×10^{-6} (1/K) depending on the type of the soil or rock. Khalili et al. (2010) showed that the thermal expansion coefficient of soils grains is the same as the skeletal thermal expansion coefficient of homogenous porous media:

$$\beta_{sT} = \beta_{DT,x} + \beta_{DT,y} + \beta_{DT,z} \quad (19)$$

The constitutive relation can therefore be written as:

$$d\boldsymbol{\sigma}' = \mathbf{M} : \left(d\boldsymbol{\varepsilon} - \mathbf{B}_{DT}\mathbf{m}\cdot dT\right) \quad (20)$$

The governing equation for the deformation model is obtained:

$$\nabla\cdot\left[\mathbf{M} : \left(d\boldsymbol{\varepsilon} - \mathbf{B}_{DT}\mathbf{m}\cdot dT\right) + \chi\, dp_w\,\mathbf{m}\right] + d\left(\rho\mathbf{g}\right) = 0 \quad (21)$$

2.4 *Heat transport*

The heat balance equation for the porous medium can be written in the following form:

$$\frac{\partial}{\partial t}\left(nS\rho_w e_w + n(1-S)\rho_v e_v + (1-n)\rho_s e_s\right) = -\nabla\cdot\left(\mathbf{J}_c + \mathbf{J}_{Aw}\right) + Q_T \quad (22)$$

in which e_w, e_v and e_s are the internal energy of water, vapor and solid phases, respectively. Q_T is the heat source term, i.e. heat generation rate per unit volume. $\mathbf{J}_{\mathrm{Aw}}$ and $\mathbf{J}_{\mathrm{c}}$ are the advective internal energy flux in water and the conductive (diffusive) heat flux in the porous medium, respectively.

The conductive heat flow is assumed to be governed by Fourier's law:

$$\mathbf{J}_c = -\lambda\nabla T \quad (23)$$

where λ is the thermal conductivity of the porous medium:

$$\lambda = (1-n)\lambda_s + nS\lambda_w + n(1-S)\lambda_g \quad (24)$$

λ_s, λ_w and λ_g are the solid, the water and the gas thermal conductivities.

The advective internal energy flux in water is:

$$\mathbf{J}_{Aw} = C_w T\mathbf{J}_w = \rho_w C_w T\left(\frac{k_{rel}}{\mu}\underline{\underline{\kappa}}^{\mathrm{int}}\left(\nabla p_w + \rho_w \underline{g}\right)\right) = \rho_w C_w \mathbf{V}_w T \quad (25)$$

in which $\mathbf{V}_w$ is the water phase velocity and C_w is the water specific heat capacity. The total heat flux in an unsaturated porous medium is a summation of diffusive heat flux and advective flux:

$$\mathbf{J}_T = \mathbf{J}_c + \mathbf{J}_{Aw} = -\lambda\nabla T + \rho_w C_w \mathbf{V}_w T \quad (26)$$

The mechanical energy conversions in fluid and solid phases are included in the source term:

$$Q_T = \boldsymbol{\sigma}_w : \nabla\mathbf{V}_w + \boldsymbol{\sigma}_s : \nabla\mathbf{V}_s = \left(nS_w p_w \nabla.\mathbf{V}_w - \tau_w\right) + (1-n)3K'\beta_{DT}\frac{\partial\varepsilon_v}{\partial t} \quad (27)$$

where $\boldsymbol{\sigma}_w$ and $\boldsymbol{\sigma}_s$ are the stress tensor in the water and solid phases, respectively. $\mathbf{V}_s$ is the solid phase velocity and τ_w is a viscous energy dissipation term. The source term Q_T is an internal/external supply which can be neglected in most practical applications.

The heat storage term, i.e. the left hand side of the heat balance equation, can be simplified as:

$$\frac{\partial}{\partial t}\left(nS\rho_w e_w + n(1-S)\rho_v e_v + (1-n)\rho_s e_s\right) = C\rho\frac{\partial T}{\partial t} \quad (28)$$

where Cρ is the heat capacity of the porous medium:

$$C\rho = (1-n)C_s\rho_s + nSC_w\rho_w + n(1-S)C_g\rho_g \quad (29)$$

C_s, C_w and C_g are the solid, the water and the gas specific heat capacities.

The right hand side of the heat balance equation can be expanded as:

$$\nabla\cdot\left(\mathbf{J}_T\right) = \nabla\cdot\mathbf{J}_c + \nabla\cdot\mathbf{J}_{Aw} = -\nabla\cdot\left(\lambda\nabla T\right) + \nabla\cdot\left(\rho_w C_w \mathbf{V}_w T\right) \quad (30)$$

in which

$$\nabla\cdot\left(\rho_w C_w \mathbf{V}_w T\right) = nS\rho_w C_w\left(\mathbf{V}_w\cdot\nabla T + T\nabla\cdot\mathbf{V}_w\right) = \rho_w C_w\left[\frac{k_{rel}}{\mu}\underline{\underline{\kappa}}^{\mathrm{int}}\left(\nabla p_w + \rho_w \underline{g}\right)\right]\cdot\nabla T + \rho_w C_w T\left[\nabla\cdot\left(\frac{k_{rel}}{\mu}\underline{\underline{\kappa}}^{\mathrm{int}}\left(\nabla p_w + \rho_w \underline{g}\right)\right)\right] \quad (31)$$

The governing equation on heat transport can therefore be written as:

$$C\rho\frac{\partial T}{\partial t} - \nabla\cdot\left(\lambda\nabla T\right) + \rho_w C_w\left[\frac{k_{rel}}{\mu}\underline{\underline{\kappa}}^{\mathrm{int}}\left(\nabla p_w + \rho_w \underline{g}\right)\right]\cdot\nabla T + \rho_w C_w T\left[\nabla\cdot\left(\frac{k_{rel}}{\mu}\underline{\underline{\kappa}}^{\mathrm{int}}\left(\nabla p_w + \rho_w \underline{g}\right)\right)\right] - Q_T = 0 \quad (32)$$

3 IMPLEMENTATION

3.1 *Finite element formulation*

The finite element formulation is obtained using a Galerkin approach applied to the mass balance, eq. (10), the non-isothermal deformation, eq. (21) and heat flow, eq. (32).

3.2 *Couplings*

The finite element formulation contains a coupled behavior which is represented by the mechanical equilibrium, mass balance and heat balance equations. The local thermodynamic equilibrium is assumed, which means that at each point the temperature in soil, water and gas is equal. The displacement of the solid skeleton, the pore water pressure and the temperature are chosen as primary variables of the problem. The spatial discretization yields the following system of equations which is non-symmetric:

$$\begin{bmatrix} \underline{\underline{K}}_{vv} & \underline{\underline{K}}_{vP} & \underline{\underline{K}}_{vT} \\ \underline{\underline{C}}_{Pv} & \underline{\underline{C}}_{PP} & \underline{\underline{C}}_{PT} \\ 0 & 0 & \underline{\underline{C}}_{TT} \end{bmatrix} \begin{bmatrix} \frac{d\underline{v}}{dt} \\ \frac{dp_w}{dt} \\ \frac{dT}{dt} \end{bmatrix} = \begin{bmatrix} 0 & 0 & 0 \\ 0 & \underline{\underline{K}}_{PP} & \underline{\underline{K}}_{PT} \\ 0 & \underline{\underline{K}}_{TP} & \underline{\underline{K}}_{TT} \end{bmatrix} \begin{bmatrix} \underline{v} \\ p_w \\ T \end{bmatrix} + \begin{bmatrix} \frac{d\underline{f}_u}{dt} \\ \underline{G}_p + \underline{q}_p \\ \underline{G}_T + \underline{q}_T + \underline{Q}_T \end{bmatrix} \tag{33}$$

In eq. (33) the matrices using the letter K represent stiffnesses, when the ones using the letter C correspond to storage. Their indices map the corresponding variables.

3.3 *Solving procedure*

Discretization in the time domain is performed by using a fully implicit finite difference scheme. The system (33) can be integrated in time, using a first order finite difference method. It can be written in a more concise form:

$$\underline{\underline{B}} \frac{d\underline{X}}{dt} + \underline{\underline{C}}\,\underline{X} = \underline{F} \tag{34}$$

The matrices $\underline{\underline{B}}$, $\underline{\underline{C}}$ and $\underline{F}$ depend on $\underline{X}$. The discretization is carried out by the generalized midpoint rule which approximates

$$\left(\frac{d\underline{X}}{dt}\right)^{i+\alpha} = \frac{\Delta\underline{X}}{\Delta t} = \frac{\underline{X}^{i+1} - \underline{X}^{i}}{\Delta t}, \qquad \underline{X}^{i+\alpha} = (1-\alpha)\,\underline{X}^{i} + \alpha\,\underline{X}^{i+1} \tag{35}$$

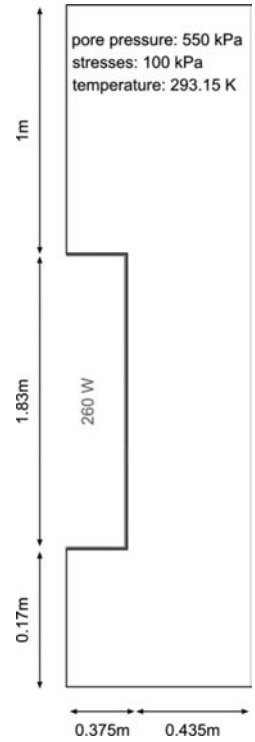


Figure 1. Geometry and boundary conditions.

By defining Δt as the time step and α as a parameter such that $0 \le \alpha \le 1$, eq. (34) at time $t^{i+\alpha}$ becomes:

$$\left[\underline{\underline{B}} + \alpha\,\Delta t\,\underline{\underline{C}}\right]^{i+\alpha} \underline{X}^{i+1} = \left[\underline{\underline{B}} - (1-\alpha)\,\Delta t\,\underline{\underline{C}}\right]^{i+\alpha} \underline{X}^{i} + \Delta t\,\underline{F}^{i+\alpha} \tag{36}$$

A fully implicit procedure is chosen using $\alpha = 1$. As $\underline{X}^{i+1} = \underline{X}^{i} + \Delta\underline{X}$, the full system can be written:

$$\begin{bmatrix} \underline{\underline{K}}_{vv} & \underline{\underline{K}}_{vP} & \underline{\underline{K}}_{vT} \\ \underline{\underline{C}}_{Pv} & \underline{\underline{C}}^{*}_{PP} & \underline{\underline{C}}^{*}_{PT} \\ 0 & -\Delta t\,\underline{\underline{K}}_{TP} & \underline{\underline{C}}^{*}_{TT} \end{bmatrix}^{i+1} \begin{bmatrix} \Delta\underline{v} \\ \Delta p_w \\ \Delta T \end{bmatrix} = \begin{bmatrix} 0 & 0 & 0 \\ 0 & \Delta t\,\underline{\underline{K}}_{PP} & \Delta t\,\underline{\underline{K}}_{PT} \\ 0 & \Delta t\,\underline{\underline{K}}_{TP} & \Delta t\,\underline{\underline{K}}_{TT} \end{bmatrix}^{i+1} \begin{bmatrix} \underline{v}^{i} \\ p_w^{\,i} \\ T^{i} \end{bmatrix} + \begin{bmatrix} \Delta\underline{f}_u \\ \Delta t(\underline{G}_p + \underline{q}_p) \\ \Delta t(\underline{G}_T + \underline{q}_T + \underline{Q}_T) \end{bmatrix} \tag{37}$$

The implementation is done in a research version of PLAXIS 2D.

4 SIMULATION

The model and its implementation are tested against the well-known FEBEX experiment as described in Martín et al. (2006). This simulation is based on Willemsen (2011). The axisymmetric geometry and the boundary conditions are provided in Fig. 1.

Table 1. Material parameters for the FEBEX bentonite.

Material parameter	Value
C_s [J/kg/K]	1000
ρ_s [kg/m^3]	2770
λ_s [J/kg/K]	1.15
β_{sT} [1/K]	$7.8 \cdot 10^{-6}$
k [m^2]	$5 \cdot 10^{-21}$

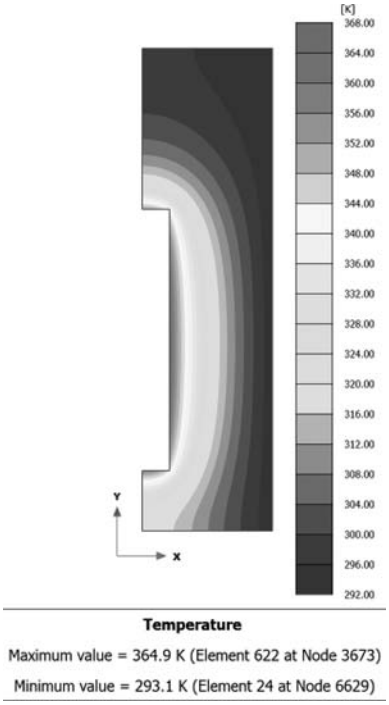


Figure 2. Temperature field after 100 days.

The initial isotropic stress inside the bentonite is set to 110 kPa and the pore water pressure to 550 kPa, for a fully saturated sample. All boundaries are closed for groundwater flow. No external mechanical action is applied to the sample. An axisymmetric radial heat flux of 260 W is used to model the heater. Top and bottom boundaries are closed for heat flux while the outer radial boundary is kept to the atmospheric temperature of 293.15 K. Figure 1 summarizes the geometry and the boundary conditions. The material parameters are given in Table 1. Figures 2, 3 and 4 present the temperature field, the heat flux and the pore pressures after 100 days.

The steady-state temperature of 90°C is found after one month. The heat flux stabilizes at the same time.

The pore pressure field is in accordance to Martín et al. 2006. The range of 5 MPa to 8 MPa is found from the outer radial boundary to the heater. These values are reached faster than in the experiment as the hydration process has not been modeled here. The lower pore pressure at the highest region of the model is due to gravity effects, as PLAXIS does not allow horizontal axisymmetry.

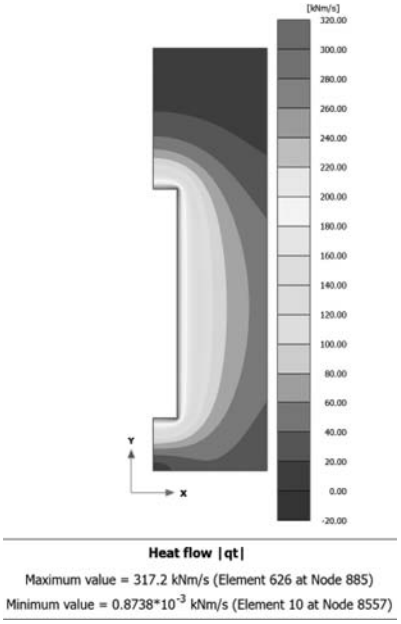


Figure 3. Heat flow after 100 days.

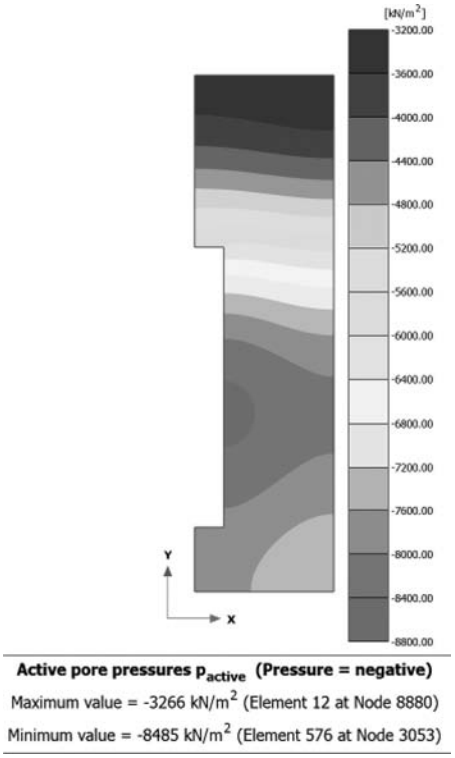


Figure 4. Pore pressure distribution after 100 days.

5 CONCLUSIONS

A THM model for partially saturated rocks has been developed. It is implemented in a research version of PLAXIS 2D. The first key strength resides in the formulation of water pressure under the assumption of constant gas pressure, simplifying the model and providing good performance. The second one is the full coupling offered by the implementation to model accurately the interactions between the phenomena in competition. The results of the first calculations are promising, yet more in depth confrontations with experimental data has to be undergone to fully validate the model and its implementation.

REFERENCES

Collin, F., Li, X., Radu, J. & Charlier, R. 2002. Thermo-hydro-mechanical couplings in clay barriers. *Engineering Geology* 64:179–193

Galavi, V., Brinkgreve, R.B.J., Bonnier, P.G. & Gonzalez, N. 2009. Fully coupled hydro-mechanical analysis of unsaturated soils. In S. Pietruszczak, G. Pande, C. Tamagnini & R. Wan (eds), *Proceedings of the 1st International Symposium on Computational Geomechanics (COMGEO I)*: 486–495, International Centre for Computational Engineering (IC^2E), Ethnarhou Makariou Str., Rhodes 85100, Greece.

Galavi, V. 2011. Fully coupled thermo-hydro-mechanical analysis of unsaturated soils. In S. Pietruszczak & G. Pande (eds), *Computational Geomechanics II (ComGeo II)*, Catvtat-Dubrovnik, 27–29 April 2011, 609–619.

Khalili, N., Uchaipichat, A. & Javadi, A. 2010. Skeletal thermal expansion coefficient and thermo-hydro-mechanical constitutive relations for saturated homogeneous porous media. *Mechanics of Materials* 42: 593–598.

Martín, P.L., Barcala, J.M., & Huertas, F. 2006. Large-scale and long-term coupled thermo-hydro-mechanic experiments with bentonite: the febex mock-up test. *Journal of Iberian Geology* 32(2): 259–282.

Rutquist, J, Borgesson, L., Chijimatsu, M., Kobayashi, A., Jing, L., Nguyen, T.S., Noorishad, J. & Tsang, C.-F. 2001. Thermohydromechanics of partially saturated geological media: governing equations and formulation of four finite element models. *International Journal of Rock Mechanics and Mining Sciences*, 38:105–127.

Schrefler, B.A. 1995. F.E. in environmental engineering: Coupled thermo-hydro-mechanical processes in porous media including pollutant transport. *Archives of Computational Methods in Engineering, State of the art reviews*, Vol. 2, 3, 1–54.

Wang, W., Kosakowski, G. & Kolditz, O. 2009. A parallel finite element scheme for thermo-hydro-mechanical (THM) coupled problems in porous media. *Computers and Geotechnics* 35: 1631–1641.

Willemsen, L.A. 2011. *Validation and Verification of Thermo-Hydro-Mechanical (THM) Coupling in Plaxis.* Master Thesis, University Luleå, Department of Civil, Environmental and Natural Resources Engineering.

Wu, W., Li, X., Charlier, R. & Collin, F. 2004. A thermo-hydro-mechanical constitutive model and its numerical modelling for unsaturated soils. *Computers and Geotechnics* 31: 155–167.

Rock Mechanics for Resources, Energy and Environment – Kwaśniewski & Łydżba (eds)
© 2013 Taylor & Francis Group, London, ISBN 978-1-138-00080-3

A study on shear characteristics of a smooth rock surface under different thermal, hydro and mechanical conditions

T. Kim, N. Zhang & S. Jeon
Department of Energy Resources Engineering, Seoul National University, Seoul, Korea

ABSTRACT: High-level radioactive waste repositories are to be designed to ensure long-term stability, and it is necessary to consider various effects at deep depth in various aspects. Especially, many uncertainties are involved in characterizing the behavior of deep rock mass in the designing process and interactions among groundwater flow, increased temperature induced by radioactive wastes and stress disturbance due to excavation should be considered. In this study, to investigate the shear characteristics of a saw-cut smooth surface of crystalline rock under various thermal-hydro-mechanical conditions, multistage triaxial tests were conducted on granitic rock. After testing, shear characteristics of the saw-cut surfaces were analyzed based on Mohr-Coulomb failure criterion. From the experimental results, it was observed that the shear characteristics of the granitic rock were sensitive to confining pressure and water pressure but not to temperature variation. Numerical analysis was conducted as well by COMSOL providing with a good agreement with experimental results.

1 INTRODUCTION

High-level radioactive waste disposal facilities are usually designed to be stable for an extended period of time as long as 10,000 years. To ensure the mechanical, hydrological and chemical stability of the facilities, long-term performance is assessed with respect to many different variables and their coupled effects. It is well-known that the international cooperative project DECOVALEX has been accumulating lots of information and knowledge of coupled processes in fractured rock masses. In addition many independent studies were carried out to investigate the T-H-M-C coupled effects in numerical and experimental methods. They include the researches by Lockner et al. (1982), Elliott & Brown (1988), Zhao & Brown (1992), Yoon & Jeon (2004) and Wanne & Young (2008).

However, few studies were carried out on the shearing behavior of a shear surface of crystalline rock under various thermal (T), hydro (H) and mechanical (M) conditions. In this study, a series of laboratory scale experiment was carried out to investigate the behavior of smooth shear surface of a crystalline rock under triaxial compression to simulate the stress condition at depth, different water pressure and temperature conditions to simulate the situation at the vicinity of a canister of high-level radioactive waste. The test results were analyzed using Mohr-Coulomb failure criterion. In addition, numerical analysis was carried out using COMSOL Multiphysics to simulate the test.

2 EXPERIMENTAL STUDY

2.1 *Sample preparation*

Granitic rock cores obtained during site investigation at KURT (KAERI Underground Research Tunnel) were taken as test samples. The samples used in the tests were cored at the depth of 70–80 m from the ground surface. The size of the specimens for triaxial compression test was approximately 47.7 mm in diameter and 100 mm in height. To make a smooth shear surface, the specimens were cut by a circular diamond saw and the angle of the saw-cut surface measured from the axis of the specimen, θ, was 28° (Fig. 1a).

Due to low permeability of granite, water injection holes of 3.0–4.0 mm in diameter were drilled on the top and bottom surfaces of the specimens only for the cases of H-M and T-H-M conditions, to apply water pressure on the shear surface (Fig. 1). Table 1 presents the specifications of the specimens.

2.2 *Experimental method*

Multistage triaxial compression tests were performed under various confining stress, temperature and water pressure conditions. Multistage triaxial test can generate a full failure envelope using a single specimen (Kovari et al. 1983). In a multistage triaxial test, the axial stress is increased under a constant confining pressure until a peak stress is observed. Once the

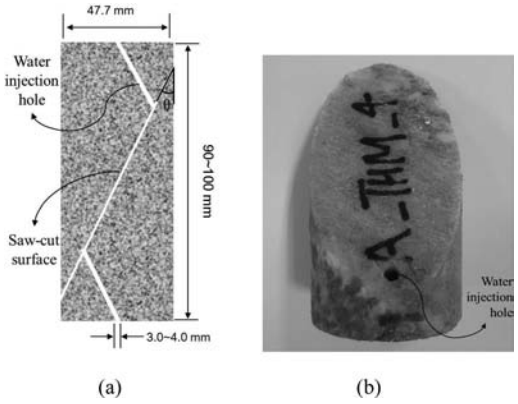


Figure 1. Configuration of the specimen. (a) Cross- sectional view of the specimen, and (b) picture of the specimen with saw-cut surface.



Figure 2. View of experimental setting of multistage triaxial compression test under thermal, hydro and mechanical condition.

Table 1. Specification of the specimens.

Testing condition	Sample ID	Diameter mm	Height mm	Inclined angle, θ (°)
M	A_M_1	47.7	96.5	28
	A_M_2	47.7	97.8	28
T-M	A_TM_1	47.7	101.6	28
	A_TM_2	47.7	86.7	28
H-M	A_HM_1	47.7	96.9	28
	A_HM_2	47.7	93.4	28
	A_HM_3	47.7	99.9	28
	A_HM_4	47.7	84.4	28
T-H-M	A_THM_1	47.7	93.4	28
	A_THM_2	47.7	92.5	28
	A_THM_3	47.7	95.0	28
	A_THM_4	47.7	103.4	28

Table 2. Variable conditions for the multistage triaxial compression test under various mechanical and thermal conditions.

Temperature of specimen °C	Water pressure MPa	Loading rate mm/min	Confining pressure MPa
20, 80	0.1, 0.5	0.3	5, 10, 15

peak stress is obtained, the confining pressure is then increased to the next step.

Under the elevated temperature condition, heat, controlled by thermo controller with an accuracy of ±5°C, is transferred to the specimen through oil inside the chamber. During heating, axial deformation of specimen was restrained to consider thermal stress built up in the specimen.

Under H-M and T-H-M conditions, water pressure was controlled by syringe pump with an accuracy of ±0.5% of full scale. To prevent leakage of water through the interface between the specimen and the membrane tube, 3 MPa of confining pressure was applied at the specimen. Figure 2 shows the view of the experimental setting under thermal, hydro and mechanical condition.

2.3 *Testing conditions*

After preliminary study, the variable conditions for the test were decided as presented in Table 2. The temperature was set at 20°C and 80°C for the test. The rock temperature around the canister was reported to reach up to 80°C according to Kwon & Cho (2009). The heating rate was set at 3°C per minute to prevent the thermal shock to the specimen. In order to reduce the thermal gradient inside the specimen, the peak temperature was maintained for 90 minutes.

The axial loading and deformation were servo-controlled during the test. Different confining pressures, i.e. 5, 10, 15 MPa, were applied to the specimen using a servo-controlled hydraulic unit with an accuracy of 0.1 MPa during the test.

0.1 MPa of water pressure was applied on A_HM_1 and A_HM_2 specimens and 0.5 MPa on A_HM_3 and A_HM_4 specimens.

2.4 *Results and discussion*

In the test, approaching to the peak axial stress, sliding occurred along the saw-cut surface with creating small amounts of gouge. Peak shear strength and friction angle of the shear surface were investigated using Mohr-Coulomb failure criterion. Results of the experiments are summarized in Table 3.

Regarding the experimental results at the elevated temperature (80°C), the two specimens showed different tendency. In case of A_TM_1 specimen, friction angle decreased compared with the results at the room temperature (20°C). However, for A_TM_2 specimen, it did not show much variation. According to Lockner et al. (1982), the frictional property of sandstone was independent of temperature at 150°C and 240°C.

Table 3. Results of multistage triaxial compression test on saw-cut specimens under various thermal, hydro and mechanical conditions.

Testing condition	Sample ID	Confining pressure, σ_3 (MPa)	Peak axial stress, σ_1 (MPa)	Normal stress, σ_n (MPa)	Shear stress, τ (MPa)	Friction angle (°)
M (20°C)	A_M_1	5	10.30	6.17	2.20	31.30
		10	24.10	13.11	5.84	
		15	41.90	20.93	11.15	
	A_M_2	5	9.80	6.20	2.08	30.20
		10	23.10	13.28	5.67	
		15	39.97	21.24	10.81	
T-M (80°C)	A_TM_1	5	13.50	6.87	3.52	24.43
		10	25.48	13.41	6.42	
		15	37.95	20.06	9.51	
	A_TM_2	5	10.17	6.14	2.14	32.88
		10	26.33	13.60	6.77	
		15	43.92	21.37	11.99	
H-M (0.1 MPa)	A_HM_1	5	9.69	6.03	1.94	25.45
		10	19.82	12.16	4.07	
		15	34.93	19.39	8.26	
	A_HM_2	5	9.86	6.07	2.01	30.37
		10	24.81	13.26	6.14	
		15	40.39	20.60	10.52	
H-M (0.5 MPa)	A_HM_3	5	10.79	6.28	2.40	35.13
		10	25.57	13.43	6.45	
		15	47.66	22.20	13.54	
	A_HM_4	5	10.42	6.19	2.25	33.02
		10	25.47	13.41	6.41	
		15	44.30	21.46	12.15	
T-H-M (80°C, 0.1 MPa)	A_THM_1	5	10.56	6.23	2.30	29.64
		10	22.70	12.80	5.26	
		15	40.10	20.53	10.40	
	A_THM_2	5	10.26	6.16	2.18	30.88
		10	19.77	12.15	4.05	
		15	40.75	20.68	10.67	
T-H-M (80°C, 0.5 MPa)	A_THM_3	5	9.79	6.06	1.99	32.40
		10	22.26	12.70	5.08	
		15	42.60	21.08	11.44	
	A_THM_4	5	9.92	6.08	2.04	31.75
		10	21.52	12.54	4.78	
		15	41.80	20.91	11.11	

Except the result of A_TM_1, we can infer that friction angle of granite is also independent on temperature variation in the range of 80°C. Figure 3 shows the relationship between the normal stress and shear stress acting on the shear surface under the room temperature and the elevated temperature.

When the water pressure was applied on the shear surface, the friction angle did not show much variation either. Under the water pressure of 0.1 MPa and 0.5 MPa, the friction angle was in the range of 25°–35° and the friction angle increased slightly with the increase of water pressure. Barton (1973) reported that shear characteristics of smooth surfaces do not or slightly change when wet. The results in this study showed a similar tendency with the observation under the water pressure of 0.1 and 0.5 MPa. Figure 4 shows the relationship between the normal stress and shear stress acting on the shear surface under the water pressure of 0.1 and 0.5 MPa.

Under the elevated temperature and water pressure, the friction angle did not vary much compared with the case of mechanical condition (Figure 5). Compared with H-M conditions, the friction angle slightly decreased but the amount of decrease was very small. Therefore, the effect of temperature is negligible at an elevated temperature of 80°C, even under T-H-M conditions.

3 NUMERICAL SIMULATION

3.1 *Model introduction*

The numerical analysis was carried out using COMSOL Multiphysics, which provides a powerful and flexible modeling environment for solving partial differential equations. The numerical simulation for multistage triaxial compression test on a saw-cut

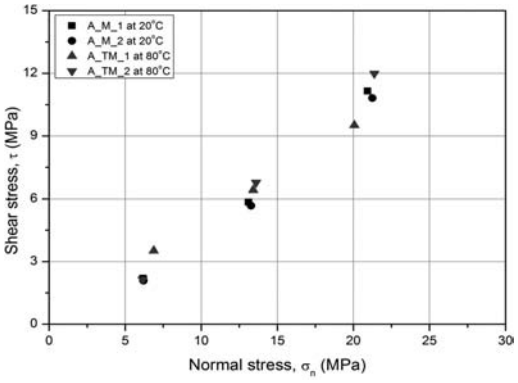


Figure 3. Relation between normal stress and shear stress acting on shear surface at room temperature (20°C) and elevated temperature (80°C) conditions.

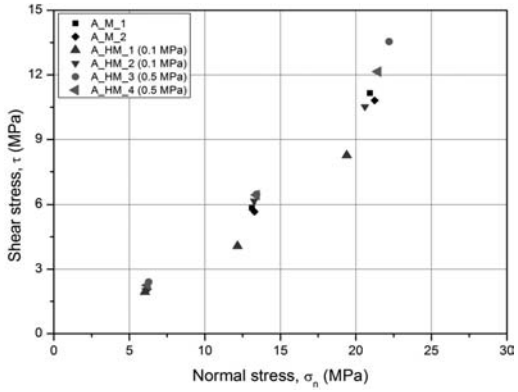


Figure 4. Relation between normal stress and shear stress acting on shear surface at water pressure of 0, 0.1, and 0.5 MPa.

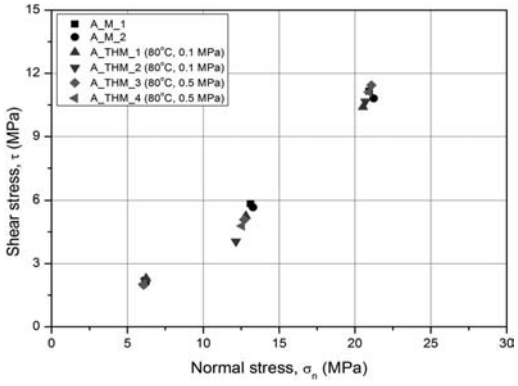


Figure 5. Relation between normal stress and shear stress acting on shear surface under mechanical and water pressure of 0.1 MPa and 0.5 MPa at an elevated temperature (80°C) conditions.

specimen was carried out under plane strain condition in a two-dimensional model. The built-in Structural Mechanics Module and Heat Transfer Module of COMSOL Multiphysics are used to simulate the

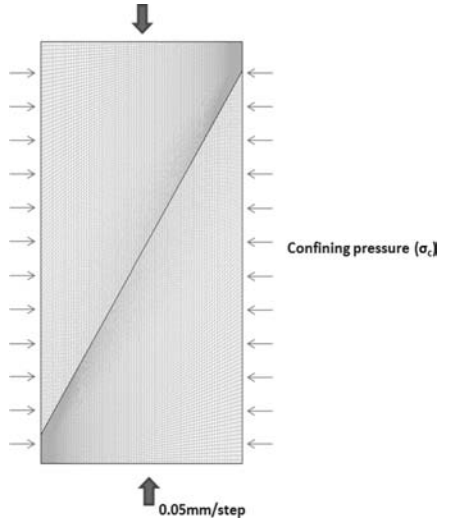


Figure 6. Two-dimensional model setup and boundary condition.

Table 4. Input parameters used in the numerical simulation.

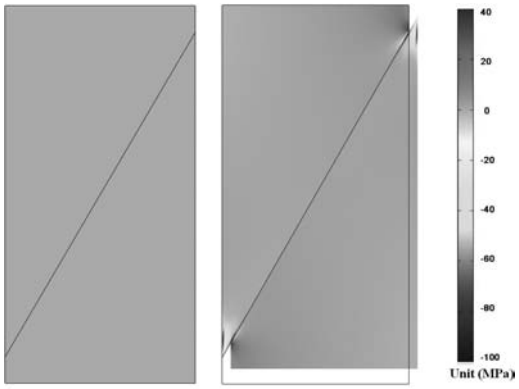
Parameter	Value
Young's modulus (GPa)	60
Poisson's ratio	0.20
Density (kg/m^3)	2660
Coefficient of thermal expansion (10^{-6}/°C)	10

thermal-mechanical coupled test. The saw-cut surface was set as boundary contact pair and frictional characteristics are modeled based on Coulomb friction criterion
(COMSOL AB., 2008). Numerical simulations under hydro-mechanical conditions and thermal-hydro-mechanical coupled conditions are not presented at this time.

The numerical model has the same dimension as the test specimen. The linear quadrilateral element was used and 14,880 quadrilateral meshes were generated in total as shown in Figure 6. Rock was assumed to be a homogeneous and isotropic material. The input parameters used in the numerical simulation are listed in Table 4. For the simulation at the elevated temperature condition, the coefficient of thermal expansion of granite specimen was as assumed to be 10×10^{-6}/°C (Kim et al., 2011). The model expands with the increase in temperature, causing thermal strain in the material. The thermal stress is induced by the thermal expansion of the model.

3.2 *Results and discussion*

Figure 7 shows the deformation and maximum principal stress distribution in the specimen during multistage triaxial compression test at room temperature. Sliding occurred along the saw-cut surface and the results of numerical analysis are listed in Table 5.



(a) Initial state (b) Final state

Figure 7. Deformation presented in the numerical model with the maximum principal stress distribution under the room temperature (20°C) condition.

Table 5. Results of numerical simulation

Testing condition	Confining pressure (MPa)	Peak axial stress (MPa)	Normal stress (MPa)	Shear stress (MPa)	Friction angle (°)
Room temperature (20°C)	5	14.07	7.00	3.76	28.97
	10	24.70	13.24	6.09	
	15	42.71	21.11	11.49	
Elevated temperature (80°C)	5	14.05	7.00	3.75	28.53
	10	24.15	13.12	5.86	
	15	42.16	20.99	11.26	

The shear behavior under multistage triaxial compression condition and the friction angle of the numerical analysis coincided with those observed in laboratory tests. Figure 8 shows the relationship between the normal and shear stress acting on the shear surface under various temperature conditions.

The shear stress increased with the increase of normal stress however the friction angle and shear stress did not vary with the increase of temperature. It was analyzed that the thermal stress due the difference in temperature, i.e. 60°C, is too small to cause the noticeable change in shearing characteristics of the specimen.

4 CONCLUSIONS

Multistage triaxial compression tests under various confining and temperature conditions were carried out on saw-cut granitic rock specimens obtained from KURT. The testing conditions were decided to consider the ground conditions at near-field of canister in the high level radioactive waste repository.

The results were analyzed using Mohr-Coulomb failure criterion and the variations of shear characteristics were investigated. Peak shear stress varied with

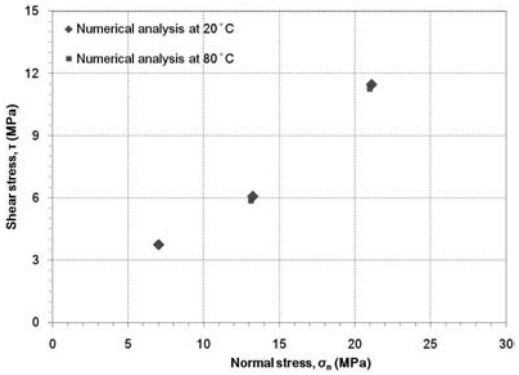


Figure 8. Relation between normal stress and shear stress acting on shear surface at the room temperature (20°C) and elevated temperature (80°C) conditions of numerical simulation.

the increase of confining stress however peak shear stress and friction angle of the granitic rock did not vary much at the elevated temperature of 80°C in the present study.

The peak shear stress and friction angle did vary much when water pressure was applied on the shear surface either. The friction angle showed slight increase with the increase of water pressure. Under T-H-M condition, friction angle also did not vary much and slight decrease of friction angle was observed compared with the case of H-M condition. According to Lockner (1982) and Barton (1973), temperature and water have small effect on frictional behavior of smooth shearing surfaces and for more clarification, additional experiments need to be performed under various conditions.

To simulate the experimental results, a series of biaxial compression tests were modeled to investigate the shear characteristics using COMSOL Multiphysics providing a good agreement with the experimental results. In the present study, thermal and hydro effect on shearing behavior of the crystalline rock was investigated. Based on the results, the shearing behavior under added hydraulic conditions and coupled thermal-hydro-mechanical conditions will be performed in the further study.

REFERENCES

Barton, N. 1973. Review of a new shear-strength criterion for rock joints. *Engineering Geology* 7: 287–332.

COMSOL AB. 2008. COMSOL Multiphysics Version 3.5, User's guide.

Elliott, G.M. & Brown, E.T. 1988. Laboratory measurement of the thermo-hydro-mechanical properties of rock. *Quarterly J. Eng. Geology* 21: 299–314.

Kim, T., Lee, C.S. & Jeon, S. 2011. A numerical study on shear characteristics of jointed rock under Thermo-mechanical coupled condition. *International Conference on Analysis of Discontinuous Deformation*, Hawaii, U.S.A.

Kovari, K., Tisa, A., Einstein, H.H. & Franklin, J.A. 1983. Suggested methods for determining the strength of rock

materials in triaxial compression: Revised version. *Int. J. Rock Mech. Min. Sci. & Geomech. Abstr.* 20: 285–290.

Kwon, S.K. & Cho, W.J. 2009. A sensitivity analysis of design parameters of an underground radioactive waste repository using a back propagation neural network. *Tunnelling and Underground Space Technology* 19(3): 203–212.

Lockner, D.A., Summers, R., Moore, D. & Byerlee, J.D. 1982. Laboratory measurements of reservoir rock from the Geysers geothermal field, California. *Int. J. Rock Mech. Min. Sci. & Geomech. Abstr.* 19: 65–80.

Wanne, T.S. & Young, R.P. 2008. Bonded-particle modeling of thermally fractured granite. *Int. J. Rock Mech. Min. Sci.* 45(5): 789–799.

Yoon, J. and Jeon, S. 2004. Experimental verification of a PTS Mode II test for rock. *Int. J. Rock Mech. Min. Sci.* 41(3): 353–354.

Zhao, J. & Brown, E.T. 1992. Thermal cracking induced by water flow through joints in heated granite. *Quarterly J. Eng. Geology*. 25: 279–290.

Rock Mechanics for Resources, Energy and Environment – Kwaśniewski & Łydżba (eds)
© 2013 Taylor & Francis Group, London, ISBN 978-1-138-00080-3

Periodic character of failure near openings in high-stress rock mass conditions

V.V. Makarov, L.S. Ksendzenko, N.A. Opanasyuk & A.M. Golosov
Far-Eastern Federal University, Vladivostok, Russia

ABSTRACT: Rock mass failure at a great depth near underground openings often has a zonal character. The mechanism of this phenomenon consists in the periodic character of the stresses in the surrounding rock mass and the development of tensile macrocracks at the places (zones) of maximum tangential stresses. A mathematical model of a highly stressed rock mass is developed on the basis of the principles of defect medium mechanics and non-equilibrium thermodynamics. A method of determining the model parameters has also been developed and a satisfactory correspondence between the experimental research on faulted zonal structures near to openings at great depths and the mathematical model calculation has been achieved. The main relationships between the width of the cracking zones and the rock mass strength property have also been determined.

1 INTRODUCTION

Failure conditions can occur in the boundary parts of the openings at great depths of excavation and wall drilling. In some cases the failure has a zonal character where tensile macrocrack zones alternate with a relatively monolithic rock mass (Shemyakin 1986, Adams & Jager 1980). Many attempts have been made to describe the zonal character of rock mass failure near openings based on classical mechanics (Shemyakin et al. 1987, Reva & Tropp 1995, Odintsev 1996; Alexeev et al. 1996). However, no one has been able to explain all of the properties of zonal failure structures without the introduction of new assumptions in each new case.

Recently, a new gauge theory has been applied to solids to describe the whirl fields of plasticity in high energy conditions (Kadich & Edelen 1983, Panin et al. 1990, Panin 1990). The main principle of gauge theory is the incompatibility of a deformation in a solid, but this does not apply to the zonal failure phenomenon of rock masses near openings. In this paper we demonstrate an example of a description of the phenomenon using the gauge mathematical model.

The description can be done from the position of consideration of the rock mass hierarchical block systems (Xu 2009). A rock sample in this conception is shown as the first level of a hierarchical system and the rock mass at the opening scale corresponds with the second one.

2 MATHEMATICAL MODEL

Rock at a great depth is modeled by a faulted structure that is far from the state of thermodynamic equilibrium; it is in constant all-around compression. The boundary-value problem is assigned as a task that concerns the stressed state of a weightless plane that is a solid damaged structure with given on an infinity stresses, which models a gravity field and is loosened by a round hole that models an unlined underground opening (Fig. 1). Due to the polar symmetry of the task, the equilibrium equations are as follows:

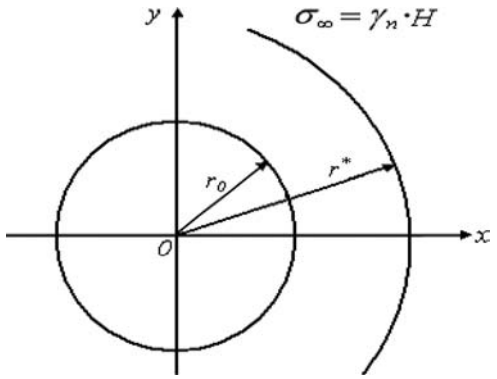


Figure 1. Design scheme of an unlined opening task.

$$\frac{\partial \sigma_{rr}}{\partial r} + \frac{1}{r}\left(\sigma_{rr} - \sigma_{\varphi\varphi}\right) = 0, \sigma_{r\varphi} = 0, r_0 \le r < \infty, \qquad (1)$$

where σ_{rr} is the normal radial stress, $\sigma_{\varphi\varphi}$ is the normal tangential stress and $\sigma_{r\varphi}$ is the shear stress.

At the opening boundary ($r = r_0$) and at infinity, the following applied forces exist:

$$\sigma_{rr} = 0 \text{ at } r = r_0; \sigma_{rr}, \sigma_{\varphi\varphi} \to \sigma_\infty \text{ at } r \to \infty, \qquad (2)$$

where $\sigma = \gamma \times H$, γ is the rock density (N/ m^3) and H is the opening depth (m).

A rock mass at a great depth is modeled by the structure where the conditions of deformation compatibility ε_{ij} are not commonly met:

$$R = \frac{\partial^2 \varepsilon_{11}}{\partial x_2^{\,2}} - 2\frac{\partial^2 \varepsilon_{12}}{\partial x_1 \partial x_2} + \frac{\partial^2 \varepsilon_{22}}{\partial x_1^{\,2}} \neq 0. \quad (3)$$

The damage parameter R is expressed by the equation (Guzev & Paroshin 2000):

$$\Delta^2 R - \gamma^2 R = 0, \quad (4)$$

where Δ is the Laplace operator and γ is the model parameter.

As the task is plane- and axi-symmetrical, Equation (4) in polar coordinates will become:

$$\left(\frac{\partial^2}{\partial r^2} + \frac{1}{r}\frac{\partial}{\partial r}\right)^2 R = \gamma^2 R. \quad (5)$$

The solution of Equation (5) decreasing at $r \to \infty$ is:

$$R(r) = aJ_0\left(\sqrt{\gamma} r\right) + bN_0\left(\sqrt{\gamma} r\right) + cK_0\left(\sqrt{\gamma} r\right), \quad (6)$$

where J_0, N_0, K_0 are the Bessel, Neumann and MacDonald functions of zero order, respectively.

3 NON-CLASSICAL BOUNDARY CONDITIONS AND TASK SOLUTION

The rock mass undergoes considerable destruction at the opening boundary; therefore, the damage parameter R should not equal zero. Assuming that all of the zones of rock destruction are equivalent and are of the same origin, we introduce the extremum of the function condition at the boundary $R(r)$ and the following zones of destruction. Therefore, the boundary conditions for the function $R(r)$ are:

$$R'(r)\big|_{r=r_0} = 0,\ R'(r)\big|_{r=r^*} = 0, \quad (7)$$

where r^* is determined experimentally.

The equation for the first invariant of stresses $\sigma = \sigma_{zz} + \sigma_{rr} + \sigma_{\varphi\varphi}$ is:

$$\Delta\sigma = \frac{E}{2(1-\nu)} R, \sigma \to 2(1+\nu)\sigma_\infty, r \to \infty, \quad (8)$$

with the determined function R, where E is the modulus of elasticity and ν is the Poisson ratio.

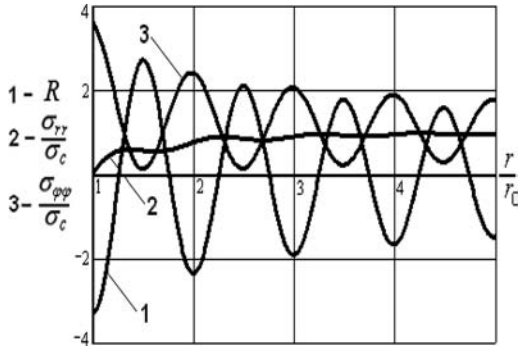


Figure 2. Oscillating character of the stresses and the R – functions in the rock mass surrounding an underground opening.

Solving the task (8) gives these formulas for the stress components:

$$\sigma_{rr} = \sigma_\infty\left(1 - \frac{r_0^{\,2}}{r^2}\right) - \frac{E}{2\left(1-\nu^2\right)\gamma^{3/2}} \cdot \frac{1}{r} \times$$
$$\times\left[aJ_1\left(\sqrt{\gamma} r\right) + bN_1\left(\sqrt{\gamma} r\right) + cK_1\left(\sqrt{\gamma} r\right)\right];$$
$$\sigma_{\varphi\varphi} = \sigma_\infty\left(1 + \frac{r_0^{\,2}}{r^2}\right) - \frac{E}{2\left(1-\nu^2\right)\gamma} \times \quad (9)$$
$$\times\left[aJ_0\left(\sqrt{\gamma}\cdot r\right) + bN_0\left(\sqrt{\gamma}\cdot r\right) - cK_0\left(\sqrt{\gamma}\cdot r\right)\right] +$$
$$+ \frac{E}{2\left(1-\nu^2\right)\gamma^{3/2}} \cdot \frac{1}{r}\left[aJ_1\left(\sqrt{\gamma}\cdot r\right) + bN_1\left(\sqrt{\gamma}\cdot r\right) + cK_1\left(\sqrt{\gamma}\cdot r\right)\right],$$

where r is the distance from the center of the opening to a selected point in the rock mass.

4 STRESS CALCULATION AND CRITERIA OF FAILURE

The stresses surrounding the opening are of an oscillating character (Fig. 2).

The zones of failure appear in the areas where the conditions of cracking under compression are met:

$$K_I = (\pi \cdot l)^{1/2} \cdot \left(\gamma_1 \cdot \sigma_1^0 - \gamma_3 \cdot \sigma_3^0\right) \geq K_{Ic}, \quad (10)$$

where l is the half-length of the fracture faults of the rock mass and is assumed to be equal to the minimum half-length of a tensile macrocrack that is unstable in stress conditions (m); σ_1^0, σ_3^0 are the maximum and minimum major stresses, respectively (MPa); γ_1, γ_3 are empirical factors; K_I is the coefficient of stress intensity (MPa $\times$ m$^{1/2}$) and K_{Ic} is the fracture toughness of the rock material (MPa$\times$ m$^{1/2}$).

The following dependence is taken as a criterion function:

$$K(r) = K_I / K_{Ic}. \quad (11)$$

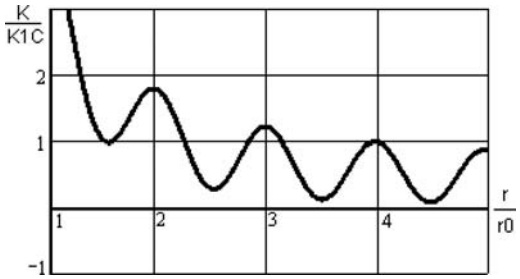


Figure 3. Character of the criterion function.

There is no failure around the opening At $K_I/K_{Ic} < 1$; the fracture starts to appear at $K_I/K_{Ic} \geq 1$. The criterion function, as well as the stress functions and R, has an oscillating character (Fig. 3).

5 PARAMETERS OF THE MODEL

The research on rock mass zonal failure was carried out on an unlined opening. In order to run the calculations, algorithms and programs were developed that included formulas for calculating the damage function $R(r)$, the stresses and the criterion function $K_r(r)$. On the basis of the programs that were developed, the experiment was carried out to analyze three types of parameters.

The first type included the parameters of model γ, c, which are determined from the experiment taking into account the all-around compression at a great depth. The second type includes the parameters that characterize the mechanical properties of the rock mass: E, the modulus of elasticity (MPa); ν, the Poisson ratio; σ_c, the uniaxial compression strength (MPa) and also the value of gravitational stresses in the rock mass, σ_∞ (MPa). The third type includes the parameters in Formula (10), which characterize the cracking structure of the rock mass: the half-length of the rock fracture faults l and the fracture toughness of the rock material K_{Ic} and also the coefficients γ_1, γ_3 (below the dependence γ_3/γ_1 is used).

Parameter γ can be determined using the procedure of statistical analysis of the natural research results of the zonal failure process in deposits in Russia (the Far Eastern part, Siberia, Donbass) and China. A linear character of dependence between the relative distance from the opening contour to the middle point of the first failure zone and the uniaxial strength of the rock was determined:

$$r^*/r_0 = 0.0083\sigma_c + 0.748, \tag{12}$$

where r^* is the distance from the opening contour to the middle point of the first failure zone that had been found from the experimental data (m).

The relationship between parameters γ and r^*/r_0 is also linear but in order to avoid a long description, the determination of its number can be achieved according to Table 1.

According to recent research, a rock mass can be seen as a hierarchical block medium (Guzev & Paroshin 2000, Guzev et al. 2005, Guzev & Makarov 2007, Kadich & Edelen 1983, Makarov 2004, Makarov et al. 2007). When the physical character of failure on the neighboring hierarchical levels is the same, the macrodefect size of the lower level can be determined as a mesodefect of the corresponding higher level (Guzev & Paroshin 2000, Guzev & Makarov 2007). Therefore, this low is reflected in the conservation shear-tensile character of the rock failure on the neighboring levels of the samples and mass in conditions of high stress (Makarov et al. 2007).

Table 1. Meanings of the parameter γ of the model

Middle part of the I-st zone, $r^* = 1 - r/r_0$	$r_0 = 1.75$	$r_0 = 2.0$	$r_0 = 2.5$	$r_0 = 3.0$
0.7	26.486	20.279	12.978	9.012
0.8	20.313	15.552	9.953	6.912
0.9	16.080	12.311	7.879	5.471
1.0	13.050	9.991	6.394	4.440

The algorithm for determining the parameters of the mathematical model consists of the following steps:

1 After the rock sample strength reaches the limit of strength σ_c, the limit of residual strength σ_c^{res}, the Young modulus E and Poisson ratio ν are determined. Then using Formula (12) the emplacement of the first failure zone's middle point r^*/r_0 can be found. The first correction parameter of the mathematical model γ can be determined after the substitution of these data in Table 1.

The maximum diameter r of the rock sample minerals d_{max} and maximum mesocrack disclosure $h^* \approx d_{max}$ are determined and after that the minimum half-length of the tensile mesocrack $l_{mezo} \approx (2.5 - 5) \times d_{max}$, is calculated. The critical half-length of the tensile macrocrack in the sample is determined by the formula

$$l_* = \frac{h_* \times E}{4\left(1-\nu^2\right)\gamma_1 \times \sigma_c} \tag{13}$$

and the stress intensity factor of the rock mass is calculated by the formula

$$K_I^{mass} = \gamma_1 \sigma_c^{rec} \sqrt{\pi l_{meso}^{mass}}. \tag{14}$$

2 Then, the stress intensity factors of both the rock sample and the rock mass are written in the equation of equality and the parameter of the model "C" is determined as the result of the calculation. In order to do this, the equation of equality is applied:

$$\begin{aligned} K_I^{mass} &= \gamma_1 \times \sigma_c^{rec} \times \sqrt{\pi l_{meso}^{mass}} = \\ &= K_1 = (\pi l)^{1/2}\left(\gamma_1 \sigma_{\varphi\varphi} - \gamma_3 \sigma_{rr}\right), \end{aligned} \tag{15}$$

where the "C" parameter is used in the right-hand part of Formula (15) (see (9)).

Table 2. Forecasted depth of the development of zonal failure in the Nikolaevskiy ore mine.

Number of failure zones	I	II	III	IV
Relative critical stress of zone formation	1.3	2.3	2.9	3.3
Depth of the appearance of the zone (m)	520	920	1160	1320

Programs for determining the last destruction zone (for lined and unlined openings: B_1 and B_2, respectively) and programs for calculating the radial length of fracture zones (for lined and unlined openings: C_1 and C_2, respectively) were developed. Program charts with brief descriptions were also developed. The patterns of the changes in the zonal structure of rock mass failure that was dependent on various factors were obtained.

The main parameters of the zone structure were identified: the number of zones of failure, the location of the furthest fracture zone from the opening boundary (the last zone of failure); the creation of the relative critical stresses of failure zones and also the value of the radial length of the failure zones.

6 RESULTS OF THE RESEARCH

As a result of the modeling experiment on the basis of the adopted mathematical model, we determined that the parameters of the zonal structure depend somewhat on the values of the elastic modulus of rocks E and the Poisson ratio ν. This conclusion corresponds to the data obtained during laboratory studies (when the elasticity varied 10 times, the critical stresses of zone creation changed by 2–5% on average). The research on fracture zones was carried out for a solid rock ($\sigma_c = 150$ MPa) and for weak rock ($\sigma_c = 15$ MPa). In order to run the calculations, algorithms and programs were developed that included formulas for calculating the expressions of defectiveness $R(r)$, stress and the criterion function $K(r)$.

The results of the solid rock case study are demonstrated by applying the method that was developed to the problem of zonal failure in the Nikolaevskij ore mine (Dalnegorsk, Russia). The forecasted depth of the development of the cracking zone is shown in Table 2.

The precision of the correlation between the theory and experiment was estimated by comparing the results of in-situ measurement of the radial displacements near the openings at a great depth (Nikolaevskiy ore mine) with the results of the model calculation (Fig. 5). It was determined that the difference between the forecasted and measured data was no more than 50% in the four radius fields around the opening.

The amplitude parameter "C" is dependent on the modulus of deformation and the Poisson ratio of the rock mass (Fig. 4).

A comparison of the results of the analytical and experimental studies of the weak rock also shows their

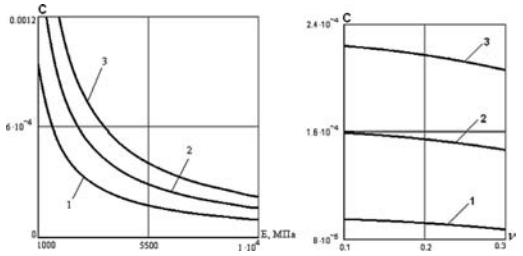


Figure 4. The relationships of the model amplitude parameter with the deformation modulus E and Poisson ratio ν under conditions with different values of rock mass failure strength: $1 - K_{Ic} = 1.5\ \text{MPa} \times \text{m}^{1/2} \times \text{d}$; $2 - K_{Ic} = 2.0\ \text{MPa} \times \text{m}^{1/2} \times \text{d}$; $3 - K_{Ic} = 2.5\ \text{MPa} \times \text{m}^{1/2} \times \text{d}$.

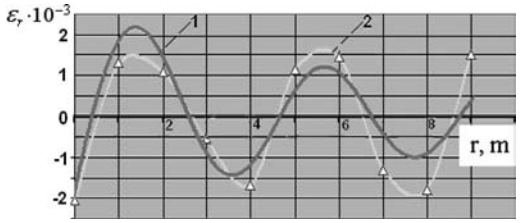


Figure 5. Comparison of the theoretical (1) and experimental (2) data of radial deformations.

Table 3. Comparison of the theoretical and experimental (Neiman et al. 1991) results (unlined opening).

		Elements of the structure of zonal failure			
Parameter	Method	1st zone	2nd zone	3rd zone	4th zone
1. Location of the furthest zone boundary, r/r_0	Experiment	1.03	2.23	3.40	4.54
	Theory	1.28	2.17	3.09	3.97
	Deviation, %	24.3	−2.7	−9.1	−12.6
2. Relative critical zone stresses, σ/σ_c^{res}	Experiment	1.1	2.2	2.7	–
	Theory	0.95	2.1	3.1	–
	Deviation, %	−13.9	−4.5	14.8	–

good convergence (Table 3). The research on the zonal failure of the rock mass was carried out for an unlined opening.

It was determined that the basic factor that influences the parameters of the structure of zonal failure is the value of the stresses that act within the rock mass (opening depth). The number of failure zones increases with an increase in the stresses and their radial length increases until it reaches neighboring zones. The closer the zone is located to the opening boundary, the faster the process. The boundary of the last zone of failure moves further into the rock mass (Fig. 6, left).

The parameters of the fracture structure of the rock mass also influence the character of zone failure. The radial length of the zones of failure decreases if the rock fracture toughness rises (Fig. 6, right). When

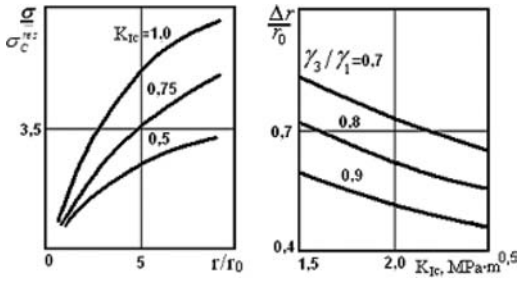


Figure 6. Dependence of the position of the last failure zone on the relative stresses acting within the rock mass (left) and the radial length of the first zone of failure on the rock fracture toughness (right).

the rock fracture toughness decreases, zones of failure appear at lower relative stresses and the distance of the last failure zone from the opening boundary increases.

The activity of rock destruction also has a strong influence on the parameters of the zone failure structure. As the length of the fracture faults increases, the radial length of the failure zones increases. This parameter decreases if the dependence γ_3/γ_1 rises. Regularities determined for the weak rock mentioned above are also true for solid rock.

7 CONCLUSIONS

The research that was conducted shows that as the depth of an opening increases, the zonal character of rock failure becomes more foreseeable, which should be taken into consideration when designing a lining for such conditions.

A method for determining the parameters of a mathematical model of zonal failure structure close to deep openings was developed. A good qualitative and quantitative correlation between the theoretical forecast and experimental research was also achieved.

ACKNOWLEDGEMENTS

The paper was supported by the FPP grant No. 14.A18.21.1980.

REFERENCES

Adams, G.R., Jager, A.J. 1980. Petroscopic observation of rock fracturing ahead of stop faces in deep-level gold mines, *Journal of South African Institute of Mining and Metallurgy* 80(6): 204–209.

Alexeev, A.D., Morozov, A.F., Metlov, L.S. et al. 1996. Synergetic models of zone disintegration phenomena, *Proc. Int. Conf. Effect. and safety of Underground Coal Mining Geomechanics*", S.-Pb., LISTEN, pp. 81–84.

Guzev, M.A. & Paroshin, A.A. 2000. Non-Euclid model of zone disintegration of rocks around the underground openings, *PMTF*, No. 3, pp. 181–195.

Guzev, M.A. & Makarov, V.V. 2007. Deformation and failure of high stressed rocks around the openings. Vladivostok: Dalnauka, 232 p.

Guzev, M.A., Makarov, V.V. & Ushakov, A.A. 2005. Modeling elastic behavior of compressed rock samples in the prefailure zone, *Journal of Mining Science* 41(6): 497–509.

Kadich, À., Edelen, D. 1983. *A Gauge Theory of Dislocations and Disclinations*. Berlin, Heidelberg, New York: Springer Verlag, 295 p.

Makarov, P.V. 2004. About the hierarchical nature of deformation and destruction of firm bodies. *Phys. Mesomech*. 7(4): 25–34.

Makarov, V.V., Ksendzenko, L.S. & Sapelkina, V.M. 2007. Periodical character of failure near the openings in high depth conditions. In *The Role of Geomechanics in the Stability of Development of Mining Industry and Civil Engineering, Proc. Int. Geomechanics Conf*., 11–15 June 2007, Nessebar, Bulgaria, II, pp. 107–115.

Neiman, L.K., Reva, V.N., Shmigol, A.V. & Kirichenko, V. Ya. 1991. Opening support on BC "Pavlogradcoal" mines, *CNIEIcoal, Review*, Moscow, 80 p.

Odintsev, V.N. 1996. *Rupture Destruction of a Brittle Rocks Mass.* Moscow: IPKON, The Russian Academy of Sciences, 166 p.

Oparin, V.N. & Tanayno, A.S. 2009. Representation of the sizes of natural separateness of rocks in an initial scale. Classification. *FTPRPI*, No. 6, pp. 40–53.

Panin, V.E. 1990. The wave nature of plastic deformation of firm bodies, *News of High Schools. Physics* 33(2): 4–18.

Panin, V.E, Egorushkin, V.E. & Panin A.V. 2006. Physical of the mesomechanics of a deformable firm body as multilevel system I. Physical bases of the multilevel approach, *Physical Mesomechanics* 9(6): 9–22.

Panin, V.E, Grinyaev, J.V. et al. 1990. *Structural Levels of Plastic Deformation and Destruction*, Science, Novosibirsk, 255 p.

Reva, V.N. & Tropp, E.A. 1995. Elastic-plastic model of zone disintegration of a vicinity of underground development, *Physicist and the Mechanic of Failure*, Sb. Proc. VNIMI, pp. 125–130.

Sadovsky, M.A. 1979 Natural lumpiness of rock, DAN USSR 247(4): 829–831.

Shemyakin, E.I., Fisenko, G.L., Kurlenya, M.V., Oparin, V.N. et al. 1986. Zone disintegration of rocks around underground developments. Part 1: The data of natural supervision, *Physicotechnical Problems of Working out of Mineral Deposits*, No. 3, pp. 3–15.

Shemyakin E. I., Fisenko G. L., Kurlenya M. V., Oparin V. N., et al. (1987). Zone disintegration of rocks around underground developments. Part 3: Theoretical representations, *Physicotechnical Problems of Working out of Mineral Deposits*, No. 1, pp. 3–8.

Xu N.-X. 2009, "Identifying rock blocks based on hierarchical rock-mass structure model", *Science in China Series D: Earth Sciences*, October 2009, Vol. 52, 10, pp. 1612–1623.

This page intentionally left blank

Rock Mechanics for Resources, Energy and Environment – Kwaśniewski & Łydżba (eds)
© 2013 Taylor & Francis Group, London, ISBN 978-1-138-00080-3

Three-dimensional modeling of a coupled shear-flow test on soft sedimentary rock

H. Park, K. Ito & M. Takahashi
National Institute of Advanced Industrial Science and Technology (AIST), Tsukuba, Japan

M. Osada
Saitama University, Saitama, Japan

G. Smolnik
Silesian University of Technology, Gliwice, Poland

ABSTRACT: It is fundamental to understand the process of crack initiation and propagation of intact rock to clarify the coupled hydro-mechanical properties due to the stress change in underground. We have been working on the study of coupled shear-flow properties on sedimentary rock using pumice tuff, Japan. The changes of shear stress, normal stress, flow rate and process of fracturing on sample surface have been investigated by using a new type coupled shear-flow test apparatus. In this study, we designed a numerical model for the coupled shear-flow test using a discrete element code. We report the comparison between the experimental results and the simulation results. The porosity changes of model showed good agreement with the flow rate behavior of the test.

1 INTRODUCTION

New fractures due to underground excavation or fault cause mechanical and hydrological problems in underground (Tsang et al., 2005, Mitchell and Faulkner, 2009). The fractures are generated through a variety of mechanisms with various scales (Bossart et al., 2002, Scholz et al., 1993). For the research of underground disposal or geological evaluation, it is necessary to investigate the coupled hydro-mechanical behavior of rock (Olsson and Barton, 2001, Li et al., 2008). We conducted an experimental study on coupled shear-flow properties of sedimentary rock, and designed a numerical model for the coupled shear-flow test using a three-dimensional simulation tool, *PFC3D* (Particle Flow Code^{3D}, Itasca Inc.). The purpose of this study is to examine the performance characteristics of the numerical model. The test system and model are briefly introduced, and the results are compared focusing on stress, permeability and crack propagation.

2 PARTICLE FLOW CODE^{3D}

PFC3D is classified as a *discrete element* code (Cundall and Strack, 1979, Potyondy and Cundall, 2004) based on the definition in the review by (Cundall and Hart, 1992). It allows finite displacements and rotations of discrete bodies (including complete detachment), and recognizes new contacts automatically as the calculation progresses. *PFC3D* can be considered as a simplified implementation of the DEM because of the restriction to rigid spherical particles.

The calculation cycle in *PFC3D* is a time-stepping algorithm that requires the repeated application of the law of motion to each particle, a force-displacement law to each contact, and a constant updating of wall positions. The calculation cycle is illustrated in Figure 1. At the start of each time-step, the set of contacts is updated from the known particle and wall positions. The force-displacement law is then applied to each contact to update the contact forces based on the relative motion between the two entities at the contact and the contact constitutive model. Next, the law of motion is applied to each particle to update its velocity and position based on the resultant force and moment arising from the contact forces and body force acting on the particle. Also, the wall positions are updated based on the specified wall velocities.

PFC3D provides a particle flow model containing the following assumptions: 1) The particles are treated as rigid bodies. 2) The contacts occur over a vanishingly small area (i.e., at a point). 3) Behavior at the contacts uses a soft-contact approach where the rigid particles are allowed to overlap one another at contact points. 4) The magnitude of the overlap is related to the contact force via the force displacement law,

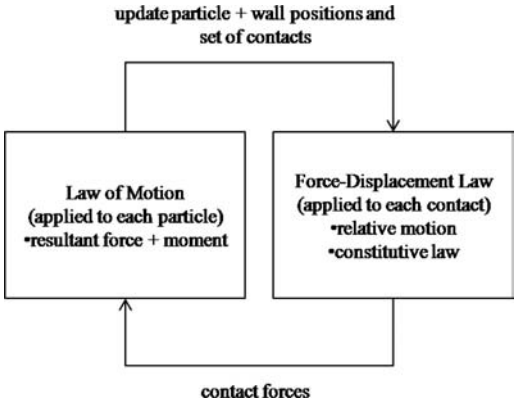


Figure 1. Calculation cycle in *PFC3D* (Itasca Consulting Group 2008).

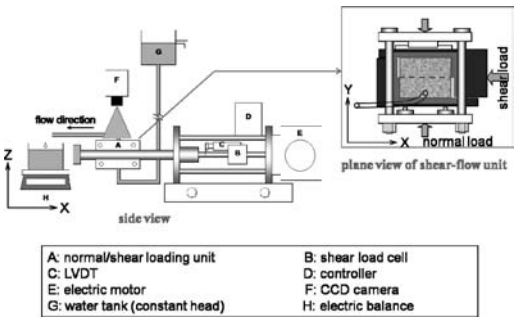


Figure 2. Schematic of coupled shear-flow-visualization test system in Saitama University, Japan.

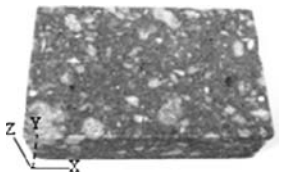


Figure 3. Pumice tuff sample from Japan (size: 60 mm × 40 mm × 20 mm).

and all overlaps are small in relation to particle sizes. 5) Bonds can exist at contacts between particles. 6) All particles are spherical. However, the clump logic (Itasca Consulting Group 2008) supports the creation of super-particles of arbitrary shape. Each clump consists of a set of overlapping particles that acts as a rigid body with a deformable boundary.

3 COUPLED SHEAR-FLOW TEST

Here, we introduce one of coupled shear-flow tests, named coupled shear-flow-visualization test. Schematic of the test system in Saitama University, Japan is presented in Figure 2. This apparatus consists of normal/shear loading unit (Fig. 2A), flow testing unit (Fig. 2A,G,H) and digital image mcapturing

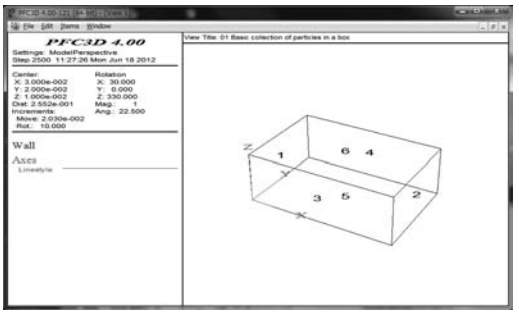


Figure 4. Design of model in *PFC3D*.

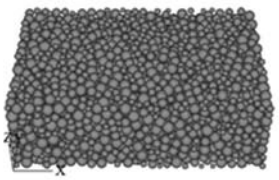


Figure 5. Particle model for coupled shear-flow test (size: 60 mm × 40 mm × 20 mm).

unit (Fig. 2A,F). Soft sedimentary rock (pumice tuff) from Japan was used for the test. Considering the size of loading unit, sample was prepared about 60 mm × 40 mm × 20 mm in size (Fig. 3). Primary normal stress which was acting in Y-direction was 0 MPa. The expansion of sample in Y-direction was restricted due to the normal loading plates which were bounded by four beams. Shear loading rate selected in the test was 0.05 mm/min. For the flow test, the constant head method was applied, and the hydraulic gradient was about 40 cm/cm. Digital images were recorded every second during shear deformation. The shear loading was continued until the shear stress reached about 50% of the peak in the post-peak regime.

4 THREE-DIMENSIONAL MODELING OF A COUPLED SHEAR-FLOW TEST

4.1 *Design of model for coupled shear-flow test*

First, the boundaries of model (i.e., the walls that contain the particles) were defined. They create a box defined by six walls. Each wall was given a unique identification number. The location of each wall is presented in Figure 4. Next, the box was filled with particles. We decided the size of model as the same with rock sample (Fig. 5). The particle size distribution and the total number of particles were 1∼2 mm in diameter and 4581, respectively. Note that the particle size distribution was selected arbitrarily.

The process of shear deformation in model is illustrated in Figure 6. Before the beginning of the deformation, half-sized walls of the Wall No. 1 and 2 (Fig. 4) were created, and the Wall No. 1 and 2 were deleted simultaneously. The half-sized wall of the Wall No. 2 was moved for shear deformation. Finally, the movement was stopped at 3.5 mm of displacement.

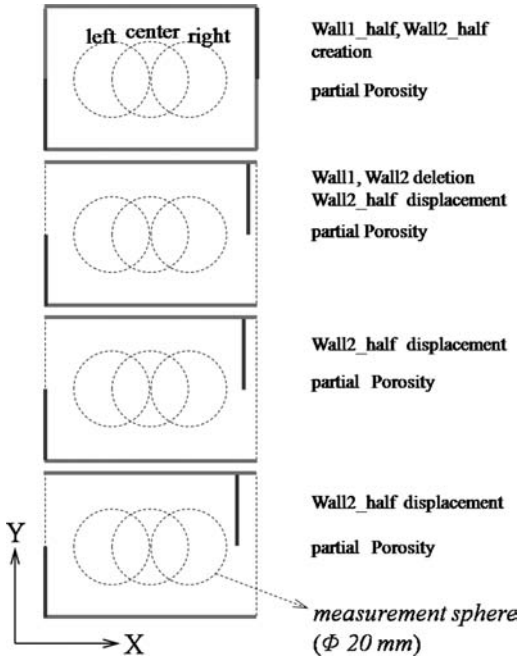


Figure 6. Shearing process and porosity measurement positions in model.

The coefficient of friction between walls and particles was set to zero.

4.2 *Change of porosity*

The permeability, unfortunately, cannot be obtained directly with this kind of deforming objects. Thus, we decided to calculate the porosity by using a *measurement sphere* as shown in Figure 6. Three positions of measurement spheres were selected along the center line of model. In this case, only these volumes are defined for the porosity calculation. The diameter of measurement spheres was 20 mm.

It will not be sufficient to simply apply the proportional relationship between porosity and permeability in rock. However, there are reports (Zhu & Wong 1997, David et al. 1994) of the proportional relationship in the case of sedimentary rocks which have high porosities. For example, David et al. (1994) reported the proportional relationship from the flow tests of four types of sandstone which have the range of porosity from 14% to 35%. In our study, the rock sample has more than 50% of porosity. We thus carried out the numerical simulation assuming the proportional relationship between porosity and permeability.

5 COMPARISON BETWEEN EXPERIMENTAL AND NUMERICAL RESULTS

5.1 *Coupled shear-flow behavior*

The changes of stress and flow rate during shear dis placement on intact sample are presented in Figure 7.

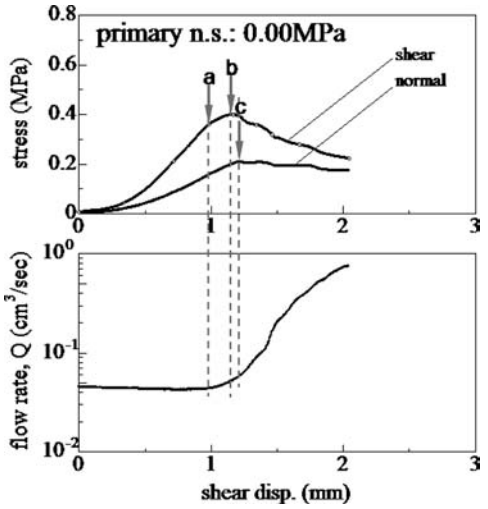


Figure 7. Coupled shear-flow behavior of rock sample.

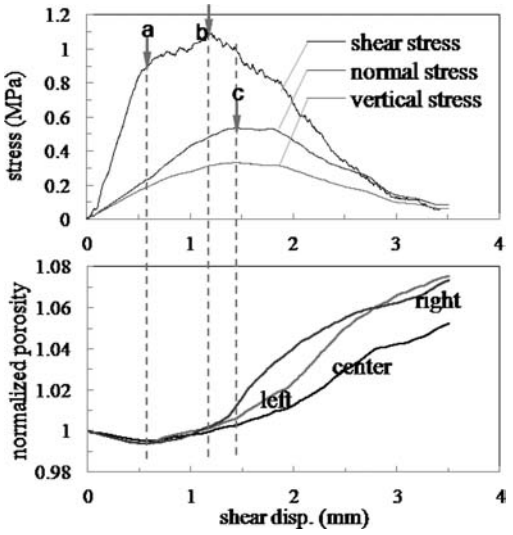


Figure 8. Coupled stress-porosity behavior of model.

Both shear stress and normal stress gradually increase with shear displacement. However, the normal stress reaches its peak later than the shear stress. The flow rate shows a slight decrease up to around the point a, and then turns to increase. The increment of flow rate continues even after the peak of shear stress, whereas the gradient of it decreases gradually as the stress becomes close to the residual strength. The dashed lines in the figure indicate; a: yield point of shear stress (0.99 mm, 90.4% of the peak), b: peak point of shear stress (1.17 mm, 0.40 MPa), c: peak point of normal stress (1.22 mm, 0.21 MPa).

Figure 8 shows the changes of stress and porosity in model. The term 'vertical stress' in the figure indicates the stress acting in Z-direction (Fig. 5), and 'normalized porosity' was obtained by dividing the initial

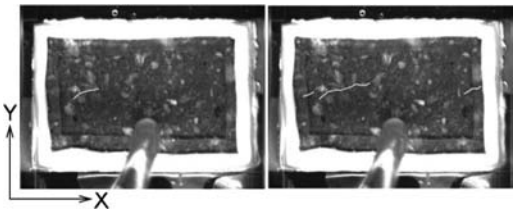


Figure 9. Crack initiation and propagation on sample surface during the coupled shear-flow-visualization test. (Left and right images correspond to the points a and b in Figure 7).

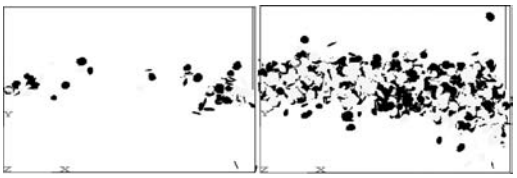


Figure 10. Shear and normal failures of contact-bond in model (Projection view. Left and right images correspond to the points a and b in Figure 8).

porosity by current porosity during shear displacement. At the early stage of shear displacement, linear increments of stresses are confirmed. It is because the model had no significant effects such as an attachment between sample and apparatus, or pre-existing micro cracks in rock sample. The peak of normal stress (point c, 1.45 mm) appears later than the peak of shear stress (point b, 1.21 mm). The normalized porosities have the minimum around the yield point of shear stress (point a, 0.52 mm), and they change almost the same up to the point b. However, the porosity of measurement sphere in right side shows the highest porosity after the point b, and then become almost the same as left side. Finally, the gradients of them decrease at the end of shear displacement.

5.2 *Crack initiation and propagation*

As shown in Figure 9, the crack initiation and propagation on sample surface were confirmed from the coupled shear-flow-visualization test. Left and right images in the figure correspond to the points a and b in Figure 7. According to the digital images of test, the visible cracks on sample surface started to appear around the point a (i.e., the yielding point of shear stress). With shear displacement, the crack propagation was continued during the point b and c. Note that the crack propagation on sample surface was not completed even after the point c. It was also identified that the fracture aperture (or area) was widened gradually with few creations of extra cracks at the end of shear displacement.

Figure 10 shows the contact-bond failures in model. Left and right images in the figure correspond to the points a and b in Figure 8. Shear and normal failures are classified in black and yellow (gray) colors respectively. Note that the images are projections of model in Z-direction. Thus, it is hard to identify the shape of fracture plane. However, according to the observation of crack distribution in 3D, it showed quite thick zone of cracks in the middle of model. Especially, right side of the model had more cracks. Further work is required to investigate the fracture geometry and connectivity in the model.

6 CONCLUSIONS

A coupled shear-flow-visualization test and its three-dimensional modeling were carried out to understand the process of crack initiation and propagation in soft sedimentary rock. The flow rate in the test decreased up to around the yield point of shear stress, and then it turned to increase. The increment of flow rate continued even after the peak of shear stress, whereas the gradient of it decreased gradually as the stress became close to the residual strength. Crack propagation on sample surface was not completed at the peak point of shear stress.

In the numerical simulation using *PFC3D* for the coupled shear-flow-visualization test, the porosity instead of measuring the permeability was calculated by using a measurement sphere. The changes of stress and porosity during shear displacement in model showed good agreement with the stress and flow rate behavior of the test. These reveal that this numerical modeling is available to investigate the coupled shear-flow properties of high porosity rocks. We expect this modeling technique can be used for the evaluation of rock mass permeability or the prediction of fault zone permeability.

ACKNOWLEDGEMENTS

This research project has been conducted as the regulatory supporting research funded by the Secretariat of Nuclear Regulation Authority (Secretariat of NRA), Japan.

REFERENCES

Bossart, P., Meier, P.M., Moeri, A., Trick, T. & Mayor, J.C. 2002. Geological and hydraulic characterisation of the excavation disturbed zone in the Opalinus Clay of the Mont Terri Rock Laboratory. *Engineering Geology* 66: 19–38.

Cundall, P.A. & Hart, R.D. 1992. Numerical modelling of discontinua. *Engineering Computations* 9: 101–113.

Cundall, P.A. & Strack, O.D.L. 1979. A discrete numerical model for granular assemblies. *Geotechnique* 29: 47–65.

David, C., Wong, T.F., Zhu, W.L. & Zhang, J.X. 1994. Laboratory Measurement of Compaction-Induced Permeability Change in Porous Rocks – Implications for the Generation and Maintenance of Pore Pressure Excess in the Crust. *Pure and Applied Geophysics* 143: 425–456.

Itasca Consulting Group 2008. *PFC3D (Particle Flow Code in 3 Dimensions) Version 4.0,* Minnesota, USA, Itasca Consulting Group, Inc.

Li, B., Jiang, Y.J., Koyama, T., Jing, L.R. & Tanabashi, Y. 2008. Experimental study of the hydro-mechanical behavior of rock joints using a parallel-plate model containing contact areas and artificial fractures. *International Journal of Rock Mechanics and Mining Sciences* 45: 362–375.

Mitchell, T.M. & Faulkner, D.R. 2009. The nature and origin of off-fault damage surrounding strike-slip fault zones with a wide range of displacements: A field study from the Atacama fault system, northern Chile. *Journal of Structural Geology* 31: 802–816.

Olsson, R. & Barton, N. 2001. An improved model for hydromechanical coupling during shearing of rock joints. *International Journal of Rock Mechanics and Mining Sciences* 38: 317–329.

Potyondy, D.O. & Cundall, P.A. 2004. A bonded-particle model for rock. *International Journal of Rock Mechanics and Mining Sciences* 41: 1329–1364.

Scholz, C.H., Dawers, N.H., Yu, J.Z. & Anders, M.H. 1993. Fault Growth and Fault Scaling Laws – Preliminary-Results. *Journal of Geophysical Research-Solid Earth* 98: 21951–21961.

Tsang, C.F., Bernier, F. & Davies, C. 2005. Geohydromechanical processes in the Excavation Damaged Zone in crystalline rock, rock salt, and indurated and plastic clays – in the context of radioactive waste disposal. *International Journal of Rock Mechanics and Mining Sciences* 42: 109–125.

Zhu, W.L. & Wong, T.F. 1997. The transition from brittle faulting to cataclastic flow: Permeability evolution. *Journal of Geophysical Research-Solid Earth* 102: 3027–3041.

This page intentionally left blank

Rock Mechanics for Resources, Energy and Environment – Kwaśniewski & Łydżba (eds)
© 2013 Taylor & Francis Group, London, ISBN 978-1-138-00080-3

Study of thermo-hydro-mechanical processes at the potential site of an Indian nuclear waste repository

A.K. Verma
Department of Mining Engineering, Indian School of Mines-Dhanbad, Jharkhand, India

T.N. Singh
Department of Earth Sciences, Indian Institute of Technology-Mumbai, Mumbai, India

R.K. Bajpai
Repository Programme Section, Bhabha Atomic Research Centre, Mumbai, India

ABSTRACT: Due to increasing gap between energy demand and supply, India is planning to build significant number of nuclear reactors which will produce significant amount of High-level radioactive waste. It can generate considerable amounts of heat as a side effect of radioactive decay of nuclear wastes which will be disposed around 400 m–1000 m below ground inside the underground nuclear repository. The rock chosen is granite and barrier near the canister is proposed to be clay. In this paper, thermo hydro mechanical (THM) analysis has been done to study the effect of heat on deformations, stresses and pore pressure variation in granite and clay barrier. For this purpose, finite difference method has been used. It has been found that both temperature and stresses at any point in the rock mass is below the design criteria which are 100°C for temperature.

1 INTRODUCTION

Nuclear energy has been a source of unlimited cheap power and is based on non-renewable energy sources. Nuclear power produces high level and low level radioactive wastes with long half life time periods. The major problem is due to the generation of long lived high level nuclear wastes (HLW) and it's safe disposal. Although the level of radioactivity of these wastes decay over time, it remains dangerously high that it must be isolated from the outer biosphere, until it has decayed to levels that pose less risk.

It is necessary to study the several processes at excavation stage in an underground repository laboratory (URL) and supplemented by surface based and traditional laboratory tests. A typical cross section of one such disposal tunnel with a disposal pit is shown in Fig. 1.

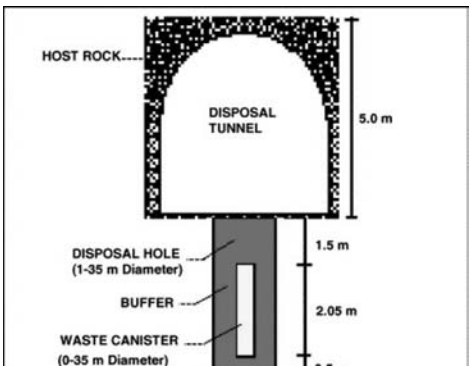


Figure 1. Cross section of a disposal tunnel with the vertical emplacement of waste overpacks in the disposal hole (AECL, 1994).

2 REGIONAL GEOLOGY AND STRUCTURE

Site near Bhima basin is found to be suitable for URL site (Fig. 2). Bhima basin is the smallest and youngest amongst the Proterozoic basins of Peninsular India. The basin receives it name after "Bhima River" a major tributary to the river Krishna. The Basin is exposed between lat. 16°20′00″N–17°35′00″N: long. 76°15′00″E–77°44′00″E on the north western fringe of eastern of Dharwar Craton. The basin has a reverse sigmoidal array of outcrops between Tandur in the northeast and Muddebihal in the Southwest, for over a stretch of 160 km with a maximum width of 40 km across Sedam. The exposed area of the basin is about 5200 sq. km. Northern and northwestern extensions are concealed under Deccan traps.

The structure comprises of a major thrust plane striking NE-SW with granitic rocks riding over limestone.

3 FIELD INVESTIGATION

The rock samples were collected from the above study area during various site visits to understand their physico mechanical, thermal and hydraulic behaviour

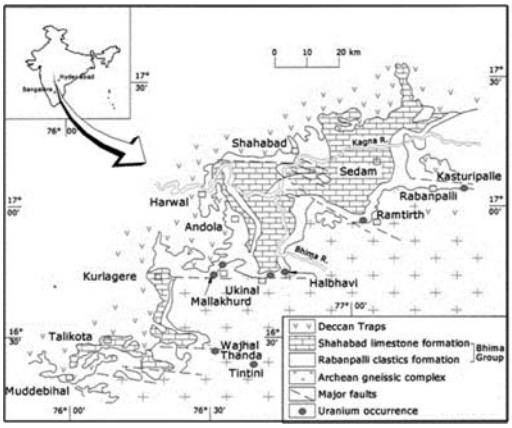


Figure 2. Geological map of the area around Bhima basin.

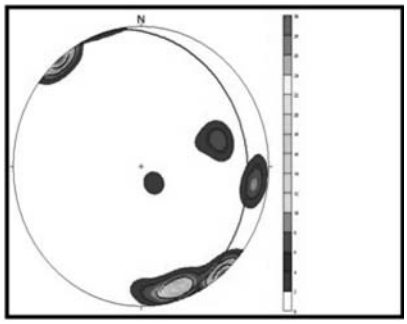


Figure 3. Equal area plot of fractures measured in outcrops.

in different states of stress. The samples were obtained from six boreholes at depth ranging from 68.0 m to 150 m.

A total of 323 fractures have been recorded in 140 m long core samples obtained from borehole number six. The average fracture frequency of the borehole is thus <3 fracture/m. The location of this borehole away from the trace of the cross faults has resulted in absence of well-defined crush/cataclastic zones. Rose diagram in Fig. 3 shows very prominent maxima of fractures striking N550E coinciding with the trace of master basement cover meta-sediment fault. The other prominent set strikes N3300W coinciding with trace of cross faults. Besides, a few random orientations are also noticed. These include N-S and E-W fractures.

4 LABORATORY INVESTIGATION

The rock samples were collected from the above study area during various site visits to understand their physico mechanical, thermal and hydraulic behaviour in different states of stress. The samples were obtained from six boreholes at depth ranging from 68.0 m to 150 m.



Figure 4. Fracture developed after UCS Test.



Figure 5. Plan view of fracture developed after triaxial loading.

Table 1. Type of rocks.

Layers	Rock types
Host Rock	Granite
Engineered Barrier (Buffer)	Clay barrier
Waste Canister	High Level Radioactive waste

5 NUMERICAL MODELING

5.1 *Model mesh*

To investigate the effect of heat flux around the single pit mode disposal with one OP (overpack), thermo-hydro-mechanical (THM) coupling analysis have been carried out using a three-dimensional dimensional FDM code, FLAC^{3D}. Mesh of the model has been generated for this case as shown in Fig. 6. Rock types for different layers is shown in table 1 and five layers of engineered barrier (EB) each with depth of 4.05 m has been modeled with dimensions shown in Table 2. Dimensions of the tunnel, barrier, spent fuel and overburden are shown in Fig. 6.

Only 10 m overburden of granitic rock has been modeled and vertical stress of 9.6 MPa has been applied on the top surface of the model to take into account of remaining 400 m overburden (which has not been modeled explicitly) as shown in Fig. 6. The properties of the spent fuel were determined with the

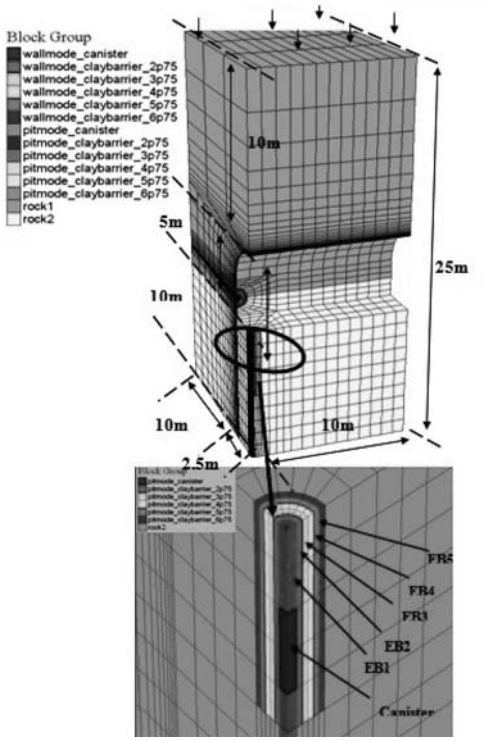


Figure 6. Model mesh for single pit mode disposal with one OP.

Table 2. Dimensions of different EB's.

Engineered Barrier	Diameter of EB (m)
EB1	0.55
EB2	0.75
EB3	0.95
EB4	1.15
EB5	1.35

assumption that the fuel and canister were uniformly mixed. Buffer and surrounding granitic properties were derived from the laboratory tests. The width, length, and height of the initial model mesh were 12.5 m, 12.5 m, and 400 m, respectively. Total numbers of zones in the model meshes were 11750.

5.2 *Heat decay*

Heat from the waste canister decays exponentially. The wastes generated from the Indian nuclear power plant follows following equations:

$$P(t)=P(t_0)e^{(3.18*e\text{-}8*deconst*t)}$$

where, deconst is −7.32496e−10 and t is the elapsed time (years) after placing the spent fuel into the pit. $P(t_0)$ is initial heat flux as a volume source of heat.

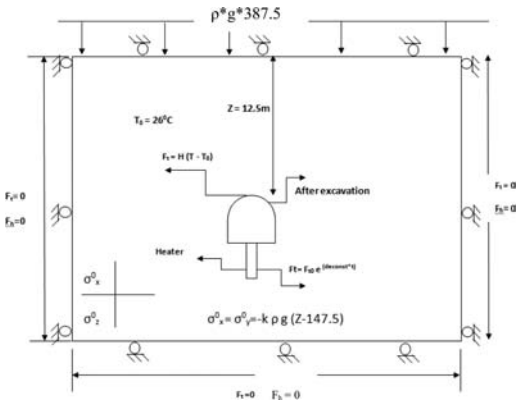


Figure 7. Boundary and Initial condition of the model.
where,
F_t = Thermal flux
F_h = Hydraulic flux
T = Temperature
P = Hydraulic pressure
t = Time
k = Coefficient of earth pressure
Z = Z-coordinate
σ_x^0, σ_z^0 – normal stresses
H, $F(t_0)$, deconst – Constant.

Table 3. Physico-mechanical properties of granitic rock samples.

Properties	Unit	Rock (Granite)	Buffer (Compacted Clay)	Canister
Shear modulus	GPa	20.10	0.243	75.15
Bulk modulus	GPa	33.05	0.321	161.3
Density	kg/m^3	2600	2050	5900
UCS	MPa	100.00	7.66	–
Tensile strength	MPa	10.5		–
Friction angle		58	48	–
Cohesion	MPa	60	1.5	–
In situ stress ratio K	–	1.5	0	–
GSI	–	70	–	–

5.3 *Intial and boundary conditions*

There are three types of boundary conditions which have been applied to the model: 1) Mechanical, 2) Flow and 3) Thermal. Roller boundary conditions have been applied to the left and right boundary, are free in X, Y and Z directions. No flow boundary conditions were applied on all the four sides of the model. Similarly, adiabatic boundary conditions were used for all sides of the model. The initial and boundary conditions for the mechanical, thermal and hydraulic effects are shown in Fig. 7.

Table 4. Thermal properties of granite and buffer

Material type	Unit	Rock (Granite)	Buffer Compacted ((lay)	Caniter
Thermal Conductivity	W/m °K	2.30	1.65	4S
Specific heat	J/kg %	1510	875	415
Thermal expansion	1/°K	2.10e-5	3.5e-4	l.5e-5

Table 5. Hydraulic properties of granite and buffer.

Material type	Unit	Rock	Buffer
Porosity	–	0.05	0.3
Permeability	m^2	4.26e-16	2.0e-19
Fluid Tensile Strength	Pa	−1.5e9	
Fluid Density	Kg/m^3	1.5e2	

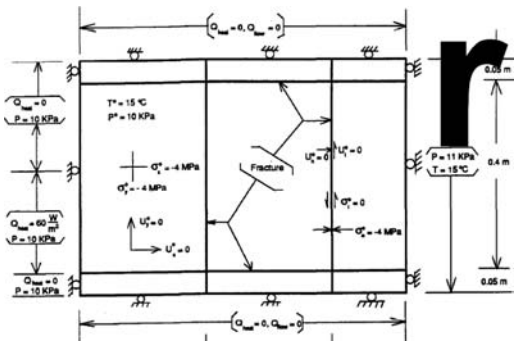


Figure 8. Geometry and boundary conditions for the multiple fracture model, bench mark test 2 (BMT2), DECOVALEX Phase I.

5.4 *Mechanical, hydraulic and thermal properties*

Table 3, Table 4 and Table 5 lists the results of physico-mechanical laboratory tests of granite and buffer samples, thermal and hydraulic properties of granite and buffer material respectively.

6 VALIDATION

The suitability and capability of FLAC^{3D} for it's application to Thermo-Hydro-Mechanical analysis has been verified and a comparison has been made with a published literature (Verma et al., 2010, Chan et al. 1995). Geometry and boundary conditions ken from the t has been shown in Figure 8.

The boundary conditions used in the FLAC^{3D} simulation is same as used in the bench mark test 2 (BMT2), DECOVALEX Phase I. A heat flux of 50 W/m^2 has been applied at the left end of the model in the region

Table 6. Physico-mechanical and thermal properties of rock.

Parameter	Value	Unit
Young's Modulus (E)	50	GPa
Poisson's ratio (ν)	0.25	–
Density (ρ_s)	2600	Kg/m^3
Uniaxial Strength (σ_c)	190	MPa
Tensile Strength (σ_t)	–	–
Thermal Conductivity (λ)	3.34	W/(m·°C)
Thermal expansion coefficient (α)	10^{-5}	C^{-1}
Solid heat capacity (c_s)	900	J/(Kg·°C)

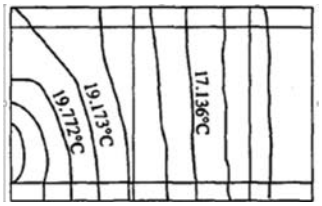


Figure 9. Temperature distribu-tion from bench mark test 2 (BMT2), DECOVALEX Phase I.

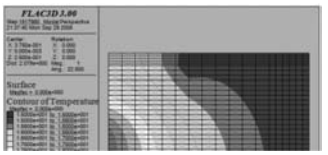


Figure 10. Temperature distributions from FLAC^{3D}.

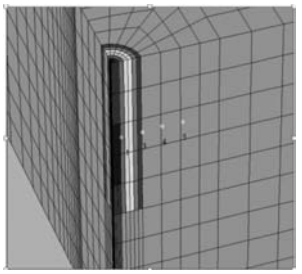


Figure 11. Location of monitoring points.

shown as in Fig. 8. Joints in the model have been simulated using interface element with given stiffness from the test case. From Figure 9 and Figure 10, it can be concluded that the temperature distribution between the two models are in good agreement.

7 RESULTS AND DISCUSSIONS

Point 1 is located at interface of the canister and barrier; points 3 is located at the interface of barrier and granite, points 4 and 5 are located in the granite (Fig. 11). Parameters like temperature, displacement, stresses

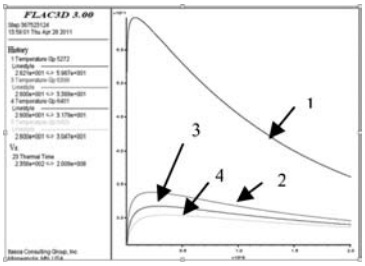


Figure 12. Temperature varia-tions with time at points 1, 3, 4 and 5.

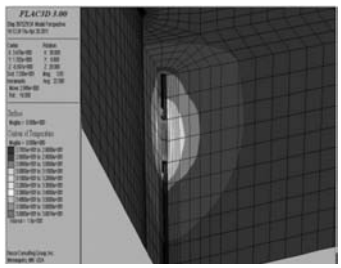


Figure 13. Temperature distributions at the Canister – Barrier interface after 6 years.

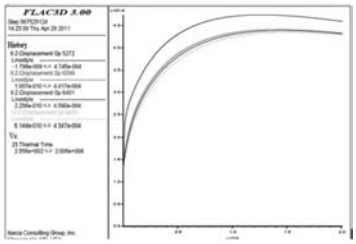


Figure 14. Vertical displacement variations with time at points 1, 3, 4 and 5.

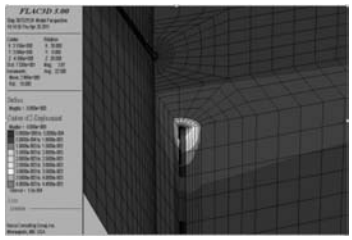


Figure 15. Convergence of the roof and heaving of the floor after 6 years.

etc. have been monitored with respect to time. Temperature at the canister and clay barrier has reached a maximum of 59°C after 60 days and then decreases exponentially to 36°C after 6 years. Figure 12 indicates that temperature at any point will never increase the designed maximum temperature of 100°C as the temperature of other monitoring points will always be less than the maximum of 59.8°C. For example, temperature at point 3 at the barrier and granite interface has reached maximum of 34°C and then decreases after 120 days. Similar are the cases with points 4 and 5. Evolution of temperature contour is shown in Figure 13, after 6 years and time at which temperature has reached it's maximum value respectively. Temperatures all along the clay barrier were 33°C–35°C after 6 years while it is 35°C–36°C at the canister and clay interface (Fig. 13). The area swept by heat front after 6 years is more than the area of heat front at the peak temperature but the magnitude of the temperature is less. This means that temperature at intersection of the floor and side wall will increase by maximum of 2–4°C.

The evolutions of the vertical displacement of the ground (uplift) and the vertical displacements of the repository structure and of the limits of the clay barrier is shown in Fig. 14. As shown in Fig. 14, vertical displacement is 0.46 mm for point, 1 which is at the interface of canister and clay barrier. The vertical displacement is increasing exponentially and reached peak of 0.46 mm after 2 years. Other monitoring points in granite follow the same trend. For example, point 3 reached peak vertical displacement of 0.44 mm.

After 6 years, crown of the tunnel has converged to 0.5 mm downward while top of the clay barrier has undergone heaving effect and has a vertical upward displacement of 0.5–1.0 mm (Fig. 15). The heaving effect was due to the heat released by the canister which has expanded the clay at the top of the clay barrier. Floor of the tunnel has undergone heaving from 0.5 mm to 4.0 mm in the upward direction. At the peak temperature of 59.8°C, top of the barrier had undergone heaving effect of 5.0 mm while bottom of the barrier had moved to 3.04 mm in negative downward direction. This is due to the expansion of clay with heating (Fig. 15).

Vertical stresses were monitored at the zones associated with the grid points 1, 3, 4 and 5. During initial few days, the vertical stresses increases suddenly to 22 MPa at the canister and clay barrier interface and reached a maximum compressive stress of 26 MPa after 60 days. The vertical compressive stress decreases after 60 days and reaches to 10 MPa after 6 years (Fig. 16). Similarly, point 3 has reached a maximum of 6 MPa and then decreases to 3.0 MPa after 6 years of heat decay from spent fuel.

Some part of the crown, floor of the tunnel and canister-clay interface experiences maximum tensile stresses of 1.17 MPa. Since rocks are weak in tension, there is greater chance of failure at these surfaces as compared to compressive stresses at the rest of the tunnel (Fig. 17). At the peak temperature, tensile stresses reached to maximum of 11 MPa which is near the tensile strength compressive strength of the granitic rock used in the URL. Hence, even at the peak temperature of 59.8°C, there is a chance of local tensile failure (Fig. 17).

Fig. 18 shows the variation of pore pressure after 6 years of heat decay. Due to heating the pore pressure front at top of canister has moved in upward direction

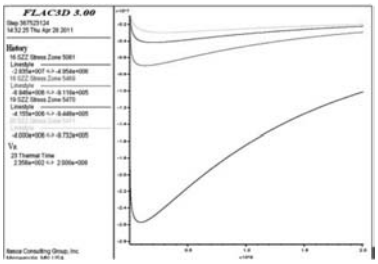


Figure 16. Vertical stresses variation with time at points 1, 3, 4 and 5.

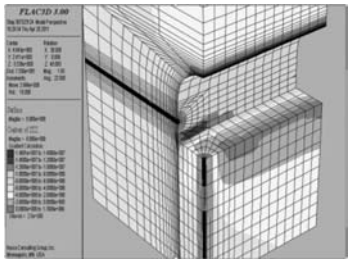


Figure 17. Vertical stress distribution of the single pit mode re-pository after 6 years.

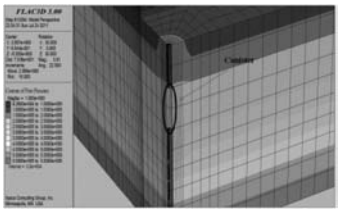


Figure 18. Pore pressure distribution after 6 years.

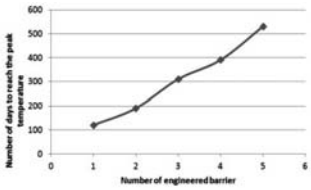


Figure 19. Variation of thickness of engineered barrier with time to reach the maximum temperature.

while the front has moved downward for the bottom of canister. 0.2–0.3 MPa of pore pressure has developed in the vicinity of the canister. Maximum pore pressure of 0.55 MPa has developed at the base of the model.

7.1 *Effect of thickness of engineered barrier*

Size of the engineered barrier has been varied from diameter of 0.55 mm to 1.35 mm (Table 2 and Fig. 6). maximum temperature were recorded at monitoring point 3 for the five cases and time taken to reach the maximum temperature were recorded as shown in fig. 8. As the thickness of the engineered barrier increases, time taken for temperature to reach the maximum value also increases (Fig. 19). This is due to increasing thickness of the engineered barrier which decreases the heat transfer capacity of the barrier (because of increase of equivalent heat capacity).

8 CONCLUSIONS

The coupled THM behavior of the porous media has been widely analyzed in this study using finite difference tool. The analysis was directed to the interaction among spent fuel canister, clay barrier and the host rock in the near field. The excavation phases were carried out in order to obtain a suitable stress state, deformations and temperature values in the near field. Once this is established, the numerical simulation covers the emplacement of canister containing spent fuel, clay barrier buffer emplacement, heating phase and cooling phase. The high heat capacity of clay barrier helps to retain heat upto it's full capacity.

Clay near to canister experienced maximum temperature of 60°C in 60 days. The simulation showed that with the granite, clay barrier and canister properties, the temperature in the repository will never increase above 60°C. At the peak temperature of 59.8°C, top of the clay barrier had undergone heaving effect with maximum vertical upward displacement of 5.0 mm after 6 years of the disposal of the vitrified waste. Clearly, most of the uplift has been attributed to the clay barrier. Hence, deformation in any part of repository will never increase 25 mm. Both the results conclude that the model satisfies the design criteria of repository. As the thickness of engineered barrier increases number of days taken to reach the maximum temperature for a particular point in the rockmass also increases. The reason being as the thickness of the buffer material increases, heat front will have to spend more time in the buffer zone as thermal conductivity of bentonite is lesser as compared to rock.

REFERENCES

AECL (1994), Environmental Impact Assessment on the Concept for Disposal of Canada's Nuclear Fuel, AECL Document, AECL-10711, COG-93-1, Atomic Energy of Canada Ltd., Whiteshell, Canada.

Chan, T., Schair, K., Jing, L., Ahola, M., Noorishad, J., Vuillod, E. (1995). International comparison of coupled thermo-hydro-mechanical models of a multiple fracture benchmark problem: DECOVALEX phase I, Bench Mark Test 2. Int. J. of Rock Mechanics and Mining Sciences & Geomechanics Abstracts, 32, pp. 435–453.

Verma, A.K., Bajpai, R. K., Singh, T. N., Narayan, P. K. and Avi Dutt (2010), "3D instability analysis of an underground geological repository-an Indian case study", Arabian J. of Geosciences, DOI 10.1007/s12517-010-0131-4.

Rock Mechanics for Resources, Energy and Environment – Kwaśniewski & Łydżba (eds)
© 2013 Taylor & Francis Group, London, ISBN 978-1-138-00080-3

Numerical modeling of induced seismicity associated with fluid injection and withdrawal using 2D discrete element fracture network model

J.S. Yoon & A. Zang
Section 2.6, Seismic Hazard and Stress Field, GFZ German Research Centre for Geosciences, Potsdam, Germany

G. Zimmermann
Section 4.1, Reservoir Technologies, International Centre for Geothermal Research ICGR. GFZ German Research Centre for Geosciences, Potsdam, Germany

O. Stephansson
Section 2.6, Seismic Hazard and Stress Field, GFZ German Research Centre for Geosciences, Potsdam, Germany

ABSTRACT: This study investigates induced seismicity in deep geothermal reservoir associated with fluid injection and production in doublet and triplet reservoir systems with a hydro-mechanical coupled numerical model. The model is using 2D discrete element model with embedded discrete fracture network. Fluid injection is performed for 6 hours with sequentially increased flow rate in three steps and the resulting induced seismicity is monitored. It is followed by constant rate fluid production at a point (doublet) and at two points (triplet) distances away from the injection point maintained for 20 hours. Spatio-temporal distribution of fluid pressure, injection/production induced seismic events, their magnitudes and source characters are investigated. The simulation shows that production induced seismic events mostly occur along the line at steep fluid pressure gradient with mostly implosion source characteristics. It was simulated that larger magnitude events can be induced in the vicinity of the production well and near pre-existing fractures when combined with abrupt slipping.

1 INTRODUCTION

Hydraulic stimulation is essential in developing Enhanced Geothermal Systems (EGS) to increase reservoir permeability and maximize heat energy extraction. Byproduct of hydraulic stimulation is induced microseismic events that can trigger some events with higher magnitudes.

As well as fluid injection, production of fluid can also induce seismic events resulting from pore pressure decline and large contraction of the reservoir, in particular increasing horizontal stresses above and below the reservoir that could lead to reverse faulting (Segall 1989). The Lacq gas field in sourth western France offers one of the best-documented cases of seismicity induced by extraction of pore fluids (Grasso & Wittlinger 1990, Segall et al. 1994).

Seismicity induced by fluid withdrawal cannot be explained without taking into account the accompanying stress changes, which are associated with the larger-scale contraction of the reservoir caused by pore pressure reduction. The magnitude of the events can be potentially large.

With this background, this numerical modelling study aims at investigating the following issues: (1) Can fluid production generate major earthquakes in the vicinity of the production well? (2) Can fluid production result in the seismic activity further away from the production well? (3) What are the source characteristics of the fluid production induced seismic events? (4) Where do they occur? (5) Can fluid production induce larger magnitude events in the already stimulated reservoir?

2 RESERVOIR MODEL

Figure 1 shows the constructed reservoir model which is represented by circular disk discrete elements bonded at their contacting points with pre-specified strength that can bear tensile and shear strength following Mohr-Coulomb failure criterion. Fluid flow algorithm is additionally implemented where the white empty space surrounded by disks is treated as pore space in geological porous media and referred to here as 'virtual pore'. Virtual pores which can store some fluid pressure are all interconnected and flow between pores occurs through the connecting flow channel governed by cubic law which is a function of hydraulic aperture (e), pressure difference (ΔP), flow channel length (L), and fluid dynamic viscosity (μ). Fluid pressure built up at the virtual pore exerts forces on

the surrounding disks, which consequently changes the stress state at the disk contacts. Mode I tensile crack occurs when the tensile stress exceeds the predefined tensile strength at the disk contact. Mode II shear crack occurs when the shear stress exceeds the Mohr-Coulomb failure envelope. Upon crack occurrence, the accumulated strain energy is released as a stress drop and seismic wave is propagated to the surrounding. Seismicity computation algorithm enables capturing the radiated seismic wave and constructs a moment tensor for each crack occurring in porous rock matrix (Hazzard & Young 2002, 2004). Yoon et al. (2013) modified the algorithm so as to compute resulting magnitude and radiated seismic energy of an induced event resulting from Mode I and Mode II failure of pre-existing joints represented by smooth joint contact model.

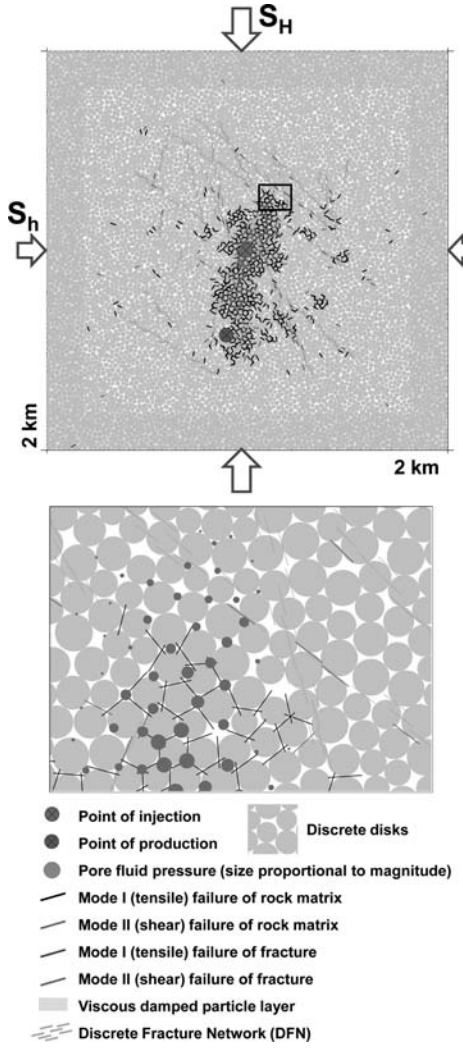


Figure 1. (a) Reservoir model (stimulated) in 2 km × 2 km size with embedded fracture network and subjected to anisotropic in-situ stress of $S_H = 75$ MPa and $S_h = 60$ MPa; (b) Close-up view of boxed area showing concept of hydro-mechanical coupling scheme: discrete particles (gray), void spaces filled with inter-connected pores.

3 SIMULATION OF DOUBLET SYSTEM

For a doublet reservoir system, one well at model centre (x = 0, y = 0) is used for massive fluid injection for stimulation of reservoir, creating induced seismicity and enhancing permeability and the other well (x = −100, y = −450, SSW of injection point) is used for fluid production.

Figure 2 shows applied flow rate for injection (sequential step-wise: 10, 12.5, 15 liter per second maintained for 2 hours each) and production (5 liter per second maintained for 20 hours) and moment magnitudes (Mw) of the induced events versus time. Events with moment magnitudes larger than 1 (over the red dashed line) are marked by red stars.

Figure 3 shows spatio-temporal distribution of fluid injection and production induced seismic events. Colour represents their time of occurrence. In general,

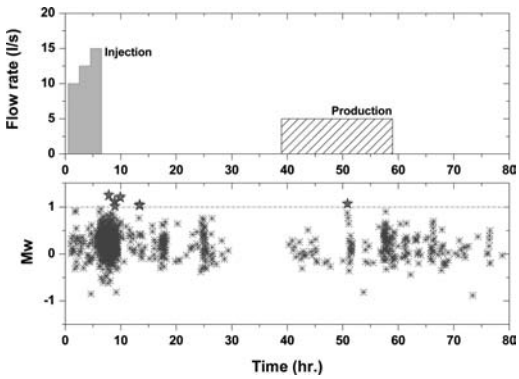


Figure 2. Sequential step-wise fluid injection (Time = 0–6.5 hr.) followed by fluid withdrawal (Time = 38–58 hr.) in doublet system. Moment magnitudes of induced seismic events versus time. Red stars are events with Mw > 1 (above the red dashed line).

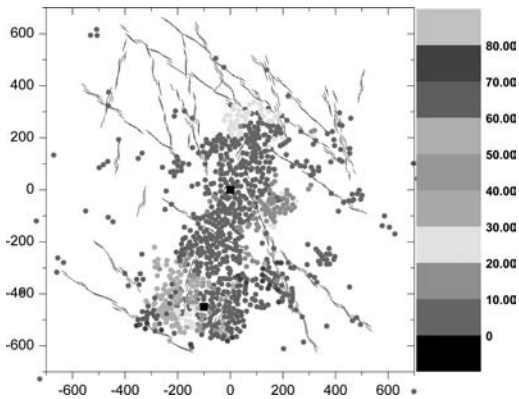


Figure 3. Spatio-temporal distribution of induced seismic events from fluid injection and withdrawal in doublet system. Colour codes according to time of occurrence in unit of hour.

the shape of the induced seismic event cloud is elliptic, extending longer in NS. Slight deviation from NS is due to presence of pre-existing discrete fracture network. Induced events associated with fluid production (occurrence time >40 hr.) are marked by green to blue, which are located at bottom tip of the induced event cloud.

Occurrence of induced seismic events are further classified into four stages in Figure 4, (a) during injection (Time = 0–6.5 hr.), (b) after shut-in (Time = 6.5–38 hr.), (c) during production (Time = 38–58 hr.), (d) after production (Time = 58–80 hr.).

Figure 5 shows contour plots of fluid pressure distribution evolving with time. Distribution of fluid pressure during injection and after shut-in (a–c) matches well with the spatial distribution of induced seismic events. Fluid production commences at 38 hr. and fluid pressure around the production well decreases and size of the fluid free area grows.

Boundary between fluid free zone and high fluid pressure zone (where the fluid pressure gradient is steep, i.e. Figure 5f, 5g) well matches with the location of induced seismic events shown in Figure 4d.

Each induced seismic event has moment magnitude which is computed from the moment tensor algorithm (Hazzard et al. 2002, 2004, Yoon et al. 2013). By analysing the moment tensor components of each induced event and decomposing it in isotropic and deviatoric parts (Jost & Hermann 1989), R values are computed using the following equation:

$$R = \frac{tr(M) * 100}{\left(|tr(M)| + \sum |mi *|\right)} \quad (1)$$

where, $tr(M)$ is the trace of the moment tensor, $tr(M) = m_1 + m_2$, representing the volume change at the source, $mi*$ are the deviatoric eigenvalues. The

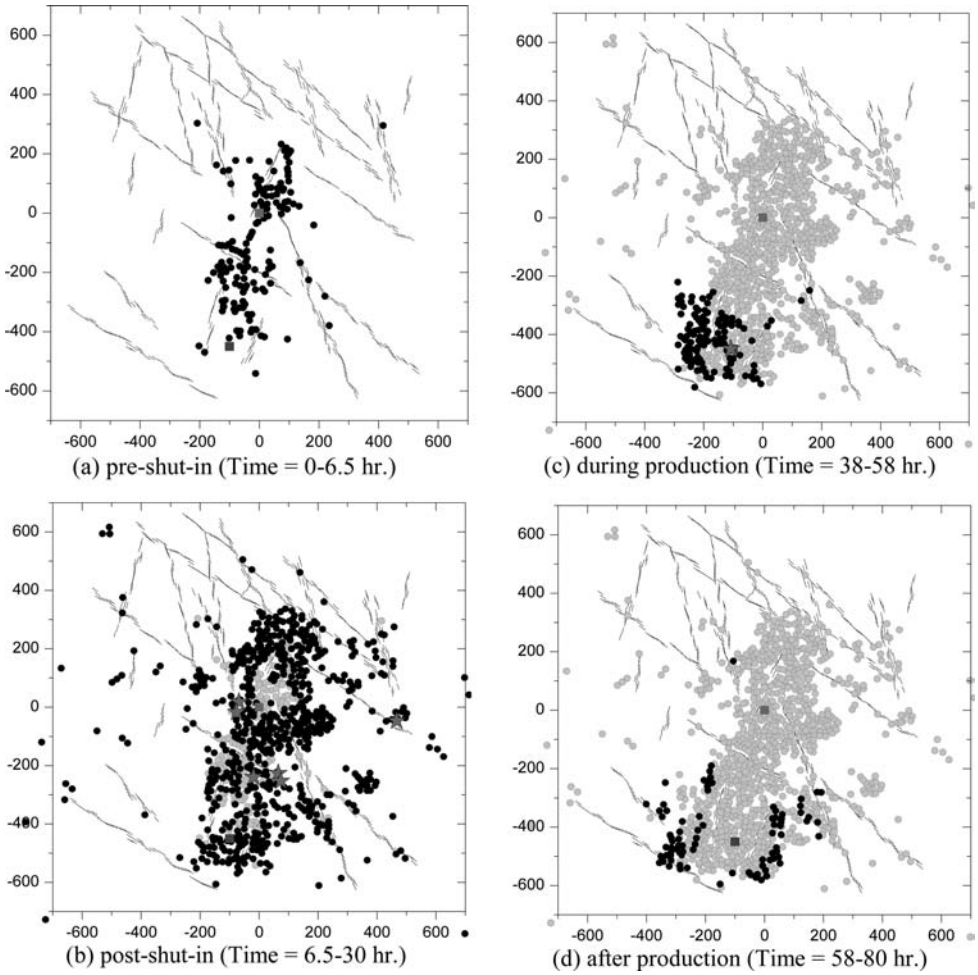


Figure 4. Distribution of induced seismic events occurred (a) during fluid injection (Time = 0–6.5 hr.), (b) after shut-in (Time = 6.5–30 hr.), (c) during fluid production (Time = 38–58 hr.), (d) after production (Time = 58–80 hr.) in doublet system. Red and blue squares are fluid injection and production points, respectively.

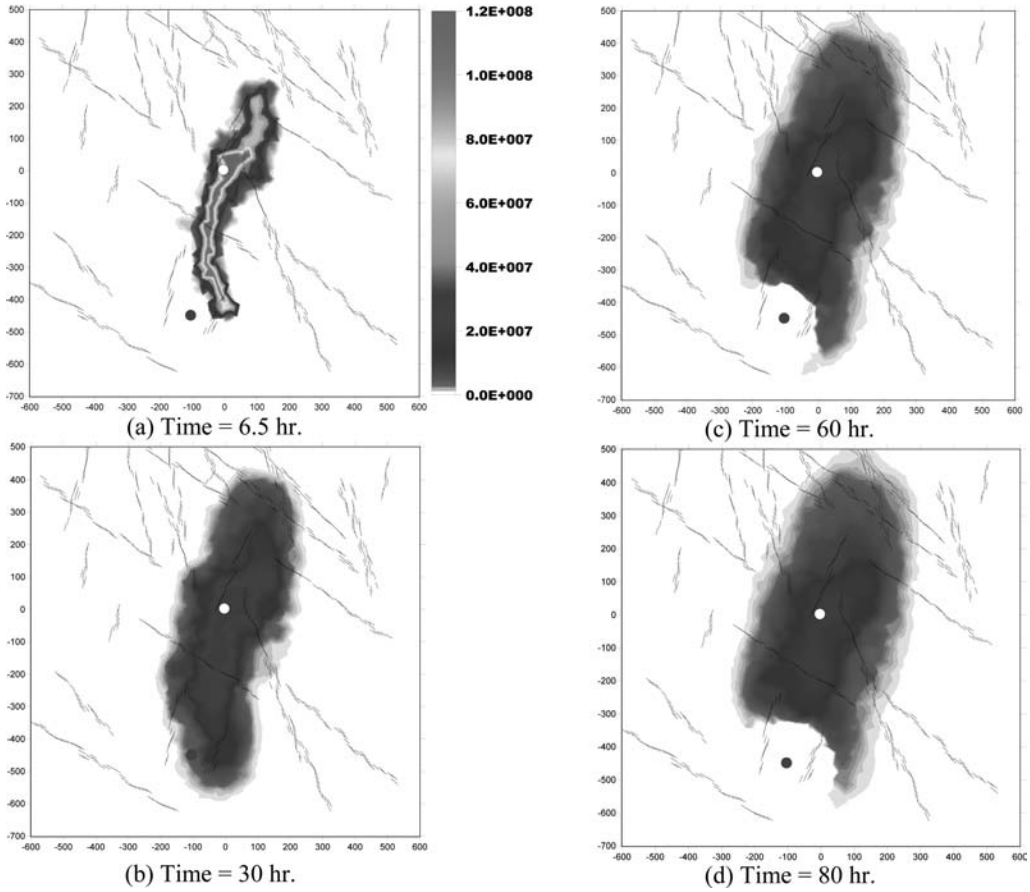


Figure 5. Distribution of fluid pressure in doublet system at time, (a) 6.5 hr., (b) 3 hr., (c) 60 hr., (d) 80 hr. Colour scale in (a) represents fluid pressure in unit of Pascal (Pa). White and blue dots are fluid injection and production points, respectively.

R varies from 66% (pure explosion) to −66% (pure implosion), and $R = 0$ indicates a pure shear failure mechanism (Feiniger & Young 1992). An event is assumed to have a significant isotropic component if the $R > 30\%$, implosional if $R < -30\%$.

Figure 6 shows the histograms of the R values of the induced seismic event that occurred in doublet system, (a) during injection, (b) after shut-in, (c) during production, (d) after production. Fluid injection results in relatively large number of positive and negative volume changing source (Fig. 6a). After shut-in, there appear more events with implosion characters, but also with explosion and shear characters. However, during and after production majority of the induced events are implosion sources.

Figure 7 shows location of induced seismic events occurred (a) during production and (b) after production and their R values. During production, there occur many events in the vicinity of the production point with mixed portion of explosion and implosion sources. After production, events are more implosional sources and occur along the outer-rim of the event cloud generated during production.

4 TRIPLET SYSTEM

This section deals with triplet reservoir system where one well at the model centre ($x = 0$, $y = 0$) is used for massive fluid injection for stimulation of reservoir and two wells (#1: $x = -100$, $y = -450$; #2: $x = 100$, $y = 300$, SSW and NNE of the injection points, respectively) are used to fluid production.

Figure 8 shows applied flow rate for injection (sequential step-wise: 10, 12.5, 15 liter per second maintained for 2 hours each) and fluid production at two wells, where 5 and 8 liter per second rate is applied to well #1 and #2 and both maintained for 20 hours and moment magnitudes (Mw) of the induced events versus time. Events with moment magnitudes larger than 1 (over the red dashed line) are marked by red stars.

Figure 9 shows spatio-temporal distribution of induced events of which time of occurrence is represented by the colour scale. Similar to the previous doublet reservoir system, induced events associated with fluid production (occurrence time >40 hr.) are marked by green to blue, which are located at top and bottom tips of the induced event cloud. Figure 10

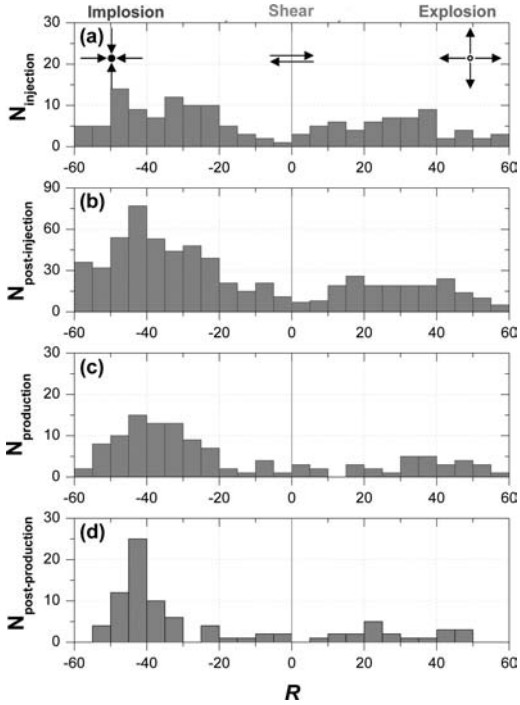


Figure 6. Histogram of the R values of the induced seismic events occurred in doublet system, (a) during fluid injection, (b) after shut-in, (c) during production, (d) after production.

displays the histograms of the *R* values of the induced seismic events occurred (a) during production and (b) after production. The histogram shows that the most of the induced events are implosional sources. Figure 11 shows location of induced seismic events occurred (a) during production and (b) after production and their *R* values. Similar to the doublet system, induced seismic events at the rim are mostly implosion sources, partially mixed with shear (green) and explosional (light blue to blue) sources.

5 SUMMARY AND CONCLUSIONS

This study deals with simulation of fluid injection and production and associated induced seismicity in fractured crystalline reservoir subjected to anisotropic in-situ stress. Stress changes due to fluid injection and production result in failure of rock matrix and pre-existing fractures in Mode I (tensile) and Mode II (shear) from which seismicity characters (magnitude and source mechanisms) are computed. Fluid injection and production are simulated in doublet system (one injection well, one production well) and triplet reservoir system (one injection well, two production wells) and the following conclusions are made.

1) Fluid production can generate induced events with relatively larger magnitudes in the vicinity of the production well.

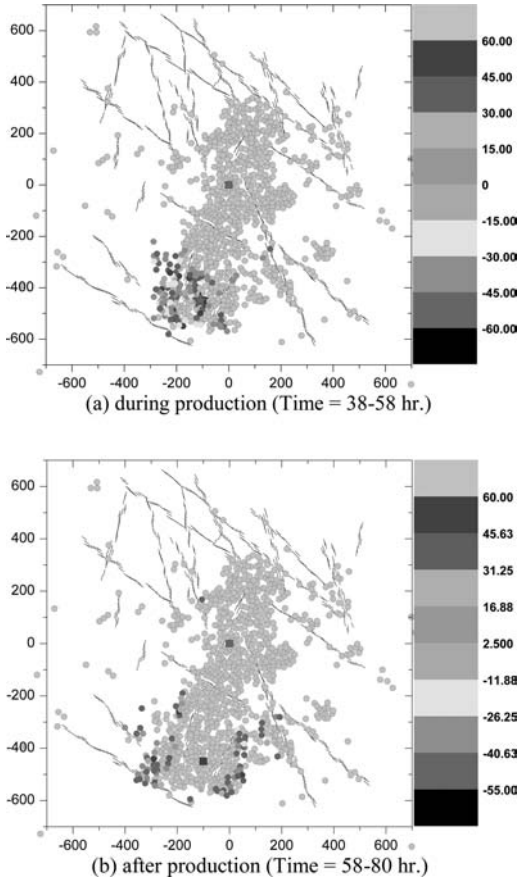


Figure 7. Distribution of induced seismic events occurred (a) during production and (b) after production and their R values in doublet system.

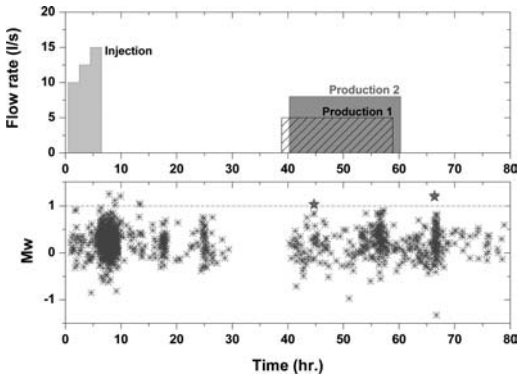


Figure 8. Sequential step-wise fluid injection (Time = 0–6.5 hr.) followed by fluid production (Time = 38–60 hr.) in triplet system and moment magnitudes of induced seismic events versus time. Red stars are events with Mw > 1 (above the red dashed line).

2) There can be a few seismic events induced at some distance away from the production well.
3) During production, densely clustered events with mixed portion of implosion and explosion

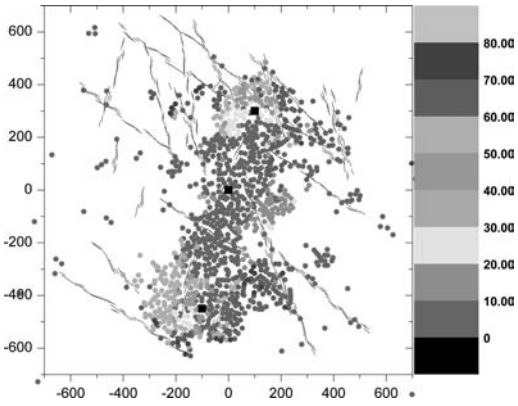


Figure 9. Spatio-temporal distribution of induced seismic events from fluid injection and withdrawal in triplet system. Colour codes according to time of occurrence in unit of hour.

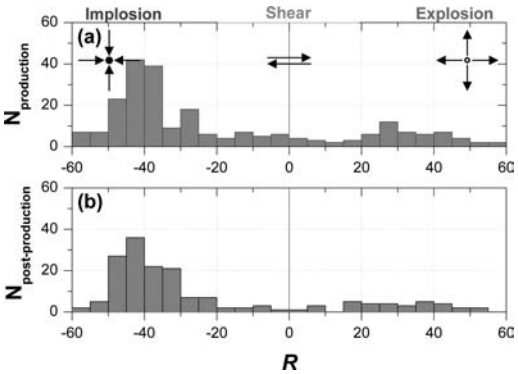


Figure 10. Histogram of the R values of the induced seismic events occurred in triplet system, (a) during production (Time = 38–60 hr.), (b) after production (Time = 60–80 hr.).

characteristics occur in the vicinity of the production point in dense cluster with larger magnitude events.

4) After production, additional events occurred along the outer rim of the event cloud generated during production. Source characters are more implosional.
5) In both doublet and triplet reservoir systems, it is shown that fluid production can result in additional induced seismic events with a few larger magnitude events occurring in the vicinity of the production well and near pre-existing fractures when combined with abrupt slipping.

ACKNOWLEDGEMENT

This work was financially supported by the German Federal Ministry for the Environment, Nature Conservation and Nuclear Safety under grant 0325451C. We thank Dr. Jim Hazzard from Itasca for the fluid flow algorithm and allowing modification and use for this study. Review and comments from Dr. Oliver Heidbach (GFZ) are appreciated.

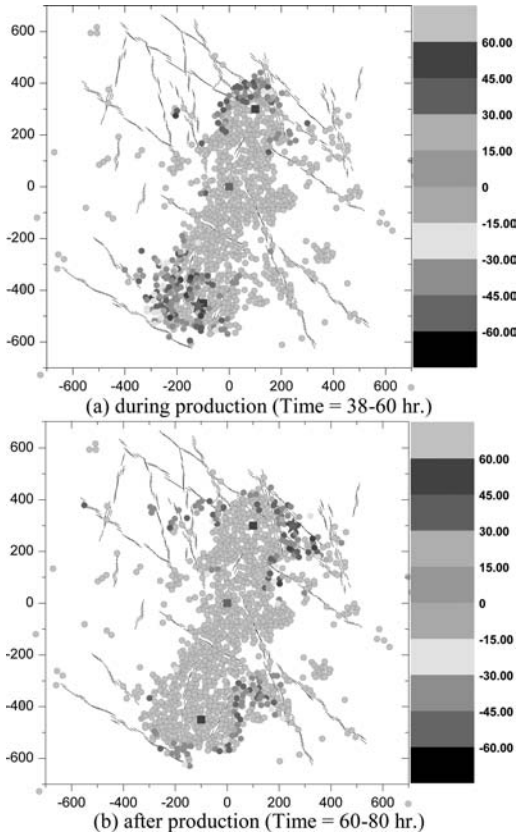


Figure 11. Distribution of induced seismic events occurred (a) during production and (b) after production and their R values in triplet system.

REFERENCES

Feignier, B. & Young, R.P. 1992. Moment tensor inversion of induced microseismic events: Evidence of non-shear-failures in the $-4 < M < -2$ moment magnitude range. *Geophysical Research Letters* 19(14): 1503–1506.

Grasso, J.R. & Wittlinger, G. 1990. Ten years of seismic monitoring over a gas field area. *Bulletin of the Seismological Society of America* 80(2): 450–473.

Hazzard, J.F. & Young, R.P. 2002. Moment tensors and micromechanical model. *Tectonophysics* 356: 181–197.

Hazzard, J.F. & Young, R.P. 2004. Dynamic modelling of induced seismicity. *International Journal of Rock Mechanics & Mining Sciences* 41: 1365–1376.

Jost, M.L. & Herrmann, R.B. 1989. A student's guide to and review of moment tensors. *Seismological Research Letters* 60: 37–57.

Segall, P. 1989. Earthquakes triggered by fluid extraction. *Geology* 17: 942–946.

Segall, P., Grasso, J.R. & Mossop, A. 1994. Poroelastic stressing and induced seismicity near the Lacq gas field, southwestern France. *Journal of Geophysical Research* 99(B8): 15423–15438.

Yoon, J.S., Zang, A. & Stephansson, O. 2013. Kaiser stress observation and simulation in deep geothermal reservoirs using hydro-mechanical coupled discrete element fracture network model. Submitted to *Geothermics* Special Issue "Induced Seismicity".

5. Mine design and ground control

This page intentionally left blank

Rock Mechanics for Resources, Energy and Environment – Kwaśniewski & Łydżba (eds)
© 2013 Taylor & Francis Group, London, ISBN 978-1-138-00080-3

Strength of faults – A concern for mining engineers?

M. Alber
Ruhr-University Bochum, Engineering Geology/Rock Engineering, Bochum, Germany

ABSTRACT: As mining operations go deeper, along with an increase of on-situ stresses, faults may be reactivated and seismic events may be induced. This paper describes several cases of mining induced seismic events and focuses on the strength of faults. From stress analyses it is known that very small amounts of induced stresses are necessary to activate faults as many faults are critically loaded. From back calculation fault friction angles are deduced which are well below published values such as the Byerlee friction angle of 40°. It has been found that friction angles as low as 18° must be present at mining depth. These values are substantiated by laboratory tests on slickensides.

1 INTRODUCTION

Several geological and geotechnical properties of the coal seam and of the coal measure rocks are observed when coal mining methods are selected. Seam undulations and seam thickness determine the longwall system. Reserves limit the cost of the mining system and the coal quality determines the price of the product. Roof and floor stability are important for gate development and longwall operations, particularly track and belt operations. Structural characteristics (dip and strike of the seam and faults) determine the blocks of reserve. During exploration focus is placed on estimating fault displacement – if exceeding seam thickness longwall mining may be excluded. In-seam seismic techniques and extensive drilling may allow accounting for the presence of faults.However, as mining operations go deeper, along with an increase of on-situ stresses, faults may be reactivated and seismic events may be induced.

Seismic events are the results of rock/rock mass failures. Failure in rock mechanics is anticipated by comparing stresses acting on and strengths of the material. There exist basically two different types of failure: rock/rock mass failure by formation of new fractures or slip of an existing discontinuity by exceeding its strength. Discontinuities include bedding planes, slickensides, joints and particularly faults. Especially slip on discontinuities is attributed to noticeable seismic events while mining. Accordingly, realistic assumption of stresses and strength is necessary but difficult to pursue.

Both types of failures may be observed on large scale during mining and allow to draw constraints for rock mass strength and especially for faults.

2 EXAMPLES FOR INDUCED SEISMICITY

Mining always means the excavation of underground opening for resource extraction. In contrast to civil engineering applictaions such as road or rail tunnels the stand-up time sought in mining is limited to the time needed for extracting the resource. Large scale failure may even be necessary for operational reasons (e.g. hang-up of strata above shield).

2.1 *Hard rock mining*

Some examples of significant mining induced seismic events in hard rock mining include:

- Klerksdorf District, South Africa. $M_L = 5.3$ in a gold mine on March 9th, 2005 (Durheim et al., 2006).
- Wyoming, USA, $M_L = 5.4$ in a trona mine (Solvay Mine) on February 3rd, 1995 (Pechmann et al., 1995)
- Coeur d'Alene District, Idaho, USA. $M_L = 3.7$ in Lucky Friday Mine on July 6th, 1989. (Whyatt et al., 1996).
- Kolar Gold Fields, Indien, $M_L = 4.6$ in 1973 (Srinivasan & Shringarputale, 1990).

Common to all events was the assumed reactivation of faults by stress redistribution from approaching underground mining operations.

2.2 *Coal mining*

Large stress redistributions are induced particularly with the longwall mining method. As a consequence numerous coal mining induced seismic events are

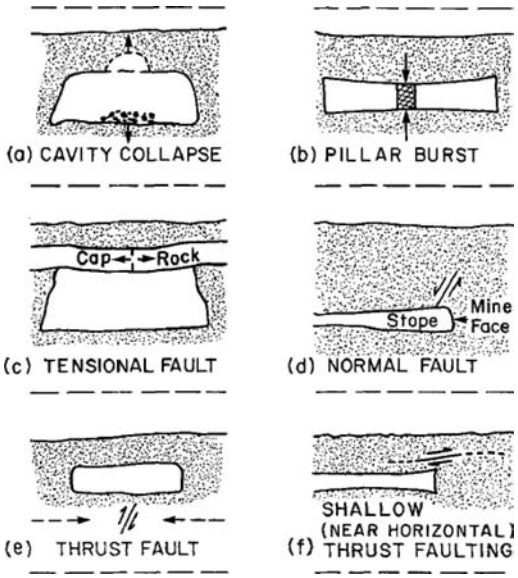


Figure 1. Six possible failure mechanisms for mining induced seismic events (Hasagewa et al., 1988).

observed. Alone in the area of the Ruhr mining district there were 13,912 seismic events for the period from 1983 to 2006 (Alber et al., 2009). Some significant events include:

- Crandall Canyon Mine, Utah, USA: $M_L = 3.7$ on August 6th, 2007 caused by collapse of a room-and-pillar section (Pechmann et al., 2008).
- Upper Silesian coal district in Poland: 55,900 seismic events $M_L > 1.6$ between 1974 and 2005. High energy seismic events are associated with tectonic zones (Stec, 2007).
- Coalbrook, Süd-Afrika: $M_L = 1$ by a collapse of a room-and-pillar section on January 21st, 1960 with 437 fatalities (van der Merwe, 2006).
- Saarwellingen, Saarland in Germany: $M_L = 4.0$ on February 23rd, 2008 while double longwall mining. Event is associated with reactivation of faults (Alber & Fritschen, 2011).

Mining induced seismic events may be traced back to 6 different failure processes (Hasegawa et al. 1988) as shown in Figure 1. Particularly the cases d-f are relevant for strong, noticeable events as discussed below.

3 BASIC ASSUMPTIONS AND MECHANISMS

The above mentioned man-made induced seismic events may be attributed to two rock mechanical defined failure processes. Failure by high strains/stresses and failure by slip on existing discontinuities/faults. Ortlepp (1992) (Fig. 2) classified various source mechanisms with their typical range of local Richter magnitudes M_L. Clearly, shear failure/fault reactivation favors seismic events with high magnitudes.

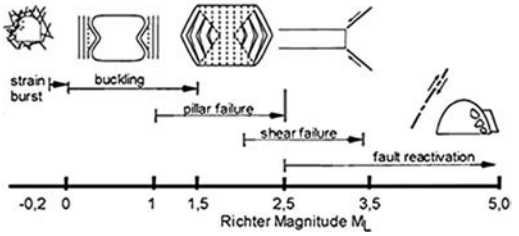


Figure 2. Relation between source mechanism and wave magnitude (simplified after Ortlepp, 1992).

It appears that shear failure of existing discontinuities and fault reactivation are of paramount relevance for mining-induced seismicity. The physical formulation of the problem is rather easy:

$$\tau > \tau_p = c + (\sigma_N\text{-}p)\cdot \tan\varphi \quad (1)$$

A discontinuity/fault fails or slips if the shear stress τ on the plane exceeds its strength τ_P. The shear strength may be estimated with knowledge about cohesion c, normal stress σ_N, water pressure p and friction angle φ. However, those rock mechanical parameters are difficult to be confidently estimated by e.g. laboratory experiments:

- The calculation of shear stress τ and the normal stress σ_N on a plane at depth requires the knowledge about the exact location and orientation of the plane as well as the primary and/or secondary stresses. Stress measurements are often executed in mining but the exact location of faults is not known even when conducting high resolution 3D seismic.
- The cohesion c of discontinuity is generally assumed to be non-existent. This assumption may hold true for a plane formed by brittle failure. Underground observations of faults or of fault zones indicate that low cohesion may be possible.
- Water pressure p on a discontinuity/fault may be estimated from water levels in a borehole.
- The estimation of friction angle φ of a discontinuity/fault is difficult. The basic friction angle φ_b (Barton & Choubey, 1977) ranges from 26°–37° for sedimentary rocks. Often, Byerlee's law (Byerlee, 1978) is applied by which $\varphi = 40°$ for $\sigma_N <$ 200 MPa.

A sound approach for estimating the strength of faults is the back-analyses of mining induced seismic events. The faults are typically known as they define the limits of longwall mining. Dimensions of underground openings as well as stresses are also often known.

4 INDUCED SEISMICITY FROM REACTIVATED FAULTS AND DERIVED FRICTION ANGLES

Numerous seismic events have been recorded during headgate development in the Ruhr mining district at a depth of 1100 m. The larger events $M_L > 0.7$ have been

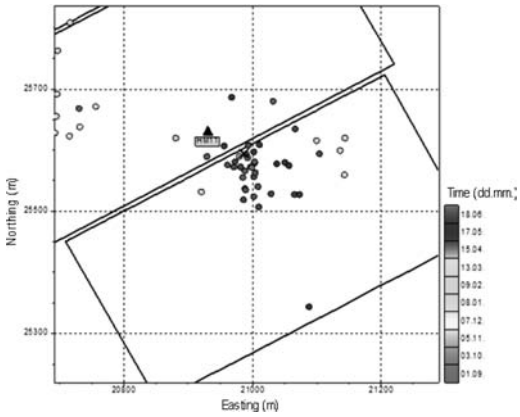


Figure 3. Location and temporal evolution of seismic events during headgate development.

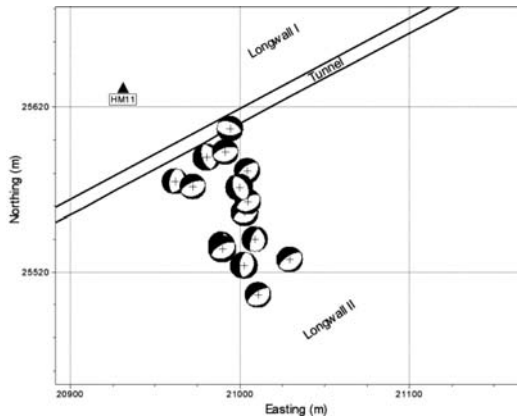


Figure 4. Focal analyses of selected seimic events.

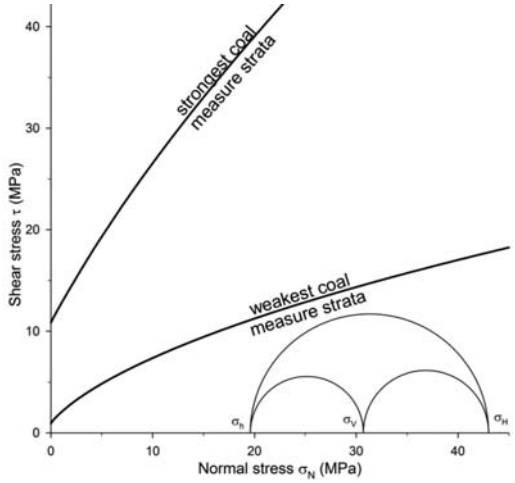


Figure 5. Mohr circles of the in situ state of stress and strength envelopes of the weakest and strongest rock mass, respectively.

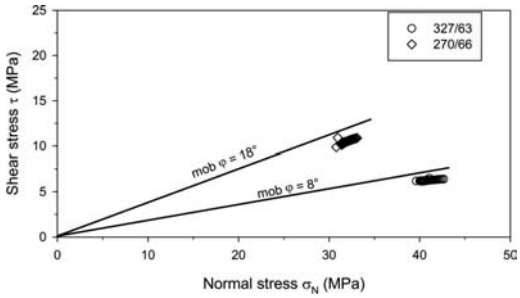


Figure 6. Numerically evaluated shear and normal stresses on assumed fault planes from focal analyses (cf. Fig. 4) and associated frictional strength of the planes. Insert denotes dipdirection and dip of the 2 fault planes.

localized (Fig. 3). The local seismological network in mine A allowed for fault plane solutions (Fig. 4). The assumed fault planes strike N-S or NE-SW with common dips of approximate 60° towards W and are in accordance with the local tectonic features in the subvariscan basin in the Ruhr area. Both, strength failure of the rock mass or fault reactivation could have been the reason for the events.

Magnitude and orientation of stresses are known from hydrofrac measurements ($\sigma_V = 29$ MPa, $\sigma_H = 39$ MPa and $\sigma_h = 21$ MPa). The intact strength of the coal and coal measure rock mass was evaluated by some 120 laboratory tests and scaled to in-situ conditions by the Hoek-Brown rock mass failure criterion in conjunction with RMR system. Rock mass strength and applied stress situation is given in Figure 5.

Evidently, even the weakest coal measure strata are strong enough and are unlikely to fail. Normal and shear stresses on planes oriented as suggested from focal analyses were calculated for the locations of the seismic events (cf. Figure 4). Figure 6 shows those stresses and the required frictional strength (mob φ) for the fault to remain stable. The respective friction angles are mob $\varphi = 18°$ and 8°.

While extracting the longwall two years later seismic events were recorded close to where events have been localized from headgate development (Figure 7). Focal analyses suggest normal faulting on both, NW-SE and NW-SW oriented planes. Again numerical modeling was employed to evaluate the normal and shear stresses on planes oriented as indicated from focal analyses.

These planes are in broad accordance with the strike of local tectonic features. The seismic events took place well ahead of the face, up to approximately 50 to 100 m in front of the actual position of the longwall. Moreover, they were localized at the same place were events were assumed when driving the tunnels two years earlier. For example, Figures 8 and 9 show the shear and normal stresses (τ, σ_N) as well as the mobilized frictional angle $\varphi_{mob} = \arctan(\tau/\sigma_N)$ for the two different planes at near the seam about 10 m north

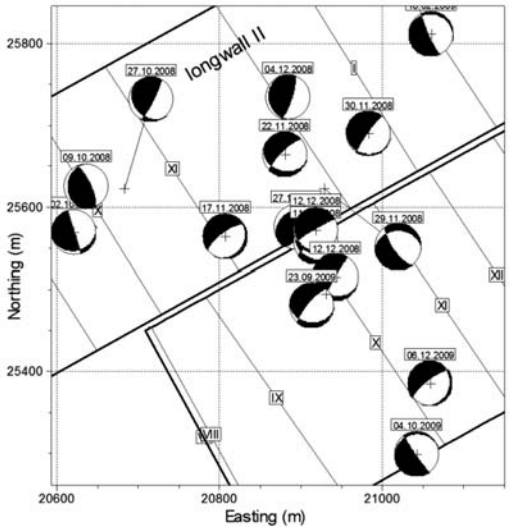


Figure 7. Location and focal analyses of the seismic events while excavating longwall II.

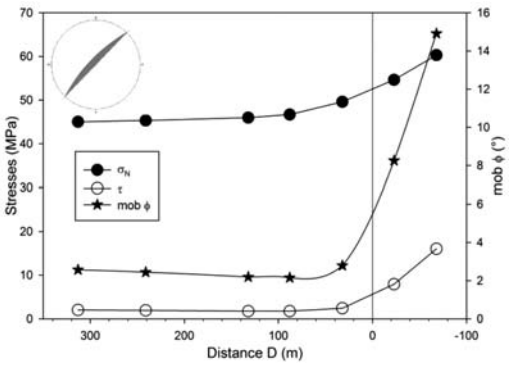


Figure 8. Shear stresses, normal stresses and mobilized friction angles on NW dipping fault plane with approaching longwall.

of the headgate. Numerical analyses were carried out at 5 positions (330 m, 241 m, 88 m, 32 m) east of the reference point and at a 2 westerly positions of the longwall when it passed through.

Clearly, the mobilized friction angle increase when the longwall face is closer than 100 m. For the NW dipping plane the mobilized friction angle would be as low as 3°, a too low value. For the SW oriented plane the mobilized friction angle at the time when the seismic event occurred, i.e. the longwall is about at a distance of 80 m from the plane is in the order of 18°. This frictional value is similar to that evaluated from the stress analyses of the seismic event during headgate development.

Shear tests on discontinuities in coal measure rock on the laboratory scale have been conducted on slickensides in shale and saw-cut sandstones. Friction

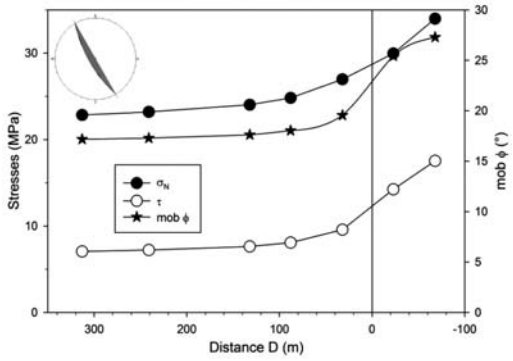


Figure 9. Shear stresses, normal stresses and mobilzed friction angles on SW dipping fault plane with approaching longwall.

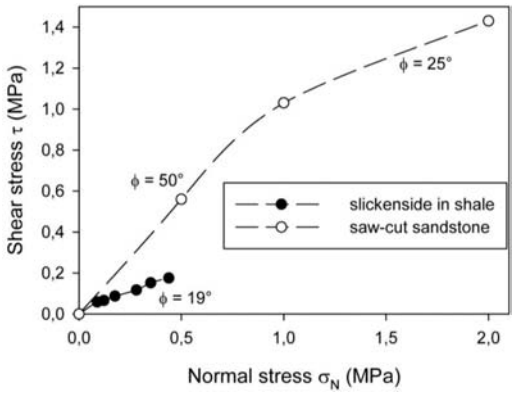


Figure 10. Frictional strength from laboratory tests on slickensides in shale and saw-cut sandstones from the mine.

angles range from 25° for the saw-cut sandstone to 19° for the slickenside in shale as shown in Figure 10. It may be assumed that for in-situ conditions the friction angles are even lower as for higher normal stresses the slope of the normal/shear stress curve gets typically smaller. This nonlinearity of shear strength is well established in rock mechanics (Patton, 1966; Barton, 1976). Moreover, when extrapolating shear strength from laboratory test to the size of fault area the roughness as well as the strength of the fault wall rock is thought to decrease (Bandis, 1990).

5 APPROACH TO EVALUATE FAULT SLIP

To evaluate the possibility of faults reactivation by mining operations the approach by Sibson (1985) is used (Fig. 11), who connects stress regimes at depth with orientation of the fault to σ_H and the fault friction angle ϕ:

$$\frac{\sigma_1'}{\sigma_3'} = (1+\mu\cdot\cot(\theta))/(1-\mu\cdot\tan(\theta)) \quad (2)$$

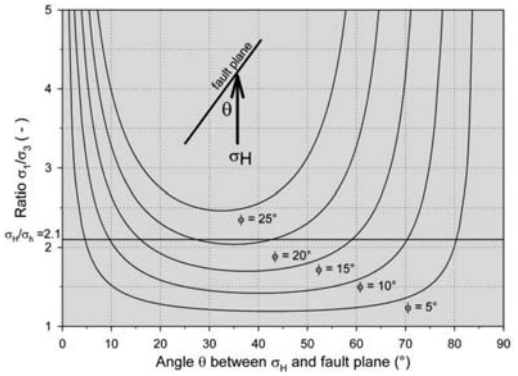


Figure 11. Application of Sibson's (1985) approach to estimate the angle θ between the major principal stress, here σ_H, and a fault plane.

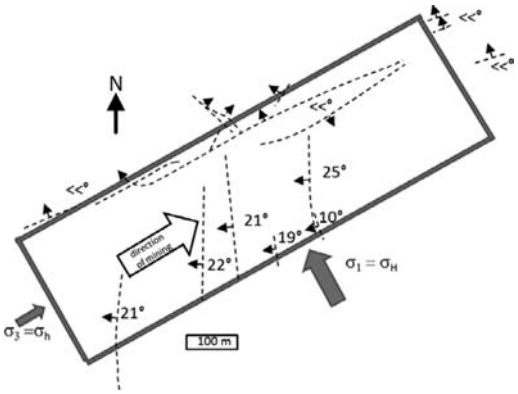


Figure 12. Plan view of a longwall in the Ruhr mining district with $\sigma_1/\sigma_3 = 2.1$. The dashed lines denote normal faults, the arrows show the dip of the fault plane. The numbers denote the required frictional angle for avoiding reactivation, <<° means that no slip may occur.

where $\mu = \tan(\varphi)$ and $\sigma_{1'}$ and $\sigma_{3'}$ are the effective principal in situ stresses at depth. As the longwall act as a sink it is often not necessary to account for water pressure at depth. For example, the stress regime in the Ruhr mining district is given by Rummel (2002) with $\sigma_H > \sigma_h > \sigma_v$ for all depths of mining. The stress ratio σ_1/σ_3 for this region is at a current mining depth of 1100 m depth $\sigma_H/\sigma_v = 2.1$.

This analysis suggests that any fault with a friction angle $\varphi < 20°$ would slip if the angle θ is between 30° to 40°. Faults with friction angles below 15° would slip in a wide range of orientations $15° < \theta < 60°$ and faults with friction angles higher than 22° would not fail in any orientation. Figure 12 shows a plan view of a longwall in the Ruhr mining district where the major variscan structures at depth as well as the orientation of the horizontal stresses are shown. All faults are steeply inclined normal faults. The required frictional values of those faults to withstand slip, as derived from Equation 2, are also shown.

6 DISCUSSION AND CONCLUSIONS

Seismic events necessarily accompany mining operations. The numerous events represent failure processes of the surrounding geologic media. These failure processes include rock mass failure and slip on faults. Rock mass failure is necessary with longwall mining and typically leads to numerous yet small seismic events. Fault reactivation may lead to rather strong events which may endanger particularly surface structures. Fine-grained coal measure rocks such as shales allow for faults with low frictional strength. The friction angle of those slickensides may be well below 20°. They may be recognized from geological mapping during gate development. The required frictional strength may be estimated from Sibson's approach which, in turn, requires knowledge about the state of stress at depth.

There is however no way to avoid fault slip but it appears possible to be prepared for it and to inform the interested parties beforehand.

In conclusion, the strength of faults is of concern for the mining engineer, if not from an operational point of view than from an environmental aspect.

ACKNOWLEDGEMENTS

This research was part of the collaborative research centre CRC 526 "Rheology of the Earth" funded by the DFG (German Research Association).

REFERENCES

Alber, M.; Fritschen, R.; Bischoff, M. & Meier, T. 2009. Rock mechanical investigations of seismic events in a deep longwall coal mine. *Int J Rock Mech Min Sci* (46): 408–420.

Alber, M & Fritschen, R. 2011. Rock mechanical analysis of a $M_l = 4.0$ seismic event induced by mining in the Saar District, Germany. *Geophys J Int* (186): 359–372.

Barton, N & Choubey, V.N. 1977. The shear strength of rock joints in theory and practice. *Rock Mechanics* (10): 1–54.

Bandis, S.C. 1990. Mechanical properties of rock joints. In N. Barton & O. Stephansson (eds.) *Proc. ISRM Symp on Rock Joints*. Rotterdam: Balkema,

Byerlee, J. 1978. Friction of rocks – *PAGEOPH* (116): 615–626.

Durrheim, R.J.; Anderson, R.L.; Cichowicz, A.; Ebrahim-Trollope, R.; Hubert, G.; Kijko, A.; McGarr, A.; Ortlepp, W.D. & N. van der Merwe, N. 2006. The Risks to Miners, Mines, and the Public posed by Large Seismic Events in the Gold Mining Districts of South Africa. In J. Hadjigeorgiou & M. Grenon (eds.), *Proc. Third Int Deep Seam and High Stress Mining*, 2–4 October 2006, Quebec City, CANADA, Université Laval, Canada.

Hasegawa; H.S.; Wetmiller, R.J. & Gendzwill, D.J. 1989. Induced Seismicity in Mines in Canada-An Overview. *PAGEOPH* (129): 423–453.

Ortlepp, W.D. 1992. The design of support for the containment of rockburst damage in tunnels; an engineering approach. In P.K. Kaiser & D.R. McCreath (eds.) *Proc Int Symp Rock Support*. Rotterdam: Balkema.

Patton, F.D. 1966. Multiple modes of shear failure in rock. *Proc. 1st Cong. ISRM.* Lisbon: ISRM.

Pechmann, J. C.; Walter, W.R.; Nava, S.J. & Arabasz, W.J. 1995. The February 3, 1995 M_L 5.1 seismic event in the trona mining district of southwestern Wyoming. *Seism Res Lett* (66): 25–34.

Pechmann, J.C.; Arabasz, W.J.; Pankow, K.L.; Burlacu, R. & McCarter, M.K. (2008). Seismological Report on the 6 August 2007 Crandall Canyon Mine Collapse in Utah. *Seism Res Lett* (79): 620–636.

Rummel; F. (2002) Crustal Stress Derived from Fluid Injection Tests in Boreholes – In V.M. Sharma & K.R. Saxena (eds.) *In-Situ Characterisation of Rocks.* Lisse: Balkema.

Sibson, R. H. 1985. A note on fault reactivation. *J Str Geol* (7): 751–754.

Srinivasan, C. & Shringarputale, S. B. 1990 Mine-induced seismicity in the Kolar gold fields. *Gerlands Beitraege zur Geophysik* (99): 10–20.

Stec, K. 2007. Characteristics of seismic activity of the Upper Silesian Coal Basin. *Geophys J Int* (168): 757–768.

van der Merwe, N. 2006. Beyond Coalbrook: what did we really learn? *J South Afr Inst Min Metall* (106): 857–868.

Whyatt, J.K.; Williams, T.J.; Blake, W.; Sprenke, K. & Wideman C. 1996. Mining-Induced Seismicity at the Lucky Friday Mine: Seismic Events of Magnitude >2.5, 1989–1994 – *DOE-Report UCRL-CR-1125338*.

Rock Mechanics for Resources, Energy and Environment – Kwaśniewski & Łydżba (eds)
© 2013 Taylor & Francis Group, London, ISBN 978-1-138-00080-3

Critical energy and mine rockburst potential

M. Al Heib, G. Lafont & C. Didier
INERIS, France

Y. Gunzburger & J.P. Piguet
Université de Lorraine, GeoRessources UMR 7359, France

W. Pytel
KGHM CUPRUM Ltd. Research & Development Centre, Poland

H. Mitri
McGill University, Canada

ABSTRACT: Rockburst is one of the most serious hazards which threaten the safety of mine operators and the underground and surface stability. Several geophysics and numerical approaches have been developed since the sixties to assess rockburst potential in underground hardrock mines. Some of the approaches are based on energy balance, Energy Release Rate (ERR) and critical energy and more recently the strain Energy Storage Rate (ESR). This paper presents the numerical results of a triaxial test of the critical energy, the critical energy depending on the confining pressure. The energy approach applied to a case study for the assessment of rockburst potential in a room-and-pillar copper mine in Poland was carried out. The Energy Storage Rate (ESR) is numerically calculated to predict burst occurrence.

1 INTRODUCTION

Rockburst causes rocks to crush and collapse together. Several factors are known to have an impact on the rockburst hazard (Hudyma, 2004): depth of mining, geology and tectonics, thickness of orebody, geomechanical characteristics of rock-mass. Some of the mining factors also have an influence on the occurrence of rockburst: mining method, roof control method, pattern of deposit cut, concentration of mining operations, spatial limits of mining operations.

To improve the control of the mining induced seismicity a methodology for managing the seismic activities of the underground coalmines was developed, it combines numerical modeling; seismic monitoring, stress measurements and back analysis of sever rockburst cases (Fig. 1). The interaction between tools allows predicting seismicity and improving the surface installation and mine safety. The numerical modeling and seismic analysis are used together to help the prediction and the evaluation of rockbursts potential.

Another approach is the consideration of energy instead of stresses. Various methods involving energy balance have been developed. The evaluation of the Energy Storage Rate (ESR) provides an indication on the state of the rock surrounding an excavation.

This paper presents a numerical modeling using FLAC-3D software to calculate the ESR and critical energy. The efficiency of the modeling technique is demonstrated for a cylindrical excavation in an infinite elastic rockmass under hydrostatic stress. A method for the calculation of critical amount of energy stored in the particular case of a triaxial test is presented. The calculation of energy is then applied to a case study of a Polish underground mine, showing the need to define accurate levels of critical energy.

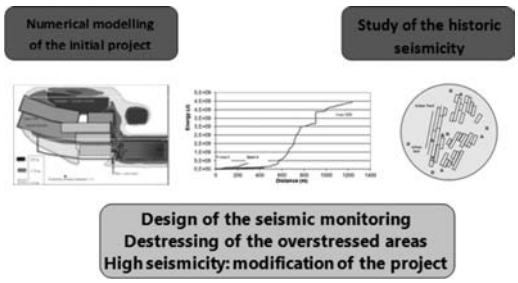


Figure 1. Methodology for the prediction of rockburst (Al-Heib 2012).

2 ENERGY BALANCE IN MINING

2.1 *Introduction*

The prediction of the occurrence of rockburst is based on detection and prevention methods used by mining companies. Primarily, micro-seismic monitoring systems (consisting of uniaxial or triaxial accelerometers)

have become an integral part of most hard rock deep mines in an effort to characterize mining induced seismicity (Trifu & Suorineni 2009, Archibald et al. 1990). The location, timing and magnitude of the induced seismic events can be determined, but the cause of these events is not directly identifiable. In fact, this seismicity can be created by high stresses, fault slip, fracture propagation, or strain burst. The main objective of monitoring is to adapt ground control support or to calibrate numerical modeling.

Optimization of the mining sequence in order to store high stresses into the free faces and good ground support practices have also been applied to reduce the proneness to rockburst.

The occurrence of strain bursts, a type of rockburst caused by the burst of a pillar, a face or a floor in a mine, has also been investigated based on analytical and numerical modeling. Various methods have been developed to locate the areas that are prone to rockburst occurrence and rockburst indicators were introduced depending on stress concentration (Tadjuś et al. 1997), energy concentration (Wang & Park 2001), ratios of stress/strength (Mitri et al. 1988).

Among them are the Energy Storage Rate (ESR) (Mitri et al. 1999) and Energy Release Rate (ERR) (Cook et al. 1966), which were introduced to relate rockburst occurrence and the amount of energy stored in rockmass. The use of ERR as a measure of underground conditions rather than an indicator of seismicity was discussed. The present study uses ESR to characterize the amount of energy that can be stored in a rockmass.

2.2 *Description of the different energy components*

As first described by Cook (1967), reviewed by Salamon (1984), and then refined by Brady and Brown (1985) and Hedley (1992), every transition from one state of equilibrium to another during a mining operation is associated with energy transfers. The energy components associated with a transition between these arbitrary states of mining are described as follows: W_{ext} is the work done by external and body forces, U_m is the elastic strain energy initially stored in rock mined during the transition between the two states, U_c is the increase in stored energy, W_r is the released energy, W_s is the work done on the support of the excavation, and W_{pla} is the work done by plastic deformation. The energy balance is therefore defined by:

$$(W_{ext} + U_m) - (U_c + W_s + W_{pla}) = W_r > 0 \qquad (1)$$

An incremental approach is used to follow the changes due to mining. The mining sequence is decomposed into different stages of excavation and the value of ESR is calculated at each stage. Hereafter, the subscript k represents the number of the current stage of excavation, *k-1*, the number of the previous one, and $\sigma_{...,k}$ $\sigma_{...,k-1}$, $\varepsilon_{...,k}$ $\varepsilon_{...,k-1}$, the corresponding components of the stress and strain tensors in a Cartesian coordinate system:

$$\overline{\overline{\sigma_k}} = \begin{pmatrix} \sigma_{xx,k} & \sigma_{xy,k} & \sigma_{xz,k} \\ \sigma_{xy,k} & \sigma_{yy,k} & \sigma_{yz,k} \\ \sigma_{xz,k} & \sigma_{yz,k} & \sigma_{zz,k} \end{pmatrix} \qquad \overline{\overline{\varepsilon_k}} = \begin{pmatrix} \varepsilon_{xx,k} & \varepsilon_{xy,k} & \varepsilon_{xz,k} \\ \varepsilon_{xy,k} & \varepsilon_{yy,k} & \varepsilon_{yz,k} \\ \varepsilon_{xz,k} & \varepsilon_{yz,k} & \varepsilon_{zz,k} \end{pmatrix}$$

As noticed by Mitri et al. (1999), an increase in stored energy in a volume V, can be separated into e_1, which is the energy due to induced stress and e_2, which is the energy due to in-situ stress (initial stress before excavation).

$$U_{c,k} = e_{1,k} + e_{2,k} \qquad (2)$$

where:

$$e_{1,k} = \frac{1}{2} * \int \overline{\overline{\Delta\varepsilon_k}} : \overline{\overline{\sigma_{ind,k}}} * dV \,, \qquad e_{2,k} = \int \overline{\overline{\Delta\varepsilon_k}} : \overline{\overline{\sigma_{k-1}}} * dV \qquad (3)$$

$\overline{\overline{\Delta\varepsilon_k}}$ is the transposed incremental strain tensor associated with the stage k

$\overline{\overline{\sigma_{ind,k}}}$ is the induced stress tensor

$$\overline{\overline{\sigma_{ind,k}}} = \overline{\overline{\sigma_k}} - \overline{\overline{\sigma_{k-1}}}$$

A FISH command was created in FLAC-3D for the purpose of this study, using a formula adapted to

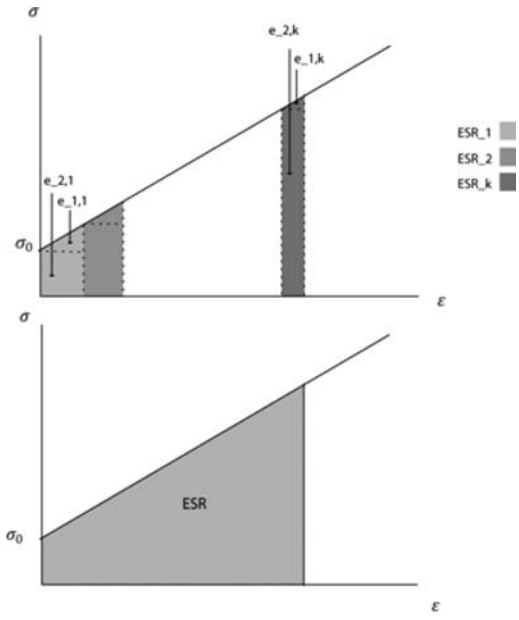


Figure 2. Energy components at mining step k (adapted from Mitri et al. 1999).

the Cartesian coordinates, applied in each zone of the model (v_{zone} is the volume of the zone considered):

$$e_{1,k,FLAC} = \frac{1}{2} * v_{zone} * (\sigma_{ind,k,xx} * \Delta\varepsilon_{xx,k} + \sigma_{ind,k,yy} * \Delta\varepsilon_{yy,k} + \sigma_{ind,k,zz} * \Delta\varepsilon_{zz,k} + 2 * (\sigma_{ind,k,xy} * \Delta\varepsilon_{xy,k} + \sigma_{ind,k,xz} * \Delta\varepsilon_{xz,k} + \sigma_{ind,k,yz} * \Delta\varepsilon_{yz,k}))$$

$$e_{2,k,FLAC} = v_{zone} * (\sigma_{xx,k-1} * \Delta\varepsilon_{xx,k} + \sigma_{yy,k-1} * \Delta\varepsilon_{yy,k} + \sigma_{zz,k-1} * \Delta\varepsilon_{zz,k} + 2 * (\sigma_{xy,k-1} * \Delta\varepsilon_{xy,k} + \sigma_{xz,k-1} * \Delta\varepsilon_{xz,k} + \sigma_{yz,k-1} * \Delta\varepsilon_{yz,k})$$

The Energy Storage Rate (ESR) is then given by (4):

$$ESR_k = \frac{d}{dV}(e_{1,k} + e_{2,k}) \quad \text{and} \quad ESR = \sum_k ESR_k \quad (4)$$

2.3 *Cylindrical excavation in elastic rockmass*

We first compare the results of a numerical modeling using the commercial codes UDEC and FLAC-3D with the analytical solution calculated by Salamon, (1984) for a cylindrical opening created instantaneously in a linearly elastic material (Fig. 3). The results of this modeling ensure that the value given by the FISH-command (developed in FLAC-3D) is correct. Table 1 presents the mechanical proprieties of material.

Stage 1 corresponds to the excavation of a 1 m-radius cylinder and stage 2 corresponds to a 2 m-radius excavation (table 2). The analytical solution can be easily found from this geometry. Work done at the outer boundary is calculated at a distance of 10 m from the center.

The absence of values for e_1 and e_2 in the column corresponding to UDEC is explained by the fact that this software does not distinguish between stored energy resulting from induced stress versus in-situ stress. The analytical solution is very close to those given by the theory. The predicted relations should be:

$$ESR_k = \frac{d}{dV}(e_{1,k} + e_{2,k}) \quad \text{and} \quad ESR = \sum_k ESI$$

$$Uc = 0.5 * W_{ext}$$

$$Uc = e1 + e2 \quad (5)$$

These relations are observed in both stages with an error of less than 4% and imply that half of the boundary work is stored into the rock mass. The other part should be dissipated by damping of the spherical waves emitted during the instantaneous excavation.

The same type of calculation was also performed for a spherical excavation in an infinite, elastic and homogenous material, and was compared with the results of the analytical solution and the boundary element program Examine-3D (Rocscience). Again, the results fit the theoretical solution, which allows us to affirm that the FISH command can efficiently predict the amount of energy stored following an excavation sequence while modeling an elastic rockmass in three dimensions.

2.4 *Calculation of critical energy*

As reported by Mitri et al. (1999), Mitri (2007), and by Xie (2009), a value of critical energy has to be determined, representing the maximum amount of elastic

Table 1. Properties of the material.

Bulk modulus (GPa)	38.9
Shear modulus (GPa)	29.7
Initial stress (MPa)	100

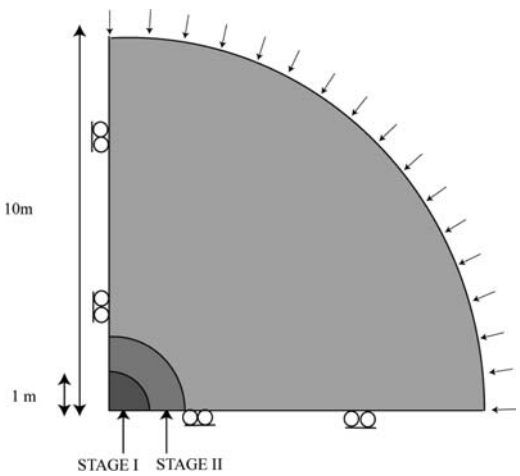


Figure 3. Dimensions of cylindrical excavation model.

Table 2. Energy balance for a cylindrical excavation in an elastic material.

	STAGE I			STAGE II		
	Analytical value	UDEC	FLAC	Analytical value	UDEC	FLAC
e_1 (MJ)	0.0266	No value	0.0264	0.0581	No value	0.0591
e_2 (MJ)	0	No value	0.002	0.00386	No value	0.0385
U_c (MJ)	0.0266	0.0266	0.0274	0.0969	0.0934	0.0976
W_{ext} (MJ)	0.0535	0.0527	0.055	0.157	0.152	0.163

energy that can be stored in a rock before it fails. Previous works chose this value based on the uniaxial compressive strength, which is a conservative assumption that does not take into account the effect of a confining pressure. The state of the stresses in the pillars was considered to be uniaxial because the failure is taking place at the pillar skin, where least principal stress is close to zero. If we consider the yielding of the center of a pillar, a confining stress does exist. During a triaxial test, the value of critical energy highly relies on the value of the confining stress. The critical value of energy stored can be obtained by considering that the plastic yielding will lead to an unstable state close to the failure of the pillar.

A triaxial test was modeled with FLAC-3D to determine the critical amount of energy that can be stored depending on the confining pressure. The energy balance during a triaxial test is conducted at a constant axial strain rate (constant downward speed of the upper plate V). A yield criterion of Mohr-Coulomb type is considered. The material is characterized by its cohesion c, its friction angle φ and its dilation angle Ψ. The dimensions of the sample are given in Figure 4. Let Ω be the volume of the sample and $d\Omega$ its surface. When the sample is compressed, a part of the work done at the external boundary is stored while the other part is dissipated by plasticity. The energy balance is given by:

$$U_c = W_{ext} - W_{pla}$$

where $W_{ext} = \int \int_0^{d\Omega} (\overline{\overline{\sigma}}, \overline{n}) \overline{V} dS$ is the boundary loading work and $W_{pla} = \int \int \int \overline{\overline{\sigma}} : \overline{\overline{\varepsilon^p}}\ dV$ is the energy dissipated by plastic work.

During the elastic phase, the work done by the loading is entirely converted into strain energy stored in the rock sample. During the plastic phase, all of the additional energy brought by the loading is dissipated as plastic work. Let t_1 be the timestep of transition between the elastic behavior and the plastic behavior. The analytical solution for the total amount of energy stored in the elastic state at a time "$t < t_1$" is:

$$U_{c,el} = \pi {R_0}^2 l_0 ({\sigma_{ax}}^2 + (2v - 1){\sigma_{conf}}^2 - 4v\sigma_{ax} * \sigma_{conf})$$

The solution for the total amount of energy dissipated by plastic work in the plastic state at a time $t < t_1$ is:

$$W_{pla} = \pi {R_0}^2 Vt\left(\left(K_p - \beta\right)\sigma_{conf} - 2 * c * \sqrt{K_p}\right)$$

Where: $K_p = \frac{1+\sin(\varphi)}{1-\sin(\varphi)}$ and $\beta = \frac{1+\sin(\psi)}{1-\sin(\psi)}$.

The solution given by the FISH command in FLAC-3D can be verified by studying the theoretical solution in the case of a triaxial test. Subsequently, the critical energy density value in the sample can be evaluated for different confining stresses (Fig. 4). The critical energy density is defined by:

$$e_c = \frac{U_{c,max}}{Volume} \tag{6}$$

When the stored energy in a zone reaches the critical energy, it starts deforming plastically.

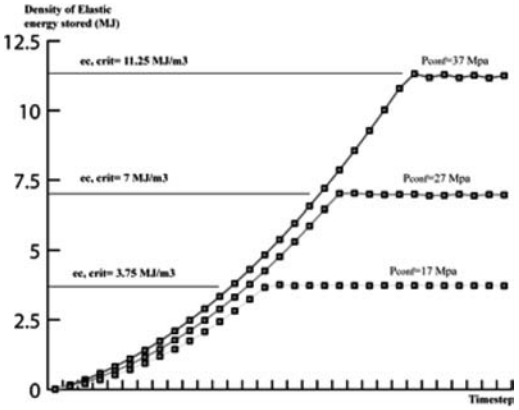


Figure 4. Evolution of the density of energy for different confining pressure.

3 CASE STUDY

3.1 *Presentation of the Rudna Copper Mine*

The Rudna mine is one of three mines in the Polish Legnica-Głogów Copper Belt, along with the Polkowice mine and the Lubin mine. The mined ore corresponds to a thin and flat rock layer, at an actual average depth of 1250 m below ground surface, exploited since the 1970's with different variants of room-and-pillar method. The production of copper ore in this mine amounts to about 12.5 Mt per year, with a grade below 2%.

Because of the mine depth, the geology and the presence of faults, this mine is subject to many rockbursts. As described by Butra (1998), even if the geological conditions above this mine are fair (thick and strong dolomite layer overlaying the ore), the size of mined out area (about 75 km^2), the number of dynamic events and the high stress concentration have made the mining environment increasingly complex. Every year, about 3000 induced tremors are registered in the LGOM district, with the energy of tremors reaching up to 10^{10} J (Orzepowski & Butra 2008).

Rock bolting and hydraulic backfilling is commonly used to support the roof and to improve the stability during the first stage of excavation. Moreover the method of yielding remnant pillars is used. This approach provides immediate roof strata protection in the working zone, as well as advantageous stress distribution due to instant support of main roof strata on yield pillars.

Control of this method constitutes a real achievement for the Polish copper mining industry. The main idea behind room-and-pillar mining with a roof-deflected system consists in the creation of pillars whose size permits yielding as the same time as lowering and deflection on the roof strata. Crushed yield pillars of wedge-column shape behave similarly to a deformable artificial support which does not accumulate elastic strain energy. For the simplicity of model,

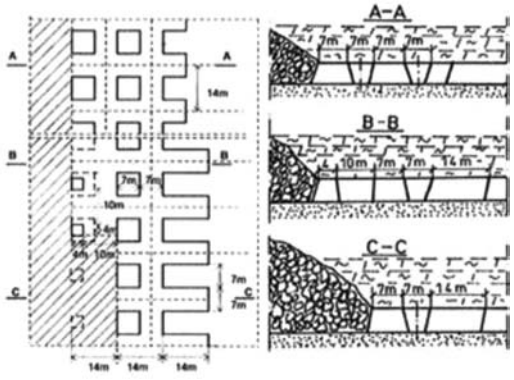


Figure 5. Mining method at Rudna mine (Pytel 2003).

Table 3. Properties of the material (adapted from Pytel 2003).

Geologic strata	Thickness (m)	γ (MN/m^3)	ν	E (MPa)	Rc (MPa)	Rt (MPa)
Dolomites	30	2.7e-2	0.24	8550	136	8.8
Orebody	3	2.7e-2	0.18	2039	67.59	3
Sandstones	30	2.7e-2	0.13	15000	18.4	0.8

the pillars were designed to be rectangular instead of wedge.

3.2 *Geometry, properties and assumptions of the model*

According to Katulski et al. (1997), horizontal principal stresses are considered to be 40% larger than the vertical stress, which is estimated to be about 30 MPa. Model geometry is taken from the map of the Rudna mine provided by KGHM. Attention was focused on a block currently under excavation. The mining method is a one-phase room-and-pillar of type J-3S, the remnant pillars have a width of 8 m.

3.3 *Description of the mining sequence*

The mining sequence is decomposed in 3 stages represented in figure 5. The dimensions of the remnants pillar and their shape shown in the figure 6 corresponds to another part of the mine which is out of the scope of the study. The cut A-A shows the first stage of development, the cut B-B the creation of the remnant pillars and the cut C-C a stage of caving of the blocks.

The numerical model aims to reproduce a room-and-pillar mining sequence. The remnant pillars of the zone modeled have the dimensions 8 m × 16 m. A distinction was made between the 2 types of excavation A and B. Steps A correspond to the development work, required to prepare the flat bedded deposit for mining and also to obtain a precise geologic description of the orebody. These panels are roadways for ore transport and communication are established inside production panels. Steps B are the ore recovery steps, corresponding to the creation of the remnant pillars.

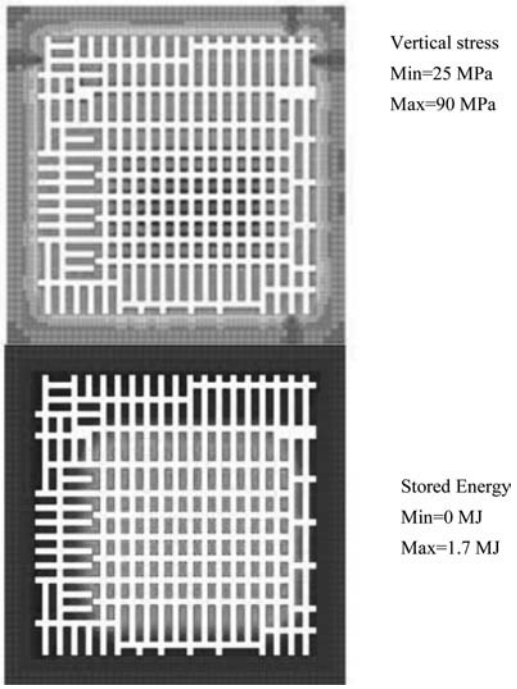


Figure 6. Vertical stress and stored energy distribution for the last step of the mining.

3.4 *Results of the modeling*

A modeling of the mine was realized with FLAC-3D. The distribution of vertical stress shows a concentration of high stresses (>90 MPa) in the center of mining area, where remnant pillars are created. The central block was excavated in 10 stages and ESR was estimated at each one. Distribution of the values of ESR and vertical stress in a plane view is summarized in figure 6 for four stages.

During the first mining steps, the energy stored in the pillars around the excavation increases, especially in the pillars at the border of the initial block. These pillars have already been disturbed during their creation and therefore this perturbation may increase the probability of strain burst occurrence. The creation of the remnant pillars leads to an increase in stored energy (from 0 to 0.29 MJ to 1.7 MJ). The evolution of the mining sequence shows a displacement of the areas of large stored energy that follows the displacement of the mining front.

The storage energy in pillars can be dissipated following tow form: static deformation of the pillars and galleries and dynamic behavior (strain burst and rock burst). The numerical modeling results indicate a real potential of rockburst phenomena in Rudna mine. Between 1990 and 2010, the high energy tremors

caused 323 events with consequences in the mines of the Legnica-Głogów Copper Region (Butra 2011). The number of events could be partially explained by a quantity of energy stored in the pillar close to a critical energy. We describe a way of calculating a critical value of the ESR to be applied in further work that would assess the probability of failure of the pillars. To continue this work, a model with accurate data and a more realistic mining sequence could also be realized.

4 CONCLUSIONS

This paper focuses on the prediction of mining induced rockbursts by the use of an energetic approach. The distinction between the different energy components involved in a mining excavation is discussed. The calculation of these components is implemented into the code FLAC-3D and tested through a comparison with the analytical solution for a cylindrical excavation in an infinite, homogenous and elastic rockmass. The evolution of the stored elastic energy was considered at each stage of exploitation and applied to an underground copper mine in Poland.

A triaxial test on an elastic-plastic sample was modeled in order to calculate the value of a critical energy density depending of the confining stress. This result is useful for the evaluation of potential rockburst in deep mines.

The next step of study will be to compare the critical energy to the energy stored in the pillars of the Rudna mine in order to determine which pillars are the most likely to be unstable and to release a high quantity of stored energy as rockbursts.

ACKNOWLEDGEMENTS

This study was sponsored by the I2Mine European Program. The authors are grateful for their support.

REFERENCES

Al Heib, M. 2012. Numerical and geophysical tools applied for the prediction of Mines induced seismicity in French coalmines. International Journal of Geosciences, 2012, 3834–846.

Archibald, J. F., Calder, P. N., Bullock, K. & Madsen, D. 1990. Development of in-situ rockburst precursor warning systems. Mining Science and Technology 11, 129–152.

Butra, J. 2011, Rockburst hazard evaluation and prevention methods in Polish copper mines, KGHM CUPRUM.

Cook, N.G.W., Hoek, E., Pretorius, J.P.G., Ortlepp, W.D., & Salamon, M.D.G. 1966. Rock mechanics applied to the study of rockbursts, J. S. Afr. Inst. of Min. and Metall. vol. 66. pp. 435–528.

Hedley, D.G.F. 1992. 'Rockburst Handbook for Ontario Hardrock Mines', CANMET, Special Report SP92-1E.

Hudyma, M.R., 2004. Mining-induced seismicity in underground, mechanized, hard rock mines – results of a worldwide survey. Australian Center for Geomechanics, University of Western Australia.

Katulski, A., Bugajski, W., Bryja, W. & Fabjanczyk, M. 1997. Measurement of pre-mining stressfield at Rudna Mine (in Polish), Proc Underground Exploitation Workshop '97, Szczyrk, Poland, 67–75.

Mitri, H.S., Tang, B. & Simon, R. 1999. FE modelling of mining-induced energy release and storage rates. JS Afr. Inst. Min. Metall 99, 103–110.

Mitri, H.S., 2007. Assessment of horizontal pillar burst in deep hard rock mines, International Journal of Risk Assessment and Management, Inderscience Publishers, pp. 695–707.

Orzepowski, S. & Butra, J. 2008. Evaluation of rock-mass state in Polish copper mines through monitoring the borehole deformations. Tectonophysics 456, 52–61.

Pytel, W. 2003. Rock mass–mine workings interaction model for Polish copper mine conditions. International Journal of Rock Mechanics and Mining Sciences 40, 497–526.

Salamon, M.D.G. 1984. Energy considerations in rock mechanics: fundamental results. JS Afr. Inst. Min. Metall 84, 233–246.

Tajduś, A., Flisiak J.& Cała, M. 1997. Estimation of rockburst hazard basing on 3D stress field analysis 273, The 4th international symposium of rockburst and seismicity in mines, Kraków, Poland.

Trifu, C.I. & Suorineni, F.T. 2009. Use of microseismic monitoring for rockburst management at Vale Inco mines. in Proceedings of 7th International Symposium on Rockburst and Seismicity in Mines (RASIM7). New York: Rinton Press 1105–1114.

Wang, J.-A. & Park, H. D. 2001. Comprehensive prediction of rockburst based on analysis of strain energy in rocks. Tunnelling and Underground Space Technology 16, 49–57.

Xie, H., Li, L., Peng, R. & Ju, Y. 2009. Energy analysis and criteria for structural failure of rocks. Journal of Rock Mechanics and Geotechnical Engineering 1, 11–20 (2009).

Rock Mechanics for Resources, Energy and Environment – Kwaśniewski & Łydżba (eds)
© 2013 Taylor & Francis Group, London, ISBN 978-1-138-00080-3

The design and results of an innovative instrumentation method for monitoring and improving the excavation of a road tunnel in a highly fractured and strained rock mass

M.I. Álvarez-Fernández, M.B. Prendes-Gero & I.N. Álvarez-Garcia
University of Oviedo, Asturias, Spain

A.O. Oliva-González
University of Las Californias, Tijuana, Mexico

ABSTRACT: This study has two aims: firstly, to develop an instrumentation and monitoring method for the excavation of a tunnel in a highly-fractured quartzite-slate mass that is subject to large stresses; secondly, to use a back-analysis with computer-based models and real instrumentation measurements to identify the properties that best model the behaviour of the mass and hence determine the best characterisation method. The results show that the monitoring procedure defined is highly effective, thanks to a number of innovations, such as the measurement of the complete convergence of the section of the tunnel and continuous, real-time data collection using GPRS. Comparing the analysis of the results with the computer-based models allows us to conclude that neither geomechanical classifications nor on-site and classic laboratory testing offer a high degree of precision when it comes to characterising masses of this nature and that the new on-site penetration test using a hydraulic cylinder (designed by the authors of this study) provides the best means of characterising highly fractured rock masses.

1 INTRODUCTION

At an international level, the current state of the art for recognising and determining general actions for operations in poor-quality underground rock masses often uses the same working method used for excavations in competent rock masses. This often results in serious errors in analysing and defining the stress-deformational properties of the soil; as such, in order to guarantee the safety of the excavation, it is necessary to establish high levels of safety using oversized supports, which increases the cost of operations and delays execution.

Furthermore, it is important to note that there is still a lack of suitable research into poor-quality or "soft" rock masses (Kurzweil 2004). The answer to this problem appears to lie in two fundamental factors:

- In recent times, a number of authors, including the authors of this study, have raised doubts as to the application of the Hoek-Brown classification to "soft" masses, since empirical evidence shows it is unable to define their behaviour.
- There is a lack of suitable laboratory and on-site testing for such materials.

This has led to different methods being used to characterise rock masses (geomechanic classifications, on-site and classic laboratory testing, and a new on-site penetration test using a hydraulic cylinder) (Isik et al. 2006; Álvarez Vigil et al. 2011). Specific excavation zones have subsequently been implemented using various devices (Chung et al. 2006).

The excavation section monitored is 11.3 m high and 11.9 m wide. Support installed along the tunnel consists in shotcrete and bolts sections (width of shotcrete and number of bolts varie as a function of terrain quality). The instruments that have been installed are load cells, convergence stations and extensometers, all of which collect and record data continuously, which can then be transmitted using GPRS. Furthermore, this research is also innovative in its attempt to design a device for measuring convergence along an entire section, in contrast to the standard approach, based on measurements form three points.

Stress and strain measurements collected by the installed instruments made it possible to analyse and monitor excavation work practically in real-time and have also served as a basis for several computer simulations based on numeric methods (Shou & Liu 2004; Bakun-Mazor et al. 2009), which have been used to calibrate the quality of rock mass characterisations obtained using different methods. Hence, the stress and strain measurements gathered from the excavation were used to create numeric models into which different values of geomechanical properties have been entered (Young's modulus, Poisson's ratio, cohesion, friction, etc.) until reaching a combination capable of reproducing the stresses and strains measured with

the instruments in the model (back-analysis method) (Vardakos et al. 2006). The values of these properties were then compared to the ones obtained using the different characterization methods.

2 CLASSIFICATION OF MATERIALS AND PROPERTIES CONSIDERED

Based on observations and tests, the materials in the zone under study have been classified into the four groups described below:

- TYPE I materials, colluvium or fault: The lithologies for this group correspond to colluvial deposits and remains of highly fragmented slates and quartzites removed by the action of the fault zones. Although this material is very weathered, it may be considered as a very weak rock mass, but not as a soil.
- TYPE II materials, slates: The lithologies found along the path of the tunnel corresponding to this group are milimetre-thin slates at 4 and 5 cm. The slate content for this group exceeds 75%, and levels of other lithologies such as quartzites (less than 25%) may also appear.
- TYPE III materials, slate-quartzite alternation: Litholologies with these properties correspond to the alternation of slates and quartzites in variable proportions. There are three types of alternations within this group:
  - Slates with quartzite intercalations, with the former clearly predominant over the latter, which appear in banks a few centimetres thick.
  - Slates between 1 and 5 cm thick, alternated with levels of quartzite of the same thickness.
  - Quartzites between 2 and 15 cm thick alternating with slates that are millimetres or a few centimetres thick.

  To summarise, this type includes alternations of slates and quartzites between the following range of proportions: 25% slate – 75% quartzite and 75% slate – 25 % quartzite.
- TYPE IV materials, quartzite: Centimetre-thick levels of quartzite (more than 75% quartzite content). The slate content is less than 25%. These materials have not been tested on-site, due to their strength.

Properties of these materials have been calculated using three different methods (geomechanical classifications, pressure meter and laboratory tests, and a new on-site penetration test using a hydraulic cylinder). This new test, designed and patented by authors (Alvarez-Vigil et al. 2011) is a stress-strain tests that consist of applying stress to the ground (using a hydraulic cylinder) and measuring the deformation produced by said stress. To perform the test, a trench approximately 1.5 m wide is first excavated in the material. The equipment is then positioned in this trench and the cylinder is positioned perpendicular to the walls. Then, pressure is applied and gradually increased until ground failure takes place. The stress-strain curve obtained for each test can be used to calculate the failure stress for each analysed material and to estimate peak and residual resistance.

Table 1, Table 2 and Table 3 show the properties of the materials calculated using the different methods,

Table 1. Properties of the materials according to their geomechanical classifications.

Lithology	RMR	Cohesion (kPa)	Friction (°)	E_m (GPa)
Type I: Colluvium/fault	23	110	16.0	2.1
Type II: Slates	32	158	20.8	3.5
Type III: Slate-quartzite alternation	43	210	26.0	6.7
Type IV: Quartzite	51	252	30.2	10.6

Table 2. Properties of the materials according to pressure meter and laboratory tests.

Lithology	Cohesion (kPa)	Friction (°)	E_m (GPa)	υ
Type I: Colluvium/fault	10400	45	2.7	0.30
Type II: Slates	11100	45	3.7	0.30
Type III: Slate-quartzite alternation	13700	45	5.2	0.30
Type IV: Quartzite	18300	46	7.6	0.29

Table 3. Properties of the materials according to penetration tests using the hydraulic cylinder.

Lithology	Cohesion (kPa)	Friction (°)	E_m (GPa)	υ
Type I: Colluvium/fault	180	25	0.43	0.3
Type II: Slates	220	25	0.93	0.3
Type III: Slate-quartzite alternation	250	27	3.40	0.3
Type IV: Quartzite	350	28	11.1	0.3

which have been used for the different computer-based models.

– In the remainder of this study, the models calculated using the properties from geomechanical, laboratory and pressure meter, and hydraulic cylinder classifications will be referred to as models A, B and C, respectively.

As can be seen properties obtained according to pressure meter and laboratory tests are for intact rock, so these values do not represent the rock mass behaviour, excepting deformation modulus obtained from pressure meter tests.

3 MONITORING AND INSTRUMENTATION METHOD

3.1 *Type of instrumentation used*

Various types of instrumentation were used:

– Complete convergence station (designed and patented by autors (González-Nicieza et al. 2012), designed to measure convergence throughout the entire section of the tunnel, including a point on the floor (Fig. 1). Data was gathered automatically and continuously.
– Pressure cells, to record the radial and tangential stresses that arise. Depending on the problems in the zone, groups of between 3 or 6 were installed per section following the layout shown in Figure 2.
– Extensometers with mechanical anchoring, specially designed by the authors of this report (Argüelles-Amado *et al.*, 2010), which offer significant advantages for installation and have a precision of ± 0.01 mm. Each installation has two extensometers with three anchorings (3, 6 and 9 m) located on each shoulder of the tunnel (see Figure 3). Data has been gathered continuously (in real time) and has been automatically processed, making it possible to detect potential problems in terms of stability in advance.
– Measurements taken using an INCREX extensometer probe in horizontal boreholes between 10 and 20 m made in the walls of the section. This borehole makes it possible to take high-precision measurements (up to thousandths of a millimetre) of any movement of the soil in the lengthwise direction of a borehole.

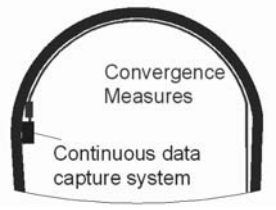


Figure 1. Example of a complete convergence station.

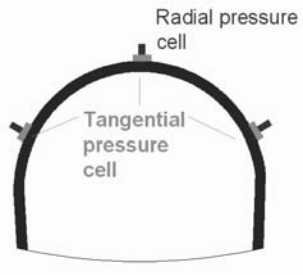


Figure 2. Example of a station with 6 pressure cells (radial and tangential).

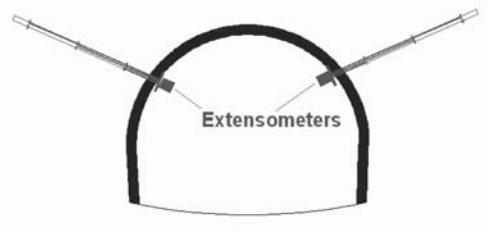


Figure 3. Example of a station with extensometers.

4 COMPUTER MODELLING OF THE TUNNEL

In order to determine which of the methods for calculating the properties of the rock mass offers the best fit to the real-world situation, the different sections of the tunnel with their support have been simulated using various computer-based models; in each case, the properties calculated using the geomechanical classifications, the pressure meter and laboratory tests, and the penetration tests using the hydraulic cylinder have been considered.

Comparing the results for each of these models with those obtained in the real world (the results of the instrumentation), it is possible to tell which of the methods allows us to obtain the results closest to a fractured rock mass.

The models have been developed using the FLAC-2D computer programme, based on finite difference numeric methods. The intense fracturation that rock mass presents makes suitable for its modelling the elastic-plastic Mohr-Coulomb criterion, because ubiquitous joints model does not represent in this case the behaviour of such fractured in all directions terrain. Taking into account the results of Poisson coefficient (approximately 0.3) calculated according to pressure meter tests and penetration tests, we have calculated a stress factor (relationship between horizontal and vertical natural stresses) of 0.43.

Models of Type I material (weakest material) have been modelled with support included simultaneously with the excavation. In the rest of models (Type II, III and IV materials) support have been included when the convergence of the section in the model reaches 10% of real convergence. Shotcrete have been modelled by

beam elements, and bolts by cable elements, both of them implemented in FLAC-2D.

5 ANALYSIS OF RESULTS

The most significant results of the monitoring and instrumentation method undertaken in the tunnel are discussed below. The majority of the instruments have been placed in areas regarded as weakest, where it is most important to monitor the movements and stresses of the soil.

5.1 *Convergences*

Figure 4 and Figure 5 show the convergence recorded in two sections created in type I materials (extremely weak materials located close to the south mouth).

The convergence is measured continuously along the entire section of the tunnel (from wall to wall). In Figure 4 the maximum convergence is 6 cm, whereas in Figure 5 the value is almost 7.5 cm. This difference in measurements is due to the fact that the zones have different coverings (180 and 300 m, respectively).

5.2 *Pressure cells*

The increase in pressure that occurs in the area surrounding the excavation has been measured using pressure cells positioned between the soil and the supporting panel. The results measured in two sections of type I materials with different coverings are shown below (Figure 6 and Figure 7).

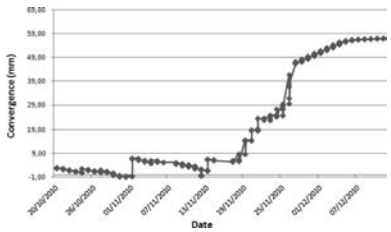


Figure 4. Convergence in type I materials with covering of 180 m.

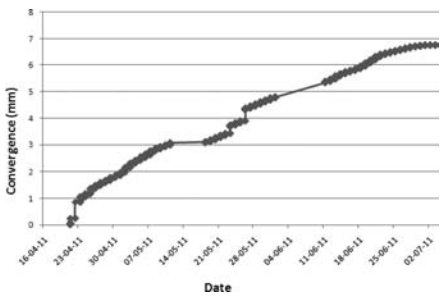


Figure 5. Convergence in type I materials with covering of 300 m.

The increase in covering entails a significant increase in the pressure of the soil on the panel: for a covering of 180 m, the increase is 4 bar (0.4 MPa); for a 300 m covering, the pressure increase is almost 12 bar (1.2 MPa).

5.3 *Extensometers*

Extensometers have been used to measure the lengthwise deformations in the area surrounding the excavation at different depths (3, 6 and 9 m). The devices have been positioned in sections of type II materials, which are most common throughout the length of the tunnel shaft. Figure 8 shows one of the graphs of measurements obtained using extensometers. The graph shows the movements of the terrain, 3, 6 and 9 m from the excavation. It is clear that the deformation is attenuated in a non-linear manner as we move away from the edge of the excavation.

5.4 *INCREX measurements*

The measurements have been taken in two 10 m boreholes located in a zone of type I materials. They have been taken at approximately monthly intervals, such that Figure 9 shows the evolution of the deformations in the area surrounding the wall over the course of four months.

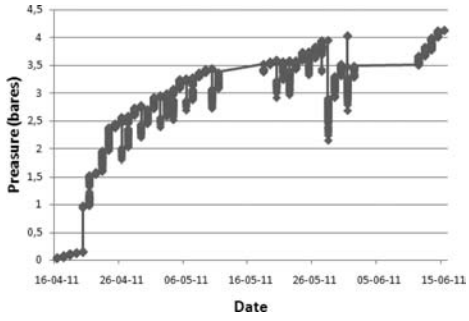


Figure 6. Pressure measured in gable for type I materials with 180 m covering.

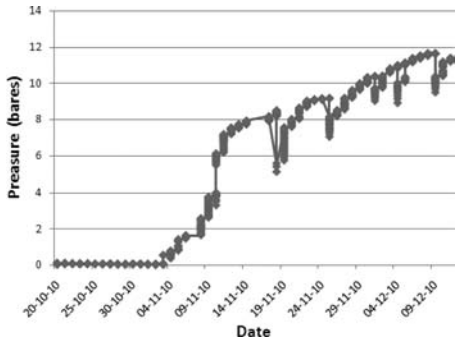


Figure 7. Pressure measured in gable for type I materials with 300 m covering.

The greatest deformations occur in the area closest to the excavation, in spite of being closest to the support. To begin with, the maximum deformations are of 5 mm at the mouth of the borehole (metre 0) and barely of 1 mm at the end (metre 10). Over time, they increase to 22 mm at the mouth of the borehole and 5 mm at the end.

5.5 *Analysis of results of back-analysis*

Let us now consider a summary of the most significant results of the models. To simplify the presentation of results, the graphs for each model (A, B and C) for a specific type of material are presented and compared with the corresponding real graphs for convergence, pressure, etc., measured in the tunnel using the instruments and detailed in the previous section. The real convergences and those obtained using the models cannot be represented on the same graph, since while the real convergence evolves over time (dates represented on the x axis), the convergence of the models varies with the steps of the calculation. Hence, the comparison must be made both based on the trend shown in the graph and the final value of the convergence.

5.5.1 *Convergences*

Figure 10 shows the convergences obtained for each of the models in a section of type I material with 300 m covering.

The different properties entered into each model mean there will be notable variations in the convergence of the set of the excavation between models. The lowest convergence is obtained using model B (properties obtained from pressure meter and laboratory testing), since the values of the strength properties were extremely high with respect to the others. The final convergence obtained in this case is barely 5 mm, well below the almost 80 mm measured in the tunnel. This is due to the fact that results of laboratory tests are for intact rock, so they don't represent the rock mass behaviour.

Convergences A and C are notably higher than those of model B. Analysing the data from Table 1 and Table 3, we can see that the values of the strength properties (cohesion and friction) are similar in both cases. However, the greatest difference between the two methods lies in the deformation modulus that is obtained, which is much lower for the tests carried out using the hydraulic cylinder.

Hence, while a convergence of 50 mm is obtained using model A, in model C the values are slightly over 70 mm, extremely close to the real value of 80 mm (see Figure 5).

5.5.2 *Pressure cells*

Figure 11 shows the simulated pressure measurements for type I materials. As can be seen, in model C (data obtained from penetration testing) the pressure increase is closest to the real value (Figure 7). The other two models exhibit similar trends, although the

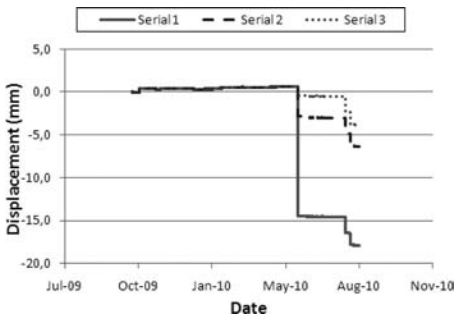


Figure 8. Extensometer measurement for type II materials.

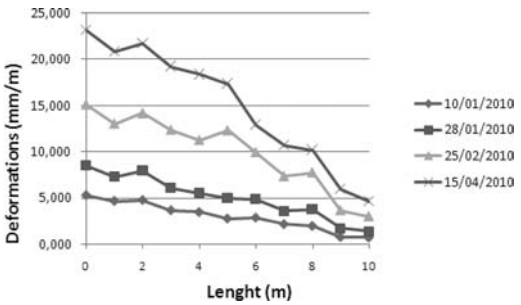


Figure 9. INCREX measurements for type II materials.

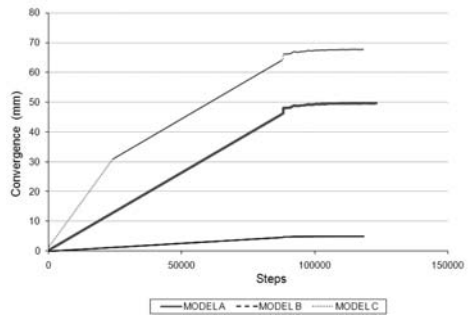


Figure 10. Convergence in type I materials with 300 m covering for the different models that were calculated.

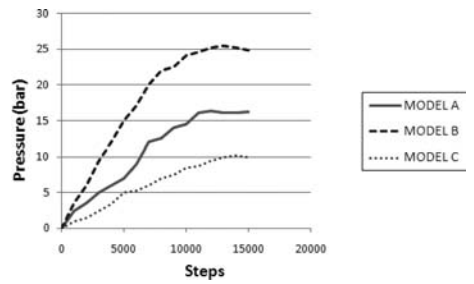


Figure 11. Pressure measured in gable in models.

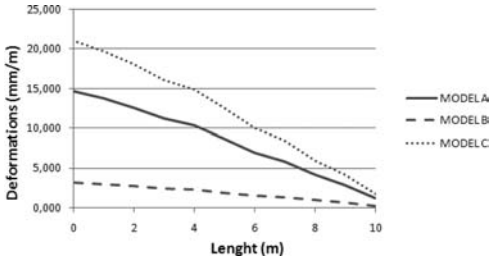


Figure 12. INCREX measurements for type I materials according to the different models calculated.

pressure increase is greater, especially in model B, due to the fact that these are materials with higher strength and deformation properties.

5.5.3 *Extensometers*

In this case, the values from the sensor located closest to the excavation (3 m) have been compared. The real sensor recorded a displacement of 18 mm in this zone. Once again, the model that gives the results closest to the real world values is model C (22 mm), although the adjustment is not as precise as in other calibrations.

5.5.4 *INCREX*

Even if the real measurements using INCREX have been taken at various moments after the excavation of the tunnel in a zone with type I materials, in the models it is not possible to establish a correlation between calculation stages and time. Hence, the comparison between the models and the real measurements has been determined based on the final measurements. If in Figure 9 we consider the measurement on 15/04/2010 and compare it to the measurements of each model represented in Figure 12 it is clear that model C is closest to the real measurement of the final deformation.

6 CONCLUSIONS

At an international level, there is a great deal of controversy over the methods for correctly characterising highly fractured rock masses.

Taking advantage of the excavation of a road tunnel in a mass with these characteristics, we have characterised the mass using three methods:

- geomechanical classifications;
- on-site and classic laboratory tests;
- on-site penetration test using the hydraulic cylinder designed by the authors of this study.

As the excavation was carried out, various continuous, real-time data collection instruments were installed to monitor displacements and pressures. Convergences and extensometers installed have been designed and patented by authors.

The properties calculated using each method were used to carry out a computer-based simulation of the excavation.

In order to verify which properties provided the best reproduction of the real-the world trend for displacements and pressure increases measured using the instruments, the graphical results were compared with the real-world graphs for each model.

In general, it was observed that for all the cases analysed, the properties calculated using the penetration tests offer the best fit, since they provide a reliable reproduction in the model of the deformations and pressure variations observed in the tunnel.

REFERENCES

Álvarez Vigil, A. E.; Álvarez Fernández, M. I.; López Gayarre, F.; González Nicieza, C. Título: Método y sistema para la realización de ensayos "in situ" y caracterización de terrenos heterogéneos o macizos rocosos intensamente fracturados. N. de solicitud: 201000902. País de prioridad: España. Fecha de prioridad: 15/07/2011. Entidad titular: Universidad de Oviedo.

Argüelles Amado, Antonio; González Nicieza, Celestino; Álvarez Fernández, M. Inmaculada. Título: Dispositivo para la medida de deformaciones en el interior del terreno (ES2331216). N. de solicitud: 200700810. País de prioridad: España. Fecha de prioridad: 28/05/2010. Entidad titular: Universidad de Oviedo.

Bakun-Mazor D., Hatzor Y. H., Dershowitz W. S. 2009. Modelling mechanical layering effects on stability of underground openings in jointed sedimentary rocks. International Journal of Rock Mechanics & Mining Sciences, Volume 46, January 2009, Pages 262–271.

Chung, H, Chun, B, Kim, B, Lee, Y. 2006. Measurement and analysis of long-term behavior of Seoul metro tunnels using the Automatic Tunnel Monitoring Systems. Tunnelling and Underground Space Technology, Volume 21 (2006) Pages 316–317.

González Nicieza, Celestino; Álvarez Vigil, Arturo E.; Álvarez Fernández, M. Inmaculada; López Gayarre, Fernando. Título: Dispositivo para la medida de la convergencia en túneles. N. de solicitud: 201001189. País de prioridad: España. Fecha de prioridad: 17/12/2012. Entidad titular: Universidad de Oviedo.

Isik N. S., Ulusay R., Doyuran V. 2008. Deformation modulus of heavily jointed–sheared and blocky greywackes by pressuremeter tests: Numerical, experimental and empirical assessments". Engineering Geology, Volume 101 (2008) Pages 269–282.

Kurzweil H. C. 2004. The LHC-project of CERN - large caverns in soft rock: A challenge for scientists and engineers. Tunnelling and Underground Space Technology, Volume 19, Issues 4-5, July-September 2004, Pages 410–411.

Shou K.J., Liu Y.C. 2004. Modelling of soft rock tunnelling in western Taiwan. Tunnelling and Underground Space Technology, Volume 19, Issues 4-5, July-September 2004, Page 419.

Vardakos S. S., Gutierrez M. S., Barton N. R. 2006. Back-analysis of Shimizu Tunnel No. 3 by distinct element modelling. Tunnelling and Underground Space Technology, Volume 22, November 2006 Pages 401–413.

Rock Mechanics for Resources, Energy and Environment – Kwaśniewski & Łydżba (eds)
© 2013 Taylor & Francis Group, London, ISBN 978-1-138-00080-3

The shape effect and rock mass structural control for mine pillar design

L.A. Ayres da Silva
Departamento de Engenharia Minas e de Petróleo da Escola Politécnica, Universidade de São Paulo, São Paulo, Brazil

A.L.M. Ayres da Silva
Netzsch Akw Equipment and Processes Ltda., São Paulo, Brazil

E.C. Sansone
Departamento de Engenharia Minas e de Petróleo da Escola Politécnica, Universidade de São Paulo, São Paulo, Brazil

ABSTRACT: The shape effect, widely studied by researchers as Hustrulid (1973), Protodyakonov (1964), Obert and Duvall (1967) and Bieniawski (1984), has had its importance recognized in the scientific and technical community since a long time ago (Bunting apud Hustrulid, 1973; Bunting, 1911). In all its technical applications however, the rock mass structure has not been taken into account. But as Bell (2000) also stresses, it is of fundamental importance for the determination of compressive strength in rock masses. This study aimed to investigate the variability of the results obtained in uniaxial compressive stress tests, using prismatic and cylindrical specimens, considering their slenderness (respectively L/H and D/H), which Bieniawski (1984a,b) defines as the relationship between the smaller size of the section and its height. In order to quantify the influence of the rock mass structure on the result of the shape effect expression, one intended to correlate its parameters with the value of Q-system of Barton (2007).

1 INTRODUCTION

The literature assigns the first attempts at rational design of pillars in underground mines to Bauschinger who, as mentioned by Bunting, verified in 1876 the compressive strength variation of 23 prismatic specimens of sandstone (Switzerland) according to the relation between their width and height, obtaining the first equation which related these two variables (Bunting apud Hustrulid, 1973).

In 1911 Bunting, studying the design of pillars in an anthracite mine, carried out tests on 13 prisms between 2″ and 6″. Based on his experience he observed the behavior of 8 pillars (from which only one failed) and obtained the same equation of Bauschinger (Bunting, 1911).

It is worth mentioning that Bunting obtained the following the equation:

$$C_P = 1750 + 750\frac{L}{H} \quad \text{(psi)} \tag{1}$$

where C_P = compressive strength in psi, L = the smallest pillar width in inch; and H = pillar height in inch.

In 1946 Obert & Duvall, performing a series of laboratory tests on various rock types, surprisingly reached the same relation (Obert & Duvall, 1967).

$$C_D = C_1\left(0.778 + 0.222\frac{D}{H}\right) \quad \text{(MPa)} \tag{2}$$

where C_1 = compressive strength in MPa for specimens having $D/H = 1$; C_D = compressive strength of specimen with $D/H \neq 1$; D = diameter of specimen in cm; and H = height of specimen in cm.

The importance attributed to such a formula is enhanced by the fact that it is to this very day still adopted by ASTM for correction of compressive strength results obtained on prismatic specimens of concrete or rock.

The same aforementioned authors in their 1967 book, not considering the scale effect (questionable for them) in their formula, proposed the use of a safety factor between 2 and 4, when applied to the pillar design, being valid for the range: $0.25 < L/H < 4$.

In 1937, Greenwald et al (cited by Bieniawski, 1969) accomplished the first "in situ" compressive strength test with a significant number of specimens of Pittsburgh coal seams in order to determine the

strength and deformation characteristics of coal specimens of large volume. The tested specimens presented all square section with widths varying between 0.8 and 1.6 m and a width/height ratio between 0.5 and 1.0. The specimens were cut with handheld saw, without the use of explosives. A thick concrete block was molded on the top of each specimen and the load was applied by means of one or two large capacity hydraulic jacks mounted between the concrete and the roof of the mine. The loading was carried out in stages and the deformations read every interval, when stabilized. Seven specimens were tested but, it has not been possible to establish any correlation between the results obtained, because they were of different dimensions. Some specimens, but not all, failed in the form of a double inverted pyramid.

The authors have obtained a relation between compressive strength and the width/height ratio that was later disregarded. However, in 1941, a different relation was obtained by the same authors with the accomplishment of five additional tests.

The second relation was obtained on a total of 7 tests. Two results of the previous series were rejected and three subsequent series (from five) were considered negligible because the widths were considered small (0.3–0.5 m).

$$\text{First relation: } C_P = 700\sqrt{\frac{L}{H}} \quad \text{(psi)} \tag{3}$$

$$\text{Second relation: } C_P = 2800\sqrt{\frac{L}{H^5}} \quad \text{(psi)} \tag{4}$$

after Bieniawski (1984a)

where C_P = compressive strength obtained on pillars of square section in psi; L = the pillar width in m; and H = height of pillar in m.

It is important to mention that slenderness is treated nowadays as a dimensionless parameter since it represents a relation between dimensions of the same order normally expressed in the same units, L/H (or D/H), i.e. width (or diameter) per height. In the initial studies of shape effect, however, there were different equations such as that proposed by Greenwald et al (see formula 4), in which slenderness correlated dimensions with different orders (L/H^5).

2 SHAPE EFFECT

Shape effect was designated as being this evident relation observed between the pillar dimensions and its ability to resist to the compressive stresses acting on it.

It is observed in laboratory compression tests that for specimens of ratio L/H around 1 or greater, there is a possibility of the rupture plan to intercept the frame plate, inducing the specimen confinement and giving as a result a higher result for the value of the rock material compressive strength. It is recommended therefore to check this property of the rock material that the specimens have a ratio L/H equal to 0.4 or 0.333. However, the effect is there, both for specimens as for rock pillars. This effect is the so-called influence of the ratio L/H or slenderness. What is important of such discussions is exactly the verification of this effect on the pillar when the exploited layer (pillar rock mass) is contained between weaker or more resistant surrounding rocks.

Thus, on the contact plan of both lithologies-discontinuities friction forces will arise in order to confine the pillar (weaker surrounding rock) or unconfine it by stress inducing, respectively of compression or traction in the contact pillar/surrounding rock.

Considering that such equations were defined based on research solely on coal, we consider questionable adopt the presented values as constants and applicable to any lithologies and rock mass structures, as stated by some of the mentioned researchers.

Bieniawski, for example, even studying coal from Witbank coalfield, obtained the following expression for the shape effect (1969,1984a,b):

$$C_D = C_1\left(0.64 + 0.36\frac{D}{H}\right) \quad \text{(MPa)} \tag{5}$$

where C_1 = compressive strength in MPa for specimens having $D/H = 1$; C_D = compressive strength of specimen with $D/H \neq 1$; D = diameter of specimen in cm; and H = height of specimen in cm.

Thus the authors of this study decided to verify the real importance of slenderness for the determination of rock pillar compressive strength.

3 PERFORMED STUDIES

Our research started with the continuation of studies conducted by Ayres da Silva (1992, 1993a,b) when he investigated various kinds of rock, testing them to observe their scale and shape effect.

3.1 *Manganese mine in the Urucum rock mass, Corumbá, Brazil*

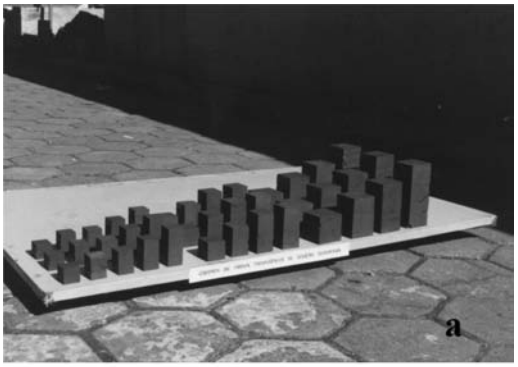
Studying the shape effect on prismatic and cubic specimens of Urucum manganese samples (see Figures 1a and 1b) of chemical sedimentary origin (deposition on the seabed), Ayres da Silva obtained the following expression:

$$C_D = C_1\left(0.344 + 0.656\frac{L}{H}\right) \quad \text{(MPa)} \tag{6}$$

defined for the range $0.4 < L/H < 4.93$.

where C_1 = compressive strength in MPa for specimens having $L/H = 1$; C_D = compressive strength of specimen with $L/H \neq 1$; L = width of specimen in cm; and H = height of specimen in cm.

The specimens from Figure 1a shown above are prismatic of square section, with nominal dimensions of



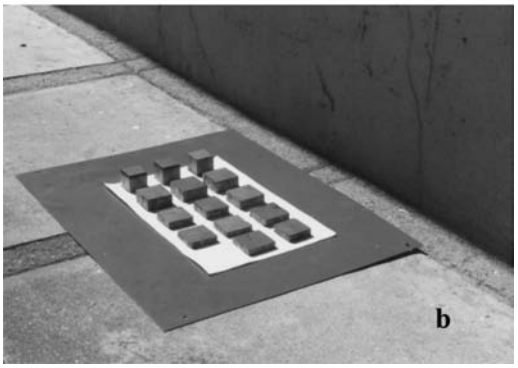


Figure 1. Prismatic specimens of square section.

respectively 4, 5.5 and 8 cm and slenderness ranging from 0.39 to 0.77. The specimens of Figure 1b are also prismatic with square section, but nominal dimensions of 4 cm and slenderness of 2.14 to 4.93.

One can observe that the manganese ore presented highly horizontal structure with an approximate spacing of 5 cm in the bedded strata.

3.2 *Basalt in the northwestern region of São Paulo State, Brazil*

Verifying the same phenomenon on the massive basalt that arises in the foundations of the road-rail bridge of 3600 m long (Ferroban) in Porto Itamarati-SP (in the design phase of those structures) on the lake of Ilha Solteira power plant, one reached to the following expression:

$$C_D = C_1\left(0.615 + 0.385\,\frac{L}{H}\right) \quad \text{(MPa)} \qquad (7)$$

where C_1 = compressive strength in MPa for specimens having $L/H = 1$; C_D = compressive strength of specimen with $L/H \neq 1$; L = width of specimen in cm; and H = height of specimen in cm.

The tests were carried out on prismatic and cubic samples.



Figure 2. Cubic basalt blocks ready to be tested, before the top rectification.



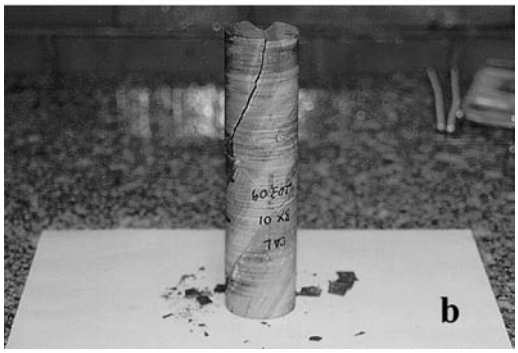


Figure 3. Compressive strength being controlled mainly by rock structure, regardless of the ratio D/H (slenderness).

3.3 *Limestone mine in Sorocaba, São Paulo, Brazil*

The tests performed by Sansone (1997) in his Master's thesis, showed the strong influence of the discontinuity planes on the limestone of São Roque Group (where the underground operation of Santa Helena mine takes place), which has structure defined by folding succeeding its stratification in a metamorphic process of marbling.

The following figures show the types of rupture that occurred for various ratios D/H, in which one can verify the control of the discontinuities on the way the specimens failed.

Table 1. Results of compressive strength tests

Type of rock	Nominal dimensions of the specimens cross sections	Number of specimens	Average dimensions L_a or D_a (cm)	H_a(cm)	Average Slenderness L_a/H_a or D_a/H_a	Average UCS (MPa)
Manganese mine in the Urucum rock mass, Corumbá,	4 cm × 4 cm	2	4.11	5.74	0.72	91.15
		3	4.12	5.99	0.69	83.90
		3	4.19	7.99	0.52	114.27
		3	4.22	9.97	0.42	58.70
	5.5 cm × 5.5 cm	3	5.32	8.23	0.65	102.83
		3	5.31	11.11	0.48	53.63
		3	5.45	12.02	0.45	58.93
	8 cm × 8 cm	3	7.88	11.97	0.66	46.93
		3	7.82	15.13	0.52	71.77
		3	7.89	19.89	0.40	78.00
	4 cm × 4 cm	2	4.32	0.88	4.91	592.50
		2	4.03	1.25	3.22	279.45
		3	4.26	1.95	2.18	210.47
Basalt in the northwestern region of São Paulo	4.5 cm × 4.5 cm	7	4.50	9.00	0.50	180.56
	4.5 cm × 4.5 cm	6	4.55	12.02	0.38	183.17
	4.5 cm × 4.5 cm	16	4.46	1.35	3.32	403.00
Limestone mine in Sorocaba, São Paulo	diameter of 3.2 cm	22	3.23	8.93	0.54	210.34
	diameter of 4 cm	24	4.18	7.26	0.80	169.28
	diameter of 5.4 cm	21	5.41	7.07	1.03	106.11
	diameter of 9.8 cm	12	9.75	8.80	1.38	129.78

As the author of the research stated: "Based on the verifications shown in the photos, one concludes that the characteristic failure mode of the studied lithology is fundamentally conditioned by the structure of the rock mass: stratification with inclined orientation, arising from alternating layers differentiated by the chemical nature."

"It was noted in the course of the tests, that during the specimens loading, there was a trend to non-mobilization of the rock intrinsic strength, but rather of the weakness plans oriented according to the stratification direction, quite suitable to rupture, varying around the value of 45°."

And the shape effect strength reproduces analytically the previous statements:

$$C_D = C_1\left(0.922 + 0.078\frac{D}{H}\right) \quad \text{(MPa)} \tag{8}$$

where C_1 = compressive strength in MPa for specimens having $D/H = 1$; C_D = compressive strength of specimen with $D/H \neq 1$; D = diameter of specimen in cm; and H = height of specimen in cm.

The table 1 summarizes data of the performed compressive strength tests.

These observations coincide with the statements of Bell (2000), who citing Barton, shows that the rock mass compressive strength has a direct relationship with the spatial orientation of discontinuity planes, varying in relation to the angle formed by them with the direction of the principal stresses acting on the sample, which is illustrated in the following figure.

In this, as in other cases, it can be verified that the results of uniaxial compressive strength of specimens are strongly affected by the dominant structure observed on them.

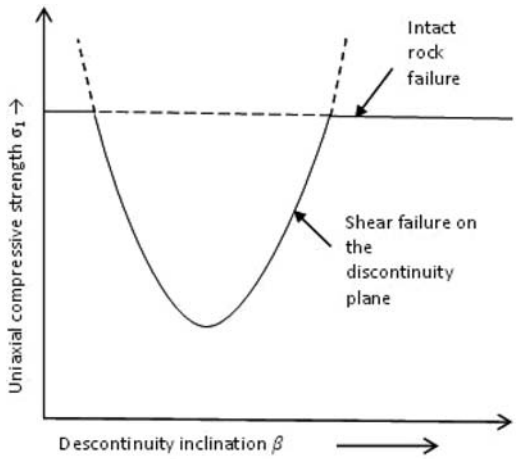


Figure 4. Illustrations of the failure plane angle and the direction of the greatest principal stress.

Thenceforward it sought to investigate the behavior of the pillars and specimens under uniaxial compression, correlating its results with the rock mass structural features.

An equation was deduced from these several experimental studies accomplished at the Rock Mechanics Laboratory of the Mining and Oil Engineering at the University of São Paulo. The completion of the research studies demonstrates the influence of rock mass structural control on the shape effect and its importance in the design of pillars in underground mining.

4 THE ROCK MASS STRUCTURAL CHARACTERIZATION

For correlation of the shape effect with the rock mass structural features, several alternatives were devised such as from Hoek & Brown and Bieniawski (1984a,b), opting finally for Barton's classification that, owing to the correlation with pillars, had its parameter Q adopted with only the first two ratios (Barton, 2000). The factor concerning the presence of water and SRF (stress reduction factor) were also, in this case, not considered necessarily applicable. The range of this modified and adopted Q was 0.1 to 100 (in the Figure 5 this parameter is presented as Q_p).

Thus based on the available data of the researches closer to the authors as well as their experience, the following conclusion was reached: $\frac{b}{a} = 0.79Q^{0.42}$ which can be expressed by the chart below.

The obtained values have demonstrated to be very consistent in many applications, and confirmed in retro analysis the verified equations. However, they are being deeper investigated through laboratory and field studies carried out in postdoctoral program by the coauthor of this paper.

What has become clear in many of these investigations and has been confirmed through the design of pillars is that the dimension of greatest importance in pillar section is that defined as more critical and not the smaller one.

The most critical dimension is the one that presents discontinuities families with smaller spacing and dips closer to 45°. Thus, when designing the pillar, this side should have such an extent that allows it to resist suitably the possible displacements occurring under these structures. Such structures, as demonstrated, which tend to control the behavior of the pillar. Consequently, the most critical side can be the larger side of a rock pillar section and not the smaller side as initially imagined.

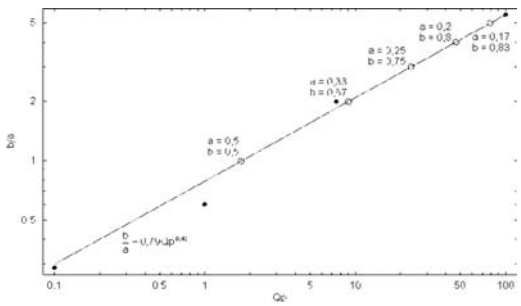


Figure 5. The correlation between the parameters a and b and the quality of the rock mass will be given by Barton's modified Q index (Q_p).

5 CONCLUSIONS

As stressed above in this work, the authors conclude that it is not only the slenderness that has to be considered in the shape effect, but in many cases the dimension to consider in the ratio has to be the side that occurs in the most unfavorable direction to the strength of the rock mass.

Therefore, to bring up the issue of slenderness of a rock pillar in this application will only make sense if the rock mass constitutes a massive or homogeneous rock material, without a defined or identifiable structure, or if it has a structure consisted of an uniform horizontally bedded or stratified planes.

The authors suggest that the designation *critical ratio width per height* for the ratio L/H will define the shape effect with greater precision and accuracy.

REFERENCES

Ayres da Silva, L.A. 1992. *Proposta de metodologia para a determinação da resistência à compressão de maciços rochosos, a partir de ensaios de laboratório*. São Paulo, 225p. Tese (Livre-Docência) – Escola Politécnica, Universidade de São Paulo.

Ayres da Silva, L.A.; Hennies, W.T. 1993. Methodology for rock mass compressive strength characterization from laboratory tests. In: International *Workshop on Scale Effects in Rock Masses, 2*, Lisbon. Proceedings. Rotterdam, Balkema, pp. 217–24.

Ayres da Silva, L.A.; Sansone, E.C.; Fujii, J. 1993. Shape effects considerations on the uniaxial compressive strength of hard rocks. In: *Safety and Environmental Issues in Rock Enginering,* EUROCK 93, 1, Lisbon. Proceedings. Rotterdam, Balkema, pp. 715–721.

Barton, N. 2000, TBM Tunneling in Jointed and Faulted Rock. Appendix, pp. 151–160. Rotterdam, Balkema

Bell, F.G. 2000. *Engineering properties of soils and rocks.* Oxford, England, Blackwell Science Ltd.

Bieniawski, Z.T. 1969. In situ large testing of coal. *African Council for Scientific and Industrial* s. n. t., pp. 67–74, paper 5. In: South Research.

Bieniawski, Z.T. 1984a. *Rock mechanics design in mining and tunneling.* Rotterdam, Balkema.

Bieniawski, Z.T. 1984b. *Strata control in mineral engineering.* Rotterdam, Balkema.

Bunting, D. 1911. Chamber-pillars in deep anthracite mines. *Transactions of the AIME*, pp. 739–748.

Hustrulid, W.A. 1973. A review of coal pillar strength formulas. *Rock Mechanics, v. 8*, pp. 115–45.

Obert, L.; Duvall, W.I. 1967. *Rock mechanics and the design of structures in rock*. New York, Wiley.

Protodyakonov, M.M. Methods if evaluating the cracked state and strength of rocks in situ. In: *International Conference On Strata Control And Rock Mechanics*, New York, 1964.

Sansone, E.C. 1997. *Estudo de aspectos geomecânicos aplicados ao projeto de minas subterrâneas.* São Paulo, 228p. Dissertação (Mestrado) – Escola Politécnica, Universidade de São Paulo.

This page intentionally left blank

Rock Mechanics for Resources, Energy and Environment – Kwaśniewski & Łydżba (eds)
© 2013 Taylor & Francis Group, London, ISBN 978-1-138-00080-3

The residual risk of an abandoned mine

D. Brambilla, L. Longoni, M. Papini, D. Arosio & L. Zanzi
Dica, Politecnico di Milano, Milano, Italy

ABSTRACT: It is well known that the mine legacy is a serious concern to present communities. The high risk associated with subsurface voids together with the lack of knowledge of geometric and geomechanical features of former mining areas make abandoned underground mines one of the current challenges for countries with a long mining history. In Italy, no long-term assessment of abandoned mine sites is required by law. In this paper we deal with the case study of Montevecchia mine, a marl mine in northern Italy abandoned in 1958 after a massive collapse. The event affected all mine levels along their middle sections and caused a large sinkhole. We initially performed geological and geophysical investigations to develop a physical model of the site. After that we carried out several numerical simulations to evaluate the stability of tunnels still in place.

1 INTRODUCTION

Abandoned mines represent a serious concern in countries with a long mine history. After being exploited for years, depleted mines are closed and abandoned; so all the monitoring activities cease and also drainage pumps are stopped, letting water flood the caves. The mine undergoes a progressive decline without any control; indeed in Italy long term assessment of abandoned mines is not required. The direct consequence is the presence of a number of closed mines whose extent and condition are unknown; even documentation is usually lost or inaccurate. These mines represent a constant threat to human settlements in terms of water pollution, subsidence and collapses. Due to this critical situation many efforts are posed to limit the hazard due to mines. The paper presents some guidelines to deal with mine through the description of a case study. The study develops through 1. historical data collection 2. geometrical and geotechnical features assessment 3. stability evaluation by numerical models 4. Risk scenarios development. The case study will show difficulties arising during the analysis of an abandoned mine and how is possible to overcome them.

1.1 *Montevecchia mine*

Montevecchia mine is located in Italy, 50 km north of Milan (Fig. 1). It has been exploited from 1930 to 1958 to extract marl, when a massive collapse interested all its seven levels. After that, the extraction stopped and the mine was never opened again. The deposit of marl is sub-vertical bed of 20 meters thickness: the stratum is limited laterally by flysch on both sides. The top of the layer, near to surface, is altered and three different zones, with different properties, can be identified. The geometry of the mine is supplied by extraction maps, schemes and drawings of the period of activity. According to workers' testimonies, some segments of the tunnels were enlarged respect to what was planned. This enlargement was done for economic reasons, but at the same time it represented a risk for the excavation stability. Therefore uncertainties in geometry assessment play a key role in stability evaluation. The first level of the mine is found at 46 m deep from the hill surface and seven tunnels were excavated with a gap of around 16 m base to base. Figure 2 illustrates the plan view of the mine: the long red region represents the excavation zone along the entire mine, while the central red spot locates the collapse area. After the collapse a large sinkhole appeared on the surface of the hill and its presence can still be spotted. The documents collected from local authorities gave an insight about geometry and plans, but no data about rock quality were recovered thus a complete geological and geophysical survey was needed.

2 ROCK QUALITY ASSESSMENT

Geo-structural conditions are usually classified in terms of rock quality. Due to the difficult and hazardous access to the mine, with the lower six levels completely flooded, two methods have been used and combined. First a geomechanical approach with survey on the visible part of Marl strip was performed, then a geophysical survey to investigate the marl properties in depth was executed. The two approaches

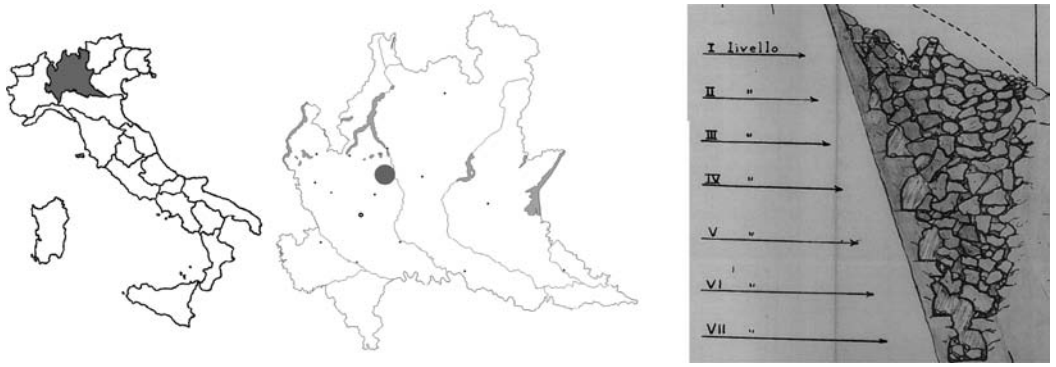


Figure 1. Montevecchia location in Italy and original document hypothesis about collapse.

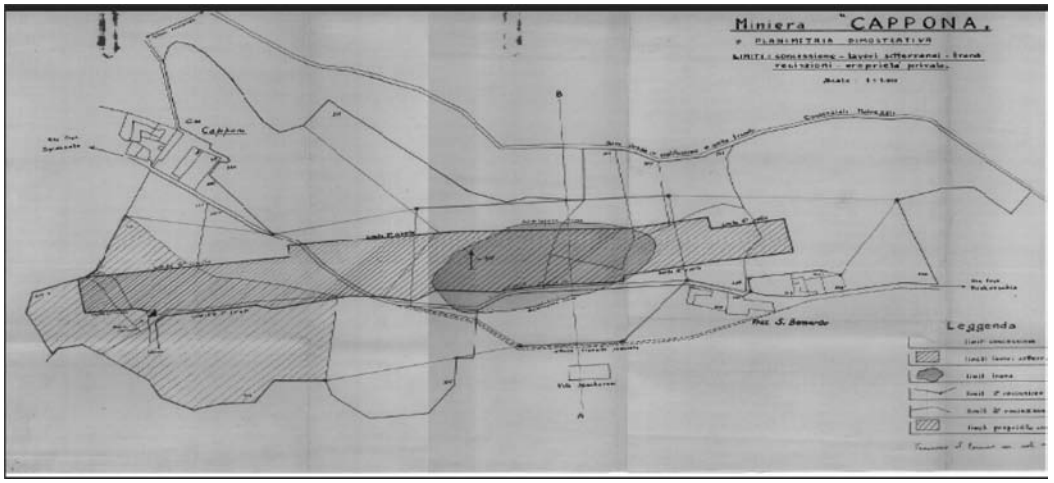


Figure 2. Montevecchia mine map, highlighted the surface area affected by collapse

and their results will be explained in the following paragraphs.

2.1 *Geological survey*

Rock mass conditions in terms of structural behavior is characterized by rock mass classifications. The selected methods were: 1. GSI (Geological Strength Index); 2. Q-System or Barton's classification; 3. RMR (Rock Mass Ratio) or Bieniawski's method.

The survey was done both on Marl and Flysch and results are reported in Table 1.

As can be seen from the values of rock mass classification the rock quality of Marl can be considered fair and the rock mass shows good mechanical properties.

Table 1. Rock mass classification values.

Geomechanics parameter	Flysch	Marl
Q	0.7	1.27
GSI	40–45	45–50
RMR (Q)	41	47
RMR (GSI)	45–50	50–55

2.2 *Geophysics*

Two different surveys were performed in Montevecchia (Arosio et al. 2012): *Seismic refraction* and multichannel analysis of surface waves (MASW) method. Seismic refraction used P-wave refraction which evaluates the compression wave generated by the seismic source with an array of receivers. The wave was generated by vertically striking a plate with a sledgehammer. *MASW* method is one of the seismic survey methods evaluating the elastic condition (stiffness) of the ground for geotechnical engineering purposes. MASW was selected for two main reasons: 1. It is based on S-wave model while refraction seismic is based on P-wave and thus gives a more complete

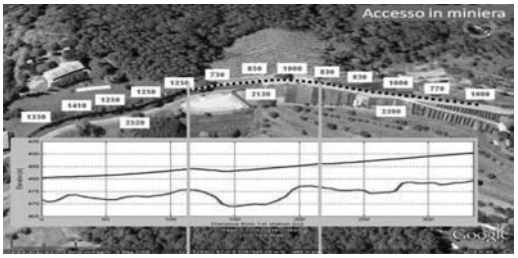


Figure 3. Geophysic survey, blue line represents surface, red line first layer thickness.

Table 2. Layer properties (mine is excavated in layer 4).

Layer	E	ν	ϕ	cohesion
Layer 1	1.39	0.27	–	–
Layer 2	5.13	0.42	–	–
Layer 3	5.91	0.44	–	–
Layer 4	11.74	0.36	40	0.7
Flysch	8.53	0.40	–	–

picture of rock mass; 2. Can detect velocity inversions. This method was performed along the mine alignment and the path was divided in three segments as it is shown in Figure 3.

2.3 *Constitutive model parameters*

The surveys focused on the definition of rock masses mechanical properties; materials will be considered elastic perfectly plastic in the model, since this law combines simplicity and a good simulation of real behavior of rocks. The mechanical properties for each layer are derived by rock mass quality indexes and by geophysics surveys, using empirical equations and Hoek-Brown criterion. Table 2 summarizes the layers properties. All the calculations are conducted with density equals to 2200 kg/m^3, but just layer 4 plastic features are calculated since the others were not needed.

3 NUMERICAL MODEL

The model was developed with 3DEC software by Itasca Ltd (Cundall et al. 1988). The model is a distinct element code coupled with a finite element model of single blocks; the main advantage is the ability to investigate the role of the two joints between Flysch and Marl which are believed to be crucial for mine stability. The first step in building a model of the Montevecchia mine was the definition of model extent; since the problem is in plain-strain condition a quasi-2D approach is possible (Fig. 4). This procedure allows to calculate boundary conditions for partial models. These are preferred because are more fast to run but

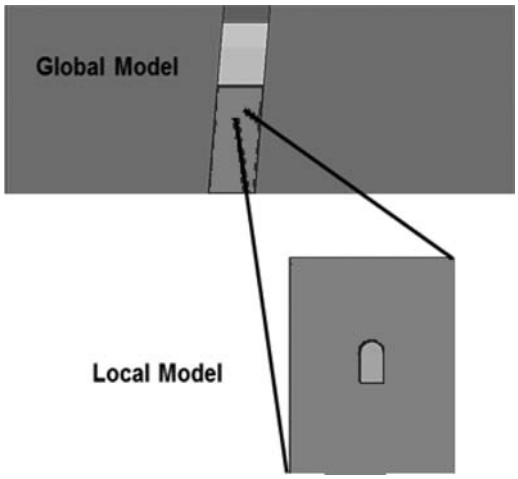


Figure 4. Local model extraction from global model.

equally representative; therefore in this way is possible to test different combinations of tunnel dimension or position and check the effects on the stability of the whole mine. Several models were considered in order to understand the behavior of the mine in different conditions in terms of geometry, deepness and tunnels section. The aim of computational modeling is to reproduce the stress-strain status of the mine according to what was designed and built. Furthermore, the results are useful to understand the possible conditions that led to the mine collapse. The proposed models are three selected from the many tested: one for shallow levels and two for deep levels. Shallow levels model: 1. Set of the three top levels. Deep levels models: 1. Set of the three last levels; 2. Proximity effect between tunnels.

3.1 *Shallow levels models*

3.1.1 *Set of the top three levels*

This case aims to model the behavior of the three shallowest levels. The three levels are found at 46, 69 and 85 m deep from the surface respectively. All the tunnels have the same dimensions 7 × 8 m and it is assumed to be small compared to the length, so the use of the plane-strain solution is permitted. Looking at the results in Figure 5, it is possible to highlight interesting behaviors: 1. the increase of tunnel depth leads the tunnel stability to worse conditions; 2. the deformation magnitude increases as the tunnel deepness increases; 3. there is low probability of intersection of plastic zones; 4. the arch effect is present around the tunnels as demonstrated by the shape of plastic regions and stresses that tends to be circular.

3.2 *Deep levels model*

The load on tunnels increases proportionally with deepness as expected; these load conditions influence the excavation stability and more attention must be

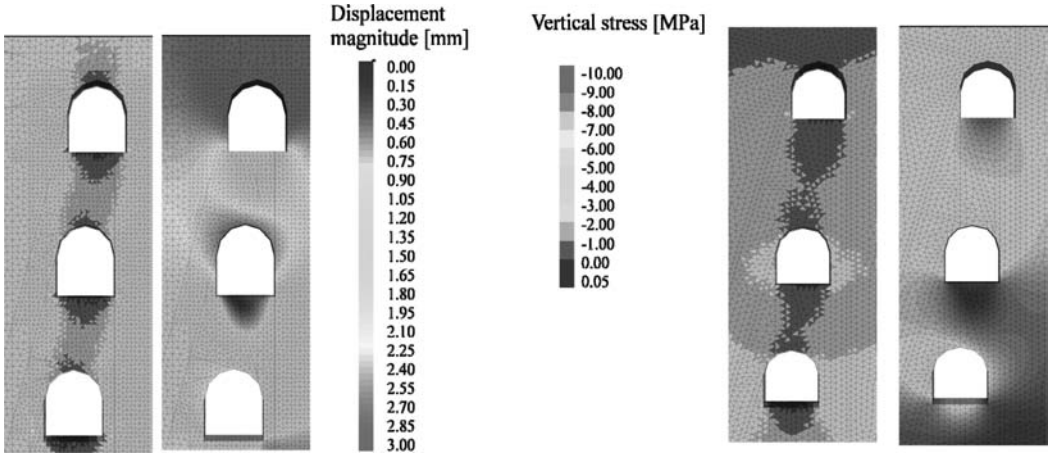


Figure 5. Shallow levels (on the right) and deep levels (on the left) stresses and displacements.

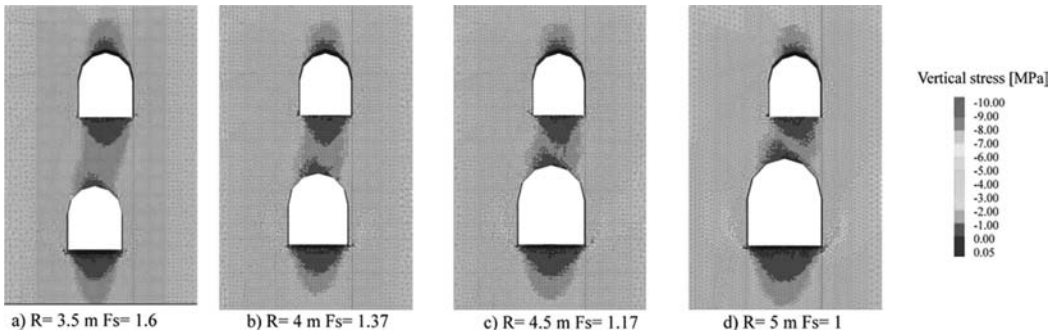


Figure 6. Tunnel proximity and safety factors.

paid to avoid possible collapses. In this section, two examples will be illustrated to understand the behavior of deep levels and explain the possible causes that led to the global collapse of 1958.

3.2.1 *Set of the three last levels*

This case is built in the same way of the previous one, but the levels considered now are the deeper three, so the stresses in the rock are significantly bigger (Fig. 5). Under these conditions the system shows acceptable displacement magnitude, smaller than 1cm. An analysis of plasticization zones highlight how the integrity of each tunnel may be critical and eventually local collapses could be possible. Note that the vertical stresses get re-distributed around the tunnels describing again the arch effect.

3.2.2 *Proximity effect between tunnels*

The first two simulations were focused on the behavior of the shallow and deep levels of the mine, tested with the mine authorized geometry; both the models do not show alarming situation. Actually some over exploitation of tunnels was reported by workers and it is probable that the collapse cause is linked to the tunnel section alteration. Due to the lack of specific indications and the inaccessibility of the tunnels different possible sections are simulated in search for critical section. The deepest tunnel enlarges progressively in the four cases (Fig. 6). The simulations are performed considering the last two levels, 133 and 149 m deep from the mountain surface, which are the most critical. Figure 6 shows how the factor of safety reduces as the lower tunnel enlarges. The critical span value, when FS is equal to 1, is 10 meters. This result suggests that in some point of the seventh level the section may have exceeded the critical values and the safety factor dropped below 1 causing the collapse that progressively interested all the levels up to the surface. The hypothesis is confirmed by the reports of minor collapse from the vault of seventh level in the months preceding the 1958 collapse.

4 HAZARD ASSESSMENT AND SCENARIOS

An effective hazard assessment for an abandoned mine is hard to be accomplished due to the reasons proposed. The main challenge is linked to the

impossibility to access the study area and recover geometry information which can be lacking or partial. It is therefore useful to analyze the main uncertainties which can affect model results and that are usually related with both geometry and material properties. In the Montevecchia study case the material properties were assessed via geophysical and geological tools and confidence level is fairly high when compared to the geometry one. In case of low level of confidence the authors are convinced that all the realistic possibilities should be investigated creating different sets of parameters combination. This approach was followed and explained in the previous paragraph, in which four cases are presented. The cases, which differ in tunnel dimension, cover combinations from tunnels of original designed section joined to standard mechanical properties to tunnel with critical section joined with the same properties. It is noticeable how the tunnel with original design dimension, vault span 7 m, shows a FS value of 1.6 assuring its stability and how an enlargement of almost 40% to 10 m span is needed to push the system to a critical status. At present is not possible to assess the span of remaining tunnels with the needed resolution, since they are not accessible, so the creation of hazard scenarios and all considerations about mine stability are mainly probability based. Therefore since no evidence of underground falls have been detected in the last 55 years, the remaining tunnels are supposed to be in a relatively stable condition with a good level of confidence. This analysis can lead to the definition of a series of scenarios in which little collapse of sections of tunnels are the most probable hazard.

5 CONCLUSIONS

As widely known abandoned mines are a source of hazard for people living and working over the extraction areas. In the previous paragraphs the hazard related to abandoned mines is analyzed and explained. After being exploited for years mines are left without long term hazard assessment plans. This situation can produce possible threat to the surface, both as sudden collapse or subsidence and water pollution problems. The authors want to propose some guidelines to deal with abandoned mines by the analysis of the study case of Montevecchia. This mine was abandoned after a collapse in 1958, unfortunately no useful information to assess the actual stability of remaining tunnels is available. A first stage of information collection should recovery all the existing data and underline missing information; then uncertainties should be investigate. A geological and geophysical survey campaign was set up to analyze deep rock mass quality and properties; obtaining reliable parameters. Geometry definition is uncertain, because of the lack of plans and the impossibility to access the tunnels; traditional underground investigation techniques, such as seismic or ground penetration radar, cannot give an image of tunnel at the needed resolution. The difference between stable condition reported in plans and critical section is a mere three meters of span, a quantity too small to be measured without direct access. Given that there is no possibility to improve the confidence in geometrical data authors suggest a probabilistic approach to analyze the stability. Different combinations of a geometrical case with geomechanical parameters lead to different scenarios with an own probability to happen. Historical considerations and absence of activity in the last 50 years, suggest that an extreme scenario is less probable. To improve the knowledge and control of the mine some actions could be taken: putting some radar reflectors would give the possibility to monitor slow subsidence with Permanent scatterers technique, giving information on movements or on a complete quiet state reached by the mine; in this way the most probable scenarios can be selected and emergency planes prepared for them.

REFERENCES

Arosio, D., Longoni, L., Papini, M. & Zanzi, L. 2013. Seismic characterization of an abandoned mine site.Acta Geophysica 61(3): 611–623, DOI: 10.2478/s11600-012-0090-0

Cundall, P.A. 1988. Formulation of a three-dimensional distinct element model – Part I: A scheme to detect and represent contacts in a system composed of many polyhedral blocks. *Int. J. Rock Mech. Min. Sci. & Geomech. Abstr.* 25: 107–116

This page intentionally left blank

Rock Mechanics for Resources, Energy and Environment – Kwaśniewski & Łydżba (eds)
© 2013 Taylor & Francis Group, London, ISBN 978-1-138-00080-3

Analysis of the consequences of mining exploitation in substantially disturbed strata based on spatial measurements of a building's tilt

L. Florkowska & A. Kanciruk
The Strata Mechanics Research Institute of the Polish Academy of Sciences, Cracow, Poland

ABSTRACT: Mining in a rock mass substantially disturbed by many years of exploitation may lead to serious consequences for the surface and buildings. This paper presents an analysis of the consequences of mining in such conditions. The analysis has been based on the measurements of the tilt of a church tower situated over the intersection point of the edges of two previously mined longwall panels. The exploitation of the next panel, in a seam below, resulted in the reactivation of the goaf. The results presented in this paper have been obtained through the use of a remote building deformation monitoring system. One of the elements of this system is a vibrating-wire (VW) tiltmeter which permits a spatial measurement of the tilt. The tests performed aimed to establish how a given building reacts to the impact of mining operations. The measurement system elaborated at the Strata Mechanics Research Institute of the Polish Academy of Sciences (SMRI PAS) is able to continuously (with a pre-set frequency) monitor the tilt. The results obtained permitted the observation of the building's behaviour during the time when the effects of mining exploitation were gradually revealed. The time of the first reaction of the building and the tilt direction justify a conclusion that the main reason for the results observed was the impact of the previously exploited longwall panels. The consequence of the fact that the panel edges were situated under the building was that it remained for a prolonged time in the area of positive strain of the ground and permanent sloping of the surface. When a lower lying seam was being mined and before the principal impact of these operations reached the church its tower tilted sharply in the direction opposite to the direction that should theoretically be expected to result from the impact of the moving mining face. Then, as the longwall panel advanced a gradual turn of the tilt plane was recorded. The measurement system described in this paper can be used in scientific research done in the context of building protection as well as an engineering tool to help evaluate the safety of buildings in mining areas. Thanks to gaining new knowledge about how buildings react to mining operations conducted in the circumstances of a substantially disturbed rock mass, appropriate methods can be elaborated to optimally design mining operations in order to protect the surface and the existing buildings.

1 INTRODUCTION

Underground mining of raw materials gives rise to a number of geotechnical problems connected with deformations of the subsoil of structures in areas affected by the exploitation. The principal mining area in Poland is the Upper Silesian Coal Basin It contains almost 80% of documented economically feasible deposits of Polish hard coal. Hard coal has been mined in this area for several dozen of years. As a consequence, the rock mass is substantially disturbed and it is difficult to predict the effects of planned exploitation operations (Florkowska 2012). Untypical stress states in the rock mass may appear as a result of reactivation of the goaf due to mining carried out in lower lying seams. This in turn causes structures to react in unexpected ways. For this reason predicting the impact that planned mining exploitation will have on a structure and evaluating the structure's safety requires a thorough analysis of the history and mining situation of the area where the structure is situated.

The traditional predicting methods often prove to be insufficient in new geotechnical conditions when the original structure of the rock mass is substantially disturbed. That is why scientific research needs to be carried out to expand the knowledge about how structures react when they are subjected to repeated mining exploitation. This research provides valuable information about how buildings react to subsoil deformations thus induced and is the basis on which new standards for predicting the impact and evaluating the safety of mining exploitation can be elaborated. Research work carried out in this field by persons with relevant knowledge and experience consists of measuring how the state of deformation of the building changes during the exploitation process and of making observations of how it behaves.

This paper presents the results of observations made using a modern tilt measuring system elaborated at the Strata Mechanics Research Institute of the Polish Academy of Sciences (SMRI PAS) in Cracow.

2 THE IMPACT OF UNDERGROUND MINING EXPLOIATATION ON THE SURFACE AND BUILDINGS

The damage to the rock mass structure resulting from mining a seam is not limited only to the most immediate neighbouring area; it transfers the undesirable impact to the higher parts of the rock mass. Just under the surface there are soil layers which, in contrast to brittle rocks, become deformed in a continuous manner. A so called subsidence trough is formed on the surface. As the process of trough formation progresses in time and space the soil of the near-surface layers, which is also the subsoil of the buildings, suffers significant deformations. The temporal aspect of trough formation depends both on the progress of mining works and the rate at which the processes in the rock mass advance, which is why trough formation is not complete the moment mining stops (Florkowska 2010).

Rock mass deformations are a source of additional loads for buildings. A building and the subsoil on which it is founded form an interacting system where the loads from the building are transferred to the ground and the ground deformations are transferred to the foundations. In the subsidence trough formation process the subsoil under the building undergoes a number of transient states of deformation. Each of these states induces a different type of load on the foundations.

The loads exerted on the structure caused by underground mining are closely linked with the movement of the face of mining exploitation. The strains of the ground brought about by the mining trough formation induce normal and tangent stresses on the contact surfaces with the foundations. The subsoil's tilt on the slopes of the trough causes an inclination of the building from the vertical and the change of directions of the principal stress. A uniform subsidence of the surface, which in itself does not pose a direct threat to the building, causes changes to the ground water level, which alters the pattern of forces the soil exerts on the foundations. Displacements of the ground may cause in multi-segment buildings with an elongated floorplan a dislocation of individual segments relative to one another or/and their pressing against one another, which induces normal and tangent contact stresses in contact areas between the segments. Mining tremors are sources of dynamic loads on structures. They can also cause radical changes in the state of stress in the disturbed rock mass.

3 THE STUDY OF THE IMPACT OF MINING EXPLOITATION ON BUILDINGS

In order to study how buildings react to underground mining exploitation a measuring system must be used which will provide data concerning the magnitude and timing of the building's state of deformation. In practice geodesic or extensometer sensor-based systems are used for this purpose. It is important to note that in both of these cases automatic measuring systems must be incorporated into a wider programme of global monitoring of a structure with the participation of specialists. It must also be remembered that the measurements of this type are point measurements. The image of how a structure works obtained on the basis of these measurements depends therefore on a proper choice of the points where to install the sensors and their number. The defects which may potentially appear in areas not covered by the measurements will remain 'invisible' to the monitoring system. Thus an additional, periodic monitoring of the whole object must be ensured

An on-going observation of the state of the building as the principal impact of exploitation becomes revealed is used to obtain measurements for the scientific research but can also be used in mining damage prevention. The standard measures of regular visits performed as part of technical supervision can be effectively supported by means of various automatic monitoring systems. Undoubtedly, remote systems are the most convenient for the user as they make it possible to monitor the changes occurring in the building without the need to take readings at the site where the device is installed. Thanks to remote data transmission results can be read on a computer of choice (Florkowska 2010, Witakowski 2010).

4 THE REMOTE TILT MONITORING SYSTEM FOR BUILDINGS

A remote-controlled building monitoring system based on measuring linear strains and the width of scratches and on spatial measuring of tilt was elaborated at the SMRI PAS. It can monitor how a building reacts to mining exploitation and it can also monitor the changes as the process progresses.

4.1 *System diagram*

Figure 1 shows the system diagram of the tilt monitoring system for buildings. It consists of a tilt transducer – the vibrating-wire (VW) tiltmeter 1 and of the remote TMS-1 VW meter 2. The tiltmeter 1 is supposed to be permanently fixed to the structure to be monitored. The remote TMS-1 meter 2 is an 8-channel

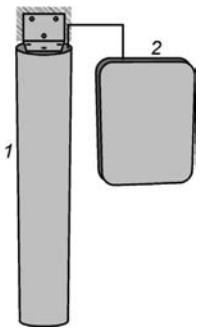


Figure 1. Tiltmeter – 1 and TMS-1 VW meter – 2.

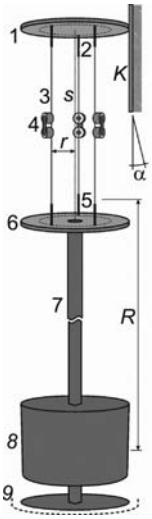


Figure 2. Tiltmeter scheme (Description in the text).



Figure 3. The tiltmeter mounted on the building.

device; the tiltmeter uses 3 of them. The remaining inputs can be used to connect other VW transducers.

4.2 *The VW meter*

The VW meter designed at the SMRI PAS can be used to make spatial measurements of tilt. Thanks to the design solution used, based on three vibrating wires, the tilt plane, tilt value and tilt plane's turn during observations can be measured (Kanciruk 2012). The scheme of the tiltmeter is shown in Figure 2 and a model of the device in Figure 3.

A disk 1 is firmly fixed to the structure *K* (Fig. 2) changes to the tilt of which should be monitored. Three grips 2 of the upper ends of the three vibrating wires 3 are fastened to the disk. The lower ends of the wires

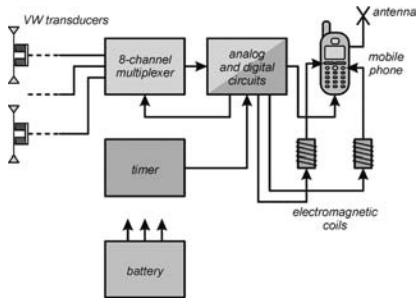


Figure 4. Block diagram of the remote TMS-1 VW meter.

are fixed to similar grips 5 of another disk 6. All the wires are hung every 120°, parallel to the axis crossing the centres of disks 1 and 6; they are also at the same distance *r* from it. The lower disk 6 has a pendulum consisting of an arm 7 and a weight 8. A swinging damper 9 equipped with a disk immersed in a liquid of appropriate viscosity dampens the free swinging of the pendulum. Each vibrating wire is equipped with an individual electromagnetic coil, the function of which is to incite the wire to vibrate and convert the vibrations to electrical signals. The electromagnetic coils 4 are fixed to the disk 1 through a ring which is not shown in the figure. The strain of individual vibrating wires 3 of the tiltmeter results from the weight of the pendulum and the tilt angle of the building α (Fig. 2). In the neutral position all the wires have equal tension and therefore their strains are also equal. As a result of the structure tilting by a certain angle α the strains of individual wires change but their sum remains unchanged. Knowing the strains of the individual wires it is possible to calculate the tilt angle α for the building and the angle θ between the vertical plane in which this tilt occurs and a predefined direction (Kanciruk, 2012). The strains of the wires are calculated based on the measurement of the period of their free vibrations.

The VW tiltmeter, like other measuring transducers, is not a self-functioning measuring device because it can only be used together with a special electronic device which would incite the wires to vibrate and measure the period of these vibrations, e.g. together with the remote TMS-1 VW meter. This meter is an automatic measuring device, which has additional functions of recording data and radio transmitting them. Figure 4 shows the block diagram of the TMS-1 meter. Eight transducers can be simultaneously connected to it and the measuring circuit can be activated every ¾; 1.5; 3; 6; 12; 24; 48 or 96 hours. The data are sent through the GSM network and the measurement results, coded as SMS, can be delivered via an internet gate in the form of an e-mail message to a declared address. The power supply battery used and the air-tight casing ensure at least 6 months of maintenance-free operation of the device in the field (Kanciruk 2012).

5 THE IMPACT OF MINING IN A DISTURBED ROCK MASS ON A SACRAL BUILDING

The measuring system described above was used in scientific research the purpose of which was to identify how buildings react to underground mining in a substantially disturbed rock mass – in conditions which prevail in the Upper Silesian Coal Basin.

5.1 *The location and structural conditions*

The monitored church is situated in the Upper Silesian Coal Basin. It is part of the remains of a 19th century historical complex of buildings situated in Bytom. The small neo-Gothic church was built in 1896 (Fig. 5). It is a two-aisle brick building, partially with a basement. The aisle is situated on the north side. The floor-plan dimensions are approximately 20×12 m. The construction of the church, typical of the sacral architecture of the period, consists of pillars, buttresses and load-bearing walls together with cross-ribbed vaults over the naves and aisles and a stellar vault ceiling over the presbytery. A quadrilateral tower is situated next to the side aisle from the north side. In 1987 the entire complex was added to the list of heritage sites.

5.2 *The geological and mining conditions*

The hard coal deposit below Miechowice was exploited in the total of 13 seams, situated both in Ruda Beds as well as in Saddle Beds. Figure 6 shows the contours of longwall panels worked between 2008 and 2010 and longwall panel 18a exploited between 2011 and 2012; the position of the church is also marked. As can be seen the church has recently been directly over longwall panels:

- 72a in seam 507wd – mined 2008 – 2009
- 97a in seam 509wd – mined 2009 – 2010
- 18a in seam 510wd – mined 2011 – 2012.

Additionally, about 220 m to the west from the building in question there is a disused Northern Shaft of the former 'Prusy' Coal Mine (Miechowitzschacht der Pressengrube). The present mining operations are mainly carried out in the shaft pillar. The deposit is mined using the longwall technique with roof caving. This is an unfavourable exploitation technique due to the lack of the installation to perform a backfilling, as a result of which the roof collapses causing damage to the surface. For this reason the principal elements of mining damage prevention are: reducing the height of the longwall and reducing the speed of exploitation.

5.3 *Installing the measuring system*

In December 2011 a measuring system was installed in the building consisting of four wire extensometers and a VW tiltmeter connected to the TMS-1 device. The extensometers were mounted in the church aisles and the tiltmeter and the TMS-1 device were placed in the tower. The system was supposed to measure the width of the scratches present in the masonry of the nave and in the vault of the aisle as well as the



Figure 5. The monitored building. Lutheran Church; Bytom.

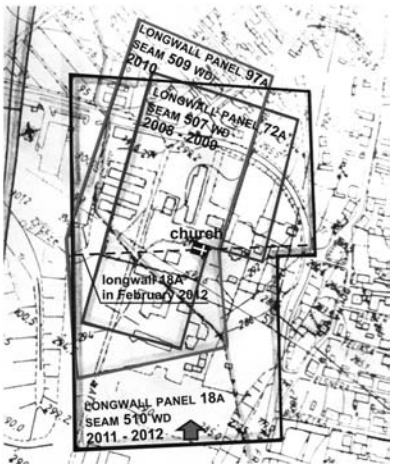


Figure 6. The position of the monitored building relative to the longwall panels mined between 2008 and 2012.

tilt of the tower; these values changed as a result of the deformation of the subsoil caused by underground mining. The meter regularly sent the measurements to one of the computers at the SMRI PAS. It was agreed that a series of measurements should be made with the starting frequency of 8/24 hours. In July 2012 this frequency was reduced to 4/24 hours and in September 2012 to 2/24 hours. In each series the vibration periods T of individual wires were measured four times. This made it possible to evaluate the repeatability of the measurements and calculate mean values of these periods. In this way, by the end of February 2013 over 2200 measurement data packages were obtained.

5.4 *Tilt measurement results*

Thanks to the results obtained with the tiltmeter a complex system of changes could be observed of the

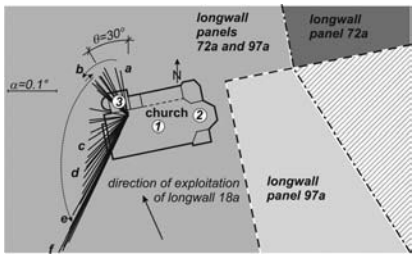


Figure 7. The floorplan of the church, its position relative to mining panels, the tower's tilt changes. 1 – the nave of the church, 2 – presbytery, 3 – church tower.

tower's tilt and its azimuth, which changed depending on how the longwall moved relative to the church site, the position of goaf and the occurrence of tremors.

Figure 7 shows a schematic floorplan of the church, its position relative to longwall panels 72a and 97a and how the tower's tilt changed. The position of longwall panel 72a (at the depth of 600 m) is very unfavourable because one of its edges (the dot-and-dash line) runs in the immediate vicinity of the church.

A bit further away runs the edge of longwall panel 97a (at the depth of 700 m). It is marked with the dashed line. The church is situated more or less centrally only relative to longwall panel 18a (at the depth of about 750 m). The figure shows the changes of the tower's tilt in weekly intervals and the changes of the tilt caused by tremors that could be felt by people. No later than the day after the equipment had been installed a powerful tremor occurred when the distance between the church and the longwall face was about 200 m. It was found that the tremor was not caused directly by the mining operations then in progress. This tremor changed rapidly the tower's tilt angle α from 0.01° to 0.11° and the change of the angle θ from −6.8° to 9.3°. These changes are illustrated by the „*a*" sections marked with a dashed line. Following the tremor the tower's tilt axis started to turn anti-clockwise, which is shown by the change of the angle θ in figure 5.3. Only at the beginning of February 2012 a minor, temporary reversal of the general tendency in the changes of the angle θ (the „*b*" case) was observed. In the first days of March 2012 the angle was almost 90°. At that time the mining face ran under the church. On 21st and 28th March two powerful tremor occurred, shown in the figure by means of pairs of sections „*c*" and „*d*" marked with a dashed line. Both tremors caused a small increase of the tilt angle α and a rapid change of the angle θ. The tremor of 28th May („*e*") did not result in any noticeable changes to the tower's tilt. Since then the tilt angle α has been increasing with the angle θ remaining stable – at about 150° (the „*f*" sections). From September 2013 the tilt angle α gradually become more stable and in December it was about 0.42°.

5.5 *Results analysis*

Figure 8 shows the measurements of the tower's tilt made between December 2011 and December

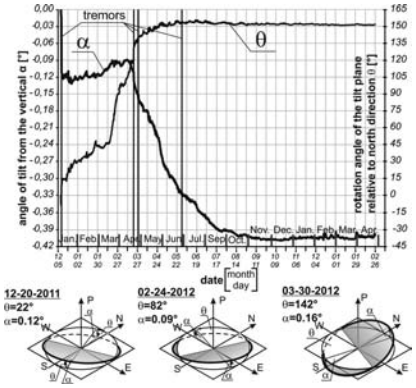


Figure 8. Recorded church tower tilt changes.

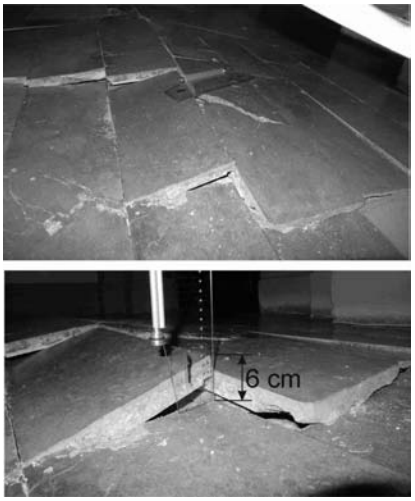


Figure 9. Example damage to the floor of the aisle following the tremor of 8th December 2011.

2012.The first clearly visible change was recorded on 8th December 2011. Then a powerful tremor occurred, which caused extensive damage, especially to the floor of the aisle (Fig. 9) and caused the tower to tilt towards the north. At that time longwall 18a was still at a considerable distance from the church. The tilt direction is therefore most probably connected with the church's position relative to the already mined longwall panels 72a and 97a.

The edges of these longwall panels intersect almost exactly under the building. The building was situated on the slope of a subsidence trough created as a result of mining the two longwall panels in the zone of permanent surface strain. As a result a complicated state of stress was induced in the subsoil on which the building was built. A powerful tremor recorded on 8th December was therefore most probably caused by a rapid stress relaxation of the rock mass caused by the then still small impact of the approaching longwall. From February 2012, at the time when the longwall ran under the building it was observed that the tilt plane turned in

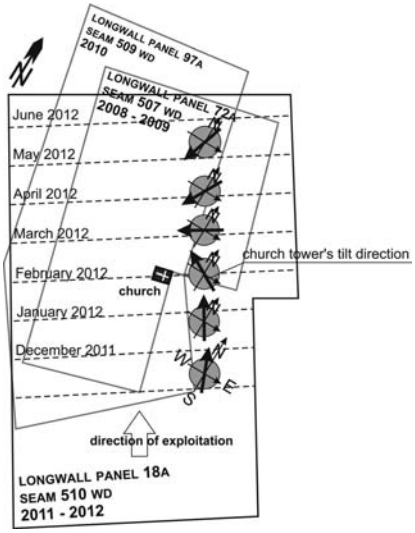


Figure 10. The change of church tower's tilt direction as longwall 18a's mining progressed.

the western direction and that the width of the scratch situated near the main entrance increased. Figure 10 shows the recorded turn of the tilt plane relative to the position of the longwall.

While longwall panel 18a was mined, the church suffered significant damage. The changes of principal stress directions caused by mining exploitation in longwall panel 18a, supported by the tiltmeter measurements, brought about a deformation to the building, the form of which was difficult to predict in advance. As we know, mining in an undisturbed rock mass should cause the surface to incline in the direction of the mining exploitation. This inclination would then increase as the longwall approached, reaching its maximum at the moment when the longwall face was under the building and then decrease (Knothe 1953a, b, 1957; Kwiatek 1997). The measurement results clearly indicate that the element that was decisive for the deformation of the church's subsoil while longwall panel 18a was being mined was a disturbance to the structure of the rock mass caused by previous mining exploitation and the reactivation of the goaf.

6 SUMMARY AND CONCLUSIONS

The completed research programme led to interesting observations of how a building reacts when it is subjected to the impact of mining exploitation in an area where intensive hard coal exploitation has been taking place for many years.

The results of the measurements made in the historical Lutheran church in Bytom-Miechowice have shown that the elaborated system proved very effective in monitoring the deformations of the building subjected to varying in time mining subsoil deformations.

The measurement results presented in this paper show the presented measuring system as an instrument of interesting scientific observations, providing knowledge about how a structure behaves when exposed to repeated mining exploitation. It is a useful tool, both as an engineering system helping to monitor buildings and as a system which can be used in scientific research.

The analysis made on the basis of the measurement data obtained confirmed that in areas where the original structure of the rock mass was substantially disturbed as a result of mining the pattern of stresses existing in the subsoil of buildings can be very complex. In such conditions even the smallest impact may cause dramatic changes. It is therefore a very difficult task to accurately predict what impact planned mining exploitation can have on the surface, buildings and technical infrastructure. An individual approach is necessary and an analysis of the history and the geological and mining situation needs to be carried out for each particular case taking into consideration its specific conditions.

REFERENCES

Florkowska, L. 2012. Building protection against the backdrop of current situation and growth perspectives for Polish mining industry. *Arch. Min. Sci.* 57(3): 655–665

Florkowska, L. 2010. Land subsidence due to mining operations in disturbed rock mass, on the example of Ruda Śląska (Poland). *Arch. Min. Sci*. 55(3): 691–701

Kanciruk, A. 2012. Methods for evaluating ground dislocations in mining areas. *Arch. Min. Sci*. 57(3): 487–496

Knothe, S. 1957. Observations of surface movements under influence of mining and their theoretical interpretation. *Proceedings of the European Congress on Ground Movement*. *The University of Leeds. April 9–12th*

Knothe, S. 1953a. Equation of subsiding trough's curvature. *Archiwum Górnictwa i Hutnictwa (Arch. of Mining and Metallurgy)* 1(1): 111–127 (in Polish)

Knothe, S. 1953b. Time influence on a formation of a subsidence through. *Archiwum Górnictwa i Hutnictwa (Arch. of Mining and Metallurgy)*. 1(1): 128–139 (in Polish)

Kwiatek, J. (ed.) 1997. Ochrona obiektów budowlanych na terenach górniczych. Katowice: Wyd. GIG

Witakowski, P. 2010. Bezprzewodowy monitoring obiektów budowlanych. *Materiały IX Sympozjum "System kompleksowego zarządzania jakością w budownictwie"*. Instytut Techniki Budowlanej (in Polish)

Rock Mechanics for Resources, Energy and Environment – Kwaśniewski & Łydżba (eds)
© 2013 Taylor & Francis Group, London, ISBN 978-1-138-00080-3

Geomechanical and geotechnical evaluation of maingate No. 080 5253 monitoring in the conditions of the Paskov mine

R. Kukutsch, K. Souček, P. Koníček, J. Ptáček, P. Waclawik & R. Šňupárek
Institute of Geonics, Institute of Clean Technologies, Academy of Sciences of the Czech Republic, Ostrava, Czech Republic

ABSTRACT: This paper addresses the monitoring results in the maingate No. 080 5253 at the Paskov Mine, in the Czech Republic. In the main longwall gate in question, the convergence of the mine affected by longwall mining 080 210, movement from loosening of the rock layers using extensometers, and the load steel frame construction reinforcement by dynamometers is monitored. In addition to in-situ measurements, research laboratory measurements were carried out to evaluate the influence of geological conditions, based on the RQD parameter of boreholes drilled before the extraction. The results show that geology, the character of the overlying rocks, and rock stress ratios play important roles in the effectiveness of the combined rock bolt and steel frame supports. The effective action of the reinforcements also shows significant adverse effects on floor lift, and these factors are reflected in the extension and retraction of anchors in the overburden and significant deformation of the profile.

1 INTRODUCTION

Even with the existing knowledge and experience of underground excavation of coal seams in the difficult mining and geological conditions of the Ostrava-Karvina coal mining district (the OKR), the installation of high-capacity and high-density support systems is unable to prevent significant deformation of mining gates at large depths (c. 800–1000 m), during the mining operations (Souček et al. 2012). The originating deformations are connected with the redistribution of stresses in the rock mass due to the excavation of the coal seams and consequently, there is deformation and fracturing of the rock mass surrounding the operating longwall gates. This is the reason for the great increase in the use of various types of anchor (e.g. stranded anchors anchored along roots, rock bolts fully encapsulated in resin) Anchoring systems are used both in an independent sense (rock bolts or anchors anchored directly to the excavated surface) and in a combined sense, where:

- anchoring elements, most frequently stranded anchors (sometime named rope anchors or string anchors) are anchored to the rock mass in various forms through steel support frames,
- rock bolts or stranded anchor heads are fixed directly to the surface of the excavated opening, and at the same time, steel support arches are installed.

For the suitable design and proper functionality of stranded anchors and all supporting systems of the mining gates, the following should be carried out:

- determination of geological and mining condition (lithological profile of overlying rock, thickness of excavated coal seam, determination of origin of overburden failure (e.g., RQD parameter, etc.) for designing the length and kind of rock anchor.
- in situ testing of tension-related characteristics of anchors and rock bolts (the so-called pull-out tests) for evaluation of the effectiveness of the designed anchors and rock bolts.
- in situ monitoring of the course of overlaying rock failure, observing and loading of the anchoring support in relation to the advance of the heading, and subsequently, the advance of the coalface for evaluation of the efficiency of the used anchors and rock bolts.
- if necessary, laboratory and in situ parametric studies on the behavior of anchoring systems (e.g., the influence of the installation borehole diameter on the tensile resistance of the anchors, the influence of the encapsulation length on the tensile resistance of the anchors, and the influence of the anchoring mixture on the tensile resistance of the anchors, etc.).

In the following chapters, we introduce some results and observations from the completed tests on the

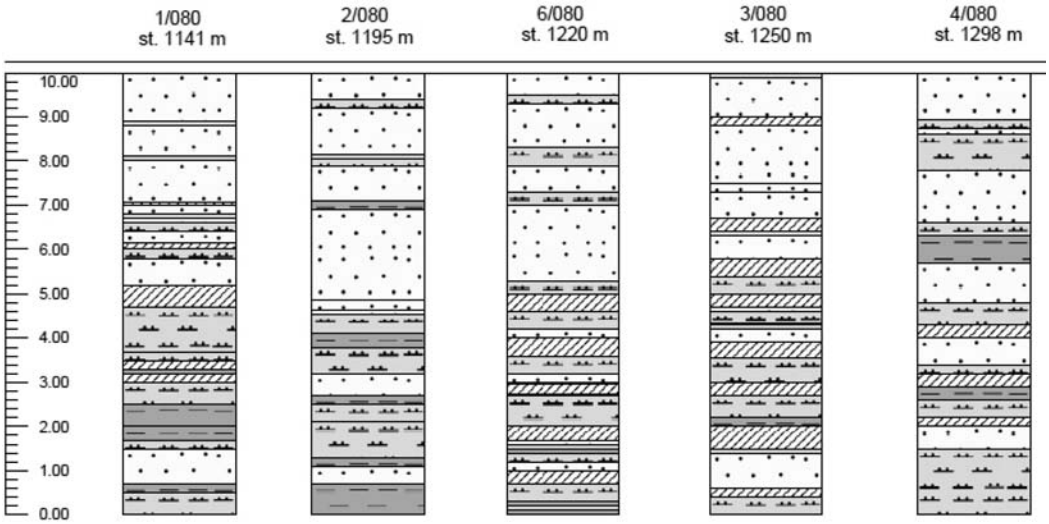


Figure 1. Overlying strata lithology of maingate No. 080 5253.

behavior of rock bolting and anchoring systems in the conditions of the longwall main gate No. 080 5253 at the Paskov Mine.

2 MINING AND GEOMECHANICAL CONDITION IN THE LONGWALL FACE 080 210

Longwall gate No. 080 5253 is located in seam No. 080 at the Paskov Mine, which is a mine without danger of rock bursts. This seam is included in the second class of coal and gas outburst risk. The seam inclination is zero. Apart from the overlying 80-cm bench of powerful position sandstones, section I comprises mainly siltstone and claystone; a firmer position occurs at a height of 5 m above the ceiling of the hall. Section II comprises regular alternations of claystone, sandstone, and siltstone with powerful position sandstone (205 cm) occurring at a height of 5 m. Section III is again alternating claystone, sandstone, and siltstone with the powerful position sandstone located above the anchor zone, from 6.5 m. In section IV, the final monitored field, there are present powerful positions of siltstone with sporadic occurrences of claystone. A thicker layer of sandstone occurs from a height of 5 m.

The assessment of the drill cores shows that the anchored overburden is composed of irregular alternating layers of siltstones, fine-grained and medium-grained sandstones, and clay stones. Irregular petrographic development is evident in both the horizontal and vertical directions (see Figure 1). The share of aleuropelitic rocks to psammitic rocks is about 1:1. The very low RQD values correspond to the petrographic structure in the area of interest. The average RQD value reaches 15.5%.

Mining of longwall face No. 080 210 commenced in November 2012 from the starting stationing of 1385 m in maingate No. 080 5253. The average mined thickness of the longwall is 112 cm, the length of the longwall face is 171 m, and the directional length of the longwall is over 1200 m. Average daily advance of the face is 5.0 m with peak levels of advance of 10 m/day.

Technologies: 113 sections Glinik, plow GH 9-38 VE and conveyor type PF 4/932

3 RESULTS OF THE PULL-OUT TESTS OF STRANDED (CABLE) BOLTS ON THE MAIN GATE NO. 080 5253

In the frame of comprehensive monitoring of the behavior and effectiveness of the stranded anchors, installed at longwall gate No. 080 5253, the tensile loading capacity of the single anchor systems used, identified as M and H below, was also tested:

- MI (in section I) – typical strand anchors 6-m in length, anchored at the their root with polyester resin HS Lokset Slow (anchorage length 2 m) subsequently grouted by using organic-mineral resin Geoflex, anchored directly to the excavated surface without a defined tensioning, stationing 1120–1160 m
- MK (section II) – typical strand anchors 6-m in length, anchored at the their root by using polyester resin HS Lokset Slow (anchorage length 2 m) anchored directly to the excavated surface without a defined tensioning, stationing 1175–1215 m
- HI (section III) typical cable bolts 6-m in length, anchored at the their root with polyester resin Lokset Slow (anchorage length 2 m), consequently grouted

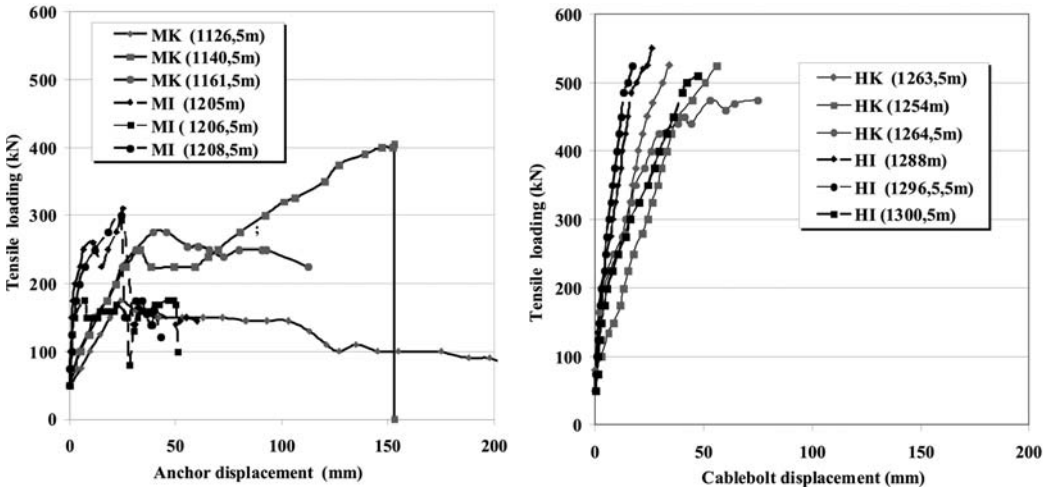


Figure 2. The pull-out test results.

with cement grout, anchored directly to the excavated surface with a defined tensioning of about 100 to 150 kN, stationing 1230–1270 m

- HK (section IV) typical cable bolts 6-m in length anchored at the base with polyester resin HS Lokset Slow (anchorage length 2 m). Anchors were tensioned during their installation on the excavated surface up to a level about 100 to 150 kN, stationing 1285–1325 m.

The purpose of the tests is to determine not only the simple pull-out strength of the installed anchors, but also to determine the overall tension-related characteristics of the anchors, which informs about the deformation curve (elongation or pulling out of the anchor) in relation to the tensile force applied. The elongation or pulling out of rock bolts is measured using a laser distance meter registering the values of the distances read. Together with data from the pressure transducer installed on the tension dynamometer, these data are recorded by means of special software on a PC into the final data set.

Figure 2 represent the typical characteristics of the tensile loading of the tested anchors. Based on the resulting tensile characteristics and pull-out strength of single anchors, it can be stated:

- From the graphs in Figure 2, it is clear that higher loading capacities have been recorded in cable anchors HI and HK, in comparison with the anchoring systems designated MI and MK, which could be caused by the poorer geological conditions (see Figure 1, borehole No. 1/080) in the overburden of the reinforced longwall gate.
- From the graphs in Figure 2, it is evident that there is minimal elongation of the anchor end of the pretensioned anchor systems HI and HK, up to level of the applied tensioning at the time of the anchors' installation.
- In both tested anchor systems, it is clear that the majority of the grouted anchors exhibit higher stiffness at all levels in comparison with those anchors anchored only at the root (see Figure 2).
- Pretensioned anchors of system HK, bonded only at the root, show similar pull-out characteristics to the grouted anchors of system HI, and they have markedly better anchor characteristic than system MK, which is anchored only at the root (see Figure 2).

4 MONITORING OF THE BEHAVIOR OF ANCHORING SYSTEMS

4.1 *Monitoring system description*

The complete monitoring system was as follows:

a) Observation of a load of selected reinforcing anchor elements by hydraulic dynamometers (Kukutsch et al. 2012). Each segment with anchor reinforcement two pairs of dynamometers (4 dynamometers to section) were installed at selected anchors. For the section of the installed anchor grouted (glued) along its entire length (MK and HK), only one pair of dynamometers has been installed. Overall, 12 dynamometers were installed. For anchors in sections MI, MK, and HK dynamometers with tensile capacity of 500 kN were installed, and for anchors installed in section HI, the dynamometers had tensile capacity of 750 kN.

b) Tensile tests of installed anchor elements were performed until their tensile strength with online recorded loads and deformations (see Figure 2).

c) Loosening monitoring of overlying rocks was performed using at least 3-level extensometers

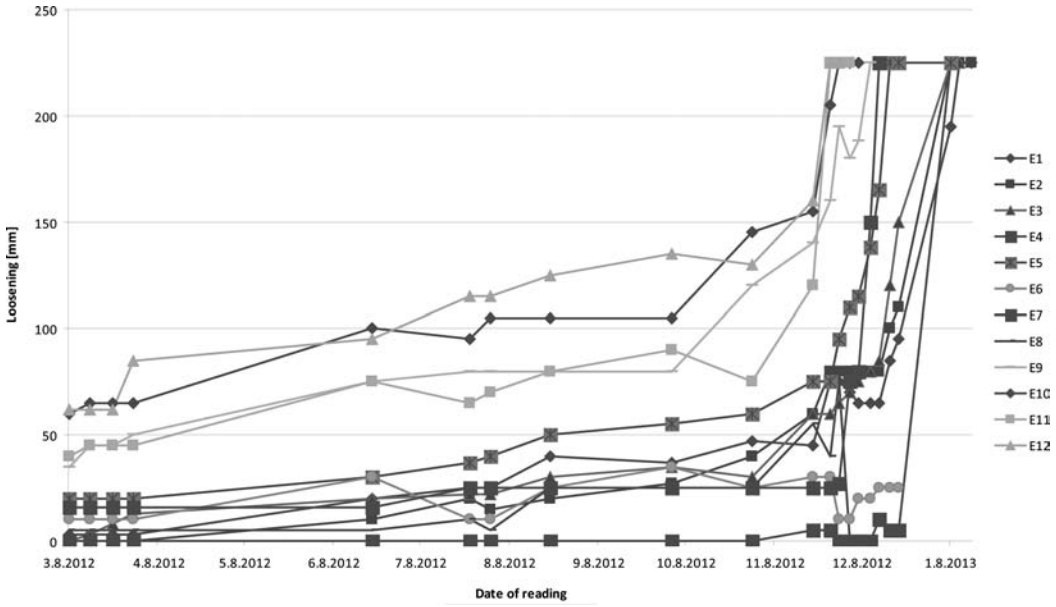


Figure 3. Overburden loosening.

(2.2, 5, and 7 m). Each section with anchorage systems had two mechanical extensometers installed (to a distance of 1 m from the load cells installed pairs), and each section without anchor reinforcement (reinforcement arc only) had just one mechanical extensometer installed (taking into account local conditions, approximately stationing 1172, 1127, 1282, and 1337 m). In total, 12 extensometers were installed.

d) Evaluation of stress of the overlying rocks through the main gate and RQD fragmentation was realized by short upward core drilling. The cores were drilled vertically upwards into the overburden of the longwall gate (approx. wellhead in the middle of the hall, according to local conditions, such that the wellhead was accessible for borehole camera inspection throughout the lifetime of the corridor).
e) Monitoring convergence in the main longwall gate with convergence profiles. The evaluation of the convergence is on the sections with anchor reinforcement installed for two convergence profiles and the stretch without anchor reinforcement after one convergence profile. There are also marked measurement points of convergence within the band (width of corridors within the agreed height above the invert, slippage between the upper and side arches TH reinforcement)
f) Borehole camera inspection in short upward boreholes of 50-mm diameter
g) In-situ stress measurement using a conical probe (CCBM).

4.2 *Monitoring and results*

Ongoing monitoring started after installation of all the elements of the monitoring system and began with performing the pull-out tests of installed cable bolts and strand anchors, and borehole camera inspection, etc. Monitoring began in November 2012, when longwall face No. 080 210 was launched

Monitoring of the extensometers consisted of control of the color scale or its part located under the roof outside the reference scale of the extensometer, and the accurate reading on the scales “A”, “B”, and “C” in millimeters is performed by the employees throughout the entire period of longwall mining at three- and four-day intervals.

Before commencing excavation, there was maximal loosening of 145 mm for extensometer E10, 130 mm for extensometer E12, and 120 mm for extensometer E9. Other extensometers showed values of loosening of 25–75 mm. From the above-mentioned extensometers with the maximum loosening, the greatest loosening was achieved at anchor “B” level, i.e., at a height of 5 m. We can determine that before starting mining, the maximum loosening was in the field of reinforcement systems HI and HK (see Figure 3).

After the start of excavation the maximum loosening at all levels was evident when the extensometers were pulled with broad front approaching 10 m before the extensometer. The exception is extensometer E6, which throughout longwall mining showed a maximum loosening of 35 mm at a time before the mining began. At the level of anchor B, at the time of deposit exploitation, the loosening was only 25 mm. Extensometer E8 was irreversibly damaged before mining.

The dynamometer readout was performed at three- and four-day intervals. With regard to the increase in values just before the approaching face, it was decided to take readout values during each shift, i.e., usually four times a day. However, incomplete data and

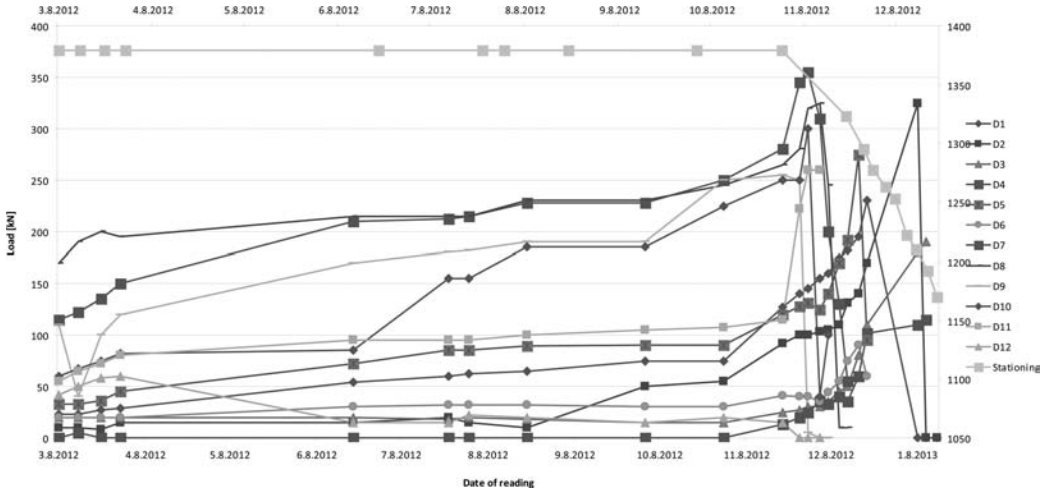


Figure 4. Development of the load.

reading errors caused inaccuracies and the data were very difficult to interpret.

During longwall mining, a significant increase of values was observed only in the immediate foreground of the longwall face (located within the influence of additional strain from the edge of the longwall face). However, in the field behind the longwall face, the pressure effects of the overlay resulted in the change of the values on the installed dynamometers.

Increased values occurred in each segment during the period prior to excavation (see Figure 4), but section HI (D7–D10) exhibited the largest increase in values of up to 250 kN. The remaining sections were loaded from 0 to 110 kN. After the start of mining, all dynamometers showed a jump in value just before the approach of the coalface. In the area behind the coalface except at dynamometer D11 (HK), another jump occurs, but this time as a reduction in value, in many cases falling to 0. Overall, the greatest load was registered in the HI section (250–355 kN), MI section showed loads of 0, 0, 190, and 115 kN, with the assumption that there will be a strain on the remaining dynamometers. Section MK showed a gradual reduction of the load behind the coalface (down from 275 to 90 and from 90 to 60 kN). The HI section showed a decrease in level of 55, 10, 0, and 40 kN. The HK section showed the maximum and minimum load, as indicated; the D11 dynamometer showed a maximum load of 260 kN and D12 exhibited minimum load of 0 kN.

The observation of this gate road was very difficult because of the "U type" ventilation, which meant that the space behind the coalface was only available until screen building. To determine how long the section behaves might have to wait until late 2013, when excavation will start on the adjacent longwall panel. However, from the results of monitoring, we conclude that the lightening of anchors behind the coalface is because of the existence of separation areas, and because the entire monitored area declined. Drop loads are demonstrated by the fact that in this section short anchors were used, whereas it would have been more appropriate to use longer anchors.

5 CONCLUSIONS

From the results obtained from the anchor pull-out tests, it can be stated that by pretensioning of the installed strand (cable), anchors in difficult geological and mining conditions can achieve better tension working characteristics of the anchors. In addition, anchors grouted along their length can affect the operating characteristics of the installed strand, and consequently, the cable anchors. In the case of disturbed and stratified overburden, anchor pretensioning and their subsequent pressure grouting can contribute to the stabilization of the overlying strata, introducing new strength bonds (bonding layer) in separation cracks. Pretensioning of the anchors up to a sufficient level can significantly affect stratification of the overlying strata during coal seam mining and eliminate loading of the longwall gates.

As the results of the pull-out tests show, the installed anchors exhibit the required capacity. However, technical mining conditions and the strain observed on the dynamometers in the area behind the coalface show that the chosen length of the anchors was less than was appropriate. Based on observations during the monitoring, it is suggested that a perfect contact between the support frames and rock mass is crucial for achieving the expected effectiveness of the application, not only of the steel support arches, but also of the entire range of combinations of anchoring support elements with steel support arches. Without meeting this fundamental condition, the efficiency of the entire support system is significantly compromised.

In addition, big problems are caused by deformations and heaving of the bottom of the entries during mining work. In the future, it will be necessary to examine the use of techniques reinforcing these areas.

ACKNOWLEDGEMENT

This article was written in connection with project Institute of clean technologies for mining and utilisation of raw materials for energy use, reg. no. CZ.1.05/2.1.00/03.0082, which is supported by the Research and Development for Innovations Operational Programme financed by the Structural Founds of the Europe Union and the state budget of the Czech Republic and Grant of the Ministry of the Interior of the Czech Republic (project No. VG20102014034).

REFERENCES

Junker, M. et al. (eds) 2009. *Strata Control in In-Seam Roadways*. Essen: VGE Verlag.

Kukutsch, R., Souček, K., Koníček, P. & Ptáček, J. 2012. High anchoring in the hallways for dual use and their monitoring. *Uhlí, rudy, geologický průzkum* 19, Special Issue: 24–28. (in Czech)

Singh, B. & Goel, R. K. 2011. *Engineering Rock Mass Classification - Tunneling, Foundations, and Landslides*. Waltham: Elsevier Science.

Souček, K., Koníček, P., Staš, L., Šňupárek, R. & Ptáček, J. 2012. The use of anchoring systems in OKR underground mines and testing of their resistance. *Tunel* 2: 4–10. (in Czech)

Stillborg, B. 1994. *Professional Users Handbook for Rock Bolting*. Clausthal-Zellerfeld: Trans Tech Publications.

Rock Mechanics for Resources, Energy and Environment – Kwaśniewski & Łydżba (eds)
© 2013 Taylor & Francis Group, London, ISBN 978-1-138-00080-3

Stability analysis of deep coal mine main roadways for pumped hydropower lower reservoir storage

A. Özarslan, H.Y. Aydıner & E. Köken
Mining Engineering, Bülent Ecevit University, Turkey

M. Alber
Engineering Geology/Rock Engineering, Ruhr-University Bochum, Germany

ABSTRACT: A grid compatible integration of fluctuating renewable energy from high capacity wind and solar energy farms to electricity systems requires large-scale energy storage methods and technologies. Currently widespread large-scale electricity storage installed is reservoir-based hydropower and Pumped Hydropower Energy Storage (PHES). Large storage volumes are necessary to deal with the relatively low volumetric storage density property of PHES plants. Investigations are made to benefit from the large volumetric storage potential of deep coal mine openings. Especially, main roadways of active and some closed hard coal mines are available and may be used as large lower reservoir volumetric storage openings for PHES plants. This paper address some basic rock engineering and stability issues associated with PHES projects in deep hard coal mines. Evaluations are made for safe and effective usage of the underground coal mine openings as PHES lower reservoir storage volumes.

1 INTRODUCTION

The electricity power sector has been undergoing changes and an increased share of electricity from renewable sources is the stated aim of many national energy policies. However, a grid compatible integration of fluctuating renewable energy from high capacity wind and solar energy farms to electricity systems requires large-scale energy storage methods and technologies. Currently widespread large-scale electricity storage installed is reservoir-based hydropower and pumped hydropower energy storage (PHES). Alternatives are underground storage of compressed air (CAES) and hydrogen gas in suitable geological formations (Meiwes 2009, Özarslan 2013). A PHES plant requires the existence of an upper and lower reservoir between which water is pumped up in off-peak periods to store hydraulic potential energy and then released down through a turbine in peak periods to produce electricity. A schematic view for a reservoir-based hydropower or PHES project is shown in Figure 1. Vertical or inclined shafts are efficiently used in pressure tunnel and shaft layouts for PHES plants. The reinforcement lining types (steel, concrete, unlined) in tunnel and shafts depends primarily on the rock conditions, depth, confinement and water pressure levels. The need for surge chambers depends on the type of turbines used, heads, length and volume of waterways, and flow velocities (Brekke & Ripley 1993).

Large storage volumes are necessary to deal with the relatively low volumetric storage density property of PHES plants. The potential for further PHES in industrialized countries in Europe is limited because of environmental considerations, lack of suitable sites and certain social acceptance issues. Investigations are made to benefit from the large volumetric storage potential of deep coal mine openings.

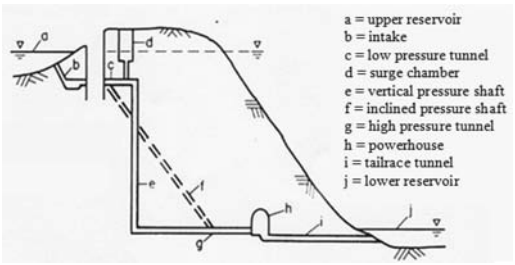


Figure 1. Typical scheme for underground hydroelectric or PHES projects (Brekke & Ripley 1993).

2 PHES CONCEPT IN DEEP COAL MINES

Major hard coal producing basins (Ruhr, Silesian etc.) and mines exist in Europe (EURACOAL 2013). These basins are well explored during their long lasting mining history and a large amount of deep underground openings has been constituted during coal mining activities. According to EU strategy for competitive,

Table 1. PHES projects in underground coal mines (Niemann 2011).

Coal Mine	Prosper H.	Auguste V.
Lower reservoir storage volume	480,000 m^3	100,000 m^3
Static head (depth)	800 m	1,200 m
Efficiency	0.65	0.65
Flow rate	11 m^3/s	2.3 m^3/s
Power installed	56 MW	17 MW
Electricity generation per year	140 GWh/a	42.5 GWh/a

sustainable and secure energy, the phase-out of subsidies for the production of coal from uncompetitive mines by the end of 2018 has been decided. Therefore, non-profitable underground coal mines will be closed.

Investigations are made to benefit from the large volumetric storage potential of deep coal mine openings. In Europe, underground hard coal mining is almost exclusively undertaken by longwall operations. The method involves driving two parallel gateroads into the coal seam, typically 200 to 300 m apart and up to 3000 m in length, before connecting both roadways to create a panel of coal. Typical coal seam heights are between 1.5–2.5 m. The temporary coal face and gateroads are allowed to collapse after production of coal. The connections from the surface to the underground coal production panels are provided by vertical shafts and horizontal main roadways. Also, inclined shafts are used to provide connection between different mining levels. Shafts and main roadways, used for transportation and ventilation, are permanent openings in underground mines, until the mine will be closed.

In many European Coal Mines (Germany, Poland, Turkey etc.) the depth of the shafts are more than 500 m below surface. Coal mine shafts can be utilized as pressure shaft and for water pump up purposes in a PHES facility. Vertical mine shafts have compared to inclined shafts usually greater overburden confinement, stronger permanent support and therefore reduced pressure shaft water leakage potential. Especially, main roadways of active and some closed hard coal mines are available and may be used as large lower reservoir volumetric storage openings for PHES plants. Kilometers of main roadway infrastructure exist in underground coal mines. For a PHES plant water will be pumped up of the mine tunnels into an artificial lake to be constructed on the surface of former mine plants. This technological concept is not yet operational, but in Germany projects are planned (Niemann 2011). Brief information is given in Table 1.

The main roadways, as the most safe and long-term stable tunnels in deep hard coal mines, are anticipated to serve as the primary storage volume for pumped hydropower lower reservoir storage. However, the usage and stability of underground openings as lower reservoir storage volumes for PHES plants must be investigated carefully considering various operating (in situ stress, water pressure, etc.) and surrounding conditions (geology, geomechanical properties of rock, support behavior, etc.).

2.1 *Operational conditions*

The German mining districts (Ruhr and Saar) are well known for their deep longwall coal mining operations and currently the average operating depth is below 1200 m. The in situ stresses at depth, resulting from the weight of the overlying strata and from locked in stresses of tectonic origin, are in the order of 19-44 MPa (Alber & Fritschen 2010). In Zonguldak Hardcoal Basin in Turkey the deepest coal mine operations are located approx. 600 m below surface. The vertical in situ stress (Pv) is normally assumed to be equal to the product of the average unit weight of the rock mass and the depth (H) below surface. The average vertical in situ stress can be estimated by Equation 1.

$$Pv\ (\text{MPa}) = 0.025\ (\text{MPa/m}) \times H\ (\text{m}) \quad (1)$$

The main roadways in coal mines are usually horseshoe shaped and typically supported by steel arch sets, and rockbolts often with shotcrete. Steel sets provide support rather than reinforcement. In permanent or long term roadways grouted (resin, cement) rockbolts are used. Steel mesh is usually used to restrain small pieces of rock between bolts and to reinforce shotcrete liner. During the development of main roadways in coal mines fault and weakness zones are crossed. Yielding steel arches, containing elements designed to slip at pre-determined loads, are usually used in coal mine roadways where large deformations are expected.

The presence of groundwater and water pressures may cause operational problems in underground openings associated with hydroelectric projects. In coal mines large amounts of groundwater are already pumped out of the deep shafts to decrease the groundwater level and to keep the mine openings dry. In German coal mines the water has to be pumped out even after mine closures.

In underground hydropower projects the criterion for deciding when a pressure tunnel should be steel lined is when the in situ minimum principal stress in the rock mass falls below the maximum dynamic water pressure in the tunnel. The internal water pressure (Pi) is a function of the maximum static head of water in the tunnel, the operation of the gates and the characteristics of the turbines (Hoek 2006). The unit weight of water is 0.01 MPa/m. The static internal water pressure ($Pi\ st$) can be calculated by Equation 2, where ΔH is the height difference of the static head in m.

$$Pi\ st\ (\text{MPa}) = 0.01\ (\text{MPa/m}) \times \Delta H\ (\text{m}) \quad (2)$$

An allowance of 30% above the maximum static head is normally used to estimate the dynamic water pressure. For an example depth of 1000 m the mains will experience high internal water pressure of up to 13 MPa. Impermeable steel lining is required in pressure shafts and tunnels where the minimum principal stress in the rock is less than 1.3 times the maximum static head water pressure for typical hydroelectric operations (Hoek 2006). The cover depths and the relatively high in situ minimum principal stress providing

confinement in the surrounding rock of concrete lined coal mine shafts and main roadways eliminate the need for steel lining, resulting in significant cost savings compared to pressure shaft and tunnels of conventional PHES projects with limited cover depths.

The mains roadways in coal mines are typically supported to withstand compressive stresses. However, for their use as PHES lower reservoir storage the mains will experience high internal water pressure and possibly dynamic effects. The main roadway support and reinforcement must be designed to withstand such loading and pressure conditions.

2.2 *Geological and geomechanical conditions*

The coal bearing strata in the Ruhr area and Zonguldak area belong to the geological Upper Carboniferous period. Clastic sediments in this regions consist usually of coal bearing strata with sandstone, siltstone, conglomerate, shale and claystone as the dominant rock types. The strata is usually jointed, faulted and folded.

Sedimentary coal measure rocks such as bedded sandstones, siltstones, conglomerates, shales, and mudstones are generally defined as weak rocks. Weak rocks may fail when subjected to the stress levels induced by the main roadway openings at deep coal mines. The strength of the rock material is variable and the rock mass is frequently more heavily jointed. The control of overbreak during excavation by drilling and blasting is more difficult, and the rock mass and the supports placed in it may be subjected to large deformations. Support is usually required immediately after excavation. In designing support and reinforcement, failure of the rock material, sliding and rotation of individual blocks of rock within the rock mass have to be considered in addition to failure along structural features such as bedding planes, shear zones and faults (Hoek 2006).

2.3 *Rock properties*

Typical coal measure rocks, such as sandstone, siltstone, and mudstone/shale usually have a wide spectrum of intact strength within the same rock type. Mean intact uniaxial compressive strength (*UCSi*) and standard deviation (*SD*) values obtained from a total of 82,500 tested rock samples taken from Ruhr and Saar coal mine districts are given in Table 2. Additionally, *UCSi* and *SD* values of intact sandstone (74 samples) and siltstone (12 samples) rock from Zonguldak coal district are shown. Similar strength results are obtained for intact sandstone and siltstone rocks.

Rock mass classification systems can be used to provide estimates of quality, strength and deformation properties of the rock mass. They are also used to provide initial estimates of support requirements. The Rock Mass Rating (*RMR*) system is used to describe the rock mass conditions of coal measure rocks. Alber et al. (2009) investigated relevant geomechanical properties (*UCSi*, *RMR*, etc.) of representative hanging and foot rock strata around coal seams. *RMR* values of sandstone and siltstone rock masses ranged usually from 50–70, within an average *RMR* value of 60 at the boundary of good-fair rock conditions.

Table 2. Coal measure rocks strength properties (Junker et al. 2009, ZEDEM 1994)

	Ruhr/Saar	Zonguldak
Rock Type	Mean $UCSi \pm SD$	Mean $UCSi \pm SD$
Sandstone	90 ± 40 MPa	96.7 ± 28.1 MPa
Siltstone	65 ± 30 MPa	66.4 ± 22.0 MPa
Mudstone/Shale	50 ± 25 MPa	NA

UCSi intact uniaxial compressive strength
SD standard deviation

The Hoek and Brown ($H - B$) failure criterion is used for estimating the strength of rock masses of sedimentary rocks. The $H - B$ failure criterion for jointed rock masses is defined by Equation 3:

$$\sigma_1^{'} = \sigma_3^{'} + \sigma_{ci}\left(m_b \frac{\sigma_3^{'}}{\sigma_{ci}} + s \right)^a \tag{3}$$

where σ_1' and σ_3' are the maximum and minimum effective principal stresses at failure, *mb* is the value of the Hoek-Brown constant *mi* for the rock mass, *s* and *a* are constants which depend upon the rock mass characteristics, and σ_{ci} is the *UCSi* value (MPa) of the intact rock pieces (Hoek 2006). m_b and s values were estimated using the Hoek–Brown failure criterion in its original approach up to 1994 (Eqs. 4-5), relating to the *RMR* system (Alber et al. 2009).

$$mb = mi \exp[(RMR\text{-}100)/28] \tag{4}$$

$$s = \exp[(RMR\text{-}100)/9] \tag{5}$$

The rock mass modulus E_M was obtained by Equation 6 (Alber et al. 2009).

$$E_{\mathrm{M}} = [UCSi/100]\text{^}0.5 \cdot 10^{(RMR\text{-}10/40)} \tag{6}$$

The two laboratory properties required for the application of the H-B failure criterion are the *UCSi* of the intact rock and the intact rock material constant *mi*. Ideally, these two parameters should be determined by uniaxial and triaxial tests. If direct laboratory testing is not possible, the value of the constant *mi*, can be estimated based upon published values (Hoek 2006). Some suggested *mi* values with ranges for sandstone and siltstone rocks are presented in Table 3. The suggested values by Gerçek & Müftüoğlu (1993) were evaluated from uniaxial and triaxial compressive strength tests of Zonguldak hardcoal mines coal measure rock samples.

Most sedimentary rocks exhibit anisotropic characteristics in terms of strength and deformational

Table 3. *mi* values for sandstones and siltstones.

	Sandstone	Siltstone
Reference	*mi*	*mi*
Hoek 2007	17.0 (13–21)*	7.0 (5–9)*
Gerçek & Müftüoğlu 1993	13.2 (7.4–25.5)*	7.4 (3.9–9.1)*

*Values in parenthesis are ranges of *mi* value

properties. Especially, siltstone, shale, and claystone rocks usually show medium to high anisotropy characteristics (Colak & Unlu 2004).

Laboratory tests should be carried out at moisture contents as close as possible to those which occur in the field. Many sedimentary rocks show a significant strength decrease with increasing moisture contents. For sandstone rock without clayey bonding material the strength decrease is usually low.

For rock mechanics and rock engineering projects, it is recommended that the dry *UCSi* is used for the purposes of strength classification, while for the actual engineering design (water tunnel, etc.) it is essential to establish the wet strength and ideally the water sensitivity of the rock, in order to assess their potential change in strength and deformability (Hoek 2006). *UCSi* tests on dry and water saturated (wet) intact sandstone and siltstone rock samples were carried out. The properties of the rocks were determined according to the ISRM suggested methods and the obtained strength values are displayed in Table 4. The low strength in dry conditions and relatively high strength decrease of water saturated siltstone rock samples is explained by anisotropic and water sensitive properties such as friction degradation. The strength decrease of dry and saturated sandstone samples was measured as approx. 25%. The values obtained for sandstone and siltstone are in good agreement with ratios predicted by Vasarhelyi (2003), and Erguler & Ulusay (2009). Junker et al. (2009) reported wet coal measure rock strength reductions as 57% for mudstone, 32 % for siltstone and 35% for sandstone with clayey bonding material.

Groundwater and water pressure influences the stability in underground excavations in several ways. When water pressure is present in a rock mass, the surfaces of the discontinuities are forced apart and shear strength is reduced by friction degradation of separation planes. Also, softening or washing out of joint fillings (clay, etc.) reduce the stability of the openings. This is especially the case with pressurized water flow. Therefore, high water inflow/outflow and external/internal water pressure conditions decrease the surrounding rock mass quality of underground openings. It is expected that this is particularly valid in the fair to very poor rock mass categories. If water inflow and outflow may not limited by reinforced linings in main roadways, stability problems are expected to occur during operational phase as PHES lower reservoir storage.

Table 4. Dry and wet/saturated strength properties of sandstone and siltstone rocks.

	Dry	Wet/Sat.	
Rock Type	*UCSi* ± *SD*	*UCSi* ± *SD*	*UCSi* sat. / *UCSi* dry
Sandstone	140.2 ± 21.9	106.9 ± 14.5	0.76
Siltstone	48.1 ± 17.7	17.4 ± 4.6	0.36

UCSi intact uniaxial compressive strength (MPa)
SD standard deviation

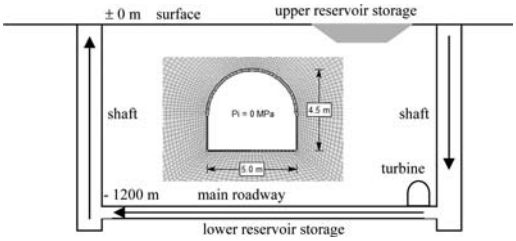


Figure 2. A schematic view of the investigated deep coal mine and main roadway conditions.

3 STABILITY ANALYSIS

Vertical primary in-situ stress can be estimated by Equation 1. The ratio of average primary horizontal stress to vertical stress is assumed as equal for the preliminary stability analyses. A simplified schematic view of a deep coal mine investigated as a potential PHES plant is given in Figure 2. The depth of a representative horseshoe shape main roadway was selected as 1200 m. The input values for the stability analyses are presented in Table 5. Phase2 software was used for the elastic and elasto-plastic stability analyses.

Elastic analyses were carried out to investigate stress distribution and concentration around a representative horseshoe shaped main roadway opening. For sandstone rock (*RMR* 60, *UCSi* 90 MPa), rock mass elastic deformation modulus (E_M) value was estimated as 16.87 GPa and Poisson's ratio (υ) as 0.25. Hydrostatic principal stress conditions (*Pv*=*Ph*) were assumed. The elastic analyses results are presented in Figures 3-5.

Without any internal water pressure (*Pi*=0) high stress concentrations occur especially at the corners where the sidewalls meet the floor (Fig. 3). Also, stress concentrations occur at the crown of the horseshoe shaped opening. The flat floor allows upward displacement and heaving of the floor (Fig. 4).

High static water pressure (*Pi*=12 MPa) at a representative depth of 1200 m provide effective support pressure and confinement of the rock surrounding the opening (Fig. 5). None stability problems are expected while this operational condition. The most critical situation will occur after the water will be pumped up from the opening in off-peak periods and none internal

Table 5. In situ stress and water pressure input values for a reference depth of 1200 m.

Property	Symbol	Value
Vertical in situ stress	*Pv*	30 MPa
Horizontal in situ stress	*Ph*	30 MPa
Max. static water pressure	*Pi st*	12 MPa
Max. dynamic water pressure	*Pi dyn*	15.6 MPa

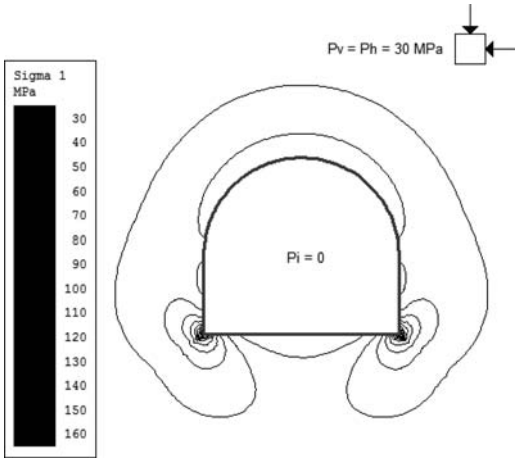


Figure 3. Major principal stress distribution ($Pi = 0$).

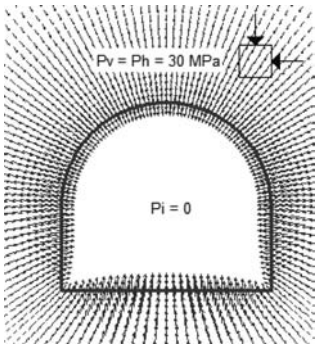


Figure 4. Relative direction of displacement vectors ($Pi = 0$).

water pressure will be active. The previous water penetration and water pressure effect will decrease strength and rock mass quality in the surrounding rock, especially for water sensitive rock conditions. Increased stability problems are expected to occur.

For underground openings at great depth and especially for waterway tunnels, the simple horseshoe shape is not a favorable choice because of high stress concentrations and increased floor heave risks. The sharp corners at the junction between the floor and the main roadway sidewalls create high stress concentrations and also generate large bending moments in any lining (shotcrete, concrete) installed in the tunnel. The

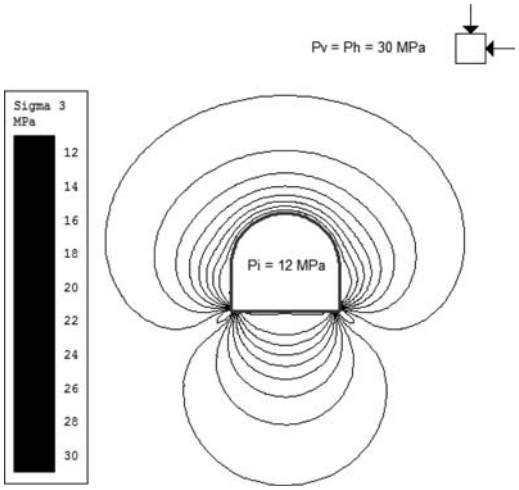


Figure 5. Minor principal stress distribution ($Pi = 12$ MPa).

stress distribution, floor heave and failure zone of the rock mass surrounding a main roadway opening can be improved by modifying the horseshoe shape with a curved invert floor (Fig. 6). The $H - B$ failure criterion was used to estimate the yielded elements and the plastic failure zone of rock masses in the vicinity of the opening. Rock mass behavior is represented as an elastic perfectly plastic material. For the example case analyzed, it was assumed that the rock mass is a good to fair quality sandstone ($RMR = 60$). The rock properties and H-B parameter values are given in Table 6. The effect of variability (*SD*) of strength (*UCSi*) values (90 ± 45 MPa) on the stability and failure zone of a representative main roadway was investigated. The higher value (135 MPa) represent hard dry and the lower value (45 MPa) weak wet/saturated sandstone rock conditions (Table 7).

A and B represent cases when the main roadway and surrounding rock is dry, with different intact strength values (hard, medium) for sandstone rocks, and without lower water reservoir storage effects. Case C represents an afterwards state of a main roadway and surrounding rock penetrated by water under high pressure. It was assumed that the former water was pumped up of the main roadway opening, while the water rock strength (wet/saturated) decrease effects still exists in the surrounding rock of the opening. Probable decrease of rock mass rating (*RMR*) and change of $H-B$ rock mass parameters (mb, s) were not taken into consideration for the stability analyses. The stability analyses showed, that even *UCSi* strength difference for dry conditions influence the extension of failure zones (Fig. 6). Especially, the strength decrease for wet/saturated rock conditions significantly affects the overall surrounding failure zone and stability of underground openings.

The main roadways in coal mines are typically supported by steel arch sets, and rockbolts often with shotcrete. Water effects on surrounding rock and support must be limited for the usage of main roadways

Table 6. *RMR* and $H - B$ rock mass parameters for sandstone.

RMR	mi	mb	s	a
60	13	3.1155	0.011744	0.5

Table 7. Investigated *UCSi* strength cases and representative conditions.

Case	*UCSi*	Remarks
A	135 MPa	hard dry sandstone rock
B	90 MPa	medium dry sandstone rock
C	45 MPa	weak wet/sat. sandstone

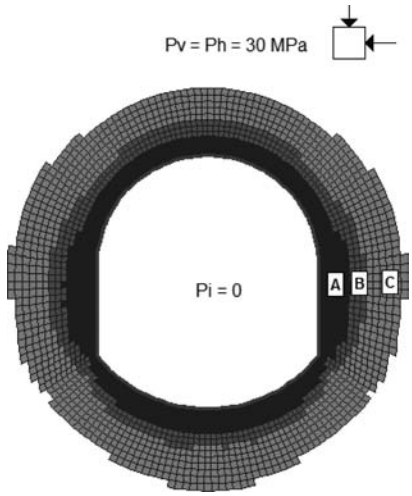


Figure 6. Failure zone development at different rock material strength cases.

for PHES lower reservoir storage openings. Therefore, liners are to be designed to withstand high water pressure and structural loads. In bolted and shotcrete lined roadways the thickness of the shotcrete liner can be increased. With thicknesses in excess of 250 mm and sufficient compressive strength, shotcrete can be designed with similar approaches as used for concrete linings. Shotcrete should be reinforced with steel mesh or fibers. For shotcrete and concrete-lined sections, the greater the deformability of the rock mass, the greater the cracking risk of the lining and the greater the potential leakage through the lining, particularly under high internal water pressures (Brekke & Ripley 2003). The rock mass surrounding the opening may be stabilized by grout injection, to improve the mechanical properties of the rock mass around the opening.

4 CONCLUSIONS

The large volumetric storage potential of deep coal mine main roadways may be used as large lower reservoir volumetric storage openings for PHES plants. Weak and water sensitive characteristics of coal measure rocks in the surrounding rock of main roadways should be considered. It is concluded that only properly designed and reinforced lined main roadways can be utilized as long-term cycling water storage volumes for a PHES plant. In addition to rock mechanics and strata control aspects, several other important factors (technology, economy, safety, legal, environment) must be considered before the usability of main roadways can be decided.

REFERENCES

Alber, M. & Fritschen, R. 2010. Lessons learned from mining-induced seismicity in two deep coal mines. In J. Zhao et al. (eds), *Rock Mechanics in Civil and Environmental Engineering*: 701–704. Leiden: CRC Press/Balkema.

Alber, M. & Fritschen, R. & Bischoff M. & Meier T. 2009. Rock mechanical investigations of seismic events in a deep longwall coal mine. *Int. J. Rock Mech. Min. Sci.* 46: 408–420

Brekke, T.L. & Ripley, B.D. 1993. Design of pressure tunnels and shafts, In J.A. Hudson (ed.), *Comprehensive Rock Engineering*, Vol. 2: 349–368. Oxford: Pergamon Press.

Colak, K. & Unlu, T. 2004. Effect of transverse anisotropy on the Hoek–Brown strength parameter 'mi' for intact rocks. *Int. J. Rock Mech. Min. Sci.* 41: 1045–1052

Erguler, Z.A. 2009. Water-induced variations in mechanical properties of clay-bearing rocks. *Int. J. Rock Mech. Min. Sci.* 46: 355–370

EURACOAL 2013. Country Profiles. European Association for Coal and Lignite, www.euracoal.be

Gerçek, H. & Müftüoğlu, Y.V. 1993. Failure characteristics of coal measure rocks. In A.G. Paşamehmetğlu et al. (eds), *Assessment and Prevention of Failure Phenomena in Rock Engineering*: 329–334. Rotterdam: Balkema.

Hoek, E. 2006. Large powerhouse caverns in weak rock. *Practical Rock Engineering*, Chapter 13, pp. 222–255.

Junker, M. (ed.) 2009. *Strata Control in Seam Roadways*. Essen: VGE Verlag.

Meiwes, H. 2009. Technical and economic assessment of storage technologies for power supply grids. *Acta Polytechnica* 49(2-3): 34–39.

Niemann, A. 2011. Machbarkeitsstudie zur Nutzung von Anlagen des Steinkohlebergbaus als Pumpspeicherwerke. PowerPoint Präsentation an der Universität Duisburg-Essen, 31.11.2011, 24 p.

Özarslan, A. 2013. Large-scale energy storage methods for renewable energy resources. *12th Energy Congress of Turkey*, 11 p. (in Turkish)

Vasarhelyi, B. 2003. Some observations regarding the strength and deformability of sandstones in dry and saturated conditions. *Bull. Eng. Geol. Env.* 62: 245–249

ZEDEM 1994. Establishment of an Industrial Support Centre in Zonguldak, Final Report, 104 p.

Rock Mechanics for Resources, Energy and Environment – Kwaśniewski & Łydżba (eds)
© 2013 Taylor & Francis Group, London, ISBN 978-1-138-00080-3

Overburden deformation and damage caused by the construction of a hard rock tunnel – An analysis and countermeasures

G. Yu, S. Lu, D. Meng & G. Ouyang
Civil Engineering Department, Qingdao Technological University, Qingdao, China

ABSTRACT: The overburden deformation and damage that were caused by subway tunnel construction in a hard rock region were studied systematically. In this paper, the lithologic characteristics of the strata in the region are analyzed. The overburden deformation and damage characteristics caused by the drilling and blasting method (mine method) are presented. The crack evolution law and scaling law in the overburden are revealed. The corresponding relation between ground subsidence and the crack evolution scaling law is established. Then, these results are used to analyze and predict the ground subsidence. The damage characteristics and laws of the building on the ground that were caused by the ground subsidence are analyzed. The quality of the existing buildings in the area and their ability to withstand deformation are also evaluated. The settlement control criterion is established scientifically. Countermeasures are given that are designed to reduce the damage to the buildings.

1 INTRODUCTION

With the rapid growth of the economy and the scale of the increase in construction in the city, the problem of traffic congestion that is common in Beijing, Shanghai and other big cities has spread to other cities such as Qingdao and Dalian. Qingdao is one of the main cities on China's eastern coast and is also an important port and tourist city. The city has a total area of 10,654 square kilometers and a total population of about 2,760,000 (as of the end of 2007). With the implementation of the strategy of "Protection along the Bay, Development around the Bay", Qingdao is facing a renewed acceleration in the expansion of city and a significant increase in the size of the population, which has resulted in more serious urban road traffic problems. Therefore, the construction of Subway Line No. 3, which is about 24.9 km long, was initiated in Qingdao in 2009.

Subway Line No. 3 is mainly being constructed using mining method. The buried depth, which is generally 16 to 25 m, is relatively shallow. The formation is mainly hard rock (granite) and the geological conditions are complex and varied. The time span of the construction is long. The construction of the subway tunnel can cause damage to the environment, including to the surrounding rock mass, overburden and surface deformation, displacement, settlement, collapse, etc. The buildings (or structures) in the area, underground pipelines, various facilities and city roads that are along the line may be subject to varying degrees of damage. In particular, damage to the buildings in the area will be intensive. The construction period is long. The foundations and structures are of various types. Some of the buildings already have some structural problems that affect their safe use because of disrepair, some alteration by the residents, coastal erosion, etc. The construction of a subway tunnel under these buildings and other structures will damage them unless effective protection measures are implemented. Therefore, finding a way to avoid or at least reduce the damage to the buildings, guarantee the progress of the construction and control the construction risks has become an urgent problem that needs to be solved in the process of the construction of the subway tunnel. Therefore, conducting research on the overburden deformation, ground subsidence, damage characteristics and mechanisms that are caused by land subsidence is very useful. These as well as effective prevention and control measures are presented in the paper.

2 THE GENESIS OF STRATA AND ROCK FEATURES IN THE AREA

The city of Qingdao is located at the southern tip of the Jiaodong Peninsula, in an area with a mountain erosion tectonic landform, a piedmont depositional landform, an intermountain depositional landform and a coastal depositional landform. The Yellow Sea lies to the east and south. The terrain is high in the east, low in the west and sags in the middle. The geology is of the sea island type (Fig. 1).

The strata are dominated by various types of metamorphic rocks of the Archean-Proterozoic Jiaonan group and various types of clastic and volcanic rocks of the Mesozoic Cretaceous period. On the sedimentary facies, which is middle-upper Pleistocene, there are residual slope sediments and rush diluvium layers. The Holocene is composed of a shallow marine sedimentary layer, alluvium and impact diluvial. The

Table 1. Interval length and their proportion of all grades of the surrounding rock.

	Grade II	Grade III	Grade IV	Grade V	Grade VI
Interval length (km)	5.207	4.021	4.801	1.984	4.082
Percentage of the total length (%)	25	20	23.9	9.9	20.3

distribution and thickness of the Quaternary layers are not very large. Because the lithologic of the coast is uneven, some places are soft, while others are hard. Because of erosion, transportation and the accumulative actions of waves, tides and sea currents, the deposits that rushed down from upstream were slowly modeled into a variety of hilly island terrains with geological tectonics. The fault structure is very developed. The five faults present in the area acted intensively during the Mesozoic period, especially during the late Mesozoic period. They controlled the action of the volcano, layer development and lava invasion of late Yanshannian period. The weathering resistance of the rock is different and the landforms are also different. The rock strata have a varied lithology. Their thickness also varies due to the transportation and accumulation activities. On the whole, the island geology has a wavy distribution. The relative elevation is high and the groundwater is relatively rich. The rock strength is uneven. There are also softer rock, soil and sand layers.

According to the geological exploration report, the rock surrounding Qingdao Subway Line No. 3 ranges from grade II to grade VI. Their lengths and their proportion are shown in Table 1. It can be seen from Table 1 that the section with better rock (grades II and III, rich water and poor permeability) account for about 45.9%, the poor surrounding rock (gradeVI, water-rich sand) accounted for about 20.3%.

From the lithological characteristics that have been revealed by the construction of the subway, the rock surrounding the tunnel can be categorized into the following 7 types:

1. Thick-bedded hard rock or hard rock with scarce joints. This kind of rock generally belongs to grade II that was revealed by the geological survey.
2. Hard rock with even vertical joints. The grade IV hard rock with vertical joints is revealed in the Qingdao Subway Line No. 3 Ling Qing interval K11 + 857.24 shaft near a horizontal passageway.
3. Hard rock with inclined joints, i.e. joints which have a certain angle with the tunnel excavation in the layers. The engineering geology of the Yonghuo interval of Qingdao Subway Line No. 3 is extremely complex due to the influence of the Cangkou fault. The rock mass is very broken and the joints are rich. There is mylonite in some places and cataclastic rock and granite are developed. There are some interpenetrated lamprophyre dykes and granite porphyry dykes. The basement is stable and joints are inclined at angles of 45 ∼ 80°.
4. Weathered soft rock in the surrounding rock. The rock mass in a natural state is relatively complete with a good structural strength. However, the rock mass will soften, disintegrate, decrease or lose structural strength after tunnel excavation because it will be contact with water or air. For example, the Lingqing interval K11 + 090.203 ∼ K11 + 10.203 section and the Yonghuo interval K24 + 220 west of the rock mass is broken and soft rock with a layer of 0.4 ∼ 6.5 m thick and the rock mass basic quality is grade V.
5. Backfill in the surrounding rock. The Lingqing interval K11 + 900 ∼ K12 + 110 section is under the backfill area of an old reservoir. The No. D13 building of 6 ∼ 7 stories is on the ground. The maximum depth of the backfill is 13.8 m. Some backfill of the original channel is mainly abandoned silt clay in the first construction process of the excavation of the foundation pit.
6. Aqueous sand layer in the surrounding rock. The Wanli interval of line No. 3 from K19 + 436 to K19 + 518 is a modern river bed. From K19 + 518 to the Licun station is the erosion depositional first terrace.
7. Lamprophyre interlayer in the surrounding rock. The layer at the Wujiang interval of line No. 3 from K7 + 959.8 to the terminal of the interval is an intermediary and slightly weathered granite layer. Another section is a piedmont erosion accumulation slope. There are lamprophyre dykes through to the surface (Fig. 2). The strongly weathered lamprophyre layer is thick and it is like sand with water softening characteristics. The strength of the intermediary weathered lamprophyre is higher, but it is lower in water and air.

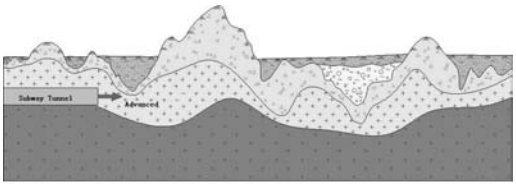


Figure 1. The geological structure of the area.

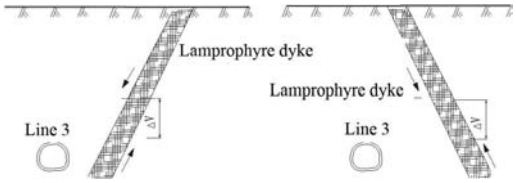
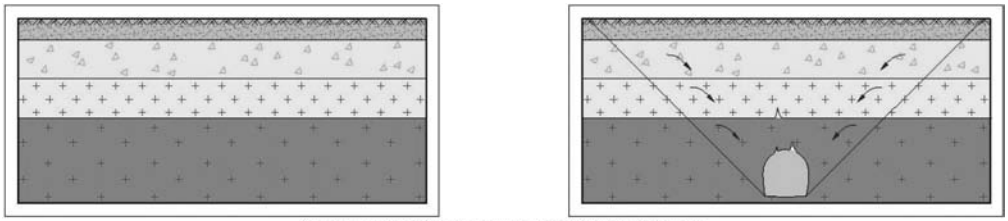
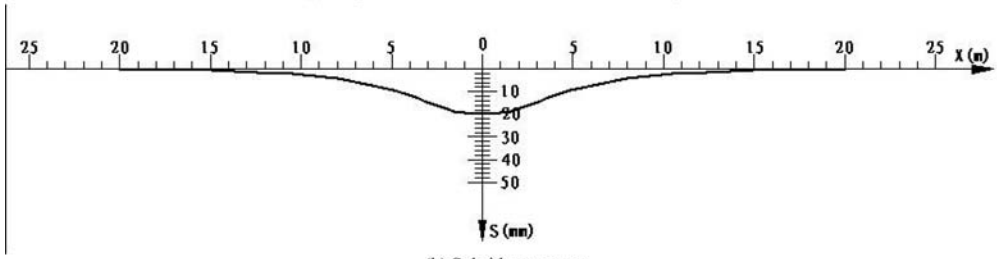


Figure 2. Strike of lamprophyre dyke in Wujiang interval.

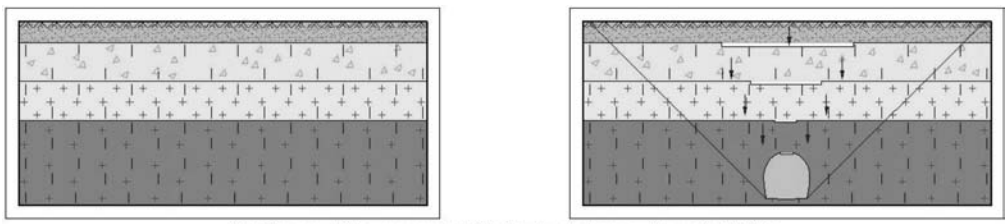


(a) Diagram of the movement of the hard rock layers.

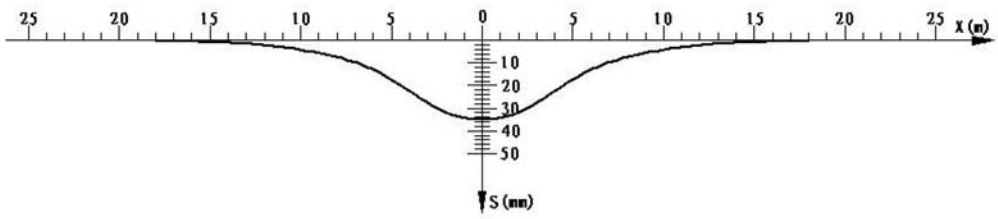


(b) Subsidence curve.

Figure 3. Diagrams of the movement of the hard rock layers and subsidence curve after the excavation of the tunnel.



(a) Diagram of the movement of the hard rock layers with vertical joints



(b) Subsidence curve.

Figure 4. Diagrams of the movement of the hard rock layers with vertical joints and subsidence curve after the excavation of the tunnel.

3 CHARACTERISTICS OF SUBSIDENCE AND THE DEFORMATION OF THE OVERBURDEN THAT IS CAUSED BY THE CONSTRUCTION OF THE TUNNEL

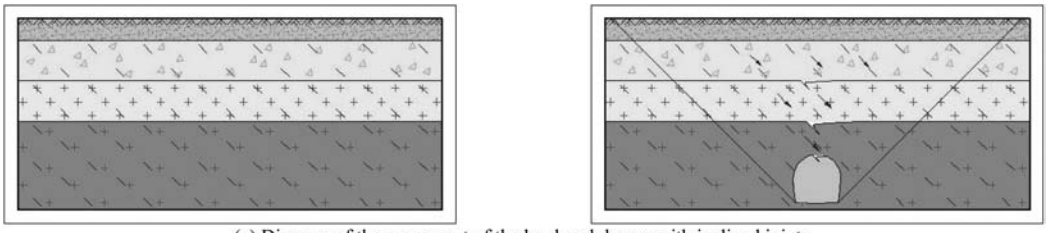
Monitoring methods are used in the tunnel and on the ground to study the characteristics of subsidence and the deformation of the overburden that is caused by the construction of the line No. 3 tunnel. Many observation data have been obtained. Seven kinds of overlying deformations and subsidence are summarized for the seven kinds of surrounding rocks mentioned above.

(1) Characteristics of the subsidence and overburden deformation of the hard rock and layered hard rock.

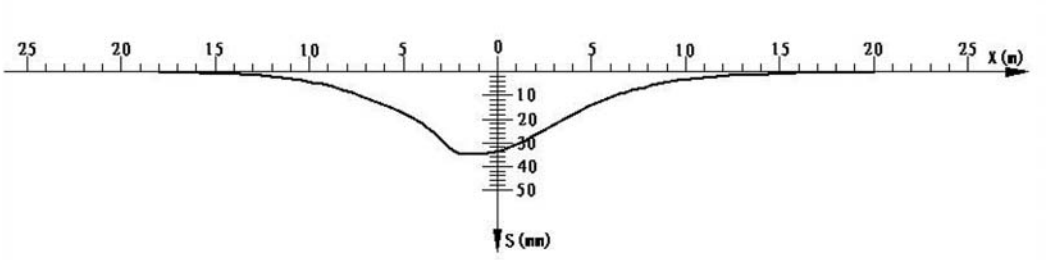
Because the hard rock mass with high strength is full and has no joints, the overlying deformation and subsidence is relatively small after the excavation of the tunnel and usually follows a normal distribution (Fig. 3); the maximum subsidence is generally within 20 mm.

(2) Overburden deformation and subsidence characteristics in the hard rock with vertical joints.

Obvious damage appears in the overburden above the tunnel. The ground subsidence is normally distributed and the maximum subsidence value, which is generally more 35 mm, increases (Fig. 4). When the water table is high in the overburden, it is easy for a collapse pit to form on the ground.

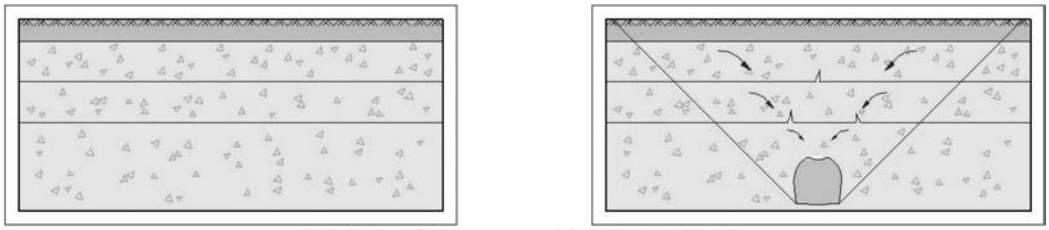


(a) Diagram of the movement of the hard rock layers with inclined joints.

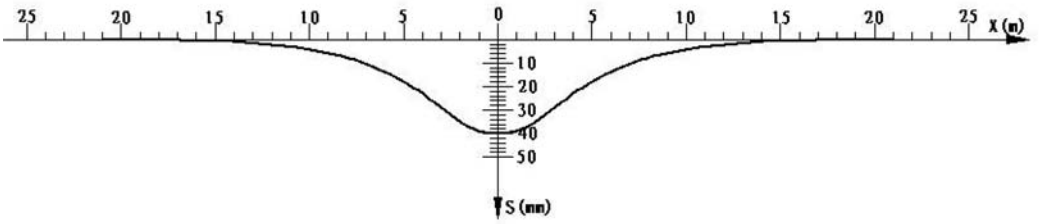


(b) Subsidence curve.

Figure 5. Diagrams of the movement of the hard rock layers with inclined joints and subsidence curve after the excavation of the tunnel.



(a) Diagram of the movement of the broken rock layers.



(b) Subsidence curve.

Figure 6. Diagrams of the movement of the broken rock layers and subsidence curve after the excavation of the tunnel.

(3) Subsidence characteristics and overlying deformation in the hard rock with inclined joints

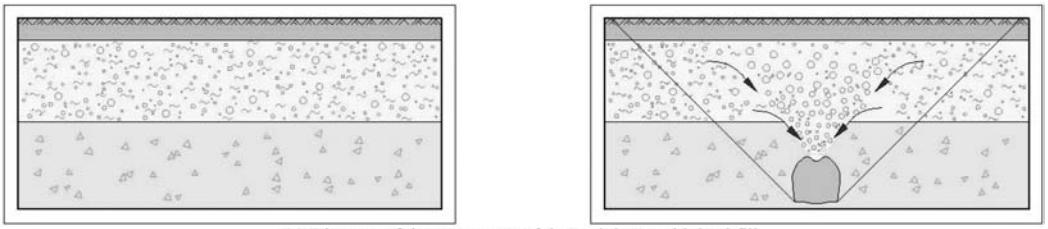
The overburden will move along the weak planes when the joints are angled with the working face of the tunnel. The subsidence has skewed distribution, the maximum subsidence point is not in the tunnel axis, as shown in Figure 5.

(4) Subsidence and overburden deformation characteristics of strongly weathered soft rock

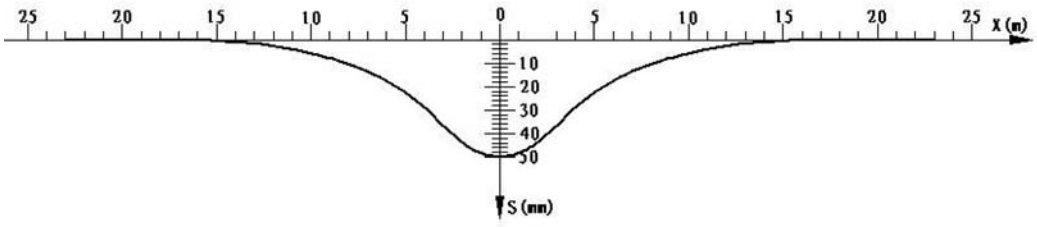
The construction of the subway tunnel leads to a subsidence curve with a normal distribution. The maximum subsidence is up to 40 mm as is shown in Figure 6; it is greater than in the situation (1). Sometimes, a funnel-shaped collapse area will appear at the surface and mouth opening cracks may appear around the area.

(5) Overburden deformation and subsidence characteristics of the backfill of the surrounding rock.

Intensive subsidence will occur when a tunnel crosses the thick backfill. The maximum subsidence will be 50 mm or even more, as is shown in Figure 7. For example, the LingQing interval K11 + 900 ~ K12 + 110 segment is under the filling area of an old reservoir. The No. D13 building of the Cuobuling block is 6 ~ 7 stories. The maximum depth of the backfill is 13.8 m. The subsidence value of observation point JC01 is 65 mm.

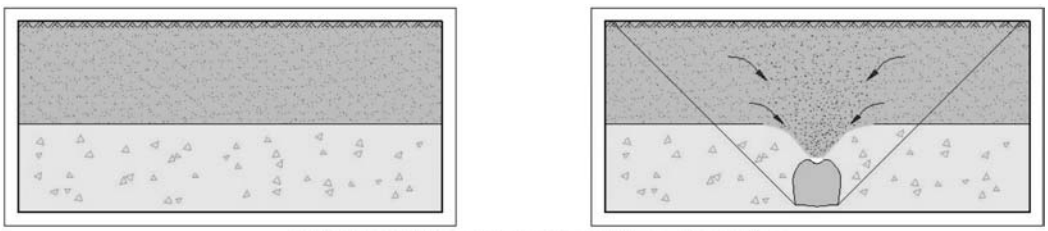


(a) Diagram of the movement of the rock layer with backfill.

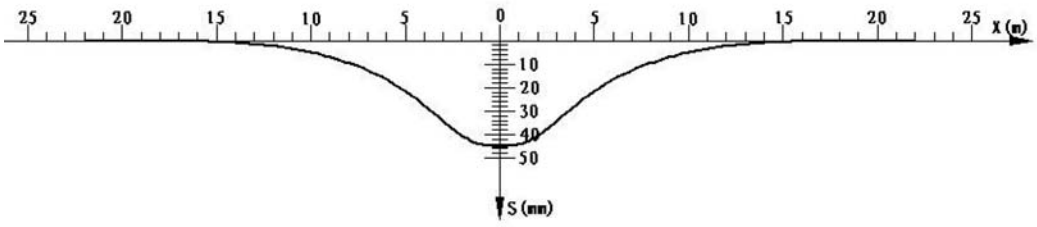


(b) Subsidence curve.

Figure 7. Diagrams of the subsidence curve and movement of the rock layer with backfill.



(a) Diagram of the movement of the rock layer with sand flow.



(b) Subsidence curve.

Figure 8. Diagrams of the movement of the rock layer with sand flow and subsidence curve after the excavation of the tunnel.

(6) Characteristics of the subsidence and overburden deformation with water-bearing sand.

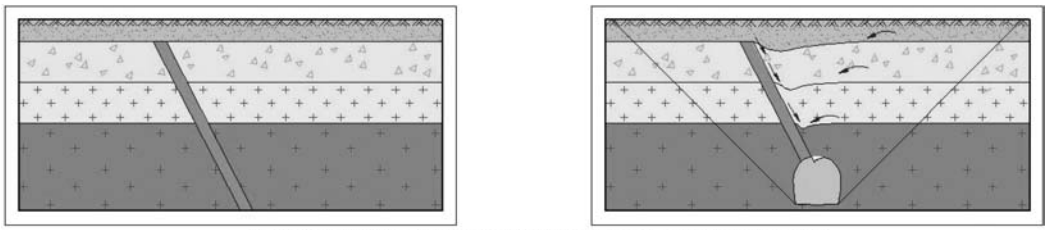
Because of its thixotropy when the tunnel passes through flow sand and silt sand, it is easy to produce sand flow and the water gushing phenomena. Tubular cavities will be formed in the surrounding rock. The structure of the rock mass will be damaged. The strength decreases and compressibility increases. A large settlement (Fig. 8) will appear on the ground, and a funnel collapse may even appear.

(7) Subsidence and deformation characteristics of an overburden with a lamprophyre dyke.

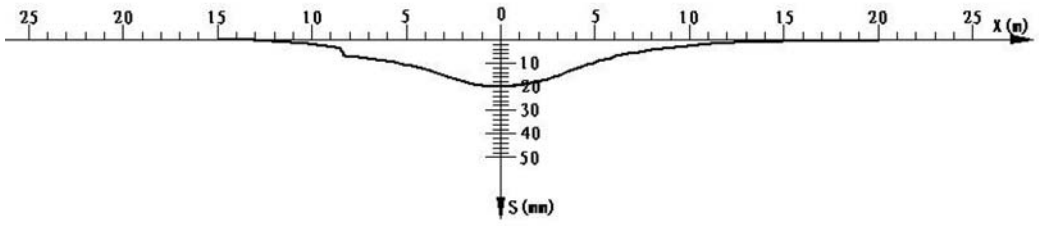
The upper and lower levels of the weak interlayer will have a movement of ΔV when there are some weak interlayers such as lamprophyre in the surrounding rock and a step subsidence will appear on the ground. This study found that when the dip angle of a weak interlayer is more than 20, the weak interlayer has a significant effect on the movement of the rock layer and ground (Fig. 9).

4 ANALYSIS OF THE SUBSIDENCE-INDUCED DAMAGE OF BUILDINGS IN THE AREA AND CONTROL STANDARDS

In order to analyze the damage caused by subsidence to buildings in the area, the buildings of Wanlong above Subway Line No. 3 were analyzed. The relative

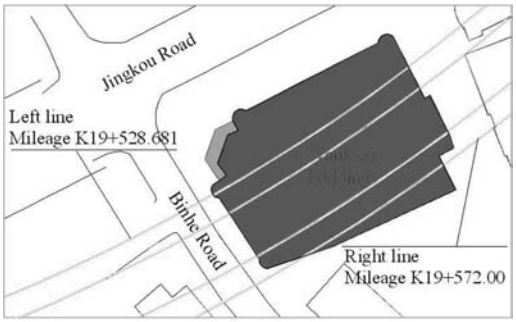


(a) Diagram of the movement of the rock layers with a lamprophyre dyke..



(b) Subsidence curve.

Figure 9. Diagrams of the movement of the rock layers with a lamprophyre dyke and subsidence curve after the excavation of the tunnel.



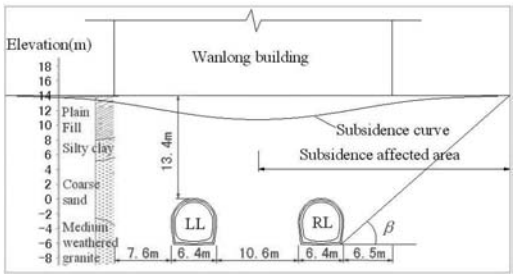


Figure 10. Relative position between the buildings and tunnel.

position between Wanlong and the tunnel is shown in Figure 10.

The back analysis method was used to determine the parameters of ground movement according to the monitoring data of the subsidence of five sections before the tunnel crosses under the buildings. In addition, the subsidence is predicted when the tunnel crosses under the buildings.

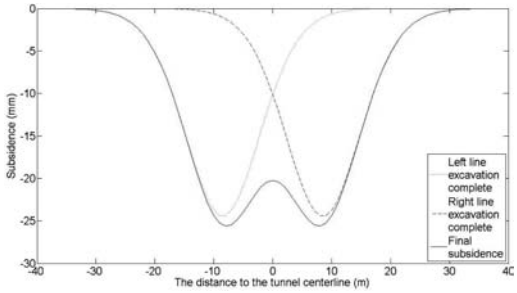


Figure 11. Predicted subsidence curve of the tunnel section in different periods.

In order to predict and quantify the damage to the buildings in Wanlong, the failure criterion of concrete materials and the Ottosen failure criterion were used in order to establish the corresponding yield proximity model.

$$f_{Ottosen}(\sigma_\pi,\tau_\pi)=\frac{-B-\sqrt{B^2-\frac{4C(H\cdot A-\sigma_\pi)}{H}}-\frac{2C\cdot\tau_\pi}{H}}{-B-\sqrt{B^2-\frac{4C(H\cdot A-\sigma_\pi)}{H}}} \quad (1)$$

where:

$$A=1/3b,\quad B=-\sqrt{1/6\lambda/b},\quad C=-a/2b,\quad H=\sqrt{3}f_c$$

and f_c is the uniaxial compressive strength of concrete.

When the degree of the safety of structural crack damage $f(\sigma_\pi, \tau_\pi)$ is [0.0, 0.1], [0.1, 0.2], [0.2, 1.0] separately, the state of a building is cracking damage, close to cracking damage and safe.

A finite element model of the buildings in Wanlong was established according to the data measured

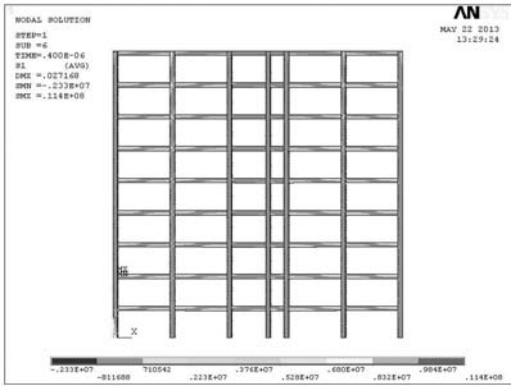


Figure 12. The first principal stress cloud chart caused by the final subsidence.

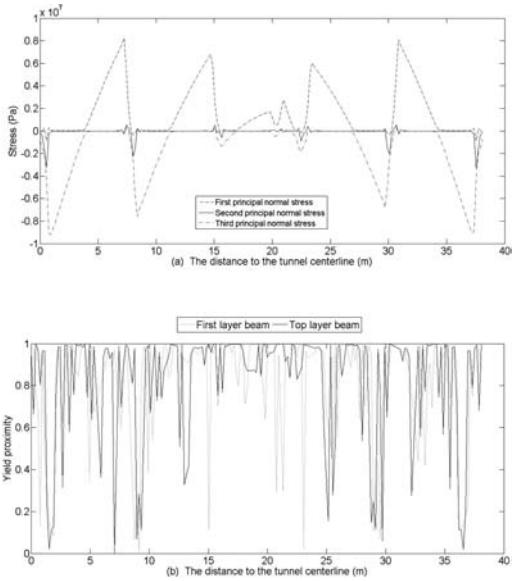


Figure 13. Yield proximity distribution curve of the framework beam of the final settlement.

in the field. According to the result of the predicted settlement in Figure 11, the settlement curve after the excavation of tunnels was added to the model as the boundary conditions. The first principal stress cloud chart is shown in Figure 12. The stress distribution of a layer and the top frame beam cracking damage are shown in Figure 13. As can be seen from that figure, parts of the building structure are undergoing cracking damage or are close to the cracking damage state.

Figure 14 shows the stress distribution in the beams of the first layer and the damage to the beams of the first and top layers of the Wanlong building after the deformation parameters of the overburden were adjusted to change the range and the size of the ground settlement and to limit the maximum surface subsidence to 18 mm. It can be seen from the figure that cracking damage does not occur when the minimum

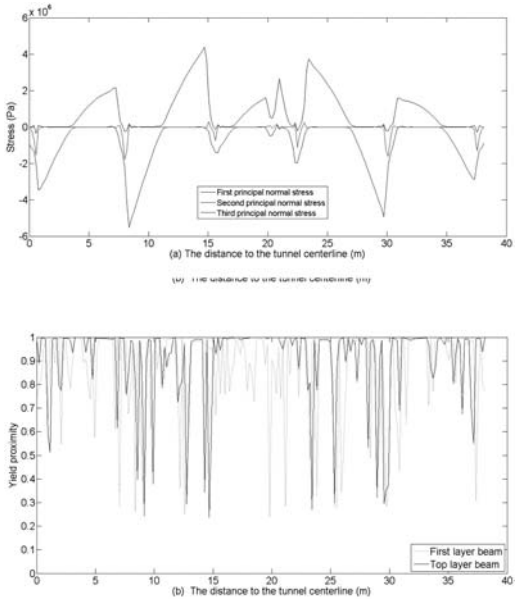


Figure 14. Distribution curve of the yield proximity of the Wanlong building for a maximum subsidence of 18 mm.

value of the yield proximity of the concrete beam is about 0.23. Therefore, if the maximum surface subsidence is controlled at a level of 18 mm, there will not be any cracking damage to the buildings in Wanlong.

5 COUNTERMEASURES TO PREVENT AND CONTROL DAMAGE TO BUILDINGS DURING THE CONSTRUCTION OF A SUBWAY TUNNEL

The damage to buildings that is caused by the construction of a subway tunnel is usually caused by a lack of building strength or an additional impact that is too large. Therefore, some preventive measures are needed for the buildings in the area that will be affected by the construction of a subway tunnel in order to ensure the normal use of the buildings. On the basis of a detailed understanding of the structure of buildings, foundations, construction time, quality status and the relative position within the area that will be affected, the safety level of buildings are divided into different grades. Buildings with poor safety levels (i.e. those that have a high degree of damage risk) should follow the principle of 'first reinforcement and second construction'. The pre-reinforcement of buildings can improve their resistance to deformation. If there are still problems after the construction, building reinforcement measures are required.

Based on the stratigraphy of the actual situation and the level of the security of the building, formation grouting and isolated piles are usually selected as the appropriate reinforcement measures.

Building foundation underpinning or structural reinforcement measures can be used when the case is serious. When the security level of neighboring buildings is general and the risk level is general, construction can proceed while strengthening is being done. However, the degree of building settlement during the construction process should be monitored in order to ensure the safety of buildings. When the security level of neighboring buildings is general or high and the risk level is low, construction can be done first followed by strengthening. However, the degree of building settlement during the construction process should be monitored in order to ensure the safety of buildings. After construction is completed, it should be determined whether there is a need to reinforce the building according to the specific circumstances.

6 CONCLUSIONS

(1) The rock lithology revealed by the Qingdao subway tunnel construction was analyzed and summarized according to the results of a field survey, reconnaissance and measurements. The rock surrounding the tunnel was divided into seven categories.
(2) The laws of the deformation of the overlying strata and surface subsidence that will be caused by the construction of a tunnel of Subway Line No. 3 were studied. Seven kinds of deformation of the overlying strata and surface subsidence are summarized for seven of the rock types.
(3) Before the tunnel crosses under the buildings of Wanlong, its deformation was analyzed according to the monitoring data. Its damage was predicted and the control standard was given scientifically. The maximum subsidence for Wanlong is 18 mm.
(4) According to the countermeasures for the prevention and control of damage to buildings, combined with the special geological characteristics in the Qingdao area, during the construction of a subway tunnel, the basic principles of the construction scheme of a shallow buried tunnel were summarized: strict standards, forepoling, enough grouting, optimal excavation, quick installation of non-yieldable (stiff) tunnel support, diligent measurements and strict management'.

ACKNOWLEDGEMENTS

Project (No. 51179080, 50874064) was supported by National Natural Science Foundation of China and the Research project for Qingdao Subway engineering (Line No. 3) with grant No. SDSITC–0108310.

REFERENCES

Meng, D., Zang, X. & Yu, G. 2012. Comparative Study of Analytical Methods for Ground Surface Settlement Induced by Subway Station Construction. *Journal of Rock Mechanics and Engineering* 31(6):1169–1177.

Ottosen, N.S. 1977. A Failure Criterion for Concrete. *Journal of the Engineering Mechanics Division* 103(4):527–535.

Yang, J. & Liu, B. 2002. *Surface Movement and Deformation Induced by Tunnel Construction in City.* Beijing: China Railway Press.

Yu, G.,Yang, L. & Su, Z. 2000. *Nonlinear Laws, Monitoring and Control of Disturbed Rock Mass Damage.* Jilin: University Press.

6. Underground storage and waste disposal

This page intentionally left blank

Rock Mechanics for Resources, Energy and Environment – Kwaśniewski & Łydżba (eds)
© 2013 Taylor & Francis Group, London, ISBN 978-1-138-00080-3

Modeling the Excavation Damaged Zones in the Bátaapáti radioactive waste repository

F. Deák
Budapest University of Technology and Economics, Budapest, Hungary

L. Kovács
RockStudy Ltd. (Kőmérő), Pécs, Hungary

B. Vásárhelyi
Department Pollack Engineering, University of Pécs, Pécs, Hungary

ABSTRACT: The program for the final disposal of low and intermediate level radioactive waste was established by Paks Nuclear Power Plant, Hungary. Preparation for final disposal of radioactive wastes has been done as part of a national program since 1993. The Central Nuclear Financial Fund and the Public Limited Company for Radioactive Waste Management (Puram) have been established to coordinate organizations and activities for all tasks in connection with nuclear waste treatment. The project started with a geological screening in order to find the most suitable formation for the radioactive waste disposal. The selected potential host rock is a granite complex in the Mórágy Granite Formation in the south-western part of Hungary, close to the village of Bátaapáti. The goal of this paper is to present the newest modeling results of the Excavation Damaged Zones around the Bátaapáti radioactive waste repository. The following zones are thoroughly investigated and modeled in both 2D and 3D: EdZ: Excavation Disturbed Zone; EDZ: Excavation Damaged Zone and HDZ: Highly Damaged Zone.

These Excavation Damaged Zones (EDZs) are very important for understanding the hydromechanical and geomechanical behavior. Therefore the EDZs were analyzed by hydrogeological, filed-survey, geophysical and Borehole Television (BHTV) methods. Our modeling was using both high number of laboratory rock tests and the field measurements. The correlation between the computed and measured values, were verified.

1 INTRODUCTION

Due to the latest studies of excavation damaged and disturbed zones three different zones are distinguished (see Figure 1):

- Excavation disturbed Zone or Excavation Influence Zone (EdZ or EIZ), which is a zone with hydromechanical and geomechanical modifications, without major changes in flow and transport properties. Stress and/or strain in EdZ zone involves only elastic change and EdZ is situated beyond the EDZ. The pore volume may be affected close to the EIZ-EDZ transition by the elastic strain.
- Excavation Damaged Zone (EDZ), is a zone with hydromechanical and geomechanical modifications inducing significant changes in flow and transport properties. The damage in this zone is in the form of grain scale fractures and minor interface dilation from the EIZ-EDZ transition to interconnected at the EDZ-HDZ. This zone could be subdivided into outer – EDZ_o and inner EDZ_i zones.
- Highly Damaged Zone (HDZ), is a zone where macro-scale fracturing or spalling may occur. The fractures are typically interconnected which results in a significant increase of the effective permeability in this zone.

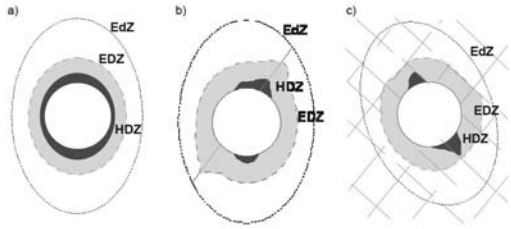


Figure 1. Schematic interpretation of the EdZ (or EIZ), EDZ and HDZ in different cases: homogeneous rock mass (a), modification of EDZ and HDZ due to one pre-existing fracture (b), modification of EDZs in jointed rock mass (c) (after Lanyon et al. 2009).

By tunneling the stress induced rock spalling which leads to damage and overbreak in excavations at higher depth in hard rock with low porosity. The spalling mechanism can lead to bursting which can be violent or non-violent and in some cases may

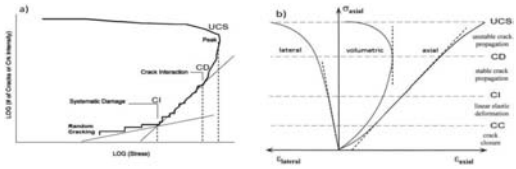


Figure 2. Damage detection using a) acoustic emissions and b) strain measurements (Diederichs & Martin 2010).

be time-dependent. Therefore in unsupported conditions with an anisotropic in situ stress field, the spalling can form notch-like geometries. Detailed researches, have demonstrated that brittle non-porous rocks behaves differently than experienced by laboratory tests (Diederichs & Martin 2010). Typically, they have a maximum long term tunnel wall strength of no more than the half of the laboratory UCS values. This lower bound strength threshold is relatively insensitive to confining stress.

$$\sigma_{1\max} = CI + (1to2)\sigma_3 \quad (1)$$

where CI is the Crack Initiation threshold, which typically ranges between 35–50% of the UCS value (Diederichs & Martin 2010).

2 LABORATORY INVESTIGATIONS

The most reliable methods are the crack volume strain method (with strain gauges) and the acoustic emission method (with AE transducers) for the determination of crack closure (CC), crack initiation (CI) and crack damage (CD) thresholds (Diederichs & Martin 2010, see Figure 2).

The damage thresholds were determined following the methods outlined by Eberhardt's & Martin's instructions (Martin 1993, Eberhardt et al. 1998).

From 208 UCS measurements using strain gauges we could use only 55 gave reliable strain results to determine the strength thresholds. This was because the strain gauges on the cores were damaged often before the failure of the samples.

To make possible the detection of the mentioned thresholds it is required the simultaneously functioning of the installed strain gauges at the CD boundary.

Based on the statistical analyses, a smaller range of values at CC and CI thresholds were observed. Typically the CI threshold is 35–50% of UCS, while the CD is around 80% of UCS (Diederich et al. 2010).

The summarized results show, that the monzogranite samples behaves as brittle material during the UCS laboratory tests (between the CD and failure stage rarely could be detected "creeping", or ductile indications).

Because of the sub-granular structure of the monzonite, it deforms ductile before the failure. This stage is somewhat larger than in the case of monzogranite. The results are summarized in Table 1 and 2.

Table 1. Damage thresholds for the monzogranite (36 samples).

Threshold	CC	CI	CD	UCS
Mean (MPa)	24.45	52.14	145.60	165.11
Standard deviation	4.50	10.65	17.09	19.25
% (of UCS)	14.81	31.58	88.18	–

Table 2. Damage thresholds for the monzonite (11 samples)

Threshold	CC	CI	CD	UCS
Mean (MPa)	24.22	53.30	134.25	163.72
Standard deviation	3.27	13.67	28.74	14.22
% (of UCS)	14.79	32.55	82.00	–

3 EXTENSION OF THE EDZ BASED ON THE HYDROLOGICAL MEASUREMENTS

Based on the measurements (with multi-packer systems) it can be stated that the thickness of EDZ in the access tunnels – determined by the several orders of magnitude increase in hydraulic conductivity – at the side walls and roof is ~0.57 m and in the floor is ~1.1 m.

With a hydrological scanning method in the vicinity of the repository chambers this value could be further specified. According to the tests it can be stated that the thickness of the EDZ in this area around the repository chamber is ~0.30 m (just as in the floor).

However – from the former EDZ-measurement data it can also be concluded – in the boreholes at the far sections from the access tunnels fractures with in excess of 1×10^{-7} m^2/s hydraulic conductivity were observed in several cases. These fractures have usually good hydraulic connection with the EDZ of tunnels.

Contrarily the measurement results from the scanning measurements carried out in the tunnel floor vary within a relatively wide range.

Since there can be fractures having direct hydraulic connection with the EDZ more than 0.30 m below the boreholes in the floor, it is statable that the EDZ is more extended in the tunnel or chamber floor, than in the side walls and roof.

Unfortunately it was not possible to determine accurately the extension of EDZ from the limited number of measurements.

Studies have shown that the thickness of EDZ is ~0.30 m, but in several cases it can extend beyond 0.50 m in the floor of the repository chamber (Andrássy et al. 2012). For more accurate determination of the extension of EDZ further studies are necessary.

In any case it can be clearly stated that the extension of the EDZ in the floor or invert of the repository chamber (the chambers have a section of 96 m^2) is

significantly lower than was observed in the access tunnels (with 21–33 m^2 tunnel section).

This is related to the different excavation modes: the access tunnels were excavated by single-phase drill and blasts, while in the repository chambers top heading (crown and bench) technique was used.

Due to the drill and blast benching in the repository chambers a large open space standing upward was available, so the explosive energy damaged less the rock mass around the excavation. The hydrogeologists use the nomenclature of Tsang therefore they didn't distinguish the EDZ (Tsang et al. 2005). The above described depths are the HDZ and/or EDZ_i boundaries.

4 ROCK MECHANICAL CHARACTERIZATION OF EDZ

In summary, the tunnel excavation process affects the rock mass producing zones of damage. These are the Excavation Damaged Zones (EDZs). Moving away from the excavation, the EDZs can be distinguished as the Highly Damaged Zone (HDZ), the inner EDZ (EDZ_i) and the outer EDZ (EDZ_o). Beyond the EDZ is a stress and/or strain influence zone that involves only elastic change, the Excavation Influence Zone (EIZ) (Perras et al. 2012).

The UCS and Brazilian tensile tests results as input parameters, as well as triaxial tests to determine the true intact rock strength (σ_{ci}) and the intact rock material constant m_i are needed for EDZs numerical modeling.

By applying the Geological Strength Index (GSI) it is possible to determine rock mass properties for input parameters when using the Hoek-Brown failure criteria (Hoek et al. 2002).

With this approach it is possible to determine rock mass properties for input into numerical models, which is applicable for rock masses with GSI < 75.

Diederichs (2007) developed a method to describe brittle behavior with the generalized Hoek-Brown peak and residual parameters. He referred to this method as the Damage Initiation and Spalling Limit (DISL). This method requires CI, UCS and tensile strength as input parameters.

4.1 *Empirical prediction of spalling*

If CI has already been determined, than it becomes possible to predict and localize the spalling. A preliminary estimate of overbreak depth can be predicted using the empirical approach of (reference) using the equation:

$$\frac{r}{a} = 0.5\left(\frac{\sigma_{max}}{CI} + 1\right), \text{ for } \sigma_{max} > CI \quad (2)$$

where r is the radial distance from the tunnel centre of the overbreak, a is the planned radius of the tunnel (Diederichs & Martin 2010). In a later work, the division of EDZs has been established by numerical modeling in the case of a circular tunnel geometry (Table 3).

Table 3. Interpreted results from numerical modeling (using DISL) for different stress levels. Predicted limits of the EDZs (after Perras et al. 2012).

EDZ-type	Relation
HDZ	$r/a = 1 + 0.2(\sigma_{max}/CI\text{-}1)^{0.5}$
EDZ_i	$r/a = 1 + 0.5(\sigma_{max}/CI\text{-}1)^{0.5}$
EDZ_o	$r/a = 1 + 0.65(\sigma_{max}/CI\text{-}1)^{0.5}$



The presented approaches have a main disadvantage. These methods can be used only in the case of circular shape tunnels.

Based on the results presented in the table above first we also carried out calibration modeling using Phase^2, a finite element program by Rocscience.

Circular tunnels were modeled using characteristic rock mechanical input parameters which of the storage chambers environment. In the output results the limits of EDZs were identified. The obtained values and modeling experience were applied during the modeling of repository chambers. Using the real geometries it was possible to define the limits and spatial extent of EDZs were defined, which theoretically occurs as a result of tunneling stress redistribution.

During the modeling process the horizontal/vertical stress values (K) were changed. Based on the in situ stress measurement we were used K = 1.00 to 1.35 values in the repository area.

For 2D modeling the Phase^2 (FEM) software, while for 3D the Examine^{3D} (BEM) codes were used.

Independently of the applied excavation modes – spalling occurs immediately and it develops notches, wedges and immediately fracturing parallel to the tunnel axis.

If the wedges are not developed by the fractures which intersect the rock mass, then the characteristic overbreaks are caused by the immediate spalling and blasting processes.

At low and intermediate in situ stress levels, the stress magnitude may reach the level, that cause localized spalling and notch formation depending on the rock strength. At greater depths the brittle failure may involve the whole boundary of the opening.

The development of brittle failure appears parallel to the excavation boundary due to the increasing of the load (Ghazvinian et al. 2011).

The existing fractures start to extend and form wing cracks parallel to the excavation surface are formed in the absence of confining stress and due to the increase in the stress magnitude around the excavation surface. The cracks propagate until they coalesce and start to interact. The interaction of the cracks causes slabbing and/or spalling around the boundary.

The mentioned brittle behavior was described in detail firstly by Hoek in 1968. He conducted experiments on glass plates and examined the fracture growth and σ_3/σ_1 relations on the plates. Hoek showed that as confining stress (σ_3) is decreased the length of the

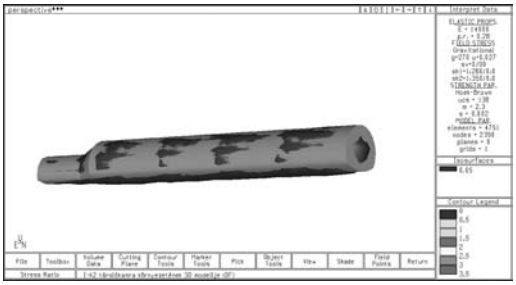


Figure 3. The $\sigma_3/\sigma_1 = 0.05$ threshold around the I-K2 repository chamber (K = 1.00).

Table 4. The distribution of EDZs based on empirical and circular tunnel modeling determinations

$\sigma_{max} = 60$ MPa, $\sigma_{max}/CI = 1.15$		
EDZ-type	r/a	σ_3/σ_1
HDZ	1.07	0.084
EDZ_i	1.19	0.176
EDZ_o	1.25	0.221

wing cracks start to extend. At a ratio of approximately $\sigma_3/\sigma_1 < 0.05$ the wing cracks significantly increase in length. The spatial arrangement of this threshold around the storage chamber is shown in the Figure 3.

As the σ_3/σ_1 ratio approaches zero, the length of the wing cracks are infinite. This can occur if the crack opening force is held constant.

5 MODELING OF THE EDZS AROUND THE REPOSITORY CHAMBERS

5.1 *Modeling results in the case K = 1.00*

During the 2D approach the extension of EDZs on the circular tunnel geometry was verified by using the analogical material and in situ primer stresses input parameters to the radioactive waste storage chambers (Table 4).

Based on the empirical and numerical modeling results the σ_3/σ_1 values were determined. These values are characteristic for the given EDZs limits. Using these σ_3/σ_1 values the damaged zones in the case of the chamber geometries were separated.

This method is capable to determine the extension of EDZs for all optional geometry shapes and dimensions if the σ_3/σ_1 values are known at the EDZs boundaries.

After the circular tunnel modeling the extension of EDZs in space for the storage chambers were examined, using the aforementioned characteristic stress ratios. After the 2D numerical modeling 3D analyses were performed to determine the spatial extent of the EDZs in the case of the two storage chambers.

Due to examination in 3D at the excavation intersections the authors found a larger extended EDZ. This phenomenon is known to us as an extra load on the intersections – its study is possible only by using 3D approach.

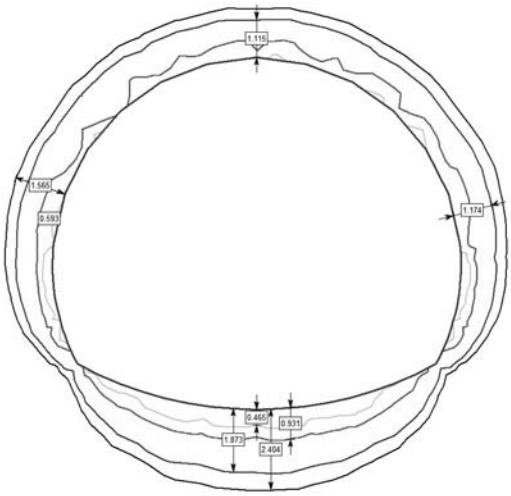


Figure 4. Extension of the EDZs around the repository chambers (threshold contours: spalling with pink, HDZ with red, EDZ_i with violet and EDZ_o with black) (K = 1.00).

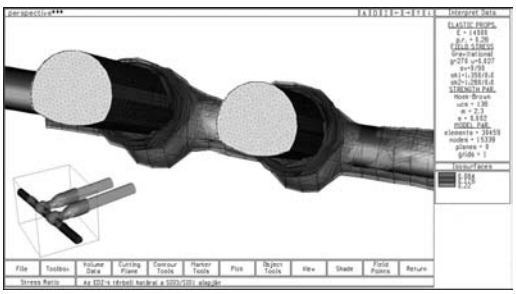


Figure 5. Excavation damaged zones in 3D (K = 1.00).

The Examine^{3D} results are shown in Figure 5.

5.2 *Modeling results in the case of in plane stress ratio K = 1.35*

After changing the horizontal/vertical stress ratio the expected results were obtained. Around the excavation floor and in the roof the excavation damaged zone appeared in a larger dimension. Our results are shown in Figure 6 and 7, and in Table 5.

5.3 *The influence of pre-existing discontinuities on the EDZs*

Even before the excavation process the rock mass can be intersected with structural discontinuities (tectonic fault planes, bedding planes, schistosity, fractures, and rock type boundaries).

These structural elements completely alter the formation of EDZs compared to the case which can be observed at the continuum mechanical approach.

Along the discontinuities stress redistributions could occur, therefore the EDZs could evolve independently of the excavation shape (Fig. 8).

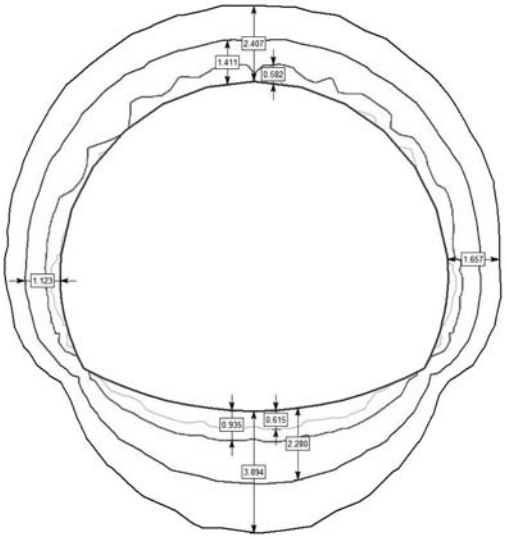


Figure 6. Extension of the EDZs around the repository chambers (threshold contours: spalling with pink, HDZ with red, EDZ_i with violet and EDZ_o with black) (K = 1.35).

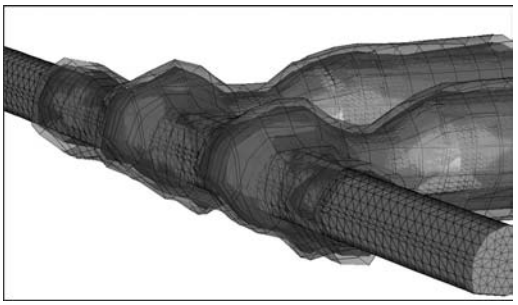


Figure 7. A sort of EDZs expansion evolve at the access tunnel and chamber intersections, further this observation will be important, due to the closing process at EDZ cutoffs (K = 1.35).

The key processes and features affecting the stability of excavation in the vertical and oblique plane are the slab-like breakouts. In the case the failure is mainly controlled by strength anisotropy (e.g. bedding) or other planes of weakness (e.g. tectonic faults, weakly cemented, silty-clay intercalations). In the horizontal plane, where wedge-like breakouts can occur, the failures are controlled mainly by stress anisotropy.

The effects of discontinuities (natural and blast generated fractures) on the EDZs can be tested and applied with very good efficiency in Phase[2].

5.4 *Further considerations in the EDZs research of Bátaapáti*

The researches of the EDZ observed at Bátaapáti supplied a high amount of results. According to these observations, the definition of the boundaries and the

Table 5. The distribution of EDZs based on empirical and circular tunnel modeling determinations

$\sigma_{max} = 65.3$ MPa, $\sigma_{max}/CI = 1.31$		
EDZ-type	r/a	σ_3/σ_1
HDZ	1.10	0.084
EDZ_i	1.25	0.187
EDZ_o	1.32	0.290

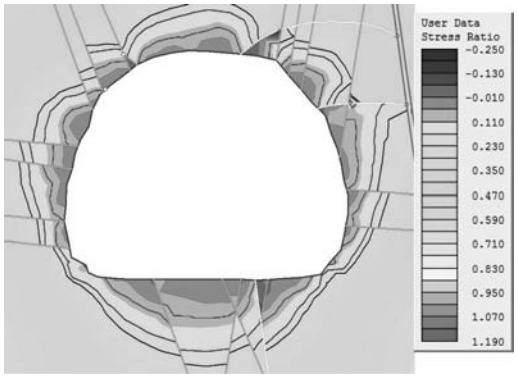


Figure 8. Extension of EDZs in the EPZS030_0045 advance, considering the documented fractures without blast damages (threshold contours: $\sigma_3/\sigma_1 = 0{,}05$ or spalling with pink, HDZ with red, EDZ_i with violet and EDZ_o with black) (K = 1.35).

rock mechanical characterization of EDZ zones are not possible.

Most of the measurements were taken for hydrological, hydraulic purposes so far. Considerably high amount of other methods applied by the research was also subordinated to these fields. The geophysical results were summarized in the geophysical monitoring reports (e.g. Bakai et al. 2012). The hydrogeological results were also presented in several documents. In the repository area a complex seismoacoustic long term monitoring system was installed before the excavation. Detailed analyses of the acoustic emissions will be finalized soon. Actually there are some preliminary elaborations on these results (Figure 9). Finally the extension and properties of the EDZ in the environment of the chambers were defined based on collectively the geophysical, BHTV, hydraulic measurements and other tests, according to hydrogeological aspects.

The results of this EDZ approach using theoretical and empirical methods should be checked in on site. Further analysis of the drilling cores from the existing radial boreholes (radial EDZ and extensometer boreholes) and data from BHTV would be a great support. From rock mechanical aspects the most practical and most applicable method is the slotting. Dye penetration of the slotting planes reveals the recently formed artificial cracks. Therefore the analysis of the amount



Figure 9. The seismoacoustic monitoring system and AE activity recorded around the repository area in Bátaapáti (Bakai et al. 2012).

and spatial distribution of the artificial cracks caused by the blasting would become more obvious (Saiang 2008).

During the following research phases identical measuring campaigns but in different location should be applied and their results should be compared. E.g. from raw data of the geophysical measurements the 3D visualization would be possible. The collective treatment of visualization and the rock mechanical models can reveal temporal trends as well.

The long-term, rheological behavior of the EDZ zones has to be analyzed by in situ measurements applied in the same time and the same place. For obtaining reliable information about the temporal behavior of the EDZs some year-long datasets are needed.

6 CONCLUSIONS

Our work highlighted, that the importance of complex laboratory measurements for accurate determination of the CC, CI, CD failure thresholds. In the Bátaapáti project the dimensions of the EDZs are identical for both in 2D and 3D numerical models and these results are very similar to the field observations.

ACKNOWLEDGEMENTS

The authors acknowledge the permission of PURAM to publish this paper. The first author is grateful to M. A. Perras and Á. Tóth for the suggestions and comments.

REFERENCES

Andrássy, M., Darvas, K., Korpai, F. & Ludmann, L. 2012: *The extension of EDZ around the repository chambers in Bátaapáti*. Golder Ltd. (in Hungarian lanquage) – RHK-K-004/12 – RHK report, 2012. June, 101 p.

Bakai, J., Kardos, J.& Szücs, I. 2012: *Operation of seismoacoustic system* (Szeiz-08, Szeiz-09, Szeiz-10) (in Hungarian) – RHK-K-045/12 – RHK report, 2012. June, 47 p.

Diederichs, M.S. 2007: Mechanistic interpretation and practical application of damage and spalling prediction criteria for deep tunneling. *Can. Geotechn. J.* 44(9): 1082–1116.

Diederichs, M.S. & Martin, C.D. 2010: *Measurement of spalling parameters from laboratory testing.* In: Zhao, Labiouse, Drudt & Mathier (eds) – EUROCK2010, ISRM, Taylor & Francis Group, London, 323–326.

Eberhardt, E., Stead, D., Stimpson, B. & Read R.S. 1998: Identifying crack initiation and propagation thresholds in brittle rock. NRC Canada, *Canada Geotech J.* 35: 222–223.

Ghazvinian, E., Diederichs, M. & Archibald, J. 2011: *Challenges related to standardized detection of crack initiation thresholds for lower-bound or ultra-long-term strength prediction of rock*. 2011 Pan-Am CGS Geotechnical Conference 8 p.

Hoek, E. 1968: *Brittle failure of rock. Rock mechanics in engineering practice*, In: K.G. Stagg & O.C. Zienkiewicz eds., Willey & Sons Ltd., London. 99–124.

Hoek, E., Carranza-Torres, C. & Corkum, B. 2002: *Hoek-Brown criterion – 2002 edition*. Proc. NARMS-TAC Conf., Toronto, 1: 267–273.

Lanyon, G.W. 2011: *OPG's Deep Geologic Repository for Low & Intermediate Level Waste – Excavation Damaged Zones Assessment*. Report prepared by Fracture System Ltd. March 2011, 95 p.

Lanyon, G.W., Marschall, P., Trick, T., Vaissiere, R., Shao, H. & Leung, H. 2009: *Hydromechanical evolution and self-sealing of damage zones around a microtunnel in a claystone fromation of the Swiss Jura mountains*. 43rd U. S. Rock Mechanics Symposium & 4th U.S.–Canada Rock Mech. Symp. paper 09-152, Asheville, North Caroline.

Martin, C.D. 1993: *The strength of massive Lac du Bonnet granite around underground opening*. Ph.D. thesis, 278 p.

Perras. M., Langford. C., Ghazvinian. E. & Diederichs, M. 2012: *Numerical deliniation of the excavation damage zones: From rock properties to statistical distribution of the dimensions*. ISRM, EUROCK2012, Stocholm, 14 p.

Saiang, D. 2008: *Behavior of blast-induced damaged zone around underground excavations in hard rock*. Diploma Thesis, Lulea University of Technology, 110 p.

Tsang, C-F., Bernier, F. & Davies, C. 2005: Geohydromechanical processes in the Excavation Damaged Zone in crystalline rock, rock salt and indurated and plastic clays – in the context of radioactive waste disposal. *Int. J. Rock Mech. & Min. Sci*. 42: 109–125.

Rock Mechanics for Resources, Energy and Environment – Kwaśniewski & Łydżba (eds)
© 2013 Taylor & Francis Group, London, ISBN 978-1-138-00080-3

Quantitative roughness profiling of fracture surfaces of a granitic host rock at a radioactive waste disposal site

Á. Krupa, F. Deák, P. Görög, I. Buocz & Á. Török
Budapest University of Technology and Economics, Budapest, Hungary

ABSTRACT: The paper provides new results on the fracture surface roughness testing from the Bátaapáti National Radioactive Waste Repository project. During the calibration of modeling and design work it was necessary to develop a simple and quantitative approach to predict the Joint Roughness Coefficient (JRC) value of fracture surfaces. To reach this goal laboratory-scale and on-site large scale surfaces were investigated. The roughness was studied on 15 smaller samples (average area of 73 cm^2), and on 5 larger in-situ granitic surfaces. The latter were documented during the excavation of the repository chambers (average area of 12 m^2). Additional specimens (more than 40) that were used for direct shear strength test (average area of 26 cm^2) were also studied by generating 3D models with the software JointMetrix3D (JMX). In order to determine the shear strength numerically, the JRC value of the surface is one of the key influencing factors. The roughness parameter (R_p) and the roughness parameter of the surface (R_s) can be calculated using several 2D profiles of the surfaces tested. The JRC values were calculated from the results of the shear strength test, and compared with the JRC values calculated from R_s. The resulting JRC values served as an input parameter to the original equation of Barton. From the evaluation of the relationship between JRC and R_s a new correlation were identified, which provided a better estimation of the JRC values of the rock types tested. The following correlations were found:

$\tau_b = \sigma_n \tan(\phi_b + (a\ln(R_S) + b)\log_{10}(\frac{JCS}{\sigma_n}))$, where a = 90.16 and b = 1.39.

The models were built in JointMetriX3D from the surfaces that were measured both in 2D (JMX profiling) and in 3D, with the OgreProject software. Unfortunately the 3D roughness profiling did not provide a reliable approximation therefore further studies are necessary in order to determine additional equations.

1 INTRODUCTION

The samples were collected from the Mórágy Granite Formation, where monzogranite is the most common lithotype. All the samples investigated were taken from this type of rock (Fig. 1). Rocks with fracture surfaces are characteristic to the region, therefore samples with natural discontinuities were investigated, as well. The bulk density of the studied samples was in between 2602–2866 kg/m^3, and the mean UCS was 136 MPa. Direct shear strength tests were carried out along the discontinuities.

There are no mathematical formulae developed by Barton & Choubey (1977) for determining the JRC values of their 10 predefined profiles. They can be evaluated only in empirical ways, depending on the experience and ability of the person who carries out the measurements.

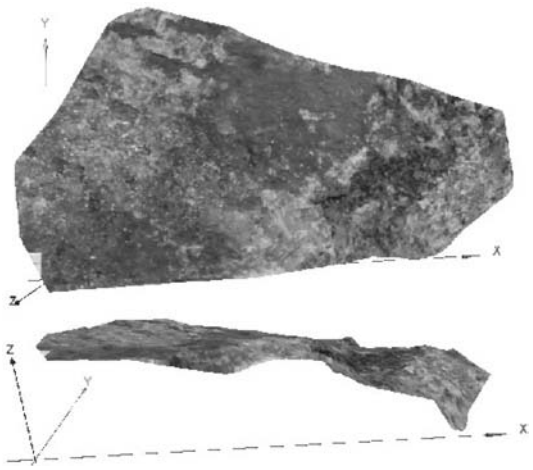


Figure 1. A sample's surface and a segment.

2 THEORICAL BACKGROUND

The most important goal of the research was to provide a good approximation for the JRC value by using both quantitative methods and correlations with the shear strength.

Using the JRC value and the strength values obtained from the direct shear strength tests, the shear

strength can be calculated with the model of Barton and Choubey (Barton 1977):

$$\tau = \sigma_n \tan(\phi_b + JRC \log_{10}(JCS / \sigma_n)) \quad (1)$$

Tse and Cruden (1979) tested more parameters, and showed that the root-mean-square expression Z_2 correlates the best with the JRC value. The formula they introduced is:

$$JRC = 32.2 + 32.47 \log Z_2 \quad (2)$$

in which:

$$Z_2 = \sqrt{\frac{\sum_{i}^{N-1}(z_i - z_{i+1})^2}{(N-1)\Delta s^2}} \quad (3)$$

z: height of the surface's points above a reference line
Δs: distance between the measured points (constant value)
N: number of measured points

According to Maerz et al. (1990) the roughness profile index has a good correlation with the JRC value, which can be described with the following formula:

$$JRC = c(R_p - 1) \quad (4)$$

in which:
c: constant assuming values equal to $c = 401$ and $c = 411$ (Maerz et al., 1990)
R_p (or R_L): roughness profile index, i.e. ratio of the length on the surface and the projection length:

$$R_p = \frac{L}{L_0} \approx \frac{\sum_{i=1}^{N-1}\sqrt{\Delta s^2 + (z_i - z_{i+1})^2}}{\Delta s(N-1)} \quad (5)$$

Haneberg (2007) described a laser 3D modelling method, which allowed measuring the roughness surface index. For this purpose, he used four profiles on the surface – vertical, horizontal and diagonal lines (Fig. 2).

Another approach was outlined by Lee et al. (2004), in which the shear strength of the surfaces was expressed by using the roughness surface index (R_S), without applying the empirically obtained JRC value. According to this method, the R_S index was calculated from the R_L value of 5 profiles. The R_S is expressed from the data of the surface:

$$R_S = \frac{A_S}{A_0} \quad (6)$$

Lee et al. (2004) performed shear strength tests, and compared the compressive strength of the samples and

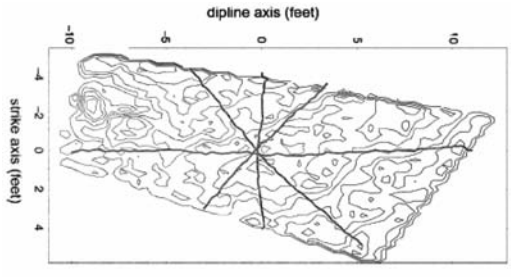


Figure 2. Haneberg's profiles (Haneberg, 2007).

shear strength results to the R_S value. To express the shear strength, the equation of Barton (1977) was used:

$$JRC = \frac{\tan^{-1}(\frac{\tau_b}{\sigma_n}) - \phi_b}{\log(\frac{JCS}{\sigma_n})} \quad (7)$$

Comparing this JRC value to the R_S value, the following expression can be outlined:

$$JRC = a \ln(R_S) + b \quad (8)$$

Starting from this formulation, the aim of this research was to find suitable values for the parameters "a" and "b" for the rock types tested, and to use these values in the original shear strength expression of Barton, in order to replace the JRC value. With the application of equation (8), the shear strength can be defined from the experiments in a quantitative way:

$$\tau_b = \sigma_n \tan(\phi_b + (a \ln(R_S) + b) \log_{10}(\frac{JCS}{\sigma_n})) \quad (9)$$

Grasselli (2001) proved that, during the shear strength test, shear initiates first at the deepest points, where the largest zones are located in the shear line. After shearing the roughest points, the points with smaller roughness participate in the process of shearing. Consequently our aim was, to analyse the surface on the shear line, where the points are deep enough to participate in the shear (the method is called GG – shear strength criterion).

3 METHODOLOGY AND TOOLS APPLIED

The approach followed in this work was based on the use of two softwares, JointMetriX3D (JMX) and OgreProject (hereafter called Ogre). In JMX, high resolution photos of the monzogranitic samples were used as input data, taken by the camera of the JMX system. A picture was taken of the same sample from two different angles, after which by matching them, a photorealistic 3D model was obtained for all the samples (Fig. 1).

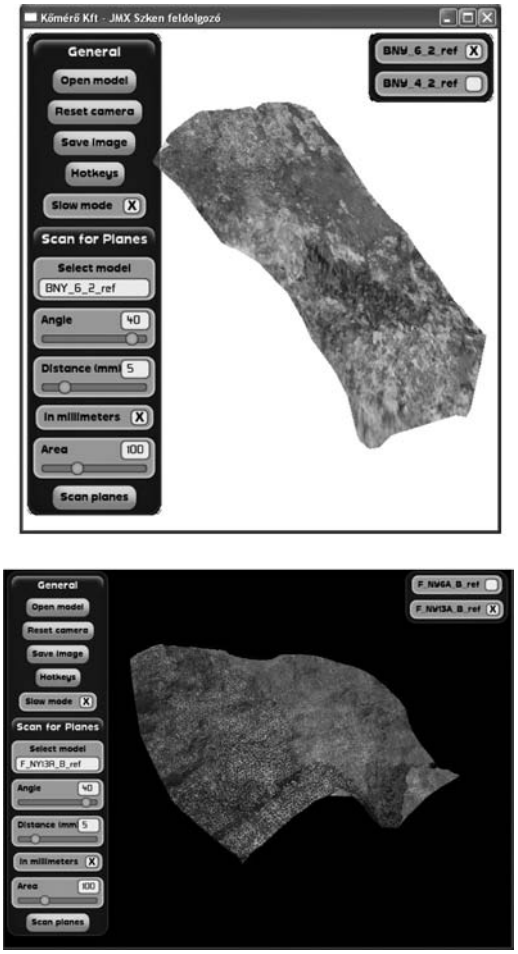


Figure 3. Users' surface in Ogreproject, and the generated areas on the sample.

The Ogre software was applied to define the roughness for the whole surface. Ogre gives the user the possibility of implementing own routines, which can help in processing the results of the graphical application by using a special programming language based on C++. An own user interface was therefore created by using C++. This allowed to access the models generated by the JMX software, and to process the data further. Three variable parameters were assigned in the software, namely (Fig. 3):

- maximum angle between the elements of the mesh and the generated plain;
- maximum difference between the surface and the generated plain (value in either millimetres or centimetres);
- minimum size of the plains (giving number of the mesh triangles)

Particular attention was paid to generate the correct density of the mesh before exporting the file.

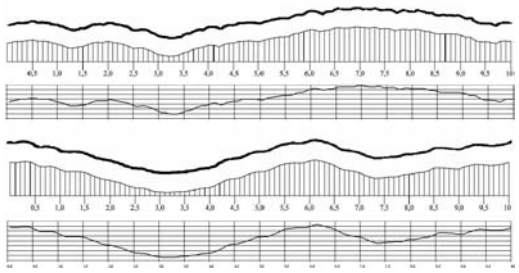


Figure 4. The 12–14 and 14–16 JRC profile's original, later in AutoCAD and finally in Microsoft Excel.

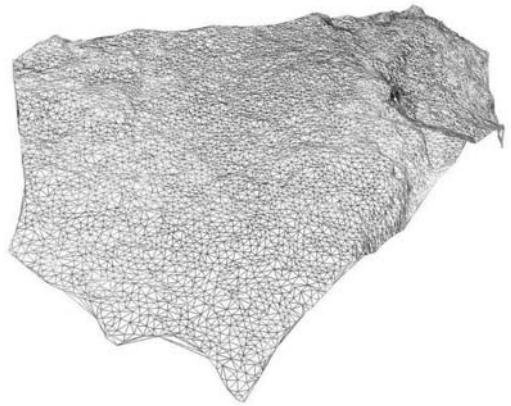


Figure 5. The generated mesh on the 3D model of the sample.

4 DIGITALIZATION OF BARTON'S PROFILE TO 2D PROFILE- AND 3D SURFACE MEASUREMENTS

The first phase of the methodology used was the digitalisation of the 2D JRC profiles. As an input data for the Ogre software, ten profiles provided by the profiling of Barton were necessary to be measured. The ten profiles were imported in AutoCAD, in which software all profiles were drawn in the form of a line following the original profile (Fig. 4). This way, the length and the height of the profiles could be determined as known values.

The 2D surface measurement was done by applying the JMX software. For each surface the grid-size of the mesh was 200,000/m^2 (Fig. 5).

Afterwards, from the surface characteristics of all samples, 4–6 profiles were chosen according to Hanaberg (2007). The inhomogeneity of the surface influences the shear strength, thus, when visible significant irregularities were observed on the surface, a profile was made along those and next to them, as well. Additional profiling was done on more regular parts of the surface, too (Fig. 6).

The profiles could be exported from JMX to a data file, in which the distances between the points and the height of the points were calculated with an accuracy of

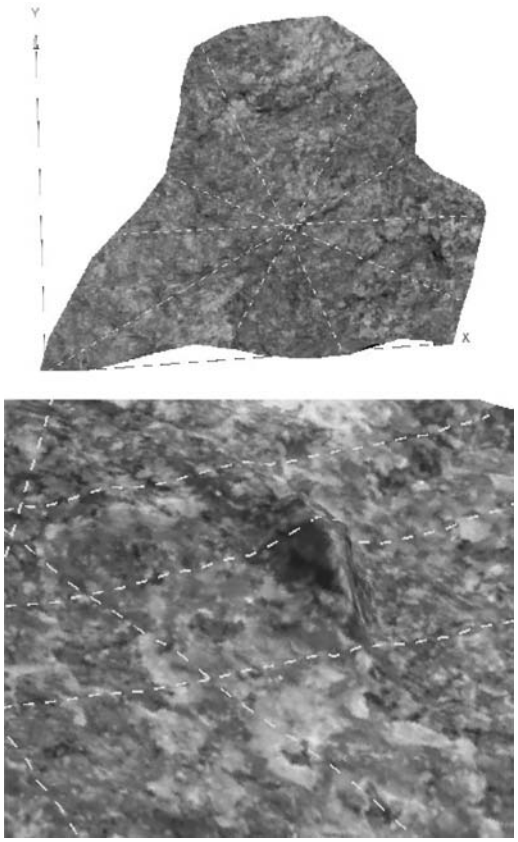


Figure 6. An average and a different surface's designated profiles.

micrometric scale. Subsequently, the distance between the highest and lowest points was calculated, allowing the determination of the JRC value (semi-quantitative method).

For the 3D surface measurements in Ogre, the profiles generated in AutoCAD were used. For all the surfaces, the parameters were chosen in order to find a reasonable correlation. More than 30 queries were performed on each sample, but even with this large amount of results, the data set showed a significant scattering. Therefore, additional samples needed to be measured, and the software algorithm refined.

5 THEORETICAL MODELS FOR THE CALCULATION OF JRC VALUES

To analyze the 2D results, it was neceessary to compare the data sets. The expression introduced by Maerz et al. (1990) was used in this phase to calculate R_P value (Eq. 3):

$$R_p \approx \frac{\sum_{i=1}^{N-1}\sqrt{\Delta s^2 + (z_i - z_{i+1})^2}}{\Delta s(N-1)} = \frac{\sum_{i=1}^{N-1}\sqrt{(s_{i+1} - s_i)^2 + (z_i - z_{i+1})^2}}{\sum_{i=1}^{N-1}(s_{i+1} - s_i)} \quad (10)$$

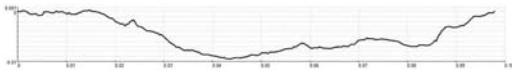


Figure 7. The profile with the highest JRC results, (16.42 and 22). The length of the profile is 9.8 cm, the maximal height difference is 9.9 mm.

The JRC was calculated from the R_P values and the mean values computed from these results were used to characterise the surfaces. According to the expression of Tse and Cruden (1979), after the transformation the Z_2 value is given by:

$$Z_2 = \sqrt{\frac{\sum_{i}^{N-1}(z_i - z_{i+1})^2}{(N-1)\Delta s^2}} = \sqrt{\frac{\sum_{i}^{N-1}(z_i - z_{i+1})^2}{\sum_{i=1}^{N-1}(s_{i+1} - s_i)^2}} \quad (11)$$

6 DETERMINATION OF THE SHEAR STRENGTH FROM SURFACE PROFILES AND JRC VALUES

The direct shear strength tests were carried out on monzogranitic samples (Buocz et al. 2010, Török et al. 2010, 2011), according to the suggestions of the ISRM. The measured and calculated values were added into the shear strength equation of Barton, and the "a" and "b" values were determined accordingly.

From the digitalised JRC profiles, the smallest height difference was obtained for the 0–2 JRC values, while the highest for the JRC values of 14–16, where a difference of 6.5 mm was determined along the 10 cm long profile. In the expression used for the calculations (Eq. 5), L is the length of the poly-line, while the L_0 value was 10 cm for all the profiles. The value of R_P could be calculated for all the JRC profiles, which allowed obtaining values of 1.001 for 0–2 JRC and 1.061 for 18–20 JRC.

The given JRC values were compared to the ones computed. For all the samples, the semi-empirical and semi-quantitative values obtained were the lowest, while the JRC calculated from R_p values were the highest. The results from the pair samples were in all three cases very similar, which provided a reliable feedback and quality control of the data set. The largest difference by the pair's samples was 4.4. Regarding the JRC values, the largest found in this study were 33.2 and 28.8 (Fig. 7), while the smallest 1.1 (calculated from $R_p = 18.3$ and 19.4) and 0.2 (calculated from $Z_2 = 16.0$ and 16.2).

The JRC was calculated from the shear strength test results obtained for the maximum and the residual strength values. Comparing the calculated and the measured JRC values to the lower calculated value, the measured values were found to be lower. The same result was observed for the higher values. Based on the

JRC values, "a" and "b" values were computed for 8 granite samples according to the following expression:

$$\tau_b = \sigma_n \tan(\phi_b + (93.63 \ln(R_S) + 2.2) \log_{10}(\frac{JCS}{\sigma_n})) \quad (12)$$

7 DISCUSSION AND CONCLUSIONS

The JRC and R_P values determined from the digitalised profiles could provide values for the "c" parameter for all the 10 profiles studied. According to the results of these analyses, Maerz et al. 1990 value of c = 401 could be well approximated for JRC values in the range 10–18. In other cases, when using value of c = 401, JRC values were either too low (0–10 JRC) or too high (JRC 18–20). When JRC is high, this value can still be used, but, conversely, for low JRC values it can give an unrealistic result.

The maximum R_p value from the digitalised profiles was 1.061; the values of the samples were on the other hand 32% higher than this, with a maximum of 1.105. By multiplying a higher R_p value than 1.061 by 401, give a result that is much higher than 20! If the c value corresponding to JRC = 18–20 is considered, instead (average 314), the calculation provides a realistic value. For 7 samples, the surface roughness index was more than 1.061, with a highest value of 1.083. With the original value of c = 401 a JRC = 33.2 was obtained, while for c = 314 JRC was equal to 26. Using the approach based on the Z_2 value, just 10% of the JRC profiles were above 20. This method seemed therefore to provide more reliable values.

In Figure 8, the three groups of values are plotted in the same R_p vs JRC diagram. The highest JRC values were computed based on R_p (both the empirical and the average values calculated from Z_2 proved to be smaller). It can be observed that the values calculated from different methods were similar.

The smaller empirical values imply smaller shear strength values. Based on the roughness measurements of the sample surfaces the introduced approach provides a better shear strength prediction in the different design phases. Therefore all the types of the calculations need to be refined and calibrated with additional laboratory testing.

Four out of the five samples of large surface were quite similar in terms of surface roughness, the fifth one was rougher. The results of the analyses confirmed these differences, since for the fifth sample extremely high values of roughness were obtained from all the three methods. Similarly to the small samples, these results yielded the highest JRC value, when this was computed from R_P, with a maximum value of 37 (Fig. 9).

All the JRC values derived from R_s and Z_2 were compared for all samples (Fig. 10). The correlation was fairly good, and it is suggested that the values can be calculated from each other (Fig. 11). This also means that, after defining R_s and JRC, other values can be easily calculated from equations and the results

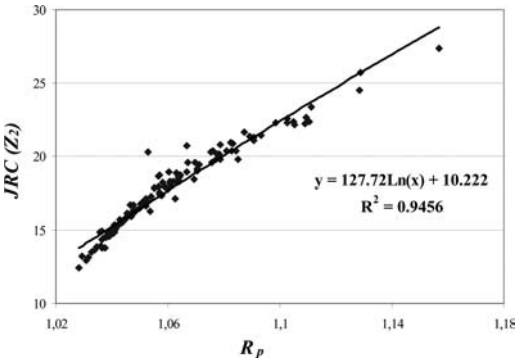


Figure 8. Calculated JRC values vs R_p (small samples).

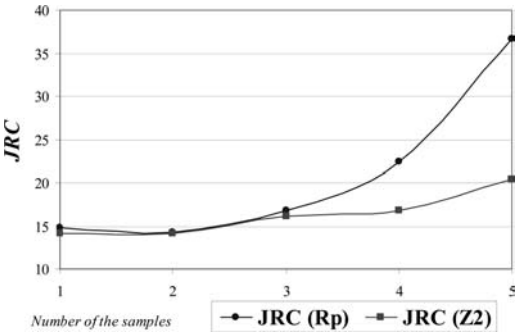


Figure 9. Comparing the calculated JRC values (Large samples).

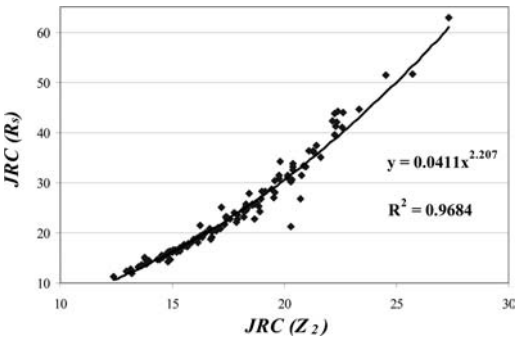


Figure 10. Correlation between JRC values calculated from R_s and Z_2.

can be used for further calculations. The relationships expressing the correlations between R_p, Z_2 and JRC, as obtained from this study, are the following:

Correlation between R_s and JRC from Z_2:

$$JRC = 127.72 \ln(R_s) + 10.22$$

JRC values counted from R_s and Z_2:

$$JRC(R_s) = 0.0411\, x^{2.207}$$

For the shear strength calculation, the mean R_s value determined for the surfaces, was used to define the

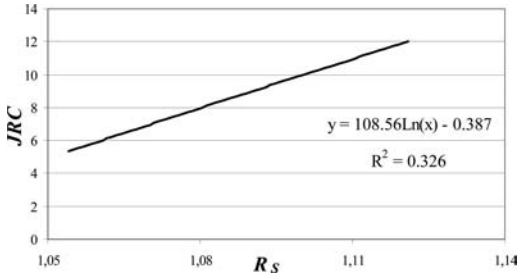


Figure 11. Correlation between JRC (calculated from the shear strength tests results) and R_s, R^2 is 0.326.

"a" and "b" values (booth for maximal and residual shear strength). A disadvantage of this approach is that when JRC and the shear strength have to be defined without any empirical method, it is necessary to have the results of shear strength tests. After obtaining this information, the JRC values have to be compared to the R_s values.

In the perspective of further developments in this research work, it is recommended to collect additional samples from different types of rocks and different rock mass quality during the next construction stage of the repository. This can allow to obtain new data sets by using the same methodology, and to outline a finer correlation between these parameters. The practical interest of the results coming from this study is that values from R_s, "a" and "b" will be available for all the main rock types of the repository and its surroundings. The results can be applied to characterize other granitic rock masses worldwide. It would become easy therefore to define the JRC values and shear strength for rock support design. This could make the process faster and would improve the current practice based on qualitative methods.

ACKNOWLEDGEMENT

The authors would like to thank RockStudy Ltd for granting the permission to work with the softwares used.

They are also thankful to PURAM (Public Limited Company for Radioactive Waste Management, Hungary) for allowing publishing the results.

REFERENCES

Barton, N., Choubey, V. 1977: The shear strength of rock joints in theory and practice. *Rock Mechanics*, **10**, pp.1–65.

Buocz I., Rozgonyi-Boissinot N., Görög P., Török Á. 2010. Laboratory determination of direct shear strength of granitoid rocks; examples from host rock of the nuclear waste storage facility of Bátaapáti (Hungary). *Central European Geology*, **53/4**, 405–417.

Grasselli G. 2001: *Shear Strength of Rock Joints based on Quantified Surface Description*, Summary of the Ph. D. thesis, EPF-Lausanne, Switzerland

Haneberg W. C. 2007: Directional roughness profiles from three-dimensional photogrammetric or laser scanner point clouds. in E. Eberhardt, D. Stead, and T. Morrison, editors, *Rock Mechanics: Meeting Society's Challenges and Demands: Proceedings, 1st Canada-U.S. Rock Mechanics Symposium*, Vancouver, May 27–31, 2007, pp.101–106.

Maerz, N.H., Franklin, J.A., Bennett, C.P. 1990: Joint roughness measurement using shadow profilometry. *Int. J. Rock Mech. Min. Sci. Geomech. Abstr*., **27**, pp.329–343.

Lee, Seok-Won, Hong, Eun-Soo, Bae, Seok-Il, Lee In-Mo 2004: Modelling of rock joint shear strength using surface roughness parameter, R_S, Konkuk University, *Proceedings of the World Tunnel Congress and 32nd ITA Assembly*, Seoul, Korea, 22–27 April 2006

Tse, R., Cruden, D.M. 1979: Estimating joint roughness coefficients., *Int. J. Rock Mech. Min. Sci. Geomech. Abstr*., **16**, pp.303–307.

Török Á., Görög P., Buocz I. 2011. Petrophysical laboratory tests of rocks from Bátaapáti repository system. (Bátaapáti tároló kőzetkörnyezetének kőzetfizikai laborvizsgálatai). In: A. Lovas ed. *Építömérnöki Kar a Kutatóegyetemért*, BME Építömérnöki Kar kiadványa, Budapest, 19–24.

Török Á., Görög P., Rozgonyi-Boissinot N., Deák F. 2010: *A Shear stenght test of samples from Bátaapáti (Bátaapátiból származó minták nyírószilárdsági vizsgálata) Report in Hungarian*, Budapest, RHK-K-083/10M01.

Rock Mechanics for Resources, Energy and Environment – Kwaśniewski & Łydżba (eds)
© 2013 Taylor & Francis Group, London, ISBN 978-1-138-00080-3

Rock mechanics for gas storage caverns with respect to optimization of operation

B. Leuger, K. Staudtmeister & D. Zapf
Institute for Geotechnical Engineering, Department for Underground Construction,
Leibniz Universität Hannover, Germany

ABSTRACT: Seasonal gas storage in rock salt caverns is a proven technology since several decades. However during the last years new operation modes with high pressure rates are aimed at. The corresponding loading of the rock salt mass differs because the change of gas temperatures during operation and the consequences of these temperature changes on the stressing of the salt rock mass must be taken into account. Within the rock mechanical design a loading history, i.e. a robust pressure versus time dependency, has to be defined which covers the possible withdrawal and injection scenarios. Alternatively the gas flow from or into the individual caverns can be taken as basic requirement. In each case, the thermodynamic influence should be considered in addition to the influence of creep. The paper discusses possible load cases which are defined pressure controlled or volume controlled respectively. It shows the differences of the time dependent state variable as well as the stress regime with respect to the assessment of the safety and economic operation.

1 INTRODUCTION

Many different aspects have to be taken into account within the dimensioning and optimization of gas storage caverns in rock salt mass for high-frequency storage. Apart of the mechanical loading the thermal loading of the surrounding rock mass is very important. Besides the determination of the operating pressures for the high-frequency gas storage there is a focus on the velocity of withdrawing the gas from the cavern. To ensure a safe operation of the cavern, next to the useable pressure regime also maximum velocities must be determined defined by pressure change rates or gas flow rates during the dimensioning or optimization. By a fast gas withdrawal from the cavern the stress condition of the surrounding rock mass is extremely influenced by the thermal load so that tensile stresses can appear in the area of the cavern wall. Due to the low tensile strength of rock salt the tensile stresses at the cavern wall must not appear in order to avoid macroscopic fracturing (Staudtmeister, May 2012, Zapf et al. 2012).

For the dimensioning of a gas storage cavern from engineering point of view a design load case has to be defined which covers all possible load scenarios. Such design load case is represented in Figure 1. The design load case contains several withdrawal and injection phases as well as phases without withdrawal or injection at maximum pressure and the pressure at lower limit of the free operating range. That procedure to determine a design load case in detail is described in Zapf et al. (2011) and Leuger et al. (2012).

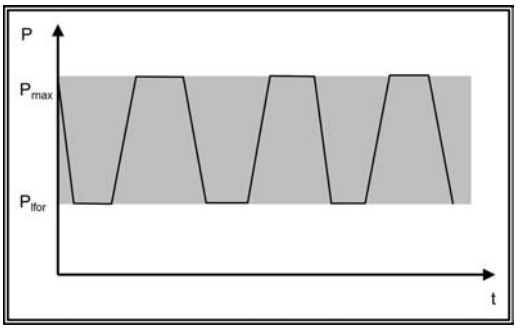


Figure 1. Example of a design load case (Staudtmeister et al., Oct. 2012).

In this paper, different withdrawal scenarios are explained and discussed with regard to an optimization from the geomechanical and economical pointof view. From geomechanical point of view an optimization means to avoid tensile stresses by a limitation of the temperature change ΔT which depends on the velocity of the internal pressure reduction in bar/day. The economical optimization means a constant and highest possible gas flow during the whole pressure range in the form of $m^3/h[V_n]$. For an example cavern different withdrawal scenarios are calculated and compared for an optimization.

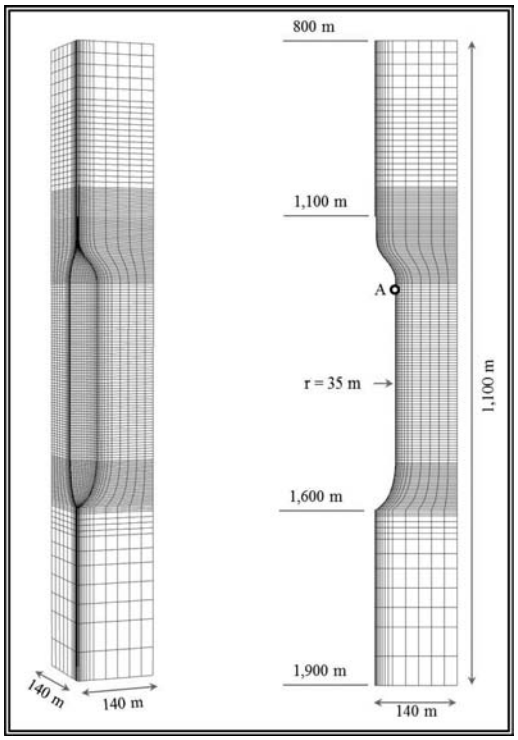


Figure 2. Calculation model and assessment point A.

2 CAVERN GEOMETRY AND INTERNAL PRESSURE CONDITIONS

The model cavern for the calculations has a cylindrical shape and is located in domal salt. The last cemented casing shoe is located at a depth of 1100 m. The cavern has a total height of 500 m and a maximum diameter of 70 m. The assumed geometrical volume of the cavern is 500,000 m^3. Figure 2 shows a schematic picture of the cavern modeled that is used for the thermo-mechanical calculation in this study. Also visible is the point of the assessment (A) of the stress redistributions versus time in the roof section of the cavern, because this is the point where tensile stresses are approached at first. The maximum pressure at the last cemented casing shoe is assumed to be 20.0 MPa (200 bar), the pressure of the lower limit of the free operation range is 8.0 MPa (80 bar).

3 CALCULATIONS

For the calculation of the internal gas temperature depending on the loading of the cavern, the program KavTec of RWE/ESK, Freiberg, Germany is used. The computed temperatures are the basis for the thermo-mechanical calculations with the Finite Differences Program FLAC^{3D} of ITASCA. In this case only the rock salt behavior is modeled. The overburden extends to a depth of 500 m. For the time depending calculations of rock salt creeping, the material law LUBBY 2 (Heusermann et al. 1983) is used. Table 1 comprises the elastic and creep parameters for the model.

Table 1. Material properties.

	E (MPa)	ν	η_M (d*MPa)	m (MPa^{-1})	l (K^{-1})
Rock Salt	18,000	0.2	4.1×10^{14}	−0.35	−0.05
	G_K (MPa)	k_1 (MPa^{-1})	η_K (d*MPa)	k_2 (MPa^{-1})	
Rock Salt	5.6×10^3	−0.08	4.3×10^3	−0.03	

Table 2. Thermal properties.

	λ (W/m/K)	c_p (J/kg/K)	α_T (K^{-1})
Overburden	2.2	700	–
Rock Salt	5.5	870	4.0×10^{-5}

For the initialization of the primary stress field densities of 2100 kg/m^3 for the overburden and 2200 kg/m^3 for the rock salt have been used. The main lateral pressure coefficient for the rock salt is $K_0 = 1.0$, because the assumption for the rock salt is homogenous and isotropic. The primary rock mass temperature is 285.15K at the top ground surface with a temperature gradient of 0.045K/m in the overburden and 0.0175K/m in the rock salt mass. For the thermo-mechanical coupling in the rock salt layer, the following properties have been applied.

The following example does not reflect the complete design load case but merely considers the first withdrawal phase. The indicated values are not used for the design load case shown in Figure 1 but are exemplarily for the description of the phenomena shown in the following sections.

3.1 *Constant pressure change rate vs. constant gas flow*

Case 1 analyzed is a withdrawal phase from the maximum pressure (200 bar) to the lower limit of the free operation range (80 bar) with a constant pressure change rate of 6.5 bar/day. The pressure versus time and the corresponding temperature versus time are shown in Figure 3. The cavern temperature at the starting point is approximately 47°C and drops down to 15.2°C within 18.5 days. The principal stresses for point A in the cavern roof region are shown in Figure 4. It can be seen that all stress components remain compressive. The lowest compressive stress is the vertical stress component with −0.65 MPa, so this component is most affected by the temperature. On one hand from

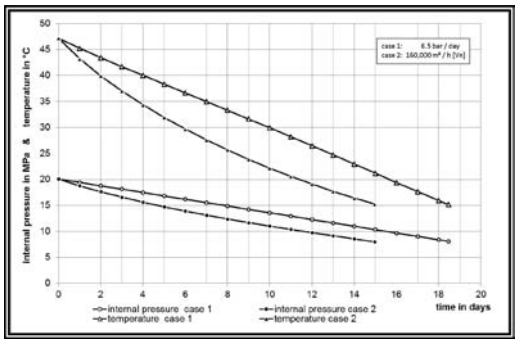


Figure 3. Pressure & temperature vs. time (case 1 & case 2).

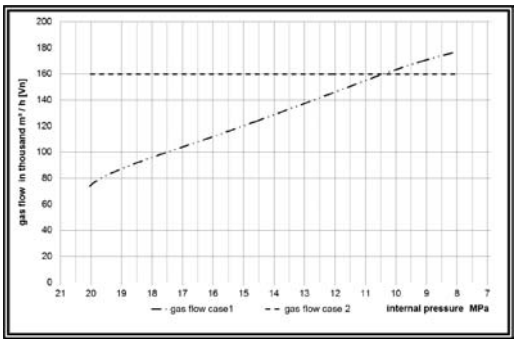


Figure 5. Gas flow vs. pressure (case 1 & case 2).

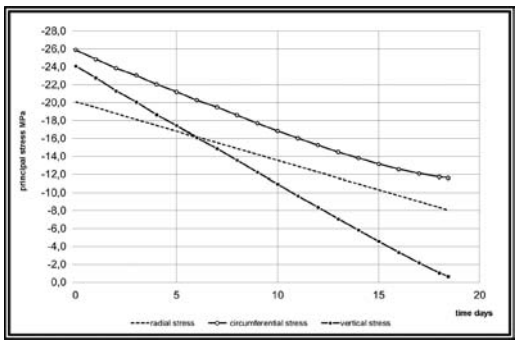


Figure 4. Principal stresses (case 1).

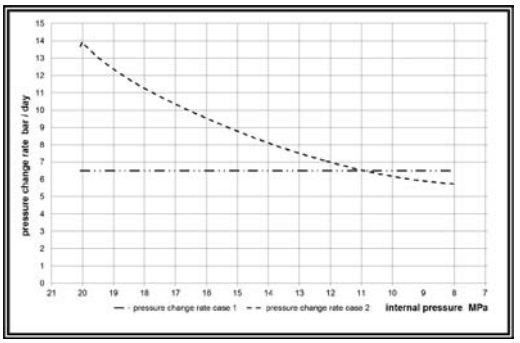


Figure 6. Pressure change rates vs. pressure (case 1 & case 2).

geomechanical point of view the withdrawal with a pressure change rate of 6.5 bar/day is optimize, but on the other hand from the economical point of view it is not. This is shown in Figure 5 where the gas flow is represented versus the internal pressure.

The gas flow value rises up from 75,000 m^3/h [V_n] on 200 bar (20 MPa) up 175,000 m^3/h [V_n] at 80 bar (8 MPa). The average gas flow is 130,000 m^3/h [V_n].

In order to optimize the gas flow case 2 represents a withdrawal from the maximum pressure (200 bar) to the lower limit of the free operation range (80 bar) with a constant gas flow of 160,000 m^3/h [V_n], also shown in Figure 5. These gas flows are calculated on the base of the temperature change of case 1. With a constant gas flow of 160,000 m^3/h [V_n] the temperature difference between the upper and the lower pressure range is the same as with 6.5 bar/day which is also shown in Figure 3. Remarkable is that a constant gas flow results in a non linear pressure change rate versus the internal pressure. It can be seen in Figure 6 that the pressure change rate is very high in the upper pressure range and decreases to less than 6.5 bar/day in the lower pressure range. The constant gas flow is much higher than the average gas flow in case 1. This depends on subside of the pressure change rate and the heat flux from the rock mass. The vertical stress component is approximately on the same level as in case 1 from the rock mass. The vertical stress component is approximately on the same level as in case 1.

From geomechanical point of view both cases are allowed for operation, because in both cases no tensile stresses occur. But it is not allowed to exceed the curve of pressure change rates shown in Figure 6, because these are the maximum pressure change rates vs. pressure to avoid tensile stresses for a continuous operation from maximum pressure to the lower limit of free operation.

From economical point of view case 2 is the optimal case, because on the one hand this case has a constant gas flow and on the other hand this gas flow is higher than the average gas flow in case 1. The usable working gas is the same in both cases, but in case 2 the cavern inventory could be withdrawn in a shorter time.

3.2 *Time periods with no gas flow*

During the operation it is rarely that there is a continuous operation of the cavern from maximum pressure to the lower limit of the free operation, but there will be periods without withdrawal. Therefore, case 3 examines an idle time of 10 days. The non linear pressure change rate from case 2 is applied. The withdrawal is stopped at an internal pressure of 140 bar. Due to the heat flux from the rock mass, the gas is heated up about 7.3°C and consequently the inside pressure raises up from 140 bar to 146.5 bar in 10 days. Figure 7 shows the development of the internal pressure and the temperature versus time. At the further withdrawal to the

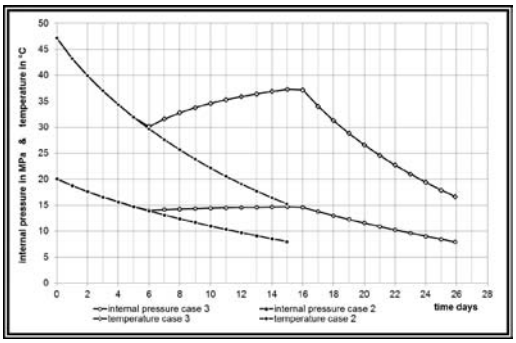


Figure 7. Pressure & temperature vs. time (case 2 & case 3).

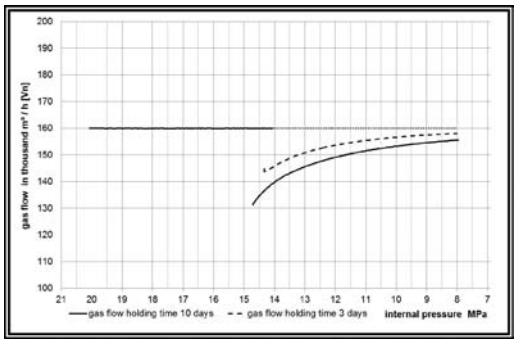


Figure 9. Gas flow vs. pressure (case 4).

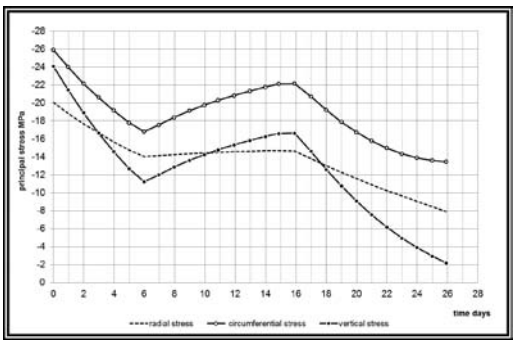


Figure 8. Principal stresses (case 3).

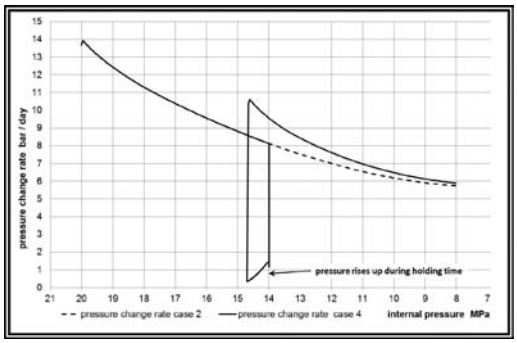


Figure 10. Pressure change rates vs. pressure (case 2 & case 4).

limit of free operation with the pressure change rate corresponding to the respective pressure, a gas temperature of 16.7°C is reached. The thermo-mechanical coupled calculation shows that the vertical stress component amounts to −2.2 MPa approximately as shown in Figure 8.

From the geomechanical point of view, an idle time during the withdrawal phase has to be assessed positive, because the vertical stress component is transferred in a higher compressive stress range. From an economic standpoint, a disadvantage arises here. Figure 9 shows the gas flow versus inside pressure. The basis of the curve for the non linear pressure change rate is a gas flow with 160,000 m^3/h [V_n]. After an idle time of 10 days, the gas flow starts with approximately 131,000 m^3/h [V_n] and reaches 158,000 m^3/h [V_n] at the end of the withdrawal (solid line). The dotted line shows an example with an idle time of 3 days. Visible is that the gas flow directly depends on the duration of the idle time and can not be calculated generally.

From the economical point of view a recommendation of a permanent constant gas flow independent on the idle time is favoured. Case 4 analyses the consequences if the gas flow starts again with a constant rate of 160,000 m^3/h [V_n] after an idle time of 10 days. Figure 10 shows the pressure change rates versus the internal pressure for a permanent gas flow for a continuous withdrawal and for a withdrawal with a idle

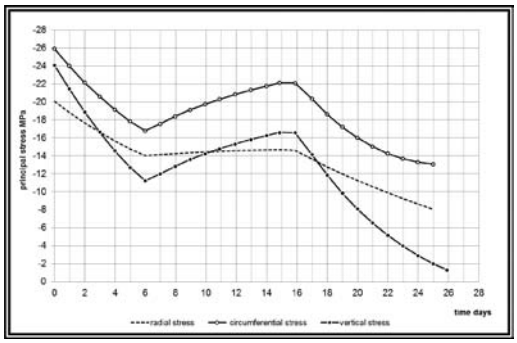


Figure 11. Principal stresses (case 4).

phase of 10 days. The gas flow rate for both examples is 160,000 m^3/h [V_n]. It appears that the pressure rate rises as expected and approaches asymptotic to the original pressure change curve. The question is whether this high pressure change rate has a negative influence on the temperature and therefore on the stress states. Figure 11 shows the stress states for case 4 versus time. The vertical stress component ends at −1.3 MPa and is higher than the vertical stress component in case 2.

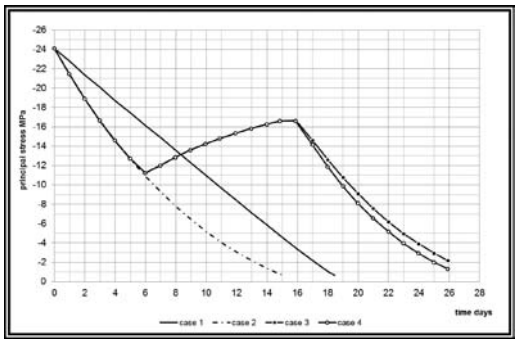


Figure 12. Vertical stresses (case 1 to case 4).

4 CONCLUSIONS

In summary, Figure 12 depicts the vertical stress components of all four cases. It shows that the influence of idle times during the withdrawal phase is positive for the stress state because the vertical stress components are transferred in a higher compressive range. Therefore idle times during a withdrawal do not have to be considered in a design load case. It also shows that during periods with no operation the stress states are influenced by the temperature change in a large extent and permanently.

The economical aim is a continuous gas flow within the whole pressure regime. The geomechanical and thermo-dynamical calculations have shown that it is possible to create a non linear pressure change regime for a permanent withdrawal with a constant gas flow. It is shown that despite greater rates of pressure change the stress regime is from geomechanical point of view to be valued positively with an idle time and a continuous gas flow. However, a cavern can only be operated with a constant gas flow, when the gas flow is controlled and monitored in an adequate manner.

REFERENCES

Heusermann, S. et al. 1983. Entwicklung mathematischer Modelle zur Beschreibung des Stoffverhaltens von Steinsalz in Abhängigkeit von der Zeit und der Temperatur auf der Grundlage von Laborversuchen mit begleitenden kontinuumsmechanischen Berechnungen nach der Methode der finiten Elemente; *Forschungsbericht T 83-218 Technologische Forschung und Entwicklung–Nichtnukleare Energietechnik*. Bundesministerium für Forschung und Technologie.

Leuger, B. et al. 2012. The Thermo-Mechanical Behavior of a Gas Storage Cavern during High Frequency Loading; *Proceedings of the 7th Conference on the Mechanical Behavior of Salt, Paris, 16–19. April 2012.* Lisse: Balkema.

Staudtmeister, K. & Zapf, D. 2012. Thermo-Mechanical Behavior of a Gas Storage Cavern under High Frequency Operations; *Proceedings of the Eurock 2012 Symposium, Stockholm, 28–30 May 2012.* Lisse: Balkema.

Staudtmeister, K. et al. 2012. Design Load Cases for Gas Storage Cavern; *Proceedings of the technical conference of the SMRI, Bremen, 01–02 October 2012.* Solution Mining Research Institute.

Zapf, D. et al. 2011. The Influence of Different Loading Scenarios on the Thermo-Mechanical Behavior of a Gas Storage; *Proceedings technical conference of the SMRI, Galveston, 18–19 April 2011.* Solution Mining Research Institute.

Zapf, D. et al. 2012. Analysis of Thermal Induced Fractures in Rock Salt; *Proceedings technical conference of the SMRI, Regina, 23–24 April 2012.* Solution Mining Research Institute.

This page intentionally left blank

Rock Mechanics for Resources, Energy and Environment – Kwaśniewski & Łydżba (eds)
© 2013 Taylor & Francis Group, London, ISBN 978-1-138-00080-3

Feasibility and behavior of a full scale disposal cell in a deep clay layer

J. Morel, F. Bumbieler, N. Conil & G. Armand
Andra, Meuse/Haute Marne Underground Research Laboratory, Bure, France

ABSTRACT: At the Meuse/Haute Marne Underground Research Laboratory, Andra is studying the possibility of disposal for intermediate to high level activity – long life nuclear waste in a 500 m deep clay formation. In particular, a specific technical and scientific program is carried out for several years to test the feasibility of realization and the behavior of disposal cells for high level – long life waste packages. Within the framework of this program, and as part of the European project LUCOEX (Large Underground Concept Experiment), a new phase has started at the end of 2012 with the realization of a full scale disposal cell demonstrator. Heat generated by waste packages is simulated by electrical heaters over a length of 15 m, with the aim to reach 90°C at the cell interface in 2 years. The thermo-mechanical behavior of the cell as well as the THM impact on the surrounding rock is monitored through a very complete instrumentation.

1 INTRODUCTION

1.1 *General context*

Andra, the French national radioactive waste management agency, is in charge of the study on the possibility of disposal for intermediate to high level activity – long life (IL/HL – LL) nuclear waste in deep geological repositories. In this aim, the Meuse/Haute Marne Underground Research Laboratory (URL) has been excavated since 2000 in a 500 m deep clay-stone layer (Callovo-Oxfordian, COX) to characterize to confining properties of the clay-stone and demonstrate the feasibility of construction and operation of a geological disposal (Delay et al. 2007).

1.2 *Callovo-Oxfordian claystones*

The main level of the URL is excavated at a depth of 490 m in the middle of a 135 m thick argillaceous rock layer, overlain and underlain by poorly permeable carbonate formations. Argillaceous rock contains a mixture of clay minerals (40 to 45% on average) and clay-size fraction of other compositions. The clay minerals offer groundwater tightness and radionuclides retention. Silica and carbonate-rich sedimentary components contribute to high strength of the rock and stability of the underground construction.

Table 1 gives Callovo-Oxfordian claystones mechanical characteristics. Sedimentation has led to a slightly anisotropic behavior of claystones. In-situ measurements indicate a strong coupling between mechanical and hydraulic processes (Armand et al. 2011).

In-situ stress field in COX claystones is anisotropic (Wileveau et al. 2007), with $\sigma_v \approx \sigma_h$ and the ratio σ_H/σ_h close to 1.3 at the main level of the URL.

Table 1. COX claystones characteristics.

Rock parameter	Notation	Value
Density	ρ	2.39 g/cm^3
Porosity	N	$7.2 \pm 1.4\%$
Intrinsic permeability	k	5×10^{-20} m^2
Water content	W	$7.2 \pm 1.4\%$
Young's modulus	E	4 ± 1.47 GPa
Poisson's ratio	ν	0.29 ± 0.05
Uniax. compress. strength	UCS	21 ± 6.8 MPa
Hoek & Brown criterion	S	0.43
	m	2.5
	σ_c	33.5 MPa
Thermal conductivity	λ	1.3–2 W/m*K

1.3 *Benchmark concept for HL-LL disposal cells*

The benchmark concept of disposal cells for HL-LL waste consists in horizontal micro-tunnels at least 40 m long and about 70 cm in diameter (Fig. 1). It comprises a body part, for packages disposal, and a head part for cell closure. They are favorably aligned with respect to the stress field. To prevent against rock deformation and allow the potential retrieval of waste containers during the reversibility period, both body and head parts have a non-alloy steel sleeve. The sleeve in the body part has a diameter slightly smaller than the one in the head part called "insert". That means it can slide in the insert. Thus, the effects of the thrust produced by its dilation, due to heat generated by the exothermic packages, are absorbed without consequence for the cell head.

The cell base is closed off by a "base plate", also made of non-alloy steel. A metal radiation-protection plug separates the cell head from the body part. For cell

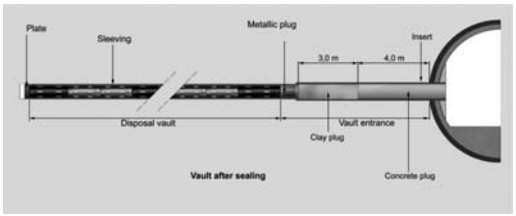


Figure 1. Concept of disposal cell for HL-LL activity waste.

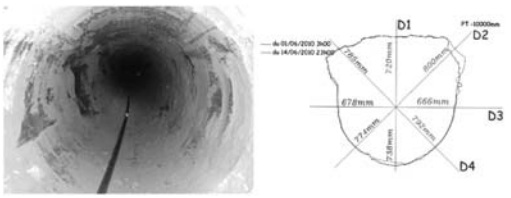


Figure 2. State of the cell wall and typical cell profile (Phase 1b).

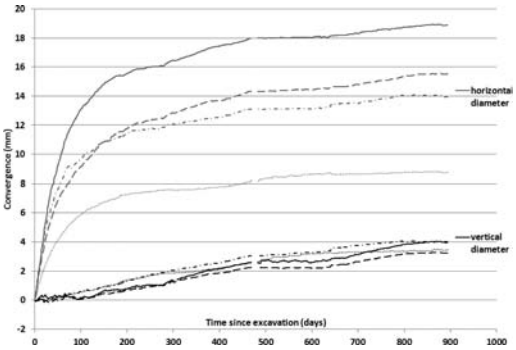


Figure 3. Convergence measured along horizontal and vertical direction in an unsleeved 20 m long cell (Phase 1b) – full line: 16 m depth; dash line: 12 m; dash/dots: 8 m; dots: 4 m.

closure, the insert is partly backfilled with a swelling-clay plug and then sealed with a concrete plug to provide additional safety.

2 EXPERIMENTAL PROGRAM

In order to check the feasibility of such disposal cells construction, and study the behavior of the cell and its impact on the surrounding rock, an experimental program has been defined and carried out through different phases since 2009.

2.1 *Drilling method*

The excavation method uses a guided auger drilling machine. The drilling head can be adapted to excavate in diameter 70 to 75 cm. It also allows the retraction of the drilling machine at the end of the excavation, by rotating in the opposite direction as for the excavation.

The drilling machine is laser-guided, what allows the control of the micro-tunnel trajectory with a precision better than +/−2 cm.

The excavation can be achieved with or without casing. The casing is made of 2 m long, 70 cm in diameter and 2 cm thick metal tubes. The 2 m long elements are welded or socketed to each other as the excavation advances.

The drilling is carried out with air.

2.2 *Experience feedback from former phases*

The first phase, carried out in 2009 (Phase 1) and 2010 (Phase 1b), aimed to check that it was possible to dig cells in several directions with respect to the stress field in the host formation, to test the excavation method (with or without advance casing) and to specify operating procedures for cell excavation in the next phases (Morel et al. 2009). It also provided initial data on the hydro-mechanical behavior of the cells and their environment: the influence distance of the cells, their mechanical behavior and damage around them.

From a technology standpoint, Phase 1 highlighted the necessity to modify the equipment and the excavation operating procedures to be able to produce a cell representative of the benchmark concept, and to make the maximum improvement to the cut quality in order to produce an annular space that is as regular as possible. These modifications were implemented for Phase 1b and showed that a 40 long sleeved cell could be produced. Production of an unsleeved 20 m long cell showed that these modifications also significantly improved the state of the cell wall, much smoother overall, although the formation of breakouts, induced by the natural stress field, is inevitable (Fig. 2).

In terms of impact of micro-tunnel digging, Phases 1 and 1b have shown that overpressures are generated during the excavation. In the horizontal plane, the over pore pressure amplitude and influence distance measured (about 35 bars at 1 m from cell wall) are much higher than the one predicted in the preliminary calculation performed for the experiment. Furthermore, convergence measurements, performed using a specifically designed system on several sections at different depth along 4 different diameters (Gay et al. 2010), show that horizontal convergence is much larger than vertical one (Fig. 3).

This anisotropic behavior, although the cell is oriented along the major stress direction and thus undergoing an isotropic stress field, was also observed for drifts of 5 m diameter with similar orientation. This is related to the shape of the excavation damaged zone (EDZ) around the cell (or drift) and to the anisotropic character of claystones. The convergence velocity decreases with time, and is of the order of 10^{-11} s^{-1} (/cell diameter) 30 months after excavation.

Phase 2, carried out in 2011, aimed to test the production of a cell head with an insert installed with a small annular space (8 mm on radius), and to produce a 40 m long cell with an instrumented sleeve, to study

how sleeve/rock clearance reduces over time (resaturation kinetics of the annular space, sleeve loading) and its influence on the mechanical behavior of the sleeve. Lessons learned from this Phase 2 were used to prepare and optimize Phase 3 corresponding to the full scale heating demonstrator.

The test of cell head production was included in the European project LUCOEX (Large Underground Concept Experiment). After 7.5 m of excavation, the insert was jammed in the rock and the thrust forces needed to pursue the excavation reached the maximum capacity of the drilling machine. Consequently, the cell head configuration was modified for Phase 3, with a length of 6 m and an annular space rock/insert of 12 mm.

Concerning the 40 m long instrumented cell, the sleeve was watertight and equipped to study its mechanical behavior (strain gages, convergence measurements, optic fibers); the annular space was instrumented with relative humidity and water pressure sensors, as well as temperature sensors. Most of the sensors (except the strain gages), as well as all cables, had to be installed after excavation by human intervention inside the sleeve, to avoid their damage during drilling. Instrumentation was installed successfully and the procedure used was thus validated for Phase 3.

2.3 *Full scale disposal cell demonstrator*

The purpose of the full scale heating demonstrator (Phase 3 of the program) is to study the behavior of a HL-LL cell under thermal loading by simulating the heat produced by waste packages. The aim is both to demonstrate production and operation of such a disposal cell, and to understand the THM behavior of the neighboring rock.

The experimental concept must thus be representative of a real disposal cell, i.e. with a head and a body part, a base plate, a plug representing the radiation protection plug, and a cover plate on the insert head. The thermo-mechanical behavior of the sleeve and insert will be monitored, as well as the cell head operation (body expansion and sliding in the insert). The impact of thermal gradient along the cell on the access drift, and the analysis of the THM behavior of the rock/sleeve interface and its impact on the mechanical loading of the sleeve will be measured. Finally, peripheral boreholes will allow the study of the THM behavior of claystones beyond the interface, mainly in terms of the overpressure induced by the heating phase.

The demonstration of cell construction and operation is included in the European project LUCOEX.

3 EXPERIMENT SET-UP

3.1 *Cell demonstrator characteristics*

The full scale demonstration cell is 25 m long, and consists in a 6 m long, 791 mm diameter head part and a 19 m long, 750 mm diameter body part. The cell is excavated in the major horizontal stress direction. Heat will be produced in the deepest 15 m. The sleeve consists in 2 m long sections (2 cm thick, 700 mm external diameter) socketed to each other; steel pieces are fixed at the junction between each sleeve section to ensure sleeve rigidity and allow its dilation and sliding in the insert. The insert consists also in 2 m long sections (2.1 cm thick, 767 mm external diameter) welded to each other. Both sleeve and insert are instrumented to monitor their thermo-mechanical behavior. Base plate, body part's head plate and insert cover plate are bolted on crowns themselves bolted on the sleeve or insert.

3.2 *Numerical modeling*

Thermal and thermo-mechanical numerical modeling has been performed to help in the preliminary design of the experiment.

A 15 m heating length has been shown highly representative with respect to the benchmark concept where waste packages are inserted over 30 m, with only 2 to 4°C of difference at the cell wall essentially at both ends of heated zone. Radial temperature profiles from the cell wall in the middle of the heated zone are extremely similar for body part lengths of 15 m and 30 m. The choice of a 25 m long demonstrator cell was thus substantiated.

Position of the heating element, centered in the sleeve or lying on the sleeve's bottom, has been found to produce temperature differences as high as 5°C between invert and crown at the outer side of the sleeve. Final position of the heaters, lying on transfer blocks (cf. next paragraph) is close to centred.

The effect of the base plate and of the body part's head plug on the thermal profile along the cell was found to be negligible.

Thermal impact of the cell on the access drift is not more than 3°C, i.e. well below the annual temperature variations associated with drift ventilation.

Finally, the thermal load to apply was modeled. Obviously, a thermal cycle representative of the repository concept (thermal peak at 10–15 years for the least exothermic packages) cannot be reproduced for the experiment, which needs results in a reasonable timeframe. It was chosen to apply a constant power to reach 90°C at the outer side of the sleeve in 2 years; the power needed was found to be around 220 W/m.

3.3 *Heaters design*

The heater device consists in five identical elements, each 3 m long, 508 mm in diameter and about 500 kg heavy. Each element is composed of 3 concentric tubes (Fig. 4): an inner cylinder providing the necessary space to allow cables path; an intermediate cylinder around which the electrical resistors are coiled; an outer cylinder to protect the resistor and provide, together with 2 lids welded on both sides of the element, water and vapor tightness for the resistors. Each cylinder is made of stainless steel.

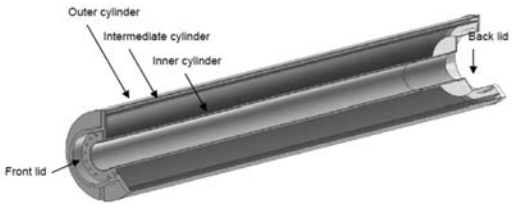


Figure 4. Heater element general design (Aitemin).

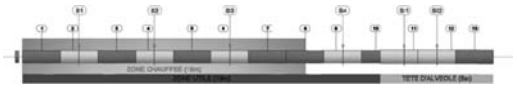


Figure 5. Location of sleeve and insert instrumented sections (Egis Géotechnique).

Each element is equipped with balls transfer blocks to facilitate its insertion in the cell by rolling on rails preliminary screwed on the sleeve and the insert. The balls transfer blocks are made of a low thermal conductivity plastic that can bear high temperature, inlaid in a stainless steel piece welded on the outer surface of the element.

In addition with temperature measurements inside and at the surface of the heaters, each element has an integrated inclinometer to measure its eventual movement induced by sleeve deformation. Moreover, sleeve convergence is measured along horizontal and vertical directions at each junction between heater elements.

Heating is controlled trough a power regulation system.

3.4 *Sleeve and insert instrumentation design*

Figure 5 shows the location of sleeve and insert instrumented sections.

Four sleeve sections (among which 3 are in the heated zone) are fitted, on their internal surface, with strain gages placed evenly around the pipe in 6 measurement areas, to measure circumferential and axial local strain. On each of these sections, the total pressure at the rock/sleeve interface is also measured at 2 locations, as well as rock/sleeve clearance reduction at the sides and vault of the sleeve through specific drillings. Relative humidity and temperature are measured in the annular space.

In addition to these instrumented sections, the sleeve's mean axial strain in the heated zone is measured with an extensometer fixed at the vault.

Two insert sections are, as for the sleeve ones, instrumented with 6 strain gages measurements area. Relative humidity is measured in the insert.

Two temperature profiles are measured along the cell (sleeve and insert), at the vault and at the side, with one measuring point per sleeve or insert section.

Sleeve and insert convergence is measured along horizontal and vertical directions for each instrumented sections outside the heated zone (inside the heated zone this measurement is made with heaters instrumentation, cf. former paragraph).

Finally, the sliding of the sleeve in the insert is measured with 3 displacement sensors fixed to the insert inner surface and in contact with the body part's head plate.

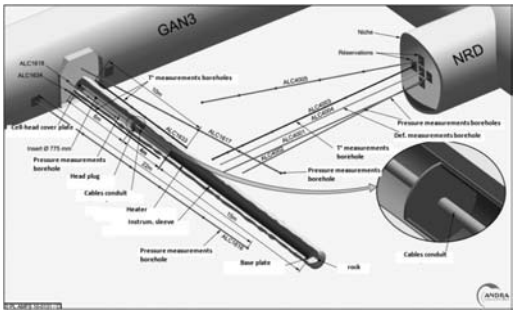


Figure 6. General view of the full scale experiment.

3.5 *Peripheral instrumentation*

Peripheral instrumentation consists in 9 peripheral boreholes drilling from the access drift and from a perpendicular one (Fig. 6), and in access drift instrumentation.

Six boreholes are equipped with pore pressure single or multipacker devices with measuring points at different distances from the cell wall in the horizontal and vertical planes. Each pore pressure measuring point is coupled with a temperature measuring point. The devices allow the realization at each measuring point of hydrogeological tests to estimate rock permeability.

Two boreholes, parallel and perpendicular to the cell, are equipped with temperature sensors. The last borehole, oriented perpendicularly to the cell, allows very fine deformation measurements at different distances from the cell wall.

The access drift instrumentation, in the immediate vicinity of the cell head, consists in support instrumentation (strain gages and displacement sensors on sliding steel arches), and displacement and tilt sensors to measure drift wall deformation induced by thermal gradient along the cell.

4 EXCAVATION AND INSTALLATION

Most of the peripheral boreholes (except two ones for temperature and pore pressure measurements parallel to the cell and at 50 cm from it, which could be damaged during excavation operation), as well as drift support instrumentation, were realized before cell excavation, to monitor the hydro-mechanical impact of excavation on surrounding rock mass and drift behavior.

The cell was excavated from 23rd to 31st October 2012, the insert first and then the body part after

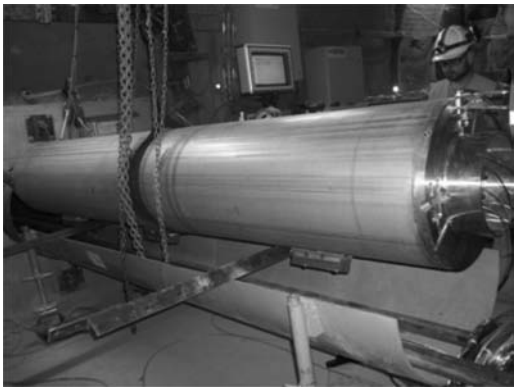


Figure 7. Positioning of a heater element at the cell entry before insertion.



Figure 8. View of the convergence instrumentation in the insert.

changing the cutting head diameter. The first 24 m were excavated in about 3 days; a technical problem that occurred on the drilling machine had then to be solved before the last meter could be excavated.

Once the base plate and the rails for heaters insertion put in place, and the last 2 peripheral boreholes drilled and equipped, instrumentation of the sleeve and insert was installed (except the strain gages that were already preinstalled) and all sensors connected to the URL data acquisition system.

Heaters were then inserted in the cell in January 2013 (Fig. 7). For this operation, sleeve and insert convergence instrumentation (Fig. 8) had to be removed, to be reinstalled just after heaters installation together with the fixation of the body part's head plate, the sleeve/insert relative displacement sensors and insert cover plate (Fig. 9).

At last, instrumentation of the access drift wall around the cell head was finalized.

5 FIRST RESULTS

A 3D scan performed before instrumentation showed that the cell trajectory was close to the theoretical one,



Figure 9. View of body part's head plate (left) and insert cover plate (right).

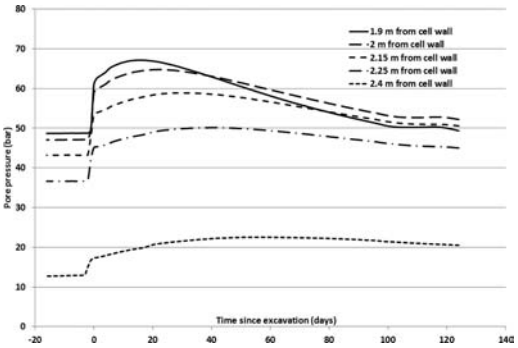


Figure 10. HM impact of cell excavation in the horizontal plane.

with a maximum deviation of 1.5 cm in the horizontal plane and 8 cm in the vertical one.

Hydro-mechanical impact of cell excavation on surrounding rock mass was found very consistent with what was measured during the former phases of the program. Induced overpressures in the horizontal plane ranged between 9 and 35 bars at distances respectively between 2.4 and 1 m from the cell wall (Fig. 10, initial pore pressure depends on the depth of the measuring point from the access drift). The time to reach the pressure peak increases with distance to cell wall.

Sleeve convergence measurements show compression in the horizontal direction and extension in the vertical one (Fig. 11). This indicates a contact with the cell wall and subsequent mechanical load of the sleeve first in the horizontal direction while no contact occurs with the sleeve vault. This behavior has been observed also in Phase 2 on the 40 m long instrumented cell as well as on smaller scale experiments of similar orientation with respect to the stress field. This observation is also consistent with convergence measurements performed in unsleeved cell (Fig. 3).

A preliminary heating test has been carried out between 30th January and 15th February 2013, to validate the operation of the heaters regulation system and the measurements acquisition. Heating power was set to 100 W/m.

Temperature on the sleeve reached 30°C (for an initial temperature of about 22°C). The test was successful, although the increase in temperature was not strong enough to measure any significant influence on sleeve behavior.

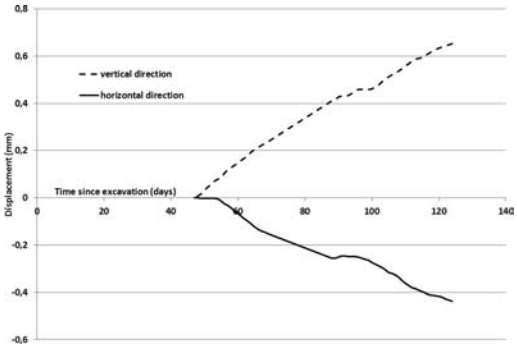


Figure 11. Sleeve diameter evolution at 8 m depth – positive displacement corresponds to extension, negative to compression.

After a slow decrease of temperature to ambient conditions, the main heating phase, at a constant power of about 220 W/m to reach 90°C on the sleeve in 2 years, will start at the end of March 2013.

6 CONCLUSIONS

Using the experience feedback from the former phases of the dedicated experimental program carried out since 2009, a full scale HL-LL waste demonstration cell has been designed and successfully realized and instrumented at the Meuse/Haute Marne URL.

First results from excavation and sleeve behavior are consistent with similar measurements performed on former demonstration cells, on drifts and on smaller scale experiments of same orientation with respect to the stress field.

Heat generated by the exothermic waste packages will be simulated with electrical heaters over a length of 15 m. The main heating phase will start at the end of March 2013 with the goal to reach 90°C on the sleeve surface in about 2 years. Numerical modeling, taking into account the back experience of smaller scale heating experiments simulation, will be performed to be compared with experimental data.

ACKNOWLEDGEMENTS

The work presented in this article has received funding from the European Atomic Energy Community's Seventh Framework Program under Grant Agreement n°269905, the LUCOEX project. The financial support is gratefully acknowledged.

REFERENCES

Armand, G., Noiret, A., Cruchaudet, M. & Conil, N. 2011. Mine by experiment performed in the Callovo-Oxfordian claystone at the Meuse Haute Marne Underground Research Laboratory (France). In Q. Qian & Y. Zhou (eds), *Harmonising Rock Engineering and the Environment, Proceedings of the 12th International Congress on Rock Mechanics, Bejing, 18–21 October* 2011: 157–162. Leiden: CRC Press/Balkema.

Delay, J., Vinsot, A., Krieger, J.M., Rebours, H. & Armand, G. 2007. Making of underground scientific experimental program at the Meuse/Haute–Marne Underground Research Laboratory, North Eastern France. *Phys Chem Earth* 32: 2–18.

Gay, O., Allagnat, D., Morel, J. & Armand, G. 2010. HA cell monitoring at the Underground Research Laboratory in the CMHM. *Tunnels et Espace Souterrain* 221: 377–382.

Morel, J., Renaud, V. & Armand, G. 2009. Feasibility of excavation of disposal cells in 500 m deep clay formation. In I. Vrkljan (ed), *Rock Engineering in Difficult Ground Conditions – Soft Rocks and Karst, Proceedings of EUROCK 2009 – The 2009 SRM Regional Symposium*: 561–566. Leiden: CRC Press/Balkema.

Wileveau, Y., Cornet, F.H., Desroches, J. & Blumling, P. 2007. Complete in situ stress determination in an argillite sedimentary formation. *Phys. & Chem Earth* 32: 866–878.

Rock Mechanics for Resources, Energy and Environment – Kwaśniewski & Łydżba (eds)
© 2013 Taylor & Francis Group, London, ISBN 978-1-138-00080-3

Temporal analysis of fracturing using acoustic emissions at the Aspö Pillar Stability Experiment

H.C. Moretti
University of Bristol, Bristol, UK
Applied Seismology Consultants Ltd., Shrewsbury, UK

J.M. Reyes-Montes & J.R. Haycox
Applied Seismology Consultants Ltd, Shrewsbury, UK

R.P. Young
University of Toronto, Toronto, Ontario, Canada

ABSTRACT: The Aspö Pillar Stability Experiment (APSE), at SKB's Hard Rock Laboratory, involved the development of a pillar by excavating two deposition holes, 1 m apart. The evolution of damage in the pillar was monitored by an ultrasonic acquisition system providing Acoustic Emission (AE) and ultrasonic surveying. This paper builds on previous work that revealed that spalling in the unconfined deposition hole pillar wall was concentrated in two 0.5 m areas at 1 m and 3 m depth which correlated to higher seismic b-values thought to be a result of the greater heterogeneity. The data set of 15,198 AEs cluster tightly around the damaged zones in sufficient quantity to allow a detailed temporal analysis of changes in the seismicity prior to spalling and assess the degree to which these changes correlate to changes to the heterogeneity, local stress regime failure in the integrity of the deposition holes. The temporal and spatial analysis of patterns in seismicity were analyzed, showing minima in b-value of induced event prior to observed periods of major damage development.

1 INTRODUCTION

Constraining the volumetric extent of excavation damage zones (EDZ) around engineered structures has benefitted from the application of remote, scaled seismic studies that passively monitor the medium using microseismic (MS), acoustic emissions (AE) and ultrasonic techniques. By mapping AE/MS locations, fracturing and rock deformation can be correlated with known changes in pressure and temperature conditions both spatially and temporally (Young et al. 2004).

Earthquakes, MS and AE, are self-similar phenomena, with scale invariability which obey a power law allowing b-value analysis in combination with fracture geometry to provide additional insights into the mechanics of rock response to changes in confining pressure and temperature.

1.1 *The Äspö Pillar Stability Experiment*

A typical nuclear waste disposal facility could require up to 4500 deposition holes to be excavated, therefore the spacing and geometry of these installations becomes of critical importance (Andersson et al. 2009).

The Äspö Pillar Stability Experiment (APSE) at SKB's Äspö Hard Rock Laboratory (HRL) was designed to examine the nature of failure processes when an ancient, deep, mildly anisotropic, fractured crystalline rock mass is subjected to both excavation and thermal-induced stresses. The development of damage and potential spalling was monitored through the remote monitoring of induced AE and ultrasonic data to determine changes in the velocity structure. The experiment was intended to demonstrate the effect of heating and subsequent cooling in the pillar between two adjacent deposition holes within a repository (Andersson & Martin 2009). One hole was simply excavated and monitored whilst the other was subject to backfill with a confining pressure of 0.8 MPa.

A tunnel boring machine was used in the excavation of two 1.75 m diameter 6 m deep holes, the first, DQ0066G01 was confined with a water-filled bladder delivering around 0.8 MPa of confining pressure. The second, separated by a 1 m thick wall, DQ0063G01 was left unconfined. Both were subjected to a two-month phase of heating from mid-May of 2004, after which the confined deposition hole was slowly depressurized.

1.2 *Acoustic emission monitoring*

At the HRL several AE and ultrasonic studies have previously been performed including the Zone of Excavation Damage Experiment (ZEDEX) (Falls &

Young 1996), Canister Retrieval Tunnel at 420 m depth (Pettitt et al. 1999) and the Prototype Repository at 450 m depth (Pettitt et al. 2002, Haycox et al. 2009).

For the APSE experiment a twenty-four ultrasonic transducer array was mounted along four borehole frames and spring loaded against the borehole wall to monitor AE and perform ultrasonic surveys of the pillar volume, details of the experiment can be found in Andersson & Martin (2009). Both passive and active monitoring addressed the objective of assessing whether an EDZ will form around the deposition boreholes, either through excavation damage or by subsequent thermal stresses, and constrain the likely spatial extent of any damage.

Typically AEs, the result of fresh fracturing, fracture coalescence or extension can be thought of as very small 'earthquakes' with a moment magnitude (M_w) of approximately -6 at these frequencies. The data acquisition parameters and calibration surveys are described in detail in Haycox et al. (2005). Thermocouples were used to measure the heat profile along the holes.

Between 21st October, 2003 and 16th August, 2004 a total of 17,360 AE events were located using the InSite Seismic Processor software (ASC 2010) using a downhill-simplex location algorithm and assuming a homogeneous-isotropic velocity structure which was varied to reflect changing velocities obtained from ultrasonic surveys, giving a mean P-wave velocity of 6,051 $m \cdot s^{-1}$ and mean S-wave velocity of 3,394 $m \cdot s^{-1}$ (Fig. 1).

AE events appeared clustered in two semi-circular EDZ that extended 20 cm into the pillar (Fig. 1) perpendicular to the direction of principal stress. Intra-pillar events were confined to the top 1 m and relate to a known shear zone. During excavation, activity in the confined hole (DQ0066G01) correlated with observed spalling damage (Andersson et al. 2009), and was probably a result of increasing stresses in a weaker part of the rock mass during deeper excavation.

For the unconfined hole (DQ0063G01), AE activity was mostly post-excavation, correlating with a zone of observed breakout damage. Similar post-excavation activity was not observed in the confined deposition hole, suggesting the confinement was sufficient to inhibit damage development.

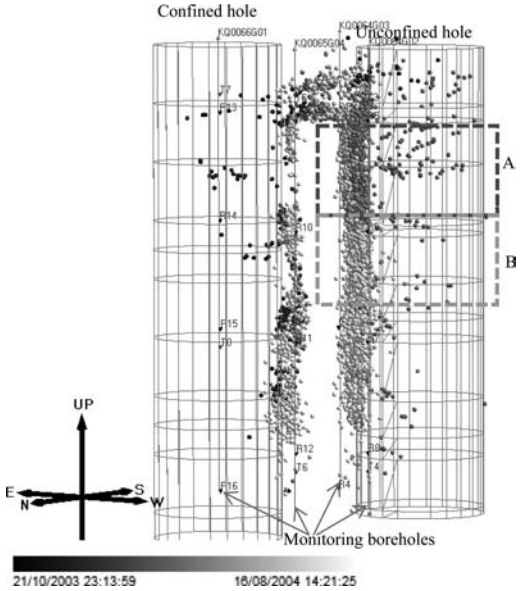


Figure 1. AE locations of all 17,360 AE events induced between 21st October, 2003 and 16th August, 2004 scaled to occurrence time. The dashed squares mark the two sub-sets analyzed in this paper: box A comprises the set of events located between 447 m and 448 m depth, box B, the subset of events located between 448 and 449 depth.

2 B-VALUE ANALYSIS

Earthquakes, MS and AE events exhibit scale invariability which obeys the exponential law defined by the event magnitude frequency distribution of Gutenberg & Richter (1942) which describes the cumulative number of earthquakes (N) occurring above a certain magnitude (M) as:

$$\log N = a - b \cdot M \qquad (1)$$

The slope of this linear relationship is close to $b = 1.0$ for the global earthquake catalogue, and describes normally stressed tectonic areas. Variations from this characterise the stress of a region (Scholz 1968, Wyss 1973). Relative variations in b-value within a fracture zone indicate changes in the stress conditions and fracture mechanism. The b-value has been observed to vary inversely with applied shear stress or effective stress (Urbancic et al. 1992; Wyss 1973), and directly with thermal gradient (Warren & Latham 1970), and material heterogeneities (Mogi 1962). A spatial variation in b-value has also been associated with changes in the tectonic stress regime (Schorlemmer et al. 2005).

Monitoring equipment sensitivity varies with event proximity and background noise, requiring considering a minimum threshold magnitude (M_c) in the estimation of b-values (Woessner & Wieman 2005). Also, saturation at large magnitudes and lack of catalogue completeness for larger events (Pacheco et al. 1992) requires considering a maximum threshold. The selection of these lower and upper magnitude boundaries can lead to different results in the calculation of b-values (Haycox et al. 2012, Wiemer & Wyss 2002).

The analysis of the complete set of induced AE events using the location magnitude (M_{Loc}) yields a b-value of 2.32 (Haycox et al. 2012), which corresponds well with data from similar deep excavation environments (Nuannin et al. 2002).

The location magnitude M_{LOC} is calculated for the events by averaging the Instrument Magnitude

(M_I) over the instruments used in the source location, regardless of the number of channels, where:

$$M_I = A.\log_{10}(r.W_{V\,RMS\,peak}) + B \qquad (2)$$

$W_{VRMSpeak}$ is the peak signal amplitude on the RMS velocity Waveform and r is distance. A and B are empirical constants.

Complexities in the excavation geometry and the presence of an EDZ causes high heterogeneity (Mogi 1962), thus raising b-values. High b-values have also been observed for high-frequency AE acquired in laboratory tests (Pettitt 1998) and dynamic numerical models of rock fracture (Hazzard 1998).

2.1 *Spatial and temporal variations of b-values at the Pillar Stability Experiment*

The analysis of spatial variations in b-values around both test holes in Haycox et al. (2012) found that the b-value varied proportionally with the spalling damage along the hole walls. This relationship is probably driven by the increase in fracture density, ductility and bulk rock heterogeneity (Mogi 1962, 2007) and suggests that remote passive seismic monitoring can determine when and where damage has undermined the integrity of a hole.

Similarly a temporal pattern was observed, with higher b-values during the excavation stage (2.19) compared with earlier background levels (1.93) (Haycox et al. 2012). This variation is likely due to the deposition holes increasing both the geometrical heterogeneity, ductility and fracture density in the host rock (Mogi 1962 2007). The events induced during the thermal stage show a higher b-value of 2.30 possibly due to the positive relationship with thermal gradients (Warren & Latham 1970).

2.2 *Temporal analysis of b-value*

Studies have shown that temporal decreases in b-value may precede the occurrence of larger magnitude events in both small-scale mining settings at Zinkgruvan mine, Sweden (Nuannin et al. 2002) and in the large-scale analysis of earthquake precursors in North-West Sumatra (Nuannin et al. 2005). This type of analysis can be applied to the spalling events that affected the deposition holes after excavation.

The unconfined hole, with over 10,000 AE events, provides a better opportunity to analyse temporal variations in the b-value and investigate their potential association with major failure in order to remotely assess failure of the engineered structure. Two adjacent 1 m-thick sections have been selected: one including a volume where heavy excavation damage was observed, located between 447 and 448 m depth near the top of the deposition hole (Fig. 1); a second volume comprises an initially competent area between 448 and 449 m depth, situated half-way along the unconfined hole.

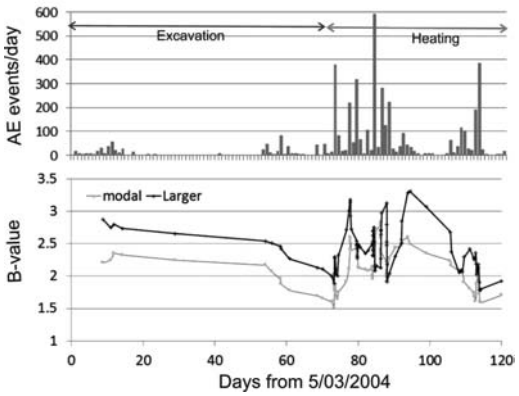


Figure 2. Event rate (top) and b-value (bottom) over the 120 day period from 5th March, 2004 for the initially competent section of deposition hole from 448 to 449 m depth.

In the following analysis, b-values were calculated using two different approaches in the selection of the magnitude range for the fitting of the linear trend. This is done to both offset and investigate the uncertainty in b-value estimation engendered by the selection of the minimum threshold magnitude (M_c) (Wiemar & Wyss 2002). The first approach, termed as 'modal', takes the interval including the mode magnitude ($1.1 \leq M_{Loc} \leq 0.7$ in this case). The second approach calculates b-values from the larger magnitude interval ($0.95 \leq M_{Loc} \leq 0.5$). Sequential temporal variations are calculated taking event bins of 300 AE events rolled forward at overlapping intervals with a 50 events step.

In the initially competent area, event rates peak between 17th May and 1st June (days 73 to 88 of the study as shown in Figure 2), however damage is observed to commence between 30th April and 3rd May (days 55 to 58), with continued fracturing occurring after that period until a second peak in damage is observed around 24th June (days 111–115) (Andersson et al. 2005).

The b-value appears to mirror the periods when stress is accumulating, falling from 30th April to 19th May and rising once the area undergoes fracturing and spalling following the heating of the hole from 14th May (day 70). This rising period is followed by a period of short-term rapid falls in b-value that precede periods of further new damage development and b-value rises coinciding with damage occurrence. Damage development was assessed through daily inspections, therefore a 1 day uncertainty must be considered when correlating observed damage with changes in b-value. The b-value finally drops as fracturing seems to stall in the build-up to the final period of damage around 24th June.

By combining AE event rate and b-value, it is evident that periods of damage development are preceded by periods of low activity rate with relative abundance of larger magnitude events. During damage development AE rates increase showing higher number of

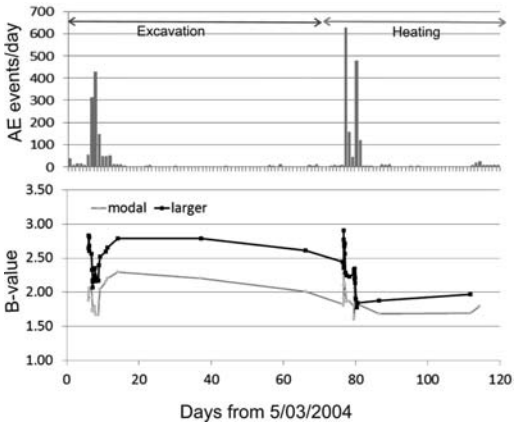


Figure 3. Event rate (top) and b-value (bottom) over the 120 day period from March 5th , 2004 for the hole section affected by excavation damage (from 447 to 448 m depth). The temporal clustering of AE activity around two short intervals does not allow the detailed analysis of b-value evolution.

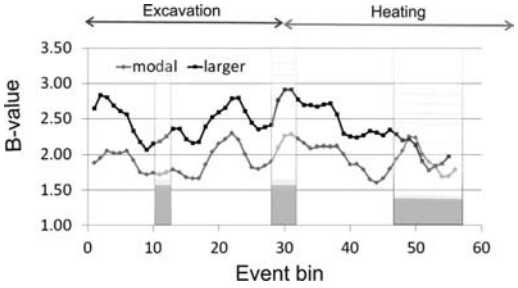


Figure 4. Evolution of b-value over the 120 day period from March 5th, 2004 for the hole section affected by excavation damage (from 447 to 448 m depth). b-value changes are plotted against sequential event bins. Overlaping bins comprise 300 AE events with a step of 50 events. Shaded bars mark observed spalling damage development and are shown to correlate with rise in b-value. A divergence towards the end of the monitoring period is only found when b-values are calculated using the larger magnitude interval (top trace).

smaller magnitude events, with the mean magnitude decreasing by 10–12% over these periods.

In the hole section affected by excavation damage, AE events concentrate in two short time periods, resulting in loss of the detail in the analysis of b-value temporal evolution (Fig. 3). An alternative way to analyse this period is to look at the change in b-values on a constant number of events basis, stretching the periods with high event rates (Fig. 4).

Figure 4 shows the degree to which the two alternative b-value calculations, using different minimum (M_c) and maximum magnitude thresholds, remain coupled throughout most of the period. Only by the end of the monitoring period both methods become uncoupled with the largest events likely being influenced by increased stresses along the known shear zone.

3 SUMMARY AND CONCLUSIONS

Changes in b-value across time reflect changes in stress accumulation and damage development. The case presented in this study indicates the potential for using b-value analysis in the remote assessment of rock failure at repository scale and use AE monitoring to remotely identify and locate failure and damage development. The temporal analysis of AE activity in the unconfined test hole showed a good correlation between drops in b-value with periods of pre-failure stress accumulation. Periods of observed damage development correlated with sharp increases in b-value. The increases are likely linked to the decrease in local stress as strain is released during damage development or to the increased heterogeneity, ductility and fracture density associated with the observed spalling damage (Haycox et al. 2012).

Importantly, for real-time monitoring, periods of consistent decrease in b-value are found to correlate with stress accumulation. These sustained drops in b-value are most evident in volumes where the structure is competent. Following damage development or failure, decreases due to stress accumulation can be partially masked by increases due to the rise in fracture density, ductility and heterogeneity (Mogi 1962, 2007).

ACKNOWLEDGEMENTS

The authors would like to thank SKB who funded the acoustic emission monitoring at the APSE. We appreciate the involvement of Christer Andersson. Will Pettitt (Itasca Consulting Group) is gratefully acknowledged for his contribution to the preparation of the original report on AE monitoring.

REFERENCES

Andersson, C., Kärnbränslehantering, S. & Eng, A. 2005. *Äspö Pillar Stability Experiment, Report R-05-02*. Swedish Nuclear Fuel and Waste Management Co, Sweden.

Andersson, C. & Martin, D. 2009. The Äspö pillar stability experiment: Part I – Experiment design. *Int. J. Rock Mech. Min*. 46: 865–878.

Andersson, C., Martin, D. & Still, H. 2009. The Äspö Pillar Stability Experiment: Part II – Rock mass response to coupled excavation-induced and thermal-induced stresses. *Int. J. Rock Mech. Min. Sci.* 46: 879–895.

ASC 2010. *InSite Seismic Processor – Technical Appendices to the User Manual version 2.14d*, Applied Seismology Consultants Ltd., Shrewsbury, U.K.

Falls, S.D. & Young, R.P. 1996. Examination of the excavation disturbed zone in the Swedish ZEDEX tunnel using acoustic emission and ultrasonic velocity measurements. In G. Barla (ed.), *Proceedings of Eurock '96*, Turin, Italy: 1337–1344. Rotterdam: Balkema.

Gutenberg, B. & Richter, C.F. 1942. Earthquake magnitude, intensity, energy and acceleration. *Bull. Seismol. Soc. Am.* 32: 163–191.

Haycox, J.R., Pettitt, W.S. & Young, R.P. 2005. *Äspö Pillar Stability Experiment, Report R-05-09.* Swedish Nuclear Fuel and waste Management Co, Sweden.

Haycox, J.R., W.S. Pettitt, J.M. Reyes-Montes, R.P. Young & Johannesson, L.-E. 2009. Acoustic Emission and Ultrasonic Survey Monitoring at the SKB Prototype Experiment During Heating and Pressurisation. In *Proceedings, Impact of Thermo-Hydro-Mechanical-Chemical (THMC) processes on the safety of underground radioactive waste repositories: An international conference and workshop in the framework of the European Commission TIMODAZ and THERESA projects*, Luxembourg, September 2009).

Haycox, J.R., Moretti, H.C., Reyes-Montes, J.M. & Young, R.P. 2012. Enhanced interpretation of fracturing from acoustic emissions and ultrasonic monitoring at the Aspö Pillar Stability Experiment. In *Proceedings, EUROCK 2012, Rock Engineering and Technology for Sustainable Underground Construction. ISRM International Symposium. Stockholm, May 2012.*

Hazzard, J.F., 1998. *Numerical modelling of acoustic emissions and dynamic rock behaviour.* Ph.D. thesis, Keele University, Staffordshire, U.K.

Mogi, K. 1962. Magnitude-frequency relationship for elastic shocks accompanying fractures of various materials and some related problems in earthquakes. *Bull. Earthquake Res. Inst. Univ. Tokyo* 40: 831–883.

Mogi, K. 2007. *Experimental Rock Mechanics*. Geomechanics Research Series. London: Taylor & Francis, 359 pp.

Nuannin, P., Kulhanek, O. & Persson, L. 2005. Spatial and temporal b-value anomalies preceding the devastating off coast of NW Sumatra earthquake of December 26, 2004. *Geophys. Res. Lett.* 32(11), doi 10.1029/2005GL022679. Issn 0094-8276.

Nuannin, P., Kulhanek, O., Persson, L. & Tillman, K. 2002. Forecasting of increased induced seismicity in the Zinkgruvan mine, Sweden, by using temporal variations of b-values. *Acta Montana, ser. A*, N 21(125): 13–25.

Pacheco, J.F., Scholz, C.H. & Sykes, L.R. 1992. Change in frequency-size relationship from small to large earthquakes. *Nature* 355: 71–73.

Pettitt, W.S. 1998. *Acoustic emission source studies of microcracking in rock*. Ph.D. thesis, Keele University, Keele, Staffordshire, U.K.

Pettitt, W.S., Baker, C. & Young, R.P. 1999. Acoustic Emission and Ultrasonic Monitoring During the Excavation of Deposition Holes in the Canister Retrieval Test. *International Progress Report IPR-01-02*, Swedish Nuclear Fuel and Waste Management Co, Sweden.

Pettitt, W.S., Baker, C., Young, R.P., Dahlström, L.O. & Ramqvist, G. 2002. The assessment of damage around critical engineering structures using induced seismicity and ultrasonic techniques. *PAGEOPH* 159: 179–195.

Scholz, C.H. 1968. The frequency-magnitude relation of microfracturing in rock and its relation to earthquakes. *Bull. Seismol. Soc. Am*. 58: 399–415.

Schorlemmer, D., Wiemer, S. & Wyss, M. 2005. Variations in earthquake-size distribution across different stress regimes. *Nature* 437: 539–542.

Urbancic, T.I., Trifu, C-I., Long, J.M. & Young, R.P. 1992. Space-time correlation of b-values with stress release, *PAGEOPH* 139(3/4): 449–462.

Warren, N.W. & Latham, G.V. 1970. An experimental study of thermal induced microfracturing and its relation to volcanic seismicity. *J. Geophys. Res*. 75: 4455–4464.

Wiemer, S. & Wyss, M. 2002. Mapping spatial variability of the frequency-magnitude distribution of earthquakes. *Adv. Geophys.* 45: 259–302.

Woessner, J. & Wiemer, S. 2005. Assessing the Quality of Earthquake Catalogues: Estimating the Magnitude of Completeness and Its Uncertainty. *Bull. Seism. Soc. Am.* 95(2): 684–698, doi: 10.1785/0120040007.

Wyss, M. 1973. Towards a physical understanding of the earthquake frequency distribution. *Geophys. J.R. astr. Soc.* 31: 441–359.

Young, R.P. Collins, D.S., Reyes-Montes, J.M. & Baker, C. 2004. Quantification and interpretation of seismicity. *Int. J. Rock Mech. Min. Sci.* 41(8): 1317–1327.

This page intentionally left blank

7. Slope and open pit stability

This page intentionally left blank

Rock Mechanics for Resources, Energy and Environment – Kwaśniewski & Łydżba (eds)
© 2013 Taylor & Francis Group, London, ISBN 978-1-138-00080-3

Conditions of stability in a marl and limestone opencast mine

Z. Bednarczyk
Institute of Opencast Mining "Poltegor-Institute" Wrocław, Poland

ABSTRACT: The objective of the work was to check the slope stability in marl and limestone mine in the city of Opole. In this mine, due to its location, blasting exploitation method was abandoned. The medium hardness rocks allowed operating the mine only by the excavators without the use of explosives. However these required the control of slope stability and the recognition of safety of exploitation processes. The scope of performed work included study of documentation, field observations, detailed engineering geology mapping and numerical analysis. In order to determine the rock strength properties, field mapping, Hoek-Brown Classification and uniaxial compression tests were used. Based on obtained data geotechnical conditions within the pit were characterized. The description of rock profiles and new cross-sections contained important information for slope stability. The field observation and mapping detected risk of displacements in strongly weathered limestone deposits to depth of 6–8 m, especially in wet conditions. The slope stability modelling included LEM analysis by Janbu and Fellenius Methods. They took into account the conditions resulting from the mining method and weather. The calculations detected that the slope was stable in dry conditions (Fs = 1.19–2.45). In the wet conditions, slope stability was reduced (Fs = 1.01–1.65). In two investigated profiles the values of relative factor of safety was very low (Fs = 0.76–1.1). Results of slope stability analysis included loads caused by the mining excavator and weather conditions. It was recommended that for mining operations at the top part of the deposit to the depth of 6–8 m, the excavator should be located at least 3 m from the slope edge. The other recommendations concerning the geotechnical instructions for mining operations were presented in the conclusions.

1 MINE LOCALIZATION AND GENERAL CHARACTERIZATION

The mine was located in the city of Opole in southwest Poland. Its owner Odra SA Cement Factory in 2011 celebrated its 100th anniversary. The Odra II Opencast mine covered area of approximately 60 ha and was founded in 1961. Its south part was located closely to the apartment buildings of the city and its east part was situated closely to the Odra River Valley. In the last years the exploitation was conducted mainly in the north-eastern and central part of the pit. The basic parameters of the mining operation are presented below:

- Mining depth: 25.0 m (148 m above the sea level)
- Exploitat. level height: lower 18.0 m, higher 7.0 m
- Actual angles of slope exploitation levels: 75°–60°
- Final slope exploitation angle: 45°
- General excavation slope angle: 32°
- Minimum mining level width: 15 m

The mine was operated by two exploitation levels: No.1/153.0–156.0 m and No.2/148.0–150.0 m. In its southern and western part mine was shaped using the explosives and already reached its target range. In these regions the slopes were exposed on the weathering processes from a few to tens of years. As a result of use of the explosives the rocks had numerous cracks, which affected slope stability. The change into the direct mining techniques resulted in reducing of mining process interference to the structure of rocks. Limestone rock exploitation was conducted by Komatsu hydraulic excavators. They was throwing output rocks directly to the operating level. (Fig. 1–4). As a result of limited operating range of mining excavator the new mining technology necessitates exploitation of several layers approximately of 3 m thick (Fig. 2).

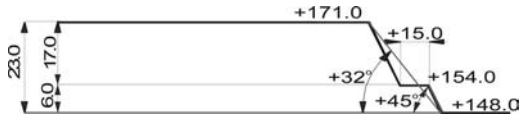


Figure 1. Slope parameters in the operated part of Odra II Mine.

The most important mining parameters are summarized in Table 1.

2 GEOLOGY AND HYDROGEOLOGY

2.1 *Geology*

The layers of limestone and chalk marl deposits in Odra II query were inclined nearly horizontally at the angles of 0.5–1° toward the SW direction. In the south part of the mine the layer inclination increased in east direction. That was caused probably by the faults. Five

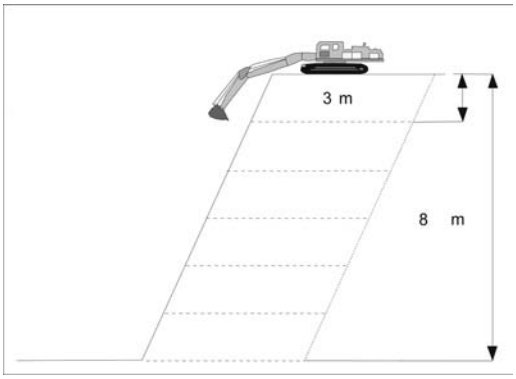


Figure 2. Schema of exploitation by Komatsu 400 excavator.

Table 1. Summary of mining and geological and parameters

Parameter	Min Value	Max Value	Mean Value
Quaternary overburden thick.[m]	0.2	1.0	1.45
Tertiary overburden thick. [m]	0.3	9.3	2.76
Limestone thickness [m]	0.5	28.0	19.40
Ratio overburden/limestone			0.03
The area of deposit [m^2]			1565424
The lower limit of the deposit [m above see level]			+148
Deposit density [g/cm^3]			2.2



Figure 3. Upper part of the mine, mining excavator.

main lithological series starting with the oldest were recognized. They are listed below:

No.1 Marly fine sands, sandstones (Cenomanian).
No.2 marly clays (Lower Turonian) high plasticity, $CaCO_3$ cont. of 22–30%, thickness of 10–14 m.
No.3 marls (Lower Turonian) parallel layered $CaCO_3$ cont. 36–41%, thickness of 10–16 m.



Figure 4. Foot part of the mine, loading and transport system.



Figure 5. Erosion in NE, not operated part of the mine.

No.4 marly limestones/Lower and Upper Turonian, stiff, $CaCO_3$ content 44–48%, thickness of 9–16 m
No.5 marly clays (Upper Turonian) fractured, $CaCO_3$ content 26–33%, thickness of 16 m.

In the investigated areas, the most regular series No.3 had thickness 16–8 m. The thickness of the series No.2 was variable. Erosion hoppers and a local discontinuities filled with Tertiary clays were recognized in the NE part of the deposit (Fig. 5). The opencast mine operated mainly limestone and marl series No.3 and No.4 within the level I and series No.2 on level II.

2.2 *Hydrogeology*

Two groundwater levels in the deposit were recognized. The first Quaternary level was formed in low thickness sands. This level was only intermittently present in the northern part of the deposit, which was not operated. The second Cretaceous aquifer was related to the Turonian limestone's marls and sandstones. This aquifer has a decisive impact on the water conditions of the deposit. The groundwater level was located on the average height of +156 m above the sea

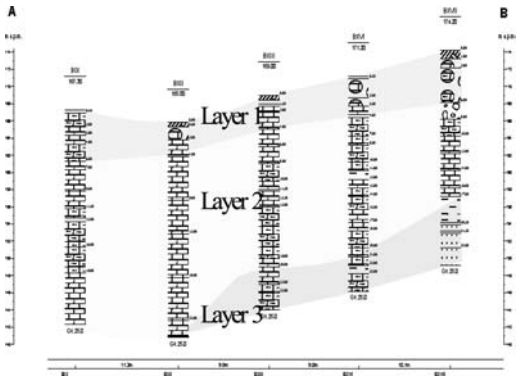


Figure 6. The geological A-B cross-section, Odra II Mine.



Figure 7. Erosion processes near the Luboszycka street

level. The mine was situated closely to the Odra river. The shortest distance from the river to the excavation was about 1200 m. The Cretaceous water level was situated few meters above the water level in river +149 m. Due to this complicated conditions mine dewatering system had to pump approximately of 35 m^3/h of water from the mining levels II and I. The depression zone has a range of about 200 m (Geological Documentation 1968). Impermeable marl clay layers were collecting the rainfall waters. The outflows of water from the open pit slopes occurred after precipitations. After intense rainfalls, they gather at the foot of the slope (Fig. 7).

3 GEOTECHNICAL INVESTIGATIONS AND SLOPE STABILITY ANALYSIS

3.1 *Site inspection and field mapping*

The field inspection, together with subsequent field mapping was combined with the analysis of documentary boreholes allowed to determine the general geotechnical conditions within the pit (Figs 5, 6). Due to the poor accessibility to the slopes, the mapping was limited to a general description of geology and slope processes characterization. It included the erosion, the weathering processes, and the presence of faults, joints, discontinuities and the water outflows and mapping. Totally sixteen profiles of the slopes of excavation were described. Based on these studies the detailed geotechnical cross-sections were constructed. They included all the gathered data and the results of laboratory tests. In order to determine the conditions of stability in geological structures documentary geological boreholes profiles were analyzed. They contained important geotechnical information necessary to comply with the interpretation of geotechnical conditions such as lithological profiles, description of the stratigraphy, the percentage of core obtained in the boreholes. For the mechanical parameters characterization percentage yields of the core (weighted average) for each of the separated layers were used. Analysis of stability included new geotechnical cross-sections, perpendicular to the edge of the excavation. They indicated the presence of high lithological variability. Three main geological layers, characterized by different physical-mechanical parameters, were recognized (Fig. 6):

- *Layer I* – limestones, heavily cracked which have the weak strength parameters. High degree of cracking occurred to a depth of 4–12.2 m. The average thickness of this layer was approximately 6 m. It was characterized by the lower percentage yield of core in boreholes (20–80%) compared with the other layers.
- *Layer II* – calcareous marls characterized by a more favourable strength parameters in relation to the layer I, thickness of 11–19 m. The yield percentage of core higher 60–90%.
- *Layer III* – marly clays, thickness of about 3–5 m. This layer was not present in the southwester part of the pit. The northern part had a thickness of 3–5 m. The yield percentage yield of the core was 60–90%.

The slopes in the west, north and south parts of the mine were shaped by explosive. Exploitation in this area had already been completed. Slopes in these regions were exposed to long-term erosion. Since the slopes had a plurality of slots from the exploitation processes they were susceptible to water washout and blowing in the wind. Traces of these influences could be seen on the slopes in the form of numerous erosion holes. In many parts of the slopes erosion processes were recognized (Fig. 7). In some lower parts of the mine water reservoirs and poor water outflow was recognized (Fig. 8).

3.2 *Laboratory tests*

In order to determine the representative rock strength parameters 36 uniaxial compression and unit weight tests were performed. They included 24 tests in dry conditions and 12 after saturation with water. The results of uniaxial compression tests are shown in Table 2.



Figure 8. Water reservoirs in foot part of the mine.

Table 2. Results of uniaxial compression strength tests.

Sample No./rock	Test No.	Strength [MPa] Dry	Wet
1/strongly fractured limestone	1	16.6	5.9
1/fractured limestone	2	25.3	9.9
1/fractured limestone	3	21.9	5.7
1/fractured limestone	4	28.2	5.6
1/strongly fractured limestone	5	17.2	6.3
2/stiff limestone	6	30.9	7.0
2/limestone	7	17.1	7.5
2/stiff limestone	8	25.1	9.4
2/stiff limestone	9	21.1	6.5
2/stiff limestone	10	32.0	5.8
2/stiff limestone	11	28.7	5.0
2/stiff limestone	12	27.3	6.5
3/soft limestone	13	29.7	–
3/soft limestone	14	19.5	–

3.3 *Slope stability analysis methods and initial data*

The analysis of slope stability were performed on the basis of site documentation, geological cross-sections taken along the slopes and field inspection on the basis on mine map in the scale of 1: 2000. The limit equilibrium (LEM) methods of slope stability analysis were used. They determined the potential slip surfaces on the slopes and to recognized the forces affecting the slope stability of rock masses (Bednarczyk 2005). The slopes formed in rock formations were characterized by a high variability of physical and mechanical parameters, and a variety of discontinuities as well as a number of other factors affecting their stability. Mass movements in marl and limestone rock quarry were caused mainly by erosion processes or by previously used blasting exploitation method. Failure in rocks could sometimes also occurred in a jointed stratum where movement was a consequence of sliding on bedding planes. Layers direction, inclination angle and occurrence of cracks or joint were very important for rocks stability. The slope stability in Odra II Mine was influenced mainly by the rock strength parameters, depended on its type, degree of weathering processes, occurrence of cracks, groundwater conditions and slope inclination. In order to determine rock strength parameters the rock samples were taken for the uniaxial compression tests. They were carried out in air-dry and saturated conditions. The main parameters determining the slope stability were shear strengths of the rock masses. To define the shear strength in the Hoek & Brown Criterion (1980) and RockLab software was used. For slopes composed of hard rocks it allowed to use conventional limit equilibrium equations. In this model internal friction angle φ and cohesion c are acting in the rock mass along a specified slip surface which is defined as:

Table 3. The material parameters A, B, T for marl and limestones rocks used in the RMR calculations.

RMR %	Value A	Value B	Value T
100	0.816	0.658	−0.140
85	0.651	0.679	−0.028
65	0.369	0.669	−0.006
44	0.198	0.066	−0.007
23	0.115	0.646	−0.002
0	0.042	0.534	0.000

$$\tan\varphi = AB\left(\sigma'/\sigma_c - T\right)^{B-1} \tag{1}$$

$$c = A\sigma_c\left(\sigma'/\sigma_c - T\right)^{B} - \sigma'\tan\varphi \tag{2}$$

where: σ_c – compressive strength, σ' – force acting on the basis of any potential slip surface, A, B, T = material parameters for different types of rocks.

The RMR classification method was also used for rock classification (Bieniawski 1989). It distinguishes five classes of rock strength parameters depend on the rock type, the degree of cracking, the size and length of cracks, their appearance, water conditions, and the percentage of core in the boreholes near the slopes. The data obtained from the laboratory tests and the strength parameters from RMR classifications were used for slope stability analysis. Analyses were performed using two different LEM methods by Fellenius and Janbu. The stability calculations were carried out in the cross-sections perpendicular to the mine edge, along all the potential circular-cylindrical surfaces. As a safety measures the relative slope stability index F_s, defined as the ratio of the total forces supporting the slope to the total forces seeking to activate the movements was calculated. In Opole mine, due to the new mining operation system, they must also take into account additional loads on the slopes caused by the mining excavator. The parameters adopted for the calculation due the complexity of the issue included the static and dynamic loads caused by the Komatsu PC

Table 4. The summary of slope stability anlysis results.

No	Dry slope Calcul. Method		Saturated slope Calcul. Method		Remarks
	Fellenius	Janbu	Fellenius	Janbu	
1	1.90	2.21	1.19	1.45	
2	1.30	1.59	1.01	1.24	+excav. upper lev.
3	0.99	1.15	0.76	0.89	+excav. lower lev.
4	1.70	1.99	1.02	1.21	+excavator
5	1.94	2.31	1.42	1.66	
6	2.41	2.56	1.51	1.65	
7	1.71	2.03	1.25	1.46	
8	2.21	2.45	1.42	1.63	
9	1.44	1.71	1.11	1.32	
10	1.16	1.37	0.90	1.14	+ excav. upper lev. 3 m from the scarp

400LC excavator. It had mass of 42,6 t, mining capacity of 3–2.2 m^3, standard track width of 600 mm and contact with the ground of 5.26 m^2. To calculate the simplified unit pressure covering static and dynamic loads Pn [kN/m^2] the following equation was used:

$$P_n = k\frac{Q}{F} \tag{3}$$

where: k – correction factor = 1.5, F = area of the contact of excavator with the ground.

The approximate estimated value of Pn = 122 kN/m^2 were included in the slope stability analysis. In those analysis it was assumed that the machine was working directly near the edge of the mine escarpment. The two values of the uniaxial compression strength in dry and saturated slope state were applied. Calculations in saturated state were carried out in order to check the behaviour of the slopes in conditions after long-term, intense rainfalls. These analyses were also performed in order to determine the impact of the excavator machine on the slope stability. Geotechnical data were obtained on the basis of documentary interpretation of the profiles, field inspection and laboratory tests. The RMR values were determined on the basis of uniaxial compression tests, the core RQD% yield, the distance between the cracks, their nature and size and approximate outflow of water from the slopes. The percentage weighted average yield of the core was calculated for each separate geotechnical layer. The correlation coefficients A, B, T used in the calculations are presented in Table 3.

3.4 *Results of numerical modelling*

Thirty-nine slope stability analyses were carried out in the project. Ten sets of slope stability calculations were performed by two different Fellenius and Janbu LEM computational methods in dry and saturated conditions. The analysis took into the account static and dynamic loads coming from the excavator. The detailed geotechnical profiles and cross-sections were

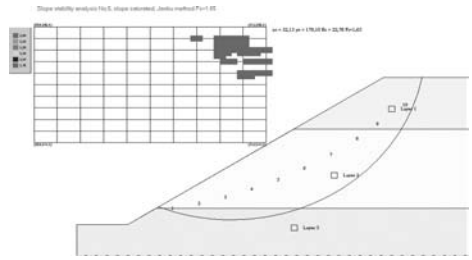


Figure 9. Slope stability analysis No.6, saturated conditions.

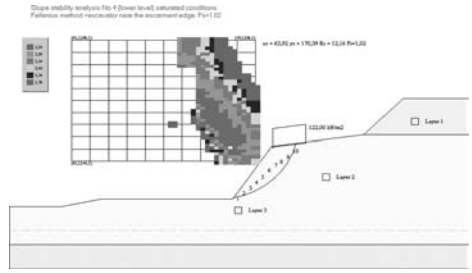


Figure 10. Slope stability analysis No.4, saturated conditions with mining excavator at the lower level, near the scarp edge.

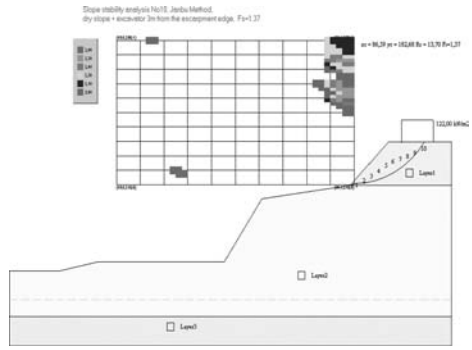


Figure 11. Slope stability analysis No.4, dry conditions with mining excavator at the upper level, 3 m from the scarp edge.

constructed in the selected for exploitation areas. The exemplar results of these calculations are shown on Figures 9–11. The summaries of the results are illustrated in Table 4. They are expressing the values of relative stability factor (F_s) of the slopes. The results from these analysis both for dry and wet conditions detected that F_s values were higher in calculations by Janbu Method. They indicated that all the investigated slopes in dry conditions (without the burden of the excavator) were stable. The stability coefficients for this condition ranged from 1.19 to 2.56. The lowest stability F_s values were obtained for these conditions in analysis No. 3–4. It should be also noted that the relative stability factor values close to $F_s = 1$ indicated the possibility of loss of stability of the slope under certain conditions. The slopes in permanently wet conditions had low stability that started from



Figure 12. Apartment buildings located closely to the mine.

0.76–1.01. The lowest, very unfavourable values of stability were obtained for saturated conditions in analysis No.3 ($F_s = 0.76–1.15$). The impact resulting from the exploitation system static and dynamic loads on slope stability were analyzed in four options. Analyses No. 2–4 was based on the assumption that the excavator was operating directly near to the edge of the escarpment. In analysis No.2 slope stability was maintained, however attention had to be paid to the very low value of the stability factor $Fs = 1.01$ in wet conditions (Fellenius Method). In analysis No. 3–4 the two option of excavator localization were considered. Type 1 was dedicated to the upper exploitation level and type 2 lower exploitation level. In this analysis the slope stability coefficients F_s range 1.02–1.70. These results indicated relatively stable conditions for dry slopes and unfavourable state when the slopes were saturated. In the most negative ranges in saturated conditions the values of F_S varied from 0.76 to 1.15. In the analysis No. 3 adverse conditions both for dry and wet conditions were observed. These conclusions eliminated the slope from the mining operations carried out directly by the excavator situated at the edge of the escarpment. It is worth to add that excluding the impact of the excavator on the slope, analysis No. 2–4 showed a relatively high stability coefficient. In order to establish the safe distance from the excavator to the escarpment edge, calculations had to took into account the several different distances.

As a result of these calculations, the safe distance from the excavator to the edge of the slope was recognized. The lowest safe distance was 3 meters. For this distance the sizes of the relative factors of safety F_s were equal 1.16–1.37 for dry conditions and 0.9–1.14 for saturated slopes (on the verge of losing stability). Therefore, it was recommended that mining by excavator should be operated with the distance of more than 3 meters from the edge of the scarp.

4 CONCLUSIONS

Presented geotechnical investigations recognized that the limestone and marl mine had very variable geotechnical conditions. The numerical slope stability analysis by LEM methods showed that in dry conditions the slopes were stable and their relative stability factors ranged from 1.19 to 2.45. The slopes saturated with water had significantly reduced stability factors, $F_s = 1.01–1.65$. Very low values of $F_s = 0.76–86$ by Fellenius Method and $F_s = 1.01–1.24$ by Janbu Method characterized the stability in these conditions in some regions. They included the average loads caused by the mining excavator. These calculations were however approximate, because of the high number of difficult to identification slope processes. The study of these influences required a detailed investigation and profiling of the slopes that was not possible in the project due to the poor slope accessibility. The previous blasting works, also significantly influenced the mechanical parameters of the rock masses. The site inspection in the northern and western parts of the pit and a field mapping indicated the presence of high-risk areas caused by weathering processes, erosion and mass movements. Some of the areas require special attention because of the potential risk to the apartment buildings and Luboszycka Street located closely to the pit (Fig. 7, 12). The risk of mass movements was considered in strongly weathered limestone deposits located in the eastern part of the open pit to the depth of approximately 6 m. Erosion processes and poor water outflow from the foot pars of the slopes especially in the western part of the pit, were recognized. These factors very adversely affected slope stability. Delivered recommendations were connected with improvement of drainage system to allow water outflow from the foot parts of the slopes. Particular caution was also advised in carrying out the mining operation by excavator. This restriction was particularly important in areas of high erosion and weathering processes occurrence on the slopes. To maintain safety mining conditions a distance of more than 3 m from the excavator to edge of the escarpment was recommended. In selected risky areas it was advised to stop the mining operations during heavy precipitations, which can cause significant deterioration of stability. This restriction and a careful monitoring of the slope behaviour were particularly important in upper part of the deposit. The slopes previously formed by the explosives had to be subjected to the reclamations and treatments. In the newly opened mine areas of the deposit it was recommended to perform additional slope stability calculations and inspections.

REFERENCES

Bednarczyk, Z. 2005. The expertise of the conditions of stability and slope performance in marl and limestone quarry for Cement Factory "Odra" SA in Opole. Institute of Opencast Mining Poltegor-Institute, Wrocław.

Bieniawski, Z.T. 1976. Rock mass classification in rock engineering. In Exploration for Rock Engineering, Proc. of the Symp., (ed. Z.T. Bieniawski), Balkema: 97–106.

Geological documentation of Odra II Marl Deposit, $A + C_1$ category 1968 Geological Company in Krakow.

Hoek, E. & Brown, E.T. 1980. Empirical strength criterion for rock masses. J. Geotech. Eng. Div., ASCE 106 (GT9): 1013–1035.

Rock Mechanics for Resources, Energy and Environment – Kwaśniewski & Łydżba (eds)
© 2013 Taylor & Francis Group, London, ISBN 978-1-138-00080-3

An on-line landslide monitoring system in flysch Carpathians

Z. Bednarczyk
Institute of Opencast Mining "Poltegor-Institute" Wrocław, Poland

ABSTRACT: The first in Poland, on-line landslide monitoring and warning system has been implemented in 2010 in Polish Carpathians. The Innovative Economy Project financed by European Agency for Regional Development was conducted at selected landslide area in Beskid Niski Mountains. In this area six landslides posed risk for infrastructure, private properties and a new bridge. Mass movements occurred in heavily saturated mixtures of rock-soil weathered deposits over the public road in the river valley. Geotechnical layers were composed mainly of saturated soft clayey soils and claystones interbeded by stiff sandstones. Colluviums depths of 7 to 18 m and shallow groundwater level characterized the investigated area. The cumulated displacements up to 193 mm were observed in seven years time. Partial stabilization implemented in 2009 included anchors, surface and internal drainage systems and buttress walls. However, after that time ground movements of 1 to 27 mm were detected in some parts of the landslides. In June 2010, displacements accelerated after extreme precipitations of 100 mm in 3 hours time. The new on-line system was consisting of four monitoring stations. Two stations included 3D continuous inclinometers – 60 sensors to the depths of 14 to 16 m. One station included 3 uniaxial in-place sensors, automatic piezometer and groundwater pore pressure transducer. Weather monitoring station performed measurements of precipitation, air pressure, air humidity and air temperature. Data were transferred by GPRS network to the Internet every 10 minutes to 6 hours. The registered displacements depths varied from 12 to 16 m depending on localization. They had complicated nature and probably numerous sliding surfaces. Its rates varied from 18 to 38 mm in last 30 months. Special software for data interpretation and recognition of high-risk conditions was implemented to allow sending SMS alarm messages to the road owner. Real-time monitoring may allow better recognition of landslide activation factors.

1 INTRODUCTION

New on-line monitoring system is high-tech equipment for measurements and early warning of rock mass movement triggers over the public road and a new bridge in risk area (Fig. 1). Four field stations enabled automatic continuous measurements of various parameters directly affecting the slope stability. During the last three years system allowed analysis of landslide activity and early warning to the owner of the road and the Polish Geological Survey. Field stations were installed on six active flysch soil-rock Carpathian landslides closely to the city of Gorlice. Data were transmitted to the Internet. Author of this paper investigated these landslides in previous years (Bednarczyk 2008). Geotechnical engineering site documentations detected that landslides had depths of 6–16 m, the area of 3.7–6 ha, the lengths of 350–500 m and the widths of 150–200 m. The recognized length of the risk zone along the road was 800 m. In 2009, the road authorities implemented a partial stabilization of the risk area by strengthening slopes over the road by the anchors and Geobrugg high tensile wire nets together with a new buttresses retaining walls system along the Bystrzanka River banks. The system of surface and deep drainage was also realized. However, partial stabilization protected only the front part of the landslides. Studies had shown that, despite of the remediation works already done, some parts of the landslides were characterized by a high movements activity after intensive precipitations.



Figure 1. On-line M1–M3 + Meteo stations location.

Threats to the road were highlighted particularly in May and June 2010, when record high precipitation and the flood in southern Poland were observed. New displacements, caused cracks on the slopes, destroyed part of the drainage ditches and stretch Geobrugg nets near the road (Figs. 2, 3, 11).

2 MEASUREMENT METHODS

The new field monitoring stations registered the ground displacements, the groundwater and the



Figure 2. New displacements, landslide No. 5.



Figure 3. Destroyed drainage ditches.

weather data continuously, in real or near-real time in the intervals from 10–60 minutes to 360 minutes depending on the selected options. Data were sent by cellular network to a web server that collected all the measurements. In this system landslide information's were shared with authorized users from any computer connected to the Internet. Data were edited in form of graphs or exported as a text files. The operation of the system was not affected by the data transmission method. This minimized the costs of administration and data management. System was powered by a rechargeable 12 V batteries and solar panels. In order to avoid accidental loss of data system provided continuous control of power supply and GSM signal strength. Data could be also downloaded manually from the datalogger by USB key. The early warning function was realized by SMS messages and e-mails. In alert conditions they were automatically sent to the system operator, the road administration and the Carpathian Branch of Polish Geological Institute

2.1 *Description of ground movement measurement methods*

Two different types of inclination sensors for measuring the ground displacements were used of: (i) 3D system of continuous inclinometer sensors and (ii) "in-place" system in standard inclinometer casings.

2.1.1 *Continuous inclinometers system*

The continuous inclinometers system is a modern measuring technology. The flexibility of the system allowed withstanding greater strains than by standard inclinometers. The installation was realized in PVC flexible protective pipes with an outside diameter 27 mm that provided protection for measuring devices. The system can be use as reusable, but this could be verified on the possibility of its removal, which depends on the size of the experienced rock mass movements. Typically, it is possible for the displacements of several centimetres in size. The system was built as a string of a special rigid segments connected by a special flexible joints with three orthogonal automatic gravitational tilt sensors sensor for measuring displacements in three axes (Fig. 4). The standard rigid segment length of 500 mm allows being bend in any direction, but preventing to be twisting. Communication between all measuring equipment was digital. The communication cables transferred obtained data to the datalogger and then by GSM/GPRS network to the Internet. Every eighth segment of the system had a microprocessor. For the correction of temperature effects every installation had ground temperature sensor. Before the installation system was stored on a special roll (Fig. 4). Each installation was built as a multiple of 8 segments so called "octets" with a length of 4 m. Devices installed in the Carpathians had multiple "octets" (×* 4 m). All the microprocessors communicated with the datalogger the same communication line. This ensures possibilities of deep installations, low power consumption, high accuracy and spatial 3D presentation. The position of the axis end of the segment length of L was calculated based on the trigonometric functions of the inclination angle θ:

$$x = L\sin(\theta) \tag{1}$$

The sensors measured the centre of angle θ according to the equation:

$$v = Cg\sin(\theta) \tag{2}$$

where: v – signal strength (usually voltage)
C – calibration coefficient
g – acceleration due to the earth gravity
θ – inclination angle

The sensors size of 1.5 mm × 4 mm × 4 mm, contained three orthogonal accelerometers from particles of pure silica (<1 mm). The measurement was based on the static inclination angle at the joints between the segments. The mobile part of the sensor was suspended on two springs that allowed the free movement

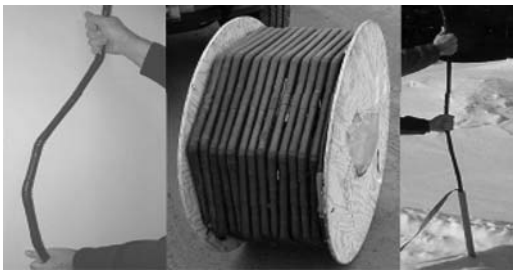


Figure 4. Continuous inclinometer system.



Figure 5. Interiour of continuous inclinometer M2 Station.

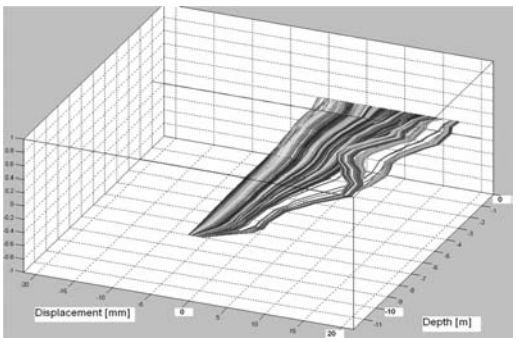


Figure 6. Continuous inclinometers 2D results.

to the left and to the right. The sensor had a number of plates separated by intervals, which were located between the fixed electrodes. The differences in a distance between the plates and the electrodes were measured as a change of electric capacitance. Realized in lower and upper part of the landslides installations included dozens of 3D sensors to monitor in a long term the ground displacements on the slopes.

The M3 field station (Poltegor_1) with depth of 12 m consisted of three octets – 24 segments, and the M2 field station (Poltegor_2) with depth of 16 m of four octets – 32 segments length of 500 mm (Fig. 4). Data interpretation software allowed reading of 2D or 3D data for the installation tilted up to 60 degrees from the vertical direction (Figs. 12, 16). The 3D displacements or shear strain data were available for the whole range of depths or at the selected ranges. In 3D mode, rotational transformation of the data, using numerical methods was used (Fig. 16). System generated alarms where movement reached a predefined threshold displacement or velocity movements.

2.1.2 *Description of inclinometers "in-place"*

The system was placed in one location at landslide No.1 in a borehole equipped with standard inclinometer casings (Fig. 7). The installation was performed using special measuring wheels to lower the sensors to a specific depth using grooves. One set of grooves was oriented in the expected direction of the slide movements, second transversely to this direction. Middle sensor was placed at the depth of expected displacement subsurface zone, wherein two others were located within the bedrock and colluviums layers. The inclination of the casings was measured by a single direction "in-place" inclinometer probe with an accuracy of +/−0.2 mm. The measurements allowed specifying the size and depth of the landslide movements. The changes in inclinations of inclinometer casings were converted into the horizontal displacement in millimetres using trigonometric functions. The displacements were calculated by comparing the current reading with the initial of the following formula:

$$\Delta u_{iy} = Lx\left[\sin\left(\theta_{iy}\right) - \sin\left(\theta_{io}\right)\right] \tag{3}$$

where: θ_{iy} – the inclination of the probe in the (i) measuring section and (y) series of measurement, θ_{io} – the inclination of the probe in the (i) measuring section in initial readings.

2.2 *Description of groundwater and wheather condition monitoring methods*

Influence of groundwater condition on slope stability and was predicted on the basis of pore pressure and groundwater level depth measurements. Devices were programmed to continuously measure and transmit data every 60 minutes. The pore pressure transducers were installed in sand filters in the boreholes. Their top parts were closed by bentonite-cement seals. The devices for measuring the groundwater depth level were installed in open piezometer boreholes. Instrumentation of the slopes included the following automatic devices for measuring water conditions: (i) one VW piezoelectric piezometer for groundwater table level measurements with filter at a depth of 10 m installed in piezometer borehole, (ii) two piezoelectric groundwater pore pressure and temperature transducers at the depth of 10 m installed in borehole in sand filters. Installed transducers converted signals frequency into pressures with usage of the diaphragm combined with tight steel wire from solenoid. Vibrations near the wire coil generated signals (Hz), which were sent to the recorder. To obtain the groundwater pressure in kPa following equation and calibration factors were used:

$$P = ax^2 + bx + c \tag{4}$$



Figure 7. In-place inclinometer and piezometer station.



Figure 8. Weather station and piezometer station.

where: x was the value read in Hz and the coefficients *a*, *b*, *c* were characteristic coefficients of the sensors. Before the installation transducers were saturated and calibrated. They worked with datalogger using special software. Recorded pore pressure values were corrected for the effect of temperatures at the installation depths.

The weather station measured the hourly amount of precipitation, the atmospheric pressure, the temperature and the humidity (Fig. 8). It works as a separate monitoring device transmitting GPRS data to a web server which collecting the data. Data could be collected also manually via RS232 interface to a laptop computer. All the measurement functions were performed automatically. Measurements were done continuously in the interval of 10 minutes. Their aggregation was possible for the selected time intervals (1 hour, daily or monthly) in the form of graphs. This allows continuous monitoring of meteorological parameters and their export as a text files. The risk and alarm conditions could be predefined in the system as emails or SMS warnings to authorized users. A lithium battery charged by a solar panel powered the station. Continuous monitoring of the battery voltage and GSM signal strength prevented accidental loss of data.

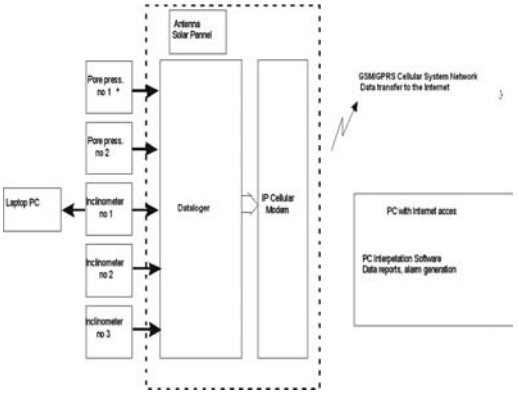


Figure 9. Block diagram of the on-line monitoring system.

3 SYSTEM SPECIFICATIONS

The on-line monitoring system included field stations collecting landslide data, multiplexers, interfaces and meteorological station. A block diagram of the monitoring system is shown in Figure 9. The system consists of the following measuring devices:

☐ *Two automatic groundwater level, pore pressure and temperature transducers* depth of 10 and 11 m.
Sensor Type: piezoelectric with temp. sensor

– Measuring range 1.5 Bar, resolution: 0.025 %

☐ *Three ground movement inclinometer systems*:

- *Inclinometer No.1 (M1)* three single-axis IP sensors, every 1 m length, multiplexing, inclinometer casings diameter of 70 mm, depths of 7– 10 m.
- Measuring range: ± 10 deg.
- *Inclinometer No.2 ÷3*, 3D inclinometers consist of
- inclinometer 2 (M2) – 4 segments, 8 transducers every 50 cm, total length of 16 m
- inclinometer 3 (M3) – 3 segments, 8 transducers every 50 cm, total length of 14 m
- Measuring range: ± 45 deg.

☐ *Weather station* consist of barometer, rain gauge, temperature sensor, humidity sensor

4 GEOTECHNICAL SITE CONDITIONS

Investigated six landslides were located over a public road, in the region of Gorlice. The new measuring stations were located over the previously installed in 2005 standard inclinometer and piezometer monitoring instrumentation. The system was locates on landslides No. 1, 5, 6 along the road length of 800 m. Landslides had size 3.7–6 ha, length of 350 m to 500 m and width of 150–200 m. Their description is given below:

– *Landslide No. 1* Large and active landslide, length of 355 m, width of 116 m, slope inclination of 9°,



Figure 10. Partially protected road (March 2010).



Figure 11. Stretch of Geobrugg nets (May 2010).

landslide depth of 6–11 m. On – line Monitoring Field Station M1 located in its central part. Meteorological station at the edge of landslide.

– *Landslide No. 5* – Very large and active landslide, length of 476 m, width of 180 m, average slope inclination of 9 – 12°, slip surface depth of 10–20 m. Seven private buildings, power, gas and water supply infrastructure in risk area. On-line Monitoring Field Station M2 located nears the top of the landslide.
– *Landslide No. 6* – M3 Large active landslide threatening the new bridge, 10 private buildings, power, gas and water supply infrastructure in risk area, length 561 m, width 147 m, average gradient 6– 9°, slip surface depth of 10–20 m. On-line Monitoring Field Stat. M1 station near the bridge.

At these landslides, partial stabilization works (2009), reduced the danger but don't lead to a complete remediation (Figs. 10, 11). Threats to the road became especially visible after record high rainfalls in May and June 2010.

5 INSTRUMENTATION AND LABORATORY

New instrumentation of the slopes included 72 m of core drillings. The work was carried out during a heavy precipitation and flood in May-June 2010, which seriously hampered the possibility to enter the landslide



Figure 12. Software for landslide data interpretation.

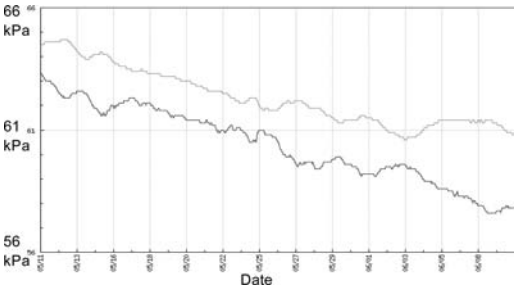


Figure 13. Results of groundwater pore pressure monitoring.

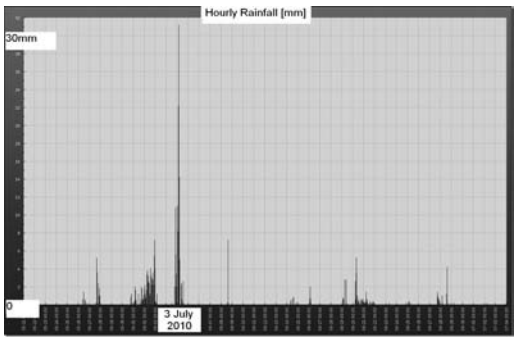


Figure 14. Precipitation s [mm], automatic weather station.

area. In two boreholes (M2, M3) continuous 3D inclinometer systems were installed. They included 54 continuous inclinometer rigid segments to a depth of 16 m and 12 m (Figs. 4, 17). The M1 in-place inclinometer was installed in a borehole depth of 14 m. This field station incorporated also two pore pressure transducers with groundwater temperature sensors and one automatic piezometer. The design depth of instrumentation was predicted to reach the bedrock layers. However, due to the complexity of the geological structures, the heterogeneity of rock – soil layers and the variable depths of slip surfaces it was complicated task. To avoid the mistakes results of previous standard monitoring measurements, the previously performed and new site investigations were used. In this region displacements up to 193 mm were observed in seven

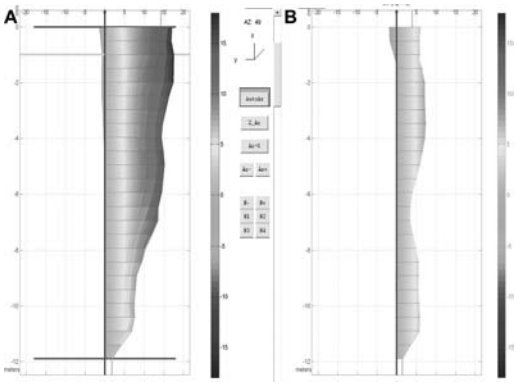


Figure 15. The results of measurements of displacement (2D), A – direction of the slope tilt, B – perpendicular direction.

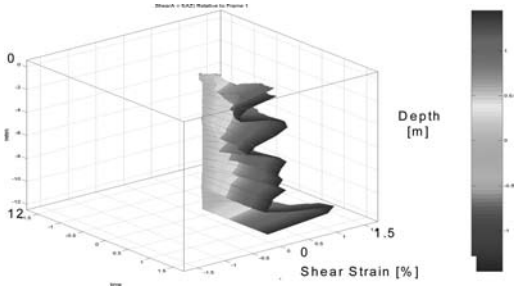


Figure 16. Shear strain, 3D diagram, M3 Field Station.

years time. The new drilling works were complemented by the laboratory tests. They included 12 field shear strength tests, 10 index tests, 2 direct shear tests, 1 IL oedometer tests, and 10 CIU and CID triaxial tests. The results showed that the colluviums to a depth of 12–15 m, had adverse strength parameters and very high natural moisture content of 20–36%. The soil types occurring on steeply inclined slopes represented heavily saturated gravely loam with a high degree of plasticity ($I_L = 0.4–0.5$). The values of effective strength parameters were variable, the internal friction angle 6.5–20°, cohesion 11–25 kPa. The colluviums depths varied 10.2–11.5 m.

6 ON-LINE MONITORING RESULTS

The results of on-line measurements indicated that the displacements were active to a depth of 11–15 m. The movements varied in size and direction. Partial stabilization implemented in 2009 included anchors, surface and internal drainage systems and buttress walls. However, after that time ground movements of 1 to 27 mm were detected in some parts of the landslides. In June 2010, displacements accelerated after extreme precipitations.

The highest movements recorded till the end of 2012 reached 35–38 mm. The largest were recorded at depths of 0–7 m. It was observed that the displacements vary with depth, which suggests the presence of multiple active slip surfaces (Figs. 15, 16). The impact of weather conditions on the activation of landslides was analysed using data from automatic weather station. The measurements allowed registration of record size precipitation including 100 mm rainfall in 3 hours on 3 June 2010 (Fig. 14). The obtained landslide data were used to determine the threshold value of alarm warnings, and to study interactions between displacement, groundwater and meteorological conditions.

7 CONCLUSIONS

New, the first in Poland landslide on-line monitoring system was presented. Region of six active landslides near the city of Gorlice was equipped with four monitoring stations. They included innovative sensors to measure 3D displacements, pore pressure, water table level and weather conditions. Monitoring started in May 2010 during heavy precipitations and a high mass movements activity. In 30 months displacement of 18–38 mm to a depths of 12–15 m were registered. Despite of partial stabilization in 2009, landslides were still active. The conclusions indicated that intense precipitation can affect stability of some parts of the slopes, especially in the area of unprotected sections of landslides No. 1, No. 5–6 and a new bridge over the Bystrzanka river. Some of the remediation works in such conditions may not be fully effective. On-line system allowed to early warning of these processes. Data will be used to improve landslides remediation and to study landslide movement activating factors.

REFERENCE

Bednarczyk, Z. (2008). Landslide geotechnical monitoring network for mitigation measures in chosen locations inside the SOPO Project Carpathian Mountains, Poland. The First World Landslide Forum, Tokyo, Japan, International Consortium of Landslides ICL, UN, UN/ISDR: 71–75.

Rock Mechanics for Resources, Energy and Environment – Kwaśniewski & Łydżba (eds)
© 2013 Taylor & Francis Group, London, ISBN 978-1-138-00080-3

Swelling rocks in an open pit mine

M.E. Bilir
Bulent Ecevit University, Zonguldak, Turkey

E. Aydıngun
Turkish Coal Enterprises, Bursa Lignite Enterprise, Bursa, Turkey

ABSTRACT: Swelling behavior is defined either as the increase in volume of unsaturated rocks containing smectite group minerals due to time-dependent water absorption or the excess stress occurring if the volume increase is obstructed. Since swelling behavior is a small process the associated problems are later realized and thus, causes the precautions taken to be either temporary or inadequate. This paper deals with obtaining the swelling parameters which can be used in solving the problems in Bursa Lignite Open Pit Mine and quantitative determination of uniaxial swelling behavior.

1 INTRODUCTION

Swelling rocks lead to damage not only to the underground structures such as tunnels, galleries, gateroads, wells but also to the surface structures like foundations, slopes, retaining walls, highways, and irrigation channels. The open pit mines are one of the surface engineering structures encountered the swelling problems. The Telnes ilmenite open pit mine in Southwestern Norway and the Goynuk lignite open pit mine in Turkey can be examples for the issue (Nilsen & Ballou 2006, Tabrizian 1989). In these mines swelling rocks caused slope failures.

The topic of this study is about swelling behavior of rocks in Turkey Coal Enterprises Bursa Lignite Open Pit Mine located in Orhaneli (Bursa). Swelling rocks are caused stability problems in Bursa Lignite Enterprise. Uniaxial swelling tests with computer controlled swelling test apparatus were performed on samples from open pit mine. Swelling stresses were found as a function of axial swelling strains. Mineralogical analyses were carried out to determine the type and percentage of swelling minerals.

2 BURSA LIGNITE ENTERPRıSE

Bursa Lignite Enterprise (BLI) is located in Gumuspinar village, Orhaneli county, Bursa, Turkey. Gumuspinar is 25 km far from Orhaneli and 83 km far from Bursa (Fig. 1). Bursa Lignite Enterprise, one of the production units of Turkey Coal Enterprises (TKİ), carries out the production of lignite coals for the Orhaneli power plant unit (1×210 MW) and for domestic use.

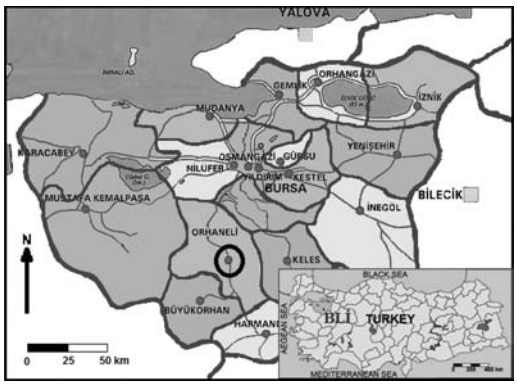


Figure 1. Location map.

Orhaneli coal basin has three coal-bearing regions, namely Gumuspinar, Sagirlar and Civili. These regions show similar stratigraphic sequences. The metamorphic schist and recrystallized limestones of Palaeozoic age and Late Cretaceous aged serpentinites form the basement of the coalfield (Esenlik et al. 2006). A coal-bearing sequence of Late Miocene age unconformably overlies the basement rocks. This sequence includes conglomerate-sandstone-claystone, lignite-claystone-siltstone and marl-tuffite. The volcanic-pyroclastic rocks of Pliocene age consist of tuff-tuffite and andesite-basalt, which are widespread in the coalfield. The sequence ends with Quaternary aged unconsolidated pebble-sand-clay, alluvium and talus deposits.

The total lignite reserve of Orhaneli basin is 39.7 million tons, of which Gumuspinar region has 22.7 million tons. In the Gumuspinar region, the lower heating value of lignite changes between 2300 and 2600 kcal/kg, also in Sagirlar between 3000 and



Figure 2. A view of the Gumuspinar region (16.9.2011).

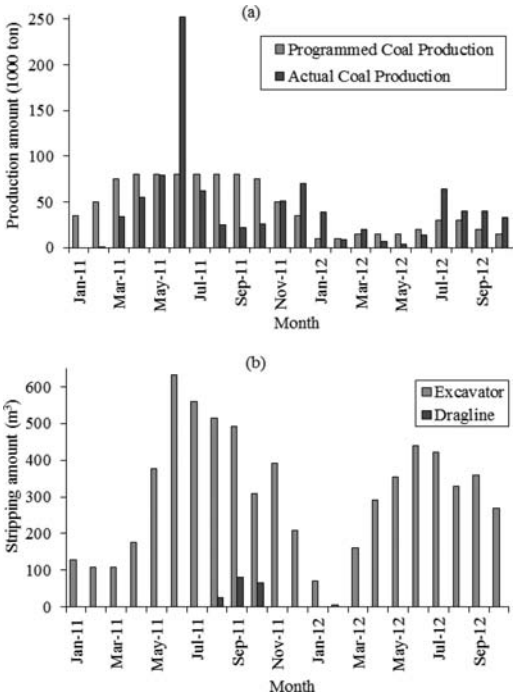


Figure 3. Programmed and actual coal production (a) and stripping operations of excavator and dragline (b) for 2011 and 2012.

3300 kcal/kg, in Civili between 1900 and 2100 kcal/kg. The thickness of seam in the Gumuspinar, Sagirlar and Civili regions is 7.05, 3.36 and 3.36 m respectively.

Currently the coal production is only performing in Gumuspinar region by open pit mining method (Fig. 2). The mining method used by BLI is a dragline/truck shovel combination. The overburden is loosened first by blasting with explosives. Then, the truck/shovel removes a certain thickness of the overburden. Finally, the dragline strips the remaining part of overburden above the seam and spoils its material on the decoaled cut. In recent years, because of poor round conditions dragline can not be used.



Figure 4. Slope failure (16.11.2011).



Figure 5. A view of poor ground conditions for excavator.

In Figure 3, stripping amounts of programmed and actual production of Gumuspınar region is shown along with the excavator and dragline of the same region. There, a decrease in lignite production and stripping operations can be seen. In this decrease, caused by the rainfall, slope instabilities and clay rocks turning in to soil had been effective.

One of the most serious slope failure in the mine occurred during a period of rain in December 2011. (Fig. 4). Removal of the slided material had finished in the middle of 2012 due to stuck of excavators to the ground (Fig. 5). In the mine slope failures still occur with lesser radius. On a village road near the establishment a bigger slope failure has occurred.

3 METHOD

To investigate the effects of the swelling rocks in the pit, specimens were taken from 10 different locations for swelling tests. 4 specimens showed important swelling behavior during the pretests.

Those specimens are: claystone (CS1 and CS4), clayey limestone (CLS), and marl (M). On other specimens low or no swelling behaviour was observed. Locations from where the 4 specimen are taken are shown in Figure 1. Sample preparation, swelling test apparatus and test method are described briefly below.

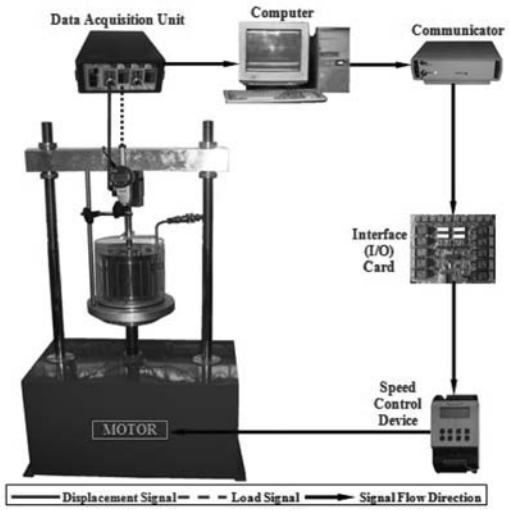


Figure 6. Swelling test apparatus.

The more information can be found in paper Bilir et al. (2012).

Cylindrical core samples usually break, crack or disintegrate from the discontinuity planes due to the fact that swelling rock has low strength and water is not used during core drilling. Thus it was not possible to prepare an undisturbed sample of the desired size. In this case, samples were ground and compacted in a mold causing some disturbance.

Because of the breakage and cracking of samples while taking cores from rock blocks, the samples were ground and then pressed by a special apparatus developed by Yesil (1991) with original dry. The cylindrical samples with a diameter of 54 mm were obtained.

Sample height and diameter/height (D/H) ratio were determined as 20 mm and 2.7, respectively by taking recommendations in ISRM (1979) and ISRM (1989) into account.

Swelling test set composed of 5 apparatus was used for uniaxial swelling test in Bulent Ecevit University. It consists of a cell, axial loading unit, and data acquisition and control unit. The general view of the apparatus is shown in Figure 6.

The purpose of the test method is to define axial swelling stress first by triggering Displacement Control Program and then uses Load Control Program a few times by which the load over the sample is reduced in certain amounts to define axial swelling strains.

4 SWELLING BEHAVIOUR

The variations in swelling stresses and swelling strains of samples with time obtained from uniaxial swelling tests and the results of these tests are given in Figures 7–11 and Table 1, respectively.

The relationship between axial swelling stress (σ_s) and axial swelling strain (ε_s) obtained from uniaxial swelling tests for samples is given in Figure 12 and obtained equations are given in Equations (1 to 4).

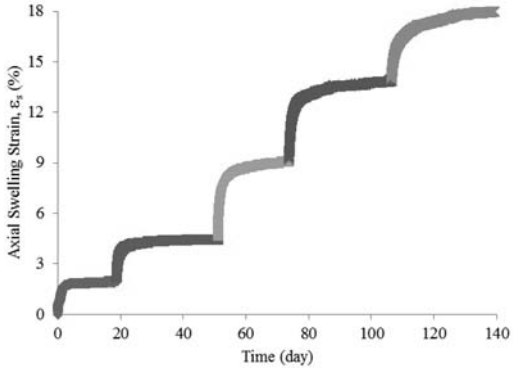


Figure 7. The variation in axial swelling strain with time for CS1.

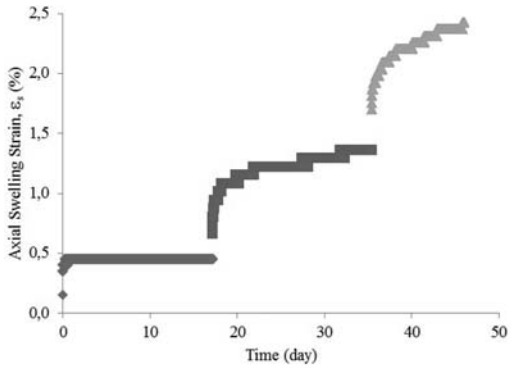


Figure 8. The variation in axial swelling strain with time for CLS.

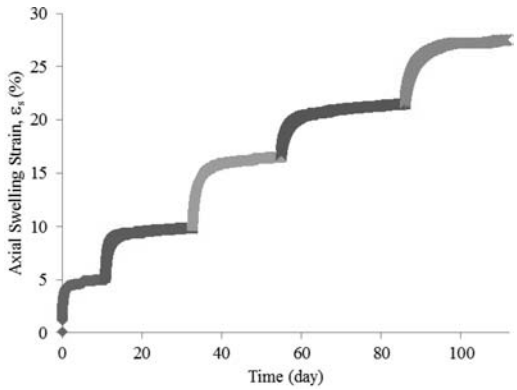


Figure 9. The variation in axial swelling strain with time for CS2.

$$\varepsilon_{s\,CS2} = -8.16 \ln \sigma_s + 16.09 \qquad R^2 = 0.99 \qquad (1)$$

$$\varepsilon_{s\,CS1} = -6.61 \ln \sigma_s + 9.05 \qquad R^2 = 0.99 \qquad (2)$$

$$\varepsilon_{s\,M} = -2.12 \ln \sigma_s + 2.79 \qquad R^2 = 0.99 \qquad (3)$$

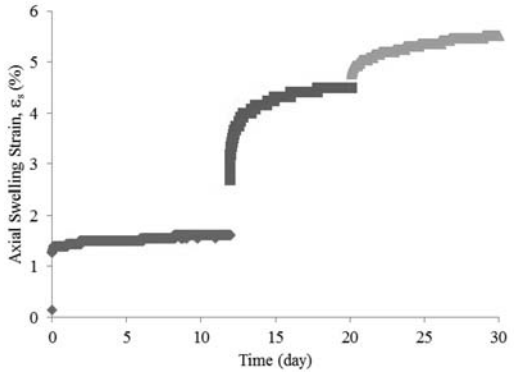


Figure 10. The variation in axial swelling strain with time for M.

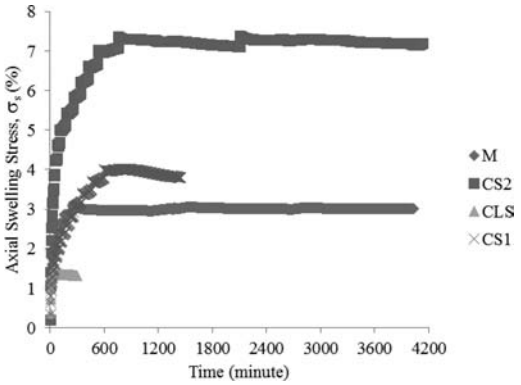


Figure 11. The variation in axial swelling stress with time for all samples.

Table 1. Swelling test results of samples.

CS1		CLS		CS2		M	
σ_s	ε_s	σ_s	ε_s	σ_s	ε_s	σ_s	ε_s
3.80	0.00	1.32	0.15	7.19	0.10	3.00	0.15
3.00	1.95	1.00	0.45	4.00	4.95	2.00	1.61
2.00	4.46	0.50	1.36	2.00	9.83	0.50	4.49
1.00	9.11	0.25	2.43	1.00	16.52	0.25	5.52
0.50	13.87			0.50	21.48		
0.25	17.98			0.25	27.55		

σ_s: Axial swelling stress (MPa); ε_s: Axial swelling strain (%)

$$\varepsilon_{s\,CLS} = -1.37 \ln \sigma_s + 0.48 \qquad R^2 = 0.99 \qquad (4)$$

X-ray identification has been done in Earthsciences Application and Research Centre of Hacettepe University. The semi-quantitative proportions were determined from the powder diffractogram following an external standard method developed by Gundogdu (1982). The detail of this method is given in Temel & Gundogdu (1996). Clay minerals and calcite dominate

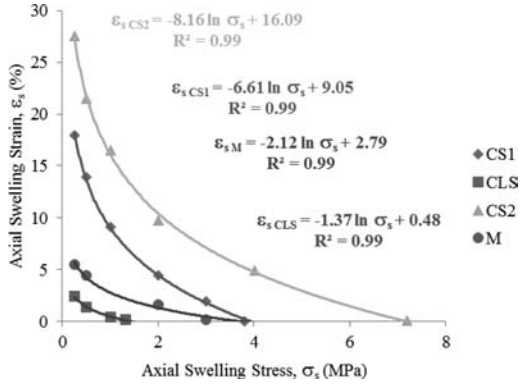


Figure 12. The relationship between axial swelling stress and axial swelling strain.

Table 2. Semi-quantitative bulk rock mineralogy and clay mineralogy of the samples based ineralogy on XRD.

	Clay and non-clay minerals (%)							Clay minerals (%)		
Sample	Clay	Mica	Calsite	Peldspar	Quartz	Dolomite	Aragonite	Smectite	Kaolmite	mite
CS1	73	8	7	6	5	1		70	20	10
CLS	18		71		1		10	91	2	7
CS2	87	6	1	2	4			71	23	6
M	64	8	10	12	5	1		90	2	8

the bulk rock composition (Table 2). The clay minerals are composed of about 70–91% smectite, 2–23% kaolinite and 6–10% illite.

The highest swelling stress and strain were obtained from the claystone samples. Then, it was followed by marl and clayey limestone, respectively. The presence of highly swelling minerals content (smectite) in the XRD analysis supports the swelling experiments' results.

When the slope stability problems at Gumuspinar region and the uniaxial swelling tests are evaluated together, the cause of sliding forces or increasing sliding forces due to high swelling potential rocks were expected. The most important factor that led to the slope failure and swelling of rocks is water. The presence of water causes swelling of rocks and an increase in pore water pressure. The slope failure and slime occurrence resulted from the rocks swelling were formed after the rainfall. The pit filled with water after rainfall. Direskeneli (2007) was stated that in the case of rocks contacted with water, the underground water level is more effective than rainfall and snow.

5 RESULTS

According to swelling experiments and mineralogical analysis, the claystone, clayey limestone and marl at Gumuspinar region, TKİ Bursa (Orhaneli) Lignite Enterprises have high swelling characteristics and smectite content. The swelled rocks were found to

be the agent to trigger the slope failure and important parameters to take into account. The accumulated water in the pit can be discharged out of the pit on time with an effective water control management and it is required to determine the slope angle and height by slope analysis.

REFERENCES

Bilir, M.E., Sari, Y.D., Muftuoglu, Y.V. & Donmez, S. 2012. Clay content effects on triaxial swelling characteristics of clay-bearing samples. *Energy Education Science and Technology Part A: Energy Science and Research* 29(2): 837–850.

Direskeneli, H. 2007. Orhaneli mine. Energy Review 9: 5–11.

Esenlik, S., Karayigit, A.I., Bulut, Y., Querol, X., Alastuey, A. & Font, O. 2006. Element behavior during combustion in coal-fired Orhaneli power plant, Bursa-Turkey. *Geologica Acta* 4(4): 439–449.

Gundogdu, M.N.G. 1982. *Geological, Mineralogical and Geochemical Investigation of the Neogeneagend Bigadic Sedimentary Basin.* PhD Thesis, Department of Geological Engineering, Hacettepe University, Ankara, Turkey (in Turkish).

ISRM, 1979. Suggested methods for determining water content, porosity, density, absorption and related properties and swelling and slake-durability index properties. *International Journal of Rock Mechanics and Mining Science & Geomechanics Abstracts* 16(2): 141–156.

ISRM, 1989. Suggested methods for laboratory testing of argillaceous swelling rocks. *International Journal of Rock Mechanics and Mining Science & Geomechanics Abstracts* 26(5): 415–426.

Nilsen, B. & Ballou, B.J. 2006. Stability problems and rock support at the Tellnes open pit mine, Norway. *The South African Institute of Mining and Metallurgy International Symposium on Stability of Rocks Slopes:* 155–165.

Tabrizian, M.G. 1989. *Examination of Three-Dimensional Swelling Characteristics and Engineering Properties of Goynuk Floor Claystone*. M.Sc. Thesis, Hacettepe Univ, Ankara, (in Turkish).

Temel, A., & Gundogdu, M.N, 1996. Zeolite occurences and erionite-mesothelioma relationship in Cappadocia region, Central Anatolia, Turkey. *Mineralium Deposita.* 31, 539–547.

Yesil, M.M. 1991. *Determination of Three Dimensional Swelling Characteristics of Clay Bearing Rocks.* Ph.D. Thesis, Middle East Technical University, Ankara, Turkey.

This page intentionally left blank

Rock Mechanics for Resources, Energy and Environment – Kwaśniewski & Łydżba (eds)
© 2013 Taylor & Francis Group, London, ISBN 978-1-138-00080-3

The role of shear surface geometry in the definition of deep-seated gravitational slope deformation thresholds

D. Brambilla, L. Longoni, M. Papini, D. Arosio & L. Zanzi
Dica, Politecnico di Milano, Milano, Italy

ABSTRACT: Deep-Seated Gravitational Slope Deformations (DSGSD) often involve complex kinematic behaviors that may vary spatially and temporally. The Alpine area counts several DSGSDs involving volumes of millions of cubic meters. In this paper we present the case study of Spriana landslide, a common example of DSGSD located in the North of Italy. Geological, geophysical and topographic investigations have been combined to develop an accurate physical model of the slope. However, some issues still need to be tackled and the definition of a reliable triggering threshold is yet a challenge. Our work focuses on the importance of the shear surface geometric features for threshold definition. We performed several 3D numerical simulations addressing the definition of groundwater table critical level. We believe our findings may improve the early warning system of Spriana landslide and we think that our approach should be used to address other complex deep seated gravitational slope deformations.

1 INTRODUCTION

Deep-seated gravitational slope deformations, also known as DSGSD, are common structures that affect mountains chains mainly as a consequence of glacial retirement after the last ice age. The scientific community has widely studied DSGSDs (Bruckl & Parotidis 2005, Guglielmi & Cappa 2010, Gutierrez-Santolalla 2005) focusing on predisposing causes of DSGSDs and on future evolution (Chemenda et al. 2009, Discenza et al. 2011). The Alpine area counts several DSGSDs that threat directly important infrastructures or villages. In Lombardy region there are a number of monitored DSGSDs i.e.: Bindo landslide, Mount Cortafò, Mount Legnoncino, Mount Piazzo, Mount Letè, Mount Ruinon and Spriana landslide. Even if DSGSDs are common in Alps and pose a serious threat to human settlements, evaluating the possibility of a reactivation is still a challenge. It is necessary to better understand predisposing and triggering causes of DSGSDs to improve accuracy in landslide prediction. The starting point for the analysis of these events deals with the definition of an equivalent physical model of the DSGSD. As a matter of fact, the model plays a key role in thresholds assessment useful for an Early Warning System. An effective monitoring system is the unique reliable way to manage landslides of this extension and volume (several millions of cubic meters). Our work focuses on a DSGSD located in the North of Italy. The authors present the case study of Spriana landslide aiming to assess alarm and pre-alarm thresholds; the process will be shown in each of its steps, focusing on the role of complex shear surfaces.

2 SPRIANA LANDSLIDE

2.1 *Location and historical data*

Spriana is a little village in Valmalenco, in the north of Italy, about 120 km north of Milan. A huge landslide is located on the hydrographical left slope of the valley. The first evidences about movements in this area can be dated to 1910. Further studies showed that during exceptional rain periods some movements were registered in the two villages, Piazzo and Cucchi, that lay directly on the landslide body. The activity continued with extensive displacement all over the area that led in 1961 to evacuate both Piazzo and Cucchi, which nowadays are completely abandoned. The period of major displacements was between 1977 and 1983 when new shallow slides detached from the slope. The landslide reactivated also in 2001 after a period of intense rainfalls and snow melt; this reactivation was completely measured by the monitoring system creating an useful database for successive analysis.

Actually Spriana landslide threats directly just few buildings in the valley but the real risk is mainly linked to a dam break. Indeed, the landslide body may occlude the river, generating a natural dam. The collapse of this dam could cause a lot of damages and victims downstream. As a matter of fact the real risk associated with this landslide is a flood for Sondrio city due to the collapse of the natural dam.

2.2 *Geology and geomorphology of the landslide*

Spriana landslide is situated on the hydrographical left of Mallero river, in the lower part of Valmalenco near

to the town of Sondrio. The flanks of the slide are identified by two minor valleys called Val Bedoglio at the north side and Val Calchera at the south one. This slope is the result of glacier and tectonic activity. The area was covered by glaciers during last ice age, 10,000 BC, that moulded the valley in the typical U shape. Then the Mallero river eroded the valley bottom and modeled the lower part in a V shape causing very steep slopes. Anyhow the river is not eroding directly the landslide foot. The local geology involves mainly Mount Canale gneiss lithology with micaschist intrusion. The surface is covered by a thick layer of debris and the slope is steep with a mean angle of 37°. Geomorphological surveys detected the presence of several faults. One of the most important for the slope is a quite vertical one, located at 1400 m asl, that acts as the crown of the landslide.

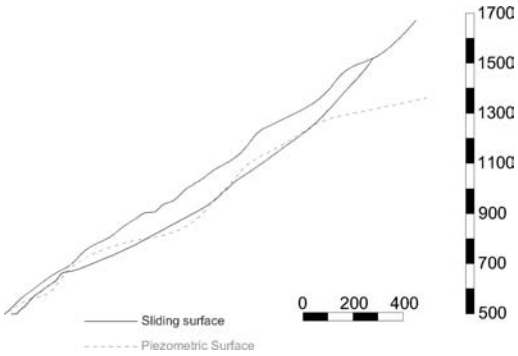


Figure 1. Spriana landslide conceptual section.

2.3 *Geological surveys*

A campaign of geological surveys was set up in the early nineties to investigate the slope condition. Twenty boreholes with continuous coring were drilled into the landslide body and equipped with piezometers and inclinometers. In addition an exploration tunnel was built to allow direct analysis of landslide body and shear surfaces. The results show extremely altered and heavily fractured rock mass; indeed rock quality designation (RQD) mean value is near to zero. Moreover the samples indicate the 50% of clasts with a diameter between 0 and 20 mm. The bed rock, massive gneiss, is in depth inside the slope, between 100 and 120 meters from surface. The foot of the slope is located at 750 m asl and this hypothesis is validated by the presence of perennial springs (Figure 1 and 2). Piezometers prove the presence of underground water located just over the foot of the landslide at 900 m asl. Unfortunately the piezometers did not allow to completely understand the dynamic of groundwater, despite that the presence of a complex groundwater system was confirmed also by other studies. Probably, a confined aquifer is present in the lower part of the slope, under 900 m asl, while an unconfined one develops above the surface of rupture especially during heavy rain falls. Another important features of the slope regards faults and joints. Indeed, the slope is rich in fault rocks. In addition to the quite vertical fault, that act as a crown, the southern side of the shear surface probably lies along a fault with an orientation varying from 255° to 265° for dip direction and from 28° to 32° for dip (fig. 3). Instead, as stated by other authors (Belloni & Gandolfo 1997) the north side of the shear surface is a plane of weakness, due to glacial retirement. This surface has a mean attitude varying from 175° to 185° for dip direction and from 28° to 32° for dip (Fig. 3). The complexity of this

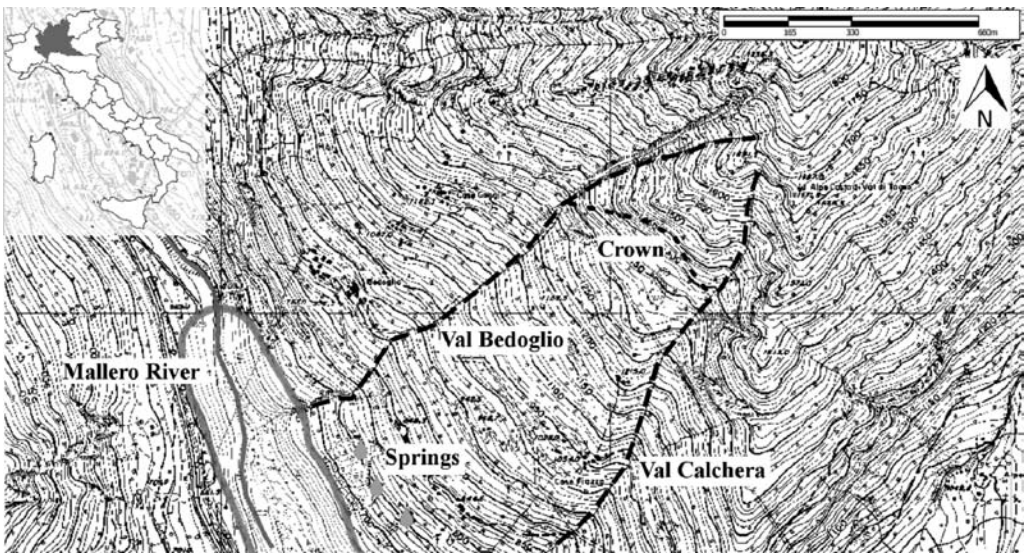


Figure 2. Spriana map with main features highlighted.

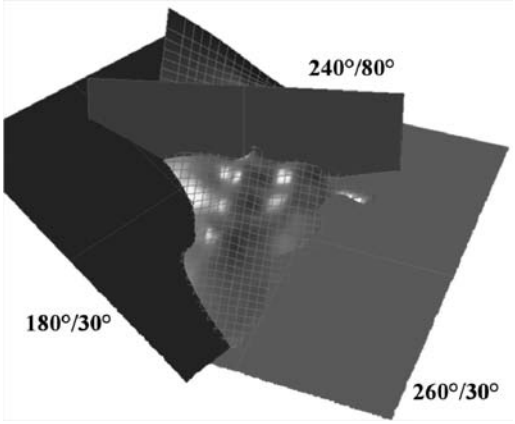


Figure 3. Faults and weakness plane attitudes.

landslide is proved by various physical model reconstruction available in literature. For instance, Belloni & Gandolfo (1997) defined a unique continuous surface of rupture. Despite that, the same authors recognized the need of new investigations in order to better characterized the shear surface. Therefore, new investigations were set up to deeply understand the slope behavior. After that, Papini et al. (2005) recognized the presence of a complex shear surface of rupture due to the intersection of fault and a weak plane. Of course, these planes are characterized by various geomechanical properties due to the different genesis. The actual physical model of the slope is depicted in Figure 3.

3 NUMERICAL MODEL

Once the geometrical and the geomechanical properties were defined, several simulation were performed in order to define suitable alarm and pre-alarm thresholds for Spriana landslide. Three Distinct Element code (3DEC) by Itasca Ltd was chosen for modeling Spriana landslide. 3DEC is a distinct element code, proposed by Cundall et al (1988), designed to explicitly include interactions between different blocks (along joints), coupled with a finite element analysis of the single blocks. The model has been built starting from a simplified topography and adding the three main structural features: the two faults and the weakness plane as shown in Figure 3. The big number of specimens allows to better define material properties. The authors performed several simulations, focusing on the role of geometry, because bias in plane attitudes will create sensible differences in stability evaluation (Kalenchuck et al. 2012). In this paper, two different models are presented. The first one showing the 1997 physical model defined by Belloni & Gandolfo, characterized by a continuum surface of rupture. The second one reproducing the 2005 hypothesis where the landslide body is wedge shaped due to the presence of a complex shear surface, characterized by the presence of a fault and weak plane. This

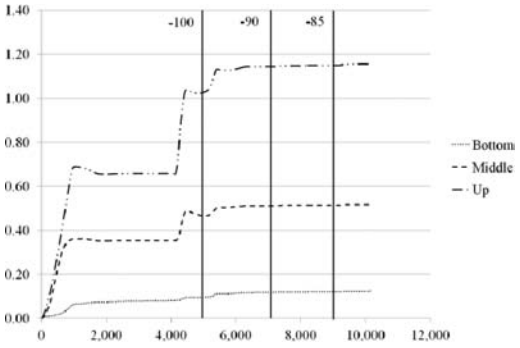


Figure 4. Continuum case displacements [m].

last model has been tested in 5 different configurations considering the range value of the attitudes of the two planes. The authors want to investigate how little change in shear surface geometry may affect the thresholds evaluation. For each model several hydrogeological conditions (groundwater tables) were tested by the use of 3DEC.

3.1 *1997 model*

This model was tested to demonstrate how the uncertainty in shear surface knowledge may affect the final outcomes. According to 1997 interpretation, the fault and the weak plane are not included in this model. Water table was added to the numerical simulations, starting from the data recorded by the piezometer installed next to the exploration tunnel at 1050 m asl. Normally the water level is about −100 m from the surface and does not change much during year except for intense rainfalls and snow-melt periods. In the simulations wa-ter level was raised by 2.5 m each step until −85 m; at these level complete collapse is expected. This value surely exceeds the level recorded during 2001 reactivation. Figure 4 depicted the displacements of three control points, showing the outcomes of the models associated with the water level. The control points are disposed one at the top, one in the middle and one at the foot of the slide. The result shows that this physical model is not reliable to reproduce the behavior of Spriana landslide. As a matter of fact, the model show only minor displacements that do not agree with the monitoring measures collected over the years.

3.2 *Wedge model*

The second model is built according to Papini et al 2005 investigations. The model has been tested in five different configurations varying the dip angle of the weak plane and fault of $+\backslash-2°$ and dip direction of $+\backslash-5°$. The different configurations are reported in Table 1. Case 1 is characterized by mean attitude values and its results reported in Figure 5.

In order to comprehend the behaviour of the wedge model two graphs are reported. The first one (Fig. 6)

deals with the results of each model, changing the groundwater level. For this graph, the control point located in the middle of the landslide body was taking into account. The second picture (Fig. 7) focuses on the behaviour of the entire slope (all control points were analyzed), considering only one hydro-geological condition. naturally the same analysis were performed also for the other piezometric levels. This graph shows that all models have a similar trend: the major displacements are located in the bottom part of the slope. As showed in this graph, the case 4 is not considered because this particular piezometric level leads to the collapse of the case 4.

Table 1. Attitude of fault and weakness plane in different model configuration.

Case	Fault Attitude	Weak Plane attitude
1	260°/30°	180°/30°
2	255°/30°	185°/30°
3	265°/30°	175°/30°
4	260°/32°	180°/32°
5	260°/28°	180°/28°

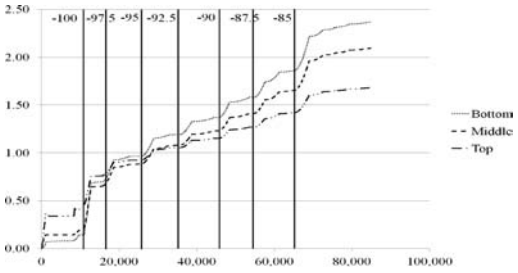


Figure 5. Displacements case 1 [m].

4 DISCUSSION

The outcomes of the models showed the importance of shear surface characterization in threshold definition. In particular, all models stated the importance in dip and dip direction of the shear surface in slope stability. Among the models, the 2001 event was better reproduced by the case 1. In this configuration a

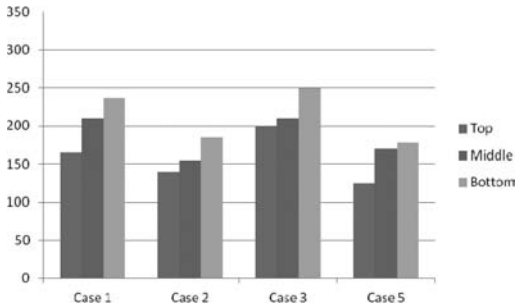


Figure 7. Maximum displacements [cm] of control points with groundwater at −87.5 meters.

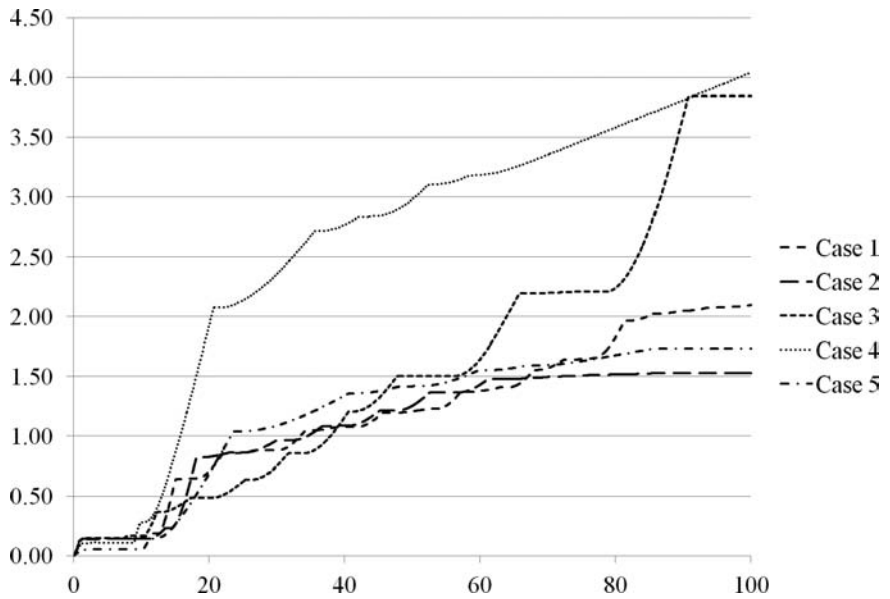


Figure 6. Displacements [m] comparison; lines represent displacements of the middle point while increasing water level up to −87.5 m for case 1,2,3,5 and −95 for case 4.

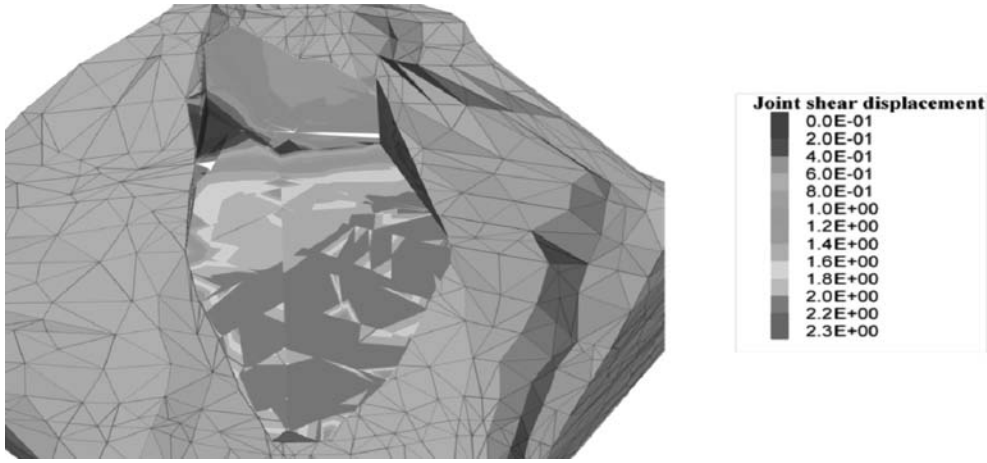


Figure 8. Landslide body is cut away to show the displacements on the joints [m].

groundwater table increment produces an effect on surface displacements comparable with the monitoring system. Moreover, as depicted in figure 8, the model one shows more displacements on the south side of the slope, where the surface of rupture corresponds to the fault. This behavior is also validated by the collected data of the inclinometers. Considering this model, it is possible to state that an increasing of 15 m compared with the normal value (100 m a.s.l). may trigger a collapse.

The second step of this paper deals with thresholds definition. Unfortunately, nowadays there are several methodologies to predict landslide events but not proved approaches for alarm and pre-alarm evaluation are available. Starting with the case 1, validated by the back analysis of the event of 2001, the limit equilibrium takes place with a groundwater level at −85 m from surface. Considering this value, the pre-alarm is defined at −95 m; instead, the alarm at −87.5 m. This analysis can be repeated for each of the five cases defining a range of values for thresholds. Finally, pre alarm threshold is ranging between −97.5 m and −90 m, while alarm threshold ranges between −90 m and −82.5 m. The pre-alarm and alarm are defined considering the role of time. Indeed, people should be alerted with enough time in order to organize the evacuation. In particular, the alarm situation should be defined evaluating the time of evacuation, the time of the emergency management but also the importance of the generation of real alarm. As a matter of fact, the false alarms have negative consequences on people.

5 CONCLUSIONS

The authors propose a method to assess hazard level for DSGSDs. DSGSDs usually extend over a considerable area and their features can vary spatially leading to the coexistence of different geometries and kinematics in the same landslide, making it difficult to thoroughly comprehend these mass movements. These unstable slopes usually comprise faults, weak areas and are sometimes divided into several blocks with different geomechanical properties, requiring demanding survey campaigns to acquire needed data. The Spriana case is chosen to show how a deep knowledge of the landslide is needed when dealing with complex landslides, whose kinematic is not clear. Moreover, this case study was chosen because it is characterized by the presence of several factors that affected the stability of the slope. The huge amount of geological and geophysical measures collected on the Spriana landslide, joined with the data collected through several years of monitoring system, allow to define a representative model, close to reality. Despite that, the uncertainty intrinsic in geological problems continue to affect the slope analysis. For instance, in this paper, the definition of the shear surface plays a key role in the stability assessment and, as stated by several numerical simulations, the geometric uncertainties strongly affect the final outcomes. A bias in geometric definition will influence the kinematic analysis of the landslide (planar failure versus wedge failure) and also the thresholds definition.

The approach used for Spriana landslide is here reported:

- define the best physical model with the available information. During this step the uncertainty must be highlighted (for instance for Spriana landslide the geometric features of the two surfaces of ruptures were taken into account).
- define the best numerical code, able to analyze the slope stability.
- generate several models that take into account all uncertainty of the problem. For Spriana, the complexity lies in the shear surface of rupture. Maybe other landslides may focus on other aspects.
- where possible, it is useful to perform a back analysis or try to validate the numerical models with a comparison of the monitoring system.

– define the same rules for the definition of thresholds and apply them to all models.
– finally a range of values of thresholds will be available in order to manage the landslide emergency.

The Spriana landslide outcomes, reported in graph 6 and 7, show how the general trend of the slope is the same but the "critical value" changes. For a reliable emergency management all these values must be considered. Then, it will be a political decision to define if considered the upper or the lower value. This decision depends on other conditions. At the end the problem is a cost benefit analysis in which it is of paramount importance taking into account several parameters: landslide volume, landslide complexity, the risk elements, the time of the emergency (depending on the morphology of the slope and on the forces available on that territory), the possible damages, the cost on new investigations and so on. Where the situation is too critical and it is not possible to take any decision regarding the critical value for evacuation, new investigations may be performed in order to improve the assessment of the slope (and, consequently, to decrease the uncertainty of the problem). The procedure of emergency is really complex, especially for natural disasters difficult to forecast. Therefore the definition of an efficient strategy is of paramount importance. The EWS is the best solution for landslide of this extension, but as stated in this paragraph there are many parameters to consider to choose the appropriate thresholds. Our approach try to make all steps transparent and, therefore, easily to update.

We believe our findings may improve the early warning system of Spriana landslide and we think that our approach should be used to address other complex deep seated gravitational slope deformations.

REFERENCES

Belloni, L. & Gandolfo, M. 1997. La frana di Spriana. Geologia tecnica & ambientale, vol. 7.

Brückl, E. & Parotidis. M. 2005. Prediction of Slope Instabilities due to Deep-Seated Gravitational Creep. *Natural Hazards and Earth System Science* 5 (2): 155–172.

Chemenda, A.I., Bois, T., Bouissou, S. & Tric, E. 2009. Numerical Modelling of the Gravity-Induced Destabilization of a Slope: The Example of the La Clapière Landslide, Southern France. *Geomorphology* 109 (3–4): 86–93.

Crosta, G.B., Chen, H. & Lee, C.F.. 2004. Replay of the 1987 Val Pola Landslide, Italian Alps. *Geomorphology* 60 (1–2): 127–146.

Cundall, P.A. 1988. Formulation of a Three-Dimensional Distinct Element model—Part I. A Scheme to Detect and Represent Contacts in a System Composed of Many Polyhedral Blocks. *International Journal of Rock Mechanics and Mining Sciences & Geomechanics Abstracts* 25 (3): 107–116.

Discenza, M.E., Esposito, C., Martino, S., Petitta, M., Prestininzi, A. & Mugnozza, G.S. 2011. The Gravitational Slope Deformation of Mt. Rocchetta Ridge (Central Apennines, Italy): Geological-Evolutionary Model and Numerical Analysis. *Bulletin of Engineering Geology and the Environment* 70 (4): 559–575.

Guglielmi, Y. & Cappa, F. 2010. Regional-Scale Relief Evolution and Large Landslides: Insights from Geomechanical Analyses in the Tinée Valley (Southern French Alps). *Geomorphology* 117 (1–2): 121–129.

Gutiérrez-Santolalla, F., Acosta, E., Ríos, S., Guerrero, J. & Lucha, P. 2005. Geomorphology and Geochronology of Sackung Features (Uphill-Facing Scarps) in the Central Spanish Pyrenees. *Geomorphology* 69 (1–4): 298–314.

Kalenchuk, K.S., Diederichs, M.S. & Hutchinson, D.J. 2012. Three dimensional numerical simulations of the Downie Slide to test the influence of shear surface geometry and heterogeneous shear zone stiffness. Comput Geosci 16:21–38.

Papini, M., Mannucci, G., Longoni, L. & Caimi, A. 2005. Il ruolo delle rocce deboli nella definizione del modello fisico della frana di Spriana. Quaderni di Geologia Applicata Vol 12 (2): 57–70.

Rock Mechanics for Resources, Energy and Environment – Kwaśniewski & Łydżba (eds)
© 2013 Taylor & Francis Group, London, ISBN 978-1-138-00080-3

Large scale field tests for slope stabilizations made with flexible facings

M. Cala
AGH University of Science and Technology, Kraków, Poland

M. Stolz, P. Baraniak & A. Rist
Bern University of Applied Sciences, Burgdorf, Switzerland

A. Roduner
Geobrugg AG, Romanshorn, Switzerland

ABSTRACT: Flexible slope stabilization systems made from wire meshes in combination with nailing are widely used in practice to stabilize soil and rock slopes (Fig. 1). They are economical solutions and a good alternative to measures based on rigid concrete liner walls or massive supporting structures. Apart from designs using conventional steel wire, meshes from high-tensile steel wire are now also available on the market. The latest can absorb substantially higher forces and transfer them onto the nailing. Special concepts have been developed for the dimensioning of flexible surface stabilization systems for use on steep slopes in more or less homogeneous soil or heavily weathered loosened rock, but also on fissured and layered rock in which the bodies liable to break out are determined by fissure and layer surfaces. Stabilizations implemented in soil and rock, with and without vegetated face, confirm that these measures are suitable for practical application (Cała, et al. 2012). The research work presented in this paper explains the latest verification of the existing dimensioning concept for superficial slope protection system based on test results coming from a large-scale field test setup. Thereby the influence of properties of the facing as well as deformations under loading and forces on the nails are tested and the results will be presented.

1 INTRODUCTION

Various aspects of slope stability are the subjects of study of many fields of engineering such as road and rail engineering, mining. There are numerous methods for stabilizing slopes that can be chosen depending on the scale of the occurrence, technical conditions and terrain characteristics. To enable the best possible solution it is necessary to take into consideration several variables that could impact the effectiveness of such protection. At the same time the technical and economic aspects of the proposed construction need to be taken into account. Another aspect to be considered is whether the construction is environmentally friendly. It is also important for the slope stabilization to ensure not only its global but also superficial stability.

In many cases the optimum solution is to use nailing in combination with the flexible facing systems. It ensures global stability (nailing) and protects the slope against the possible local instabilities and rockfalls. High effectiveness of such solutions was proved in the recent years' installations.

It can be claimed that the aspects of nailing are relatively well known, whereas, in the case of slope facing there are still many questions. In order to understand better how the nailing and slope facing work together and what the role of mesh is in bearing and transferring the forces to the nailing system, first results of the full scale tests, setup and equipment that was used will be presented in this article.



Figure 1. Example of slope stabilization with the use of nails and flexible facing, Source: Geobrugg Polska Sp. z o.o.

The entire project is supported with CTI Swiss funds and lead by Bern University of Applied Sciences with cooperation with Geobrugg AG and AGH University of Science and Technology.

2 OBJECTIVES

The objective of the full scale tests is to investigate the nature of failure in the superficial layer of slopes stabilized by nailing and steel mesh system. The information gathered will be used as the basis for the creation of the overall concept measuring such occurrences, what will enable its further optimization. The data will also allow for the creation and calibration of the calculation model which is based on the 3D numerical methods. Until now, only 2D numerical calculations concerning interaction between soil, nails and mesh were performed (Cała & Kowalski 2008).

In the full scale tests it is planned to investigate a number of different types of steel meshes in the same testing setup. Several types of soil samples will be used and the arrangement of nails will vary. The tests are to be conducted by changing the inclination angle of the box. This is done by raising one of its sides while the opposite side is positioned on the concrete panel. The change of inclination should be done continuously and gradually at 5-degree intervals until one of the system's elements fails or until it reaches the maximum inclination of 85 degrees.

Recorded during the tests are: the forces and the moments of forces, forces on the mesh and in the connections between the mesh and nails as well as failures of the mesh and nails when pressured with the sliding soil.

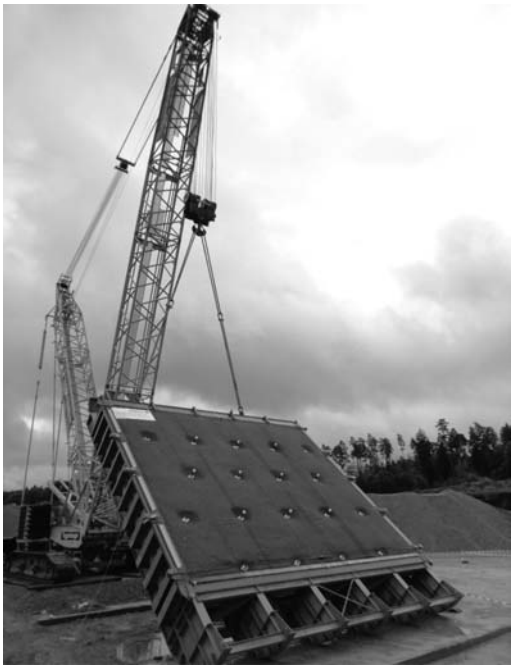


Figure 2. Experimental setup for the full scale test of nails and flexible facing combination.

3 FULL SCALE TESTS

The first series of tests was conducted in Winterthur, Switzerland, at the end of 2012 and beginning of 2013. The aim of the tests was to check whether the tests objectives were correct and to ensure the settings would imitate the real slopes conditions in the best possible way.

Thanks to the initial tests also the methodology and the process of conducted tests could be improved and the choice of measurement equipment could be more adequate.

3.1 *Test set-up*

The experimental setup allowed to physically simulate a slope section in unconsolidated soil reinforced with a flexible facing and untensioned anchors (Fig. 2). Therefore, soil material was filled in a large inclinable box and covered by a flexible facing which was tightened onto the surface by anchors installed at the floor of the box and fastened at the edges of the box by wire ropes. Then the box was lifted at one end by a crane while the other end was unrolled on round skids bearing on a concrete base plate. The inclinable box was a rigid steel construction whose floor and inner walls were faced with wooden planks. The inner width, length and filling height of the box were 12.08 m, 9.99 m and 1.20 m, respectively. These dimensions resulted in a total volume of 144.82 m^3. This also means that, depending on the soil, total weight of 300 tons of fill-up material might be expected. In order to ensure that the failure plain developed within the soil but not between the soil and the floor of the box, squared timber bars of 60 mm width and 30 mm height were fastened across the wooden floor at a distance of 500 mm.

In the experimental setup anchors of the type GEWI with 28 mm diameter were used. In order to simulate the injection of the grout around the nails, which in reality results in pile skin friction, steel bars for the experimental setup were prefabricated with a mantle of grout filled into a surrounding fluted PVC-tube with 100 mm diameter. This grout mantle started 240 mm below the upper end of the steel bar in order to fasten the spike plates by a screw nut. At the bottom part the nail was welded to the steel plate (240 mm × 240 mm) which was in the next step screwed onto a bigger steel plate (490 mm × 700 mm) which was finally fastened to one of the steel beams under the wooden floor of the box. Due to various holes in the bigger steel plates the nail positions could be varied allowing their distance to be chosen freely within a large range. Nails pattern, type and diameter were chosen as for applications of flexible facings in reality. It is important to note that during the testing phase nails were installed the way that the rows of nails were offset to each other by half of a horizontal nails distance. This means that the maximum possible local body liable to break out between the individual nails was limited to a width "a" and a length of 2 × "b" as shown in Figure 3 (Geobrugg AG 2011).

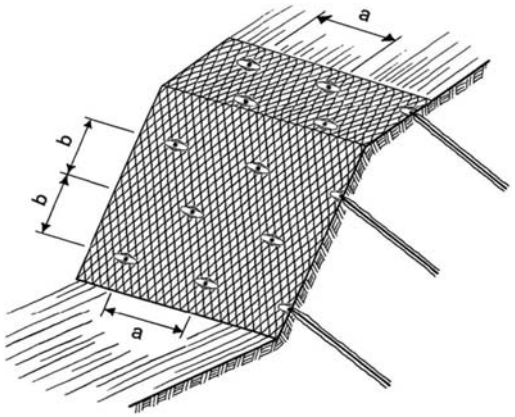


Figure 3. Arrangement of the nails with an offset.

Table 1. Parameters of fill-up materials.

Soil type	Grain size [mm]	Friction angle [°]	Cohesion [kPa]	Bulk density [kg/m^3]
Round gravel	16/32	33	0	1670
Recycling gravel	0/63	38	0	1800

In the final version of the experimental setup the flexible facing was fastened along the four margins of the box by means of wire ropes, strong enough to bear all expected forces (top rope diameter of 22 mm and rapture load of 305 kN, on both sides and at the bottom a 14 mm wire rope with a breaking force of 91 kN). The top boundary rope was fastened to the steel frame in the way simulating additional row of upper nails. The bottom boundary rope was fastened to the lowest row of the nails in order to imitate the real boundary conditions of protected continuous slope. To avoid slipping off the fill-up material through the individual mesh of flexible facing, geotextile with smaller openings was used. This was also to simulate commonly used erosion control mat under the steel mesh.

For the first three tests of the series round gravel (16/32 mm) was used as a fill-up material. It was changed into recycling gravel (0/63 mm) for the following tests. The parameters of both materials are presented in Table 1. The recycling gravel was compacted by means of a vibrating plate at 0.6 m and on the top surface. The round gravel only was only be compacted at the surface. In the top layer around the nail heads small depressions were formed in order to allow mesh to be pretensioned.

3.2 *Response variables and instrumentation*

As response variables (1) the forces in the upper and lower horizontal wire ropes, (2) the downslope displacement of one anchor head, (3) the surface deformation of the artificial slope in three-dimensions, as well as (4) the inclination angle at failure of the protection system were measured. The forces in the wire ropes were measured by means of load cells (typ: strain gauges on aluminum plates, measuring range until max. 200 kN, resolution $\leq$50 Hertz in the tests 0.5–2 Hertz). The downslope displacement was measured by pull-cable encoder (rope potentiometer type CD115-3000-R01K-L15-K01, measuring range 0–3'000 mm, resolution depending on reporting device) which was installed in stable position onto the steel frame and the cable itself was attached to the nail head in the second row from the top. This allowed to measure nail head deformation without an influence from the boundaries of the box or from the occurring deformation.

The load-cells and the pull-cable encoder measured continuously throughout the whole test. Received data were transferred and formatted by a measuring amplifier (HBM, Spider 8) and finally stored on a laptop. The electrical cables from the sensors to the amplifier had to be protected from the consequences of potential slope failures and superficial rolling and saltation of grains by means of an adequate cable guiding. Furthermore, the cables' length had to account for the increasing distance between the sensors and the amplifier when inclining the box and thus to prevent rupture.

The three-dimensional surface deformations of the slope were measured by the Terradata AG company at every inclination step using a laser-scanner (Riegl VZ-400). The angular horizontal and vertical measuring resolution was set to 0.02 degrees resulting in a spatial resolution between 7 mm and 10 mm for the given scanning distance between 20 m and 30 m. Higher resolutions were intentionally avoided in order to limit the scanning time and the amount of data.

To measure displacement of the nail heads by means of laser scanning, white balls with a diameter of $\sim$100 mm were placed on top of the nails for better resolution for the laser-scanner.

The inclination angle of the artificial slope was continuously measured during each test by a simple manual goniometer mounted onto one skid at the lower margin of the box and also with the inclination sensor measuring amplifier (HBM Spider 8). By these continuous measurements also the inclination angles at which any part of the artificial slope failed were recorded. Such failures were defined as events of discontinuous movements, namely when the soil grains underneath the flexible facing started to roll, when a complete layer started to slide downslope, when grains started to pass the holes of the mesh in a large volume, when a nail noticeably broke, or when the flexible facing or any other element was damaged.

The load on the crane hook was measured at 30 degrees inclination of the testing box, sporadically also at higher inclinations. This information was mainly important to control that the carrying load did not exceed the crane's limit of 500 tons. However, the

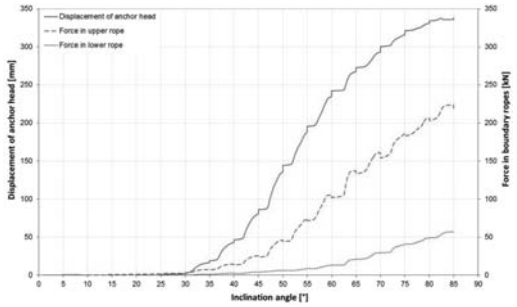


Figure 4. Displacement of equipped anchor head and boundary rope forces depending on inclination.

measurements were also interesting for the result of the tests.

4 TEST RESULTS

At the time of releasing this paper the first series of eight individual tests were performed. Due to the fact that during the first four tests unexpected setup defects were found all tests results were classified as the provisional tests of the equipment. Because the results of the last three tests of the first series have not been analysed yet, in this article only the outcomes of the first liable test (test number 5) are included. It is expected that all the results of series one and series two will be presented soon.

Test no. 5 was carried out with the high tensile strength steel wire mesh (mesh type TECCO 65/3 made of 3 mm diameter wires, steel strength 1770 N/mm^2). The test itself was performed from the initial setup inclination of 0 degrees. However, the first forces in the load cells were measured at the inclination of 30 degrees. This was due to the friction angle of the fill-up material. Starting from that point all inclination changes were performed in assumed intervals of 5 degrees. The original data contains the measured response variables, i.e. the displacement of the nail head as well as the forces in the upper and lower boundary ropes as function of time (Fig. 4).

First deformations of the slope surface and tensioning of the mesh were visible at the inclination of 45 degrees, however, up to this point the measurement showed the displacement of 80 mm of the equipped nail head. At 50 degrees the first slips of the surface were observed close to the lower boundary of the box. At 55 degrees the cracks due to the slips reached halfway between the lowest and the second row of nails. When the slope was inclined to 85 degrees the mesh was elongated further, up to 400 mm, but the slope remained stable and the material was fully kept back without any destruction of installed mesh or nails.

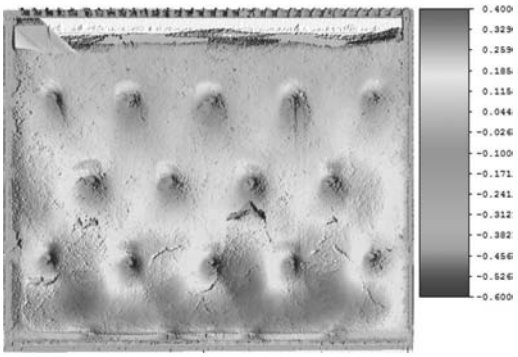


Figure 5. Test 5 – Visualization of the soil surface resulting from laser scanning at 85 degrees. Elevations and depressions relative to the initial planar reference surface are indicated by colors with the corresponding values given in meters. Source: Terradata AG (2012).

Figure 5 shows the final elongation of the mesh reached at the inclination of the slope of 85 degrees.

5 CONCLUSIONS AND OUTLOOK

It can be concluded that the method and setup for flexible slope facing in large scale gives a great opportunity to have better understanding of the nature of superficial slope movements and further improvement of protection measures. It is believed that the following series of experiments will show advantages and limits of application of all tested mesh types. For the future the test setup will be used as a tool for optimization nails grid and flexible facing depending on local ground conditions. These experiments can also be used to check the current stage of calculation methods and as a tool for their improvement as well as the basis for the numerical modelling of the entire complex slope stabilization systems based on nails and flexible facing.

REFERENCES

Cała M., Kowalski M. 2008. Reinforced slope stability analysis with FLAC. Continuum and distinct element numerical modeling in geo-engineering. 1st international FLAC/DEM Symposium : Minneapolis, Minnesota. (eds. R. Hart, Ch. Detournay, P. Cundall) Minneapolis: Itasca Consulting Group, Inc.

Cała, M., Flum D., Roduner A., Rüegger, R., Wartmann, S. 2012. *TECCO Slope Stabilization System and RUVOLUM Dimensioning Method.* Bad Langesalza: Beltz Bad Langesalza GmbH.

Geobrugg AG. 2011. *TECCO Slope Stabilization System Summary of Published Technical Papers 1998–2011.*

Rock Mechanics for Resources, Energy and Environment – Kwaśniewski & Łydżba (eds)
© 2013 Taylor & Francis Group, London, ISBN 978-1-138-00080-3

Application of stochastic methods for the strain and stability analysis of a slope

E. Hrubešová, B. Luňáčková & T. Petřik
Faculty of Civil Engineering, VSB-TU Ostrava, Czech Republic

ABSTRACT: The paper specifies the fundamentals of stochastic simulation Latin Hypercube Sampling Method (LHS) and presents examples of application of this method for the solution of the stress-strain and stability state of the slope. The stochastic simulation methods enable to involve into the calculation the stochastic character of the input parameters. In the first example the stochastic character of shear strength characteristics of soils is considered. The second example takes into account the stochastic character of the basic parameters of dynamic load (frequency and amplitude of the dynamic load) for the solution of dynamic response (stability factor and displacements) of the slope subjected to surface blasting seismic effect. On the basis of the stochastic analysis we can determine the probability of the model response.

1 INTRODUCTION

The stress-strain and stability analysis of the slope is the very often solved problem in the geotechnical practice. For the solution of such problem there can be used many computational methods based on limit equilibrium methods (LEQM) or numerical methods (for example finite element method (FEM)), which more or less reflect the various factors determining the behavior of slope. Predicative power of the modeling results is always fundamentally determined by the reliability of the input data. To increase the predicative power of model results (model response) can be used stochastic simulation methods, which are based on the assumption, that the input values of the model are considered as stochastic variables governed by certain laws of probability. Based on the accepted type of the probability distribution of the input parameters of the model and the type of simulation methods the specific values of input parameters are generated. To determine the appropriate random model responses the series of repeated parametric calculations with the generated input values are carried out. Based on the statistical evaluation of the model responses (stochastic variables) the determination of probability range of response results can be obtained.

2 GENERAL PRINCIPLE OF STOCHASTIC SIMULATION METHODS

The LHS stochastic simulation method enables to reduce the number of necessary parametric calculations (the order of tens calculations are sufficient). The method was described for the first time by McKay et al. (1979) and was further developed by e.g. Iman et al. (1981) and others. The LHS method ranks among the so-called stratified methods, where random realizations of a particular parameter are obtained on the basis of the random selection of intervals, which ensures that the whole range of values of the input parameter being generated is covered (Baecher 2003). The range of values of the distribution function of a given input parameter X_j is divided into N intervals, where N is equal to the number of the repeated parametric calculations made later. Subsequently, an interval number is generated using a uniform probability distribution generator (each interval has therefore the same probability of selection $1/N$). By using random permutations of interval numbers (without repetitions) for each input random parameter we obtain a table of random values of N rows and k columns, where k is the number of the calculation input random parameters. The value of the inverse distribution function, corresponding usually to the middle of a given randomly chosen interval, then determines the random realization of each parameter entering a simulation calculation.

For the purposes of generation using this stochastic simulation method, the GLHS software module was applied. This module, which enables to generate input data with various probability distribution types, was developed at the Department of Geotechnics and Underground Engineering of VSB – Technical University of Ostrava.

3 APPLICATION OF THE LHS METHOD IN A NUMERICAL MODEL FOR EVALUATING THE STABILITY OF A SLOPE

The stochastic simulation method was used to assess the stability situation of the Ujala slope in the village

of Doubrava (the Karvina area, Czech Republic). Both the finite element method (the Plaxis 2D software) and the limit equilibrium method (the Galena software) were used for the calculations. In addition to analyzing the stability response determined directly from the two mentioned calculation methods, also the so-called response surface were determined for both calculation types – the approximation of the original model using a simpler model, which is very significant in terms of reducing the time requirements of simulation methods. In the case solved the response area Y was considered in the form of the first degree polynomial (1):

$$Y = a + \sum_{i=1}^{k} b_i X_i \qquad (1)$$

where X_i, $i = 1, \ldots k$ are the stochastic parameters entering the calculations, a, b_i, $i = 1, \ldots, k$ are the coefficients of polynomial.

The behavior of the rock materials in the model based on the finite element method was described using the Mohr-Coulomb elastic-perfectly plastic constitutive model. The LHS simulation method was applied to the strength characteristics of the soils in the geological profile (determining the stability), the other calculation input characteristics (the geometric characteristics, the deformation characteristics of the soils, the unit weight of the soils) were considered to be deterministic. The quantification itself of the slope stability was then carried out by comparing the active and passive forces in the slope in the case of the application of the limit equilibrium method (Bishop's method) and by applying the strength characteristics reduction method, the so-called φ-c reduction method, in the case of the application of the finite element method.

The slope assessed has a height of 25.5 m and consists of three types of soils. A layer of glacial loams of a depth of 3–5 m is situated near the surface and Miocene layers (upper and bottom) are situated under them. The slope body is divided into three subsections with a different slope. The top part of the slope has a slope of 35°, the inclination of the middle layer is 16°, and the inclination of the bottom part is 7° . The uninclined horizontal groundwater level is localized at a depth of approx. 2.8 m under the glacial loam layer outcrop in the base of the slope (Fig. 1).

The assumption of the normal probability distribution of cohesion and of the friction angle is taken into account and the corresponding parameters of this distribution for the rock types result from the statistical analysis of properties of the soils in the given locality (Table 1). The values of the previously mentioned input parameters, which are not subject to the simulation process, are given in Table 2.

A total of 22 realizations of random values of the strength characteristics of all three rock types in the geological profile of the model were generated using the LHS method (so that6 stochastic input parameters in total enter the model). The scatter of random generated value of cohesion of glacial loam corresponding to normal distribution $N(\mu, \sigma^2) = N(21, 2.8)$ is presented in Figure 2.

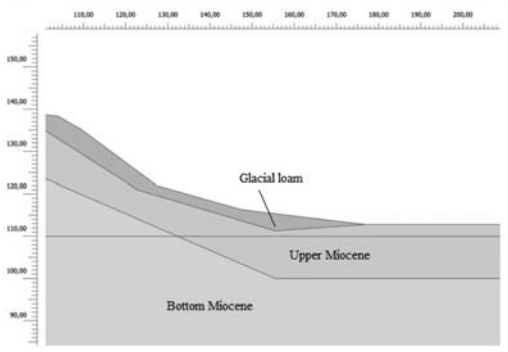


Figure 1. Geometry and the geological profile of the slope Ujala.

Table 1. Parameters of normal distribution function of stochastic input parameters.

	Cohesion		Friction angle	
	μ^* kPa	σ^{**} kPa	μ^* deg	σ^{**} deg
Glacial loam	21	1.7	20	0.7
Upper Miocene	12	1.3	23	1
Bottom Miocene	50	3.3	26	1

*Mean value, **Standard deviation

Table 2. Non-stochastic input parameters.

	Unit weight kN/m^3	Young's modulus MPa	Poisson's ratio
Glacial loam	21	6	0.3
Upper Miocene	22	8	0.25
Bottom Miocene	19.8	20	0.2

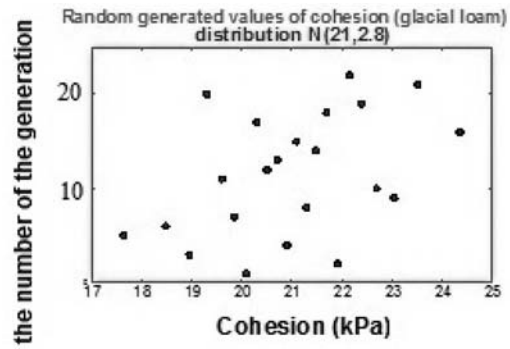


Figure 2. The scatter of random generated value of cohesion (glacial loam).

Table 3. Statistical evaluation of the stability factor.

	Simulation variants				
Statistics	1	2	3	4	5
Mean value	1.21	1.22	1.2	1.2	1.22
Variance	0.0019	0.0019	0.0026	0.0026	0.0018
Percentile 0.05	1.16	1.16	1.14	1.13	1.15
Percentile 0.95	1.27	1.27	1.3	1.3	1.29

On the basis of the 22 simulated calculations the localization and shape on the critical slip surface and the corresponding values of the stability factor on this slip surface were determined. To compare the results of the application of the LHS simulation method with the Monte Carlo method, calculations were further made using the Monte Carlo method with 25,000 randomly generated values of the strength characteristics.

There were analyzed five simulation variants:

- 1-LHS method applied to Galena software (LEQM)
- 2-LHS method applied to Response Surface based on Galena software (LEQM)
- 3-LHS method applied to Plaxis software (FEM)
- 4-LHS method applied to Response Surface based on Plaxis Software (FEM)
- 5-MC method applied to Galena software (LEQM)

The models indicated the independence of the position and shape of the critical slip surface on the randomly generated realizations of the strength characteristics, however, in the case of the application of the finite element method the critical slip surface was deeper to a certain extent in comparison with the results of Bishop's method (see Figure 3).

The results of the statistical evaluation of the stability factor according to the individual previously specified calculation variants are given in Table 3. The box graphs, corresponding to the statistical evaluation, are presented in the Figure 4.

On the basis of the aforementioned quantitative statistical characteristics of the sets corresponding to the individual simulation variants the following conclusions can be formulated:

- A mean value of the stability factor is within a range of 1.2–1.22, differences in individual simulation variants are therefore minimal in practical terms.
- A variance of the stability factor value is in a range of 0.0018–0.0026; the minimum value is reached in the case of variant 5 and the maximum value corresponds to variants 3 and 4 (i.e. the variants based on the calculation of the stability factor using the finite element method).
- There is a 90% probability that the stability factor values in all realized simulation calculations will be within a range of 1.13–1.3.

Despite differences in the computational methods, it results from the comparison of the results that all

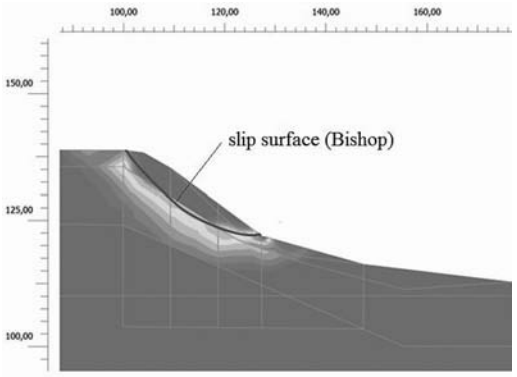


Figure 3. Localization of critical slip surface in the slope.

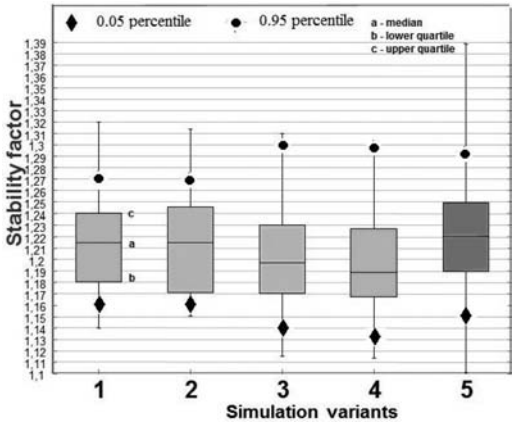


Figure 4. The box graphs corresponding to the statistical evaluation of the simulation variants.

simulation variants 1–5 give, in practical terms, an almost identical stochastic quantification of the stability factor of the analyzed slope body, both in terms of its mean value and the relevant percentiles. It was however necessary to realize all 22 parametric calculations using the relevant response model (the limit equilibrium method and the finite element method) in variants 1 and 3, in the case of variants 2 and 4 it was only 7 parametric calculations to determine the response area (simulation was made on this response area) and in the case of variant 5, 25,000 parametric calculations were made using the Monte Carlo simulation method on the assumption of the model based on Bishop's limit equilibrium method.

4 STOCHASTIC MODELLING OF STRESS-STRAIN AND STABILITY STATE OF SLOPE EXPOSED TO DYNAMIC EFFECTS

The stress-strain state and stability state of brown-coal open cast mine closing slopes exposed to dynamic effects of a surface blast were also analyzed using the LHS stochastic simulation method. In doing so,

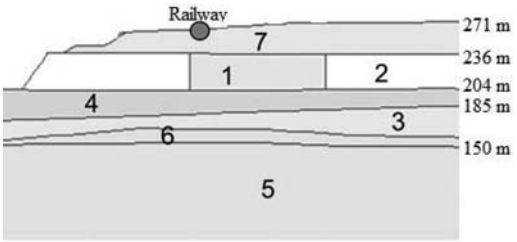


Figure 5. Slope geometry and the geological profile (1-old workings, 2-coal seam, 3-volcanic rocks, 4-subsoil (saturated), 5-gneiss, 6-kaolin gneiss, 7-overburden).

the stress-strain analysis was focused especially on the evaluation of the state in the place of the railway situated at a distance of approx. 50 m from the edge of the slope. The slope height is 55 m. The slope geometry and the soil interfaces in the geological profile are shown in Figure 5.

The descriptive, physical and mechanical properties of the soils are given in Table 4 (γ-unit weight, ν-Poisson's ratio, E-Young's modulus, c-cohesion, φ-friction angle).

The Plaxis dynamic module was used for modeling. To characterize seismic loading, the Plaxis dynamic module requires entering the loading amplitude and frequency, the size of the area in which the considered seismic loading is primarily activated, and the time for which this loading is applied (Hori 2006, Towhata 2008). The amplitude and frequency of dynamic loading in the model were of a stochastic nature and the other input parameters were considered to be deterministic. According to the results of seismic monitoring, the frequency of seismic loading due to a surface blast was in a range of 2–4 Hz and the amplitude of loading was in a range of 400–600 kPa (Kalab & Knejzlik 1999). The simulation generation generated 20 values in total for the two mentioned characteristics of dynamic loading, on the assumption of the normal probability distribution. The seismic loading application time is t = 2 sec, the size of the activation area of seismic loading corresponds to a surface blast activation width of 60 m, and the distance of the source of dynamic loading from the base of the closing slopes in the model varies within a range of 80–430 m. Material damping is not considered in the model (Rayleigh damping parameters are zero).

The Plaxis dynamic module was used for modeling. To characterize seismic loading, the Plaxis dynamic module requires entering the loading amplitude and frequency, the size of the area in which the considered seismic loading is primarily activated, and the time for which this loading is applied (Hori 2006, Towhata 2008). The amplitude and frequency of dynamic loading in the model were of a stochastic nature andthe other input parameters were considered to be deterministic. According to the results of seismic monitoring, the frequency of seismic loading due to a surface blast was in a range of 2–4 Hz and the amplitude of loading was in a range of 400–600 kPa (Kalab & Knejzlik1999). The simulation generation generated 20 values in total for the two mentioned characteristics of dynamic loading, on the assumption of the normal probability distribution. The seismic loading application time is t = 2 sec, the size of the activation area of seismic loading corresponds to a surface blast activation width of 60 m, and the distance of the source of dynamic loading from the base of the closing slopes in the model varies within a range of 80–430 m. Material damping is not considered in the model (Rayleigh damping parameters are zero).

Twenty parametric calculations for evaluating the deformation and stability response of the considered slope body were made for each modeled distance of blasting operations from the base of the closing slopes with the twenty generated values of the frequency and amplitude of loading. The results of the model calculations did not prove any significant effect of the variability of the input characteristics of seismic loading on the stability of the slope body (differences in hundredths only). The variability of the input data influenced more markedly the strain situation in the slope body. By evaluating the basic statistical characteristics of the obtained sets of results – the mean values, the variances and the relevant 5% and 95% percentiles – the range (a, b) in which the values of horizontal u and vertical w displacements in the place of the railway will be determined with a 90% probability – Table 5).

To verify the reliability of the results of the model study on the effect of blasting operations on the stress-strain state of the closing slopes, the modeled results of the vibration velocity were compared with the results of the experimental measurements published in (Kalab 2006). The maximum velocity amplitude, recorded by the seismic station located at a distance of 1 km from

Table 4. Properties of the soil and rock material.

Type	γ kN/m^3	ν	E MPa	c kPa	φ deg
Old workings	8	0.3	5	6	26
Coal seam	11	0.3	50	35	25
Volcanic rocks	19.5	0.3	150	70	25
Subsoil	20	0.3	150	70	23
Gneiss	20	0.3	3000	200	40
Kaolin gneiss	20	0.3	150	70	25
Overburden	17.5	0.3	56	20	12

Table 5. Range of the displacements u, w in the place of railway with 90% probability.

	Unit	330 m*	230 m*	180 m*	130 m*	80 m*
u	mm	(4,3)	(5,4)	(9,8)	(8,5)	(16,14)
w	mm	(8,7)	(11,8)	(21,15)	(21,13)	(40,34)

*Distance of the dynamic source from the toe of the slope

the surface localization of the blast, did not exceed 5 mm.s^{-1} and this corresponds with the results of modeling.

5 CONCLUSIONS

The application of the LHS stochastic simulation method enabled to take the stochastic nature of the selected input characteristics in consideration in computational models. The two illustrative examples documented the major advantage of this simulation method – a reduction of the number of necessary simulation calculations in comparison with the often used Monte Carlo simulation method. This advantage is determining especially when simulation methods are applied in combination with numerical modeling methods. The result of the application of stochastic simulation methods can give an idea of the range in which the analyzed results of modeling will be with a certain probability, which increases the information value of results of mathematical modeling.

ACKNOWLEDGEMENTS

The authors are grateful for support of this work from the Ministry of Education, Youth and Sports of the Czech Republic – student grantSP2013/139 “Increasing the reliability of modeling of technical seismic impact in rock mass using simulation based on LHS method”.

REFERENCES

Baecher, G.B., 2003. *Reliability and Statistics in Geotechnical Engineering.* Chichester: John Wiley.

Hori, M. 2006. *Introduction to Computational Earthquake Engineering*. London: Imperial College Press.

Iman, R.L., Helton, J.C. & Campbell, J.E. 1981. An approach to sensitivity analysis of computer models, Part 1. Introduction, input variable selection and preliminary variable assessment. *Journal of Quality Technology* 13 (3): 174–183.

Kalab, Z. 2006. Measurements of seismic vibrations induced by quarry blasts at the Mostecka basin. *Zeszyty Naukowe Politechniki Śląskiej* 271: 49–58.

Kalab, Z. 2008. *Seismic Measurements in Geotechnics.* Ostrava: VSB - Technical University Ostrava. (in Czech)

Kalab, Z. & Knejzlik, J. 1999. The Influence of Basinal Structures on the Shape of Wave Patterns of Induced Seismic Events: An Example from the North Bohemian Brown Coal Basin. *Exploitation and Utilization of Coal* 74(2):185-190.

McKay, M.D., Beckman, R.J. & Conover, W.J. 1979. A Comparison of Three Methods for Selecting Values of Input Variables in the Analysis of Output from a Computer Code (JSTOR Abstract). *Technometrics (American Statistical Association)* 21 (2): 239–245.

Towhata, I. 2008. *Geotechnical Earthquake Engineering.* Berlin Heidelberg: Springer Verlag.

This page intentionally left blank

Rock Mechanics for Resources, Energy and Environment – Kwaśniewski & Łydżba (eds)
© 2013 Taylor & Francis Group, London, ISBN 978-1-138-00080-3

Physical modeling and simulation of slope failure by means of centrifuge acceleration

S. Kramadibrata, R.K. Wattimena, M.A. Azizi & Y. Wicaksana
Mining Engineering Department, Institut Teknologi Bandung, Indonesia

I.D. Sidi
Civil Engineering Department, Institut Teknologi Bandung, Indonesia

ABSTRACT: Slope stability in open pit mines is an important issue. Most open pit coal mines are located in Kalimantan in which rainfall is very high and as such so is the probability of slope failure. It has been well accepted that slope failure risk consists of probability times consequence of the slope failure. In order to have a study on the consequences of slope failure as a function of various geotechnical parameters, a laboratory scale investigation was conducted. A centrifuge with a diameter of 3.65 m, a load capacity of 3 kN and a maximum rotation of 70 rpm was designed and built in house by the Laboratory of Geomechanics & Mining Equipment of ITB in Indonesia. Dimensional analysis was used to scale down the model from a real slope condition in an open pit coal mine. The material used in this study is consolidated clayey sand with slope heights of 10 cm, slope angles of 45°, 60° and 75°; the centrifugal acceleration were 0.15g, 0.23g, 0.33g; 0.46g, 0.59g, 0.75g, and 0.93g. By running the centrifuge at different levels of rpm and slope dimensions, the volume and mode of the slope failures can be obtained and can be used for the input data for assessing risk analysis of slope stability in an open pit coal mine. In order to confirm the results of the physical modeling tests, numerical modeling using the limit equilibrium method and direct monitoring in the field are also carried out

1 INTRODUCTION

Slope stability is the one of the most important factors in the surface mining operation. The factors affected slope stability are shear strength, rainfall, ground water, blasting intensity, probability of earthquakes, etc. Those parameters should be carefully considered, otherwise, the risk of slope failure will increase. It is well known that slope failure risk consists of probability times consequence of the slope failure.

To study the impact of a slope failure as a function of geotechnical parameters, then a laboratory scale research was conducted. By using a centrifuge that has been built in the laboratory, gravitational acceleration can be modeled with various scenarios. The mode of failure caused by the gravitational acceleration can be clearly investigated and the volume of collapsed material can also be calculated.

By using the centrifugal experimentation, the scenario can be planned to fit the field prototype condition. Small scale experimentation has a lot of advantages to determine failure mechanisms, namely, easily-controllable test conditions, adjustable slope geometry and material used.

In this experiment, a centrifugal test was conducted to evaluate the slope stability due to gravitational acceleration which was represented as *Ng*. The slopes, which were made using clayey-sand material was placed inside a plexiglass box which was located at the end of the centrifuge. It was then spun, gradually increasing in speed so the gravitational acceleration went from 1g to *Ng*.

2 CENTRIFUGE MODELING

Laboratory tests using centrifuge physical modeling has been conducted by some previous researchers such as Hoek (1966), Joseph et al. (1988), Misich (1997), Ling et al. (2009), and others. The test was conducted to study the behavior of a rock mass model both in open pit and underground mines.

The basic principle of modeling is the centrifugal stresses at the same point in the geometry of the prototype and the model should be the same. Bucky (1931) suggested a method to conduct centrifuge physical modeling: "to produce at corresponding points in a small scale model, the same unit stresses that exist in a full scale structure, the weight of the material of the model must be increased in the same ratio that the scale of the model is decreased with respect to the full scale structure. The effect of an increase in weight may be obtained by the use of centrifugal force, the model being placed in a suitable revolving apparatus".

According to Joseph et al. (1988), if the model and prototype are made of materials with identical mechanical properties, then the strains in the model and prototype will also be identical. In other words, if a model with scale L of a prototype is spun at Ng on the centrifuge, then the model's behavior is thought to be similar to the prototype's behavior. To make the statement true, there are three assumptions that are made, namely: 1) the model is a correctly scaled version of the prototype; 2) when the scaled model, subject to an ideal Ng gravity field, behaves like the prototype at 1g; and 3) the centrifuge produces this ideal gravitational field.

3 PHYSICAL AND MECHANICAL PROPERTIES

Physical properties test of the sample was conducted to determine the condition of the material for the experimentation. With an average water content of 13%, it will cause a difference between natural and dry density. It is known that the material has an average natural density of 1380 kg/m^3. Sieve test results indicate that the composition of sand has a larger portion than clay and silt with 55.7%. This supports the information that the tested material is classified as clayey sand.

Direct shear strength test was conducted to determine the mechanical properties of the tested material. Tested material is clayey sand that has undergone a process of compaction. Mechanical properties provide cohesion value (C) at 15.5 kPa and internal friction angle (ϕ) of 41.7°.

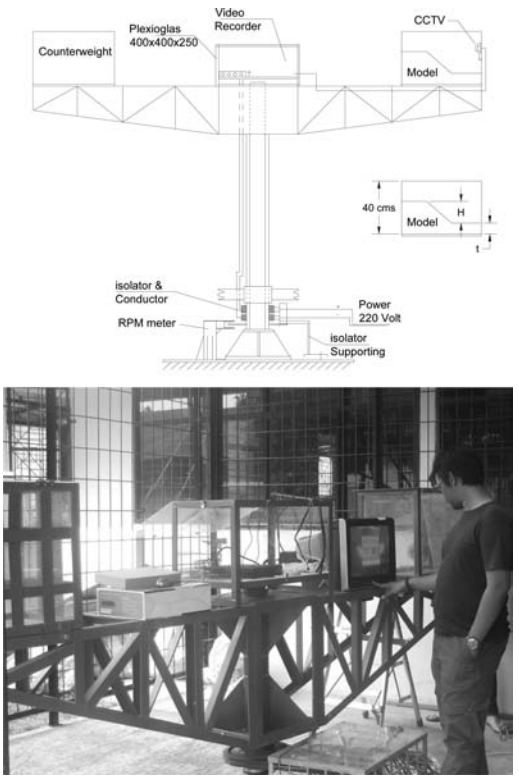


Figure 1. Design of centrifuge equipment.

4 EXPERIMENTATION

Physical modeling of slope stability uses a conventionally compacted clayey sand material with -20 mesh undersize. The slope model dimension is adjusted for various slope angles and two different base heights. The slope model is placed inside the plexiglass box which is located at the end of the centrifuge's swing arm. The slope model direction is set to the opposite direction of the center of rotation. With this scheme, the centrifugal force will be generated parallel to the slope direction.

The test is performed to obtain the value of centrifugal acceleration which acts as the acceleration (a) that represents the gravitational acceleration. Testing is done by rotating the slope model which is generated by the electric motor that is connected to the pulleys with a maximum rotation of 70 rpm. The centrifugal acceleration will be calculated by the equation of rotational motion and also by recording results from the rpm meter which is attached in the central rod of the centrifuge. By using this rpm meter, the angular velocity of the centrifuge can be recorded to reach a desired velocity.

Acceleration on this modeling is derived from the angular velocity with a certain rotational radius. In rotational motion, centrifugal acceleration ($a_{centrifugal}$) can be represented by $\omega^2 R$ which means the value of $a_{centrifugal}$ is depending on the distance of the center of rotation to the point of observation (R/Radius).

The angular velocity (ω) is controlled by the rotation motor control which adjusts the resistance for the actual current. The slope face condition during the test can be monitored in real time by CCTV video camera and can also be recorded.

There are two different base thicknesses (t) of 10 cm and 20 cm which is combined with a variety of slope angles, namely (α_1) 45°, (α_2) 60° and (α_3) 75°. The angular velocities (ω) given are 10 rpm, 12.5 rpm, 15 rpm, 17.5 rpm, 20 rpm, 22.5 rpm and 25 rpm. If they are converted to the acceleration, the range of acceleration is 0.15g–0.93g. The total numbers of experiments are 42 tests with the different scenarios using the constant slope height of 10 cm.

Despite the fact that the maximum ω that can be generated by the centrifuge was 70 rpm, the experiments were carried out only at ω of 25 rpm. This can be understood because the slope model started to fail at an ω of 15 rpm.

An example of an rpm meter result can be shown in Figure 2 and the sketch of slope model is depicted in Figure 3.

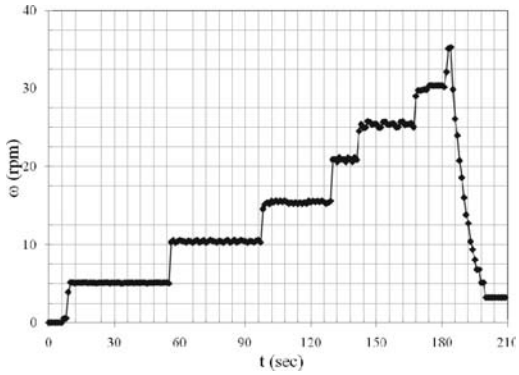


Figure 2. Example of the rpm meter result.

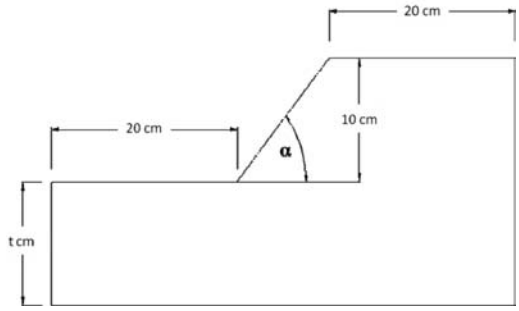


Figure 3. Sketch of the slope model.

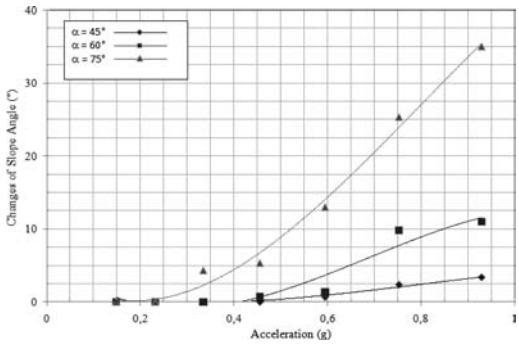


Figure 4. Changes of slope angle vs acceleration at $t = 10$ cm.

5 DISCUSSION

5.1 *Changes in slope angle*

The slope angles were measured both prior as well as subsequent to the testing. Changes of the slope angle in the sides and the center of the model is measured for the average value.

In Figures 4 and 5, it can be clearly seen that the greater the acceleration, the larger the changes in the slope angle. This phenomenon is seen for all scenarios, and is caused by the larger magnitude of the external force for the larger acceleration.

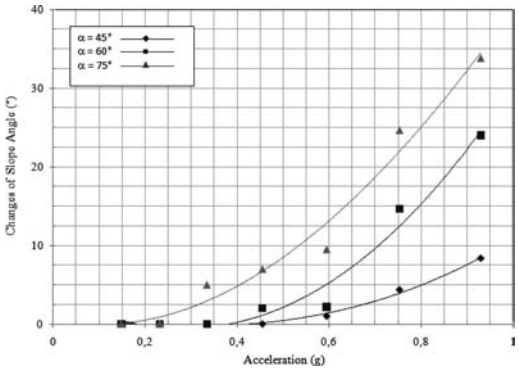


Figure 5. Changes of slope angle vs. acceleration at $t = 20$ cm.

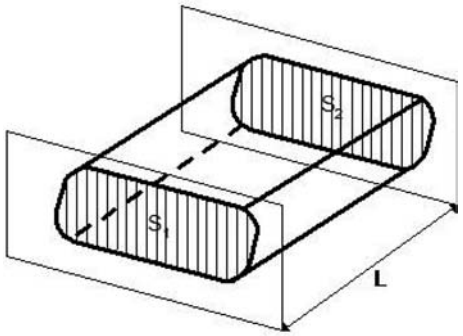


Figure 6. The illustration of volume calculation using cross-sectional method.

It can be seen in Figures 4 and 5 that for the slope angle = 45°, the changes of the slope is around 35° for both $t = 10$ cm and $t = 20$ cm. However, there is a significant difference for slope angles 60° and 75°. In the scenario of $t = 20$ cm, the change is larger than at $t = 10$ cm. This phenomenon might be due to the fact that different geometry has different centre of gravity that then leads to the changing of the point where the acceleration works at, and subsequently change the volume of failed material. However, further research on this issue is required.

5.2 *Volume of collapsed material*

The volume of collapsed material can be calculated using a cross-sectional method with the following equation:

$$Volume = \left(\frac{S_1 + S_2}{2} \right) \times L \quad (1)$$

In which S_1 = area of section 1, S_2 = area of section 2 and $L =$ distance between section 1 and section 2.

In this experiment, L is equal to the width of the plexiglass box which is 37.7 cm in width. The result of the experiments can be seen in Table 1.

Table 1. Comparison of collapsed volume based on base thickness.

Slope angle (α) – (°)	Angular vel. (ω)$^{-}$ rpm	Centrifugal acc. (a) – g	Volume of collapsed material (mm^3)	
			t/H = 1	t/H = 2
45	10.0	0.15	–	–
	12.5	0.23	–	–
	15.0	0.33	–	–
	17.5	0.46	–	–
	20.0	0.59	21,082	95,562
	22.5	0.75	526,932	143,213
	25.0	0.93	1,186,136	1,777,367
60	10.0	0.15	–	–
	12.5	0.23	–	–
	15.0	0.33	–	–
	17.5	0.46	29,845	87,882
	20.0	0.59	38,806	289,607
	22.5	0.75	714,296	1,142,357
	25.0	0.93	1,796,688	2,218,598
75	10.0	0.15	–	–
	12.5	0.23	–	–
	15.0	0.33	56,550	536,660
	17.5	0.46	164,650	533,314
	20.0	0.59	551,424	545,708
	22.5	0.75	1,896,641	2,054,886
	25.0	0.93	2,776,605	stopped

Table 1 shows that a steeper slope angle will result in a larger volume of collapsed material in the slope with a similar rate of acceleration. For example, in the rate of acceleration of 0.75 g with t/H = 1, slope with 45° produces 526 cm^3 of collapsed material whereas 60° and 75° produce 714 cm^3 and 1896 cm^3, respectively.

From Table 1 it can also be seen that a higher t/H will generate a larger volume of collapsed material. It supports the previous statement that t/H = 2 is more stable than t/H = 1, so the external factor produced by centrifugal acceleration is foccused in the slope face area.

From Table 1, in the scenario of slope angle 45°, the slope starts to fail when 0.59 g is applied. On the other hand, the tests with a 75° slope angle starts to fail when 0.33 g is applied. This might mean that the steeper slope angle, the easier it is to fail.

6 CONCLUSIONS

The conclusions from this experiment are as follows:

- The change of the slope angle as a result of the centrifugal test gets larger when the acceleration and the initial slope angle increase
- It can be proved that the thickness of the base model influences the distribution of the weakness zone. The thicker the base of the model, the larger the volume of collapsed material. This is due to the concentration of the external factor that might be more focused to the slope face than to the base of the model.

REFERENCES

Bucky, P.B. 1931. The use of models for study of mining problems. Technical Publication 425. New York: Am. Inst. of Min. & Met. Engng.

Joseph, P.J., Einstein, H.H. & Whitman, R.V. 1988. A Literature Review of Geotechnical Centrifuge Modeling with Particular Emphasis on Rock Mechanics. Massachusetts: MIT.

Joseph, P.J. & Einstein, H.H. 1988. Rock Modeling Using the Centrifuge. Massachusetts: MIT.

Ling, H.I., Wu, M.H., Leshchinsky, D. & Leshchinsky, B. 2009. Centrifuge Modeling of slope instability. Journal of geotechnical and geo-environmental engineering. ASCE.

Misich, I. 1997. Subsidence prediction and mine design for underground coal mining in the collie basin. PhD Thesis. Curtin University of Technology: Western Australia.

Rock Mechanics for Resources, Energy and Environment – Kwaśniewski & Łydżba (eds)
© 2013 Taylor & Francis Group, London, ISBN 978-1-138-00080-3

A safety inspection system for large-scale slopes in Korea

J.G. Lee, B.S. Jang & S.W. Bae
Korea Infrastructure Safety Corporation, Goyang, Korea

J.S. Moon
Kyungpook National University, Daegu, Korea

H.J. Sin & J.H. Park
Ministry of Land, Transport and Maritime Affairs, Sejong, Korea

ABSTRACT: Large slopes constructed during road or building construction contain a number of potential risk factors, and consequently they require a more detailed inspection. In Korea, large slopes more than 200 m long and with a cut height of more than 50 m have been designated as large-scale slopes for special inspections. The total number of large-scale slopes located on the national highways is 146 and their average lengths and heights are 329 m and 64 m, respectively. The safety inspection for large-scale slopes consists of an assessment of their stability and condition and an evaluation of the level of damage and potential risk factors. The final safety rating for slope stability is determined based on these assessment results and the future plan for periodic inspection is decided based on the final safety rating. In this study the safety ratings for all 146 large-scale slopes were evaluated and the economic efficiency of operating the current inspection system was assessed.

1 INTRODUCTION

As approximately 60% of the national land in Korea consists of mountainous areas, it is essential to form a cut slope or an embanked slope as a prerequisite to construction work in many cases. In particular, more cut slopes are being formed for road construction than for other construction work as these construction zones are long, with most passing through mountainous areas. Most road slopes are distributed along expressways and the national highway, and their number is increasing year by year.

Currently, Korea has 4789 km of expressways along which approximately 7000 slopes are distributed. In addition, there are 13,797 km of national highway, more than twice the length of the expressways that have 29,757 slopes, which is more than four times the number of slopes as on the expressways.

The Ministry of Land, Transport and Maritime Affairs has been operating the Cut Slope Management System since 1997 in order to prevent slope disasters on the national highway and to minimize any damage. A complete enumeration of the slopes on the national highway through the Cut Slope Management System was conducted and a master plan was established based on the result and is in operation. Continued observation of these slopes is required, but only 124 sites on which it is difficult to apply reinforcement methods remain under real-time monitoring.

Of these cut slopes, slopes more than 200 m long and with a cut height of more than 50 m are designated as large-scale slopes under the "Special Act on the Safety of the Facility", regular safety inspection and maintenance must be conducted. The Cut Slope Management System includes safety inspections of the large-scale slopes that are distributed on the national highway, which contributes to reducing the damage that can result from slope collapse and also secures the safety of roads through safety inspections and maintenance.

2 SAFETY INSPECTIONS

2.1 *Status*

Currently 146 large-scale slopes in Korea are distributed along the national highway, all of which have been identified to be rock slopes due to Korea's geological characteristic of shallow soil depth. The average length of large-scale slopes is 329 m and the average height is 64 m.

Figure 1 shows the length distribution of large-scale slopes. Most large-scale slopes have a length of less than 400 m.

Figure 2 shows the height distribution of large-scale slopes. Most large-scale slopes have a height of less than 80 m, while 48% have a height of 50∼60 m.

The rock types comprising large-scale slopes are igneous rocks, sedimentary rocks and metamorphic rocks at ratios of 33%, 33%, and 34%, respectively, which is slightly different from the findings of a previous study (35%, 25%, and 40%).

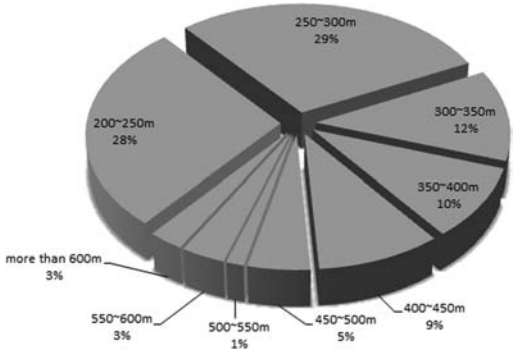


Figure 1. Length distribution of large-scale slopes.

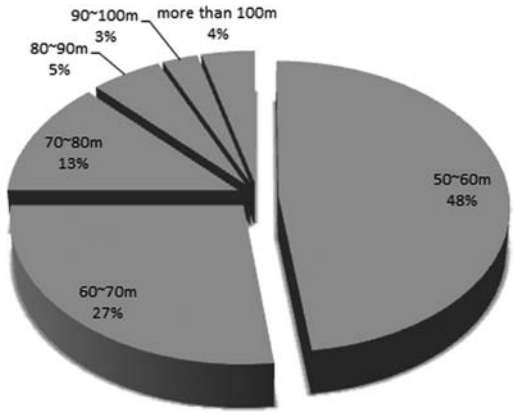


Figure 2. Height distribution of large-scale slopes.

2.2 *Inspection method*

A safety inspection is conducted in order to assess whether facilities meet the requirements for use by correctly assessing the current condition of the facilities. A safety inspection includes a close visual inspection (condition assessment) and a simple site test. The condition assessment is divided into the damage level and potential risk factors.

The damage level consists of tensile cracks, ground deformation, structural deformation and a collapse occurrence scale, and the potential risk factors include the ground state (relationship between joint condition and the slope), slope shape, natural factors (rainfall or groundwater conditions) and artificial factors (drainage conditions, condition of the reinforcement method). Based on an assessment norm, the defect index was calculated by giving each item a defect score and dividing the aggregate of the defect scores by the total sum of items.

In addition, the final safety rating of large-scale slopes was calculated and the lower rating between the stability rating based on stability assessment (conducted if necessary) and the condition rating based on the defect index was chosen.

Table 1 shows the condition of the facilities along with their safety rating.

Table 1. Safety rating of facilities.

Safety rating	Slope condition
A (Excellent)	Safety facilities
B (Good)	Simple repair & maintenance required
C (Average)	Prompt reinforcement or replacement of some facilities required
D (Insufficient)	Urgent reinforcement required & decision has to be made about whether to limit use
E (Bad)	Prohibited use or reconstruction required

Table 2. Execution cycle for safety inspection.

Safety rating	Execution cycle (slope)
A class	More than once every 3 years
B, C class	More than once every 2 years
D, E class	More than once a year

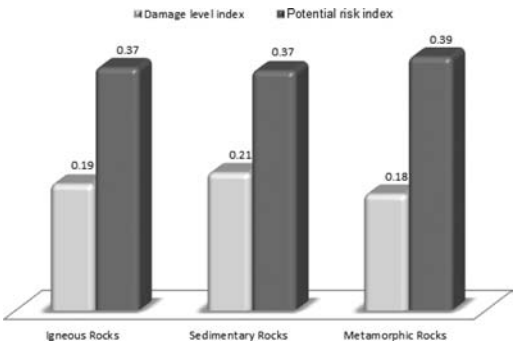


Figure 3. Damage level index & potential risk index distribution by rock type.

In order to ensure the continued safety of facilities, a safety inspection is carried out periodically, and the inspection cycle is decided by the safety rating of the final safety inspection, as shown in Table 2.

2.3 *Safety inspection result*

After an initial safety inspection of 146 large-scale slopes, 71 were found to have a B rating, 72 locations had a C rating and 3 locations had a D rating, and thus most were found to be either a B or C rating.

Figure 3 shows the damage level index and potential risk index by rock type. The damage level index and potential risk index by rock type were not found to show any distinct differences from each other. However, sedimentary rock was in the highest position for the damage level index, while metamorphic rock showed the highest potential risk index.

Of the 146 large-scale slopes, a second safety inspection was made for 67 after the initial safety inspection. During the second safety inspection, the

safety rating was lowered from class B down to class C for 14 of the 67. These have doubled from 0.11 to 0.22 in the average damage level index and have risen from 0.33 to 0.42 in the average potential risk index. In addition, the item of 'structural deformation' was shown to have the greatest degree of change among items that were evaluated for the damage level, while the item of 'protection/reinforcement condition' that had the greatest degree of change among the items that were evaluated for potential risk factors. The result of such an analysis indicates that the condition of the slope followed by the passage of time affects not only the condition of the slope itself, but also the condition of the different structures that have been installed on the slope in order to ensure the safety of the road.

3 COST-BENEFIT ANALYSIS

3.1 *Theoretical background*

The main analysis technique for a cost-benefit analysis includes the B/C ratio, Net Present Value (NPV), Internal Rate of Return (IRR), etc. Of these, for a case designed to analyze the economy of a project, it is desirable to judge from the B/C ratio (Kim, 2009). In this study, as we reviewed the feasibility of safety inspections for each slope on a limited budget, this B/C ratio analysis technique was applied.

In this study, a cost-benefit analysis was performed for one safety inspection on 146 of the large-scale slopes that are different from each other in terms of the protection-method, volume of traffic, inspection cycle, etc. The calculation premises for the analysis were as follows:

1) The social discount for calculating the percentage value of 5.5% was applied, which the Korea Development Institute has used since 2008.
2) The standard year for present value was 2012.
3) The inspection cost was calculated by applying the "Standard for Cost of Safety Inspection and Precision Safety Inspection, Ministry of Land, Transport and Maritime Affairs, 2009."
4) In order to reduce accidents, the damage amount and restoration cost incurred due to the collapse of large-scale slopes in 2012 was applied.

3.2 *Benefit analysis*

In this study, the benefit that resulted from the safety inspection of Large-scale Slopes was set as the benefit of a reduction in accidents and delays through the prevention of collapses.

The benefit of accident reduction was applied to all of the objects by analyzing the example of the collapse of a large-scale slope in 2012. The collapsed slope was 422 m long and 70 m high. Approximately 720 m^3 of the collapse occurred after heavy rainfall due to a typhoon. As shown in Table 3, the amount of damage due to the collapse was approximately 57,655 USD, and the restoration cost for maintaining the slope and ancillary facilities was estimated to be 192,186 USD.

Table 3. Damage amount & restoration cost for the collapsed slope.

Collapse volume (m^3)	Damage amount ($)	Restoration cost ($)
720	57,655	192,186

Table 4. Vehicular travel time value.

Year	Price index	Car ($/unit)	Bus ($/unit)
2009	97.1	13	53
2012	109.9	15	60

* The 2010 price index was applied based on 100.

Table 5. Examples of the delay reduction benefit calculation.

Site	Delay reduction benefit
A	8 hr × 38 ($/car.hr) × 322 (car) = 97,888 ($)
B	8 hr × 38 ($/car.hr) × 417 (car) = 126,768 ($)
C	8 hr × 38 ($/car.hr) × 526 (car) = 159,904($)

The benefit of a reduction in delays means the cost for the delayed movement of cars that was incurred by the collapse of the slope. For the national highway, the average traffic delay time was about 8 hours and this figure was used. In our traffic facility projects, the travel time value is often in various applications, one of which is in estimating traffic demand, and the other is the benefit estimation from an economic analysis (Kim, 2009). In the modified and complemented 'Standard Guidelines on Pre-feasibility Survey for Projects in the Sector of Road & Railroad (Korea Development Institute, 2008), the average travel time value of a car is classified into business use and non-business use. In this study, the above criteria were applied and the average travel time value of cars and buses was calculated including inflation. Additionally, the traffic volume was calculated for each slope (the average daily traffic volume and hourly traffic volume of which were calculated by analyzing the traffic volume from 2009 to 2011) (Table 4).

The delay reduction benefit of each slope was calculated as the product of the average delay time, the travel time value of car and the average traffic volume (Table 5).

For the total benefits, the present value was calculated based on the standard year using the discount rate after calculating the benefit value of each year during the evaluation period and the total amount of benefits is the sum of the percentage value amount of each benefit (Sin 2003).

$$BPV_j = \sum_t \left(\frac{B_{jt}}{(1+i)^t} \right) \quad (1)$$

Table 6. Examples of the calculations of total benefits.

Site	Accident reduction benefit ($)	Delay reduction benefit ($)	Total benefit ($)
A	236,817	92,652	328,469
B	236,817	118,826	355,643
C	236,817	149,939	386,757

*When calculating the total benefit, the social discount rate (5.5%) was applied

Table 7. Examples of the calculation of the cost of safety inspections.

Site	Basic compensation ($)	Coordination cost			Applied compensation ($)
		Length	Height	Use	
A	19,309	1.3	1.1	1.2	33,134
B	19,309	1.1	1.1	1.2	27,249
C	19,309	1.4	1.0	1.2	33,134

where BPV_j = the present value of the benefit j; t = the annual time; B_{jt} = the benefit of j at the t-th year after the initiation for public use; i = the social discount rate; and j = the benefit by type.

In this study, because the cost-benefit analysis was followed by a one-time inspection of each slope, the total benefit can be described as the sum of the accident reduction benefit and the delay reduction benefit that corresponds to the inspection cycle of each slope (Table 6).

3.3 *Cost analysis*

In this study, the costs that followed the inspection cycle of large-scale Slopes were classified as the cost of the safety inspection, the cost of the reinforced method, the cost of maintenance and the cost of periodic inspections.

For the cost of the safety inspection, the "Safety Inspection & Precision Safety Diagnosis Payment (cost calculation) Standard (Ministry of Land, Transport and Maritime Affairs, 2009)" was used, which was calculated by reflecting the scale (length, height) of a slope (Table 7).

The protection-method cost is the one that is necessary in order to apply the reinforcement method that is required for securing the stabilization of each slope and the safety of a road after a safety inspection. As the methods and cost required for each slope are different from each other, the protection-method and required cost for each slope were estimated and applied (Table 8).

The daily management cost includes the cost of removing fallen rocks, drainage dredging, etc. during the daily management of slope. As the daily management cost for large-scale slopes is not collected separately at the moment, the ratio (0.5%) of the daily management costs for the 29,757 large-scale slopes on the national highway was estimated and applied (Table 9).

Table 8. Examples of the calculation of the protection-method cost.

Site	Protection-method 1	Counter-method 2	Cost ($)
A	Retaining wall	Anchor	138,951
B	Rockfall Protection Fence	Greenification	129,026
C	Rockfall Protection Net	Banquette drain	66,768

*Only the typical methods by site are expressed.

Table 9. Calculation of daily maintenance costs.

Year	Total cost ($)	Ratio (%)	Applied cost ($/location)
2010	713,048	0.5	24
2011	2,299,673	0.5	78
2012	3,366,290	0.5	115
Average			73

Table 10. Examples of the calculation of the daily inspection costs.

Inspection labor (persons)	Labor cost ($)	Car driving cost ($)	Total cost ($/year)
8	1437	433	1870

*Labor cost is 199,093/day, car applied based on the lease.

The daily inspection cost is the cost that is required for the periodic inspections to maintain the slopes that are conducted annually. As the daily inspections are classified into spring inspections, rainfall inspections, autumn inspections and winter inspections, the cost was calculated on the basis of the annual total of four inspections (2 persons/1 time) (Table 10). The cost was applied based on the lease cost for cars, the fuel economy of the car was set at 5 km/L and the driving distance was set at 50 km/hour.

The total cost can be also calculated using the same method as that for calculating the total benefit (Sin 2003).

$$CPV_j = \sum_t \left(\frac{C_{jt}}{(1+i)^t} \right) \quad (2)$$

where, CPV_j = the present value of cost j; t = annual time; C_{jt} = value of cost j at the t-th year; i = social discount rate; and j = cost by type.

In this study, as a cost-benefit analysis followed by one-time inspection of large-scale slopes was conducted, the total cost can be defined as the sum of

Table 11. Example of the calculation of the total costs.

Site	Cost ($)				Total benefit ($)
	Safety inspection	Protection method	Daily maintenance	Daily inspection	
A	31,405	0	137	3545	35,087
B	25,827	46,182	137	3545	75,691
C	31,405	0	137	3545	35,087

*In calculating the total cost, the social discount rate (5.5%) was applied

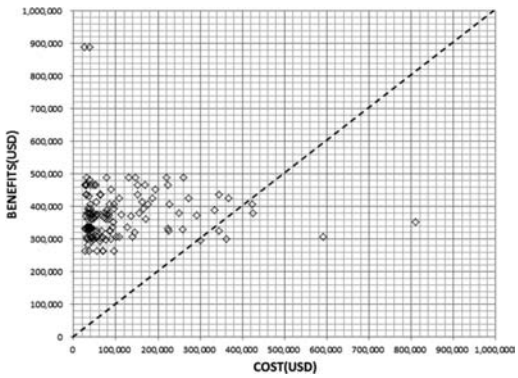


Figure 4. Cost-benefit analysis result.

the costs for the safety inspections, the protection-method, daily maintenance and daily inspection during a one-time inspection cycle (Table 11).

3.4 *Result*

When analyzing the cost-benefit for safety inspections of large-scale slopes, most were found to be economically feasible, as the benefit/cost ratio (B/C ratio) for 139 of them was calculated to be higher than 1.0. Additionally, when a separate protection-method was necessary due to good slope conditions, the B/C ratio proved to be relatively high due to the lower total cost. Among the result values, the two locations with very high B/C ratios of 23.8 and 33.8 have the biggest difference between the benefit and cost due to the fact that the cost of the protection-method is 0 and the traffic volume is the highest.

4 CONCLUSIONS

In this study, the results of safety inspections of the 146 large-scale slopes that are distributed along the Korean national highway and their economic efficiency were analyzed.

The analysis found that most of the 146 large-scale slopes were calculated as class B or C, and their conditions were determined to be good. In addition, 14 of the 67 large-scale slopes that were inspected twice were lowered from class B down to class C in their safety rating, as these were analyzed to have been greatly affected by changes in the condition of the structure that was installed on the slope to secure the safety of the road.

Additionally, the B/C ratio was calculated to be higher than 1.0 for the safety inspections of 139 of the 146 large-scale slopes, and thus they were analyzed to be economically feasible. In particular, the analysis of the cost and benefit for the safety inspections of the large-scale slopes, affected the protection-method cost and traffic volume for each slope.

ACKNOWLEDGEMENTS

This study was conducted with support from the 'Cut Slope Management System Operation Business' of the Ministry of Land, Transport and MariTime Affairs.

REFERENCES

Kim, Y.S. 2009. Economic evaluation on slope investigation techniques using a cost-benefit analysis. *Korea Geotechnical Society Spring National Conference 2009*: 157–160.

Korea Infrastructure Safety Corporation. 2009. *Detailed instructions for safety inspection and precise safety diagnosis*. Goyang: ministry of Land, Transport and Maritime Affairs.

Korea Development Institute. 2008. *Standard guidelines on pre-feasibility survey for projects in the sector of road & railroad*. Seoul: Korea Development Institute.

Ministry of Land, Transport and Maritime Affairs. 2009a. *Standard for cost of safety inspection and precision safety inspection*. Seoul: Korea Infrastructure Safety Corporation.

Ministry of Land, Transport and Maritime Affairs. 2009b. *Safety inspection & precision safety diagnosis payment(cost calculation) standard*. Seoul: Ministry of Land, Transport and Maritime Affairs.

Sin, M.H. et al. 2003. Development of cost-benefit analysis technique for rockfall measures method. *Korean Society for Railway's autumnal symposium collection of dissertations*: 417–422.

This page intentionally left blank

Rock Mechanics for Resources, Energy and Environment – Kwaśniewski & Łydżba (eds)
© 2013 Taylor & Francis Group, London, ISBN 978-1-138-00080-3

Basic kinematic analysis of a rock slope using terrestrial 3D laser scanning on the M-22 highroad pilot site

M. Marjanović
Faculty of Mining and Geology, University of Belgrade, Belgrade, Serbia
Faculty of Science, Palacky University, Olomouc, Czech Republic

B. Abolmasov, U. Djurić, S. Zečević & V. Šušić
Faculty of Mining and Geology, University of Belgrade, Belgrade, Serbia

ABSTRACT: Terrestrial laser scanning has propelled recent advancements in rock slope engineering. Building models with millions of points to discretize an actual slope has provided resolutions which empower computer-based analysis/measurements of rock slopes as a supplement/substitute for conventional data acquisition. Herein, we are following-up such trends at a pilot site on the M-22 highroad near Ljig (Serbia). The site is composed of stratified Cretaceous flysch sediments, traversed by several joint sets, making a convenient setting for potential failures. Prior to the kinematic analysis, modeling of the 3D surface has been performed on 1 cm resolution point cloud, obtained by Leica Scan Station 2. The 3D surface model was then mapped for the planar discontinuities, forwarded to the kinematic analysis for planar, wedge and toppling failures. The analysis matches with previous findings, indicating that the most dominant failure type is a planar slide, showing that proposed methodology yields reliable and concurrent results.

1 INTRODUCTION

Recent development in terrestrial laser scanning technology has resulted in advancements in numerous engineering branches, and rock slope engineering is one representative example. Collecting spatial information on millions of points, usually called point clouds has found its use in modeling of actual slopes and allowed high-resolution, computer-based analysis as a supplement/substitute for conventional field data acquisition (Tonon & Kottenstette 2006, Kemeny & Turner 2008).

There are a number of benefits in using point clouds as discrete models of the rock slopes:

- they enable more objective and more accurate measurements (of distances, areas, volumes) and mapping (of planar and linear structures) on accessible and inaccessible slope parts (high and steep rock faces)
- high-precision cross-sections and contour lines, which are for instance required in stability analysis, can be obtained.
- advanced visualization of slopes and objects on them.
- the models (saved in digital form) are available for reuse at any time with no additional expenses, unlike the field investigation revisits
- they provide a very good base for the monitoring of the particular slope sites, where each change can be accurately determined and interpreted or predicted.

On the other hand, the drawbacks could be recognized in the following:

- the equipment and the processing software/hardware are expensive
- field day lasts long and requires skilled, multidisciplinary team of Engineering Geologists and Surveying specialists/technicians
- the scanning conditions should be optimal (vegetation, draped mesh or other objects can screen the laser signal, resulting in noise and shadows)
- there might be a considerable manual labor involved in removing of the screens mentioned above or alternatively, scanning could be limited to optimal, low-vegetation seasons and cleared slope faces.

There is already a host of case studies where 3D terrestrial laser scanning has been applied in the context that will be followed herein (Lato & Vöge 2012, Lato et al. 2012, Sturzenegger & Stead 2009, Brodu & Lague 2012). As inspired by these examples, our goals are to demonstrate how reliable measurements and analyses can be performed on a point cloud based model of a rock slope. The principal objective was to analyze the potential for development of different types of failures (kinematic analysis) at one particular rock slope (Fig. 1) along the M-22 highroad near Ljig (Serbia).

Finally, this research is an extension of some preceding preliminary attempts on acquisition and processing

of the point cloud models collected at the same study site by using 3D terrestrial scanning and photogrammetric techniques (Zečević et al. 2012).

2 STUDY SITE

The study site (E20°14′35″, N44°12′2″) is located in the Western Serbia near the town of Ljig (some 4 km southward). It rests alongside to a very important and very frequent roadway, M-22 highroad. One of the motifs for investigating this rock slope arises from the necessity of maintaining the safety along the road, since this slope is not particularly well protected despite the fact that block failures have been witnessed in the past.

The site is composed of a solid rock mass represented by a flysch formation, so called "Ljiški flysch". It is an upper Cretaceous (Campan-Maastricht) stratified (rhythmic) succession of mica-sandstone shale and conglomerate. Thus, there are units that are alternating rhythmically and have different mechanical properties, which further complicates the investigation of the slope. Conveniently though, the area around the slope site is not particularly tectonized. The strata follow the monotonous trends of the flank of an anticline structure located southward (Fig. 2). The closest regional structure is "Boljkovački" fault which is deflected in eastward direction, several kilometers away from the site (Filipović et al. 1978).

The investigated rock slope (Fig. 1) is not very easy to characterize for several reasons:

- as mentioned before, the units alternate while their strength and other mechanical properties differ
- the units have different susceptibility to weathering (shale are most susceptible, followed by sandstone which is generally richer in carbonate than silicate components, which makes it less compact).
- in addition the slope face is faceted and roughed.

The structural set could be generalized by the three distinctive discontinuity sets, which are described as follows:

- stratification, which significantly varies in spacing and aperture and detritus filling (average spacing of sandstone units is 1.9 m, for conglomerate 1.1 m, and for shale 0.3 m)
- near-parallel joint system (the origin is most likely due to the decompression related to the valley opening or perhaps in relation to cleavage of axial plane of the near anticline) with relatively smooth surfaces with small aperture, regular spacing (cca. 1.5 m) and no fill.
- near-perpendicular joint system (most likely tension joints, parallel to the longitudinal, beta-axis of regional stress direction) also with relatively smooth surfaces with small aperture, regular spacing (1.5 m) and no fill.

Considering the general rock slope metrics (measured *in-situ*) it is important to mention that the investigated part of the slope is some 6 m high (the entire slope is more than 20 m high) and 7 m long (the entire slope is more than 50 m long). The average dip of the slope part face is 75° and its approximate azimuth is 180°.

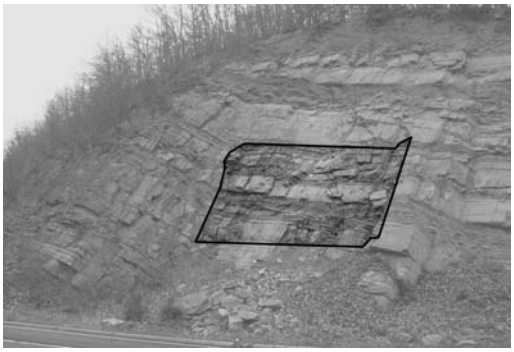


Figure 1. A photo of the study site taken in winter 2010/11. The investigated (scanned) part of the slope is highlighted (photo by the authors).

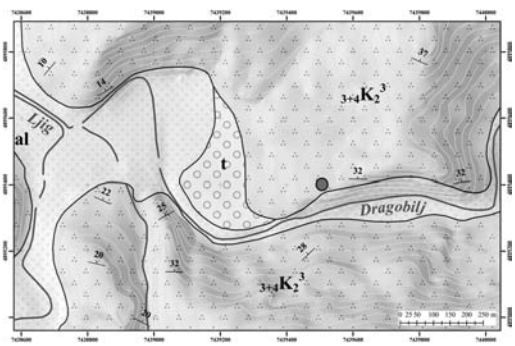


Figure 2. Geological setting of the wider area of the site. The site is marked by red dot, the symbols are standard geological map symbols (according to Filipović et al. 1978).

3 METHODOLOGY

Methodology could be systematized in two subsections, one regarding the technology of collecting and processing of the data and the second regarding the kinematic analysis of the rock slope over the acquired data.

3.1 *3D terrestrial laser scanning*

The data have been acquired by the Leica Scan Station 2, a terrestrial long-range laser pulse scanner, with relatively narrow beam (range goes to 300 m in optimal conditions, but in realistic operative conditions it is usually 80–120 m, and the beam is 4 mm thick). The system has a built-in high-resolution digital camera. As in any other LiDAR (Light Detection and Ranging) system, the data is represented by a point cloud which contains information on X, Y, Z relative coordinates of each collected point, as well as



Figure 3. Referencing the marks on the investigated slope part. Note also the displaced blocks in the foot of the slope, witnessing of a recent rockfall (photo by the authors).

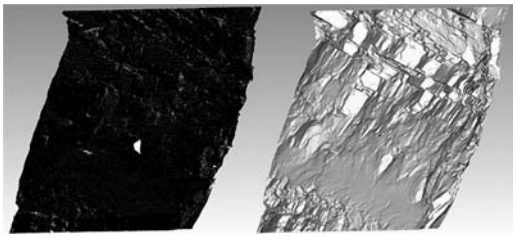


Figure 4. Processed point cloud (left) and corresponding meshed model (right).

the intensity (reflectance) of the laser beam and also the recorded R, G, B values (Red, Green, Blue values of RGB color model) recorded by a camera and related to each point. The points have been scanned at 1 cm resolution at 50000 points/s. Unfortunately, only one taking from a single viewing angle was conducted due to the organizational circumstances. The positioning of the laser scanner has been configured according to the spatial orientation of the slope face (180/75°). The initial point cloud offset was measured *in-situ* and equaled −70°, although this offset could have been disregarded, because the relative coordinate system analysis for the case of the site-specific kinematic analysis is also plausible. An important detail is the placing of the referent marks for this relative coordinate system (Fig. 3) which allows a quick and simple registration between successive scans (point clouds), although there are available (global) algorithms for automatic registration of the point clouds.

In result, a point cloud containing 435,314 points has been acquired (each with seven coordinates: X, Y, Z, R, G, B, intensity). Prior to the triangulation, a raw point cloud has been preprocessed (co-registered) and manually cleaned from the bias information, such as vegetation, passing vehicles traces. Finally, a geometrically simplified (meshed) model of the slope face has been generated and further analyses have been performed either on that mesh or preprocessed cloud (Fig. 4).

3.2 *Kinematic analysis*

Given the geometrical slope model, kinematic analysis, i.e. the preliminary analysis of the failure potential had taken place. In brief, it implies graphical stereonet analysis of geometrical conditions (with addition of mechanical parameter – estimated internal friction angle along the slip surfaces) required for different types of slope failures. In rock slopes, this usually comes down to the plane, wedge or toppling failures. It is assumed that these failures happen once the geometrical conditions are met (Goodman 1989, Hoek & Bray 1981, Kliche 2009). These are usually referred as Markland's condition/test for planar or wedge failure (Eq. 1) and toppling failure (Eq. 2). Thus, spatial relations of the mapped planar discontinuities (defined by v_d and α_d as strike and dip of the discontinuity/intersection plunge and φ_d as the internal friction angle along the slip surface of the discontinuity) and the slope face (defined by v_s and α_s as the average strike and dip of the slope face) determine whether there is a potential for failure development. If all of the conditions for any of the plane, wedge or toppling failures are met, the slope is declared unstable, giving way to further, more detailed slope stability analysis.

$$\alpha_s > \alpha_d > \varphi_d; \quad \gamma_s = \gamma_d \pm 20°; \tag{1}$$

$$\alpha_d > \varphi_d; \quad \gamma_s = \gamma_d \pm 20°; \quad \exists(\perp v_d) \tag{2}$$

To perform kinematic analysis first requires one to classify the types of the geological discontinuities (bedding, joint/fault, cleavage, foliation etc.), to group them into the systems of common origin (stratification, tension, relaxation, shear joints etc.) and to measure their orientation (strike and dip angles). Assuming that the slope can be accurately fitted with the point cloud, and that the quintessential discontinuity systems are evident on the slope face, kinematic analysis can be routinely conveyed (Jaboyedoff et al. 2007).

4 RESULTS AND DISCUSSION

Visually, the investigated slope indicated apparent potential for block failures, especially in the upper, weathered sections (which unfortunately have not been captured by the scanning scene). Piles of fallen blocks in the foot of the slope witness of recent rockfall activity that has most likely been a consequence of above mentioned block failure potential. Thus, planar failures were apparently expected to be confirmed by the kinematic analysis, while wedge and toppling failures have not been that apparent, since wedge failure for instance, has slightly less restrictive condition (Eq. 1) for plunge azimuth than planar case (Hoek & Bray 1981).

Proposed three planes of discontinuity systems (see Chapter 2) have been adopted as a guideline for the actual, on-screen selection of the discontinuity sets (Fig. 5). In turn, over 70,000 of 435,000 points

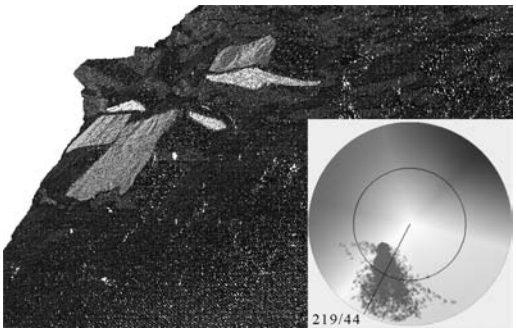


Figure 5. Screen shot of interactive selection of discontinuity sets on a point cloud. Note that highlighted selections correspond to the proposed systems js1 and ss. In the inset, ss set has been displayed on the stereonet and assigned with a yellow color code.

Table 1. Basic parameters of the selected joint sets.

set	strike/dip °	sample size %	Fisher's K	stereonet color
ss	39/44	15	21.4	yellow
js1	187/62	75	140.9	magenta
js2	148/79	10	267.9	blue

have been assigned to according discontinuity sets. The selection has further been filtered, because such amount of strike/dip information with such level of detail (both coordinates were set to have one decimal precision) is unnecessary. Instead the set has been reduced to a reasonable 5000 randomly selected points, with balanced (proportional) sample sizes for all three systems (Table 1). Set representing stratification, denoted ss, has orientation 39/44°, parallel joint system (js1) 187/79° and perpendicular joint system (js2) 148/79°. According to the Fisher's K parameter (Table 1), all of the systems have been generalized well enough (Fisher 1982).

Further difficulty was the absence of any *in-situ* testing of the internal friction angle along the slip surfaces or any other mechanical parameter, for that matter. There is also mentioned difficulty with variability of the rock units, but however, a single friction angle, i.e. a range of friction angle values has been proposed for a given rock mass. Some guidelines for similar masses have been found in the literature (Hoek & Bray 1981). As the most adverse case $\varphi_d = 20°$ has been adopted and denoted as Model-φ_{min}. The other extreme was $\varphi_d = 30°$ (denoted Model-φ_{max}). It has been shown that the selection of the friction angle has not been too influential, since similar spatial setting, thus similar results of kinematic analysis, has been preserved in both cases (Fig. 6–7).

The results are clearly showing that the conditions for planar are met by js1 system, which has been expected (Fig. 6–7). According to the extended criteria for wedge failures, there is also possibility of wedge failures along intersection of conjugated js1-js2, which plunges within the critical zone (Fig. 6–7)

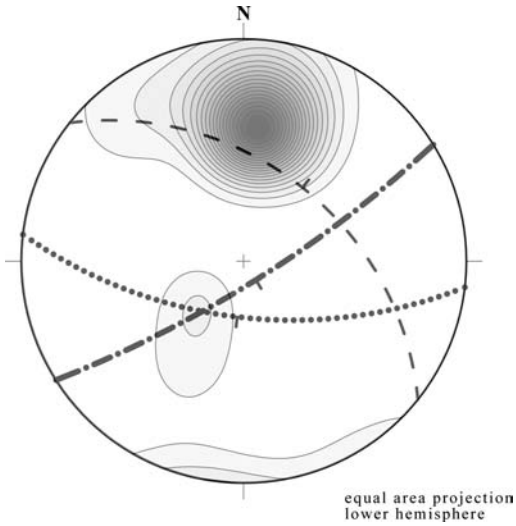


Figure 6. Computation of the systems from the point data. Contours represent the point density of the sample. Dashed line represents the great circle of the ss system, dotted line represents js1 and dash-dotted line represents the js2 system.

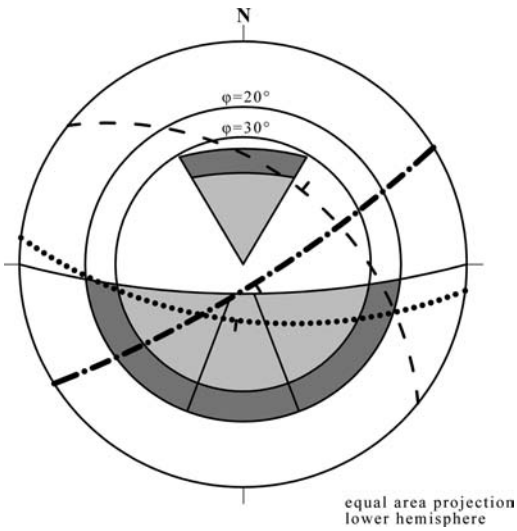


Figure 7. Stereonet display of kinematic analysis results for two cases: $\varphi_d = 20°$ and $\varphi_d = 30°$ (darker shaded areas represent the extension of the $\varphi = 20°$ critical zone to the $\varphi = 30°$ zone shaded in lighter tone). The great circle of the slope is represented by the thin solid line. Other great circles are the same as in the Figure 6.

failure. Regarding the isometric spacing of these two systems, it is likely that relatively large blocks ranging from 0.001–0.01 m^3 can be deployed as results of both, planar and wedge failures. Finally, the results are showing that there is no toppling failure potential of js2 for a few reasons:

– the dip of the ss is not steep enough
– there is no perpendicular undercutting system

– spacing is rather broad for sandstone units, which is why these units are not expected to topple (material bridges are likely to remain more intact in thicker monoliths).

5 CONCLUSIONS

The study demonstrates a successful application of the field measurements based on terrestrial LiDAR technology and their direct use in the kinematic analysis of the rock slope. The results are showing that the most severe threat is block slide emerging along the frontal plane of the slope (js1) or along the wedge (js1–js2). Additional slope stability analysis is required for more detailed and more elaborated results (safety factor calculation). It would also require a more detailed laboratory (e.g. bulk density) and field testing (e.g. friction angle and cohesion along the slip surfaces, residual strength etc.) of the separate rock units. Such slope stability could also benefit from the LiDAR technology, since it would be provided with the very accurate cross-sections and contour lines, yielding precise slope geometry. Only after such robust analyses, the remediation measures (stabilization or protection) could be proposed. Further plans for analysis also include the seasonal monitoring of the same site (in the local coordinate system) in order to estimate the volumes of displaced material and the source areas by tracking changes in successive scans. Also, kinematic analysis alone can be further improved by performing analysis over the entire (faceted) slope, as proposed by some previous researchers (Gurocak et al. 2008).

ACKNOWLEDGEMENT

The research has been supported by the project of the Ministry of science and technological development of Republic of Serbia: “The application of GNSS and LiDAR technology in monitoring of the infrastructure and terrain stability” (TR 36009).

REFERENCES

Brodu, N. & Lague, D. 2012. 3D terrestrial LiDAR data classification of complex natural scenes using a multi-scale dimensionality criterion: Applications in geomorphology. *ISPRS Journ. of Photogram. and Rem. Sens*. 68: 121–134.

Filipović, I., Marković, B., Pavlović, Z., Rodin, V. & Marković, O. 1978 *Osnovna Geološka Karta 1:100,000 – Tumač za list Gornji Milanovac L 34-137*. Federal Geological Bureau, Belgrade.

Fisher, N.I. 1982. Robust estimation of the concentration parameter of Fisher’s distribution on the sphere. *Journal of the Royal Statistical Society (Series C, Applied Statistics)* 31/2: 152–154.

Gurocak, Z., Alemdag, S. & Zaman, M.M. 2008. Rock slope stability and excavatability assessment of rocks at the Kapikaya dam site, Turkey. *Engineering Geology* 96: 17–27.

Goodman, R.E. 1989. *Introduction to Rock Mechanics*. New York: John Wiley & Sons

Hoek, E. & Bray, J.W. 1981. *Rock Slope Engineering*. London: Institution of Mining and Metallurgy.

Jaboyedoff, M., Metzger, R. Oppikofer, T. et al. 2007. New insight techniques to analyze rock-slope relief using DEM and 3D-imaging cloud points: COLTOP-3D software. In E. Eberhardt, D. Stead & T. Morrison (eds), *Rock Mechanics: Meeting Society’s Challenges and Demands* 1: 61–68. New York: Taylor & Francis.

Kemeny, J. & Turner, K. 2008. Ground-based LiDAR rock slope mapping and assessment. Lakewood: Central Federal Lands Highway Division.

Kliche, C.A. 2009. *Rock Slope Stability*. Society for Mining, Metallurgy and Exploration, Inc., Littleton.

Lato, M.J., Diederichs, M.S., Hutchinson, J.D. & Harrap, R. 2012. Evaluating roadside rockmasses for rockfall hazards using LiDAR data: optimizing data collection and processing protocols. *Nat. Hazards* 60: 831–864.

Lato, M.J. & Vöge, M. 2012. Automated mapping of rock discontinuities in 3D lidar and photogrammetry models. *Int. J. Rock Mech. Min. Sci*. 54: 150–158.

Sturzenegger, M. & Stead, D. 2009. Quantifying discontinuity orientation and persistence on high mountain rock slopes and large landslides using terrestrial remote sensing techniques. *Nat. Hazards Earth Syst. Sci.* 9: 267–287.

Tonon, F. & Kottenstette, J. 2006. *Laser and Photogrammetric Methods for Rock Face Characterization*. Alexandria: American Rock Mechanics Association.

Zečević, S., Šušić, V. & Pandžić J., Erić V. 2012. The application of new slope survey technologies in geotechnics. *Proceedings of XIV Symposium of Engineering Geology and Geotechnics, Belgrade, 19–22 September 2012*. Belgrade: DGEITS.

This page intentionally left blank

Rock Mechanics for Resources, Energy and Environment – Kwaśniewski & Łydżba (eds)
© 2013 Taylor & Francis Group, London, ISBN 978-1-138-00080-3

Microseismicity due to gravity-induced rock-mass deformations and a related alarm system

S. Martino, A. Prestininzi & S. Rivellino
"Sapienza" Università di Roma, Dipartimento di Scienze della Terra e Centro di Ricerca Previsione, Prevenzione e Controllo dei Rischi Geologici (CERI), Roma, Italy

L. Lenti
Institut Français des Sciences et Technologies des Transports, de l'Aménagement et des Réseaux (IFSTTAR), Paris Cedex 15, France

A. Paciello
Agenzia Nazionale per le Nuove Tecnologie, l'Energia e lo Sviluppo Economico Sostenibile (ENEA) S. Maria di Galeria (Roma), Italy

ABSTRACT: Gravity-induced deformations due to Rock-Mass Creep (RMC) affect the carbonate Peschiera Springs slope (Italy) which hosts the most important drainage plant for the Rome's water supply. This water resource is due to a major regional karst aquifer with an average discharge exceeding 18 m^3/s. The interaction of the RMC with the karst ground water seepage is responsible for underground failures, including cave collapses which generally occur very close to the spring area. On September 2008, an accelerometric array was installed within the tunnels of the drainage plant for integrating a pre-existing stress-strain monitoring system. The integrated monitoring system provided many data on: i) continuous deformations due to the RMC which affects the slope; ii) microseismicity due to the underground failures occurring within the slope; ii) underground failures and rock-mass deformations induced by earthquakes. The up to now collected data, were fundamental for deriving an alarm system devoted to the drainage plant management and based on some characteristic parameters of the seismic records. This alarm system provides three possible levels of alarm, which can be independently reached in the different sectors of the drainage plant: the "ordinary" level; the "alert" level and the "emergency" level. Some recently occurred events of underground failures made it possible to experience the reliability of the adopted alarm system.

1 INTRODUCTION

This study used the data from an accelerometric array to record precursors, post-failure events and triggering impulsive events within a karst rock mass hosting the major drainage system of Rome's aqueduct. The pre-failure behaviour of rock masses represents a complex geomechanical problem because the stress and jointing conditions as well as the joint setting can strongly constrain pre-failure effects, such as generation of cracks, opening or closing of joints and readjustment of the stress field within the rock mass. Recognizing pre-failure events by geological surveys as well as monitoring natural and anthropogenic systems is a major goal for the mitigation of risks due to the "unexpected" and "rapid" rock failure events (Szwedzicki 2003). More complex scenarios of failure involving rock masses can be associated with impulsive triggers (i.e. explosions, collapses) or earthquakes. In these last cases precursors do not necessarily occur, while the events representing possible triggers can be monitored.

Some experiments have been performed in mines or in landslide areas with the aim of monitoring failure precursors by use of acoustic as well as seismometric devices (Miller et al. 1989, Lei et al. 2004, Lai et al. 2006, Paskaleva et al. 2006, Deparis et al. 2008, Senfaute et al. 2009). On the other hand hypogeous instabilities triggered by impulsive events were recorded during experiments of controlled explosions and collapses of caves in mine areas (Phillips et al. 1997, Yang et al. 1998). Many authors (Miller et al. 1989, Phillips et al. 1997, Heng 2009) have analysed spectral features of microseismic emissions due to rock falls, collapses and explosions, both natural and artificially induced, distinguishing specific signal features for different types of events.

The analysis of sequences of precursors as well as of post-failure events (i.e. underground instabilities induced by impulsive triggers) can be considered a very useful tool for the security managing of the plant. In this regard, the Peschiera Springs monitoring system slope is devoted to evaluate possible trigger thresholds

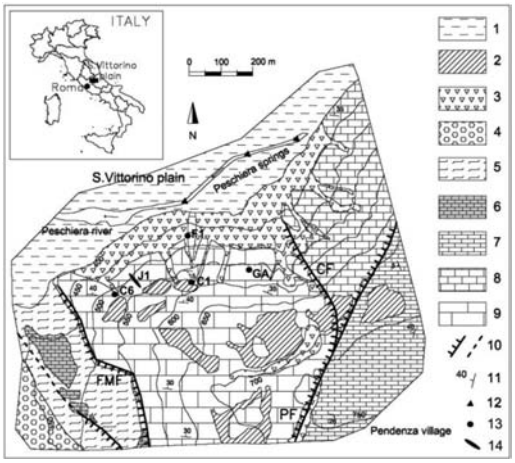


Figure 1. Location and geological sketch of the Peschiera Springs slope: (1) Recent alluvia of the Velino River; (2) Reddish soils; (3) Slope debris; (4) Gravel and conglomerate (upper-Pliocene and lower-Pleistocene parts); (5) Sandy-clayey flysch (upper Miocene); (6) Marly limestone (upper Cretaceous–lower Miocene); (7) Birdseye micritic limestone (lower Cretaceous); (8) Coral limestone (upper Malm); (9) Coral and echinoids limestone (Malm part); (10) Fault (dashed if estimated): FMF Fiamignano-Micciani Fault, CF Canalone Fault, PF Pendenza Fault; (11) Strike and dip of strata; (12) Springs; (13) accelerometric station installed within the drainage plant; (14) monitored joint within the drainage plant.

or to recognize different levels of alarm, based on the observed trends of events, in terms of frequency and energy.

2 THE PESCHIERA SPRING SLOPE

The Peschiera Springs slope corresponds to the south-western flank of Mt. Nuria (Central Apennines, Italy) and it is composed of Malm-Lower Cretaceous limestones (Capotorti et al. 1995, Ciotoli et al. 2001, Bigi & Costa Pisani 2002) (Fig. 1). The structural setting of the slope is monoclinic, with EW-trending and N-dipping (30°–40°) strata; many fault lines cross the slope with roughly NS and N35E trends (Fig. 1).

The slope hosts a major karst aquifer which represents the drainage system of the Nuria-Velino-western Fucino and western Marsica (Velino-Sirente) mountains (total area: 1016 km^2), whose main springs are the Peschiera-Canetra ones (measured total discharge: roughly 18 to 21 m^3/s according to Boni et al., 1986; Boni et al., 1995). The Peschiera Springs drainage plant, which consists of a complex system of drainage and collector tunnels and related connection halls, is part of the Rome aqueduct system managed by the ACEA-ATO2 S.p.A. Italian company.

Geomorphological surveys performed on the slopes as well as a digital, high-resolution (2 m), elevation model of the slope (DEM) derived by a LIDAR (Light Detection And Ranging) radar remote survey,

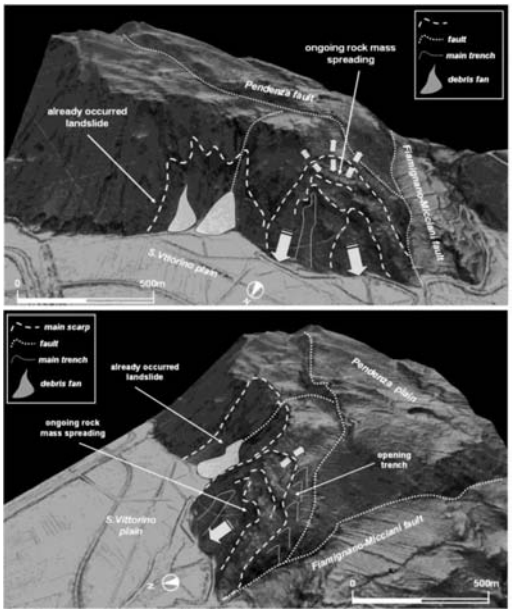


Figure 2. 3D views of the DEM showing the already occurred landslide and the ongoing rock mass spreading which involves the Peschiera Springs slope.

enabled to identify numerous gravity-induced morphological elements (e.g. scarps, trenches, sinkholes and tension cracks) (Fig. 2) (Lenti et al., 2012). These landforms are indicative of slow, intense and pervasive slope deformations, which affect the entire slope. These deformations correspond to different evolutionary stages ascribable to specific portions of the slope, as proved by already published outputs of a stress-strain monitoring system installed within the drainage plant (Martino et al., 2004, Maffei et al., 2005).

3 SEISMOMETRIC MONITORING

3.1 *Monitoring system*

Since 4 September 2008, four accelerometric stations (GA, C1, F1 and C6 in Figure 2) were installed at the Peschiera Springs drainage plant to record seismic events and underground failures, i.e. events due to collapses and rock-mass cracking. Each station is equipped with a triaxial accelerometer (KINEMETRICS EPISENSOR: range set 2 g, sensitivity 1.25 V/g, bandwidth – −3 dB at 1 g–200 Hz) directly installed on the bedrock, connected via cable to a 12-channel digital data-logger (K2 KINEMETRICS: 24 bit and 130 dB digital data logger) which is set to the absolute local time and using through a GPS device and samples with a 250 Hz frequency for full trace record.

The trigger criteria of the data logger were set to record events characterised by different durations and large-band frequency content. To this end purpose, station C1 was set in the STA/LTA (short time amplitude/long time amplitude) trigger mode, which is devoted to the detection of low-magnitude

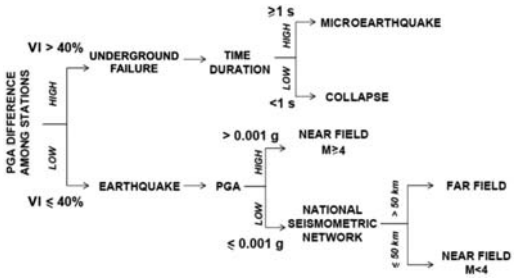


Figure 3. Flowchart showing the detection procedure adopted to distinguish different types of events recorded by the accelerometric network within the Peschiera Springs slope.

earthquakes. The other stations were set with a threshold trigger fixed according to the local noise level (i.e., 10^{-5} g).

3.2 *Recorded events*

Until February 2013, more than 1300 events were recorded by the accelerometric network. These events were separated into earthquakes and micro-earthquakes, i.e., cracks and collapses associated with underground failures. To automatically detect the different kinds of recorded events, a specific script was implemented (Fig. 3) through SAC (Seismic Analysis Code) and Fortran codes on Unix platform, taking into account the records obtained from the accelerometric network (Lenti et al., 2012).

The script provides a processing of the recorded accelerometric time-histories in both time and frequency domains to compute the following physical properties of the records: time duration, Fast Fourier Transform, cumulative Arias intensity and Peak of Ground Acceleration (PGA). Based on these computed properties and following the flowchart of Figure 3 it is possible to classify the recorded events and, in particular, to recognize among earthquakes, cracks (micro-earthquakes) and underground collapses. The signal analysis performed up to now does not provide the event localization; at this aim far field earthquakes (epicentral distances >50 km) are located according to Italian Accelerometric Network (data available on the web-site: www.ingv.it).

As a further analysis, the time distribution of the detected earthquakes and micro-earthquakes enables the recognition of sequences, taking into account "anomalous" rises (increases) in the frequency of events (i.e., more than 10 events per day for earthquakes and more than 3 events per day for micro-earthquakes).

Among the observed seismic and microseismic sequences the most relevant are (Fig. 4):

1. L'Aquila seismic sequence, started with the M_w 6.3 mainshock occurred on 6 March 2009 at 3.32 a.m.;
2. the Valle dell'Aterno – Gran Sasso – Monti della Laga sequence, with a M_w 5.1 main shock, which started on 9 April 2009 and ended in June 2009;
3. the Reatini mountains sequence, 25 June 2009 to July 2009, which was characterised by intermediate-to-low magnitude earthquakes (i.e., up to M_w 4.0);
4. a micro-earthquake sequence due to cracks, occurred from 22 December 2009 to the beginning of January 2010 and characterised by 9 cracks with PGA values between 10^{-3} g and 10^{-4} g.
5. a micro-earthquake sequence due to collapses occurred on 27 April 2010 with 4 events within a few minutes (maximum PGA value of 5×10^{-3} g) and followed by 3 further events with minor intensity;
6. the Reatini mountains sequence, 11 August 2010 to the end of October 2010, with approximately 40 events of M_w in the range 2–3.6;
7. the 11 March 2011 M_w 8.9 Japan teleseismic event;
8. a rock-fall event of approximately 100 m^3 occurred (22 March 2011) from a scarp located on the slope surface, that was recorded with a maximum PGA of 3×10^{-4} g;
9. a micro-earthquake sequence (5 June 2011) due to 8 collapses occurred within 8 minutes, which reached a maximum PGA of 2×10^{-2} g;
10. a micro-earthquake sequence (23 September 2011) due to 15 collapses occurred within approximately half an hour, with a maximum PGA of 2×10^{-2} g;
11. the Emilia seismic sequence started with the M_w 5.9 mainshock occurred on May 20, 2012;
12. the 13 September 2012 micro-earthquake sequence with a time duration of ten of minutes and PGA values between 10^{-3} g and 10^{-4} g, due to underground collapses of karst caves within the slope.

The recorded data point out that the micro-earthquakes, related to cracks and collapses, generally originate in the slope's eastern portion of the slope, where stations GA and C1 are located. The here presented evidence is in good agreement with the evolutionary model of the gravity-induced deformation that affects the slope, which indicates that the eastern sector (stations C1 and GA) is involved in more intense and diffuse deformations and is characterised by an intensely jointed rock mass (Martino et al. 2004, Maffei et al. 2005).

4 ALARM SYSTEM

The analysis of the recorded events is a useful tool for managing the natural risk due to underground failures at the Peschiera Springs slope. For this purpose, the frequencies of the earthquakes and underground failures as well as the cumulative Arias intensity (Lenti et al. 2012) of the underground failures are plotted as a function of time.

To provide an alarm system for the plant in the case of underground events, a frequency index (FI(P, t)) was defined as the sum of an earthquake frequency index (FI_er(P, t)) and a micro-earthquake frequency index (FI_me(P, t)).

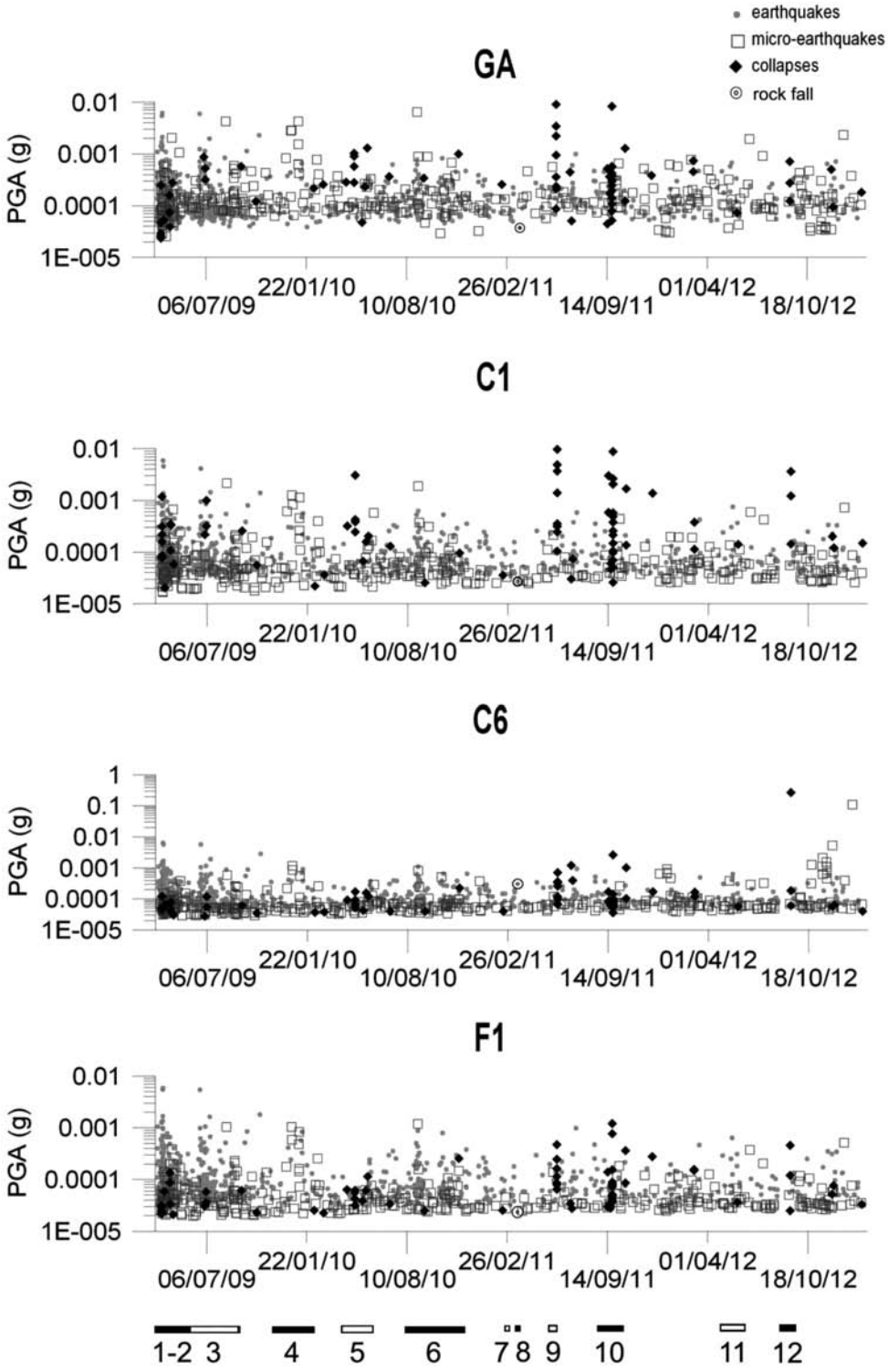


Figure 4. Example of earthquake and micro-earthquake sequences recorded the Peschiera Springs slope from March 28, 2009 to February 16, 2013 (see the bars below the last plot: numbers are referred to the text list). The average values of the horizontal PGA components (PGA_h) computed by the specifically implemented SAC-Fortran script are here plotted for each accelerometric station (see Fig. 1 for the location).

Table 1. Parameters used to evaluate the control index (CI(P, t)).

Earthquake frequency (event/day)	Micro-earthquake frequency (event/day)	FI_er/me(P, t)
0–10	0–3	0
11–20	4–10	1
>20	>10	4
Energy rate (g^2)		EI (P, t)
$\leq 10^{-3}$		0
$10^{-3}/10^{-2}$		1
$\geq 10^{-2}$		4
Alarm level	FI(P, t) + EI(P, t)	CI(P, t)
Ordinary	0	1
Alert	1–3	2
Emergency	4–12	3

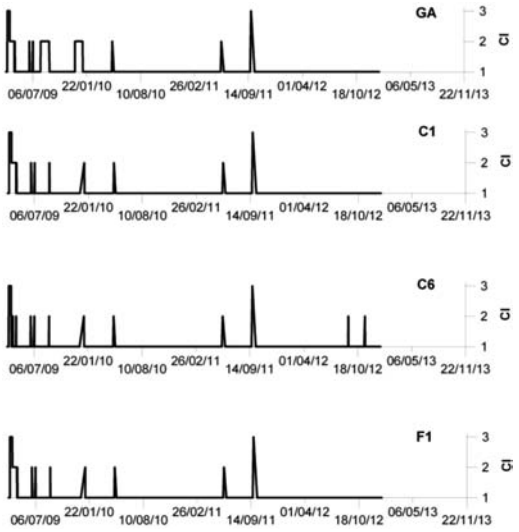


Figure 5. Control index for each accelerometric station within the time interval 28 March 2009 to 16 February 2013.

These indexes are daily assigned to each station according to the daily frequency of recorded events (Table 1). Moreover, the rate of the cumulative Arias intensity of the recorded micro-earthquakes was used to define an energy index (EI(P, t)) which can be attributed to each station (Table 1).

A final control index (CI(P, t)) is daily computed for each station of the network as a function of the sum of the frequency and energy indexes (FI(P, t) + EI(P, t). This last index enables the association of each specific sector of the plant (represented by the corresponding accelerometric station) with three possible levels of alarm: the "ordinary" level (OL) (CI(P, t) = 1); the "alert" level (AL) (CI(P, t) = 2); and the "emergency" level (EL) (CI(P, t) = 3). To take into account additional individual events of significant intensity, an alert threshold was fixed at a PGA value of 10^{-3} g based on the local PGA-magnitude curve derived thus far (Lenti et al. 2012).

The attributed range-values of the frequency indexes as well as of the CI(P, t) are based on the empirical observation performed up to now in the plant, i.e. comparing the recorded events with the observed stress-strain effects within monitored structural elements of the drainage plant. Due the complexity of the natural system a physically-based co-relation among triggering events (i.e. external to the slope such as the earthquakes) and local microseismic events (i.e., referable to rock mass cracks and underground collapses) is not available, but several objective evidences have been collected up to now, which can be grouped in the three following categories:

1. deformational effects clearly related to external actions such as near field seismic sequences and teleseismic earthquakes;
2. deformational effects related to local micro-seismic sequences and corresponding to cracks or collapses occurred within the slope;
3. deformational effects which were not related to seismic records.

According to the above listed categories of effects, many underground failure sequences can be directly attributed to the continuous slope deformation because triggering seismic events were not recorded by the accelerometric array. Nevertheless, near-field seismic sequences (i.e., sequences characterised by epicentral distances <450 km) with $M_w > 4$ and underground failures are generally strongly correlated, as observed during the 2009 L'Aquila seismic sequence and the June–July 2009 and August–October 2010 Reatini mountains seismic sequences.

Based on the above described warning system, in the total period of monitoring, the "alert" level was reached 7 times, due to seismic or micro-seismic sequences, while the "emergency" level was reached only twice (Fig. 5): i) during the near field L'Aquila seismic sequence on April 2009 and ii) during the local micro-seismic sequence associated to the 15 collapses occurred on September 2011.

5 CONCLUSIONS

The gravity-induced deformations involving the Peschiera Springs slope (Central Italy), where Rome's aqueduct drainage plant is located, cause underground instabilities that affect the rock mass. Over approximately 4 years (from September 2008 to February 2013), an accelerometric array installed at the drainage plant recorded more than 1300 seismic and microseismic events.

A physical analysis of the seismic records enabled the recognition of different types of events, such as earthquakes, collapses and cracks, in terms of characteristic parameters, i.e. PGA, duration and M_w.

Based on the analysis of the recorded sequences of earthquakes and micro-earthquakes, an "alert strategy" was developed for the Peschiera Springs drainage plan. This strategy consists in associating a level of alarm (ordinary, alert and emergency) with different plant sectors, each represented by an accelerometric station. The levels of alarm determine different procedures to manage the geological risk to the plant due to underground failures. Even if the here discussed "alert strategy" is mainly based on empirical observations, i.e. referred to the specific case-study, the same approach could be applied to manage similar natural risks affecting underground infrastructures, after specifically re-defining the values of the parameters used to evaluate the control index (CI(P, t)).

REFERENCES

Bigi, S. & Costa Pisani, P. 2002. Structural setting of the Cicolano-M. Calvo area (Central Apennines, Italy). *Bollettino Società Geologica Italiana Speciale* 1: 141–149.

Boni, C.F, Capelli, G. & Petitta, M. 1995. *Carta idrogeologica dell'alta e media Valle del F. Velino*. Elaborazione cartografica e stampa System Cart, Roma.

Boni, C.F., Bono, P. & Capelli, G. 1986. Schema idrogeologico dell'Italia Centrale. *Memorie Società Geologica Italiana* 35: 991–1012.

Capotorti, F., Fumanti, F. & Mariotti, G. 1995. Evoluzione tettonico-sedimentaria e strutturazione del settore di piattaforma carbonatica laziale-abruzzese nell'alta Valle del F. Velino. *Studi Geologici Camerti Speciale* 2: 101–111.

Ciotoli, G., Di Filippo, M., Nisio, S. & Romagnoli, C. 2001. La Piana di S. Vittorino: dati preliminari sugli studi geologici, strutturali, geomorfologici, geofisici e geochimici. *Memorie Società Geologica Italiana* 56: 297–308.

Deparis, J., Jongmans, J., Cotton, F., Bailler, L., Thouvenot, F. & Hantz, D. 2008. Analysis of rock-fall and rock-fall avalanche seismograms in the French Alps. *Bull Seism Soc Am* 98(2): 1781–1796.

Heng, IS. 2009. Rotating stellar core-collapse waveform decomposition: a principal component analysis approach. *Class Quantum Grav* 26: 105005.

Lai, X.P., Cai, M.F. & Xie, M.W. 2006. In situ monitoring and analysis of rock mass behavior prior to collapse of the main transport roadway in Linglong Gold Mine, China. *Int J Rock Mech Min Sci* 43: 640–646.

Lei, X., Masuda, K., Nishizawa, O., Jouniaux, L., Liu, L., Ma, W., Satoh, T. & Kusunose, K. 2004. Detailed analysis of acoustic emission activity during catastrophic fracture of faults in rock. *J Struct Geol* 26: 247–258.

Lenti, L., Martino, S., Paciello, A., Prestininzi, A. & Rivellino, S. 2012. Microseismicity within a karstified rock mass due to cracks and collapses triggered by earthquakes and gravitational deformations. *Nat Hazards* 64: 359–379.

Maffei, A., Martino, S. & Prestininzi, A. 2005. From the geological to the numerical model in the analysis of the gravity-induced slope deformations: an example from the Central Apennines (Italy). *Eng Geol* 78: 215–236.

Martino, S., Prestininzi, A. & Scarascia Mugnozza, G. 2004. Geological-evolutionary model of a gravity-induced slope deformation in the carbonate central Apennines (Italy). *Q J Eng Geol Hydroge* 37(1): 31–47.

Miller, A., Richards, J.A., McCann, D.M., Browitt, C.W.A. & Jackson, P.D. 1989. Microseismic techniques for monitoring incipient hazardous collapse conditions above abandoned limestone mines. *Q J Eng Geol* 22: 1–18.

Paskaleva, I., Aronov, A.G., Seroglazov, R.R. & Aronova, T.I. 2006. Characteristic features of induced seismic processes in mining regions exemplified by the potassium salt deposits in Belarus and Bulgaria. *Acta Geod Geoph Hung* 41(3–4): 293–303.

Phillips, W.S., Pearson, D.C., Edwards, C.L. & Stump, B.W. 1997. Microseismicity induced by a controlled, mine collapse at white pine, Michigan. *Int J Rock Mech Min Sci* 34(3–4), Paper No. 246.

Senfaute, G., Duperret, A., & Lawrence, J.A. 2009. Microseismic precursory cracks prior to rock-fall on coastal chalk cliffs: a case study at Mesnil-Val, Normandie, NW France. *Nat Hazards Earth Syst Sci* 9: 1625–1641.

Szwedzicki, T. 2003. Rock mass behaviour prior to failure. *Int J Rock Mech Min Sci* 40: 573–584.

Yang, X., Stump, B.W. & Phillips, W.S. 1998. Source mechanism of an explosively induced mine collapse. *Bull Seism Soc Am* 88(3): 843–854.

Rock Mechanics for Resources, Energy and Environment – Kwaśniewski & Łydżba (eds)
© 2013 Taylor & Francis Group, London, ISBN 978-1-138-00080-3

Comparison between the mechanical behavior of barriers against rock fall vs debris flows

A. Segalini & R. Brighenti
Department of Civil, Environmental and Territory Engineering, University of Parma, Italy

A.M. Ferrero
Department of Earth Sciences, University of Turin, Italy

G. Umili
Department of Civil, Environmental and Territory Engineering, University of Parma, Italy

ABSTRACT: A debris flow is represented by a mixture of solid particles of various sizes and water, flowing along a laterally confined channel-shaped region whilst a rock fall is represented by singular rock blocks moving along the path with different kind of motion like sliding, rolling bouncing etc.

The assessment of the energy associated to such a phenomena is very important for the proper design of retention devices that are useful in populated area or generally where it is necessary to limit the destructive effects of such a phenomenon. In this paper, a simplified parametric analysis of the mechanics of the debris flow impact is considered in order to estimate the forces that develop on the main structural elements of a retention barrier (Brighenti et al, in prep.) and evaluate their dependency from the various input parameters.

1 INTRODUCTION

The debris flows are rapid mass movements – composed by a mixture of grains, water and air – that develops under the effect of gravitational forces. The amount of energy involved in such phenomena is enormous and their mobility is such to allow them to propagate for several hundreds of meters without losing their destructive potential. Due to these characteristics, debris flows are ascribed among the most dangerous and catastrophic natural events (Takahashi 1983).

On the other hand rock fall is the motion of a rock block under gravitational forces that could be simplified as a lumped mass entity whose energy could be computed as the kinetic energy of the blocks along its path. In the case of rock fall, retention barrier are designed with an energy approach considering that the kinetic energy of the block is instantaneously transferred to the barrier that completely stops the block. In the debris flow case the energy dissipation is not instantaneous and consequently the design approach cannot be exclusively based on energy balance since the flow speed, duration, quality etc.. can heavily influence the barrier loading rate. Although the retention structures are similar, the working mechanics is sensibly different and the design approach must be different in coherence with the loading rate and the induced state of stress.

Flexible barriers are designed to resist to large deformation, above the 10% in the impact direction. Barrier design can be done with two different approaches:

- The energy approach that is similar in both phenomena (rock fall and debris flow) design to dissipate the kinetic energy of the debris flow; however, also with this approach, the computation of maximum induced forces is needed to define critical load condition.
- Force approach that is based on the determination of the acting forces to be compared with the barrier resistance.

The energetic approach is based on the lumped mass assumption and is usually too conservative for debris flow since it do not consider the energy dissipation of the debris due to inelastic deformation and to the formation of a debris heap behind the barrier that partially absorb the debris impact.

Wartmann & Salzmann (2002) proposed an energy method based on their flow test during which they could measure the impact time and estimate the global kinetic energy (EB) absorbed by the barrier. The method is based on the mass conservation although details are not given by the authors.

Numerical models with the Distinct Element Method with the PFC3D code (Itasca 2003) have been developed by Sun & Law (2012) and they showed the

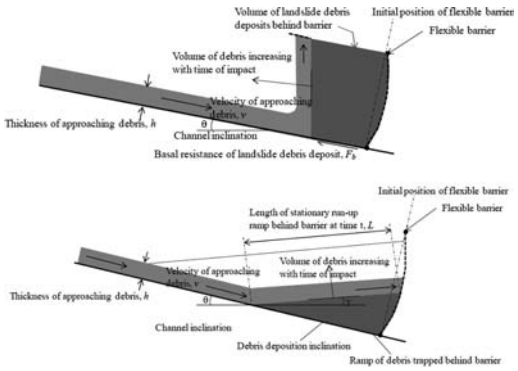


Figure 1. (a) Pile up mechanism, (b) run up mechanism (Sun & Law 2012).

different impact modes induced by the flow rheology: the pile up mechanism (Fig. 1a) and run up mechanism (Fig. 1b). They traduced the different barrier loading mechanism into design methods.

In the pile up mechanism the debris heap behind the barrier activate a friction force at the debris slope contact. Sun & Law (2012) believe that the friction force increases with the debris impacts that when the two forces are equal the barrier energy is constant. In the run up mechanism the debris commute its kinetic energy into frictional and potential energy during the impact phase. In this way the energy can be computed in both mechanisms and compared with the barrier capacity.

In the force approach the loading scheme consider the sum of dynamic and the static load components (Suwa & Okuda 1983). The dynamic impact can be theoretically estimated by assuming the incompressible fluid hypothesis against a rigid barrier, and can be the assessed based on momentum conservation for a steady fluid motion (Hungr 1985, Van Dine 1996) whilst a theoretical solution for cable-like retention barriers is not yet available.

The pressure produced by the debris flow impact on the barrier can be estimated as the sum of static plus kinetic energy. By considering the well-known Bernoulli theorem, the kinetic energy of the flowing material, expressed as:

$$E_k = \frac{1}{2} \cdot \rho_d \cdot v_0^2 \tag{1}$$

is converted in a pressure load when the velocity vanish due to the impact. The dynamic pressure on the barrier can thus be estimated as:

$$q_d(x) = \alpha \cdot \rho_d \cdot v_0^2 \tag{2}$$

where α is an empirical coefficient that can be assumed to be equal to 2.0 (Ferrero et al. 2010) while ρ_d is the mass density and v_0 the arrival velocity of the debris. On the other hand when the debris start to accumulate behind the barrier static pressure can be assumed to take place. The static pressure acting at the depth $d(t)$,

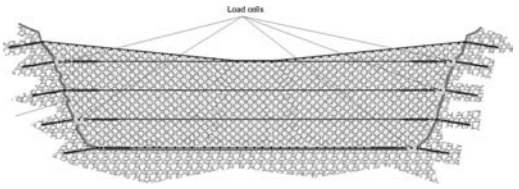


Figure 2. Typical structural lay-out of a net retention barrier against debris-flow. Single elements features as well as geometrical lay-out can vary with make and model of the barrier and with particular installation conditions (channel size, depth, etc.).

measured with respect to the top free surface of the material, can be assessed through the relation:

$$q_s(d,x) = q_s(x,z) = k \cdot d(t) \cdot \rho_d \cdot g \tag{3}$$

where the depth can be expressed as:

$$d(t) = h_0 + h(t) - z \tag{4}$$

and k is the coefficient of earth pressure (assumed equal to 1.0), g the acceleration of gravity and z is the vertical position of the point under consideration.

Once the flow depth overtakes the barrier height a further force may be considered:

$$\tau = h \cdot \rho_d \cdot g \cdot \tan\varphi \tag{5}$$

where h is the barrier height and φ the debris friction.

The proposed method consider the 3 forces components and it distribute them on the barrier net with a series of assumptions allowing for the computation of the stresses acting in the main structural parts of the barrier such as the horizontal and vertical cables and the brakes.

2 MECHANICS OF CABLE-LIKE RETENTION BARRIERS

The typical channelized debris flow barrier has a nearly trapezoidal shape and is anchored to the ground (generally at the channel sides) by means of grouted anchors or cables. The main structural cables are horizontal and their number depends on the overall height and on the expected flow parameters (Fig. 2).

By considering the barrier made of n cables at a relative distance equal to p, the load $q_i(x)$ acting on the i-th cable located at the vertical coordinate z_i, can be simply calculated.

A dissipating element that would limit the amount of force transferred to its foundations during the debris flow impact can be connected to each horizontal cable. The governing equation of the equilibrium of a loaded cable can be usefully employed to describe the mechanical behavior of such a structural system.

Let us consider the barrier constituted by several horizontal cables mounted at a reciprocal constant distance equal to p. The i-th cable – having its extremities

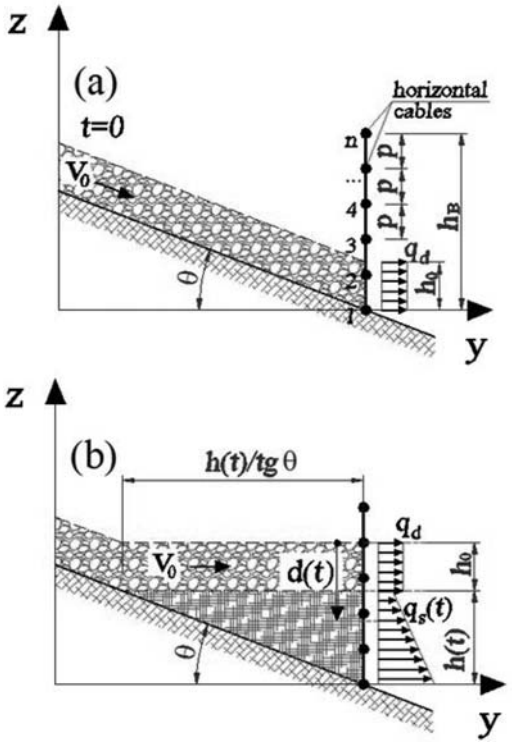


Figure 3. Debris accumulation behind the barrier and corresponding loads at different time steps: (a) t = 0, (b) t > 0.

fixed at the points A and B – is characterized by a horizontal length equal to l_i, while its total effective length (when elongated under loading) is assumed to be equal to L_i (Fig. 4). The distributed load acting on such a cable is assumed to lie in an horizontal plane and to be constant with respect to the x coordinate at a fixed time t. The load is, however, variable with time, since the depth $d(t)$ of the cable with respect to the top surface of the flowing material increases with t (Fig. 1b).

The present model, for sake of simplicity, considers the main resisting cables to be loaded only in the horizontal direction by the forces produced by the debris impact on the barrier, while the resultant of the vertical forces transmitted by the connecting net to the single cable is considered as negligible. As a consequence, only the deformation of the cables in the horizontal plane will be assumed to be significant in the resistant mechanism of the structure.

Starting from the equilibrium equation of the i-th cable in differential form at the time instant t,

$$\frac{d^2u_i}{dx^2} = -\frac{q_t(z_i,x)}{H_i} = -\frac{q_{ti}(x)}{H_i} \tag{6}$$

where u_i is the horizontal displacement of a generic point, with coordinate x, of the cable (in the y direction).

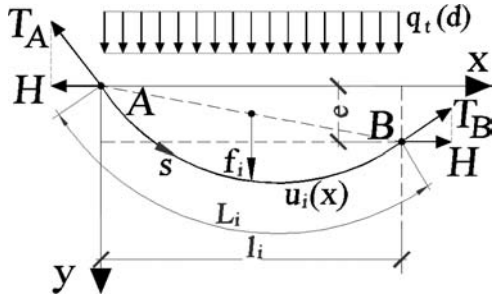


Figure 4. Scheme of the single cable under the forces produced by the impact of a debris-flow, with related geometrical and static quantities.

After a double integration and by assuming a constant distributed load at a given time instant the tensile axial force $T_i(x)$ in the cable can be computed as:

$$T_i(x) = H_i \cdot \frac{ds}{dx} = H_i \cdot \sqrt{1+\left[\frac{q_{ti}}{2H_i}\left(l_i - 2x\right)\right]^2} \cong H_i \tag{7}$$

based on a direct relation between the cable deformation (u) and the loading pressure:

$$q_{ti}(\bar{u}_i) = \frac{64\,E_i A_{ti}}{3l_i^4} \cdot \bar{u}_i^{\,3} \tag{8}$$

where A_{ti} is cross section of the equivalent cable representing the transversal net and E_i is the Young modulus of the equivalent transversal cables representing the net.

It must be also recalled that, in debris flow net barriers, the presence of brakes is quite common; such a devices operate by dissipating energy and by increasing the cable length once the maximum allowable force of the brake is reached. Such an increased length produces a beneficial effect by inducing a decrease of the tension forces in the cables, while neglecting the brakes usually leads to a conservative design of the barriers.

$$f_b = \begin{cases} T_i \cong H_i & \text{if } T_i < f_{b,\max} \text{ and } s_b = 0 \\ f_{b,\max} & \text{if } T_i > f_{b,\max} \text{ and } s_b \le s_{b,\max} \\ T_i \cong H_i & \text{if } s_b > s_{b,\max} \end{cases} \tag{9}$$

where f_b, $f_{b,max}$ are the generic force and maximum allowable force in the brake, respectively, and s_b, $s_{b,max}$ the generic displacement and maximum allowable displacement in the brake, respectively.

Since the horizontal cables are connected by the barrier net, it can be assumed that they are joined together by 'equivalent' vertical cables having the effect to distribute a portion of the load directly applied to each horizontal cable to the adjacent ones. In order to determine the load distribution among the cable a parameter

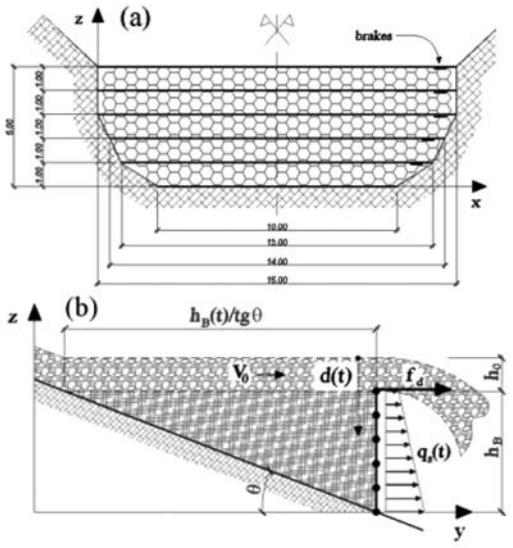


Figure 5. (a) Barrier geometry, (b) flow data.

r that relate the displacement u to the load q has been define as:

$$\frac{d^2u_i}{dx^2} = -\frac{\beta_i \cdot q_{ti} \cdot \dfrac{r^3(z_i,z_i)\cdot C_i}{\sum_{k=1}^{n} r^3(z_k,z_i)\cdot C_k}}{H_i} + \\ -\frac{\sum_{\substack{j=1 \\ j\neq i}}^{n} \beta_j \cdot q_{tj} \dfrac{r^3(z_j,z_i)\cdot C_i}{\sum_{k=1}^{n} r^3(z_k,z_j)\cdot C_k}}{H_i} = -\frac{Q_i}{H_i} \tag{10}$$

where $r(z_j, z_i)$ is equal to:

$$r(z_j,z_i) = \frac{1}{\left(\left|z_j - z_i\right| + 1\right)^{m_{ji}}} \tag{11}$$

and the coefficient $\beta_j = 1.0$ if $q_j \neq 0$ and $\beta_j = 0$ if $q_j = 0$.

The function $r(z, z_i)$, if properly tuned through its coefficient m_{ij}, can represent the relation between the displacements of two connected cables.

The coefficient m and the consequent relation r have been determined by the authors based on a specific calibration test.

The method allows to calculate (by solving the obtained non-linear problem) the effective cable length and the corresponding force H_i at the equilibrium state. the system is solved by a genetic algorithm in a iteration way: a starting random configurations are defined and an error function determined. The algorithm determines the configuration that minimizes the error.

The above described mechanical model has been implemented in a simple in-house made Fortran code.

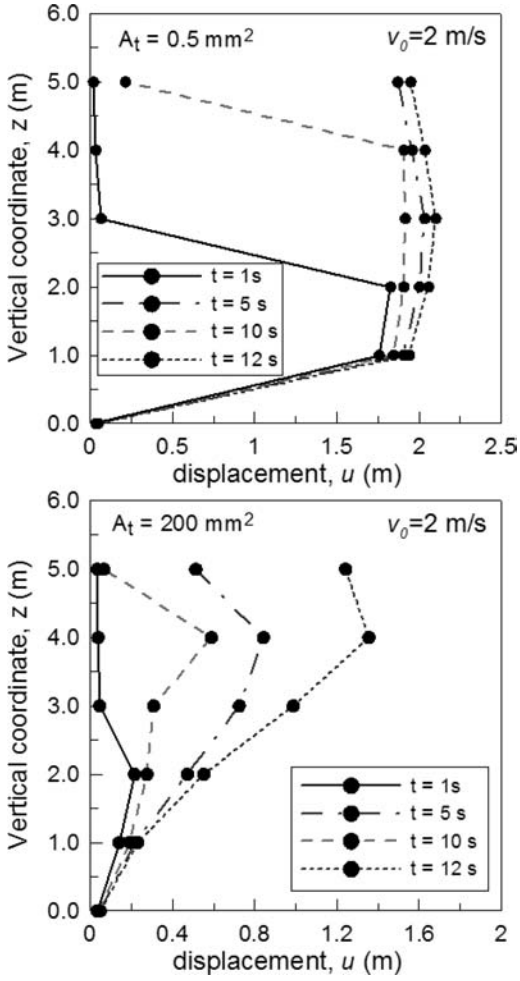


Figure 6. Vertical deformed sections of the barrier mid span at different time instants: (a) $A_t = 0.5\,mm^2$, (b) $A_t = 200\,mm^2$.

3 PARAMETRICAL ANALYSIS

Considering the scheme in Figure 5, where the barrier geometry and the flow data are reported, and considering a flow velocity equal to 2, 4 and 8 m/s and A_t equal to 0.5, 50 and 2000 mm^2 respectively, one can obtain the following results (Fig. 6 and Fig. 7), in terms of vertical middle deformed sections at different loading times, acting forces, brake sliding, brake energies and elastic energy on the 6 cables.

For each cable the maximum force has been calculated by considering a fixed velocity v_0 equal to 2 m/s and by varying the "apparent" transversal section of the net (Fig. 8); then the maximum force has been calculated by considering a fixed transversal section A_t of the net equal to 0.5 mm^2 and by varying the velocity v_0 (Fig. 9).

The practical example reported shows as the cable are loaded in different times depending on the flow velocity and that the central cables (3 and 4 in Figure 7)

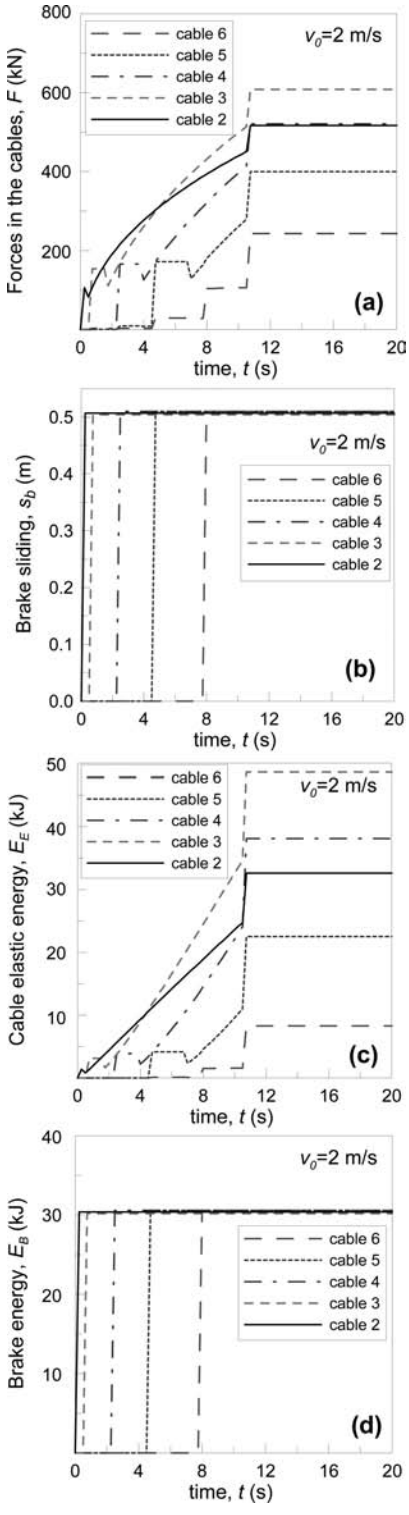


Figure 7. Results obtained by the proposed model for a fixed $A_t = 0.5\,mm^2$ vs time: (a) forces acting in the cables; (b) brakes sliding; (c) elastic energy stored in the cables and (d) brakes dissipated energy.

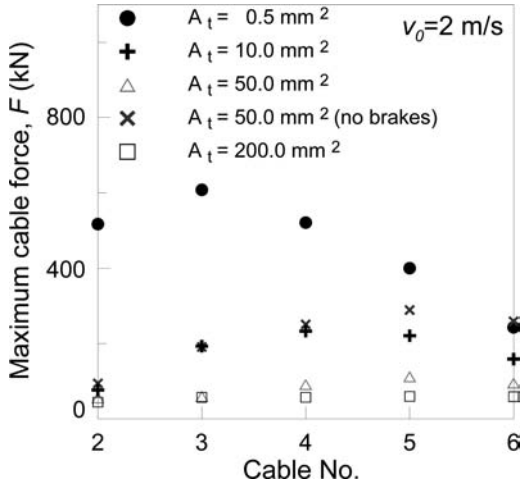


Figure 8. Maximum forces in the cables for a fixed flow velocity and variable "apparent" cross section of the net A_t.

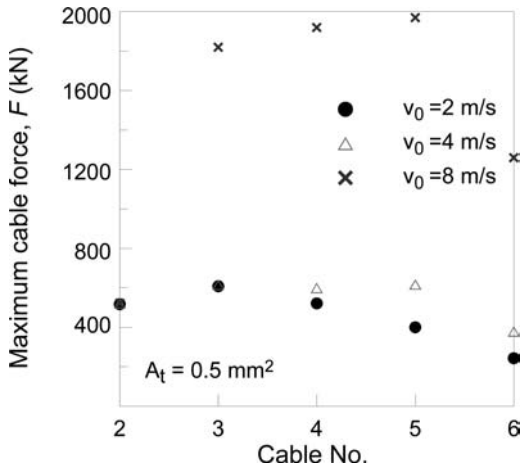


Figure 9. Maximum forces in the cables for different velocities and fixed "apparent" cross section of the net A_t.

are those where a larger state of stress is induced. The brakes are activated at different time but they reach the same stress rate. In Figure 8 the influence of the resisting sections is shown while in figure 9 the flow velocity influence is reported. One can observe as the choice of the optimal resisting section can be made by comparing the maximum induced force in the cable with the cable resistance obtained from the UNI EN-12385-4 code. Figure 8 also shows as the brake presence decreases the cable induce forces and consequently improves the barrier performance with a fixed cable section.

Finally in Figure 9 the increase of the flow velocity results in an increment of the induced maximum cable load in a nonlinear way, since it is connected to the energy balance.

4 CONCLUSIONS

The obtained results show as the impact of a debris flow need a more complicate analysis than that of a single block during a rock fall phenomena. The design of deformable barriers requires a deep knowledge of the slope geology and morphology in order to estimate the velocity of the flow and its rheology that can determine different impact mechanics and conseguent acting forces. More over, during the impact of a debris flow a large part of the kinetic energy is dissipated by friction forces and collision whilst with rock fall all the kinetic energy is dissipated by the barrier in a nearly instantateous impact. The energy dissipation determines a different energy balance during the barrier loading phase with different induced state of stresses.

The above mentioned consideration are accounted for in the proposed analytical method that can consider a realistic distribution of the load, either in time and space. The model simplification makes the proposed method easier and quicker to be applied if compared with numerical model while still taking the major aspects of the phenomena into account. This method allows for parametric analysis that are always suggested when dealing with natural phenomena where a large variability of the ruling parameters are expected.

REFERENCES

Brighenti et al. (in prep.) Debris flow hazard mitigation: a simplified analytical model for the design of flexible barriers. *Computers and Geotechnics.*

Canelli, L., Ferrero, A.M., Migliazza, M., Segalini, A. 2013. Debris flow risk mitigation by the means of rigid and flexible barriers – experimental tests and impact analysis. *Nat. Hazards Earth Syst. Sci.* 12: 1–7 (www.nat-hazards-earth-syst-sci.net/12/1/2012/ doi:10.5194/nhess-12-1-2012).

Ferrero, A.M., Giani, G.P., Segalini, A. 2010. Numerical and experimental analysis of debris flow protection fence efficiency. Proc. European Rock Mechanics Symposium (Eurock 2010), Lausanne, CH. Balkema, Rotterdam: 578–578.

Hungr, O. 1985. A model for the runout analysis of rapid flow slides, debris flows, and avalanches. *Can Geotech J.* 32: 610–623.

Itasca Consulting Group Inc. 2003. PFC3D (Particle Flow Code in 3 Dimensions), Version 3.0. Minneapolis: ICG.

Sun, H.W. & Law, R.P.H. 2012. A preliminary study on impact of landslide debris on flexible barriers. Geotechnical Engineering Office. Standard and Testing Divison. Technical Note 1/2012. The Government of Hong Kong Special Administrative Region.

Suwa, H., & Okuda, S. 1983. Deposition of debris flows on a fan surface, Mt. Yakedake, Japan. *Z. Geomorphol. Suppl.* 46: 79–101.

Takahashi, T. 1983. Debris flow and debris flow deposition. In M. Shahinpoor (ed.), *Advances in the Mechanics and Flow of Granular Materials*, Vol. II: 57–77. Clausthal-Zellerfeld: Trans Tech Publications.

Van Dine, D.F. 1996. Debris Flow Control Structures for Forest Engineering. Province of British Columbia Ministry of Forests Research Program, 68.

Wartmann, S.T. & Salzmann, H. 2002. Debris flow and floating tree impacts on flexible barriers. Natural Terrain – A Constraint to Development? The Institution of Mining and Metallurgy – Hong Kong Branch, pp. 125–131.

Rock Mechanics for Resources, Energy and Environment – Kwaśniewski & Łydżba (eds)
© 2013 Taylor & Francis Group, London, ISBN 978-1-138-00080-3

Rock fall modeling for protection barrier design and validation in the Sungun copper mine

R. Tajaddodian Far & N. Behi
Pars Olang Consultant Eng. Co., Tehran, Iran

F. Alilou
Copper Industries Company Sungun Copper Complex, Tabriz, Iran

ABSTRACT: A rock fall is significant phenomenon in rock engineering. happens quickly. In 2009, a rock fall occurred in a slope located above a concentration plant in the Sungun copper mine (northwest of Iran) and damaged structures. After the occurrence of the rock fall, both a stability analysis and stabilization system design were executed for the slope. In this study, the Sungun concentration plant slope was rated using the RHRS system and was determined to be a dangerous region. In addition, behavior parameters were determined based on the back analysis method. Laboratory test results and information about the fall were used in this method. Sections in the dangerous region and analysis models were prepared after determining the behavior parameters. The result of the modeling specifies the rock fall profile, energy of the fall and the point at which the rock stopped. Finally, stabilization systems were designed using the results of the modeling.

1 INTRODUCTION

The text The Sungun copper mine, which is the second largest open pit mine in Iran, is located 100 km northwest of Tabriz City. This area is a mountainous region. The Sungun ore body is a porphyry copper deposit and the mine was designed to produce 7 million tons of ore with future expansions of up to 14 million tons. The ore body is located in a deep valley and the local topography ranges from 1700 to 2450 m.

The Sungun concentration plant is situated south of the Sungun mine. The concentration area is mountainous. A big slope 70 m high and 500 m wide was constructed in order to build this plant. There are some blocks of trachyte at the top of the slope, which can cause rock fall. This matter was reported during the construction of the slope. In addition, a rock fall occurred in this region in June 2009.



Figure 1. Location of the Sungun area in Iran.

The following are discussed in this paper. Firstly, the geology of the area is described, followed by a description of how the region was rated using the RHRS system and determined to be a high-risk area. Next, the behavior parameters that were determined by laboratory tests and back analysis are presented. Finally, there is a discussion of how the slope was modeled using RocFall software and how suitable support systems were designed for each region.

2 GEOLOGY

The geology of the area is very complicated. There are three active tectonic areas in this region (Tajaddodianfar 2009) and there are several blocks of trachyte at the top of the slope (Fig. 2).

The trachyte blocks have undergone intensive weathering have been converted to soil in some parts. Many factors such as mine blasting, dynamic forces, freezing and unfreezing all had an on the rock fall.

For analysis of the rock fall, the slope was separated into seven regions based on the RHRS system and geological parameters. The geological parameters, slope height, weathering and fall history were rated to 0 to 81 scores according to this system (Tajaddodianfar 2009).



Figure 2. The slope of the concentration plant.

Table 1. Result of rating in different regions.

Row	Region	RHRS Rate	Comment
1	A region	245	Low danger
2	RF3-RF1	464	Medium danger
3	RF1-RF2	476	High danger
4	RF2-RF4	498	High danger
5	RF4-RF5	489	High danger
6	RF5-RF6	572	High danger
7	RF6-RF7	549	High danger

In RHRS system, regions with a score of 500 or more are considered to be in the dangerous range (Maerz 2000, Pierson et al. 2001).

The RHRS system that is used in the construction of railways and roads was modified by the authors for the concentration plant (Tajaddodianfar 2009). AVR and DSD have a maximum rate because the plant is the constant. The rating results in different regions are listed in Table 1.

3 BEHAVIOR PARAMETERS

The back analysis method was used to determine the behavior parameters. Initially, a profile of the rock fall was drawn. Then, pairs of the coefficient of restitution (RN and RT) were determined. In the next step, the fall profile was modeled using these pairs. The best profile, the one that was most similar to the actual fall, was selected and the pairs of this model showed the behavior parameters of the region of the rock fall (Fig. 3).

The behavior parameters that were determined using the back analysis method are presented in Table 2.

The weight of the blocks is an important parameter in a rock fall. Three types of blocks including small, medium-size and large are located in several regions. Table 3 presents the classification of the properties of the blocks that were determined using field survey and statistical studies.



Figure 3. Profile of the actual rock fall.

Table 2. Behavior parameters of the rock fall.

Row	Litho	RN	Std.	RT	Std.	Friction Angle
1	Soil-Rock	0.33	0.007	0.8	0.003	25
2	Rock	0.2	0.01	0.78	0.005	22
3	Concrete	0.45	0	0.73	0	38

Table 3. Block properties (weight [kg]) in different regions.

	Small Block		Medium-size Block		Large Block	
Region	Mean	Std.	Mean	Std.	Mean	Std.
Rf3-rf1	552	253	2505	1213	10615	6092
Rf1-rf2	451	262	2090	948	7601	3150
Rf2-rf4	491	249	2173	904	11588	4509
Rf4-rf5	432	281	2268	864	9307	4913
Rf5-rf6	480	315	1921	772	10999	8254
Rf6-rf7	408	281	2153	1016	11870	8271

4 STABILITY ANALYSIS

Stability analysis was performed in different regions with RocFall software based on the results of the back analysis (Schwegl 2003). The main objective in this analysis was to determine the place where the block stopped and the energy of the falling blocks. Generally, Monte Carlo simulation method utilizing 100 blocks was used in the stability studies. Furthermore, a probability analysis, which determines the accuracy of the results, was carried out on the RocFall results. As the results indicate, the concentration plant is susceptible to rock falls.

Table 4 compares the stability results, while Figure 4 presents a stability analysis of regions Rf6-rf7

Table 4. Fall energy [kJ] in different regions.

	Small Block		Medium-size Block		Large Block	
Region	Mean	Re%	Mean	Re%	Mean	Re%
Rf3-rf1	36	62	182	68	761	62
Rf1-rf2	19	65	41	68	294	59
Rf2-rf4	9	69	34	70	204	66
Rf4-rf5	12	68	61	68	241	65
Rf5-rf6	11	67	83	71	256	63
Rf6-rf7	31	63	73	71	412	67

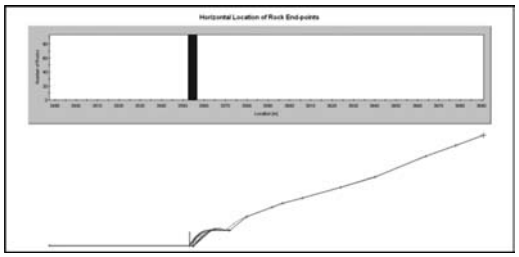


Figure 4. Rock fall analysis and the place where the fall stopped in regions Rf6-rf7.

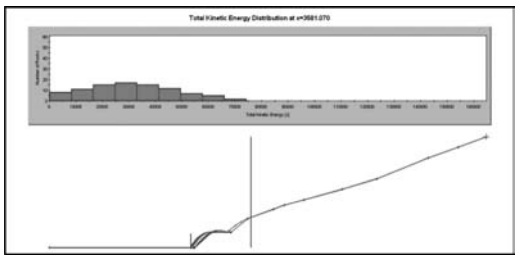


Figure 5. Fall energy for small blocks.

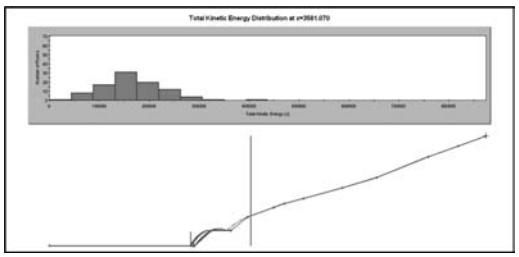


Figure 6. Fall energy for medium-size blocks.

and Figures 5–7 illustrate fall energy in this area for different blocks (Tajaddodianfar & Shariar 2004).

5 SUPPORT SYSTEM DESIGN

Considering the importance of the concentration, a proper support system had to be designed to protect it from rock falls.

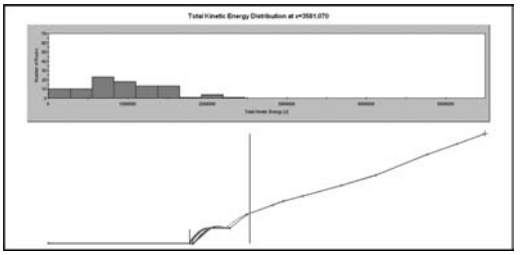


Figure 7. Fall energy for large blocks.

Table 5. Results of fall control system.

Region	Stabilization sys.	Barrier Height	Barrier Capacity
Rf3-rf1	Elastic Sys.	2	350
Rf1-rf2	Elastic Sys.	1.5	300
Rf2-rf4	Elastic Sys.	2	300
Rf4-rf5	Elastic Sys.	1	200
Rf5-rf6	Elastic Sys.	1	150
Rf6-rf7	Elastic Sys.	2	350

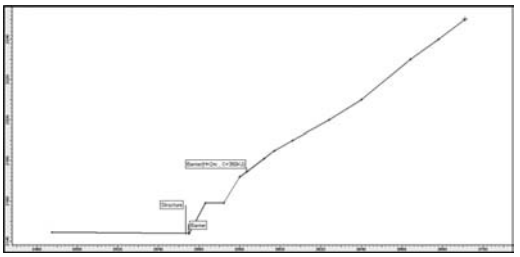


Figure 8. Stabilization systems in regions Rf6-rf7.

The main objectives of the design of the support system were as follows:

a) to control the movement of unstable blocks,
b) to control the falling blocks in an area with low energy,
c) to guarantee safety for different areas,
d) to design an economical system.

A support system that met the above-mentioned objectives was designed for the concentration slope. The best system was an elastic barrier, which can control blocks with a fall energy of 500 kJ.

After designing the supporting system, a statistical simulation was carried out using the Monte Carlo method for different regions and the efficiency of the control system was determined for each region.

Table 5 shows the results of the support system that was designed.

Figure 8 presents the stabilization system in regions Rf6-rf7.

Figure 9 shows the model of regions Rf6-rf7 after the designed support system was installed.

An elastic barrier has a good efficiency and it can control falling blocks. Table 6 presents the results

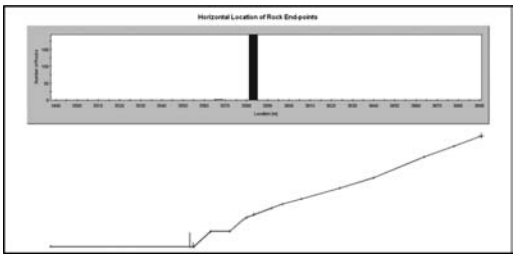


Figure 9. End point of a falling block after the installation of the support system in regions Rf6-rf7.

Table 6. Simulation results of the control system for rock falls.

Region	System Accuracy*	Risk Reduction
Rf3-rf1	82%	93.5%
Rf1-rf2	84%	92.5%
Rf2-rf4	75%	89.2%
Rf4-rf5	75%	82.3%
Rf5-rf6	63.5%	79.2%
Rf6-rf7	72%	83.7%



Figure 10. Passive protection system installed on the slope above the concentration plant at the Sungun copper mine.

of the Monte Carlo simulation method that was performed for the stabilization systems.

In summary, rock fall protection systems, including both active and passive systems together with gabion walls, were designed using a compilation of the results of modeling, probability analysis and a technical and economic evaluation (Figs 10–12).

6 EARTHQUAKES AND THE REACTION OF THE PROTECTION SYSTEMS

After installing the protection systems, two earthquakes with magnitudes of 6 and 6.5 on the Richter scale occurred near the Sungun mine and caused some of the blocks located above the concentration plant



Figure 11. Active protection system installed on slope above the concentration plant, Sungun copper mine.



Figure 12. Active protection system installed on the slope above the concentration plant at the Sungun copper mine.



Figure 13. Reaction of the passive system, which controlled the 7-ton block.

to fall. Support cables in the active support system were extended after the occurrence of the first earthquake. They controlled the blocks. Then, the passive system controlled the moving blocks (7 tons and 300 kg) and prevented them from falling down and striking the concentration plant (Figs 13–14).



Figure 14. Control of the 7-ton block that fell towards the concentration plant.



Figure 15. Control of the 300 kg block that fell towards the concentration plant.

7 CONCLUSIONS

The results of this study are as follows:

1. The blocks above the Sungun concentration plant slope are susceptible to rock fall.
2. The RHRS system was used to rate the slope.
3. The RHRS system was modified for the slope because it is designed for the construction of railways and roads.
4. The scores of AVR and DSD were changed in order to modify the system.
5. The modeling result shows that rock falls threatens the concentration plant.
6. The accuracy of the stability analysis was determined by Mont Carlo simulation method and the average result was 79.2%.
7. The best stabilization system for controlling a falling block with a 500 kJ capacity for all of the regions was an elastic barrier.
8. The accuracy of the stabilization system is 68.2%.
9. An earthquake occurred in Azerbaijan Province near the Sungun copper mine on August 11, 2012. It destroyed many buildings, but the protection systems prevented the blocks that were located above the concentration plant and conveyor from falling.

ACKNOWLEDGEMENTS

The authors appreciate the individuals who supported and helped us in completing this project. Special thanks to the NICICO personnel, Mr. Almasi (POC Direct Manager), Mr. Baghernezhad (Sungun mine manager) and Ms. Kimia Kalantari.

REFERENCES

Maerz, N.H. 2000. Highway Rock Cut Stability Assessment in Rock Mass Not Conducive to Stability Calculations. Proceeding of the 51th Annual Highway Geology Symposium; Seattle, Washington. USA.

Pierson, L.A. Gullixson, C.F. & Chassie, R.G. 2001. *Rockfall Catchment Area Design Guide*. Final Report SPR-3(032). Oregon Department of Transportation and Federal Highway Administration, Salem.

Schwegl, J. 2003. Geotechnical Characterization and Rockfall Simulation of a Slope: A Practical Case Study from South Tyrol (Italy). *Engineering Geology*, 67.

Tajaddodianfar, R. & Shariar, K. 2004. Rockfall analysis in mineral processing plant site of Sungun copper mine. Proceedings of the 5th international symposium on mining science and technology. China.

Tajaddodianfar, R. 2009. Rock fall analysis and stabilization systems technical report. Pars Olang Consultant Engineering Company; Tehran, Iran.

This page intentionally left blank

Rock Mechanics for Resources, Energy and Environment – Kwaśniewski & Łydżba (eds)
© 2013 Taylor & Francis Group, London, ISBN 978-1-138-00080-3

Slope optimization and design based on geotechnical and hydrogeological assessments for a new deep open pit coal mine

R. Ulusay, M. Ekmekci & E. Tuncay
Hacettepe University, Department of Geological Engineering, Beytepe, Ankara, Turkey

N. Hasancebi
EnerjiSa Power Generating Company, Balgat, Ankara, Turkey

ABSTRACT: Isikdere open pit mine has been operating since late 2009 by the Turkish Coal Enterprises to provide lignite for a thermal power plant. The technical objectives of this study are to evaluate stability of the final pit slopes and to recommend necessary modifications on the current pit project and remedial measures. The analysis results indicate that stability of the final pit slopes is sensitive to multiplanar failures and pressurized water in the coal seam is also another factor adversely affecting the stability. Problems associated with groundwater at the site were also assessed with the analyses of piezometric level and groundwater inflow. Remedial measures investigated suggest that at some parts of the pit, original project should be modified by flattening or shifting the final slopes towards north or stripping them to a certain elevation.

1 INTRODUCTION

The Isikdere open pit mine, with a length of 2.5 km, width of 750 m and maximum depth of about 150–170 m located at western Turkey, has been operating since late 2009 by the Turkish Coal Enterprises (TKI) to extract lignite for a thermal power plant in the vicinity (Figure 1a). Excavation of the pit has been initiated at the SE boundary of the coal sector and is progressing towards NW (Figure 1b). The current width and face angle of the working benches are 7–10 m and 60°, respectively, and overall angle of the final sidewall slopes is planned as 30°–32°.

The technical objectives of this study is to evaluate stability of the final pit slopes throughout the coal field, to assess hydrogeological conditions affecting the pit slope stability, and to recommend necessary modifications on the initial pit project and remedial measures based on geotechnical and hydrogeological conditions.

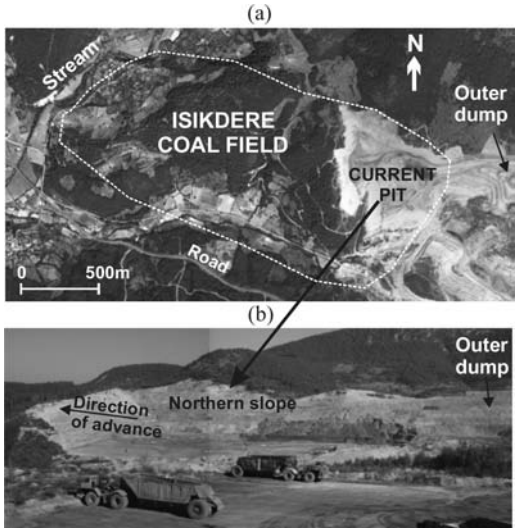


Figure 1. (a) Satellite view of the coal field (www.google.com), (b) a view from the current pit.

2 ENGINEERING GEOLOGY OF THE PIT

At the Isikdere coal field, Tertiary coal measures, which consist of Turgut, Sekköy and Yatagan formations, overlie the basement rocks (Palaeozoic schist and Mesozoic crystallized limestone at south and north, respectively). The Sekköy formation consists of thick-bedded compact marls overlying the coal seam, thinly laminated marls and limestone alternation and a weak zone at the top at north. The coal seam is underlined by the plastic underclay of Turgut formation (Fig. 2). Yatagan formation is the youngest section of the coal measures mainly consisting of tuffites and marls and exposes at the SE boundary of the pit. An alluvial sequence of 2–8.5 m thick and slope debris composed of fine grained material surrounding small pieces of limestone overlie the coal measures at the west and north, respectively.

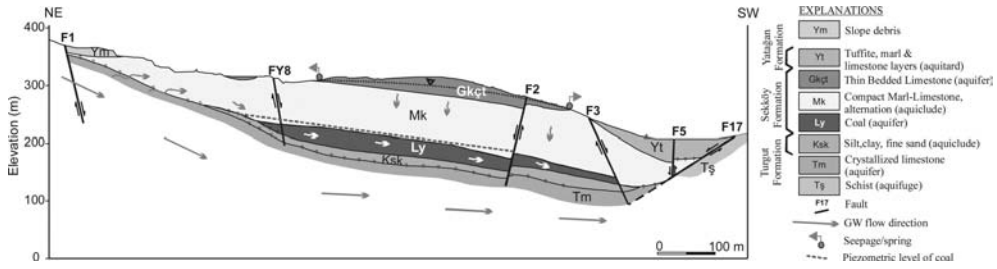


Figure 2. Geological and hydrogeological cross-section from the Isikdere coal field.

The coal measures and coal seam have evident smooth bedding planes and are dissected by nearly vertical (75°–85° and moderately persistent three main joint sets. While the bedding is nearly horizontal at the central part of the field, it dips to south and north with inclinations ranging between 2° and 26° at north and southeast, respectively (Fig. 2). The coal field was divided into blocks by a number of normal faults with dips between 65° and 70° and slickensided surfaces. Particularly, the two longest faults (Faults F1 and F17 in Figure 2) have an important role on the stability of the pit walls due to their continuity.

3 HYDROGEOLOGICAL CONCEPTUAL MODEL

The hydrogeological study ultimately aimed at construction of a hydrogeological conceptual model which provided a thorough understanding of occurrence and movement of groundwater at and around the open pit. Field studies to define the hydrostratigraphic units and the extension and thickness of the water-bearing layers included geological and hydrographic mapping, geophysical survey, drilling 32 exploration/observation wells, in-situ tests, water sampling for hydrochemical and isotopic analyses by following the procedure and steps defined in ASTM (1999) (Fig. 3).

The Paleozoic schist forms the impervious basement rock. The Mesozoic crystallized limestone is highly fractured and karstified, and forms one of the major aquifers with hydraulic head lower than the bottom of the ultimate pit in the region. Groundwater occurrence and permeability of the coal seam, reaching up to as high as 84 Lugeon, suggested that it forms an aquifer confined by the impervious Turgut formation from the bottom and the thick, impervious claystone-compact marl sequence from the top. Hydraulically, the coal seam is not connected to the Mesozoic crystallized limestone.

The thin bedded limestone at the most upper section of the Sekköy formation with permeability of between 5 and 70 Lu (moderate-to-high) is fractured and locally karstified along major fractures and faults. However, this unit does not form an aquifer in the site due to two reasons; firstly, the secondary openings (fractures) and karstic cavities are mostly filled by the fines of the overlying Yatagan formation, and

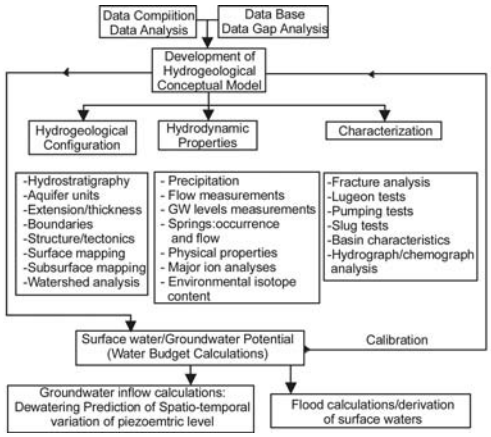


Figure 3. Flowchart of the methodology applied for hydrogeological conceptualization.

secondly this unit has been dissected by incision by creeks forming small caps which do not allow formation of permanent saturated zone. The hydrogeological conceptualization is depicted in Figure 2. The alluvial sequence is an unconfined aquifer with a local extension of 0.2 km^2 and fully penetrated by the intermittent stream along the western pit boundary. During high water level (rainy) periods, the aquifer is recharged by the stream. As the recession (low water level) period starts the flow direction is inversed and the groundwater discharges back to the stream valley. Based on this fact, it was recommended that the streambed should be excavated during the low water level (dry) period, when the alluvial aquifer will not create dewatering problems.

4 PIEZOMETRIC LEVEL AND GROUNDWATER INFLOW

Hydrogeological analyses were performed to calculate (a) the temporal change of the piezometric level of the coal seam at the vicinity of the excavated surface and (b) the total ground inflow to the pit. The compact marl sequence overlying the coal layer does not contain groundwater, and therefore, groundwater flow into the pit will occur only when the coal seam is cut by excavations. The drop of the piezometric level

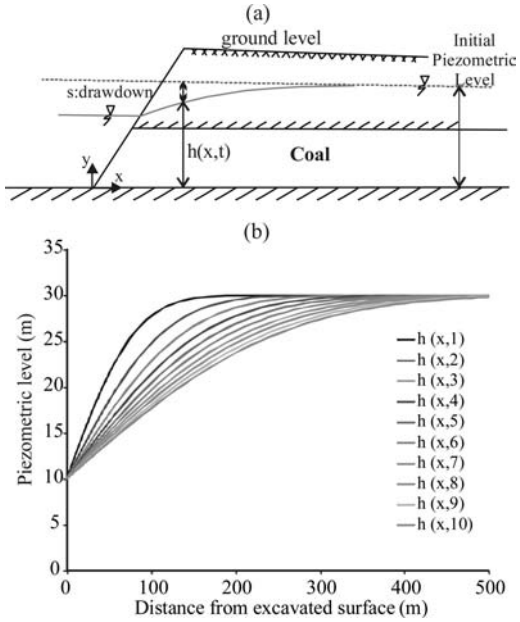


Figure 4. (a) Conceptualization of groundwater flow into the pit, (b) piezometric level predictions for x and t.

at and behind the excavated surface was estimated by an analytical solution of the partial differential equation simulating the groundwater flow in confined aquifers (Fig. 4a). The field conditions well satisfy the assumptions and the boundary conditions defined for the analytical solution given by Nguyen & Raudkivi (1982). The solution for a certain cross-section is given in Figure 4b as a set of curves depicting the piezometric level change with respect to distance from the excavated surface (x) and time (t). The groundwater inflow to the pit was calculated using the extended solution of Nguyen & Raudkivi (1982). Owing to the hydraulic characteristics and the limited thickness of the coal aquifer, the groundwater flow into the pit was found to be in the order of less 0.3 l/s per unit length of the excavated surface of the coal.

5 GEOMECHANICAL TESTING

Detailed laboratory testing of discontinuities (bedding planes of coal measures, fault gouges) and underclay were conducted to investigate their geomechanical characteristics. Since the alluvial sequence at the western pit boundary is very thin and will be stripped during mining, no geomechanical test was performed on this unit. The slickensided bedding surfaces of the marls in the main overburden have the lowest shear strength (Table 1a). The rock mass shear strengths of the overburden units and the coal seam were also determined using Hoek-Brown failure criterion (Hoek et al. 2002) and the input parameters used in the calculations for different overburden units and coal seam are given in Table 1b.

Table 1. (a) Shear strength parameters of discontinuities and soil materials with materials' unit weight.

	Shear strength				
	Peak		Residual		Unit
Material/ Discontinuity	c (kPa)	ϕ (°)	c (kPa)	ϕ (°)	weight (kN/m^3)
Non-slickensided bedding in marl	5.4	28	4.4*	15.4*	14.9
Slickensided bedding in marl	0.9	14	0	12.5	
Bedding in tuffite	0	34.2	0*	32.9*	14.4
Underclay	20.9	19.2	13.4*	13.1*	18.0
Fault gauge	16.3	29.4	14*	19.1*	–
Slope debris	8.9	21.7	8*	15.8*	17.6

*Employed in the stability analysis

(b) Hoek-Brown parameters for the rock masses

Unit	GSI	UCS (MPa)	m_i	D
Marl/marl-limestone	50	17.9	4	1
Weak zone (Northern slope)	45	4.3	3	1
Lignite	40	7.8	18	1
Tuffite	26	3.6	15	1

GSI: Geological strength index (estimated from the quantified GSI chart by Sonmez & Ulusay (2002), UCS:Uniaxial compressive strength, m_i: constant m for rock material, D: Disturbance factor

6 BACK-ANALYSIS OF LOCAL BENCH FAILURES

In the current pit, three local instabilities including a few benches constructed in the marls of Sekköy formation occurred in the form of planar failure along bedding planes. Two slope sections from instability 1 and one section from instabilities 2 and 3 were back analysed using the Hoek & Bray (1977)'s method and the back-calculated shear strength of bedding planes were compared with experimentally determined shear strength parameters (Fig. 5). The back-analyses suggested that the use of the residual shear strength parameters of the bedding planes will be more representative in the stability assessments of the pit slopes.

7 STABILITY AND RE-DESIGN OF THE FINAL PIT SLOPES

7.1 *Methodology*

On the basis of the initial pit slope project, the crest and toe of the final pit slopes are shown in Figure 6. The most critical stability conditions for the final pit slopes, which were previously planned throughout the coal field with an overall angle of 30°, was investigated along 19 cross-sections (Fig. 6) by a

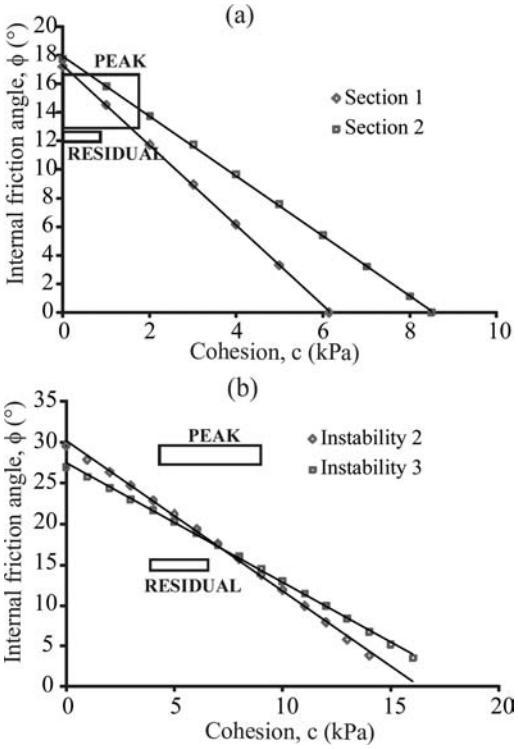


Figure 5. Back analysis results of (a) Intsability-1 and (b) Instabilities 2 and 3.

series of limit equilibrium analysis considering three main modes of failure illustrated in Figure 7. The expected piezometric level through each section analysed was estimated from the solutions discussed in hydrogeology section. By considering the previous studies (Apaydın & Ulusay 1990, Ulusay 1991) and the back-analysis results, shear strength parameters of discontinuities and soil materials in Table 1a and input parameters for rock masses in Table 1b were utilized in the analyses. Practical experience (Hoek & Bray 1977, Huang 1983) suggests that for critical slopes, a minimum safety factor (SF) of 1.2–1.25, preferably 1.3, is used if the design is based on residual shear strength. If the ground acceleration is not taken into consideration, safety factors between 1.3 and 1.4 are more preferable. In this study, SF values between 1.3 and 1.4 for final slopes and 1.1 for benches were considered to be suitable. The computer code Slide (Rocscience 2009) for circular and non-circular failures, and the one developed by Hoek (1987) based on Sarma (1979)'s method for analysing multiplanar failures were employed.

7.2 *Assessments for redesign of the pit*

In the first stage of analyses, stability of the slopes in the slope debris at the northern part of the pit and possibility of rock mass circular failure through the main overburden (Sekköy formation) were investigated. For SF = 1.3, a general slope angle in the slope debris was found as 25°–26°. The analyses suggest that no rock mass failure is expected throughout slopes in the overburden if the overall final slope angle (30°) considered in the original pit project is applied.

The stability of the northern final slope, striking NW-SE, was analysed based on the types of instability in Figure 7 using initial slope profiles on the cross-sections 1–5, 7–9, 16 and 19 (Figure 6). If a SF $\geq$ 1.3 was calculated for each slope profile in the original pit project, it was concluded that a final slope angle of 30° for the analysed cross-section is acceptable for design. In the case of SF < 1.3, additional analyses were performed to redesign (slope flattening or overburden stripping to a certain elevation or shifting the position of the preliminary slope) the slope until the calculation gave an SF $\geq$ 1.3 for each analysed slope profile. Only the stages of the analysis carried out for the redesign of sections 1 and 5 are given in detail herein.

The analyses indicated that circular and non-circular failures are more critical than translational failures along Section 1 and the lowest SF was obtained for a compound failure surface passing through the slope debris, weak zone in the Sekköy formation and its marly sequence and following the bedding plane in the Sekköy formation (SF = 1.24). If the toe of the slope is shifted towards south, depth of the slope will increase and consequently SF will decrease. Therefore, as a redesign alternative, without changing the position of toe of the slope in the original project, the effect of a stripping procedure (starting from +346 m to +310 m; Fig. 8a) on stability was analysed. As it will be seen from Figure 8a, at the end of the fifth stripping stage SF increases up to 1.31 which is a suitable value for design.

Because the final slope in the original project is critical (non-circular failure, SF = 0.94) and stripping cannot contribute significantly to increase SF (1.08), slope flattening was considered as a solution for Section 5. The results indicate that a final slope angle of 23° will provide a safe slope design (Fig. 8b).

The results obtained from other cross-sections representing the northern final slope are shown in Figure 6.

The overall angle of the southern final pit slope was also planned as 30° in the original project. This slope was analysed using slope profiles along the cross-sections 1–3, 5–7, 9 and 11–13. Due to the presence of a continuous basin margin fault (Fault 17) and associated adversely dipping strata at the south of the pit (Fig. 2), mutiplanar failure becomes more critical than others. The analysis results showed that circular and non-circular failures were not critical for the southern final slope. The calculated SF values indicated that the slope profiles along sections 1 (SF = 0.74), 2 (SF = 084), 3 (SF = 0.87) and 6 (SF = 1.16) were critical in terms of multiplanar failure. Therefore, without changing the position of the slope crest and considering the water pressure, slope flattening from 30° to 17° and 20° was analysed (slopes 1 and 2 in Figure 9).

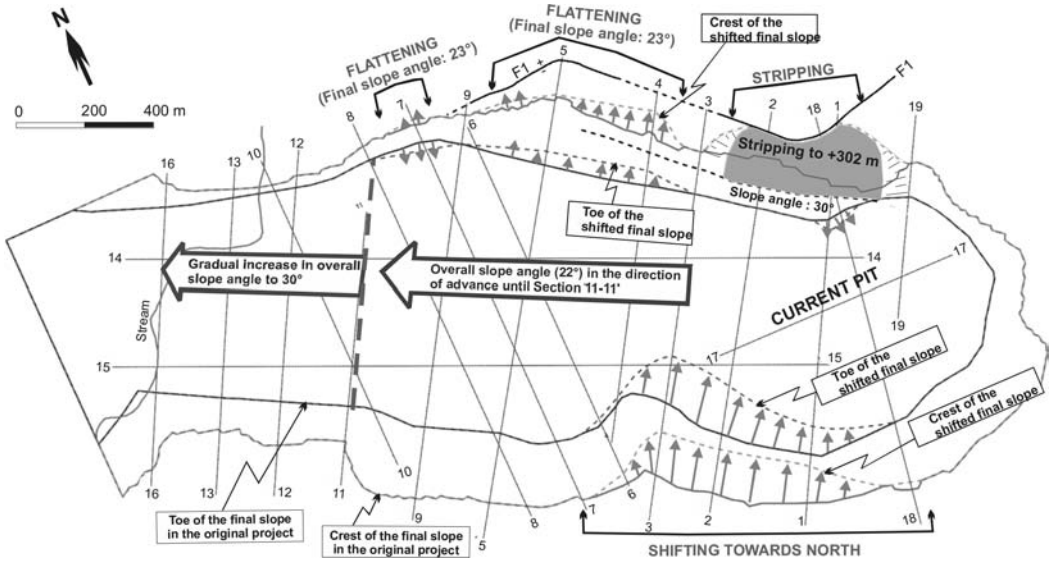


Figure 6. Comparison of the final pit slopes based on original project and stability analyses.

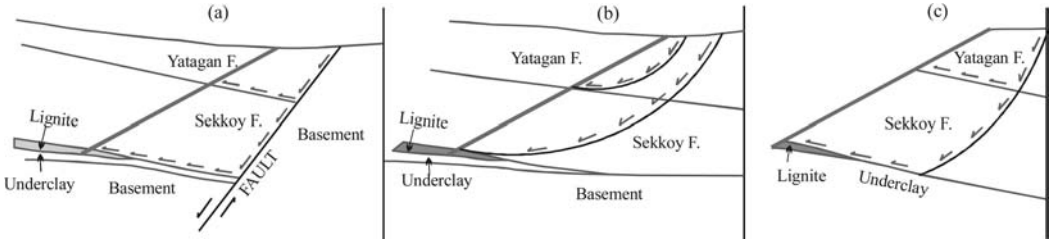


Figure 7. Modes of failures considered in pit slope stability analyses.

Although the calculated SF values increased, they were still less than 1.3. The other re-design alternatives with and without water pressure are given in Figure 9 with the calculated SF values (Slopes 3–6). In case of flattening the slope from 30° to 20°, SF value increased to 1.28 (Slope 4 in Figure 9). But this alternative will result in more overburden removal and leaving more coal. Slope 6 (Fig. 9), which also considers water pressure and is obtained shifting the planned slope towards NE, seems as the best solution. These redesign considerations were also applied to the slope profiles along cross-sections 2, 3 and 6. For these sections, shifting the original position of the slope with an overall angle of 30° towards NE was also found to be necessary. The analyses performed along other sections, which represent the southern final slope, yielded SF $\geq$ 1.3 indicating that the original slope project is applicable at the western part of the southern slope (Fig. 6). The analyses based on different failure types for the western final pit slope revealed that an overall final slope angle of 30° will provide safety in terms of stability (Fig. 6). However, the analyses suggested that the overall angle of the advancing slope should be kept as 22° until section 11 and then should be gradually increased to 30° as shown in Figure 6.

On the basis of the analyses, in order to achieve stable conditions, eastern part of the northern final pit slope should be flattened or stripped to a certain elevation or shifted towards north. As seen in Figure 6, shifting back the final pit slope towards north without any change in its overall angle is necessary at the eastern part of the southern final slope.

8 CONCLUSIONS

The orientation of strata in the coal measures and faults along the sidewalls of the pit lead to unstable conditions in mining practice in the Isikdere pit. The most critical slope instabilities are expected to occur in the form of multiplanar and non-circular failures, and therefore, advancing to north and south by following the current design seems to be troublesome. This situation calls the modification of the current pit slope design at different parts of the pit by stripping the overburden at a certain elevation or slope flattening or shifting the position of the slopes in the original

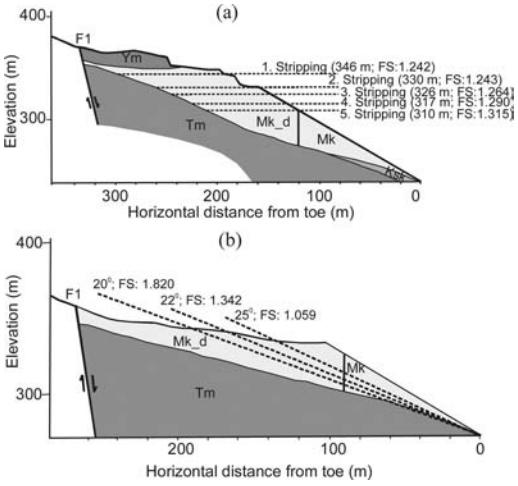
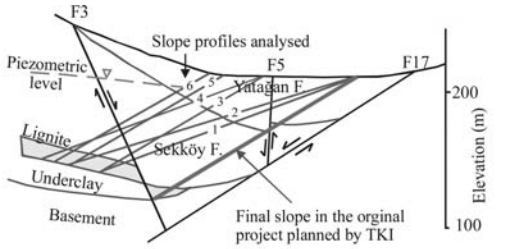


Figure 8. (a) Variation of SF depending on the elevation of overburden stripping (Section 1), (b) variation of SF with slope flattening along Section 5.



Slope No.	Slope angle (°)	Safety factor (without pore water pressure)	Safety factor (with pore water pressure)
1	20	1.13	-
2	17	1.28	-
3	30	1.05	-
4	20	1.42	1.28
5	30	1.32	1.18
6	30	1.44	1.32

Figure 9. Different slope configurations investigated to increase the stability of the southern final slope along Cross-section 1 and the values of SF calculated for each alternative considering two different water conditions.

project to achieve stability. The coal seam forms a confined aquifer which is important factor affecting the pit stability. The piezometric level was found to decline about 20 m in about one week at the excavated surface. The distance of influence was calculated to extend about 300 m from the excavated surface. Groundwater inflow per unit length of the excavated surface of the aquifer was found to be insignificant.

REFERENCES

Apaydın, N. & Ulusay, R. 1990. *Geotechnical investigation report on TKİ-GELİ Milas-Sekköy open pit*. General Directorate of Mineral Research and Exploration, Ankara (in Turkish).

ASTM, 1999. *Guide for Conceptualization and Characterization of Groundwater Systems (D5979-96). Standards on Design, Planning and Reporting of Groundwater and Vadose Zone Investigations.* Second Edition. Philadelphia, PA: ASTM Publication.

Hoek, E. 1987. General two-dimensional slope stability analysis. In: E.T. Brown (ed.), *Analytical and Computational Methods in Engineering Rock Mechanics*, London: Allen and Unwin.

Hoek, E. & Bray, J.W. 1977. *Rock Slope Engineering*. London: Institute of Mining and Metallurgy.

Hoek, E., Carranza-Torres, C.T. & Corkum, B. 2002. Hoek-Brown failure criterion-2002 edition. *5th North American Rock Mechanics Symposium, Toronto, Canada* 1: 267–273.

Huang, Y.H. 1983. *Stability Analysis of Earth Slopes*. New York: Van Nostrand Reinhold Comp.

Nguyen, V.U. & Raudkivi, A.J. 1982. Transient two-dimensional groundwater flow. *Hydrological Sciences – Journal – des Sciences Hydrologiques* 4(12): 427–438.

Rocscience 2009. *Slide V5.043- 2D limit equilibrium analysis*. Rocscience Inc., Toronto, Canada

Sarma, S.K. 1979. Stability analysis of embankments and slopes. *Journal of the Geotechnical Engineering Division ASCE* 105(GT12): 1511–1524.

Sonmez, H. & Ulusay, R. 2002. A discussion on the Hoek-Brown failure criterion and suggested modifications to the criterion verified by slope stability case studies. *Yerbilimleri* 26: 77–99 (www.yerbilimleri.hacettepe. edu.tr)

Ulusay, R. 1991. *Geotechnical evaluations and deterministic design considerations for pitwall slopes at Eskihisar (Yatagan-Mugla) strip coal mine*. PhD Thesis, Middle East Technical University, Department of Geological Engineering, Ankara

Rock Mechanics for Resources, Energy and Environment – Kwaśniewski & Łydżba (eds)
© 2013 Taylor & Francis Group, London, ISBN 978-1-138-00080-3

Influence of accuracy in specifying design input data on stability safety factors for excavated slopes in an open pit mine

V.K. Vavilova
Geodynamics Research Center – Branch of JSC "Hydroproject Institute", Moscow, Russia

ABSTRACT: The accuracy of the basic input data is extremely important in slopes stability analysis. Primarily such inputs include orientation of the planes of weakness (joints) existing in the rock mass in question, as well as parameters of the shear strength along these joints and across the rock mass. More accurate knowledge of the inputs permits reliability of the analyses to be enhanced and excessive safety margins to be avoided. The task of this study was to assess the impact of the key input parameters on slope stability of the open pit mine in Yakutia. A parametric analysis of such input data such as: dip angles of flat and steep fractures, their parameters of shear strength (tan φ and C) and of the rock mass, rock density, and angle of inclination of the open pit mine slope was performed.

1 INTRODUCTION

Effectiveness of an open cut mining as well as creation of high engineered slopes and rock excavations depend on correct determination of the general angle of slope inclination. The accuracy of the main input data is extremely important in stability analysis.

Assuming that the safety factor of a rock mass k is the product of combination of the basic design parameters p_i such as:

- dip angles of potential sliding surfaces,
- parameters of shear strength along these surfaces,
- rock density,
- dip angles of the slope,
- method of stability analysis applied,

it is possible to assess the effect of potential influence of each parameter by a value of the safety factor $\partial k/\partial \rho_i$: $k = f(\rho_i)$ ($i = 1, 2, \ldots$) using the parametric analysis method (Londe 1984, 1988, Gaziev & Rechitski 1985). This method permits to define the most sensitive parameters, and efforts should be concentrated on their more precise specification.

2 OPEN PIT MINE AND ITS GEOLOGICAL STRUCTURE

The task of this study was to assess the impact of the key input parameters on stability of the open pit mine slope of one of the deposits in Yakutia.

The main host rock is sandstone of variable preservation. The designed depth of the open cut works out to be 300 m (Fig. 1).

The southern slope of the open cut with three joint sets dipping towards the cut face was investigated: joint set I dip at 30°–60°, joint set IV dip at 70°–90°, and joint set V dip at 50°–60°. The results of geological mapping of the rock mass show that the joint of sets IV and V occur more frequently in the rock mass are longer than the joints of set I, and therefore potential failure of the rock mass in the form of rotational block slide was also considered in the analysis.



Figure 1. Open pit mine in Yakutia.

3 METHOD OF PARAMETRIC ANALYSIS

The stability on polygonal sliding surfaces were analyzed by the Bishop method, while the circular failure surfaces were analyzed using the Fellenius solution.

Parametric analysis of impact of the input parameters in question was carried applying the following typical computational schemes with due account for the rock mass structure.

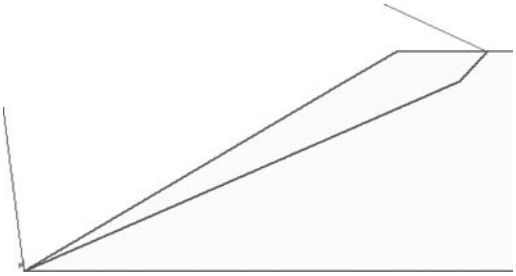


Figure 2. Computational scheme No. 1.

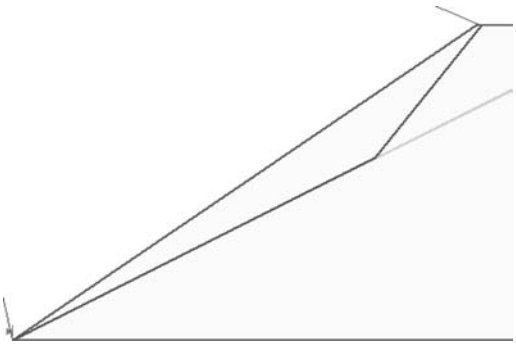


Figure 3. Computational scheme No. 2.

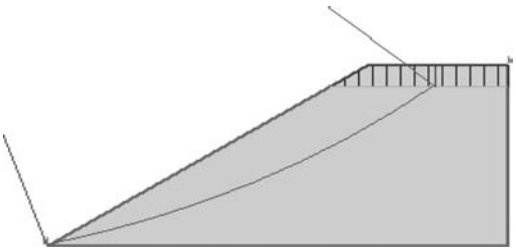


Figure 4. Computational scheme No. 3.

Computational scheme No. 1. Movement on polygonal-shaped surface formed by the combination of a steeply dipping joint of set V and gently dipping surface of set I with the length of steeply dipping joints being limited to 50 m (Fig. 2).

Computational scheme No. 2. Movement on polygonal-shaped surface formed by the combination of steeply dipping joint of set V and gently dipping slide surface of set I with the unlimited length of the steeply dipping joint (Fig. 3).

Computational scheme No. 3 (Fig. 4). Movement on circle-shaped surface bounded by a fissure tensional crack (or by one of the joints from set IV or V).

The following 8 parameters were used as inputs: coefficient of friction tan φ_1 and cohesion C_1 on gently dipping slide surface; coefficient of friction tan φ_2 and cohesion C_2 on steeply dipping slide surface; dip angle of gently dipping slide surface α_1; dip angle of steeply dipping slide surface α_2; rock density ρ and angle of inclination of the open cut face β (Fig. 5).

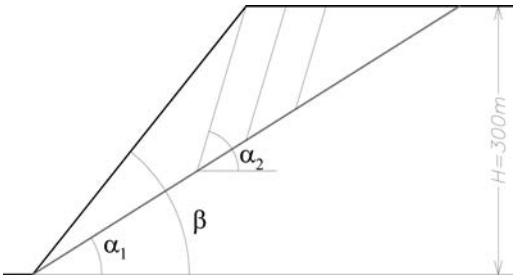


Figure 5. Parameters for the slope stability analysis.

Table 1. Average values of inputs ($\rho = 2460\,\text{kg/m}^3$).

Scheme No.	α_1	α_2	tan φ_1	C_1 (MPa)	tan φ_2	C_2 (MPa)
1	30	55	0.90	0.20	0.60	0.10
2	30	55	0.87	0.55	0.80	0.25
3	Curved sliding surface		0.87	0.55	Curved sliding surface	

In the slope stability analysis the slope for each parameter has been assigned considering its several deviations ΔX from the average value. The rest parameters remained constant. Variations of the stability factor of the open cut face Δk were determined basing on the analysis results. Extent of impact of this or that parameter on stability of the open cut face was assessed by the ratio of dimensionless values $\partial k/\partial X$ where ∂k and ∂X represent relative variations of the parameters: $\partial k = \Delta k/k_{av.}$ and $\partial X = \Delta X/X_{av}$.

4 RESULTS OF PARAMETRIC ANALYSIS

Based on the results of measurements carried by geologists, the average values of dip angles of gentle and steep of displacement surfaces were taken equal to $(\alpha_1)_{av} = 30°$, $(\alpha_2)_{av} = 55°$; according to the laboratory tests, the average value of rock density was taken equal to $\rho_{av} = 2460\,\text{kg/m}^3$.

Shear strength parameters along the joints or for the rock massive conditionally were taken basing on the Russian Building Code specification (SNIP 2011).

The average values of the input parameters used in the analysis are given in Table 1.

In the analysis, the average value of the angle of the cut face inclination is taken equal to $\beta = 38°$.

The average values of other parameters were defined basing on the results of preliminary analysis on condition that the stability factor of the cut face stays within $k = 1.3$–1.6.

Computational scheme No. 1 represents 50 m long steeply dipping joints existing in the rock mass (such a dimension is close to the maximum length of steeply dipping joints measured in the open cut).

Table 2. Results of analysis assessing impact of various factors on slope stability.

		Computational scheme				
		1		2		3
		Slide surface				
Impact of parameter	Design formula	gentle	steep	gentle	steep	circular
$\tan\varphi$	$\partial k/\partial(\tan\varphi)$	0.97	0.025	0.70	0.20	0.99
C	$\partial k/\partial C$	0.029	0.0013	0.09	0.013	0.18
Dip angle of slide surface α	$\partial k/\partial\alpha$	−(0.90–0.95) ($\alpha_2 = 50^0$–60^0)	Rather small	0.95	0.25	–
Rock density ρ	$\partial k/\partial\rho$	−0.032		−0.11		−0.032
Inclination of slope face β	$\partial k/\partial\beta$	–		−4(0.55–1.17) ($\alpha_2 = 30°$–$55°$)		–

Computational scheme No. 2 assumes that gently and steeply dipping slide surfaces are coincident with the existing joints of sets I and V. As in this case when the size of both slide surfaces exceeded the design length of the joints, the analysis was based on the given values of parameters $\tan\varphi$ and C considering the presence of joint blocks and using the method proposed in (Fishman & Miroshnikova 1984).

The given shear properties were used as the average values in the parametric analysis.

Computational scheme No. 3 simulated the slope with a circle failure surface whose stability has been analyzed using the method of algebraic summation of forces (Fellenius solution).

The results of analysis for relative influence of the above listed strength and structural parameters of the open cut face 300 m high with the slope face dipping at about 38°, on its stability factor k are given in Table 2.

5 CONCLUSIONS

Computations show that in the studied case stability of the slope is most affected by two parameters: the coefficient of friction $\tan\varphi$ along the gently dipping sliding surface and of its dip angle α_1. The factor of $\tan\varphi$ impact on stability of the cut face in all the computational schemes is approximately the same – 0.70–1.0. The value of cohesion is of subordinate importance.

Extent of influence of the strength parameter along the steeply dipping slide surface and its dip angle tend to differ in computational schemes No. 1 and No. 2. With the limited length of the steeply dipping slide surface (computational scheme No. 1), this influence is tangibly less than with its bigger length. As for the rock density, its impact on extent of the slope stability is not so great.

Computations confirm great influence of the cut slope inclination β on its stability. Increase in the inclination of the open cut face by 2° and 4° may be compensated by increasing of the coefficient of friction along the gently dipping sliding surface by 10 and 20 percent respectively.

Reliable appraisal of the strength properties of the rock mass is a very important objective whose achievement would permit excessive safety margins stemming from the lack of knowledge to be avoided and project economic efficiency to be increased.

REFERENCES

Fishman, Yu.A. & Miroshnikova, L.S. 1984. Experience in the development and use of engineering-geological models in hydrotechnical construction practice. *Inzh. Geol.,* No. 5.

Gaziev, E.G. & Rechitski, V.I. 1985. *Probability Assessment of Rock Mass Safety.* Moscow: Stroyizdat.

Londe, P. Reflexion sur la securité des barrages. Comité Française des Grands Barrages. Colloque technique, Paris, avril 1984, avril 1988.

Russian Building Code SNIP 2.02.02-85, 2011. Ministry of Regional Development, R. F., Moscow.

This page intentionally left blank

Rock Mechanics for Resources, Energy and Environment – Kwaśniewski & Łydżba (eds)
© 2013 Taylor & Francis Group, London, ISBN 978-1-138-00080-3

Monitoring unstable slopes using Persistent Scatterers Interferometry: opportunities and challenges

J. Wasowski
CNR-IRPI (National Research Council), Bari, Italy

F. Bovenga
CNR-ISSIA (National Research Council), Bari, Italy

D. Nitti & R. Nutricato
GAP srl, Bari, Italy

ABSTRACT: Advanced space-borne Persistant Scatterers Interferometry (PSI) can provide wide-area coverage (thousands km^2) and precise (mm-cm resolution), spatially dense information (from hundreds to over thousand measurement points/km^2) on ground surface deformations. Furthermore, new application opportunities are emerging thanks to i) the greater data availability offered by recent launches of radar satellites, ii) the improved capabilities of the new space radar sensors (Cosmo-SkyMed, TerraSAR-X) in terms of resolution (from 3 to 1 m) and revisit time (from 11 to 4 days). Although, the applicability of radar interferometry to regional and local-scale investigations of slope instability have been demonstrated in several studies, more progress is needed in the integration of PSI results with ground data and in their validation in order to foster a more profitable use of this technique. It is also expected that numerical modeling slope deformations detected by radar satellites should help to constrain the data interpretation.

1 INTRODUCTION

The satellite-based Synthetic Aperture Radar (SAR) Differential Interferometry (DInSAR) can be used to measure ground surface deformations with millimeter-centimeter precision. However, the applicability of DInSAR is limited to areas with scarce vegetation cover. The advanced multi-temporal InSAR techniques such as Persistent Scatterer Interferometry (PSI) (e.g. Ferretti et al. 2001) mitigate this limitation by focusing on selected radar targets (PS) exhibiting coherent radar backscattering properties (mainly man-made structures and rock outcrops). This allows detecting and monitoring with millimeter precision displacements occurring between successive satellite overpasses of the same area. With their capability to provide wide-area coverage (thousands km^2) and precise spatially dense measurements (from hundreds to over thousand measurement points/km^2), the PSI techniques can assist in both regional and local scale investigations of landslides (e.g. Hilley et al. 2004, Bovenga et al. 2006, Colesanti & Wasowski 2006, Farina et al. 2006, Cascini et al. 2010).

Furthermore, new application opportunities have emerged thanks to i) the greater data availability offered by recent launches of radar satellites, and ii) the improved capabilities of the new space radar sensors (X-band Cosmo-SkyMed, C-band RADARSAT-2, TerraSAR-X; see Table 1) in terms of resolution (from 3 to 1 m) and revisit time (from 11 to 4 days for X-band acquisitions). The availability of higher spatial and temporal resolution information about ground surface displacements implies improved slope instability investigation and monitoring capabilities (e.g. Bovenga et al. 2012).

It appears that the geotechnical community is not fully aware of the actual potential and limitations of PSI as applied to landslide investigations. Some skepticism, especially among practitioners and end users, may have resulted from the initial enthusiastic promotion of the technique, which has not paid enough attention to its limitations.

This work aims to contribute to a better informed use of PSI in slope instability detection and monitoring by presenting application examples from areas characterized by different geological settings. We will illustrate i) the potential of the technique to provide, under suitable conditions (favorable slope aspect/inclination, limited vegetation), reconnaissance and site-specific information on slope instability, ii) the difficulties in inferring the exact cause(s) of slow displacements (mm-cm/year) commonly registered on radar targets.

2 RADAR DATASETS AND PROCESSING

For this work two slope failure-prone areas were selected. One study site is located in the Italian Alps,

Table 1. Selected characteristics of principal SAR sensors, including the upcoming Sentinel-1.

Satellite mission	Wave length (cm)	Resolution Az./Range (m)	Repeat Cycle (days)	Max. Vel. (cm/yr)	Incident Angle (degree)
ALOS PALSAR	23.6	≈5/8.6	46	46.8	8÷60
ALOS PALSAR-2	22.9	1/3 3 ÷ 10/3 ÷ 10 100/100	14	149.2	8 ÷ 70
ENVISAT	5.6	≈6/24	35	14.6	19÷44
RADARSAT-1	5.5	≈8/30	24	20.4	20÷50
RADARSAT-2	5.5	≈3/3 ≈8/8 ≈26/25	24	20.4	20÷50
SENTINEL-1	5.6	≈ 5/5 ÷ 24	12 6	42.5 85	20÷45
COSMO -SkyMED	3.1	≈ 2.5/2.5 1.0 / 1.0	16 8 4 2	17.7 35.4 70.7 141.4	20 ÷ 60
TerraSAR-X	3.1	≈3.3/2.8	11	25.7	20÷55

around the town of Madesimo, and the other in the Southern Gansu Mountains (China) near the town of Zhouqu.

2.1 *Radar data*

In the Madesimo, Italy case study we relied on the medium resolution imagery acquired by the ENVISAT C-band radar sensor of the European Space Agency. Over 30 images were used covering about five year period, from June 2005 till August 2010.

In the Zhouqu, China case study, over 20 high resolution COSMO-SkyMed X-band images acquired by the Italian Space Agency (ASI) were used (Table 1). The radar data span the period from January 2011 to February 2012.

2.2 *PSI processing approach*

In this work SPINUA PSI processing algorithm (Bovenga et al. 2004, Bovenga et al. 2006) was applied to process both C- and X-band datasets. SPINUA adopts a patch-wise approach based on processing of limited portions of radar imagery (usually a few km^2), which are selected according to the density and the distribution of initially identified potential PS. This solution enables obtaining fast results by processing small number of SAR images.

3 PSI RESULTS AND INTERPRETATION

3.1 *The case of Madesimo, Italy*

3.1.1 *Background information*

The study area is in the municipality of Madesimo, which represents the northernmost portion of the Lombardy Region, bordering with Switzerland. The town Madesimo, located in a north-south trending valley at 1550 m a.s.l. (Central Alps of Italy), is well known to the enthusiasts of winter sports.

With high local relief and intensely deformed and fractured rocks, the Central Alps are susceptible to a variety of mass movements ranging from deep seated gravitational slope deformations to very shallow failures (rockfalls, debris flows). This is also the case of the Madesimo area where many peaks exceed 3000 m a.s.l.

At Madesimo of particular concern is the west facing slope of the Mount Mater, because of its proximity to the town (Apuani et al. 2012). The pre-Permian paragneiss forms the slope bedrock, often being covered by rock debris. This, the presence of debris fans at the base of the Mount Mater and the overall morphology of the slope facing the town (Fig. 1) denotes potential instability. However, so far, slope hazard assessments were hampered by the lack of information on the history and amount of slope movements.

3.1.2 *PSI results*

The PSI results obtained by processing the ENVISAT images are presented in Figure 1, which also offers a Google Earth-supported 3D visualization of the geomorphologic context of the Mount Mater. The instability of the slope facing the town of Madesimo is marked by the presence of two clusters of PS showing similar velocity displacements, typically exceeding 20 mm/year (Fig. 1). We interpret these two apparently coherent deformations fields as indicative of slow rock slide movements within a larger deep-seated slope failure.

The detection and quantification of the velocity of the displacements is important for a preliminary slope hazard assessment. In particular, this initial PSI-derived information can be used to better focus future

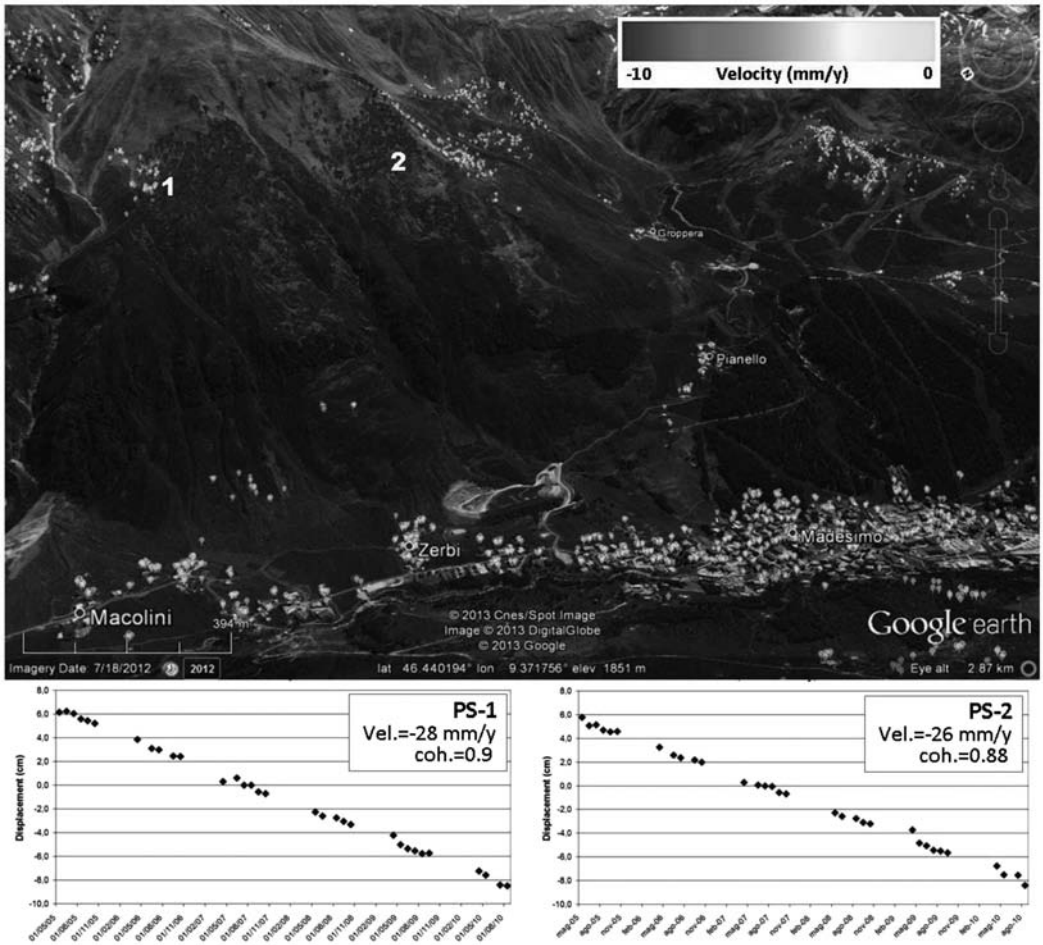


Figure 1. (Upper) Distribution and average line of sight (LOS) velocity of radar targets (marked by light grey to dark color dots) in the town of Madesimo area, Italian Alps, overlaid on optical image from GoogleEarth^{TM}; velocity saturated at −10 mm/year for vi-sualization purposes. Numbers 1 and 2 mark radar targets (PS) showing typical velocities (>420 mm/year) of two clusters of moving radar targets in the upper part of Mount Mater; the town of Madesimo is in the lower right of image; (Lower) Time series of mov-ing radar targets PS-1 and PS-2.

in situ investigation of the Mount Mater slope. Furthermore, given the high elevation and difficult access to the middle-upper part of the Mount Mater, PSI could be used to provide continued remote monitoring of the slope movements.

3.2 *The case of Mundan slope at Zhouqu, China*

3.2.1 *Background information*

The study area is located in the southern part of the Gansu Province, northwestern China, characterized by steep mountains with elevations reaching 4000 m. The town of Zhouqu develops in the Bailong river valley at an altitude of about 1340 m. The bedrock geology in the valley mainly comprises Silurian and Carboniferous slates and phyllites. The upland, mountainous topography is predominantly formed in metamorphosed limestones of Permian and Devonian age.

Slope failures are widespread around Zhouqu, reflecting the fragility of this high relief environment characterized by the presence of tectonically sheared weak rocks and frequent recurrence of large magnitude earthquakes. The region was also affected by the 12th May 2008 Mw7.9 Wenchuan earthquake.

The Mundan landslide is located just to the southeast Zhouqu, on the NE facing valley slope of the Bailong river (Fig. 2). This deep failure is nearly 1 km long and about 500 meters wide with the average slope gradient of about 15 degrees. The slide, involving intensely sheared shales and phyllites, descends towards the river in approximately ENE direction.

In spite of some recent stabilization efforts the slide shows signs of activity and poses a threat to the settlements and infrastructure (e.g. road) along the river. There is also a risk that the slide could even block the Bailong river.

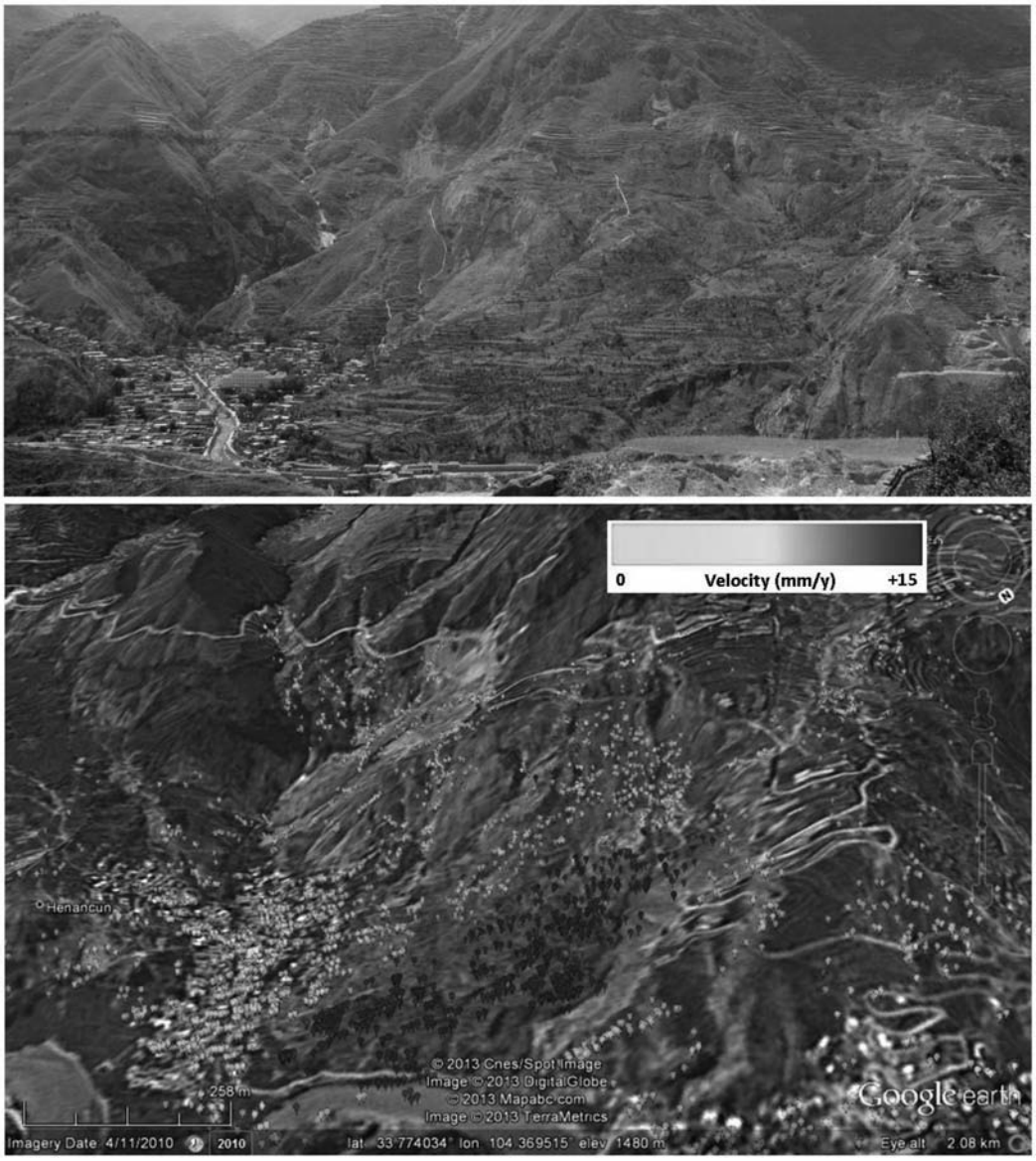


Figure 2. (Upper) Frontal view of the slope affected by the Mundan landslide complex (in the center); SW viewing direction. Ac-tive collateral slope failure and surface drainage (white tracks) are visible at the right (southern) flank of the main slide, upslope the village of Hunan (lower left); photo taken in September 2012; (Lower) Distribution and average line of sight (LOS) velocity of PS (marked by light grey to dark color dots) in the area affected by the Mudan landslide (in center); velocity saturated at 15 mm/year for visualization purposes. Note a cluster (dark dots) of moving PS (below center) with velocities reaching 400 mm/year. Back-ground image is from GoogleEarth™.

3.2.2 *PSI results*

Figure 2 shows the frontal view of the slope area affected by the Mudan landslide and relevant PSI results overlaid on Google Earth image. The PS are mainly present on the middle-lower slopes in the northern and apparently less active portion of the landslide. The PS velocities in the northern segment of the slide typically exceed 15 mm/yr, with maximum displacement rates reaching 40 mm/yr (in LOS).

Upon inspection in 2011, the middle-upper slopes in the central and southern parts of the landslide showed evident geomorphic signs (e.g. intensely deformed ground, fractures) indicative of the recent occurrence of significant movements (in particular in the southern part of the landslide).

These and the associated ground surface disturbance can explain the lack of PS there. However, the presence of slowly moving PS on the lower slopes of

the southern segment of the slide deserves attention, because this area is urbanized including the village of Henan.

4 DISCUSSION AND CONCLUSIONS

The interpretation of the significance of mm-cm/year displacements detected on slopes through PSI is not straightforward, because such slow deformations may arise from a wide variety of causes (e.g. Colesanti & Wasowski 2006). It is recognized that subsurface changes to ambient stresses, by geomorphological processes, civil engineering works, mining, fluid and gas extraction or seismic activity can all generate similarly small surface strains. But slope failure case records do indicate that the most significant impacts are often those related to climatic variations and their control on hydrogeology, groundwater pressures and effective strength. The magnitudes and timing of deformations arising from such changes will depend on the hydraulic and geotechnical characteristics of slope materials, which can range from rocks to engineering soils.

In the case of rock slopes, their structurally controlled characteristics and climate will have a direct impact on average water levels, which can be found at variable depths below the ground surface. For slope instability are important outcrops of confined aquifers and valley landforms underlain by unconfined groundwater rock aquifers consisting of poor water bearing materials with both high fracture hydraulic conductivity and low groundwater storage. Although intense precipitation can cause sudden and high water level fluctuations and thus effective stress changes and thus considerable changes in mass effective strengths within such aquifers, the associated temporal surface deformations on rock slopes are generally unknown.

Nevertheless, it is known that accelerating strain rates occur prior to shear failure in rocks (e.g. Turner & Schuster 1996). Such strains are not registered routinely, especially in regional scale investigations, because of the high cost involved in field instrumentation and in situ monitoring. This limitation can be overcome by exploiting PSI for the detection of any form of long-term wide-area surface strain. Hence satellite radar-based remote sensing can provide a useful contribution to slope stability studies. However, as pointed out above, the parameter and geological boundary uncertainties which control small ground surface deformation changes need to be investigated and better understood before they can be confidently used in slope hazard assessments or for early warning purposes. In this context, it is expected that useful constraints for the proper interpretation of PSI data will come from numerical modeling of slope deformations detected by PSI.

ACKNOWLEDGEMENTS

Work supported in part by the Italian Space Agency (ASI) – COSMO-SkyMed AO Project ID 1820. ENVISAT and COSMO-SkyMed data were provided, respectively, by the European Space Agency (ESA) under CAT-1 project ID 2653 and by ASI.

REFERENCES

Apuani, T., Arosio, D., De Finis, E., Stucchi, E., Zanzi, L. & Ribolini, A. 2012. Preliminary seismic survey on the unstable slope of Madesimo. *Proceedings of SAGEEP (Symposium on the Application of Geophysics to Engineering & Environmental Problems*) 2012, Tucson AZ, 8 pp.

Bovenga, F., Refice, A., Nutricato, R., Guerriero, L. & Chiaradia, M.T. 2004. SPINUA: a flexible processing chain for ERS/ENVISAT long term Interferometry. *Proc. ESA-ENVISAT Symposium*, 6–10 September, 2004, Salzburg, Austria.

Bovenga, F., Wasowski, J., Nitti, D.O., Nutricato, R. & Chiaradia, M.T. 2012. Using COSMO/SkyMed X-band and ENVISAT C-band SAR interferometry for landslides analysis. *Remote Sensing of Environment* 119: 272–285.

Cascini, L., Fornaro, G. & Peduto, D. 2010. Advanced low- and full-resolution DInSAR map generation for slow-moving landslide analysis at different scales. *Engineering Geology* 112: 29–42.

Colesanti, C. & Wasowski, J. 2006. Investigating landslides with space-borne Synthetic Aperture Radar (SAR) interferometry. *Engineering Geology* 88(3–4): 173–199.

Farina, P., Colombo, D., Fumagalli, A., Marks, F. & Moretti, S. 2006. Permanent Scatterers for landslide investigations: outcomes from ESA-SLAM project, *Engineering Geology* 88(3–4): 200–217.

Ferretti, A. Prati, C. & Rocca, F. 2001. Permanent scatterers in SAR interferometry. *IEEE Transactions on Geoscience and Remote Sensing* 39: 8–20.

Hilley, G.E., Burgmann, R., Ferretti, A., Novali, F. & Rocca, F. 2004. Dynamics of slow-moving landslides from Permanent Scatterer analysis. *Science* 304: 1952–1955.

Turner A.K. & Schuster R.L. (eds). 1996. *Landslides – investigation and mitigation, Special Report 247*. Transportation Research Board. Washington, D.C.: National Academy Press.

This page intentionally left blank

8. Dynamic phenomena in rock masses

This page intentionally left blank

Rock Mechanics for Resources, Energy and Environment – Kwaśniewski & Łydżba (eds)
© 2013 Taylor & Francis Group, London, ISBN 978-1-138-00080-3

Large scale field tests of rock bolts and high-tensile steel wire mesh subjected to dynamic loading

M. Cala
AGH University of Science & Technology, Kraków, Poland

A. Roth & A. Roduner
Geobrugg AG, Romanshorn, Switzerland

ABSTRACT: Rockburst means stress induced violent ejection of rock mass in tunneling and mining. Rock mass comes off under high energy release. To determine this energy, different approaches exist, depending on different countries and regions. Rockburst phenomena mostly occur in deep tunnels and mines but also in regions, where high stress concentrations appear. A major engineering challenge for mines experiencing significant seismicity is the performance of the support systems. The development of an adequate retaining system, such as dynamic rock bolts together with high-tensile steel wire mesh and their behavior during rockburst had been tested and quantified. The special large scale test facility was constructed for that purpose. It allowed the estimation of portions of energy transmitted by rock bolts and wire mesh.

1 INTRODUCTION

As more and more near surface deposits are mined out, deeper mines are required in order to continue the exploitation of resources. This inevitably leads to the occurrence of more rock bursting, deformation problems and safety issues. Rock burst means stress induced loosening of parts of the rock mass under enormous energy release. It seems to be similar to damage from natural seismic phenomena. Rock burst events occur mostly in deep tunnels and mines but also in regions with high horizontal stresses.

There are different methods to mitigate rock burst risks thus reducing exposure of personnel. Changes include mine design, layout and extraction sequence (Potvin 2012). In addition the ground support needs to be chosen and designed in such a way that it can cope with the conditions. In deep mines the ground support is complex and cost is high. Static ground support is not satisfactory for such a demanding environment. The ground support consists of the rock reinforcement (e.g. bolt), a surface support (e.g. mesh) and the connection between the two (e.g. plate). For dynamic loads it is essential that these components fit and work together as a system (Cala & Roth 2007). The observations of Heal (2007) show that most of the damage done from rock bursting led to the failure of the surface support or the rupture of the reinforcement.

In order to investigate the dynamic behavior of reinforcement elements and surface support, extensive testing was carried out at various test sites. Some tests were done in South Africa, Canada and Australia. Hadjigeorgiou (2011) put the results of the various tests together and tried to make them comparable. However the boundary conditions of the test sites were different making comparison difficult. There are two active test sites at the moment, one is in Canada at CANMET and the other in Australia at WASM (Player et al. 2004). The WASM test site is the best instrumented facility and is based on the momentum transfer concept. It can test reinforcement, surface support and to a certain extent combinations of the two.

2 MOTIVATION

Mining engineers design support systems for their operations, based on the work done in Canada which resulted in the Canadian Rockburst Manual (Kaiser et al. 1995) and the above mentioned testing of reinforcement and surface support. It is widely known that the support scheme should work together, but there is little research data available on the dynamic interaction of the main components. In many cases the energy absorption capacities are added together in a superposition for obtaining the capacity of the system as a whole.

Both in static and dynamic loading it is important that the surface support can bear the load of the rock mass and transfer it to the reinforcement. Furthermore in dynamic loading the reinforcement should start yielding in order to absorb energy without the surface support failing beforehand. Heal (2007) comes to the conclusion that using the dynamic capacity of the reinforcement alone for the design would likely overestimate the capacity of the system. Potvin (2012)

therefore proposes to look at the weakest link of the support system and since this is in most cases the surface support, makes the assumption to use the capacity of the surface support as the capacity of the system.

In this study it is believed that the above mentioned approach is too conservative and that more data on the interaction between the reinforcement, the surface support and the connection elements is required. This is one reason for using the test site in Walenstadt, Switzerland, where a 3.6 m × 3.6 m surface support can be dynamically tested with four dynamic rock bolts in a regular bolt pattern. The other motivation comes from the need to translate the results of the individual component tests at test sites like the WASM site (Player et al. 2004) into full-scale tests for proving the suitability and fitness for use of the overall system. Another option is to use blast tests for this (Heal et al. 2004), but there the loading is questionable and the testing is hardly repeatable.

The hypothesis of this work is based on the assumption that during dynamic loading of a surface support scheme, the surface support is loaded by a part of the fractured mass. The resulting force in the surface support will then be transferred to the connection element (e.g. plate) and then on to the reinforcement, with the other part of the load going directly to the reinforcement. The rock mass around the bolt is bonded to the bolt and held by the plate. There will be an arching effect in the rock mass in between the bolts, depending on the fracturing. Consequently part of the loading will go directly on the bolts and not on the mesh. To verify the difference in loading, load cells were used in the test set-up at both ends of the bolts. It is the aim of the test setup to measure the loads in the different elements and then back calculate what load was borne by the surface support and how much was carried by the dynamic reinforcement directly. This is of course dependent on the type of rock mass and cannot be seen as a general ratio.

For these large scale field tests and their analysis, the calculation of the energy output during a rock burst event is the main topic. Additionally important is the development of adequate retaining elements, such as reinforcement and surface support. Their behaviors during rock burst have to be proven and their interaction has to be observed and described as well. The test construction should be able to test this so called interaction and show, how much energy will be absorbed by reinforcement, surface support and the test set-up itself. This may be compared to the breakage of the rock in a real rock burst event which also absorbs energy.

3 LARGE SCALE FIELD TESTS

Many tests regarding the behavior of dynamic reinforcement and surface support alone have been carried out already. Thus the behavior of the individual retaining elements is well known. But for safety in tunneling and mining projects it is of great interest to have a complete support scheme, which protects the underground workers from risks, such as rock burst. This large scale field tests are supposed to show the behavior of dynamic high-tensile mesh and dynamic rock bolts installed together. The tests should indicate the load and energy distribution between the components.

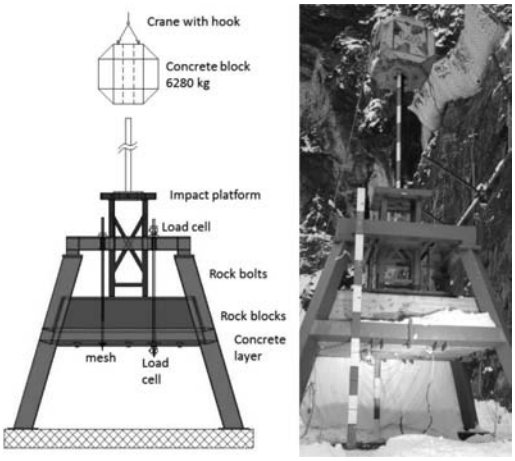


Figure 1. Large scale field test setup.

The main goal of these trials is to evaluate a dimensioning concept, where the retaining elements can be designed for dynamic conditions. These calculations are based on the energy distribution between the reinforcement and the surface support. In this project, research for the energy release during a rock burst phenomena is not considered. The input energy for the tests has been assessed and classified based on the dynamic tests conducted at WASM (Thompson et al. 2012).

3.1 *Test setup*

The main frame of the test set-up is made of steel, with a high tensile chain link mesh horizontally connected to the frame by lacing wire rope through mesh and frame (see Figure 1). The mesh is hold back by four dynamic rock bolts in a typical pattern.

Formwork was installed underneath the wire mesh. A plastic foil was placed on top of the wire mesh, before concrete was poured onto the formwork. The plastic foil was used to keep the mesh separated from the concrete slab. Before the tests were conducted, the plastic foil was removed. Natural rock boulders and an equalizing layer of gravel were then placed on the top of the thin concrete slab. This layered build-up of concrete, rocks and gravel is intended to simulate the pre-fractured rock mass prior to the rock burst, with the concrete plate as a base to prevent mesh and bolts from preloading. The concrete slab is designed to crack under load as there is no reinforcement in the concrete. On top of the gravel layer, a load distribution plate is installed to initiate the energy impact caused by the test block's impact. The test block is lifted by a crane.

To start the test, the crane will disengage the test block which then falls onto the impact platform on the top of the construction. The impact platform on the steel stamp is connected with the load distribution grid lying on the equalizing gravel layer.

While following physical laws, the energy impact on the whole construction is the difference of the potential energy of the test block before and after the impact. The maximum height to lift the test block is limited by the length of the guiding steel column to approximately 3.25 m (see Figure 1). The mass of the test block used is 6280 kg.

For the rock burst trials, a high tensile steel wire mesh of 3.6×3.6 m (mesh type TECCO G80/4, aperture 80 mm, wire diameter 4 mm, wire strength 1770 N/mm^2) and four dynamic rock bolts of 3 m length (bolt type D-Bolt, diameter of 20 mm) were used. The dynamic bolts have a deformable length of 1.5 m and according to the manufactures' specification would elongate by about 15%, meaning an elongation of about 225 mm is possible. The bolts were grouted into steel tubes (wall thickness 8 mm) which are separated into two parts. This gives a defined position for the elongation of the bolt (simulating the detachment point of the fractured rock mass). For the load transmission from the mesh to the bolts, special spike plates are used whose geometry fit exactly for the diamond shaped steel wire mesh. The spike plates ensure that six wires are always grasped by each plate.

3.2 *Instrumentation*

In order to determine factors affecting the system, devices including load cells, high speed cameras and accelerometers were installed to evaluate the distribution of the forces on the mesh, bolt and system as a whole.

The forces and the elongation of the bolts as well as the deflection of the mesh are the primary factors used to calculate the energy absorption capacity of the mesh and the bolts. Based on the results from the test, the energy capacity of the elements can be calculated by the area under the Load–Displacement curve. By knowing the input energy calculated by the potential energy difference of the test block before and after the impact, the energy absorbed by the test setup can be back calculated. The procedure is explained in section 3.5.

The high speed cameras and accelerometers generate measurements of displacement, velocity and acceleration. Therefore, the measurements are redundant and can be cross checked.

3.2.1 *Load cells*

Two load cells were installed on one of the four dynamic bolts. One cell is at the collar of the bolt the other one at its end (see Figure 2). The upper cell measures the total force on anchor and mesh together while the lower cell only measures the vertical load taken up by the mesh.



Figure 2. Lower (left) and upper (right) load cell.

3.2.2 *High speed cameras*

Two high speed cameras were installed in front of the steel frame, from where several measuring points on the bolts, the mesh and the test block were filmed. With a computer tracking program the displacement of mesh and bolts can be evaluated out of the grouped pictures per time by pursuit of a measure point on the pictures. The velocity can be calculated by the first differentiation of the displacement and the acceleration by the second differentiation of the displacement. An upper camera films the movement of the test block and the impact whilst a lower camera films the deformation of the mesh and the bolts.

3.2.3 *Accelerometers*

The accelerometers measure the acceleration in time. By a double integration, the deformation can be calculated. This is used to cross check the data output from the high speed camera. Sensors are fixed to the mesh, bolts, the test block and the impact platform. The mesh sensor is able to measure a three dimensional movement of the mesh.

3.3 *Test execution*

As already mentioned in section 3.1, the rock burst is simulated by releasing a heavy concrete test block in free fall on the test set-up. Due to the potential energy difference of the test block before and after the impact, a certain amount of energy is put into the system. This input energy is absorbed by the bolts, the mesh and the test set up itself (including breakage of the concrete slab).

After the dynamic movement of the rock mass, the effect of plastic elongation and deformation of bolts and mesh is plain to see. All the extra elastic deformation can be discovered by analyzing the data output from high speed cameras and accelerometers. This will show the maximum deformation of the support elements during the dynamic impact.

Different tests were carried out with various stiffness of the assembly, mainly by varying the thickness of the concrete slab and the assembly of the natural stones which are build-in more or less interlocked. Those adjustments resulted in different loading conditions of the anchors and the mesh which directly refers to variable behavior of the rock mass in reality.



Figure 3. Elongation of anchors for a stiff assembly (left) and pressing of the concrete plate into the mesh for a stiff assembly (right).



Figure 4. Elongation of anchors for a softer assembly (left) and deflection of the mesh for a softer assembly (right).

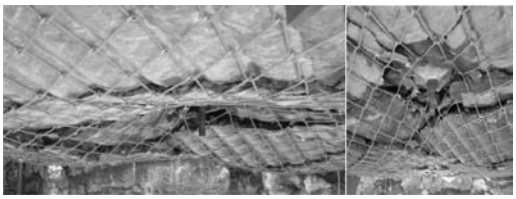


Figure 5. Loading of the mesh and transferring the loads to the plates.

The following pictures show the plastic deformation of the mesh and the bolts. Firstly for a stiff assembly, secondly for a softer one.

For the stiff setup, the elongation of the bolts is very well seen (Fig. 3 left). The elongation was 150 mm, or 10% of the dynamic length of the bolt. As noted above, the bolts used in this test are able to elongate about 15% of their elongation length.

For the stiff assembly, the deflection of the mesh was about 140 mm which is quite moderate (Fig. 3 right). Due to the thickness and therefore stiffness of the concrete slab, the slab only broke up into a few large pieces. Therefore, the loading on the mesh was not in a parabolic shape as expected with more fragmented rock. The shape had a more triangle character due to the big concrete pieces pressed into the mesh. This loading results in higher forces on the bolts compare to the forces on the mesh and therefore, in combination with the major deformation of the mesh, to more energy absorption by the bolts than by the mesh.

The nearly parabolic shape can be noticed, when looking at the deflection of the mesh of the softer setup (Fig. 4 right and Fig. 5). At its highest deformation, the deflection of the mesh is around 300 mm.

In comparison, when the test was setup with a thinner and less stiff concrete slab, the loading on the mesh resulted in a more parabolic shape, due to the higher fracturing rate in the concrete. As a consequence, the plate and bolt only see the loading from the material directly above the bolt and plate, having a cone shape.

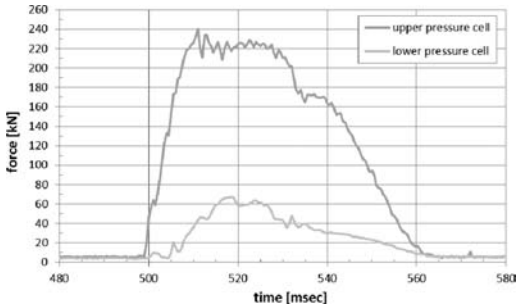


Figure 6. Forces measured by the load cells for a stiff assembly.

In this test setup the mesh absorbs more energy than the bolts. Figure 4 left shows the movement of the bolts of about 25 mm for the softer setup.

3.4 *Test results*

Using a drop height of approx. 3.25 m and the test block's weight of 6280 kg, the energy input in the system can be calculated to 200 kJ. Depending on the stiffness of the test setup the energy absorbed by the mesh and the bolts will vary. The stiffer the test setup, the more energy is absorbed by the bolts. This refers to rock types which do not break into small pieces during a seismic event. If they do so, then there is more load going into the mesh because these small blocks are ejected between the bolts into the mesh. Nevertheless in both cases support elements have to be able to absorb their share of energy without rupture. Only the distribution of the energy absorption varies depending on the stiffness described above. This distribution is analyzed in section 3.5.

With regards to the energy absorbed by mesh and bolt it is necessary to have a look at the forces measured at the collar and the end of the bolt. The diagrams 6 and 7 show those forces for a stiffer and for a softer test setup. The maximum force in the bolt for the stiffer test setup has been about 240 kN. This value is located in the yielding area of the bolt. Regarding the mesh, the maximum measured force is about 65 kN. For this range of forces, no rupture of the mesh around the plates appears. Figure 7 shows the loads in the bolts during the stiff assembly event with time.

For the softer test setup, forces are generally lower and impact times longer caused by the smoother behavior of the whole system. The maximum force measured by the upper load cell belongs to the dynamic bolt and its value is around 165 kN. This value is below the yielding load and the bolts were only lightly activated (25 mm). The maximum force from the mesh is about 50 kN. The forces for the soft assembly can be seen in Figure 7.

3.5 *Analysis*

As described above, the trials show that bolts and mesh work together, meaning that both support elements

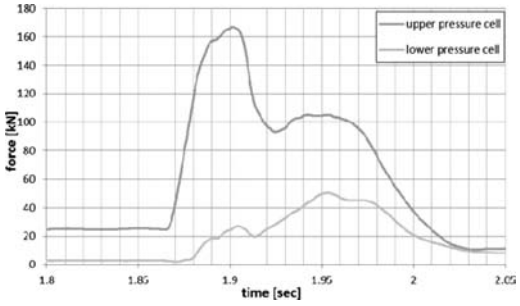


Figure 7. Forces measured by the load cells for a softer assembly.

absorb a part of the energy without being overloaded. The amount of energy each part of the support will take, depends on the type, stiffness and the behavior of the rock mass.

The energy distribution in the stiff test setup using the integration of the load-displacement has been back calculated as follows. The energy absorbed by the bolts is about 32 kJ in total (about 8 kJ per bolt). The mesh absorbs about a third of this amount namely about 10 kJ. In this setup a total of 42 kJ was absorbed by the support system where the bolts took 75% and the mesh 25%.

Investigating the energy distribution of the softer setup it can be seen that the bolts only dissipate a small amount of energy of about 10 kJ (2.5 kJ per bolt) while the mesh absorbs about 26 kJ. In this case the mesh takes about 70% of the total energy of 36 kJ and the bolts only 30%.

These two examples presented so far are rather extreme cases (although relatively small energies), with a very stiff and a very soft test setup. The energy distribution for other cases will be in between these ratios. Based on the type of rock material and the magnitude of the seismic event the ratio will change. If the rock does not tend to break into small pieces during a rock burst and if the magnitude of the rock burst is big, then more energy will go onto the bolts. If this is not the case then more energy has to be absorbed by the mesh (see Figure 8).

By knowing the energy dissipated by mesh and bolts, the energy absorbed by the test facility can be back calculated. By subtracting the energy dissipated by bolts and mesh the left over amount of energy refers to the energy absorbed by the test setup (in the above mentioned two cases about 160 kJ each).

3.6 *Energy distribution between mesh and bolts*

As shown in the sketch in Figure 9, the energy distribution on both support elements in regards to the stiffness of the test setup can be described by a simple model. The distribution of the load between reinforcement and surface support could be described by using a ratio of the mass or energy distribution between mesh and bolts. The rock mass acting directly on the bolts will have a cone shape around the bolts. Between the

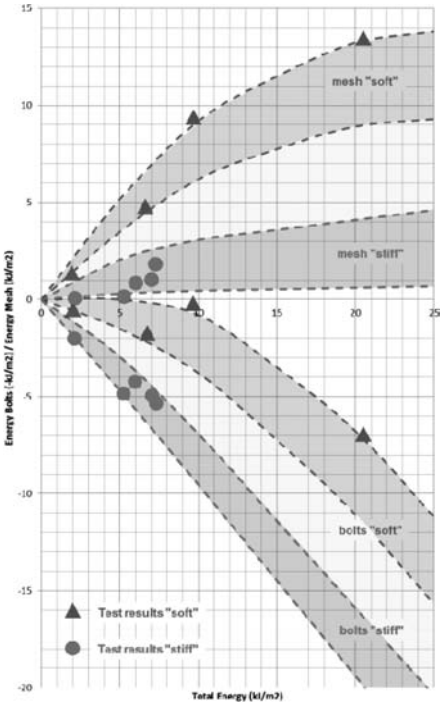


Figure 8. Ratio of the energy which is going into the mesh and the bolts based on the results of the executed tests.

bolts, arching effects are observed, meaning that the mass above the arch loads the bolt as well as the cone. The rock mass below the arch will then impact the surface support.

For further considerations the ratio can be estimated by evaluating the properties and the behavior of the rock mass. A stiffer rock mass which does not disintegrate much during a rock burst results in more mass and energy which have to be absorbed by the bolts. If the rock mass is breaking into quite small pieces then a bigger share of the mass and energy is going on the mesh. It has to be kept in mind, that rock burst events primarily occur in relatively high stressed brittle rock. Thus too heavily broken up rock mass is unlikely.

The results of the two presented tests suggest that in a rock mass where the rock is not breaking into small pieces an energy distribution of 25% mesh and 75% bolt can be assumed. If the rock breaks into smaller pieces then this can be the opposite: Energy distribution of 70% mesh and 30% bolt. This ratio will also vary with the magnitude of the rock burst loading. The higher the loading the more mass has to be activated and the deeper the failure zone in the rock which consequently leads to an increase of the energy share for the bolts.

In Figure 8 the results of all the tests with the two setups is put into a graph which shows the relation between the total energy, the energy going onto the mesh and into the bolts (in kJ/m^2). The type “soft” is related to rock types where the failure mode creates a disintegrated rock mass with ejection of rocks between

the bolts. In contrary the rock type "stiff" does fracture and displace during an event but does not break up in small pieces which are ejected.

4 CONCLUSIONS AND OUTLOOK

It can be concluded that the test site Walenstadt has been successfully commissioned and that it can be used to apply a dynamic rock burst loading to a larger panel of surface support and four bolts. The instrumentation with load cells, accelerometers and high speed video cameras does work as intended and allows an analysis and back calculation of the system behavior and energy absorption. With the stiff setup it was possible to show that the test setup can impose enough energy to activate four strong dynamic bolts. With the soft setup, mainly the mesh was loaded and the anchors were lightly activated. This result will lead to the next step in subjecting the setup to higher energies and thus simulate stronger rock bursts which should lead to the loading of the mesh and the yielding of the dynamic bolts.

The test setup proved to be suitable to show the overall performance of such a ground support system. It was demonstrated that high-tensile mesh works together with the dynamic bolts. The method of connecting the two systems was shown to be suitable. However this test cannot be compared to more repeatable lab testing since it includes breakage of the concrete slab and also the compaction of the rock mass. From that point of view it will be very interesting to test different rock mass setups and see the influence on energy distribution ratio between bolts and mesh. This will lead to a small data base of such values which then may be compared to conditions in real applications.

An additional option would be to create a three-dimensional numerical model of the test facility. The database of previous experiments would serve to validate the numerical model. Then the simulation of other configurations of rock mass and support elements would be possible and reliable.

Based on this initial work it is hoped to be able to suggest a dimension factor for different ground conditions with a proven ratio of load which has to be absorbed by the surface support during a dynamic impact. This load then has to be transferred by the plate into the bolt without puncturing around the plate. Together with this information it will be possible to choose a dynamic bolt for the surface support which yields before the surface support is rupturing. These factors of the load distribution between mesh and bolts seem to be dependent on the rock type and the magnitude of the rock burst.

REFERENCES

Cala M., Roth A. (2007) Application of steel wire mesh for ground support under rockburst hazard. Gornictwoi Geoinzynieria. AGH University of Science & Technology. Kraków. Vol. 31 b. 3/1 pp. 125–133 (in polish).

Hadjigeorgiou, J. and Potvin, Y. (2011) A critical assessment of dynamic rock reinforcement and support testing facilities, Rock Mech Rock Eng (2011) 44, Springer Verlag, pp. 565–578.

Heal, D., Hudyma, M. and Potvin, Y. (2004) Assessing the in-situ performance of ground support systems subjected to dynamic loading, in Proceedings Fifth International Symposium on Ground Support in Mining and Underground Construction, E. Villaescusa and Y. Potvin (eds), 28–30 September 2004, Perth, Australia, Taylor & Francis Group, London, pp. 319–326.

Heal, D. (2007) Observations and analyses of incidences of rock burst damage in underground mines, University of Western Australia, Perth.

Kaiser et al. (1995) Canadian Rockburst Research Program. Vol. 2, Camiro Mining Division, Sudbury, Ontario, Canada

Player, J.R., Villaescusa, E. and Thompson A.G. (2004) Dynamic testing of rock reinforcement using momentum transfer concept, in Proceedings Fifth International Symposium on Ground Support in Mining and Underground Construction, E. Villaescusa and Y. Potvin (eds), 28–30 September 2004, Perth, Australia, Taylor & Francis Group, London, pp. 327–339.

Potvin, Y. (2012) An interpretation of ground support capacity submitted to dynamic loading, Newsletter Australian Centre for Geomechanics, Australian Centre for Geomechanics, Vol. 39, December 2012, Perth, Australia, pp. 1–5.

Thompson, A.G., Villaescura, E. and Windsor, C.R. (2012) Ground support terminology and classification: an update, GeotechGeolEng, Springer, published online.

Rock Mechanics for Resources, Energy and Environment – Kwaśniewski & Łydżba (eds)
© 2013 Taylor & Francis Group, London, ISBN 978-1-138-00080-3

Unifying energetic approach for the control of ground vibrations

C. Dinis da Gama
IST Lisbon, Portugal

ABSTRACT: The phenomena of ground vibrations may be originated either by natural causes (earthquakes, volcanic eruptions, landslides and meteorite impacts) or by man-made activities (industry, traffic, construction, demolition and rock blasting) and their consequences sometimes represent the most relevant factor for ground and structural damage, as well as for people nuisance.

It is obvious that greater vibration intensities are associated with both the magnitude of released energies and to shorter distances from their sources, thus involving the role of ground attenuation on the propagation of stress waves from their origin to the monitoring points.

Determination of relevant safety criteria for structures affected by ground vibrations has been achieved by many institutions under different approaches, according to the specific events that are occurring. However, an overall analysis of those criteria indicates that it is possible to encompass all such events under an unifying approach based on the energy transmitted to the ground, which may lead to reliable solutions for safety control and protection purposes. Examples of this criterion are provided.

1 INTRODUCTION

Ground vibrations are dynamic phenomena that must be adequately understood and quantified by means of appropriate scientific concepts, followed by specialized engineering applications. This knowledge should be dominated by operators and local authorities in order to specify the acceptability of plant or equipment, the permissible working hours (not including emergency operations) and the maximum allowable levels of vibration and noise at the boundaries of the site (Sarsby, 2000). Those problems should be solved before work starts, providing an assessment to the feasibility of most engineering projects, whatever its stage is (initial conception, design, tender, construction, regular activity, etc.).

Besides empirical approaches for such a control, there are means of predicting those effects if quantification of the main influencing variables is performed, in order to establish their specific involvement in the resulting magnitudes of vibration at any site that is to be protected.

An important factor of dealing with vibrations and their effects is the definition of three categories, which are (according to Sarsby, 2000):

a) Steady state or continuous – when an approximately constant level of vibration is maintained for a substantial time (examples of large pumps, compressors, etc.).
b) Transient or impact – if the vibration intensity decreases suddenly from its peak level to zero, before a new maximum is attained some time after (cases of dynamic compaction, pile-driving with drop hammer, etc.)
c) Intermittent – a string of vibration phenomena happens, with each one is of short duration, separated by intervals with low or zero intensity, such as in the rock blasting with a succession of charges, or a diesel pile-driver.

As the reaction of a structure depends on the time factor, as far as vibration intensities are reaching its foundation, it is obvious that the mathematical models proposed for their modeling must take in due account these three category types.

2 GROUND VIBRATIONS – SOURCES, TYPES AND MEASUREMENTS

The origin of ground vibrations can be ascribed to natural or man-made causes when earth's surface is put into periodic displacements whose magnitude and frequency may cause damage to structures and panic to people. Under the first group of phenomena, either seismic events or landslides may release vibrations of great intensity which may induce damage to cities or engineering workings (nuclear power stations, for instance) thus causing relevant human insecurity and even life losses, as well as for animals and plants.

The second type includes such man-made activities as heavy industries, vehicle traffic, constructions, demolitions and specialized operations as rock blasting and events of war. Their resulting consequences may produce high levels of ground vibrations, which lead to various kinds and degrees of structural damage and also to people nuisance.

The main advantage of the second type with respect to the first one is related to the common absence of a

surprise effect (unfortunately not always), regarding people awareness and their preparation for sustaining ground vibration effects.

Obviously, methods and equipment for vibration measurements are essential for its characterization, both in terms of intensity and frequency of the waves that are generated by man-made events, in opposition to most natural phenomena, except in specialized logging earthquake laboratories.

Furthermore, there is a consensus that such man-made vibrations must be previously submitted to calculations for predicting their harmful results, based on the existence of official legislation and/or technical standards which are supposed to control those effects.

However, problems may arise when in a certain construction site, for example, where different types of mechanical equipment are operating, located at various distances from nearby structures that must be protected.

A methodology for such cases is required, under an unifying criterion that may be implemented in accordance with engineering regulations, such as the one that is presented below.

Other solutions to reduce vibration levels at certain locations may involve their own protection by means of installing anti-vibrating tools or shock-absorbers, as well as creating wave reflectors in the surrounding ground, such as excavated trenches or artificial discontinuities.

3 WAVE ATTENUATION FUNDAMENTALS

3.1 *Basic concepts*

The amplitude of vibrations can be quantified in terms of displacement, velocity or acceleration and each one can be stated in either time or frequency domain. Issues related to vibration-sensitive facilities are generally treated in the frequency domain, although most approaches to vibration propagation in soils and rocks is very much limited to the time domain, which is typical of construction and mining engineering.

In terms of Physics, the attenuation is ascribed to internal friction mechanisms which may be divided in two groups: intrinsic (such as anelasticity of rocks, visco-elasticity, thermic effects, dislocations and scattering) and extrinsic (mostly due to frictional losses at fractures, joints and other discontinuities, due to solid friction).

For its importance in dealing with vibration problems, the *Boltzmann superposition principle* should always be remembered. It states that the mechanical behavior of a solid is a function of its previous history, because when it suffers a series of deformations, whose individual effects are independent from the previous ones, the resulting behavior may be evaluated by the addition of effects that each deformation has caused in the solid.

In order to determine the attenuation characteristics of waves, a distinction between earth and air propagations must be pointed out.

3.2 *Ground vibrations*

Three options are available for quantifying the reduction with distance of the seismic waves amplitude, which is a characteristic property of any type of ground: the attenuation coefficient n, the attenuation factor α and the quality factor Q:

i) The first one is a dimensionless number n which is an exponent of the distance D between two points 1 and 2, where peak magnitude A is monitored. The relation between both magnitudes may be expressed by:

$$A_2 = A_1 D^{-n} \tag{1}$$

where n is a dimensionless parameter that depends on the ground type.

ii) The attenuation factor α involves more variables (propagation velocity c and wave frequency f) and it is involved in the relationship between two amplitudes in the form of:

$$A_2 = \frac{A1}{D}\, e^{-\alpha(D-1)} \tag{2}$$

It can be demonstrated that:

$$\alpha = \frac{f}{2c}\frac{\Delta E}{E} = \frac{\pi f}{cQ} \tag{3}$$

where E is the energy supplied to the movement and ΔE is the part that is dissipated between the two points.

iii) Quality factor

The capacity of a ground material for attenuating seismic waves can be measured by a dimensionless quantity Q, called the quality factor for measuring the internal friction, which is obtained by ratio of energy of seismic wave E and the energy dissipated per wave cycle ΔE, or:

$$Q = 2\pi \frac{E}{\Delta E} \tag{4}$$

Typical values of Q range from 5 to 20 (soils) through 100 (rocks) to 10,000 (steel). According to Knopoff (1964) the average value of Q in the Earth's crust is 110.

For the sake of simplicity, Q is assumed to be independent of wave frequency in the useful seismic bandwidth. When various ground layers exist, they interfere in the Q value, so its value in a certain place indicates the composition of existing layers. Therefore, measured Q values are able to identify changes in material properties.

Assuming elastic behavior with a linear relationship between stress and strain, the wave amplitude A is proportional to $E^{1/2}$. Hence,

$$\frac{1}{Q} = \frac{\Delta A}{\pi A} \tag{5}$$

from which we can obtain the amplitude fluctuations due to attenuation.

That is, given initial amplitude A_0, let λ be the wavelength given in terms of frequency ω and phase velocity c by $\lambda = 2\pi\ c/\omega$, then

$$\Delta A = \lambda \frac{dA}{dz} \tag{6}$$

as a consequence

$$\frac{dA}{dz} = \frac{\omega A}{2cQ} \tag{7}$$

resulting in a exponential decaying solution

$$A(\omega, z) = A_0(\omega) e^{-\frac{\omega z}{2cQ}} \tag{8}$$

From observation of exponentially decaying values of A(ω,z) the Q value may be obtained, so the relation becomes:

$$ln \frac{A}{A_0} = \frac{\omega z}{2cQ} = \frac{\omega t}{2Q} \tag{9}$$

It is assumed that the phase velocity c does not depend on frequency, ie, that there are no dispersion effects. This has the added effect of correlating well the time of travel of the reflected wave with the depth of the layer from which the reflection occurs.

Hence, by recording the $\ln(A/A_0)$ versus t graph, and then estimate the *average* slope, the value of Q can be determined. This concept is known as *log spectral ratio* method.

3.3 *Noise*

For quantifying the attenuation of sound vibrations with distance, the Decibel is an unit used to express relative differences in signal strength. It is expressed as the base 10 logarithm of the ratio of the energies of two waves:

$$1\ dB = 10\ log\left(\frac{E_1}{E_2}\right) \tag{10}$$

Wave amplitude can also be expressed in dB. Since energy is proportional to the square of a signal's amplitude (e.g., an energy ratio of 100 is equivalent to an amplitude ratio of 10), dB is expressed as follows:

$$1\ db = 20\ log\left(\frac{A_1}{A_2}\right) \tag{11}$$

Logarithms are useful as the unit of measurement because (a) their signal power tends to span several orders of magnitude and (b) its signal attenuation loss and gain can be expressed in terms of subtraction and addition.

For example, suppose that a signal that passes through two ground segments is first attenuated in the ratio of 20 to 1 on the first leg and 7 to 1 on the second.

The total signal degradation is in the ratio of 140 to 1. Expressed in dB, this becomes

$$10\ log 20 + 10\ log 7 = 13.01 + 8.45 = 21.46\ dB \tag{12}$$

Table 1. Values of attenuation and of input power survives for different levels of attenuation.

Levels of attenuation	Values of Attenuation *dB*	Values of input power survives Adimensional
Very High	1	0.79
High	3	0.50
Medium	10	0.1
Small	20	0.01
Very Small	30	0.001
Minimum	40	0.0001

Table 1 helps to indicate the order of magnitude associated with dB.

Many times dB ratios are expressed using a third letter (or letters), e.g. dBm where the third letter is a reference level for the log operation.

For instance, dBm is used to define dB levels in a 50 Ohm RF system, using a 1 milliwatt reference level.

3.4 *Indirect methods to evaluate internal friction*

Two other factors may be utilized to evaluate attenuation related to wave propagation: the logarithm decrement δ (for free vibrations) and the curtosis of the resonance curve (under forced vibrations).

The first one involves the amplitudes of two successive peaks (see Figure 1), by the expression:

$$\delta = log_e \frac{A_i}{A_i + 1} \tag{13}$$

The second is again the definition of Q, the already defined quality factor, by means of the resonance curve, as the ratio of its frequency at the maximum amplitude, divided by the bandwidth of the system, or distance between half power points (see Fig. 1):

$$Q = \frac{f_r}{\Delta f} \tag{14}$$

The two concepts are related, in cases of low damping, by the ratio of stored energy E and energy lost ΔE in a stress cycle:

$$\delta = \frac{2E}{\Delta E} \tag{15}$$

which leads to a remarkable relation between δ and Q:

$$\delta = \frac{\pi}{Q} \tag{16}$$

3.5 *Vibration insulation*

In order to reduce or avoid the consequences of ground vibrations disturbing humans, there are artificial systems for their reduction. One of the simplest ones

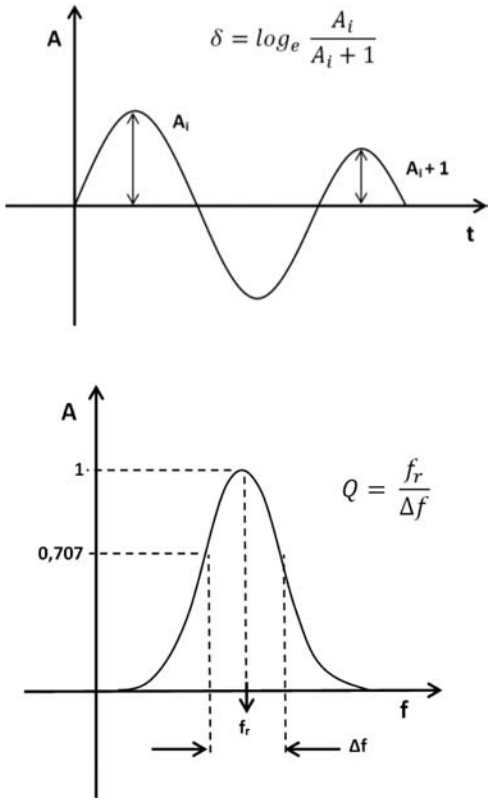


Figure 1. Graphic representation of the two indirect factors for determining internal friction.

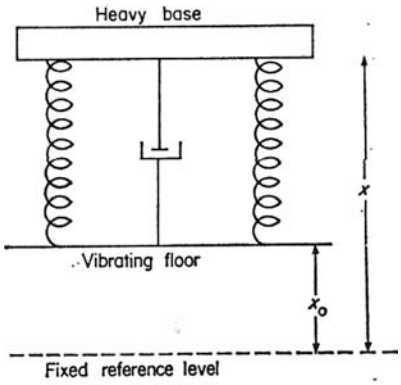


Figure 2. Schematic composition of a vibration insulator (after Pain 1968).

is shown in Figure 2 where the vibrations induced by a vibrating floor are reduced by a system of springs and one viscous resistance, or dashpot. This insulator usually operates at the mass-controlled end of the frequency spectrum, and its resonant frequency is designed to be lower than the range of the expected frequencies.

4 EARTHQUAKE BORNE VIBRATIONS

4.1 *Basic concepts*

Three main types of earthquakes may be defined (Bolt 1978):

a) Tectonic earthquakes – caused by rock breakage suddenly in response to the various geological forces that act underground, mainly in the vicinity of large faults, sometimes caused by great surface fault ruptures.
b) Volcanic earthquakes – when they occur in conjunction with volcanic activity.
c) Collapse earthquakes – small seismic activity occurring in regions of underground caverns and mines, when the induced stresses around those openings causes large masses of rock to burst, producing seismic waves, or ground vibrations.

Their relative importance may be evaluated by two parameters: magnitude and intensity. The first one deals with the amount of energy liberated at their origin (or hypocenter). Four types of magnitudes exist: M_L (local magnitude), M_S (surface wave magnitude), M_b (body or P-wave magnitude) and M_w (seismic moment magnitude scale). The first one was proposed in 1935 by Richter for quantifying medium-size earthquakes in California, considering that it can be evaluated by means of using the logarithm to base ten of the maximum seismic wave amplitude (in microns) recorded in a standard seismograph at a distance of 100 km from the earthquake epicenter.

For greater magnitudes and distances, another criterion was suggested by Gutenberg, due to the fact that higher frequency vibrations are attenuated and seismic surface waves (Rayleigh and Love waves) are dominated by waves with a 20 second period (or a wavelength of about 60 km), so their magnitude was called surface wave scale (M_S). Gutenberg later on combined compressional P-waves and transverse S-waves, so he created the body-wave magnitude scale (M_b), measured for periods between 1 and 10 seconds.

A very well-known formula suggested by Gutenberg and Richter in 1956 was the approximate calculation of the released energy E (ergs) from an earthquake of Ms magnitude, by:

$$\log E = 11.8 + 1.5 M_S \tag{17}$$

More recently, Hanks and Kanamori (1979) introduced the moment magnitude scale as a dimensionless number given by the expression:

$$M_W = \frac{2}{3} \log M_0 - 9.1 \tag{18}$$

where M_0 is the so-called seismic moment (in $N \cdot m$ units) with the following relation:

$$M_0 = \mu A \delta \tag{19}$$

In this formula, μ represents the shear modulus of the ground (around 30 GPa), A is the shearing area

Table 2. Modified Mercalli Intensity Scale with equivalent values of ground vibrations velocity and acceleration (according to Bolt, 1978).

MM Intensity Scale	Peak Vibration Velocity cm/s	Peak Acceleration ($g = 980\ cm/s^2$)
I	Hardly felt	–
II	“	–
III	“	–
IV	1–2	0.015 g–0.02 g
V	2–5	0.03 g–0.04 g
VI	5–8	0.06 g–0.07 g
VII	8–12	0.10 g–0.15 g
VIII	20–30	0.25 g–0.30 g
IX	45–55	0.50 g–0.55 g
X	> 60	>0.60 g
XI	Destructive	Destructive
XII	“	“

along the geologic fault that collapsed and δ its average displacement. Because of the logarithm scale, an increase of 1 step corresponds to $10^{1.5} = 31.6$ times the amount of released energy, and a step of 2 to 1000 times that energy.

As far as seismic intensity is concerned, it is defined as the measure of ground vibration obtained from the damage done to structures built by man, changes in the Earth’s surface and extent of animal reactions to the shaking.

The most used intensity scale is the Modified Mercalli, which contain 12 levels of damage expressed in roman numbers. For its importance with respect to engineering quantities, the following table can correlate them with peak vibration velocities and peak accelerations (Bolt 1978).

4.2 *Correlations with explosive detonations*

Because of the similitude between their effects, it has been proposed by many authors the correlation between earthquakes and large explosions, in particular nuclear blasts.

Such a correlation has been based on the practical rule that a one megaton of trinitrotoluene or TNT equivalent explosion creates a seismic signal with a magnitude of 4, by the expression of earthquake magnitude:

$$M = \frac{2}{3} \times (\log P + 6) \tag{20}$$

where P the weight of TNT detonated in Mton. This charge has a specific energy of 4.18 MJ/kg so the formula indicates that only 0.5% of bomb energy is converted in radiated seismic energy.

Therefore, the amount of liberated energy is the most important factor in any earth vibration phenomenon.

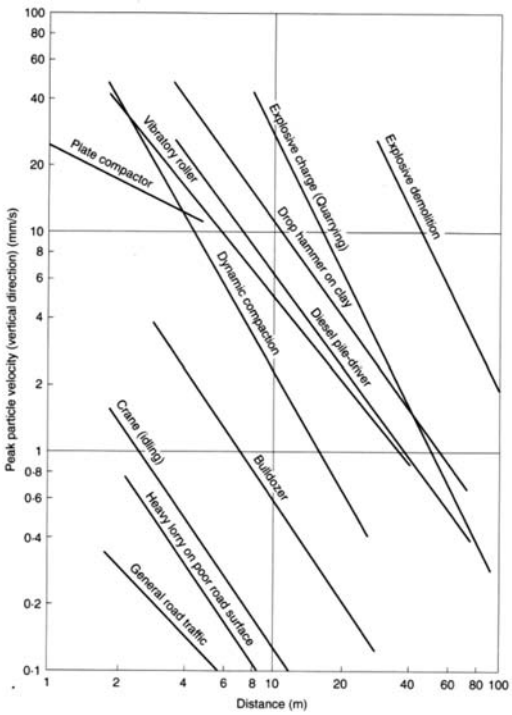


Figure 3. Vibrations from typical construction operations (Sarsby, 2000).

5 THE CORRELATION OF INTEREST

Figure 3 contains a diagram between peak particle velocity and distance for a series of different vibration phenomena, according to the British Standard 5228, Part 4 (BSI, 1996), as edited by Sarsby, 2000.

In order to reach an equation for such a family of curves, it is required to determine which energy was spent in each situation, since a bulldozer, a pile driver or an explosive charge in quarrying only have that variable attached. Several forms of energy were consumed, from mechanical (vehicles), to potential (drop hammer), or chemical (explosive), etc.

Such variable may be called “liberated energy” and represents the main cause for transmitting vibrations to the ground. In a certain number of cases, as it is the case of explosives, it is not common the use energy, but the detonated explosive weight, which is less correct because each explosive type liberates a certain energy, and only total energy or energy per time delay may correspond to the correct reality.

Upon substituting numerical data, a multiple regression was performed between two independent variables (released energy E and distance D) and one dependent variable (peak vibration velocity v), thus giving the following equation:

$$v = 0.013 \times E^{1.29} \times D^{-1.47} \tag{21}$$

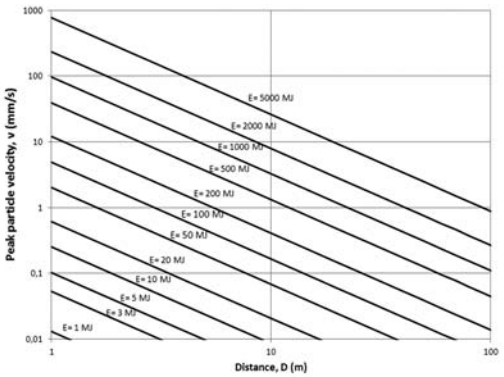


Figure 4. Variation of ground vibration's peak particle velocity with distance and in function of the energy released by any phenomena inducing such disturbances.

The utilized units were, respectively, mm/s for v, MJ for E and m for D. The corresponding correlation coefficient was 0.82. Its graphical presentation is shown in Figure 4.

It is obvious that such an equation may be applicable for various types of grounds (rocks and soils) so its results must be considered approximations for each specific situation.

6 CONCLUSIONS

Human response levels to ground vibrations, air blast and noise are considerable below those levels necessary to induce damage to residential structures (Nicholls et al., 1971). The human response level is a major factor contributing to complaints, rather than actual failure or fracturing of the construction materials.

It is obvious that geology and direction have great effects on both the amplitude level and its decay with distance. Most safety rules and national standards establish limits of vibration intensities, in order to prevent such damage, so their prediction in advance may constitute a good form of avoiding those inconveniences.

The mathematical expression that was presented above may be considered one more tool to conduct safe engineering workings, not only to prevent damage, but also to avoid human opposition reactions, thus contributing to a better life for everyone involved.

REFERENCES

Bolt, B. A. 1978. *Earthquakes, a Primer*. W. H. Freeman and Company, San Francisco.

BSI. 1996. *British Standard 5228: Noise and Vibration Control on Construction and Open Sites*. Parts 1 to 5, London.

Gama, C.D., Torres, V.N. & Paneiro, G. 2010. Ground Borne Vibration Environmental Impacts in Urban Railway Construction Projects (in Portuguese). *Proceedings of the XII National Geotechnics Congress, pp. 201 – 210, Guimarães.*

Hanks, T. & Kanamori, H. 1979. A Moment Magnitude Scale. *Journal of Geophysical Research*, Vol. 84, N^o B5, pp. 2348–2350.

Kolsky, H. 1963. *Stress Waves in Solids*. Dover Publications, Inc., New York.

Krylov, V. 1996. Computation of Ground Vibrations Generated by Accelerating and Braking Road Vehicles. *Journal of Vibration and Control*, Vol. 2, pp. 299–321.

Nicholls, H.R. et. al. 1971. Blasting Vibrations and Their Effects in Structures. *U.S. Bureau of Mines Bulletin 656, Washington, D.C.*

Pain, H.J. 1968. *The Physics of Vibrations and Waves.* John Wiley & Sons Ltd, London.

Sarsby, R. 2000. *Environmental Geotechnics*. Thomas Telford, London.

Srbulov, M. 2011. *Practical Soil Dynamics.* Springer.

Rock Mechanics for Resources, Energy and Environment – Kwaśniewski & Łydżba (eds)
© 2013 Taylor & Francis Group, London, ISBN 978-1-138-00080-3

A numerical study on the ground amplifications in areas above abandoned room and pillar mines and old longwall mines

M. Geniş
Department of Mining Engineering, Bülent Ecevit University, Zonguldak, Turkey

Ö. Aydan
Institute of Oceanic Research and Development, Tokai University, Shizuoka, Japan

ABSTRACT: In this article, the authors present the outcomes of their studies on the dynamic characteristics of ground and amplification of ground motions above abandoned mines and discuss their implications. In addition to the effects of some parameters associated with extraction, some topographic effects on ground motions in areas with abandoned mines are also investigated and results are presented. It will be clearly shown that ground amplifications may be quite large on the abandoned mines where extraction is carried out by room and pillar technique or open-pit mines. The ground amplifications may be 3–5 times that at the base. Particularly these amplifications may be quite large particularly near steep cliffs.

1 INTRODUCTION

There are many abandoned mines in various parts of Japan and the recent earthquakes showed these mines are quite vulnerable to cause sinkholes and subsidence (Aydan & Tano 2012a,b). Therefore, there is a growing concern on the safety of areas above such abandoned mines in relation to the anticipated Nankai-Tonankai-Tokai earthquake. Unfortunately, the present seismic risk assessment of Japan does not consider the effect of abandoned mines on ground motions in such areas. The authors have been carrying out researches on the short and long-term stability of ground above these abandoned mines.

There are almost no studies on the dynamic characteristics of ground and amplification of ground motions induced by earthquakes above abandoned mines exploited by room and pillar technique as well as long-wall mining techniques except those by the authors. In this article, the authors present the outcomes of their studies on the dynamic characteristics of ground and amplification of ground motions above abandoned mines and discuss their implications. In addition to the effects of some parameters associated with extraction, some topographic effects on ground motions in areas with abandoned mines are also investigated and results are presented.

2 CHARACTERISTICS OF ABANDONED COAL AND LIGNITE MINES

The shallow lignite seams are commonly exploited using the room and pillar technique. The extraction ratio of lignite seam is generally in the order of 60–80%. Pillars of lignite support roof layers.

The long-wall technique was employed for exploiting the coal/lignite seams. The overburden ground would subside into the excavated space following the extraction of coal/lignite seams. Depending upon backfilling state, the overall subsidence would be a fraction of the total height of extraction (Aydan 1994). For longwall mining operations in Japan, Hiramatsu et al. (1979) reports that the overall subsidence would be 70 to 90 percent of the total extraction height due to bulking of the broken overburden layers when no backfilling is employed. However, the broken overburden layers or goaf (gob) might further subside in long-term due to creep, degradation and vibration resulting from earthquakes or other sources. It should be also noted that the geomechanical characteristics of the goaf would be different from the original unbroken ground.

3 CHARACTERISTICS AND AMPLIFACTION OF GROUND MOTIONS ABOVE ABANDONED ROOM AND PILLAR MINES

Aydan et al. (2004, 2013) performed some model experiments to investigate the dynamic characteristics and amplification of ground motions using a shaking table. In those experiments, the effects of excavation ratio, depth and overburden the dynamic characteristics and amplification of ground motions at ground surface were investigated. However, it is very difficult to investigate the effects topography and complex earthquake acceleration is such model experiments.

Table 1. Parameters used finite element analyses.

Layers	$(G/\rho)^{1/2}$ (m/s)	η/ρ (m^2/s)	(b/ρ) (m/s^2)
Layer 1 (30–40 m)	320	32	10
Layer 2 (28–30 m)	160	16	10
Layer 3 (0–28)	320	32	10

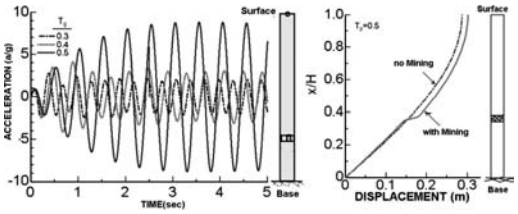


Figure 1. The acceleration response at ground surface and maximum displacement response of lignite pillars.

In this section, the authors utilized some numerical techniques to investigate the effect of depth, layer inclination and topographic effects.

3.1 *One-dimensional shear layer modeling of a mine with flat ground*

Aydan et al. (2004, 2007) also developed a shear layer model utilizing the tributary area concept for assessing the shaking characteristics of ground above abandoned lignite mines. The lignite mine was assumed to be 2 m thick with excavation ratio of 50%. Table 1 gives the properties of materials used in the finite element analyses. Figure 1(a) shows the acceleration response at ground surface for sinusoidal shaking with various periods. The largest amplification occurs when the period of ground shaking coincides with the natural period of the domain, as expected. Figure 1(b) shows the maximum ground displacement response with respect to the base with a wave period of 0.5 s. As expected, large relative displacement occurs at the level of extracted lignite seam. The amplitude of the amplification entirely depends upon the viscous properties of layers and frequency characteristics of the ground motions.

The same numerical model was used to assess the shaking characteristics of ground above the abandoned mine located at a depth of 16 m in Mitake town for an exploitation ratio of 70%. Results are shown in Figure 2 for the abandoned lignite subjected to the base acceleration obtained according to the method proposed by Sugito (2000) for the anticipated M9 Nankai-Tonankai-Tokai earthquake. The material properties used in the analyses are given in Table 2. The maximum amplitude of the base acceleration is about 250 gals. The ground motions are amplified up to 3.7 times at the ground surface. This implies that the ground motions above the abandoned lignite mines can reach very high level of shaking, which may be critical for surface structures.

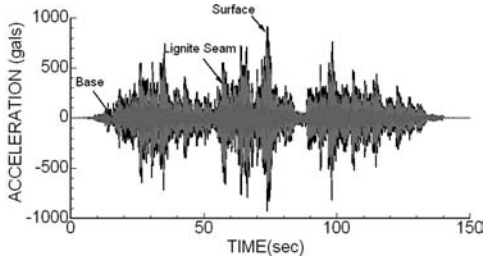


Figure 2. The acceleration response at ground surface and lignite seam.

Table 2. Parameters used finite element analyses.

Layers	$(G/\rho)^{1/2}$ (m/s)	η/ρ (m^2/s)	(b/ρ) (m/s^2)
Layer 1 (36–31 m)	900	45	19
Layer 2 (18–31 m)	600	30	19
Layer 3 (16–18)	400	20	14
Layer 4 (5–16 m)	500	25	19
Layer 5 (0–5)	300	15	19

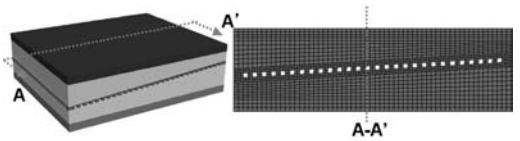


Figure 3. A three-dimensional view of analyzed domain and its cross-section along layer dip direction.

Table 3. Parameters used numerical analyses.

Layer	Vs (m/s)	ρ (kN/m^3)	E (MPa)	Poisson ratio	Damping ratio (%)
Soil	300	19	270	0.35	5
Mst-Sst	500	19	750	0.30	5
Lignite	400	14	400	0.30	5
Mst-Sst	600	19	1073	0.30	5
Chert	1000	19	3647	0.30	5

3.2 *Three-dimensional analyses of mine with flat ground and inclined lignite seam*

The dynamic response of an actual abandoned lignite mine with a flat ground surface and inclined lignite seam in Mitake town was chosen and its dynamic response is analysed using the strong motion due to the M9 anticipated Nankai-Tonankai-Tokai earthquake. The strong motion estimation was obtained according to the method proposed by Sugito et al. (2000). Figure 3 shows a three-dimensional perspective view of the mine and a cross section. The material properties used in the analyses are given in Table 3. The method is based on the finite difference technique utilizing

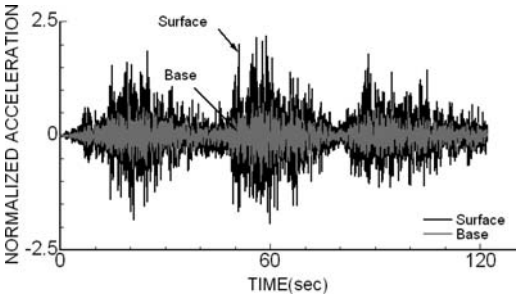


Figure 4. The acceleration response at ground surface and lignite seam.

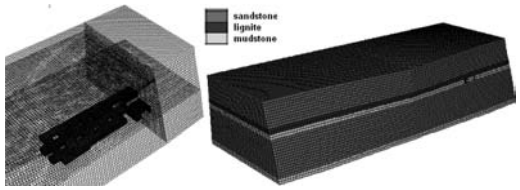


Figure 5. Mesh, geology and geometry of abandoned lignite mine.

Table 4. Rock material properties used in numerical analyses.

Unit	γ (kN/m^3)	E (MPa)	G (MPa)	Damping Ratio (%)
Lignite	20	557	229	5
Sandstone	20	257	103	5
Mudstone	20	76	30	5

silent boundary conditions and Rayleigh type damping of 5%. The details of the numerical method can be found in a publication by Geniş & Aydan (2008). Figure 4 shows the computed ground acceleration at the surface normalized by that of the base at the middle section denoted in Figure 3. The amplification of the ground motion is about 2.2 times that of the base.

3.3 *Three-dimensional analyses of abandoned mine with flat ground adjacent to Cliff*

The dynamic response of abandoned lignite mine is chosen as an actual example and its dynamic response is analysed. Figure 5 shows a three-dimensional perspective view, geometry and geology of the abandoned mine. The material properties used in the analyses are given in Table 4. The input ground motion is first assumed to be sinusoidal with a chosen period. Figure 6(a) shows the selected points of observation. The acceleration responses of the selected points are shown in Figure 6(b). The method is based on the finite difference technique utilizing silent boundary conditions and Rayleigh type damping was 5%. As noted from the

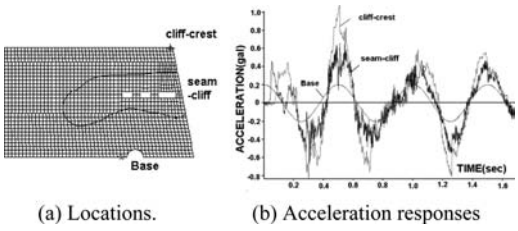


Figure 6. Locations and acceleration responses of selected points.

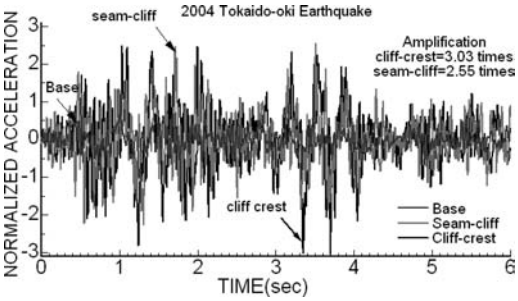


Figure 7. Acceleration responses of selected points during the 2004 Tokaido-oki earthquake.

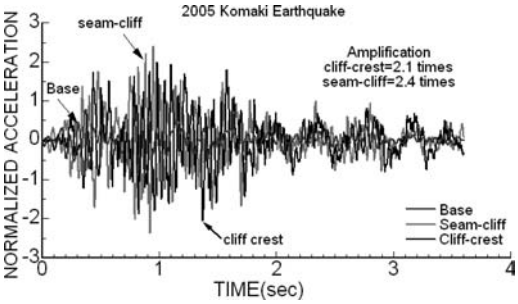


Figure 8. Acceleration responses of selected points during the 2005 Komaki earthquake.

figure, the ground motion is amplified to 3 times at the seam level near the cliff and 5 times at the cliff crest. This example also shows the importance of ground amplification due to topography.

The abandoned mine was subjected to ground shaking due to 2004 Tokaido-oki earthquake (Mj 7.2) (236 km away) and 2005 Komaki earthquake (Mj 4.7) (25 km away). The accelerations recorded at Mino-kamo strong motion station of K-NET as base accelerations. Figures 7 and 8 shows the acceleration responses at the same selected points normalized by the maximum value of the base ground acceleration. Far-distant earthquakes induce larger ground motions in the vicinity of the cliff crest above the abandoned mines compared to those by the near-field earthquakes.

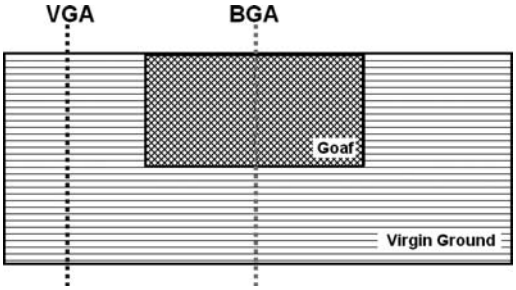


Figure 9. Illustration of ground conditions of old mine workings with longwall mining technique.

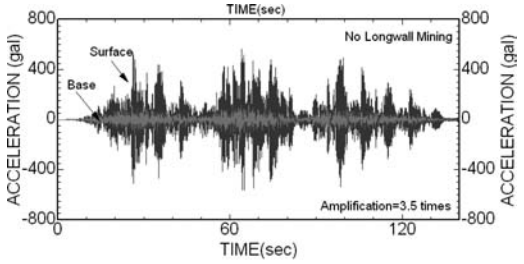
Table 5. Parameters used finite element analyses.

Layers	$(G/\rho)^{1/2}$ (m/s)	η/ρ (m^2/s)	(b/ρ) (m/s^2)
Virgin ground	900	45	25
Goaf	300	15	18

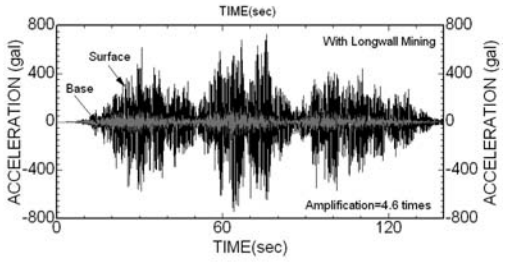
4 CHARACTERISTICS AND AMPLIFACTION OF GROUND MOTIONS ABOVE ABANDONED MINES WITH LONGWALL MINING TECHNIQUE

As mentioned in the introduction, long-wall mining is one of the commonly used extraction technique for coal and lignite seams. The ground above the coal seam is forced to fail following the extraction of the coal. The broken rock mass above the mined areas is called goaf or gob and its properties are reduced greatly with respect to virgin ground. There are few reports on the in-situ investigations of the characteristics of the goaf such as by Fujii et al. (2011). The in-situ investigations showed that the reduction of wave velocity of goaf can be between 30% and 65% of the virgin ground. As pointed out by Aydan et al. (2013), there is no report about the possible ground amplifications above the goaf of old mine workings. The authors have been now performing three dimensional ground response analyses for such grounds in addition to preliminary shear layering dynamic analyses. In this article, we just report the results of analyses using the shear layering dynamic analysis method. Analyses were carried out for two ideals situations, namely, virgin ground and ground with goaf with a depth of 30 m, which is relatively shallow (Figure 9). Material properties are shown in Table 5 and the ground motion was assumed to be due to the M9 anticipated Nankai-Tonankai-Tokai earthquake as used in the previous sections.

Figure 10 shows the computed acceleration responses for ground surface for old mine workings without/with long wall mining. As expected ground amplification occurs due to free surface even there is no mining. However, the ground amplification on the ground surface above the goaf becomes much larger when it is compared with that of the virgin ground.



(a) acceleration responses for virgin ground (VGA).



(b) acceleration responses for mined ground (BGA).

Figure 10. Acceleration response of ground surface for virgin ground and the mine ground.

5 CONCLUSIONS

Although there are many abandoned mines in various parts of Japan and the recent earthquakes showed these mines are quite vulnerable to cause sinkholes and subsidence, the present seismic risk assessment of Japan does not consider the effect of abandoned mines. The outcomes of the numerical studies on the dynamic characteristics of ground above abandoned mines showed that ground amplifications may be quite large on the abandoned mines where extraction is carried out by room and pillar or long-wall mining technique. The ground amplifications may be 3–5 times that at the base. Particularly these amplifications may be quite large particularly near steep cliffs. Furthermore, the frequency content of ground accelerations may have some pronounced effects on ground amplifications when the responses induced by nearby and far distant earthquakes are compared. Further studies on the effect of multiple seam extraction or of new large underground excavations beneath abandoned mines on the ground motions and their amplifications should be carried out.

ACKNOWLEDGEMENTS

The authors greatly acknowledge Emeritus Prof. Dr. T. Kawamoto of Nagoya University for the encouragement and suggestions and Prof. Dr. M. Sugito for the acceleration record for the anticipated M9 Nankai-Tonankai-Toukai earthquake.

REFERENCES

Aydan, Ö. 1994. A model study on the caving mechanism of longwalls in heavily jointed media. *The 3rd Int. Symp. on Mine Planning and Equipment Selection,* Istanbul, October, 765–770.

Aydan, Ö. 2004. Damage to abandoned lignite mines induced by 2003 Miyagi-Hokubu earthquakes and some considerations on its possible causes. J. of School of Marine Science and Technology, 2(1): 1–17.

Aydan, Ö. 2007. Monitoring. In Mine Closure and Post-Mining Management – International State of Art, C. Didier (Ed.). International Commission on Mine-Closure, ISRM, 111–123.

Aydan Ö. & Kawamoto T. 2004. The damage to abandoned lignite mines caused by the 2003 Miyagi-Hokubu earthquake and some considerations on its causes. *3rd Asian Rock Mechanics Symposium*, Kyoto, 525–530.

Aydan, Ö. & Geniş, M. 2007. Assessment of dynamic stability of an abandoned room and pillar underground lignite mine, (in Turkish), 23–44, Turkish Journal of Rock Mechanics Bulletin, Turkish National Rock Mechanics Group, No. 16,

Aydan, Ö. & Tano, H. 2012a. The damage to abandoned quarries and mines by the M9.0 east Japan Mega Earthquake on March 11, 2011. The 41st Rock Mechanics Symposium of Japan, Paper No. 410011, Tokyo, 129–134.

Aydan, Ö. & Tano, H. 2012b. Sinkholes and subsidence above abandoned mines and quarries caused by the great east Japan earthquake on March 11, 2011 and their implications. The damage to abandoned mines and quarries by the Great East Japan Earthquake on March 11, 2011. Journal of Japan Association for Earthquake Engineering, (Special Issue), 12(4): 229–248.

Aydan, Ö., Daido, M., Ogura, Y. & Kawamoto, T., 2004. A research on dynamic characteristics of areas with abandoned mines. 15th Central Japan Geotechnical Symp. (Geotechnical Environmental Problems) (in Japanese). Nagoya, 19–24.

Aydan, Ö., Sakamoto, A., Yamada, N., Sugiura, K. & Kawamoto, T. 2005. The characteristics of soft rocks and their effects on the long term stability of abandoned room and pillar lignite mines. Post Mining 2005, Nancy.

Aydan, Ö., Sakamoto, A., Yamada, N., Sugiura, K. & Kawamoto, T. 2005. A real time monitoring system for the assessment of stability and performance of abandoned room and pillar lignite mines. Post Mining 2005, Nancy.

Aydan, Ö., Daido, M., Ito, T., Tano, H. & Kawamoto, T. 2006. Instability of abandoned lignite mines and the assessment of their stability in long term and during earthquakes. 4th Asian Rock Mechanics Symposium, Singapore, Paper No. A0355 (on CD).

Aydan, Ö., Tano, H. & Geniş, M. 2007. Assessment of long-term stability of an abandoned room and pillar underground lignite mine. Turkish Journal of Rock Mechanics Bulletin, Turkish National Rock Mechanics Group, ISRM, No. 16, 1–22.

Aydan Ö., Daido M., Ito T., Tano H. & Kawamoto T. 2006. Instability modes of abandoned lignite mines and the assessment of their stability in long-term and during earthquakes. *3rd Asian Rock Mechanics Symposium*, Singapore, on CD.

Aydan Ö, Sugiura K. & Sakamoto, A. 2013. Dynamic characteristics of ground above abandoned mines. 13th *Japan Rock Mechanics Symposium*, Okinawa, 519–524

Geniş, M. & Aydan, Ö. 2008. Assessment of dynamic response and stability of an abandoned room and pillar underground lignite mine. The 12th International Conference of International Association for Computer Methods and Advances in Geomechanics (IACMAG), Goa, India, 3899–3906.

Geographical Information Authority of Japan (GSI) (2011): Special web site for East Japan mega earthquake.http://www.gsi.go.jp/BOUSAI/

Fujii, Y., Ishijima, Y., Ichihara, Y., Kiyama, K., Kumakura, S., Takada, M., Sugawara, T., Narita, T., Kodama, J., Sawada, M. & Nakata, E. 2011. Mechanical Properties of Abandoned and Closed Roadways in the Kushiro Coal Mine, Japan. International Journal of Rock Mechanics and Mining Sciences, 48(4): 585–596.

Hiramatsu, Y., Okamura, H. & Sugawara, K. 1979. Surface subsidence and horizontal displacament caused by mining induced coal seams. Proc. 4th Congress International Society for Rock Mechanics, 665-670, Vol. 1, Balkema.

Kawamoto, T. Aydan Ö, Okura, K. & Fujii, K. 2004. Reconnaissance report on the sinkholes in the abandoned lignite mine area caused by the 2003 Miyagi-Hokubu earthquake, Japan Filling Association (Nihon Juten Kyokai), 36 p.

Sugito, M., Furumoto,Y. & Sugiyama, T 2000. Strong Motion Prediction on Rock Surface by Superposed Evolutionary Spectra, 12th World Conference on Earthquake Engineering, 2111/4/A, CD-ROM.

This page intentionally left blank

Rock Mechanics for Resources, Energy and Environment – Kwaśniewski & Łydżba (eds)
© 2013 Taylor & Francis Group, London, ISBN 978-1-138-00080-3

Spatio-temporal analysis of the influence of mining on the surface – A case study from the Ostrava-Karviná Coal Field

E. Jiránková
Institute of Geodesy and Mine Surveying, VSB-Technical University, Ostrava, Czech Republic

P. Waclawik
Institute of Geonics, Department of Geomechanics and Mining Research, Academy of Sciences of the Czech Republic, Ostrava, Czech Republic

ABSTRACT: If coal seams are mined by longwall mining, the original stress balance in the rock mass is changed. The stress increases around the mined-out area. As a result, increased stress causes compression around the excavation. The compression around the excavation is shown by exact measurable subsidence. The impact of mining can be theoretically determined by a limiting impact angle. The paper deals with the assessment of mining in the ninth and seventh blocks at Karvina Mine Lazy Plant and its influence on the surface. The process of failure of the mining seam's rigid roof in both areas will be explained. On the basis of spatio-temporal relationships of real surface subsidence, mined longwalls, and geomechanical events, the character of overlying rock deformations can be evaluated. The character of rigid overlying strata will be evaluated by means of an inflexibility coefficient which has the advantage of including the main factors of influence: the thickness of the seam and the rigidity and compactness of the overlying strata. It is possible to specify the time of breakthrough by synchronous evaluation of seismic events at the mining seam's overlying strata because surface measurements are usually done once every half-year.

1 INTRODUCTION

In every case, measured subsidence at the surface occurs as a result of higher stress, which arises in the surroundings of mined areas (Jirankova 2010). Determination of the value of subsidence at the surface with regard to the extent and thickness of mined longwalls is important for distinguishing situations where the deformation of solid overlying strata occurs (Mučková et al. 2010). In many cases a strutting vault forms over the mined area and breakthrough of the whole thickness of the intact firm overburden does not occur. At the origin of the strutting vault this can lead to an enormous concentration load of formation and the occurrence of geomechanical events. But in cases where the intact overlying strata break, the breaking cannot extend further. Incurred overhangs of intact firm strata by its restraint to the no undermine overburden contribute to considerable additional load on the affected areas.

Dimensioning of the mined-out area in which get in concrete conditions to breakthrough unyielding hanging rock strata has a very important meaning for consideration of the changes in the state of stress in rock massif. It is possible to obtain the proportions of the mined-out area at the time of breakthrough by backward evaluation of mine surveys and seismic observations in the locality in which they exist (Jirankova et al. 2012). Backward evaluation also provides a survey of the break overburden earlier dig for seam which has substantial meaning for the correct interpretation of the actual evaluation break overburden at the same time dig for strata.

2 NATURAL CONDITIONS

This paper evaluates the overlying strata of seam 40 in the area of the seventh and ninth blocks of the Karvina Mine Plant Lazy. The area is situated in Karvina subbasin in the Czech part of the Upper Silesian basin. The seams are mined by the longwall method by controlled caving.

In the area of the ninth block of Karvina Mine Plant Lazy, the mining of seams 39 and 40 has been finished. The last panel to be mined in seam 40, panel 140 908 – 2, was finished in February 2013. In accordance with further progress, only the seams of the Ostrava strata will be mined. Seam 39 appears at an average depth of 640 m and seam 40 at an average depth of 710 m. The given seams belong to the Sedlova member of the Karvina strata. The general incline of the ninth strata block is 6–7° NNE. Structural and tectonic conditions are clear from the geological cross-section (see Fig. 2). The distance between seam 39 and the overlying strata of seam 38 is 15 m. Seam 39 has

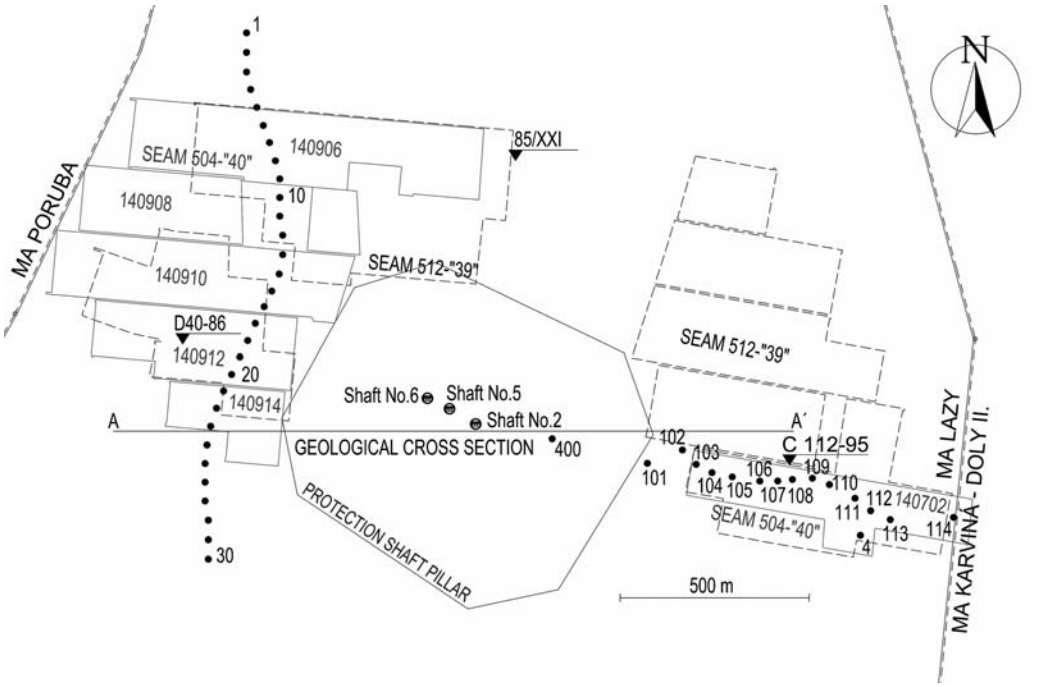


Figure 1. The scheme of the mining in 39 and 40 seams. The position of surface points regarding mining.

a thickness of 4–6 m in the area. Interbedded strata between seams 38 and 39 are built mostly by fine-grained and medium-grained sandstones. Interbedded strata between seams 40 and 39 have an average thickness of approximately 60 m. The thickness of seam 40 is variable and is often reduced by erosion. Where no erosion has developed, the seam reaches a thickness of 3–6 m. In the area of erosion the thickness is less than 1 m. The average mined thickness of the seam is around 4 m. Interbedded strata between seams 39 and 40 are built mostly by fine-grained and medium-grained sandstones. Fine-grained and medium-grained conglomerates create intercalations in some places. Information about the lithology of the overlying strata is provided especially by exploration borehole No. 85/XXI and D40 – 86 (Fig. 1).

In the area of Karvina Mine, Plant Lazy, seam 39 has already been mined out. In the seam 40 is in the seventh block; panel 140 702 has already been mined out and panel 140 705 has been prepared for mining. Seam 39 is found at an average depth of 685 m and seam 40 at an average depth of 740 m below the surface. The incline of the strata in the seventh block is variable. The anticline bend of strata so-called Sušská Saddle divided this area into two parts (Grygar & Waclawik, 2011). The seams have an incline of 8° to WNW in the western part and 7° to NNE in the eastern part. The interbedded strata between seam 39 and the overlying seam 38 has a thickness of 27 m. Seam 39 has a thickness of 4–6 m in the area. The interbedded strata between seams 38 and 39 are built mostly by fine-grained and medium-grained sandstones. The interbedded strata between seams 40 and 39 have an average thickness of 55 m and are built mostly by fine-grained and medium-grained sandstones. Medium-grained conglomerates create intercalations in some places. The thickness of the seam is very variable here too; on average it reaches about 4.5 m. In the eastern part, erosive sandstones lies on the seam, whose thickness is about 3 m. In the seventh block, seam 40 is developed in a direct roof of irregular siltstone, with a variable thickness of 1–13 m, which is locally eroded by superposed sandstones. Information about the lithology of the overlying strata of a given seam is provided, especially for exploration borehole No. C 112/95 (Fig. 1).

3 SEISMIC MONITORING

The monitoring of seismic activities proceeds continually. At present, local area network (LAN) seismic stations and regional nets operate in Ostrava Krasne Pole. The local net comprises stations. The stations operated by individual mines for monitoring their own mining areas in the Karvina part of OKD. The regional net comprises stations of the seismic polygons of Green Gas DPB, a.s. Seismic polygons comprise ten stations together. Six surface stations of the seismic polygon are situated in shallow boreholes, the seventh station is situated in a gallery of mining measured base in Ostrava Krasne Pole and three mining reference stations of the seismic polygon are situated in the underground part of Karvina basin. The mining reference stations serve to join regional nets to local nets.

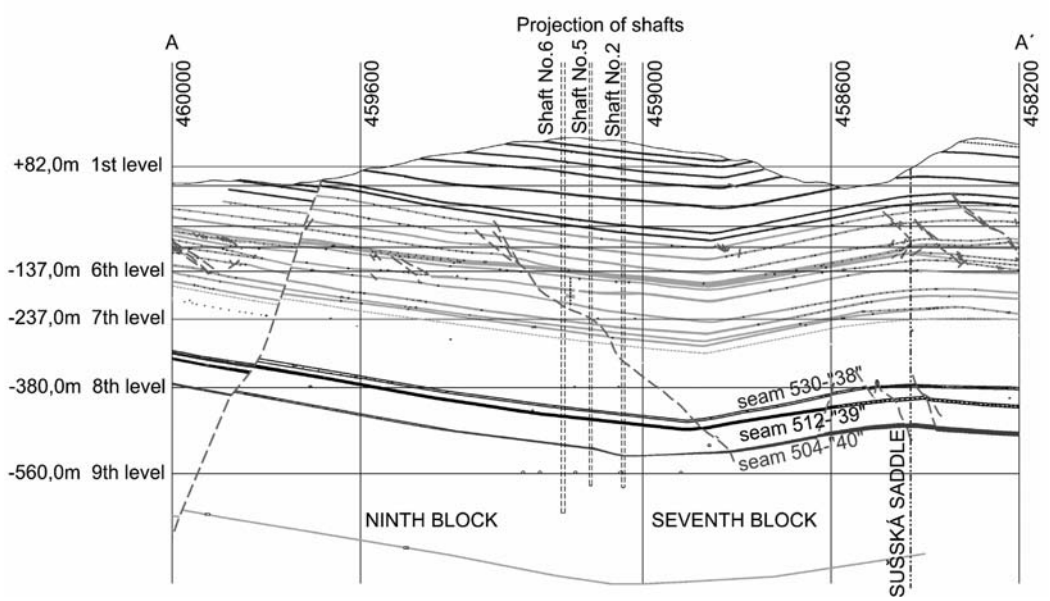


Figure 2. The geological cross section in line A–A′.

Plotting of the data of the local net together with those of seismic polygon stations has taken place since 2002 in the scoring centre at Green Gas DPB a.s. in Paskov.

4 SURFACE MONITORING

Surface levelling points of a surveyor's straight line are compiled at half-yearly intervals. The first measurement in the area of the ninth block was performed before the beginning of mining in seam 38. Surface spots are stabilized with the help of spikes fitted to the surface of the road. The distance between points is about 50 m. The relative positions of points on a surveyor's straight line and single mined-out faces are shown in Figure 1.

The first surface measurements of the heights of surface points were done before the beginning of mining of seam 40 in the seventh block. Subsequently two measurements were performed at the time interval of two months. The relative positions of the mined panel 140 702 and the surface points of a surveyor's straight line are displayed in Figure 1.

Successful evaluation and correct illustration showing the mechanism of disruption depends above all on location surface points towards mining, on frequency surface measurement and on sufficient knowledge of the natural conditions of mining and the technical information of mining.

5 ANALYSIS OF MEASURED VALUES

The solid overburden is a bedded inhomogeneous beam that is formed of variously powerful and variously firm strata. Those strata are corrupted by a complicated system of tectonic faults. The bedded overburden rocks have different mechanical properties so their different deformations happen. The overburden is built by firm strata which have a large bearing but small deflection ability. Those strata are brittle deformed when the strength limit is exceeded. Furthermore, there are strata able to big deflection as well as strata which changed conditions they may suit to plastic. This means that at the time of breakthrough of the firm overburden, fragile deformation occurs only for those strata which have small deflection ability. The deformation of the flexibile strata is not brittle at the time of breakthrough of firm overburden. Those strata are brittle deformed as far as subsequently with progressive mining (Jirankova 2012).

The conclusions regarding the evaluation of breakthrough in seam 40 in the ninth block of Karvina Mine Plant Lazy are as follows. The mining in seam 39 is accompanied by regular breakthrough of the overburden. The interlayer between seams 39 and 38 has a thickness of only 15 m and the overburden of seam 38 is already disturbed. The coefficient of inflexibility of the interlayer between seams 38 and 39 is 4.9.

At the time when mining of the last panel of seam 39, panel 139 908, was being carried out, mining of panel 140 914 in seam 40 began simultaneously. From the results of the surface measurement of heights it was found that during the period between 24 May 2008 and 11 October 2008 the subsidence of the surface increased (Fig. 3). From the interpretation of surface subsidence and simultaneous seismic activity it is possible to determine the probable time of breakthrough of the firm overburden in August 2008. The width of the mined-out area at the time of breakthrough was about 260 m, the coefficient of inflexibility of the interlayer

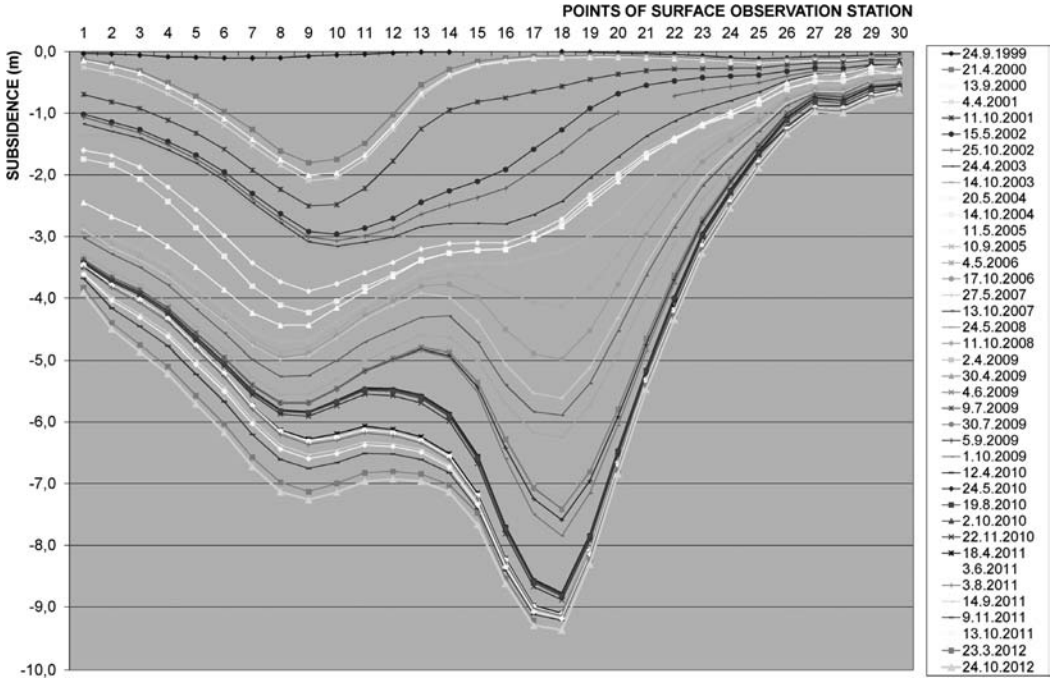


Figure 3. The formation of the subsidence trough in the line surveyor's straight line 1–30.

stratum between seams 39 and 40 is 16.3, and the average depth of mining in seam 40 is 710 m. The progress of other mining in seam 40 led to a gradual fracture of the overhang over the layer of carboniferous rock strata and spreading of the formed subsidence trough.

The evaluation of the disruption of the firm overburden of seam 40 in the seventh block of Karvina Mine Plant Lazy indicates that breakthrough of the firm overburden above the mined-out area of panel 140 702 did not happen until this time. From measurement of surface heights, only a decline in the strutting vault formed above the area mined-out until this time was ascertained. The biggest measured subsidence, with a value of 165 mm, was ascertained at surface point No. 109. At the time of mining of panel 140 702 no significant seismological event were registered. The width of the panel at the beginning of mining was 120 m after mining approximately 250 m life of face was panel extended on 195 m and subsequently reduce on width 120 m. The total life of face is 860 m. The parameters of the area mined-out until this time do not reach the width of the mined-out area in probable time breakthrough firm overburden seam 40 in the area of the ninth block, see above.

6 CONCLUSIONS

The practical signification evaluation fracture of overburden consists in dimensioning the surface of the mined out area at which come to breakthrough firm overburden and in evaluation of the current state of failure of the overburden at the time of the last surface levelling.

Dimensioning of the mined-out area at which get in factual conditions to breakthrough firm hanging rock strata has a very large importance for assessment of changes stress state of rock mass. Extraction of this area is a basic strategic prerequisite for the effective improvement of geomechanical conditions of subsequent mining activities in underlying seams.

The evaluation of the actual state of failure is based on measured of the surface subsidence and registered seismic events. The knowledge of the failure of the overburden in previously mined out seams and experiences from the assessment of similar localities is necessary. In this regard is evaluation of the current state of failure always prediction because the accuracy of the evaluation of current results will evidence as far as from evaluation at the time of the next surface levelling.

The question arises of how it is possible to use experience from earlier evaluations of similar localities. The rock mass is an environment with no homogenous natural conditions, as not only every area but also every mined-out coal face is unique. The selection of similar locations must be performed on the basis of generalized parameters. The main influential factors which should be included are the thickness of intact the overburden, the strength and integrity of the intact overlying rock strata, the number of bedding surface on one meter intact overburden, the number of significant tectonic faults, and the depth of mining, seam thickness, range and seismic effect of free

haul blasting, and average speed of panel advance. The generalized parameters mentioned influencing factors offer only rough selection similar locations. Indeed, nor after retrieval acceptable similar locations it is not possible results evaluation simply take over and think of them as prediction currently assessed areas. Evaluation of the current state of failure of the overburden has to be done, above all, from the measured values in the existent locality alone, and then a practical evaluation of the records should be done.

In the paper, the results and practical meaning of a method for evaluating the failure of firm overburden are introduced. The method is based on contemporary assessment of mine surveyors' observations and seismic observations depending on the character of the rock mass. The method allows specify the state when the firm overburden cracked. When the firm overlying rock strata are not breakthrough, the surroundings of the mined-out area are over-loaded and danger of anomalous geomechanical events increases.

ACKNOWLEDGEMENT

This article was written in connection with grant project SGS No. SP2013/34 – The geodetic and geophysical monitoring of changes of the physical characteristics of the rock environment in the subsidence trough areas.

REFERENCES

Grygar, R. & Waclawik, P. 2011. Structural-tectonic conditions of Karviná Subbasin with regard to its position in the apical zone of Variscan accretion wedge. *Acta Montanistica Slovaca* 16(2): 159–175.

Jiránková, E. 2010. Assessment of rigid overlying strata failure in face mining. *Central European Journal of Geosciences* 2(4): 524–530.

Jiránková, E., Petroš, V. & Šancer, J. 2012. The assessment of stress in an exploited rock mass based on the disturbance of the rigid overlying strata. *International Journal of Rock Mechanics and Mining Sciences* 50: 77–82.

Jiránková, E. 2012. Utilisation of surface subsidence measurements in assessing failures of rigid strata overlying extracted coal seams. *International Journal of Rock Mechanics and Mining Sciences* 53: 111–119.

Mučková, J., Černota, P., Barták, P. & Mikoláš, M. 2012. Mining subsidence monitoring of highway between Ostrava and Frýdek-Místek. *Journal of the Polish Mineral Engineering Society* 1(28): 31–40.

This page intentionally left blank

Rock Mechanics for Resources, Energy and Environment – Kwaśniewski & Łydżba (eds)
© 2013 Taylor & Francis Group, London, ISBN 978-1-138-00080-3

Control of rockburst risk in hard coal longwall mining – A case study

P. Koniček, R. Kukutsch, J. Ptáček, K. Souček, L. Staš & P. Waclawik
Institute of Geonics, Institute of Clean Technologies, Academy of Sciences of the Czech Republic, Ostrava

ABSTRACT: Rockburst represents a very dangerous phenomenon in the Upper Silesian Coal Basin (USCB). The rockburst problem relates to the natural and mining conditions in the rock mass. It is very difficult to decide which of the factors prevails, but we generally assume that the existence of competent adjacent rocks in the roof of the seams and incomplete seam extraction in the overburden, cause irregular stress distribution in the rock mass and stress overflow in those regions with the highest stress concentration. Destress blasting in overlying competent rocks is a very important rockburst control technique. The case study describes the control of rockburst risk by destress blasting in an example of the longwall of the Czech part of the USCB. Destress blasting, in the competent overburden of the exploited seam, was applied as the main rockburst prevention method. Groups of boreholes were fired ahead of the longwall face with explosive charges of up to 4500 kg during the longwall mining of the thick coal seam. An analysis of the effectiveness of stress release following destress blasting and generally, during the course of mining was realized. Despite its rarity, rockburst in the longwall face was induced by the applied destress blasting during the course of longwall mining. The authors evaluate the causes and effects of the induced rockburst from in situ stress and deformation measurements. The case study presented confirms that destress blasting is a very important mine safety tool that contributes to the reduction of rockburst hazard.

1 INTRODUCTION

Ostrava-Karvina coalfield (hereafter OKR) is the only hard coal deposit in the Czech Republic. It is a part of the Upper Silesian Coal Basin (USCB), which mostly belongs to Poland (see Fig. 1). Owing to the geological and geomechanical characteristics of the rock massif and because of long-term mining activity, irregular stress distribution occurs in the rock mass. Irregular distribution of stress and of its concentration in certain parts of the rock mass, when exceeding the rock strength limit, can lead to a sudden release of elastic deformation energy and to the occurrence of a rockburst. Considerable attention has been dedicated to this problem in the OKR for about one hundred years, as the first reports of rockburst are dated from the very beginning of the last century (Holecko et al. 1999). In the OKR, a multiseam sedimentary hard coal deposit is exploited. The Czech part comprises an area of about 1550 km^2. The total thickness of the Carboniferous strata extends up to 2000 m. The geological structure is the result of several geological genesis cycles. It is essentially changing in a west-east direction and based on geological differentiation, the Czech part of the deposit has been structured into a western part (Ostrava part of basin), and into an eastern part (Karvina part of basin). It should be mentioned here that at the present time only the eastern Karvina part of the OKR

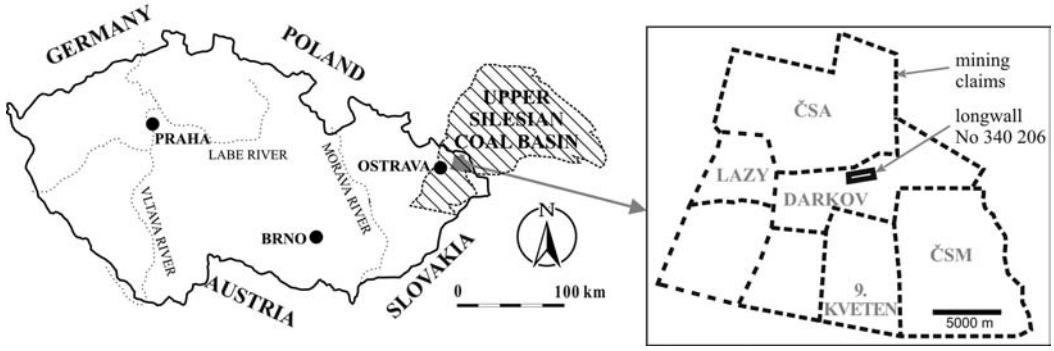


Figure 1. Geographic location of the USCB within the Czech Republic.

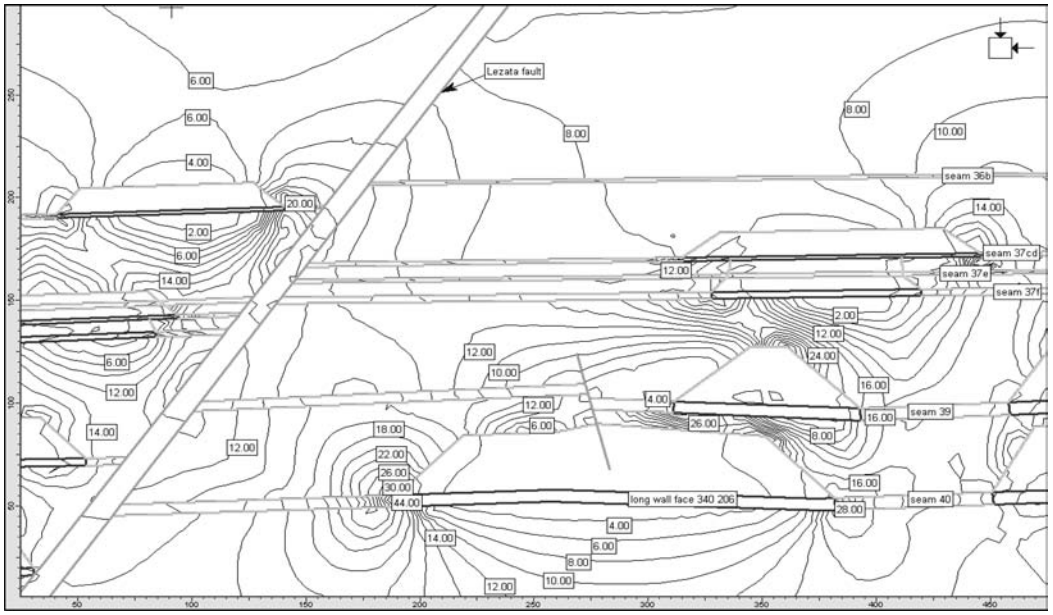


Figure 2. Mathematical model of the vertical stress component in the N-S cross section.

is exploited, whereas mining in the western Ostrava part of the OKR has been halted. In the Karviná subbasin, the paralic series were covered by sedimentation of continental molasse beds. In contrast to the lithological nature of the western part of the OKR, the sedimentary cycles are conspicuously longer and moreover, very competent sandy rocks prevail (Dopita et al. 1997). The compression strength of such rocks is distinctly higher than that of mudstones and siltstones. Higher stress concentrations occur in thicker banks of rigid rock components than in other parts of the rock massif. This condition has been manifested most conspicuously in the Sedlové member, which is a basal part of the Karvina series of the carboniferous strata. The Sedlové member features several tens of meters of thick banks of rigid rocks (sandstones, sandy siltstones and conglomerates). Equally, as a rule, the coal seams are several meters thick. The vertical distances between coal seams mostly reach several tens of meters. Between the mined coal seams, there are frequently vertical distances of up to 100 m. For stress distribution, irregular sedimentation is important with a rather variable thickness of strata; some parts of the strata are more-or-less eroded. An important feature of the rock mass is not only the considerable difference between the compression strengths of the different lithological types of rock, but also the difference in rock strength within the same lithological type. The resultant distribution of stress in the rock massif is affected equally by the nature of the structural build, which differs between the western and eastern parts of the OKR. In the eastern part (Karviná subbasin), a calm, almost horizontal deposition of strata prevails with a rather simple fault structure, comprising mostly two systems of normal faults, roughly perpendicular to each other. In addition to the above-mentioned geological characteristics, which affect primarily the distribution of stress in the rock massif, the mining activity itself also contributes to the irregularity in the stress concentration. In the OKR, hard coal has been mined since the second half of the 18th century. Since that time, the exploitation of the coal seams has advanced gradually downwards to ever-bigger mining depths. The development of new mining methods, the introduction of new technology, and economic reasons have led frequently to the abandonment of many non-excavated parts of the coal deposit. Currently, when coal is mined at a depth of roughly 1000 m below the surface, a non-uniform distribution of stress is caused by all of the afore-mentioned factors; thus, coal mining is very unfavorably affected (Drzewiecki & Kabiesz 2008, Dubiński & Konopko 2000). Considering that currently, the coal seams of the Sedlové member (the properties of which are generally the least favorable) are being worked almost exclusively, the high risk of rockburst occurrence in the rock massif, loaded in such a way, is obvious.

2 GEOLOGICAL PROPERTIES OF ROCK MASS IN THE LONGWALL 340 206

The area of longwall No. 340 206 mining discussed here, is situated to the east of the former safety shaft pillar in the Karvina subbasin (see Fig. 2). The principal structures that influence the stress state in the described area are tectonic fault zones Gabriela in the west (dip 70°, amplitude 80 m) and Lezata in the north

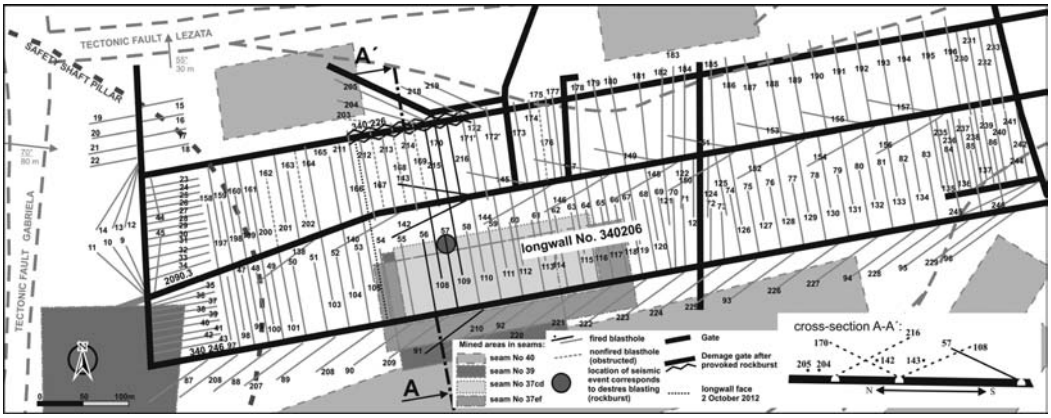


Figure 3. Longwall situation and design of the rock blasting boreholes.

(dip 50°, amplitude from 20 to 80 m). The Gabriela fault is a wide tectonic zone (30–100 m) with frequent opposite dip faults that indicate tensile stress conditions at the time of origin. The sediment layer formation is slightly folded (general dip from 5–8° to the N–NW). Seam No. 40 with a thickness of 6–7 m is a basal seam of the Sedlove member. Competent rigid rocks (sandstones and conglomerates) comprise the predominant part of the interbed of seams 40 and 39 (from 60% to 90%) and increase from east to west (towards the safety shaft pillar). The share of competent rigid rocks in the overburden (up to seam No. 36) is also large (from 44% to 64%) (Kratky & Macura 2011).

3 MINING AND GEOMECHANICAL CONDITIONS IN THE LONGWALL NO. 340 206

Seam No. 40 was mined out by the longwall No. 864 123.24 CM the locality of Gabriela in the Darkov mine. The longwall area belongs to the areas with the highest rockburst risk, according to the results of geological and geomechanical analyzes of stress distribution in the rock mass. The longwall was mined out using the controlled caving method using SL – 500F combine and reinforced by the advancing support DBT 2.6/5.5. The depth under the surface was around 800 m and the dip of the strata around 5° to the northeast. The mined seam thickness was 5.5 m and the width of the longwall block was 200 m. Seams Nos. 37cd, 37e, 37f, and 39 were mined out in the overburden of seam No. 40 (see Fig. 2). The irregularity of their mining caused irregular stress distribution within the surroundings of the mined block. All the abovementioned seams were mined out only in independent areas in connection with the geological structure of the rock mass. In addition, the influence of the goaf in seam No. 40 must be taken into consideration. The mathematical model of the geomechanical properties of the rock mass was compiled to verify the idea of the stress-strain changes during mining. The model was constructed in the vertical north-south cross section. The commercial software Phase 2 by Rocscience was used. It applies the plane deformation model using the finite element method. The specific density of the rock mass of 0.026 MN/m^3 was taken into consideration. The relation of the vertical and horizontal components was considered in a ratio of 1:1, according to the former by hydrofracturing measured stress interpretation. All model materials were interpreted as elastic isotropic. The model of the vertical stress component is demonstrated as an example in Fig. 2. The stress distribution in Fig. 2, according to the theoretical idea, shows considerable irregularity and high stress concentration, mainly in the north edge of longwall No. 340 206. This corresponds to the rock mass behavior in the course of the mining.

4 ROCKBURST PREVENTION, DESTRESS ROCK BLASTING

Destress rock blasting in the overburden is considered the most effective method in the system of the rockburst prediction for the geological and geomechanical rock conditions of the Sedlove member (Comeau et al. 1999, Dvorsky & Konicek 2005, Konicek et al. 2011). It was projected as the rockburst prevention measure for mining longwall No 340 206 in the Darkov mine (Kratky & Macura 2011). The design of destress blasting is presented in Fig. 3. The destress blasting boreholes were drilled upwards (from $+8°$ to $+30°$) from coal seam level No. 40 (see small cross section A-Á in Fig. 3). The lengths of the holes varied from 30 m to 90 m. In light of the design parameters and the destress blasting task, borehole diameters of 93 mm were selected. Borehole spacing was designed according to the natural and mining conditions, e.g., 8 m in the start area of the longwall and from 10 m to 12 m in the rest of the area of the longwall. The

drill hole bottoms were situated at a distance of 26 m to 32 m above coal seam No. 40. Plastic explosives in charges, as well as pneumatic sand stemming, were applied to the boreholes. The lengths of particular charges varied from 18 m up to 70 m and the lengths of sand stemming from 15 m up to 30 m. All charges in each stage were fired simultaneously without using delays. Detonators DEM-ZB-S, produced by Austin Detonator, Czech Republic, were used for ignition. The weight of particular charges varied according to the length of the drill hole; from 75 kg up to 600 kg per hole. In certain stages, groups of 2 to 10 drill holes with total charges of 800 kg up to 4325 kg were blasted. A gelatinous ammonium nitrate explosive Supergel 30 (cartridges diameter 28 mm and length 200 mm) from Maxam Deutschland GmbH was used.

The main goals of destress blasting in the area of longwall No. 340 206 were the softening of the competent rock layers and reduction of their effective modulus of elasticity ahead of the longwall face, and to decrease additional stress levels of unmined areas of coal seams in the overburden. Another advantage of this blasting method is the release of stress in the absence of the miners.

The destress blasting was designed in advancing stages. 12 stages of destress blasting were realized before the provoked rockburst on 2 October 2011 during the mining of longwall No. 340 206 from July 2011 until October 2011. There was released greater seismic energy than would correspond to the workings performed with the explosives for the specific physical-mechanical conditions in all stages. According to the site conditions, the first 3 stages were fired before the start of mining. Other stages were fired ahead of the longwall face according to site conditions, longwall advance and registered seismic activity (Knotek et al. 1985).

No. 13 destress blasting stage provoked the rockburst. It comprised 10 boreholes and was fired on 2 October 2012 (marked in Fig. 3). Two boreholes from maingate No. 340 226 (Nos. 215 and 216) situated southward had the following characteristics: borehole length 70 and 63 m, explosive charge 400 and 325 kg, length of explosive charge in boreholes 68% and 71% total length of borehole. Three boreholes from middlegate No. 2090.3 (Nos. 108, 109 and 170) situated northward and southward had the characteristics: explosive charge 275, 450 and 250 kg, length of explosive charge in boreholes 67%, 73% and 60% to total length of borehole. Two boreholes from middlegate No 2090.3 (Nos. 142 an 143) situated in stemming area of boreholes Nos. 108, 109 and 170 had the characteristics: explosive charge 250 and 175 kg, length of explosive charge in boreholes 60% and 56% to total length of borehole. Three boreholes from tailgate No. 340 246 (Nos. 56, 57 and 91) situated northward in the area of the longwall panel and southward in the area of the left pillar between the previous longwall panel and longwall No. 340 206 had the characteristics: explosive charge 576, 500 and 500 kg, length of explosive charge in all boreholes was 75% to total length of borehole. Distance of longwall face from the first borehole of stage (No. 56) was 50 m at the time of firing. Explosive charges in all boreholes were fired succesfully and all stemmings were held (Konicek et al. 2012).

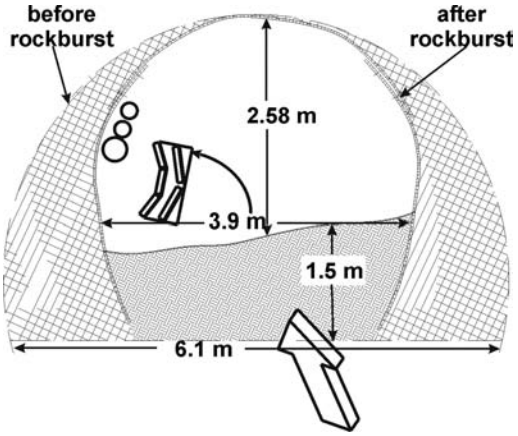


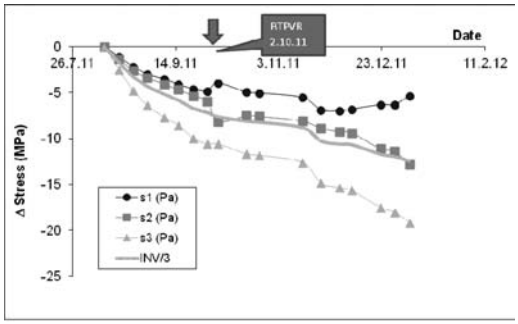
Figure 4. Reconstruction of probably action of forces during provoked rockburst in main gate No. 340 226 in stationing 260 m boreholes.

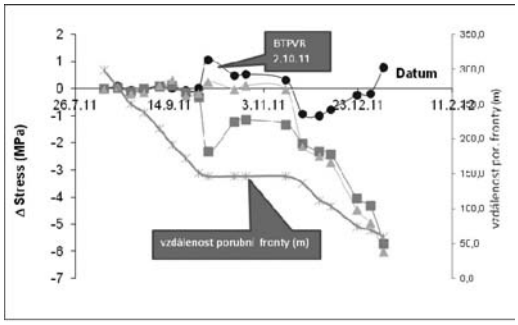
5 PROVOKED ROCKBURST

The rockburst induced by rock blasting in the overburden, realized within the rockburst prevention, occurred on 2 October 2012 in the area of the longwall. Gates inspection after blasting verified a provoked rockburst with impact in maingate No. 340 226. The rockburst manifested itself as: deformation of the main gate of length 131 m (marked in Fig. 3) as a bottom swelling of up to 3.5 m, deformation of steel arch, broken hydraulic probes, yield of steel arches by up to 0.6 m, damage to conveyor belt and scattering of facilities. The probable action of force during the rockburst was evaluated from the deformation of roadway (Fig. 4). Generally, we can say that the main action of the force was from the bottom of the roadway about 3 m left of the coal.

6 STRESS MONITORING IN GATEWAY 340 226

The monitoring of stress-strain processes and their interpretation during the course of mining the longwall No. 340 206 was projected for the irregularity in the stress distribution and was to be expected. The tensometric conical measuring probe – compact conical borehole monitoring (CCBM) (Stas et al. 2011) was installed next to the other experimental monitoring facilities on gateway No. 340 206. The reason for





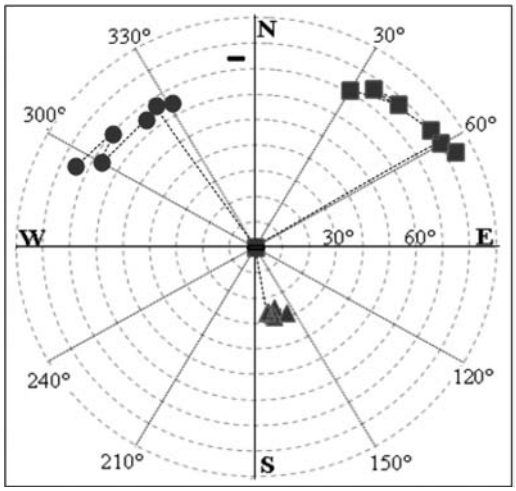


Figure 5. Interpreted stress changes with the ductile compo-nets (a), the orientation of pricipal stress dirrections inter-preted according to the ductile components (b).

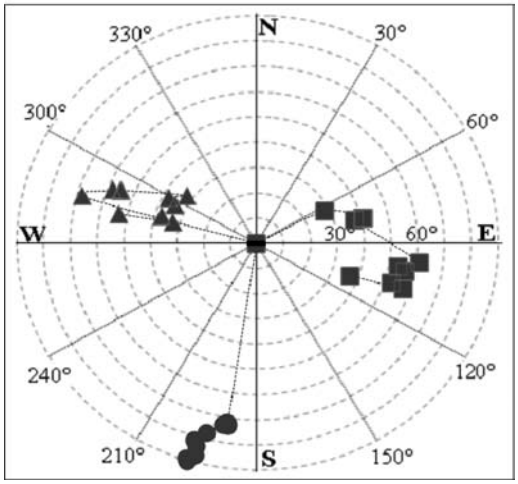


Figure 6. Interpreted stress changes without the ductile componets (a), the orietation of pricipal stress changes dir-rections (b).

its use was stress tensor monitoring during the course of the longwall mining. The probe was installed in the longwall face on gateway No. 340 206. The stress data reading was realized once a week. The gradual deformation in the face of the measuring hole and the progressive increase of the stress tensor components is possible to determine from the monitoring data. Thus, it would be possible to estimate the orientation and mutual ratio of the principal stress tensor components. The basic orientation of the principal stress components, without the influence of the longwall face stress, is documented in the Fig. 5b. The value of component S3 is the highest, and according to the assumption, nearly perpendicular. The order of the deviation reaches 30°. The stress vector component S2 is oriented horizontally (deviation 10° to 20°) and its direction is 30° to 60°. Similarly, the S1 component is oriented horizontally with the direction 300° to 330°. The relation of the magnitude of the particular components is obvious from Fig. 5a and is as follows: S3:S2:S1 = 2.2:1.2:1.

The rockburst induced by rock blasting in the overburden, realized within the rockburst prevention, occurred on 2 October 2012 in the area of the longwall. Due to the impact of the rockburst on gateway No. 340 226 a part of the stress measurement installation was damaged, but the stress changes induced by the rockburst were at least partially monitored.

The long-term ductile deformation and the connected stress tensor changes are visible from Fig. 6a and 6b. The rockburst induced by the rock blasting was manifested by a discontinuity in the magnitude of all interpreted stress components. Afterwards, the stress values were stabilized as the longwall mining was interrupted. The stress increase induced by the longwall mining is evident from the longwall distance from the tensometric probe 130 m in its fore field. After the mining started anew, the qualitative changes of the stress component were monitored.

The results of the interpretation of the stress tensor changes could show the stress changes before and after the rockburst demonstration in maingate No. 340 226. It is possibly the first time that a record of the stress changes induced by a rockburst has been obtained. The correct interpretation will require extended comparison with the normal and other anomalous data measured in the rock mass areas with high stress concentration.

7 CONCLUSIONS

Destress rock blasting plays a significant role in the system of rockburst prevention, and it is a very useful rockburst prevention technique; mainly with the rockburst focus in the overlying competent roof strata. This technique of a proactive rockburst measure decreases the risk of rockburst occurrence in high-risk areas. The example of the use and the definition of the geological and geomechanical properties of rock mass were described above. Over 30 years' experience of destress rock blasting in hard coal longwall mining in the Czech part of the USCB, have shown that it is a very useful method of rockburst control in difficult stress conditions.

More than 2000 cases of destress rock blasting have been realized since the 1980s (Konicek et al. 2011). Many of the cases that have been carried out show high seismic effects, which document stress release in the rock mass, but only in a very few cases was the rockburst was induced by the blasting. Rockburst can be provoked in specific conditions, as shown by the cases presented. However, problems such as the distribution of stress fields near the boreholes after blasting, the range of the resulting rock deformation, and more precise determination of the stress concentration area, must be resolved in the future. Nevertheless, destress rock blasting contributes to make safe longwall mining of hard coal in conditions of substantial rockburst risk, especially through stress reduction in the rock mass without employees present.

ACKNOWLEDGEMENT

This article was written in connection with project Institute of clean technologies for mining and utilisation of raw materials for energy use, reg. no. CZ.1.05/2.1.00/03.0082, which is supported by the Research and Development for Innovations Operational Programme financed by the Structural Founds of the Europe Union and the state budget of the Czech Republic and Grant of the Ministry of the Interior of the Czech Republic (project No. VG20102014034).

REFERENCES

Comeau, W., Mitri, H. S., Marwan, M. M. & Baoyao, T. 1999. World-wide survey of destress blasting practice in deep hard rock mines. *Proceedings of the 25th Annual Conference on Explosives and Blasting Technique* Vol. I, Nashville: 189–205

Dopita, M. et al. 1997. *Geology of the Czech Part of the Upper Silesian Coal Basin* (in Czech). Prague, Ministry of the Environment of the Czech Republic.

Drzewiecki, J. & Kabiesz, J., 2008. Dynamic events in roof strata – occurrence and prevention, *Coal Science & Technology Magazine*, No. 235 Huaihai Road (W) Xuzhou, Jiangsu, China, 221006, 55–57.

Dubinski, J. & Konopko, W. 2000. *Rockbursts – Assessment, Prediction and Control* (in Polish), Central Mining Institute, Katowice.

Dvorsky, P. & Konicek, P. 2005. Systems of Rock Blasting as a rock burst measure in the Czech Part of the Upper Silesian Coal Basin. *Proceedings of the Sixth International Symposium on Rockburst and Seismicity in Mines*, Perth, 493–496.

Holecko, J., Ptacek, J., Takla, G. & Konecny, P. 1999. Rock bursts in the Czech part of the Upper Silesian Coal Basin – Features, theoretical models and conclusions for practice, *Proceedings 9th International Congress on Rock Mechanics*, Paris, France, A. A. BALKEMA.

Knotek, S. et al. 1985. Research into Geomechanics Evaluation of Rock Mass Due to Geophysical Methods (in Czech): *Final Report of Research* SP ZV II-6-1/2.09 11 381, VVUU, Ostrava.

Konicek, P., Konecny, P. & Ptacek, J. 2011. Destress Rock Blasting as a Rockburst Control Technique, *Proceedings of the 12th International Congress on Rock Mechanics*, Bejing, 18–21 October 2011, Taylor & Francis Group, pp. 1221–1226.

Konicek, P., Soucek, K., Stas, L. & Przeczek A. 2012: Rockbursts provoked by destress blasting in hard coal longwall mining, *Proceedings of the 10th International Symposium on Rock Fragmentation by Blasting*, New Delhi, India, pp. 193–202.

Kratky, D. & Macura, M. 2011. General design of destress blasting in area of longwall No. 340 206 (in Czech), *unpublished, Darkov Colliery*, pp. 20.

Stas, L., Knejzlík, J., Palla, L., Soucek, K., Waclawik, P. 2011. Measurement of stress changes using compact conical-ended borehole monitoring. *Geotechnical Testing Journal*. 34, 6 (2011), pp. 685–693.

Rock Mechanics for Resources, Energy and Environment – Kwaśniewski & Łydżba (eds)
© 2013 Taylor & Francis Group, London, ISBN 978-1-138-00080-3

Integration of geomechanical and geophysical analysis methods for the prediction of seismic events in underground mining

B. Orlecka-Sikora
Institute of Geophysics PAN, Kraków, Poland

W. Pytel
Wroclaw University of Technology and KGHM CUPRUM CBR, Wrocław, Poland

ABSTRACT: The main objective of the presented analyses is to find the bridge between the solutions of the geomechanical and related geophysical problems addressed to the selected archival seismic events. This permitted finding such geomechanical formulae, involving components of rock mass' strain/stress states and the material characteristics, which on the basis of the long-term path of rock mass loading due to mining predicted by numerical modeling, could indicate the necessary conditions which should be fulfilled if the anticipated by methods of geophysics failure mechanism could develop.

1 INTRODUCTION

The Legnica-Głogów Copper Basin is the area where the underground copper mining operations are usually associated with a high seismic activity. For better understanding of this type of seismicity, the stronger tremors' focal mechanisms are investigated on the routine bases in the local mines' seismic stations. These investigations permit recognizing stress-deformation processes which occur during a given tremor's occurrence.

The largest risk for the mining operations are created by high-energy tremors which hypocenters are located within the main roof strata, about 40–200 m above the excavated copper ore body. The most often encountered focal mechanisms of the such tremors are the slipping type mechanism with the rupture plane which spatial location is frequently correlated with tectonic structures located nearby. However, seismic tremors in Polish copper mines occur equally often in the areas which are virtually free of tectonic disturbances. Therefore one may conclude that the unique conjunction of stress induced by mining, the coseismic alterations of stress field and the primary stress in rock mass involving also the tectonic residual components, are the most important cause of such tremors' occurrence. Since changes of stress in rock mass during the mining process may be effectively tracked using the solutions offered by the appropriate 3D geomechanical models (e.g. FEM), the assessment of these changes due to mining face progress is very possible also in the location where the seismic tremor has occurred and afterwards was characterized by its focal mechanism by using the appropriate geophysical methods.

Therefore the main goal of the presented analyses is to find the bridge between the solutions of the geomechanical and related geophysical problems addressed to the selected archival seismic events. This permitted finding such geomechanical formulae, involving components of rock mass' strain/stress states and the material characteristics, which on the basis of the long-term path of rock mass loading due to mining predicted by numerical modeling, could indicate the necessary conditions which should be fulfilled if the anticipated by methods of geophysics failure mechanism could develop.

The developed approach for a seismic event prediction, based on the integration of the geophysical methods and geomechanical numerical modeling techniques, is illustrated using example of strong seismic event occurred in 2005 in one of the areas of the Rudna mine.

2 SEISMICITY IN UNDERGROUND MINES

2.1 *Seismic processes analyzes based on geophysical methods*

Mining activities change in time, which results in more or less irregular time variability of the local stress field inducing the seismicity and hence in the variability of the seismicity itself (Lasocki 2008, Gibowicz & Lasocki 2001).

These time dependences of the stress state and the seismic process are properties probably the most distinctly differentiating the mining-induced from the natural, tectonic seismicity. Due to these the mining seismic hazard assessment problem is also virtually time-dependent as well as it is related strongly to mining activities.

Most of the techniques aiming at determining the local time-dependent seismic hazard deduce the present and future hazard from past-to-present time variations of a parameter or parameters obtained from seismic series. Every value of such indicative parameters is related to a particular moment of time and is usually estimated from respective values of appropriate parameterization of a number of consecutive events that occurred just before this time-moment. It is usually assumed that the seismic process changes slowly enough to reach a reasonable compromise between the number of consecutive values needed to keep the estimation error within an acceptable limit and a relative stationarity of these values, which is required for statistical estimation.

It is assumed at the same time that the data samples used in the estimation are free from an internal stochastic coupling. A review of some of such techniques can be found in (Gibowicz & Lasocki 2001); more recent publications on this subject are e.g. (Feit et al. 2002, Tang & Xia 2010).

Recent works indicate, however, that the lack of interactions between the mining seismic events can be accepted as a first approximation only. Weglarczyk & Lasocki (2009) have evidenced by means of rigorous statistical testing that parameterizations of the seismic process in mines can have long and/or short memory. They showed, in particular, that series of distances between epicenters and series of times elapsed between occurrences of every two consecutive events are internally correlated over short as well as long time perspectives. It can be, therefore, expected that including reliable models of interrelations among events into hazard estimation methods will increase the accuracy of the resultant estimates.

The static stress transfer due to coseismic deformation and its impact on subsequent earthquakes is one of the better recognized models of the event interrelations in natural seismicity. It has been shown also that it plays a role in modifying the seismic processes in mines. Orlecka-Sikora et al. (2009) applied the stress transfer model to study interactions between events in a time-ordered series comprising of stronger tremors from Rudna copper ore mine in Poland. In the recent work (Orlecka-Sikora et al. 2012) however, they analyzed for a first time a modifying impact of the static stress transfer due to stronger tremors on the seismic process directly linked to mining works in one of the mine section. It turns out that the stress change due to coseismic slip of two stronger tremors that occurred quite close in time influenced significantly the location and rate of smaller subsequent events in the next few months. Moreover, it appears, contrary to the results of previous analyses, that the negative Coulomb stress changes played a major role in this respect. The obtained results indicate that accounting for the static stress changes due to coseismic deformations can improve considerably the seismic hazard estimation in mines. Furthermore, the static stress change analysis can be valuable for optimizing the exploitation strategy.

2.2 *Mine workings instability potential assessed by FEA approach*

As a result of many years' experience, the KGHM mines have developed an effective and relatively safe room-and-pillar mining technology mostly based on a one-phase almost complete extraction approach. For many years this kind of mining operations has been successfully complemented with 3D FEA analyses performed by KGHM Cuprum R&D Center using NE/Nastran software. This approach based on multiplate analogue has proved to be an effective tool which may be used in any prognosis of the stress-strain effects of mining operations conducted below a stiff, stratified roof strata, especially in the area where important mine objects and structures are located (Pytel 2010).

This approach offers the possibility for rock bursts hazards' assessing before the event occurrence, however due to the 3D model complexity the solutions are usually confined to a preliminary indication of the areas of the higher hazard level and a rough description of the most likely mechanism of rock mass failure.

3 SITE AND SEISMIC EVENT CONSIDERED

3.1 *Geology and mining operations*

The seismic data studied in the present work is associated with mining exploitation in the section G-11/8 of Rudna mine. The Rudna mine is one of the three copper ore mines in Legnica–Glogow Copper District (LGCD) in south–west Poland. A productive level located at the depth from 900 to 1200 m is over-lain by some 15 m thick dolomite layer followed upwards by rigid anhydrite strata of around 50 m thickness. Below the deposit a thin layer of quartzite sandstones precedes some 300 m thick layer of hard Rotliegendes sandstones. In the geophysical analyses an average rock mass compressive strength was 136.6 MPa for the strata above the copper ore deposit, 77.6 MPa for the deposit layer and 44.4 MPa for the floor layer. The depth of the ore body, an ability to accumulate strain energy by both the upper layer of anhydrites and the lower sandstone layer as well as highly variable tectonic conditions constitute grounds for generating violent seismicity and rockbursts.

The mine operates an in-mine seismic system, consisting of 32 Wilmore MK2 and MK3 uniaxial–vertical seismometers. The distance between sensors ranges from 0.5 to 11 km. The system records statically all events from magnitude completeness 1.2. Event epicenters are determined with the location error less than 50 m, however the seismic network is nearly flat and the hypocentral depth is poorly constrained.

Ore is extracted in the Rudna mine by means of a room-and-pillar exploitation system. In this system, the ore-seam is cut into passages and chambers separated by structural pillars. In the course of removal of rock the pillars degrade enabling gradual roof subsidence. In the panel G-11/8 the dimension in the axle of designed chambers and passages are 14 m by 21 m on

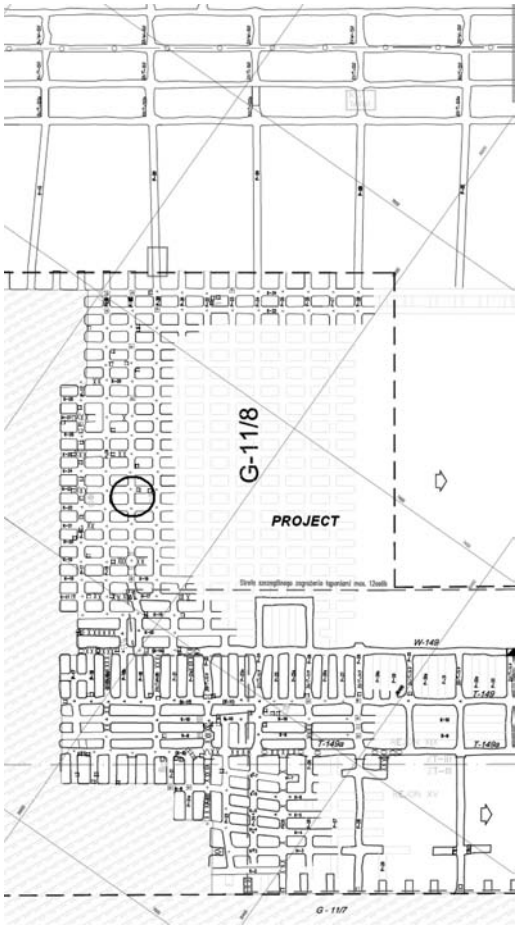


Figure 1. Mine workings plan at the beginning of January 2005 with the tremor of the January 7th 2005 location within the G-11/7 panel.

both wings of the excavation front (Fig. 1). Throughout the rest of this paper we distinguish mined out parts as those where excavation has been finished but the pillars are still in the degradation process and goaf where the pillar degradation and subsiding process has ended. Productive blasting is carried out in each section twice a day at fixed hours in the morning and afternoon. Occasionally, destressing blasting is done.

3.2 *Seismic events analyses using geophysical methods*

Mining works in the section G-11/8 began in 2002 and have been continued until present. The length of the exploitation front is 600 m. From the beginning the works in this section have been accompanied by seismic activity with occasional strong tremors.

At the beginning of 2005 two strong tremors took place: 3.7 ML on 7.01.2005 and 3.5 ML on 20.01.2005. The first event was triggered successfully by destressing blasting. The second event took place

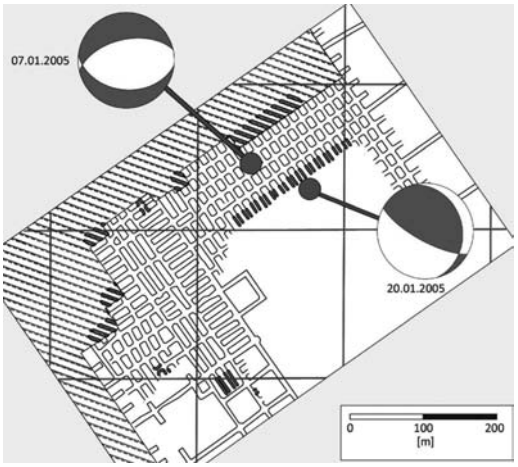


Figure 2. Location of two strong seismic events: ML3.7 from 7.01.2005 and ML3.5 from 20.01.2005, with respect to mining works in the section G-11/8 (Orlecka-Sikora et al. 2012).

during excavation works and was considered as a natural rock mass relaxation. The source parameters and focal mechanisms were calculated using the moment tensor inversion in time domain and the spectral analysis (e.g. Wiejacz, 1992; Domanski & Gibowicz, 2008). Strike, dip and rake errors are not greater than 201, 51 and 101, respectively, for both events.

The moment tensor analysis shows that shear components (DC) dominate for both events, although some 25 percent of the overall mechanisms is left for non-double-couple components. However, the DC nodal planes parameters remain the same within the estimation errors when the full moment tensor solutions are replaced by the sole shearing mechanisms. Due to that and for the sake of simplicity the DC solutions are accepted. Figure 2 presents locations of these two events against the map of mining works in G-11/8 and the events focal mechanisms.

The mechanisms of the both tremors are identified to be different since the first one is associated with the normal type of fault, while the second one with the reversal type. The tremors occurred at almost the same hypocentral coordinates, i.e. about 150 m above the floor of extracted copper ore body, within the middle of the massive deposit or salt rock of 150 m of thickness. There has been assumed (Orlecka-Sikora et al. 2011) however that the instability within the relatively stiff anhydrite layers above mined-out area was the direct cause of the following strong tremor comprising weaker and thick salt rock located in main roof body.

Furthermore, the local geological conditions suggested that both considered seismic events may be linked to the existing faults system with strike W-E and inclined by 50° from the direction of the mining face progress.

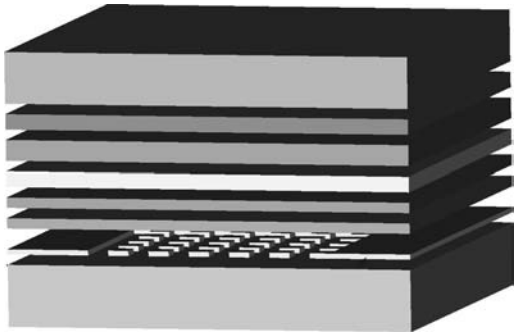


Figure 3. General view of the numerical model.

3.3 *Analyses based on geomechanical modeling*

3.3.1 *Introduction*

As a basic physical model for the problem, the multi-plate overburden model has been accepted with the following simplifying assumptions (Fig. 3):

- overburden strata consists of several homogeneous rock plates reflecting the real lithology in the area,
- technological and remnant pillars work effectively within post-critical phase (elastic-plastic with strain softening behavior),
- the value of carried loads depends on pillar size and actual extraction ratio.

Geomechanical problem solution and results visualization were based on the NEi/NASTRAN computer program code utilizing FEM in three dimensions. It was understood that all but the pillars' materials reveal a linear-elastic characteristics, whereas copper ore rock mass behavior is represented by elasto-plastic with strain softening kind of mechanical model. The entire numerical model general boundary conditions were described by displacement based relationships. More information on the applied solution method may be find elsewhere (Pytel 2003).

Numerical experiments modeling the three-dimensional mine layout were performed, using two boundary condition sets defined by presence or absence of horizontal additional stress. The determined stress/deformation states were used afterwards for quantitative characterization of the effect of horizontal tectonic stress on system behavior and safety using the indicators called safety margins related to well known shear type failure criterion based on the Coulomb's theory (Jaeger et al. 2007)

$$\sigma_1 = \sigma_{cm} + A \cdot \sigma_3 \tag{1}$$

(where: σ_{cm} – unconfined compression strength in rock mass scaled down acc. to the Hoek's (2007) approach, $\sigma_{1,3}$ – major and minor principal stress respectively, compression – positive), A – positive material constant dependent on angle of internal friction ϕ in rock mass:

$$A = \frac{1+\sin\phi}{1-\sin\phi}. \tag{2}$$

Table 1. Geological data in the analyzed area.

Rock	Thickness m	Strength C_o MPa	Strength σ_{cm}* MPa	Deformation parameters ϕ* deg	E GPa	ν –
Quaternary	47	–	–	–	0.07	0.30
Tertiary	345	–	–	–	0.07	0.30
Sandstone	219	60.5	6.0	30	4.4	0.16
Clayey shale	22	42.3	2.3	27	2.0	0.19
Anhydrite A3	30.5	109.9	30.0	38	19.9	0.24
Dolomite Ca3	1.5	148.2	62.9	46	40.8	0.23
Anhydrite A2	22.5	110.7	30.6	38	20.3	0.24
Dolomite Ca2	9.7	157.9	73.3	48	47.3	0.24
Anhydrite A1g	50	100.5	23.9	36	16.0	0.26
Salt rock	94	24	1.5	24	2.90	0.4
Anhydrite A1d	64	111.6	31.2	38	20.7	0.26
Limestone Ca1	15	214.2	148.9	60	82.2	0.25
Copper ore**	4	94.8	–	–	32.2	0.23
Gray sandstone	7	28.5	–	–	8.1	0.16
Red sandstone	200	15.6	–	–	5.0	0.13

*Compression strength and angle of internal friction in rock mass assessed acc. to Hoek's (2007) approach (see Fig. 6)
**Laboratory assessed strength values

The respective safety margin has been formulated as follows:

$$F_c = \sigma_{cm} + A \cdot \sigma_3 - \sigma_1 \tag{3}$$

Rock mass instability potential is indicated by safety margin value smaller than zero. The safety margins' spatial distribution served then as a basic measure helpful in identifying areas of higher failure risk.

3.4 *Geological conditions in the site*

The copper ore deposit, located at the depth of 1130 m is almost horizontally flat and is covered immediately by very thick and stiff main roof strata consisting of 15 m layer of coherent limestone/dolomite overlaid by 64 m thick strong anhydrite plate and 311 m thick competent sandstone stratum. The averaged geological data over the considered area and the estimated rock mass parameters are given in Table 1.

3.5 *In-situ stress*

Only few field measurements of in-situ stress has been performed in the area of KGHM's copper mines within the hard lower dolomite stratum (Katulski et al. 1997, Fabich et al. 2002). Stress tensor components originally expressed in the principal stress coordinate system (1-2-3) has been transformed into the (h-H-z) – system (h – direction of the least horizontal component, H – direction of the greatest horizontal component, z – direction of the vertical component (the greatest horizontal stress component $\sigma_H = 44.41$ MPa acts at the angle of 301 deg from the

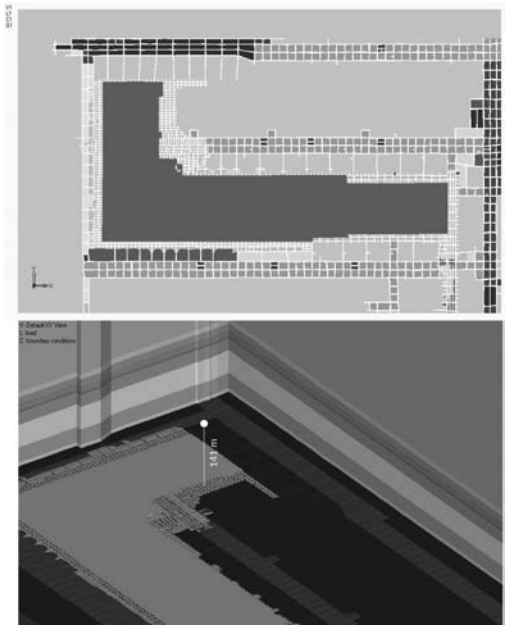


Figure 4. View of the FEM model of G-11/8 panel; copper ore level (top), entire 3D model cross-section (bottom).

North, while the smallest $\sigma_h = 19.8$ MPa). The additional stress within different rock mass strata have been set up according to the ratio of the rocks module of deformation – the stronger strata are loaded more than weaker ones.

3.6 *Analysis of safety margins distribution*

To illustrate the effect of mining face geometry as well as high horizontal stress involvement, G-11/8 on stress distribution in rock mass, Rudna mine's district has been modeled and analyzed using the finite element method formulated in three dimensions (Fig. 4). The mine workings basic geometry was evaluated from safety point of view with:

(a) no tectonic stress,
(b) with presence of horizontal tectonic stress characterized as above.

Calculated safety margin F_c contours within anhydrite A1d strata, 23, 39, 55, and 71 m m above the immediate roof stratum are shown in Figures 5–8.

4 CONCLUSIONS

The obtained analysis results have proved generally a significant and positive agreement between the geophysically based seismic events occurrence's explanation and their interpretation obtained using FEA. The presented analyzes have prove that in the considered case, the shear mode is a dominant mode of main roof failure. The estimated failure plane's strike of about 50 deg against the mining face progress

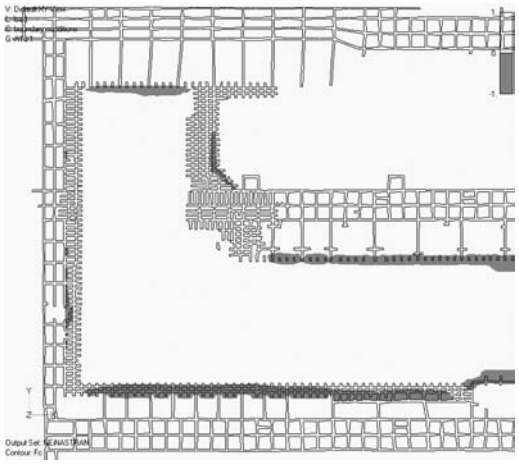


Figure 5. Simplified safety margin Fc contour for a case without of tectonic horizontal stress, within A1d anhydrite deposit 23 m above the immediate roof strata (gray colour – negative Fc value, i.e. shear type instability possible).

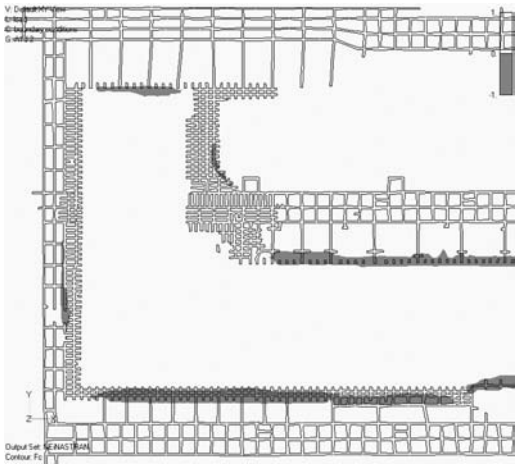


Figure 6. Simplified safety margin Fc contour for a case without of tectonic horizontal stress, within A1d anhydrite deposit 39 m above the immediate roof strata (gray colour – negative Fc value, i.e. shear type instability possible).

direction (Fig. 4) is also in agreement with results of seismological analysis. Moreover, the dip of the failure plane within the anhydrite layer (Figs 5–8) suggests the normal type of the induced fault, however this numerical approach did not involve any existing planes of discontinuities which, if existed, could significantly change the obtained results. Both the geophysical and numerical analytical tools both have proved that main roof strata instability could be triggered within the thick anhydrite stratum at the elevation of about 150 m above immediate roof strata and may be transmitted into relatively weak salt rock deposit resting at higher elevation.

The obtained analysis results have also proved generally a significant and positive effect of a large value

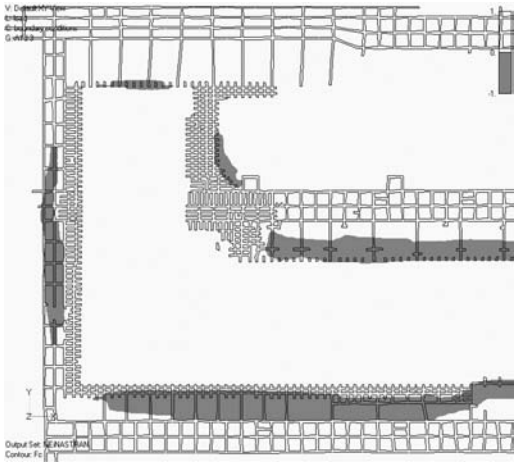


Figure 7. Simplified safety margin Fc contour for a case without of tectonic horizontal stress, within A1d anhydrite deposit 55 m above the immediate roof strata (gray colour – negative Fc value, i.e. shear type instability possible).

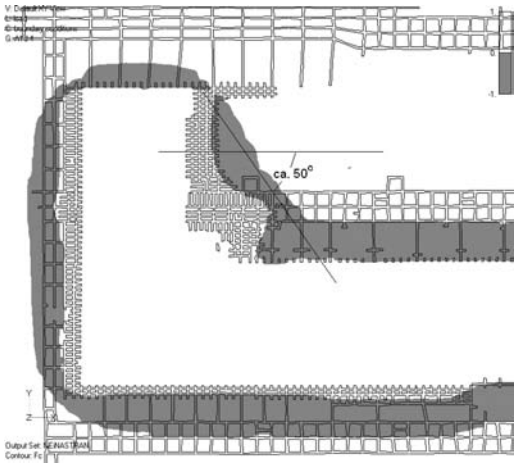


Figure 8. Simplified safety margin Fc contour for a case without of tectonic horizontal stress, within A1d anhydrite deposit 71 m above the immediate roof strata (gray colour – negative Fc value, i.e. shear type instability possible).

horizontal (tectonic) stress presence on main roof strata stability (safety margins values exlusively positive). This mean that in such a case a bump hazard (instability within main roof strata) has much lower potential than one could expect. However, since safety margin contours differ depending on the mode of possible mechanism of failure, these conclusions may be addressed only to particular strength hypothesis used in numerical analysis.

REFERENCES

Domanski, B. & Gibowicz, S.J. 2008. Comparison of source parameters estimated in the frequency and time domains for seismic events at the Rudna copper mine, Poland. *Acta Geophys* 56: 324–343.

Fabich, S. & Pytel, W. 2003. Określenie naprężeń w górotworze w różnych warunkach geologiczno-górniczych na podstawie badań in-situ, Res. Rep. CBPM Cuprum, Wroclaw

Feit GN., Malinnikova ON., Zykov VS. & Rudakov VA. 2002. Prediction of rockburst and sudden outburst hazard on the basis of estimate of rock-mass energy. *J Min Sci* 38(1): 61–63.

Gibowicz, S.J. & Lasocki, S. 2001. Seismicity induced by mining: ten years later. *Adv Geophys* 4: 39–181

Hoek, E. 2007. *Practical Rock Engineering*. www.rocscience.com/hoek/Hoek.asp

Jaeger J.C., Cook N.G.W. & Zimmerman, R. 2007. *Fundamen-tals of Rock Mechanics*. Blackwell Publ.

Katulski A., Bugajski, W., Bryja, Z., & Fabjanczyk, M. 1997. Pomiar przedeksploatacyjnego pola naprężeń w KGHM Polska Miedź, O/ZG Rudna. Proc. Underground Exploitation Workshop, Szczyrk: 67–75

Lasocki S. 2008. Some unique statistical properties of the seismic process in mines. In: Proceedings of the 1st Southern Hemisphere International Rock Mechanics Symposium, Vol. 1: Mining and Civil. Nedlands, Western Australia: Australian Centre for Geomechanics; pp. 667–78.

Orlecka-Sikora B., Papadimitriou, E.E. & Kwiatek, G.A. 2009. A study of the interaction among mining induced seismic events in the Legnica Glogow Copper District, Poland. *Acta Geophys* 57(2): 413–434.

Orlecka-Sikora, B. Lasocki, S. Lizurek, G. & Rudzinski, L. 2012. Response of seismic activity in mines to the stress changes due to mining induced strong seismic events, *Int. J. Rock Mech. Min. Sci.* 53: 151–158.

Pytel, W. 2003. Rock mass-mine workings interaction model for Polish copper mine conditions, *Int. J. Rock Mech. Min. Sci.* 40: 497–526.

Pytel, W. 2010. Room-and-pillar mine workings design in high level horizontal stress conditions. Case of study from the Polish underground copper mines. In F. Xie (ed.), *Rock Stress and Earthquakes*: 505–511. Leiden: CRC Press/Balkema.

Tang, L. & Xia, K.W. 2010. Seismological method for prediction of areal rockbursts in deep mine with seismic source mechanism and unstable failure theory. J Centr South Univ Technol 17: 947–53.

Weglarczyk, S. & Lasocki, S. 2009. Studies of short and long memory in mining induced seismic processes. *Acta Geophys* 57(2): 696–715.

Wiejacz, P. 1992. Calculation of seismic moment tensor for mine tremors from the Legnica-Glogow Copper Basin. *Acta Geophys Pol* 40: 103–22.

Rock Mechanics for Resources, Energy and Environment – Kwaśniewski & Łydżba (eds)
© 2013 Taylor & Francis Group, London, ISBN 978-1-138-00080-3

Determination of dynamic rock strength to assess blasting efficiency

F.L. Pellet, V.K. Dang, C. Baumont, M. Dusseux & G.J. Huang
INSA-University of Lyon, France

ABSTRACT: Dynamic tests using the Split Hopkinson Pressure Bar test (SHPB) were conducted on granite specimens in order to study the efficiency of the drill and blast method and the environmental impact of the excavation of a tunnel in urban areas. The tests were performed at different strain rates of loading corresponding to variable energy levels. Compared to the static uniaxial strength, the dynamic strength of the rock was found to be much higher. The dynamic strength clearly increases with the strain rate of the loading but decreases with the duration of load application. The same conclusions can be drawn for the Young's modulus. Using the experimental results, the strength parameters of the rock were back calibrated using a Finite Element model of the test; preliminary numerical simulations of SHPB tests gave good results. These results can therefore be used to correlate the blasting load to the damage observed in the tunnel during excavation.

1 INTRODUCTION

It has long been known that rock materials behave quite differently under dynamic loadings compared to static loading. Recent studies (Bohloli 1997, Zhou et al. 2012) showed that the Unconfined Compressive Strength (UCS) of rock increases when the loading pulse value increases.

In the present paper, the results of an experimental program performed on Lavasan granite in dynamic loading are presented and compared with static loading tests results (Pellet et al. 2011). This program was conceived to assess the efficiency of the drill and blast excavation method as well as to evaluate the environmental impact of tunnel excavation in an urban area.

2 EXPERIMENTAL PROGRAM

2.1 *Experimental set up for SHPB test*

The Split Hopkinson Pressure Bar test (SHPB) was developed by Kolsky (1949) as a modification of the Hopkinson pressure bar test (Hopkinson 1914). Several studies have been carried out with this equipment on different materials (Forquin et al. 2010, Johnson 2010, Kaiser 1998, Weimin and Jinyu 2009).

The SHPB system is composed of two axial bars (input bar and output bar) and a striker launched by a gas gun. Figure 1 shows a general view of SHPB while Figure 2 presents a schematic of the device.

A short cylindrical specimen is installed between the two main bars. The impact between the striker and the input bar generates a compressive wave (loading wave and unloading waves) which is the output to the specimen.



Figure 1. General view of the Split Hopkinson Pressure Bar (SHPB) device in the University of Lyon.

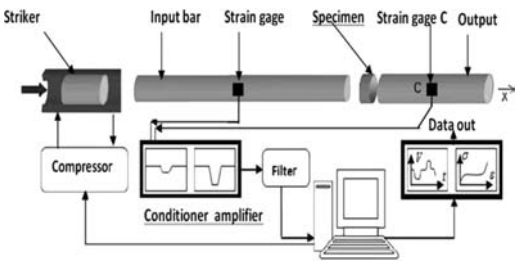


Figure 2. Diagram of the Split Hopkinson Bar Pressure (SHPB) test facility.

The main objective of the SHPB experiments is to perform indirect strain measurements: strains are measured in the bars rather than directly in the specimen. Strain gauges give the values of the strike, the reflected and output strain waves in the bars. From these measurements, the values of the forces and displacements (stress and strain) can be determined at any point along the bars and the specimen at any time.

Table 1. Physical and mechanical properties of Lavasan granite.

Bulk specific gravity	(g/cm^3)	2.65
Porosity	(%)	1.0
P-wave velocity	(m/sec)	3994 ± 35
S-wave velocity	(m/sec)	2550 ± 20
Poisson's ratio	–	0.25
Young's modulus	[GPa]	45 ± 5
UCS	[MPa]	148 ± 15

2.2 *Rock under study*

Tests were performed on Lavasan granite; this has been extensively studied (Keshavarz et al. 2008, Keshavarz et al. 2009). The previous experimental investigations consisted mostly of static uniaxial compression tests with acoustic emission records. Prior to the SHPB tests, the physical properties and the sonic wave velocities (V_p and V_s) of each specimen were measured. The mechanical and physical properties of this granite are summarized in Table 1.

2.3 *Tests preparation*

For each SHPB test the following data were determined and recorded:

- Distance of each strain gauge pair from the strike/specimen bar interface,
- Orientation of the strain gauge pair (axial or circumferential),
- Length of the striker bar,
- Gain of each amplifier determined by shunt calibration,
- Elapsed time for the striker bar to cross the laser timer distance,
- Photograph of the specimen bar before and after impact,
- Additional notes including any damaged gauges and the damage distances,
- Gas gun firing pressure.

The specimen was aligned to the input bar axis using a flashlight and adjusting the support wires until no light could be seen at the interface. The data logger was set to the number of channels to be read. The trigger voltage level for the incident gauges was determined by practice and was set depending on the velocity of the striker bar.

The raw data files consist of ordered pairs of time and voltage for each gauge; these basic time-voltage data sets are used for all subsequent data reductions. Mathematical computations such as zeroing, converting the voltage to strain, time-shifting the reflected wave, super positioning of the incident and reflected waves, calculation of the strain and stress at the interface, and calculation of the loading and unloading strain rate of a wave were facilitated. The data processing involved the following basic steps, some of which are explained in more detail in the following subsections (Johnson 2010):

- Zero the data by subtracting the initial voltage reading from each channel,
- Time-shift the reflected wave in the input bar data,
- Convert zeroed voltage to strain for each channel,
- Calculate stress and strain applied to the specimen bar,
- Tabulate the arrival time, peak strain and plastic strain for each channel.

3 MEASURED AND CONTROLLED PARAMETERS

Measuring the deformation of both the input bar and the output bar allows the applied force, the deformation and the strain rate of the specimen to be obtained. The possibility of obtaining additional measurements includes the displacement of targets using a dynamic strain gauge. A video recording was produced using a fast camera (Phantom V4).

3.1 *Time-shift of the reflected wave*

The incident wave passes through the strain gages near the center of the bar and continues to the interface between the incident bar and specimen. At the interface, part of the wave is transmitted to the specimen bar and part is reflected back into the input bar. Therefore a single channel of data contains both the incident and reflected waves. The start or "zero" of the reflected wave must be determined in order to isolate it from the single channel of data. The time difference or time-shift of the reflected wave must be computed before the incident and reflected strain waves can be superimposed. The time-shift of the reflected wave (Δt_R) is the time required for the wave to travel from the gauge to the interface and return. The time-shift for the reflected incident stress wave is:

$$\Delta t_R = \frac{2l}{c} \tag{1}$$

where c is the sonic wave velocity in the input bar, l is distance from the center of the strain gauge pair on the input bar to the incident bar – specimen interface.

The experimental measurements confirm that the wave velocity in the input bar is in close agreement with that calculated by its elastic modulus and density using the following equation:

$$c = \sqrt{\frac{E}{\rho}} \tag{2}$$

where E is the elastic modulus of the bar or of the specimen (MPa), ρ is the density of the bars or of the specimen (N/m^3).

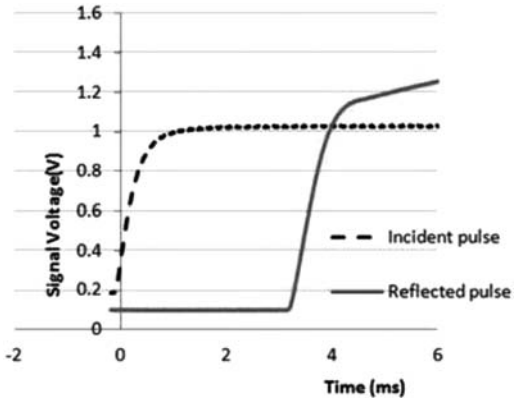


Figure 3. Signal voltage in gauges (1) and (3) for a 300 kPa loading pulse.

From this formula the dynamic elastic modulii of the bars and of the specimen can be calculated using the equation:

$$E_{dyn} = \rho c^2 \tag{3}$$

3.2 *Converting voltage to strain*

The objective of the testing program is to study the dynamic behavior of the Lavasan granite at very high strain rates. It is therefore necessary to extract the stress-strain curve from the signals recorded by each gauge. Indeed, the strain gauges used consist of a Wheatstone bridge, which is characterized by a gauge factor κ.

The relationship between the resistance, R, and the longitudinal deformation undergone by the gauges can be determined by

$$\frac{\Delta R}{R} = \kappa \varepsilon_l \tag{4}$$

Therefore, it is possible to relate the supply voltage to the voltage measured in the longitudinal deformation, V_{ex}.

$$\varepsilon_l = \frac{2}{(1+\nu)\kappa}\frac{V_{out}}{V_{ex}} \tag{5}$$

where ε_l is longitudinal deformation of the bars, ν is Poisson's ratio, V_{out} is the output voltage and V_{ex} is the excitation in volts (20 V, ±0.1 V). For this case, the gauge factor was 2.115.

Figure 3 shows the output voltage with respect to time for both the incident and the reflected waves for a 300 kPa loading pulse.

3.3 *Stress in the specimen*

The average stress in the specimen can be expressed in terms of the forces applied on each surface of the specimen. A schematic representation of any specimen is shown in Figure 4.

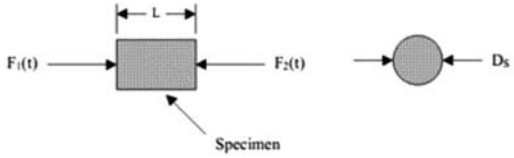


Figure 4. Schematic diagram of the cylindrical specimen.

When the specimen is sandwiched between the pressure bars, forces $F_1(t)$ and $F_2(t)$ are applied to the specimen of diameter D_s. The average force on the specimen is given by:

$$F_{AVG}(t) = \frac{F_1(t) + F_2(t)}{2} \tag{6}$$

Hence the average stress on the cylindrical specimen is computed by:

$$\sigma_{AVG}(t) = \frac{F_{AVG}(t)}{\pi D_s^2 / 4} \tag{7}$$

The stress at the contact surface between the specimen and the input and the output bars can be calculated using the formula:

$$\sigma_I(t) = E_b\left[\varepsilon_I(t) + \varepsilon_R(t+\Delta t)\right] \tag{8}$$

$$\sigma_I(t) = E_b\,\varepsilon_T(t) \tag{9}$$

where, $\varepsilon_I(t)$ is the incident strain wave, $\varepsilon_R(t)$ is reflected strain wave, $\varepsilon_T(t)$ is the transmitted strain wave and E_b is the elastic modulus of the bar (equation 3).

The forces $F_1(t)$ and $F_2(t)$ acting on the specimen surfaces are due to the pressure bars. For a specimen in dynamic equilibrium, the forces at the ends of the pressure bars may be expressed in terms of the incident and reflected pressure bar strains as follows:

$$F_1(t) = A_1.\sigma_I(t) = E\left[\varepsilon_I(t) + \varepsilon_R(t)\right]\frac{\pi D_b^2}{4} \tag{10}$$

$$F_1(t) = A_1.\sigma_T(t) = E\,\varepsilon_T(t)\,\frac{\pi D_b^2}{4} \tag{11}$$

Substituting equations (10) and (11) into equation (6) gives an expression for the average stress on the specimen in terms of the pressure bar strains:

$$\sigma_{AVG}(t) = \frac{E D_b^2}{2D_s^2}\left[\varepsilon_I(t) + \varepsilon_R(t) + \varepsilon_T(t)\right] \tag{12}$$

where D_b is the diameter of the pressure bars.

3.4 *Strain and strain rate in the specimen*

Particle velocity at the end of the input and output bars (V_{inc} and V_{tr}) can be calculated from the equations:

$$V_I(t) = C_{inc}\left[\varepsilon_I(t) - \varepsilon_R(t\right] \tag{13}$$

Table 2. Geometry and material properties of SHPB components.

Properties	Striker*	I- bar**	T-bar***
Young modulus [Pa]	2e11	7.363e11	7.363e11
Density (kg/m^3)	7700	2810	2810
Poisson's ratio	0.3	0.3	0.3
Diameter [m]	0.05	0.05	0.05
Length (m)	900 (50)	3.0	2.0

*Steel
**Input bar (aluminum)
***Output bar (aluminum)

$$Vtr(t)=C_{inc}\,\varepsilon_T(t) \tag{14}$$

Then, the average strain rate of the specimen is given by equation (15):

$$\dot{\varepsilon}_m = \frac{V_T(t)-V_T(t)}{l_{spec}} \tag{15}$$

where, l_{spec} is the length of the specimen. For a point in the specimen, the strain is expressed as follows:

$$\dot{\varepsilon}_2 = \frac{\Delta\varepsilon}{\Delta t}=\frac{\varepsilon_2-\varepsilon_1}{t_2-t_1} \tag{16}$$

We can obtain the strain value at any instant in time based on the strain rate and the above strain value:

$$\varepsilon_2 = \varepsilon_1 + \dot{\varepsilon}_2\left(t_2-t_1\right) \tag{17}$$

where t_1, t_2 are the times corresponding to the ε_1 and ε_2 values which are recorded by the gauges.

3.5 *Preliminary tests*

Initially, the bars were tested without any specimen to determine their own properties. The properties of the SHPB components are reported in Table 2. The location of each strain gauge pair on the bars is identified by a number. In this study, the gauges are located in the center of the bars.

4 SHPB TEST RESULTS

For experiments carried out on rock specimens, the loading pulse was progressively increased from 100 kPa to 350 kPa. Using a striker of 900 mm in length, the specimen was destroyed at a 350 kPa loading pulse.

The measured signal (60.000 values) allows one the computation of the dynamic elastic modulus of the specimen, which was found to be 76.5 GPa. The travel time of the striker, Δt, was equal to 3.26 μs for a pulse of 300 kPa. As the distance between two gauges is 50 mm, the velocity of the striker bar is 15.34 m/s (17.34 m/s for a pulse of 350 kPa).

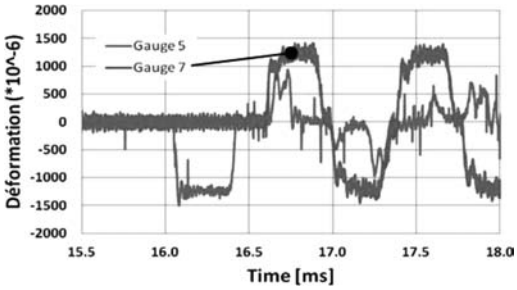


Figure 5. Strain of input bar (gauges 5) and output bar (gauge 7) versus time for a 300 kPa loading pulse (specimen 38).

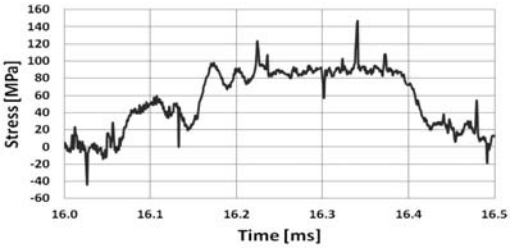


Figure 6. Stress in the input bar versus time for a 300 kPa loading pulse (specimen 38).

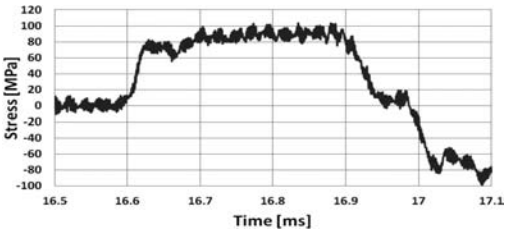


Figure 7. Stress in the output bar versus time for a 300 kPa loading pulse (specimen 38).

Using the signal measured by the gauges, and combining the above equations for the longitudinal deformation, the incident strain wave $\varepsilon_I(t)$, reflected strain wave $\varepsilon_r(t)$ and transmitted strain wave $\varepsilon_T(t)$ in the bars were calculated based on equation (5). Figure 5 shows the strains versus the time measured in both the input bar and the output bar.

From these results, the stress in the bars at the two contact surfaces $\sigma_I(t)$, $\sigma_T(t)$, as well as the average stress on the specimens were computed (eq. (12)). Using the particle velocity values at the end of input and output bars $V_I(t), V_T(t)$, the average strain rate and strain values of the specimen can also be determined by using the equations (15) and (17). Stresses in the input bar and the output bar are represented with respect to time in Figures 6 and 7. From these results, it can be clearly seen that the maximal stress values in the specimen increase when the loading pulse value is larger.

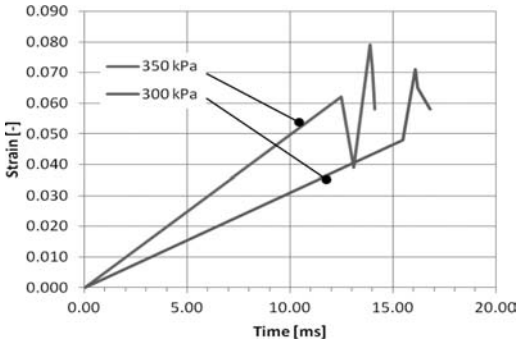


Figure 8. Strain versus time in specimen 38 for 300 kPa and 350 kPa loading pulse.

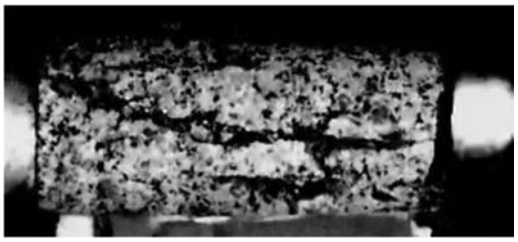


Figure 9. Photo of a specimen after failure; a longitudinal fracture can clearly be seen after the strike.

The relationships between stress and strain in specimen 38 for the 300 kPa and 350 kPa loading pulses are presented in Figure 8. As the force applied by the striker bar is proportional to its velocity, an increase in the velocity increases both the strain and the strain rate in the specimen.

Figure 9 shows a photo of the specimen after failure; a longitudinal fracture can clearly be seen after the strike.

Additional tests were performed with a shorter striker and a higher pulse pressure (up to 500 kPa). The goal was to reduce the time during which the load is applied to the specimen in order to be closer to the in situ conditions for tunnel blasting.

When using a shorter striker (50 mm in length instead of 900 mm) it was found that the duration of load application is reduced, dropping from 350 μs to 50 μs. Consequently, the dynamic strength of the specimen is substantially increased up to 205 MPa.

5 PRELIMINARY NUMERICAL SIMULATIONS OF SHPB TESTS

In order to determine the efficiency of blasting for tunnel excavation in granite, some numerical simulations of the SHPB tests were performed using the Finite Element code ABAQUS/Explicit (Abaqus, 2010). The material properties of bars used in the SHPB tests were presented in Table 2. A 3-D axisymmetric model of the SHPB was built using 8-node brick elements

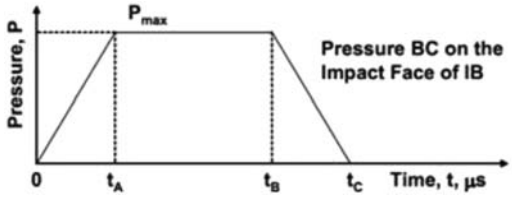


Figure 10. Loading pulse history on the impacted face of the input bar.

(C3D8R). The longitudinal axis of the bars is the z-axis.

A surface contact interface condition without friction is defined between the bar-specimen interfaces. The displacements of bars in X- and Y-axes (cross section) and in the end face of the output bar were assumed to be zero. The specimen is represented as a circular cylinder. The bars remain elastic at all times during the SHPB experiments, and therefore can be considered as a linear-elastic isotropic material. The specimens are modeled with a linear-elasto-plastic constitutive law using a Mohr-Coulomb failure criterion whose parameters were deduced from the properties given in Table 1.

The input bar is divided into 6240 elements (approximate global size 0.02). The number of elements in the output bar is 3900 (approximate global size 0.02). The approximate global size of the specimen element is chosen to be smaller (0.015); it is therefore divided into 129 elements. The total number of elements in this model is 10255 with 13024 nodes.

The impact velocity of the striker is converted to a pressure pulse applied on the impact face of the input bar. The pressure applied to the face is introduced directly in the form of a slot as shown in Figure 10. Its magnitude is given by:

$$P_{max} = \frac{1}{2}\rho\ S_b\ C\ V_{st} \tag{18}$$

where ρ is the density of the striker, S_b is the section of the bars, C is the velocity of wave propagation in the striker (equation 2), V_{st} is the velocity of the striker bar (17.34 m/s in the case of a 350 kPa pressure pulse).

The duration of the application of the force is a function of the striker length. The stress pulse applied to the input bar is defined using the four parameters: t_A, t_B, t_C and $P_{max.}$

In this study, the time parameters were chosen as follows: $t_A = 99\,\mu s$, $t_B = 101\,\mu s$, $t_C = 200\,\mu s$, $T = 200\,\mu s$. The amplitude of the loading pulse, calculated using equation (18), is equal to $P_{max} =$ 34234052 Pa.

The results of the SHPB numerical simulation are presented in Figures 11, 12 and 13. The comparison of the numerical results to the experimental results shows good agreement for the stresses and strains in the specimen despite the fact that the computed maximum stress is smaller than the value obtained from the tests.

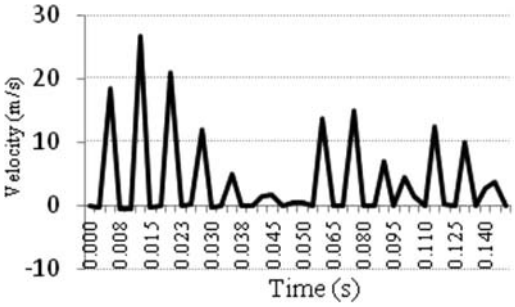


Figure 11. Particle velocity versus time in the input bar.

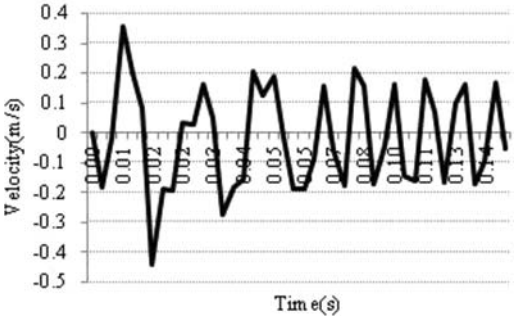


Figure 12. Particle velocity versus time in the output bar.

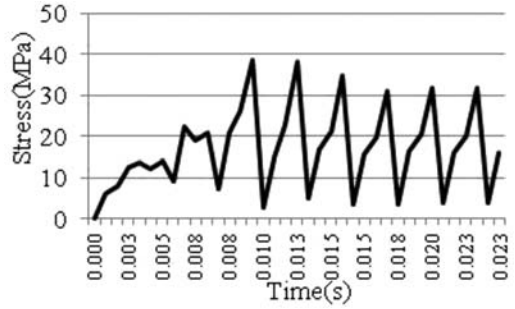


Figure 13. Stress versus time in the specimen.

The reason for this discrepancy may be due to imperfect contact at the interfaces between the bars and the specimen. Another issue is related to the boundary condition of the bar: In the model, displacements were assumed to be equal to zero at the end of the bar. This is not necessarily true in the experiments.

6 CONCLUSIONS

This study allows us to highlight the effect of dynamic loading on the mechanical properties of Lavasan granite. It was found that both the uniaxial compressive strength (UCS) and Young's modulus substantially increase with the rate of loading. It was also observed that the duration of the loading depends on the length of the striker; the longer the striker the larger the loading time and therefore is the lower the UCS. Additional tests are therefore required to assess this effect. The results of numerical modeling show that it is possible to compute realistic strain and stress in the rock specimen. This approach will be extended in the future to model the entire tunnel excavation process.

REFERENCES

ABAQUS, 2010. Getting Started with ABAQUS Version 6.10, ABAQUS, Inc.

Bohloli, B. 1997. Effects of the geological parameters on rock blasting using the Hopkinson split bar. International Journal of Rock Mechanics and Mining Sciences. 34: 32.e1–32.e9.

Forquin, P. Safa, K. Gary, G. 2010. Influence of free water on the quasi-static and dynamic strength of concrete in confined compression tests. Journal of Cement and Concrete Research. 40: 321–333.

Hopkinson, B. 1914. A method of measuring the pressure produced in the detonation of high explosives or by the impact of bullets. Philosophical Transactions of the Royal Society (London) A. 213: 437–456.

Johnson, J.C. 2010. The Hustrulid bar – a dynamic strength test and its application to the cautious blasting of rock. PhD Thesis, University of Utah.

Kaiser, M.A. 1998. Advancements in the Split Hopkinson Bar Test, Master of Science in Mechanical Engineering – Virginia Tech University, Blacksburg, Virginia.

Keshavarz, M. Pellet, F.L. Amini Hosseini, K. Rousseau, C. 2008. Comparing the results of acoustic emission monitoring in Brazilian and uniaxial compression tests. Proc. 5th Asian Rock Mechanics Symposium, Tehran, Iran: 357–363.

Keshavarz, M. Pellet, F.L. Amini Hosseini, K. 2009. Effectiveness of energy and hit rate parameters of acoustic emission for prediction of rock failure. Proc. Sinorock Symposium, Hong Kong, China, CDRom.

Kolsky, H. 1949. An investigation of the mechanical properties of materials at very high rates of loading. Proceedings of the Physical Society of London, B62: 676–700.

Pellet, F. L. Keshavarz, M. Amini Hosseini, K. 2011. Mechanical damage of a crystalline rock having experienced ultra high deviatoric stress up to 1.7 GPa. International Journal of Rock Mechanics and Mining Sciences. 48: 1364–1368.

Weimin, L. Jinyu, X. 2009. Impact characterization of basalt fiber reinforced geopolymeric concrete using a 100-mm-diameter split Hopkinson pressure bar, Journal Materials Science and Engineering. A 513–514: 145–153.

Zhou, Y.X. Xia, K. Li, X.B. Li, H.B. Ma, G.W. Zhao, J. Zhou, Z.L. Dai, F. 2012. Suggested methods for determining the dynamic strength parameters and mode-I fracture toughness of rock materials. International Journal of Rock Mechanics and Mining Sciences. 49: 105–112.

Rock Mechanics for Resources, Energy and Environment – Kwaśniewski & Łydżba (eds)
© 2013 Taylor & Francis Group, London, ISBN 978-1-138-00080-3

Dynamic modelling of a mining-induced fault slip

A. Sainoki & H. Mitri
McGill University, Montreal, QC, Canada

ABSTRACT: Fault slip bursts induced by mining activities could inflict severe damage to mine openings. In this paper, dynamic modelling of mining-induced fault slip is demonstrated with the purpose of examining an effect of a variety of factors, such as mining depth and the angle of friction, on seismic response of the fault slip, using a numerical model with a fault parallel to a steeply dipping ore body that is mined out with sublevel stoping method. The results obtained from the analyses show that fault-slip could become significantly violent when mining depth increases or when the angle of friction decreases, while the shear stiffness and dilation angle of the fault do not exert a severe influence on the behaviour of the fault. It is also shown that significantly high shear rupture velocity could be induced by extracting the orebody parallel to the fault.

1 INTRODUCTION

Fault slip burst could pose a severe threat to nearby openings in underground hard rock mines, where existence of faults is not uncommon. Many attempts have been made in order to estimate a magnitude and location of the fault slip in underground mines, considering progress of mining activities. Hofmann & Scheepers (2011) simulated fault-slip areas by comparing results obtained from numerical analysis with data captured by microseismic monitoring system. Estimating cumulative seismic moment while simulating progress of mining sequences over a long period has been performed (Sjoberg et al. 2012). In terms of the locations of fault-slip, Alber et al. (2008) attempted to associate mining activities with the occurrence of seismic events in geological structures. Owing to the studies, better understanding of fault slip related seismic events has been achieved.

However, fault-slip burst is a dynamic phenomenon, which gives rise to seismic waves that propagate through rockmasses and could cause severe damage when hitting surfaces of mine openings where stresses are concentrated. According to Blake & Hedley (2003), fault-slip burst that took place in Wright-Hargreaves Mine in 1964 caused significant damage to mine openings from 2550 level to 3750 level, which resulted from seismic waves. Although static analysis is capable of simulating shear displacement increments and stress change induced by the fault slip, dynamic analysis is indispensable to simulate the seismic waves.

Significant efforts to model fault-slip dynamically have been mainly made in geophysics and seismology. As a result, a number of dynamic friction laws taking into consideration dynamic behaviour of faults, such as slip-weakening and-strengthening behaviour, have been developed (Ida 1972). Employing the dynamic friction laws makes it possible to investigate characteristics of the dynamic behaviour of faults. Importantly, fault-slip that occurs in underground mines has similar mechanism to shallow earthquakes (Gibowicz & Kijko 1994). Hence, the knowledge is presumably applicable to dynamic modelling of fault-slip in mining contexts.

In the present study, dynamic modelling of fault-slip that occurs in an underground hard rock mine is performed. A numerical model with a fault parallel to an orebody is generated, and a parametrical study is conducted to examine factors that possibly exert an influence on the behaviour of the fault, such as mining depth, the angle of friction, and the distance between the fault and orebody. Through the study, dynamic behaviour of the fault, such as slip rate and shear rupture velocity, are also examined for better understanding of the dynamic behaviour of fault-slip in underground mines. Thus, the present study focuses on gaining fundamental knowledge of seismic response of a fault to mining activities in underground hard rock mines.

2 NUMERICAL ANALYSIS

To examine the response of a fault to mining activities, a numerical model encompassing a fault parallel to a steeply dipping, tabular ore body is generated by means of FLAC3D code (Itasca 2009). Subsequently, static and dynamic analyses are carried out with the code. In this section, the detailed descriptions of the numerical model and analyses are given.

2.1 *Mining sequence proposed*

A typical example of sublevel stoping method employed in the present study is shown in Figure 1. With the mining method, large blocks referred to as

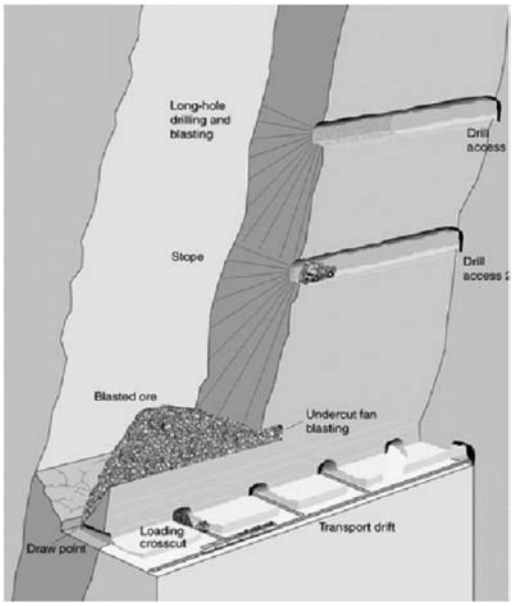


Figure 1. Typical sublevel stoping method (AtlasCopco).

stope are extracted at each sublevel by blasting. Afterwards, the cavities created due to the extraction of the stopes are backfilled in order to minimize an effect of the extraction on in-situ stress fields. In this study, bottom-up mining is carried out.

2.2 *Model geometries & analysis procedure*

The numerical model encompassing the geological features is illustrated in Figure 2. As shown in the figure, the length, width and height of the model are 300 m, 332 m, and 300 m, respectively. The width of the ore body is 22 m, and a dip angle is 80°. The fault running parallel to the ore body is located 30 m away from the ore body; and interface elements are utilized to model the fault. A positional relationship between the fault and orebody is one of the factors examined in the parametric study; thus an effect of the fault location on a magnitude of the fault-slip is investigated. To do that, models where a fault is situated at positions different from that shown in Figure 1 are also generated and analyzed.

It is postulated that mining rates, at which stopes are extracted, have an influence on the behaviour of the fault. Therefore, two types of stope geometries that take the mining rates into consideration are modelled. Stope geometry for high mining rates is depicted in Figure 2. The height and strike length of the stopes are 30 m and 200 m, respectively. On each sublevel, two stopes are extracted from hanging wall to footwall side. The stope strike length is modelled to be long enough to simulate the high mining rates. Conversely, the stope strike length of 25 m is modelled for low mining rates. In that case, 16 stopes are modelled at each level, which are separately extracted in retreat.

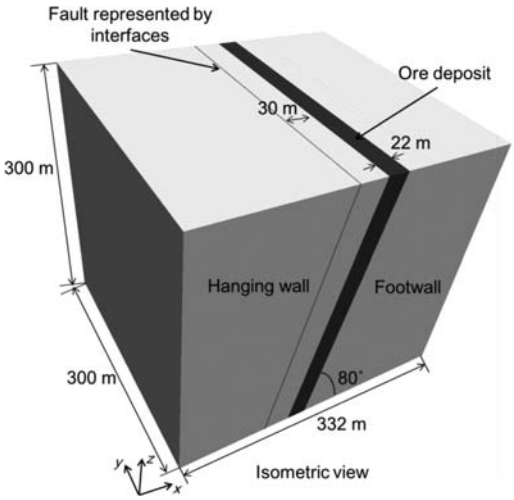


Figure 2. Geometries of a numerical model analyzed.

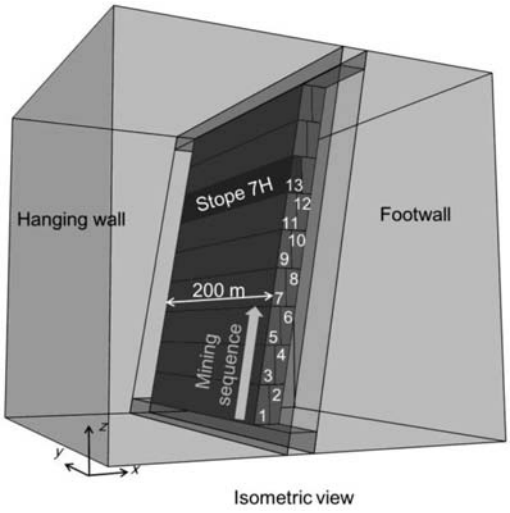


Figure 3. Stopes and mining sequence representing sublevel stoping method.

In either case, backfill is conducted after each extraction of the stopes.

2.3 *Analysis procedure*

First, static analysis is carried out while extracting the stopes with delayed backfill. The numbers in Figure 3 illustrate the mining sequence. Extracting the stopes with static analysis prior to dynamic analysis aims to reduce computation time; it continues until the stress state on the fault is deemed to be burst- prone, at which time the fault-slip is simulated with dynamic analysis.

After extracting stopes numbered 1 to 12 in Figure 3 with static analysis, stope7H shown is extracted with dynamic analysis. Fault slip induced by the extraction is examined and compared between the models for the

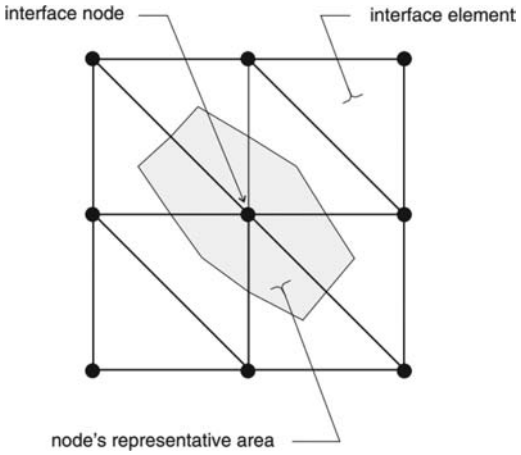


Figure 4. Interface elements used for modelling a fault.

parametrical study. In the case of the low mining rates, dynamic analysis is conducted when extracting a stope located at the center of the orebody on hanging wall side on the same level as stope7H.

2.4 *Interface*

The fault shown in Figure 2 is modelled with interface elements that consist of collections of triangular elements, each of which is defined by three nodes as shown in Figure 4. Each interface node has an associated representative area; and the interface element, which is zero-thickness, is attached into target faces in a numerical model.

During each timestep, normal and shear force are computed at each node as follows (Itasca 2009).

$$F_n^{(t+\Delta t)} = k_n u_n A + \sigma_n A \tag{1}$$

$$F_{si}^{(t+\Delta t)} = F_{si}^{(t)} + k_s \Delta u_{si}^{(t+(1/2)\Delta t)} A + \sigma_{si} A \tag{2}$$

where $F_n^{(t+\Delta t)}$, u_n, k_n, and A are normal force at time $(t+\Delta t)$, absolute normal penetration of the interface node into the target face, normal stiffness, and the representative area associated with interface node, respectively, and $F_{si}^{(t+\Delta t)}$, u_{si}, k_s, σ_{si} are shear force vector at time $(t+\Delta t)$, incremental relative shear displacement vector, shear stiffness, and additional shear stress vector due to interface stress initialization, respectively. When the shear force exceeds shear strength determined by Mohr-Coulomb failure criterion, stresses on the fault are modified, which results in slip arising excess shear stress along the fault.

2.5 *Mechanical properties of rockmass & initial stress states*

The mechanical properties of the rockmass used for the models are based on test results obtained from rock samples of Bousquet 2 Mine (Henning 1998).

Table 1. Mechanical properties of rockmass.

	E GPa	C MPa	φ °	ν	γ kN/m^3	σ_T MPa	ψ °
HW	31	2.6	38	0.21	25.5	1.1	9.3
Ore	115	11.5	48	0.1	25.5	5.9	12.0
FW	49	4.3	39	0.15	25.5	1.8	9.75
BF[1]	2.5	0.1	35	0.35	23.0	N/A	0.0

[1]Backfill.

Table 2 lists the elastic modulus, E, cohesion, C, internal friction angle, φ, Poisson's ratio, ν, tensile strength, σ_T, and dilatancy angle, ψ, of rockmass and backfill material.

Initial stress states are simulated with the equations proposed by Diederichs (1999), which are given as:

$$k_{\max} = 1 + \frac{25}{\sqrt{H}} \tag{3}$$

$$k_{\min} = 1 + \frac{8}{\sqrt{H}} \tag{4}$$

where H is the distance from the ground surface. Maximum and minimum horizontal-to-vertical stress ratios are derived from equations 3 and 4; and the direction of maximum horizontal stress is perpendicular to the ore body. As discussed by Ryder (1988), mining depth could affect the behaviour of the fault, so that in the present study, the depth at the top boundary of the model is set at 1500 m, 2000 m, and 2500 m, assuming that the unit weight of overlying rockmass is 25.5 kN/m^3.

2.6 *Model analyzed*

Models for the parametrical study are generated changing the mechanical properties of the fault and model geometries. The variables taken for this study are fault location, the strike length of the fault, mining depth, the distance between the fault and ore body, the friction angle of the fault surface, shear and normal stiffness, and the dilatancy angle. Tables 2a and 2b list the models analyzed to examine an influence that each factor exerts on fault behaviour.

2.7 *Analysis conditions*

The boundaries of the models are fixed in the direction perpendicular to the boundaries, and the initial stress fields are applied to the models. For the dynamic analysis, the boundary conditions are changed to viscous in order to prevent the model boundaries from reflecting elastic waves arising from fault slip and the extraction of the stope. With regard to the attenuation of elastic waves, local damping embodied in FLAC3D is utilized. This is deemed to be sufficient at this stage, considering the focus of the present study.

Table 2a. Model properties (No. 1–7).

Model No.	1	2	3	4	5	6	7
FL[1] (m)	HW[3]	HW	HW	HW	HW	HW	HW
SL[2] (m)	200	200	200	200	200	200	200
H (m)	1500	1500	1500	1500	1500	1500	1500
D[4] (m)	30	30	30	30	30	60	90
φ (°)	30	30	30	30	30	30	30
k_n (GPa/m)	3.1	3.1	3.1	6.2	9.3	3.1	3.1
k_s (GPa/m)	1.28	1.28	1.28	2.56	3.84	1.28	1.28
ψ (°)	0	5	10	0	0	0	0

[1]Fault location.
[2]Stope strike length.
[3]Hanging wall.
[4]Distance between fault and orebody.

Table 2b. Model properties (No. 8–13).

Model No.	8	9	10	11	12	13
FL (m)	HW	HW	HW	HW	HW	FW[1]
SL (m)	200	200	200	200	25	200
H (m)	2000	2500	1500	1500	1500	1500
D (m)	30	30	30	30	30	30
φ (°)	30	30	25	15	30	30
k_n (GPa/m)	3.1	3.1	3.1	3.1	3.1	3.1
k_s (GPa/m)	1.28	1.28	1.28	1.28	1.28	1.28
ψ (°)	0	0	0	0	0	0

[1]Footwall.

3 RESULTS AND DISCUSSION

Based on the results obtained from the dynamic analysis, each model is compared in terms of maximum shear displacement, seismic source parameters, and slip rate. Note that all the values above are calculated from increments of shear displacement and shear stress during the dynamic analysis.

3.1 *Maximum shear displacement, seismic source parameters and slip rate*

Figure 1 depicts the summation of normalized the maximum shear displacement, seismic moment, energy released during the fault-slip, and slip rate based on the result for Model 1. The summation of normalized values is given as:

$$Sum = \frac{d_s^i}{d_s^1} + \frac{M_0^i}{M_0^1} + \frac{E_s^i}{E_s^1} + \frac{SR^i}{SR^1} (i = 1 \sim 13) \quad (5)$$

where d_s, M_0, E_s, and SR represent the maximum shear displacement, seismic moment, energy radiated during the fault-slip, and slip rate (m/s), respectively. The summation of the normalized values can be considered an index representing the degree to which fault-slip becomes violent, compared to that for Model 1. Each component of the bars in the figure, on the other hand,

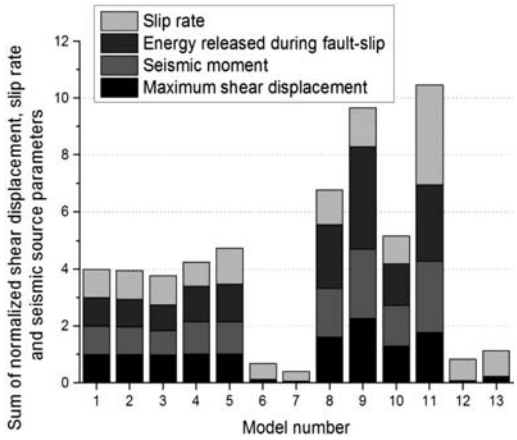


Figure 5. Sum of normalized shear displacement, slip rate and seismic source parameters based on the result of Model 1.

shows how each factor, such as mining depth, affects the behaviour of the fault.

It is found out from the figure that the dilatancy angle of the fault and shear and normal stiffness do not significantly affect the behaviour of the fault; the value of the summation does not differ widely from that of Model 1. In contrast, a significant increase in the summation can be seen for Model 9 and 11, which correspond with the case for the mining depth of 2500 m and the friction angle of 15°. Hence, these results imply that the behaviour of the fault is strongly dependent on these factors and that estimating a magnitude of fault slip properly necessitates taking the factors into consideration.

The figure also shows factors that decrease the magnitude of the fault-slip. As can be seen, the summation are quite low for Models 6, 7, 12, and 13; the distance between the fault and orebody has been increased for Models 6 and 7; low mining rates have been employed for Model 12; the location of the fault has been moved to footwall side for Model 13. As the mining rate only is controllable among them, determining proper mining rates would play a key role in controlling the occurrence of large seismic events.

As discussed above, the two factors, namely mining depth and the angle of friction, significantly exert a negative influence on the behaviour of the fault. Therefore, the effect of the factors is furthermore examined. Figure 6 depicts a relation between an increase in mining depth and the behaviour of the fault. As shown in the figure, all the normalized values increase with increasing mining depth. It should be noted that there is a large discrepancy between the increases in the values. Normalized seismic moment rises to 2.45 due to the increase in the mining depth. On the other hand, normalized energy released during fault-slip rises to 3.57. The results in the figure indicate that energy released during fault-slip is the most susceptible to mining depth of the normalized values. Considering the fact that energy released during the fault-slip is an important index to evaluate the severity of the fault-slip

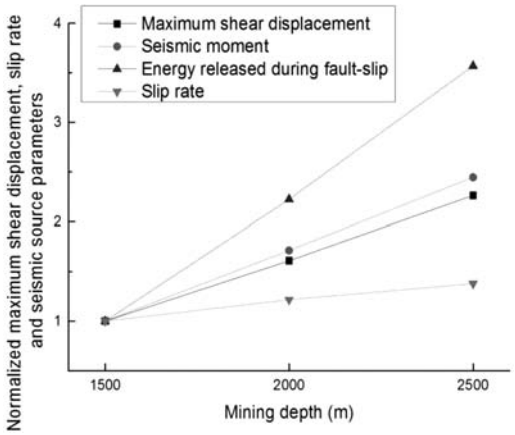


Figure 6. Relation between mining depth and behaviour of fault.

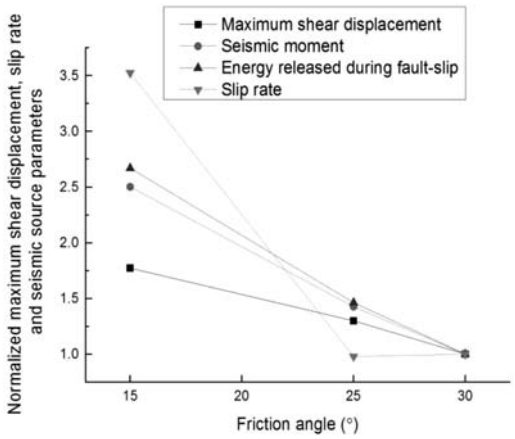


Figure 7. Relation between the angle of friction and behaviour of fault.

(Hedley 1992), better understanding of this tendency would be indispensable for operations in deep hard rock mines. Figure 7 depicts a relation between the angle of friction and the behaviour of the fault. As is the case with mining depth, a decrease in the angle of friction increase the maximum shear displacement, slip rate, and seismic source parameters. In this case, the discrepancy between seismic moment and energy released during the fault-slip is smaller compared to that for mining depth. However, a large rise in slip rate induced by the reduction in the angle of friction is remarkable. Slip rate can be considered to be directly related to peak particle velocity (PPV). Hence, this result implies that extremely high PPV could be caused given that infill materials, such as clay, that decrease the angle of friction exist on fault surfaces.

3.2 *Rupture velocity*

Characteristics of shear rupture velocity that could be experienced in deep hard rock mines are examined

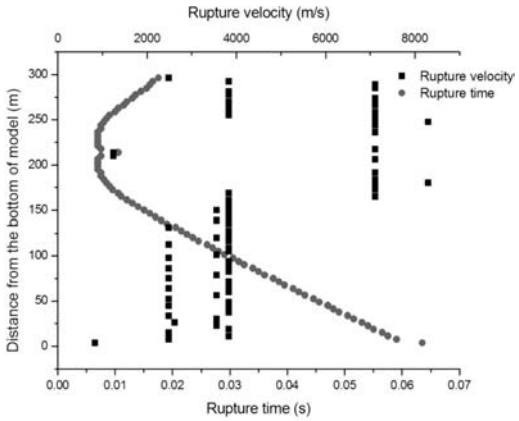


Figure 8. Rupture time and rupture velocity at points on the center line of the fault.

as the rupture velocity is strongly associated with the generation of seismic waves. The rupture velocities at points on the center line of the fault, i.e. the line of $y = 150$ m on the fault, are investigated. Figure 8 depicts rupture time, at which shear rupture starts, and rupture velocity, at which shear failure expands on the fault. In the present study, the nodes on the line at which a slip rate exceeds 0.1 m/s are considered to be ruptured. It can be seen from the figure that rupture time takes the minimum value 250 m above the bottom of the model. The location can be considered as a hypocenter of the induced fault-slip. Rupture velocities are computed by dividing the difference in the rupture time by the distance between the nodes. It is found out from the figure that extremely high rupture velocities arises around the hypocenter, ranging from 7500 m/s to 8000 m/s; then, the rupture velocities decrease to approximately 2500 m/s for nodes remote from the hypocenter.

Shear rupture velocity that exceeds S-wave velocity is termed "supershear" (Bizzarri & Spudich 2008). As S-wave velocity can be estimated to be 2200 m/s, supershear is found to occur. Furthermore, it is found out that the positional relationship that the fault runs parallel to the orebody leads to the generation of supershear as stress waves induced by extracting the stope reach the fault at the same time. Although it is not always straightforward to relate the occurrence of fault-slip to specific extraction of stope, this result indicates a possibility that supershear occurs in underground mines where faults run parallel to an orebody.

3.3 *Limitations of Mohr-Coulomb criterion for dynamic modelling of fault-slip*

Table 3 shows seismic moment, energy released during the fault-slip, and moment magnitude for Model 1. The moment magnitude shown in the table is 2.15, which can be regarded as a relatively large seismic event. However, considering that the fault-slip is induced by

Table 3. Computed seismic source parameters.

	M_0 dyne·cm	E_s J	M_w
Model 1	1.87×10^{19}	6.64×10^{8}	2.15

extracting a stope of which strike length is 200 m, it is not unconceivable that more violent seismic events are simulated. In fact, much larger seismic events in underground mines have been reported (Blake & Hedley 2003). It is thus postulated that this is attributed to the use of Mohr-Coulomb criterion for modelling of fault-slip. In reality, a number of phenomena, such as slip-weakening behaviour, are involved in dynamic behaviour of faults, whereas the dynamic analysis does not consider such phenomena. This result implies that it is necessary to employ other friction laws allowing for the phenomena to estimate a magnitude of fault slip related seismic events properly.

4 CONCLUSIONS

Static and dynamic analyses are performed in order to simulate fault-slip that occurs in deep hard rock mines. A parametrical study is conducted to examine the factors that possibly exert an influence on the behaviour of the fault. The results show that mining depth and friction angle of fault-surface as well as the distance between the fault and orebody significantly affect the behaviour of the fault, while stiffness of the fault and dilatancy angle do not have a large influence. It is also found out that when mining depth increases, the increase in energy released during fault-slip is much larger than those in seismic moment, the maximum shear displacement increment and slip rate. Furthermore, the results indicate that a decrease in the angle of friction leads to extremely high slip rate, which could in turn result in high peak particle velocity. Investigation of shear rupture velocity demonstrates that supershear is induced by extracting stopes when a fault runs parallel to an orebody. Finally, limitations of Mohr-Coulomb criterion when modelling dynamic behaviour of the fault are indicated. The present study has served toward better understanding of fundamental behaviour of faults in deep underground mines.

ACKNOWLEDGEMENTS

This work is financially supported by a grant from the Natural Science and Engineering Research Council of Canada (NSERC) – Discovery Grant Program, and McGill University (MEDA Fellowship Program); the authors are grateful for their support.

REFERENCES

Alber, M., Fritschen, R., Bischoff, M. & Meier, T. 2009. Rock mechanical investigations of seismic events in a deep longwall coal mine. *Int. J. Rock Mech. Min. Sci*. 46: 408–420.

Bizzarri, A. & Spudich, P. 2008. Effects of supershear rupture speed on the high-frequency content of S waves investigated using spontaneous dynamic rupture models and isochrones theory. *Journal of Geophysical Research: Solid Earth* 113(B5), DOI: 10.1029/2007JB005146.

Blake, W. & Hedley, D.F.H. 2003 *Rockbursts: Case Studies from North American Hard-Rock Mines*. Littleton CO: Society for Mining, Metallurgy, and Exploration, Inc.

Diederichs, M.S. 1999. *Instability of Hard Rockmasses: The Role of Tensile Damage and Relaxation.* PhD Thesis, University of Waterloo, Waterloo, Ontario, Canada.

FLAC3D software, 2009. Itasca, Minneapolis.

Gibowicz, S.J. & Kijiko, A. 1994. *An Introduction to Mining Seismology*. New York: Academic Press.

Hedley, D.G.F. 1992. *Rockburst Handbook for Ontario Hardrock Mines*. Canada Center for Mineral and Energy Technology.

Henning, J.G. 1998.*Ground Control Strategies at the Bousquet 2 Mine* [MEng]. Montreal: McGill University.

Hofmann, G. F. & Scheepers, L.J. 2011. Simulating fault slip areas of mining induced seismic tremors using static boundary element numerical modelling *Mining Technology* 120: 53–64.

Ida, Y. 1972. Cohesive force across the tip of a longitudinal-shear crack and Griffith's specific surface energy. *Journal of Geophysical research* 77(20): 3769–3778.

Ryder, J.A. 1988 Excess shear stress in the assessment of geologically hazardous situations. *J. S. Afr. Inst. Min. Metall*. 88: 27–39.

Sjoberg, J., Perman, F., Quinteiro, C., Malmgren, L., Dahner-Lindkvist, C. & Boskovic, M. 2012. Numerical analysis of alternative mining sequences to minimise potential for fault slip rockbursting. *Mining technology* 121(4): 226–235.

Rock Mechanics for Resources, Energy and Environment – Kwaśniewski & Łydżba (eds)
© 2013 Taylor & Francis Group, London, ISBN 978-1-138-00080-3

The estimation of the effectiveness of torpedo blasting based on an analysis of focal mechanisms of induced mining tremors in the Bielszowice coal mine

Ł. Wojtecki
"Bielszowice" Coal Mine, Kompania Węglowa S.A., Ruda Śląska, Poland

M.J. Mendecki, A. Talaga & W.M. Zuberek
Faculty of Earth Sciences, University of Silesia in Katowice, Sosnowiec, Poland

ABSTRACT: Coal exploitation in the Upper Silesian Coal Basin is associated with rockburst hazard. This hazard is minimalized by active rockburst prevention, where torpedo blastings in roof-rocks take very important place. The estimation of the torpedo blasting effectiveness becomes significant under exploitation in difficult geological and mining conditions, where the high danger of rockburst occurs.

Pioneer investigations lead to estimate of the torpedo blastings effectiveness on the basis of an analysis of focal mechanisms of the induced mining tremors. The study has been carried out in the Bielszowice coal mine in cooperation with the Faculty of Earth Sciences of the University of Silesia. The torpedo blastings were performed during exploitation of the seam 507 with the longwall 307b. Each blasting provoked a tremor immediately. The parameters of the focal mechanisms for each provoked event were estimated by the FOCI software.

Beside tremors foci with an explosive mechanism, related only to the detonation of an explosive, the occurrence of tremor foci with a shear mechanism has been confirmed. Shear mechanism in provoked tremors proves that blastings caused the motion of rock masses, what is connected with stress drop in the rock mass. The results have been associated with geological and mining conditions.

1 INTRODUCTION

Coal exploitation under condition of a rockburst hazard determines active rockburst prevention applying, where torpedo blastings occupy a prominent place. An estimation of the blasting efficiency becomes particularly important during the exploitation in difficult geological and mining conditions.

The focal mechanism studies with seismic moment tensor inversion method were performed for the tremors induced by torpedo blastings in the longwall 307b during exploitation of the seam 507 in the Bielszowice coal mine. Focal mechanisms were calculated by the seismic moment tensor inversion based on the analysis of seismic waves generated in the focus and registered by the appropriate number of seismometers surrounding the source.

2 GEOLOGICAL AND MINING CONDITIONS IN LONGWALL 307B AREA

The seam 507 in the Bielszowice coal mine, in longwall 307b area is located at depths of about −620–−660 m below sea level and its thickness varies from 2.7 m to 3.8 m. The direct roof of the seam 507 is composed of alternating layers of shale, sandy shale and sandstone. Most of these rocks has high compressive strength (tens of MPa). At a distance of more than 50 m above the seam 507 a thick layer (up to 60 m) of sandstone occurs. The floor of the seam 507 consists of shale and sandy shale with small thickness (several meters). Thick seam 510 (up to 8 m) is deposited below.

The exploitation of longwall 307b in the seam 507 was started on January, 2011 and was ended on June, 2012. The longwall begun its run from area of pillar for flank drifts and was running along the abandoned gobs of longwalls 306 and 306b. In November, 2011 the longwall 307b crossed the mine filled drift to the level 900 m. At the end, this longwall was running in the area of pillar for "Bielszowice" shafts and was approaching to the pillar for main drifts. On the runway of longwall 307b mining edges in seams 501 and 502 (laying approximately 150 m and 135 m above the seam 507) occurred.

High seismic activity appearing in the longwall 307b area has indicated that rockburst hazard in this excavation was at high level. Total number of recorded seismic events was 6273 with a total released tremors energy $2.62 \cdot 10^8$ J, including 3341 events with energy of the order of 10^2 J, 1840 events with energy of the order of 10^3 J, 897 events of the order of 10^4 J, 160 events of the order of 10^5 J, 34 events of the order of 10^6 J and one tremor of energy of $2 \cdot 10^7$ J. In the

period from August, 2011 to March, 2012, the level of rockburst hazard in the longwall 307b was the highest. During these eight months about 70% of seismic events with energy of the order of 10^5 J, about 97% of seismic events with energy of the order of 10^6 J and the strongest tremor with energy of $2 \cdot 10^7$ J occurred. In this time longwall 307b was running beneath mining edges in upper seams 501 and 502 (generally parallel to the longwall) and was approaching to the edge of the pillar for "Bielszowice" shafts. These conditions influenced on stress state in the roof rocks.

3 TORPEDO BLASTINGS FROM THE LONGWALL 307B

Because of high level of rockburst hazard during longwall 307b runway, the passive and active rockburst prevention were applied. Active rockburst prevention in the longwall 307b was carried out mainly with the torpedo blastings in roof rocks. The main purpose of these blastings was to destress the rock mass ahead of longwall 307b. Emulinit PM explosive material has been used for each blasting. For each torpedo blasting 6 blastholes with a length of 40 m (arranged in pairs – one pair in the middle of the longwall, and the other at a distance of 60 m from longwall headings) were drilled. Blastholes were deviated from the longwall face to the north-east and south-east at the angle of about 40°, and they were inclined at an angle of 35° to the horizon. Explosive material occupied near 15 m of each blasthole, and the rest was filled with the tamping. During each torpedo blasting 432 kg of emulinit PM was detonated. In accordance to the presented parameters 11 torpedo blastings were performed, which provoked an immediate tremors with seismic energy range of $3 \cdot 10^4$ J to $9 \cdot 10^4$ J. These blastings were performed at the average 25 m intervals of longwall advance. Because of mentioned above increased level of rockburst hazard, which appeared in August, 2011, the torpedo blastings from the longwall were performed by using a larger amount of explosives. From this time 96 kg of emulinit PM was loaded to each blasthole and occupied near 20 m of it. During each torpedo blasting 576 kg of explosives was detonated. In addition, the inclination of blastholes was increased up to 40° relative to horizon, what was an optimal solution due to the geological structure and technical capability. At the end of October, 2011 the localization of blastholes pairs in longwall 307b was modified appropriately to occurrence of spontaneous high-energy tremors. In the period of increased seismic activity, occurring up to the end of January, 2012, thirteen torpedo blastings with described parameters were performed. These blastings provoked an immediate tremors with energy range from $4 \cdot 10^4$ J to $9 \cdot 10^4$ J. These blastings were performed at the average 15 m intervals of longwall advance. Since February, 2012, a stable distribution of blastholes pairs in the longwall 307b had been restored. Decrease of seismic activity and associated rockburst hazard caused reduction of the frequency of torpedo blasting from the longwall (at the average 23 m intervals of longwall advance). Nine torpedo blastings were performed and provoked an immediate tremors with energy range from $4 \cdot 10^4$ J to $8 \cdot 10^4$ J.

The effectiveness of the torpedo blastings performed from the longwall 307b had important significance for the safety exploitation under high rockburst hazard. An attempt of the estimation of torpedo blastings effectiveness was performed, based on the analysis of the focal mechanism of provoked tremors.

4 CALCULATION OF FOCAL MECHANISM

The method of seismic moment tensor inversion is useful to determine processes, which take place in tremor source. The tensor decomposition into the isotropic component (I), the compensated linear vector dipole (CLVD) and a double pair of forces (DBCP) is the most used characterization of the tremor source (Gibowicz & Kijko 1994, Marcak & Zuberek 1994, Gibowicz 1995, Stec 2009, Stec & Wojtecki 2011). Part I describes the volumetric changes in the source ("+" – explosion, "−" – implosion), CLVD describes a mechanism similar to the uniaxial compression ("−") or tension ("+") and DBCP relates to processes of shearing. The advantage of the isotropic part in focal mechanism of induced tremors suggests explosive mechanism and a destruction of the rock mass mainly by the detonation of the explosives (change of pressure in the source). The advantage of the double pair of indicates shear mechanism, what is connected with a shear displacement of rock masses and associated with stress drop in the rock mass (Gibowicz & Kijko 1994).

5 RESULTS

Seismic moment tensor calculations were performed in the FOCI software based on an inversion of P-wave arrival, taking into account the directions of the first deflection in the time domain. Mechanisms of all 33 events provoked by torpedo blastings have been estimated. Focal mechanisms were determined on the basis of records registered by seismological network of the Bielszowice coal mine. Seismic stations were distributed evenly and optimally around the longwall 307b. The error of epicenter location ranged from about 20 to about 35 m and it depended on the number of seismic stations which had been taken into calculations. The error of hypocenter location in the area of the longwall 307b was larger and in extreme cases reached over 60 m. For this reason, the vertical components of focus location were improved by the FOCI software (Kwiatek 2009), testing the seismic moment tensor solution and assuming the value corresponding to the highest values of quality coefficient and the smallest error of estimation.

Table 1. Focal mechanisms of tremors provoked by torpedo blastings from January, 2011 to the first half of July, 2011.

Date	Time h	Time m	Energy [J]	Mass of explosives [kg]	Coordinates in Sucha Gora System X [m]	Y [m]	Z[1] [m]	Tensor components [%] I	CLVD	DBCP	Type mechanism[2]
2011-02-14	5	44	3.0E+04	432	15774	3931	−616	42.8	28.8	28.5	EXPL
2011-03-21	6	13	9.0E+04	432	15734	3949	−621	44.3	34.1	21.6	EXPL
2011-04-04	5	41	5.0E+04	432	15789	3874	−594	37.9	25.6	36.6	EXPL
2011-04-18	6	30	4.0E+04	432	15806	3826	−632	46.2	37.1	16.7	EXPL
2011-05-02	3	30	5.0E+04	432	15804	3814	−629	37.7	27.7	34.6	EXPL
2011-05-16	12	6	5.0E+04	432	15798	3794	−629	45.6	34.3	20.1	EXPL
2011-05-30	7	28	6.0E+04	432	15769	3796	−622	48.6	43.9	7.5	EXPL
2011-06-13	2	34	5.0E+04	432	15732	3745	−626	43.3	24.8	31.8	EXPL
2011-06-27	5	16	3.0E+04	432	15761	3734	−622	47.0	31.7	21.3	EXPL
2011-07-11	5	16	4.0E+04	432	15706	3725	−594	46.4	431	10.5	EXPL

[1] foci depth determined from the best fitting solution the FOCI software.
[2] EXPL – explosive mechanism of source.

Table 2. Focal mechanisms of tremors provoked by torpedo blastings from the second half of July, 2011 to the first half of March, 2012.

Date	Time h	Time m	Energy [J]	Mass of explosives [kg]	Coordinates in Sucha Gora System X [m]	Y [m]	Z[1] [m]	Tensor components [%] I	CLVD	DBCP	Type mechanism[2]
2011-07-18	7	7	7.0E+04	432	15753	3708	−625	25.2	23.2	51.6	RE
2011-08-01	5	16	4.0E+04	576	15760	3667	−631	2.8	21.2	75.9	RE
2011-08-21	17	56	4.0E+04	576	15800	3660	−627	6.5	2.7	90.9	RE
2011-09-04	18	59	5.0E+04	576	15776	3633	−628	31.1	15.3	53.7	RE
2011-09-19	5	29	4.0E+04	576	15771	3612	−627	9.1	9.3	81.6	RE
2011-10-10	5	48	8.0E+04	576	15766	3605	−618	15.3	21.4	63.3	RE
2011-10-30	23	26	7.0E+04	576	15759	3585	−624	5.7	27.9	66.3	RE
2011-11-14	0	10	7.0E+04	576	15759	3564	−582	0.8	21.5	77.7	RE
2011-11-20	23	16	8.0E+04	576	15756	3564	−624	7.7	22.4	69.9	RE
2011-11-28	0	4	8.0E+04	576	15743	3531	−624	22.6	18	59.4	RE
2011-12-11	23	9	9.0E+04	576	15742	3533	−625	5.8	22.9	71.3	RE
2011-12-26	22	43	7.0E+04	576	15743	3505	−631	31.2	28.7	40.1	RE
2012-01-08	22	50	7.0E+04	576	15748	3513	−632	11.1	26.1	62.8	RE
2012-01-22	23	33	6.0E+04	576	15714	3482	−627	12.9	24.5	62.7	RE
2012-02-13	6	28	6.0E+04	576	15738	3415	−628	29.4	27.1	43.5	RE
2012-02-27	5	11	8.0E+04	576	15761	3420	−625	26.6	25.9	47.5	RE
2012-03-12	0	32	6.0E+04	576	15770	3410	−619	18.3	14.6	67.1	RE

[1]foci depth determined from the best fitting solution the FOCI software
[2]RE – reverse slip mechanism of source.

Events induced by the torpedo blastings obtained the best solutions for the depth range from about −580 to about −640 m below sea level (in average −620 m). This depth corresponds to roof-rocks, where torpedo blasting were performed.

From January, 2011 up to the first half of July, 2011, provoked tremors (10 cases) were characterized by explosive mechanism (Table 1). Participation of isotropic component in full solution of the focal mechanism for these events ranged from 37.7% to 48.6% (mean 44%). Average participation of CLVD was 33.1%, while of DBCP was only 22.9%. Only in two cases, the participation of DBCP component was at a similar level as isotropic (tremors from 04-04-2011 and 02-05-2011). The rock mass destruction were caused only by detonation of explosives and the shear mechanism was negligible.

From the second half of July, 2011 up to the first half of March, 2012 in foci of provoked tremors (17 cases), reverse slip mechanism was dominated (Table 2). The participation of DBCP in full seismic moment tensor solution varied from 40.1% to 90.9% (mean 63.8%). Other components had a lower share (on the average 15.4% of explosion, and on the average 20.8% of uniaxial tension). Therefore, the torpedo blastings had provoked the rock mass movement along

Table 3. Focal mechanisms of tremors induced by torpedo blastings in the period from the second half of March, 2012 to the end of June, 2012.

Date	Time h	Time m	Energy [J]	Mass of explosives [kg]	Coordinates in Sucha Gora System X [m]	Y [m]	Z[1] [m]	Tensor components [%] I	CLVD	DBCP	Type mechanism[2]
2012-03-26	6	29	4.0E+04	576	15743	3371	−635	40.4	39.6	20	EXPL
2012-04-09	11	40	7.0E+04	576	15770	3360	−633	44	43.7	12.3	EXPL
2012-04-22	23	41	8.0E+04	576	15801	3298	−618	47.7	47.3	5	EXPL
2012-05-06	23	57	8.0E+04	576	15810	3270	−614	48.7	49	2.3	EXPL
2012-05-20	22	51	7.0E+04	576	15750	3305	−639	46.4	46.3	7.3	EXPL
2012-06-03	23	23	6.0E+04	576	15661	3240	−606	46.7	45.7	7.6	EXPL

[1,2] – analogous to table 1.

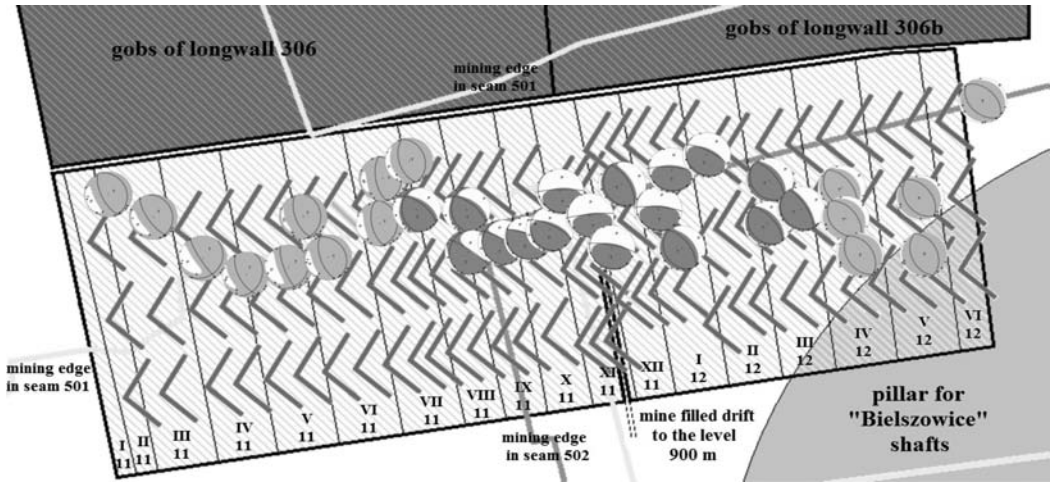


Figure 1. Map of the seam 507 with marked blastholes (red lines) and beach balls representing mechanisms of provoked tremors (grey – explosive mechanism, blue – shear mechanism).

the cracking plane and associated stress drop in the rock mass.

Due to the large share of DBCP in focal mechanism of provoked tremors during the second half of July, 2011 to the first half of March, 2012, the parameters of nodal planes have been calculated. In each case, the movement of rock mass probably occurred along the cracking plane corresponding to the nodal plane B. An azimuth of nodal plane B for nearly 90% of events was parallel in range of ±25° to the position of the longwall 307b front. Only in two cases the differences were larger (34° and 44°). A dip angle of nodal plane B ranged from 10.2° to 53.6° (mean 21.5°). A rake angle of rock mass displacement in the focus for the nodal plane B ranged from 82.2° to 152.4° (mean 118°). Because of the occurrence of mining edges in seams 501 and 502 (parallel to the longwall 307b front) and the edge of pillar for "Bielszowice" shafts the additional stress in layers of strong roof rocks (bending in the direction of longwall 307b gobs) were presented. Blastings in such geomechanical situation created cracking planes, which probably allowed the displacement of strong rocks blocks upward and mechanism of reverse slip.

Since the second half of March 2012 to the end of June 2012, the tremor foci induced by torpedo blastings (6 cases) started dominating the explosive mechanism again (Table 3).

Explosion component share in the full tensor solution of each event exceeded 40% (average 45.6%). A significant participation in the solution had the uniaxial tension and it was averaging 45.3%. The share of the shear component was marginal, and ranged from 2.3% to 20% (mean 9.1%). In the final stage of the longwall 307b runway the torpedo blastings did not cause slip displacement of rock mass and rock destruction was mainly associated with the detonation of explosives.

6 DISSCUSION AND SUMMARY

Among the 33 tremors foci, induced by torpedo blastings from the longwall 307b, two types of dominating mechanisms have been observed (explosion and

shear). The identified mechanisms appeared in alternating groups of tremors. Without presence of additional stresses, destruction of roof rocks by torpedo blastings was mainly a result of explosives detonation. Shear mechanism of provoked tremors occurred during exploitation in presence of mining factors causing an increase of stress in the roof rocks (when the level of rockburst hazard was the highest). The occurrence of shear mechanisms in provoked tremors foci coincide almost exactly with the period of the highest seismic intensity in the longwall 307b (and the higher stresses in rock mass). Correlation between the occurrence of shear mechanism in provoked tremors foci and disadvantageous mining conditions is clear. Mechanisms of all tremors provoked by the torpedo blastings from longwall 307b are presented on the map of seam 507 in the form of beach balls (Fig. 1). The monthly progress of the longwall 307b was also marked.

Effectiveness of torpedo blastings in longwall 307b can be confirmed by fact, that any of high-energy seismic events did not cause any destructive effects in the openings. Occurrence of shear mechanism in provoked tremors foci is associated with the destressing effect.

Therefore, it can be concluded that the method of seismic moment tensor inversion may become useful for fast estimation of the torpedo blastings effectiveness during exploitation in difficult mining conditions, corresponding with high rockburst hazard.

REFERENCES

Gibowicz, S.J. & Kijko, A. 1994. *An Introduction to Mining Seismology*. Int. Geoph. Series, Vol. 55. San Diego, New York: Academic Press.

Gibowicz, S.J. 1995. Mining tremors – Mechanism, location and energy. *Proceedings, School of Underground Mining, Szczyrk, 27 February – 3 March, 1995*: 5–30. (in Polish)

Król, M. 1998. *Application of seismic moment tensor and spectral analysis of seismic waves for mine tremor study in copper mine "Polkowice-Sieroszowice",* Ph.D. Thesis, Institute of Geophysics, Polish Academy of Sciences. (in Polish)

Kwiatek, G. 2009. *Foci – seismic moment tensor – spectral parameters, a description of the program*. www.sejsmologia-gornicza.pl/focirockburst/download.php (in Polish)

Marcak, H. & Zuberek, W.M. 1994. *Mining Geophysics*. Katowice: Śląskie Wydawnictwo Techniczne. (in Polish)

Stec, K. 2009. The focal mechanism and methods of its determination. *Proceedings, Workshop on the Natural Hazards in Mining Industry*: 287–305. (in Polish)

Stec, K. & Wojtecki, Ł. 2011. Characteristics of the mine tremor source mechanism associated with the mining in the seam 510, the longwall 502 in the "Bielszowice" Coal Mine. *Prace Naukowe GIG. Górnictwo i Œrodowisko* 1/2011: 61–77. (in Polish)

This page intentionally left blank

9. Design methodology in rock engineering

This page intentionally left blank

Rock Mechanics for Resources, Energy and Environment – Kwaśniewski & Łydżba (eds)
© 2013 Taylor & Francis Group, London, ISBN 978-1-138-00080-3

Rock engineering design and the evolution of Eurocode 7

L.R. Alejano
University of Vigo, Spain

A. Bedi
Imperial College, UK

A. Bond
Geocentrix, UK

A.M. Ferrero
University of Parma, Italy

J.P. Harrison
University of Toronto, Canada

L. Lamas
LNEC, Portugal

M.R. Migliazza
University of Milan, Italy

R. Olsson
NGI, Norway

Á. Perucho
CEDEX, Spain

A. Sofianos
NTUA, Greece

H. Stille
KTH, Sweden

D. Virely
Laboratoire régional des Ponts et chaussées de Toulouse, France

ABSTRACT: The Eurocode for Geotechnical Design, EN-1997-1:2004, informally known as Eurocode 7 or EC7, was fully implemented within the European Union in 2010. This Eurocode is intended to apply to all geotechnical engineering design, including rock engineering. In recognition that all codes must continue to evolve in order to remain applicable, and the long time that such evolution takes, work is already underway under the auspices of the European Committee for Standardisation, CEN, to identify how the code should develop for future revisions. This paper presents a summary of the maintenance procedures for Eurocodes in general and the specific maintenance work currently being undertaken on EC7 in respect of rock engineering design. It also highlights potential future development of EC7, and the need for enthusiastic involvement by the European rock engineering community to direct these developments.

1 INTRODUCTION

Standardisation is an integral part of a number of important EU policies that are concerned with better regulation, simplification of legislation, increase in competitiveness and removal of barriers to trade. As a result, the standardisation process is highly developed with the EU.

In the realm of structural engineering, the standardisation process has led to the development of a linked coherent set of standards — the so-called Structural Eurocodes — that govern construction and design.

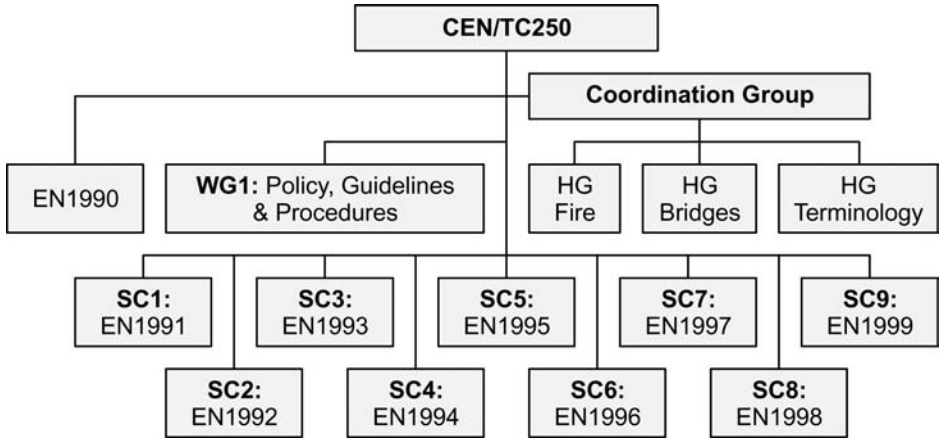


Figure 1. Structure of CEN/TC/250 (http://eurocodes.jrc.ec.europa.eu).

In this paper we explain the EU's standardisation process, the development and introduction of the standard for Geotechnical Design, EN-1997-1:2004 (CEN, 2004), informally known as Eurocode 7 or EC7, and the manner in which this standard is maintained. We present in detail the maintenance work that is currently underway, and highlight some issues of long-term, and hence future, importance.

2 DEVELOPMENT OF EUROPEAN STANDARDS

Within the EU, the process of standardisation is based on consensus amongst different groups such as industry and public authorities, and is undertaken by independent standards bodies. The development of formal European Standards (EN) is the responsibility of the European Standards Organisations (ESO), of which there are three:

- CEN (Comité Européen de Normalisation/ European Committee for Standardisation) which deals with all sectors except electrotechnology and telecommunication;
- CENELEC (Comité Européen de Normalisation Electrotechnique/European Committee for Electrotechnical Standardisation) which deals with electrotechnical standards; and
- ETSI (European Telecommunications Standards Institute) which covers telecommunications and some aspects of broadcasting.

In addition to the formal EN standards, these organisations also produce Technical Specifications, Technical Reports and Guides.

The organisation that has responsibility for standards that apply to rock engineering design and construction is CEN.

2.1 *CEN and structural Eurocodes*

CEN comprises a number of Technical Committees, of which one — CEN/TC250 — is responsible for all of the so-called 'Structural Eurocodes'. These govern all aspects of design and construction related to structural engineering, including geotechnical engineering. The tangible history of the Eurocodes can be traced to 1971, as shown in Table 1.

Table 1. History of Eurocodes.

Year	Event
1971	Public Procurements Directive 1971/305 issued
1975	Eurocode development started
1980	International Inquiry with regard to construction codes performed
1984	First Eurocodes published
1989	Construction Products Directive 1989/106 issued
1990	Work on draft standards (ENVs) started
1992	Publication of ENV Eurocodes commenced
1998	Conversion of ENVs to ENs initiated
2003	EC recommendation on implementation and use of Eurocodes
2004	Directive on Public Works contracts, Public Supply contracts and Public Service contracts issued
2006	Publication of ENs completed
2010	Full EN implementation; conflicting National Standards withdrawn

One aspect of the development shown in Table 1 that is often not grasped is that in 2010 the EN Eurocodes became reference design codes for the purposes of the following: proving compliance with the essential requirements of the Construction Products Directive; offering a basis for specifying contracts; and, giving a framework for drawing up harmonised technical specifications for construction. In As a result, the EN Eurocodes are now the standard technical specification for all European public works contracts, and all designs must demonstrate that they are technically equivalent to an EN Eurocode solution. Taken together, these statements show that it is critical for designers of rock engineering solutions within the European Union to be fully conversant with the relevant EN Eurocodes.

Table 2. Sub-committees of CEN/TC250 and the Eurocode for which they are responsible.

Sub-committee	Eurocode	Title
SC1	EN1991	Actions on structures
SC2	EN1992	Design of concrete structures
SC3	EN1993	Design of steel structures
SC4	EN1994	Design of composite steel and concrete structures
SC5	EN1995	Design of timber structures
SC6	EN1996	Design of masonry structures
SC7	EN1997	Geotechnical design
SC8	EN1998	Design of structures for earthquake resistance
SC9	EN1999	Design of aluminium structures

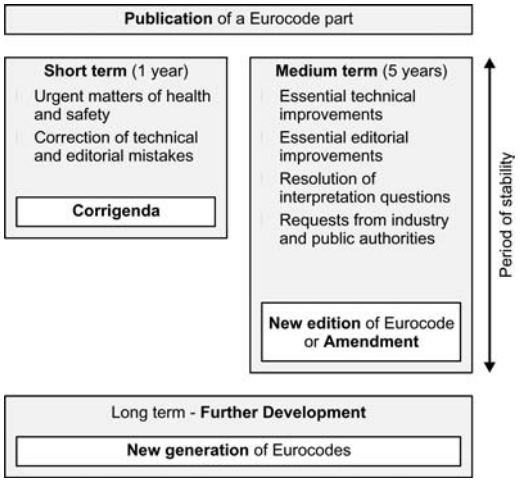


Figure 2. The Eurocode maintenance work programme (http://eurocodes.jrc.ec.europa.eu).

CEN/TC250 has the responsibility of establishing general policies, programmes and strategies for the Structural Eurocodes, and to oversee their implementation. It also supports and guides its sub-committees in achieving these policies and objectives during any code drafting work.

The membership of CEN/TC250 and its sub-committees comprises delegates of the 29 CEN National Members, together with delegates from the 5 Affiliates (i.e. countries likely to become members of the EU or EFTA) participating as observers. The general structure of CEN/TC250 is shown in Figure 1. In addition to three Horizontal Groups (HG) that work across subject boundaries and a group (WG1) that ensure policy, guidelines and procedures are being followed, there are nine specialist sub-committees each of which is responsible for a particular Eurocode (Table 2). Thus, CEN/TC250/SC7 is responsible for Eurocode 7.

3 MAINTENANCE OF EUROCODES

In addition to the development of the EN Eurocodes, under the rules governing the operation of CEN, its committees and sub-committees, a critical responsibility is that of code maintenance. This activity is essential in order to preserve the credibility, integrity and relevance of the Eurocodes, as well as to ensure that they do not contain errors.

As a balance between the competing desires of frequent correction and a period of stability that supports industrial implementation, the normal maintenance cycle has been set at five years. Maintenance commences as soon as a draft Eurocode has been accepted (i.e. when an ENV is published as an EN), and comprises all activities connected with the updating of the codes in the light of practical experience of their use. The maintenance process is illustrated in Figure 2 and is arranged as follows:

– Short term (immediate or within one year). This includes urgent correction of errors, preparation of essential technical amendments with regard to urgent matters of health and safety, essential technical and editorial improvements (e.g. mistakes in symbols, typographical mistakes), elimination of inconsistencies and misleading statements, and resolution of questions of interpretation, resulting from feedback from the use of the Eurocodes.
– Medium term (the normal five-year review cycle). Technical and editorial improvements, the resolution of questions of interpretation, and requests from industrial organisations and public authorities fall into this category. If necessary, a new edition or amendment to the Eurocodes may be published.
– Long term (greater than five years). This contains matters relating to development of new items (e.g. emerging requirements that are not covered by the existing Eurocodes). It includes new material and concepts that require research, and thus may be considered as development.

Thus, CEN/TC250 is now involved in the first of these five-year maintenance cycles, the outline programme for which is shown Table 3.

A key event in this cycle is the publication by the EU of Programming Mandate M/466. Although broad in its content, this specifically asked for the following developments:

– reduction in the number of Nationally Determined Parameters (NDPs);
– incorporation of results from recent international studies, including performance-based and sustainability concepts;
– simplification of rules for limited and well-identified fields of application;
– development of auxiliary guidance documents to facilitate implementation

These all support the principles of maintaining credibility, integrity and relevance of the Eurocodes.

Table 3. Maintenance programme for the Structural Eurocodes.

Year	Event
2010	March: National Standards withdrawn
2010	May: EU issues programming mandate M/466
2013	October: deadline for receipt of 5-year review comments
2015	October: Draft revisions of Eurocodes available
2018	October: Second generation of Eurocodes available

4 MAINTENANCE OF EUROCODE 7

In response to Programming Mandate M/466, CEN/TC250/SC7 undertook a survey of National Standards Bodies (NSBs) in order to identify the key maintenance issues regarding EC7. The responses covered the entire range of geotechnical design, but tended to emphasise soil mechanics issues. The ten most popular topics identified for development were:

1. improved guidance on selection of water pressures;
2. simplification/reduction of Design Approaches;
3. guidance on use of numerical modelling;
4. new content regarding reinforced soil;
5. improved general guidance on selecting characteristic soil parameters;
6. improved link to EC8 for seismic design;
7. harmonisation of NDPs;
8. partial factors for different classes of consequence;
9. removal from EC7 Part 2 of material readily found in text books; and
10. improved guidance on buoyancy and hydraulic failure.

Despite the use in item 5 of the word 'soil', items 2, 3, 5, 6, 7, 8 and 9 are directly relevant to rock engineering.

In late 2011 CEN/TC250/SC7 formed a number of Evolution Groups (EGs), shown in Table 4, to further identify both the immediate maintenance requirements and future development of EC7. The membership of the EGs comprises over one hundred experts from industry and academia across the whole of Europe.

The subjects represented by these groups clearly correspond with both the wishes of M/466 (e.g. reduction in NDPs, simplification of rules for well-identified applications) and the topics identified by the NSBs.

To realise the EGs, in late 2011 SC7 appointed members to EG0, who in turn identified a small number of initial provisional members for each EG. Following this, and with guidance from EG0, each EG revised and expanded its own membership. For each EG, the aim has been to ensure representation from across as much of Europe as possible, subject to the constraint of keeping a modest membership. In accordance with the operating procedures of CEN/TC250/SC7, the membership of all individuals appointed to each EG is required to be ratified by the NSB of the country the individual represents. The current (March 2013) membership of EG 13 is shown in Table 5.

Table 4. EC7 Evolution Groups.

Group	Subject	Group	Subject
EG0	Management and oversight	EG1	Anchors
EG2	Maintenance and simplification	EG3	Model solutions
EG4	Numerical methods	EG5	Reinforced soil
EG6	Seismic design	EG7	Pile design
EG8	Harmonisation	EG9	Water pressures
EG10	Calculation models	EG11	Characterisation
EG12	Tunnelling (not convened)	EG13	Rock Mechanics
EG14	Ground improvement		

Table 5. Membership of EG13.

Member	Country	Member	Country
L.R. Alejano	Spain	A. Bedi	UK
A. Bond	UK	A.M. Ferrero	Italy
J.P. Harrison	UK	L. Lamas	Portugal
M.R. Migliazza	Italy	R. Olsson	Norway
Á. Perucho	Spain	A. Sofianos	Greece
H. Stille	Sweden	D. Virely	France

As for all EGs, the principal duty of EG13 is to produce by the end of September 2013 a report outlining the medium- and long-term maintenance requirements of EC7.

5 THE WORK OF EG13

In order to develop its work programme and hence the structure its report to EG0, the members of EG 13 sought comments from rock engineering practitioners, held regular teleconferences, and on those occasions when circumstances permitted (e.g. Eurock 2012) small groups of members met in person. In addition, liaison with the other EGs took place both by correspondence and at occasional Convenors' Meetings. The work of EG13 is set out below.

5.1 *Interaction with other EGs to improve integration of rock mechanics within EC7*

Early in the work of EG13 a general view developed among the members that the integration of rock engineering within EC7 was suboptimal. As a result, it was felt that there was the potential for substantial interaction with the work of the other EGs. The intention was that such interaction would help the other EGs recognise the special design challenges posed by those

attributes of fractured rock masses with which rock engineering designers are familiar (e.g. discontinuities, heterogeneity, anisotropy), thereby improving the embodiment of rock engineering requirements within EC7. As a result, interaction took place with EG2, EG3, EG4, EG8, EG10 and EG11.

5.2 *Critical review of EC7 with regard to rock mechanics*

As written, although many sections of EC7 are directly applicable to rock engineering they either omit to specifically refer to rock engineering or suggest nomenclature, approaches or techniques that are not in general use in rock engineering. This has the effect of making EC7 difficult to apply, or even seemingly inapplicable, to rock engineering. The first of these shortcomings is unintended, and the second manifestly untrue. Thus, a critical review of EC7 was undertaken, specifically to allow identification and suggestions for improvement of those clauses that are deficient with respect to rock engineering practice.

5.3 *National Annexes*

The detail to which rock mechanics and rock engineering is included within National Annexes varies, possibly as a result of the varying balance of soils to rock engineering within different countries. Given the deficiencies noted in 5.2 above, a review of all NAs was undertaken to identify those procedures and concepts that could be included within the main body of the code.

5.4 *Vocabulary and definitions*

In many places, EC7 uses vocabulary and definitions that are inconsistent with those generally encountered in rock engineering. Thus, a thorough review of EC7 was performed in order to identify all vocabulary and definitions that differ from those in customary rock engineering use, and make suggestions for improved wording.

5.5 *Design implementation and monitoring*

Generally, the rock excavation process (e.g. blasting) leads to an excavation geometry that differs from the one assumed in the design, and may also reduce the strength and stiffness of the surrounding rock mass. Consequently, design implementation is a critical aspect of the rock engineering design process. Associated with this is the issue of monitoring: instrumentation is installed in many rock slopes and most underground openings in order to both guide the construction process and confirm the final performance of the structure. Although both design implementation and monitoring procedures are considered briefly in EC7, they are not covered to the detail required for rock engineering. As such, recommendations are being made regarding improvements to these important aspects.

5.6 *Laboratory and field tests*

Part 2 of EC7 includes a large number of rock mechanics laboratory and field tests, but the appropriateness of some of these and the comprehensiveness of the list (e.g. there is no guidance on determining the strength of anisotropic rock) is questionable. A list of recommended rock mechanics laboratory and field tests is thus being prepared.

An additional question is whether — as a reference design code — it is necessary for EC7 to refer to other ENs, or whether it can refer to documents such as the ISRM Suggested Methods. This is not a question that EG13 can answer, but it is one that will be presented to SC7.

5.7 *Characterisation of rock and rock mass model*

Current rock engineering practice is based on the characterisation of rock masses in order to determine appropriate methods of analysis. Unfortunately, EC7 offers insufficient guidance on this critical aspect of engineering practice.

The work of EG13 is to review characterisation philosophies and methods in general rock engineering practice, and identify those that are suitable for inclusion in EC7. In addition, recommendations are being made regarding potential contextual locations (i.e. related to the subject matter, not absolute section numbers) within EC7 for the inclusion of guidance on characterisation methods and their use in rock engineering design.

5.8 *Design by prescriptive measures*

EC7 suggests that prescriptive measures may be applied in those situations where calculation models are not necessary, and generally 'involve conventional and generally conservative rules in the design, and attention to specification and control of materials, workmanship, protection and maintenance procedures'. Although some countries use prescriptive measures for some rock engineering designs, in general it is not clear to which rock engineering situations this applies or how it connects to the use of empirical or observational approaches, both or which are widely used in rock engineering. These issues are being investigated, and suggestions will be made as to how the concept of prescriptive measures can be clarified and improved with regard to rock engineering.

5.9 *Analytical and empirical model*

A spectrum of models ranging from the completely analytical through to wholly empirical are used in rock engineering practice, with selection of a particular model for a given project being made by various informal, subjective and *ad hoc* methods. Currently,

EC7 gives no guidance on how an appropriate modelling approach should be selected. This is intimately connected with the issue of characterisation described in 5.7 above.

EG13 will make suggestions as to how guidance in respect of model selection could be included in EC7.

5.10 *Use of partial factors*

As a limit state design code that assumes variability in loads and materials properties is a stochastic phenomenon, EC7 makes extensive use of partial factors to characterise this variability. Although this approach has a long history in structural engineering, and to some extent in soils-related geotechnical engineering, there has been very little development of partial factors in rock engineering. Why this is so is not clear, but it may be due either to a simple lack of the development of such factors by the rock engineering community or the recognition that some characteristic of rock mechanics properties precludes their development. Both of these aspects are being explored by EG13, and the Group's report will offer suggestions as to how the use of partial factors in rock engineering can be clarified.

5.11 *Observational method*

The observational approach is widely used in rock engineering, and represents a close coupling of the construction and design processes such that both the design and design implementation are continually revised during the construction process. It is not clear that the provisions within EC7 for use of the observational method are properly appropriate for rock engineering works, and so suggestions will be made for improving these provisions.

6 FUTURE DEVELOPMENT OF EUROCODE 7

As has been explained above, EC7 is currently undergoing a normal five-year review as part of the standard maintenance cycle. This review will identify medium term revisions. The maintenance cycle also includes long term developments, and it is important that the rock engineering community comes together to identify what is required in this respect. Some required future developments seem clear: for example, EC7 gives no guidance on how to measure and characterise *in situ* stress, nor is it currently applicable to underground excavations (this is one reason why EG12, Tunnelling, was not convened as part of the current five-yearly review). There is also no guidance on the design of rock slopes, which may be the largest single area of work in rock engineering.

The development of EC7 to incorporate these, and other as yet unidentified areas of rock engineering endeavour is a major undertaking that will require many years of dedicated work. By necessity, this work will need to involve the whole rock engineering community of constructors, designers and academics from across the entire EU.

As a first step, and building on the work of EG13, the organisers of Eurock 2014 in Vigo, Spain, are intending to convene a workshop that will hopefully initiate this development. The amount and nature of the work required to develop EC7 for rock engineering means there is the potential for many such meetings in the coming years.

7 CONCLUSIONS

The introduction of EC7 will dramatically affect the practice of rock engineering throughout the EU. Although EC7 only became a reference design code in 2010, the first five-yearly cycle of medium term maintenance is now underway. Under the auspices of a CEN Technical Committee, an Evolution Group comprising experts representing a wide number of countries is engaged on identifying those aspects of EC7 that deserve revision. Finally, the long term development of EC7 is yet to be decided, and it seems that the entire rock engineering community within the EU has a critical role to play in this regard.

ACKNOWLEDGEMENTS

The work undertaken by two earlier members of Evolution Group 13 — namely, Dr Claus Erichsen (Germany) and Dr Tatiani Rotunda (Italy) — is warmly appreciated.

REFERENCE

CEN (European Committee for Standardisation). 2004. Geotechnical Design: Part 1, General Rules. EN-1997-1. Brussels, Belgium: CEN.

Rock Mechanics for Resources, Energy and Environment – Kwaśniewski & Łydżba (eds)
© 2013 Taylor & Francis Group, London, ISBN 978-1-138-00080-3

Risk management approach for the design of underground constructions

B. Amusin
ACI, New York, USA

J. Eisenberg
Rutgers, New Jersey, USA

ABSTRACT: Traditional design methods for mining, tunneling and public underground constructions use deterministic approaches. Reliability requirement for these constructions became very high and deterministic approaches lead to introduction of overpriced Factors of Safety (FS). It is more appropriate to select an optimal support based on the risk focused management approach. The Monte-Carlo method for statistical simulation is recommended for the design of underground constructions. As the first step we use simplified approach based on a plausible assumption that variation in the stress and the strength of rock mass, rock pressure manifestation, and support capacity can be described by the normal distribution law.

1 INTRODUCTION

Karl Terzaghi was one of the first specialists who underlined the importance of risk management in the design of geotechnical structures (Terzaghi 1982). He considered risk management as a process of balancing economy and safety. During the last 50 years of quantitative analysis of probability failure for different constructions was developed and discussed in numeral workshops and international conferences (Whitman 1984, Baecher & Christian 2003, Chowdhury & Flentje 2008). However, application of modern probabilistic solutions in design practice is still limited because of rather poor current statistical estimates of the initial data and results. These solutions can not adequately describe the complicated multifactorial process of rock deformations around underground openings and interaction support with rock mass. Risk management for the design of underground construction shall take into account uncertainties associated with the stress and the strength of rock mass as well as uncertainties of construction and technology:

- Uncertainties of the initial geological, geomechanical parameters:
  - strength and creep properties of the rock mass around opening
  - stress state in the rock mass
  - dip angle of the rock seams
- Uncertainties of the technological condition:
  - dimension of the opening cross-section
  - rate of opening driving
  - opening direction in respect to strike direction
  - type of construction: drill-and-blast or TBM
  - distance and time support installation from the face
  - type of support: concrete, anchor or yielding support
  - contact condition: full contact or contact with rubblework behind contour
  - type of opening: separate, chamber, parallel or junction of the openings
- Uncertainties of the strength and deformation characteristics of the support
- Uncertainties of the design methods

These uncertainties have different effect on bottom-line results. Method of Monte Carlo can provide a sensitivity analysis to determine factors which have the maximum impact on the results. Traditional design methods for mining, tunneling, and public underground constructions use different deterministic approaches: empirical, theoretical, and the theoretical-experimental. All these methods also require statistic of field measurements of rock pressure manifestation for their calibration.

The empirical methods, based on poor statistical and verisimilar hypothesis, are often unreliable, especially for prediction load on the support. Theoretical methods are still not very practical because of uncertainty of the initial data and inadequately theoretical models to the real mechanism of the rock pressure manifestation.

A more reliable design approach would be the theoretical-experimental method TEM (Amusin 1994, Amusin & Eisenberg 2009).

In this method, the theoretical model describes the mechanism deformation and interaction support with rock mass. Discrepancies of the model are corrected

with the introduction of empirical and semi-analytical factors, which take into account important geomechanical and technological parameters.

Reliability requirement for underground constructions became very high. At the same time deterministic approach leads to introduction of overpriced safety factors.

The optimal support shall be selected based on the risk management approach. This approach determines the optimal solution based on two criteria: minimal cost and permissible safety.

The purpose of this paper is to develop a risk design management approach for calculation of an optimal factor of safety.

The factor of safety is considered optimal if it provides minimum total cost with maximum relia- bility of the opening. The total cost is determined by summing the construction and the maintenance cost.

The construction cost includes the cost of opening advance coupled with the cost of the support with reinforcement. The construction cost for important and expensive projects can also include expenses for additional geological exploration and/or simple short term measurements (Amusin et al. 1992), in order to decrease deviation in the initial data. The maintenance cost during construction includes cost of demurrage and cost of support repair. The maintenance cost can also include additional cost of periodic inspections and repair work during and after completion of construction. Such approach could be particularly well suited for minor openings, to decrease construction cost without compromising safety. For collecting statistics and to conduct statistical analysis, we recommend using the Monte-Carlo method of numerical simulation. Initial parameters, according to the Monte-Carlo, are introduced as mean values with coefficients of variation. They are calculated randomly for each cycle of simulation from all diapason of the initial parameters using a random number generator. Finally, the statistic of the results can be collected, after multiple cycles of calculations.

As the first step, we use a simplified risk management approach based on verisimilar assumption that variation of the stress and strength of the rock mass, rock pressure manifestation, and support capacity can be described by normal distribution law. To calculate the maximum, minimum, and mean values of the rock pressure manifestation and the required support capacity deterministic method can be used. We recommend using the program TUNNEL, which is developed based on the deterministic TEM.

2 SIMPLIFIED RISK MANAGEMENT APPROACH

The simplified risk management approach is based on the following verisimilar assumptions:

- Statistics of the initial data and results can be described by normal distribution (bell curve);
- Maximum, mean and minimum values of the rock pressure manifestation are determined based on deterministic design method;
- The maximum is determined by the same design method for increased initial stress state by value $(1 + \nu_i)$ and decreased initial strength of rock mass by value $(1 - \nu_i)$, where ν_i is the coefficient variation for the initial data. For simplification we use the same coefficient variation for all initial data;
- The minimum of the rock pressure manifes- tation is determined for decreased initial stress state by value $(1 - \nu_i)$ and for increased initial strength of rock mass by value $(1 + \nu_i)$;
- The maximum value $x_{\max}$ corresponds to 3σ; the minimum $x_{\min}$ corresponds to -3σ;
- Coefficient variation of the support capacity ν_s does not change with support reinforcement;
- Standard deviation σ of the results is deter- mined by Eq.:

$$\sigma = (x_{\max} - \bar{x})/3 \tag{1}$$

Table 1. z – values depend on probability (p).

p, %	70	80	90	95	99.7
z	0.53	0.84	1.28	1.64	2.75

Based on the program TUNNEL we estimate mean, maximum and minimum values of the rock pressure manifestation: load on the support (P) and support capacity (P_{sc}). The mean values $\bar{x}$ are calculated for $\nu_i = 0$ and they are designated accordingly as: $\bar{P}$, $\bar{P}_{sc}$. Calculation procedure for finding the optimal risk and confidence level of the opening reliability can be done as follows:

a) Find load, which does not exceed maximum value of the load P with probability$p$, %:

$$P = \overline{P} + z \times \sigma \tag{2}$$

where standard z – score is determined from the standard z – table of the normal distribution law depending on probability p.

b) Find required factor of safety (FS) for given support with mean value of the support capacity $\bar{P}_{sc}$ corresponds to the maximum load P from Eq.:

$$x = \bar{x} + z \times \sigma \tag{3}$$

where: $x = P$; $\bar{x} = \bar{P}_{sc} \times FS$; $\sigma = \bar{P}_{sc} \times FS \times v_s$; v_s is coefficient variation for the support capacity; z – value corresponds to probability of the opening failure p_f: Finally, factor safety can be found from Eq. (3), after substitution all values in it:

$$FS = P / \overline{P}_{sc} \times (1 + z \times v_s) \tag{4}$$

c) Repeat calculations steps a) and b) for different probability levels: $p = 70\%$; $p = 80\%$; $p = 90\%$;

Table 2. z – values as function of probability (p_f).

p_f	30	20	10	5	0.3
z	−0.53	−0.84	−1.28	−1.64	−2.75

$p = 95\%$; $p = 99.7\%$ and risk levels of construction failure accordingly: $p_f = 30\%$; $p_f = 20\%$; $p_f = 10\%$; $p_f = 5\%$; $p_f = 0.3\%$.

d) Estimate construction cost and maintenance cost for each risk level p_f.

e) Find optimal confidence level of the opening reliability corresponding to minimum total cost.

3 EXAMPLE OF THE RISK MANAGEMENT FOR SUPPORT SELECTION

The optimal safety factor is determined according to sequence a)–e) above. Let's consider an opening with width and height B = 6 m located at depth $\bar{H} = 1000$ m in siltstone ($\gamma = 2.5\, t/m^3$) with compressive sample strength $\bar{S}_c = 75$ MPa, angle of internal friction $\varphi = 30^0$; RQD = 40; opening is advanced with rate V = 5 m/d by drill & blast method; rigid reinforce concrete support is installed in $t_1 = 2$days at L = 10 m from the face of opening ($L = V \times t_1$). All voids behind the support are back filled with rubblework and cementation to create a full contact support with rock mass. Parameters of the rock pressure manifestation were calculated by the program TUNNEL. The maximum values $x_{\max}$ were determined for the maxi- mum initial stress (γH) and the minimum strength S_c:

$$\gamma H = \gamma \bar{H} \times (1 + v_i); \quad S_c = \bar{S}_c \times (1 - v_i) \tag{5}$$

The minimum stress and maximum strength were used as initial data in order to determine minimum rock pressure manifestation $x_{\min}$:

$$\gamma H = \gamma \bar{H} \times (1 - v_i); \quad S_c = \bar{S}_c \times (1 + v_i) \tag{6}$$

Calculations were provided for two variants of the coefficients variation of the initial data: $v_i = 0.2$ and $v_i = 0.1$. Results of calculations are shown in Table 3.

Bell curves were constructed for the load on the support for the final time t = 15 years (see Fig.1a), based on our verisimilar assumptions and results of calcu- lations, presented in Table 3.

Finally, for our example we received: for $v_i = 0.2$ $\bar{P} = 539$ kPa, $\sigma = 116.3$ kPa, $v_r = 0.215$ and for $v_i = 0.1$ $\bar{P} = 539$ kPa, $\sigma = 56.7$ kPa, $v_r = 0.105$. Our approach for calculation factor of safety (FS) for $v_i = 0.2$ and probability levels, p = 70% (risk factor $p_f = 30\%$ accordingly) is illustrated on Fig 1b. The load P can be determined by Eq. (2) and Table 1: $P = \bar{P} + z \times \sigma = 539 + 0.53 \times 116.3 = 600$ kPa. So for acceptable stability level $p = 70\%$ max load on the support does not exceed $\bar{P} = 600$ kPa. Values of the load P for other probability levels p and coefficients variation $v_i = 0.2$ and $v_i = 0.1$ are presented in Table 4.

Table 3. Load on the support (P) depends on time (t) and coefficient variation (v_i).

v_i	t, days	1	10	30	90	15 years
0	$\bar{P}$, kPa	31	138	288	405	539
0.2	max P, kPa	44	241	442	526	888
	min P, kPa	21	79	190	279	305
0.1	max P, kPa	36	172	340	442	709
	min P, kPa	24	114	240	352	428

Table 4. Maximum load (P) depends on probability (p) and coefficients variation (v_i).

p, %		70	80	90	95	99.7
P, kPa	$v_i = 0.2$	600	637	688	730	859
	$v_i = 0.1$	569	587	612	632	695

Table 5. Required factor of safety (FS) depends on probability p_f and coefficients variation v_i and v_s.

	$v_i = 0.2$		$v_i = 0.1$	
p_f	$v_s = 0.2$	$v_s = 0.1$	$v_s = 0.2$	$v_s = 0.1$
30	1.34	1.27	1.27	1.20
20	1.53	1.38	1.41	1.28
10	1.85	1.58	1.64	1.40
5	2.17	1.75	1.88	1.51
0.3	3.82	2.37	3.09	1.92

Reinforce concrete support with capacity $\bar{P}_{sc} = 500$ kPa is recommended for mean condition by the program TUNNEL. Assume a coefficient variation for the support capacity is $v_s = 0.2$. The factor of safety for the risk factor $p_f = 30\%$ is determined by Eq. (4) and Table 2:

$$FS = P / \bar{P}_{sc} \times (1 + z \times v_s) = 600/500 \times (1 - 0.53 \times 0.2) = 1.34.$$

So, capacity of the support shall be increased in 1.34 times in order to provide stability level $p = 70\%$.

The same procedure is used to determine FS for all other diapasons of the risk level (probability of the failure) p_f and coefficients of variation for initial data v_i and support capacity v_s.

Results of calculation of the required FS are presented in Table 5.

If the project is an important tunnel or major mining opening (transportation or ventilation arteries), for which failure would cause huge or even catastrophic losses, designer introduces a high value factor of safety sometimes without sufficient justification.

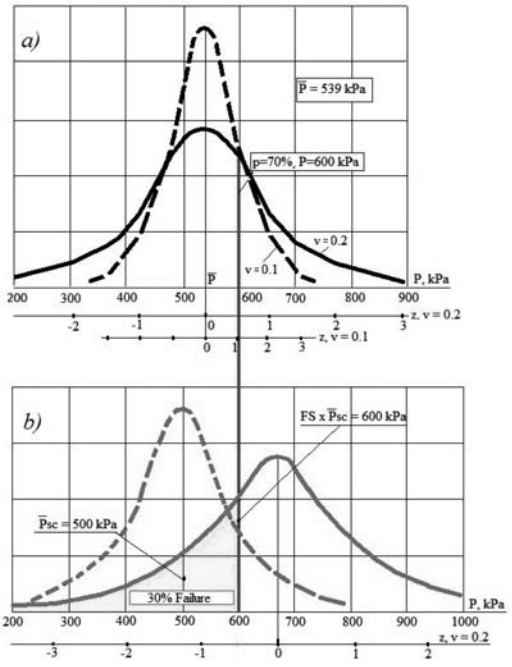


Figure 1. Determination of the factor safety (FS)
a) bell curve of the load distribution for $v_i = 0.2$ and $v_i = 0.1$
b) bell curve of the support capacity distribution for $v_s = 0.2$
– – bell curve for a given capacity of the support
—— bell curve for required support capacity

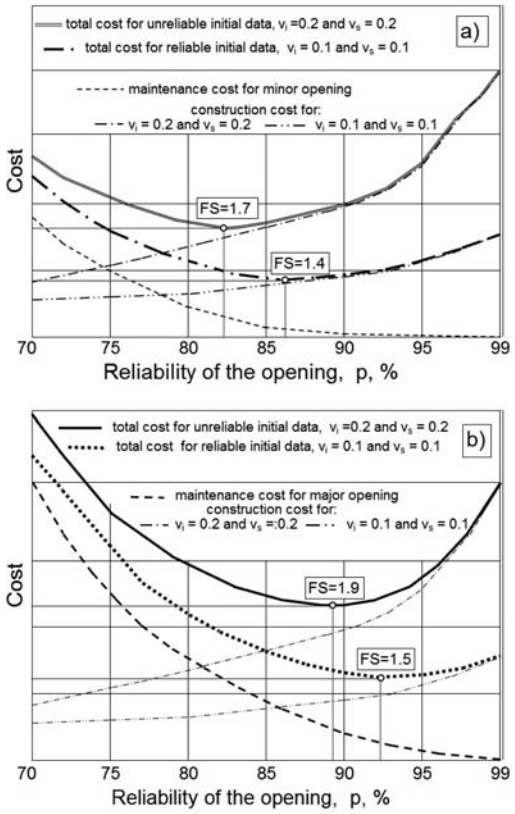


Figure 2. Optimal reliability for minor (a) and major (b) openings.

A cost of construction and maintenance cost substantially depend on the factor of safety. It becomes unreasonably high if uncertainties of the initial data and support parameters are high. For example, the required factor of safety for confidence level $p = 95\%$ could be decreased in 1.44 times from FS = 2.17 to FS = 1.51 if coefficients of variation decrease from $v_i = 0.2$ and $v_s = 0.2$ to $v_i = 0.1$ and $v_s = 0.1$. The factor of safety for confidence level $p = 99.7\%$ could be decreased in 2 times from FS = 3.82 to FS = 1.92.

Approach for the finding of optimal solutions is presented in the Fig 2a and 2b for the minor and major openings respectively.

We did not estimate the cost of construction and maintenance cost in our example, leaving it to be done by a professional estimator based on standard routines. Nevertheless, we use a conditional cost for the analysis since cost and safety factor are almost proportional. Important quantitative analysis can be done even based on the conditional cost.

The optimal cost of the construction can be substantially decreased and reliability of the opening can be increased if we diminish dispersion of the initial data and support capacity.

Additional geological survey can sometimes provide a more economical design solution for major constructions because it decreases factor of safety without compromising the safety of construction. Designer may choose to go one step further to provide clarification of the initial data using back analysis method during the construction (Amusin et al. 1992).

Another resource for decreasing factor of safety and accordingly decreasing the total cost is minimization of the uncertainties for support capacity. For example, proper quality control of the cast in place concrete might substantially decrease uncertainties due to human performance and accordingly decrease coefficient variation of the support capacity.

Replacement monolithic concrete support with tubing, precast segments, or block support can eli-minate requirement for the field quality control of the concrete and decrease required safety factor.

Proper filling space behind support with rubblework and cementation can increase support capacity, decrease the coefficient variation of the support capacity and accordingly decrease required safety factor.

4 CONCLUSIONS

The purpose of the risk management includes finding a rational balance between cost and safety. Design solutions for an appropriate support of underground

construction can be found through minimization of the total cost with variation of the safety factors.

It was shown that the optimal safety factor for the different type of underground constructions can be found even based on the simplified approach. Our analysis confirms that the higher factor of safety and the respective higher cost of construction are required for higher scatter of geomechanical and technological initial data. That is why more extensive exploration can decrease uncertainties of the initial data and accordingly decrease total cost, while providing the same level of reliability. Short term measurements in the opening or prototype opening, driven in similar condition, can also decrease deviation of the initial data. The designer can modify the project during the construction based on analysis of the preliminary field measurements. This approach is especially effective for important and expensive underground constructions. In addition, quality control of the construction can substantially decrease dispersion of the support capacity and accordingly decrease required safety factor as well as the respective cost of construction.

If the project involves a minor opening, for which a partial failure would cause only modest economic loss, the designer could try to achieve greater economy by allowing a greater risk of failure without compromising the safety such as to provide periodic inspection and the required repair. One direct result of our approach is the ability to identify the parameters whose uncertainty contributes most strongly to the probability of failure.

We hope that our presentation will serve as a catalyst to promote a more comprehensive study by engineers, scientists, economists, and contractors who have extensive experience in dealing with risk and cost management in geomechanical projects.

REFERENCES

Amusin B., Shick V. & Lama R. 1992. Using back analysis to estimate geotechnical field parameters for the design of support system for tunnels. *Tunneling and Underground Space Technology*, Vol.7, N.3, 281–284.

Amusin, B. 1994. Method for design support of underground constructions. *International Conference "Underground Opening for Public Use" Glovik, Norway 14–17 June, 1994*, 65–77.

Amusin, B. & Eisenberg, J. 2009. Rock mass classifications and support design for underground construction. 5th Colloquium "Rock Mechanics – Theory and Practice. Mitteilungen für Ingenieurgeologie und Geomechanik", Nov. 26–27, 2009, TU-Wien, Austria.

Baecher, G. & Christian, J. 2003. Reliability and statistics in geotechnical engineering, 618p

Chowdhury, R. & Flentje, P. 2008. Strategic approaches for management of risk in geomechanics. In *Proceedings of the 12th International Conference of International Association for Computer Methods and Advances in Geomechanics. Goa, India, 1–6 October 2008*, 3031–3042.

Terzaghi Lectures, 1974–1982, ASCE 1982, 435 p.

Whitman R.V. 1984 Evaluating 'calculated risk' in geotechnical engineering. *Journal of Soil Mechanics and Foundation Division, ASCE, vol. 110*, No. 2, p 145–188.

This page intentionally left blank

Rock Mechanics for Resources, Energy and Environment – Kwaśniewski & Łydżba (eds)
© 2013 Taylor & Francis Group, London, ISBN 978-1-138-00080-3

A new design approach for rockfall barriers

A. Grimod
Maccaferri Canada Ltd, Cambridge, Canada

G. Giacchetti
Officine Maccaferri SpA, Bologna, Italy

ABSTRACT: the design of rockfall barriers requires analytical simulations of the trajectories of the falling blocks along the slope. The easiest way to design these structures is by comparing the energy level defined by the numerical analysis with the results of the full-scale test carried out according to ETAG 027/2008 ("Guideline for European Technical Approval of Falling Rock Protection Kits"). This is the guideline used by the manufacturers to test their rockfall fences. Unfortunately this approach has a lot of uncertainties because it does not take into consideration all the technological limits of the rockfall barriers and the installation issues. This paper illustrates the procedure of a new design approach based on the Italian norm UNI 11211:12, the European Guideline ETAG 027/2008 and the in-situ experience of Maccaferri in the rockfall protection field.

1 INTRODUCTION

1.1 *Rockfall barrier*

Rockfall barriers are generallycomprised of a number of components:

- steel posts (support structure), spaced from 8 to 12 m;
- upper and lower longitudinal steel cables;
- lateral and upslope steel bracing cables;
- energy dissipation devices, able to increase the energy absorption of the fence;
- an interception structure (steel mesh).

The barriersare then anchored to the soil by foundations. These elements have the function to transmit the loads of the impact to the ground.

ETAG 027/2008 (reference paragraph 2.4.3.2 of ETAG 027/2008) classifies asa deformable rockfall barrier, a structure able to absorb an energy no lower than 100 kJ (350 kg travelling at 90 km/h). It does not define any upper energy limits, but at the present the record for the highest energy capacity fence belong to the RMC 850/A, which is able to absorb an energy higher than 8500 kJ (27 t travelling at 90 km/h).

Rockfall barriers are passive measures used to protect structures and infrastructures from rockfall events. Their main advantages are: they are able to protect largerock surfaces, which would be impossible, for economic reasons, to cover with drapery mesh, they are able to absorb high energy levels, they can be installed in most location and morphological conditions, they can be easily installed on vertical slopes, and they are systems that have been tested and certified byrecognized Approval Bodies.

1.2 *The European Guideline ETAG 027-2008*

The European Guideline for Technical Approval of Falling Rock Protection Kits (ETAG 027) was issued in 2008 by the European Organization for Technical Approval (EOTA). Nowadays, it is the stricter standard around the word on rockfall barriers. It defines several aspects, such us:

- The components of the barriers (called kit), as described in the previous paragraph;
- The minimum lifespan of the barrier: 25 years in standard environmental condition and 10 years for aggressive environments;
- Maximum Energy Level (MEL) of the barrier;
- Serviceability Energy Level (SEL) of the barrier, as 1/3 of MEL;
- 9 different energy level classifications, as shown in table 1;
- The procedures to carry out full-scale crash tests in term of minimum dimension of the tested barrier, minimum requirement for the tested block (shape, weight, diameter), geometry and feature of the test facility, impact dynamics, test energy levels and number of tests;
- The measurements that have to be done on the barrier before, during and after the test;
- Maximum elongation of the barrier (in the dynamic condition);
- Residual height of the barrier (height of the fence after the impact);
- Classification of the barriers according to their residual height, as shown in table 2;
- The factory controls that manufacturers must follow on the material composing the kit.

Table 1. Energy level classification according to ETAG 027/2008.

Class	SEL	MEL
0	–	100 kJ
1	85 kJ	250 kJ
2	170 kJ	500 kJ
3	330 kJ	1000 kJ
4	500 kJ	1500 kJ
5	660 kJ	2000 kJ
6	1000 kJ	3000 kJ
7	1500 kJ	4500 kJ
8	>1500 kJ	>4500 kJ

Table 2. Classification for residual height of the barrier after the MEL test.

Category	Nominal height/Residual height
A	>50%
B	from 30 to 50%
C	>30%

Table 3. Values of residual height and maximum dynamic elongation measured during the MEL crash test on the Maccaferri rockfall barriers.

Barrier	Energy	Residual height	Max dynamic elongation	Certified heights
RMC 050/A	500 kJ	75%	3.70 m	3.0 to 3.5 m
RMC 050/ICAT2	500 kJ*	61%	3.40 m	3.0 to 3.5 m
RMC 100/A	1000 kJ	69%	4.45 m	3.5 to 4.0 m
RB 1500	1500 kJ	62%	5.80 m	4.0 to 5.0 m
RMC 200/A	2000 kJ	72%	5.25 m	4.0 to 5.0 m
RMC 300/A	3000 kJ	73%	6.05 m	5.0 to 6.0 m
RMC 500/A	5000 kJ	70%	6.50 m	6.0 to 7.0 m
RMC 850/A	8500 kJ	58%	8.10 m	7.0 to 8.0 m

* Barrier without up-slope bracing cables.

During the tests manufacturers must measure the residual height, the maximum dynamic deformation and the forcestransferred by the impact on the foundations. With these parameters, designers can clearly specify their performance requirement for the designed rockfall barriers and they are able to design the best foundation type for the specific site.

The table below shows the values recorded during the MEL testsfor different rockfall barriers tested by Maccaferri.

The European Guideline allows increasing the height of the tested kit no more than 1 m, if the tested height is higher or equal to 4 m, and 0.5 m, if the tested height is lower than 4 m. No reductions on high are permitted.

Nowadays, ETAG 27/2008 represent a milestone for the rockfall tenders, and even if it is a European Guideline, it is accepted all around the world.

2 ROCKFALL SIMULATION

2.1 *Input data*

The first step in the design of a rockfall barrier is the numerical and analytical simulation of the rock fall trajectories along the slope. The input data necessary for a reliable analysisis based upon the results of 3 main surveys:

- Geomechanical: to define the type of rock, the dimensions of the potential unstable blocks and the type of failure;
- Geological: to define the type of soil present on the slope, in order to identify the restitution coefficients (which define the bounces of the blocks on the slope) and the friction between the soil and the boulder (which define both the rebounds and the rolling of the boulders during their falls);
- Topography: to define the cross section most likely to fail, identify the location of the unstable masses and to figure out the best position of the fence on the slope.

All these parameters can be analyzed with a different level of accuracy: with in-situ analysis or with visual investigation (i.e. pictures) or simply using literature and maps. As it will be described in the next chapter, some safety coefficients should be introduced to take into consideration the reliability and the precision of the surveys.

2.2 *Simulation of the rock trajectories*

The rockfall simulations are normally carried out with commercial software that can be based on different algorithms. These toolsare able to identify the trajectory of the falling blocks at every point on the slope. Thus, users can easily find the dynamic parameters of the block during its falling motion, such as energy, velocity and height above the ground level.To obtain reliable results, the simulation should be performed considering at least 1000 trajectories.

During the numerical analysis designers should take into consideration several aspects (Giacchetti & Zotti 2012):

- It is not recommended to use the energy directly calculated by the software. It is better to calculate it knowing the block velocity and mass: $E = 1/2\, m\, v^2$. In this way it is possible to control anomalous values, evaluate the quality of the simulation, and apply the safety factors as described in the next chapter;
- The rotational energy represents approximately 10–15% of the total kinetic energy. For this reason it can be neglected;
- The statistical analysis of the output of the simulations should allow for a risk of 5%, thus the probability distributionsto take into consideration have to be referred to the 95° percentile;
- The simulation in "seismic" condition can be carried out considering an initial velocity of the block

at the starting point. The seismic analysis is foreseen only if the barrier is designed close to the detachment area, and the initial velocity is quite high.

To validate the rockfall simulation a back analysis is always recommended to compare the numerical distribution of the end points of the blocks with the in-situ evidence. If the comparison differs, the restitution coefficients have to be calibrated according with the real conditions. When the model is well calibrated, the rockfall barrier design can start with the procedure illustrated in the next chapter.

3 NEW DESIGN APPROACH

3.1 *Ideal condition vs. Real conditions*

The easiest way to design a rockfall barrier is bythe direct comparison of the results obtained with the rock fall simulations and the nominal energy of the barriers tested according to ETAG 027/2008 (i.e. if from the rockfall simulation the energy obtained is 1000 kJ, theoretically the barrier to be use would have a nominal capacity of 1000 kJ). Although rockfall barrier are in common use, designers and consultants do not have a clear overview of the real performances and the technological limits of these structures.

Some questions should be solved: how do the site specific aspects of installation affect the barrier performances? What is the behavior of the barriers under extreme condition? What is the functional reliability of ETAG 027/2008?

First of all it is important to underline that the crash tests are carried out in ideal conditions, where the barriers are installed with:

- A perfect planimetric alignment;
- The bases of the posts are all at the same level;
- The impact is only in the center of the central span of the fence;
- The barrier is impacted by a single block only;
- The barrier is always composed by 3 spans and the distance between the post is 10 m;
- The posts are perfectly parallels (in the same hypothetical plane).

The evidence shows that the barriers are always installed in a non-ideal condition. The practical consequences of an impact can be listed below:

- If the barrier has a downslope concave-angle deviation,it can have a lager downslope deformation;
- If the barrier has a downslope convex-angle deviation, it can tilt upslope. In this case a downslope bracing cable is always recommended in the deviation post;
- If there is a difference on the level between the adjacent posts, the interception structure is low stressed in one direction and high stressed in the other. The consequence is the increasing of the compression force on the upper post, which can suffer of normal stress;
- The barrier can be impacted everywhere: lateral span, post, lower part, etc., thus the results of the crash test must be considered as a sort of index, because they cannot describe the barrier behavior for any impact condition;
- The barrier can be impacted by several blocks which can provoke high stresses on all the components of the structure;
- It is always recommended to design barriers with a length 30 to 70–80 m. Short barriers, composed by 1 or 2 spans, can be installed, but their performance are generally reduced in term of energy capacity, residual height and deformation. Longest barriers (more than 100 m long) can be difficult to install, they have a relevant impact on the environment (the passage of animals and people is difficult), and they have high maintenance costs. If the zone to be protected has a length higher then 80–100 m, it is recommended the installation of two parallel barriers alignments. These 2 fences must have an overlap and the distance between each other has to be able to guarantee the maximum elongation of the upslope barrier (see figure 1);
- If the distance between the posts is lower than 10 m, the energy capacity of the barrier can be reduced (the energy absorption of these structures is directly related to the surface of the interception structure), while if the distance exceed the 10 m, the max elongation can rise and the residual height generally is reduced. In order to guarantee optimal performances, the barrier installed should have the post spacing as in the test facility. Generallya post-to-post distance between 8 to 12 m is allowed;
- If the posts are not in the same hypothetical plane, thus they are not parallel each other, the barrier can suffers of anomalous stress conditions and the deformations are generally higher.

To minimize all the technological limits due to the real in-situ conditions, it is recommended to choose barriers that can guarantee high performance: the maximum dynamic deformation has to be the lowest, and the residual height the highest one. Even if ETAG 027/2008 defines a barrier in category A if its residual height is higher than 50%, to increase the safety margin Maccaferri suggests to rise this minimum value. In this way, the barrier, after the first impact, will be able to intercept falling blocks with a higher height above the ground.

3.2 *Energy Level*

The European Guideline ETAG 027/2008 introduces the concept of Maximum Energy Level (MEL) and Serviceability Energy Level (SEL) of the barrier. Designers are able to refer their design to one of these 2 energy capacities of the barrier.

The Ultimate Limit State design (MEL) is normally adopted if the frequency of the rock falls is low, if only one block is expected to fall, or, if the risk level allowed is high and/or if the maintenance can be easily

done. The MEL criterion is typically used for temporary works or installations at the base of re-profiled slope (i.e. mining industry).

The Serviceability Limit State design (SEL) is generally adopted in order to reduce the maintenance costs of the fence, when the risk permitted is low (i.e. entrance of a tunnel) and/or if multiple impacts are expected. The SEL criterion is obviously the most expensive, because the barrier must have a capacity 3 times more (SEL = 1/3 of MEL) than a barrier designed with MEL approach, but it increases the safety condition of the zone.

According to their specific cases, designers can chose the MEL or SEL approach. Moreover, several safety coefficients must be introduced to increase the driving actions of the impact and to reduce the resistances of the fence. The following paragraphs will describe the steps in the design a rockfall barrier according to the approach proposed by Peila & Oggeri (2006) and implemented by the UNI 11211:4-2012 standard (Rockfall Protective Measure).

The most important parameter to be identified during the rockfall barrier design is the energy level of the barrier, which can be defined as following:

$$E_{sd} < \frac{E_b}{\gamma_E} \tag{1}$$

where E_{sd} = design energy level of the block; E_b = nominal energy of the barrier (MEL or SEL, as defined during the crash tests in accordance with ETAG 027/2008); γ_E = safety coefficient related to the energy level adopted during the design (1.20 with MEL approach; 1.00 with SEL approach; 2.00 if the barrier is composed by 1 or 2 spans).

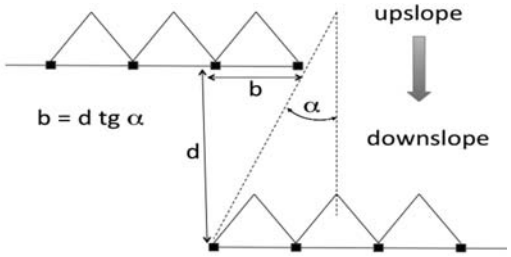


Figure 1. Procedure to calculate the spacing between 2 parallel barrier alignments; where: b = overlap between the barriers, d = distance between the barriers, α = deviation angle of the trajectory from the maximum gradient (generally between 10° and 45°) (Giacchetti & Zotti, 2012).

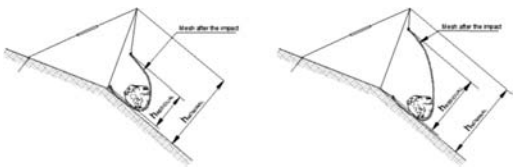


Figure 2. Advantage having a high residual height of the barrier. Left: barrier with a residual height >50%; Right: barrier with a residual height = 75%. Both are classified in Category A (according to ETAG 027/2008), but the second barrier has an higher safety margin if impacted by a second block.

The design energy level (E_{sd}) is defined by multiplying the classical formula of the kinetic energy by a safety coefficient (γ_R) that takes into consideration the risk for the human life. As discussed in the paragraph 2.2, the rotational energy is neglected):

$$E_{sd} = \left(\frac{1}{2} M_d \cdot v_d^2\right) \gamma_R \tag{2}$$

where M_d = design mass of the block; v_d = design velocity of the block; γ_R = safety coefficient related to human risk (according to the risk analysis done ad hoc for the site; or from 1.00: for low economic value and it can be easily repaired, to 1.20 for high economic value and it cannot be repaired).

The design mass (M_d) of the block is defined as:

$$M_d = (V_B \cdot \gamma)\, \gamma_{VOL} \cdot \gamma_\gamma \tag{3}$$

where V_B = volume of the block; γ = unit weight of the block; γ_{VOL} = safety coefficient related to the precision of the block survey (from 1.02: high precision, to 1.10: low precision); γ_γ = safety coefficient related to the evaluation of the unit weight of the rock (generally equal to 1.00).

The design velocity (v_d) of the block is:

$$v_d = (v_t \cdot \gamma)\, \gamma_{Tr} \cdot \gamma_{Dp} \tag{4}$$

where v_t = velocity calculated with the rockfall simulation and referred to the 95% of the velocity distribution; γ_{Tr} = safety coefficient related to the reliability of the rockfall simulation (from 1.02: if a back analysis is done, to 1.10: if the restitution coefficients are based on literature); γ_{Dp} = safety coefficient related to the quality of the topographic survey (from 1.02: high quality, to 1.10: low quality).

The safety coefficient shown in the formulas 1 to 4 must to be equal or higher than 1. The Italian Standard (UNI 11211:4-2012) gives their exact values, but designers outside Italy may change the value of these coefficients based on their experience and their specific site conditions.

3.3 *Height*

The minimum height of the barrier must be evaluated considering a free area on the barrier where the blocks cannot impact. Moreover, the dimension of the block has to be taken into consideration.

$$H_b > H_d + f_{\min} \tag{5}$$

$$H_d = H_t \cdot \gamma_{Tr} \cdot \gamma_{Dp} + R \tag{6}$$

where H_b = minimum height of the barrier; H_d = height of the trajectories calculated with the rockfall simulation and referred to the 95% of the height distribution; f_{min} = safety zone (usually no lower than 50 cm); γ_{Tr} = safety coefficient related to the reliability of the rockfall simulation (from 1.02 to 1.10); γ_{Dp} = safety coefficient related to the quality of the topographic survey (from 1.02 to 1.10); R = radius of the design block.

3.4 *Deformation*

The last aspect to be evaluated during the rockfall barrier design is the minimum distance between the barrier and the protected structure. This parameter is fundamental in order to avoid any interaction between the deformed fence after the impact and the area to be protected (road, railway, building, etc.).

$$H_d = H_t \cdot \gamma_{Tr} \cdot \gamma_{Dp} + R \quad (7)$$

where D_A = minimum distance between the barrier and the area to be protected; D_b = maximum dynamic elongation of the barrier, measured during the MEL test (ETAG 027/2008); γ_d = safety coefficient related to energy level adopted during the design, to the length of the barrier, and the zone of the barrier impacted by the design block (see table 4).

The deformation of the barrier increases if the energy level of the fence is larger; it is always recommended to place the barrier at least 10 m far from the protected area.

3.5 *Rockfall barrier performances*

During the design, designers and consultants must characterize the barriers in term of residual height and maximum deformation. As shown in table 3, all the manufacturers must know these values, which are recorded during the full-scale test in accordance with ETAG 027/2008.

Barriers with high residual height and low deformations can increase the safety level of the protected area after the first impact.

Maccaferri, with its 130+ years of experience in the field of rockfall protection, developed its barriers with the intention of realizing very high performance. Maccaferri's barriers can be classified among the best on the market because they are able to distribute the impulsive forces over a larger surface.

Table 4. Values of the coefficient γ_d introduced by the UNI 11211:4-2008.

Coefficient	Value
γ_d	= 1.0 for SEL design approach
	> 1.0 for MEL design approach
	= 1.0 if the length of the barrier is at least 30 m
	> 1.0 if the barrier is shorter than 30 m
	= 1.0 if the impact is not on the lateral spans
	> 1.0 if the impact is on the lateral spans

4 FOUNDATION DESIGN

4.1 *Load analysis*

During the full-scale tests, manufacturers have to measure the forces transmitted to the foundations during the impact. Usually the systems to measure the forces on the foundations consist on a data logger connected to different load cells disposed on all the main foundations of the barriers: post bases, upslope cables and lateral cables.

Even if ETAG 027/2008 requires that the foundations forces must be measured during the full-scale tests, the guideline does not define the foundations of the barrier as a component of the rockfall kit. The reason is due to fact that barriers are never installed in the same type of soil (loose soil, rock, etc.), thus every barrier should have its proper anchoring system according to the geology observed on the job site and of course the type of barrier.

During the design it is impossible specify one type of foundation for every anchor.Normally designers divide the foundation in 3 categories taking into consideration the worst load for each anchor:

- Post foundations: compression and shear stresses;
- Up-slope foundations: tensile stress (pull-out);
- Lateral foundations: tensile stress (pull-out).

Table 5 describes an example of the maximum loads acting on the foundations of Maccaferri 3000 kJ barrier (RMC 300/A).The values listed in the table are the one recorded during the MEL full-scale test. These are the values at ultimate limit state of the barrier: they are the forces corresponding at the maximum capacity of the barrier. Designers should consider these loads for their designs.

4.2 *Type of foundations*

Foundations have to be able to transmit the load on the ground. Deep-foundations are normally used in order to guarantee the best performance with a minimum cost.Generally the anchoring systems are designed as following:

- Post foundations: steel bars (usually for rock) or micropiles (usually for loose soil);

Table 5. Values of maximum forces acting on the foundation of the RMC 300/A.

Foundation	Value
POST	Compression 275.55 kN
	Shear 207.63 kN
UP-SLOPE	Pull-out 243.37 kN
LATERAL	Pull-out 300.00 kN

– Up-slope and lateral foundations: flexible cable anchors (steel bars can be used, but they are not recommended because they suffer the dynamic loads, which can pull out the anchor in every direction. A flexible system is preferred).

All the anchor systems are considered passives, because they start to work only if they are stressed by the impact, no pre-tensioning is required. They are installed in drilled-holes and they are full grunted along their entire length in order to develop the maximum friction anchor-grout and grout-soil. The length and the diameter of the anchors as well as the drilling diameter depend on the design requirement. If the barrier is installed in a uneven soil, a little concrete plinth (i.e. dimensions $50 \times 50 \times 50$ cm) can be foresee to give a flat base for the posts of the fence.

The foundations of the posts must not be too large and stiff, first of all for economic reasons, and then because the anchoring system has to be able to dissipate the energy itself. If the post of the barrier is founded on a rigid and stiff foundation during the impact the post would be high stressed in correspondence of the footplate and no movement would be allowed. This phenomenon can create problem to the post that can be seriously damaged due to the high compression stress on it. On the other hands, a lighter and flexible post foundation is strongly recommended because it is deformable and can dissipate the energy of the impact.

The problem of the reduction of the residual height of the barrier could rise if flexible foundations for the posts are used. In fact, after a large impact the base footplate can collapse into the ground. This behavior could be accepted in order to reduce the maintenance of the barrier: in this way the negative effects on the foundations can decrease. Vice versa, by using stiff foundations it could be possible to maintain the effective residual height of the barrier, but with serious consequences for the foundations: in these cases foundations often need to be replaced.

5 CONCLUSIONS

The European Organization for Technical Approval issued in 2008 a Guideline (ETAG 027) which defines a standardized procedure that manufactures may follow to test their rockfall fences at the full scale, in order to understand the performances of their barriers and consequently obtain the European Technical Approval (ETA) and the CE marking. This guideline is essentially the only test and construction framework utilized by manufacturers all around the world, but unfortunately it describes the performance of the barrier only in ideal conditions and it does not take into consideration all the technological limits of these structures which must be considered during the design phase. A new approach had been defined by the Italian Standard (UNI 11211:4-2012) in order to design the barrier at ultimate and serviceability limit state. To increase the safety level of the protected area, the forces acting on the barrier are increased and the barrier resistances are reduced.

Even if the foundations of the rockfall fences are not part of the kit defined by the ETAG 027/2008, these elements are really important on the global behavior of the barrier. These anchoring systems have to be able to dissipate themselves the energies in order to reduce the negative consequence on the barrier and reduce the maintenance costs.

REFERENCES

EOTA 2008. ETAG 027: Guideline for European technical approval of falling rock protection kits. Brussels, www.eota.be

Giaccheti G., Zotti I.M. 2012.Design approach for rockfall barriers. *Proceedings of the XI National Congress of Geotechnics – 9–10 August 2012.* San José: Costa Rica

Peila, D., Oggeri, C. & Baratono, P. 2006. Barriere paramassi a rete. Interventi e dimensionamento. *GEAM, Quaderni di studio e di documentazione n26*

UNI. 2012. UNI 11211-4:2012 Rockfall protection measures – Part 4: definitive and executive design. Milano. www.uni.com

Rock Mechanics for Resources, Energy and Environment – Kwaśniewski & Łydżba (eds)
© 2013 Taylor & Francis Group, London, ISBN 978-1-138-00080-3

Influence of in-situ stress variation on results of back analyses – an open pit case study

M. Grošić & D. Vidović
Geotech Ltd., Rijeka, Croatia

Ž. Arbanas
University of Rijeka, Faculty of Civil Engineering, Rijeka, Croatia

ABSTRACT: One of the crucial points in performing stress-strain back analyses is knowledge of the magnitudes and directions of insitu stresses. Although vertical insitu stress mostly depends on weights of overlaying strata, horizontal stress is more complex to determine and depends on vertical stresses, locked stresses of tectonic origin, topography and other complex geological conditions. To obtain the deformation modulus of rock mass, except from insitu measurements, back analyses based on monitoring data are often carried out. Direct approach from the back analysis is based on iterative procedure, correcting the trial values of unknown parameters by minimizing the error function. This paper presents a case study of an open pit excavation reinforced by rockbolts and shotcrete that was monitored during the construction phase. Back analyses were performed with variation of in situ horizontal stresses as an unknown in thenumerical model. Analyses have shown significant scattering of obtained deformation moduliof rock mass, which vary a few dozen times. Results of the back analyses and comparison with measured data are presented.

1 INTRODUCTION

Knowledge of the virgin stress field is very important in many problems dealing with rock mechanics and related projects. The need to understand the insitu stresses in rock mass has been recognized by engineers for a long time and many methods to measure these stresses have been proposed since the early 1930s.

These in situ stress measuring tests are relatively expensive and are used only at significant projects in civil and mining engineering. For smaller projects tests are not performed and certain indirect estimations of rock mass deformation properties are used.

Horizontal stress direction and magnitudes vary significantly on local and global scales and incorrect predictions can lead to incomprehension of geotechnical construction behavior and to possible collapse and failure.

2 PREVIOUS RESEARCH

2.1 *The deformation modulus of rock mass*

Deformability is characterized by a modulus describing the relationship between the applied loadsand the resulting strains. The fact that jointed rock masses do not behave elastically has prompted the usage of the term modulus of deformation rather than modulus of elasticity or Young's modulus (Palmström & Singh 2001).

According to the Commission onTerminology, Symbols and Graphic Representation of the International Society for Rock Mechanics (ISRM),there are several important definitions of deformation properties of rock and rock mass (ISRM 1975). Modulus of elasticity or Young's modulus (E) is defined as the ratio of stress to corresponding strain below the limit of proportionality of a material. Modulus of deformation of a rock mass (E_m) is the ratio of stress to corresponding strain during loading of a rock mass, including elastic and inelastic behavior. Modulus of elasticity of a rock mass (E_{em}) is the ratio of stress to corresponding strain during loading of a rock mass, including only the elastic behavior.

2.2 *Indirect estimation of the deformation modulus*

The deformation modulus can be measured in situ using one of the following methods: flat jack tests, cable jacking tests, radial jack tests, dilatometer tests and pressure chamber. Because of the high costs of the tests, the deformation modulus of rock mass is rarely measured in situ and is often obtained by indirect estimations.

Deformation parameters of rock mass are often estimated through approximate equations that are based on one of the rock mass classifications (RMR, GSI, Q classification, RMi). Several authors have proposed empirical relationships for estimating the value of rock

mass deformation modulus on the basis of classification schemes: Bieniawski (1978), Serafim & Pereira (1983), Grimstad & Barton (1993), Clerici (1993), Palmström (1995), Hoek & Brown (1997), Hoek et al. (2002), Hoek & Diederichs (2006) and many others.

All these correlations are based on insitu measurements and back analyses in underground projects and assume that rock mass is isotropic, but at engineered rock mass slopes completely different conditions are present.

Proposed expressions provide significant deviations of rock mass deformation modulus compared to the measured values obtained from monitoring results during excavation of cuts and underground openings in rock mass (Palmström & Singh 2001, Kayabasi et al. 2003 Arbanas et al. 2004).

2.3 *In situ stress state*

Rock at depth is subjected to stresses resulting from the weight of the overlying strata and from locked in stresses of tectonic origin. When an opening is excavated in this rock, the stress field is locally disrupted and a new set of stresses is induced in the rock surrounding the opening. Knowledge of the magnitudes and directions of these insitu and induced stresses is an essential component of underground excavation design since, in many cases, the strength of the rock is exceeded and the resulting instability can have serious consequences on the behavior of the excavations (Hoek 2007).

Measurements of vertical stresses confirmedthe assumption that the vertical stress is approximately equal to depth times unit weight of rock mass. Horizontal stresses of rock mass at specific depth are much more difficult to estimate then vertical stresses.

2.4 *Estimating horizontal stress*

There are two basic assumptions when estimating the state of stress at any depth (z) in a rock mass. The first assumption refers to predicting a vertical stress component (σ_v) due to weight of overlaying rock mass. The second assumption involves estimating the horizontal stress component $\sigma_h = K_0\sigma_H$ which is equal to coefficient K_0 times vertical stress σ_v.

Different expressions have been proposed in the literature for the horizontal stressesby many authors: Terzaghi & Richart (1952), Talobre (1967), Brown & Hoek (1978), Herget (1988), Sheorey (1994) and others. Most of these expressions were based on worldwide stress measurements in mining and civil engineering projects.

In many cases it is shown that horizontal stresses are equal or rather even greater than vertical stresses even by several times: Terzaghi & Richart (1952), Isaacson (1957), Terzaghi (1962), Maritinetti & Ribacchi (1980), Rummel et al. (1986), Cooling et al. (1988), Ribacchi (1988), Cristescu (1989), Hyett & Hudson (1989), Zoback (1992) and others. According to Aytmatov (1986), stress measurements conducted in different parts of the world have shown that in 65–70% of cases horizontal stresses exceed vertical stress.Cristescu & Hunsche (1998) proposed the constant K_0 to have values between 0.3 and 3.0. Occasionally, K_0 can be either smaller than 0.3 or greater than 3.0. In weak and highly fractured rock masses, horizontal stress can be obtained through one of the friction angle methods, such as the simplified form introduced by Jaky (1948).

These differences between predicted and measured stresses are present due to tectonic stresses, residual and thermal stresses, erosion, lateral straining, anisotropy, topography and other geological settings.

Scattering in horizontal stress variations should be taken into account and should not be neglected in the designing phase of a project.

2.5 *Observation methods and back analyses*

The observational method was introduced by Terzaghi & Peck (1967) and Peck (1969) and developed further by Powderham (1998), Nicholson et al. (1999) and others. This method is based on continuous field measurements on installed equipment and back analyses, the results of which are then compared with numerical modeling predictions.

According to Cividini et al. (1981), there are two different ways to conduct back analyses: the inverse approach and the direct approach. For the inverse approach, the formulation is the reverse of that in ordinary stress analyses, even though the governing equations are identical. According to this approach, the number of measured values should be greater than the number of unknown parameters, but it is unclear whether the method could be applied in geotechnical problems in which there is scattering of measured values. The direct approach to back analysis is based on an iterative procedure of correcting the trial values of unknown parameters by minimizing the error function. Gioda & Maier (1980) pointed out that an advantage of direct approach methods is that they may be applied to non-linear back analysis problems without having to rely on a complex mathematical background. Cividini et al. (1981) stated that standard algorithms of mathematical programming might be adopted for numerical solutions. Iterative solutions require very time-consuming computations.

3 CASE STUDY OF OPATIJA SPORTSHALL OPEN PIT

3.1 *Project overview*

The Sports Hall “Marino Cvetkoviæ” is planned as a part ofthe sports center in the City of Opatija in the Republic of Croatia. The SportsHall is designed as a 88.0 m long and 52.0 m wide rectangular building with a garage and service facilities. Excavation of the pit and geotechnical works were the most demanding part of the construction because of the requirement for



Figure 1. Panorama view of the reinforced open pit during work execution.

a deep open excavation in an urban area which at some parts exceeded the height of 25.0 m – Figure 1. The location has an inclined ravine shape, running in direction NW-SE. The elevation of the ravine varied from 48.0 m a.s.l. while the bottom of the pit was designed to be at 22.1 m a.s.l.

The open pit was constructed in several phases, using a retaining wall construction in the soil layers and reinforcement by rock bolts and multilayered reinforced sprayed concrete in the rock mass.

3.2 *Geological setting*

In order to design the excavation, its support system, and the building foundation, a detailed complex geotechnical field investigation was performed which consisted of geotechnical drilling, laboratory testing and engineering-geological mapping of terrain.

The location is made up of two types of limestone and dolomite breccias covered with terra rossa and superficialdeposit. In the central part of the site, a 10.0 m wide fault zone is present which runs in direction W-E.

The bedrock consists of limestone and dolomite breccias with carbonate or clay matrix. Both breccias are massive and non-stratified. On the surface, where the bedrock is in contact with the cover material, breccias are more intensely fissured and jointed. The rock is mostly medium to weakly carstificated, except in the surface and tectonically jointed fault zone.

Based on field investigation and laboratory testing the following rock mass characteristics were assigned: uniaxial compression strength 75.0 to 100.0 MPa, geological strength index (GSI) from 30 to 40, and disturbance factor of D = 0.7. Based on these parameters numerical modeling was performed.

3.3 *Monitoring data and interpretation*

During the open pit construction, a monitoring system was established consist of horizontal extensometers and vertical inclinometers, and other observations such as geodetic surveying and measuring of forces in the rockbolts. This provided the necessary data for a stress-strain back analysis of the response of the excavated and reinforced rock mass.

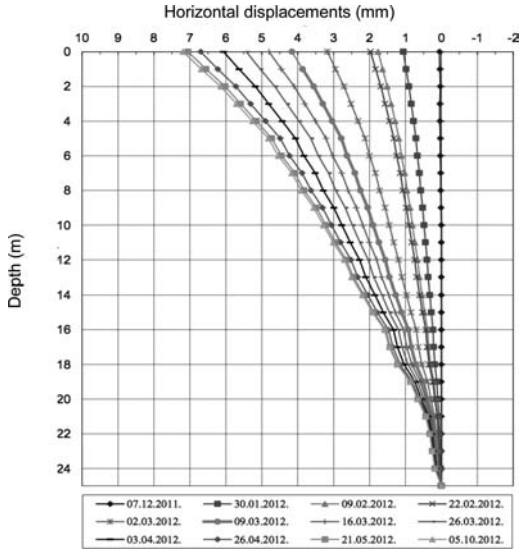


Figure 2. Horizontal displacements measured at vertical inclinometer VI-4.

Verification and back analyses were performed based on horizontal displacements from the inclinometer situated at the south part of the open pit at engineering-geological section B-B' – Figure 2. Excavation reached the bottom of the pit in early March 2012 and the maximum horizontal displacements reached a value of 4.2 mm (measured on 09/03/2012 – Figure 2) at the top of inclinometer.

It was observed that a significant amount of displacements occurred even after excavation reached its final level – up to 75%. These displacements are caused by time-dependent behavior of reinforced rock mass and stress redistribution and should not be neglected. These deformations should be processed in more detail in future research.

4 NUMERICAL MODELING

4.1 *Numerical model*

Numerical modeling of behavior of reinforced cuts was performed using a two-dimensional explicit finite

Table 1. Properties of geotechnical unit 1 and 2.

Properties	Geotechnical units		
	Symbol	U1	U2
Geological strength index	GSI	30	40
Uniaxial compressive strength (MPa)	σ_c	70	100
Parameter mi	m_i	8	8
Disturbance factor	D	0.7	0.7
Unit weight (kN/m$^{3)}$	γ_k	23.0	23.0
Poisson's ratio	ν	0.25	0.25
Model	–	HB	HB
Shear modulus	G	varied	varied

*HB – Hoek-Brown elasto-plastic model

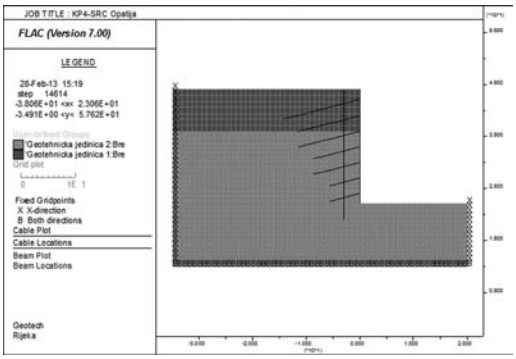


Figure 3. Model used in numerical simulations – cross section B-B'.

difference method software for engineering mechanics computation – FLAC V7.0 (Itasca Consulting Group Inc 2011).

Rock mass was modeled as Hoek-Brown elastoplastic material divided into two geotechnical units. The first stage of numerical modeling involved defining in situ conditions where horizontal stresses were varied with different coefficient K_0 as follows – 0.3, 0.5, 1.0, 1.5 and 3.0. Properties of geotechnical units used in numerical modeling are presented in Table 1.

4.2 *Modeling of open pit construction*

After defining in-situ stresses the second part of numerical modeling started – the construction phase. Excavation was simulated by defining null elements and recalculating stress-strain condition for each phase. Rockbolts were simulated as cable elements installed after each excavation phase – Figure 3.

To obtain rock mass deformation modulus the back analysis method was used. The direct approach to back analysis based on an iterative procedure of correcting the trial values of the deformation modulus by minimizing the error function was used to approximate

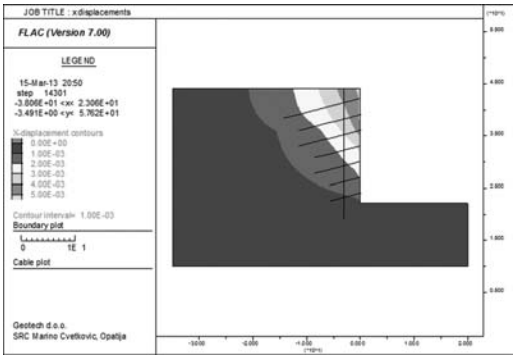


Figure 4. Results of numerical simulation for coefficient $K_0 = 1.0$ – horizontal displacements at final state of excavation.

Table 2. Properties of deformation modulus of geotechnical units 1 and 2 due to coefficient K_0 variation.

Properties	K_0	E_1	E_2	Unit
Case 1	0.3	8.5e1	8.5e2	MPa
Case 2	0.5	1.6e2	1.6e3	MPa
Case 3	1.0	3.5e2	3.5e3	MPa
Case 4	1.5	5.3e2	6.0e3	MPa
Case 5	3.0	1.3e3	1.6e4	MPa

measured values (horizontal displacements) obtained from the inclinometer for each case – Figure 4.

In total, 5 different cases were calculated with varying horizontal stresses and 5 different deformation moduli were obtained for each geotechnical unit from the back analyses results.

5 RESULTS AND PARAMETER STUDY

Numerical modeling was performed to analyze the influence of variation of in situ horizontal stresses to the construction behavior. Five cases were back analyzed varying the coefficient of horizontal stress K_0 from 0.3 to 3.0.

For each case numerical back analysis was performed and a deformation modulus for each of the two geotechnical units was obtained – Table 2.

Based on the results of back analyses from Table 2 it is obvious that the deformation modulus significantly depends on the horizontal stress value. For the geotechnical unit 1 the deformation modulus varies from $E = 8.5e1$ MPa for $K_0 = 0.3$ to $E = 1.3e3$ MPa for $K_0 = 0.3$ which is 15 times higher than the minimum value. For the geotechnical unit 2 differences are even greater and vary from $E = 8.5e2$ MPa for $K_0 = 0.3$ to $E = 1.6e4$ MPa for $K_0 = 3.0$ which is 18 times higher than the minimum value.

A comparison of measured horizontal displacements for inclinometer VI-4 and results of back analyses for variation of coefficient K_0 are presented in

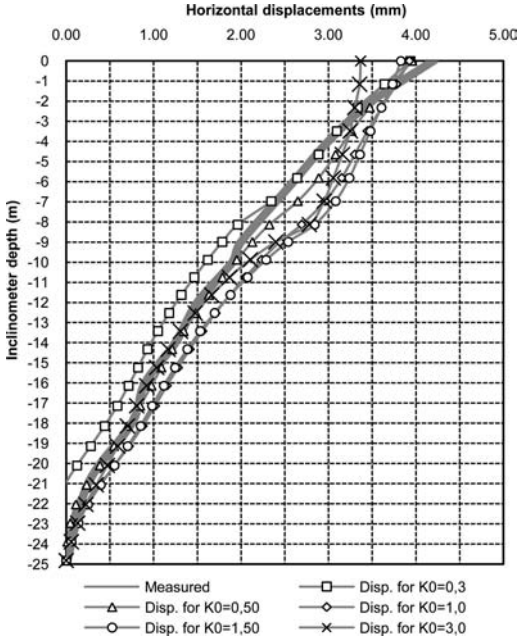


Figure 5. Measured and simulated horizontal displacement at inclinometer VI-4 for variation of coefficient K_0.

Figure 5. Relationship of deformation modulus of rock mass vs. coefficient K_0 variation is presented in Figure 6.

Based on results obtained from back analyses it is obvious that minimum and maximum values of the deformation modulus vary up to 18 times. This indicates that horizontal stress value is crucial for performing back analyses and its variation should be taken into account during design and monitoring processes.

During performing of the numerical stress-strain analyses of excavation of the reinforced openpit yield stress condition was not reached.

6 CONCLUSIONS AND RECOMMENDATIONS FOR FURTHER RESEARCH

One of the crucial points in performing stress-strain back analyses is knowledge of the magnitudes and directions of in-situ stresses. Although vertical insitu stresses mostly depend on weights of overlaying strata, horizontal stresses are more complex to determine.

To obtain the rock mass deformation modulus, the back analysis method is often used. In this open pit case study numerical modeling was performed to analyze the influence of variation of insitu horizontal stresses to the construction behavior. Five cases were analyzed varying the horizontal stress coefficient K_0 from 0.3 to 3.0.

Based on the results of back analyses, it is obvious that the deformation modulus significantly depends on the horizontal stress value. For geotechnical unit

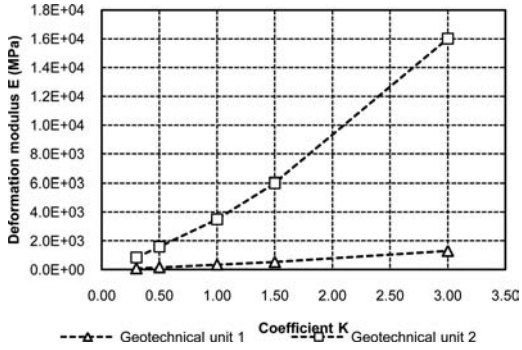


Figure 6. Deformation modulus E for geotechnical units 1 and 2 vs. coefficient $K_0 = 1.0$ variation.

1 deformation moduli varied from E = 8.5e1 MPa for $K_0 = 0.3$ to E = 1.3e3 MPa for $K_0 = 0.3$ which is 15 times higher than the minimum value. For geotechnical unit 2 differences are even bigger and deformation modulivary from E = 8.5e2 MPa for $K_0 = 0.3$ to E = 1.6e4 MPa for $K_0 = 3.0$ which is 18 times higher than the minimum value.

From obtained results from back analyses it could be seen that for very low stress conditions ($K_0 = 0.3$) extremly low and very unlikely deformation modulus of the rock mass are required to reach the displacements measured by inclinometer. These result should be taken with greater attention.

Deformation modulus and insitu horizontal stresses should be taken into account as unknowns when performing back analyses. Varying one of these unknowns significantly affects the results of numerical analyses and reinforced rock mass behavior.

Implementing observational methods and monitoring during the construction phase enables minimization and reduces the possibility of incomprehension of geotechnical construction behavior and possible collapse and failure of the structure.

This paper presents the back analysis of deformation modulus based on the monitoring data with assumption that horizontal stresses are unknown. Back analysis could also be performed to obtain the horizontal stresses based on the monitoring data for constant deformation modulus.

REFERENCES

Arbanas, Ž., Jardas, B. & Kovačević, M.S. 2004. Excavation of Open Pit Zagrad in Rijeka, Croatia – A case history. *Proc. 5th Int. Conf. on Case Histories in Geotechnical Engineering* (New York, 13–17 April 2004). Paper No. 5.64, pp. 1–6.

Aytmatov, I.T. 1986. On virgin stress state of a rock mass in mobile folded areas, In O. Stephansson (ed.), *Proc. Int. Symp. on Rock Stress and Rock Stress Measurements*: 55–59. Luleå: Centek Publishers.

Bieniawski, Z.T., 1978. Determining rock mass deformability: Experience from case histories. *Int. J. Rock Mech. Min. Sci. & Geomech. Abstr.* 15: 237–247.

Brown, E.T. & Hoek, E. 1978. Trends in relationships between measured rock in situ stresses and depth. *Int. J. Rock Mech. Min. Sci. & Geomech. Abstr.* 15: 211–215.

Clerici, A., 1993. Indirect determination of the modulus of deformation of rock masses – Case histories. In L. Ribeiro e Sousa & N.F. Grossmann (eds), *Safety and Environmental Issues in Rock Engineering, Proc. Int. Symp. Eurock '93* 1: 509–517. Rotterdam: Balkema.

Cividini, A., Jurina, L. & Gioda, G. 1981. Some aspects of characterization problems in geomechanics. *Int J. Rock Mech. Min. Sci. & Geomech. Abstr.* 18: 487–503.

Cooling, C.M., Hudson, J.A. & Tunbridge, L.W. 1988. In situ rock stresses and their measurements in the U.K. Part II, Site experiments and stress field interpretation. *Int. J. Rock Mech. Min. Sci. & Geomech. Abstr.* 25(6): 371–382.

Cristescu, N.D. 1989. *Rock Rheology*. Dordrecht: Kluwer Academic.

Cristescu, N.D. & Hunsche, U. 1998. *Time Effects in Rock Mechanics*. New York: John Wiley & Sons.

Gioda, G. & Maier, G. 1980. Direct search solution of an inverse problem in elastoplasticity: Identification of cohesion, friction angle and *in situ* stress by pressure tunnel tests. *International Journal for Numerical Methods in Engineering* 15(12): 1823–1848.

Grimstad, E. & Barton, N. 1993. Updating the Q-system for NMT. *Proceedings of the International Symposium on Sprayed Concrete* (Fagernes, Norway 1993): 46–66. Oslo: Norwegian Concrete Association

Herget, G. 1988. *Stresses in Rock*. Rotterdam: Balkema.

Hoek, E., 2007. *Practical Rock Engineering* – Course notes. http://www.rocscience.com/education/hoeks_corner

Hoek, E. & Brown, E.T. 1997. Practical Estimates of Rock Strength. *Int. J. Rock Mech. Min. Sci. & Geomech. Abstr.* 34(8): 1165–1187.

Hoek, E., Carranza-Torres, C.T. & Corkum, B. 2002. Hoek-Brown failure criterion-2002 edition. In *Proceedings of the 5th North American Rock Mechanics Symposium* (Toronto, 7–10 July 2002) 1: 267–273. Toronto: University of Toronto Press.

Hoek, E., & Diederichs, M. 2006. Empirical estimates of rock mass modulus. *Int. J Rock Mech. Min. Sci.* 43: 203–215

Hyett, J.A. & Hudson J.A. 1989. In situ stress for underground excavation design in a naturally fractured rock mass. In A. Wahab Khair (ed.), *Rock Mechanics as a Guide for Efficient Utilization of Natural Resources, Proceedings of the 30th U.S. Symposium of Rock Mechanics*: 293–300. Rotterdam: Balkema.

Isaacon, E. de St. Q. 1957. Research into the rock burst problem on the Kolar gold field. *Mine and Quarry Engineering, December*: 520–526.

ISRM 1975. *Commission on Terminology, Symbols and Graphic Representation*. International Society for Rock Mechanics (ISRM).

Itasca Consulting Group Inc 2002. *FLAC version 7.0, User Manual.* Minneapolis: Itasca Consulting Group Inc.

Jaky, J. 1948. Pressure in silos. *International Proceedings of 2nd International Conference on Soil Mechanics and Foundation Engineering, Rotterdam*, Vol. 1: 103–107.

Kayabasi, A., Gokceoglu, C. & Ercanoglu, M., 2003. Estimating the deformation modulus of rock masses: a comparative study. *Int. J. Rock Mech. Min. Sci.* 40: 45–63.

Martinetti, S. & Ribacchi, R. 1980. In situ stress measurements in Italy. *Rock Mechanics* 9: 31–47.

Nicholson, D., Tse, C.-M. & Penny, C. 1999. *The Observational Method in Ground Engineering: Principles and Applications,* Report 185. London: CIRIA.

Palmström, A., 1995. *RMi – A Rock Mass Characterization System for Rock Engineering Purposes.* Ph.D. thesis, University of Oslo.

Palmström, A. & Singh, R. 2001. The deformation modulus of rock masses — comparisons between in situ tests and indirect estimates. *Tunnelling and Underground Space Technology* 16(2): 115–131.

Peck, R.B. 1969. Advantages and limitations of the observational method in applied soil mechanics. *Geìotechnique* 19 (2): 171–187.

Powderham, A.J. 1998. The observational method–application through progressive modification. *Civil Engineering Practice: Journal of the Boston Society of Civil Engineers Section/ASCE* 13(2): 87–110.

Ribacchi, R. 1988. Rock mass deformability: In situ tests, their implementation and typical results in Italy. In S. Sakurai (ed.), *Proceedings of 2nd International Symposium on Field Measurements in Geomechanics*: 171–192. Rotterdam: Balkema.

Rummel, F. 1986. Stresses and tectonics of upper continental crust – a review. In O. Stephansson (ed.), *Proc. Int. Symp. on Rock Stress and Rock Stress Measurements*: 177–186. Luleå: Centek Publishers.

Serafim, J.L. & Pereira, J.P. 1983. Consideration of the Geomechanics Classification of Bieniawski. In *Proceedings of the International Symposium on Engineering Geology and Underground Constructions*, Vol. 1: II.33–II.42.

Sheorey, P.R. 1994. A theory for in situ stresses in isotropic and transversely isotropic rock, *Int. J. Rock Mech. Min. Sci. & Geomech. Abstr.* 31(1): 23–34.

Talobre, J.A. 1967. *La Mecanique des Roches* (2nd edn). Paris: Dunod.

Terzaghi, K. 1962. Measurements of stresses in rock, *Géotechnique* XII(2), June 1962: 105–124.

Terzaghi, K. & Richart, F.E. 1952. Stresses in rock about cavities. *Géotechnique* III(2): 57–90.

Terzaghi, K. & Peck, R.B. 1967. *Soil Mechanics in Engineering Practice.* New York: John Wiley.

Zoback, M.L. 1992. First- and second-order patterns of stress in the lithosphere: the World Stress Map Project. *J. Geophys. Res.* 97(B8): 11761–11782.

Rock Mechanics for Resources, Energy and Environment – Kwaśniewski & Łydżba (eds)
© 2013 Taylor & Francis Group, London, ISBN 978-1-138-00080-3

The contribution of rock mechanics to small-scale mining in Indonesia

P.N. Hartami & B. Nugroho
Mining Engineering Department, Trisakti University, Indonesia

S. Mayangsari
Economic Faculty, Trisakti University, Indonesia

Nurhardono
Department of Energy and Mineral Resources, Indonesia

ABSTRACT: Generally small-scale mining does not pay attention to the Health and Safety (HSE) aspect. This is due to the fact that the knowledge and awareness of the miners is limited. The miners do not use personal protective equipment and they work in unsafe conditions, such as working in unsupported holes, digging and excavating below unstable slopes, which consequently causes many mining accidents. on the research site is a small-scale gold mine in Sekotong, West Lombok. In recent years, many people of Sekotong, a small village that is located about 40 kilometers from Mataram, West Nusa Tenggara (NTB), Indonesia, have become gold miners. The small-scale mining in this area is sporadic, disorganized, and used the underground mining method and simple equipment such as crowbars, hammers and chisels. The mining activities are carried out at a depth of approximately 40 meters below the surface with a very narrow entrance that sometimes only is large enough to fit a body. It is not surprising that there are many mining accidents. This paper aims to describe the contribution of rock mechanics to small-scale mining in Indonesia in order to decrease the number of mining accidents because people are not aware of good mining practices, safety and the behavior of rocks.

1 INTRODUCTION

Indonesia is a country that has many natural resources and because of this mining activitities in Indonesia are not only done by big companies but also by individuals and small companies. However, actually, small-scale mining is often counter productive because it creates many problems. Usually, the operators of small-scale mines do not pay attention to the Health and Safety aspect due to their lack of knowledge as well as the lack of awareness ofthe miners. The miners do not use personal protective equipment and they work in unsafe conditions, such as working in unsupported locations or digging and excavating on unstable slopes. Therefore there are frequently many accidents which is some cases are fatal.

According to the report of N.D. Soemantri (2010), several mining accidents caused by underground collapses that resulted in dozens of deaths were recorded. Furthermore, there are many mining accidents that result in either injuries or fatalities that are not reported. Therefore, to date there is no accurate data regarding mining accidents in Indonesia.

Rock mechanics is a science that studies the characteristics and behavior of a rock mass that can be used for designing underground stability. The application of the principles of rock mechanics can assist miners in performing their activities safely. Using the case study from West Lombok, Indonesia as one of small-scale mining centers, it is expected that methodology and principles of rock mechanics can be applied to other small-scale mines.

2 SMALL-SCALE MINING IN WEST LOMBOK, INDONESIA

West Lombok is located on Lombok Island, West Nusa Tenggara Province, Indonesia (Fig. 1). Geographically, Lombok Island lies between 115°46'–116°28' E and 8°12' – 8°55' S.



Figure 1. Map of Indonesia.

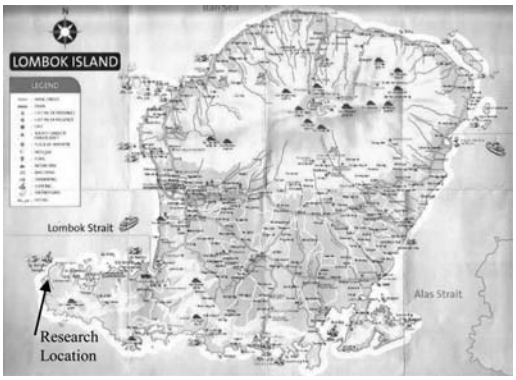


Figure 2. Lombok Island, Indonesia.

Generally, small-scale mining on West Lombok is located in the Pelangan Forest and Kedaro Forest. Starting at the exploration area of PT. Newmont Nusa Tenggara and PT. Indotan Inc., small-scale mining spread to other locations on Central Lombok and East Lombok. A map of Lombok Island is presented in Figure 2.

This research was carried out in one of small-scale underground mines on Selindungan Mountain, West Pelangan.

3 SMALL-SCALE MINING ACTIVITIES IN PELANGAN VILLAGE, WEST LOMBOK

The underground mining method used at the research location is *gophering/coyoting*. This method is an unsupported method or one that uses very few supports. Usually, the gophering method uses unskilled laborers and simple methods. The mine tunnel is dug toward the ore bodies in an irregular manner.

3.1 *Access development*

The access tunnel in small-scale mining is developed using simple equipment such as hammers, crowbars, chisels and head lamps. Generally, the dimensions of a tunnel are 0.8–1.5 m and can only be used by one person. There are two types of access to the ore, horizontal and vertical openings.

3.2 *Supporting system*

One problem of underground mining activities is the stability of excavations. To maintain the stability of an underground excavation, it is necessary to build a supporting system in the weak areas of both the vertical and horizontal openings. The type of supporting wood depends on the type of mine. A mining operation or individual miner who has made a large investment uses high-quality wood such as mahogany, albacia and coconut, while those who have a smaller investment use other wood such as caruy, carelang and kilimari.



Figure 3. Supporting system for a horizontal tunnel.



Figure 4. Supporting system for a raise.

Figure 3 and Figure 4 show examples of supporting systems in mine tunnels.

3.3 *Process for accessing and mining the ore*

As is the case with the development of access into and within the mine, the ore bodies are excavated using simple tools such as hammers, crowbars and chisels. The excavation follows the direction (strike) of the orebody, moving from the top to the bottom of the orebody. During the excavation process, the miner usually leaves a pillar, called an "ambuhan" (usually any ore bodies that are not profitable or those that are of a low grade).

The "ambuhans" are also intended to be the pillars that maintain the stability of the underground tunnels. When all of the ore bodies that could be mined are exhausted, some miners then excavate the "ambuhans" from the bottom to the top of the tunnel. Figure 5 shows the process that is used to access and mine the ore.

3.4 *Ore transport system*

The transport of the ore and waste rock is conducted semi-mechanically and manually via a main haulage



Figure 5. Manual ore mining.



Figure 6. Ore transport using pulleys.

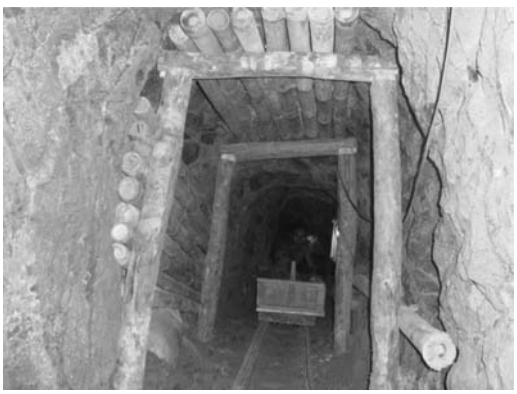


Figure 7. Ore transport using a lorry.

system. The broken ore and rock are placed in a sack and then it is transported to the surface. The transport system in vertical holes uses pulleys (Fig. 6), while the transport system in a horizontal system uses timber lorries (Fig. 7).



Figure 8. A fan for a ventilation system.



Figure 9. Drainage system using a pump.

3.5 *Ventilation system*

Underground mines are not directly connected to the surface. Therefore, a fan is necessary to draw the air from the surface into the underground tunnels. If the temperature in the tunnel increases, a fan will be installed at the entrance to draw the air out of the mine through the entrance.

In several mine tunnels, there are many entrances and many holes are connected to the surface. Thus, the air will be drawn to the mine entrance. This will reduce the number of fans that are required. Figure 8 shows the type of fan that is used to draw air into the underground tunnels.

3.6 *Drainage system*

To expel the water from underground tunnels, the miners transfer the water into an unused tunnel either manually or by using a pump. If the water is shallow, the water is drained out to the surface. Figure 9 shows the types of pumps that are used to drain water into an unused hole.

4 ROCK MASS CLASSIFICATION FOR SMALL-SCALE MINES

Hoek et al. (1995) stated that during the feasibility and preliminary design stages of a project, when very little detailed information is available on the rock mass and its stress and hydrologic characteristics, the use of a rock mass classification scheme can be of considerable benefit.

Small-scale mining comprises mining that is usually done by people that have little or no education, a small capital investment and for which there is a limited amount of information about the rock characteristics. The application of the principles of rock mechanics such as rock mass classification should be done as they are both practical and easy to understand. The rock sampling methods, gathering of laboratory data and the determination of rock class must be simple and practical in order to reccomend ways to increase underground stability.

4.1 *Rock sampling*

Rock sampling in small-scale mining activities cannot use full core drilling. Rock samples are taken from a tunnel wall and placed into a plastic sample container to be tested in the laboratory.

4.2 *Rock Description*

Obtaining a rock description is usually done megascopically without using a microscope. The rock type in the investigated location is dominated by tuff and sandstone tuff, the majority are a brown or white-grayish color, the hardness is between 2–6, fine-to-medium grained and have a good porosity.

The rock density was obtanied by doing a comparison between the volume and weight of the rock samples using a simple method. The apparatus used a beakers to calculate the volume of the rock sample and digital scales to obtain the weight of the rock samples. The density of the rock at the research location is between 1.7–2.6 g/cm^3.

4.3 *Rock Mass Rating*

4.3.1 *Point Load Test*

The point load test was conducted to determine the strength of a rock sample when the sample is subjected to force at a single focal point. The results of a point load test are used to get the value of the point load index that can be used to predict the uniaxial compressive strength value of these samples (see Table 1).

Table 1. Point load strength test results.

Depth m	P N	De cm	Is (N/m^2)	UCS MPa	Rating
0–1	0.1	5.02	39.68	0.95	0
1–2	0.8	3.73	575.01	13.8	2
5–6	0.1	4.14	58.34	1.40	1
10–11	0.3	7.80	49.31	1.18	1
16	1.0	4.13	586.27	14.07	2
18	0.8	4.85	340.10	8.16	2
19	0.5	5.07	194.52	4.67	1

4.3.2 *Rock Quality Designation (RQD)*

RQD is a parameter that describes the quality of a rock mass based on the rock core. If there no full coring activities can be performed, Palmström (1982) suggested that the RQD can be estimated from the number of discontinuities per unit volume using the following equation:

$$RQD = 115 - 3.3Jv \quad (1)$$

where Jv is the sum of the number of joints per unit length for all of the joints (the volumertic joint count)

The value of the RQD indicated that the rock mass is in either a good or very good condition (see Table 2).

4.3.3 *Spacing and Condition of Discontinuities*

The spacing of the discontinuites was measured using a compass and measurement apparatus. Table 3 and Table 4 show the ratings for the spacing and condition of the discontinuities the in mine tunnel.

4.3.4 *Groundwater condition*

The majority groundwater conditions in mine tunnels are dry. Therefore, the rating for the groundwater condition is 15.

Table 2. Rock Quality Designation.

Distance m	Joint	RQD (%)	Description	Rating
0–1	6	95.2	Very good	20
1–2	8	88.6	Good	17
5–6	7	91.9	Very good	20
6–7	7	91.9	Very good	20
10–11	8	88.6	Good	17
11–12	7	91.9	Very good	20
18–19	8	88.6	Good	17
19–20	8	88.6	Good	17

Table 3. Spacing of discontinuities in a mine tunnel.

Distance m	Spacing cm	Rating
0–1	11.2	8
1–2	12.4	8
5–6	11.8	8
6–7	12.3	8
10–11	9.8	8
11–12	8.8	8
18–19	7.4	8
19–20	8.1	8

4.3.5 *Orientation of the discontinuities relative to the mine tunnel axis*

The discontinuity orientation is a parameter that is used to adjust the rock mass rating. It depends on the orientation of the mine tunnel axis and the excavation direction relative to the dip and strike of the discontinuities that occur in rock masses. Table 6 shows the adjustment rating because of the effect of the orientation of discontinuities to the mine tunnel axis.

4.3.6 *Rock Mass Classification*

From the observations and measurements, this will have a rating of five parameters. The final RMR will be obtained after it is reduced with an adjustment rating (Table 5) and this will be used to determine the rock class. Table 6 shows the RMR value and the Rock Mass Classification.

Table 4. Conditions of discontinuities in a mine tunnel.

Distance m	L cm	W mm	Surface	Filling	Weathered	Rating
0–1	66	4	Slighty rough	Tuff <5 mm	Slighty	15
1–2	112	9	Slighty rough	Tuff <5 mm	Slighty	11
5–6	117	5	Slighty rough	Clay >5 mm	Slighty	7
6–7	132	20	Slighty rough	Clay <5 mm	Slighty	9
10–11	33	20	Slighty rough	Clay <5 mm	Slighty	13
11–12	46	2	Slighty rough	Tuff >5 mm	Slighty	13
18–19	65	24	Slighty rough	Clay >5 mm	Slighty	11
19–20	83	30	Slighty rough	Clay <5 mm	Slighty	13

Table 5. Effect of the orientation of the discontinuities relative to the mine tunnel axis.

Tunnel Axis N E	Distance m	Strike/ Dip N E/^{0}	Effect	Rating
210–230	1–2	295/64^0	Very favorable	0
		276/65^0	Very favorable	0
160–190	5–17	272/14^0	Unfavourable	−10
		115/59^0	Fair	−5
		39/64^0	Fair	−5
		29/71^0	Very unfavorable	−12
		243/49^0	Very favorable	0
		69/74^0	Very favorable	0
		234/31^0	Favorable	−2
		234/39^0	Favorable	−2
130–150	17–20	217/72^0	Very favorable	0
		246/70^0	Very favorable	0

An RMR value between 43–60 indicates that the rock mass is within the fair rock categories, but it must be kept in mind that at some locations, the rock mass is on the border between the fair rock and poor rock categories.

The value of RMR can be used to predict the Stand-up time of a tunnel with certain dimensions. Lauffer (1958) stated that the stand-up time for an unsupported span is related to the quality of the rock mass in which the span is excavated. In a tunnel, the unsupported span is defined as the span of the tunnel or the distance between the face and the nearest support, if this is greater than the span of the tunnel.

In this research, the span of the mine tunnel was 65 cm. According to Figure 9, no support is required for the mine tunnel in Selindungan. If, however, there are stability problems during the excavation process and it is necessary to stabilize it, then it should be possible to install the support.

Table 6. RMR value and rock quality.

Parameter	Value	Rating
Point load		2
RQD	88.6–95.2	17–20
Spacing of discontinuities	7.4–11.4	8
Condition of discontinuities	Slightly rough Separation <5 mm Slightly weathered	7–15
Groundwater condition	dry	15
Adjustment (orientation of discontinuities)		−3
RMR		43-60
Rock Class		III
Rock Quality		Fair
Stand-up time		

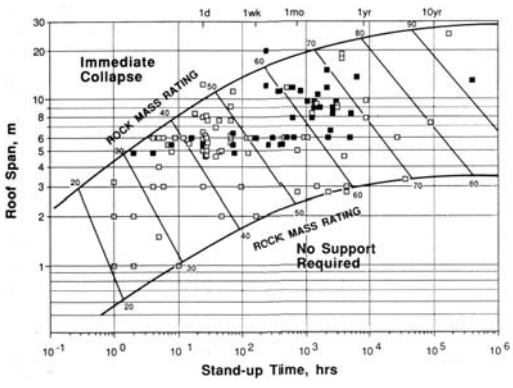


Figure 10. Relationship between stand-up time, span and RMR classification after Bieniawski (1989).

5 CONCLUSIONS

Based on the calculation, the RMR value of mine tunnels are between 43–60 and the rock class is fair rock (class III).

The dimensions of the mine tunnel of 65 cm has some advantages for underground stability. No support is required.

If the span of the mine tunnel is enlarged, the stand-up time will decrease, and therefore a support system will be required.

The methodology of rock mechanics, especially rock mass classification, can be applied in practice for small-scale mining in order to assist domineers in performing their activities safely.

ACKNOWLEDGEMENTS

The authors would like to acknowledge the Department of Energy and Mineral Resources, Republic of Indonesia on behalf of N. Diding Soemantri, M. Dipha Kurnia and Sandi Firmanulhaq for permission to do the research.

REFERENCES

Bieniawski, Z.T. 1989. *Engineering Rock Mass Classifications.* New York: Wiley.

Dinas Pekerjaan Umum Pertambangan dan Energi, 2008. *Kebijakan Pertambangan Umum di Kabupaten Lombok Barat*. Mataram: Unpublished

Soemantri, N.D. 2010. *Laporan Koordinasi Penertiban Pertambangan Liar di Lombok Barat*. Dinas Pertambangan dan Energi Provinsi Nusa Tenggara Barat. Mataram: Unpublished.

Hoek, E. & Brown, E.T. 1980. *Underground Excavation in Rock*. London: Institution of Mining and Metallurgy.

Hoek, E., Kaiser, P.K. & Bawden, W.F. 1995. *Support of Underground Excavations in Hard Rock.* Rotterdam: Balkema.

Lauffer, H. 1958. Gebirgsklassifizierung für den Stollenbau. *Geologie und Bauwesen* 24(1): 46–51, in E. Hoek et al. 1995. *Support of Underground Excavations in Hard Rock.* Rotterdam: Balkema

Milne, D., Hadjigeorgiou, J. & Pakalnis, R. 1998. Rock mass characterization for underground hard rock mines. *Tunnelling and Underground Space Technology* 13(4): 383–391.

Palmström, A. 1982. The volumetric joint Mount – a useful and simple measure of the degree of rock jointing. In *Proc. 4th Int. Congress of IAEG,* New Delhi, pp. V.221–V.228.

Rusnak, J. & Mark, C. 2000. Using the point load test to determine the uniaxial compressive strength of coal measure rock. In S.S. Peng & C. Mark (eds), *Proceedings of the 19th International Conference on Ground Control in Mining,* Morgantown, WV, pp. 362–371.

Tony S. 2002. *Analisa Kestabilan Terowongan Menggunakan Metode RMR di PT ANTAM*. Jakarta: Unpublished.

Rock Mechanics for Resources, Energy and Environment – Kwaśniewski & Łydżba (eds)
© 2013 Taylor & Francis Group, London, ISBN 978-1-138-00080-3

Index of time-dependency for rock and its application for the assessment of the long-term stability of underground structures

K. Hashiba & K. Fukui
Department of Systems Innovation, University of Tokyo, Tokyo, Japan

ABSTRACT: Previous experimental and theoretical studies showed that rock strength was proportional to the $1/(n+1)$-th power of loading-rate and creep lifetime was inversely proportional to the n-th power of creep stress, where n was the constant value depending on rock type and testing environment. This paper introduced the n values of various rocks and analyzed the relation of the n value to the loading condition, testing environment and other mechanical properties. The n values were almost constant in unconfined various loading conditions if rock type and testing environment were same. The n value decreased in water-saturated condition and increased under confining pressure in proportion to strength. The effect of time was incorporated into Rock Mass Rating (RMR) with the aid of the n value. A formula representing the reduction of RMR due to time was proposed.

1 INTRODUCTION

Understanding time-dependency of rock is indispensable for geotechnical applications to estimate long-term deformation and stability of underground structures. In previous studies the authors investigated the time-dependent behaviors of rock such as loading-rate dependency of strength (Hashiba et al. 2006, Hashiba et al. 2011) and creep (Shin et al. 2005, Okubo et al. 2010). The results showed that peak and residual strengths were proportional to the $1/(n+1)$-th power of loading-rate, where n was the constant value depending on rock type and testing environment. It was also found that creep lifetime was inversely proportional to the n-th power of creep stress, where n was the same value as the loading-rate dependency under the same loading condition and testing environment. Therefore the n value can be an index of time-dependency for rock. The smaller the n value, the larger the time-dependency of rock, that is the larger the increase of strength with an increase in loading-rate and the larger the increase of creep lifetime with a decrease in creep stress. Okubo et al. (2013) reported the n values obtained in previous studies for ten Japanese rocks and a Chinese coal. This paper introduces the results and analyzes the relation of the n value to the loading condition, testing environment and other mechanical properties of rock.

Up to now many researchers and engineers have proposed various rock mass classification systems for engineering design and stability analysis of underground structures (Singh & Goel 2011). However, time dependent effects have been considered only in few classification systems (Kalamaras & Bieniawski 1995), because an appropriate index of time-dependency for rock mass is missing. The n value representing the time-dependency of rock specimens is probably a useful index for rock mass characterization. In this study, with the aid of the n value, the effect of time is incorporated into Rock Mass Rating, RMR (Bieniawski 1989), which is one of the famous classification systems used in the world.

2 INDEX OF TIME-DEPENDENCY FOR ROCK

2.1 *Loading-rate dependency and creep*

Previous studies showed that rock strength σ_f increased with an increase in loading-rate C. The following formula has been used for the relation between σ_f and C (Sano et al. 1981, Lajtai et al. 1991, Fukui et al. 2004, Hashiba et al. 2006).

$$\sigma_f \propto C^{\frac{1}{n+1}} \tag{1}$$

Stress-rate, strain-rate or a linear combination of them have been used as the loading-rate C (Okubo et al. 1990).

The relation between loading-rate dependency and creep will be examined theoretically as follows. Speed λ of process leading to failure is assumed to be proportional to the n-th power of stress σ.

$$\lambda = a\sigma^n \tag{2}$$

The failure process has to be interpreted as crack growth from a microscopic view (Sano et al. 1981) or as stiffness degradation from a macroscopic view (Okubo & Fukui 2006). Failure criterion is assumed as follows;

$$\Lambda = \int \lambda dt \tag{3}$$

where t is time and Λ is the value affected by rock types and testing conditions. In a strength test with a constant stress-rate, the following relation between strength σ_f and stress-rate C is obtained by substituting $\sigma = Ct$ into Equation 2 and then 3.

$$\sigma_f = \left\{ \frac{(n+1)\Lambda C}{a} \right\}^{\frac{1}{n+1}} \quad (4)$$

Testing results with constant stress-rate, strain-rate and a linear combination of them are similar in pre-failure region, and therefore Equation 4 indicates that strength is proportional to the 1/(n + 1)-th power of loading-rate as Equation 1.

In a creep test, the following relation between creep lifetime t_{cr} and creep stress σ_{cr} is obtained by substituting $\sigma = \sigma_{cr}$ into Equations 2 and then 3.

$$t_{cr} = \frac{\Lambda}{a\sigma_{cr}^{\,n}} \quad (5)$$

This equation shows that creep lifetime is inversely proportional to the n-th power of creep stress. In previous studies the n value obtained from strength tests with Equation 1 corresponded to the one from creep tests with Equation 5 (Hashiba et al. 2006). The experimental and theoretical results indicate that the n value can be an index of time-dependency for rock.

2.2 *Testing methods to obtain n values*

Figure 1 (a)–(c) shows the testing methods used to obtain the n value in strength tests. In this paper, "strain rate" indicates "axial strain rate". In the multi-strain rate test (MS) shown in (a), a specified strain rate C is applied to each specimen and the peak strength σ_f is recorded. Figure 2 provides some examples of testing results of MS. The n value can be obtained from the straight line in Figure 2(b) which slope is 1/(n + 1). This is a conventional method, which is dependable if one can use homogeneous rock blocks. However, this method has the disadvantage that a large number of specimens has to be tested. For example, if four loading rates and five specimens for each loading rate are tested, a total of twenty specimens is needed for a single set of tests with a homogeneous rock block.

Okubo et al. (1990) proposed the SS method in Figure 1(b); the stepwise strain rate increase is conducted while observing the stress-strain curve. As an example of the testing result of SS shown in Figure 3, the strain rate is increased just before peak strength, and the n value can be obtained by substituting σ_1 and σ_2 into Equation 1. This method allows the researcher to obtain the n value from a single specimen, but it takes sophisticated technology and much experience to appropriately select the time to raise the strain rate. In particular it is difficult to apply this method to brittle rocks.

Figure 1(c) shows the most recently developed method (AS) (Hashiba et al. 2006). The strain rate is alternated between two stages of high and low values during the test, for example the rates are 10^{-4} and 10^{-5}/s. As an example of the testing result of AS shown in Figure 4, inner and outer envelope curves of the stress-strain curve are assumed to be the stress-strain curves corresponding to the two loading-rates. The n value can be obtained by substituting the peak strength σ_1 and σ_2 along the envelope curves into Equation 1. In this method, the n value can be obtained from a single specimen and the strain rate is simply alternated between two values, so no sophisticated technology is needed. This method is a recommended one, which has wide applicability to various rock types.

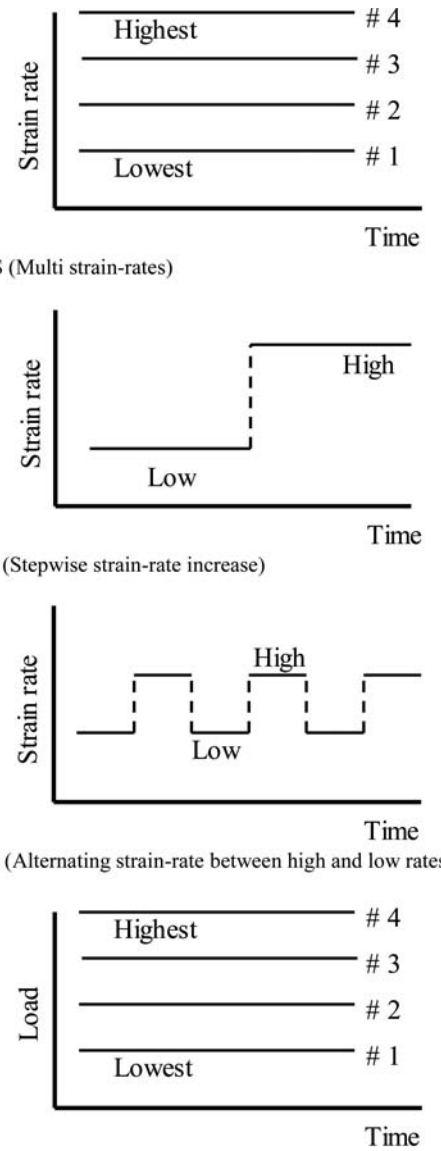
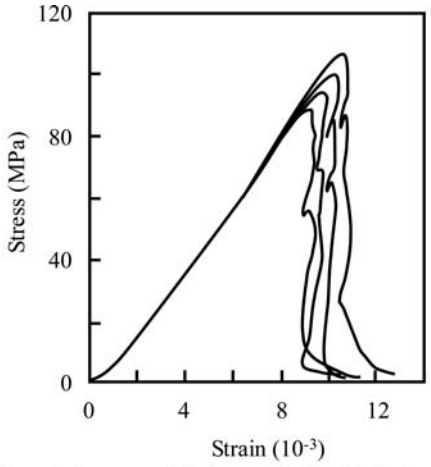
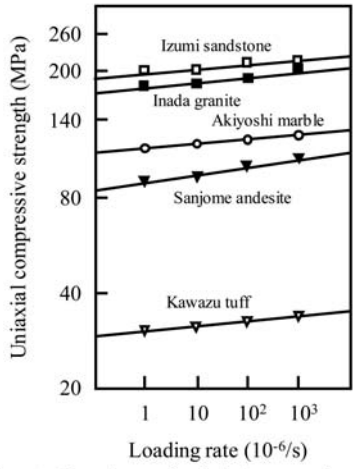


Figure 1. Four testing methods to obtain n values (Okubo et al. 2013).



(a) Stress-strain curves of Sanjome andesite with the loading-rates 10^{-6}, 10^{-5}, 10^{-4} and 10^{-3} /s.



(b) Loading-rate dependency of uniaxial compressive strength.

Figure 2. Testing results of MS method (Okubo et al. 1990). Tests were conducted with constant loading-rate, which was a linear combination of stress- and strain-rates.

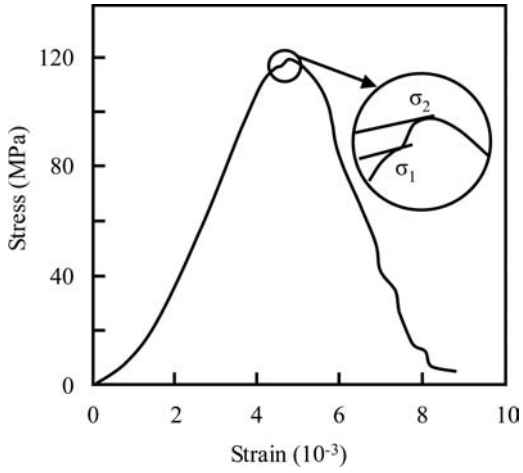


Figure 3. Testing result of SS method with Akiyoshi marble (Okubo et al. 1990). Strain-rate was increased by tenfold just before the peak strength.

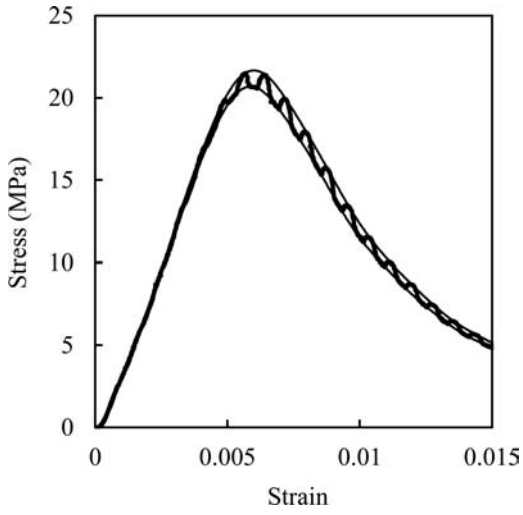


Figure 4. Testing result of AS method with Tage tuff (Hashiba et al. 2006). Strain-rate was alternated between 10^{-4} and 10^{-5}/s. Two thin lines are inner and outer envelope curves.

As mentioned in the foregoing chapter, the n value can be obtained from creep tests. In the multi-level creep test (ML) shown in Figure 1(d), the n value can be obtained by substituting creep lifetime t_{cr} and creep stress σ_{cr}, into Equation 5. For the specimen to fail in the creep test, a long time is needed, so this cannot be considered a common method.

3 N VALUES FOR VARIOUS ROCKS

Okubo et al. (2013) reported the n values for ten Japanese rocks with testing environment, loading conditions and testing methods, which we used for a detailed analysis. The n values were almost constant in various testing methods shown in Figure 1 if rock type, testing environment and loading conditions were same as described in Okubo et al. (2013), so the values in unconfined condition are rearranged and shown in Table 1.

The rock, for which the greatest amount of test data was available, was Sanjome andesite. Tests were conducted intermittently over a long period and specimens were made from several blocks. However, the coefficient of variation of the n value 5.3% was much smaller than that of strength 13% in uniaxial compression and air-dried condition. In air-dried condition the n values of Sanjome andesite were between 35 and 41 in uniaxial compression, uniaxial tension, Brazilian tension, three point bending and shear tests, which indicates that the n value did not depend on the loading conditions. The n value in uniaxial compression tests corresponded to that in Brazilian tension tests under

Table 1. Testing results under unconfined condition.

Rock	Test	Air-dried Strength (MPa)	n	Water-saturated Strength (MPa)	n
Sanjome andesite	UC	85	37	69	29
	UT	5.4	38		
	BT	5.6	41	4.1	28
	BD	6.7	35		
	SH	20	38		
Tage tuff	UC	18	47	8.0	22
	UT	1.2	46		
	BT	1.3	45		
Inada granite	UC	183	47	184	42
Kawazu tuff	UC	34	60	23	42
Oya tuff	UC	12	40	5.0	16
Izumi sandstone	UC	200	59		
Kimachi sandstone	UC	40	42		
Tako sandstone	UC	33	72		
Akiyoshi marble	UC	112	68		
Dotan (hardpan)	UC	4.2	30		

UC: Uniaxial compression test, UT: Uniaxial tension test, BT: Brazilian tension test, BD: Three point bending test, SH: Direct shear test. Strength: Strain-rates were 10^{-5} and 10^{-6}/s in compression and tension.

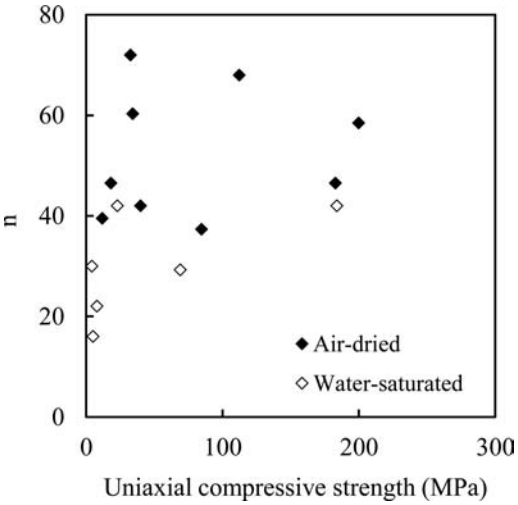


Figure 5. Relation between the n value and uniaxial compressive strength.

water-saturated condition. The strength and n value in water-saturated condition were 70–80% of those in air-dried condition, which was probably due to chemical reaction with water.

The n values of Tage tuff were almost constant in uniaxial compression, uniaxial tension and Brazilian tension tests. The strength and n value in water-saturated condition were less than half of those in air-dried condition. The strengths and n values of Kawazu and Oya tuff also decreased notably with water. The strength did not change but the n value decreased slightly with water for Inada granite. The

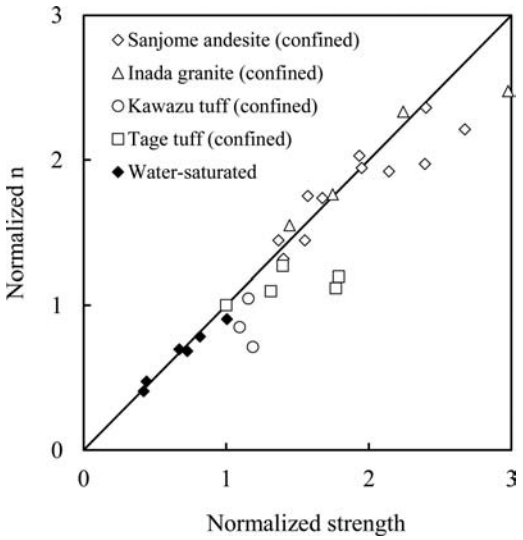


Figure 6. Relation between normalized n and normalized strength in water-saturated and confined conditions. Results of Sanjome andesite, Inada granite, Kawazu tuff, Oya tuff and Tage tuff in water-saturated condition are included.

n values of ten rocks are between 30 and 80 in air-dried condition, and some n values are less than 30 in water-saturated condition. Figure 5 shows the relation between the uniaxial compressive strength and n value of each rock. There is no definite correlation between them and therefore the n value cannot be estimated from rock strength.

Okubo et al. (2013) investigated the relation between the confined strength and n value normalized with the values in unconfined condition. The relation between them was approximated with a straight line as shown in Figure 6. In this paper the uniaxial compressive strength and n value in water-saturated condition are normalized with the values in air-dried condition and shown in the same figure. The relation between them was approximated with the same straight line whose slope is one.

The strength σ_f and n in air-dried condition are assumed to change to σ_f' and n′ with water or confining pressure. The strength increases $\Delta\sigma_f$ and $\Delta\sigma_f'$ with an increase in loading-rate from C_1 to C_2 are calculated with Equation 1 and expansion into power series as follows;

$$\Delta\sigma_f = \left\{\left(\frac{C_2}{C_1}\right)^{\frac{1}{n+1}} - 1\right\}\sigma_f \approx \frac{\sigma_f}{n+1}\ln\frac{C_2}{C_1} \tag{6}$$

$$\Delta\sigma_f' = \left\{\left(\frac{C_2}{C_1}\right)^{\frac{1}{n'+1}} - 1\right\}\sigma_f' \approx \frac{\sigma_f'}{n'+1}\ln\frac{C_2}{C_1} \tag{7}$$

The following formula can be obtained from the equations.

$$\frac{\Delta\sigma'_f}{\Delta\sigma_f}=\frac{n+1}{n'+1}\frac{\sigma'_f}{\sigma_f}\approx\frac{n}{n'}\frac{\sigma'_f}{\sigma_f} \tag{8}$$

where n, n′ ≫ 1. Normalized σ'_f/σ_f and n′/n are almost equivalent under water-saturated or confined condition as shown in Figure 6 and therefore $\Delta\sigma'_f \approx \Delta\sigma_f$. The result indicates that the strength increase with an increase in loading-rate is constant in air-dried/water-saturated and unconfined/confined conditions, and that the n value in water-saturated or confined condition can be estimated from the air-dried and unconfined data.

4 RMR AND N VALUES

In previous studies various rock mass classification systems were proposed, but time effects have been considered only in few systems. To classify rock masses, RMR uses six parameters; Uniaxial compressive strength of rock material, rock quality designation (RQD), spacing of discontinuities, condition of discontinuities, groundwater conditions and orientation of discontinuities. Kalamaras & Bieniawski (1995) examined the effect of time on RMR and proposed the following formula;

$$RMR_t = RMR - 0.14T_m \tag{9}$$

where RMR_t represents the RMR after T_m years. Equation 9 indicates that RMR decreases with time, but the decrement $0.14T_m$ seems to be arbitrary. In this paper, with the aid of the n value, the effect of time is incorporated into *RMR*.

Rock mass strength is assumed to decrease with time as Equation 5.

$$\frac{\sigma_{FL}}{\sigma_F}=\left(\frac{T_{FL}}{T_F}\right)^{-\frac{1}{n}} \tag{10}$$

where σ_F is the stress under which rock mass will fail immediately in the short period of time T_F, namely commonly-used rock mass strength. σ_{FL} is the stress under which rock mass will fail after the long period of time T_{FL}. As shown in Figure 7 providing the relation between σ_{FL}/σ_F and T_{FL}/T_F, rock mass strength decreases with an increase in the period of time or a decrease in the n value.

Relation between RMR and rock mass properties has been researched, and the following empirical equation was proposed for the relation between RMR and rock mass strength (Zhang 2010).

$$\frac{\sigma_F}{\sigma_f}=\exp\left\{\frac{\alpha(RMR-100)}{\beta}\right\} \tag{11}$$

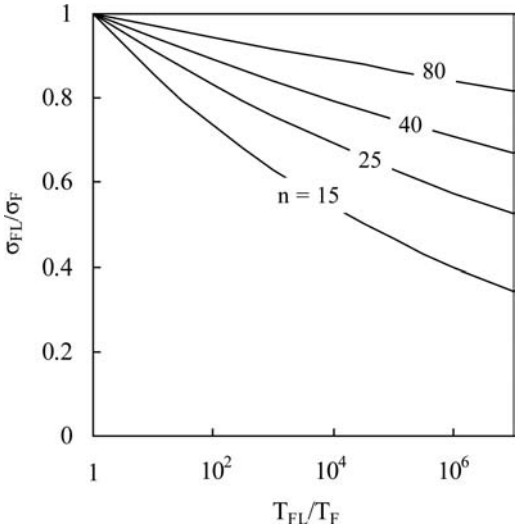


Figure 7. Relation between σ_{FL}/σ_F and T_{FL}/T_F in Equation 10. σ_{FL} and σ_F are the stresses under which rock mass will fail after the period of time T_{FL} and T_F, respectively.

Table 2. Values of α and β in Equation 11 proposed in previous studies (Zhang 2010).

Proposed by	α	β
Yudhbir & Prinzl	7.65	100
Ramamurthy	1	18.75
Kalamaras & Bieniawski	1	24
Sheorey	1	20

where σ_F and σ_f are unconfined compressive strength of rock mass and intact rock, respectively. α and β are constants, and their values proposed in previous studies are in Table 2. The following formula is obtained by changing σ_F into σ_{FL} and RMR into RMR_t in Equation 11.

$$\frac{\sigma_{FL}}{\sigma_f}=\exp\left\{\frac{\alpha(RMR_t-100)}{\beta}\right\} \tag{12}$$

The following formula is obtained from Equations 10, 11 and 12:

$$RMR_t = RMR-\frac{\beta}{(\alpha\log e)n}\log\left(\frac{T_{FL}}{T_F}\right) \tag{13}$$

Equation 13 resembles Equation 9 but considers not only time but also the n value representing the degree of time-dependency of rock. The second term of the right side in Equation 13 is *RMR*'s decrement ΔRMR. When the values of α and β are constant, ΔRMR increases with an increase in T_{FL}/T_F or a decrease in the *n* value.

Figure 8 shows the relation between ΔRMR and T_{FL}, when T_F in which immediate collapse occurs is

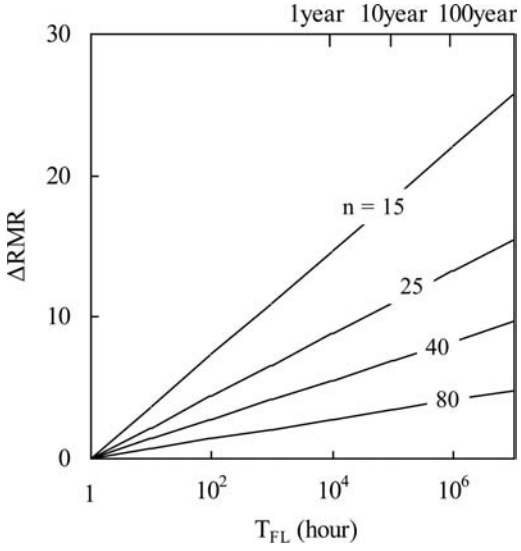


Figure 8. Relation between ΔRMR and T_{FL} calculated with Equation 13. In the equation ΔRMR is the second term of the right side, T_F, α and β are set to 1 hour, 1 and 24, respectively.

1 hour, α is 1 and β is 24. The values of α and β were employed in Kalamaras & Bieniawski (1995). According to the figure, when $n = 80$, ΔRMR after 100 years is less than 5, so the effect of time is not so critical. When $n = 15$, for example tuff in water-saturated condition as shown in Table 1, ΔRMR after 10 years is ca. 20, so the reduction of RMR due to time should be considered. The subjects of future research are to investigate whether the n values of rock masses are the same as those of rock specimens, and then to validate Equation 13 and Figure 8.

5 SUMMARY AND CONCLUSIONS

Previous experimental and theoretical studies showed that rock strength was proportional to the 1/(n + 1)-th power of loading-rate and creep lifetime was inversely proportional to the n-th power of creep stress, where n was the constant value depending on rock type and testing environment. This paper introduced the n values of various rocks and analyzed the relation of the n value to the loading condition, testing environment and other mechanical properties of rock. The n values were almost constant in unconfined various loading conditions if rock type and testing environment were same. The n value decreased in water-saturated condition and increased under confining pressure in proportion to strength.

The effect of time was incorporated into RMR with the aid of the n value. A formula representing the reduction of RMR due to time was proposed. The n value will probably be an appropriate index of time-dependency for not only rock specimen but also rock mass. Validation of the application of the n value to rock mass classification systems is the subject of future investigation.

REFERENCES

Bieniawski, Z.T. 1989. *Engineering rock mass classifications*, Chapter 4, New York, Wiley-Interscience.

Fukui, K. Okubo, S. & Ogawa, A. 2004. Some aspects of loading-rate dependency of Sanjome andesite strengths, *Int. J. Rock Mech. Min. Sci.* 41: 1215–1219.

Hashiba, K. Okubo, S. & Fukui, K. 2006. A new testing method for investigating the loading rate dependency of peak and residual rock strength, *Int. J. Rock Mech. Min. Sci.* 43: 894–904.

Hashiba, K. Okubo, S. & Fukui, K. 2011. Alternating loading-rate test and its application in estimating long-term behavior of rock, *Proceedings of 45th US Rock Mechanics/Geomechanics Symposium*, No.11–202.

Kalamaras, G.S & Bieniawski, Z.T. 1995. A rock mass strength concept for coal seams incorporating the effect of time, *Proceedings eighth international congress on rock mechanics*, 1, 295–302.

Lajtai, E.Z. Scott Duncan, E.J. & Carter, B.J. 1991. The effect of strain rate on rock strength, *Rock Mech. Rock. Engng.* 24: 99–109.

Okubo, S. & Fukui, K. 2006. An analytical investigation of a variable-compliance-type constitutive equation, *Rock Mech. Rock Engng.* 39: 233–253.

Okubo, S. Nishimatsu, Y. & He, C. 1990. Loading rate dependence of class II rock behavior in uniaxial and triaxial compression tests – An application of a proposed new control method, *Int. J. Rock Mech. Min. Sci. & Geomech. Abstr.* 27: 559–562.

Okubo, S. Fukui, K. & Hashiba, K. 2010. Long-term creep of water-saturated tuff under uniaxial compression, *Int. J. Rock Mech. Min. Sci.* 47: 839–844.

Okubo, S. Hashiba, K. & Fukui, K. 2013. Loading rate dependency of the strengths of some Japanese rocks, *Int. J. Rock Mech. Min. Sci.* 58: 180–185.

Sano, O. Ito, I. & Terada, M. 1981. Influence of strain rate on dilatancy and strength of Oshima granite under uniaxial compression, *J. Geophys. Res.* 86(B.10): 9299–9311.

Shin, K. Okubo, S. Fukui, K. & Hashiba, K. 2005. Variation in strength and creep life of six Japanese rocks, *Int. J. Rock Mech. Min. Sci.* 42: 251–260.

Singh, B. & Goel, R.K. 2011. *Engineering rock mass classification*, Waltham, Butterworth-Heinemann.

Zhang, L. 2010. Estimating the strength of jointed rock masses, *Rock Mech. Rock Engng.* 43: 391–402.

Rock Mechanics for Resources, Energy and Environment – Kwaśniewski & Łydżba (eds)
© 2013 Taylor & Francis Group, London, ISBN 978-1-138-00080-3

Rock ledge support design. A deterministic and stochastic approach

J. Jakubowski
AGH University of Science and Technology, Krakow, Poland

J.B. Stypulkowski
CDM Smith, Doha, Qatar

ABSTRACT: In engineering practice, rock ledge stability analysis is often performed as a two-dimensional failure analysis, where the single sliding plane is defined by the problem geometry and not the actual joints geometry. This was the case with the Yard Trench Lead in Sunnyside Yard, an element of the East Side Access Project in NYC. A probabilistic wedge stability analysis, including surcharge load and rock bolt reinforcement, was presented and discussed as a design alternative. The transition from 2D to 3D and from a deterministic to a stochastic approach, with the use of the geological joint orientation data, was shown to provide a more realistic view of the initial support design and to have the potential of leading to reductions in the initial support costs.

1 INTRODUCTION

Reinforcement and support requirements in blocky rock mass have commonly been assessed by means of a rigid blocks limit equilibrium stability analysis. This approach has been confirmed by site observations and proven in engineering practice when empirical, rock mass quality classification-based methods are unable to project structural failure. The relevant solutions have been presented, *inter alia*, by Wittke (1965), Priest (1980), Lucas (1980) and Bray & Brown (1976). The problem of arbitrary polyhedral block stability analysis was solved by Warburton (1981), Goodman and Shi (1985), Lin and Fairhurst (1988) and others. The method put forward by Goodman and Shi (1985) was used in this study for computations. It is popular and refers not only to a particular block, but to blocky rock mass in general, as well. While most of the methods consider the sliding and falling modes of failure, the problem of rotational failure has also been addressed (Mauldon 1995a, Wittke 1990).

As a result of the limited information on discontinuities and their highly stochastic nature, uncertainty constitutes the central problem of analyses and their interpretation in jointed, blocky rock mass. A solution to this problem is brought about by probabilistic methods, either analytical or simulation (for example, McMahon 1971, Priest & Brown 1983, Park et al. 2005, Hatzor 1993, Hoerger & Young 1990, Mauldon 1995b, Jakubowski & Tajdus 1995, Jakubowski 2011). The statistical description of a joint network is crucial for stochastic joint geometry modeling and probabilistic stability analysis in a blocky rock mass (Hudson & Priest 1983, Mauldon et al. 2001, Zhang & Einstein 2000, Kulatilake 2001, Shanley & Mahtab 1976, Chiles 1987, Dershowitz & Einstein 1988).

A good alternative for the rigid block, limit equilibrium methods is provided by the Discrete Element Methods (Cundall 1988, Shi 2001), also used as a stochastic DEM (Jakubowski & Starzec 2002).

2 YARD TRENCH LEAD CONSTRUCTION

Metropolitan Transit Authority Capital Construction's East Side Access Project is designed to provide Long Island commuters with direct access to Manhattan's Grand Central Terminal. The connection in Sunnyside Yard involved tunneling and a cut-and-cover structure. This served as launch pad for the construction of four tunnels in Queens. Three TBMs with a diameter of 6.55 m were launched through the semi-circular slurry wall and one through the rock outcrop below it. Launching the lowest TBM for the tunnel required the excavation of the long trench known as the Yard Trench Lead (YTL), where the TBM could be assembled as shown in Figure 1. The entire north wall rock ledge was designed to be supported by pattern bolting. Five 2.5-cm diameter bolts, spaced every 1.5 m were applied to support the TBM and the rock ledge. A shotcrete layer was placed in selected areas to prevent raveling.

3 GEOLOGY AND JOINTS

The rock was mapped as the Hartland Formation. At the site, it is hard to medium-hard, slightly weathered,

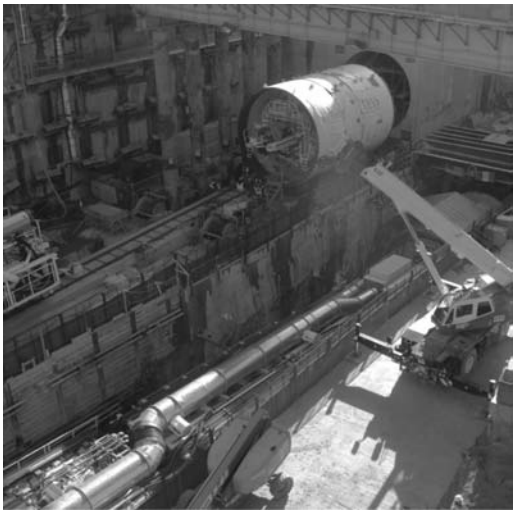


Figure 1. The top TBM was launched through the slurry wall and the bottom one through rock below the wall.

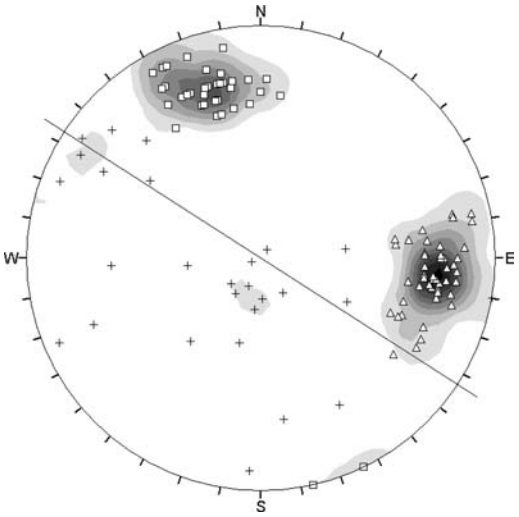


Figure 2. The two main joint sets identified.

fine to coarse grained black and white gneiss, trace pegmatite, jointed to massive, with joints that are slightly weathered, iron stained or mineral-coated with calcite, pyrite, and/or chlorite. The rock mass is generally blocky to massive. Geological data on rock cuts describing joint orientations was collected, however without the complete geological mapping and positioning of joint traces. There was thus insufficient information to enable the identification of the key blocks actually existing in the north wall rock ledge. Dominant joint sets include joints which run along the foliation and joints that cross the foliation, with some sub-horizontal joints. 121 highly persistent joints with no missing data, were qualified for analysis. Two major, distinct joint sets, plus several randomly distributed joints of various orientations, were identified (Fig. 2).

4 BLOCK SLIDE MODELS AND INPUT DATA

The 2D single plane sliding model geometry used for the original design at the YTL is presented in Figure 3, as are the minor modifications made for the purpose of this study. The top of the cut was horizontal and the rock cut face was vertical, $h = 9.14$ m high. For the 2D model, the critical slide plane was fixed by the width of TBM platform $b = 6.71$ m, giving the sliding plane dip angle of $\alpha = 53.8°$. A Coulomb strength model with a sliding plane friction angle of $\phi = 38°$ and zero cohesion was applied. The TBM platform load was assumed to be distributed uniformly on upper face with a pressure of $q_u = 88$ kPa. Rock bolts acted as passive support. The pattern bolting effect was represented by uniformly distributed force on wall face, and was specified by support traction (force per

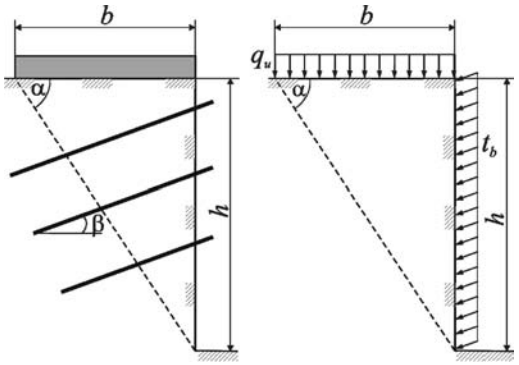


Figure 3. 2D slide model geometry.

unit area) magnitude t_b (Fig. 3). It was inclined similar to the rock bolts, at a plunge of $\beta = 20°$, and (unlike pressure) had both normal and tangential components. The surcharge load and bolt force acting on a block were assumed to be proportional to its respective face areas.

The factor of safety for the 2D sliding model and passive bolts can be obtained from:

$$FS = \frac{(Q+W)\cos\alpha\tan\phi + T\sin(\alpha+\beta)\tan\phi + \zeta T\cos(\alpha+\beta)}{(Q+W)\sin\alpha}$$
$$\alpha+\beta \le 90°, \zeta = 1; \quad \alpha+\beta > 90°, \zeta = 0 \qquad (1)$$

where W, Q and T are the magnitudes of block weight, surcharge load and ultimate rock bolt force, respectively.

The factor of safety formula is adjusted for steeply dipping rock wedges by the coefficient ζ when the bolt force tangent projection on the sliding direction lowers the factor of safety. An alternative adjustment

in the formula rejects both the tangential and normal components of bolt force only if their sum becomes negative. Since formula (1) was applied for the YTL support design, it was thus also used for the 3D sliding model in this study, in the form shown below:

$$FS = \frac{S\{\mathbf{Q}+\mathbf{W}+\mathbf{T}\} - \zeta(\mathbf{T}\cdot\mathbf{s})}{(\mathbf{Q}+\mathbf{W})\cdot\mathbf{s}};\ \zeta = \begin{cases} 1 & \mathbf{T}\cdot\mathbf{s} \le 0 \\ 0 & \mathbf{T}\cdot\mathbf{s} > 0 \end{cases} \quad (2)$$

where **W**, **Q**, **T** stand for vectors of block weight, surcharge load and ultimate rock bolt force, respectively; $S\{\}$ is a shear strength function of the above force vectors sum; and **s** = sliding direction vector.

The 3D double- or single-plane sliding of the tetrahedral wedge model assumes that the joints are planar and the blocks are rigid. The maximum block height is h and the maximum width on the upper face, perpendicular to the crest, is b. Block length along the slope strike was limited to 50 m and the volume, down to 1 m^3.

The kinematic and kinetic wedge sliding analysis was performed using vector calculus and the author's code, verified with Swedge and Rocplane software (Rocscience).

5 2D SLIDING STABILITY ANALYSIS

Deterministic 2D stability analysis with the requisite $FS = 2.0$ was originally applied for the YTL support design. Using the 2D single plane sliding model (Fig. 3), the pattern bolting support traction t_b necessary to meet the $FS = 1.0$ and $FS = 2.0$ conditions was calculated as 52 kPa and 173 kPa, respectively. For the 2D model, the critical sliding plane was not fixed on the basis of geological data, but by the width of the TBM platform and it was understood as being the 'worst case'. A question can be posed as to whether the assumption was correct. Computations show that, for support traction $t_b = 173$ kPa, the assumption is met. However, for $t_b = 52$ kPa and $\alpha = 72°$, $FS(\alpha)$ drops to a value of 0.89. In this situation $t_b = 66$ kPa must be applied in order to provide $FS \geq 1$ for the 2D sliding model.

6 GEOMETRICAL COMPARISON

Let us consider a simple 2D unit slice and 3D tetrahedral wedge, loaded by self-weight only, without external loads, bolt support or cohesion. Let the 2D sliding plane dip angle be equal to the wedge intersection line plunge. In this situation, the FS of the 3D wedge sliding along the intersection line is larger than the FS assessed from the 2D sliding model (Hoek & Bray 1981). This conclusion results from geometrical relations valid for such a simplified model. It does not have to be valid for a single plane wedge sliding mode or when external loads are added.

For a simple comparison of a 2D and a 3D sliding model with external loads, what might be imagined is a tetrahedral, symmetrical wedge of very great length along a slope strike, having an intersection plunge equal to the sliding plane dip angle and the same h, b, q_u and t_b as the 2D sliding model (Fig. 3). If the FS for the 2D sliding model equals 2.0, then the 3D wedge model FS is higher and equals 2.35.

Another simple comparison between the 2D unit slice and 3D wedge models can be obtained when taking only the obvious geometrical differences between the block in both models into account. To do this, the 2D sliding FS formula must be modified by multiplying the volume, upper face area and slope face area by 1/3, 1/2 and 1/2, respectively, in order to reflect the geometrical relations between the right prism and the tetrahedron. For the data considered in this paper, $FS = 2.35$ is again obtained for the wedge model, whereas it was 2.0 for the 2D sliding model.

These are purely theoretical deliberations; however, they serve to illustrate some of the geometrical reasons for a higher wedge FS, as compared to a 2D sliding model and taking into account external loads.

The intersection lines of all the wedges having a width equal to, or lower than, upper face width b, can be inclined much more steeply than in the 2D model with a fixed width b. Wedge sliding can also tend to occur along a single plane, and not necessarily along an intersection line. In such cases, the FS for wedges can be lower than the FS for a 2D sliding model. The results may also depend on the previously mentioned FS formula adjustment.

7 MEAN WEDGE STABILITY

For the specific conditions of the YTL, the joints data show (Fig. 2) that there are clearly two main joint sets and a third group of joints of diverse orientation and origin. The two mean planes of these two joint sets best represent the mean orientation of joints in this region. So, if we are to conduct a deterministic analysis and have to select a single wedge representing the whole wedge population, it is reasonable to single out the wedge formed by these two mean planes. Computations show $FS = 3.91$ for the mean wedge while it was 2.0 for the 2D sliding model The mean wedge geometry is presented in Figure 4.

8 NOTES ON PROBABILISTIC ANALYSIS

We were unable to analyze all the real rock wedges in the wall given that we did not know their exact locations. In evaluating a 3D wedge model, dealing with the 3D joint orientations was unavoidable. This was the reason for employing a simplified probabilistic analysis based on site measurements.

With the exception of the joint plane orientations, all the model parameters were used as deterministic values, and are the same for both the 2D and 3D models. Technically, they could be considered as random variables if reliable data on their probability distributions

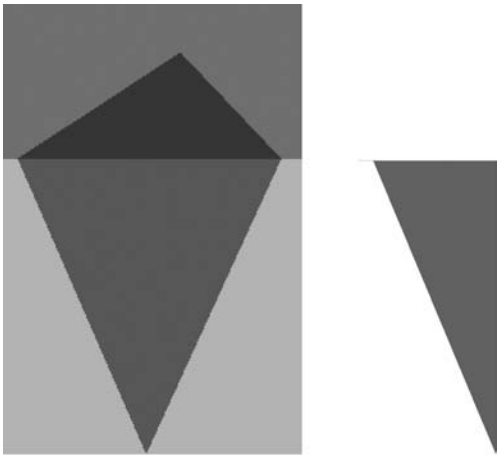


Figure 4. Geometry of the mean wedge.

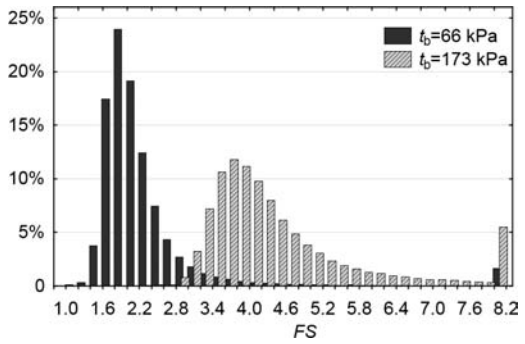


Figure 5. Empirical probability densities of *FS* for two support traction levels. Stochastic simulation results.

Table 1. *FS* estimates for two support traction levels.

Model	$t_b = 66.0$ kPa	$t_b = 173.0$ kPa
Deterministic 2D	1.00	2.00
Deterministic 3D	1.90	3.91
Probabilistic 3D		
0.001 quantile	1.20	2.49
0.01 quantile	1.49	2.99
0.1 quantile	1.63	3.37

was available and the variable independency issue was tackled. However, these factors were not relevant to the purpose of this study.

It was assumed that the measured joint orientations represent a statistically homogeneous region. A large extension of discontinuity planes was posited for both the 2D and 3D wedge models. Features such as joint density, trace length or persistency, and waviness were not considered. The probability of failure was assigned for the set of blocks having the same geometry, in the sense of Joint Pyramid and Block Pyramid, and represented by the largest wedge.

A probabilistic analysis of discontinuity nets and blocky rock mass stability can involve the analysis not only of joint orientations, but also of spacing, trace lengths, block size and location. A broader approach of this kind, carried out with model calibration and verification, allows a better assessment of the probabilities of failure, despite the fact that numerous significant factors remain simplified.

The term 'probability of failure' refers to a conditional probability of failure upon the model assumptions being met. This is a kind of relative measure of the chances that failure occurs for one particular data configuration more often than it does for others.

Here we assume that the probability of failure refers to all the joint plane combinations under consideration and not just to the number of kinematically removable wedges.

Probability of failure can be considered as the sum of the probability of 2D sliding failure, the probability of wedge sliding failure and the probability of rotational failure. The survey data for the YTL (Fig. 2) did not indicate a plane having a strike parallel to the slope face and a dip greater than the friction angle, as is necessary for a 2D failure. This does not eliminate 2D failure, but it does make it unlikely. The bolt reinforcement applied means that toppling failure is also unlikely. This justifies the assumption that, in this case, the probability of failure is estimated as the probability of the 3D wedge failure.

9 STOCHASTIC SIMULATION

Since there were two main joint sets, it was reasonable to assume that they would create the most frequent wedges. For each joint set, we estimated a Fisher distribution parameter quantifying the circular dispersion around a mean orientation: $k_1 = 48.0$, $k_2 = 42.2$. Then we sampled 100,000 pairs of planes, with each plane in the pair coming from a separate joint set and a separate Fisher orientation distribution. To reduce variance, we used a stratified sampling. For each pair of joint planes a wedge stability analysis was performed giving an output sample.

The standard result of a stochastic simulation, probabilistic slope stability analysis is a *FS* empirical density for the assumed support and other slope parameters. A stochastic simulation for pattern bolting support traction $t_b = 62$ kPa and 173 kPa was performed and the results are presented in Figure 5 and Table 1. A large *FS* value was assigned for each infinite and tapered block, so that they fell to the far right of the unbounded intervals in the relative frequency histograms presented in Figure 5 and had an impact on the analysis results.

In addition to *FS* characteristics, the support traction t_b necessary to provide $FS = 1.0$ and $FS = 2.0$ was estimated for each block. Empirical probability density functions of t_b and the respective quantiles were estimated and are presented in Figure 6 and

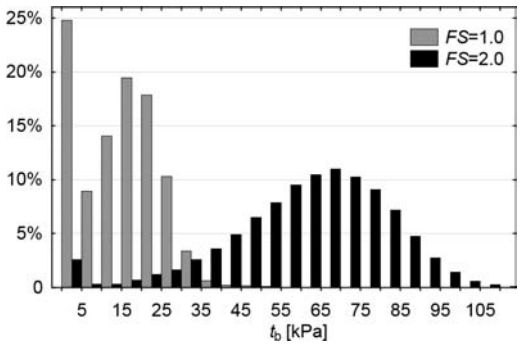


Figure 6. Empirical probability densities of support traction for two *FS* levels. Stochastic simulation results.

Table 2. Support traction estimates for two *FS* levels.

Model	$FS = 1.0$ kPa	$FS = 2.0$ kPa
Deterministic 2D	66.0	173.0
Deterministic 3D	18.0	71.4
Probabilistic 3D		
0.999 quantile	50.0	131.6
0.99 quantile	35.7	101.4
0.9 quantile	26.9	85.2

Table 2. Pairs of sampled planes which did not produce a kinematically removable wedge were considered as requiring $t_b = 0$ and fell to the far left of the unbounded intervals in the relative frequency histograms (Fig. 6).

10 DISCUSSION

The results shown provide a fairly comprehensive description of the stability conditions at the YTL north face, in line with the models applied.

According to the 2D sliding model, the values of *FS* corresponding to $t_b = 62$ kPa and 173 kPa equal 1.0 and 2.0 respectively (Table 1). A deterministic model of the mean wedge indicates much larger *FS* values, at 1.90 and 3.91 respectively. The mean wedge cannot really be used for the purpose of design because it neither represents the 'worst case' deterministic nor quantifies the uncertainty related to joint orientations.

According to the stochastic simulation results, $t_b = 66$ kPa provides $FS > 1.49$ and $t_b = 173$ kPa provides $FS > 2.99$, with a probability of 0.99 (Table 1).

A detailed examination of the data presented in Figure 5 proves that no unstable wedge were encountered in the output sample of 100,000 for either 66.0 kPa or 173 kPa. Taking into consideration the sample size and the estimation error, this means that the probability of failure is very low in both cases, and the 173 kPa value, in particular, has been oversized in terms of probability of failure.

A designer would wish to compare both approaches in terms of the required support, rather than *FS* and for this purpose, the results presented in Figure 6 and Table 2 might prove more useful. If 0.001 is an acceptable probability of failure, one can apply a pattern bolting of $t_b = 50.0$ kPa. Explicitly accepting any specific probability of failure is often difficult for engineers. So a possible alternative is an approach based on the t_b distribution for a preferred *FS* value, not for $FS = 1$ indicating failure. For $FS = 2.0$ one might accept a 0.9 quantile of t_b estimated at 85.2 kPa as a design value (Table 2).

The 50.0 kPa and 85.2 kPa values state 29% and 49% of the original 173 kPa given by the 2D slide, analysis. This is understandable when we recall that the 3D probabilistic model employs wedge geometry and incorporates information on the actual joint orientations, apparently favorable as regards the north face of the YTL. The particular criteria which should be applied and the decision as to whether 50.0 kPa, 85.2 kPa or another design value should be accepted depends on the engineer's judgment and industry standards. A probabilistic 3D wedge analysis provides tools for the evaluation of each option.

11 SUMMARY AND CONCLUSIONS

The main goal of this study was to compare a 2D deterministic and a 3D probabilistic model based on joint orientation data for the particular conditions of the YTL, where the rock ledge was surcharge loaded and reinforced with rock bolts. The same, simple rigid block limit equilibrium condition was examined. Some purely geometrical reasons for a larger *FS* for a 3D wedge than for a comparable 2D unit slice were noted. The probabilistic, simulation model allowed a wedge stability analysis to be performed despite the uncertainty related to the joints orientation and wedge geometry. The results of 3D wedge simulations presented in the paper include *FS* probability density functions and quantile estimates for given pattern bolting traction t_b magnitudes and t_b density functions and quantile statistics for given *FS* values.

For the conditions particular to the YTL, the joint orientations appeared to be favorable and the 3D probabilistic model could incorporate this feature into the stability analysis. The required rock bolt support force indicated by the 3D probabilistic analysis appeared to be significantly lower than that provided by the 2D deterministic sliding model, allowing the required rock bolt pattern to be lighter. The 3D wedge model is also more realistic, gives more confidence in the results, and has the capability of identifying dangerous wedges. Finally, using the 3D wedge probabilistic model makes it possible both to judge the stability conditions better and, at times, to lighten the rock bolt reinforcement substantially.

ACKNOWLEDGEMENTS

The paper was prepared for AGH UST research project No. 11.11.100.197.

REFERENCES

Bray, J.W. & Brown, E.T. 1976. A short solution for the stability of a rock slope containing a tetrahedral wedge. *International Journal of Rock Mechanics and Mining Sciences & Geomechanics Abstracts* 13: 227–229.

Chiles, P. 1987. Three-Dimensional geometric modelling of a fracture network. In *Geostatistical, Sensitivity and uncertainty methods for ground water flow and radionuclide transport modeling*. San Francisco.

Cundall, P.A. 1988. Formulation of a Three-dimensional Distinct Element Model – Part I. A Scheme to Detect and Represent Contacts in a System Composed of Many Polyhedral Blocks. *International Journal of Rock Mechanics and Mining Sciences & Geomechnics Abstracts* 25(3): 107–116.

Dershowitz, W.S. & Einstein, H.H. 1988. Characterizing rock joint geometry with joint system models. *Rock Mechanics and Rock Engineering* 21: 21–51.

Goodman, R.E. & Shi, G.H. 1985. *Block Theory and Its Application to Rock Engineering*. Englewood Cliffs: Prentice-Hall.

Hatzor, Y.H. 1993. The Block Failure Likelihood. A Contribution to Rock Engineering in Blocky Rock Masses. *International Journal of Rock Mechanics and Mining Sciences & Geomechanics Abstracts* 30(7): 1591–1597.

Hoek, E. & Bray, J.W. 1981. *Rock Slope Engineering.* London: The Institution of Mining and Metallurgy.

Hoerger, S.F. & Young, D.S. 1990. Probabilistic prediction of keyblock occurrences. In *Rock Mechanics Contributions and Challenges*: 229–236. Balkema.

Hudson, J.A. & Priest, S.D. 1983. Discontinuity frequency in Rock Masses. *International Journal of Rock Mechanics and Mining Sciences & Geomechanics Abstracts* 20: 73–89.

Jakubowski, J. 2011. Probabilistic stability analysis of a tunnel in a fracture zone. *Archives of Mining Sciences* 56(3): 405–413.

Jakubowski, J. & Starzec, P. 2002. Deformable and rigid blocks modelling within the scheme of statistical simulation. In *Mining and Tunnelling, Innovation and Opportunity*. Toronto: University of Toronto Press.

Jakubowski, J. & Tajdus, A. 1995. The 3D Monte-Carlo simulation of rigid blocks around a tunnel. In H.P. Rossmanith (ed.), *Mechanics of Jointed and Faulted Rock*. Rotterdam: Balkema.

Kulatilake, P.H.S.W. 2001. *Fracture characterization and network modeling.* Eurock Pre-Symposium Course. Helsinki University of Technology.

Lin, D. & Fairhurst, C. 1988. Static analysis of the stability of three-dimensional blocky systems around excavations in rock. *International Journal of Rock Mechanics and Mining Sciences & Geomechanics Abstracts* 25(3):139–147.

Lucas, J.M. 1980. A general stereographic method for determining the possible mode of failure of any tetrahedral rock wedge. *International Journal of Rock Mechanics and Mining Sciences & Geomechanics Abstracts* 17:57–61.

Mauldon, M. 1995a. A generalisation of block theory for edge rotation. In *Proceedings of the Conf. on Fractured and Jointed Rock Masses*: 295–301. Rotterdam: Balkema.

Mauldon, M. 1995b. Keyblock Probabilities and Size Distributions: A First Model for Impersistent 2-D Fractures. *International Journal of Rock Mechanics and Mining Sciences & Geomechanics Abstracts* 32: 575–583.

Mauldon, M., Dunne, W.M. & Rohrbaugh, M.B. 2001. Circular scanlines and circular windows: new tools for characterizing the geometry of fracture traces. *Journal of Structural Geology* 23: 247–258.

McMahon, B.K. 1971. Statistical methods for the design of rock slopes. In *Proceedings of the 1st Australian-New Zealand Conference on Geomechanics*: 314–321.

Park, H.J., West, T.R. & Woo, I. 2005. Probabilistic analysis of rock slope stability and random properties of discontinuity parameters, Interstate Highway 40, Western North Carolina, USA. *Engineering Geology* 79: 230–250.

Priest, S.D. 1980. The use of inclined hemisphere projection methods for the determination of kinematic feasibility, slide direction and volume of rock blocks. *Int. Journal of Rock Mechanics and Mining Sciences & Geomechanics Abstracts* 20: 43–47.

Priest, S.D. & Brown, E.T. 1983. Probabilistic stability analysis of variable rock slopes. *Trans. Inst. Min. Metall.* 92:A1–12.

Shanley, R.J. & Mahtab, M.A. 1976. Delineation and analysis of clusters in orientation data. *Mathematical Geology* 8(1): 9–23.

Shi, G.H. 2001. Three dimensional discontinuous deformation analyses. In *Proceedings of the 38th US Rock Mechanics Symposium*: 1421–8. Washington.

Warburton, P.M. 1981. Vector stability analysis of an arbitrary polyhedral block with any number of free faces. *International Journal of Rock Mechanics and Mining Sciences & Geomechanics Abstracts* 18: 415–427.

Wittke, W. 1965. Methods to analyze the stability of rock slopes with and without additional loading. *Rock Mechanics and Engineering Geology, Suppl. 2*. Vienna: Springer-Verlag.

Wittke, W. 1990. *Rock Mechanics – Theory and Applications*. Berlin: Springer.

Zhang, L. & Einstein, H.H. 2000. Estimating the intensity of rock discontinuities. *International Journal of Rock Mechanics and Mining Sciences* 37(5): 819–837.

Rock Mechanics for Resources, Energy and Environment – Kwaśniewski & Łydżba (eds)
© 2013 Taylor & Francis Group, London, ISBN 978-1-138-00080-3

Protection of a tunnel entrance from rockfall risk

C. Mignelli, K. Daneshmand & D. Peila
Department of Environment, Land and Infrastructure Engineering (DIATI), Politecnico di Torino, Torino, Italy

ABSTRACT: In mountainous areas, tunnel portals and job sites for tunnel construction are often located in areas prone to rockfall events. Providing the safety of roads close to tunnel portals, subjected to rockfall risk, is an unavoidable issue that should be taken into account. In this paper, a risk management approach has been introduced to evaluate rockfall risk on the road stretch at the entrance and exit of tunnels. The event tree method is improved to achieve a flexible solution to calculate the rockfall risk for tunnels. Furthermore, some design abacuses are developed to provide the input parameters related to the event tree. Afterwards, a parametrical analysis is presented to explain the methodology. The elaborated approach can be useful to choose best technical solutions and design protection devices against rockfall.

1 INTRODUCTION

The rock block collapse from slopes is one of the most frequent hazards for public transportation systems in mountainside areas. The effects of these instabilities can led to vehicle damages, injury or death of drivers and passengers as well as economic loss due to road closure (Duncan & Norman 1996).

Referring to tunnelling engineering, sometimes tunnel portals and job sites for tunnel construction are located in areas prone to rockfalls and the rock block detachments can occur while the tunnel is in service or during construction.

In order to deal with this issue, several geometry configurations of a rock slope prone to rockfall overhanging a tunnel portal have been defined and the results of trajectographic analysis have been analysed. The rockfall trajectographic analysis has been performed to evaluate the number of rock blocks that can reach the road and their percentage. This analysis has been done with a 2D method and a lumped mass model has been utilized. The geotechnical restitutional parameters (k_n, k_t, ϕ) are set as standard values available in technical literature (Giani 1992, Hungr & Evans 1988, Azzoni et al. 1995). The goal of this research is to provide a design procedure and suggest somemeasures to prevent the falling rock blocks toward the road such as rockfall barriers and/or artificial protruding tunnels (Fig. 1a,b,c).

From the phenomenological point of view, a rockfall is induced by the rock detachment from a rock slope and its downfall movement. Despite of the relatively small size of the blocks in comparison with other landslides, they are a destructive and dangerous event since the blocks move with high speedup to 25–30 m/s (Bunce et al. 1997, Evans & Hungr 1993, Giani 1992).

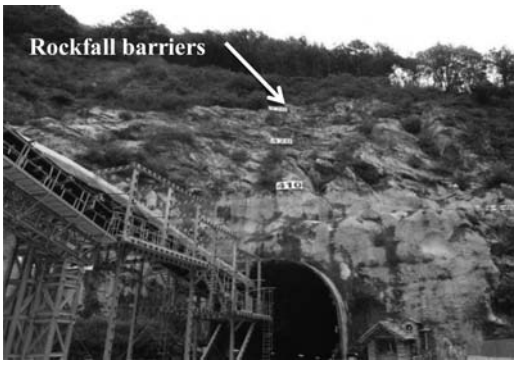


Figure 1a. Job site of Monte Ceneri tunnel, tunnel portal protected by rockfall barriers.



Figure 1b. Job site of Monte Ceneri tunnel, excavated rock mass deposit before treatment and transportation to final disposal.

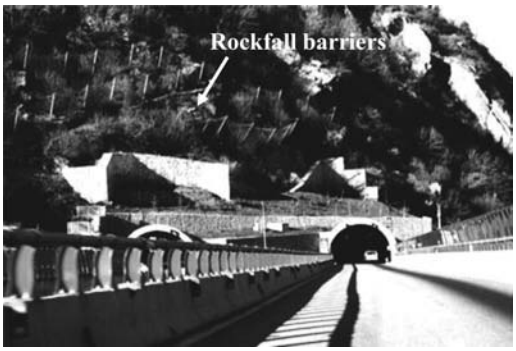


Figure 1c. Tunnel Entrance of the Torino-Frejus highway.

The trajectories of falling rock can be described as combinations of four motion types: free fall, rolling, sliding and bouncing. The occurrence of each motion type is strongly depended on the slope angle.

The most frequent reason of rock-fall are linked with water pressure and the growth of tree roots in cracks which can open fractures and loosen blocks on the slope. Other important factors affecting stability of rock slopes are represented by the geological and geotechnical conditions of each site, adverse dip of the joints, soil decomposition as well as earthquakes that can trigger the collapse (Duncan & Norman 1996).

2 ROCKFALL RISK

The risk analysis associated with these types of instabilities is a complex operation requiring the assessment of both the hazard and the vulnerability of the traffic. Moreover, the risk assessment plays a key role in the selection of the protective measures.

Rockfall hazard can be defined as the probability that a falling block reaches a specific stretch of a road with given intensity (Fell et al. 2008).While the simplest method to define the rockfall risk consists of analysing the distribution of elements at risk with different vulnerability levels and hazards (Guzzetti et al. 2003; 2004). Risk analysis is used to assess the consequences of expected rockfall events and evaluate both the technical suitability and the cost-benefits of different protection devices (Corominas et al. 2005, Straub & Schubert 2008, Mignelli et al. 2012). Referring to the design of tunnel portals it is possible to use an artificial protruding tunnel for a certain length or to install structures such as rockfall barriers or embankments on the slope to intercept the falling block trajectory (Peila et al. 2002). These latter solutions can prevent the blocks falling on the road thus reducing the frequency of collapses and control, intercept or deviate the blocks during their movement and in this way reducing the risk (Peckover & Kerr 1977, Peila et al. 2006). For this analysis the even tree approach is a widely used tool (Bunce et al. 1997, Hoek 2000, Peila & Guardini 2008, Mignelli et al. 2012).

A specific applicationof this method has been developed to evaluate rockfall risk on the road stretch at the entrance and exit of a tunnel.

2.1 *The event tree approach*

Event tree approach is the logical representation of all the possible incidental sequences that begins from an initiating event, specifically a rockfall. The event tree method calculates the risk (number of fatalities/year) due to the impact of a rock block on the road that can induce a car accident or directly impact on the moving vehicles. The proposed approach is illustrated in Figure 2. The starting point of this analysis is the rockfall event frequency and the first node of the tree is the probability that a falling rock can hit or not a moving vehicle.

This approach is repeated for each node to calculate all the possible incidental sequences. The probability of each branch can be evaluated by different approaches including: numerical evaluation based on the principal probabilistic methods such as the binomial theorem or Bayes' theorem (Benjamin & Cornell 1970), predefined assumptions, elaboration of statistical data coming from international databases and probabilistic analysis. The main input parameters are: number of rocks that can fall from the slope during a predefined time interval (i.e. one year) and the probability that a rock block can reach the road. A better and more complete description of the used event tree can be found in Mignelli et al. (2012). The number of rockfall events per year is the basis of the calculation and a design input parameter.This number can be obtained from a rock slope historical data bases (if available), and/or through an analysis of the geo-structural conditions of the slope.The probability that a falling rock can reach the road is computed by a trajectographic analysis.

Other required input data for this analysis are: the length of the studied slope, speed of the vehicles, the average vehicle length, the number of vehicles travelling on the road per day and the average number of passengers on the vehicle.

The methodology takes into account several probability values in each node:

- R1 and R1': are respectively probabilities that a falling rock hits a moving vehicle or not, which means a car with a pre-defined speed is at the same time and position of the falling rock block;
- R2 and R2': are respectively probabilities that the falling block hitting the car can cause or not some fatal accidents;
- R3 and R3': are respectively probabilities that a vehicle hits a fallen rock laying on the road evaluated based on the road layout, car speed and driver standard reaction time;
- R4 and R4': are respectively probabilities of fatal or no fatal accidents if a car impacts a block laying on the road. This value is defined based on the Italian road administration statistics of car accidents.

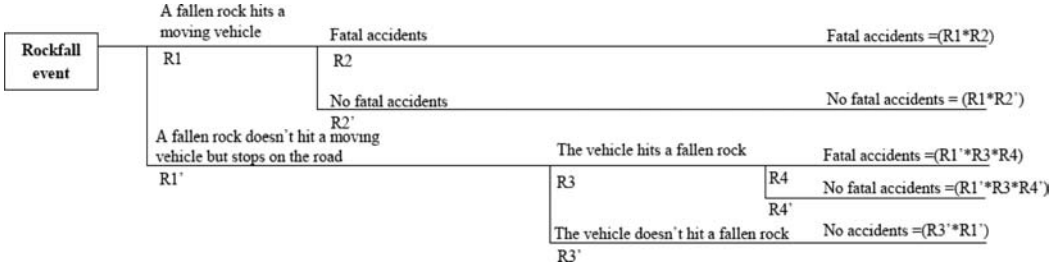


Figure 2. Event tree approach to calculate rockfall risk for roads close to tunnel portals.

The risk of no accident, no fatal accident and fatal accident is then obtained by adding the values of each incidental sequence.

3 DESIGN ABACUSES

3.1 *The proposed method*

The geometry of the studied slope is shows in Figure 3. In this Figure it is assumed that the tunnel and some parts of the slope, from which the blocks arrive, can be described as debriswhile the slope is rock mass.

The height of the tunnel portal is 8 m, the horizontal length of the debris (L) ranges as 20 m; 40 m; 80 m and the angle of debris (α), referring to horizontal direction, ranges from 20° to 40°.

The rockfall source areas arelocated at the top of the slopeand 5000 rock blocks events aresimulated. The most frequent rock-block sizes range between 0.5 and 2 m^3.

The rockfall trajectory models, with a lumped mass scheme, utilize normal (k_n) and tangential (k_t) restitution coefficients to calculate the rebound of simulated rock on the slope surface and rolling friction coefficient (Giani 1992; Ferrari et al. 2011). The used considered restitution coefficient and their statistic distributions arereported in Table 1; whereas Figure 4 shows some trajectographic analysis. The design abacuses in Figure 5 have been developed based on the downfall height and stoppage point of the falling block considering the angle of debris slop with horizontal direction equals to 20° and 40°.

Taking into account a debris slope with the angle of 20°, the percentage of rock blocks that reach the road is reported in Figure 6. For example if the debris length is 20 m and the height of the slope is 105 m, the stoppage point is 40 m far from the tunnel entrance and the number of falling block is 84%. It should be mentioned that increasing the debris angle and the height of the rock slope, the distance between stoppage point and the axis origins will increase. Obviously, the number of rock blocks that reach the road is a function of the rock slope height and the angle of the debris.

These results are useful to design protruding tunnel, if it is necessary, or to implement rockfall barriers above the tunnel.

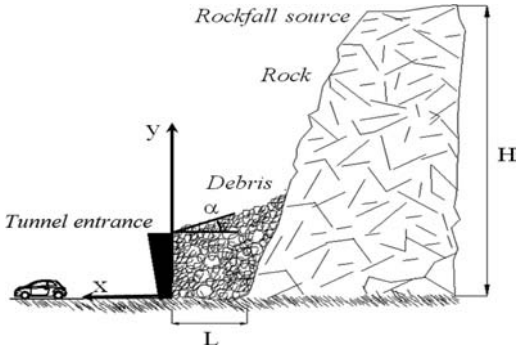


Figure 3. Geometry of the studied slope.

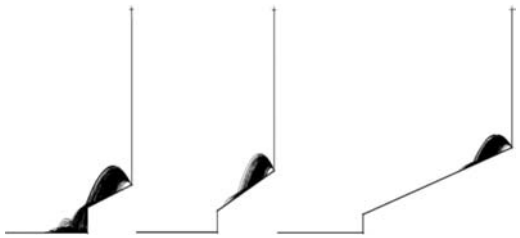


Figure 4. Trajectographic analysis; the debris slope angle was set as 20° and the debris length was ranged as 20 m; 40 m; 80 m (as shown respectively from left to right in this figure).

Table 1. The values of the normal and tangential restitution parameters used in the trajectographic analysis.

Material	k_t	k_n	ϕ
Debris	0.55 ± 0.04	0.30 ± 0.04	$30° \pm 0.5$
Rock	0.80 ± 0.04	0.55 ± 0.04	$30° \pm 0.5$
Asphalt	0.90 ± 0.04	0.40 ± 0.04	$30° \pm 0.5$

3.2 *Parametrical analysis*

To discuss the results that could be achieved with the proposed method, a parametrical analysis has been developed, based on standard geo-parameters, that

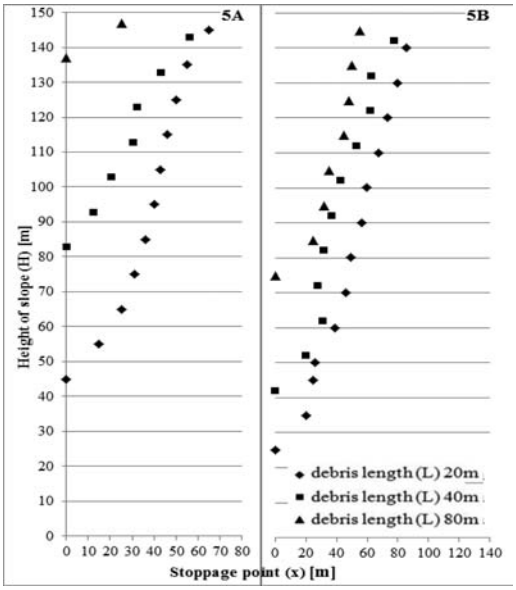


Figure 5. Stoppage point of the block that are detached from different slope height when the debris angle is 20° (5A) and when the debris angle is 40° (5B).

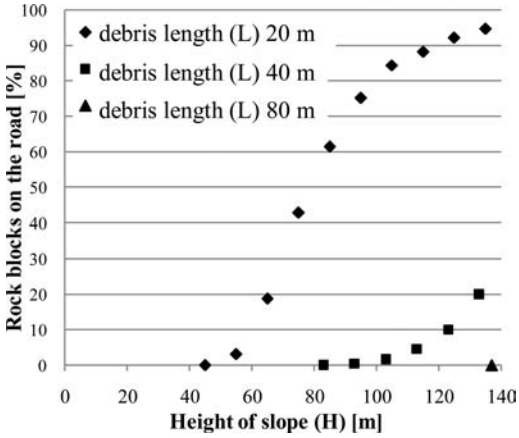


Figure 6. The percentage of rockfall blocks that hits the road according to the height of the slope when the debris angle is 20°.

can be found in real cases. The analysis concerns an application of the methodfortwo slope configurations:

- geometry (A): the debris angle is 20° and the debris length is 20 m;
- geometry (B): the debris angle is 20° and the debris length is 40 m.

This calculation has been done in absence and presence of rockfall barrier alignments taking into account their level of efficacy.

The efficacy of the protection has been considered as the percentage of rock block interception; for instance, an efficacy of 100% means that all the rockfall events are stopped by the considered protection device. A lower efficacy is due to the probabilistic distribution of a stochastic event, such as a rockfall, where some of the collapse can bypass the protection and cannot be computed on the design stage with the used procedure.

Rockfall protection barriers have been designed to be located at 8 meters from the tunnel entrance in the debris, in order to intercept the blocks detached from the upper slope. Figure 6 shows the percentage of rockfall blocks that hits the road according to the height of the slope.

It should be mentioned that in presence of rockfall barriers the number of blocks that have reached the road is significantly reduced.

The developed event tree approach has been applied to these configurations. In this analysis the traffic volume is considered as 1000 vehicles/day and 6000 vehicles/day, in order to provide a low and a high intensity traffic scenario for an extra-urban road. The speed limit is posed to 70 km/h and the number of passengers on the vehicle are three. Two return periodshave been considered: one falling block with return period of ten years and the other falling block with return period of five years.

The number of blocks that can reach the road,used as input parameter in the event tree, is the number of blocks that are detachedin the considered return period multiplied by the percentage of blocks that can reach the road, obtained from the trajectographic analysis (Fig. 5).

The rockfall risk for both geometries and traffic configurations have been calculated and shown in Figure 7 and Figure 8. The maximum risk level with a peak of 3.63E-3 (number of fatalities/year) is provided by the geometry (A) with the return period of 5 years. With increasing the debris length, the number of rocks that reach the road decreases as well as the risk level.

Rockfall barriers provide a useful tool to reduce the risk level but in some cases their protective impact is not enough therefore it is also necessary to introduce protruding.

4 CONCLUSIONS

In mountainous regions, the collapse of rock blocks that are detached from slopes overhanging roads and railways poses a common public hazard. Tunnel portals and tunnel job sites are often unsafe areas with reference to rockfall events. Considering the importance of this issue, the event tree method is developed to achieve a flexible solution to calculate the rockfall risk for tunnels. Some important input parameters to be implemented in the even tree method are extracted from design abacuses. These design abacuses take into account the most widespread geometries of the slope above a tunnel. The combination of design abacuses and the even tree method proposes an effective

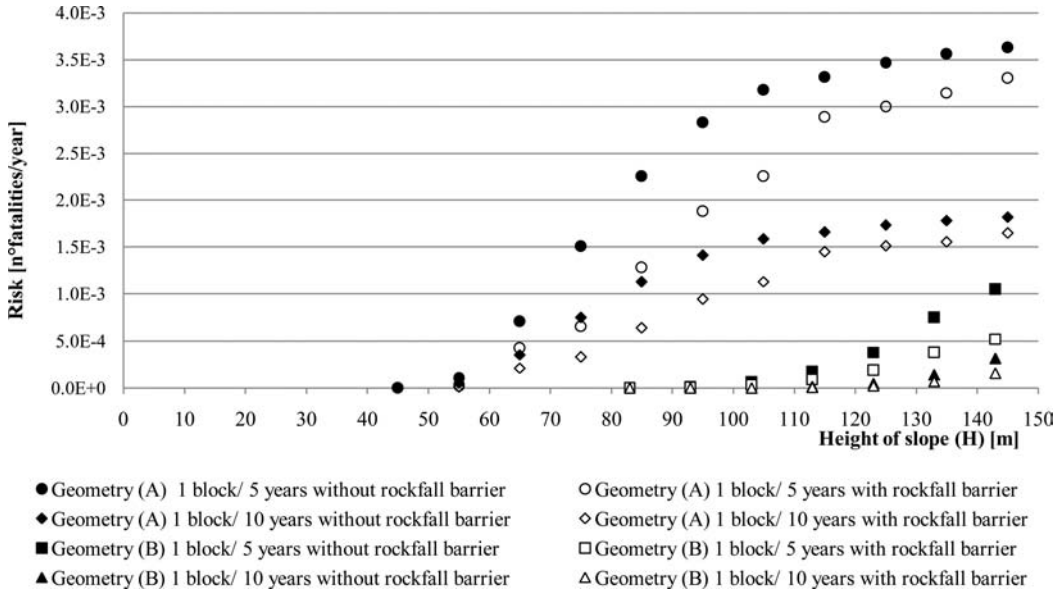


Figure 7. Rockfall risk calculated, considering a traffic of 1000 vehicles/day.

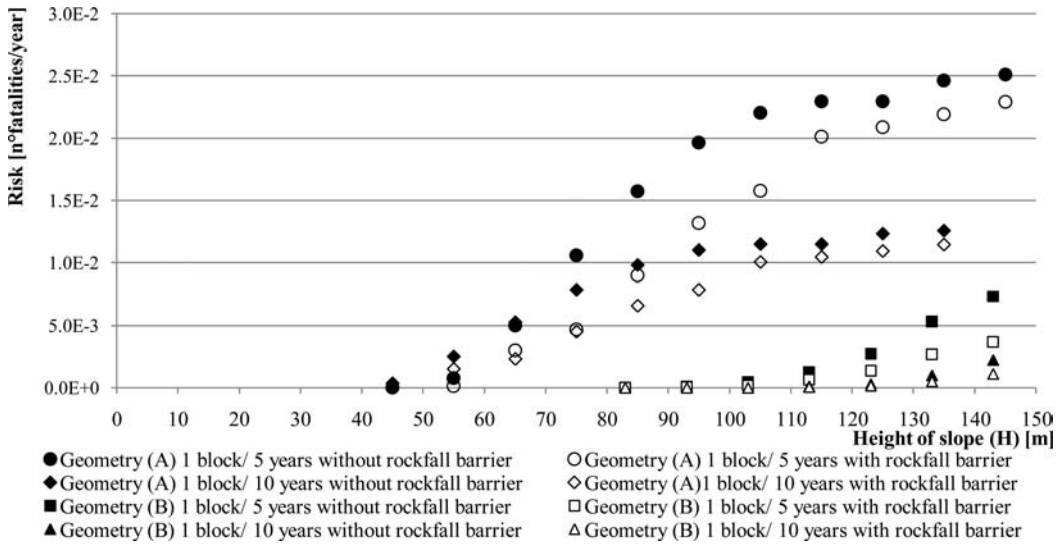


Figure 8. Rockfall risk calculated, considering a traffic of 6000 vehicles/day.

approach to calculate the rockfall risk considering standard geometry of the slope. Finally, the elaborated approach can be useful to choose the best technical solution (rockfall barriers or protruding artificial tunnels) and design protection devices against rockfall.

REFERENCES

Azzoni, A., La Barbera, G. & Zaninetti, A. 1995. Analysis and prediction of rock falls using a mathematical model. *International Journal of Rock Mechanics and Mining Sciences* 32: 709–724.

Benjamin, J.R. & Cornell, C.A. 1970. *Probability, statistics and decision for civil engineers.* New York: McGraw-Hill.

Bunce, C.M., Crude, D.M. & Morgenstern, N.R. 1997. Assessment of the hazard from rockfall on a highway. *Canadian Geotechnical Journal* 34: 344–356.

Corominas, J., Copons, R.J.M., Vilaplana, J., Altimir, J. & Amigo, J. 2005. Quantitative assessment of the residual risk in a rockfall protected area. *Landslides* 2: 343–357.

Duncan, C.W. & Norman, I.N. 1996. *Stabilization of rock slopes. Landslides investigations and mitigation*, *Special Report 247*: 474–506. Washington: Transportation Research Board, National Research Council.

Evans, S.G. & Hungr, O. 1993. The assessment of rockfall hazard at the base of talus slopes. *Canadian Geotechnical Journal* 30(4): 620–636.

Fell, R., Corominas, J., Bonnard, C., Cascini, L., Leroi, E. & Savage, W.Z. on behalf of the JTC-1 Joint Technical Committee on Landslides and Engineered Slopes 2008. Guidelines for landslide susceptibility, hazard and risk zoning for land use planning. *Engineering Geology* 102: 85–98.

Ferrari, F., Apuani, T. & Giani, G.P. 2011. Study of rockfalls in middle San Giacomo Valley (SO) using kinematic models. *Geoingegneria Ambientale e Mineraria* 132: 55–64.

Giani, G.P. 1992. *Rock Slope Stability Analysis.* Rotterdam: Balkema.

Guzzetti, F., Reichenbach, P. & Wieczorek, G.F. 2003. Rockfall hazard and risk assessment in the Yosemite Valley, California, USA. *Natural Hazards and Earth System Sciences* 3(6): 491–503.

Guzzetti, F., Reichenbach, P.& Ghigi, S. 2004. Rockfall hazard and risk assessment along a transportation corridor inthe Nera Valley, central Italy. *Environmental Management* 34: 191–208.

Hoek, E. 2000. *Practical Rock Engineering*: 115–136, available at: www.rocscience.com.

Hungr, O. & Evans, S. 1988. Engineering evaluation of fragmental rockfall hazards. In C. Bonnard (ed.), *Landslides, Proceedings of the 5th International Symposium on Landslides, Lausanne,* 1: 685–690. Rotterdam: Balkema.

Mignelli, C., Peila, D. & Lo Russo, S. 2012. ROck-fall risk management assessment: the RO.MA. approach. *Natural Hazards* 62(3): 1109–1123.

Peckover, F.L. & Kerr, W.G. 1977. Treatment and maintenance of rock slopes on transportation routes. *Canadian Geotechnical Journal* 14(4): 487–507.

Peila, D. & Guardini, C. 2008. Use of the event tree to assess the risk reduction obtained from rockfall protection devices. *Natural Hazards and Earth System Sciences* 8: 1441–1450.

Peila, D., Oggeri, C. & Barantonio, P. 2006. *Barriere paramassi a rete, interventi e dimensionamento*. *Quaderni e studi di documentazione*. Torino: GEAM.

Peila, D. & Pelizza, S. 2002. Criteria for technical and environmental design of tunnel portals. *Tunnelling and Underground Space Technology* 17: 335–340.

Straub, D. & Schubert, M. 2008. Modeling and managing uncertainties in rock-fall hazards. *Georisk* 2: 1–15.

Rock Mechanics for Resources, Energy and Environment – Kwaśniewski & Łydżba (eds)
© 2013 Taylor & Francis Group, London, ISBN 978-1-138-00080-3

Infrared thermography methodology applied to detect localized rockfalls in self-supporting underground mines

M.B. Prendes-Gero & F.J. Suárez-Domínguez
Department of Construction and Manufacturing Engineering, Engineering Polytechnic School of Gijón, Gijón, Asturias, Spain

C. González-Nicieza & M.I. Álvarez-Fernández
Department of Mining Engineering, Mining Engineering School, University of Oviedo, Asturias, Spain

ABSTRACT: There are several factors that affect the formation of localized rockfalls in self-supporting underground mines. Between these factors we can point out the type of material, the environmental conditions, the process of exploitation or the redistribution of stresses. All of them contribute to the alteration of the rock and the formation of cracks, and their spreading produces rockfalls and increase in the temperature of the surrounding material. The measure, all through the time, of the temperature of the rock with thermic images allows us to identify variations in it. These changes in the thermic conditions of the rock mass identify areas with a high probability of rockfalls. Following this principle, researchers of the University of Oviedo have developed a methodology for the prevention of localized rock falls in self-supporting underground mines using infrared thermography techniques. To test its goodness, they have applied it in an underground mine of limestone located in the north of Spain. This work has been realized in the last year and it has realized that the infrared thermography technique is a quantitative way to know the risk of rockfalls, that lets to prepare the adequate proceedings in order to avoid accidents or situations of risk within the exploitation. In this paper the methodology developed and its application on a real mine, as well as the results of the job are described.

1 INTRODUCTION

The purpose of this article is to develop and validate a procedure for quantitatively determining the location and probability of localised detachments of material in self-supporting underground excavations through the evaluation of thermal alterations to reduce the risk of accidents in such situations.

When an excavation is made inside a fractured rock mass and the spacing of joints is considerable, large blocks of rock may appear. If these blocks are unstable, may come loose inside the excavated cavity, causing significant personal and material damages. For this reason it is important to have analytical tools for identifying such blocks before or during the execution of work.

For straight galleries with a constant cross-section and tetrahedral blocks made up of three families of joints and the surface of the gallery itself, the problem of identifying blocks has been widely studied and solved (Goodman & Shi 1985, González et al. 2005). For pentahedral blocks made up of four families of joints and the surface of the gallery, both the problems of identification and support have also been studied in considerable depth and solutions found (González et al. 2005).

All the studies conclude that there are various factors that affect the formation of localised detachments of rock on mine ceilings and walls. These include the type and properties of material, the environmental conditions and the operating process, among others.

For self-supporting limestone mines, the formation of blocks does not only depend on the properties of the mass, but also on the formation and the propagation of cracks that occur during the operation process (e.g. blasting, machinery) and which, together with the environmental conditions (temperature, humidity) favour the weathering of the limestone. This problem is generally overcome by healing the area in which operations are carried out.

However, there is the possibility of localised detachments on a smaller scale which are nonetheless capable of causing material and human damages and which have not been studied in depth.

For limestone mines, the propagation of cracks causes an increase in the temperature of the surrounding material until reaching breaking point.

The use of thermography makes it possible to detect anomalies and thermal variations that occur as a result of humidity differences in the material and which are a symptom of the detachment. Similarly, by analysing the data obtained, it is possible to evaluate the risk of detachment and monitor susceptible areas. This procedure improves the state of the current technique since it is based on objective and quantifiable data and not a subjective visual assessment.

The procedure makes it possible to precisely determine the potential for localised detachments in rock masses based on objective criteria, taking the thermal variations obtained using thermography techniques as data to eliminate their inherent risk. Analysing the data that is obtained, a protocol is followed to undertake a "back analysis", providing a quantitative evaluation of the risk of detachment and monitoring it over the course of time.

This article begins with a brief description of the physical laws of thermography, and the various factors that influence the measurement of thermal radiation. In the third point it is collected the steps of the proposed methodology that is developed in the point fourth. In it, they are explained the different steps of the methodology: locating and marking the points of interest, data collection, the management and analysis of data, and the protocol to follow. These are applied into an underground limestone mine owned by Cantera de Campanzar, S.A. in Arrasate, situated in Gipuzkoa, Spain. Finally the conclusions are described.

2 PHYSICAL BASIS OF THERMOGRAPHY

Thermography is a technique that makes it possible to determine the temperature of an object by capturing its infrared radiation.

This radiation is directly proportional to the emissivity, or rather the quotient of the radiation emitted by the body being measured and that emitted by a black body (which absorbs all the incident radiation) at the same temperature. This quotient makes it possible to classify bodies as black when $\varepsilon = 1$ and grey when $\varepsilon < 1$.

In practice the emissivity value can be regarded as a constant inherent to each material, although it is in fact a function of wavelength, temperature and angle of incidence.

Similarly, the radiation that is emitted is not constant for all wavelengths. For the ambient temperature, the maximum level of radiation is produced for wavelengths located on the infrared band of the spectrum, particularly on the near and mid infrared bands, which comprise wavelengths between 700 nm and 20000 nm.

In addition to emissivity, there are other factors that influence the measurement of the thermal radiation emitted by a body. The radiation that reaches the receptor contains radiation from other bodies or nearby light sources, referred to as parasite radiation, which can cause temperatures in excess of the real values.

Furthermore, the measurement depends on the angle of incidence of the observation, since the emissivity of a material varies depending on its direction, and is zero for grazing angles.

Finally, the atmosphere, the medium in which the thermal radiation is transmitted, also exerts an influence, absorbing or dispersing part of the radiation. There are windows of transmission or intervals of wavelengths for which the atmosphere is practically transparent. At ambient temperature, these intervals are between 8 and 13 μm.

3 GENERAL METHODOLOGY FOR THE PROCEDURE

In order to apply this methodology in a practical and straightforward manner, it is established the criteria to be followed for a correct implementation of the steps of the procedure and the models of documents to be generated during each phase. The objective is to ensure repeatability when it comes to gathering data (obtaining thermograms). These criteria are (Figure 1):

a) Location and signage
   - Choosing and identifying the points for taking samples
   - Applying signage to the points for taking samples
   - Preparing the file for location and signage

b) Data collection
   - Frequency of data collection
   - Determining the physical and environmental parameters (ambient temperature, reflected temperature, relative humidity, dew point, emissivity of the material)
   - Taking the thermogram
   - Preparing the file for data collection

c) Data management and analysis
   - Establishing the protocol for managing and analysing the data
   - Preparing the file for managing and analysing the data

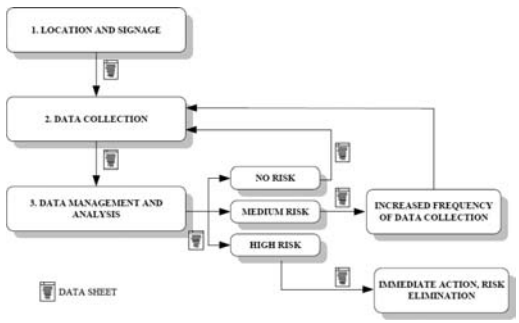


Figure 1. General schema for the procedure.

– Establishing the protocol for identifying and evaluating risks
– Preparing the file for evaluating risks and measures to be taken

4 METHODOLOGY APPLICATION

The methodology has been applied in the Campanzar Quarry that nowadays is being transformed into an underground mine. The rock mass (slate) is being exploited by the room and pillar system where the material is removed to create subterranean rooms and areas in the form of columns are left intact to support the roof weigh. The system of exploitation and the features of the rock mass (Table 1) produce the apparition of critical points that can lead to rock falls (Alcalde-Gonzalo et al. 2013). It is necessary to find and control these points to avoid damages in the exploitation.

4.1 *Location and signage*

This phase entails the selection and identification of the points for taking the samples, based on criteria such as accessibility, repeatability and the operational requirements of the operation itself. The identification of the points is carried out in the operation of advance by scanning the mined areas with the thermography camera. This step is simple and fast because of the camera shows on-line the images captured. The operator chooses those points with temperatures between 3 and 5°C above the background temperature. This range joined to the higher levels of humidity and the operation of machinery that generates CO_2 favour the dissolution process and hence the rupture of the rock.

Once they have been selected and identified, the points are marked using markers that can be identified on site, their geodesic coordinates are recorded, and the frequency with which data will be collected is determined. All this information is recorded on a file for each point, together with a plane that showed the exact location of the point (Fig. 2). In this point it is necessary to emphasize the influence that in the results of the process has the frequency of the measurements. A lot of measurements let to know the evolution of the temperature although with a high cost. Otherwise too few measurements will not let to carry out the actions that prevent the rockfalls or the damages. So, the frequency is not a fixed data. At general the interval is reduced when there are high increments in the temperature of the critical points with respect the surrounding rock mass.

4.2 *Data collection*

Once the critical points have been marked, the data is collected on site, or rather the thermograms are taken and the physical and environmental parameters are determined at that point (Table 2).

The majority of the thermographic cameras on the market store the information on digital memory, which facilitates its subsequent processing and management. Here it should be noted the requirement for strict compliance with the protocol that is established, both when it comes to the location for taking the thermograms, as well as for determining the additional data required to guarantee repeatability when it comes to gathering data and its subsequent correct management and analysis (Thomas 1999, Maldage 2001). Finally, the data collection file should be filled as Figure 3 shows.

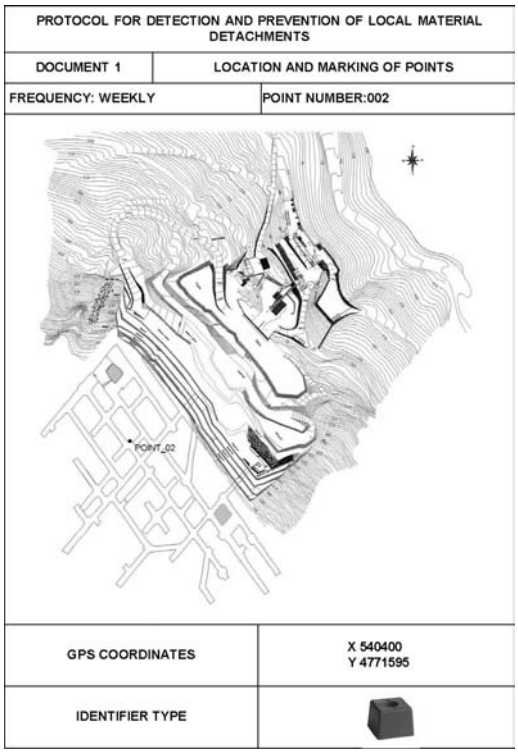


Figure 2. Example of location and marking of points file.

Table 1. Property of the rock mass: Campanzar Quarry.

Property	Value
Specific weight	27 kN/m^3
Tensile strength	5.57 MPa
Young's modulus	100 GPa
Friction angle	30°
Cohesion	2 MPa
Poisson's ratio	0.25

Table 2. Physical and environmental parameters.

Temperature (°C)	Rel. humidity (%)	Dew point (°C)	Emissivity
4.50	90	3.00	0.90

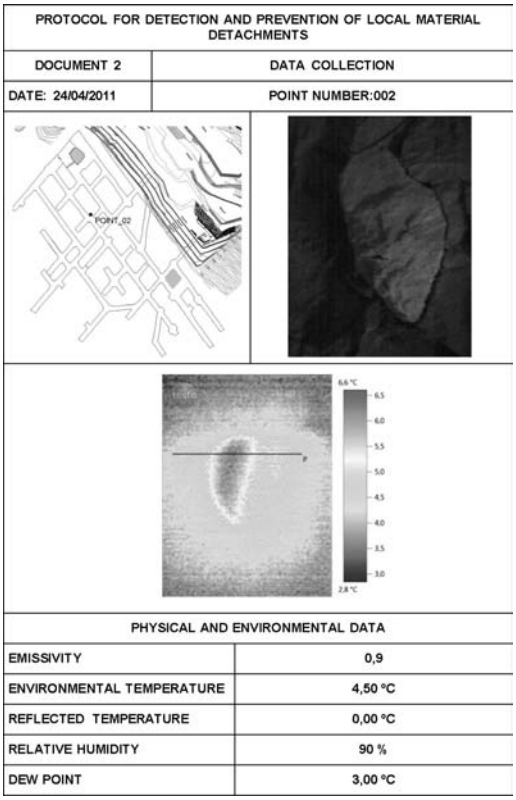


Figure 3. Example of data collection file.

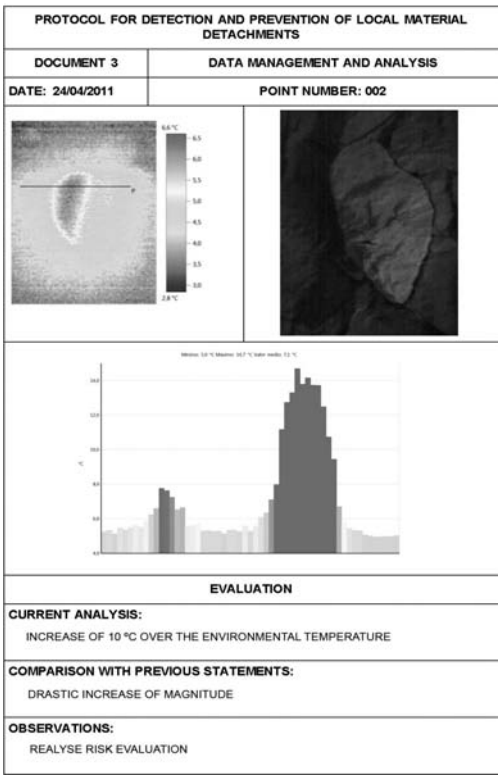


Figure 4. Sample data management and analysis file.

4.3 *Data management and analysis*

The information gathered on site is transferred to a database for management and analysis (Kaplan 2001, Krapez et al. 1991). The existence and maintenance of this database makes it possible to determine not just the actual state of the areas being studied but also their behaviour and evolution over time. The protocol for the procedure for managing and handling data essentially consists for the critical areas identified:

a) Analysis of the current state
b) Comparing the current state with previous states
c) Preparing the analysis and management file (Fig. 4)

Based on the previous analysis it is possible to identify and evaluate the areas of risk. Three levels are established with different protocols for action and the corresponding action sheet is prepared (Fig. 5).

The actions to be carried out for each area are:

– No risk: continue gathering and monitoring data with the established frequency.
– Medium risk: increase the frequency for gathering and monitoring data.
– High risk: proceeded to carry out the required operations to avoid a potential accident, generally by healing the material susceptible to detachment or, under certain conditions, applying support methods.

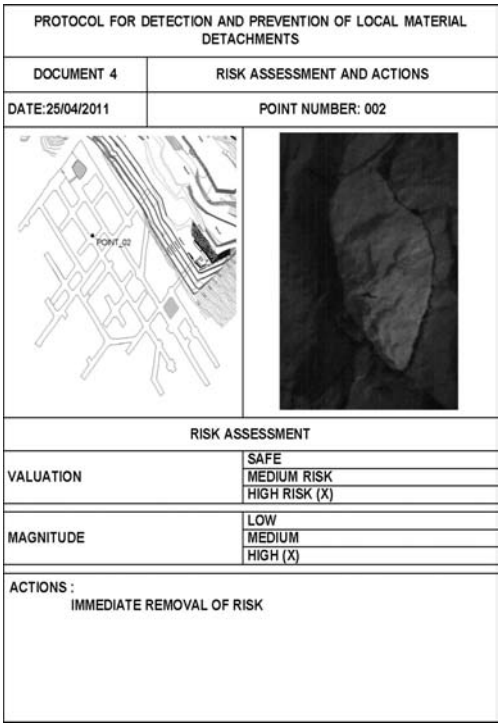


Figure 5. Example of the risk assessment and action file.

5 CONCLUSIONS

From this paper it is possible to conclude that infrared thermography:

- It is a diagnostic or preventive maintenance technique whose capacity for on-site analysis makes it possible to monitor processes or materials where the temperature and the emissivity of the services provide valid information.
- It is a non-destructive technique that makes it possible to measure the surface temperature without coming into direct contact with the system being studied, facilitating its application in complex environments such as sub-surface mining.
- It is a technique that provides real-time information that can be stored digitally, allowing greater flexibility when it comes to studying the data that is obtained.

Finally, once the data has been obtained and properly analysed, it is possible to locate and identify areas that are susceptible to detachments, establish a quantitative evaluation of the inherent risk, and establish a protocol for monitoring and preventive actions.

It should be noted that this technique makes it possible to obtain objective data of the situation, since at present checks are carried out visually and there are areas for which, on account of their distance or location, such a check is not possible. Furthermore, this technique can be applied systematically.

ACKNOWLEDGEMENTS

The authors are grateful to Cantera de Campanzar, S.A. of Grupo Calcinor (Arrasate, Gipuzkoa, Spain) for their support in carrying out this work.

REFERENCES

Alcalde-Gonzalo, J., Prendes-Gero, M.B., Álvarez-Fernández, M.I., Álvarez-Vigil, A.E. & González-Nicieza, C. 2013. Roof tensile failures in underground excavations. *International Journal of Rock Mechanics and Mining Sciences* 58: 141–148.

González Palacio, C. Menéndez Díaz, A., Álvarez Vigil, A.E. & González-Nicieza, C. 2005. Identification of non-pyramidal key blocks in jointed rock masses for tunnel excavation. *Computers & Geotechnics* 32: 179–200.

Goodman, R.E. & Shi, G. 1985. *Block Theory and Its Application to Rock Engineering.* London: Prentice-Hall.

Kaplan, H. 2001. *ASNT Level III Study Guide: Infrared and Thermal Testing Method.* American Society for Nondestructive Testing.

Krapez, J.C., Maldague, X. & Cielo, P. 1991. Thermographic Non-Destructive Evaluation: Data inversion procedures, Part II: 2-D Analysis and Experimental Results. *Research in Nondestructive Evaluation* 3: 101–124.

Maldague, X. 2001. *Theory and Practice of Infrared Technology for Nondestructive Testing.* New York: Wiley-Interscience.

Thomas, R.A. 1999. *Thermography Monitoring Handbook.* Oxford: Coxmoor Publishing Company.

This page intentionally left blank

Rock Mechanics for Resources, Energy and Environment – Kwaśniewski & Łydżba (eds)
© 2013 Taylor & Francis Group, London, ISBN 978-1-138-00080-3

Are classification systems outdated?

W. Schubert
Graz University of Technology, Graz, Austria

ABSTRACT: Lacking appropriate mathematical, mechanical, investigation and testing methods to realistically characterize the ground and predict the ground and system behaviours, for many centuries purely empirical methods for tunnel design have been used. Initially the used experience was bound to single persons. Later, formalized procedures have been developed, using a few, relatively easily collectable parameters, and by weighting them, arrive at a ground quality indicator. It is obvious that the complex properties of the ground cannot be adequately described by a single number or expression. Basis for the selection of parameters and weighting and rating is experience under specific conditions, making a use under other conditions questionable. The authors of some of the systems extended their classification systems to tunnel design tools by including additional parameters and input in the system. The assignment of e support measures is strongly biased, and does not consider different behavioural modes of the ground and its interaction with excavation and support. Thus tunnel designs based on such systems necessarily are inaccurate and sometimes even entirely wrong. From the legal point of view, the sole use of "classification systems" for tunnel design is inacceptable, as there is no proof of stability or serviceability. Due to the reasons mentioned above and a number of other shortcomings, like oversimplification, so called "classification systems" are not adequate to the problem, leading to inadequate designs, and thus to uneconomical construction.

1 WHY CLASSIFICATION?

The reasons for establishing a classification system can be manifold. The main purpose generally is to group items with similar features or properties into one category. This requires the definition of classification criteria. Those criteria need to be clear and meaningful. It is quite obvious that a small number of classification criteria leads to a quite heterogeneous distribution of individual members of one category.

As an example the classification of children, which should enter school may serve. The main criterion in most countries is that they are six years of age. If this is the only criterion applied, any six year old kind falls into the category of school beginners, regardless of their origin, mother tongue, weight and height, and what other differences might exist among that group.

To arrive at a more homogeneous group, additional criteria are required. Naturally the single criteria are not of the same importance, thus the different criteria need to be weighted. The weight of each criterion again depends on which specific requirements the target group should meet. It is quite clear that different persons would put different weights on the single criteria due to their personal preferences or experience. With adding more criteria to apparently arrive at a more homogeneous group the bias increases. There is no guarantee that the group eventually fits together, as one group member may have strong qualifications with respect to some criteria, while another group member has high qualification in other aspects.

The question arises why we need classification at all if the result probably is not satisfying? The answer is quite simple: to enable also inexperienced people to form a group, meeting certain requirements with some degree of probability of success. But while an expert can correct unwanted results from the classification process, a layperson uncritically has to believe that the result is appropriate.

2 CLASSIFICATION IN TUNNELING

Tunneling in a larger scale started in the mid nineteenth century with the world wide boom in railway construction. Knowledge about the mechanical processes during tunnel excavation practically did not exist. The fields of soil or rock mechanics were developed only in the mid nineteen hundreds. Consequently education in the field of geotechnics was absent. This led to the need to develop tools allowing also miners and engineers with lack of experience or education to make decisions on the construction method. Classification systems were in use in mining for a long time. Mining is a more or less stationary industry, with only slightly varying ground conditions throughout the mine. There it is relatively easy to develop empirical rules, as due to the abundant number of underground

openings a lot of experience can be gained. In contrast, civil engineering projects generally are located in different geological conditions, have different boundary conditions and requirements. Applying the empirical rules, developed for certain conditions on all the different "prototypes" can be rather hazardous, as situations may be encountered, which the authors did not think of.

The background of the common classification systems is not known, thus it is impossible to judge, for which conditions they may yield reasonable results, and under which conditions they are simply not applicable.

2.1 *Common classification systems*

Two approaches were used in the past. In one case the ground was classified according to the behaviour (Lauffer 1958, Pacher et al. 1974), in the other case certain rock mass features are used to arrive at an index (Bieniawski 1973, 1983, Barton et al. 1974). The system using the behaviour, frequently in use in combination with NATM due to lack of definition was abandoned was abandoned, and replaced by an engineering approach (OeGG, 2001, 2008, 2010). What remained in use are the "quantitative" classification systems.

Necessarily the classification systems are rather simple, in order to allow easy use. They cannot consider specific hazards or failure modes. If the rating results in a certain number, then always the same support is recommended, regardless of the specific rock mass structure and potential hazards. There is no way of assessing the safety margin of a certain support under certain conditions, as the assignment was done based on a rule and not engineering analysis. Another deficiency is the collection of the data. Considered in the rating is only what can be seen, for example at the tunnel face. It should be well known that the behaviour of the system is strongly influenced by geological features like foliation, or slickensides and faults outside the underground opening. Thus for assessing the potential hazards a representative volume around the tunnels needs to be considered. In particular singularities in the vicinity of the tunnel can be a hazard for the stability. "Homogenizing" the rock mass by reducing its properties to a single index can easily lead to overlooking potential failure mechanisms. The effect of a single persistent discontinuity, located close to the tunnel sidewall and striking +/− parallel to the tunnel axis is shown in Figure 1. It can be easily seen that shearing along the discontinuity can lead to a collapse.

The inherent "homogenization" of the rock mass leads to a loss of information. This again can result in a completely wrong assessment of the behaviour of the tunnel. It is well known that in foliated rock mass under higher overburden the behaviour of the system is strongly influenced by the relative orientation of the foliation to the tunnel. Not only can the displacements be up to an order of magnitude higher, when tunneling parallel to the foliation strike, also the development

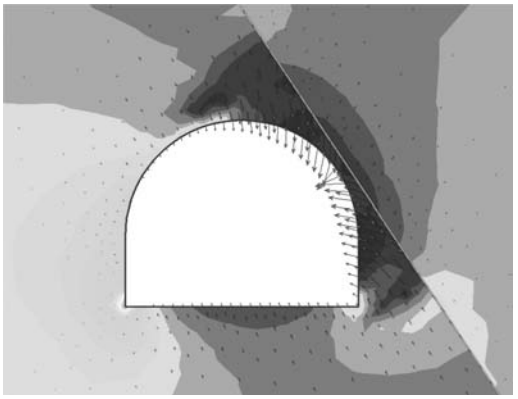


Figure 1. Simple numerical simulation of the influence of a singularity close to the tunnel wall.

of the displacements in relation to the face advance differs considerably, compared to the case with excavation perpendicular to the foliation strike (Goricki et al. 2005).

The inconsistency of quantitative classification systems has been demonstrated by Palmstrom & Broch (2006), in particular addressing the factor SRF in the Q-System (see Figure 2).

Proponents of the quantitative classification methods always claim that the system worked well in the past. But the fact that a tunnel does not collapse is no proof at all that we did everything right. Sometimes it is mere luck, respectively the high potential of the rock mass for self stabilization; in other cases the support may have been grossly overdesigned, without of the people responsible even realizing it.

One of the most serious setbacks of classification systems however is that engineers are not required to think in hazards and associated consequences. Thus they will have a limited understanding of the mechanical processes associated with tunnelling. If the processes are not fully understood, it is also difficult to predict the expected behaviour, and interpret observation results. Consequently also the learning effect will be very limited, and the chance to better engineer the next section or project is minimal.

3 REQUIREMENTS AND LEGAL ASPECTS

Underground structures are rather costly, and consequences of unfavorable behaviour or failure may be extremely severe, hence they demand proper engineering. The hazards during construction are significant, and need to be dealt with properly. Meanwhile in underground engineering it is a general requirement to proof stability and serviceability in all construction stages (for example EUROCODE 7, 1997). In EC 7 tunnels in general belong to the category 3 structures, requiring detailed investigation and analysis. Rule of

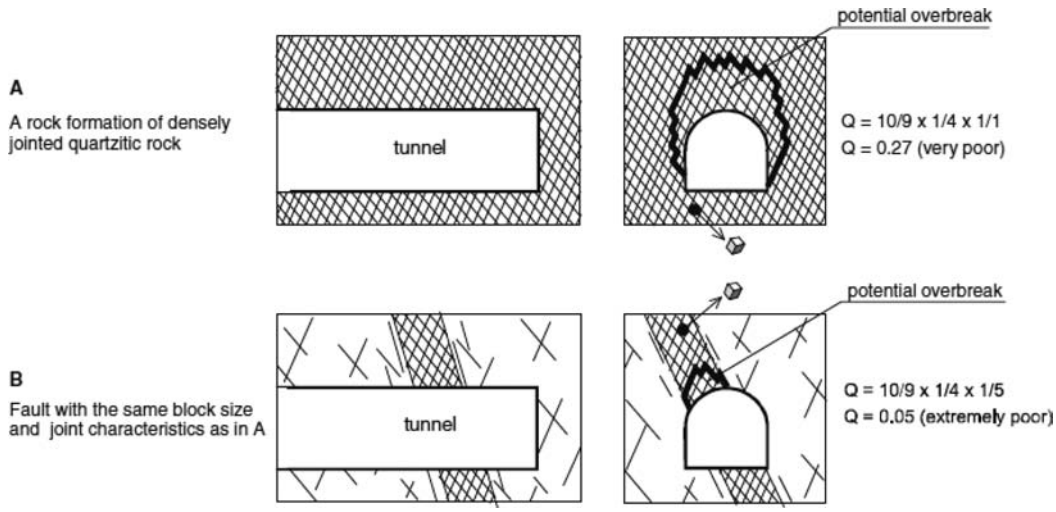


Figure 2. Misleading result of classification (from Palstrom & Broch, 2006).

thumb methods as a sole means of design are not allowed. Although currently available standards will have to be adjusted to better fit the requirements of underground engineering, designs have to be traceable, consistent and audible. Empirical methods – like classification systems – do not fulfill this requirement. The increasing "legalization" of our society makes it extremely hazardous to apply such empirical methods.

What if an accident happens? Who would take the responsibility? The authors of the classification system? I doubt that. In the end the user will be held responsible, and in the worst case brought to court.

Also insurance companies are increasingly reluctant to make business with the tunnel industry, as the risk for them is extremely high.

4 CONCLUSIONS

Extensive experience in tunneling over the last fifty to sixty years has allowed accumulating enormous experience. Considerable research and development now allows engineering underground structures in a way as usual for other buildings. Nobody would accept to use a major bridge or high rise building, which was designed just based on a set of simple rules.

Today tools allow appropriate modeling of underground structures, addressing the project and site specific issues with reasonable effort. There is no need using empirical methods with unknown background any longer. Education in geotechnics and tunneling meanwhile has a high standard, allowing engineers to perform a design job properly.

Being entrusted with large and important projects, engineers should be aware of their responsibility against clients and the public. Using outdated methods for design and construction frequently not only leads to unsafe and uneconomical construction, as specific problems cannot be addressed appropriately.

It has also to be kept in mind that tunnel engineering is not a simple task and is associated with high responsibility. Owners and authorities increasingly become aware of the deficiencies of the traditional empirical approach, and it can be expected that such methods will not be accepted in near future. It can be observed that slowly the community is becoming aware of the problem, and risk oriented design approaches are becoming more common. The call for engineering approaches to tunnel design and construction continuously spreads (see Palmstrom & Stille 2007).

With legal aspects becoming more important, one should be aware that in the case of an accident many questions will be asked. Then one should be well prepared to properly explain why one did this or that. With the current state of the art in engineering and legal as well as insurance issues in mind, abandoning empirical methods, such as classification system should be abandoned as quickly as possible.

REFERENCES

Barton, N., Lien, R. & Lunde, J. 1974. Engineering Classification of Rock Masses for the Design of Tunnel Support. *Rock Mechanics and Rock Engineering* 6(4): 189–236.

Bieniawskí, Z. T. 1973. Engineering Classification of Jointed Rock Masses. *Trans. S. Afr. Inst. Civ. Eng.* 15: 335–344.

Bienìawski, Z. T. 1983. The Geomechanics Classification (RMR System) in Design Applications to Underground Excavations. *Proc. Int. Symp. Eng. Geol. Underground Constr.* Rotterdam: Balkema.

CEN/TC 250, 2006. EN 1997-1, EUROCODE 7 Geotechnical design – Part 1: General rules

Goricki, A., Button, E.A., Schubert, W., Poetsch, M. & Leitner, R. 2005. The Influence of Discontinuity

Orientation on the Behaviour of Tunnels. *Felsbau* 23(5): 12–18.
Lauffer, H. 1958. Gebirgsklassifizierung für den Stollenbau. *Geologie und Bauwesen* 24(1): 46–51.
OeGG, 2001, 2008. Guideline for the geotechnical design of underground structures. OeGG, Salzburg
OeGG, 2010. Guideline for the geotechnical design of underground structures with conventional excavation. Austrian Society for Geomechanics, Salzburg
Pacher, F., Rabcewicz, L. v. & Golser, J. 1974. Zum derzeitigen Stand der Gebirgsklassifizierung im Stollen- und Tunnelbau. *Schriftenreihe Strassenforschung. Bundesministerium für Bauten und Technik, Heft 18*, Wien.
Palmstrom, A. & Broch, E. 2006. Use and misuse of rockmass classification systems with particular reference to the Q-system. *Tunnelling and Underground Space Technology* 21: 575–593.
Palmstrom, A. & Stille, H. 2007. Ground behaviour and rock engineering tools for underground excavations. *Tunnelling and Underground Space Technology* 22: 363–376.

Rock Mechanics for Resources, Energy and Environment – Kwaśniewski & Łydżba (eds)
© 2013 Taylor & Francis Group, London, ISBN 978-1-138-00080-3

Sensitivity analysis of the generalized Hoek-Brown failure criterion

P. Ván
Department of Theoretical Physics, Wigner FK, RMI; Department of Energy Engng, BME; Montavid Thermodynamic Research Group, Budapest, Hungary

B. Vásárhelyi
Department of Structural Engng, Pollack M Faculty of Engineering, University of Pécs, Pécs, Hungary

ABSTRACT: Recently, the Hoek-Brown failure criterion is one of the mostly used failure criterion for rock mass. The constants of this failure criterion depend on, among the others, the Geological Strength Index (*GSI*) and the disturbance factor (*D*). The purpose of this paper is to analyze the sensitivity of the various constants of this equation, which depends on the *GSI* value and the *D* factor. The results show that the Hoek-Brown constants are very sensitive to both the *GSI* and the *D* factor, so to determine them exactly is very important for the rock engineering design. The sensitivity of the strength of the rock mass is also calculated. Thus these input parameters can be not determinable exactly, the results shows to take into account to use these relationships, mostly for risk analysis.

1 INTRODUCTION

The purpose of this paper is to determine the sensitivity of the Hoek-Brown failure criterion of rock mass based on the Geological Strength Index (*GSI*) and the disturbance factor (*D*). The sensitivity of different empirical formulas to parameter uncertainty is an important factor for a rock engineering designer.

The Hoek-Brown rock mass failure criterion is frequently applied in rock engineering calculations one should have some idea about the effect of variations in the input parameters for judging the acceptability of the design. Accordingly, we analyze the generalized Hoek-Brown formula from this point of view, and give some practical tools for rapid sensitivity analyses.

The first steps of this analysis were carried out by Ván & Vásárhelyi (2007). According to their results, the *GSI* based equations for calculating the deformation moduli of rock mass (Hoek & Diederichs 2006) can be not used in the practice without any risk.

It has to be noted, that the origin of all of these *GSI* based equations is empirical, they do not have any theoretical foundation. Moreover, their empirical foundation is questionable, it was never published, as it was pointed out by Anagnostou & Pimentel (2012). Recently, Ván & Vásárhelyi (2013) analyzed the advantage and disadvantage of the *GSI* system.

2 GEOLOGICAL STRENGTH INDEX (GSI) AND THE DISTURBANCE FACTOR (D)

The Geological Strength Index (*GSI*), as a system of rock-mass characterization, was introduced by Hoek (1994) and Hoek et al. (1995). The goal of this engineering geological system was to present input data, particularly those related to rock-mass properties required as inputs into numerical analysis or closed form solutions for designing tunnels, slopes or foundations in rocks. It provides a field method, so the geological character of rock material, together with the visual assessment of the mass it forms, is used as a direct input to the selection of parameters relevant for the prediction of different mechanical parameter of the rock-mass. This approach enables a rock mass to be considered as a mechanical continuum. Marinos et al. (2005) deeply review the application and the limitation of the Geological Strength Index. According to the definition of *GSI*, "*From the lithology, structure and surface conditions of the discontinuities, estimate the average value of GSI. Do not try to be too precise. Quoting a range from 33 to 37 is more realistic than starting that GSI = 35*" (Marinos & Hoek 2000). This mean, that if the $GSI = 10$, ($7 < GSI < 12$) the sensitivity of this value reaches the 20%, but minimum 5%!

According to the authors, *GSI* can be used in case of very weak and sheared rock masses, ie. flysch and

schist, where $GSI < 30$ (Marinos & Hoek 2001 and Hoek et al. 1998, respectively).

The determination of these parameters is not easy and is not exact; it is encumbered by several uncertainties. Also with the more exact methods for the calculation of the *GSI* value (see Sonmez & Ulusay 1999, Cai et al. 2004 and Russo 2009) there are several possibilities of errors. Moreover, the different input (in situ measured) parameters for determining exactly the *GSI* value depend on the site investigators (e.g. see the results of Deák et al., 2012). It is the well known subjectivity of the results, thus the differences for the same tunnel face can reach as much as 30%.

The influence of blast damage on the near surface rock mass properties have been taken into account in the 2002 version of the Hoek-Brown criterion (Hoek et al., 2002). *D* is a factor which depends upon the degree of disturbance due to blast damage and stress relaxation. It varies from 0 for undisturbed in situ rock masses to 1 for very disturbed rock masses. Up to now, there is only one guidelines for the selection of *D* factor (Hoek et al., 2002). The exact determination of the disturbance factor *D* is more difficult – up to now it is not standardized and not any possibility to measure it. One can see, this parameter is very sensitive, as well.

3 BASICS OF THE GENERALIZED HOEK-BROWN FAILURE CRITERION

The Hoek-Brown criterion is one of the most popular failure criterion for determining the failure envelope of the rock mass. For jointed rock masses it is given by the following generalized formula (Hoek et al., 2002):

$$\sigma_1' = \sigma_3' + \sigma_{ci}\left(m_b \frac{\sigma_3'}{\sigma_{ci}} + s\right)^a, \tag{1}$$

where

- σ_1' and σ_3' are the maximum and minimum effective principal stresses at failure;
- σ_{ci} is the uniaxial compressive strength of intact rock;
- m_b is the value of the Hoek-Brown constant for the rock mass, depending on the Hoek-Brown constant of intact rock (m_i), the Geological Strength Index (*GSI*) and the disturbance factor (*D*):

$$m_b = m_i \exp\left(\frac{GSI - 100}{28 - 14D}\right) \tag{2}$$

- *s* and *a* are parameters that also depend on the rock mass characteristics:

$$s = \exp\left(\frac{GSI - 100}{9 - 3D}\right) \tag{3}$$

and

$$a = \frac{1}{2} + \frac{1}{6}\left(e^{-GSI/15} - e^{-20/3}\right) \tag{4}$$

According to the Hoek-Brown equation (1) the ratio of the uniaxial compressive strength of the rock mass (σ_{cm}) and to that of the intact rock (σ_{ci}) is:

$$\sigma_{cm}/\sigma_{ci} = s^a \tag{5}$$

where *s* and *a* can be calculated by Eq. (3) and (4), respectively.

The Hoek-Brown equation is suggested by ISRM for using as failure criterion of jointed rock mass (Eberhard 2012)

Eqs. (1)–(3) are empirical equations, results of experimental observations, without theoretical background.

4 SENSITIVITY ANALYSIS

The sensitivity of a function *f* regarding the uncertainties of the variables can be characterized by the formula commonly known as propagation of uncertainty or propagation of error (Bronstein & Semendyayev 2004). Let us suppose that f is a real function which depends on *n* random variables $x_1, x_2, \ldots x_n$. From their uncertainties Δx_1, Δx_2, ... Δx_n we can calculate the uncertainty Δf of *f*:

$$\Delta f = \left(\sum_{i=1}^{n}\left(\left.\frac{\partial f}{\partial x_i}\right|_{x_1,\ldots,x_{i-1},x_{i+1},\ldots,x_n} \Delta x_i\right)^2\right)^{\frac{1}{2}} \tag{6}$$

Here it was assumed that the variables are uncorrelated and the underlying distribution which these errors represent is Gaussian.

Therefore if the variables x_i are measured with an experimental error, $x_i \pm \Delta x_i$, we can estimate the uncertainty of their arbitrary function with the above formula. This formula is robust; the Gaussian distribution is a reasonable assumption is several cases. If the variables are correlated we should apply a modified equation for sensitivity estimates.

In this paper the relative sensitivity of the Hoek-Brown parameters, the rock mass strength of the rock mass were calculated in case of $\Delta GSI/GSI = 0.05$ and $\Delta GSI/GSI = 0.10$ and values for $D = 0$; 0.5 and 1.0.

5 RESULTS OF THE SENSITIVITY ANALYSES

5.1 *Analysis of the sensitivity of the m_b value*

The dependence of *GSI* on the ratio of the m_b/m_i is plotted in Figure 1 in the case of 0; 0.5 and 1.0 values of disturbance factor *D*.

The 5% and 10% *GSI* deviations were calculated and presented in Figures 2 and 3, respectively. We can see that the relative sensitivity of m_b is at least double the uncertainties of the *GSI* and *D* values, and may be 7 times higher in case of large disturbance parameters and low and high *GSI* values.

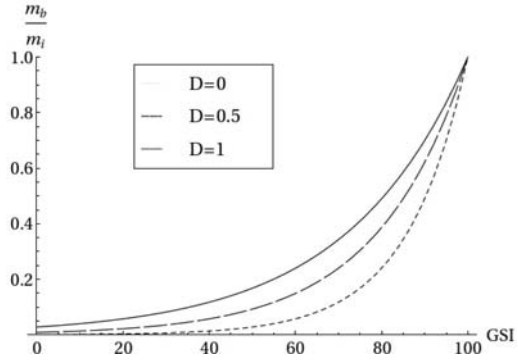


Figure 1. The *GSI* dependence of the ratio of the m_b/m_i (see Eq. (2)) in case of different disturbance factors *D*.

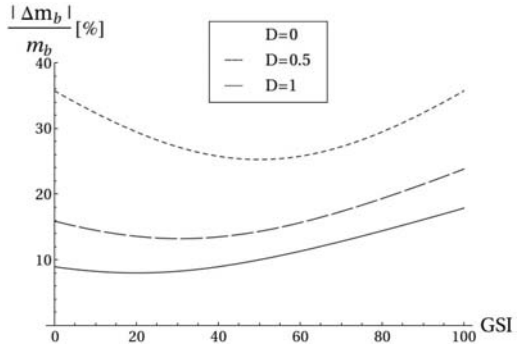


Figure 2. The relative sensitivity of m_b in case of 5% measurement errors ($GSI \pm 0.05GSI$ and $D \pm 0.05D$).

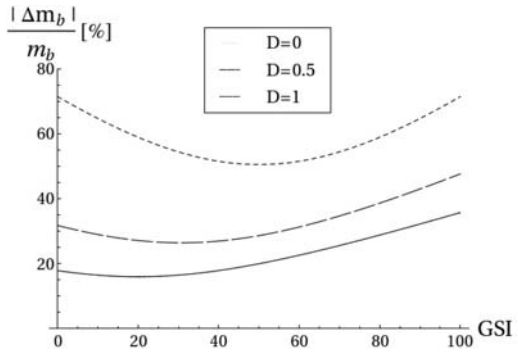


Figure 3. The relative sensitivity of m_b in case of 10% measurement errors ($GSI \pm 0.1GSI$ and $D \pm 0.1D$).

5.2 *Analysis of the sensitivity of the s value*

The dependence of *s* parameter on *GSI* is plotted in Figure 4, in the case of 0; 0.5 and 1.0 values of disturbance factor *D*.

Figures 5 and 6 show that the relative sensitivity of the s parameter is at least the triple of the uncertainties of the variables, and may even be 15 times higher (!) in the case of large disturbance parameters and high *GSI* values.

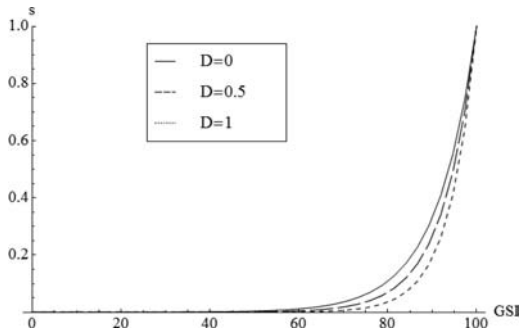


Figure 4. The *GSI* dependence of the s parameter (see Eq. (3)) in case of different disturbance factors *D*.

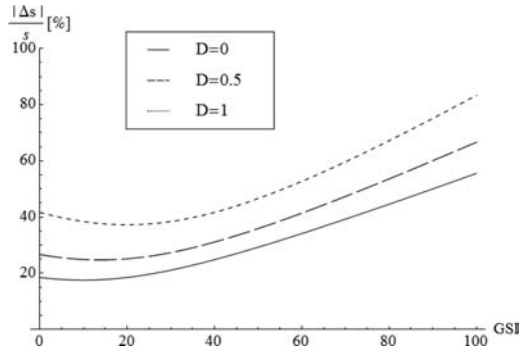


Figure 5. The relative sensitivity of *s* in case of 5% measurement errors ($GSI \pm 0.05GSI$ and $D \pm 0.05D$).

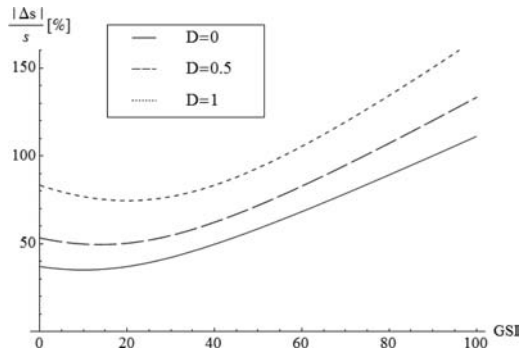


Figure 6. The relative sensitivity of *s* in case of 10% measurement errors ($GSI \pm 0.1GSI$ and $D \pm 0.1D$).

5.3 *Analysis of the sensitivity of the a parameter*

The *a* parameter is independent of the disturbance factor and not sensitive to the uncertainties in *GSI* (Eq. 4, Fig. 7).

The maximum relative sensitivity of *a* is about equal to the uncertainty of the variables at *GSI* value 20. The relative sensitivity of *a* in the case of 5% and 10% measurement errors are plotted in Figs. 8 and 9, respectively.

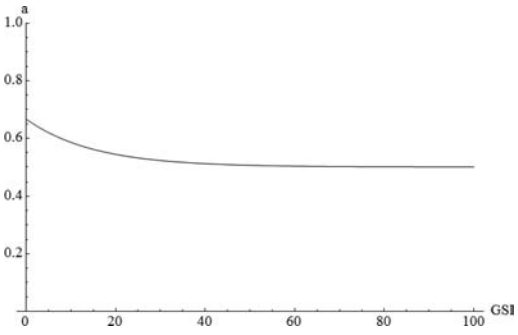


Figure 7. The *GSI* dependence of the a parameter (see Eq. (4)).

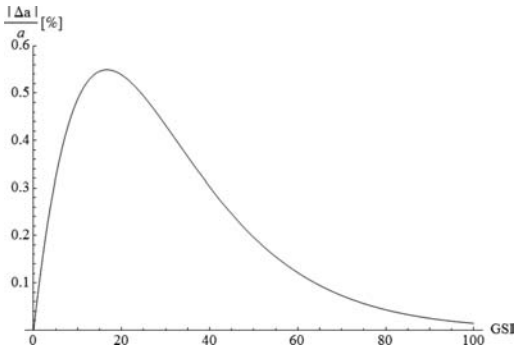


Figure 8. The relative sensitivity of a in case of 5% measurement errors ($GSI \pm 0.05GSI$).

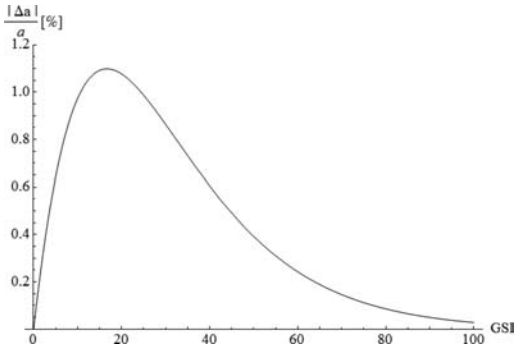


Figure 9. The relative sensitivity of a in case of 10% measurement errors ($GSI \pm 0.1GSI$).

Finally, in Figure 10 the Hoek-Brown failure envelope is presented in 3D visualization (Eq. 1) and the sensitivity of this criterion is plotted in Figure 11 in case of 10% errors (i.e.: $GSI \pm 0.1GSI$ and $D \pm 0.1D$)

5.4 *Analysis of the sensitivity of the strength of the rock mass*

The dependence of the rock mass strength σ_1 on *GSI* (see Eq. (1)) in the case of various disturbance factors D is presented in Figure 12.

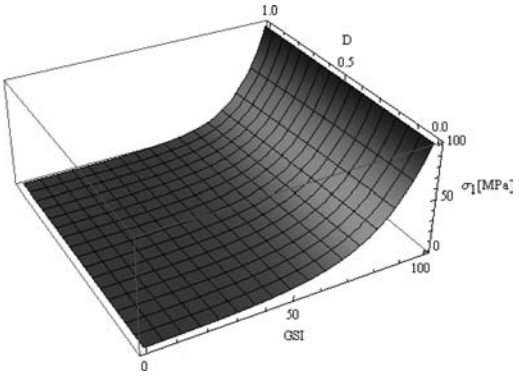


Figure 10. 3D Visualization the Hoek-Brown failure criterion.

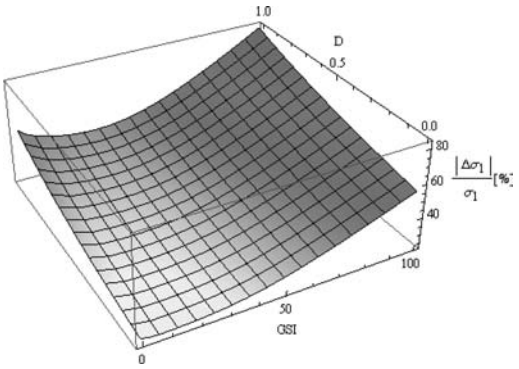


Figure 11. The sensitivity of the Hoek-Brown failre criterion in case of 10% errors ($GSI \pm 0.1GSI$ and $D \pm 0.1D$).

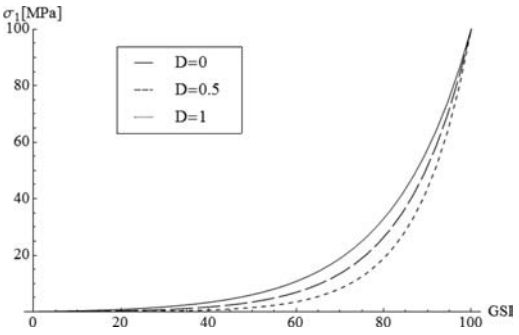


Figure 12. The *GSI* dependence of the rock mass strength σ_1 (see Eq. (1)) in case of different disturbance factors D.

According to Figures 13–14 at low *GSI* values the uncertainty in the disturbance parameter determines the sensitivity of the rock mass strength, at high *GSI* values the uncertainty in *GSI* dominates and the disturbance parameters have less influence.

Figures 15–16 show that the relative sensitivity of the rock mass strength σ_1 is at least double of the uncertainties in the *GSI* and disturbance parameter, and may be 8 times higher in the case of large disturbance parameter and high *GSI* values.

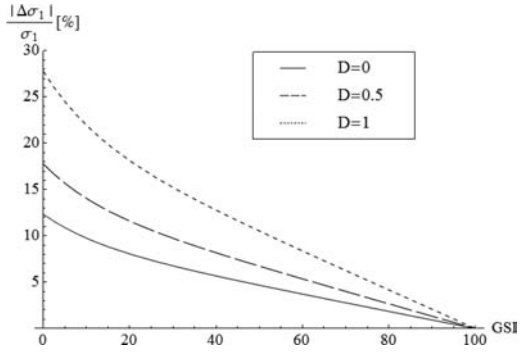


Figure 13. The relative sensitivity of the rock mass strength σ_1 in case of 5% measurement error in the damage parameter and exact *GSI* values ($D \pm 0.05D$)

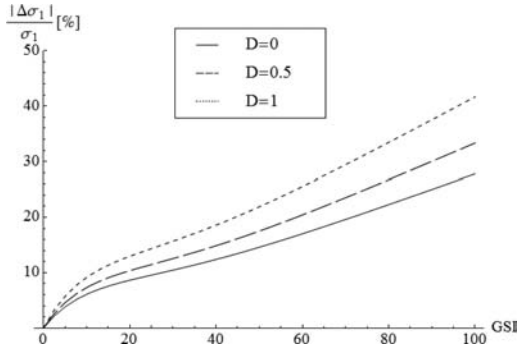


Figure 14. The relative sensitivity of the rock mass strength σ_1 in case of 5% measurement error in the *GSI* and exact damage parameter determination ($GSI \pm 0.05GSI$).

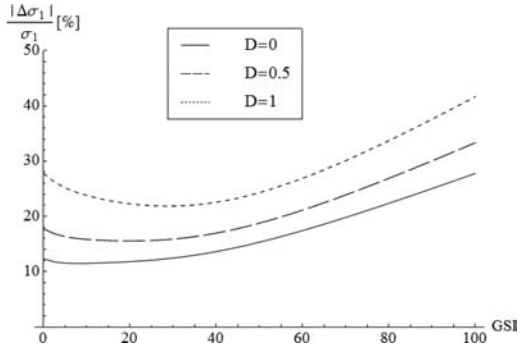


Figure 15. The relative sensitivity of the rock mass strength σ_1 in case of 5% measurement errors ($GSI \pm 0.05GSI$ and $D \pm 0.05D$).

6 DISCUSSION

The sophisticated empirical Hoek-Brown formula is sensitive to the uncertainties of the *GSI* and disturbance parameter (D) values. Its relative sensitivity may reach a value 8 times higher than the relative uncertainties of the *GSI* and D factors in the case of high

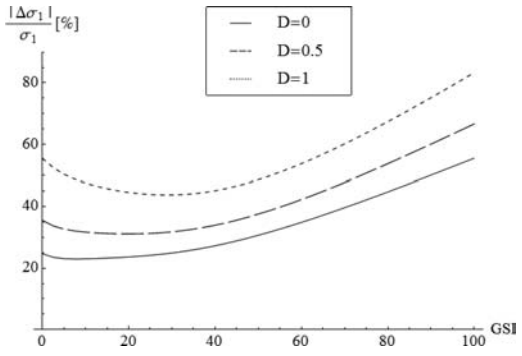


Figure 16. The relative sensitivity of the rock mass strength σ_1 in case of 10% measurement errors ($GSI \pm 0.1GSI$ and $D \pm 0.1D$)

disturbance and *GSI* values, if these relative uncertainties are uniform. With more exact measurements and *GSI* determination at high *GSI* values and disturbance factor determination at low *GSI* values, the relative sensitivity of the Hoek-Brown formula can be considerably reduced.

According to our analysis the Hoek-Brown failure criterion can be highly sensitive to the uncertainties in the *GSI* and disturbance parameters. This sensitivity is due to the complex structure of the function, criterion containing a lower number of parameters may be less sensitive. In any case the rock engineering design should consider the uncertainties of the design parameters and calculate them routinely.

Finally, the GSI value can be connected to thermodynamic based damage models, see Ván & Vásárhelyi (2010). Thermodynamics reveals an interrelation between the deformation modulus and rock mass strength. Rock mass characterizations are interpreted as damage classifications and failure as loss of thermodynamic stability. For intact rock and polynomial free energy it has resulted in a three dimensional failure criterion as that was shown by Ván & Vásárhelyi (2001).

ACKNOWLEDGEMENTS

P. Ván acknowledges the financial support of the OTKA K81161, K104260 and TT 10-1-2011-0061/ZA-15-2009 for this research.

REFERENCES

Anagnostou, G. & Pimentel, E. 2012. Zu den Felsklassifikationen mit Indexwerten im Tunnelbau. *Geotechnik* 35(2): 83–93.

Bronstein, I.N. & Semendyayev, K.A. 2004. *Handbook of Mathematics*, Springer, Berlin (4th edition).

Cai, M.; Kaiser, P.K.; Uno, H.; Tasaka, Y. & Minami, M. 2004. Estimation of rock mass deformation modulus and strength of jointed hard rock masses using GSI system. *Int. J. Rock Mech. Min. Sci*. 41: 3–19.

Deák, F.; Kovács, L. & Vásárhelyi, B. 2012. Comparison of Different Rock Mass Classifications at Bátaapáti Radioactive Waste Repository. *Proc. Eurock 2012,* p. 12.

Eberhard, E. 2012. The Hoek-Brown failure criterion – ISRM suggested method. *Rock Mech. Rock Eng*. 45(5): 981–988.

Hoek, E., Carranza-Torres, C. & Corkum, B. 2002. *Hoek-Brown failure criterion – 2002 Edition*. Proc. 5. North American Rock Mech. Conf. 1: 267–271.

Hoek, E. 1994. Strength of rock and rock masses. *News J ISRM* 2(2):4–16.

Hoek, E. & Diederichs, M.S. 2006. Empirical estimation of rock mass modulus. *Int. J. Rock Mech. Min. Sci*. 43: 203–215.

Hoek, E.; Kaiser, P.K. & Bawden, W.F. 1995. *Support of Underground Excavations in Hard Rock*. Rotterdam: Balkema.

Marinos, P. & Hoek, E. 2000. *GSI*: *A geologically friendly tool for rock mass strength estimation*. Proc. GeoEng2000 Conference, pp. 1422–1442

Marinos, P. & Hoek, E. 2001: Estimating the geotechnical properties of heterogeneous rock masses such as flysch. *Bull. Eng. Geol. Env*. 60: 85–92.

Marinos, V., Marinos, P. & Hoek, E. 2005: The Geological Strength Index: Applications and Limitations. *Bull. Eng. Geol. Environ.* 64(1): 55–65.

Russo, G. 2009: A new rational method for calculating the GSI. *Tunneling & Underground Space Technology* 24: 103–111.

Sonmez, H. & Ulusay, R. 1999: Modifications to the geological strength index (GSI) and their applicability to stability of slopes. *Int. J. Rock Mech. Min. Sci*. 36: 743–760.

Ván, P. & Vásárhelyi, B. 2001. Second law of thermodynamics and the failure of rock materials. In D. Elsworth, J.P. Tinucci & K.A. Heasley (eds), *Rock Mechanics in the National Interest* I: 767–773. Lisse: A.A. Balkema Publishers.

Ván, P. & Vásárhelyi, B. 2007. Sensitivity analysis of the Hoek-Diederichs rock mass modulus estimating formula. In L.R. Sousa, C. Olalla & N.F. Grossmann (eds), *The Second Half Century of Rock Mechanics, Proc. 11th Congress of ISRM* I: 411–414. Leiden: Taylor & Francis/Balkema.

Ván, P. & Vásárhelyi, B. 2010. Relation of rock mass characterization and damage. In: I. Vrkljan (ed.), *Rock Engineering in Difficult Ground Conditions – Soft Rocks and Karst, Proc. Eurock 2009*: 399–404. Leiden: CRC Press/Balkema.

Ván, P. & Vásárhelyi, B. 2013. GSI system based sensitivity analysis of Hoek-Brown failure envelope of the rock mass. *Rock Mech. Rock Eng*. (under submission)

Rock Mechanics for Resources, Energy and Environment – Kwaśniewski & Łydżba (eds)
© 2013 Taylor & Francis Group, London, ISBN 978-1-138-00080-3

Analysis and treatment of a diversion tunnel in adverse geological conditions: A case study from south-western China

J.K. Yang & Y.F. Wang
China Three Gorges Corporation, Beijing, China

D.F. Chen
Key Laboratory of Ministry of Education on Safe Mining of Deep Metal Mines, Northeastern University, Shenyang, Liaoning, China

ABSTRACT: The #3 and #4 diversion tunnels of Wudongde Hydropower Station pass through a long surrounding rock of adverse geological condition. The rock formation of the adverse geological tunnel sections is thin-layer marbleized dolomite with steep dip angle, with existing interlayer cleavages and microfissures. The tunnel orientation and the strata layer's strike intersect at small angle. During the excavation of the upper layer sections, local collapses and fall-blocks were frequently observed, most of which are in the left crown. This brought serious instability concerns. A numerical model was established using finite element method to analyze the mechanism and characteristics of such instability. Thin layer and steep dip angle rock formations with lower dip angle joints and fissures generally has lower strength; therefore, affected by excavation, unstable failures occur at the left crown. A series of actions have been taken to treat the collapse areas, including shotcrete-rock bolt support, steel arch, concrete backfill, and consolidation grouting without concrete covering. The treatment results are satisfactory per construction requirements.

1 INTRODUCTION

1.1 *Project overview*

Wudongde Hydropower Station is located in lower reaches of Jinsha River, where Sichuan Province marches with Yunnan Province. As a large-sized hydropower station, it has a 406,100 km^2 watershed area, a 7.408 billion m^3 total storage capacity, and a 10,200 MW total installed capacity. The under construction hydropower station will be completed by 2020, and will be the fourth-largest hydropower station in China.

There are five diversion tunnels in both left and right banks. The #3, #4, and #5 diversion tunnels are in the right bank. The spacing distance between the tunnel axes is 38 to 50 m, the thickness of the middle wall between the tunnels is 28.1 to 30.1 m. The maximum embedment depth of the tunnels is 560 m. #3 and #4 division tunnels are a bit lower than #5 tunnel. The elevation of #3 and #4 tunnels' entrance is 812.0 m, and the exit is 800.0 m high. The length of #3 division tunnel is 1472.4 m (stake number is 0 + 000 to 1 + 472.4) and 1613.6 m for the #4 division tunnel (stake number is 0 + 000 to 1 + 613.6). #3 and 4 # division tunnel both have a horseshoe-shaped tunnel portal, and the lined tunnel dimension is 16.5 m × 24.0 m (width × height).

1.2 *Geological condition of adverse geological sections*

The dam site of Wudongde Hydropower Station belongs to the landform of middle mountain and ravine. The mountain's elevation on both sides is about 2000 to 3000 m. Jinsha River is the lowest erosion base level of the region. The dam site has a folded basement strata of Presinian System Huili Group epimetamorphic rock and a cover strata of Sinian System sedimentary rock and igneous rock. The strata of #3 and #4 diversion tunnels is folded basement. The surrounding rock of adverse geological sections is classified to be the IV grade. The overall length of #3 diversion tunnel's adverse geological section is 443 m, and 649 m for #4 tunnel (Fig. 1). The strata of adverse geological sections is Yinmin Formation of Mesoproterozoic Erathem Huili Group (Pt^2_{2y}), and consists of thin-layer hoary marbleized dolomite with steep dip angle. There are few limestone and dolomite in the strata. The single layer thickness of marbleized dolomite is 5 to 15 mm, and there are phyllite films of 0.5 to 1 mm thick between the layers. The dip of the strata is 120° to 130° , inclined downstream. The dip angle of the strata is 50° to 65°. The included angle between the strata's strike and the tunnel axis is 20° to 30° . There are three large faults across the adverse geological sections. The width of the fault zone is 1 to 2 m.

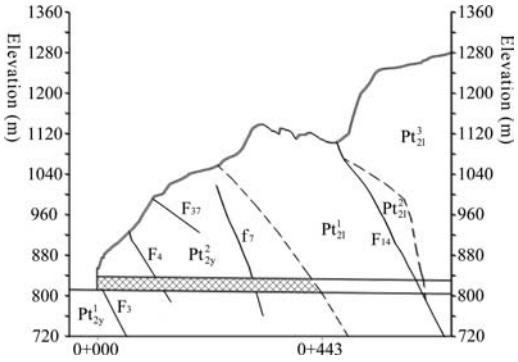


Figure 1. Adverse geological section of diversion tunnel #3.

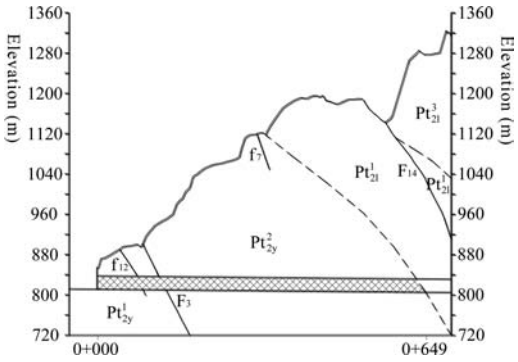


Figure 2. Adverse geological section of diversion tunnel #4.

Table 1. Surrounding rock engineering geological classification of diversion tunnel #3 and #4.

		Diversion tunnel #3	Diversion tunnel #4
Diversion tunnel length (m)		1472.2	1613.6
Grade II	Length (m)	128.0	106.6
	Proportion (%)	8.7	6.6
Grade III	Length (m)	463.2	369.0
	Proportion (%)	31.5	22.9
Grade IV	Length (m)	881.0	1138.0
	Proportion (%)	59.8	70.5

The included angle between the faults and tunnel axis is about 65° . Interlayer cleavages and microfissures are well developed, while large fissures are relatively rare. Influenced by tectogenesis, crumpled bedding was developed in the thin layer formation, which made part of the surrounding rock incline upstream.

The grade IV surrounding rock can be divided into grade IV_1 and grade IV_2. The main features of grade IV_1 surrounding rock can be summarized as the following: the stratum's layer is very thin and microfissures are well developed; the interbedded cohesive strength is relatively low but with a certain degree of strength; and the surrounding rock has a limited stability. The main features of grade IV_2 sur-rounding rock are: the surrounding rock has strong corrosion and weathering, the microfissures are con-siderably developed; most of the rock mass has cloddy and granular structure with a very low strength that can be crushed by hand; the diameter of the rock fragment is 1 to 3 cm; the surrounding rock has very low stability and it is easy to collapse during excavation; concrete fragments occasionally fall even after being shotcreted.

Table 2. Summary of collapses during layer I excavation.

Diversion tunnel	Stake number	Collapse area	Maximum depth (m)
3#	0 + 073~0 + 077	Left crown	1.4
	0 + 092~0 + 155	Left crown	3.3
	0 + 168~0 + 193	Left crown	9.5
	0 + 205~0 + 230	Left crown	2.9
	0 + 260~0 + 265	Left crown	1.5
	0 + 295~0 + 320	Middle crown	3.0
	0 + 345~0 + 363	Left crown	3.5
	0 + 372~0 + 388	Left crown	2.4
	0 + 402~0 + 410	Left crown	1.8
	0 + 415~0 + 430	Left crown	1.7
4#	0 + 050~0 + 057	Left crown	1.7
	0 + 057~0 + 080	Left crown	1.3
	0 + 093~0 + 098	Left crown	1.0
	0 + 115~0 + 125	Left crown	0.9
	0 + 135~0 + 145	Left crown	1.4
	0 + 177~0 + 198	Left crown	3.4
	0 + 240~0 + 275	Left crown	1.9
	0 + 310~0 + 340	Left crown	2.5
	0 + 354~0 + 400	Left crown	3.7
	0 + 400~0 + 450	Left crown	2.5
	0 + 470~0 + 497	Left crown	7.4
	0 + 500~0 + 525	Left crown	3.0
	0 + 545~0 + 640	Left crown	3.6

2 CHARACTERISTICS OF SURROUNDING ROCK INSTABILITY

2.1 *The condition of surrounding rock instability*

The layer I excavation of adverse geological tunnel sections started in April 2012 (there are four layers, the height of layer I is 9 m, the height of layer II–IV is 6 m), ended in November 2012. During the exca-vation, instability problems such as collapse and fall-block are exceedingly serious, which delayed the construction progress. 10 collapse occured in diversion tunnel #3, and 13 collapses in diversion tunnel #4. The general depth of the collapse is 1.5 to 2.5 m while the maximum depth is 9.5 m. The minimum volume of the collapse is 5 m^3 while the maximum volume is 900 m^3 (Tab. 2). There are horizontal cracks and slip in the side wall during the excavation of layer II and III. The cracks have a length of 3 to 8 m, width of 0.3 to 0.5 m, depth of 1 to 2 m.

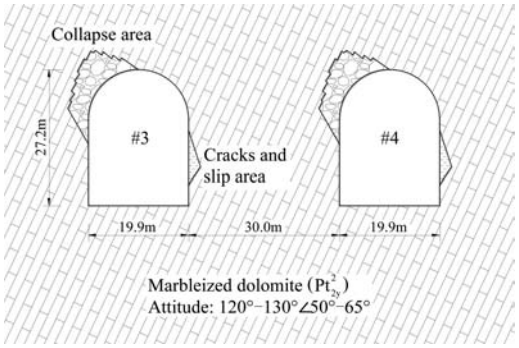


Figure 3. Caption of instability of adverse geological sections.

2.2 *Characteristics of surrounding rock instability*

The characteristics of surrounding rock instability of diversion tunnels #3 and #4 can be summarized as follows:

a) All the collapse happened in thin layer sur-rounding rock;
b) Almost all the instabilities happened in left crown and right side wall (Fig. 3). To be specific, the collapse happened during the excavation of layer I and mostly in the left crown; the cracks and slip happened during the excavation of layer II to IV and mostly in the right side wall. Geophysical characterization showed that the excavation-disturbed zone of the left crown is 4 to 5 m deep while the other area is 2 to 4 m deep;
c) Part of the shotcreted crown had fell concrete blocks, and most of the falling was in the left side. The concrete blocks have various sizes, and the maximum size is more than 2 m^2 in area. Water leakage was observed near the side wall and crown of some sections.

3 PATTERN ANALYSIS OF SURROUNDING ROCK INSTABILITY

3.1 *Numerical simulation*

There are in-situ tests of crustal stress at the dam site but no in-situ test at the diversion tunnel of adverse geological condition. To make a reliable numerical simulation, a back analysis had been introduced to acquire the initial crustal stress field (Yang 1996, Fu et al. 2006). In this study, the initial crustal stress field was simulated in the adverse geological sections with a 3-D finite element method ($FLAC^{3D}$). The simulated crustal stress field can provide the stress boundary conditions for the simulation of excavation using a 2-D finite element method ($FLAC^{3D}$).

3.1.1 *3D-simulation of crustal stress field*

During the hydropower station's pre-feasibility study, some boreholes near diversion tunnels were drilled to test the crustal stress by using hydraulic fractured method and strain release borehole wall stress relief method (BWSRM) (Wang 1991). According to the measurement of the test, the area's stress field shows a typical self-weight stress field feature. This study adopted self-weight stress field to simulate the initial stress field of the adverse geological sections. The rock mass of the sections have orthotropy mechanical property; therefore, the Bilinear Strain-Hardening/Softening Ubiquitous-Joint Model was used in the simulation. It is an elastic-plastic model which consider the layered structural plane.

Table 3. Physico-mechanical parameters of rock mass and faults in the adverse geological sections.

Parameters		Rock mass	Fault
Modulus of deformation	E (GPa)	10.0	1.0
Poisson ratio	v	0.28	0.35
Dilation angle of RM	ψ(°)	10.0	7.5
Tensile strength of RM	σ^t (MPa)	2.0	0.5
Initial cohesion of RM	c_0 (MPa)	8.0	2.0
Residual cohesive of RM	c_d (MPa)	1.0	1.0
Internal friction angle of RM	ϕ_0 (°)	20	15
Residual friction angle of RM	ϕ_d (°)	40	30
Equivalent plastic strain of RM	$\bar{\varepsilon}_c^p$	3	3
	$\bar{\varepsilon}_\phi^p$	5	5
Initial cohesion of joint	c_{j0}(MPa)	4.0	1.0
Residual cohesive of joint	c_{jd} (MPa)	0.1	0.1
Internal friction angle of joint	ϕ_{j0} (°)	15	10
Residual friction angle of joint	ϕ_{jd} (°)	40	25
Equivalent plastic strain of joint	$\bar{\varepsilon}_{cj}^p$	3	3
	$\bar{\varepsilon}_{\phi j}^p$	5	5
Angle of dip of RM	dip (°)	75	75
Dip of RM	dd (°)	90	90
Dilation angle of joint	ψ_j (°)	7.5	6.0
Tensile strength of RM	σ_j^t (MPa)	0.20	0.01

*RM is rock mass.

The result of the 3-D crustal stress simulation indicates that there is a close link between the principal stress and the depth of the tunnel. Generally the orientation of the excavation area's maximum principal stress is trending towards the river valley. The value of the maximum principal stress is −6.5 to −11.5 MPa, the angle of dip is 80° to 90°. The minimum principal stress is trending upstream of the river valley. The value of the minimum principal stress is −2.0 to 4.0 MPa, the angle of dip is 0° to 10°. The stress components and side pressure coefficients of the surrounding rock are as follows:

S_{xx} = –3.0∼–4.0 MPa
λ_x = 0.45∼0.55
S_{yy} = – 4.0∼– 5.0 MPa
λ_y = 0.55∼0.65

where S_{xx} = stress components of xx direction; λ_x = side pressure coefficient of x direction (perpendicular to the orientation of river valley); S_{yy} = stress

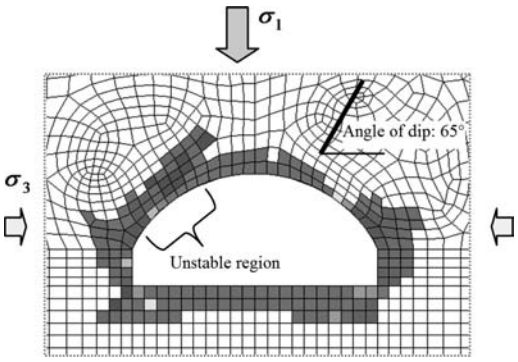


Figure 4. Yield region of layered rock mass.

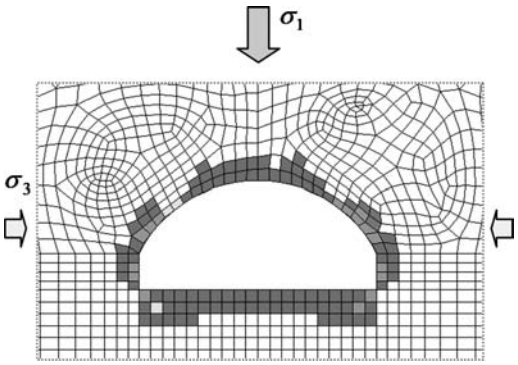


Figure 5. Yield region of homogenous rock mass.

components of yy direction; and $\lambda_y =$ side pressure coefficient of y direction (parallel to the orientation of river valley).

3.1.2 *Simulation results*

By using stress boundary condition from the 3-D crustal stress simulation, a 2-D simulation of layer I excavation was made. Two models were made with the same gravity field values and physico-mechanical parameters. One model has layered rock mass of steep dip angle; the other has homogenous rock mass without layers. The simulations indicated that:

a) The yield region of layered rock mass is relatively big (dip angle is 65°) (Fig. 4). The yield region is at the left crown;
b) There is no obvious bigger yield region of homogenous rock mass without layering structure (Fig. 5).

According to rock mechanics and engineering practice, large-scale structural plane has significant impact on rock mass stress distribution (Xie et al. 2006, Cundall 1971). For this reason a numerical model using distinct element method (UDEC) was built to simulate excavation. The model only has one large-scale bedding plane of steep dip angle and one large-scale joint of lower dip angle. The simulation also indicates left crown collapse. The whole process of the instability is as follows: the surrounding rock of left crown starts to loose → left crown falls block → discontinuous cracks inside the left crown take shape → cracks connect and form whole collapse. This means that the bedding plane and the joints caused a penetrating pull apart plane. The plane is the inner boundary surface of the whole collapse.

3.2 *Pattern analysis*

According to the simulation results, the surrounding rock instability of adverse geological sections can be summarized as follows:

(1) Due to the low interlayer cohesive strength, well developed microfissures and cleavages, exceedingly corrosion and weathering, and particularly fragmented rock, the surrounding rock has a very short self-stabilization time;
(2) Rock mass of thin layer and steep dip angle tend to unload under excavation. The bedding plane of the rock mass tends to unfold. The rock mass under the cut of joints and fissures that intersect the bedding with large-angle became cataclastic shaped blocks, which eventually results in whole collapse;
(3) The strata strike and the tunnel axis intersect with small angle. It will form an unstable combination in the left tunnel crown;
(4) There are two kinds of rock mass collapses, either with or without structural strengths:
    a) Collapse with structural strength (Fig. 6): thin layer rock mass with certain degree of strength under the cut of single structural plane or fissure;
    b) Collapse without structural strength (Fig. 7): thin layer rock mass with highly developed structural planes will form cracked body of loosen texture. The collapsed rock mass are granular mixtures.

4 TREATMENT MEASURES OF INSTABILITY

To ensure stability of the tunnel crown and side wall during the excavation of lower layers, the following construction schemes were implemented:

(1) First anchor and shotcrete were used in the instable area to prevent further collapse. To form an arc-shaped shell with enough bearing capacity, the shotcrete layer should have adequate thickness. The anchor rod should penetrate the excavation disturbed zone of surrounding rock (Read 2004, Martino & Chandler 2004). With shotcrete outside and anchor inside, a load-bearing ring is formed in the surrounding rock.
(2) Then the collapse area was backfilled with concrete and steel arch was used to support. As a passive support form, steel arch is usually used in

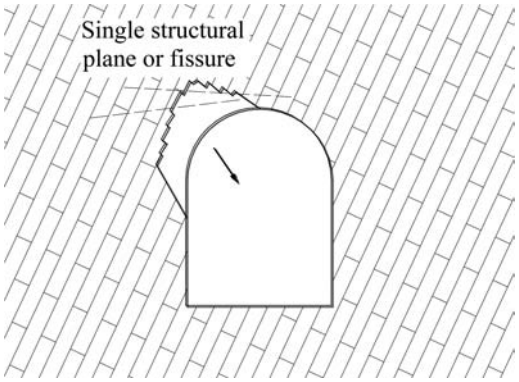


Figure 6. Collapse with single structural plane or fissure.

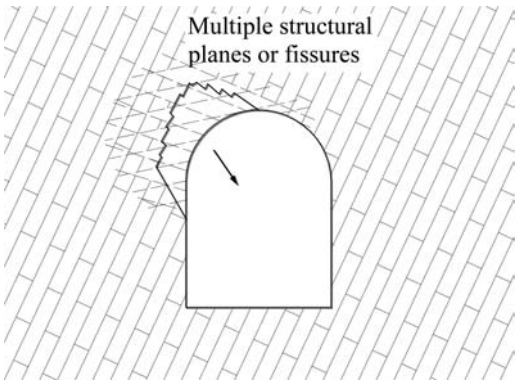


Figure 7. Collapse with multiple structural planes or fissures.

soft rock tunnel, since soft rock deformation has the features of oversize and timeliness. Steel arch has the features of strong rigidity and high resist deformation ability, which make steel arch fit the surrounding rock relatively well in the adverse geological section.

(3) Finally, consolidation grouting without cover weight was applied in the left crown and side wall depends on the surrounding rock's specific circumstance. According to geophysical detection, after grouting the wave velocity of surrounding rock (V_p) increases by about 10%.

There are two construction schemes about backfilling the collapse area with concrete and steel arch. Scheme A first use steel arch to support and then set up formwork to backfill concrete; scheme B first set up formwork to backfill concrete then use steel arch to support. A 2-D numerical model was established by using finite element method (FLAC^{3D}) to compare these two construction schemes. The planar diversion tunnel model is based on one steel arch. The simulation use solid units to simulate the steel arch which composed by H-section steel. The two situations use the same crustal stress, physico-mechanical parameters and material parameters.

According to the numerical simulation, conclusions are drawn as follows:

(1) Given its strong rigidity, steel arch works well on the deformation control in both schemes;
(2) After the excavation of layer II, the maximum pressure stress of the steel arch is about 16 MPa, the maximum tensile stress is about 3 MPa. Both of the stresses are lower than steel arch's design strength of 215 MPa;
(3) The maximum pressure stress of the steel arch in scheme A is about 14 MPa, the maximum deformation is 20 to 22 mm; the maximum pressure stress of the steel arch in scheme B is about 13.9 MPa, the maximum deformation is 20 to 22 mm. The steel arch stress distribution, the surrounding rock deformation value, and the surrounding rock deformation distribution range are generally consistent in both schemes.

When set up sheet steel form to backfill concrete, the steel arch can be used as temporary support structure. This can save the cost and shorten the construction period. Therefore, scheme A was chosen in the practical construction and the improvements were satisfactory.

5 CONCLUSIONS

Rock mass of thin layer and steep dip angle tend to unload under excavation. The bedding plane of the rock tends to unfold. The rock mass under the cut of joints and fissures that intersect the bedding with large-angle became cataclastic shaped blocks, which eventually resulted in whole collapse. The strata strike and the tunnel axis intersect with small angle, which formed an unstable combination that made most of the collapse happened in the left crown.

A series of construction procedures was made to cope with the collapse area and achieved expected results. First anchor and shotcrete were used in the instable area to prevent further collapse. Then the collapse area was backfilled with concrete and use steel arch to support. Finally, consolidation grouting without cover weight was carried out in the left crown and side wall to improve the rock mass's strength. By far the #3 and #4 diversion tunnels' ex-cavation of layer II and III are largely finished. No more large-scale instability accidents occurred during the excavation, and according to the deformation monitoring, the deformation of the crown are con-verged.

The #3 and #4 diversion tunnel excavation of Wudongde Hydropower Station has the features of large excavating section, poor geological condition, and long adverse geological section. The successful excavation procedure can provide reference to simi-lar domestic and oversea large span underground cavern projects.

REFERENCES

Cundall, P.A. 1971. A computer model for simulating large scale movements in blocky rock systems. *Proceedings of the International Symposium on Rock Mechanics.* Nancy, France: 2–8.

Fu, C., Wang, W. et al. 2006. Back analysis study on initial geostress field of dam site for Xiluodu hydropower Project. *Chinese Journal of Rock Mechanics and Engineering*: 25(11): 2305–2312 (in Chinese).

Martino, J. & Chandler, N. 2004. Excavation-induced damage studies at the Underground Research Laboratory. *International Journal of Rock Mechanics and Mining Sciences.* 41(8): 1413–1426.

Read, R.S. 2004. 20 years of excavation response studies at AECL's Underground Research Laboratory. *International Journal of Rock Mechanics and Mining Sciences* 41(8): 1251–1275.

Wang, L., Zhou, P. et al. 1991. *Geostress survey and its application in project.* Beijing: Geology Publishing House (in Chinese).

Xie, Y., Liu, J. et al. 2006. Stability ananlysis of block in surrounding rock mass of large underground excavation. *Chinese Journal of Rock Mechanics and Engineering* 25(2): 306–311 (in Chinese).

Yang, L. 1996. *Back analysis theory for geotechnical engineering and its engineering application.* Beijing: Science Press (in Chinese).

Rock Mechanics for Resources, Energy and Environment – Kwaśniewski & Łydżba (eds)
© 2013 Taylor & Francis Group, London, ISBN 978-1-138-00080-3

Excavation and monitoring of the main tailrace tunnels of the Xiangjiaba underground power station

Z. Yi
China Three Gorges Corporation, China

ABSTRACT: The main tailrace tunnel of the Xiangjiaba right bank underground power station has the biggest designed cross-section dimension of its kind in the world. Due to this fact, its construction is complex. The principle of "top arch" lining first, then "excavation down" was adopted based on the location conditions during construction and thus addressed the issue of super-big cross-section tunneling works. The safety monitoring data of the project indicate that the stress strain develops in line with the project development law and demonstrate that the parameters designed for the excavation and support are reasonable. Construction safety meets the design requirements and the tunnel remains safe and stable. Therefore, the method for this tailrace tunnel can be used as a reference for other similar projects.

1 SUMMARY OF THE PROJECT

The Xiangjiaba Hydropower Station is developed at the last cascade of the Jinsha River. Its main function is power generation, combined with the auxiliary functions of improving the ship channel, flood control, irrigation, trapping sediment, etc. The total installed capacity of the power station is 6400 MW, which includes four units that are each capable of 800 MW on the right bank underground power station.

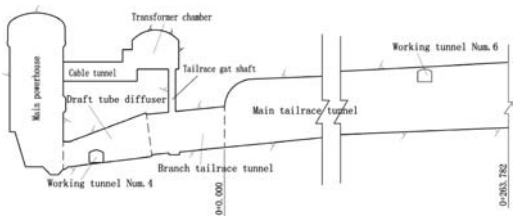


Figure 1. Longitudinal profile of the tailrace system.

1.1 *Design of the project*

The tailrace system of the right bank underground power station is composed of a diffusion section, a tailrace adit and the main tailrace tunnel (the top elevation varies). Every two tailrace adits converge into one main tailrace tunnel and the two main tailrace tunnels are deployed. Please refer to Figures 1 and 2 for the profile and plan arrangement of the tailrace system.

The two main tailrace tunnels are quite large. They are 263.78 m and 199.78 m long and have a longitudinal grade of 3% and 4% , respectively. The tunnels are D-shaped, their excavation height is between 35.10 m and 38.20 m and their excavation width is between 22.40 m and 24.40 m. A conventional support with rockbolts, anchors and lining concrete was adopted. In addition, certain safety supports were utilized during the construction period. During the later stages, the tunnels were lined with C25 concrete 1.0 m, 1.5 m and 2.0 m thick, respectively based on the type of cross-section. The lined tunnel has a net width of 20.0 m and a net height of 34.0 m. Additionally, backfill grouting for the crown at 120° and full-section consolidation were carried out.

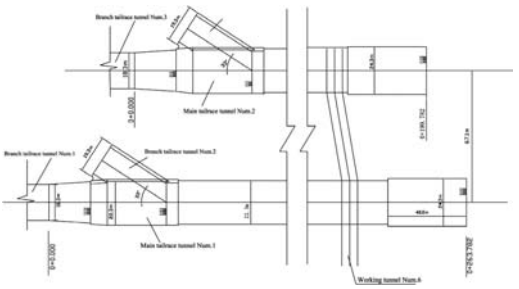


Figure 2. Level layout of tailrace system.

1.2 *Geological conditions*

The tailrace tunnel is buried in low-angle dip rock strata T_3^{2-6-2} and T_3^{2-6-3}. Generally the strata is composed of thick even super-thick sandstone, and locally of thin to moderately thick sandstone. Most of the rocks are of grade II∽III; they are slightly weathered or fresh. Locally at the developed joints, the rocks are mainly of grade III except for some soft rocks of grade

V. The tunnel outlet is located in a strong stress-release zone, where a long, wide fissure with mud sandwich exists and the rocks are of grade IV. No significant fault was observed in the rock strata and most of the exposed fractured mud sandwich was JC2-2 and JC2-3. The unstable rock masses were mainly located at the tunnel crown, generally in the form of a falling mass. In addition, the columnar blocks formed from the cut between the crown laminar and the joints were quite unstable. The angle between the joints of group NWW and NEE and the axis of the main tailrace tunnel is small. The mass between the weak laminar in the lower part (if it exists) and the NW joints may result in a toppling failure. When the joints of group NWW and NEE in the rock mass of the tunnel wall are near the tunnel wall, a buckling failure may occur in the platy rock mass cut (HydroChina 2005).

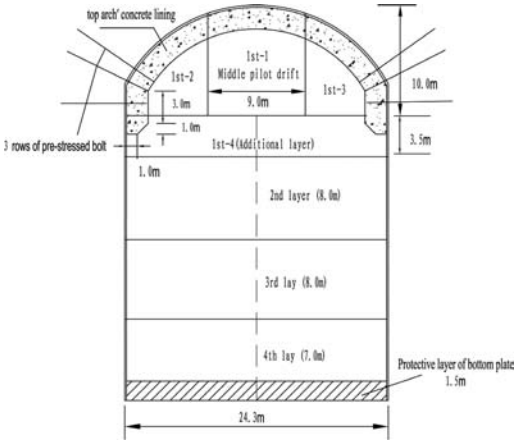


Figure 3. Sketch of the excavation layers and top arch concrete lining of the main tailrace tunnel.

2 TUNNEL EXCAVATION AND SUPPORT

Though the main tailrace tunnels of the Xiangjiaba Hydropower Station are not very long, they were excavated in a big cross section, which had a maximum width of 24.30 m and a maximum height of 38.15 m. It is the biggest tailrace tunnel of its kind in the world. In addition, the complex geological conditions led to variations in the cross-section dimensions and a quantitative rise in the complexity of its construction which created some additional difficulties.

2.1 *Method of excavation and support*

Based on the structural characteristics of the tailrace tunnels the layout of the construction adits and the performance of the equipment, the tunnels were excavated in four layers in a descending manner. A protective layer was reserved on the invert. Please refer to Figure 3 for the arrangement of the layers and Table 1 for method of the construction of each layer. Due to the huge dimensions of the cross-section of the main tailrace tunnel when the top arch lining was excavated after the cross-section, then lining the top arch is difficult to carry out because of the huge difference in altitudes, therefore a sequence of construction that is different from the conventional one was used. It is described as follows: the top arch lining was executed shortly after excavation, then the down excavation continued and finally the bottom plate and sidewall were poured, thus completing the lining of the cross-section.

2.2 *Matters that required attention*

The relation between excavation and support construction must be dealt with correctly. During any underground construction, there are many uncertain factors due to complicated geological conditions. In addition, the rock stress will be redistributed after excavation, which leads to rock deformation, thus a landslip will occur. A large-span main tailrace tunnel with a high sidewall must be supported in order to adjust the rock stress as soon as possible in order to provide the balance necessary to hold the tunnel steady. Therefore weak blasts, strong supports and frequent observations should be the principle that is executed during the construction (Yin & Yang 2009).

For example, in the construction of the top arch of a main tailrace tunnel support, in addition to the temporary support that is used due to geological conditions, a permanent support should be promptly constructed after excavation .in order to avoid interference between the support and the excavation due to the distance. The control principle is described as follows: based on different rock grades, the distance for II and III are 30∼50 m and 5∼30 m separately, as far as IV is concerned, the support should closely follow the excavation.

3 SAFETY MONITORING

3.1 *Instrument arrangement*

Each of the two main tailrace tunnels has three sections buried multipoint displacement meter and anchor dynamometer and four sections buried bolt stress meter and reinforced meter. Figure 4 shows a typical monitoring section. The process of burying the instrument and collecting data closely follow the progress of the civil construction During the construction process, when abnormal measured values were found, they were analyzed in a timely manner and measures such as strengthening support were taken to ensure the safety of the construction process.

3.2 *The monitoring results of the multipoint displacement meter*

By the middle of October 2011, the maximum deformation of the all of the monitoring section, which

Table 1. Method of excavation and support in the layers for the main tailrace tunnels.

Location	Excavation Procedure	Excavation Method	Support Method	Remark
Layer I	Middle pilot tunnel → alternate enlargement excavation on both sides → excavation of sub-layer I-4 on the bottom	YT28 pneumatic drill for horizontal drilling, smooth blasting, tunneling advanced 2–3 m in each cycle	BOOMER353E for drilling rockbolt holes, Master grout injection machine for grouting the rockbolts and Master robotic sprayer for shotcreting. YG80 drill for drilling anchor holes	To distance the blasting of the layer II with the top arch lining, Sub-layer I-4 high 3.5 m was excavated prior to top arch lining
Layer II, III & IV	Pre-splitting the structural line → drilling & blasting excavation on the left and right	100Y downhole drill for drilling pre-splitting holes, YT28 pneumatic drill for alternate excavation on the left and right	ditto	To minimize the impact by blasting layer II, the pre-splitting of layer II was carried out prior to the top arch′ lining
Protective layer on invert	drilling & blasting excavation on the left and right	YT28 pneumatic drill for drilling horizontal holes. Side wall and the invert structural line were excavated by smooth blasting	ditto	

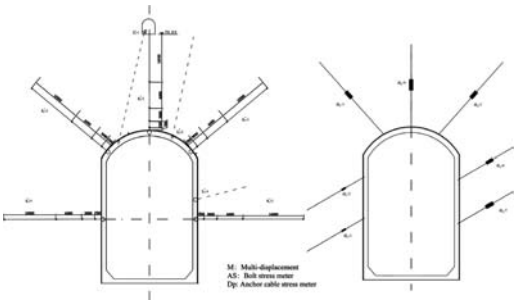


Figure 4. Typical monitoring profile of the main tailrace tunnel.

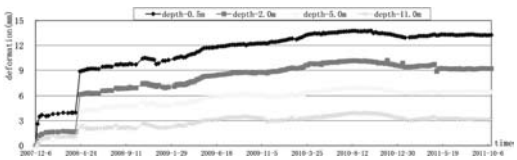


Figure 5. Curve of surrounding rock deformation – time.

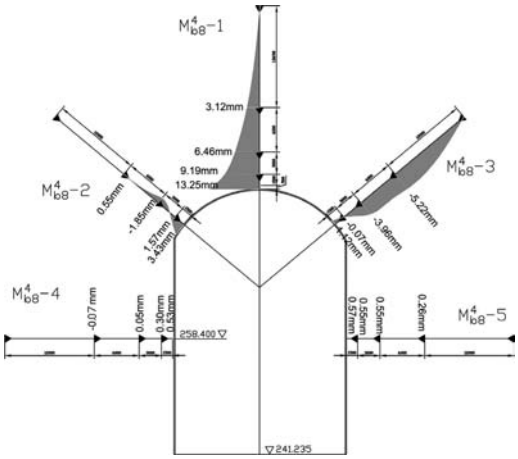


Figure 6. Layout of surrounding rock deformation.

happened in the surface of top arch centerline of the section closest to the exit of the #2 main tailrace tunnel, was 13.25 mm. Figure 5 shows the line of the deformation process. Figure 6 presents the distribution of the deformation surrounding rock at each of the measurement points.

Monitoring data showed that most of the top surrounding rock deformations occurred during the excavation of the vault while the lower sections were less affected by the excavation of caverns. When the cavern was dug further, the surrounding rock deformation gradually inclined to stability. The excavation of the vault of the main tailrace tunnel was divided into three steps, the excavation of the middle guide hole, the expansion of the left and right sides. According to the general rules, the surrounding rock deformation should also show three steps of growth (Fan et al. 2011), but Figure 6 shows only two steps. The reason for this is that the multipoint displacement meter is buried after the excavation of the middle guide hole. Once the excavation commences, the deformation of the surrounding rock begins. Thus, the multipoint displacement meter fails to capture the surrounding rock deformation in the middle guide hole.

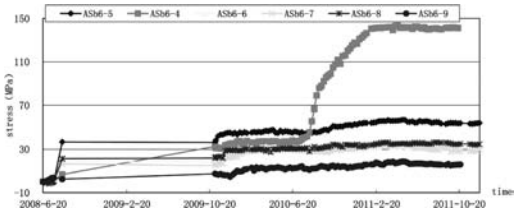


Figure 7. Typical relationship curve of anchor bolt stress–time.

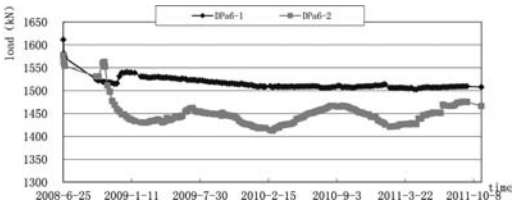


Figure 8. Typical relationship curve of anchor cable load–time.

Therefore, Figure 6 lacks one incremental step. This also indicates that the monitoring data accorded with practice.

After the completion of the excavation of the #2 main tailrace tunnel at the end of 2010, the surrounding rock deformation inclined to stability. The annual change of vault deformation was less than 1.5 mm (The measured value of most instruments is less than 0.5 mm). Due to cable damage, the instruments of the sidewalls of this section could not be used to observe. The cable was reinstated with the sidewall casting. Figure 6 shows that the surrounding rock deformation in the surface is biggest and that it decreases from the outside to the inside. From the analysis of the deformation data of each section, the deformation near the section of the exit side is the largest and the deformation near inside section is relatively small, which is consistent with the topography and geological conditions of the sections.

According to the design numerical calculation, the theoretical value of the surrounding rock deformation of the vault of the main tailrace tunnel is 15.72 mm (HydroChina 2003), which is slightly different from the most measured deformation value, 13.25 mm. If the value of the deformation that is not captured by the instrument in the excavation of the middle guide hole is added, it will be closer to the theoretical value. This shows that the design parameter of excavation and support is reasonable and the construction results are consistent with the design.

3.3 *The monitoring results of the bolt stress meter*

Figure 7 shows the typical process line of the bolt stress meter of the main tailrace tunnel. According to the analysis, the bolt stress of the main tailrace tunnel has the following features: (i) Most of the bolt stress is small. The measured value of a vast majority is less than 50 MPa and the largest is about 200 MPa. (ii) Most of the bolt stress is tension and little is pressure. (iii) Most of the bolt stress had a large increase during the early burial, the measured values were stable and the annual change was smaller. (iv) Bolt stress is negatively correlated with temperature changes. (v) Due to the poor geological conditions of the cavern, the tailrace blasting excavation, the overloaded vehicle traffic of the roof top and other factors, the bolt stress of the export section was larger relative to the cave section. The above features are in accordance accord with the practical engineering conditions and general engineering rules.

3.4 *The monitoring results of the anchor dynamometer*

The anchor cable load of the #1 main tailrace tunnel is between 1180.55 and 1603.33 kN. The anchor cable load of the #2 main tailrace tunnel is between 1011.66 and 1469.95 kN. The current load of only one measurement point is greater than the locking load. The remaining points are under the unloading state. Since the completion of the excavation and section lining, the anchor cable load has been relatively stable. Figure 8 shows the typical change line of the anchor cable load of main tailrace tunnel.

4 SUMMARY

Construction of the main tailrace tunnel has been completed and the entire construction process went relatively smoothly. Due to the features and the difficulty of the project, the construction scheme of the main tailrace tunnel of the Xiangjiaba right bank underground power station is different from any conventional scheme. It adopts the overall construction program of "top arch" lining first, then "excavation down" and this program effectively resolves the problem of the huge height difference of the lining. The safety monitoring system guided the construction effectively. The monitoring data show that the stress and strain of the rock surrounding the main tailrace tunnel have inclined to stability and the project is in a safe and stable state. The measured data of the deformation of the surrounding rock are consistent with the numerical calculation results. This shows that the parameters of the tunnel support are reasonable and that the quality of the construction meets the design requirements.

All in all, the overall construction program of the main tailrace tunnel of the Xiangjiaba right bank underground power station solves the problems of the construction of a super large section of a cavern. It can be a reference for similar projects.

REFERENCES

Fan, Q., Liu, Y. & Wang, Y. 2011. Construction and monitoring study of large underground powerhouse caverns of Xiangjiaba hydropower station. Chinese Journal of Rock Mechanics and Engineering 30(4):666–676. (in Chinese)

HydroChina ZhongNan Engineering Corporation 2003. Feasibility Study Report of Xiangjiaba Hydropower Station. (in Chinese)

HydroChina ZhongNan Engineering Corporation 2005. Bidding Documents of Construction of Xiangjiaba Right Bank Underground Power Station. (in Chinese)

Yin, Q. & Yang, J. 2009. Cavern excavation method for underground powerhouse complex at Xiangjiaba Hydropower Station. Sichuan Water Power 28(4):1–6. (in Chinese)

This page intentionally left blank

Rock Mechanics for Resources, Energy and Environment – Kwaśniewski & Łydżba (eds)
© 2013 Taylor & Francis Group, London, ISBN 978-1-138-00080-3

Periphery mapping in NATM tunnels

B. Yilmaz
Statkraft Energy, Cetin Hydroelectric Power Plant Construction Project, Siirt, Turkey

H. Keskin Citiroglu
Department of Geological Engineering, Engineering Faculty, Bulent Ecevit University, Zonguldak, Turkey

ABSTRACT: In this study; to get different approach to periphery mapping technique the application of tunnels opened by NATM (New Austrian Tunneling Method) method is aimed. Surface settlements due to excavation are important to keep under control in every stage of tunnels are opening by NATM method. During the progress of the tunnel, weak zones must be identified and spreading of weak zones should be estimated. As a result of detection of weak zones and other geological structures, stability can be achieved by applying additional support systems (additional rock bolt, cement and/or chemical injection, temporary invert concrete with strut etc.) before geological structure cause of the surface settlement. All geological structures encountered along the route are saved on the periphery map. Periphery map allows for three dimensional observation and estimation. Because of NATM is a gradual excavation method, periphery map allows to estimate of the geological structure of other stages. Dimensions and orientations of discontinuities (faults, beddings etc.) encountered along the tunnel progress is saved on the periphery map. Existing faults in progress of the tunnel can be estimated with the help of periphery map. Also, bedding orientation is an important parameter in tunneling works can be estimated with the help of periphery map. According to estimated fault and bedding orientation, additional precautions (AGF umbrella arc, fore pilling, face bolt, additional steel support, gradual excavation etc.) are taken to the stability of the excavation surface. It is important to hold to existing water level to keep under control of surface settlement in NATM tunnels. During the progress of the tunnel, periphery map is prepared to showing to status of water on tunnel surface. While excavations continuing, geotechnical values such as RMR, Q, GSI, are calculated with geotechnical data which was collected according to observational standards published by ISRM (International Society for Rock Mechanics) in 1981, are processed on periphery maps. So the areas, additional support measures to be taken, will be selected. NATM is a method of gradual excavation. The NATM tunnels which is designed to initially opening of the pilot tunnel, geological and geotechnical properties of the tunnel on the main section are determined with the help of periphery map prepared with pilot tunnel data. Also, after the excavation of the top heading, estimating the other stage's (such as Upper Medium Heading UMH, Lower Medium Heading LMH, bench and invert) geological and geotechnical properties, collectively showing the concerned data to be provided.

1 INTRODUCTION

Is it possible to prediction of discontinuities directions and spreading of weak zones? It is important to prediction of geological parameters of the tunnels in advance in terms of the tunnel stability which opened in especially weak rock by NATM method. Nowadays in tunneling works, with the aim of the prediction of concerned geological parameters, geological data are obtained during tunnel work, together with the evaluation of different methods and computer applications, some assumptions are made. Periphery mapping technique in tunneling works, the first by the U.S. Army Corps of Engineers (1970), was applied. In this study, predictability with the help of periphery mapping technique to geological properties of different stages of tunnels which are opened by NATM method is presented. In addition, representation on the periphery maps of rock classification values which are calculated by the help of geotechnical properties were obtained according to observational standards published by ISRM in 1981, and correlation between other geological data is sampled. With the help of the water periphery map that is another kind of species of periphery mapping technique, before the tunnel concrete lining work, give information about the actual location of the status of water in tunnel, is provided.

Many times the importance of geological periphery mapping has been proven. Although many application areas of periphery mapping technique are existing, some of the application areas are considered in this study are listed below:

- By estimating orientations of geological formations, geological condition of NATM excavation stages to be determined.
- Estimation of discontinuities (faults and beddings) orientations.

- Projecting geology from the pilot drift to the full bore of a tunnel before enlarging is started (U.S. Army Corps of Engineers 2001).
- Planning tunnel support systems and selecting the best location and inclination of supplemental rock bolts (U.S. Army Corps of Engineers 2001).
- Correlation between rock classification values and other geological data.
- Preparation of water periphery maps which is shown water situation on tunnel surface, before concrete lining works.

2 PERIPHERY MAPPING METHOD

The peripheral geologic mapping method is simple, easy to use, and is applicable to large- and small-diameter tunnels, shafts, and adits with either circular, horseshoe, or irregular shapes (ASTM 2002).

The full peripheral method of mapping provides an advantage over planar or section maps in that the three dimensional perspective allows assessments of strike and dips of rock mass features without the use of pocket transit compasses which are often affected by the metal and electrical systems installed in the underground opening (ASTM 2002).

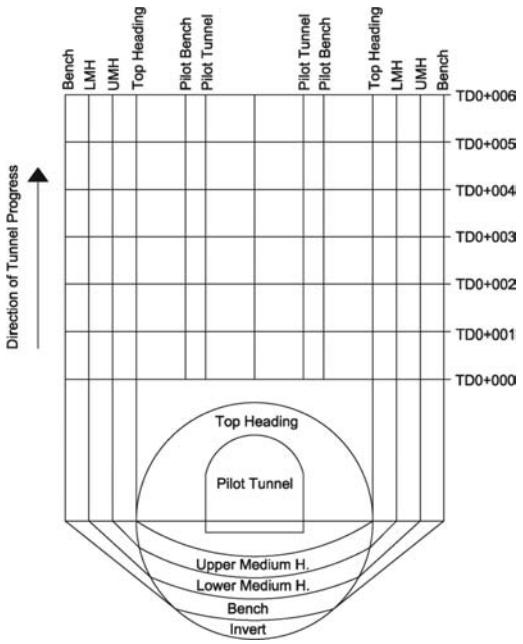


Figure 1. Plan for "Geological Periphery Map of NATM Tunnel".

2.1 *Preparation of periphery maps*

The map is drawn by observing features on the tunnel wall or crown and then sketching the features on the map (U.S. Department of Energy 1994). Therefore, preparing of geological tunnel face maps for effective periphery mapping is important. Information on tunnel geological face maps are transferred to periphery map sheet. Water features on excavation surface, such as faults and discontinuities in the bedding orientations, orientations of the main joint systems, weak zones; the boundaries of geological units are available on concerned geological face maps.

The method is useful for plotting curving or irregular discontinuities which are difficult to project to a flat plane as in other methods (USBR 2009). In this method, the entire circumference of the excavation is represented by a flat sheet. The walls of the tunnel are "unrolled" such that the centerline of the tunnel crown is located longitudinally on the centre of the map area. The base of the left and right walls is located at the top and bottom of the sheet (U.S. Department of Energy 1994). Plot scales on either side of the plan to provide distance control while mapping (USBR 2009). The advantage of this method is that features can be located on the tunnel wall and then sketched onto the map without any compensation or projection. Strike and dip symbols are placed on the map at the location where the measurement was taken. The locations of both geologic and non-geologic features such as rock reinforcement, photogrammetry targets and samples can also be recorded on the map. The viewer should keep in mind the map is representation of the tunnel surface and not a plan view of the tunnel. The view shown here is as if the viewer were outside and above the tunnel (U.S. Department of Energy 1994).

Periphery mapping plan is related with tunnel that is opened by NATM method, is shown in Figure 1. NATM tunnel shown in the figure, the first stage is planned to open a pilot tunnel. At later stages in order of top heading, upper medium heading UMH, lower medium heading LMH, bench and invert excavations were performed. Due to the rock surfaces are usually covered with muck or invert segments, tunnel invert is not shown on periphery plan.

2.2 *Implementation of periphery mapping technique in NATM tunnels*

NATM method developed by Rabcewicz (1964) and introduced to the world. This method is based on the measurement of deformations and sensitive monitoring during opening of the tunnel, a method which controls the behaviour of the rock mass. NATM is a gradual excavation method. This method is common with larger openings and involves excavating smaller drifts, one at a time, stabilizing that opening, and then excavating the next portion of the drift (U.S. Department of Energy 1994). Sensitive geological and geotechnical monitoring is important in tunnels which is opened by NATM method. During the excavations, the face mapping work should be done at frequent intervals. Face mapping work within the range of 2–3 m excavation is appropriate for determination of persistence, and exact locations of discontinuities and

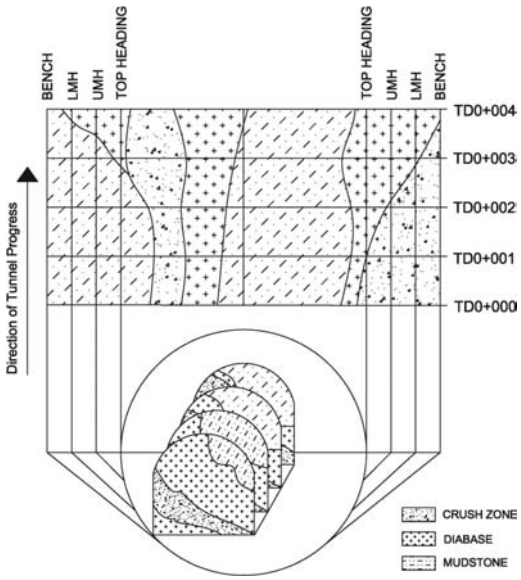


Figure 2. Geological periphery map for determination of spreading of weak zones.

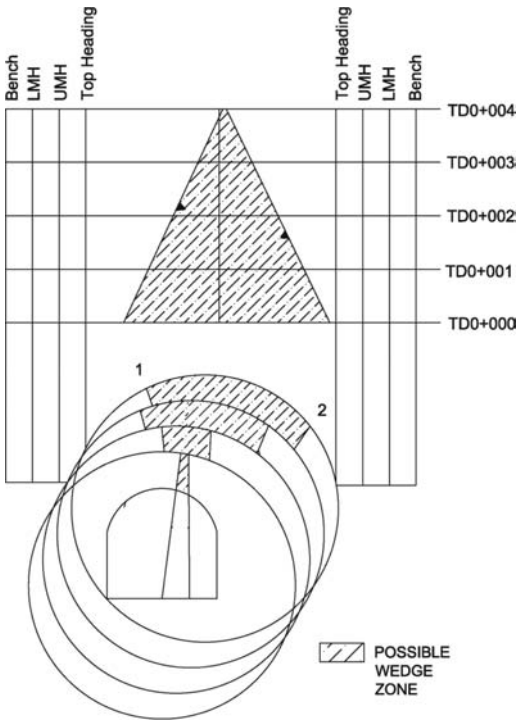


Figure 3. Geological periphery map for determination of fault directions.

other geological structures. Geological information saved on tunnel geological face maps which are prepared regularly, are transferred to periphery map sheet which is prepared for NATM tunnels (Fig. 1). Geological data is optional, based on the project needs and it can be selected major datas according to usage of periphery map. Periphery mapping sheet that is prepared for NATM tunnels includes all of the stages (UMH, LMH, and bench) of NATM tunnels. The tunnel invert is not mapped because rock surfaces usually are covered with muck or invert segments (USBR 2009). In the NATM tunnels which is designed to initially opening of the pilot tunnel, also pilot tunnel section takes place on periphery mapping sheet as a stage of NATM tunnel.

3 PREDICTION OF NATM TUNNEL GEOLOGY WITH THE HELP OF THE PERIPHERY MAPPING TECHNIQUE

Surface settlements due to excavation are important to keep under control in every stage of tunnels are opening by NATM method. During the progress of the tunnel, weak zones must be identified and spreading of weak zones should be estimated. With the aim of identification of discontinuities' orientations and spreading of weak zones in tunnels which is opened by NATM method, periphery mapping technique is used.

3.1 *Prediction of orientation of weak zones and other geological structures*

In Figure 2; horseshoe shaped pilot tunnel its dimensions are 4.50 m × 4.50 m is planned to open inside the cylindrical shaped a NATM tunnel its dimensions are 10.60 m × 10.60 m, is seen. Borders of geological structures that are encountered during opening of pilot tunnel were transferred onto main NATM tunnel profile. In the light of the geological assessment before enlargement of the tunnel started, dashed areas indicates estimation of spreading of concerned weak zones and other geological structures that is encountered along the pilot tunnel excavation, on NATM tunnel stages. After opening of each different NATM tunnel stages, spreading of geological units is estimated in next stage.

3.2 *Prediction of discontinuities orientations*

Fault and bedding orientations are directly effective on tunnel stability. In this section, fault and bedding orientations, with the help of periphery mapping technique, predictability has been introduced. The movement of fault and beddings, in the NATM tunnel stages, were sampled.

3.3 *Prediction of faults orientations*

In Figure 3, No. 1 and No. 2 faults are encountered during excavation of pilot tunnel (4.50 m × 4.50 m), has been transferred on the periphery map. When projections and orientations of these faults on the main tunnel

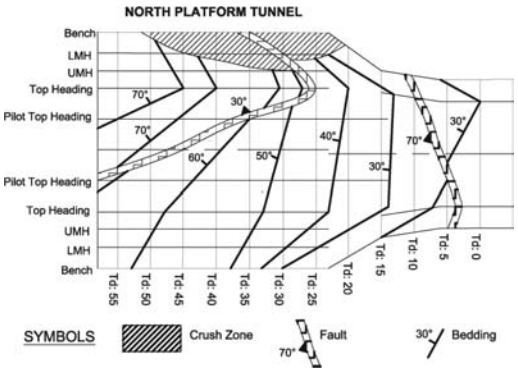


Figure 4. Geological periphery map for determination of bedding directions.

are analyzed, the hatched area in Figure 3 shows exact location of possible wedge type of sliding.

3.3.1 *Prediction of bedding orientations*

In tunneling works, bedding orientations are directly effective on tunnel stability. Sample periphery modeling has been made on Figure 4. In a tunnel which is excavated by NATM method; exact locations and orientations of beddings encountered during excavation of pilot tunnel, has been transferred to the upper heading excavation part, on the periphery map. Positions and orientations of the beddings likely to be encountered in other stages of NATM tunnel (UMH, LMH, bench), was estimated.

4 CORRELATIONS OF ROCK MASS VALUES WITH OTHER GEOLOGICAL DATAS, WITH THE HELP OF PERIPHERY MAPPING TECHNIC

While evaluating the tunnel geology; estimating the orientation of discontinuities alone is not a reliable approach. At the same time, discontinuities properties should be evaluated on the basis of empirical standards which were published by ISRM in 1981. And, rock strength parameters that are effective on tunnel stability should be determined. Correlation between discontinuities estimation and rock strength parameters provides a more efficient estimate of the stability of a tunnel. In Figure 5; in a tunnel which is opened with NATM method, the boundaries of geological units encountered during excavation of the pilot tunnel and rock strength parameters of geological units, was shown. Discontinuities (faults and beddings) that are mentioned in Figures 3–4 were transferred to periphery map. In this example; (Fig. 5) as a result of correlation of taking into account of discontinuities orientations, rock mass rates and weak zones; specified part of tunnel in figure, is possible to mention of existence of a possible fold zone and fold axis. Hatched area in the figure, represents to the spread of the crush zone.

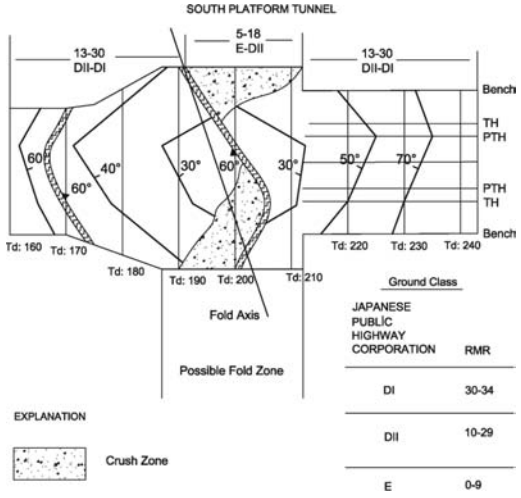


Figure 5. Geological periphery map for correlation between rock mass values and other geological data (Research Report 1992).

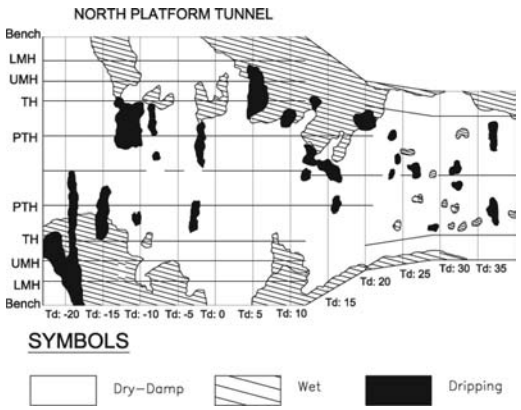


Figure 6. Water Periphery Map. North Platform Tunnel of Marmaray Project – Sirkeci Station – Turkey.

5 WATER PERIPHERY MAPS

In tunneling works, it is important to take control of water flow. The chemical composition of the water coming from the surface of the tunnel has direct impact on the steel support and concrete lining which is used for tunnel support. It is a major cost item to take out of the water in the tunnel for especially in the subway tunnels that are in use. The limit of allowable leakage is determined on project phase of tunneling studies. After completion of the tunnel excavation, amount of the water coming from the surface of the tunnel must be taken to the limits that are indicated on project phase. With the help of the water periphery map that is another kind of species of periphery mapping technique, before the tunnel concrete lining work, give information about the actual location of the status of

water in tunnel, is provided. In Figure 6; a part of Marmaray Project Sirkeci Station Tunnels that is opened with NATM method is modeling with periphery mapping technique to status of water on tunnel surface is seen. Marmaray project is a railway project connecting the Asian and European sides (13.6 km). Bosporus has been passed with the immersed tube tunnels (1.4 km). At the both side of Bosporus which is connected with immersed tubes; underground station constructions (3 stations with a length between 225 m and 242 m) with using of NATM tunneling method, were performed. In addition, the project has 37 surface stations (Marmaray 2013). In Sirkeci Station, after the completion of NATM excavation, before beginning of concrete lining work; to minimize the flow of water within the limits by applying of cement injection on water flow areas, was tried. At a later stage, waterproofing was provided by coating of the membrane to the tunnel walls.

6 CONCLUSIONS

Periphery mapping technique is projecting geology from the pilot drift to the full bore of a tunnel which is excavated by NATM method before enlarging is started. In this way, periphery maps allows to estimation of excavation stages of NATM. It is appropriate approach to take advantage of periphery maps while pre-planning and pre-selection of support systems phase for the next stage of excavation. In addition, following of the tunnel support system at the same time with tunnel progress, with help of periphery maps, is performed. Best location and inclination of additional support systems can be chosen with the help of periphery map, if required. Preparation of water periphery maps before the start of lining concrete work is important for the measures phase and evaluation of underground water location in tunnel.

Periphery maps should be assessed necessarily in conjunction with other methods during re-design and stability analysis related with NATM tunnels.

REFERENCES

ASTM, 2002. *Standard Guide for Geotechnical Mapping of Large Underground Openings in Rock.* D4879–02.

ISRM, 1981. *ISRM Suggested Methods: Rock Characterization, Testing and Monitoring.* E.T. Brown (ed.). London: Pergamon Press, 211 pp.

Marmaray, 2013. Marmaray Project General and Technical Information. Republic of Turkey, Ministry of Transport, Maritime Affairs and Communications. www.marmaray.com.tr. Date of Access: 12.02.2013.

Rabcewicz, L. 1964. The New Austrian Tunnelling Method, Part one. *Water Power* November 1964: 453–457.

Research Report, 1992. *Full Face Excavation Methods*. Japan Tunnelling Association, Part 3.

U.S. Army Corps of Engineers, 1970. *Geologic Mapping of Tunnels and Shafts by the Full Periphery Method.* DOA Office of the Chief of Engineers. Washington, DC, Engineering Technical Letter No. 1110-1-37.

U.S. Army Corps of Engineers, 2001. *Engineering and Design Geotechnical Investigations.* Washington DC. 20314-1000. EM 1110-1-1804.

USBR 2009. *Geological Mapping and Documentation.* Engineering Geology Field Manual, Vol. 1. Chapter 6.

U.S. Department of Energy 1994. *Underground Geological Mapping. North Ramp-Starter Tunnel, Geologic Mapping of the Exploratory Studies Facility. Technical Procedure. Yucca Mountain Project Exploratory Studies Facility.* Prepared by U.S Bureau of Reclamation and U.S Geological Survey. Principal Investigator: Steven C. Beason, SCP No.8.3.14.2.2.4,1994, Effective data 1997.

This page intentionally left blank

10. Mechanical breakage of rocks

This page intentionally left blank

Rock Mechanics for Resources, Energy and Environment – Kwaśniewski & Łydżba (eds)
© 2013 Taylor & Francis Group, London, ISBN 978-1-138-00080-3

Investigations on the fracture behaviour of rocks in a triaxial compression test

L. Baumgarten & H. Konietzky
Geotechnical Institute, Chair for Rock Mechanics, TU Bergakademie Freiberg, Germany

ABSTRACT: For the determination of rockmechanical parameters uni- and triaxial compression tests as well as tests for the determination of tensile strength were conducted in the lab. Triaxial compression tests can be conducted as conventional single stage tests, multi-stage tests or continuous failure state tests. The determination of the tensile strength can be performed e.g. by direct tensile tests, Brazilian tests and flexural tension tests. Within a research project the failure behaviour of sandstone is investigated in respect to the different types of triaxial compression tests. The stress-strain behaviour, the fracture pattern including the post-failure behaviour was simulated with PFC^{3D}. This paper presents the results obtained with this research project so far.

1 INTRODUCTION

Triaxial tests with several limit states or continuous failure states have some advantages: less material is necessary, data scatter is reduced and tests are more economical. On the other hand it is difficult is estimate to what extent the different stress paths influence the obtained failure envelope. Therefore, a research programme was initiated and a homogeneous sandstone (Postaer Sandstone, Elbe-Valley, Saxony) was used to investigate the influence of the different types of triaxial tests on the obtained failure envelope. The lab test programme comprises uniaxial compression and tension tests in different directions to the bedding planes as well as different types of triaxial tests (continuous failure state tests, single stage tests and multi-stage tests) perpendicular to the bedding. In parallel numerical simulations were performed using PFC^{3D} (Itasca 2008), which has the advantage, that different stress paths can be applied to identical samples and deeper inside into the micromechanical damage process in the pre- and post-failure region can be obtained. The aim is to deduce recommendations for the application of the different types of triaxial tests especially in relation to the deduction of the failure envelope.

2 TRIAXIAL COMPRESSION LAB TESTS

As documented by Fig. 1 the results of conventional single triaxial tests (CSTT), continuous failure state tests (CFST) and multi-stage triaxial tests (MSTT) show good agreement. In general, MSTT results in slightly lower strength values compared to CSTT because the next loading step is applied just before the peak strength is reached and the damage is increasing with increasing number of loading steps. Therefore, the failure envelope deduced from MSTT can be considered only as a first approximation. On the other side, the uncertainties are smaller as those produced by the natural scatter between different rock samples of the same material. Currently under investigation is the influence of the stress path on the damage and failure pattern. It seems, that for the stability of the rock sample during the MSTT stress paths with reduced axial load and simultaneously increased circumferential stress are favourable. The concept of CFST was applied successfully with a continuously applied circumferential stresses of 3 up to 20 MPa (Fig. 2).

3 NUMERICAL SIMULATIONS

The numerical simulations are based on the Discrete Element Method by using the Particle Flow Code PFC^{3D}. In a first phase the samples were generated by particles considering the determined grain size distribution (including a shift to reduce the number of particles but also guarantying that the largest particle is smaller than 25% of the sample diameter). During the simulation the linear contact stiffness model and the parallel bond model were used. Within a calibration procedure a good agreement between lab test results and numerical simulations were achieved for CSTT and confining pressures between 10 and 40 MPa. Also the simulated fracture pattern agree well with the observations in the lab (Fig. 3 and 4). However, the simulations reveal too small lateral extensions, especially for confining pressures below 30 MPa. The reason is, that for the application of the confining pressure a cylindrical wall was used, which allows only uniform lateral deformation instead of the development

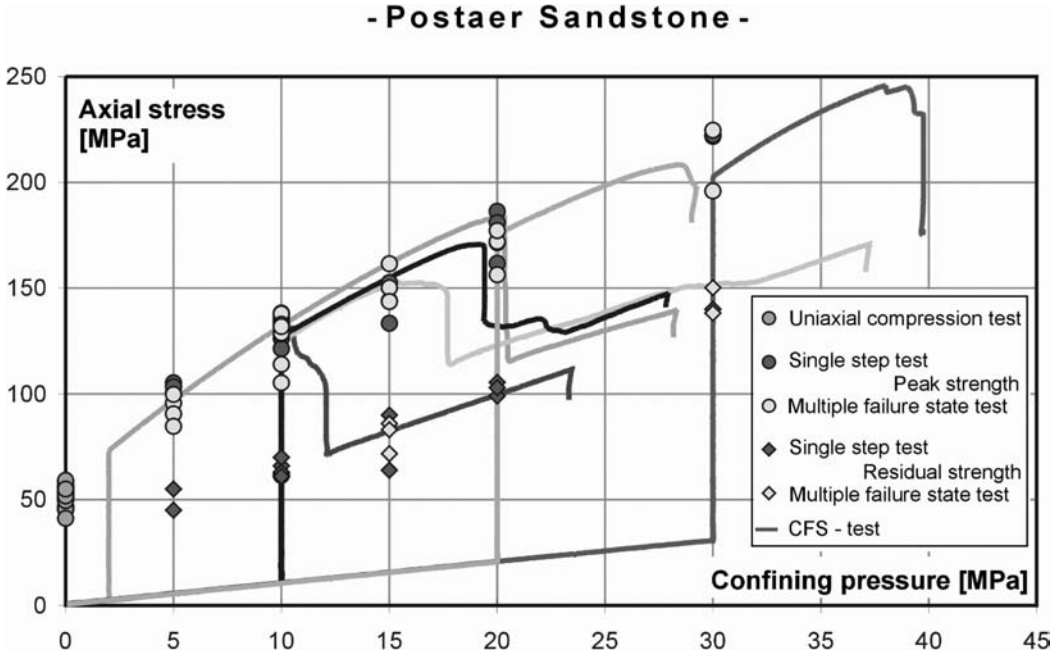


Figure 1. Postaer Sandstone – Peak and Residual Strength (Baumgarten & Konietzky 2010).

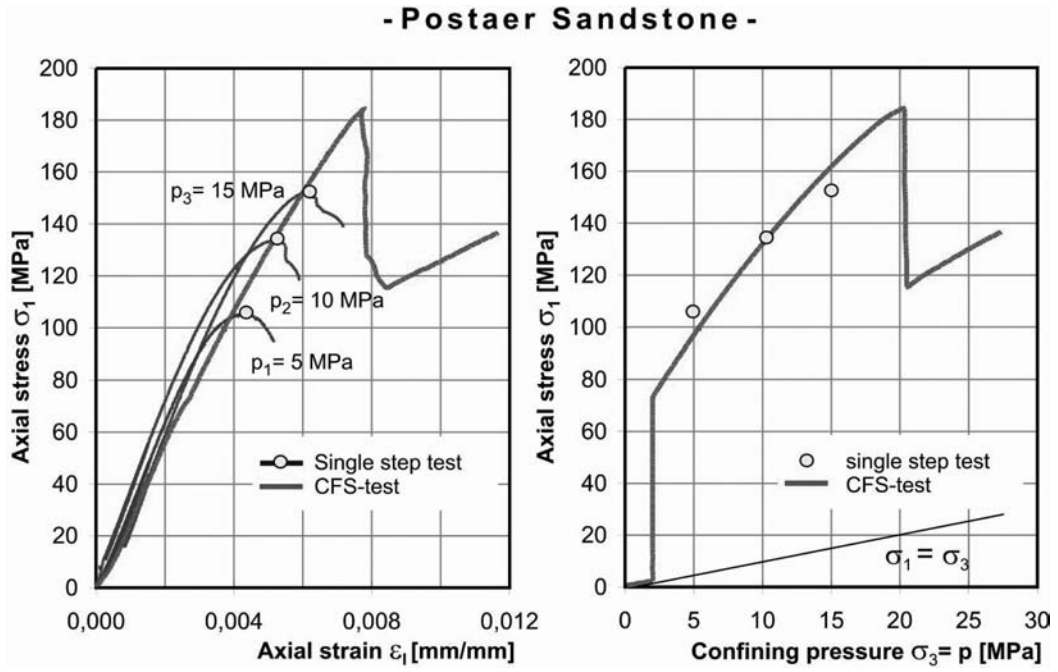


Figure 2. Single Step Tests and Continuous Failure State Test (Baumgarten & Konietzky 2010).

of a barrel-shaped contour like observed in the lab. In the consequence, the radial pressure is not any more uniform and restricts the lateral deformation. To overcome this restriction a new procedure was developed: after reaching the required circumferential stress, the wall elements, which represent the confinement, were deleted and replaced by equivalent contact forces. This procedure allows the development of realistic radial deformations. Fig. 5 shows the corresponding results by comparing lab test results and numerical simulations. Whereas the sphere model can reproduce the stress-strain and strength behaviour quite

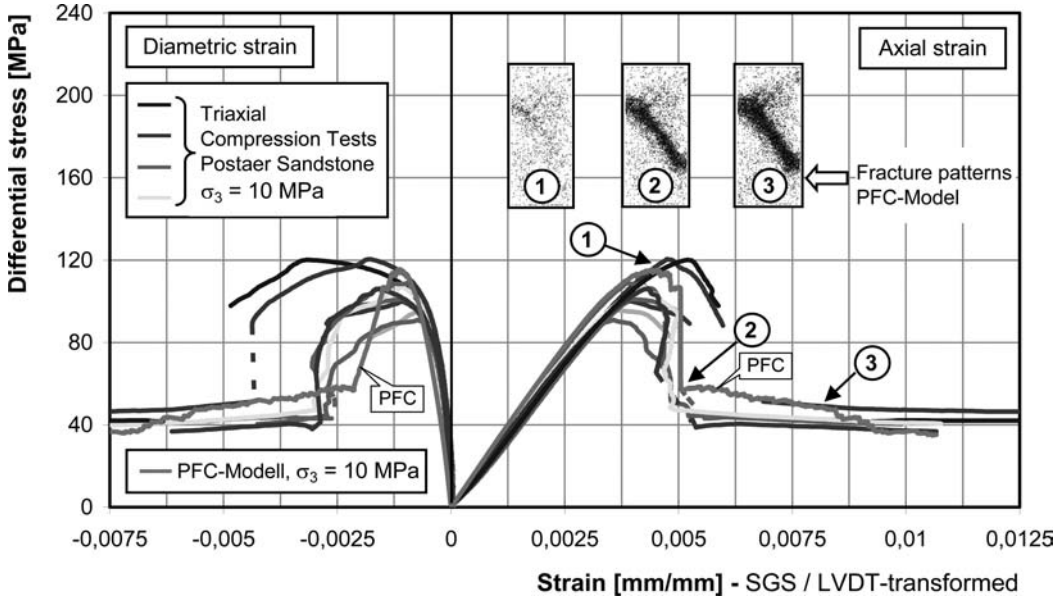


Figure 3. Triaxial Compression Tests with a Confining Pressure of 10 MPa, Laboratory tests/PFC3D – simulation – stress-strain-curves (Baumgarten & Konietzky 2010).

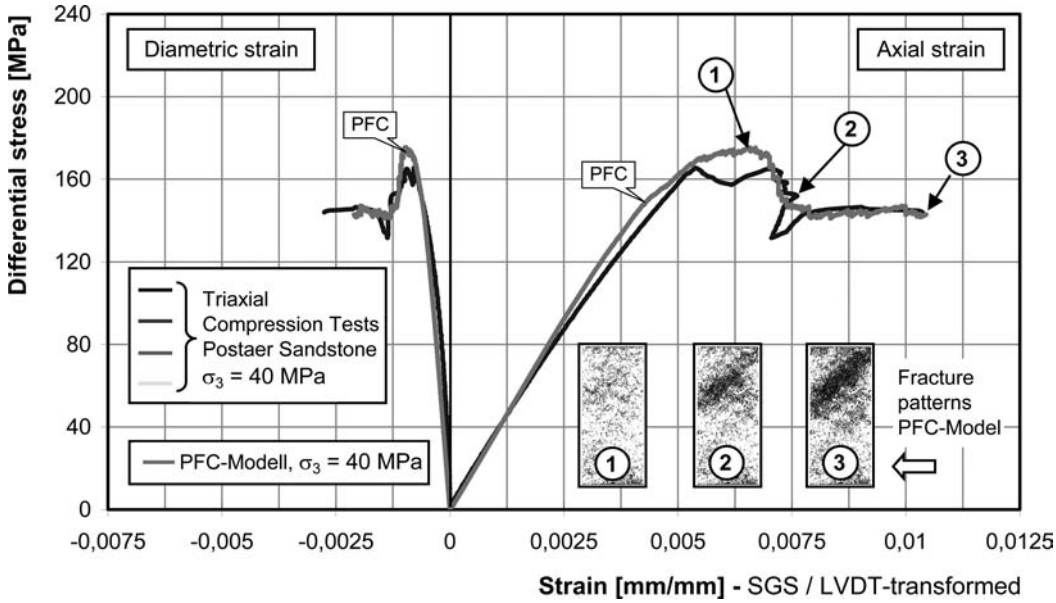


Figure 4. Triaxial Compression Tests with a Confining Pressure of 40 MPa, Laboratory tests/simulation – stress-strain-curves (Baumgarten & Konietzky 2010).

well for confining pressures between 10 and 40 MPa, significant deviations were observed for the uniaxial tension and compression tests. The sphere model can not follow the quite non-linear failure envelop for low confining pressure values and the tensile region (Fig. 6). To overcome these restrictions a new model was set-up, which replaces the balls by clumps (slaved particles), which represent the particle shape in a more realistic manner. Investigations have shown, that only 15% of the grains of the investigated sandstone can be considered as nearly spherical (Baumgarten & Konietzky 2010). The comparison between lab test results and numerical simulations show, that the clump model is well suited to model the pre-failure range, but has still some problems to simulate the post-failure range. The clumps lead to a more realistic interlocking

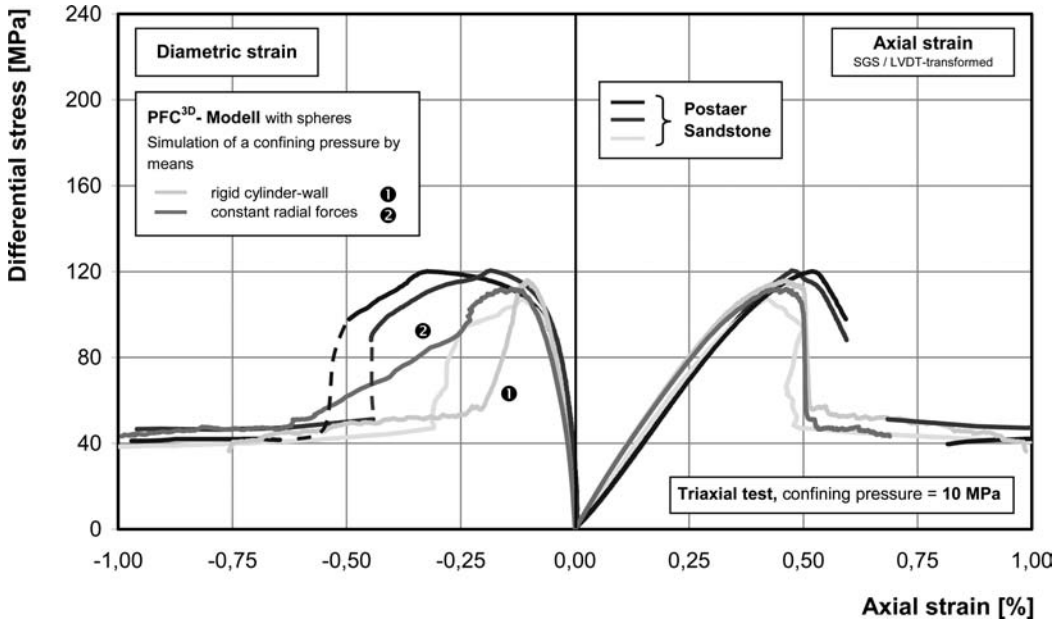


Figure 5. Triaxial Compression Tests with a Confining Pressure of 10 MPa, Laboratory tests/simulation – stress-strain-curves (Baumgarten & Konietzky 2012).

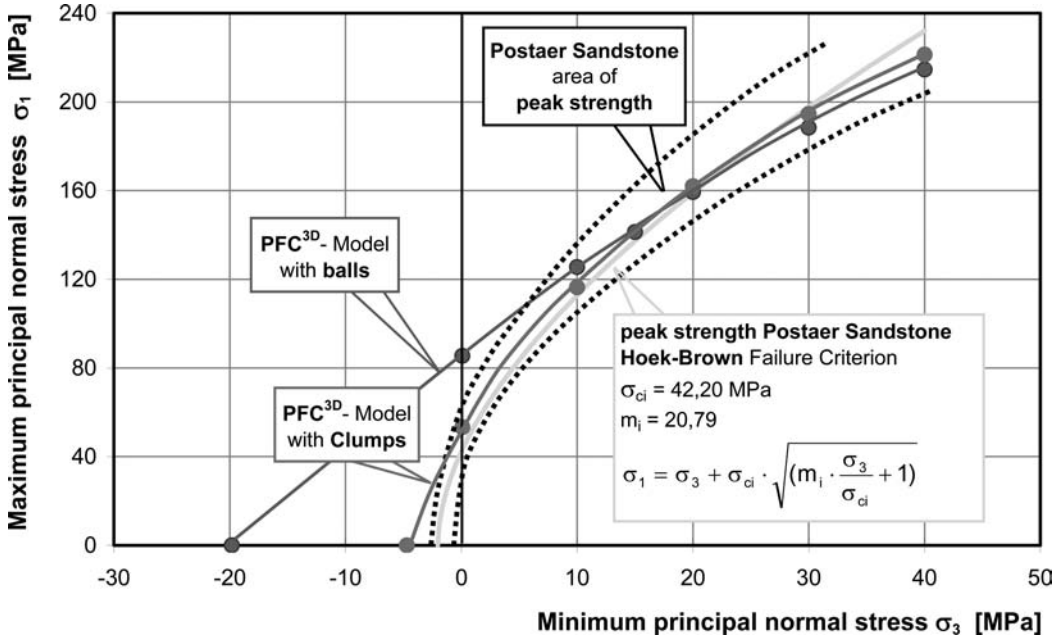


Figure 6. Failure Envelope, Peak Strength – Laboratory tests/PFC3D – simulations (Baumgarten & Konietzky 2010).

of the grains and restrict the translational and rotational movements. Also, under higher stresses the number of contacts (coordination number) is increasing. Consequently, bond strength could be reduced, which leads to lower tensile strength while compressive strength is still high. Progressive bond breakages are observed if app. 50 to 60% of the peak strength is reached. This is confirmed by ultrasonic wave speed measurements in the lab and also documented by corresponding numerical simulations (Baumgarten & Konietzky 2012). The numerical simulations show a further increase in damage (crack development) even after the peak strength

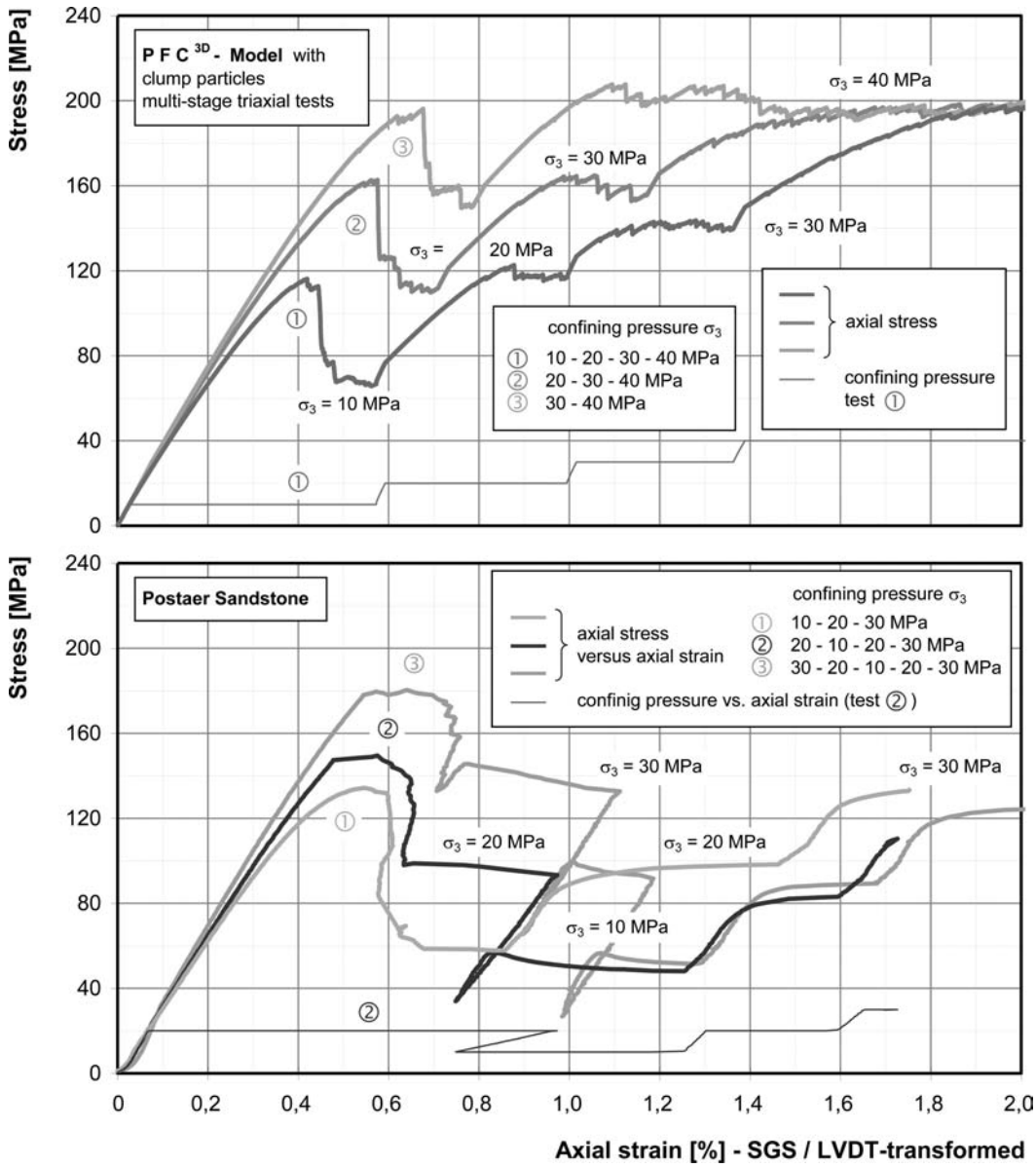


Figure 7. Multi-Stage Triaxial Tests – Simulations (PFC3D-Clump-Model)/Laboratory-Tests, Stress-Axial Strain-Characteristics (Baumgarten & Konietzky 2012).

was reached, whereas lab tests have revealed only very slightly further reduction in ultrasonic wave speed, which is interpreted as only minor additional cracking in that phase. To simulate the decay from peak to residual strength, local reduction of friction for broken bonds was implemented. The degree of reduction is a function of confining pressure and number of broken bonds per particle. This leads, similar to the observations in the lab, to the accumulation of cracks inside a band (creation of shear bands).

As shown by Fig. 7, after reaching the residual strength level the numerical simulations were continued by an isotropic loading stage followed by a deviatoric loading stage until reaching a new residual strength level. During the isotropic loading stage the particle contact friction is set back to the initial value, but locally reduced again if new cracks are created. This procedure allows to simulate the post failure range and the residual strength, respectively. Not yet solved is the problem of massive ongoing damage inside the post failure region, which leads to partly unrealistic fracture pattern and to strong loss of stiffness. At the current stage the mechanical behaviour of the Postaer Sandstone can be simulated quite well for the pre-failure

range up to the peak strength. Especially in the post-failure range some discrepancies between simulation results and lab tests are still observed.

4 CONCLUSIONS

A particle based simulation approach is well suited to model the stress-strain behaviour and the internal micromechanical damage development of rocks. The ball-model gives satisfying results when only compression has to be considered, although the non-linearity of the failure envelope can not be reproduced. The clump-model instead overcomes the disadvantages of the ball model, because the non-linearity can be reproduced and the tensile strength is modelled properly. This documents the great influence of the grain shape on the micromechanics.

REFERENCES

Baumgarten, L. & Konietzky, H. 2010: Numerical Investigations about Damage and Fracture of Sandstone under 3-axial Compression. 18th European Conference on Fracture – Fracture of Materials and Structures from Micro to Macro Scale. Proceedings-CD (C.06.2-5), Dresden.

Baumgarten, L. & Konietzky, H. 2012: Stress-Strain, Strength and Failure Behaviour of Postaer Sandstone in Tension and Compression Tests – Laboratory Investigations and Numerical Modelling with PFC-3D. In Veröffentlichungen des Instituts für Geotechnik der TU Bergakademie Freiberg 1: 41–61.

Itasca Consulting Group, Inc. 2008: PFC3D-Particle Flow Code in 3 Dimensions, Ver. 3.10-305. Minneapolis, Minnesota, USA.

Mittelbach, L; Konietzky, H. & Baumgarten, L. 2012: Ultraschallmessungen bei Triaxialversuchen – Laborversuche und numerische Simulation. Mitteilungen der Bundesanstalt für Wasserbau 95: 71–78.

Rock Mechanics for Resources, Energy and Environment – Kwaśniewski & Łydżba (eds)
© 2013 Taylor & Francis Group, London, ISBN 978-1-138-00080-3

The relationships between Drilling Rate Index (DRI), physico-mechanical properties and specific cutting energy for some carbonate rocks

G. Ekincioglu
Ahi Evren University, Kaman Vocational School, Kırsehir, Turkey

R. Altindag, N. Sengun & S. Demirdag
Department of Mining Engineering, Süleyman Demirel University, Isparta, Turkey

A. Guney
Department of Mining Engineering, Mugla University, Mugla, Turkey

ABSTRACT: In this study, the relationships between Drilling Rate Index (DRI) values and the Specific Cutting Energy (SCE) were investigated by experimental work for twelve different carbonate rocks which are produced as natural stones in various regions of Turkey. Physical and mechanical properties of rocks were determined on rock samples in excavation laboratory prior to determining the DRI values of each rock type. In order to determine the SCE of the rocks, the samples were prepared in compliance with the testing standards. Cutting tests were carried out on prepared rock samples using the equipment having a circular saw. The relationships between the DRI values and physico-mechanical properties of rocks were investigated by using simple regression analyses, which yielded relationship equations with meaningful correlation coefficients of 0.81–0.94 between the DRI and physical properties of rocks whereas the relations between the DRI and mechanical properties of rocks yielded as well significant correlation coefficients ranging between 0.79–0.87. A high correlation coefficient of 0.91 between the DRI and SCE may suggest that the SCE of rocks be a useful tool in estimating the value of the DRI of rocks and vice versa.

1 INTRODUCTION

The parameters influencing the efficiency of an excavation may be divided into two major groups depending on the rock medium and excavation equipment. Although it is possible to alter the parameters of the excavation equipment, changing the parameters of rock medium is not. Therefore, identification of the parameters depending on rock properties by taking into account the excavation equipment is important in terms of efficiency.

Cutting processes constitute a significant share in natural stone quarries and factories. Thus, determination of excavation parameters and carrying out related performance tests become important to optimize the cost inputs.

Energy spent during the cutting varies depending on the rock type and the parameters of sawing machine. Physical and mechanical properties of the rock and hard mineral content will affect the sawing process. In addition, the rotation speed (peripheral speed), the feed rate (cutting speed), the depth of cut, the structure of cutter socket and the machine's power will affect the specific energy. Various researchers have studied the specific energy values for several rock types and established meaningful relations between specific energy, cutting parameters and the physico-mechanical properties of rocks.

Ucun et al. (2008) have carried out sawing tests on two different rock types to determine the cutting forces, power consumption, specific energy and noise values. Sengun et al. (2009) have performed sawing tests on 4 different rocks of magmatic origin and calculated specific energy values for each rock based on the values measured at constant cutting parameters. Regression analyses were performed to determine the effect of rock physico-mechanical properties on cutting energy. Their results indicated that porosity, a physical rock property, and uniaxial compressive strength, a mechanical rock property, had the greatest influence on cutting process. Bayram et al. (2011) have implemented sawing tests on Afyon White marble at different peripheral cutting speeds and different rates of cut progress and analyzed the relationships between the parameters of cutting and the noise level. At the end of the study, it was reported that noise level was related to the cutting force, unit wear and unit energy values.

In Mining and Civil Engineering, drilling is the process of making a hole into the rock mass and filling the hole with explosives for blasting by which mechanical energy is created to fragment the rock. Difficulty

or ease of drilling the rock depends on the resistance of the rock against drilling. This resistance varies according to the physical and mechanical properties of rocks.

Drillability of the rock indicates the rate that the drill bit makes progress into the rock. Rock drillability depends on rock hardness, strength, abrasion ability, fabric and brittleness. Field and laboratory studies are conducted to determine the role of rock properties which are effective in rock drilling. Some researchers have investigated the relationship between the physical properties of the rock and impact drilling speeds (Paone et al, 1966; Tandanand & Unger, 1975; Scholar & Hero, 2003).

Olsen & Blindheim (1970), in their drilling efforts in the field, have analyzed their results from the device named Siewers miniature drill test and obtained significant relationships. Jain & Singh (1993) have conducted laboratory drilling work on the rocks of different geological classes, applying different drilling thrust and rotation speeds to calculate the specific energy needed for the drilling operation. They found significant correlations between specific energy and Schmidt hardness, compressive strength and tensile strength. Dunn et al. (1993) have investigated the relationships between the specific energy and rock drillability for basalt and ultramafic talc carbonate rocks. Yaralı (2007) has determined the brittleness test and the drilling rate index (DRI) values based on Siewers miniature drill test on 16 different rocks. He then investigated the relationships between the DRI and three different rock brittleness values which are calculated based on uniaxial compressive strength and Brazillian tensile strength. Ekincioglu (2008) has examined the relationship between drillability of limestones and sawability of circular saws. Yaralı & Kahraman (2011) have determined the relationship between the DRI and two different brittleness values obtained from the compressive and tensile strength values on 32 different rock types. Recently, Yagiz (2009) introduced a brittleness index obtained from the indentation test.

In this study, the relationships between drilling rate index values and the specific cutting energy were investigated by experimental work for twelve different carbonate rocks.

2 DRILLING RATE INDEX (DRI)

Drilling rate index (DRI) of the rocks is used as a measure of the ease or difficulty of rock drillability. This index has been developed by N. Von Matern and A. Hjelmer in Switzerland in 1943. This test method has become the standard following a few changes and has begun to be used in determining the drillability of rocks since the end of 1950s. The DRI is determined based on brittleness (S_{20}) and Siewers miniature drill (SJ) tests (Tamrock, 1984).

In brittleness (S20) test; a weight of 14 kg is dropped 20 times at a height of 25 cm on crushed rock samples of about 500 g (16–11.2 mm lump size) and the percentage of undersize the sieve of 11.2 mm is taken as the rock brittleness value (S_{20}).

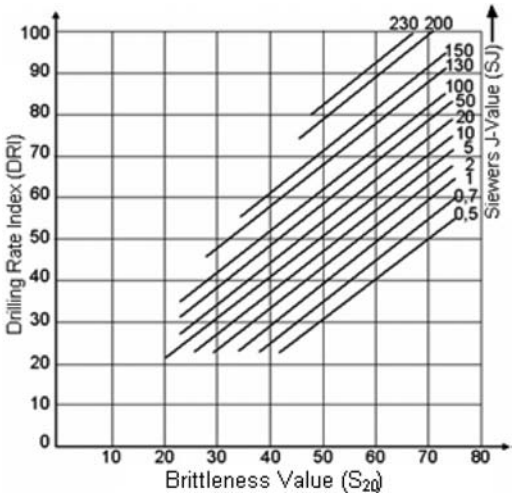


Figure 1. Diagram used to determine the DRI.

Table 1. Classification of the DRI value (Bruland, 1998).

Rock Class	DRI
Extremely low	≤25
Very low	26–32
Low	33–42
Medium	43–57
High	58–69
Very high	70–82
Extremely high	≥83

Siewers miniature drill test (SJ); a 8.5 mm diameter wedge tip made of tungsten-carbide (WC) is rotated 200 laps on the rock sample applying a force of 20 kg. The length of the drill hole is taken as the value (SJ) specified in 1/10 mm.

The DRI value is estimated using the diagram given in Figure 1, in which (S_{20}) value is intersected with the value obtained from Siewers miniature drill experiment (SJ) to find the DRI value, which is then classified depending on Table 1 (Bruland, 1998).

3 SPECIFIC CUTTING ENERGY

Specific energy is defined as the amount of energy needed to cut the rock per unit volume and is expressed as J/mm^3 in unit. Efficient cutting process requires maximum cutting speed and minimum specific cutting energy. Provided such conditions are satisfied, cutting is considered as the most economical. Therefore, the specific energy becomes a measure of cutting efficiency and a criterion as well. Several researchers take into account the cutting forces (normal and tangential), specific energy and specific wear values as sawability parameters.

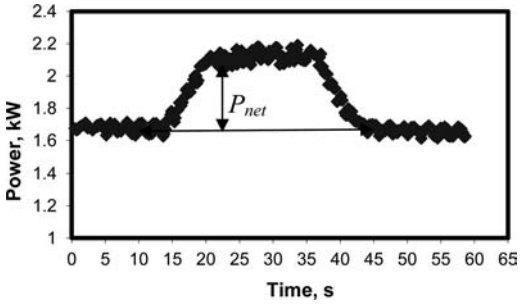


Figure 2. Power-time graph of Hacilar Beige sample.

Since vertical and lateral forces and wear values cannot be measured precisely in experimental set-up, total tangential force and specific energy values only are taken into account as the sawability parameters. During the test, real-time readings of voltage (V), frequency (f), and current (I) values are recorded via CX-drive software as the data file, and then converted and stored as the plain text data files. In Microsoft Excel, the instantaneous power consumed during the cutting is automatically calculated by multiplying the real-time values of current (I) and voltage (V) using Equation 1:

$$P = V * I \tag{1}$$

where P = instantaneous power consumed during cutting, watt, V = real-time voltage, volt, I = real-time current, amper.

Following the calculation of real-time power consumed, power-time graph is drawn as seen in Figure 2, through which it is possible to determine the power values during the full cut (P_c) and when the saw machine is idle (P_i). The difference between these two values will result in the net power (P_{net}) consumed by the saw machine (Equation 2).

$$P_{net} = P_c - P_i \tag{2}$$

where P_{net} = net power consumed during the cutting, watt, P_c = power consumed at full cut, watt, P_i = power consumed when machine is idle, watt.

For each rock type used in this work, specific removal rate and specific cutting energy values were calculated via Equation 3 and Equations 4–5, respectively. Sengun et al. (2009) was referred in calculating the values of the power consumed at full-cut and specific energy.

$$Q = V_a * h \tag{3}$$

$$F_r = P_{net} / V_t \tag{4}$$

$$SE = (F_r * V_t)/(h * W_s * V_a) \tag{5}$$

where SE = specific energy, J/mm^3, Q = specific removal rate, cm^2/min, F_r = radial force, N, V_t = tangential speed, m/s, h = cut depth, m, W_s = socket width, m, V_a = cutting advance speed, m/min.

Table 2. Rock types used in this study.

Rock type	Code	Class	Location
Marmara Grey	M-1	Metamorphic	Balıkesir
Tiger Skin	M-2	Metamorphic	Afyon
Mugla White	M-3	Metamorphic	Mugla
Bucak Travertine	TRV-1	Sedimentary	Burdur
Denizli Travertine	TRV-2	Sedimentary	Denizli
Aglasun Beige	KT-1	Sedimentary	Burdur
Tundra Grey	KT-2	Sedimentary	Afyon
Burdur Beige	KT-3	Sedimentary	Burdur
Lymra	KT-4	Sedimentary	Antalya
Karia Beige	KT-5	Sedimentary	Burdur
Hacilar Beige	KT-6	Sedimentary	Burdur
Calcerus Tuff	KT-7	Sedimentary	Denizli

Table 3. Physical properties of rocks.

Rock code	UVW, g/cm^3	SH	Vp m/s	BSA cm^3/50 cm^2	Source
M–1	2.706	41.6	3577	21.3	A
M–2	2.710	43.5	4720	29.8	A
M–3	2.715	47.5	4408	24.0	A
TRV-1	2.485	36.7	4257	28.0	A
TRV-2	2.384	43.9	4425	29.0	A
KT–1	2.682	31.5	5521	13.0	A
KT–2	2.652	53.6	5868	14.5	A
KT–3	2.677	62.6	5705	11.6	A
KT–4	2.415	56.6	4362	40.8	B
KT–5	2.688	61.5	5849	17.0	B
KT–6	2.690	63.0	5997	15.1	B
KT–7	2.013	14.6	3635	40.9	B

A: Sengun, 2009; B: Ekincioglu, 2008

4 EXPERIMENTAL WORK

For this work, 12 different rock types were collected from different locations in Turkey (Table 2). Physical and mechanical properties of the rocks were determined in compliance with the standards of TS 699 (1987), TS EN 12372 (2001), TS EN 14157 (2005), ISRM (1981) and ISRM (2007). The samples were prepared and tested in Natural Stones Technology Laboratory at Mining Engineering Department of the Suleyman Demirel University (Isparta).

4.1 *Physical properties of rocks*

Physical rock properties such as unit volume weight (UVW) and Bohme surface abrasion (BSA) were determined in compliance with the standards of TS 699 (1987) and TS EN 14157 (2005), respectively. Ultrasound velocity (Vp) and Shore hardness (SH) tests were implemented in compliance with the standards of ISRM (1981, 2007), which is based on the ISRM suggested method proposed by Altindag & Guney (2006). Average values obtained from the tests are displayed in Table 3.

Table 4. Mechanical properties of rocks.

Rock code	UCS MPa	BTS MPa	Is_{50}, MPa	BS MPa	Source
TRV-1	60.7	4.4	3.99	4.4	A
M–1	74.6	6.0	3.26	14.0	A
M–2	70.3	5.4	3.46	13.5	A
M–3	85.7	4.7	3.52	11.7	A
TRV-2	62.5	3.4	3.58	19.1	A
KT–1	109.8	5.6	4.66	12.8	A
KT–2	145.5	7.0	5.39	13.4	A
KT–3	129.9	8.0	5.33	11.5	A
KT–4	34.9	3.9	3.21	11.1	B
KT–5	130.6	8.1	3.38	25.8	B
KT–6	92.3	6.7	6.51	13.8	B
KT–7	18.3	2.1	1.51	9.6	B

A: Sengun, 2009; B: Ekincioglu, 2008

4.2 *Mechanical properties of rocks*

Mechanical rock properties such as uniaxial compressive strength (UCS), Brazillian tensile strength (BTS), point load index (Is_{50}) and bending strength (BS) were determined in accordance with the standards of TS EN 1926 (2000), ISRM (1981), ISRM (1985) and TS EN 12372, respectively. Average values of the results obtained are shown in Table 4.

4.3 *Drillability properties of rocks*

Rock drillability values may be calculated in many ways. In this study, rock drillability value was estimated based on the drilling rate index (DRI) value, which was approximated using the values of brittleness test (S_{20}) and Siewers miniature drilling tests (SJ).

In order to test the brittleness (S_{20}), rock samples were crushed down to the range of 16–11.2 mm sieve. Then, using the device which appears in Figure 3, the weight of 14 kg was dropped 20 times on the rock samples and the weight of undersize material of the sieve of 11.2 mm was rated to the weight of original rock to find the brittleness value (S_{20}). The experiments were repeated 3 times and the arithmetical means were taken into consideration.

For the Siewers miniature drilling tests, NX core samples of 30 mm length were prepared and the experiments were carried out as described in the second section using the device which appears in Figure 4. Drilling tests were performed on 5 samples for each rock type. For the rocks tested in this study, DRI values were determined via Figure 1, based on the values obtained from brittleness (S_{20}) and the Siewers miniature drilling tests (SJ). During the experiments, a new drill bit was used for each hole. Arithmetical means of the DRI test results are displayed in Table 5.

4.4 *Specific cutting energy*

The amount of energy spent to cut per volume per unit time is defined as specific energy (SCE) and the



Figure 3. Brittleness test device.



Figure 4. Siewers miniature drill test device.

Table 5. The DRI and SCE values of the rocks.

Rock code	DRI	DRI class	SCE J/mm^3
M–1	59	High	0.491
M–2	54	Medium	0.517
M–3	58	High	0.521
TRV-1	61	High	0.491
TRV-2	64	High	0.471
KT–1	47	Medium	0.622
KT–2	57	Medium	0.694
KT–3	37	Low	0.760
KT–4	61	High	0.306
KT–5	45	Medium	0.849
KT–6	42	Low	0.815
KT–7	84	Very high	0.139



Figure 5. Computer controlled rock cutting machine.

area cut per unit time is defined as the specific bearing rate (Q). The specific cutting energy values of the rocks were determined using the block samples of $50 \times 100 \times 200$ mm in size. In the experiments, cutting depth of 20 mm, saw peripheral velocity of 50 m/s and the cut advance speed of 0.5 m/min values were kept constant. The data obtained from the tests are exhibited in Table 5.

Cutting experiments were implemented using the disc with a diameter of 350 mm and diamond concentration of 18–24% on the blade. The blade contains 25 sockets with dimensions of $3.7 \times 6.7 \times 40$ mm. Each segment is cooled via a pump at a constant water flow rate of average 10 liter/min in order to eliminate the effect of external cooling water. A view of the computer-controlled cutting machine used in the tests is shown in Figure 5.

5 STATISTICAL EVALUATION

In addition to the relationships between the DRI values and physical and mechanical properties of rocks, existence of the relationships between specific cutting energy and the DRI values was examined by simple regression analyses by using least squares regression. Linear, logarithmic, exponential and power curve fitting was undertaken and the best approximation equation with highest correlation coefficient determined.

The relationships between the DRI and physical and mechanical rock properties are shown in Figures 6–13 while the relationships between the DRI and specific cutting energy values are given in Figure 14. The regression analysis yielded a high correlation coefficient of 0.81–0.94 between the DRI and physical rock properties while the significant correlation coefficients between the DRI and mechanical properties were obtained as 0.79–0.87.

A considerably high correlation coefficient of 0.91 was obtained between the DRI and SCE, implying that the DRI possesses more meaningful relation with specific cutting energy as shown in Figure 8.

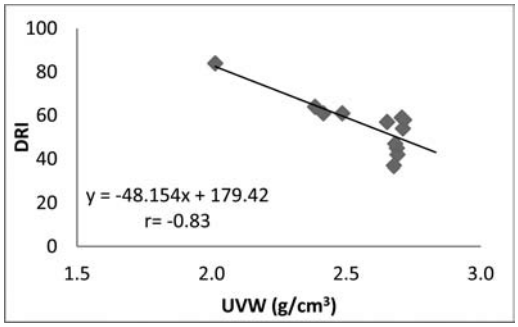


Figure 6. Relationship between the DRI and UVW.

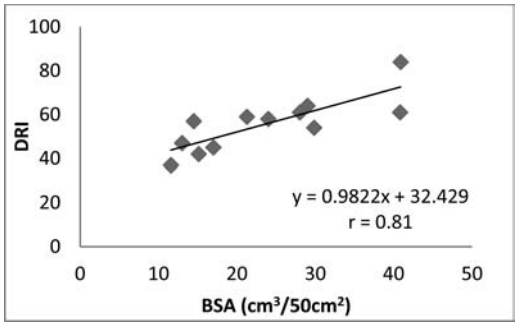


Figure 7. Relationship between the DRI and BSA.

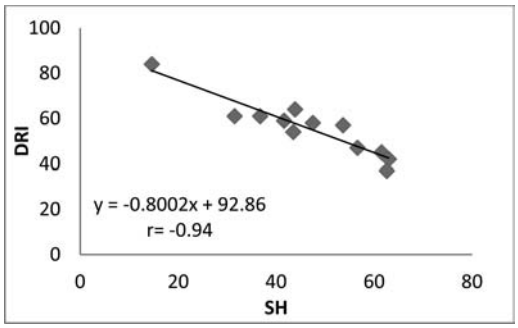


Figure 8. Relationship between the DRI and SH.

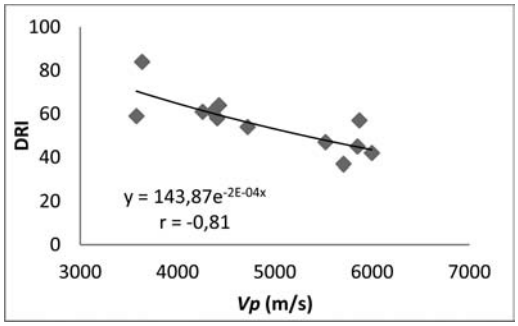


Figure 9. Relationship between the DRI and V_p.

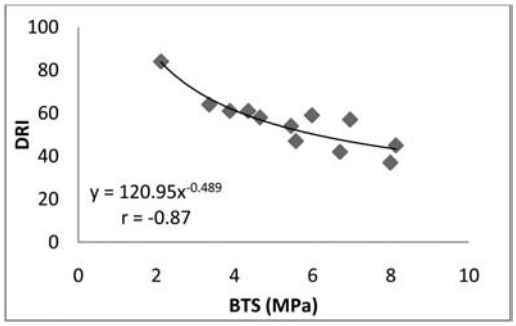


Figure 10. Relationship between the DRI and BTS.

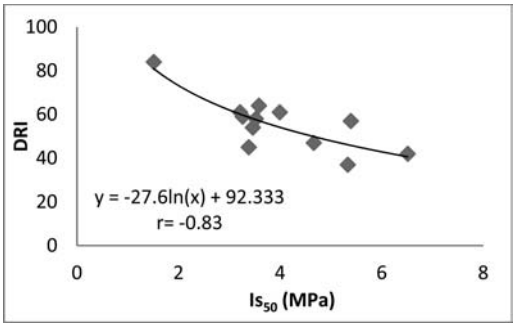


Figure 11. Relationship between the DRI and $Is_{(50)}$.

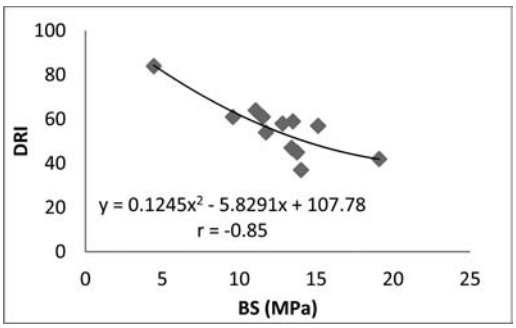


Figure 12. Relationship between the DRI and BS.

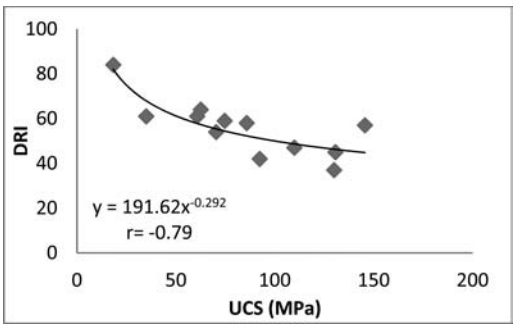


Figure 13. Relationship between the DRI and UCS.

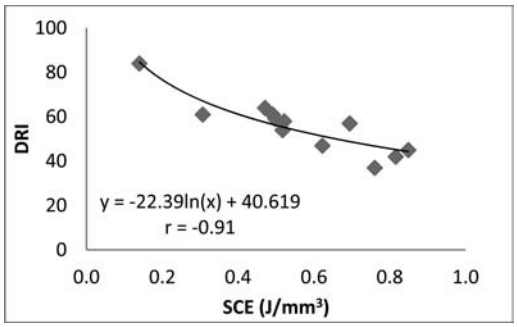


Figure 14. Relationship between the DRI and SCE.

Table 6. Hypothesis test results of the relations between the properties.

Depend. variable	Independ. variable	n	r	t calc.	t table	Comment
	UVW		−0.83	−4.71		Meaning
	BSA		0.81	4.37		Meaning
	SH		−0.94	−8.71		Meaning
	Vp		−0.81	−4.37		Meaning
DRI	BTS	12	−0.87	−5.58	±2.23	Meaning
	Is(50)		−0.83	−4.71		Meaning
	BS		−0.85	−5.10		Meaning
	UCS		−0.79	−4.07		Meaning
	SCE		−0.91	−6.94		Meaning

A hypothesis test was conducted to justify the significancy of the correlation coefficients found for the relationships between the DRI, physico-mechanical properties and SCE values. In result of statistical evaluations carried with 95% confidence level, the correlation coefficients of the relations between the DRI and other rock properties were found to be considerably significant (Table 6).

6 CONCLUSIONS

In this study, the DRI value which represents rock drillability was taken into consideration and its relations with other physical and mechanical rock properties were investigated. In addition, relations between the DRI and specific energy of cutting process with circular saws were assessed. Therefore, physical and mechanical properties of 12 different rock types and their SCE values were determined at constant work parameters. Brittleness (S_{20}) and Siewers miniature drill (SJ) tests were carried out to determine the DRI values of the samples. In the result of statistical assessments, quite high correlations were found between the DRI, physical and mechanical properties and SCE such that the highest correlation coefficient of ($r = 0.94$) was found between the DRI and SH. Similarly, a meaningful correlation ($r = 0.91$) was found between the DRI and SCE.

In conclusion, certain physico-mechanical properties of rocks may be taken into account in estimating the DRI values of rocks. Consequently, the estimated DRI value may be used in making a decision prior to the sawing process whether or not a certain rock type with known physico-mechanical properties can be sawn with a circular saw.

REFERENCES

Altindag, R., Guney, A., 2006. ISRM Suggested Method for Determining Shore Hardness Value for rock. International Journal of Rock Mechanics and Mining Sciences, 43, 996–997.

Bayram, A., Yaşıtlı, N., E., Özçelik, Y., 2011. Dairesel testereli kesimde gürültü seviyesinin kesim parametreleriyle ilişkileri. Türkiye 22. Uluslararası Madencilik kongresi Ve sergisi bildirile kitabı, 407–413.

Bilgin, N., Kahraman, S., 2003, Drillability Prediction in Rotary Blast Hole Drilling, 18th International Mining Congress and Exhibition of Turkey, Haziran 10–13, Antalya.

Bruland, A., 1998. Hard rock Tunnel Boring, 13A-98, Drillability Test Methods, NTNU Angleggdrift.

Dunn, P., Roberts C., Ballardin B.,1993. The Use of Specific Energy As a Drillabiliyt İndex. Geotecnical Instrumentaion and Monitoring in Open pit anda Underground Mining, Swzedzicki (ed.), 125–132.

Ekincioğlu, G., 2008. Çeşitli Kireçtaşlarının Delinebilirlik İndeks Özellikleri ve Kayaç Kesilebilirliği Arasındaki İlişkilerin Değerlendirmesi, Yüksek Lisans Tezi, SDÜ Fen Bilimleri Enst.

ISRM, 1981. Rock Characterization, Testing and Monitoring – ISRM Suggested Methods. Brown, E.T. (ed), Pergamon Pres, 211p.

ISRM, 1985. Suggested Method for Determining Point Load Strength. Int. J. Rock Mech. Min. Sci. And Geomech., 22 (2), 51–60.

ISRM, 2007. The complete ISRM suggested methods for rock characterization, testing and monitoring: 1974–2006, (Ulusay, R., Hudson, J.A., Editors), Kozan Ofset, s.628, Ankara.

Jain A.K., Singh D.,1993. Specific Energy As a Criterion for Drillability of Rocks- A Labratory Study. Geotecnical Instrumentaion and Monitoring in Open pit and Underground Mining, Swzedzicki(ed.), 253–263.

Olsen, R., Blindheim, O., 1970. On the Drillabilty of Rock by Percussive Drilling. Proceedings of the second congress of the International Society for Rock Mechanics, Belgrade, 65–70.

Paone, J., Bruce, W. E., Virciglio, P. R., 1966. Drillability Studies Statistical Regression Analysis of Diamond Drilling. RI-USBM 6880.

Sengun, N., 2009. Kayaçların Kırılma Tokluğu Ve Gevrekliğinin Dairesel Testereler İle Kesme Verimi Üzerine Etkileri. Süleyman Demirel Üniversitesi Fen Bilimleri Enstitüsü, Doktora Tezi,165s, Isparta.

Sengun, N., Altındağ, R., Koçcaz, C., E., 2009. Isparta Yöresinde Bulunan Bazı Mağmatik Kökenli Kayaçların Kesilebilirlik Analizi. DEÜ mühendislik fakültesi fen ve mühendislik dergisi, cilt 11, sayı 31.

Tamrock, 1984, Handbook on Surface Drilling and Blasting, Painofaktorit, Finland.

Tandanand S., Unger H.F., 1975, Drillability determination-A drillability index of percussive drills. USBM RI 8073.

TS 699, 1987. Tabii Yapı Taşları Muayene ve Deney Metotları. Türk Standartları Enstitüsü, Ankara.

TS EN 12372, 2001. Doğal Taşlar – Deney Metodları- Yoğun Yük Altında Bükülme Dayanım Tayini. Türk Standartları Enstitüsü, Ankara

TS EN 14157, 2005. Doğal Taş –Aşınma Direncinin Tayini. Türk Standartları Enstitüsü, Ankara.

TS EN 1926, 2000. Doğal Taşlar –Deney Metodları- Basınç Dayanım Tayini. Türk, Standartları Enstitüsü, Ankara.

Ucun, İ., Aslantacs, K., Büyüksağiş, S. İ., 2008. Kayaç kesme işleminde kullanılan elmas soketli kesici diskin kesme performansının incelenmesi. Makine teknolojileri dergisi, sayı 3, 33–40.

Yagiz S. 2009. Assessment of brittleness using rock strength and density with punch penetration test. *Tunneling and Underground Space Technology*, 24, 66–74.

Yaralı, O., 2007. Kayaç Kırılganlığı ve Delme Oranı İndeksi Arasındaki İlişkilerin Araştırılması. Türkiye 20. Uluslararası Madencilik Kongresi, 217–224, Ankara.

Yaralı, O., Kahraman, S., 2011. The drillability assessment of rocks using the different brittleness values. Tunnelling and Underground Space Technology, 26, 406–414.

This page intentionally left blank

Rock Mechanics for Resources, Energy and Environment – Kwaśniewski & Łydżba (eds)
© 2013 Taylor & Francis Group, London, ISBN 978-1-138-00080-3

A new small scale rock cutting test

M. Entacher, S. Lorenz & R. Galler
Montanuniversität Leoben, Chair of Subsurface Engineering, Austria

G. Winter
Montanuniversität Leoben, Chair of Mechanical Engineering, Austria

ABSTRACT: Full scale linear cutting tests are regarded as a reliable basis for performance prediction of hard rock Tunnel Boring Machines (TBM). However, obtaining suitable specimen is difficult and the effort to perform a feasible number of cutting tests is significant. This paper presents a newly developed small scale rock cutting test apparatus which can be installed in conventional hydraulic testing machines typically available in common rock mechanics laboratories. The specimen are obtained from drill cores which are available at early project stages. Results are compared with full scale rock cutting tests and geotechnical standard parameters. Consequently, the new test might prove a valuable tool for performance prediction of mechanically excavated underground structures.

1 INTRODUCTION

Accurate performance prediction is one of the main concerns in determining the construction time of excavations utilizing mechanical excavators such as tunnel boring machines (TBM). Typically, performance prediction models are based on geotechnical parameters like uniaxial compressive and indirect tensile strength as their main input parameters. The most established model of this kind is the semi-empirical/ semi-theoretical performance prediction model of the Colorado School of Mines (Rostami 1997). It was developed by combining basic theoretical relationships with laboratory data obtained from full scale rock cutting tests.

Besides the use of models, the best net penetration rate prediction can be obtained by conducting full scale linear cutting tests. The first well-known linear cutting machine was built in the 1970's at the Earth Mechanics Institute of the Colorado School of Mines (Ozdemir et al. 1976). Today, there are several linear cutting rigs which are used for the evaluation of rock cuttability (e.g. Balci & Bilgin 2007, Jeon et al. 2006, Abu Bakar & Gertsch 2012).

Inspite of providing reliable results, the conduction of full scale cutting tests is costly and time-consuming. In addition, large rock blocks are needed which are typically not available during an exploration phase of a tunnel project. Hence, full scale cutting tests are rarely carried out for performance prediction purposes before TBM excavation starts. In order to overcome these downsides, cutting tests on a smaller scale might prove useful because rock failure mechanisms are identical to the real excavation process except from scale effects.

Roxborough & Philipps (1974) developed a rock cutting rig for testing the performance of drag picks. The rig was built as a modification of an industrial shaping machine. It was mainly used to conduct full scale cutting tests with drag picks but also small scale cutting tests with disc cutters. McFeat-Smith & Fowell (1979) used the same test rig for numerous investigations such as the determination of specific rock cutting energy (MJ/m^3 yield).

While Öztürk et al. (2004) used the same cutting rig at Istanbul Technical University, Bilgin et al. (2010) subsequently developed an improved cutting rig (portable linear cutting machine, PLCM) that was presented at EUROCK 2010. The PLCM is capable of testing small scale disc cutters and rock blocks of about $20 \times 20 \times 10$ cm. It is equipped with a triaxial load cell with an accuracy of about 1 kN. The conducted test series is compared with full scale linear cutting tests and proves that small scale cutting tests are very promising.

This paper presents an evaluation of a scaled rock cutting laboratory test developed at the Chair of Subsurface Engineering, Montanuniversität Leoben, that is designed as an attachment fixture for hydraulic presses typically available in rock mechanics laboratories. As it uses existing infrastructure, the test rig is cheap and easy to use. The precision of the used load cell allows for fundamental investigations of rock breakage mechanisms. It is shown that high-quality results applicable for TBM performance prediction are obtained with standard specimen geometries that are available during exploration. The results are validated by a comparison will full scale rock cutting tests.

2 DEVELOPMENT OF A SCALED ROCK CUTTING TEST

2.1 *Design and assembly*

The design of the scaled cutting test was governed by the following boundary conditions:

- Specimen should be available at early project phases, i.e. drill cores,
- sufficient confinement should eliminate edge effects,
- a rotating scaled disc cutter should be used,
- indentation depth (penetration) should be adjustable very precisely,
- the test apparatus should be cheap and easy to use.

According to these constraints, it was chosen to use rock cores with a diameter of 10 cm that are cut in half and a height of approximately 9 cm because the maximum stroke of a typical hydraulic press is about 10 cm. The size of the disc cutter was estimated in order to suit such sample sizes without inducing cracks that reach to the edge of the specimen. It was chosen to use a steel cutter with a carbonitrided surface that approximately represents a 1:8 model of a typical 17″ constant cross-section cutter.

During assembly, the disc cutter is heated up and shrunk onto a shaft which is attached to a housing with combined needle/ball bearings to ensure sufficient maximum load capacity and smooth rotation. The cutter housing is attached to a linear bearing that ensures a straight cutting path when the cutter is thrusted into the sample. The specimen holder is a stiff steel block into which the rock sample is cemented with a two-component epoxy resin that ensures optimal confinement. It can be attached to its counterpart with bolts either in a central position or with an offset to simulate interacting cuts with spacing. Steel spacers are put between specimen holder and disc cutter in order to be able to adjust the necessary indentation depth of the cutter. A photograph of the test apparatus and an assembly drawing is shown in Figure 1.

2.2 *Measurement instrumentation*

Forces in rolling direction (F_R) are measured with a load cell that is part of the hydraulic press. Normal and side forces are not measured for the sake of simplicity. It was shown that rolling and normal forces (F_N) are closely related to each other. Hence, it was decided that it is tolerable to disregard the direct measurement of normal forces.

One of the assumptions of the performance prediction model of the Colorado School of Mines is that rolling (F_R) and normal force (F_N) are not independent from each other. One can be converted into the other with a conversion factor that is a function of penetration depth and cutter radius. The calculation is based on the assumption that there is a constant pressure distribution between cutter and rock over the whole contact length which is described by angle ϕ. For a constant pressure distribution, the angle of load application β becomes $\phi/2$ which is a reasonable assumption. This

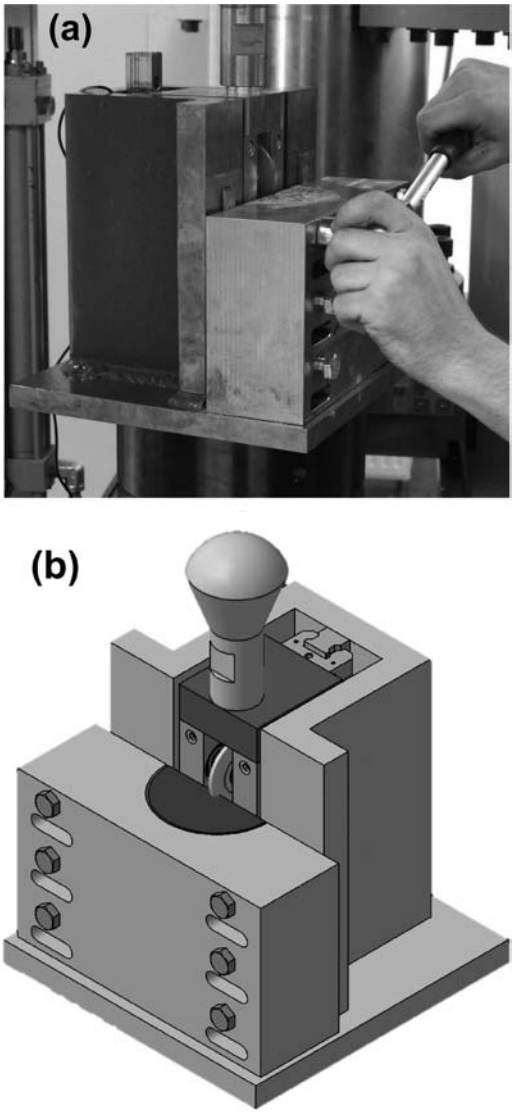


Figure 1. Cut-view of the scaled rock cutting test (a), experiment setup (b).

pressure distribution was thoroughly investigated by Rostami (2013) with a strain gauge equipped disc cutter. After the calculation of β, normal and rolling force can be found using trigonometric functions (R: cutter radius, p: penetration, in-depth explanations can be found in Rostami 1997):

$$\varphi = \arccos\left(\frac{R-p}{R}\right) \tag{1}$$

$$\beta = \varphi / 2 \tag{2}$$

$$F_N = F_T \cos(\beta), F_R = F_T \sin(\beta) \tag{3}$$

$$F_N = \frac{F_R}{\tan(\beta)} \tag{4}$$

Table 1. Geotechnical parameters and mineral composition of the investigated lithologies.

Rock type	ρ g/cm^3	σ_c MPa ± sd	σ_t MPa ± sd	E GPa ± sd
Augengneiss (AG)	2.6	206 ± 21	19 ± 0.5	35 ± 4
Calcareous mica schist (CMS)	2.7	83 ± 5	9.9 ± 0.5	38 ± 14
Brixen granite (BG)	2.7	160 ± 16	13.2 ± 1.1	43 ± 8

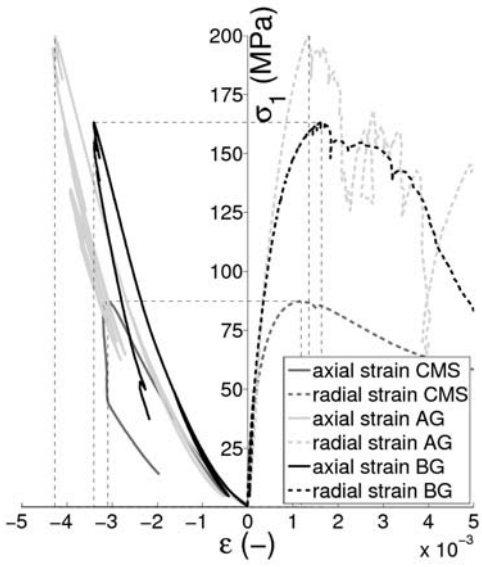


Figure 2. Stress-strain curves and rock texture of the investigated lithologies.

For the scaled cutting test ($R = 28$ mm, $p = 1.5$ mm), β comes out as 9.42°. Hence, $F_N \approx 6\, F_R$. Gertsch et al. (2007) conducted a large series of full scale linear cutting tests with Colorado Red Granite. They experimentally proved that the ratio F_R/F_N increases almost linearly as penetration goes up. 1.5 mm penetration for the scaled disc cutter is equivalent to 12 mm on a 17″ disc cutter. For such penetrations, a cutting coefficient (F_R/F_N) of 1/6 is very reasonable compared to the results of Gertsch et al.

3 LABORATORY TESTING

3.1 *Description of lithologies and geotechnical parameters*

Three different lithologies are presented in this paper. Their uniaxial compressive and Brazilian tensile strength, Young's modulus (secant modulus), specific weight and mineralogical composition (Rauch 2012) are given in Table 1.

Uniaxial compressive strength tests were carried out load-controlled until elasticity parameters were obtained. Afterwards, circumferential strain was used as the control parameter in order to be able to investigate post-failure behaviour.

Kahraman (2007) suggested that besides rock strength parameters, rock brittleness strongly influences cuttability. It is commonly accepted that rocks with characteristics such as little elongation at failure, high Young's modulus or high compressive to tensile strength ratio are regarded as brittle. However, there is no standard definition of brittleness that was proven to be useful for the prediction of rock cuttability. Consequently, uniaxial compressive strength tests were used to qualitatively investigate the post-failure behaviour of the tested lithologies in order to be able to assess their brittleness. Figure 2 shows one typical stress-strain curve for each rock type obtained from uniaxial compressive strength tests. It shows that AG can be considered very brittle, BG brittle and CMS rather ductile.

3.2 *Results of scaled rock cutting tests*

From each lithology at least five specimen were tested with the new scaled rock cutting apparatus. Anisotropic samples were prepared such that the foliation was approximately perpendicular to the cutting kerf. Each sample was cut five times in same kerf at the center of the specimen. Spacers were reduced after each cut so that penetration remained constant at 1.5 mm. Hence, the only difference between subsequent cuts was the pre-damage of the sample. Figure 3 shows the measured rolling forces of all five cuts from an Augengneiss specimen. It can be seen that the characteristics of cutting forces are different when cutting undamaged or pre-damaged rock. The corresponding photograph of the sample after all cuts is shown in Figure 4.

3.3 *Comparison with full scale rock cutting tests*

A series of full scale linear cutting tests was conducted at the Earth Mechanics Institute of the Colorado School of Mines under the supervision of Christian Frenzel and Brian Asbury with the three presented lithologies. All tests were carried out with a commercial 17″ single disc cutter with a tip width of 5/8″ (15.9 mm). Augengneiss (AG) and calcareous mica schist (CMS) were tested by Lisa Mori (2012) with a special focus on size and shape of the excavated material. An analysis of cutting forces of these tests was done by Entacher & Lassnig (2012). The results are used in this paper to evaluate the newly developed scaled rock cutting test. The results are only taken from samples that were cut in similar directions relative to the foliation as the scaled cutting tests, i.e. the foliation was approximately perpendicular to the cutting kerf. The third lithology, Brixen granite (BG), was tested by the first author with the purpose of comparing the results with TBM operational data. Figure 5 shows the

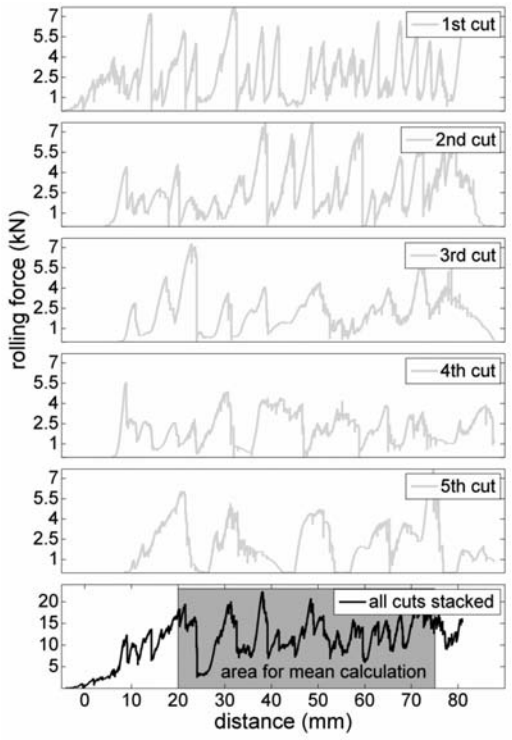


Figure 3. Results from scaled rock cutting tests (specimen AG02), 1st (top) to 5th cut and summation of all cuts (bottom).

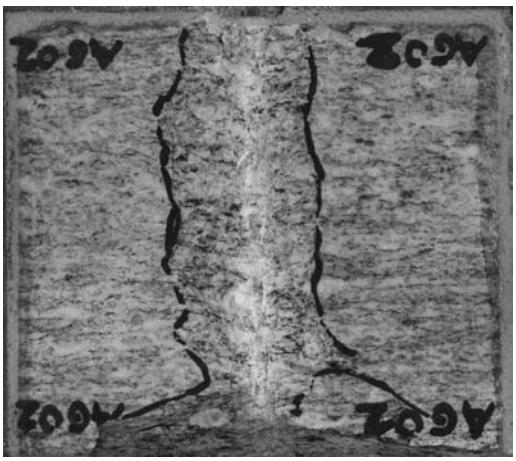


Figure 4. Specimen AG02 after testing.

results of the mentioned test series in the form of a penetration – mean normal force graph. In addition, it shows the results of the TBM performance prediction model of the Colorado School of Mines (CSM) with input parameters from Table 1.

As indicated in the figure, different penetration depths and spacings were used. In order to be able to use consistent data from all lithologies, it was decided to use a spacing (s) of 80 mm and a penetration depth

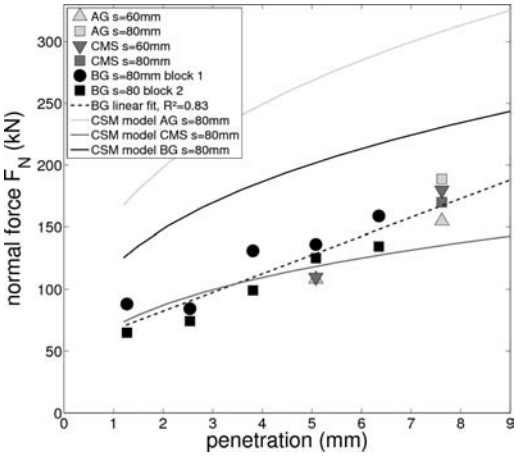


Figure 5. Results of full scale cutting tests and corresponding prediction of the CSM model.

of 0.3″ (7.6 mm) for comparison purposes. In order to be able to do so, BG results were extrapolated to this penetration value as indicated by the linear fit line. Consequently, one value was found for each of the three lithologies.

Figure 6 shows a comparison between scaled rock cutting tests, full scale rock cutting tests, uniaxial compressive and brazilian tensile strength. The results for the scaled cutting tests are the average equivalent normal force (*equivalent* $F_N = F_R \times 6$) of the last three cuts which represent a steady-state predamaged surface. The results of the first two cuts were not considered because they represent an undamaged rock surface which is not representative for the condition of the tunnel face during mechanical excavation.

It is notable that uniaxial compressive and brazilian tensile strength are the most widespread input values for performance prediction models while it is clear from Figure 6 that the distribution of these parameters deviates significantly from the distribution of the actual cutting forces. It is obvious that results from the scaled rock cutting test are much closer to the reference results than uniaxial compressive and Brazilian tensile strength.

4 DISCUSSION

The newly developed scaled rock cutting test proved to have superior applicability for TBM performance prediction than geotechnical standard tests such as uniaxial compressive strength and brazilian tensile strength tests. Advantages of these tests are however that not only cuttability, but also basic physical properties such as elasticity parameters Young's modulus E and Poisson's ratio ν are derived. Hence, they are used for a large variety of tasks such as design

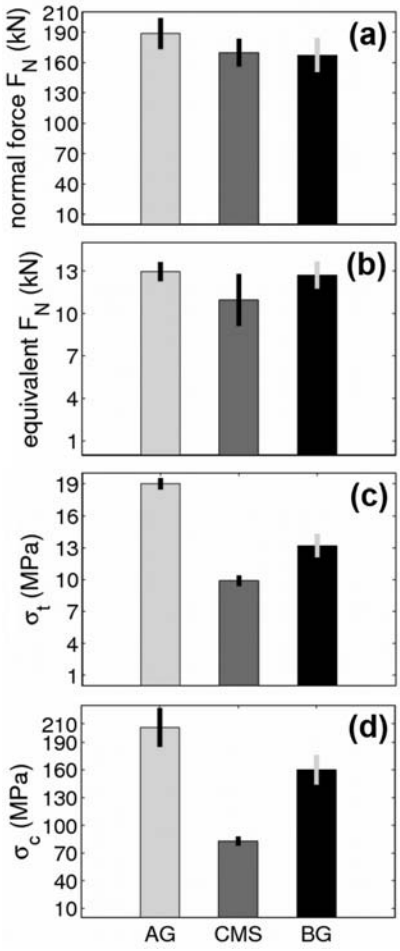


Figure 6. A comparison between full scale cutting tests (a), scaled cutting tests (b), uniaxial compressive (c) and Brazilian tensile strength (d) including standard deviations.

of underground structures. For the prediction of cuttability however, it was shown that these standard tests have a very limited applicability. Consequently, full scale or scaled rock cutting cannot substitute geotechnical standard tests, they have to be conducted additionally in order to be able to assess rock cuttability.

Bilgin et al. (2010) presented scaled rock cutting tests with single disc cutters at EUROCK 2010. Their results are equally promising than the results of the present study. The applicability of their test rig is different however because it is a specially built rig and uses rock blocks as specimen. In contrast to this, the present scaled rock cutting apparatus is designed as an easy and low-cost, yet very precise attachment device to hydraulic presses commonly available in rock mechanics laboratories. The used samples are 10 cm diameter cores cut in half which are available even in very early stages of a tunnelling project.

To summarize, scaled rock cutting tests are closing a gap between geotechnical standard tests which have serious limitations for TBM performance prediction and full scale rock cutting tests which are expensive and time-consuming and sometimes impossible to conduct due to the lack of appropriate samples.

5 CONCLUSIONS

A scaled rock cutting test rig has been developed. It is designed as an attachment for hydraulic presses commonly available in rock mechanics laboratories. The main innovation lies in its simplicity, accurate test results and the standard specimen size which can be obtained easily during all phases of a tunnelling project. Thus, it proved to be a promising tool for TBM performance prediction which is superior to geotechnical standards tests and much cheaper than full scale rock cutting tests.

ACKNOWLEDGEMENTS

We are grateful for the financial support by the Austrian Research Promotion Agency (FFG) within the Eurostars project E!5514. We are indebted to Martin Gimpel who helped us with geotechnical testing and in-depth discussions. The supervision of Dr. Christian Frenzel and Brian Asbury during the conduction of rock cutting tests at Colorado School of Mines was greatly appreciated. We thank Lisa Mori and Klaus Lassnig for the provision of rock cutting data.

REFERENCES

Abu Bakar, M.Z., Gertsch, L.S. 2012. Disc cutting tests on dry and saturated sandstone: muck as a performance estimator. *SME Annual Meeting; Proc., Seattle, February 2012.*

Balci, C. & Bilgin, N. 2007. Correlative study of linear small and full-scale rock cutting tests to select mechanized excavation machines. *International Journal of Rock Mechancis and Mining Sciences* 44: 468–476

Bilgin, N., Balci, C., Tumac, D., Feridunoglu, C., Copur, H. 2010. Development of a portable rock cutting rig for rock cuttability determination. *European Rock Mechanics Symposium, Proc., Lausanne, June 2010.*

Entacher, M. & Lassnig, K. 2012. Findings from disc cutting tests on alpine lithologies. *Geomechanics and Tunnelling* 5: 547–556.

Gertsch, R., Gertsch, L. & Rostami, J. Disc cutting tests in Colorado Red Granite: Implications for TBM performance prediction. *International Journal of Rock Mechancis and Mining Sciences* 44: 238–246.

Jeon, S., Chang, S., Choi, S., Bae, G. & Park, K.I. 2006. Performance estimation of TBM disc cutter by linear cutting machine. *41st US Rock Mechanics Symposium; Proc., Golden, 1–6 June 2006.*

Kahraman, S. 2002. Correlation of TBM and drilling machine performances with rock brittleness. *Engineering Geology* 65: 269–283.

McFeat-Smith, I., Fowell, R.J. 1979. The selection and application of roadheaders for rock tunnelling. *Rapid Excavation Tunneling Conference; Proc., Atlanta, 261–278, October 1979*.

Mori, L. 2012. Results of linear cutting tests on different alpine lithologies. *MSc thesis, Montanuniversität Leoben*.

Ozdemir, L. Miller, R. & Wang, F.D. 1976. Mechanical tunnel boring prediction and machine design. *National Science Foundation.*

Öztürk, C.A., Nasuf, E. & Bilgin, N. 2004. The assessment of rock cutability, and physical and mechanical rock properties from a texture coefficient. *The Journal of the South African Institue of Mining and Metallurgy* 8: 397–402.

Rostami, J. 1997. Development of a force estimation model for rock fragmentation with disc cutters through theoretical modeling and physical measurement of crushed zone pressure. *PhD Thesis, department of mining engineering, Colorado School of Mines*.

Rostami, J. 2013. Study of pressure distribution within the crushed zone in the contact area between rock and disc cutters. *International Journal of Rock Mechancis and Mining Sciences* 57: 172–186.

Roxborough, F., Philipps, H.W. 1974. Experimental studies on the excavation of rock using picks. *3rd ISRM Congress; Proc., Denver, 1407–1412 September 1974*.

Rock Mechanics for Resources, Energy and Environment – Kwaśniewski & Łydżba (eds)
© 2013 Taylor & Francis Group, London, ISBN 978-1-138-00080-3

Emission analysis of the cutting tools used for hard rock cutting with regard to status monitoring

K. Nienhaus, C. Kuchinke & D. Röllinger
RWTH Aachen University, Institute for Mining and Metallurgical Machinery, Aachen, Germany

ABSTRACT: For the extraction of medium hard rock cutting machines such as road headers, continuous miners or longwall shearers are often used. The defining parts of these machines are one or more rotary drums equipped with picks. While the picks are in interaction with the rock they emit a wide variety of physical effects like vibration, transient shock emissions, infrared emission, or others which can be analyzed to derive present machine parameters, present tool conditions as well as properties of the material actually being cut.

The objective of the present paper is an analysis of these emissions investigating if and how they can be used for status monitoring of the cutting process under laboratory as well as under real conditions. In this case, real conditions refer primarily to cutting speed and cutting forces.

1 INTRODUCTION

The automation of mining machinery is a major task in the modern mining industry in order to increase safety and productivity. In many industrial branches partially or fully automated machines and processes are common and lead to highly efficient operations. The mining industry is facing difficulties due to the rough conditions in the mining environment, and, therefore, high demands on machine safety are formulated.

Extraction machines like roadheaders, continuous miners or long wall shearers are often used to extract coal, salt or ore. The cutting process is of special interest because its optimization and monitoring are the key factors for minimizing the energy input and maximizing the equipment durability. Especially to be emphasized as a major task are the material identification and the condition monitoring of cutting tools. Material identification or "boundary layer detection" is fundamental for a highly automated machine. Sharp picks are vital for effective cutting. Worn or even damaged picks cause higher cutting forces, increase airborne dust and decrease the cutting efficiency. Additionally, they can lead to tool holder damage and drum damage.

Depending on the cutting conditions encountered in the mine, different types of picks can be used. The conventional chisel pick is used in coal ploughs. Most modern extraction machines use point-attack type picks. The point-attack pick is renowned for being robust and hard wearing since it is self-sharpening. Shearer loaders or continuous miners are equipped with cutter drums. The cutting drums rotate about a horizontal axis and are equipped with point-attack picks. As the drum rotates, the picks start to cut with zero depth of cut as they enter the coal at roof or floor, and the depth of cut increases to a maximum at mid-drum level and then decreases until the pick exits at zero depth of cut.

The cutting process seems simple, but consists of a high number of factors. Therefore, it is complicated to analyze the cutting process in its entirety.

This paper analyzes the different emissions in a cutting process and investigates if and how they can be used for status monitoring of the cutting process under laboratory as well as under real conditions.

2 POTENTIAL SOURCE LOCATIONS

An analysis of the cutting process with regard to possible origins for information carrier and possible locations for the application of appropriate sensor gives as a result 5 locations, which are tagged in Figure 1. Thereby, it is useful to distinguish between locations where physical effects have their origin and those locations where signals can be detected with the help of any sensor. Complementary, Table 1 illustrates the phases of crack initiation, crack propagation and flacking off chips during rock cutting.

The contact point between a single cutting tool and the material to be cut (1) represents the point, where most of the signals and information carriers, which will be discussed in this article, have their origin. The underlying cause is the high amount of released energy while the tool interacts with the material. During this interaction changes within the material to be cut,and at its surface (2), as well as inside the tool and its surface (3) take place. Additionally, changes with regard to the environment around the contact point such as dust and acoustic noise can be observed (4). Furthermore,

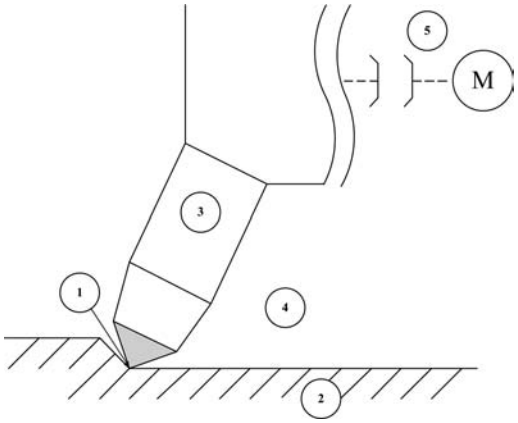
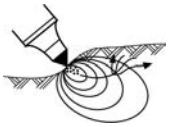
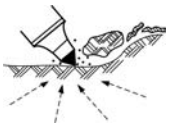


Figure 1. Origin of information carrier.

Table 1. Phases of rock cutting with a round-shaft pick (Thuro 2002).

	Phase 1: – application of force – forming an area of tension
	Phase 2: – initiation of cracks and crack propagation – ductile deformation
	Phase 3: – tear and removing of chips

some changes occurring during the interaction of the tool with the material are visible at the power input (5).

In the following it will be investigated which signals and information carriers are emitted at the respective location.

2.1 *Contact point*

At the contact point the cutting tool touches the material and the energy required for the destruction of the material is transferred into the rock. Consequently, a concentrated area of tension is formed by pressing the tool into the rock mass and moving the tool forward, Table 1 – Phase 1 (Gehring 1973, Thuro 2001). If the induced stress is higher than the stress resistance of the rock, cracks are initiated. In the further process of rock cutting, the cracks widen while the external loads are applied and the stress resistance is locally exceeded after ductile deformation, Table 1 – Phase 2 and Wahab Khair et al. 1989. If the rock mass is stressed further, chips are flaked off, Table 1 – Phase 3.

During these phases of rock cutting, at the contact point shock waves are induced through the material to be cut and through the tools material. This includes structure-borne sound, acoustic emission and acoustic noise as well, e.g. Becker et al. 1981, Yamada et al. 1989.

During the cutting process the cutting tool is moved forward through the material depending on the cutting head and the arrangement of the single tools at the tool carrier. Due to the friction between the tool and the material both are warmed up and emit thermal radiation (Cools 1993, Rogers & Roberts 1991). In addition, mechanical vibrations of the cutting tool are induced, which are caused by an uneven locomotion of the tool over the material surface, and by the effects of lateral forces and contact pressure (Vorona 2012, Wahab Khair et al. 1989).

The value and the direction of the cutting forces vary with changes of the cutting tools' geometry which is the result of wear and tear (Gehring 1973, Nishimatsu 1972, Vorona 2012). With increasing wear and tear, the geometry of the cutting trace, e.g. cutting depth and cutting width, and the geometry of the product, e.g. particle size, particle size contribution, and particle shape, change (Gehring 1973, O'Dogherty & Burney 1963, Tuncdemir et al. 2008).

2.2 *Material*

Within the material a wide range of physical effects can be observed caused by changes within the structure of the material induced by crack initiation, crack propagation and flaking off of chips and by the slipping of the cutting tool over the materials surface. In the following the most important signals are discussed.

Studies suggest that the measured emissions that mean both structure-borne sound and acoustic emission are unique for each material and for the amount of released energy by a relation between appearing cutting forces and the recorded signals (Becker et al. 1981, Nienhaus 2012). However, a correlation between sound signals and the used cutting tools needs to be verified.

Furthermore, tests have been carried out investigating the occurrence of acoustic emissions and electromagnetic emissions during uniaxial compression tests. Additionally, Brazilian tests of different types of material, e.g. coal, potash salt, gypsum were carried out (Grosse & Finck 2006, Lockner 1993, Yamada et al. 1989, Zang et al. 1998). An investigation concerning the correlation of acoustic emissions recorded during rock cutting and during compression tests and Brazilian tests will be contemporarily published. If the relation is confirmed, acoustic fingerprints for boundary layer detection could be recorded with little effort.

Along with the occurrence of changes of sound waves, changes in the field of mechanic loads can be measured. Based on cutting force-time-diagrams, a periodically swelling and fading is expected. Numerous studies show a dependence on the cutting force-time curve of the wear affected tool geometry

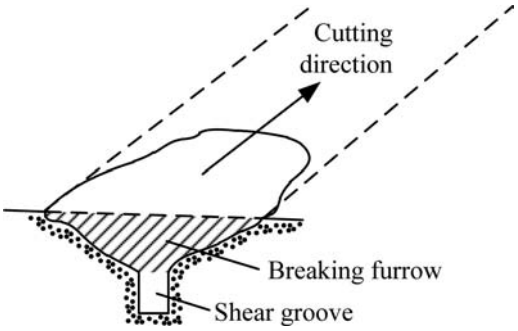


Figure 2. Cross-sections of a Cutting trace (Gehring 1973).

and other process parameters, e.g. Gehring 1973, Vorona 2012.

Changes of the cutting track, Figure 2, evoked by changes of the tool geometry have not been considered yet with a focus on status monitoring, but on the optimization of rock cutting processes (Gehring 1973, Vorona 2012).

2.3 *Cutting tool*

The waves, which can be detected at the surface of the cutting tool or inside the tool and their origin, are very similar to the effects which can be recorded at the surface or in the material. They represent a superposition of waves which have their origin within the material to be cut and the tool. The amplitude of sound waves induced within the tool is significantly lower due to the small amount of released potential energy because less material is removed from the tip of the tool compared to the longwall face.

As mentioned in section 2.1, the resulting friction phenomena are able to cause high temperatures at the cutting surface of the tool (Cools 1993, Glowka 1989). Based on this experiences not only the temperature, but also the temperature-time course as well as the development of the corresponding temperature field have to be taken into consideration for status monitoring of cutting tools.

2.4 *Environment*

In the present paper under "Environment" effects and information carriers recorded around the contact point in the ambient space are understood.

The objective of rock cutting is to loose rock fragments out of the rock mass. The product can be analyzed with focus on a variety of parameters, such as particle size, particle size distribution, particle shape, particle surface and some derived parameters (Tuncdemir et al. 2008).

Additionally, dust is generated during the cutting process, which can also be analyzed analogical (Vorona 2012). The mineralogical composition and the particle size contribution are the most interesting parameters.

Table 2. Signals and information carriers and their corresponding place of localization.

	Location, Fig. 1.				
signal/information carrier	1	2	3	4	5
electromagnetic emission		x	x		
acoustic emission		x	x		x
structure-borne sound		x	x		x
mechanical vibrations		x	x		x
acoustic noise				x	
thermal radiation	x	x	x	x	x
changes in geometry		x	x	x	
mechanical loads		x	x		x
power consumption					x

2.5 *Power train*

The current power consumption of the cutting machine contains a reflection of the processes that happen in front of the cutting tool and is a result of fluctuations in tool loads and any losses within the power train. Studies such as Gajewski & Jonak (2011) show unique patterns for different cases. Further apparently unpublished reports of the Institute of Mining and Metallurgical Machinery (IMR) at RWTH Aachen University consider missed tools as well as tools with different degrees of wear and tear.

3 SUITABILITY FOR STATUS MONITORING AND STATE DESCRIPTION

After naming and describing appearing signals and information carriers the following section will deduces how information for condition cutting drum monitoring and for in-situ state description of single cutting tools can be derived.

Table 2 lists the identified signals and the information carriers and shows where they can be recorded.

3.1 *Electromagnetic emission*

In the context of status monitoring of rock cutting processes "electromagnetic radiation" describes changes of the electromagnetic field around the material to be cut and around the cutting tools.

Yamada et al. (1989) describe that during rock fracture processes electromagnetic emissions are observable. The emissions were recorded during compression tests on a variety of materials. As during the rock cutting process many microcrack processes take place, it is assumed, that during changes of the electromagnetic field are also observable.

Whether the intensity of the measured electromagnetic events is sufficient for status monitoring is to be verified by tests.

3.2 *Structure-borne sound*

Structure-borne sound is the sum of mechanic waves within a frequency spectrum from 0 to 20 kHz which

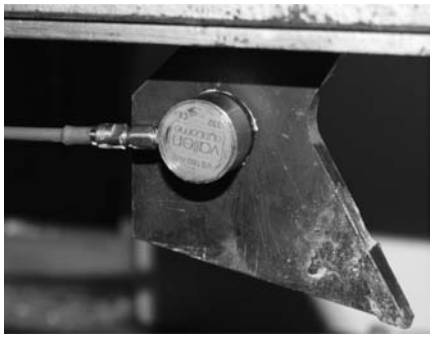


Figure 3. Cutting tool with AE-sensor.

are induced or propagated by vibrating solid bodies. Structure-borne sound can be detected at the surface of solid bodies with accelerometers. The propagation and the intensity of structure-borne sound are strongly influenced by the amount of boundary layers during the transmission path, by the length of the path and by material parameters. Present challenges in condition monitoring using structure-borne sound are the improvement of evaluation algorithms and identifying characteristics of influence factors. For further information see e.g. Möser (2010).

Principles of non-destructive testing with structure-borne sound can be applied to status monitoring of rock cutting processes because structure-borne sound is induced both by the relative movement between the cutting tool and the material and by the fracture processes within the materials. Thus, influencing parameters of this signal are material properties, process parameters and the geometry of the cutting tool.

3.3 *Acoustic emission*

Acoustic emissions (AE) are stress waves caused by structural changes within a solid body, e.g. slides, crack initiation and crack propagation, whereby potential energy is released, which is led by mechanical waves through solid bodies. The energy of acoustic emission events is proportional to the velocity of the trigger event and is significantly less than the energy of structure-borne sounds.

The technique of AE testing is well known for monitoring of Concrete structures, e.g. bridges, or condition monitoring of pressure vessels (Grosse 2008).

In rock cutting AE-signals are induced during the same processes where structure-borne sound is induced, this means structural changes within the material to be cut as well as wear and tear processes of the cutting tool. Figure 3 depicts an AE-sensor mounted on a cutting edge pick.

The challenge is to record the different but similar signals and to separate unique characteristics within the signals since AE signals are transferred from material to be cut into the tool and vice versa.

Present studies show that boundary layer detection with the help of the interpretation of characteristic



Figure 4. Temperature at the tip of a cutting tool.

values and feature spaces of AE-signals is possible. AE-signals induced during rock cutting with worn tools are analyzed at the moment. A correlation between the signal and the cutting forces is currently investigated (Nienhaus 2012).

3.4 *Mechanical vibrations and acoustic noise*

During rock cutting, acoustic noise is evoked when stress waves within the material to be cut or within the cutting tool are transferred to the ambient air. This happens through microscale movement of the free material surface and by a flow of ambient air into cracks and crevices with an access to the ambient air (Becker et al. 1981). The objective of the presented investigation was to reduce the required cutting forces and the generated noise during rock cutting. The results of experiments show a relationship between the applied cutting energy and the measured sound pressure levels. If the named changes are recognizable during rock cutting under real conditions, a status monitoring system could be supported by conclusions drawn on generated noise. The signals underlie overlapping of other acoustic noise generators like the cutting engine.

3.5 *Thermal radiation*

As mentioned above, tool and material heat up every cutting sequence with increasing cutting duration. Figure 4, made with an IR-camera, shows the tip of a cutting tool (Fig. 3) directly before (a) and after a cooling off phase(b)of a cut through a gypsum block. In this illustration the color "red" indicates a high temperature compared to the environment. Hence, the tip of the tool has been heated up during the cutting process. Similar experiments were carried out in the past, showing similar results by Cools 1993, Glowka 1989, Rogers & Roberts 1991.

If a temperature monitoring succeeds, algorithms used for condition monitoring of electrical machines and of bearings where temperature monitoring is state of the art in condition monitoring, can be taken for status monitoring and state description in rock cutting.

Hypothetically, with the help of temperature monitoring selective jetting of cutting tools in potentially explosive atmospheres could be realized for reducing water consumption and improving safety at work. Furthermore, if temperature changes occur very fast at the tip of tools, changes in the material properties can be

assumed. Conversely, if only one tool shows abnormalities at every cutting sequence, a damaged tool can be assumed.

3.6 *Changes in geometry*

As a result of rock cutting the surface of the material to be cut and of the cutting tools is changed. These changes depend on characteristic material properties and process parameters as it has been described for the previous signals and information carriers.

As Gehring (1973) has shown, the cross-section geometry of the cutting trace depends on cutting tool geometry. Other authors are concerned with wear and tear of cutting tools for the improvement of the cutting process but not for status monitoring, e.g. Rother 1980, Vorona 2012.

Due to the presence of dust, steam and material flying around during the cutting process an observation of geometry changes of the cutting tools is only possible if the affected tools are not in interaction with the material. The same requirements are valid for an observation of the cutting trace. Therefore, a real-time observation of geometry changes is difficult to realize, but a suitable and compared to other methods, a method which provides a clear statement for condition monitoring and state description.

3.7 *Mechanical loads*

As shown in Table 1, the area of mechanical tensions changes during a cutting sequence. At the contact point of tool and material a small homogeneous field of tensions is built up which becomes more asymmetric and inhomogeneous with progressive process duration. After flacking off the respective chip the field collapses.

Simultaneously, an area of tensions is formed in the tool.

The characteristic of the stress distribution and the chronological development during the cutting process depend on specific material parameters, the tool geometry and process parameters like feeding rate or cutting velocity.

Currently, no attempts have been made to observe the formation of the area of tensions at the tip of the cutting tool and at the contact point in the material.

3.8 *Power consumption*

The power consumption of the engines mounted on rock cutting machines is directly influenced by the processes that occur at the tip of the cutting tool (Becker et al. 1981, Gajewski & Jonak 2011, Gehring 1973).

However, in order to analyze the input parameters current and voltage, high-performance measurement equipment and respective evaluation devices are required. In addition, a real-time model is needed which processes the given input parameters and describes the present cutting process with a sufficient accuracy.

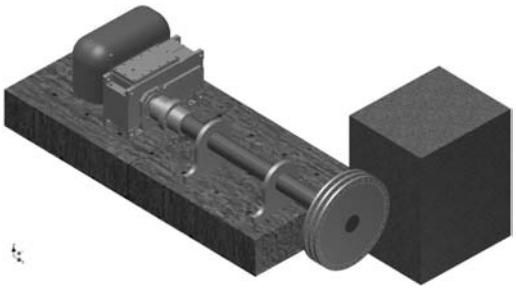


Figure 5. Scheme of the 1:1 test bench.

Currently, no methods for a sufficiently accurate modeling of these processes are known. Hence, research projects to provide methods for modeling cutting processes of hard rock cutting are in preparation.

An essential question is whether changes occur during the cutting process at the tip of the tools can be discovered time course of the power consumption. Due to that, the original signal is superimposed with fluctuations within the energy supply and the occurring changes are supposed to be on a very low level of intensity.

4 FURTHER PROCEEDING

Based on the presented research results, it can be concluded that a variety of physical effects and information carriers are emitted during the rock cutting process. These indicate a large potential for status monitoring and state description of cutting processes. Since there is no available holistic status monitoring system for rock cutting processes in rough underground operations, a suitable one has to be developed. As mentioned above, the objective is to achieve a high degree of automation of extraction machinery in general. Therefore, the cluster "Rock Cutting" was constituted to accomplish a group of research institutes and mining companies. The aim of this cluster is an application-oriented development of machine-compatible status monitoring systems and highly efficient cutting devices for hard rock extraction.

As a first step the IMR is carrying out tests within the EU-project i2mine. These tests will be made on a newly developed test rig. This test rig will utilize a model-like cutting drum. Cutting speeds of up to 3 m/s will be realized, allowing application-oriented research in the fields of material identification and condition monitoring of mining machinery.

As a second step, a test bench, shown in Figure 5, has been developed, that simulates cutting processes under real conditions. The cutting drum will have a diameter of 1000 mm and will rotate with 2.5 s^{-1}.

5 CONCLUSIONS

The paper shows a variety of spots where physical effects and information carriers have their origin.

These include relevant information for status monitoring and state description of the cutting process which can be recorded by sensors. Further on the paper explains potential benefits of the proven effects and information carriers with regard to status monitoring and state description.

The result of this extensive study also reveals a great demand for rock cutting tests under real conditions to comprehend the behavior of cutting tools and raw materials. These tests will show which sensors and applied techniques are actually applicable for status monitoring and state description.

Further on, the IMR is establishing a research cluster "Rock Cutting" with the aim of research and development in fundamentals of rock fracturing and rock mechanics, process optimization and rock cutting simulation as well as the development of methods for material-recognition und process parameter monitoring. Therefore, tests with a real cutting drum and with cutting speeds up to 8 m/s will carried out.

REFERENCES

Becker, R.S., Anderson, G.R. & Kovac, J. 1981. Investigation of the mechanics and noise associated with coal cutting. *Journal of Engineering for Industry* 103: 257–269.

Cools, P. 1993. Temperature measurements upon the chisel surface during rock cutting. *International Journal of Rock Mechanics and Mining Sciences & Geomechanics Abstracts* 30(1): 25–35.

Gajewski, J. & Jonak, J. 2011. Towards the identification of worn picks on cutter drums based on torque and power signals using artificial neural networks. *Tunnelling and Underground Space Technology* 26(1): 22–28.

Gehring, K. 1973. Möglichkeiten zur Beurteilung des Arbeitsverhaltens von Werkzeugen zur schneidenden Gesteinsbearbeitung, *Berg- und Hüttenmännische Monatshefte* 118: 319–327.

Glowka, D.A. 1989. The thermal response of rock to friction in the drag cutting process. *Journal of Structural Geology* 11(7): 919–931.

Grosse, C.U. & Finck, F. 2006. Quantitative evaluation of fracture processes in concrete using signal-based acoustic emission techniques. *Cement and Concrete Composites* 28(4): 330–336.

Grosse, C.U. & Ohtsu, M. (ed.) 2008. *Acoustic Emission Testing*. Berlin Heidelberg: Springer-Verlag.

Lockner, D. 1993. The role of acoustic emission in the study of rock fracture. *International Journal of Rock Mechanics and Mining Sciences & Geomechanics Abstracts* 30(7): 883–899.

Möser, M. & Kropp, W. 2010. *Körperschall: Physikalische Grundlagen und technische Anwendungen.* Berlin Heidelberg: Springer-Verlag.

Nienhaus, K. et al. 2012. Accoustic emission and pick forces in rock cutting. In *Seventh International Symposium Rockbolting and Rock Mechanics in Mining: 30–31 May 2012, RWTH Aachen University.*

Nishimatsu, Y. 1972. The mechanics of rock cutting. *International Journal of Rock Mechanics and Mining Sciences & Geomechanics Abstracts* 9(2): 261–270.

O'Dogherty, M. & Burney, A. 1963. A laboratory study of the effect of cutting speed or the performance of two cutter picks. *Colliery Engineering* 40(469): 51–54.

Rogers, S. & Roberts, B. 1991. Wear mechanisms associated with rock excavation using attack picks. *Mining Science and Technology* 12(3): 317–323.

Rother, E. 1980. Experimentelle Untersuchungen zum Verschleiss von hartmetallbestückten Keilmeisseln beim Zerspanen von Gestein, PhD thesis, Rheinisch-Westfälische Technische Hochschule Aachen, Aachen.

Thuro, K. 2001. Geologisch-felsmechanische Grundlagen der Gebirgslösung im Tunnelbau, Habilitation, Technische Universität München, München.

Tuncdemir, H. et al. 2008. Control of rock cutting efficiency by muck size. *International Journal of Rock Mechanics and Mining Sciences* 45(2): 278–288.

Vorona, M. 2012. Optimierung des Schneidprozesses und Prognose der relevanten Arbeitsgrößen bei der Gesteinszerstörung unter Berücksichtigung des Meißelverschleißes, PhDthesis, TU Bergakademie Freiberg, Freiberg.

Wahab Khair, A., Reddy, N. & Quinn, M. 1989. Mechanisms of coal fragmentation by a continuous miner. *Mining Science and Technology* 8(2): 189–214.

Yamada, I., Masuda, K. & Mizutani, H. 1989. Electromagnetic and acoustic emission associated with rock fracture. *Physics of the Earth and Planetary Interiors* 57(1–2): 157–168.

Zang, A. et al. 1998. Source analysis of acoustic emissions in Aue granite cores under symmetric and asymmetric compressive loads. *Geophysical Journal International* 135(3): 1113–1130.

Rock Mechanics for Resources, Energy and Environment – Kwaśniewski & Łydżba (eds)
© 2013 Taylor & Francis Group, London, ISBN 978-1-138-00080-3

3D elastic solutions for point load and Brazilian indirect tensile strength tests

Mehdi Serati
CSIRO Earth Science and Resource Engineering, Queensland Centre for Advanced Technologies, Pullenvale, Australia
The University of Queensland, School of Civil Engineering, Australia

Habib Alehossein
CSIRO Earth Science and Resource Engineering, Queensland Centre for Advanced Technologies, Pullenvale, Australia

Nazife Erarslan & David J. Williams
The University of Queensland, School of Civil Engineering, Australia

ABSTRACT: In this paper, an analytical solution is developed of the stress and displacement components in a three-dimensional solid disc subjected to Brazilian and point load test boundary conditions. The methodology is initially based on introducing the load distribution in both tests using the double Fourier series technique. The displacement vector in cylindrical polar coordinates (r, θ, z) is then presented by means of harmonic potentials according to the Papkovich-Neuber scheme. Stresses are then recovered by searching for acceptable potentials that satisfy both the domain Laplacian equation and the prescribed Fourier boundary expression. Several solutions are developed in terms of design graphs, and the effect of influencing parameters on the calculated results, e.g. material elastic properties, loading configurations and specimen geometries, are discussed.

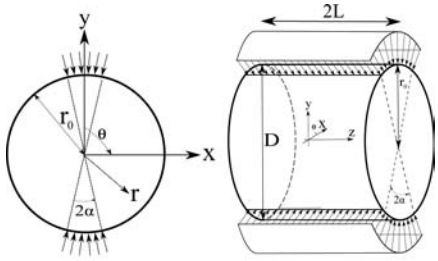
1 INTRODUCTION

The Brazilian test (Hondros 1959, ISRM 1978, ASTM 008a) and Point load test (Wijk 1978, ISRM 1985, ASTM 008b) have a rich history in the field of engineering applications. Both tests provide a measure of the indirect tensile strength of a given material for which testing under direct tension is difficult. Investigation for the critical value of stresses induced in a target brittle material subjected to these tests, has long been studied experimentally, theoretically and numerically. A review of the state of art, especially for the testing of rock specimen, can be found in Chau (1998) and Diyuan and Louis (2012). However, a generic three-dimensional (3D), elastic, closed-form solution has not yet been proposed for the Brazilian test. Moreover, reported results obtained by analytical methods for the point load test generally employ excessively complex 3D mathematical derivations (Wei and Chau 2000). Therefore, in the study presented herein, the mathematical hurdles for the calculation of elastic field variables in a solid disc subjected to Brazilian and point load boundary tractions are investigated with a relatively simple 3D elasticity procedure. The proposed formulation can also be conveniently used to solve a variety of other problems in which the curved boundary of a solid disc is under arbitrary loading with different frequencies applied in the axial and circumferential directions., e.g. strip-loaded (Barton 1941) or fully-loaded cylinders (Serati et al. 2012).

2 CONSTRUCTION OF SOLUTION

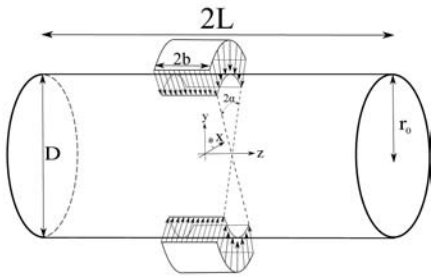
2.1 *Geometry and loading distribution*

To achieve the objectives, the specimen geometry in both the Brazilian and point load tests is considered as an isotropic, circular cylinder of radius r_0 and length $2L$, having a uniform cross-section aligned in the z-direction. The two ends ($z = \mp L$) are further assumed to be traction-free and the centre of the disc coincides with the origin of the coordinates (see Fig. 1(b) and 1(c)). The loading configuration in the Brazilian test is simulated by a pair of radial loads of magnitude F, which are then assumed to be uniformly distributed over a $2\alpha r_0$ strip of the disc surface at each end of a diameter (Fig. 1(b)). The concentrated diametral forces in the point load test are considered as loads of magnitude F, which are then assumed to be uniformly distributed over a region with length $2b$ in the axial direction ($b << L$) and $2\alpha r_0$ in the circumferential direction (Fig. 1(c)). Based on these assumptions, the vertical cross-sections of stress in both the Brazilian and point load tests on the xoy plane become similar, as shown in Fig. 1(a). A double Fourier series of the



(a) Vertical cross section of Brazilian and point load tests on xoy domain

(b) 3D loading configuration of the Brazilian test



(c) 3D loading configuration of the point load test

Figure 1. Schematic boundary conditions of a solid cylinder subjected to Brazilian and point load testing conditions.

assumed radial stress ($\sigma_{rr\,(r=r_0)}$) can then be expressed by equations (1) and (2) for the Brazilian and point load tests, respectively.

$$\sigma_{rr\,(r=r_0,BT)} = -\frac{2\,P}{\pi\,\alpha\,L}\left(\sum_{n=1}^{\infty}\frac{\alpha f(n)}{2\pi}\cos(\gamma_n z)\right.$$

$$\left.+\sum_{m=2,4,6}^{\infty}\sum_{n=1}^{\infty}\frac{f(n)\sin(m\alpha)}{m\,\pi}\cos(\gamma_n z)\cos(m\theta)\right) \quad (1)$$

$$\sigma_{rr\,(r=r_0,PLST)} = -\frac{P}{\pi^2\,b\,\alpha}\left(\frac{b\,\alpha}{L}\sum_{n=1}^{\infty}f(n)\cos(\gamma_n z)\right.$$

$$+\alpha\sum_{n=1}^{\infty}\frac{sin(\beta_n b)}{n}\cos(\beta_n z)$$

$$+\frac{2b}{L}\sum_{m=2,4,6}^{\infty}\sum_{n=1}^{\infty}\frac{f(n)\sin(m\alpha)}{m}\cos(\gamma_n z)\cos(m\theta)$$

$$\left.+2\sum_{m=2,4,6}^{\infty}\sum_{n=1}^{\infty}\frac{sin(\beta_n b)\sin(m\alpha)}{mn}\cos(\beta_n z)\cos(m\theta)\right) \quad (2)$$

where, P is the total force per radial length acting on one side of the specimen (or F/r_0), $\gamma_n = \frac{n\,\pi}{4\,L}$, $\beta_n = \frac{n\,\pi}{L}$ representing the frequency of the applied load in z-direction, and $f(n)$ is a function of n only given by:

$$f(n) = \frac{1-\cos(n\,\pi)}{n}\sin(\frac{n\,\pi}{2}) \quad (3)$$

Accordingly, the other two boundary conditions on the curved surface for both problems are:

$$\sigma_{rz\,(r=r_0,\,\theta,\,z)} = 0 \quad (4)$$

$$\sigma_{r\theta\,(r=r_0,\,\theta,\,z)} = 0 \quad (5)$$

It should be pointed out that the loadings in equations (1) and (2) are assumed to be simple uniform radial distributions, for the sake of mathematical simplicity. Other load distributions on the curved surface such as parabolic, circular or Hertzian, can also be modelled using the methodology presented herein, provided that a double Fourier series form of the desired loading is known.

2.2 *Solution methodology in (r, θ, z) domain*

The starting point of the 3D elastic field determination of deformations and stresses is the Navier's equation of equilibrium, which gives the unique solution for a given problem based on displacements only (Timoshenko & Goodier 1969, Little 1973, Sadd 2009, Barber 2010). The Navier's displacements are obtained on eliminating the strains (ϵ_{ij}) and stresses (σ_{ij}) from the fundamental system of partial differential equations in linear elasticity. Navier's equation in vector notation is:

$$\nabla^2\boldsymbol{u} + \frac{1}{1-2\nu}\nabla(\nabla\,.\,\boldsymbol{u}) = 0 \quad (6)$$

where ν is the Poisson's ratio, u is the displacement vector and ∇, $\nabla.$ and ∇^2 are the gradient, divergence and Laplace operators, respectively. To find the general solution of equation (6), Papkovich (1932) and Neuber (1934) proposed a technique based on the Helmholtz decomposition theorem, substituting u with a harmonic vector $\boldsymbol{\psi}$ and a harmonic scalar potential ϕ (Eubanks & Sternberg 1956, Youngdahl 1969, Barber 2010). Generally, the Papkovich-Neuber (PN) solution is expressed as:

$$2\,\mu\,\boldsymbol{u} = -4\,(1-\nu)\,\boldsymbol{\psi} + \nabla(\boldsymbol{r}\,.\,\boldsymbol{\psi} + \phi) \quad (7)$$

$$\nabla^2\boldsymbol{\psi} = \boldsymbol{0} \quad (8)$$

$$\nabla^2\phi = 0 \quad (9)$$

where r represents the position vector of a field point and μ denotes the Lamé constant. Completeness and

uniqueness of the PN solution has long been investigated through extensive studies. It is also evident that in the solution of a cylinder subjected to no body forces and loaded periodically on its axial direction, the component of $\boldsymbol{\psi}$ aligned with the axis of the cylinder (i.e. ψ_z) may be taken as zero without impairing the generality of the solution (Eubanks & Sternberg 1956, Youngdahl 1969, Barber 2010). This elimination technique ($\psi_z = 0$) is used, since otherwise the Papkovich-Neuber stress components retain ψ_z, with z coefficient, leading to difficulties in expressing the boundary conditions of the Brazilian and point load problems with the double Fourier series. Reformulating equation (6) in cylindrical polar coordinates and using the PN solution with $\psi_z = 0$, displacements and stresses in terms of ϕ and $\boldsymbol{\psi}_{(\psi_r,\,\psi_\theta,\,0)}$ are then recovered (Alehossein & Serati 2013). This means that:

$$2\,\mu\,u_r = -4\,(1-\nu)\,\psi_r + \frac{\partial}{\partial r}(r\,\psi_r + \phi) \quad (10)$$

$$2\,\mu\,u_\theta = -4\,(1-\nu)\,\psi_\theta + \frac{\partial}{r\,\partial\theta}(r\,\psi_r + \phi) \quad (11)$$

$$2\,\mu\,u_z = -4\,(1-\nu)\,\psi_z + \frac{\partial}{\partial z}(r\,\psi_r + \phi) \quad (12)$$

$$\sigma_{rr} = \frac{-2\,\nu}{r}\left(\psi_r + r\,\psi_{r,\,r} + \psi_{\theta,\,\theta}\right) + r\,\psi_{r,\,rr} - 2(1-2\nu)\,\psi_{r,\,r} + \phi_{,\,rr} \quad (13)$$

$$\sigma_{r\theta} = \psi_{r,\,r\theta} - 2(1-\nu)\,\psi_{\theta,\,r} + \frac{1}{r}\left[2(1-\nu)(\psi_\theta - \psi_{r,\,\theta}) + \phi_{,\,r\theta}\right] - \frac{\phi_{,\theta}}{r^2} \quad (14)$$

$$\sigma_{rz} = r\,\psi_{r,\,rz} - (1-2\,\nu)\psi_{r,\,z} + \phi_{,\,rz} \quad (15)$$

It is worth noting that the only harmonic function in the governing field equations (equations 10 to 15) is ϕ, and the two vector components ψ_r, ψ_θ do not necessarily satisfy the Laplace equation (Moon & Spencer 1988, Simmonds 1994).

With the boundary conditions defined by equations (1 to 5) and the stresses obtained from equations (13 to 15), the remaining step is to find the $\boldsymbol{\psi}$ and ϕ that give the boundary conditions upon substitution in equations (13 to 15), and also satisfy equations (8) and (9), simultaneously. For the Brazilian test, this is achieved by selecting trial functions for ϕ, ψ_r and ψ_θ according to equations (16 to 18).

$$\phi = \sum_{n=1}^{\infty} B_{0n} I_0(\gamma_n r)\cos(\gamma_n z) + \sum_{m=2,4,6}^{\infty}\sum_{n=1}^{\infty} D_{mn} I_m(\gamma_n r)\cos(\gamma_n z)\cos(m\theta) \quad (16)$$

$$\psi_r = \sum_{n=1}^{\infty} B'_{0n} I_1(\gamma_n r)\cos(\gamma_n z) + \sum_{m=2,4,6}^{\infty}\sum_{n=1}^{\infty} D'_{mn} I_{m+1}(\gamma_n r)\cos(\gamma_n z)\cos(m\theta) + \sum_{m=2,4,6}^{\infty}\sum_{n=1}^{\infty} D''_{mn} I_{m-1}(\gamma_n r)\cos(\gamma_n z)\cos(m\theta) \quad (17)$$

$$\psi_\theta = \sum_{n=1}^{\infty} B''_{0n} I_1(\gamma_n r)\cos(\gamma_n z) + \sum_{m=2,4,6}^{\infty}\sum_{n=1}^{\infty} D'_{mn} I_{m+1}(\gamma_n r)\cos(\gamma_n z)\sin(m\theta) - \sum_{m=2,4,6}^{\infty}\sum_{n=1}^{\infty} D''_{mn} I_{m-1}(\gamma_n r)\cos(\gamma_n z)\sin(m\theta) \quad (18)$$

In a similar fashion, potentials (16 to 18), with additional terms corresponding to the stresses induced by $\cos\beta_n z$ in equation (2), can also be used for the point load test, e.g. the harmonic scalar ϕ becomes:

$$\phi = \sum_{n=1}^{\infty} B_{0n1} I_0(\gamma_n r)\cos(\gamma_n z) + B_{0n2} I_0(\beta_n r)\cos(\beta_n z) + \sum_{m=2,4,6}^{\infty}\sum_{n=1}^{\infty} D_{mn1} I_m(\gamma_n r)\cos(\gamma_n z)\cos(m\theta) + \sum_{m=2,4,6}^{\infty}\sum_{n=1}^{\infty} D_{mn2} I_m(\beta_n r)\cos(\beta_n z)\cos(m\theta) \quad (19)$$

where $I_m(\gamma_n r)$ (or $I_m(\beta_n r)$) denotes the modified Bessel function of the first kind of order m and argument $\gamma_n r$ (or $\beta_n r$), and B_{0n}, B'_{0n}, B''_{0n}, D_{mn} ... are the as yet undetermined integral constants for each m and n.

It can readily be verified that equations (16 to 18) satisfy $\nabla^2\phi = 0$ and $\nabla^2\boldsymbol{\psi}_{(\psi_r,\psi_\theta,0)} = 0$. Therefore, substituting the potentials obtained from equations (16 to 18) into equations (13–15) and comparing the coefficients of each group in the final stresses, i.e. $\cos(\gamma_n z)\cos(m\theta)$, with those given from the boundary conditions in (1) or (2), all of the constants for each pair of m and n are recovered. For instance, if the first term of the potentials with only $\cos(\gamma_n z)$ in equations (16 to 18) are selected, the generated σ_{rr}, $\sigma_{\theta\theta}$ and σ_{zz} of the stress tensor take the form:

$$\sigma_{rr} = \sum_{n=1}^{\infty}\frac{B_{0n}}{r}\left[r\,\gamma_n^2\,I_0(\gamma_n r) - \gamma_n I_1(\gamma_n r)\right]\cos(\gamma_n z) + \sum_{n=1}^{\infty}\frac{B'_{0n}}{r}\left[r\,\gamma_n(2\nu-3)I_0(\gamma_n r) + (\gamma_n^2 r^2 + 4 - 4\nu)I_1(\gamma_n r)\right]\cos(\gamma_n z) \quad (20)$$

$$\sigma_{r\theta} = -\sum_{n=1}^{\infty} \frac{2(1-\nu)}{r}\Big[r\,\gamma_n I_0(\gamma_n r) - 2I_1(\gamma_n r)\Big] B''_{0n}\cos(\gamma_n z) \quad (21)$$

$$\sigma_{rz} = -\sum_{n=1}^{\infty} \Big[B'_{0n}\big(r\,\gamma_n^2 I_0(\gamma_n r) - 2(1-\nu)\gamma_n I_1(\gamma_n r)\big) + B_{0n}\gamma_n^2 I_1(\gamma_n r)\Big]\sin(\gamma_n z) \quad (22)$$

Alternatively, the abbreviated equations (20 to 22) are

$$\sigma_{rr} = \sum_{n=1}^{\infty} f(n,r)\cos(\gamma_n z) \quad (23)$$

$$\sigma_{r\theta} = \sum_{n=1}^{\infty} g(n,r)\cos(\gamma_n z) \quad (24)$$

$$\sigma_{rz} = \sum_{n=1}^{\infty} h(n,r)\sin(\gamma_n z) \quad (25)$$

where $f(n,r)$, $g(n,r)$ and $h(n,r)$ are functions of n and r only. Stresses calculated from equations (20 to 25), when $r = r_0$, must satisfy the applied stress, given by the first term in equation (1), at the boundary. With this in mind, all three constants B_{0n}, B'_{0n} and B''_{0n} for each n are then determined by solving the system of simultaneous algebraic equations as follows (Alehossein & Serati 2013).

$$f(n,r_0) = -\sum_{n=1}^{\infty} \frac{2P\left(1-\cos(n\,\pi)\right)\sin(\frac{n\,\pi}{2})}{2\pi^2\, n\, L} \quad (26)$$

$$g(n,r_0) = 0 \quad (27)$$

$$h(n,r_0) = 0 \quad (28)$$

Stress and displacement components induced in a solid disc subjected to Brazilian and point load test conditions can then be recovered by following procedures identical to those used for the $\cos(\gamma_n)$ term, extended for all the trigonometric terms in the potential functions.

3 RESULTS AND DISCUSSION

Once stresses in the (r, θ, z) domain are known, the stress components can be transformed to other coordinates, based on the contravariant transformation behaviour of elastic stress tensors. Schematic contour plots of calculated stresses in (x, y, z) and (r, θ, z) domains are shown in Fig. 2, in which dashed lines denote regions in compression (or negative values of stress components) and solid lines represent regions in tension (or positive values of stress components). Distributions of normalised σ_{xx} along horizontal and loading lines in a Brazilian specimen are illustrated in Fig. 3. The effect of Poisson's ratio and the shape effect on the tensile hoop stress induced at the centre of a point load specimen are also depicted in Fig. 4. In all figures, stresses have also been nondimensionalised for convenience in verifying the results against available solutions from experimental or 2D analytical studies (ISRM 1978, ISRM 1985, ASTM 008a, ASTM 008b), i.e. the classical suggested formula for the maximum tensile stress at the centre of a Brazilian disc (equation 29), or the point load strength index (equation 30).

$$\sigma_{t,Max} = \frac{F}{2\,\pi\, L\, r_0} \quad (29)$$

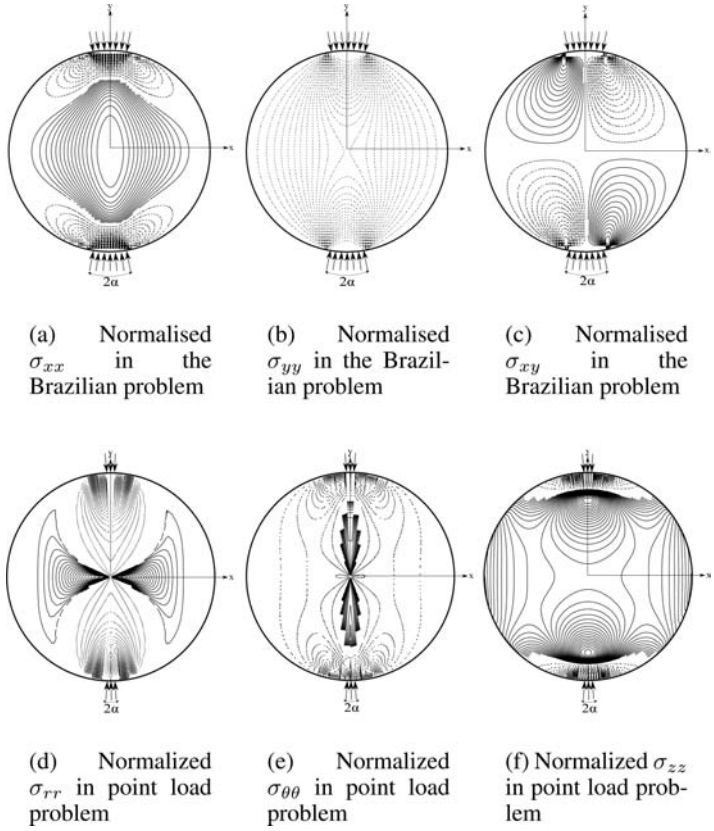
$$I_{(s)} = \frac{F}{D^2} \quad (30)$$

In equations (29) and (30), F is the applied compressive load at failure, $2L$ is the thickness of the disc, and r_0 and D are radius and diameter of the disc, respectively (see also Fig. 1).

Parametric studies of the calculated results reveal that stresses in discs with different geometries under both both Brazilian and point load boundary conditions (equations 1 and 2) always satisfy the given boundary configurations on the curved surface ($r = r_0$). Moreover, the traction-free assumption on the two ends of solid discs subjected to Brazilian and point load testing is also achieved in an average sense in the light of the Saint Venant's approximation principle, e.g.

$$\int_0^{2\pi}\int_0^{r_0} \sigma_{rz,\,(z=\pm L)}\, dr\, d\theta = 0 \quad (31)$$

Results for the Brazilian problem show that for small values of arc loading, or $2\alpha \leq 15°$, equation (29) is eventually confirmed, at which the maximum tensile stress occurs at the centre of the disc and persisting nearly uniformly in the vertical direction along the loading line (Fig. 3(b)). It is further concluded that the induced stresses are less affected by elastic material parameters and more dominated by the loading condition (e.g. the effect of 2α). That is, by increasing the loading angle, the maximum tensile stress decreases and tensile zone becomes more confined to a narrower region in the vicinity of the disc centre. This behaviour continues until $2\alpha = \pi$, at which the condition of a fully-loaded disc is met, and the stresses become equal to the applied compressive radial pressure ($-\frac{F}{2\alpha r_0 2L}$) everywhere inside the domain. The distribution and orientation of the biaxial compressive stress near the two contacts is also influenced by 2α. That is, more of the region close to the point of loading comes under high compressive stress with increasing the arc loading. In other words, for an individual material of known tensile strength and high ratio of compressive to tensile



(a) Normalised σ_{xx} in the Brazilian problem

(b) Normalised σ_{yy} in the Brazilian problem

(c) Normalised σ_{xy} in the Brazilian problem

(d) Normalized σ_{rr} in point load problem

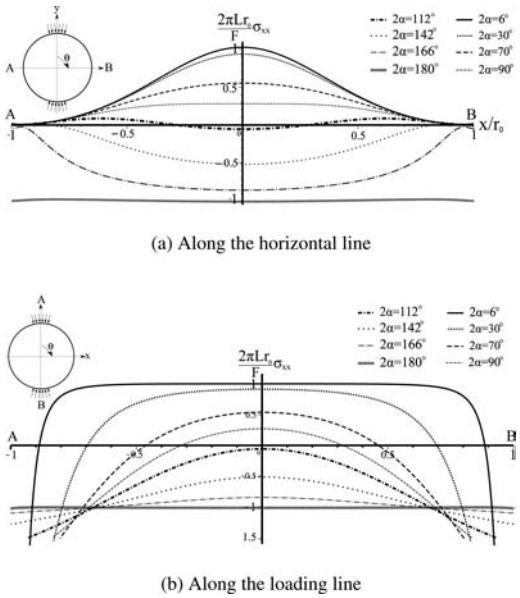
(e) Normalized $\sigma_{\theta\theta}$ in point load problem

(f) Normalized σ_{zz} in point load problem

Figure 2. Schematic contour plots of normalised stress components inside a disc sample under Brazilian and point load tractions, when $\nu = 0.25$. For the Brazilian test $2\alpha = 20^\circ$ and $r_0 = 2L$, while for the point load test, $2\alpha = 2^\circ$ and $r_0 = 0.5L$.

strength, e. g. rocks, a general increase in the tensile failure load is expected on increasing the loading angle to compensate for the decrease in the maximum induced tensile stress.

With reference to Fig. 2 for the point load problem, it can be seen that both $\sigma_{\theta\theta}$ and σ_{zz} are tensile over more that 80% of the loading line. It is also clear that the majority of the loading plane (the *xoy* plane) is under uniform tension in the z-direction. This in return can explain the published experimental results in which a disc-shaped specimen under diametrical point loading generally fails along the loading plane in a tensile fashion (ISRM 1985, ASTM 008b). Furthermore, as shown in Fig. 4, the results indicate that the hoop tensile stress at the centre of a point load specimen is affected both by the shape of the specimen (L/r_0) and Poisson's ratio of the material. The greater the Poisson's ratio, the lower the tensile induced at the centre of the disc. On the other hand, the shape of a point load specimen influences the point load strength index only if the ratio of thickness/diameter (or L/r_0) is less than one. This outcome coincides with ASTM and ISRM point load test standards (ISRM 1985, ASTM 008b), and the data provided in Fig. 4 can be considered valid for specimens with geometry of $\frac{L}{r_0} < 1$.



(a) Along the horizontal line

(b) Along the loading line

Figure 3. Variation of the normalised σ_{xx} induced in a solid disc under Brazilian testing with different loading angles (2α) when $\nu = 0.25$ and $\frac{L}{r_0} = 0.5$.

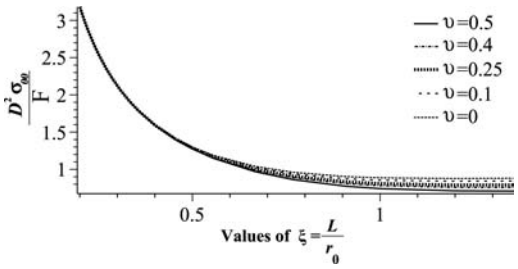


Figure 4. Variation of tensile hoop stress at the centre of a disc sample subjected to point load testing.

4 CONCLUSION

Brazilian and point load strength tests have attracted the attention of many researchers due to their extensive use in many engineering problems. In the present paper, a three dimensional elastic solution for a solid circular disc under these two testing conditions is provided. The methodology is based on the Papkovich-Neuber scheme and the double Fourier series technique. A parametric study of the influence of specimen shape, material parameters and loading configurations has been conducted in order to provide a comprehensive understanding of stresses and deformations induced in disc specimen subjected to Brazilian and point load testing.

ACKNOWLEDGEMENT

The first author acknowledges the scholarships support provided by Commonwealth Scientific and Industrial Research Organization (CSIRO) through Minerals Down Under Flagship Scholarship and the University of Queensland (UQ) through UQ Postgraduate Scholarship from the School of Civil Engineering.

REFERENCES

Alehossein, H. & M. Serati (2013). 3D Fourier-Papkovich-Neuber elastic analysis of laterally loaded circular bars. *submitted to Rock Mechanics and Rock Engineering*.

ASTM (2008a). *D3967-08: Standard test method for splitting tensile strength of intact rock core specimens*. West Conshohocken, USA: ASTM International.

ASTM (2008b). *D5731-08: Standard test method for determination of the Point Load Strength Index of rock and application to rock strength classifications*. West Conshohocken, USA: ASTM International.

Barber, J. R. (2010). *Elasticity*. Springer.

Barton, M. V. (1941). The circular cylinder with a band of uniform pressure on a finite length of the surface. *J. Appl. Mech 8*, 97–104.

Chau, K. T. (1998). Analytic solutions for diametral point load strength tests. *Journal of Engineering Mechanics 124*(8), 875–883.

Diyuan, L. & N. Y. W. Louis (2012). The Brazilian disc test for rock mechanics applications: review and new insights. *Rock Mechanics and Rock Engineering*, 1–19.

Eubanks, R. A. & E. Sternberg (1956). On the completeness of the boussinesq-papkovich stress functions. *Journal of Rational Mechanics and Analysis 5*(1), 735–746.

Hondros, G. (1959). The evaluation of Poisson's ratio and the modulus of materials of a low tensile resistance by the brazilian (indirect tensile) test with particular reference to concrete. *Aust J Appl Sci 10*, 243–268.

ISRM (1978). Suggested methods for determining tensile strength of rock materials. *Int. J. Rock Mech. Min. Sci. Geomech. Abstr. 15*(3), 99–103.

ISRM (1985). Suggested method for determining point load strength. *Int. J. Rock Mech. Min. Sci. Geomech. Abstr. 22*, 51–60.

Little, R.W. (1973). *Elasticity*. Civil engineering and engineering mechanics series. Englewood Cliffs, NJ: Prentice Hall.

Moon, P. & D. E. Spencer (1988). *Field Theory Handbook, Including Coordinate Systems, Differential Equations, and Their Solutions* (Second ed.). New York: Springer-Verlag.

Sadd, M. H. (2009). *Elasticity: theory, applications, and numerics* (second ed.). Boston, Massachusetts, USA: Elsevier, Academic Press.

Serati, M., H. Alehossein, & D. J.Williams (2012). Elastic stress analysis of partially loaded hollow discs. *International Journal of Engineering Science 53*(0), 19–37.

Simmonds, J. G. (1994). *A Brief on Tensor Analysis* (Second ed.). New York: Springer-Verlag.

Timoshenko, S. P. & J. N. Goodier (1969). *Theory of Elasticity* (Third ed.). New York: McGraw-Hill.

Wei, X. X. & K. T. Chau (2000). Finite solid circular cylinders subjected to arbitrary surface load. part II – application to double-punch test. *International Journal of Solids and Structures 37*(40), 5733–5744.

Wijk, G. (1978). Some new theoretical aspects of indirect measurements of the tensile strength of rocks. *Int. J. Rock Mech. Min. Sci. Geomech. Abstr. 15*(4), 149–160.

Youngdahl, C. K. (1969). On the completeness of a set of stress functions appropriate to the solution of elasticity problems in general cylindrical coordinates. *International Journal of Engineering Science 7*(1), 61–79.

11. Rock tunnel excavation and support

This page intentionally left blank

Rock Mechanics for Resources, Energy and Environment – Kwaśniewski & Łydżba (eds)
© 2013 Taylor & Francis Group, London, ISBN 978-1-138-00080-3

Underground construction at high altitudes: A case history on Mont Blanc in Italy

G. Bragonzi & P. Cancelli
Studio Cancelli Associato, Milan, Italy

R. Castellanza
DISAT, University Milano Bicocca, Milan, Italy

G. Frigerio
SIPOS, Terni, Italy

ABSTRACT: As a result of reaching its design life the existing Monte Bianco aerial cableway, operating on the Italian side, had to be replaced by a new one, which is currently under construction. The new aerial cable way will connect the lower station in Pontal d'Entreves (1300 m.a.s.l.) with the intermediate station at Pavillon de Mont Frety (2160 m.a.s.l.), and with the top station at Helbronner Peak (3460 m.a.s.l.). A new underground link between Helbronner Peak station to New Torino Hut (3370 m.a.s.l.) had also to be built. The link is basically composed by two sections: the first, which is a 80 meters deep vertical pit, descending underground from Helbronner Peak station, and the second which is a 160 meters long sub horizontal tunnel emerging at Torino Refuge. The vertical pit will also perform as a deep shaft foundation for the heavy loads required by rope anchors. On the top of Helbronner peak the presence of two adjacent stations (Italian and French) has led to the realization of vertical structures consisting in a series of micropiles connected in head by concrete curbs, to allow the excavation works on the Italian side without causing displacements to the existing French station. After a first introduction focused on the project general description, the paper will present the intensive geomechanical in situ and laboratory tests. Due to the necessity of ensuring coexistence between the construction works and the existing cableway serviceability (at least for the main part of the works), a series of 3D numerical analysis of the construction processes have been performed in order evaluate the force variation in the pre-tensioned anchors of the French cableway. The entire construction process has been modeled and the results was useful to support the final design of the new station leaving in service the French cableway.

1 INTRODUCTION

The new cable way will connect the lower station in Pontal d'Entreves with the top station at Helbronner Peak and its territory, as well as link with France and, through the French territory, with the town of Chamonix. The overall layout is divided into two sections (Fig. 1), the first "Pontal d'Entreves – Mont Frety" with a length of 1700 m and a capacity of 800 persons/hour, the cable cars can carry up to 80 passengers. The second one "Mont Frety – Punta Helbronner" with a length of 2630 m and a capacity of 600 persons/hour, the cable cars can carry up to 75 passengers. The new system is designed for fully rotating cable cars and the system's rated speed is a constant 9.0 m/s. The track requires constructing special line supports, three for the first section and two for the second one.

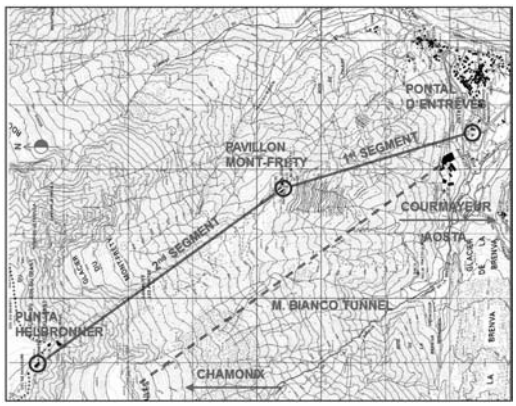


Figure 1. General framework of the area.

2 PONTAL D'ENTREVES

The location of the valley station is placed immediately downstream of Pontal d'Entreves. The design foresees the realization of underground parking. Their foundation is set at the altitude of about 1300 m a.s.l. The lowest basement, containing the winches, is located at the depth of 12 m from ground level.

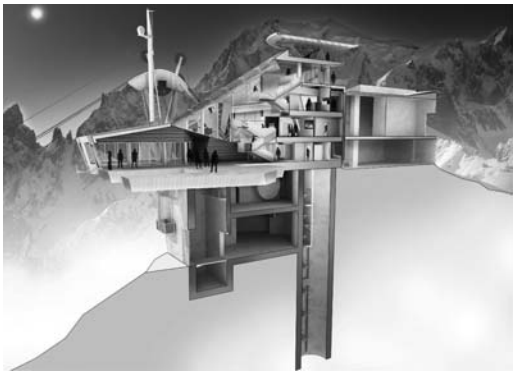


Figure 2. Upper station section.

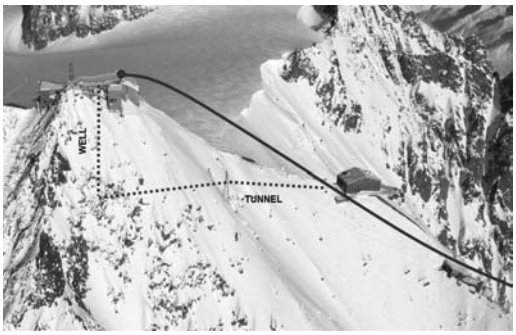


Figure 3. Schematic section of the underground link and the new cableway line (blue line).

3 PAVILLON MONT FRETY

The structure of the new intermediate station at Pavillon is placed west of the current station. The distribution of the spaces according to the new line gives rise to several leaps of the building's foundations, that imposes demanding conditions of redistribution of loads on foundations. The lowest basement is located at the deep of 11 m from ground level.

4 HELBRONNER PEAK

The upper station (Fig. 2), instead, due to the restricted space, is going to be located exactly where the current station is. Because of the extremely limited space available, the station will be constructed in a mostly vertical manner with cantilevered terraces. The entire project is developed on the various slopes as a result of the small area available on the ridge and, while to the south it borders with the Italian station overlooking the steep incline of Helbronner Peak, to the North it rests on the rocky peak right next to the French Liaison station. Since the new project will no longer stop near the Torino Refuge (3370 m.a.s.l.), a new underground link between Helbronner to Torino Hut had also to be built (Fig. 3). The facilities have the dual function of structurally anchoring the new Pointe Helbronner station to the rocky bedrock and of hosting safety staircases and elevators that will connect with the tunnel (154 m) leading to the Torino Hut. The vertical well will be approximately 70 meters deep with a finished internal diameter of 5 m and will be created using the "Raise Boring" technique, which is characterized by the integrity of the walls (since they are not affected by explosions) and by the possibility of constantly removing debris that accumulate at the base of the wells during the work. The structure therefore consolidates the whole mountain section where the new station is to be erected and allows properly anchoring the cableways load bearing structures, considering that its cables bear over 100 tons of tension each, and will be anchored to specifically designed reinforced concrete drums.

5 GEOMECHANICAL SETTING

Punta Helbronner station and the surrounding areas, including the Col de Saussure and the ridge on which take place Torino Refuge are located entirely within the Plutonic granitic – granodiorite Monte Bianco, Upper Carboniferous age. The excavation will take place entirely in the Granite of Monte Bianco.

The ridge consists of intensely fractured granitic mass. It divides the East and West sides with steep slopes, which are hosting at the current French-Italian station. Also to the South slope is nearly 70%.

The element that ensures the consolidation of bedrock and provides maximum safety to anchorages ropes is well above mentioned.

In addition to a preliminary analysis to define the initial conditions, were identified potential failure surfaces on the slopes more steep and was simulated mechanical effect that will have the new building on rocky cluster structure investigated.

The interpretation of geotechnical investigations results made it possible to define the framework of discontinuities in the rock mass and the engineering parameters usable for the design process. Were performed 4 core drilling, borehole expansion test, geotechnical survey, borehole TV camera and laboratory tests.

The borehole TV camera (Fig. 4), when the depth and transit time are known, allowed the identification and positioning of discontinuities (fractures, layers, etc.) and the acquisition of information relative to the geometric characteristics of the borehole (radius, volume, sections)

The slope stability depens on joint filling materials. Despite of the discontinuities are filled with non-systematic frequency (Fig. 5), they ensure the stability of wedge.

It was possible to recognize the presence of obvious crack patterns generally linkable with seasonal thermal fluctuations. Without significant changing stress state the slope stability is preserved. Because of, not only the new cableway, but also excavations leads to a new

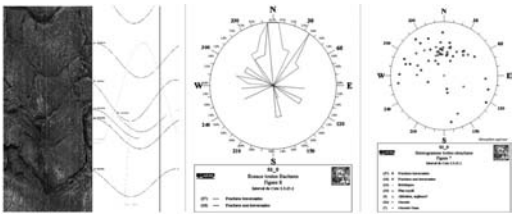


Figure 4. Report on the analysis of image product by TV camera (the rose and Wulff diagram).

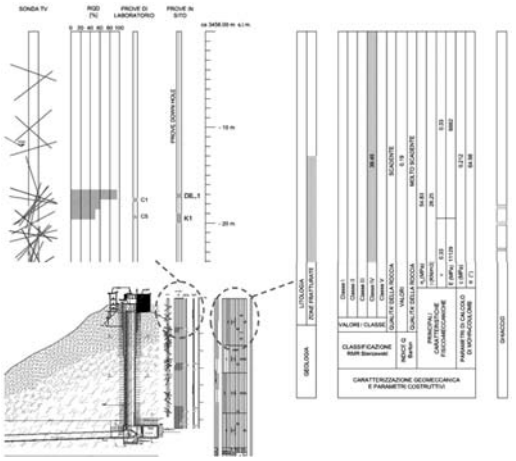


Figure 5. Geotechnical profile.

stress state, a series of 3D numerical analysis of the construction processes were performed.

6 FEM ANALYSES

Due to the necessity of ensuring coexistence between the construction works and the existing cableway serviceability (at least for the main part of the works), a series of 3D numerical analysis of the construction processes have been performed. In particular the goal of numerical analyses is to evaluate the force variations in the pre-tensioned anchors of the French cableway that should be maintained in service during the entire construction stages of the new Italian cableway.

A continuum numerical model based on the 3D finite element analyses has been chosen and the 3D MIDAS GTS code is used. As shown in the following pictures the entire excavation process has been simulated. Despite the presence of several families of joints the continuum approach has been preferred for the level of accuracy in the 3D geometry that allow this method. Of course the equivalent continuum rock mass properties have been evaluated by using the Hoek-Brown criterion that consider the GSI value. The adopted parameters are show in Table 1.

Table 1. Parameters of rock mass.

σ_{ci}	MPa	55
GSI	–	53
m_i	–	33
D	–	0.7

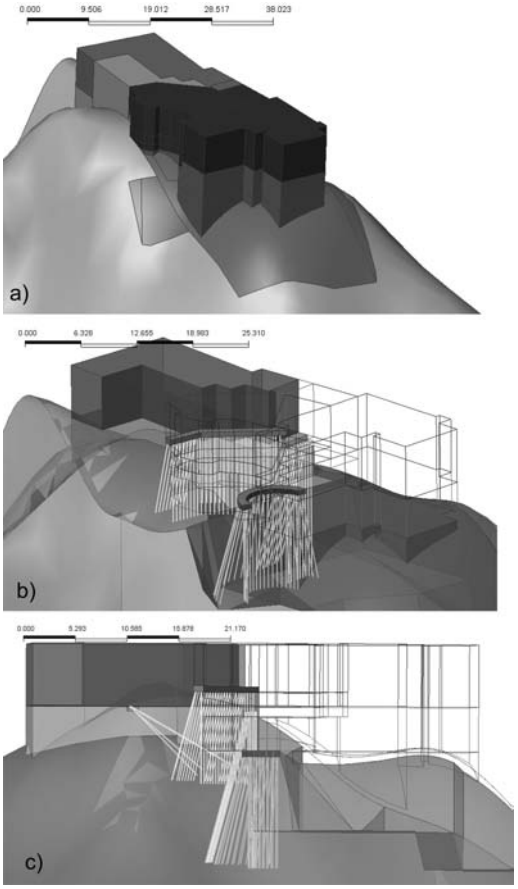


Figure 6. 3D geometrical model.

6.1 *3D geometrical model, construction stages and mesh*

In Figure 6 are reported some pictures about the 3D model of French and Italian cableways (Fig. 6a). The main structural and geotechnical works of this project are represented by three foundations formed by micropiles that will allow the security of the French cableway during the excavation phases (Fig. 6b). In particular, the French cableway anchors located behind the future excavation should not undergo tensional variations due the works phases (Fig. 6c).

The numerical modelling has taken into consideration the main phases of works: in Figure 7 are reported the construction stages: 7a) current state; 7b) initial demolition of Italian cableway and realization of first

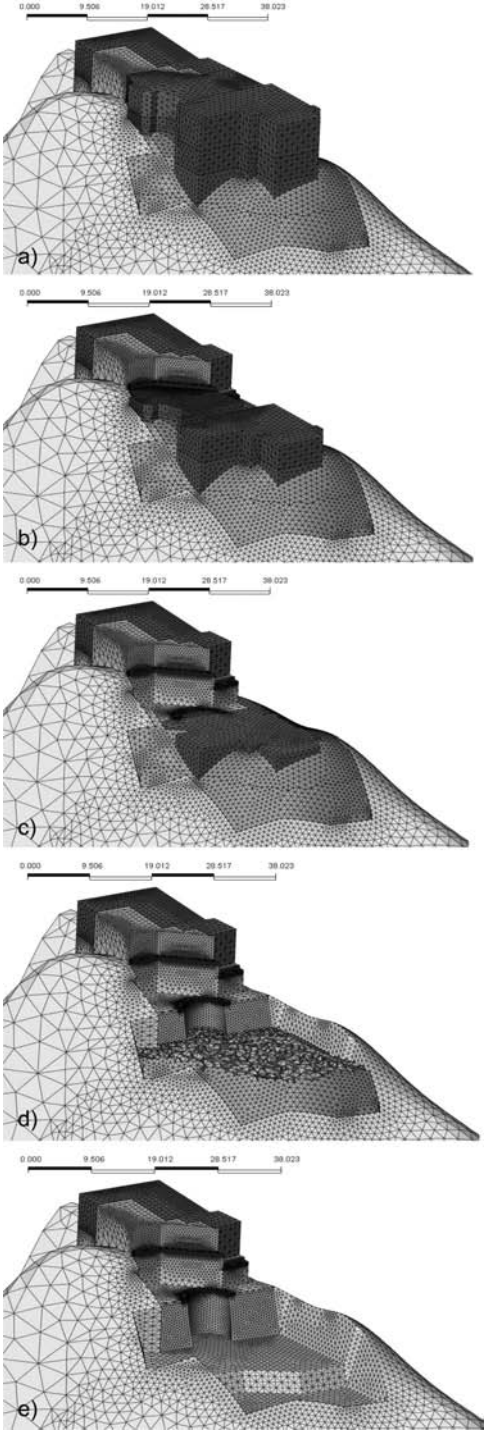


Figure 7. Construction stages: activated mesh.

two sets of micropiles; 7c) completion of demolition of Italian building, excavation and realization of third set of micropiles; 7d, 7e) rock excavation.

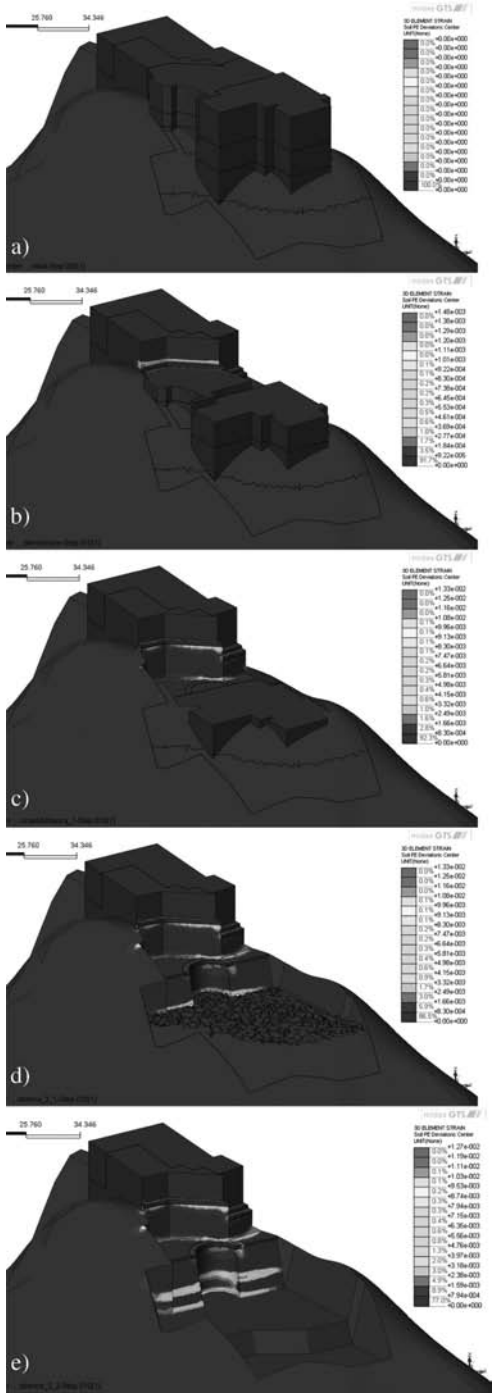


Figure 8. Construction stages: plastic strains.

6.2 *Numerical results*

The numerical results of elastoplastic analysis are reported in Figure 8 (plastic strains) and Figure 9 (displacements) for each of the construction stages shown in Figure 7.

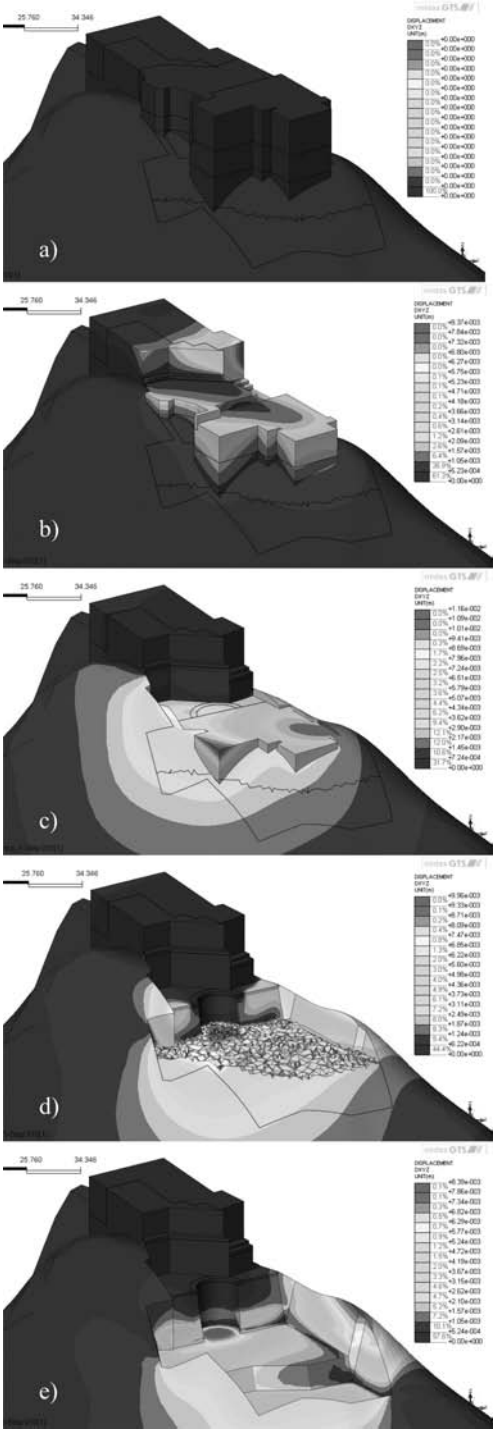


Figure 9. Construction stages: displacements.

In the first stage of analysis (Fig. 9a) the displacements due to the gravity have been deleted.

In Figure 7b is possible to note the displacements due to the initial demolition of Italian cableway: the

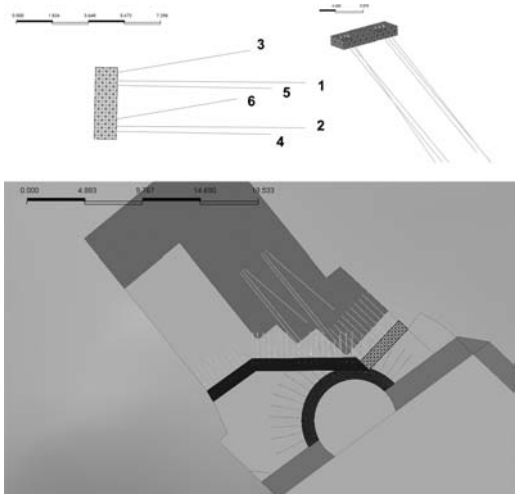


Figure 10. French cableway anchors.

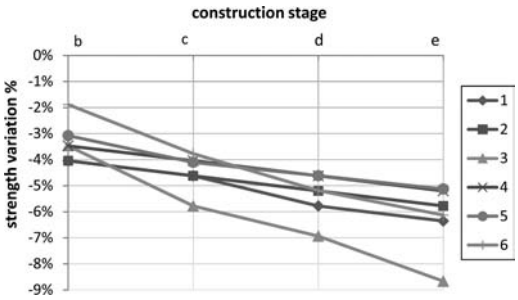


Figure 11. Strength variation % of French cableway anchors during the construction stages.

displacements are lower than 1 cm. At this time of works there is the realization of the first two set of micropiles necessary for the next steps of excavation. In the numerical analysis, after the stage b, have been reset the displacement in order to view displacements only due to the next rock excavation stages after the realization of micropiles.

The French cableway is currently anchored in rock mass by 10 anchors; six of this ten are located behind the Micropiles that will be realized (Fig. 6c and Fig. 10). The anchors not have the same geometry: anchors 1and 2 are longer and have a lower dip inclination therefore seem to interact more with micropiles.

In particular the goal of numerical analyses is to evaluate the force variations in the pre-tensioned anchors of the French cableway that sure be maintained in service during the entire construction stages of the new Italian cableway (Fig. 11).

In Figure 11 the numerical result shows that for all anchors there is a loss of tension strength in a range of 5–6% excluding the anchor 3 for which this reduction is approximately 9%.

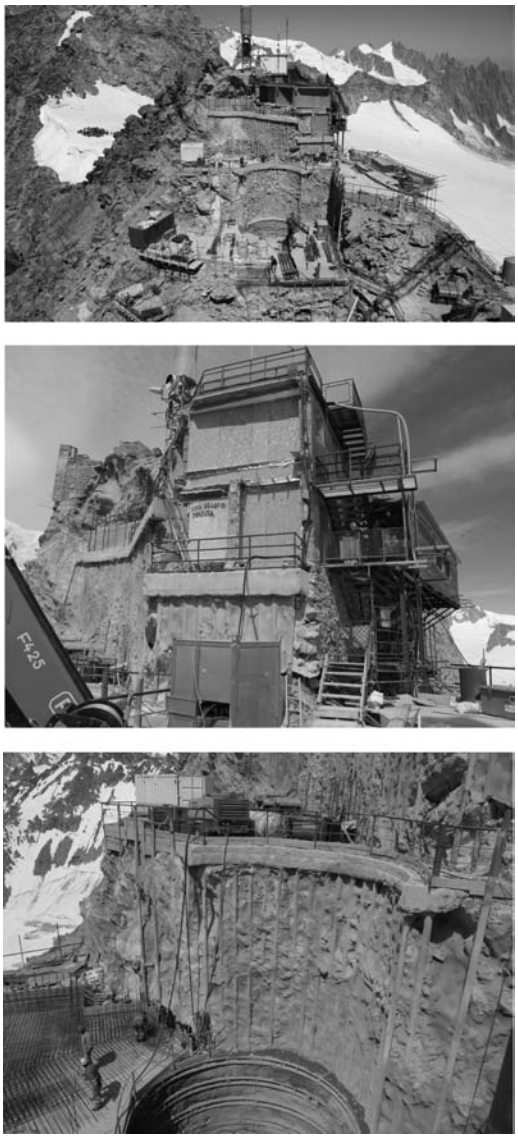


Figure 12. Picture of the works at Helbronner Peak.

7 CONSTRUCTION WORKS

Below there are some pictures of works in progress in Helbronner Peak, related to the construction stage shown in Figure 7e.

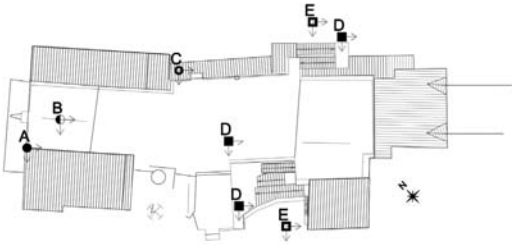


Figure 13. Monitoring instruments.

8 MONITORING SYSTEM

The first monitoring system was installed in April 2007. In 2011 additional tools (Extensometer and Extensoinclinometer) were added at the beginning of excavation. In June 2012 new extensoinclinometers for boreholes close to the micropiles wall were installed.

The monitoring network installed is shown in Figure 13. 'A' Inverted pendulums; 'B' Electric level; 'C' Joint meter; 'D' Inclinometers for bore holes; 'E' Long-base extensometer.

9 CONCLUSIONS

In the present work the main aspects of the construction design, geomechanical characterization and numerical analyses has been presented.

The entire process of the 3D construction stage excavation has been modeled in detail with a FEM continuum approach in order to evaluate the force variation in the pre-tensioned anchors of the French cableway. A limited variation of 9% has been predicted so that the construction work are going ahead according the final design.

All sensors are connected to two automatic data acquisition unit, equipped with a GSM modem for remote transmission of data. The measurements obtained are contained within a range of 3.5–4 mm.

Rock Mechanics for Resources, Energy and Environment – Kwaśniewski & Łydżba (eds)
© 2013 Taylor & Francis Group, London, ISBN 978-1-138-00080-3

Evaluation of geological conditions ahead of a tunnel face using the Tunnel Seismic Prediction method (TSP) – Lesson learned from the Pahang-Selangor raw water transfer tunnel, Malaysia

M.A.M. Ismail, R. Azit & S.M. Ng
School of Civil Engineering, Universiti Sains Malaysia

H. Zabidi
School of Materials and Mineral Resources Engineering, Universiti Sains Malaysia

N. Bakhudin
Shimizu-Nishimatsu-UEMB-IJM (SNUI) Joint Venture, Hulu Langat, Selangor Malaysia

Z. Nordin
Phang-Selangor Raw Water Transfer Tunnel Project, Ministry of Energy, Green Technology and Water, Cyberjaya, Selangor Malaysia

ABSTRACT: In this study, Tunnel Seismic Prediction method (TSP) was used to predict the geological condition ahead of the tunnel face. The tunnel which extends 44.6 km is intersected by several major faults and few lineaments. The ability of the TSP system was investigated to predict one the anticipated fault which had been inferred from the geological map. Then, the TSP results were applied to delineate the relation between seismic velocities and geological parameters for the predicted fault ahead of the tunnel face. The results show a velocities drop 10 to 40 m ahead of the tunnel face which had indicated the initial findings of the unfavorable geological condition from geological map. From the verification analyses, the TSP results are substantially correlated with the Tunnel Boring Machine (TBM) driving data, geological mapping, rock class grade point and uniaxial compressive strength obtained using Rock Schmidt Hammer. In this case, the TSP was a helpful tool for the tunnel contractor in predicting zones of geological instabilities during the excavation process of long deep tunnel. Thus, such prediction method can be used as a decision support in the observational design and construction system especially in determining suitable tunnel support system in the expected unfavourable geological conditions.

1 INTRODUCTION

The tunnel boring machine has been used all over the world because of its advantages such as higher excavation advance rate compare to drill and blast, smooth tunnel face which lead to less excavation disturbed zone and suitable to be used for long tunneling, thus reducing the number of adit of shaft that need to be constructed. However, if there is some unfavorable geological conditions such as collapse, overbreak, or weak zone due to the existence of faults and fractured zones, the progress of the excavation is disrupt, making it impossible to fully achieve the high advance rate capability of the TBM. It is important, especially in the construction of long tunnel like Gotthard Base Tunnel and Seikan Tunnel that have hugh challenge due to its complex and changing geological conditions to have a reliable and detailed information of the ground conditions especially ahead of the tunnel face to foresee any ground diificulties that might be encountered and to prepare appropriate countermeasures to lease the effects.

To predict the geological condition ahead of the tunnel face, many researchers have developed the TBM excavation control and monitoring system (Shirasagi et al. 2000), which can combine the results of the drill logging (Aoki et al. 1990), TBM driving data, an amount of muck measured by conveyer belt scales (Inou et al. 2001). A ground evaluation method based on the state of muck is developed (Inou et al. 2000) and display in one system to predict geological conditions ahead of and surrounding the tunnel face and to help the TBM operator to control excavation. Furthermore, to link the various data derived from excavation, Yamamoto et al. (2003) have developed the comprehensive geological evaluation methods by calculating the rock mass grade from drill logging data and TBM driving data. In addition, geostatistical method, for instance Kriging and Sequential Indicator Simulation are applied to create distribution maps of rock mass properties to visualize the probability distribution of weak rock (Mito et al. 2003).

The prediction method as discussed above assess the rock mass properties samples directly and therefore

can determine the rock mass properties with relatively high precisions. However the prediction system based on the information such as from probe drilling can be time consuming, costly and the data obtained is limited to 20–40 meters ahead of the tunnel face with point wise information. To speed up the evaluation process, a non-destructive geophysical methods such as seismic reflection and refraction have been developed and improved significantly in the recent years.

Although the geophysical methods bear low costs and can be carried out faster than probe drilling, the results should be intepreted carefully due to the nature of the method which cannot access the rock samples directly. Thus, the verification of the seismic results with the TBM driving data and tunnel face mapping is essential in the observational design and construction method.

In the long tunnel alingment, the seismic reflection method are normally used to predict the geological condition ahead of the tunnel face at the anticipated faults, lineaments or when there is a significant changes in topographical condition and tunnel overburden (Murakami et al. 2002).

2 OVERVIEW OF THE PAHANG-SELANGOR RAW WATER TRANSFER TUNNEL

The Pahang Selangor Raw Water Transfer Tunnel is located in the central zone of Peninsular Malaysia. The project is to convey and transfer raw water from the Semantan River through a transfer tunnel to the Selangor/Kuala Lumpur region for domestic and industrial uses to mitigate future water shortages. The project is divided into four construction while lot 1-1 consist of a 44.6 km long water transfer tunnel contracted to joint venture company of Shimizu Corporation, Nishimatsu Construction, UEM Builders Bhd and IJM Construction (SNUI JV). The long tunnel is divided into seven faces, three long TBM drives of 11.77 km, 11.80 km and 11.30 km, from Adits 4, 3, and 2 respectively, plus four NATM headings, one in each direction from Adit 1 upstream, another from the inlet to Adit 1, and the fourth from the outlet portal to Adit 4 (Fig. 1).

The first 5.2 m diameter TBM was launched on November 10, 2010, followed shortly after by the second on December 30, 2010. The third machine began boring in March 2011. Tunneling is taking place in the high overburden up to 1200 m (3900 ft) below the Titiwangsa Mountain Range. The main rock type is granite which forms several batholitic intrusions collectively termed the main range granite. The petrology varies but in general a medium to coarse grained porphyritic biotite quartz biotite granite. This is of Paleozic Age (about 200 m.y. age) and intrudes rock of the Silurian age Karak Formation. Due to the existence of multi-topograhical scale from shallow (12 m) to very high tunnel overburden (1246 m) the tunnel alignment is intersected by several major geological structures (i.e. Krau Fault, Karak Fault, Bukit Tinggi fault, Kongkoi Fault, Tekali fault and a few lineaments) with various lithilogies units (Fig. 2). Thus, the tunneling project serve as an excellent test site for the prediction of geological condition ahead of the tunnel face using the seismic method. The tunnels are being supported with ring beams, rock bolts, and shotcrete depending on the conditions. The subsequent data is taken from TBM-3 heading on December 2011 where the measurements are carried out to predict the geological over break.

3 METHODOLOGY

In this study, the TSP system is used to forecast the geological condition ahead of the tunnel face and the later obtained findings from real geology and rock mass condition such as TBM driving data, Rock Schmidt hammer and rock class grade point obtained from tunnel side wall mapping and rock mass classification system were used to verify the forecasting geological condition obtained by TSP.

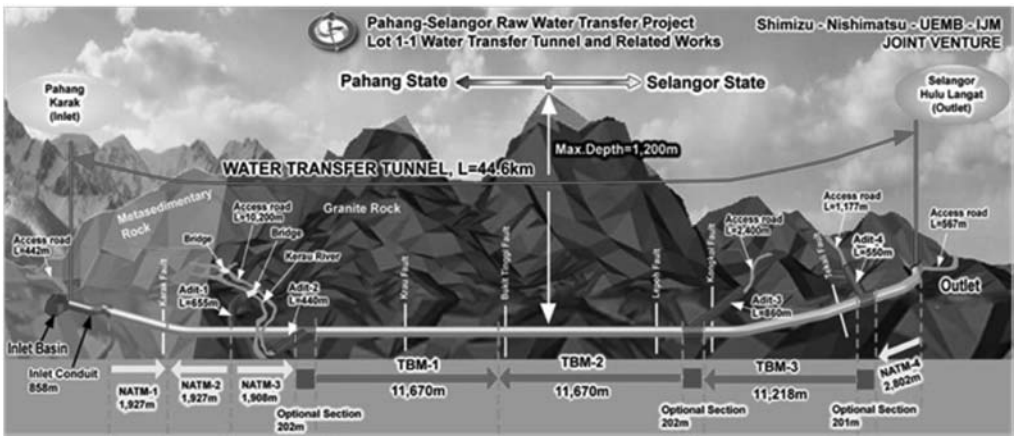


Figure 1. Tunnel structure of Pahang Selangor Raw Water Transfer Tunnel (Tsuri 2008).

3.1 *Tunnel Seismic Prediction*

Tunnel Seismic Prediction system is used to obtain the position of fracture zone and geological features 100 m to 150 m ahead of the tunnel face (Yamato et al. 2001). A sequential detonation of small charges embedded in the rock along the tunnel wall creates acoustic signal, spherical seismic wave fronts will propagate through the rock mass and the ground in the form of body wave such as compression (primary) or shear (secondary) wave. Any changes in rock strength or mechanical properties for example at fracture zones or at changes of rock formations will reflect a certain portion of the signals and the remaining portion will be transmitted as shown in Figure 3. The time taken for the reflected signals to arrive back at the highly sensitive receivers is measured. The transmission velocity, delay time, waveforms, and direction of the echo signal are proportional to the properties and distribution of the corresponding rock (Chen et al. 2011).

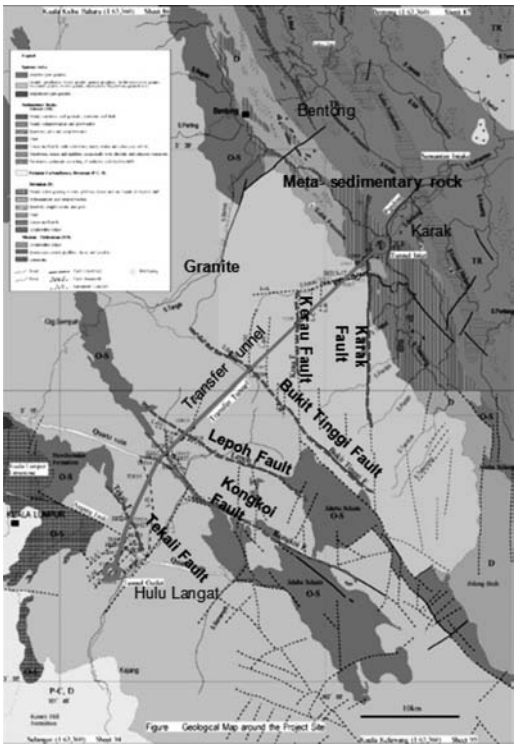


Figure 2. Geological condition along the tunnel alignment.

Seismic body waves passing through homogeneous, isotropic media have well-defined equations of motion (Keaton 2009). Utilizing these equations, computations for the wave speed may be uniquely determined. The field surveys can readily obtain primary and secondary wave velocities, V_p and V_s. A homogeneous isotropic medium's engineering properties of Young's or elastic modulus (E) and shear modulus (G) and either density (r) or Poisson's ratio (υ) can be determined, if V_p and V_s are known.

$$\upsilon = \frac{(V_p / V_s)^2 - 2}{2[(V_p / V_s)^2 - 1]} \tag{1}$$

$$E = \rho V_p{}^2 \frac{(1-2\upsilon)(1+\upsilon)}{1-\upsilon} \tag{2}$$

$$G = \frac{E}{2(1+\upsilon)} \tag{3}$$

$$\rho = \frac{G}{V_s^2} \tag{4}$$

3.2 *TBM driving data*

TBM data consist of thrust load, cutter torque, penetration rate, cutter revolutions, and muck amount are generated during the TBM excavation. These data can be used to perform real time calculations of the rock

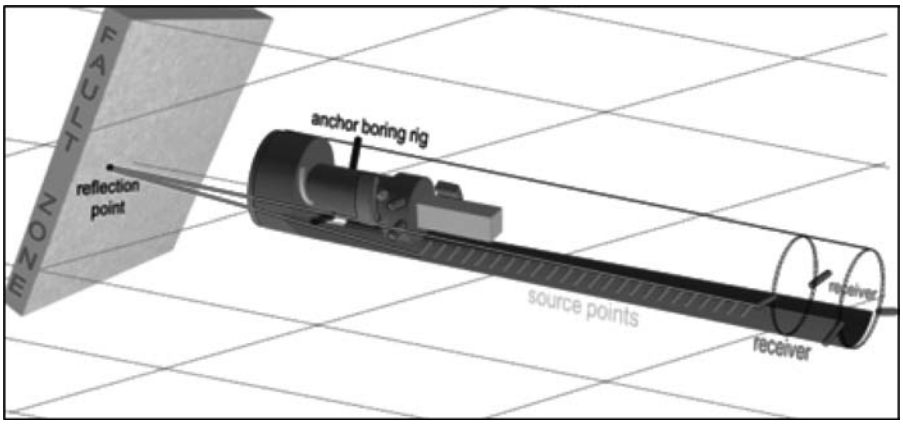


Figure 3. Standard Tunnel Seismic Prediction layout in TBM tunneling. The acoustic waves released by small explosive charges (only wave rays shown) hit a geological discontinuity (e.g. fault zone) and are being reflected and then picked up by the 3-component receivers (Dickmann & Pittard 2012).

mass strength value, σ_c proposed by Fukui et al. (2000) and excavating energy, Q_v as proposed by Yamamoto et al. (2003).

$$\sigma_c = \frac{F_N}{C \times P_e} \tag{5}$$

where $F_N =$ resultant thrust force; $P_e =$ penetration rate; and $C =$ constant.

$$Q_v = \frac{F}{A} + 2\pi N \frac{T_r}{A \times V} \tag{6}$$

where $F =$ thrust load; $A =$ are of cross section of TBM; $N =$ cutter revolutions per minutes; $T_r =$ cutter torque; $V =$ excavation speed.

TBM driving data is collected during the excavation of TBM. TBM automatically record and save the data to server when it operates. The data consist of the data such as TBM boring energy, TBM cutter head thrust force, TBM cutter head revolutions, TBM stroke speed and TBM penetration rate. The data is collected when the cutting wheel of TBM face is in operation to excavate the rock and recorded in real time as the tunnel moving forward.

3.3 *Rock Schmidt Hammer test*

Rock Schmidt hammer test obtained the compressive strength of the rock condition by pushing the hammer towards the tunnel wall (Aydin 2009, Hack & Huisman 2002). The extent to which this energy is recovered depends on the hardness of the material, which is expressed as a percentage of the maximum stretched length of the key spring before the release of the piston to its length after the rebound. The rebound number is shown on the hammer after the plunger is pressed against the rock mass. Using the correlation chart to estimate joint wall compressive strength from Schmidt hardness (Hoek 2007), the uniaxial compressive strength is then calculated from the rebound number shown on the Schmidt hammer. When applying the Schmidt Hammer test, the tunnel wall must be in intact and representative of the rock mass domain. The rock must be free of other material that will affect the reading such as shotcrete. It is also essential that the hammer be held in right angle, there is a danger of frictional sliding of the plunger tip, material removal by chipping and a partial transfer of energy to and from the hammer if the hammer is not held properly.

3.4 *Rock class grade point*

Rock class grade point is determined based on the Japanese Highway Public Corporation Rock Mass classification system or referred as JH Classification system. The classification system described a quantitative method for describing the quality and strength of the rock mass by obtaining the grade point from the geological observation of parameters such as rock strength from uniaxial compressive strength (UCS) test, point load or UCS by Rock Schmidt Hammer, weathering and alteration of rock, spacing of discontinuities, condition of discontinuities, groundwater condition, orientation of discontinuities and degradation of rock. The comparison of rock conditions between JH classification systems with Rock Mass Rating system (RMR) which is widely used for underground construction is shown in Table 1.

Table 1. Comparison between JH and RMR rock classifications and conditions.

JH	Rock conditions	RMR	Rock conditions
A	Very good rock, hard and fresh	I	Very good rock
B	Good rock, hard and fresh but affected by weathering	I–II	Good rock
CI	Fair rock, rock is weathered	II	Fair rock
CII	Fair to poor rock weathered	III	
DI, DII	Very poor rock	IV–V	Poor rock
E	Fault and crushed rock zone	V	Very poor rock

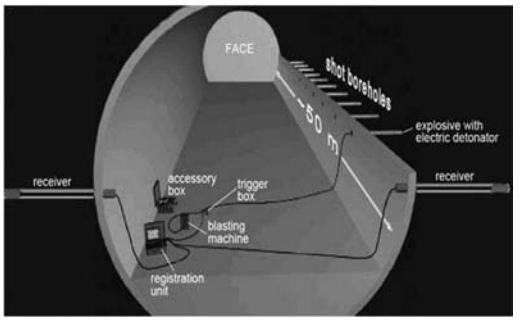


Figure 4. TSP shot holes and data acquisition layout (after Dickmann 2008).

3.5 *Aspect data processing and evaluation in TSP*

TSP is carried out by a sequential detonation of small charges embedded in the rock along the tunnel wall. Usually, the seismic data acquisition will be carried out with a layout consisting of one shot profile (line up of shots) on either the right or the left side of the tunnel according to the main strike direction of rock boundaries as shown in Figure 4.

The measurement profile such as the position of receiver and shot hole need to be determined at the preliminary stage. For measurement profile marking, the chainage of the TBM face is determined first as it will be for the scheduled TSP measurement. The receiver position is defined by approximately 55 m back from the TBM face. The reference location (REF) on the tunnel axis to link the relative coordinate system (X, Y, Z) of the TSP measurement within the global coordinate system of the tunnel is defined afterwards.

All receiver and shot positions have to be defined relative to the reference location (REF). For simplification, the REF position is set to the receivers point and fixed it as zero point. Relevant receiver and shot hole positions are defined according to the standard layout. The distance between the receiver and the first shot hole should be in the range of 15–20 m. The interval between shot points should be approximately 1.5 m, but can be less if TSP measurement layout is imperative due limited space. 24 shot holes with minimum penetration of 1.5 m into the tunnel side wall were drilled with 32 to 45 mm in diameter and 1.5 m spacing. Two receiver boreholes, one placed at left wall and one at right wall are drilled with approximately 1.5 m in depth and 45 mm in diameter.

To performed TSP measurement, the recording unit and laptop are set up for data acquisition. The receivers are installed before starting the recording unit and laptop was connected to the recording unit. The shot hole is charged afterward, detonating-cord and blasting cap is connected together and the hole is filled by water for tamping reasons. After the shot hole is blasted, the data is acquired using the TSPwin software.

The TSPwin software has a flexible ways of data visualization and straightforward user interaction guiding the operators of the software from data acquisition, data analysis until final results output and present the results in a comprehensive manner. When all process or procedures of analysis are completed, results which include the P-wave velocities, V_p to V_s ratio, Poisson ratio, Density, Dynamic Young Modulus, Static Young Modulus, Shear Modulus and Bulk Modulus will be obtained and presented. A longitudinal view showing the extracted reflector segments extracted for P, SH and SV wave type with their extrapolated intersection points to the tunnel axis and plan view showing the computed strike angles for each reflector segment with a fixed length and centered at the tunnel will be presented.

4 RESULTS AND DISCUSSION

4.1 *Prediction result using TSP*

The forecast results of TSP prediction and the latter findings of real rock mass/geological conditions are presented in Figure 5. The results are divided into three sectors. The upper sectors show the results from the TSPwin software. The results reflect the curve progression of the rock parameters along the tunnel axis such Primary waves (P-waves) velocity, V_p–V_s ratio, Poisson Ratio, Density and Dynamic Young's Modulus. Meanwhile, the red line indicates result from left receiver which is in line with the shot holes location and the blue line indicates the result of the receiver on the right of the side wall. At the time of measurements, the tunnel face was at TD 185 m. The measured P-wave velocity in the area of moderately jointed granite was 5000 m/s from TD 116 m to TD 185 m. Beyond this area, the velocity drop to about 4300 m/s. This indicates the rock mass condition beyond TD 185 m to TD 220 m is likely to be less favorable in term of rock mass strength and the overall geological conditions. The result of V_p–V_s ratio show a increasing value from TD 190 m to TD 220 m which might indicate the presence of water bearing zone due to the nature of Vs (shear waves) which does not propagates through fluid. The Poisson ratio is the ratio of transverse strain to longitudinal strain. The value of Poisson ratio is higher between TB 195 m to TD 220 m which might indicate the changes in rock mass quality. At TD 210 m, the density of the rock further decreases and indicates the rock is weak and poor. The value of dynamic Young's modulus also decreases at the between TD 190–220 indicating high possibilities weaker rock mass.

4.2 *Verification of the predicted TSP result*

The lower sector of Figure 5 contains information of rock properties from the TBM driving data. The TBM driving data can be regarded as the continuous measure of rock mass properties. It was used to validate the results of TSP obtained before excavation. The boring energy graph show a good correlation with the TSP results whereas the consumed energy to excavate the rock drop down at the area of TD 185 m to TD 220 m, indicates the rock is poor and the energy consumed to penetrate the rock is thus lesser. The second graph in the sector is the cutter head thrust force, the value of cutter head thrust force show significant decreases beyond TD 175 m to TD 220 m indicating the rock in the region is weaker and required lesser additional force from TBM to penetrate through. The penetration of the TBM tells the rate of TBM penetrate through a unit volume of rock in a revolution of cutter head. The penetration graph point out the area of weak rock at TD 175 m to 210 m as the value of the graph increases sharply at the region. From the TBM data, comparison is made and the results of TSP can be said to be in good correlation with the TBM data.

The last sector of the Figure 5 includes the description and details of the geological findings from rock class grade point (from JH classification system), UCS (from Rock Schmidt Hammer) and tunnel face mapping. The first information is the uniaxial compressive strength obtained from the Rock Schmidt hammer test. It can be clearly seen from the UCS graph where the value drops to about less than 10 MPa at the region of TD 175 m to TD 210 m. This explained the existence of weak rock mass zone in this area. As from the second graph, the rock class in the extent of TD 175 m to TD 210 m is very poor. The rock class grade point reduced from about 60 in the slightly weathered area to 18 grade points in the fault zone. The important geological information is mapped in the geological tunnel plan. The details and features of rock condition were described in the mapping, the map show the encountered fault zone and geological overbreak in extent from TD 185 m to TD 210 m.

The result from the TBM data and geological findings validate the prognosis of TSP and show good correlation and agreement within the three different

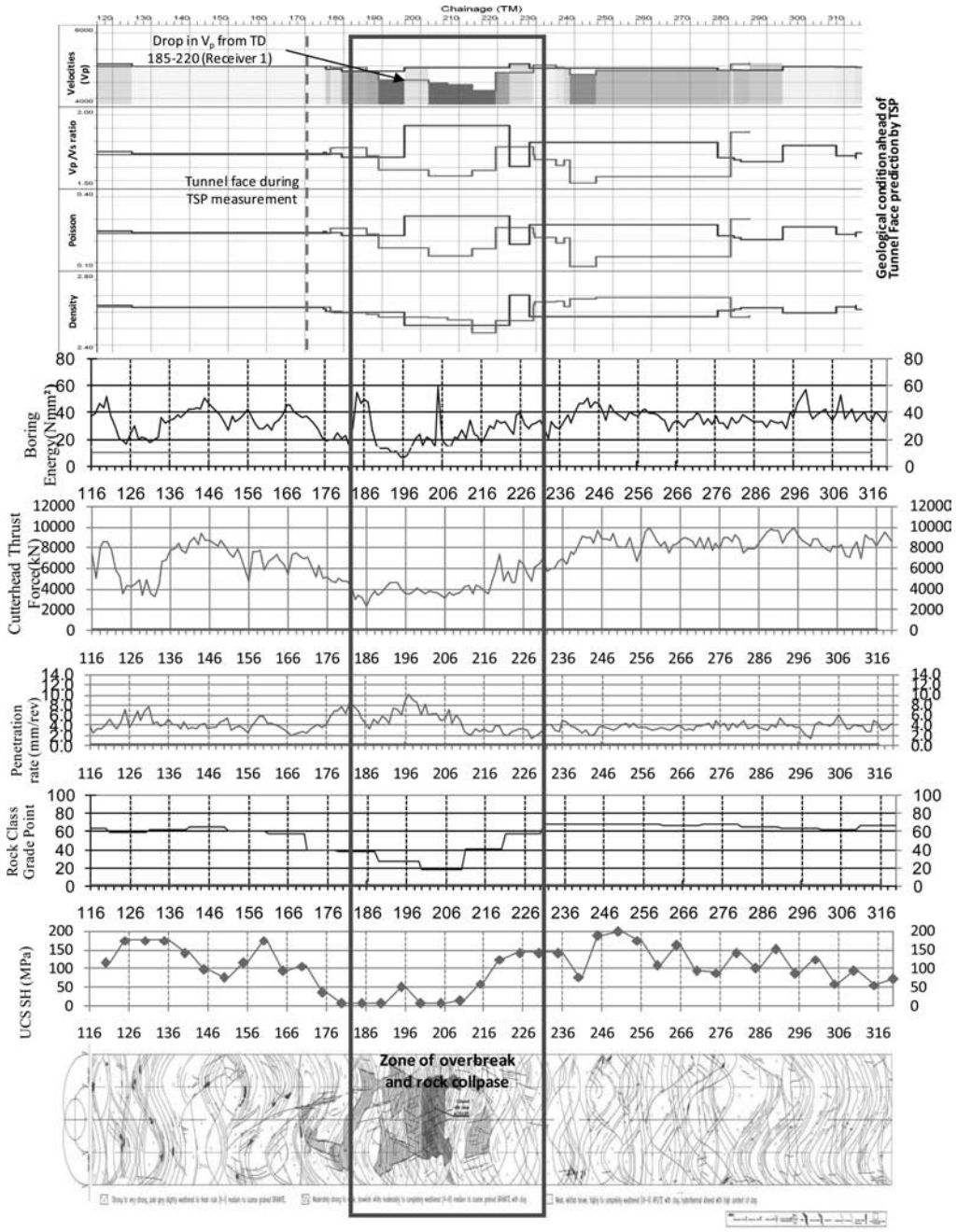


Figure 5. Result of TSP and correlation with TBM driving data, rock mass rating and geological mapping.

types of data. The closely jointed and highly weathered granite zone (which contributed to small collapsed) exists in the region of TD 185 m to TD 210 m. The TSP did predicted changes of weaker rock properties in this region and from that result, the engineer has a view of ground condition to be excavated and appropriate action has been taken to protect the TBM and the tunnel itself.

5 CONCLUSIONS

In this study, it is achieved to apply the Tunnel Seismic Prediction to predict the geological conditions ahead of the tunnel face. The TSP results show good agreement with the latter empirical data and geological findings based on TBM driving data, rock strength, rock mass rating and geological mapping. The TBM

data and geological observation show the weak rock area in the region of TD 185 m to TD 210 m. The prognosis of TSP before the excavation gave an early information of rock condition in the extent and this allow the engineer to take appropriate action to protect the tunnel by predetermined the suitable support and mitigate the risk of collapse and thus save the construction time and cost.

The advantages of this prediction are:

i) The construction of tunnel can be improved by predicting the geological condition in high accuracy in real time.
ii) The risk management system and planning judgment can be established earlier before any adverse ground condition is encountered.

In short, this system contributed to realize a more advanced observational design construction method and the implementation of reasonable TBM construction method in long deep tunnel construction.

ACKNOWLEDGEMENT

The authors gratefully acknowledge the support by Pahang-Selangor Raw Water Transfer Project, Ministry of Energy, Green Technology and Shimizu-Nishimatsu-UEM and IJM Joint Venture. The authors also greatly appreciate the financial assistance from USM Short Term Grant and Special Research Program for Alumni Members Grant (under AUNSEED-Net JICA Project) that made this research possible.

REFERENCES

Aoki, K., Mito, Y., Yamamoto, T. & Shirasagi, S. 2007. Geostatistical evaluation of the mechanical properties of rock mass for TBM tunnelling by seismic reflection method. *Rock Mech. Rock Engng.* 40(6): 591–602.

Amberg Technologies AG. TSP 203*PLUS* Field Operation & Data Acquisition Manual Version 2.7.

Amberg Technologies AG. TSPwin PLUS Processing & Evaluation Software Manual Version 2.6.

Aydin, A. 2009. ISRM Suggested method for determination of the Schmidt hammer rebound hardness: Revised version. *International Journal of Rock Mechanics and Mining Sciences* 46: 627–634.

Chen, G., Wu, Z., Wang, F. & Ma, Y. 2011. Study on the application of a comprehensive technique for geological prediction in tunneling. *Environmental Earth Sciences* 62(8): 1667–1671.

Dickmann, T. 2008. Theoretical and applied case studies of seismic imaging in tunnelling. *Geomechanics and Tunnelling* 1(5): 436–441.

Dickmann, T. & Pittard, F. 2011. An engineering view of the seismic prediction during tunnelling. In Q. Qian & Y. Zhou (eds), *Harmonising Rock Engineering and the Environment, Proceedings of the 12th International Congress on Rock Mechanics*: 953–956. Leiden: CRC Press/Balkema.

Hack, H.R.G.K. & Huisman, M. 2002. Estimating the intact rock strength of a rock mass by simple means. In J.L. van Rooy & C.A. Jermy (eds), *Engineering Geology for Developing Countries, Proceedings of 9th Congress of the International Association for Engineering Geology and the Environment*: 1971–1977. Durban: South African Institute of Engineering Geologists (SAIEG).

Hoek, E. 2006. *Practical Rock Engineering,* URL: http://www.rocscience.com/hoek/corner/Practical_Rock_Engineering.pdf (accessed on November 2012).

Inou, M., Yamamoto, T., Shimodera, S. 2001. Evaluation method for tunnel face using muck weight by TBM's excavation (in Japanese). In *Proc. of the 56th JSCE Annual Meeting*: 104–105. (in Japanese)

Inou, M., Miura, S., Yamamoto, T., Kuronuma, I. & Tanaka, H. 2000. Development of evaluation methods for tunnel face using muck by TBM's excavation. In *Proc. of the 55th JSCE Annual Meeting*: 116–117. (in Japanese)

Keaton, J.R. 2009. Rock Quality, Seismic Velocity, Attenuation, and Anisotropy (a book review). *Environmental & Engineering Geoscience* 15(1): 50–52.

Mito, Y., Yamamoto, T., Shirasagi, S., Aoki, K. 2003. Prediction of the geological condition ahead of the tunnel face in TBM tunnels by geostatistical simulation technique. In *Technology Roadmap for Rock Mechanics, Proceedings of the 10th International Congress on Rock Mechanics* 1: 683–688. Johannesburg: The South African Institute of Mining and Metallurgy.

Murakami, K., Murayama, M., Terada, K., Fuke, Y., Miyajima, Y. & Aoki, K. 2007. Development and application of the new TBM risk management system. In J. Barták et al. (eds), *Proceedings of the World Tunnel Congress 2007 and 33rd ITA/AITES Annual General Assembly*: 833–836. London: Taylor & Francis.

Shirasagi, S., Yamamoto, M., Mito, Y., Ashraf, M. 2011. The intergrated prediction system for geological conditions ahead of tunnel faces. In Q. Qian & Y. Zhou (eds), *Harmonising Rock Engineering and the Environment, Proceedings of the 12th International Congress on Rock Mechanics*: 1809–1812. Leiden: CRC Press/Balkema.

Tsuri, T. 2008. Detailed Engineering Design Report. Part 5: Water Transfer Tunnel. Tokyo Electric Power Services Co., Ltd.

Yamamoto, T. Shirasagi, S., Inou,M., Aoki, K. 2001. Correlation with various systems for forward prediction of geological condition ahead of the tunnel face. In P. Särkkä & P. Eloranta (eds), *Rock Mechanics – A Challenge for Society*: 393-398. Lisse: Swets & Zeitlinger.

Yamamoto, T., Shirasagi, S., Yamamoto, S., Mito, Y., Aoki, K. 2003. Evaluation of the geological condition ahead of the tunnel face by geostatistical techniques using TBM driving data. *Tunnelling and Underground Space Technology* 18: 213–221.

This page intentionally left blank

Rock Mechanics for Resources, Energy and Environment – Kwaśniewski & Łydżba (eds)
© 2013 Taylor & Francis Group, London, ISBN 978-1-138-00080-3

Tunnel behaviour and support in molassic rocks. Experience from 12 tunnels in Greece

V. Marinos
Aristotle University of Thessaloniki, Greece

G. Prountzopoulos & P. Fortsakis
National Technical University of Athens, Greece

ABSTRACT: Molasse consists of a series of tectonically undisturbed sediments of sandstones, conglomerates, siltstones and marls, produced by erosion of mountain ranges after the orogenesis. Molassic rock masses may have very different structure close to the surface as compared to those confined in depth, where bedding planes, do not appear as clearly defined discontinuity surfaces. The present paper focuses on the tunnelling experience through molassic formations, based on data from the design and construction of twelve tunnels in Egnatia Highway in northern Greece. The fundamental tool for this research was TIAS database, which has been used for the storage, retrieval and correlation of the available data. The rock mass behaviour that was anticipated during construction is described and the molasse specific GSI chart is validated. In conclusion, a standardization of the geotechnical behaviour of molassic rock mass types and the temporary support categories that have been successfully implemented is presented.

1 INTRODUCTION

The present paper addresses the issue of tunnelling through molassic rocks, based on the experience gained from the design and construction of tunnels in Egnatia Highway in northern Greece. The scope of this work is to set a framework concerning the different types of molassic rocks, the geotechnical behaviour of each type in tunnelling and the temporary support philosophy, both for underground construction and portal areas. The main characteristics of the geomaterial in question that cause its particular behaviour are (a) the lithological heterogeneity, as the formation consists of almost uninterrupted series of sandstones, siltstones, marls or claystones and conglomerates, with alternations of layers from just some centimeters to even few meters thick, (b) the low to moderate strength of the intact rock of these alternations, (c) the compact, almost intact structure in depth, even when sandstone beds alternate with siltstones and (d) the problematic behaviour of the formation close to the surface, due to slaking and weathering, especially of the siltstone parts.

A fundamental tool of this research was a database specifically established, where all relevant to investigation, tunnel design and construction data were stored and retrieved, the TIAS database (Tunnel Information and Analysis System, Marinos et al. 2012). The 12 tunnels in the molassic formation of the Panagia - Grevena section of Egnatia Highway. are shown in Table 1.

Table 1. Tunnels through molasse in the Egnatia Highway.

Tunnel name	Length (m)	Maximum overburden (m)
Sirtos	1520	112
Ag. Triadas	385	14
Ag. Paraskeuis	500	35
Agnanteros	720	40
Prionia	780	40
Velanidia	640	40
Nika	465	45
Lagadia	425	60
Zigra	385	50
Kiloma	1040	80
Karantza	715	80
Venetikos	700	50

2 ENGINEERING GEOLOGICAL FEATURES

2.1 *Geological setting*

The term molasse comes from a Swiss local name assigned initially to soft sandstones associated with marls and conglomerates belonging to the Tertiary and had a great development in the lowland parts of Switzerland. They have resulted from debris of weathering and erosion of the Alps mountain belt. The term is now used to describe the deposits from the erosion of an entire mountain range, after the final phase of orogenesis behind the mountain building area.

The environment is geologically "quiet" and compression effects are mainly confined to the peripheries of new basins.

As molasse characterizes a series of sediments formed and developed after the main orogenesis, it has not suffered compression, shears and thrusts, thus deterioration of the quality of the rock mass is limited. Only in few cases the molassic formations may be deformed and present thrusts due to the final advance of tectonic napes, but such a decrease of their quality is localized. In such cases, mild folds or minor tectonic slips are present. Gravity faults are common, but their impact in the deterioration of the quality of the rock is limited. Hence, there are no extensively developed poor zones, i.e. fractured, folded or sheared. The inclination of strata is generally low and cases with more than 30° dips are rare.

2.2 *Engineering geological characteristics*

The particularity of the molassic rock masses focuses on the variable heterogeneity, the presence of low strength geomaterials and the compact structure with depth. The principal engineering geological characteristics of molassic formations are the following:

- Alternations of competent sandstone and/or conglomerate beds and incompetent – generally of low/moderate strength – siltstone or claystone,
- Poor – weak diagenesis in some cases,
- Weathering of siltstone – claystone due to the phenomenon of fission (slaking),
- Detrimental effect of water on the siltstones – clay members and their discontinuities.
- Differentiation of the structure with depth (expressed stratification and discontinuous structure at the surface and close to it, continuous and tight structure in depth).

The various types of molasses, as reported below, mainly concern sandstone and siltstone alternations of different quota and thicknesses. There is also a rather common occurrence of conglomerates that range from very compact (calcitic) to loose (clayey). These rocks can alternate in layers of tens of centimetres to few metres or appear as massive strata. Lateral transitions between layers are common.

2.3 *Differences in depth and on surface*

Molassic rocks present significant differences between surface and depth. These differences lie on rock mass structure, weathering and permeability and consequently are very important for the rock mass quality and behaviour in tunnelling.

Molassic rocks, particularly with sandstone and well-cemented conglomerates, tend to be highly frictional. Due to the limited deformation to which they have been subjected during deposition, the joints in these rocks are generally free from the effects of shear movement (slickensides). Siltstone or claystone beds, being confined soon under the surface, are compact enough to form an almost continuous medium. Their presence may however reduce the strength of the overall mass. Yet, in few cases where siltstones are fairly strong and under low stress, their behaviour does not significantly differ from that of sandstones.

The bedding is the essential joint set in a molassic rock mass, but is only expressed on and near the surface. In depth it is mainly concealed. For the cases analysed in this paper, RQD values near the surface range from 0% to 50%. After some metres (~5 m) rock masses become medium fractured and weathered, while bedding planes are still evident. In depths larger than 10–15 m, rock masses are usually homogeneous in structure and compact with RQD values >60%.

Weathering alters the rock mass strength significantly. Siltstone (or marly) members are very vulnerable to weathering and fissility may be developed parallel to the bedding when these rocks are exposed to the surface or are very close to it. Siltstone (or marly) members in outcrops appear thinly layered and when they alternate with sandstones, the appearance of the rock mass resembles to flysch. This appearance in outcrops can be misleading when considering the behaviour of molassic rocks in a confined underground environment, in which the process of air slaking is restricted and the rock mass is continuous and massive.

In some cases, sandstones are loose and may be treated as dense sands. In such weak molasses, clays and silts also appear and the material can be treated like a soil. This paper does not address these soil-like molasses that have limited spatial distribution. Yet, it should be noted that molasses near the surface may create a cover with such soil characteristics.

The overall permeability of the molassic formation decreases very rapidly with depth according to the results of in-situ permeability tests presented by Marinos et al. (2008). More specifically, the permeability of sandstone molasse is significantly higher than in the case of the siltstone one. In the case of alternations of the two rock types, permeability approaches the value of the siltstone, since the siltstone layers do not allow the water flow through the rock mass and decrease the overall permeability. Furthermore, the frequent lateral transitions do not permit the development of a uniform aquifer. Fault zones, although more permeable are neither numerous nor wide. Hence, although the water table will usually be above the tunnel elevation, only limited water inflows are anticipated, although in some situations it may be necessary to relieve water pressures by drillholes.

2.4 *Molasse rock mass types*

The mollasic formations are distinguished and classified in rock mass types (I to VI) mainly based on the participation ratio of sandstone and siltstone members (Fig. 1).

2.5 *Molasse classification*

The GSI classification system for molassic formations was used along the 12 tunnels (Hoek et. al. 2005).

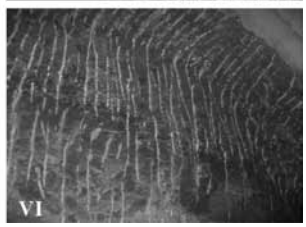
Type I Thick to medium thickness sandstone beds with sporadic thin films of siltstone	• Thick sandstone layers (>5m), separated by sparse thin siltstone intercalations (few cm). • Sandstones have generally high strength, which can be lower when they are silty or marly. • Compactin depth, but near the surface silty or marly sandstones may exhibit separation parallel to the bedding.	
Type II Sandstone with siltstone interlayers	• Sandstone beds with thickness from 50cm to few meters (~ 5m). They are separated by siltstone intercalations, few cm to 30cm thick. • In depth, though heterogeneous, is uniform and compact. Near the surface may exhibit some separation and loosening with friable parts.	
Type III Rockmass with sandstone and siltstone similar amounts	• Systematic alternations of siltstones and sandstones, with banks thickness of few tens of centimeters to few meters (~5m), in similar proportions. • At depths (>~ 6-10m), rock mass is massive and continuous. Near the surface is laminated. • Lithologic heterogeneity and other discontinuities, only at the surface due to splitting.	
Type IV Siltstone with sandstone interlayers	• Low degree of weathering in depth but high near the surface. • Siltstone beds are formed by thin to medium thick layers. Sandstone layer are usually thin (~10-20cm). • Main discontinuity is the bedding, showing great persistence (>10m) but is strongly sealed and "virgin".	
Type V Siltstone with sparse sandstone interlayers	• Main level of weakness is the bedding. • Large strength variation. Can be fresh to completely weathered. • In the non-weathered nature (depths>~6-10m), formation is massive (the bedding is unnoticeable or "virgin"). • In surface, bedding and discontinuities separate the siltstone (air-slaking), resulting in complete collapse of the fabric. May have expandable clay minerals.	
Type VI Conglomerate	• Found in intercalations and less as an independent thick horizon. • Cementation may be weak to moderate, when comprised of silty-clayey materials, and strong when matrix is calcitic.	

Figure 1. Typical types of molassic rock masses on tunnel faces in Egnatia Highway.

The use of this GSI chart assisted to the construction of almost all tunnels with much lighter support measures than what was initially foreseen.

The GSI classification for molasses (Hoek et al. 2005) was based on the observations and evaluations from the design of the 12 tunnels along the Egnatia Highway. This approach led to two charts, one for surface and one for depth. The validation of the proposed GSI charts for molasses is hereafter discussed.

Since molassic rock masses are confined in depth and bedding planes do not appear as clearly defined discontinuity surfaces as in flysch and the rock mass is massive, the use of the initial GSI chart (Marinos & Hoek 2000) is recommended and a value of 50–60 or more is to be applied. These values were validated

Table 2. Molasse intact rock properties (Marinos & Tsiambaos 2010).

	σ_{ci} (MPa)					E_i (GPa)					$MR = E_i/\sigma_{ci}$			
Rock material	n	min	max	μ	σ	n	min	max	μ	σ	n	range	μ	R^2
Sandstone	238	10.8	116.7	35.1	21.1	132	2.0	31.3	8.8	7.4	123	100–260	170	0.87
Siltstone	152	1.92	51.1	16.9	10.8	58	0.7	9.1	3.0	1.9	58	120–220	160	0.87
Conglomerates	165	5.0	68.2	23.1	13.9	82	1.1	19.4	7.4	5.1	79	180–670	375	0.69

σ_{ci}: intact rock uniaxial compressive strength, E_i: intact rock deformation modulus, MR: Modulus Ratio, n: number of samples, min: minimum values, max: maximum values, μ: mean value, σ: standard deviation.

during construction. If no discontinuities are present, GSI is very high (GSI > 75) and the rock mass can be treated as intact with engineering parameters given by laboratory testing. When fault zones were encountered in depth, GSI values generally lied in the range of 35–50 (Blocky-Disturbed structure). This is a difference with the original chart (area M2 in Hoek et al. 2005) that suggested more disturbed and disintegrated rocks and accordingly lower GSI values.

On the surface, the heterogeneity of the formation is discernible and similarities exist with the structure of some flysch types. Hence the GSI chart for heterogeneous rock masses (Marinos et al. 2011) can be used. This version of the chart, for fissile molassic rocks had been presented by Hoek et al. (2005). These values were also confirmed during tunnel construction.

2.6 *Intact rock properties*

A large number of results from laboratory tests regarding the intact rock properties have been presented by Marinos & Tsiambaos (2010). It is evident that the strength and deformability parameters of siltstone are lower than the corresponding values of sandstone, but this difference is not as significant as in the case of flysch ground types (Table 1).

3 BEHAVIOUR TYPES

The high strength of the molassic rock mass compared to the in situ stresses at shallow to medium depths, does not qualify serious stress-induced phenomena. The dominant failure mode in tunnels is the gravity driven falls and slides of blocks and wedges defined by intersecting joints and bedding planes. It should be underlined though, that this behaviour has been verified during construction of tunnels under a maximum overburden of 110 m and shall not be considered for much greater depths.

Generally, the behaviour of the molassic formations during tunnelling depends on three major parameters. That is (a) the structure, (b) the dominant rock type intact strength and (c) the depth of the tunnel. Therefore the expected behaviour types can be illustrated in Fig. 2. These behaviour types are distinguished in two areas (M1 and M2, see Fig. 2):

– Stable (St), in the case of intact, massive structure and shallow to medium depths. As the tunnel depth increases, stable behaviour with negligible deformation is observed for sandstone or conglomerate dominated formations.
– Stable (St), with only limited deformation (Sh), especially in cases of siltstone dominated formations, under significant overburden. The magnitude of the resulting deformation depends on the strength of the siltstone and the tunnel depth. Serious deformation has not been encountered in the Egnatia tunnels, as the maximum depth was limited to 110 m.
– Wedge failure (Wg), in cases of blocky structures and shallow to medium depths. As the tunnel depth increases, the same behaviour with insignificant

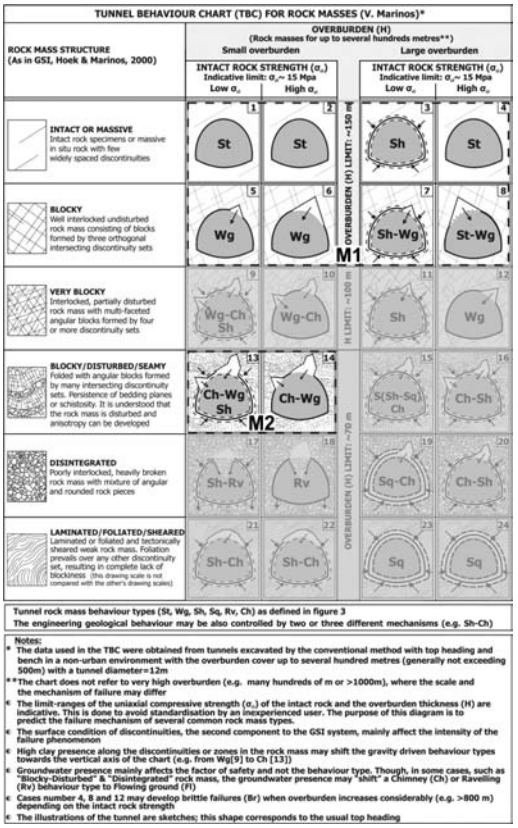


Figure 2. Tunnel behaviour chart for typical molassic rock masses, based on the chart produced by Marinos (2012).



Figure 3. Landslide in mollasic formation at the entrance portal of the Karatzas tunnel in Egnatia Odos.

deformation is observed for sandstone or conglomerate dominated formations. The increasing confinement with depth may result in less frequent wedge failure incidents (St-Wg). A slightly different failure mechanism can manifest in the case of thin-bedded formations with almost horizontal bedding planes. Failure of rock plates due to self-weight from the crown area may be frequent and intense once their base is exposed, due to deconfinement that may cause subvertical tension cracks. Such unfavourable conditions have to be faced, in order to avoid systematic overbreaks.

- Wedge failure, with only limited deformation (Sh-Wg), in the case of siltstone dominated formations, under significant overburden. The magnitude of the resulting deformation again depends on the strength of the siltstone and the depth of the tunnel.
- Extensive wedge failure that can evolve into chimney type failure (Ch-Wg), in the case of weathered and disturbed structure, close to the surface (portal areas or tunnelling in shallow depth under streams or gullies), due to slaking of the siltstone parts.
- Frequent wedge failure that can evolve into chimney type failure (Wg-Ch), in the case of very blocky rock masses due to faulting. In the case of siltstone dominated formations in medium to large depths, limited deformation (Sh) can occur. It is reminded that serious deformation has not been encountered in the tunnels of the Egnatia Highway, as the maximum depth of the tunnels was 110 m.

Concerning water inflows, limited presence of water has been met in the 12 tunnel projects, which occur mainly in the form of increased moisture to drip. In some rare cases, occasional or continuous low flow at various locations mainly in sandstone-siltstone contact layers and along major discontinuities has been encountered. Nevertheless, this presence degrades the characteristics of the discontinuities and should be taken into account when assessing the geotechnical characteristics of the formation.

The low geotechnical properties of the molassic formations close to the surface have led to several slope failures in the portal areas. These failures were not guided from preexisting discontinuities such as the bedding planes, but they were associated with the development of a new circular-shaped surface through the weak rock mass. Fig. 3 shows a typical slope failure in conglomerates at the entrance of Karatzas tunnel in Egnatia Highway.

4 TUNNEL SUPPORT

The support philosophy in molassic formations shall take into account the rock mass structure and the observed failure mechanisms, in relation to the tunnel depth as described above. These approaches for the philosophy of temporary support categories have been shaped based on the geotechnical behaviour of the molassic formation, as well as on construction data. In the Egnatia Highway tunnels through molassic formations 54% of the total length has been excavated implementing a support category with shotcrete shell, bolts, steel sets and light spilling. A very light support category containing a thin shotcrete shell and a sparse grid of bolts has been adopted for the 38% of the total length. Finally a heavy support category with thick shotcrete shell, steel sets, forepolling and fibreglass nails have been implemented in only 6.5% of the total length and mainly at the area of the portals. Therefore, away from the ground surface, where the rock mass is subjective to surface weathering conditions and any possible fault zones, there are two basic types of temporary support sections that could be applied.

The first type concerns stable conditions with only local gravity type failures and small to insignificant deformation (Fig. 4). This is the most common case for all molasse types in depth and shall be applied for low to medium overburden, or even under higher overburden in cases of sandstone or conglomerate domination. The temporary support consists of a thin shotcrete layer and a pattern of rock bolts, whereas the excavation step can be 3–4 m. Additionally, it is proposed to apply wire mesh to avoid small rock falls instead of fibre reinforced shotcrete. The first 3–5 cm thick layer of shotcrete applied on the exposed rock mass surfaces as soon as possible seals and protects the siltstone layers from slaking. The rock bolts pattern strengthens the rock mass, keeps it confined and prevents possible gravity driven falls of relaxed, structurally defined blocks or wedges, or falls due to decompression of the, otherwise, sealed bedding planes. The addition of a second layer of shotcrete, reinforced either by wire mesh or by fibres, creates a complementary shell, incorporating the rock bolts' heads and ensuring overall stability of the excavation.

The second support section type (Fig. 5) for sound molasse away from portals or faults refers (a) to conditions with frequent wedge failures due to the geometry of major discontinuities and the conditions already presented (horizontal bedding planes) and/or (b) to cases of weak rock (e.g. siltstone) dominated molassic formations under considerable to high overburden. Additionally to the shotcrete and the rock bolts, light steel sets may be required, whereas the excavation step has to be limited (around 2 m), in order to avoid any

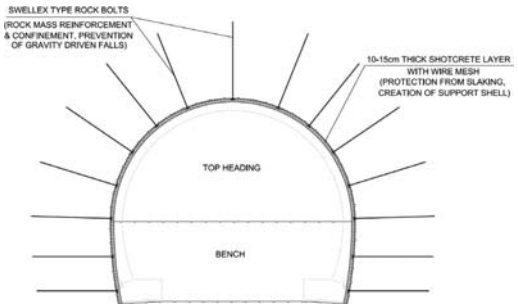


Figure 4. Typical support design for the molassic formations of category M1 (see Fig. 2).

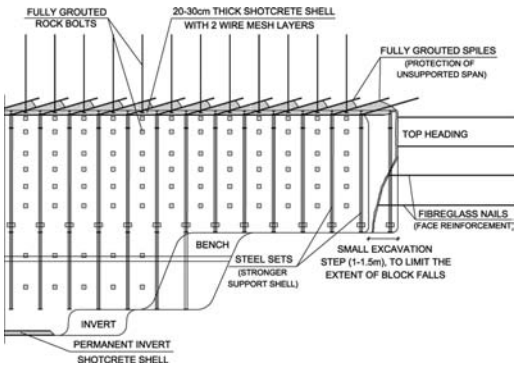


Figure 5. Typical support design for the molassic formations at portal areas, near the surface or in the vicinity of faults/shear zones (Category M2, see Fig. 2).

wedge formation or significant deformation in the case of large depths.

For the weathered molassic formations close to the tunnel portals or the heavily jointed and weak molassic rock masses within fault zones, there is need for a more stiff support, by means of heavier steel sets and a stronger shotcrete shell. Attention shall be given to cause minimum disturbance to the surrounding geomaterial, by minimizing the excavation step (~1 m). Additionally, it may be necessary to stabilize the tunnel face, using face reinforcement measures (e.g. fibreglasss nails) or face protection schemes (e.g. spiles, forepole umbrella), in order to avoid progressive detachment, deconfinement and creation of chimney type failures.

5 CONCLUSIONS

The paper concentrates on the engineering assessment of the molassic formation, on the issues of design parameters and tunnel support. Detailed records from the design and construction of 12 tunnels with lengths of 385 m to 1520 m and under maximum cover up to 110 m were evaluated.

The molasses characterize a sequence of alternations of sandstones, siltstones-mudstones and conglomerates. The molasses form rock masses with dramatically different structure when they outcrop or are close to the surface and when they are confined in depth. In depth they are undisturbed and massive since they have not suffered from compression, shears and thrusts. In outcrops they appear heterogeneous, disturbed and sometimes loose to disintegrate. For the assessment of rock mass properties, GSI charts for molasses (Hoek et. al. 2005) were used. This assisted to the construction of almost all tunnels with lighter support measures. The validation of the proposed GSI charts for molasses is discussed.

The dominant failure mode in the tunnels was wedge falls and slides of blocks. Deformation problems experienced under the maximum overburden of 110 m were minor. A medium support class was generally applied and in many cases steel sets have not been applied and the support class has changed to a light category with rock bolts and thin to medium layer of shotcrete. Tunnel face pre-support with spiles was only used when immediate gravity driven failures were anticipated, due to the geometry of formations and the loosening of the rock mass.

REFERENCES

Hoek, E., Marinos, P. & Marinos, V. 2005. Characterisation and engineering properties of tectonically undisturbed but lithologically varied sedimentary rock masses. *International Journal of Rock Mechanics and Mining Sciences*, 42(2): 277–285.

Marinos V. 2012. Assessing rock mass behavior for tunnelling. *Journal of Environmental and Engineering Geoscience*, Vol. XVIII, No. 4, pp. 327–341.

Marinos, P., Marinos V., Fortsakis, P. & Prountzopoulos G. 2008. Permeability of flysch and mollase. Distribution, comparison and decrease with depth. Grouting under dams. *Proceedings of the 8th International Hydrogeological Congress, Athens, Greece*, 2: 587–596.

Marinos, V., Fortsakis, P. & Prountzopoulos, G. 2011. Estimation of geotechnical properties and classification of geotechnical behaviour in tunnelling for flysch rock masses. In Anagnostopoulos, A. Pachakis, M. & Tsatsanifos, C. (eds), *Geotechnics of Hard Soils – Weak Rocks; Proceedings of the 15th European Conference on Soil Mechanics and Geotechnical Engineering, Athens, Greece, 12–15 September*, 1: 435–440. Amsterdam: IOS Press.

Marinos, P. & Hoek, E. 2000. GSI: a geologically friendly tool for rock mass strength estimation. *Proceedings of the GeoEng2000 at the International Conference on Geotechnical and Geological Engineering*, *Melbourne, Australia*, 1422-1446. Lancaster: Technomic publishers.

Marinos, V., Prountzopoulos, G., Fortsakis, P., Koumoutsakos, D. & Papouli, D. (2012) Tunnel Information and Analysis System: A geotechnical database for tunnels. *Geotechnical and Geological Engineering*. doi: 10.1007/s10706-012-9570.

Marinos, V. & Tsiambaos, G. 2010. Strength and deformability of specific sedimentary and ophiolithic rocks. In Koukis, G., Zelilidis, A. Koukouvelas, I., Papatheodorou, G., Geraga, M. & Zygouri V. (eds), *Planet Earth: Geological Processes and Sustainable Development, Bulletin of the Geological Society of Greece and Proceedings of the 12th International Congress. Patras, Greece, 19–22 May*, XLIII, 3:1259–1266.

Rock Mechanics for Resources, Energy and Environment – Kwaśniewski & Łydżba (eds)
© 2013 Taylor & Francis Group, London, ISBN 978-1-138-00080-3

New yielding elements for tunnel linings: Design requirements, layout and influence on system behavior

W. Schubert
Graz University of Technology, Graz, Austria

N. Radončić
GeoConsult ZT GmbH, Wals bei Salzburg, Austria

ABSTRACT: The expansion of the current European infrastructure demands the construction of several major and challenging tunnelling projects, such as Gotthard and Ceneri in Switzerland, Lyon-Turino in Italy/France and Koralm, Brenner and Semmering tunnels in Austria. Due to their length and alignment as "base tunnels", they encounter various geological formations and tectonical faults under high overburden. This leads to a frequent combination of weak ground and high primary stresses, causing high displacement magnitudes. Loads unsustainable by a stiff support, support damage and costly re-profiling are a usual consequence. Over the past decades, various approaches for creation of ductile tunnel linings have been proposed and sometimes successfully applied. While most systems fulfilled their role of "deforming element", the imperatives of costs and operational feasibility, as well as their general interaction with shotcrete and deforming ground are seldom discussed. This publication concentrates on a new yielding element type developed at the Institute for Rock Mechanics and Tunnelling, Graz University of Technology. It is based on the venerable Lining Stress Controllers. Their drawbacks such as relatively large amount of machined parts (load bearing pipe, inner and outer leading pipes) have been addressed and removed, while the already favourable load-displacement relationship has been considerably improved. The new element's interaction with shotcrete lining and its overall influence on the system behaviour is discussed in detail.

1 INTRODUCTION

Due to the general requirements of high capacity traffic infrastructure, long and deep tunnels in alpine regions are unavoidable. The expansion of the current European infrastructure results in construction of numerous long tunnels, especially in the middle Europe: Lyon-Turin in Italy/France, Gotthard and Ceneri in Switzerland, and Semmering, Koralm and Brenner Tunnel in Austria. This can lead to a combination of weak ground in extended tectonic faults and high overburden. In case the conventional approach of obtaining displacement compatibility by increasing the support stiffness and load bearing capacity is followed, extreme support requirements and an unsafe and uneconomical design are the result. The application of stiff support concepts has proven itself unsafe and uneconomical due to:

- Suppressing of the displacements, thus removing the ability to observe, measure and predict the system behaviour and analyse the stabilisation process.
- Much higher amount of potential energy is present, both in the ground and in the support. This leads to a more violent release of energy (as external work) in case the support fails. In addition, the re-profiling in such cases is much more costly, since the amount of clearance violation is higher (if stiff support is applied, lower amount of overexcavation is required). In the end, the massive, however failed, lining has to be replaced in a costly manner.
- The extreme support requirements (shotcrete linings with thickness above 50 cm) considerably slow down the construction progress.
- Contrary to the two-dimensional approaches such as convergence confinement method, the installation of a stiff support not only leads to an other equilibrium point between the support and the ground, but also actively attracts additional loads by changing the amount of the displacements ahead of the face (Barlow 1986).

These problems have been successfully circumvented in the last four decades by initially leaving open shotcrete gaps in the lining and applying systematic rock bolting (Pöchhacker 1974, John 1980, Schubert 1993) and later by inserting yielding elements into the lining gaps (Pöttler 1996, Schubert 1996, John & Mattle 2007, Barla 2009, Ramoni & Anagnostou 2010). The insertion of yielding elements allows direct control of the support characteristic and represents state-of-the-art now. However, while their application has been wide and frequently successful in the past years, the requirements on the yielding

elements and on the overall support characteristic are seldom discussed in detail. In this publication, a new element prototype is discussed, which has been developed in a reverse manner. The exemplary theoretical requirements on the load-displacement relationship have been determined, and *then* the elements have been as finely tuned to the requirements as possible.

2 DESIGN REQUIREMENTS

The design requirements on a ductile lining are straightforward:

- The mobilised resistance level has to lead to final displacements compatible with the amount of the overexcavation – clearance profile must not be violated.
- The mobilised resistance level has to be higher than the maximal assumed loosening load. By fulfilling this requirement, no dead weight loading can occur in the system.
- The support resistance should be as high as possible, thus minimising the rock mass disintegration in the vicinity of the cavity.

The position of the yielding elements in the liner should comply with the overall displacement field – in case of a strongly asymmetrical displacement field (due to ground anisotropy), the element position in the cross section is to be accordingly adjusted. Deduced from the reasoning presented above, the requirements on the ductile elements are as follows:

- The mobilized load has always to be below the time-dependent shotcrete strength, but as high as possible. In a theoretical, "perfect" case, the load-displacement characteristic should follow the shotcrete capacity curve with an offset – allowing displacements and stress release in the ground while keeping the shotcrete "just below" the point of overstressing.
- The load-displacement characteristic has to incorporate the influence of the shotcrete rheological behaviour in combination with the respective time and face position dependent displacement characteristic.

Although the basic concept appears simple and straightforward, incorporating all of the requirements presented above represents a highly complex endeavour. Since this publication concentrates on the new element development and its interaction with the overall system behaviour, full re-production of the mathematical background is omitted. For additional information, please refer to (Hoek et al. 2008, Schubert 2008, Ramoni & Anagnostou, 2010, Radoncic et al. 2009, Radoncic 2011).

3 THE "IDEAL ELEMENT"

The idealized element characteristic has been derived from an assumed displacement development characteristic (based on absolute displacement monitoring data from various tunnels in Austria) and rheological behaviour of shotcrete. The applied mechanical approach is as follows:

- Determination of the time-dependent strength of shotcrete;
- Determination of the shotcrete strains occurring due to the stresses equalling the shotcrete strength – (multiplied with a chosen safety margin);
- Determination of the face position (and through the assumption of an advance rate) and time-dependent displacements;
- subtracting the occurring shotcrete strains from the overall strain due to displacements (determined above);
- the "ideal" load-displacement relationship is thus determined by assigning the shotcrete stress to the respective displacement not taken by the shotcrete.

3.1 *Calculation basics*

The shotcrete strength is determined by applying the Eurocode 2 relationship for time-dependent strength development, under the assumption of rapidly curing cement:

$$\beta(t) = \beta_{28} \cdot e^{\left(s\left(1-\left(\frac{28}{t}\right)^{1/2}\right)\right)} \tag{1}$$

where: t – time in days, β – shotcrete strength at the age t, β_{28} – shotcrete strength at the age of 28 days and s – cement-dependent parameter, in this case equalling 0.5.

The rheological behaviour of shotcrete is assessed by applying the flow-rate method (Schubert 1988). The shotcrete strain ε_2 at time "2" is given as:

$$\varepsilon(t_2) = \varepsilon(t_1) + \\ + \frac{\sigma(t_2) - \sigma(t_1)}{E(t_2)} + \sigma(t_2)\Delta C(t) + \Delta\varepsilon_d + \Delta\varepsilon_{sh} \tag{2}$$

where: $\varepsilon(t_1)$ – axial strain at the time "1" (begining of interval), $\varepsilon(t_2)$ – axial strain at the time "2" (end of interval), $\sigma(t_1)$ – axial stress at the time "2", $\sigma(t_2)$ – axial stress at the time "1", $E(t_2)$ – Time-dependent Young's modulus, $\Delta C(t_2)$ – Time- dependent plastic creep rate, $\Delta\varepsilon_d$ – increment of reversible creep strain and $\Delta\varepsilon_{sh}$ – increment of shrinkage strain.

The time-dependent Young's modulus is defined as:

$$E(t) = E_{28}\sqrt{\left(\frac{t}{1.8 + 0.93t}\right)} \tag{3}$$

with E_{28} representing the Young's modulus at 28 days of shotcrete age, and t the current shotcrete age. The plastic creep rate increment $\Delta C(t)$ is given as

$$\Delta C(t) = A'\left(t_2^{\frac{1}{3}} - t_1^{\frac{1}{3}}\right) \tag{4}$$

with A' as material parameter. The reversible viscous strain increment $\Delta\varepsilon_d$ is dependent on the already accumulated total viscous strain ε_d and writes as:

$$\Delta\varepsilon_d = \left(\sigma_2 C_{d\infty} - \varepsilon_d\right)\left(1 - e^{\frac{-\Delta C(t)}{Q}}\right) \tag{5}$$

with $C_{d\infty}$ and Q as additional empirical parameters. Finally, the shotcrete shrinkage increment is defined as:

$$\Delta\varepsilon_{sh} = \frac{\varepsilon_{sh\infty} t_2}{B + t_2} - \frac{\varepsilon_{sh\infty} t_1}{B + t_1} \tag{6}$$

with B as curvature parameter and $\varepsilon_{sh\infty}$ as final shrinkage strain.

Apart from shotcrete "swelling" due to hydration heat in the early stages, the above set of equations enables very good assessment of the rheological behaviour of the shotcrete (Müller 2001). The maximum attainable shotcrete strains are given by assuming a strength-dependent stress $\sigma(t)$ and applying it in the relationship (2):

$$\sigma(t_i) = \frac{\beta(t_i)}{\gamma_C} \tag{7}$$

where γ_C denotes a constant safety factor and ti arbitrary time step in the presented forward-difference scheme.

3.2 *Determination of the load-displacement characteristic*

The displacements imposed on the yielding element-shotcrete support system have been calculated by the relationship presented by Sulem et al. (1987):

$$u_r(x) = u_{end} \cdot \left[1 - \left(\frac{X}{X + x}\right)^2\right] \tag{8}$$

where: $u_r(x)$ – radial displacement at the face distance x, u_{end} – final displacement at infinite face distance, X – displacement development characteristic parameter and x – relative face distance. The face distance x is calculated by assuming constant advance rate a: $x = at$. The tangential shortening of the support is given as

$$u_t(x) = u_r(x) \cdot 2 \cdot \pi \tag{9}$$

thus allowing the direct determination of the required element shortening $\Delta l_{element}$, by inserting the strains calculated by applying the equation (2):

$$\Delta l_{element} = \frac{u_t(x) - \left(2R\pi - n_{Gaps} h_{Gap}\right) \cdot \varepsilon_{Shot}(t)}{n_{Gaps.}} \tag{10}$$

with $u_t(x)$ – tangential shortening, R – tunnel radius, n_{Gaps} – number of element gaps in the lining, h_{Gap} – average height of every element gap and $\varepsilon_{Shot}(t)$ being the calculated shotcrete strain. The pairing of the element shortening required for displacement compatibility with the assumed shotcrete stress (multiplied with the shotcrete lining cross-section area) yields the load-displacement relationship of the "ideal" element.

3.3 *Case study*

A case study regarding the influence of various parameters has been conducted. The basic parameters are listed in Table 1.

The influence of the advance rate is shown on Figure 1. It demonstrates the relevance of the advance rate on the load-displacement characteristic: a higher advance rate requires elements with lower initial stiffness, while slow progress allows the shotcrete to cure and develop its strength, and the issue of the initial stiffness becomes less important. The characteristic of the displacement development (controlled by parameter X) influences the results in a similar manner: if the displacement development is acute (rapid convergence towards final value, represented by low X values), the initial stiffness of the elements has to be

Table 1. Analysis parameters.

Parameter	Unit	Value
Tunnel radius R	[m]	5
Shotcrete thickness t_{shot}	[cm]	30
Safety factor γ_C	[–]	1.50
Number of element gaps n_{Gaps}	[–]	4
Gap height h_{Gap}	[cm]	40
Final displacement u_{end}	[m]	0.2
Creep constant A'	[$d^{2/3}$/MPa]	0.0001
Final reversible creep $C_{d\infty}$	[1/MPa]	0.00009
Reversible creep constant Q	[1/MPa]	0.0001
Final shrinkage strain $\varepsilon_{sh\infty}$	[–]	0.00125
Shrinkage constant B	[d]	600
28-days strength β_{28}	[MPa]	40
Young's modulus E_{28}	[MPa]	20000

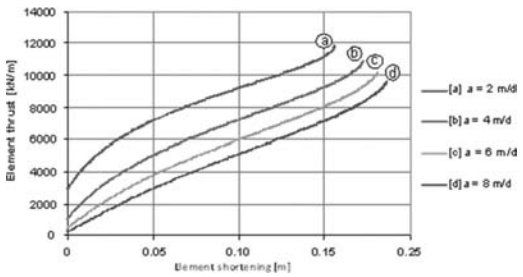


Figure 1. Influence of the advance rate on the required load-displacement characteristic of the yielding elements.

much lower than in case of a long lasting displacement development (X is high) – Figure 2.

Based on the results of a systematic parameter study conducted by Sitzwohl (2011) (exemplarily represented above), following conclusions regarding the development of a new element have been drawn:

- The initial stiffness has primary importance, since shotcrete has the lowest capacity at this stage. Even slight fluctuations in other boundary conditions (advance rate, weaker ground, other displacement characteristic et cetera) result in strong variation of the ideal load-displacement curve.
- The resistance can be allowed to continuously rise and thus match the shotcrete capacity. Ideally plastic behaviour of elements is therefore not imperative, a linear or curved characteristic (element acting as a spring) is desirable. The only imperative is that the element thrust never exceeds the shotcrete capacity; otherwise damages to the lining would occur.

Due to the experience with the Lining Stress Controllers (LSCs) and their low initial stiffness (Moritz 1999, Schubert 2008, Radoncic 2011), they have been chosen as starting point for further development. In addition, the issue of low initial stiffness can be easily addressed by staged activation of the lining stress controllers in the deformation gap (Fig. 3), thus allowing on-site fine tuning to the observed behaviour.

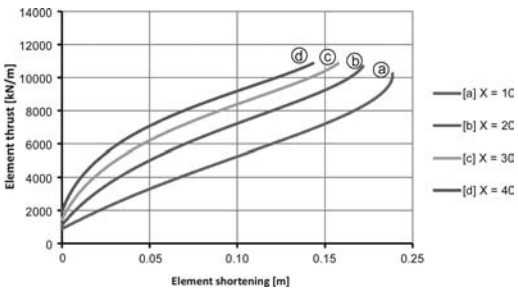


Figure 2. Influence of the displacement development on the required yielding element behaviour.

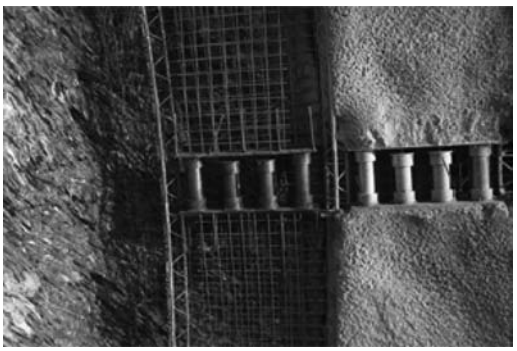


Figure 3. Installed LSC elements – middle pair shorter and with higher capacity, in order to obtain delayed activation and low initial stiffness. (Photo: R. Vergeiner).

4 LABORATORY TESTING

The initial idea of enhancing the lining stress controllers' behaviour was by filling them by a porous mixture. It was expected that the gradual internal pressure build-up would lead to a stiffening effect as described above (gradual increase in resistance) and ensure concentrical buckling of the steel pipe. In order to identify a usable material, systematic study of various mixtures of sand, cement and porous clay granulate (market name: Liapor) has been conducted (Sitzwohl 2011). The addition of cement has been chosen in the early testing stages, since the transport and assembly of the yielding elements could be done separately: before the elements are built in, the deformable porous "filler" has only to be inserted into the LCS pipe. The initial testing programme on the filling materials was as follows:

- uniaxial compressive strength tests (displacement controlled) in order to determine the post-failure behaviour of the specimen.
- Oedometric tests in order to determine the mechanical behaviour under constrained volumetric conditions.

After the most promising mixtures have been identified, the large scale testing of the compound elements (LSC + mixture) has been conducted. The results have proven that the insertion of the porous core results in an almost perfectly symmetric buckling (Fig. 4). The buckling figure occurred systematically in all tests (clearly caused by the axial loading of the pipe and favourable additional internal pressure caused by compression of the filling), and the observed load-displacement behaviour has been greatly improved (Fig. 5).



Figure 4. Cut through a deformed element with porous filling.

The stable thrust mobilisation is obtained without the co-axial leading tubes (typical for LCSs), and the entire element now requires only one filled tube. Due to the high initial porosity, the initial stiffness is not influenced at all.

5 INFLUENCE ON SYSTEM BEHAVIOR

The comparison of the "ideal" load-displacement relationship based on displacement monitoring data from the Lavanttal Fault zone, with an average advance rate of 4 m/d and displacement parameter X set to 20, shows that the obtained behaviour is already very close to the ideal one. All other parameters have been used as presented in Table 1.

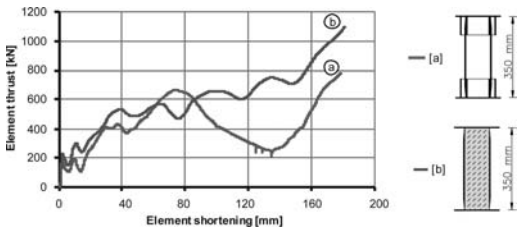


Figure 5. Comparison between regular type IIa LSC and its filled counterpart.

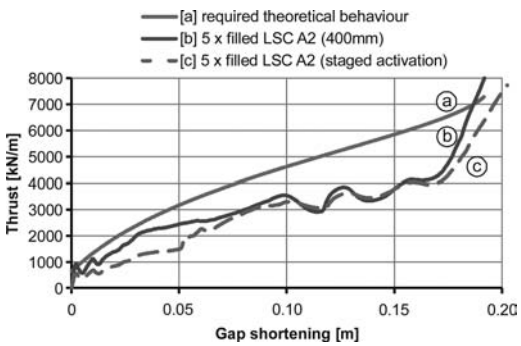


Figure 6. Comparison between the observed and "ideal" load-displacement characteristics.

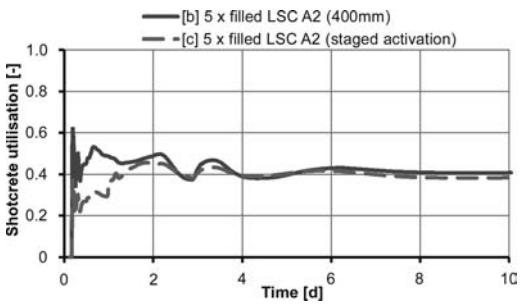


Figure 7. Shotcrete utilization.

The shotcrete utilisation for the first ten days is already very steady, apart from the initial fluctuations at low shotcrete age (Fig. 7). The staged activation of elements (dashed line) leads to an even more continuous characteristic, never exceeding the maximal envisioned utilisation of 0.67 (due to the safety factor of 1.50 – see Table 1) and never falling below 0.40.

6 FURTHER DEVELOPMENT

The tested concept of filled lining stress controllers has proven to be very promising. Additional work will be invested in further laboratory testing on a broader range of dimensions and filling recipes. The final product will be, in an analogy to the PhD thesis by Moritz (1999), a "cookbook" with a set of element types and their respective load-displacement characteristics. The desired final load-displacement characteristic of the entire yielding element set (inserted in the lining gap) can be easily obtained by combining various elements and choosing the correct element offset.

In addition, an entirely different type of element has been devised in the course of the work as well, featuring telescoping pipes and relying on the porous filling to bear the load in the initial stages. The obtained load-displacement relationship is very steady, however the initial stiffness is still too high and the concept features a strong "shock" after the tubes come into contact with the endplates on the other side. However, the concept appears promising as well, due to its simplicity and a load-displacement characteristic featuring no load fluctuations over a large range of displacement.

7 CONCLUSIONS

The developed porous filling of the lining stress controllers has led to a considerable enhancement of the load-displacement relationship while simplifying them. Reductions of the load oscillation, increase in maximum shortening and a considerable load increase in later stages have been proven in the tests.

REFERENCES

Barla, G. 2009. Innovative tunneling construction method to cope with squeezing at the Saint Martin La Porte access adit Lyon – Turin Base Tunnel. In I. Vrkljan (ed.), *Rock Engineering in Difficult Ground Conditions – Soft Rocks and Karst, Proceedings of EUROCK 2009 – The 2009 ISRM Regional Symposium* 15–24. Leiden: CRC Press/Balkema.

Barlow, J.P. 1986. Interpretation of tunnel convergence measurements. *MSc Thesis*, Department of Civil Engineering, University of Alberta, Canada.

Hoek, E., Carranza-Torres, C., Diederichs, M. & Corkum, B. 2008. Integration of geotechnical and structural design in tunnelling. 2008 Kersten Lecture. *Proc. University of Minnesota 56th Annual Geotechnical Engineering Conference*. Minneapolis.

John, M. 1980 Construction of the Arlberg expressway tunnel tube 3. *Tunnels and Tunnelling International* 12(5): 45–50.

John, M. & Mattle, B. 2007. Auswirkungen stark druckhafter Gebirgsverhältnisse auf den TBM-Vortrieb. *Felsbau* 25(6): 14–21.

Kovari, K., Ehrbar, H. & Theiler, A. 2005. Druckhafte Strecken im TZM Nord: Projekt und bisherige Erfahrungen. In S. Löw et al. (eds): *Geologie und Geotechnik der Basistunnel am Gotthard und am Lötschberg*: 239–252. Vdf. Hochschulverlag an der ETH Zürich.

Moritz, A.B. 1999. Ductile Support System for Tunnels in Squeezing Rock. In: G. Riedmüller, W. Schubert & S. Semprich (eds), *Schriftenreihe Gruppe Geotechnik Graz*, Heft 5, Graz University of Technology, Austria.

Müller, M. 2001. Kriechversuche an jungen Spritzbetonen zur Ermittlung der Parameter für Materialgesetze, *Diplomarbeit,* Institut für Geomechanik, Tunnelbau und konstruktiven Tiefbau, Montanuniversität Leoben.

Pöchhacker, H. 1974. Moderner Tunnelvortrieb in sehr stark druckhaftem Gebirge. *Porr Nachrichten* 57/58.

Radoncic, N. 2011. Tunnel design and prediction of system behaviour in weak ground. *Doctoral thesis,* Institute for Rock Mechanics and Tunnelling, Graz University of Technology.

Radoncic, N., Moritz, A.B. & Schubert, W. 2009. Ductile lining design. *Geomechanics and Tunnelling* 2: 561–577.

Ramoni, L. & Anagnostou, G. 2010. The interaction between shield, ground and tunnel support in TBM tunnelling through squeezing ground. *Rock Mechanics and Rock Engineering* 44(1): 37–61.

Schubert, P. 1988. Beitrag zum rheologischen Verhalten vom Spritzbeton. *Felsbau* 6(3): 150–153.

Schubert, W. 1996. Dealing with squeezing conditions in Alpine tunnels. *Rock Mechanics and Rock Engineering* 29(3): 145–163.

Schubert, W. 2008. Design and construction of tunnels in poor and faulted rock masses. In A. Majdi & A. Ghazvinian (eds), *Proc. 5th Asian Rock Mechanics* Symposium, 24–26 November 2008, pp. 827–835.

Sitzwohl, M. 2011. Optimierung der Lining Stress Controller durch zementgebundene poröse Füllung. *Master Thesis*, Graz University of Technology.

Sulem, J., Panet, M. & Guenot, A. 1987. An analytical solution for time-dependent displacements in a circular tunnel, *Int. J. Rock Mech. Min. Sci. & Geomech. Abstr.* 24(3): 155–164.

Rock Mechanics for Resources, Energy and Environment – Kwaśniewski & Łydżba (eds)
© 2013 Taylor & Francis Group, London, ISBN 978-1-138-00080-3

A Rock Mass Rating system for predicting TBM utilization

S. Yagiz
Pamukkale University, Department of Geological Engineering, Denizli, Turkey

T. Kim
Parsons Brinckerhoff, Inc., New York City, NY, USA

O. Frough & S.R. Torabi
Faculty of Mining, Petroleum and Geophysics, Shahrood University of Technology, Shahrood, Iran

ABSTRACT: Prediction of utilization based on rock mass properties is critical for any mechanized tunneling project, since the utilization have an influence on duration and costs of project. Using some case studies including Queens, Milyang, Manapouri, Karaj, Varzo, Maen, Pieve mechanized tunneling project around the world, the attempt is made to estimate utilization via Rock Mass Rating (RMR) System herein. It is concluded that the machine utilization has some reasonable correlations with RMR; however, this relationship is depend on not only rock mass properties but also machine specifications. In other words, the utilization may change with both rock mass conditions and utilized machine type. Due to that rock properties and other related downtimes should be examined together to obtain the reliable equations for predicting the utilization. Further, developed relationships may be used for similar rock type to estimate utilization from RMR.

1 INTRODUCTION

Utilization (U) is defined as the percentage of machine boring time to the shift time. It is summarily the function of the advance rate, (AR) and the rate of penetration, (ROP), ($U = AR/[ROP \times Shift\ Hour]$). In this function, the ROP is the ratio of excavated distance to the operating time during continues excavation phase, while the AR is the ratio of both mined and supported actual distance to the total time (Yagiz 2008). In mechanical tunneling, type of operation, management, maintenances, geological conditions, capacity of the backup system and other factors that cause downtimes -*including the times of support installation, re-gripping, grouting, maintenance, machine break down, cutter change, mucking delays, stoppage caused by geological adverse conditions and other components such as shift changes*- to the operation, have an influence on the utilization.

A wide variety of TBM performance prognosis models and principles with special focus on rate of penetration are introduced in the literature since the early use of TBM. Some methods simply focus on rock parameters such as uniaxial compressive strength and rock abrasion value, while other methods consider a combination of comprehensive laboratory, field and machine data. Although CSM, NTNU and Q_{TBM} models have suggested some equations and graphs for estimating the utilization factor (Rostami & Ozdemir 1993, Bruland 1998, Barton 1999, Yagiz 2002), there are a few documents in the literature about estimating TBM utilization with relevant parameters.

Also several researchers have applied different soft computation techniques for TBM performance prediction. Benardos & Kaliampakos (2004) correlate TBM performance with geological and geotechnical site conditions by using artificial neural network. Kim (2004) developed a utilization predictor model based on fuzzy logic method. Also two-dimensional numerical analyses were performed to explore the effect of joint orientation and joint spacing on rock fragmentation by a TBM (Gong et al. 2005). Yagiz (2008) developed an empirical equation to estimate the rate of penetration by the use of rock mass properties. Khademi Hamidi et al. (2010) studied the relationship between the RMR and TBM performance. Frough et al. (2012) also made attempts to develop the relationship between RMR and some TBM performance parameters.

The present study is attempted to develop the relationship between the RMR and TBM utilization using the data obtained and examined from seven different tunnel sites around the world.

2 CASE STUDIES

To estimate the utilization via RMR system, the case studies are examined and the result of findings is

introduced herein. Following projects are examined for this purpose.

2.1 *Queens Tunnel (USA)*

The Queens Water tunnel was constructed to improve distribution of freshwater throughout the City of New York, especially in district of Queens (Yagiz 2002). The Queens Water tunnel was located in New York City where the geological formation was highly complex and composed of different type of metamorphosed igneous rock with shear zones, faults, joints and other local fractures. The combination of mineral assemblage and rock texture demonstrated that the rock had several episodes of high degree metamorphic recrystallizations. The tunnel site composed of rhyodacite dyke, granitic gneiss intermixed with orthogneiss, gneiss, amphibolite, pegmatite, and the combination of gneiss-schist (Yagiz 2002, 2008).

2.2 *Manapouri Tunnel (New Zealand)*

The second tailrace tunnel of the Manapouri hydro project that is an underground hydroelectric power station located in the Fiordland area of southwestern New Zealand. The objective of adding the tailrace tunnel was to increase the overall cross-sectional area of flow, thereby reducing the flow velocities and associated frictional head losses (Yagiz et al. 2010).

The Paleozoic age metamorphic rocks dominate the region of the Fiordland National Park, which is bounded by the tectonic boundary between the Australian and the Pacific crustal Plates in New Zealand. The principal rock types were: gneiss with varying degrees of intrusion by pegmatite and other granitic rocks; gabbro; diorite and minor amounts of mixed meta-sediments like marble, quartzite and calc-silicates (Kim 2004, MacFarlane et al. 2008, Yagiz et al. 2009, 2010).

2.3 *Milyang Tunnel (South Korea)*

The Milyang tunnel was constructed to deliver clean water from Milyang dam to Yangsan area through 2.6 m-diameter hydro-tunnel in South Korea (Kim 2004, Yagiz et al. 2010). According to geological site investigation studies, most of the tunnel alignment consisted of igneous rocks, such as granite and andesite (Kim 2004). The rock formations were generally composed of biotite-rich and fine to medium grained granite (Kim 2004, Yagiz et al. 2010).

2.4 *Karaj Tunnel (Iran)*

The Karaj–Tehran water conveyance tunnel with 30 km length is located northwest of Tehran in Iran, between Karaj and Tehran, and was designed for transferring 16 m^3/s of water from Amir–Kabir dam to Tehran (Frough et al. 2012). The Karaj Water tunnel is divided into two sections: Data collected from first section of the tunnel that is 16 km long at the southeast end is used for this study. The lithology of this section of the tunnel consists of a sequence of Karaj formations and is composed of variety of pyroclastic rocks, often interbedded with sedimentary rocks (Hassanpour et al. 2010, Frough et al. 2012).

2.5 *Maen Tunnel (Italy)*

Rock units consist of meta-ophiolites (serpentinite, metagabbro, metabasite, chlorite schist, talc schist) and meta-sediments (calc-schist and silicate marble) belonging to the Zermatt-Saas Zone of the Pennidic Domain (Dal Piaz 1988, Reinecke 1991). The parent rocks were carbonate pelagic sequences and mafic crystalline rocks that underwent high-pressure low-temperature metamorphism during the early phases of the alpine orogenesis. Schists and serpentinites show a foliated texture a metagabbro and metabasite are generally weakly foliated (Sapigni et al. 2002).

2.6 *Varzo Tunnel (Italy)*

The Varzo tunnel is excavated entirely in the Antigorio Gneiss Formation, a massive or weakly foliated rock generated by high-grade metamorphism of granite and granodiorite rocks (Milnes 1973, Steck 1987). Metaaplite and metabasite dikes locally traverse the tunnel axis, but the area may be considered essentially homogenous. The geological structure is a monocline gently dipping in a southerly direction, slightly complicated by folds and minor fault zones related to the Sempione-Centovalli fault, a major tectonic structure located 2 km to the south (Mancktelow 1985, Sapigni et al. 2002).

2.7 *Pieve Tunnel (Italy)*

Most of the Pieve Vergonte tunnel is located in the Sesia-Lanzo Zone of the Austroalpine Domain (Reinhardt 1966, Compagnoni et al. 1977). Excavated rocks consist of two metamorphic complexes made up of gneiss and micaschists separated by a meta-diorite intrusive body with minor masses of meta-quartzdiorite and metagabbro. The geological structure is complicated by multiple folding associated with shear zones and brittle fault zones (Sapigni et al. 2002).

In this study, analyzing the data obtained from literature (such as Maen and Varzo) and collected data from the sites (i.e., Queens and Manapouri), some correlations is obtained between the RMR system and rock mass related TBM utilization that is one of the main parameters to estimate the cost and time of mechanical tunnels.

3 TBM – RMR INTERACTION

Seven tunnel projects were studied to examine the relationship between the RMR and TBM utilization.

Table 1. RMR and utilization obtained from relevant projects (Sapigni et al. 2001, Yagiz 2002, Kim 2004, Hasanpour et al. 2010, Forough et al. 2012).

Karaj		Varzo		Maen		Pieve		Manapouri		Milyang		Queens	
RMR	U	RMR	U	RMR	U	RMR	U	RMR	U	RMR	U	RMR	U
21	0.09	28	0.23	16	0.07	29	0.32	39	0.21	42	0.18	29	0.18
35	0.23	32	0.25	23	0.08	34	0.26	40	0.28	51	0.21	36	0.22
46	0.16	45	0.31	36	0.08	47	0.25	48	0.33	57	0.24	43	0.23
49	0.21	55	0.19	44	0.09	54	0.39	58	0.38	62	0.29	53	0.34
50	0.21	64	0.31	56	0.12	65	0.41	69	0.42	70	0.32	62	0.39
57	0.16	74	0.37	65	0.10	74	0.43	75	0.46	76	0.37	71	0.41
63	0.16	85	0.51	74	0.16	83	0.44	85	0.505	85	0.405	76	0.42
64	0.22	94	0.53	85	0.20	92	0.42	90	0.52	93	0.41	91	0.46
72	0.17	–	–	93	0.17	–	–	94	0.55	95	0.42	95	0.48

Table 2. Machine specifications for relevant projects (Sapigni et al. 2001, Yagiz 2002, Kim 2004, Hasanpour et al. 2010, Frough et al. 2012).

	Karaj	Varzo	Maen	Pieve	Manapouri	Milyang	Queens
Tunnel length (km)	16	6.6	1.75	9.6	9.6	5.4	7.6
Cutterhead dia (m)	4.66	4.05	4.2	4.05	10.05	2.6	7.1
Cutters dia (mm)	432	432	432	432	432	432	482
Cutter disk spacing (mm)	70	75	66	75	82	65	82
TBM Model	*Herrenknecht, Double	*Robbins 1214-240-1	Wirth 340/420E Open	*Robbins 1111-234-3	*Robbins Model 323–288	Wirth, TB260E Open	Robbins, 235–282 Open
Number of cutters	31	27	36	27	68	22	50
Cutterhead speed (rpm)	11	4.5–8.6	5.5–11	11.3	2.53–5.07	13	8.3
Max cutterhead thrust (kN)	17000	8827	7920	4602	18165	4300	15500

*Double shield.

According to the dataset, it is observed that the RMR values rages from around 16 to 95, while the utilization rages from 9 to %53 in the dataset. Each tunnel case includes different rock type and also machine specification that used for excavation. Due to that, the wide range of utilization in these dataset is likely as wanted (Table 1).

Tunnel boring machines (TBMs) for these projects are various from open type through double shield machine. Also, their cutter size, thrust, rpm, torque and other specifications are also different as the diameter and length of studied tunnels. The specifications of utilized TBMs for studied tunnels are given in Table 2. Manapouri tunnel has the maximum cutter size and number, while the Varzo and Pieve tunnels have the minimum cutter size and numbers among the examined projects.

Even though TBM performance parameters such as the rate of penetration and advanced rate together with utilization are evaluated for these projects, but only the utilization and RMR system relationships are examined herein.

4 DISCUSSION

Seven tunnel projects examined have variety of rock mass properties and conditions. It is found that the rock mass properties and TBM performance has some relationship. In this study, rock mass properties via RMR system and TBM utilization that is related to rock mass properties are examined using regression analysis.

Various regression equations are developed and some meaningful relationship is obtained among the RMR and TBM utilization. In this study, linear ($y = ax + b$); non-linear ($y = ax^b$); exponential ($y = ae^x$); polynomial ($y = ax^2 + bx + c$) and logarithmic ($y = a + \ln x$) relationships are examined in order to develop the most reliable and accurate empirical equations between the RMR and the utilization. In fact, the simple regression is developed to estimate the utilization as a function of RMR.

In this approach, the RMR is independent input variable whereas measured utilization is dependent variable. So, the statistics were used to generate different regression models among the variables. Eventually the maximum coefficient of determination (r^2) was obtained between the RMR and utilization by the use of quadratic regression. Due to that, the obtained relationships are introduced as quadratic in Table 3 and so in Figure 1.

So, the obtained relationships among the variables are quadratic but developed empirical equations are different due to variety of excavated rock mass properties and utilized TBM specifications. So, the utilization

Table 3. Obtained quadratic relationship between RMR and utilization for each project.

Project	U(%) = f(RMR)	r^2
Queens	$U = 5 \times 10^{-5} \times RMR^2 + 0.01 \times RMR - 0.95$	0.93
Manapouri	$U = 4 \times 10^{-5} \times RMR^2 + 0.01 \times RMR - 0.90$	0.97
Milyang	$U = 3 \times 10^{-5} \times RMR^2 + 0.009 \times RMR - 0.17$	0.98
Karaj	$U = 9 \times 10^{-5} \times RMR^2 + 0.0095 \times RMR - 0.049$	0.44
Pieve	$U = 1 \times 10^{-5} \times RMR^2 + 0.0045 \times RMR + 0.15$	0.69
Maen	$U = 2 \times 10^{-5} \times RMR^2 - 0.0003 \times RMR + 0.071$	0.85
Varzo	$U = 1 \times 10^{-4} \times RMR^2 - 0.0075 \times RMR + 0.38$	0.88

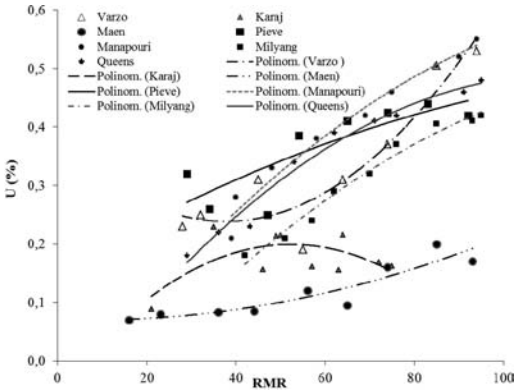


Figure 1. The relationship between the RMR and TBM utilization for each project.

depends on rock mass properties and machine specifications rather than only RMR.

5 CONCLUSIONS

In this study seven mechanical tunnel projects is evaluated from the scope of relationship between the RMR and percentage of TBM utilization. It is found that the RMR and utilization shows various correlations for each project. The best correlations are obtained between the utilization and RMR in quadratic for all tunnels. That means the relationship seems to be quadratic between the variables. However, the utilization depends on excavated rock type, RMR, machine specifications, maintenance, tunnel support time, and so. Due to that, U (%) may be estimated using machine specifications and rock mass properties rather than only RMR. However, the obtained empirical relationship may be useful for same type of project and rock type in early stage of the tunneling.

REFERENCES

Barton, N. 1999. TBM Performance estimation in rock using Q_{TBM}. *Tunnels and Tunneling International* 31(9): 30–33

Benardos, A.G. & Kaliampakos, D.C. 2004. Modelling TBM performance with artificial neural networks. *Tunnelling and Underground Space Technology* 19: 597–605.

Bruland, A., 2000. *Hard Rock Tunnel Boring*, Vol. 3 – *Advance Rate and Cutter Wear*. Doctoral Thesis, Norwegian University of Science and Technology, Trondheim, Norway.

Compagnoni, R., Dal Piaz, G.V., Hunziker, J.C., Gosso, G., Lombardo, B. & Williams, P.F. 1977. The Sesia-Lanzo Zone, a slice of continental crust with alpine high pressure-low temperature assemblages in the Western Italian Alps. *Rend Soc Ital Mineral Petrol* 33: 281–334.

Dal Piaz, G.V. 1988. Revised setting of the Piedmont zone in the northern Aosta valley, Western Alps. *Ofioliti* 13: 157–62.

Frough, O., Torabi, S.R., Yagiz, S. & Tajik, M. 2012. Effect of rock mass conditions on TBM utilization factor in Karaj–Tehran water conveyance tunnel. In N. Phienwej & T. Boonyatee (eds), *Tunnelling and Underground Space for a Global Soci*ety, *Proceedings of ITA-AITES World Tunnel Congress & 38th General Assembly*, 9 p. May 18–23, 2012, Bangkok. Engineering Institute of Thailand.

Gong, Q.M., Zhao, J. & Jiao, Y.Y. 2005. Numerical modeling of the effects of joint orientation on rock fragmentation by TBM cutters. *Tunnelling and Underground Space Technology* 20(2): 183–191.

Hassanpour, J., Rostami, J., Khamechian, M. & Tavakoli, H.R. 2010. TBM performance analysis in pyroclastic rocks: case history of Karaj water conveyance tunnel. *Rock Mechanics and Rock Engineering* 43(4): 427–445.

Khademi Hamidi, J., Shahriar, K., Rezai, B. & Rostami, J. 2010. Performance prediction of hard rock TBM using rock mass rating (RMR) system. *Tunnelling and Underground Space Technology* 25(4): 333–345.

Kim, T. 2004. *Development of a Fuzzy Logic Based Utilization Predictor Model for Hard Rock Tunnel Boring Machines.* PhD Thesis, 254 p., Colorado School of Mines, Colorado USA.

MacFarlane, D.F., Watts, C.R. & Nilsen, B. 2008. Field applica-tion of NTH fracture classification at the Second Manapouri Tailrace tunnel, New Zealand. In M.F. Roach et al. (eds), *Proceedings of North American Tunneling Conference*: 236–242. Littleton: Society for Mining, Metallurgy, and Exploration.

Mancktelow, N. 1985. The Simplon line: a major displacement zone in the western Lepontine Alps. *Eclogae Geol Helv* 78: 73–96.

Milnes, A.G. 1973. Structural reinterpretation of the classic Simplon Tunnel Section of the Central Alps. *Geol Soc Am Bull* 84: 269–74.

Reinecke, T. 1991. Very-high-pressure metamorphism and uplift of coesite-bearing meta-sediments from the Zermatt-Saas zone, Western Alps. *Eur J Mineral* 3: 7–17.

Reinhardt, B. 1966. Geologie und Petrographie der Monte Rosa-Zone, der Sesia-Zone und des Canavese im Gebiet zwischen Valle d'Ossola und Valle Loana (Prov. di Novara, Italien). *Schweiz Mineral Petrogr Mitt* 46: 553–678.

Rostami, J. & Ozdemir, L. 1993. A new model for performance prediction of hard rock TBMs. Rapid Excavation and Tunneling Cogress. 793-809. Boston, USA.

Sapigni, M., Berti, M., Bethaz, E., Busillo, A. & Cardone, G. 2002. TBM performance estimation using rock mass classification. *Int J Rock Mech Min Sci* 39: 771–778.

Steck, A. 1987. Le massif du Simplon – Réflexions sur la cinématique des nappes de gneiss. *Schweiz Mineral Petrogr Mitt* 67: 27–45.

Yagiz, S. 2002. *Development of Rock Fracture and Brittleness Indices to Quantifying the Effects of Rock Mass Features and Toughness in the CSM Model Basic Penetration for Hard Rock Tunneling Machines.* PhD Thesis, 289 p., Colorado School of Mines, Colorado, USA

Yagiz, S. 2008. Utilizing rock mass properties for predicting TBM performance in hard rock condition. *Tunnelling and Underground Space Technology* 23: 326–339.

Yagiz, S. 2009. Assessment of brittleness using rock strength and density with punch penetration test. *Tunnelling and Underground Space Technology* 24: 66–74.

Yagiz, S., Rostami, J., Kim, T., Ozdemir, L. & Merguerian, C. 2009. Factors influencing performance of hard rock tunnel boring machine. In I. Vrkljan (ed.), *Rock Engineering in Difficult Ground Conditions – Soft Rocks and Karst, Proceedings of Eurock 2009 – The ISRM Regional Symposium, Cavtat, Croatia*: 695–700. Leiden: CRC Press/Balkema.

Yagiz, S., Merguerian, C. & Kim, T. 2010. Geological controls on the breakthrough of tunnel boring machines in hard rock crystalline terrains. In J. Zhao et al. (eds), *Rock Mechanics in Civil and Environmental Engineering, Proceedings of Eurock 2010 – The ISRM Regional Symposium, Lausanne, Switzerland*: 401–404. Leiden: CRC Press/Balkema.

This page intentionally left blank

12. Petroleum rock mechanics

This page intentionally left blank

Rock Mechanics for Resources, Energy and Environment – Kwaśniewski & Łydżba (eds)
© 2013 Taylor & Francis Group, London, ISBN 978-1-138-00080-3

Observations of the intrinsic acoustic anisotropy of sands in various geologic settings

L.A. Hathon & M.T. Myers
Shell International E & P, Inc., Houston, TX, USA

ABSTRACT: Acoustic anisotropy in unconsolidated sediments and sedimentary rocks is a function of both the intrinsic character of the material and variability in the externally applied stress field. This paper reports measured intrinsic, acoustic anisotropy in unconsolidated sands from fold-thrust belts, from sub-salt settings, and for sands in extensional basin settings. In the latter, vertical effective stress has been the principal stress throughout the sand's burial history. In contrast in thrust belt settings the principal stress is non-vertical for some portion of the burial history. Similarly, in sub-salt settings horizontal stress gradients arise due to rapid changes in salt thickness. Polar and azimuthal acoustic properties were measured under isostatic stress conditions at in situ stress. Azimuthal anisotropy in thrust belt sands averaged 15% in both crestal and flank structural positions. Polar anisotropies tend to be substantially lower than azimuthal values, averaging half the azimuthal anisotropy. In sub-salt settings the degree of azimuthal anisotropy in sands ranged from 5–10%. Polar anisotropies are low, typically less than 1%. In extensional basin settings, measured azimuthal anisotropy ranged from 0–3%. In these samples, polar anisotropy is larger than the azimuthal value, and varies with the compaction state of the sands. In all cases the level of anisotropy measured in the core plugs was directly tied to textural changes observed in thin section, and is in good agreement with log measures of anisotropy. These observations suggest that a TI medium assumption may be inappropriate in fold/thrust belt and subsalt settings.

1 INTRODUCTION

Predicting reservoir properties ahead of the bit in fold-thrust belts and in sub-salt settings must account for the action of elevated horizontal stresses that are commonly active in these settings. Elevated horizontal stresses result in enhanced compaction of reservoir sands and bounding mudrocks, although the magnitude of these effects is not well understood. One method for estimating the magnitude of the layer parallel compaction is the measurement of directional acoustic properties. This paper reports on the development of laboratory techniques for measuring acoustic anisotropy (polar and azimuthal) on single vertical plugs taken from full diameter core. The laboratory measurements were made under isostatic stress conditions. This implies that any directional differences in acoustic properties are intrinsic to the material and not related to stress state.

2 MEASUREMENT TECHNIQUES

The azimuthal anisotropy measurements were performed by surrounding the sample with a ring of transducers spaced by 45 degrees (Figure 1). This technique was developed so that both axial (vertical) and azimuthal (horizontal) velocities could be measured on a single plug. The axial velocity may cross several discrete beds in the sample, whereas the azimuthal velocities are measured in a single bed in an appropriately oriented plug (perpendicular to bedding). The transducer ring is separated from the plug by a confining fluid; therefore *only compressional* velocity can be measured azimuthally. In addition, both compressional and shear velocities were measured along the plug axis.



Figure 1. Measurement apparatus for simultaneous measurement of azimuthal and axial velocities on a single plug. The dashed lines represent the approximate ray paths of the acoustic measurements.

An isostatic stress condition was chosen for making the measurements. Because the stress state during measurement was the same in all directions, azimuthal differences in the measured acoustic properties are inferred to arise from some directional difference in material properties intrinsic to the core material. These directional differences in material properties are referred to as intrinsic anisotropy. Anisotropy in the applied stress field can also give rise to directional variations in acoustic properties. In general as the applied stress in any direction increases, the velocity in that direction also increases. The isostatic stress condition imposed during measurement eliminates stress as a source of the laboratory measured anisotropy in acoustic properties.

3 POST-TEST IMAGE ANALYSIS

After the acoustic properties were measured, the plugs were impregnated with epoxy and marked with the position of the maximum and minimum azimuthal velocities. Three mutually perpendicular thin sections were prepared from each plug; one cut in the bedding plane (end trim), one cut parallel to the fast direction, and one cut parallel to the slow direction (Fig. 2). Several representative images from each thin section were analyzed using Computer Assisted Petrography (CAP), Shell's proprietary image analysis tool. CAP analysis allows the user to define grain contacts, identify the mineralogy of detrital and authigenic phases, and to classify pore types (such as grain fracture pores). Orientation of individual grain contacts, grain long axes, and pore body long axes can then be calculated from the analyzed images.

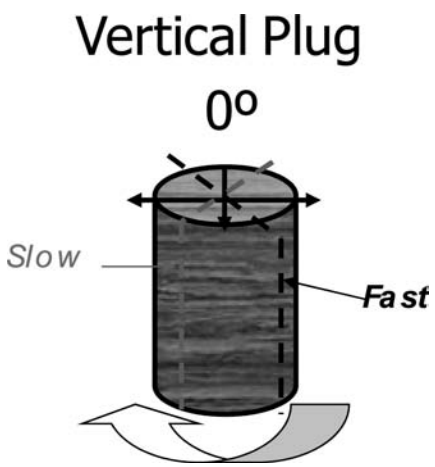


Figure 2. Illustration of an oriented vertical plug on which azimuthal velocity measurements have been made. The position of the zero transducer is marked at the beginning of the test. Once the data have been analyzed, the positions of the fast and slow directions with respect to the zero transducer are determined and transferred to the epoxy impregnated plug. A circular end trim thin section with fast and slow directional marks and longitudinal sections in the fast and slow directions are cut. Representative images from those thin sections are analyzed.

The centroid of each framework grain is also found during a routine CAP analysis. When a sand is deposited, a statistically uniform distribution of grains typically arises because the grains have a characteristic initial size. This means that the center to center separations of nearest neighbors is controlled by the geometric constraints of the packing of the grains. This condition is necessary for the estimation of strain in granular media, in which the grains themselves are not plastically deformed. The strain ellipse is found in CAP using a graphical technique called Fry analysis (Fry 1979). First, the center of each grain is located. Each grain in turn is placed at a reference origin and the positions of all other grain centers in the image are recorded. What results is a distribution of points with a central region which is vacant or shows a low concentration of points. This region results because no two original particles can come closer together than the sum of their radii. The shape and orientation of the strain ellipse are directly recorded by the elliptical form of this vacant region (Ramsay & Huber 1983; Figures 6b–8b).

4 RESULTS AND DISCUSSION

Six measurements of azimuthal and polar anisotropy in compressional velocity were made, three at the crestal location, and three at the flank location, in laterally equivalent strata. Figure 3 illustrates an example of the raw data and the quality of curve fits to the measurements. The anisotropy based on the azimuthal velocities is defined as:

$$\text{Azimuthal Anisotropy} = \\ = (\text{maximum velocity}/\text{minimum velocity}) - 1$$

For the sample shown the calculated anisotropy is 0.16, or 16%. Summary data are shown in Table 1. The average azimuthal anisotropy observed in the thrust belt sands was 15% at the crest, 16.7% on the flank of the structure, and 15.8% overall. Higher values were observed locally and appear to be associated with the presence of small scale (sub-seismic) faults or the presence of deformation bands in the material.

Average polar anisotropy measured in these sands is much lower than the azimuthal values, with an average of 7.5%. The maximum and minimum polar anisotropy show a wide variability (Table 1). As described above, the axial plug velocity may be measured over several discrete beds within the sample, whereas azimuthal anisotropy is more likely to be measured within a single bed. Controls on the development of polar anisotropy include the presence of fine scale laminations, changes in framework mineralogy (e.g. the presence of abundant lignitic fragments at the flank

location which are rare at the crest), changes in depositional facies between the two well locations, as well as the compaction state and stress history. Because the interpretation of polar anisotropy is complicated by all of these variables, as a first look at the magnitude and implications of polar anisotropy, using the average value is appropriate. Although the maximum and minimum values are reported in the data table, for the purposes of this article, discussion is limited to the average polar anisotropy.

The magnitude of the laboratory measurements of compressional azimuthal anisotropy is in good agreement with estimates of shear anisotropy from log data (Fig. 4; Rob Vines, pers. comm.). Although shear splitting is typically interpreted to reflect anisotropy in far field stresses, the laboratory data suggest that the logs may be responding at least in part to intrinsic anisotropy in these sands. These data further suggest that in certain thrust belt settings, a transverse isotropic (TI) medium should not be assumed for seismic processing and interpretation. A transverse isotropic medium exhibits polar anisotropy (perpendicular to bedding) but is isotropic in the bedding plane.

In contrast to the thrust belt sands, for normally consolidated sands (in extensional basins), azimuthal

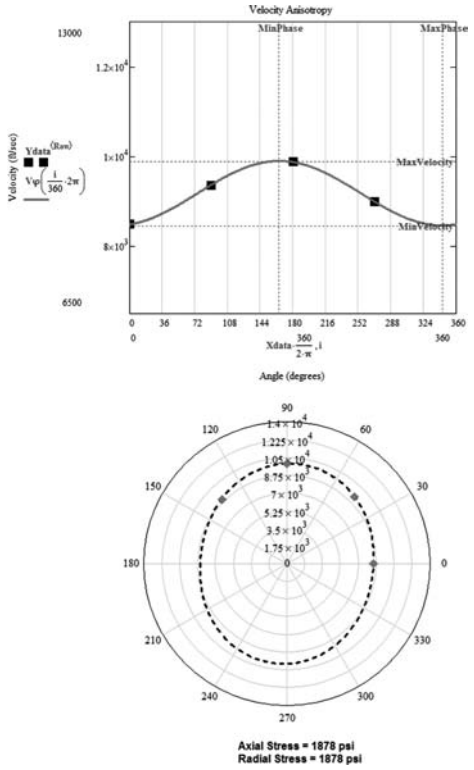


Figure 3. Measured azimuthal anisotropy in a vertical (bedding plane perpendicular) plug from depth A highlighted in Figure 5 at 8166.6 ft. (2489.2 m). Because the transducers are fixed at an arbitrary orientation with respect to the sample a curve is fit to the data and the maximum and minimum azimuthal velocities are picked from the curve. There are two ways to view the data, the curve fit to the left and an azimuthal fit to the right in which the outer circle shows the azimuth around the core plug, the green grid lines are velocity contours, the red points are the measured data and the dashed line is the ellipse that best fits the data. Note that the velocities are in units of ft./sec.

Table 1. Summary of azimuthal and polar anisotropy data for sands from both crestal and flank positions in the thrust structure.

Sample ID	Sample Depth (m)	Vp Hmin (m/sec)	Vp Hmax (m/sec)	VpV (m/sec)	Vp Vlog (m/sec)	AZ anisotropy	Anisotropy	Max Polar Anisotropy	Min Polar Anisotropy
8166.70	2489.2	2591	3011	2869	2667	16%	2.40%	10.70%	4.10%
8023.25	2445.5	2753	3284	3418	3207	17%	13%	24.20%	4.10%
8598.85	2620.9	2611	2963	2979	2855	12%	6.80%	14.10%	0.50%
8568.35	2611.6	2621	3367	2869	2745	28%	4.20%	9.40%	17.40%
8675.00	2644.1	3005	3227	3062	3074	7%	1.70%	1.90%	5.40%
8565.70	2610.8	2597	3002	3280	3103	15%	17.10%	26.30%	9.20%
Average:						16%	7.53%	14.43%	6.78%
Extension 1		2360	2379	2195		0%	8.00%	8.40%	7.50%
Extension 2		2237	2317	2403		1.04%	5.60%	7.40%	3.70%

Extension 1 and 2 are samples taken from extensional basin settings in which vertical effective stress (VES) is the principal stress, and no azimuthal anisotropy was observed (or expected). Acoustic log velocities are also reported for the sands to illustrate agreement between laboratory and log data (B. Couzens, pers. comm.). Average polar anisotropy is the ratio of the average azimuthal velocity to the axial velocity measured in the plug. Measurement uncertainty is on the order of ~2% for the axial velocities and on the order of 3–4% for the horizontal velocities.

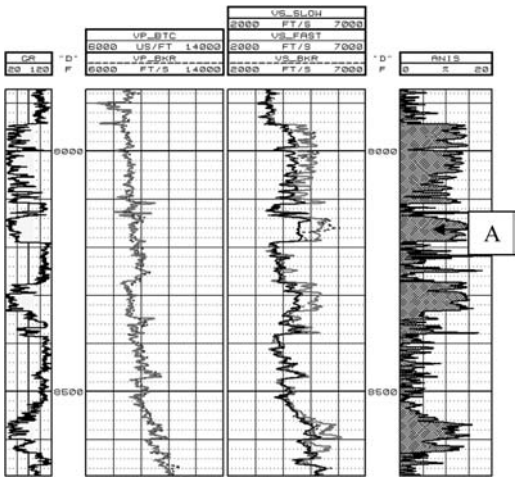


Figure 4. Log data from the crestal well (R. Vines). In this vertical well we see shear anisotropy in the sands. The polarization of the faster wave is inferred to be aligned with the regional stress field. Shear splitting suggests that the "stress-induced" anisotropy in the sands is on the order of 15%. Location A is the depth at which the plug measurements shown in Figure 4 were made. Note that the magnitude of the intrinsic anisotropy in the core plugs, as reflected in the compressional anisotropy measured under isostatic stress conditions, is in good agreement with the magnitude of the log measured shear anisotropy.

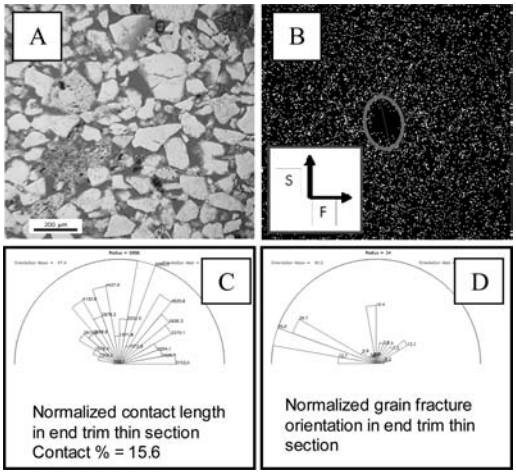


Figure 5. Image analysis from sample at 8166.7 ft. (2489.2 m) **A**. Plane light image from an end trim thin section interpreted to generate data in B, C, and D. Arrows indicate grain fractures. Red arrows indicate representative grain contacts. Black arrows indicate grain typical grain fractures. **B**. Strain ellipse from Fry analysis performed on end trim thin section. Note that significant shortening has occurred parallel to the fast velocity direction (indicated by the F arrow on the inset; S refers to the slow direction). **C**. Normalized grain contact orientation. Grain contacts tend to be oriented nearly perpendicular to the fast velocity direction. **D**. Normalized grain fracture orientation. Fracture long axes (see arrows on plane light image) are oriented nearly perpendicular to the slow direction.

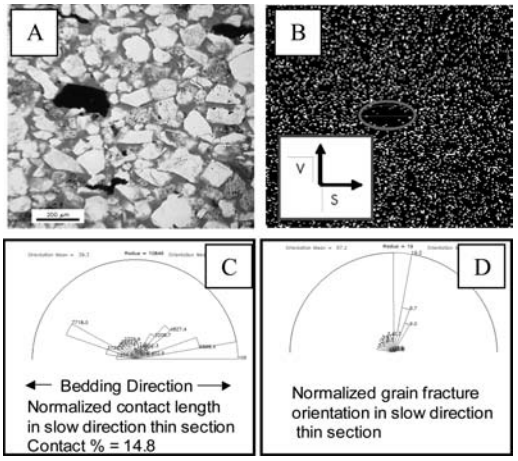


Figure 6. Image analysis from sample at 8166.7 ft. (2489.2 m) **A.** Plane light image from a slow direction thin section interpreted to generate data in B, C, and D. **B.** Red arrows indicate representative grain contacts. Black arrows indicate grain typical grain fractures. Strain ellipse from Fry analysis performed on slow direction thin section. Note that significant shortening has occurred due to vertical (normal burial) compaction (indicated by the V arrow on the inset; S refers to the slow direction). **C.** Normalized grain contact orientation. Grain contacts are in the bedding plane, parallel to the slow velocity direction. **D.** Normalized grain fracture orientation. Fracture long axes are oriented perpendicular to the slow direction.

anisotropy is nearly zero. Polar anisotropy is substantial, however, even in first cycle basins and at relatively low effective stresses. In extensional basins where elevated horizontal stresses have not developed, a TI medium is an appropriate assumption.

As shown in Figures 5–7 the influence of layer parallel compaction in the thrust belt samples is evidenced by the rotation of grain contacts out of the bedding plane and into a direction perpendicular to the fast azimuthal velocity direction. Figure 5 is from the end trim, Figure 6 is from the measured slow direction and Figure 7 is from the measured fast direction. Each figure shows a representative plane light image (A) from one of the three mutually perpendicular thin sections. Examples of areas in thin section that are interpreted as grain contacts are indicated by red arrows while grain fractures are indicated by black arrows in Figures 5a–7a.

The strain ellipse for each direction is labeled B in Figures 5–7. The end trim section, Figure 5, contains both the fast and the slow azimuthal velocity directions. A substantial shortening is observed along the fast direction as indicated by the significantly smaller axis of the strain ellipse in this direction. In the slow direction, the strain recorded in the sample is consistent with normal burial compaction (Fig. 6). Here the shortening is parallel to the vertical direction. The data from the thin section in the fast direction show the measured horizontal strain due to layer parallel compaction

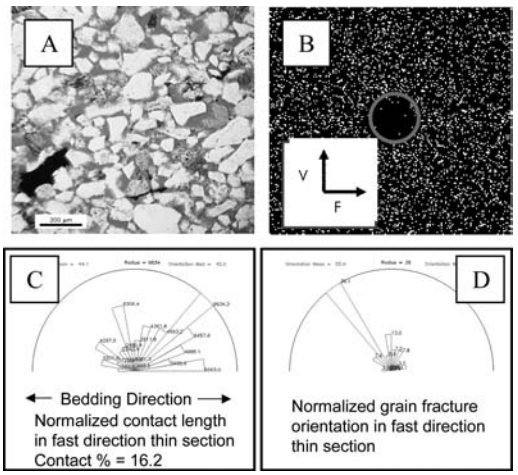


Figure 7. Image analysis from sample at 8166.7 ft. (2489.2 m) **A**. Plane light image from a fast direction thin section interpreted to generate data in B, C, and D. Red arrows indicate representative grain contacts. Black arrows indicate grain typical grain fractures. **B**. Strain ellipse from Fry analysis performed on fast direction thin section. Note that the magnitude of compaction in the fast direction is equal to compaction in the vertical (normal burial) direction (indicated by the V arrow on the inset; F refers to the fast direction). **C**. Normalized grain contact orientation. Although some grain contacts remain in the bedding plane, significant rotation out of the bedding plane has occurred. **D**. Normalized grain fracture orientation. Fracture long axes are oriented at a high angle to the fast velocity direction.

is equal to the vertical strain due to burial (Fig. 7). Therefore the strain and measured velocities are nearly identical in the fast and vertical directions in this sample. This is consistent with the generally low values for minimum polar anistropy shown in Table 1.

Acoustic energy is transmitted through a granular material at points of grain contact. Therefore, the greater the degree of grain contact perpendicular to the transmission direction of the acoustic energy, the faster that energy can be transmitted through the sample. Grain contact orientations are shown in part C of each figure. As shown in these rose diagrams, the total length of contacts in a particular direction determines the size of the section in any orientation around the half-circle. In the end trim section, grain contact orentations are strongly aligned perpendicular to the fast direction (Fig. 5c).

In the slow direction (the vertical-VHmin plane), nearly all grain contacts are in the bedding plane (horizontal), perpendicular to the axial velocity direction (Fig. 6c). In all cases the vertical velocity is faster than the horizontal minimum velocity (see maximum polar anisotropy, Table 1), consistent with the bedding plane parallel orientation of the grain contacts. In the fast direction, although bedding plane parallel contacts are still present, grain contacts have rotated out of the bedding plane and into a high angle to the fast velocity direction (Fig. 7c). Contact orientation in the fast direction (the vertical-VHmax plane) is distinctly different to that in the slow direction (compare Figures 6c and 7c).

Grain fractures, which are rarely observed in normal compaction settings, are often found in materials that have experienced significant lateral strain. Grain fracture pores tend to be oriented perpendicular to, or at a high angle to, associated grain contacts. Normalized grain fracture orientations are shown in part D of each figure. In each case, grain fracture long axes are preferentially oriented perpendicular to the slow direction. This is expected because the direction of the highest compliance of the fracture is consistent with the lowest velocity.

5 CONCLUSIONS

For thrust belt settings in which the onset of elevated horizontal stress occurs while the sediments are still unconsolidated azimuthal anisotropies can be high. In the Northwest Borneo fold-thrust belt, compressional azimuthal anisotropy averages 15%. Average polar anisotropies are substantially lower than azimuthal values. Laboratory measures of compressional acoustic anisotropy are the same order of magnitude as estimates from shear splitting observed in log data. This observation suggests that the logs are responding at least in part to accumulated strain in the material, and not solely to far field stresses. A TI medium assumption is inappropriate, because the sands are anisotropic in the bedding plane as well as perpendicular to it.

Sands displaying azimuthal anisotropy have characteristic textural features that have given rise to their anisotropic acoustic properties, and reflect the layer parallel compaction that has resulted from elevated horizontal stress. Grain contacts tend to be oriented perpendicular to the fast direction. Grain fractures tend to be oriented perpendicular to the slow direction. It is thought that both the fractures and the contact anisotropy discussed above contribute to the total velocity anisotropy. Strain analysis of oriented thin sections shows that the degree of horizontal compaction in thrust belts can be as high as compaction resulting from vertical stresses. For the thrust belt structure, accumulated strain in the sands, as indicated by the magnitude of the azimuthal acoustic anisotropy, is independent of structural position (whether on the crest or flank) but can be elevated proximal to sub seismic faults and deformation bands.

REFERENCES

Fry, N. 1979. Random point distributions and strain measurement in rocks. *Tectonophysics* 60: 69–105.

Ramsay, J.G. & Huber, M.I. 1983. *The Techniques of Modern Structural Geology: Strain Analysis.* London: Academic Press.

This page intentionally left blank

Rock Mechanics for Resources, Energy and Environment – Kwaśniewski & Łydżba (eds)
© 2013 Taylor & Francis Group, London, ISBN 978-1-138-00080-3

Well stimulation on the basis of preliminary triaxial tests of reservoir rock

V.I. Karev & Yu.F. Kovalenko
Ishlinskii Institute for Problems in Mechanics of Russian Academy of Sciences, Moscow, Russia

ABSTRACT: The purpose of the paper is the presentation of the geomechanical approach to the development and the improvement of methods for increasing well productivity and reservoir recovery. Control stress-strain state in the vicinity of a well to enhance the permeability of the well drained zone increases significantly efficiency of stimulation of a well. It is carried out by directed unloading of the reservoir on the basis of knowledge of the deformation, strength and filtration properties of specific field rocks. Examination of rock mechanical properties is made by laboratory tests of rock samples at the true triaxial apparatus. The methodic and the results of laboratory studies of rocks and of pilot field works on wells are presented on the example of a specific field. They have shown high efficiency of this approach.

1 INTRODUCTION

As the result of mudding while drilling, siltation of a reservoir during the operation, plastic deformation of rocks under the influence of shear stresses, wells are often surrounded by poorly permeable zone. In addition, efficiency of many widespread EOR methods, such as acid treatment, hydropulse impact, is caused by the existence of a good hydrodynamic link between the reservoir and the well.

The permeability of well drained zone can be restored by a simple and effective way – by creating a new artificial system of filtration channel by rock cracking using directional unloading reservoir. This method, known as the "geoloosening method" (Khristianovich et al. 2000), has successfully passed pilot field tests, and is based on the capability of majority of rocks to fracture and to disintegrate in case of the emergence of certain level shear stresses. The required stress state can be created by decreasing the pressure in the well, combined with certain operations, intended priory to form a bottom geometry (more perforation, slot cutting, etc.). The value of pressure drawdown and bottom hole design can be established by the direct physical modeling of the conditions that occur near the well. For this purpose, the Triaxial Independent Load Test System was created at Institute for Problems in Mechanics of Russian Academy f Science. It is a unique research complex that allows using rock specimens to recreate any stress conditions, arising in the reservoir during any process operations in the well and to study their effect on permeability. Tests are carried out on rock specimens, extracted from the particular reservoir core. The facility is equipped with the automatic control system, which allows to set the required loading program and to conduct control as by force and by displacement. Loading trajectories are determined based on calculations: in simple cases, such as simulation of the conditions in the vicinity of the open borehole – analytically, in more complex cases – numerically.

2 PHYSICAL MODELING OF MECHANICAL PROCESSES IN THE VICINITY OF A WELL

2.1 *Ways to control and calculate stress state in the vicinity of a well*

Stress state around a well can be controlled in fact by only two ways: by changing pressure in it or by creating certain bottom hole geometry. There are two main designs of a bottom hole: an open hole when cementing the production string is made up to the reservoir and an cased hole when the production string is lowered and cemented to the bottom of a well. In the second case, the hydrodynamic link between a reservoir and a well is done by perforation of the intervals of oil layers. Perforation, creating holes in the production string can be different type by a number of holes, their geometric form and depth. It is also possible to cut slits on the bottom hole of vertical or horizontal orientation. Respectively, stress-strain state near a well will be changed differently in dependence on the bottom hole design when changing pressure in a well.

In the case of an open hole, stresses in the vicinity of a well can be determined analytically by solving the Lame's problem. In general case, it is necessary to use numerical methods. Deformation of rock can switch to non elastic phase in dependence on rock properties and pressure drawdown value. Then it is necessary to solve an elastic-plastic problem in order to determine stresses and the size of the plastic zone.

2.2 *Open hole*

Before drilling a well initial stresses act in the reservoir. They were formed by weight of overlying rocks, reservoir fluid pressure, geological structure, tectonic processes. Rock pressure in the vertical and horizontal directions can be different and depends on the rheological properties of the rock, geological structure and the degree of tectonics. For simplicity, we assume that rock massif is initially compressed in all directions rock pressure $q = -\gamma H$, with reservoir pressure p_0, where γ is specific weight of the overlying rocks, H is depth of the reservoir. Then effective stresses acting on soil matrix will (Khristianovich 1941).

$$s_n = q + p_0(1-\delta), \quad s_n, q < 0, p_0 > 0 \tag{1}$$

where s_n = normal stresses, acting on the plate with the normal $\boldsymbol{n}$; δ = the share of contact areas relative to the entire grain surface of soil matrix.

If the contact areas between the grains of soil matrix are small ($\delta \approx 0$), the pressure compressing soil matrix equals to the total rock pressure at a given depth minus reservoir pressure. The most characteristic values of δ for rocks are in the range from 0 to 0.2.

After drilling a well there is a redistribution of stresses in its vicinity. Figure 1 shows schematically a section of the well and the stresses acting in its vicinity: radial σ_r, ring σ_θ and axial σ_z.

Since the diameter of a well is usually much less than formation thickness we can assume, that plane strain conditions are created in the vicinity of a well. If we consider the formation as an elastic body (yield strength is high), the stresses arising in the vicinity of an open hole filled with fluid under pressure p_w are determined by the well-known from the theory of elasticity solution of Lame'problem for a cylindrical cavity under the action of external compression and internal pressure (Lyav 1935).

$$\sigma_r = -(q + p_w)(R_w / r)^2 + q \tag{2}$$

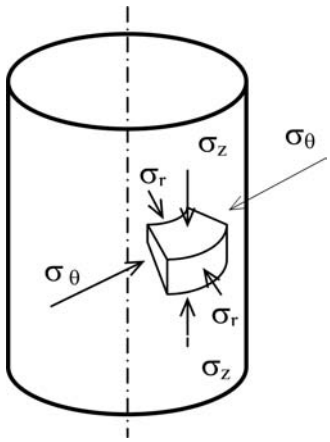


Figure 1. Stresses acting in the vicinity of the well.

$$\sigma_\theta = (q + p_w)(R_w / r)^2 + q \tag{3}$$

$$\sigma_z = q \tag{4}$$

where $p(r)$ = pressure at a distance r from the axis of a well; R_w = radius of a well.

Stresses in the soil matrix using (1) are expressed by

$$s_r = -(q + p_w)(R_w / r)^2 + q + p(r)(1-\delta) \tag{5}$$

$$s_\theta = (q + p_w)(R_w / r)^2 + q + p(r)(1-\delta) \tag{6}$$

$$s_z = q + p(r)(1-\delta) \tag{7}$$

The maximum shear stresses are:

$$\tau = 1/2(s_r - s_\theta)$$

They are expressed by:

$$\tau = -(q + p_c)(R_c / r)^2 \tag{8}$$

The stresses on the wall of the well, i.e. at $r = R_w$ are:

$$s_r = -\delta p_c \tag{9}$$

$$s_\theta = 2(q + p_c) - \delta p_c \tag{10}$$

$$s_z = q + (1-\delta) p_c \tag{11}$$

$$\tau = -(q + p_c) \tag{12}$$

Taking into account that pressure drawdown in a well is equal by definition

$$\Delta p = p_0 - p_c, \tag{13}$$

Formulas (9)–(11) can be easily expressed as dependences on the value of pressure drawdown

$$s_r = -\delta(p_0 - \Delta p) \tag{14}$$

$$s_\theta = 2q + (2-\delta)(p_0 - \Delta p) \tag{15}$$

$$s_z = q + (1-\delta)(p_0 - \Delta p) \tag{16}$$

Pressure drawdown can be expressed by the components of stresses, such as:

$$\Delta p = p_0 - \frac{s_\theta - 2q}{2-\delta} \tag{17}$$

2.3 *Description of facility*

Physical modeling of the processes occurring in the vicinity of a well during certain production operations and studying how the permeability of a specific field changes is conducted by using a special experimental setup. Figure 2 shows a photograph of Triaxial Independent Load Test System (TILTS). TILTS is the setup allowing a study of the deformation, strength and filtration properties of rocks by testing rock samples of a cubic shape with an edge of 40 or 50 mm (Karev & Kovalenko 2013). The original kinematic scheme applied in the design of the loading assembly allows the press plates to converge in three directions, without creating obstacles to each other, which makes it possible to load a sample independently for each of the three axes.

TILTS belongs to a class of electro-hydraulic testing machines, it is equipped with an automated control system with feedback. TILTS has an automated system of permeability, which allows to measure the permeability of a sample along one of its axes in the automatic mode.

Permeability is determined by blowing air through the sample due to the presence of perforation in two opposing press plates of the setup. Permeability is calculated by an air flow rate.

Figure 3 shows a rock sample after the test.

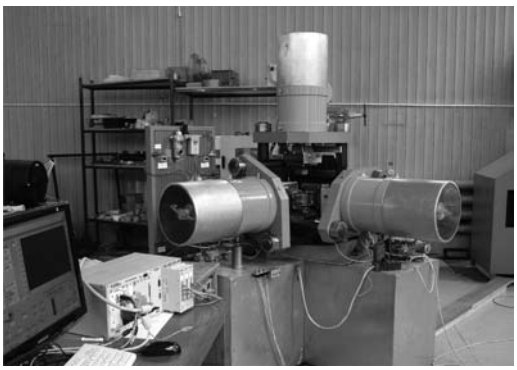


Figure 2. Triaxial Independent Load Test System (TILTS).

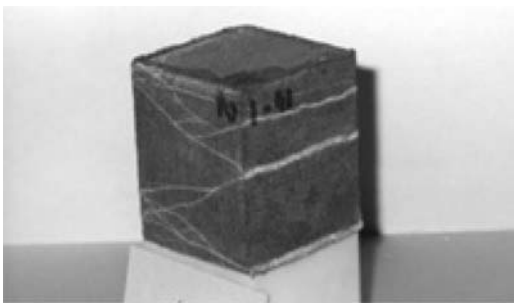


Figure 3. The cracked sample after the test.

2.4 *Test programs*

There are three main programs of sample loading, simulating the conditions of rock compression with increasing pressure drawdown in a well. These programs allow to determine the mechanical properties of the specific field rock in the preliminary stage:

program 1 – "generalized shift";
program 2 – "generalized stretch";
program 3 – "generalized compression."

Figure 4 shows the program 1, which simulates the stresses in the vicinity of an open hole. The stresses σ_1, σ_2, σ_3 are the absolute values of the stresses applied to the sample on axes 1, 2, 3. They correspond to the effective stresses s_z, s_θ, s_r, acting in the vicinity of a well.

The strains of the sample are measured in three directions and its permeability is recorded in any of the directions during the experiment. Tests are carried out in three stages:

Stage 1. A sample is pressed evenly on all the sides to a stress equal to the difference between the value of rock pressure at the depth- and the value of reservoir pressure with a coefficient $p_0(1-\delta)$ (segment OA on Figure 4). Point A corresponds to the stresses acting in the soil matrix before the well drilling.
Stage 2. One component of stress σ_2 is continuing to grow (segments AB), the second σ_1 remains constant, and the third σ_3 is decreasing. The loading is developed so that the average stress $\sigma = (\sigma_1 + \sigma_2 + \sigma_3)/3$ all through the Phase 2 retains, it follows from (5)–(7). Endpoint phase (point B) corresponds to the state when the well is drilled. Vertical stress on the wall of the well is equal to

$$q + (1 - \delta)p_w$$

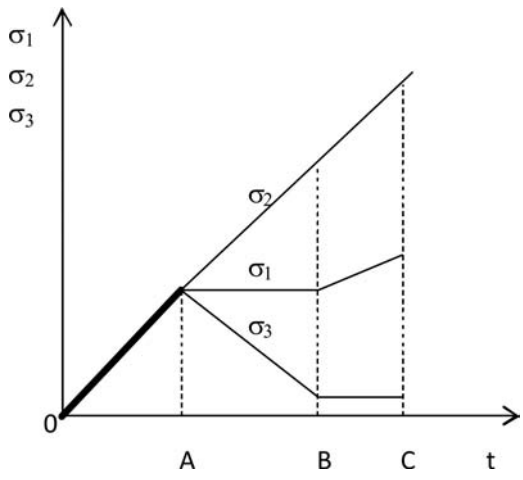


Figure 4. Test program modeling the stresses in the vicinity of an open borehole.

Stage 3. The process of reducing the pressure in the well (segment BC) is simulated in the third stage. Thus, as it can be seen from expressions (5)–(7), the stress σ_3 corresponding to the radial stress in the soil matrix s_r is falling slightly with decreasing bottom hole pressure, and the circular and vertical stresses are rising, but the vertical stress is increasing about two times slower.

The third stage lasts as long as the sample is not destroyed or stresses do not reach the values corresponding to the maximum possible pressure drawdown (complete draining of the well). In the second case, the sample is unloaded in order to determine its permeability during the unload. Process of unloading is developed in exactly the opposite manner to the loading program of the sample.

2.5 *Geoloosening phenomenon*

In the result of a large amount of conducted on TILTS investigations of rock properties of many fields which have a different lithological composition, deposit in the wide range of depths, it was found out that the most of the rocks have the following property (Karev & Kovalenko 2006). When shear stresses reach a certain value, depending on the rock properties, rock is cracking, disintegrating, which results in a sharp irreversible increase in rock permeability. This effect is called "geoloosening". On the basis of its use the technology of increasing well productivity and reservoir recovery was developed and patented. It was successfully pilot-tested in a number of fields in Siberia and the Urals, and has proved to be very efficient.

We should note that up to date the development of enhanced oil recovery methods has not taken into account this phenomenon of rock permeability dependence on stresses, although under certain conditions it is crucial to select some optimal parameters of well drilling and operation. Practice has shown the high efficiency of the joint application of the geoloosening technology and others widely used methods to increase well production, in particular, the treatment of oil layers with chemicals.

3 REALISATION OF THE PROPOSED APPROACH

3.1 *Essence of the proposed method*

The proposed method consists in the following. Rock samples are selected from productive strata. Compression conditions that occur in the bottom hole in different designs of the bottom hole and different pressure drawdown are modeled by using TILTS. Deformations and permeability of the samples are measured during the process of loading. The stresses at which the cracking and irreversible permeability increasing of the samples occurs, are determined on the base of the test results. Corresponding bottom hole design and pressure drawdown are chosen. Then these conditions are realized on the well. An additional perforation can be produced before wellbore treatment to initiate a process of structural changes in the stratum. This can be made both on the casing boreholes and on the open holes. The perforation type – the number of holes, their size and form is determined on the base of tests by using TILST and calculations.

Pressure drawdown is supported either until an increasing of the flow rate, or until the termination of its increase. After that, chemical reagent is pumped into the reservoir. It is kept in the reservoir during the time required to complete the chemical reaction. Then the reaction products are pumped from the reservoir, and the wellbore is switched to the operating mode.

After processing the reservoir using chemical reagent repeat working out the well is produced with a long-term pressure drawdown at the same conditions. Recreating pressure drawdown, which has to have the value not less than selected and keeping its value allow to increase the permeability of the bottom hole rock due to more complete removal of the reaction products and additional destruction of reservoir rocks which are partially dissolved (or weakened) under chemical treatment.

Mud acid of different composition and concentration can be used for clay-containing low-permeability reservoirs of fields in Western Siberia as a chemical reagent, for example, "PFC-A" etc. Selection of chemicals, volumes of injection in the well, time of its impact on the reservoir rock are determined through special laboratory experiments on chemical exposure of chemicals to reservoir rock of the field. Nature and impact of chemicals to rock permeability should be established and appropriate calculations are to be conducted.

This way of processing layer zones can significantly reduce operating costs and reduce the risk of irreversible changes in the bottom zone of the reservoir, which can lead to poor operational capacity of the well.

Creating the pressure drawdown at the bottom hole, no less than one selected on the base of rock sample tests and its maintenance either until increase the flow rate, or until termination of its increase allows to implement the process of rock fracture at the bottom hole for an essential increase in its permeability and, as a consequence, growth of the flow rate of fluid. Increasing the fluid flow rate gives an indication of the beginning of the geoloosening process in the wellbore drained zone, and termination of its increase indicates that the geoloosening process has been completed. In the result of geoloosening a high permeability zone is formed in the vicinity of the well.

Injection of the chemical reagent into the bottom zone of the well can further extend the filtration channels in the reservoir due to chemical reactions. If this zone has a poor permeability, the chemical reagent can penetrate into the formation only for a short distance. Preliminary increasing permeability of wellbore zone by geoloosening allows the chemical reagent to penetrate into the reservoir faster and deeper and as a result, the chemical treatment efficiency of reservoir is much higher.

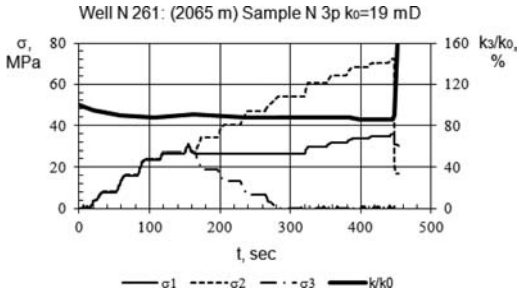


Figure 5. Change of the stress components and permeability during the test.

Pumping from the reservoir allows to clear the filtration channels from the reaction products and thus contributes to the target output of the fluid to the well.

3.2 *Test results*

The described approach has been implemented at the Kislorskoye field of Russian Innovation Fuel and Energy Company "RITEC".

Samples for tests with edge 50 mm were prepared of core taken from the well N 261 drilled on Jurassic sediments of Kislorskoye field. The samples were tested by TILTS by the method described above. During the tests, it was established that the samples begin to break down at pressure drawdown equal 100–120 at.

Figures 5, 6 show the graphs obtained in tests of a sample on program 1, which simulates the stresses in the vicinity of the open borehole. Coring depth is 2065 m. Initial permeability k0 = 19 mD. In this test, it was taken $\delta = 0$.

During the test of the sample when the loading parameter $\sigma 2$ (monotonically increasing stress components) reached value of 72 MPa, which corresponds to pressure drawdown 110 at (17), it began to deform intensive inelastically (creep), that was accompanied by a sharp increase in permeability that can be seen from the strain curves and permeability change curve. After the test macrocracks system was formed in the sample (see Figure 3.), which was the reason for a significant increase in its permeability.

3.3 *Field works on the wells*

Field works were conducted on the wells N 302 and N 331 at Kislorskoye field. As a chemical reagent, 12% of mud acid was used in the well N 301.

The well had the following parameters:

1. Operating horizon is Tyumen formation, stratum is J_{3-4}, the depth of the reservoir is 2050 m.
2. Lateral horizontal borehole.
3. Production rate was 5 m^3 per day.

Jet pump and packer were lowered in the well for treatment (Figure 7). By their using the pressure drawdown of 110 at was created, which value was monitored by the deep gauge. Simultaneously rate of flow was being controlled, and it was increasing gradually. On

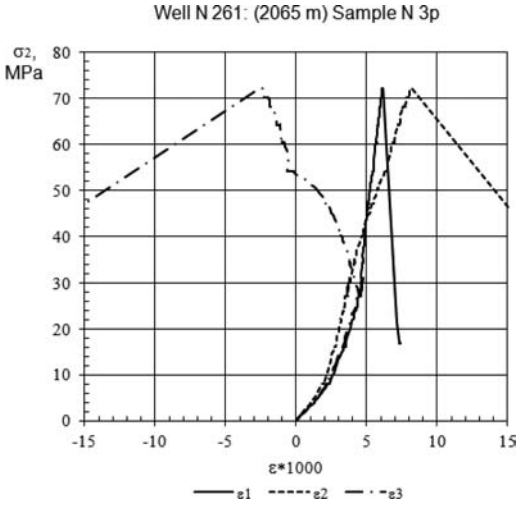


Figure 6. Sample strain curves.

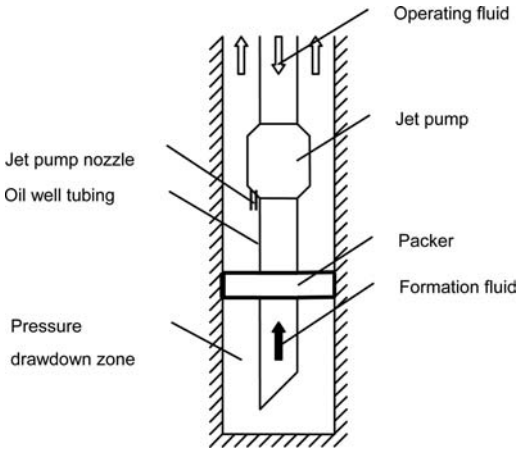


Figure 7. Scheme of jet pump work.

the expiration of 10 hours flow rate to the well reached 19 m^3 per day and its growth stopped, that indicated the completion of cracking and breaking the soil in the bottom zone of the well.

After this the injection of 6 m^3 12% mud acid was made into the formation. The well was left for 2 hours to react. Then the evacuation of reaction products was carried out from the reservoir using the jet pump at pressure drawdown equal 100 at in volume 7 m^3.

After repairing the well was put into operation, and its production rate became 9 m3 per day.

Similarly the well N 331 was treated with the use of other chemicals – a mixture of organic acid PFK-A and hydrochloric acid.

The well had the following parameters:

1. Operating horizon is Tyumen formation; strata are J_2 and J_{3-4}.
2. The well was perforated at depth 2200 m.
3. Production rate was 4 m^3 per day.

After repairing the well was put into operation and its production rate became 8.5 m^3 per day. Thus the production rate of both wells increased by about two times due to the joint use of the geoloosening method and chemical treatment.

It should be noted that the experience of using only the chemical treatment of the well drained zone at this field practically has not worked out. The resulting low permeability around the well did not let any chemical agents penetrate deep into the formation. The use of the geoloosening method alone at other wells of this field gave a production rate increase of about one and half times. It can be concluded that the overall result of increasing the permeability of the well drained zone by the use of geoloosening and chemical treatment is significantly higher than from the use of each of these methods separately.

4 CONCLUSIONS

Well stimulation on the basis of a preliminary study of the mechanical properties of reservoir rocks by triaxial tests and a choice of an optimal method of impact on a reservoir became a very effective way to increase the well production rate. The results of the joint use of the geoloosening method and the acid treatment of the wells, presented in the paper, show this. A preliminary geoloosening operation may increase the effectiveness of other well-known methods which need a good hydrodynamic link well and reservoir, for example, hydropulse impact (Karev & Kovalenko 2012).

REFERENCES

Karev, V.I. & Kovalenko, Yu.F. 2013. Triaxial loading system as a tool for solving geotechnical problems of oil and gas production. In M. Kwaśniewski et al. (eds), *True Triaxial Testing of Rocks*: 301–310. Leiden: CRC Press/Balkema.

Karev, V.I. & Kovalenko, Yu.F. 2006. Dependence of permeability layer zones from depression and design face for various types of rocks. *Technologies of FEC* 6: 59–63. (in Russian)

Karev, V.I. & Kovalenko, Yu.F. 2012. Joint application of wave technology and reservoir directional unloading for increase in well production. In *Proc. Int. Conf.* (Moscow, 27–29 November 2012). Moscow: Institute of Computer Studies. (in Russian)

Khristianovich, S.A., Kovalenko, Yu.F., Kulinich, Yu.V. & Karev, V.I. 2000. Improvement of productivity of oil wells using the geo-loosening method. *Oil & Gas Eurasia* 2: 90–94.

Khristianovich, S.A. 1941. On flow gas-saturated liquid in porous rocks. *J. Appl. Math. Mech.* 2: 277–282. (in Russian)

Lyav, A. 1935. *Mathematical Theory of Elasticity.* Moscow: ONTI. (in Russian)

Rock Mechanics for Resources, Energy and Environment – Kwaśniewski & Łydżba (eds)
© 2013 Taylor & Francis Group, London, ISBN 978-1-138-00080-3

Evaluation of stress changes due to multi-stage hydraulic fracturing – Consideration of field results

N.B. Nagel, F. Zhang, M.A. Sanchez-Nagel & B. Lee
Itasca Houston, Inc., Houston, Texas, USA

ABSTRACT: In horizontal well completions for unconventional reservoirs, multiple hydraulic fracturing stages, each often with multiple clusters, are used to provide sufficient stimulated area to make an economic well. Each created hydraulic fracture alters the stress field around it. When hydraulic fractures are placed close enough together, the well-known stress shadow effect occurs in which subsequent fractures are affected by the stress field from the previous fractures. The effects include higher net pressures, smaller fracture widths and changes in the associated 'complexity' of the stimulation. In this paper, we present the results of a numerical evaluation of the effect of multiple hydraulic fractures on stress shadowing for a horizontal well in North America and attempt to highlight the potential cause of the deviation between numerical predictions and field results. The study provides insight into understanding stress shadow effects under field conditions as well as the potential impact on hydraulic fracture stimulations. In addition, the results may help explain the relationship between stress shadowing and microseismic behavior seen in multi-stage horizontals.

1 INRODUCTION

The world-wide boom in shale gas, shale oil and other unconventional developments is now well-known, and the boom has had a marked impact on the balance of hydrocarbon production. For example, where states such as Texas and Alaska have been hydrocarbon production leaders for decades, the Energy Information Agency (EIA 2012) notes that North Dakota has become the second largest oil producer in the United States due to production from the Bakken shale. These shale developments, notably beginning in the Barnett in the 1990s, have been driven by: 1) the application of horizontal wells; 2) the application and improvements in multi-stage hydraulic fracturing; and 3) significant commodity prices (GWPC 2009 and King 2010).

In multi-stage hydraulic fracturing, dozens, and perhaps 50 or more, hydraulic fractures are created along a long horizontal wellbore. Due to the inflation of the hydraulic fracture, and placement of proppant to keep the fracture permanently open, the stress field around the hydraulic fracture is altered. As far back as Sneddon's work on the evaluation of stress near a crack (Sneddon 1946), numerous authors have looked at the impact of stress field changes around hydraulic fractures (Nagel & Sanchez-Nagel 2011, Rios et al. 2013 and Warpinski et al. 2012). The stress field change, principally the increase in the minimum horizontal stress, Shmin, caused by a hydraulic fracture (typically the final, propped hydraulic fracture) is called the stress shadow effect or simply the stress shadow.

As noted by Nagel & Sanchez-Nagel (2011): 1) the increase in Shmin (stress shadow) extends significant distances (as much as or more than 1000 m) behind a fracture and spreads out above and below it; 2) the increase in Shmin due to a stress shadow is largely unaffected by either the in-situ rock mechanical properties or the stress ratio (though these do appear to affect changes in the vertical stress, Sv, and the maximum horizontal stress, SHmax); 3) reducing hydraulic fracture stage spacing results in a greater minimum Shmin stress increase in the inter-fracture region as the stress shadow from each fracture overlaps more as stage spacing is reduced, and 4) the stress shadow tends to stabilize the natural fracture system behind the fracture tip.

Within this paper, the numerical results from several stress shadow modeling studies, conducted in support of completion operations for a horizontal well in North America, are presented. Using a continuum code, stress shadow evaluations are first presented with a focus on the magnitude and behavior of stress changes between hydraulic fracture stages. Following this, numerical results for the full well are compared to field results. The results show a good fit in early stages, but a poor fit towards the heel of the well. Finally, numerical results using a discrete element model are used to consider the cause of the miss-match between the original numerical predictions and the field data.

2 CONTINUUM SIMULATIONS

2.1 *Numerical model*

The continuum simulations were performed with ageneral-purpose, three-dimensional, explicit, finite-difference program for engineering mechanics computations. The simulation domain was represented by

polyhedral elements within a three-dimensional grid. Each element behaved according to the prescribed linear stress/strain lawin response to applied forces or boundary restraints. All simulations were performed in large-strain mode, and closure on proppant was simulated by inserting beam elements once the hydraulic fracture was fully open.

2.2 *Field conditions*

For the initial stress shadow evaluations, the well conditions were as follows:

- Depth, TVD: ~1450 m
- Horizontal Length: ~650 m
- Vertical Stress: 35.3 MPa
- Max. Horz. Stress: 32.6 MPa
- Min. Horz. Stress: 23.8 MPa
- Pore Pressure: 17.7 MPa
- Rock Bulk Modulus: 8.9 GPa
- Rock Shear Modulus: 4.7 GPa
- Fracture Net Pressure: 1.4 MPa

2.3 *Simulation of a hydraulic fracture*

Simulated hydraulic fracture dimensions and net pressures were initially determined from a commercial hydraulic fracture simulator (used for design purposes). These hydraulic fracture dimensions and net pressures were then used as boundary conditions within the continuum model. Figure 1 shows a cutaway view (in both the vertical and horizontal planes) of an example stress shadow resulting from a single hydraulic fracture. Locations for subsequent hydraulic fracture stages are also shown to indicate the potential influence of the stress shadow at these locations.

2.4 *Single hydraulic fracture stress shadow results as a function of fracture height*

A series of initial simulations were conducted to evaluate the influence of hydraulic fracture height (for a set fracture half-length) and stage spacing prior to the simulation of the field case horizontal well (with 15 stages). For a constant fracture half-length of 120 m, fracture height was varied from 40 m to 60 m to 80 m. Stage spacing was varied from 54 m to 70 m to 154 m. Figures 2 through 4 show the stress shadow effect on Shmin, SHmax, and Sv, respectively, along the wellbore as a function of hydraulic fracture height. The hydraulic fracture was at position 465 m along the wellbore.

From the figures, it is clear that: 1) the stress shadow effect will occur on both sides of a hydraulic fracture;

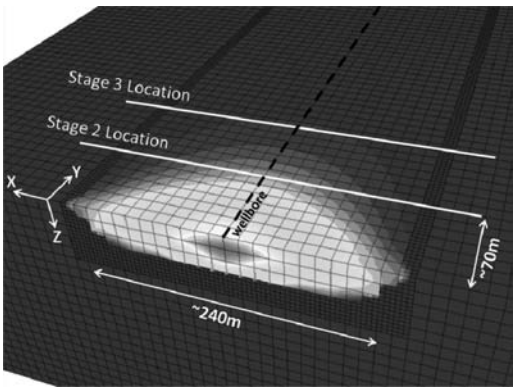


Figure 1. Example stress shadow from a single hydraulic fracture. Warmer colors are greater stress.

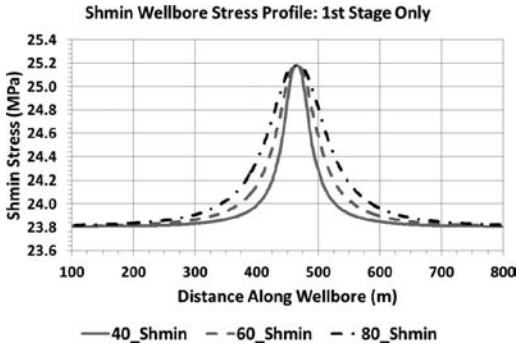


Figure 2. Stress shadow Shmin results for single, variable height, hydraulic fractures. Fracture half-length was 120 m.

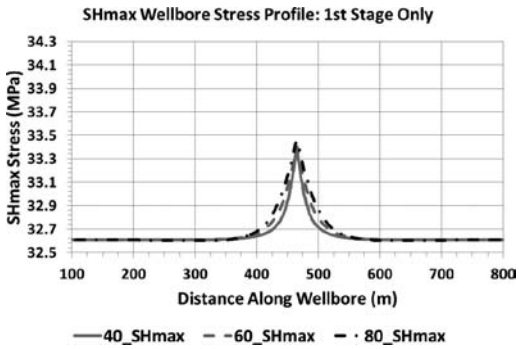


Figure 3. Stress shadow SHmax results for single, variable height, hydraulic fractures. Fracture half-length was 120 m.

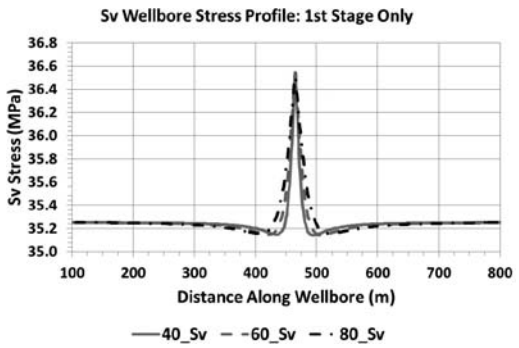


Figure 4. Stress shadow Sv results for single, variable height, hydraulic fractures. Fracture half-length was 120 m.

2) as fracture height increases, the distance of influence for the stress shadow effect also increases; 3) the distance of influence of a stress shadow is much smaller for SHmax than for Shmin and smaller still for Sv; and 4) the maximum increase in SHmax is half that of the maximum increase in Shmin, while the maximum increase in Sv is very similar to that of Shmin.

The important implications of the single hydraulic fracture stress shadow results include: 1) hydraulic fracture height plays a key role in the influence distance of the stress shadow; and 2) the influence distance is different for the three principal stresses – suggesting that the shear stress changes induced by a hydraulic fracture also become a function of distance from the hydraulic fracture.

2.5 *Dual hydraulic fracture stress shadow results as a function of fracture height and stage spacing*

Following the single fracture simulations, simulations were conducted to evaluate the influence of hydraulic fracture height (for a set fracture half-length) and stage spacing using two hydraulic fractures. A single hydraulic fracture was first simulated (and propped open) and then a second hydraulic fracture was simulated (including closure on proppant). The results, like the single stage simulations, looked at the influence of stress shadows on Shmin, SHmax, and Sv. Figures 5 through 7 show the stress shadow effect on Shmin for dual hydraulic fractures of constant height and variable stage spacing. Figures 8 through 10 show the stress shadow effect on Shmin for dual hydraulic fractures for constant spacing and variable fracture height.

Figures 5 through 7 show that not only does the stress shadow effect on Shmin overlap when stage spacing is small enough, but the stress shadow magnitude also increases (additively) when the stages are small enough. At a 40 m fracture height, Figure 5 shows that there is a small, additive stress effect when the spacing is less than two times the fracture height and at a spacing of four times the fracture height, the additive effect is nearly gone. In contrast, Figure 7 shows that the additive effect can nearly double the stress shadow for small stage spacings.

Figures 8 through 10 show that, for a given stage spacing, increasing hydraulic fracture height increases the additive effect of stress shadows from dual hydraulic fractures. Further, the figures suggest that when stage spacing is greater than about twice the fracture height, the additive effect is negligible, though

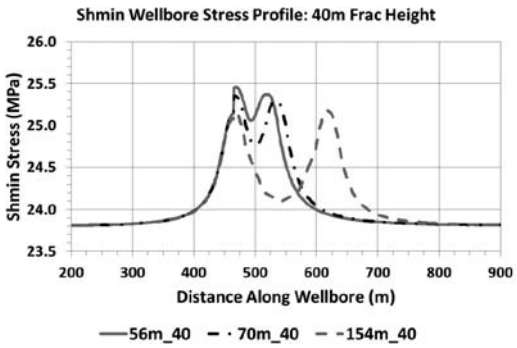


Figure 5. Stress shadow effects on Shmin for dual hydraulic fractures with variable spacing for a 40 m fracture height.

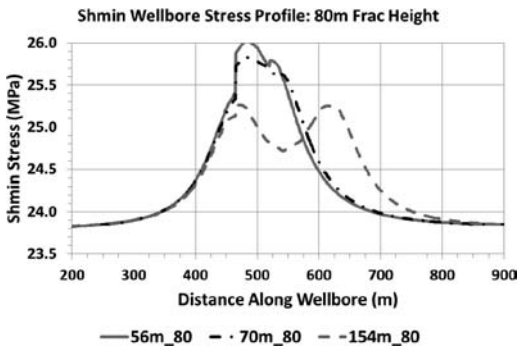


Figure 7. Stress shadow effects on Shmin for dual hydraulic fractures with variable spacing for an 80 m fracture height.

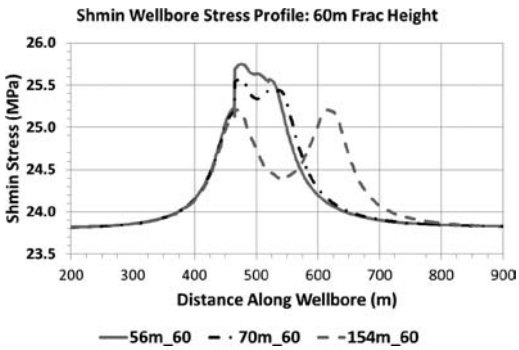


Figure 6. Stress shadow effects on Shmin for dual hydraulic fractures with variable spacing for a 60 m fracture height.

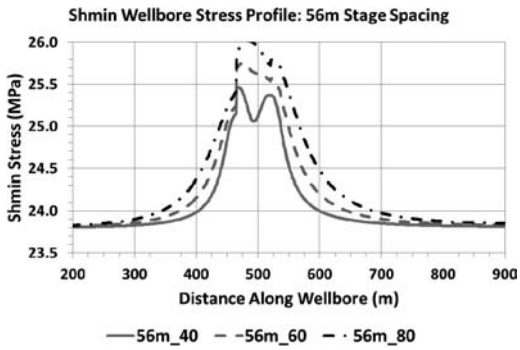


Figure 8. Stress shadow effects on Shmin for dual hydraulic fractures with variable height for a 56 m stage spacing.

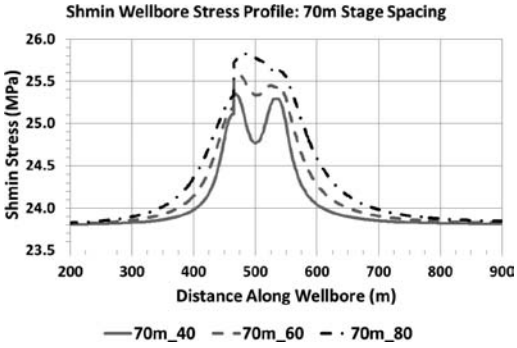


Figure 9. Stress shadow effects on Shmin for dual hydraulic fractures with variable height for a 70 m stage spacing.

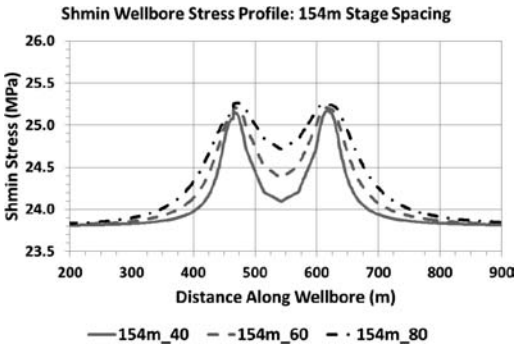


Figure 10. Stress shadow effects on Shmin for dual hydraulic fractures with variable height for a 154 m stage spacing.

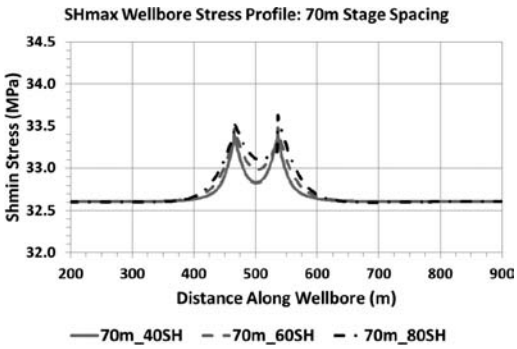


Figure 11. Stress shadow effects on SHmax for dual hydraulic fractures with variable height for a 70 m stage spacing.

the inter-fracture region still experiences a potentially significant increase in stress.

The stress shadow effects seen in Figures 5 through 10 also occur for the other principal stresses, though the difference in influence distance reduces the additive effect as seen in Figure 11.

Because of the variable influence distance of the stress shadow effect on the principal stresses, the

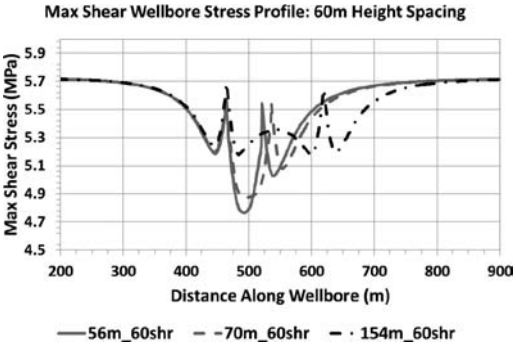


Figure 12. Stress shadow effects on the maximum shear stress for dual fractures with variable stage spacing and 60 m fracture height.

change in the shear stress around the hydraulic fracture also varies with fracture height and stage spacing as shown in Figure 12.

The important implications of the dual hydraulic fracture stress shadow results include: 1) at a stage spacing less than about twice the hydraulic fracture height, there is an additive effect on Shmin due to stress shadows wherein the increase in Shmin can be double or more the single fracture stress shadow; 2) the additive effect is significantly influenced by both fracture height and stage spacing; 3) the additive effect is much less for SHmax and Sv due to their much smaller influence distance; and 4) only at a stage spacing greater than about four times the fracture height do stages effectively act independently of each other.

3 15 STAGE FIELD CASE

3.1 *Numerical model*

Like the single and dual hydraulic fracture simulations, the simulation of multi-stage hydraulic fracturing for the field case was performed with ageneral-purpose, three-dimensional, explicit, finite-difference program for engineering mechanics computations in large-strain mode. In contrast, however, stage spacing was very irregular (as shown in Table 1 and Figure 13) and the simulation domain was much larger. In addition, fracture height was set to 130 m and fracture length to 220 m for each stage.

3.2 *Field case simulation results*

Like the single and dual hydraulic fracture simulations, the multi-stage fracture simulations were conducted in a serial fashion in which each fracture was created, equilibrated, then propped, and the model re-equilibrated before the next fracture stage was simulated. Figure 14 shows the simulated increase in Shmin due to stress shadowing along the wellbore for all 15 hydraulic fracturing stages.

The results in Figure 14 confirm and reinforce the additive effect noted from the dual fracture simulations. Clearly from such small stage spacings (which

Table 1. Stage spacing for the field case.

Stage	Spacing	Stage	Spacing	Stage	Spacing
1	–	6	42 m	11	77 m
2	91 m	7	42 m	12	49 m
3	49 m	8	28 m	13	35 m
4	42 m	9	28 m	14	28 m
5	28 m	10	77 m	15	49 m

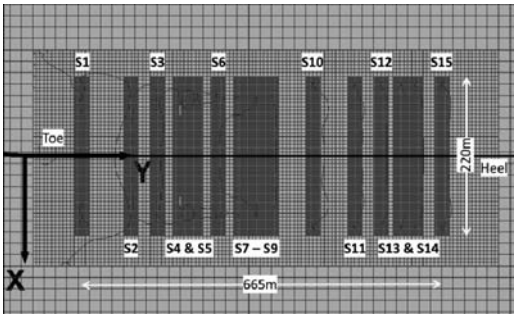


Figure 13. Schematic (plan view) of the multi-stage hydraulic fractures for the field case horizontal well. The location of the 15 fracture stages is labeled S1 to S15.

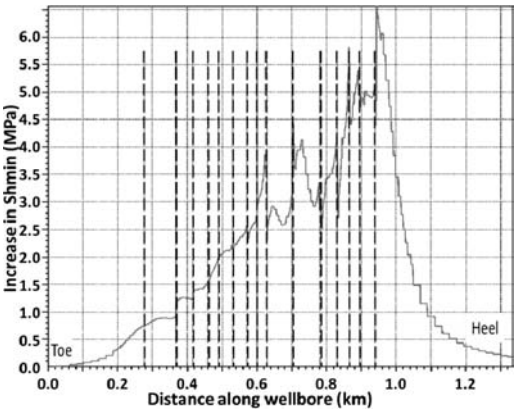


Figure 14. Profile of simulated Shmin increase along the wellbore due to stress shadowing from 15 irregularly spaced hydraulic fractures. Dashed black lines indicate the position of the 15 hydraulic fractures.

range from 21% to 70% of the hydraulic fracture height), there is cumulative stress shadow effect along the wellbore such that, though each stage net pressure was 1.4 MPa, at the 15th stage the Shmin increase was more than 6.5 MPa. However, the increase in Shmin is not purely monotonic as when the stage spacing increases (as in the 10th and 11th stages), there is a local decrease in the stress shadow effect.

The comparison of the simulation results in Figure 14 to field data (field instantaneous shut-in pressure, ISIP) is shown in Figure 15. As in many field situations, the field data was somewhat limited. First, ISIP

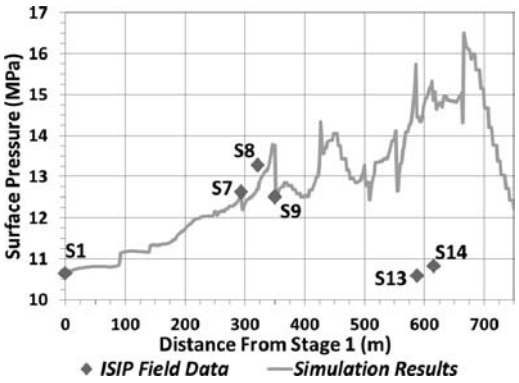


Figure 15. Comparison of field ISIP data to the simulated stress shadow data from Figure 14. Stage numbers are as shown.

data from only six of the 15 stages was available for comparison due to the use of a sliding-sleeve completion. In addition, the measure of in-situ stress change, ISIP, is often close, but not equal, to Shmin and the values represent surface data and not downhole data (as the model data does). However, even given these limitations, there is an excellent match between the simulated stress shadow effect on Shmin and the field data through at least the 9th of the 15 stages. With the later, heel-side-of-the-well stages, the field ISIP drops back to essentially equal or less than the ISIP value after the first stage.

4 EVALUATION OF HEEL-SIDE ISIP REDUCTION

4.1 *Review of causes*

The behavior noted in Figure 15 – the reduction in stress towards the heel of a multi-stage wellbore instead of the anticipated continued increase –has been noted in many field cases and a number of causes have been postulated (Nagel et al. 2013). One obvious potential cause for the reduction of ISIP towards the heel of the well is that these stages are in a different stress compartment. However, for the field case presented there is no evidence to support this possibility. The presence of compliant natural fractures might also serve to reduce or change the stress shadow effect. Again, however, for the field case presented there is no evidence that the natural fracture density or behavior changes from the toe to the heel of the well. Another cause that could potentially explain the reduction in ISIP is hydraulic fracture rotation; that is, rather than creating a series of parallel planar hydraulic fractures, the stress shadow effect induces non-planarity and even full rotation.

4.2 *Stress shadow-induced fracture rotation*

As shown in Rios et al. (2013), the stress shadow effect on Shmin varies with both distance from the previous

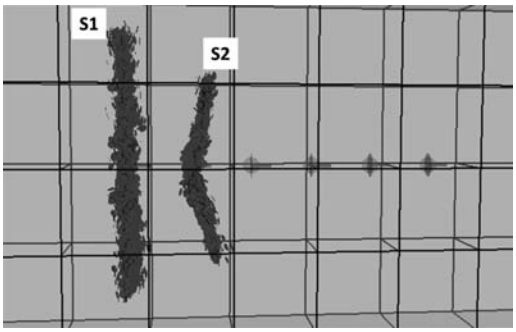


Figure 16. Example of hydraulic fracture rotation of a second fracture due to stress shadow effects froma previous fracture.

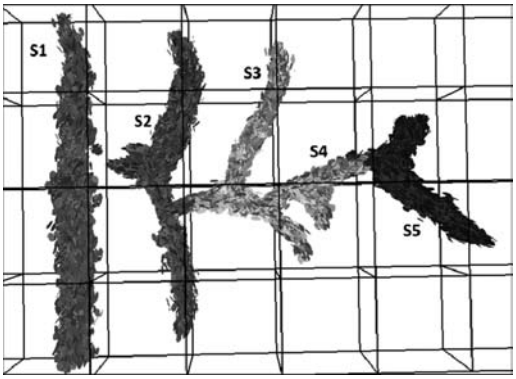


Figure 17. Hydraulic fracture rotation due to the additive effect of stress shadows for a five stage well. Each color represents a separate stage. The ratio of stage spacing to fracture height is approximately one.

stage and distance from the wellbore (often the widest part of the propped hydraulic fracture). As a result, a propagating hydraulic fracture, in the stress shadow from a previous stage, will tend to grow away from that stage. This is shown in Figure 16.

The hydraulic fracture rotation seen in Figure 16 (generated from a discrete element model with a stage spacing to fracture height ratio less than one) is caused by a small, local rotation in the principal stresses due to the stress shadow effect from the first hydraulic fracture. However, as noted from the dual hydraulic fracture simulations and seen in the field case simulation of the increase in Shmin due to the stress shadow effect from multiple hydraulic fractures, there is an additive effect of stress shadows. As shown in Figure 17, which shows five hydraulic fracture stages, the additive effect of stress shadows can lead to severe fracture rotation and alteration of the local principal stresses.

5 CONCLUSIONS

Based upon the simulations conducted, the comparison to field data, and evaluation of the miss-fit between simulation results and field results, the following conclusions are made:

1) The greatest impact of the stress shadow effect is on the minimum horizontal stress, Shmin, and the influence distance of the increase in Shmin is much greater than that for the increase in the maximum horizontal stress, SHmax, or the vertical stress, Sv.
2) The stress shadow effect from a single hydraulic fracture is strongly controlled by the fracture height. For multiple hydraulic fractures, stage spacing also plays a critical role.
3) For closely spaced fractures (less than two times the fracture height), there is an additive effect of the stress shadow and, as shown in a field case, the increase in Shmin can exceed four times or more the net pressure from a single hydraulic fracture.
4) The continuum simulations provided a good fit to field-measured stress shadow effects through the first two-thirds of the stages for a 15 stage field case; however, there was a significant miss-match to near-heel measurements. While there are multiple potential causes, the most likely cause is hydraulic fracture rotation due to the stress shadow effect.

REFERENCES

Ground Water Protection Council and ALL Consulting, 2009. Modern Shale Gas Development in the United States: A Primer, prepared for the US DOE, Office of Fossil Energy, DE-FG26-04NT15444.

King, G.E. 2010. Thirty Years of Gas Shale Fracturing: What Have We Learned?. Paper SPE 133456 presented at the SPE Annual Technical Conference and Exhibition, Florence, Italy, 19–22 September.

Nagel, N. & Sanchez-Nagel, M. 2011. Stress Shadowing and Microseismic Events: A Numerical Evaluation. Paper SPE 147363 presented at the SPE Annual Technical Conference and Exhibition, Denver, Colorado, USA, 30 October–2 November.

Nagel, N.B., Sanchez-Nagel, M., Zhang, F., Garcia, X. & Lee, B. 2013. Coupled Numerical Evaluations of the Geomechanical Interactions Between a Hydrualic Fracture Stimulation and a Natural Fracture System in Shale Formations. *Rock Mechanics and Rock Engineering,* DOI 10.1007/s00603-013-0391-x

Rios, A.M., Gutierrez, G., Nagel, N.B., Zhang, F., Sanchez-Nagel, M. & Lee, B. 2013. Stress Shadow Evaluations For Chicontepec – Evaluating New Completion Options, ARMA 13-200, presented at the 47th US Rock Mechanics/ Geomechanics Symposium, San Francisco, CA, USA, 23–26 June.

Sneddon, I.N. 1946. The Distribution of Stress in the Neighbourhood of a Crack in an Elastic Solid. *Proc. R. Soc. London, Ser. A.* 195: 229–260.

U.S. Energy Information Administration, 2012. Annual Energy Outlook 2012 Early Release Overview. U.S. Dept. of Energy, Washington D.C., USA, www.eia.gov

Rock Mechanics for Resources, Energy and Environment – Kwaśniewski & Łydżba (eds)
© 2013 Taylor & Francis Group, London, ISBN 978-1-138-00080-3

Analysis of the hydromechanical behavior of fault zones in petroleum reservoirs

G.L. Righetto, C.E.R. Lautenschläger, N. Inoue & S.A.B. da Fontoura
ATHENA – Computational Geomechanics Group, GTEP – Group of Technology in Petroleum Engineering, PUC-Rio – Pontifical Catholic University of Rio de Janeiro, Brazil

ABSTRACT: Aiming to increase hydrocarbon production, the oil industry has developed recovery methods whose purpose is to get more production. Thus, several problems may be encountered when making use of these techniques, mainly the conventional one. In addition, consideration of geological structures in reservoir engineering, such as fault zones, has fundamental character for determining realistic response for the production of hydrocarbons. In the case of faults zones, its consideration in the model has significant importance currently, especially with regard to the possibility of reactivation and possible loss of tightness of the reservoir. Thus, the aim of this study was assess reservoir models with a fault zone using partially coupled hydro-mechanical simulations. The methodology considers a fault zone whose behavior is given by the Mohr-Coulomb yield criterion. The plasticity model showed consistent results with the process of reactivation for the models. Thus, for the case where the objective is to determine the maximum flow rate of injection as well as its spatial configurations aimed at maintaining the field production, it is possible to establish the flow rate that may result in the initiation of the fault reactivation. Furthermore, the effect of surrounding rocks had a great influence in the time required to initiate the process of reactivation. As a general conclusion, it is stated that the consideration of fault zones in reservoirs, as well as surrounding rocks, must be taken into account to obtain more accurate response to the field behavior.

1 INTRODUCTION

The exploitation of petroleum began from the drilling of the first well of petroleum in the XIX century in the United States. From this point, aiming increase the petroleum recovery, the oil industry developed recovery methods whose objective is to obtain a higher production than that which would be obtained only as a result of the natural energy of the reservoir (Thomas 2001). In this context, several problems can be faced when one uses recovery techniques, mainly through the fluid injection, in geologically complex reservoirs.

Besides that, the consideration of geological structures in the reservoir engineering, for instance faults, has fundamental importance for determining realistic responses related to oil recovery factor, compaction of reservoir, seafloor subsidence, among others. In the specific case of faults, its consideration and analyses has been reported for several authors (Morris et al. 1996, Wiprup & Zoback 2000, Mildren et al. 2002, Streit & Hillis 2004, Chiaramonte et al. 2006, Færseth et al. 2007, Rutqvist et al. 2007, 2008, Soltanzadeh & Hawkes 2008, Zhang et al. 2009, Cappa & Rutqvist 2010, Ducellier et al. 2011, Jain et al. 2012, McDonald et al. 2012; Leclère & Fabbri 2012), due, mainly by its reactivation possibility. In the fault reactivation perspective during the field development, the objective is to prescribe the highest injection flow rate or the highest bottom hole pressure that can be applied in injector wells in order to maintain the reservoir pressure, without the failure of the faults. The process of fault reactivation, due the stress state variation, can result in an emergence of a preferential path for the hydrocarbon, implying in the most critical cases, in the leakage of fluid and possible loss of tightness of the reservoir.

The concern about the possibility of fault reactivation became important, mainly due the CCS (Carbon Capture and Sequestration) projects, once these components are re-injected within reservoirs, and for using in EOR (Enhanced Oil Recovery) technologies.

Thus, the following part refers to the consideration of fault zones in a simplified reservoir model, taking into account the hydromechanical behavior through the use of a strong coupling methodology developed by Computation Geomechanics Group – ATHENA/GTEP – PUC-Rio.

2 HYDROMECHANICAL MODELING IN FAULT ZONES

2.1 *Flow-stress coupling*

Studies conducted by the Computational Geomechanics Group – ATHENA/ GTEP – PUC-Rio showed substantial influence of geomechanical effects on the history of fluid pressures during the development of

a reservoir, and also on other aspects such as subsidence and compaction. The coupling methodology developed consists of a one and two-way partial coupling scheme, where the flow variables (pore pressure and saturation of the phases) and the stress variables (displacement field, stress and strain state) are calculated separately and sequentially, by a conventional reservoir simulator and a stress analysis program, respectively. The coupling parameters are exchanged at each time step until reaching the convergence. The quality of this methodology was ensured by the rigorous development of a coupling parameter which approximates the geomechanical response to the fully coupled behavior (Biot 1941). In this work, it will be shown just the equations of the flow problem and the stress analysis problem. For more details about the development of the formulation see Inoue & Fontoura (2009a).

The flow equation can be obtained by combining the mass conservation equation and the Darcy's law. The law of mass conservation is a material-balance equation written for a component in a control volume. In hydrocarbon reservoirs, a porous medium can contain one, two and three fluid phases. The governing flow equations (single-phase) for the conventional reservoir simulation and the fully coupled scheme are given by Eq. (1) and Eq. (2), respectively. In the conventional reservoir simulation, the porosity is related to pore pressure through the rock compressibility using a linear relation, and in the fully coupled scheme, the porosity equation is composed of four components that contribute to the fluid accumulation term.

$$\left(c_f\phi^0 + c_r\phi^0\right)\frac{\partial p}{\partial t} - \frac{k}{\mu}\nabla^2 p = 0 \tag{1}$$

$$\left[c_f\phi^0 + c_S\left(\alpha - \phi^0\right)\right]\frac{\partial p}{\partial t} - \frac{k}{\mu}\nabla^2 p = -\alpha\frac{\partial \varepsilon_v}{\partial t} \tag{2}$$

where ϕ is the porosity, p is the pore pressure, t is the time, k is the permeability, μ is the viscosity, c_f is the fluid compressibility, c_s is the solid matrix compressibility, c_r is the rock compressibility, α is a Biot's coefficient and ε_v is the bulk volumetric strain.

The formulation of the geomechanical problem takes into account the equilibrium equations, stress-strain-displacement equations, rock-flow interaction and the boundary conditions. The governing equation of the geomechanical problem may be written as indicated in Eq. (3).

$$G\nabla^2 \mathrm{u} + \frac{G}{1-2\nu}\nabla\nabla\cdot\mathrm{u} = \alpha\nabla p \tag{3}$$

where G is the shear modulus, u is the nodal displacement and ν is the Poisson ratio.

The methodology used herein for the coupling between flow and stress problem was described in Inoue & Fontoura (2009a, 2009b). The coupling is achieved through a convenient approximation between of the flow equation of the conventional reservoir simulation and the flow equation of the fully coupled scheme. In this methodology, the effect of solids compressibility is removed from the fully coupled scheme and the effect of volumetric strain of the porous medium is added to conventional reservoir simulation.

The parameters responsible for the coupling, which honor the fully coupling equation, are the porosity ϕ and the pseudo-compressibility c_p, presented in Eq. (4) and (5) respectively. These parameters are updated during each iteration through the coupled analysis.

$$\phi = \phi^o + \alpha\left(\varepsilon_v - \varepsilon_v^o\right) + \frac{1}{Q}\left(p - p^o\right) \tag{4}$$

$$c_p = \frac{\varepsilon_v^{n+1} - \varepsilon_v^n}{\phi^o\left(p_i^{n+1} - p_i^n\right)} \tag{5}$$

Furthermore, the partial coupling between the stress analysis program and the conventional reservoir simulator is reached using a staggered procedure, implemented in a C++ code (Inoue & Fontoura, 2009b).

2.2 *Geometrical model*

According to the structural geology literature, ideally, a numerical model that aims modeling fault reactivation and leakage should consider its real geomorphology. Nevertheless, a realistic representation of these structures can face several numerical difficulties related to the mesh/grid generation, once it will be necessary refined discretization to model them properly.

Therefore, it was built one model composed by reservoir, surrounding rocks and fault zone (inclination of 60° relative to the horizontal axis). Figures 1 and 2 show the top, front and fault zone view in details, respectively. Table 1 resume the properties used in the analyses. A constant flow rate of 1100 m^3/day was assumed in each well and each one was completed in all layers along the depth.

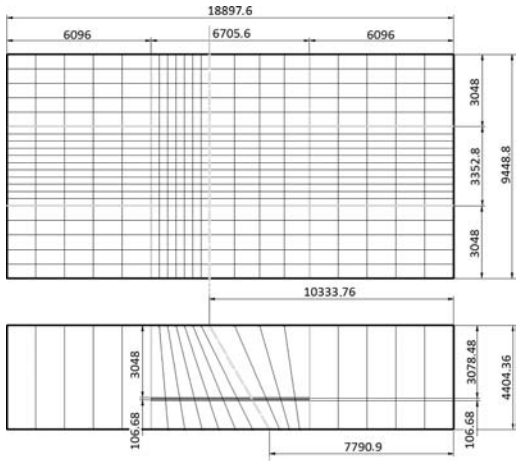


Figure 1. Geometrical model: top and front view (meters).

After the idealization of the geometry of the model, the next item will present the numerical procedures to build the mesh/grid as well as the insertion of the failure criterion for the fault zone in the hydromechanical coupling code.

2.3 *Numerical approach for fault reactivation*

As can be observed in the works available in the technical literature, evaluate numerically the fault reactivation process is not an easy task, moreover, there is not a single and well-known methodology. Besides that, there is another issue to be analyzed, once faults can be a plane or zone with thickness (Davis & Reynolds 1996). Thus, the definition of numerical technique to analyze this process properly must take into account the real geomorphology of the fault (Righetto 2012).

In this work, the stress analysis software (ABAQUS®) evaluates the fault reactivation mechanism considering a fault as a zone with thickness pre-established. Thereby, this region can be modeled with a continuum approach combined with constitutive models, for instance Mohr-Coulomb. Indeed, Mohr-Coulomb yield criterion was adopted to evaluate the failure of material constituting the fault zone. In the reservoir simulator (ECLIPSE®), the fault zone was considered also, however, its core was held sealant.

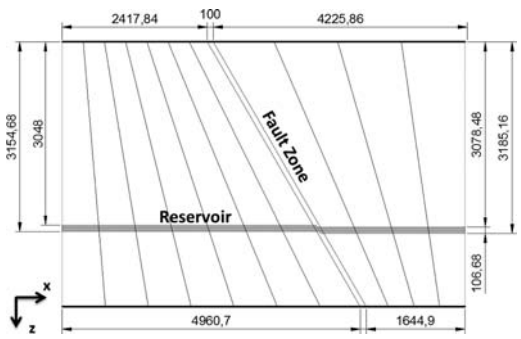


Figure 2. Geometrical model: detail of fault zone (meters).

Table 1. Rock, fluid and fault zone properties.

Properties	Values
Formation volume factor at 0.1013 MPa	1
Viscosity	1cp
Fluid density at 0.1013 MPa 0.1013 MPa	10^3 kg/m^2
Fluid Compressibility	2.2×10^9 Pa
Permeability in x and y directions	1×10^{-13} m^2
Permeability in z directions	1×10^{-14} m^2
Initial porosity	0.25
Young's modulus (reservoir)	5 GPa
Young's modulus (fault zone)	1 GPa
Cohesion of fault zone	0.5 MPa
Friction angle of fault zone	31°
Dilatancy angle of fault zone	11°
Young's modulus (surrounding rocks)	7 GPa
Poisson's ratio (all rocks)	0.25

All hydraulic characteristics, for instance permeability, flow rates, compressibility, were defined in the flow simulator. It should the mentioned that the grid of finite difference method (used in the flow simulation) was coincident with the mesh of finite element method (used in the stress analyses).

The flowchart shown in Figure 1 presents the main steps for the implementation of a fault reactivation model in the partial hydromechanical code.

The six steps shown in the Figure 3 will be presented in details following. It will be emphasizing just the characteristics related to fault zone model.

- (1) *Finite element mesh generation*
  To generate the finite element mesh composed by reservoir and surrounding rocks, use has been made of the software PATRAN® and ABAQUS®. Figure 4 shows a tridimensional view of the whole geomechanical model.
- (2) *Finite difference grid generation*
  The finite difference grid was generated using the flow simulator ECLIPSE®. It should be mentioned that in the flow simulator, it is generate only the reservoir grid. The surrounding rocks are not considered in conventional reservoir simulation, as already discussed previously. Figure 5 shows a

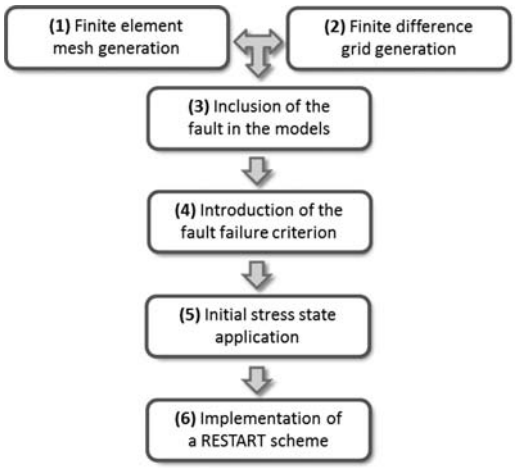


Figure 3. Flowchart with the steps for implementation of the fault reactivation model.

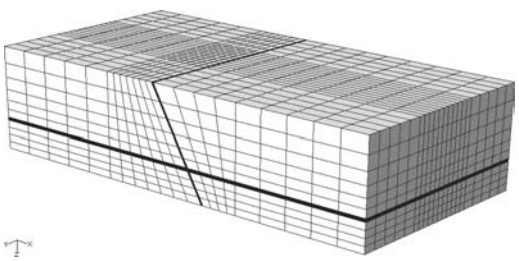


Figure 4. Panorama of the whole geomechanical model.

tridimensional view of the reservoir as well as the injector wells position.

- (3) *Inclusion of the faults in the model*
  As the fault zone was considered through the continuum approach, its discretization (grid and mesh) was made in a conventional way. The sealant core of fault zone was defined in this step of model development.
- (4) *Introduction of the fault failure criterion*
  Mohr-Coulomb yield criterion was adopted to evalu-ate the failure of the fault zone. This constitutive model was chosen due its wide use in the Geotechnical Engineering. Besides that, this model needs just three strength parameters, which are: friction angle, cohesion and dilatancy. Another advantage of Mohr-Coulomb criterion is related to the use of conventional laboratory tests to obtain these parameters.
- (5) *Initial stress state application*
  To apply the initial stress state in the model, was used the principle of virtual stress equilibrium (Herwanger & Koutsabeloulis, 2011). The steps are:
  a) The displacements in x, y, z directions were prevented in all nodes of the model;
  b) The lithostatic stresses were applied in all elements of the model;
  c) ABAQUS® was run with the imposed boundary conditions (a) and the imposed initial conditions (b);
  d) As a result, ABAQUS® calculated the reaction forces in all nodes;
  e) Before the beginning of hydromechanical analyses, the reaction forces (d) were applied as nodal forces aiming to guarantee the equilibrium, i.e, null values of displacements and strains.
- (6) *Implementation of a Restart scheme*
  In each time step of the flow-stress analysis, the coupling code uses an iterative scheme to reach the equilibrium. Thus, it was implemented a *Restart* scheme in the stress analysis program, once the Mohr-Coulomb yield criterion needs to be updated due the stress history. Figure 6 shows the *Restart* scheme used in the flow and stress program, respectively.

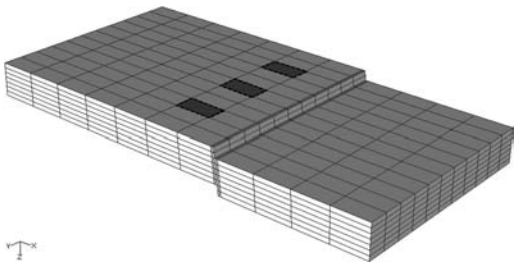


Figure 5. Panorama of the reservoir, fault zone and the position of the injection wells.

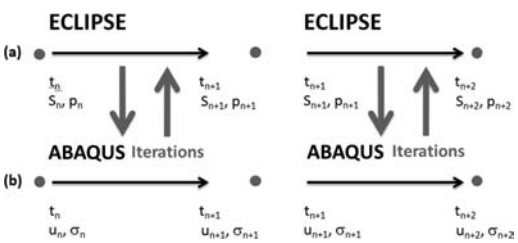


Figure 6. Restart scheme for: (a) ECLIPSE® and (b) ABAQUS®.

2.4 *Mohr-Coulomb yield criterion*

As mentioned in the previously sections, it was adopted Mohr-Coulomb yield criterion (see Figure 7) to perform the fault zone reactivation analyses. Thus, as it was used ABAQUS® in the geomechanical analyses, it will be present the equations available in the theoretical manual.

The yield function is defined, properly, according to the three stress invariants (Desai & Siriwardane, 1984). The first stress invariant (p), named equivalent pressure stress, can be defined as:

$$p = -\frac{1}{3} trace(\boldsymbol{\sigma}) \tag{6}$$

The second stress invariant (q), named Mises equivalent stress, can be defined as:

$$q = \sqrt{\frac{3}{2}(\boldsymbol{S} : \boldsymbol{S})} = \sqrt{3 \cdot J_{2D}} \tag{7}$$

where $\boldsymbol{S}$ and J_{2D}, are the deviatoric stress and second deviatoric stress invariant, respectively.

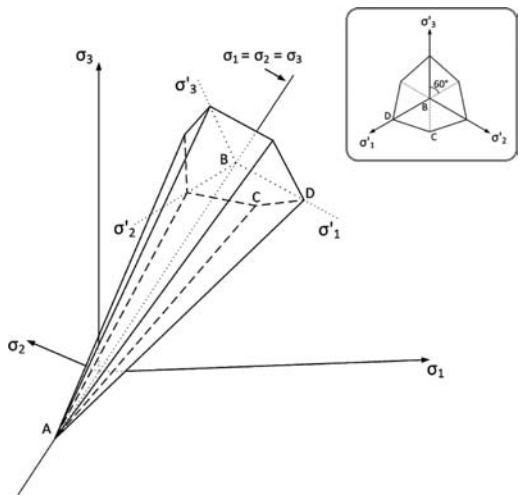


Figure 7. Mohr-Coulomb failure criterion: pyramidal surface in principal stress space and, in a detail, the cross-section in the equipressure plane (Labuz & Zang, 2012).

The third stress invariant (r) can be defined as:

$$r = \sqrt[3]{\frac{9}{2}(\boldsymbol{S}\cdot\boldsymbol{S}:\boldsymbol{S})} = J_{3D} \quad (8)$$

where J_{3D} is the third deviatoric stress invariant.

Therefore, the Mohr-Coulomb yield function (f) can be written as:

$$f = R_{mc}\cdot q - p\cdot\tan\phi - c = 0 \quad (9)$$

where ϕ and c are the friction angle and cohesion of the geomaterial. R_{mc} is the Mohr-Coulomb deviatoric stress measure written as:

$$R_{mc} = \frac{1}{\sqrt{3}\cdot\cos\phi}\,sen\left(\theta+\frac{\pi}{3}\right)+\frac{1}{3}\cos\left(\theta+\frac{\pi}{3}\right)\cdot\tan\phi \quad (10)$$

where θ is the deviatoric polar angle defined as:

$$\cos(3\theta) = \left(\frac{r}{q}\right)^3 \quad (11)$$

After the variables definition, the Mohr-Coulomb yield criterion can be verified through the failure envelope as shown in Figure 8.

Thus, the stress path resulting from the hydromechanical simulations can be plotted together with the failure envelope to verify the fault zone reactivation.

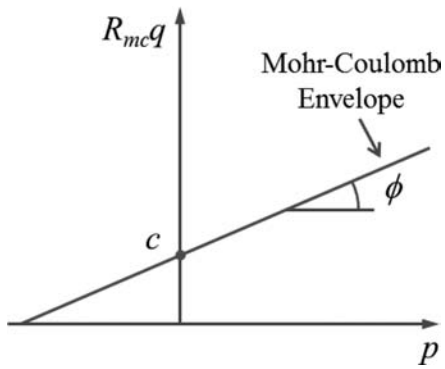


Figure 8. Mohr-Coulomb surface in the meridional plane (adapted from Abaqus, 2010).

3 FAULT REACTIVATION ANALYSIS

The results presented here regards to the plasticity analysis performed in the fault zone of reservoir model. The right side of Figure 9 shows the face of fault zone analyzed in relation to the right portion of the complete model. The portion of the model that contains the reservoir was highlighted in front view on the left side of Figure 9, in order to facilitate the visualization of the region where the failure process was started in the following figures.

Figure 10 illustrates the yielding development in the region of the fault zone, in terms of plastic deformation. In Figure 10(a) is indicated the injection time of 1 day, without evidences of plastic deformation. In Figure 10(b) is shown the injection time of 2163 days, where it was observed the onset of the material failure in the fault zone. Figure 10(c) shows the injection time of 4000 days, where the collapse extends throughout fault zone.

It can be seen that the beginning of yielding occurred in an isolated form at the ends of fault zone, spreading throughout the extent of the fault zone with the injection process, with greater intensity at its ends. In the end of analysis, it can be observed that the entire fault zone presents plastic deformations, thereby emphasizing the generalized rupture of the material that composes it. Furthermore, when comparing the evolution of the yielding with time, it is evident the horizontal and vertical spread of the rupture process.

According to Eqs. (6), (7) and (8), it was calculated the values of the three stress invariants along the analysis time. Knowing the three stress invariants, it can be performed the calculation of the Mohr-Coulomb yielding function, observing their variation in time with the injection process. The function value tends towards zero when occurs rupture of the material of the fault zone as shown in Figure 11.

It was also verified that the yield criterion was fulfilled correctly through the Mohr-Coulomb failure envelope and the stress path in the meridional plane, as shown in Figure 12. When the yield function (Eq. 9) tends to reach a value equal to zero, the stress path touches the Mohr-Coulomb envelope, indicating the collapse.

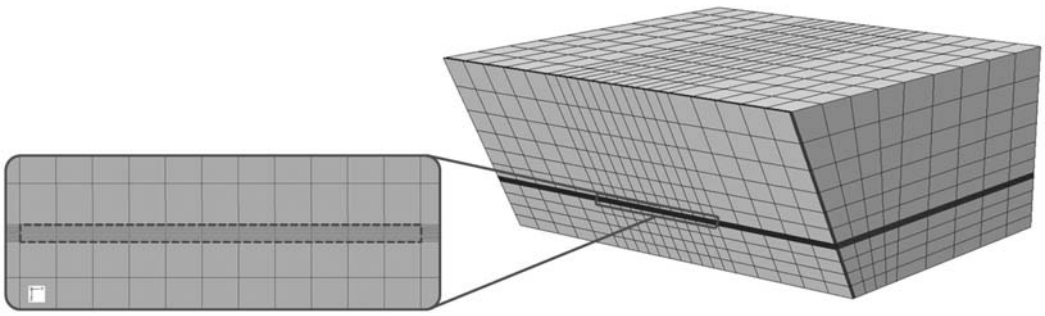


Figure 9. Indication of the fault zone in the amplified region of reservoir.

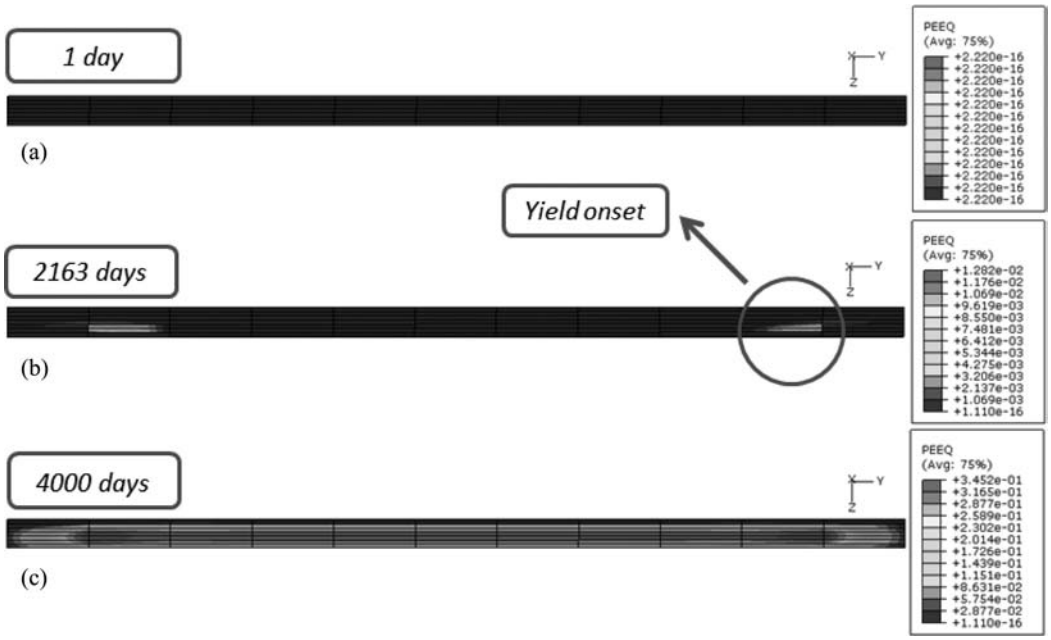


Figure 10. Appearance of plastic deformations along the fault zone at injection times of (a) 1 day; (b) 2163 days and (c) 4000 days.

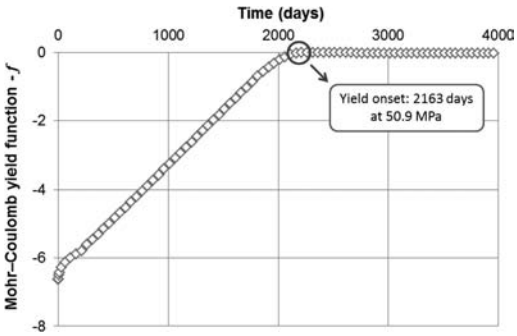


Figure 11. Yield function variation along the time injection.

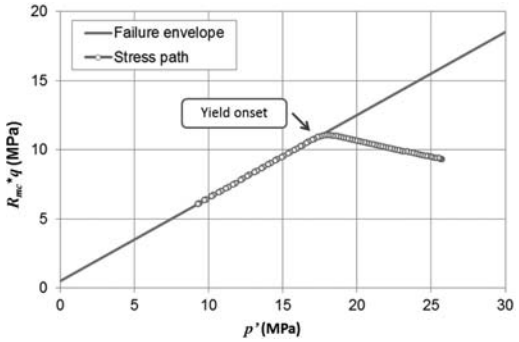


Figure 12. Stress path defined along the time injection in function of Mohr-Coulomb envelope.

It was observed that from 2163 days, the yielding function has a practically zero value, indicating that the criterion was reached in the material composing the fault zone. This fact corroborates the picture 12, since the trajectory of the envelope touches Mohr-Coulomb envelope after 2163 days of analysis.

Using the two-way partial coupling it was found that the pore pressure causing the occurrence of yielding was equal to 50.9 MPa. With increasing of the fluid pressure within the reservoir, due to the injection process, it was observed the occurrence of significant vertical displacements in the reservoir and overburden. Figure 13(a) illustrates the displacement field generated in a vertical middle section of the full model at the end of 4000 days. Figures 13(b) and 13(c) respectively show the vertical displacements and plastic deformations in the region of the fault zone after 4000 days of injection.

It is observed that the geomechanical effects caused by injection were significant not only in the reservoir, but also in the surrounding rocks, indicating the importance to its consideration in coupled analyses involving reactivation of faults. Due to the propagation of displacements observed, it is clear that the properties attributed to the materials, of reservoir and overburden, are influential in the system response when assessed in a coupled way. In this aspect, the reactivation process can be affected in terms of pressure to be reached to cause yielding of the material of zone fault.

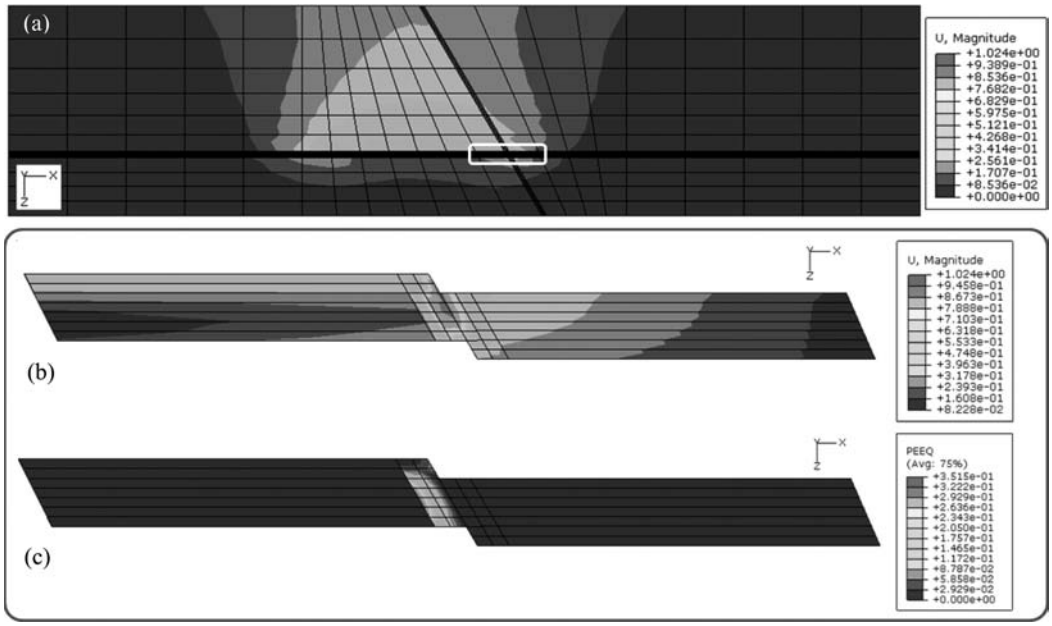


Figure 13. Model panorama after 4000 days of injection (a) vertical displacements of a central cross section in whole model, (b) vertical displacements of a central cross section near to the fault zone and (c) plastic strain values in the yield region of the fault zone.

4 CONCLUSIONS

At the end of this study, it can be stated that the consideration of complex geological structures such as fault zones, has fundamental character to perform a realistic numerical modeling in petroleum geomechanics. Allied to this, there is the use of robust methodologies for solving the problem of flow-stresses, as were applied in this work. Therefore, in the case of risk analysis of fault reactivation, the approach employed in this study show great potential for application and can be used in the workflow of reservoirs analysts. This approach can assist in decision making regarding possible well configurations and flow rates/bottom hole pressure that can be applied in injection wells, whose goal is to increase/ maintain production of oil or even storing carbon dioxide, besides the analysis of risks associated with loss of seal and leakage of reservoirs.

ACKNOWLEDGEMENTS

The authors would like to thank to SIMULIA and Schlumberger for providing the academic licenses of the software ABAQUS® and ECLIPSE®, respectively. Thanks are also extended to Petrobras for the financial support.

REFERENCES

ABAQUS. 2010. *ABAQUS User's Manual*. Dassault Systèmes, Simulia Corporation. Rhode Island, USA.

Biot, M.A. 1941. General theory of three-dimensional consolidation. *Journal of Applied Physics* 12(2): 155–164.

Cappa, F. & Rutqvist, J. 2010. Modeling of coupled deformation and permeability evolution during fault reactivation induced by deep underground injection of CO_2. *International Journal of Greenhouse Gas Control* 5: 336–346.

Chiaramonte, L.; Zoback, M. D.; Friedmann, J.; Stamp, V. 2006. CO_2 sequestration, fault stability and seal integrity at Teapot Dome, Wyoming. In *Proc. 8th International Conference on Greenhouse Gas Control Technologies, Trondheim, Norway, 19-22 June 2006*.

Davis, G.H. & Reynolds, F.J. 1996. *Structural Geology of Rocks and Regions* (2nd edn). New York: John Wiley & Sons, Inc.

Desai, C.S. & Siriwardane, H.J. 1984. *Constitutive Laws for Engineering Materials with Emphasis on Geologic Materials.* New Jersey: Prentice-Hall.

Ducellier, A.; Seyedi, D.; Foerster, E. 2011. A coupled hydromechanical fault model for the study of the integrity and safety of geological storage of CO_2. *Energy Procedia* 4: 5138–5145.

Færseth, R.B., Johnsen, E. & Sperrevik, S. 2007. Methodology for risking fault seal capacity: implications of fault zone architecture. *American Association of Petroleum Geologists Bulletin* 91(9): 1231–1246.

Herwanger, J.V. & Koutsabeloulis, N. 2011. *Seismic geomechanics: how to build and calibrate geomechanical models using 3D and 4D seismic data*. EAGE Publications.

Inoue, N. & Fontoura, S.A.B. 2009a. Answers to some questions about the coupling between fluid flow and rock deformation in oil reservoirs. In *Proc. SPE/EAGE Reservoir Characterization and Simulation Conference*, SPE Paper Number 125760-MS.

Inoue, N. & Fontoura, S.A.B. 2009b. Explicit coupling between flow and geomechanical simulators. In *Proc. International Conference on Computational Methods for Coupled Problems in Science and Engineering. Ischia Island, Italy, 8–10 June 2009.*

Jain, A., Verma, A.K., Vishal, V. & Singh, T.N. 2012. Numerical simulation of fault reactivation phenomenon. *Arabian Journal of Geosciences*, DOI 10.1007/s12517-012-0612-8

Labuz, J. F. & Zang, A. 2012. ISRM Suggested Method: Mohr–Coulomb Failure Criterion. *Rock Mechanics and Rock Engineering* 45: 975–979.

Leclère, H. & Fabbri, O. 2013. A new three-dimensional method of fault reactivation analysis. *Journal of Structural Geology* 48: 153–161.

Macdonald, J.; Backé, G.; King, R.; Holford, S.; Hillis, R. 2012. Geomechanical modelling of fault reactivation in the Ceduna Sub-basin, Bight Basin, Australia. *Geological Society London Special Publications 2012* 367: 71–89.

Mildren, S.D., Hillis, R.R. & Kaldi, J. 2002. Calibrating predictions of fault seal reactivation in the Timor Sea. *Australian Petroleum Production and Exploration Association Journal*: 187–202

Morris, A., Ferril, D.A. & Henderson, D.B. 1996. Slip tendency analysis and fault reactivation. *Geology* 24: 275–278.

Righetto, G. L. 2012. *Hydromechanical Simulation of Fault Reactivation in Petroleum Reservoirs: Approaches by Contact Interactions and Plasticity.* M.Sc. Thesis, Department of Civil Engineering, Pontifical Catholic University of Rio de Janeiro. (in Portuguese)

Rutqvist, J.; Birkholzer, J. T.; Cappa, F.; Tsang, C. F. 2007. Estimating maximum sustainable injection pressure during geological sequestration of CO_2 using coupled fluid flow and geomechanical fault-slip analysis. *Energy Conversion and Management* 48: 1798–1807.

Rutqvist, J.; Birkholzer, J. T.; Tsang, C. F. 2008. Coupled reservoir-geomechanical analysis of the potential for tensile and shear failure associated with CO_2 injection in multilayered reservoir-caprock systems. *International Journal of Rock Mechanics and Mining Sciences* 45: 132–143.

Soltanzadeh, H. & Hawkes, C.D. 2008. Semi-analytical models for stress change and fault reactivation induced by reservoir production and injection. *Journal of Petroleum Science and Engineering* 60: 71–85.

Streit, J.E. & Hillis, R.R. 2004. Estimating fault stability and sustainable fluid pressures for underground storage of CO_2 in porous rock. *Energy* 29: 1445–1456.

Thomas, J.E. 2001. *Fundamentals of Petroleum Engineering*. Rio de Janeiro: Interciência. (in Portuguese)

Wiprut, D. & Zoback, M. D. 2000. Fault reactivation and fluid flow along a previously dormant normal fault in the northern North Sea. *Geology* 28: 595–598.

Zhang, Y., Gartrell, A., Underschultz, J.R. & Dewhurst, D.N. 2009. Numerical modeling of strain localization and fluid flow during extensional fault reactivation: Implications for hydrocarbon preservation. *Journal of Structural Geology* 31: 315–327.

13. Geological CO_2 sequestration

This page intentionally left blank

Rock Mechanics for Resources, Energy and Environment – Kwaśniewski & Łydżba (eds)
© 2013 Taylor & Francis Group, London, ISBN 978-1-138-00080-3

AE monitoring of hydraulic fracturing experiments conducted using CO_2 and water

T. Ishida, Y. Nagaya, S. Inui, K. Aoyagi, Y. Nara & Y. Chen
Kyoto University, Kyoto, Japan

Q. Chen & Y. Nakayama
3D Geoscience, Inc., Tokyo, Japan

ABSTRACT: Use of carbon dioxide (CO_2) as a fluid for hydraulic fracturing has been considered to stimulate oil production, to enhance shale gas recovery and to extract hot dry rock geothermal energy. In these projects, CO_2 is usually injected into rocks at a depth more than 1,000 m. In the temperature and pressure at that depth CO_2 usually becomes a supercritical state (SC-CO_2), and viscosity of the SC-CO_2 is very low around 5% of that of water. So, it is important to understand the behavior of SC-CO_2 in rock. Thus, we made hydraulic fracturing experiments using SC-CO_2 and water in two granite specimens for each fracturing fluid under a true tri-axial loading condition. The results of the experiments suggested that low viscosity fluid like SC-CO_2 is expected to induce more three dimensionally and widely spreading cracks under considerably lower breakdown pressure than water.

1 INTRODUCTION

Carbon dioxide (CO_2) is injected into the underground rock for a variety of purposes. It is often used for miscible flooding to enhance oil recovery in depleted petroleum reservoirs, and the use of CO_2 as a fracturing fluid for well stimulation has been considered because it eliminates formation damage and residual fracturing fluid (Sinal & Lancaster 1987, Liao et al. 2009). Using CO_2 as fracturing and circulating fluid has also been proposed in hot dry rock geothermal energy extraction, because it eliminates scaling in the surface piping due to the inability of CO_2 to dissolve mineral species (Brown, 2000). Recently, since shale has a greater affinity for CO_2 than methane (Nuttall et al. 2006), the CO_2 injection to enhance shale gas recovery has been considered as well (Kalantari-Dahaghi 2010). For all of these purposes, it is necessary to understand the behavior of CO_2 in rock. It is also important to know how injected CO_2 infiltrate into the surrounding rock mass in CO_2 capture and storage projects (Xue et al. 2006, Nooner et al. 2007).

In these projects, CO_2 is usually injected into rocks at a depth of more than 1,000 m. The temperature and pressure at that depth usually makes CO_2 a supercritical state, while the lower temperatures in special geological conditions create a liquid state. The viscosity of liquid CO_2 (L-CO_2) is one order lower than that of normal liquid water, while that of the supercritical state (SC-CO_2) is much lower still. To clarify fracture behavior induced with injection of the low viscosity fluid, we have already conducted hydraulic fracturing experiments using SC- and L-CO_2 in granite specimens under hydrostatic loading, and have discussed differences in the results between the two fluids (Ishida et al. 2012). In this paper, we report the hydraulic fracturing experiments using SC-CO_2 and water in granite specimens under a true tri-axial loading condition. From the results, we discuss differences between the two fluids focusing on the breakdown pressure and distribution of located acoustic emission (AE) sources, adding data of our experiments with injection of oil having a few hundred times larger viscosity than water.

2 EXPERIMENTAL METHOD

2.1 *Specimens and confining pressure*

Four cubic (17 cm × 17 cm × 17 cm) samples of Kurokamijima granite were used as specimens. Two of the four, the specimens G1115 and G1202, were subjected to SC-CO_2 injection, while the other two, the specimens G1102 and G1103, were subjected to water injection. The samples had a 2 cm diameter central hole, and the inherent rift plane of the granite specimen was oriented so as to correspond to the YZ-plane in the Cartesian coordinate system, as shown in Figure 1. To monitor AE events induced with the injection, as an AE sensor, sixteen cylindrical PZT (Pb(lead) zirconium titanate) elements in total were glued on the lateral four surfaces of the specimen. Since the

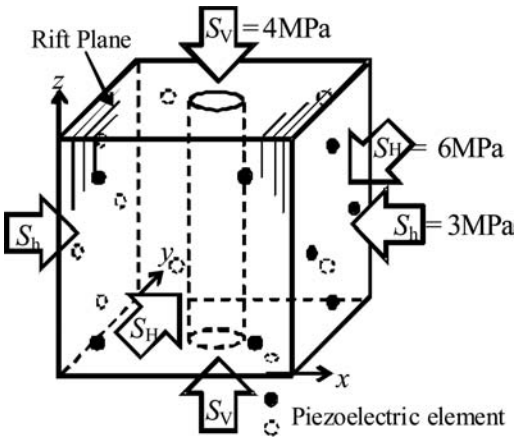


Figure 1. Coordinate system, loading condition of the specimen and setting positions of PZT elements used as AE sensors.

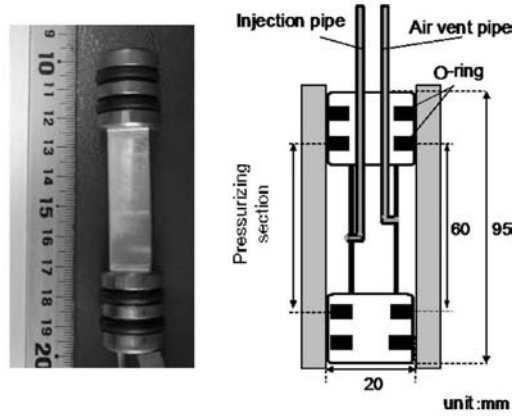


Figure 2. Straddle packer used to inject CO_2. Photo (left) and illustration of a sectional view of the packer (right).

PZT elements measured 3 mm in diameter and 4 mm in thickness, to apply confining pressure, 6 mm thick hard nylon plates having 5 mm diameter holes at the positions of the PZT elements and grooves to pass signal wires from them were glued to the four surfaces of the specimen. After filling silicon caulking compound in the holes and the grooves for waterproofing, the every plate was covered with another 4 mm thick plate.

The specimen was placed in a cylindrical pressure cell. Four bow-shaped spacer blocks were inserted between the specimen and the inner wall of the pressure cell, and a flat jack was placed between the specimen and each spacer block to apply pressure in the X- and Y-directions. In the Z-direction, flat jacks were placed between the specimen and loading plates supported by the end caps on the top and bottom of the pressure cell. In all experiments, confining pressures of 3, 6 and 4 MPa were applied in the X-, Y- and Z-directions respectively.

2.2 *CO_2 injection method*

To inject CO_2 and water, a packer shown in Figure 2 was inserted into the center hole of the specimen. The packer had a 60 mm pressurizing section sealed with two O-rings at each end. The pressurizing section was centered along the hole.

CO_2 becomes supercritical when the temperature is higher than 31.1°C and the pressure is greater than 7.38 MPa as shown in Figure 3. To satisfy the condition, the injection system shown in Figure 4 was made. CO_2 was fed from a bomb to a cylinder of the syringe pump, which has a capacity of 266 mL. To fill the cylinder as full as possible, the CO_2 was cooled and kept in liquid form by circulating coolant in a cooling unit located above the cylinder. The liquid form CO_2 (L-CO_2) was discharged from the cylinder of the syringe pump at a constant flow rate of 10 mL/min. It

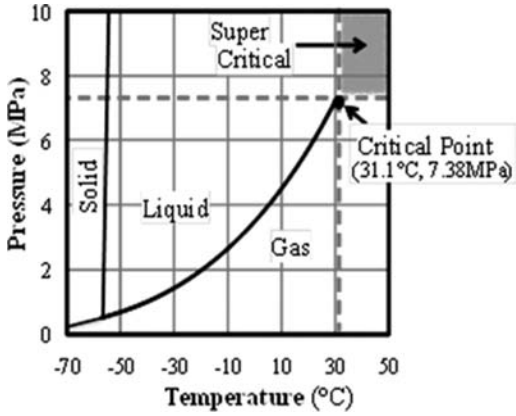


Figure 3. Phase diagram of CO_2.

was passed through a heater unit and the temperature was maintained at 55°C by bandaging electric resistance heating ribbon along the pipe connecting the heating unit to the packer as shown in Figure 4. In addition, the cell in which the specimen was contained was filled with hot water at a temperature of around 45°C to prevent the injected CO_2 from cooling. Although the specimen was soaked in hot water for around one hour, we believed that water does not infiltrate into around the injection hole due to its low permeability and the hydraulic fracturing was induced in dry condition from our experience on previous similar experiments.

For the water injection, water was injected under room temperature directly from the syringe pump at the same flow rate of 10 mL/min as for the SC-CO_2. In this case, the cell was also kept at room temperature without filling water.

For the both cases of SC-CO_2 and water, the injection was stopped just after hydraulic fracturing was induced, which was indicated by a sudden pressure drop.

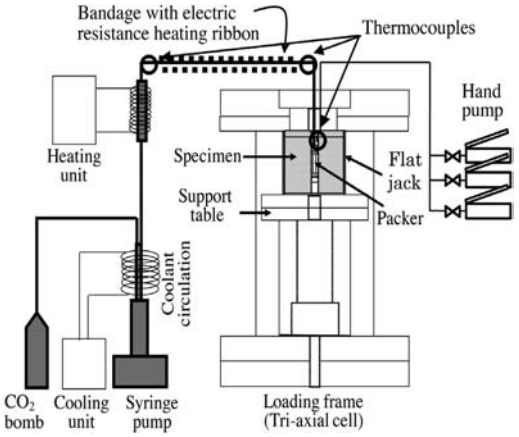


Figure 4. System for injecting fracturing fluid and loading confining pressure.

2.3 Monitoring methods

The AE signals detected at the PZT elements having a resonance frequency of 300 kHz were amplified by 66 to 84 dB in total (36 dB in a pre-amplifier and 30 to 48 dB in a signal conditioner), and recorded on a hard disk through an A/D converter. For each event, the record length and sampling time of the A/D converter were selected to be 2048 words and 0.1 μs respectively, while the amplitude was digitized with 12 bits resolution. The dead time was set to be 1 ms after recording an event, to prevent the hard disk from recording too much noise due to "ringing," which is the vibration following a large AE event. The recording of an AE event was triggered when one of the signals from 16 AE sensors exceeded 0.3 V. In addition, the number of AE events per second was counted for each AE sensor when the signal exceeded 0.3 V. Every 0.1 s, the injected fluid pressure was measured through transducers set at the top of the packer, and the flat jack pressures in the three directions, X, Y and Z, were measured through transducers set on the connecting pipes of opposing pairs of flat jacks.

In the case of SC-CO_2 injection, temperature changes were measured with a thermocouple buried with plaster just above the packer in the hole. Thermocouples were also placed at the both ends of the section of a pipe bandaged with electric resistance heating ribbon, as shown in Figure 4.

3 RESULTS

3.1 *Change of fluid pressure, temperature and AE count rate*

SC-CO_2 was injected into the specimens, G1115 and G1202, while water was injected into G1102 and G1103 in the same flow rate 10 cm^3/min.

Figure 5 shows changes of the injected fluid pressure, the confining pressures, the AE count rate and the

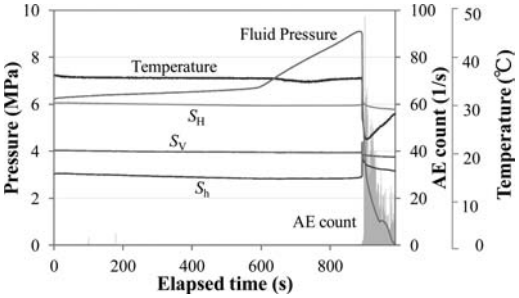


Figure 5. Changes of the injected fluid pressure, the confining pressures the AE count rate and the temperature in the specimens, G1115, for SC-CO_2 injection.

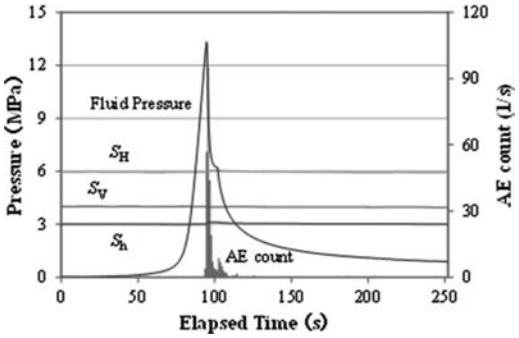


Figure 6. Changes of the injected fluid pressure, the confining pressures the AE count rate and the temperature in the specimens, G1103, for water injection.

temperature when SC-CO_2 was injected into the specimens, G1115. The injected fluid pressure decreases suddenly just after recording the breakdown pressure, 9.10 MPa. The temperature was measured with a thermocouple buried with plaster just above the packer was 35.5°C at the breakdown, which indicates that the fracturing was induced by SC-CO_2. However, the temperature decreased just after the breakdown. This is most likely due to adiabatic expansion of CO_2 by leakage through the cracks induced by the fracturing. The AE count rates increased sharply just after the breakdown and the events continued to occur for several second. The confining pressure S_H, S_V, and S_h were kept at the almost constant pressure set at 6, 4 and 3 MPa, with small fluctuations due to crack extensions at the breakdown.

Figure 6 shows those when water was injected into the specimen, G1103. The breakdown pressure was 13.33 MPa, which is considerably larger than 9.10 MPa in the SC-CO_2 injection. In spite of the same flow rate, the pressure increased to the breakdown pressure in a shorter time than SC-CO_2 due to the difference in compressibility of the fluid. Thus, the time necessary for the test run is quite different between SC-CO_2 and water.

The pressure records in the other two specimens, G1202 with SC-CO_2 injection and G1102 with water

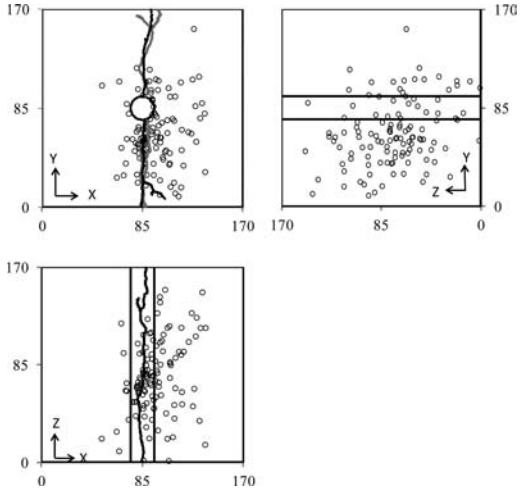


Figure 7. AE source distribution and cracks visible on the surfaces of the specimen G1115 with SC-CO_2 injection.

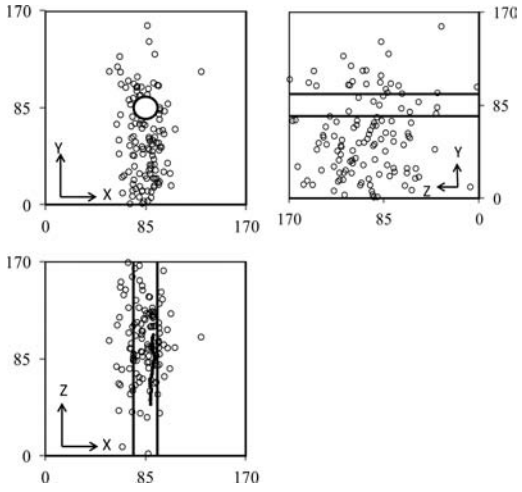


Figure 8. AE source distribution and cracks visible on the surfaces of the specimen G1103 with water injection.

injection, were similar to those in G1115 and G1103 shown above. The respective breakdown pressures were 10.16 and 12.96 MPa showing the same tendency that the breakdown pressure with water injection is larger than that with SC-CO_2.

3.2 *Induced visible cracks and located AE sources*

Figures 7 and 8 show the located AE sources projected onto the three orthogonal planes, XY, YZ and ZX, in the SC-CO_2 injection into the specimen, G1115, and in the water injection into G1103, respectively. The figures show only the AE sources that occurred for 15 second just after the breakdown. AE sources were located taking into account the anisotropy of the P-wave velocity (Rothman et al. 1974), with accuracy expected to fall within a few mm. This was possible because only AE events satisfying the following conditions were considered (Ishida & Sasaki 2011) (i) P-wave initial motions detected by more than five sensors; and (ii) standard deviation and the maximum of differences between the observed and back-calculated arrival times were within 3 μs. With satisfying the conditions, 118 and 119 sources were obtained in the specimen G1115 for SC-CO_2 and in G1103 for water injection, respectively.

In the all experiments including the other two specimens, the cracks were induced along the inherent rift plane, which also corresponds to the direction of maximum confining pressure. After the experiments, we closely observed the induced cracks on the specimen surfaces macroscopically Figure 7 and 8 shows the visible cracks sketched on the projection planes of the specimens with the located sources. Only on the XY plane of Figure 7, since the cracks observed on the two opposite planes, those observed on the planes $Z = 0$ and $Z = 170$ mm were distinguished with the dark and light lines respectively. In the other cases, the cracks observed on only one plane.

When we compare the two figures, Figure 7 seems to show more three dimensional large distributions rather than Figure 8. To present the difference in numbers, at first, the most likely flat plane for the distribution of the AE sources was estimated for each specimen, by minimizing the sum of squares of distances from a located source to the flat plane. After that the average distance from a source to the estimated flat plane, *L*av, was obtained. The average distance, *L*av, was 12.1 mm in the specimen G1115 for SC-CO_2 injection, while that was 9.7 mm in G1103 for water injection. This indicates that the cracks induced with SC-CO_2 extends more three dimensionally than that with water, for example, wavelike with more secondary braches rather than along a flat plane.

The source distributions in the other two specimens, G1202 with SC-CO_2 injection and G1102 with water injection, were similar to those in G1115 and G1103 shown above, and the respective average distance, *L*av, were 11.44 and 9.27 mm showing the same tendency.

4 DISCUSSION

Figure 9 shows a relation between the breakdown pressure and viscosity of the fracturing fluid. Since we have also conducted injection experiments with viscous oil having a few hundred mPa · s (Mahha Super Transmission Oil, 75W-90, Fuji Kosan Co. Ltd.) under the same condition as those for the SC-CO_2 and the water injection, the figure includes the results of the oil injection. In the figure, the viscosity of SC-CO_2 was calculated from the temperature and the pressure at the breakdown, using the equation of state for CO_2 of T. Ohmori (http://hp.vector.co.jp/authors/VA030090/) based on the theory by Fenghour et al. (1998). Those of the water and the oil were revised for the fluid

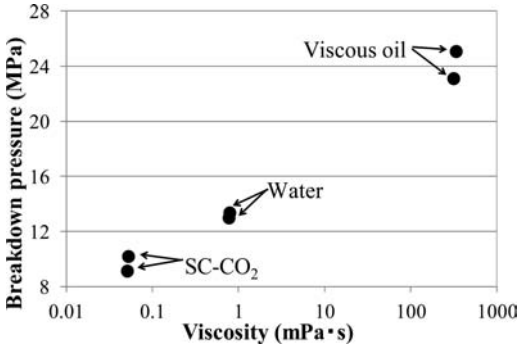


Figure 9. Relation between the breakdown pressure and the viscosity of fracturing fluid.

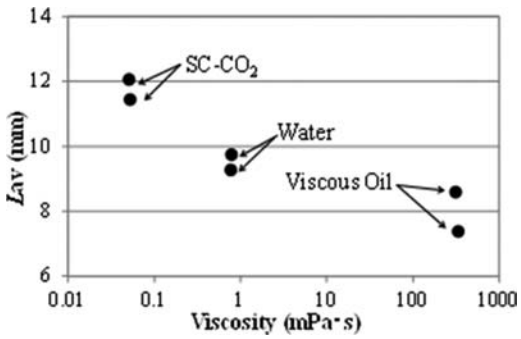


Figure 10. Relation between the average distance from a source to the estimated most likely flat plane, *L*av, and the viscosity of fracturing fluid.

temperatures measured at the respective experiments. This figure clearly indicates that the breakdown pressure increases with the viscosity, being consistent with the facts elucidated in experimentally by Schmitt & Zoback (1993) and theoretically by Bunger et al. (2010). Thus, the breakdown pressure with injection of low viscosity fracturing fluid like SC-CO_2 is expected to be considerably lower than those with injection of water and viscous fluid like gel, when it is injected into the same rock type stratum under the same in situ stress condition and flow rate.

Figure 10 shows a relation between viscosity of the fracturing fluid and the average distance from a source to the estimated most likely flat plane, Lav. This figure clearly indicates that the average distance, *L*av, decreases with the viscosity, suggesting that the low viscosity fracturing fluid like SC-CO_2 induces more three dimensionally and widely spreading cracks, for example, wavelike with more secondary braches rather than along a flat plane than water and viscous fluid like gel. Ishida et al. (2004) conducted hydraulic fracturing experiments on the same kind of cubic Kurokami-jima granite using normal water and viscous oil, with viscosities of 1 and 80 mPa · s respectively. The results indicate that viscous oil tends to generate thick and planar cracks with few branches, while water tends to generate thin and wavelike cracks with many secondary branches. Our results obtained in the experiments are consistent with their results. On the other hand, Warpinski et al. (2005) made hydraulic fracturing using slick water and viscous gel in a shale gas reservoir, and compared the microseismic maps associated with the two fracturings. The map associated with slick water fracturing outlines a much larger area than that achieved with the gel fracturing. Our results including those in Ishida et al. (2004) are consistent with the field experience, in the viewpoint of the difference in the fracturing fluid viscosity.

5 CONCLUDING REMARKS

We conducted the hydraulic fracturing experiments using SC-CO_2 and water in cubic granite blocks under a true tri-axial loading condition. Including data of our experiments with injection of oil having a few hundred times larger viscosity than water, we discussed effects of viscosity of fracturing fluid on the breakdown pressure and distribution of located AE sources. The results can be summarized as follows.

(1) We obtained clear tendency that the breakdown pressure increases with the viscosity of the fracturing fluid, which is consistent with the results elucidated in experimentally and theoretically by other researchers. From the tendency, the breakdown pressure with injection of low viscosity fracturing fluid like SC-CO_2 is expected to be considerably lower than that with injection of water, when it is injected into the same rock type stratum under the same in situ stress condition and flow rate.

(2) We also obtained clear tendency that the average distance from an AE source to the estimated most likely flat plane, *L*av, decreases with the viscosity of the fracturing fluid. The tendency is consistent with the microseismic maps associated with hydraulic fracturing in a shale gas reservoir using slick water and viscous gel; the microseismic maps shows that slick water fracturing outlines a much larger area than that achieved with the gel fracturing. From the tendency, it is expected that hydraulic fracturing with low viscosity fluid like SC-CO_2 can induce more three dimensionally and widely spreading cracks, for example, wavelike with more secondary braches rather than along a flat plane than water.

ACKNOWLEDGEMENTS

This work was financially supported by JSPS (Japan Society for the Promotion of Science) Grant-in-Aid for Scientific Research (B), Grant Number 21360446 and ENEOS Hydrogen Trust Fund of 2012. We appreciate their supports.

REFERENCES

Brown, D.W. 2000. A hot dry rock geothermal energy concept utilizing supercritical CO_2 instead of water. In *Proc. 25th Workshop on Geothermal Reservoir Engineering* (January 24–26, 2000, Stanford, CA), SGP-TR-165, 233–238.

Bunger, A.P., Lakirouhani, A. & Detournay, E. 2010. Modelling the effect of injection system compressibility and viscous fluid flow on hydraulic fracture breakdown pressure. In F. Xie (ed.), Rock Stress and Earthquakes: 59–67. London: Taylor & Francis.

Fenghour, A. et al. 1998. The viscosity of carbon dioxide, *J. Phys. Chem. Ref. Data* 27(1): 31–44, doi:10.1063/1.556013.

Ishida, T. et al. 2012. Acoustic emission monitoring of hydraulic fracturing laboratory experiment with supercritical and liquid CO_2. *Geophysical Research Letters* 39, L16309, doi:10.1029/2012GL052788.

Ishida, T. & Sasaki, S. 2011 Numerical simulation to examine accuracy of AE source location and its applications to in-situ rock monitoring. *J. Acoust. Emission* 29: 260–272.

Ishida, T. et al. 2004. Influence of fluid viscosity on the hydraulic fracturing mechanism. *J. Energy Resour. Technol.* 126: 190–200, doi:10.1115/1.1791651.

Kalantari-Dahaghi, A. 2010. Numerical simulation and modeling of enhanced gas recovery and CO_2 sequestration in shale gas reservoirs: A feasibility study. Paper presented at SPE International Conference on CO_2 Capture, Storage, and Utilization (10–12 November 2010, New Orleans, Louisiana, USA). Society of Petroleum Engineers.

Liao, S., Brunner F. & Matter L. 2009. Impact of ignoring CO_2 injection volumes on post-frac PTA. In *Proceedings of the Canadian International Petroleum Conference* (16–18 June 2009, Calgary, Alberta, Canada): 1146–1150. Society of Petroleum Engineers.

Nooner, S.L. et al. 2007. Constraints on the in situ density of CO_2 within the Utsira formation from time-lapse seafloor gravity measurements. *Int. J. Greenhouse Gas Control* 1: 198–214, doi:10.1016/ S1750-5836(07)00018-7.

Nuttall, B.C. 2006. Sequestration in gas shale of Kentucky. 5th Annual Conference on Carbon Capture and Sequestration, Alexandria, Virginia, UAS, Poster No. 106.

Rothman, R.L. et al. 1974. Errors in Hypocenter Location due to Velocity Anisotropy. *Bull. Seismol. Soc. Am.* 64: 1993–1996.

Schmitt, D.R. & Zoback, M.D. 1993. Infiltration effects in the tensile rupture of thin walled cylinders of glass and granite: Implications for the hydraulic fracturing breakdown equation. *Int. J. Rock Mech. Min. Sci. Geomech. Abstr.* 30: 289–303, doi:10.1016/0148-9062(93)92731-5.

Sinal, M.L. & Lancaster, G. 1987. Liquid CO_2 fracturing: Advantages and limitations. *J. Can. Pet. Technol.* 26(5): 26–30.

Warpinski, N.R. et al. 2005. Comparison of single- and dual-array microseismic mapping techniques in the Barnett shale. In *Proceedings of the 2005 Annual Technical Conference and Exhibition* (9–12 October 2005, Dallas, Texas, USA). Society of Petroleum Engineers.

Xue, Z. et al. 2006. Estimation of CO_2 saturation from time-lapse CO_2 well logging in an onshore aquifer, Nagaoka, Japan. *Explor. Geophys.* 37: 19–29, doi:10.1071/EG06019.

Rock Mechanics for Resources, Energy and Environment – Kwaśniewski & Łydżba (eds)
© 2013 Taylor & Francis Group, London, ISBN 978-1-138-00080-3

Effects of vertical stress on fracture propagation using super critical carbon dioxide

A. Kizaki
Graduate School of Environmental Studies, Tohoku University, Sendai, Japan

K. Ohashi
City Government of Ageo City, Japan

H. Tanaka
Tohoku Electric Power Co., Inc., Sendai, Japan

K. Sakaguchi
Graduate School of Environmental Studies, Tohoku University, Sendai, Japan

ABSTRACT: To clarify the effects of the vertical stress along the borehole on the hydraulic fracture formation, we conducted hydraulic fracturing experiments using the fracturing fluids of the water and the super critical carbon dioxide. A borehole was bored perpendicular to the weak plane of the rock, and horizontal stresses of 5 and 3 MPa and a vertical stress of 12 MPa were applied. The obtained results were compared with the results obtained at a lower applied vertical stress of 1 MPa.

The total length of the fractures measured at the specimen surfaces for the vertical stress of 12 MPa tended to be smaller than that for a vertical stress of 1 MPa. This suggests that the horizontally oriented pores and microcracks were compressed by the high vertical stress and that the infiltration of the fracturing fluids significantly affected fracture propagation.

1 INTRODUCTION

Japan is one of the most volcanically active countries in the world and has rich geothermal resources. Geothermal power generation does not result in discharges of greenhouse gases, such as carbon dioxide, to the same extent as other energy generation methods that combust fossil fuels. This form of energy generation is also stable, not being dependent on weather or season. Geothermal energy therefore constitutes an eco-power generation method that mitigates global warming. To promote geothermal research and development, Muraoka et al. proposed the Japan Beyond-Brittle Project (JBBP) (Asanuma et al. 2012). This international project is designed to demonstrate the feasibility of a new type of power generation method, using an artificial brittle fracture reservoir system in high temperature ductile zones.

Figure 1 shows the relation between shear strength and depth obtained by Byerlee's law and the plastic flow law for various strain rates ($\dot{\varepsilon}$) at a high geothermal gradient of 130°C/km. This high geothermal gradient was observed at the Kakkonda geothermal field, Japan (Muraoka et al. 1998). The creep parameters obtained by Jaoul et al. (1984) were used to produce this figure. In brittle failure, shear strength increases with depth, since confining pressure (σ_n) increases with depth. Contrastively, in ductile failure, shear strength decreases with depth, since temperature increases with depth.

As a result, the shear strength of an intact rock is at a maximum at a certain depth. Herein, this depth is defined as the depth of Brittle-Ductile transition,

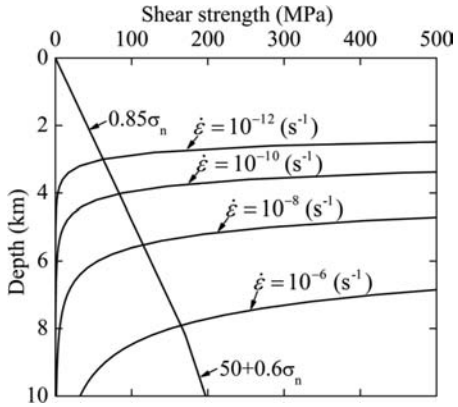


Figure 1. Relation between the shear strength and the depth obtained by Byerlee's law and the plastic flow law for the various strain rates ($\dot{\varepsilon}$) at the high geothermal gradient of 130°C/km.

although this latter depth is not a single point and is a zone instead. In ductile failure, shear strength depends strongly on the strain rate and the temperature, and accordingly, the depth of the Brittle-Ductile transition also depends strongly on these parameters. The natural fracture system created by shear failure does not develop well in the high temperature ductile zone because creep behavior is considered to be dominant for the intact rock at high temperatures. Therefore, in order to obtain a large surface area for heat extraction, methods are needed to create complex fracture systems in rock masses having low fracture density.

To control fracture formation, a hydraulic fracturing method using various types of fluids has been proposed (Ishida et al. 1996, Ishida et al. 2004, Ito et al. 2011, Ishida et al. 2012). In this study, we mainly used super critical CO_2 ($SCCO_2$) as the fracturing fluid since it has lower viscosity compared to water and is considered to be preferable to operational fluids, given its inability to dissolve and transport mineral species (Brown 2000).

Kizaki et al. (2012) conducted hydraulic fracturing experiments for Inada granite and Ogino tuff specimens using $SCCO_2$ and water, with the aim of understanding the effects of viscosity of hydraulic fluids and the weak planes of the rock on fracture formation. They reported that vertical fractures were created in the specimen along the borehole through the injection of water, while complicated horizontal fractures along the rift or bedding planes tended to be created by the injection of $SCCO_2$. These results suggest that both viscosity of the hydraulic fluid and weak planes of the rocks influence the formation of hydraulic fractures. However, only a weak vertical stress of 1 MPa was applied to the specimens in this case, since this was adequate for the purpose of the fracturing experiment.

This study aims to clarify our understanding of the fundamental processes of hydraulic fracture formation, using $SCCO_2$. Hydraulic fracturing experiments using water and $SCCO_2$ as fracturing fluids were conducted, and the effects of vertical stress on fracture formation were investigated.

2 EXPERIMENTAL METHOD

2.1 *Rock specimens*

Inada granite and Ogino tuff were used as the rock specimens for this study. Inada granite, which was quarried from Ibaraki Pref., Japan, has allotriomorphic granular textures, and mainly consists of quartz, orthoclase, and biotite. The quartz has many microcracks and the orthoclase has developed cleavages. This granite is typically used for mechanical experiments in Japan. Ogino tuff, which was quarried from Fukushima Pref., Japan, is fine glassy tuff and mainly consists of fine volcanic glasses (Kobayashi, et al. 1980, Kobayashi, et al. 1987). We used this Ogino tuff as a typical volcanic sedimentary rock from the Tohoku region of Japan.

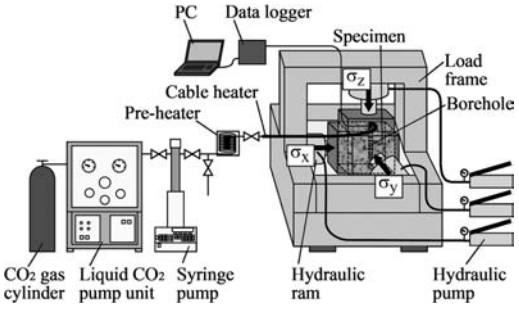


Figure 2. Schematic illustration of the experimental system.

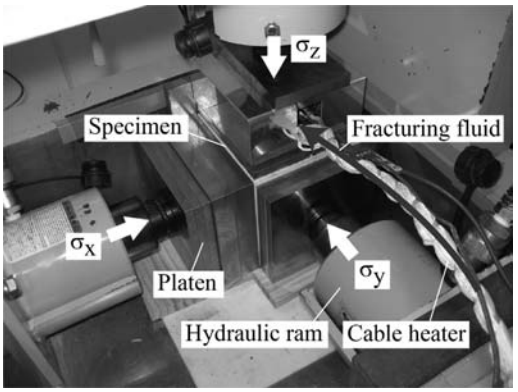


Figure 3. Photograph of the loaded specimen.

The size of the specimen was 15 cm-cubic. A borehole with a diameter of 2 cm was created in a direction perpendicular to the rift or bedding planes of the rock specimens. The characteristics of the rift or bedding planes were confirmed through the measurement of P-wave velocities, as described later.

2.2 *Experimental system*

Figure 2 shows a schematic illustration of the experimental system. The experimental system mainly consists of a true triaxial compression machine, a supplying system of hydraulic fluids, and a measuring system. The rock specimen was placed in the true triaxial compression machine. Figure 3 shows a photograph of the rock specimen placed in the true triaxial compression machine. Three compressive stresses were applied to the rock specimen using three hydraulic rams. $SCCO_2$ and water were used as the fracturing fluids and injected into the borehole within the specimen.

The carbon dioxide gas was supplied from the gas cylinder and was compressed and chilled by the liquid carbon dioxide pump unit. To supply sufficient volume of carbon dioxide for the experiments, liquid carbon dioxide was filled in the syringe pump that supplied it at a constant flow rate. The liquid carbon dioxide was heated to super critical condition by the pre-heater and the cable heater situated in the flow lines.

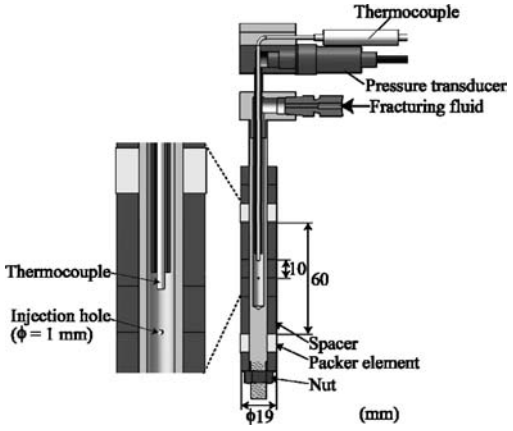


Figure 4. Details of the straddle packer.

Table 1. Experimental conditions for hydraulic fracturing experiments.

Fracturing fluid	Specimen	Flow rate (q) (ml/min)	Stress condition (MPa) σ_H	σ_h	σ_v	Specimen No.
CO_2	Inada granite	10	5	3	12	I-10
		50				I-50
		150				I-150
	Ogino tuff	10				O-10
		50				O-50
		150				O-150
Water	Inada granite	50	5	3	12	Iw-50
	Ogino tuff					Ow-50

The rock specimens with natural water content were warmed to approximately 40°C and adopted in the experiments that used $SCCO_2$. The specimens at an ambient temperature of approximately 10°C were used for the experiments using water.

Figure 4 shows details of the packer used in this study. This is a straddle-type packer and has two packer elements made of urethane rubber. These packer elements were compressed to seal the borehole by screwing the nut attached at the bottom of the packer. The distance between the two packer elements was 60 mm in this study. To measure the pressure and temperature near the borehole, we installed a pressure transducer and thermocouple in the packer.

2.3 *Experimental conditions*

Table 1 lists the experimental conditions for the hydraulic fracturing experiments. We used $SCCO_2$ and water as fracturing fluids. The flow rates (q) were 10, 50 and 150 ml/min for the experiments using $SCCO_2$, and 50 ml/min for the experiments using water. Figure 5 shows the stress conditions applied to the rock

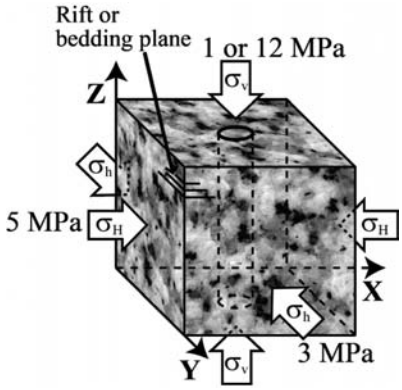


Figure 5. Stress conditions and the direction of borehole.

Table 2. P-wave velocities of the specimens.

Specimen	Specimen No.	P-wave velocity (m/s) V_{PH} (V_{PH}/V_{PH})	V_{Ph} (V_{Ph}/V_{PH})	V_{PV} (V_{PV}/V_{PH})
Inada granite	I-10	4385 (1)	4063 (0.93)	3933 (0.90)
	I-50	4554 (1)	4236 (0.93)	4064 (0.89)
	I-150	4627 (1)	4310 (0.93)	4290 (0.93)
	Iw-50	4067 (1)	4037 (0.99)	3619 (0.89)
Ogino tuff	O-10	2807 (1)	2743 (0.98)	2672 (0.95)
	O-50	2952 (1)	2868 (0.97)	2745 (0.93)
	O-150	2858 (1)	2711 (0.95)	2670 (0.93)
	Ow-50	2883 (1)	2795 (0.97)	2678 (0.93)

specimen. Three confining pressures of 5, 3, and 12 MPa were applied to the specimen for the two horizontal (σ_H, σ_h) and vertical (σ_v) directions, respectively. This vertical stress was determined so as to measure breakdown pressures, which are estimated from the elastic theory and with the tensile strengths of the rocks used in this study, and are found to be smaller than the vertical stress.

Table 2 lists the P-wave velocities of the specimens. The velocities normalized by each maximum velocity are also given in the table. The rift or bedding planes were confirmed as the perpendicular plane against the direction of the minimum P-wave velocity. The boreholes were created in a direction perpendicular to the rift or bedding planes. The maximum and minimum horizontal stresses were applied in the direction of the maximum (V_{PH}) and second (V_{Ph}) P-wave velocities, respectively, and the vertical stress was applied in the direction of the minimum P-wave velocity (V_{PV}). The ratios between the maximum (V_{PH}) and the minimum (V_{PV}) P-wave velocities ranged from 0.89 to 0.95.

To visualize the fractures created by the hydraulic fracturing, the fractures were colored using red water-based ink. The colored specimens were cut with a diamond cutter, and the surfaces and cut surfaces were scanned using an image scanner. We traced the fractures from the scanned images manually and measured the length of the visible fractures using NIH

ImageJ (Abramoff, M.D. et al. 2004). The traced images were arranged to develop views that would allow an understanding of the hydraulic fracture shapes obtained under each experimental condition.

3 RESULTS AND DISCUSSION

3.1 *View of the development of fractures created by hydraulic fracturing experiments*

Figure 6 shows the development of fractures in specimens of Inada granite, through hydraulic fracturing experiments conducted at a flow rate of 50 ml/min. Figure 6(a) and (b) show the results obtained using $SCCO_2$ at vertical stresses (σ_v) of 1 and 12 MPa, respectively. Figure 6(c) and (d) show the results obtained using water at vertical stresses (σ_v) of 1 and 12 MPa, respectively. The direction of maximum horizontal stress (σ_H) is also shown in the figure.

The directions of the fractures were generally oriented in the direction of maximum horizontal stress (σ_H). Several fracture branches were observed for the results obtained using $SCCO_2$, while single fractures were generally obtained for those obtained using water. The orientation of the fracture obtained at the lower vertical stress of 1 MPa was slightly oblique to the direction of maximum horizontal stress (σ_H). The reason for this result is that the microcracks were not compressed to a significant degree by the low vertical stress, and as a result, the anisotropy of the rock could strongly affect the fracture orientation at such a low vertical stress.

3.2 *Pressure and temperature changes during hydraulic fracturing experiments*

Figures 7 and 8 show temperature and pressure changes that occurred during the hydraulic fracturing experiments for Inada granite at a flow rate of 50 ml/min and at a vertical stress of 12 MPa, using $SCCO_2$ and water, respectively. After the hydraulic fluid injection started, the pressure increased, and subsequently, the breakdown occurred.

After the CO_2 was supplied, the pressure increased rapidly and was kept constant at the vapor pressure of CO_2 at that temperature. The pressure was increased by the injection of CO_2, and the temperature increased due to an adiabatic compression of CO_2. The temperature showed a small decrease during 67∼75 s (Fig. 7). This suggests that latent heat was consumed due to the phase change of the liquid CO_2 remaining in the flow line.

When the breakdown occurred, since pressure and temperature satisfied the critical condition, the CO_2 was in super critical state. After the breakdown, pressure rapidly decreased and temperature rapidly decreased due to the adiabatic expansion of CO_2. The temperatures of the water were kept approximately constant during the experiment (Fig. 8).

Table 3 summarizes the breakdown pressures and temperatures obtained at the two vertical pressures (σ_v) of 1 (Kizaki et al. 2012) and 12 MPa. Although

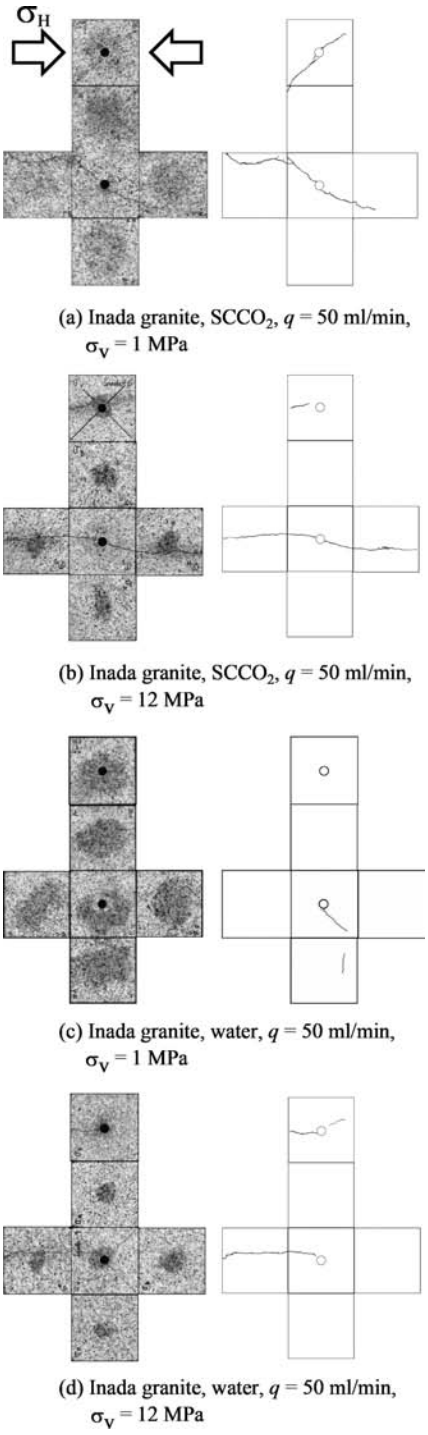


Figure 6. View of the development of fractures in the specimens through the hydraulic fracturing experiments, and a view of the traces of the fractures. (a) Inada granite, $SCCO_2$, $q = 50$ ml/min and $\sigma_v = 1$ MPa. (b) Inada granite, $SCCO_2$, $q = 50$ ml/min and $\sigma_v = 12$ MPa. (c) Inada granite, water, $q = 50$ ml/min and $\sigma_v = 1$ MPa. (d) Inada granite, water, $q = 50$ ml/min and $\sigma_v = 1$ MPa.

the breakdown pressure for Ogino tuff at a flow rate of 10 ml/min and at a vertical stress of 12 MPa using CO_2 was smaller than the critical pressure, we assumed this result was obtained using $SCCO_2$ in this study. The breakdown pressures obtained in this study were smaller than the vertical stress of 12 MPa applied in this study. The breakdown pressures obtained using $SCCO_2$ tended to be smaller than those obtained using water. These results indicate that low viscosity fluids such as $SCCO_2$ tend to create cracks in the rock at lower breakdown pressures. Moreover, the breakdown pressures generally decreased with a decrease in the flow rate (q). The results obtained for the breakdown pressure showed qualitatively better agreements with Haimson-Fairhurst equation where the effect of pore pressure is considered in the evaluation of the breakdown pressure rather than classical Hubbert-Willis-Scheidegger breakdown formula. Accordingly, these results suggest that the hydraulic fluid permeates into the rock before the breakdown and increases pore pressure around the borehole. As a result, the breakdown pressure is considered to decrease due to the reduction of effective stress around the borehole.

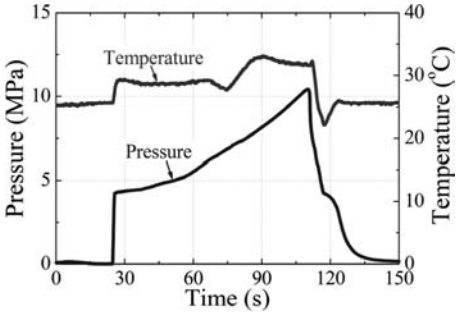


Figure 7. Pressure and temperature changes during hydraulic fracturing using $SCCO_2$ for the Inada granite ($q = 50$ ml/min, $\sigma_v = 12$ MPa).

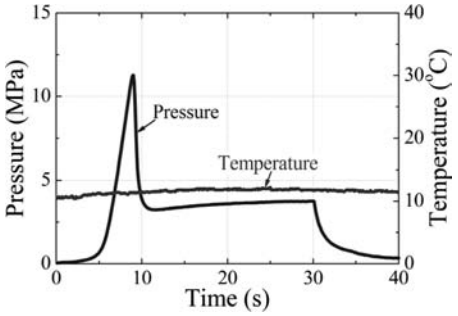


Figure 8. Pressure and temperature changes during the hydraulic fracturing using water for the Inada granite ($q = 50$ ml/min, $\sigma_v = 12$ MPa).

3.3 *Total length of fractures*

Figures 9 and 10 show the total length of fractures obtained for the Inada granite and Ogino tuff,

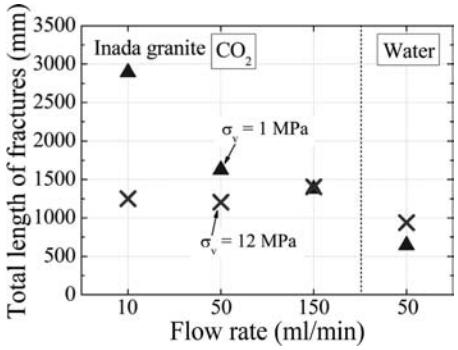


Figure 9. Total length of fractures obtained for the Inada granite.

Table 3. Breakdown pressures and temperatures.

Fracturing fluid	Specimen	Stress condition σ_H (MPa)	σ_h (MPa)	σ_v (MPa)	Flow rate, q (ml/min)	Breakdown pressure (MPa)	Breakdown temperature (°C)
CO_2	Inada granite	5	3	1	10	8.52	38.0
					50	9.56	40.5
					150	11.20	44.2
	Ogino tuff				10	n/a	n/a
					50	10.04	38.1
					150	n/a	n/a
Water	Inada granite				50	11.84	9.1
	Ogino tuff				50	10.51	9.1
CO_2	Inada granite	5	3	12	10	9.22	31.4
					50	10.38	31.7
					150	11.84	41.0
	Ogino tuff				10	6.84	39.0
					50	9.53	37.8
					150	7.26	36.1
Water	Inada granite				50	11.27	11.4
	Ogino tuff				50	8.58	13.0

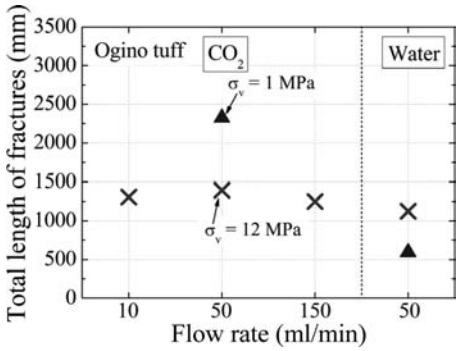


Figure 10. Total length of fractures obtained for the Ogino tuff.

respectively. The total length of fractures obtained using $SCCO_2$ at a vertical stress of 1 MPa tended to be larger than that obtained at 12 MPa. This suggests that the vertical stress compressed the microcracks and that the anisotropy of the fracture orientation decreased with vertical stress in this study. In contrast, the total length of fractures obtained using water at a vertical stress of 1 MPa was smaller than that obtained at 12 MPa. This is because the selectively propagated fracture was reached at the outer wall of the specimen at low vertical stress, and as a result, the total length of the fracture did not increase so much.

The total length of fractures obtained using $SCCO_2$ was larger than that obtained using water. This indicates that low viscosity fluid creates more branched fractures since hydraulic fluid tends to permeate into microcracks or fine pores with decrease in viscosity.

4 CONCLUSIONS

In this study, hydraulic fracturing experiments were conducted on 15 cm-cubic Inada granite and Ogino tuff specimens, using $SCCO_2$ and water as fracturing fluids. A borehole was created in a direction perpendicular to the rift or bedding planes, and two horizontal stresses of 5 and 3 MPa and a vertical stress of 12 MPa were applied to the specimens. To better understand the effects of vertical stress along the borehole on hydraulic fracture formation, the created fractures were observed and the total lengths of visible fractures were measured. The main results obtained from this study can be summarized as follows:

(1) The breakdown pressures obtained using $SCCO_2$ tended to be smaller than those obtained using water, and the breakdown pressures approximately decreased with the decrease in flow rate. These results suggest that low viscosity fluids such as $SCCO_2$ permeate into the rock and increase the pore pressure around the borehole. As a result, the breakdown pressure is considered to have decreased due to the reduction of effective stress around the borehole.

(2) The total length of fractures measured at the specimen surfaces for a vertical stress of 12 MPa tended to be smaller than that for a vertical stress of 1 MPa. This suggests that the horizontally oriented microcracks were compressed by the larger vertical stress and that the infiltration of fracturing fluid significantly affects fracture propagation.

ACKNOWLEDGEMENT

The authors thank Prof. Ito and Dr. Shimizu for their assistance in conducting the hydraulic fracturing experiments.

REFERENCES

Abramoff, M.D., Magalhaes, P.J. & Ram, S.J. 2004. Image Processing with Image. *J. Biophotonics International* 11(7): 36–42.

Asanuma, H., Muraoka, H., Tsuchiya, N. & Ito, H. 2012. The Concept of the Japan Beyond-Brittle Project (JBBP) to Develop EGS Reservoirs in Ductile Zones. *GRC Transactions* 36: 359–364.

Brown, D.W. 2000. A Hot Dry Rock Geothermal Energy Concept Utilizing Supercritical CO_2 Instead of Water. *Proceedings of the Twenty-Fifth Workshop on Geothermal Reservoir Engineering*, Stanford, California: 233–238.

Ishida, T., Chen, Q & Mizuta, Y. 1996. Effects of fluid viscosity in hydraulic fracturing deduced from acoustic emission monitoring, *Journal of Geotechnical Engineering (III)* 547, III-36, 183–198.

Ishida, T., Chen, Q., Mizuta, Y. & Roegiers, J. C. 2004. Influence of fluid viscosity on the hydraulic fracturing mechanism. *Transactions of the ASME, Journal of Energy Resource Technology* 126: 190–200.

Ishida, T., Aoyagi, K., Niwa, T., Chen, Y., Murata, S., Chen, Q. & Nakayama, Y. 2012. Acoustic emission monitoring of hydraulic fracturing laboratory experiment with supercritical and liquid CO_2 *Geophysical Research Letters* 39(16), DOI: 10.1029/2012GL052788

Ito, T., Igarashi, A. & Yamamoto, K. 2011. Laboratory experiments of hydraulic fracturing in unconsolidated sands, *Journal of MMIJ* 127: 243–248.

Jaoul, O., Tullis, J. & Kronenberg, A. 1984. The effect of varying water contents on the creep behavior of Heavitree quartzite. *Journal of Geophysical Research* 89(B6): 4298–4312.

Kizaki, A., Tanaka, H., Ohashi, K., Sakaguchi, K. & Matsuki, K. 2012. Hydraulic fracturing in Inada granite and Ogino tuff with super critical carbon dioxide. *Proceedings of the 7th Asian Rock Mechanics Symposium* (Seoul, Korea, October 15–19, 2012): 1026–1033.

Kobayashi, R., Matsuki, K. & Otsuka, N. 1980. Fracture toughness of rock in splitting test – Size effect of tuff specimens on fracture toughness, *Journal of MMIJ* 96: 313–318.

Kobayashi, R., Sakai, N., Matsuki, K. & Okumura K. 1987. Triaxial testing machine for properties of rocks in water circumstance at elevated temperature and results of tests by using it. *Journal of the Geothermal Research Society of Japan* 9(3): 185–195.

Muraoka, H., Uchida, T., Sasada, M., Yagi, M., Akaku, K., Sasaki, M., Yasukawa, K., Miyazaki, S., Doi, N., Saito, S., Sato, K. & Tanaka, S. 1998. Deep Geothermal Resources Survey Program: igneous, metamorphic and hydrothermal processes in a well encountering 500°C at 3729 m depth, Kakkonda, Japan, *Geothermics* 27(5–6): 507–534.

Rock Mechanics for Resources, Energy and Environment – Kwaśniewski & Łydżba (eds)
© 2013 Taylor & Francis Group, London, ISBN 978-1-138-00080-3

Assessing the geomechanical effects of CO_2 injection in a depleted gas field in Poland by field scale modelling

B. Orlic
TNO, Earth, Environmental and Life Sciences, Utrecht, The Netherlands

M. Mazurowski
Polish Oil & Gas Company, Warsaw, Poland

B. Papiernik & S. Nagy
AGH University of Science & Technology, Cracow, Poland

ABSTRACT: A field scale geomechanical model was developed in an early phase of the feasibility study considering geological CO_2 storage in a depleted gas field in Poland. Geomechanical model of the gas field was adequate to evaluate the induced stress changes, the geomechanical effects on the top seal and induced surface deformation. The estimated geomechanical effects on the top seal are weak and do not pose a risk for the containment. The effects on the regional sub-vertical faults intersecting the reservoir are not expected to cause fault destabilization, except in the case of partial re-pressurization of non-connected neighbouring compartments. However, the reliability of fault stability assessment is low due to the lack of seismic data that would have made detailed mapping of faults at field scale possible. Our future work will include updating the existing model with a more detailed fault interpretation and dynamic reservoir simulation results when they become available.

1 INTRODUCTION

Gas extraction and CO_2 injection into depleted hydrocarbon reservoirs will change the state of stress in the reservoir and the surrounding rock. As a result of induced stress changes natural fracture systems and faults can be reactivated, and new fractures formed. Open and connected fracture systems in the mechanically damaged seal pose the risk for loss of containment of injected CO_2. Besides the effects on the containment, stress changes due to withdrawal and injection of fluids into the subsurface will induce deformation of the storage reservoir (compaction/expansion), surrounding rock (various deformation modes) and ground surface (subsidence/uplift). Sudden slip on pre-existing faults can lead to induced micro-seismic and (felt) seismic events.

In this paper we describe a geomechanical modelling study carried out to evaluate the geomechanical effects associated with gas extraction and possible future CO_2 injection in a depleted gas field in Poland. The study area is located in southwestern Poland on the Fore-Sudetic Monocline (Fig. 1). The two largest fields located in the study area are the Załęcze and the Żuchlów gas fields. In this paper we report preliminary results of 3D field-scale geomechanical modelling of the Załęcze gas reservoir.

The focus of this geomechanical study, conducted within the EU-funded *SiteChar* project (www.sitechar-co2.eu), was to assess the impact of pore pressure changes on the integrity of top seal and stability of faults. Assessment of depletion- and injection-related mechanical effects allows defining the geomechanical constraints for safe injection and storage of CO_2 (Hawkes et al. 2004).

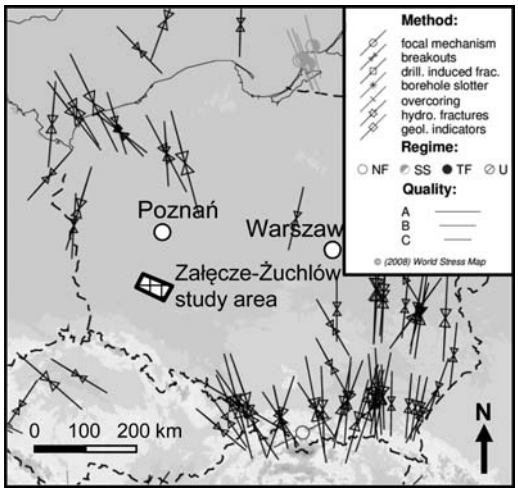


Figure 1. Map showing location of the study area and orientations of the maximum horizontal stress based on the World Stress Map database (Heidbach et al. 2008).

The geomechanical effects are frequently assessed by developing 2D, field scale, numerical geomechanical models of the storage site under study (e.g. Orlic, 2013). A site-specific geomechanical model is usually based on a vertical cross-section through the storage site interpreted from seismic and borehole data. Plain strain conditions are assumed, which are applicable for elongated reservoirs in a normal faulting or compressional stress regimes, but cannot be used in the case of a strike-slip regime. 3D field scale geomechanical modelling overcomes these limitations. However, this approach requires much more effort and extensive input for model development, such as a 3D structural geological model with interpreted overburden, sideburden and underburden. Hence, 3D field scale modelling of CO_2 storage sites tend to be postponed to project's late phase when the results of site characterization (e.g. Vidal-Gilbert et al. 2009 and Olden et al. 2012) and field monitoring (e.g. Rutqvist et al. 2010 and Morris et al. 2011) become available. Nevertheless, it may be advantageous to develop an initial version of 3D geomechanical model early in the project and update it later, when new information becomes available.

In this paper we describe development of a field scale model of the Załęcze gas reservoir, which was developed in an early phase of the feasibility project, and its use for preliminary assessment of depletion- and injection-related geomechanical effects.

2 FIELD DESCRIPTION

2.1 *Geological setting*

The Załęcze gas field is located in the Silesian basin, which represents the marginal part of the Southern Permian Basin (SPB). In the SPB, the Upper Rotliegend sandstones together with the overlaying Zechstein Limestone (Ca_1) form the reservoir of the Carboniferous Total Petroleum System (Pletsch et al. 2010). The Załęcze gas field is located in the central part of the Silesian basin dominated by aeolian sandstones deposited in the Southern Erg. Marginal parts of the basin are dominated by fluvial sandstones with aeolian intercalations. The source rocks of this petroleum system are Carboniferous deposits.

A detailed reservoir scale static model of the study area (50 × 20 km) was developed in the course of the *SiteChar* project by Papiernik et al. (2012). The model was built using data from 190 wells located within the study area, geological maps and 2D seismic data with incomplete coverage of the study area. The static model was used as the basis for deriving the structural framework model of a smaller area (17 × 17 km) that encompasses the Załęcze gas field, which was needed for construction of the numerical mesh (Fig. 2).

2.2 *Reservoir, top seal and faults*

The Załęcze gas reservoir occupies an area of 20.3 km^2 and has an average thickness of 130 m (Fig. 3). The gas accumulation is formed in a small anticlinal structure at a depth of 1300 mbsl. The reservoir is composed of the Saxonian aeolian and fluvial deposits (Upper Rotliegend). Average porosity of the reservoir sandstone is 15% and permeability 400 mD. The initial reservoir pressure at discovery in 1971 was 15 MPa. The reservoir is now depleted down to 2 to 3 MPa. The Rotliegend sandstone reservoir is covered by a 15m-thick Basal Zechstein Limestone layer (Ca_1) of poor reservoir quality.

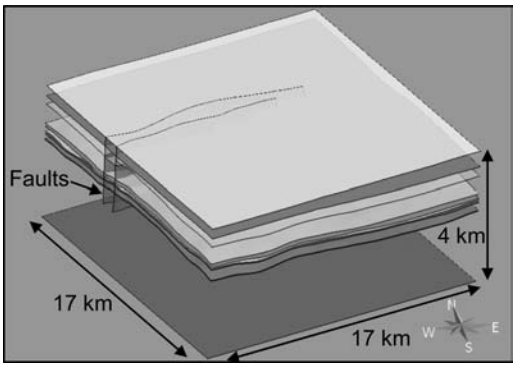


Figure 2. Perspective view of the structural framework with horizons and faults used to build a mesh for the numerical model of the Załęcze gas field.

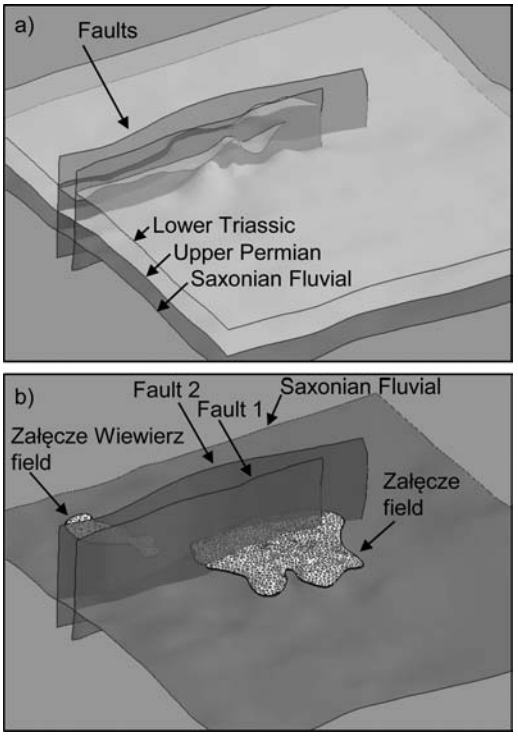


Figure 3. a) Enlarged view of the structural framework with the main horizons and faults; b) outline of the Załęcze gas reservoir intersected by two regional faults.

Zechstein evaporites form the top seal of the Rotliegend reservoir. The total thickness of the top seal ranges from 250 to 500 m. The seal consists of several cyclothems, i.e. alternating stratigraphic sequences of various evaporites: halite, anhydrite, dolomite and gypsum. The immediate caprock to the reservoir rocks is an anhydrite layer, which is over-lain by a continuous rock salt layer. Rock salt is an excellent seal that can ensure safe and stable containment in the long-term. A 20 m-thick dolomite layer (Ca_2), located at a depth of about 1100 mbsl, represents the secondary Zechstein reservoir which is considered for CO_2 storage. The secondary reservoir is overlain by a 100 m-thick Zechstein seal. The shallow overburden above the Zechstein comprises clastic deposits of Buntsandstein, Muschelkalk carbonates and Quaternary deposits.

Two regional fault systems were interpreted, one in the Zechstein substratum and the other in the shallow overburden above the Zechstein. These two systems are largely independent. Deep faults below the Zechstein deposits intersect the Permian deposits and terminate below the Zechstein salt layer. These faults have small vertical offsets and do not impede or retard across-fault flow in the gas reservoir. Faults developed above the Zechstein have a vertical throw of up to 200 m and form a system of grabens (Fig. 3a). Local salt diapirs could also be interpreted, although their geometry is poorly controlled by the input data. Two major sub-vertical faults intersecting the Załęcze gas reservoir are incorporated in the structural framework model (Fig. 3b).

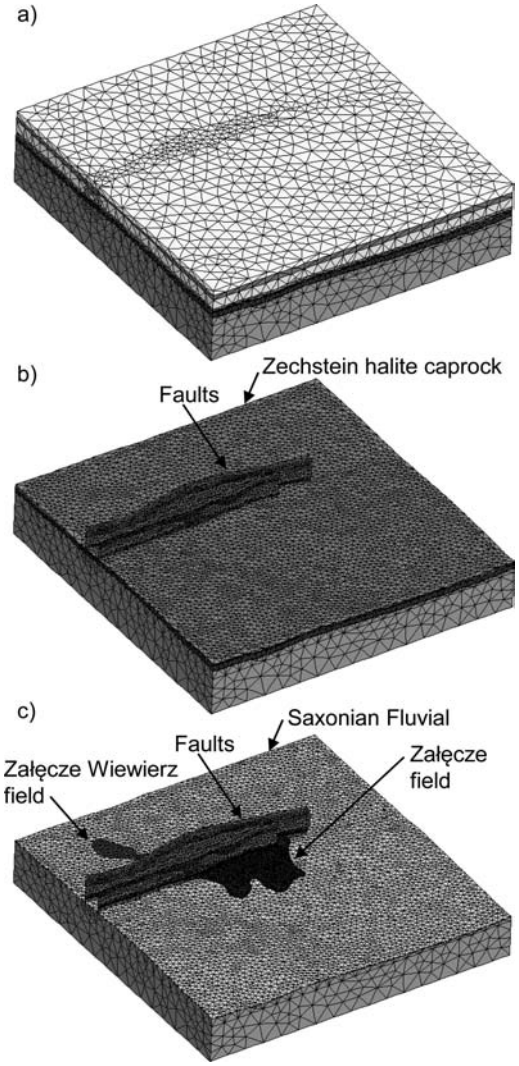


Figure 4. Perspective view of the finite element geomechanical model of the Załęcze gas field. a) Complete model; b) part of the model showing the Zechstein halite seal; c) part of the model showing outline of the two gas fields and two major regional faults.

3 FIELD SCALE GEOMECHANICAL MODEL

Field scale geomechanical model was built from the structural framework model of the Załęcze gas field (Fig. 2). The model comprises the geomechanical units characterized by the material properties and constitutive laws, the initial state of stress and pore pressure loading of the reservoir caused by gas extraction and CO_2 injection. A general purpose finite-element package DIANA was used to develop the finite elements model and perform calculations (TNO Diana, 2012).

3.1 *Mesh construction and boundary conditions*

The modelled domain is $17 \times 17 \times 4$ km (Fig. 2). The gas reservoir is located at the approximate centre of the model. The size of the model was selected in such a way to minimize the effects of model boundaries on the induced stresses and deformation in, nearby, and below the compacting/inflating reservoir. For example, the rigid model base is set at 4000 mbsl, which is equal to 3 times the depth of the gas reservoir. The model is rotated in the horizontal plane to align the model boundaries with the regional directions of the two principal horizontal stresses (Fig. 1).

The geomechanical model consists of ten layers (listed in order of increasing depth):

- three overburden layers,
- the upper Zechstein anhydrite and dolomite layer,
- the Zechstein salt (halite) layer,
- the lower Zechstein anhydrite layer,
- the Zechstein carbonate reservoir (Ca_1),
- the Saxonian aeolian reservoir,
- the Saxonian fluvial reservoir,
- the underburden.

The geometry of the reservoir structure and juxtaposition of various geological units across two major faults intersecting the reservoir was fully preserved

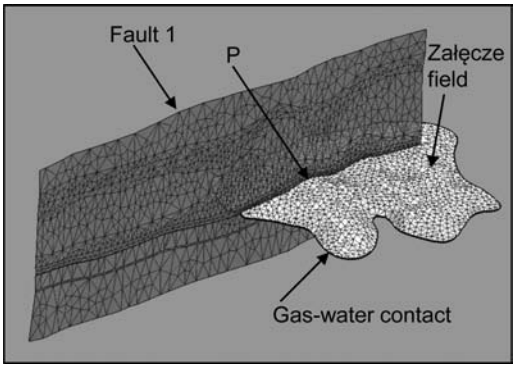


Figure 5. Detailed view of the Załęcze gas reservoir intersected by a regional fault.

in the geomechanical model. The faults are extended through the Zechstein halite layer to avoid artificial stress concentrations at fault edges close to the reservoir-caprock interface.

The finite element mesh is made of tetrahedral solid elements and triangular planar interfaces (Fig. 4a). 295,000 quadratic second-order ten-node solid pyramid elements are used to represent the geomechanical units. The fault surfaces are modelled by 6,000 triangular 6+6 nodded interface elements of zero thickness (Fig. 4b). Mesh resolution increases towards the reservoir structure and fault surface where the induced stress changes are the largest (Figs 4c, 5). The presence of a few thin layers (the Zechstein carbonate reservoir and the Zechstein salt layer are locally less than 10 m thick) required fine meshing of thin layers throughout the whole model (Fig. 4b).

The structural boundary conditions imposed on model boundaries constrain displacements perpendicular to the sides and base of the geomechanical model.

3.2 *Geomechanical units and material properties*

The material properties for the differentiated geomechanical units are summarized in Table 1. The elastic properties for the reservoir rock are derived from uniaxial compressive strength tests executed in the rock mechanics laboratory of the AGH University in Cracow. Physical and elastic properties of other geomechanical units were derived by interpretation of abundant well log data. All the geomechanical units were assumed to be elastic besides the Zechstein salt layer, which was modelled as a viscoelastic material. A composite creep material law was used for the salt combing a linear term for the solution-precipitation creep and a non-linear term for the dislocation creep (Fokker, 1995). The values of creep properties for halite are taken over from the literature on deep solution salt mining in the Netherlands (Van Heekeren et al. 2009).

Table 1. Geomechanical units and material properties.

Geomechanical unit	Density kg/m^3	Young's modulus GPa	Poisson's coefficient –
Overburden 1 (Quat.)	2000	5	0.30
Overburden 2 (Musch.)	2300	10	0.30
Overburden 3 (Bunts.)	2300	15	0.30
Upper Ze anhydrite	2500	22	0.25
Ze salt*	2170	30	0.26
Lower Ze anhydrite	2950	28	0.31
Carbonate reservoir	2760	39	0.18
Saxonian aeolian res.	2410	13	0.23
Saxonian fluvial res.	2670	21	0.23
Underburden	2650	30	0.25
Faults	Friction coef. (–)	Cohesion MPa	
	0.6	0	

*The Zechstein salt is modelled as a viscoelastic material in scenario 3.

The frictional behaviour of faults is modelled using a Coulomb friction criterion with a friction coefficient value of $\mu = 0.6$ and zero cohesion.

3.3 *Initial stress and loading by the pore pressure*

The orientations and the magnitudes of three principal *in situ* stresses are required for initialization of stresses in the geomechanical numerical model.

The present day stress regime in the southwestern part of Poland is extensional. Although measured stress data close to the study area are not available from the World Stress Map database, it is likely that the maximum horizontal stress direction follows the regional NNW-SSE trend (Heidbach et al. 2008, Fig. 1). This is confirmed by interpretation of borehole breakouts from well Za-21 carried out by Jarosiñski (2005). For a depth range of 1250 to 2195 m, the orientation of the maximum horizontal stress varies in the range of $166 \pm 26°$, which is in agreement with the regional stress data. The magnitude of the largest *in situ* (vertical) principal stress was derived from the rock density values given in Table 1. The magnitudes of other two principal horizontal stresses were not available. It was assumed that two horizontal principal stresses have the same magnitude and this parameter was varied in sensitivity analysis.

Dynamic loading of the gas reservoir by the pore pressures is realized by applying uniform pressure changes in the gas reservoir. The initial reservoir pressure in the gas reservoir was set at 15 MPa. The reservoir is depleted by 95% over a period of 30 years. During the subsequent 10-year period of CO_2 injection, the reservoir pressure increases uniformly up to 13.5 MPa (90% of the pre-depletion pressure). It was assumed that the pressure in aquifers connected to the Załęcze gas reservoir do not change, due to lack of field measurements and/or reservoir simulation scenarios which would suggest the opposite.

3.4 *Sensitivity scenarios*

The base case (BC) scenario was calculated using the following input parameters: fault friction coefficient $\mu = 0.6$; the initial effective stress ratio $K_0' = 0.6$; elastic behaviour of the Zechstein salt layer; and uniform re-pressurization of the whole gas reservoir. Besides the base case, four additional scenarios were calculated which considered:

1. Low fault friction ($\mu = 0.017$, i.e. $\varphi = 1°$).
2. Low minimum horizontal stress ($K_0' = 0.3$).
3. Viscoelastic behaviour of the Zechstein salt layer.
4. Re-pressurization of single reservoir block.

4 MODELLING RESULTS

Non-linear analysis was used to initialize the stresses in the finite element model and calculate the geomechanical effects resulting from pore pressure change in the reservoir. Subsidence data over the past production period were not available to calibrate the geomechanical model.

4.1 *Stress change and top seal integrity*

The largest stress changes in the reservoir and the surrounding rock occur at the end of depletion period, when the reservoir is nearly fully depleted. Stress perturbations around the compacting reservoir follow the general pattern of unloading (and decompaction) of the layers above the reservoir and loading (i.e. an increase in the compressive stress and compaction) of the side-seal near reservoir edges. The side-seal takes over part of the overburden load previously carried by the undepleted reservoir. Because the reservoir top has a form of an undulating surface, local stress concentrations occur in the top seal above the surface peaks and depressions (Fig. 6a, b). For example, unloading (due to vertical stress change) occurs above local surface peaks and loading above local depressions (Fig. 6a).

The maximum magnitudes of induced stress changes affecting the top seal range from −1 to 1 MPa (negative sign is used for loading). Such magnitudes are small to mechanically damage the Lower Zechstein anhydrite, which represents the immediate top seal to the gas reservoir. This was confirmed by checking expected magnitudes and ranges of the principal stresses obtained by simulations. Tensile failure was evaluated by looking at the minimum effective principal stress. Tensile stresses were not detected anywhere in the caprock and no significant risk was identified. Shear failure of the existing fractures in the caprock was evaluated by looking at the ratio of the largest to the smallest principal stress. For cohesionless fractures with a coefficient of friction of $\mu = 0.6$, shear slip would be induced if the maximum principle effective stress exceeds three times the minimum principal effective stress on preferentially oriented fractures. Shear failure was not detected anywhere in the caprock and no significant risk was identified.

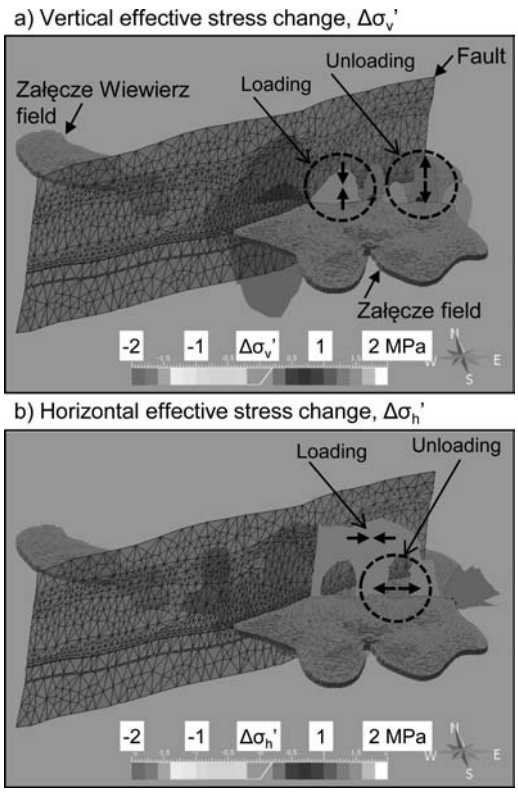


Figure 6. Depletion-induced stress perturbations (relative to the initial state) at the end of depletion period. a) Vertical effective stress change plotted on an east-west cross-section through the Załęcze reservoir; b) horizontal effective stress. Negative sign denotes an increase in the compressive stress, i.e. loading.

4.2 *Fault stability*

Faults intersecting the gas reservoir are sub-vertical and have small vertical offset. Equal compaction or expansion of the faulted reservoir blocks on either side of a fault does not effect fault stability (Fig. 7, base case). Fault reactivation at the level of the gas reservoir can only occur in a hypothetical case of partial reservoir re-pressurization (Fig. 7, scenario 4). In this scenario, the CO_2 injected in the fully depleted reservoir causes re-pressurization of the faulted reservoir block on one side of the fault, while the other block stays fully depleted. Differential deformation on either side of the fault leads to fault destabilization and fault slip. This scenario is unlikely because there was no indication of reservoir compartmentalization during the period of gas production.

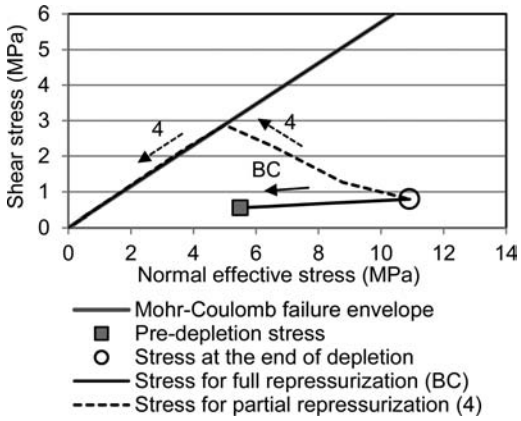


Figure 7. Stress path for the observation point P located on the fault section intersecting the Załęcze gas reservoir. Stress paths are shown for the scenario of simultaneous re-pressurizing of both reservoir compartments (BC = base case) and the scenario of re-pressurizing a single compartment (scenario 4). Location of point P is shown in Figure 5.

4.3 *Reservoir compaction and surface deformation*

The maximum amount of surface subsidence at the end of depletion period amounts to about 5 cm (Fig. 8a). Relatively small amounts of subsidence are due to: (i) small thickness of the gas-bearing, compacting sediments; (ii) presence of stiff evaporite layers in the overburden; and (iii) absence of depletion in supporting aquifers.

In the case of an elastic subsurface response, reservoir re-pressurization due to CO_2 injection would lead to almost full subsidence reversal.

The amount of reservoir compaction is slightly larger than the surface subsidence (Fig. 8b). The spatial pattern of compaction contours at the reservoir top is also more complex than at the ground surface. It deviates from concentric circles (observed at the surface) due to the varying thickness of the gas-bearing part of the reservoir.

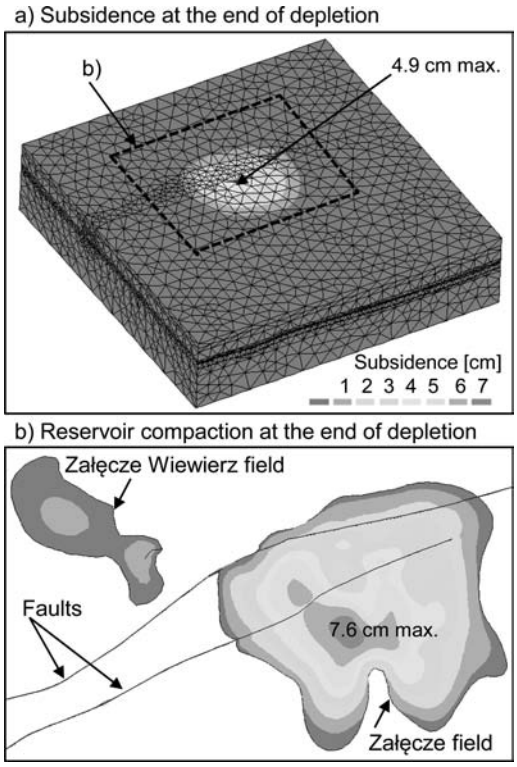


Figure 8. a) Perspective view of the numerical model showing vertical deformation at the end of depletion period. Maximum surface subsidence amounts to 4.9 cm. b) Map showing compaction of the top of the Załęcze reservoir and the Załęcze Wiewierz reservoir. Maximum reservoir compaction amounts to 7.6 cm.

5 CONCLUSIONS

A field scale geomechanical model of a depleted gas field in Poland was developed in an early phase of the CO_2 storage feasibility study and used for preliminary assessment of depletion- and injection-related geomechanical effects. The study yielded the following conclusions:

- Geomechanical model of the gas field, built from the static geological model, was sufficient to estimate the extent and magnitude of stress changes around the gas reservoir, the geomechanical effects on top seal as well as the induced subsurface and surface deformation.
- Both the static geological model and the geomechanical model contain regional faults only. Developing a more detailed field scale faulted model was not possible due to the lack of high quality seismic data.
- The reliability of fault stability assessment based on model predictions is therefore low.
- Vertical stress perturbations around the compacting reservoir follow the general pattern of unloading of the overburden above the reservoir and loading of the side-seal near reservoir edges.
- Deviations from the general pattern of stress perturbations occur in the top seal above the reservoir. Because of the undulating shape of the reservoir top, local stress concentrations arise above surface peaks and depressions.
- The geomechanical effects on the top seal are weak and there is no significant risk for tensile or shear failure.
- The geomechanical effects on regional subvertical faults intersecting the reservoir do not lead to fault destabilization except in an unlikely case of partial reservoir re-pressurization.

– The maximum amount of surface subsidence at the end of depletion period is small and amounts to about 5 cm.

The following recommendations are given:

– Update the existing geomechanical model with a more detailed fault interpretation when it becomes available.
– Update the pore pressure loads by using dynamic reservoir simulation outputs when they become available.

ACKNOWLEDGEMENTS

The research leading to these results has received funding from the European Union Seventh Framework Programme (FP7/2007-2013) under grant agreement n° 256705.

REFERENCES

Fokker, P.A. 1995. *The behaviour of salt and salt caverns*. PhD Thesis, Delft University of Technology, The Netherlands.

Hawkes, C., McLellan, P.J., Zimmer, U. & Bachu, S. 2004. Geomechanical factors affecting geological storage of CO_2 in depleted oil and gas reservoirs: risks and mechanisms. Gulf Rocks 2004, *6th North American Rock Mechanics Symposium*, Houston, Texas, 5–9 June 2004, paper no 04-579.

Heidbach, O., Tingay, M., Barth, A., Reinecker, J., Kurfeß, D. & Müller, B. 2008. The World Stress Map database release 2008. doi:10.1594/GFZ.WSM.Rel2008.

Jarosiński, M. 2005. Ongoing tectonic reactivation of the Outer Carpathians and its impact on the foreland: Results of borehole breakout measurements in Poland. *Tectonophysics* 410: 189–206.

Morris, J.P., Hao, Y, Foxall, W. & McNab, W. 2011. A study of injection-induced mechanical deformation at the In Salah CO_2 storage project. *Int. J. Greenhouse Gas Control* 5: 2670–280.

Olden, P., Pickup, G., Jin, M., Mackay, E., Hamilton, S., Sommerville, J. & Todd, A. 2012. Use of rock mechanics laboratory data in geomechanical modelling to increase confidence in CO_2 geological storage. *Int. J. Greenhouse Gas Control* 11: 304–315.

Orlic, B. 2013. Site-specific geomechanical modeling for predicting stress changes around depleted gas reservoirs considered for CO_2 storage in the Netherlands. *47th US Rock Mechanics/Geomechanics Symposium*, San Francisco, 23–26 June 2013, paper no ARMA 13-446.

Papiernik B., Kiersnowski, H., Machowski, G. & Górecki, W. 2012. Upper Rotliegend Reservoir and Facies Models of Geomorphological and Structural Gas Traps in Silesian Basin – South-West Poland. *74th EAGE Conference & Exhibition.*

Pletsch, T., Appel, J., Botor, D., Clayton, C.J., Duin, E.J.T., Faber, E., Gorecki, W., Kombrink, H., Kosakowski, P., Kuper, G., Kus, J., Lutz, R., Mathiesen, A., Ostertag-Henning, C., Papiernek, B. & Van Bergen, F. 2010. *Petroleum generation and migration*. In J.C. Doornenbal & A.G. Stevenson (eds), *Petroleum Geological Atlas of the Southern Permian Basin Area.* EAGE Publications, Houten, 225–253.

Rutqvist J., Vasco, D. & Myer, L. 2010. Coupled reservoir-geomechanical analysis of CO_2 injection and ground deformations at In Salah, Algeria. *Int. J. Greenhouse Gas Control* 4: 225–230.

TNO Diana 2012. DIANA: *Finite element program and User Documentation*, version 9.4.4 (tnodiana.com).

Van Heekeren, H., Bakker, T., Duquesnoy, T., de Ruiter, V. & Mulder, L. 2009. Abandonment of an extremely deep cavern at Frisia salt. In *Proceedings of the SMRI Spring 2009 Technical Conference*, Kraków, Poland, 27–28 April 2009.

Vidal-Gilbert, S., Nauroy, J.-F. & Brosse, E. 2009. 3D geomechanical modelling for CO_2 geologic storage in the Dogger carbonates of the Paris Basin. *Int. J. Greenhouse Gas Control* 3: 288–299.

This page intentionally left blank

This page intentionally left blank

This book contains the Proceedings of EUROCK 2013 – The 2013 ISRM International Symposium, which was held on 23-26 September 2013 in Wrocław, Poland. The Symposium was organized by the ISRM National Group POLAND and the Institute of Geotechnics and Hydrotechnics of the Wrocław Institute of Technology.

The focus of the Symposium was on recent developments in the field of rock mechanics with an emphasis on the application of rock mechanics to the extraction of natural resources, securing energy supplies and protecting of the environment surrounding rock that is subjected to engineering activities.

The main topics, which were covered in the 150 papers (including six keynote papers) that make up this book are: rock mass characterization, laboratory and in-situ testing, constitutive models and numerical modeling, mathematical modeling of THM processes in rocks, mine design and ground control, underground storage and waste disposal, slope and open pit stability, dynamic phenomena in rock masses, design methodology in rock engineering, mechanical breakage of rocks, rock tunnel excavation and support, petroleum rock mechanics and geological CO_2 sequestration.

The book also includes the 2013 ISRM Franklin Lecture by A. Goricki on the engineering aspects of geotechnical tunnel design.

The book will be of interest and value to rock mechanics researchers as well as to professionals who are involved in the various branches of rock engineering.

Politechnika Wrocławska

CRC Press
Taylor & Francis Group
an **informa** business
www.crcpress.com

6000 Broken Sound Parkway, NW
Suite 300, Boca Raton, FL 33487
Schipholweg 107C
2316 XC Leiden, NL
2 Park Square, Milton Park
Abingdon, Oxon OX14 4RN, UK

ISBN 978-1-138-00080-3

an **informa** business